Relationships Between Tectonics, Volcanism, and Hydrothermal Venting in the New Hebrides and Mariana Back-Arc Basins, Western Pacific

Melissa Anderson

A thesis submitted to the Faculty of Graduate and Postdoctoral Studies
in partial fulfillment of the requirements for the Doctor of Philosophy degree in Earth Sciences

Department of Earth Sciences
Faculty of Science
University of Ottawa

© Melissa Anderson, Ottawa, Canada, 2018

Abstract

Understanding the controls on the distribution and type of hydrothermal venting in modern oceanic spreading environments is key to developing tools for exploration and understanding the metallogeny of ancient massive sulfide deposits. Compared to mid-ocean ridges, subduction zones are characterized by additional tectonic complexities, including arc-ridge collisions, arc rotations, pre-existing structures, and variable distances to the arc. This thesis addresses the question, "How do tectonic complexities associated with subduction influence the structure and volcanic evolution of a back-arc basin, and how do they affect the distribution and type of hydrothermal venting?" A multi-scaled approach was used to address this question in the nascent back-arc region of the New Hebrides and in the more advanced stages of opening of the Mariana back-arc basin. In the New Hebrides, an arc-ridge collision segmented the volcanic front and affected the southern and northern back-arc regions in different ways. In the southern Coriolis Troughs (CT), voluminous eruptions are closely linked to the ridge collision, forming a large shield volcano in the near-arc region (Nifonea Volcano). The caldera-hosted eruptions produced high-temperature but short-lived magmatic-hydrothermal activity restricted to the shield volcano. In the northern Jean Charcot Troughs (JCT), ridge collision caused a reversal in the rotation of the arc, reducing extension in the south and increasing extension in the north. Unlike the CT, extension in the JCT is strongly affected by pre-existing structures, which form irregular widely-spaced grabens and volcanic ridges and magmatism in the central part of the back-arc. Here, hydrothermal venting is focused along deeply penetrating faults, associated with widespread tectonic extension. Detailed studies of the mineralogy and geochemistry of the ore and alteration at the Tinakula deposit reveal that massive sulfide accumulation in the region dominated by tectonic extension is characterized by longer-lived, lower-temperature venting than at Nifonea. Hydrothermal activity in the JCT at

Tinakula is dominated by (1) long-lived heat from an underlying magma source; (2) fluid circulation along a fissure with long-lived or reactivated permeability; (3) enrichment in fluid-mobile elements such as Ba that are transported at low temperature; (4) mixing of cold seawater with hydrothermal fluids within the permeable volcaniclastic substrate and at the seafloor; (5) water depth controls on maximum hydrothermal vent temperatures; and (6) reduced permeability of the host volcaniclastic succession at the site of mineralization caused by precipitation of alteration minerals and sulfates, focusing fluid flow. The different styles of volcanic and hydrothermal activity closely resemble those of mid-ocean ridge environments in areas that are dominated by tectonic rather than magmatic extension. A comparison with the more advanced stages of rifting and segmentation of the Mariana back-arc demonstrates that Mid-Ocean Ridge (MOR)-type structural and magmatic controls on hydrothermal activity are important during all stages of back-arc basin evolution. This work highlights the diversity of volcanic eruption styles and hydrothermal venting from the earliest stages of back-arc rifting to the advanced stages of basin opening and shows that processes normally associated with MOR-type spreading are directly analogous to back-arc basin systems. However, additional tectonic complexities (e.g., ridge-arc collisions) have a major impact on the location and type of magmatic and hydrothermal activity at back-arc spreading centers, with important implications for understanding ancient volcanic-hosted massive sulfide deposits that mainly formed in back-arc basins.

Acknowledgements

First and foremost, I would like to acknowledge my PhD supervisor Mark Hannington, who provided me with the support and the freedom to pursue my dream project. Thank you for having confidence in me and for encouraging me through it all. Your feedback and thorough edits have made me a better researcher and writer, and I couldn't have asked for a better supervisor.

Thank you to the examining committee of this thesis (P. Audet, D. Schneider, B. Cousens, and S. Piercey), and to the reviewers of the manuscripts, who have improved this thesis tremendously.

I would also like to thank Tim McConachy and Neptune Minerals Inc. for allowing me to work this project and providing logistics and support along the way. I would also like to thank Katie Allen and James Carpenter for their help on-site.

Thank you to the PIs and research groups who allowed me to join their cruises, including (but not limited to) Karsten Haase (Erlangen), Uli Schwarz-Schampera (BGI), Joe Resing and Bill Chadwick (NOAA), and Mark Hannington and Sven Petersen (GEOMAR). I acknowledge the many sources of funding for this research, including NSERC, SEG, IAVCEI, and DAAD.

I would also like to acknowledge my students, Maria Anders and Henning Wienkenjohann, who have both contributed to this project with their theses. A big thanks also goes to all of those who have assisted me with the analytical work: Nico Augustin, Sabine Lange, Mario Thöner, and Jutta Heinze. In addition, I thank the many interns who have worked on this project with me, in particular: Anna Jegen, Megan Williams, Thomas Dols, Frederica van Dehl, Michael Sims, Falk Brüggemeier. Thank you to the support staff at GEOMAR and uOttawa: Sabine Lange, Sandy Sheperd, Helene de Gouffe, Caroline Bisson, and Lisa-Robin Murphy for administration assistance. Also, many thanks to David Diekrup for being my go-to person in Ottawa while I'm not there, and for the support along the way. Thank you to the wonderful scientists at GEOMAR (past and present) who have supplied me with limitless expertise and have given me a home-away-from-home. I am grateful for the opportunity to be around such talented people all day. In particular, thank you to Hannah Grant for providing spell-checks on the many drafts of this thesis.

I'd like to thank all of the mentors I've had throughout the years, who have encouraged me to undertake this adventure and provided reference letters to help me get there, including: Hamid Mumin, Dave Lentz, Hendrick Falck, John Jamieson, and Sven Petersen.

I would like to thank my family and friends for the love and support along the way. And finally thank you Marek Anderson, my incredible partner, for the continuous love and support and for believing in me, even at times when I didn't. This thesis is dedicated to you.

Table of Contents

Abstract ii
Acknowledgements iv

Chapter 1: Introduction 1
1.1. Background 1
1.2. Research objective 2
1.3. Thesis organization 2
1.4. Statement of original contribution 4
References 11

Preface to Chapter 2 13
Chapter 2: The southern New Hebrides back-arc: Tectonic focusing of voluminous basaltic eruptions in magma-deficient back-arc rifts 14
Abstract 15
2.1. Introduction 15
2.2. Tectonic setting 17
2.3. Methods 19
2.4. Geology of the Vate Trough 23
2.4.1. Old arc crust 23
2.4.2. Basin Floor 25
2.4.3. Other structural features of the Vate Trough 26
2.5. Geology of the Nifonea axial volcano 28
2.5.1. Summit caldera 29
2.5.2. Hydrothermal activity 32
2.6. Discussion 34
2.6.1. Geodynamic controls on the style of rifting 34
2.6.2. Link to shield-type volcanism 36
2.6.3. Controls on the distribution and type of hydrothermal venting 40
2.7. Conclusions 41
References 42

Preface to Chapter 3 48
Chapter 3: Magmatism and hydrothermal venting in the Jean Charcot Troughs, SW Pacific: Influence of the geodynamic evolution of the northern New Hebrides back-arc 49
Abstract 50
3.1. Introduction 50
3.2. Tectonic setting 52

3.3. Methods 58
3.3.1. Bathymetry and geological mapping 58
3.3.2. Sample collection and petrography 60
3.3.3. Whole-rock geochemistry 60
3.4. Regional geology 60
3.4.1. Structures of the Jean Charcot Troughs (JCT) 60
3.4.2. Structures of the Starfish area 63
3.5. Geology of the Tinakula area 65
3.6. Volcanic rock samples 74
3.6.1. Petrography 74
3.6.2. Geochemistry 78
3.7. Hydrothermal deposits 88
3.8. Discussion 92
3.8.1. Geodynamic controls on the style of rifting in the JCT 92
3.8.2. Magma chemistry 96
3.8.3. Controls on hydrothermal venting at Tinakula 102
3.9. Conclusions 103
References 105

Preface to Chapter 4 *114*
Chapter 4: Mineralogy, geochemistry, S-isotopes, and fluid inclusion systematics of the Tinakula seafloor massive sulfide deposit, Jean Charcot Troughs, SW Pacific 115
Abstract 116
4.1. Introduction 116
4.2. Geology of the Tinakula deposit 117
4.3. Methods 121
4.3.1. Sample collection and petrography 121
4.3.2. Whole-rock geochemistry 122
4.3.3. Trace-element geochemistry by EPMA 122
4.3.4. S-isotope analyses 122
4.3.5. Fluid inclusion analyses 124
4.3.6. ^{226}Ra/Ba geochronology 125
4.4. Results 126
4.4.1. Ore mineralogy and paragenesis 126
4.4.2. Ore geochemistry 138
4.4.3. Element correlations and principal component analysis (PCA) 142
4.4.4. Iron and manganese oxyhydroxides 149
4.4.5. Sulfide mineralogy and chemistry 153
4.4.6. Sulfur isotopes 161

4.4.7. Fluid inclusion analyses 165
4.4.8. Barite dating 172
4.5. Discussion 176
4.5.1. Behavior of trace elements in different sulfide minerals 176
4.5.2. Conditions of mineralization at Tinakula 180
4.5.3. Comparison of Tinakula sulfides with global SMS deposits 186
4.6. Conclusions 194
References 196

Preface to Chapter 5 *205*
Chapter 5: Mineralogical and geochemical characteristics of hydrothermal alteration in the volcaniclastic-hosted Tinakula seafloor massive sulfide deposit (New Hebrides back-arc, SW Pacific) 206
Abstract 207
5.1. Introduction 208
5.2. Subsurface geology 208
5.3. Methods 213
5.3.1. Core logging, sample collection, and petrography 213
5.3.2. SWIR spectroscopy 215
5.3.3. Clay-size separations and XRD analyses 219
5.3.4. Whole-rock geochemistry 220
5.3.5. Oxygen and hydrogen isotopes 220
5.4. Drill sites 221
5.4.1. Site A 221
5.4.2. Site B 222
5.4.3. Site C 226
5.4.4. Site D 228
5.4.5. Site E 230
5.4.6. Site F 230
5.5. Analytical results 231
5.5.1. SWIR spectroscopy results 231
5.5.2. XRD results 238
5.5.3. Immobile and mobile element geochemistry 247
5.5.4. Mass balance changes 254
5.5.5. Oxygen and hydrogen isotopes 263
5.6. Discussion 265
5.6.1. Explosive volcanism at Tinakula 265
5.6.2. Alteration processes 267
5.6.3. Hydrothermal fluids and ore formation 275

5.7. Conclusions 278
References 280

Preface to Chapter 6 *287*
Chapter 6: Geological interpretation of volcanism and segmentation of the Mariana back-arc spreading center between 12.7°N and 18.3°N **288**
Abstract 289
6.1. Introduction 289
6.2. Tectonic setting 292
6.3. Methods 296
6.4. Mapped features 303
6.4.1. Old BAB crust 303
6.4.2. Neovolcanic terrain 304
6.4.3. Volcanoes 305
6.4.4. Deep sedimented basins 305
6.4.5. Structures 306
6.5. Segment geology 306
6.5.1.Southern Mariana back-arc 306
6.5.2. Central Mariana back-arc 309
6.6. Regional structures 325
6.7. Discussion 327
6.7.1. Large-scale segmentation and cross-arc structures of the Mariana back-arc 327
6.7.2. Segment-scale fault patterns and spreading direction 330
6.7.3. Axial morphology and magma supply rates 331
6.7.4. Relationship to hydrothermal venting 337
6.8. Conclusions 339
References 340

Chapter 7: Global summary and conclusions **354**
7.1. Chapter highlights 354
7.3. Future directions 363
References 364

Appendices
Appendix A: Supplementary information for Chapter 2 367
Appendix B: Supplementary information for Chapters 3 and 4 389
Appendix C: Sample list and maps 396
Appendix D: Petrographic reports of volcanic rocks 410

Appendix E: Petrographic reports of sulfides 469
Appendix F: Petrographic reports of oxides 631
Appendix G: Petrographic reports of altered volcaniclastic rocks 656
Appendix H: Whole-rock geochemistry of volcanic rocks 792
Appendix I: Whole-rock geochemistry of sulfides 803
Appendix J: Whole-rock geochemistry of oxides 829
Appendix K: Whole-rock geochemistry of altered volcaniclastic rocks 840
Appendix L: EPMA analyses on sulfide minerals of the Tinakula deposit 856
Appendix M: Supplementary information for Chapter 5 894
Appendix N: Graphical drillcore summary logs 910
Appendix O: SWIR spectroscopy analyses of altered volcaniclastic rocks 929
Appendix P: XRD analyses of altered volcaniclastic rocks 969
Appendix Q: Supplementary information for Chapter 6 1003

Chapter 1

Introduction

1.1. Background

Submarine back-arc basins are important environments for the formation of seafloor hydrothermal systems, accounting for approximately one-third of known sites to date (Hannington et al., 2005). The majority have been discovered along intra-oceanic back-arc basins (e.g. Mariana Trough, Lau Basin, North Fiji Basin), which form as a result of prolonged arc rifting caused by extension during slab-rollback (Leat and Larter, 2003). Recent studies have begun to document the variability of hydrothermal deposits in back-arc basins compared to deposits that form along mid-oceanic ridges. Diverse eruption styles, host rock lithology, hydrothermal fluid composition, mineralogy of hydrothermal precipitates, trace element signatures, and isotopic systematics result from variable rates of back-arc spreading, magma supply, crustal thickness, depth to the heat source, magma composition, and volatile flux (Franklin et al., 2005; Hannington et al., 2005). Unlike mid-ocean ridges, tectonic effects, including collisions between a variety of oceanic and continental blocks, asymmetric rifting, and influence of pre-existing structures, contribute to the complexity of these systems. In particular, arc-ridge collisions are common (e.g., Lesser Antilles, Sumatra, South America, Japan, SW Pacific) and may cause increased plate coupling and significant variations in the horizontal velocity along the convergent boundary (e.g., Calmant et al., 1995; 2003; Taylor et al., 1995). The geodynamic evolution of different back-arc basins involves a unique combinations of these tectonic effects, which influence the overall metallogenic potential of the region.

Modern seafloor massive sulfide (SMS) deposits are important analogues of ancient volcanic-hosted massive sulfide deposits and are now considered viable targets for advanced mineral exploration; therefore, understanding the tectonic and volcanic controls on the siting of hydrothermal deposits is crucial for guiding exploration activities. The majority of ancient volcanogenic massive sulfide deposits are interpreted to have formed in subduction-related arc and back-arc environments (Hannington et al., 2005), so a robust understanding of the magmatic and

tectonic evolution of modern back-arc basins is important for interpreting the metallogeny of these ancient submarine environments.

1.2. Research objective

The main research objective of this thesis is to understand how tectonic complexities associated with subduction can influence the structural, magmatic, and hydrothermal evolution of a back-arc basin, which affects the distribution and type of mineral deposits that are formed. This objective is addressed using a multi-scale approach in three areas: the Coriolis Troughs (southern New Hebrides back-arc), the Jean Charcot Troughs (northern New Hebrides back-arc), and the Mariana back-arc. The New Hebrides back-arc basins are very young (<6.5 Ma; Monjaret et al., 1991; Pelletier et al., 1998) and therefore represent an important stage of early arc rifting, a major gap in our understanding of back-arc evolution. Previous work in the area has been limited and inadequate to constrain the evolution of the earliest back-arc rifting and the link to hydrothermal venting in this region. Recent discoveries of venting at the Nifonea volcano (Coriolis Troughs) and in the area of the Tinakula-Starfish volcano area (Jean Charcot Troughs) provide the first opportunity to understand the geological controls on magmatic-hydrothermal activity in nascent back-arc rifts. The Mariana back-arc, by contrast, is an example of a mature end-member of back-arc spreading that can be compared to the nascent New Hebrides back-arcs. Recent exploration of 600 km of the southern and central Mariana back-arc revealed 19 active vent sites, allowing comprehensive investigation of the tectonic and volcanic controls on hydrothermal venting along the length of the back-arc region. Together, these studies provide insights into the fundamental controls on the metallogenic potential of back-arc environments.

1.3. Thesis organization

This thesis comprises seven chapters. The introductory chapter describes the background and rationale for the research, the over-arching goals, and specific objectives. It also outlines the organization of the thesis and the original contributions of the author. The following five chapters are manuscripts written by the author. These chapters are organized according to geographical location: the Coriolis Troughs in the southern New Hebrides back-arc (Chapter 2), the Jean

Charcot Troughs in the northern New Hebrides back-arc (Chapters 3–5), and the southern and central Mariana back-arc spreading center (Chapter 6). Each of these chapters begins with a preface that relates it to the previous chapters and links it to the overall research objective. The final chapter provides a global summary and conclusions, as well as implications of the research.

Chapter 2 is a manuscript published in *Earth and Planetary Science Letters* in 2016, and focuses on the relationships between tectonism, volcanism, and hydrothermal venting in the Coriolis Troughs (southern New Hebrides back-arc), specifically unexpected shield-type volcanism (Nifonea volcano) in the young Vate Trough and hydrothermal venting in the summit caldera. These relationships are explored from basin- to deposit-scales, including the influence of subduction zone collisions and asymmetric slab rollback on focusing magma in an otherwise magma-deficient back-arc rift.

Chapter 3 is the companion to Chapter 2, focusing on the Jean Charcot Troughs (northern New Hebrides back-arc). This chapter examines how the tectonic events that affected the volcanism and hydrothermal venting in the northern New Hebrides have a profoundly different manifestation than in the south. The role of pre-existing structures on the morphology of the back-arc is investigated, together with the implications for the formation of the recently-discovered Tinakula massive sulfide deposit, which is described in detail in the next two chapters.

Chapter 4 focuses on deposit-scale investigations of the mineralogy, geochemistry, and S-isotope systematics of the Tinakula deposit (Jean Charcot Troughs). This chapter explores the genetic aspects of the deposit in relation to the local and regional magmatic and tectonic framework outlined in Chapter 3, with implications for understanding the broader metallogeny of the Jean Charcot Troughs (summarized in Chapter 7).

Chapter 5 is a study of hydrothermal alteration in the shallow footwall of the Tinakula deposit, examining elemental exchanges relative to the unaltered volcanic precursor described in Chapter 3. Relationships between explosive volcanism and hydrothermal alteration are investigated, leading to a model for how hydrothermal fluids can become focused in a highly-permeable volcaniclastic substrate.

Chapter 6 is a manuscript published in *Geochemistry, Geophysics, Geosystems* in 2016 exploring the relationships between regional tectonics, volcanism, and hydrothermal venting in the southern and central Mariana back-arc. This chapter investigates how subduction-zone processes influence magmatic and hydrothermal activity in a mature back-arc basin, including the entire range of back-arc spreading morphologies, from fast-spreading at ~13°N to slow-spreading at ~18°N. In particular, the impact of subduction-zone collisions, pre-existing structures, and the effects of arc proximity are explored in relation to magma supply rates, which in turn affect the siting of hydrothermal venting along different back-arc segments.

Chapter 7 summarizes the main findings of the research, with a focus on the influence of subduction zone complexities on volcanism and hydrothermal venting in different back-arc settings. It discusses the implications for this work and makes recommendations for future work.

Appendices are included as a digital supplement. They provide the data not included in the manuscripts, including entire geochemical datasets, QA/QC, and additional details on methodology.

1.4. Statement of original contribution

This thesis encompasses original research conducted by Melissa Ovedia Anderson under the supervision of Professor Mark Hannington at the University of Ottawa. This section outlines the contribution of the author, collaborators, and colleagues to each chapter.

Chapter 1: Introduction

- M.O. Anderson wrote the chapter, including: background, research rationale, objectives, thesis organization, and contributions

Chapter 2: The southern New Hebrides back-arc: Tectonic focusing of voluminous basaltic eruptions in magma-deficient back-arc rifts

M.O. Anderson, M.D. Hannington, K.M. Haase, U. Schwarz-Schampera, N. Augustin, T.F. McConachy, K. Allen

Contributions:

- M.O. Anderson participated in expedition SO-229, including data collection and initial interpretations
- M.O. Anderson wrote the chapter and supplementary material, with the following contribution: K. Allen jointly processed and interpreted water column data collected by Mini-Autonomous Plume Recorders included in Appendix A
- M.O. Anderson produced all figures and tables with the following contribution: N. Augustin created Fig. 2.2 as per the specifications of M.O. Anderson
- M.O. Anderson produced the seafloor geological maps and interpretations
- T.F. McConachy provided additional bathymetric data to complement the data collected during the SO-229 cruise, used for geological interpretations, and provided reviews on the manuscript
- N. Augustin processed the bathymetric maps using Terrain Texture Shading software, used as the base layer for the geological maps (visualized using ArcGIS by M.O. Anderson), in addition to reviewing the manuscript
- K.M. Haase and U. Schwarz-Schampera were the chief scientists on the SO-229 cruise and provided additional reviews on the manuscript
- M.D. Hannington provided valuable guidance throughout the research and preparation of the manuscript
- M.O. Anderson acted as the corresponding author during the submission and review process
- The final manuscript was peer-reviewed by D. Fornari and an anonymous reviewer

This article was published in *Earth and Planetary Science Letters* in 2016:

Anderson, M.O., Hannington, M.D., Haase, K.M., Schwarz-Schampera, U., Augustin, N., McConachy, T.F., Allen, K., 2016. Tectonic focusing of voluminous basaltic eruptions in

magma-deficient backarc rifts. Earth and Planetary Science Letters 440, 43–55, doi:10.1016/j.epsl.2016.02.002.

Preliminary interpretations were published in a cruise report in 2013:

Haase, K.M., and Shipboard Scientific Party, 2013. R/V Sonne SO-229 Cruise Report: Volcanism, hydrothermal activity and vent biology in the Coriolis Troughs, New Hebrides Island Arc, 244p., doi:10.13140/RG.2.1.1718.2323.

Aspects of this work were published as an extended abstract and presented orally:

Anderson, M.O., Hannington, M.D., Haase, K.M., Schwarz-Schampera, U., 2015. Geological controls on hydrothermal venting at the Nifonea Volcano, Vate Trough, Vanuatu. SGA Biennial Meeting, 24–27 August, 2015, Nancy, France.

This paper provided the geological context for interpretations made in a subsequent publication in 2017:

Schmidt, K., Garbe-Schönberg, D., Hannington, M.D., Anderson, M.O., Bühring, B., Haase, K., Haruel, C., Lupton, J., Koschinsky, A., 2017. Boiling vapour-type fluids from the Nifonea vent field (New Hebrides Back-Arc, Vanuatu, SW Pacific): Geochemistry of an early-stage post-eruptive hydrothermal system. Geochimica et Cosmochimica Acta, 185–209, doi:10.1016/j.gca.2017.03.016.

Chapter 3: Magmatism and hydrothermal venting in the Jean Charcot Troughs, SW Pacific: Influence of the geodynamic evolution of the northern New Hebrides back-arc

M.O. Anderson, M.D. Hannington, McConachy

Contributions:

- M.O. Anderson wrote the chapter and supplementary sections, and produced all tables
- M.O. Anderson produced the figures with the following contributions: T.F. McConachy provided seafloor images (Fig. 3.10 and 3.11), 3D bathymetric images (Fig. 3.12), and map of earthquake epicenters (Fig. 3.23); N. Augustin processed the bathymetry with Terrain Texture Shading software (Fig. 3.6b)

- T.F. McConachy (Neptune Minerals Inc.) provided data (bathymetry, samples, ROV dive videos and photos, and whole-rock geochemistry data for eight samples)
- M.O. Anderson collected samples from Neptune Minerals Inc. repository in Gosford, Australia with the assistance of K. Allen
- M.O. Anderson produced the seafloor geological and structural maps, and visualized the datasets using ArcGIS software
- Interns M. Anders and M. Sims prepared samples for whole-rock geochemistry (ActLabs) under the supervision of M.O. Anderson
- M.O. Anderson conducted petrography at GEOMAR
- M.D. Hannington provided guidance throughout the research and preparation of the manuscript.

This manuscript is in preparation for publication, and aspects of this work were published as an abstract presented orally:

> Anderson, M.O., Hannington, M.D., McConachy, T.F., 2015. Massive sulfide accumulation along a submarine scoria cone row at the Tinakula Deposit, New Hebrides Arc, Solomon Islands. GeoBerlin Annual Conference, 4–7 October, 2015, Berlin, Germany.

Chapter 4: Mineralogy, geochemistry, S-isotopes, and fluid inclusion systematics of the Tinakula seafloor massive sulfide deposit, Jean Charcot Troughs, SW Pacific

M.O. Anderson, M.D. Hannington, T.F. McConachy, J.W. Jamieson, M. Anders, T. Hansteen, S. Petersen, H. Wienkenjohann, H.A. Strauss

Contributions:

- M.O. Anderson wrote the chapter and supplementary sections
- M.O. Anderson produced all tables and figures, with the following contributions: H. Wienkenjohann provided data for Table 4.8; M. Anders provided the data for Table 4.9; T.F. McConachy provided seafloor images (Fig. 4.2)
- T.F. McConachy provided data (bathymetry, samples, ROV dive videos and photos)

- M.O. Anderson collected samples from Neptune Minerals Inc. repository in Gosford, Australia with the assistance of K. Allen
- M.O. Anderson processed the datasets using ArcGIS software
- M.O. Anderson prepared samples for whole-rock geochemistry (ActLabs) with the assistance of interns A. Jegen and F. van Diehl
- M.O. Anderson conducted petrography at GEOMAR
- M.O. Anderson conducted EPMA analyses at GEOMAR with the assistance of Mario Thörner (lab manager) and interns T. Dols, M. Williams, and F. Brüggemeier; reduction of EPMA data was conducted by Mario Thörner
- J.W. Jamieson conducted ^{226}Ra/Ba geochronology at the University of Ottawa and reviewed the manuscript
- H. Wienkenjohann collected samples for S-isotopes at GEOMAR under the supervision of M.O. Anderson, and performed S-isotopes analyses at Wilhelms-Universität Munster for his B.Sc. thesis, supervised by H.A. Strauss and co-supervised by M.O. Anderson; M.O. Anderson provided additional interpretations of S-isotope data for this manuscript
- M. Anders performed fluid inclusion petrography and microthermometry at GEOMAR for her M.Sc. thesis under the supervision of M.O.Anderson, M.D. Hannington, T. Hansteen, and S. Peterson; M.O. Anderson provided additional interpretations of microthermometry data for this manuscript
- M.D. Hannington provided guidance throughout the research and preparation of the manuscript

This manuscript is in preparation for publication, and aspects of this work were published as abstracts presented orally and as a poster:

Anderson, M.O., Hannington, M.D., McConachy, T.F., 2015. Massive sulfide accumulation along a submarine scoria cone row at the Tinakula Deposit, New Hebrides Arc, Solomon Islands. GeoBerlin Annual Conference, 4–7 October, 2015, Berlin, Germany. (Oral presentation)

Anderson, M.O., Hannington, M.D., Haase, K., Schwartz-Shampera, U., McConachy, T., 2014. Insights into magmatic-hydrothermal processes in the newly-discovered seafloor

massive sulfide deposits of the New Hebrides arc-backarc, SW Pacific. AGU Annual Fall Meeting, 12–19 December, 2014, San Francisco, CA. (Poster presentation)

Chapter 5: Mineralogical and geochemical characteristics of hydrothermal alteration in the volcaniclastic-hosted Tinakula seafloor massive sulfide deposit (New Hebrides back-arc, SW Pacific)

M.O. Anderson, M.D. Hannington, McConachy, T.F., Augustin, N.

Contributions:

- M.O. Anderson wrote the chapter and produced all tables and figures, with the following contribution: T.F. McConachy provided the 3D bathymetry (Fig. 5.3.)
- T.F. McConachy provided data (bathymetry) and samples
- M.O. Anderson produced graphical summary core logs and collected drill core samples from the Neptune Minerals Inc. repository in Honiara, Solomon Islands, assisted by J. Carpenter
- M.O. Anderson processed the datasets using ArcGIS software
- M.O. Anderson performed petrography and clast-matrix separations of samples
- Intern A. Jegen collected SWIR spectra under the supervision of M.O. Anderson
- N. Augustin helped set up the particle-size separation lab and provided valuable guidance to M.O. Anderson
- M.O. Anderson prepared samples for clay-size separates, including sonic disaggregation, wet sieving, particle separation in standing cylinders, and freeze drying with the assistance of S. Lange and interns A. Jegen, M. Williams, and H. Sauer
- M.O. Anderson conducted XRD analyses at GEOMAR assisted by J. Heinze (lab manager), S. Lange, and A. Jegen; XRD interpretations were performed by M.O. Anderson
- M.O. Anderson prepared samples for whole-rock geochemistry provided by ActLabs and O-isotope data provided by QFIR
- M.O. Anderson performed mass-balance calculations, temperature calculations, and created geological cross-sections
- M.D. Hannington provided guidance throughout the research and preparation of the manuscript

Chapter 6: Geological interpretation of volcanism and segmentation of the Mariana back-arc spreading center between 12.7°N and 18.3°N

M.O. Anderson, Chadwick, W.W., Jr., Hannington, M.D., Merle, S.G., Resing, J.A., Baker, E.T., Butterfield, D.A., Walker, S.L., Augustin, N.,

Contributions:

- M.O. Anderson participated in the sea-going expedition FK151121, including data collection and initial interpretations
- M.O. Anderson wrote the chapter and produced all tables and figures, with the following contribution: N. Augustin created Fig. 6.2 per the specifications of M.O. Anderson
- S.G. Merle processed the raw bathymetry and N. Augustin processed the data using Terrain Texture Shading software; M.O. Anderson visualized the data using ArcGIS software
- M.O. Anderson generated all geological maps and cross-sections
- W.W. Chadwick, J.A. Resing, E.T. Baker, and D.A. Butterfield were co-chief scientists on the FK151121 cruise, and provided edits and valuable feedback for the manuscript
- S.L. Walker and N. Augustin reviewed the manuscript
- M.D. Hannington edited the manuscript and provided valuable feedback
- M.O. Anderson acted as the corresponding author during the submission and review process
- The final manuscript was peer-reviewed by an anonymous reviewer

This article was published in *Geochemistry, Geophysics, Geosystems* in 2017:

Anderson, M.O., Chadwick, W.W, Hannington, M.D., Merle, S.G., Resing, J.A., Baker, E.T., Butterfield, D.A., Walker, S.L., Augustin, N., 2017. Geological interpretation of volcanism and segmentation of the Mariana back-arc spreading center between 12.7°N and 18.3°N. Geochemistry, Geophysics, Geosystems 18, 2240–2274, doi:10.1002/2017GC006813.

Preliminary geological maps and interpretations were published in a cruise report in 2016:

Resing, J.A., and Shipboard Scientific Party, 2016. R/V Falkor FK151121 Cruise Report: Hydrothermal Hunt in the Mariana Back-Arc, 103 p., doi:10.7284/906519.

Aspects of this work were published as abstracts and presented orally and as a poster:

Anderson, M.O., Chadwick, W.W. Jr., Merle, S.G., Resing, J., Walker, S., Baker, E., Hannington, M.D., Augustin, N., 2017. Relationship between tectonism, volcanism, and hydrothermal venting along the Mariana back-arc spreading center between 12.7°N and 18.3°N. AGU Chapman Conference on Submarine Volcanology, 29 January–3 February, 2017, Hobart, Australia. (Oral presentation)

Baker, E.T., Walker, S.L, Resing, J.A., Chadwick, W.W., Merle, S.G., Anderson, M.O., 2016. Hydrothermal plume surveys of the backarc Mariana Trough (12.7°–18.3°N) by surface-ship and submersible find an unexpectedly high vent site frequency. AGU Annual Fall Meeting, 12–16 December, 2016, San Francisco. (Poster presentation)

This paper provided the geological context for interpretations made in a subsequent publication:

Baker, E.T., Walker, S.L, Resing, J.A., Chadwick, W.W. Jr., Merle, S.G., Anderson, M.O., Butterfield, D.A., Buck, N.J., Michael, S., 2018. The effect of arc proximity on hydrothermal activity along spreading centers: New evidence from the Mariana back-arc (12.7°–18.3°N). Geochemistry, Geophysics, Geosystems 18, doi:10.1002/2017GC007234.

References

Calmant, S., Lebellegard, P., Taylor, F., Bevis, M., Maillard, D., Recy, J., Bonneau, J., 1995. Geodetic measurements of convergence across the New Hebrides subduction zone. Geophys. Res. Lett. 22, 2573–2576, doi:10.1029/95GL01780.

Calmant, S., Pelletier, B., Labellegard, P., Bevis, M., Taylor, F.W., Phillips, D.A., 2003. New insights on the tectonics along the New Hebrides subduction zone based on GPS results. J. Geophys. Res. 108, 2319, doi:10.1029/2001JB000644.

Franklin, J.M., Gibson, H.L., Jonasson, I.R., Galley, A.G., 2005. Volcanogenic massive sulfide deposits, Econ. Geol. 100, 523–560.

Hannington, M.D., de Ronde, C.E.J., Petersen, S., 2005. Sea-Floor Tectonics and Submarine Hydrothermal Systems. Econ. Geol. 100, 111–141.

Leat, P.T., Larter, R.D., 2003. Intra-oceanic subduction systems: Tectonic and magmatic processes: Geol. Soc. London, Spec. Pub. 219, 1–17.

Monjaret, M.C., Bellon, H., Maillet, P., 1991. Magmatism of the troughs behind the New Hebrides island arc (RV Jean Charcot SEAPSO 2 cruise): K-Ar geochronology and petrology. J. Volcanol. Geotherm. Res. 46, 265–280, doi:10.1016/0377-0273(91)90088-H.

Pelletier, B., Calmant, S., Pillet, R., 1998. Current tectonics of the Tonga-New Hebrides region. Earth Planet. Sci. Lett. 164, 263–276, doi:10.1016/S0012-821X(98)00212-X.

Taylor, F.W., Bevis, M.G., Schutz, B.E., Kuang, D., Récy, J., Calmant, S., Charley, D., Regnier, M., Perin, B., Jackson, M., Reichenfeld, C., 1995. Geodetic measurements of convergence at the New Hebrides island arc indicate arc fragmentation caused by an impinging aseismic ridge. Geology 23, 1011–1014, doi:10.1130/0091-7613(1995)023<1011:GMOCAT>2.3.CO;2.

Preface to Chapter 2

This chapter focuses on the Coriolis Troughs in the southern New Hebrides back-arc. These are some of the youngest back-arc features on Earth, and provide important insight into the earliest stages of back-arc rifting. This chapter investigates the influence of geodynamic processes on back-arc structures and magmatic activity. The geology of the youngest basin, the Vate Trough, is examined in detail using novel seafloor geological mapping techniques in order to understand the structural and volcanic evolution of the basin. The study highlights the importance of subduction-zone collisions and asymmetric slab rollback, which acted together to create a local stress field that has focused magma in an otherwise magma-deficient back-arc rift. In particular, the unexpected occurrence of a large shield-type volcano (Nifonea) in the young magma-deficient Vate Trough is attributed to local extension resulting from transtension and asymmetric slab rollback caused by the collision of the d'Entrecasteaux ridge with the subduction zone. These findings have important implications for hydrothermal venting, which are discussed here and in greater detail in Chapter 7.

Chapter 2

The southern New Hebrides back-arc: Tectonic focusing of voluminous basaltic eruptions in magma-deficient back-arc rifts

Published in: Anderson, M.O., Hannington, M.D., Haase, K.M., Schwarz-Schampera, U., Augustin, N., McConachy, T.F., Allen, K., 2016. Tectonic focusing of voluminous basaltic eruptions in magma-deficient backarc rifts. Earth Planet. Sci. Lett. 440, 43–55, doi:10.1016/j.epsl.2016.02.002.

Abstract

The Coriolis Troughs of the New Hebrides subduction zone are among the youngest back-arc rifts in the world. They reach depths of >3 km, despite their small size (<100 km in length and only 25–45 km wide) and their proximity to the arc front (~50 km). The narrow, deep graben morphology is characteristic of magma-deficient arc rifts in the early stages of back-arc extension, where the rate of extension and subsidence exceeds the magmatic input. Unexpectedly, the youngest graben, the Vate Trough, contains a centrally-located 1000-m tall and 14-km wide shield volcano with a large, 5 × 8 km breached summit caldera. The Nifonea axial volcano has a volume of ~126 km^3, reflecting unusually high extrusion rates, given its young age (<3 Ma), and the summit caldera hosts the remnants of a large lava lake, the first described from a submarine back-arc setting. Extensive diffuse hydrothermal venting and several clusters of black smoker chimneys, with the highest recorded fluid temperatures (368°C) in the SW Pacific, occur on the youngest lava flows. Comparison with similar axial volcanoes on the mid-ocean ridges suggests that the 46 × 10^6 m^3 of sheet flows in the caldera could have been erupted in <30 hours. The focusing of voluminous basaltic eruptions into an otherwise magma-deficient back-arc has been linked to strong left-lateral transtension caused by clockwise rotation and segmentation of the southern portion of the arc after collision with d'Entrecasteaux ridge. This study shows that the upper plate stresses can result in dramatic variability in magma supply and hydrothermal activity at the earliest stages of arc rifting and could explain the wide range of melt compositions, volcanic styles and mineral deposit types found in nascent back-arc rifts.

2.1. Introduction

Back-arc basins form as a result of extension in response to different combinations of hinge rollback, anchoring of the subducting slab, anomalous melting in the mantle wedge, and mantle diapirism (e.g., Karig, 1971; Schellart et al., 2002). A correlation between back-arc stresses and slab dip has also been documented (e.g., Sdrolias and Müller, 2006). Steep subduction angles (up to 90°) occur when the downgoing slab is significantly older and more dense than the overriding plate, such as along the Mariana Trench (Fryer, 1995). This interplay of plate kinematics, subducting slab properties, and mantle wedge dynamics contribute to a wide range of back-arc basin morphologies (see Appendix A: Suppl. Table A1). Early arc rifts are characterized by deep

linear troughs bounded by rift-parallel normal faults (e.g., Central Volcanic Region in N.Z.; Jean Charcot and Coriolis Troughs, New Hebrides; Fonualei Rifts in north Tonga), progressing to asymmetrical and disorganized extension with intrusion of magma into the thinned faulted basement (e.g., Southern Havre Trough; Okinawa Trough). The extreme variability in magma supply and hydrothermal activity depends on the structural evolution of the rift zones. True seafloor spreading and associated magnetic anomalies develop when crustal accretion in the opening basin is eventually dominated by passive upwelling of shallow mantle material (e.g., Lau Basin and North Fiji Basin: Martínez and Taylor, 2006).

At the rifting stage of back-arc basin formation, the geochemical signatures of the magmas range from arc-like to MORB-like, reflecting contributions from different melt sources (Pearce and Stern, 2006). At the same time, a wide range of volcano types may form, including simple monogenetic to polygenetic cones, domes, and tuff rings. This contrasts with mid-ocean ridges (MORs), which are characterized by effusive basaltic fissure eruptions, complex hummocky volcanoes, pillow volcanoes, and large flat-topped volcanoes, with very few pyroclastic eruptions. Where low-viscosity basaltic magma dominates, large shield volcanoes are common, especially at MOR-plume intersections, such as Axial Volcano on the Juan de Fuca Ridge and near the Lucky Strike Seamount on the Mid-Atlantic Ridge. Shield volcanoes, commonly with broad steep-walled summit calderas, result from the high magma supply rates associated with mantle upwelling. The voluminous effusive eruptions are typically accompanied by widespread hydrothermal activity (e.g., Chadwick et al., 1985; Embley et al., 1990; Langmuir et al., 1997), the evolution of which reflects the caldera dynamics (Stix et al., 2003).

Few examples of shield-type volcanoes are known in volcanic arcs and back-arc basins. Rarely, structurally-focused and/or flux-induced partial melting in the mantle produces a high magma supply in intra-arc basins above the mantle wedge (e.g., Ambrym Volcano, Vanuatu: Picard et al. 1994). In deeper back-arc basins, the supply of melt varies with proximity to the volcanic front and is regulated by the rate of subduction and slab geometry, which control melt extraction from the mantle wedge (e.g., Martínez and Taylor, 2006). Here, we report the results of geological mapping of a large shield-type axial volcano (named Nifonea after “hook” in the local vernacular) in the Vate Trough of the New Hebrides, carried out during R/V Sonne cruise SO-

229 (Haase and Shipboard Scientific Party, 2013). New data are combined with results from previous cruises to develop the first coherent picture of unexpected effusive volcanism associated with the early rifting of the Vate Trough. We examine the volcanic and structural evolution of the axial volcano and suggest a direct link between the unusual style of volcanism and the regional tectonic stresses induced by asymmetric rollback of the subducting Australian plate and fragmentation of the New Hebrides arc.

2.2. Tectonic setting

During the Oligocene to early Miocene, the New Hebrides Island Arc formed part of the continuous Melanesian Arc along the Vitiaz Trench where the Pacific Plate was being subducted beneath the Indo-Australian Plate (Hall, 2002). A regional reversal of subduction occurred in the Late Miocene when the Ontong Java Plateau was introduced into the subduction zone. Subsequent eastward subduction of the Australian Plate beneath the Pacific Plate along the New Hebrides Trench was accompanied by slab rollback and the opening of the North Fiji Basin (Auzende et al., 1995). Seismic data indicate that the angle of subduction along the New Hebrides Trench is currently 60–70°, and the convergence rates vary significantly from 30 mm y^{-1} in the north to 170 mm y^{-1} in the south (Fig. 2.1a; Pysklywec et al., 2003). Collision with the d'Entrecasteaux Ridge (DER), a chain of fossil submarine volcanoes, occurred at ~3 Ma and has since caused progressive segmentation of the arc.

Shortening and thickening of the central segment of the arc at the present location of the DER resulted in a lack of extension in the associated back-arc (Charvis and Pelletier, 1989; Meffre and Crawford, 2001). Collision with the West Torres Massif (WTM), a large (>35000 km^2) submarine plateau, also contributed to the shortening and thickening of the arc crust (Yan and Kroenke, 1993; Schellart et al., 2002). The central segment has the lowest convergence rates (Bergeot et al., 2009) and is now moving east relative to the adjacent arc segments (Taylor et al., 1995). These complexities have allowed Indian-type mantle to migrate into the central arc segment, where Pacific-type mantle sources have dominated (Crawford et al., 1995). The structural consequences of collision with the aseismic DER are well documented (Collot et al., 1992; Greene et al., 1992). The regular spacing of the arc volcanoes was severely disrupted, and

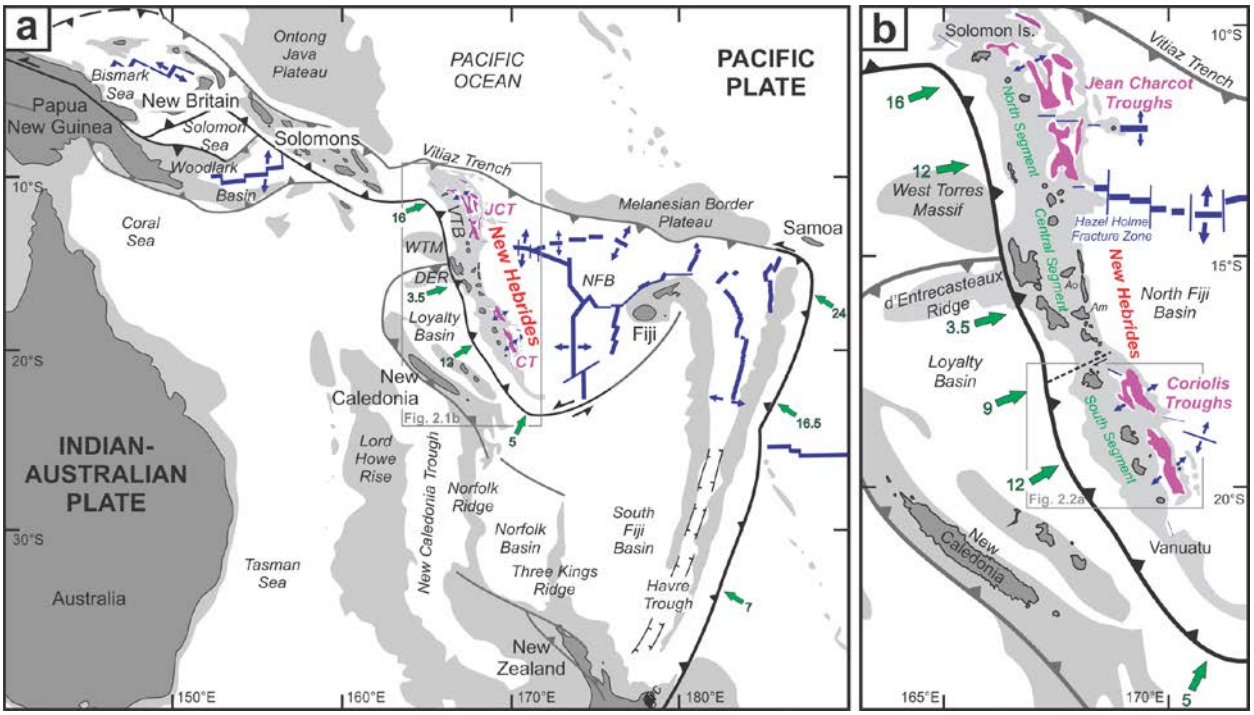


Fig. 2.1. Geographic location and tectonic features: (a) southwest Pacific, and (b) the New Hebrides arc-back-arc system (southern Solomon Islands and Vanuatu). Light grey areas are shallower than 2000 mbsl, green arrows indicate convergence directions and rates (cm y^{-1}; Pysklywec et al., 2003), blue lines represent spreading centers, and the New Hebrides back-arc rifts are indicated in purple. The location of Fig. 2.2a is indicated. AO = Aoba Volcano, AM = Ambrym Volcano, CT = Coriolis Troughs, JCT = Jean Charcot Troughs, DER = d'Entrecasteaux Ridge, WTM = West Torres Massif. Modified from Hall (2002).

arc-parallel and arc-transverse faults produced a number of intra-arc grabens in which unusually deep sedimentary basins formed. Several large low-profile basaltic shield volcanoes (Ambrym and Aoba) formed along major transverse faults in the basins. These faults acted as magma conduits for primitive picritic and ankaramitic lavas from which these volcanoes formed (Crawford et al., 1988).

North of 13°30'S, the arc has been rotating counterclockwise with respect to the North Fiji Basin, causing rapid NE-SW back-arc extension (41–84 mm y^{-1}; Bergeot et al., 2009) and producing a series of complex horsts, grabens, and half grabens with diffuse magmatism that comprise the Jean Charcot Troughs (JCT). The JCT are bound in the south by the western extension of the Hazel Holme Fracture Zone and to the east by the volcanic Duff Ridge. South of the DER, clockwise rotation of the New Hebrides Arc resulted in NE-SW extension of the basement at a rate of 20–35 mm y^{-1} (Bergeot et al., 2009) and produced the back-arc Coriolis Troughs between 6.5–3.5 Ma (Fig. 2.1b: Monjaret et al., 1991; Pelletier et al., 1998). The clockwise rotation and extension of the basement block have been described by Arculus and Shipboard Scientific Party (2006). Despite its young age, the rifting has developed several flat-bottomed grabens, 70–100 km in length and with deep bounding structures. The youngest trough is the Vate Trough, with a maximum width of 25 km. The Coriolis Troughs were previously thought to be similar to the intra-arc basins to the north, but the recent discovery of young ocean floor in the Vate Trough confirms that they are true back-arc basins (McConachy et al., 2005; Haase and Shipboard Scientific Party, 2013). The narrow, deep grabens are situated only ~50 km from the arc front but reach depths of more than 3 km (2840 mbsl in the north to 3400 mbsl in the south; Fig. 2.2). This morphology is characteristic of magma-deficient arc rifts in the early stages of back-arc extension, where the rate of extension and subsidence exceeds the magmatic input (Martínez and Taylor, 2006).

2.3. Methods

Ship-based multibeam bathymetric data from the Vate Trough were collected during R/V Southern Surveyor CoTroVE cruise in 2004 (COriolis TROughs Vents Expedition: Arculus and Shipboard Scientific Party, 2006) and are supplemented here with new data from R/V Sonne

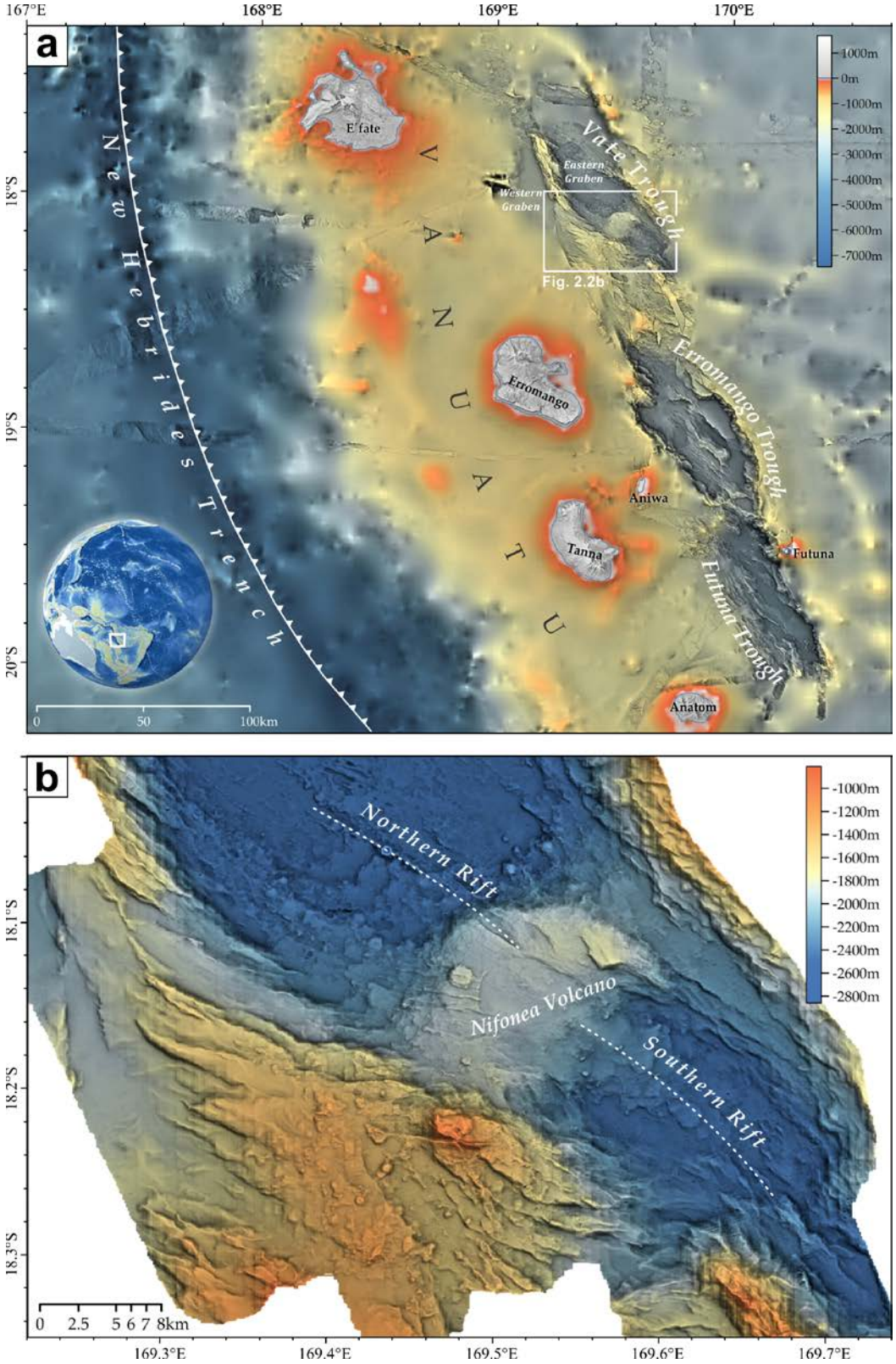


Fig. 2.2. Kongsberg EM 300 multibeam bathymetric map of the Coriolis Troughs, New Hebrides Back-arc, Vanuatu, overlain on global marine altimetry data (Sandwell et al., 2014).

cruise SO-229 (CoVolVe, COriolis VOLcanism and Vents: Haase and Shipboard Scientific Party, 2013). The Southern Surveyor was equipped with a Kongsberg-Simrad EM 300 multibeam echo sounder with an operating frequency of 30 kHz, and the R/V Sonne was equipped with a Kongsberg-Simrad EM 120 multibeam echo sounder with an operating frequency of 12 kHz. The combined surveyed area is 17,694 km^2 and included the Vate, Erromango, and Futuna Troughs. The data were gridded using the weighted moving average method in QPS Fledermaus software with a cell size of 30 m. These data were reprocessed using the "Terrain Texture Shading" (TTS) technique developed by Brown (2010) as an interpretive tool in applied geomatics to reveal subtle surface and structural features that can be directly correlated with volcanic geomorphology (see Appendix A).

The processed bathymetric maps were interpreted together with backscatter data from the GLORIA sidescan sonar survey of Price et al. (1993; Suppl. Fig. A1) to create a new geological map of the Vate Trough, covering an area of ~3000 km^2 (Fig. 2.3). Bottom observations from ROV dives in the Trough, together with TV grabs, wax rock coring, and other rock sampling, were used to "ground truth" the legend derived from seafloor texture and bathymetric features (Suppl. Figs. A2 and A3, Tables A2 and A3; Haase and Shipboard Scientific Party, 2013). Six dives were conducted with the ROV Kiel 6000 during the 2013 SO-229 CoVolVe cruise. Four dives were on the Nifonea axial volcano; one dive examined the eastern margin of the volcano and another examined the western rift flank of the Vate Trough. Additional ROV dives carried out by Neptune Minerals Inc. in 2010 also provided coverage at the summit of Nifonea. Although some areas lack direct ROV or camera observations, the comparison with sidescan data and seafloor observations in other similar studies show that we can confidently assign different volcanic facies to different terrain textures (cf. Perfit and Chadwick, 1998; McClinton and White, 2015).

A more detailed map of the structure, volcanology, and hydrothermal activity covering 70 km^2 at the summit of the Nifonea axial volcano was created by analyzing digital SD and HD video and still camera records from the ROV dives. Fully georeferenced measurements of structural features, including faults, lineaments, fissures and dikes, were compiled. Relative ages of the mapped units were established from overlapping and cross-cutting relationships, sediment cover

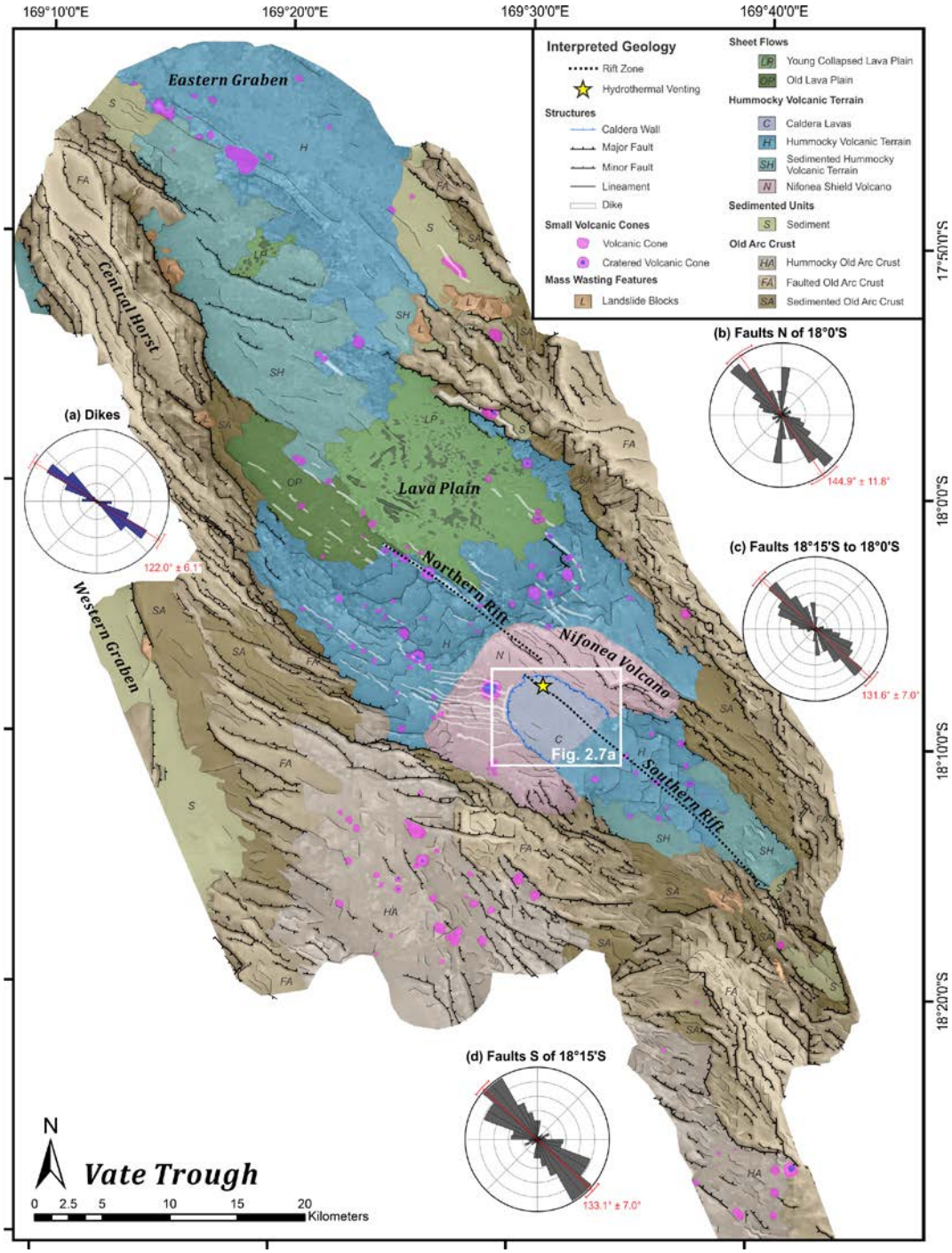


Fig. 2.3. Predicted geological map and structures of the Vate Trough, New Hebrides Back-arc, Vanuatu, overlain on Kongsberg EM 300 multibeam bathymetry gridded at 30 m. The geological legend, arranged in order of increasing apparent age of units, is described in the text. Included in this diagram are rose diagrams of the structures in the Vate Trough, with a class interval of 10° and a circle spacing of 10: (a) dikes (entire area), n = 93, (b) major and minor faults north of 18°S, n = 151; (c) major and minor faults between 18°15'S and 18°0'S, n = 266; (d) major and minor faults south of 18°15'S, n = 318. The location of the detailed map in Fig. 2.7a is outlined in white.

thickness recorded during ROV dives, and morphological and backscatter evidence of young volcanic flow features and mass wasting. This type of mapping provides the most reliable picture currently available of the volcanic geomorphology of the seafloor at scales of 1:50,000 to 1:100,000.

2.4. Geology of the Vate Trough

The Vate Trough is the northernmost and youngest (<3.5 Ma: Monjaret et al., 1991) of three arc-parallel *en echelon* grabens of the Coriolis Troughs located between 17°41'S and 20°3'S (Futuna, Erromango, and Vate: Fig. 2.2). It comprises two NW-SE trending flat-bottomed grabens separated by a normally-faulted central horst. The smaller western graben has a width ~15 km and a maximum depth of 2150 mbsl, whereas the main eastern graben has a width of ~25 km and a maximum depth of 2840 mbsl. The eastern graben is bordered by terraced escarpments that expose the New Hebrides arc basement. It consists of two deep sub-basins, separated by the Nifonea axial volcano. The two sub-basins originally formed a single elongate basin that is now subdivided by the emerging Nifonea axial volcano.

2.4.1. Old arc crust

The walls of the Vate Trough expose mainly old arc crust (Figs. 2.3, 2.4 and Suppl. Fig. A1). At the top of the graben walls the seafloor is hummocky with a rough ("high rugosity") surface dotted by numerous small volcanic edifices and minor faulting. Towards the basin walls, the arc crust is heavily faulted, with steep slopes. Samples collected from the western wall of the trough all consist of basalt with MgO contents between 4.5–10.6 wt. % (Haase and Shipboard Scientific Party, 2013). Large angular blocks, up to 2 km in size, occur on the basin floor adjacent to the steep walls of the northern sub-basin. They are interpreted to be foundered arc crust that has been transported very short distances. Sedimented arc crust outside the trough shows less relief, characterized by fewer normal faults, flatter slopes and a generally smooth morphology. Sidescan sonar data reveal an uneven, low to moderate backscatter intensity, and gradational contacts between substrates of different texture. The hummocky arc crust outside the trough

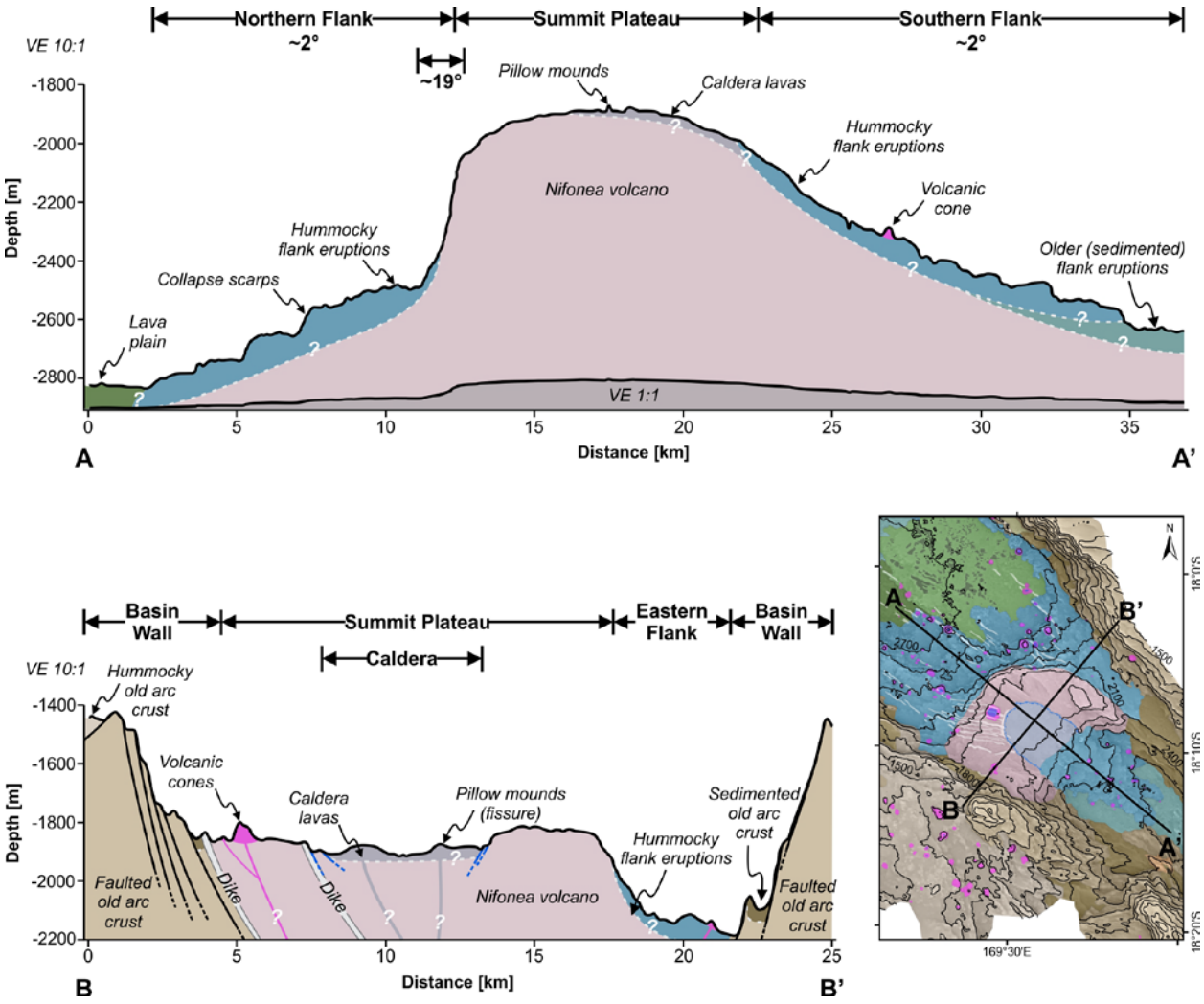


Fig. 2.4. Cross-sections of the Nifonea axial volcano showing interpreted geology and structures. The inset shows the cross-section locations with 150 m contour spacing, with the same legend as Fig. 2.3. Grey dashed lines represent gradational contacts between units. In A-A' the caldera wall is indistinguishable due to recent eruptions in the caldera that have increased the height of the caldera floor, while in B-B' nested caldera walls are visible. The volcanic flanks have slope angles of ~2°, which is consistent with the classification of Nifonea as a shield volcano. 10× vertical exaggeration (VE).

covers ~13% of the area mapped (399 km^2 of the ~3000 km^2), the faulted arc crust covers ~32% (967 km^2), and the more heavily sedimented arc crust covers ~9% (255 km^2).

2.4.2. Basin floor

The main features of the basin floor are lightly sedimented hummocky volcanic terrain, extensive lava plains, and volcanic cones (Figs. 2.3, 2.4). The hummocky volcanic terrain is centered along the axial part of the basin, north and south of the Nifonea volcano, and dominates the basin floor in the far north. There is a distinct lack of faulting in this terrain compared with the older arc crust, reflecting relatively recent volcanism. It has a rough surface morphology (high rugosity) and a high backscatter in the sidescan data. 'Hummocks' up to 200 m high are interpreted to be thick onlapping flows (pillows and lobes) oriented perpendicular to the slope and with steep flow fronts and collapse features (cf. Yeo et al., 2012), some of which are distinguishable in the GLORIA data of Price et al. (1993). These flows cover ~19% of the mapped area (581 km^2), including on the distal flanks of the Nifonea axial volcano. The hummocky volcanic terrain in the northern part of the trough is covered by sediment with a relatively smooth surface morphology, but the volcanic character of the substrate is still evident beneath the sediment based on the moderate rugosity and slight decrease in the backscatter intensity. These flows are interpreted to be the oldest volcanic features in the graben, and cover ~9% of the mapped area (254 km^2). Sediment-filled topographic lows in the basin floor occupy ~5% of the mapped area (159 km^2) and are characterized by smooth surfaces, an absence of faults, and low mottled backscatter, reflecting uneven sediment thickness.

More than 160 small volcanic cones, typically less than 0.5 km^2 in size, are found throughout the trough. They are readily identifiable in the multibeam data by their circular morphology, steep sides, and high relief relative to the surrounding lavas (width:height of ~10:1). They are most common as part of the hummocky volcanic terrain, in many cases showing a close spatial association strong lineaments (dike-like features) crossing the basin floor, but they also occur in older arc crust on the flank of the trough.

Two flat areas of the northern sub-basin, between the hummocky flows, have a very high and even backscatter, suggesting little sediment cover. These areas are interpreted to be broad, lightly sedimented 'lava plains' and possibly sheet flows (cf. Perfit and Chadwick, 1998; McClinton and White, 2015). A slightly older lava plain occurs centrally on the west side of the northern sub-basin, in the deepest part of the trough, and covers 56 km^2 (Fig. 2.3). This area is cut by many dike-like features and overlain by a much larger field of younger collapsed flows to the east. The surface of the younger flows is flat and pock-marked by many irregular depressions interpreted to be collapse features (large drain-backs). The collapse features occupy ~10% of the area of the flows and range in size from ~10 m to 2 km in diameter and <10–40 m in depth. The backscatter in this area is very high, indicating little or no sediment, and there are far fewer dike-like features or small cones. Contacts with the older lightly sedimented flows are sharp. The younger lava plain covers a single large area of 154 km^2 (Fig. 2.3), but it is interpreted to represent multiple stacked flows with individual thicknesses of between 14 and 40 m (Fig. 2.5). The total volume of lava in this area is estimated to be ~16 km^3.

The large lava plains in the northern sub-basin and the northern flank of the Nifonea volcano are cut by a large number of elongate ridges (~3–80 m in height: Fig. 2.3). Individual ridges range from ~250 m in length up to more than 5 km, with a strike of 122° ± 6° (95% confidence), following the orientation of other structural features in the Vate Trough (see below). However, on the northwest flank of Nifonea volcano they are rotated ~23° towards the basin axis (Fig. 2.3a). Several are identifiable in GLORIA sidescan as lineations with high backscatter but no displacement on either side (i.e., not associated with fault scarps), consistent with volcanic dikes or fissure ridges. More than 70 of these dike-like features are observed in the northern sub-basin, and a third of them are associated with small volcanic cones. They clearly mark areas of tectonic activity and extension of the graben floor, and some are obscured by the youngest lava flows.

2.4.3. Other structural features of the Vate Trough

Numerous other types of lineaments occur throughout the Vate Trough (Fig. 2.3). Scarps >100 m in height are classified as major faults; those with <100 m scarps are minor faults. Other lineaments may represent fractures, abrupt changes in seafloor morphology, erosional features,

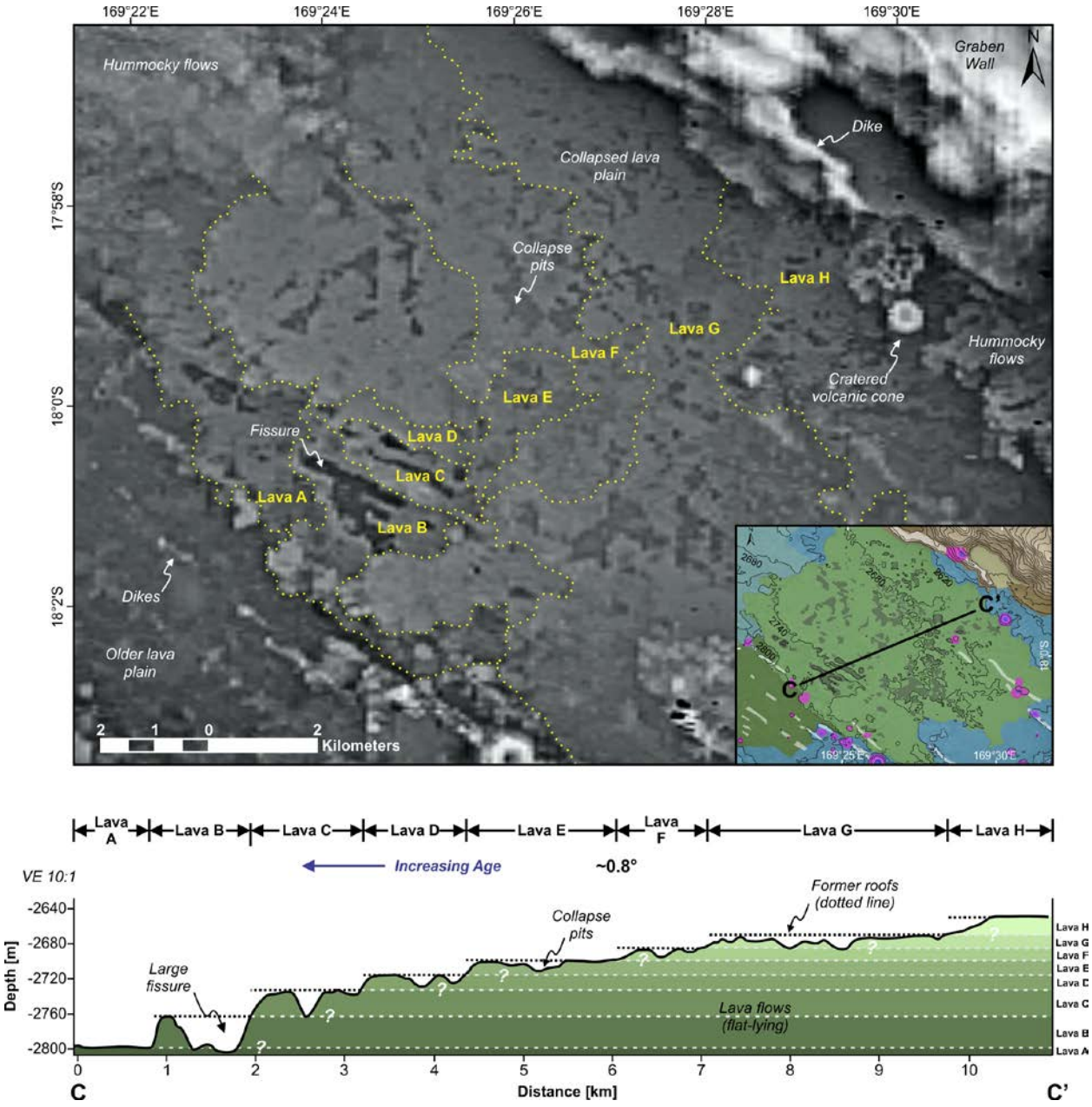


Fig. 2.5. EM 300 multibeam bathymetry of the extensive lava plain in the Vate Trough showing terrain texture shading and interpreted geological features and flow boundaries. Yellow dotted lines represent the extent of the interpreted flows. The upper panel shows the use of terrain texture in areas that lack direct ROV observations to confidently assign flow boundaries. The inset shows the location of cross-section C-C' with 150 m contour spacing, with the same legend as Fig. 2.3. In the cross section C-C', the collapse features are approximately the same thickness as the flat-lying lava flow units, which become older to the west. The size and depth of the collapsed features increases to the west, where the oldest flows are exposed. 10× vertical exaggeration (VE).

or buried structures. Many of the major structures that are recognizable in the sidescan sonar images have linear to curvilinear traces with high backscatter that reveal dip directions. Asymmetries in cross section vary near the center of the trough and at the top of the horst separating the east and west grabens, but the inferred faults are generally east-dipping on west side of the trough and west-dipping on the east side. The largest faults occur in old arc crust on the eastern and western walls. They commonly display a zig-zag pattern, typical of *en echelon* basins and reflecting oblique extension. More than 230 major fault segments with lengths between ~250 m to nearly 8 km were measured. Although the minor faults (more than 500) have relatively low scarps, many can also be traced for considerable distances (up to 10s of km).

These features define a tectonic fabric north of 18°S that has an orientation of 145° ± 12° (n = 151, 95% confidence interval), parallel to the elongation of the rift basin (Fig. 2.3b). Near the Nifonea axial volcano, between 18°S and 18°15'S (Fig. 2.3c), the faults rotate counterclockwise and are oblique to the rift basin, with an orientation of 132° ± 7° (n = 266). South of 18°15'S (Fig. 2.3d), the fault pattern is more complex with a vector mean of 133.1° ± 7.0° (n = 318). This area represents the beginning of the transfer zone between the Vate and Erromango Troughs (Fig. 2.2a).

2.5. Geology of the Nifonea axial volcano

The large Nifonea axial volcano is more than 1 km high above the surrounding rift floor, rising to a minimum depth of 1770 mbsl, is at least 14 km wide, and has a volume of ~126 km^3. It spans the entire width of the Vate Trough, forming a dramatic crescent-shaped topographic high. Two prominent but low volcanic ridges extend ~13 km southeast and ~15 km northwest of the volcano. The southern ridge is characterized by hummocky lava flows and numerous small volcanic cones up to 90 m high and can be traced onto the basin floor at a depth of 2600 mbsl (Fig. 2.3). It appears to represent part of voluminous rift-axis eruptions, emanating in part from the Nifonea volcano. This 'Southern Rift' can be traced through the caldera and appears to be coextensive with the 'Northern Rift' which reaches the deepest part of the basin in the north (Fig. 2.3). A second ridge, on the northwest flank of the volcano is dominated by hummocky flows and abundant subparallel dike-like features that terminate abruptly at the summit caldera. This

ridge, which forms part of the west wall of the trough, may have formed at the earliest stages of opening of the basin and emergence of the Nifonea volcano. Two small (0.7 km and 1.5 km diameter) cratered, flat-topped volcanoes on the upper rampart of Nifonea also appear to belong to an earlier phase of pre-caldera volcanism (Fig. 2.3).

The 149 km^2 summit area of the volcano is dominated by the large, 5 × 8 km, horseshoe-shaped caldera. In 2001, hydrothermal activity was detected within the northern part of the caldera, coincident with a large area of ponded sheet flows (McConachy et al., 2005). Subsequent dredging and deep-towed camera surveys in 2004 confirmed the presence of vent fauna and high-temperature black smoker chimneys (Arculus and Shipboard Scientific Party, 2006). However, it was apparent that the large hydrothermal plume discovered in 2001 was already diminished when the area was revisited in 2004.

2.5.1. Summit caldera

The summit caldera is open towards the SE, and the caldera-related lava flows grade into hummocky volcanic terrain that defines the south rift zone. The caldera walls rise stepwise to the rim about 40 m above the caldera floor, with sediment draped over some of the steps. Older pillow lavas and minor sheet flows are exposed in vertical scarps, up to 20 m high, observed in the caldera wall during the ROV dives. In contrast, the caldera floor is dominated by a mix of much younger (unsedimented) sheet flows and lobate flows, with local pillow mounds (Fig. 2.6). NW-SE trending fissures are common, punctuated by young pillow mounds up to 20 m high.

The geology of the caldera floor is depicted in Figure 2.7a. It shoals gradually to the NE from ~2080 to 1875 mbsl. Lobate flows with abundant fractured and drained lobes are the most common lava morphology observed. Their interpreted map distribution suggests that they were sourced from a NW-striking fissure that cuts across the caldera floor and is co-extensive with prominent faults on the northern caldera wall. This flow type extends for several hundreds of meters on either side of the fissure, with sediment thickness, estimated from observations during ROV dives, increasing away from the fissure. At least two major eruptions of lobate flows are recognized. The youngest, which lack sediment, are interpreted occupy an area of 15.7 km^2.

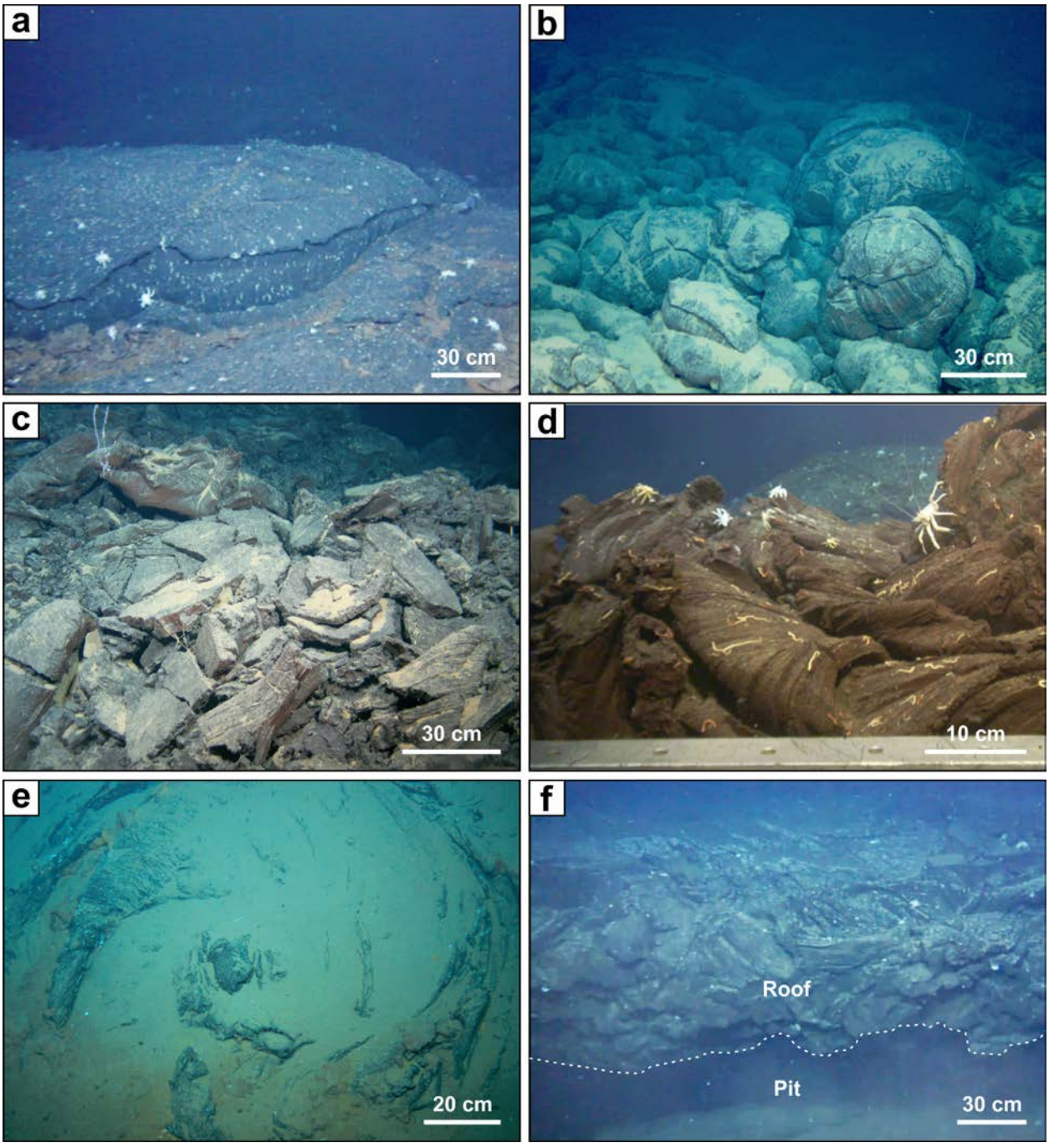


Fig. 2.6. Lava morphologies in the Nifonea caldera: (a) lobate lava flow (SO-229 ROV 60); (b) pillow flow (SO-229 ROV dive 83); (c) jumbled sheet flow (SO-229 ROV dive 77); (d) ropey sheet flow (SO-229 ROV dive 60); (e) lava whorl (SO-229 ROV dive 77); (f) the edge of a collapse pit (below) with jumbled sheet flow on top (SO-229 ROV dive 60). The locations of the photos are shown in Suppl. Fig. A3.

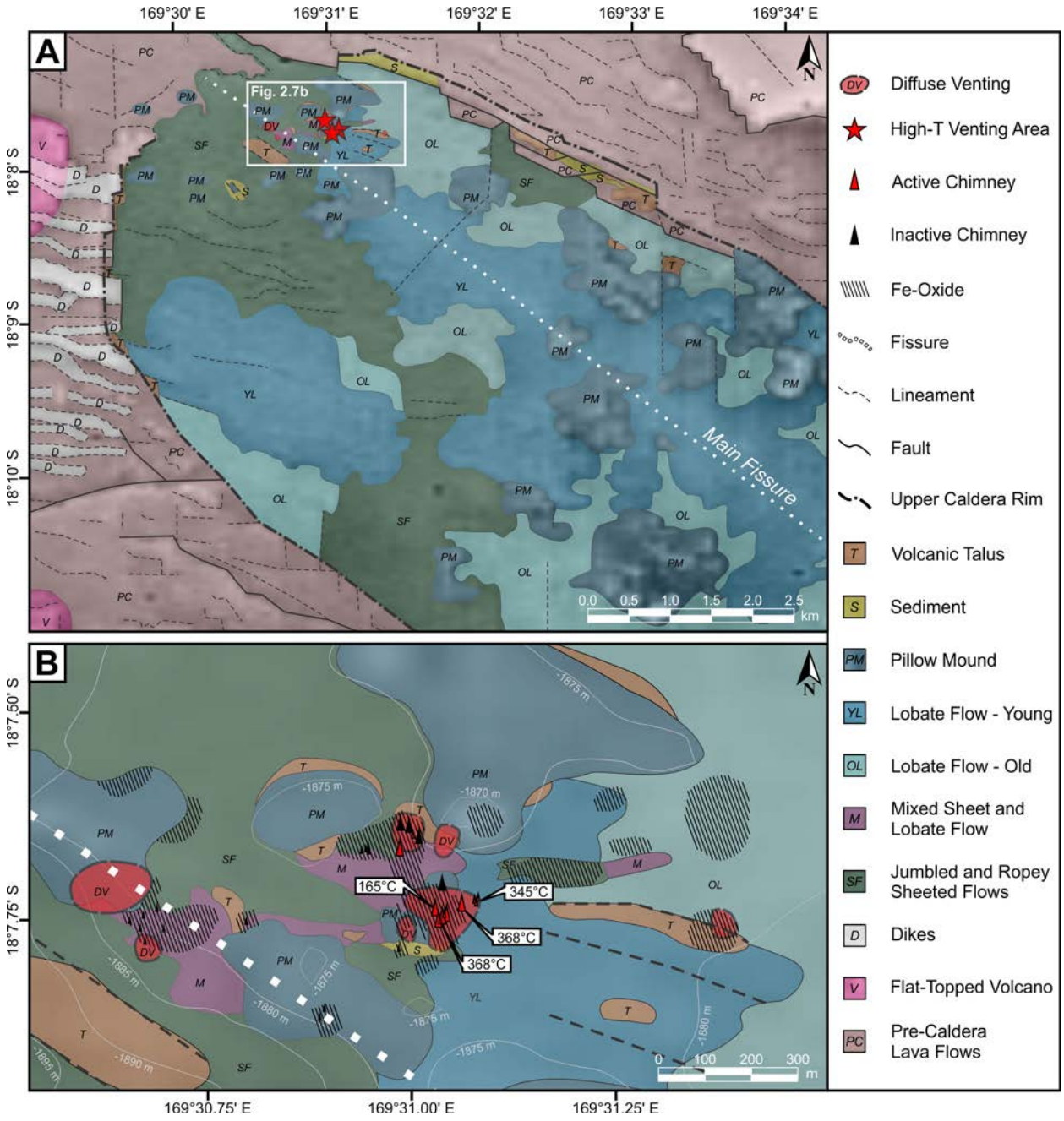


Fig. 2.7. Detailed geological maps within the Nifonea caldera: (a) lava morphologies and structures throughout the caldera; (b) detailed geological map of hydrothermal venting in the Nifonea caldera, including measured vent temperatures in the Main Vent Field from Haase and Shipboard Scientific Party (2013) and Schmidt et al. (2017).

Older lobate lavas with up to 1 cm of sediment occupy an area of 9.3 km^2. Small pillow mounds, generally 10–20 m tall and 50–100 m in diameter, occur on top of the lobate flows. These have coalesced locally into more extensive fields of pillow mounds, especially in the SE of the caldera.

The northwest part of the caldera floor is covered by extensive jumbled and ropey sheet flows. These flows cover an area of 11.4 km^2, and their distribution suggests that they have ponded against the caldera wall in several locations. Flow morphologies typical of a lava lake are evident everywhere in this part of the caldera, including 'lava whorls', collapse features and fissures with clear evidence of drain-back (Fig. 2.6e,f; cf. Fornari et al., 1998). The predominance of jumbled flows, abundant lava curtains, and fragile broken crusts on the surfaces of the sheet flows indicate low viscosity and high effusion rates of the erupted lavas (Gregg and Fink, 1995). The collapse features are 7–10 m in diameter and >4 m deep, and many are aligned in the same direction as the main NW-trending fissure interpreted to be the source of most of the lavas in the caldera. Locally, the collapse pits (or skylights) occur in rows that mark the locations of eruptive centers (Suppl. Fig. A4). Assuming the depth of the collapse pits represent the flow thickness (~4 m), the total sheet flow volume is ~45.6 $\times 10^6$ m^3.

2.5.2. Hydrothermal activity

A large area of diffuse hydrothermal venting (~1 km^2) occurs near the intersection of the northern caldera wall and the main NW-SE trending fissure (Figs. 2.7b, 2.8a). The venting is associated with a cluster of small pillow mounds, most likely marking local eruptive fissures, on top of the surrounding sheet flows. Extensive areas are characterized by shimmering and milky water discharging from the spaces between the pillows and lobes. Several large areas of diffuse venting were also with patches of tubeworms, mussels, barnacles, and other vent fauna. The venting produces a white cloud of "smoke", locally accompanied by bacterial floc, and is likely the source of a persistent low-lying particle plume over much of the caldera (Fig 2.8a; Suppl. Fig. A5).

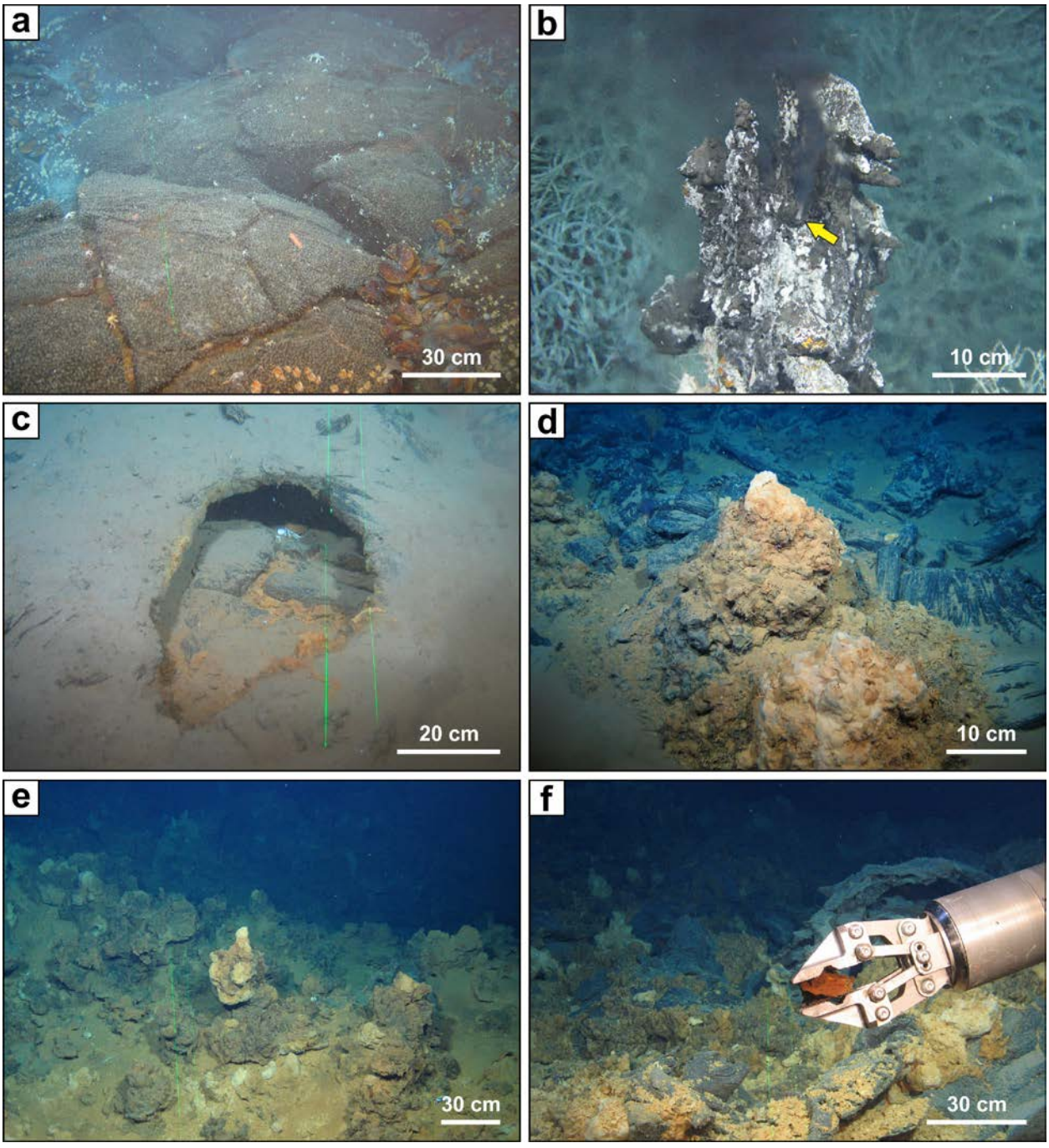


Fig. 2.8. Different styles of hydrothermal venting in the Nifonea caldera: (a) diffuse interlobe and interpillow venting producing milky plume (SO-229 ROV dive 77); (b) black smoker with two-phase venting, indicated by the yellow arrow, resulting from boiling at the seafloor (SO-229 ROV dive 66); (c) Small collapse pit in sheet flows with iron oxide crust (SO-229 ROV dive 27); (d) iron oxide chimney growing on jumbled sheet flows (SO-229 ROV dive 77); (e) abundant iron oxide crusts and chimneys (SO-229 ROV dive 66); (f) sampling of iron oxide crust (SO-229 ROV dive 66). The locations of the photos are indicated in Suppl. Fig. A3.

Several clusters (~20 × 20 m each) of black smoker chimneys occur near the base of one of the small pillow mounds where more focussed, high-temperature flow was found (Fig. 2.8b). These include a main cluster of six black smoker chimneys (0.5–4 m tall) at a depth of 1862 mbsl, several isolated ~50–80 cm tall chimneys venting grey to black smoke, and a cluster of much smaller chimneys (0–2 cm tall) venting grey to clear liquid. Measured temperatures of the vent fluids were between 354°C and 368°C (Haase and Shipboard Scientific Party, 2013; Schmidt et al., 2017). Two-phase venting was observed at all of the chimneys, indicating that the fluids are boiling at the seafloor. All of the chimneys have grown directly on pillow lava, with no significant chimney talus or other hydrothermal substrate. The dominant mineralogy is pyrite, chalcopyrite, and anhydrite, with minor Fe-rich sphalerite (Haase and Shipboard Scientific Party, 2013). The Cu-rich nature of the chimneys and a lack of significant barite are consistent with high mineralization temperatures.

Outside the areas of high-temperature venting, there is an abrupt transition from fresh pillows with abundant vent fauna to lightly-sedimented lobate and jumbled sheet flows with abundant Fe-oxide crusts and chimneys (Fig. 2.8c–f). Large area of Fe-oxide sediment and crusts occur immediately northwest of the main vent field, covering an area of ~150 × 200 m, and up to 600 m to the east and west of the main vent field over, similar-sized areas up to 200 m across (Fig. 2.7b). The crusts and chimneys are composed mainly of Fe-stained bacterial floc that is extremely friable and becomes suspended in the water column when disturbed. Although a weak temperature anomaly was detected in the sediments at one location, no focused discharge was observed. Much of this Fe-oxide may be related to past eruptions, as indicated by the heavier sediment cover on adjacent sheet flows.

2.6. Discussion

2.6.1. Geodynamic controls on the style of rifting

The evolution of the Coriolis Troughs can be compared to other young arc rifts of similar size and subsidence rates for their age (e.g., Sumisu Rift in the Izu-Bonin Trough: Ishizuka et al., 2003). In the earliest stages of arc rifting, back-arc volcanism is generally diffuse, reflecting a

highly variable magma supply behind the arc front (e.g., Martínez and Taylor, 2006). Numerical modeling confirms that the most rapid subsidence occurs at the beginning of basin opening, accelerated by heat loss to the surrounding cold lithosphere (Wang et al., 1991). Because the rifting is disorganized and magma flow is unfocused, the formation of large shield-type volcanoes in immature back-arc rifts is rare. In the Coriolis Troughs, early rifting of the arc crust has been characterized by high rates of tectonic extension and subsidence, resulting in the narrow, deep grabens observed today. The basins are progressively deeper from north to south (~2840 mbsl in the Vate Trough, ~3130 mbsl in the Erromango Trough, and ~3400 mbsl in the Futuna Trough) tracking an increase in age from ~3.5 Ma for the Vate Trough, ~4.1 Ma for the Erromango Trough, and ~6.5 Ma for the Futuna Trough (K-Ar ages of basalts and andesites on the rift flanks: Monjaret et al., 1991; Maillet et al., 1995). The calculated rates of subsidence, based on the ages and depths, are between 400 and 500 m my^{-1}. However, the troughs are much older than one would infer from their widths and the present-day spreading rate (~20–35 mm y^{-1}: Bergeot et al., 2009). Thus, early opening may have been much slower than it is today, consistent with the evolution of other back-arc rifts (e.g., Wiens et al., 2006). However, the highly focused magmatism observed in the Vate Trough is not observed in most other early arc rifts.

The different graben morphologies reflect different styles of rifting, with tectonic extension and deep faults dominating in Futuna and Erromango and magma intrusion and diking dominating in Vate Trough. In particular, large shield-type volcanoes do not occur in the Futuna or Erromango Troughs, likely because these troughs started rifting ~1–5.5 m.y. prior to the collision with the DER, whereas the younger Vate Trough has been strongly affected by the stress regime established by the ridge subduction. As observed in most of the active back-arc basins in the SW Pacific, rifting was likely triggered by changes in the subduction rate, with the deepest basins forming above steep slab dips (~60–70°). Highly variable stress regimes in the overriding plate result from large-scale rotation of arc segments, commonly associated with the subduction of ridges or seamount chains (e.g., Louisville Ridge beneath the Lau Basin). The magnitude of the arc disruptions is related to the size of the colliding ridge, the plate trajectory (i.e., the span of the ridge segment that is introduced to the subduction zone), and the compositional contrast between the ridge and the overlying plate.

The particular rift dynamics of the New Hebrides back-arc and the strong focusing of magma into the Vate Trough are interpreted to reflect mechanically induced stresses caused by the rotation of the southern arc segment, with a Euler Pole defined by GPS measurements (Bergeot et al., 2009). The Australian hinge line is migrating westward at ~8.9 cm y^{-1} in the south, compared to only 0.8 cm y^{-1} along the central segment, resulting in significant left-lateral transtension in the southern back-arc region (Fig. 2.9a; Schellart et al., 2002). This oblique shear forms large open conduits in the rifted arc crust, where Arculus and Shipboard Scientific Party (2006) suggested that the melt that formed the Nifonea axial volcano was localized at the approximate position of maximum opening. This contrasts with large axial volcanoes on mid-ocean ridges, where magma intrusion is strongly focused under the shallowest part of the ridge and especially where magma supply is enhanced by hotspot intersections. A more detailed bathymetric survey outside the Vate Trough may reveal the larger-scale structural control on magmatism at this location (e.g., Fig. 2.2).

The voluminous eruptions in the Vate Trough are thought to be associated with rapid melt extraction, which is reflected in the unusual alkalic composition of the volcanic rocks recovered from the Nifonea volcano (basalt, trachybasalt, and trachyandesite: McConachy et al., 2005; Haase and Shipboard Scientific Party, 2013). Notably, these volcanic rocks lack the arc-like trace element signature that usually characterizes back-arc rifts close to the arc front, such as in the Lau Basin (e.g., high SiO_2 magmas along the Valu Fa Ridge: Fretzdorff et al., 2006). The compositions indicate relatively low-degree partial melting of mixed enriched and depleted mantle material that must have been efficiently extracted during rifting of the back-arc (McConachy et al., 2005; Lima et al., 2017)

2.6.2. Link to shield-type volcanism

The large Nifonea axial volcano has a complex structural, magmatic, and hydrothermal history that closely resembles other submarine shield volcanoes. It closely resembles Axial Volcano on the Juan de Fuca Ridge (Embley et al., 1990) and is comparable in size and shape to a number of subaerial shield volcanoes (e.g., Mokuoweoweo caldera on Mauna Loa, Hawaii; Fernandina

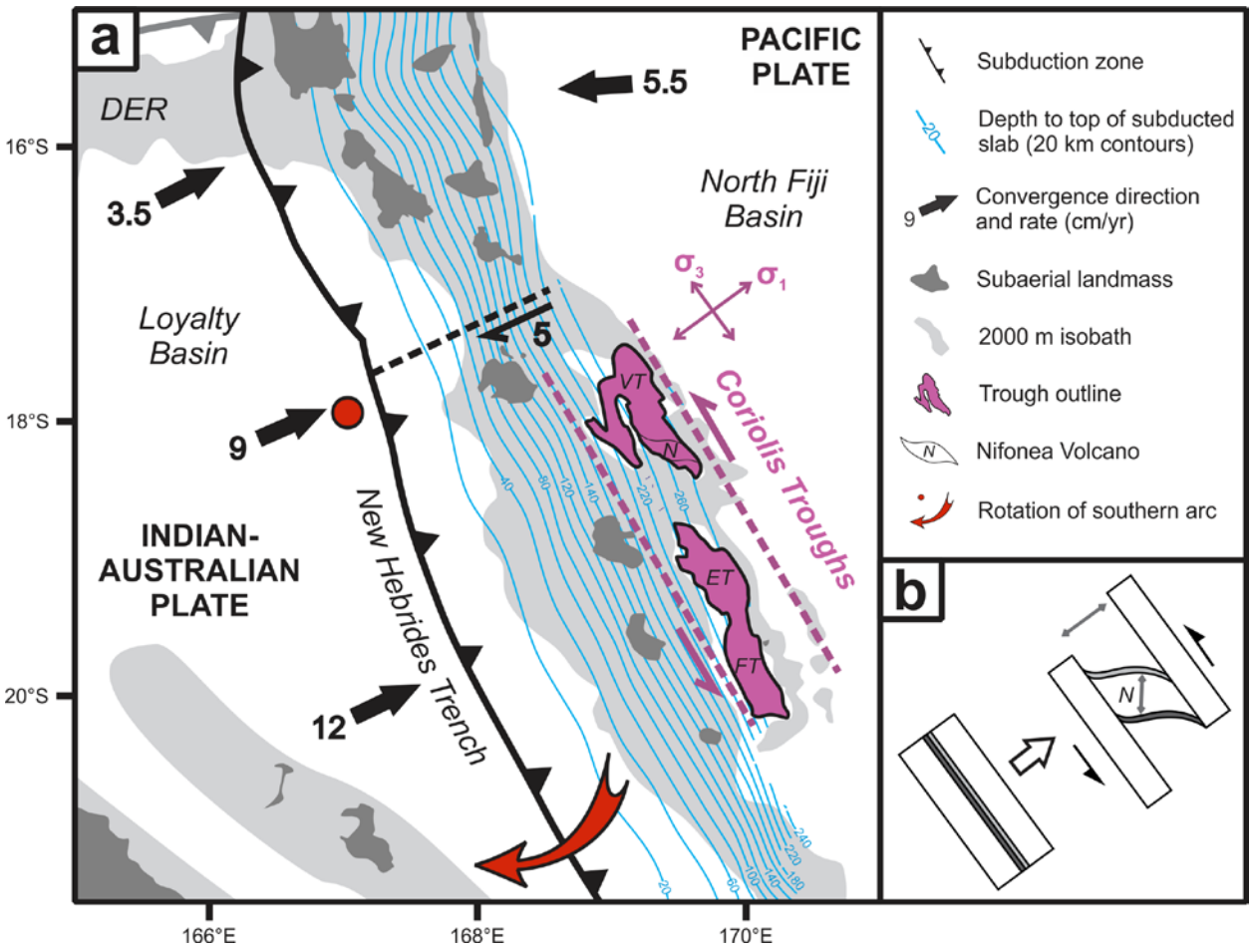


Fig. 2.9. Geodynamic setting of the southern half of the New Hebrides arc: (a) the collision of the d'Entrecasteaux Ridge (DER) causes plate coupling in the associated back-arc, while subduction continues in the south. Slab rollback causes opening of the Coriolis Troughs, and the incongruent subduction rates from north to south results in rotation of the southern section of the arc (red circle indicates Euler Pole, red arrow indicates rotation direction; Bergeot et al., 2009) and the left-lateral transtensive stress regime in the back-arc region; (b) cartoon schematic of the opening of the Vate Trough under left-lateral transtension, with the Nifonea axial volcano forming at the maximum opening extent (after Arculus and Shipboard Scientific Party, 2006). VT = Vate Trough, N = Nifonea axial volcano, ET = Erromango Trough, FT = Futuna Trough.

caldera, Galápagos Islands; Krafla caldera in Iceland: Fig. 2.10). Volcanoes of this type have a polygenetic circular form, a central feeder system, shallow flank slopes (<10°) and a height to diameter ratio of about 1:20. The large volumes reflect exceedingly high extrusion rates. Extensive sheet flows, collapse structures and drain-back features indicate eruption of low viscosity lavas, typical of axial volcanoes affected by mantle plumes (e.g., Langmuir et al., 1997). Caldera subsidence on these volcanoes originates from the drainage of magma rather than by explosive eruptions (e.g., Wood, 1984), and the causative flank eruptions commonly occur along major rift zones (e.g., Embley et al., 1990). The latter are controlled by the regional seafloor spreading axis and closely resemble the north and south rift zones at Nifonea. Importantly, episodic volcanism can alternate between the rift zones and the caldera (e.g., Chadwick and Howard, 1991), as some magmas encounter hydraulic resistance beneath the summit of the volcano and inject laterally away from the magma chamber, while other low-viscosity magmas possess less hydraulic resistance and erupt at the summit (Floyd, 1991). The ponded sheet flows in the Nifonea caldera are typical of a solidified lava lake, the first seafloor lava lake of this type described in a back-arc basin. Lava lakes are common on fast-spreading ridges (e.g., Fornari et al., 1998) and on slower-spreading ridges where shallow plume-related axial magma chambers promote high effusion rates of low viscosity lava (e.g., Fouquet et al., 1995). The volume of sheet flows erupted in the Nifonea caldera (~45.6 × 10^6 m^3) is similar to that erupted during the 1998 eruption of Axial Volcano on the Juan de Fuca Ridge (31 × 10^6 m^3, covering 7.1 km^2 to an average thickness of 3.5 m: Chadwick et al., 2013). The eruption rates at Axial were estimated to be 1.8–8.8 × 10^6 m^3 h^{-1}, which would have been sufficient to produce the jumbled sheet flows in the northern part of the Nifonea caldera in <30 h. This has important implications for the nature of any associated hydrothermal activity (see below). The ponded flows post-date the most recent evidence of rifting in the summit caldera, covering the NW-trending fissures on the caldera floor.

There is strong evidence for younger effusive volcanism also in the north-central part of the Vate Trough, where the large lava plain with collapse features was mapped. These extensive flows may be an indication of a second major magma conduit opening near the eastern wall of the basin. The lava plain represents an eruption of ~16 km^3 of lava, which is comparable in size to the largest recorded subaerial flood basalt eruption (e.g., the 934 AD Eldgjá flow in Iceland

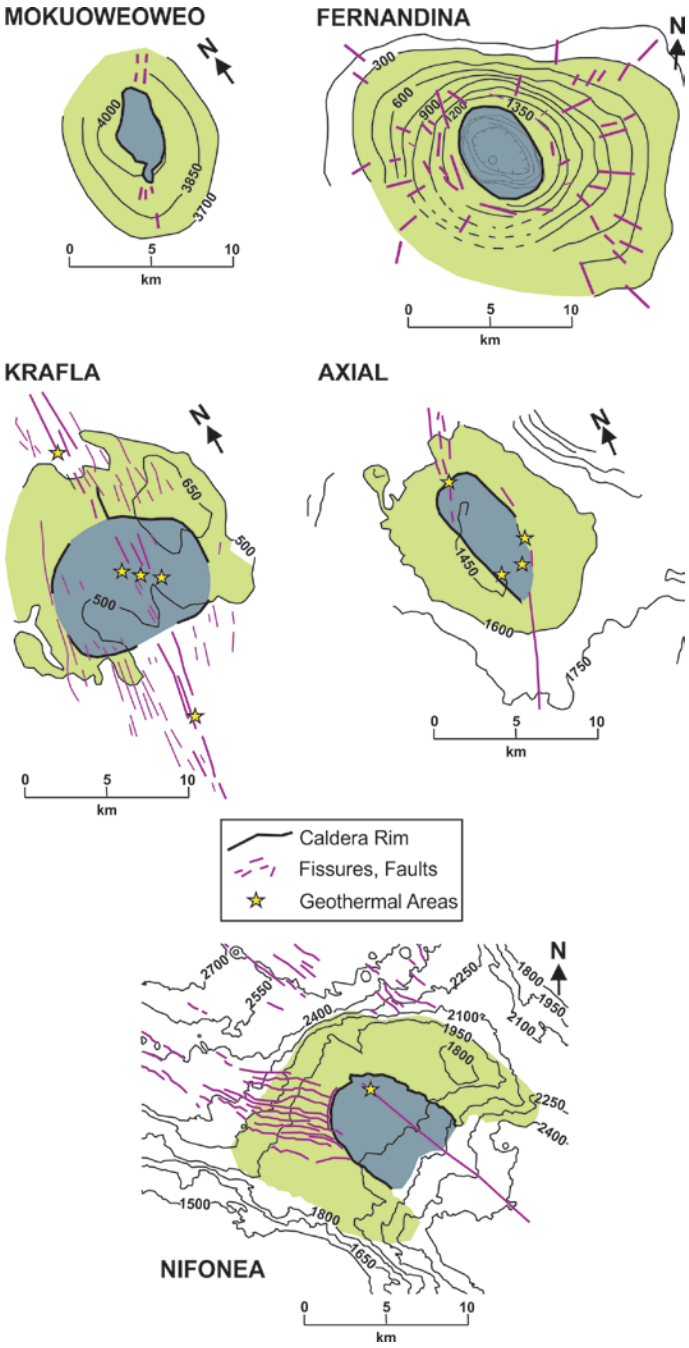


Fig. 2.10. A comparison of calderas (blue) in large basaltic shield volcanoes, after Embley et al. (1990). The contour interval is 150 m. Mokuoweoweo is the caldera of Mauna Loa, Hawaii, Fernandina is in the Galápagos Islands, Krafla is in northern Iceland, and Axial is Axial Seamount on the Juan de Fuca Ridge.

produced 18.3 km^3 of lava over 3–8 years: Thordarson et al., 2001). In the Icelandic fissure systems, such lava plains are often precursors to the development of large shield-like volcanic complexes (e.g., Walker, 1993).

2.6.3. Controls on the distribution and type of hydrothermal venting

Hydrothermal activity in the Nifonea caldera is dominated by diffuse flow rather than focused discharge. A history of widespread and poorly focused venting is indicated by the extensive Fe-oxides covering the caldera floor. The highly permeable lava morphologies in the summit caldera, characteristic of lava lakes (cf. Fouquet et al., 1995), appear to have prevented the development of focused discharge. Instead, these types of eruptions commonly release massive amounts of high-temperature hydrothermal fluid over very large areas and at short time intervals (i.e., megaplumes or 'event plumes': Baker et al., 1995), followed by rapid cooling and poorly focused low-temperature discharge. This style of eruption and hydrothermal activity has been documented at Axial Volcano (e.g., at the ASHES vent site, where localized high-temperature upflow is surrounded by large areas of diffuse flow: Hammond, 1990) and at CoAxial Site on the Juan de Fuca Ridge (e.g., the FLOC site, where diffuse "snow-blower" vents emitted bacterial floc after an eruption and 'event plume' in 1993: Butterfield et al., 1997). The large particle plume still hanging in the water column above the Nifonea caldera may be a remnant of an earlier plume associated with a major eruption (Haase and Shipboard Scientific Party, 2013).

High-temperature venting is localized only where large permeability contrasts exist to focus the fluids. The pillow mounds, where high-temperature venting is now occurring in the Nifonea caldera, likely present such a contrast. The measured temperatures of the black smoker chimneys are among the highest recorded in the SW Pacific (Haase and Shipboard Scientific Party, 2013), but the vents are isolated and not parts of larger sulfide mounds. No chimney talus is present, despite their fragile construction and the frequent seismic activity, suggesting that the vents are extremely young and possibly date from the latest eruption. This is consistent with the observation by Arculus and Shipboard Scientific Party (2006) that a robust hydrothermal plume centered above the caldera in 2001 was no longer present in 2004. The absence of old sulfide chimneys or mounds among the Fe-oxide deposits suggests that any earlier hydrothermal activity

that may have been related to successive eruptions of sheet flows also quickly faded and failed to produce a sustained hydrothermal system.

Similar deposits of Fe-Si oxyhydroxides, like those in the Nifonea caldera, have been reported in the other troughs (Iizasa et al., 1998; Maillet et al., 1995), as well as in other nascent back-arc rifts (e.g., in the Sumisu Rift in the northern Izu-Bonin arc: Urabe and Kusakabe, 1990). This type of mineralization may be typical of hydrothermal activity during early arc rifting, before large-scale magmatic extension takes place, and could represent a setting for some analogous Fe-oxide deposits in the geological record (e.g., some banded iron formations: Bekker et al., 2010).

2.7. Conclusions

The nascent Coriolis Troughs have several remarkable features that are unique in a back-arc basin environment. These include the narrow, deep graben morphology, the unusual alkalic compositions of some of the lavas that lack any subduction-zone signatures and, in the case of the Vate Trough, a large shield-type volcano and lava lake. Such early arc rifts are normally characterized by low rates of magma production. The focusing of voluminous basaltic eruptions into an otherwise magma-deficient back-arc is thought to be related to the opening of structural conduits in the rifted arc crust that promoted rapid extraction and localization of melt to form the Nifonea volcano. Left-lateral transtension in the back-arc was caused by clockwise rotation of the southern arc segment following collision of the d'Entrecasteaux ridge with the steeply-dipping New Hebrides subduction zone. High-resolution geological mapping has revealed the impact of these events on the structural and volcanic features in the Vate Trough.

Extensive sheet and lobate flows formed from the rapid extrusion of lava along the axial rift zones, ponding in the summit caldera of the Nifonea volcano and also on the rift valley floor. The style of volcanism is similar to that of other large MOR axial volcanoes. Eruptions at these volcanoes have been linked to 'megaplume' events that release large amounts of high-temperature hydrothermal fluid over short time intervals, followed by collapse of the main hydrothermal flow into localized feeder dikes with widespread but diffuse venting. The

persistent low-lying particle plume and widespread Fe-oxide deposits may be the 'smoking gun' for similar eruptions in the Nifonea caldera.

Appendix A. Supporting Information

Supplementary data associated with this article is found in Appendix A.

References

Arculus, R.J., Shipboard Scientific Party, 2006. Coriolis Troughs and southern New Hebrides Arc: Primary tectonic results from the CoTroVe (SS06/2004) Research Voyage [ext. abstract]. ASEG Annual Meeting, 2006 Jul 2–6, Melbourne, Australia, CISRO Publishing, 6 p., doi:10.1071/ASEG2006ab003.

Auzende, J., Pelletier, B., Eissen, J., 1995. The North Fiji basin: Geology structure, and geodynamic evolution. In: Taylor, B. (Ed.), Back-arc Basins: Tectonics and Magmatism. Plenum, New York, pp. 139–175.

Baker, E.T., German, C.R., Elderfield, H., 1995. Hydrothermal plumes over spreading-center axes: Global distributions and geological inferences. In: Humphries, S., Zierenberg, R.A., Mullineaux, L.S., Thomson, R.E. (Eds.), Seafloor Hydrothermal Systems: Physical, Chemical, Biological, and Geological Interactions. Geophys. Monogr. 91, AGU, Washington D.C., pp. 47–71.

Bekker, A., Slack, J.F., Planavsky, N., Krapež, B., Hofmann, A., Konhauser, K.O., Rouxel, O.J., 2010. Iron formation: The sedimentary product of a complex interplay among mantle, tectonic, oceanic, and biospheric processes. Econ. Geol. 105, 467–508, doi:10.2113/gsecongeo.105.3.467.

Bergeot, N., Bouin, M.N., Diament, M., Pelletier, B., Régnier, M., Calmant, S., Ballu, V., 2009. Horizontal and vertical interseismic velocity fields in the Vanuatu subduction zone from GPS measurements: Evidence for a central Vanuatu locked zone. J. Geophys. Res. 114, 1–20, doi:10.1029/2007JB005249.

Brown, L., 2010. A new technique for depicting terrain relief [abstract]. NACIS Annual Meeting, 2010 Oct 13–17, St. Petersburg, Florida.

Butterfield, D.A., Jonasson, I.R., Massoth, G.J., Feely, R.A., Roe, K.K., Embley, R.E., Holden, J.F., McDuff, R.E., Lilley, M.D., Delaney, J.R., 1997. Seafloor eruptions and evolution of hydrothermal fluid chemistry. Phil. Trans. R. Soc. A 355, 369–386, doi:10.1098/rsta.1997.0013.

Chadwick, J.W.W., Embley, R.W., Fox, C.G., Nooner, S.L., Zumberge, M.A., 1985. Hydrothermal Vents on an Axis Seamount of the Juan de Fuca Ridge. Lett. Nat. 313, 121–214.

Chadwick, J.W.W., Howard, K.A., 1991. The pattern of circumferential and radial eruptive fissures on the volcanoes of Fernandina and Isabela islands, Galápagos. Bull. Volcanol. 53, 259–275, doi:10.1007/BF00414523.

Chadwick, J.W.W., Clague, D.A., Embley, R.W., Perfit, M.R., Butterfield, D.A., Caress, D.W., Paduan, J.B., Martin, J.F., Sasnett, P., Merle, S.G., Bobbitt, A.M., 2013. The 1998 eruption of Axial Seamount: New insights on submarine lava flow emplacement from high-resolution mapping. Geochem. Geophys. Geosyst. 14, 3939–3968, doi:10.1002/ggge.20202.

Charvis, P., Pelletier, B., 1989. The northern New Hebrides back-arc troughs: history and relation with the North Fiji Basin. Tectonophysics 170, 259–277, doi:10.1016/0040-1951(89)90275-8.

Collot, J.Y., Lallemand, S., Pelletier, B., Eissen, J.-P., Glaçon, G., Fisher, M.A., Greene, H.G., Boulin, J., Daniel, J., Monzier, M., 1992. Geology of the d'Entrecasteaux-New Hebrides Arc collision zone: results from a deep submersible survey. Tectonophysics 212, 213–241, doi:10.1016/0040-1951(92)90292-E.

Crawford, A.J., Greene, H.G., Exon, N.F., 1988. Geology, petrology and geochemistry of submarine volcanoes around Epi Island, New Hebrides island arc. In: Green, H.G., Wong, F.L. (Eds.) Geology and offshore resources of the Pacific island arcs—Vanuatu region. Circum-Pacific Council for Energy and Mineral Resources Earth Sci. Ser. 8, Houston, Texas, pp. 301–327.

Crawford, A.J., Briqueu, L., Laporte, C., Hasenaka, T., 1995. Coexistence of Indian and Pacific oceanic upper mantle reservoirs beneath the Central New Hebrides Island Arc. In: Taylor, B. & Natland, J. (Eds.), Active Margins and Marginal Basins of the Western Pacific. Geophys. Monogr. 88, AGU, Washington D.C. pp. 199–217.

Embley, R.W., Murphy, K.M., Fox, C.G., 1990. High-resolution studies of the summit of Axial Volcano. J. Geophys. Res. 95, 12,785–12,812.

Floyd, P.A., 1991. Oceanic islands and seamounts. In: Floyd P.A. (Ed.), Oceanic Basalts. Blackie, Glasgow, pp. 174–218.

Fornari, D.J., Haymon, R.M., Perfit, M.R., Gregg, T.K.P., Edwards, M.H., 1998. Axial summit trough of the East Pacific Rise 9°-10°N: Geological characteristics and evolution of the axial zone on fast spreading mid-ocean ridges. J. Geophys. Res. 103, 9827–9855, doi:10.1029/98JB00028.

Fouquet, Y., Ondréas, H., Charlou, J.-L., Donval, J.-P., Radford-Knoery, J., Costa, I., Lourenço, N., Tivey, M.K., 1995. Atlantic lava lakes and hot vents. Nature 377, 201, doi:10.1038/377201a0.

Fretzdorff, S., Schwarz-Schampera, U., Gibson, H.L., Garbe-Schönberg, C.-D., Hauff, F., Stoffers, P., 2006. Hydrothermal activity and magma genesis along a propagating back-arc basin: Valu Fa Ridge (southern Lau Basin). J. Geophys. Res. 111, 1–17, doi:10.1029/2005JB003967.

Fryer, P., 1995. Geology of the Mariana Trough. In: Taylor, B. (Ed.), Back-arc Basins: Tectonics and Magmatism. Plenum, New York, pp. 237–280.

Greene, H.G., Collot, J.Y., Pelletier, B., Lallemand, S., 1992. Observation of forearc seafloor deformation along the North d'Entrecasteaux Ridge—New Hebrides Island Arc collision zone from Nautile Submersible. Proc. ODP, Init. Reports 134, 43–53.

Gregg, T.K.P., Fink, J.H., 1995. Quantification of submarine lava-flow morphology through analog experiments. Geology 23, 73–76, doi:10.1130/0091-7613(1995)023<0073:QOSLFM>2.3.CO;2.

Haase, K.M., Shipboard Scientific Party, 2013. Volcanism, hydrothermal activity and vent biology in the Coriolis Troughs, New Hebrides Island Arc. RV Sonne SO-229 Cruise Report, 244 p., doi:10.2312/cr_so229.

Hall, R., 2002. Cenozoic geological and plate tectonic evolution of SE Asia and the SE Pacific – computer-based reconstructions, model and animations. J. Asian Earth Sci. 20, 353–431, doi:10.1016/S1367-9120(01)00069-4.

Hammond, S.R. 1990. Relationships between lava types, seafloor morphology, and the occurrence of hydrothermal venting in the ASHES Vent Field of Axial Volcano. J. Geophys. Res. 95, 12,875–12,893, doi:10.1029/JB095iB08p12875.

Iizasa, K., Kawasaki, K., Maeda, K., Matsumoto, T., Saito, N., Hirai, K., 1998. Hydrothermal sulfide-bearing Fe-Si oxyhydroxides deposits from the Coriolis Troughs, Vanuatu back-arc, southwestern Pacific. Mar. Geol. 145, 1–21, doi:10.1016/S0025-3227(97)00112-6.

Ishizuka, O., Uto, K., Yuasa, M., 2003. Volcanic history of the back-arc region of the Izu-Bonin (Ogasawara) arc. In: Larter, R.D., Leat, P.T. (Eds.) Intra-oceanic Subduction Systems: Tectonic and Magmatic Processes. Geol. Soc. London, Spec. Pub. 219, 187–205.

Karig, D., 1971. Origin and development of marginal basins in the western Pacific. J. Geophys. Res. 76, 343–357, doi:10.1007/s11192-012-0776-8.

Langmuir, C., Humphris, S., Fornari, D., Van Dover, C.L., Von Damm, K., Tivey, M.K., Colodner, D., Charlou, J.-L., Desonie, D., Wilson, C., Fouquet, Y., Klinkhammer, G.P., Bougault, H., 1997. Hydrothermal vents near a mantle hot spot: the Lucky strike vent field at 37°N on the Mid-Atlantic Ridge. Earth Planet. Sci. Let. 148, 69–91.

Lima, S.M., Haase, K.M., Beier, C., Regelous, M., Brandl, P.A., Hauff, F., Krumm, S., 2017. Magmatic evolution and source variations at the Nifonea Ridge (New Hebrides Island Arc). J. Pet. 0, 1 – 22, doi:10.1093/petrology/egx023.

Maillet, P., Ruellan, E., Gérard, M., Person, A., Bellon, H., Cotton, J., Joron, J.-L., Nakada, S., Price, R.C., 1995. Tectonics, Magmatism, and evolution of the New Hebrides back-arc troughs (southwest Pacific). In: Taylor, B. (Ed.), Back-arc Basins: Tectonics and Magmatism. Plenum, New York, pp. 177–235.

Martínez, F., Taylor, B. 2006. Modes of crustal accretion in back-arc basins: Inferences from the Lau Basin. In: Christie, D.M., Fisher, C.R. (Eds.), Back-arc Spreading Systems: Geological, Biological, Chemical, and Physical Interactions. Geophys. Monogr. 166, 5-30.

McClinton, J.T., and White, S.M., 2015. Emplacement of submarine lava flow fields: A geomorphological model from the Niños eruption at the Galápagos Spreading Center. Geochem. Geophys. Geosyst. 16, 899–911, doi:10.1002/2014GC005632.

McConachy, T.F., Arculus, R.J., Yeats, C.J., Binns, R.A., Barriga, F., McInnes, B., Sestak, S., Sharpe, R., Rakau, B., Tevi, T., 2005. New hydrothermal activity and alkali volcanism in the back-arc Coriolis Troughs, Vanuatu. Geology 33, 61–64, doi:10.1130/G20870.1.

Meffre, S., Crawford, A.J., 2001. Collision tectonics in the New Hebrides arc (Vanuatu). Isl. Arc 10, 33–50, doi:10.1046/j.1440-1738.2001.00292.x.

Monjaret, M.C., Bellon, H., Maillet, P., 1991. Magmatism of the troughs behind the New Hebrides island arc (RV Jean Charcot SEAPSO 2 cruise): K-Ar geochronology and petrology. J. Volcanol. Geotherm. Res. 46, 265–280, doi:10.1016/0377-0273(91)90088-H.

Pearce, J., Stern, R., 2006. Origin of back-arc basin magmas: Trace element and isotope perspectives. Geophys. Monogr. 166, AGU, Washington, D.C., pp. 63–86, doi:10.1029/166GM06.

Pelletier, B., Calmant, S., Pillet, R., 1998. Current tectonics of the Tonga-New Hebrides region. Earth Planet. Sci. Lett. 164, 263–276, doi:10.1016/S0012-821X(98)00212-X.

Perfit, M.R., Chadwick, W.W.J., 1998. Magmatism at mid-ocean ridges: Constraints from volcanological and geochemical investigations. In: Buck, R., et al. (Eds.) Faulting and Magmatism at Mid-Ocean Ridges, Geophys. Monogr. Ser. 106, AGU, Washington, D.C., pp. 59–115.

Picard, C., Monzier, M., Eissen, J.-P., Robin, C., 1994. Concomitant evolution of tectonic environment and magma geochemistry, Ambrym volcano (Vanuatu, New Hebrides arc). Geol. Soc. London, Spec. Pub. 81, 135–154, doi:10.1144/GSL.SP.1994.081.01.08.

Price, R.C., Maillet, P., Johnson, D.P., 1993. Interpretation of GLORIA side-scan sonar imagery for the Coriolis Troughs of the New Hebrides back-arc. Geo-Mar. Lett. 13, 71–81, doi:10.1007/BF01204548.

Pysklywec, R.N., Mitrovica, J.X., Ishii, M., 2003. Mantle avalanche as a driving force for tectonic reorganization in the southwest Pacific. Earth Planet. Sci. Lett. 209, 29–38, doi:10.1016/S0012-821X(03)00073-6.

Sandwell, D.T., et al., 2014. New global marine gravity model from CryoSat-2 and Jason-1 reveals buried tectonic structure. Science 346, 65–67.

Schellart, W.P., Lister, G.S., Jessel, M.W., 2002. Analogue modeling of arc and back-arc deformation in the New Hebrides arc and North Fiji Basin. Geology 30, 311–314, doi:10.1130/0091-7613(2002)030<0311:AMOAAB>2.0.CO;2.

Schmidt, K., Garbe-Schönberg, D., Hannington, M.D., Anderson, M.O., Bühring, B., Haase, K., Haruel, C., Lupton, J., Koschinsky, A., 2017. Boiling vapour-type fluids from the Nifonea vent field (New Hebrides Back-Arc, Vanuatu, SW Pacific): Geochemistry of an early-stage, post-eruptive hydrothermal system. Geochim.Cosmochim. Acta 207, 185–209, doi:10.1016/j.gca.2017.03.016.

Sdrolias, M., Müller, D. 2006. Controls on back-arc basin formation. Geochem. Geophys. Geosyst. 7, Q04015, doi:10.1029/2005GC001090.

Stix, J., Kennedy, B, Hannington, M., Gibson, H., Fiske, R., Mueller, W., Franklin, J., 2003. Caldera-forming processes and the origin of submarine volcanogenic massive sulfide deposits. Geology 31, 375–378, doi:10.1130/0091-7613(2003)031<0375:CFPATO>2.0.CO;2.

Taylor, F.W., Bevis, M.G., Schutz, B.E., Kuang, D., Récy, J., Calmant, S., Charley, D., Regnier, M., Perin, B., Jackson, M., Reichenfeld, C., 1995. Geodetic measurements of convergence at the New Hebrides island arc indicate arc fragmentation caused by an impinging aseismic ridge. Geology 23, 1011–1014, doi:10.1130/0091-7613(1995)023<1011:GMOCAT>2.3.CO;2.

Thordarson, T., Miller, D.J., Larsen, G., Self, S., Sigurdsson, H., 2001. New estimates of sulfur degassing and atmospheric mass-loading by the 934 AD Eldgjá eruption, Iceland. J. Volcanol. Geotherm. Res. 108, 33–54.

Urabe, T., Kusakabe, M., 1990. Barite silica chimneys from the Sumisu Rift, Izu-Bonin Arc; possible analog to hematitic chert associated with Kuroko deposits. Earth Planet. Sci. Lett. 100, 283–290, doi:10.1016/0012-821X(90)90191-Y.

Walker, G.P.L., 1993. Basaltic-volcano systems. Geol. Soc., London, Spec. Pub. 76, 3–38, doi:10.1144/GSL.SP.1993.076.01.01.

Wang, C.-Y., Kastens, K., Hwang, W.-T., 1991. Rapid subsidence of small oceanic basins: A study of the Marsili Basin, Central Mediterranean. J. Geophys. Res., 96, 4413–4421, doi:10.1029/90JB02366.

Wiens, D.A., Seama, N., Conder, J.A., 2006. Mantle structure and flow patterns beneath active back-arc basins inferred from passive seismic and electromagnetic methods. In: Christie, D.M., Risher, C.R., Lee, S.-M., Givens, S. (Eds.), Back-arc Spreading Systems: Geological, Biological, Chemical, and Physical Interactions 166. AGU, Washington D.C., pp. 43–62, doi:10.1029/166GM05.

Wood, C.A., 1984. Calderas: A planetary perspective. J. Geophys. Res. 80, 8391–8406, doi:10.1029/JB089iB10p08391.

Yan, C., Kroenke., L., 1993. A plate tectonic reconstruction of the Southwest Pacific 0-100 Ma. In: Berger, W. (Ed.) Proc. ODP, Sci. Results 130. Ocean Drilling Program, College Station, TX, pp. 697–709.

Yeo, I., Searle, R.C., Achenbach, K.L., Le Bas, T.P., Murton, B.J., 2012. Eruptive hummocks: Building blocks of the upper ocean crust. Geology 40, 91–94, doi:10.1130/G31892.1.

Preface to Chapter 3

This chapter examines the Jean Charcot Troughs (JCT) in the northern New Hebrides back-arc. In contrast to the deep but simple graben morphology of the Coriolis Troughs (CT), the seafloor morphology of the JCT is a complex series of shallow and discontinuous grabens and volcanic ridges. The strikingly different morphology of the JCT is related to the complex local geodynamics characterized by dominantly tectonic extension and reduced magmatism compared to the CT. In addition, the recent discovery of hydrothermal venting at the Tinakula deposit is investigated in order to better understand the relationships between volcanism and hydrothermal activity in this dramatically different back-arc setting. In-depth examinations of the processes of ore deposition and alteration at Tinakula are presented in subsequent chapters (*Chapters 4* and *5*).

Chapter 3

Magmatism and hydrothermal venting in the Jean Charcot Troughs, SW Pacific: Influence of the geodynamic evolution of the northern New Hebrides back-arc

Abstract

The Jean Charcot Troughs in the northern New Hebrides consist of a broad expanse of irregular grabens and volcanic ridges, extending up to ~120 km east of the volcanic front, and reaching depths of less than 1000 mbsl. Individual grabens have lengths of 20–65 km and widths of 5–15 km, separated by volcanic ridges. The back-arc rifting initiated at ~4 Ma in response to steepening of the subducting Indo-Australian slab following detachment. Two phases of extension characterize the evolution of the back-arc: (1) initial extension controlled by structures in the upper plate (North Fiji Basin crust); and (2) asymmetric rollback of the eastward subducting slab caused by the collision with the buoyant d'Entrecasteaux ridge at ~3 Ma, reversing the direction of arc rotation from clockwise to counter-clockwise. The latter resulted in a prolonged episode of extension in the northern part of the back-arc. The compositions of the volcanic rocks reflect an enriched mantle source (i.e., high Yb and Nb), contributions from the deep subducting slab (indicated by high Ba and Th), fractional crystallization, and bimodal volcanism. Long-lived magmatism near the Starfish stratovolcano provided the heat source for hydrothermal venting and the formation of the Tinakula seafloor massive sulfide deposit. This newly-discovered deposit formed along a row of basaltic to andesitic submarine scoria cones at water depths of 1070–1204 mbsl. This setting differs from that of typical seafloor massive sulfide deposits in arc-front calderas or back-arc spreading centers and highlights the diversity of mineralizing environments that may be developed. This study adds to our understanding of the controls on early stages of back-arc rifting.

3.1. Introduction

Active back-arc extension, rifting, and seafloor spreading characterizes the regions behind many of the volcanic arcs in the western Pacific (e.g., the Taupo-Havre-Lau system, the North Fiji basin, the New Hebrides back-arc, the Manus basin, the Mariana trough, and the Okinawa trough; Taylor, 1995). The study of back-arc basins has largely concentrated on crustal-accretion processes associated with seafloor spreading in mature back-arcs (e.g., Martínez and Taylor, 2002). These processes share many similarities with mid-ocean ridge spreading centers (e.g., Parson et al., 1990; Ruellan et al., 1994; Taylor et al., 1996; Livermore et al., 1997; Zellmer and Taylor, 2001).

Considerably less attention has been paid to juvenile back-arc magmatism, with studies focused primarily on the transition between rifting and spreading in the Lau, Manus, and Mariana basins (e.g., Martínez and Taylor, 2002). An important missing piece of the puzzle is the earliest developmental stage. Young or 'immature' back-arc rifting is associated with complex styles of magmatism and deformation, which are strongly influenced by upper plate stresses induced by tectonic complexities, such as asymmetric slab rollback and subduction-zone collisions (e.g., Collot et al., 1985; Stern, 2002; Mason et al., 2010; Anderson et al., 2016). In response to oblique convergence, most arc-backarc systems display significant variations along their lengths, including highly variable subduction rates, spreading rates, slab geometry, crustal thickness, magmatic production, and faulting (cf. Taylor, 1995). Therefore, a full understanding of back-arc rifting requires comprehensive studies of a range of tectonic conditions from the initiation of rifting to more advanced stage of back-arc basin opening.

Back-arc regions in the earliest stages of rifting are generally characterized by narrow linear grabens that are <100 km long and <45 km wide (e.g., Izu-Bonin arc: Fryer et al., 1990; Coriolis Troughs: Anderson et al., 2016; Suppl. Table A1). These rifts widen and deepen over several millions of years until they are large enough to allow passive mantle upwelling and true seafloor spreading (Martínez and Taylor, 2002; Hannington et al., 2005). Bimodal volcanism is a common feature of early back-arc rifting, producing both basaltic and felsic lavas. Mafic end-member compositions (back-arc basin basalt or BABB: Stern, 2002) lie between mid ocean ridge basalt (MORB) and island arc basalt (IAB), but a wide range of magma compositions is now being recognized in immature back-arc rifts (e.g., McConachy et al., 2005; Keller et al., 2008; Jenner and O'Neill, 2012), reflecting processes in the underlying mantle and interactions between the mantle and the fluids derived from the subducting slab. Contributions from the slab enhance melting and also influence the chemistry of the erupted lavas (e.g., Pearce et al., 1995; Bézos et al., 2009).

The region of the Jean Charcot Troughs in the northern New Hebrides is one of the youngest back-arcs in the world, forming only ~4 m.y. ago. However, unlike the Izu-Bonin arc and the Coriolis Troughs, back-arc extension is characterized by a complex series of grabens with different depths and orientations that are widely spaced over ~120 km from the arc front. The crustal thickness is

poorly constrained, estimated to be 10–20 km (Suppl. Table A1; Johnson et al. 1993; Maillet et al., 1995). In this paper, we consider the underlying causes and the structural, petrological, and hydrothermal consequences of this style of back-arc extension. A number of research cruises in the late 1980s to early 1990s provided most of the data that we now have (summarized by Maillet et al., 1995), but high-resolution (50-m or better) bathymetric coverage is almost non-existent and most of the New Hebrides back-arc region is virtually unexplored, particularly in the north. More recently, exploration in this area has been driven by the search for seafloor massive sulfide deposits. Neptune Minerals Inc. discovered the Tinakula deposit in 2011, which they investigated during five cruises between 2011 and 2012. This study examines the morpho-tectonic and volcanic features of the Jean Charcot Troughs where the Tinakula deposit is located and considers how broad-scale tectonic processes have influenced the locations of the hydrothermal activity and the geochemical characteristics of the deposit and its host volcanic rocks. Using a combination of high-resolution (1-m) geological mapping and volcanic rock sampling, new insight is provided into the magmatic and hydrothermal evolution of the particular mode of extension of the JCT.

3.2. Tectonic setting

The tectonically complex New Hebrides volcanic arc acquired its current configuration as a result of opposing subduction along the fossil Vitiaz Trench and contemporary New Hebrides Trench. In the early Cenozoic, the Pacific plate was initially subducting south- or southwest-ward beneath the NW-trending Melanesian volcanic arc, and a continuous archipelago that extended from northern coastal New Guinea to Fiji (Fig. 3.1; Hall and Spakman, 2002). Espiritu Santo, Malekula, and the Torres islands (now the Western Volcanic Belt of the New Hebrides arc) formed between 25 Ma and 14 Ma in response to this southwest subduction (Fig. 3.1b; Coleman, 1970; Gill and Gorton, 1973; Kroenke and Rodda, 1984; Falvey et al., 1991). Subduction ceased when the arc collided with two large volcanic plateaus, first the Ontong Java Plateau in the Early to Middle Miocene (Auzende et al., 1988, 1995; Collot et al., 2011), followed by the Melanesian Border Plateau in the Middle Miocene (Hathway, 1993; Schellart et al., 2006). This caused a subduction reversal along the proto-New Hebrides arc at 12–10 Ma, resulting in NE-dipping subduction of the Indo-Australian plate beneath the Pacific plate (Hall and Spakman, 2002). With this, volcanism shifted to the Eastern Volcanic Belt of the New Hebrides arc, forming the islands of Maewo and

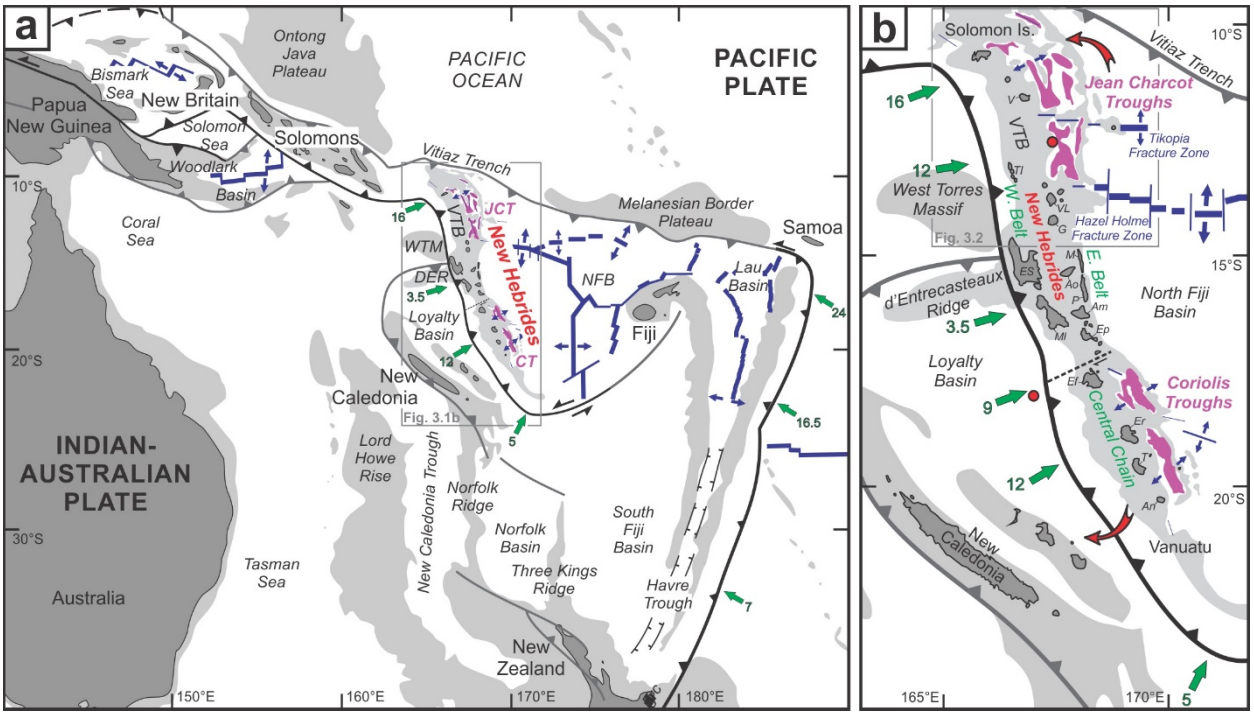


Fig. 3.1. Geographic location and tectonic features: (a) southwest Pacific; and (b) the New Hebrides arc-back-arc system (southern Solomon Islands and Vanuatu). Light grey areas are shallower than 2000 mbsl, green arrows indicate the convergence directions and rates (cm yr^{-1}; Pysklywec et al., 2003), blue lines represent spreading centers, the New Hebrides back-arc troughs are indicated in purple, and the red circles and arrows indicate the current Euler Poles and rotation directions of the northern and southern segments (Bergeot et al., 2009). The location of Fig. 3.2 is indicated. From north to south, the Western Volcanic Belt includes the Torres Islands (TI), Espiritu Santo (ES), and Malekula (Ml); the Eastern Volcanic Belt includes Maewo (M) and Pentecost (P), and the Central Volcanic Chain includes Vanikoro (V), Vanua Lava (VL), Gaua (G), Aoba (Ao), Ambrym (Am), Epi (Ep), Efate (Ef), Erromango (Er), Tanna (T), and Aneityum (An). CT = Coriolis Troughs, DER = d'Entrecasteaux Ridge, JCT = Jean Charcot Troughs, VTB = Vanikoro-Torres Basin, WTM = West Torres Massif. Modified from Hall (2002).

Pentecost in the Early Pliocene (7–3.5 Ma; Mitchell and Warden, 1971) and the Central Volcanic Chain initiated in the Late Miocene (5.8–5.3 Ma until present; Bellon et al., 1984), forming the regularly-spaced Banks Islands (Vanua Lava, Gaua), Aoba, Ambrym, Epi, Efate, Erromango, Tanna, and Aneityum islands (Fig. 3.1b). The formation of parallel volcanic belts may be due to early focusing of volcanism along a seismically active fracture zone forming the Eastern Volcanic Belt (Hanuš and Vaněk, 1983). Notably, there are no subaerial arc volcanoes between the islands of Vanikoro and the Banks Islands (between ~13°30'S and ~11°45'S). In this region, there is a large fore-arc basin, known as the Vanikoro-Torres Basin (or the Torres-Santa Cruz Basin), which is ~1900 m deep and heavily sedimented (up to 6 km thick: Holmes, 1988). Seismic reflection profiles reveal that faulting and folding extends to the seafloor (Falvey and Greene, 1988). Several submarine volcanoes along the easternmost part of the Vanikoro-Torres Basin represent the northern extension of the Central Volcanic Chain.

The Miocene subduction reversal was associated with significant asymmetric rollback of the Indo-Australian plate, with rapid clockwise rotation of the New Hebrides arc and simultaneous counter-clockwise rotation of the Fiji Platform, opening the North Fiji Basin (NFB; Hall, 2002). Widely-accepted early models of the NFB described the opening in three distinct phases: NE-SW opening from 12 to 7 Ma, N-S opening from 7 to 3 Ma, and E-W opening from 3 Ma to the present (Auzende et al., 1988, 1995). However, Martin (2013) proposed a model of single-phase "double saloon door" tectonics to account for back-arc spreading with both arc-parallel and arc-perpendicular components from 12–10 Ma until 1.5 Ma, and single "saloon door" rotation of the New Hebrides arc after 1.5 Ma. Opposite arc rotations associated with double saloon door tectonics may have been driven by divergent slab pull forces along a curved subduction zone (Martin, 2007, 2011). The northern extent of the New Hebrides is associated with a ~90° bend in the orientation of the trench (Fig. 3.1a), where there is a gap between the Vanuatu and Solomon slabs that likely originated from slab tearing during the collision of the Ontong Java Plateau (Hall, 2002; Hall and Spakman, 2002). Toroidal flow entering the mantle wedge from the northwest through this gap may have facilitated arc rotation by causing deviatoric tensile stresses in the overlying plate (Schellart, 2004; Martin, 2013).

Rifting of the New Hebrides arc, in response to eastward subduction and rollback of the Indo-Australian plate, formed the Coriolis Troughs (CT) beginning at 6.5–3.5 Ma, and the Jean Charcot Troughs (JCT) at ~4 Ma (Fig. 3.1; Monjaret et al., 1991; Pelletier et al., 1998). The early stages of opening of these basins was interrupted by collisions with two oceanic plateaus, the d'Entrecasteaux Ridge (DER) at 2–3 Ma (Collot et al., 1992; Greene et al., 1992) and the West Torres Massif (WTM) at 0.7–1 Ma (Meffre and Crawford, 2001; Schellart et al., 2002). Increased plate coupling along the collision zone resulted in large variations in convergence rates, with a maximum of 170 mm yr^{-1} at Vanikoro to 27 mm yr^{-1} opposite the DER (relative to the Australian Plate; Bergeot et al., 2009). This segmented the arc and resulted in shortening and thickening of the central segment (13°–17°S), while back-arc extension continued in the southern segment (17°–21°S) and in the northern segment (10°–13°S; Pelletier and Louat, 1989; Calmant et al., 1995, 2003; Taylor, 1995). Following the collision with the DER, the southern segment continued to rotate clockwise relative to the NFB at a rate of 8.97 ± 0.14 ° Ma^{-1} with a Euler Pole located at 17°68'S/166°55'E (red circle, Fig. 3.1b; Bergeot et al., 2009) and resulting in strong left-lateral transtension in the back-arc troughs (Anderson et al., 2016). In the northern segment, a counter-clockwise rotation relative to the NFB began with a Euler Pole located at 12°31'S/167°32'E (red circle, Fig. 3.1b), rotating at a rate of 20.79 ± 4.95 ° Ma^{-1} (Bergeot et al., 2009).

The CT in the south comprise three volcanically-active *en echelon* grabens situated ~50 km from the volcanic arc, extending 70–100 km in length, up to 25 km in width, and reaching depths of 2840–3400 mbsl (Fig. 3.1; Arculus et al., 2006; Anderson et al., 2016). The current rate of extension of the troughs varies from 20 mm yr^{-1} to 35 mm yr^{-1}, increasing southwards (Bergeot et al., 2009). In sharp contrast, the JCT in the north comprise a series of complex grabens and volcanic ridges that rise to minimum depths of ~800 mbsl (Figs. 3.1 and 3.2; Pelletier et al., 1993; Maillet et al., 1995). Individual grabens range in size from 20–65 km in length and 5–15 km in width. GLORIA sidescan surveys of Johnson et al. (1992) covering the southern half of the JCT (south of ~12°15'S) reveal sedimented basins separated by highly reflective volcanic ridges. The current rate of extension of the troughs increases northwards from 36–55 mm yr^{-1} to 70–81 mm yr^{-1} (Bergeot et al., 2009); however, this extension may be over the entire width of the back-arc, in which case individual troughs may be opening much more slowly than the CT.

The JCT are bound in the south at ~13°36'S by the Hazel Holme Fracture Zone (HHFZ), a seismically-active ridge that is considered to be an extensional zone related to the opening of the NFB (Fig. 3.2; Maillet et al., 1995). East of ~168°30'E, this fracture zone is characterized by an E-W trending trough, with a depth of 3300–4400 mbsl, bound by parallel ridges that rise to depths of ~2400 mbsl (Fig. 3.2). The HHFZ becomes more difficult to distinguish west of ~168°30'E, where it is comprised of a series of narrow troughs and ridges that merge towards the Banks Islands. A second E-W trending extensional zone occurs at ~12°20'S, known as the Tikopia Fracture Zone (TFZ; Fig. 3.2). Similar to the HHFZ, the TFZ displays a slow-spreading trough morphology east of Tikopia Island at ~168°55'E, where it reaches depths of ~4200 mbsl. To the west of ~168°55'E, E-W trending volcanic ridges and aligned seamounts suggest that the controlling basement structure extends westward toward the volcanic arc (Fig. 3.2). Recently formed volcanic complexes at this location obscure the horst-and-graben morphology of the back-arc rift. A notable bathymetric high bisects the northern and southern JCT where the TFZ crosses the back-arc region at the location of the Tinakula deposit (see below). The JCT are separated from the North Fiji Basin by the West Tikopia Ridge and the Duff Ridge, which are interpreted to be part of the pre-rifted fossil volcanic arc (Auzende et al., 1995). There is no consensus on the northern extent of the JCT, although here we consider them to include the NW-SE trending trough between the Duff Ridge and the Reef Islands. At ~10°30'S, the Santa Cruz Trough forms an E-W trending intra-arc basin.

A fundamental question in the evolution of the New Hebrides arc is what triggered the second phase of rifting at ~6–5 Ma, during the development of the North Fiji Basin. Back-arc extension is thought to be caused mainly by rollback of the subduction hinge, driven by the downward pull of the slab (Elsasser, 1971; Dewey, 1980; Faccenna et al., 2001; Hall et al., 2003; Schellart et al., 2002; 2003; Sdrolias and Müller, 2006). Numerical models suggest that hinge rollback occurs when the gravity-driven velocity of the down-going slab exceeds the convergence rate (Hall et al., 2003). Furthermore, there is a well-established correlation between back-arc stresses and slab dip (Jarrard, 1986; Heuret and Lallemand, 2005; Lallemand et al., 2005; Sdrolias and Müller, 2006). Currently, the east-dipping Australian slab is dipping at an angle of 60–70°, reaching maximum depths of 300–350 km, with an average down-dip length of only 200 km (Richards et al., 2011; Hayes et al., 2012). The truncated slab length is thought to be the result of the complete detachment

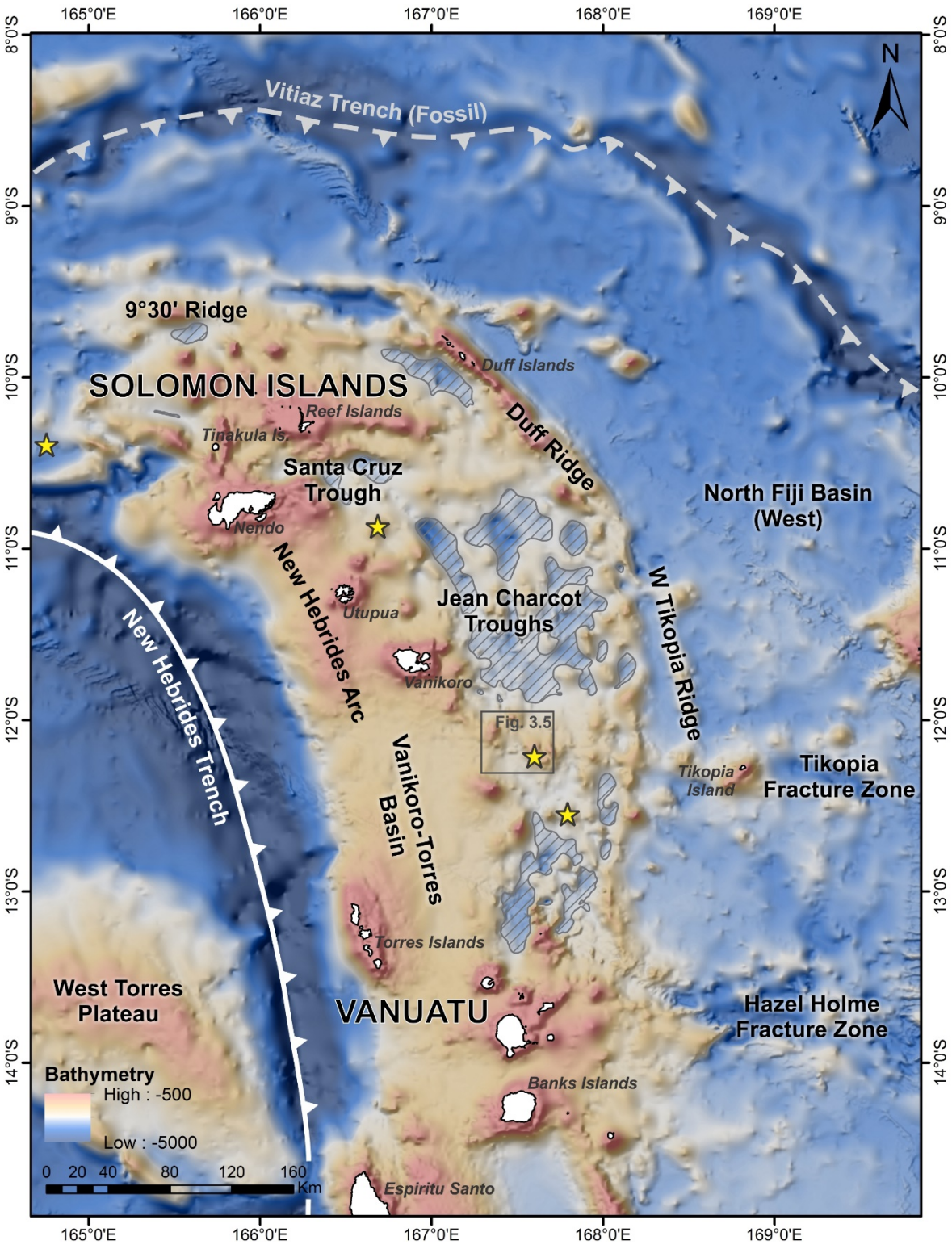


Fig. 3.2. Global marine altimetry of the Jean Charcot Troughs from Sandwell et al. (2014). Back-arc troughs deeper than 2800 mbsl are indicated by the grey hatched pattern. The location of Fig. 3.5 (Starfish area) is shown, with the locations of hydrothermal venting (after Beaulieu, 2013) indicated by yellow stars.

of the lower slab (Barazangi et al., 1973), which has since migrated eastwards and collided with the west-dipping Pacific slab below the Tonga subduction zone (Richards et al., 2011). The timing of slab break-off was poorly constrained by Richards et al. (2011), who estimated it to have initiated around 5 Ma, beginning in the southeast and propagating to the northwest (Fig. 3.3a,b). Complete detachment could have occurred in as little as 1 m.y. (Burkett and Billen, 2010; Richards et al., 2011). Following this, the slab-pull force remained strong enough to continue driving subduction of the Australian plate due to its negative buoyancy. Steepening of the down-going slab (Fig. 3.3c,d) also may have been facilitated by lateral mantle flow around the slab edges (e.g., Schellart, 2004). A similar process has been described, for example, in the central Mediterranean basins by Carminati et al. (1998) and Martin (2006). Sudden steepening of the subducting Australian slab at 5 Ma could have altered the stress regime in the upper plate, resulting in extension and the formation of the New Hebrides back-arc rifts at ~6–5 Ma. Initiation of tearing in the southeast and propagating to the northwest is consistent with the development of the southern Coriolis Troughs first, followed by the northern Jean Charcot Troughs, according to K-Ar ages determined by Monjaret et al. (1991) and Pelletier et al. (1998). This mechanism of slab detachment-induced back-arc extension resulting in renewed or more efficient basin development remains a poorly explored—yet potentially significant—tectonic process in subduction zones of the western Pacific.

3.3. Methods

3.3.1. Bathymetry and geological mapping

Ship-based multibeam bathymetric data and seafloor samples from the JCT and Tikopia Ridge in the "Starfish" area was collected by Neptune Minerals Inc. aboard the *MV Dorado Discovery*, *MV Nor Tigerfish*, and *MV Skandi Hawk* (2011–2012). RESON SeaBat 8160 multibeam bathymetry operating at 50 kHz was collected over 685.5 km^2, and the data were gridded with a cell size of 50 m. Detailed bathymetry was collected around the Tinakula deposit (within the Starfish region) with an ROV-mounted RESON SeaBat 7125-ROV2 400 kHz multibeam equipped with an Inertial Navigation System over an area of ~223,200 m^2 (~2.2 km^2) and gridded with a cell size of 0.2 m. Extensive bottom observations were made during 13 ROV dives (55 hours total dive time; Suppl.

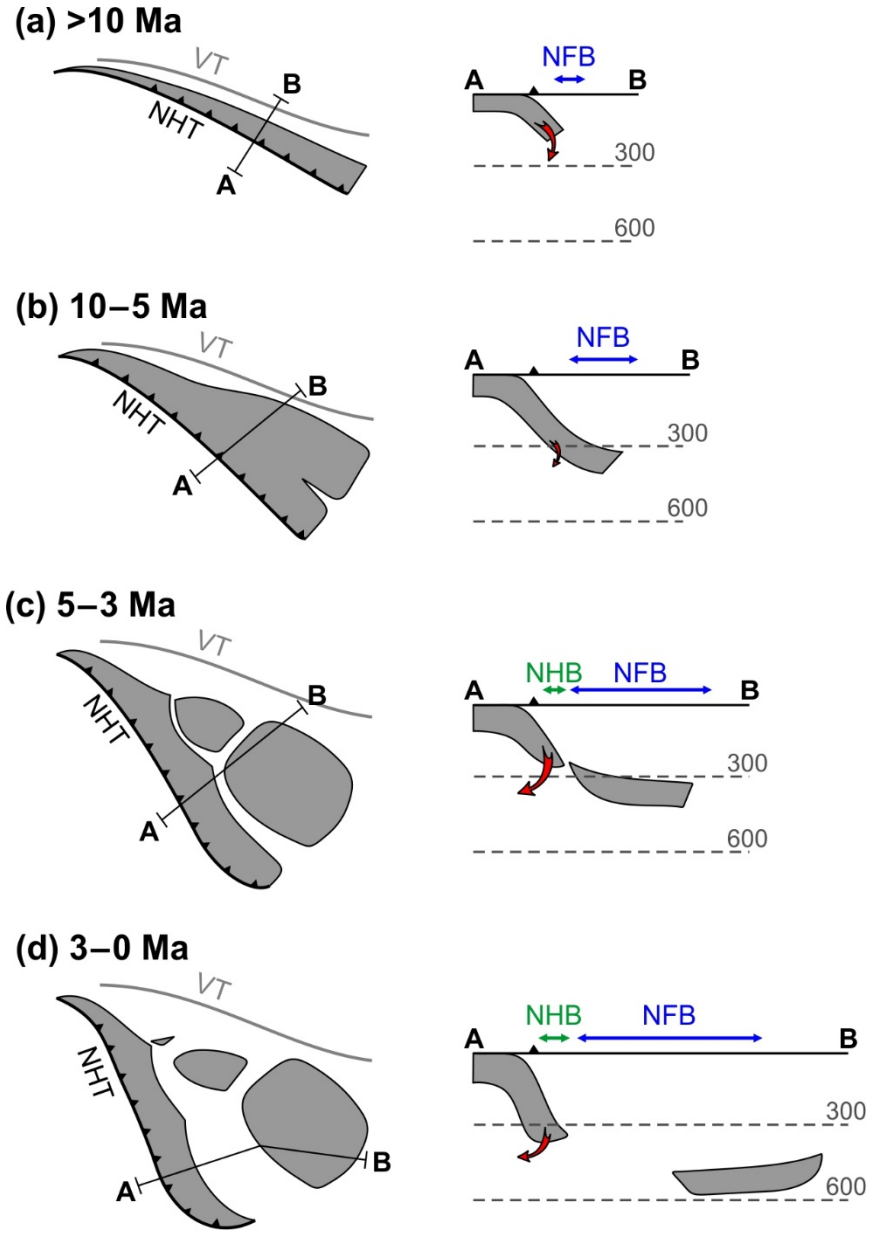


Fig. 3.3. Simplified model of the progressive horizontal tearing and detachment of the Australian slab, modified from Richards et al. (2011): (a) orientation of the Australian slab (grey) beneath the North Fiji Basin (NFB) as subduction along the New Hebrides trench (NHT) begins, ca. 10 Ma, with a cross-section from A–B shown on the right with depths below seafloor in km; (b) initial tearing beginning in the south at a depth of ~300 km, ca. 5 Ma (or earlier); (c) complete detachment of the slab associated with steepening of the remaining slab forming the New Hebrides back-arc (NHB) indicated by the red arrow; (d) progressive eastward migration of the detached slab beneath NFB, and continued steepening of the remaining slab, ca. 3–0 Ma. VT = fossil Vitiaz Trench.

Fig. B1). Using these data, plus fully georeferenced digital ROV dive videos, photos, and grab sampling, we produced a detailed geological map of the Tinakula area including all volcanic features, structures and hydrothermal activity, following the approach of Anderson et al. (2016).

3.3.2. Sample collection and petrography

Seafloor samples from the Tinakula-Starfish area collected by Neptune Minerals Inc. in 2011–2012 were examined in detail. A subset of 14 samples of fresh volcanic rocks (see Appendix C for full sample list and maps) were prepared as polished thin sections and analyzed by transmitted and reflected light microscopy. Petrographic descriptions included mineral identification, textures, abundances, and paragenesis and are compiled in Appendix D.

3.3.3. Whole-rock geochemistry

Samples of glass from fresh volcanic rocks (n = 13) from the Starfish-Tinakula area were hand-picked, taking care to note the presence of crystals or alteration, before being milled. Samples were analyzed at ActLabs (Ontario, Canada). A lithium metaborate/tetraborate fusion followed by ICP-OES and MS was used to analyze major elements (SiO_2, Al_2O_3, $Fe_2O_{3(T)}$, MnO, MgO, CaO, Na_2O, K_2O, TiO_2, and P_2O_5) and trace elements (Ag, As, Ba, Bi, Ce, Co, Cr, Cs, Cu, Ga, Ge, Ge, Hf, In, Mo, Nb, Ni, Pb, Rb, Sb, Sn, Sr, Ta, Th, Tl, U, V, W, Y, Zn, Zr, REEs). Additional trace elements were determined by INAA using a high-purity Ge detector: Au, Br, Cr, Ir, Sc, Se, Sb, and As. Cold vapor analysis was used to determine Hg, and infrared spectroscopy was used to determine total S. Additional geochemical data was provided for eight volcanic rock samples by Neptune Minerals Inc., including major elements (XRF) and trace elements (ICP-MS and ICP-AES). Full results are in Appendix H.

3.4. Regional geology

3.*4.1. Structures of the Jean Charcot Troughs (JCT)*

Using a bathymetric model based on satellite altimetry (Fig. 3.2) and vertical gravity gradient

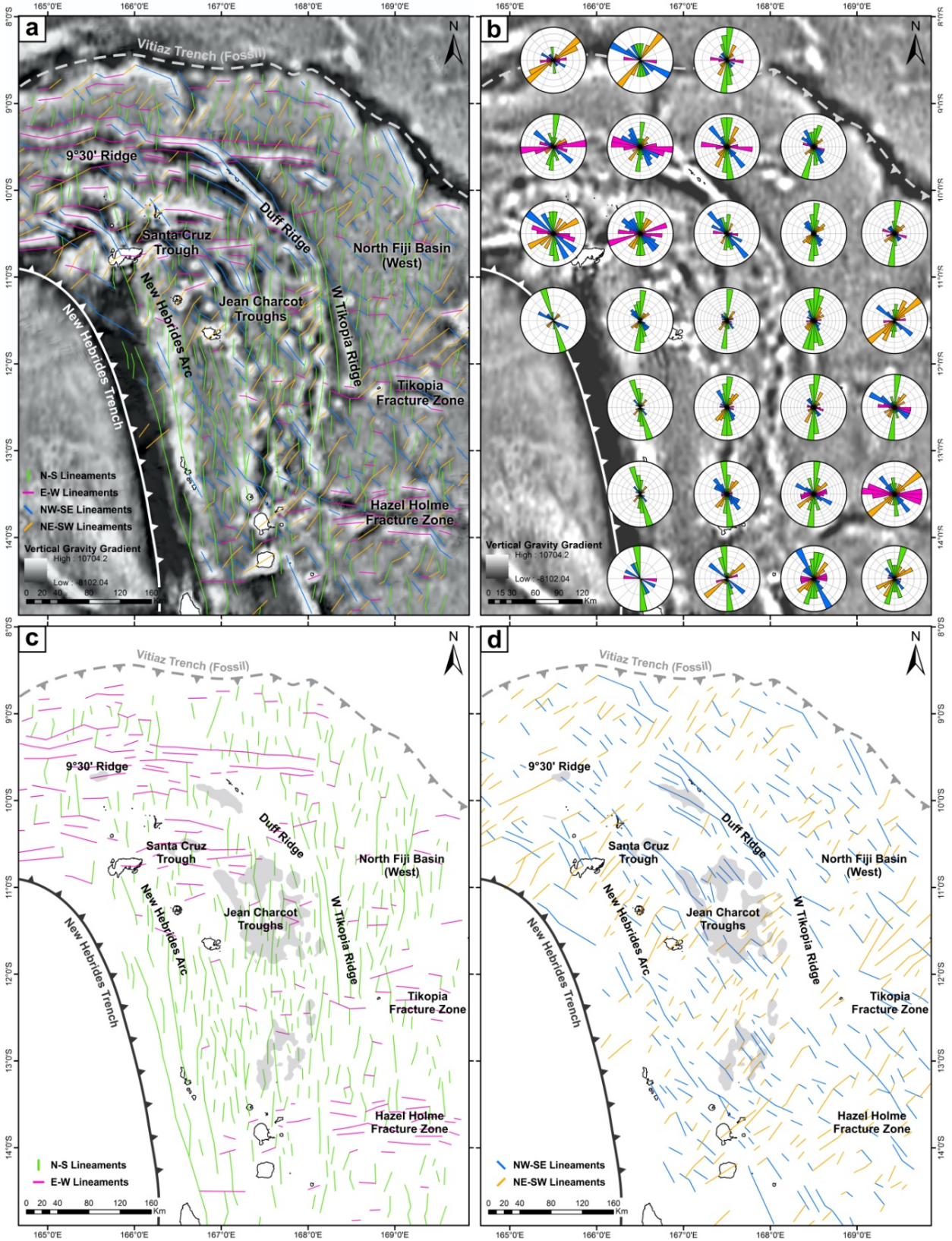

a
b
c
d
N
Vitiaz Trench (Fossil)
9°30' Ridge
Duff Ridge
Santa Cruz Trough
North Fiji Basin (West)
New Hebrides Arc
Jean Charcot Troughs
W Tikopia Ridge
New Hebrides Trench
Tikopia Fracture Zone
Hazel Holme Fracture Zone
N-S Lineaments
E-W Lineaments
NW-SE Lineaments
NE-SW Lineaments
Vertical Gravity Gradient
High : 10704.2
Low : -8102.04
0 20 40 80 120 160 Km
0 15 30 60 90 120 Km
165°0'E
166°0'E
167°0'E
168°0'E
169°0'E
8°0'S
9°0'S
10°0'S
11°0'S
12°0'S
13°0'S
14°0'S

Fig. 3.4. Structural lineaments of the Jean Charcot Troughs (same view as Fig. 3.2): (a) vertical gravity gradient of Sandwell et al. (2014) with interpreted lineaments categorized as N-S (green), E-W (pink), NW-SE (blue), and NE-SW (orange); (b) rose diagrams of the main lineament trends for every 1-degree latitude and longitude; (c) N-S and E-W trending lineaments; (d) NW-SE and NE-SW trending lineaments. Back-arc troughs are shown in light grey in (c) and (d).

(VGG) data of Sandwell et al. (2014; Fig. 3.4), we conducted a detailed fabric analysis of the JCT. Importantly, the most recent VGG data from CryoSat-2 and Jason-1 missions has revealed buried structures throughout the region not visible in the bathymetric model, including in the Vanikoro-Torres fore-arc basin and the western NFB. Figure 3.4a shows the interpreted lineaments, which are categorized into N-S (green), E-W (pink), NW-SE (blue), and NE-SW (orange) trending features. These data are shown in Figure 3.4b as rose diagrams for each degree of latitude and longitude using GEOrient software. The most common structures are the N-S trending lineaments with a mean trend of 358.3° ± 2.0° (n = 459), which dominate the fore-arc and the JCT and occur throughout the NFB (Fig. 3.4c). They also define the West Tikopia Ridge separating the JCT from the NFB. In contrast, the E-W trending lineaments, with a mean trend of 90.6° ± 3.7° (n = 196), are the least common. These are located primarily in the northern part of the map area near the 9°30' Ridge and the Santa Cruz Trough, but they also are dominant in the Tikopia and Hazel Holme fracture zones (Fig. 3.4c) formed during N-S opening of the NFB. The lineament analysis shows that the Tikopia fracture zone extends from the NFB to the volcanic arc, crossing the eastern margin of the JCT, contrary to interpretations by previous authors (Pelletier et al., 1993, 1998; Charvis and Pelletier, 1989; Auzende et al., 1995). The NW-SE lineaments (136.4° ± 3.1°; n = 308) occur throughout the map area (Fig. 3.4d). They are most common in the northern JCT – Santa Cruz Trough area and define the Duff Ridge. NE-SW lineaments (43.2° ± 2.9°; n = 278) also occur throughout the map area (Fig. 3.4d) but are most common in the NFB (Fig. 3.4b). Notably, the northern JCT (north of ~12°S) are dominated by NW-SE trending lineaments, whereas the southern JCT are mainly associated with NE-SW trending lineaments (Fig. 3.4b).

3.4.2. Structures of the Starfish area

The "Starfish" area, named for the Starfish volcano, is located between 11°55'S and 12°20'S, and 167°15'E and 167°45'E (inset Fig. 3.2; Fig. 3.5). It straddles the poorly-defined boundary between the Central Volcanic Chain of the volcanic arc and the back-arc JCT. It is also located at the intersection with the E-W trending Tikopia Fracture Zone. Ship-based multibeam bathymetry (Fig. 3.5) reveals heavy faulting and the formation of 2400-m deep grabens in the west of the map area. At 12°3'S/167°22'E, an old volcanic edifice, likely part of the volcanic arc, has been rifted in half.

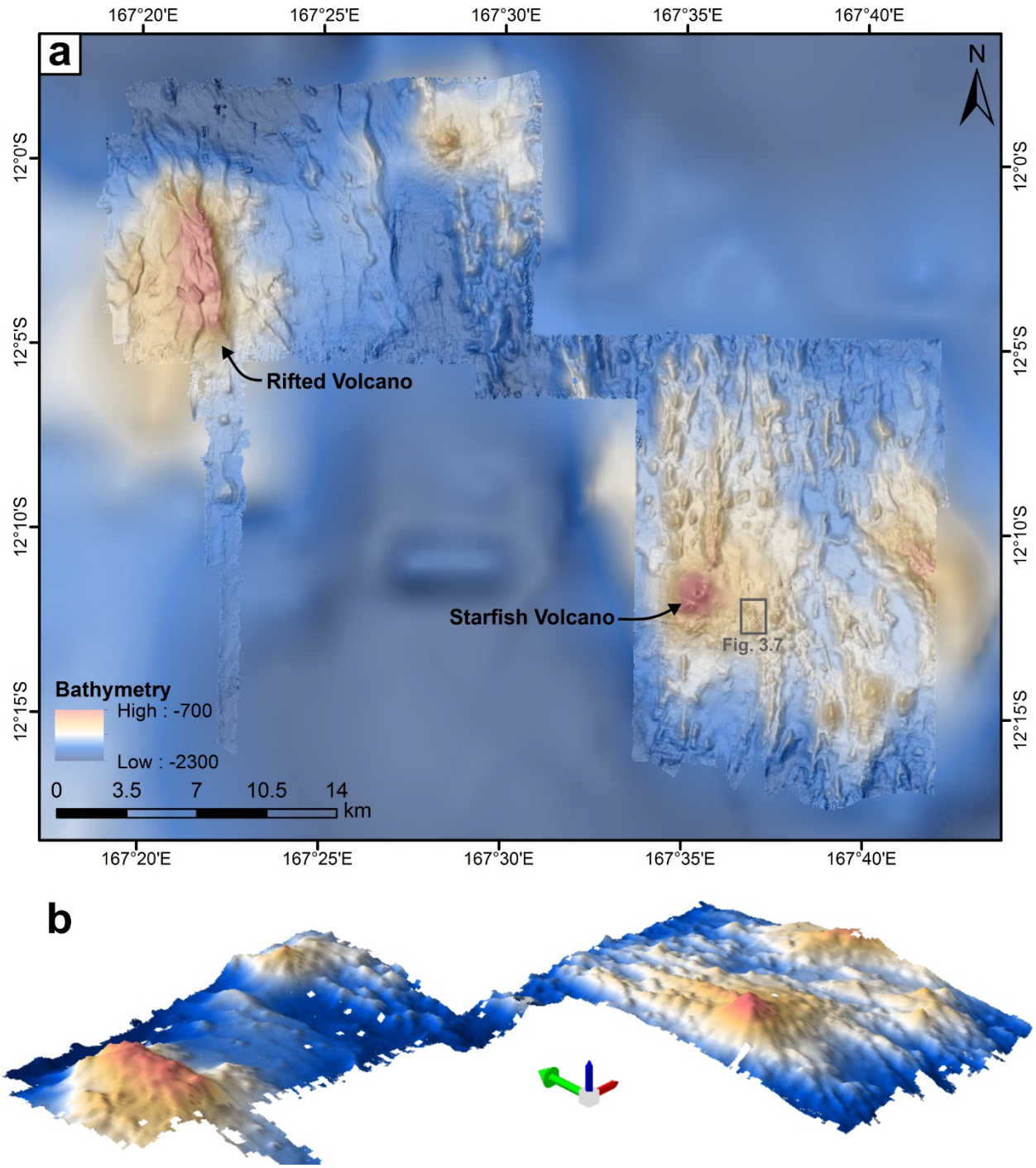


Fig. 3.5. RESON SeaBat 8160 50 kHz multibeam bathymetry of the Starfish area (50 m resolution), collected by Neptune Minerals Inc.: (a) hill- and slope-shaded bathymetry overlain on satellite altimetry of Sandwell et al. (2014), with the location of Fig. 3.7 (Tinakula deposit) shown; (b) 3D view looking NE (2× vertical exaggeration).

This style of heavy faulting is in sharp contrast with the east of the map area, which is characterized by elongate volcanic ridges and rows of discrete volcanic cones (Fig. 3.5). Recent volcanism in this area is confirmed by the GLORIA sidescan sonar survey of Johnson et al. (1992), which reveals a series of closely-spaced, N-S-trending linear reflections individually continuous over distances of 30 km or more. The survey area covers much of the volcanic platform surrounding the Starfish volcano, which rises to a minimum water depth of ~460 m.

Structures in the eastern half of the map area include N-S, E-W, NW-SE, and NE-SW lineaments that consist mainly of elongate volcanic ridges and aligned volcanic cones, with some faults (Fig. 3.6). The most common are the N-S lineaments (0.7° ± 2.4°; n=233; Fig. 3.6b), indicating a strong extensional control in the E-W direction in this area. NE-SW lineaments are also common, especially in the northern map area (40.4° ± 3.5°; n = 217; Fig. 3.6b). These appear to offset the N-S trending lineaments with a dextral sense of motion. In contrast, NW-SE lineaments are not abundant, and occur predominantly in the central part of the map area (145.4° ± 6.5°; n = 50; Fig. 3.6b). They partially offset some of the N-S lineaments with a sinistral sense of motion. The E-W trending lineaments are the least abundant (101.1° ± 6.9°; n = 38; Fig. 3.6b), possibly because structures related to the E-W Tikopia Fracture Zone are concealed by recent volcanic products. The mean orientation of the lineaments in the Starfish area closely follows that of the larger Jean Charcot Troughs (Fig. 3.6c).

3.5. Geology of the Tinakula area

The Tinakula seafloor massive sulfide (SMS) deposit is centered at 167°36’50”E/12°12’10”S at a depth of 1070–1204 mbsl, located on the volcanic platform ~2 km ESE of the Starfish volcano, which is centered at 167°36’50”E/12°12’10”S (Fig. 3.7). Detailed bathymetry and seafloor observations reveal a strong structural control on volcanic and hydrothermal features associated with Tinakula. The deposit sits at the intersection of a regional N-S structure with a NE-SW structure (Fig. 3.8). The NE-SW structure offsets the N-S trending structure with a dextral sense of motion. Minor faults, fractures, and aligned volcanic and hydrothermal features are common at the local scale. These secondary features are most common in close proximity to the regional

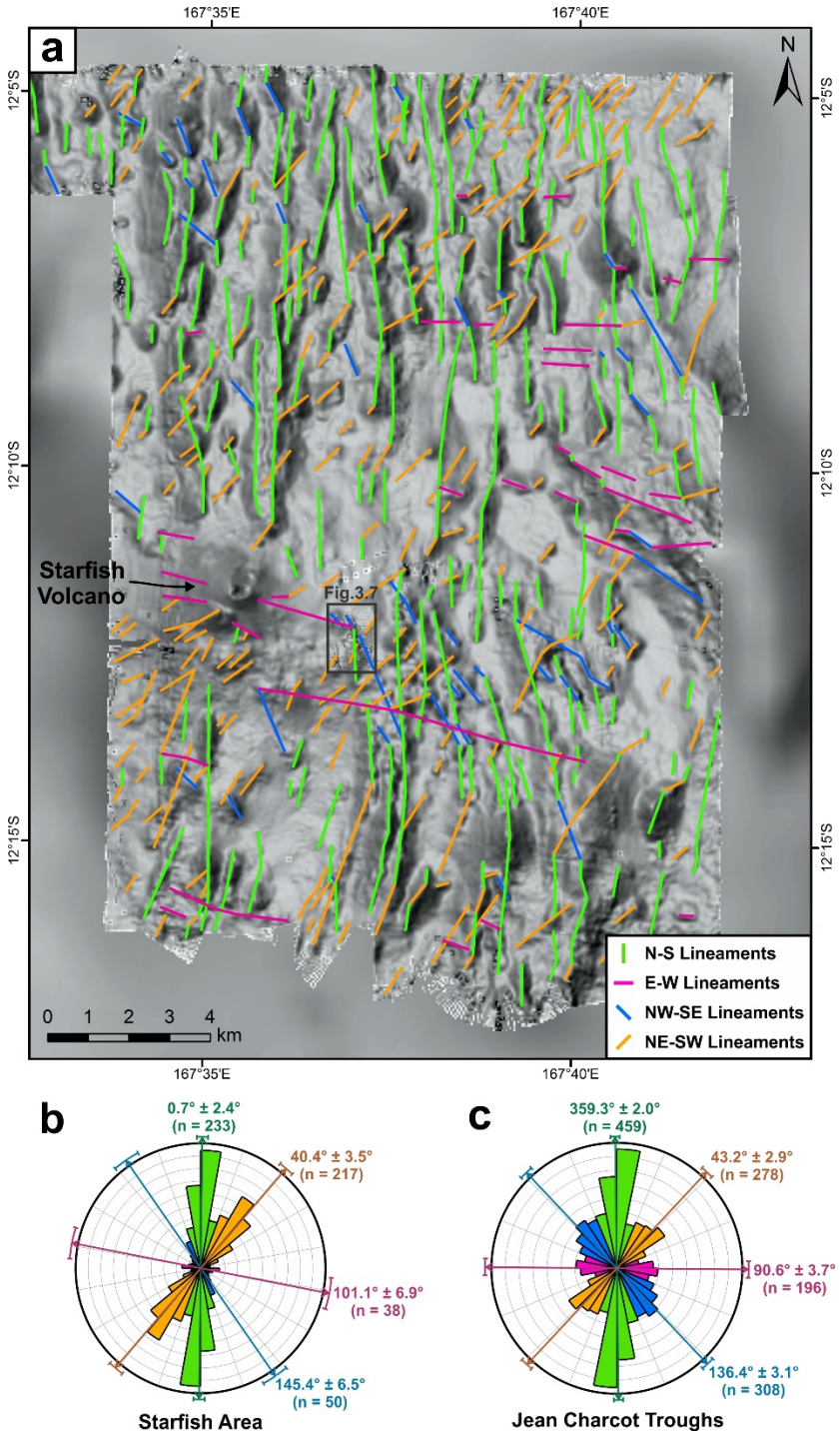


Fig. 3.6. Interpreted lineaments of the Starfish area: (a) N-S (green), E-W (pink), NW-SE (blue), and NE-SW (orange) lineaments consisting of volcanic ridges, aligned volcanic cones, and faults, overlain on hill- and slope-shaded RESON SeaBat 8160 50 kHz multibeam bathymetry, with the location of Fig. 3.7; (b) rose diagram of the lineaments of the Starfish area, dominated by N-S and NE-SW trending lineaments (mean values shown); (c) structural trends of the entire Jean Charcot Troughs (see Fig. 3.4) for comparison (mean values shown). This shows the dominance of N-S and NE-SW trending structures in the Starfish area.

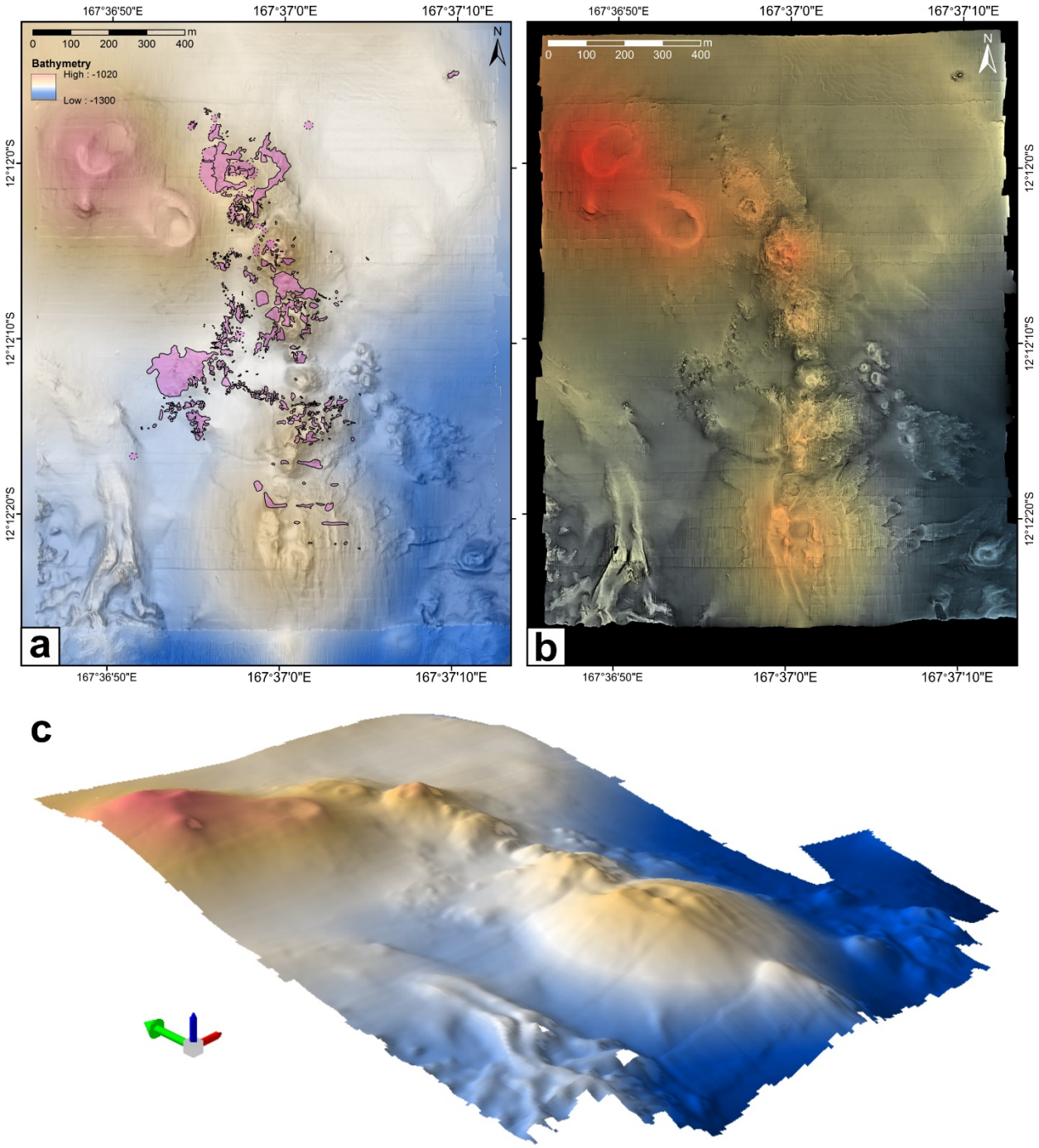


Fig. 3.7. Detailed RESON SeaBat 7125-ROV2 400 kHz multibeam bathymetry of the Tinakula area (0.2 m resolution): (a) traditional hill- and slope-shaded bathymetry with massive sulfide chimneys and mounds shown in pink (solid lines = exposed chimneys and mounds; dashed lines = buried chimneys an mounds); (b) terrain texture shaded bathymetry (using method of Brown, 2010), which enhances features such as craters and sedimentary ripples (upper right corner); (c) 3D view looking NE (no vertical exaggeration).

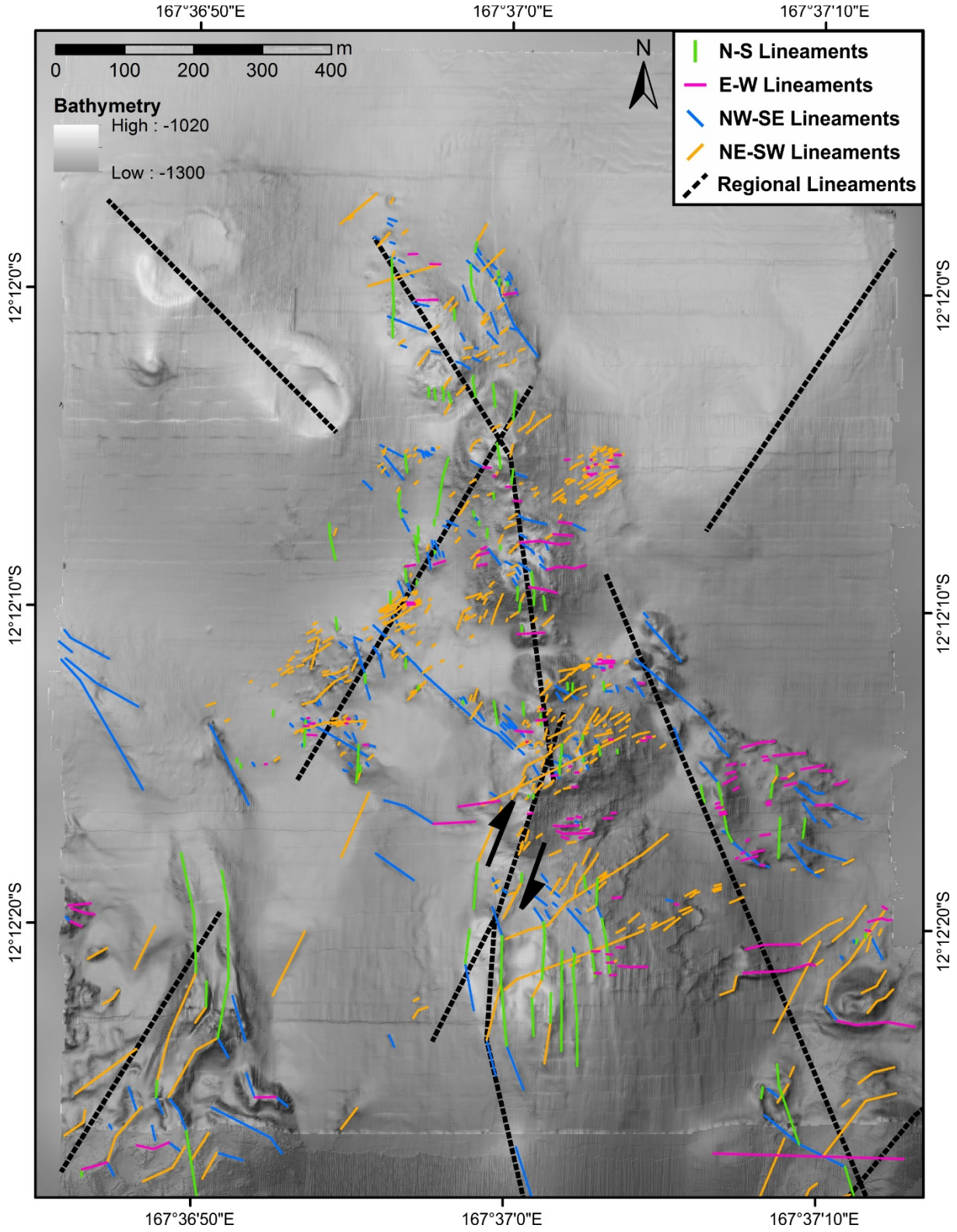


Fig. 3.8. Detailed and regional lineaments in the Tinakula area overlain on greyscale hill- and slope-shaded RESON SeaBat 7125-ROV2 400 kHz multibeam bathymetry (same view as Fig. 3.7a,b). This shows the close association of local structures with regional structural corridors.

structures and generally coincident with larger volcanic features at the seafloor, especially on the flanks of volcanic cones. Volcanic cones in the NW corner of the map area (Fig. 3.8) are also aligned with regional NW-SE structures. This trend is also followed by secondary fractures and fissures on the surrounding seafloor that appear to have no volcanic association. In the central part of the map area, the main N-S structure is marked by a row of cratered volcanic cones that define a large fissure. The volcanoes include composite cones (n = 3), cinder cones (n = 36), and maars (n = 3). They are classified here according to morphology (compiled in Suppl. Table B1), seafloor observations, and sampling. The composite cones are 55–140 m high with basal diameters of 327–691 m and low aspect ratios compared to cinder cones ($H/W_{cone,avg}$ = 0.18; Fig. 3.9a). These volcanoes have relatively small craters (52–86 m in diameter and 11–26 m deep) relative to the basal diameter of the cone ($W_{crater}/W_{cone,avg}$ = 0.16; Fig. 3.9b). Cinder cones vary in size, with heights of just 3 m up to 73 m, and basal diameters of 13–1158 m ($H/W_{cone,avg}$ = 0.27; Fig. 3.9a). These are both uncratered (n = 16) and cratered (n = 20), with crater diameters of 5–35 m and crater depths of 1–13 m ($W_{crater}/W_{cone,avg}$ = 0.27; Fig. 3.9b). Volcanic maars have the lowest aspect ratios ($H/W_{cone,avg}$ = 0.06), with heights of only 1–2 m and basal diameters of 17–32 m (Fig. 3.9a). They also have the largest crater widths relative to their basal diameters ($W_{crater}/W_{cone,avg}$ = 0.73), with crater diameters of 9–43 m (Fig. 3.9b). The defining feature of the maars is a crater floor that is at the same elevation, or even below, the surrounding seafloor depth, with crater depths of 2–4 m. The morphology of the Tinakula edifices is similar to subaerial basaltic volcanoes, but they are generally smaller in diameter (Fig 3.9).

The interpreted geology of the Tinakula area, based on ROV dive observations, geomorphological features interpreted from bathymetry, and sampling is shown in Figure 3.10. A large composite cone dominates the central N-S fissure in the south, with a row of basaltic cinder cones and two small maars (craters without cones) at the northern end of the fissure. Two additional composite cones in the NE corner of the map appear to be unrelated to the central fissure. The larger composite cones are associated with felsic or bimodal eruptive products. Large felsic lava flows in the SW corner of the map area (Fig. 3.10) have a distinctly different morphology that may indicate channelized flow or volcanic ridges. Coherent mafic-intermediate flows have been observed throughout the map area (Fig. 3.11a) with abundant autobreccia and/or hyaloclastite (Fig. 3.11b) and blocky volcanic talus (Fig. 3.11c). Massive sulfide chimneys and mounds display a

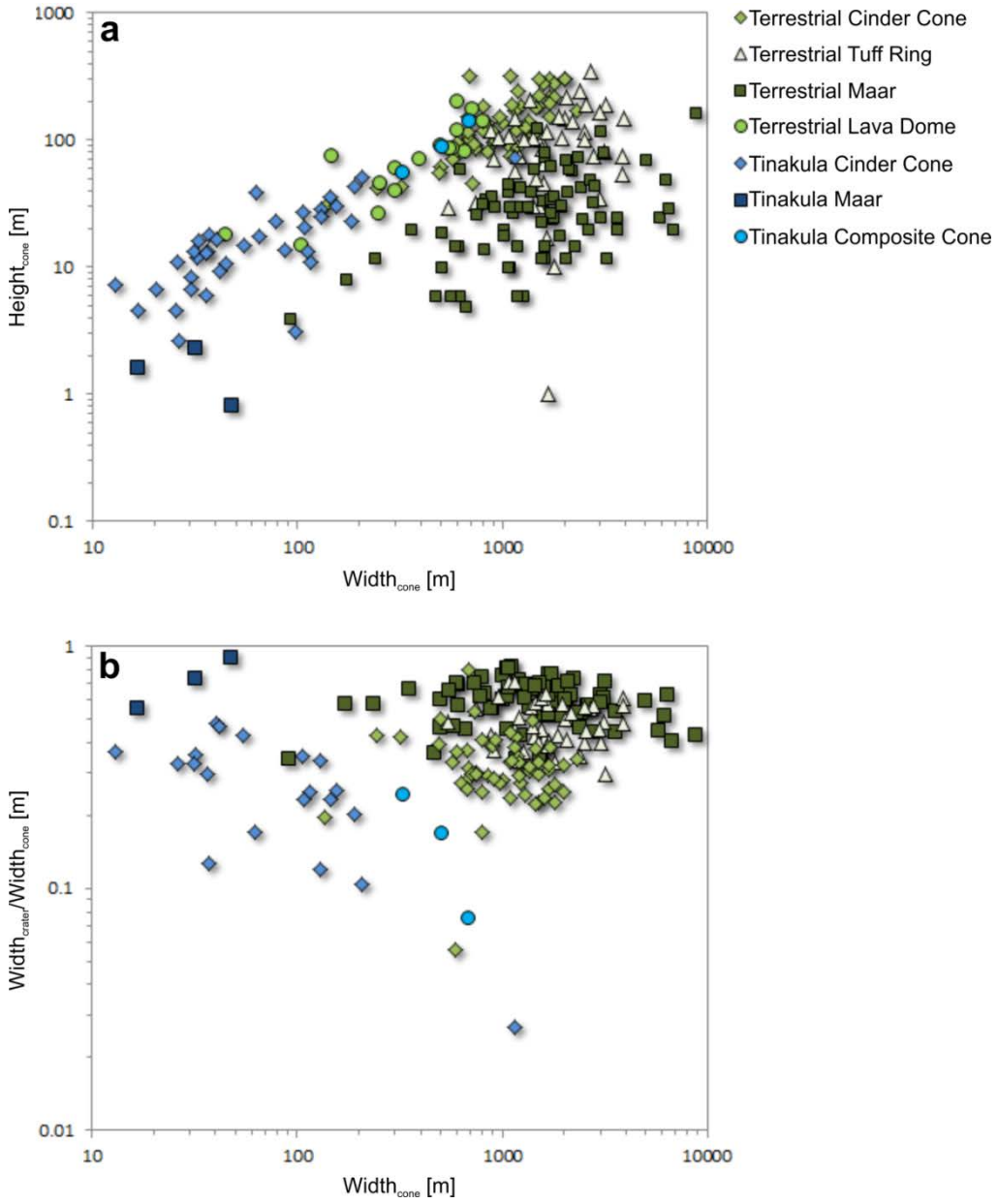


Fig. 3.9. Aspect ratios of volcanic edifices in terrestrial environments (green: Pike, 1978) and at the submarine Tinakula deposit (blue; this study), with logarithmic scales: (a) cone width vs. cone height; (b) cone width vs. crater/cone width. Parameters are tabulated in Suppl. Table B1. This highlights the morphological similarity of volcanic cones at Tinakula with subaerial volcanoes, with smaller cone widths for all volcanic edifice types at Tinakula.

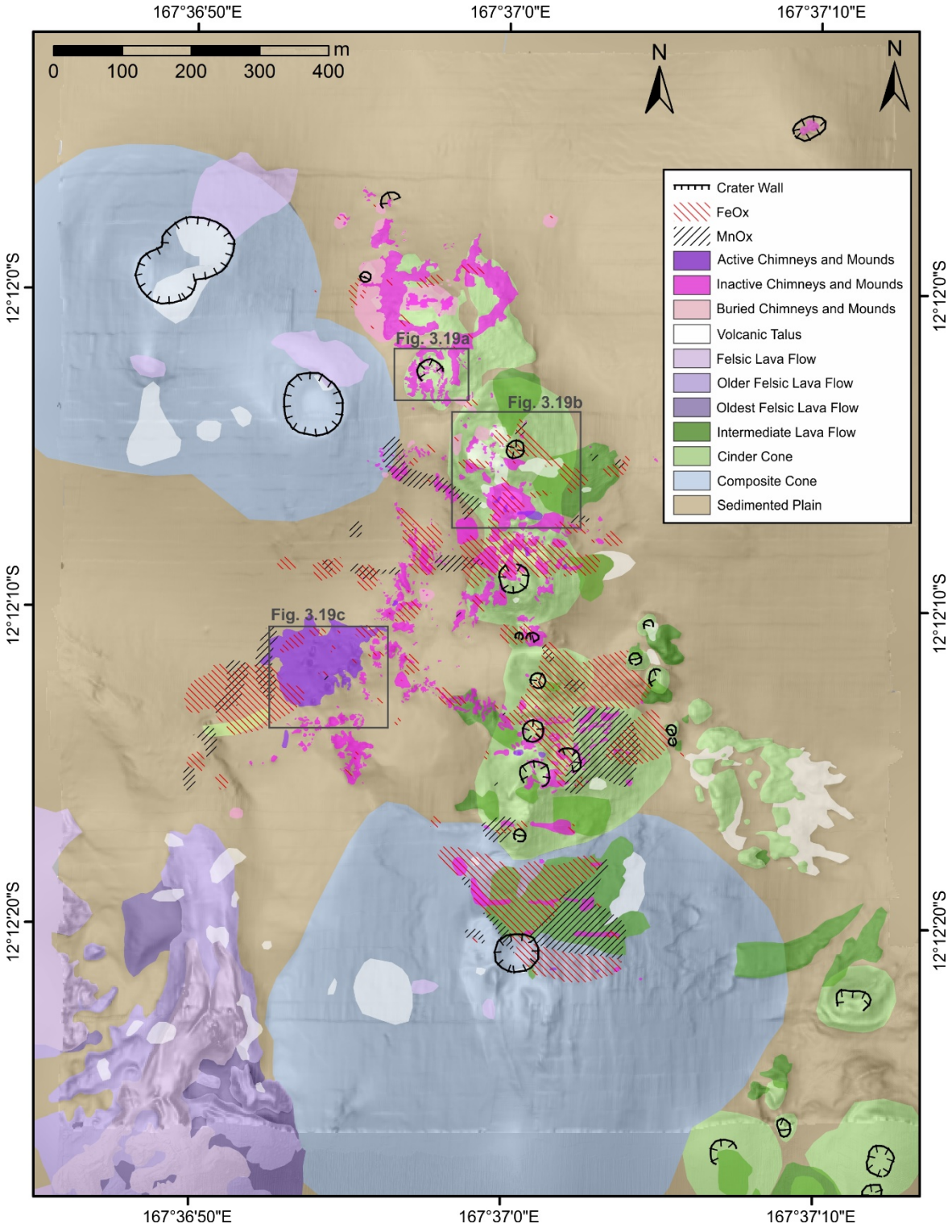


Fig. 3.10. Geology of the Tinakula area interpreted from ROV dive videos and sampling overlain on hill- and slope-shaded RESON SeaBat 7125-ROV2 400 kHz multibeam bathymetry (same view as Fig. 3.7). Craters without cones are classified as maars in Fig. 3.9.

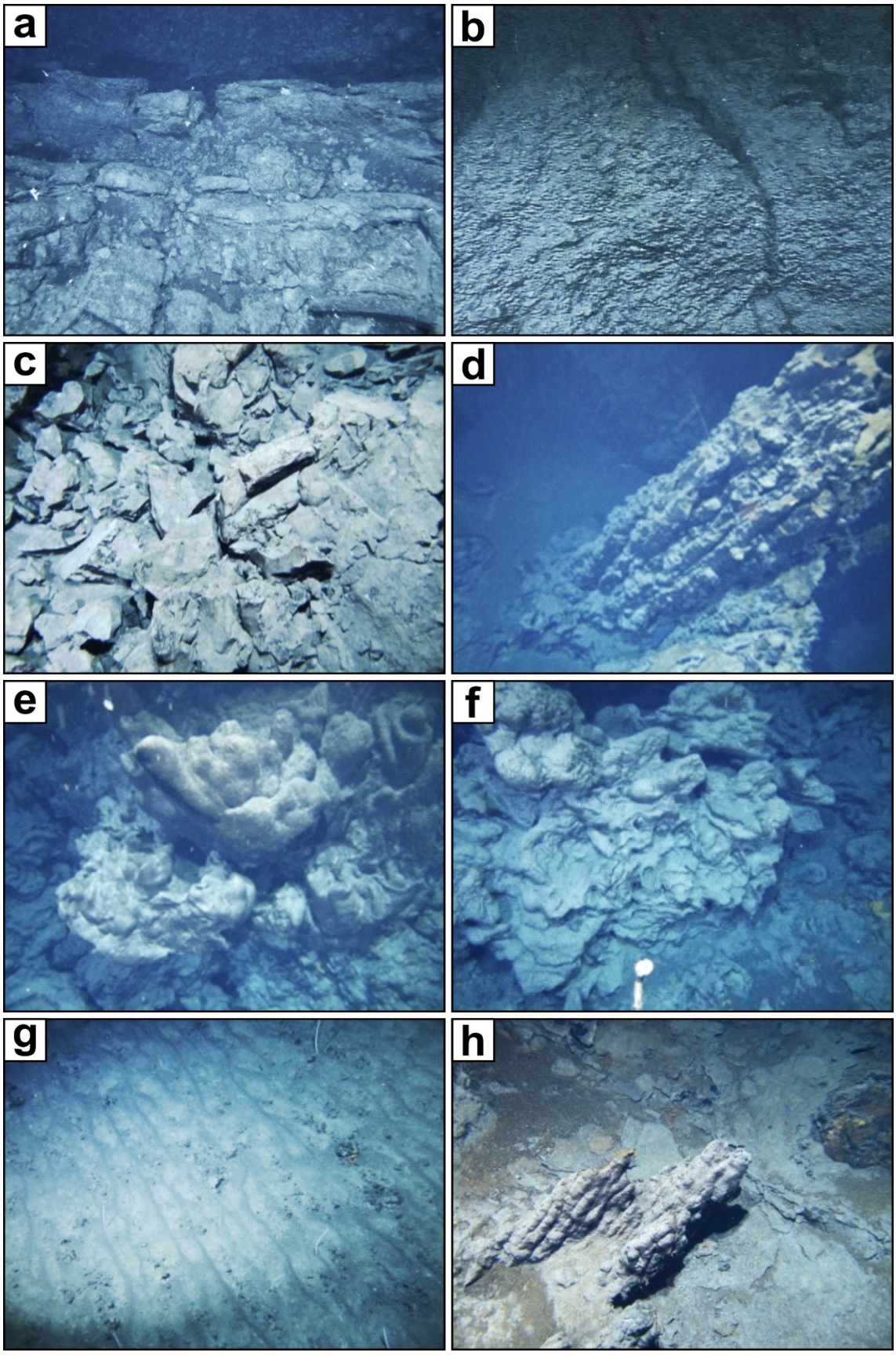

a
b
c
d
e
f
g
h

Fig. 3.11. Mappable seafloor units observed during ROV dives: (a) banded lava flow; (b) volcaniclastic breccia; (c) volcanic talus; (d) multi-spired sulfide chimney; (e) bulbous sulfide chimney with ‘tulip’ morphology; (f) bulbous to layered sulfide chimney; (g) rippled unconsolidated volcaniclastic sediment (fallout tephra); (h) indurated sediment partially burying a chimney.

range of morphologies, from spired to bulbous (Fig. 3.11d–f). Mafic-intermediate(?) volcaniclastic sediment covers the volcanic cones. The material ranges from coarse sand- to pebble-sized, with a few larger volcanic fragments or bombs (with elongate vesicles and quenched margins). The sediment is 1.5 m to >8 m deep in places, and is massive to crudely bedded with weak grading. Abundant ripple marks are observed in the sediment (Fig. 3.11g), with large-scale ripples visible in the bathymetry (Fig. 3.7). Locally, the sediment is hydrothermally indurated (Fig. 3.11h).

3.6. Volcanic rock samples

3.6.1. Petrography

Details of the petrography of 14 fresh volcanic rocks samples from Tinakula are summarized in Table 3.1. The samples include coherent lava (Fig. 3.12a) and autobrecciated lava (Fig. 3.12b). They are dark aphyric to weakly porphyritic and vesicular with a glassy or microcrystalline matrix, with up to 1-cm thick glass rinds. Palagonite alteration of variable intensity occurs at the sample margins (Fig. 3.12c). Abundant sub-mm vesicles are rounded to elongate and typically constitute 15–35 vol. % of the samples (avg. 23 vol.%), indicating that the magma was volatile-rich (Fig. 3.12). The vesicles and (micro-)phenocrysts commonly display flow-foliation. Local domains of pumice with stretched vesicles indicate a frothy flow-top in three autobrecciated samples (Fig. 3.12e). Sub-rounded xenoliths are present in seven samples, comprised of vesicular volcanic fragments likely picked up during flow (Fig. 3.12f). The samples show a wide range phenocryst abundance from 3–29 vol.%, mostly plagioclase with minor clinopyroxene, orthopyroxene, magnetite, and rare maghemite. The phenocrysts commonly occur as glomeroporhyritic aggregates (Fig. 3.12d). Samples collected from the cinder cones that host the Tinakula deposit have the lowest abundance of phenocrysts, generally <10 vol.%. The groundmass contains either tachylite or sideromelane glass, with microphenocrysts of plagioclase, and minor clinopyroxene, orthopyroxene, and magnetite. Most of the samples contained globules of immiscible sulfide (<1 vol.%), indicating the melts were sulfur saturated. Trace sulfides are also present in the vesicles, typically chalcopyrite, with rare pyrite or galena. Samples GMA13-036 and GMA13-065 have minor alteration (3–4 vol.% alteration minerals), and samples P0015, P0016, and P0040 have

Table 3.1. Summary of petrographic observations of volcanic rocks from the Starfish-Tinakula area, with rock classifications using the TAS diagram of Le Bas et al. (1986; Fig. 3.13)

	GMA13-001	GMA13-015	GMA13-023	GMA13-035	GMA13-036	GMA13-039	GMA13-043	GMA13-044	GMA13-057	GMA13-063	GMA13-065	P0015	P0016	P0040
	D	**A**	**B-A**	**A**	**A(?)**	**A**	**D**	**D**	**B-A**	**D**	**D**	**B-A**	**B-A**	**B-A**
	Starfish	Tinakula	N Tinakula	Tinakula	Tinakula	Tinakula	W Tinakula	W Tinakula	Tinakula	N Tinakula	Starfish	Tinakula	Tinakula	TKAD021
Phenocrysts	**10**	**5**	**5**	**10**	**3**	**15**	**25**	**10**	**3**	**29**	**15**	**2**	**3**	**3**
Pl	+	+	+	+	+	++	++	+	+	++	++	+	+	+
Cpx	Tr	+	+	+	Tr	+	+	+		+	+	Tr	Tr	+
Opx	+	Tr	Tr	+	+	+	+	+		+	+	Tr		Tr
Mag	Tr	Tr	Tr	+	Tr	Tr	+	Tr		+	+			Tr
Mgh	Tr			Tr			Tr	Tr		Tr	Tr			
Groundmass	**75**	**60**	**60**	**58**	**72**	**65**	**74**	**75**	**82**	**65**	**48**	**53**	**28**	**43**
$Glass_{(Sid)}$	++						+++	+		+++	+++			
$Glass_{(Pal)}$		+							+					
$Glass_{(Pum)}$		+		+		+								
$Glass_{(Tac)}$		++	+++	+++	++	++			+++			+++	++	++
Pl	+++	+++	++	++	+++	+++	+++	+++	+++	+++	++	+++	++	++
Cpx	Tr	Tr	+	+	+	+	+	+	++		Tr	+	+	+
Opx	Tr	Tr	+	+	+	+	+	+	+	+	+	+	+	+
Mag	+	+	+	+	+	+	+	+	+	+	Tr	+	++	+
Mgh	Tr			Tr			Tr	Tr						
Xenoliths		**<1**		**2**	**1**						**2**	**2**	**2**	**5**
Vesicles	**15**	**35**	**35**	**30**	**20**	**20**	**1**	**15**	**15**	**5**	**30**	**30**	**35**	**35**
Immiscible S	**<1**	**<0.1**	**<1**	**<1**		**<1**	**<1**	**<1**	**<0.1**	**1**	**<1**		**<0.1**	
Py	Tr		Tr	Tr		Tr	Tr	Tr	Tr	+	Tr		Tr	
Ccp		Tr				Tr								
Icb(?)						Tr								
Late Sulfides	**<0.1**	**<1**	**<0.1**	**<0.1**	**<0.1**	**<1**		**<0.1**			**<0.1**	**1**	**<1**	**<1**
Ccp	Tr	Tr	Tr	Tr	Tr	Tr					Tr	+	Tr	Tr
Py						Tr		Tr				Tr	Tr	Tr
Gn														Tr
Alteration	**<0.1**	**<1**	**<1**	**<0.1**	**4**	**<1**	**<0.1**	**<0.1**	**<1**	**<1**	**3**	**12**	**32**	**14**
Hem	Tr	Tr	Tr		Tr	Tr			Tr			Tr	+	+
Goe(?)	Tr		Tr	Tr		Tr	Tr	Tr	Tr			Tr	Tr	
FeO_x		Tr	Tr	Tr	+	Tr			Tr	Tr	+	Tr	+	Tr
MnO_x									Tr		Tr			
$Pal_{(Gel)}$					+						Tr		Tr	Tr
Clay		Tr			Tr						+		++	++
Cv	Tr	Tr			Tr	Tr						Tr		
Ser												Tr	+	
Cal												+	+	
Qz(?)													+	
Rt													+	+

D = dacite; A = andesite; B-A = basaltic-andesite

Bold values are in vol. %

+++ = abundant (>25%); ++ = major (10-25%); + = minor (1-9%); Tr = Trace (<1%)

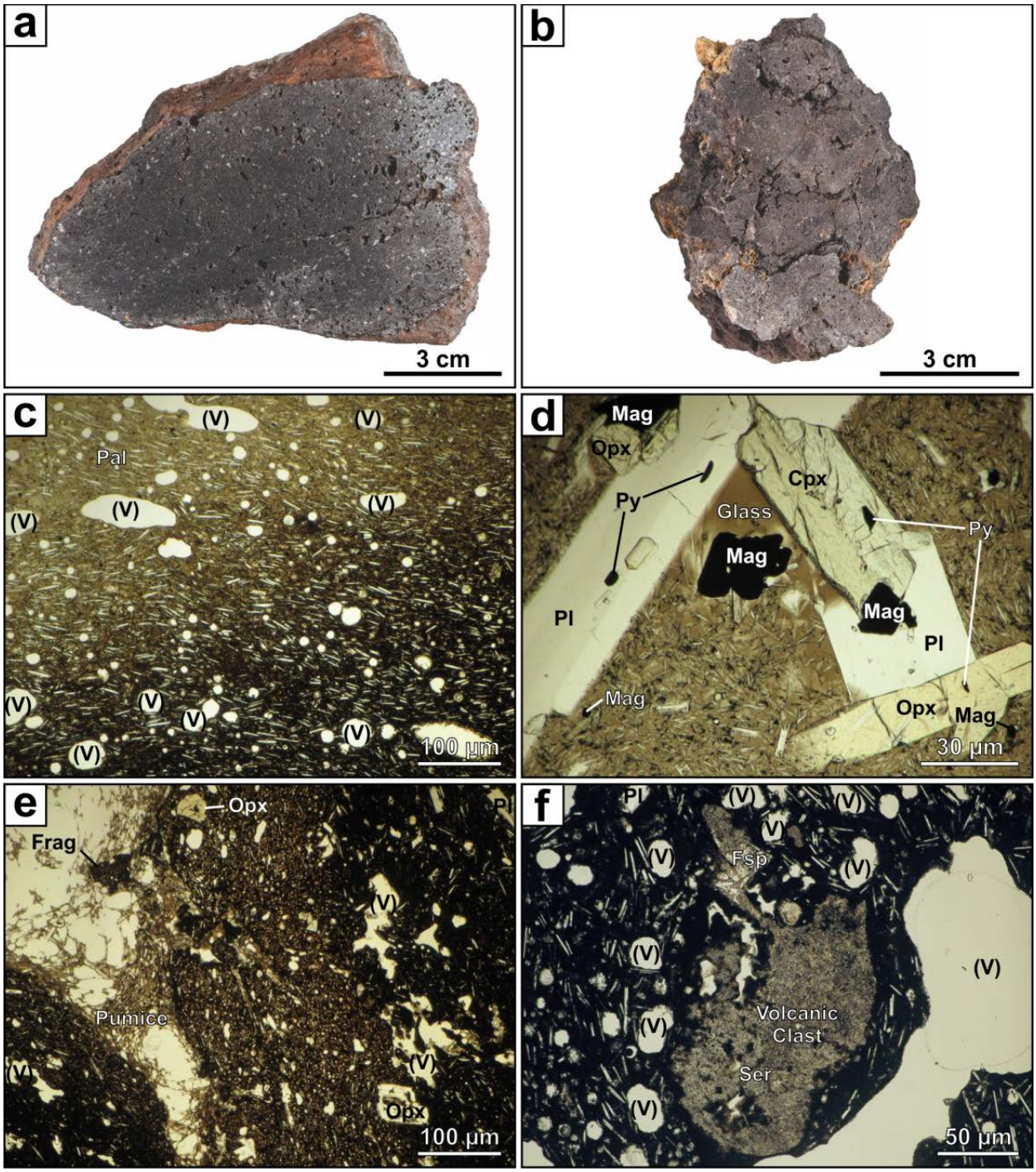


Fig. 3.12. Representative volcanic rocks recovered from the Starfish-Tinakula area; (a) coherent weakly porphyritic vesicular lava, sample GMA13-001; (b) autobrecciated aphyric vesicular lava, sample GMA13-039; (c) transmitted light photomicrograph (PPL) of flow-foliated vesicular lava, with microphenocrysts of plagioclase and a glassy matrix that is palagonitized near the sample margin (top), sample GMA13-057; (d) transmitted light photomicrograph (PPL) showing the glomeroporphyritic phenocryst assemblage of plagioclase, clinopyroxene, orthopyroxene, and magnetite, with sulfide inclusions and a glassy to microcrystalline groundmass, sample GMA13-063; (e) transmitted light photomicrograph (PPL) of autobrecciated vesicular lava with pumaceous

flow-top froth and rare phenocrysts of orthopyroxene, sample GMA13-039; (f) transmitted light photomicrograph (PPL) of strongly-altered sub-rounded lithic fragment in a vesicular flow-foliated lava, sample P0015. Cpx = clinopyroxene; Fsp = feldspar; Mag = magnetite; Opx = orthopyroxene; Pal = palagonite; Pl = plagioclase; Py = pyrite(?); Ser = sericite; (V) = vesicle.

moderate alteration (12–32 vol.% alteration minerals) with rare clay minerals altering the glassy groundmass and lining vesicles.

3.6.2. Geochemistry

Major and trace element analyses were performed on 13 volcanic glasses collected over a wide area around the Tinakula deposit, including from the nearby Starfish volcano (Tables 3.2, 3.3, and Appendix H). Loss on ignition (LOI) values are low, from 0.15% to 2.32%, with only one sample having 4.08%, and major element alteration monitored using the Hashimoto alteration index [AI = 100 × (K_2O + MgO) / (K_2O + MgO + Na_2O + CaO)] of Ishikawa et al. (1976), which indicates the samples are mostly unaltered (AI values of 17.4–28.1). The total alkali-silica (TAS) diagram of Le Bas et al. (1986) reveals two chemically-distinct groups of volcanic rocks: Group I corresponding to basaltic-andesites to andesites and Group II corresponding to dacites (Table 3.4 and Fig. 3.13). The map distribution of these rock types is shown in Figure 3.14. The dacites have MgO contents of 1.03–1.76 wt.% (avg. 1.30 wt.%; n = 9); andesites contain 2.12–2.98 wt.% MgO (avg. 2.48 wt.%; n = 3), and basaltic-andesites 2.84–4.93 wt.% MgO (avg. 3.77 wt.%; Fig. 3.15). These compositions are similar to those of other samples from the Jean Charcot Troughs (Maillet et al., 1995), but are distinct from samples recovered in the Coriolis Troughs (Fig. 3.13; McConachy et al., 2005; Lima et al., 2017). Concentrations of SiO_2, Na_2O, K_2O, and P_2O_5 all increase with decreasing MgO (Fig. 3.15), whereas TiO_2, Al_2O_3, FeO_T, and CaO decrease, within the range of other samples from the JCT. However, samples from the Starfish-Tinakula area have generally higher SiO_2 and Na_2O, and lower FeO_T and CaO contents than volcanic rocks from the Coriolis Troughs (CT), New Hebrides Arc (NHA), and North Fiji Basin (NFB) (Fig. 3.15). Group I basaltic-andesites and andesites from this study show some overlap with the NHA; Group II dacites show no overlap with volcanic rocks from other settings.

Concentrations of incompatible trace elements are shown in Figures 3.16 and 3.17, reflecting separate trends for Group I basalts to basaltic-andesites and Group II dacites, indicating that the two are not related by simple fractionation processes. The trace element concentrations (normalized to N-MORB) are slightly higher than published values from the JCT but within the range of samples from the CT (Fig. 3.17). Dacites are distinguished from basaltic-andesites by

Table 3.2. Whole-rock geochemistry of ROV grab samples of volcanic glass from the Starfish-Tinakula area (this study), normalized to 100% volatile-free, with rock classifications using the TAS diagram of Le Bas et al. (1986; Fig. 3.13)

		GMA13-001	GMA13-015	GMA13-023	GMA13-035	GMA13-039	GMA13-043	GMA13-044	GMA13-057	GMA13-063	GMA13-065	P0015	P0016	P0040
		D	A	B-A	A	A	D	D	B-A	D	D	B-A	B-A	B-A
	Method	Starfish	Tinakula	N Tinakula	Tinakula	Tinakula	Tinakula	W Tinakula	W Tinakula	Tinakula	N Tinakula	Starfish	Tinakula	Tinakula
SiO_2 - %	FUS-ICP	67.53	57.43	55.96	57.15	58.26	63.49	66.37	54.56	67.15	66.92	53.53	53.22	55.40
TiO_2	FUS-ICP	0.87	1.40	1.60	1.23	1.20	1.09	0.96	1.29	0.78	0.87	1.32	1.28	1.31
Al_2O_3	FUS-ICP	15.19	16.96	16.50	16.65	17.08	16.25	15.37	17.38	15.71	15.52	16.15	17.07	17.37
$Fe_2O_{3(T)}$	FUS-ICP	4.78	8.92	9.74	9.43	8.40	6.20	5.16	9.39	4.64	4.76	11.21	11.06	9.50
MnO	FUS-ICP	0.164	0.165	0.206	0.189	0.169	0.184	0.176	0.212	0.166	0.165	0.188	0.188	0.168
MgO	FUS-ICP	1.11	2.33	3.19	2.98	2.12	1.76	1.27	3.99	1.03	1.14	3.99	3.90	2.84
CaO	FUS-ICP	3.12	7.47	7.09	7.09	7.34	4.37	3.50	8.29	2.89	3.08	8.80	8.57	8.63
Na_2O	FUS-ICP	6.08	4.53	4.57	4.36	4.53	5.71	6.07	4.20	6.47	6.33	4.10	4.02	4.05
K_2O	FUS-ICP	0.97	0.62	0.80	0.69	0.67	0.73	0.85	0.55	1.02	0.98	0.52	0.52	0.60
P_2O_5	FUS-ICP	0.20	0.20	0.33	0.19	0.20	0.23	0.26	0.14	0.17	0.21	0.15	0.14	0.15
$FeO_{(T)}$		4.30	8.02	8.77	8.49	7.55	5.58	4.65	8.45	4.17	4.29	10.09	9.95	8.55
Mg#		20.4	22.5	26.7	26.0	21.9	24.0	21.4	32.1	19.8	21.0	28.3	28.1	24.9
AI		18.4	19.7	25.5	24.2	19.1	19.8	18.1	26.6	17.9	18.3	25.9	26.0	21.3
S - ppm	TD-ICP	60	200	140	170	120	50	80	120	20	40	250	310	220
Cu	TD-ICP	7	57	9	47	76	3	3	86	3	6	109	95	39
Zn	TD-ICP	87	83	85	87	79	85	86	79	86	82	77	86	128
Cd	TD-ICP	<0.5	<0.5	<0.5	<0.5	<0.5	<0.5	<0.5	<0.5	<0.5	<0.5	<0.5	<0.5	<0.5
Ga	FUS-MS	17	18	18	17	17	17	18	17	18	17	17	17	17
Ge	FUS-MS	1.6	1.2	1.0	1.3	1.0	1.3	1.3	1.2	1.2	1.3	1.1	1.1	1.5
Ag	TD-ICP	0.3	<0.3	<0.3	<0.3	<0.3	<0.3	<0.3	<0.3	<0.3	<0.3	<0.3	<0.3	<0.3
As	INAA	3.5	<0.5	<0.5	<0.5	<0.5	<0.5	4.1	2.4	2.3	<0.5	<0.5	2.6	<0.5
Sb	FUS-MS	0.6	0.6	0.4	0.5	0.7	0.6	0.5	0.6	0.6	0.5	0.5	0.5	0.5
Bi	FUS-MS	<0.1	<0.1	<0.1	<0.1	<0.1	<0.1	<0.1	<0.1	<0.1	<0.1	<0.1	<0.1	<0.1
In	FUS-MS	0.1	0.1	0.1	<0.1	<0.1	0.1	0.1	0.1	0.1	0.1	<0.1	0.1	0.1
Se	INAA	<3	<3	<3	<3	<3	<3	<3	<3	<3	<3	<3	<3	<3
Sn	FUS-MS	8	7	7	7	7	8	7	7	8	7	7	7	7
Tl	FUS-MS	0.09	0.06	<0.05	0.06	<0.05	0.06	0.06	0.08	0.07	0.08	<0.05	<0.05	0.09
Hg - ppb	1G	<5	5	<5	7	14	<5	<5	11	<5	<5	7	6	10

D = dacite; A = andesite; B-A = basaltic andesite

Mg# = 100 x [MgO / (MgO + FeO)]

AI = 100 x [(MgO + K_2O) / (Na_2O + K_2O + CaO + MgO)]

Table 3.2. Continued

		GMA13-001	GMA13-015	GMA13-023	GMA13-035	GMA13-039	GMA13-043	GMA13-044	GMA13-057	GMA13-063	GMA13-065	P0015	P0016	P0040
		D	A	B-A	A	A	D	D	B-A	D	D	B-A	B-A	B-A
	Method	Starfish	Tinakula	N Tinakula	Tinakula	Tinakula	Tinakula	W Tinakula	W Tinakula	Tinakula	N Tinakula	Starfish	Tinakula	Tinakula
Au - ppb	INAA	<2	9	<2	<2	<2	<2	<2	<2	<2	<2	<2	<2	<2
Ir - ppm	INAA	<5	<5	<5	<5	<5	<5	<5	<5	<5	<5	<5	<5	<5
Mo	FUS-MS	<2	<2	<2	<2	<2	<2	<2	<2	<2	<2	<2	<2	<2
Co	FUS-MS	3	15	15	18	14	5	3	26	3	3	25	26	18
Cr	INAA	<5	<5	<5	<5	<5	<5	<5	<5	<5	<5	<5	<5	15
Ni	TD-ICP	2	3	3	3	5	1	1	10	<1	2	10	9	5
Sc	INAA	10.6	23.5	19.4	21.4	20.1	13.9	11.9	26.6	9.4	10.6	24.2	23.9	24.0
V	FUS-ICP	36	299	202	232	229	66	43	354	30	37	356	353	347
Rb	FUS-MS	14	8	8	9	8	10	12	6	15	14	6	6	7
Cs	FUS-MS	0.3	0.2	0.2	0.2	<0.1	0.2	0.3	0.2	0.3	0.3	0.2	0.1	0.2
Sr	FUS-ICP	166	269	263	266	258	210	179	278	159	172	286	278	278
Ba	FUS-ICP	218	136	100	126	130	166	192	105	222	219	106	107	112
Pb	TD-ICP	6	<3	<3	3	<3	<3	<3	<3	<3	<3	<3	<3	<3
Zr	FUS-ICP	219	113	112	103	100	171	206	90	239	225	85	87	89
Hf	FUS-MS	4.9	2.4	2.6	2.6	2.6	3.7	4.4	2.0	5.4	4.9	2.0	2.0	2.0
Nb	FUS-MS	7.1	4.2	4.2	3.6	4.0	5.8	6.8	2.9	7.8	7.3	2.8	2.9	2.8
Ta	FUS-MS	0.43	0.25	0.25	0.23	0.20	0.32	0.43	0.19	0.48	0.47	0.18	0.17	0.18
Th	FUS-MS	1.61	0.84	0.69	0.78	0.90	1.24	1.43	0.63	1.71	1.65	0.62	0.66	0.75
U	FUS-MS	0.63	0.39	0.28	0.37	0.40	0.48	0.57	0.28	0.65	0.65	0.28	0.32	0.55
Be	FUS-ICP	1	1	1	<1	<1	1	1	<1	2	1	<1	<1	<1
Br	INAA	9.2	6.4	<0.5	7.6	<0.5	<0.5	4.7	<0.5	6.6	4.1	6.3	<0.5	4.2
W	FUS-MS	0.9	<0.5	<0.5	<0.5	<0.5	<0.5	1.6	<0.5	<0.5	1.9	<0.5	1.2	<0.5
Y	FUS-MS	56.3	34.3	39.0	32.8	36.0	50.7	57.2	28.1	59.1	55.9	28.2	29.2	30.4
La	FUS-MS	15.60	8.92	8.59	8.02	8.60	13.60	14.20	6.80	16.60	15.00	6.64	6.61	7.25
Ce	FUS-MS	34.9	20.8	21.6	18.9	20.3	30.1	33.5	15.6	37.4	34.8	15.3	15.9	16.8
Pr	FUS-MS	5.06	2.99	3.30	2.80	2.93	4.34	4.95	2.31	5.46	5.07	2.34	2.39	2.57
Nd	FUS-MS	22.7	13.6	15.6	13.3	13.3	18.8	22.7	10.7	23.5	23.4	10.8	11.0	11.3
Sm	FUS-MS	6.34	4.23	4.57	3.98	4.20	5.55	6.30	3.19	6.61	6.65	3.29	3.19	3.59
Eu	FUS-MS	1.86	1.48	1.75	1.43	1.52	1.87	1.88	1.24	1.95	1.86	1.22	1.21	1.35
Gd	FUS-MS	7.30	5.11	5.87	4.49	5.00	6.72	7.56	4.07	7.87	7.62	4.14	3.99	4.39
Tb	FUS-MS	1.36	0.90	1.03	0.81	0.90	1.23	1.36	0.70	1.45	1.34	0.72	0.75	0.74
Dy	FUS-MS	8.70	5.74	6.70	5.19	5.80	7.88	9.08	4.76	8.99	8.83	4.79	4.69	4.95
Ho	FUS-MS	1.85	1.16	1.38	1.11	1.10	1.64	1.87	0.99	1.92	1.87	0.96	1.00	1.02
Er	FUS-MS	5.31	3.31	3.75	3.22	3.50	4.93	5.63	2.78	5.76	5.58	2.80	2.77	3.00
Tm	FUS-MS	0.796	0.506	0.515	0.474	0.520	0.749	0.863	0.406	0.908	0.857	0.40	0.430	0.444
Yb	FUS-MS	5.45	3.35	3.52	3.25	3.50	5.00	5.61	2.72	5.80	5.95	2.69	2.86	2.97
Lu	FUS-MS	0.879	0.525	0.582	0.535	0.560	0.795	0.902	0.430	0.955	0.956	0.413	0.473	0.458
LOI	FUS-ICP	0.46	1.09	1.77	1.48	2.320	0.720	0.950	0.840	-1.17	0.45	0.4	0.15	1.14

D = dacite; A = andesite; B-A = basaltic andesite

Table 3.3. Whole-rock geochemistry of ROV grab samples of volcanic rocks from the Starfish-Tinakula area (data from Neptune Minerals Inc.), normalized to 100% volatile-free

		650A	660	813	TGS10-79B	93	601	624	763
		B-A	B-A	B-A	B-A	D	D	D	D
	Method	Tinakula	Tinakula	Tinakula	Tinakula	Starfish	Tinakula	Tinakula	Tinakula
SiO_2 - %	XRF	53.90	52.70	51.90	55.10	66.35	64.80	66.38	66.18
TiO_2	XRF	1.22	1.51	1.23	1.23	0.83	0.91	0.92	0.95
Al_2O_3	XRF	17.00	16.60	17.20	17.00	16.00	15.95	15.68	15.69
$Fe_2O_{3(T)}$	XRF	2.30	3.51	2.34	3.19	1.54	1.68	1.30	1.38
FeO	Titrations	8.06	7.61	8.01	6.58	2.88	3.50	3.46	3.48
MnO	XRF	0.20	0.67	0.19	0.18	0.17	0.18	0.18	0.18
MgO	XRF	3.97	3.93	4.93	3.23	1.29	1.59	1.26	1.29
CaO	XRF	8.44	8.28	10.00	8.06	3.40	3.89	3.49	3.56
Na_2O	XRF	4.32	4.72	3.62	4.57	6.47	6.40	6.27	6.21
K_2O	XRF	0.44	0.36	0.40	0.63	0.85	0.87	0.80	0.80
P_2O_5	XRF	0.16	0.16	0.14	0.16	0.22	0.22	0.27	0.28
Mg#		33.0	34.1	38.1	32.9	30.9	31.2	26.7	27.0
AI		25.7	24.8	28.1	23.4	17.8	19.3	17.4	17.6
S - ppm	ICPAES	152	405	202	202	50	255	101	50
Cu	ICPAES	81.0	28.0	121.0	83.0	8.1	14.3	14.1	10.1
Zn	ICPAES	93	95	93	99	95	98	95	99
Cd	ICPMS	<0.5	<0.5	<0.5	<0.5	<0.5	<0.5	<0.5	<0.5
Ga	ICPMS	19.4	20.3	19.4	19.2	19.2	18.6	19.2	19.8
Ag	ICPMS	0.51	0.51	<0.5	<0.5	<0.5	<0.5	<0.5	<0.5
As	ICPMS	2	1	1	1	1	2	1	2
Bi	ICPMS	<0.1	<0.1	<0.1	<0.1	<0.1	<0.1	<0.1	<0.1
In	ICPMS	0.06	0.06	0.06	0.06	0.08	0.08	0.08	0.10
Se	ICPMS	<5	<5	<5	<5	<5	<5	<5	<5
Sn	ICPMS	<1	<1	<1	<1	2	1	2	1
Au - ppb	ICPMS	2	2	2	2	<2	3	2	<2
Mo - ppm	ICPMS	0.91	12.30	0.61	0.81	1.70	1.60	1.60	1.60
Cr	ICPAES	<10	<10	30.4	<10	70.6	30.6	10.1	<10
Ni	ICPAES	14.1	10.1	20.2	10.1	6.0	10.2	8.1	6.1
Sc	ICPAES	28.3	28.4	34.4	26.3	12.1	12.2	12.1	16.1
V	ICPAES	343	345	374	323	40	61	30	30
Li	ICPMS	7.1	12.7	6.1	5.6	15.1	10.2	14.7	16.1
Rb	ICPMS	6.5	4.9	6.9	10.1	15.3	12.9	12.9	13.7
Sr	ICPMS	262	270	307	263	177	186	174	184
Ba	ICPMS	101	94	116	107	196	188	188	188
Pb	ICPMS	2.00	2.00	2.00	2.00	3.02	4.08	4.04	3.03
Zr	ICPMS	111	107	82	122	261	240	251	244
Hf	ICPMS	2.42	2.43	1.82	2.60	5.44	5.31	5.46	5.45
Nb	ICPMS	3.5	3.0	2.5	4.0	8.6	7.7	8.1	8.1
Ta	ICPMS	0.20	0.20	0.10	0.20	0.40	0.41	0.40	0.40
Th	ICPMS	0.81	0.71	0.71	1.11	1.81	1.63	1.62	1.72
U	ICPMS	0.30	0.30	0.20	0.40	0.60	0.61	0.61	0.61
Be	ICPMS	0.51	0.41	0.40	0.61	1.21	1.02	1.21	1.01
Y	ICPMS	28.3	29.3	23.9	30.5	52.1	48.0	54.6	55.3
La	ICPMS	6.57	5.98	5.36	7.38	13.81	12.86	14.35	14.22
Ce	ICPMS	16.06	16.32	13.26	19.00	34.89	31.64	34.55	33.90
Pr	ICPMS	2.40	2.45	2.00	2.71	5.04	4.70	4.97	5.12
Nd	ICPMS	11.01	11.86	9.51	12.63	22.89	21.33	22.63	23.51
Sm	ICPMS	3.38	3.55	2.83	3.69	6.40	5.97	6.47	6.61
Eu	ICPMS	1.31	1.47	1.21	1.36	2.02	1.89	2.12	2.12
Gd	ICPMS	4.04	4.86	3.64	4.85	7.86	7.35	8.08	8.47
Tb	ICPMS	0.71	0.81	0.61	0.81	1.41	1.28	1.41	1.41
Dy	ICPMS	5.05	5.37	4.20	5.41	9.23	8.42	9.24	9.38
Ho	ICPMS	1.05	1.13	0.89	1.15	2.00	1.84	1.96	2.06
Er	ICPMS	3.13	3.34	2.53	3.49	5.80	5.56	5.96	6.10
Tm	ICPMS	0.46	0.51	0.38	0.53	0.93	0.84	0.89	0.93
Yb	ICPMS	3.03	3.19	2.38	3.39	6.05	5.46	6.01	6.20
Lu	ICPMS	0.46	0.51	0.38	0.53	0.95	0.84	0.95	0.97
LOI	1000°C	0.84	1.51	0.91	1.73	1.22	4.08	1.63	1.52

D = dacite; A = andesite; B-A = basaltic andesite

Mg# = 100 x [MgO / (MgO + FeO)]

AI = 100 x [(MgO + K_2O) / (Na_2O + K_2O + CaO + MgO)]

Table 3.4. Average whole-rock geochemistry of basaltic andesites (Group I), andesites (Group I), and dacites (Group II) from the Starfish-Tinakula area

	Basaltic-Andesite n = 10	Andesite n = 3	Dacite n = 9		Basaltic-Andesite n = 10	Andesite n = 3	Dacite n = 9
SiO_2 - %	54.03	57.61	66.13	Ni - ppm	10	4	4
TiO_2	1.33	1.28	0.91	Sc	26.2	21.7	12.1
Al_2O_3	16.92	16.90	15.71	V	333	253	41
$Fe_2O_{3(T)}$	6.92	8.91	3.49	Li	7.9	N/A	14.0
FeO	8.45	8.02	4.03	Rb	7	8	13
MnO	0.24	0.17	0.17	Cs	0.2	0.2	0.3
MgO	3.77	2.48	1.30	Sr	276	264	179
CaO	8.46	7.30	3.48	Ba	105	131	197
Na_2O	4.24	4.48	6.22	Pb	2	2	3
K_2O	0.53	0.66	0.87	Zr	98	105	228
P_2O_5	0.17	0.20	0.23	Hf	2.2	2.5	5.0
				Nb	3.2	3.9	7.5
Mg#	30.9	23.5	24.7	Ta	0.19	0.23	0.42
				Th	0.74	0.84	1.60
S - ppm	222	163	78	U	0.32	0.39	0.60
Cu	72.3	60	8	Be	<1	<1	1
Zn	93	83	90	Br	2.3	4.8	5.0
Cd	<0.5	<0.5	<0.5	W	<0.5	<0.5	1.0
Ga	18.3	17.3	18.2	Y	29.7	34.4	54.4
Ge	1.2	1.2	1.3	La	6.80	8.51	14.47
Ag	<0.3	<0.3	<0.3	Ce	16.6	20.0	34.0
As	1.2	<0.5	1.8	Pr	2.50	2.91	4.97
Sb	0.5	0.6	0.6	Nd	11.60	13.40	22.38
Bi	<0.1	<0.1	<0.1	Sm	3.48	4.14	6.32
In	0.1	<0.1	0.1	Eu	1.35	1.48	1.95
Se	<3	<3	<3	Gd	4.43	4.87	7.65
Sn	4	7	5	Tb	0.76	0.87	1.36
Tl	<0.05	0.05	0.07	Dy	5.10	5.58	8.86
Hg - ppb	7	9	<5	Ho	1.06	1.12	1.89
Au	<2	4	<2	Er	3.07	3.34	5.63
Ir - ppm	<5	<5	<5	Tm	0.45	0.50	0.86
Mo	2	<2	<2	Yb	2.97	3.37	5.73
Co	22	16	3	Lu	0.47	0.54	0.91
Cr	8	<5	14				

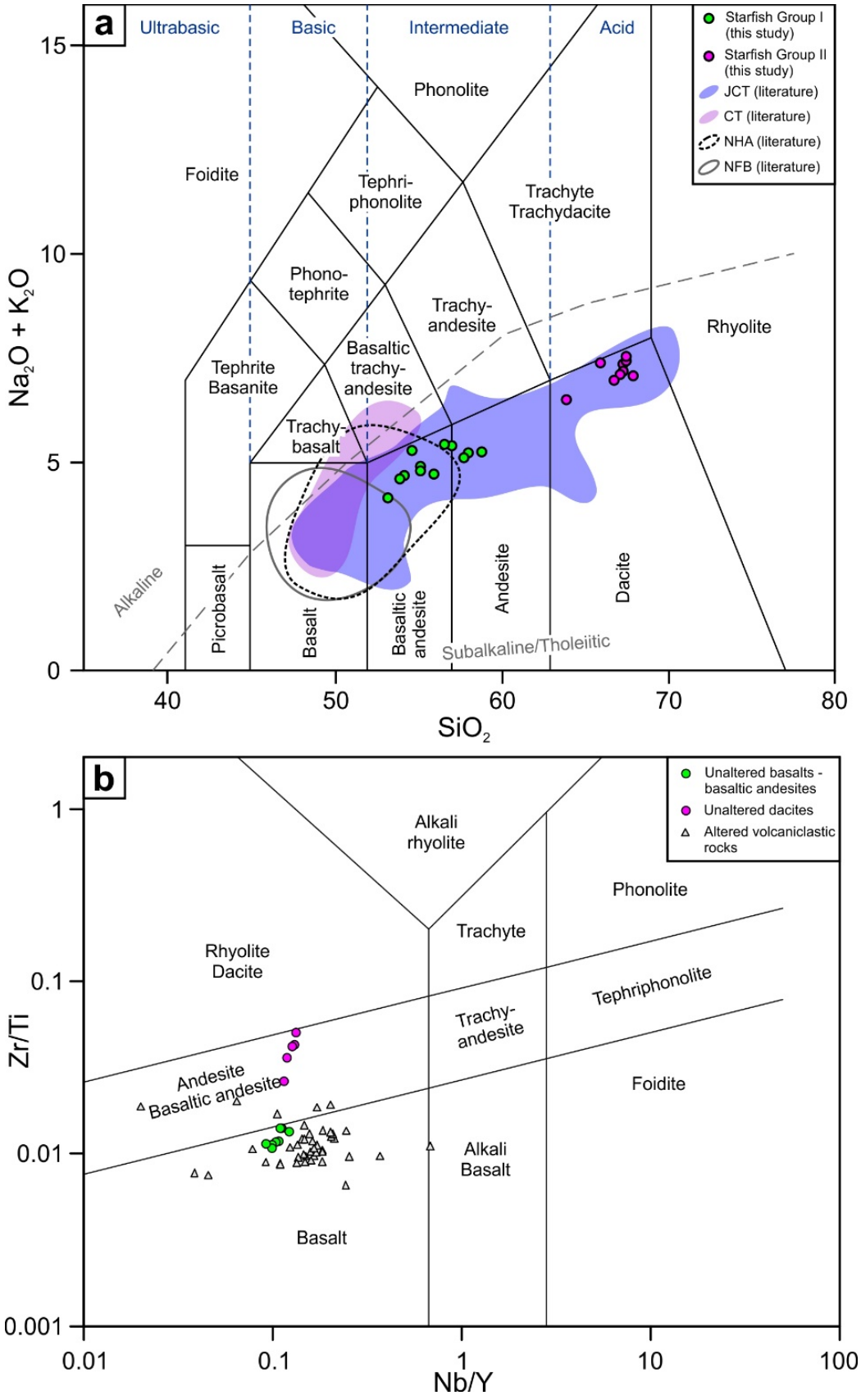

a
Ultrabasic
Basic
Intermediate
Acid
Starfish Group I (this study)
Starfish Group II (this study)
JCT (literature)
CT (literature)
NHA (literature)
NFB (literature)
Phonolite
Foidite
Tephri-phonolite
Trachyte Trachydacite
Phono-tephrite
Trachy-andesite
Rhyolite
Basaltic trachy-andesite
Tephrite Basanite
Trachy-basalt
Alkaline
Picrobasalt
Basalt
Basaltic andesite
Andesite
Dacite
Subalkaline/Tholeiitic
Na2O + K2O
SiO2
15
10
5
0
40
50
60
70
80
b
Unaltered basalts - basaltic andesites
Unaltered dacites
Altered volcaniclastic rocks
Alkali rhyolite
Phonolite
Trachyte
Rhyolite Dacite
Tephriphonolite
Trachy-andesite
Andesite Basaltic andesite
Foidite
Alkali Basalt
Basalt
Zr/Ti
Nb/Y
1
0.1
0.01
0.001
0.01
0.1
1
10
100

Fig. 3.13. Composition of volcanic rocks from the Starfish-Tinakula area: (a) total alkali-silica (TAS) diagram of Le Bas et al. (1986), revealing two compositional groups: basaltic-andesite to andesite (green circles) and dacite (pink circles); (b) Immobile element Nb/Y vs. Zr/Ti classification plot (modified by Pearce, 1996) of whole-rock geochemical data, with samples appearing to have less felsic compositions compared to the TAS diagram. Altered samples (*Chapter* 5) plot near unaltered basalts–basaltic andesites. Literature data compilation: Jean Charcot Troughs (JCT) from Maillet et al. (1995); Coriolis Troughs (CT) from McConachy et al. (2005) and Lima et al. (2017); New Hebrides Arc (NHA) from Peate et al. (1997), Sorbadere et al. (2011; 2013); North Fiji Basin (NFB) from Eissen et al. (1991; 1994) and Nohara et al. (1994).

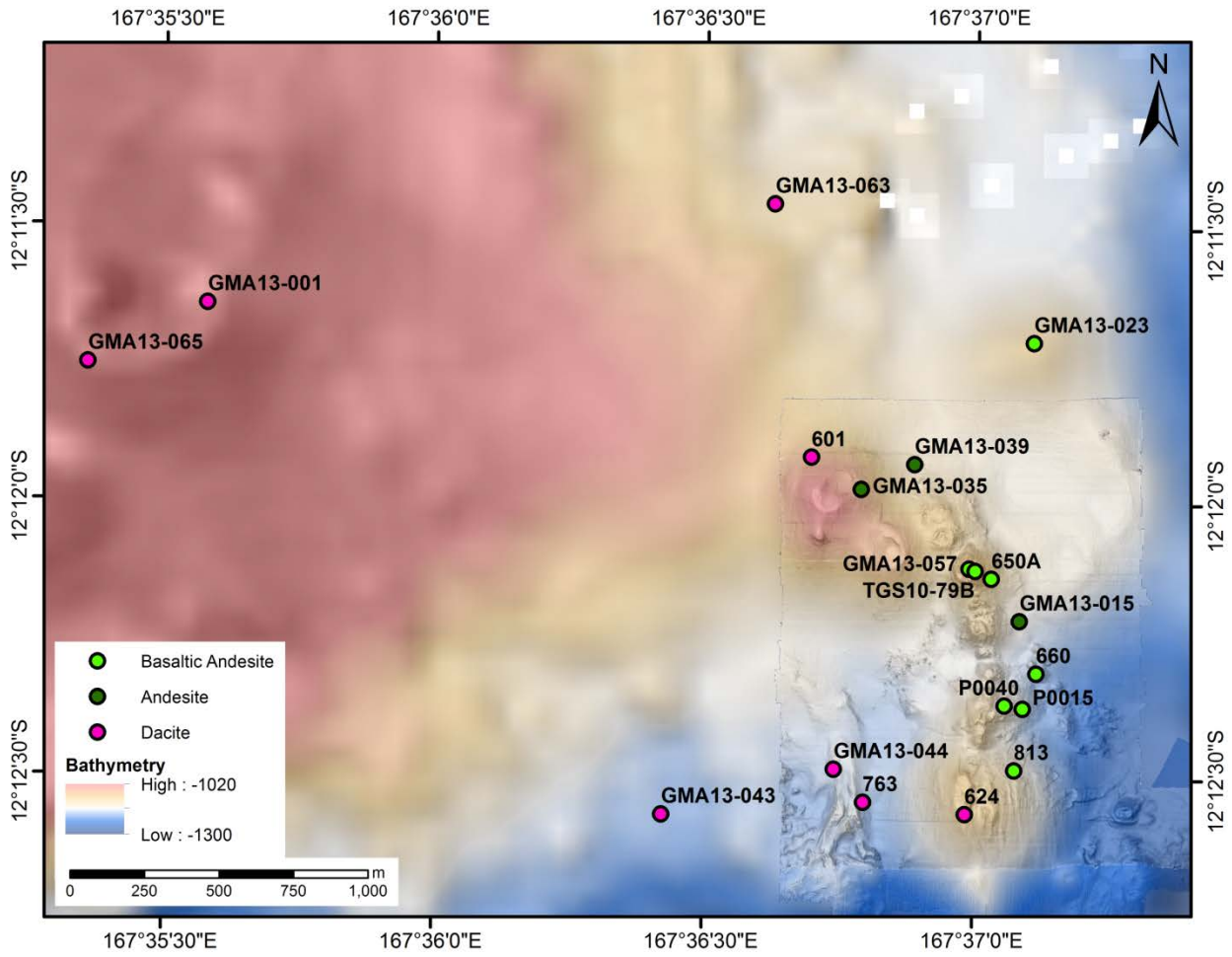


Fig. 3.14. Map of the distribution of volcanic rock types in the Starfish-Tinakula area, including samples analyzed in this study and data provided by Neptune Minerals Inc., overlain on RESON SeaBat 8160 and SeaBat 7125-ROV2 multibeam bathymetry.

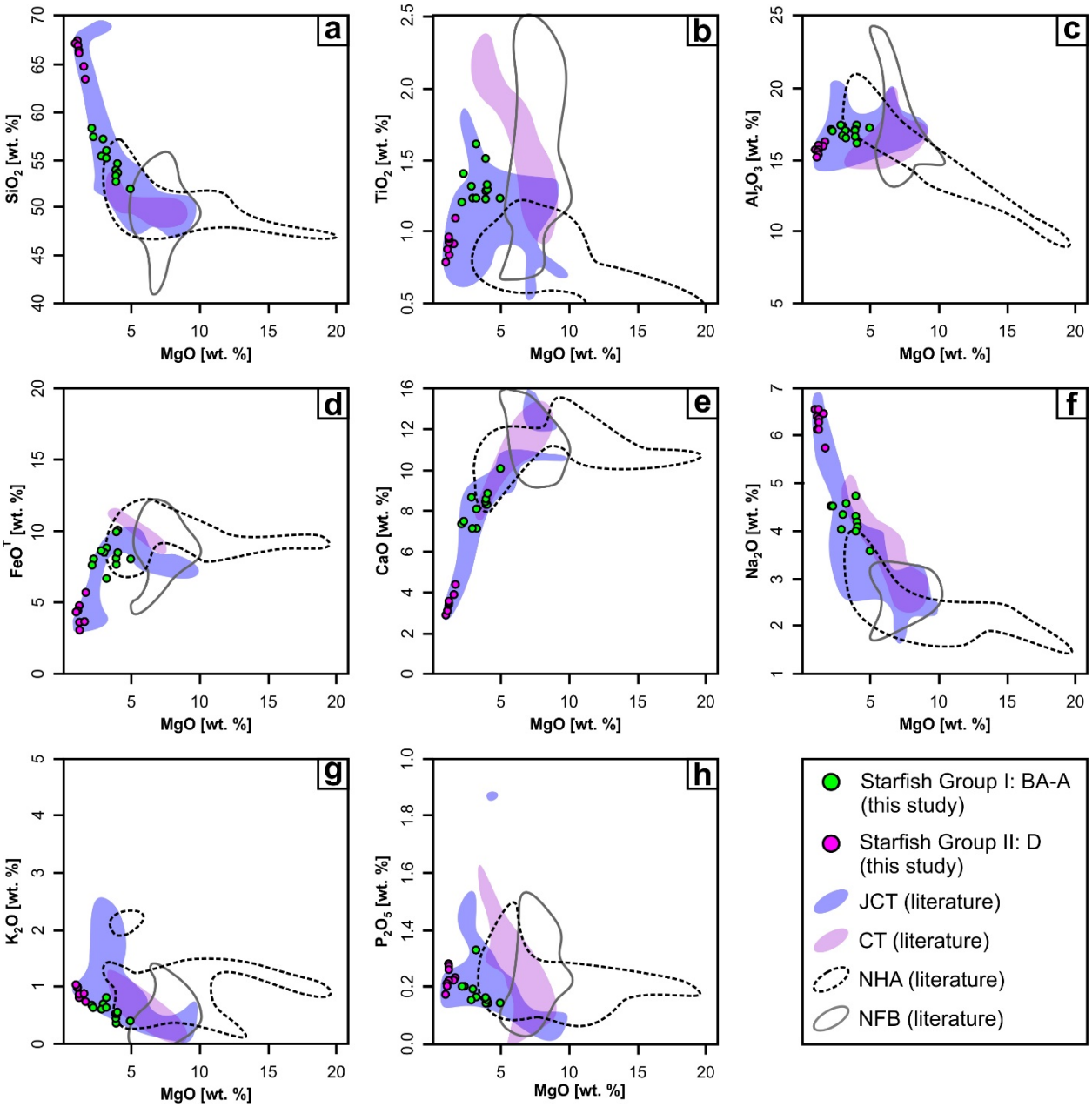


Fig. 3.15. Major element compositions of Group I basaltic-andesites to andesites (BA-A; green circles) and Group II dacites (D; pink circles), compared with other samples from the Jean Charcot Troughs (JCT) Coriolis Troughs (CT) New Hebrides Arc (NHA), and North Fiji Basin (NFB); see Literature data compilation: Jean Charcot Troughs (JCT) from Maillet et al. (1995); Coriolis Troughs (CT) from McConachy et al. (2005) and Lima et al. (2017); New Hebrides Arc (NHA) from Peate et al. (1997), Sorbadere et al. (2011; 2013); North Fiji Basin (NFB) from Eissen et al. (1991; 1994) and Nohara et al. (1994).

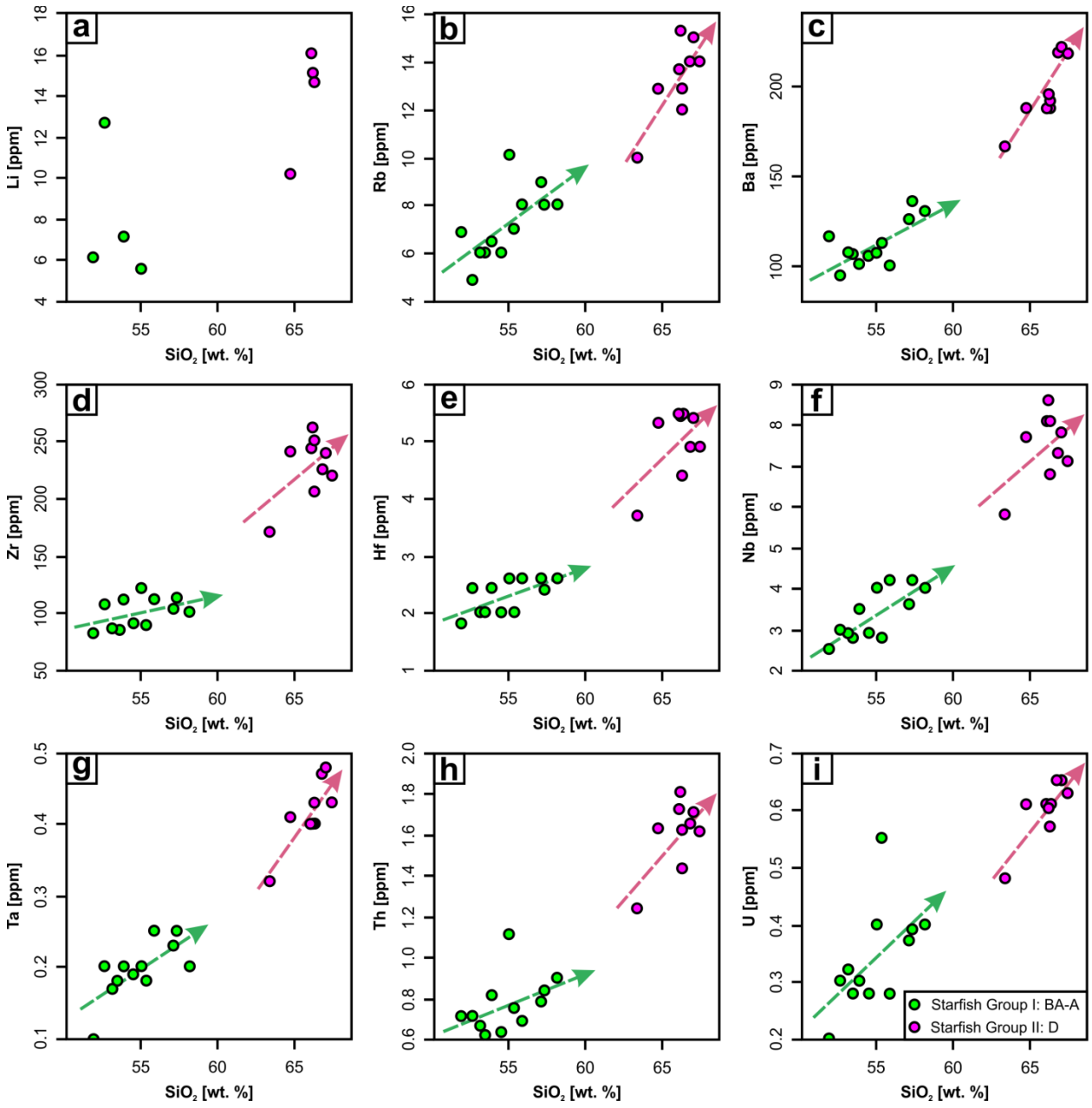


Fig. 3.16. SiO_2 versus incompatible trace elements in Group I basaltic-andesites to andesites (BA-A; green circles) and Group II dacites (D; pink circles) from the Starfish-Tinakula area. Green arrows indicate the fractionation trends of Group I samples, and pink arrows indicate the fractionation trends of Group II samples. Distinct fractionation trends of each suite indicate that they are not related through simple fractionation processes; Group II dacites are interpreted to form through partial melting of a basaltic crustal parent.

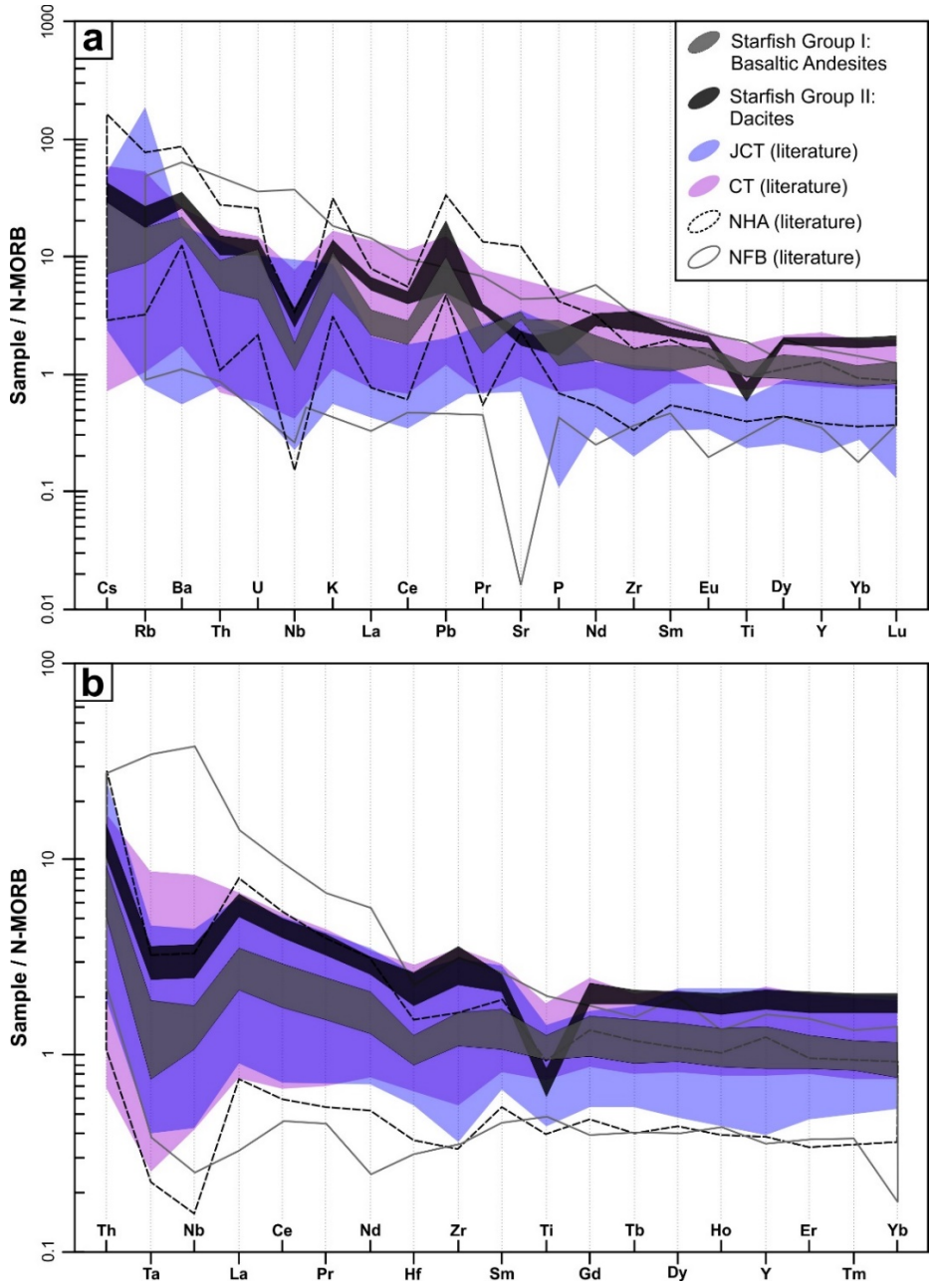


Fig. 3.17. Trace element compositions of Group I basaltic andesites to andesites (grey) and Group II dacites (black) from the Starfish-Tinakula area normalized to N-MORB: (a) after Sun and McDonough, (1989); (b) after Sun and McDonough (1989) in Pearce (2014). Fields for lavas from other samples in the JCT, the CT, the NHA, and the NFB are shown. Group II dacites show higher overall concentrations of trace-elements relative to Group I basaltic-andesites to andesites and published values from the JCT. The volatile element signature (e.g., Ba, Th) reflects a slab signature, while immobile incompatible elements (e.g., Ta, Nb) reflect the melt source. Literature data compilation: Jean Charcot Troughs (JCT) from Maillet et al. (1995); Coriolis Troughs (CT) from McConachy et al. (2005) and Lima et al. (2017); New Hebrides Arc (NHA) from Peate et al. (1997), Sorbadere et al. (2011; 2013); North Fiji Basin (NFB) from Eissen et al. (1991; 1994) and Nohara et al. (1994).

higher trace element concentrations and negative Ti-anomalies. REE concentrations of Group II volcanic rocks (REE_{Total} = 153.90–184.27 ppm) show negative Eu anomalies in chondrite-normalized spider plots with Eu/Eu* = 0.80–0.94, whereas Group I andesites have lower REE (REE_{Total} = 73.08–117.76 ppm) and positive Eu anomalies in most samples with Eu/Eu* = 0.97–1.15 (Fig. 3.18). Both groups have flat profiles with slight enrichment of LREE over HREE.

3.7. Hydrothermal deposits

An overlay of hydrothermal features is also shown on Figure 3.10, including active, inactive, and buried chimneys and mounds, as well as large areas of iron and manganese oxyhydroxide. Individual chimneys and mounds are distinguishable in the SeaBat 7125-ROV2 multibeam bathymetry. They occur primarily along the central row of cinder cones over a strike length of ~1050 m (Fig. 3.10) and are widely distribued at the tops and along the flanks of these cones, as well as inside the summit craters (Fig. 3.19a,b). They also occur in the center of each of the maars in the north, suggesting that some of these craters could have a hydrothermal origin (cf. Monecke et al., 2012). West of the row of cinder cones, the chimneys and mounds are not associated with observable volcanic features at the seafloor (Fig. 3.10; Fig. 3.19c), but instead appear to occur mainly along a NE-SW structure over a strike length of ~400 m, and a smaller NW-SE buried structure.

The hydrothermal features of the Tinakula deposit are mostly inactive (Fig. 3.10), with only a few small chimneys venting grey smoke (Fig. 3.20a). Larger, inactive sulfide chimneys are <1 to 15m high and commonly surrounded by sulfide talus (Fig. 3.20d–g). Intact chimneys show a wide range of morphologies, including: (1) single- and multi-spired chimneys, with rough outer surfaces (Fig. 3.20d); (2) horned to tulip-shaped forms with smooth, bulbous exteriors and no central conduits (Fig. 3.20e); and (3) low-relief, composite or layered chimneys with ‘drooping’ bulbous protrusions (Fig. 3.20f). The intact inactive chimneys with bulbous morphologies do not display significant weathering and were hard to sample owing to a high barite content. Variably-weathered sulfide talus is abundant near the base of many of the chimneys, and locally dominates the mound-shaped substrate (Fig. 3.20g). The volcaniclastic sediment that drapes the volcanic cones also

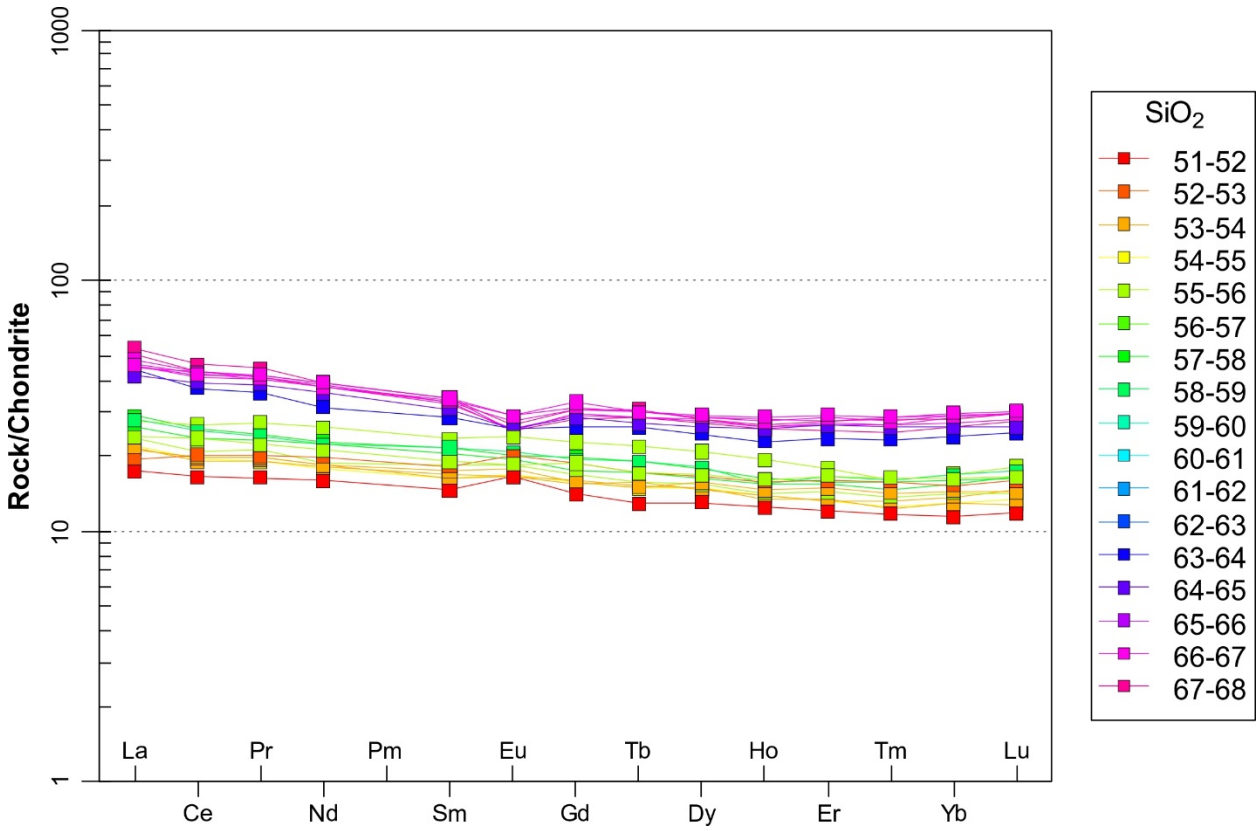


Fig. 3.18. Chondrite-normalized REE plot of volcanic rocks from the Starfish-Tinakula area according to SiO_2 contents (after Boynton, 1984). SiO_2 values > 63 % represent Group I dacites (pink and blue colors), which have higher overall REE contents and negative Eu anomalies (Eu/Eu* = 0.80–0.94). SiO_2 values < 59 % represent Group II andesites (red to green colors), which have positive Eu anomalies in most samples (Eu/Eu* = 0.97–1.15). Both groups have flat profiles with slight enrichment of LREE over HREE.

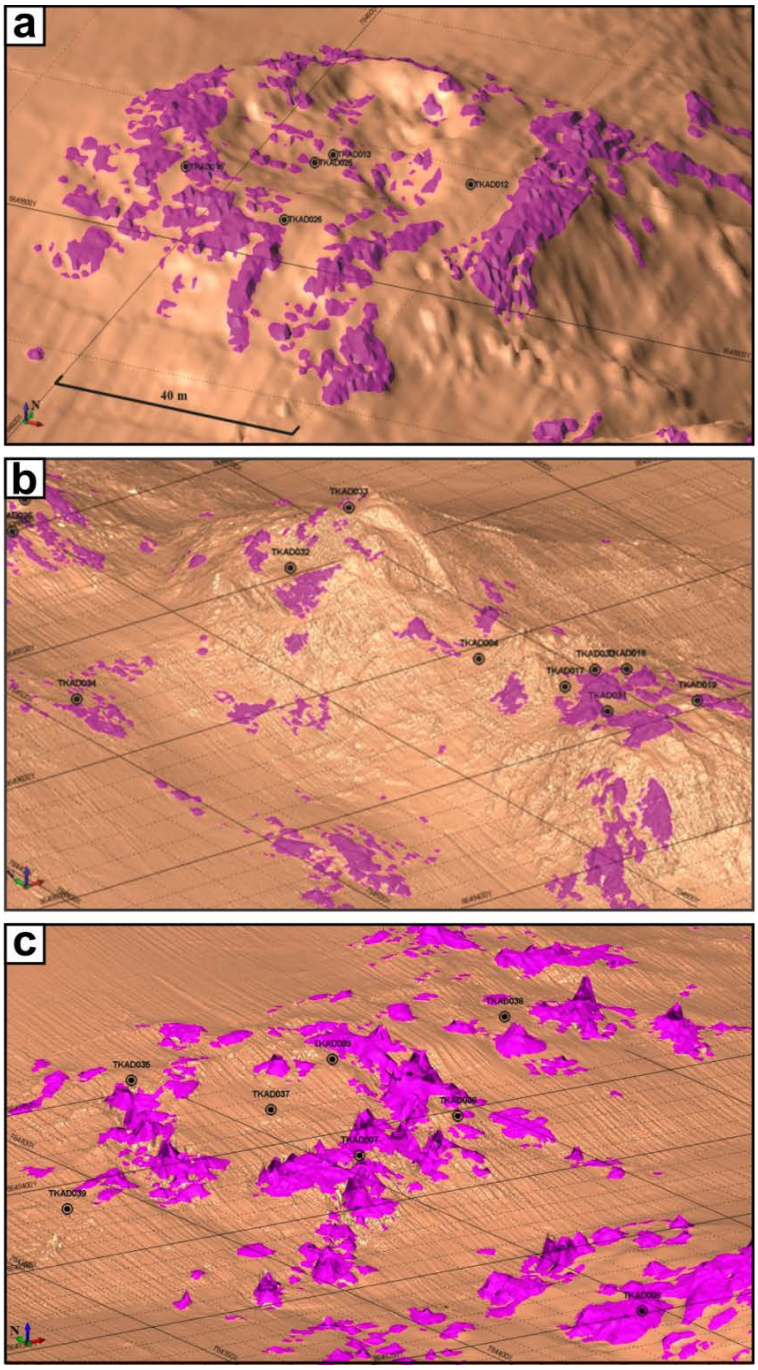


Fig. 3.19. Distribution of chimney complexes and mounds (purple) in selected areas of the Tinakula deposit revealed by RESON SeaBat 7125-ROV2 400 kHz multibeam bathymetry (0.2 m resolution), with locations shown in Fig. 3.10: (a) chimney complexes and mounds primarily distributed around the rim of a cratered cinder cone (facing ENE); (b) chimney complexes and mounds on the flank of a cinder cone on slump features, with additional mounds on the surrounding plain not associated with volcanic features (facing NE); (c) chimney complexes and mounds not associated with volcanic cones (facing NE). Chimney features are identified based on steep-sided morphologies and direct seafloor observations. Black circles indicate drillhole collars. Images courtesy of Neptune Minerals Inc.

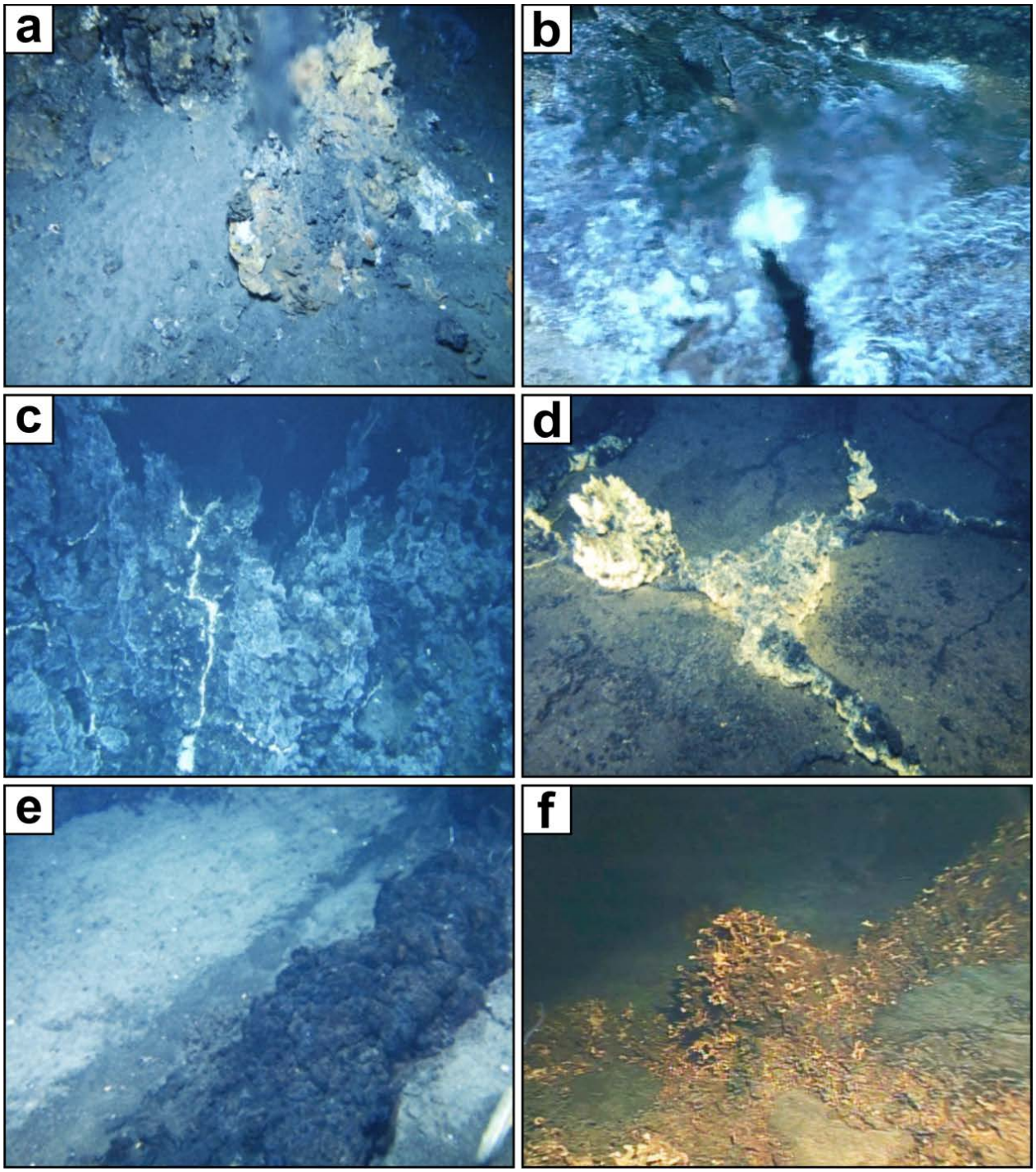


Fig. 3.20. Styles of hydrothermal venting at the Tinakula deposit: (a) small oxidize chimney venting grey smoke; (b) diffuse venting of shimmering water with bacterial matting; (c) diffuse and fracture-controlled venting and bacterial mat in a chimney field; (d) fracture-controlled iron- and manganese oxides forming small branching 'chimneys'; (e) fracture-controlled manganese oxide; (f) fracture-controlled iron oxide chimney with abundant fossil worm tubes. Images courtesy of Neptune Minerals Inc.

partially buries many of the chimneys and mounds (Fig. 3.20h, i). Diffuse low-temperature venting occurs in faulted areas, indicated by shimmering water and bacterial mats localized along fractures in the indurated sediment (Fig. 3.20b,c). Siliceous iron- and manganese-oxide crusts with clear fracture control extend up to 140 m away from the sulfide chimneys. The crusts for irregular, low-relief textures deposits, locally with branching 'chimneys' (Fig. 3.20d,e), some with fossilized worm tubes (Fig. 3.20f). Secondary oxides (gossans) are found locally with the chimneys and mounds.

The surface expression of hydrothermal precipitates consists of 13,812 m^2 of active chimneys and mounds, 50,842 m^2 of inactive chimneys and mounds, and 9,260 m^2 of partially buried chimneys and mounds, for a total area of 76,914 m^2 (Fig. 3.10). In addition, iron oxides occur over an area of 90,974 m^2 and manganese oxides occur over an area of 38,112 m^2, although these areas of low-temperature venting can overlap with each other and with the chimneys and mounds. These values reflect the minimum areal footprint of the deposit due to irregular coverage by ROV limiting direct seafloor observations (Suppl. Fig. B1), and the burial of chimneys and mounds by volcaniclastic sediment. The areal extent of this deposit is significant compared to others discovered along mid-ocean ridges, sedimented ridges, arcs, and back-arc basins, of which less than 10% have dimensions on the order of 5,000+ m^2 (Hannington et al., 2010). Deposits with comparable sizes (by area) include the Solwara 1 deposit in the Eastern Manus Basin (90,000 m^2), and the Mir zone, Ashadze-1 and Ashadze-2 deposits on the Mid-Atlantic Ridge (50,000 m^2 each), which have massive sulfide tonnages ranging from 1–3 Mt (Hannington et al., 2010, 2011). The cumulative amount of hydrothermal precipitates at Tinakula is 1.85 Mt based on comparisons with area estimates in Hannington et al. (2010, 2011).

3.8. Discussion

3.8.1. Geodynamic controls on the style of rifting in the JCT

The back-arc region of the northern Jean Charcot Troughs (JCT) reflects a starkly different morphology compared to the southern Coriolis Troughs (CT). Extension in the JCT is distributed over a wide area characterized by complex grabens, horsts, and volcanic ridges, compared to the

simple narrow and deep graben morphology of the CT (Fig. 3.2). Lineament analysis reveals that E-W oriented extension dominates the back-arc over this area, producing mainly arc-parallel N-S structures (Fig. 3.4). However, well-developed NE-SW, NW-SE, and E-W structures are also present that appear to be linked to opening of the North Fiji Basin (especially the TFZ and HHFZ). Seafloor spreading and associated magnetic lineations in the NFB are both arc-parallel and arc-perpendicular, with rifts propagating in nearly all directions and structures of different orientations opening contemporaneously (Martin, 2013). The similar orientations of structures in the adjacent JCT suggest that they have developed, at least in part, above NFB crust and have inherited the same fracture pattern. This idea is supported by magnetic anomaly patterns that cross from the northwestern NFB into the JCT (Fig. 3.21: Charvis and Pelletier, 1989). Our data confirm that key structures crossing the JCT are colinear with the Tikopia Fracture Zone (a former spreading center in the NFB) forming an orthogonal fracture network and on the inter-trough high that hosts the Tinakula deposit (Fig. 3.4c). Previous authors considered that the TFZ was terminated at the West Tikopia Ridge and offset to the north where it continued as the 9°30' Ridge (e.g., Auzende et al., 1995). This study finds no evidence to support transform motion along the West Tikopia Ridge.

The collision with the d'Entrecasteaux Ridge (DER) at ~3 Ma had a strong impact on the most recent development of the back-arc troughs, both in the JCT and CT (*Chapter 2*). In the northern JCT, the collision with the DER 'pinned' the southern end of the arc segment, halting the previous clockwise rotation. Continued rollback of the Indo-Australian slab induced a rapid counter-clockwise rotation in the north (Calmant et al., 2003), which appears to have had the largest impact on the JCT, producing the better-developed grabens in the north compared to the poorly-defined complex grabens in the south (Fig. 3.2). The northern JCT are opening at a rate of 70–81 mm yr^{-1} compared to 36–55 mm yr^{-1} in the south (Bergeot et al., 2009), reflecting proximity to the pole of rotation at 12.51°S / 167.54°E (red circle in Fig. 3.1b; Bergeot et al., 2009). The broad "V"-shape of the JCT (Fig. 3.1b and Fig. 3.2) may indicate progressive westward jumping of the active rift over time as the arc was rotated. Thus, the opening of the JCT has been primarily controlled by extension of the upper plate along complex pre-existing structures, noted above, and rapid shift in rotation of the arc caused by collision with the DER.

Deep earthquake epicenters along the New Hebrides arc and adjacent back-arc indicate active

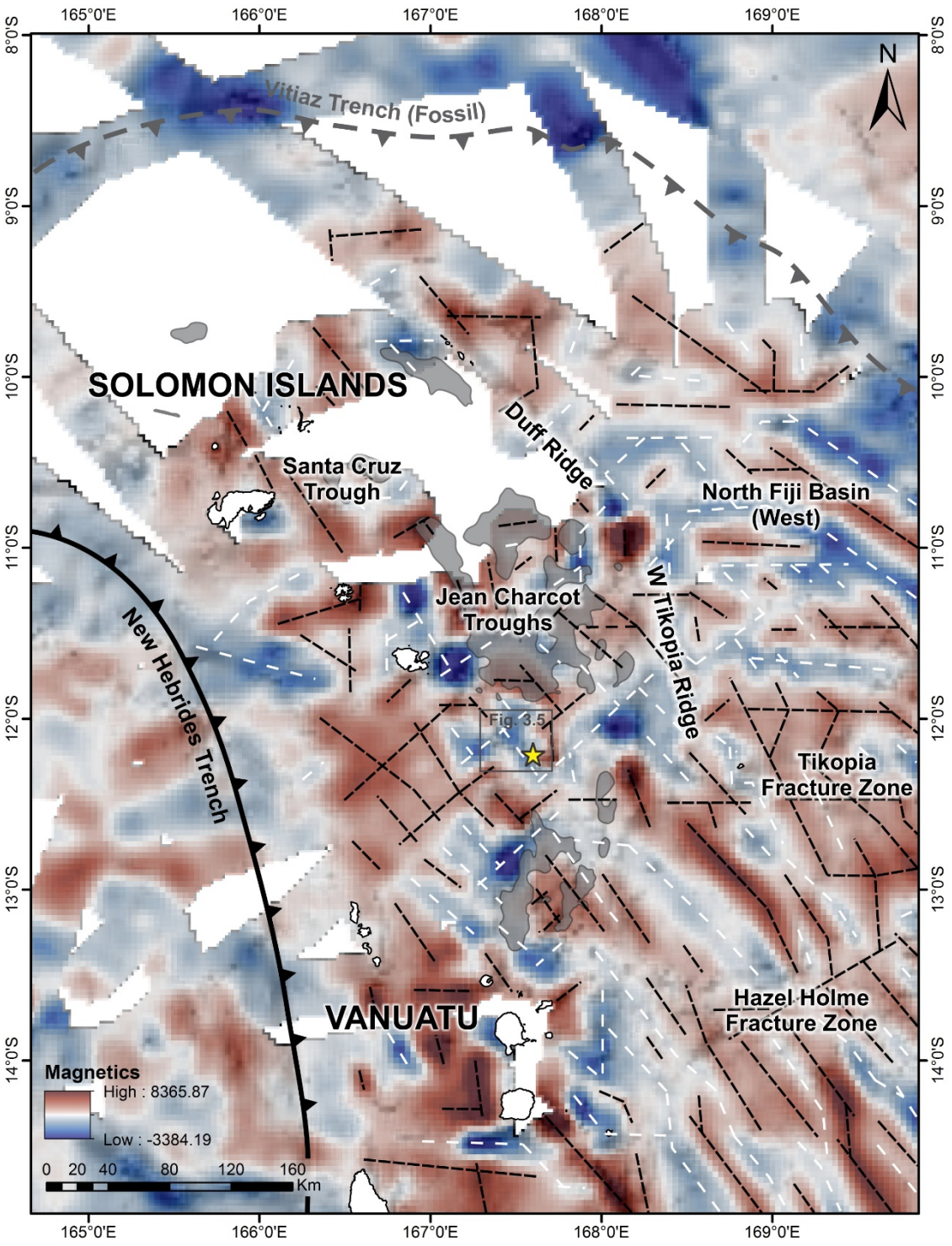


Fig. 3.21. Magnetic anomalies interpreted from the 2-arc min Earth Magnetic Anomaly Grid (50% transparency; Maus et al., 2009) overlain on hill-shaded bathymetry. Dashed black lines indicate positive anomalies, dashed white lines indicate negative anomalies. Tectonic features are named, as shown in Fig. 3.2, back-arc grabens are shaded in grey, and the Tinakula deposit is indicated by the yellow star. Note that magnetic lineations extend from the North Fiji Basin into the back-arc region of the Jean Charcot Troughs.

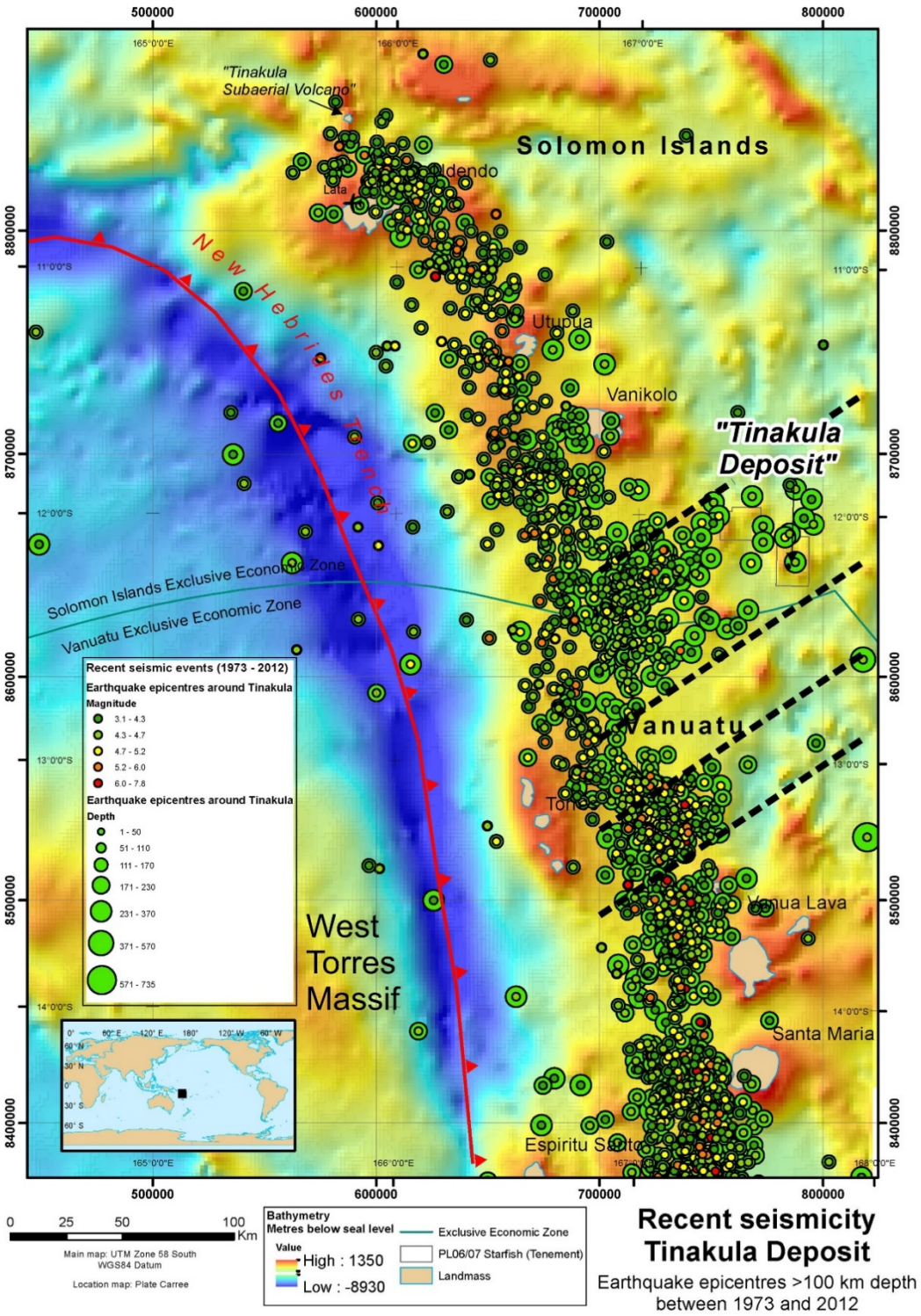


Fig. 3.22. Map of epicenters recent earthquakes along the northern segment of the New Hebrides arc from the USGS Earthquake Catalogue (https://earthquake.usgs.gov/earthquakes/), showing active seismicity along several ENE-trending corridors (dashed black lines), proximal to the Tinakula deposit. These deep structures may be related to the trench collision with the West Torres Masif. Image courtesy of Neptune Minerals Inc.

seismicity along several corridors that cross the back-arc region and extend at least as far east as the Tinakula area (Fig. 3.22). These may be reflecting fractures or other features of the down-going Indo-Australian slab that are manifested in the deforming upper plate, which may be related to slab tearing associated with the subduction zone collision with the West Torres Massive. It is therefore possible that deep subduction-related tectonic fabrics may further influence magmatism and hydrothermal venting in the back-arc by modifying the mantle flow regime.

3.8.2. Magma chemistry

In the area of the Tinakula deposit, magmatism appears to be focused in an area of shallower seafloor where the TFZ crosses the back-arc region (Fig. 3.2). Active arc volcanism in the west of the mapped area is dominated by felsic rocks, whereas volcanoes in the back-arc region are mainly basaltic to andesitic. The most mafic samples recovered from the Starfish-Tinakula area are basaltic-andesites with SiO_2 values of >51 wt.%. The phenocryst assemblage is consistent with fractionation from a basaltic parent (Table 3.1; Fig. 3.12d), and the evolution from basaltic to andesitic compositions can occur rapidly during magma ascent (e.g., Turner et al., 2000). Some andesitic magmas stall at the shallow crustal level, where they may continue to fractionate to dacitic compositions (Pearce and Stern, 2006). However, the dacitic samples from this study show distinct fractionation trends (Fig. 3.16 and Fig. 3.17) that may reflect partial melting of mafic crustal rocks more typical of bimodal volcanism (e.g., Tamura and Tatsumi, 2002). Clearly defined arrays in plots of SiO_2 versus incompatible elements for both of these groups (Fig. 3.16) indicate that these melts underwent extensive fractionation prior to eruption.

The wide range of SiO_2 contents of fresh volcanic rocks in the JCT (53.22–67.15 wt.%), together with high Al_2O_3 (15.19–17.38 wt.%) and low TiO_2 (0.78–1.60 wt.%; Table 3.2 and Fig. 3.15) are consistent with previous sampling (Maillet et al., 1995) and typical of the arc to back-arc transition (e.g., Fryer, 1990). The major elements show that the sampled rocks in this study are distinct from both NHA and NFB rocks, but also notably different from the volcanic rocks of the CT. In particular, the JCT has higher overall SiO_2 and Na_2O contents, and lower MgO, TiO_2, FeO_T, and CaO contents than the CT (e.g., Lima et al., 2017). This reflects the effects of contrasting mantle

source compositions, variable source enrichment through mantle wedge and subducting slab processes, degrees of partial melting, and melt extraction processes in the JCT and the CT.

The New Hebrides subduction system has two distinct mantle domains, including Pacific-type and Indian-type signatures (Crawford et al., 1995; Peate et al., 1997; Heyworth et al., 2011). The Indian-type mantle migrated from the NFB into the central arc segment during the subduction zone collision of the d'Entrecasteaux Ridge (Crawford et al., 1995), displacing Pacific-type mantle. This Indian-type mantle subsequently flowed southward into the back-arc CT following pressure gradients developed during asymmetric rollback of the Australian plate (Heyworth et al., 2011). Variation in distinct mantle sources between the JCT and the CT are shown by the plot of Nb versus Yb (Fig. 3.23). Dacite and andesite samples from Starfish-Tinakula area (JCT) are both enriched in Nb and Yb (Fig. 3.23) and fall along the same linear array indicating a common mantle source, which is interpreted to be Pacific-type based on previous Pb-isotopic studies (e.g., Crawford et al., 1995; Heyworth et al., 2011). Note that trace-element signatures alone are not sufficient to distinguish Indian-type from Pacific-type mantle. In contrast, a mixed depleted- (low-Nb) and enriched- (high-Nb) mantle source has been described for the Nifonea Volcano in the CT (purple triangles in Fig. 3.23; Lima et al., 2017), consistent with influx of mantle material from the NFB. These source characteristics are attributed to small-scale (<20 km) heterogeneities in the refractory mantle (Lima et al., 2017). Enrichment of the mantle beneath the JCT and the CT may reflect metasomatism during earlier subduction events (e.g., along the fossil Vitiaz trench or the initial opening of the NFB: Hofmann and White, 1982; Sobolev et al., 2005; Grove et al., 2006). Mantle enrichment through a process of "preconditioning" is described by Kincaid and Hall (2003), whereby small melt fractions are extracted from the mantle asthenosphere during flow to the site of initial magma generation, associated with extraction of HSF, LIL, and LREE (mantle depletion), followed by fluxing of the depleted mantle with hydrous slab-derived fluids (LIL and LREE). This results in a mantle signature with depleted HSF relative to LIL and LREE. If the pre-conditioned mantle is heterogeneous, this process could account for the differences in trace elements between the JCT and CT (e.g., Pearce and Stern, 2006).

An important subduction component in the JCT basaltic-andesite is indicated by enrichment of mobile elements (Rb, Ba, Sr, K, Th, U, LREE, middle REE) relative to N-MORB in Fig. 3.17,)

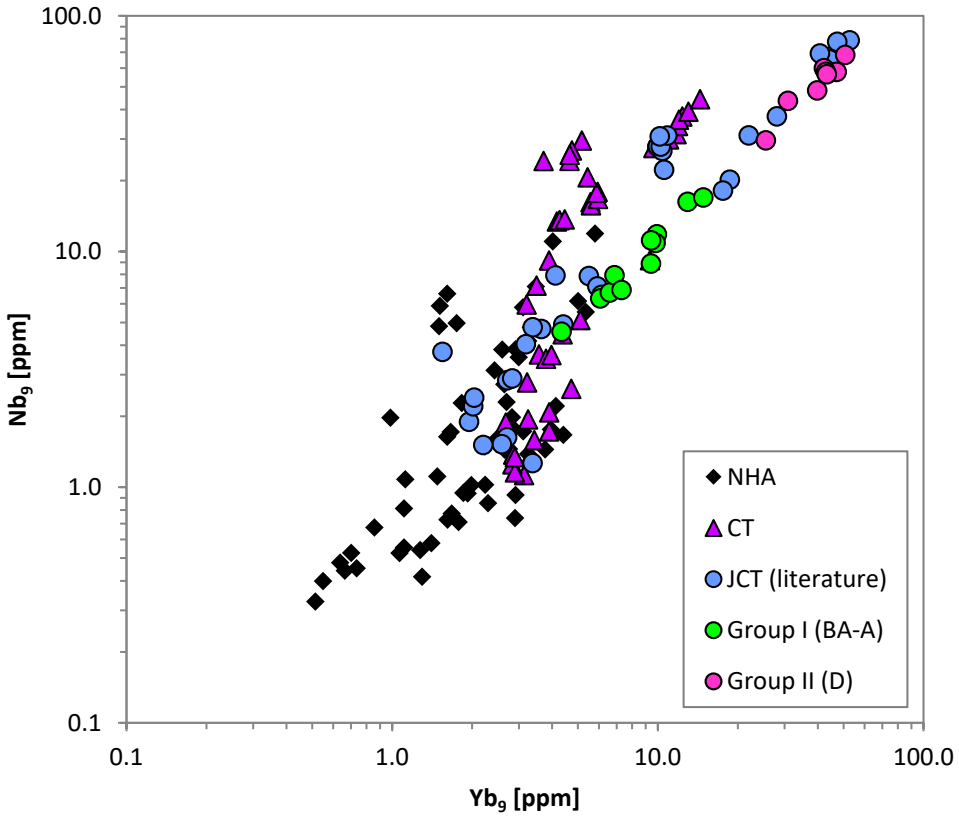


Fig. 3.23. Plot of Yb versus Nb, normalized to MgO = 9 wt.% by applying a simple normalization factor to each element. Samples from the Starfish-Tinakula area (Group I basaltic andesites to andesites and Group II dacites) plot along a linear trend, indicating a common mantle source. CT = Coriolis Troughs; JCT = Jean Charcot Troughs; NHA = New Hebrides Arc. See Fig. 3.13 for literature compilation references.

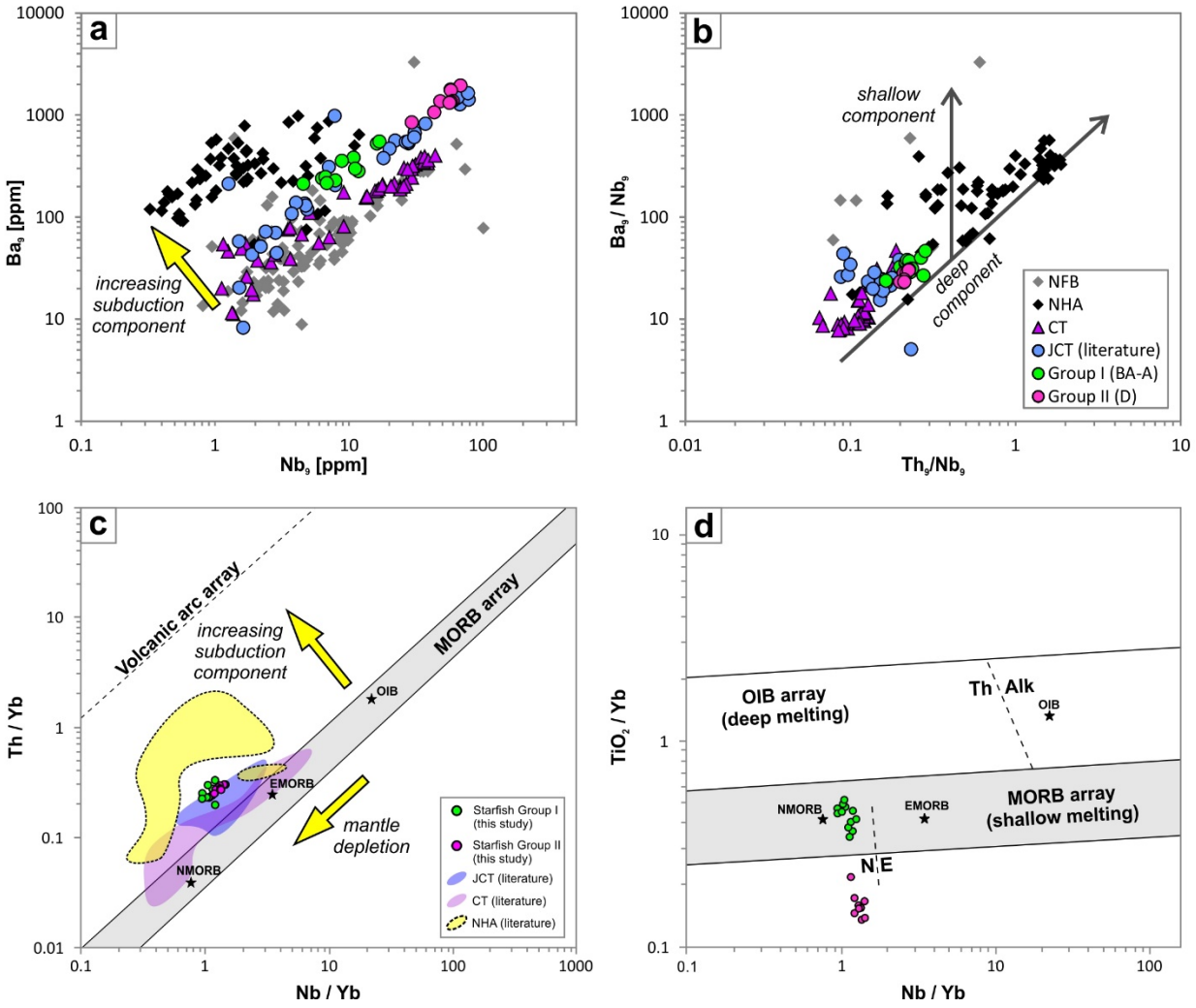


Fig. 3.24. Contributions of subduction components for samples from the New Hebrides subduction zone with trace elements normalized to MgO = 9 wt.%: (a) plot of Nb vs. Ba indicating total subduction component (increasing contributions in the direction of the yellow arrow), with significant contributions in samples from the Starfish-Tinakula area; (b) plot of Th/Nb vs. Ba/Nb showing relative contributions from the deep subduction components (aligned along a diagonal vector), and shallow subduction components (aligned along a vertical vector); (c) plot of Nb/Yb versus Th/Yb after Pearce (2008) to discriminate the subduction component (Th/Yb) from mantle depletion; (d) plot of Nb/Yb versus TiO_2/Yb after Pearce (2008) to discriminate NMORB from EMORB. Samples from this study (Group I andesites and Group II dacites) show slight mantle enrichment relative to NMORB and a significant subduction component typical for BABB. CT = Coriolis Troughs; JCT = Jean Charcot Troughs; NFB = North Fiji Basin; NHA = New Hebrides Arc. Literature data compilation: Jean Charcot Troughs (JCT) from Maillet et al. (1995); Coriolis Troughs (CT) from McConachy et al. (2005) and Lima et al. (2017); New Hebrides Arc (NHA) from Peate et al. (1997), Sorbadere et al. (2011; 2013); North Fiji Basin (NFB) from Eissen et al. (1991; 1994) and Nohara et al. (1994).

and relative to chrondrite in Fig. 3.18. Ratios of subduction-mobile to subduction-immobile elements reflect the total subduction input (e.g., Ba/Nb) and can distinguish deep subduction input (sediment melting: e.g., Nb/Th) versus shallow input (aqueous fluid: e.g., Ba/Th (Pearce and Stern, 2006). This is shown for the Starfish-Tinakula samples in Figure 3.24. Relative to the North Fiji Basin basalt, the trace elements reveal a significant subduction component in the Starfish-Tinakula samples (Ba/Nb > 22), but less input than in the New Hebrides Arc (Fig. 3.24a). In general, the back-arc lavas are dominated by a deep subduction component compared to the arc front (Fig. 3.24b) and a slight enrichment in the mantle compared to N-MORB (Fig. 3.24c,d). The samples from the Starfish-Tinakula area have higher overall subduction contributions than in the CT, which may reflect greater arc crust contributions to the back-arc magmas during diffuse extension.

Trace metal concentrations in least-altered whole-rock glasses in the Starfish-Tinakula area are similar to those of N-MORB glasses, suggesting that there has been no systematic metal enrichment of the back-arc lavas. Cu and Zn concentrations in basaltic-andesite and andesite are 69 ppm and 93 ppm, respectively (n = 13; Fig. 3.25). Dacitic lavas are generally depleted in Cu (8 ppm; n = 9) but still contain appreciable Zn (90 ppm; n = 9). This reflects sulfur saturation of the melt and the presence of Cu-rich immiscible sulfides mainly in the basaltic end-members. Petrographic studies reveal two types of primary sulfides in the volcanic rocks: (1) fine-grained globular monosulfides, representing an early immiscible phase; and (2) very fine-grained late vesicle-lining sulfides, including chalcopyrite, pyrite, and rare galena (Table 3.1). Many of the sulfide globules are associated with magnetite (Appendix D), which is a common feature found in back-arc magmas affected by a subduction component (e.g., Valu Fa ridge; Keith et al., 2017). The crystallization of Fe-Ti oxides has been shown to trigger the saturation of S in back-arc silicate melts, as fO_2 is an important control on S-saturation due to the conversion of sulfates into less-soluble sulfides (e.g., Sun et al., 2004; Jenner et al., 2010, 2015). The behavior of Cu is followed closely by other chalcophile elements (Co, Ni, and Hg), which are also enriched in the andesites. Pb, and especially Ba, are enriched in both basaltic-andesite and dacite compared to N-MORB, as noted in other back-arc basins (Fouquet et al., 1993; Jenner et al., 2012). These are important slab-derived components, along with As, Sn, and Ga (Pearce, 2008). The latter are elevated in Group II dacites (up to 4 ppm, 8 ppm, and 20 ppm, respectively) relative to Group I basaltic-andesites, reflecting the common behavior of these elements in silicic melts (e.g., Stanton, 1994). These

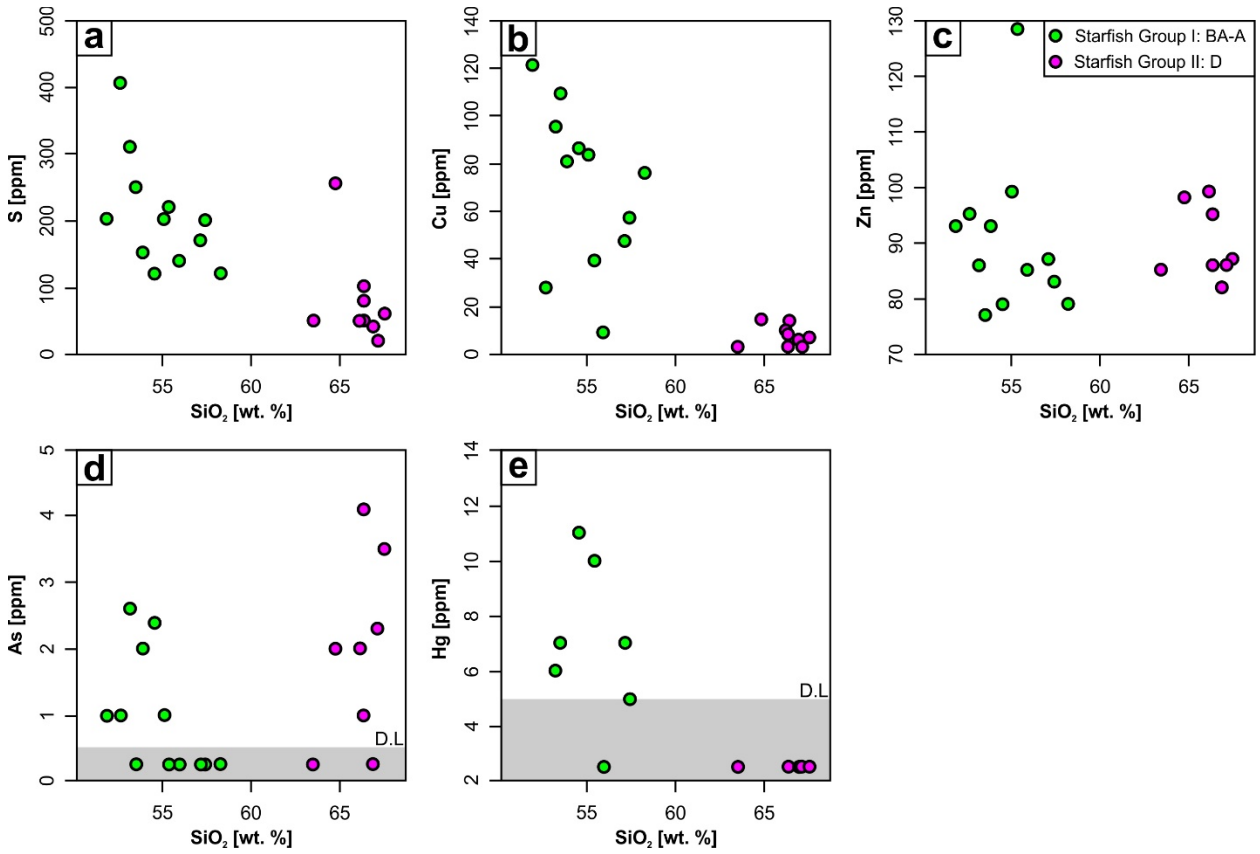


Fig. 3.25. Concentrations of selected chalcophile elements in volcanic glass from the Starfish-Tinakula area. Grey shaded areas indicate the lower detection limit (D.L.). BA-A = basaltic andesite to andesite; D = dacite.

enrichments are also reflected in the hydrothermal precipitates (see *Chapter 4*). However, background concentrations of the precious metals, Au and Ag, are generally low in all of the rocks, and typical of N-MORB and BABB (Jenner et al., 2010). The abundance of vesicles in all rock types is noteworthy (Table 3.1), and the presence of rare chalcopyrite, pyrite, and galena lining the vesicle walls, highlights the possibility of vapor transport of the metals in the melt (e.g., Williams-Jones and Heinrich, 2005).

3.8.3. Controls on hydrothermal venting at Tinakula

The Starfish-Tinakula area is characterized by a strongly tectonized seafloor, dominated by E-W directed extension and a strong N-S structural fabric (Figs. 3.5 and 3.6). Volcanism along these structures occurs as continuous elongate ridges or aligned smaller cones. Hydrothermal venting is controlled by the same structures and may include: (1) short-lived, high-temperature venting associated with the shallow intrusion of dikes (e.g., forming the volcanic ridges in the Starfish area in Fig. 3.5a); or (2) long-lived, lower-temperature venting associated with more diffuse flow in permeable volcaniclastic units. The Tinakula seafloor massive sulfide deposit is located in an area of intense intersecting faults, above an inflated portion of the back-arc (including the Starfish volcano) where magmatic activity is notably enhanced (Fig. 3.5). Here, the regional N-S and NE-SW structures intersect (Figs. 3.6 and 3.8), and enhanced magmatism related to the nearby TFZ impinges on the area of back-arc extension. The area is seismically-active, undergoing extension at a maximum rate of ~80 mm yr^{-1} (Calmant et al., 2003), which enhances permeability along the faults that may otherwise become sealed by mineral precipitation. Enhanced magmatism and a potentially long-lived magma chamber are confirmed by the large size of the Starfish volcano and the presence of highly-fractionated melts.

An important control on hydrothermal venting at Tinakula is the abundance of volcanicastic material, which is analogous to the host volcanic successions of many large-tonnage VMS deposits (e.g., Franklin et al., 2005). Hydrothermal fluids tend to migrate laterally within permeable volcaniclastic host rocks and form stratiform ore lenses both on and below the seafloor. The impressive areal extent of mineralization at Tinakula may partly reflect this style of subseafloor hydrothermal replacement. This is underscored by the occurrence of chimneys along linear trends

with no association to volcanic features on the seafloor (Figs. 3.10 and 3.19c). The nature of the footwall and the implications for hydrothermal fluid flow are discussed in detail in *Chapter 5*.

Massive sulfide accumulation at Tinakula occurs primarily along the central row of andesitic cinder cones. The cones likely formed over a few days to weeks (Sigurdsson, 2000) and therefore are not the source of heat for hydrothermal venting. Rather, they delineate a major fissure that has likely been intruded by dikes. Heat from the dikes, and possibly a larger subvolcanic magma chamber, was sufficient to drive widespread hydrothermal circulation to form the Tinakula deposit. The hydrothermal fluids exploited the same structural pathways as the magmas. Currently, however, active venting is restricted to a few sites of diffuse shimmering water and rare white-grey smoke, with very little vent fauna. Thus, the hydrothermal system is interpreted to be in a waning phase.

3.9. Conclusions

The northern New Hebrides back-arc (the Jean Charcot Troughs, or JCT) is characterized by a distinct morphology unlike any back-arc setting known in the world today, consisting of irregular grabens and volcanic ridges spread out over a wide area. The geodynamic evolution of the JCT is reflected in the morpho-tectonic fabrics on the seafloor, which is linked to diffuse extension on an upper plate along pre-existing structures developed on crust of the North Fiji Basin. The collision of the d'Entrecasteaux ridge (DER) with the trench resulted in reversed block rotation and enhanced extension rates in the northern part of the JCT, and slower extension rates in the south associated with deep sedimentation.

The composition of volcanic rocks in the JCT reveals an enriched mantle source with contributions from the deep subducting slab. The primary basaltic melts are significantly modified by processes of fractional crystallization, evolving to basaltic-andesitic to andesitic compositions. Dacitic melts were subsequently produced through a process of bimodal volcanism. The major and trace element geochemical signature of the JCT is distinct from the CT, resulting from distinct mantle source compositions and source evolution.

Extension in the back-arc produced highly-tectonized crust, providing pathways for both magmas and hydrothermal fluids along deeply-penetrating faults. The Tinakula seafloor massive sulfide (SMS) deposit formed near the back-arc Starfish stratovolcano at a water depth of 1070–1204 mbsl, with sulfide precipitation over an area ~77,000 m^2. There is a close spatial association of mineralization with a row of basaltic-andesitic cinder cones on the broad axial high between the two main clusters of troughs adjacent to the TFZ. Similarly prospective areas may be located at the intersection with the HHFZ and in the high areas between the northern JCTs. The inflated areas of the back-arc may be analogous to mid-segment axial highs associated with slow-spreading MORs (e.g., Devey et al., 2010) and represent an enhanced supply of magma in areas that are otherwise dominated by tectonic extension. Despite the overall high rate of basin opening, the JCT have many similarities to slow-spreading crust. Distributed extension across more than 120 km of the back-arc gives rise to stable, long-lived faults similar to slow-spreading ridges. This style of extension is in sharp contrast with the simple narrow-graben morphology of the Coriolis Troughs (CT) in the southern back-arc.

The New Hebrides is one of the least-explored back-arc systems in the world. It is an excellent natural laboratory for understanding early back-arc rifting processes, which remains a missing piece of the puzzle in our understanding of the subduction zone factory. Further work is required to reveal the deep architecture of the Jean Charcot Troughs, and continued exploration for hydrothermal vent sites will aid our understanding of where and when hydrothermal systems become established during the early phases of back-arc rifting. This study is an important step towards understanding the links between subduction-zone complexities, such as the DER collision, and the overall metallogenic potential of the New Hebrides back-arc.

Appendix B. Supporting Information

Supplementary data associated with this article is found in Appendix B.

References

Anderson, M.O., Hannington, M.D., Haase, K., Schwarz-Schampera, U., Augustin, N., McConachy, T.F., Allen, K., 2016. Tectonic focusing of voluminous basaltic eruptions in magma-deficient back-arc rifts. Earth Planet. Sci. Lett. 440, 43–55, doi:10.1016/j.epsl.2016.02.002.

Arculus, R.J., and Shipboard Scientific Party, 2006. Coriolis Troughs and southern New Hebrides Arc: primary tectonic results from the CoTroVe (SS06/2004) Research Voyage. ASEG Extended abstracts 2006, 1–6, doi:10.1071/ASEG2006ab003.

Auzende, J.-M., Lafoy, Y., Marsett, B., 1988. Recent geodynamic evolution of the North Fiji Basin (SW Pacific), Geology 16, 925–929, doi:10.1130/0091-7613(1988(016<0925:RGEOTN>2.3.CO;2.

Auzende, J.-M., Pelletier, B., Eissen, J.-P., 1995. The North Fiji basin geology, structure, and geodynamic evolution. In: Taylor, B. (Ed.), Backarc Basins: Tectonics and Magmatism. Springer, New York, pp. 139–175, doi:10.1007/978-1-4615-1843-3.

Barazangi, M., Isacks, B.L., Oliver, J., Dubois, J., Pascal, G., 1973. Descent of lithosphere beneath New Hebrides, Tonga-Fiji and New Zealand: Evidence for detached slabs. Nature 242, 98 –101, doi:10.1038/242098a0.

Beaulieu, S.E., 2013. InterRidge Global Database of Active Submarine Hydrothermal Vent Fields: prepared for InterRidge, Version 2.3. http://vents-data.interridge.org.

Bellon, H., Marcelot, G., Lefevre, C., Maillet, P., 1984. Le volcanisme de l'île d'Erromango (République du Vanuatu): calendrier de láctivité (données ^{40}K-^{40}Ar). C.R. Acad. Sci., Paris, 299, pp. 257–262.

Bergeot, N., Bouin, M.N., Diament, M., Pelletier, B., Régnier, M., Calmant, S., Ballu, V., 2009. Horizontal and vertical interseismic velocity fields in the Vanuatu subduction zone from GPS measurements: Evidence for a central Vanuatu locked zone. J. Geophys. Res. 114, 1–20, doi:10.1029/2007JB005249.

Bézos, A., Escrig, S., Langmuir, C.H., Michael, P.J., Asimow, P.D., 2009. Origins of chemical diversity of back-arc basin basalts: a segment scale study of the Eastern Lau Spreading Center. J. Geophys. Res. 114, B06212, doi:10.1029/2008JB005924.

Boynton, W.V., 1984. Cosmochemistry of the rare earth elements; meteorite studies. In: Henderson, P. (Ed.), Rare earth element geochemistry, Elsevier Sci. Publ. Co., Amsterdam, pp. 63–114.

Brown, L., 2010. A new technique for depicting terrain relief [abstract]. NACIS Annual Meeting, 2010 Oct 13–17, St. Petersburg, Florida.

Burkett, E.R., Billen, M.I., 2010. Three-dimensionality of slab detachment due to ridge-trench collision: Laterally simultaneous boudinage versus tear propagation. Geochem. Geophys. Geosyst. 11, Q11012, doi:10.1029/2010GC003286.

Calmant, S., Lebellegard, P., Taylor, F., Bevis, M., Maillard, D., Récy, J., Bonneau, J., 1995. Geodetic measurements of convergence across the New Hebrides subduction zone. Geophys. Res. Lett. 22, 2573–2576, doi:10.1029/95GL01780.

Calmant, S., Pelletier, B., Lebellegard, P., Bevis, M., Taylor, F.W., Phillips, D.A., 2003. New insights on the tectonics along the New Hebrides subduction zone based on GPS results. J. Geophys. Res. 108, 2319, doi:10.1029/2001JB000644.

Carminati, E., Wortel, M.J.R., Spakman, W., Sabadini, R., 1998. The role of slab detachment processes in the opening of the western-central Mediterranean basins: some geological and geophysical evidence. Earth Planet. Sci. Lett. 160, 651 – 665, doi:10.1016/S0012-821X(98)00118-6.

Charvis, P., Pelletier, B., 1989. The northern New Hebrides back-arc troughs: history and relation with the North Fiji Basin. Tectonophysics 170, 259–277, doi:10.1016/0040-1951(89)90275-8.

Coleman, P.J., 1970. Geology of the Solomon and New Hebrides Islands as part of the Melanesian re-entrant, southwest Pacific. Pac. Sci. 24, 289–314.

Collot, J. Y., Daniel, J., Burne, R.V., 1985. Recent tectonics associated with the subduction/collision of the d'Entrecasteaux zone in the central New Hebrides. Tectonophysics 112, 325–356, doi:10.1016/0040-1951(85)90185-4.

Collot, J.Y., Lallemand, S., Pelletier, B., Eissen, J.-P., Glaçon, G., Fisher, M.A., Greene, H.G., Boulin, J., Daniel, J., Monzier, M., 1992. Geology of the d'Entrecasteaux-New Hebrides Arc collision zone: results from a deep submersible survey. Tectonophysics 212, 213–241, doi:10.1016/0040-1951(92)90292-E.

Collot, J.Y., Vendé-Leclerc, M., Rouillard, P., Lafoy, Y., Géli, L., 2011. Structural provinces of the Southwest Pacific Map, Geological Survey of New Caledonia – DIMENC, IFREMER.

Crawford, A.J., Briqueu, L., Laporte, C., Hasenaka, T., 1995. Coexistence of Indian and Pacific oceanic upper mantle reservoirs beneath the Central New Hebrides Island Arc. In: Taylor, B. & Natland, J. (Eds.), Active Margins and Marginal Basins of the Western Pacific. Geophys. Monogr. 88, AGU, Washington D.C. pp. 199–217.

Devey, C.W., German, C.R., Haase, K.M., Lackschewitz, K.S., Melchert, B., Connelly, D.P, 2010. The relationships between volcanism, tectonism and hydrothermal activity on the Mid-Atlantic Ridge south of the equator. In: Rona, P.A., et al. (Eds.), Diversity of hydrothermal systems on slow spreading ocean ridges, vol. 188. AGU, Washington, D.C., pp. 133–152, doi:10.1029/2008GM000756.

Dewey, J.F., 1980. Episodicity, sequence and style at convergent plate boundaries. In: Strangeway, D.W. (Ed.), The Continental Crust and its Mineral Deposits. Spec. Pap. Geol. Assoc. Can., Toronto, 20, pp. 553–573.

Eissen, J.-P., Lefèvre, C., Maillet, P., Morvan, G., Nohara, M., 1991. Petrology and geochemistry of the central North Fiji Basin spreading centre (Southwest Pacific) between 16°S and 22°S. Mar. Geol. 98, 201–239, doi:10.1016/0025-3227(91)90104-C.

Eissen, J.-P., Nohara, M., Cotten, J., Hirose, K., 1994. North Fiji Basin basalts and their magma sources: Part I. Incompatible element constraints. Mar. Geol. 116, 153–178, doi:10.1016/0025-3227(94)90174-0.

Elsasser, W.M., 1971. Existence of an asthenosphere. J. Geophys. Res. 76, 7296–7297, doi:10.1029/JB076i029p07296.

Faccenna, C., Funiciello, F., Giardini, D., Lucente, P., 2001. Episodic back-arc extension during restricted mantle convection in the central Mediterranean. Earth Planet. Sci. Lett. 187, 105–116, doi:10.1016/S0012-821X(01)00280-1.

Falvey, D.A., Greene, H.G., 1988. Origin and evolution of the sedimentary basins of the New Hebrides arc. In. Greene, H.G., Wong., F.L. (Eds.). Geology and Offshore Resources of Pacific Island Arcs – Vanuatu Region. Circum-Pacific Council for Energy and Mineral Resources, Earth Sci. Series 8, Houston, TX, pp. 413–442.

Falvey, D.A., Colwell, J.B., Coleman, P.J., Greene, H.G., Vedder, J.G., Burns, T.R., 1991. Petroleum prospectivity of Pacific island arcs: Solomon Islands and Vanuatu. APEA J. 31, 191–212, doi:10.1071/AJ90015.

Fouquet, Y., von Stackelberg, U., Charlou, J.L., Erzinger, J., Herzig, P.M., Mühe, R., Wiedicke, M., 1993. Metallogenesis in back-arc environments: The Lau Basin example. Econ Geol. 88, 2154–2181, doi:10.2113/gsecongeo.88.8.2154.

Franklin, J.M., Gibson, H.L., Jonasson, I.R., Galley, A.G., 2005. Volcanogenic massive sulfide deposits. Econ. Geol. 100, 523–560.

Fryer, P., Taylor, B., Langmuir, C.H., Hochstaedter, A.G., 1990. Petrology and geochemistry of lavas from the Sumisu and Torishima backarc rifts. Earth Planet. Sci. Lett. 100, 161–178, doi:10.1016/0012-821X(90)90183-X.

Gill, J.B., Gorton, M., 1973. A proposed geological and geochemical history of eastern Melanesia. In: Coleman, P. (Ed.), The western Pacific: Island arcs, marginal seas, geochemistry. Western Australia Univ. Press, Perth, pp. 543–566.

Greene, H.G., Collot, J.Y., Pelletier, B., Lallemand, S., 1992. Observation of forearc seafloor deformation along the North d'Entrecasteaux Ridge—New Hebrides Island Arc collision zone from Nautile Submersible. Proc. ODP, Init. Reports 134, 43–53.

Grove, T.L., Chatterjee, N., Parman, S.W., Médard, E., 2006. The influence of H_2O on mantle wedge melting. Earth Planet. Sci. Lett. 249, 74–89, doi:10.1016/j.epsl.2006.06.043.

Hall, R., 2002. Cenozoic geological and plate tectonic evolution of SE Asia and the SE Pacific – computer-based reconstructions, model and animations. J. Asian Earth Sci. 20, 353–431, doi:10.1016/S1367-9120(01)00069-4.

Hall., R., Spakman, W., 2002. Subducted slabs beneath the eastern Indonesia-Tonga region: insights from tomography. Earth Planet. Sci. Lett. 201, 321–336, doi:10.1016/S0012-821X(02)00705-7.

Hall, C.E., Gurnis, M., Sdrolias, M., Lavier, L.L., Müller, R.D., 2003. Catastrophic initiation of subduction following forced convergence across fracture zones. Earth Planet. Sci. Lett. 212, 15–30, doi:10.1016/S0012-821X(03)00242-5.

Hannington, M.D., de Ronde, C.E.J., Petersen, S., 2005. Sea-Floor Tectonics and Submarine Hydrothermal Systems. Econ. Geol. 100, 111–141. Society of Economic Geologists, Littleton, CO, pp. 325–356.

Hannington, M.D., de Ronde, C.E.J., Petersen, S., 2010. Modern sea-floor massive sulfides and base metal resources: Toward an estimate of global sea-floor massive sulfide potential. Econ. Geol. 15, 317–338.

Hannington, M.D., hann, J., Monecke, T., Petersen, S., Beaulieu, S. 2011. The abundance of seafloor massive sulfide deposits. Geology 39, 1155–1158, doi:10.1130/G32468.1.

Hanuš, V., Vaněk, J., 1983. Deep structure of the Vanuatu (New Hebrides) island arc: intermediate depth collision of subducted lithospheric plates. N.S. J. Geol. Geophys. 26, 133–154, doi:10.1080/00288306.1983.10422513.

Hathway, B., 1993. The Nadi Basin: Neogene strike-slip faulting and sedimentation in a fragmented arc, western Viti Levu, Fiji. Geol. Soc. London 150, 563–581, doi:10.1144/gsjgs.150.3.0563.

Hayes, G.P., Wald, D.J., Johnson, R.L., 2012. Slab 1.0: A three-dimensional model of global subduction zone geometries. J. Geophys. Res. 117, B01302, doi:10.1029/2011JB008524.

Heuret, A., Lallemand, S., 2005. Plate motions, slab dynamics, and back-arc deformation. Phys. Earth Planet. Int. 149, 31–51, doi:10.1016/j.pepi.2004.08.022.

Heyworth, Z., Knesel, K.M., Turner, S.P., Arculus, R.J., 2011. Pb-isotopic evidence for rapid trench-parallel mantle flow beneath Vanuatu. J. Geol. Soc. London 168, 265–271, doi:10.1144/0016-76492010-054.

Hofmann, A.W., White, W.M., 1982. Mantle plumes from ancient oceanic crust. Earth Planet. Sci. Lett. 57, 421–436, doi:10.1016/0012-821X(82)90161-3.

Holmes, M.L., 1988. Seismic refraction measurements in the summit basins of the New Hebrides arc. In: Greene, H.G., Wong, F.L. (Eds.) Geology and Offshore Resources of Pacific Island Arcs – Vanuatu Region. Circum-Pacific Council for Energy and Mineral Resources, Earth Sci. Series 8, Houston, TX, pp. 163–176.

Ishikawa, Y., Sawaguchi, T., Iwaya, S., Horiuchi, M., 1976. Delineation of prospecting targets for Kuroko deposits based on modes of volcanism of underlying dacite and alteration halos. Mining Geol. 26, 105–117, doi:10.11456/shigenchishitsu1951.26.105 (in Japanese with English abs.).

Jamieson, J.W., Clague, D.A., Hannington, M.D., 2014. Hydrothermal sulfide accumulation along the Endeavour Segment, Juan de Fuca Ridge. Earth Planet. Sci. Let. 395, 136–148, doi:10.1016/j.epsl.2014.03.035.

Jarrard, R.D., 1986. Relations among subduction parameters. Rev. Geophys. 24(2), 217–284, doi:10.1029/RG024i002p00217.

Jenner, F.E., O'Neill, H.S.C., 2012. Analysis of 60 elements in 616 ocean floor basaltic glasses. Geochem. Geophys. Geosyst. 13, Q02005, doi:10.1029/2011GC004009.

Jenner, F.E., O'Neill, H.S.C., Arculus, R., Mavrogenes, J.A., 2010. The magnetite crisis in the evolution of arc-related magmas and the initial concentration of Au, Ag and Cu. J. Pet 51, 2445–2464, doi:10.1093/petrology/egq063.

Jenner, F.E., Hauri, E.H., Bullock, E.S., Konig, S., Arculus, R.J., Mavrogenes, J.A., Mikkelson, N., Goddard, C., 2015. The competing effects of sulfide saturation versus degassing on the behavior of the chalcophile elements during the differentiation of hydrous melts. Geochem. Geophys. Geosyst. 16, 1490–1507, doi:10.1002/2014GC005670.

Johnson, D.P., Maillet, P.C., Rice, R.C., 1992. The seabed morphology of the Hazel Holme Fracture Zone and the New Hebrides arc, northern Vanuatu – Solomon Islands Region. SOPAC Technical Report 138, pp. 28.

Keith, M., Haase, K.M., Klemd, R., Schwarz-Schampera, U., Franke, H., 2017. Systematic variations in magmatic sulphide chemistry from mid-ocean ridges, back-arc basins and island arcs. Chem. Geol. 451, 67–77, doi:10.1016/j.chemgeo.2016.12.028.

Keller, N.S., Arculus, R.J., Hermann, J., Richards, S., 2008. Submarine back-arc lava with arc signature: Fonualei Spreading Center, northeast Lau Basin, Tonga. J. Geophys. Res. 113, B08S07, doi:10.1029/2007JB005451.

Kincaid, C., Hall, P.S., 2003. Role of back-arc spreading in circulation and melting at subduction zones. J. Geophys. Res. 108, 2240, doi:10.1029/2001JB001174.

Kroenke, L.W., Rodda, P. 1984. Cenozoic tectonic development of the southwest Pacific. U.N. ESCAP, CCOP/SOPAC Tech. Bull. 6, pp. 122.

Lallemand, S., Heuret, A., Boutelier, D., 2005. On the relationships between slab dip, back-arc stress, upper plate absolute motion, and crustal nature in subduction zones. Geochem. Geophys. Geosyst. 6, Q09006, doi:10.1029/2005GC000917.

Le Bas, M.H., Le Matre, R.W., Streckeisen, A., Zanettini, B., 1986. A chemical classification of volcanic rocks based on the total alkali-silica diagram. J. Petrol. 27, 745–750, doi:10.1093/petrology/27.3.745.

Lima, S.M., Haase, K.M., Beier, C., Regelous, M., Brandl, P.A., Hauff, F., Krumm, S., 2017. Magmatic evolution and source variations at the Nifonea Ridge (New Hebrides Island Arc). J. Pet. 0, 1 – 22, doi:10.1093/petrology/egx023.

Livermore, R., Cunningham, A., Vanneste, L., Larter, R., 1997. Subduction influence on magma supply at the East Scotia Ridge. Earth Planet. Sci. Lett. 150, 261–275, doi:10.1016/S0012-821X(97)00074-5.

Maillet, P., Ruellan, E., Gérard, M., Person, A., Bellon, H., Cotton, J., Joron, J.-L., Nakada, S., Price, R.C., 1995. Tectonics, Magmatism, and evolution of the New Hebrides back-arc troughs (southwest Pacific). In: Taylor, B. (Ed.), Back-arc Basins: Tectonics and Magmatism. Plenum, New York, pp. 177–235.

Martin, A.K., 2006. Oppositely directed pairs of propagating rifts in back-arc basins: Double saloon door seafloor spreading during subduction rollback. Tectonics 25, TC3008, doi:10.1029/2005TC001885.

Martin, A.K., 2007. Gondwana breakup via double-saloon-door rifting and seafloor spreading in a backarc basin during subduction rollback. Tectonophysics 445, 245–272, doi:10.1016/j.tecto.2007.08.011.

Martin, A.K., 2011. Double saloon door tectonics in the Japan Sea, Fossa Magna, and the Japanese Island Arc. Tectonophysics 498, 45–65, doi:10.1016/j.tecto.2010.11.016.

Martin, A.K., 2013. Double-saloon-door tectonics in the North Fiji Basin. Earth Planet. Sci. Lett. 374, 191–203, doi:10.1016/j.epsl.2013.05.041.

Martínez, F., Taylor, B., 2002. Mantle wedge control on back-arc crustal accretion. Nature 416, 417–420, doi:10.1038/416417a.

Mason, W.G., Moresi, L., Betts, P.G., Miller, M.S., 2010. Three-dimensional numerical models of the influence of a buoyant oceanic plateau on subduction zones. Tectonophysics 483(1–2), 71–79, doi:10.1016/j.tecto.2009.08.021.

Maus, S., et al., 2009. EMAG2: A 2-arc min resolution Earth Magnetic Anomaly Grid compiled from satellite, airborne, and marine magnetic measurements. Geochem. Geophys. Geosyst. 10(8), Q08005, doi:10.1029/2009GC002471.

McConachy, T.F., Arculus, R.J., Yeats, C.J., Binns, R.A., Barriga, F., McInnes, B., Sestak, S., Sharpe, R., Rakau, B., Tevi, T., 2005. New hydrothermal activity and alkali volcanism in the back-arc Coriolis Troughs, Vanuatu. Geology 33, 61–64, doi:10.1130/G20870.1.

Meffre, S., Crawford, A.J., 2001. Collision tectonics in the New Hebrides arc (Vanuatu). Isl. Arc 10, 33–50, doi:10.1046/j.1440-1738.2001.00292.x.

Mitchell, A.H.G., Warden, A.J., 1971. Geological evolution of the New Hebrides island arc. J. Geol. Soc. 127, 501–529, doi:10.1144/gsjgs.127.5.0501.

Monecke, T., Petersen, S., Hannington, M.D., Anzidei, M., Esposito, A., Giordano, G., Garbe-Schönberg, D., Augustin, N., Melchert, B., Hocking, M., 2012. Explosion craters associated with shallow submarine gas venting off Panarea island, Italy. Bull. Volcanol. 74, 1937–1944, doi:10.1007/s00445-012-0651-8.

Monjaret, M.C., Bellon, H., Maillet, P., 1991. Magmatism of the troughs behind the New Hebrides island arc (RV Jean Charcot SEAPSO 2 cruise): K-Ar geochronology and petrology. J. Volcanol. Geotherm. Res. 46, 265–280, doi:10.1016/0377-0273(91)90088-H.

Nohara, M., Hirose, K., Eissen, J.-P., Urabe, T., Joshima, M., 1994. The North Fiji Basin basalts and their magma sources: Part II. Sr-Nd isotopic and trace element constraints. Mar. Geol. 116, 179–195, doi:10.1016/0025-3227(94)90175-9.

Parson, L.M., Pearce, J.A., Murton, B.J., Hodkinson, R.A., and Shipboard Scientific Party, 1990. Role of ridge jumps and ridge propagation in the tectonic evolution of the Lau back-arc basin, southwest Pacific. Geology 18, 470–473, doi:10.1130/0091-7613(1990)018<0470:RORJAR>2.3.CO;2.

Pearce, J.A., 2008. Geochemical fingerprinting of oceanic basalts with applications to ophiolite classification and the search for Archean oceanic crust. Lithos 100, 14–48, doi:10.1016.j.lithos.2007.06.016.

Pearce, J., Stern, R., 2006. Origin of back-arc basin magmas: Trace element and isotope perspectives. Geophys. Monogr. 166, AGU, Washington, D.C., pp. 63–86, doi:10.1029/166GM06.

Pearce, J.,A., 2014. Immobile element fingerprinting of ophiolites. Elements 10, 101–108, doi:10.2113/gselements.10.2.101.

Pearce, J.A., Ernewein, M., Bloomer, S.H., Parson, L., Murton, B.J., Johnson, L.E., 1995. Geochemistry of Lau Basin volcanic rocks: influence of ridge segmentation and arc proximity. Geol. Soc. London, Spec. Publ. 81, 53– 75, doi:10.1144/GSL.SP.1994.081.01.04.

Peate, D.W., Pearce, J.A., Hawkesworth, C.J., Colley, H., Edwards, C.M.H., Hirose, K., 1997. Geochemical variations in Vanuatu arc lavas: The role of subducted material and a variable mantle wedge composition. J. Pet. 38, 1331– 1358, doi:10.1093/petroj/38.10.1331.

Pelletier, B., Louat, R., 1989. Seismotectonics and present-day relative plate motions in the Tonga-Lau and Kermadec-Havre region. Tectonophysics 165, 237–250, doi:10.1016/0040-1951(89)90049-8.

Pelletier, B., Lafoy, Y., Missegue, F., 1993. Morphostructure and magnetic fabric of the northwestern North Fiji Basin. Geophys. Res. Lett. 20, 1151–1154, doi:10.1029/93GL01240.

Pelletier, B., Calmant, S., Pillet, R., 1998. Current tectonics of the Tonga-New Hebrides region. Earth Planet. Sci. Lett. 164, 263–276, doi:10.1016/S0012-821X(98)00212-X.

Pike, R.J., 1978. Volcanoes on the inner planets: Some preliminary comparisons of gross topography. Proc. Lunar Planet. Sci. Conf. 9th Proc., 3239–3273.

Pysklywec, R., Mitrovica, J.X., Ishii, M., 2003. Mantle avalanche as a driving force for tectonic reorganization in the southwest Pacific. Earth Planet. Sci. Lett. 209, 29–38, doi:10.1016/S0012-821X(03)00073-6.

Richards, S., Holm, R., Barber, G., 2011. When slabs collide: A tectonic assessment of deep earthquakes in the Tonga-Vanuatu region. Geology 39, 787–790, doi:10.1130/G31937.1.

Ruellan, E., Lafoy, Y., Auzende, J.M., Foucher, J.P., Dupont, J., 1994. Oblique spreading in the southern part of the Lau back-arc basin (S.W. Pacific). In: Stevenson, A.J., Herzer, R.H., Balance, P.F. (Eds.), Geology and Submarine Resources of the Tonga-Lau Fiji Region, SOPAC, Suva, Fiji, pp. 319–327.

Sandwell, D.T., et al., 2014. New global marine gravity model from CryoSat-2 and Jason-1 reveals buried tectonic structure. Science 346, 65–67.

Schellart, W.P., 2004. Kinematics of subduction and subduction-induced flow in the upper mantle. J. Geophys. Res. 109, B07401, doi:10.1029/2004JB002970.

Schellart, W.P., Lister, G.S., Jessel, M.W., 2002. Analogue modeling of arc and back-arc deformation in the New Hebrides arc and North Fiji Basin. Geology 30, 311–314, doi:10.1130/0091-7613(2002)030<0311:AMOAAB>2.0.CO;2.

Schellart, W.P., Jessell, M.W., Lister, G.S., 2003. Asymmetric deformation in the backarc region of the Kuril arc, northwest Pacific: New insights from analogue modeling. Tectonics 22, 1074, doi:10.1029/2002TC001473.

Schellart, W.P., Lister, G.S., Toy, V.G., 2006. A Late Cretaceous and Cenozoic reconstruction of the Southwest Pacific region: Tectonics controlled by subduction and slab rollback processes. Earth-Sci. Rev. 76, 191–233, doi:10.1016/j.earscirev.2006.01.002.

Sdrolias, M., Müller, D. 2006. Controls on back-arc basin formation. Geochem. Geophys. Geosyst. 7, Q04015, doi:10.1029/2005GC001090.

Sigurdsson, H., 2000. Volcanic episodes and rates of volcanism. In: Sigurdsson, H., et al. (Eds.), Encyclopedia of Volcanoes. Academic Press, San Diego, Calif., pp. 271–279.

Sobolev, A.V., Hofmann, A.W., Sobolev, S.V., Nikogosian, I.K., 2005. An olivine-free mantle source of Hawaiian shield basalts. Nature 434, 590–597, doi:10.1038/nature03411.

Sorbadere, F., Schiano, P., Métrich, N., Garaebiti, E., 2011. Insights into the origin of primitive silica-undersaturated arc magmas of Aoba volcano (Vanuatu arc). Contrib. Mineral. Petrol. 162, 995–1009, doi:10.1007/s00410-011-0636-1.

Sorbadere, F., Schiano, P., Métrich, N., Bertagnini, A., 2013. Small-scale coexistence of island-arc- and enriched-MORB-type basalts in the central Vanuatu arc. Contrib. Mineral. Petrol. 166, 1305–1321, doi:10.1007/s00410-013-0928-8.

Stanton, R.L., 1994. Ore elements in arc lavas. Oxford Mono. Geol. Geophys. 29, Clarendon Press, London.

Stern, R.J., 2002. Subduction zones. Rev. Geophys. 40(4), 1–13, doi:10.1029/2001RG000108.

Sun, W., McDonough, W.F., 1989. Chemical and isotopic systematics of oceanic basalts: Implications for mantle composition and processes. Geol. Soc. London Spec. Pub. 42, 313–345, doi:10.1144/GSL.SP.1989.042.01.19.

Sun, W., Arculus, R.J., Kamenetsky, V.S., Binns, R.A., 2004. Release of gold-bearing fluids in convergent margin magmas prompted by magnetite crystallization. Nature 431, 975–978, doi:10.1038/nature02972.

Tamura, Y., Tatsumi, Y., 2002. Remelting of an andesitic crust as a possible origin for rhyolitic magma in oceanic arcs: An example from the Izu-Bonin Arc. J. Petrol. 43, 1029–1047, doi:10.1093/petrology/43.6.1029.

Taylor, B. (Ed.), 1995. Back-arc Basins: Tectonics and Magmatism. Springer, New York, doi:10.1007/978-1-4615-1843-3.

Taylor, B., Zellmer, K.E., Martínez, F., Goodliffe, A., 1996. Sea-floor spreading in the Lau back-arc basin. Earth Planet. Sci. Lett. 144, 35–40, doi:10.1016/0012-821X(96)00148-3.

Turner, S.P., George, R.M.M., Evans, P.J., Hawkesworth, C.J., Zellmer, G.F., 2000. Time-scales of magma formation, ascent and storage beneath subduction-zone volcanoes. Phil. Trans. R. Soc. London 358, 1443–1464, doi:10.1098/rsta.2000.0598.

Williams-Jones, A.E., Heinrich, C.A., 2005. Vapor transport of metals and the formation of magmatic-hydrothermal ore deposits. Econ. Geol. 100, 1287–1312.

Zellmer, K.E., Taylor, B., 2001. A three-plate kinematic model for Lau Basin opening. Geochem. Geophys. Geosyst. 2, 1020, doi:10.1029/2000GC000106.

Preface to Chapter 4

Chapter 3 examined the geodynamic evolution of the Jean Charcot Troughs (JCT) and the influence on the geological setting of the Tinakula seafloor massive sulfide deposit and the geochemistry of its volcanic host rocks. This chapter presents a detailed study of the mineralogy and geochemistry of the hydrothermal precipitates at Tinakula, providing further insight into the relationships between regional geodynamics, volcanism, and hydrothermal venting in a young back-arc rift. Compared to the Nifonea vent field in the Coriolis Troughs (described in *Chapter 2*), which is strongly influenced by the evolution of the large Nifonea shield volcano, the Tinakula deposit presents the characteristics of a large, relatively low-temperature hydrothermal system in a shallow tectonized terrane that has not yet reached the same stage of rifting.

Chapter 4

Mineralogy, geochemistry, S-isotopes, and fluid inclusion systematics of the Tinakula seafloor massive sulfide deposit, Jean Charcot Troughs, SW Pacific

Abstract

Tinakula is the first seafloor massive sulfide deposit described in the Jean Charcot Troughs of the New Hebrides back-arc. The mineralization is characterized by several unusual features: (1) a high proportion of barite-to-sulfide, with locally barite-dominant chimneys, but also high-temperature Cu-rich chimneys composed almost entirely of chalcopyrite; (2) bulbous to complexly layered Zn-rich chimneys formed by low-temperature (<250°C) venting; and (3) widespread low-temperature siliceous and iron oxide-rich deposits resulting from diffuse venting through volcaniclastic sediments. Chalcopyrite-rich chimneys are highly enriched in Au, As, Mo, In, and Ga. Lower-temperature Zn-rich chimneys are dominated by low-Fe sphalerite (avg. <2.3 mol% FeS) and are enriched in Cd, Ge, Sb, and Ag. Barite chimneys are enriched in Si, Sr, Pb, and Hg. Free gold is present locally in the Cu-rich chimneys (grades up to 9.26 ppm Au), but it is also locally enriched as invisible (or nano-particulate) gold in low-temperature Zn-rich chimneys (grades up to 7.81 ppm Au). Other trace elements (Cd, Ge, Hg, and In) are notably enriched compared to other arc-related massive sulfide deposits. High concentrations of Ba and Hg in the massive sulfides can be directly related to enrichments in the host volcanic rocks. Sulfur from the volcanic host rocks and thermochemical reduction of seawater sulfate are the primary sources of sulfur in the deposit, with little or no contribution from magmatic volatiles or biogenic sources. Although the ~5,500-year-old vent field is in a waning stage of hydrothermal activity, abundant barite and silica has resulted in remarkable preservation of chimneys. The barite-rich chimneys bear a close resemblance to unusual layered barite-sulfide chimneys and mounds in the East Diamante caldera (Mariana back-arc) and may be typical of seafloor massive sulfides at the earliest stages of back-arc rifting.

4.1. Introduction

Recent studies have begun to document the variability of hydrothermal deposits in arc and back-arc environments compared to deposits that form along mid-oceanic ridges. Diverse host rocks, hydrothermal fluid compositions, mineralogy of hydrothermal precipitates, trace element signatures, and isotopic systematics result from variable rates of back-arc spreading, melt supply, crustal thickness, depth to the heat source, magma composition, and volatile flux (Franklin et al., 2005; Hannington et al., 2005). The composition of the volcanic rocks provides a first-order

control on the composition of seafloor massive sulfide (SMS) deposits, as metals are leached from the host rocks during hydrothermal circulation (Hannington et al., 2005).

The first indication of the presence of an active hydrothermal field in the JCT was the detection of a methane anomaly in the water column near the Starfish seamount during the KAIYO 89 cruise (Urabe et al., 1990). This anomaly was investigated further during the SOLAVENTS cruise, during which fresh and altered rhyodacite samples were recovered by dredging, and a number of temperature anomalies were recorded by CTD (McConachy et al., 2002). Additional research and exploration cruises in the area included the SEAPSO Leg 2 cruise (Récy et al., 1986), a GLORIA survey (Johnson et al., 1992), and the SOPACMAPS cruise (Kroenke, 1995). The Tinakula SMS deposit was discovered by Neptune Minerals Inc. in September, 2011, during the ASHR Leg 2 cruise aboard the MV Dorado Discovery. It is located in the Temotu Province within the exclusive economic zone of the Solomon Islands, approximately 890 km east-southeast of Guadalcanal, centered at 167°36’50”E/12°12’10”S, and at a water depth of 1070–1204 mbsl. The discovery was initially made by locating the source of a seafloor-hugging plume, followed by the discovery of sulfide chimneys during ROV dive operations. Four subsequent cruises (2011–2012) performed additional mapping, ROV grab sampling, resource drilling, and ocean floor electromagnetic (OFEM) geophysical surveys.

This chapter examines the mineralogy and geochemistry of hydrothermal precipitates at the Tinakula deposit in order to identify the controls on ore formation, including the influence of temperature, fluid mixing, host rock compositions, and the possible magmatic contributions to the hydrothermal system. The extent of seafloor weathering and massive sulfide preservation is also evaluated and the minimum age of the deposit is determined.

4.2. Geology of the Tinakula deposit

The Tinakula deposit is located in the Jean Charcot Troughs (JCT) in the northern New Hebrides back-arc, centered at 167°36’50”E/12°12’10”S (Fig. 4.1). This part of the JCT is characterized by intersecting regional structures and enhanced magmatism along the E-W trending Tikopia Fracture Zone that bisects the back-arc (Fig. 4.1, inset). Here, active extension and long-lived magmatism

has promoted circulation of hydrothermal fluids along deeply-penetrating faults near the Starfish back-arc volcano, forming the Tinakula seafloor massive sulfide deposit. This deposit occurs at a depth of 1070–1204 mbsl, and is characterized by a series of largely-inactive chimneys and mounds that are closely associated with structures on the seafloor (Fig. 4.1). In particular, mineralization is spatially associated with a row of volcanic cinder cones, with chimneys occurring within the volcanic craters, on the flanks, and on the surrounding seafloor. The chimneys and mounds have been partially buried by sand-sized volcaniclastic sediment. The volcaniclastic cover is locally indurated and mineralized, and therefore was deposited syn- to post-mineralization. Active hydrothermal venting is limited to a few sites of low-temperature shimmering water at the base of chimneys or along fractures in indurated sediments, and is widely associated with bacterial mats (Fig. 4.2a). Venting of white- to grey- smoke from chimney spires is rare (Fig. 4.2b).

Sulfide chimneys at Tinakula display two distinct morphologies: (1) multi-spired chimneys with central vent orifices typical of black-smokers (Figs. 4.2a,b); and (2) bulbous chimneys that lack central vent orifices, with irregular morphologies (tulip-shaped, layered, drooping, with smooth or popcorn-textured outer surfaces: Figs. 4.2c,d). The irregular and bulbous chimney morphologies are more common than ‘normal’ multi-spired chimneys. The lack of central vent orifices in the bulbous chimneys suggests a ‘beehive’ or flange-style of venting (e.g., Zhu et al., 2007). However, the irregular or bulbous chimney morphologies at Tinakula have not previously been described on the seafloor. The layered hydrothermal barite-sulfide mounds are most similar to features described by Hein et al. (2014) from the East Diamante caldera in the Mariana arc. They were attributed to fracture-controlled versus point-source venting, extensive subseafloor mixing, lateral fluid flow and diffuse discharge, which may be a typical feature of hydrothermal systems hosted by permeable volcaniclastic rocks. This type of discharge is also consistent with the bottom-hugging plume signal originally detected by McConachy et al. (2002).

In addition to sulfide chimneys, there are abundant <1 m-tall iron and manganese oxyhydroxide “chimneys,” including silica-rich chimneys associated with bacterial mats (Fig. 4.2e) and silica-poor branching Fe-Mn oxide chimneys formed along fractures on the seafloor (Fig. 4.2f). Precipitation of Fe-Mn oxides along fractures is widespread, extending up to 100 m away from the chimney complexes and mounds (Fig. 4.1).

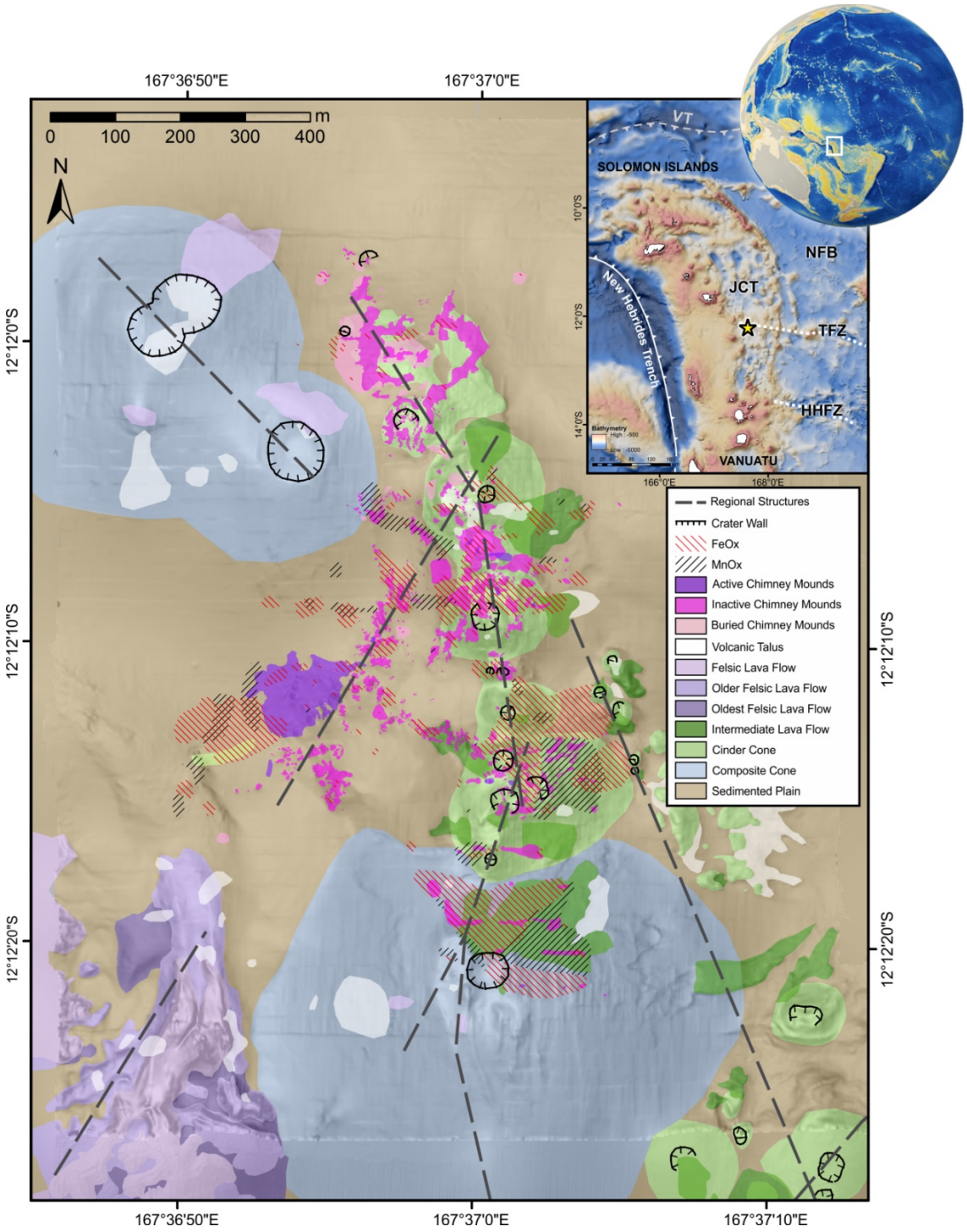


Fig. 4.1. Geology of the Tinakula area interpreted from ROV dive videos and sampling overlain on hill- and slope-shaded RESON SeaBat 7125-ROV2 400 kHz multibeam bathymetry. Location shown as a star on inset map with global marine altimetry from Sandwell et al. (2014). HHFZ = Hazel Holme Fracture Zone; JCT = Jean Charcot Troughs; NFB = North Fiji Basin; TFZ = Tikopia Fracture Zone; VT = Vitiaz Trench (fossil).

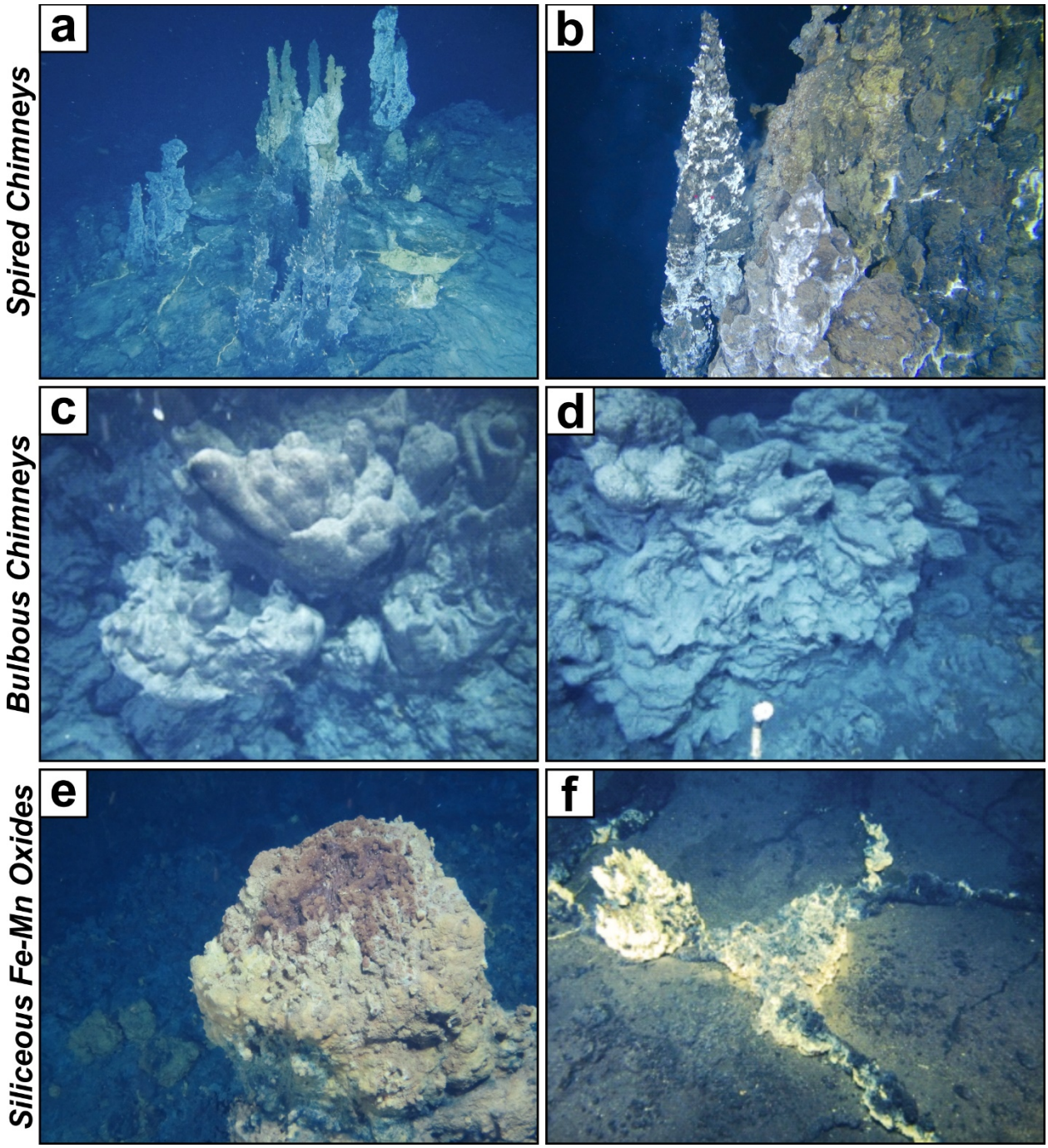


Fig. 4.2. Chimney morphologies encountered during ROV dive operations: (a) partly oxidized inactive spired chimneys with bacterial mat; (b) weakly-venting spire with minor oxidation; (c) inactive bulbous chimney; (d) inactive layered to droopy bulbous chimney; (e) siliceous iron oxide chimney with small worm casts; (f) fracture-controlled iron and manganese oxyhydroxides, locally forming dendritic oxide 'chimneys.' Images courtesy of Neptune Minerals Inc.

The host volcanic rocks are dominantly mafic-intermediate volcaniclastic material associated with the row of cinder cones. Nearby larger composite cones with dacitic lavas or bimodal volcanic rocks do not host mineralization (Fig. 4.1). A detailed study of the hydrothermal alteration of the host volcanic rocks is provided in *Chapter 5*.

4.3. Methods

4.3.1. Sample collection and petrography

Seafloor samples from the Tinakula-Starfish area were collected by Neptune Minerals Inc. in 2011–2012. This study examines a subset of 75 ROV grab samples, including 63 samples of sulfide-sulfate chimneys and mound material, and 12 samples of oxyhydroxides (see Appendix C for full sample list and maps). Of the mineralized samples, 23 were selected for ^{226}Ra dating (see below). In addition, seafloor drilling at the Tinakula deposit was undertaken by Neptune Minerals Inc. in 2012 aboard the MV Skandi Hawk using Benthic Geotech's Portable Remotely Operated Drill "PROD 3." During drilling, retrievable metal casings were used to stabilize the hole to prevent collapse and contamination of the drillhole. Drilling tools included: (1) a 75-mm diameter double-tube push-core barrel used primarily for unconsolidated material and highly clay-altered volcanic rocks and (2) a 72-mm diameter rotary core barrel with diamond bit assembly for competent rock. The combination of these drilling tools achieved an average recovery of 79.1%. Sub-samples from the drilling program were included in this study and are considered in greater detail in *Chapter 5* (see Appendix C for full sample list and drillhole locations),

Samples of sulfide-sulfate chimneys and oxyhydroxides were prepared as polished thin sections and analyzed by transmitted and reflected light microscopy. Petrographic descriptions included mineral identification, textures, mineral abundances, and paragenesis. Detailed petrographic descriptions of the sulfide-sulfate chimney samples are in Appendix E, and oxyhydroxides in Appendix F.

4.3.2. Whole-rock geochemistry

Bulk whole-rock geochemistry was performed on hydrothermal precipitates from the Tinakula deposit in order to document the lateral and vertical variations of major and trace elements. A total of 45 sulfide-sulfate samples and 7 oxyhydroxide samples were analyzed at ActLabs (Ontario, Canada). Major and minor elements, including Cu, Al, Ca, Fe, Mg, Na, K, P, S, Si, Ti, B, Be, Bi, Cd, Co, Cs, Cu, REEs, Ga, Ge, In, Li, Mn, Mo, Nb, Ni, Pb, Rb, Se, Sn, Sr, Te, Tl, Ta, Th, U, V, W, Y, and Zn were analyzed using ICP-OES and ICP-MS using a sodium peroxide fusion method for total metal recovery. Cold vapor AAS was used to determine Hg. Instrumental neutron activation analysis (INAA) was used to determine Au, Ag, As, Ba, Br, Cr, Fe, Hf, Ir, Sb, Sc, and Zn. Total S was determined by infrared spectroscopy. Full results are in Appendix I (sulfide-sulfates) and Appendix J (oxyhydroxides). The precision and accuracy of the data was determined by analyzing duplicate samples and standard reference materials after every 15 samples (minimum), resulting in precision of better than 10% and accuracy of better than 5% for most analyses (Appendix I).

4.3.3. Trace-element geochemistry by EPMA

Mineral compositions were determined on 16 sulfide-sulfate samples using a JEOL JXA 8200 electron probe micro-analyzer (EPMA) equipped with five wavelength-dispersive spectrometers and one energy-dispersive detector at the GEOMAR Helmholtz Centre for Ocean Research Kiel (Appendix L). A 15 keV accelerating potential and a 50 nA probe (cup) current were used for the analyses. Standards used were: chalcopyrite (FeK_α, SK_α, CuK_α), rhodonite (MnK_α) gallium arsenide (GaL_α, AsK_β), sphalerite (ZnK_α), silver telluride (AgL_α), indium antimonide (InL_α, SbL_α), cadmium sulfide (CdL_α), gold (AuL_α), cinnabar (HgM_α), and galena (PbM_α). Germanium and molybdenum were not analyzed due to a lack of suitable standard reference materials.

4.3.4. S-isotope analyses

Sulfide and sulfate mineral separates, including anhydrite, gypsum, barite, chalcopyrite, and sphalerite, were hand-picked from 25 sulfide-sulfate samples from the Tinakula deposit, totaling

54 mineral separates collected from ROV grab samples and 15 from one ~24-m deep drillhole (TKAD001). Mineral-specific chemical pre-treatment and S-isotope analyses were performed at the Laboratory for Stable Isotope Geochemistry at the Westfälische Wilhems-Universität Münster, Germany, described in detail by Wienkenjohann (2015). Samples were first powdered using an agate mortar, and then quantitatively separated using mineral-specific wet-chemical separation methods. Chemical pre-treatment of anhydrite and gypsum followed the method of Wotte et al. (2012) for water-soluble sulfates, whereas the pre-treatment of barite followed a modified wet-chemical extraction technique of Canfield et al. (1986) and Zhabina and Volkov (1978) for acid-insoluble sulfates. Sphalerite mineral separate pre-treatment followed the method of Canfield et al. (1986), modified according to Rice et al. (1993). Chalcopyrite and pyrite mineral separates pre-treatment followed the method of Canfield et al. (1986) for chromium-reducible sulfur. Each mineral phase was converted to silver sulfide following the technique of Thode and Monster (1961).

Analysis of $\delta^{34}S$ was performed on all samples via element analyzer-isotope ratio mass spectrometry (EA-IRMS). Each sample was placed in a tin capsule with ~300–800 μg of V_2O_5, acting as an oxygen donor (Gavelin et al., 1960; Ricke, 1964). The solid sulfur minerals were transformed into gaseous SO_2 by combustion in a Carlo Erba EA before being introduced to a Thermo Finnigan MAT DeltaPlus IRMS. Results are stated in standard delta notation relative to the Canyon Diablo Triolite. Precision was attained via replicate analysis of every subsample, with reproducibility better than ±0.3 ‰ (1σ). Accuracy was observed through repeat analysis of standard reference materials (IAEA-S1, IAEA-S2, IAEA-S3, NBS-127) and two lab internal standard materials (Ag_2S and CdS), showing an external reproducibility of ±0.2 ‰ (1σ).

^{34}S isotopes were measured for select subsamples via fluorination-IRMS, following the procedure outlined by Ono et al. (2006), and described by Wienkenjohann (2015). Approximately 2.5 mg of silver sulfide precipitates were packed in aluminum foil and placed in nickel reactors to be fluorinated to sulfur hexafluoride (SF_6) by injecting F_2 in fivefold excess. The reaction lasted eight hours at 300°C. The resulting SF_6 was cryogenically purified using liquid nitrogen cold traps and then a gas chromatograph. Purified SF_6 was introduced into a Thermo Finnigan MAT 263 IRMS. Results are stated in standard delta notation $\delta^{34}S$. Reproducibility was attained by measuring

emerged SF_6 from each sample eight times, and accuracy was evaluated by repeat analysis of a standard reference material (IAEA-S1), with a reproducibility (1σ) of ±0.03 ‰.

4.3.5. Fluid inclusion analyses

Five samples were selected from the one drillhole (TKAD001) for fluid inclusion analyses, consisting of hydrothermally-altered and sulfate-cemented volcaniclastic material. Doubly-polished thick sections (~130 μm) were prepared at Dettmar Dissection Technology (Bochum, Germany), using an industry-standard water-free kerosene technique. Fluid inclusion petrography was done using an optical polarizing microscope, documenting fluid inclusion sizes, vapor-liquid ratios, host minerals, fluid inclusion generations, and occurrence as separate inclusions or groups (described in detail by Anders, 2016). Microthermometric analyses were done using a Leitz Laborlux 12 Pol S microscope equipped with a Linkam™ THMS 600 gas-flow heating and freezing stage at the GEOMAR Helmholtz Centre for Ocean Research in Kiel, Germany. Accuracy was maintained by measuring phase transitions within synthetic fluid inclusions (Syn Flinc). Replicate measurements of homogenization and freezing point depression temperatures were performed every five to ten analyses. Salinities were calculated from freezing-point depression temperatures following Bodnar and Vityk (1994), as follows:

$$Salinity = (1.78|T_m|^1 - 0.0442|T_m|^2 + 0.000557|T_m|^3)$$

(Equation 1)

Where T_m is the melting temperature, and salinity is expressed as wt.% NaCl equivalent. Homogenization temperatures were corrected for pressure effects of the overlying water column at the sample location (1107.61 mbsl; 108.65 bar) following Zhang and Frantz (1987). Errors are estimated as ± 0.2°C for salinity measurements and ± 4°C for homogenization temperature measurements. The critical points, bulk molar volumes, densities, and P-T isochores were determined using the program FLINCOR (Brown, 1989).

4.3.6. ^{226}Ra/Ba geochronology

^{226}Ra/Ba dating of hydrothermal barite from the Tinakula deposit was carried out following the methods of Ditchburn et al. (2004), de Ronde et al. (2005), and Jamieson et al. (2013), to establish the recent history of magmatism in the Tinakula-Starfish area. The long half-life of ^{226}Ra (1600 years) allows samples to be dated that are in the age range of ~200 to 20,000 years old (Jamieson et al., 2013). A sample collected from an actively-venting chimney was used as a "zero-age" end member and proxy for the initial ^{226}Ra/Ba ratio, with the assumption that this ratio does not vary over time (e.g., Butterfield et al., 1994). Ages were calculated as follows:

$$t = \frac{\ln(N_0/N) \times \lambda}{\ln 2}$$

(Equation 2)

Where N_0 is the initial ^{226}Ra/Ba at the time of formation, N is the current ^{226}Ra/Ba of the sample, λ is the half-life of ^{226}Ra (1600 years), and t is the age in years. A total of 22 additional samples were selected to encompass the full age range of hydrothermal materials, including active chimneys, inactive chimneys, and talus. Samples were crushed and powdered, with one split sent to ActLabs (Ontario) to determine Ba concentrations by INAA (full geochemistry in Appendix I), and a split used to determine ^{226}Ra activity via gamma spectrometry at the University of Ottawa. Prior to measurements, the sample tubes were sealed for 21 days to prevent the escape of ^{222}Rn gas, following the technique described in Jamieson et al. (2013). ^{214}Pb, a daughter isotope from the decay of ^{222}Rn, was measured as a proxy for ^{226}Ra, to avoid peak overlap with ^{235}U. Measurements were made using a XLB-GWL-SV digital gamma spectrometer (DSPec, Ortec®), containing a high-purity germanium crystal, 54.7 mm × 66.2 mm, with an active well depth of 40 mm. Counting times ranged from 2 to 12 hours, depending on the activity of ^{226}Ra in each sample. The spectral signatures were calibrated using IAEA-312 reference material, and analyzed using a custom program developed and provided by Dr. Peter Appleby (University of Liverpool) to correct for background, detector efficiency, sample volumes, and matrix effects. All ages determined are considered minimum values, as hydrothermal barite can be remobilized and mixed with 'young' barite (Ditchburn and de Ronde, 2017).

4.4. Results

4.4.1. Ore mineralogy and paragenesis

Samples analyzed in this study were collected along the main N-S row of cinder cones in the Tinakula map area (Fig. 4.3). Detailed petrography is reported in Appendix E and F, and is summarized in Table 4.1. The mineralogy is dominated by sphalerite [(Zn,Fe)S], chalcopyrite [$CuFeS_2$], pyrite [FeS], marcasite [FeS], and barite [$BaSO_4$], with subordinate galena [PbS], Pb-As-Sb sulfosalts (most likely jordanite-geocronite [$Pb_{14}(Sb,As)_6S_{23}$] solid solution), and amorphous silica [SiO_2], with rare visible gold (as native Au or electrum [Au,Ag]). Minor secondary bornite [Cu_5FeS_4], covellite [CuS], digenite [Cu_9S_5], atacamite [$Cu_2(OH)_3Cl$] are present. Iron and manganese oxyhydroxides [Fe-$MnOO_x$] and clay are common. Anhydrite is notably rare. All of the chimneys are characterized by a high overall porosity.

The samples are classified into four main chimney types: (1) chalcopyrite-rich chimneys (n = 2); (2) zoned chalcopyrite-rich chimneys (n = 18); (3) dendritic sphalerite-rich chimneys (n = 28); and (4) dendritic barite-rich chimneys (n = 10), including silicified barite-rich chimneys (n = 7; Table 4.1). The areal distribution of the different chimney types is shown in Figure 4.3, with no obvious spatial controls on mineralogy; different chimney types commonly occur in close proximity to one another. Mineralized volcanic breccia was recovered from the base of several chimney complexes (n = 3), where the chimneys have overgrown volcaniclastic material. Mixed chimney talus with rounded clasts of sulfides was recovered in drill core (n = 3). Oxide samples, dominated by silica and iron- and manganese oxyhydroxides, with subordinate barite and clay, were also investigated. Mineralized samples in the drillcore that do not display identifiable chimney textures, and contain abundant hydrothermally-altered volcanic rock are considered to be part of the stringer zone (n = 7) and are described further in *Chapter 5*.

Chalcopyrite-rich chimneys

Chalcopyrite-rich chimneys comprise abundant massive coarse-grained chalcopyrite with both early minor fine- to medium-grained pyrite and later fine-grained pyrite lining former vent

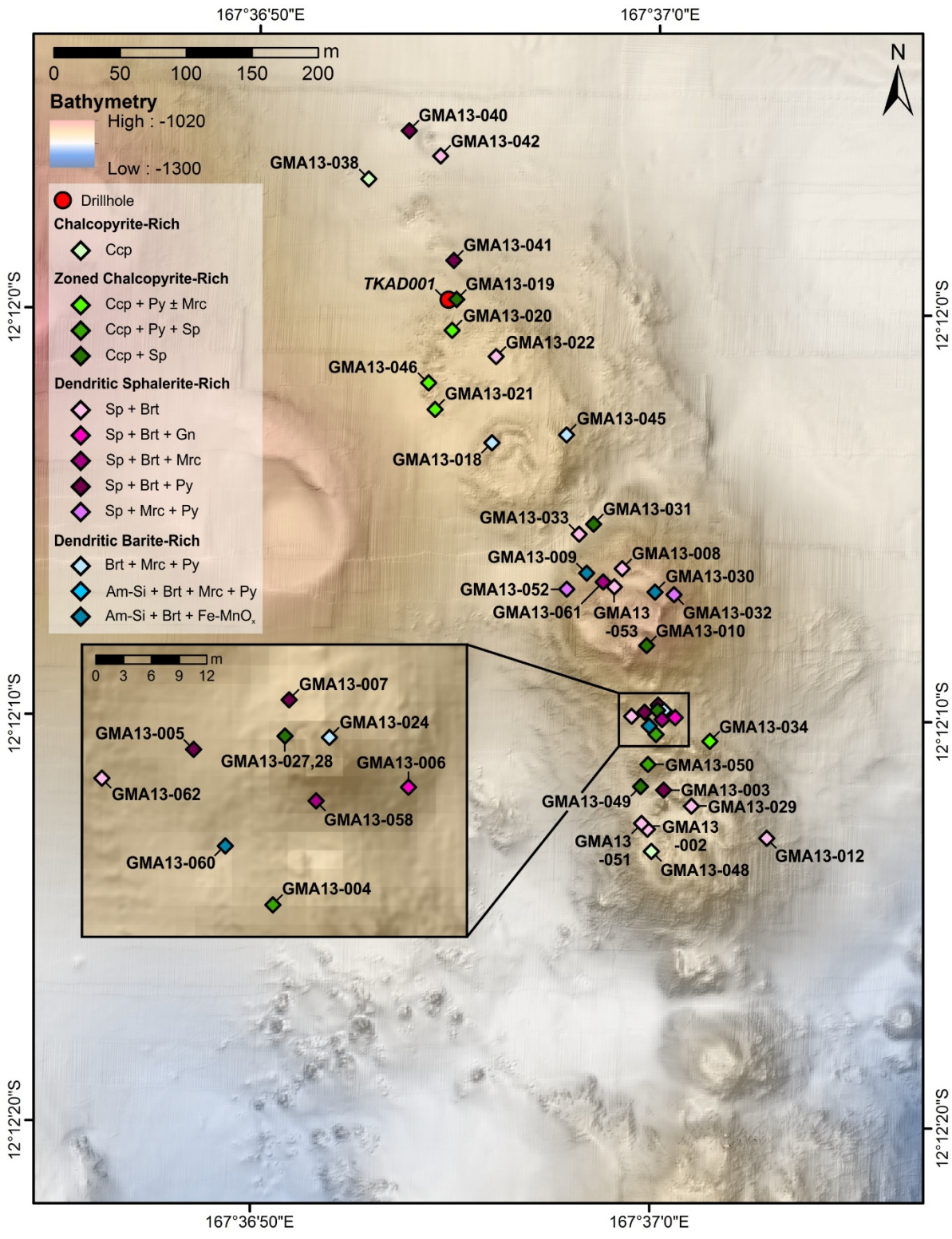


Fig. 4.3. Map of the distribution of sulfide-sulfate chimney types in the Tinakula area overlain on RESON SeaBat 7125-ROV2 multibeam bathymetry. See text for chimney classification. Am-Si = amorphous silica; Brt = barite; Ccp = chalcopyrite; Mrc = marcasite; Py = pyrite; Sp = sphalerite.

Table 4.1. Summary of petrographic observations of chimney samples from the Tinakula deposit

Sample	Chimney Type	Sp	Ccp	Py	Mrc	Gn	Jd	Au	Brt	Anh	Gp	Am-Si	Bn	Dg	Cv	Ata(?)	FeOx	Hem	Goe(?)	MnOx	Volc. Clasts	Clay	Cal
Chalcopyrite-rich																							
GMA13-038	Ccp	+	+++	+					+						Tr	+	+						
GMA13-048	Ccp	+	+++	+				Tr	Tr			+			Tr		Tr						
Zoned chalcopyrite-rich																							
GMA13-020	Ccp + Py ± Mrc	+	+++	++	+				+			++			+								
GMA13-021	Ccp + Py ± Mrc	+	+++	++	+				+			++			+	+	+		+				
GMA13-034	Ccp + Py ± Mrc	+	+++	++	+++				+			+	Tr	Tr	+		+		+				
GMA13-046	Ccp + Py ± Mrc	+	+++	++					+						+		+						
GMA13-004a	Ccp + Mrc + Sp	++	+++	+	+++		Tr		+			++			+								
GMA13-004b	Ccp + Mrc + Sp	++	+++	+	+++				+			++			Tr								
GMA13-050	Ccp + Mrc + Sp	+++	+++	+	+++		Tr		+						+								
MA13-028	Ccp + Mrc + Sp	++	+++		+++				+	++			+			Tr							
MA13-041	Ccp + Mrc + Sp	++	+++		++		+		++							+	Tr					Tr	
MA13-048	Sp + Brt	+++	++	+			+		+++				+			Tr	+					+	
GMA13-010	Ccp + Sp	++	+++		+				+			+	+	Tr	Tr		+			+			
GMA13-019b	Ccp + Sp	++	+++						+			++					Tr						
GMA13-027	Ccp + Sp	++	+++	+	+	Tr	+		+			+		Tr	+								
GMA13-028	Ccp + Sp	+	+++	+					+						+		+						
GMA13-031	Ccp + Sp	++	+++	+	+				+			+		Tr	+		+			+			
GMA13-049	Ccp + Sp	++	+++		+							++											
MA13-046	Ccp + Sp	++	+++	+			+		++				Tr			Tr	+					+	
P0042	Ccp + Sp	++	+++	+					++				Tr		Tr		+					Tr	
Dendritic sphalerite-rich																							
GMA13-002	Sp + Brt	+++		+					+++			+					Tr	+					
GMA13-012	Sp + Brt	+++		+					+++														
GMA13-019a	Sp + Brt	+++	++	+	+	Tr			+++			+			Tr								
GMA13-022	Sp + Brt	+++	+	Tr		Tr	Tr		+++														
GMA13-029	Sp + Brt	+++	Tr	+		+	Tr		+++	+													
GMA13-033	Sp + Brt	+++		+		Tr			++								+			+			
GMA13-042	Sp + Brt	+++	+	+		+			+++			+			+		+	+		+			
GMA13-051	Sp + Brt	+++	+	Tr		+	+		+++			++		Tr	+		+	+				++	
GMA13-053a	Sp + Brt	++	+	+	++	+			+++			+					Tr		Tr				
GMA13-062	Sp + Brt	+++	+	+	+	Tr			++			+					Tr						
MA13-003	Sp + Brt	+++	+	Tr					++				Tr										
MA13-011	Sp + Brt	+++	+	+			+		+++			+					Tr						
MA13-029	Sp + Brt	+++	+	+		+			+++			Tr					Tr					+	
MA13-043	Sp + Brt	+++	+	+					+++			++											
MA13-065	Sp + Brt	+++		+			+		+++								+						
P0043	Sp + Brt	+++		+			+		+++			++					+					+	
GMA13-003a	Sp + Brt + Py	+++	Tr	++	+	Tr			++						Tr								
GMA13-003b	Sp + Brt + Py	+++	+	++	+	+			+						Tr		Tr						
GMA13-005	Sp + Brt + Py	+++	+	++	+	+			+++														
GMA13-007	Sp + Brt + Py	+++	Tr	++		+	Tr		+++														
GMA13-040	Sp + Brt + Py	+++	+	++		+			+++			+			Tr		+	Tr		+			
GMA13-041	Sp + Brt + Py	+++	+	++	+	+			+++			+		Tr	+		+	+	Tr				
GMA13-058	Sp + Brt + Mrc	+++	+	+	+++	+	Tr		+++										+				
GMA13-061	Sp + Brt + Mrc	++	+	+	++	+	Tr		+++			+		+	+		Tr		Tr				
GMA13-006	Sp + Brt + Gn	+++	+	+		+++	+		++								+						
GMA13-032	Sp + Mrc/Py	+++	+	+++	+	+	Tr		+			++			Tr		Tr		Tr				
GMA13-052	Sp + Mrc/Py	+++	+	+	++	+			+			+					+						
MA13-098	Sp + Mrc/Py	++	++	+++					++			++					Tr					+	

+++ = abundant (>25%); ++ = major (10-25%); + = minor (1-9%); Tr = Trace (<1%)

Sp = sphalerite; Ccp = chalcopyrite; Py = pyrite; Mrc = marcasite; Gn = galena; Jd = jordanite; Au = gold; Brt = barite; Anh = anhydrite; Gp = gypsum

Am-Si = amorphous silica (opal-A); Bn = bornite; Dg = digenite; Cv = covellite; Ata = atacamite; FeOx = iron oxyhydroxie; Hem = hematite; Goe = goethite; MnOx = manganese oxyhydroxide; Volc. = volcanic; Cal = calcite

Table 4.1. Continued

Sample	Chimney Type	Sp	Ccp	Py	Mrc	Gn	Jd	Au	Brt	Anh	Gp	Am-Si	Bn	Dg	Cv	Ata(?)	FeOx	Hem	Goe(?)	MnOx	Volc. Clasts	Clay	Cal
Barite-rich																							
GMA13-18b	Brt + Mrc ± Py	+		++	++				+++			+		Tr	Tr		Tr						
GMA13-024	Brt + Mrc ± Py	+			+++				++								+		+				+
GMA13-045	Brt + Mrc ± Py	+		+	++	+	+		+++			+					Tr		Tr				
Silicified barite-rich																							
GMA13-009b	Am-Si + Brt ± Fe-MnOx	+		+	+	Tr	Tr		+++			++					+			+			
GMA13-018a	Am-Si + Brt ± Fe-MnOx			+					++			+++					+			+++			
GMA13-030a	Am-Si + Brt ± Fe-MnOx			+	++							++					+++	+		+			
GMA13-060	Am-Si + Brt ± Fe-MnOx	+	+		Tr				+++			++					+	+	+	+		+	
GMA13-017a	Am-Si + Brt + Mrc/Py			++	++				+++			+++					++	+		+			
GMA13-017b	Am-Si + Brt + Mrc/Py	+		++	++				+++			+++					Tr						
GMA13-030b	Am-Si + Brt + Mrc/Py	+		++	++				+++			++					+						
Mineralized volcanic breccia																							
GMA13-008	Sp + Brt + Volc. Clasts	++	Tr	+		+			++	+		+			Tr		+			+	+++	+	
GMA13-009a	Sp + Brt + Volc. Clasts	++		+	Tr	Tr	Tr		+++	+							+	+		+	+++		
GMA13-053b	Sp + Brt + Volc. Clasts	++	+	+	+	+			+++			++					+				++	+	
Mineralized volcanic breccia - stringer																							
MA13-010	Sp + Brt + Volc. Clasts	+++	+	+					+++			+									+		
MA13-012	Sp + Brt + Volc. Clasts	++	+	+			+		+++			++									+++		
MA13-032	Sp + Brt + Volc. Clasts	++	+	+					+++			++					+				++		
MA13-066	Sp + Brt + Volc. Clasts	++	+	Tr					+++			++				Tr					+		
MA13-013	Py + Brt + Volc. Clasts	+	+	++					++			+									++	+++	
MA13-031	Ccp + Brt + Volc. Clasts	+	++	+					+++			++									+++		
P0011	Ccp + Brt + Volc. Clasts		+++	++					+++			++	Tr		Tr		Tr				++		
Mixed chimney talus																							
MA13-030	Sp + Py + Brt + Gp	+++	+	++					++	+	++											++	
MA13-033	Ccp + Sp + Py + Brt/Anh	++	+++	++						++	+												
P0010	Ccp + Sp + Py + Brt/Anh	++	++	+++					++		++		+										

+++ = abundant (>25%); ++ = major (10-25%); + = minor (1-9%); Tr = Trace (<1%)

Sp = sphalerite; Ccp = chalcopyrite; Py = pyrite; Mrc = marcasite; Gn = galena; Jd = jordanite; Au = gold; Brt = barite; Anh = anhydrite; Gp = gypsum
Am-Si = amorphous silica (opal-A); Bn = bornite; Dg = digenite; Cv = covellite; Ata = atacamite; FeOx = iron oxyhydroxie; Hem = hematite; Goe = goethite;
MnOx = manganese oxyhydroxide; Volc. = volcanic; Cal = calcite

conduits (Table 4.1; Fig. 4.4a–c; Fig. 4.5a). Locally, minor low-Fe sphalerite and barite also line former vent conduits and are interpreted to be late. Covellite, iron oxyhydroxides, and atacamite(?) are minor oxidation products. In one sample, there were trace amounts of visible gold occurring as very fine-grained inclusions within the chalcopyrite (sample GMA13-048; Fig. 4.4c).

Zoned chalcopyrite-rich chimneys

Three types of zoned chalcopyrite-rich chimneys are identified (Table 4.1; Fig. 4.4d–f): (1) chalcopyrite + pyrite ± marcasite chimneys; (2) chalcopyrite + marcasite + sphalerite chimneys; and (3) chalcopyrite + sphalerite chimneys. The mineralogical zonation occurs as bands around former vent conduits (Fig. 4.4d–f). The mineral paragenesis lining the chimney conduits is summarized in Figure 4.5b. In general, early dendritic to colloform marcasite, which has locally been altered to porous secondary pyrite, is followed by primary euhedral pyrite, and then abundant coarse-grained chalcopyrite. The inner conduit is dominated by banded chalcopyrite and high-Fe sphalerite, followed by a second generation of marcasite, and then low-Fe sphalerite with inclusions of fine-grained Pb-As-Sb sulfosalts (jordanite) and minor galena. This sequence is sometimes repeated. A late-stage of tabular coarse-grained barite, colloform amorphous silica and iron oxyhydroxides occupies remaining open spaces, and the chalcopyrite is locally altered to secondary Cu-sulfides (covellite, digenite, and bornite).

Dendritic sphalerite-rich chimneys

Sphalerite-rich chimneys consist of dendritic barite, sphalerite, and pyrite/marcasite (Table 4.1; Fig. 4.4g–i). Several different types are recognized: (1) sphalerite + barite chimneys; (2) sphalerite + barite + pyrite chimneys; (3) sphalerite + barite+ marcasite chimneys; (4) sphalerite + barite + galena chimneys; and (5) sphalerite + marcasite/pyrite chimneys. Clearly defined vent conduits are rare, typical of “beehive” chimneys formed by diffuse fluid venting (Fig. 4.4g–i). Similar dendritic sphalerite + barite occurs in mineralized volcanic breccia (Fig. 4.6a; Table 4.1) at the base of the chimneys. The mineral paragenesis of the chimneys is shown in Figure 4.5c; the earliest mineral phase is dendritic barite (Fig. 4.4h), followed by variable amounts of high- to low-Fe sphalerite, galena, and colloform pyrite (Fig. 4.4i). Locally, the early marcasite is replaced by

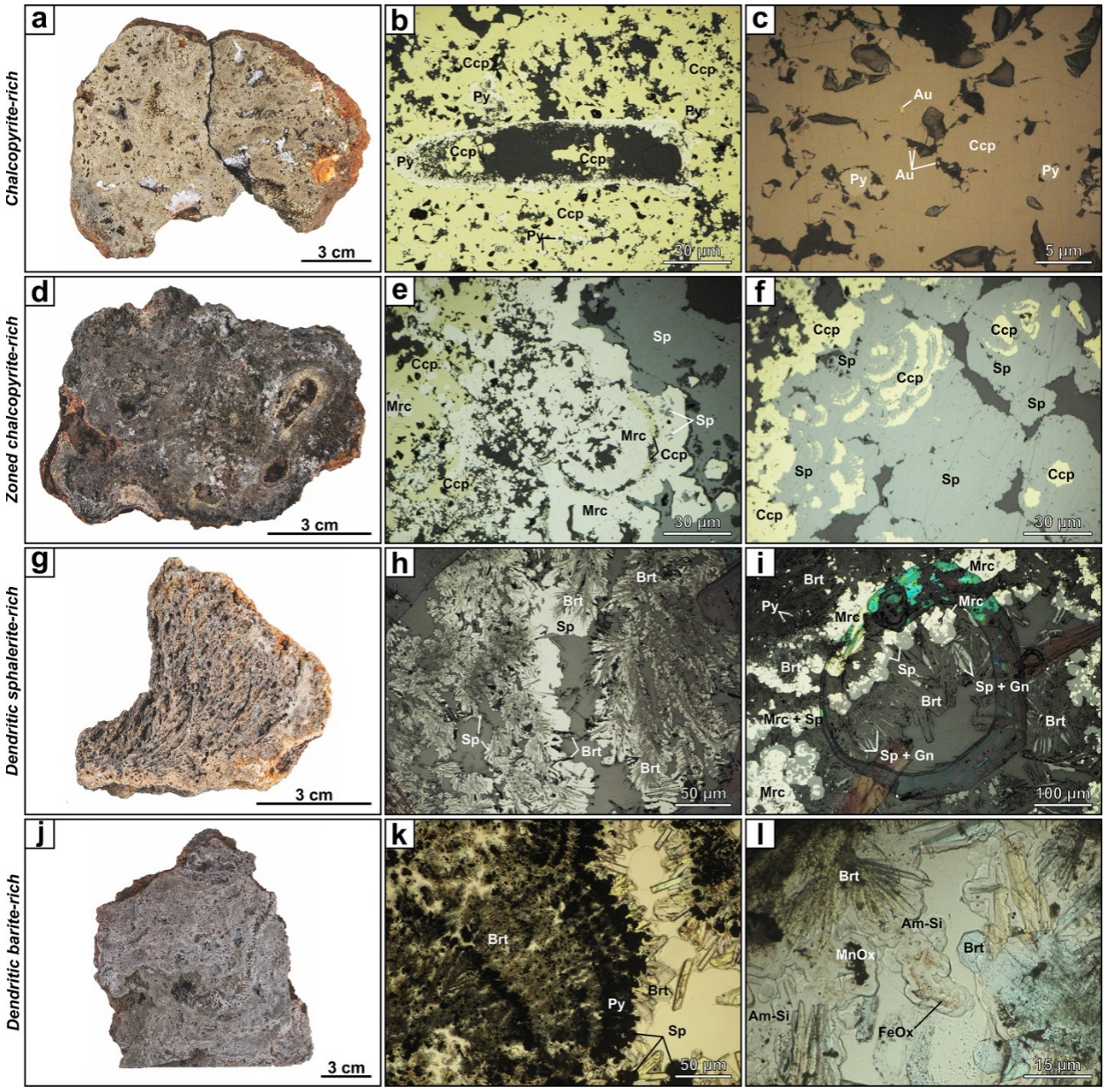


Fig. 4.4. Features of chimney types at the Tinakula deposit: (a) hand sample photo of a chalcopyrite-rich chimney, sample GMA13-048; (b) reflected light photomicrograph (PPL) of chalcopyrite-rich chimney with pyrite lining a former vent conduit, sample GMA13-038; (c) reflected light photomicrograph (PPL) of chalcopyrite-rich chimney with fine-grained gold inclusions within chalcopyrite, sample GMA13-048; (d) hand sample photo of zoned chalcopyrite-rich chimney, sample GMA13-031; (e) reflected light photomicrograph (PPL) of zoned chalcopyrite-rich chimney with chalcopyrite, marcasite (filling a former vent conduit), and sphalerite, sample GMA13-050; (f) reflected light photomicrograph (PPL) of zoned chalcopyrite-rich chimney with banded chalcopyrite and sphalerite, sample GMA13-031; (g) hand sample photo dendritic sphalerite-rich chimney, sample GMA13-012; (h) reflected light photomicrograph (PPL) of dendritic to acicular barite, followed by sphalerite with minor late barite, sample GMA13-022; (i) reflected light photomicrograph (PPL) of dendritic sphalerite-rich chimney, with early barite +

spherulitic pyrite, followed by intergrown marcasite + sphalerite, coarse-grained barite, and late sphalerite + galena, sample GMA13-058; (j) hand sample photo of dendritic barite-rich chimney, sample GMA13-045; (k) transmitted light photomicrograph (PPL) of banded dendritic barite + pyrite, with minor sphalerite, and late tabular barite, sample GMA13-018B; (l) transmitted light photomicrograph (PPL) of dendritic to radial barite, tabular barite, and late amorphous silica with very fine-grained inclusions of iron and manganese oxyhydroxides, sample GMA13-009B. Detailed petrography for all sulfide-sulfate samples is available in Appendix E. Am-Si = amorphous silica; Au = gold; Brt = barite; Ccp = chalcopyrite; Cv = covellite; Fe-MnOx = iron and manganese oxyhydroxides; Gn = galena; Mrc = marcasite; Py = pyrite; Sp = sphalerite.

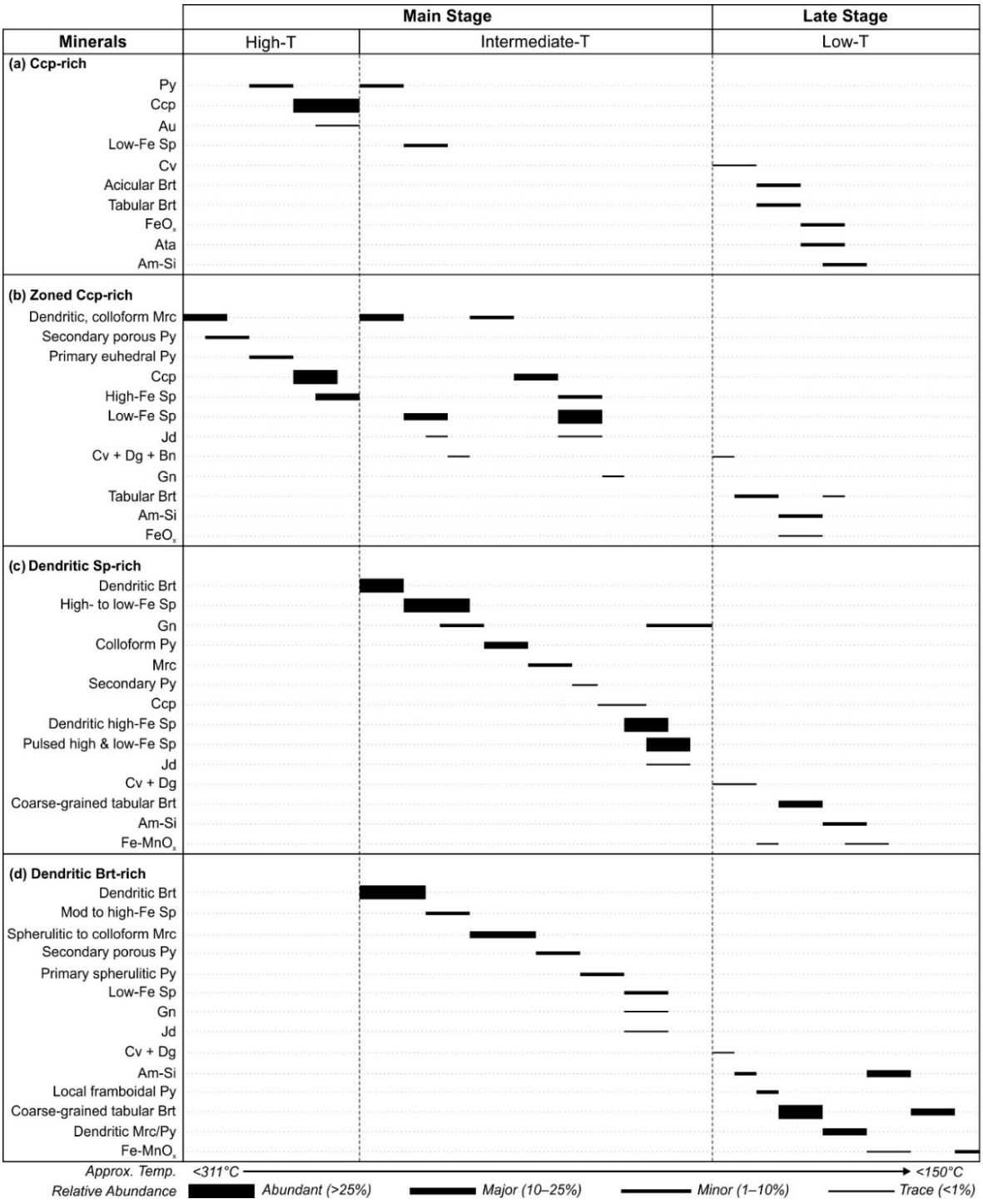


Fig. 4.5. General paragenesis of chimney types at the Tinakula deposit: (a) chalcopyrite-rich chimneys; (b) zoned chalcopyrite-rich chimneys; (c) dendritic sphalerite-rich chimneys; (d) dendritic barite-rich chimneys. Note that these generalized mineralization sequences are locally repeated within individual chimneys. Detailed paragenesis for all sulfide-sulfate samples is available in Appendix E. Am-Si = amorphous silica; Ata = atacamite; Au = gold; Bn = bornite; Brt = barite; Dg = digenite; Ccp = chalcopyrite; Cv = covellite; Fe-MnOx = iron-manganese oxyhydroxide; Gn = galena; Jd = jordanite; Mrc = marcasite; Py = pyrite; Sp = sphalerite.

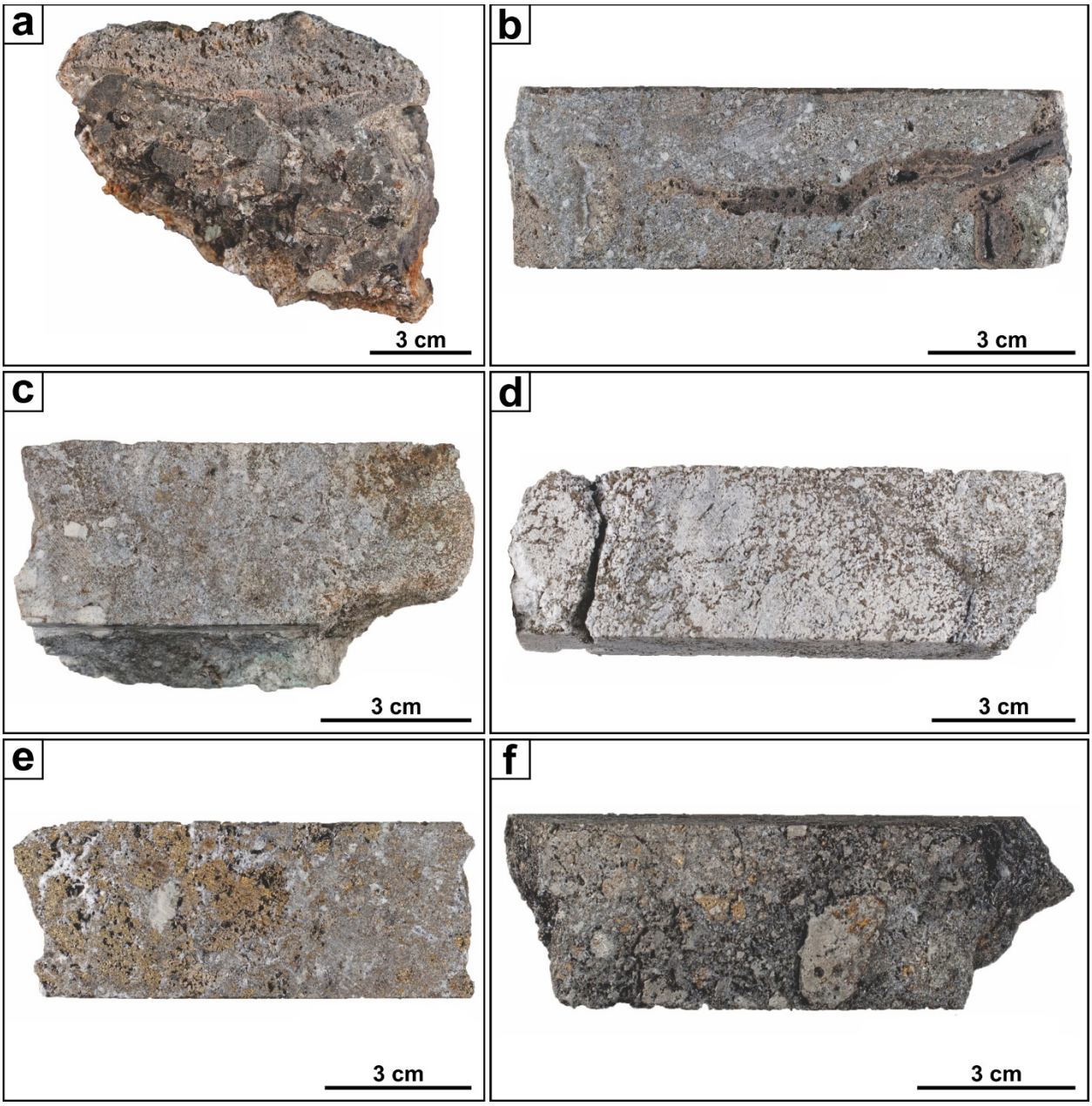


Fig. 4.6. Additional mineralized lithologies at the Tinakula deposit: (a) base of a sphalerite + barite chimney (top) with altered volcanic clasts (bottom) cemented by barite + sphalerite (sample GMA13-009); (b) stringer-zone mineralization with intensely-altered volcanic clasts cemented by barite with disseminated and fracture-controlled sphalerite + barite (sample MA13-012); (c) stringer-zone mineralization with intensely-altered volcanic clasts, cemented by barite, with disseminated chalcopyrite and minor pyrite (sample MA13-031); (d) stringer-zone mineralization with intensely-altered volcanic clasts, cemented by barite, with disseminated pyrite (sample MA13-013); (e) stringer-zone mineralization with intensely-altered volcanic clasts, cemented by barite, with disseminated chalcopyrite and minor pyrite (sample P011); (f) chimney talus consisting of clasts of various sizes, shape and mineralogy, cemented by fine-grained sulfides and minor sulfates (sample MA13-030).

pyrite. Multiple generations of dendritic high-Fe sphalerite and banded high- and low-Fe sphalerite (± jordanite and galena) often occur. Chalcopyrite is rare, generally occurring as fine-grained inclusions at the margins of sphalerite bands. Late-stage tabular barite is common, followed by minor amounts of amorphous silica, and trace iron- and manganese oxyhydroxides. Trace amounts of secondary covellite and digenite have replaced sphalerite. Additional petrographic details are found in Appendix E.

Dendritic barite-rich chimneys

Barite-rich chimneys consist mainly of dendritic barite, marcasite, and pyrite, with variable late-stage amorphous silica and minor or no sphalerite, chalcopyrite, galena, or Pb-As-Sb sulfosalts (Table 4.1 and Fig. 4.4j–l). Three subtypes are recognized: (1) barite + marcasite ± pyrite chimneys; (2) amorphous silica + barite ± iron and manganese oxyhydroxides; and (3) amorphous silica + barite + marcasite and pyrite. The mineral paragenesis is shown in Fig. 4.5d, beginning with abundant fine-grained dendritic barite (Fig. 4.4k), followed by colloform or dendritic marcasite that has locally been replaced by porous pyrite. Minor to rare sphalerite ranges from dark to black (moderate- to high-Fe). Late-stage dendritic pyrite and marcasite are associated with low-Fe sphalerite containing inclusions of galena and jordanite. Sphalerite is locally altered to covellite and digenite. Late-stage amorphous silica line or fills open spaces and locally is associated with framboidal pyrite, coarse-grained tabular barite, and minor iron and manganese oxhydroxides (Fig. 4.4l).

Mineralized volcanic breccia

Seven samples from shallow drill core (less than 6 m deep) are highly mineralized volcanic breccias, interpreted to represent the upper parts of a stringer zone. The breccias contain variably-altered volcanic clasts cemented by barite and amorphous silica but retaining a high porosity (Table 4.1 and Fig. 4.6b–e). Minor disseminated sulfides and lesser amounts of vein-controlled mineralization are present, including pyrite, marcasite, sphalerite, and chalcopyrite. Three main types of breccias are recognized based on the cementing material: (1) sphalerite + barite; (2) pyrite

+ barite; (3) chalcopyrite + barite. Samples from the stringer zone and deeper footwall alteration are described in *Chapter 5*.

Mixed chimney talus

Three samples from shallow drill core consist of mixed chimney talus with variably-rounded sulfide clasts (mm- to cm-size) in a matrix of sulfates (barite, anhydrite, and gypsum) and/or fine-grained sulfides (Table 4.1 and Fig. 4.6f). The sulfide clasts consist of sphalerite, pyrite, and chalcopyrite-rich chimney fragments, suggesting that they are sourced from different chimney types. Most do not contain amorphous silica. The clasts appear to have been transported variable distances from their sources. Additional petrographic details are found in Appendix E.

Iron and manganese oxyhydroxides

Iron and manganese oxyhydroxides are precipitated widely around the Tinakula deposit, occurring in close proximity to sulfide chimneys, and along fractures in the indurated crust on the seafloor (Fig. 4.2f), interpreted to form via primary precipitation of a low-temperature late-stage oxidizing fluid. These crusts are very friable, resulting in a sampling bias towards silicified or barite-rich samples (Suppl. Fig. C1 and Appendix F). The samples are subdivided into three main types: (1) Si-rich samples with variable proportions of Fe- and Mn-oxhydroxides (n = 8); (2) dendritic Mn-rich oxides (n = 3); and (3) oxide-cemented sediment (n = 1).

The silica-rich samples are dominated by amorphous silica, chalcedony, and minor microcrystalline quartz with variable amounts of amorphous to dendritic iron and manganese oxyhydroxides. The macroscopic texture has a wispy appearance, and the samples contain abundant fossilized worm tubes (Fig. 4.7a,b), suggesting that biogenic processes may have been important in the early stages of growth. The samples are generally soft and friable, and locally have a layered appearance or delicate banded chimney-like textures. Very few sulfides are present in these samples; minor fine-grained pyrite is present locally, with trace amounts of chalcopyrite and sphalerite. Several samples contain locally abundant dendritic- to coarse-grained barite. The Mn-dominated samples display banded chimney-like textures with bands of dendritic to colloform

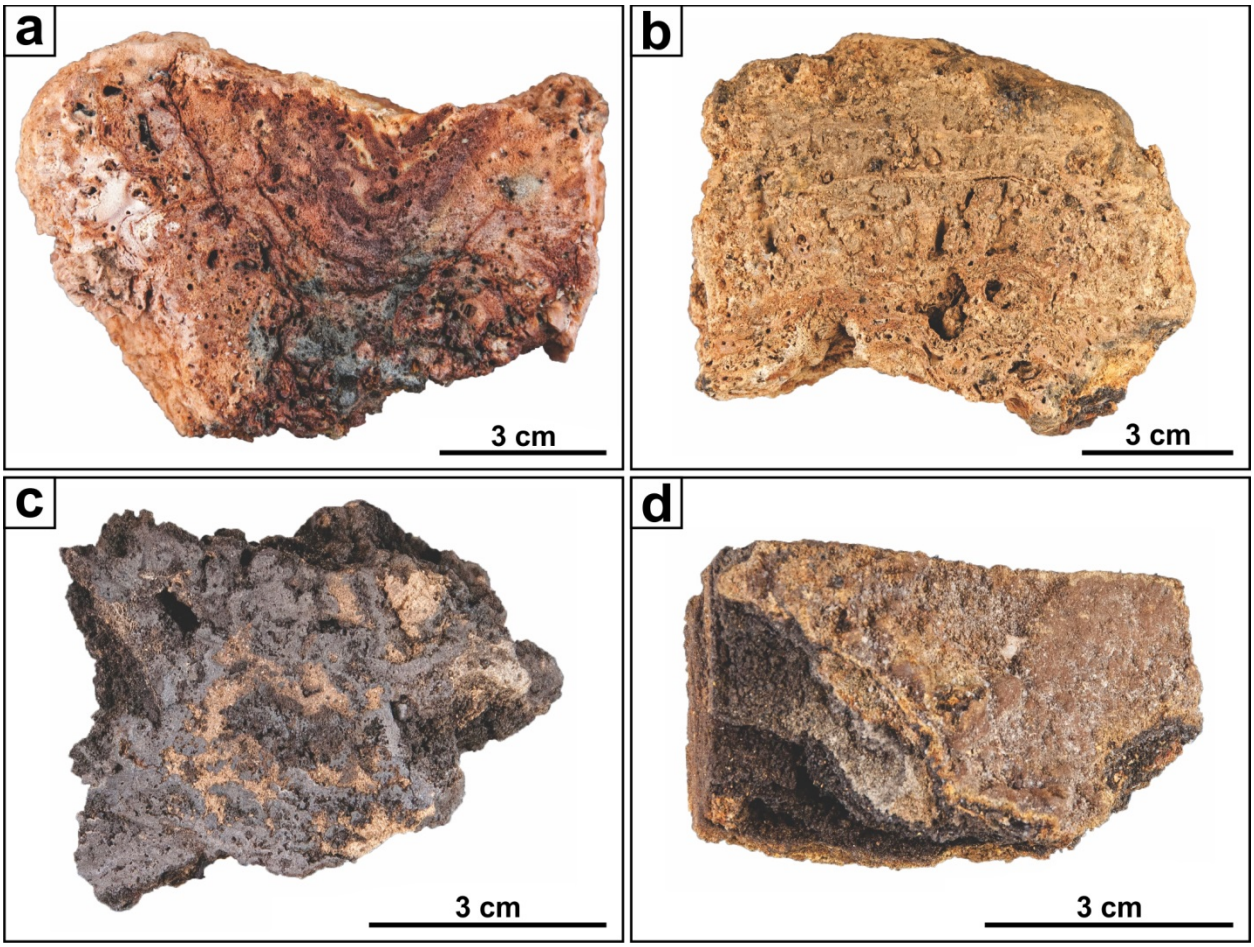


Fig. 4.7. Oxide lithologies at the Tinakula deposit: (a) Si-rich chimney with minor Fe and Mn oxides and abundant worm casts, sample GMA13-037; (b) Si-rich chimney with minor Fe oxides, with a layered appearance and abundant worm casts, sample GMA13-054; (c) Mn oxide, with bands of dense dendritic Mn oxide, infilled by lighter Fe oxide, sample GMA13-011; (d) laminated volcaniclastic sediment with late Fe and Mn oxide infill of permeable space, sample GMA13-014.

Mn-oxyhydroxides that locally appear to define vent conduits (Fig. 4.7c), and are very soft and friable with a high porosity. The samples overall have a minimum pore space of 20 vol.%. One sample contained finely-bedded volcanic sandstone that has been impregnated with iron and manganese oxides (Fig. 4.7d). The planar laminated beds of sand-sized volcanic(?) particles are a few mm-thick, infilled by alternating Fe-Mn oxides, with a higher proportion of Mn oxides at the top of the sample where it was exposed at the seafloor. In this sample, the Fe-Mn oxides apparently precipitated from primary low-temperature hydrothermal fluids permeating through the sediment.

4.4.2. Ore geochemistry

The bulk compositions of each mineralization style are listed in Table 4.2, with additional details in Appendix I. Average Zn concentrations for all chimney samples in the deposit are high (0.06–52.60 wt.%; avg. 19.20 wt.%, n = 36), reflecting the dominance of sphalerite-rich chimneys, and an average of 5.82 wt.% Cu (0.01–30.00 wt.%, n = 36), but very low Pb contents (<0.01–2.93 wt.%; avg. 0.35 wt.% , n = 36) compared to other back-arc basin sulfide deposits (e.g., Fig. 4.8; cf. Hannington et al., 2005; Monecke et al., 2016). Trace element concentrations of chimney samples are highly variable, with average concentrations (in order of decreasing abundance): 708 ppm Cd, 610 ppm As, 154 ppm Sb, 118 ppm Ag, 56 ppm Mo, 50 ppm Ge, 50 ppm In, 37 ppm Ga, 23 ppm Tl, 21 ppm Hg, 11 ppm Se, and 2.36 ppm Au (n = 36). Values of Ni, Bi, Co, Sn, W, Te, and REEs are generally below detection limits. The concentrations of Ba are 6.49 wt.% (n = 36), reflecting the abundant barite, but the Ca concentrations are low (avg. 0.06 wt.%; n = 36). Strontium is notably enriched (avg. 2157 ppm; n = 36), with concentrations up to 0.85 wt.% in barite-rich samples. The average Si concentrations are 5.45 wt.% (n = 36). One silicified barite-rich chimney contained 35.1 wt.% Si, with very low concentrations of most other trace elements except Sr.

Chalcopyrite-rich chimneys contain up to 30.00 wt.% Cu, associated with elevated Mo (avg. 343 ppm; n = 2) and In (avg. 262 ppm; n = 2; Table 4.2). Gold concentrations range from 124–9260 ppb (Suppl. Table I1), averaging 4692 ppb Au (n = 2). Zoned chalcopyrite-rich chimneys have moderate Cu contents (avg. 12.1 wt.%; n = 11) and a wide range of Zn concentrations (0.48–24.40 wt.%; Table 4.2), averaging 13.16 wt.% (n = 11). Lead concentrations are unexpectedly low (avg.

Table 4.2. Average whole-rock geochemistry of sulfide-sulfate samples by chimney type at the Tinakula deposit (after Appendix I)

		Ccp-Rich	Zoned chalcopyrite-rich			Dendritic sphalerite-rich				Barite-rich	Silicified barite-rich
		Ccp	Ccp + Py ± Mrc	Ccp + Mrc + Sp	Ccp + Sp	Sp + Brt	Sp + Brt + Py	Sp + Brt + Mrc	Sp + Mrc/Py	Brt + Mrc ± Py	Am-Si + Brt + Mrc/Py
		n = 2	*n = 3*	*n = 5*	*n = 3*	*n = 13*	*n = 1*	*n = 2*	*n = 3*	*n = 2*	*n = 2*
S_{Total}	wt. %	33.3	35.4	34.4	27.6	23.0	19.8	21.9	30.1	35.8	5.1
Au	ppb	4692	1014	2670	3517	1133	4270	5455	3510	3905	171
Fe	wt. %	25.65	27.97	21.78	12.05	2.88	2.10	6.60	14.80	22.80	2.35
Cu	wt. %	30.00	17.03	10.14	10.52	0.68	0.81	0.38	1.52	0.51	0.02
Mo	ppm	343	85	53	66	14	110	46	67	11	9
In	ppm	262	59	57	125	14	27	5	5	<0.2	<0.2
Ni	ppm	<10	<10	<10	<10	<10	10	20	<10	<10	<10
Bi	ppm	<2	<2	<2	<2	<2	<2	<2	<2	<2	<2
Co	ppm	2	<0.2	<0.2	<0.2	<0.2	<0.2	<0.2	2	1	2
Zn	wt. %	1.99	1.54	1.54	21.50	30.92	27.10	15.61	25.02	3.39	0.23
Cd	ppm	144	61	15.12	963	1008	1120	601	761	155	3
Ga	ppm	23	21	682	91	31	65	18	26	13	4
Ge	ppm	9	24	72	74	69	51	30	50	21	2
Se	ppm	9	8	54	11	13	12	11	13	7	1
Tl	ppm	1	26	12	32	17	8	38	47	11	12
Pb	ppm	44	428	1401	1927	4441	5300	6600	2444	12600	1545
Hg	ppb	535	11080	30122	10697	19145	6480	19050	35100	27300	35880
As	ppm	54	568	1091	579	641	425	567	625	488	112
Sb	ppm	9.3	55	158	193	143	179	364	299	119	46
Ag	ppm	42	42	66	138	139	124	272	112	210	32
Te	ppm	<6	<6	<6	<6	<6	<6	<6	<6	<6	<6
Sn	ppm	14	6.3	19	5	9	4	1	<0.5	<0.5	<0.5
W	ppm	7	1	4	2	3	1	<0.7	<0.7	<0.7	1
Ba	wt. %	0.05	0.65	1.10	4.06	9.49	9.15	13.49	2.33	8.58	15.18
Ca	wt. %	0.02	0.03	0.05	0.04	0.07	0.06	0.11	0.08	0.08	0.11
Sr	ppm	3	209	434	1445	2781	2730	6235	1539	4135	3137
Mg	wt. %	0.03	0.02	<0.01	<0.01	<0.01	<0.01	<0.01	<0.01	<0.01	0.03
Mn	ppm	10	205	41	189	36	227	311	2338	578	63
K	wt. %	<0.1	<0.1	<0.1	<0.1	<0.1	<0.1	<0.1	<0.1	<0.1	<0.1
Na	wt. %	0.09	0.15	0.11	0.19	0.07	0.21	0.10	0.16	0.04	0.23
Si	wt. %	0.6	3.3	3.2	5.1	4.3	9.1	5.0	6.7	2.3	27.0
Al	wt. %	0.22	0.21	0.18	0.10	0.03	0.17	0.17	0.09	0.02	0.14
Ti	wt. %	<0.01	<0.01	<0.01	<0.01	<0.01	<0.01	<0.01	<0.01	<0.01	<0.01
V	ppm	37	43	27	35	19	59	20	39	24	27
P	wt. %	0.053	0.033	0.017	0.022	<0.005	0.012	<0.005	0.053	0.007	<0.005

Am-Si = amorphous silica; Anh = anhydrite; Brt = barite; Ccp = chalcopyrite; Gp = gypsum; Mrc = marcasite; Py = pyrite; Sp = sphalerite; Volc. = volcanic

Table 4.2. Continued

		Min. volc. breccia	Min. volc. breccia - stringer			Mixed chimney talus	
		Sp + Brt + Volc. Clasts	Sp + Brt + Volc. Clasts	Py + Brt + Volc. Clasts	Ccp + Brt + Volc. Clasts	Sp + Py + Brt + Gp	Ccp + Sp + Py + Brt/Anh
		n = 1	*n = 3*	*n = 1*	*n = 2*	*n = 1*	*n = 1*
S_{Total}	wt. %	10.2	17.4	13.7	24.9	22.2	31.7
Au	ppb	221	2397	1220	255	356	552
Fe	wt. %	1.39	5.09	11.70	18.95	0.91	22.20
Cu	wt. %	0.05	0.77	5.40	10.18	0.86	7.86
Mo	ppm	10	29	17	163	22	143
In	ppm	2	9	48	44	<0.2	30
Ni	ppm	<10	<10	<10	<10	<10	<10
Bi	ppm	<2	<2	<2	<2	<2	<2
Co	ppm	6	2	7	11	<0.2	2
Zn	wt. %	3.39	16.74	2.09	2.45	35.60	5.16
Cd	ppm	20	562	77	109	1610	263
Ga	ppm	9	20	33	19	3	24
Ge	ppm	22	79	11	19	66	32
Se	ppm	5	10	8	10	12	12
Tl	ppm	6	27	3	15	<0.1	49
Pb	ppm	3890	6918	97	79	539	217
Hg	ppb	25200	23103	1770	905	13700	1070
As	ppm	221	830	441	255	659	306
Sb	ppm	47	243	19	13	530	14
Ag	ppm	56	110	<5	<5	401	bdl
Te	ppm	<6	<6	<6	<6	<6	<6
Sn	ppm	<0.5	<0.5	1	1	3	11
W	ppm	10	11	2	5	5	8
Ba	wt. %	15.40	6.02	0.09	0.71	9.42	0.97
Ca	wt. %	0.64	0.13	0.09	0.09	0.04	0.02
Sr	ppm	5060	2038	6	164	1740	303
Mg	wt. %	0.27	0.01	0.08	0.04	<0.01	<0.01
Mn	ppm	272	58	12	36	11	192
K	wt. %	<0.1	<0.1	0.8	0.3	<0.1	<0.1
Na	wt. %	0.43	0.19	0.26	0.14	0.10	0.04
Si	wt. %	12.2	15.6	25.5	14.5	1.7	10.9
Al	wt. %	1.79	0.55	2.95	1.30	0.09	0.13
Ti	wt. %	0.11	0.05	0.33	0.10	<0.01	<0.01
V	ppm	109	44	160	94	18	66
P	wt. %	0.019	<0.005	0.009	0.020	<0.005	0.012

Am-Si = amorphous silica; Anh = anhydrite; Brt = barite; Ccp = chalcopyrite; Gp = gypsum; Mrc = marcasite; Py = pyrite; Sp = sphalerite; Volc. = volcanic; Min. = mineralized

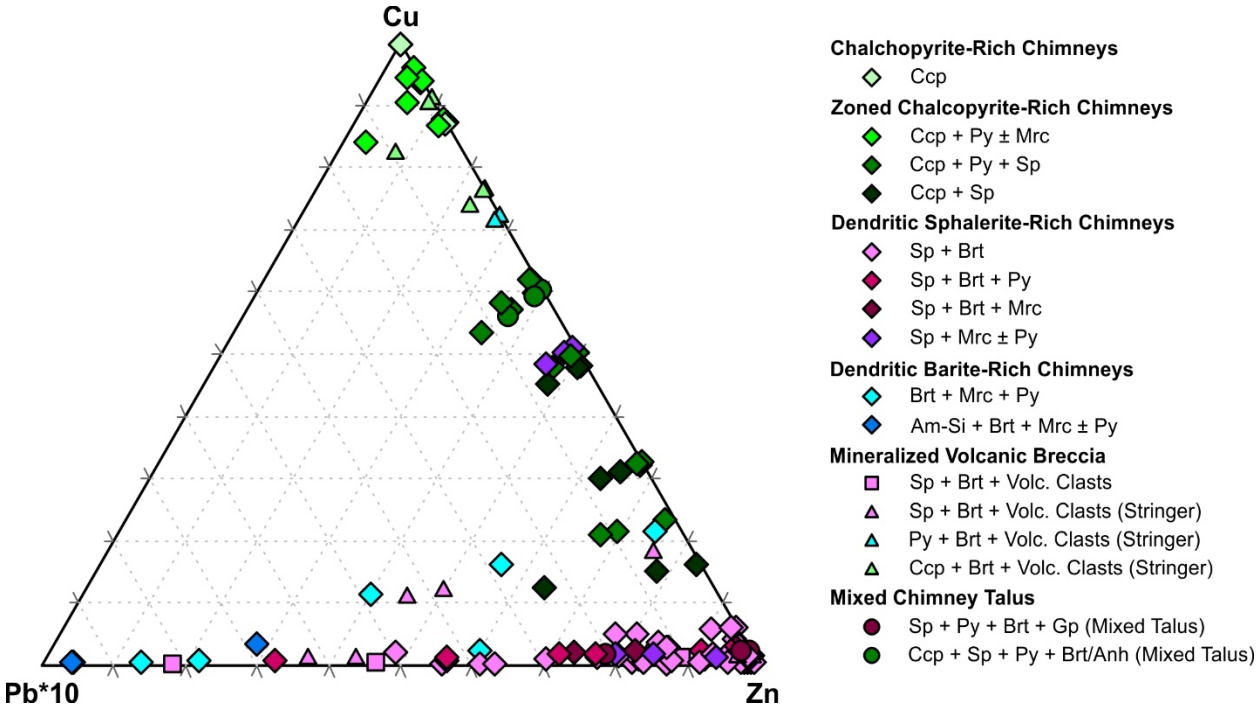


Fig. 4.8. Ternary diagram of Cu, Pb, and Zn concentrations in bulk whole-rock chimney samples from the Tinakula deposit, classified according to sample type (see text for classification). Detailed data is available in Appendix I. Am-Si = amorphous silica; Brt = barite; Ccp = chalcopyrite; Mrc = marcasite; Py = pyrite; Sp = sphalerite; Volc. = volcanic.

1279 ppm; n = 11), but As and Sb concentrations are high (avg. 809 ppm As; 139 ppm Sb; n = 11), reflecting variable amounts of Pb-As-Sb sulfosalts in the samples. Most Zn-rich samples contain very high concentrations of Ga (up to 1540 ppm), Ge (up to 99 ppm), Hg (up to 95 ppm), and Se (up to 20 ppm); Au concentrations are 1014–3517 ppb. Dendritic sphalerite-rich chimneys have low Cu contents (avg. 0.79 wt.%; n = 19) and slightly more Pb (avg. 4398 ppm; n = 19; Table 4.2). Concentrations of Ag (avg. 148 ppm, up to 424 ppm), Sb (avg. 193 ppm, up to 594 ppm), As (avg. 619 ppm, up to 1520 ppm), and Au (avg. 2128 ppb; up to 7810 ppb) are also higher than in the zoned chalcopyrite chimneys, generally following Zn and Pb concentrations (Suppl. Table I1, Table 4.2). The four sampled barite-rich chimneys contain 11.88 wt.% Ba (avg.), low Zn (avg. 1.81 wt.%) and Cu (avg. 0.26 wt.%), and high Pb (avg. 7073 ppm), As (avg. 299 ppm) and Sb (avg. 82 ppm). In addition, concentrations of Au and Ag reach 5370 ppb Au (avg. 2038 ppb) and 229 ppm Ag (avg. 121 ppm), with the highest concentrations in chimneys that are not silicified.

High As contents are found in both high- and low-temperature assemblages at Tinakula (Table 4.2). In bulk whole-rock samples from Tinakula, As contents range from 10–1940 ppm (avg. 610 ppm; n = 36; Appendix I), which is within the range of average As contents reported from massive sulfide deposits in arc-related rift settings (avg. 45–43,481 ppm; Monecke et al., 2014). The concentrations of In, particularly in the Cu-rich chimneys, are higher than 75% of reported In concentrations in seafloor massive sulfide deposits, with values of up to 280 ppm (avg. 105 ppm; n = 13). Mercury concentrations are elevated in samples containing marcasite and late sphalerite + galena, particularly samples GMA13-024, -031, -045, -052, and -058 (Appendix L), with slightly higher concentrations in low-temperature assemblages.

4.4.3. Element correlations and principal component analysis (PCA)

The behavior of trace and selected major elements has been analyzed using Pearson correlations and principal component analysis in the XLSTAT add-on for Microsoft Excel. The data were grouped based on petrography into chalcopyrite-rich and sphalerite-rich samples, which are interpreted to reflect high-temperature (>250°C) and low-temperature (<250°C) assemblages, respectively (Hannington et al., 2005). The Pearson correlation matrices are shown in Tables 4.3 and 4.4, and bivariate plots for selected trace elements of each chimney type are shown in

Table 4.3. Correlation matrix (Pearson) for high-temperature chimneys (chalcopyrite-rich and zoned chalcopyrite-rich chimney types) from the Tinakula deposit. Correlation coefficients indicating strong positive correlations are highlighted in red, and strong negative correlations are highlighted in green (minimum 99% confidence interval; n = 13)

	S	Fe	Pb	Zn	Cd	Ga	Ge	Se	As	Sb	Tl	Ag	Au	Cu	Hg	In	Mo	Mn	Si	Ba	Ca	Sr
S	1																					
Fe	**0.85**	1																				
Pb	-0.38	-0.55	1																			
Zn	-0.58	**-0.91**	0.57	1																		
Cd	-0.53	**-0.86**	0.50	**0.98**	1																	
Ga	-0.46	**-0.76**	0.45	**0.88**	**0.94**	1																
Ge	-0.46	**-0.78**	**0.80**	**0.88**	**0.84**	**0.72**	1															
Se	-0.24	-0.56	0.14	**0.74**	**0.80**	**0.77**	0.64	1														
As	0.13	0.03	0.40	0.11	0.08	0.12	0.23	-0.15	1													
Sb	-0.63	**-0.83**	0.54	**0.85**	**0.76**	0.63	**0.76**	0.47	0.36	1												
Tl	-0.18	-0.13	**0.71**	0.12	0.10	0.22	0.35	-0.19	0.65	0.23	1											
Ag	-0.58	-0.69	0.25	0.66	0.62	0.47	0.42	0.22	-0.15	0.60	-0.07	1										
Au	-0.36	-0.34	-0.02	0.22	0.24	0.23	0.05	0.13	-0.32	0.06	-0.21	0.23	1									
Cu	0.17	0.41	-0.57	-0.49	-0.43	-0.43	-0.57	-0.07	**-0.75**	-0.64	-0.56	-0.21	0.24	1								
Hg	0.10	-0.18	0.70	0.36	0.25	0.14	0.56	0.09	0.30	0.41	0.32	0.11	-0.13	-0.32	1							
In	-0.25	-0.07	-0.31	-0.09	-0.03	-0.02	-0.36	-0.08	**-0.73**	-0.32	-0.45	0.27	0.42	0.63	-0.37	1						
Mo	-0.05	0.18	-0.34	-0.37	-0.35	-0.31	-0.45	-0.25	-0.48	-0.43	-0.31	-0.22	**0.79**	0.59	-0.29	0.51	1					
Mn	-0.12	-0.16	0.06	-0.01	-0.05	0.04	0.11	-0.09	0.00	0.07	0.07	-0.18	-0.10	-0.44	-0.17	-0.27	-0.05	1				
Si	-0.18	0.01	0.20	-0.10	-0.12	-0.11	-0.07	-0.51	0.63	0.14	0.61	0.11	-0.16	-0.55	-0.20	-0.25	-0.21	0.11	1			
Ba	-0.64	**-0.71**	0.49	0.50	0.40	0.40	0.51	0.11	0.06	0.63	0.19	0.30	0.10	-0.54	0.21	-0.10	-0.13	0.68	0.05	1		
Ca	-0.16	-0.15	-0.09	0.20	0.28	0.33	-0.03	0.24	0.37	0.18	-0.03	-0.03	0.14	-0.08	-0.28	0.10	-0.07	-0.35	0.14	-0.10	1	
Sr	-0.61	**-0.73**	0.60	0.55	0.45	0.43	0.57	0.09	0.08	0.64	0.25	0.37	0.12	-0.58	0.33	-0.09	-0.15	0.62	0.07	**0.98**	-0.16	1

Table 4.4. Correlation matrix (Pearson) for low-temperature chimneys (dendritic sphalerite-rich and barite-rich chimney types) from the Tinakula deposit. Correlation coefficients indicating strong positive correlations are highlighted in red, and strong negative correlations are highlighted in green (minimum 99% confidence interval; n = 23)

	S	Fe	Pb	Zn	Cd	Ga	Ge	Se	As	Sb	Tl	Ag	Au	Cu	Hg	In	Mo	Mn	Si	Ba	Ca	Sr
S	1																					
Fe	**0.77**	1																				
Pb	-0.11	-0.12	1																			
Zn	0.01	**-0.56**	0.01	1																		
Cd	0.04	-0.44	-0.08	**0.88**	1																	
Ga	0.18	0.05	-0.24	0.32	**0.63**	1																
Ge	-0.02	-0.50	0.08	**0.74**	**0.54**	0.09	1															
Se	0.19	-0.37	0.19	**0.88**	**0.76**	0.24	**0.71**	1														
As	0.08	0.08	0.20	0.00	-0.05	0.02	0.27	0.23	1													
Sb	0.12	-0.09	0.01	0.41	0.42	0.21	-0.01	0.45	-0.01	1												
Tl	0.22	0.14	-0.08	0.22	0.07	0.11	0.08	0.28	0.38	**0.58**	1											
Ag	0.08	-0.15	0.34	0.12	0.06	-0.13	0.17	0.24	0.09	**0.60**	0.20	1										
Au	0.36	0.27	-0.06	0.00	0.11	0.29	-0.06	0.23	-0.02	**0.63**	0.35	**0.56**	1									
Cu	0.46	**0.63**	-0.19	-0.30	-0.18	0.28	-0.22	-0.13	**0.55**	-0.13	0.32	-0.33	0.01	1								
Hg	0.26	0.12	-0.10	0.18	0.39	**0.68**	0.00	0.23	-0.09	0.22	0.08	0.02	0.33	0.07	1							
In	0.21	0.18	-0.19	0.04	0.26	**0.67**	0.17	0.11	0.34	-0.13	0.02	-0.20	0.23	**0.63**	0.27	1						
Mo	0.00	0.07	-0.07	0.05	0.20	0.40	-0.17	0.11	0.00	0.18	0.17	-0.26	0.28	0.10	0.25	0.11	1					
Mn	0.03	0.09	-0.04	0.00	0.12	0.21	-0.14	0.06	0.05	0.16	0.03	-0.10	0.18	-0.06	0.44	-0.14	**0.65**	1				
Si	**-0.63**	-0.12	-0.08	-0.36	-0.30	-0.10	-0.38	-0.51	-0.13	-0.16	-0.01	-0.38	-0.27	-0.05	-0.24	-0.11	0.10	-0.03	1			
Ba	-0.37	-0.49	0.21	-0.09	-0.15	-0.33	0.13	-0.07	-0.08	0.09	-0.43	0.41	-0.06	-0.45	-0.10	-0.22	-0.21	-0.09	-0.35	1		
Ca	0.10	0.08	0.00	-0.14	-0.16	-0.06	-0.17	-0.05	0.14	-0.17	-0.02	0.22	0.14	-0.09	0.10	-0.29	0.32	**0.56**	-0.38	0.38	1	
Sr	-0.22	-0.26	0.24	-0.19	-0.22	-0.24	-0.17	-0.16	-0.22	0.05	-0.27	0.45	0.15	-0.41	0.05	-0.28	-0.04	0.16	-0.34	**0.85**	**0.59**	1

Figures 4.9 and 4.10. Trace elements with strong lattice substitution in different minerals, such as Sr in barite and Cd in sphalerite, show the strongest correlations in both high- and low-temperature assemblages (e.g., Ba versus Sr: r = 0.98 and 0.85, respectively; Zn versus Cd: r = 0.98 and 0.88, respectively: Fig. 4.9a,b). Statistically-significant correlations also occur between Ga, Ge, Se, and Sb and Zn (Cd), strongly suggesting the substitution of the elements in sphalerite (Figs. 4.9c–f). The correlation between Ga/Zn is greatest in high-T chimneys (r = 0.88), but not in low-T chimneys (r = 0.32; Fig. 4.9c), which is followed by strong positive correlations between Ga/Ge in high-T chimneys (r = 0.72) but not in low-T chimneys (r = 0.09; Fig. 4.9f). In high-T chimneys, Cu is negatively correlated with As (r = -0.75), reflecting the low total As concentrations of these samples (Fig. 4.9g). In low-T chimneys, both As and In are positively correlated with Cu (r = 0.55 and 0.63, respectively; Fig. 4.9g,h), indicating that chalcopyrite (or other Cu-rich trace minerals: e.g., roquesite) are the main hosts for these elements. Lead is positively correlated with Tl in high-T chimneys (r = 0.71) but not in low-T chimneys (r = -0.08; Fig. 4.9i). Similarly, there is only a correlation between Pb/Hg in high-T chimneys (r = 0.70; Table 4.3). There is variable correlation between As and Sb; high-temperature chimneys generally contain some As but low Sb, whereas low-temperature chimneys contain both As and Sb. There is a moderate correlation between Ag and Sb in both high- and low-T chimneys (r = 0.60; Fig. 4.10a), and a moderate correlation between Ag/Zn in high-T chimneys only (r = 0.66; Fig. 4.10b). In low-T chimneys, there is a moderate correlation between Ag and Au (r = 0.56; Fig. 4.10c) and Sb and Au (r = 0.63; Fig. 4.10d). In high-T chimneys, Au only correlates with Mo (r = 0.79; Table 4.3).

Principal components analysis was performed on the combined data set (n=36) to analyze and visualize the combinations of elements that account for most of the variance. Factor 1 captures the maximum variability in the data. The factor loadings for the first four factors are shown in Table 4.5. They account for 61.3% of the total variance. Factor 1 is related to the formation of the low-temperature mineral assemblage, with positive loadings for Zn, Cd, Ge, Pb, Sb, Ag, Ba, and Sr. Negative loadings for Fe, Cu, Mo and In in Factor 1 reflect the high-T mineral assemblage. Positive loadings for Ga, Se, and Hg in Factor 2 reflect lattice substitutions in sphalerite in high-T chimneys. Positive loadings for Mn, V, and Mo in Factor 3 likely reflect adsorption of oxyanions from seawater by iron and manganese oxyhydroxides. There are additional positive loadings for

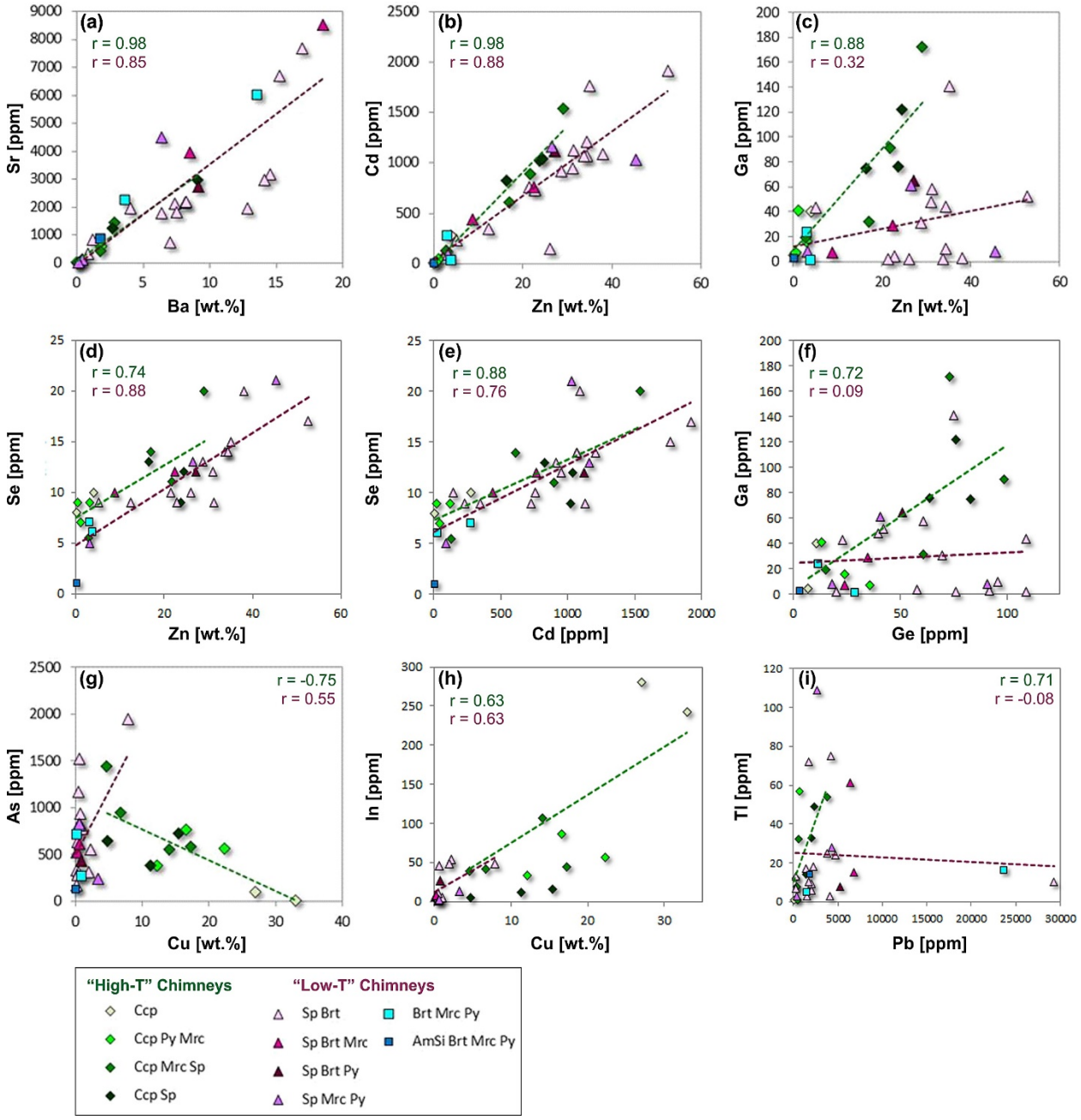


Fig. 4.9. Bivariate plots for selected whole-rock major and trace elements for high-temperature chimneys (trendlines and r-values shown in green) and low-temperature chimneys (trendlines and r-values shown in purple) from the Tinakula deposit. Am-Si = amorphous silica; Brt = barite; Ccp = chalcopyrite; Mrc = marcasite; Py = pyrite; Sp = sphalerite.

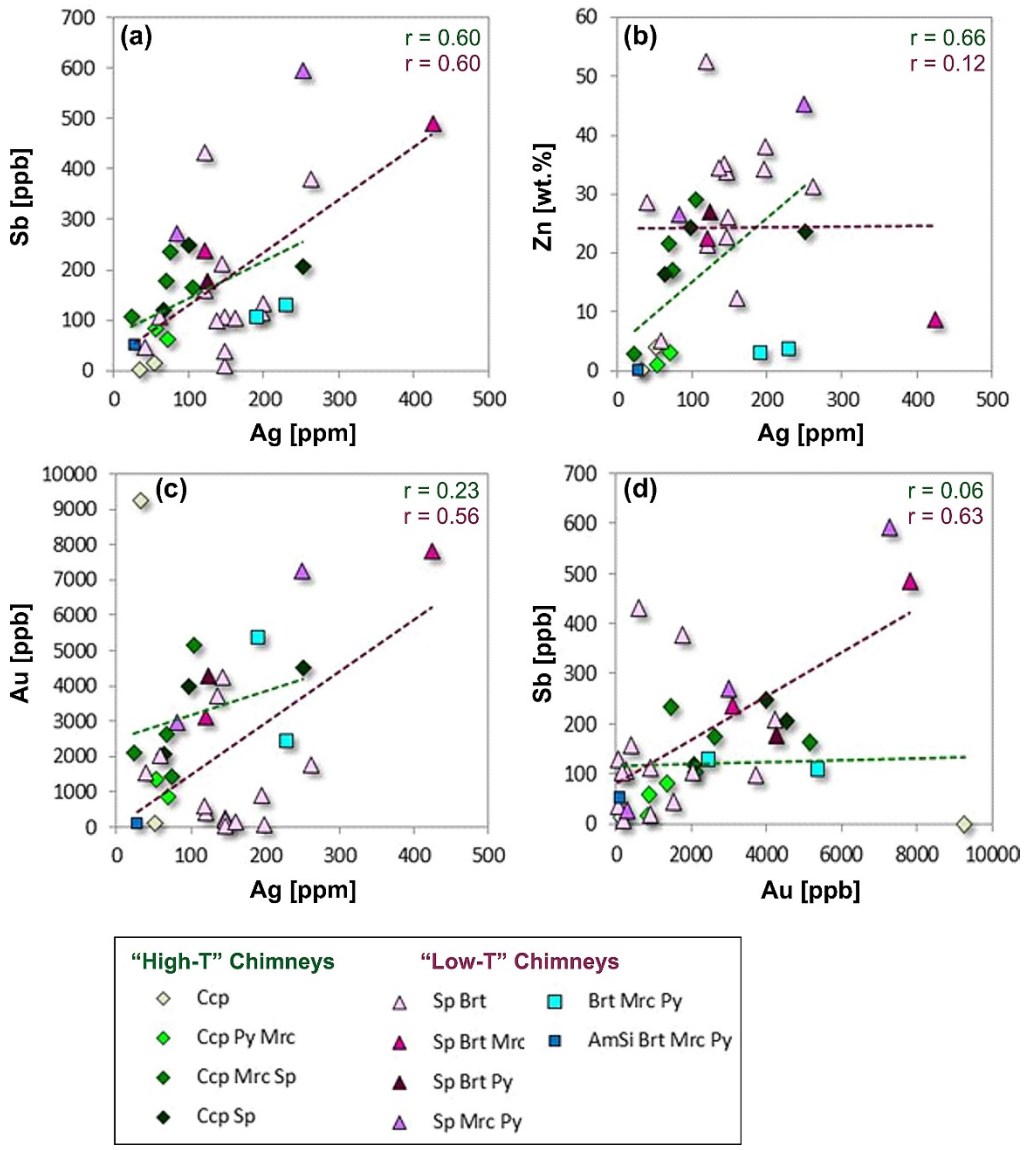


Fig. 4.10. Bivariate plots for selected whole-rock trace elements versus Ag and Au for high-temperature chimneys (trendlines and r-values shown in green) and low-temperature chimneys (trendlines and r-values shown in purple) from the Tinakula deposit. Am-Si = amorphous silica; Brt = barite; Ccp = chalcopyrite; Mrc = marcasite; Py = pyrite; Sp = sphalerite.

Table 4.5. Factor loadings for the principal component analyses of high-and low-T chimneys from the Tinakula deposit (n = 36)

	Factor 1	Factor 2	Factor 3	Factor 4
Eigenvalue	5.9	3.6	2.5	2.1
Variability (%)	25.5	15.7	11.0	9.1
Cumulative %	25.5	41.2	52.2	61.3
Au	0.015	0.436	**0.443**	-0.439
Fe	**-0.792**	0.156	0.124	0.080
Cu	**-0.774**	0.405	0.047	-0.277
Mo	**-0.535**	0.278	0.309	-0.408
In	**-0.611**	0.479	0.124	-0.366
Zn	**0.804**	0.424	-0.221	-0.024
Cd	**0.684**	0.589	-0.139	-0.030
Ga	0.103	**0.735**	0.076	0.083
Ge	**0.640**	0.402	-0.320	0.024
Se	0.591	**0.614**	-0.167	-0.141
Tl	0.196	0.295	0.130	**0.528**
Pb	**0.406**	-0.276	0.038	-0.055
Hg	0.306	**0.307**	0.268	0.210
As	0.220	0.011	-0.012	**0.528**
Sb	**0.591**	0.335	0.240	0.028
Ag	**0.661**	-0.090	0.217	-0.323
Ba	**0.616**	-0.561	0.160	-0.337
Ca	0.397	-0.348	**0.544**	-0.091
Sr	**0.562**	-0.544	0.418	-0.327
Mn	0.142	0.048	**0.746**	0.278
Si	-0.145	-0.339	-0.141	**0.519**
V	-0.244	0.087	**0.648**	0.389
Low-T Chimneys	**0.664**	-0.466	-0.049	-0.053
High-T Chimneys	**-0.664**	0.466	0.049	0.053

Values in bold correspond for each variable to the factor for which the squared cosine is the largest

Au and Ca in Factor 3, reflecting the occurrence of both of these elements in both high- and low-T assemblages. Positive loadings for Tl, As, and Si in Factor 4 reflect low amounts of late-stage low-temperature precipitation or adsorption of these elements in the amorphous silica. The factor loadings, which are shown graphically in Figure 4.11, indicate a combination of both temperature and mineralogical controls on the behavior of the trace elements.

The respective high- and low-temperature assemblages are clearly separated by F1 and F2 (e.g., Sr, Ba, and Ca in barite, along with Pb, and Ag in low-T chimneys; Cu, Fe, Mo, and In in high-T chimneys). Vectors for Zn, Ge, Cd, and Se reflect incorporation of these elements into the lattice of sphalerite and plot in the upper right quadrant because sphalerite occurs in both high- and low-T mineral assemblages. Plots of F2 and F3 plus F2 and F4 show the association of Au and Mo with Cu in the high-T chimneys. The plot of F2 and F4 also shows the association of As and Tl in the low-temperature oxide and Si-rich chimneys.

4.4.4. Iron and manganese oxyhydroxides

Whole-rock geochemical analyses of 7 oxide samples that displayed “chimney-like” textures, are tabulated in Table 4.6 (details in Appendix J) and compared graphically in Figure 4.12. The samples have Si concentrations from 11.10 wt.% to 43.10 wt.%, with 2.09–11.10 wt.% Fe and 0.10–7.99 wt.% S_{total}. Concentrations of Mn are variable, from a few ppm to >1 wt.%, and Ba concentrations range from 56 ppm to 28.6 wt.%. Cu and Zn contents are generally low (37–481 ppm and 70–3840 ppm Zn, respectively), but certain trace metals are enriched relative to the sulfur content (e.g., 41-1310 ppm Pb, and up to 440 ppm As, 69 ppm Hg, and 247 ppb Au). The latter are consistent with the low-temperature origin of the Fe-oxide and silica chimneys and crusts (e.g., Hannington et al., 1991; Hein et al., 2000; Hein et al., 2014). High concentrations of Mo (up to 485 ppm), V (up to 193 ppm), and Cr (up to 77 ppm) likely reflect the strong adsorption of these elements onto Fe- and Mn-oxyhydroxide precipitates (e.g., Hein et al., 2000).

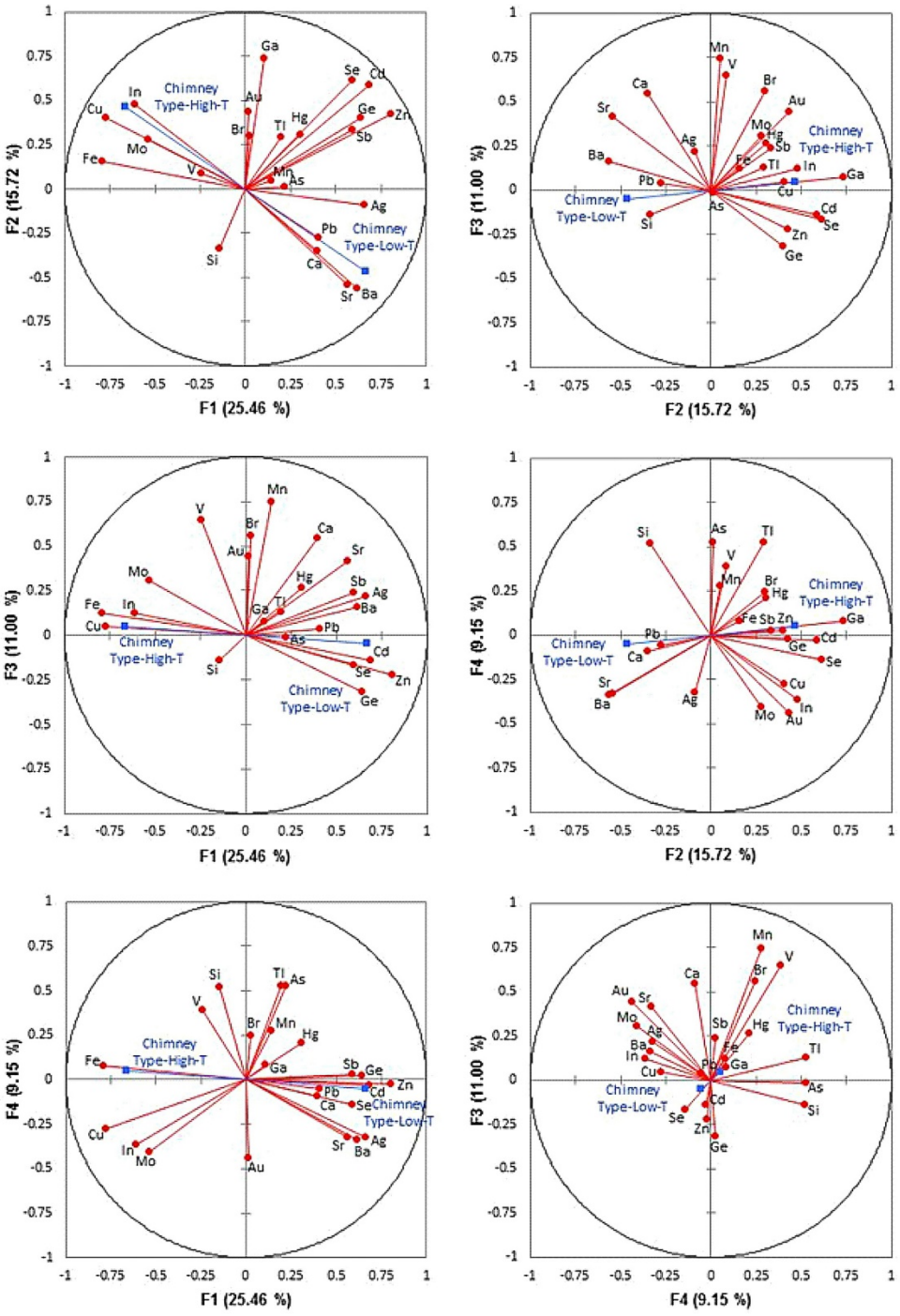


Fig. 4.11. Factor loadings of the principal component analyses of chimneys from the Tinakula deposit (n = 36). Narrow angles between vectors reflect positive correlations between elements, right angles reflect elements that are not related to one another, and obtuse angles reflect negative correlations between elements. Short vectors indicate elements that are not well represented in the chosen dimensions. These data are grouped into high- and low-temperature chimney types and displayed as blue vectors (see text for chimney type descriptions) in order to detect which of these explanatory variables have the strongest effects on the dependent variable (see Table 4.5).

Table 4.6. Whole-rock geochemistry of siliceous Fe-Mn oxyhydroxides at the Tinakula deposit

	Unit	D.L.	Analysis Method	GMA13-025 Fe-Mn	GMA13-026 Si-Fe	GMA13-037 Si-Fe	GMA13-047 Si-Fe	GMA13-054 Si-Fe	GMA13-055 Si-Fe	GMA13-059 Si-Fe-Mn	Average
Si	%	0.01	FUS-Na_2O_2	11.10	> 30.0	43.10	29.60	> 30.0	> 30.0	25.60	19.91
Fe	%	0.01	INAA	11.10	4.75	2.37	8.77	6.91	6.72	12.90	7.65
Mg	%	0.01	FUS-Na_2O_2	0.80	0.18	0.02	0.28	0.14	0.36	0.32	0.30
Mn	ppm	3	FUS-MS-Na_2O_2	>10000	451	6	9230	3340	247	>10000	4753
S	%	0.01	FUS-Na_2O_2	0.10	2.42	0.20	1.10	0.03	0.12	0.13	0.59
S_{Total}	%	0.01	CS	0.13	2.55	0.19	1.06	0.10	0.18	0.16	0.62
Au	ppb	2	INAA	<2	24	<2	<2	26	37	<2	13
Cu	ppm	2	FUS-MS-Na_2O_2	481	165	58	357	37	44	60	172
Mo	ppm	1	INAA	485	29	1	26	26	32	92	99
In	ppm	0.2	FUS-MS-Na_2O_2	0.3	<0.2	<0.2	<0.2	<0.2	<0.2	<0.2	<0.2
Ni	ppm	10	FUS-MS-Na_2O_2	40	10	<10	60	10	10	20	22
Bi	ppm	2	FUS-MS-Na_2O_2	<2	<2	7	<2	<2	<2	<2	<2
Co	ppm	0.2	FUS-MS-Na_2O_2	62.7	16.0	<0.2	2.9	1.0	2.5	49.4	19.2
Zn	ppm	30	FUS-MS-Na_2O_2	880	360	70	1090	90	100	620	459
Cd	ppm	2	FUS-MS-Na_2O_2	2	bdl	<2	3	6	<2	4	3
Ga	ppm	0.2	FUS-MS-Na_2O_2	33.3	6.3	2.0	4.6	1.6	0.9	4.5	7.6
Ge	ppm	0.7	FUS-MS-Na_2O_2	7.6	22.3	5.0	9.2	12.7	11.1	9.9	11.1
Se	ppm	0.8	FUS-MS-Na_2O_2	<0.8	2.1	4.0	2.5	2.1	<0.8	3.3	2.1
Tl	ppm	0.1	FUS-MS-Na_2O_2	9.3	61.0	2.0	0.7	0.9	0.1	4.0	11.1
Pb	ppm	0.8	FUS-MS-Na_2O_2	110.0	41.2	465.0	1330.0	65.1	171.0	1310.0	498.9
Hg	ppb	5	1G	24	479	2910	140	8980	2180	1250	2280
As	ppm	0.5	INAA	159	189	105	415	444	71	292	239
Sb	ppm	0.1	INAA	7.6	25.6	14.7	21.6	39.9	13.3	31.9	22.1
Ag	ppm	5	INAA	<5	<5	<5	<5	<5	<5	<5	<5
Te	ppm	6	FUS-MS-Na_2O_2	<6	<6	<6	<6	<6	<6	<6	<6
Sn	ppm	0.5	FUS-MS-Na_2O_2	<0.5		<0.5	<0.5	4.6	1.3	<0.5	1.0
W	ppm	0.7	FUS-MS-Na_2O_2	2.9	<0.7	2.0	2.5	2.5	0.8	3.0	2.0
Ba*	ppm	3	FUS-Na_2O_2	2080	56	2980	29000	90	211	96	4930
Ca	%	0.01	FUS-Na_2O_2	0.73	0.10	0.04	0.24	0.16	0.15	0.47	0.27
Sr	ppm	3	FUS-MS-Na_2O_2	354	34	89	2080	75	52	176	409
K	%	0.1	FUS-Na_2O_2	0.8	0.1	<0.1	0.2	0.2	0.2	0.3	0.30
Na	%	0.01	INAA	1.75	0.87	0.10	1.78	1.01	1.76	1.68	1.16
Al	%	0.01	FUS-Na_2O_2	0.15	0.08	<0.01	0.08	0.05	0.03	0.03	0.06
Ti	%	0.01	FUS-Na_2O_2	<0.01	<0.01	<0.01	<0.01	<0.01	<0.01	<0.01	<0.01
P	%	0.005	FUS-Na_2O_2	-	-	0.017	-	-	-	-	-
B	ppm	10	FUS-MS-Na_2O_2	110	20	<5	60	90	40	120	63
Be	ppm	4	FUS-MS-Na_2O_2	<3	<3	<3	<3	<3	<3	6	<3
Cr	ppm	5	INAA	18	62	<5	71	50	77	55	48
Cs	ppm	0.1	FUS-MS-Na_2O_2	<0.1	0.4	<0.1	<0.1	<0.1	<0.1	<0.1	<0.1
Hf	ppm	1	INAA	<1	<1	<1	<1	<1	<1	<1	<1
Ir	ppb	5	INAA	<5	<5	<5	<5	<5	<5	<5	<5
Li	ppm	3	FUS-MS-Na_2O_2	47	<3	<3	3	5	<3	33	13
Nb	ppm	2.4	FUS-MS-Na_2O_2	<2.4	<2.4	<2.4	<2.4	<2.4	<2.4	<2.4	<2.4
Rb	ppm	0.4	FUS-MS-Na_2O_2	5.5	2.8	<0.4	1.9	1.6	2.1	1.9	2.3
Ta	ppm	0.2	FUS-MS-Na_2O_2	<0.2	<0.2	<0.2	<0.2	<0.2	<0.2	<0.2	<0.2
Th	ppm	0.1	FUS-MS-Na_2O_2	<0.1	<0.1	<0.1	<0.1	<0.1	<0.1	<0.1	<0.1
U	ppm	0.1	FUS-MS-Na_2O_2	3.6	2.2	2.0	3.1	4.4	10.5	2.7	4.1
Sc	ppm	0.1	INAA	0.6	0.3	<0.1	0.2	0.2	<0.1	0.2	0.2
Y	ppm	0.1	FUS-MS-Na_2O_2	8.7	<0.1	<0.1	<0.1	<0.1	<0.1	3.2	1.7
La	ppm	0.4	FUS-MS-Na_2O_2	2.2	0.7	<0.4	0.6	<0.4	<0.4	1.6	0.8
Ce	ppm	0.8	FUS-MS-Na_2O_2	5.0	1.2	<0.8	1.4	<0.8	<0.8	2.0	1.5
Pr	ppm	0.1	FUS-MS-Na_2O_2	0.6	0.1	<0.1	0.2	<0.1	<0.1	0.2	0.2
Nd	ppm	0.4	FUS-MS-Na_2O_2	3.1	0.8	1.0	1.2	<0.4	<0.4	1.5	1.1
Sm	ppm	0.1	FUS-MS-Na_2O_2	0.6	<0.1	<0.1	0.3	<0.1	<0.1	0.1	0.2
Eu	ppm	0.1	FUS-MS-Na_2O_2	0.4	<0.1	<0.1	1.2	<0.1	<0.1	<0.1	0.3
Gd	ppm	0.1	FUS-MS-Na_2O_2	1.2	0.2	<0.1	0.9	<0.1	<0.1	0.4	0.4
Tb	ppm	0.1	FUS-MS-Na_2O_2	0.2	<0.1	<0.1	<0.1	<0.1	<0.1	<0.1	<0.1
Dy	ppm	0.3	FUS-MS-Na_2O_2	1.1	<0.3	<0.3	<0.3	<0.3	<0.3	0.5	0.3
Ho	ppm	0.2	FUS-MS-Na_2O_2	0.3	<0.2	<0.2	<0.2	<0.2	<0.2	<0.2	<0.2
Er	ppm	0.1	FUS-MS-Na_2O_2	0.9	0.1	<0.1	0.1	<0.1	0.2	0.4	0.3
Tm	ppm	0.1	FUS-MS-Na_2O_2	0.1	<0.1	<0.1	<0.1	<0.1	<0.1	<0.1	<0.1
Yb	ppm	0.1	FUS-MS-Na_2O_2	0.7	0.1	<0.1	1.6	<0.1	0.1	0.3	0.4
Lu	ppm	0.05	INAA	0.20	<0.05	<0.05	<0.05	0.13	0.18	0.07	0.09

D.L. = detection limit; > = above detection limit; *Ba values >10000 measured by INAA (D.L. 50 ppm)

Averages calculated using half detection limit when below detection limits, and the upper detection limit when above

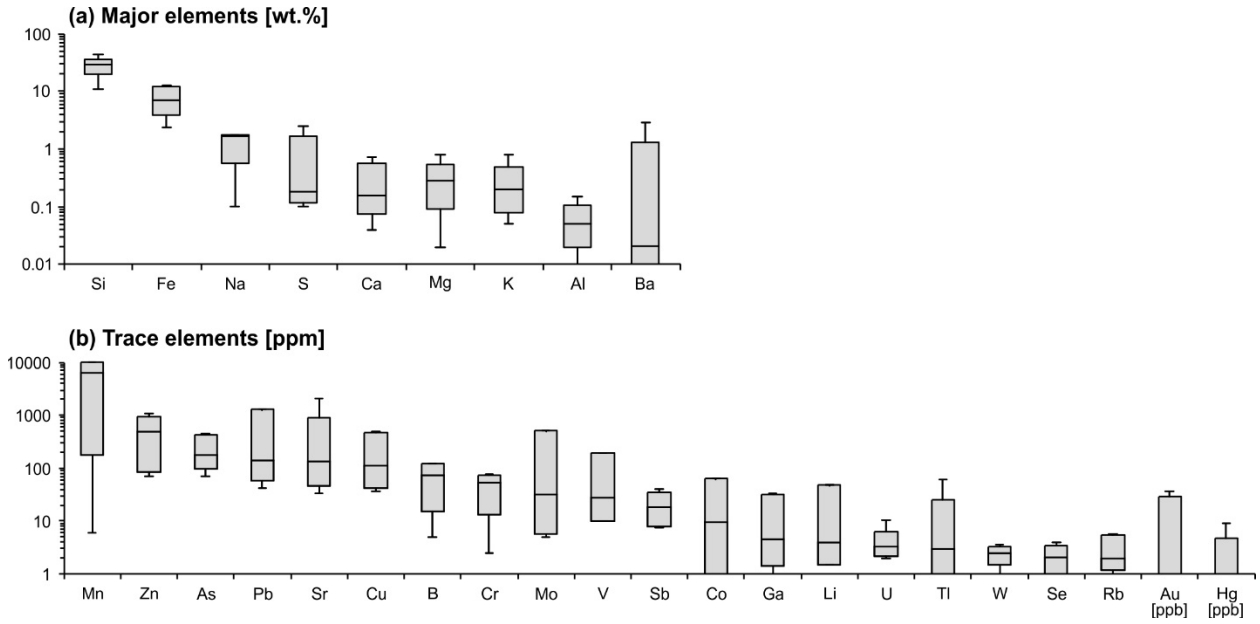


Fig. 4.12. Box-and-whisker plots of whole-rock geochemistry of oxide samples (n = 7) from the Tinakula deposit: (a) major elements, expressed as wt.%; (b) trace elements, expressed as ppm, except for Au and Hg (ppb). Below detection limit values have been replaced by half of the detection limit. The top of the box represents the 90th percentile of the data, the bottom of the box represents the 10th percentile, the central line represents the median, the bars represent the range of the data, and outliers are indicated by stars (*). The complete data are in Table 4.6.

4.4.5. Sulfide mineralogy and chemistry

EPMA analyses were performed on sulfide phases from 16 chimney samples. In addition to the major elements (Cu, Fe, Zn, Pb, As, and S), selected trace elements were also measured (Ag, As, of the Sb, Cd, Ga, Hg, and In). Germanium was not analyzed due to the lack of an available standard, and visible gold grains in sample GMA13-048 were too small to analyze. Results are summarized on Table 4.7 and Figures 4.13 and 4.14 (details are provided in Appendix L).

Chalcopyrite

Chalcopyrite is mainly stoichiometric $CuFeS_2$ (Suppl. Table L18). Traces of Zn and Pb are most likely due to inclusions of sphalerite and galena, especially where intergrown with sphalerite in the Zn-rich chimneys. An average of ~1 wt.% Zn was recorded in all analyses of chalcopyrite in the Zn-rich chimneys. Indium concentrations were generally below detection limits, reaching a maximum concentration in chalcopyrite of 0.18 wt.% from the zoned chalcopyrite-rich chimneys. However, no discrete In-bearing phases (e.g., roquesite inclusions) were observed. Mercury was detected in two analyses of chalcopyrite from chalcopyrite-rich chimneys (up to 0.13 wt.%), but was below detection in most other samples. Lead (up to 0.27 wt.%), together with As (up to 1.25 wt.%), Sb (up to 1.40 wt.%), and Ag (up to 0.06 wt.%) were detected in chalcopyrite from the Zn-rich chimneys, and may represent inclusions of sulfosalts, although Ag-rich chalcopyrite is known from some ancient massive sulfide deposits (see below). The highest concentration of Ag occurs in chalcopyrite from the dendritic sphalerite-rich chimneys. Gold was detected in chalcopyrite from the chalcopyrite-rich chimneys (avg. 0.1 wt.%; n = 47), with up to 0.78 wt.% Au in sample GMA13-048, corresponding to a bulk concentration of 9.26 ppm Au (Appendix I).

Pyrite and marcasite

Pyrite and marcasite are both close to stoichiometric FeS_2 (Suppl. Table L18), but locally contain up to 4.7 wt.% Cu and 5.1 wt.% Zn, most likely as submicroscopic inclusions of chalcopyrite and sphalerite. Arsenic concentrations are high in both marcasite (up to 1.42 wt.%) and pyrite (up to 2.7 wt.%) and may reflect lattice substitution, although submicroscopic inclusions of Pb-As-Sb

Table 4.7. Range and average trace-element concentrations measured by EMPA for sulfide minerals from the Tinakula deposit, depicted in Figs. 4.13 and 4.14, and detailed in Appendix L

Chalcopyrite	**Fe**	**S**	**Cu**	**In**	**Zn**	**Cd**	**Ga**	**Hg**	**Pb**	**As**	**Sb**	**Ag**	**Au**	**Mn**
Chimney Type	wt.%	wt.%	wt.%	wt.%	wt.%	wt.%	wt.%	wt.%	wt.%	wt.%	wt.%	wt.%	wt.%	wt.%
Ccp-rich														
Min	29.60	33.56	34.04	<0.01	<0.01	<0.01	<0.01	<0.01	NA	NA	NA	NA	<0.01	<0.01
Max	30.97	35.33	35.05	<0.01	2.05	0.02	0.05	0.13	NA	NA	NA	NA	0.78	0.03
Avg	30.52	34.49	34.65	<0.01	0.07	<0.01	<0.01	0.01	NA	NA	NA	NA	0.10	<0.01
n	*47*	*47*	*47*	*47*	*47*	*47*	*47*	*23*	*NA*	*NA*	*NA*	*NA*	*47*	*23*
Zoned Ccp-rich														
Min	28.43	33.6	29.31	<0.01	<0.01	<0.01	<0.01	<0.01	<0.01	<0.01	<0.01	<0.01	<0.01	<0.01
Max	33.37	38.09	37.53	0.18	2.80	0.03	0.08	0.11	0.39	1.25	0.38	0.04	0.44	0.03
Avg	30.28	34.61	34.41	<0.01	0.35	0.01	0.01	0.01	0.13	0.06	0.02	0.01	0.08	0.01
n	*185*	*185*	*185*	*185*	*185*	*185*	*185*	*160*	*140*	*160*	*160*	*58*	*83*	*42*
Dendritic Sp-rich														
Min	27.52	33.77	32.48	<0.01	<0.01	<0.01	<0.01	<0.01	<0.01	<0.01	<0.01	<0.01	<0.01	<0.01
Max	31.03	35.67	35.24	0.08	4.19	0.06	0.05	0.07	0.27	0.96	1.40	0.06	0.26	0.03
Avg	29.68	34.70	34.01	<0.01	1.22	0.01	0.01	0.01	0.13	0.05	0.06	0.02	0.06	<0.01
n	*88*	*88*	*88*	*88*	*88*	*88*	*88*	*88*	*72*	*88*	*88*	*31*	*31*	*62*
Dendritic Brt-rich														
Min	29.15	34.51	33.41	<0.01	1.09	<0.01	<0.01	0.05	0.19	<0.01	<0.01	0.01	0.04	NA
Max	29.15	34.51	33.41	<0.01	1.09	<0.01	<0.01	0.05	0.19	<0.01	<0.01	0.01	0.04	NA
Avg	29.15	34.51	33.41	<0.01	1.09	<0.01	<0.01	0.05	0.19	<0.01	<0.01	0.01	0.04	NA
n	*1*	*1*	*1*	*1*	*1*	*1*	*1*	*1*	*1*	*1*	*1*	*1*	*1*	*1*

Pyrite	**Fe**	**S**	**Cu**	**In**	**Zn**	**Cd**	**Ga**	**Hg**	**Pb**	**As**	**Sb**	**Ag**	**Au**	**Mn**
Chimney Type	wt.%	wt.%	wt.%	wt.%	wt.%	wt.%	wt.%	wt.%	wt.%	wt.%	wt.%	wt.%	wt.%	wt.%
Ccp-rich														
Min	43.92	51.12	0.04	<0.01	<0.01	<0.01	<0.01	<0.01	NA	NA	NA	NA	<0.01	<0.01
Max	47.88	53.44	2.1	<0.01	4.10	0.02	0.03	0.02	NA	NA	NA	NA	0.36	0.03
Avg	46.97	52.63	0.8	<0.01	0.19	<0.01	<0.01	<0.01	NA	NA	NA	NA	0.07	<0.01
n	*33*	*33*	*33*	*33*	*33*	*33*	*33*	*15*	*NA*	*NA*	*NA*	*NA*	*33*	*15*
Zoned Ccp-rich														
Min	43.7	51.29	0.01	<0.01	0.01	<0.01	<0.01	<0.01	0.17	<0.01	<0.01	0.01	<0.01	<0.01
Max	48.09	53.34	1.93	<0.01	1.30	0.02	0.01	0.04	2.40	0.70	0.04	0.01	0.17	0.99
Avg	46.74	52.40	0.31	<0.01	0.25	0.01	<0.01	<0.01	0.42	0.07	0.01	0.01	0.06	0.06
n	*43*	*43*	*43*	*43*	*43*	*43*	*43*	*35*	*34*	*35*	*35*	*1*	*9*	*35*
Dendritic Sp-rich														
Min	41.23	49.16	<0.01	<0.01	0.01	<0.01	<0.01	<0.01	0.11	<0.01	<0.01	<0.01	<0.01	<0.01
Max	48.32	54.08	4.73	<0.01	6.14	0.03	0.03	0.18	4.57	1.42	0.26	0.08	0.28	0.23
Avg	45.64	52.40	0.31	<0.01	1.04	0.01	<0.01	0.01	1.20	0.12	0.02	0.02	0.07	0.04
n	*96*	*96*	*96*	*96*	*96*	*96*	*96*	*96*	*82*	*96*	*96*	*46*	*46*	*91*

Marcasite	**Fe**	**S**	**Cu**	**In**	**Zn**	**Cd**	**Ga**	**Hg**	**Pb**	**As**	**Sb**	**Ag**	**Au**	**Mn**
Chimney Type	wt.%	wt.%	wt.%	wt.%	wt.%	wt.%	wt.%	wt.%	wt.%	wt.%	wt.%	wt.%	wt.%	wt.%
Zoned Ccp-rich														
Min	45.11	51.26	0.01	<0.01	<0.01	<0.01	<0.01	<0.01	0.05	<0.01	<0.01	<0.01	<0.01	<0.01
Max	48.09	53.56	2.19	<0.01	2.39	0.02	0.01	0.03	0.55	0.89	0.04	0.01	0.28	0.01
Avg	47.29	52.85	0.47	<0.01	0.21	0.01	<0.01	<0.01	0.18	0.07	0.01	<0.01	0.05	<0.01
n	*82*	*82*	*82*	*82*	*82*	*82*	*82*	*45*	*37*	*45*	*45*	*13*	*50*	*9*
Dendritic Sp-rich														
Min	42.54	50.45	<0.01	<0.01	0.01	<0.01	<0.01	<0.01	0.07	<0.01	<0.01	<0.01	<0.01	<0.01
Max	48.26	53.9	3.11	<0.01	5.14	0.02	0.01	0.05	4.82	2.71	0.11	0.13	0.22	0.18
Avg	46.74	52.60	0.30	<0.01	0.31	0.01	<0.01	0.01	0.61	0.26	0.02	0.04	0.04	0.02
n	*51*	*51*	*51*	*51*	*51*	*51*	*51*	*51*	*51*	*51*	*51*	*18*	*18*	*51*
Dendritic Brt-rich														
Min	43.9	51.53	<0.01	<0.01	<0.01	<0.01	<0.01	<0.01	0.13	<0.01	<0.01	<0.01	<0.01	NA
Max	47.94	54.73	4.46	<0.01	1.19	0.02	0.01	0.05	1.73	0.96	0.05	0.04	0.24	NA
Avg	46.81	53.42	0.58	<0.01	0.18	<0.01	<0.01	<0.01	0.38	0.06	0.01	<0.01	0.05	NA
n	*43*	*43*	*43*	*43*	*43*	*43*	*43*	*43*	*18*	*43*	*43*	*43*	*43*	*NA*

Sphalerite	**Zn**	**S**	**Fe**	**Cu**	**In**	**Cd**	**Ga**	**Hg**	**Pb**	**As**	**Sb**	**Ag**	**Au**	**Mn**
Chimney Type	wt.%	wt.%	wt.%	wt.%	wt.%	wt.%	wt.%	wt.%	wt.%	wt.%	wt.%	wt.%	wt.%	wt.%
Ccp-rich														
Min	54.30	32.57	0.53	0.08	<0.01	<0.01	<0.01	NA	NA	NA	NA	NA	<0.01	<0.01
Max	66.07	34.54	7.39	3.91	0.10	0.67	0.26	NA	NA	NA	NA	NA	0.34	0.01
Avg	64.35	33.23	1.54	0.07	0.01	0.33	0.17	NA	NA	NA	NA	NA	0.11	<0.01
n	*16*	*16*	*16*	*16*	*16*	*16*	*16*	*NA*	*NA*	*NA*	*NA*	*NA*	*16*	*3*
Zoned Ccp-rich														
Min	52.24	31.08	0.08	0.07	<0.01	<0.01	0.13	<0.01	0.11	<0.01	<0.01	<0.01	<0.01	<0.01
Max	66.33	33.48	8.21	7.00	0.14	2.04	1.03	0.13	7.24	1.83	0.50	0.07	0.44	0.03
Avg	62.76	32.75	1.72	1	0.01	0.40	0.23	0.01	0.69	0.07	0.09	0.01	0.15	0.01
n	*196*	*196*	*196*	*196*	*196*	*196*	*196*	*144*	*127*	*144*	*144*	*53*	*105*	*27*
Dendritic Sp-rich														
Min	54.06	31.52	0.04	0.03	<0.01	<0.01	0.13	<0.01	0.03	<0.01	<0.01	<0.01	<0.01	<0.01
Max	66.66	34.33	11.06	2.83	1.31	2.01	0.65	1.28	4.86	1.44	1.64	0.38	0.57	0.06
Avg	63.24	32.79	1.30	0.78	0.01	0.33	0.21	0.03	1.03	0.09	0.21	0.10	0.19	0.01
n	*300*	*300*	*300*	*300*	*300*	*300*	*300*	*300*	*266*	*300*	*300*	*132*	*132*	*253*
Dendritic Brt-rich														
Min	56.11	30.31	0.01	0.01	<0.01	<0.01	<0.01	<0.01	0.15	<0.01	<0.01	<0.01	<0.01	<0.01
Max	65.91	34.61	4.98	2.36	0.02	0.12	0.26	0.64	8.39	1.80	2.10	0.77	0.43	0.02
Avg	62.93	32.80	0.97	0.47	<0.01	0.03	0.16	0.04	1.56	0.13	0.24	0.12	0.14	0.01
n	*79*	*79*	*79*	*79*	*79*	*79*	*79*	*79*	*63*	*79*	*79*	*79*	*79*	*16*

Table 4.7. Continued

Galena	Pb	S	Fe	Cu	In	Zn	Cd	Ga	Hg	As	Sb	Ag	Au	Mn
Chimney Type	wt.%	wt.%	wt.%	wt.%	wt.%	wt.%	wt.%	wt.%	wt.%	wt.%	wt.%	wt.%	wt.%	wt.%
Zoned Ccp-rich														
Min	86.42	13.24	0.02	0.17	<0.01	0.05	0.04	<0.01	<0.01	<0.01	0.07	NA	NA	NA
Max	86.69	13.37	0.03	0.20	0.01	0.07	0.05	0.02	0.08	0.30	0.09	NA	NA	NA
Avg	86.56	13.31	0.03	0.18	<0.01	0.06	0.05	0.01	0.04	0.15	0.08	NA	NA	NA
n	*2*	*2*	*2*	*2*	*2*	*2*	*2*	*2*	*2*	*2*	*2*	*NA*	*NA*	*NA*
Dendritic Sp-rich														
Min	67.03	12.35	<0.01	<0.01	<0.01	<0.01	<0.01	<0.01	<0.01	<0.01	<0.01	<0.01	<0.01	<0.01
Max	88.02	17.85	0.77	1.14	0.01	18.02	0.14	4.69	0.11	1.62	2.36	0.29	0.38	0.03
Avg	84.58	13.66	0.06	0.14	<0.01	2.65	0.05	0.09	0.02	0.15	0.47	0.04	0.05	<0.01
n	*59*	*59*	*59*	*59*	*59*	*59*	*59*	*59*	*59*	*59*	*59*	*14*	*14*	*45*
Dendritic Brt-rich														
Min	69.93	12.87	<0.01	0.05	<0.01	<0.01	0.02	<0.01	<0.01	<0.01	<0.01	<0.01	<0.01	NA
Max	87.02	17.75	0.09	0.91	<0.01	8.32	0.08	0.04	0.13	9.93	2.84	1.23	0.27	NA
Avg	83.59	13.65	0.01	0.17	<0.01	1.99	0.05	0.01	0.04	0.65	0.50	0.19	0.05	NA
n	*37*	*37*	*37*	*37*	*37*	*37*	*37*	*37*	*37*	*37*	*37*	*37*	*37*	*NA*

Pb-As-Sb Sulfosalt	Pb	S	As	Sb	Fe	Cu	In	Zn	Cd	Ga	Hg	Ag	Au	Mn
Chimney Type	wt.%	wt.%	wt.%	wt.%	wt.%	wt.%	wt.%	wt.%	wt.%	wt.%	wt.%	wt.%	wt.%	wt.%
Zoned Ccp-rich														
Min	72.08	16.68	6.11	0.10	<0.01	0.04	<0.01	1.96	0.04	<0.01	<0.01	NA	NA	NA
Max	74.88	17.71	9.34	0.14	0.06	0.17	<0.01	2.65	0.06	<0.01	0.10	NA	NA	NA
Avg	73.48	17.20	7.73	0.12	0.03	0.10	<0.01	2.31	0.05	<0.01	0.05	NA	NA	NA
n	*2*	*2*	*2*	*2*	*2*	*2*	*2*	*2*	*2*	*2*	*2*	*NA*	*NA*	*NA*
Dendritic Sp-rich														
Min	65.93	17.70	8.53	<0.01	<0.01	0.17	<0.01	0.02	0.03	<0.01	<0.01	NA	NA	NA
Max	72.96	18.42	10.01	0.07	0.08	3.28	<0.01	2.63	0.06	<0.01	0.08	NA	NA	NA
Avg	70.37	18.01	9.38	0.03	0.04	1.28	<0.01	1.76	0.05	<0.01	0.03	NA	NA	NA
n	*3*	*3*	*3*	*3*	*3*	*3*	*3*	*3*	*3*	*3*	*3*	*NA*	*NA*	*NA*
Dendritic Brt-rich														
Min	69.32	14.56	8.95	0.03	<0.01	0.09	<0.01	0.31	0.03	<0.01	<0.01	0.11	<0.01	NA
Max	71.77	18.21	11.91	0.28	0.03	0.15	<0.01	1.86	0.05	<0.01	0.12	0.37	0.21	NA
Avg	70.47	16.81	9.76	0.09	0.01	0.12	<0.01	1.12	0.04	<0.01	0.04	0.20	0.03	NA
n	*6*	*6*	*6*	*6*	*6*	*6*	*6*	*6*	*6*	*6*	*6*	*6*	*6*	*NA*

Covellite	S	Cu	Fe	In	Zn	Cd	Ga	Hg	Pb	As	Sb	Ag	Au	Mn
Chimney Type	wt.%	wt.%	wt.%	wt.%	wt.%	wt.%	wt.%	wt.%	wt.%	wt.%	wt.%	wt.%	wt.%	wt.%
Ccp-rich														
Min	31.10	54.31	0.28	<0.01	0.84	<0.01	<0.01	NA	NA	NA	NA	NA	<0.01	NA
Max	33.51	64.44	0.81	0.01	12.38	0.13	0.03	NA	NA	NA	NA	NA	<0.01	NA
Avg	31.97	60.95	0.46	<0.01	4.87	0.05	0.01	NA	NA	NA	NA	NA	<0.01	NA
n	*3*	*3*	*3*	*3*	*3*	*3*	*3*	*NA*	*NA*	*NA*	*NA*	*NA*	*3*	*NA*
Zoned Ccp-rich														
Min	32.21	62.58	<0.01	<0.01	<0.01	<0.01	<0.01	<0.01	0.13	<0.01	<0.01	0.07	0.05	<0.01
Max	33.46	66.41	2.15	0.03	1.56	0.01	0.02	0.03	0.46	0.7	0.03	0.07	0.05	0.01
Avg	32.89	64.53	0.40	0.01	0.54	<0.01	0.01	0.01	0.23	0.24	0.01	0.07	0.05	0.01
n	*10*	*10*	*10*	*10*	*10*	*10*	*10*	*10*	*9*	*10*	*10*	*1*	*1*	*3*
Dendritic Sp-rich														
Min	29.62	63.06	0.06	<0.01	1.85	0.04	0.01	<0.01	0.53	<0.01	<0.01	NA	NA	NA
Max	29.90	64.78	0.15	<0.01	6.09	0.05	0.4	<0.01	1.49	<0.01	0.02	NA	NA	NA
Avg	29.76	63.92	0.10	<0.01	3.97	0.04	0.02	<0.01	0.96	<0.01	0.01	NA	NA	NA
n	*2*	*2*	*2*	*2*	*2*	*2*	*2*	*2*	*2*	*2*	*2*	*NA*	*NA*	*NA*

Bornite	Fe	S	Cu	In	Zn	Cd	Ga	Hg	Pb	As	Sb	Ag	Au	Mn
Chimney Type	wt.%	wt.%	wt.%	wt.%	wt.%	wt.%	wt.%	wt.%	wt.%	wt.%	wt.%	wt.%	wt.%	wt.%
Zoned Ccp-rich														
Min	15.28	32.18	48.46	<0.01	<0.01	<0.01	<0.01	<0.01	<0.01	<0.01	<0.01	0.06	<0.01	<0.01
Max	16.19	33.43	51.22	<0.01	<0.01	0.01	0.03	<0.01	<0.01	2041	0.03	0.17	0.19	0.02
Avg	15.68	32.91	49.75	<0.01	<0.01	0.01	0.01	<0.01	<0.01	0.05	0.02	0.13	0.06	0.01
n	*4*	*4*	*4*	*4*	*4*	*4*	*4*	*4*	*4*	*4*	*4*	*4*	*4*	*4*

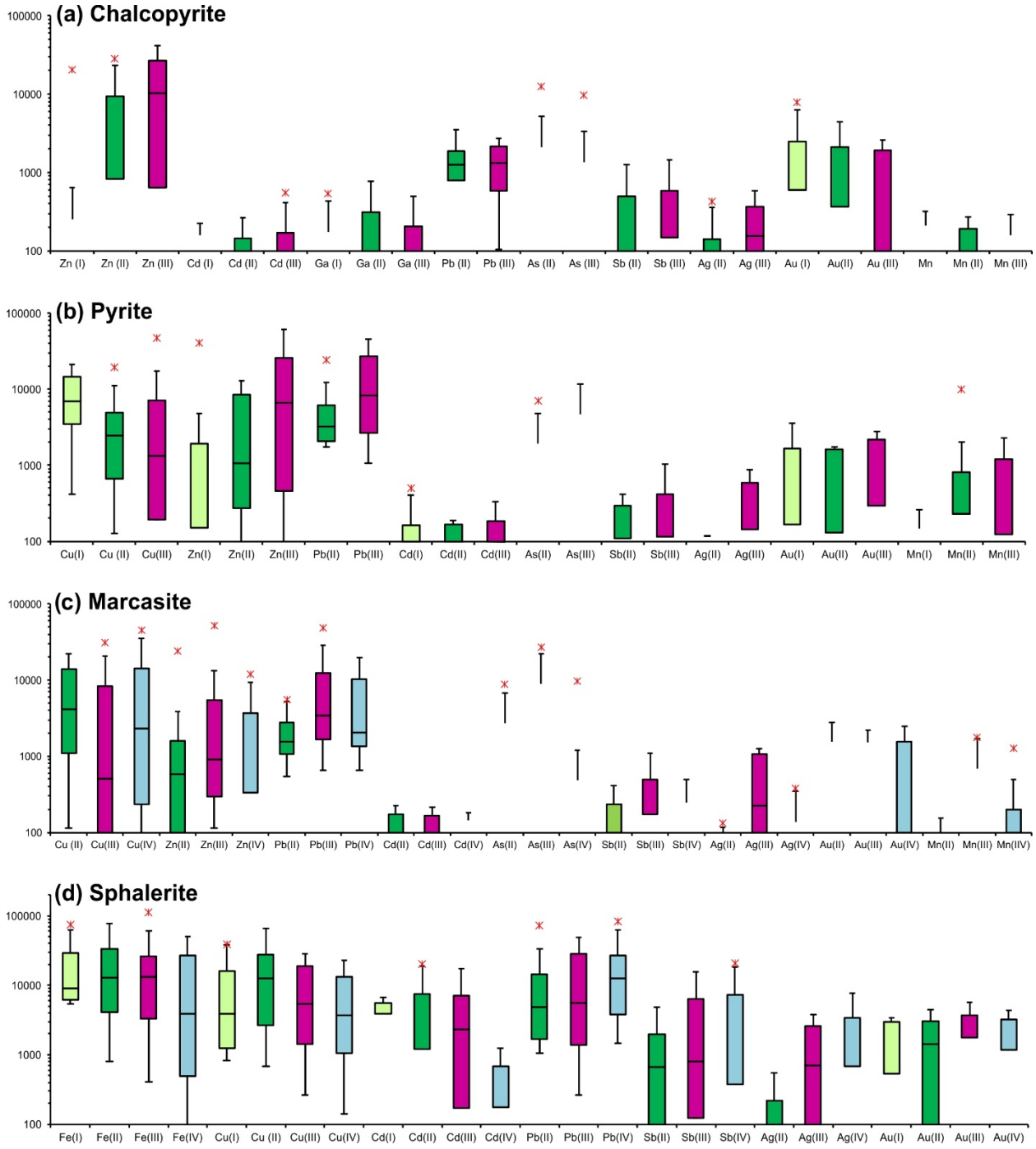


Fig. 4.13. Box-and-whisker plots of selected trace elements (in ppm) analyzed by EPMA for sulfide minerals from the Tinakula deposit: (a) chalcopyrite; (b) pyrite; (c) marcasite; and (d) sphalerite. The top of the box represents the 90th percentile, the bottom of the box represents the 10th percentile, the central line represents the median, the bars represent the range of the data, and outliers are indicated by stars (*). Boxes are colored and labelled according to chimney type: light green (I) represents the chalcopyrite-rich chimneys; dark green (II) represents the zoned chalcopyrite-rich chimneys; purple (III) represent dendritic sphalerite-rich chimneys; light blue (IV) represents dendritic barite rich chimneys. The complete data are in Appendix L.

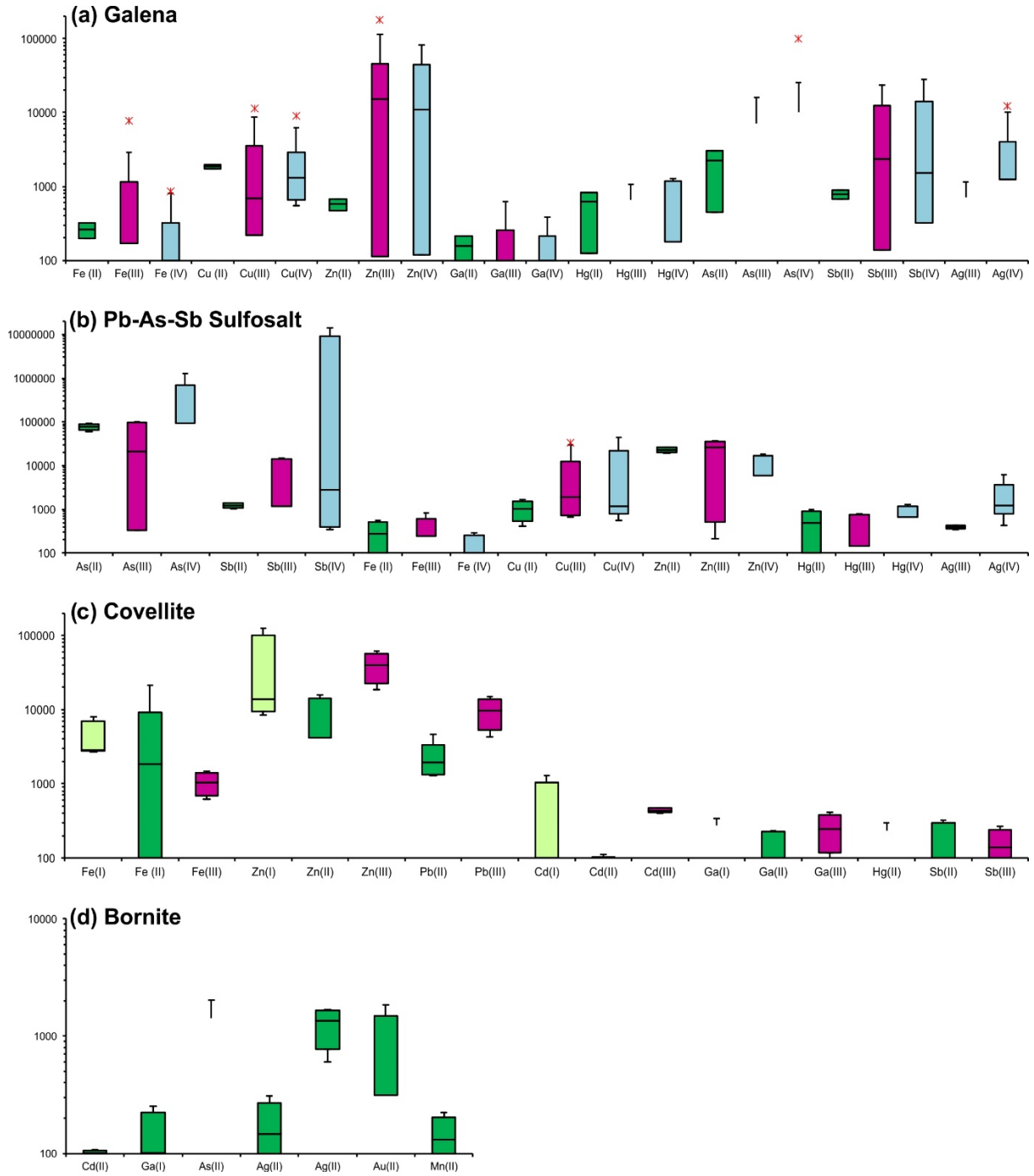


Fig. 4.14. Box-and-whisker plots of selected trace elements (in ppm) analyzed by EPMA for sulfide minerals from the Tinakula deposit: (a) galena; (b) Pb-As-Sb sulfosalts; (c) covellite; and (d) bornite. The top of the box represents the 90th percentile, the bottom of the box represents the 10th percentile, the central line represents the median, the bars represent the range of the data, and outliers are indicated by stars (*). Boxes are colored and labelled according to chimney type: light green (I) represents the chalcopyrite-rich chimneys; dark green (II) represents the zoned chalcopyrite-rich chimneys; purple (III) represent dendritic sphalerite-rich chimneys; light blue (IV) represents dendritic barite rich chimneys. The complete data are in Appendix L.

sulfosalts are also likely present, particularly in dendritic sphalerite-rich chimneys where there is a weak correlation between As and Pb in individual analyses. Lead reaches a maximum concentration of 4.57 wt.% in pyrite and 4.82 wt.% in marcasite in dendritic sphalerite-rich chimney types. This chimney type also has the highest Hg concentration in pyrite (up to 0.18 wt.%), although the concentrations in marcasite are lower (0.05 wt.%). There is a moderate correlation between Hg, Pb, and Sb among individual microprobe analyses of pyrite, indicating that Hg likely occurs within Pb-As-Sb sulfosalt inclusions (Appendix L). Manganese concentrations reach a maximum of 0.99 wt.% in pyrite and 0.18 wt.% in marcasite. Where pyrite and marcasite occur together in the same chimney (zoned chalcopyrite-rich and dendritic sphalerite-rich chimney types), pyrite phases tend to have higher Zn, Pb, and Mn, whereas marcasite tends to have higher As. Gold was detected (up to 0.36 wt.%) in pyrite from the chalcopyrite-rich chimney in which microscopic gold grains were observed (sample GMA13-048).

Sphalerite

The FeS content of sphalerite ranges from 0.02 to 13.98 mol%, with more than 50% of the analyses reporting <2 mol% FeS (uncorrected for chalcopyrite: Fig. 4.15; Suppl. Table L18). The CuS content ranges from 0.02 to 10.71 mol% (Suppl. Tables L17). The Cu/Fe ratios indicate the presence of submicroscopic inclusions of chalcopyrite in many cases (Suppl. Fig. L1); however, a large proportion of the analyses do not contain enough Fe to account for all of the Cu as chalcopyrite. All chimney types display both “high” and “low” Fe sphalerite, with the highest concentrations of Fe in chalcopyrite-rich assemblages, and the widest range of values in the dendritic barite-rich chimneys (Fig. 4.13d). Many grains of dark-colored sphalerite contain less than ~2 mol% FeS, and several contain <1 mol% (e.g., 52_C1_sp12 and 62_C2_sp1; Suppl. Table L17). These analyses include high concentrations of Cu (up to 3.21 mol% CuS) or Pb (up to 2.04 wt.% Pb), suggesting that very fine- grained disseminated inclusions of other sulfide phases may cause the color of sphalerite to appear darker in transmitted light. In contrast, although most light-colored sphalerite has FeS contents lower than ~2 mol%, several had concentrations >5 mol% FeS, even when corrected for chalcopyrite (e.g., 31_C10_sp3 and 50_C3_sp3; Suppl. Table L17). These samples may contain submicroscopic inclusions of pyrite that are not abundant enough to cause the sphalerite to appear dark. Cadmium (up to 2.0 wt.%), In (up to 1.3 wt.%), Ga (up to 1.0 wt.%),

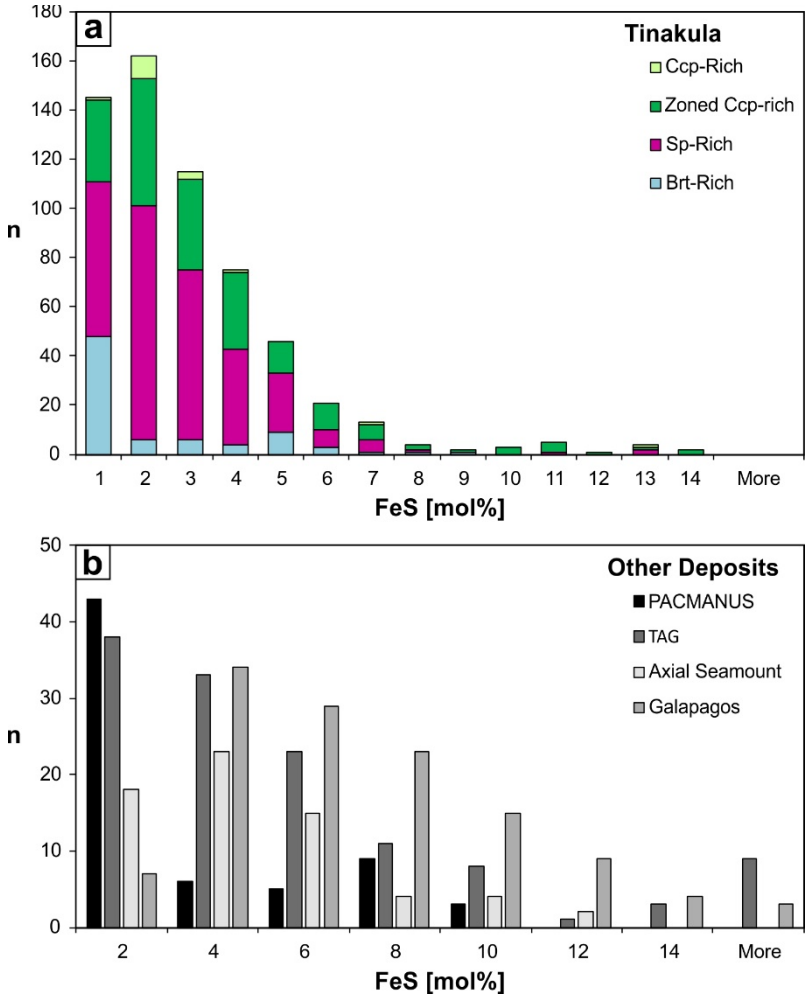


Fig. 4.15. Frequency histograms of FeS (mol%) concentrations in sphalerite from: (a) different chimney types at the Tinakula deposit (n = 598), calculated following Scott and Barnes (1971; see Suppl. Table L17 for data); and (b) other hydrothermal deposits dominated by low-Fe sphalerite, including PACMANUS (from Moss and Scott, 2001), TAG, Axial Seamount, and the Galapagos rift (from Hannington and Scott, 1989).

and Hg (up to 1.3 wt.%) are likely present in solid solution in sphalerite (e.g., Cook et al., 2009). Cadmium concentrations decrease in the lower-temperature assemblages, from an average of 0.33 wt.% in the chalcopyrite-rich chimneys to 0.03 wt.% in the dendritic barite-rich chimneys (Fig. 4.13d; Table 4.7). This suggests a strong temperature dependence, which is also reflected in the Fe content of sphalerite. Within individual chimneys, there is a tendency towards cooler temperatures (i.e., lower-Fe concentrations) in paragenetically late stages of growth, although these patterns are complicated by pulsed hydrothermal events leading to the complexly banded sphalerite in many cases. Concentrations of Pb, As, Sb, and Ag are locally very high, increasing from the zoned chalcopyrite-rich chimneys to the dendritic sphalerite-rich chimneys, to the dendritic barite-rich chimneys (Table 4.7). These data mainly indicate galena or sulfosalt inclusions, but bands of uniformly-bright sphalerite were observed with backscattered electron imaging that appear to indicate doping by Pb, or at least ultrafine dispersions of galena and sulfosalt nanoparticles in the sphalerite. In sphalerite from the dendritic barite-rich chimneys, As concentrations reach a maximum of 1.8 wt.%, Sb reaches a maximum of 2.1 wt.%, and Ag reaches a maximum of 0.77 wt.%.

Galena

Galena contains up to several wt.% of Cu and Zn in many samples, most likely representing micro-inclusions of chalcopyrite and sphalerite (including with trace Cd). Concentrations of Ga and Hg are low, averaging less than 0.08 wt.% in all of the chimney types (Table 4.7). In contrast, As, Sb, and Ag are locally enriched (Fig. 4.14a). Galena in the dendritic barite-rich chimneys has the highest concentrations of As (up to 9.93 wt.%) and Sb (up to 2.84 wt.%) and likely reflect As and Sb solid-solution with Pb-As-Sb sulfosalts. Silver concentrations in this galena reach 1.2 wt.%, which may reflect coupled substitution mechanisms (e.g., Renock and Becker, 2011; Grant et al., 2015), in particular, a positive correlation between Ag and Sb in the microprobe analyses indicate coupled substitution of Ag^{+} and Sb^{3+} for Pb^{2+} (Appendix L).

Pb-As-Sb sulfosalts

The Pb-As-Sb sulfosalts in the Tinakula chimneys have an average composition of 71.0 wt.% Pb, 9.3 wt.% As, 0.08 wt.% Sb, and 17.21 wt.% S (n = 11), which is close to the arsenic end-member of the jordanite-geocronite series (Fig. 4.16; Suppl. Table L18). The slightly higher Pb and lower As and S than pure jordanite (69.4 wt.% Pb, 10.8 wt.% As, 17.6 wt.% S) may indicate the presence of submicroscopic inclusions of galena. The concentrations of As and Sb are highest in the lower-temperature barite-rich assemblages, and they are associated with higher concentrations of Ag (up to 0.37 wt.%) and detectable Au (up to 0.21 wt.%; Table 4.7).

Covellite and bornite

Secondary covellite, which mainly replaces sphalerite, contains significant Zn, averaging 1.86 wt.% (n = 15; Appendix L) and reaching a maximum of 12.38 wt.%. The latter is likely due to a mixture of CuS and ZnS. Lead reaches a maximum of 1.49 wt.% in covellite, but all other trace elements are low (Fig. 4.14c). Bornite mostly replaces chalcopyrite. Four spots measured in covellite within one zoned chalcopyrite-rich sample indicate slightly elevated As (up to 0.20 wt.%, Ag (up to 0.17 wt.%), and detectable Au (up to 0.19 wt.%: Fig. 4.14d and Table 4.7). In the single sample containing bornite (zoned chalcopyrite-rich chimney GMA13-010), Ag concentrations are significantly increased (avg. 1253 ppm; n = 4) relative to co-existing chalcopyrite (avg. 89.5 ppm; n = 21; Appendix L), suggesting possible secondary remobilization of both Cu and Ag on a small scale.

4.4.6. Sulfur isotopes

Results of sulfur isotope measurements of mineral separates from 54 ROV grab samples and 15 drill-core subsamples from drillhole TKAD001 (maximum depth 22.32 mbsf) are provided in Table 4.8. Chalcopyrite has $\delta^{34}S$ values that range from -0.8 to 2.4 ‰ and are, on average, slightly lower in the chalcopyrite-rich chimneys than in the sphalerite-rich and zoned sphalerite-chalcopyrite chimneys (Fig. 4.17a). Pyrite has $\delta^{34}S$ values from -0.4 to 3.1 ‰, with slightly higher values in the sphalerite-rich chimneys, ranging from 0.3 to 11.0 ‰ (Fig. 4.17b). Light-colored

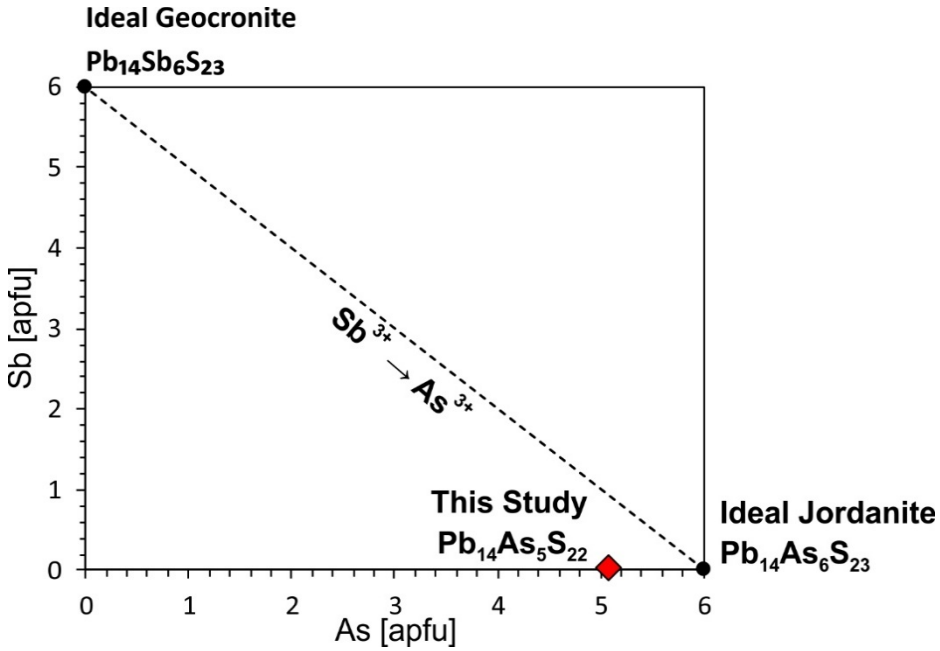


Fig. 4.16. Average composition of Pb-As-Sb sulfosalts from Tinakula (red diamond; n = 11) compared to ideal jordanite-geocronite (dashed line; after Biagioni et al., 2016). Lower As and S concentrations relative to Pb at Tinakula may result from submicroscopic inclusions of galena within jordanite. The complete data are in Appendix L.

Table 4.8. Results of S-isotope measurements of sulfide and sulfate minerals at the Tinakula deposit

			No Pretreatment *DeltaPlus*		Chemical Pretreatment *MAT 253*
Sample	Sample Type	Mineral	$\delta^{34}S$ (‰)	± 1 σ (‰)	$\delta^{34}S$ (‰)
GMA13-004	Zoned Ccp-rich	Ccp	0.3	0.12	
GMA13-010	Zoned Ccp-rich	Ccp	0.3	0.09	0.46
GMA13-019A	Sp-rich	Ccp	0.7	0.17	
GMA13-021	Zoned Ccp-rich	Ccp	0.6	0.13	
GMA13-034	Zoned Ccp-rich	Ccp	1.9	0.07	
GMA13-038	Ccp-rich	Ccp	-0.8	0.13	
GMA13-046	Zoned Ccp-rich	Ccp	1.3	0.12	1.22
GMA13-048	Sp-rich	Ccp	1.6	0.23	
GMA13-049	Zoned Ccp-rich	Ccp	2.4	0.09	1.98
GMA13-021	Zoned Ccp-rich	Py	0.9	0.02	
GMA13-024	Brt-rich	Py	-0.4	0.05	
GMA13-029	Sp-rich	Py	3.1	0.13	
GMA13-038	Ccp-rich	Py	-0.4	0.06	
GMA13-045	Brt-rich	Py	1.3	0.08	1.07
GMA13-046	Zoned Ccp-rich	Py	1.6	0.08	1.74
GMA13-048	Sp-rich	Py	1.9	0.13	1.79
GMA13-050	Zoned Ccp-rich	Py	2.0	0.12	
P005	Alt. FW; 19.14 mbsf	Py			0.90
GMA13-010	Zoned Ccp-rich	Sp (dark)	1.2	0.36	
GMA13-012	Sp-rich	Sp (dark)	2.4	0.27	
GMA13-012	Sp-rich	Sp (dark)	**11.0**	0.21	
GMA13-019A	Sp-rich	Sp (dark)	1.2	0.10	1.15
GMA13-022	Sp-rich	Sp (dark)	**8.4**	0.14	
GMA13-022	Sp-rich	Sp (light)	**11.0**	0.32	
GMA13-024	Brt-rich	Sp (dark)	0.3	0.00	
GMA13-032	Sp-rich	Sp (dark)	0.9	0.03	1.31
GMA13-032	Sp-rich	Sp (light)	1.1	0.07	
GMA13-038	Ccp-rich	Sp (dark)	1.1	0.17	
GMA13-040	Sp-rich	Sp (dark)	2.4	0.24	
GMA13-040	Sp-rich	Sp (light)	**7.0**	0.36	
GMA13-042	Sp-rich	Sp (dark)	2.5	0.11	
GMA13-042	Sp-rich	Sp (light)	3.4	0.14	
GMA13-045	Brt-rich	Sp (dark)	1.1	0.08	1.15
GMA13-049	Zoned Ccp-rich	Sp (dark)	3.4	0.05	
GMA13-050	Zoned Ccp-rich	Sp (dark)	1.4	0.07	
GMA13-052	Sp-rich	Sp (dark)	3.1	0.34	
GMA13-061	Sp-rich	Sp (dark)	1.6	0.11	
GMA13-061	Sp-rich	Sp (dark)	2.0	0.34	
GMA13-062	Sp-rich	Sp (dark)	2.6	0.22	
GMA13-062	Sp-rich	Sp (dark)	1.9	0.06	
P005	Alt. FW; 19.14 mbsf	Sp (dark)			0.55
P003	Alt. FW; 14.81 mbsf	Anh	21.2	0.39	22.17
P004	Alt. FW; 15.65 mbsf	Anh			21.96
MA13-087	Alt. FW; 16.05 mbsf	Anh			21.88
MA13-088	Alt. FW; 17.40 mbsf	Anh			21.27
MA13-089	Alt. FW; 17.90 mbsf	Anh	20.5	0.02	21.46
MA13-090	Alt. FW; 18.40 mbsf	Anh	20.6	0.18	
P005	Alt. FW; 19.14 mbsf	Anh			21.07
MA13-091	Alt. FW; 20.77 mbsf	Anh			20.80
P003	Alt. FW; 14.81 mbsf	Gp			21.79
P004	Alt. FW; 15.65 mbsf	Gp	21.3	0.50	
GMA13-002	Sp-rich	Brt	21.7	0.25	
GMA13-012	Sp-rich	Brt	21.0	0.01	
GMA13-019A	Sp-rich	Brt	20.9	0.19	
GMA13-024	Brt-rich	Brt	19.5	0.08	
GMA13-029	Sp-rich	Brt	19.3	0.04	
GMA13-031	Zoned Ccp-rich	Brt	22.5	0.06	
GMA13-034	Zoned Ccp-rich	Brt	**15.9**	0.12	21.04
GMA13-040	Sp-rich	Brt	**9.6**	0.24	
GMA13-045	Brt-rich	Brt	20.5	0.19	21.67
GMA13-049	Zoned Ccp-rich	Brt	**2.1**	0.01	
GMA13-058	Sp-rich	Brt	20.1	0.05	
GMA13-061	Sp-rich	Brt			21.15
GMA13-062	Sp-rich	Brt	**5.5**	0.14	

$d^{34}S$ values measured relative to Canyon Diablo Troilite (V-CDT)
Alt. FW = altered footwall; Anh = anhydrite; Gp = gypsum; Brt = barite;
Ccp = chalcopyrite; Py = pyrite; Sp = sphalerite
Bold values reflect contaminated sulfide/sulfate samples

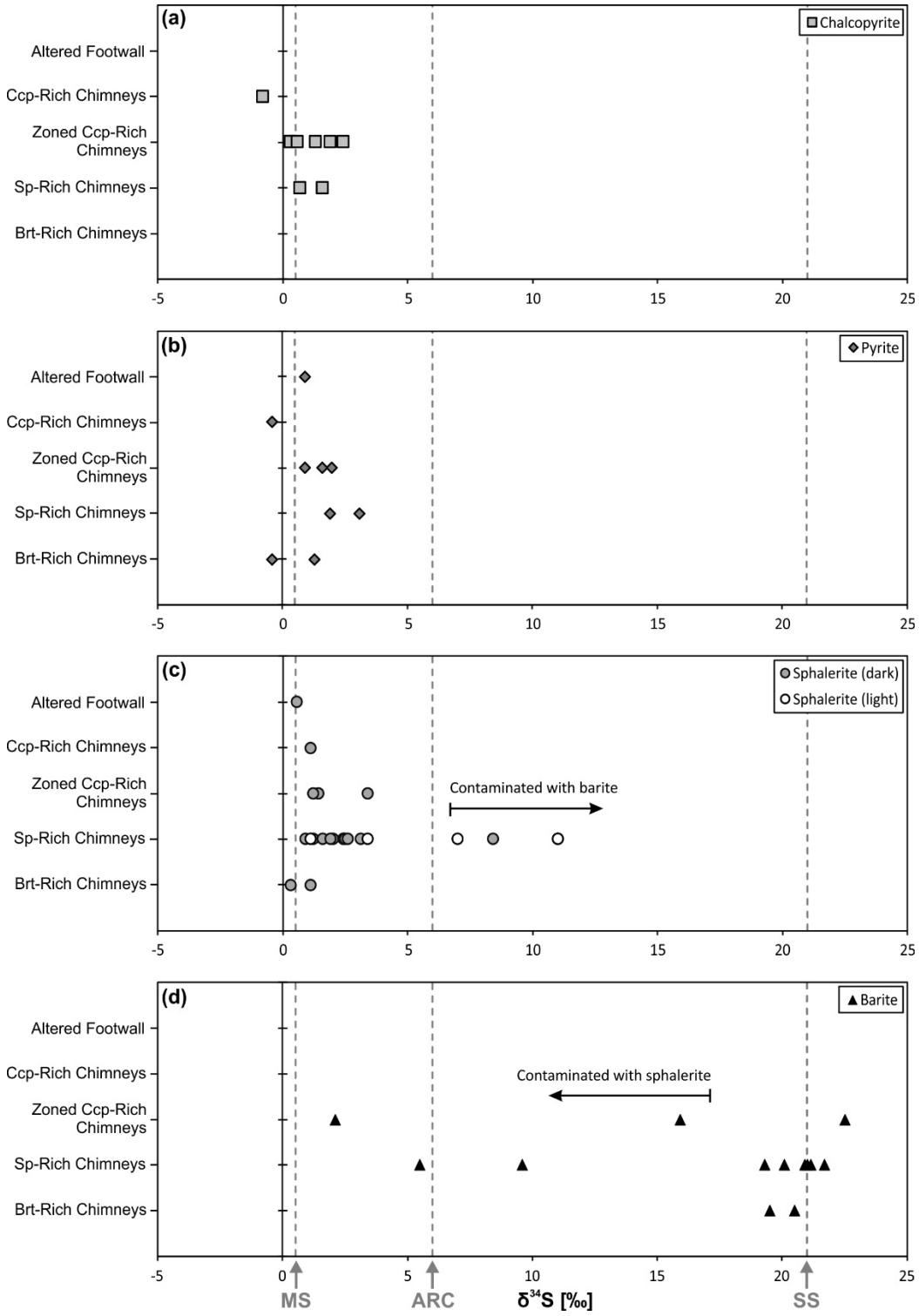


Fig. 4.17. Variations in $\delta^{34}S$ (V-CDT) and in minerals from chimneys at the Tinakula deposit: (a) chalcopyrite; (b) pyrite; (c) sphalerite (dark and light); and (d) barite. Lithologies are shown on the left, and the composition of MORB sulfur (MS: $\delta^{34}S$ = +0.5 ± 0.6 ‰; Sakai et al., 1984), island arc andesite sulfur (ARC: $\delta^{34}S$ = 6.00 ‰; Alt et al., 1993), and seawater sulfate (SS: $\delta^{34}S$ = 21.0 ‰; Rees et al., 1978) are shown by dashed lines. Detailed S-isotope data are shown in Table 4.8.

sphalerite has slightly higher $\delta^{34}S$ values than dark-colored sphalerite from the same samples, generally higher than 1.0 ‰; the lowest $\delta^{34}S$ value of sphalerite is 0.6. Unusually high $\delta^{34}S$ values in some sphalerite samples (>7 ‰) compared to MOR and arc-related chimneys may indicate contamination by included sulfate minerals (GMA13-012, -022, -040; shown in bold in Table 4.8). These hand-picked samples were not chemically purified, and the closely intergrown nature of dendritic sphalerite and barite suggests that contamination up to 50% is possible, which would result in an isotopic composition of 11.0 ‰. Anhydrite collected from the altered footwall of TKAD001 has $\delta^{34}S$ values between 20.5 and 22.2 ‰, typical of seawater sulfate ($\delta^{34}S$ = 21.0 ‰; Rees et al., 1978). Gypsum has $\delta^{34}S$ values from 21.3 to 21.8 ‰; the $\delta^{34}S$ values of anhydrite and gypsum show a slight decrease with depth (Fig. 4.18). Barite collected from chimney samples yielded $\delta^{34}S$ values from 2.1 to 22.5 ‰ (Fig. 4.17d). Unusually low $\delta^{34}S$ values (<16 ‰) reflect contamination of barite with included sphalerite in samples that have not been chemically purified (GMA13-034, -040, -049, -062; bold values in Table 4.8), as described above. This is supported by re-analysis of sample GMA13-034, which has an initial $\delta^{34}S$ value of 15.9 ‰, and after chemical pre-treatment yields a more reliable value of 21.04 ‰.

4.4.7. Fluid inclusion analyses

Five samples from the hydrothermally-altered volcaniclastic footwall from drillhole TKAD001 were prepared as doubly-polished thick sections in order to investigate the temperature and salinity of hydrothermal fluids responsible for sulfate and sulfide precipitation to a maximum depth of19.3 mbsf. The petrography of the footwall is outlined in *Chapter 5* and described in detail in Appendix G. The full list of fluid inclusion characteristics, and microthermometry and salinity measurements are shown in Table 4.9, with inclusions grouped according to crystal (capital letter), petrographic group (g0x), and sub-group (lower-case letter), taking freezing and heating measurements into account. Fluid inclusions occur within three distinct phases of sulfate precipitation (sequence I to III on Table 4.9), consisting of early irregular anhydrite veining and later phases of anhydrite and barite, and within sphalerite precipitated along the margins of the early anhydrite veins in the deepest samples (MA13-090 and P005).

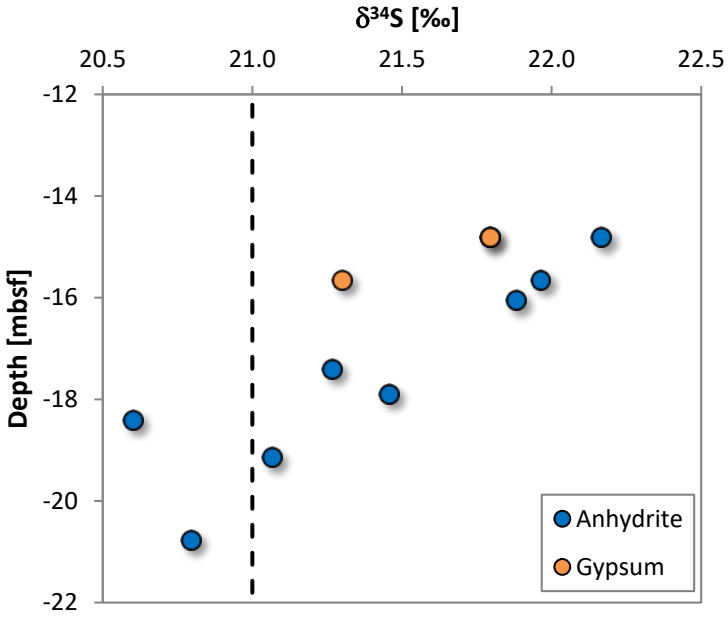


Fig. 4.18. Variations in $\delta^{34}S$ (top; V-CDT) in anhydrite and gypsum with depth in drillhole TKAD001 (Tinakula deposit). Errors are within the symbol size. The dashed line indicates the value of seawater sulfate ($\delta^{34}S$ = 21.0 ‰; Rees et al., 1978). Detailed S-isotope data are shown in Table 4.8.

Table 4.9. Fluid inclusion (FI) characteristics, homogenization temperatures (T_h), entrapment temperatures (T_e), and salinities (wt.% NaCl equivalent) from drillhole TKAD001

FI Group	Host Mineral	No. of FI	Size [µm]	V [%]	Phases	Generation	Paragenetic Sequence	T_h [°C]	T_e [°C]	Salinity [wt.% NaCl eq.]	Notes
P003_A_g01	anh	2	4–7	1–10	L + V	primary	I	N/A	N/A	N/A	
P003_B_g01	anh	4	4–6	1–5	L + V	secondary	I	N/A	N/A	N/A	
P003_B_g02	anh	2	3–4	1	L + V	secondary	I	N/A	N/A	N/A	lie on crack within crystal
P003_B_g03	anh	17	4–10	1–10	L + V	primary	I	N/A	N/A	N/A	lie on crack within crystal
P003_C_g01	anh	2	1–16	1–10	L + V	secondary	II	N/A	N/A	N/A	
P004_D_g01a	anh	2	9–20	5–15	L + V	primary	I	269	273	3.6	
P004_D_g01b	anh	2	3–4	4–8	L + V	primary	I	232	238	3.6	parallel to crystal margins
P004_E_g03	anh	6	4–22	10	L + V	primary	I, II	230	236	0.0	secondary chain next to it
P004_K_g01a	anh	1	16	10	L + V	primary	II, III	254	259	3.8	lies separate
P004_K_g01b	anh	3	6–9	10	L + V	primary	II, III	200	206	3.8	
P004_L_g01	anh	10	7–10	2–8	L + V	secondary	I	262	267	3.9	many generations in different layers
P004_L_g02	anh	4	8–10	7	L + V	secondary	I	251	256	4.1	
P004_L_g03	anh	1	8	7	L + V	secondary	I	237	243	3.4	
P004_N_g02	brt	2	4–38	2–10	L + V	secondary	II	211	217	2.8	some inclusions necking down
P004_N_g03	brt	3	4–10	2–4	L + V	secondary	II	207	213	3.0	some inclusions necking down
P004_N_g04	brt	1	8	5	L + V	secondary	II	250	256	3.1	some inclusions necking down
P004_N_g05	brt	2	10–12	1–10	L + V	secondary	II	213	219	3.1	some inclusions necking down
P004_N_g07a	brt	7	2–10	5–10	L + V	secondary	II	196	202	3.1	some inclusions necking down
P004_N_g07b	brt	3	2–4	8–10	L + V	secondary	II	261	266	3.1	some inclusions necking down
P004_P_g01	anh	5	8–16	2–10	L + V	primary	I	225	231	3.6	smaller inclusions surrounding
P004_R_g01a	brt	2	10–40	5	L + V	secondary	II	252	257	3.4	along row above crack
P004_R_g01b	brt	2	10–17	5	L + V	secondary	II	203	209	3.4	along row above crack
P004_U_g01a	anh	2	28–38	5–10	L + V	secondary	I	288	291	2.6	
P004_U_g01b	anh	12	3–7	5–10	L + V	secondary	I	225	231	2.6	
P004_U_g02	anh	1	20	5	L + V	secondary	I	221	227	2.3	
P004_V_g01	anh	4	3–5	4–8	L + V	secondary	I	225	234	2.8	
P004_V_g02	anh	2	2–5	4	L + V	primary	I	231	231	2.8	
P004_W_g01	anh	7	5–15	4–8	L + V	secondary	I	258	264	2.6	
MA13-089_A_g01	anh	2	15-42	2–5	L + V	secondary	II	N/A	N/A	N/A	part of large group, most are empty
MA13-089_B_g01	anh	1	20	1	L + V	secondary	I	N/A	N/A	N/A	part of large group, most are empty
MA13-089_C_g01	anh	1	18	10	L + V	primary	I	N/A	N/A	N/A	
MA13-090_G_g01	sp	1	20	10	L + V	secondary	I	242	248	3.4	
MA13-090_H_g01	sp	1	25	5	L + V	primary	I, II	240	246	3.4	
MA13-090_H_g02	sp	1	25	7	L + V	primary	I, II	295	298	3.1	
MA13-090_H_g07	sp	19	8–20	8–20	L + V	secondary	I, II	269	274	4.5	along row
MA13-090_H_g10	sp	3	10–22	4–10	L + V	secondary	I, II	270	275	3.3	implosion (?) of one inclusion
MA13-090_I_g01	sp	7	6–10	5–10	L + V	secondary	I	265	270	2.6	FI chain
MA13-090_J_g01	sp	5	2–11	10–20	L + V	secondary	I	288	291	3.3	FI chain/cluster
P005_F_g01	sp	8	4–13	2–20	L + V	secondary	I	258	263	3.9	FI chain
P005_G_g01a	sp	7	5–50	5–10	L + V	secondary	I	249	254	3.6	mostly empty
P005_G_g01b	sp	4	6–16	5–10	L + V	secondary	I	232	238	3.6	some necking down
P005_G_g01c	sp	6	6–15	5–10	L + V	secondary	I	232	238	2.6	
P005_G_g01d	sp	3	6–12	5–10	L + V	secondary	I	249	257	3.9	
P005_L_g01a	sp	5	4–15	3–7	L + V + S	secondary	I	230	238	3.8	two inclusions show 3 and 5% solids
P005_L_g01b	sp	2	5	2–3	L + V	secondary	I	220	225	3.8	
P005_L_g01c	sp	2	5–7	7–10	L + L + V	secondary	I	249	254	4.5	one inclusion with 3% second L phase
P005_L_g01d	sp	5	5	2–7	L + V	secondary	I	230	235	3.9	
P005_L_g02	sp	29	2–7	3–10	L + V	secondary	I	225	230	3.4	
P005_M_g01	sp	12	2–6	5–15	L + V	secondary	I	221	227	4.1	
P005_P_g02	sp	9	5–20	7–10	L + V	secondary	I	272	277	4.7	
P005_P_g03	sp	11	1–9	5–7	L + V	primary	I	251	257	3.6	

anh = anhydrite; brt = barite; sp = sphalerite; L = liquid; V = vapor; S = solid; N/A = not analyzed

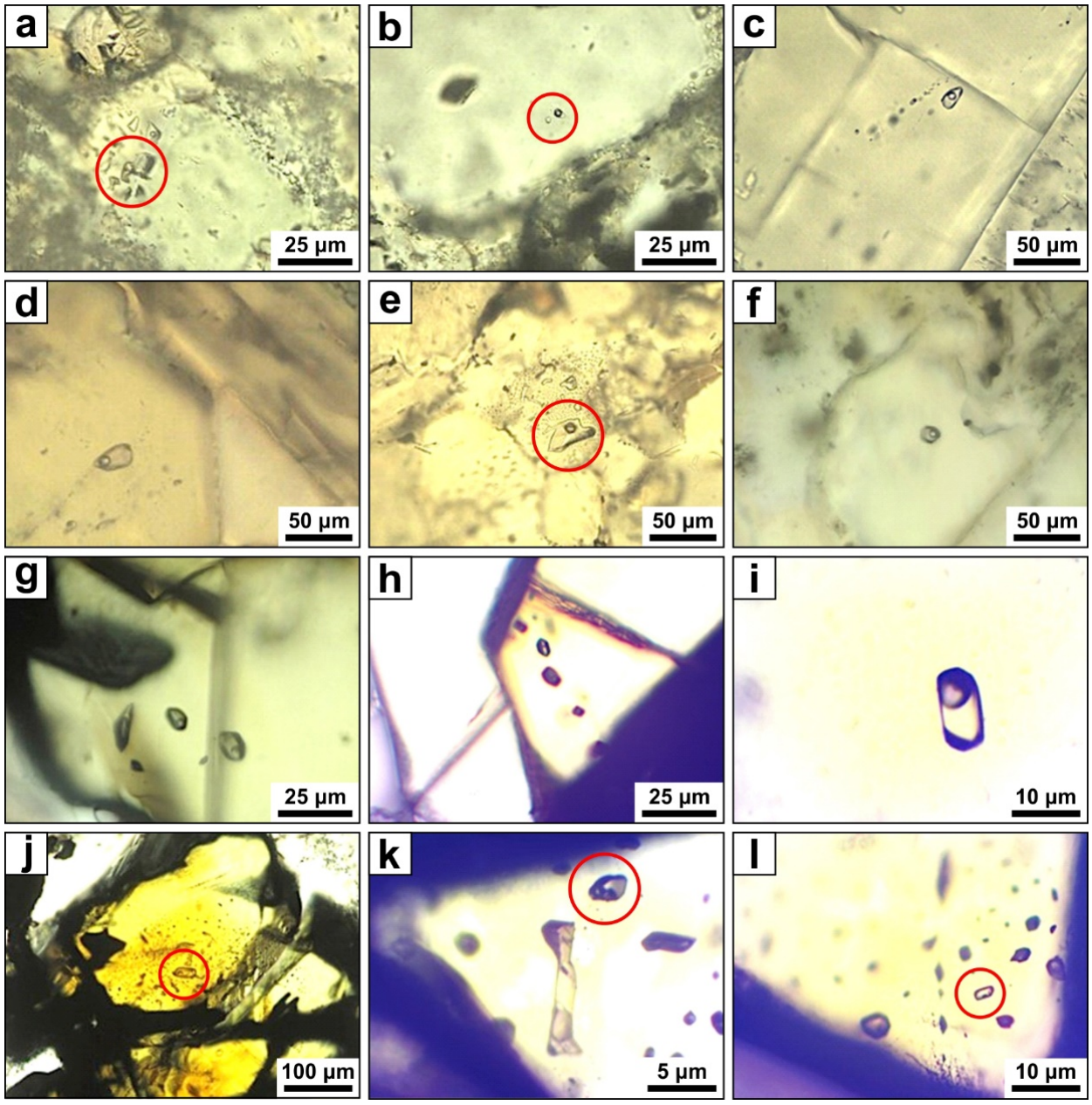


Fig. 4.19. Transmitted light photomicrographs (PPL) of fluid inclusion characteristics from samples from drillhole TKAD001: (a) a large secondary inclusion (red circle) within anhydrite from sample P003_C_g01; (b) two primary fluid inclusions with a vapor phase and a thick, black meniscus (red circle) within anhydrite (sample P003_A_g01); (c) a single primary fluid inclusion within tabular anhydrite next to secondary inclusions formed as a result of crack-healing (sample P004_E_g03); (d) a large primary inclusion in barite (sample P004_R_g01); (e) secondary inclusions within anhydrite (red circle; sample MA13-089_A_g01); (f) a primary inclusion within anhydrite (sample MA13-089_C_g01); (g) primary fluid inclusions with negative crystal shapes within sphalerite (sample MA13-090_H_g02); (h) secondary fluid inclusions in a row with negative crystal shapes in sphalerite (sample MA13-090_I_g01); (i) a large primary inclusion within sphalerite (sample P005_P_g03); (j) a sphalerite crystal with numerous secondary fluid

inclusions, including one very large one in red circle (sample P005_G_g01); (k) a secondary fluid inclusion within sphalerite showing a second liquid phase (red circle; sample P005_L_g01c); and (l) a secondary fluid inclusion within sphalerite with a liquid, vapor, and solid phase (red circle; sample P005_L_g01a). Fluid inclusion groups are outlined in Table 4.9.

Fluid inclusions from sample P003 (14.8 mbsf) are found exclusively within anhydrite/gypsum precipitated on hydrothermally-altered volcanic clasts (Table 4.9). These inclusions are generally <10 µm, reaching maximum sizes of 10–16 µm (Fig. 4.19a). All inclusions are composed of a liquid phase with up to 10% vapor (Fig. 4.19b). Microthermometry measurements of inclusions in sample P003 were not possible.

Sample P004 (15.7 mbsf) contains fluid inclusions within both anhydrite/gypsum and barite crystals (Table 4.9). Most inclusions occur as primary and secondary inclusions within large tabular anhydrite crystals precipitated directly on clay-altered clasts. Inclusion sizes vary between 2–60 µm, but are generally >20 µm, and are composed of a liquid and vapor phase with an average of <10% vapor (Fig. 4.19c). Barite occurs as large crystals after anhydrite, associated with numerous secondary inclusions between 4–38 µm and a maximum vapor phase of 10%, with a single large (40 µm) primary inclusion with ~5% vapor identified (Fig. 4.19d). Entrapment temperatures (T_e) of anhydrite range from 206 to 291˚C, with a median temperature of 238˚C, whereas barite has slightly lower T_e (median = 218˚C), with a bimodal distribution of temperatures from 202–220 ˚C and 256–266 ˚C (Fig. 4.20a). Anhydrite salinities range from 0.0 to 4.1 wt.% $NaCl_{equiv}$, with a median value of 3.3 wt.% $NaCl_{equiv}$, whereas barite salinities cover a narrower range from 2.8 to 3.4 wt.% $NaCl_{equiv}$ (median 3.1 wt.% $NaCl_{equiv}$; Fig. 4.20b).

Fluid inclusions occur within three different anhydrite/gypsum crystals in sample MA13-089 (18.0 mbsf), consisting mainly of secondary inclusions (Fig. 4.19e), with one exception (Fig. 4.19f). The fluid inclusions have both liquid and vapor phases (1–10% vapor), and are of relatively large size (15–42 µm; Table 4.9). Due to the high porosity of this sample, none of the inclusions survived preparation for microthermometry.

Sample MA13-090 (18.5 mbsf) contains abundant fluid inclusions within sphalerite that precipitated after earlier generations of anhydrite (Table 4.9). The inclusions include relatively large primary inclusions up to 25 µm with 5–30% vapor phase (Fig. 4.19g) and groups of smaller secondary inclusions (<10 µm) along healed cracks in the crystal (Fig. 4.19h). All inclusions consist of a vapor and liquid phase. Entrapment temperatures range from 246 to 298˚C (median

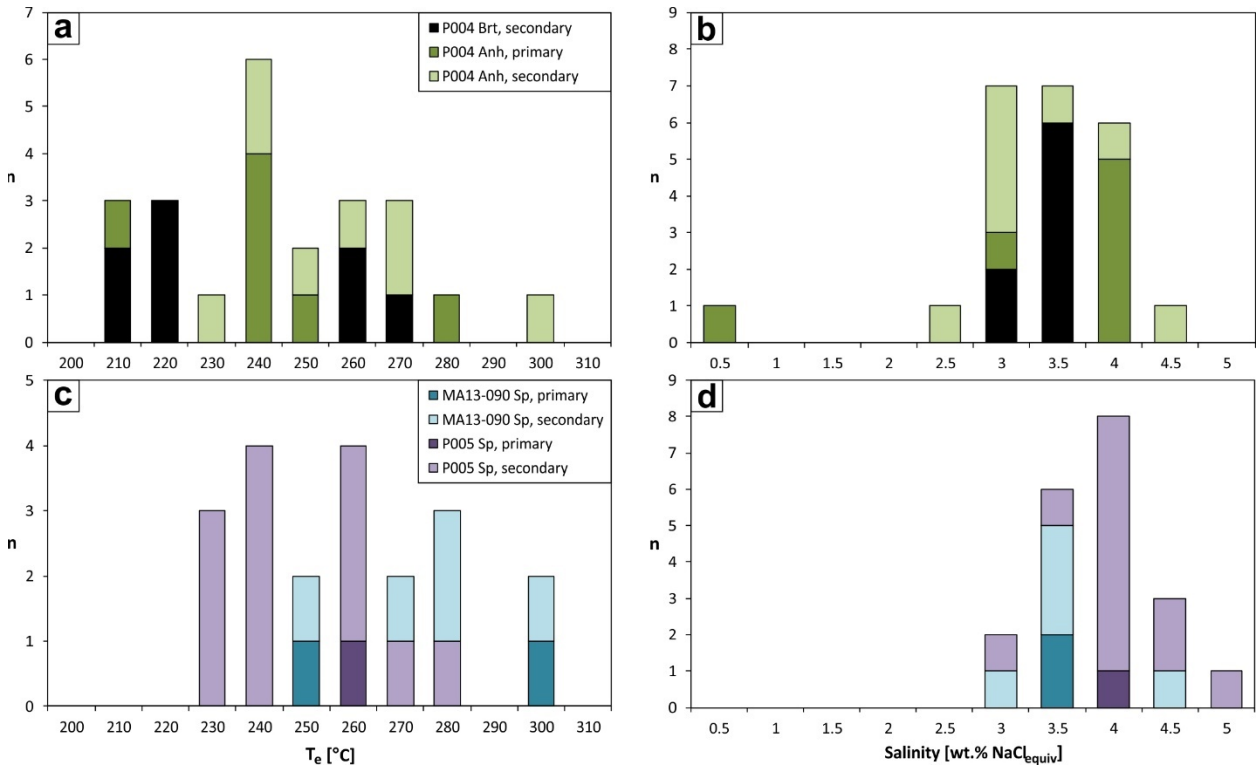


Fig. 4.20. Microthermometry and salinity measurements of fluid inclusions (primary and secondary) in samples from drillhole TKAD001: (a) entrapment temperatures (T_e) of inclusions in barite and anhydrite from sample P004 (15.7 mbsf); (b) salinities of inclusions in barite and anhydrite from sample P004 (15.7 mbsf); (c) entrapment temperatures (T_e) of inclusions in sphalerite from samples MA13-090 (18.5 mbsf) and P005 (19.3 mbsf); and (d) salinities of inclusions in sphalerite from samples MA13-090 (18.5 mbsf) and P005 (19.3 mbsf). Data are shown in Table 4.9. Anh = anhydrite; Brt = barite; Sp = sphalerite.

274 ˚C; Fig. 4.20c) with salinities between 2.6 and 4.5 wt.% $NaCl_{equiv}$ (median 3.3 wt.% $NaCl_{equiv}$; Fig. 4.20d).

Fluid inclusions in sample P005 (19.3 mbsf) also occur within sphalerite, and mostly consist of secondary inclusions (<10 µm), with few large primary inclusions up to 50 µm (Figs. 4.19i,j). The majority of the inclusions consist of a vapor and fluid phase, with up to 20% vapor (generally between 1–10%). Several inclusions contain a second liquid phase (2–5%) in addition to the vapor phase (Fig. 4.19j). Two single inclusions contain a dark solid phase (3% and 5%) with a tabular habit, likely a sulfide mineral (Fig. 4.19k). Entrapment temperatures are generally lower than sample MA13-090, ranging from 225 to 277˚C (median 238˚C; Fig. 4.20c), which reflects the high number of secondary inclusions measured in this sample. Salinities vary from 2.6 to 4.7 wt.% $NaCl_{equiv}$ (median 3.8 wt.% $NaCl_{equiv}$; Fig. 4.20d).

4.4.8. Barite dating

The results of ^{226}Ra dating of hydrothermal barite from the Tinakula deposits are shown in Table 4.10. Details of the analyzed samples are provided in Appendix E. A “zero-age” sample from an actively-venting chimney (sample GMA13-024) had the highest calculated $^{226}Ra/Ba$ ratio (1022 ± 68 Bq/kg·wt.%), which was used as the initial ratio of the entire deposit. One sample had insufficient Ba for measurement (MA13-028). The results indicate that hydrothermal venting at Tinakula has been ongoing for at least 5597 ± 240 years. The spatial distribution of samples with their calculated ages is shown in Figure 4.21. Approximately 75% of the data are between 988 and 2369 years; other samples from drillcore are younger than ~1400 years. Although there is no consistent spatial variation with age, the two oldest samples (MA13-011 and MA13-030) were collected from drillcore at 1.1 and 3.6 m depth, respectively (Fig. 4.21). Of the 22 measured samples, only these two have ages >4000 years. Taken together, the barite dating suggest that the Tinakula hydrothermal systems has been active for at least the last 5,500 years (Fig. 4.22).

Based on this minimum deposit age, the estimated growth rate for Tinakula is ~330 t/yr. This is comparable to the calculated mass accumulation rates of other large deposits, including the 2,700,000-t TAG deposit on the Mid-Atlantic Ridge (~360 t/yr: Hannington et al., 1998), and the

Table 4.10. Results of ^{226}Ra dating of hydrothermal barite from the Tinakula deposit

Sample	Comment	Latitude	Longitude	Depth [mbsl]	Ba (wt.%)	^{226}Ra Activity (Bq/kg)	^{226}Ra/Ba (Bq/kg·wt.%)	Age (years)
GMA13-002	Inactive Chimney	784711.71	8649565.62	1109.4	14.50	3323 ± 181	229	3450 ± 229
GMA13-010	Active Chimney	784711.11	8649704.58	1074.5	2.72	2593 ± 209	953	160 ± 267
GMA13-019A	Talus	784567.23	8649966.57	1100.6	7.34	3102 ± 157	423	2038 ± 224
GMA13-021	Inactive Chimney	784550.95	8649883.22	1087.5	0.04	24 ± 4	666	988 ± 390
GMA13-022	Talus	784597.25	8649923.31	1090.3	14.10	5162 ± 252	366	2369 ± 222
GMA13-024	Active Chimney	784724.27	8649655.45	1094.1	3.65	3729 ± 162	**1022**	**0**
GMA13-029	Inactive	784745.09	8649583.14	1109.7	16.90	9187 ± 407	544	1457 ± 217
GMA13-031	Talus	784671.02	8649796.42	1103.3	9.04	5322 ± 248	589	1273 ± 220
GMA13-032	Inactive Chimney	784731.90	8649743.06	1074.3	0.46	188 ± 15	411	2101 ± 265
GMA13-034	Active Chimney	784758.96	8649632.2	1108.3	1.85	1333 ± 71	720	807 ± 227
GMA13-040	Inactive Chimney	784531.45	8650094.08	1123.4	9.15	2828 ± 162	309	2760 ± 233
GMA13-045	Talus	784650.47	8649863.99	1089.7	13.50	5153 ± 247	382	2273 ± 221
GMA13-061	Talus	784678.16	8649752.78	1081.6	8.48	3319 ± 170	391	2215 ± 225
GMA13-062	Talus	784699.65	8649651.04	1099.7	6.36	1728 ± 100	272	3057 ± 234
MA13-011	Drillhole TKAD018	784756.43	8649604.73	1110.2	12.80	1158 ± 73	90	5597 ± 240
MA13-028	Drillhole TKAD013	784616.18	8649922.38	1091.5	0.07	-	-	-
MA13-029	Drillhole TKAD013	784616.18	8649922.38	1091.5	4.07	2950 ± 149	725	792 ± 224
MA13-030	Drillhole TKAD013	784561.08	8649940.06	1091.8	9.42	1337 ± 87	142	4556 ± 244
MA13-031	Drillhole TKAD013	784588.91	8649829.11	1088.7	0.64	420 ± 36	659	1014 ± 274
MA13-065	Drillhole TKAD026	784609.20	8649820.32	1089.0	8.19	3691 ± 187	451	1891 ± 224
P0010	Drillhole TKAD003	784726.01	8649576.46	1110.3	0.97	583 ± 40	599	1234 ± 248
P0011	Drillhole TKAD003	784765.73	8649281.14	1113.8	0.78	699 ± 47	896	304 ± 247
P0043	Drillhole TKAD031	784765.73	8649281.14	1113.8	1.21	963 ± 56	795	578 ± 234

Latitude and longitude coordinates are in WGS84 UTM projection

Bold values indicate the initial ^{226}Ra/Ba ratio of the "zero-age" chimney

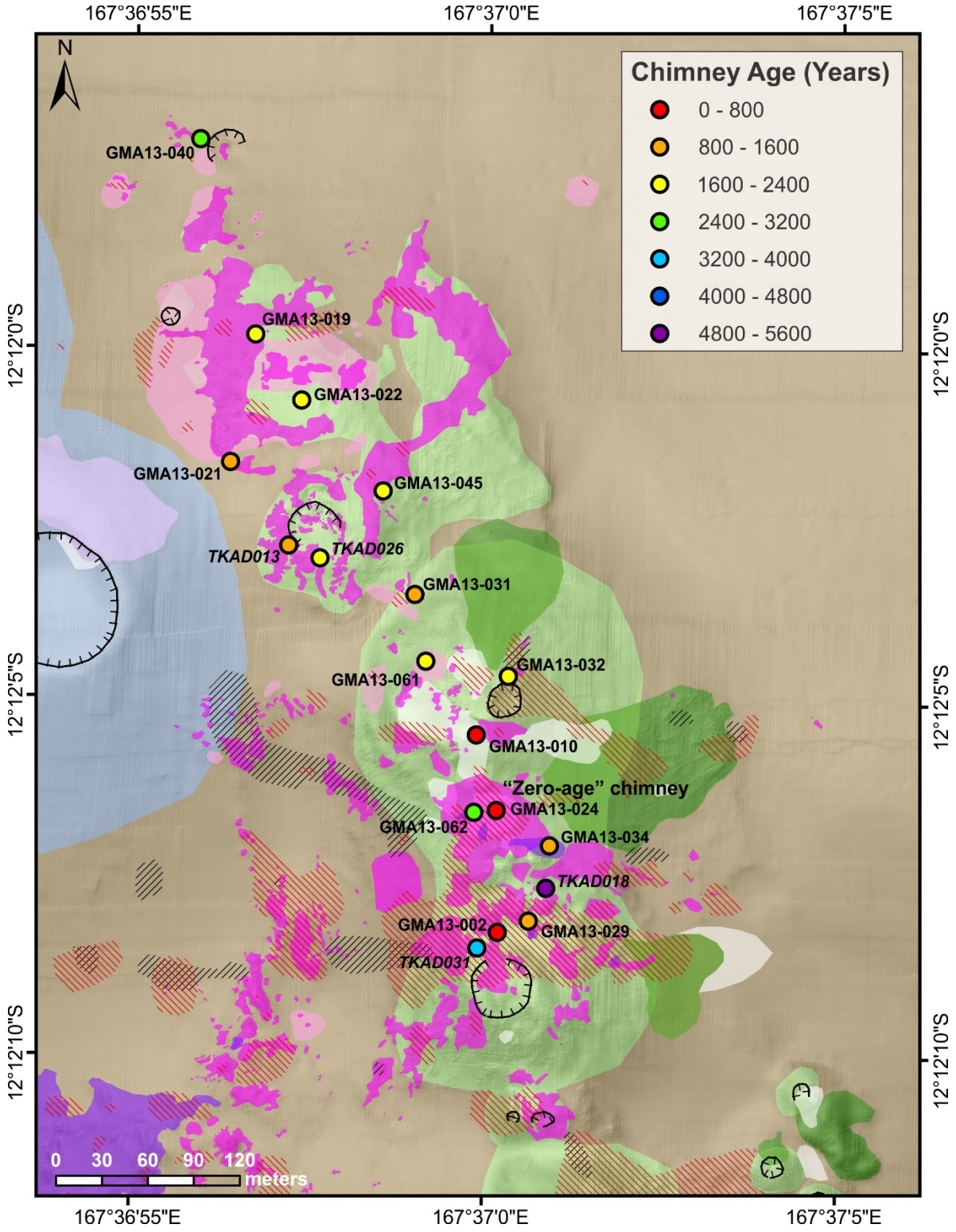


Fig. 4.21. Ages measured by ^{226}Ra dating of hydrothermal barite at the Tinakula deposit, overlain on a close-up of the geology map from Fig. 3.10. Grab samples are labelled; drillholes are in italics. Data are in Table 4.10.

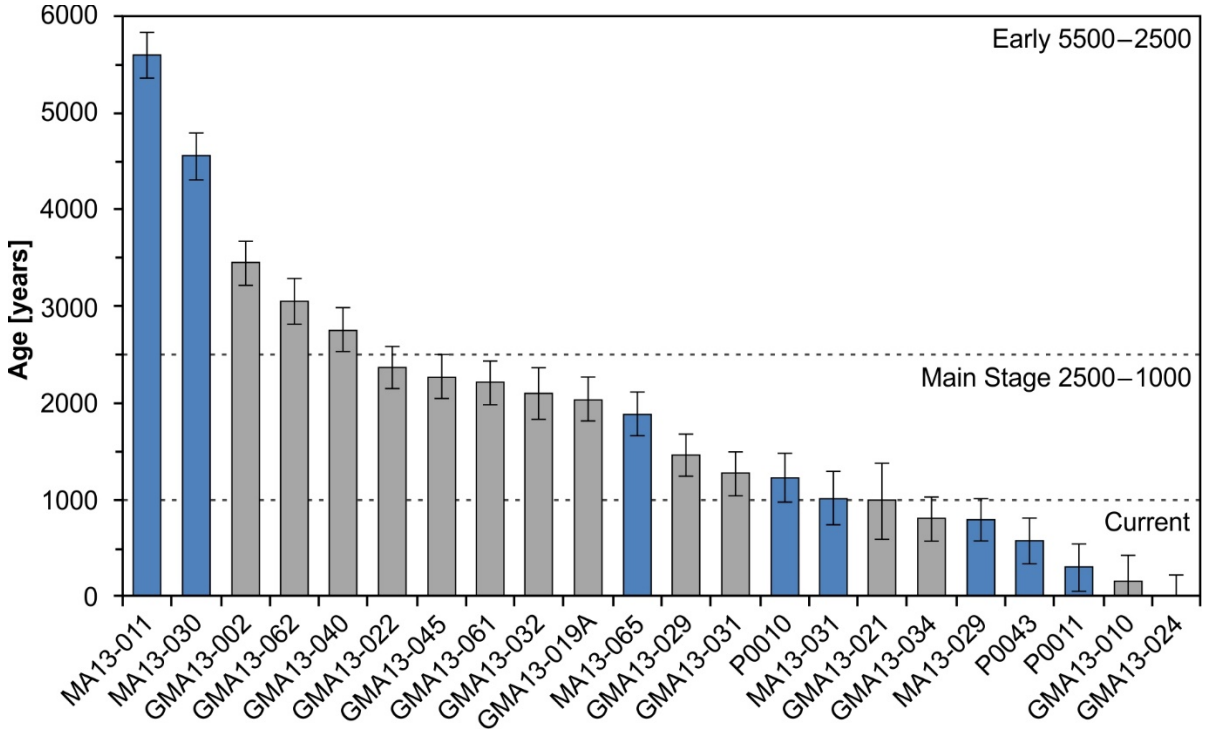


Fig. 4.22. Distribution of ^{226}Ra ages of hydrothermal barite from sulfide chimney samples at the Tinakula massive sulfide deposit, with samples collected from shallow drillcore highlighted in blue. Ages are relative to the "zero-age" sample (GMA13-024). Data are in Table 4.10.

~1,155,00-t Endeavour segment of the Juan de Fuca Ridge (~395 t/yr; Jamieson et al., 2014). This may reflect the efficiency of sulfide chimneys with diffuser or "beehive" structures in sequestering metals from vent fluids (Fouquet et al., 1993a),

4.5. Discussion

4.5.1. Behavior of trace elements in different sulfide minerals

Figure 4.23 compares the concentrations of different trace metals in the Tinakula sulfides with similar data for massive sulfides in other arc environments. Samples from Tinakula have unusually high Cd concentrations, primarily contained within sphalerite-rich chimneys. Concentrations of Sb, As, Ga, Ge, Hg, In, Mo, Se, and Tl are similar to but in some cases higher (e.g., Ge and Hg in low-T chimneys; In and Mo in high-T chimneys) than in other rifted arc-related deposits. These minor elements are mostly present in sulfide phases as fine-grained (submicroscopic) mineral inclusions or substituting for major elements within the crystal lattice. Simple substitutions occur between elements with similar Z/r ratios, such as those between Zn^{2+}, Fe^{2+}, Cu^{2+}, Cd^{2+}, Ga^{2+}, Ge^{2+}, Hg^{2+}, and Mn^{2+}. Elements with different valences follow more complex coupled-substitution processes.

Cadmium

Cadmium is strongly correlated with Zn, reflecting a simple substitution of $Cd^{2+} \leftrightarrow Zn^{2+}$ in the sphalerite crystal lattice. Concentrations of Cd in sphalerite are up to 20,400 ppm, with the highest values in zoned chalcopyrite-rich chimneys (avg. 4024 ppm; n = 196; Table 4.7), and lowest values in dendritic barite-rich chimneys (avg. 283 ppm; n = 79). Enrichment of Cd in sphalerite above 1.0 wt.% has previously been recorded from a few localities on the seafloor, including Menez Gwen (Lein et al., 2010) and Palinuro (Petersen et al., 2014). At Tinakula, Cd is also abundant in galena, averaging 468–493 ppm, with a maximum measured value of 1438 ppm, reflecting substitution of Cd^{2+} with Pb^{2+}. This is higher than previously recorded at a seafloor massive sulfide deposit, which has been measured at up to ~1100 ppm at the Palinuro seamount in Italy (Petersen et al., 2014) and at Hook Ridge in the Bransfield Strait, Antarctica (Petersen et al., 2004).

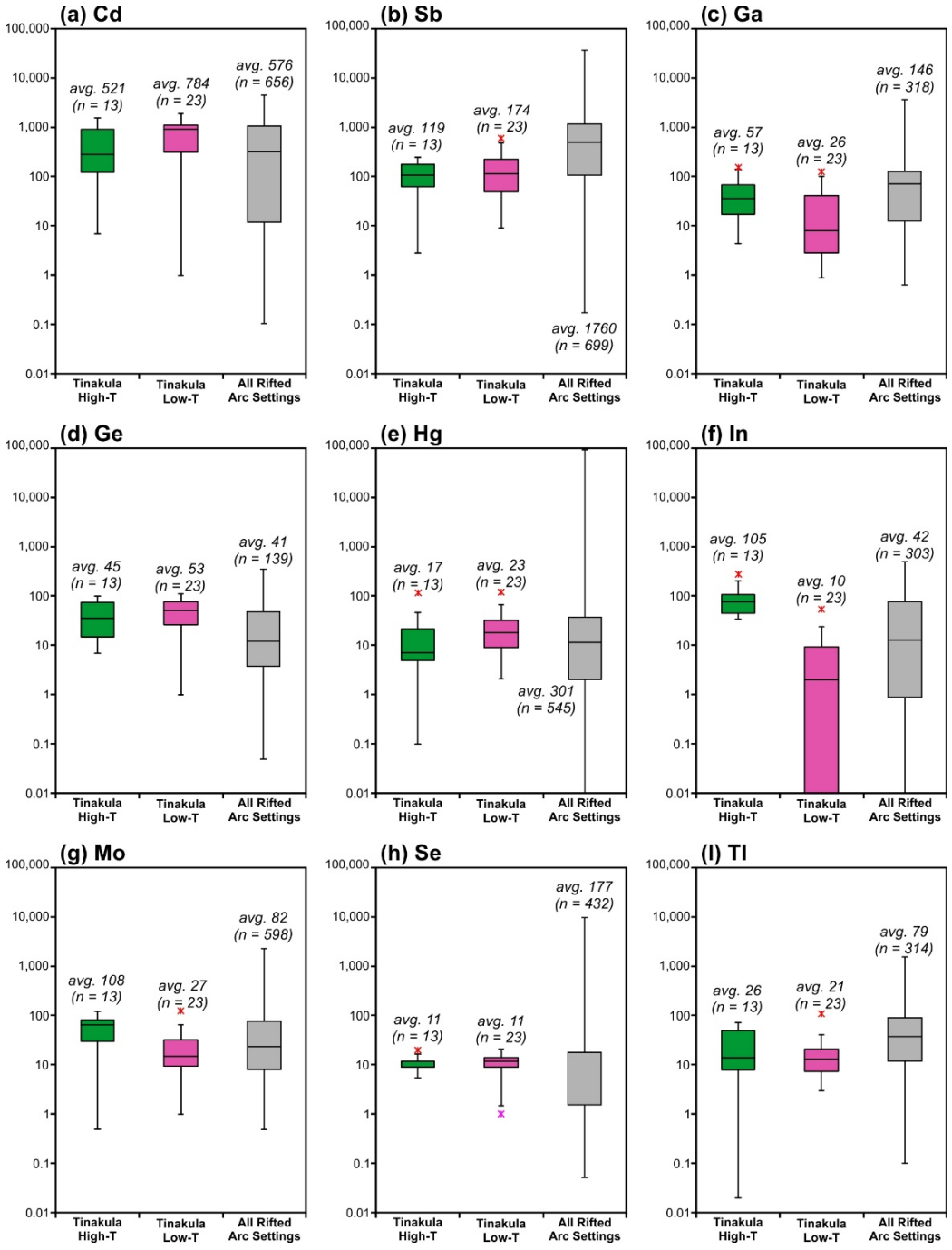


Fig. 4.23. Box-and-whisker plots of whole-rock geochemistry of selected trace elements from chimney samples from the Tinakula deposit, including high-temperature assemblages (chalcopyrite-rich and zoned chalcopyrite-rich chimney types) shown in green, and low-temperature assemblages (dendritic sphalerite-rich and barite-rich chimney types) shown in pink, compared to samples from literature from all rifted arc settings shown in grey (Monecke et al., 2016; and references therein). Below detection limit values have been replaced by half of the detection limit. The top of the box represents the 75th percentile of the data, the bottom of the box represents the 25th percentile, the middle line represents the median, the bars represent the range of the data, and outliers are indicated by stars (*). All data are shown as ppm.

Antimony

The highest concentrations of Sb are in the low-temperature barite-rich chimneys associated with a Pb-As-Sb sulfosalt, galena, and sphalerite. Concentrations of Sb in the Pb-As-Sb sulfosalt from a dendritic barite-rich chimney reach a maximum of 2.63 wt.% (Table 4.7). The occurrence of jordanite or jordanite-geocronite solid solution has been well documented in many seafloor massive sulfide deposits, including Axial seamount (Hannington and Scott, 1989; Hannington et al., 1991), Palinuro seamount (Tufar, 1991), Brothers volcano (Berkenbosch et al., 2012), and the PACMANUS hydrothermal field (Binns, 2014). High Sb concentrations in galena, up to 2.84 wt.%, reflect the extensive solid solutions throughout the Pb-As-Sb series (e.g., Biagioni et al., 2016). High concentrations in sphalerite from the barite-rich chimneys, up to 2.10 wt.%, reflect submicroscopic inclusions of the Sb-bearing sulfosalts as both Sb and As correlate well with Pb in most analyses. In dendritic sphalerite-rich chimneys, Sb is included in chalcopyrite (up to 1.40 wt.%), pyrite (up to 0.26 wt.%), and marcasite (up to 0.11 wt.%). Elevated Sb in the main sulfide phases of arc-related seafloor massive sulfide deposits is well documented (e.g., Monecke et al., 2016). At Palinuro seamount, sphalerite contains up to 3.49 wt.% Sb, galena contains up to 2.7 wt.%, pyrite contains up to 2.71 wt.%, and chalcopyrite contains up to 1.14 wt.% (Petersen et al., 2014).

Arsenic

The Pb-As-Sb sulfosalts contains up to 11.91 wt.% As (4.10–8.37 wt.%; Table 4.7). High As concentrations are also found in all of the major sulfide phases. In high-temperature zoned chalcopyrite-rich chimneys, sphalerite contains up to 1.83 wt.% As, chalcopyrite up to 1.25 wt.%, and covellite up to 0.70 wt.%. In sphalerite, As may be directly incorporated into the crystal lattice, or it may be hosted in micro-inclusions of Pb-As-Sb sulfosalts. Less is known about substitution of As in chalcopyrite. In low-temperature dendritic sphalerite-rich chimneys, As is most abundant in marcasite (up to 2.71 wt.% As) and pyrite (up to 1.42 wt.% As). This may result from direct substitution under low temperatures (Maslennikov et al., 2009), non-stoichiometric substitution (e.g., Huston et al., 1995), or the presence of As-nanoparticles (Deditius et al., 2011). In low-

temperature barite-rich chimneys, As is most abundant in galena (up to 9.93 wt.% As), likely occurring as sub-microscopic inclusions as As does not correlate with any other element in galena.

Gallium

Gallium is primarily hosted in sphalerite with average values of 0.15–0.23wt.% for the different chimney types; because Ga is trivalent, a coupled substitution mechanism is required. Ga/Cu are <1, indicating a possible coupled substitution of $Cu^{+} + Ga^{3+} \leftrightarrow 2Zn^{2+}$, as suggested by Cook et al. (2012). The highest concentrations are in sphalerite from zoned chalcopyrite-rich chimneys (maximum of 1.0 wt.%), and the lowest concentrations are from dendritic barite-rich chimneys (maximum of 0.26 wt.%: Table 4.7). These values are higher than previously recorded for sphalerite in seafloor massive sulfide deposits (maximum of 0.15 wt.%: Petersen et al., 2004) but few analyses have been reported. In the lower-temperature assemblages, significant Ga is also contained in galena, with up to 4.7 wt.% in galena from dendritic sphalerite-rich chimneys (avg. 0.09 wt.%; n = 59).

Indium

Indium is also enriched in Tinakula sphalerite, with concentrations of up to 1.3 wt.% in sphalerite from dendritic sphalerite-rich chimneys (Table 4.7). Sphalerite from the dendritic barite-rich chimneys is generally In-poor. Indium can be hosted in sphalerite by coupled substitution with monovalent copper (i.e., $Cu^{+} + In^{3+} \leftrightarrow 2Zn^{2+}$). Previous studies have shown that In may be enriched in higher-temperature (high-Fe) sphalerite (e.g., Schwarz-Schampera and Herzig, 1997), but this relationship was not observed in the Tinakula samples. Monecke et al. (2016) suggested that the bulk of In occurs as micro-inclusions (e.g., the Cu-In-sulfide, roquesite) in the main sulfide minerals. This is consistent with the common association of In in sphalerite with chalcopyrite-disease (e.g., Kieft and Damman, 1990). Chalcopyrite from Tinakula also has elevated In concentrations, with up to 0.18 wt.% in chalcopyrite from zoned chalcopyrite-rich chimneys (Table 4.7). This may reflect substitution into the iron site in chalcopyrite (e.g., Huston et al., 1995). The In concentrations in Tinakula sphalerite and chalcopyrite are higher than previously reported for other seafloor massive sulfide deposits (up to 0.09 wt.% and 0.12 wt.%, respectively,

in the Menez Gwen hydrothermal field: Lein et al., 2010), but like Ga few analyses for In have been reported. Elevated In has been reported from a large siliceous pyritic chimney from the PACMANUS hydrothermal field in the Manus basin, with concentrations of up to 130 ppm (Binns, 2014), but the host mineral of the In was not identified.

Mercury

Mercury is present in all minerals from the lowest-temperature assemblages, including low-Fe sphalerite, galena, and the Pb-As-Sb sulfosalts. Mercury-rich galena and jordanite are both present in sphalerite and micro-inclusions may account for some of the Hg reported in sphalerite. Concentrations of Hg in sphalerite are up to 1.3 wt.% in a dendritic sphalerite-rich chimney (Table 4.7). Galena and jordanite from a dendritic barite chimney both contain up to 0.13 wt.% Hg. Pyrite and chalcopyrite contain up to 0.18 wt.% and 0.11 wt.% respectively, where the minerals are associated Hg-rich sphalerite (e.g., sample GMA13-031; Appendix L). Similar Hg concentrations have been found in sphalerite from other arc-related seafloor sulfide deposits (e.g., Petersen et al., 2004), and very high concentrations have been reported from several minerals in a sediment-hosted deposit at Palinuro seamount (up to 7.41 wt.% Hg in sphalerite, up to 0.69 wt.% in pyrite, up to 7.24 wt.% in tetrahedrite-tennantite, and up to 21.5 wt.% in a Hg-rich sulfosalt: Petersen et al., 2014).

4.5.2. Conditions of mineralization at Tinakula

Minimum trapping temperature of primary fluid inclusions in anhydrite reach 295°C with salinities close to that of seawater (2.8 to 3.8 wt.% $NaCl_{equiv}$) at ~16 mbsf. Trapping temperatures of primary fluid inclusions in sphalerite were up to 298°C at ~18 mbsf. These temperatures are only about 10–20°C lower than the minimum temperature of boiling of the Tinakula fluids (308–311°C at 1070–1204 m water depth: Fig. 4.24), strongly suggesting that the highest-temperature fluids have boiled at depth and cooled by mixing on the way to the seafloor. Temperatures on the boiling curve higher than 350°C could be expected less than 500 m below the seafloor. Cooling of deep fluids from this temperature would have resulted in deposition of most of the high-temperature (e.g., Cu-

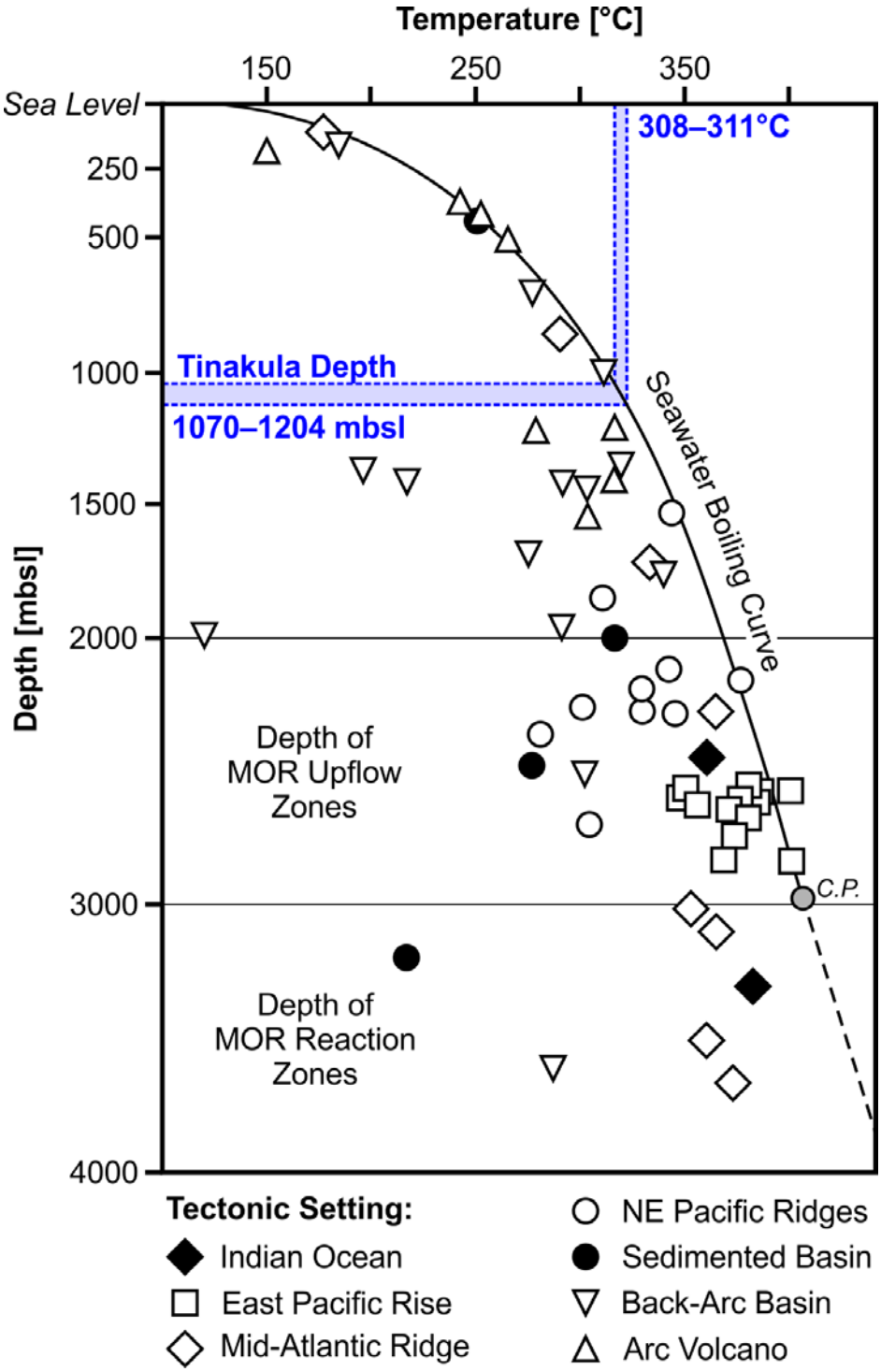


Fig. 4.24. Seawater boiling curve showing maximum temperatures of submarine hydrothermal vents, with examples from different tectonic settings, after Hannington et al. (2005) with data from Stoffers et al. (2006). The depth range of the Tinakula deposit (blue) corresponds to a maximum temperature range of 308–311°C. C.P. = critical point of seawater; depths of MOR upflow and reaction zones are approximate.

rich) minerals in the subseafloor, accounting for the predominance of Zn-rich ore at the seafloor. The presence of a number of very Cu-rich inactive chimneys in the Tinakula field suggests that the fluids had temperatures capable of transporting significant Cu in the past (Hannington et al., 1999) and could have been boiling at the seafloor.

"High-temperature" chimneys from Tinakula included both chalcopyrite-rich (n = 2) and zoned-chalcopyrite-rich (n = 18) samples (Fig. 4.5) and were collected from structures with 'normal' spire-like chimney morphologies (Figs. 4.2a,b). They are characterized by high concentrations of In and Mo (Table 4.3; Fig. 4.11), as well as microscopic grains of native gold. The latter may have formed as a result of precipitation during boiling, as recently documented in other seafloor hydrothermal systems (e.g., Hannington et al., 2016; Gartman et al., 2017). Gold concentrations correlates well with Mo (r = 0.79), reaching maximum whole-rock concentrations of 9260 ppb Au and 620 ppm Mo (Table 4.3).

The widespread occurrence of dendritic sphalerite-rich (n = 28) and barite-rich (n = 20) assemblages indicates that vent temperatures were commonly $\leq$250°C (e.g., Hannington, 2013). Chimney-like structures formed at these temperatures correspond to the bulbous chimney morphologies shown in Figure 4.2c,d. These chimneys are enriched in Ba, Sr, Ca, and Si, as well as Pb, Sb, and As, reflecting the abundance of galena and Pb-As-Sb sulfosalts. The low-temperature, sphalerite-rich assemblages show a well-known Au association with Sb (r = 0.63) and Ag (0.56), reaching maximum whole-rock concentrations of 7810 ppb Au, 489 ppm Sb, and 424 ppm Ag (e.g., Hannington et al., 1986). Gallium is incorporated mainly in galena, whereas in higher-temperature assemblages it is mainly in sphalerite. Arsenic precipitation appears to occur in both low- and high-temperature assemblages, reflecting the different mineral phases that contain As (e.g., pyrite at high temperature; galena and sulfosalts at lower temperatures). Most of the sphalerite has a low Fe content ($\leq$3 mol% in more than 70% of analyses; Fig. 4.15), consistent with lower temperatures of formation of most of the Zn-rich chimneys (e.g., Scott and Barnes, 1971; Barton and Skinner, 1979; Hannington et al., 1991). These data are compared to the range of sphalerite compositions from other seafloor massive sulfide systems dominated by low-Fe sphalerite in Figure 4.15. Figure 4.25 shows the equilibrium FeS content of sphalerite at different temperatures and sulfur activities for typical seafloor vent systems and the relevant compositions

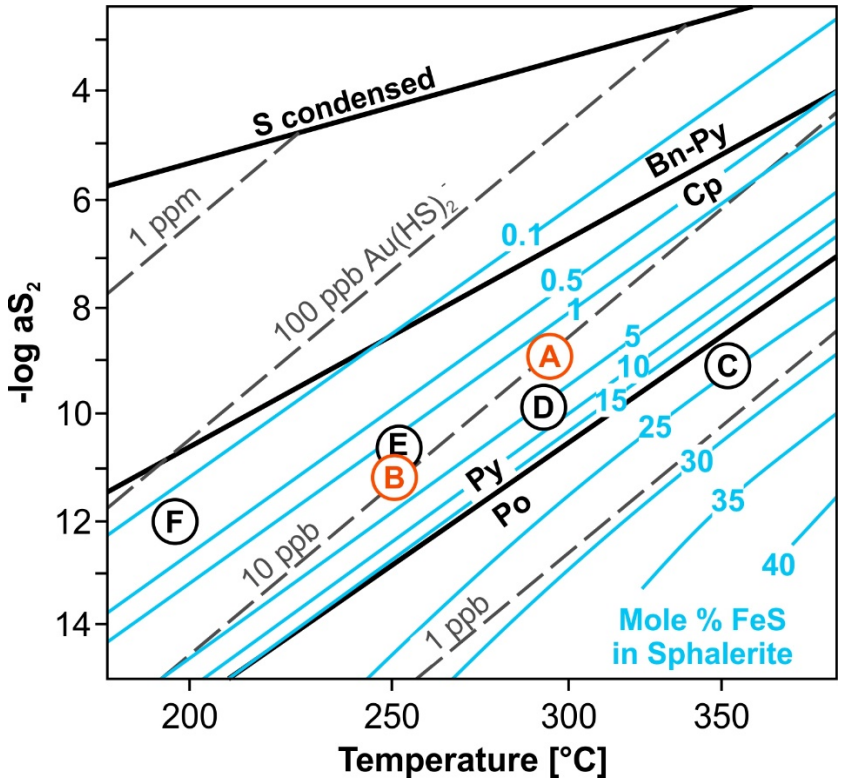


Fig. 4.25. Temperature-a_{S2} diagram showing the equilibrium FeS contents of sphalerite at different temperatures and sulfur activities for typical seafloor vent systems and the compositions of Tinakula sphalerite, with gold solubility contours (in ppb $Au[HS]_2^-$; dashed lines), and sulfidation boundaries for pyrite-pyrrhotite and bornite + pyrite-chalcopyrite (bold lines), from Hannington and Scott (1989) and references therein. Data from Tinakula are shown in orange: (A) sample MA13-090; and (B) sample P005 (full data in Suppl. Table L18); sphalerite compositions from other deposits is shown for 21°N EPR (C), Explorer Ridge (D), and Axial Seamount (E and F; Hannington and Scott, 1989).

of Tinakula sphalerite. Gold solubility contours (in ppb $Au[Hs]_2^-$) are also plotted, showing the higher concentrations of gold that could be transported in Tinakula fluids compared to typical MOR black smokers in equilibrium with pyrite and pyrrhotite. The polymetallic assemblages (pyrite, chalcopyrite, sphalerite, galena, and Pb-As-Sb sulfosalts) and low- to medium-FeS contents in sphalerite suggest an intermediate sulfidation state of the fluids (cf. Hannington, 2014). Elevated concentrations of most trace elements are found in low-Fe sphalerite, including Cd and Hg, whereas concentrations of Ga are higher in sphalerite with moderate-Fe contents (maximum at ~6 mol% FeS; Fig. 4.26). Notably, sphalerite from low-temperature barite-rich chimneys have low concentrations of Cd and Ga, and elevated concentrations of Hg compared to other chimney types, following trends in bulk geochemistry (Fig. 4.26; Table 4.2).

High- and low-temperature chimneys occur in close proximity (Fig. 4.3), which may reflect complex fluid paths or temperature variations. Many of the samples exhibit a complex paragenesis regardless of sample type, displaying overprinting bands of high- and low-temperature minerals (Appendix E), supporting changing or pulsed hydrothermal temperatures during the growth of a single chimney. Evidence for discrete hydrothermal events at a single location is given by the occurrence of a barite-sphalerite chimney growing directly on an older silicified barite-rich chimney (sample GMA13-053; Appendix E). However, there is no evidence for deposit-scale zone refining, such as that described in the TAG hydrothermal field (Hannington et al., 1998). Rather, the system appears to be in a waning phase of hydrothermal activity, with widespread late-stage precipitation of low-temperature amorphous silica and Fe- and Mn-oxyhydroxides. Because of the high preservation potential of barite, reflecting its low solubility (Blount, 1977), even the oldest chimneys are well preserved. These chimneys are particularly sturdy, and one fully intact (inactive) chimney has a calculated age of 3450 ± 229 years (Table 4.10).

The abundance of barite reflects the important role of mixing between the Ba-rich hydrothermal fluids and SO_4-rich seawater (e.g., Hannington and Scott, 1989; Herzig et al., 1993). Cooling of the fluids and mixing near the seafloor was particularly likely given the highly permeable volcaniclastic substrate. Mineralization appears to have been widespread, with limited development of a deep, highly focused upflow zone. Mixing at the seafloor has led to strong thermal and chemical gradients in the chimneys, and precipitation of minerals under disequilibrium

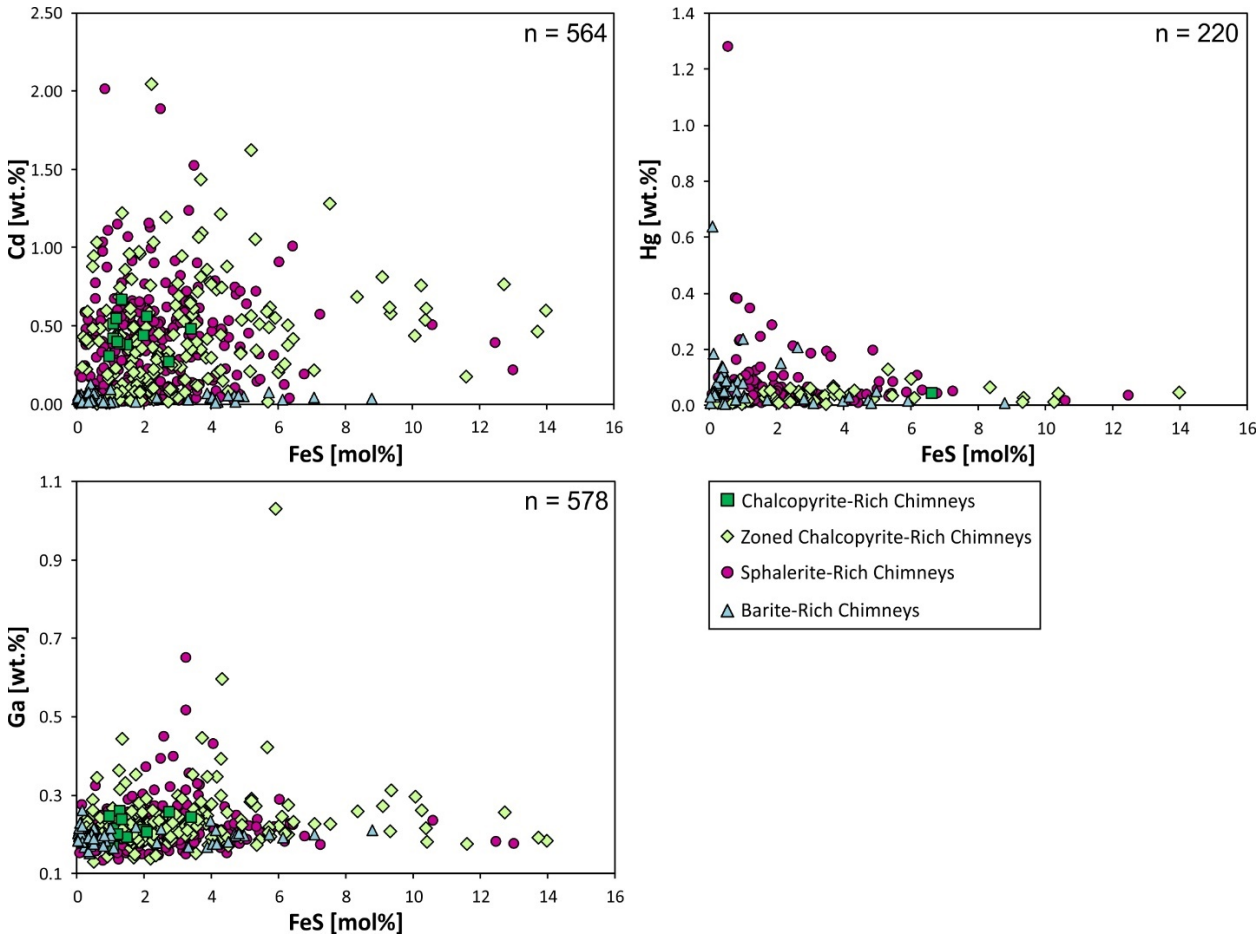


Fig. 4.26. Selected trace-element concentrations versus mol% FeS in sphalerite measured by EPMA (values above detection limits only). Complete data are in Appendix L.

crystallization conditions (e.g., minerals rapidly precipitated under highly supersaturated conditions to create the widespread dendritic textures: Turcotte, 1997). A study of hydrothermal barite by Jamieson et al. (2016) showed a high proportion of seawater mixing responsible for dendritic barite (<40% hydrothermal component) compared to well-formed crystalline barite. This mode of precipitation is likely responsible for the formation of porous beehive-like structures and the unusual bulbous chimneys observed at Tinakula. During early phases of chimney formation, seawater was able to percolate through the porous structure, resulting in the precipitation of multiple generations of dendritic sulfides and dendritic barite. Strong thermal gradients are reflected in the presence of cm-thick rims of white dendritic barite, with cores of sphalerite + barite. While most hydrothermal chimneys are characterized by disequilibrium textures only in early phases or in the outer chimney walls, disequilibrium conditions persisted during the growth of the majority of chimneys at Tinakula, ultimately leading to the unusual bulbous and layered morphologies. This style of mineralization, previously described in layered barite-sulfide mounds in the East Diamante caldera (Hein et al., 2014) and at Clark Seamount (de Ronde et al., 2014), may be common where chimney/mound formation is controlled by diffuse, low-temperature fluid flow and permeable volcaniclastic substrates.

4.5.3. Comparison of Tinakula sulfides with global SMS deposits

Massive sulfide deposits in rifted arc environments have overall higher base metal contents than most deposits on mid-ocean ridges, with average concentrations of 2.7 wt.% Cu, 17.0 wt.% Zn, and 0.7 wt.% Pb (Petersen et al., 2016). Tinakula has relatively few Cu-rich chimneys, with an average concentration of 5.82 wt.% Cu for all sulfide chimneys analyzed (n = 36; Appendix I). The average Zn concentration (19.20 wt.%) and Pb concentration (0.35 wt.%) of the chimney samples are consistent with the abundant sphalerite chimneys in the Tinakula field. The total combined base metal content (Cu + Zn + Pb) of the chimneys is 28.64 wt.% (median value; n = 36; Appendix I). The individual chimneys span the full range of Cu:Zn:Pb ratios (Fig. 4.8); chalcopyrite-rich, zoned chalcopyrite-rich, and dendritic sphalerite-rich chimneys are similar to massive sulfide deposits along sediment-free mid-ocean ridges; whereas the dendritic barite-rich chimneys have higher proportions of Pb, Ba, and As + Sb, similar to other deposits at volcanic arcs or in back-arc basins. The average of all samples shows a bulk composition much closer to

that of basalt-hosted massive sulfide deposits than to most arc-related deposits (e.g., Figs. 4.27 and 4.28; Table 4.11). The metal ratios bear the closest resemblance to deposits of the Juan de Fuca Ridge (unsedimented), which are characterized by an enriched-MORB source, with higher Pb, As, Sb, and Ba than N-MORB (e.g., Ames et al., 1993; Goodfellow and Franklin, 1993; Koski et al., 1994; Bjerkgard et al., 2000). In particular, Tinakula is characterized by very high As + Sb compared to all other all other tectonic settings (Fig. 4.28). This is consistent with the basaltic-andesite host rocks of the deposit and the apparent lack of influence from the nearby dacitic lavas. In contrast, the average sulfide composition from the Nifonea vent field in the Coriolis Troughs (southern New Hebrides back-arc) have a lower proportion of Ba and a higher proportion of As + Sb, similar to other arc and back-arc deposits (Figs. 4.27; Haase et al., 2014).

Gold concentrations in the Tinakula sulfide chimneys, which range from <0.04–9.26 ppm Au (avg. 2.36 ppm, n = 36), are higher than the average for MOR but somewhat lower than other arc-related massive sulfide deposits, which have a median gold content of 7.5 ppm Au (Monecke et al., 2014; Table 4.10). The high gold relative to MOR sulfides likely reflects a combination of enrichment in the back-arc basin lavas and the generally low-temperature of the deposits (i.e., strong Zn-Pb-As-Sb association typical of Au-enriched sulfides at MOR: Hannington et al., 1986; Hannington and Scott, 1989; Hannington et al., 1991; Herzig et al., 1993; Hannington et al., 1995). However, there is little evidence for a direct magmatic contribution of Au to the hydrothermal system, as has been suggested for very Au-rich deposits at some arc-front volcanoes (e.g., Moss et al., 2001; Yang and Scott 2005; Berkenbosch et al., 2012). The lack of elements such as Bi or Te, which are commonly associated with the Au in Cu-rich chimneys of other arc-related systems, is also consistent with little or no direct magmatic input. Native gold or electrum was found in high-temperature Cu-rich assemblages (<1 μm grains in chalcopyrite sample GMA13-048; Fig 4.4c), which may be related to boiling rather than magmatic input (see below). “Invisible” Au was also detected in pyrite (up to 0.36 wt.%) and sphalerite (up to 0.57 wt.%), where it may be incorporated as nanoparticles associated with the formation of vacancies and defects during disequilibrium crystallization rather than by direct substitution in the crystal structure (e.g., Cook et al., 2009; Vikentyev, 2015).

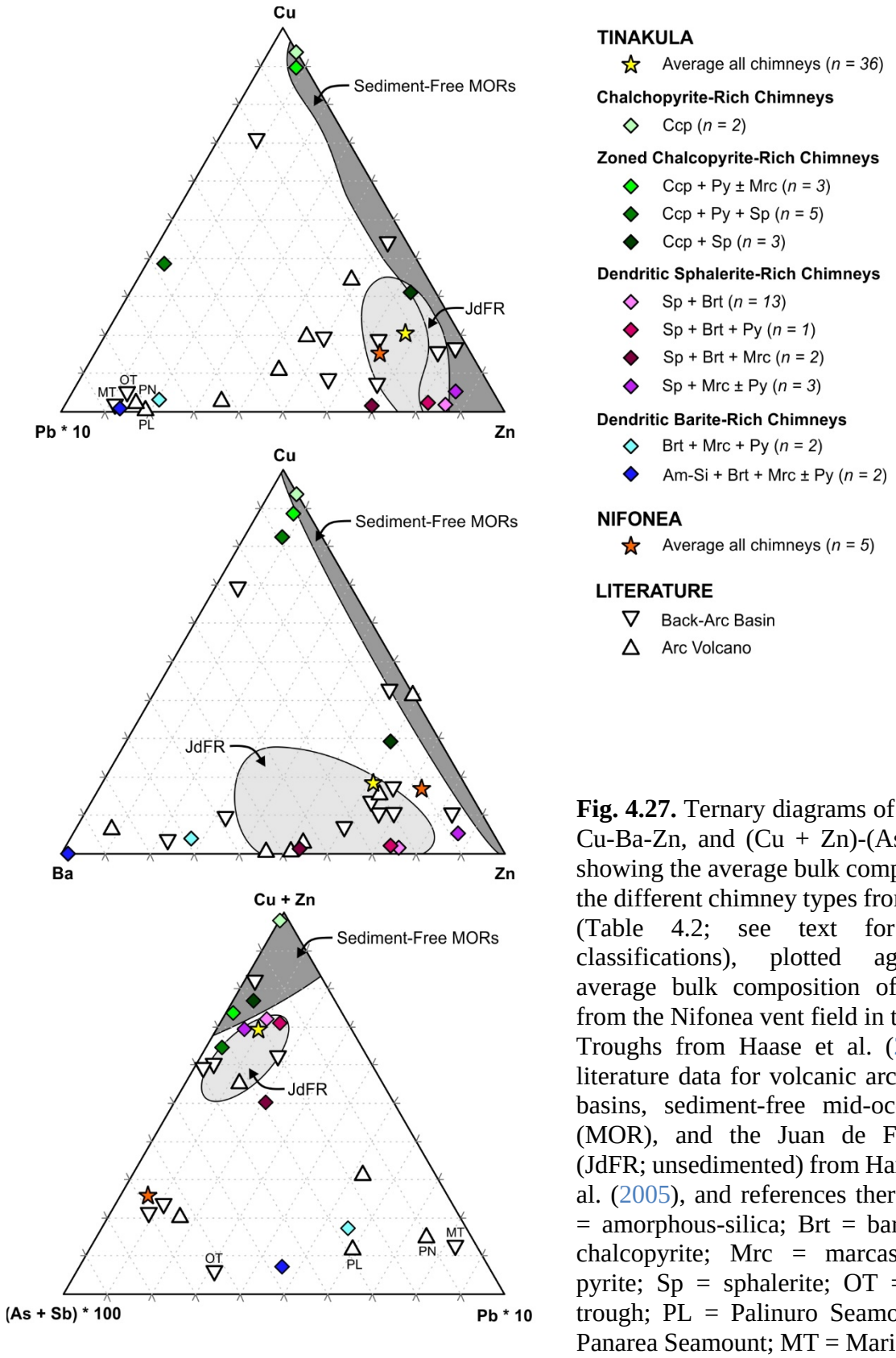


Fig. 4.27. Ternary diagrams of Cu-Pb-Zn, Cu-Ba-Zn, and (Cu + Zn)-(As + Sb)-Pb showing the average bulk compositions of the different chimney types from Tinakula (Table 4.2; see text for chimney classifications), plotted against the average bulk composition of chimneys from the Nifonea vent field in the Coriolis Troughs from Haase et al. (2014), and literature data for volcanic arcs, back-arc basins, sediment-free mid-ocean ridges (MOR), and the Juan de Fuca Ridge (JdFR; unsedimented) from Hannington et al. (2005), and references therein. Am-Si = amorphous-silica; Brt = barite; Ccp = chalcopyrite; Mrc = marcasite; Py = pyrite; Sp = sphalerite; OT = Okinawa trough; PL = Palinuro Seamount; PN = Panarea Seamount; MT = Mariana trough.

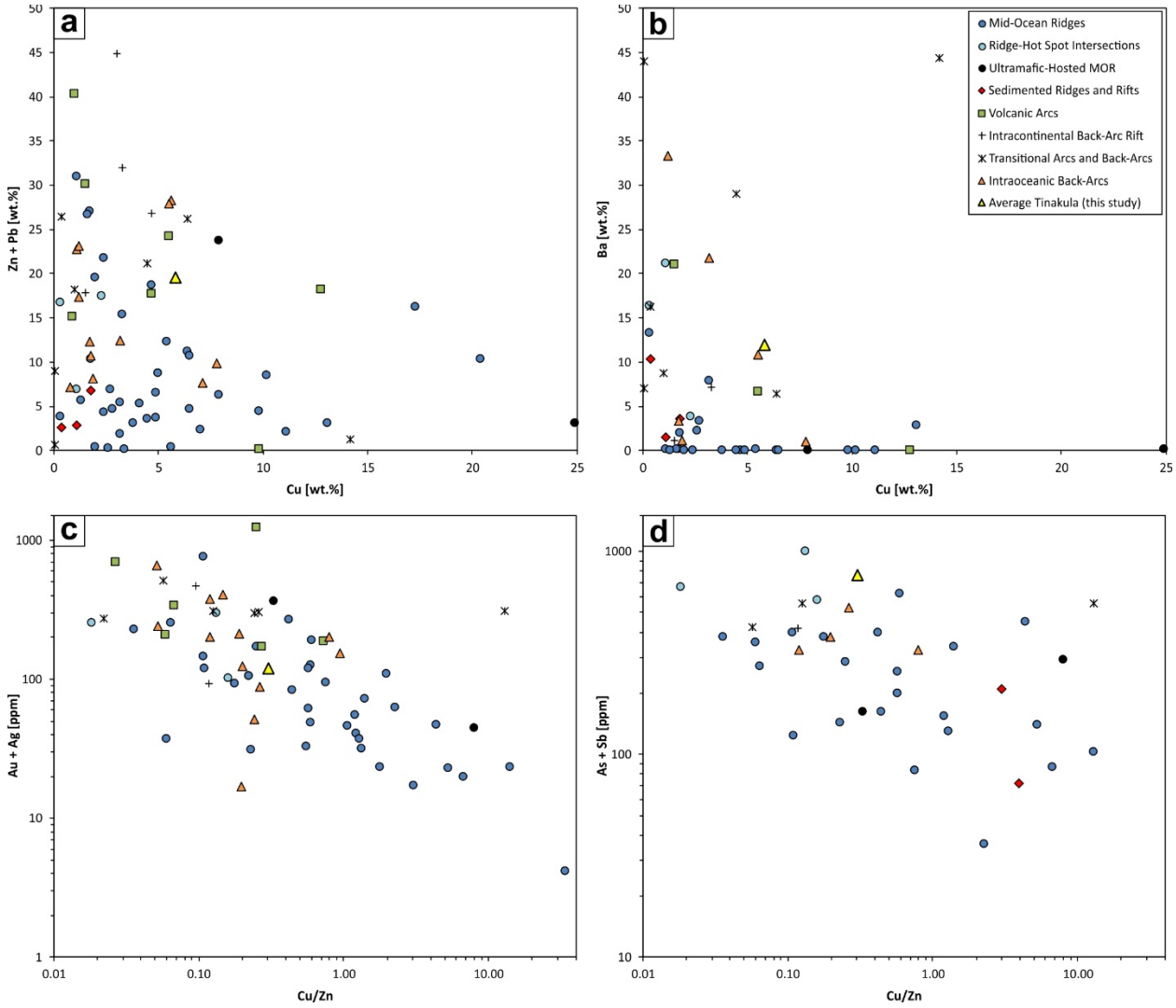


Fig. 4.28. Average bulk compositions of sulfide seafloor massive sulfide deposits compared to the average values at the Tinakula deposit (summarized in Table 4.11): (a) Zn + Pb vs. Cu ; (b) Ba vs. Cu; (c) Au + Ag vs. Cu/Zn; (d) As + Sb vs. Cu/Zn. Tinakula has moderate Cu, Zn + Pb, and Au + Ag contents, with slightly enriched Ba compared to mid-ocean ridge environments, and very high As + Sb compared to all other all other tectonic settings.

Table 4.11. Average bulk compositions of sulfide samples from seafloor massive sulfide deposits compared to the Tinakula deposit (chimney samples only)

	n	Cu [wt.%]	Zn [wt.%]	Pb [wt.%]	Fe [wt.%]	Ba [wt.%]	Au [ppm]	Ag [ppm]	As [ppm]	Sb [ppm]
Mid-Ocean Ridges										
Juan de Fuca Ridge										
S. Explorer Ridge	51	3.2	5.4	0.1	25.2	7.9	0.72	125	575	42
High Rise, Endeavour	51	1.8	10.1	0.3	24.7	2	0.33	93	350	31
Main Field, Endeavour	83	2.7	6.4	0.5	30.1	3.3	0.11	267	356	42
Clam Bed, Endeavour	5	0.3	2.8	1.1	14.8	13.3	0.12	145	316	80
Mothra	20	3.3	14.9	0.5	-	-	0.05	105	-	-
Co-axial	6	-	23.2	-	-	-	0.98	59	-	-
Northern Cleft	26	1.7	26.6	0.5	15.8	0.1	0.25	255	220	51
Southern Cleft	16	1.1	30.9	0.1	18.6	0.1	0.11	230	360	18
East Pacific Rise										
21°N	46	5.4	12.2	0.1	17.2	0.1	0.12	83	140	23
21°N, Green Seamount	6	2.6	0.2	<0.1	26.5	2.3	0.16	<1	95	8
14°N	5	2.8	4.7	<0.1	9.0	-	0.51	48	-	-
13°N	71	6.4	11.1	0.1	28.2	0.01	0.45	61	245	11
13°N Seamount	13	2.4	4.3	0.03	-	-	0.80	32	-	-
11°30'N	23	3.2	1.8	<0.1	29.5	-	0.25	23	-	-
11°32'N	32	3.4	0.1	<0.1	-	-	0.13	4	-	-
11°N	18	1.6	26.6	0.1	20.5	0.1	0.15	37	330	26
09°50'N	29	7.9	6.3	<0.1	-	-	-	-	-	-
07°24'S	14	11.1	2.1	<0.1	34.6	<0.1	0.05	23	135	4
16°43'S	19	10.2	8.5	<0.1	31.3	<0.1	0.32	55	140	15
17°26'S	1	1.3	5.6	<0.1	36.3	<0.1	0.10	31	135	9
18°25'S	35	4.7	18.6	0.1	21.9	<0.1	0.58	170	280	6
21°30'S	28	9.8	4.3	0.1	37.4	<0.1	0.41	62	35	1
21°50'S	1	2.4	21.7	0.1	28.6	<0.1	0.36	120	110	14
37°40'S	24	3.8	3.1	<0.1	-	-	0.82	40	-	-
Galapagos Rift										
86°W	128	4.5	3.5	<0.1	28.3	0.01	0.29	37	120	10
Indian Ocean										
Sonne Field, CIR	35	13.1	3.0	<0.1	31.2	2.9	1.02	46	400	48
Kairei Field, CIR	8	20.4	10.3	<0.1	-	-	7.99	101	-	-
Endmond Field, CIR	17	6.5	10.7	<0.1	-	-	4.01	188	-	-
Mt. Jourdanne, SWIR	7	2.0	18.4	1.2	15.6	-	5.17	750	5760	450
Mid-Atlantic Ridge										
Broken Spur	76	4.9	3.7	<0.1	-	-	1.64	30	-	-
24 30'N, MAR	16	4.1	<0.1	5.3	-	-	-	-	-	-
TAG	310	4.9	6.5	<0.1	27.2	<0.1	1.80	92	55	28
Mir Zone	137	5.0	8.7	<0.1	27.9	-	4.20	115	145	54
Alvin Zone	4	2.0	0.3	<0.1	40.7	<0.1	0.88	19	83	3
Snakpit	93	6.5	4.6	0.1	34.9	<0.1	1.66	70	320	20
Krasnov Field	137	5.6	0.4	<0.1	-	-	1.11	22	-	-
Turtle Pits, 5°S	43	7.0	2.3	<0.1	-	-	0.26	17	-	-
Nibelungen, 8°S	9	17.3	16.2	0.1	-	-	8.95	37	-	-
Ridge-Hot Spot Intersections										
Lucky Strike	3	1.1	6.8	0.1	21.5	21.2	-	102	573	-
CASM, Axial volcano	31	0.3	16.3	0.4	4.3	16.4	4.12	250	435	230
ASHES, Axial volcano	90	2.3	17.3	0.2	15.0	3.8	1.56	295	780	220
Ultramafic-Hosted										
Rainbow, MAR	9	7.9	23.7	<0.1	29.0	<0.1	3.10	362	163	-
Logatchev	54	24.9	3.1	<0.1	23.7	0.2	8.36	36	265	29
Sedimented Ridges and Rifts										
Middle Valley	100	1.1	2.8	<0.1	26.0	1.5	0.16	7	61	11
Excanaba Trough	51	1.8	5.6	1.2	30.5	3.6	1.29	163	4914	860
Guaymas Basin	22	0.4	2.2	0.4	17.4	10.4	0.15	82	100	110
Intracontinental Back-Arc Rift										
Okinawa Trough										
Izena Cauldron	40	3.3	20.2	11.8	6.2	7.2	3.13	2305	17500	6710
North Iheya Ridge	6	3.0	31.4	13.5	10.5	-	1.23	465	1725	1136
Minami Ensei Knolls	6	1.5	12.8	5.0	3.3	1.1	2.43	90	420.0	-
Yonuguni Knoll	8	4.7	17.0	9.8	-	-	-	-	-	-

Table 4.11. Continued

	n	Cu [wt.%]	Zn [wt.%]	Pb [wt.%]	Fe [wt.%]	Ba [wt.%]	Au [ppm]	Ag [ppm]	As [ppm]	Sb [ppm]
Volcanic Arcs										
Izu-Bonin Arc										
Sunrise, Myojin Knoll	37	5.5	21.9	2.3	10.5	6.7	20.00	1215	5045	3565
Kita Bayonnaise	3	4.7	17.3	0.4	-	-	9.13	162	-	-
Hakurei	24	1.0	37.2	3.1	-	-	6.00	692	-	-
Myojinsho caldera	3	1.5	25.5	4.6	1.9	21.0	1.71	205	1410	475
Suiyo Seamount	13	12.8	17.5	0.7	15.0	<0.1	27.73	160	1170	585
Kermadec Arc										
Brothers Seamount	37	0.9	13.2	1.9	-	-	0.50	340	-	-
Rumble II	1	9.8	0.1	<0.1	-	-	-	-	-	-
Transitional Arcs and Back-Arc Basins										
Manus Basin										
Central Manus	152	1.0	17.6	0.6	11.6	8.7	-	514	425	-
Pacmanus, SER	111	6.4	24.8	1.4	12.4	6.4	13.49	290	4600	670
SuSu, SER	19	14.2	1.1	0.2	20.8	44.4	13.12	294	255	300
Franklin Seamount	34	<0.1	0.4	0.2	0.7	44.0	13.12	294	255	300
Tyrrhenian Sea										
Panarea Seamount	5	<0.1	6.2	2.8	10.5	7.0	-	11	505	-
Palinuro Seamount	15	0.4	17.9	8.6	15.1	16.3	3.40	270	3400	750
Bransfield Strait	7	4.5	18.5	2.6	1.1	29.0	0.54	300	7590	573
Intraoceanic Back-Arc Basins										
Mariana Trough										
Alice Springs, 18°N	11	1.2	10.0	7.4	2.4	33.3	0.78	200	270	58
Forecast, 13°N	13	0.8	6.7	0.5	-	-	22.90	355	-	-
Manus Basin										
Solwara 11	17	1.8	9.4	1.3	-	-	1.07	213	-	-
Solwara 3	31	1.1	21.3	1.4	-	-	15.15	642	-	-
Solwara 2	44	1.2	22.9	0.2	-	-	6.73	234	-	-
Solwara 10	13	7.1	7.5	0.1	-	-	2.31	152	-	-
North Fiji Basin	93	7.8	9.8	0.1	26.3	1.0	2.55	200	270	58
Lau Basin										
Kings Triple Junction	78	5.6	28.2	0.1	8.7	-	-	17	380	-
Northern Valu Fa Ridge	63	3.2	12.1	0.4	6.8	21.8	2.68	86	450	75
Central Valu Fa Ridge	87	5.5	27.6	0.3	7.4	10.8	3.21	120	1900	76
Southern Valu Fa Ridge	25	1.7	11.6	0.7	32.3	3.3	1.43	405	3815	21
New Hebrides Back-Arc										
Nifonea, CT*	5	1.9	7.8	0.3	19.2	1.1	0.11	51	2567	34
Tinakula, JCT (this study)	**36**	**5.8**	**19.2**	**0.4**	**11.9**	**6.5**	**2.36**	**118**	**610**	**154**

*Data from Haase et al. (2014); all other data compiled by Hannington et al. (2005), and references therein

Whole-rock concentrations of Ag in the Tinakula chimneys range from <5–424 ppm (avg. 118 ppm Au, n = 36) and are similar to Zn-rich MOR hydrothermal systems (Table 4.11). Similar to other Zn-rich deposits, the Ag is mainly associated with galena (up to 1.23 wt.%; mostly <0.60 wt.%), Pb-As-Sb sulfosalts (up to 0.37 wt.%), and sphalerite (up to 0.37 wt.%), typical of low-temperature assemblages. The abundance of sphalerite throughout the deposit indicates that it accounts for a large portion of the silver budget. The overall highest concentrations of Ag were found in low-temperature dendritic barite-rich chimneys (Table 4.2). Silver-rich galena has been identified in low-temperature assemblages at many other massive sulfide deposits, including Eastern Australian VMS deposits (up to 1.07 wt.% at the Rosebury deposit; Huston et al., 1996), Kidd Creek (up to 0.73 wt.% Ag; Gemmell, 2013), and Hackett River (up to 0.58 wt.% Ag; Grant et al., 2015). Thermodynamic constraints indicate that silver can be accommodated in galena as a solid solution at ore-forming temperatures (e.g., Chutas and Sack, 2004). Silver-bearing sphalerite has also been documented in hydrothermal chimneys at several locations, such as the Edmond hydrothermal field on the Central Indian Ridge (Wu et al., 2016, 2018).

The sulfur isotope signature in a seafloor hydrothermal system reflects: (1) the isotopic composition of sulfur leached from the host rock; (2) contributions from seawater sulfate (both oxidized and reduced); (3) the extent of reduction of seawater sulfate by hydrothermal fluids; and (4) the amount of mixing between these sources (Ohmoto, 1996). The $\delta^{34}S$ of sulfur in MORB is between -0.6 and +1.6 ‰, with a global mean value of +0.5 ± 0.6 ‰ (Sakai et al., 1984), but arc lavas typically have higher $\delta^{34}S$ values, as high as +6 to +8 ‰ (Ueda and Sakai, 1984; Alt et al., 1993), with a slab-influenced mantle source of +5 ‰ (McDermott et al., 2015). Modern seawater sulfate has a $\delta^{34}S$ value of 21.0 ‰ (Rees et al., 1978). $\delta^{34}S$ values of sulfides at Tinakula are 3–7 ‰ lower than arc-related volcanic values. This may result from degassing of magmatic volatiles from the underlying intermediate-felsic magma chamber(s), which can produce H_2S with low $\delta^{34}S$ values from the disproportionation of SO_2 during cooling below ~400°C (Gamo et al., 1997; Kusakabe et al., 2000). For example, magmatically-derived $\delta^{34}S$ values of from Conical Seamount and Palinuro seamount reach -17.5 ‰ and -39.3 ‰, respectively (Fig. 4.29; Gemmell et al., 2004; Petersen et al., 2014). There is no additional mineralogical evidence for a magmatic contribution to the hydrothermal system (e.g., advanced argillic alteration minerals such as alunite and jarosite). Seawater sulfate also may be reduced by bacteria, resulting in negative $\delta^{34}S$ values at least as low

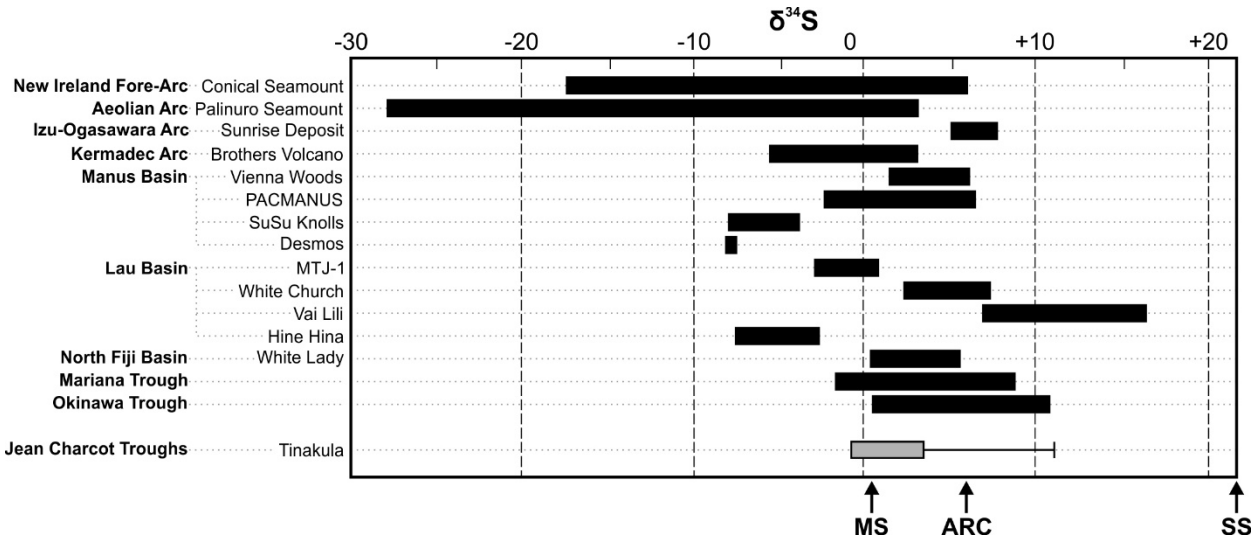


Fig. 4.29. Sulfur isotope compositions of sulfides from seafloor massive sulfides in arc and back-arc environments from Petersen et al. (2014) and Hannington et al. (2005), and references therein. Samples from this study (shown in grey) range from -0.8 to 3.4 ‰; higher values between 7.0 and 11.0 ‰ are considered suspect, likely resulting from mineralogical impurities with barite (Table 4.8). MS = MORB sulfur of (+0.5 ‰; Sakai et al., 1984); SS = seawater sulfate (21.0 ‰; Rees et al., 1978); ARC = island arc andesites (6.00 ‰; Alt et al., 1993).

as -40 ‰ (Canfield and Raiswell, 1999). All of these processes could result in sulfide that is isotopically lighter than the arc-related igneous source. However, there are no systematic spatial variations in S-isotope compositions of chimneys along the main structure at Tinakula, suggesting that the sulfur source was very uniform. The highest values in sphalerite (>7 ‰) likely reflect mineralogical impurities (fine-grained barite) in samples that were not chemically purified, as sphalerite and barite is closely intergrown and difficult to distinguish even at the microscopic scale (see Appendix I). $\delta^{34}S$ values of barite are close to that of seawater sulfate, ranging from 19.3 to 22.5 ‰. Values that were significantly lower (between 2.1 and 15.9 ‰) reflect impure samples that were mixed with sphalerite; this was confirmed by chemical treatment to remove sulfide producing $\delta^{34}S$ values with a narrow range of 21.04 to 21.67 ‰ (Table 4.8). Chalcopyrite has the lowest $\delta^{34}S$ values (avg. 0.9 ‰; n = 9), pyrite has intermediate values (avg. 1.2 ‰; n = 8) and sphalerite displays the highest $\delta^{34}S$ values (avg. 3.1 ‰; n = 22; Fig. 4.17). This can be explained by more oxidized conditions in the lower-temperature assemblages (Ohmoto and Rye, 1979) but also a larger contribution of reduced seawater sulfate mixing with the igneous sulfur. Hydrothermal circulation at Tinakula resulted in the precipitation of anhydrite in the footwall at temperatures >150°C, with sulfate derived from seawater, and Ca derived from leaching of the host rock. The $\delta^{34}S$ values of anhydrite and gypsum in the footwall (down to 20.77 mbsf) range from 21.96 to 20.5 ‰. Interaction of the reduced hydrothermal fluids with this sulfur could also have resulted in an increase in the $\delta^{34}S$ of the sulfides (e.g., Alt et al., 1989; Shanks, 2001).

4.6. Conclusions

The Tinakula seafloor massive sulfide deposit is the in the young Jean Charcot troughs is one of the first well-documented examples of SMS developed mainly in volcaniclastic rocks associated with the first mafic (basaltic to andesitic) lavas erupted in an early back-arc rift. The particular mineralization and alteration styles are a direct result of the volcanic setting, which is dominated by permeable volcaniclastic substrate, rather than the coherent lava flows typical of mid-ocean ridges, promoting lateral fluid flow, mixing with cold seawater, and widespread diffuse venting at relatively low temperatures. This ultimately led to the formation of abundant distinctive beehive-like chimneys with unusual bulbous and layered morphologies over ~5,500 years. In addition, Tinakula displays a wide range of mineralization styles, including: (1) high-temperature

chalcopyrite-rich chimneys, with elevated concentrations of Au (up to 9260 ppb), Mo (up to 620 ppm), and In (up to 280 ppm); (2) zoned chimneys with high-temperature cores of pyrite and chalcopyrite and low-temperature margins of sphalerite, with elevated concentrations of Ga (up to 172 ppm) and Ag (up to 251 ppm); (3) low-temperature chimneys containing dendritic sphalerite and barite, with elevated concentrations of Au (up to 7810 ppb), Ag (up to 424 ppm), Cd (up to 1920 ppm), As (up to 1520 ppm), Sb (up to 594 ppm), and Hg (up to 61.8 ppm); (4) low-temperature dendritic barite-rich chimneys, with elevated concentrations of Pb (up to 2.37 wt.%) and Hg (up to 39.5 ppm); and (5) late-stage low-temperature siliceous iron oxide chimneys, with low concentrations of base and precious metals.

The tectonic setting of the Tinakula deposit also plays a first-order role in the composition of the massive sulfide chimneys. Geochemical analyses of volcanic rocks in the Starfish-Tinakula area reveal an enriched mantle source and contributions from the subducting slab, and a combination of partial melting and fractionation have produced a chemically diverse suite of intermediate (basaltic-andesite to andesite) and felsic (dacites) rocks. Major and trace elements from both suites may have been leached during hydrothermal circulation. For example, very small enrichments of Ba in the host rocks of seafloor hydrothermal systems are known to result in significant enrichment of Ba in the fluids (e.g., Hannington et al., 2005). However, the Tinakula massive sulfides have unexpectedly low Pb contents for arc-related hydrothermal systems. This likely reflects the importance of dominantly mafic volcanic rocks along the row of cinder cones that host the deposit, although the massive sulfides also have low Co and Ni concentrations that might have been expected from a mafic source. The sulfides are also depleted in trace metals commonly associated with direct magmatic contributions to the hydrothermal fluids, such as Bi, Te and Se in mafic-intermediate magmatic suites or Sn and W in felsic magmatic suites. Thus the Tinakula metal assemblage is transitional between a purely mafic-dominated back-arc system and something more typical of an arc-front volcano (e.g., Fouquet et al., 1993b; Hannington et al., 2005; Berkenbosch et al., 2012; Monecke et al., 2016). The distribution of the trace elements reflect both mineralogical controls (e.g., co-precipitation, mineral substitution) and the effects of mixing, cooling, and possibly boiling. In addition, $\delta^{34}S$ isotopes show that crustal host rock and thermochemical reduction of sweater sulfate are the primary sources of sulfur. SO_4–H_2S isotopic exchange in the shallow subsurface, resulting from entrainment of seawater and reaction with sulfate minerals,

may be a dominant process. This study adds to our knowledge about the diversity of seafloor massive sulfides in early back-arc settings, as well as the influence of tectonism and volcanism on mineralization at the earliest stages of arc rifting.

Appendix B. Supporting Information

Supplementary data associated with this article is found in Appendix B.

References

Alt, J.C., Anderson, T.F., Bonnell, L., 1989. The geochemistry of sulfur in a 1.3 km section of hydrothermally altered oceanic crust, DSDP Hole 504B. Geochim. Cosmochim. Acta 53, 101–1023, doi:10.1016/0016-7037(89)90206-8.

Alt, Shanks, W.C. III., Jackson, M.C., 1993. Cycling of sulfur in subduction zones: the geochemistry of sulfur in the Mariana island arc and back-arc trough. Earth Planet. Sci. Lett. 119, 477–494, doi:10.1016/0012-821X(93)90057-G.

Anders, M., 2016. Fluid inclusions and mineralogy at the seafloor massive sulfide deposit, New Hebrides arc/backarc, Solomon Islands. Unpublished master's thesis, Christian Albrechts University of Kiel, Kiel, Germany, 96 p.

Ames, D.E., Franklin, J.M., Hannington, M.D., 1993. Mineralogy and geochemistry of active and inactive chimneys and massive sulfides, Middle Valley, Northern Juan de Fuca Ridge: An evolving hydrothermal system. Can. Mineral. 31, 997–1024.

Barton, P.B., Jr., Skinner, B.J., 1979. Sulfide mineral stabilities. In: Barnes, H.L. (Ed.), Geochemistry of hydrothermal ore deposits. Wiley, New York, NY, pp. 278–403.

Berkenbosch, H.A., de Ronde, C.E.J., Gemmell, J.B., McNeill, A.W., Goemann, K., 2012. Mineralogy and formation of black smoker chimneys from Brothers submarine volcano, Kermadec arc. Econ. Geol. 107, 1613–1633, doi:10.2122/econgeo.107.8.1613.

Biagioni, C., Dini, A., Orlandi, P., Moëlo, Y., Pasero, M., Zaccarini, F., 2015. Lead-antimony sulfosalts from Tuscany (Italy). XX. Members of the jordanite-geocronite series from the Pollone Mine, Valdicastello Carducci: Occurrence and crystal structures. Minerals 6, 15, doi:10.3390/min6010015.

Binns, R., 2014. Bikpela: A large siliceous chimney from the PACMANUS hydrothermal field, Manus Basin, Papua New Guinea. Econ. Geol. 109, 2243–2259, doi:10.2113/econgeo.109.8.2243.

Bjerkgard, T., Cousens, B.L., Franklin, J.M., 2000. The Middle Valley sulfide deposits, northern Juan de Fuca Ridge: Radiogenic isotope systematics. Econ. Geol. 95, 1473–1488, doi:10.2113/gsecongeo.95.7.1473.

Blount, C.W., 1977. Barite solubilities and thermodynamic quantities up to 300-degrees-C and 1400 bars. Amer. Mineral. 62, 942–957.

Bodnar, R., Vityk, M., 1994. Interpretation of microthermometric data for H_2O-NaCl Fluid Inclusions. In: De Vivo, B., Frezzotti, M. (Eds.), Fluid Inclusions in Minerals, Methods and Applications. Virginia Tech, Blacksburg, VA, pp. 117–130.

Brown, P.E., 1989. FLINCOR: A computer program for the reduction of and investigation of fluid inclusion data. Am. Mineral. 74, 1390–1393.

Butterfield, D.A., McDuff, R.E., Mottl, M.J., Lilley, M.D., Lupton, J.E., Massoth, G.J., 1994. Gradients in the composition of hydrothermal fluids from the Endeavour segment vent field: Phase separation and brine loss. J. Geophys. Res. 99, 9561–9583, doi:10.1029/93JB03132.

Canfield, D.E., Raiswell, R., Westrich, J.T., Reaves, C.M., Berner, R.A., 1986. The use of chromium reduction in the analysis of reduced inorganic sulfur in sediments and shales. Chem. Geol. 54, 149–155, doi:10.1016/0009-2541(86)90078-1.

Canfield, D.E., Raiswell, R., 1999. The evolution of the sulfur cycle. Am. J. Sci. 299, 267–723, doi:10.2475/ajs.299.7-9.697.

Chutas, N.I., Sack, R.O., 2004. Ore genesis at La Colorado Ag-Zn-Pb deposit in Zacatecas, Mexico. Mineral. Mag. 68, 923–937, doi:10.1180/0026461046860231.

Cook, N., Ciobanu, C.L., Pring, A., Skinner, W., Shimizu, M., Danyushevsky, L., Saini-Eidukat, B., Melcher, F., 2009. Trace and minor elements in sphalerite: A LA-ICPMS study. Geochim. Cosmochim. Acta 73, 4761–4791, doi:10.1016/j.gca.2009.05.045.

Cook, N.J., Ciobanu, C.L., Brugger, J., Etschmann, B., Howard, D.J., de Jonge, M., Ryan, C.G., Paterson, D., 2012. Determination of the oxidation state of Cu in substituted Cu-In-Fe-bearing sphalerite via μ-XANES spectroscopy. Am. Mineral. 97, 476–479, doi:10.2138/am.2012.4042.

de Ronde, C.E.J., Hannington, M.D., Stoffers, P., Wright, I.C., Ditchburn, R.G., Reyes, A.G., Baker, E.T., Massoth, G.J., Lupton, J.E., Walker, S.L., Greene, R.R., Soong, C.W.R., Ishibashi, J., Lebon, G.T., Bray, C.J., Resing, J.A., 2005. Evolution of a submarine magmatic-hydrothermal system: Brothers volcano, southern Kermadec arc, New Zealand. Econ. Geol. 100, 1097–1133, doi:10.2113/gsecongeo.100.6.1097.

de Ronde, C.E.J., Walker, S.L., Ditchburn, R.G., Caratori Tontini, F., Hannington, M.D., Merle, S.G., Timm, C., Handler, M.R., Wysoczanski, R.J., Dekov, V.M., Kamenov, G.D., Baker, E.T., Embley, R.W., Lupton, J.E., Stoffers, P., 2014. The anatomy of a buried submarine hydrothermal system, Clark Volcano, Kermadec Arc, New Zealand. Econ. Geol. 109, 2261–2292, doi:10.2113/econgeo.109.8.2261.

Deditius, A.P., Utsunomiya, S., Kesler, S.E., Reich, M., Ewing, R.C., 2011. Trace elements nanoparticles in pyrite. Ore Geol. Rev. 42, 32–46, doi:10.1016/j.oregeorev.2011.03.003.

Ditchburn, R.G., de Ronde, C.E.J., 2017. Evidence for remobilization of barite affecting radiometric dating using ^{228}Ra, ^{228}Th, and ^{226}Ra/Ba values: Implications for the evolution of sea-floor volcanogenic massive sulfides. Econ. Geol. 112, 1231–1245, doi:10.5382/econgeo.2017.4508.

Ditchburn, R., Graham, I., Barry, B., de Ronde, C.E.J., 2004. Uranium series disequilibrium dating of black smoker chimneys. N. Z. Sci. Rev. 61, 54–56.

Fouquet, Y., Wafik, A., Cambon, P., Nevel, C., Gente, P., 1993a. Tectonic setting and mineralogical and geochemical zonation in the Snakepit sulfide deposit (Mid-Atlantic Ridge at 23°N). Econ. Geol. 88, 2018–2036.

Fouquet, Y., von Stackelberg, U., Charlou, J.L., Erzinger, J., Herzig, P.M., Mühe, R., Wiedicke, M., 1993b. Metallogenesis in back-arc environments: The Lau Basin example. Econ Geol. 88, 2154–2181, doi:10.2113/gsecongeo.88.8.2154.

Franklin, J.M., Gibson, H.L., Jonasson, I.R., Galley, A.G., 2005. Volcanogenic massive sulfide deposits. In: Hedenquist, J.W., et al. (Eds.), 100th Anniversary Volume of Economic Geology, Society of Economic Geologists, Littleton, CO, pp. 523–560.

Gamo, T., Okamura, K., Charlou, J.-L., Urabe, T., Auzende, J.-M., Ishibashi, J., Shitashima, K., Chiba, H., and Shipboard Scientific Party, 1997. Acidic and sulfate-rich hydrothermal fluids from the Manus back-arc basin, Papua New Guinea. Geology 25, 139–142, doi:10.1130/0091-7613(1997)025<0139:AASRHF>2.3.CO;2.

Gartman, A., Hannington, M.D., Jamieson, J.W., Peterkin, B., Garbe-Schönberg, D., Findlay, A.J., Fuchs, S., Kwasnitschka, T., 2017. Boiling-induced formation of colloidal gold in black smoker hydrothermal fluids. Geology 46, 39–42, doi:10.1130/G39492.1.

Gavelin, S., Parwel, A., Ryhage, R., 1960. Sulfur isotope fractionation in sulfide mineralization. Econ. Geol. 55, 510–530, doi:10.2113/gsecongeo.55.3.510.

Gemmell, J.B., Sharpe, R., Jonasson, I.R., Herzig, P.M., 2004. Sulfur isotope evidence for magmatic contributions to submarine and subaerial gold mineralization: Conical Seamount and the Ladolam gold deposit, Papua New Guinea. Econ. Geol. 99, 1711–1725, doi:10.2113/gsecongeo.99.8.1711.

Gemmell, T.P., 2013. Geology of the Kidd Creek deep orebodies – Mine D, western Abitibi Subprovince, Canada. Unpublished master's thesis, University of Ottawa, Ottawa, Canada, 178 p.

Goodfellow, W.D., Franklin, J.M., 1993. Geology, mineralogy, and geochemistry of sediment-hosted massive sulfides in shallow cores, Middle Valley, northern Juan de Fuca Ridge. Econ. Geol. 88, 2037–2068, doi:10.2113/gsecongeo.88.8.2037.

Grant, H.L.J., Layton-Matthews, D., Peter, J.M., 2015. Distribution and controls on silver mineralization in the Hackett River Main Zone, Nunavut Canada: An Ag- and Pb-enriched Archean volcanogenic massive sulfide deposit. Econ. Geol. 110, 943–982, doi:10.2113/econgeo.110.4.943.

Haase, K.M., Shipboard Scientific Party, 2014. Volcanism, hydrothermal activity and vent biology in the Coriolis Troughs, New Hebrides Island Arc. RV Sonne SO-229 Status Report, 60 p.

Hannington, M.D., 2013. The role of black smokers in the Cu mass balance of the oceanic crust. Earth Planet. Sci. Lett. 374, 215–226, doi:10.1016/j.epsl.2013.06.004.

Hannington, M.D., 2014. Volcanogenic massive sulfide deposits. In: Turekia, k., Holland H. (Eds.), Treatise on Geochemistry 2nd Ed. 13, Elsevier Ltd., Oxford, UK, pp. 463–488, doi:10.1016/B978-0-08-095975-7.01120-7.

Hannington, M.D., Peter, J.M., Scott, J.D., 1986. Gold in sea-floor polymetallic sulfide deposits. Econ. Geol. 81, 1867–1883, doi:10.2113/gsecongeo.81.8.1867.

Hannington, M.D., Scott, S.D., 1989. Sulfidation equilibria as guides to gold mineralization in volcanogenic massive sulfides: Evidence from sulfide mineralogy and the composition of sphalerite. Econ. Geol. 84, 1978–1995, doi:10.2113/gsecongeo.84.7.1978.

Hannington, M.D., Herzig, P., Scott, S., Thompson, G., Rona, P., 1991. Comparative mineralogy and geochemistry of gold-bearing sulfide deposits on the mid-ocean ridges. Mar. Geol. 101, 217–248, doi:10.1016/0025-3227(91)90073-D.

Hannington, M.D., Jonasson, I.R., Herzig, P.M., Petersen, S., 1995. Physical and chemical processes of seafloor mineralization at mid-ocean ridges. Geophys. Monogr. Ser. 91, 178–193, doi:10.1029/GM091p0115.

Hannington, M.D., Galley, A., Herzig, P., Petersen, S., 1998. Comparison of the TAG mound and stockwork complex with Cyprus-type massive sulfide deposits. In: Herzig, P.M., et al. (Eds.), Proc. ODP, Sci. Results 158, pp. 389–415.

Hannington, M.D., Poulsen, K.H., Thompson, J.F.H., Sillitoe, R.H., 1999. Volcanogenic gold in the massive sulfide environment, In: Barrie, C.T., Hannington, M.D. (Eds.), Volcanic-Associated Massive Sulfide Deposits: Processes and Examples in Modern and Ancient Settings. Rev. Econ. Geol. 8, 319–350, doi:10.5382/Rev.08.014.

Hannington, M.D., de Ronde, C.E.J., Petersen, S., 2005. Sea-Floor Tectonics and Submarine Hydrothermal Systems. In: Hedenquist, J.W., et al. (Eds.), 100th Anniversary Volume of Economic Geology, Society of Economic Geologists, Littleton, CO, pp. 111–141.

Hannington, M.D., Harðardóttir, V., Garbe-Schönberg, D., Brown, K.L., 2016. Gold enrichment in active geothermal systems by accumulating colloidal suspensions. Nat. Geosci. 9, 299–302, doi:10.1038/ngeo2661.

Hein, J.R., Koschinsky, A., Bau, M., Manheim, F.T., Kang, J.-K., Roberts, L., 2000. Cobalt-rich ferromanganese crusts in the Pacific. In: Cronan, D.S. (Ed.), Handbook of Marine Mineral Deposits, CRC Press, Boca Raton, FL, pp. 239–269.

Hein, J.R., de Ronde, C.E.J., Koski, R.A., Ditchburn, R.G., Mizell, K., Tamura, Y., Stern, R.J., Conrad, T.A., Ishizuka, O., Leybourne, M.I., 2014. Layered hydrothermal barite-sulfide mound, East Diamante Caldera, Mariana Volcanic Arc. Econ. Geol. 109, 2179–2206, doi:10.2113/econgeo.109.8.2179.

Herzig, P.M., Hannington, M.D., Fouquet, Y., von Stackelberg, U., Petersen, S., 1993. Gold-rich polymetallic sulfides from the Lau back arc and implications for the geochemistry of gold in sea-floor hydrothermal systems of the southwest Pacific. Econ. Geol. 88, 2182–2209, doi:10.2113/gsecongeo.88.8.2182.

Huston, D.L., Sie, S.H., Suter, G.F., Cooke, D.R., Both, R.A., 1995. Trace elements in sulfide minerals from eastern Australian volcanic-hosted massive sulfide deposits: Part I. Proton microprobe analyses of pyrite, chalcopyrite, and sphalerite, and Part II. Selenium levels in Pyrite: Comparison with $\delta^{34}S$ values and implications for the source of sulfur in volcanogenic hydrothermal systems. Econ. Geol. 90, 1167–1196, doi:10.2113/gsecongeo.90.5.1167.

Huston, D.L., Jablonski, W., Sie, S.H., 1996. The distribution and mineral hosts of silver in eastern Australian volcanogenic massive sulfide deposits. Can. Mineral. 34, 529–546.

Jamieson, J.W., Wing, B.A., Hannington, M.D., Farquhar, J., 2006. Evaluating isotopic equilibrium among sulfide mineral pairs in Archean ore deposits: Case study from the Kidd Creek VMS deposit, Ontario, Canada. Econ. Geol. 101, 1055–1061, doi:10.2113/gsecongeo.101.5.1055.

Jamieson, J.W., Hannington, M.D., Clague, D.A., Kelley, D.S., Delaney, J.R., Holden, J.F., Tivey, M.K., Kimpe, L.E., 2013. Sulfide geochronology along the Endeavour segment of the Juan de Fuca Ridge. Geochem. Geophys. Geosyst. 14, 2084–2099, doi:10.1002/ggge.20133.

Jamieson, J.W., Clague, D.A., Hannington, M.D., 2014. Hydrothermal sulfide accumulation along the Endeavour Segment, Juan de Fuca Ridge. Earth Planet. Sci. Lett. 395, 136–148, doi:10.1016/j.epsl.2014.03.035.

Jamieson, J.W., Hannington, M.D., Tivey, M.K., Hansteen, T., Williamson, N.M.-B., Stewart, M., Fietzke, J., Butterfield, D., Frische, M., Allen, L., Cousens, B., Langer, J., 2016. Precipitation and growth of barite within hydrothermal vent deposits from the Endeavour Segment, Juan de Fuca Ridge. Geochim. Cosmochim. Acta 173, 64–85, doi:10.1016/j.gca.2015.10.021.

Johnson, D.P., Maillet, P.C., Rice, R.C., 1992. The seabed morphology of the Hazel Holme Fracture Zone and the New Hebrides arc, northern Vanuatu – Solomon Islands Region. SOPAC Technical Report 138, 28 p.

Kieft, K., Damman, A.H., 1990. Indium-bearing chalcopyrite and sphalerite from the Gasborn area, West Bergslagen, central Sweden. Mineral. Mag. 54, 109–112, doi:10.1180/minmag.1990.054.374.12.

Koski, R.A., Jonasson, I.R., Kadko, D.C., Smith, V.K., Wong, F.L., 1994. Compositions, growth mechanisms, and temporal relations of hydrothermal sulfide-sulfate-silica chimneys at the northern Cleft segment, Juan de Fuca Ridge. J. Geophys. Res. 99, 4813–4832, doi:10.1029/93JB02871.

Kroenke, L.W., 1995. A morphotectonic interpretation of SPOACMAPS 1:500,000 charts: Central Solomon Islands – Southern Tuvalu, Vol. 220. South Pacific Applied Geoscience Commission.

Kusakabe, M., Komoda, Y., Takano, B., Abiko, T., 2000. Sulfur isotopic effects in the disproportionation reaction of sulfur dioxide in hydrothermal fluids: implications for the $\delta^{34}S$ variations of dissolved bisulfate and elemental sulfur from active crater lakes. J. Volcanol. Geoth. Res. 97, 287–307, doi:10.1016/S0377-0273(99)00161-4.

Lein, A., Bogdanov, Y., Maslennikov, V., Li, S., Ulyanova, N., Maslennikova, S., Ulyanov, A., 2010. Sulfide minerals in the Menez Gwen nonmetallic hydrothermal field (Mid-Atlantic Ridge). Lithol. Miner. Resour. 45, 305–323, doi:10.1134/S0024490210040012.

Maslennikov, V.V., Maslennikova, S.P., Large, R.R., Danyushevsky, L.V., 2009. Study of trace element zonation in vent chimneys from the Silurian Yaman-Kasy volcanic-hosted massive sulfide deposit (southern Urals, Russia) using laser ablation-inductively coupled plasma mass spectrometry (LA-ICPMS). Econ. Geol. 104, 1111–1141, doi:10.2113/gsecongeo.104.8.1111.

McConachy, T.F., Yeats, C.J., and Shipboard Scientific Party, 2002. Final Cruise FR03-2002, SOLAVENTS-2002, Solomons Australia vents expedition aboard the RV Franklin, 26 March – 21 April 2002: CSIRO Exploration and Mining Report 1026F, 440 p.

McDermott, J.M., Ono, S., Tivey, M.K., Seewald, J., Shanks, W.C. III, Solow, A.R., 2015. Identification of sulfur sources and isotopic equilibria in submarine hot-springs using multiple sulfur isotopes. Geochim. Cosmochim. Acta 160, 169–187, doi:10.1016/j.gca.2015.02.016.

Monecke, T., Petersen, S., Hannington, M.D., 2014. Constraints on water depth of massive sulfide formation: Evidence from modern seafloor hydrothermal systems in arc-related settings. Econ. Geol. 109, 2079–2101, doi:10.2113/econgeo.109.8.2079.

Monecke, T., Petersen, S., Hannington, M.D., Grant, H., Samson, I., 2016. The minor element endowment of modern sea-floor massive sulfides and comparison with deposits hosted in ancient volcanic successions. I: Verplanck, P.L, Hitzman, M.W. (Eds.), Reviews in Economic Geology 18, Society of Economic Geologists, Knoxville, TN, pp 245–306.

Moss, R., Scott, S.D., 2001. Geochemistry and mineralogy of gold-rich hydrothermal precipitates form the eastern Manus Basin, Papua New Guinea. Can. Mineral. 39, 957–978, doi:10.2113/gscanmin.39.4.957.

Moss, R., Scott, S.D., Binns, R.A., 2001. Gold content of eastern Manus Basin volcanic rocks: implications for enrichment in associated hydrothermal precipitates. Econ. Geol. 96, 91–107, doi:10.2113/gsecongeo.96.1.91.

Ohmoto, H., 1996. Formation of volcanogenic massive sulfide deposits: The Kuroko perspective. Ore Geol. Rev. 10, 135–177, doi:10.1016/0169-1368(95)00021-6.

Ohmoto, H., Rye, R.O., 1979. Isotopes of sulfur and carbon. In: Barnes, H.L. (Ed.), Geochemistry of Hydrothermal Ore Deposits, 2nd Ed., Wiley, New York, NY, pp. 509–567.

Ono, S., Wing, B.A., Johnston, D., Farquhar, J., Rumble, D., 2006. Mass-dependent fractionation of quadruple sulfur isotope system as a new tracer of sulfur biogeochemical cycles. Geochim. Cosmochim. Acta 70, 2238–2252, doi:10.1016/j.gca.2006.01.022.

Ono, S., Shanks, W.C. III, Rouxel, O.J., Rumble, D., 2007. S-33 constraints on the seawater sulfate contribution in modern seafloor hydrothermal vent sulfides. Geochim. Cosmochim. Acta 71, 1170–1182, doi:10.1016/j.gca.2006.11.017.

Peters, M., Strauss, H., Petersen, S., Kummer, N.-A., Thomazo, C., 2011. Hydrothermalism in the Tyrrhenian Sea: Inorganic and microbial sulfur cycling as revealed by geochemical and multiple sulfur isotope data. Chem. Geol. 280, 217–231, doi:10.1016/j.chemgeo.2010.11.011.

Petersen, S., Herzig, H.M., Schwarz-Schampera, U., Hannington, M.D., Jonasson, I.R., 2004. Hydrothermal precipitates associated with bimodal volcanism in the Central Bransfield Strait, Antarctica. Miner. Deposita 39, 358–379, doi:10.1007/s00126-004-0414-3.

Petersen, S., Monecke, T., Westhues, A., Hannington, M.D., Gemmell, J.B., Sharpe, R., Peters, M., Strauss, H., Lackschewitz, K., Augustin, N., Gibson, H., Kleeberg, R., 2014. Drilling shallow-water massive sulfides at the Palinuro volcanic complex, Aeolian Island Arc, Italy. Econ. Geol. 109, 2129–2158, doi:10.2113/econgeo.109.8.2129.

Petersen, S., Krätschell, A., Augustin, N., Jamieson, J., Hein, J.R., Hannington, M.D., 2016. News from the seabed – Geological characteristics and resource potential of deep-sea mineral resources. Mar. Pol. 70, 175–187, doi:10.1016/j.marpol.2016.03.012.

Récy, J., Charvis, P, Ruellan, E., Monjaret, M.-C., Gérard, M., Auclair, G., Baldassari, C., Boirat, J.-M., Brown, G.R., Butscher, J., Collot, J.Y., Daniel, J., Louat, R., Monzier, M., Pontoise B., 1986. Tectonique et volcanis,me sous-marin à l'arrière de l'arc des Nouvelles- Hébrides (Vanuatu): résultats préliminaires de la campagne SEAPSO (leg 2) du N.O. Jean Charcot. C.R. Acad. Sci. 303, 685–690.

Rees, C.E., Jenkins, W.J., Monster, J., 1978. Sulfur isotopic composition of ocean water sulfate. Geochim. Cosmochim. Acta 42, 377–381, doi:10.1016/0016-7037(78)90268-5.

Renock, D., Becker, U., 2011. A first principles study of coupled substitution in galena. Ore Geol. Rev. 42, 71–83, doi:10.1016/j.oregeorev.2011.04.001.

Rice, C.A., Tuttle, M.L., Reynolds, R.L., 1993. The analysis of forms of sulfur in ancient sediments and sedimentary rocks: Comments and cautions. Science 107, 83–95, doi:10.1016/0009-2541(93)90103-P.

Ricke, W., 1964. Präparation von Schwefeldioxid zur massenspektrometrischen Bestimmung des Schwefel-Isotopen-Verhältnisses 32S/34S in natürlichen Schwefelverbindungen. Zeitschrift für Anal. Chemie 199, 401–413, doi:10.1007/BF00493595 (In German).

Sakai, H., Marais, D., Ueda, A., Moore, J., 1984. Concentrations and isotope ratios of carbon, nitrogen, and sulfur in ocean-floor basalts. Geochim. Cosmochim. Acta 48, 2433–2441, doi:10.1016/0016-7037(84)90295-3.

Sandwell, D.T., et al., 2014. New global marine gravity model from CryoSat-2 and Jason-1 reveals buried tectonic structure. Science 346, 65–67.

Schwarz-Schampera, U., Herzig, P., 1997. Geochemistry of in in VMS deposits: implications from active hydrothermal vents in the southern Lau Basin. In: Paunen, H. (Ed.), Mineral Deposits. Balkema, Rotterdam, pp. 379–382.

Scott, S.D., Barnes, H.L., 1971. Sphalerite geothermometry and geobarometry. Econ. Geol. 66, 653–669, doi:10.2113/gsecongeo.66.4.653.

Shanks, W.C. III, 2001. Stable isotopes in seafloor hydrothermal systems: vent fluids, hydrothermal deposits, hydrothermal alteration, and microbial processes. Rev. Mineral. Geochem. 43, 469–525, doi:10.2138/gsrmg.43.1.469.

Stoffers, P., Worthington, T.J., Schwarz-Schampera, U., Hannington, M.D., Massoth, G.J., Hekinian, R., Schmidt, M., Lundsten, L.J., Evans, L.J., Vaiomo'unga, R., Kerby, T., 2006. Submarine volcanoes and high-temperature hydrothermal venting on the Tonga arc, southwest Pacific. Geology 34, 45 –456, doi:10.1130/G22227.1.

Thode, H.G., Monster, J., 1961. Sulphur isotope geochemistry. Geochim. Cosmochim. Acta 25, 159–174, doi:10.1016/0016-7037(61)90074-6.

Tufar, W., 1991. Paragenesis of complex massive sulfide ores from the Tyrrhenian Sea. Mitt. Österr. Geol. Ges. 84, 265–300.

Turcotte, D., 1997. Fractals and Chaos in Geology and Geophysics, Cornell University, New York.

Ueda, A., Sakai, H., 1984. Sulfur isotope study of Quaternary volcanic rocks from the Japanese island arc. Geochim. Cosmochim. Acta 48, 1837–1848, doi:10.1016/0016-7037(84)90037-1.

Urabe, T., Auzende, J.-M., Deplus, C., Eissen, J.-P., Grimaud, D., Huchon, P., Ishibashi, J., Joshima, M., LaGabrielle, Y., Mevel, C., Naka, J., Tanaka, T., Tanahashi, M., 1990. Hydrothermal deposits at the central spreading axis of the North Fiji Basin (SW Pacific): Preliminary report of the Nautile dives of the STARMER cruise. Min. Geol. 40, 117–124 (in Japanese with English abs.).

Vikentyev, I.V., 2015. Invisible and microscopic gold in pyrite: Methods and new data for massive sulfide ores of the Urals. Geol. Ore Dep. 57, 237–265, doi:10.1134/S1075701515040054.

Wienkenjohann, H., 2015. A sulfur isotope study of the Tinakula deposit, New Hebrides island arc, Solomon Islands. Unpublished bachelor's thesis, Westfälische Wilhelms-Universität Münster, Münster, Germany, 67 p.

Wotte, T., Shields-Zhou, G.A., Strauss, H., 2012. Carbonate-associated sulfate: Experimental comparisons of common extraction methods and recommendations toward a standard analytical protocol. Chem. Geol. 132–144, doi:10.1016/j.chemgeo.2012.07.020.

Wu, Z., Sun, X., Xu, H., Konishi, H., Wang, Y., Wang, C., Dai, Y., Deng, X., Yu, M., 2016. Occurrences and distribution of "invisible" precious metals in sulfide deposits from the Edmond hydrothermal field. Central Indian Ridge. Ore Geol. Rev. 79, 105 – 132, doi:10.1016/j.oregeorev.2016.05.006.

Wu, Z., Sun, X., Xu, H., Konishi, H., Wang, Y., Lu, Y., Cao, K., Wang, C., Zhou, H., 2018. Microstructural characterization and in-situ sulfur isotopic analysis of silver-bearing sphalerite from the Edmond hydrothermal field, Central Indian Ridge. Ore Geol. Rev. 92, 318–347, doi:10.1016/j.oregeorev.2017.11.024.

Yang, K., Scott, S.D., 2005. Vigorous exsolution of volatiles in the magma chamber beneath a hydrothermal system on the modern sea floor of the eastern Manus back-arc basin, western Pacific: Evidence from melt inclusions. Econ. Geol. 100, 108 –1096, doi:10.2113/gsecongeo.100.6.1085.

Zhabina, N.N., Volkov, I.I., 1978. A method of determination of various sulfur compounds in sea sediments and rocks. In: Krumbein, W.E. (Ed.), Environmental Biogeochemistry and Geomicrobiology. Vol. 3: Methods, Metals and Assessment, Ann Arbor Sci. Publ., Ann Arbor, MI, pp. 735–746.

Zhang, Y., Frantz, J.D., 1987. Determination of the homogenization temperatures and densities of supercritical fluids in the system NaCl-KCl-$CaCl_2$-H_2O using synthetic fluid inclusions. Chem. Geol. 64, 335–350, doi:10.1016/0009-2541(87)90012-X.

Zhu, W., Tivey, M.K., Gittings, H., Craddock, P.R., 2007. Permeability-porosity relationships in seafloor vent deposits: Dependence on pore evolution processes. J. Geophys. Res. 112, B05208, doi:10.1029/2006JB004716.

Preface to Chapter 5

This chapter investigates the shallow subseafloor of the Tinakula system from drilling by combined push and rotary coring. The nature of the subseafloor hydrothermal alteration has been characterized by a combination of detailed mineralogy based on SWIR and XRD and mass gains and losses in the hydrothermally-altered footwall relative to the unaltered volcanic precursor described in *Chapter 3*. It also explores the temperatures and compositions of the hydrothermal fluids. The study examines the impact of the highly permeable volcaniclastic facies on hydrothermal fluid flow, with comparisons to ancient volcaniclastic-hosted deposits in the geological record.

Chapter 5

Mineralogical and geochemical characteristics of hydrothermal alteration in the volcaniclastic-hosted Tinakula seafloor massive sulfide deposit (New Hebrides back-arc, SW Pacific)

Abstract

Nineteen sites were drilled at the Tinakula deposit in the Jean Charcot Troughs to examine the vertical and lateral variations in hydrothermal alteration. This study presents new data on the subseafloor geology, clay mineral assemblages, whole-rock geochemistry, and clay mineral isotopic compositions in order to investigate water-rock reactions and associated elemental changes, as well as hydrothermal fluid temperatures and composition. The subsurface geology of the Tinakula deposit comprises dominantly pyroclastic rocks associated with a row of cinder cones along an eruptive fissure. The volcaniclastic succession has been intensely hydrothermally altered by: (1) replacement of volcanic glass and primary minerals by clays; (2) infill of pore space by clays; (3) cementation by anhydrite; and (4) formation of sulfate-sulfide veins. Clay alteration is broadly conformable with five alteration zones developed with increasing depth below the seafloor: (1) montmorillonite/nontronite; (2) nontronite + corrensite; (3) illite/smectite + pyrite; (4) illite/smectite + chamosite; and (5) chamosite + corrensite. Mass balance calculations indicate that these assemblages are accompanied by different chemical changes relative to an unaltered basaltic-andesite precursor. Zones of argillic alteration are distinguished from zones of chloritic alteration by mass changes in ΔK_2O, ΔMgO, and ΔFe_2O_3. Increasing temperature of alteration with depth is recorded by a transition from argillic to chloritic alteration, increasing phyllosilicate crystallinity and increasing proportions of illite in mixed-layer I/S clays. Oxygen and hydrogen isotopes of clay mineral separates and fluid inclusions in anhydrite support increasing temperature with depth (124–256°C) and seawater-dominated hydrothermal fluids at high water:rock ratios. Based on the stabilities of the dominant alteration phases, the hydrothermal fluids were neutral to slightly acidic. Local changes in alteration zonation and temperatures were caused by fluid focusing along inferred faults and by permeability contrasts created by infilling and cementation of volcaniclastic units. Over-pressuring and fracturing of the more coherent volcaniclastic rocks is thought to have been responsible for the local sulfate-sulfide veining. Several phases of chimney growth punctuated by subsequent burial by volcaniclastic cover sequences is indicated by multiple oxidized paleoseafloor horizons. The study shows how hydrothermal fluids can become focused in permeable volcaniclastic rocks by progressive low-temperature hydrothermal alteration and mineralization, leading to a large area of intense alteration close to the seafloor; what is unique is that this alteration covers such a large area so close to the seafloor.

5.1. Introduction

The Tinakula deposit is a modern analogue of volcaniclastic-dominated seafloor massive sulfide mineralization that is common in the geological record. It differs from normal MOR-type hydrothermal systems and deposits at spreading centers in deeper back-arc basins by the style of volcanism and hydrothermal upflow focused along a row of young cinder cones (Fig. 5.1). The character of volcanic eruptions in the shallow seafloor plays a first-order control on the localization of hydrothermal fluids and the morphology of the footwall alteration zones. Coherent lavas formed through effusive processes are relatively impermeable, with hydrothermal fluids focused along faults with minimal influx of cold seawater, forming discordant pipe-like alteration zones (e.g., Noranda district, QC; Gibson and Galley, 2007; TAG hydrothermal mound, 26°N on the MAR; Rona et al., 1993). In contrast, volcaniclastic-dominated strata have high permeability and porosity, resulting in lateral fluid flow, widespread mixing with seawater, and stratiform alteration zones (e.g., Sturgeon Lake district, ON; Morton et al., 1990). Precipitation of sulfates and secondary clay minerals in the footwall reduces the overall permeability (Figs. 5.2 and 5.3; e.g., Browne, 1978), allowing fluids to become focused and discharge at the seafloor as high-temperature vents. Shallow seafloor drilling at Tinakula provides the unique opportunity to examine the third dimension of an actively-forming deposit in a volcaniclastic-dominated nascent back-arc setting. In particular, we investigate of the hydrothermally-altered footwall in order to understand the environmental influence on the morphology of the deposit, mechanisms of sulfide accumulation and composition, and the geometry and mineralogy of alteration assemblages.

5.2. Subsurface geology

The footwall of the Tinakula deposit is composed of intensely altered volcaniclastic material with vertical and lateral variations in facies, including changes in clast size, shape, and proportion, degree of sorting, and alteration mineralogy and intensity, as revealed by core logging (Appendix N) and detailed petrographic observations (Appendix G; Figs. 5.2 and 5.3). Three footwall facies are recognized, classified according to McPhie et al. (1993): (1) hyaloclastite breccia, with monomict clasts characterized by glassy curviplanar margins, flow-banded phenocrysts, and local

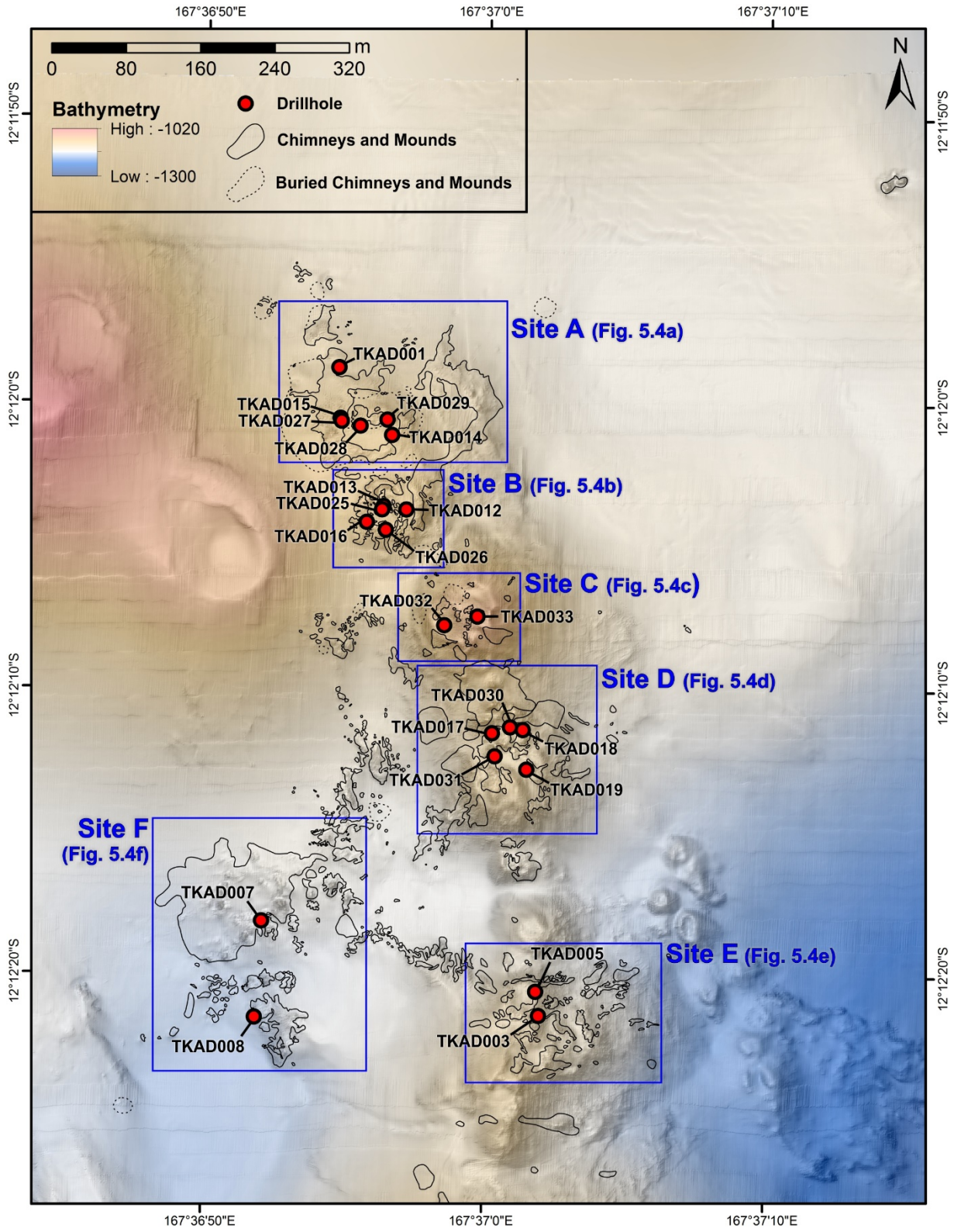


Fig. 5.1. Hill and slope-shaded RESON SeaBat 7125-ROV2 400 kHz multibeam bathymetry of the Tinakula area (0.2 m resolution), with chimney complexes and mounds outlined in black. The locations of drillholes examined in this study shown by red circles.

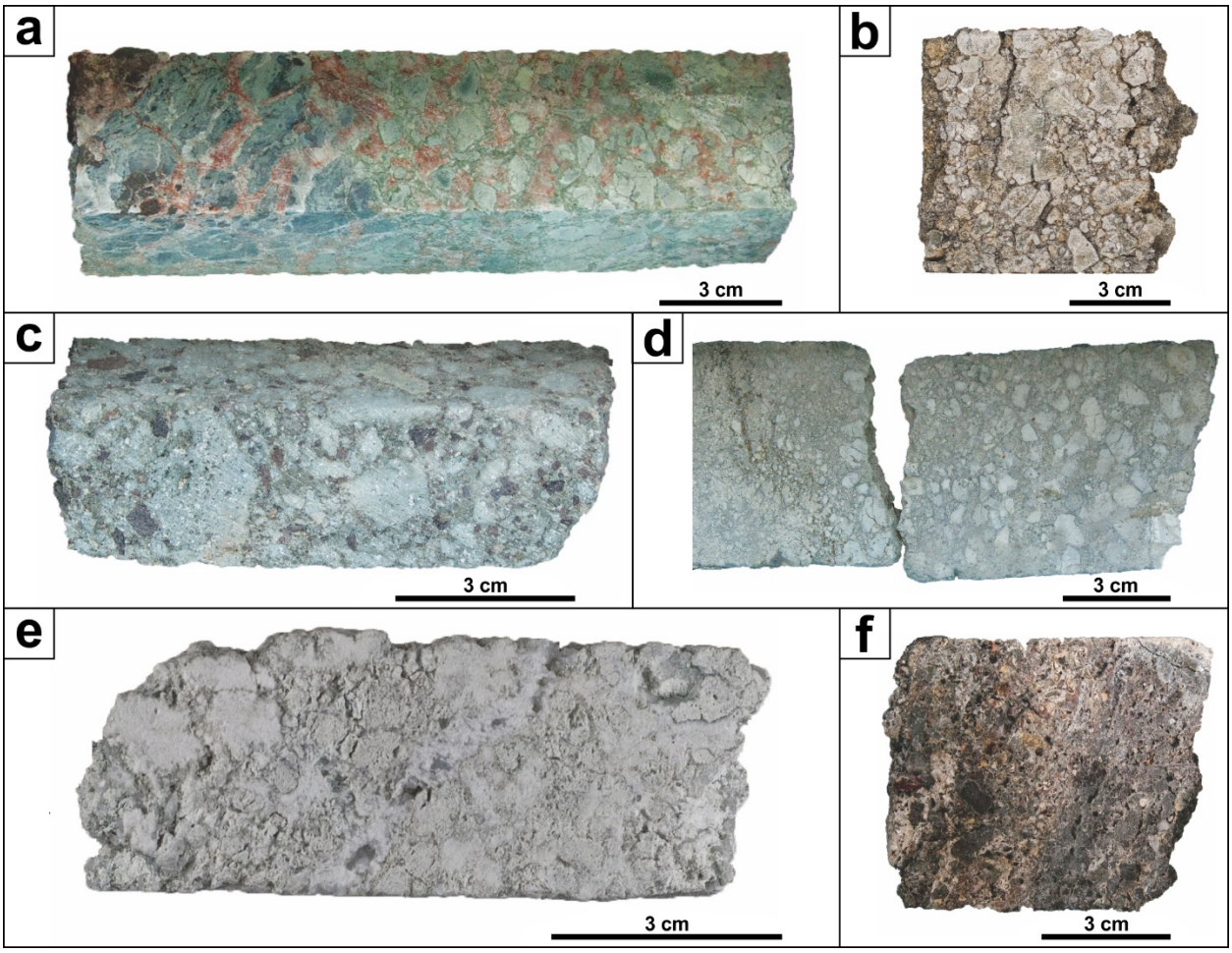


Fig. 5.2. Volcanic and hydrothermal features of the footwall of the Tinakula deposit: (a) variably clay-altered monomict matrix-supported hyaloclastite breccia with flow foliation and local jigsaw fit, sulfate-cemented with minor iron oxide staining, sample P003; (b) intensely clay-altered monomict clast-supported volcanic breccia (hyaloclastite), weakly sulfate-cemented, sample MA13-074; (c) variably clay-altered polymict clast-supported lapillistone, sulfate-cemented, sample P002; (d) intensely clay-altered monomict clast-supported lapillistone, sulfate-cemented and weakly graded, sample MA13-092; (e) intensely clay-altered monomict matrix-supported lapillistone, sulfate-cemented, sample P013; (f) variably-altered polymict matrix-supported proximal reworked volcanic breccia, silicified, sample MA13-023.

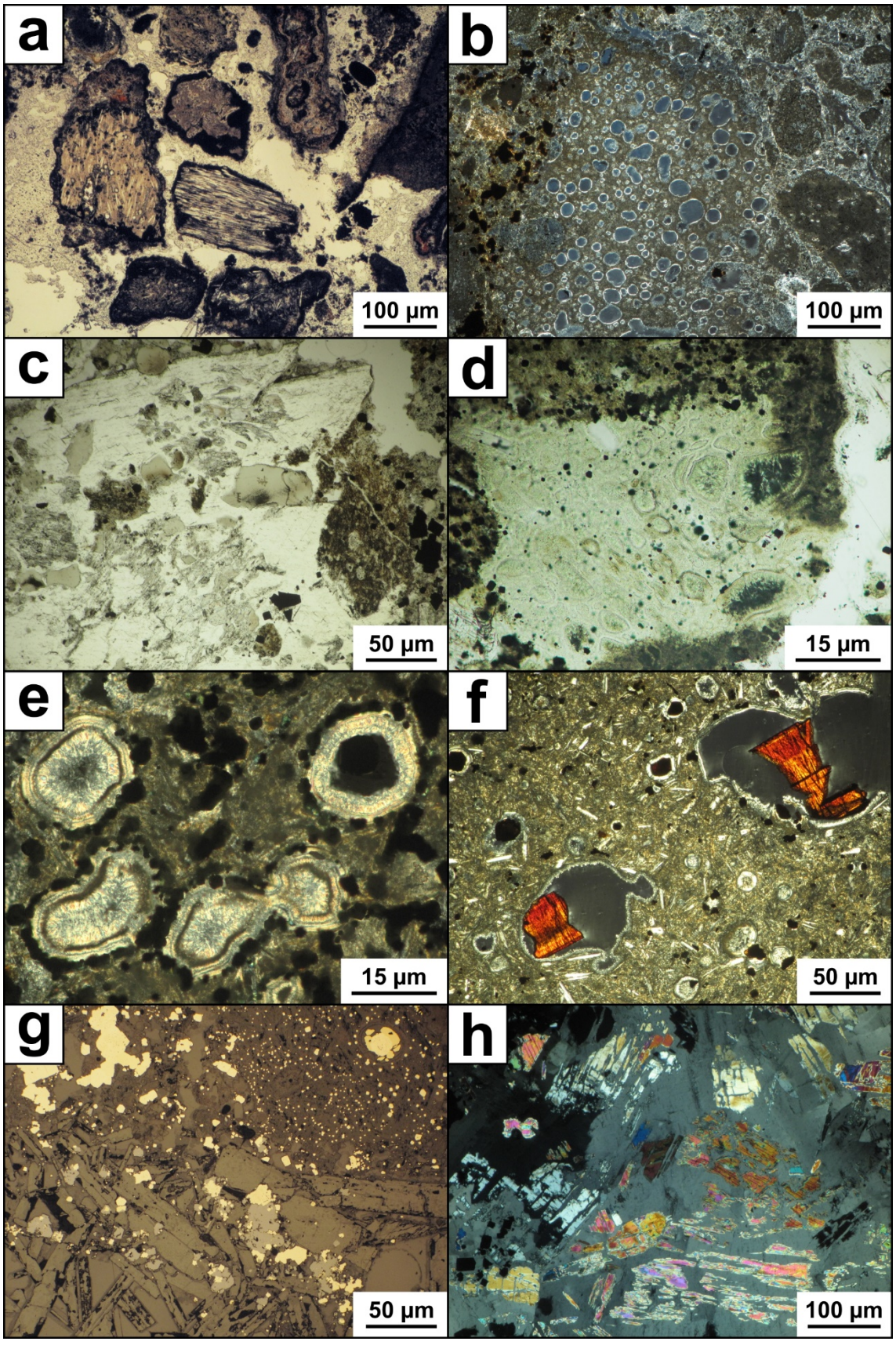

a
100 µm
b
100 µm
c
50 µm
d
15 µm
e
15 µm
f
50 µm
g
50 µm
h
100 µm

Fig. 5.3. Microscopic volcanic and hydrothermal features of the footwall of the Tinakula deposit: (a) transmitted light photomicrograph in plane-polarized light (PPL) of polymict clast types, including glass-rich volcanic clasts and tube pumice, cemented by amorphous silica, sample MA13-023 (2.5×); (b) transmitted light photomicrograph in cross-polarized light (XPL) of clay-altered scoriaceous clasts with intense clay alteration of the clasts and matrix, sample MA13-068 (2.5×); (c) transmitted light photomicrograph in PPL of volcanic clasts and glass shards surrounded by gypsum after anhydrite, sample MA13-040 (5×); (d) transmitted light photomicrograph in PPL of tube pumice with late chlorite infill, sample MA13-053 (2.5×); (e) transmitted light photomicrograph in PPL of an intensely clay-altered clast with multiple generations of clay infilling vesicles, sample MA13-044 (20×); (f) transmitted light photomicrograph in XPL of a clay-altered clast, with clay lining of vesicles and late sphalerite precipitation, sample MA13-072 (5×) (g) reflected light photomicrograph in PPL of fine-grained pyrite disseminated through an altered clast, and late sulfides (pyrite, sphalerite, chalcopyrite) surrounded by anhydrite, sample MA13-045 (5×); (h) transmitted light photomicrograph in XPL of anhydrite altered to gypsum, sample MA13-040 (2.5×).

jigsaw-fit textures (Figs. 5.2a,b and 5.3b); (2) phreatomagmatic breccia (lapillistone or tuff), characterized by vesicular volcanic clasts associated with variable amounts of juvenile clasts, glass shards and crystal fragments (Figs. 5.2c–e and 5.3c); and (3) proximal resedimented volcanic breccia, characterized by mass-flow bedforms with rounded to subangular polymictic clasts, ranging from relatively unaltered to completely clay-altered clasts (Fig. 5.2f). The volcanic clasts are generally vesicular, with up to 20% mm-sized vesicles. Samples with uncertain lithologies are referred to only as volcanic mudstone/sandstone/breccia. Although the primary composition of the different clast types may be the same, highly variable alteration intensity was observed (Fig. 5.2f). Alteration and late infill by patchy sulfate cement obscures the primary textures, resulting in a high degree of uncertainty regarding facies interpretations. Pyrite, chalcopyrite, and sphalerite, where present, are generally disseminated and locally associated with sulfate veins (Fig. 5.3g). Stringer mineralization, comprising disseminated and veinlet sulfides and abundant barite, occurs in a narrow horizon in the uppermost volcaniclastic units of most drillholes.

5.3. Methods

5.3.1. Core logging, sample preparation, and petrography

Shallow seafloor drilling was undertaken by Neptune Minerals Inc. in 2012 aboard MV Skandi Hawk using the Benthic Geotech Portable Remotely Operated Drill PROD-3 (Fig. 5.1). During drilling, retrievable metal casings were used to stabilize the hole to prevent collapse and contamination of the drillhole. Push coring was used for unconsolidated material, using a 75 mm double tube push coring barrel. A rotary coring technique was used for competent rocks, using a using a 72 mm core diameter assembly. The average depth of the drillholes is 7.1 mbsf, with one longer drillhole (TKAD001) reaching 22.32 mbsf, with an average core recovery of 79.1%. The drillcore was stored at 4°C in a refrigerated container in Honiara, Solomon Islands, where it dried completely. Drillcore examined in this study was re-logged and sampled to establish between-hole correlations along the length of the N-S trending row of scoria cones that mark the eruptive fissure (Sites A–D; Figs. 5.1 and 5.4). Samples of the altered footwall were collected at regular 1-m spaced intervals or where there were significant changes in primary lithology, or alteration type/intensity.

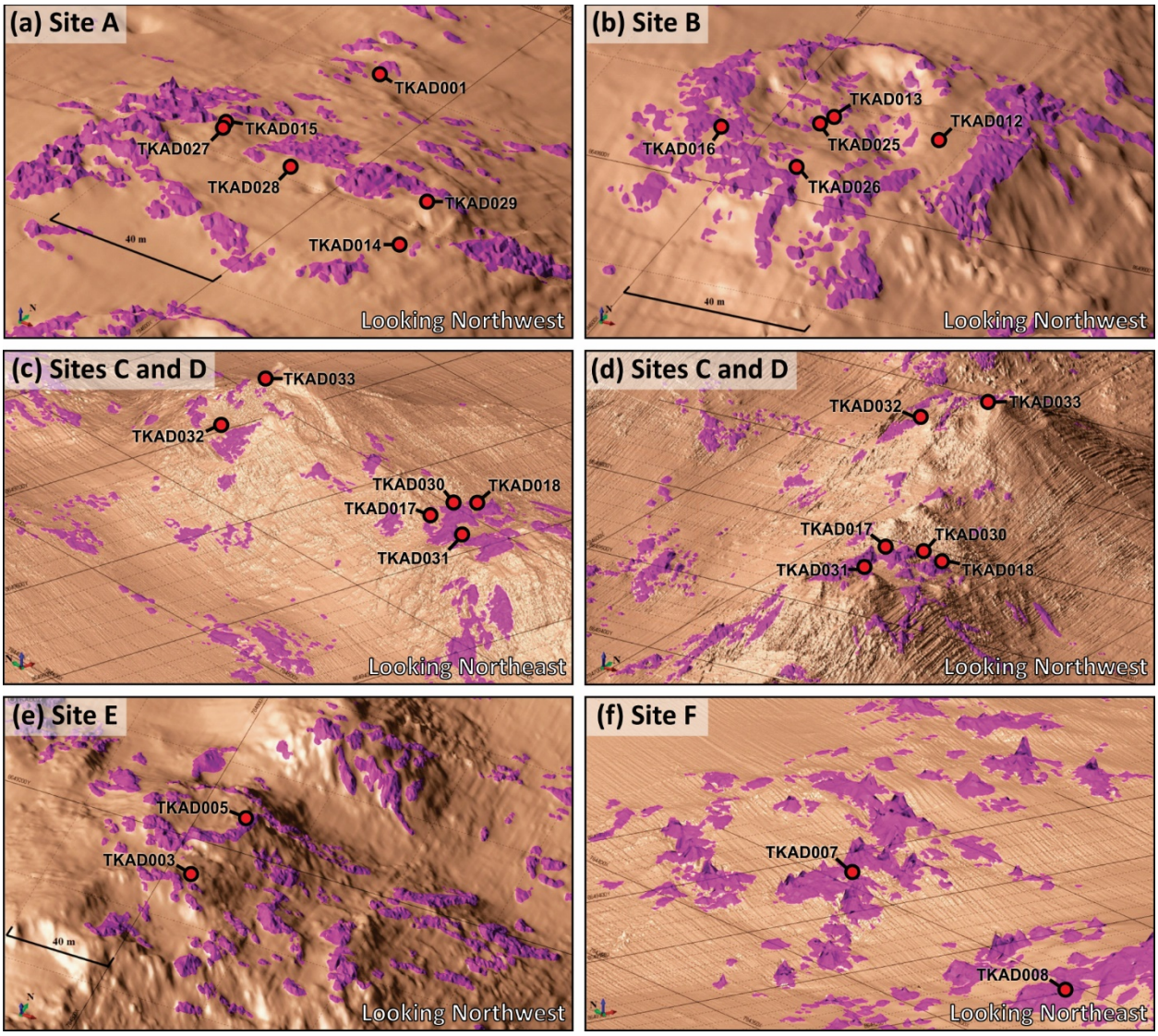


Fig. 5.4. 3D close-up of the bathymetry of study sites in the Tinakula area (hill-shaded RESON SeaBat 7125-ROV2 400 kHz multibeam bathymetry; 0.2 m resolution), with chimney complexes and mounds shown in purple and the locations of drillholes (red circles) examined in this study: (a) Site A, looking NW; (b) Site B, looking NW; (c) Sites C and D, looking NE; (d) Sites C and D, looking NW; (e) Site E, looking NW; and (f) Site F, looking NE. All images courtesy of Neptune Minerals Inc.

Where drillcore was less competent due to alteration, entire core samples were collected (including plastic liners); otherwise, quarter-core sections ≥10 cm were cut from the half core using a dry saw. A subset of 63 drillcore samples encompassing all of the hydrothermally-altered volcaniclastic sequences was selected for detailed study (see Table 5.1 for sample list). Representative off-cuts were sent to Dettmar Dissection Technology (Bochum, Germany) to be prepared as polished thin sections. The samples were vacuum impregnated with epoxy, and cut and polished into thin sections using kerosene instead of water in order to eliminate clay swelling, slaking, and dissolution of anhydrite. Polished thin sections were examined by transmitted and reflected light microscopy. Petrographic details were recorded, including primary lithological characteristics (e.g., vesicularity, phenocrysts, and groundmass textures) and alteration-related features (e.g., mineralogy, paragenetic relationships, and intensity). Despite the locally intense alteration, it was generally possible to reconstruct the volcanic facies based on observations made during both core logging and detailed petrography.

Samples from the volcaniclastic footwall were hand-separated into clast (suffix –C) and matrix (suffix –M) components. The clasts comprise clay-altered volcanic fragments and the matrix consists of either fine-grained clay-altered material or sulfate cement (primarily anhydrite and gypsum). Samples where the clasts and matrix could not be distinguished are labelled –CM (Table 5.1). The samples were then treated separately for whole-rock geochemistry and shortwave infrared spectroscopy.

5.3.2. SWIR spectroscopy

For SWIR spectroscopy, the samples were gently hand-crushed using a mortar and pestle, and were dry sieved to separate fine (<63 μm) and coarse (<63 μm) fractions. SWIR spectroscopy was used to measure absorption features in the infrared region (~1300–2500 nm) in order to identify alteration minerals and investigate compositional variations amongst mineral groups (e.g., Thompson et al., 1999; Jones et al., 2005; Hinchey, 2011). These absorption features reflect the transformation of radiant energy to vibrational energy within molecular bonds of the crystal lattice, including OH, H_2O, Al-OH, Fe-OH, and Mg-OH bonds, which vibrate at different wavelengths as a function of bond length (Thompson et al., 1999). Analyses were performed on the hand-separated

Table 5.1. List of samples and analytical methods from shallow drillcore at the Tinakula deposit, with drillholes arranged from north to south (see Fig. 5.1 for drillhole locations)

Location		From	To			Clay fraction	Clay fraction	Fluid	Clast-matrix*	Whole-rock	
Drillhole	Sample	[mbsf]	[mbsf]	Lithology	Name	oriented XRD	O-isotope	inclusion	sub-sample	geochemistry	SWIR
Site A *(North)*											
TKAD001	MA13-078	4.54	4.68	Cover	Intensely clay-altered monomict volcanic breccia, unconsolidated	X			MA13-078-C	X	
	MA13-082	7.00	7.10	Cover	Moderately clay-altered monomict(?) volcanic breccia, unconsolidated	X			MA13-082-C	X	
	P002	10.39	10.5	Cover	Variably clay-altered polymict clast-supported breccia, silicified	X					
	MA13-085	12.90	13.00	Cover	Moderately clay-altered monomict(?) volcanic breccia, unconsolidated	X			MA13-085-CM	X	
	MA13-086	14.00	14.12	Stringer	Variably clay-altered monomict(?) matrix-supported resedimented lapillistone, cemented	X			MA13-086-C	X	X
									MA13-086-M	X	
	P003	14.81	14.95	Stringer	Intensely clay-altered monomict matrix-supported hyaloclastite breccia, cemented	X		X			
	P004	15.65	15.80	Stringer	Intensely clay-altered monomict clast-supported volcanic breccia, cemented and mineralized	X		X			
	MA13-087	16.05	16.22	Stringer	Intensely clay-altered bedded monomict matrix-supported lapillistone, cemented and mineralized	X	X		MA13-087-C	X	X
	MA13-088	17.40	17.00	Footwall	Intensely clay-altered monomict(?) matrix-supported pumaceous lapillistone, cemented and wealky mineralized	X			MA13-088-C	X	X
	MA13-089	17.90	18.00	Footwall	Intensely clay-altered monomict(?) matrix-supported hyaloclastite breccia, cemented and mineralized	X		X			
	MA13-090	18.40	18.60	Footwall	Intensely clay-altered bedded monomict matrix-supported lapillistone, cemented and mineralized	X		X	MA13-090-C	X	
	P005	19.14	19.30	Footwall	Intensely clay-altered monomict clast-supported volcanic breccia, cemented and mineralized	X		X	P0005-C		X
	MA13-091	20.80	21.00	Footwall	Intensely clay-altered bedded monomict clast-supported lapilli tuff, cemented and mineralized	X			MA13-091-CM	X	X
	MA13-092	21.30	21.45	Footwall	Intensely clay-altered bedded monomict matrix-supported lapillistone, cemented and mineralized	X					
TKAD015	MA13-050	3.49	3.63	Stringer	Variably clay-altered volcanic breccia and chimney sediment, unconsolidated	X			MA13-050-C	X	
	MA13-051	4.34	4.43	Footwall	Intensely clay-altered monomict matrix supported shard-rich pumaceous lapillistone, unconsolidated	X			MA13-051-CM	X	
	MA13-052	6.42	6.52	Footwall	Intensely clay-altered monomict matrix-supported shard-rich scoriaceous lapillistone, cemented	X			MA13-052-C	X	X
									MA13-052-M	X	
	MA13-053	7.23	7.34	Footwall	Intensely clay-altered scoriaceous monomict matrix-supported hyaloclastite breccia, cemented and weakly mineralized	X	X		MA13-053-C	X	X
TKAD027	MA13-056	2.50	2.60	Footwall	Chimney talus and minor clay-altered monomict volcanic breccia, unconsolidated	X			MA13-056-CM	X	
	MA13-057	4.60	4.70	Footwall	Intensely clay-altered scoriaceous monomict matrix-supported resedimented hyaloclastite breccia, cemented	X	X		MA13-057-C	X	
	MA13-058	6.50	6.59	Footwall	Intensely clay-altered monomict matrix-supported scoriaceous shard-rich lapillistone, cemented	X			MA13-058-C	X	
TKAD028	MA13-099	4.50	4.60	Footwall	Variably clay-altered monomict(?) lapillistone(?), cemented	X			MA13-099-C		X
TKAD029	MA13-095	3.60	3.70	Cover	Strongly clay-altered polymict(?) volcanic breccia, unconsolidated	X					
Site B											
TKAD016	MA13-034	2.02	2.13	Footwall	Pervasively clay-altered matrix supported monomict coarse granular volcanic breccia, cemented	X			MA13-034-C	X	X
	MA13-035	5.65	5.71	Footwall	Pervasively clay-altered polymict clast-supported pumaceous shard-rich lapillistone, weakly cemented	X			MA13-035-C	X	
	MA13-036	7.00	7.05	Footwall	Pervasively clay-altered massive scoriaceous and pumaceous polymict matrix-supported lapillistone, weakly mineralized and weakly	X			MA13-036-C	X	X
TKAD025	MA13-039	5.50	5.60	Footwall	Intensely clay-altered pumaceous shard-rich polymict matrix-supported lapillistone, moderately cemented and mineralized	X	X		MA13-039-C	X	X
	MA13-040	6.91	7.00	Footwall	Intensely clay-altered shard-rich scoriaceous monomict clast-supported laipllistone, cemented	X	X		MA13-040-C	X	X

*C = clast separate; M = matrix separate; CM = clast + matrix

Table 5.1. Continued

Location		From	To			Clay fraction	Clay fraction	Fluid	Clast-matrix*	Whole-rock	
Drillhole	Sample	[mbsf]	[mbsf]	Lithology	Name	oriented XRD	O-isotope	inclusion	sub-sample	geochemistry	SWIR
TKAD026	MA13-067	2.90	3.00	Stringer	Intensely clay-altered massive polymict matrix-supported pumaceous lapillistone, mineralized	X	X		MA13-067-C	X	X
	MA13-068	3.60	3.68	Footwall	Intensely clay-altered massive scoriaceous polymict matrix-supported coarse tuff,	X			MA13-068-C	X	X
	MA13-069	5.64	5.75	Footwall	Intensely clay-altered polymict matrix-supported scoriaceous lapillistone, cemented	X	X		MA13-069-C	X	
TKAD012	MA13-062	2.81	2.90	Footwall	Intensely clay-altered polymict(?) clast-supported lapilli tuff, weakly cemented and mineralized	X	X		MA13-062-C	X	X
	MA13-063	4.25	4.36	Footwall	Variably clay-altered polymict(?) volcanic breccia, unconsolidated	X	X		MA13-063-CM	X	
	MA13-064	6.49	6.60	Footwall	Variably clay-altered monomict(?) volcanic sandstone, unconsolidated	X			MA13-064-C	X	
Site C											
TKAD032	MA13-072	2.05	2.17	Footwall	Moderately clay-altered and silicified massive monomict matrix-supported shard-rich lapillistone, cemented and mineralized	X			MA13-072-C	X	X
	MA13-073	3.90	4.00	Footwall	Moderately clay-altered massive monomict matrix-supported shard-rich lapillistone, weakly cemented and mineralized	X			MA13-073-C	X	X
	MA13-074	5.31	5.40	Footwall	Moderately clay-altered massive monomict clast-supported volcanic breccia, weakly cemented	X			MA13-074-C	X	X
	MA13-075	6.42	6.54	Footwall	Intensely clay-altered matrix-supported monomict hyaloclastite breccia, cemented and weakly mineralized	X	X		MA13-075-C	X	X
TKAD033	MA13-023	1.51	1.60	Footwall	Silicified and intensely clay-altered polymict matrix-supported resedimented volcanic breccia				MA13-023-C	X	
	MA13-024	2.55	2.66	Footwall	Variably clay-altered polymict clast-supported resedimented volcanic breccia, weakly				MA13-024-C	X	
	MA13-025	3.00	3.10	Footwall	Moderately clay-altered monomict shard-rich lapilli tephra, unconsolidated	X			MA13-025-C	X	
	MA13-026	4.76	4.88	Footwall	Moderately clay-altered polymict matrix-supported shard-rich lapilli tephra, unconsolidated	X			MA13-026-C	X	X
									MA13-026-M		X
	MA13-027	7.30	7.40	Footwall	Moderately clay-altered polymict matrix-supported lapilli tephra, unconsolidated	X			MA13-027-CM	X	X
									MA13-027-M		X
Site D											
TKAD017	MA13-019	5.00	5.10	Footwall	Variably clay-altered clast-supported monomict volcanic breccia, poorly consolidated with chimney fragments and patchy anhydrite cement				MA13-019-CM	X	
	MA13-020	6.90	7.00	Footwall	Intensely clay-altered volcanic breccia, weakly cemented	X			MA13-020-CM	X	
TKAD030	MA13-005	5.06	5.21	Stringer	Pervasively clay-altered massive monomict matrix-supported hyaloclastite sandstone, mineralized	X			MA13-005-M	X	X
	MA13-006	6.45	6.60	Footwall	Pervasively clay-altered monomict matrix-supported hyaloclastite breccia, cemented	X			MA13-006-C	X	X
TKAD018	MA13-014	3.00	3.10	Stringer	Pervasively clay-altered massive volcanic mudstone, mineralized	X			MA13-014-C	X	
	MA13-015	5.00	5.10	Footwall	Pervasively clay-altered monomict matrix-supported granular hyaloclastite, cemented	X			MA13-015-C	X	X
	MA13-016	6.60	6.71	Footwall	Pervasively clay-altered monomict matrix-supported hyaloclastite breccia, unconsolidated	X			MA13-016-C	X	
TKAD031	MA13-044	5.64	5.69	Stringer	Pervasively clay-altered massive resedimented granular hyaloclastite, mineralized and unconsolidated	X			MA13-044-C	X	X
									MA13-044-M	X	
	MA13-045	6.60	6.67	Stringer	Pervasively clay-altered massive resedimented hyaloclastite breccia, mineralized and unconsolidated	X			MA13-045-C	X	

*C = clast separate; M = matrix separate; CM = clast + matrix

Table 5.1. Continued

Location		From	To			Clay fraction	Clay fraction	Fluid	Clast-matrix*	Whole-rock	
Drillhole	Sample	[mbsf]	[mbsf]	Lithology	Name	oriented XRD	O-isotope	inclusion	sub-sample	geochemistry	SWIR
Site E *(South)*											
TKAD005	P020	20.55	20.67	Footwall	Intensely clay-altered monomict clast-supported volcanic breccia, irregularly cemented	X					
TKAD003	P012	11.11	11.20	Footwall	Intensely clay-altered polymict matrix-supported resedimented hyaloclastite breccia, cemented	X	X				
	P013	13.40	13.50	Footwall	Intensely clay-altered monomict clast-supported volcanic breccia, cemented	X			P0013-C		X
	P014	16.41	16.50	Footwall	Intensely clay-altered monomict matrix-supported hyaloclastite breccia, cemented	X	X		P0014-C		X
Site F *(West)*											
TKAD007	P021	3.50	3.60	Footwall	Silicified and intensely clay-altered monomict matrix-supported resedimented hyaloclastite breccia, cemented and mineralized	X					
	P022	11.23	11.34	Footwall	Intensely clay-altered monomict matrix-supported volcanic breccia, weakly cemented	X	X		P0022-C		X
	P023	22.35	22.45	Footwall	Intensely clay-altered monomict clast-supported volcanic breccia, cemented	X	X				
TKAD008	P025	7.50	7.56	Footwall	Intensely clay-altered monomict clast-supported volcanic breccia, cemented	X					
	P024	18.13	18.20	Footwall	Intensely clay-altered monomict clast-supported hyaloclastite(?), cemented	X					

*C = clast separate; M = matrix separate; CM = clast + matrix

clast and matrix components of the volcaniclastic footwall, using a Fieldspec® Pro spectroradiometer at the University of Ottawa. The Fieldspec® Pro has a spectral bandwidth of 3–10 nm and a scan time of 100 ms. Duplicate measurements were made for every sample, and white reference measurements were made every fifth sample. The data were normalized using The Spectral Geologist (TSG) 7 software by removing the convex hull continuum fitted over the spectrum in order to allow comparisons between absorption features from a common baseline (e.g., Jinfeng et al., 2014). The absorption-band positions were then automatically analyzed by TSG 7 using an inbuilt reference library of spectra of common minerals and a proprietary algorithm in order to identify the mineral phases and their relative abundances in each sample. The spectra were then manually assessed to confirm mineral identifications based on the shape and wavelength minima of the absorption features.

5.3.3. Clay separations and XRD analyses

For X-ray diffraction analysis, bulk samples from the altered footwall were gently hand-crushed and introduced to a sonic bath to further disaggregate each sample. Each sample was divided into a fine (<63 μm) and a coarse fraction (>63 μm) by wet sieving. Further grain size separation into a silt (2–63 μm) and clay fraction (<2 μm) was performed by settling of particles in standing water cylinders following the technique of Moore and Reynolds (1997). A small quantity of sodium hexametaphosphate was added to neutralize the electrostatic surface charges on the clay particles and thereby prevent flocculation during settling. After the silt fractions settled, the clay-sized fraction was siphoned off and separated from the water through the addition of a flocculating agent (magnesium chloride) followed by decanting. The concentrated water-saturated samples were repeatedly washed with de-mineralized water and separated by centrifuging, followed by freeze-drying for disintegration. These clay-sized fractions were then treated separately for XRD spectroscopy and O-isotope analyses.

The mineralogy of the clay-sized fractions of 58 samples was determined using a Philips X-ray diffractometer PW 1710, equipped with a Co-tube and an automatic divergence slit and monochromator, located at the GEOMAR Helmholtz Centre for Ocean Research Kiel, Germany. Operating conditions were 40 kV and 35 mA. Oriented mounts were prepared by placing wet

dispersed clay particles onto glass slides and allowing the suspension to dry. Air-dried samples were measured with a 2-theta scanning angle of 3–40°, at a scan rate of 1 second per 0.01° step. Subsequently, the samples were saturated by ethylene glycol (EG)-solvation following a standard vaporization technique under a vacuum for 24 hours, and measured using the conditions described above. MacDiff v.4.2.6 software was used for mineral identification and display of XRD data. Determination of the proportion of illite to smectite (expressed as % illite) in mixed-layer I/S clays was done by measuring the difference in d-spacings (Δd) between the 001-illite/002-EG-smectite and 002-illite/003-EG-smectite, following Moore and Reynolds (1997). The accuracy of this method is ± 2%. The ordering type (i.e., Reichweite) of the mixed-layer I/S clays was determined by the position of the reflection at low diffraction angles (10–17 Å) for glycol-solvated samples (Moore and Reynolds, 1997). Comparisons between SWIR spectroscopy and XRD methods are outlined in Appendix M.

5.3.4. Whole-rock geochemistry

Whole-rock geochemical analyses were performed at ActLabs (Ontario, Canada) on 47 samples of fine (<63 μm) clay-altered material, separated into clast and matrix components as described above and avoiding sulfate matrix. A lithium metaborate/tetraborate fusion ICP technique was used to analyze major elements (SiO_2, Al_2O_3, $Fe_2O_{3(T)}$, MnO, MgO, CaO, Na_2O, K_2O, TiO_2, and P_2O_5) and trace elements (Ba, Be, Bi, Co, Cs, Ga, Ge, Hf, In, Mo, Nb, Rb, Sr, Ta, Th, Tl, U, V, W, Y, Zr, REEs). A total-digestion ICP technique was used to analyze Ag, Cd, Cu, Ni, Pb, and Zn, with upper detection limit assays of Cu and Zn re-analyzed using a four acid ICP-OES technique. Additional trace elements were analyzed by INAA (Au, Br, Cr, Ir, Sc, Se, Sb, and As). Cold vapor analysis was used to determine Hg, and infrared spectroscopy was used to determine total S. Precision and accuracy was better than 5% for most analyses (Appendix K), as determined by analysis of duplicate samples and standard reference materials after every 10 samples.

5.3.5. Oxygen and hydrogen isotopes

Oxygen and hydrogen isotope analyses were performed on 14 samples with monominerallic clays (<2 μm), free from Fe- and Mn-oxides (as determined qualitatively by XRD). The analyses were

carried out by the Queen's Facility for Isotope Research (Ontario, Canada). Oxygen was extracted from 5 mg samples at 550–600°C using the BrF_5 technique of Clayton and Mayeda (1963). Samples were analyzed via dual inlet on a Thermo-Finnigan Delta^{Plus} XP isotope-ratio mass spectrometer (IRMS). For hydrogen isotope measurements, samples were weighed into silver capsules, degassed for one hour at 100°C, and then crushed and loaded into a zero-blank auto sampler. Hydrogen isotopic compositions were measured using a Finnigan thermos-combustion elemental analyzer coupled to a Thermo-Finnigan Delta^{Plus} XP continuous-flow IRMS. All values are expressed in the conventional δ-notation as per mil (‰) deviation from V-SMOW (Vienna Standard Mean Ocean Water) after McKinney et al. (1950):

$$\partial^{18}O = \frac{\left(^{18}O/^{16}O\right)_{Sample} - \left(^{18}O/^{16}O\right)_{VSMOW}}{\left(^{18}O/^{16}O\right)_{VSMOW}} \times 1000\ ‰$$

(Equation 1)

$$\delta D = \frac{\left(\ ^{2}H/\ ^{1}H\right)_{Sample} - \left(\ ^{2}H/\ ^{1}H\right)_{VSMOW}}{\left(\ ^{2}H/\ ^{1}H\right)_{VSMOW}} \times 1000\ ‰$$

(Equation 2)

The analytical precision and accuracy for $\delta^{18}O$ values are both 0.1 ‰, and the precision and accuracy of δD are 3 ‰ and 1.5 ‰, respectively.

5.4. Drill sites

5.4.1. Site A

Site A in the northern area of Tinakula is a topographic high that rises ~10 m from background sediments over an area of ~100 m by 80 m (Figs. 5.1, 5.4a). In the west there is a steep slope, whereas in the north and east the slopes are more gradual. Chimneys are clustered around a central plateau, which may be a crater. Drillholes TKAD001, 015, 027, 028, and 029 were examined in this study (see Appendix N for graphical summary core logs). The geology of Site A is

characterized by a cover sequence of variable thickness and smectite alteration, followed by a horizon of chimney talus, and an altered footwall. Drillhole *TKAD001* is the deepest drillhole of those studied, reaching a depth of 22.3 mbsf. It is also the northernmost drillhole, located next to an inactive chimney complex (Fig. 5.4a), but it did not intersect massive sulfides. The upper ~13.8 m of the recovered core consist of variably altered hanging-wall volcaniclastic tuff (cover sequence) and strongly oxidized mud and sand with chimney fragments, interpreted to be paleoseafloor horizons. The transition from the strongly oxidized mud and sand to the footwall sequence at ~14.0 m is gradational, with intensely clay-altered monomictic lapillistone that is crudely bedded with matrix-supported and clast-supported horizons. Below this, the volcaniclastic material is cemented by anhydrite with lesser gypsum and cut by a few sulfate veins. Pyrite and sphalerite, with minor chalcopyrite, galena, covellite, and bornite, are associated with the sulfate infill and veins. *TKAD015* (Fig. 5.5) and *TKAD027* were drilled in close proximity (~3 m apart) on top of a buried chimney mound composed of chimney talus overlain by <1 m of volcaniclastic material. The occurrence of chimney talus in the cover sequence indicates mass wasting from nearby chimneys. Intensely clay-altered, poorly-sorted monomict matrix-supported lapillistone occurs below the chimney talus in both drillholes. The upper part of the lapillistone unit is unconsolidated, with minor disseminated pyrite and rare chalcopyrite, with an increase in sulfate infill/cement down hole and a few sulfate veins (2–5 mm wide) at high angles to the core axis near the bottom. *TKAD028* is located to the east of TKAD015/027, intersecting 0.5 m of similar volcaniclastic material, followed by a narrow sulfide horizon (0.7 m) dominated by barite and sphalerite at the top, and becoming pyrite-rich down hole. The clay-altered lapillistone at the bottom of the hole is similar to that found in TKAD015/027 but somewhat better sorted. *TKAD029* in the east encountered only the variably-altered volcaniclastic material to a depth of 7.8 mbsf, with crudely bedded sand-sized fragments, grading to gravel-sized downhole, and a few larger vesicular clasts. Patchy iron oxide and green clay alteration occur in the fine-grained matrix and in some larger clasts.

5.4.2. Site B

Site B is a crater-like feature south of Site A, also in the northern area of the Tinakula deposit (Figs. 5.1 and 5.4b). The crater is approximately 70 m by 80 m in size, with chimneys and mounds

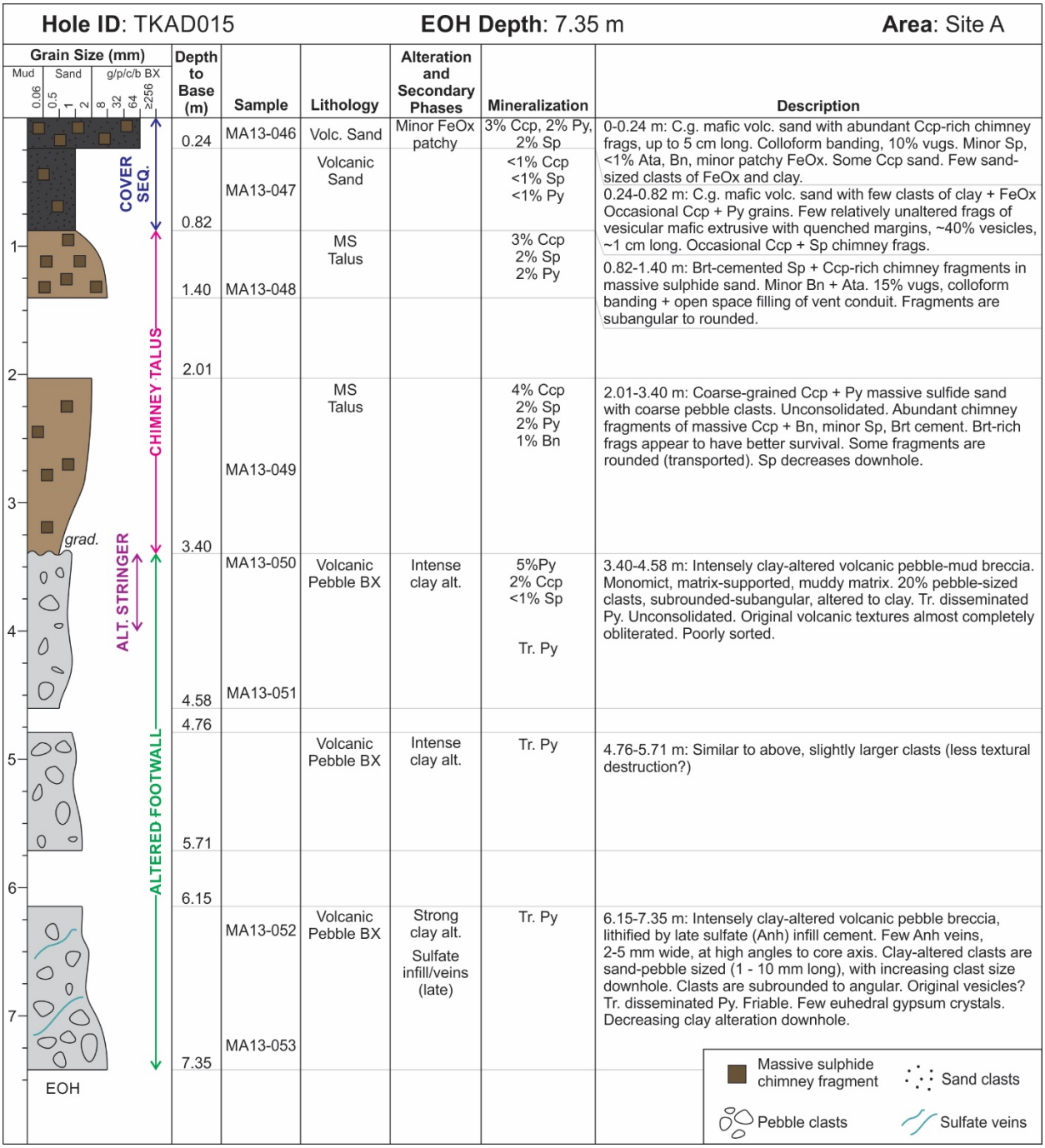


Fig. 5.5. Graphical drillcore summary log of TKAD015 from Site A (location shown on Fig 5.1; see Appendix N for additional logs from Site A).

along the crater walls and on the outer flanks of the cone. The area is characterized by massive sulfide chimney growth on top of chimney talus, with variable amounts of volcaniclastic cover sequence (see Appendix N for graphical summary core logs). *TKAD016* is located on the western edge of the crater at the margin of an inactive pyrite-rich chimney complex and mound. The recovered core consists of poorly-sorted monomict lapillistone. The upper part is cemented by sulfates (gypsum with a few large crystals up to 7 mm long); the lower part is mostly unconsolidated with patchy sulfate cement, a few cross-cutting veinlets of anhydrite, and weak silicification. Mineralization consists of minor disseminated pyrite associated with sulfate infill, minor sphalerite near the top, and minor to trace chalcopyrite near the bottom. *TKAD025* is located in the center of the crater. It did not intersect massive sulfides, but encountered intensely-altered lapilli with a few clasts of sphalerite-rich chimney fragments, and several sulfate-rich horizons (Fig. 5.6). Below 4 mbsf, the core contains a chaotic mix of volcanic and chimney fragments, with polymict sub-angular to angular volcanic clasts that are matrix supported. Gypsum is abundant in the volcaniclastic material and chimney talus, with the proportion of sulfate generally decreasing down hole. Two horizons at 3.1–4.0 and 6.0–6.5 mbsf contain sulfate mud with abundant gypsum crystals up to 3 cm long. There is weak late-stage silicification. These features are consistent with explosive hydraulic explosions (e.g., Rona, 2003) causing reworking of the volcanic pile, consistent with the crater-like topography of the bathymetry. *TKAD013* is located 3.7 m from TKAD025 within the volcanic crater. It intersected massive sulfide chimney talus, containing abundant sphalerite, chalcopyrite, pyrite, and barite. The talus is cemented by sulfate-rich and clay-altered mud and fine-grained sulfides. Minor sulfate-cemented lapillistone and matrix-supported monomict volcaniclastic breccia with minor disseminated chalcopyrite and pyrite, and pervasive sulfate-silica cement was cored between 4.8 and 4.9 mbsf. *TKAD026* was drilled on the southern wall of the crater, where it intersected fragments of massive sphalerite-barite chimney material to a depth of 1.4 mbsf, followed by an intensely-altered footwall sequence consisting of monomict, matrix-supported, and moderately rounded lapillistone with intense grey-white clay-alteration that decreases down hole. Minor chalcopyrite and pyrite are disseminated throughout, decreasing downhole, and there is minor patchy barite cement in the upper portion and anhydrite cement in the lower portion (increasing down hole). There is no apparent bedding or grading of the lapilli. *TKAD012* is the easternmost drillhole at Site B, located on the upper rim of the volcanic cone, with volcanic facies similar to TKAD026. This drillhole encountered a thin 62 cm cover sequence of

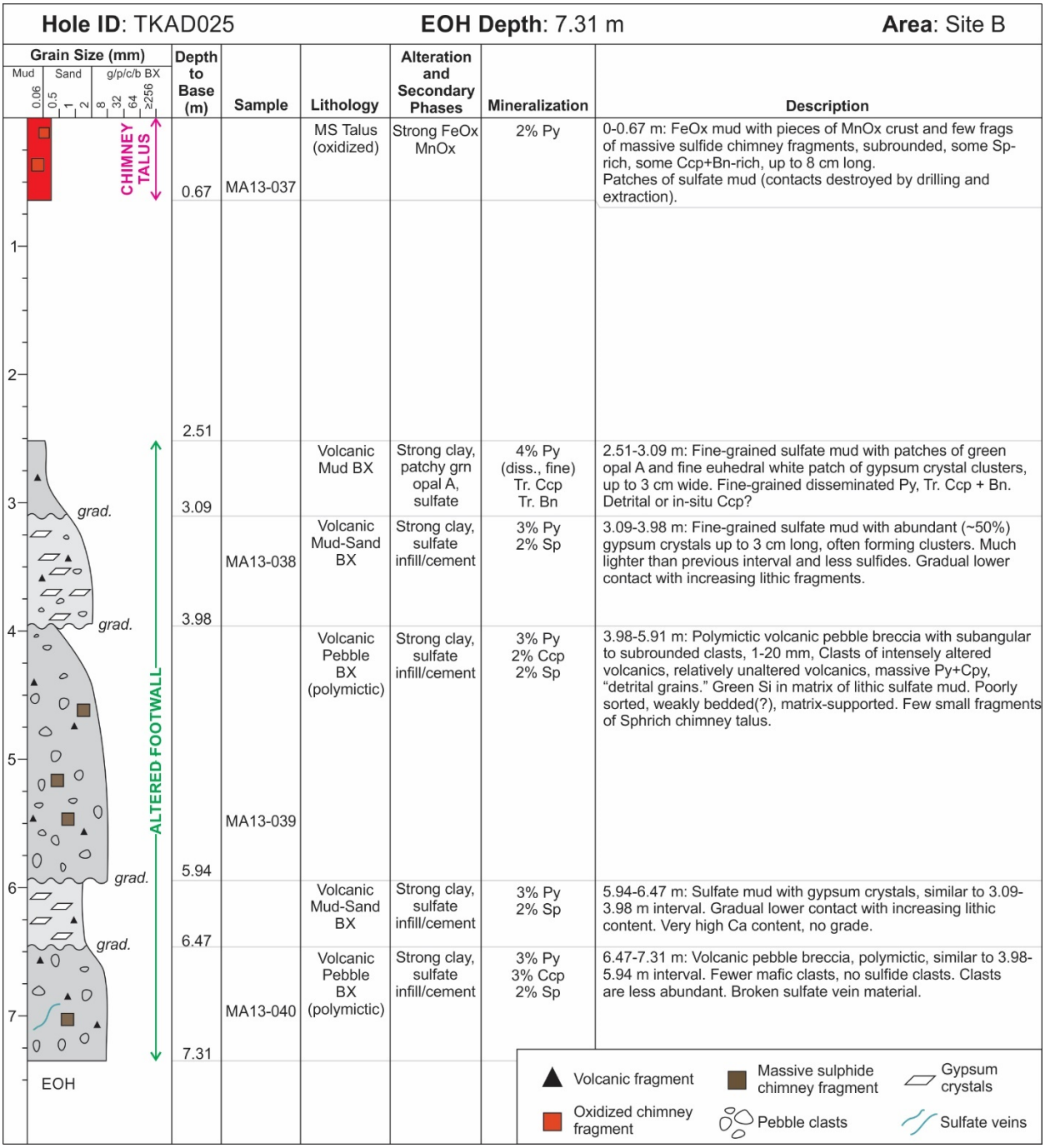


Fig. 5.6. Graphical drillcore summary log of TKAD025 from Site B (location shown on Fig 5.1; see Appendix N for additional logs from Site B).

unconsolidated volcaniclastic material, followed by the footwall volcaniclastic sequence to a depth of 7.4 mbsf. The footwall breccia contains sub-rounded vesicular clasts with variable degrees of alteration, ranging in color from black to grey to white, with a slight decrease in intensity of white clay-alteration down hole. The matrix is fine clay-altered mud at the top, with sulfate cement increasing down hole. There are minor finely disseminated sulfides (pyrite and sphalerite) throughout, with decreasing sphalerite down hole.

5.4.3. Site C

Site C is a large volcanic cinder cone, rising to a maximum height of ~70 m above the seafloor, with a diameter of ~120 m by 90 m (Fig. 5.4c,d). It is located in the central Tinakula area (Fig. 5.1), south of Site B along the N-S row of cinder cones (see Appendix N for graphical summary core logs). *TKAD032* occurs on the flank of the cinder cone, associated with a circular collapse feature with nearby chimney complexes and mounds. This drillhole encountered unconsolidated cover consisting of sand-to gravel-sized volcaniclastic material in the first 1.8 m, followed by intensely-altered footwall volcaniclastics and breccia to 6.9 mbsf. The footwall breccia consists of sub-rounded to sub-angular vesicular monomictic clasts, variably altered to white-grey clay, with the most intense alteration at the clast margins. The uppermost breccia is matrix-supported (30–40% clasts) with fine dark grey clay, fine-grained pyrite, variable sulfate cement, and a few cross-cutting veins of sulfate. Minor disseminated sphalerite and chalcopyrite occur in the top meter of breccia, and finely-disseminated pyrite occurs throughout the matrix in the lower section, associated with the sulfate cement (up to 25 vol.% anhydrite/gypsum). Several horizons in the lower footwall are clast-supported (up to 60% clasts) with angular monomict clasts that are interpreted to be autobreccias. *TKAD033* was drilled near the summit of the cone at the edge of a small crater or collapse feature. Similar to TKAD032, this drillhole encountered unconsolidated volcaniclastic material in the first 1.1 m, followed by intensely-altered footwall lapillistone to a depth of 7.5 mbsf (Fig. 5.7). In this core, the fine-grained (ash?) matrix of the breccia facies is strongly clay-altered with weaker alteration of the clasts, primarily at the margins. Variable alteration intensity gives this rock a polymict appearance. The proportion of matrix decreases down hole, becoming variably clast-supported at ~5.0 mbsf. There are minor fine-grained sulfides

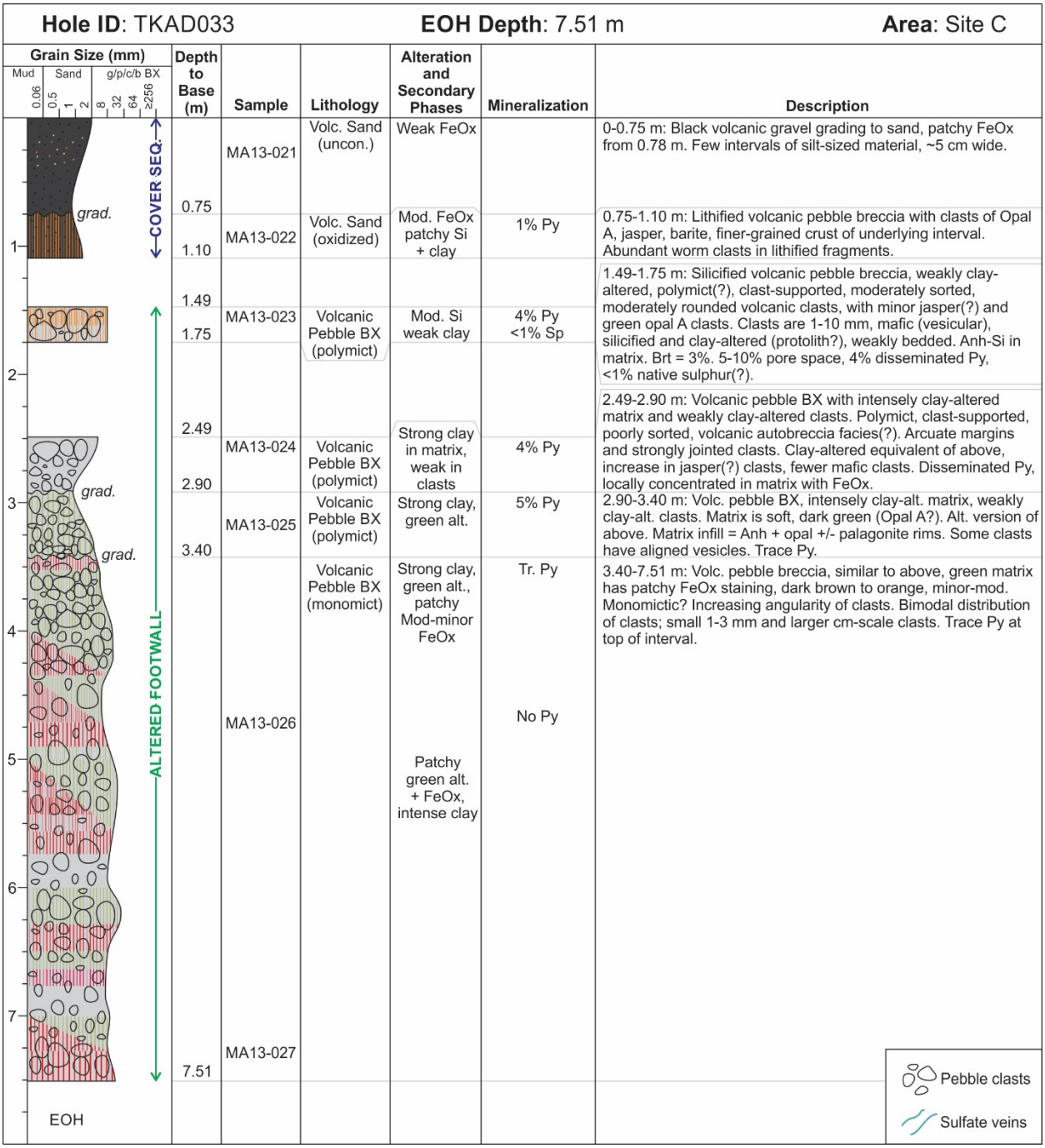


Fig. 5.7. Graphical drillcore summary log of TKAD033 from Site C (location shown on Fig 5.1; see Appendix N for additional logs from Site C).

in the matrix, ranging down hole from sphalerite, to pyrite + chalcopyrite, to pyrite. Minor anhydrite infill and veins, and minor late-stage silica occur at the bottom of the hole.

5.4.4. Site D

Site D is an irregularly-shaped topographic high, ~70 m by 80 m in diameter (Figs. 5.1 and 5.4c,d), with chimneys clustered on the northern flank, in the saddle between two cinder cones (see Appendix N for graphical summary core logs). Here, there is localized low-temperature venting of milky fluids from fractures near the base of inactive chimneys. *TKAD017* cored a thin cover of unconsolidated volcaniclastic material, followed by chimney talus and oxidized mud and sand with chimney fragments, interpreted to be paleoseafloor horizons, in the first 5.2 m (Fig. 5.8). Altered footwall breccia extends from this depth to the bottom of the drillhole at 7.4 mbsf. It consists of strongly clay-altered monomict breccia, with sub-rounded cm-sized clasts that are matrix-supported. There are a few sub-rounded chimney fragments, along with disseminated pyrite throughout (2–3 vol.%) and minor chalcopyrite veinlets towards the base, associated with very white clay alteration. Patchy gypsum cement, with a few coarse-grained crystals, increases in abundance down hole. *TKAD030* intersected ~2.3 m of cover unconsolidated volcaniclastic material, followed by 10 cm of oxidized mud and sand, ~3 m of sphalerite-rich angular chimney talus, and ~2 m of intensely-altered footwall to a depth of 7.3 mbsf. The footwall breccia consists of strongly clay-altered lapilli tuff, with monomict clasts from ~0.2 mm up to 1 cm. There are several beds distinguished by changes in grain size and several horizons that are clast-supported with lapilli-sized clasts. These rocks are cemented by abundant sulfate that obscures primary volcanic textures. The sulfate cement is associated with minor disseminated chalcopyrite in the upper part, and minor disseminated pyrite throughout. *TKAD018* encountered ~1.2 m of chimney talus with intense oxidation at the seafloor to a depth of 0.6 mbsf, followed by altered footwall volcaniclastics to a depth of 6.7 mbsf. From 1.1 to 1.8 mbsf, the footwall breccia consists of angular, monomict, matrix-supported lapilli tuff, with moderate to strong clay alteration that mainly affects the clasts. The matrix consists of clay-altered material (ash?), cemented by silica. Below 1.8 mbsf, the breccia is clast-supported, moderately sorted, and unconsolidated, with patchy anhydrite cement below 3.8 mbsf. Intense alteration obscures primary volcanic textures, making it difficult to distinguish facies changes. Minor disseminated sphalerite and chalcopyrite occur

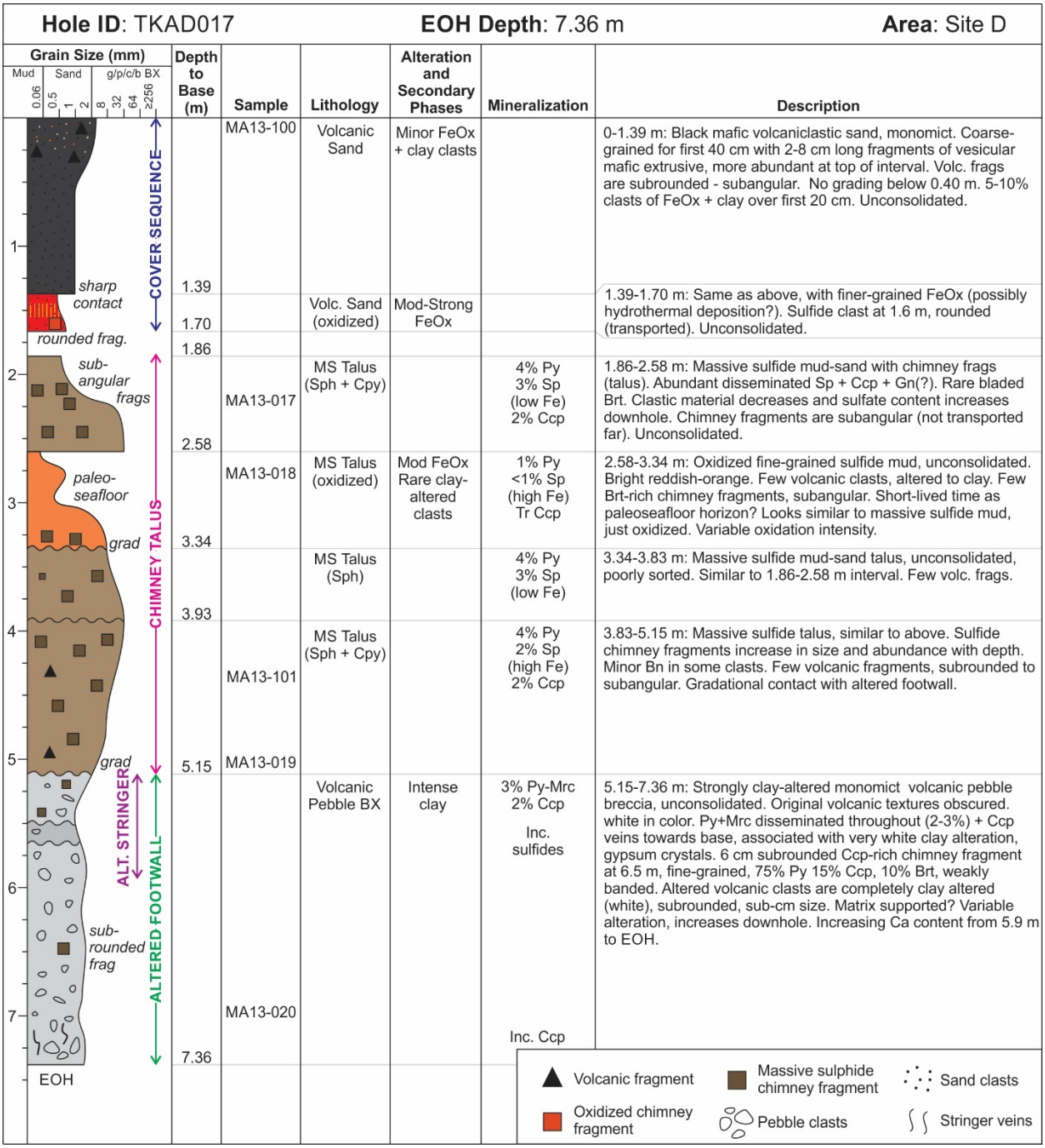


Fig. 5.8. Graphical drillcore summary log of TKAD017 from Site C (location shown on Fig 5.1; see Appendix N for additional logs from Site D).

within the matrix, decreasing in abundance down hole. Minor disseminated pyrite occurs throughout. *TKAD031* intersected massive sulfide talus in the first ~5 m, with layers of oxidized mud and sand (paleoseafloor horizons) at ~2.1 mbsf and ~3.5 mbsf, followed by intensely clay-altered and matrix-supported footwall volcaniclastics with ~30% sub-rounded clasts that decrease in abundance and size down to 7.3 mbsf. The matrix is fine-grained and light grey, and the breccia is unconsolidated, with only minor patchy sulfate cement. There is no obvious bedding or grading of the footwall sequence.

5.4.5. Site E

Site E is on the southernmost cinder cone (Figs. 5.1 and 5.4e). *TKAD005* is located near an inactive chimney complex on a narrow ridge or circular crater-like feature. The drillhole recovered monomict, clast-supported, moderately-sorted lapillistone that shows weak grading. The clasts are vesicular and sub-rounded, and are strongly altered to white clay. The matrix consists of sulfate cement with minor disseminated sphalerite and pyrite that decrease in abundance down hole. *TKAD003* is located along a small ridge south of TKAD005, near a scarp that may represent a crater wall or mass-wasting slump. This drillhole recovered monomict, clast-supported lapillistone, with angular to sub-angular clasts that are intensely altered to white clay, with strong sulfate cement and minor disseminated pyrite that is locally oxidized to hematite.

5.4.6. Site F

TKAD007 is the western sulfide field, where there is evidence for structural control of actively-venting chimney complexes and mounds but no constructional volcanic features (Figs. 5.1 and 5.4f). Core from this drillhole consists of monomict clast-supported lapillistone, with moderately-sorted sub-angular clasts that have been pervasively altered to clay. The matrix consists of sulfate cement that increases in abundance down hole, with minor disseminated pyrite and fracture-controlled patchy iron-oxide alteration. There are a few cm-wide pyrite-chalcopyrite veinlets associated with the most intense clay alteration near the top of the volcaniclastic sequence. *TKAD008* is located along a NW-SE trending structure that is associated with a low-relief ridge and numerous inactive chimney complexes and mounds. The recovered core consists of a

monomict matrix-supported lapillistone, grading down hole to a clast-supported lapillistone, associated with a general increase in clast size and angularity. The clasts are moderately altered to clay, with a decrease in alteration intensity down hole and weak alteration of clast margins below 6 mbsf. The breccia is variably cemented by sulfate, which is locally fracture-controlled. Minor patchy disseminated pyrite is limited to the upper part of the section. There are patches of strong iron-oxide alteration throughout the matrix.

5.5. Analytical results

5.5.1. SWIR spectroscopy results

Results of SWIR spectroscopy are summarized in Table 5.2 and Figure 5.9, with full results reported in Appendix O. Identified minerals include: white micas, montmorillonite ($[Na,Ca]_{0.33}[Al.Mg]_2[Si_4O_{10}[OH]_2 \cdot nH_2O$), nontronite ($Ca_{0.5}[Si_7Al_{0.8}Fe_{0.2}][Fe_{3.5}Al_{0.4}Mg_{0.1}]O_{20}[OH]_4$), chlorite ($[Fe,Mg_5Al][AlSi_3]O_{10}[OH]_8$), and gypsum ($CaSO_4$). White mica is the most abundant mineral group, ranging in composition from paragonite ($Na_2Al_4[Si_6Al_2O_{20}][OH]_4$) to muscovite ($K_2Al_4[Si_6Al_2O_{20}][OH,F]_4$) and illite ($K_{1.5\text{-}1.0}Al_4[Si_{6.5\text{-}7.0}Al_{1.5\text{-}1.0}O_{20}][OH]_4$). These white micas are identified by the distinct Al-OH absorption feature between 2180 and 2228 nm, with wavelengths between 2189–2195 nm for paragonite and 2200–2213 nm for muscovite and illite (this study; Thompson et al., 1999). In addition, small absorption features are present at 2350 and 2450 nm. Montmorillonite is also identified by the Al-OH absorption feature; however, pure montmorillonite has a narrow and symmetrical 2200 nm feature with a small shoulder on the H_2O+OH absorption feature at 1450–1460 nm. Chlorite is identified by the strong absorption feature at 2340 nm, the wavelength of which increases from 2324 nm for Mg-rich compositions to >2350 nm for Fe-rich compositions. Gypsum is identified by the OH+H_2O feature at 1400 nm, along with the OH feature at 1800 nm. The alteration mineral assemblages generally progress downhole from smectite (montmorillonite/nontronite), to white mica (paragonite, paragonitic-illite, muscovitic-illite, and illite), to chlorite. Samples containing montmorillonite and white mica may reflect mixed-layer clays rather than discrete end-member phases. Comparisons between drillholes also reveal variations in mineral assemblage according to drill site: Site A is dominated by smectite and white mica that progresses downhole to chlorite; Site B contains minor smectite

Table 5.2. Clay minerals identified by SWIR spectroscopy from samples of the altered volcaniclastic footwall from the Tinakula deposit, with drillholes arranged from north to south, see Fig. 5.1.

Location		Depth	Smectite		Chlorite	White Mica				Sulfate	AlO(OH)
Drillhole	Sample	[mbsf]	Mnt [%]	Non [%]	Chl [%]	Pg [%]	Pgl [%]	Msl [%]	Ms [%]	Gp [%]	Dsp [%]
Site A *(North)*											
TKAD001	MA13-086-C	14.00-14.12	●							○	
	MA13-087-C	16.05-16.22	●				◑				
	MA13-088-C	17.40-17.50						(?)	●		
	P005-C	19.11-19.30	(?)					●			
	MA13-091-CM	20.77-21.00			◑				◑		
TKAD015	MA13-052-C	6.42-6.52			(?)	●				○	
	MA13-053-C	7.23-7.34			(?)	●				◑	
TKAD028	MA13-099-C	4.50-4.60								◑	●*
Site B											
TKAD016	MA13-034-C	2.02-2.13								◑	●*
	MA13-036-C	7.00-7.05	(?)		●	◑					
TKAD025	MA13-039-C	5.50-5.60	(?)		(?)					●	
	MA13-040-C	6.91-7.00			●					○	
TKAD026	MA13-067-C	2.90-3.00	◑			●					
	MA13-068-C	3.60-3.68	(?)		(?)	●					
	MA13-069-C	5.64-5.75				(?)*				(?)*	
TKAD012	MA13-062-C	2.81-2.90	◑		(?)		◑				
Site C											
TKAD032	MA13-072-C	2.05-2.17	●								
	MA13-073-C	3.90-4.00	●								
	MA13-074-C	5.31-5.40	●		(?)		◑				
	MA13-075-C	6.42-6.54	●		(?)		◑				
TKAD033	MA13-026-C	4.76-4.88	●								
	MA13-026-M	4.76-4.88	●								
	MA13-027-C	7.30-7.40	●								
	MA13-027-M	7.30-7.40									●*
Site D											
TKAD030	MA13-005-C	5.06-5.21	(?)			●					
	MA13-006-C	6.45-6.60	(?)			●					
TKAD018	MA13-015-C	5.00-5.10				◑				●	
TKAD031	MA13-044-C	5.64-5.69		◑			●				
Site E *(South)*											
TKAD003	P013-C	13.40-13.50	◑		(?)		●				
	P014-C	16.41-16.50	(?)		◑			◑			
Site F *(West)*											
TKAD007	P022-C	11.23-11.34	(?)		◑		●				

Amounts indicated are >50% (●), 25–50% (◑), <25% (○); * = unreliable results

(?) indicates manual search of the spectral library; all others by Spectral Assist automated identification using TSG 7 software

C = clast separate; M = matrix separate; CM = clast + matrix; Mnt = montmorillonite; Chl = chlorite; Pg = paragonite; Pgl = paragonitic-illite; Msl = muscovitic illite; Ms = muscovite; Gp = gypsum; Dsp = diaspore

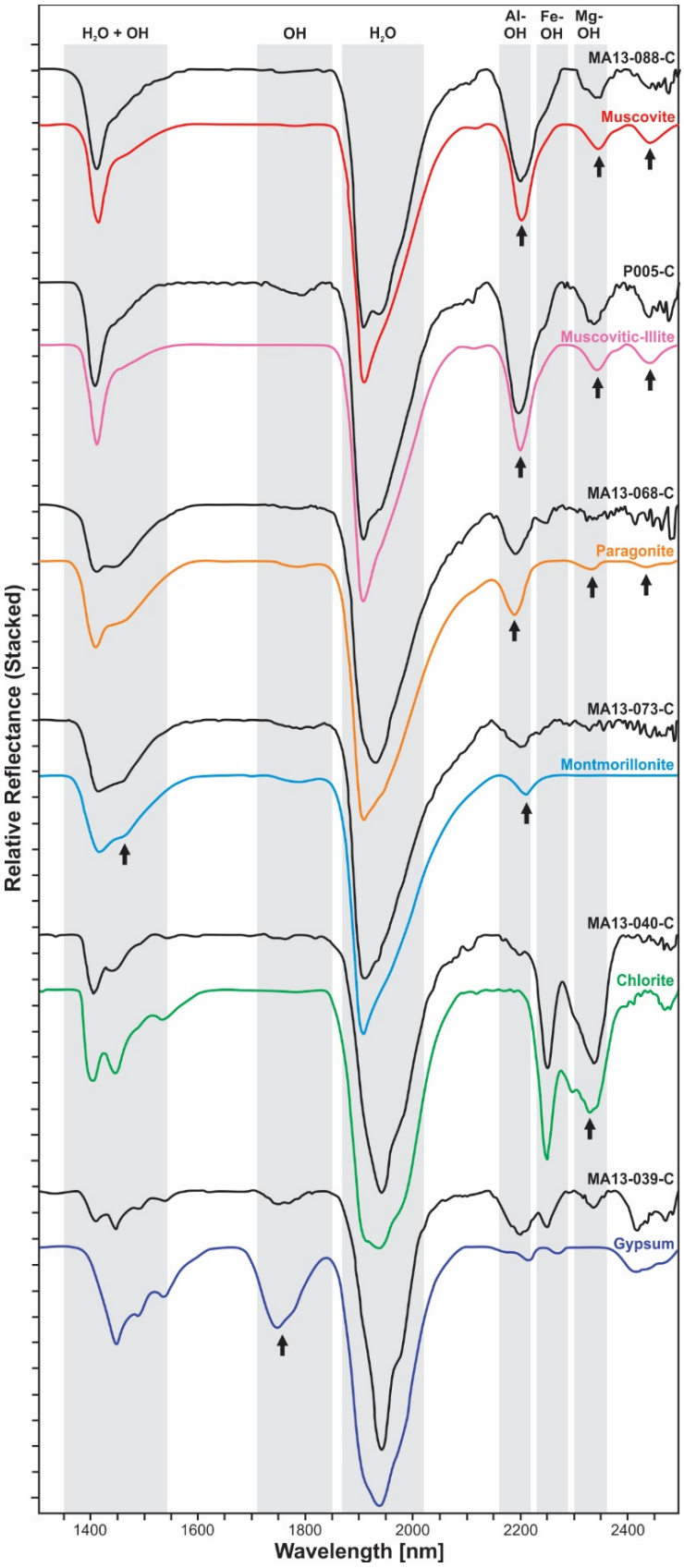


Fig. 5.9. Main minerals identified by SWIR spectroscopy, with reference spectra (colored lines) and examples of samples from the intensely-altered footwall from the Tinakula deposit (Hull Quotient normalized). Diagnostic absorption features are shown by black arrows (see text).

above ~3 mbsf, with variable chlorite and white mica downhole; Site C is dominated by montmorillonite with minor white mica (and chlorite?) below ~5 mbsf; Site D is dominated by white mica; Site E progresses downhole from smectite + white mica at ~13.5 mbsf to chlorite + white mica at ~16.5 mbsf; and Site F contains chlorite and white mica. These variations are outlined in detail below for each drillhole according to site.

Site A

Drillhole *TKAD001* is the best example of a progressive change in alteration mineralogy downhole in the Tinakula deposit (Fig. 5.10; Table 5.2; Appendix O). The shallowest sample from a depth of 14.0 mbsf is characterized by a mixture of montmorillonite and gypsum. A shallow absorption feature at 2300 nm indicates slightly higher Fe contents than pure montmorillonite, with a composition between montmorillonite and nontronite. This peak becomes less pronounced at 16.0 mbsf, which contains a mixture of montmorillonite and paragonitic illite. Below this, the mineralogy becomes more potassic, ranging from muscovitic illite to muscovite. At a depth of 17.4 mbsf, the mineralogy was identified using the TSG 7 software as 100% muscovite, characterized by a feature at 1909 nm. A weak absorption feature at 1940 nm suggests the additional presence of minor muscovitic illite. At 19.4 mbsf, the 1944 nm feature is more pronounced, characteristic of muscovitic illite. A broad feature between 1700–1800 nm suggests the presence of minor montmorillonite. At 20.8 mbsf, the spectra quality is degraded, but is consistent with a mixture of chlorite and muscovite. The position of the feature at 2340 nm reflects an Fe- and Mg-rich chlorite composition. The downhole transition from smectite to muscovite is reflected in the ratio of the depth of the 2200 nm feature to the depth of the 1909 nm feature, which progressively increases from 0.16 in the shallowest sample of montmorillonite (MA13-086-C; 14.0 mbsf), to 0.45 in the sample of muscovite (MA13-088-C; 17.4 mbsf), to 0.73 in the sample of muscovitic illite (P005-C; 19.1 mbsf). *TKAD015* contains a mixture of paragonite and gypsum. There is a very slight shift in the position of the Al-OH absorption feature from 2192 nm at 6.4 mbsf to 2195 nm at 7.2 mbsf. Manual inspection of the spectra reveal a strong feature at 2340 nm, suggesting the presence of chlorite. The position of this feature together with an Fe-OH absorption peak at 2252 nm and an Mg-OH absorption peak at 2340 suggest that this chlorite is Fe- and Mg-rich.

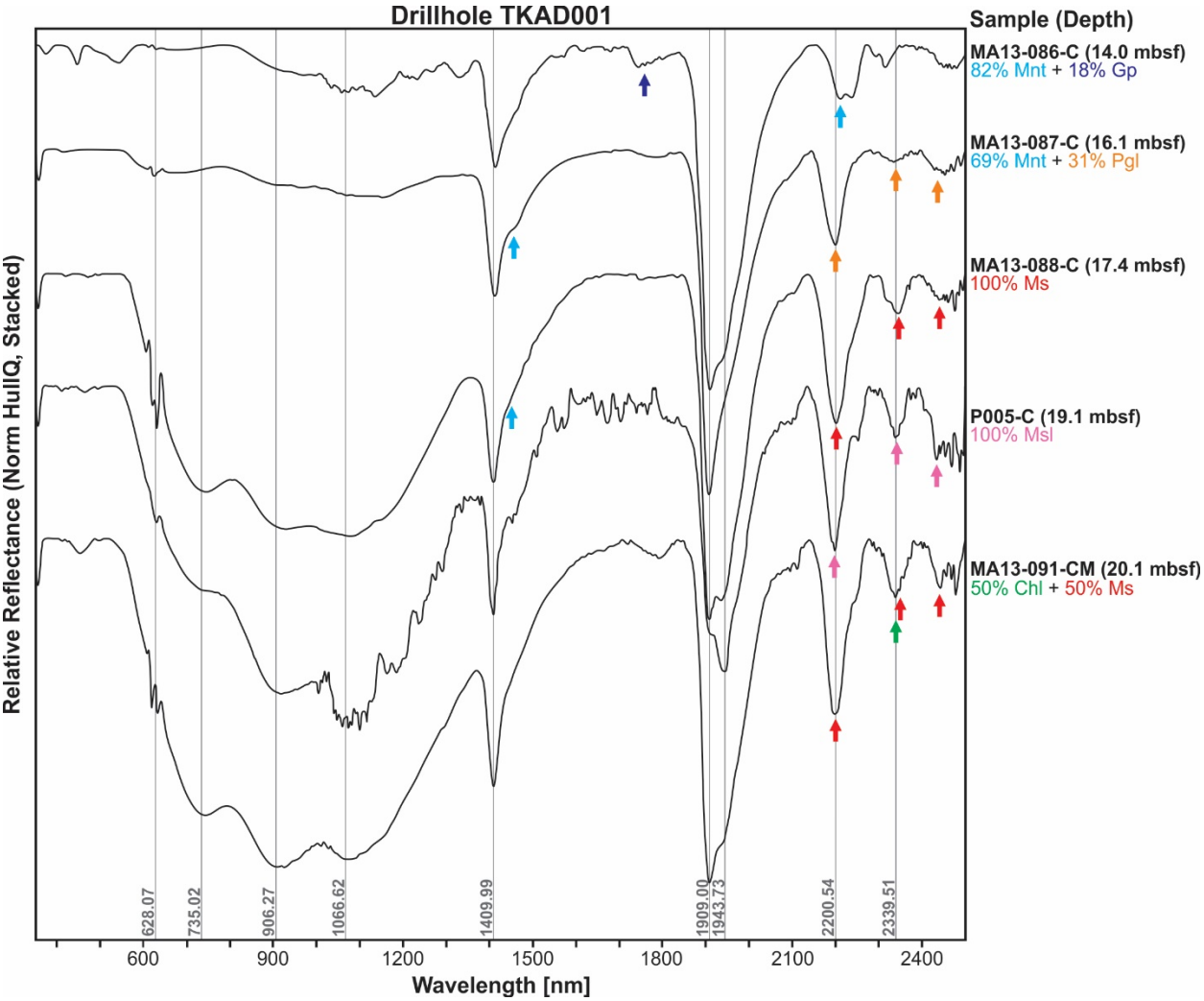


Fig. 5.10. Stacked SWIR spectra for samples from drillhole TKAD001 showing changes in mineralogy with depth (Hull Quotient normalized). Diagnostic absorption features are shown by colored arrows (see Appendix O for additional details). Mnt = montmorillonite; Gp = gypsum; Pgl = paragonitic-illite; Ms = muscovite; Msl = muscovitic-illite; Chl = chlorite.

Site B

The hydrous phyllosilicates in *TKAD016* consist of 60% chlorite and 40% paragonite at a depth of 7.0 mbsf, which is the only reliable spectra obtained for this drillhole (Table 5.2; Appendix O). The Mg-OH absorption peak at 2329 nm suggests that this chlorite is Mg-rich. A distinct shoulder on the H_2O+OH feature at 1450 nm may indicate the presence of montmorillonite, although interferences from the chlorite spectra do not allow a positive identification. *TKAD025* is dominated by gypsum at a depth of 5.5 mbsf, but a distinct feature at 2340 nm suggests the presence of Fe-Mg chlorite. This feature becomes much stronger and narrower at 6.9 mbsf, with chlorite comprising 90% of the sample. The location of this feature does not change downhole. A shoulder feature at 1450 nm may indicate the presence of montmorillonite in the shallow sample. *TKAD026* is characterized by a mixture of paragonite (63%) and montmorillonite (37%; Table 5.2) at 2.9 mbsf. At 3.6 mbsf, the spectra is dominated by paragonite, although a shoulder feature at 1450 nm suggests that montmorillonite persists to this depth. In addition, a weak feature at 2329 nm suggests the presence of Mg-chlorite. The wavelength of the Al-OH feature of the paragonite increases slightly downhole from 2190 nm to 2194 nm, similar to drillhole TKAD015. *TKAD012* contains 72% montmorillonite and 38% paragonitic illite at a depth of 2.8 mbsf. A very weak absorption feature at 2340 nm suggests the presence of minor Mg-chlorite.

Site C

TKAD032 reveals a downhole trend from montmorillonite to mixed montmorillonite and paragonitic-illite (Table 5.2; Appendix O). Samples from 2.0 mbsf and 3.9 mbsf contain 100% montmorillonite, with an distinct downhole-increase in wavelength of the Al-OH feature from 2173 nm to 2200 nm. Samples from 5.3 mbsf and 6.4 mbsf contain a 2:1 mix of montmorillonite and paragonitic illite. In these samples, the 2190 nm feature is broad and remains consistent. The deeper samples are also characterized by the appearance of Fe-OH and Mg-OH features at 2243 nm and 2329 nm, respectively, suggesting the presence of Fe-Mg chlorite. *TKAD033* was sampled at depths of 4.8 mbsf (two samples) and 7.3 mbsf. The two samples from 4.8 mbsf represent separate analyses of clast and matrix material. Both analyses consist of 100% montmorillonite, with a weak feature at 2243 nm that is slightly stronger in the matrix material. This may reflect an

Fe-rich smectite composition (nontronite). The sample from 7.3 mbsf is also composed of 100% montmorillonite (nontronite?). There is a slight increase in the position of the Al-OH feature downhole, from 2205 nm to 2209 nm, consistent with previous measurements.

Site D

TKAD030 consists of an alteration mineralogy dominated by paragonite at depths of 5.1 mbsf and 6.5 mbsf (Table 5.2; Appendix O). Manual inspection of the spectra reveal a shoulder feature at 1450 nm, suggesting the likely addition of montmorillonite in both of these samples, becoming more distinct downhole. A weak, broad feature near 1800 nm in the deeper sample is consistent with increasing montmorillonite concentration downhole. The locations of the main features remain consistent between samples. *TKAD018* reveals a mineral assemblage consisting of a simple mixture of 59% gypsum and 41% paragonite at a depth of 5.0 mbsf. There is a very weak Fe-OH feature at 2265 nm, possibly indicating minor amounts of an Fe-bearing phase, such as nontronite, although this cannot be confirmed. *TKAD031* contains of a 2:1 mix of paragonitic-illite and nontronite from a similar depth of 5.6 mbsf. This is the only sample with a positive identification of nontronite (Fe-rich smectite).

Site E

TKAD003 contains 67% paragonitic-illite, with 33% montmorillonite at relatively deep depths of 13.4 mbsf, although there is a high degree of uncertainty with this sample (Table 5.2; Appendix O). A strong feature at 2336 nm, along with a Fe-OH feature at 2249 nm, suggests the presence of Fe-Mg chlorite. This feature becomes more distinct downhole at a depth of 16.4 mbsf, where the sample contains 50% Fe-Mg chlorite and 50% muscovitic-illite. A shoulder feature at 1450 nm indicates that montmorillonite persists to this depth. *TKAD007* consists of 51% paragonitic illite and 49% chlorite at a depth of 11.2 mbsf. The position of the feature at 2235 nm, along with the Fe-OH feature at 2251 nm, suggests that this chlorite is Fe- and Mg-rich. A weak shoulder at 1450 nm suggests the presence of minor montmorillonite.

5.5.2. XRD results

Results of XRD analyses from drillcore samples from the Tinakula deposits are shown in Table 5.3, arranged according to sample location as shown in Figure 5.1. Complete XRD spectra are reported in Appendix P. The samples included variably-altered tuff (i.e., cover sequence), and intensely altered volcaniclastic breccias (i.e., footwall sequence) with stringer mineralization. The identified alteration minerals include: dioctahedral smectite (montmorillonite and nontronite), chlorite (mainly chamosite, with minor clinochlore and chloritoid), illite, and mixed-layer clays (corrensite, aliettite(?), rectorite, and illite/smectite. Small amounts of quartz, pyrite, marcasite, hematite, and anhydrite were also identified, and possibly paratacamite, barite, and barian celestine. Mixed-layer illite/smectite (I/S) contain variable proportions of illite and smectite, ranging from 50% illite (defining the mineral rectorite) to ~91% illite (denoted 0.9 I/S; Table 5.4), averaging 74% illite (n = 30). Five alteration assemblages are distinguished (outlined in Fig. 5.11): (1) montmorillonite/nontronite ± plagioclase; (2) nontronite + corrensite; (3) I/S + pyrite; (4) I/S + chamosite; and (5) chamosite + corrensite. Each has a distinct color, which is apparent in drillcore (Table. 5.3): montmorillonite/nontronite ± plagioclase is associated with yellow-orange to red-brown hues; nontronite + corrensite is associated with greenish yellow to greenish gray hues; I/S + pyrite is associated with yellow-gray hues; I/S + chamosite shows a wide range of hues from bluish white to olive and greenish yellow; and chamosite + corrensite shows dominantly greenish hues, ranging from greenish yellow to pale olive. As seen in the SWIR data, the alteration assemblages vary with location (Sites A–E; Fig. 5.1) and depth (Table 5.3), generally progressing downward in the order: montmorillonite/nontronite ± plagioclase to nontronite + corrensite, to I/S + pyrite, to I/S + chamosite, to chamosite + corrensite. Sites A is dominated by chamosite + corrensite alteration, with localized illite/smectite + chamosite alteration that varies over short distances, interpreted to reflect local changes associated with inferred syn-volcanic faulting (Fig. 5.12). Alteration at Site B is semi-conformable, varying downhole from I/S + pyrite, to I/S + chamosite, to chamosite + corrensite (Fig. 5.13). Site C is characterized by nontronite near the surface, followed by nontronite + corrensite and chamosite + corrensite at depth (Fig. 5.14). Alteration at Site D varies from I/S + pyrite near the surface, to I/S + chamosite at depth (Fig. 5.15). End-member illite is present in all of the samples from this site, indicative of high

Table 5.3. Clay minerals identified by XRD from samples of the altered volcaniclastic footwall from the Tinakula deposit, with drillholes arranged from north to south (see Fig. 5.1)

Location		Depth	Munsell	Smectite		Chlorite			Mixed Layer Clays				Illite		Feldspar	Non-Clay Minerals								Alteration
Drillhole	Sample	[mbsf]	Clay Color	Mnt	Non	Cld	Clc	Cham	Corr	Alie(?)	Rect	I/S	Ill	Pg	Pl	Qz	Py	Mrc	Hem	Ata(?)	Anh	Brt	Cel	Assmeblage
Site A *(North)*																								
TKAD001	MA13-078	4.54-4.68	Mod. yellowish brown	●											●									Mnt/Non + Pl
	MA13-082	7.00-7.10	Light yellowish orange	●											●									Mnt/Non + Pl
	P002	10.39-10.50	Dusky yellow		●						(?)				◑									Mnt/Non + Pl
	MA13-085	12.90-13.00	Dark yellowish orange		●										●									Mnt/Non + Pl
	MA13-086	14.00-14.12	Mod. reddish brown	(?)	●														○					Mnt/Non + Pl
	P003	14.81-14.95	Greenish gray		●	○			◑															Non + Corr
	P004	15.65-15.80	Light greenish gray			○			●		●		○											Non + Corr
	MA13-087	16.05-16.22	Pale greenish yellow	(?)	●				○															Non + Corr
	MA13-088	17.40-17.50	Light greenish gray					●	●			●									○			I/S + Cham
	MA13-089	17.90-18.00	Light gray					●			●					○								I/S + Cham
	MA13-090	18.40-18.57	Light greenish gray					●			●	○	○											I/S + Cham
	P005	19.11-19.30	Very light gray					◑			●	○	○				(?)							I/S + Cham
	MA13-091	20.77-21.00	Pale greenish yellow	○				◑				●					(?)							I/S + Cham
	MA13-092	21.30-21.45	Light greenish gray					●	○			○	◑											I/S + Cham
TKAD015	MA13-050	3.49-3.63	Pale olive	○				○				●	○							(?)				I/S + Cham
	MA13-051	4.34-4.43	Pale greenish yellow					●				◑												Cham + Corr
	MA13-052	6.42-6.52	Grayish yellow green					●				○												Cham + Corr
	MA13-053	7.23-7.34	Grayish yellow green					●				○												Cham + Corr
TKAD027	MA13-056	2.50-2.60	Light olive					●			●									(?)		(?)	(?)	I/S + Cham
	MA13-057	4.60-4.70	Light greenish gray					●				○												I/S + Cham
	MA13-058	6.50-6.59	Grayish yellow green					●				◑												I/S + Cham
TKAD028	MA13-099	4.50-4.60	Pale greenish yellow					●			(?)	◑					○							I/S + Cham
TKAD029	MA13-095	3.60-3.70	Light yellowish orange		●										●									Non + Pl
Site B																								
TKAD016	MA13-034	2.02-2.13	Greenish gray							(?)	●							○						I/S + Py
	MA13-035	5.65-5.71	Pale greenish yellow					◑			●	(?)												I/S + Cham
	MA13-036	7.00-7.05	Yellowish gray					●	(?)	◑														Cham + Corr
TKAD025	MA13-039	5.50-5.60	Pale olive					●				○												I/S + Cham
	MA13-040	6.91-7.00	Pale olive	(?)				●	○															Cham + Corr
TKAD026	MA13-067	2.90-3.00	Light bluish gray					○			●						○							I/S + Cham
	MA13-068	3.60-3.68	Light greenish gray	○				●			(?)	●												I/S + Cham
	MA13-069	5.64-5.75	Light greenish gray					●			(?)	◑												I/S + Cham
TKAD012	MA13-062	2.81-2.90	Pale olive					○	●															Cham + Corr
	MA13-063	4.25-4.36	Light greenish yellow				○		●					○										Cham + Corr
	MA13-064	6.49-6.60	Greenish gray						●			(?)							○					Cham + Corr

Amounts indicated are major (●), minor (◑), and trace (○); uncertain identifications are indicated by (?)

Mnt = montmorillonite; Non = nontronite; Cld = Chloritoid; Clc = Clinochlore; Cham = chamosite; Corr = corrensite; Ali = aliettite; Rect = rectorite; I/S = illite/smectite; Ill = illite; Pg = paragonite; Ph = phillipsite; Pl = plagioclase; Qz = quartz; Py = pyrite; Mrc = marcasite; Hem = hematite; Ata = paratacamite(?); Anh = anhydrite; Brt = barite; Cel = celestine

Table 5.3. Continued

Location		Depth	Munsell	Smectite		Chlorite			Mixed Layer Clays				Illite		Feldspar	Non-Clay Minerals								Alteration
Drillhole	Sample	[mbsf]	Clay Color	Mnt	Non	Cld	Clc	Cham	Corr	Alie(?)	Rect	I/S	Ill	Pg	Pl	Qz	Py	Mrc	Hem	Ata(?)	Anh	Brt	Cel	Assmeblage
Site C																								
TKAD032	MA13-072	2.05-2.17	Yellowish gray		●																○			Mnt/Non + Pl
	MA13-073	3.90-4.00	Greenish gray		●				○										○		○			Non + Corr
	MA13-074	5.31-5.40	Grayish yellow		●				○												○			Non + Corr
	MA13-075	6.42-6.54	Greenish gray		●				○								○				(?)			Non + Corr
TKAD033	MA13-025	3.00-3.10	Dusky yellow		●										●		○				(?)			Mnt/Non + Pl
	MA13-026	4.76-4.88	Moderate brown		●		(?)								●				○					Mnt/Non + Pl
	MA13-027	7.30-7.40	Moderate brown				○		●						○				(?)					Cham + Corr
Site D																								
TKAD017	MA13-020	6.90-7.00	Yellowish gray	○							○	●	◑				◑				◑			I/S + Py
TKAD030	MA13-005	5.06-5.21	Grayish yellow		●						◑		○				○				○			I/S + Py
	MA13-006	6.45-6.60	Yellowish gray								●	◑	○						◑		◑			I/S + Py
TKAD018	MA13-014	3.00-3.10	Light grayish yellow	◑								●	○				○				○			I/S + Py
	MA13-015	5.00-5.10	Yellowish gray	○							○	●	○						○		○			I/S + Py
	MA13-016	6.60-6.71	Light grayish yellow	◑				○				●	◑						○		○			I/S + Cham
TKAD031	MA13-044	5.64-5.69	Grayish Yellow	○								●	○				(?)				○			I/S + Py
	MA13-045	6.60-6.67	Grayish Yellow	○								●	○				(?)				○			I/S + Py
Site E *(South)*																								
TKAD005	P020	20.55-20.67	Mod. greenish gray	(?)				●			●	(?)												I/S + Cham
TKAD003	P012	11.11-11.20	Light greenish gray	(?)				●				◑												I/S + Cham
	P013	13.40-13.50	Bluish white					●				●												I/S + Cham
	P014	16.41-16.50	Bluish white					●				◑												I/S + Cham
Site F *(West)*																								
TKAD007	P021	3.50-3.60	Light olive gray						●			(?)					○							I/S + Py
	P022	11.23-11.34	Bluish white					●			(?)	○												I/S + Cham
	P023	22.35-22.45	Pale greenish yellow					●				○	(?)											I/S + Cham
TKAD008	P025	7.50-7.56	Mod. reddish brown	○				◑	●										(?)					Cham + Corr
	P024	18.13-18.20	Mod. reddish brown		●														(?)					Mnt/Non + Pl

Amounts indicated are major (●), minor (◑), and trace (○); uncertain identifications are indicated by (?)

Mnt = montmorillonite; Non = nontronite; Cld = Chloritoid; Clc = Clinochlore; Cham = chamosite; Corr = corrensite; Ali = aliettite; Rect = rectorite; I/S = illite/smectite; Ill = illite; Pg = paragonite; Ph = phillipsite; Pl = plagioclase; Qz = quartz; Py = pyrite; Mrc = marcasite; Hem = hematite; Ata = paratacamite(?); Anh = anhydrite; Brt = barite; Cel = celestine

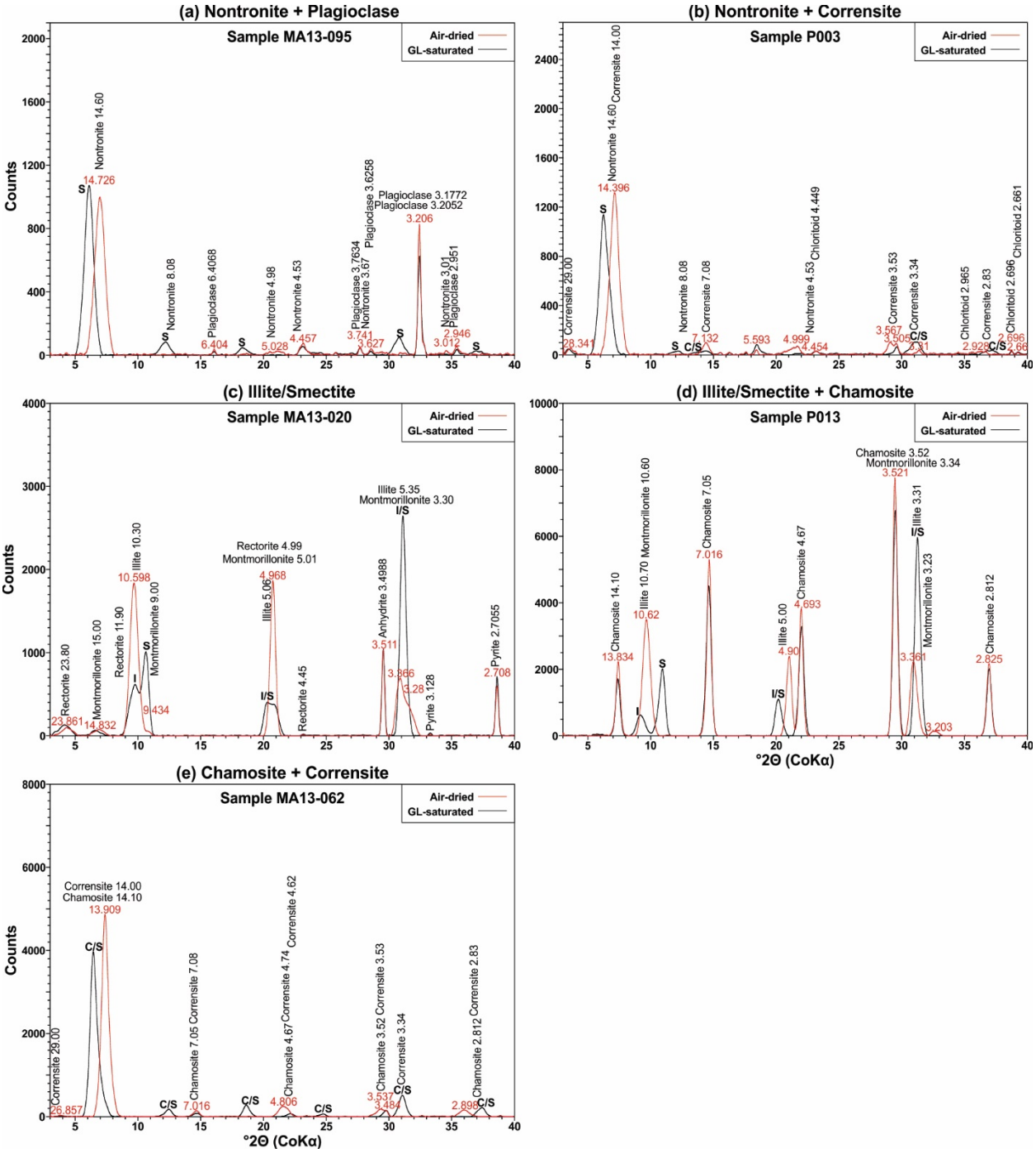


Fig. 5.11. Examples of XRD spectra of background-corrected air-dried (red) and glycol-saturated (black) samples showing the main alteration assemblages from the Tinakula deposit: (a) nontronite + plagioclase; (b) nontronite + corrensite; (c) illite/smectite + pyrite; (d) illite/smectite + chamosite; (e) chamosite + corrensite.

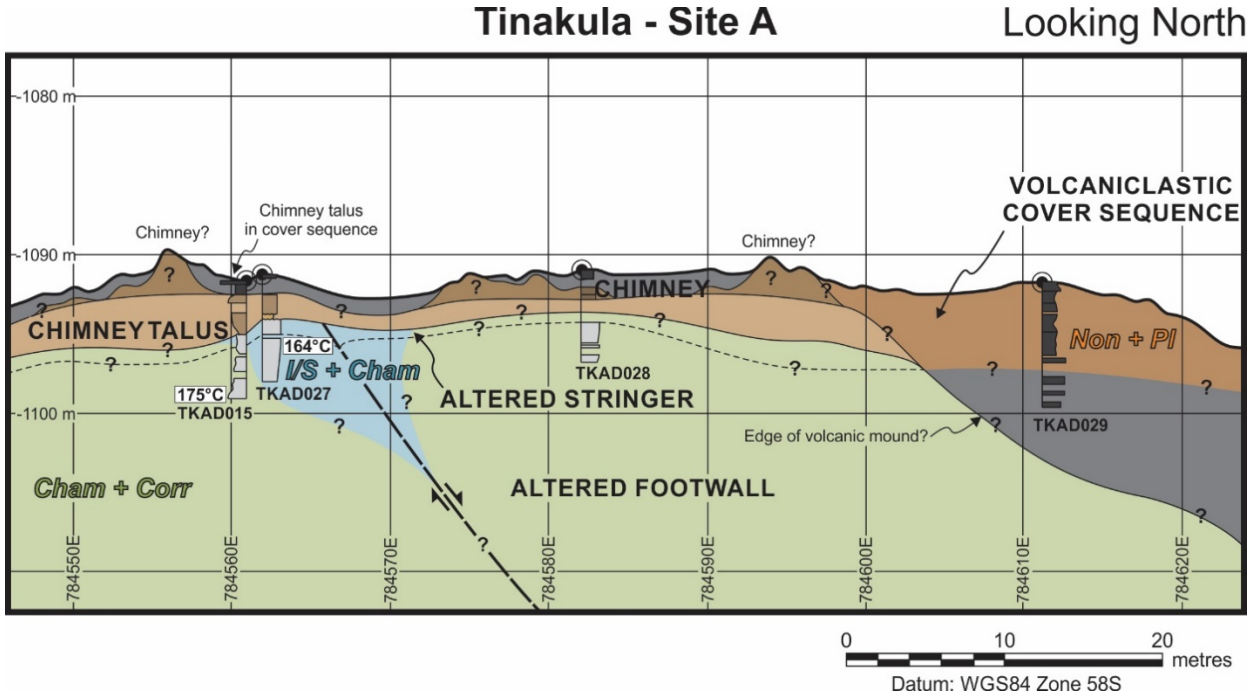


Fig. 5.12. East-west cross-section of the geology and alteration of Site A interpreted from drillcore and seafloor morphologies. Temperatures calculated from δ^{18}O-isotopes. Cham = chamosite; Corr = corrensite; I/S = illite/smectite; Non = nontronite; Pl = plagioclase.

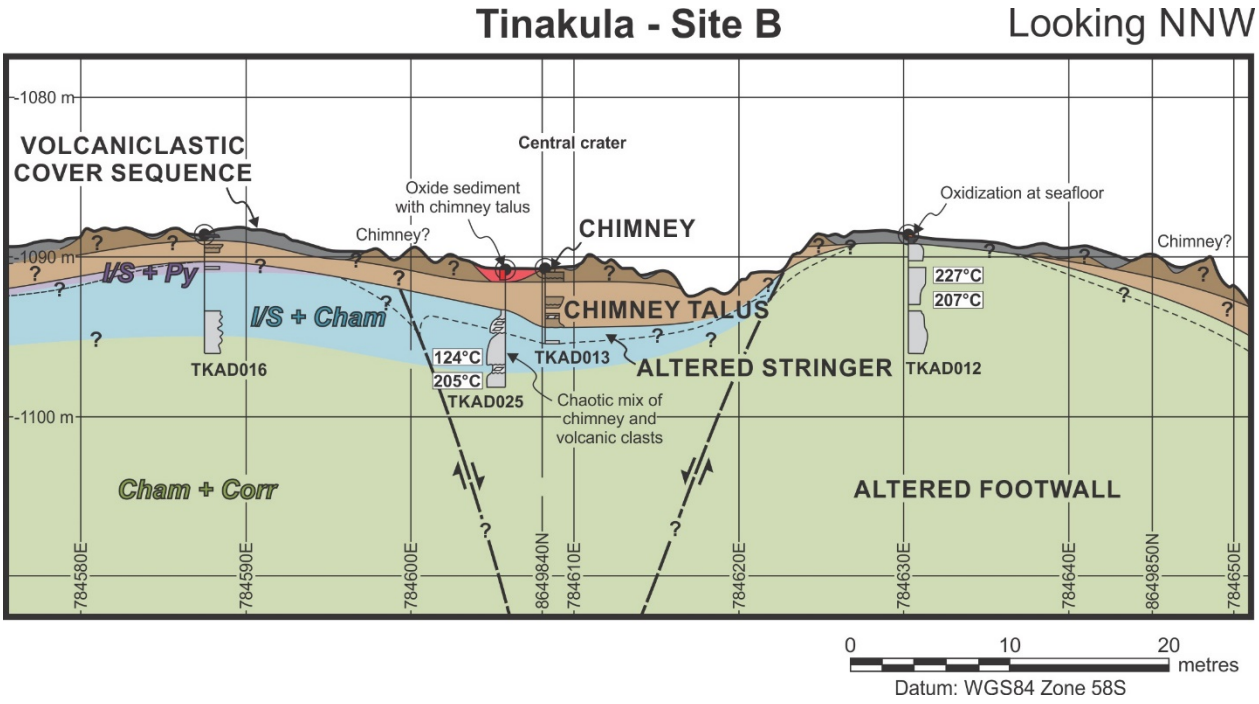


Fig. 5.13. ENE-WSW cross-section of the geology and alteration of Site B interpreted from drillcore and seafloor morphologies. Temperatures calculated from δ^{18}O-isotopes Cham = chamosite; Corr = corrensite; I/S = illite/smectite; Py = pyrite.

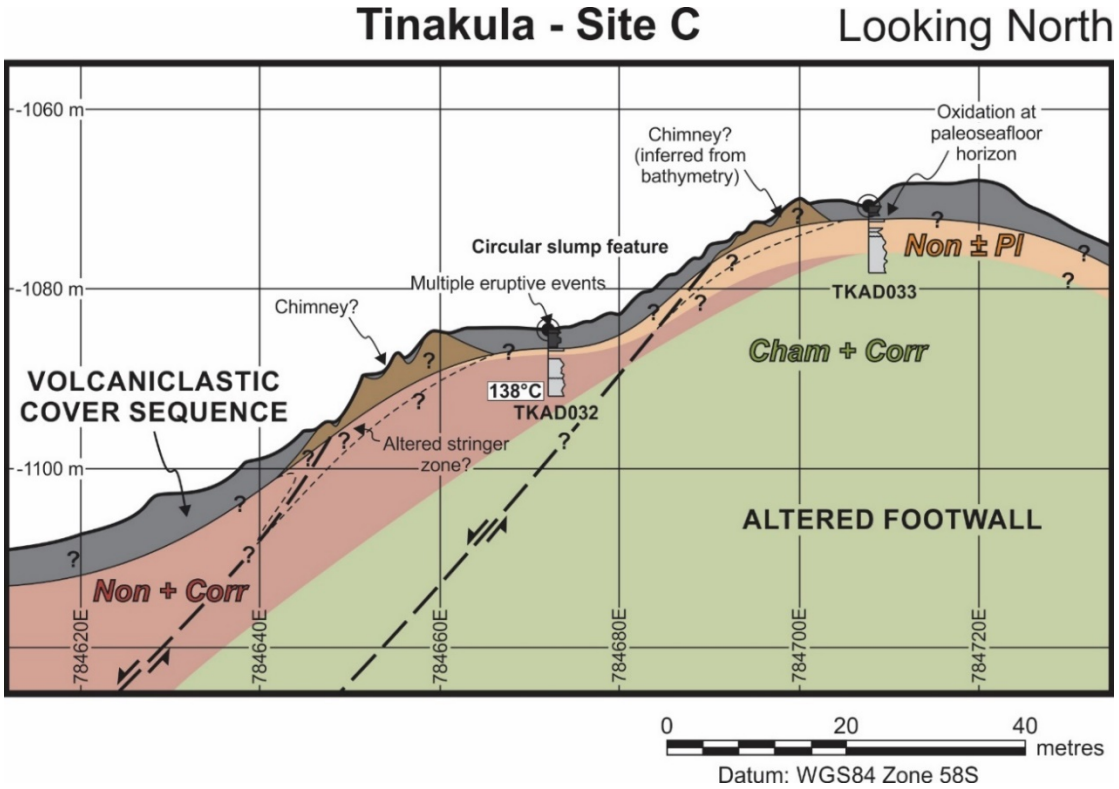


Fig. 5.14. East-west cross-section of the geology and alteration of Site C interpreted from drillcore and seafloor morphologies. Temperature calculated from δ^{18}O-isotopes Cham = chamosite; Corr = corrensite; Non = nontronite; Pl = plagioclase.

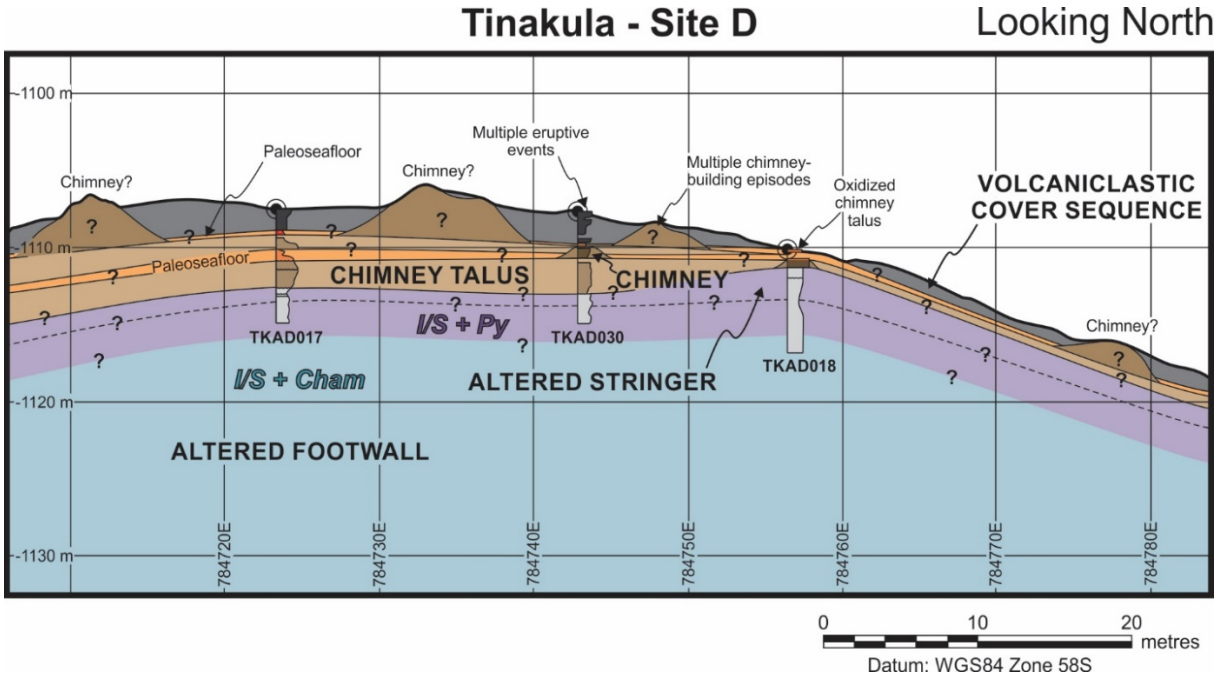


Fig. 5.15. East-west cross-section of the geology and alteration of Site D interpreted from drillcore and seafloor morphologies. Cham = chamosite; I/S = illite/smectite; Py = pyrite.

temperatures suggesting that argillic alteration is grading towards phyllic alteration. These variations are outlined in detail below for each drillhole according to site.

Site A

Drillhole *TKAD001* shows a distinct downhole change in alteration mineralogy (Table 5.3; Appendix P). Alteration of the cover sequence of the upper part of the drillhole is dominated by montmorillonite, transitioning to nontronite (Fe-rich smectite) at 10.2 mbsf associated with an increase in alteration intensity. Plagioclase of unknown composition is also present in the upper ~13 m of the drillhole, which may be primary igneous feldspar or part of the alteration assemblage. In the strongly-altered footwall section of the drillhole (below 14.0 mbsf), there is a clear downhole progression in alteration mineralogy. Chlorite-group minerals appear at ~14.8 mbsf with the appearance of minor amounts of chloritoid (14.8–15.8 mbsf) and mixed-layer chlorite-smectite (i.e., corrensite; 14.8–17.5 mbsf), followed by abundant chamosite from ~17.4 mbsf to the end of the drillhole. The occurrence of chamosite corresponds with mixed-layer I/S, which contains an increasing proportion of illite downhole, from 0.6 I/S to 0.85 I/S. Discrete illite also occurs below ~18.4 mbsf. Non-clay minerals include minor hematite (at 14.0 mbsf), anhydrite (at 17.4 mbsf), silica (at 17.9 mbsf), and possible pyrite (at 19.1 and 20.8 mbsf). *TKAD015* is dominated by mixed-layer I/S in the upper footwall, with minor discrete montmorillonite and illite at ~3.5 mbsf. The I/S clays show a downhole decrease in the proportion of illite, ranging from 0.9 I/S at 3.5 mbsf to 0.75 I/S at 7.2 mbsf. Chamosite is also present, with increasing relative abundance downhole. Possible atacamite (minor) is present near the top of the drillhole. *TKAD027* is also dominated with mixed-layer I/S in the upper footwall, with a downhole decrease in the proportion of illite from 0.8 I/S at 4.6 mbsf to 0.75 I/S at 6.5 mbsf. Similarly, the proportion of chamosite increases downhole. Minor amounts of possible paratacamite and Ba-rich sulfates (barite and Ba-celestine) are present at the top of the drillhole at 2.5 mbsf. *TKAD028* reveals abundant chamosite, minor mixed-layer 0.6 I/S, and possible minor pyrite at 4.5 mbsf. *TKAD029* contains abundant montmorillonite and plagioclase at 3.6 mbsf, similar to the mineralogy of the cover sequence in drillhole TKAD001.

Site B

TKAD016 shows a downhole trend in mineralogy, beginning with abundant rectorite, minor marcasite, and possible aliettite (minor) at 2.0 mbsf (Table 5.3; Appendix P). At 5.7 mbsf, there is abundant chamosite, rectorite, and 0.6 I/S. At 7.0 mbsf, abundant chamosite, possible corrensite, and aliettite are present. *TKAD025* contains abundant chamosite and minor 0.8 I/S at 5.5 mbsf. At 7.0 mbsf, the mineralogy consists of abundant chamosite, possible corrensite, and possible montmorillonite (very minor). *TKAD026* consists of abundant rectorite, minor chamosite, and minor pyrite at 2.9 mbsf. At 3.6 mbsf, the mineralogy consists of abundant 0.6 I/S, possible montmorillonite, and an increasing proportion of chamosite. At 5.6 mbsf, the mineralogy is dominated by chamosite, with minor 0.7 I/S (downhole-increasing illite). *TKAD012* is dominated by corrensite at 2.8 mbsf, with minor end-member chamosite. At 4.2 mbsf, the mineralogy consists of corrensite, minor chloritoid, and very minor illite. At 6.4 mbsf, the mineralogy is dominated entirely by corrensite, with possible I/S and hematite (very minor).

Site C

TKAD032 is dominated by corrensite over the entire depth with possible minor endmember nontronite and anhydrite (Table 5.3; Appendix P). There is minor hematite at 3.9 mbsf, and pyrite at 6.4 mbsf. *TKAD033* is dominated by plagioclase, with minor nontronite and pyrite, and possible anhydrite (very minor) at 3.9 mbsf. The relative proportion of nontronite increases slightly at 4.8 mbsf, along with the appearance of hematite rather than pyrite. Very minor clinochlore may also be present. The deepest sample at 7.3 mbsf is dominated by mixed-layer chlorite-smectite, with minor plagioclase, and possible hematite (very minor).

Site D

Site D is distinguished by the presence of minor end-member illite in all of the samples. *TKAD017* consists of abundant 0.7 I/S, minor rectorite, and minor end-member illite and montmorillonite at 6.9 mbsf (Table 5.3; Appendix P). Anhydrite and pyrite are also present. *TKAD030* represents the gradational stringer zone between massive sulfide mineralization and the altered footwall. At 5.1

mbsf, the mineralogy is dominated by nontronite, with minor rectorite, and very minor end-member illite. Minor anhydrite and possible minor pyrite is also present. The amount of illite increases downhole; at 6.5 mbsf, the mineralogy is dominated by rectorite, 0.75 I/S and end-member illite, with minor anhydrite and hematite. *TKAD018* has an alteration mineralogy consisting of 0.7 I/S, minor discrete montmorillonite and illite, and anhydrite and pyrite at 3.0 mbsf. At 5.0 mbsf, there is a slight decrease in the proportion of illite to 0.65 I/S, along with the addition of minor rectorite. Here, pyrite has oxidized to hematite. At 6.6 mbsf, the mineralogy is dominated by discrete illite and montmorillonite, with minor 0.75 I/S, anhydrite, and hematite. *TKAD031* has a similar mineral assemblage at 5.6 mbsf and 6.6 mbsf, dominated by 0.7 I/S, with minor discrete montmorillonite and illite, as well as minor anhydrite.

Site E

TKAD005 is dominated by chamosite, with minor rectorite and 0.7 I/S at a depth of 20.6 mbsf, with possible minor discrete montmorillonite (Table 5.3; Appendix P). *TKAD003* is also dominated by chamosite over the sample interval, with minor I/S with slightly increasing proportions of illite, from 0.7 I/S at 11.1 mbsf to 0.75 I/S at 16.4 mbsf.

Site F

TKAD007 is dominated by corrensite, with minor pyrite, and possible minor 0.7 I/S at a depth of 3.5 mbsf (Table 5.3; Appendix P). At 11.2 mbsf, the alteration assemblage is dominated by chamosite, with minor 0.75 I/S and possible rectorite. At 22.4 mbsf, chamosite remains the dominant phase, with minor 0.75 I/S and possible discrete illite (minor). *TKAD008* is also dominated by corrensite at a depth of 7.5 mbsf, with discrete chamosite, and possible minor discrete montmorillonite. At 18.1 mbsf, the mineralogy is dominated by nontronite. Minor amounts of hematite may be present in both of these samples.

5.5.3. Immobile and mobile element geochemistry

Representative whole-rock geochemical analyses of altered volcaniclastic rocks from the shallow footwall of the Tinakula deposit are shown in Table 5.5, with associated alteration assemblages (full results in Suppl. Table K1; downhole changes outlined in Appendix M). Variations in selected immobile and mobile elements for each alteration assemblage are shown in Fig. 5.16. Immobile elements cover a narrow range, with average concentrations of 99.78 ppm Zr, 24.57 ppm Y, and 19.08 ppm Sc (n = 47). Concentrations of Ba, Si, Al, Fe, S, Mg, Ca, Na and K show significant variation, consistent with their mobility during hydrothermal alteration (e.g., Humphries and Thompson, 1978). Concentrations of Ba and CaO likely reflect the abundance of barite and anhydrite/gypsum, respectively, rather than mass balance changes of silicates. In addition, concentrations of $Fe_2O_{3(T)}$ and $S_{(T)}$ are associated with pyrite mineralization, which is most abundant in the illite/smectite + pyrite alteration assemblage. The whole-rock geochemistry reveals alteration trends associated with Na-metasomatism, Na-loss, and K-metasomatism (Fig. 5.17a,b). The alteration box plot in Figure 5.17c after Large et al. (2001) plots the Hashimoto alteration index (AI) and the chlorite-carbonate-pyrite index (CCPI) with a box for the least-altered samples, and nodes for the main alteration minerals. At Tinakula, anhydrite replaces carbonate as the main source for Ca in the samples; as a result, intensely-altered samples with varying proportions of anhydrite may plot within the least-altered field. Illite-rich and chlorite-rich alteration assemblages are better distinguished by relative proportions of MgO, Na_2O, K_2O, and Al_2O_3 as shown in the triangular diagram in Figure 5.18a,b. Note that there is significant overlap between smectite-rich and chlorite-rich samples, and these cannot be easily distinguished from one another. In these diagrams, increasing alteration intensity is reflected by increasing distance from the unaltered precursor composition. This diagram also highlights the transitional nature of alteration assemblages from illite/smectite + pyrite to illite/smectite + chamosite to chamosite + corrensite, and may provide a useful tool for exploration in intermediate volcanic environments where there is abundant anhydrite/gypsum and pyrite associated with alteration.

In general, REEs are considered immobile during hydrothermal alteration, particularly the HREEs (e.g., Bau, 1991). The chondrite-normalized plot for the altered volcaniclastic rocks and the unaltered basaltic-andesitic precursors are shown in Figure 5.19. All alteration assemblages show

Table 5.5. Representative whole-rock geochemical analyses of altered volcaniclastic rocks from the Tinakula deposit with associated alteration assemblages, normalized to 100% LOI-free

			MA13-026-C	MA13-073-C	MA13-006-C	MA13-088-C	MA13-036-C
			TKAD033	TKAD032	TKAD030	TKAD001	TKAD016
Element	**D.L.**	**Method**	Mnt/Non ± Pl	Non + Corr	I/S + Py	I/S + Cham	Cham + Corr
SiO_2 - %	0.01	FUS-ICP	53.95	51.72	41.65	52.34	35.27
TiO_2	0.001	FUS-ICP	1.592	1.718	2.467	1.983	1.804
Al_2O_3	0.01	FUS-ICP	22.48	21.93	27.00	23.80	22.85
$Fe_2O_{3(T)}$	0.01	FUS-ICP	7.69	13.69	20.24	8.99	23.18
MnO	0.001	FUS-ICP	0.041	0.045	0.010	0.253	0.079
MgO	0.01	FUS-ICP	2.72	7.65	0.63	6.42	9.11
CaO	0.01	FUS-ICP	6.06	0.65	0.69	1.16	3.43
Na_2O	0.01	FUS-ICP	4.97	2.34	1.50	1.05	1.33
K_2O	0.01	FUS-ICP	0.32	0.24	5.72	3.94	2.85
P_2O_5	0.01	FUS-ICP	0.16	0.04	0.07	0.06	0.11
$S_{(T)}$	0.01	CS	0.56	7.00	13.30	2.73	12.70
Cu - ppm	1	TD-ICP*	83	237	128	141	2250
Zn	1	TD-ICP*	117	1080	135	928	120
Ag	0.3	TD-ICP	0.6	3.1	1.3	0.6	0.6
As	0.5	INAA	11.8	56.3	226.0	24.5	28.4
Bi	0.1	FUS-MS	< 0.1	< 0.1	< 0.1	< 0.1	< 0.1
Cd	0.5	TD-ICP	< 0.5	1.4	< 0.5	2.1	< 0.5
Ga	1	FUS-MS	22	17	28	23	22
Ge	0.5	FUS-MS	2.3	0.9	< 0.5	1.0	< 0.5
Au - ppb	2	INAA	< 2	42	94	82	51
Hg	5	1G	82	902	14	298	0.6
In - ppm	0.1	FUS-MS	< 0.1	0.3	0.3	0.3	< 0.2
Sb	0.2	INAA	0.5	10.4	3.4	1.3	< 3
Se	3	INAA	< 3	< 3	< 3	< 3	1
Sn	1	FUS-MS	< 1	< 1	< 1	1	0.34
Tl	0.05	FUS-MS	0.66	1.14	0.40	0.76	30
Ir	5	INAA	< 5	< 5	< 5	< 5	< 5
Mo	2	FUS-MS	< 2	12	8	< 2	7
Co	1	FUS-MS	9	27	11	17	17
Cr	5	INAA	< 5	26	< 5	13	< 5
Ni	1	TD-ICP	8	24	5	7	6
Sc	0.1	INAA	28.2	24.8	32.6	28.8	21.2
V	5	FUS-ICP	361	316	350	360	283
Ba	2	FUS-ICP	8162	7194	2228	1559	395
Pb	3	TD-ICP	39	522	40	30	< 3
Rb	1	FUS-MS	5	4	64	56	28
Cs	0.1	FUS-MS	0.4	0.2	0.3	0.3	0.2
Sr	2	FUS-ICP	414	202	234	88	58
Zr	1	FUS-ICP	884	91	163	156	139
Hf	0.1	FUS-MS	2.2	2.1	3.6	3.9	3.3
Nb	0.2	FUS-MS	3.8	3.8	6.6	6.7	5.8
Ta	0.01	FUS-MS	0.18	0.18	0.43	0.36	0.22
Th	0.05	FUS-MS	0.78	0.67	1.25	1.35	1.03
U	0.01	FUS-MS	4.68	13.20	16.6	12.90	8.15
Be	1	FUS-ICP	2	2	< 1	1	< 1
W	0.5	FUS-MS	1.1	0.6	178.0	2.8	124.0
Y	0.5	FUS-MS	21.2	20.8	38.4	33.3	37.1
La	0.05	FUS-MS	6.18	4.98	75.50	14.90	15.20
Ce	0.05	FUS-MS	14.40	12.10	157.00	31.90	33.90
Pr	0.01	FUS-MS	2.17	1.76	18.80	4.37	4.45
Nd	0.05	FUS-MS	9.93	8.86	74.00	19.20	20.10
Sm	0.01	FUS-MS	2.89	2.89	13.60	4.89	5.23
Eu	0.005	FUS-MS	1.40	1.41	7.58	2.53	2.67
Gd	0.01	FUS-MS	3.36	3.25	8.24	5.58	5.90
Tb	0.01	FUS-MS	0.61	0.6	1.13	0.95	1.01
Dy	0.01	FUS-MS	3.82	3.91	7.48	6.12	6.61
Ho	0.01	FUS-MS	0.78	0.77	1.45	1.31	1.37
Er	0.01	FUS-MS	2.42	2.25	4.50	3.77	4.11
Tm	0.005	FUS-MS	0.357	0.333	0.656	0.545	0.608
Yb	0.01	FUS-MS	2.34	2.27	4.39	3.39	4.12
Lu	0.002	FUS-MS	0.361	0.365	0.726	0.521	0.655

*O.L. = 4acid ICP-OES; D.L. = detection limit; Cham = chamosite; Corr = corrensite; I/S = illite/smectite; Mnt = montmorillonite; Non = nontronite; Pl = plagiolcase; Py = pyrite

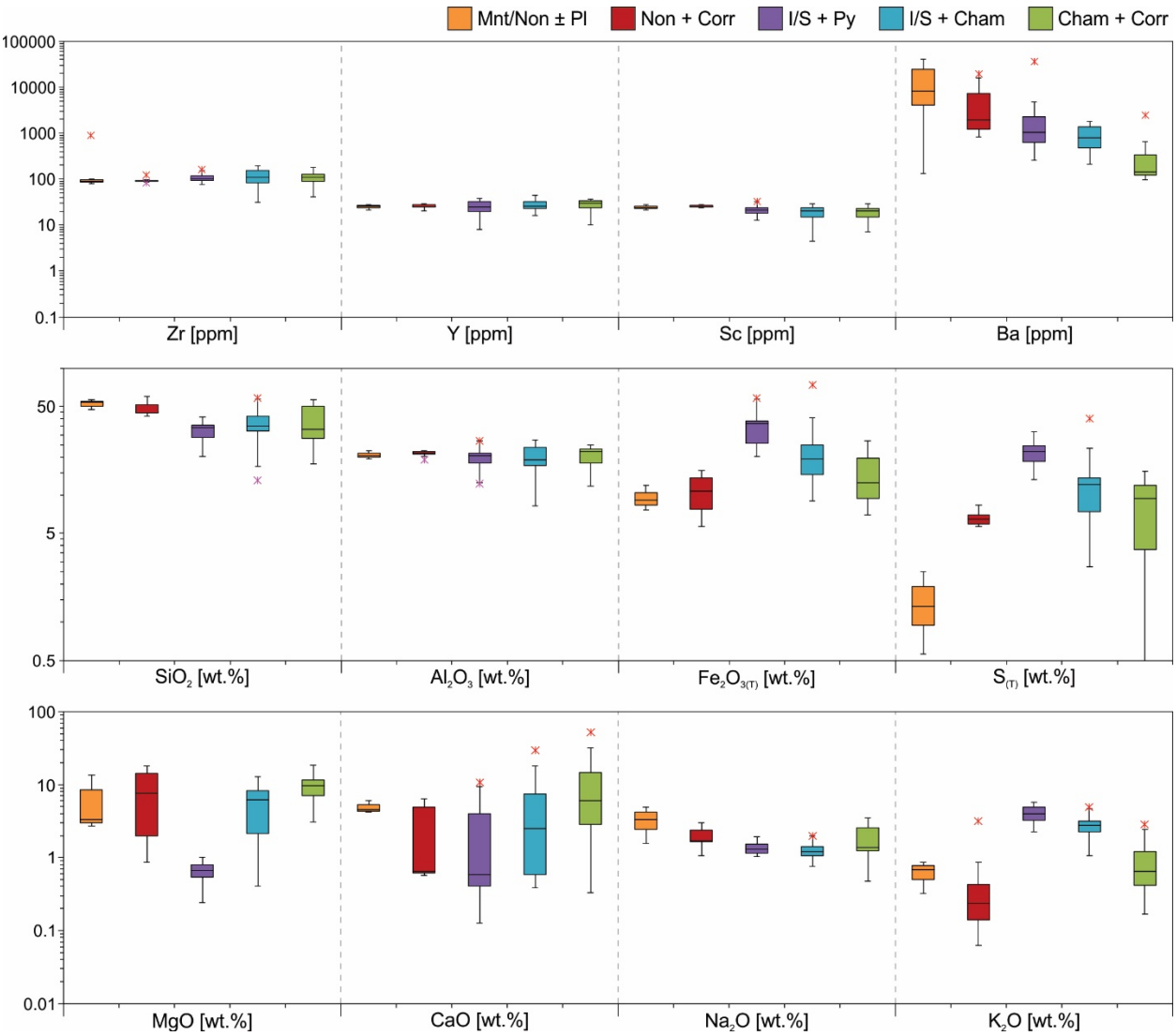


Fig. 5.16. Box plots of selected whole-rock immobile and mobile elements associated with each alteration assemblage (full data in Appendix K). The top of the box represents the 75th percentile, the bottom of the box represents the 25th percentile, the central line represents the median, the bars represent the range of the data, and outliers are indicated by stars (*). Cham = chamosite; Corr = corrensite; I/S = illite/smectite; Mnt = montmorillonite; Non = nontronite; Pl = plagioclase; Py = pyrite.

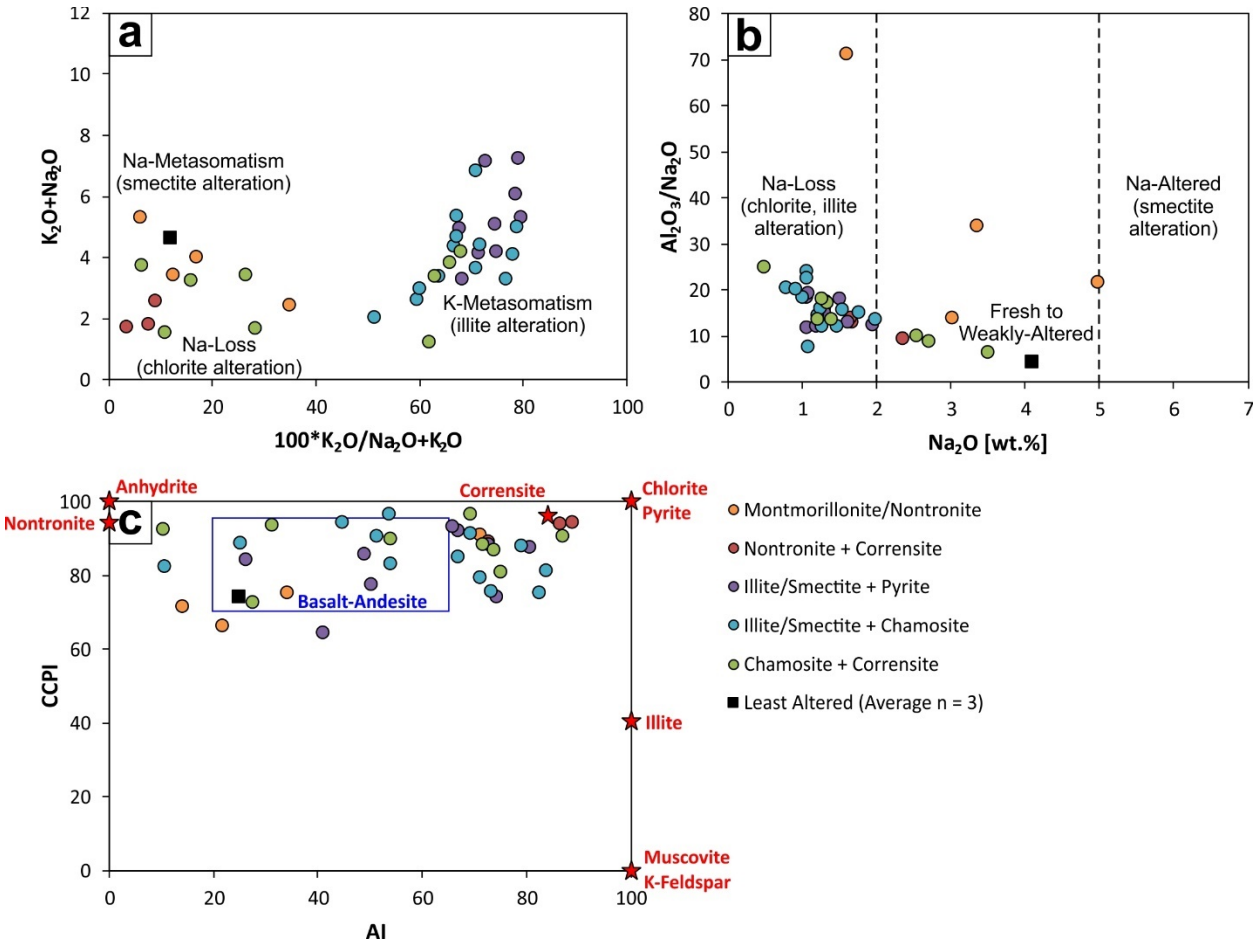


Fig. 5.17. Whole-rock geochemistry associated with hydrothermal alteration: (a) modified Hughes (1973) diagram outlining fresh basaltic-andesite, Na-loss associated with chlorite alteration, Na-metasomatism associated with smectite alteration, and K-metasomatism associated with illite alteration; (b) Al_2O_3/Na_2O versus Na_2O plot distinguishing fresh to weakly-altered rocks from smectite-altered rocks (Na-gain) and illite-chlorite-altered rocks (Na-loss) after Ruks et al. (2006); and(c) the alteration box plot with the Hashimoto alteration index (AI = $100*[K_2O+MgO]/[K_2O+MgO+CaO+Na_2O]$; Ishikawa et al., 1976) versus the chlorite-carbonate-pyrite index (CCPI=$100*[Fe_2O_{3T}+MgO]/[Fe_2O_{3T}+MgO+K_2O+Na_2O]$) after Large et al. (2001) with the least-altered field for basalt and andesite and the main alteration minerals and anhydrite. Note that overlapping mineralogy and the presence of anhydrite may cause intensely-altered samples to plot in the least-altered field.

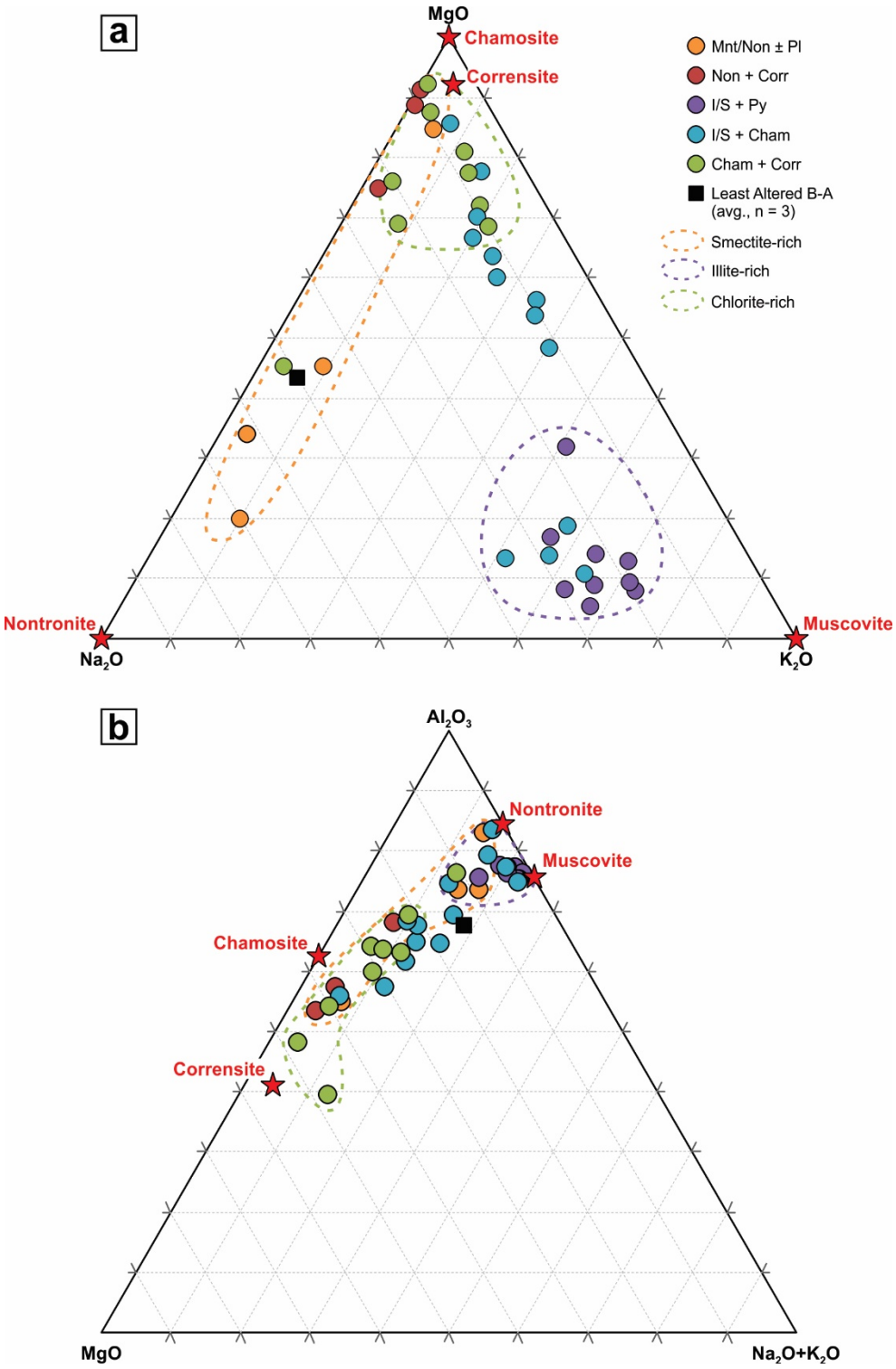


Fig. 5.18. Ternary plots of whole-rock geochemistry distinguishing alteration types: (a) MgO-Na_2O-K_2O diagram distinguishing chlorite + smectite from illite alteration (b) Al_2O_3-MgO-Na_2O+K_2O diagram distinguishing chlorite from illite alteration (modified from MacDonald et al., 1996). B-A = basaltic andesite; Cham = chamosite; Corr = corrensite; I/S = illite/smectite; Non = nontronite; Pl = plagioclase; Py = pyrite.

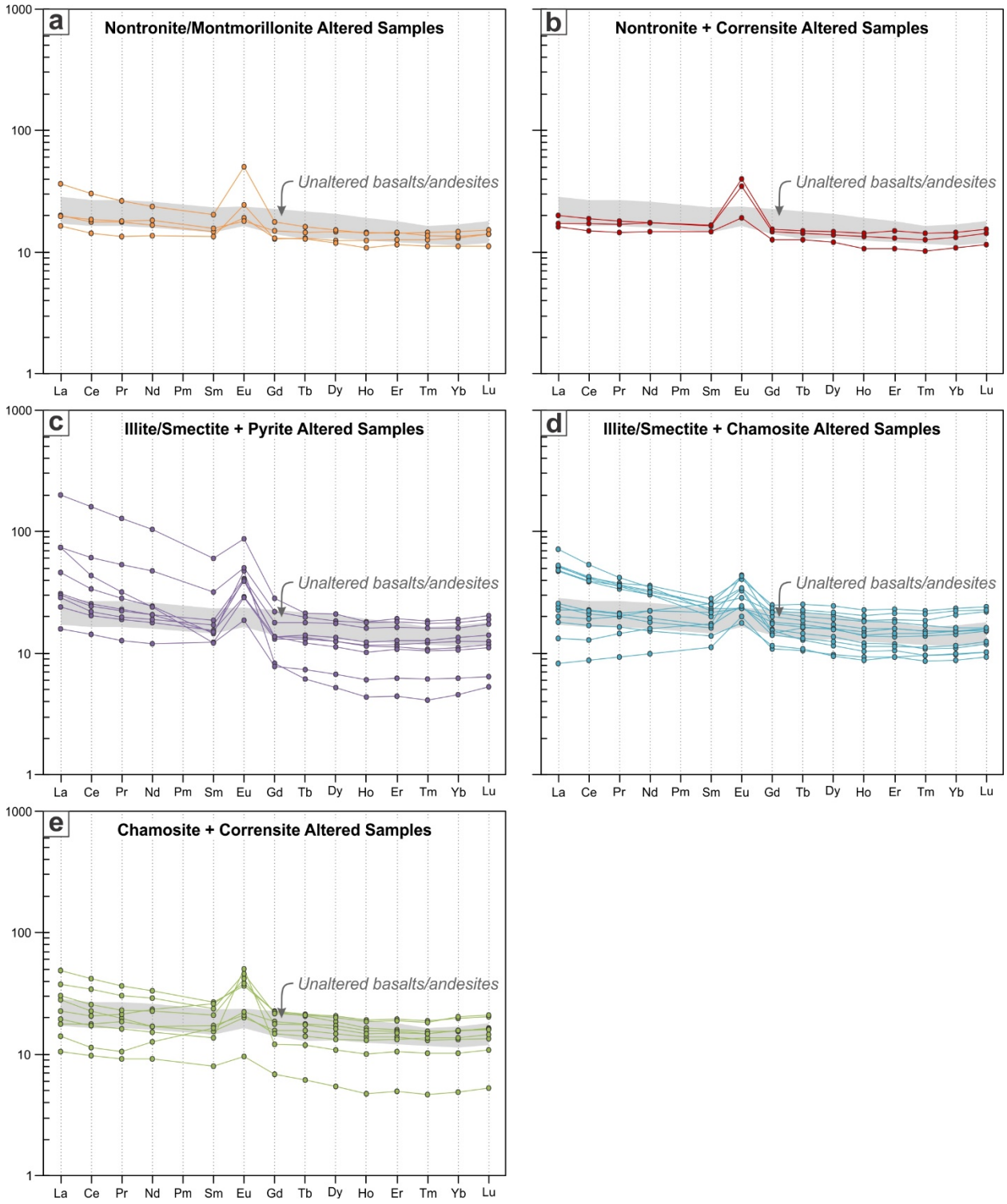


Fig. 5.19. Chondrite-normalized REE plot (after Boynton, 1984) of different alteration assemblages compared to unaltered basalts/andesites (Fig. 3.18): (a) nontronite/montmorillonite altered samples with REE depletion and flat profiles; (b) nontronite + corrensite altered samples with REE depletion and flat profiles; (c) illite/smectite + pyrite altered samples with LREE enrichment in some samples and downwards-sloping REE profiles; (d) illite/smectite + chamosite

altered samples with moderate LREE enrichment in some samples and flat to downward-sloping profiles; (e) chamosite + corrensite altered samples with slight LREE enrichment in most samples and slightly downward-sloping profiles. All alteration types are associated with pronounced positive Eu anomalies.

pronounced positive Eu anomalies. Smectite-rich assemblages (nontronite/montmorillonite and nontronite + corrensite) show slight REE depletion relative to unaltered basaltic-andesites and have flat profiles. The I/S + pyrite assemblage shows significant LREE enrichment in some samples and downwards-sloping profiles, whereas the chamosite-rich assemblages (I/S + chamosite and chamosite + corrensite) show moderate LREE enrichment in some samples and flat to down-ward-sloping profiles. These data show the strong mobility of REE during alteration of the volcanic rocks and the mobilization of Eu in the reduced hydrothermal fluid. In particular, LREE appear to be mobile in higher-temperature assemblages.

5.5.4. Mass balance changes

Unaltered volcanic rocks from the Tinakula deposit range in composition from basaltic-andesites and andesite to dacites, with basaltic-andesites most abundant near the volcanic cones (described in *Chapter 3*). In the immobile element classification plot of Nb/Y versus Zr/Ti (Fig. 5.20, modified by Pearce, 1996) altered volcanic rocks plot closest to the unaltered basalt-basaltic andesite compositions, suggesting a single basaltic-andesite immobile element precursor. In order to determine the composition of the precursor for the altered volcanic rocks, whole-rock geochemical data is compared to least-altered volcanic rocks in Figure 5.21. Least-altered volcanic rocks were identified through petrography to select samples with no alteration minerals or textures (Appendix D), followed by whole-rock geochemistry to select samples with LOI values <1.2%, low base metal values, and minimal Na_2O depletions (Table 5.6). The three unaltered basaltic-andesites lie on linear trends in TiO_2/Zr, TiO_2/Al_2O_3, and Nb/Zr plots (Fig. 5.21), and these linear trends demonstrate the immobility of these elements during hydrothermal alteration (e.g., Maclean, 1990). Mass balances were calculated for all alteration assemblages from the footwall of the Tinakula deposit following the single precursor method of MacLean and Barrett (Maclean, 1990; Maclean and Barrett, 1993; Barret and MacLean, 1994a, 1994b, 1999), using the average concentrations of the three unaltered samples as the precursor value. In this method, the displacement of immobile elements in altered rocks from the least-altered precursor is proportional to the mass change (Maclean, 1990). The least-mobile element Zr (avg. 89 ppm) was used for calculation of the enrichment factor (EF) as follows:

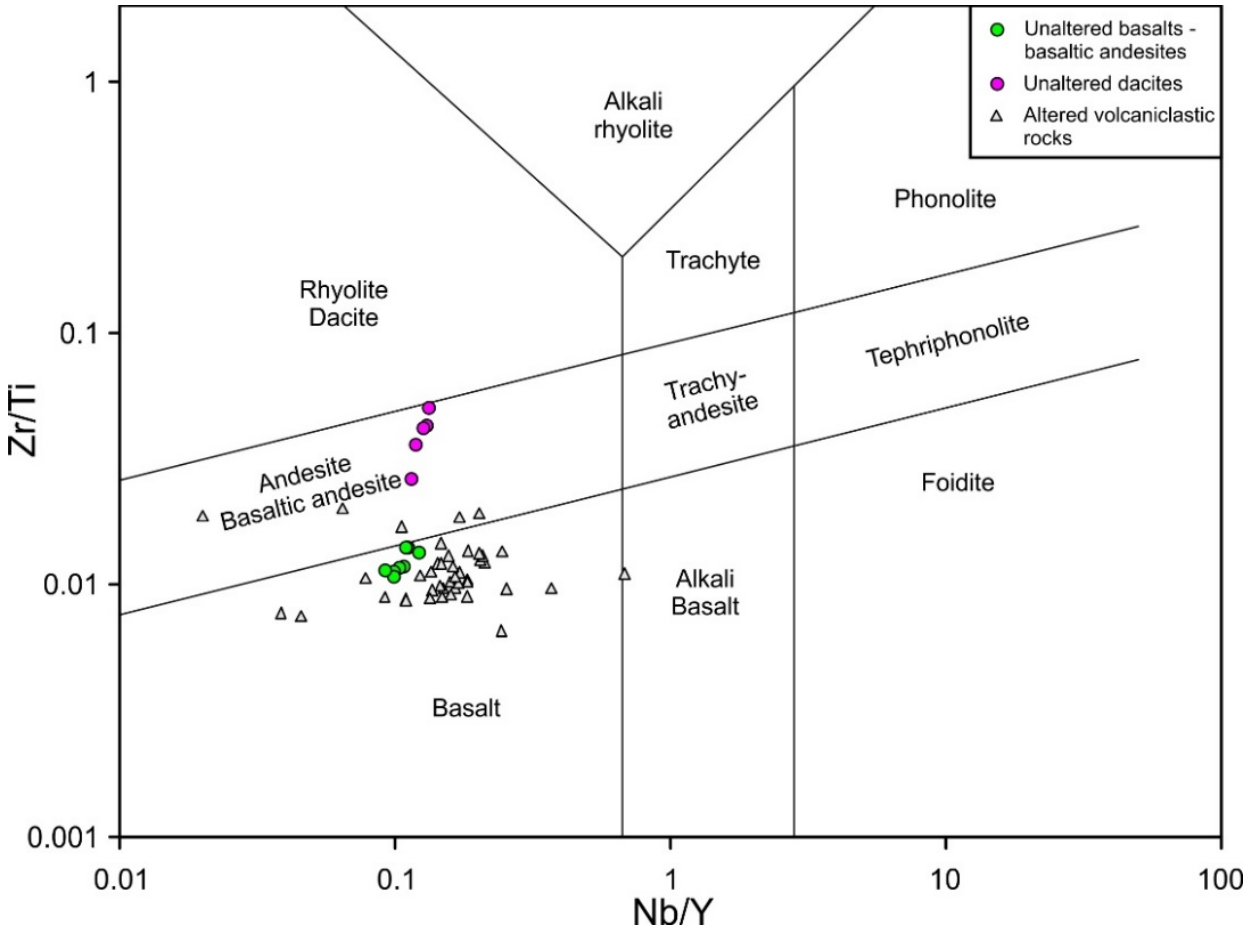


Fig. 5.20. Immobile element Nb/Y vs. Zr/Ti classification plot (modified by Pearce, 1996) of whole-rock geochemical data, with altered samples plotting near unaltered basalts–basaltic andesites; note that all samples plot in less felsic fields due to high Ti contents. These plots are consistent with a basaltic-andesite precursor for all altered samples.

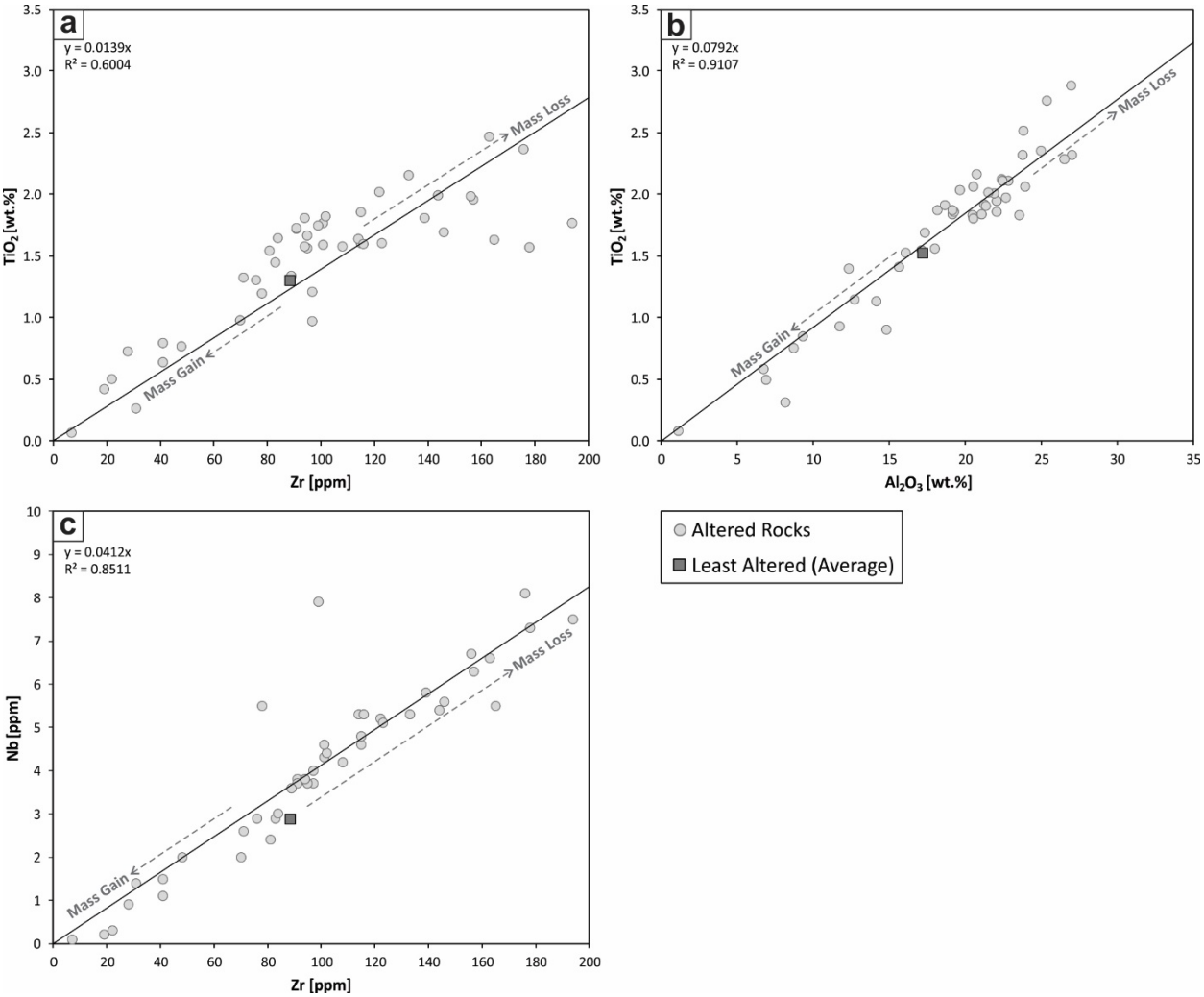


Fig. 5.21. Immobile element ratios of altered volcanic rocks and the least-altered precursor (average of three samples) showing linear trends with relative mass gains and losses.

$$EF = Zr_{precursor}/Zr_{altered\ sample}$$

(Equation 3)

The reconstructed composition (RC) of the altered samples was calculated for each element (normalized to 100% volatile free):

$$RC = EF \times C_{altered\ sample}$$

(Equation 4)

where $C_{altered\ sample}$ is the elemental concentration of a given element of the altered sample in wt.%, ppm, or ppb. Finally, the mass change (MC) for each element in each sample was calculated by subtracting the precursor value of that element from the reconstructed composition as follows:

$$MC = RC - C_{precursor}$$

(Equation 5)

where $C_{precursor}$ is the concentration of a given element in the unaltered sample in wt.%, ppm, or ppb. Full results of mass changes for each element are in Suppl. Table K2. The largest mass changes at Tinakula are associated moderate to intense alteration, with changes associated with depth (Figs. 5.22 and 5.23) and with alteration mineral assemblage (Table 5.7; Fig. 5.24). Titanium is conserved in all alteration assemblages. The mass changes of major elements for each mineral assemblage are outlined below:

(1) Montmorillonite/nontronite ± plagioclase alteration is associated with Si and Na losses in smectite-rich samples; Si gains with no Na change in plagioclase-rich samples; Ca losses in all samples; no gains in Al or Fe (either conserved or lost); and no change in K;

(2) Nontronite + corrensite alteration is associated with Si, Ca and Na losses, Mg gains, no losses of Al or Fe (either conserved or gained), and no change in K;

(3) Illite/smectite + pyrite alteration is associated with losses in Si, Mg, Na, and Ca, and gains in both Fe (due to pyrite) and K;

(4) Illite/smectite + chamosite alteration is associated with Si, Na, and K losses, and mixed gains and losses in Fe and Mg, with Mg losses when I/S is more abundant than chamosite, and Fe losses when I/S is in equal proportion to chamosite;

Table 5.6. Whole-rock geochemistry of the least-altered volcanic rocks (basaltic-andesites)

	D.L.	Method	GMA13_057	P0016	P0040	Average
SiO_2 - %	0.01	FUS-ICP	54.56	53.22	55.40	54.39
TiO_2	0.001	FUS-ICP	1.29	1.28	1.31	1.30
Al_2O_3	0.01	FUS-ICP	17.38	17.07	17.37	17.27
$Fe_2O_{3(T)}$	0.01	FUS-ICP	9.39	11.06	9.50	9.98
MnO	0.001	FUS-ICP	0.212	0.188	0.168	0.189
MgO	0.01	FUS-ICP	3.99	3.90	2.84	3.57
CaO	0.01	FUS-ICP	8.29	8.57	8.63	8.50
Na_2O	0.01	FUS-ICP	4.20	4.02	4.05	4.09
K_2O	0.01	FUS-ICP	0.55	0.52	0.60	0.55
$S_{(T)}$	0.01	CS	0.012	0.031	0.022	0.022
LOI		FUS-ICP	0.84	0.15	1.14	0.71
A.I.			26.63	25.96	21.30	
Al/Na			2.95	3.03	3.06	
Cu - ppm	1	TD-ICP*	86	95	39	73
Zn	1	TD-ICP*	79	86	128	98
Ag	0.3	TD-ICP	<0.3	<0.3	<0.3	<0.3
As	0.5	INAA	2.4	2.6	<0.5	1.75
Bi	0.1	FUS-MS	<0.1	<0.1	<0.1	<0.1
Cd	0.5	TD-ICP	<0.5	<0.5	<0.5	<0.5
Ga	1	FUS-MS	17	17	17	17
Ge	0.5	FUS-MS	1.2	1.1	1.5	1.3
Hg - ppb	5	1G	11	6	10	9
In - ppm	0.1	FUS-MS	0.1	0.1	0.1	0.1
Sb	0.2	INAA	0.6	0.5	0.5	0.5
Se	3	INAA	<3	<3	<3	<3
Sn	1	FUS-MS	7	7	7	7
Tl	0.05	FUS-MS	0.08	<0.05	0.09	0.07
Au - ppb	2	INAA	<2	<2	<2	<2
Ir - ppm	5	INAA	2.5	2.5	2.5	2.5
Mo	2	FUS-MS	<2	<2	<2	<2
Co	1	FUS-MS	26	26	18	23
Cr	5	INAA	<5	<5	15	7
Ni	1	TD-ICP	10	9	5	8
Sc	0.1	INAA	26.6	23.9	24.0	24.8
V	5	FUS-ICP	354	353	347	351
Rb	1	FUS-MS	6	6	7	6
Cs	0.1	FUS-MS	0.2	0.1	0.2	0.2
Sr	2	FUS-ICP	278	278	278	278
Ba	2	FUS-ICP	105	107	112	108
Pb	3	TD-ICP	<3	<3	<3	<3
Zr	1	FUS-ICP	90	87	89	89
Hf	0.1	FUS-MS	2.0	2.0	2.0	2.0
Nb	0.2	FUS-MS	2.9	2.9	2.8	2.9
Ta	0.01	FUS-MS	0.19	0.17	0.18	0.18
Th	0.05	FUS-MS	0.63	0.66	0.75	0.68
U	0.01	FUS-MS	0.28	0.32	0.55	0.38
Be	1	FUS-ICP	<1	<1	<1	<1
Br	0.5	INAA	<0.5	<0.5	4.2	1.6
W	0.5	FUS-MS	<0.5	1.2	<0.5	0.57
Y	0.5	FUS-MS	28.1	29.2	30.4	29.2
La	0.05	FUS-MS	6.80	6.61	7.25	6.89
Ce	0.05	FUS-MS	15.6	15.9	16.8	16.1
Pr	0.01	FUS-MS	2.31	2.39	2.57	2.42
Nd	0.05	FUS-MS	10.7	11.0	11.3	11.0
Sm	0.01	FUS-MS	3.19	3.19	3.59	3.32
Eu	0.005	FUS-MS	1.24	1.21	1.35	1.27
Gd	0.01	FUS-MS	4.07	3.99	4.39	4.15
Tb	0.01	FUS-MS	0.70	0.75	0.74	0.73
Dy	0.01	FUS-MS	4.76	4.69	4.95	4.80
Ho	0.01	FUS-MS	0.99	1.00	1.02	1.00
Er	0.01	FUS-MS	2.78	2.77	3.00	2.85
Tm	0.005	FUS-MS	0.406	0.430	0.444	0.427
Yb	0.01	FUS-MS	2.72	2.86	2.97	2.85
Lu	0.002	FUS-MS	0.430	0.473	0.458	0.454

*O.L. = 4acid ICP-OES; A.I. = Alteration Index (Ishikawa et al., 1976)

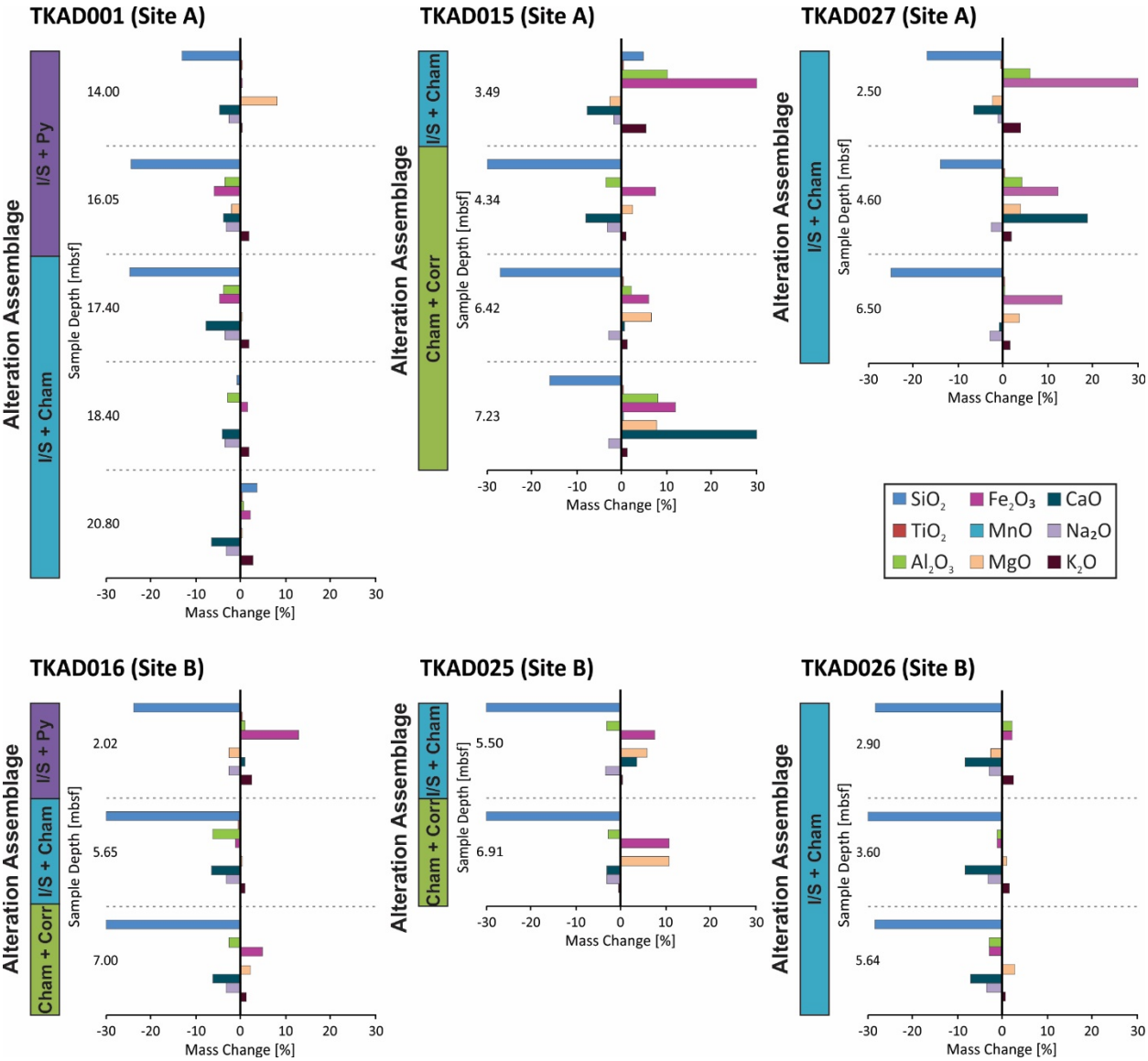


Fig. 5.22. Mass changes downhole associated with changes in alteration mineral assemblages (%Δ). Cham = chamosite; Corr = corrensite; I/S = illite/smectite; Non = nontronite; Pl = plagioclase; Py = pyrite.

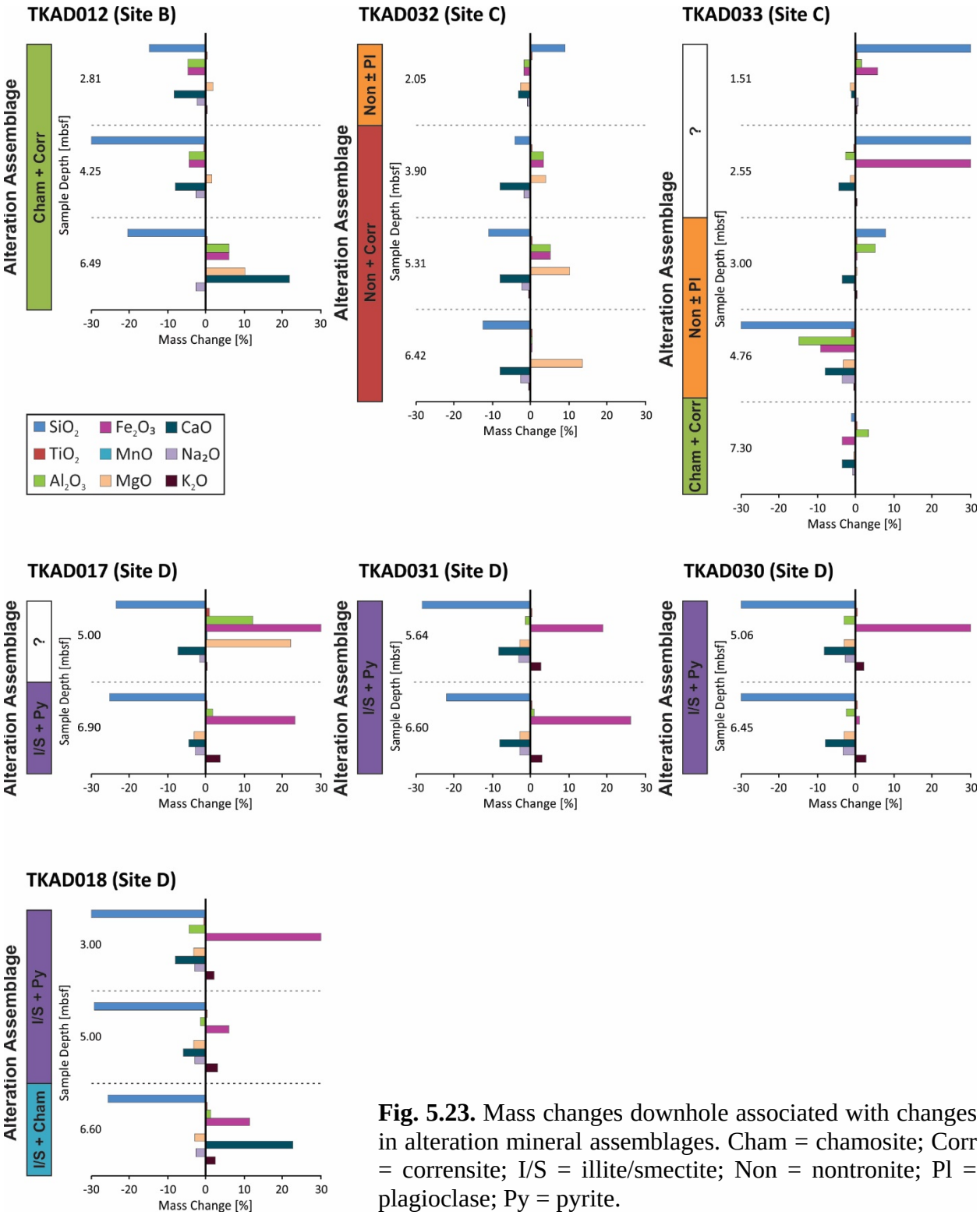


Fig. 5.23. Mass changes downhole associated with changes in alteration mineral assemblages. Cham = chamosite; Corr = corrensite; I/S = illite/smectite; Non = nontronite; Pl = plagioclase; Py = pyrite.

Table 5.7. Mass balance changes associated with alteration mineral assemblages in altered volcaniclastic rocks relative to a least-altered basaltic-andesite precursor (full results in Suppl. Table K2)

Alteration	Sample	SiO_2	TiO_2	Al_2O_3	Fe_2O_3	MnO	MgO	CaO	Na_2O	K_2O	Comment
Mnt/Non ± Pl											
	MA13-086-C	○	–	–	–	–	●	○	○	–	Non-rich
	MA13-025-C	●	–	–	–	–	–	○	–	–	Pl-rich
	MA13-026-C	○	–	○	○	–	○	○	○	–	Non = Pl
	MA13-072-C	●	–	○	○	–	○	○	○	–	Non-rich
Non + Corr											
	MA13-073-C	○	–	●	●	–	●	○	○	–	Corr > Non
	MA13-074-C	○	–	●	●	–	●	○	○	–	Corr > Non
	MA13-0745-C	○	–	–	–	–	●	○	○	–	Corr > Non
I/S + Py											
	MA13-087-C	○	–	○	○	–	○	○	○	●	Minor Corr
	MA13-034-C	○	–	●	●	–	○	●	○	●	Rect
	MA13-019-CM	○	–	●	●	–	●	○	○	●	
	MA13-020-CM	○	–	●	●	–	○	○	○	●	I/S, Mnt, Rect
	MA13-044-C	○	–	○	●	–	○	○	○	●	I/S
	MA13-045-C	○	–	●	●	–	○	○	○	●	I/S, Mnt, Pl?
	MA13-005-M	○	–	○	●	–	○	○	○	●	Non, Rect
	MA13-006-C	○	–	○	●	–	○	○	○	●	Rect, I/S
	MA13-014-C	○	–	○	●	–	○	○	○	●	Mont, I/S
	MA13-015-C	○	–	○	●	–	○	○	○	●	I/S, Mont, Rect
I/S + Cham											
	MA13-088-C	○	–	○	○	–	–	○	○	●	I/S = Cham
	MA13-090-C	○	–	○	●	–	–	○	○	●	Cham > I/S
	MA13-091-CM	●	–	–	●	–	–	○	○	●	Cham > I/S
	MA13-050-C	●	–	●	●	–	○	○	○	●	I/S > Cham
	MA13-056-CM	○	–	●	●	–	○	○	○	●	I/S > Cham
	MA13-057-C	○	–	●	●	–	●	●	○	●	Cham > I/S
	MA13-058-C	○	–	–	●	–	●	○	○	●	Cham > I/S
	MA13-035-C	○	–	○	○	–	–	○	○	●	Rect = Cham
	MA13-039-C	○	–	○	●	–	●	●	○	●	Cham > I/S
	MA13-067-C	○	–	●	○	–	○	○	○	●	I/S > Cham
	MA13-068-C	○	–	○	○	–	●	○	○	●	I/S = Cham
	MA13-069-C	○	–	○	●	–	●	○	○	●	I/S = Cham
	MA13-016-C	○	–	●	●	–	○		○	●	I/S > Cham
Cham + Corr									○		
	MA13-051-CM	○	–	○	●	–	●	○	○	●	Minor I/S
	MA13-052-C	○	–	●	●	–	●	●	○	●	Minor I/S
	MA13-053-C	○	–	●	●	–	●	●	○	●	Minor I/S
	MA13-036-C	○	–	○	●	–	●	○	○	●	Minor I/S(?)
	MA13-040-C	○	–	○	●	–	●	○	○	–	Cham > Corr
	MA13-062-C	○	–	○	○	–	●	○	○	–	Corr > Cham
	MA13-063-C	○	–	○	○	–	●	○	○	–	Corr > Cham
	MA13-064-C	○	–	●	●	–	●	●	○	–	Cham > Corr
	MA13-027-CM	○	–	●	○	–	–	○	○	–	Corr > Cham

● = gain; ○ = loss; – = no change; Cham = chamosite; Corr = corrensite; I/S = illite/smectite; Mnt = montmorillonite; Non = nontronite; Pl = plagioclase; Py = pyrite; Rect = rectorite

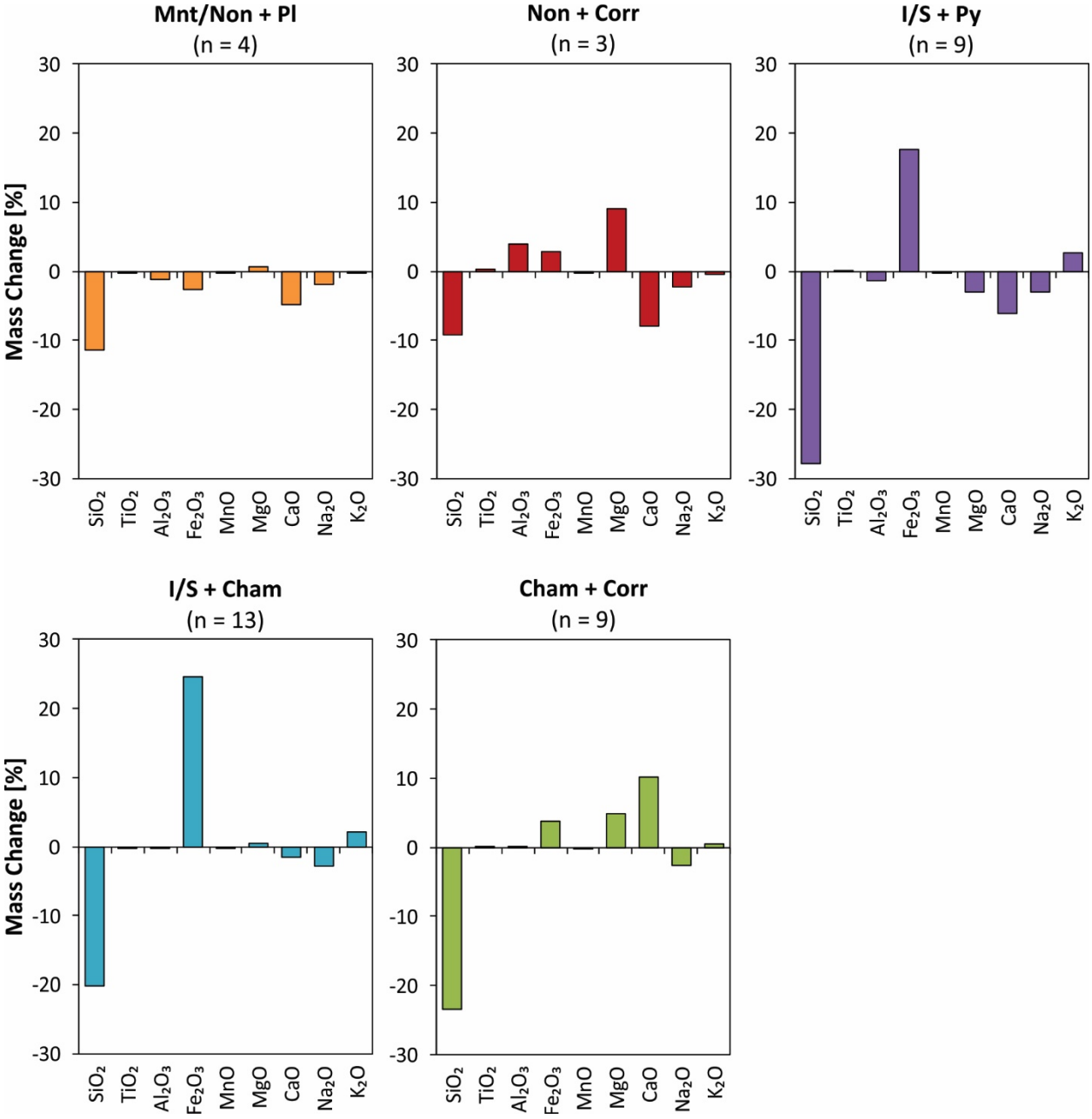


Fig. 5.24. Average mass changes for each alteration mineral assemblage. Cham = chamosite; Corr = corrensite; I/S = illite/smectite; Non = nontronite; Pl = plagioclase; Py = pyrite.

(5) Chamosite + corrensite alteration is associated with Si and Na losses, Mg gains, Fe gains when chamosite is more abundant than corrensite (and Fe losses when corrensite is more abundant), K gains when minor I/S is present, and no changes in K when there is no I/S.

5.5.5. Oxygen and hydrogen isotopes

Samples analyzed for O-isotopes include monomineralic nontronite (n = 2), chamosite (n = 9), corrensite (n = 2), and rectorite (n = 1). The results are shown in Table 5.8 and Figure 5.25. Values of $\delta^{18}O_{VSMOW}$ range from +12.3 to +12.5 ‰ for nontronite, +2.2 to +8.3 ‰ for chamosite, +9.6 to +11.1 ‰ for corrensite, and is +5.9 ‰ in one analysis of rectorite. The large range and high $\delta^{18}O$ values reflect substantial fractionation relative to the hydrothermal fluids (e.g., Huston, 1999). Values of δD_{VSMOW} range from -92 to -86 ‰ for nontronite, -65 to -52 ‰ for chamosite, -85 to -80 ‰ for corrensite, and is -69 ‰ in one analysis of rectorite. Temperatures were calculated using the following equation, assuming a $\delta^{18}O$ of the hydrothermal fluid close to that of average seafloor hydrothermal vent fluids ($\delta^{18}O$ = +1.3 ‰: de Ronde, 1995),

$$1000 \ln \alpha_{mineral-water} = \partial^{18}O_{mineral} - \partial^{18}O_{water} = A \times 10^6/T^2 - B$$

(Equation 6)

where *A* and *B* represent published mineral-water fractionation factors, as outlined in Table 5.8. The calculated temperatures range from 124°C to 251°C, with an error of ±10% (Fig. 5.25c), showing a systematic increase from to nontronite (136–138°C), to chamosite (124–205°C), to corrensite (207–227°C), to rectorite (256°C),. There is a general decrease in $\delta^{18}O_{VSMOW}$ with depth, associated with an increase in δD_{VSMOW}, reflecting a progressive increase in the subsurface temperature during clay formation; in particular, drillhole TKAD025 increases from 124°C at 5.5 mbsf to 205°C at 6.9 mbsf. Drillhole TKAD026 shows a reverse trend, decreasing from 256°C at 2.9 mbsf to 161°C at 5.6 mbsf, resulting from contrasting permeabilities in the substrate that control lateral fluid flow.

Table 5.8. Oxygen and hydrogen isotopic measurements and calculated temperatures of formation of clay minerals from the footwall of the Tinakula deposit

Site	Drillhole	Sample	Depth [mbsf]	Mineral	δD [‰ VSMOW]	$\delta^{18}O$ [‰ VSMOW]	Fractionation Factors A	B	Reference	Temperature [°C]
A	TKAD001	MA13_087	16.1–16.2	Nontronite	-86	+12.5	2.55	4.05	[1]	136
A	TKAD027	MA13_057	4.6–4.7	Chamosite	-53	+4.9	3.10	12.63	[3]	164
A	TKAD015	MA13_053	7.2–7.3	Chamosite	-53	+4.1	3.10	12.63	[3]	175
B	TKAD025	MA13_039	5.5–5.6	Chamosite	-65	+8.3	3.10	12.63	[3]	124
B	TKAD025	MA13_040	6.9–7.0	Chamosite	-52	+2.2	3.10	12.63	[3]	205
B	TKAD026	MA13_067	2.9–3	Rectorite	-69	+5.9	2.458	4.19	[2]	256
B	TKAD026	MA13_069	5.6–5.8	Chamosite	-61	+5.1	3.10	12.63	[3]	161
B	TKAD012	MA13_062	2.8–2.9	Corrensite	-85	+9.6	4.28	8.78	[3]	227
B	TKAD012	MA13_063	4.3–4.4	Corrensite	-80	+11.1	4.28	8.78	[3]	207
C	TKAD032	MA13_075	6.4–6.5	Nontronite	-92	+12.3	2.55	4.05	[1]	138
E	TKAD003	POO12	11.1–11.2	Chamosite	-56	+4.6	3.10	12.63	[3]	169
E	TKAD003	POO14	16.4–16.5	Chamosite	-57	+4.0	3.10	12.63	[3]	177
F	TKAD007	POO22	11.2–11.3	Chamosite	-54	+5.8	3.10	12.63	[3]	152
F	TKAD007	POO23	22.4–22.5	Chamosite	-53	+3.3	3.10	12.63	[3]	187

Fractionation factors used in Equation 6 after: [1] Sheppard and Gilg (1996); [2] Savin and Lee (1988) ; [3] Buatier et al. (1995)

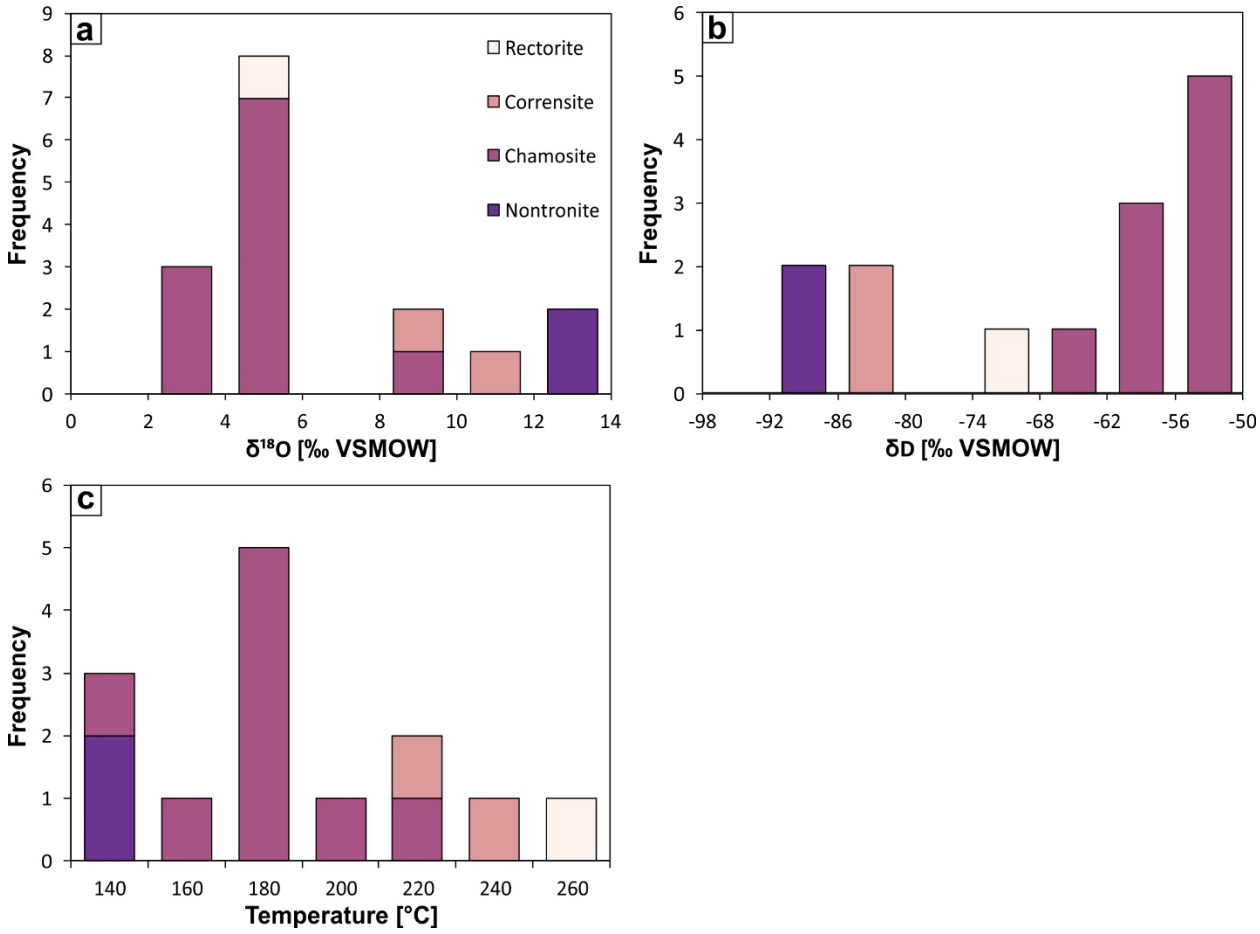


Fig. 5.25. Frequency distribution histograms for $\delta^{18}O$, δD, and calculated temperatures for the different clay mineral phases.

5.6. Discussion

5.6.1. Explosive volcanism at Tinakula

Volcanic facies in the subseafloor at Tinakula include hyaloclastite breccia, phreatomagmatic breccia (lapillistone or tuff), and resedimented volcanic breccia. The distribution of these facies plays a first-order control on lateral hydrothermal fluid flow. The dominance of volcanic breccia, which locally grades downwards to coherent volcanic facies (hyaloclastite), is consistent with the formation of cinder cones (e.g., McPhie et al., 1993). The seafloor topography reveals multiple craters formed via explosive volcanism or through explosive hydrothermal (steam) brecciation. Hydrothermal explosions likely formed the maars in the northern part of the study area (e.g., Monecke et al., 2012; *Chapter 3*), and are associated with reworking of the volcanic pile resulting in rounded chimney clasts entrained within the hydrothermally-altered volcaniclastic footwall to depths of ~7.3 mbsf (drillholes TKAD017 and TKAD025; Appendix N). The formation of sulfide chimneys is locally related to crater rims, syn-volcanic faults, or slump scarps, in addition to regional structures not associated with constructional volcanic features on the seafloor (*Chapter 3*). The chimneys are susceptible to mass-wasting, with abundant sulfide talus in the volcaniclastic material. Drilling also reveals several paleoseafloor horizons characterized by oxidized sediments and chimney fragments, indicating episodic ore formation.

Continued exploration of the seafloor has documented explosive eruptive products occurring at depths in excess of 3 km (Clague et al., 2009), with variations in eruption style, intensity, duration, and volume in different tectonic settings. Volcanism along mid-ocean ridges is dominated by effusive basaltic eruptions producing complex hummocky volcanoes, pillow volcanoes, and large flat-topped volcanoes associated with passive mantle upwelling (e.g., Yeo et al., 2012). In contrast, arc volcanism tends to produce pyroclastic eruptions from high-Si melts, associated with hydrous melting in the mantle wedge (e.g., Grove et al., 2012). Volcanism in back-arc basins may be similar to either MOR or arc environments, depending in part on the stage of rifting and the tectonic evolution of the basin (e.g., Pearce and Stern, 2006). The site of the Tinakula deposit is typical of early back-arc rifting, with rows of basaltic cinder cones developed along eruptive fissures but few large volcanoes, like the nearby Starfish volcano (Figs. 3.7, 3.9 and 5.1). However, the Starfish-

Tinakula area is located on an inflated segment that bisects the Jean Charcot Troughs, rather than within the basin itself, indicating enhanced magmatism on a regional scale (see *Chapter 3*). Immobile trace-element geochemistry of the volcaniclastic rocks confirms that the cinder cones are basaltic to andesitic, whereas other nearby volcanic features are mainly dacitic. Volcanic products recovered in drillcore from Tinakula have a substantial pyroclastic component, dominated by lapilli tuff, volcanic breccia facies and low fine-ash content. Similar ash-poor volcanic breccias described on land have been considered diagnostic of deep water eruptions, interpreted to result from low explosivity because of the greater hydrostatic pressures; alternatively, ash may be removed from the deposits by suspension in the water column (Busby, 2005).

The volcanic clasts recovered in drillcore are notably dense, with mm-sized vesicles that comprise no more than 20 vol.% of the clasts. In contrast to Strombolian eruptions, including in submarine environments (e.g., Head and Wilson, 2003), the cinder cones at Tinakula are generally broad (~15–200 m) and have a low-relief (Fig. 3.9; Suppl. Table B1). The eruption processes at Tinakula are, therefore, very different from those of pyroclastic deposits described along oceanic spreading centers (e.g., Clague et al., 2009). In particular, the more felsic composition and higher viscosities likely contributed to magma overpressure and greater explosive fragmentation. However, the magma was not as felsic as the high-viscosity silicic melts typical of arc-front volcanoes (e.g., Carey et al., 2018). The Tinakula volcanoes reflect the eruption styles associated with mafic-intermediate volcanism in a young back-arc basin in seawater depths of ~1,000–1,200 mbsl (*Chapter 3*).

Another notable volcanic product at Tinakula is a layer of crudely-bedded coarse sand-sized volcaniclastic fragments that drape the entire deposit, ranging in thickness from <1 to ~13 m and partially burying the sulfide chimneys. This material is interpreted to represent fallout from a nearby volcanic eruption. Near the chimney complexes and mounds, it is highly indurated (i.e., baked), forming crusts with weak sulfide mineralization and smectite alteration. Cracks in the indurated crust have focused ongoing low-temperature fluid flow, forming extensive networks of fracture-controlled iron and manganese oxides away from the chimneys and mounds (Fig. 3.20d–f). This indurated crust may have been an important factor is controlling the flow of higher-

temperature fluids in the subseafloor breccias and therefore influencing the distribution of the sulfide chimneys at the seafloor.

5.6.2. Alteration processes

Petrographic observations of the volcaniclastic footwall rocks at Tinakula reveals the formation of alteration minerals through initial replacement of primary phases (volcanic glass and feldspar crystals), followed by direct precipitation from solution into open spaces, and then further replacement by dissolution-precipitation or transformation processes (Figs. 5.2 and 5.3; Appendix G). The alteration assemblages at Tinakula are similar to proximal footwall alteration zones associated with ancient Kuroko-type VMS deposits (e.g. Shikazono et al., 1995), and fall into the broad categories of argillic (smectite, illite, and pyrite) and chloritic (chamosite, corrensite) alteration types.

The alteration assemblages are all associated with Si losses, with mass changes as much as -48.98% (Suppl. Table K2). In contrast, Si gains occur at the tops of drillholes TKAD015, TKAD032, and TKAD033, representing local silicification near the seafloor (Figs. 5.22 and 5.23) in the form of late opaline silica filling void spaces. Similarly, strong gains in Ca near the bottom of drillholes TKAD015, TKAD012, and TKAD018 reflect the presence of anhydrite/gypsum regardless of alteration type, resulting in CaO mass gains of up to 324.85% (Suppl. Table K2). Smectite is ubiquitous throughout the footwall in every alteration assemblage as discrete montmorillonite/nontronite and/or mixed layer clays. It primarily replaces volcanic glass, and is associated with losses of Si, Ca, and Na (Fig. 5.24). Similar Si losses associated with smectite-alteration of volcanic glass has been reported at the PACMANUS hydrothermal system in the Manus back-arc basin (Monecke et al., 2007). Illite alteration is associated with gains in K and losses of Na, Ca, and Si (Fig. 5.24), and occurs as pore-space filling, and replacement of volcanic glass and phenocrysts, following the simplified reaction:

$$2Ca_{0.5}Na_{0.5}Al_{1.5}Si_{2.5}O_8\ [\text{andesine}] + K^+ + H_2O\ [\text{seawater}] \rightarrow KAl_3Si_3O_{10}(OH)_2\ [\text{muscovite}] + 2SiO_2\ [\text{quartz}] + Na^+ + Ca^{2+} + O_2$$

Alternatively, illite may have been formed from smectite either directly or through continuous transformation of mixed-layer phases (e.g., Inoue et al., 1990). The high abundance of mixed-layer clays, with illite increasing down hole, supports the process of continuous transformation of smectite to illite. The whole-rock concentrations of Fe_2O_3 primarily reflect pyrite mineralization, which is most strongly associated with illite alteration. The formation of chlorite is associated with gains in Mg and losses of Si (Fig. 5.24). It occurs as pore-space fill, replacement of primary volcanic material, or through alteration of illite at high temperatures, following the general reactions:

$$4Ca_{0.5}Na_{0.5}Al_{1.5}Si_{2.5}O_8\ [\text{andesine}] + 15(Fe,Mg)^{2+} + 12H_2O\ [\text{seawater}] \rightarrow$$
$$3(Fe^{2+},Mg)_5Al_2Si_3(OH)_8\ [\text{chlorite}] + SiO_2\ [\text{quartz}] + 2Na^{2+} + 2Ca^{2+} + 9O_2$$

$$2KAl_3Si_3O_{10}(OH)_2\ [\text{muscovite}] + 15(Fe,Mg)^{2+} + 10H_2O\ [\text{seawater}] \rightarrow$$
$$3(Fe^{2+},Mg)_5Al_2Si_3(OH)_8\ [\text{chlorite}] + 3SiO_2\ [\text{quartz}] + 2K^{+} + 2O_2$$

Alternatively, chlorite may have been formed from smectite directly or through an intermediate corrensite step (e.g., Shau et al., 1990). However, at Tinakula chamosite appears before corrensite in the downhole progression of alteration assemblages, suggesting that corrensite forms as an alteration product of mixed layer illite/smectite clays. Smectite, illite-pyrite and chlorite alteration can be graphically distinguished through plots of mass balance changes of ΔMgO, ΔK_2O, ΔFe_2O_3, and ΔNa_2O, as shown in Figure 5.26, in which increasing alteration intensity is shown by increasing distance from the unaltered precursor composition.

The formation of Mg-bearing chlorite is likely related to seawater entrainment into ascending hydrothermal fluids, as water-rock interactions at temperatures above 150°C effectively remove Mg from solution due to precipitation of Mg-OH-Si minerals (e.g., Bischoff and Dickson, 1975). The geochemical mass transfer of Mg from seawater to rock provides constraints on the chemical water:rock (w/r) ratios (Mottl, 1983) as follows:

$$\frac{\Delta C_{i(rock)}}{\Delta C_{i(water)}} = \frac{W}{M}$$

(Equation 7)

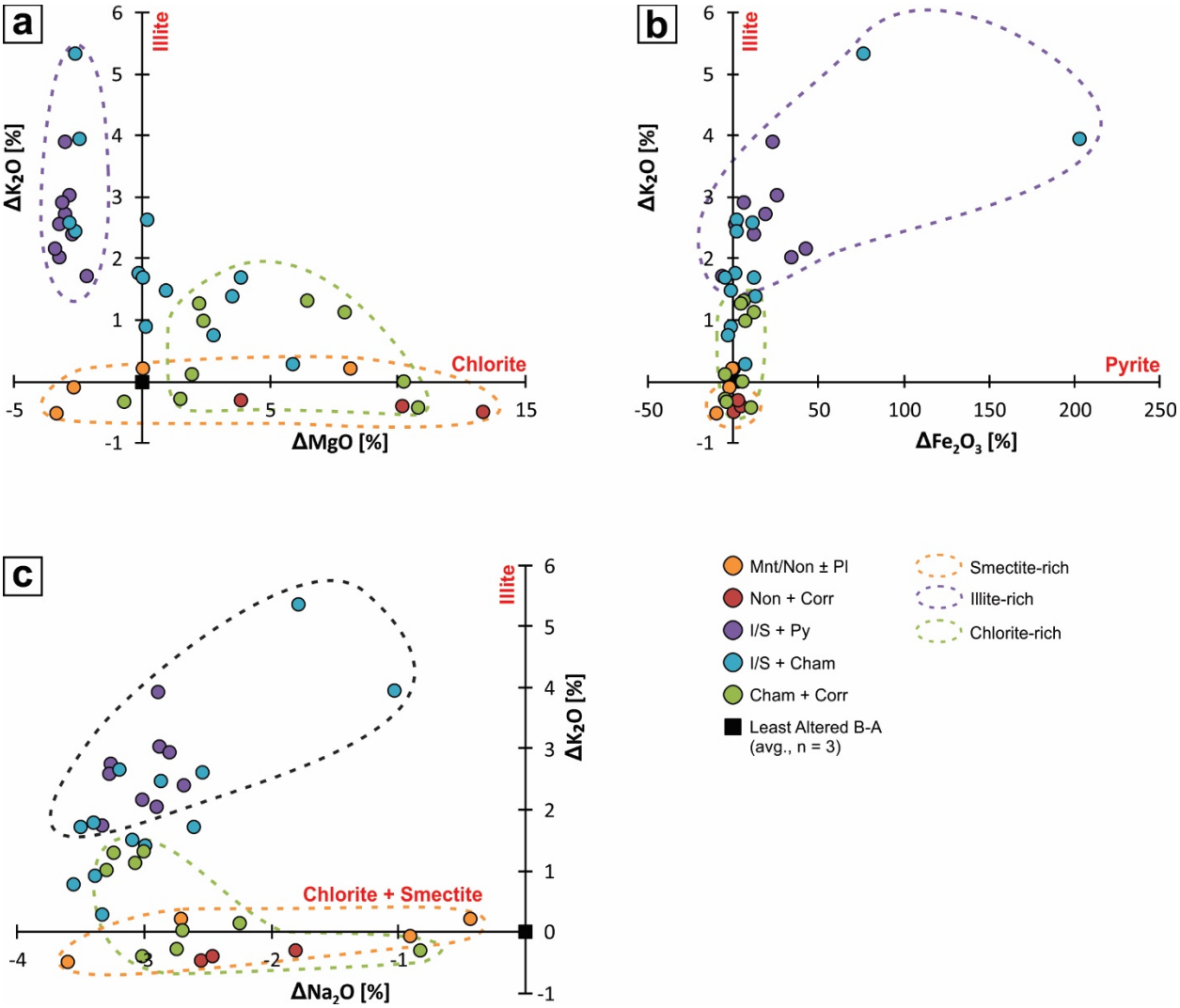


Fig. 5.26. Plots of mass changes of major elements for different alteration assemblages: (a) mass increases of K_2O reflecting illite alteration, and mass increases of MgO reflecting increased chlorite; (b) mass increases of Fe_2O_3 primarily reflecting pyrite alteration rather than chlorite alteration; and (c) mass decreases of Na_2O reflecting chlorite and smectite alteration. B-A = basaltic andesite; Cham = chamosite; Corr = corrensite; I/S = illite/smectite; Non = nontronite; Pl = plagioclase; Py = pyrite.

Where $\Delta C_{i(rock)}$ is the loss/gain of species *i* per kilogram of rock (mol $kg_{(rock)}^{-1}$), $\Delta C_{i(water)}$ is the loss/gain of species *i* in the fluid phase, *W* is the mass of water in contact with rock, *M* is the mass of rock, and *W/M* defines the chemical w/r ratio. This method assumes a steady flow rate over the duration of deposit formation (minimum 5597 ± 240 years; *Chapter 4*), a homogenous initial composition of the rock, and that local equilibrium and chemical steady state is reached between the fluid and the rock. The w/r mass ratios at Tinakula have been estimated from the MgO flux by assuming an initial seawater concentration of 1295 ppm (53.3 mmol/kg) Mg, and that 100% of the Mg has been transferred to the altered rock (Table 5.9). Similarly, K_2O is added to the rock primarily from hydrothermal fluids, with w/r mass ratios estimated assuming an initial seawater concentration of 390 ppm (9.97 mmol/kg) K. The calculated w/r ratios are considered minimum values as seawater with unreacted Mg and K may be added to the system during hydraulic flow-through (Mottl, 1983). The results reveal positive w/r ratios calculated from MgO fluxes in alteration assemblages containing abundant chlorite minerals (chamosite/corrensite). There is a general downhole-increase in w/r ratios; for example, drillhole TKAD032 increases from 1.81 to 6.22 between 3.90–6.42 mbsf (nontronite + corrensite assemblage), and TKAD012 increases from 0.91 to 4.7 between 2.81–6.49 mbsf (chamosite + corrensite assemblage). Ratios calculated from K_2O fluxes are positive in assemblages dominated by illite (illite/smectite + pyrite and illite/smectite + chamosite). The w/r ratios tend to increase with depth, with two notable exceptions: TKAD027 decreases from 8.37 to 2.95 between 2.50–6.50 mbsf, and TKAD026 decreases from 5.20 to 1.59 between 2.90–5.64 mbsf. This likely results from extensive lateral fluid flow along contrasting permeabilities. The overall average w/r ratio is 4.19 (calculated from the highest w/r in each sample), consistent with a fluid-dominated system (e.g., Mottl, 1983).

The Tinakula drilling shows that distinct alteration assemblages can form within ~10 m of the seafloor in a volcaniclastic substrate. Several lines of evidence indicate increasing temperature with depth: (1) increasing abundance of anhydrite down-hole; (2) increasing phyllosilicate crystallinity down-hole indicated by increases in the Al-OH absorption feature in SWIR analyses; (2) transitions from smectite to mixed-layer I/S with increasing proportions of illite to corrensite and chamosite; and (4) decreasing $\delta^{18}O$ and increasing δD of monomineralic clays. Calculated temperatures of formation increase by ~130°C from nontronite → chamosite → corrensite →

Table 5.9. Water:rock (w/r) ratios calculated from mass changes in Mg and K in altered rocks for each mineral assemblage

Sample	MA13-086-C	MA13-072-C	MA13-025-C	MA13-026-C	MA13-073-C	MA13-074-C	MA13-075-C	MA13-087-C
Location	Site A	Site C	Site C	Site C	Site C	Site C	Site C	Site A
Drillhole	TKAD001	TKAD032	TKAD033	TKAD033	TKAD032	TKAD032	TKAD032	TKAD001
Depth	14.00	2.05	3.00	4.76	3.90	5.31	6.42	16.05
Assemblage	Mnt/Non	Mnt/Non	Mnt/Non	Mnt/Non	Non + Corr	Non + Corr	Non + Corr	I/S + Py
ΔMg [mmol/kg]	0.20	-0.07	0.00	-0.08	0.10	0.25	0.33	-0.05
w/r[1]	3.80	-1.24	0.04	-1.54	1.81	4.74	6.22	-1.00
ΔK [mmol/kg]	0.00	0.00	0.00	-0.01	-0.01	-0.01	-0.01	0.04
w/r[2]	0.42	-0.21	0.41	-1.11	-0.69	-0.89	-1.05	3.65

Sample	MA13-034-C	MA13-020-CM	MA13-044-C	MA13-045-C	MA13-005-M	MA13-006-C	MA13-014-C	MA13-015-C
Location	Site B	Site D	Site D	Site D	Site D	Site D	Site D	Site D
Drillhole	TKAD016	TKAD017	TKAD031	TKAD031	TKAD030	TKAD030	TKAD018	TKAD018
Depth	2.02	6.90	5.64	6.60	5.06	6.45	3.00	5.00
Assemblage	I/S + Py	I/S + Py	I/S + Py	I/S + Py	I/S + Py	I/S + Py	I/S + Py	I/S + Py
ΔMg [mmol/kg]	-0.07	-0.07	-0.07	-0.07	-0.08	-0.08	-0.08	-0.08
w/r[1]	-1.25	-1.39	-1.38	-1.30	-1.50	-1.50	-1.56	-1.45
ΔK [mmol/kg]	0.05	0.08	0.06	0.06	0.04	0.05	0.05	0.06
w/r[2]	5.08	8.29	5.79	6.42	4.30	5.45	4.58	6.21

Sample	MA13-088-C	MA13-090-C	MA13-091-CM	MA13-050-C	MA13-056-CM	MA13-057-C	MA13-058-C	MA13-035-C
Location	Site A	Site A	Site A	Site A	Site A	Site A	Site A	Site B
Drillhole	TKAD001	TKAD001	TKAD001	TKAD015	TKAD027	TKAD027	TKAD027	TKAD016
Depth	17.40	18.40	20.80	3.49	2.50	4.60	6.50	5.65
Assemblage	I/S + Cham	I/S + Cham	I/S + Cham	I/S + Cham	I/S + Cham	I/S + Cham	I/S + Cham	I/S + Cham
ΔMg [mmol/kg]	0.00	0.00	0.01	-0.06	-0.06	0.10	0.09	0.00
w/r[1]	0.04	-0.04	0.11	-1.20	-1.12	1.80	1.66	0.08
ΔK [mmol/kg]	0.04	0.04	0.06	0.11	0.08	0.04	0.03	0.02
w/r[2]	3.59	3.74	5.60	11.34	8.37	3.60	2.95	1.89

Sample	MA13-039-C	MA13-067-C	MA13-068-C	MA13-069-C	MA13-016-C	MA13-051-CM	MA13-052-C	MA13-053-C
Location	Site B	Site B	Site B	Site B	Site D	Site A	Site A	Site A
Drillhole	TKAD025	TKAD026	TKAD026	TKAD026	TKAD018	TKAD015	TKAD015	TKAD015
Depth	5.50	2.90	3.60	5.64	6.60	4.34	6.42	7.23
Assemblage	I/S + Cham	I/S + Cham	I/S + Cham	I/S + Cham	I/S + Cham	Cham + Corr	Cham + Corr	Cham + Corr
ΔMg [mmol/kg]	0.15	-0.06	0.02	0.07	-0.07	0.06	0.16	0.20
w/r[1]	2.76	-1.21	0.46	1.31	-1.31	1.14	3.03	3.69
ΔK [mmol/kg]	0.01	0.05	0.03	0.02	0.05	0.02	0.03	0.02
w/r[2]	0.56	5.20	3.15	1.59	5.48	2.10	2.77	2.38

Sample	MA13-036-C	MA13-040-C	MA13-062-C	MA13-063-CM	MA13-064-C	MA13-027-CM
Location	Site B	Site B	Site B	Site B	Site B	Site C
Drillhole	TKAD016	TKAD025	TKAD012	TKAD012	TKAD012	TKAD033
Depth	7.00	6.91	2.81	4.25	6.49	7.30
Assemblage	Cham + Corr	Cham + Corr	Cham + Corr	Cham + Corr	Cham + Corr	Cham + Corr
ΔMg [mmol/kg]	0.06	0.27	0.05	0.04	0.26	-0.02
w/r[1]	1.04	5.04	0.91	0.71	4.78	-0.31
ΔK [mmol/kg]	0.03	-0.01	0.00	-0.01	0.00	-0.01
w/r[2]	2.69	-0.90	0.24	-0.63	-0.01	-0.70

ΔMg, ΔK= mass change in whole-rock Mg and K concentrations (see Suppl. Table K2)

1 - w/r calculated from initial seawater concentration of 53.3 mmol/kg Mg

2 - w/r calcualted from initial seawater concentration of 9.97 mmol/kg K

rectorite. All drillholes indicate progressive alteration from I/S + pyrite to I/S + chamosite to chamosite + corrensite with increasing temperature (e.g., Figs. 5.12 and 5.13). The relatively high formation temperatures of corrensite are consistent with late alteration of illite/smectite clays after the first appearance of chamosite. The inferred temperatures are within the thermal stability of mixed layer clays (Fig. 5.27), which have been found in geothermal systems up to 250°C (e.g., Jennings and Thompson, 1986; Harvey and Brown, 1991). Downhole temperature gradients are extreme, with increases in temperature of up to 80°C in just over one meter (e.g., TKAD025 at Site B). These steep temperature gradients reflect the influence of upwelling hydrothermal fluids and an influx of cold seawater, indicated by anhydrite cement at depth and increasing barite near the seafloor. Two drillholes show reverse temperature gradients, reflecting highly variable subseafloor permeability (e.g., calculated temperatures from 256°C at 2.9 mbsf to 161°C at 5.6 mbsf in TKAD026).

Alteration of the substrate by lateral fluid flow through the highly permeable volcaniclastic rocks at all of the drill sites is similar to the alteration described from ancient volcaniclastic-hosted VMS deposits (e.g., Mattabi deposit, Sturgeon Lake, ON: Galley et al., 2007); what is unique is that this alteration covers such a large area so close to the seafloor. In ancient VMS this type of alteration is commonly observed at depths of up to 200 m below the seafloor, commonly in association with subseafloor deposition of massive sulfide (e.g., Allen et al. 2002; Doyle and Allen, 2003). At Tinakula, alteration assemblages vary laterally across the deposit, as shown in Figure 5.28. In this figure, the lateral extent of the hydrothermal alteration is constrained by magnetic lows revealed by ocean-floor electromagnetic surveys (Neptune Minerals unpublished data). Montmorillonite/nontronite is localized at Site A and Site D, whereas nontronite + corrensite is localized at Site C. Illite/smectite + pyrite alteration occurs in the north (Site A) and in the central portions of the deposit (Site D), whereas illite/smectite + chamosite and chamosite + corrensite are widespread and proximal to hydrothermal chimneys. Site D is interpreted to be at the center of the highest-temperature upflow, associated with extensive formation of illite. This is consistent with observations of ongoing active venting and the presence of chalcopyrite-rich chimneys and likely reflects focusing of hydrothermal fluids along intersecting structures (Fig. 5.1; Fig. 3.8). Site A is also dominated by chamosite + corrensite near the seafloor and is associated with chalcopyrite-rich chimneys. Sites B, C, E, and F have relatively lower temperatures, with greater variability in

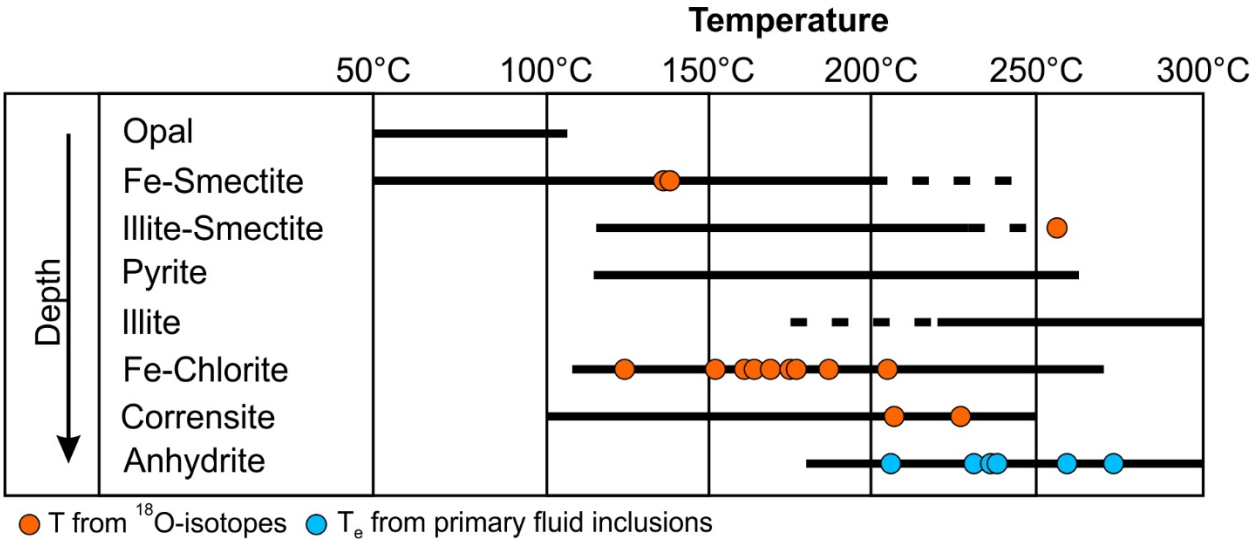


Fig. 5.27. Temperature ranges for the formation of hydrothermal alteration minerals from Reyes (1990), with significant overlap between minerals. Temperature calculations from the Tinakula deposit using ^{18}O-isotopes (orange circles; Table 5.8) and primary fluid inclusions in anhydrite and sphalerite (blue circles; Table 4.9) are shown.

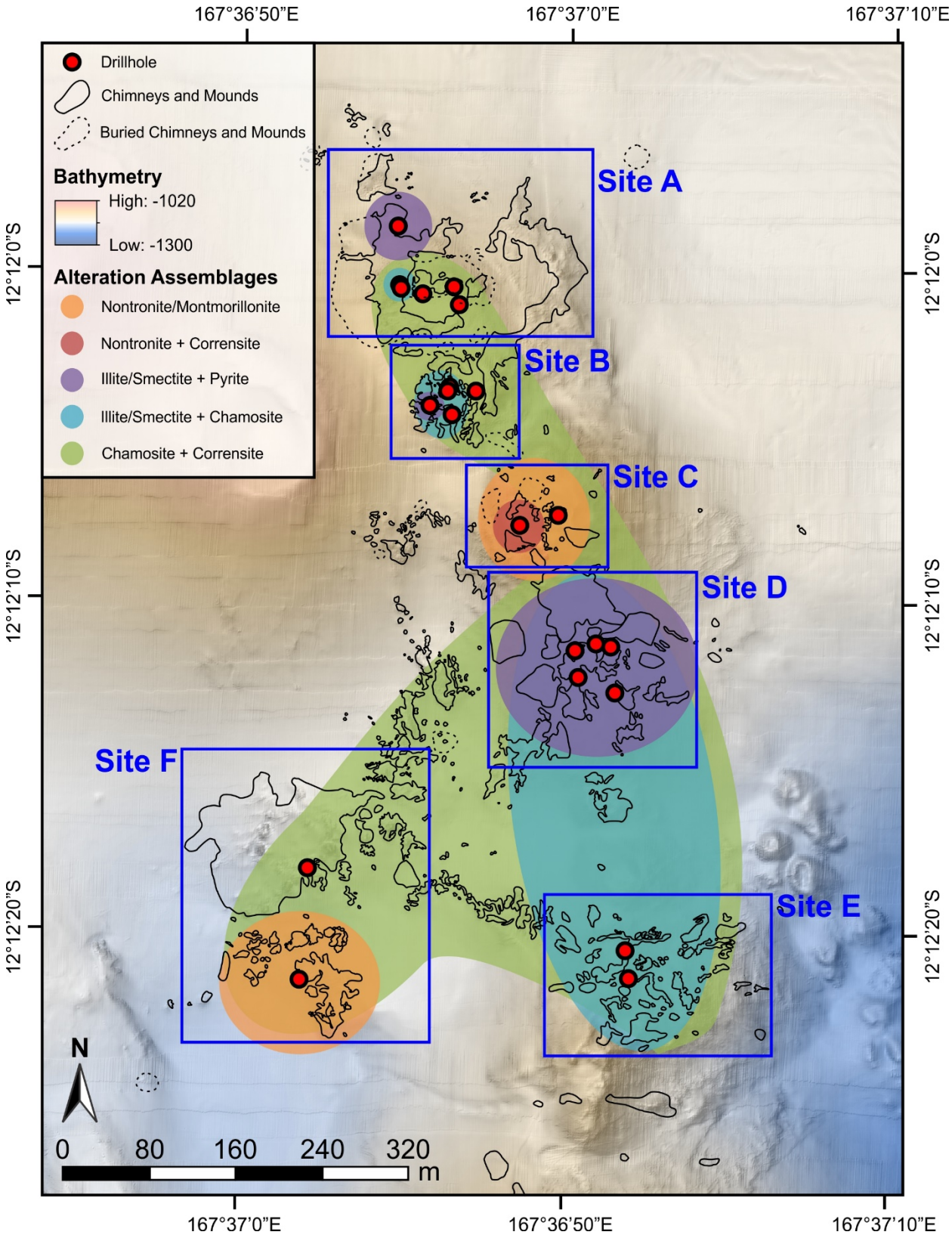


Fig. 5.28. Map showing the lateral distribution of alteration assemblages in the subseafloor of the Tinakula deposit encountered during drilling.

alteration assemblages and few mainly sphalerite-rich and barite-rich chimneys.

5.6.3. Hydrothermal fluids and ore formation

The alteration assemblages at Tinakula are consistent with a near-neutral or slightly acidic pH (cf. Reyes, 1990; Corbett and Leach, 1998). Abundant fluid mixing between hydrothermal fluids and ambient seawater is indicated by subseafloor precipitation of anhydrite. Salinities of primary inclusions between 2.8–3.8 wt.% $NaCl_{equiv}$ indicate seawater-dominated fluids, possibly with a component of condensed vapor-phase liquid (*Chapter 4*). The calculated temperatures of clay formation are ~20°C lower than the measured homogenization temperatures of primary fluid inclusions in anhydrite (T_e ≤273°C), and ~40°C lower than the measured homogenization temperatures of primary fluid inclusions in sphalerite (T_e ≤298°C; *Chapter 4*). This suggests that the initial $\delta^{18}O$ of the hydrothermal fluid may be heavier than the assumed value of 1.3 ‰, and the calculated temperatures, therefore, represent minimum values. The initial $\delta^{18}O$ of the hydrothermal fluid is calculated from Equation 6 assuming the rocks equilibrated with the hydrothermal fluid at the same temperature of most of the primary inclusions and within the thermal stability of clay formation, around 240°C (Table 5.10), ranging from 0.8 ‰ in rectorite to a maximum of 9.2 ‰ in chamosite. There are no accepted hydrogen isotope fractionation factors for 2:1 phyllosilicates to calculate initial δD_{water} values. Gilg and Sheppard (1996) propose approximating fractionation factors of Al-rich, Fe- and Mg-free smectites using kaolinite factors; however, the smectites in this study are Fe-rich nontronite. Initial δD_{water} values are calculated from chamosite samples using chlorite-water fractionation factor $\alpha = 0.954$ after Marumo et al. (1980), yielding δD_{water} values of -18.7 ‰ to -9.8 ‰ (Table 5.10). It is important to note that H-isotope fractionation in chlorite is strongly dependent on mineral chemistry (e.g., Savin and Lee, 1988; Marumo et al., 1980), resulting in a high level of uncertainty in these calculations. The $\delta^{18}O$-δD diagram in Figure 5.30 reveals isotopic signatures that generally fall outside of the seawater field; this may be due in part to the wide range of temperatures associated with chamosite formation. The sample within the field has a $\delta^{18}O_{water}$ value of 3.1 ‰ and δD_{water} value of -9.8 ‰. Most VMS deposits are estimated to form from hydrothermal fluids with $\delta^{18}O_{water}$ values between -1 and +4 ‰ (Huston, 1999), which is lighter than the $\delta^{18}O_{water}$ at Tinakula. Similarly heavy $\delta^{18}O_{water}$ values have been reported from ancient VMS deposits, including O-isotopes measured in minerals from the Kuroko ore bodies (up

Table 5.10. Initial oxygen and hydrogen isotope values for the hydrothermal fluid calculated at 240°C

Site	Drillhole	Sample	Depth [mbsf]	Mineral	Reference	$\delta^{18}O_{water,\ initial}$ [% VSMOW]	$\delta D_{water,\ initial}$ [% VSMOW]
A	TKAD001	MA13_087	16.1–16.2	Nontronite	[1]	+6.9	
A	TKAD027	MA13_057	4.6–4.7	Chamosite	[3]	+4.8	-11.3
A	TKAD015	MA13_053	7.2–7.3	Chamosite	[3]	+5.0	-10.5
B	TKAD025	MA13_039	5.5–5.6	Chamosite	[3]	+9.2	-23.1
B	TKAD025	MA13_040	6.9–7.0	Chamosite	[3]	+3.1	-9.8
B	TKAD026	MA13_067	2.9–3	Rectorite	[2]	+0.8	
B	TKAD026	MA13_069	5.6–5.8	Chamosite	[3]	+6.0	-18.7
B	TKAD012	MA13_062	2.8–2.9	Corrensite	[3]	+2.1	
B	TKAD012	MA13_063	4.3–4.4	Corrensite	[3]	+3.6	
C	TKAD032	MA13_075	6.4–6.5	Nontronite	[1]	+6.7	
E	TKAD003	POO12	11.1–11.2	Chamosite	[3]	+5.4	-14.1
E	TKAD003	POO14	16.4–16.5	Chamosite	[3]	+4.9	-15.1
F	TKAD007	POO22	11.2–11.3	Chamosite	[3]	+6.7	-11.7
F	TKAD007	POO23	22.4–22.5	Chamosite	[3]	+4.2	-10.6

Oxygen fractionation factors used in Equation 6 after: [1] Sheppard and Gilg (1996);
[2] Savin and Lee (1988) ; [3] Buatier et al. (1995) (see Table 5.9)
Hydrogen fractionation factor for chlorite-water ($\alpha = 0.954$) after Maruno et al. (1980)

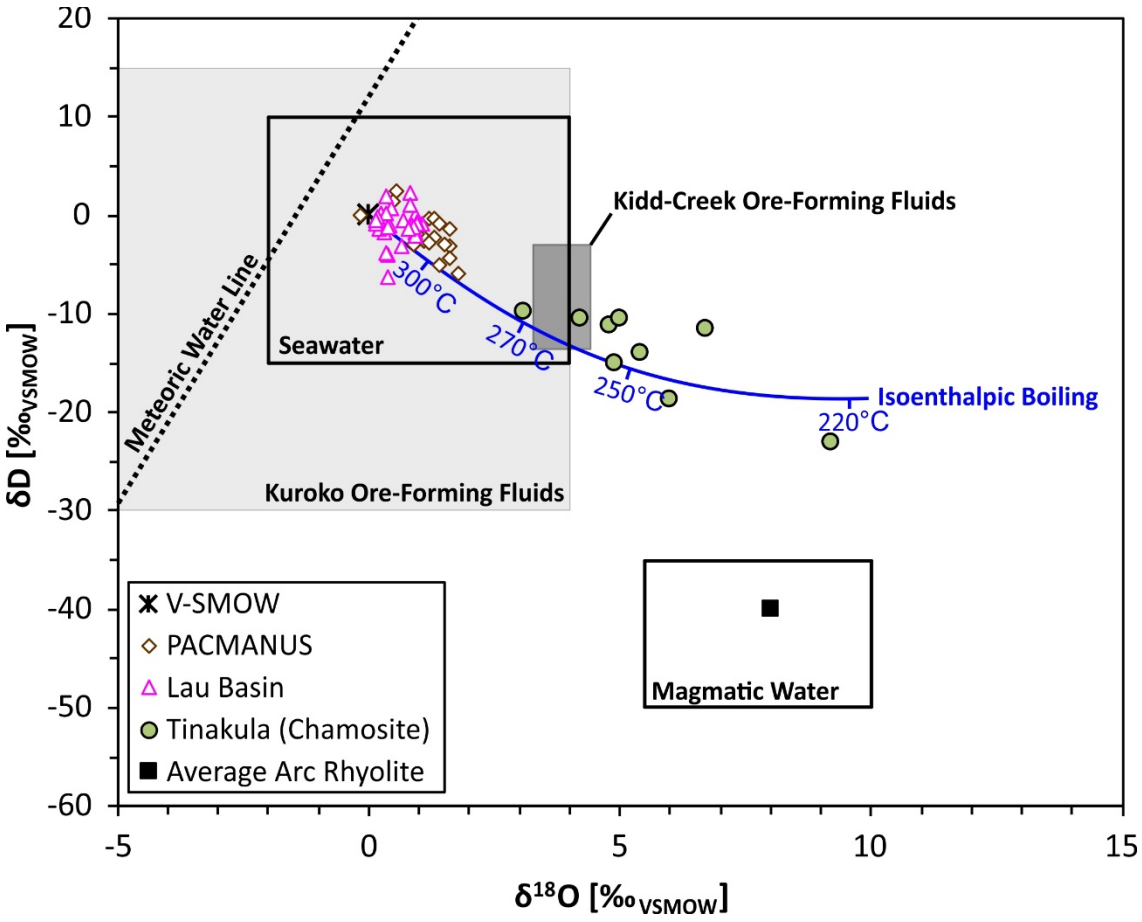


Fig. 5.30. $\delta^{18}O$-δD diagram showing the isotopic values for the hydrothermal fluid at Tinakula equilibrated at a temperature of 240°C (see Table 5.10), compared to data from the Lau basin (Mottl et al., 2011) and the PACMANUS deposit in the Manus Basin (Reeves et al., 2011), the Kuroko ore forming fluids (Ohmoto, 1996), and the Kidd Creek deposit (Huston and Taylor, 1999). The fields of seawater and magmatic water (Sheppard, 1986; Taylor, 1992) and the global meteoric water line (Craig, 1961) are also shown. Samples from Tinakula closely follow the adiabatic boiling path from Huston (1999), associated with increasing $\delta^{18}O$ values and slightly decreasing δD values with progressive boiling.

to 10.8 ‰; Ohmoto, 1983, 1996). $\delta^{18}O_{water}$ at Tinakula shifts towards lighter values in alteration assemblages associated with higher temperatures near chalcopyrite-rich chimneys, to a minimum value of 0.8 ‰ associated with rectorite. This trend has been noted in stringer zones of other ore deposits (e.g., Cathles, 1993). The source of the ^{18}O-rich hydrothermal fluids at Tinakula may partly derive from isotopic exchange with ^{18}O-rich rocks, boiling of the ore fluid, or direct contributions from magmatic fluids. At high temperatures, water-rock interactions may shift the $\delta^{18}O_{water}$, but not δD_{water}. The $\delta^{18}O_{water}$ values at Tinakula are heavier than those of average igneous rocks in arc-back-arc environments (~8 ‰; Huston, 1999), so this alone cannot account for the heavy isotope signature, and does not account for the low δD. Adiabatic boiling of the hydrothermal fluid can further increase $\delta^{18}O_{water}$, and may also decrease δD_{water}. This is supported by the fact that samples from Tinakula closely follow the isoenthalpic boiling path calculated by Huston (1999; Fig. 5.30). Sub-seafloor boiling is inferred at Tinakula based on the seawater boiling curve, with boiling temperatures higher than 350°C at <500 m below the seafloor (Fig. 4.24). Similar shifts in the O- and H-isotopic signatures may result from interaction with magmatic fluids; however, there is no additional evidence to support magmatic contributions at Tinakula (e.g., low-pH alteration assemblages, strongly negative S-isotope values). Many ancient VMS deposits with anomalous $\delta^{18}O_{water}$ and δD_{water} values are attributed to metamorphic fluids; this study demonstrates that these values may be obtained through normal ore-forming processes.

5.7. Conclusions

Mineralogical and geochemical characteristics of shallow subsurface alteration at Tinakula reflect the evolved mafic composition of the source rocks, high permeability of the volcaniclastic substrate, hydrothermal fluid composition, and temperature gradients. Combined processes of upwelling hydrothermal fluids and influx of ambient seawater result in zonation of the alteration mineral assemblages, which show a progression with depth from argillic (smectite, illite, pyrite) to chloritic (chamosite, corrensite) zones. In addition to zoned alteration assemblages, increasing temperatures with depth are recorded by increasing phyllosilicate crystallinity, increasing proportions of illite in mixed-layer I/S clays, and calculations of temperatures from $\delta^{18}O$-isotopes and fluid inclusions. These alteration zones are semi-conformable resulting from lateral fluid flow within the highly-permeable volcaniclastic substrate, with local interruptions in the downhole

progression of temperature caused by changes in permeability associated with deposition of finer-grained tuffs. There are also broader-scale changes in alteration assemblages with temperature along the main N-S trending fissure, with the highest temperatures associated with increasing proximity to the inferred heat source and intersecting structures.

Five alteration assemblages are identified, associated with mass changes in major elements relative to an unaltered basaltic-andesite precursor: (1) montmorillonite/nontronite, associated with losses of Si and alkalis; (2) nontronite + corrensite, associated with losses of Si, Ca, Na, and K, with gains in Al, Fe, and Mg; (3) illite/smectite + pyrite, associated with losses of Si, Al, Mg, Ca, and Na, and gains in K; (4) illite/smectite + chamosite, associated with losses of Si, Ca, and Na, and gains in Fe, Mg, and K; and (5) chamosite + corrensite, associated with losses of Si and Na, and gains in Fe, Mg, Ca, and K.

Hydrothermal alteration consists of replacement of volcanic glass and primary minerals by clay minerals, and infill of pore space by clay minerals. Clay alteration occurs at temperatures between ~124℃ and ~256℃. This is followed by irregular precipitation of anhydrite into pore spaces at temperatures of ≤273°C as seawater mixed with the hydrothermal fluids, with increasing anhydrite abundance downhole. Precipitation of clays and anhydrite reduced the overall permeability of the volcaniclastic substrate. This had the effect of insulating deeper hydrothermal fluid circulation, which locally led to over-pressurization and fracturing of the overlying rock, forming sulfate veins with minor sulfides, including sphalerite at temperatures of ≤ 298°C. This process demonstrates how hydrothermal fluids can become focused in a highly-permeable volcaniclastic substrate, leading to high-temperature venting at the seafloor and the formation of chalcopyrite-, sphalerite-, and barite-rich chimney mounds. The Tinakula deposit represents a modern analogue for mafic-intermediate pyroclast-dominated volcanogenic massive sulfide deposits (e.g., Sturgeon Lake, Ontario, Canada), demonstrating the potential of large ore deposits to form at the early stages of back-arc rifting.

Appendix M. Supporting Information

Supplementary data associated with this article is found in Appendix M.

References

Allen, R.L., Weihed, P., The Global VMS Research Project Team, 2002. Global comparisons of volcanic-associated massive sulfide deposits. In: Blundell, D.J. Neubauer, F., Quadt, A. von (Eds.), The Timing and Location of Major Ore Deposits in and Evolving Oregen. Geol. Soc. London Spec. Publ., pp, 13–38, doi:10.1144/GSL.SP.2002.204.01.02.

Barret, T.J., MacLean, W.H., 1994a. Chemostratigraphy and hydrothermal alteration in exploration for VHMS deposits in greenstones and younger volcanic rocks. In: Lentz, D.R. (Ed.), Alteration and alteration processes associated with ore-forming systems, Geol. Assoc. Can., Short Course Notes Vol. 11, Waterloo, ON, pp. 433–467.

Barret, T.J., MacLean, W.H., 1994b. Mass changes in hydrothermal alteration zones associated with VMS deposits of the Noranda area. Explor. Min. Geol. 3, 131–160.

Barret, T.J., MacLean, W.H., 1999. Volcanic sequences, litho-geochemistry, and hydrothermal alteration in some bimodal volcanic-associated massive sulfide systems. In: Barrie, C.T., Hannington, M.D. (Eds.), Volcanic-Associated Massive Sulfide Deposits: Processes and Examples in Modern and Ancient Environments. Soc. Econ. Geol., Reviews in Economic Geology Vol. 8, pp. 101–131, doi:10.5382/Rev.08.05.

Bau, M., 1991. Rare-earth element mobility during hydrothermal and metamorphic fluid-rock interaction and the significance of the oxidation state of europium. Chem. Geol. 93, 219–230, doi:10.1016/0009-2541(91)90115-8.

Bischoff, J.L., Dickson, F.W., 1975. Sea water-basalt interaction at 200°C and 500 bars – Implications for origin of sea-floor heavy-metal deposits and regulation of sea water chemistry. Earth Planet. Sci. Lett. 25, 385–397, doi:10.1016/0012-821X(75)90257-5.

Boynton, W.V., 1984. Cosmochemistry of the rare earth elements; meteorite studies. In: Henderson, P. (Ed.), Rare earth element geochemistry, Elsevier Sci. Publ. Co., Amsterdam, pp. 63–114.

Browne, P.R.L., 1978. Hydrothermal alteration in active geothermal fields. Ann. Rev. Earth. Planet Sci. 6, 229–250, doi:10.1146/annurev.ea.06.050178.001305.

Buatier, M.D., Früh-Green, G.L., Karpoff, A.M., 1995. Mechanism of Mg-phyllosilicate formation in a hydrothermal system at a sedimented ridge (Middle Valley, Juan de Fuca). Contrib. Mineral. Petrol. 122, 134–151, doi:10.1007/s004100050117.

Busby, C., 2005. Possible distinguishing characteristics of very deepwater explosive and effusive silicic volcanism. Geology 33, 845–848, doi:10.1130/G21216.1.

Carey, R., Soule, S.A., Manga, M., White, J.D.L., McPhie, J., Wysoczanski, R., Jutzeler, M., Tani, K., Yoerger, D., Fornari, D., Caratori-Tontini, F., Houghton, B., Mitchell, S., Ikegami, F., Conway, C., Murch, A., Fauria, K., Jones, M., Cahalan, R., McKenzie, W., 2018. The largest deep-ocean silicic volcanic eruption of the past century. Sci. Adv. 4, e1701121, doi:10.1126/sciadv.1701121.

Cathles, L.M., 1993. Oxygen isotope alteration in the Noranda mining district, Abitibi greenstone belt, Quebec. Econ. Geol. 88, 1483–1511, doi:10.2113/gsecongeo.88.6.1483.

Clague, D.A., Paduan, J.B., Davis, A.S., 2009. Widespread strombolian eruptions of mid-ocean ridge basalt. J. Volcanol. Geotherm. Res. 180, 171–188, doi:10.1016/j.jvolgeores.2008.08.007.

Clayton, R.N., Mayeda T.K., 1963. The use of bromine pentafluoride in the extraction of oxygen from oxides and silicates for isotopic analysis. Geochim. Cosmochim. Acta, 27, 43–52, doi:10.1016/0016-7037(63)90071-1.

Corbett, G.J., Leach, T.M., 1998. Southwest Pacific rim gold-copper systems: Structure, alteration and mineralization. Soc. Econ. Geol. Spec. Publ. 6, Littleton, CO, 238 p.

Craig, H., 1961. Standard for reporting concentrations of deuterium and oxygen-18 in natural waters. Science 133, 1833–1834, doi:10.1126/science.133.3467.1833.

de Ronde, C.E.J., 1995. Fluid chemistry and isotopic characteristics of seafloor hydrothermal systems and associated VMS deposits: potential for magmatic contributions. In: Thompson, J.F.H. (Ed.), Magmas, Fluids and Ore Deposits. Mineral. Assoc. Can. Short Course Ser. 23, 479–509.

Doyle, M.G., Allen, R.L., 2003. Subsea-floor replacement in volcanic-hosted massive sulfide deposits. Ore Geol. Rev. 23, 183–222, doi:10.1016/S0169-1368(03)00035-0.

Galley, A.G., Hannington, M.D., Jonasson, I., 2007. Volcanogenic massive sulfide deposits. In: Goodfellow, W.D. (Ed.), Mineral Deposits of Canada: A Synthesis of Major Deposit-Types, District Metallogeny, the Evolution of Geological Provinces, and Exploration Methods. Mineral. Dep. Div., Geol. Assoc. Can., Spec. Publ. 5, pp 141–161.

Gibson, H.L., Galley, A.G., 2007. Volcanogenic massive sulphide deposits of the Archean, Noranda district, Quebec. In: Goodfellow, W.D. (Ed.), Mineral Deposits of Canada: A Synthesis of Major Deposit-Types, District Metallogeny, the Evolution of Geological Provinces, and Exploration Methods. Mineral. Dep. Div., Geol. Assoc. Can., Spec. Publ. 5, pp 533–552.

Gilg, H.A., Sheppard, S.M.F., 1996. Hydrogen isotope fractionation between kaolinite and water revisited. Geochim. Cosmochim. Acta 60, 529–533, doi:10.1016/0016-7037(95)00417-3.

Grove, T.L., Till, C.B., Krawczynski, M.J., 2012. The role of H_2O in subduction zone magmatism. Annu. Rev. Earth Planet. Sci. 40, 413–439, doi:10.1146/annurev-earth-042711-105310.

Harvey, C.C., Brown, P.R., 1991. Mixed-layer clay geothermometry in the Wairakei geothermal field, New Zealand. Clays Clay Miner. 39, 614–621.

Hinchey, J.G., 2011. Visible/infrared spectroscopy (VIRS) of volcanogenic massive sulphide hydrothermal alteration products, Tulks volcanic belt, central Newfoundland: An additional exploration technique?. Newfoundland and Labrador Dept. of Nat. Res. Geol. Survey Report 11-1, 97–108.

Hughes, C.J., 1973. Spilites, keratophyres, and the igneous spectrum. Geol. Mag. 109, 513–527, doi:10.1017/S0016756800042795.

Humphries, S.E., Thompson, G., 1978. Trace element mobility during hydrothermal alteration of oceanic basalts. Geochim. Cosmochim. Acta 42, 127–136, doi:10.1016/0016-7037(78)90222-3.

Huston, D.L., 1999. Stable isotopes and their significance for understanding the genesis of volcanic-hosted massive sulfide deposits: A review. In: Barrie, C.T., Hannington, M.D. (Eds.), Volcanic-Associated Massive Sulfide Deposits: Processes and Examples in Modern and Ancient Environments. Soc. Econ. Geol., Reviews in Economic Geology Vol. 8, pp. 157–179, doi:10.5382/Rev.08.07.

Huston, D.L., Taylor, B.E., 1999. Genetic significance of oxygen and hydrogen isotope variations at the Kidd Creek volcanic-hosted massive sulfide deposit, Ontario, Canada. In: Hannington, M.D., Barrie, C.T. (Eds.), The Giant Kidd Creek Volcanogenic Massive Sulfide Deposit, Western Abitibi Subprovince, Canada. Econ. Geol. Mono. Ser. 10, Littleton, CO, pp. 335–350, doi:10.5382/Mono.10.12.

Inoue, A., Watanabe, T., Kohyama, N., Brusewitz, A.M., 1990. Characterization of illitization of smectite in bentonite beds at Kinnekulle, Sweden. Clays Clay Min. 38, 241–249.

Ishikawa, Y., Sawaguchi, T., Iwaya, S., Horiuchi, M., 1976. Delineation of prospecting targets for Kuroko deposits based on modes of volcanism of underlying dacite and alteration haloes. Mining Geol. 26, 105–117.

Jennings, S., Thompson, G.R., 1986. Diagenesis of Plio-Pleistocene sediments of the Colorado River Delta, southern California. J. Sediment. Petrol. 56, 89–98, doi:10.1306/212F8891-2B24-11D7-8648000102C1865D.

Jinfeng, Y., Xing, L., Liang, L., Pan, J., Meng, T., 2014. Application of short-wave infrared (SWIR) spectroscopy in quantitative estimation of clay mineral contents. IOP Conf. Series: Earth Environ. Sci. 17, 6 p.

Jones, S., Herrmann, W., Gemmell, J.B., 2005. Short wavelength infrared spectral characteristics of the HW horizon: Implications for exploration in the Myra Falls volcanic-hosted massive sulfide camp, Vancouver Island, British Columbia, Canada. In: Hedenquist, J.W., et al. (Eds.), 100th Anniversary Volume of Economic Geology, Society of Economic Geologists, Littleton, CO, pp. 273–294, doi:10.2113/gsecongeo.100.2.273.

Large, R.R., Gemmell, B., Paulick, H., Huston, D.L., 2001. The alteration box plot: A simple approach to understanding the relationship between alteration mineralogy and lithogeochemistry associated with volcanic-hosted massive sulfide deposits. Econ. Geol. 96, 957 – 971, doi:10.2113/gsecongeo.96.5.957.

MacDonald, R., Barrett, W.J., Sherlock, R.L., 1996. Geology and lithogeochemistry at the Hidden Creek massive sulfide deposit, Anyonx, west-central British Columbia. Explor. Min. Geol. 5, 369 – 398.

Maclean, W.H., 1990. Mass change calculation in altered rock series. Mineral. Deposit. 25, 44–49, doi:10.1007/BF03326382.

Maclean, W.H., Barrett, T.J., 1993. Lithogeochemical techniques using immobile elements. J. Geochem. Expl. 48, 109–133, doi:10.1016/0375-6742(93)90002-4.

Marumo, K., Nagasawa, K., Kuroda, Y., 1980. Mineralogy and hydrogen isotope geochemistry of clay minerals in the Ohnuma geothermal area, northeastern Japan. Earth Planet. Sci. Lett. 47, 255–262, doi:10.1016/0012-821X(80)90041-2.

McKinney, C.R., McCrea, J.M., Epstein, S., Allen, H.A., Urey, H.C., 1950. Improvements in mass spectrometers for the measurement of small differences in isotope abundance ratios. Rev. Sci. Instr. 21, 724–730, doi:10.1063/1.1745698.

McPhie, J., Doyle, M., Allen, R., 1993. Volcanic textures: A guide to the interpretation of textures in volcanic rocks. Centre for Ore Deposit and Exploration Studies, University of Tasmania, 196 p.

Monecke, T., Giorgetti, G., Scholtysek, O., Kleeberg, R., Götze, J., Hannington, M.D., Petersen, S., 2007. Textural and mineralogical changes associated with the incipient hydrothermal alteration of glassy dacite at the submarine PACMANUS hydrothermal system, eastern Manus Basin. J. Volcanol. Geotherm. Res. 160, 23 – 41, doi:10.1016/j.jvolgeores.2006.08.007.

Monecke, T., Petersen, S., Hannington, M.D., Anzidei, M., Esposito, A., Giordano, G., Garbe-Schönberg, D., Augustin, N., Melchert, B., Hocking, M., 2012. Explosion craters associated with shallow submarine gas venting off Panarea island, Italy. Bull. Volcanol. 74, 1937–1944, doi:10.1007/s00445-012-0651-8.

Moore, D.M., Reynolds, C.R. Jr., 1997. X-ray diffraction and the identification and analysis of clay minerals, 2nd Ed. Oxford University Press, New York, 400 p.

Morton, J.L., Koski, R.A., Normark, W.R., Ross, S.L., 1990. Distribution and composition of massive sulfide deposits at Escanaba Trough, southern Gorda Ridge. In: McMurray, G.R. (Ed.), Gorda ridge - A sea floor Spreading Center in the United States' Exclusive Economic Zone, pp. 77–92, doi:10.1007/978-1-4612-3258-2_5.

Mottl, M.J., 1983. Metabasalts, axial hot springs, and the structure of hydrothermal systems at mid-ocean ridges. Geol. Soc. Am. Bull. 94, 161–180, doi:10.1130/0016-7606(1983)94<161:MAHSAT>2.0.CO;2.

Mottl, M., Seewald, J., Wheat, C., Tivey, M., Michael, P., Proskurowski, G., McCollom, T.M., Reeves, E., Sharkey, J., You, C.F., 2011. Chemistry of hot springs along the Eastern Lau Spreading Center. Geochim Cosmochim Acta 75, 1013–1038, doi:10.1016/j.gca.2010.12.008.

Ohmoto, H., 1983. Geologic setting of the Kuroko deposits, Japan: Part I. Geologic history of the Green Tuff region: Econ. Geol. Mono. 5, 9–24.

Ohmoto, H., 1996. Formation of volcanogenic massive sulfide deposits: The Kuroko perspective. Ore Geol. Rev. 16, 491 – 559, doi:10.1016/0169-1368(95)00021-6.

Pearce, J.A., 1996. A user's guide to basalt discrimination diagrams. In: Wyman, D.A. (Ed.), Trace element geochemistry of volcanic rocks: Applications for massive sulphide Exploration. Geol. Assoc. Can. Short Course Notes Vol. 12, pp. 79–113.

Pearce, J., Stern, R., 2006. Origin of back-arc basin magmas: Trace element and isotope perspectives. Geophys. Monogr. 166, AGU, Washington, D.C., pp. 63–86, doi:10.1029/166GM06.

Reeves, E.P., Seewald, J.S., Saccocia, P., Bach, W., Craddock, P.R., Shanks, W.C., Sylva, S.P., Walsh, E., Pichler, T., and Rosner, M., 2011. Geochemistry of hydrothermal fluids from the PACMANUS, Northeast Pual and Vienna Woods hydrothermal fields, Manus basin, Papua New Guinea. Geochim. Cosmochim. Acta, 75, 1088−1123, doi:10.1016/j.gca.2010.11.008.

Reyes, A.G., 1990. Petrology of Philippine geothermal systems and the application of alteration mineralogy to their assessment. J. Volcanol. Geotherm. Res. 42, 279–309, doi:10.1016/0377-0273(90)90057-M.

Rona, P.A., Hannington, M.D., Raman, C.V., Thompson, G., Tivey, M.K., Humphris, S.E., Lalou, C., Petersen, S., 1993. Active and relict sea-floor hydrothermal mineralization at the TAG hydrothermal field, Mid-Atlantic Ridge. Econ. Geol. 88, 1989–2017, doi:10.2113/gsecongeo.88.8.1989.

Rona, P.A., 2003. Resources of the seafloor. Science 299, 673–674, doi:10.1126/science.1080679.

Ruks, T.W., Piercey, S.J., Ryan, J.J., Villeneuve, M.E., Creaser, R.A., 2006. Mid- to Late Paleozoic K-feldspar augen granitoids of the Yukon-Tanana Terrain, Yukon, Canada: Implications for crustal growth and tectonic evolution of the Northern Cordillera. Geol. Soc. Amer. Bull. 118, 1212–1231, doi:10.1130/B25854.1.

Rye, R.O., Roberts, R.J., Snyder, W.S., Lahusen, G.L., and Motica, J.E., 1984. Textural and stable isotope studies of the Big Mike cupriferous volcanogenic massive sulfide deposit, Pershing County, Nevada. Econ. Geol. 79, 124–140, doi:10.2113/gsecongeo.79.1.124.

Savin, S.M., Lee, M., 1988. Isotopic studies of phyllosilicates. In: Bailey, S.W. (Ed.), Hydrous Phyllosilicates (Exclusive of Micas), Rev. Mineral. 19, pp. 189–223.

Shau, Y.H., Peacor, D.R., Essene, E.J., 1990. Corrensite and mixed-layer chlorite=corrensite in metabasalt from northern Taiwan: TEM=AEM, EMPA, XRD, and optical studies. Contrib. Mineral. Petrol. 105, 123–142, doi:10.1007/BF00678980.

Sheppard, S.M.F., 1986. Characterization and isotopic variations in natural waters. In: Valley, J.W., Taylor, H.P., Jr., and O'Neil, J.R. (Eds.), Stable isotopes in high temperature geological processes: Reviews in Mineral- ogy, Mineral. Soc. Amer., Washington, D.C., Vol. 16, pp. 165–183.

Sheppard, S.M.F., Gilg, H.A., 1996. Stable isotope geochemistry of clay minerals. Clay Minerals 31, 1–24, doi:10.1180/claymin.1996.031.1.01.

Shikazono, N., Utada, M., Shimizu, M., 1995. Mineralogical and geochemical characteristics of hydrothermal alteration of basalt in the Kuroko mine area, Japan: Implications for the evolution of a back arc basin hydrothermal system. Appl. Geochem. 10, 621–642, doi:10.1016/0883-2927(95)00032-1.

Taylor, B.E., 1992. Degassing of H_2O from rhyolite magma during eruption and shallow intrusion, and the isotopic composition of magmatic water in hydrothermal systems. In: Hedenquist, J.W. (Ed.), Magmatic Contributions to Hydrothermal Systems. Geol. Survey Japan, Reports, Tsukuba, 279, pp. 190–194.

Thompson, A.J.B., Hauff, P.L., Robitaille, J.A., 1999. Alteration mapping in exploration: Application of short-wave infrared (SWIR) spectroscopy. Soc. Econ. Geol. Newslett. 39, 1–27.

Urabe, T., Scott, S.D., Hattori, K., 1983. A comparison of footwall- rock alteration and geothermal systems beneath some Japanese and Canadian volcanogenic massive sulfide deposits. Econ. Geol. Mono. 5, 345–364, doi:10.5382/Mono.05.21.

Head III, J.W., Wilson, L., 2003. Deep submarine pyroclastic eruptions: Theory and predicted landforms and deposits. J. Volcanol. Geotherm. Res. 121, 155–193, doi:10.1016/S0377-0273(02)00425-0.

Yeo, I., Searle, R.C., Achenbach, K.L., Le Bas, T.P., Murton, B.J., 2012. Eruptive hummocks: Building blocks of the upper ocean crust. Geology 40, 91–94, doi:10.1130/G31892.1.

Preface to Chapter 6

The previous chapters focused on the relationships between tectonics, volcanism, and hydrothermal venting in young back-arc basins, with a focus on the influence of subduction zone complexities on metallogenic potential. This chapter will now investigate how these processes operate in a mature back-arc spreading center. The southern and central Mariana back-arc is the target of investigations, providing insight into the influence of subduction-zone collisions, pre-existing structures, and the effects of arc proximity on magma supply rate and the siting of hydrothermal vent sites. This work has implications for evaluating the overall resource potential of each of the back-arc segments. Additional investigations on the effects of arc proximity on hydrothermal venting are published in Baker et al. (2017).

Chapter 6

Geological interpretation of volcanism and segmentation of the Mariana back-arc spreading center between 12.7°N and 18.3°N

Published in: Anderson, M.O., Chadwick, W.W. Jr., Hannington, M.D., Merle, S.G., Resing, J.A., Baker, E.T. Butterfield, D.A., Walker, S.L., Augustin, N., 2017. Geological interpretation of volcanism and segmentation of the Mariana back-arc spreading center between 12.7°N and 18.3°N. Geochem. Geophys. Geosyst. 18, doi:10.1002/2017GC006813.

Abstract

The relationships between tectonic processes, magmatism, and hydrothermal venting along ~600 km of the slow-spreading Mariana back-arc between 12.7°N and 18.3°N reveal a number of similarities and differences compared to slow-spreading mid-ocean ridges. Analysis of the volcanic geomorphology and structure highlights the complexity of the back-arc spreading center. Here, ridge segmentation is controlled by large-scale basement structures that appear to pre-date back-arc rifting. These structures also control the orientation of the chains of cross-arc volcanoes that characterize this region. Segment-scale faulting is oriented perpendicular to the spreading direction, allowing precise spreading directions to be determined. Four morphologically-distinct segment types are identified: dominantly magmatic segments (Type I); magmatic segments currently undergoing tectonic extension (Type II); dominantly tectonic segments (Type III); and tectonic segments currently undergoing magmatic extension (Type IV). Variations in axial morphology (including eruption styles, neovolcanic eruption volumes, and faulting) reflect magma supply, which is locally enhanced by cross-arc volcanism associated with N-S compression along the 16.5°N and 17.0°N segments. In contrast, cross-arc seismicity is associated with N-S extension and increased faulting along the 14.5°N segment, with structures that are interpreted to be oceanic core complexes—the first with high-resolution bathymetry described in an active back-arc basin. Hydrothermal venting associated with recent magmatism has been discovered along all segment types.

6.1. Introduction

The Mariana back-arc in the western Pacific is a slow-spreading center with highly complex tectonics with variable magmatic and hydrothermal activity (Fig. 6.1). Processes of crustal accretion in the Mariana back-arc share some similarities with the Mid-Atlantic Ridge, both being characterized by strong ridge segmentation along large shear zone offsets and non-transform ridge-axis discontinuities. Individual segments on slow-spreading ridges may exhibit several important variations along strike: (1) increased magmatic activity towards the center of the segment; (2) increased crustal thickness towards the ends of the segment; and (3) increased fault size towards the ends of the segment (e.g., Devey et al., 2010). However, ridges associated

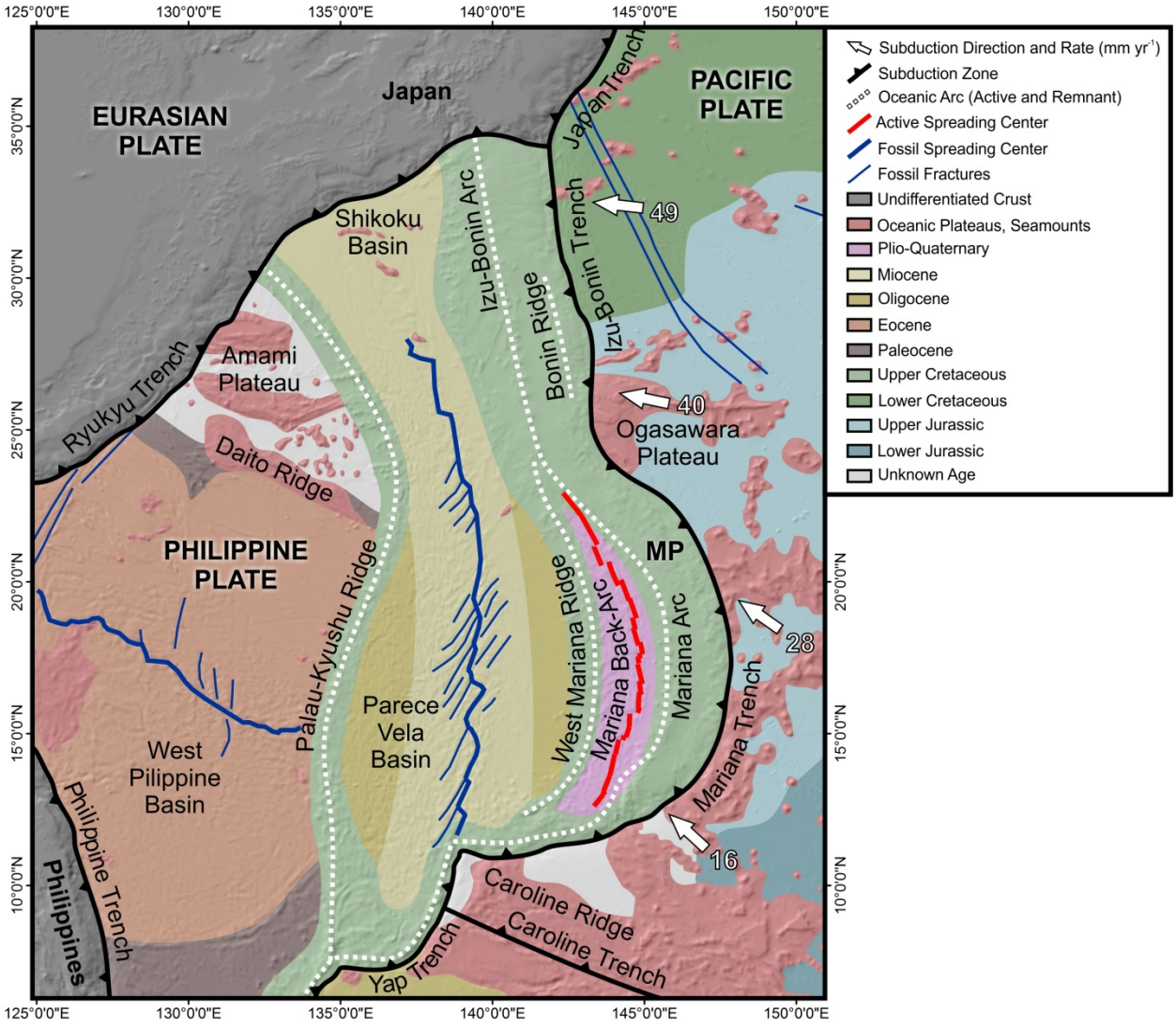


Fig. 6.1. Tectonic setting of the Mariana subduction zone, overlain on regional bathymetry (GMRT v.3.2; Ryan et al., 2009). Ages of oceanic crust are from Bouysse (2010) and references therein. Seafloor fractures are from Matthews et al. (2011) and Wessel et al. (2015). Subduction rates are relative to the Philippine Plate, from deMets et al. (2010). MP = Mariana Microplate.

with back-arc spreading have additional complexities resulting from oblique subduction, irregular trench geometries, strongly asymmetric spreading, subduction-zone collisions, slab re-orientation, variations in spreading rates, and variable contributions of arc magmas (e.g., Jenner et al., 1987; Vallier et al., 1991; Taylor et al., 1995; Stern, 2002; Kato et al., 2003; Stern, 2010; Stern et al., 2013). The structure of the Mariana back-arc is highly variable and reflects a number of these effects; for example, deep axial valleys with variable depths and cross-sectional morphologies north of 13.6°N versus axial volcanic ridges lacking valleys and resembling fast-spreading centers such as the East Pacific Rise south of 13.6°N (Fryer, 1995; Martínez et al., 2000; Deschamps and Fujiwara, 2003; Deschamps et al., 2004; Asada et al., 2007).

Early investigations of the Mariana region were driven by the discovery of hydrothermal activity in the central back-arc during a series of *Alvin* dives in 1987, which located the Alice Springs (including Central Peak), Burke (including Snail Pits and Anemone Heaven), and Illium vent fields near 18°12'N, and the Central Trough vent field near 18°2'N (Craig et al., 1987; Campbell et al., 1987; Hessler et al., 1988; Hessler and Martin, 1989; Hessler and Lonsdale, 1991, Gamo and Shipboard Scientific Party, 1993; Fujikura et al., 1997; Ishibashi et al., 2015). Venting was subsequently discovered in the southern back-arc near 13°N, beginning with the Forecast Seamount vent field in 1992 (Johnson et al., 1993; Gamo and Shipboard Scientific Party, 1993), the 13°N Ridge low-temperature vent field in 1999 (Mitsuzawa et al., 2000; Masuda et al., 2001), the Snail (also known as the "Fryer" site), Yamanaka (also known as the "Y" site), Pika, and Archean (3030–2980 mbsl) vent fields in 2003, and the Urashima vent field in 2010 (Wheat et al., 2003; Ishibashi et al., 2004; Urabe et al., 2004; Baker et al., 2005; Kakegewa et al., 2008; Yoshikawa et al., 2012; Nakamura et al., 2013; Ikehata et al., 2015). However, the regional geological context of the different vent sites was poorly understood.

Here, we use nearly-continuous high-resolution multibeam bathymetry collected by the *R/V Falkor* expedition FK151121 (20 November to 17 December 2015) over ~600 km of the Mariana back-arc spreading axis between ~13°N and ~18°N to assess the large-scale variations in axial morphology, and the relationships between tectonic processes, faulting, magma supply, and hydrothermal activity (Resing and Shipboard Scientific Party, 2016; Baker et al., 2016). The study area is divided into 11 segments, separated by first-, second-, and third-order

discontinuities. We identify four morphologically-distinct segment types, reflecting variable magma supply and structural evolution along the back-arc. We discuss the relationships between these features and the influence on hydrothermal venting. We also investigate the regional controls on ridge segmentation, and the effect of cross-arc structures on segment morphologies. Finally, segment-scale fault orientations are measured to reveal precise spreading directions along the Mariana back-arc.

6.2. Tectonic setting

The ~2800 km long Izu-Bonin-Mariana (IBM) trench is characterized by the oblique subduction of some of the oldest oceanic lithosphere in the world, ranging in age from Early Cretaceous in the north and to Mid-Jurassic along the Mariana trench (Fig. 6.1; Jarrard, 1986; Müller et al., 1997; Stern et al., 2003). The relative motions of the Pacific plate and the Philippine Sea plate result in a southward decrease in convergence rates along the IBM (deMets et al., 1994). Near the southern end of the Philippine Sea plate (8°N 137°18'E; deMets et al., 1994), the Pacific plate is moving NW relative to the Mariana trench at a rate of 16–28 mm yr^{-1}, while along the Izu Bonin trench the Pacific plate is moving WNW at a rate of 40–49 mm yr^{-1} (Fig. 6.1; deMets et al., 2010). Several phases of clockwise rotation of the Philippine Sea plate, beginning in the Eocene, affected the region (Uyeda and Ben-Avraham, 1972; Koyama et al., 1992; Hall et al., 1995; Sdrolias et al., 2004), first with the northward migration of the Izu-Bonin trench and opening of the West Philippine back-arc basin between 55 and 33–30 Ma (Fig. 6.1; Hilde and Lee, 1984; Deschamps and Lallemand, 2002). By 30–15 Ma, the Izu-Bonin trench had migrated almost ~1000 km to the north, accompanied by the opening of the Shikoku basin, while the Mariana trench migrated ~400 km to the north, accompanied by the opening of the Parece Vela basin (Fig. 6.1; Seno and Maruyama, 1984; Seno, 1985; Okino et al., 1998; Sdrolias et al, 2004). At ~25 Ma, the arrival of much older oceanic lithosphere (110–130 Ma crust from the Pacific plate) caused southward steepening of the IBM slab that is thought to have increased back-arc spreading and trench migration (Seno, 1985; le Pichon and Huchon, 1987; Carlson and Mortera-Gutierrez, 1990). In the late Miocene-Pliocene, subduction initiated farther south along the Philippine trench, and clockwise rotation of the Philippine Sea plate resumed, retreating from the Mariana trench faster than from the Izu-Bonin trench (Seno, 1985). This resulted in renewed

spreading in the Mariana back-arc at ~7 Ma, with true seafloor spreading initiating at 3–4 Ma, forming the Mariana Microplate (Figs. 6.1, 6.2; Scott et al., 1981; Masuda et al., 1994; Martínez et al., 1995; Stern et al., 2003). Spreading continues today in the Mariana back-arc basin, with an opening rate of ~15 to 45 mm yr^{-1}, increasing southwards (Kato et al., 2003; Stern et al., 2003).

Differences in the rate of trench migration in the Izu-Bonin and Mariana subduction zones correspond to different slab dips and morphologies (van der Hilst and Seno, 1993; Miller et al., 2004). Seismic tomography indicates that the Izu-Bonin slab deflects horizontally at the 670 km discontinuity in the upper mantle, whereas the Mariana slab dips almost vertically into the lower mantle (van der Hilst and Seno, 1993; Engdahl et al., 1998; Widiyantoro et al., 1999). The dramatic change in slab trajectory is accommodated by tearing at the junction of the Izu-Bonin and Mariana arcs (Miller et al., 2004). A possible slab tear also has been suggested at the southern end of the Mariana arc, where there is a sharp curve in the Challenger Deep segment (Fryer et al., 2003; Gvirtzman and Stern, 2004; Miller et al., 2006).

Several different mechanisms have been proposed to explain the modern crescent shape of the Mariana trench (Figs. 6.1, 6.2). Karig (1971a,b) suggested that the shape of the back-arc and variations in spreading rate are related to the non-rigid behaviour of the arc and forearc. Bracey and Ogden (1972) suggested that the basin formed as a result of rifting of the arc first at the center and then progressing northwards and southwards, contributing to the crescent shape of the arc. Le Pichon et al. (1985) proposed a rigid plate model with a single pole of rotation at ~21°N/138°E, although several studies demonstrated that a single pole cannot account for the basin geometry (Karig et al., 1978; Fryer and Hussong, 1981; Stern et al., 1984). Most authors agree that collisions of buoyant oceanic plateaus with the IBM subduction zone effectively 'pinned' the top and bottom of the Mariana trench, while continued eastward rollback at the center produced the curved shape (Vogt, 1973; Vogt et al., 1976; McCabe and Uyeda, 1983; Hsui and Youngquist, 1985; Carlson and Mortera-Gutierrez, 1990; Taylor, 1992; Scholz and Small, 1997; Miller et al., 2004; Miller et al., 2005; Wallace et al., 2005; Miller et al., 2006). In the south at ~10°N, the Mariana trench abuts the Caroline Ridge (Fig. 6.1). In the north at ~26°N, the Ogasawara Plateau (also known as the Marcus-Necker Ridge, Michelson Ridge, or Mid-Pacific Mountains) occurs at the junction between the Izu-Bonin and Mariana trenches

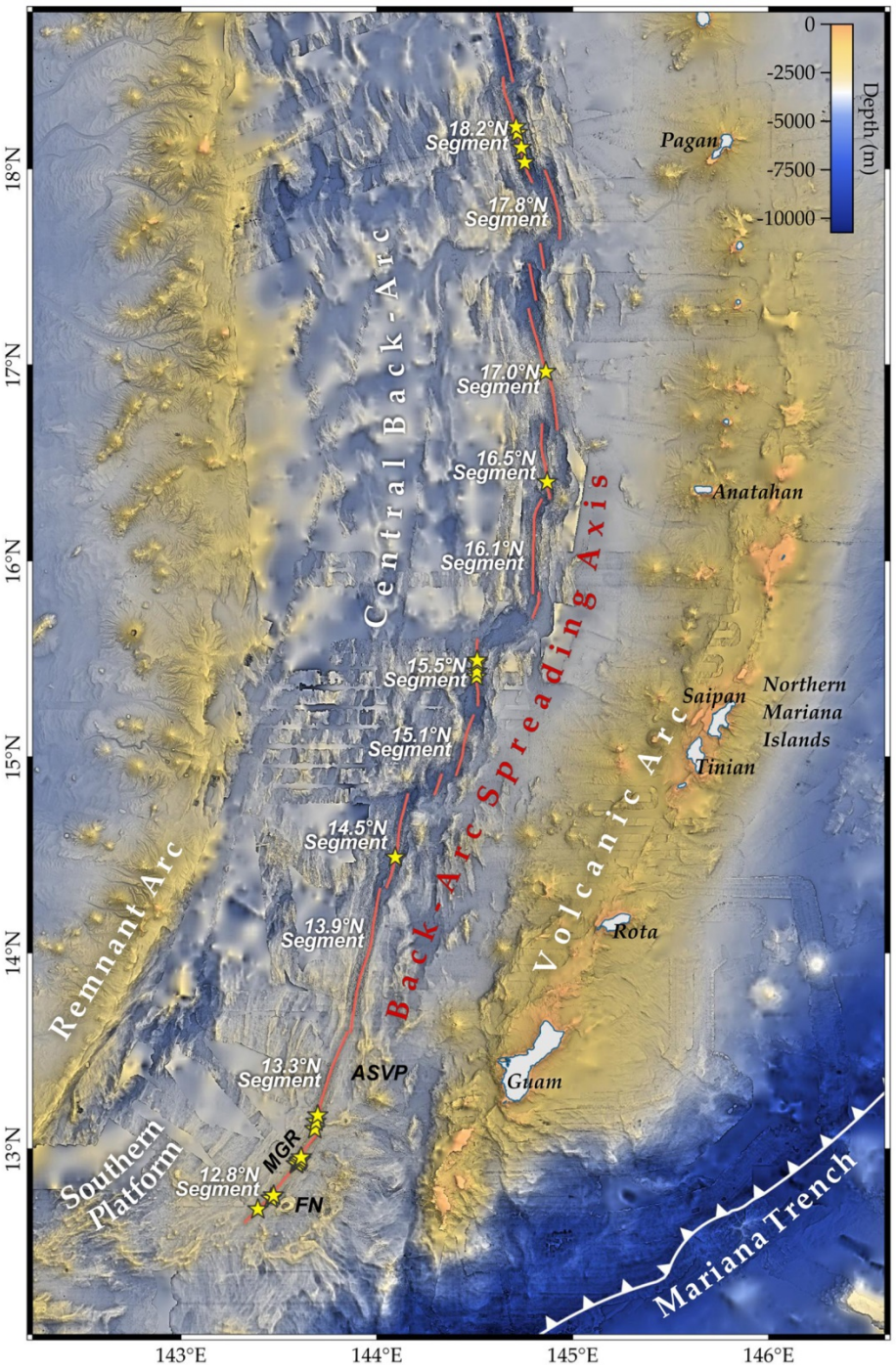


Fig. 6.2. Bathymetry of the Mariana back-arc with the segment nomenclature, with data from the Global Multi-Resolution Topography Synthesis (GMRT v3.2; Ryan et al., 2009), the FK151121 expedition aboard the *R/V Falkor* in 2015 (Resing and Shipboard Scientific Party, 2016), and the EX1605L1-2 expeditions aboard the *R/V Okeanos Explorer* in 2016 (Gray, 2016; Lobecker, 2016). Yellow stars indicate hydrothermal vent sites discovered along the back-arc from Resing and Shipboard Scientific Party (2016) and Baker et al. (2016). ASVP = Alphabet Seamount Volcanic Province; FN = Fina Nagu volcanic complex; MGR = Malaguana-Gadao Ridge.

(Fig. 6.1). Trench modification by collision of oceanic plateaus is supported by the three-dimensional numerical modelling of Mason et al. (2010), and is currently the most widely-accepted explanation for the highly arcuate shape of the Mariana trench.

De Mets et al. (2010) showed that extension in the back-arc is associated with the eastward displacement of the Mariana trench at ~20 mm yr^{-1} relative to the Philippine plate. The southern segments of the Mariana back-arc have full-spreading rates of 45 mm yr^{-1} (Kato et al., 2003). The central segments have slow spreading rates of 25–40 mm yr^{-1} (Kato et al., 2003), and the spreading is two to three times faster to the west than to the east (Deschamps and Fujiwara, 2003). In the central Mariana back-arc near 18°N, Fryer (1981) noted a major difference in seafloor morphology between the western and eastern sides of the basin. The western side is characterized by extensively block-faulted terrain over 60 km in width, whereas the eastern side contains evenly spaced ridges and troughs that resemble abyssal hill morphologies adjacent to the active spreading axis (Fig. 6.2). Fryer (1981) suggested that this morphology resulted from a two-stage evolution of the back-arc basin, with initial stretching and collapse of the arc during the first few million years of extension producing the block-faulted terrain, followed by a transition to true seafloor spreading producing the ridge-transform morphology. Major fracture zones (deep valleys that extend across the back-arc region) were originally identified by Kong (1993), and Hawkins et al. (1990) described numerous minor discontinuities in the back-arc spreading axis. Near the back-arc spreading center, these fracture zones are associated with major ridge offsets that display a strong sinistral shear component (referred to here as shear zone offsets, or SZOs), and are highly oblique to the spreading axis, unlike transform fractures at mid-ocean ridges. The morphology of the seafloor also varies considerably between the northern, central, and southern parts of the back-arc (Fig. 6.2; Fryer and Hussong, 1981; Hussong and Uyeda, 1981; Macdonald, 1982; Sinton and Hussong, 1983; Kong et al., 1992; Seama and Fujiwara, 1993; Fryer, 1995; Baker et al., 1996; Stüben et al., 1998; Martínez et al., 2000; Deschamps and Fujiwara, 2003; Deschamps et al., 2004; Asada et al., 2007). The slow-spreading morphology of the central segment is thought to correspond to a greater crustal thickness in this region of 4–7 km (Ambos and Hussong, 1982; Bibee et al., 1980; LaTraille and Hussong, 1980; Sinton and Hussong, 1983). In the north (21°N to 22°N latitude), the full-spreading rate is even slower, at ~10–15 mm yr^{-1} (Yamazaki et al., 1993). Progressive changes in isotopic and

geochemical compositions of basaltic glasses along the length of the Mariana back-arc were reported by Gribble et al. (1996) and Gribble et al. (1998), who identified a mature arc component with increased partial melting in the northernmost rift compared to the "true" back-arc basin basalts of the central back-arc. The proportion of the subduction component also decreases southwards in the central back-arc (Gribble et al., 1996).

A notable feature of the Mariana back-arc is the occurrence of cross-arc chains of volcanoes that extend westward from the presently active volcanic arc and are also present on the remnant arc (Fryer and Hussong, 1982; Dixon and Stern, 1983; Fryer, 1995; Heeszel et al., 2008; Stern et al., 2014). Several of these 'cross-arc chains' are seismically active (Heeszel et al., 2008). Near the active volcanic arc, these structures are undergoing ~N-S extension (Heeszel et al., 2008), consistent with GPS measurements of the islands, which are moving apart in a N-S direction (Kato et al., 2003). The regime where the cross-arc chains are located shifts from extension at the volcanic front to compression further to the west, reflecting the stresses associated with the bend in the arc (Heeszel et al., 2008). Fryer and Hussong (1982) suggested the volcanism associated with the cross-arc chains results from a complex interaction of pre-existing structures, fore-arc tectonics, arc magmatism, and back-arc rifting. Here, we examine these structures and their role in back-arc segmentation, segment morphology, and magmatism in the southern and central back-arc.

6.3. Methods

Ship-based multibeam bathymetric data from the active Mariana back-arc was collected during the *R/V Falkor* expedition FK151121 (Resing and Shipboard Scientific Party, 2016) and the *R/V Okeanos Explorer* expedition EX1605L1-2 (Gray, 2016; Lobecker, 2016), as shown in Figure 6.2. The *Falkor* and the *Okeanos Explorer* were both equipped with Kongsberg Maritime EM 302 multibeam echo sounders with operating frequencies of 30 kHz, capable of mapping seawater depths of up to 7,000 m. The data were gridded with a cell size of 40 m. To create geological maps of the active back-arc spreading center, the bathymetric data were interpreted with the aid of acoustic backscatter, slope shading, and rugosity and were further processed using the "Terrain Texture Shading" (TTS) technique (see Appendix Q: Suppl. Fig. Q1) developed by

Brown (2010). Terrain Texture Shading combines traditional hill shading with curvature analysis to add texture to shaded relief (e.g., Kennelly, 2008; Kennelly and Stewart, 2014; Augustin et al., 2016). This technique can increase the contrast of geological and structural features, and has recently been applied to bathymetric data in different tectonic settings (e.g., Anderson et al., 2016; Augustin et al., 2016).

We identified 11 separate segments along the Mariana back-arc spreading center that are between 33 and ~82 km long and ~6 to 25 km wide (Fig. 6.2). The mapped segments are between 12°52'N and 18°36'N and cover an area of ~23,250 km^2. Individual segments are separated by first- and second-order discontinuities, including three major shear zone offsets and numerous minor discontinuities. These include overlapping spreading centers (OSCs) and deviations in axial linearity (DEVALS) defined by sharp changes in spreading axis orientation with very little offset. Both OSCs and DEVALs are characterized by zones of discordant topography and highly variable structural orientations. Compared to previous work on the segmentation of the Mariana back-arc spreading center by Stüben et al. (1998), this study provides higher-resolution bathymetry, improved geographical precision, and a more precise identification of the spreading axis, leading to a better understanding of the relationships between geological units and the nature of the ridge offsets. The eight ridge segments identified by Stüben et al. (1998) broadly correlate with the segments identified here (Fig. 6.2): segment 1 (Stüben et al., 1998) = the 17.0°N segment (this study); segments 2, 3, and 4 (Stüben et al., 1998) are likely misidentified and occur to the west of the 16.5°N segment (this study); segment 5 (Stüben et al., 1998) = the 16.1°N segment (this study); segment 6 (Stüben et al., 1998) = the 15.5°N segment (this study); segment 7 (Stüben et al., 1998) = the 15.1°N segment (this study); and segment 8 (Stüben et al., 1998) = the 14.5°N segment (this study).

Different styles of faulting in this study were identified in the gridded bathymetry from scarps associated with high-intensity linear backscatter reflectors when facing inwards and low-backscatter shadows when facing outwards. The faults were mapped with the fault scarp direction indicated, and the vertical offsets were estimated using the depth differences between two points on either side of the scarp at the center of the fault in map view. The geometry and

spatial arrangement of faults, including azimuth distribution, were compiled and analyzed to distinguish areas of pure extension from those with a strike-slip component.

The map legend used in subsequent figures (also shown in Suppl. Fig. Q2) follows Anderson et al. (2016) and is based on established classifications of volcanic geomorphology and seafloor structure (cf. Walker, 1993; Thouret, 1999; Sigurdsson, 2000). Interpretation of map units was based on ground-truth data from earlier observations made during submersible dives with *Alvin* at ~18°N in 1987 (Craig et al., 1987; Campbell et al., 1987; Hessler et al., 1988; Gamo and Shipboard Scientific Party, 1993), with *Shinkai 6500* near ~13°N in 1992 (Y9204 TRANSARC expedition; Johnson et al., 1993; Gamo and Shipboard Scientific Party, 1993) and at ~17°N in 2008 (JAMSTEC expedition YK08-08 Leg-1; Fujiwara et al., 2008), from seafloor images captured by the towed ocean floor observation system and TV-grab between 14°45'N and 17°40'N during the *Sonne* SO-69 cruise in 1990 (Stüben et al., 1998), from near-bottom photo surveys at 15.5°N and 17°N by AUV *Sentry* in 2015 (expedition FK151121; Resing and Shipboard Scientific Party, 2016), ROV *Deep Discoverer* dives at 15.5°N and 17°N in 2016 (expedition EX1605L1; Gray, 2016), and ROV *SuBastian* dives at 15.5°N, 17°N, and 18°N in 2016 (expedition FK161129; Butterfield and Shipboard Scientific Party, 2017; Fig. 6.3). Comparisons with ground-truthed acoustic backscatter in other similar studies (e.g., Yeo et al., 2012; 2016; Anderson et al., 2016) provide additional confidence in our interpretations. Relative ages of the geological units were interpreted from overlapping relationships and sediment cover from backscatter intensity (cf. Hewitt et al., 2010). All contacts are inferred. Hydrothermal vent sites (yellow stars, Fig. 6.2) along the back-arc were identified during plume surveys of the FK151121 cruise (Resing and Shipboard Scientific Party, 2016; Baker et al., 2016), with seafloor observations confirming active venting during the EX1605L-1 cruise (Gray, 2016) and the FK161129 cruise (Butterfield and Shipboard Scientific Party, 2017).

Quantitative map data are reported in terms of the parameters shown in Figure 6.4 and summarized in Table 6.1: (1) segment length, measured along the back-arc spreading axis; (2) segment width, *W*, measured perpendicularly between the tops of the axial valley walls; (3) axial valley relief, *d*, measured from the deepest part of the axial valley to the highest point of the axial wall; (4) skewness, *s*, as the difference in height across an axial valley; (5) axial volcanic ridge

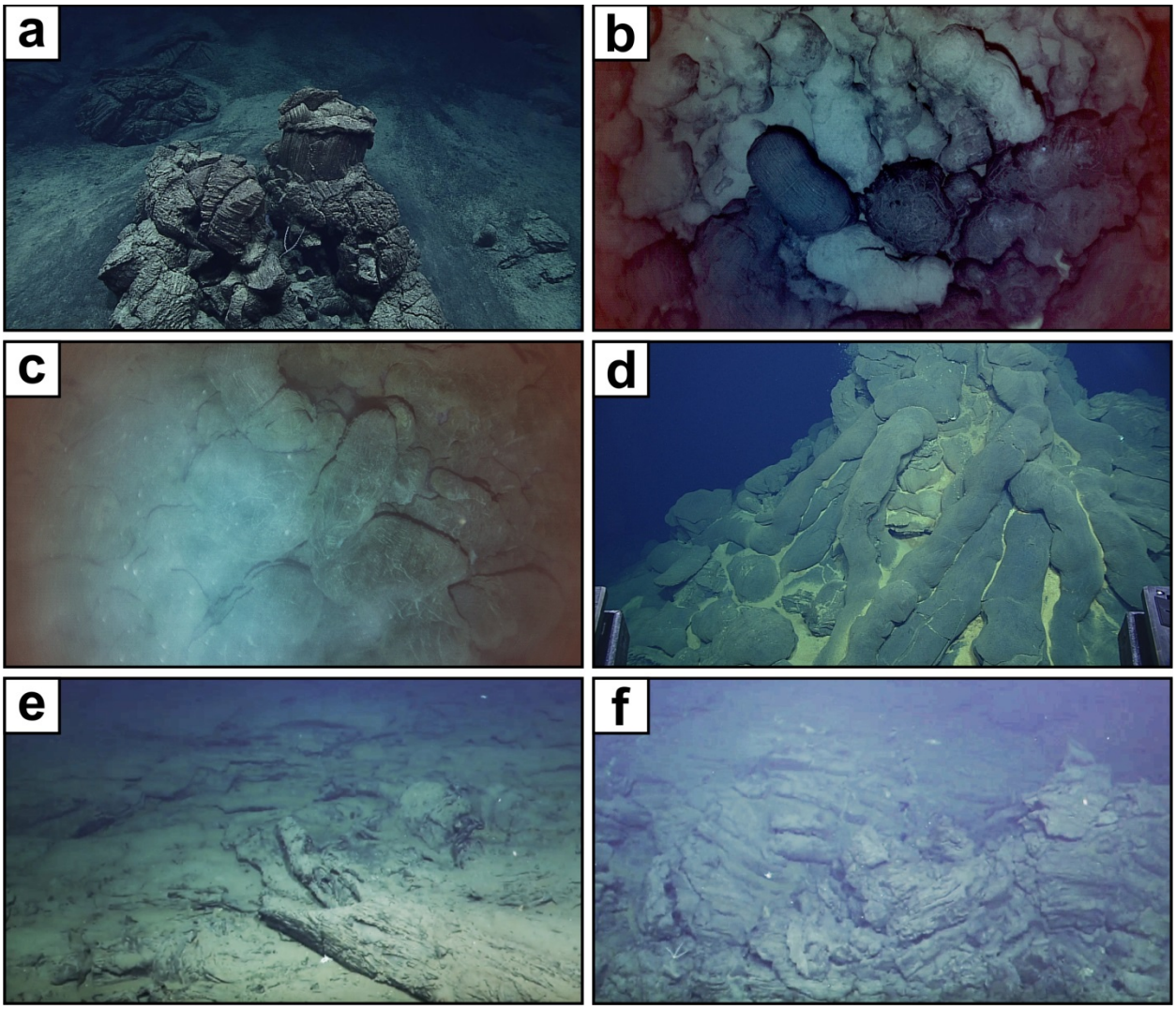


Fig. 6.3. Seafloor observations of lava morphologies and hydrothermal venting along the Mariana back-arc: (a) small isolated pillow lava outcrop surrounded by thick sediment (EX1605L-1 cruise; ROV dive 9; Gray, 2016); (b) older sedimented pillow flows overlain by young pillow flows (FK151121 cruise; AUV *Sentry* dive 367; Resing and Shipboard Scientific Party, 2016); (c) diffuse low-temperature diffuse venting emanating from a young pillow flow (FK151121 cruise; AUV *Sentry* dive 367; Resing and Shipboard Scientific Party, 2016); (d) large pillow mound with low-temperature iron-stained hydrothermal precipitates (EX1605L-1 cruise; ROV dive 9; Gray, 2016); (e) sedimented ropey sheet flows that characterize the 'smooth volcanic terrain' of the 17.0°N segment (FK161129 cruise; ROV dive S41; Butterfield and Shipboard Scientific Party, 2017); and (e) jumbled sheet flows along the 17.0°N segment (FK161129 cruise; ROV dive S41; Butterfield and Shipboard Scientific Party, 2017).

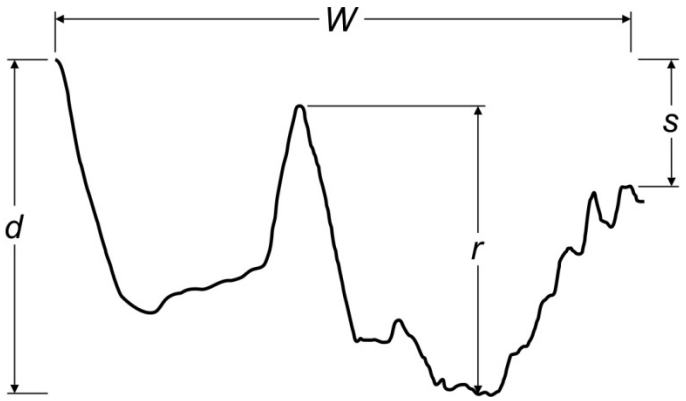


Fig. 6.4. Example of a cross-axis bathymetric profile with morphological parameters used in Table 6.1 and described in text: *W* = segment width, *d* = axial valley depth, *r* = axial volcanic ridge height, *s* = skewness.

Table 6.1. Morphologies and important features of the back-arc segments

	Segment Length (km)	Distance to Arc (km)	Full Spreading Rate (mm yr^{-1})*	Neo-Volcanic Volume (km^3)**	Segment Width *W* (km)†	Eruption Rate per km (m^3 yr^{-1} km^{-1})**	Maximum Seafloor Depth (mbsl)	Axial Valley Relief *d* (m)†	Skewness *s* (m)†	Axial Volcanic Ridge Relief *r* (m)†	Segment Type§	Hydro-thermal Venting ?
Southern Back-Arc												
12.8°N Segment	65	25	–	–		–					I	Y
A-A'					17		3400	N/A	0	500		
13.3°N Segment	59	25	45	–		–					I	Y
B-B'					14		3450	400	200	550		
C-C'					18		3700	400	50	550		
Central Back-Arc												
13.9°N Segment	82	68	~42.5	145		9377					III	N
D-D'					11		3350	550	0	200		
E-E'					8		3600	250	50	100		
F-F'					13		4300	700	150	250		
14.5°N Segment	49	86	~41.5	271		9979					III	Y
G-G'					12		4350	600	50	300		
H-H'					23		4500	1100	200	800		
I-I'					25		4550	1200	600	650		
15.1°N Segment	33	84	40	118		6219					III	N
J-J'					17		4400	800	100	250		
K-K'					23		3950	1050	200	450		
L-L'					13		4550	1300	700	200		
15.5°N Segment	34	101	~38	84		3912					IV	Y
M-M'					22		4650	1300	500	300		
N-N'					24		4400	1300	100	1050		
O-O'					25		4350	950	400	350		
16.1°N Segment	64	95	35	163		11143					III	N
P-P'					25		4300	1200	150	350		
Q-Q'					8		4200	850	300	150		
R-R'					10		4100	600	400	200		

Table 6.1. Continued

	Segment Length *L* (km)	Distance to Arc (km)	Full Spreading Rate (mm yr^{-1})*	Neo-Volcanic Volume (km^3)**	Segment Width *W* (km)†	Eruption Rate per km (m^3 yr^{-1} km^{-1})**	Maximum Seafloor Depth (mbsl)	Axial Valley Relief *d* (m)†	Skewness *s* (m)†	Axial Volcanic Ridge Relief *r* (m)†	Segment Type§	Hydro-thermal Venting?
16.5°N Segment	42	97	~32	108		10286					II	Y
S-S'					10		4050	650	400	350		
T-T'					8		3950	500	250	N/A		
U-U'					13.5		4500	1100	300	500		
17.0°N Segment	70	103	28	474		31600					II	Y
V-V'					18		4150	600	100	200		
W-W'					6		3300	450	100	0		
X-X'					11		3350	500	50	150		
Y-Y'					19		4550	1500	1400	200		
17.8°N Segment	39	97	~26	83		3458					III	N
Z-Z'					15		4300	1000	200	250		
AA-AA'					16		4250	1250	550	350		
BB-BB'					10		4650	1300	200	500		
18.2°N Segment	61	113	25	401		11739					IV	Y
CC-CC'					16		4750	1350	150	950		
DD-DD'					14		3900	600	0	250		
EE-EE'					16		4400	1300	650	800		

* Full spreading rates determined by GPS for some latitudes (Kato et al., 2003); extrapolated for intervening segments (indicated by ~)

** See Supplementary Information and Suppl. Table Q2 for neovolcanic volume and eruption rate calculations

† See Fig. 5.4 for definitions of parameters

§ See text for segment type classification (summarized in Fig. 6.17)

height, *r*, measured from the deepest part of the axial valley to the top of the central volcanic ridge. These measurements were made along 31 profiles across the mapped segments of the back-arc, perpendicular to spreading direction. Cross-sectional profiles were generated in ArcGIS®v.10.1 and were drafted to include the mapped geological features.

6.4. Mapped features

Despite variations in gross segment morphologies, we identify the fundamental geological units that occur throughout the southern and central back-arc. These units are classified as "old BAB crust," "neovolcanic terrain," "volcanoes," "deep sedimented basins," and "structures," as described below, which form the basis of the legend in Figures 6.5–6.14. We present a series of geological maps along each segment to show the distribution of these features (Section 5; Figs. 6.5–6.14), in order to provide insight into the evolution of the back-arc and the relationship between tectonics and volcanism along the spreading center.

6.4.1. Old BAB crust

The axial valley walls of the central Mariana trough expose old back-arc basin (BAB) crust associated with back-arc spreading that is now at the flanks of the active spreading center. This unit is stratigraphically older than the neovolcanic products that occupy the axial valley floor. The features of the old BAB crust are classified here based on the surface morphology and backscatter intensity. "Hummocky old crust" is characterized by a rough surface (high rugosity), with a low to moderate slope, numerous small volcanic edifices, and minor faulting. The backscatter is uneven with a low to moderate intensity. "Faulted old crust" has a lower surface roughness but numerous normal faults with steep slopes identified as bright, curvilinear reflectors in otherwise low-intensity backscatter. "Sedimented old crust" is characterized by smooth surfaces with low relief, few normal faults, shallow slopes, and low and even backscatter intensity. The contacts between these different types of old crust are gradational. Dome-shaped bathymetric features with clear corrugated surfaces at the sides of the axial valley are interpreted here to be "oceanic core complexes," similar to those now commonly found on the slow-spreading Mid-Atlantic Ridge (MAR; e.g., Tucholke et al., 1998; MacLeod et al., 2009). While

no sampling has been performed to confirm the presence of upper mantle rocks, these distinct bathymetric features are associated with mappable large-offset low-angle faults along the axial valley walls, and the corrugations on their upper surfaces extend ~6–7 km parallel to the direction of spreading. Near the tops of the core complexes, the seafloor morphology becomes more rugged with complex faulting patterns, which is consistent with observations of core complexes along the MAR, where sampling indicates that these elevated massifs are exposed magmatic crust (e.g., MacLeod et al., 2009). Such structures are widely interpreted to form by detachment faulting in areas of extension with relatively reduced magma supply (e.g., Buck et al., 2005).

6.4.2. Neovolcanic terrain

The neovolcanic terrain occupies the central portion of the spreading axis, and can be clearly distinguished from the older BAB crust. It is dominated by high-amplitude backscatter intensity and categorized as hummocky, smooth, or sedimented. The "hummocky neovolcanic terrain" forms long, linear volcanic ridges at the center of the axial valley (axial volcanic ridges, or AVRs). Characteristic features include a high rugosity, highly variable slopes, and moderately high to high backscatter. This is interpreted to reflect multiple thick onlapping pillow and lobate flows with steep flow fronts, most likely formed by multiple diking events during phases of magmatic extension (Fig. 6.3d; e.g., Yeo et al., 2012). It is difficult to distinguish individual flows based only on backscatter (i.e., sediment cover) because of the surface roughness and numerous steep-sloped reflectors. However, an AUV *Sentry* photo survey from 2015 (dive 367, FK151121; Resing and Shipboard Scientific Party, 2016) and ROV dives from 2016 (dive 9, EX1605L-1; and dive S45, FK161129; Gray, 2016; Butterfield and Shipboard Scientific Party, 2017) reveal both young and old pillow flows (Fig. 6.3b,c). The hummocky volcanic terrain grades locally into "smooth neovolcanic terrain," which is characterized by a low rugosity, low slopes, and high even backscatter. This is interpreted to represent flat-lying sheet flows that were erupted at a higher effusion rate, and is the dominant volcanic morphology in the southern segments where it comprises the main part of the ridge axis. In the central segments, smooth neovolcanic terrain generally occurs at the periphery of the hummocky flows near the axial valley walls and in deep basins. Seafloor observations during an AUV *Sentry* photo survey (dive

370, FK151121; Resing and Shipboard Scientific Party, 2016) and ROV dives (dive 11, EX1605L-1; and dive S41, FK161129; Gray, 2016; Butterfield and Shipboard Scientific Party, 2017) near 17°N confirmed the presence of jumbled to ropy sheeted flows with minor lobate flows (Fig. 6.3e,f) and numerous lava channels. "Sedimented neovolcanic terrain" also has a low rugosity and low slopes but is distinguished from the smooth volcanic terrain by a lower backscatter intensity. It occurs at variable distances from the hummocky AVRs within the broad axial valley, and fills in topographic lows around pillow mounds (Fig. 6.3a).

6.4.3. Volcanoes

Numerous volcanic edifices are found throughout the back-arc. These are classified as large rifted volcanoes, large volcanic cones, and smaller volcanic edifices. Only "small volcanic edifices" with diameters greater than 1 km were mapped; smaller edifices are numerous but difficult to distinguish from large hummocky mounds. The features that are clearly volcanoes are up to ~3 km in diameter and commonly have flat tops or dome shapes; obvious cones are less common. They have a clear circular shape and well-defined steep edges; some also have summit craters. They are common throughout the neovolcanic zone but also occur in hummocky old crust on the tops of the axial walls. "Large volcanic edifices" are ~4 to ~16.5 km in diameter, ~500 to ~2200 m in height, and have very high relief in addition to circular shapes and steep sides. Numerous off-axis examples can be seen at 13°0'N, and a particularly large cone occurs near the segment end at 16°20'N. A single large "rifted-volcano" near 17°N has a flat, circular morphology and is clearly split by the axial valley.

6.4.4. Deep sedimented basins

Deep, sedimented basins separate the ridge segments along the shear zone offsets (SZOs) and non-transform discontinuities at the segment ends. Near the segment centers, sedimented basins are less common and only occur distal to the spreading axis. They are low depressions with smooth bottoms and low, even backscatter interpreted to represent thick sediment cover. The sediment cover is greatest in areas of low magmatic activity at the segment ends and away from

the narrow spreading center. Faulting is rare; where present, the basins are designated “faulted basins.”

6.4.5. Structures

Features with strongly linear to curvilinear traces and scarps >100 m in height are identified as “major faults”; those with scarps <100 m high are referred to as “minor faults”. A total of 1664 major faults were measured with strike lengths of less than 100 m to a maximum of 8478 m; another 5148 minor faults were measured with strike lengths to a maximum of 11540 m. Both are identified as highly reflective linear features in the backscatter data. All fault surfaces are moderately to steeply dipping (generally east-dipping on the west side of the back-arc segments and west-dipping on the east side) with apparent normal sense of movement. Some distinctive lineaments, interpreted to be eruptive fissures, occur along the AVRs. In the middle of each ridge segment, the lineaments all have similar strike directions, whereas at the segment ends they show many orientations, reflecting the structural complexity of the transfer zones.

6.5. Segment geology

In this section, we describe the geology of 11 segments that comprise the active spreading center in the southern and central back-arc region (Figs. 6.5–6.14). The mapped area includes two segments along the 124 km of the southern back-arc, and 9 segments along 474 km of the central back-arc. The segments are named according to the latitude at the segment centers. For each segment, the cross-sectional morphologies are shown along profiles at the segment middle and end points. Structural azimuths are also examined, including major and minor faults and volcanic ridge axes.

6.5.1. Southern Mariana back-arc

The southern Mariana back-arc between 11°50’N and 13°40’N was first described in detail by Martínez et al. (2000). It is shallower than the central part of the back-arc (~3000 mbsl along the in the south, compared to ~3500–5000 m in the central back-arc), and the spreading axis

approaches to within ~25 km of the presently active arc-front volcanoes, owing to the sharp westward curvature of the trench (Fig. 6.2). The active spreading center is morphologically similar to a fast-spreading ridge, including a broad "inflated" zone with a narrow axial rise (the Malaguana-Gadao Ridge), a smooth flanking morphology, and a general lack of transform offsets, despite sharp changes in the trend of the spreading center (Fig. 6.5). The presence of a shallow axial magma chamber along the Malaguana-Gadao Ridge was documented by Becker et al. (2010).

The 12.8°N and 13.3°N segments

The 12.8°N and 13.3°N segments are ~58 km in length and located ~25 km from the volcanic arc. They are morphologically similar and broadly symmetrical (low 'skewness'), with widths of ~14–17 km, maximum seafloor depths of ~3400 to ~3700 mbsl (increasing northwards), and ~500–550 m-tall axial topographic highs (Fig. 6.5; Table 6.1). Profile A-A' in Figure 6.5 shows topography similar to the fast-spreading EPR (cf. MacDonald, 2001). At ~13°10'N (profiles B-B' and C-C' in Fig. 6.5), clear valley walls up to 400 m high first appear and the axial zone bears a closer resemblance to the intermediate-rate spreading segments of the EPR (cf. MacDonald, 2001). Along the spreading axis, the seafloor is dominated by heavily faulted but smooth and hummocky neovolcanic terrain. Minor sedimented neovolcanic terrain occurs along a narrow graben to the west of the spreading axis (Fig. 6.5). The smooth flows are interpreted to represent the products of volcanic eruptions close to the center of the spreading axis, with the hummocky terrain on the flanks. The latter is thought to be dominated by lobate and pillow flows, possibly related to increased magma transport along lava tubes or greater eruptive volumes along faults on the eastern side of the back-arc spreading axis. The dominant structures along the 12.8°N segment have a mean orientation of 39.3° ± 1.7° (95% confidence interval; n = 325; Fig. 6.5). There is an abrupt change in the orientation at 13°4'N, where an OSC has an offset of ~4.6 km with the 13.3°N segment. The dominant structures along the 13.3°N segment have a mean orientation of 23.8° ± 1.2° (n = 488; Fig. 6.5). There are more outward-dipping faults on this segment, and individual faults have vertical throws of less than ~300 m.

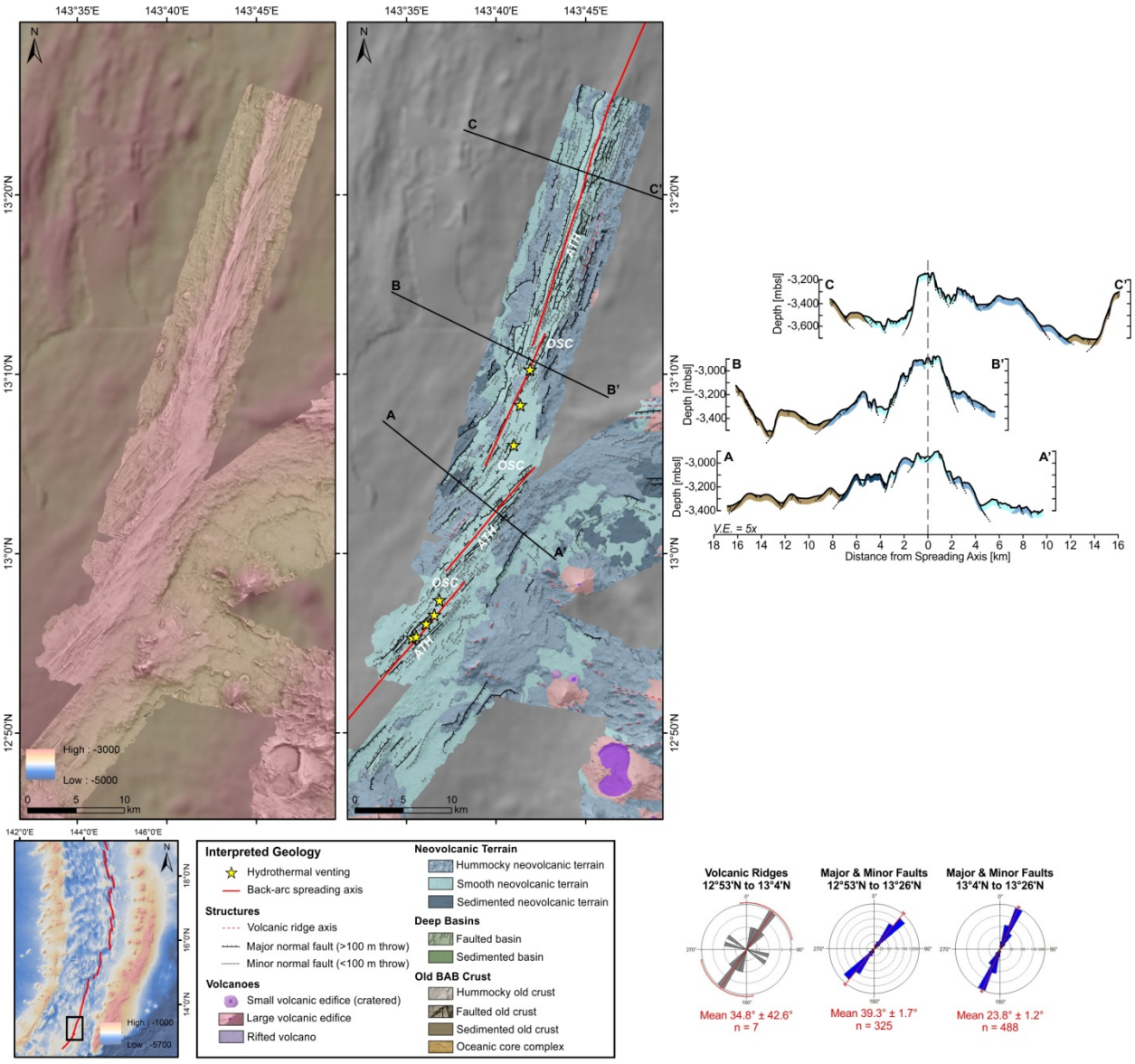


Fig. 6.5. (left) Bathymetry, (middle) interpreted geological map, and (right) across-axis profiles of the 12.8°N and 13.3°N segments, with the segment location in the back-arc shown as a black square in the lower left map. Azimuths of the major and minor faults from 12°53'N to 13°4'N, and 13°4'N to 13°26'N are shown in blue, and the volcanic ridge axes for the entire area are shown in grey (lower right corner). ATH = axial topographic high; OSC = overlapping spreading center; V.E. = vertical exaggeration (5×). A larger geological map is available in Appendix Q (Suppl. Fig. Q3).

6.5.2. Central Mariana back-arc

Between ~13°40'N and 18°40'N the central Mariana back-arc more closely resembles a slow-spreading (<50 mm yr^{-1}) mid-ocean ridge. Segmentation is controlled by major SZOs, OSCs, and DEVALs. The axial valley is pronounced, with relief up to ~1500 m, with the highest relief at the segment ends. In cross-section, the axial walls are highly skewed (i.e., have different heights on either side of the spreading center), and this skewness becomes more pronounced towards the segment ends. As noted by previous workers, the magmatic activity in this part of the back-arc is strongly focused at the segment centers (e.g., Fryer and Hussong, 1981; Hussong and Uyeda, 1981; Macdonald, 1982; Martínez et al., 2000). The axial depths are greater than on mid-ocean ridge crust of the same age, a regional characteristic of the Mariana back-arc, and the orientations of faults are more variable with a wider zone of axial deformation, indicated by recent faulting far off-axis (Fryer and Hussong, 1981; Macdonald, 1982). The axial zone of each segment is bound by heavily faulted old BAB crust along the valley walls. Hummocky neovolcanic terrain dominates the valleys, forming long volcanic ridges dotted by numerous small volcanic edifices. The axial zone is variably faulted, with individual segments dominated by either recent magmatic or tectonic extension.

The 13.9°N segment

The 13.9°N segment is ~82 km in length and is located ~68 km from the volcanic arc. It is separated from the 13.3°N segment to the south by an OSC with an offset of ~1.8 km. The segment is characterized by a narrow (~8–13 km wide) axial valley bound by faulted old crust in the west and hummocky old crust in the east (Fig. 6.6; Table 6.1). The valley relief ranges from ~550 in the south, ~250 m midway along its length, and ~700 m in the north, with a progressive northward deepening of the seafloor (3350 mbsl to 4300 mbsl; Table 6.1). The valley has a low degree of skewness in cross section with <100 m height difference between the western and eastern walls (Fig. 6.6; Table 6.1). The axial valley is dominated by hummocky and smooth neovolcanic terrain, with numerous small flat-topped volcanic edifices (Fig. 6.6). Short volcanic ridges occur throughout the hummocky terrain. The lack of an axial volcanic high and the presence of a central graben (up to ~250 m deep) suggest a relatively low rate of magma supply

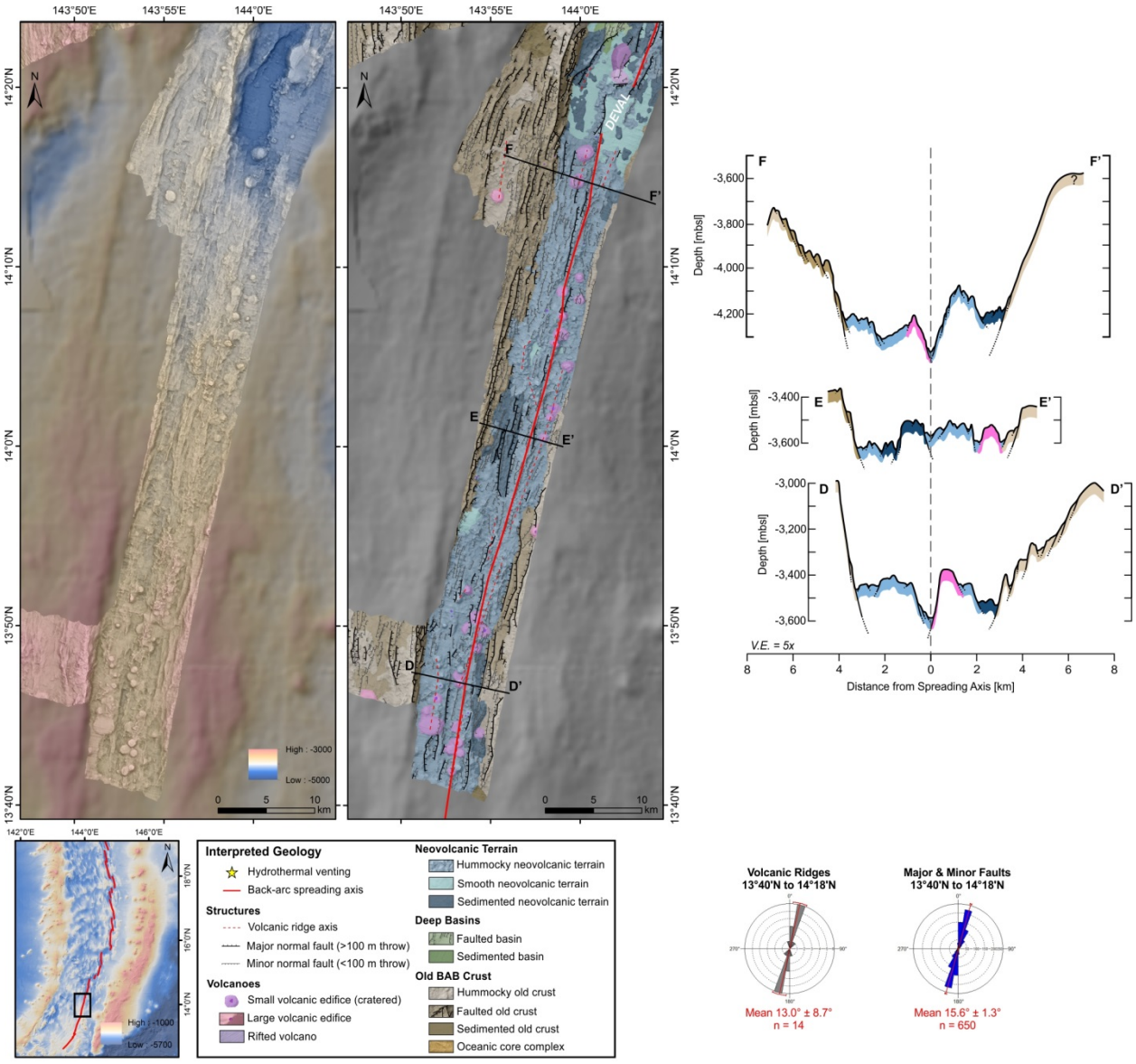


Fig. 6.6. (left) Bathymetry, (middle) interpreted geological map, and (right) across-axis profiles of the 13.9°N segment, with the segment location in the back-arc shown as a black square in the lower left map. Azimuths of the major and minor faults and the volcanic ridge axes for the entire segment from 13°40'N to 14°18'N are shown in blue and grey, respectively (lower right corner). DEVAL = deviation in axial linearity; V.E. = vertical exaggeration (5×). A larger geological map is available in Appendix Q (Suppl. Fig. Q4).

(Fig. 6.6). The total estimated volume of the neovolcanic products is ~334 km^3 (see Appendix Q for volume calculations). Intense faulting within the old crust and neovolcanic zone has a uniform orientation over the entire segment length of 15.6° ± 1.3° (n = 662). The maximum throw on the faults is ~400 m.

The 14.5°N segment

The 14.5°N segment is ~49 km long and located ~86 km from the volcanic arc, offset ~1 km to the east from the 13.9°N segment by a DEVAL. This segment is characterized by a northward deepening of the seafloor from ~4350 mbsl to a maximum depth of ~4550 mbsl and widening of the back-arc from ~12 km to ~25 km (Fig. 6.7; Table 6.1). The relief of the axial valley increases progressively from ~600 m in the south to ~1200 m in the north (Fig. 6.7; Table 6.1). The ~1100-m high western flank of the axial valley wall at ~14°40'N is interpreted to be an inside corner high (IC; e.g., Severinghaus and Macdonald, 1988) and oceanic core complex (as described in Section 4.1; Fig. 6.7; Table 6.1). An additional complex occurs on the opposite side of the axial valley, with rough corrugations parallel to the spreading direction, and N-S extension indicated by an 800-m wide E-W trending graben. These features confirm the formation of core complexes in the Mariana back-arc, following the earlier discovery of upper mantle peridotites in dredge samples at 20°N (Stern et al., 1996). They the second to be identified in a back-arc basin environment based on high-resolution bathymetric features, following the discovery of the Godzilla megamullion structures in the extinct Parece Vela basin (Ohara et al., 2001). The axial valley walls at this location are composed of heavily sedimented, faulted to hummocky old crust, and the basin floor is dominated by an 800-m high axial volcanic ridge. The heavily faulted neovolcanic terrain forming the ridge is clearly split along its axis forming a deep graben, with sedimented hummocky neovolcanic terrain in the west, and younger hummocky neovolcanic terrain to the east (Fig. 6.7). Smooth neovolcanic terrain occurs only at the segment ends. The volume of neovolcanic products in the axial valley is estimated to be ~271 km^3 (see Appendix Q). Fault orientations between 14°10'N and 14°53'N have a wide range with a mean of 16.7° ± 1.8° (n = 944), parallel to the volcanic ridges (16.7° ± 16.0°, n = 10; Fig. 6.7). A subset of faults trending ~ENE forms a small graben at 14°30'N/144°0'E,

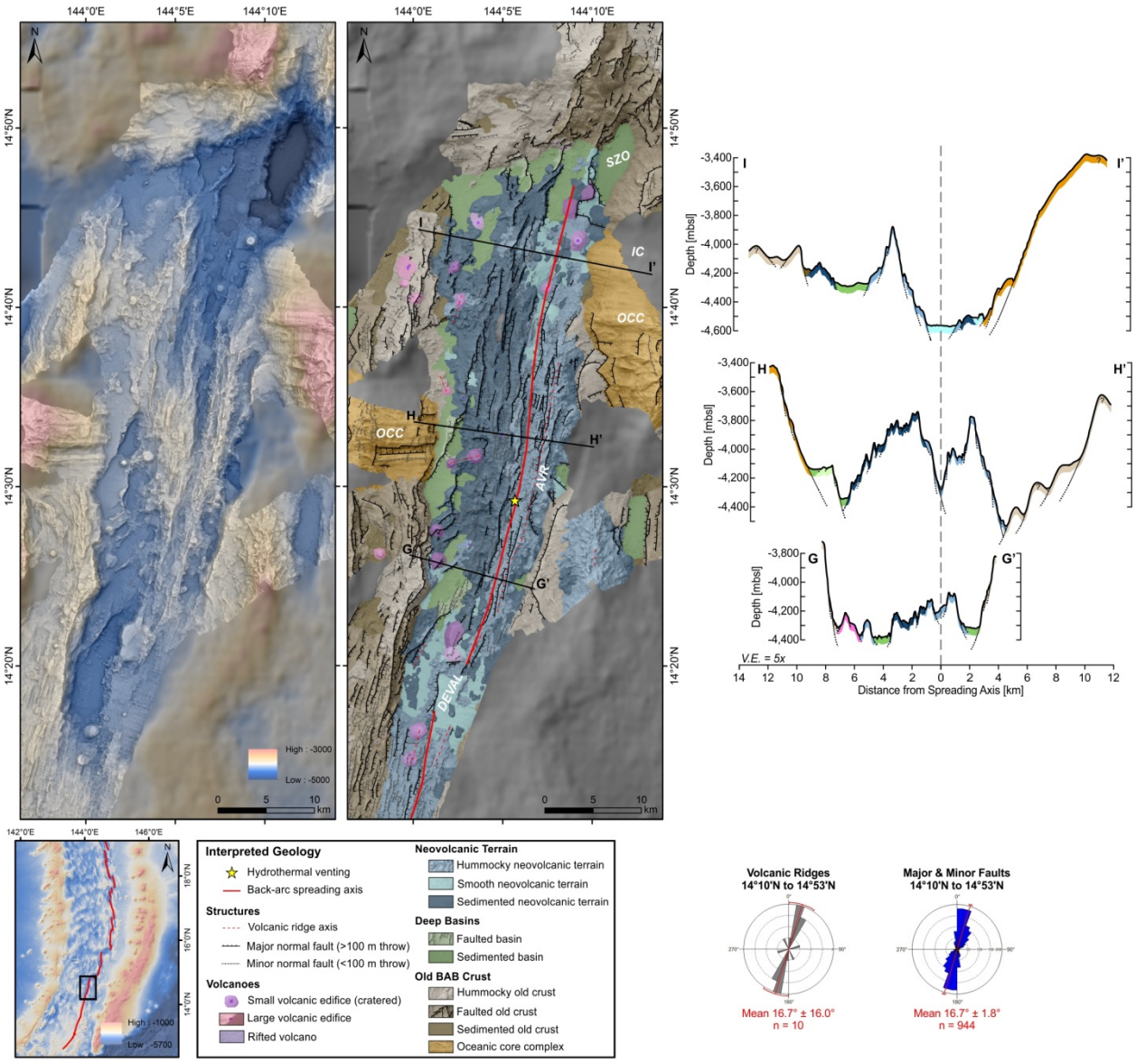


Fig. 6.7. (left) Bathymetry, (middle) interpreted geological map, and (right) across-axis profiles of the 14.5°N segment, with the segment location in the back-arc shown as a black square in the lower left map. Azimuths of major and minor faults and the volcanic ridge axes and for the entire segment from 14°18'N to 14°53'N are shown in blue and grey, respectively (lower right corner). AVR = axial volcanic ridge; DEVAL = deviation in axial linearity; IC = inside corner high; OCC = oceanic core complex; SZO = shear zone offset; V.E. = vertical exaggeration (5×). A larger geological map is available in Appendix Q (Suppl. Fig. Q5).

consistent with a component of N-S extension (Fig. 6.7). Individual fault throws along this segment are up to ~550 m in height.

The 15.1°N segment

The 15.1°N segment is ~33 km long and located ~84 km from the volcanic arc (Fig. 6.8; Table 5.1). It is separated from the 14.5°N segment by a SZO comprising a series of deep sedimented basins in a northeast-trending *en echelon* arrangement. The offset between the 15.1°N and 14.5°N segments is ~31 km, and is associated with a fracture zone that extends a further ~57 km to the west. The axial valley widens from ~17 km to ~23 km midway along its length and narrows to ~13 km in the north, but the depth is similar to the 14.5°N segment, shallowing to ~3950 mbsl in the center (Fig. 6.8; Table 6.1). The axial high is dominated by heavily faulted and sedimented hummocky neovolcanic terrain. In the southern portion of the segment, the neovolcanic zone is dominated by a narrow ~450 m-tall hummocky axial volcanic ridge, with smooth and sedimented neovolcanic terrain towards the valley walls and sedimented basins (Fig. 6.8). Axial valley relief increases northwards from ~800 m to 1300 m, with approximately ~700 m difference in height in the northern part of the segment (Fig. 6.8; Table 6.1). It has a documented spreading rate of ~40 mm yr^{-1} (Kato et al., 2003). The volume of neovolcanic products is estimated to be ~118 km^3 (see Appendix Q). The axial walls are dominated by hummocky old crust, which contains most of the faults, having a wide range of orientations (mean of 14.6° ± 7.3°, n = 217; Fig. 6.8). The maximum throw on the faults is ~600 m. Subordinate E-W and NW-SE trending faults are also present. Notably corrugated surfaces at 15°8'N on the western side of the valley suggest the presence of another core complex. Of all the segments studied, the 15.1°N segment most closely resembles the slow-spreading MAR (e.g., near 37°N: MacDonald, 2001).

The 15.5°N segment

The 15.5°N segment is ~34 km long and located ~101 km from the volcanic arc. It is offset from the 15.1°N segment by an abrupt change in the trend of the spreading axis. The axial valley is ~22–25 km wide, shallowing northwards from ~4650 to 4350 mbsl. The axial valley relief also

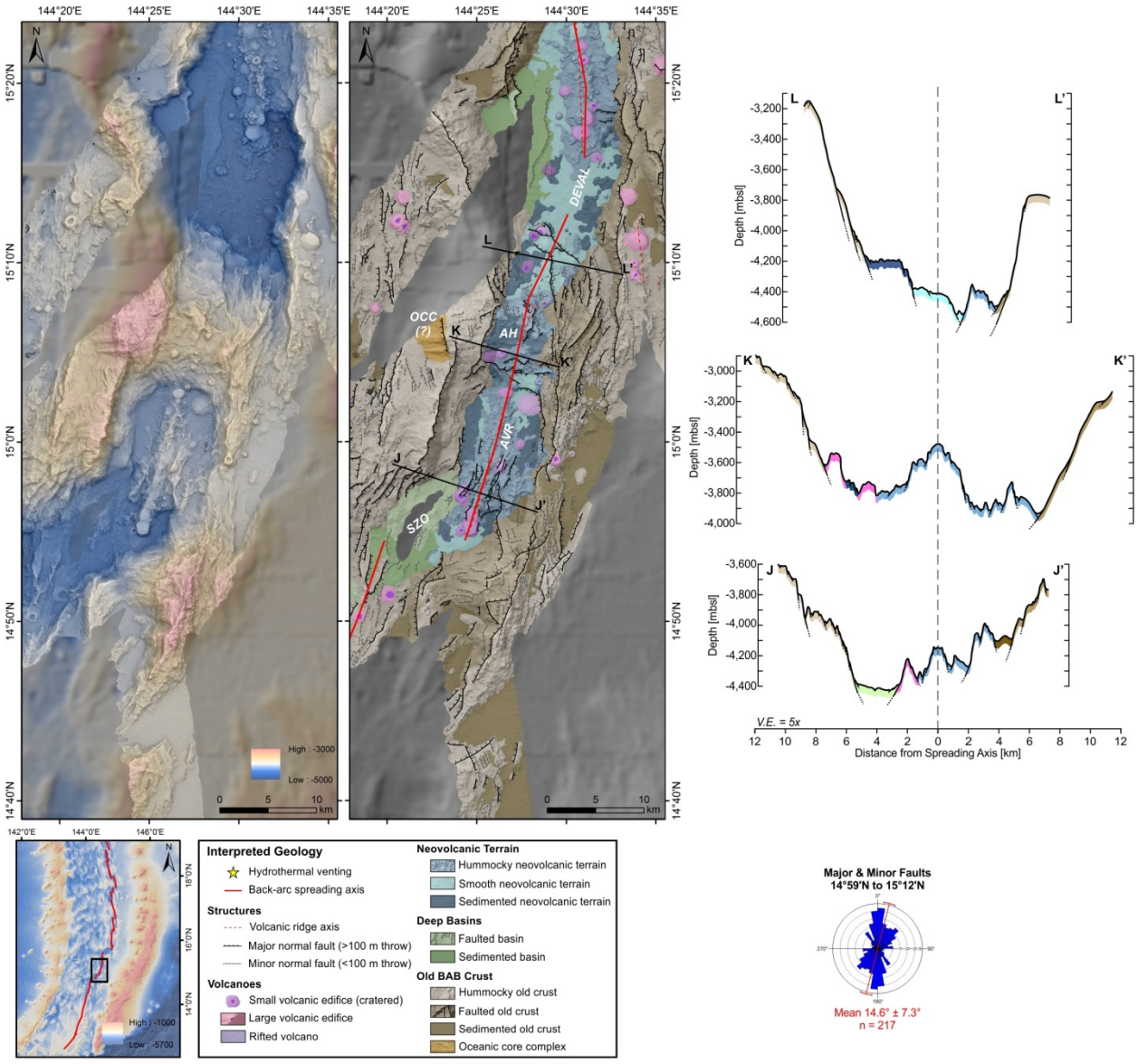


Fig. 6.8. (left) Bathymetry, (middle) interpreted geological map, and (right) across-axis profiles of the 15.1°N segment, with the segment location in the back-arc shown as a black square in the lower left map. Azimuths of the major and minor faults of the entire segment from 14°59'N to 15°12'N are shown in blue (lower right corner). AH = axial high; AVR = axial volcanic ridge; DEVAL = deviation in axial linearity; OCC(?) = possible oceanic core complex; SZO = shear zone offset; V.E. = vertical exaggeration (5×). A larger geological map is available in Appendix Q (Suppl. Fig. Q6).

decreases from ~1300 to 950 m (Fig. 6.9; Table 6.1). There is a large height difference of ~400 m at the northeastern end of the segment forming an inside corner high (Fig. 6.9; Table 6.1). The neovolcanic zone shows almost no faulting and has a tall axial volcanic ridge that rises up to ~1050 m above the surrounding seafloor (Fig. 6.9). The ridge is composed of hummocky neovolcanic terrain surrounded by smooth and sedimented neovolcanic terrain (Fig. 6.9; Table 6.1), with an estimated total volume of ~84 km^3 (see Appendix Q). An AUV *Sentry* photo survey (dive 367) conducted during the FK151121 cruise identified newly-erupted pillow lavas occupying an area 7.3 km long and 300–600 m in width at this spreading axis (Fig. 6.3a; Resing and Shipboard Scientific Party, 2016). Two ROV *Deep Discoverer* dives (numbers 9 and 10) during cruise EX1605L-1 and one ROV *SuBastian* dive (number S45) during cruise FK161121 also found multiple generations of extensive pillow flows and minor lobate flows, and large steep-sided pillow mounds topped by smaller pillow mounds called "haystacks" (Fig. 6.3b; Gray, 2016; Butterfield and Shipboard Scientific Party, 2017). The volcanic ridges along the axial valley have a mean orientation of 15.9° ± 13.5° (n = 151; Fig. 6.9), whereas faulting in the old BAB crust adjacent to the axial valley has a mean orientation of 7.5° ± 4.9° (n = 151) with throws of up to 800 m.

The 16.1°N segment

The 16.1°N segment is ~64 km long and located ~95 km from the volcanic arc. It is offset ~35 km to the east by a first-order ENE-trending SZO, associated with a fracture zone that extends for ~164 km across the width of the back-arc. Like the other segments, it shallows northwards from ~4300 to 4100 mbsl (Fig. 6.10; Table 6.1). Axial relief also decreases northwards from ~1200 to 600 m, with a height difference of 300–400 m between the central and northern parts of the segment (Fig. 6.10, Table 6.1). The entire segment has an hourglass-shape, with the axial zone being ~25 km wide in the south, ~8 km wide in the center, and ~10 km wide in the north (Fig. 6.10; Table 6.1). A discontinuous axial volcanic ridge, 100–350 m in height, occupies an area of low relief at the center of the mid-segment high (Fig. 6.10). In the south, the axial volcanic ridge is slightly offset to the east where the valley widens near the SZO. The full spreading rate is ~35 mm yr^{-1} (Kato et al., 2003), and the estimated volume of the neovolcanic products is ~163 km^3 (see Appendix Q). The hummocky and smooth volcanics of

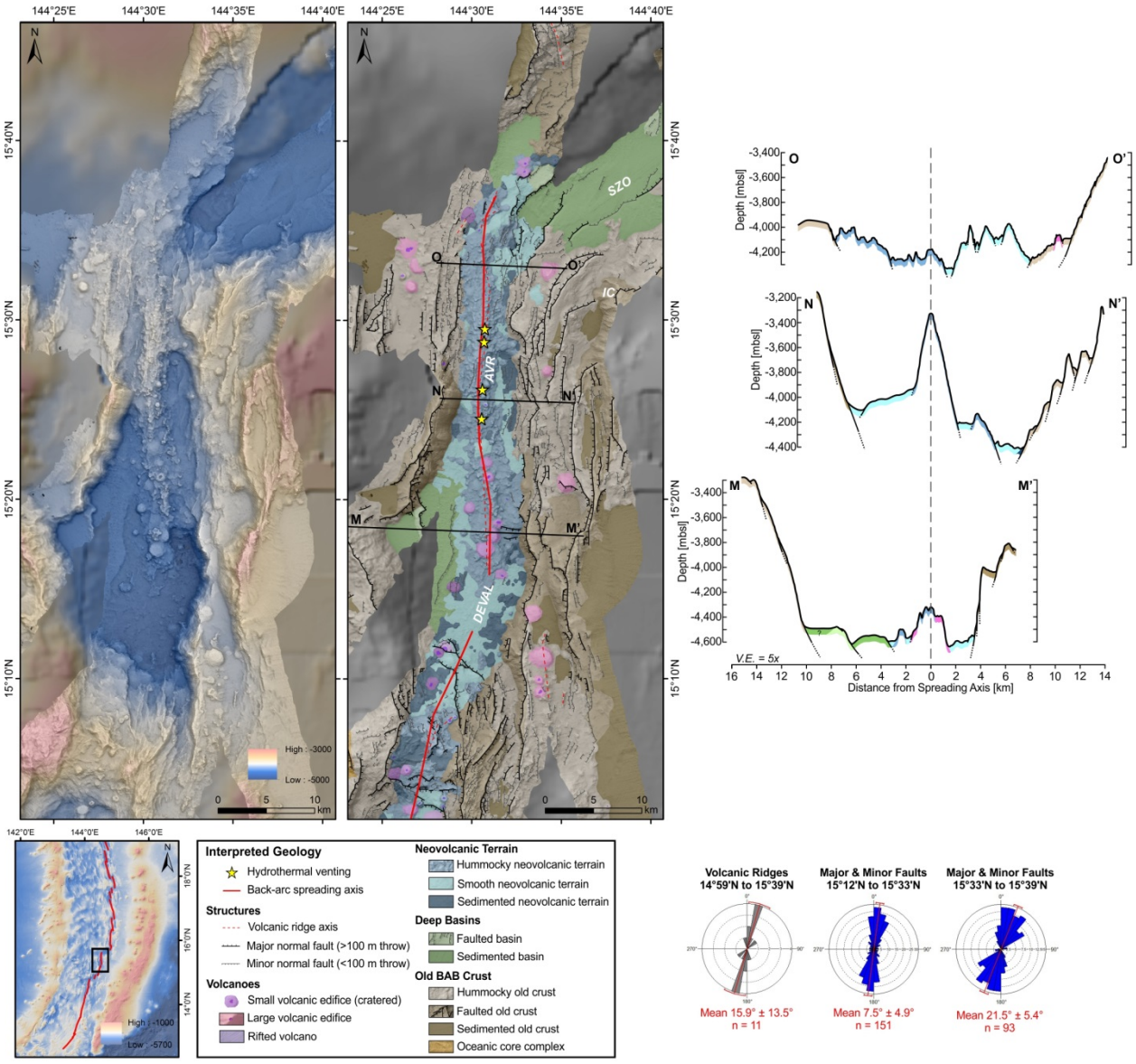


Fig. 6.9. (left) Bathymetry, (middle) interpreted geological map, and (right) across-axis profiles of the 15.5°N segment, with the segment location in the back-arc shown as a black square in the lower left map. Azimuths of the major and minor faults from 15°12'N to 15°33'N, and 15°33'N to 15°39'N are shown in blue, and the volcanic ridge axes from 14°59'N to 15°39'N are shown in grey (lower right corner). AVR = axial volcanic ridge; DEVAL = deviation from axial linearity; IC = inside corner high; SZO = shear zone offset; V.E. = vertical exaggeration (5×). A larger geological map is available Appendix Q (Suppl. Fig. Q7).

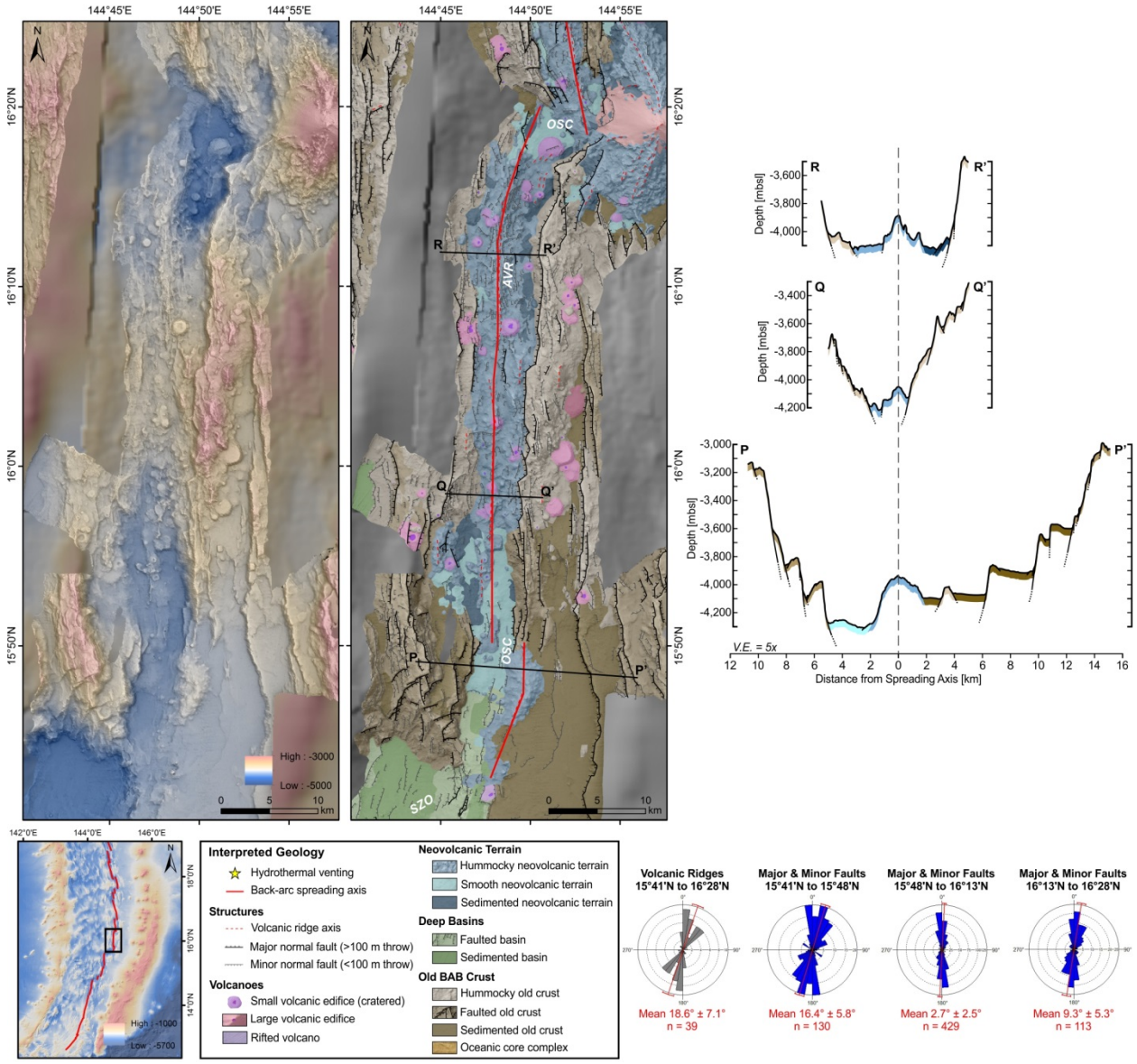


Fig. 6.10. (left) Bathymetry, (middle) interpreted geological map, and (right) across-axis profiles of the 16.1°N segment, with the segment location in the back-arc shown as a black square in the lower left map. Azimuths of the major and minor faults from 15°41'N to 15°48'N, 15°48'N to 16°13'N, and 16°13'N to 16°28'N are shown in blue, and the volcanic ridge axes for the entire segment are shown in grey (lower right corner). AVR = axial volcanic ridge; OSC = overlapping spreading center; SZO = shear zone offset; V.E. = vertical exaggeration (5×). A larger geological map is available in Appendix Q (Suppl. Fig. Q8).

the neovolcanic zone are moderately faulted, with throws of <100 m. Larger faults with throws of 600 m occur off-axis in the old crust between 15°48'N and 16°13'N and have an orientation of 2.7° ± 2.5° (n = 429; Fig. 6.10), although a number of faults and ridges with different orientation are related to the radial pattern of faulting at the base of a large off-axis volcanic cone (Fig. 6.10). The axial walls are moderately-faulted hummocky and sedimented old crust (Fig. 6.10).

The 16.5°N segment

The 16.5°N segment is ~42 km long and located ~97 km from the volcanic arc. It is offset ~8.5 km to the east from the 16°20'N segment by a second-order OSC. A large volcanic cone occurs at the southern end of the segment to the east of the spreading center (Fig. 6.11). The axial zone, which also has an hour-glass shape, ranges from 10 km in width in the south to 8 km in the center and 20 km in the north (Fig. 6.11; Table 6.1), shallowing from ~4050 mbsl in the south to ~3950 mbsl in the center, before rapidly deepening to ~4500 mbsl in the north. In the south, the axial valley is ~650 m deep and dominated by heavily-faulted hummocky to smooth neovolcanic terrain with a ~300 m-tall axial volcanic ridge (Fig. 6.11; Table 6.1). Midway along the segment, the axial valley is ~500 m deep and consists of unfaulted smooth volcanic terrain and large, dome-shaped volcanoes (Fig. 6.11). In the north, it is ~1100 m deep and contains a ~500 m-tall axial volcanic ridge with minor faulting (Fig. 6.11). The neovolcanic products along this segment have an estimated volume of ~108 km^3 (see Appendix Q). Faulting between 16°19'N and 16°54'N trends ~N-S, with a mean orientation of 1.0° ± 1.7° (n = 1161); however, the mean orientation of the volcanic ridges is closer to 174.3° ± 4.7° (n = 43; Fig. 6.11). The irregular axial walls consist of hummocky to sedimented old crust.

The 17.0°N segment

The 17.0°N segment is ~70 km and located ~103 km from the volcanic arc. It is offset from the 16.5°N segment by an OSC, with a jump of ~8 km. The segment has a pronounced hourglass shape, with the width of the axial zone ranging from ~19 km in the south, to ~6 km in the center, and ~18 km in the north (Fig. 6.12; Table 6.1). The axial valley is ~600 m deep in the south with

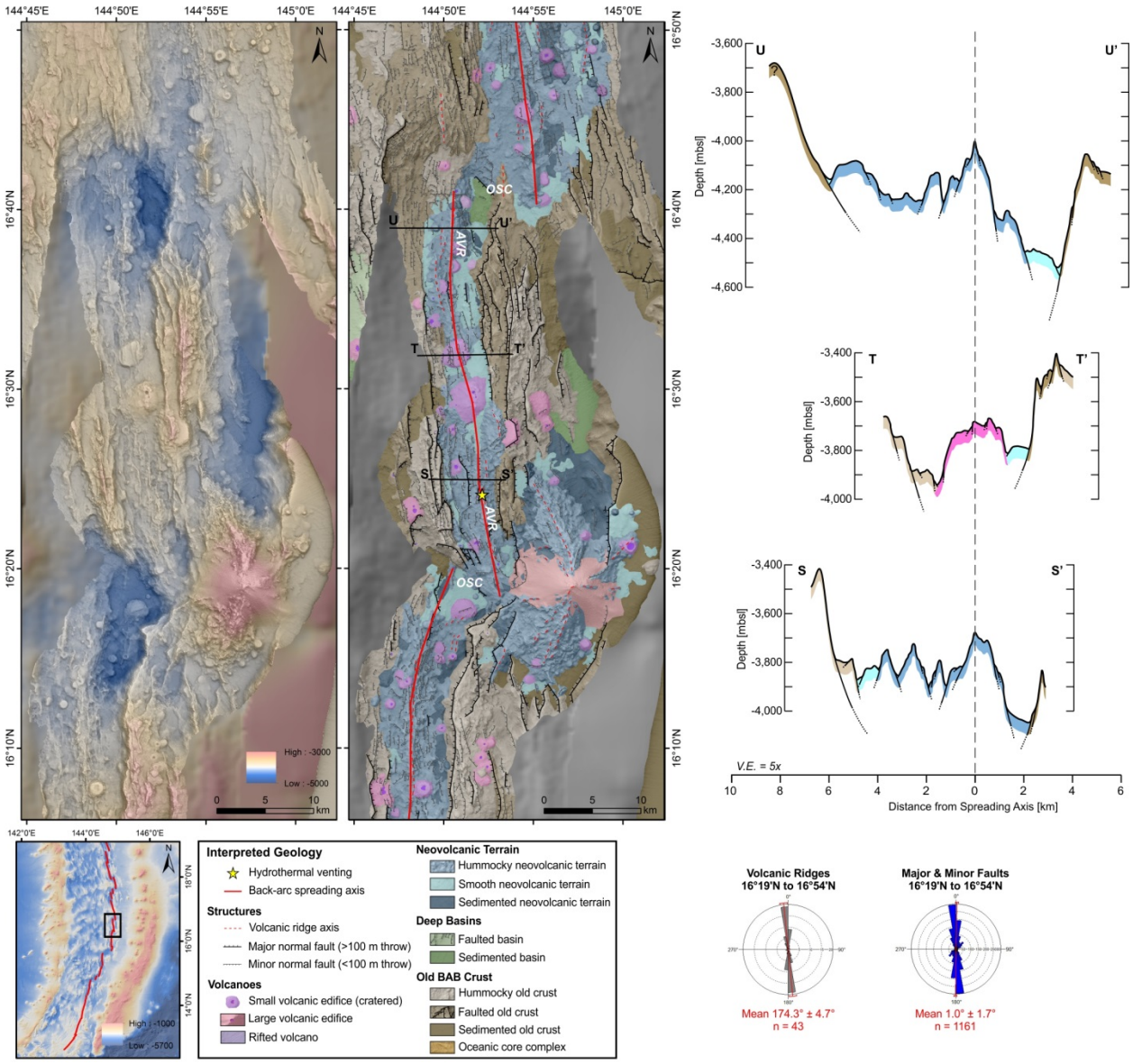


Fig. 6.11. (left) Bathymetry, (middle) interpreted geological map, and (right) across-axis profiles of the 16.5°N segment, with the segment location in the back-arc shown as a black square in the lower left map. Azimuths of the major and minor faults and the volcanic ridge axes for the entire segment from 16°19'N to 16°54'N are shown in blue and grey, respectively (lower right corner). AVR = axial volcanic ridge; OSC = overlapping spreading center; V.E. = vertical exaggeration (5×). A larger geological map is available in Appendix Q (Suppl. Fig. Q9).

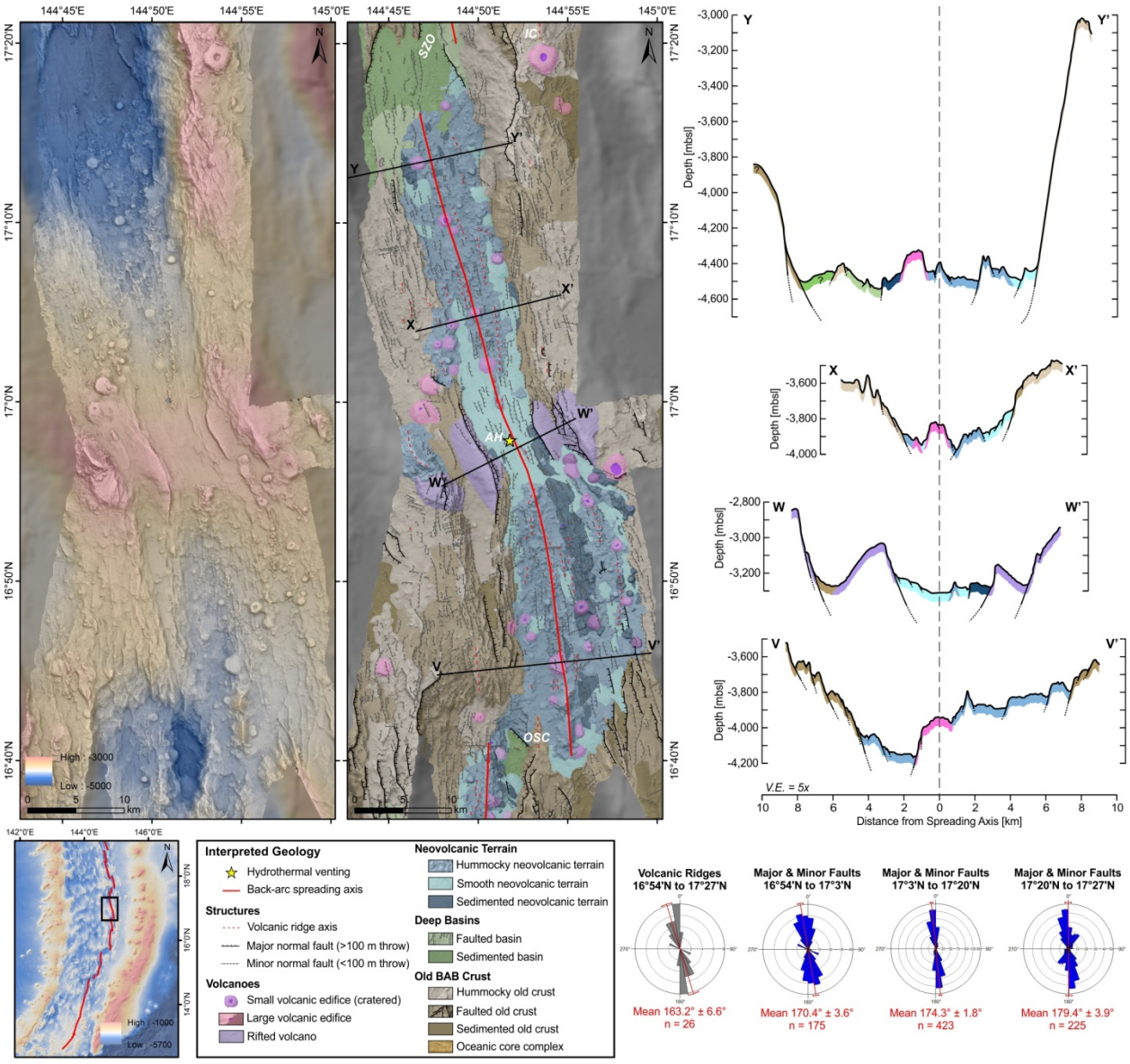


Fig. 6.12. (left) Bathymetry, (middle) interpreted geological map, and (right) across-axis profiles of the 17.0°N segment, with the segment location in the back-arc shown as a black square in the lower left map. Azimuths of the major and minor faults from 16°54'N to 17°3'N, 17°3'N to 17°20'N, and 17°20'N to 17°27'N are shown in blue, and the volcanic ridge axes for the entire segment are shown in grey (lower right corner). AH = axial high; IC = inside corner high; OSC = overlapping spreading center; SZO = shear zone offset; V.E. = vertical exaggeration (5×). A larger geological map is available in Appendix Q (Suppl. Fig. Q10).

a seafloor depth of ~4150 mbsl, shallowing to ~3300 mbsl midway along the segment where the axial valley is ~450 m deep. The orientation of the axial zone follows a gently-sigmoidal shape, and then drops into a 1500-m deep valley at a water depth of ~4550 mbsl in the north (Fig. 6.12; Table 6.1). The southern neovolcanic zone occupies a broad area of unsedimented hummocky and smooth volcanic flows separated by sedimented volcanic flows (Fig. 6.12). The eastern half has higher backscatter intensity, suggesting that this area may be the location of a new spreading axis. This is supported by near-bottom side-scan surveys conducted in 2003 (Deschamps and Fujiwara, 2003; Deschamps et al., 2004; Deschamps et al., 2005; Asada et al., 2007). There are abundant minor faults within the axial valley, but mainly within the sedimented flows and near the basin walls. The central part of the neovolcanic zone is characterized by a large, split flat-topped volcano (Fig. 6.12). Further away from the spreading center, a second split volcano is mirrored on either side of the axial valley, indicating multiple episodes. A magma lens was imaged at this location at ~4 km depth in multichannel seismic surveys (Taylor et al., 2002), and the site was visited by submersible in 2008 (Fujiwara et al., 2008). It was also the focus of an AUV *Sentry* photo survey during dive 370 in 2015 (Resing and Shipboard Scientific Party, 2016), and ROV dives in 2016 (Gray, 2016; Butterfield and Shipboard Scientific Party, 2017). The center of the volcano is smooth and unfaulted, and multiple ROV dives revealed extensive jumbled and ropey sheet flows and minor lobate flows, indicating high effusion rates (Fig. 6.3e,f). This smooth seafloor morphology is in sharp contrast to the other segments of the central back-arc, which are dominated by hummocky axial volcanic ridges. Fujiwara et al. (2008) observed almost no sediment in the axial portion, and our data show a decrease in backscatter intensity toward the eastern wall. In the northern part of the segment, the axial valley is dominated by hummocky neovolcanic terrain along discontinuous low-relief volcanic ridges with little faulting; smooth neovolcanic terrain occurs at the flanks (Fig. 6.12a). The overall spreading rate of the segment is ~30 mm yr^{-1} (Kato et al., 2003), and the estimated volume of material within the neovolcanic zone is ~474 km^3 (see Appendix Q). The axial valley walls are dominated by hummocky old crust, with minor faulting (throws <100 m: Fig. 6.12). Between 17°3’N and 17°20’N, faults have a mean orientation of 174.3° ± 1.8° (n = 423**;** Fig. 6.12). Between 17°20’N and 17°27’N, fault orientations are variable (mean of 179.4° ± 3.9°,–n = 225; Fig. 6.12), reflecting the shape of the spreading axis. North of 17°20’N, an inside-corner high on the eastern

flank of the valley is dominated by a large detachment fault (~22° dip) with a maximum throw of ~3000 m (Fig. 6.12).

The 17.8°N segment

The 17.8°N segment is ~39 km long and located ~97 km from the volcanic arc (Fig. 6.13; Table 6.1). This segment marks the apex of the curved subduction zone, where the back-arc is the widest. It is separated from the 17.0°N segment by another SZO, with a total offset of ~42 km to the east. This offset is associated with the extensive Pagan Fracture Zone, which extends ~226 km westward across the width of the back-arc and reflects the curvature of the arc, which changes from NE-SW to ~N-S (Fig. 6.2). The segment widens and deepens northwards, from ~15 to 17 km in width and from ~4300–4650 mbsl (Fig. 6.13; Table 6.1). The axial valley walls increase in height from ~1000 to 1300 m, with a ~550 m height difference ('skewness') between the eastern and western axial walls in the central portion of the segment (Fig. 6.13; Table 6.1). The old crust that forms the walls is heavily faulted on the west and dominated by hummocky volcanics in the east. A narrow hummocky axial volcanic ridge up to 500 m high occurs within the neovolcanic zone, surrounded by sedimented and smooth neovolcanic terrain (Fig. 6.13). The total volume of neovolcanic products is estimated to be ~83 km^3 (see Appendix Q). Between 17°40'N and 18°0'N, the major and minor faults have a mean orientation of 172.8° ± 3.6° (n = 386; Fig. 6.13). The volcanic ridges follow the dominant fault orientation, with a mean orientation of 167.1° ± 3.9° (n = 31; Fig. 6.13).

The 18.2°N segment

The 18.2°N segment is ~61 km long and located ~113 km from the volcanic arc. It is separated from the 17.8°N segment by an OSC with a total offset of ~9 km to the west and occupies the widest part of the Mariana back-arc. The segment morphology has been described previously by Asada et al. (2007), and the early discovery of hydrothermal activity along this segment (Alice Springs vent field) made it the target of several investigations. It ranges in width from ~16 km at the segment ends to ~14 km in the segment center (Fig. 6.14; Table 6.1), and it has a spreading rate of ~25 mm yr^{-1} (Kato et al., 2003). This is the shallowest segment of the central back-arc, at

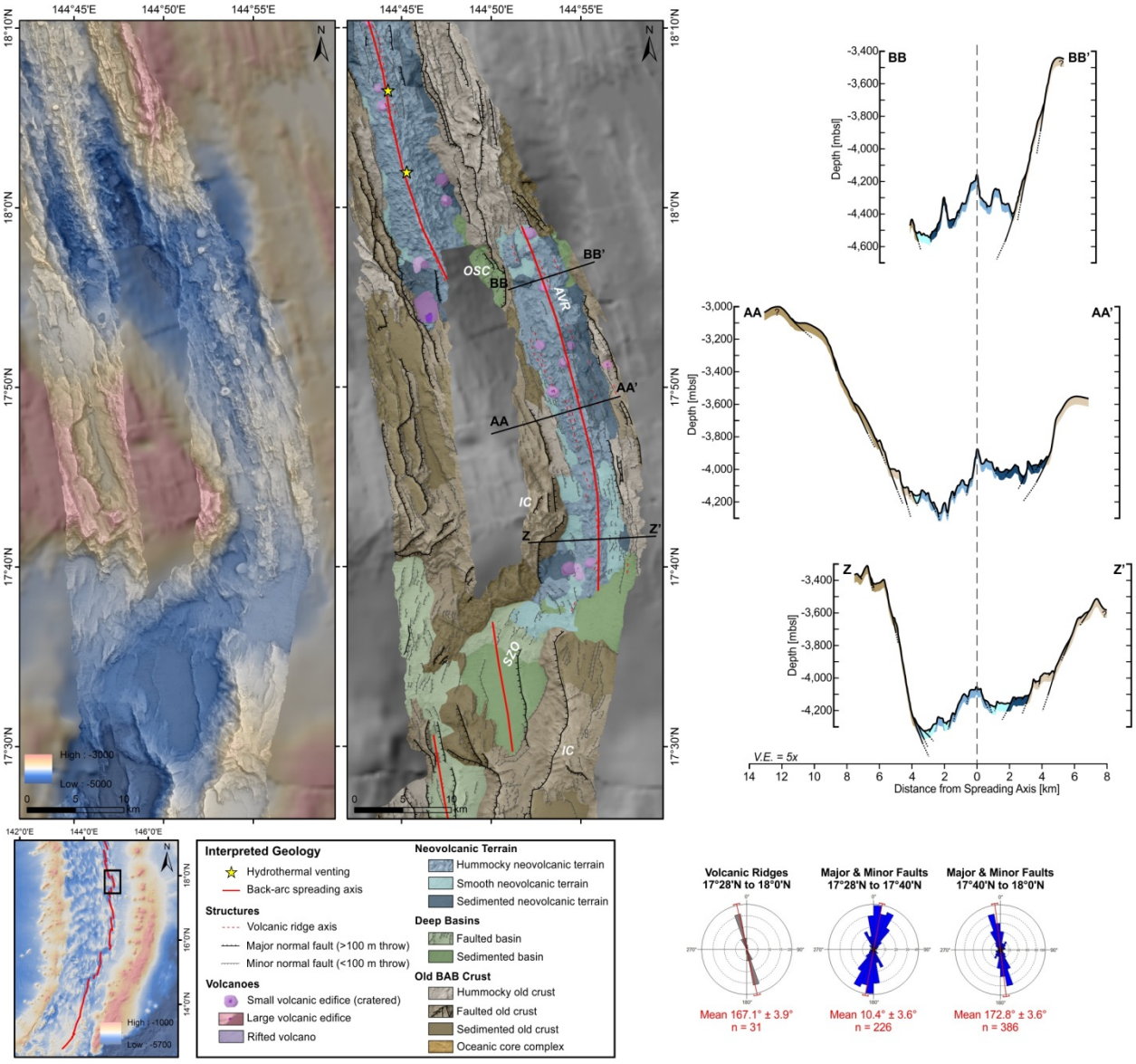


Fig. 6.13. (left) Bathymetry, (middle) interpreted geological map, and (right) across-axis profiles of the 17.8°N segment, with the segment location in the back-arc shown as a black square in the lower left map. Azimuths of the major and minor faults from 17°28'N to 17°40'N, and 17°40'N to 18°0'N are shown in blue, and the volcanic ridge axes for the entire segment are shown in grey (lower right corner). AVR = axial volcanic ridge; IC = inside corner high; OSC = overlapping spreading center; SZO = shear zone offset; V.E. = vertical exaggeration (5×). A larger geological map is available in Appendix Q (Suppl. Fig. Q11).

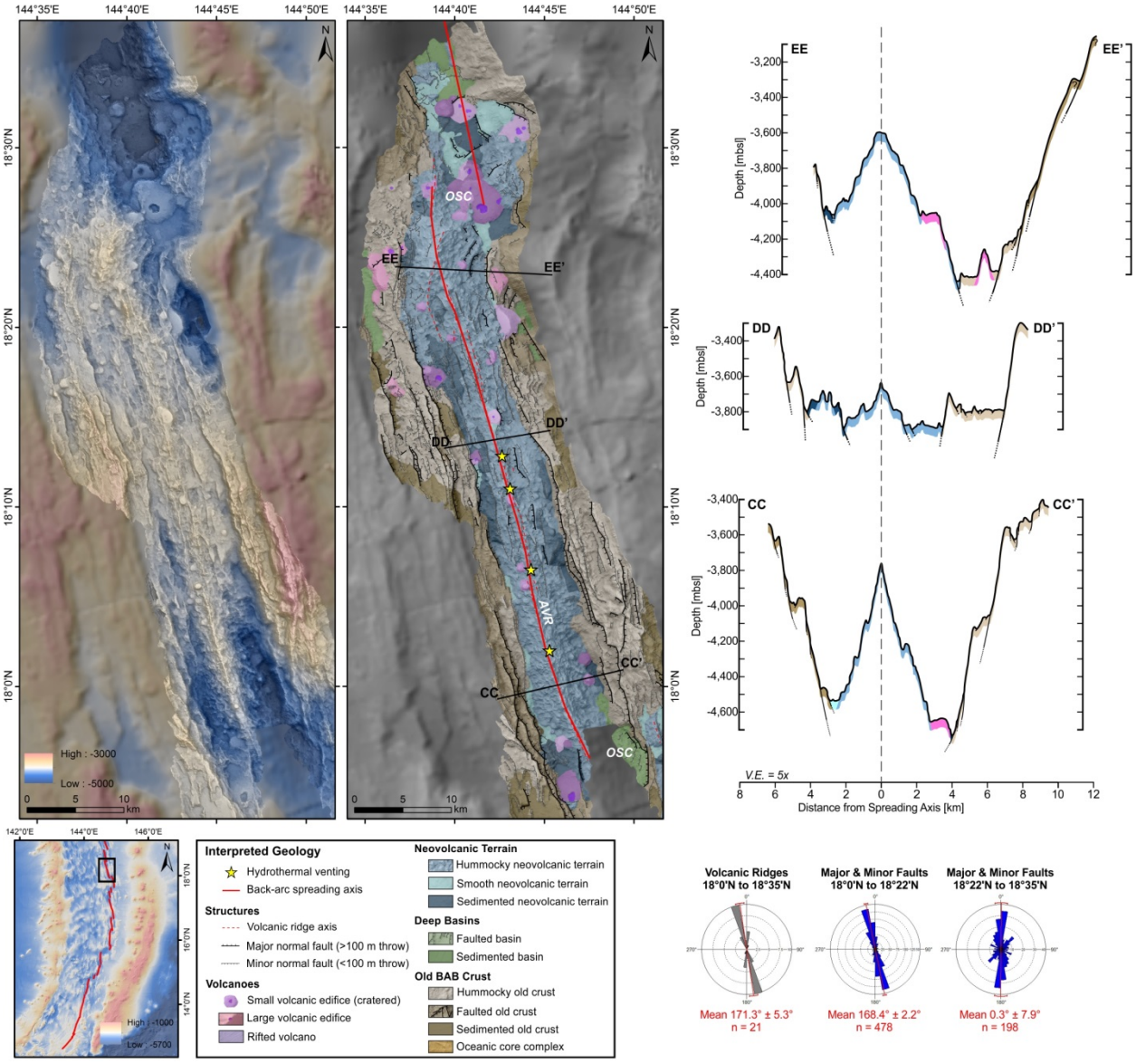


Fig. 6.14. (left) Bathymetry, (middle) interpreted geological map, and (right) across-axis profiles of the 18.2°N segment, with the segment location in the back-arc shown as a black square in the upper right map (lower left corner). Azimuths of the major and minor faults for 18°0'N to 18°22'N, and 18°22'N to 18°35'N are shown in blue, and the volcanic ridge axes for the entire segment are shown in grey (lower right corner). AVR = axial volcanic ridge; OSC = overlapping spreading center; V.E. = vertical exaggeration (5×). A larger geological map is available in Appendix Q (Suppl. Fig. Q12).

3900 mbsl, with an axial valley relief of ~600 m, deepening to 4400 mbsl in the south and 4750 mbsl in the north (Fig. 6.14; Table 6.1). Along the southern half of the spreading segment, the axial zone is dominated by an unfaulted volcanic ridge, 800 to 950 m in height, comprised of hummocky volcanic terrain (Fig. 6.14). Along the northern half of the axial zone, there is increased faulting and abundant sedimented neovolcanic terrain with a narrow hummocky volcanic ridge that is 200 m in height (Fig. 6.14). The total volume of neovolcanic material is estimated to be ~401 km^3 (see Appendix Q). Between 18°0'N and 18°22'N, the faults have a narrow range of orientations with a mean of 168.4° ± 2.2° (n = 478; Fig. 6.14), similar to the volcanic ridges (171.3° ± 5.3°, n = 21).

6.6. Regional structures

The regional bathymetry (GMRT v3.2; Ryan et al., 2009) and the vertical gravity gradient (Sandwell et al., 2014) reveal the major structural lineaments throughout the back-arc (Fig. 6.15a). The heavily block-faulted terrain described by previous authors that characterizes most of the back-arc bears a close resemblance to the abyssal hill fabric of slow-spreading mid-ocean ridges. The southern back-arc has fewer lineaments overall, transitioning from relatively smooth terrain over much of its width to block-faulted terrain towards the remnant arc in the west (near 143°0'E at 13°30'N; Fig. 6.15). A series of N-S trending lineaments in the southern half of the back-arc, which are characterized by deep sub-parallel valleys (Fig. 6.15a), are also seen in the northern half of the back-arc where they turn towards NW-SE, following the orientation of the volcanic front. Both the N-S and NW-SE lineaments are interpreted to be rift basins formed during back-arc opening (Fig. 6.15b). Cross-cutting these structures are major E-W and NE-SW trending lineaments (Fig. 6.15a), which include deep, linear valleys as well as topographic highs. The valleys are interpreted to be ancient transform faults (primary structures), several of which extend across the basin, including major fracture zones at 15.6°N and 17.5°N (the Pagan Fracture Zone; Fig. 6.15b). Secondary structures (i.e., those that are not directly linked to pre-existing structures) are not as well developed as the primary structures (which are distinct linear features), and do not appear to cross-cut other structures (Fig. 6.15b). The topographic highs that follow this orientation are thought to be related to cross-arc volcanic chains described briefly by Oakley et al. (2009; Fig. 6.15b). These cross-arc chains are heavily faulted across most of the back-arc,

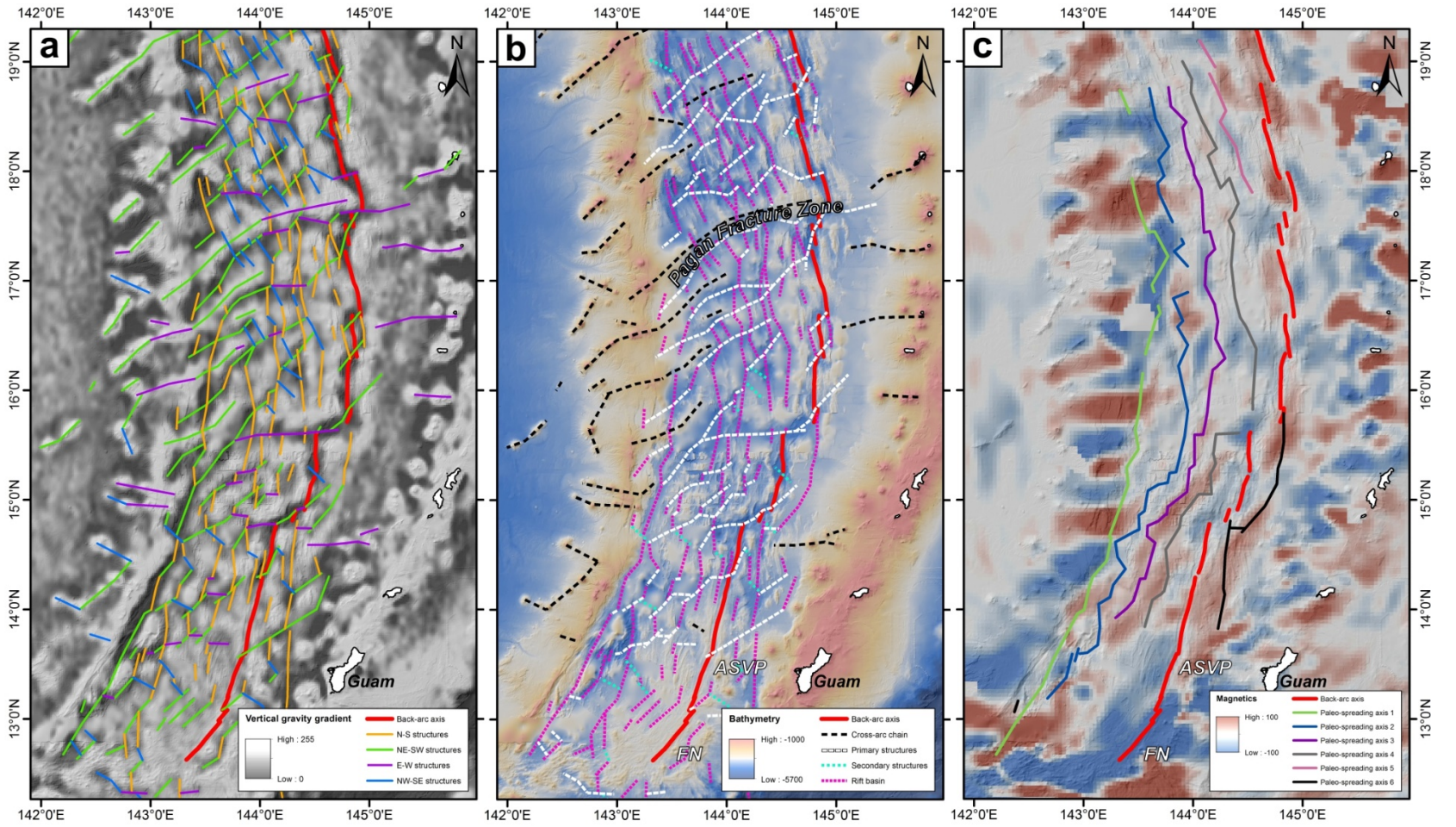


Fig. 6.15. Regional structural interpretation of the Mariana back-arc: (a) lineaments classified according to orientation, interpreted from the vertical gravity gradient (50% transparency) (Sandwell et al., 2014) overlain on hill-shaded bathymetry; (b) interpretation of structures, with the regional bathymetry (GMRT v.3.2; Ryan et al., 2009); and (c) paleo-spreading axes interpreted from continuous rift basins that broadly coincide with magnetic anomalies, with the 2-arc min Earth Magnetic Anomaly Grid (50% transparency; Maus et al., 2009) overlain on hill-shaded bathymetry. Subaerial volcanoes are shown in white. ASVP = Alphabet Seamount Volcanic Province; FN = Fina Nagu volcanic complex.

with discrete volcanoes observed only along the cross-arc chains closest to the active volcanic arc (including the Guguan, Diamante, and Pagan cross-arc chains; Stern et al., 2006; Stern et al., 2014) and those that extend westward from the remnant arc (Fig. 6.15b).

Magnetic anomalies visible in the global 2-arc min Earth Magnetic Anomaly Grid (Maus et al., 2009) reveal linear features that are sub-parallel to the active spreading center (Fig. 6.15c). These anomalies broadly correlate with several nearly-continuous rift basins and may represent paleo-spreading centers formed as the back-arc rifting 'jumped' progressively eastward (e.g., Fryer, 1981). The strongest magnetic anomaly closely follows the present-day spreading axis between 20°0'N and ~15°40'N. South of ~15°40'N, this anomaly is located east of the spreading axis (Fig. 6.15c), suggesting that the spreading axis at this location has recently jumped westward, in contrast to the general evolution of the back-arc. Abandoned rift valleys are clearly visible in the bathymetry along this magnetic anomaly, further supporting the interpretation as a paleo-spreading center (Suppl. Fig. Q13). South of 13°40'N, a cluster of near-arc volcanoes (the Alphabet Seamount Volcanic Province) formed on young (Late Neogene) thin back-arc crust where the arc magmas appear to have exploited an earlier back-arc structure (Stern et al., 2013). The increased magmatism in this part of the southern back-arc, the westward rift jump of the southern back-arc spreading axis, and the re-organization of the southern arc volcanoes appear to be closely related to the separate and complex evolution of the southern termination of the Mariana arc (cf. Stern et al., 2013).

6.7. Discussion

6.7.1. Large-scale segmentation and cross-arc structures of the Mariana back-arc

The eastward migration of the Mariana trench relative to the Philippine Sea plate has resulted in sinistral shearing in the southern and central back-arc that is accommodated by three major shear zone offsets at 14.8°N, 15.6°N, and 17.5°N (Fig. 6.15). These discontinuities offset the ridge segments by 31–42 km each. At 14.8°N and 17.5°N, sinistral shearing is accommodated by short ~N-S-trending faults producing a series of *en echelon* trench-parallel basins (Fig. 6.16a,c). Along the 14.8°N SZO, the eastward-stepping basins trend ~3–24°, are ~10–12 km long, ~4–8

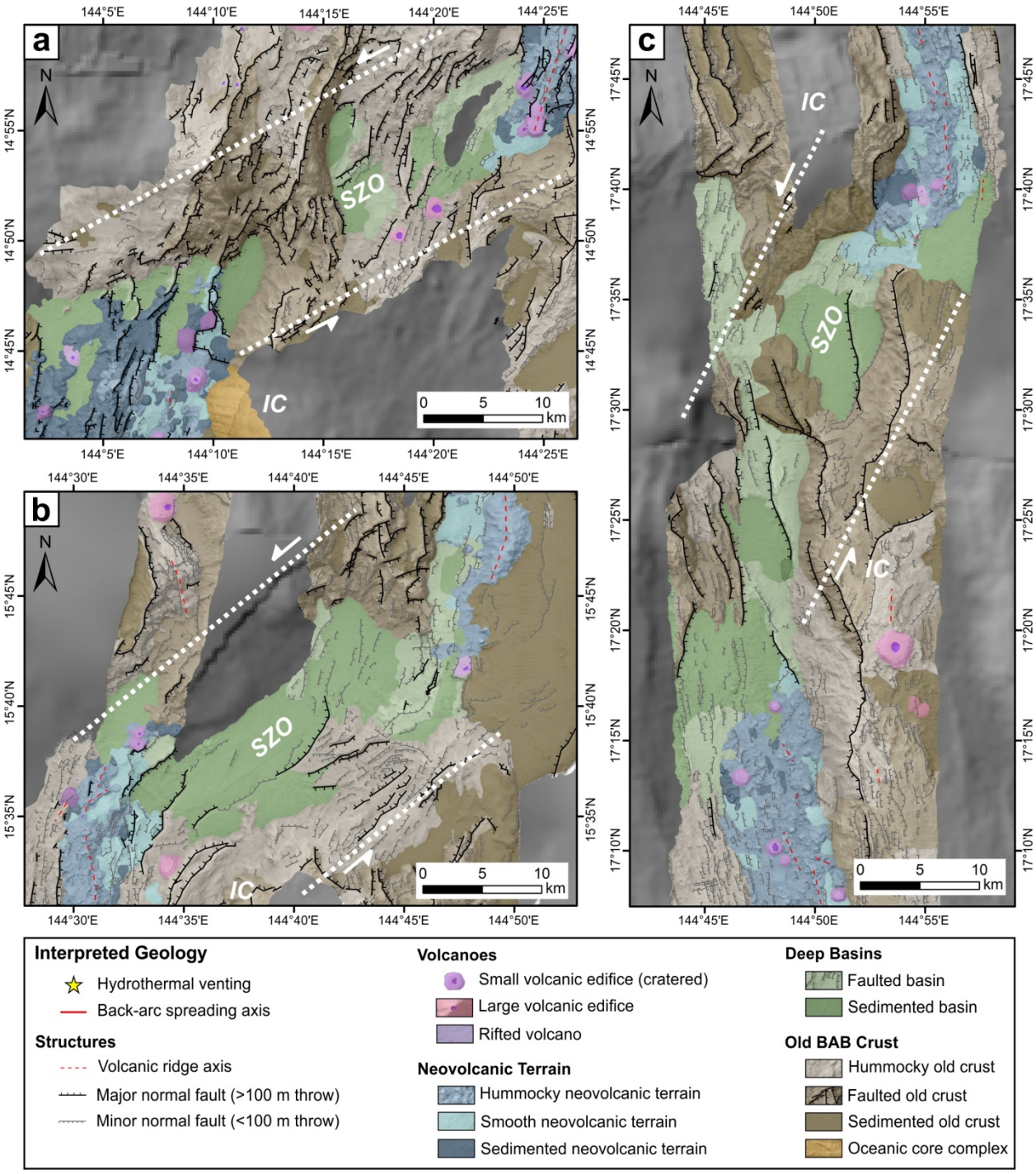


Fig. 6.16. Structures and interpreted geology of the major shear zone offsets along the spreading axis, highlighting the sinistral shear components with orientations indicated by dotted white lines and arrows: (a) the 14.8°N SZO with a general trend of ~61°; (b) the 15.6°N SZO with a general trend of ~51°, and (c) the 17.5°N SZO with a general trend of ~21°. These offsets are associated with major fracture zones that extend westward across the back-arc (Fig. 6.15). IC = inside corner high; SZO = shear zone offset.

km wide, ~2.5–6 km apart, and reach depths of over 5000 mbsl. Along the 17.5°N SZO, the eastward-stepping basins trend ~349–351°, are ~14–20 km long, ~7–8 km wide, ~3 km apart, and reach depths of over 4900 mbsl. This type of faulting is common in propagating rifts (e.g., Einarsson and Eiriksson, 1982; Sigmundsson, 2006) and likely results from the asymmetry of the back-arc opening. The deep, magma-starved sedimentary basin corresponding to the 15.6°N SZO (~30 km long and reaching depths of over 4600 mbsl: Fig. 6.16b) also appears to be related to left-lateral shearing. This style of ridge segmentation contrasts with the first-order discontinuities that characterize the global mid-ocean ridge system, which may offset segments by hundreds of kilometers (Macdonald et al., 1982). Smaller-offset discontinuities are common between the slow-spreading MAR (e.g., Schouten et al., 1985) and the Mariana back-arc, which contains at seven second-order OSCs and DEVALs in the study area. The overlap between segments includes both along-axis gaps (negative offsets) and true overlaps up to ~9 km. In the central segments, OSCs are associated with oblique extensional faulting with segment ends pointing slightly towards each other. In contrast, OSCs in the southern back-arc are characterized by abrupt changes in the orientations of the spreading axis. This may be due to the thermal structure of the segments and the relative importance of magmatic *versus* tectonic extension (Grindlay et al., 1991).

Oakley et al. (2009) proposed a model of magmatic segmentation for the Mariana back-arc in which cross-arc volcanic chains have acted as focal points for magmatism and nucleation of back-arc segments. However, not every segment center is associated with a clearly defined cross-arc chain of volcanoes. Instead, the cross-arc chains that cross the entire width of the back-arc (not just the volcanically-active portions that extend westward from the arc; shown as black dashed lines in Fig. 6.15b) are parallel to major E-W and NE-SW trending structures (shown as white dashed lines in Fig. 6.15b), indicating that these structures were probably conduits for increased volcanism at the seafloor. Similar cross-arc chains that extend westward from the remnant West Mariana Ridge are colinear with NNE-trending fractures in the Parece-Vela Basin, and generally appear to follow the same structural trend (Suppl. Fig. Q14). These observations suggest that the cross-arc chains follow long-lived basement structures, inherited from or even pre-dating successive back-arc opening episodes (Fryer and Hussong, 1982; Fryer, 1995). Zhang et al. (2016) considered that transform faults in the South China Sea, Okinawa Trough, West

Philippine Basin, and Shikoku-Parece Vela basins are similarly inherited structures, the highly oblique orientation of which reflects complex plate convergence and rotation. Thus, the segmentation of the Mariana back-arc spreading center may be controlled by an early fabric in the arc crust, with all of the major and minor offsets associated with a major E-W or NE-SW trending structures at the regional scale (Fig. 6.15b). These pre-existing structures may also have influenced the locations of volcanoes along the island arc, as suggested by Fryer (1995).

6.7.2 Segment-scale fault patterns and spreading direction

Segment-scale faulting in the back-arc region closely follows the regional structural trends, in particular the curvature of the subduction zone from south to north along the length of the arc. Some segments are undergoing nearly pure extension, while others show a strong a component of oblique extension. However, axis-perpendicular extension is dominant, allowing precise spreading directions to be determined.

On the southern segments (12.8°N, 13.3°N, and 13.9°N), the faulting is remarkably consistent between the neovolcanic zone and the valley bounding faults, both dominated by almost pure extension. The spreading directions are 129.3° ± 1.7° along the 12.8°N segment, 113.8° ± 1.2° along the 13.3°N segment, and 105.6° ± 1.3° along the 13.9°N segment, perpendicular to the measured faulting. At 14.5°N, the spreading direction is 106.7 ± 1.3°, but the faults show an anastomosing pattern, and there is a subset of ~E-W-trending faults that appear to be associated with N-S extension. The latter form a graben at 14°30'N/144°0'E (Fig. 6.7), near which small volcanic edifices are aligned in the E-W faulting direction. At 15.1°N, the spreading direction is 104.6 ± 7.3° but with a large uncertainty related to minor left-lateral shearing of the segment and displacements in the spreading axis. This complexity decreases northwards and disappears along the 15.5°N segment where there is a notable lack of faulting within the neovolcanic zone and the spreading direction is 97.5° ± 4.9°.

On the central segments (16.1°N, 16.5°N, and 17.0°N), the faults show increasing curvature and evidence of oblique offsets. The spreading direction is 92.7° ± 2.5° at 16.1°N but then shifts progressively from 91.0° ± 1.7° at 16.5°N to 80.4° ± 3.6° in the southern part of the 17.0°N

segment and 84.3° ± 3.9° in the northern part of the 17.0°N segment. As noted by Deschamps et al. (2005), the faulting in the center of the 17.0°N segment is oblique to the distal faults and abyssal hill fabric, which trend ~N-S. This is thought to reflect an early episode of spreading that was dominantly E-W followed by a shift to the present orientation at ~1 Ma. Geodetic measurements indicate that the whole of the basin along 17.0°N segment has been widening in a direction of ~73° (Kato et al., 2003; Deschamps et al., 2005), but local spreading is clearly oblique to that opening. This may be explained by a hot magmatic center that has responded more quickly than the cold segment ends (Deschamps et al., 2005). The spreading directions along the 17.8°N and 18.2°N segments are 82.8° ± 3.6° and 78.4° ± 2.2°, respectively.

6.7.3 Axial morphology and magma supply rates

The morphology of the southern Mariana back-arc bears a strong resemblance to fast-spreading mid-ocean ridges, despite its slow spreading rate. Martínez et al. (2000) proposed several mechanisms that could account for the enhanced magmatism: (1) trench-parallel extension and inward-radiating faulting that reflects the geometry of the trench; (2) decoupling of the spreading centers from the regional stress field affecting the eastern flank of the basin; and (3) input of arc magmas from the nearby volcanic front (Fryer, 1995; Fryer et al., 1998). The latter is supported by geochemical studies that indicate an arc component in the Alphabet Seamount Volcanic Province (ASVP; Fryer et al., 1998; Stern et al., 2013) and the Fina Nagu volcanic complex (FN; Brounce et al., 2016). The contribution of arc magmas may also explain the thicker crust and shallower depth of the southern back-arc (Martínez et al., 2000). New mapping shows a gradual transition from a “fast-spreading” morphology in the south to an “intermediate-spreading” morphology farther north, with pronounced axial valley walls first appearing at ~13°20’N. At 13°40’N, there is a sudden increase in the distance to the volcanic front of the arc and the development of a “slow-spreading” morphology. Distinctive mid-segment highs are evident, with narrow (8–13 km wide), deep axial valleys, and the farther away from the arc, the deeper the axial valley becomes. These observations support a model of decreasing influence of arc-enhanced magmatism in the central back-arc.

The eruption style, degree of faulting, and gross segment morphologies are closely linked to magma supply (cf. Eason et al., 2016). We observed 4 distinct types of back-arc spreading segments, summarized in Figure 6.17: (I) *magmatic segments*, characterized by significant axial volcanic rises (~500–550 m) that lack deep valleys and are dominated by smooth volcanic terrain; (II) *magmatic segments currently undergoing tectonic extension*, characterized by an hourglass shape (focused magmatism at a mid-segment high), moderate axial valley relief (450–500 m), and abundant smooth volcanic terrain with few hummocky volcanic ridges at the segment centers; (III) *tectonic segments*, characterized by axial valleys with moderate-to-high relief at the segment center (~800–1250 m), low hummocky axial volcanic ridges (~100–450 m) with central grabens, and abundant faulting within the axial valley; and (IV) *tectonic segments currently undergoing magmatic extension*, characterized by axial valleys with moderate-to-high relief at the segment center (600–1300 m), prominent hummocky axial volcanic ridges (~800–1050 m) that lack central grabens, and limited faulting within the axial valley. The southern segments, 12.8°N and 13.3°N, are type I; segments 16.5°N and 17.0°N are type II; segments 13.9°N, 14.5°N, 15.1°N, 16.1°N, and 17.8°N are type III; segments 15.5°N and 18.2°N are type IV (Table 6.1; Fig. 6.18). Figure 6.19 shows an along-axis profile along the Mariana back-arc spreading center, highlighting the magmatically-robust versus tectonically-dominated segment types. The diversity of across-axis segment morphologies and seafloor depths is similar to the MAR (e.g., Devey et al., 2010), associated with along-axis variations in crustal thickness related to magma supply. For example, the within-axis high and hourglass-shaped segment morphology of the Turtle Pits area (3°S, MAR; Devey et al., 2010) is similar to the Type II segment in the Mariana back-arc at 17.0°N.

The volume of neovolcanic material in conjunction with spreading rates determined by Kato et al. (2003) can be used as a first-order estimate of the eruption rates and magma supply along each of the segments studied here (Table 6.1; Appendix Q). The eruption rate per kilometer along each segment appears to decrease northwards from 9377 m^3 yr^{-1} km^{-1} along the 13.9°N segment to 3912 m^3 yr^{-1} km^{-1} along the 15.5°N segment. There is an increase in eruption rates and magma supply along the 16.1°N, 16.5°N, and 17.0°N segments. The highest eruption rates along the 17.0°N type II segment (31600 m^3 yr^{-1} km^{-1}), consistent with the abundance of sheet flows at the center of this segment. Estimated eruption rates are highly variable for the

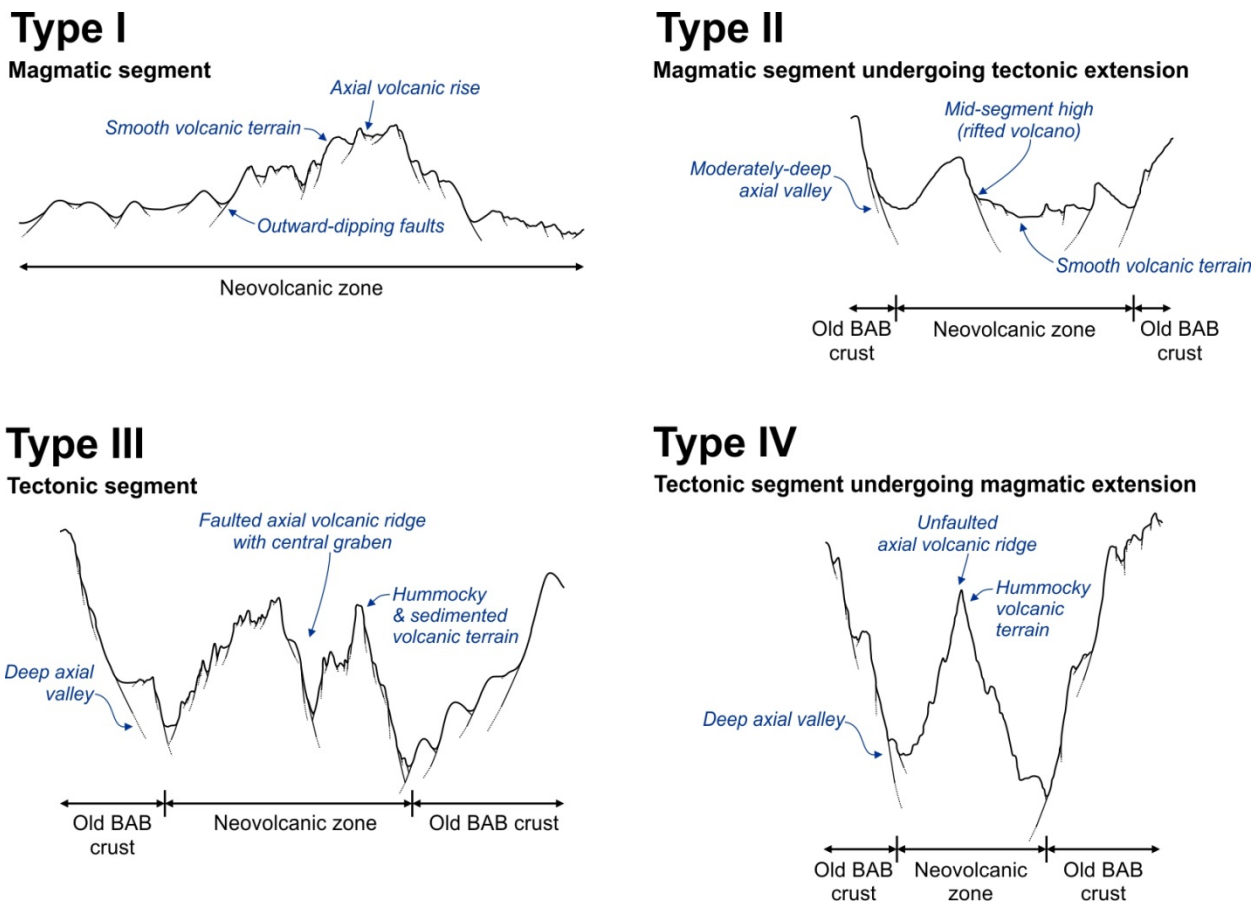


Fig. 6.17. Distinguishing cross-sectional features of the back-arc segment types found in the southern and central Mariana back-arc.

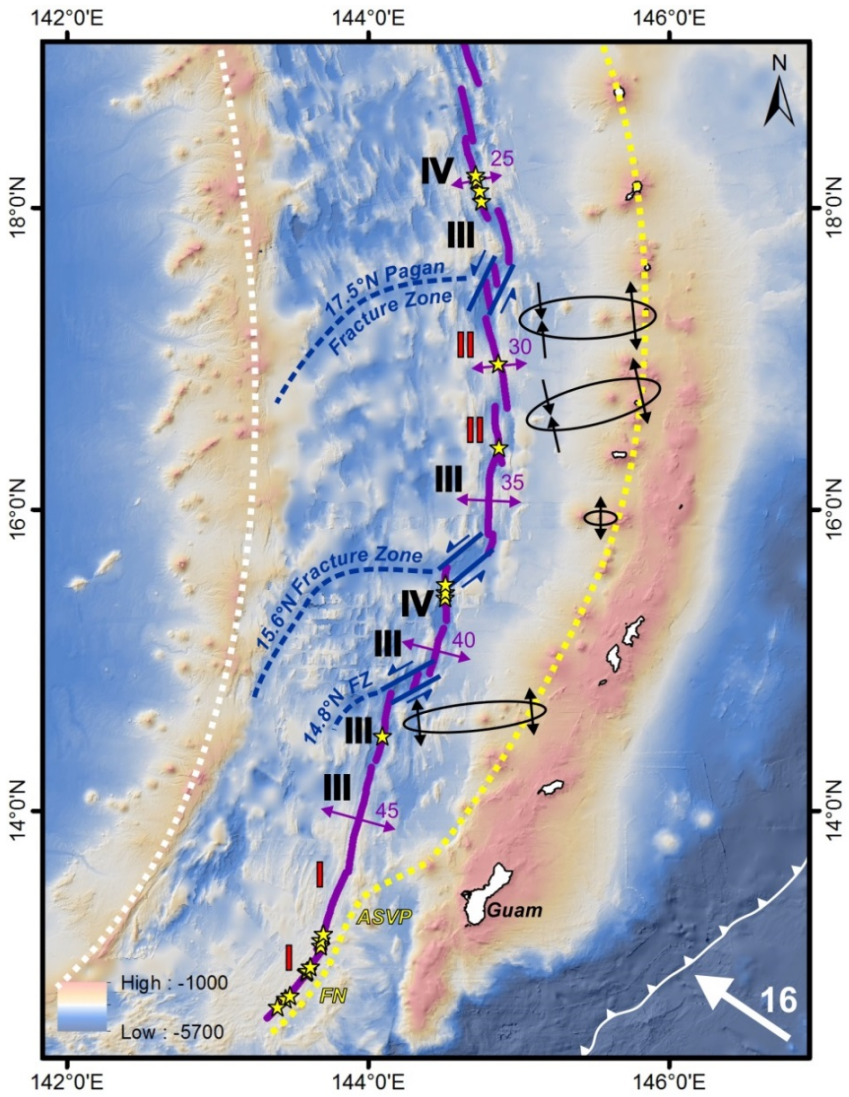


Fig. 6.18. Important tectonic features that affect magma supply and segment morphology in the central and southern Mariana back-arc include: (1) oblique subduction; (2) a curved plate margin; (3) arc volcanism near the spreading axis in the south; (4) southward-increasing spreading rates (5) three major shear zone offsets associated with regionally-extensive fracture zones; and (6) ~N-S extension and/or compression along active volcanic cross-chains associated with westward-convex plate curvature. White dotted line = remnant volcanic arc (West Mariana Ridge); yellow dotted line = active volcanic arc; white arrow = convergence direction and rate (mm yr^{-1}; deMets et al., 2010); purple line = back-arc spreading axis, with spreading direction (this study) and rate (mm yr^{-1}; Kato et al., 2003); blue lines = sinistral shear zone offsets and associated fracture zones; black ellipses = zones of cross-chain extension-compression indicated by seismicity (Heeszel et al., 2008); red numbers (I, II) = magmatically-robust segments; and black numbers (III, IV) = tectonic segments (see text for segment classification); yellow stars = hydrothermal vent sites (Resing and Shipboard Scientific Party, 2016; Baker et al., 2016); ASVP = Alphabet Seamount Volcanic Province; FN = Fina Nagu volcanic complex; FZ = fracture zone.

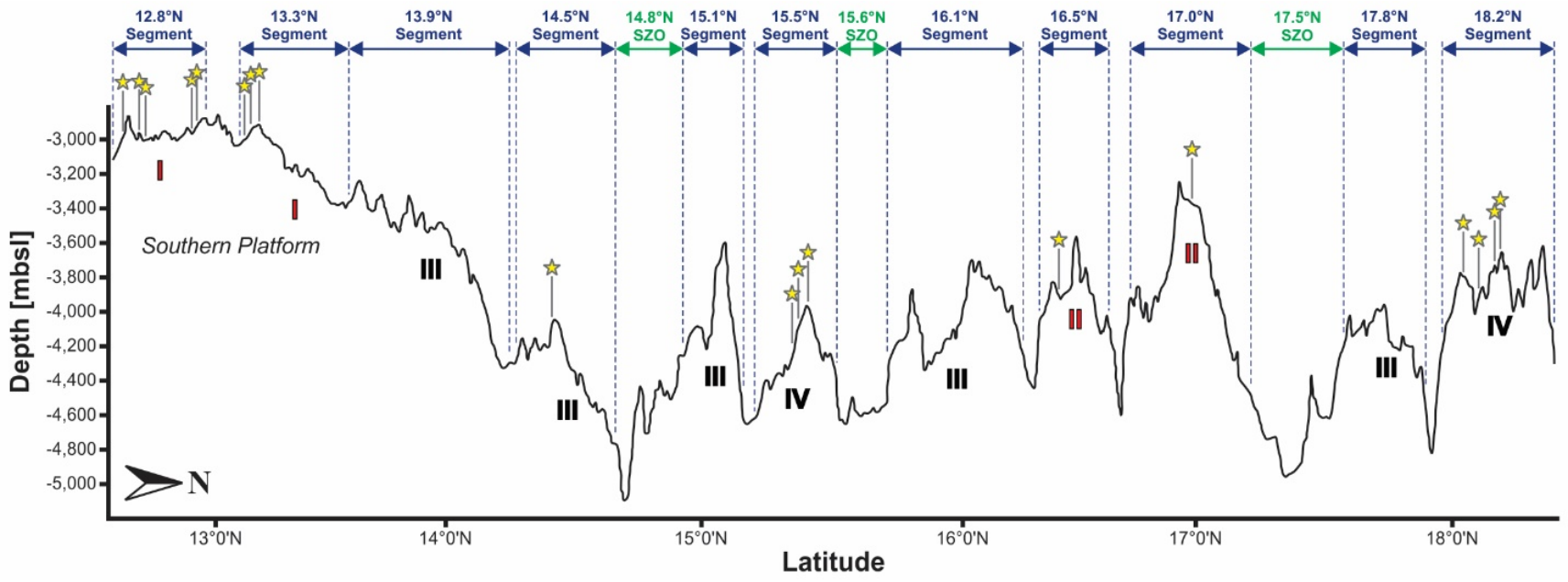


Fig. 6.19. An along-axis bathymetric profile from south to north along the Mariana back-arc spreading axis, highlighting the different segment types: red numbers (I, II) indicate magmatically-robust segments, and black numbers (III, IV) indicate tectonically-dominated segments (see text and Fig. 6.17 for detailed descriptions). Yellow stars = hydrothermal vent sites (Resing and Shipboard Scientific Party, 2016; Baker et al., 2016); SZO = shear zone offset.

tectonic segments (types III and IV), all of which are dominated by hummocky pillow lava flows.

The rate of magma supply on the global mid-ocean ridges is on the order of 18 km^3 yr^{-1} (Sigurdsson, 2000). Volcanic arcs account for a much smaller proportion of submarine magmatism, on the order of 2–5 km^3 yr^{-1} (Arculus, 1999). The global MOR average is equivalent to about 300 km^3 per kilometer of ridge length every 1 million years. By comparison, the estimated eruption rates along the Mariana back-arc are less than 11 km^3 per kilometer of ridge length over the same time period. Although about 20 or 30 times smaller than on global mid-ocean ridges, the eruption rate at the center of one segment (17.0°N) was large enough to have produced a neovolcanic ridge with a volume comparable to some of the largest shield-type MOR axial volcanoes (e.g., >470 km^3 Axial Volcano on the Juan de Fuca Ridge). Along this segment, additional crustal permeability may be associated with segment-scale shearing produced by the reactivation of the adjacent shear zone (Deschamps et al., 2005).

Local variations in magma supply in the back-arc may be influenced by magmatism associated with cross-arc volcanic chains. These cross-arc chains are associated with either extension or compression in the back-arc as a result of the arcuate geometry of the subduction zone (Fig. 6.18; Heeszel et al., 2008). The cross-arc chains at 16°35’N and 17°15’N are associated with ~N-S extension in the arc, while the back-arc is undergoing compression. These corridors may provide the structural pathways for focusing magmatic activity, contributing to the development of the large volcanic cone at the southern end of the 16.5°N segment and increased magmatism at the centers of the 16.5°N and 17.0°N segments, as described by Asada et al. (2007). In contrast, the cross-arc volcanic chain at 14°40’N beginning near Northwest Rota seamount (Fig. 6.18) is associated with increased seismicity and ~N-S extension in both the arc and back-arc (Heeszel et al., 2008). The back-arc spreading center at this latitude is heavily faulted and appears to be undergoing mainly tectonic extension, with reduced magma supply and the occurrence of two oceanic core complexes (Fig. 6.7). It appears, therefore, that not all cross-arc structures are necessarily exploited by rising magma.

6.7.4 Relationship to hydrothermal venting

Eighteen individual hydrothermal vent sites have been identified along seven of the back-arc segments; twelve of which were discovered during the FK151121 expedition (Fig. 6.18; Resing and Shipboard Scientific Party, 2016; Baker et al., 2016). Hydrothermal venting was located on every segment type in the Marianas back-arc (Figs. 6.18, 6.19). In every case, the venting occurs near the segment centers where magmatic activity is also focused (Fig. 6.19).

Magmatic segments (type I) in the southern back-arc are associated with several hydrothermal vents. The similarity of these 'magmatic' segments with fast-spreading ridges suggests the influence of a shallow axial magma chamber that may drive numerous closely-spaced hydrothermal systems (e.g., Hannington et al., 2009; 2011; German et al., 2016). At these high magmatic intensities, the crust behaves ductilely, prohibiting the formation of deeply-penetrating faults, thus confining the hydrothermal circulation to the shallow crust (e.g., Devey et al., 2010).

The slower spreading rates of central back-arc segments (<40 mm yr^{-1}: Kato et al., 2003) provide more favorable conditions for larger but more widely-spaced hydrothermal upflow (Baker and German, 2004; Baker, 2007). German et al. (2016) noted that hydrothermal activity on slow-spreading ridges may, in fact, be significantly enhanced by the strong tectonic control on fluid flow. Deeply penetrating faults in these settings allow circulation of seawater to considerable depths and, in some cases, at some distance off axis, so that some unusually large hydrothermal systems are found on slow (20–50 mm yr^{-1}) and ultraslow-spreading (<20 mm yr^{-1}) ridges where few were expected at all. All of the hydrothermal prospecting along the central Mariana back-arc to date has been confined to the spreading axis.

Type II segments are characterized by focussed magmatism with moderate magmatic intensities, resulting in frequent magmatic events that may maintain continuous hydrothermal circulation over long periods of time (e.g., Turtle Pits region on the MAR; Devey et al., 2010). The largest mid-segment high occurs at 17.0°N, where large, vigorously-venting chimneys have been observed (Gray, 2016; Butterfield and Shipboard Scientific Party, 2017). However, repeated

volcanic eruptions may frequently “pave-over” the hydrothermal vent sites, preventing large accumulations of massive sulfides at the seafloor (e.g., Fouquet, 1997; Anderson et al., 2016).

Tectonic segments (type III) may be associated with increased crustal permeability, which is the primary factor governing the location, intensity, and temperature of hydrothermal circulation (Wilcock, 1998). One small plume on a type III segment at 14.5°N is associated with heavy faulting and N-S extension related to cross-arc volcanism, producing the most structurally-complex segment in the back-arc. The oceanic core complexes along this segment are important targets for exploration, as some of the world’s largest seafloor massive sulfide deposits have been discovered on core complexes along mid-ocean ridges (e.g., Semenov ore district, MAR, 13°31’N; Pertsev et al., 2012).

Tectonic segments currently undergoing magmatic extension (type IV) were also found to have large plumes along the axial volcanic ridges, associated with observations of both focused and diffuse venting (15.5°N, 18.2°N; Resing and Shipboard Scientific Party, 2016; Butterfield and Shipboard Scientific Party, 2017). High acoustic backscatter and direct seafloor observations suggest that some of the hydrothermal venting is directly related to recent volcanism (Resing and Shipboard Scientific Party, 2016). Hydrothermal activity along the 18.2°N segment (including the Central Trough, Burke, Alice Springs and Illium vent sites) has been ongoing for at least 35 years (Craig et al., 1987; Gamo and Shipboard Scientific Party, 1994; Butterfield and Shipboard Scientific Party, 2017). However, along these segments, volcanic events are rare and have a generally low volume, driving only short-lived (i.e., <1200 y) hydrothermal circulation.

Compared to slow-spreading mid-ocean ridges, the Mariana back-arc is associated with additional tectonic complexities (including cross-arc volcanism, oblique extension, and input of arc magmas; Fig. 6.18) that promote increased crustal permeability (e.g., 14.5°N segment) or enhanced magmatism (e.g., 12.8°N and 17.0°N segments), providing favorable sites for the accumulation of large massive sulfide deposits.

6.8. Conclusions

Back-arc spreading centers share a number of features in common with both fast- and slow-spreading mid-ocean ridges but have additional tectonic complexities related to oblique convergence, plate rotation, asymmetric extension, and subduction-zone collisions (Hannington et al., 2005). Within the Mariana back-arc, large-scale structures control the segmentation of the back-arc spreading axis, some potentially related to inherited basement structures marked by distinctive cross-arc volcanic chains. Along the southern and central back-arc spreading center, most of the offset occurs along three major shear zone offsets, which are oblique to the spreading axis as a result of asymmetric extension. In contrast to mid-ocean ridges, which are characterized by transform faults oriented perpendicular to the ridge axis, this can result in large-scale crustal permeability of the type previously described for extensional transform boundaries, for example, in the Eastern Manus Basin (Taylor et al., 1994). In the Mariana back-arc, this is best illustrated by the re-activation of the shear zone offset at 17.5°N, which has induced oblique spreading in the adjacent segments.

Magmatism in the southern Mariana back-arc is highly influenced by proximity to the volcanic arc, which may contribute melt to the spreading center. Where magma supply rates are enhanced by melt from the arc, ridge morphologies resemble fast-spreading mid-ocean ridges. Farther away from the arc, the central Mariana spreading centers strongly resemble slow-spreading mid-ocean ridges, with deep axial valleys containing axial volcanic ridges, strong magma focusing at mid-segment highs, large-scale detachment faulting, and ridge segmentation dominated by second- and third-order discontinuities (OSCs and DEVALS). Melts may be focused into the spreading segments where long-lived cross-arc structures are present. Four different segment types are recognized: magmatic segments (type I); magmatic segments currently undergoing tectonic extension (Type II); tectonic segments (type III); and tectonic segments currently undergoing magmatic extension (Type IV). Type I segments occur in the southern back-arc and—despite the slow-spreading rate—closely resemble fast-spreading mid-ocean ridges with high-level magmatism and shallow-crustal hydrothermal circulation. The gradual change in segment morphology with proximity to the volcanic arc supports earlier suggestions of a strong influence by melt contributions from the arc. Tectonically-influenced segments (type II, III, and

IV) occur in the central Mariana back-arc, and bear a closer resemblance to slow-spreading mid-ocean ridges in terms of ridge morphology, structure, magma supply rates, and hydrothermal activity. North-south extension occurs along cross-arc structures near the arc front (Heeszel et al., 2008). One such structure extends into the back-arc near the 14.5°N segment, which is characterized by abundant faulting and the development of oceanic core complexes. Further from the volcanic arc towards the back-arc, cross-chains are associated with N-S compression and focused magmatism along the 16.5°N and 17.0°N segments. This focused magmatism produces the characteristic hourglass segment morphology, where the axial valley is dominated by smooth sheet flows along central axial volcanic highs, in sharp contrast to the hummocky pillow mounds and ridges that occur throughout most of the central back-arc.

Hydrothermal activity in the Mariana back-arc is broadly similar to that on mid-ocean ridges, and is localized where a heat source is present to drive hydrothermal circulation, and faulting focuses fluid flow. Recent discoveries along the spreading axis of every segment type indicate a primary magmatic control on venting. By comparison with slow-spreading ridges (e.g., Devey et al., 2010; German et al., 2016), the greatest potential for large massive sulfide accumulations is in the type II segment at 17.0°N and the type III segment at 14.5°N. As hydrothermal outflow is strongly influenced by crustal permeability, our mapping of the fault patterns provides a means to examine the relationships between large-scale tectonic processes (and associated volcanism) with hydrothermal venting as discoveries continue to be made.

Appendix Q. Supporting Information

Supplementary data associated with this article is found in Appendix Q.

References

Ambos, E. L., Hussong, D.M., 1982, Crustal Structure of the Mariana Trough. J. Geophys. Res. 87(B5), 4003–4018, doi:10.1029/JB087iB05p04003.

Anderson, M.O., Hannington, M.D., Haase, K., Schwarz-Schampera, U., Augustin, N., McConachy, T.F., Allen, K., 2016. Tectonic focusing of voluminous basaltic eruptions in magma-deficient back-arc rifts. Earth Planet. Sci. Lett. 440, 43–55, doi:10.1016/j.epsl.2016.02.002.

Arculus, R.J., 1999. Origins of the continental crust. J. Proc. Roy. Soc. New South Wales 132, 83–110.

Asada, M., Deschamps, A., Fujiwara, T., Nakamura, Y., 2007. Submarine lava flow emplacement and faulting in the axial valley of two morphologically distinct spreading segments of the Mariana back-arc basin from Wadatsumi side-scan sonar images. Geochemistry, Geophys. Geosyst. 8, Q04001, doi:10.1029/2006GC001418.

Augustin, N., van der Zwan, F.M., Devey, C. W., Ligi, M., Kwasnitschka, T., Feldens, P., Bantan, R.A., Basaham, A. S., 2016. Geomorphology of the central Red Sea Rift: Determining spreading processes. Geomorphology 274, 162–179, doi:10.1016/j.geomorph.2016.08.028.

Baker, E.T., 2007. Hydrothermal cooling of midocean ridge axes: Do measured and modeled heat fluxes agree?. Earth Planet. Sci. Lett. 263(1–2), 140–150, doi:10.1016/j.epsl.2007.09.010.

Baker, E.T., German, C.R., 2004. On the global distribution of hydrothermal vent fields. In: German, C.R., Lin, J., Parson, M. (Eds.), Mid-Ocean Ridges: Hydrothermal Interactions Between the Lithosphere and Oceans. AGU, Washington, D.C., pp. 245–266,

Baker, E.T., Massoth, G.J., Nakamura, K., Embley, R.W., de Ronde C.E.J., Arculus, R.J., 2005. Hydrothermal activity on near-arc sections of back-arc ridges: Results from the Mariana Trough and Lau Basin. Geochem. Geophys. Geosyst. 6, Q09001, doi:09010.01029/02005GC000948.

Baker, E.T., Chadwick, W.W.J., Walker, S.L., Merle, S.G., Resing, J.A., Anderson, M.O., 2016. Hydrothermal plume surveys of the Mariana Back-arc (12.7°–18.3°N) by surface-ship and AUV find an unexpectedly high spatial frequency of vent sites. In: 2016 Fall Meeting. AGU, San Francisco, Calif.

Baker, N., Fryer, P., Martínez, F., Yamazaki, T., 1996. Rifting history of the northern Mariana Trough: SeaMARC II and seismic reflection surveys. J. Geophys. Res. 101(B5), 11427–11455.

Becker, N.C., Fryer, P.F., Moore, G.F., 2010. Malaguana-Gadao Ridge: Identification and implications of a magma chamber reflector in the southern Mariana Trough. Geochem. Geophys. Geosyst. 11, Q04X13, doi:10.1029/2009GC002719.

Bibee, L.D., Shor, G.G., Lu, R.S., 1980. Inter-arc spreading in the Mariana Trough. Mar. Geol. 35(1–3), 183–197, doi:10.1016/0025-3227(80)90030-4.

Bouysse, P., et al., 2010. Geological map of the world at 1:25 M. 3rd ed., 2 sheets, CGMW, UNESCO, Paris.

Bracey, D.R., Ogden, T.A., 1972. Southern Mariana Arc: Geophysical observations and hypothesis of evolution. Bull. Geol. Soc. Am. 83, 1509–1522, doi:10.1130/0016-7606(1972)83(1509:SMAGOA)2.0.CO;2.

Brounce, M., Kelley, K.A., Stern, R., Martínez, F., Cottrell, E., 2016. The Fina Nagu volcanic complex: Unusual submarine arc volcanism in the rapidly deforming southern Mariana margin. Geochem. Geophys. Geosyst. 17, 4078–4091, doi:10.1002/2016GC006457.

Brown, L. (2010), Texture shading: A new technique for depicting terrain relief [abstract]. In: NACIS Annual Meeting. 2010 Oct 13–17, St. Petersburg, Florida.

Buck, W.R., Lavier, L.L., Poliakov, A.N.B., 2005. Modes of faulting at mid-ocean ridges. Nature 434(7034), 719–723, doi:10.1038/nature03358.

Butterfield, D., and Shipboard Scientific Party, 2017. Hydrothermal hunt at the Mariana back-arc, Leg 2. In: Cruise Report for FK161129 on RV Falkor, Seattle, Washington, doi:10.7284/907181.

Campbell, A.C., Edmond, J.M., Colodner, D., Palmer, M.R., Falkner, K.K., 1987. Chemistry of hydrothermal fluids from the Mariana Trough back-arc basin in comparison to mid-ocean ridge fluids. In: EOS Trans. AGU 68(44), San Francisco, Calif., pp. 1531,

Carlson, R.L., Mortera-Gutiérrez, C.A., 1990. Subduction hinge migration along the Izu-Bonin-Mariana arc, Tectonophysics 181(1–4), 331–344, doi:10.1016/0040-1951(90)90026-5.

Craig, H., Horibe, Y., Farley, K.A., 1987. Hydrothermal vents in the Mariana Trough: results of the first Alvin dives. In: EOS Trans. AGU 68(44), San Francisco, Calif, pp. 1531.

deMets, C., Gordon, R.G., Argus, D.F., Stein, S., 1994. Effect of recent revisions to the geomagnetic reversal time scale on estimate of current plate motions. Geophys. Res. Lett. 21(20), 2191–2194, doi:10.1029/94GL02118.

deMets, C., Gordon, R.G., Argus, D.F., 2010. Geologically current plate motions. Geophys. J. Int. 181, 1–80, doi:10.1111/j.1365-246X.2009.04491.x.

Deschamps, A., Fujiwara, T., 2003. Asymmetric accretion along the slow-spreading Mariana Ridge. Geochem. Geophys. Geosyst. 4(10), 8622, doi:10.1029/2003GC000537.

Deschamps, A., Lallemand, S., 2002. The West Philippine Basin: An Eocene to early Oligocene back arc basin opened between two opposed subduction zones. J. Geophys. Res. Solid Earth. 107(B12), 1–24, doi:10.1029/2001JB001706.

Deschamps, A., Fujiwara, T., Asada, M., Gente, P., Nakamura, Y., Heuret, A., Naito, K., Horikawa, H., Suganuma, S., 2004. Deep-tow sonar survey of the Mariana spreading axis: initial results of the KR03-12 cruise. InterRidge News 13, 6–9.

Deschamps, A., Fujiwara, T., Asada, M., Montési, L., Gente, P., 2005. Faulting and volcanism in the axial valley of the slow-spreading center of the Mariana back arc basin from Wadatsumi

side-scan sonar images. Geochem., Geophys. Geosyst. 6(5), Q05006, doi:10.1029/2004GC000881.

Devey, C.W., German, C.R., Haase, K.M., Lackschewitz, K.S., Melchert, B., Connelly, D.P, 2010. The relationships between volcanism, tectonism and hydrothermal activity on the Mid-Atlantic Ridge south of the equator. In: Rona, P.A., et al. (Eds.), Diversity of hydrothermal systems on slow spreading ocean ridges, vol. 188. AGU, Washington, D.C., pp. 133–152, doi:10.1029/2008GM000756.

Dixon, T.H., Stern, R.J., 1983. Petrology, chemistry, and isotopic composition of submarine volcanoes in the southern Mariana arc. Geol. Soc. Am. Bull., 94, 1159–1172, doi:10.1130/0016-7606(1983)94<1159:PCAICO>2.0.CO;2.

Eason, D.E., Dunn, R.A., Canales, J.P., Sohn, R., 2016. Segment-scale variations in seafloor volcanic and tectonic processes from multibeam sonar imaging, mid-Atlantic Ridge Rainbow region (35°45'-36°35'N). Geochem., Geophys. Geosyst. 17, 3560–3579, doi:10.1002/2016GC006433.

Einarsson, P., Eiríksson, J., 1982. Earthquake fractures in the Districts Land and Rangárvellir in the South Iceland Seismic Zone. Jökull 32, 113–120.

Engdahl, R.E., van der Hilst, R., Buland, R., 1998. Global teleseismic earthquake relocation with improved travel times and procedures for depth determination. Bull. Seismol. Soc. Am. 88(3), 722–743, doi:10.1130/0-8137-2349-3.461.

Evans, J.S., Oakleaf, J., Cushman, S.A., Theobald, D., 2014. An ArcGIS Toolbox for surface gradient and geomorphometric modeling, version 2.0-0. Available: http://evansmurphy.wix.com/evansspatial. Accessed: 2016 Nov 1.

Fouquet, Y., 1997. Where are the large hydrothermal sulphide deposits in the oceans?. In: Philosophical Transactions: Mathematical, Physical and Engineering Sciences, vol. 355, pp. 247–441.

Fryer, P., 1981. Petrogenesis of basaltic rocks from the Mariana Trough. Doctoral dissertation, Univ. of Hawai'i., Honolulu, Hawai'i, pp. 157.

Fryer, P., 1995. Geology of the Mariana Trough, in Back-arc Basins. In: Taylor, B. (Ed.), Tectonics and Magmatism. Springer, New York, pp. 237–279, doi:10.1007/978-1-4615-1843-3.

Fryer, P., Hussong, D.M., 1981. Seafloor spreading in the Mariana Trough: Results of leg 60 drill site selection surveys. Initial Rep. Deep Sea Drill. Proj. 60, 45–55, doi:10.2973/dsdp.proc.60.103.1982.

Fryer, P., Hussong, D.M., 1982. Arc volcanism in the Mariana Trough. In: EOS Trans. AGU, 63(45), San Francisco, Calif, pp. 1135.

Fryer, P., Fujimoto, H., Sekine, M., Johnson, L.E., Kasahara, J., Masuda, H., Gamo, T., Ishii, T., Ariyoshi, M., Fujioka, K., 1998. Volcanoes of the southwestern extension of the active Mariana Island arc: New swath-mapping and geochemical studies. Isl. Arc 7(3), 596–607, doi:10.1111/j.1440-1738.1998.00212.x.

Fryer, P., Becker, N., Appelgate, B., Martínez, F., Edwards, M., Fryer, G., 2003. Why is the Challenger Deep so deep?. Earth Planet. Sci. Lett. 211(3–4), 259–269, doi:10.1016/S0012-821X(03)00202-4.

Fujikura, K., Yamazaki, T., Hasegawa, K., Tsunogai, U., Stern, R.J., Ueno, H., Yamamoto, H., Sun, C.-H., Okutani, T., 1997. Biology and earth scientific investigation by the submersible "Shinkai 6500" system of deep-sea hydrothermalism and lithosphere in the Mariana back-arc basin. JAMSTEC J. Deep Sea Res. 13, 1–20.

Fujiwara, T., Umino, S., Asada, M., Koike, Y., Kimoto, K., Kanamatsu, T., Okada, S., 2008. A submersible study of the Mariana Trough back-arc spreading center at 17°N. JAMSTEC J. Deep Sea Res. 8, 61–73, doi:10.5918/jamstecr.8.61.

Gamo, T., and Shipboard Scientific Party, 1993. Revisits to the mid-Mariana Trough hydrothermal site and discovery of new venting in the southern Mariana region by the Japanese submersible Shinkai 6500. InterRidge News 2, 11–14.

Gamo, T., and Shipboard Scientific Party, 1994. Mariana 1992 diving surveys by "Shinkai 6500" (Y9204 cruise): Revisits to the Mid-Mariana hydrothermal area and discovery of hydrothermal vents in the southern Mariana region. JAMSTEC J. Deep Sea Res. 10, 153–162

German, C.R., Petersen, S., Hannington, M.D., 2016. Hydrothermal exploration of mid-ocean ridges: Where might the largest sulfide deposits be forming?. Chem. Geol. 420, 114–126, doi:10.1016/j.chemgeo.2015.11.006.

Gray, L.M., 2016. Mapping data acquisition and processing summary report. In: Cruise EX-16-05 Leg 1: 2016 Deepwater Exploration of the Marianas. NOAA Off. of Ocean Explor. and Res., Silver Spring, Md., pp. 1–19.

Gribble, R.F., Stern, R.J., Bloomer, S.H., Stüben, D., O'Hearn, T., Newman, S., 1996. MORB mantle and subduction components interact to generate basalts in the southern Mariana Trough back-arc basin. Geochim. Cosmochim. Acta 60, 2153–2166, doi:10.1016/0016-7037(96)00078-6.

Gribble, R.F., Stern, R.J., Newman, S., Bloomer, S.H., O'Hearn, T., 1998. Chemical and isotopic composition of lavas from the Northern Mariana Trough: Implications for magmagenesis in back-arc basins. J. Petrol. 39, 125–154, doi:10.1093/petroj/39.1.125.

Grindlay, N.R., Fox, P.J., Macdonald, K.C., 1991. 2nd-Order Ridge Axis Discontinuities in the South-Atlantic - Morphology, Structure, and Evolution. Mar. Geophys. Res. 13(1), 21–49.

Gvirtzman, Z., Stern, R.J., 2004. Bathymetry of Mariana trench-arc system and formation of the Challenger Deep as a consequence of weak plate coupling. Tectonics 23(2), 1–15, doi:10.1029/2003TC001581.

Hall, R., Ali, J.R., Anderson, C.D., Baker, S.J., 1995. Origin and motion history of the Philippine Sea Plate. Tectonophysics 251, 229–250, doi:10.1016/0040-1951(95)00038-0.

Hannington, M., Jamieson, J., Monecke, T., Petersen, S., Beaulieu, S., 2011. The abundance of seafloor massive sulfide deposits. Geology 39(12), 1155–1158, doi:10.1130/G32468.1.

Hannington, M.D., 2009. Modern submarine hydrothermal systems — A global perspective on distribution, size, and tectonic setting. In: Cousens, B., Piercey, S.J. (Eds.), Submarine Volcanism and Mineralization: Modern Through Ancient. In: Short Course Notes, vol. 19. Geol. Assoc. of Can. Min. Deposits Div., St. John's, N.L., pp. 91–148.

Hannington, M.D., de Ronde, C.E.J., Petersen, S., 2005. Sea-Floor Tectonics and Submarine Hydrothermal Systems. Econ. Geol. 100, 111–141.

Hawkins, J.W., Lonsdale, P.F., Macdougall, J.D., Volpe, A.M., 1990. Petrology of the axial ridge of the Mariana Trough back-arc spreading center. Earth Planet. Sci. Lett. 100, 226–250, doi:10.1016/0012-821X(90)90187-3.

Heeszel, D.S., Wiens, D.A., Shore, P.J., Shiobara, H., Sugioka, H., 2008. Earthquake evidence for along-arc extension in the Mariana Islands. Geochem. Geophys. Geosyst. 9(12), 1–13, doi:10.1029/2008GC002186.

Hessler, R.R., Lonsdale, P.F., 1991. Biogeography of Mariana Trough hydrothermal vent communities. Deep Sea Res. Part A 38(2), 185–199, doi:10.1016/0198-0149(91)90079-U.

Hessler, R.R., Martin, J.W., 1989. Austinograea williamsi, New Genus, New Species, a hydrothermal vent crab (Decapoda: Bythograeidae) from the Mariana Back-Arc basin, western Pacific. J. of Crustacean Biol. 9(4), 645–661, doi:10.2307/1548594.

Hessler, R.R., Lonsdale, P., Hawkins, J., 1988. Patterns on the ocean floor. New Sci. 24, 47–51.

Hewitt, A., Salisbury, R., Wilson, J., 2010. Using multibeam echosounder backscatter to characterize seafloor features. Sea Technol. 51(9), 10–13, doi:10.4043/20672-MS.

Hilde, T.W.C., Lee, C.-S., 1984. Origin and evolution of the West Philippine Basin: A new interpretation. Tectonics 102, 85–104.

Hsui, A.T., Youngquist, S., 1985. A dynamic model of the curvature of the Mariana Trench. Nature 318(5), 455–457, doi:10.1038/314731a0.

Hussong, D.M., Uyeda, S., 1981. Tectonic processes and the history of the Mariana Arc: A synthesis of the results of Deep Sea Drilling Project Leg 60. Initial Rep. Deep. Drill. Proj. 60, 909–929, doi:10.2973/dsdp.proc.60.154.1982.

Ikehata, K., Suzuki, R., Sazuhiko, S., Ishibashi, J., Urabe, T., 2015. Mineralogical and geochemical characteristics of hydrothermal minerals collected from hydrothermal vent fields in the southern Mariana spreading center. In: Ishibashi, J., Okino, K., Sunamura, M. (Eds.), Subseafloor Biosphere Linked to Hydrothermal Systems: TAIGA Concept. Springer Japan, pp. 275–287.

Ishibashi, J., Yamanaka, T., Kimura, H., Hirota, A., Toki, T., Tsunogai, U., Gamo, T., Utsumi, M., Roe, K., Miyabe, S., Okamura, K., 2004. Geochemistry of hydrothermal fluids in south Mariana back-arc spreading center. In: Eos Trans. AGU 85(47), Fall Meet. Suppl. Abstract V44A-05.

Ishibashi, J.-i., Tsunogai, U., Toki, T., Ebina, N., Gamo, T., Sano, Y., Masuda, H. Chiba H., 2015/ Chemical composition of hydrothermal fluids in the central and southern Mariana Trough back-arc basin. Deep. Res. Part II 121, 126–136, doi:10.1016/j.dsr2.2015.06.003.

Jarrard, R.D., 1986. Relations among subduction parameters. Rev. Geophys. 24(2), 217–284, doi:10.1029/RG024i002p00217.

Jenner, G.A., Cawood, P.A., Rautenschlein, M., White, W.M., 1987. Composition of back-arc basin volcanics, Valu Fa Ridge, Lau Basin: Evidence for a slab-derived component in their mantle source. J. Volcanol. Geotherm. Res., 32(1–3), 209–222, doi:10.1016/0377-0273(87)90045-X.

Johnson, L.E., Fryer, P., Masuda, H., Ishii, T., Gamo, T., 1993. Hydrothermal vent deposits and two magma sources for volcanoes near 13°20’N in the Mariana back-arc basin: a view from Shinkai 6500. In: EOS Trans. AGU, 74(43), San Francisco, Calif., pp. 681.

Kakegawa, T., Utsumi, M., Marumo, K., 2008. Geochemistry of sulfide chimneys and basement pillow lavas at the southern Mariana trough (12.55°N–12.58°N). Resour. Geol. 58(3), 249–266, doi:10.1111/j.1751-3928.2008.00060.x.

Karig, D.E., 1971a. Origin and development of marginal basins in the western Pacific. J. Geophys. Res. 76(11), 2542–2561, doi:10.1007/s11192-012-0776-8.

Karig, D.E., 1971b. Structural history of the Marianas island arc system. Geol. Soc. Am. Bull. 82, 323–344, doi:10.1130/0016-7606(1971)82(323:shotmi)2.0.co;2.

Karig, D.E., Anderson, R.N., Bibee, L.D.T., 1978. Characteristics of back arc spreading in the Mariana Trough. J. Geophys. Res. 83(B3), 1213–1226, doi:10.1029/JB083iB03p01213.

Kato, T., Beavan, J., Matsushima, T., Kotake, Y., Camacho, J.T., Nako, S., 2003. Geodetic evidence of back-arc spreading in the Mariana Trough. Geophys. Res. Lett. 30(12), 1–4, doi:10.1029/2002GL016757.

Kennelly, P.J., 2008. Terrain maps displaying hill-shading with curvature. Geomorphology 102(3–4), 567–577, doi:10.1016/j.geomorph.2008.05.046.

Kennelly, P.J., Stewart, A.J., 2014. General sky models for illuminating terrains. Int. J. Geogr. Inf. Sci. 28(2), 383–406, doi:10.1080/13658816.2013.848985.

Kong, L.S.L., 1993. Seafloor spreading in the Mariana Trough. In: Segawa, J. (Ed.), Preliminary Report of the Hakuhu-Maru Cruise KH92-1. Ocean Res. Inst., Univ. Tokyo, Tokyo, pp. 5–16.

Kong, L.S.L, Seama, N., Fujimoto, H., Kasahara, J., KH92-1 Shipboard Scientific Party, 1992. Segmentation of the Mariana Trough back-arc spreading center at 18°N. InterRidge News 1(1), 2–5.

Koyama, M., Cisowski, S., Pezard, P., 1992. Paleomagnetic evidence for northward drift and clockwise rotation of the Izu-Bonin forearc since the early Oligocene. In: Taylor, B., et al. (Eds.), Proceedings of the Ocean Drilling Program, Scientific Results, vol. 126. Ocean Drilling Program, College Station, Tex., pp. 353–370.

LaTraille, S., Hussong, D., 1980. Crustal structure across the Mariana island arc. In: Hayes, D. (Ed.), The Tectonic and Geologic Evolution of Southeast Asian Seas and Islands. AGU, Washington, D.C., pp. 209–221.

Le Pichon, X., Huchon, P.H., 1987. Central Japan triple junction revisited. Tectonics 6, 35–45, doi:10.1029/TC006i001p00035.

Le Pichon, X., Huchon, P.H., Barrier, E., 1985. Pangea, geoid and the evolution of the western margin of the Pacific Ocean. In: Nasu, N., et al. (Eds.), Formation of Active Ocean Margins. Terra-pub, Tokyo, pp. 3–42.

Lobecker, E., 2016. Oceanographic Data Collected During the EX1605L2 (CAPStONE CNMI & Mariana Trench MNM (Mapping)) on NOAA Ship OKEANOS EXPLORER in the North Pacific Ocean from 2016-05-20 to 2016-06-11 (NCEI Accession 0155917), version 1.1 [data set]. NOAA Natl. Cent. For Environ. Inform., doi:10.7289/V5Z03663.

Macdonald, K.C., 1982. Mid-ocean ridges: Fine scale tectonic, volcanic and hydrothermal processes within the plate boundary zone. Annu. Rev. Earth Planet. Sci. 10, 155–190, doi:10.1146/annurev.ea.10.050182.001103.

Macdonald, K.C., 2001. Mid-ocean ridge tectonics, volcanism, and geomorphology. Encycl. Ocean Sci. 3, 1798–1813, doi:10.1016/B978-012374473-9.00094-1.

MacLeod, C.J., Searle, R.C., Murton, B.J., Casey, J.F., Mallows, C., Unsworth, S.C., Achenbach, K.L., Harris, M., 2009. Life cycle of oceanic core complexes. Earth Planet. Sci. Lett. 287(3–4), 333–344, doi:10.1016/j.epsl.2009.08.016.

Martínez, F., Fryer, P., Baker, N.A., Yamazaki, T., 1995. Evolution of back-arc rifting: Mariana Trough, 20°–24°N. J. Geophys. Res. 100(B3), 3807–3827, doi:10.1029/94JB02466.

Martínez, F., Fryer, P., Becker, N., 2000. Geophysical characteristics of the southern Mariana Trough, 11°50′N–13°40′N. J. Geophys. Res. 105(B7), 16591–16607, doi:10.1029/2000JB900117.

Mason, W.G., Moresi, L., Betts, P.G., Miller, M.S., 2010. Three-dimensional numerical models of the influence of a buoyant oceanic plateau on subduction zones. Tectonophysics 483(1–2), 71–79, doi:10.1016/j.tecto.2009.08.021.

Masuda, H., Lutz, R.A., Matsumoto, A., Masumoto, S., Fujioka, K., 1994. Topography and geochemical aspects on the most recent volcanism around the spreading axis of the southern Mariana Trough at 13°N. JAMSTEC J. Deep Sea Res. 10, 176–185.

Masuda, H., Mitsuzawa, K., Seama, N., Masumoto, S., and YK-99-11 Shipboard Scientific Party, 2001. Bathymetry and hydrothermal activities in the southern Mariana Trough—reconnaissance results of YK-99-11. JAMSTEC J. Deep Sea Res. 18, 83–88.

Matthews, K.J., Miller, R.D., Wessel, P., Whittaker, J.M., 2011. The tectonic fabric of the ocean basins. J. Geophys. Res. Solid Earth 116(12), 1–28, doi:10.1029/2011JB008413.

Maus, S., et al., 2009. EMAG2: A 2-arc min resolution Earth Magnetic Anomaly Grid compiled from satellite, airborne, and marine magnetic measurements. Geochem. Geophys. Geosyst. 10(8), Q08005, doi:10.1029/2009GC002471.

McCabe, R., Uyeda, S., 1983. Hypothetical model for the bending of the Mariana Arc. In: Hayes, D.E. (Ed.), The Tectonic and Geologic Evolution of Southeast Asian Seas and Islands: Part 2. AGU, Washington, D.C., pp. 281–293.

Miller, M.S., Kennett, B.L.N., Lister, G.S., 2004. Imaging changes in morphology, geometry, and physical properties of the subducting Pacific plate along the Izu-Bonin-Mariana arc. Earth Planet. Sci. Lett. 224, 363–370, doi:10.1016/j.epsl.2004.05.018.

Miller, M.S., Gorbatov, A., Kennett, B.L.N., 2005. Heterogeneity within the subducting Pacific slab beneath the Izu-Bonin-Mariana arc: Evidence from tomography using 3D ray tracing inversion techniques. Earth Planet. Sci. Lett. 235(1–2), 331–342, doi:10.1016/j.epsl.2005.04.007.

Miller, M.S., Gorbatov, A., Kennett, B.L.N., 2006. Three-dimensional visualization of a near-vertical slab tear beneath the southern Mariana arc. Geochem. Geophys. Geosyst. 7(6), Q06012, doi:10.1029/2005GC001110.

Mitsuzawa, K., Masuda, H., Seama, N., Hasegawa, Y., Miyamoto, M., Togashi, N., So, A., Yamanobe, H., 2000. Preliminary report of Deep-Tow/Yokosuka Cruise at hydrothermal areas in the mid and southern Mariana. JAMSTEC J. Deep Sea Res. 17, 73–87.

Müller, R.D., Roest, W.R., Royer, J.Y., Gahagan, L.M., Sclater, J.G., 1997. Digital isochrons of the world's ocean floor. J. Geophys. Res. 102(B2), 3211–3214, doi:10.1029/96JB01781.

Nakamura, K., Toki, T., Mochizuki, N., Asada, M., Ishibashi, J.I., Nogi, Y., Yoshikawa, S., Miyazaki, J.I., Okino, K., 2013. Discovery of a new hydrothermal vent based on an underwater, high-resolution geophysical survey. Deep Sea Res. Part I 74, 1–10, doi:10.1016/j.dsr.2012.12.003.

Oakley, A.J., Taylor, B., Moore, G.F., Goodliffe A., 2009. Sedimentary, volcanic, and tectonic processes of the central Mariana Arc: Mariana Trough back-arc basin formation and the West Mariana Ridge. Geochem. Geophys. Geosyst. 10(8), Q08X07, doi:10.1029/2008GC002312.

Ohara, Y., Yoshida, T., Kato, Y., Kasuga, S., 2001. Giant megamullion in the Parece Vela back-arc basin. Mar. Geophys. Res. 22, 47-61, doi:10.1023/A:1004818225642.

Okino, K., Kasuga, S., Ohara, Y., 1998. A new scenario of the Parece Vela Basin genesis. Mar. Geophys. Res. 20(1), 21–40, doi:10.1023/A:1004377422118.

Park, C.-H., Tamaki, K., Kobayashi, K., 1990. Age-depth correlation of the Philippine Sea back-arc basins and other marginal basins in the world. Tectonophysics 181(1–4), 351–371, doi:10.1016/0040-1951(90)90028-7.

Pertsev, A.N., Bortnikov, N.S., Vlasov, E.A., Beltenev, V.E., Dobretsova, I.G., Ageeva, O.A., 2012. Recent massive sulfide deposits of the Semenov ore district, Mid-Atlantic Ridge, 13°31′ N: Associated rocks of the oceanic core complex and their hydrothermal alteration. Geol. Ore Depos. 54(5), 334–346, doi:10.1134/S1075701512050030.

Resing, J.A., and Shipboard Scientific Party, 2016. Hydrothermal hunt at Mariana back-arc. In: Cruise Report for FK151121 on RV Falkor. Seattle, Wash., pp. 107, doi:10.7284/906519.

Ryan, W.B.F., Carbotte, S.M., Coplan, J.O., O'Hara, S., Melkonian, A., Arko, R., Weissel, R.A., Ferrini, V., Goodwillie, A., Nitsche, F., Bonczkowski, J., Zemsky. R.. 2009. Global multi-resolution topography synthesis. Geochem. Geophys. Geosyst. 10(3), Q03014, doi:10.1029/2008GC002332.

Sandwell, D.T., Müller, R.D., Smith, W.H.F., Garcia, E., Francis, R., 2014. New global marine gravity model from CryoSat-2 and Jason-1 reveals buried tectonic structure. Science 346(6205), 65–7, doi:10.1126/science.1258213.

Scholz, C.H., Small, C., 1997. The effect of seamount subduction on seismic coupling. Geology 25(6), 487–490, doi:10.1130/0091-7613(1997)025<0487:TEOSSO>2.3.CO;2.

Schouten, H., Klitgord, K.D., Whitehead, J.A., 1985. Segmentation of mid-ocean ridges. Nature 317, 225–229, doi:10.1038/317225a0.

Scott, R.B., Kroenke, L., Zakariadze, G., Sharaskin, A., 1981. Evolution of the South Philippine Sea: Deep Sea Drilling Project Leg 59 results. In: Orlofsky, S. (Ed.), Initial Report of the Deep Sea Drilling Project 59. U.S. Gov. Print. Off., Washington, D.C., pp. 909–929.

Sdrolias, M., Roest, W.R., Müller, R.D., 2004. An expression of Philippine Sea plate rotation: The Parece Vela and Shikoku Basins. Tectonophysics 394(1–2), 69–86, doi:10.1016/j.tecto.2004.07.061.

Seama, N., Fujiwara, T., 1993. Geomagnetic anomalies in the Mariana Trough 18°N. In: Segawa, J. (Ed.), Preliminary Reports of the Hakuho-Maru Cruise KH92-1. Ocean Res. Inst., Univ. Tokyo, Tokyo, pp. 70–71.

Seno, T., 1985. Age of subducting lithosphere and back-arc basin formation in the Western Pacific since the middle Tertiary. In: Nasu, N., et al. (Eds.), Formation of Active Ocean Margins. Terra Sci., Tokyo, pp.469–481.

Seno, T., Maruyama, S., 1984. Paleogeographic reconstruction and origin of the Philippine Sea. Tectonophysics 102, 53–84, doi:10.1016/0040-1951(84)90008-8.

Severinghaus, J.P, Macdonald, K.C., 1988. High inside corners at ridge-transform intersections. Mar. Geophys. Res. 9, 353–367, doi:10.1007/BF00315005.

Sigmundsson, F., 2006. Iceland Geodynamics: Crustal Deformation and Divergent Plate Tectonics. Springer, Chichester, U.K..

Sigurdsson, H., 2000. Volcanic episodes and rates of volcanism. In: Sigurdsson, H., et al. (Eds.), Encyclopedia of Volcanoes. Academic Press, San Diego, Calif., pp. 271–279.

Sinton, J.B., Hussong, D.M., 1983. Crustal structure of a short length transform fault in the central Mariana Trough. In: Hayes, D.E. (Ed.), The Tectonic and Geologic Evolution of Southeast Asian Seas and Islands: Part 2. AGU, Washington, D.C., pp. 236–254, doi:10.1029/GM027p0236.

Stern, R.J., 2002. Subduction zones. Rev. Geophys. 40(4), 1–13, doi:10.1029/2001RG000108.

Stern, R.J., 2010. The anatomy and ontogeny of modern intra-oceanic arc systems. In: Kusky, T.M., Zhai, M.-G., Xiao, W. (Eds.), The Evolving Continents: Understanding Processes of Continental Growth, vol. 338. Geol. Soc. Spec. Publ., pp. 7–34.

Stern, R.J., Smoot, N.C., Rubin, M., 1984. Unzipping of the volcano arc, Japan. Tectonophysics 102, 153–174, doi:10.1016/0040-1951(84)90012-X.

Stern, R.J., Bloomer, S. H., Martínez, F., Yamazaki, T., Harrison, T. M., 1996. The composition of back-arc basin lower crust and upper mantle in the Mariana Trough: A first Report. Isl. Arc 5, 354–372, doi:10.1111/j.1440-1738.1996.tb00036.x.

Stern, R.J., Fouch, M.J., Klemperer S.L., 2003. An overview of the Izu-Bonin-Mariana subduction factory. Geophys. Monogr. 138, 175–222.

Stern, R.J., Kohut, E., Bloomer, S.H., Leybourne, M., Fouch, M., Vervoort, J., 2006. Subduction factory processes beneath the Guguan cross-chain, Mariana Arc: no role for sediments, are serpentinites important?. Contrib. Mineral. Petrol. 151, 202–221, doi:10.1007/s00410-005-0055-2.

Stern, R.J., Tamura, Y., Masuda, H., Fryer, P., Martínez, F., Ishizuka, O., Bloomer, S.H., 2013. How the Mariana Volcanic Arc ends in the south. Isl. Arc 22, 133–148, doi:10.1111/iar.12008.

Stern, R.J., Tamura, Y., Ishizuka, O., Shukano, H., Bloomer, S.H., Embley, R.W., Leybourne, M., Kawabata, H., Nunokawa, A., Nichols, A.R.L., Kohut, E., Pujana, I., 2014. Volcanoes of the Diamante cross-chain: evidence for a mid-crustal felsic magma body beneath the Southern Izu-Bonin-Mariana arc. In: Gomez-Tuena, A., Straub, S.M., Zellmer, G.F. (Eds.), Orogenic Andesites and Crustal Growth. Geol. Soc., Spec. Publ., pp. 235–255.

Stüben, D., Neumann, T., Taibi, N.E., Glasby, G.P., 1998. Segmentation of the southern Mariana back-arc spreading center. Isl. Arc 7, 513–524, doi:10.1111/j.1440-1738.1998.00207.x.

Taylor, B., 1992. Rifting and the volcanic-tectonic evolution of the Izu-Bonin-Mariana arc. In: Taylor, B., et al. (Eds.), Proceedings of the Ocean Drilling Program, Scientific Results, vol. 126. Ocean Drill. Program, College Station, Tex., pp. 627–651.

Taylor, B. (Ed.), 1995. Back-arc Basins: Tectonics and Magmatism. Springer, New York, doi:10.1007/978-1-4615-1843-3.

Taylor, B., Crook, K., Sinton, J., 1994. Extensional transform zones and oblique spreading centers. J. Geophys. Res. 99(B10), 19707–19718, doi:10.1029/94JB01662.

Taylor, B., Goodliffe, A.M., Moorel, G.F., Oakley, A.J., Fryer, P., and EW0202 Scientific Party, 2002. Multi-channel seismic images of the Mariana Trough: EW0202 initial results. EOS Trans. AGU 83(47), Fall Meet. Suppl. Abstract, T72A-1228.

Thouret, J.-C., 1999. Volcanic geomorphology—an overview. Earth-Science Rev. 47, 95–131, doi:10.1016/S0012-8252(99)00014-8.

Tucholke, B.E., Lin, J., Kleinrock, M.C., 1998. Megamullions and mullion structure defining oceanic metamorphic core complexes on the Mid-Atlantic Ridge. J. Geophys. Res. 103, 9857–9866, doi:10.1029/98JB00167.

Urabe, T., Ishibashi, J., Maruyama, A., Marumo, K., Seama, N., Utsumi, M., 2004. Discovery and drilling of on- and off-axis hydrothermal sites in back-arc spreading center of southern Mariana Trough, western Pacific. EOS Trans. AGU 85(47), Fall Meet. Suppl. Abstract, V44A-03.

Uyeda, S., Ben-Avraham, Z., 1972. Origin and development of the Philippine Sea. Nature 238, 37.

Vallier, T., Jenner, G.A., Frey, F.A., Gill, J.B., Davis, A.S., Volpe, A.M., Hawkins, J.W., Cawood, P.A., Morton, J.L., Scholl, D.W., Rautenschlein, M., White, W.M., Williams, R. W., Stevenson, A. J., White, L.D., 1991. Subalkaline andesite from Valu Fa Ridge, a back-arc spreading center in southern Lau Basin: petrogenesis, comparative chemistry, and tectonic implications. Chem. Geol. 91, 227–256, doi:10.1016/0009-2541(91)90002-9.

van der Hilst, R., Seno, T., 1993. Effects of relative plate motion on the deep structure and penetration depth of slabs below the Izu-Bonin and Mariana island arcs. Earth Planet. Sci. Lett. 120, 395–407, doi:10.1016/0012-821X(93)90253-6.

Vogt, P.R., 1973. Subduction and aseismic ridges. Nature 242, 189–191, doi:10.1038/242117a0.

Vogt, P.R., Lowrie, A., Bracey, D.R., Hey, R.N., 1976. Subduction of aseismic oceanic ridges: Effects on shape, seismicity, and other characteristics of consuming plate boundaries. Spec. Pap. Geol. Soc. Am. 172, 1–59, doi:10.1130/SPE172-p1.

Walker, G.P.L., 1993. Basaltic-volcano systems. In: Prichard, H.M., et al. (Eds.), Magmatic Processes and Plate Tectonics, vol. 76. Geol. Soc. Spec. Publ., pp. 3–38.

Wallace, L., McCaffrey, R., Beavan, J., Ellis, S., 2005. Rapid microplate rotations and back-arc rifting at the transition between collision and subduction. Geology 33(11), 857–860, doi:10.1130/G21834.1.

Wessel, P., Matthews, K.J., Müller, R.D., Mazzoini, A., Whittaker, J.M., Myhill, R., Chandler, M.T., 2015. Semiautomatic fracture zone tracking. Geochem. Geophys. Geosyst. 16, 2462–2472, doi:10.1002/2015GC005853.

Wheat, C.G., Fryer, P., Hulme, S., Becker, N., Curtis, A., Moyer, C., 2003. Hydrothermal venting in the southernmost portion of the Mariana back-arc spreading center at 12°57'N. EOS Trans. AGU 84(46), Fall Meet. Suppl. Abstract, V32A-0920.

Widiyantoro, S., Kennett, B.L.N., van der Hilst, R.D., 1999. Seismic tomography with P and S data reveals lateral variations in the rigidity of deep slabs. Earth Planet. Sci. Lett. 173(1–2), 91–100, doi:10.1016/S0012-821X(99)00216-2.

Wilcock, W.S.D., 1998. Cellular convection models of mid- ocean ridge hydrothermal circulation and the temperatures of black smoker fluids. J. Geophys. Res. 103(B2), 2585–2596, doi:10.1029/97JB03252.

Yamazaki, T., Murakami, F., Saito, E., 1993. Mode of seafloor spreading in the northern Mariana Trough. Tectonophysics 221(2), 207–222, doi:10.1016/0040-1951(93)90333-F.

Yeo, I., Searle, R.C., Achenbach, K.L., Le Bas, T.P., Murton, B.J., 2012. Eruptive hummocks: Building blocks of the upper ocean crust. Geology 40(1), 91–94, doi:10.1130/G31892.1.

Yeo, I.A., Devey, C.W., LeBas, T.P., Augustin, N., Steinführer, A., 2016. Segment-scale volcanic episodicity: Evidence from the North Kolbeinsey Ridge, Atlantic Earth Planet. Sci. Lett. 439, 81–87, doi:10.1016/j.epsl.2016.01.029.

Yoshikawa, S., Okino, K., Asada, M., 2012. Geomorphological variations at hydrothermal sites in the southern Mariana Trough: Relationship between hydrothermal activity and topographic characteristics. Mar. Geol. 303–306, 172–182, doi:10.1016/j.margeo.2012.02.013.

Zhang, Y., Li, S.Z., Suo, Y.H., Guo, L.L., Yu, S., Somerville, I.D., Guo, R.H., Zang, Y.B., Zheng, Q.L., Mu, D. L., 2016. Origin of transform faults in back-arc basins: examples from Western Pacific marginal seas. Geol. J. 51(S1), 490–512, doi:10.1002/gj.2807.

Chapter 7

Global Summary and Conclusions

7.1. Chapter highlights

This thesis examined the deep, grabens of the Coriolis Troughs (CT) with focused magmatism, versus the shallow, diffuse extension in the Jean Charcot Troughs (JCT), versus the mature back-arc spreading in the Marianas, and the structural, petrological, and hydrothermal consequences of these different scenarios. The CT and the JCT illustrate two distinct styles of the initial stages of arc rifting in the New Hebrides. The Mariana back-arc illustrates mature seafloor spreading, characterized by fast-spreading ridge morphologies in the south and slow-spreading ridge morphologies in the central back-arc. In each of these settings, the influence of subduction-related tectonic complexities (e.g., arc rotations, arc-ridge collisions, pre-existing structures, and proximity to the volcanic arc) on basin evolution and hydrothermal venting was investigated using a multi-scale approach. The main points of each chapter are summarized below.

Chapter 2: The southern New Hebrides back-arc: Tectonic focusing of voluminous basaltic eruptions in magma-deficient back-arc rifts

- The formation of the Nifonea shield-type volcano in the young Vate trough is linked to arc segmentation resulting from collision with the d'Entrecasteaux Ridge.
- Arc-transverse faults act as magma conduits for voluminous basaltic eruptions during rifting.
- The Nifonea volcano hosts the first large lava lake described in a submarine back-arc
- Effusive eruptions in the Nifonea caldera produced short-lived hydrothermal venting and an "event plume."
- High-temperature fluids are focused along permeability contrasts between lava morphologies.

- This chapter describes the structural, volcanological, and hydrothermal consequences of back-arc rifting forming deep grabens with focused magmatism, providing the basis for comparisons with other modes of back-arc rifting.

Chapter 3: Geodynamic evolution of the northern New Hebrides back-arc: Influence on magmatism and hydrothermal venting in the Jean Charcot Troughs, SW Pacific

- Rifting of the New Hebrides back-arc at ~6.5 Ma is linked to steepening of the subducting slab following detachment, along with asymmetric slab rollback.
- Irregular grabens extending ~120 km from the arc result from extension along pre-existing structures in the upper plate, with enhanced magmatism along structural intersections.
- A reversal of arc rotation associated with the collision of the d'Entrecasteaux ridge (DER) led to distributed extension in the northern back-arc and narrower grabens in the south.
- Igneous geochemistry reflects an enriched mantle source, contributions from the deep subducting slab, fractional crystallization and bimodal volcanism.
- A row of basaltic cinder cones, marking early back-arc rifting on a volcanic high between the JCTs, are host to the Tinakula massive sulfide deposit.
- This chapter describes the structural, petrological, and hydrothermal consequences of back-arc rifting dominated by diffuse extension, providing the basis for comparisons of hydrothermal and magmatic processes associated with other modes of back-arc rifting.

Chapter 4: Mineralogy, geochemistry and S-isotope systematics of the Tinakula seafloor massive sulfide deposit, Jean Charcot Troughs, SW Pacific

- Mineralization of the Tinakula deposit is controlled by faulting and the different volcanic facies of the cinder cones, deposited over ~5,500 years.
- Dendritic barite and sphalerite, precipitated by low-temperature diffuse venting through the permeable volcaniclastic substrate are the dominant style of mineralization.
- Local high-temperature chalcopyrite-rich chimneys are formed at several sites, reflecting more focused fluid flow.
- The geochemistry of the Tinakula sulfides is similar to other rifted arc settings, with enrichments in Cd, Ge, Hg, and In, and Ba compared to MOR systems.

- Multiple sulfur isotopes show that crustal host rock and thermochemical reduction of seawater-derived dissolved sulfate are the primary sources of sulfur at Tinakula, with no contributions from magmatic volatiles or biogenic sources.
- This chapter explores the hydrothermal processes in a back-arc rift setting associated with diffuse extension, highlighting the influence of mafic (basaltic to andesitic) explosive volcanism on fluid flow and the composition of hydrothermal precipitates, providing a basis of comparison to hydrothermal processes in magmatically-robust back-arc environments.

Chapter 5: Mineralogical and geochemical characteristics of hydrothermal alteration in the volcaniclastic-hosted Tinakula seafloor massive sulfide deposit (New Hebrides back-arc, SW Pacific)

- Shallow drilling at Tinakula revealed mainly pyroclastic lithofacies that have been variably altered by hydrothermal fluids mixed with cold seawater.
- Hydrothermal alteration consists of: (1) replacement of volcanic glass and primary minerals by clays; (2) infill of pore space by clays; (3) cementation by anhydrite, further reducing permeability; and (4) fracturing, leading to the precipitation of sulfate-sulfide veins and high-temperature venting at the seafloor.
- Five distinct alteration types are recognized with increasing depth to ~20 m below the seafloor: (1) montmorillonite/nontronite; (2) nontronite + corrensite; (3) illite/smectite + pyrite; (4) illite/smectite + chamosite; and (5) chamosite + corrensite.
- Zones of argillic alteration are distinguished from zones of chloritic alteration by mass changes in ΔK_2O, ΔMgO, ΔFe_2O_3 relative to an unaltered basaltic-andesite precursor.
- Increasing temperature with depth is recorded by a transition from argillic to chloritic alteration, increasing phyllosilicate crystallinity, increasing proportions of illite in mixed-layer I/S clays, oxygen isotope geothermometry on clay minerals (119–220°C) and fluid inclusions in anhydrite and sphalerite (up to 291°C).
- Hydrothermal fluids were neutral to slightly acidic, with slight shifts to higher salinity, possibly resulting from phase separation and seawater mixing.

- Tinakula may be typical of the type of SMS deposit developed mainly in volcaniclastic rocks associated with the first mafic (basaltic to andesitic) lavas erupted in an early back-arc rift.
- This chapter explores the fluid-rock interactions in permeable mafic volcaniclastic substrate, highlighting the influence of volcanism in a back-arc rift setting associated with diffuse extension, providing a basis of comparison to hydrothermal processes in magmatically-robust back-arc environments.

Chapter 6: Geological interpretation of volcanism and segmentation of the Mariana back-arc spreading center between 12.7°N and 18.3°N

- Ridge segmentation along the back-arc spreading center is controlled by pre-existing basement structures that appear to pre-date back-arc rifting.
- Four morphologically-distinct segment types are identified: dominantly magmatic segments (Type I); magmatic segments currently undergoing tectonic extension (Type II); dominantly tectonic segments (Type III); and tectonic segments currently undergoing magmatic extension (Type IV).
- Variations in segment morphology reflect changes in magma supply, which is locally enhanced by proximity to cross-arc volcanoes.
- Spatial density of vent sites is highest in areas of enhanced magma supply associated with arc proximity.
- This chapter describes the structural, volcanological, and hydrothermal consequences of mature back-arc spreading ranging from fast-spreading to slow-spreading ridges, providing the basis for comparisons of the influence of tectonism on volcanism and hydrothermal processes in immature back-arc rifts.

This thesis examined the basin morphologies and structural features of the New Hebrides and Mariana back-arcs to identify the geodynamic factors that influence the evolution of back-arcs at different stages of formation, from early rifting to mature seafloor spreading. New ship-based bathymetric mapping in the CT reveal three simple narrow and deep grabens that are typical of early back-arc rifts where the rate of extension and subsidence exceeds the magmatic input (e.g., Sibuet et al., 1987; Giba et al., 2010). These grabens are <100 km long, 25–45 km wide, and reach

depths of >3 km. The grabens are arranged en echelon, ~50 km from the arc front. Structural interpretations made from the bathymetry reveal left-lateral transtension in the back-arc, with the strongest influence in the youngest graben (the Vate Trough). This transtension is ascribed to the subduction-zone collision with the d'Entrecasteaux Ridge (DER) at ~3 Ma, which segmented the arc (e.g., Collot et al., 1992; Green et al., 1992) and resulted in the clockwise block-rotation of the southern segment about a new pole near the DER. These upper plate stresses resulted in focusing of voluminous eruptions forming the Nifonea shield volcano in the center of the otherwise magma-deficient back-arc rift. In contrast, satellite altimetry of the JCT reveal a series of irregular grabens and volcanic ridges extending up to ~120 km from the volcanic arc. Regional structures in the back-arc are interpreted from vertical gravity gradient data and regional magnetic data, which indicate that many of the structures were formed during the opening of the North Fiji Basin (NFB). In particular, E-W lineaments extend from the Tikopia paleo-spreading center in the NFB across the JCT, associated with an inflated region of enhanced magmatism that bisects the basin morphology of the back-arc. Therefore, the irregular back-arc morphology is strongly controlled by extension along pre-existing structures in the back-arc region. These structures appear to have played a greater role in the evolution of the JCT compared to the CT. This study also examines systematic variations in the basin morphologies in the JCT; the basins in the north are deeper with simple graben morphologies, while the basins in the south have irregular morphologies and are highly sedimented. These observations are consistent with a reversal of the arc rotation from clockwise to counter-clockwise following the collision with the DER, which reduced extension in the south and promoted extension in the north. Therefore, the DER collision had profound yet disparate impacts on the morphological and structural evolution of both the CT and JCT.

The contrasting styles of volcanism in the CT and JCT were also examined in the broader geodynamic context. In the CT, ROV dives reveal effusive volcanism and ponding of a lava lake in the summit caldera of the Nifonea axial volcano. This type of volcanism is typical of mid-ocean ridges, particularly near ridge-hotspots intersections (e.g., Axial Volcano, Juan de Fuca Ridge: Embley et al., 1990), and is therefore an unexpected style of volcanism for a young back-arc rift. The volcano has an unusual alkalic composition not previously documented in a back-arc rift, which may be related to efficient removal of low-degree partial melts along arc-transverse faults or tapping of a heterogeneous mantle source (e.g., Lima et al., 2017). This style of tectonically-

focused magmatism in the CT contrasts with the style of volcanism in the JCT, as revealed by ship-based and high-resolution ROV bathymetry, seafloor observations during ROV dives, and sampling of volcanic rocks. In the JCT, there are a wide range of volcanic styles, including arc-like volcanism forming the bimodal basaltic-dacitic Starfish composite volcano, as well as fissure eruptions forming volcanic ridges and rows of mafic (basaltic to andesitic) cinder cones. The steep slopes near the summit of the Starfish volcano reflect viscous dacitic lava flows that do not travel far from the vent, whereas the gentle slopes near the base (i.e., the 'platform') reflect accumulated pyroclastic and eroded material. Cinder cones tend to form on the flank of the composite volcanoes during later stages of eruption as magmas exploit fractures that extend from the magma chamber outwards towards the unstable flank (Sigurdsson, 2000). Volcanic rocks from the JCT show a larger subduction component (more arc-like signature) compared to the CT. The contrasting styles of volcanism in the CT and JCT further reflect the distinct geodynamic evolution of each back-arc.

In the Mariana back-arc, examination of satellite altimetry, regional magnetic data, and newly-acquired ship-based multibeam bathymetry reveals complex basin evolution and volcanism. Along the spreading center, four distinct ridge morphologies indicate variable magma supply and style of extension (tectonic versus magmatic). In particular, magmatism is enhanced in the southern back-arc associated with increasing proximity to the volcanic arc, indicating contributions of arc magmas to the back-arc. Additionally, cross-arc volcanic chains are identified, which locally enhance magmatism along the 16.5°N and 17.0°N segments. These cross-arc volcanic chains follow the trends of structures that extend across the back-arc, following the trends of structures in the adjacent Parece Vela basin, which suggests that they may pre-date back-arc rifting. These structures are spatially associated with first- and second-order offsets in the spreading ridge, indicating that pre-existing structures may have been a key factor in segmentation and magma focusing during back-arc evolution. The arcuate shape of the present-day volcanic front in the Marianas results from subduction-zone collisions with buoyant oceanic plateaus. A collision with the Ogasawara Plateau at ~26°N segmented the arc, pinning the northern tip of the Marianas. At ~10°N a collision with the Caroline Ridge pinned the southern end of the Marianas. These collisions caused rotation of the arc, resulting in double saloon-door style back-arc spreading (e.g., Wallace et al., 2005). A comparison of the double-saloon-door style of opening in the New

Hebrides and the Marianas is shown in Fig. 7.1a. In both cases, buoyant oceanic plateaus caused significant modification of the subduction zone. Complex back-arc evolution, including asymmetric extension and block-rotations, is a direct result of these collisions. Examination of the basin morphologies and structural features of the New Hebrides and Mariana back-arcs demonstrates the continued importance of subduction-zone collisions and pre-existing structures on back-arc evolution and volcanism from early back-arc rifting to mature seafloor spreading.

Finally, the influence of geodynamics and volcanism on hydrothermal venting was explored in each back-arc setting. In the CT, the Nifonea vent field is magmatically robust, associated with voluminous basaltic sheet flows and pillow mounds in the summit caldera of the Nifonea shield volcano. Hydrothermal venting is dominated by high-temperature but apparently short-lived venting, indicated by a lack of chimney talus and the predominance of high-temperature minerals (chalcopyrite, anhydrite; Haase et al., 2014). Attempts to date the chimneys at Nifonea by ^{226}Ra/Ba dating of barite were unsuccessful due to the low barium content (Suppl. Table B2); however, the initial ratio is higher than other arc-related deposits in the western Pacific (e.g., de Ronde et al., 2011; 2014). This may be due to an excess in ^{226}Ra, which supports the short-lived nature of the system (Anderson et al., 2016) and limited water-rock exchange at extremely high water:rock ratios (Schmidt et al., 2017). The high temperatures promote widespread boiling of the hydrothermal fluids, despite the deep water depth (~1875 mbsl). The asymmetrical slab rollback and associated block-rotation of the southern New Hebrides produced transtension in the CT, which focuses robust magmatism in one large volcano; this directly leads to high-temperature, short-lived hydrothermal venting that is driven by effusive eruptions in the summit caldera. In contrast, the Tinakula deposit in the JCT occurs at a depth of only ~1070-1204 mbsl, and venting is mainly lower-temperature, indicated by the abundance of sphalerite-barite and barite-silica chimneys. The abundance of barite in the hydrothermal precipitates also reflects the increased influence of a deep subduction component in the JCT. Compared to Nifonea, Tinakula is a long-lived system, with minimum ages of barite dated by ^{226}Ra/Ba dating of 5597 ± 240 years. Diffuse extension in the JCT is associated with a highly tectonized seafloor, promoting fissure-type eruptions along deep-seated faults. The volcaniclastic material produced by these fissure eruptions results in a highly permeable substrate, allowing extensive seawater mixing, indicated by abundant

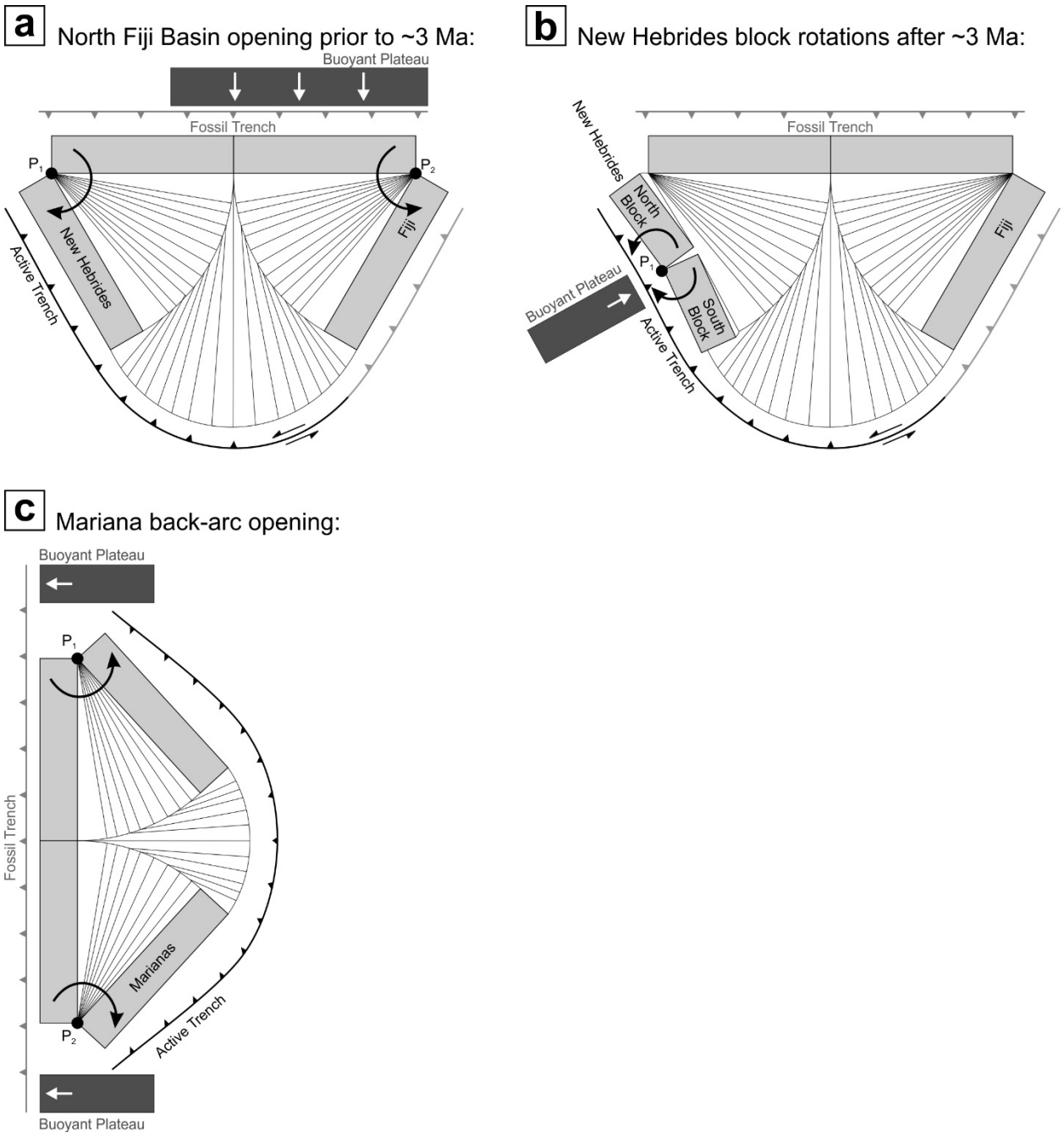


Fig. 7.1. Cartoon schematic of the double-saloon-door rifting and spreading model (a) opening of the North Fiji basin until ~3 Ma; (b) block rotations of the New Hebrides following the collision with the DER at ~3 Ma, with reversed rotation of the northern block; and (c) opening of the Mariana back-arc. Buoyant oceanic plateaus interrupt subduction at both locations, and the resulting back-arc opening is associated with both arc-parallel and arc-perpendicular rifts. Modified from Martin (2013) to include buoyant oceanic plateaus and trenches in (a), additional impact of the subduction-zone collision ~3 Ma in (b), and drafted in the same style for the Marianas in (c).

anhydrite in the footwall and widespread subseafloor deposition of the sulfides. Seawater mixing also results in abundant low-temperature venting.

Recent discoveries along Mariana spreading axis reveal hydrothermal venting at the segment centers of every segment type where magmatic activity is also focused, indicating a primary magmatic control on venting. In particular, vigorously-venting high-temperature chimneys have been observed at the large mid-segment high at 17.0°N, where magmatism may follow cross-arc structures, and may be tectonically focused from transtension resulting from movement along the adjacent shear zone offset. There is also a strong magmatic control on the overall distribution of vent sites, with numerous closely-spaced sites in the southern back-arc where magmatism is enhanced by proximity to the volcanic arc. Hydrothermal venting in the New Hebrides and Mariana back-arcs is broadly similar to that on mid-ocean ridges, forming where a heat source is present to drive hydrothermal circulation and faults focus fluid flow. However, compared to mid-ocean ridges, the geodynamic evolution of these back-arc environments is influenced by additional tectonic complexities, such as pre-existing structures, arc-transverse faults, and contributions from arc magmas, that promote crustal permeability or enhanced magmatism, which promote the formation of massive sulfide deposits.

The southern CT, northern JCT, and Mariana Trough represent the complete spectrum of early arc rifting to mature back-arc spreading. Until now, the description of tectonic, magmatic, and hydrothermal activity at western Pacific submarine arcs has focused on either the arc front (e.g., Izu-Bonin and Tonga-Kermadec arcs: Embley et al., 2004; de Ronde et al., 2005; Stoffers et al., 2006) or deeper back-arc basins where active seafloor spreading is already occurring (e.g., North Fiji Basin and Lau Basin: Kim et al., 2006; Ferrini et al., 2008). This thesis documented the structural, volcanic, and hydrothermal characteristics of the young New Hebrides back-arcs and the Mariana Trough, which are directly influenced by the complex geodynamic evolution of each back-arc.

7.2. Future directions

The comparison of the New Hebrides and Mariana back-arcs shows that their magmatic and hydrothermal evolution have been strongly affected by subduction-related tectonic complexities at a range of different scales. This has important implications for understanding the fundamental controls on ore formation in ancient back-arc settings and for developing exploration tools for massive sulfide deposits. 80% of VMS deposits mined on land were formed in subduction zones, closely related to the rifting of arc crust and seafloor spreading in more mature back-arc settings (Franklin et al., 2005). Yet the details of this relationship remain poorly understood. The Nifonea volcano is a modern analogue for mafic flow-dominated submarine environments in greenstone terranes, and the Tinakula setting is more typical of volcaniclastic-dominated settings, with very different styles of associated hydrothermal activity and mineralization. The volcanic centers of the more mature back-arc basin of the Marianas are indistinguishable from MOR spreading centers and are modern analogues of the settings for typical Cyprus-type massive sulfide deposits. Seafloor mapping techniques developed in this study highlight the particular conditions wherein enhanced magmatism and pre-existing structures may contribute to ore formation in both nascent back-arc rifts and mature back-arc spreading centers, but some important questions remain:

(1) When does rifting of an arc begin? Do rifts jump, as spreading ridges do, or is initial extension more diffuse over the whole area? Limited geochronological data are available in most back-arc rifts (e.g., the best data from JCT is from 30 years ago).

(2) Where does the arc crust stop and the back-arc crust begin? In some settings, this transition happens within 20 km, but in others, it may be more widely manifested.

(3) Why does arc volcanism stop in some segments and continue in others? In the JCT, arc volcanism between ~11°S and 12°S has terminated, with magmatism shifted into the back-arc. Is this related to the recent collision with the West Torres Plateau (~1.5 Ma)?

(4) At what stage of early arc rifting do large hydrothermal systems develop?

(5) What is the deep crustal structure? How does the crustal thickness influence the structure and composition of the newly formed back-arc crust?

In addition, isotopic studies (Sm-Nd, Pb) of the unaltered volcanic host rocks of the Tinakula deposit (*Chapter 3*) will shed greater light on the provenance of the melts and mantle composition.

The geological mapping techniques developed in this study represent a manual adaptation of land-based remote-predictive mapping methods that have the potential to transform our maps of the seafloor (currently almost exclusively topographic). This will require continued refinement, including machine learning techniques that may further improve our geological interpretations.

References

Anderson, M.O., Hannington, M.D., Haase, K., Schwarz-Schampera, U., Augustin, N., McConachy, T.F., Allen, K., 2016. Tectonic focusing of voluminous basaltic eruptions in magma-deficient back-arc rifts. Earth Planet. Sci. Lett. 440, 43–55, doi:10.1016/j.epsl.2016.02.002.

Collot, J.Y., Lallemand, S., Pelletier, B., Eissen, J.-P., Glaçon, G., Fisher, M.A., Greene, H.G., Boulin, J., Daniel, J., Monzier, M., 1992. Geology of the d'Entrecasteaux-New Hebrides Arc collision zone: results from a deep submersible survey. Tectonophysics 212, 213–241, doi:10.1016/0040-1951(92)90292-E.

de Ronde, C.E.J., Hannington, M.D., Stoffers, P., Wright, I.C., Ditchburn, R.G., Reyes, A.G., Baker, E.T., Massoth, G.J., Lupton, J.E., Walker, S.L., Greene, R.R., Soong, C.W.R., Ishibashi, J., Lebon, G.T., Bray, C.J., Resing, J.A., 2005. Evolution of a submarine magmatic-hydrothermal system: Brothers volcano, southern Kermadec arc, New Zealand. Econ. Geol. 100, 1097–1133, doi:10.2113/gsecongeo.100.6.1097.

de Ronde, C.E.J., Massoth, G.J., Butterfield, D.A., Christenson, B.W., Ishibashi, J., Ditchburn, R.G., Hannington, M.D., Brathwaite, R.L., Lupton, J.E., Kamenetsky, V.S., Graham, I.J., Zellmer, G.F., Dziak, R.P., Embley, R.W., Dekov, V.M., Munnik, F., Lahr, J., Evans, L.J., Takai, K., 2011. Submarine hydrothermal activity and gold-rich mineralization at Brothers Volcano, Kermadec Arc, New Zealand. Miner. Dep. 46, 541–584, doi:10.1007/s00126-011-0345-8.

de Ronde, C.E.J., Walker, S.L., Ditchburn, R.G., Caratori Tontoni, F., Hannington, M.D., Merle, S.G., Timm, C., Handler, M.R., Wysoczanski, R.J., Dekov, V.M., Kamenov, G.D., Baker, E.T., Embley, R.W., Lupton, J.E., Stoffers, P., 2014. The anatomy of a buried submarine hydrothermal system, Clark Volcano, Kermadec arc, New Zealand, Econ. Geol. 109, 2261–2292, doi:10.2113/econgeo.109.8.2261.

Embley, R.W., Murphy, K.M., Fox, C.G., 1990. High-resolution studies of the summit of Axial Volcano. J. Geophys. Res. 95, 12,785–12,812.

Embley, R.W., Baker, E.T., Chadwick, W.W. Jr., Lupton, J.E., Resing, J.A., Massoth, G.J., Nakamura, K., 2004. Explorations of Mariana arc volcanoes reveal new hydrothermal systems. EOS, Trans. AGU 85, 37–44, doi:10.1029/2004EO040001.

Giba, M., Nicol, A., Walsh, J.J., 2010. Evolution of faulting and volcanism in a back-arc basin and its implications for subduction processes. Tectonics 29, 1–18, doi:10.1029/2009TC002634.

Ferrini, V.L., Tivey, M.K., Carbotte, S.M., Martinez, F., Roman, C., 2008. Variable morphologic expression of volcanic, tectonic, and hydrothermal processes at six hydrothermal vent fields in the Lau back-arc basin. Geochem. Geophys, Geosyst. 9, Q07022, doi:10.1029/2008GC002047.

Greene, H.G., Collot, J.Y., Pelletier, B., Lallemand, S., 1992. Observation of forearc seafloor deformation along the North d'Entrecasteaux Ridge—New Hebrides Island Arc collision zone from Nautile Submersible. Proc. ODP, Init. Reports 134, 43–53.

Haase, K.M., Shipboard Scientific Party, 2014. Volcanism, hydrothermal activity and vent biology in the Coriolis Troughs, New Hebrides Island Arc. RV Sonne SO-229 Status Report, 59 p.

Kim, J., Lee, I., Halbach, P., Lee, K.-Y., Ko, Y.-T., Kim, K-H, 2006. Formation of hydrothermal vents in the North Fiji Basin: Sulfur and lead isotope constraints. Chem. Geol. 233, 257–275, doi:10.1016/j.chemgeo.2006.03.011.

Lima, S.M., Haase, K.M., Beier, C., Regelous, M., Brandl, P.A., Hauff, F., Krumm, S., 2017. Magmatic evolution and source variations at the Nifonea Ridge (New Hebrides Island Arc). J. Pet. 0, 1 – 22, doi:10.1093/petrology/egx023.

Martin, A.K., 2013. Double-saloon-door tectonics in the North Fiji Basin. Earth Planet. Sci. Lett. 374, 191–203, doi:10.1016/j.epsl.2013.05.041.

Monjaret, M.C., Bellon, H., Maillet, P., 1991. Magmatism of the troughs behind the New Hebrides island arc (RV Jean Charcot SEAPSO 2 cruise): K-Ar geochronology and petrology. J. Volcanol. Geotherm. Res. 46, 265–280, doi:10.1016/0377-0273(91)90088-H.

Pelletier, B., Calmant, S., Pillet, R., 1998. Current tectonics of the Tonga-New Hebrides region. Earth Planet. Sci. Lett. 164, 263–276.

Schmidt, K., Garbe-Schönberg, D., Hannington, M.D., Anderson, M.O., Bühring, B., Haase, K., Haruel, C., Lupton, J., Koschinsky, A., 2017. Boiling vapour-type fluids from the Nifonea vent field (New Hebrides Back-Arc, Vanuatu, SW Pacific): Geochemistry of an early-stage, post-eruptive hydrothermal system. Geochim.Cosmochim. Acta 207, 185–209, doi:10.1016/j.gca.2017.03.016.

Sibuet, J.-C., Letouzey, J., Barbier, F., Charvet, J., Foucher, J.-P., Hilde, T.W.C., Kimura, M., Ling-Yun, C., Marsset, B., Muller, C., Stéphan, J.-F. 1987. Back arc extension in the Okinawa Trough. J. Geophys. Res. 92, 14,041 – 14,063, doi:10.1029/JB092iB13p14041.

Sigurdsson, H., 2000. Volcanic episodes and rates of volcanism. In: Sigurdsson, H., et al. (Eds.), Encyclopedia of Volcanoes. Academic Press, San Diego, Calif., pp. 271–279.

Stoffers, P., Worthington, T.J., Schwarz-Schampera, U., Hannington, M.E., Massoth, G.J., Hekinian, R., Schmidt, M., Lundsten, L.J., Evans, L.J., Vaiomo'unga, R., Kerby, T., 2006.

Submarine volcanoes and high-temperature hydrothermal venting on the Tonga arc, southwest Pacific. Geology 34, 453–456, doi:10.1130/G22227.1.

Wallace, L., McCaffrey, R., Beavan, J., Ellis, S., 2005. Rapid microplate rotations and back-arc rifting at the transition between collision and subduction. Geology 33(11), 857–860, doi:10.1130/G21834.1.

Appendix A

Supplementary Information for Chapter 2: The southern New Hebrides back-arc: Tectonic focusing of voluminous basaltic eruptions in magma-deficient back-arc rifts

Contents of this file:

1. Data collection and processing
2. Seafloor observations
3. Hydrothermal plume data
4. Supplementary Tables:
    - **Table A1.** A comparison of active backarc basins in the southwest Pacific
    - **Table A2.** Description of the mapped features of the Vate Trough
    - **Table A3.** Types of seafloor observations used to ground-truth maps
5. Supplementary Figures:
    - **Fig. A1.** GLORIA sidescan sonar image of the Vate Trough
    - **Fig. A2.** Stations and ROV dive tracks from the SO-229 CoVolVe cruise
    - **Fig. A3.** Stations and ROV dive tracks from the SO-229 CoVolVe cruise
    - **Fig. A4.** Screen shot of the forward-looking sonar on the ROV Kiel 6000
    - **Fig. A5.** Turbidity and redox anomalies measured by MAPR devices
6. Supplementary References

1. Data Collection and Processing

Bathymetric data used in this study includes EM 300 multibeam bathymetry collected in 2004 aboard the R/V Southern Surveyor and EM 120 multibeam bathymetry collected in 2013 aboard the R/V Sonne. The data were combined and gridded using the weighted moving average method and QPS Fledermaus software with a cell size of 30 m, and then reprocessed using a terrain texture shading approach that combines basic hill shading with curvature analysis to add texture to shaded relief (e.g., Kennelly, 2008; 2014). The method is an enhancement of techniques

widely used in automated landform classification and now standard practice in remote sensing and applied geomorphology (e.g., Pike et al., 2000; Lindsay et al., 2015; among many examples). The process has been captured by dedicated algorithms in the Terrain Texture Shading (TTS Shader) software of L. Brown, now available as freeware from Natural Graphics (http://www.naturalgfx.com/tts.htm). The modeler reads digital elevation data (DEMs) and creates a visual hierarchy of texture and elevation that solves many of the problems associated with traditional hill shading, improving edge detection and maintaining contrast ratios at every zoom level. The tool can reveal patterns that are hidden in conventional displays of bathymetric surfaces by increasing the contrast of features such as faults and geological contacts in low relief terrain. Figure 2.5 in the manuscript shows the application of the technique to identify flow boundaries. After processing, the rendered images were merged in Global Mapper with weighted shaded relief (translucency of 40%) and slope maps (maximum slope 40°, 65% translucency) to create shaded GeoTiffs as base maps for Figs. 2.3 and 2.7. We are currently using this approach to analyze bathymetric surfaces in a wide range of settings (e.g., Yeo et al., 2012; Augustin et al., 2016). Other applications of TTS Shader are described by T. Patterson of the U.S. National Park Service (http://www.shadedrelief.com/texture_shading/).

The geological maps of the Vate Trough (Fig. 2.3) and the Nifonea volcano (Fig. 2.7) were constructed from interpreted seafloor texture, slope, and rugosity derived from the bathymetric surfaces, supplemented by direct seafloor observations and sampling. The different features in the terrain models and the corresponding geological units are shown in Table A2. Data from a GLORIA (Geologic LOng Range Inclined Asdic) sidescan sonar survey collected during the 1989 *HMAS Cook* cruise and reported by Price et al. (1993; Suppl. Fig. A1) were also used to guide the geological interpretations. The backscatter intensity in Fig. A1 is related to the nature of the seafloor, in particular the slope angle and surface roughness (Blondel, 2009), which can be directly linked to sediment cover; heavily sedimented surfaces are less reflective, whereas high relief and unsedimented surfaces are highly reflective. Bright backscatter on the basin floor represents unsedimented lava; highly reflective lineaments on the basin walls represent fault scarps. The eastern wall casts an acoustic shadow, and the older arc crust is variably sedimented (Price et al., 1993). The combination of interpreted bathymetric surfaces, backscatter data, and seafloor observations, compared with observations in other similar studies (e.g., Fornari, 1986;

Fornari et al., 1998; Perfit and Chadwick, 1998; Yeo et al., 2012; Chadwick et al., 2013; McClinton and White, 2015) allows us to confidently assign geological contacts following well-established approaches for classifying volcanic geomorphology (cf. Walker et al., 1993; Thouret, 1999; Sigurdsson, 2000).

2. Seafloor Observations

Direct seafloor observations were made during ten ROV dives including Kiel 6000 and the Neptune data over 22 line kilometers with a total combined bottom time of ~70 hours (Suppl. Figs. A2 and A3). The Kiel 6000 contains seven thrusters that allow precise positioning and automatic station-keep mode stationary operation. The underwater navigation system includes: (1) an RDI Workhorse Navigator 1200 Doppler Velocity Logger (DVL) to provide 3D differential motion tracking at sub-centimeter resolution, (2) a Posidonia 6000 Ultra Short Baseline Logger (USBL) pinger used in association with a ship-mounted USBL antenna to determine absolute ROV position, and (3) a Precision Navigation TCM2-50 compass to provide information on the vehicle heading. In addition, depth and altitude measurements were provided by a Paroscientific Digiquartz pressure sensor and a Seabird Electronics FastCat SBE 49 CTD sensor. Vehicle heading, pitch and roll were provided by a Crossbow VG700CA orientation sensor. Visual observations of the seafloor made at a flying height of 0–8 m were recorded using a Kongsberg OE14-366 MKII navigation camera, a Kongsberg OE15-500 HD camera, and a Kongsberg OE14-208 HD still camera.

The ROV Kiel 6000 was also equipped with a Kongsberg-Maritime MS 1000 forward-looking obstacle avoidance sonar mounted vertically to the front of the ROV, which provided a continuous acoustic scan of the seafloor up to 400 m in front of the vehicle with a resolution of ±1 m. These data revealed features beyond the visual range of the video, such as small faults, pillow mounds, and collapse pits (e.g., Suppl. Fig. A4).

Additional data on the seafloor was obtained from rock sampling, both during the ROV dives, and during TV grabs and by wax coring (Suppl. Figs. A2 and A3; Haase and Shipboard Scientific Party, 2013). Sampling was focused on the Nifonea axial volcano and along the

northern and southern rift zones. Direct observations of the seafloor were possible with the TV grab; evidence of the relative age of the lavas was obtained from the wax coring. Major differences between units were also evident from selected whole-rock geochemical data reported in Haase and Shipboard Scientific Party (2014).

3. Hydrothermal Plume Data

Two Mini-Autonomous Plume Recorder – Oxidation-Reduction Potential (MAPR-ORP) devices were deployed during SO-229 to detect hydrothermal plume signals in the water column (Baker and Milburn, 1997). The MAPR-ORP devices were used during each wax rock core deployment, CTD hydrocast, and TV grab (attached to the cable, 20 to 50 m above the instruments), and also on the frame of the ROV. A total of 43 MAPR deployments were made at Nifonea and throughout the Vate Trough (Haase and Shipboard Scientific Party, 2013). Temperature, pressure, turbidity (optical backscatter) and oxidation-reduction potential (ORP) were measured at five second intervals. Optical backscatter was measured using a nephelometer, which converts nephelometric turbidity (NTUs) to volts. The ORP sensor measures the oxidation-reduction potential of the water column in millivolts and plotted as ΔE, which is the difference between measurements at 5-second intervals.

Unequivocal hydrothermal plume signals (i.e., ΔE anomalies with or without corresponding turbidity anomalies) were detected during 22 of the 43 MAPR-ORP deployments (Haase and Shipboard Scientific Party, 2013; Suppl. Fig. A5). ΔE anomalies were recorded within the Nifonea caldera over an area of ~1 km^2, corresponding to the locations of intense light transmission and methane anomalies originally mapped by McConachy et al. (2005). The largest anomalies measured in 2013 were at depths of between 1540 and1805 mbsl in two separate areas situated ~500 m apart; one directly over the main vent field, where largest ΔE anomalies were recorded (from -0.68 mV to 17.45 mV), and the other corresponding to the area of diffuse venting (-0.43 mV to -8.53 mV). A single ΔE anomaly and coincident NTU anomalies were also located 1 km to the south of the main vent sites, at 1620 m and 1740 m water depths. It is possible that these anomalies correspond to another area of diffuse venting, but the similar depth suggests that they emanate from the known vent field. Neptune Minerals Inc. visually inspected

an area near this location (~300 m to the east) during ROV operations in 2010 and found no direct evidence of venting.

In contrast to the ΔE anomalies, which are located mainly in the area of known venting, the particle plume at Nifonea is widespread, covering ~65 km^2. The intensity of the turbidity signal ranges from 0.07 to 1.16 V, comparable to the measurements made directly over the vent site but many kilometers away. The particle plume occurs in distinct layers at ~1540 to 1580 mbsl and ~1620 to 1680 mbsl, ~100 to 300 m above the seafloor, with the largest NTU values within the ~1620 to 1680 mbsl layer. A weaker particle layer was also detected at ~1710 to 1740 mbsl at some stations. The particle layers appear to coincide with the depths of measured ΔE anomalies closer to the main vent field, and then spread across the main volcanic platform, plunging to the southeast, most likely due to the prevailing current direction.

4. Supplemental Tables

Table A1. A comparison of active backarc basins in the southwest Pacific

	Basin	Setting[1]	Age (Ma)	Basin Width (km)	Basin Length (km)	Graben Width (km)	Graben Length (km)	Depth (mbsl)	Spreading Rate (mm/yr)	Distance from Arc (km)	Subduction Rate (mm/yr)	Slab Dip[2] (°)	Slab Age[3] (Ma)	Crustal Thickness (km)
Earliest Rifting:														
[1]	Fonualei Rift	IO	<1	50	250	20–30	50	1200–2700	47–94	20–75	165–200	40–50	>100	10–20
[2]	Izu-Bonin Rifts	IO	1–2	10–60	240	10–60	20–120	1000–1615	1.5–3	0	50–60	40–80	>100	16
[3]	Taupo Volcanic Zone (New Zealand)	IC	4	20–30	250	20–30	25–45	0	6–8	0	45–50	60	>100	15
[4]	Jean Charcot Troughs (N. New Hebrides)	IO	2–3	50–80	300	3–9	20–35	2400–3000	41–84	35–55	170	60–70	30	10–20
[5]	Coriolis Troughs (S. New Hebrides)	IO	3–6	25–45	312	25–45	70–100	2840–3400	20–35	50	90–120	70	50	10–20
Early to Late Rifting:														
[6]	Southern Havre Trough	T	5	120	1300	6–10	15–35	2000–4000	15–20	30–45	53–90	30–60	>100	<6–11
[7]	Okinawa Trough	IC	2–13	100–200	1200	10–20	50–100	1000–2500	16–45	30–60	52	40–50	60–100	>10–30
Late Rifting to Early Ocean Spreading:														
[8]	Mariana Trough	IO	7	50–250	933	10–40	20–30	3000–4500	16–45	0–80	21–45	70–90	~152	3–7

Table A1. Continued

	Basin	Setting[1]	Age (Ma)	Basin Width (km)	Basin Length (km)	Graben Width (km)	Graben Length (km)	Depth (mbsl)	Spreading Rate (mm/yr)	Distance from Arc (km)	Subduction Rate (mm/yr)	Slab Dip[2] (°)	Slab Age[3] (Ma)	Crustal Thickness (km)
Early Ocean Spreading:														
[9]	Lau Basin	IO	5-6	200–600	1100	8–30	80–200	<1000–3300	40–240	20–150	164–240	40–50	>100	6–9
[10]	Manus Basin	T-IO	4	150–340	900	NA	NA	1600–2700	14-100 (W); 115–145 (E)	50–300	80–150	70	~45	
Late Ocean Spreading:														
[11]	North Fiji Basin	IO	12	900	>1000	NA	NA	2000–3600	15–80	500	35–170	60–70	103–118	2.8–8

[1]Setting: IC = intracontinental; T = transitional; IO = intraoceanic; VRM = volcanic rifted margin

[2]Slab dip angles from Hayes et al. (2012)

[3]Subducting slab age from Leat and Larter (2003)

Sources: [1] Zellmer and Taylor (2001); [2] Taylor et al. (1990), Klaus et al. (1992), Stern (2002); [3] Cole et al. (1995), Acocella et al. (2003), Spinks (2005); [4,5] Johnson et al. (1993), Maillet et al. (1995); Bergeot et al. (2009), this study; [6] Gamble and Write (1995); Delteil et al. (2002); Wysoczanski et al. (2006); [7] Kimura (1985), Sibuet et al. (1987), Sibuet et al. (1995), Fournier et al. (2001); [8] Fryer (1995), Martínez and Taylor (2003), Gvirtzman and Stern (2004), Kitada et al. (2006); [9] Parson et al. (1990), Parson and Tiffin (1993), Martínez and Taylor (2003); Ruellan et al. (2003); [10] Taylor et al. (1991), Martínez and Taylor (2003); [11] Auzende et al. (1995), Zhang and Pysklywec (2006)

Table A2. Description of the mapped features of the Vate Trough (Fig. 2.3) in order of increasing age, type area shown as greyscale Kongsberg EM 300 multibeam bathymetry gridded at 30 m and processed using the TTS technique of Brown (2010), with a field of view of 2 km across each image unless otherwise stated

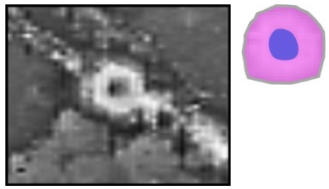
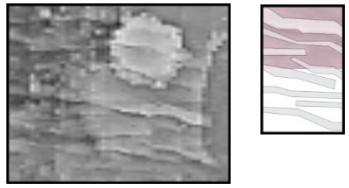
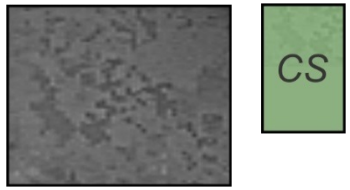
Image of Type Area and Unit Label	Unit Name and Description	Distinguishing Features	Interpretations and Assumptions	Area [km^2]
	**Volcanic Cones** Occur throughout the Vate Trough, primarily associated with the *hummocky volcanic terrains* on the flanks of the *Nifonea Volcano* and the *hummocky old arc crust* on the basin wall. Many volcanoes are associated with *dikes*. Include cone-shaped and flat-topped volcanoes, with a few containing summit craters (shown in blue). The majority have an area <0.5 km^2, and six volcanoes have an area >1 km^2.	Circular morphology, steep flanks, high relief relative to the surrounding geology, and height:width ratios of 1:10.	The volcanoes are interpreted to be younger than the units that they formed on top of. The volcanoes that occur on top of the *dikes* are interpreted to form coincidentally with the diking event; the large cratered flat-topped volcano on the summit of the *Nifonea Volcano* is cut by *dikes* and is interpreted to be younger than the dike event. Interpretation as collapsed pillow mound is rejected due to the size and flat-tops of most of the features.	NA
	**Dike-Like Features** Occur in the central part of the Vate Trough along the flank of the *Nifonea Volcano*, and on the NW summit of the volcano abruptly terminating at the Nifonea Caldera. Protrude 3–80 m from the surrounding geology. Cross-cuts the *old sheet flows*, *hummocky volcanic terrains*, and the *Nifonea Volcano*.	Elongate ridge morphology, several are identifiable in the sidescan sonar as high backscatter lineations not associated with fault scarps.	May be compositionally similar to other lava units. Interpreted to be younger than the units it cuts, but older than the Nifonea Caldera. May be alternatively termed "fissure ridges," but “dike” is preferred to distinguish it from eruptive fissures mapped in the caldera. Interpretation as a tectonic feature is rejected due to the lack of fault scarp.	NA
	**Landslide Blocks** Occur proximal to the walls of the basin in the north and south Vate Trough. Consists of angular blocks up to 2 km in size.	Strongly inclined slopes that indicate minor rotation, proximal occurrence to graben walls.	Interpreted to be foundered arc crust that has been transported very short distances. May alternatively be arc crust, but the steep slopes suggest a secondary process of transportation.	21
	**Young Collapsed Lava Plain** Occur at low relief on the basin floor in the center of the Vate Trough, slightly topographically higher than the *old sheet flow*. Sharp contacts with all other units.	Flat surface morphology marked by large irregular depressions and high even backscatter.	The absence of faulting and dykes suggests that this unit is younger than the *hummocky volcanic terrains* and the *older sheet flow unit*. The depressions are interpreted to be collapse pits after lava was drained, and the lava plain is interpreted to be sheet flows. Terraced relief is interpreted to reflect multiple flows that may have variable composition. The flow morphology is interpreted to be sheet flows based on the diagnostic pits.	154

Table A2. Continued

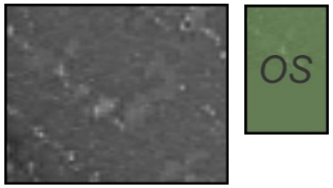
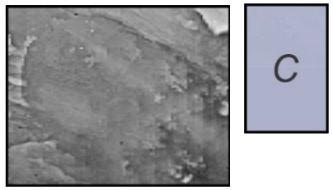
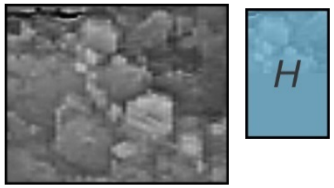
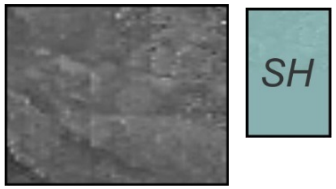
Image of Type Area and Unit Label	Unit Name and Description	Distinguishing Features	Interpretations and Assumptions	Area [km^2]
	**Old Lava Plain** Occur at the deepest part of the basin floor in the center of the Vate Trough. It is cut by many *dikes* and is overlain by *young collapsed sheet flows*. The contacts with all other units are sharp.	Very flat surface morphology with high even backscatter.	Interpreted to be sheet flows based on the high backscatter and occurrence next to another large lava plain of sheet flows, although other lava flow morphologies may be present. It may consist of multiple flows of variable composition.	56
	**Caldera Lavas** Consist of lava flows within the Nifonea Caldera, including young mixed sheet flows, lobate flows, and pillow mounds (determined from ROV dives). Grades into the *hummocky volcanic terrain* where the caldera is open to the south. (Field of view = 8 km)	Bound by caldera walls, relatively smooth morphology with discrete mounds, identification based primarily on ROV observations.	Interpreted to be the youngest volcanic products of the Nifonea Volcano but may be compositionally similar to the caldera wall lavas. Presence of lava flows, including very young flows and active venting, confirmed through ROV dives and assumed to be present throughout the caldera.	34
	**Hummocky Volcanic Terrains** Occur on the basin floor in the north of the Vate Trough and along the flanks of the *Nifonea Volcano* forming an "S" shape following the regional stress field. Gradational contacts with the *Nifonea Volcano*, *caldera lavas*, and *sedimented hummocky volcanic terrain*; sharp contacts with other units.	Rugose surface morphology with 'hummocks' up to 200 m high, some identifiable in backscatter, very high backscatter overall.	High backscatter suggests a volcanic substrate. Hummocks are interpreted to be thick onlapping pillows and lobes with steep flow fronts and collapse features oriented normal to the slope of the seafloor (e.g., Yeo et al., 2012), although other lave flow types may be present. It likely consists of multiple lava flows that may have variable compositions. This unit may reflect backarc rifting or flank eruptions of the *Nifonea Volcano*.	581
	**Sedimented Hummocky Volcanic Terrain** Occur in the north and south parts of the trough adjacent to the hummocky volcanic terrain. Gradational contacts with hummocky lava flows and sediment; sharp contacts with other units.	Rugose surface morphology, smoother than the hummocky volcanic terrain, but hummocks remain identifiable. The backscatter is high but uneven.	Gradational transition from hummocky flows with a similar but smoother morphology and uneven backscatter (interpreted to represent light sediment cover) suggest that this unit is a sedimented (i.e., older) hummocky volcanic unit.	254

Table A2. Continued

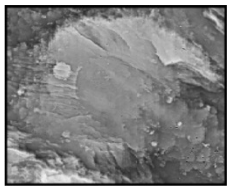
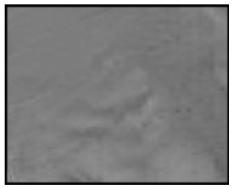
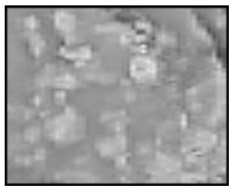
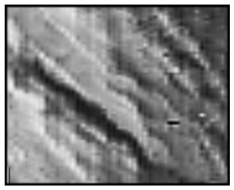
Image of Type Area and Unit Label	Unit Name and Description	Distinguishing Features	Interpretations and Assumptions	Area [km^2]
 	**Nifonea Volcano** This unit outlines the top flat summit of the volcano. Gradational contacts with the *hummocky volcanic terrain* on the flanks. (Field of view = 18.5 km)	A large crescent-shaped volcano with shallow slopes (~2°) spanning the width of the Vate Trough, characterized by a large 5 × 8 km caldera.	The volcano is interpreted to be a shield volcano based on the size and slope, and may consist of various volcanic morphologies.	149
 	**Sediment** Occurs at topographic lows on the basin floor. Gradational contacts with basin floor units and *sedimented hummocky arc crust*.	Smooth surface morphology, faulting absent, low-moderate (dark grey) mottled backscatter.	Assumed to be comprised of pelagic muds and volcaniclastic material, considered to be older than unsedimented units. Depth of sediment is unknown and may vary considerably. Alternative interpretations included sedimented lava flows, but here it is simplified as sediment as there is no evidence for recent volcanic activity.	159
 	**Hummocky Old Arc Crust** Occurs at high relief on the basin walls. Gradational contacts with other arc crust units, sharp contacts with other units.	Rugose surface dotted with numerous small volcanic cones and minor normal faulting.	Interpreted to be rifted arc crust based on position (comprises walls of trough) and evidence from geochemistry. High backscatter and volcanic features in bathymetry suggest that this part of the arc crust has recent volcanic activity and is therefore considered the youngest arc crust unit. Interpreted to be older than the volcanic units on the basin floor as it formed prior to rifting.	399
 	**Faulted Old Arc Crust** Occurs at high relief on the basin walls. Gradational contacts with other arc crust units, sharp contacts with other units.	Steep slopes and abundant normal faults. Rough acoustic shadow and bright backscatter lineaments identify fault scarps.	Interpreted to be rifted arc crust based on position (comprises walls of trough) and evidence from geochemistry. This unit is identified based on abundance of faults and no evidence for recent volcanic activity. Interpreted to be older than the *hummocky arc crust* and younger than the *sedimented arc crust*, but compositions may be similar.	967

Table A2. Continued

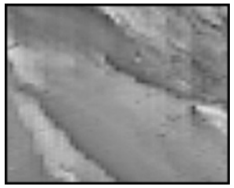
Image of Type Area and Unit Label	Unit Name and Description	Distinguishing Features	Interpretations and Assumptions	Area [km^2]
	**Sedimented Old Arc Crust** Occurs on the basin walls topographically lower than the *faulted* or *hummocky arc crust*, but higher than the basin floor. Gradational contacts with other arc crust units and *sediment*, sharp contacts with other units.	Contains relatively less normal faults and flatter slopes than the faulted arc crust and an overall smooth morphology.	Interpreted to be rifted arc crust based on position (comprises walls of trough) and evidence from geochemistry. Increased sedimentation indicated by backscatter, a lack of faults, and a smooth morphology, grading towards "sediment". Considered to be the oldest arc crust unit due to increased sedimentation.	255

Table A3. Types of seafloor observations used to ground-truth maps in Figs. 2.3 and 2.7, with locations shown in Figs. A2 and A3

Mapped Feature	ROV Dive Number	TV Grab Station	Wax Rock Corer Station	GLORIA Backscatter Observations
Vate Trough (Fig. 2.3)				
Volcanic Cones		28TVG, 74TVG	69VSR, 32VSR, 76VSR, 54VSR	High, generally not distinguishable from other fresh volcanics on basin floor
Dike-Like Features		36TVG, 78TVG	75VSR, 53VSR	High, several distinguishable as linear features with no fault scarp
Landslide Blocks				Uneven, low-moderate
Young Collapsed Lava Plain				High, even
Old Lava Plain			55VSR	High, even
Caldera Lavas	D12, D14, D16, D17, 27ROV, 60ROV, 66ROV, 77ROV, 83ROV	35VSR, 29VSR, 71VSR, 82VSR, 34VSR, 31VSR, 64VSR, 70VSR, 63VSR		No coverage
Hummocky Volcanic Terrain	72ROV	68TVG, 37TVG	33VSR, 63VSR, 58VSR, 57VSR	High, hummocks distinguishable
Sedimented Hummocky Volcanic Terrain			59VSR	High, slightly lower than unsedimented hummocky volcanic terrain
Nifonea Shield Volcano	83ROV	67TVG	81VSR, 80VSR	No coverage
Sediment				Uneven, low-moderate
Hummocky Old Arc Crust				Uneven, low-moderate
Faulted Old Arc Crust				Uneven, low-moderate, faults distinguishable
Sedimented Old Arc Crust	72ROV			Uneven, low

Table A3. Continued

Mapped Feature	ROV Dive Number	TV Grab Station	Wax Rock Corer Station	GLORIA Backscatter Observations
Nifonea Caldera (Fig. 2.7)				
Diffuse Venting	D12, D14, D16, D17, 27ROV, 60ROV, 66ROV, 77ROV			No coverage
Active Chimney	D12, 27ROV, 60ROV, 66ROV, 77ROV			No coverage
Inactive Chimney	D14, D17, 27ROV, 66ROV, 77ROV			No coverage
Fe-oxide	D12, D14, D17, 27ROV, 60ROV, 66ROV, 77ROV			No coverage
Fissure	D12, D14, 77ROV			No coverage
Volcanic Talus	D12, D14, D16, D17, 27ROV, 60ROV, 66ROV, 77ROV, 83ROV			No coverage
Sediment	D12, D14, 77ROV, 83ROV			No coverage
Pillow Mound	D12, D14, D16, D17, 27ROV, 60ROV, 66ROV, 77ROV, 83ROV	37TVG, 61TVG, 62TVG	63VSR, 64VSR, 70VSR, 31VSR, 71VSR	No coverage
Lobate Flow - Young	D14, D16, D17, 60ROV, 66ROV, 77ROV, 83ROV		33VSR, 82VSR, 29VSR	No coverage
Lobate Flow - Old	D14, D16, D17, 60ROV, 83ROV			No coverage
Mixed Sheet and Lobate Flows	D14, D16, D17, 60ROV, 27ROV, 66ROV, 77ROV			No coverage
Jumbled and Ropey Sheeted Flows	D12, D14, D17, 27ROV, 66ROV, 77ROV		34VSR, 29VSR	No coverage
Dike-Like Features		36TVG		No coverage
Flat-Topped Volcano		28TVG		No coverage
Pre-Caldera Lava Flows	83ROV	67TVG	81VSR, 80VSR	No coverage

5. Supplemental Figures

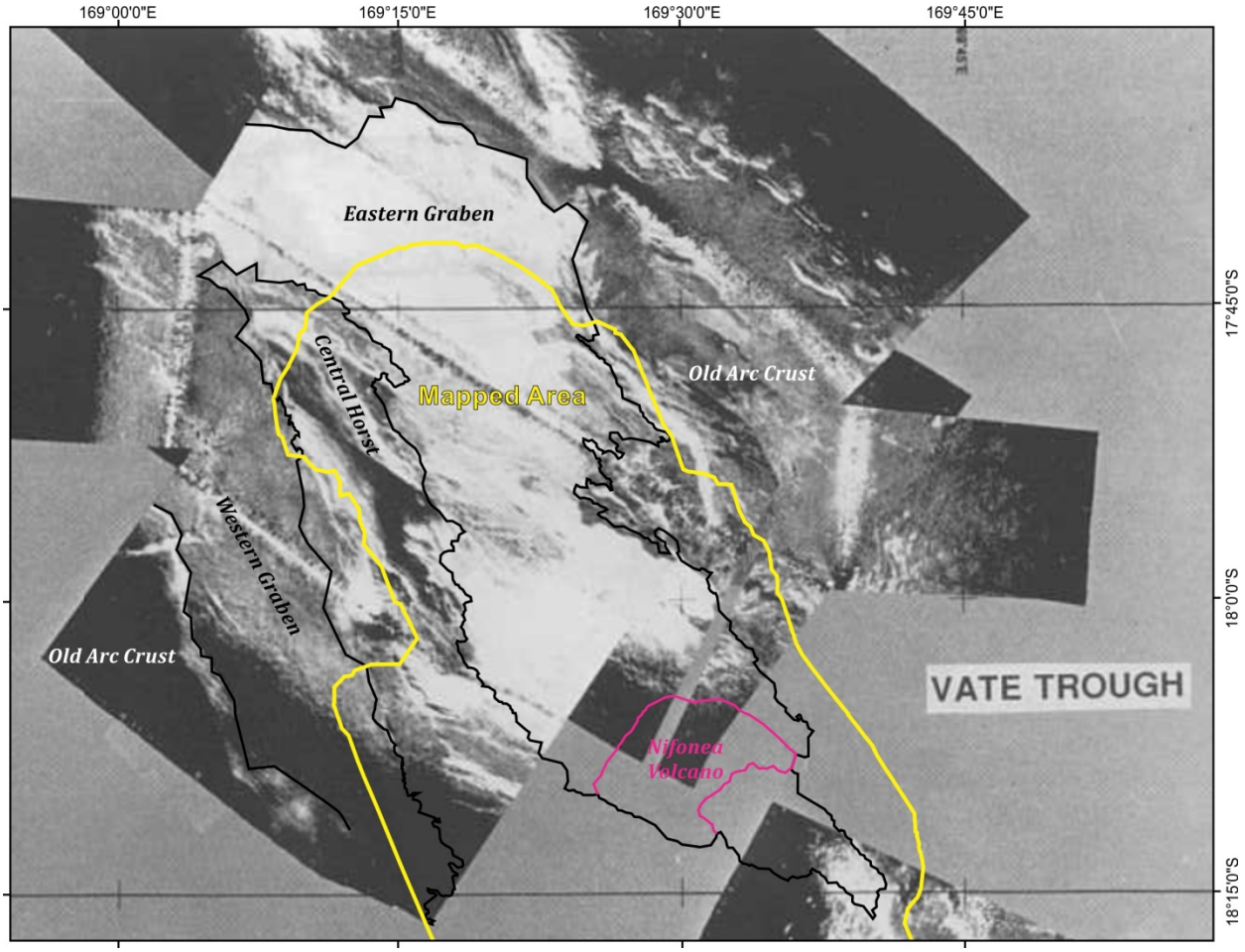


Fig. A1. GLORIA sidescan sonar image of the Vate Trough from Price et al. (1993) showing the basin walls (black) and the area of geological mapping (yellow; Fig. 2.3). Equipment failure prevented the imaging of the Nifonea Volcano.

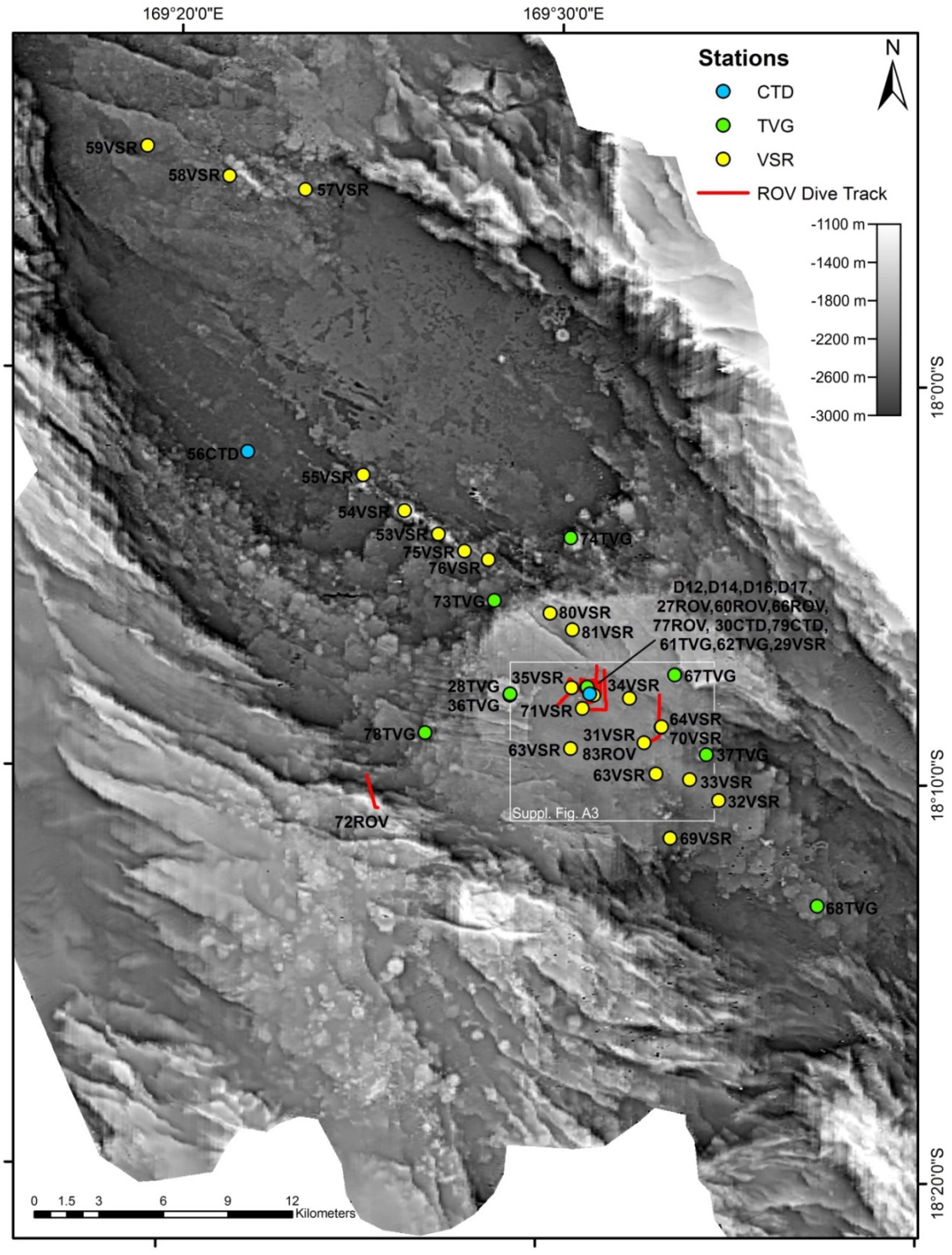


Fig. A2. Stations (circles) and ROV dive tracks (red lines) from the SO-229 CoVolVe cruise and data collected by Neptune Minerals Inc., used for sample collection and ground-truthing the geological mapping, overlain on TTS-processed Kongsberg EM 300 multibeam bathymetry gridded at 30 m. CTD = conductivity-temperature-depth device, TVG = TV grab, VSR = wax rock corer.

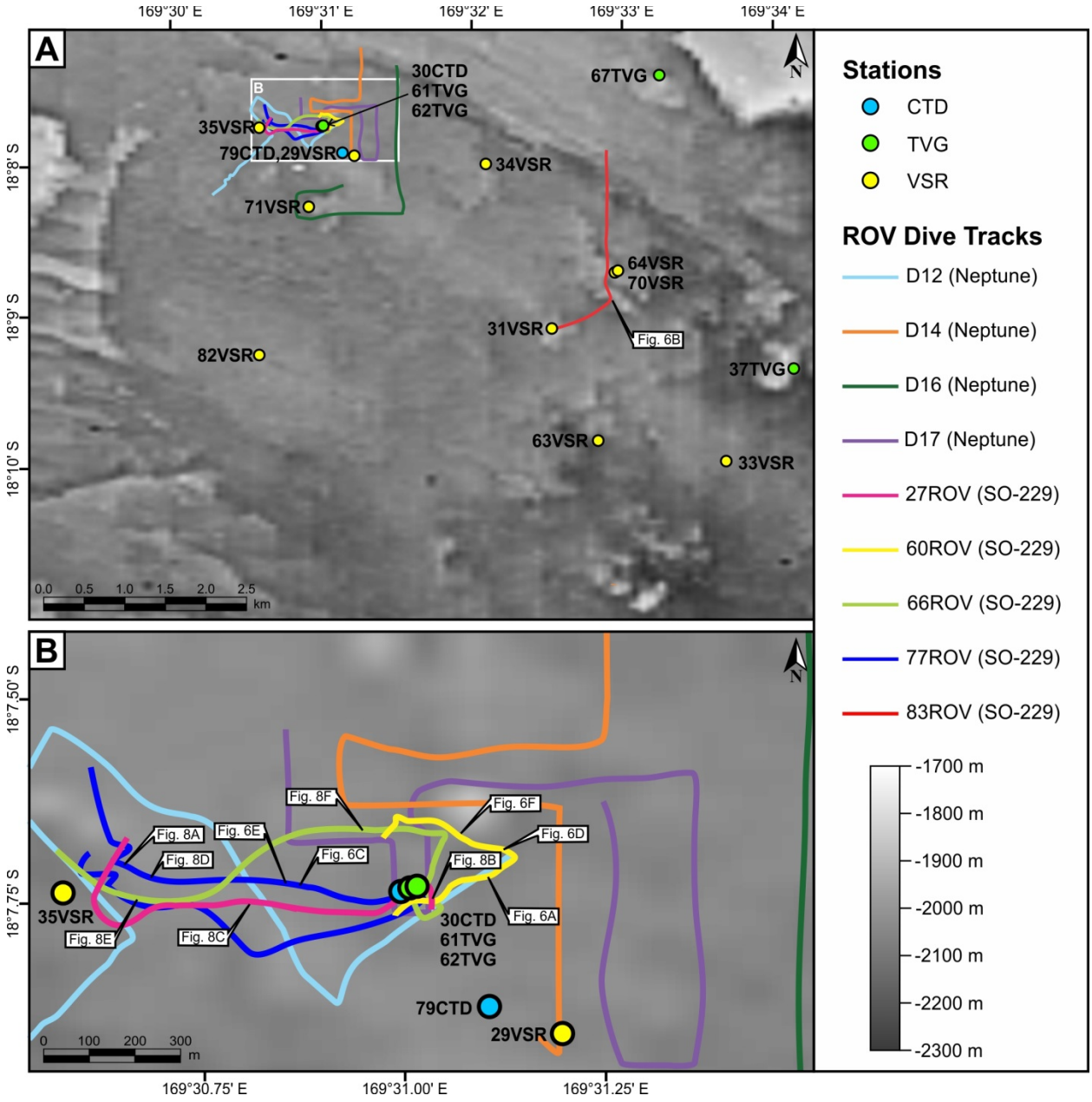


Fig. A3. Stations (circles) and ROV dive tracks (colored lines) from the SO-229 CoVolVe cruise and data collected by Neptune Minerals Inc., used for sample collection and ground-truthing the geological mapping, overlain on TTS-processed Kongsberg EM 300 multibeam bathymetry gridded at 30 m. Map extent is the same as Fig. 2.7 for (a) the Nifonea Caldera (Fig. 2.7a), and (b) the Nifonea Main Vent Field (Fig. 2.7b). CTD = conductivity-temperature-depth device, TVG = TV grab, VSR = wax rock corer.

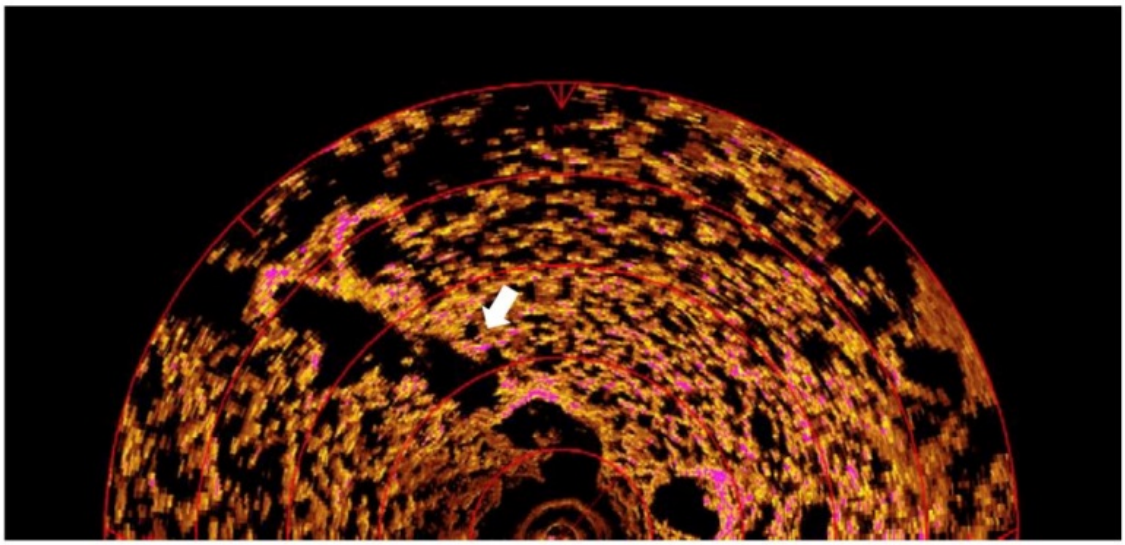


Fig. A4. Screen shot of the forward-looking sonar on the ROV Kiel 6000 during dive operations in 2013. The arrow indicates a row of five collapse structures located along the NW-trending fissure to the west of the main vent field, interpreted to represent an eruptive fissure. The individual craters are 5 to 10 m in diameter and 3 to 4 m deep, with clear drain-back features. The line spacing is 10 m.

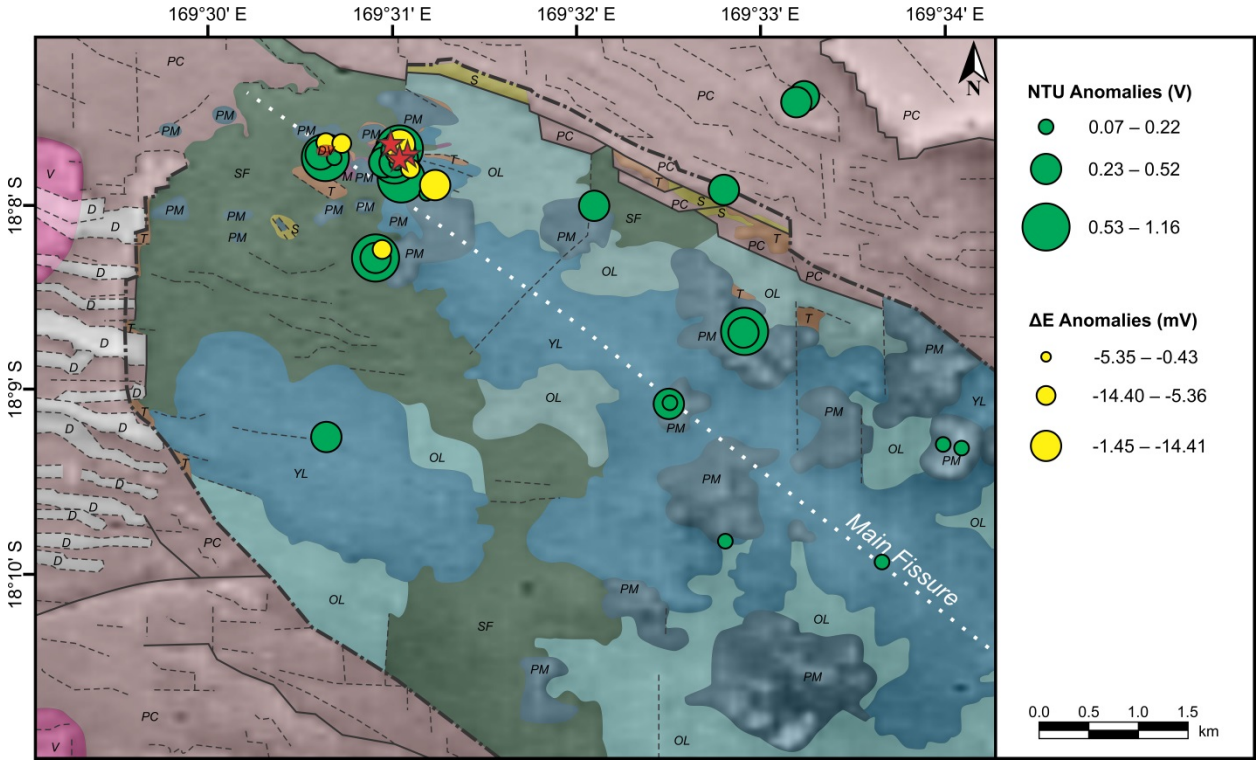


Fig. A5. Turbidity (NTU) and redox (ΔE) anomalies measured by Mini Autonomous Plume Recorder (MAPR) devices in the water column in the Nifonea Caldera (data from Haase and Shipboard Scientific Party, 2013). The geological legend is the same as Figure 2.8.

6. Supplemental References

Acocella, V., Spinks, K., Cole, J., Nicol, A., 2003. Oblique back arc rifting of the Taupo Volcanic Zone, New Zealand. Tectonics 22 (4), 1–18, doi:10.1029/2002TC001447.

Augustin, N., van der Zwan, F.M., Devey, C.W., Ligi, M., Kwasnitschka, T., Feldens, Bantan, R.A., Basaham, A.S., 2016. Geomorphology of the Central Red Sea Rift: Determining spreading processes. Geomorphology 274, 162–179, doi:10.1016/j.geomorph.2016.08.028.

Auzende, J., Pelletier, B., Eissen, J., 1995. The North Fiji basin: Geology structure, and geodynamic evolution. In: Taylor, B. (Ed.), Back-arc Basins: Tectonics and Magmatism. Plenum, New York, pp. 139–175.

Baker, E.T., Milburn, H.B., 1997. MAPR: A new instrument for hydrothermal plume mapping, RIDGE Events 8, January 1997, 23–25.

Bergeot, N., Bouin, M.N., Diament, M., Pelletier, B., Régnier, M., Calmant, S., Ballu, V., 2009. Horizontal and vertical interseismic velocity fields in the Vanuatu subduction zone from GPS measurements: Evidence for a central Vanuatu locked zone. J. Geophys. Res. 114, 1–20, doi:10.1029/2007JB005249.

Blondel, P.C., 2009. Sidescan Sonar Data Processing. In: The Handbook of SideScan Sonar. Springer, Berlin, pp. 49–84, doi:10.1007/978-3-540-49886-5.

Brown, L., 2010. A new technique for depicting terrain relief [abstract]. NACIS Annual Meeting, 2010 Oct 13–17, St. Petersburg, Florida.

Chadwick, J.W.W., Clague, H.A., Embley, R.W., Perfit, M.R., Butterfield, D.A., Caress, D.W., Paduan, J.B., Martin, J.F., Sasnett, P., Merle, S.G., Bobbitt, A.M., 2013. The 1998 eruption of Axial Seamount: New insights on submarine lava flow emplacement from high-resolution mapping. Geochem. Geophys. Geosyst. 14, 3939–3968, doi:10.1002/ggge.20202.

Cole, J.W., Darby, D.J., Stern, T.A., 1995. Taupo Volcanic Zone and Central Volcanic Region backarc structures of North Island, New Zealand. In: Taylor, B. (Ed.), Back-arc Basins: Tectonics and Magmatism. Plenum, New York, pp. 1–28.

Delteil, J., Ruellan, E, Wright, I., Matsumoto, T., 2002. Structure and structural development of the Havre Trough (SW Pacific). J. Geophys. Res. 107, 1–17, doi:10.1029/2001JB000494.

Fornari, D.J., 1986. Submarine lava tubes and channels. Bull. Volcanol. 48, 291–298, doi:10.1007/BF01081757.

Fornari, D.J., Haymon, R.M., Perfit, M.R., Gregg, T.K.P., Edwards, M.H., 1998. Axial summit trough of the East Pacific Rise 9°-10°N: Geological characteristics and evolution of the axial zone on fast spreading mid-ocean ridges. J. Geophys. Res. 103, 9827–9855, doi:10.1029/98JB00028.

Fournier, M., Fabbri, O., Angelier, J., Cadet, J.-P., 2001. Regional seismicity and on-land deformation in the Ryukyu arc: Implications for the kinematics of opening of the Okinawa Trough. J. Geophys. Res. 106, 13,751–13,768, doi:10.1029/2001JB900010.

Fryer, P., 1995. Geology of the Mariana Trough. In: Taylor, B. (Ed.), Back-arc Basins: Tectonics and Magmatism. Plenum, New York, pp. 237–280.

Gamble, J.A., Wright, I.C., 1995. The Southern Havre Trough: Geological structure and magma petrogenesis of an active backarc rift complexes. In: Taylor, B. (Ed.), Back-arc Basins: Tectonics and Magmatism. Plenum, New York, pp. 29–62.

Gvirtzman, Z., Stern, R.J., 2004. Bathymetry of Mariana trench-arc system and formation of the Challenger Deep as a consequence of weak plate coupling. Tectonics 23, 1–15, doi:10.1029/2003TC001581.

Haase, K.M., Shipboard Scientific Party, 2013. Volcanism, hydrothermal activity and vent biology in the Coriolis Troughs, New Hebrides Island Arc. RV Sonne SO-229 Cruise Report, 244 p., doi:10.2312/cr_so229.

Haase, K., Shipboard Scientific Party, 2014. RV Sonne cruise SO-229 status report: Volcanism, hydrothermal activity and vent biology in the Coriolis Troughs, New Hebrides Isl. Arc, 59 p.

Hayes, G.P., Wald, D.J., Johnson, R.L., 2012. Slab 1.0: A three-dimensional model of global subduction zone geometries. J. Geophys. Res. 117, 1–15, doi:10.1029/2011JB008524.

Johnson, D.P., Maillet, P.C., Price, R., 1993. Regional setting of a complex backarc: New Hebrides Arc, northern Vanuatu-eastern Solomon Islands. Geo-Mar. Lett. 13, 82–89, doi:10.1007/BF01204549.

Kimura, M. (1985) Back-arc rifting in the Okinawa Trough. Mar. Petrol. Geol. 2, 222–240, doi:10.1016/0264-8172(85)90012-1.

Kitada, K., Seama, N., Yamazaki, T., Nogi, Y., Suyehiro, K., 2006. Distinct regional differences in crustal thickness along the axis of the Mariana Trough, inferred from gravity anomalies. Geochem. Geophys. Geosyst. 7 (4), Q04011, doi:10.1029/2005GC001119.

Kennelly, P.J., 2008. Terrain maps displaying hill-shading with curvature. Geomorphology 102, 567–577, doi:10.1016/j.geomorph.2008.05.046.

Kennelly, P.J., 2014. General sky models for illuminating terrains. Int. J. Geogr. Inf. Sci. 28, 383–406, doi:10.1080/13658816.2013.848985.

Klaus, A., Taylor, B., Moore, G.F., Murakami, F., Okamura, Y., 1992. Back-arc rifting in the Izu-Bonin Island Arc: Structural evolution of the Hachijo and Aoga Shima Rifts. Isl. Arc 1, 16–31.

Leat, P.T., Larter, R.D., 2003. Intra-oceanic subduction systems: introduction. Geol. Soc. Spec. Pub. 219, 1–17, doi:10.1144/GSL.SP.2003.219.01.01.

Lindsay, J.B., Cockburn, J.M.H., Russell, H.A.J., 2015. An integral image approach to performing multi-scale topographic position analysis. Geomorphology 245, 51–61, doi:10.1016/j.geomorph.2015.05.025.

Maillet, P., Ruellan, E., Gérard, M., Person, A., Bellon, H., Cotton, J., Joron, J.-L., Nakada, S., Price, R.C., 1995. Tectonics, Magmatism, and evolution of the New Hebrides backarc troughs (southwest Pacific). In: Taylor, B. (Ed.), Back-arc Basins: Tectonics and Magmatism. Plenum, New York, pp. 177–235.

Martínez, F., Taylor, B., 2003. Controls on back-arc crustal accretion: Insights from the Lau, Manus, and Mariana Basins. In: Larter, R., Leat, P. (Eds.) Intra-Oceanic Subduction Systems: Tectonic and Magmatic Processes. Geol. Soc. London, Spec. Pub. 219, 19–54., doi:10.1144/GSL.SP.2003.219.01.02.

McClinton, J.T., White, S.M., 2015. Emplacement of submarine lava flow fields: A geomorphological model from the Niños eruption at the Galápagos Spreading Center. Geochem. Geophys. Geosyst. 16, 899–911, doi:10.1002/2014GC005632.

McConachy, T.F., Arculus, R.J., Yeats, C.J., Binns, R.A., Barriga, F., McInnes, B., Sestak, S., Sharpe, R., Rakau, B., Tevi, T., 2005. New hydrothermal activity and alkali volcanism in the backarc Coriolis Troughs, Vanuatu. Geology 33, 61–64, doi:10.1130/G20870.1.

Parson, L.M., Pearce, J.A., Murton, B.J., Hodkinson, R.A., RRS Charles Darwin Scientific Party, 1990. Role of ridge jumps and ridge propagation in the tectonic evolution of the Lau back-arc basin, southwest Pacific. Geology 18, 470–473.

Parson, L.M., Tiffin, D.L., 1993. Northern Lau Basin: Backarc extension at the leading edge of the Indo-Australian Plate. Geo-Mar. Lett. 13, 107–115, doi:10.1007/BF01204552.

Perfit, M.R., Chadwick, W.W.J., 1998. Magmatism at mid-ocean ridges: Constraints from volcanological and geochemical investigations. In: Buck, R., et al. (Eds.) Faulting and Magmatism at Mid-Ocean Ridges, Geophys. Monogr. Ser. 106, pp. 59–115. AGU, Washington, D.C.

Pike, R.J., 2000. Geomorphometry – diversity in quantitative surface analysis. Prog. Phys. Geogr. 24, 1–20, doi:10.1177/030913330002400101.

Price, R.C., Maillet, P., Johnson, D.P., 1993. Interpretation of GLORIA side-scan sonar imagery for the Coriolis Troughs of the New Hebrides backarc. Geo-Mar. Lett. 13, 71–81, doi:10.1007/BF01204548.

Ruellan, E., Delteil, J., Wright, I., Matsumoto, T., 2003. From rifting to active spreading in the Lau Basin – Havre Trough backarc system (SW Pacific): Locking/unlocking induced by seamount chain subduction. Geochem. Geophys. Geosys. 4 (5), 8909, doi:10.1029/2001GC000261.

Sibuet, J.-C., Letouzey, J., Barbier, F., Charvet, J., Foucher, J.-P., Hilde, T.W.C., Kimura, M., Ling-Yun, C., Marsset, B., Muller, C., Stephan, J.-F., 1987. Back arc extension in the Okinawa Trough. J. Geophys. Res. 92, 14,041–14,063, doi:10.1029/JB092iB13p14041.

Sibuet, J.-C., Hsu, S.-K., Shyu, C.-T., Liu, C.-S., 1995. Structural and kinematic evolutions of the Okinawa Trough backarc basin. In: Taylor, B. (Ed.), Back-arc Basins: Tectonics and Magmatism. Plenum, New York, pp. 343–380.

Sigurdsson, H., 2000. Volcanic episodes and rates of volcanism. In: Sigurdsson, H., Houghton, B., McNutt, S.R., Rymer, H., Stix, J. (Eds.), Encyclopedia of Volcanoes. Academic Press, San Diego, pp. 271–279.

Spinks, K.D., Acocella, V., Cole, J.W., Basset, K.N., 2005. Structural control of volcanism and caldera development in the transtensional Taupo Volcanic Zone, New Zealand. J. Volcanol. Geotherm. Res. 144, 7–22, doi:10.1016/j.jvolgeores.2004.11.014.

Stern, R.J., 2002. Subduction Zones. Rev. Geophys. 40, 1012, doi:10.1029/2001RG000108.

Taylor, B., Brown, G., Fryer, P., Gill, J.B., Hochstaedter, A.G., Hotta, H., Langmuir, C.H., Leinen, M., Nishimura, A., Urabe, T., 1990. ALVIN-Seabeam studies of the Sumisu Rift, Izu-Bonin arc. Earth Planet. Sci. Lett. 100, 127–147, doi:10.1016/0012-821X(90)90181-V.

Taylor, B., Klaus, A., Brown, G.R., Moore, G.F., 1991. Structural development of Sumisu Rift, Izu-Bonin Arc. J. Geophys. Res. 91, 16,113–16,129, doi:10.1029/91JB01900.

Thouret, J.-C, 1999, Volcanic geomorphology — an overview. Earth Sci. Rev., v. 47, p. 95–131, doi:10.1016/S0012-8252(99)00014-8.

Walker, G.P.L., 1993. Basaltic-volcano systems. Geol. Soc., London, Spec. Pub. 76, 3–38, doi:10.1144/GSL.SP.1993.076.01.01.

Wysoczanski, R.J., Wright, I.C., Gamble, J.A., Hauri, E.H., Luhr, J.F., Eggins, S.M., Handler, M.R., 2006. Volatile contents of Kermadec Arc-Havre Trough pillow glasses: Fingerprinting slab-derived aqueous fluids in the mantle sources of arc and back-arc lavas. J. Volcanol. Geotherm. Res. 152, 51–73, doi:10.1016/j.jvolgeores.2005.04.021.

Yeo, I., Searle, R.C., Achenbach, K.L., Le Bas, T.P., Murton, B.J., 2012. Eruptive hummocks: Building blocks of the upper ocean crust. Geology 40 (1), 91–94, doi:10.1130/G31892.1.

Zellmer, K.E., Taylor, B., 2001. A three-plate kinematic model for Lau Basin opening. Geochem. Geophys. Geosyst. 2, 1020, doi:10.1029/2000GC000106.

Zhang, N., Pysklywec, R.N., 2006. Role of mantle flow at the North Fiji Basin: Insights from anomalous topography. Geochem. Geophys. Geosyst. 7 (12), Q12002, doi:10.1029/2006GC001376.

Appendix B

Supplementary Information for Chapters 3 and 4

Contents of this file:

1. Supplementary Figures

   Fig. B1. ROV dive tracks covering the Tinakula deposit.

2. Supplementary Tables

   Table B1. Compilation of geomorphological features of terrestrial volcanoes from Pike (1987), and submarine volcanoes at Tinakula (this study)

   Table B2. ^{226}Ra/Ba ratios measured for chimneys from the Nifonea vent field

1. Supplementary Figures

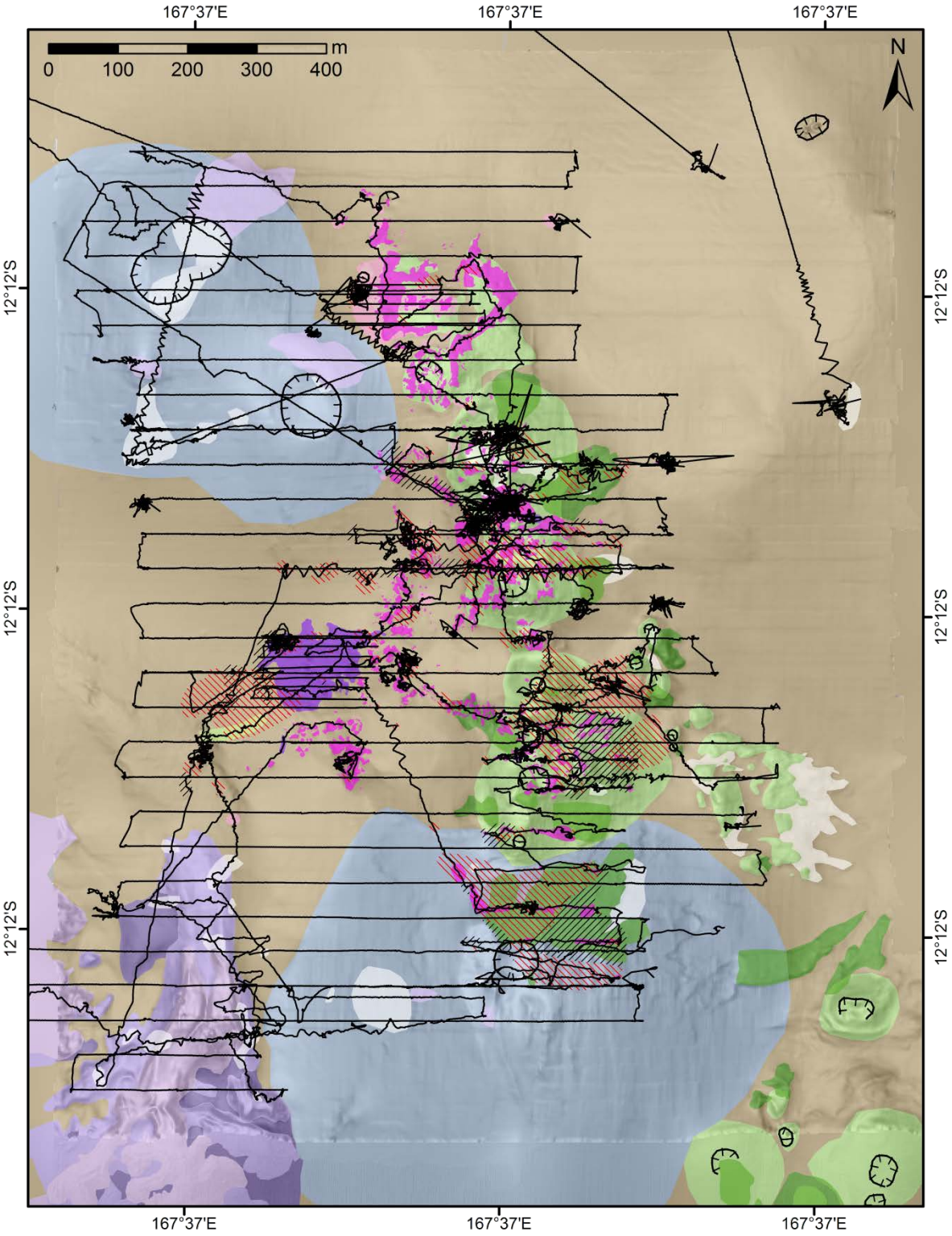


Fig. B.1. ROV dive tracks covering the Tinakula deposit.

2. Supplementary Tables

Table B1. Compilation of geomorphological features of terrestrial volcanoes from Pike (1987), and measured geomorphological features of submarine volcanoes at Tinakula (this study)

Feature Class	Crater Diameter *Wcr* (m)	Crater Depth (m)	Edifice Height *H* (m)	Flank Width (m)	Basal Diameter *Wco* (m)	Wcr/Wco	H/Wco
*Terrestrial Volcanoes**							
Cinder cone	190	37	153	245	680	0.28	0.23
Cinder cone	135	11	43	93	321	0.42	0.13
Cinder cone	171	19	90	230	631	0.27	0.14
Cinder cone	342	51	183	580	1502	0.23	0.12
Cinder cone	252	56	111	214	680	0.37	0.16
Cinder cone	137	27	182	332	801	0.17	0.23
Cinder cone	33	58	81	280	593	0.06	0.14
Cinder cone	342	80	80	255	852	0.40	0.09
Cinder cone	366	48	89	367	1100	0.33	0.08
Cinder cone	414	57	117	470	1354	0.31	0.09
Cinder cone	220	40	95	190	600	0.37	0.16
Cinder cone	250	49	137	300	850	0.29	0.16
Cinder cone	250	23	61	125	500	0.50	0.12
Cinder cone	335	85	183	450	1235	0.27	0.15
Cinder cone	225	18	91	260	745	0.30	0.12
Cinder cone	280	22	137	360	1000	0.28	0.14
Cinder cone	415	66	122	383	1181	0.35	0.10
Cinder cone	353	32	95	275	903	0.39	0.11
Cinder cone	265	48	152	353	971	0.27	0.16
Cinder cone	495	41	118	338	1171	0.42	0.10
Cinder cone	528	51	153	585	1698	0.31	0.09
Cinder cone	440	39	219	630	1700	0.26	0.13
Cinder cone	485	55	215	655	1795	0.27	0.12
Cinder cone	785	132	169	758	2301	0.34	0.07
Cinder cone	380	58	97	275	930	0.41	0.10
Cinder cone	488	32	74	306	1100	0.44	0.07
Cinder cone	258	40	116	326	910	0.28	0.13
Cinder cone	555	83	320	68	691	0.80	0.46
Cinder cone	215	35	100	237	689	0.31	0.15
Cinder cone	430	55	139	460	1350	0.32	0.10
Cinder cone	350	98	244	425	1200	0.29	0.20
Cinder cone	550	107	305	575	1700	0.32	0.18
Cinder cone	690	61	111	355	1400	0.49	0.08
Cinder cone	210	20	45	250	710	0.30	0.06
Cinder cone	410	85	280	695	1800	0.23	0.16
Cinder cone	195	37	55	150	495	0.39	0.11
Cinder cone	191	42	70	190	571	0.33	0.12
Cinder cone	260	150	315	420	1100	0.24	0.29
Cinder cone	380	85	275	610	1600	0.24	0.17
Cinder cone	450	120	305	530	1510	0.30	0.20
Cinder cone	650	75	300	675	2000	0.33	0.15
Cinder cone	200	30	120	300	800	0.25	0.15
Cinder cone	220	49	85	260	740	0.30	0.11
Cinder cone	440	88	171	355	1150	0.38	0.15
Cinder cone	396	6	94	168	732	0.54	0.13
Cinder cone	550	80	115	450	1450	0.38	0.08
Cinder cone	175	50	115	250	675	0.26	0.17
Cinder cone	315	35	125	485	1285	0.25	0.10
Cinder cone	400	102	89	400	1200	0.33	0.07
Cinder cone	500	100	300	750	2000	0.25	0.15
Cinder cone	105	28	42	70	245	0.43	0.17

Table B1. Continued

Feature Class	Crater Diameter *Wcr* (m)	Crater Depth (m)	Edifice Height *H* (m)	Flank Width (m)	Basal Diameter *Wco* (m)	Wcr/Wco	H/Wco
Cinder cone	375	109	189	370	1115	0.34	0.17
Cinder cone	653	140	195	525	1703	0.38	0.11
Cinder cone	27	8	30	55	137	0.20	0.22
Cinder cone	330	30	140	235	800	0.41	0.18
Cinder cone	500	100	225	500	1500	0.33	0.15
Cinder cone	325	60	180	563	1451	0.22	0.12
Tuff Ring	1500	320	345	600	2700	0.56	0.13
Tuff Ring	1010	120	150	500	2010	0.50	0.07
Tuff Ring	410	60	75	400	1210	0.34	0.06
Tuff Ring	1000	55	117	750	2500	0.40	0.05
Tuff Ring	950	77	192	1125	3200	0.30	0.06
Tuff Ring	667	83	65	465	1597	0.42	0.04
Tuff Ring	265	24	29	138	541	0.49	0.05
Tuff Ring	1600	92	75	600	2800	0.57	0.03
Tuff Ring	960	60	45	315	1590	0.60	0.03
Tuff Ring	770	136	206	300	1370	0.56	0.15
Tuff Ring	770	74	108	150	1070	0.72	0.10
Tuff Ring	850	260	245	775	2400	0.35	0.10
Tuff Ring	800	183	152	537	1874	0.43	0.08
Tuff Ring	520	90	150	315	1150	0.45	0.13
Tuff Ring	700	100	100	420	1540	0.45	0.06
Tuff Ring	2400	150	150	750	3900	0.62	0.04
Tuff Ring	613	60	75	295	1203	0.51	0.06
Tuff Ring	820	56	56	165	1150	0.71	0.05
Tuff Ring	1125	57	105	410	1945	0.58	0.05
Tuff Ring	1875	60	54	1000	3875	0.48	0.01
Tuff Ring	600	21	104	410	1420	0.42	0.07
Tuff Ring	955	6	17	350	1655	0.58	0.01
Tuff Ring	335	45	70	285	905	0.37	0.08
Tuff Ring	1400	105	100	550	2500	0.56	0.04
Tuff Ring	845	135	215	600	2045	0.41	0.11
Tuff Ring	1150	84	139	515	2180	0.53	0.06
Tuff Ring	1535	68	80	800	3135	0.49	0.03
Tuff Ring	860	47	49	300	1460	0.59	0.03
Tuff Ring	465	60	100	400	1265	0.37	0.08
Tuff Ring	690	25	25	500	1690	0.41	0.01
Tuff Ring	600	20	30	450	1500	0.40	0.02
Tuff Ring	600	10	10	600	1800	0.33	0.01
Tuff Ring	650	45	30	375	1400	0.46	0.02
Tuff Ring	950	80	85	300	1550	0.61	0.05
Tuff Ring	1040	117	117	300	1640	0.63	0.07
Tuff Ring	415	31	32	165	745	0.56	0.04
Tuff Ring	1200	30	35	900	3000	0.40	0.01
Tuff Ring	2200	70	75	825	3850	0.57	0.02
Tuff Ring	648	63	1	505	1658	0.39	0.00
Tuff Ring	1350	160	165	810	2970	0.45	0.06
Tuff Ring	380	60	120	250	880	0.43	0.14
Tuff Ring	590	60	105	180	950	0.62	0.11
Tuff Ring	1140	210	190	700	2540	0.45	0.07
Maar	760	60	40	300	1360	0.56	0.03
Maar	1100	80	43	650	2400	0.46	0.02
Maar	1245	225	40	400	2045	0.61	0.02
Maar	31	16	4	30	91	0.34	0.04
Maar	2730	60	20	2000	6730	0.41	0.00
Maar	136	32	12	50	236	0.58	0.05
Maar	300	74	19	100	500	0.60	0.04
Maar	820	256	74	390	1600	0.51	0.05

Table B1. Continued

Feature Class	Crater Diameter *Wcr* (m)	Crater Depth (m)	Edifice Height *H* (m)	Flank Width (m)	Basal Diameter *Wco* (m)	Wcr/Wco	H/Wco
Maar	1525	160	33	600	2725	0.56	0.01
Maar	1900	116	25	550	3000	0.63	0.01
Maar	1300	48	24	575	2450	0.53	0.01
Maar	975	37	18	460	1895	0.51	0.01
Maar	1000	37	12	300	1600	0.63	0.01
Maar	610	153	20	200	1010	0.60	0.02
Maar	100	26	8	36	172	0.58	0.05
Maar	1500	75	20	560	2620	0.57	0.01
Maar	425	26	6	95	615	0.69	0.01
Maar	1200	131	30	350	1900	0.63	0.02
Maar	560	41	34	495	1550	0.36	0.02
Maar	2280	67	12	450	3180	0.72	0.00
Maar	2600	110	25	1600	5800	0.45	0.00
Maar	1600	56	20	1000	3600	0.44	0.01
Maar	4000	61	29	1200	6400	0.63	0.00
Maar	1250	43	12	380	2010	0.62	0.01
Maar	915	37	27	100	1115	0.82	0.02
Maar	1630	80	15	300	2230	0.73	0.01
Maar	550	50	12	490	1530	0.36	0.01
Maar	793	21	15	185	1163	0.68	0.01
Maar	1020	165	25	375	1770	0.58	0.01
Maar	763	30	18	122	1007	0.76	0.02
Maar	1500	192	49	565	2630	0.57	0.02
Maar	1037	61	15	275	1587	0.65	0.01
Maar	1070	75	27	315	1700	0.63	0.02
Maar	1900	150	80	600	3100	0.61	0.03
Maar	1100	150	80	250	1600	0.69	0.05
Maar	1300	138	35	200	1700	0.76	0.02
Maar	1350	143	37	200	1750	0.77	0.02
Maar	1233	119	74	545	2323	0.53	0.03
Maar	235	50	20	60	355	0.66	0.06
Maar	425	25	15	90	605	0.70	0.02
Maar	350	90	60	130	610	0.57	0.10
Maar	930	90	60	235	1400	0.66	0.04
Maar	650	45	40	200	1050	0.62	0.04
Maar	520	80	35	150	820	0.63	0.04
Maar	720	75	10	175	1070	0.67	0.01
Maar	850	124	10	100	1050	0.81	0.01
Maar	3750	367	167	2500	8750	0.43	0.02
Maar	2950	265	70	1000	4950	0.60	0.01
Maar	1750	190	120	625	3000	0.58	0.04
Maar	1245	99	44	780	2805	0.44	0.02
Maar	3200	160	50	1500	6200	0.52	0.01
Maar	500	70	30	200	900	0.56	0.03
Maar	800	40	30	250	1300	0.62	0.02
Maar	1305	138	31	300	1905	0.69	0.02
Maar	1360	115	58	400	2160	0.63	0.03
Maar	1075	97	23	230	1535	0.70	0.01
Maar	1950	66	25	825	3600	0.54	0.01
Maar	1500	232	60	300	2100	0.71	0.03
Maar	888	148	63	400	1688	0.53	0.04
Maar	490	70	37	195	880	0.56	0.04
Maar	490	45	32	150	790	0.62	0.04
Maar	600	45	14	100	800	0.75	0.02
Maar	875	115	30	162	1199	0.73	0.03
Maar	880	150	30	100	1080	0.81	0.03
Maar	870	35	6	190	1250	0.70	0.00

Table B1. Continued

Feature Class	Crater Diameter *Wcr* (m)	Crater Depth (m)	Edifice Height *H* (m)	Flank Width (m)	Basal Diameter *Wco* (m)	Wcr/Wco	H/Wco
Maar	360	28	6	95	550	0.65	0.01
Maar	300	32	5	180	660	0.45	0.01
Maar	270	55	15	155	580	0.47	0.03
Maar	480	140	45	285	1050	0.46	0.04
Maar	170	20	6	150	470	0.36	0.01
Maar	230	20	10	135	500	0.46	0.02
Maar	515	50	26	110	735	0.70	0.04
Maar	520	65	43	350	1220	0.43	0.04
Maar	400	25	6	385	1170	0.34	0.01
Maar	915	130	30	200	1315	0.70	0.02
Maar	1230	170	70	400	2030	0.61	0.03
Maar	1000	20	125	225	1450	0.69	0.09
Cinder-Spatter Cone	200	18	19	150	500	0.40	0.04
Cinder-Spatter Cone	150	23	31	110	370	0.41	0.08
Cinder-Spatter Cone	80	27	55	130	340	0.24	0.16
Cinder-Spatter Cone	215	45	45	113	441	0.49	0.10
Cinder-Spatter Cone	130	31	36	110	350	0.37	0.10
Cinder-Spatter Cone	125	27	18	70	265	0.47	0.07
Cinder-Spatter Cone	115	30	70	138	391	0.29	0.18
Cinder-Spatter Cone	60	14	23	60	180	0.33	0.13
Cinder-Spatter Cone	75	15	31	83	241	0.31	0.13
Cinder-Spatter Cone	130	45	52	360	850	0.15	0.06
Cinder-Spatter Cone	160	40	49	145	450	0.36	0.11
Cinder-Spatter Cone	90	27	42	205	500	0.18	0.08
Cinder-Spatter Cone	70	35	3	70	210	0.33	0.01
Cinder-Spatter Cone	80	21	23	60	200	0.40	0.12
Cinder-Spatter Cone	138	10	15	86	310	0.45	0.05
Cinder-Spatter Cone	660	47	45	270	1200	0.55	0.04
Lava Dome, Cratered	75	20	80	290	655	0.11	0.12
Lava Dome, Cratered	75	25	175	320	715	0.10	0.24
Lava Dome, Cratered	98	42	120	250	598	0.16	0.20
Lava Dome, Cratered	150	30	85	210	570	0.26	0.15
Lava Dome, Cratered	95	5	45	80	255	0.37	0.18
Lava Dome, Cratered	25	5	15	40	105	0.24	0.14
Lava Dome, Cratered	200	30	140	300	800	0.25	0.18
Lava Dome, Cratered	170	70	200	215	600	0.28	0.33
Lava Dome, Cratered	185	50	85	185	555	0.33	0.15
Lava Dome, Cratered	170	50	90	165	500	0.34	0.18
Lava Dome, Cratered	150	21	26	50	250	0.60	0.10
Lava Dome, Cratered	60	40	60	120	300	0.20	0.20
Lava Dome, Cratered	95	20	70	150	395	0.24	0.18
Lava Dome, Cratered	40	9	75	53	146	0.27	0.51
Lava Dome, Cratered	17	16	18	14	45	0.38	0.40
Lava Dome, Cratered	120	10	40	90	300	0.40	0.13
Tinakula Volcanoes							
Tinakula Maar	23.4	2.0	2.3	-	32.0	0.73	0.07
Tinakula Maar	9.3	1.6	1.6	-	16.8	0.55	0.10
Tinakula Maar	43.1	4.2	0.8	-	48.1	0.90	0.02
Tinakula Cinder Cone	0	0	3.1	-	97.2	-	0.03
Tinakula Cinder Cone	28.8	4.9	11.0	-	115.6	0.25	0.10
Tinakula Cinder Cone	21.4	8.2	50.9	-	205.4	0.10	0.25
Tinakula Cinder Cone	38.5	4.4	42.9	-	190.5	0.20	0.23
Tinakula Cinder Cone	4.7	3.3	18.1	-	37.3	0.13	0.49
Tinakula Cinder Cone	11.5	2.9	12.0	-	32.2	0.36	0.37
Tinakula Cinder Cone	15.7	5.2	28.4	-	130.7	0.12	0.22
Tinakula Cinder Cone	37.4	12.6	27.4	-	106.5	0.35	0.26

Table B1. Continued

Feature Class	Crater Diameter *Wcr* (m)	Crater Depth (m)	Edifice Height *H* (m)	Flank Width (m)	Basal Diameter *Wco* (m)	Wcr/Wco	H/Wco
Tinakula Cinder Cone	25.4	5.73	20.8	-	108.5	0.23	0.19
Tinakula Cinder Cone	31.0	1.3	72.7	-	1157.5	0.03	0.06
Tinakula Cinder Cone	10.7	3.3	38.6	-	62.5	0.17	0.62
Tinakula Cinder Cone	10.4	2.8	13.3	-	31.5	0.33	0.42
Tinakula Cinder Cone	10.8	3.5	13.4	-	36.4	0.30	0.37
Tinakula Cinder Cone	19.6	3.7	16.6	-	40.5	0.48	0.41
Tinakula Cinder Cone	0	0	13.0	-	35.6	-	0.37
Tinakula Cinder Cone	8.5	1.8	11.1	-	26.1	0.33	0.43
Tinakula Cinder Cone	4.8	1.1	7.2	-	13.0	0.37	0.55
Tinakula Cinder Cone	0	0	8.4	-	30.5	-	0.28
Tinakula Cinder Cone	0	0	4.5	-	25.4	-	0.18
Tinakula Cinder Cone	0	0	22.8	-	79.0	-	0.29
Tinakula Cinder Cone	0	0	15.9	-	33.0	-	0.48
Tinakula Cinder Cone	0	0	6.0	-	36.0	-	0.17
Tinakula Cinder Cone	0	0	4.6	-	16.8	-	0.27
Tinakula Cinder Cone	0	0	6.7	-	30.1	-	0.22
Tinakula Cinder Cone	0	0	13.8	-	86.6	-	0.16
Tinakula Cinder Cone	0	0	2.6	-	26.3	-	0.10
Tinakula Cinder Cone	0	0	6.6	-	20.5	-	0.32
Tinakula Cinder Cone	0	0	13.3	-	112.0	-	0.12
Tinakula Cinder Cone	0	0	22.8	-	182.6	-	0.12
Tinakula Cinder Cone	43.7	5.8	24.8	-	130.2	0.34	0.19
Tinakula Cinder Cone	33.8	5.9	35.6	-	145.8	0.23	0.24
Tinakula Cinder Cone	0	0	10.8	-	44.5	0.00	0.24
Tinakula Cinder Cone	19.4	7.5	9.3	-	41.8	0.46	0.22
Tinakula Cinder Cone	0	0	17.3	-	64.8	-	0.27
Tinakula Cinder Cone	23.4	5.0	14.9	-	54.8	0.43	0.27
Tinakula Cinder Cone	39.6	10.0	30.3	-	154.8	0.26	0.20
Tinakula Composite Cone	51.7	11.0	140.2	-	690.7	0.07	0.20
Tinakula Composite Cone	79.1	10.2	55.2	-	326.9	0.24	0.17
Tinakula Composite Cone	86.2	26.3	86.8	-	512.0	0.17	0.17

*from Pike (1987)

Table B2. ^{226}Ra/Ba ratios measured for chimneys from the Nifonea vent field

Sample	Comment	Latitude	Longitude	Depth [mbsl]	Ba [wt.%]	^{226}Ra Activity [Bq/kg]	^{226}Ra/Ba [Bq/kg·wt.%]
SO229-060-ROV 14-2b	Active Chimney	18°7.734'S	169°31.106'E	1873	5.45	4580.06	**840 ± 63**
SO229-066-ROV 04-2a	Active Chimney	18°7.758'S	169°31.039'E	1862	bdl	13.08	N/A
SO229-066-ROV 04-4b	Active Chimney	18°7.758'S	169°31.039'E	1862	0.066	20.15	305 ± 26
SO229-066-ROV 04-16	Active Chimney	18°7.758'S	169°31.039'E	1862	0.051	10.00	196 ± 27

bdl = below detection limits; initial ^{226}Ra/Ba in bold

Appendix C

Sample List and Maps – Starfish-Tinakula Deposit Area

Contents of this file:

1. Supplemental Tables:
    - **Table C1.** ROV grab samples
    - **Table C2.** Drillcore samples
    - **Table C3.** Drillcore collars
2. Supplemental Figures
    - **Fig. C1.** Map of ROV grab sample locations in the Tinakula deposit area
    - **Fig. C2.** Map of ROV grab samples of volcanic rocks of the Starfish-Tinakula deposit area
    - **Fig. C3.** Map of drillcore collar locations in the Tinakula deposit area

Notes:

Datum WGS 1987

1. Supplemental Tables

Table C1. ROV grab samples from the Tinakula deposit and surrounding area

Sample	Parent ID	X	Y	Z	ROV Dive	Venting	Sample Type	Sample Name
GMA13-001	096	782144.8	8650638.1	-653.2	ROV10	N	Volcanic	Porphyritic vesicular dacite flow
GMA13-002	754	784711.7	8649565.6	-1109.3939	ROV121	N	Sulfide talus	Sphalerite + barite chimney talus
GMA13-003	632	784724.0	8649595.3	-1109.0408	ROV111	N	Sulfide	Sphalerite + barite chimney
GMA13-004	633	784718.2	8649637.3	-1099.0464	ROV111	Y	Sulfide	Zoned marcasite + chalcopyrite + sphalerite chimney
GMA13-005	636	784709.6	8649654.2	-1097.721	ROV111	N	Sulfide	Sphalerite + barite chimney
GMA13-006	634	784732.8	8649650.1	-1099.3033	ROV111	N	Sulfide talus	Sphalerite + galena + barite chimney talus
GMA13-007	635	784719.9	8649659.5	-1095.2905	ROV111	N	Sulfide	Sphalerite + barite chimney
GMA13-008	646	784692.6	8649762.8	-1081.9095	ROV112	N	Altered volcaniclastic	Mineralized monolithic clay-altered volcaniclastic breccia
GMA13-009	647	784665.8	8649759.3	-1089.1438	ROV112	N	Altered volcaniclastic	Mineralized polylithic volcaniclastic breccia with barite chimney
GMA13-010	649	784711.1	8649704.6	-1074.4598	ROV112	Y	Sulfide talus	Zoned chalcopyrite + sphalerite chimney talus
GMA13-011	657	784665.2	8649570.8	-1133.376	ROV114	N	MnOx	MnOx Chimney
GMA13-012	659	784802.0	8649558.9	-1128.3	ROV114	N	Sulfide	Sphalerite + barite chimney
GMA13-013	651	784884.0	8649703.3	-1134.7844	ROV112	N	MnOx	MnOx Chimney
GMA13-014	655	784834.2	8649561.3	-1142.8955	ROV114	N	Volcanic	Hyaloclastite
GMA13-015	658	784867.6	8649563.5	-1154.28	ROV114	N	Volcanic	Glassy vesicular andesite flow with xenoliths
GMA13-016	652	784555.1	8649732.4	-1099.26	ROV112	N	MnOx	MnOx chimney
GMA13-017	707	784593.9	8649858.1	-1088.8327	ROV118	N	Silicified caprock + sulfide	Silicified iron-oxide caprock with barite + pyrite chimney
GMA13-018a	706	784594.1	8649858.0	-1088.81	ROV118	N	Silicified caprock	Silicified biogenic(?) caprock
GMA13-018b	706	784594.1	8649858.0	-1088.81	ROV118	N	Sulfide talus	Pyrite/marcasite + barite chimney talus
GMA13-019a	701	784567.2	8649966.6	-1100.6264	ROV118	N	Sulfide talus	Sphalerite + barite chimney talus overgrown by zoned chalcopyrite + sphalerite chimney
GMA13-019b	701	784567.2	8649966.6	-1100.6264	ROV118	N	Sulfide talus	Zoned chalcopyrite + sphalerite chimney talus
GMA13-020	703	784563.8	8649943.2	-1093.9473	ROV118	N	Sulfide	Zoned chalcopyrite + marcasite chimney
GMA13-021	704	784551.0	8649883.2	-1087.533	ROV118	N	Sulfide	Zoned chalcopyrite + pyrite chimney

Table C1. Continued

Sample	Parent ID	X	Y	Z	ROV Dive	Venting	Sample Type	Sample Name
GMA13-022	705	784597.3	8649923.3	-1090.2988	ROV118	N	Sulfide talus	Sphalerite + barite chimney talus
GMA13-023	594	784917.9	8650496.1	-1092.19	ROV108	N	Volcanic	Glassy vesicular basaltic-andesite flow
GMA13-024	588	784724.3	8649655.5	-1094.0507	ROV108	Y	Sulfide	Marcasite + barite chimney
GMA13-025	590	784605.4	8649877.1	-1090.5476	ROV108	N	FeOx	FeOx chimney talus
GMA13-026	595	785157.4	8649925.2	-1147.319	ROV108	N	FeOx	FeOx chimney talus
GMA13-027	592	784719.5	8649655.6	-1095.8328	ROV108	N	Sulfide	Zoned chalcopyrite + sphalerite chimney
GMA13-028	586	784719.5	8649655.6	-1097.52	ROV108	N	Sulfide	Zoned chalcopyrite + sphalerite chimney
GMA13-029	598	784745.1	8649583.1	-1109.7398	ROV109	Y	Sulfide	Barite + sphalerite chimney
GMA13-030	604	784717.4	8649745.0	-1074.882	ROV109	N	Silicified caprock + sulfide	Silicified iron oxide caprock with barite + pyrite chimney
GMA13-031	603	784671.0	8649796.4	-1103.3315	ROV109	N	Sulfide	Zoned chalcopyrite + sphalerite chimney
GMA13-032	606	784731.9	8649743.1	-1074.335	ROV109	N	Sulfide	Zoned sphalerite + pyrite chimney
GMA13-033	602	784660.0	8649788.9	-1103.665	ROV109	N	Sulfide talus	Sphalerite + barite chimney talus
GMA13-034	608	784759.0	8649632.2	-1108.2709	ROV109	Y	Sulfide	Zoned pyrite/marcasite + chalcopyrite chimney
GMA13-035	611	784337.5	8650007.6	-1052.75	ROV109	N	Volcanic	Glassy porphyritic vesicular andesite flow with xenoliths
GMA13-036	607	784712.3	8649661.3	-1094.45	ROV109	N	Volcanic	Subtly clay-altered vesicular andesite(?) flow with xenoliths
GMA13-037	687	784572.3	8649536.4	-1144.741	ROV116	N	Silicified FeOx	Siliceous
GMA13-038	695	784500.8	8650057.7	-1115.578	ROV118	N	Sulfide	Chalcopyrite chimney
GMA13-039	696	784516.6	8650090.5	-1126.66	ROV118	N	Volcanic	Autoclastic vesicular andesite flow
GMA13-040	697	784531.5	8650094.1	-1123.3665	ROV118	N	Sulfide	Barite + sphalerite chimney
GMA13-041	700	784565.3	8649996.1	-1108.6958	ROV118	Weak	Sulfide	Sphalerite + barite chimney
GMA13-042	698	784555.2	8650074.9	-1122.1306	ROV118	N	Sulfide	Sphalerite + barite chimney
GMA13-043	711	783664.4	8648919.8	-1195.95	ROV118	N	Volcanic	Porphyritic dacite flow
GMA13-044	712	784243.3	8649069.3	-1167.24	ROV119	N	Volcanic	Vesicular porphyritic dacite flow
GMA13-045	708	784650.5	8649864.0	-1089.694	ROV118	N	Sulfide talus	Barite + marcasite chimney talus
GMA13-046	710	784546.0	8649903.4	-1089.596	ROV118	N	Sulfide	Chalcopyrite + pyrite chimney
GMA13-047	743	784694.7	8649577.9	-1117.9191	ROV121	Patchy	FeOx	FeOx chimney
GMA13-048	750	784714.6	8649548.9	-1108.722	ROV121	N	Sulfide talus	Chalcopyrite chimney talus

Table C1. Continued

Sample	Parent ID	X	Y	Z	ROV Dive	Venting	Sample Type	Sample Name
GMA13-049	742	784706.5	8649598.0	-1111.684	ROV121	N	Sulfide talus	Zoned chalcopyrite + sphalerite chimney talus
GMA13-050	741	784712.1	8649614.7	-1100.6417	ROV121	N	Sulfide talus	Zoned chalcopyrite + marcasite + sphalerite chimney talus
GMA13-051	746	784707.3	8649570.0	-1110.5646	ROV121	N	Sulfide talus	Barite + sphalerite chimney talus
GMA13-052	727	784650.6	8649747.2	-1092.0702	ROV120	N	Sulfide	Sphalerite + marcasite chimney
GMA13-053	729	784686.6	8649749.0	-1078.3188	ROV120	N	Sulfide talus	Barite + sphalerite chimney, growing on silicified barite + sphalerite chimney talus with entrained volcanic clasts
GMA13-054	723	784671.9	8649531.5	-1136.5111	ROV120	N	FeOx	FeOx chimney
GMA13-055	722	784675.8	8649494.2	-1143.306	ROV120	N	FeOx	FeOx chimney
GMA13-056	725	784607.8	8649727.5	-1107.1881	ROV120	N	Silicified FeOx	Siliceous iron oxyhydroxide
GMA13-057	732	784698.6	8649739.9	-1068.93	ROV120	N	Volcanic	Vesicular basaltic andesite flow
GMA13-058	736	784722.8	8649648.6	-1096.154	ROV120	N	Sulfide talus	Barite + sphalerite + marcasite chimney talus
GMA13-059	734	784715.6	8649686.0	-1085.4637	ROV120	N	FeOx	FeOx chimney
GMA13-060	733	784713.0	8649643.7	-1101.7145	ROV120	N	Silicified sulfide	Silicified barite chimney
GMA13-061	738	784678.2	8649752.8	-1081.5789	ROV120	N	Sulfide talus	Barite + marcasite + sphalerite chimney talus
GMA13-062	737	784699.7	8649651.0	-1099.6825	ROV120	Y	Sulfide talus	Sphalerite + barite chimney talus
GMA13-063	768	784049.8	8650965.1	-1116.89	ROV123	N	Volcanic	Vesicular porphyritic dacite flow
GMA13-064	091	781606.9	8650201.1	-630.17	ROV10	N	Altered Volcaniclastic BX	Variably altered polymict clast-supported volcaniclastic breccia, silicified
GMA13-065	097	781742.7	8650441.4	-498.97	ROV10	N	Volcanic	Vesicular porphyritic dacite flow with xenoliths
P0015	821	784877.4	8649270.0	-1163.09	Unknown	N	Volcanic	Subtly-altered vesicular basaltic-andesite flow with xenoliths
P0016	828	784891.9	8649249.0	-1175.25	Unknown	N	Volcanic	Moderately-altered vesicular basaltic-andesite flow with xenoliths

Table C2. Drillcore samples from the Tinakula deposit area

Sample	Parent ID	Drillhole	From (mbsf)	To (mbsf)	Interval (m)	Sample Type	Sample Name
MA13-001	2545	TKAD030	0.6	0.7	0.1	Cover sequence	Mafic volcaniclastic sand (fallout)
MA13-002	2547	TKAD030	2.08	2.15	0.07	Cover sequence	Oxide sediment
MA13-003	2548	TKAD030	2.41	2.55	0.14	Sulfide talus	Sphalerite + barite chimney talus
MA13-004	2549	TKAD030	3.9	4	0.1	Sulfide talus	Sphalerite-rich massive sulfide sediment
MA13-005	2551/2552	TKAD030	5.06	5.21	0.15	Altered footwall	Clay-altered monomict matrix-supported hyaloclastite sandstone, mineralized
MA13-006	2554	TKAD030	6.45	6.6	0.15	Altered footwall	Clay-altered monomict matrix-supported hyaloclastite breccia, cemented
MA13-007	2439	TKAD019	2	2.1	0.1	Volcanic	Sand- to pebble-sized vesicular oxidized mafic volcanic talus
MA13-008	2442	TKAD019	4.7	4.8	0.1	Volcanic	Pebble-sized vesicular slightly oxidized mafic volcanic talus
MA13-009	2443	TKAD019	6	6.1	0.1	Volcanic	Sand- to pebble-sized vesicular mafic volcanic talus
MA13-010	2427	TKAD018	0.74	0.84	0.1	Sulfide talus	Sphalerite + barite chimney talus
MA13-011	2427	TKAD018	1.1	1.19	0.09	Sulfide talus	Sphalerite + barite chimney talus
MA13-012	2428	TKAD018	1.35	1.45	0.1	Stringer zone	Mineralized, hydrothermally-altered volcaniclastic breccia (stringer zone)
MA13-013	2430	TKAD018	1.67	1.83	0.16	Stringer Zone	Mineralized, hydrothermally-altered volcaniclastic breccia (stringer zone)
MA13-014	2431	TKAD018	3	3.1	0.1	Altered footwall	Clay-altered massive volcanic mudstone, mineralized
MA13-015	2433	TKAD018	5	5.1	0.1	Altered footwall	Clay-altered monomict matrix-supported granular hyaloclastite, cemented
MA13-016	2434	TKAD018	6.6	6.71	0.11	Altered footwall	Clay-altered monomict matrix-supported hyaloclastite breccia, unconsolidated
MA13-017	2416	TKAD017	2.25	2.32	0.07	Sulfide talus	Sphalerite- and chalcopyrite-rich massive sulfide sediment
MA13-018	2417	TKAD017	2.77	2.84	0.07	Sulfide talus	Oxidized pyrite-rich massive sulfide sediment
MA13-019	2421	TKAD017	5	5.1	0.1	Altered footwall (transition)	Clast-supported monomict volcanic breccia and chimney talus, poorly cemented
MA13-020	2424	TKAD017	6.9	7	0.1	Altered footwall	Clay-altered volcanic breccia, weakly cemented
MA13-021	2578	TKAD033	0.3	0.4	0.1	Cover sequence	Mafic volcaniclastic sand (fallout)
MA13-022	2579	TKAD033	0.9	1	0.1	Cover sequence	Mafic volcaniclastic sand (fallout), oxidized
MA13-023	2581	TKAD033	1.51	1.6	0.09	Stringer zone	Silicified clay-altered polymict matrix-supported resedimented volcanic breccia
MA13-024	2582	TKAD033	2.55	2.66	0.11	Stringer zone	Clay-altered polymict clast-supported resedimented volcanic breccia, weakly mineralized
MA13-025	2583	TKAD033	3	3.1	0.1	Altered footwall	Moderately clay-altered monomict shard-rich lapilli tephra, unconsolidated
MA13-026	2585	TKAD033	4.76	4.88	0.12	Altered footwall	Moderately clay-altered polymict matrix-supported shard-rich lapilli tephra, unconsolidated

Table C2. Continued

Sample	Parent ID	Drillhole	From (mbsf)	To (mbsf)	Interval (m)	Sample Type	Sample Name
MA13-027	2588	TKAD033	7.3	7.4	0.1	Altered footwall	Moderately clay-altered polymict matrix-supported lapilli tephra, unconsolidated
MA13-028	2382	TKAD013	0.58	0.67	0.09	Sulfide talus	Zoned chalcopyrite + sphalerite chimney talus
MA13-029	2384	TKAD013	2.17	2.27	0.1	Sulfide talus	Sphalerite + barite chimney talus
MA13-030	2386	TKAD013	3.61	3.68	0.07	Sulfide talus	Mixed chimney talus
MA13-031	2387	TKAD013	4.88	4.95	0.07	Stringer zone	Mineralized, hydrothermally-altered volcaniclastic breccia (stringer zone)
MA13-032	2405	TKAD016	0.7	0.74	0.04	Stringer zone	Mineralized, hydrothermally-altered volcaniclastic breccia (stringer zone)
MA13-033	2405	TKAD016	0.91	1	0.09	Sulfide talus	Mixed chimney talus
MA13-034	2406	TKAD016	2.02	2.13	0.11	Altered footwall	Clay-altered monomict matrix-supported coarse granular volcanic breccia, cemented
MA13-035	2409	TKAD016	5.65	5.71	0.06	Altered footwall	Clay-altered polymict clast-supported pumaceous shard-rich lapillistone, weakly cemented
MA13-036	2410	TKAD016	7	7.05	0.05	Altered footwall	Clay-altered polymict matrix-supported scoriaceous and pumaceous lapillistone, weakly cemented and mineralized
MA13-037	2536	TKAD025	0.58	0.67	0.09	Oxide	Intensely oxidized volcanic(?) mud
MA13-038	2538	TKAD025	3.54	3.7	0.16	Stringer zone	Clay-altered monomict volcanic breccia, unconsolidated
MA13-039	2540	TKAD025	5.5	5.6	0.1	Stringer zone	Clay-altered polymict matrix-supported pumaceous shard-rich lapillistone, moderately cemented, mineralized
MA13-040	2542	TKAD025	6.91	7	0.09	Stringer zone	Clay-altered monomict clast-supported scoriaceous shard-rich lapillistone, cemented
MA13-041	2557	TKAD031	0.78	0.9	0.12	Sulfide talus	Zoned chalcopyrite + sphalerite chimney talus
MA13-042	2559	TKAD031	2.17	2.25	0.08	Sulfide talus	Sphalerite-rich massive sulfide sediment
MA13-043	2563	TKAD031	4.91	5	0.09	Sulfide talus	Sphalerite + barite chimney talus
MA13-044	2564	TKAD031	5.64	5.69	0.05	Altered footwall	Clay-altered matrix-supported monomict breccia resedimented granular hyaloclastite, mineralized, unconsolidated
MA13-045	2565	TKAD031	6.6	6.67	0.07	Altered footwall	Clay-altered polymict matrix-supported resedimented hyaloclastite breccia, mineralized and unconsolidated
MA13-046	2392	TKAD015	0.05	0.12	0.07	Sulfide talus	Zoned chalcopyrite + sphalerite chimney talus
MA13-047	2393	TKAD015	0.56	0.7	0.14	Cover sequence	Mafic volcaniclastic sand (fallout)
MA13-048	2394	TKAD015	1.3	1.39	0.09	Sulfide talus	Zoned sphalerite + barite + chalcopyrite chimney talus
MA13-049	2396	TKAD015	2.67	2.82	0.15	Sulfide talus	Chalcopyrite-rich massive sulfide sediment and chimney talus

Table C2. Continued

Sample	Parent ID	Drillhole	From (mbsf)	To (mbsf)	Interval (m)	Sample Type	Sample Name
MA13-050	2398	TKAD015	3.49	3.63	0.14	Stringer zone	Clay-altered volcaniclastic breccia with chimney talus
MA13-051	2400	TKAD015	4.34	4.43	0.09	Altered footwall	Clay-altered monomict(?) matrix-supported shard-rich pumaceous lapilli tephra, unconsolidated
MA13-052	2402	TKAD015	6.42	6.52	0.1	Altered footwall	Clay-altered monomict matrix-supported shard-rich scoriaceous lapilli tephra, cemented
MA13-053	2403	TKAD015	7.23	7.34	0.11	Altered footwall	Clay-altered monomict matrix-supported scoriaceous resedimented hyaloclastite, cemented
MA13-054	2517	TKAD027	0.05	0.21	0.16	Cover sequence	Mafic volcaniclastic sand (fallout)
MA13-055	2519	TKAD027	1.7	1.84	0.14	Sulfide talus	Chalcopyrite-rich massive sulfide sediment
MA13-056	2520	TKAD027	2.5	2.6	0.1	Sulfide talus	Unconsolidated chimney talus with minor monomict volcanic clasts
MA13-057	2522	TKAD027	4.6	4.7	0.1	Altered footwall	Clay-altered monomict matrix-supported scoriaceous resedimented hyaloclastite, cemented
MA13-058	2524	TKAD027	6.5	6.59	0.09	Altered footwall	Clay -altered monomict matrix-supported shard-rich lapilli tephra, cemented
MA13-059	2370	TKAD012	0	0.1	0.1	Cover sequence	Oxide sediment
MA13-060	2370	TKAD012	0.25	0.32	0.07	Oxide	Oxidized chimney talus
MA13-061	2370	TKAD012	0.33	0.44	0.11	Cover sequence	Mafic volcaniclastic sand (fallout)
MA13-062	2374	TKAD012	2.81	2.9	0.09	Altered footwall	Clay-altered polymict(?) clast-supported shard-rich lapilli tuff, weakly mineralized and cemented
MA13-063	2376	TKAD012	4.25	4.36	0.11	Altered footwall	Clay-altered unconsolidated polymict volcanic breccia
MA13-064	2378	TKAD012	6.49	6.6	0.11	Altered footwall	Clay-altered unconsolidated monomict volcanic sandstone, unconsolidated
MA13-065	2526	TKAD026	0.5	0.65	0.15	Sulfide talus	Sphalerite + barite chimney talus
MA13-066	2528	TKAD026	1.18	1.27	0.09	Stringer zone	Mineralized, hydrothermally-altered volcaniclastic breccia (stringer zone)
MA13-067	2530	TKAD026	2.9	3	0.1	Altered footwall	Clay-altered polymict matrix-supported pumaceous lapillistone, mineralized
MA13-068	2531	TKAD026	3.6	3.68	0.08	Altered footwall	Clay-altered polymict matrix-supported scoriaceous coarse tuff, mineralized
MA13-069	2533	TKAD026	5.64	5.75	0.11	Altered footwall	Clay-altered polymict matrix-supported scoriaceous lapillistone, cemented
MA13-070	2567	TKAD032	0.2	0.3	0.1	Cover sequence	Mafic polymictic volcaniclastic sand (fallout), oxidized
MA13-071	2568	TKAD032	0.9	1	0.1	Cover sequence	Mafic volcaniclastic sand (fallout)
MA13-072	2570	TKAD032	2.05	2.17	0.12	Stringer zone	Clay-altered clast-supported monomict lapillistone, silicified and mineralized

Table C2. Continued

Sample	Parent ID	Drillhole	From (mbsf)	To (mbsf)	Interval (m)	Sample Type	Sample Name
MA13-073	2573	TKAD032	3.9	4	0.1	Altered footwall	Clay-altered clast-supported monomict lapillistone, weakly cemented and mineralized
MA13-074	2575	TKAD032	5.31	5.4	0.09	Altered footwall	Clay-altered monomict clast-supported volcanic breccia, weakly cemented
MA13-075	2576	TKAD032	6.42	6.54	0.12	Altered footwall	Clay-altered monomict matrix-supported hyaloclastite breccia(?), cemented and weakly mineralized
MA13-076	2000	TKAD001	0.2	0.3	0.1	Cover sequence	Mafic volcaniclastic sand (fallout)
MA13-077	2002	TKAD001	1.72	1.9	0.18	Cover sequence	Mafic volcaniclastic sand (fallout) and clay, fine sulfides
MA13-078	2006	TKAD001	4.54	4.68	0.14	Altered footwall	Clay-altered monomict volcanic breccia, unconsolidated
MA13-079	2006	TKAD001	4.9	5	0.1	Altered footwall	Clay-altered monomict volcanic breccia, unconsolidated
MA13-080	2007	TKAD001	5.5	5.6	0.1	Altered footwall	Clay-altered polymict clast-supported volcanic breccia, silicified
MA13-081	2008	TKAD001	5.7	5.8	0.1	Altered footwall	Oxidized clay-altered monomict(?) volcanic breccia, unconsolidated
MA13-082	2009	TKAD001	7	7.1	0.1	Altered footwall	Weakly clay-altered monomict volcanic breccia, unconsolidated
MA13-083	2011	TKAD001	8.4	8.5	0.1	Altered footwall	Oxidized clay-altered monomict(?) volcanic breccia, unconsolidated
MA13-084	2013	TKAD001	11.1	11.3	0.2	Altered footwall	Clay-altered polymict(?) volcanic breccia, unconsolidated
MA13-085	2015	TKAD001	12.9	13	0.1	Altered footwall	Fe- and clay-altered monomict(?) volcanic breccia, unconsolidated
MA13-086	2017	TKAD001	14	14.12	0.12	Altered footwall	Fe- and clay-altered monomict matrix-supported resedimented(?) lapilli tephra, cemented
MA13-087	2020	TKAD001	16.05	16.22	0.17	Stringer zone	Clay-altered bedded matrix-supported monomict lapillistone, mineralized and cemented
MA13-088	2021	TKAD001	17.4	17.5	0.1	Altered footwall	Clay-altered matrix-supported monomict pumaceous lapilli tephra, cemented and weakly mineralized
MA13-089	2022	TKAD001	17.9	18	0.1	Altered footwall	Clay-altered matrix-supported monomict hyaloclastite breccia, cemented and mineralized
MA13-090	2022/2023	TKAD001	18.4	18.57	0.17	Altered footwall	Clay-altered bedded matrix-supported monomict lapilli tephra, cemented and mineralized
MA13-091	2024	TKAD001	20.77	21	0.23	Altered footwall	Clay-altered bedded monomict clast-supported lapilli tuff, cemented and mineralized
MA13-092	2025	TKAD001	21.3	21.45	0.15	Altered footwall	Clay-altered bedded matrix-supported lapilli tephra, cemented and mineralized

Table C2. Continued

Sample	Parent ID	Drillhole	From (mbsf)	To (mbsf)	Interval (m)	Sample Type	Sample Name
MA13-093	2497	TKAD029	0.83	0.95	0.12	Cover sequence	Mafic volcaniclastic sand (fallout)
MA13-094	2499	TKAD029	2.28	2.4	0.12	Cover sequence	Mafic volcaniclastic sand (fallout), oxidized
MA13-095	2502	TKAD029	3.6	3.7	0.1	Cover sequence	Clay-altered polymict(?) volcanic breccia, unconsolidated
MA13-096	2505	TKAD029	6.32	6.4	0.08	Cover sequence	Mafic volcaniclastic sand (fallout), oxidized
MA13-097	2510	TKAD028	0.3	0.4	0.1	Cover sequence	Mafic volcaniclastic sand (fallout)
MA13-098	2512	TKAD028	1.56	1.65	0.09	Sulfide talus	Zoned pyrite + sphalerite chimney talus
MA13-099	2514	TKAD028	4.5	4.6	0.1	Altered footwall	Clay-altered monomict matrix-supported lapilli tephra(?), cemented
MA13-100	2413	TKAD017	0	0.1	0.1	Cover sequence	Mafic volcaniclastic sand (fallout)
MA13-101	2419	TKAD017	4.35	4.5	0.15	Chimney talus	Sphalerite- and chalcopyrite-rich massive sulfide sediment
P0001	2003	TKAD001	2.67	2.8	0.13	Oxide	FeOx chimney
P0002	2013	TKAD001	10.39	10.5	0.11	Altered footwall	Variably clay-altered polymict clast-supported volcanic breccia, silicified
P0003	2018	TKAD001	14.81	14.95	0.14	Stringer zone	Variably clay-altered monomict matrix-supported hyaloclastite breccia, cemented
P0004	2019	TKAD001	15.65	15.8	0.15	Stringer zone	Clay-altered monomict clast-supported volcanic breccia, cemented and mineralized
P0005	2023	TKAD001	19.14	19.3	0.16	Altered footwall	Clay-altered monomict clast-supported volcanic breccia, cemented and mineralized
P0010	2033	TKAD003	0.99	1.1	0.11	Chimney talus	Mixed chimney talus
P0011	2037	TKAD003	5.8	5.9	0.1	Stringer zone	Mineralized, hydrothermally-altered volcaniclastic breccia (stringer zone)
P0012	2043	TKAD003	11.11	11.2	0.09	Altered Footwall	Clay-altered polymict matrix-supported resedimented(?) hyaloclastite sand-cobble breccia, cemented
P0013	2045	TKAD003	13.4	13.5	0.1	Altered Footwall	Clay-altered monomict clast-supported volcanic breccia, cemented
P0014	2047	TKAD003	16.41	16.5	0.09	Altered Footwall	Clay-altered monomict matrix-supported hyaloclastite sand-cobble breccia, cemented
P0020	2132	TKAD005	20.55	20.67	0.12	Altered Footwall	Clay-altered monomict clast-supported volcanic breccia, irregularly cemented
P0021	2174	TKAD007	3.5	3.6	0.1	Stringer zone	Clay-altered monomict matrix-supported resedimented(?) hyaloclastite sand breccia, mineralized and cemented

Table C2. Continued

Sample	Parent ID	Drillhole	From (mbsf)	To (mbsf)	Interval (m)	Sample Type	Sample Name
P0022	2185	TKAD007	11.23	11.34	0.11	Altered Footwall	Clay-altered monomict matrix-supported volcanic breccia, weakly cemented
P0023	2201	TKAD007	22.35	22.45	0.1	Altered Footwall	Clay-altered monomict clast-supported volcanic breccia, cemented and mineralized
P0024	2229	TKAD008	18.13	18.2	0.07	Altered Footwall	Clay-altered monomict clast-supported hyaloclastite(?) breccia, cemented
P0025	2215	TKAD008	7.5	7.56	0.06	Altered Footwall	Clay-altered monomict clast-supported volcanic breccia, cemented
P0040	2209	TKAD021	4.41	4.45	0.04	Volcanic	Moderately-altered vesicular basaltic-andesite flow with xenoliths
P0042	2557	TKAD031	0.38	0.45	0.07	Sulfide talus	Zoned chalcopyrite + sphalerite chimney talus
P0043	2560	TKAD031	2.86	3	0.14	Sulfide talus	Sphalerite + barite chimney talus
P0044	2561	TKAD031	3.61	3.68	0.07	Sulfide talus	Sphalerite-rich massive sulfide talus, oxidized

Table C3. Drillcore collars from the Tinakula deposit area

Hole ID	End of hole depth (mbsf)	x	y	z	Azimuth	Dip
TKAD001	22.32	784559.69	8649995.52	-1107.61	0.00	-90.00
TKAD002	4.60	784765.41	8649279.24	-1113.95	0.00	-90.00
TKAD003	21.21	784765.73	8649281.14	-1113.84	0.00	-90.00
TKAD004	21.16	784705.96	8649636.13	-1103.65	0.00	-90.00
TKAD005	20.94	784770.85	8649318.94	-1121.74	0.00	-90.00
TKAD006	23.84	784760.86	8649319.46	-1122.88	0.00	-90.00
TKAD007	23.79	784469.39	8649400.09	-1161.27	0.00	-90.00
TKAD008	20.76	784476.30	8649298.22	-1171.89	0.00	-90.00
TKAD009	4.38	784487.62	8649438.89	-1152.23	0.00	-90.00
TKAD010	21.16	784764.40	8649252.70	-1116.19	0.00	-90.00
TKAD011	10.25	784755.86	8649288.58	-1116.27	0.00	-90.00
TKAD012	7.51	784631.38	8649842.16	-1088.93	0.00	-90.00
TKAD013	5.91	784606.66	8649845.93	-1090.82	0.00	-90.00
TKAD014	6.71	784616.18	8649922.38	-1091.76	0.00	-90.00
TKAD015	7.35	784561.08	8649940.06	-1091.80	0.00	-90.00
TKAD016	10.00	784588.91	8649829.11	-1088.73	0.00	-90.00
TKAD017	7.36	784723.31	8649601.46	-1107.68	0.00	-90.00
TKAD018	6.71	784756.43	8649604.73	-1110.18	0.00	-90.00
TKAD019	6.88	784760.22	8649562.25	-1109.44	0.00	-90.00
TKAD020	7.16	784787.60	8649281.12	-1125.01	0.00	-90.00
TKAD021	5.70	784816.78	8649280.51	-1131.64	0.00	-90.00
TKAD022	6.99	784813.22	8649303.06	-1137.14	0.00	-90.00
TKAD023	6.03	784781.64	8649266.13	-1118.82	0.00	-90.00
TKAD024	6.00	784658.52	8649363.21	-1146.64	0.00	-90.00
TKAD025	7.31	784605.04	8649842.58	-1090.91	0.00	-90.00
TKAD026	6.31	784609.20	8649820.32	-1089.04	0.00	-90.00
TKAD027	6.75	784562.04	8649937.83	-1091.36	0.00	-90.00
TKAD028	5.87	784582.16	8649932.63	-1091.00	0.00	-90.00
TKAD029	8.79	784611.16	8649938.92	-1091.81	0.00	-90.00
TKAD030	7.26	784742.79	8649607.79	-1107.72	0.00	-90.00
TKAD031	7.33	784726.01	8649576.46	-1110.26	0.00	-90.00
TKAD032	6.92	784672.04	8649717.82	-1084.40	0.00	-90.00
TKAD033	7.51	784707.86	8649726.84	-1070.68	0.00	-90.00
TKAD034	5.47	784557.94	8649707.06	-1107.54	0.00	-90.00
TKAD035	6.20	784445.85	8649454.80	-1154.15	0.00	-90.00
TKAD036	7.17	784497.24	8649403.68	-1157.83	0.00	-90.00
TKAD037	8.51	784464.32	8649427.63	-1157.03	0.00	-90.00
TKAD038	7.06	784533.70	8649440.75	-1150.65	0.00	-90.00
TKAD039	5.43	784403.48	8649415.56	-1166.43	0.00	-90.00

2. Supplementary Figures

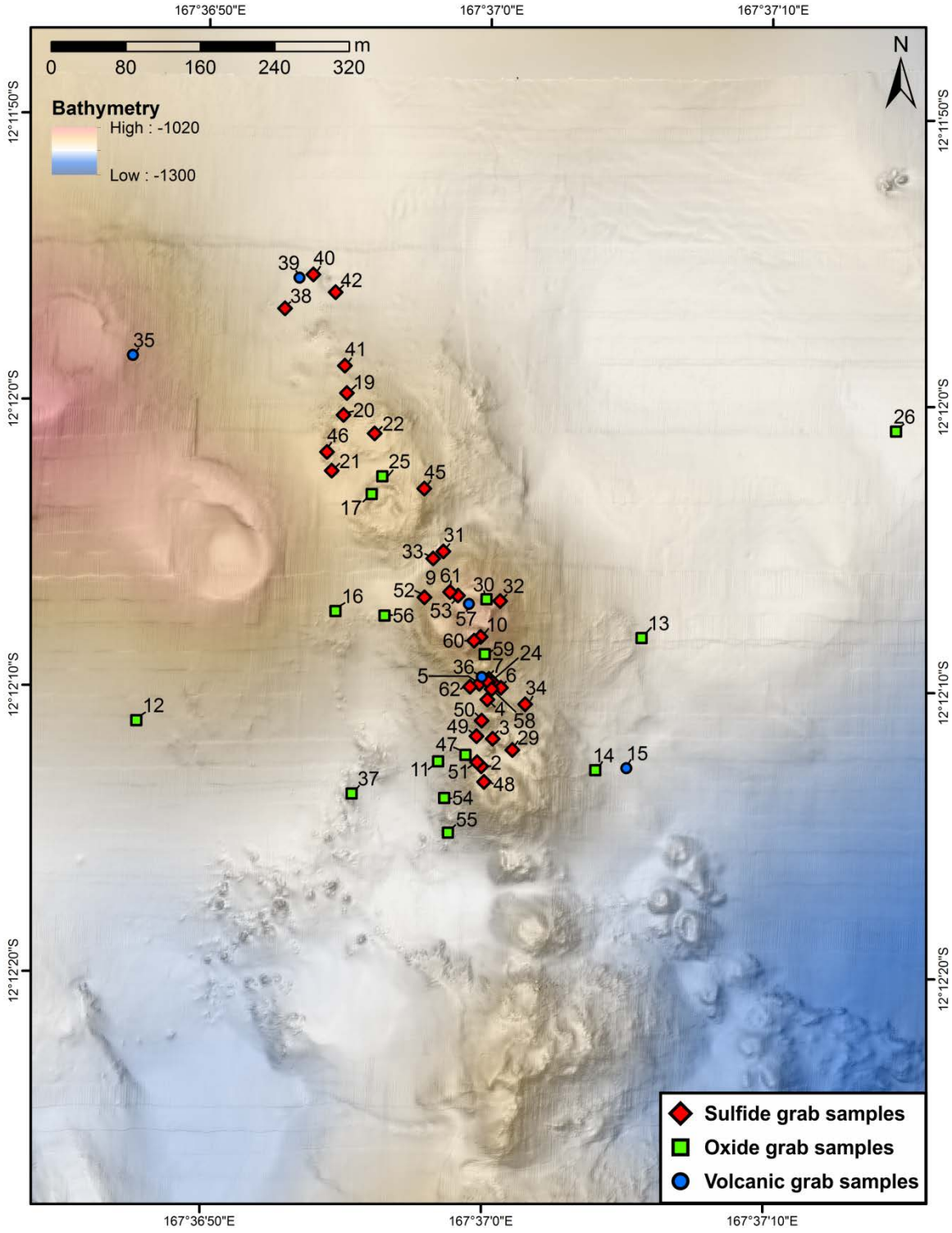


Fig. C1. Locations of ROV grab samples at the Tinakula deposit area used in this study (GMA-##): red diamonds = sulfides, green squares = oxyhydroxides, blue circles = volcanics.

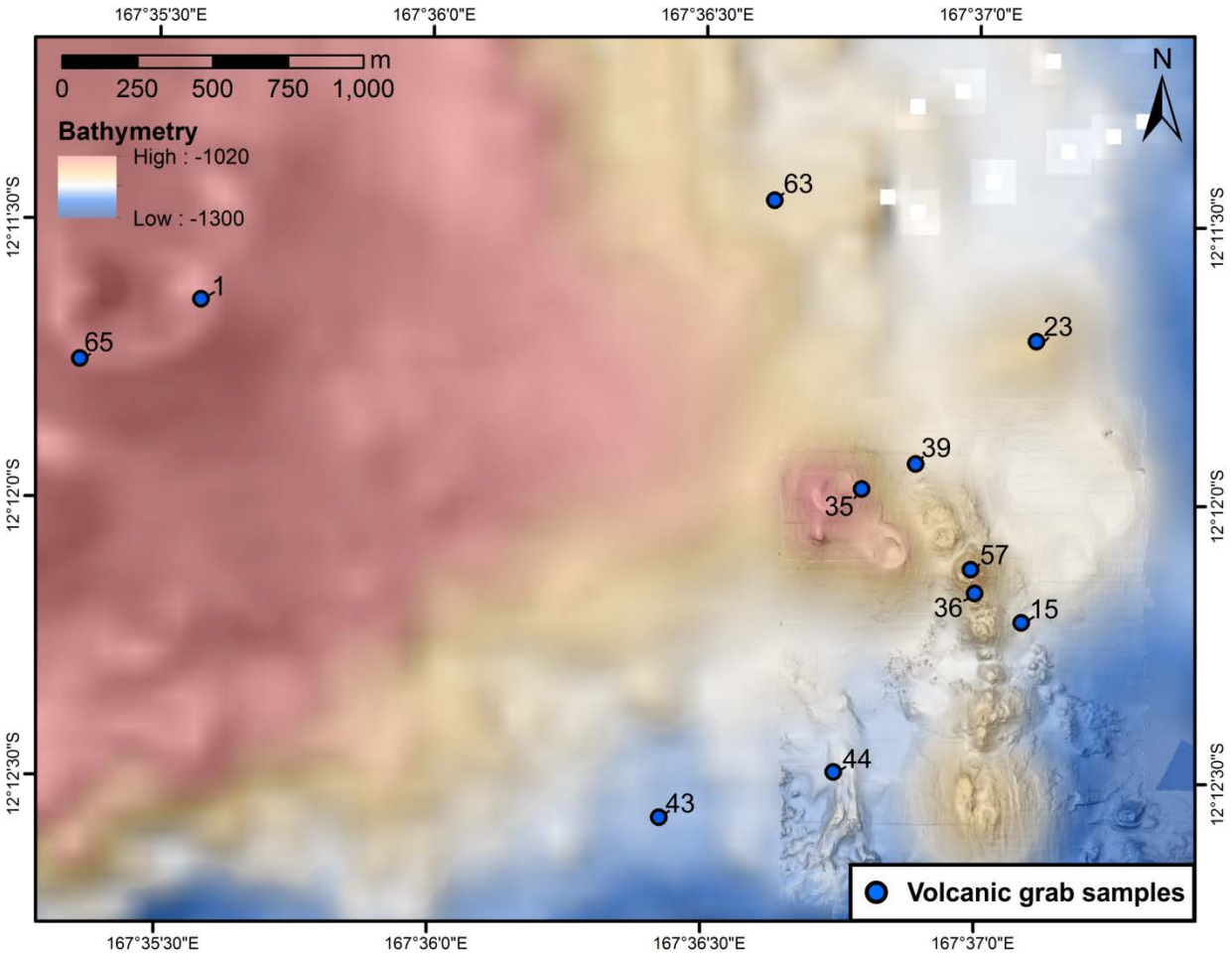


Fig. C2. Locations of ROV grab samples of volcanic rocks of the Starfish-Tinakula area (GMA-##).

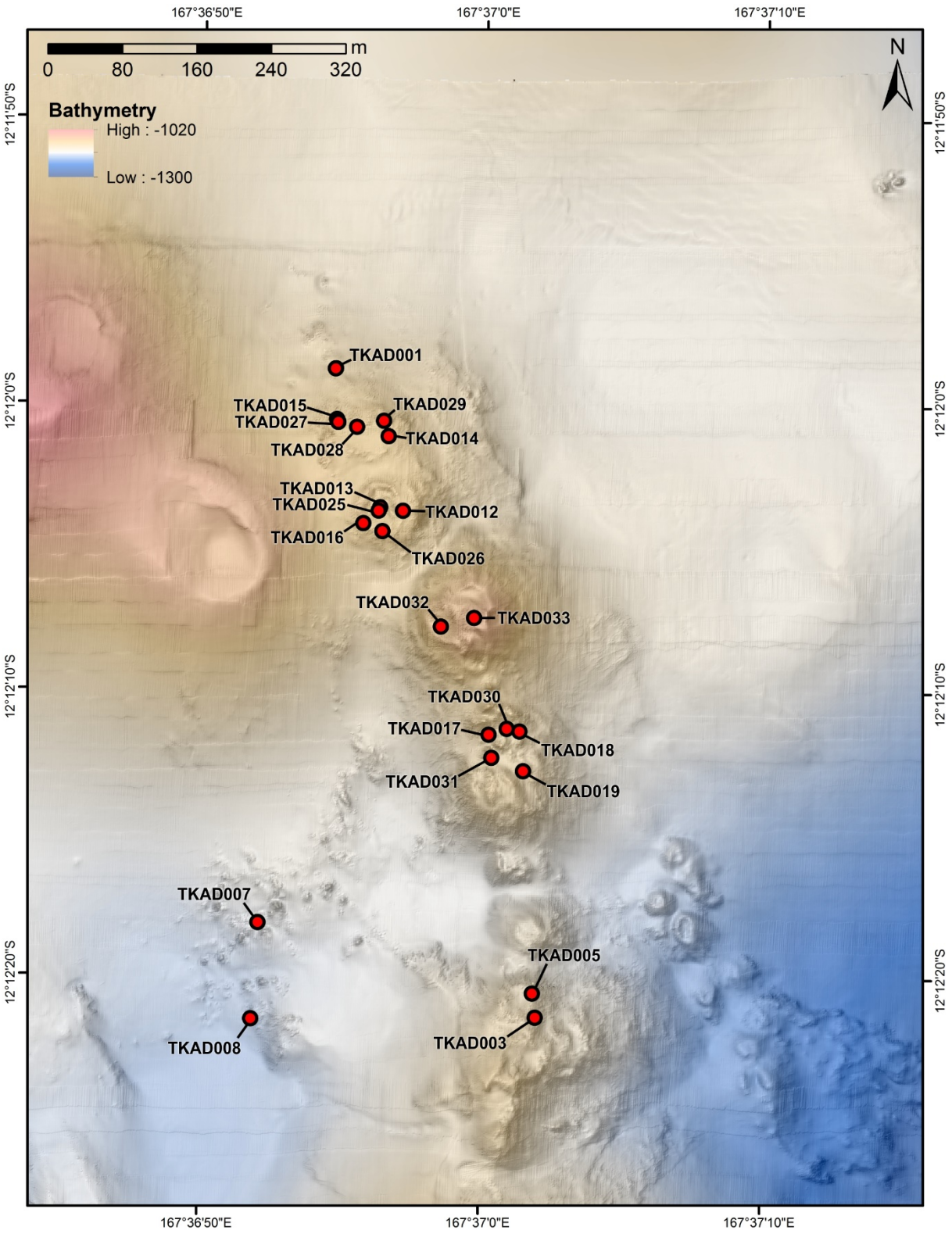


Fig. C3. Locations of drillhole collars (red circles) at the Tinakula deposit area used in this study.

Appendix D

Petrographic Reports – Volcanic Rocks

List of Samples

ROV GRAB SAMPLES 411

SAMPLE: GMA13-001 411

SAMPLE: GMA13-015 415

SAMPLE: GMA13-023 419

SAMPLE: GMA13-035 423

SAMPLE: GMA13-036 427

SAMPLE: GMA13-039 431

SAMPLE: GMA13-043 435

SAMPLE: GMA13-044 439

SAMPLE: GMA13-057 443

SAMPLE: GMA13-063 447

SAMPLE: GMA13-065 451

SAMPLE: P0015 455

SAMPLE: P0016 458

DRILLCORE SAMPLES 462

SAMPLE: P0040 462

SAMPLE: MA13-007 466

SAMPLE: MA13-008 467

SAMPLE: MA13-009 468

Notes:

Mineral abbreviations after Whitney and Evans (2010). Detailed whole rock geochemistry (this study) is reported in Appendix H.

+++ = abundant (>25%); ++ = major (10-25%); + = minor (1-9%); Tr = trace (<1%); - = none

ROV GRAB SAMPLES

SAMPLE: GMA13-001 **PARENT ID:** 096	**LOCATION:** 782144.8E/8650638.1N *(Big Starfish)* **WATER DEPTH:** 653 mbsl

Geochemical Notes

SiO_2 = 67.53%; Dacite (TAS)

Video Description

N/A

Hand Sample Description



Hand sample of GMA13-001.

Fine-grained black volcanic extrusive rock with 20% vesicles, <1-4 mm, rounded. 5% feldspar phenocrysts, <1-2 mm, randomly oriented. Slightly mottled texture on cut surface from alteration? Weathered surface has brown-orange FeOx, surficial coating.

Thin Section Description



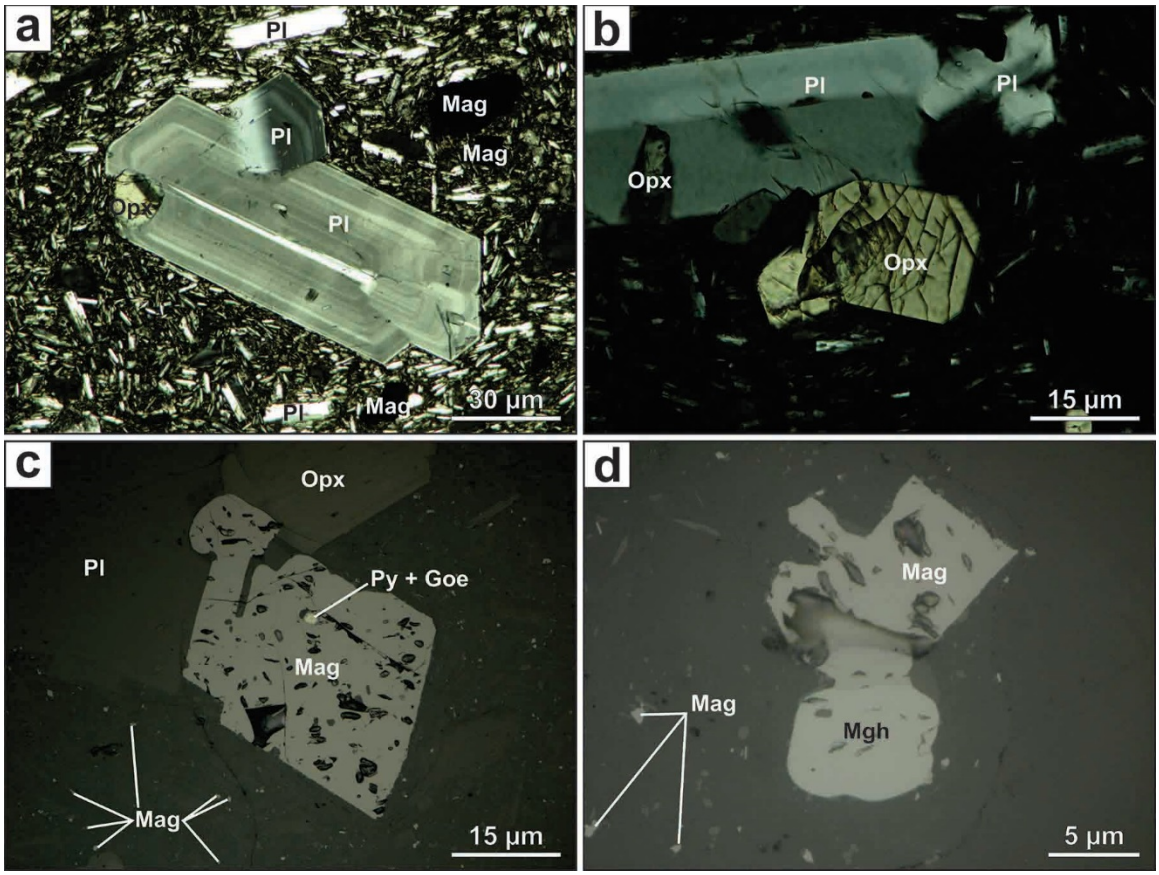
Thin section scan of GMA13-001.

This section is a massive porphyritic volcanic rock, with local weak flow-foliation. It contains ~15% vesicles, up to a few mm wide, with irregular margins. It contains ~10% phenocrysts, and ~75% microcrystalline to glassy groundmass.

The phenocryst assemblage is dominated by subhedral to euhedral plagioclase, which locally displays oscillatory chemical zoning. Twinning is dominated by Carlsbad twins, with minor albite twinning. Using the Michel-Lévy method, the plagioclase composition is An_{35}, while the Carlsbad-Albite method yields a composition of An_{43}. The next most common phenocryst is anhedral to euhedral orthopyroxene. It locally is surrounded by plagioclase phenocrysts (poikolitic texture). Phenocrysts of clinopyroxene also occur to a lesser extent, associated with the orthopyroxene and plagioclase crystals.

The groundmass consists of abundant fine-grained plagioclase crystals, surrounded by brownish glass (sideromelane?). The crystals are locally aligned along the flow direction, surrounding the phenocrysts.

Fine-grained magnetite (+ maghemite?) is regularly disseminated throughout the groundmass. Larger euhedral crystals also occur as phenocrysts. One large phenocryst contains an inclusion of rounded pyrite (immiscible sulfide melt?) that has been altered to secondary goethite(?) around the margins. Several opaque cubic phenocrysts are associated with the magnetite, displaying a slightly lighter grey color and greater relative hardness, likely maghemite(?). Trace amounts of very fine-grained chalcopyrite occurs in a few of the vesicles, locally altered to fine-grained covellite. Trace amounts of iron oxyhydroxides also occur in some vesicles.



Photomicrographs of GMA13-001: ***(a)*** *transmitted light (XPL) photomicrograph of chemical zonation of coarse-grained plagioclase phenocrysts, with plagioclase laths in the groundmass showing flow foliation around the larger phenocrysts;* ***(b)*** *transmitted light (XPL) photomicrograph of the phenocryst assemblage, including plagioclase with orthopyroxene inclusions;* ***(c)*** *reflected light (PPL) photomicrograph of magnetite phenocryst with an inclusion of pyrite, partially altered to goethite(?), and fine-grained magnetite (+ maghemite?) in the groundmass;* ***(d)*** *reflected light (PPL) photomicrograph of magmatite and maghemite(?) phenocrysts, with fine-grained magnetite (+maghemite) disseminated in the groundmass.*

	Abundance [modal %]	Relative Abundance
Vesicles	**15**	
Immiscible S	**<1**	
Py	<1	Tr
Ccp	-	
Icb(?)	-	
Phenocrysts	**10**	
Pl	7	+
Cpx	<1	Tr
Opx	2	+
Mag	<1	Tr
Mgh	<1	Tr
Groundmass	**75**	
$Glass_{(Sid)}$	15	++
$Glass_{(Pal)}$	-	
$Glass_{(Pum)}$	-	
$Glass_{(Tac)}$	-	
Pl	58	+++
Cpx	<1	Tr
Opx	<1	Tr
Mag	2	+
Mgh	<0.1	Tr
Xenoliths	**-**	
Late Sulfides	**<0.1**	
Ccp	<0.1	Tr
Py	-	
Alteration	**<0.1**	
Hem	-	
Goe(?)	<0.1	Tr
FeO_x	<0.1	Tr
MnO_x	-	
$Pal_{(Gel)}$	-	
Clay	-	
Cv	<0.1	Tr

Paragenesis: Pyrite immiscible sulfide droplets → goethite(?), local → magnetite phenocrysts → maghemite replacement of magnetite → orthopyroxene + clinopyroxene phenocrysts → vesicular groundmass (plagioclase + magnetite + minor pyroxene + sideromelane? glass) → fine-grained chalcopyrite in some vesicles → minor covellite alteration of chalcopyrite + iron oxyhydroxides (trace) in some vesicles.

Interpretation: Coherent lava flow

Name: Porphyritic vesicular dacite flow

SAMPLE: GMA13-015 **PARENT ID:** 658	**LOCATION:** 784867.6E/8649563.5N **WATER DEPTH:** 1154 mbsl

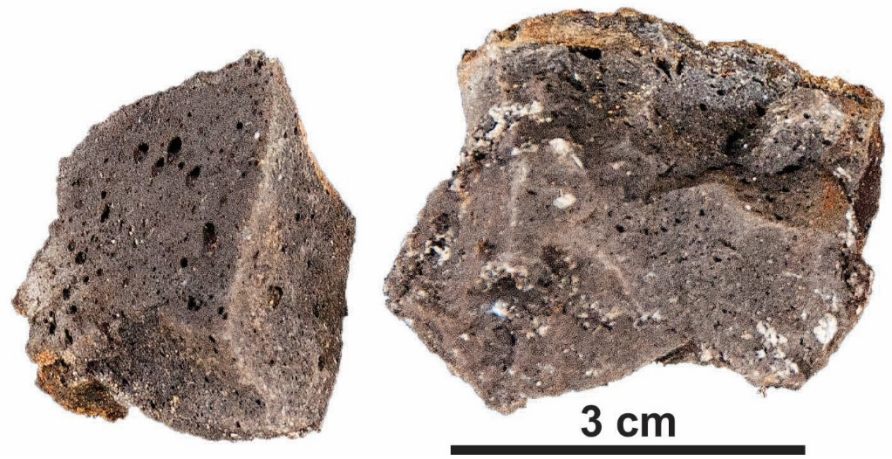
Geochemical Notes

SiO_2 = 57.43%; Andesite (TAS)

Video Description

Buried lava flow, ropey, easily broken.

Hand Sample Description



Hand sample of GMA13-015.

Fragments of vesicular mafic extrusive. 20-25% vesicles, some elongate/aligned. Quench margins? Mostly unaltered. Fragments originated from one sample, broke while cutting.

Thin Section Description

This sample is a very vesicular volcanic rock, containing ~35% rounded vesicles ranging in size from a few microns up to a few mm across. It contains ~5% phenocrysts and ~60% groundmass overall.

There are a few coarse-grained subhedral to anhedral phenocrysts up to 10 mm across, ~5% overall. It is locally glomeroporphyritic. These phenocrysts consist of plagioclase, orthopyroxene, and clinopyroxene. The plagioclase phenocrysts have a composition of An_{23} (M.L. method); the low number of measurable phenocrysts results in a high uncertainty in this number.



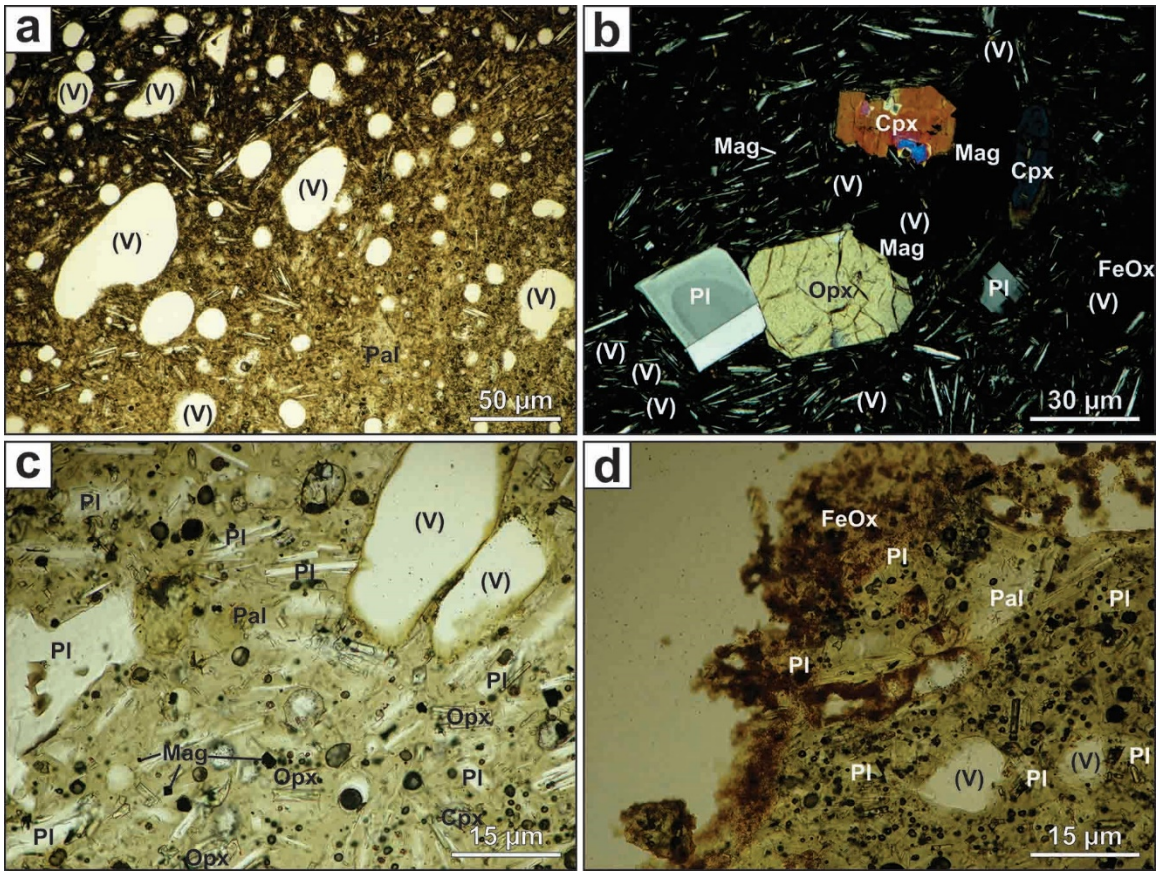
Thin section scan of GMA13-015.

The groundmass consists of fine-grained plagioclase crystals, locally aligned along a flow direction, and minor pyroxene. Glass (tachylite) is abundant and irregular dark brown in color, and contains abundant microlites (indicative of undercooling or supersaturation), with occasional microlite-free patches. The color is uneven, occasionally appearing as rounded clasts/xenoliths(?). There are minor patchy iron oxides near some vesicles. A few areas containing large vesicles are partially filled in by pumice that is lighter-brown to colorless, containing a few plagioclase crystals and abundant vesicles.

Magnetite is evenly distributed as fine-grained disseminated crystals in the groundmass, with a few larger phenocrysts, one displaying a skeletal texture.

One possible rounded immiscible sulfide droplet of chalcopyrite was observed, weakly altered to covellite around the margin, included in magnetite.

A glassy margin occurs on the bottom-left part of the section. It is marked by a change in color from dark brown to lighter orange-ish brown (palagonite) with a decrease in the abundance of microlites. This area contains patchy dark brown coloring, and contains both phenocrysts and magnetite. The margin of the section is bright orange from iron oxyhydroxide alteration. Trace chalcopyrite forms in some vesicles. A fine-grained colorless unknown tetragonal mineral (zeolite?) with first-order birefringence also forms in some vesicles. Late hematite fills cracks, locally.



Photomicrographs of GMA13-015: ***(a)*** *transmitted light (PPL) photomicrograph at the contact between unaltered tachylitic glass (top left) and plagonitized glassy margin (bottom right), with abundant rounded vesicles and fine-grained plagioclase laths in the groundmass;* ***(b)*** *transmitted light (XPL) photomicrograph of the phenocryst assemblage, including plagioclase, orthopyroxene, clinopyroxene, and magnetite, with local flow foliation of plagioclase laths in the groundmass;* ***(c)*** *transmitted light (PPL) photomicrograph of the glassy palagonite margin, with fine-grained plagioclase, orthopyroxene, clinopyroxene, and magnetite, with few microlites;* ***(d)*** *transmitted light (PPL) photomicrograph of iron oxhyhydroxides at the edge of the sample associated with palagonite glass. (V) = vesicle.*

	Abundance [modal %]	Relative Abundance
Vesicles	**35**	
Immiscible S	**<0.1**	
Py	-	
Ccp	<0.1	
Icb(?)	-	
Phenocrysts	**5**	
Pl	3	+
Cpx	2	+
Opx	<1	Tr
Mag	<1	Tr
Mgh	-	
Groundmass	**60**	
$Glass_{(Sid)}$	-	
$Glass_{(Pal)}$	5	+
$Glass_{(Pum)}$	2	+
$Glass_{(Tac)}$	15	++
Pl	38	+++
Cpx	<1	Tr
Opx	<0.1	Tr
Mag	<1	+
Mgh	-	
Xenoliths	**<1**	
Late Sulfides	**<1**	
Ccp	<1	Tr
Py	-	
Alteration	**<1**	
Hem	<1	Tr
Goe(?)	-	
FeO_x	<1	Tr
MnO_x	-	
$Pal_{(Gel)}$	-	
Clay	-	
Cv	<0.1	Tr
Zeo(?)	<0.1	Tr

Paragenesis: Chalcopyrite immiscible sulfide droplets(?) → covellite alteration→ magnetite phenocrysts → plagioclase phenocrysts → clinopyroxene + orthopyroxene phenocrysts → vesicular groundmass (plagioclase + magnetite + pyroxene + tachylitic glass) + quenched palagonite margin + xenoliths(?) → pumaceous glass in some open areas → chalcopyrite along vesicles → zeolite(?) and iron oxyhydroxides in some vesicles + hematite along local fractures.

Interpretation: Coherent lava flow with glassy rim, and xenoliths(?) picked up during flow

Name: Glassy vesicular andesite flow with xenoliths(?)

SAMPLE: GMA13-023 **PARENT ID:** 594	**LOCATION:** 784917.9E/8650496.1N *(N. Plateau)* **WATER DEPTH:** 1092 mbsl

Geochemical Notes

SiO_2 = 55.96%; Basaltic-andesite (TAS)

Video Description

Round rock from between sheeted lava rocks.

Hand Sample Description

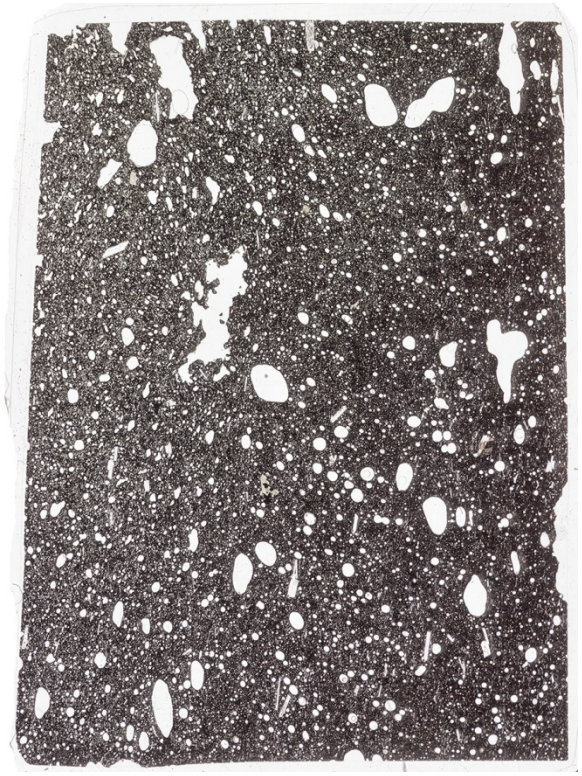


Hand sample of GMA13-023.

Fine-grained black vesicular mafic extrusive. Contains 10% vesicles, rounded, <1 - 10 mm. 2% Feldspar phenocrysts, sub-mm scale. Outer surface is rough. Weathering (white clay) alteration extends 0.5 cm into sample, outer surface is slightly brown-orange Mn-oxide. Glass rind on two sides suggests lobe flow.

Thin Section Description

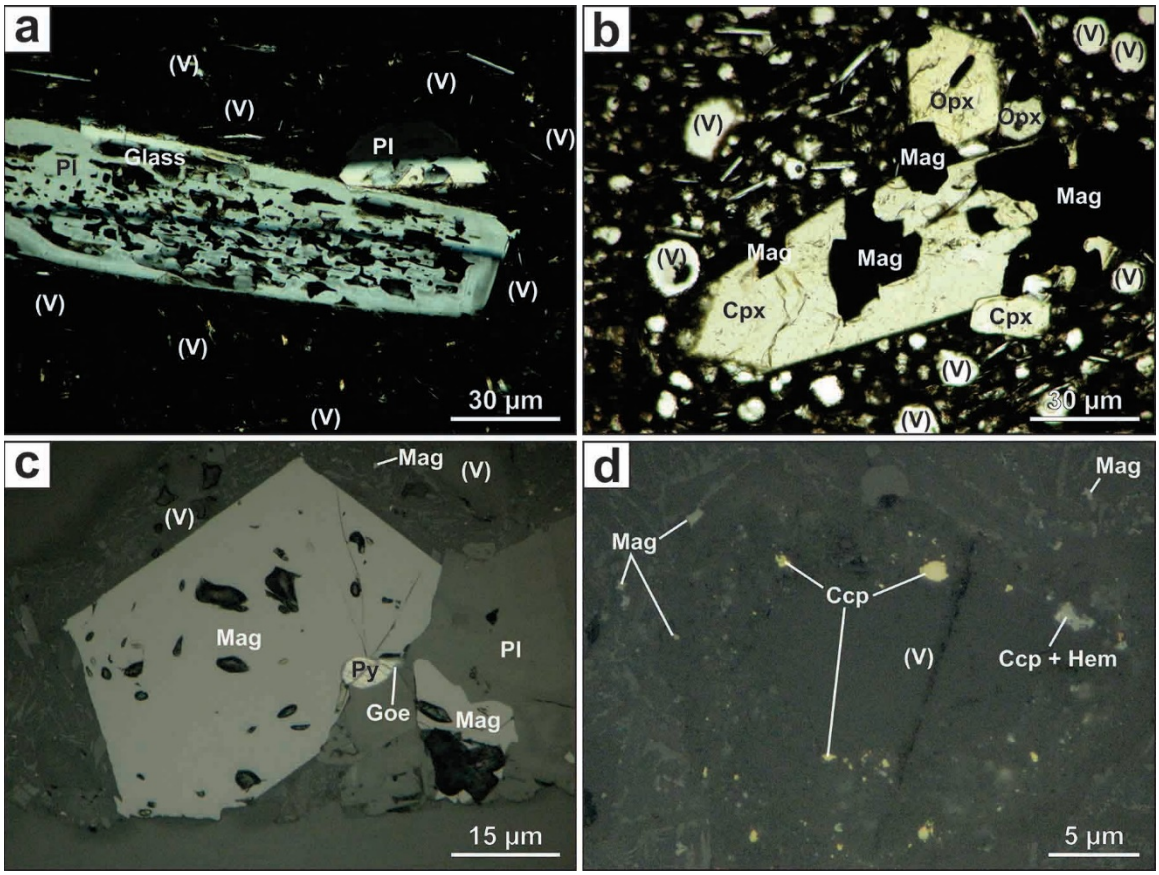
This section is a massive, flow-foliated volcanic rock, containing ~35% rounded spherical to elongate vesicles that range in size from 0.01 to 2 mm in length. It contains ~5% large phenocrysts (“megacrysts”) of plagioclase with subordinate clinopyroxene and orthopyroxene. The subhedral plagioclase phenocrysts have a composition of An_{23} (M.L. method) to An_{27} (C.A. method), and commonly display oscillatory chemical zonation. Several of the phenocrysts contain abundant inclusions of brownish-black isotropic glass.



Thin section scan of GMA13-023.

The groundmass (60% overall) contains brownish-black glass (tachylite), plagioclase crystals ("microphenocrysts") up to 1 mm long, and fine-grained scattered pyroxene. The plagioclase crystals show a strong flow-foliation, which is generally followed by the megacrysts and elongated vesicles.

Fine-grained magnetite is disseminated throughout the groundmass, with a few larger crystals up to 3 mm long, associated rounded inclusions of pyrite (immiscible sulfide melt?), locally altered to goethite. Minor very fine-grained chalcopyrite (± hematite) occurs in several of the vesicles, ~1% overall. Some vesicles contain inward-growing microlites (oxides?) and trace amounts of iron oxyhydroxides.



Photomicrographs of GMA13-023: ***(a)*** *transmitted light (XPL) photomicrograph of plagioclase phenocryst with abundant inclusions of isotropic glass;* ***(b)*** *transmitted light (PPL) photomicrograph of highly vesicular groundmass of tachylitic glass and fine-grained plagioclase, with orthopyroxene and clinopyroxene phenocrysts with inclusions of magnetite;* ***(c)*** *reflected light (PPL) photomicrograph of subhedral magnetite phenocryst, with minor rounded pyrite, altered to goethite;* ***(d)*** *reflected light (PPL) photomicrograph of fine-grained chalcopyrite (+ hematite?) forming within a vesicle, and fine-grained magnetite within the groundmass assemblage. (V) = vesicle.*

	Abundance [modal %]	Relative Abundance
Vesicles	**35**	
Immiscible S	**<1**	
Py	<1	Tr
Ccp	-	
Icb(?)	-	
Phenocrysts	**5**	
Pl	4	+
Cpx	1	+
Opx	<1	Tr
Mag	<1	Tr
Mgh	-	
Groundmass	**60**	
$Glass_{(Sid)}$	-	
$Glass_{(Pal)}$	-	
$Glass_{(Pum)}$	-	
$Glass_{(Tac)}$	30	+++
Pl	21	++
Cpx	3	+
Opx	5	+
Mag	1	+
Mgh	-	
Xenoliths	**-**	
Late Sulfides	**<0.1**	
Ccp	<0.1	Tr
Py	-	
Alteration	**<1**	
Hem	<0.1	Tr
Goe(?)	<1	Tr
FeO_x	<0.1	Tr
MnO_x	-	
$Pal_{(Gel)}$	-	
Clay	-	
Cv	-	

Paragenesis: Pyrite immiscible sulfide droplets → goethite(?) alteration → magnetite phenocrysts → plagioclase phenocrysts → clinopyroxene + orthopyroxene phenocrysts → vesicular groundmass (plagioclase + pyroxene + magnetite + tachylitic glass) → chalcopyrite in vesicles → hematite and iron oxyhydroxides in vesicles.

Interpretation: Coherent lava flow

Name: Glassy vesicular basaltic-andesite flow

SAMPLE: GMA13-035 **PARENT ID:** 611	**LOCATION:** 784337.5E/8650007.6N **WATER DEPTH:** 1053 mbsl

Geochemical Notes

SiO_2 = 57.15%; Andesite (TAS)

Video Description

N/A

Hand Sample Description

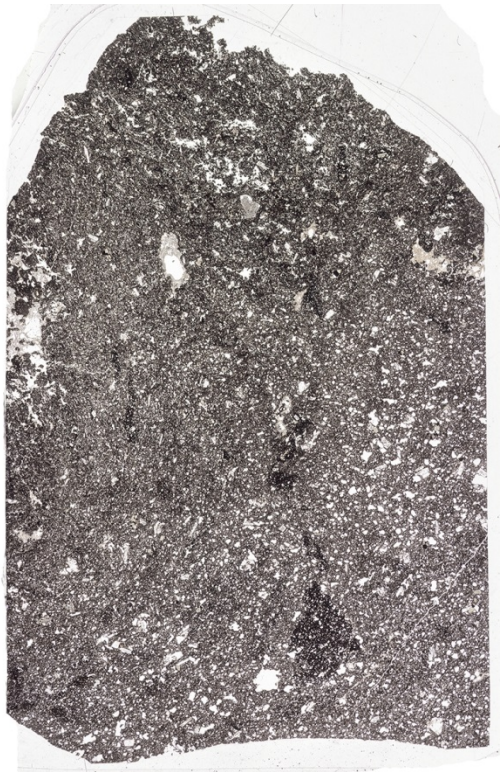


Hand sample of GMA13-035.

Fragments of fine-grained mafic extrusive, with very small (sub-mm to mm scale) vesicles, up to 5%, no elongation. Aphyric. Very minor FeOx coating.

Thin Section Description

This section contains abundant vesicles with irregular margins, ~30% overall. It also contains ~10% anhedral to euhedral phenocrysts, locally glomeroporphyritic, and ~58% groundmass. The color is dark brown, with very dark brown patches that appear to outline subangular tachylitic glassy clasts/xenoliths(?), ~2% overall.

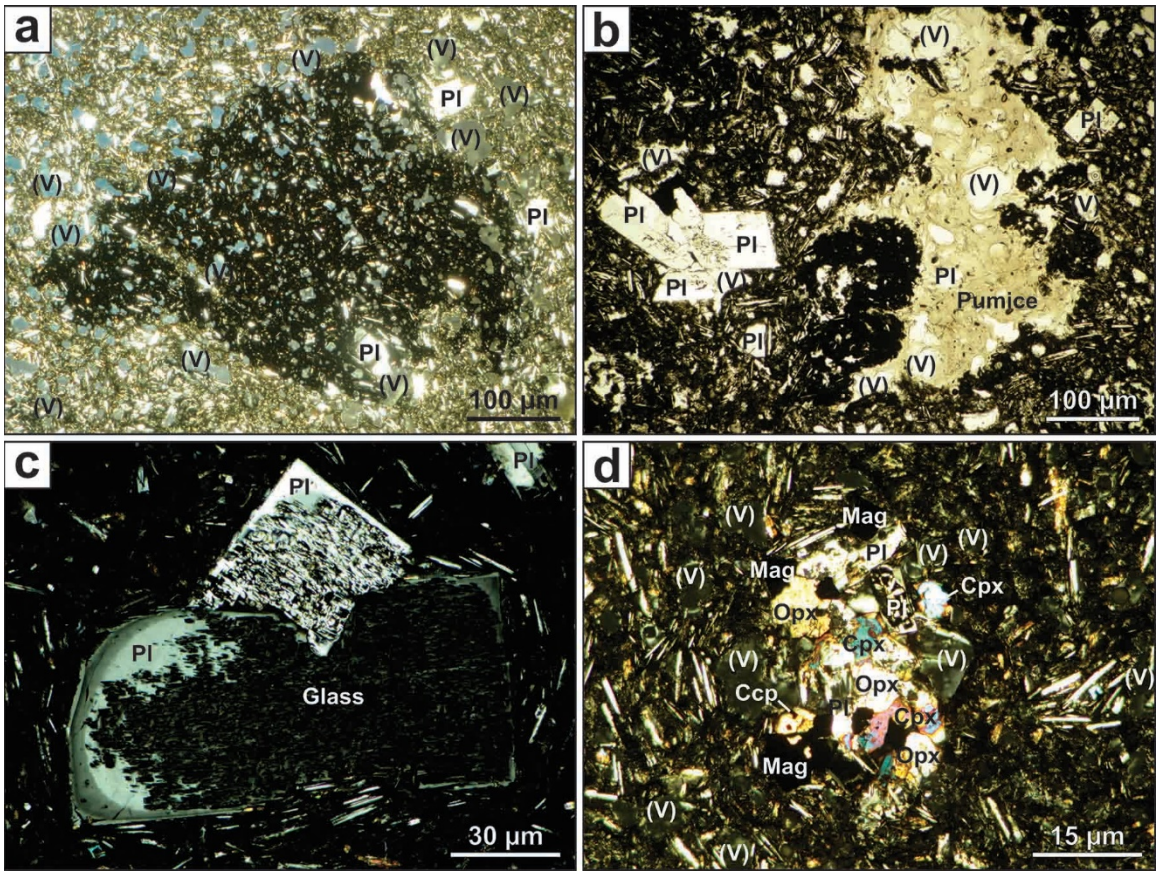


Thin section scan of GMA13-035.

The phenocrysts consist of plagioclase, orthopyroxene, clinopyroxene, and magnetite. The plagioclase locally contains black melt inclusions. It has a composition of An_{11} (M.L. method). Clinopyroxene locally contains melt inclusions as well. The magnetite is associated with minor amounts of maghemite(?) and contains inclusions of rounded pyrite, partially altered to iron oxide (goethite ± hematite?).

The groundmass consists of plagioclase, tachylitic glass, orthopyroxene, clinopyroxene, and finely-disseminated magnetite. Moderate flow foliation is defined by aligned plagioclase phenocrysts. The glass is heterogeneous dark brown (tachylitic) with abundant microlites. A few areas appear to be clasts/xenoliths with irregular margins. These dark brown 'clasts' contain a higher proportion of glass (tachylite). The shape is subangular to wispy. They are irregularly distributed through the section.

There are patchy areas, associated with larger vesicles, which contain light brown relatively clear pumaceous glass with very few microlites, but containing the occasional plagioclase + orthopyroxene phenocryst. Trace chalcopyrite occurs in several vesicles.



Photomicrographs of GMA13-035: ***(a)*** *transmitted light (XPL) photomicrograph of irregular coloring of the glassy groundmass, possibly a tachylitic xenolith(?);* ***(b)*** *transmitted light (PPL) photomicrograph of pumaceous highly-vesicular glass, irregularly distributed in a vesicular tachylitic glassy groundmass with phenocrysts of plagioclase;* ***(c)*** *transmitted light (XPL) photomicrograph of plagioclase with sieve texture / abundant glass inclusions;* ***(d)*** *transmitted light (XPL) photomicrograph of the phenocryst assemblage, including plagioclase, orthopyroxene, clinopyroxene (with rare inclusions of chalcopyrite), and magnetite. (V) = vesicle.*

	Abundance [modal %]	Relative Abundance
Vesicles	**30**	
Immiscible S	**<1**	
Py	<1	Tr
Ccp	-	
Icb(?)	-	
Phenocrysts	**10**	
Pl	5	+
Cpx	3	+
Opx	1	+
Mag	1	+
Mgh	<0.1	Tr
Groundmass	**58**	
$Glass_{(Sid)}$	-	
$Glass_{(Pal)}$	-	
$Glass_{(Pum)}$	3	+
$Glass_{(Tac)}$	22	+++
Pl	20	++
Cpx	5	+
Opx	6	+
Mag	2	+
Mgh	<0.1	Tr
Xenoliths	**2**	
Late Sulfides	**<0.1**	
Ccp	<0.1	Tr
Py	-	
Alteration	**<0.1**	
Hem	-	
Goe(?)	<0.1	Tr
FeO_x	<0.1	Tr
MnO_x	-	
$Pal_{(Gel)}$	-	
Clay	-	
Cv	-	

Paragenesis: Pyrite immiscible sulfide droplets → goethite → magnetite → maghemite replacement of magnetite → plagioclase phenocrysts → clinopyroxene phenocrysts → orthopyroxene phenocrysts → vesicular groundmass (plagioclase + magnetite + pyroxene + tachylitic glass) + tachylitic xenoliths(?) → pumaceous glass in some large open spaces → late chalcopyrite in vesicles → iron oxyhydroxides in vesicles.

Interpretation: Coherent lava flow with glassy xenoliths picked up during flow

Name: Glassy porphyritic vesicular andesite with xenoliths(?)

SAMPLE: GMA13-036 **PARENT ID:** 607	**LOCATION:** 784712.3E/8649661.3N **WATER DEPTH:** 1094 mbsl

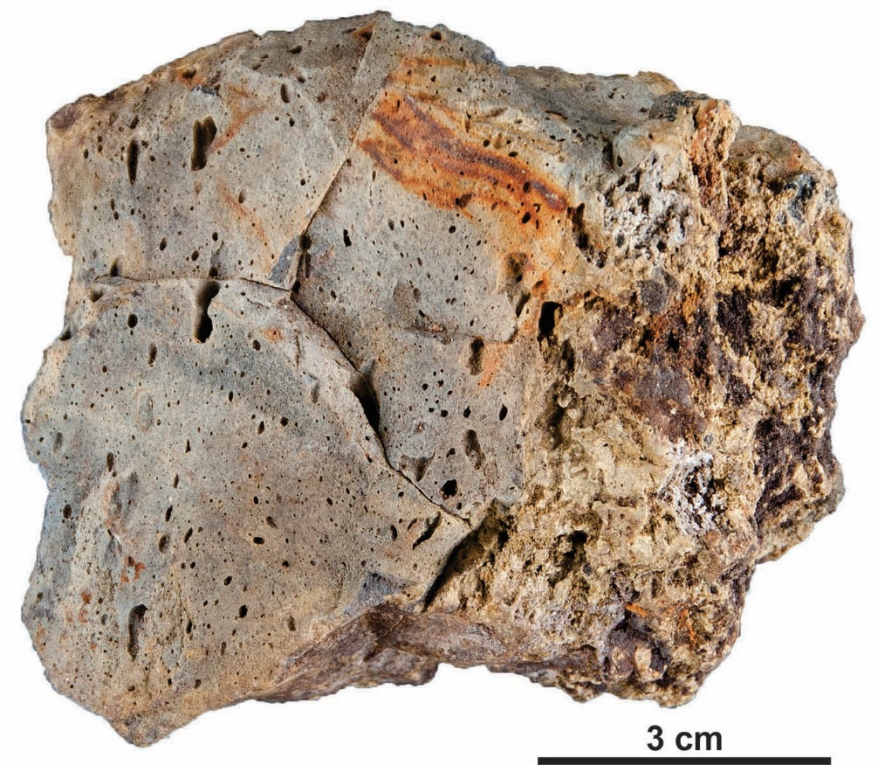
Geochemical Notes

N/A

Video Description

Volcanic sample located close to hydrothermal center.

Hand Sample Description



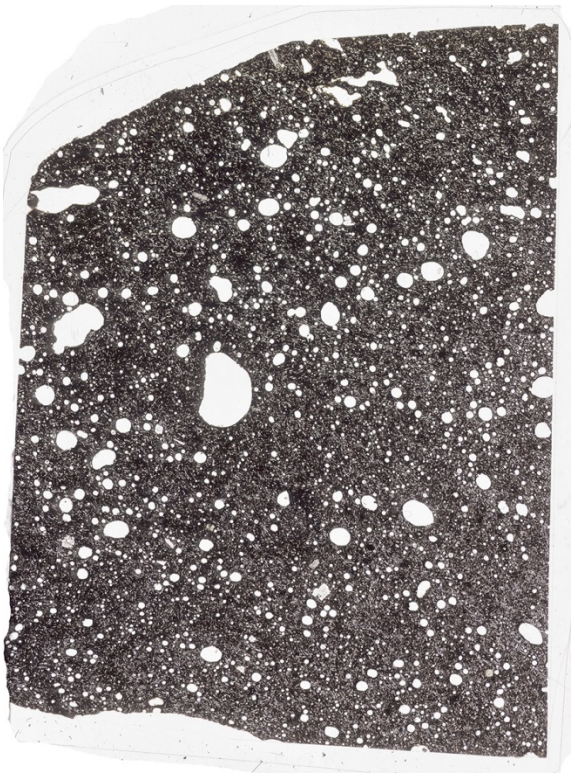
Hand sample of GMA13-036.

Slightly bleached/clay altered fine-grained vesicular mafic extrusive. 5-7% vesicles, <1-4 mm, elongate (flow fabric). Sample is light grey to yellow. Exterior has FeOx, clay, MnOx alteration. Interior of the sample displays less alteration.

Thin Section Description

This section has ~20% rounded vesicles, ~3% phenocrysts, and 72% groundmass. There is no whole-rock geochemistry for this sample (due to alteration), but the lack of phenocrysts is consistent with basaltic rocks observed in this study.

The phenocrysts consist of orthopyroxene and plagioclase, both with abundant glass inclusions, and rare clinopyroxene. Several orthopyroxene phenocrysts have thin coronas of plagioclase. There are also

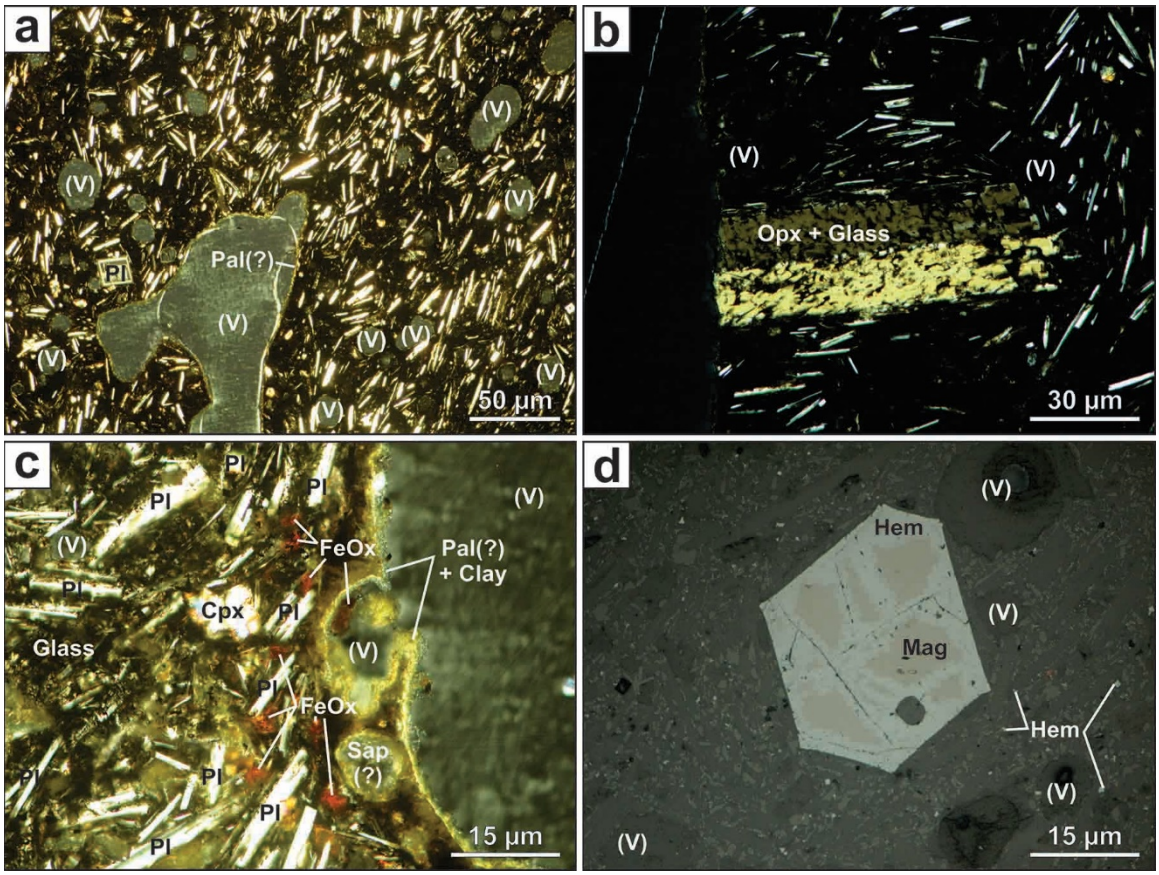


Thin section scan of GMA13-036.

three euhedral to subhedral hexagonal to cubic crystals of magnetite that is being altered to hematite (martite) along fractures. The plagioclase phenocrysts have a composition of An_{17} (M.L. method), although there is high uncertainty as a result of the low number of crystals measured.

The groundmass contains abundant dark brown to orange glass (tachylitic) with abundant microlites, with rims of dark brown (oxide?) around vesicles. There are patches of dark brown areas with irregular margins, possibly relict glassy clasts/xenoliths (tachylitic?). There are fine- to medium-grained plagioclase displaying strong flow foliation. There is minor clay alteration associated with the glassy groundmass. There is also fine-grained orthopyroxene and clinopyroxene, minor fine-grained magnetite and hematite (altered).

Several of the vesicles are lined by very fine-grained gel-palagonite(?) and/or other clays, and are partially infilled by rare bright red-orange iron oxyhydroxides, particularly near the bottom of the section. Trace very fine-grained chalcopyrite occurs in several vesicles, locally altered to covellite.



Photomicrographs of GMA13-036: ***(a)*** *transmitted light (XPL) photomicrograph of irregular vesicules, locally lined by gel-palagonite(?), and flow-foliation of plagioclase laths in the glassy tachylitic groundmass;* ***(b)*** *transmitted light (XPL) photomicrograph of orthopyroxene phenocryst with abundant glass inclusions, and foliation of plagioclase laths in the groundmass around the phenocryst;* ***(c)*** *transmitted light (XPL) photomicrograph of iron oxyhydroxides and very fine-grained gel-palagonite(?) and other clays(?) along a vesicle;* ***(d)*** *reflected light (PPL) photomicrograph of magnetite altered to hematite along cracks, also known as martitization. (V) = vesicle.*

	Abundance [modal %]	Relative Abundance
Vesicles	**20**	
Immiscible S	**-**	
Py	-	
Ccp	-	
Icb(?)	-	
Phenocrysts	**3**	
Pl	1	+
Cpx	<1	Tr
Opx	2	+
Mag	<1	Tr
Mgh	-	
Groundmass	**72**	
$Glass_{(Sid)}$	-	
$Glass_{(Pal)}$	-	
$Glass_{(Pum)}$	-	
$Glass_{(Tac)}$	21	++
Pl	38	+++
Cpx	4	+
Opx	8	+
Mag	1	+
Mgh	-	
Xenoliths	**1**	
Late Sulcides	**<0.1**	
Ccp	<0.1	Tr
Py	-	
Alteration	**4**	
Hem	<1	Tr
Goe(?)	-	
FeO_x	1	+
MnO_x	-	
$Pal_{(Gel)}$	3	+
Clay	<1	Tr
Cv	<0.1	Tr

Paragenesis: Magnetite phenocrysts → orthopyroxene phenocrysts + clinopyroxene phenocrysts → plagioclase phenocrysts → vesicular groundmass (plagioclase + pyroxene + magnetite + tachylitic glass) + tachylitic xenoliths(?) → chalcopyrite in vesicles → covellite alteration of chalcopyrite → incipient hematite alteration of magnetite + iron oxhydroxides near vesicles → gel-palagonite (+ other clays?) lining vesicles.

Interpretation: Coherent flow with subtle alteration, and a few xenoliths(?) picked up during flow.

Name: Subtly clay-altered vesicular andesite(?) flow with xenoliths(?)

SAMPLE: GMA13-039 **PARENT ID:** 696	**LOCATION:** 784516.6E/8650090.5N **WATER DEPTH:** 1127 mbsl

Geochemical Notes

SiO_2 = 58.26%; Andesite (TAS)

Video Description

Banded piece from volcanic talus at base of chimney.

Hand Sample Description

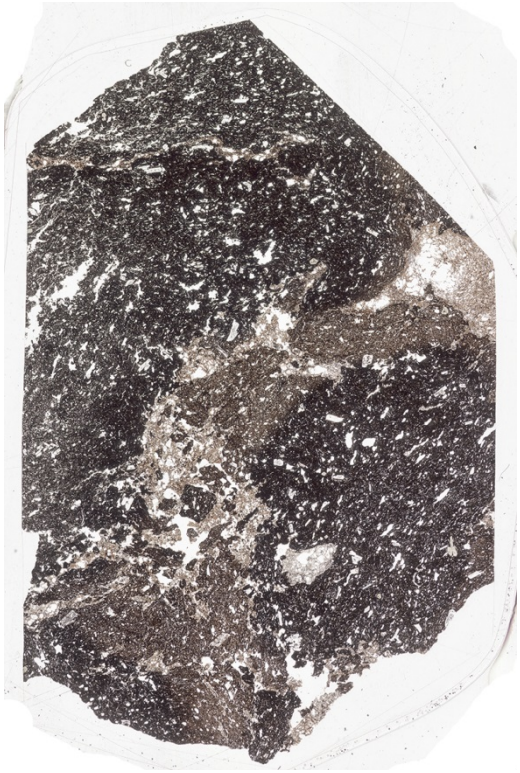


Fine-grained vesicular mafic extrusive, dull black, aphanitic, mildly vitric, with 5-10% small vugs up to 2 mm across, spheroidal to weakly elongate. Rare plagioclase microphenocrysts. Strongly jointed, in-situ fracturing. 3% fine feldspar phenocrysts, sub-mm size. Weak MnOx alteration near fractures.

Hand sample of GMA13-039.

Thin Section Description

This section is heterogeneous, with dark brown-black areas containing ~20% vesicles, 15% phenocrysts, and 65% groundmass, lighter brown with ~50% vesicles, ~10% phenocrysts, and ~40% groundmass, and a pumaceous area with open spaces filled with wispy orange-brown glass arranged in a rectilinear network, with 85% vesicles, 5% phenocrysts, and 10% glass. The bulk proportions are: 35% vesicles, 15% phenocrysts, and 50% groundmass. The dark brown (least altered) domain has a phenocryst assemblage that includes subhedral to euhedral plagioclase, orthopyroxene, clinopyroxene, and minor magnetite. The distribution of phenocrysts is even, although it locally displays a glomeroporphyritic texture. The



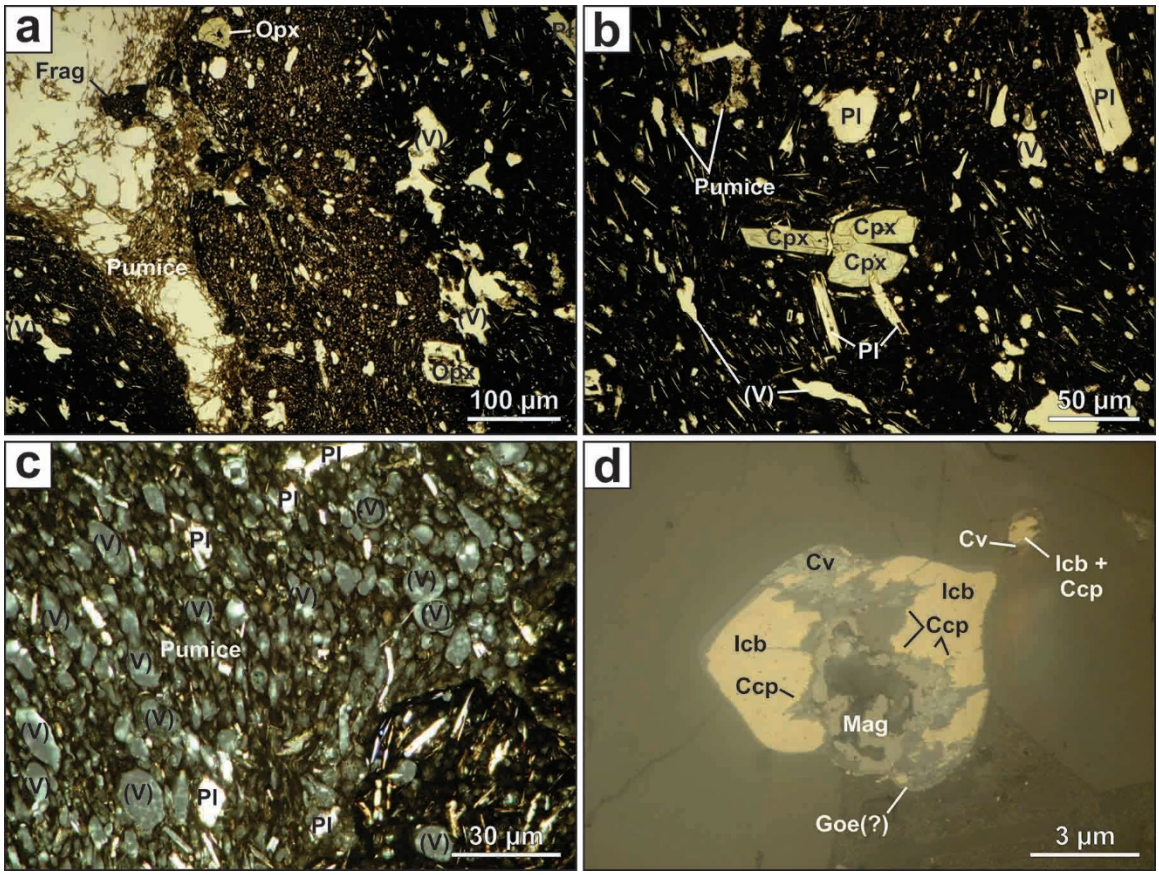
Thin section scan of GMA13-039.

plagioclase and orthopyroxene phenocrysts contain abundant black melt inclusions. The plagioclase phenocrysts have a composition of An_{25} (M.L. method). The magnetite contains rare fine-grained inclusions of globlular pyrite, altered to trace goethite. Following magnetite, there is local isocubanite(?) with exsolved chalcopyrite, weakly altered to covellite and goethite(?).

The groundmass contains abundant tachylitic glass, abundant fine- to medium-grained plagioclase aligned along a flow foliation (flowing around phenocrysts), and minor fine-grained pyroxene and magnetite. The vesicles associated with this domain are irregular and elongate in the flow direction. A few vesicles are lined with minor amounts of iron oxyhydroxides.

This domain grades into the light-brown vesicle-rich domain over a short distance. This domain contains abundant small rounded vesicles, and a few larger vesicles elongate with the flow foliation. Phenocrysts are still present, as are opaque phases. There is a sharp contact between this domain and the glassy, pumaceous domain.

The pumaceous domain forms along fractures/joints in the lava flow, and contains large clasts or inclusions of the previous light-brown domain. It occurs as a vesicle-rich network of banded glass that flows around the edges of the rock. The vesicles are rounded to ellipsoidal/rectilinear, resulting from stretching during flow. It contains evenly distributed phenocrysts of plagioclase and minor pyroxene, as well as opaque phases. Fine-grained sulfides (chalcopyrite, pyrite) form within the pore spaces.



Photomicrographs of GMA13-039: ***(a)*** *transmitted light (PPL) photomicrograph of dark brown-black tachylitic domain (right) with irregular vesicles and plagioclase + othopyroxene phenocrysts, followed by highly vesicular slightly lighter-colored domain (middle) with rounded vesicles and an orthopyroxene phenocryst (middle), followed by a highly vesicular glassy/pumaceous domain along a crack, containing fragments of the previous domain;* ***(b)*** *transmitted light (PPL) photomicrograph of the dark brown-black tachylitic domain with phenocrysts of plagioclase and clinopyroxene, grading into slightly lighter-brown domain (top) with abundant rounded vesicles, and minor glassy/pumaceous domain in open spaces;* ***(c)*** *transmitted light (XPL) photomicrograph of the highly vesicular/pumaceous domain showing rounded to elongate/stretched vesicules from flow foliation, and sharp contact with the dark brown domain;* ***(d)*** *reflected light (PPL) photomicrograph of magnetite, followed by isocubanite with chalcopyrite phenocrysts (immiscible sulfide droplet?), partially altered to covellite and goethite(?).*

	Abundance [modal %]	Relative Abundance
Vesicles	**20**	
Immiscible S	**<1**	
Py	<1	Tr
Ccp	<0.1	Tr
Icb(?)	<0.1	Tr
Phenocrysts	**15**	
Pl	11	++
Cpx	2	+
Opx	2	+
Mag	<1	Tr
Mgh	-	
Groundmass	**65**	
$Glass_{(Sid)}$	-	
$Glass_{(Pal)}$	-	
$Glass_{(Pum)}$	5	+
$Glass_{(Tac)}$	21	++
Pl	33	+++
Cpx	4	+
Opx	8	+
Mag	2	+
Mgh	-	
Xenoliths	**-**	
Late Sulfides	**<1**	
Ccp	<1	Tr
Py	<0.1	Tr
Alteration	**<1**	
Hem	<1	Tr
Goe(?)	<0.1	Tr
FeO_x	<1	Tr
MnO_x	-	
$Pal_{(Gel)}$	-	
Clay	-	
Cv	<0.1	Tr

Paragenesis: Pyrite immiscible sulfide droplet → goethite (?) alteration → magnetite phenocrysts → isocubanite(?) with exsolved chalcopyrite immiscible sulfide droplet → covellite + goethite(?) alteration → plagioclase phenocrysts → clinopyroxene + orthopyroxene phenocrysts → vesicular groundmass (plagioclase, pyroxene, magnetite, tachylitic glass) → vesicular pumaceous (flow-top froth) → chalcopyrite and pyrite in vesicles → hematite alteration of magnetite + iron oxyhydroxides.

Interpretation: Autoclastic lava flow with frothy flow-top breccia.

Name: Autoclastic vesicular andesite flow

SAMPLE: GMA13-043 **PARENT ID:** 711	**LOCATION:** 783664.4E/8648919.8N **WATER DEPTH:** 1196 mbsl

Geochemical Notes

SiO_2 = 63.49%; Dacite (TAS)

Video Description

N/A

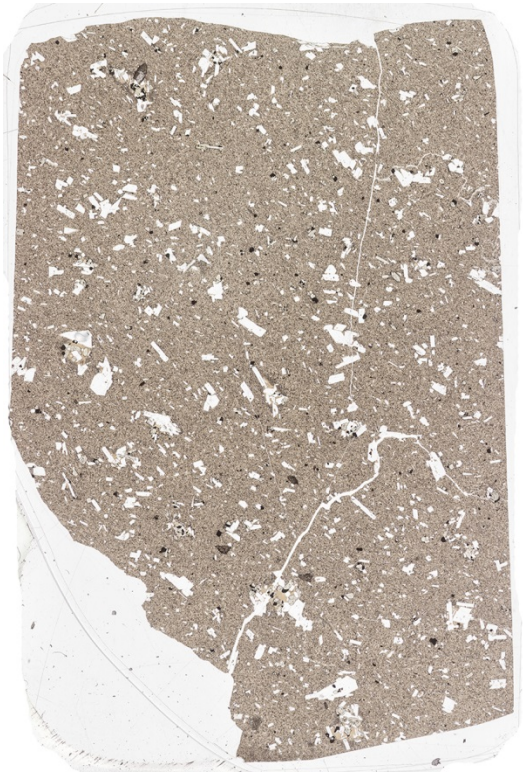
Hand Sample Description



Hand sample of GMA13-043.

Massive Fspr-Pyx-Ol(?)-phyric fine-grained mafic extrusive, non-vesicular. 25% mm-scale phenocrysts. Up to 5% Ol(?), 5% Pyx. Minor jointing.

Thin Section Description

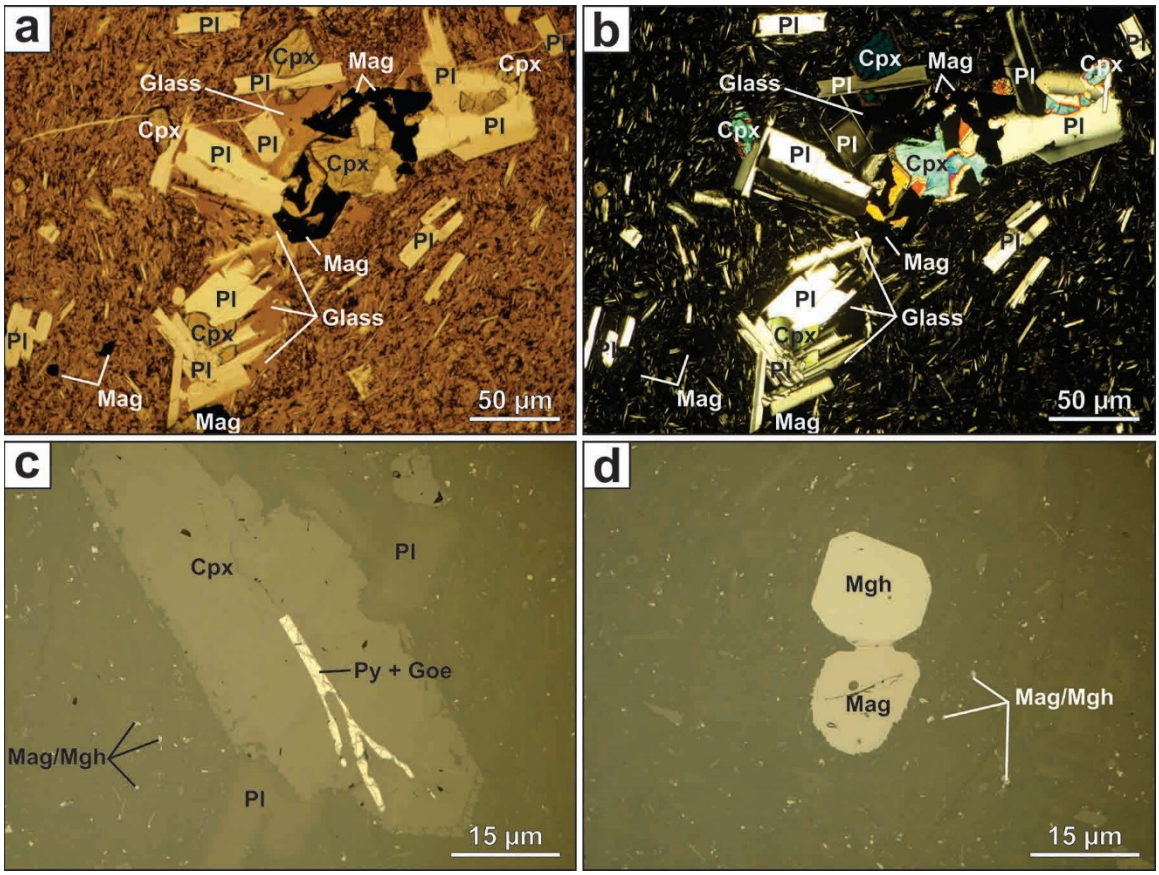


Thin section scan of GMA13-043.

This section is a massive volcanic rock with only ~1% small vesicles, abundant phenocrysts (~25%), and ~74% groundmass.

The phenocryst assemblage includes orthopyroxene, clinopyroxene, and plagioclase (with rare inclusions of pyroxene and magnetite), and magnetite (with rare fine-grained globular pyrite inclusions). There are also minor phenocrysts of maghemite(?). The clinopyroxene also locally contains rare pyrite that is being altered to goethite(?). The phenocrysts are evenly distributed throughout the section, and are locally glomeroporphyritic. The plagioclase phenocrysts display compositional zoning, and have a composition of An_{55} (M.L. method).

The groundmass contains abundant fine-grained plagioclase, disseminated magnetite (and maghemite?), minor pyroxene, and light orange-brown sideromelane glass with few microlites. The plagioclase crystals are locally aligned along a weak flow foliation.



Photomicrographs of GMA13-043: ***(a)*** *transmitted light (PPL) photomicrograph of glomeroporphrytic texture, containing phenocrysts of plagioclase, clinopyroxene, and magnetite, associated with trapped glass, in a fine-grained to glassy (sideromelane) goundmass;* ***(b)*** *transmitted light (XPL) photomicrograph the same view as (a) showing minor flow-foliation of fine-grained plagioclase laths in the glassy groundmass;* ***(c)*** *reflected light (PPL) photomicrograph of pyrite altered to goethite, along the cleavage plane of a clinopyroxene phenocryst;* ***(d)*** *reflected light (PPL) photomicrograph of magnetite and maghemite phenocrysts, with fine-grained disseminated magnetite ± maghemite in the groundmass.*

	Abundance [modal %]		Relative Abundance
Vesicles	**1**		
Immiscible S	**<1**		
Py		<1	Tr
Ccp		-	
Icb(?)		-	
Phenocrysts	**25**		
Pl		10	++
Cpx		6	+
Opx		6	+
Mag		3	+
Mgh		<1	Tr
Groundmass	**74**		
$Glass_{(Sid)}$		37	+++
$Glass_{(Pal)}$			
$Glass_{(Pum)}$			
$Glass_{(Tac)}$			
Pl		33	+++
Cpx		1	+
Opx		1	+
Mag		2	+
Mgh		<1	Tr
Xenoliths	**-**		
Late Sulfides	**-**		
Ccp		-	
Py		-	
Alteration	**<0.1**		
Hem		-	
Goe(?)		<0.1	Tr
FeO_x		-	
MnO_x		-	
$Pal_{(Gel)}$		-	
Clay		-	
Cv		-	

Paragenesis: Pyrite immiscible sulfide droplet → goethite(?) alteration → magnetite phenocrysts → maghemite replacement of magnetite → clinopyroxene phenocrysts → orthopyroxene phenocrysts → plagioclase phenocrysts → massive groundmass (plagioclase + pyroxene + magnetite + maghemite? + sideromelane glass).

Interpretation: Coherent lava flow

Name: Porphyritic dacite flow

SAMPLE: GMA13-044 **PARENT ID:** 712	**LOCATION:** 784243.3E/8649069.3N **WATER DEPTH:** 1167 mbsl

Geochemical Notes

SiO_2 = 66.37%; Dacite (TAS)

Video Description

N/A

Hand Sample Description



Massive very fine grained glassy mafic extrusive with 15-20% mm-scale phenocrysts of feldspar, 5% phenocrysts of Pyx (<1 mm). Cooling fractures. 5-7% elongate vesicles, <1-5 mm long, flow banding.

Hand sample of GMA13-044.

Thin Section Description

This section contains ~15% elongate vesicles aligned along a strong flow foliation, ~10% phenocrysts, and ~75% groundmass.

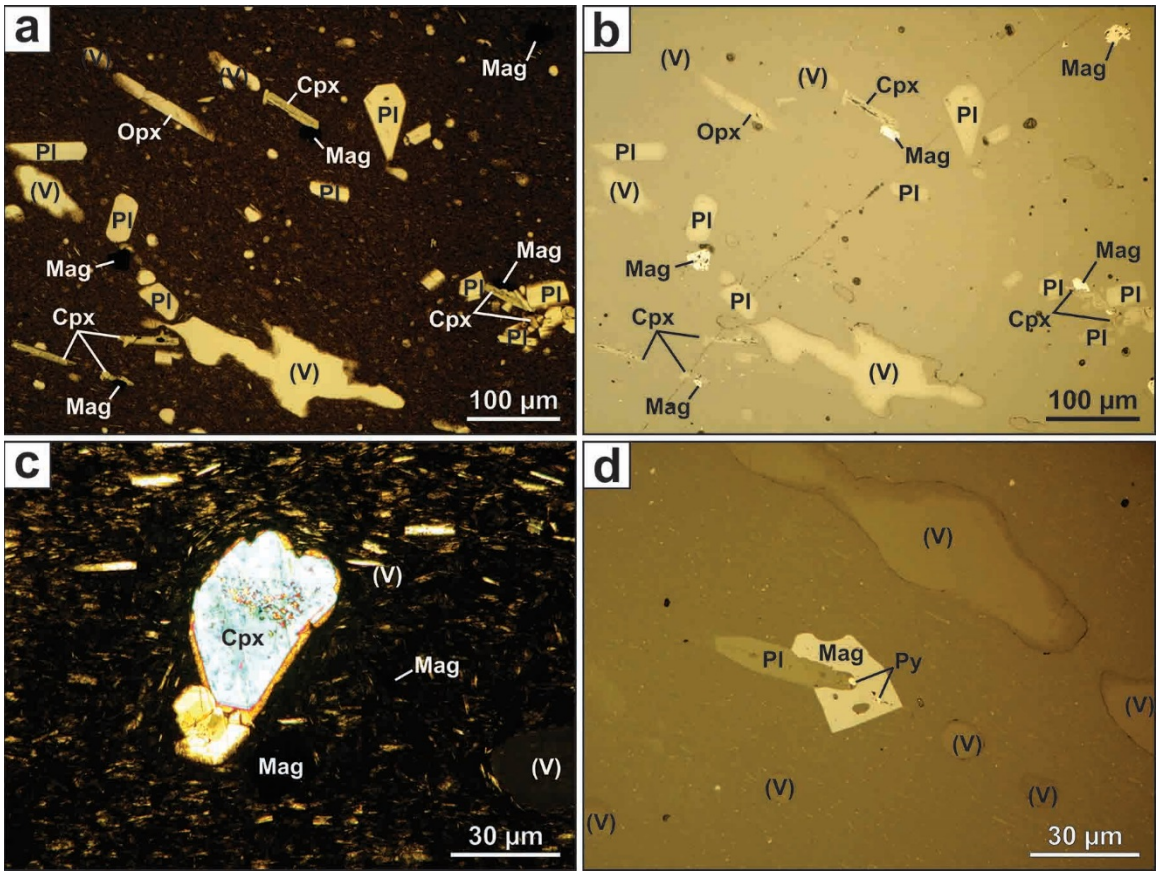
The phenocrysts consist primarily of plagioclase (An_{50}, M.L. method), with long tabular crystals aligned along the flow foliation. It contains minor inclusions of glass and clinopyroxene. There are minor medium-grained orthopyroxene and clinopyroxene phenocrysts. There are also minor medium-grained



Thin section scan of GMA13-044.

magnetite, with rare inclusions of rounded pyrite (immiscible sulfide melt?). There are a few crystals of maghemite(?). Orthopyroxene also contains rare inclusions of pyrite. One medium-grained subhedral grain of pyrite (pseudomorph?) partly being replaced by magnetite(?) is not associated with any other phenocryst. The phenocrysts are locally glomeroporphritic.

The groundmass contains abundant fine- to very fine-grained plagioclase, orange-brown sideromelane(?) glass containing abundant microlites, and very fine-grained magnetite (and possible maghemite?). Fine-grained pyroxene is rare. The color of the groundmass lightens slightly towards the top left of the section, indicating slight palagonitization towards a quenched margin. Locally, pyrite (partly altered to goethite?) lines vesicles.



Photomicrographs of GMA13-044: ***(a)*** *transmitted light (PPL) photomicrograph of irregular vesicles in a glassy sideromelane groundmass, with phenocrysts of clinopyroxene, orthopyroxene, plagioclase, and magnetite;* ***(b)*** *reflected light (PPL) photomicrograph the same view as (a) showing distribution of magnetite;* ***(c)*** *transmitted light (XPL) photomicrograph of clinopyroxene and magnetite phenocrysts, with flow-foliated laths of plagioclase in a glassy groundmass, flowing around the phenocrysts;* ***(d)*** *reflected light (PPL) photomicrograph of magnetite with fine-grained chalcopyrite inclusions. (V) = vesicle.*

	Abundance [modal %]	Relative Abundance
Vesicles	**15**	
Immiscible S	**<1**	
Py	<1	Tr
Ccp	-	
Icb(?)	-	
Phenocrysts	**10**	
Pl	5	+
Cpx	3	+
Opx	2	+
Mag	<1	Tr
Mgh	<0.1	Tr
Groundmass	**75**	
$Glass_{(Sid)}$	16	++
$Glass_{(Pal)}$	3	+
$Glass_{(Pum)}$	-	
$Glass_{(Tac)}$	-	
Pl	50	+++
Cpx	2	+
Opx	2	+
Mag	2	+
Mgh	<1	Tr
Xenoliths	**-**	
Late Sulfides	**<0.1**	
Ccp	-	
Py	<0.1	Tr
Alteration	**<0.1**	
Hem	-	
Goe(?)	<0.1	Tr
FeO_x	-	
MnO_x	-	
$Pal_{(Gel)}$	-	
Clay	-	
Cv	-	

Paragenesis: Pyrite immiscible sulfide droplets → minor alteration to goethite(?) → magnetite phenocrysts → maghemite locally replacing magnetite → clinopyroxene + orthopyroxene phenocrysts → plagioclase phenocrysts → vesicular groundmass (plagioclase + pyroxene + magnetite + maghemite? + sideromelane and palagonite glass) → late pyrite in vesicles → alteration of pyrite to goethite(?).

Interpretation: Flow-foliated massive lava flow

Name: Vesicular porphyritic dacite flow

SAMPLE: GMA13-057 **PARENT ID:** 732	**LOCATION:** 784698.6E/8649739.9N **WATER DEPTH:** 1069 mbsl

Geochemical Notes

SiO_2 = 54.56%; Basaltic-andesite (TAS)

Video Description

Large black piece, looks like basalt. Talus slope, rubble and flat slabby material, to lobate banded style chimney fragments - appears to be loose rubble but everything cemented.

Hand Sample Description



Hand sample of GMA13-057.

Very fine grained glassy vesicular mafic extrusive, dark grey, aphanitic, with 7-10% spheroidal vesicles, sub-mm to 4 mm across, weakly elongate. 5% very fine grained feldspar phenocrysts. 2 mm wide vitric zone. Patchy MnOx with minor FeOx on outer surface.

Thin Section Description



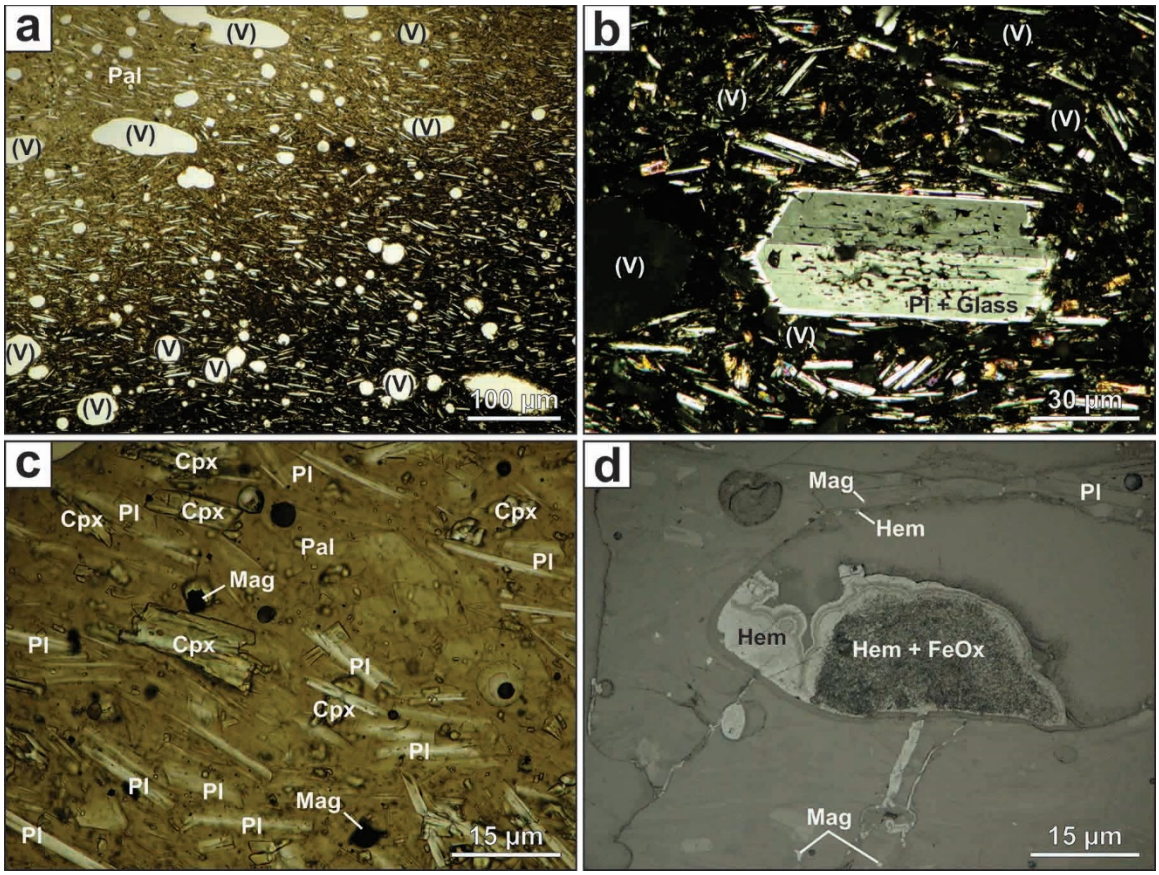
Thin section scan of GMA13-057.

This section contains ~15% rounded to elongate vesicles, aligned along a flow foliation. It contains ~3% phenocrysts and ~82% groundmass.

The phenocrysts are entirely composed of plagioclase crystals (composition not determined) with abundant melt inclusions, and rare thin coronas of additional plagioclase.

Immiscible pyrite droplets are rare, and are altered to goethite(?).

The groundmass consists of fine- to medium-grained plagioclase aligned along the flow foliation, fine- to medium-grained orthopyroxene and clinopyroxene, and minor very fine-grained magnetite. The remainder is dark brown tachylitic glass. In the top right part of the section there is a gradual transition to light brown palagonitized glass with minor microlites. There is an increase in plagioclase abundance here. The vesicles and fractures here are lined with minor fine-grained iron oxides (including hematite) and oxyhydroxides, locally displaying colloform textures. This appears to be a partially altered quench margin.



Photomicrographs of GMA13-057: ***(a)*** *transmitted light (PPL) photomicrograph of transition from dark brown tachylitic glass to light brown palagonitized glassy margin, with rounded to elongate vesicles, and fine-grained plagioclase laths aligned along a flow foliation;* ***(b)*** *transmitted light (XPL) photomicrograph of plagioclase phenocryst with glass inclusions, with a corona of additional plagioclase, and a groundmass of pyroxene and plagioclase laths aligned along a flow foliation;* ***(c)*** *transmitted light (PPL) photomicrograph close-up of the groundmass assemblage of plagioclase, clinopyroxene, and magnetite, with palagonitized glass and few microlites;* ***(d)*** *reflected light (PPL) photomicrograph of late colloform hematite filling in late cracks and pore space. (V) = vesicle.*

	Abundance [modal %]	Relative Abundance
Vesicles	**15**	
Immiscible S	**<0.1**	
Py	<0.1	Tr
Ccp	-	
Icb(?)	-	
Phenocrysts	**3**	
Pl	3	+
Cpx	-	
Opx	-	
Mag	-	
Mgh	-	
Groundmass	**82**	
$Glass_{(Sid)}$	-	
$Glass_{(Pal)}$	5	+
$Glass_{(Pum)}$	-	
$Glass_{(Tac)}$	30	+++
Pl	29	+++
Cpx	12	++
Opx	4	+
Mag	2	+
Mgh	-	
Xenoliths	**-**	
Late Sulfides	**-**	
Ccp	-	
Py	-	
Alteration	**<1**	
Hem	<1	Tr
Goe(?)	<0.1	Tr
FeO_x	<1	Tr
MnO_x	<0.1	Tr
$Pal_{(Gel)}$	-	
Clay	-	
Cv	-	

Paragenesis: Pyrite immiscible sulfide droplet → altered to goethite(?) → plagioclase phenocrysts → vesicular groundmass (plagioclase + pyroxene + magnetite + tachylitic and palagonite glass) → late hematite + manganese oxide + iron oxyhydroxides.

Interpretation: Flow-foliated vesicular andesite, partially altered along a glassy margin

Name: Vesicular basaltic-andesite flow

SAMPLE: GMA13-063 **PARENT ID:** 768	**LOCATION:** 784049.8E/8650965.1N **WATER DEPTH:** 1117 mbsl

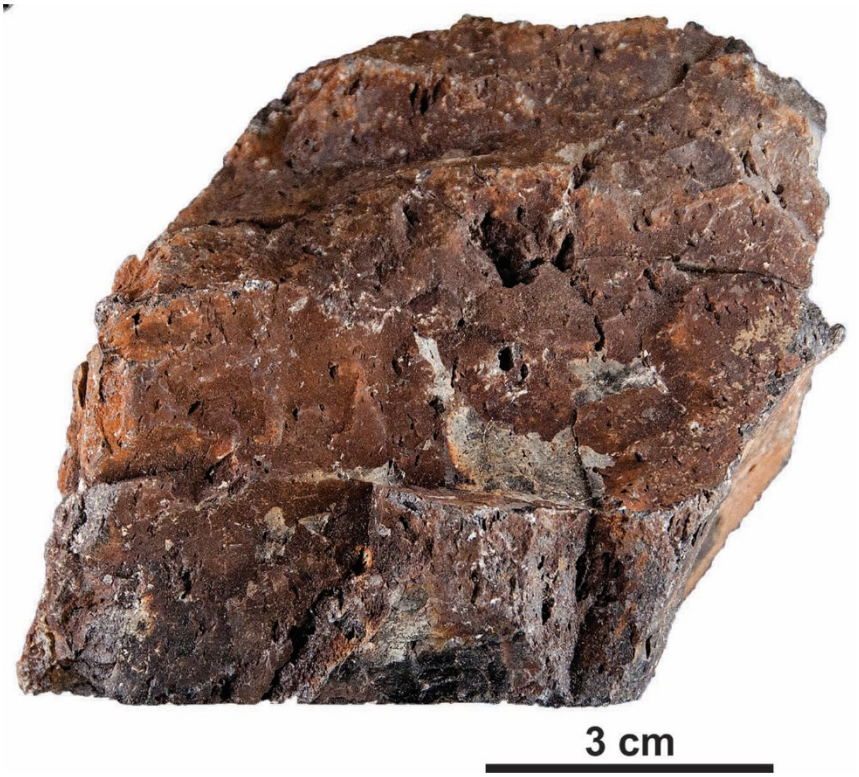
Geochemical Notes

SiO_2 = 67.15%; Dacite (TAS)

Video Description

N/A

Hand Sample Description



Hand sample of GMA13-063.

Very fine grained mafic extrusive (basaltic andesite), dark grey, aphanitic, with 3-5% vesicles, sub-mm to 5 mm in length, small spheroidal and larger irregular. 5% sub-mm feldspar phenocrysts. Glassy margins. Trace Ol(?) phenocrysts, ~1% Pyx phenocrysts. No obvious glass rind, but one outer surface has vitric spicules and is coated with possible siliceous chimney material with scattered sulphides (Py?). Fine grained Py also lines fractures near this surface.

Thin Section Description

This section contains ~5% elongated vesicles with irregular margins, ~30% phenocrysts aligned along a flow foliation, and ~65% fine-grained groundmass.

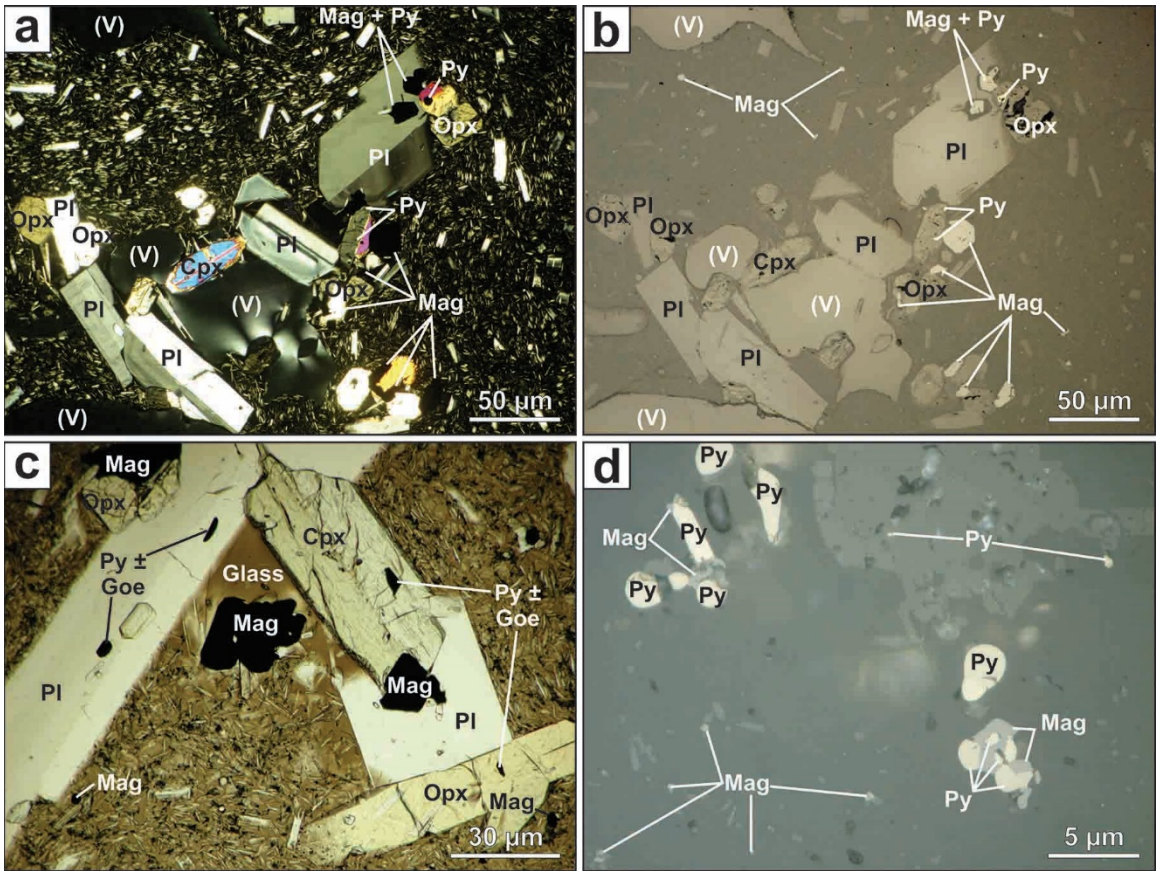
The phenocrysts have a bimodal distribution of sizes, both medium-grained and coarse-grained. They are evenly distributed and locally glomeroporphyritic. The phenocrysts include plagioclase with a composition of An_{65} (M.L. method), with frequent compositional zonation and local melt inclusions.



There is also minor orthopyroxene and clinopyroxene. There is also abundant cubic magnetite, with a few inclusions of globular pyrite (immiscible sulfide melt?). Fine-grained pyrite is also locally included in plagioclase and pyroxene, locally altered to iron oxide. There are minor maghemite(?) phenocrysts.

The groundmass consists primarily of fine-grained plagioclase, weakly aligned along a flow foliation, with minor fine-grained orthopyroxene, and evenly disseminated very fine-grained magnetite. There is abundant light brown volcanic glass (sideromelane) with rare microlites. Minor very fine-grained iron oxyhydroxides line a few vesicles.

Thin section scan of GMA13-063.



Photomicrographs of GMA13-063: ***(a)*** *transmitted light (XPL) photomicrograph of glomeroporphyritic phenocryst assemblage, including plagioclase, clinopyroxene, orthopyroxene, and magnetite, with a fine-grained glassy (sideromelane) groundmass;* ***(b)*** *reflected light (PPL) photomicrograph of the same view as (a) showing distribution of magnetite, with minor inclusions of pyrite;* ***(c)*** *transmitted light (PPL) photomicrograph of plagioclase and pyroxene phenocrysts, with inclusions of pyrite (locally altered to goethite), and magnetite, with trapped crystal-free sideromelane glass;* ***(d)*** *reflected light (PPL) photomicrograph of magnetite and rounded pyrite. (V) = vesicle.*

	Abundance [modal %]		Relative Abundance
Vesicles	**5**		
Immiscible S	**1**		
Py		1	+
Phenocrysts	**29**		
Pl		20	++
Cpx		3	+
Opx		4	+
Mag		2	+
Mgh		<1	Tr
Groundmass	**65**		
$Glass_{(Sid)}$		20	+++
$Glass_{(Pal)}$		-	
$Glass_{(Pum)}$		-	
$Glass_{(Tac)}$		-	
Pl		40	+++
Cpx		-	
Opx		4	+
Mag		1	+
Mgh		-	
Xenoliths	**-**		
Late Sulfides	**-**		
Ccp		-	
Py		-	
Alteration	**<1**		
Hem		-	
Goe(?)		-	
FeO_x		<1	Tr
MnO_x		-	
$Pal_{(Gel)}$		-	
Clay		-	
Cv		-	

Paragenesis: Pyrite immiscible sulfide droplets → magnetite phenocrysts → orthopyroxene phenocrysts → clinopyroxene phenocrysts → plagioclase phenocrysts → vesicular groundmass (plagioclase + orthopyroxene + magnetite + sideromelane glass) → local iron oxides/oxyhydroxides lining vesicles.

Interpretation: Moderately flow-foliated lava flow, with two stages of phenocryst formation

Name: Vesicular porphyritic dacite flow

SAMPLE: GMA13-065 **PARENT ID:** 097	**LOCATION:** 781742.7E/8650441.4N *(Big Starfish)* **WATER DEPTH:** 449 mbsl

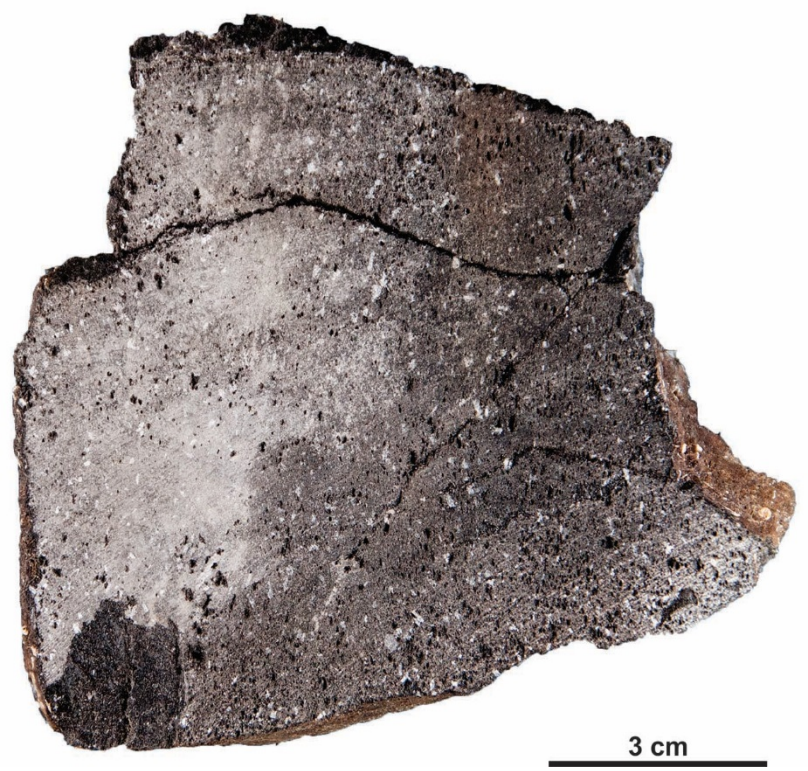
Geochemical Notes

SiO_2 = 66.92%; Dacite (TAS)

Video Description

N/A

Hand Sample Description

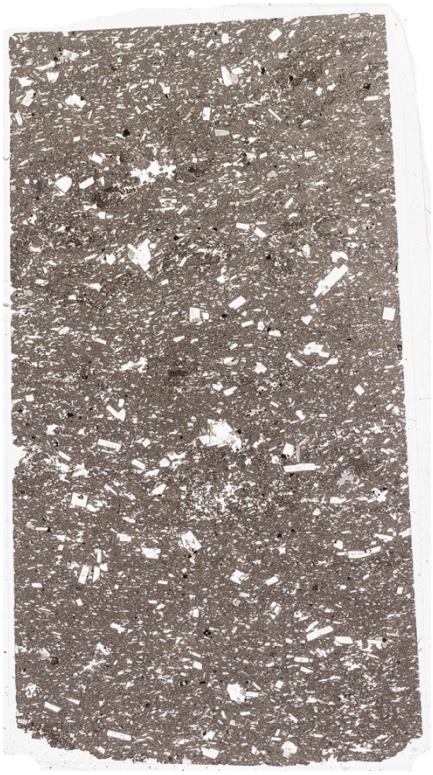


Vesicular very fine grained mafic extrusive rock (feldspar-phyric dacite) with 10% small irregular vesicules, 10% sub-mm scale feldspar phenocrysts, aphanitic groundmass. Few cooling fractures. Glassy exterior.

Hand sample of GMA13-065.

Thin Section Description

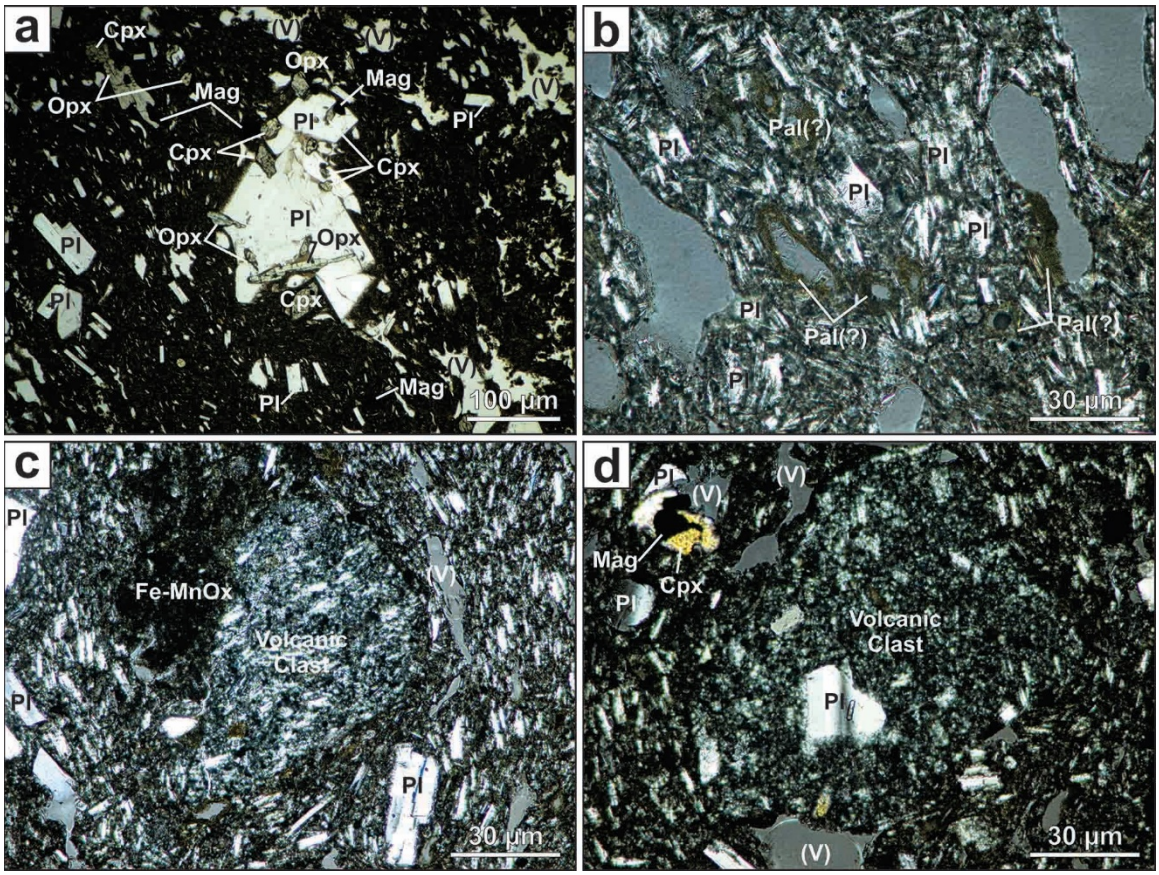
This section contains ~30% irregular elongate vesicles, ~15% phenocrysts, and ~51% groundmass. The phenocrysts primarily consist of plagioclase, with lesser amounts of orthopyroxene and magnetite, with minor clinopyroxene. The magnetite contains a few inclusions of rounded pyrite (immiscible sulfide?), and is locally replaced by maghemite(?). The plagioclase phenocrysts have a composition of An_{60} (M.L. method). The phenocrysts are aligned along a flow-foliation. They are mostly evenly distributed, but locally are glomeroporphyritic.



The groundmass is also aligned along a strong flow foliation. It contains fine-grained plagioclase, magnetite (+maghemite?), and lesser amounts of orthopyroxene and clinopyroxene, and abundant brown glass (sideromelane). The groundmass has heterogeneous color, either from increased oxide content or melted clasts. The glass is partially altered to clays. A few angular to subrounded clasts (xenoliths) are characterized by a different color (tachylite?), increased magnetite, and plagioclase crystals that do not align with the flow foliation. There are ~2% xenoliths overall. The groundmass shows a flow-foliation directed around these xenoliths.

Patchy iron oxyhydroxides form in many of the vesicles, and are associated with the xenoliths. A few vesicles are lined with gel-palagonite(?). Minor fine-grained chalcopyrite also forms in a few of the vesicles.

Thin section scan of GMA13-065.



Photomicrographs of GMA13-065: ***(a)*** *transmitted light (PPL) photomicrograph of glomeroporphyritic phenocryst assemblage, including plagioclase, clinopyroxene, orthopyroxene, and magnetite, with a fine-grained glassy (sideromelane) groundmass;* ***(b)*** *transmitted light (XPL) photomicrograph of the plagioclase-rich groundmass assemblage, with elongate vesicles and gel-palagonite(?) in some vesicles;* ***(c)*** *transmitted light (XPL) photomicrograph of a volcanic clast (xenolith) associated with iron-manganese oxides;* ***(d)*** *reflected light (XPL) photomicrograph of clay-altered volcanic clast, with plagioclase crystals in the host groundmass flowing around it. (V) = vesicle.*

	Abundance [modal %]	Relative Abundance
Vesicles	**30**	
Immiscible S	**<1**	
Py	<1	Tr
Ccp	-	
Icb(?)	-	
Phenocrysts	**15**	
Pl	10	++
Cpx	1	+
Opx	3	+
Mag	1	+
Mgh	<1	Tr
Groundmass	**48**	
$Glass_{(Sid)}$	27	+++
$Glass_{(Pal)}$	-	
$Glass_{(Pum)}$	-	
$Glass_{(Tac)}$	-	
Pl	20	++
Cpx	<1	Tr
Opx	1	+
Mag	<1	Tr
Mgh	-	
Xenoliths	**2**	
Late Sulfides	**<0.1**	
Ccp	<0.1	Tr
Py	-	
Alteration	**3**	
Hem	-	
Goe(?)	-	
FeO_x	2	+
MnO_x	<1	Tr
$Pal_{(Gel)}$	<1	Tr
Clay	3	+
Cv	-	

Paragenesis: Pyrite immiscible sulfide droplets → magnetite phenocrysts → maghemite replacing magnetite → orthopyroxene phenocrysts → clinopyroxene phenocrysts → plagioclase phenocrysts → vesicular groundmass (plagioclase + pyroxene + magnetite + sideromelane glass) + altered xenoliths → vesicle-lining chalcopyrite → clay alteration of glass + gel-palagonite(?) lining some vesicles + manganese and iron oxyhydroxides.

Interpretation: Coherent lava flow with entrained xenoliths (clasts) of another flow, subtly altered

Name: Subtly-altered vesicular porphyritic dacite flow with xenoliths

SAMPLE: P0015 **PARENT ID:** 821	**LOCATION:** 784877.4E/8649270.0N **WATER DEPTH:** -1163.09 mbsl

Geochemical Notes

SiO_2 = 53.53%; Basaltic-andesite (TAS)

Hand Sample Description

N/A

Thin Section Description



Thin section scan of P0015.

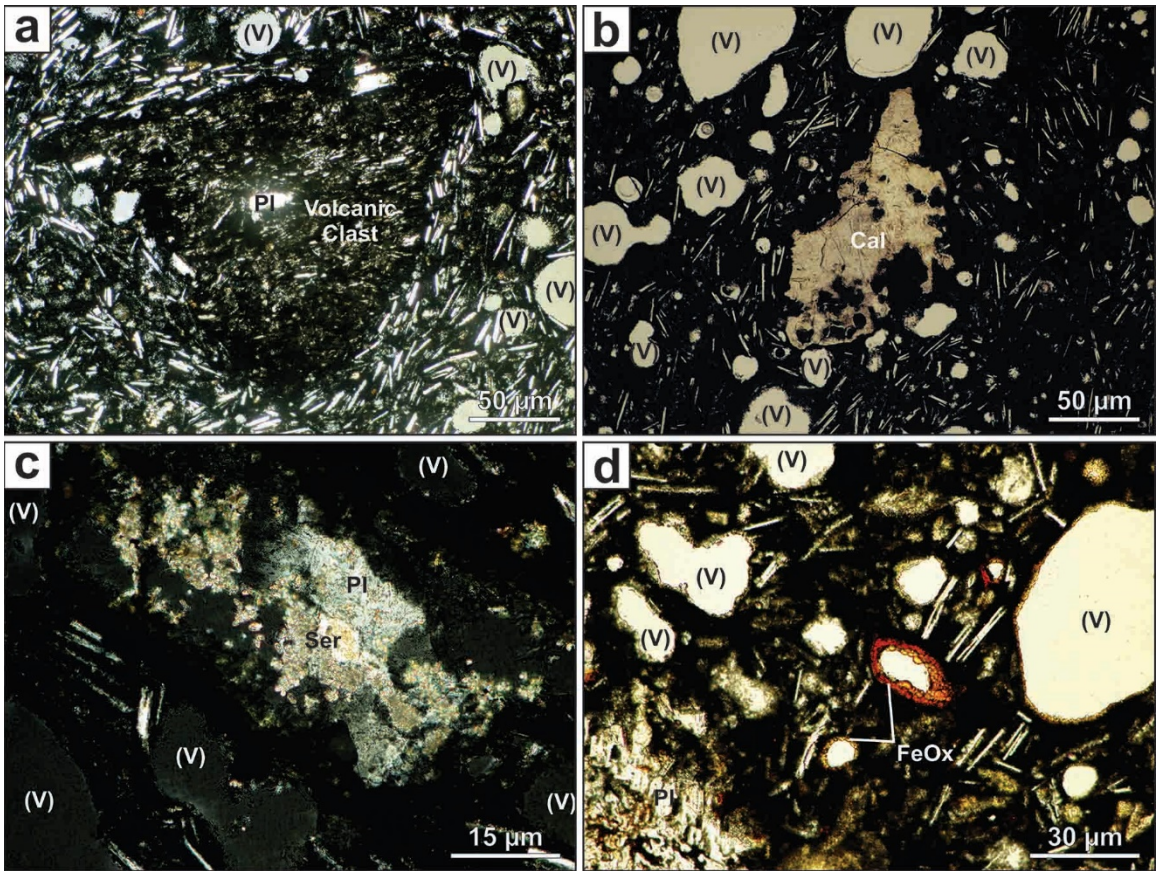
This section contains abundant rounded vesicles, ~30% overall. There are ~2% phenocrysts, ~2% xenoliths, and ~64% groundmass. The phenocrysts consist of plagioclase with minor clinopyroxene and orthopyroxene. The phenocrysts have abundant sieve texture and/or melt inclusions. One plagioclase phenocryst has been partially altered to sericite, associated with increased porosity. Unlike the previous samples described, there are no magnetite phenocrysts. There are also no convincing immiscible sulfide droplets.

The groundmass consists of abundant dark brown (tachylitic) glass, fine- to medium-grained plagioclase, fine-grained orthopyroxene and clinopyroxene, and only minor very fine-grained magnetite. The groundmass shows a strong flow foliation with aligned plagioclase laths. This flow foliation trends around the xenoliths.

The color of the groundmass is heterogeneous, with some very dark areas with irregular margins, which may be melted xenoliths. One obvious sub-rounded xenolith is present in this section, ~2 mm wide. The flow foliation of the host groundmass flows around this xenolith.

The xenolith is dark brown, with plagioclase crystals and moderate clay alteration.

Very fine-grained chalcopyrite forms in many of the vesicles. The vesicles are also locally lined by hematite or iron oxyhydroxides, and rare gel-palagonite(?).



Photomicrographs of P0015: ***(a)*** *transmitted light (XPL) photomicrograph of a volcanic clast (xenolith), with plagioclase crystals in the host groundmass flowing around it;* ***(b)*** *transmitted light (PPL) photomicrograph of a calcite-altered volcanic clast (xenolith);* ***(c)*** *transmitted light (XPL) photomicrograph of a plagioclase phenocryst mostly altered to sericite;* ***(d)*** *transmitted light (PPL) photomicrograph of late iron oxyhydroxides in some vesicles. (V) = vesicle.*

	Abundance [modal %]	Relative Abundance
Vesicles	**30**	
Immiscible S	**-**	
Py	-	
Ccp	-	
Icb(?)	-	
Phenocrysts	**2**	
Pl	1	+
Cpx	<1	Tr
Opx	<1	Tr
Mag	-	
Mgh	-	
Groundmass	**53**	
$Glass_{(Sid)}$	-	
$Glass_{(Pal)}$	-	
$Glass_{(Pum)}$	-	
$Glass_{(Tac)}$	40	+++
Pl	38	+++
Cpx	7	+
Opx	3	+
Mag	1	+
Mgh	-	
Xenoliths	**2**	
Late Sulfides	**1**	
Ccp	1	+
Py	<0.1	Tr
Alteration	**12**	
Hem	<1	Tr
Goe(?)	<0.1	Tr
FeO_x	<1	Tr
MnO_x	-	
$Pal_{(Gel)}$	1	
Clay	10	
Ser	<0.1	Tr
Cal	1	+
Cv	<0.1	Tr

Paragenesis: Clinopyroxene + orthopyroxene phenocrysts → plagioclase phenocrysts → vesicular groundmass (plagioclase + pyroxene + magnetite + tachylitic glass) + xenoliths → chalcopyrite + pyrite lining vesicles → covellite alteration of chalcopyrite + goethite(?) alteration of pyrite → local sericite alteration of plagioclase → hematite + other iron oxyhydroxides lining vesicles

Interpretation: Weakly-altered coherent volcanic flow with entrained clasts/xenoliths.

Name: Weakly-altered vesicular basaltic-andesite flow with xenoliths

SAMPLE: P0016 **PARENT ID:** 828	**LOCATION:** 784891.9E/8649249.0N **WATER DEPTH:** 1175.25 mbsl

Geochemical Notes

SiO_2 = 53.22%; Basaltic-andesite (TAS)

Hand Sample Description

N/A

Thin Section Description



Thin section scan of P0016.

This section is very vesicular, with ~35% rounded to elongate vesicles, 3% phenocrysts, 2% xenoliths, and ~58% groundmass, which has been pervasively altered.

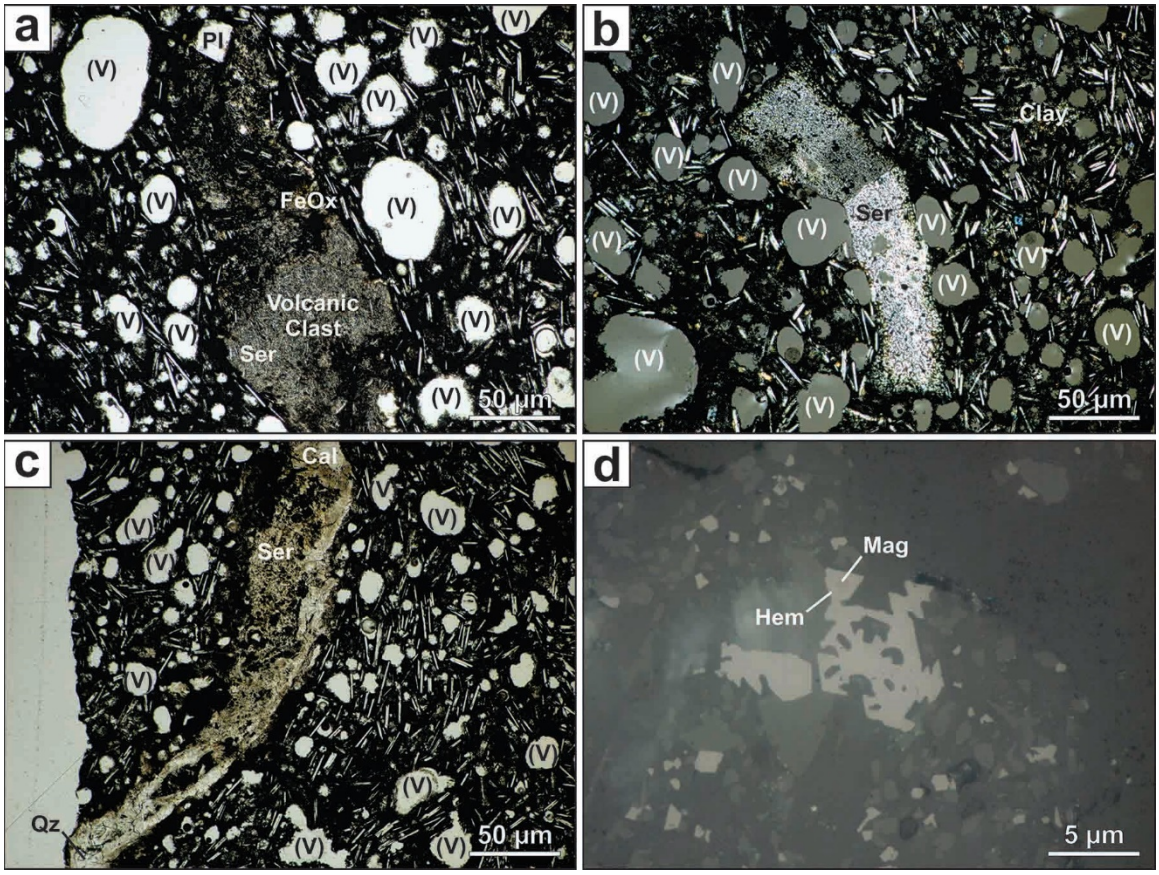
The phenocrysts are glomeroporphyritic, and include plagioclase, and clinopyroxene. A few of the larger plagioclase phenocrysts are almost completely altered to clay (sericite), or have coronas of clay alteration. A few plagioclase crystals display sieve texture. There are only a few clinopyroxene phenocrysts, all unaltered. There are no magnetite phenocrysts, but what appear to be rutile pseudomorphs of magnetite in one area.

The groundmass is composed of fine- to medium-grained plagioclase crystals, moderately aligned along a flow foliation, which changes direction frequently, as well as fine-grained clinopyroxene + orthopyroxene. Abundant fine- to very fine-grained magnetite (or maghemite?) is scattered throughout the groundmass, locally displaying snowflake texture. Very fine-grained rounded inclusions of pyrite within the magnetite suggest an immiscible sulfide precursor. In other areas where pyrite occurs, it is partially to almost completely altered to goethite(?). The remaining tachylitic glass has been pervasively altered to very fine-grained clay minerals.

The entrained xenoliths have irregular sub-rounded margins, and are intensely and pervasively altered to clay minerals (including sericite), calcite(?), and iron oxides.

Late fine-grained chalcopyrite forms in some vesicles. Gel-palagonite(?) also lines a few of the vesicles, along with reddish-orange iron oxyhydroxides that occur locally in some vesicles. A large crack or vesicle at the top of the section appears to have been filled in by carbonate (calcite or siderite?), clays, and

recrystallized quartz(?). There are iron oxides (including hematite and goethite) and oxyhydroxides along the margin of this crack.



Photomicrographs of P0016: ***(a)*** *transmitted light (PPL) photomicrograph of a pervasively altered (sericite and iron oxide) volcanic clast (xenolith), with plagioclase crystals in the host groundmass showing flow foliation;* ***(b)*** *transmitted light (XPL) photomicrograph of sericite-altered plagioclase phenocryst (relict);* ***(c)*** *transmitted light (PPL) photomicrograph of crack filled in with calcite, recrystallized quartz, and sericite;* ***(d)*** *reflected light (PPL) photomicrograph of snowflake-textured magnetite crystal mostly altered to hematite. (V) = vesicle.*

	Abundance [modal %]	Relative Abundance
Vesicles	**35**	
Immiscible S	**<0.1**	
Py	<0.1	Tr
Ccp	-	
Icb(?)	-	
Phenocrysts	**3**	
Pl	3	+
Cpx	<1	Tr
Opx	-	
Mag	-	
Mgh	-	
Groundmass	**28**	
$Glass_{(Sid)}$	-	
$Glass_{(Pal)}$	-	
$Glass_{(Pum)}$	-	
$Glass_{(Tac)}$	12	++
Pl	10	++
Cpx	5	+
Opx	1	+
Mag(?)	10	++
Mgh	-	
Xenoliths	**2**	
Late Sulfides	**<1**	
Ccp	<0.1	Tr
Py	<1	Tr
Alteration	**32**	
Hem	5	+
Goe(?)	<1	Tr
FeO_x	1	+
MnO_x	-	
Pal_{Gel}	<1	Tr
Cal	2	+
Qz(?)	1	+
Ser	2	+
Clay	10	++
Rt	1	+
Cv	-	

Paragenesis: Pyrite immiscible sulfide droplets → magnetite phenocrysts (relict) → clinopyroxene phenocrysts → plagioclase phenocrysts → vesicular groundmass (plagioclase + pyroxene + magnetite + tachylitic glass) + altered xenoliths → chalcopyrite crystallization in vesicles → alteration: magnetite phenocrysts altered to rutile, glassy groundmass partially altered to clay and iron oxides/hydroxyoxides, plagioclase phenocrysts altered to sericite, pyrite altered to goethite(?) → gel-palagonite(?) + iron oxides and hydroxyoxides lining vesicles, calcite + clay + recrystallized quartz(?) filling fracture.

Interpretation: Moderately altered volcanic flow with entrained intensely-altered xenoliths picked up during flow.

Name: Moderately-altered vesicular basaltic-andesite flow with xenoliths

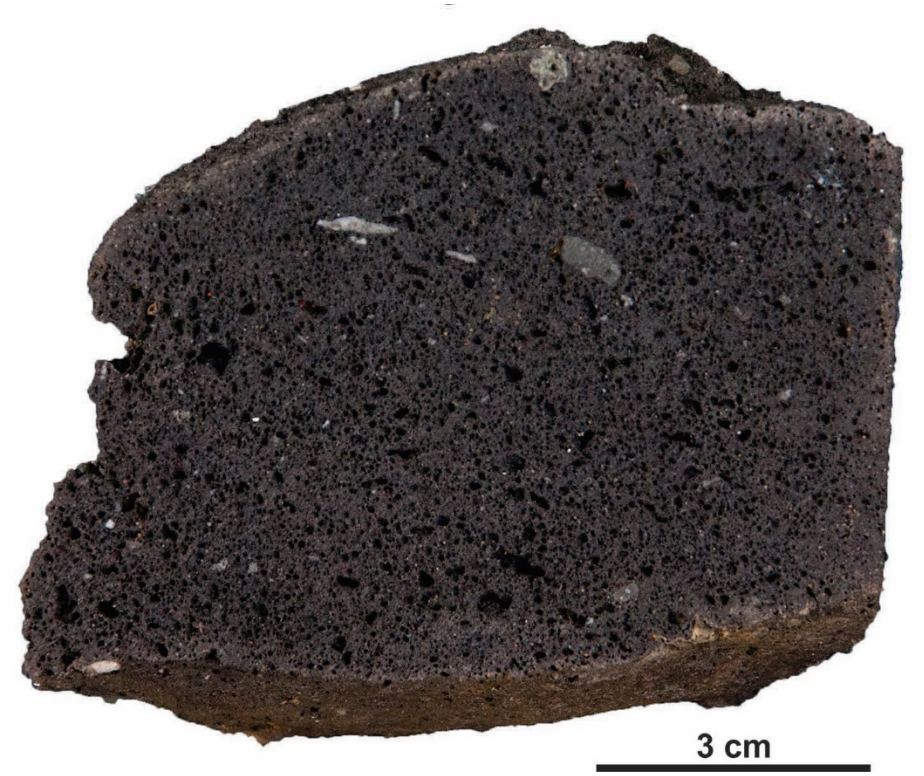
DRILLCORE SAMPLES

SAMPLE: P0040 **PARENT ID:** 2209 **SAMPLE DEPTH:** 4.41-4.45 mbsf	**DRILLHOLE:** TKAD021 **DRILLHOLE LOCATION:** 784816.78E/8649280.51N **WATER DEPTH:** 1131.64 mbsl

Geochemical Notes

SiO_2 = 55.40%; Basaltic-andesite (TAS)

Hand Sample Description



Hand sample of P0040.

Micro-vesicular feldspar-phyric volcanic flow. Elongate vesicles and aligned phenocrysts suggest a weak flow texture. A few subangular phenocrysts a few mm across are visible, and appear lighter grey in color.

Thin Section Description

This section contains ~35% rounded to elongate, irregular vesicles, ~3% phenocrysts, ~5% xenoliths, and ~56% glassy groundmass that has been partially altered.



Thin section scan of P0040.

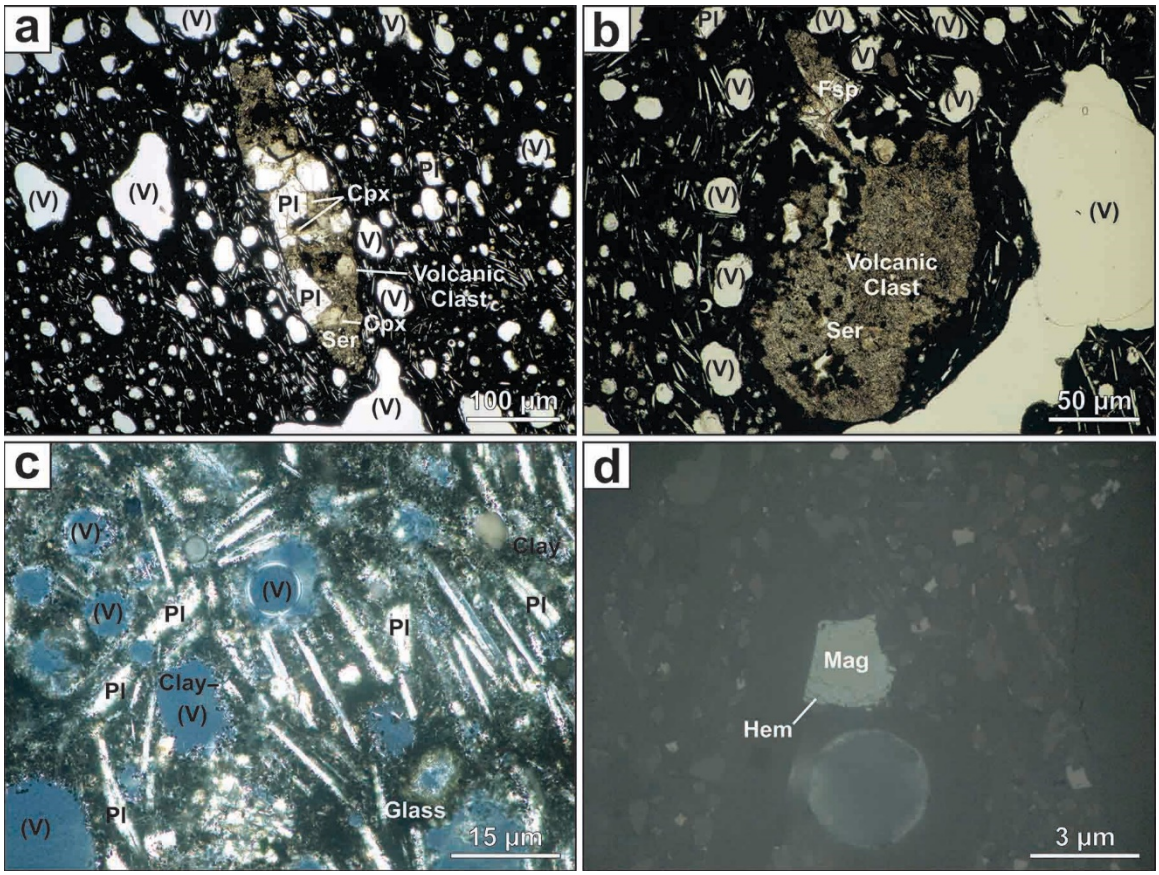
The vesicles are elongate along the direction of flow, which is followed by the alignment of plagioclase crystals.

The phenocrysts are dominated by plagioclase, magnetite, orthopyroxene, and clinopyroxene. They are locally glomeroporphyritic. Locally, the magnetite phenocrysts have been completely pseudomorphed by porous hematite. A few very-coarse grained plagioclase phenocrysts have been completely removed or altered to fine-grained clays. No immiscible sulfide droplets were observed.

The groundmass is composed of fine- to medium-grained plagioclase, and minor fine-grained clinopyroxene, orthopyroxene, and magnetite, which locally displays snowflake texture. Some of the magnetite has been partially to completely altered to hematite. The remaining groundmass is composed of dark brown glass (tachylite), which has been partially altered to fine-grained clay minerals (incipient alteration)

Entrained xenoliths have irregular subrounded margins, and are intensely pervasively altered to iron oxides, carbonate, rutile, and very-fine grained clays. These clasts appear to be aligned along one horizon, possibly related to flow dynamics.

Rare fine-grained chalcopyrite and pyrite (+ galena?) form in some of the vesicles. Rarely, vesicles are lined by irregular gel-palagonite(?), or iron oxyhydroxides.



Photomicrographs of P0040: ***(a)*** *transmitted light (PPL) photomicrograph of a partially altered volcanic clast (xenolith), with plagioclase crystals in the host groundmass showing flow foliation;* ***(b)*** *transmitted light (PPL) photomicrograph of pervasively sericite-altered xenolith;* ***(c)*** *transmitted light (XPL) photomicrograph of the plagioclase-rich groundmass assemblage, with partial clay alteration of glass;* ***(d)*** *reflected light (PPL) photomicrograph of a magnetite crystal mostly partially altered to hematite. (V) = vesicle.*

	Abundance [modal %]	Relative Abundance
Vesicles	**35**	
Immiscible S	**-**	
Py	-	
Ccp	-	
Icb(?)	-	
Phenocrysts	**3**	
Pl	2	+
Cpx	1	+
Opx	<1	Tr
Mag	<1	Tr
Mgh	-	
Groundmass	**43**	
$Glass_{(Sid)}$	-	
$Glass_{(Pal)}$	-	
$Glass_{(Pum)}$	-	
$Glass_{(Tac)}$	15	++
Pl	20	++
Cpx	1	+
Opx	2	+
Mag	5	+
Mgh	-	
Xenoliths	**5**	
Late Sulfides	**<0.1**	
Ccp	<0.1	Tr
Py	<0.1	Tr
Gn	<0.1	Tr
Alteration	**14**	
Hem	3	+
Goe(?)	-	
FeO_x	<1	Tr
MnO_x	-	
$Pal_{(Gel)}$	<1	Tr
Clay	10	++
Rt	1	+
Cv	-	

Paragenesis: Magnetite phenocrysts → plagioclase phenocrysts → orthopyroxene + clinopyroxene phenocrysts → vesicular groundmass (plagioclase + pyroxene + magnetite + tachylitic glass) + altered xenoliths → sulfide precipitation in vesicles (chalcopyrite + pyrite + galena?) → hematite alteration of magnetite + rutile pseudomorph of magnetite + clay alteration of glassy groundmass → gel-palagonite(?) + iron oxyhydroxides lining vesicles.

Interpretation: Weakly altered volcanic flow with entrained intensely-altered xenoliths picked up during flow.

Name: Weakly-altered vesicular basaltic-andesite flow with xenoliths

SAMPLE: MA13-007 **PARENT ID:** 2439 **SAMPLE DEPTH:** 2.00-2.10 mbsf	**DRILLHOLE:** TKAD019 **DRILLHOLE LOCATION:** 784760.22E/8649562.25N **WATER DEPTH:** 1109.44 mbsl

Hand Sample Description



Hand sample of MA13-007.

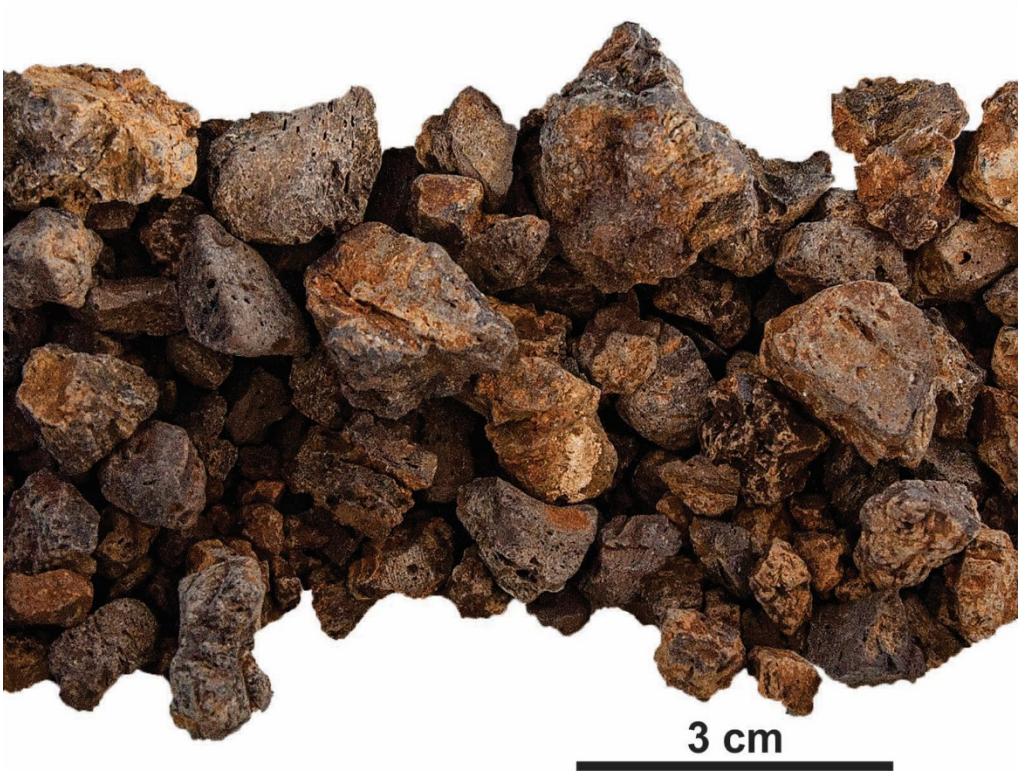
Moderately oxidized orange-brown volcaniclastic sand, with subtle clay alteration. Contains fresh to slightly oxidized volcanics (vesicular, aphyric, aphanitic, black). Sample contains both sand and volcanic fragments.

Interpretation: Hyaloclastic volcanic flow

Name: Sand- to pebble-sized vesicular oxidized intermediate(?) volcanic talus

SAMPLE: MA13-008 **PARENT ID:** 2442 **SAMPLE DEPTH:** 4.70-4.80 mbsf	**DRILLHOLE:** TKAD019 **DRILLHOLE LOCATION:** 784760.22E/8649562.25N **WATER DEPTH:** 1109.44 mbsl

Hand Sample Description



Hand sample of MA13-008.

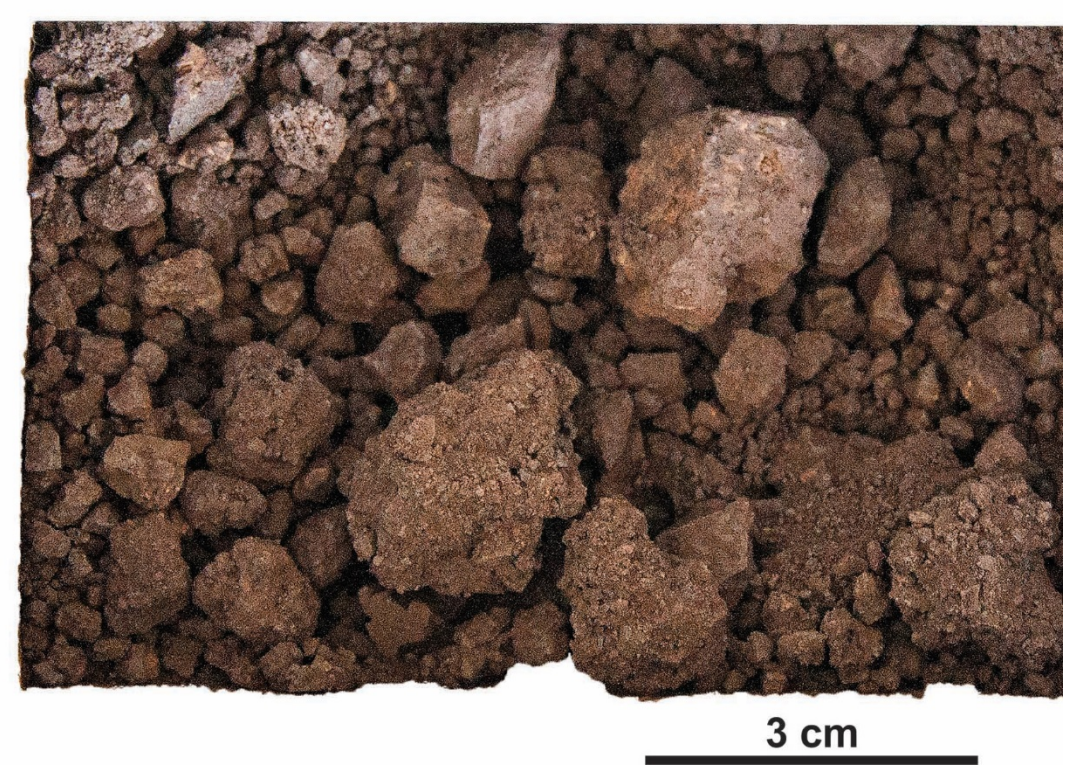
Blocks of vesicular mafic extrusive, black, 5-15% vesicles ranging in size from 1 mm to 5 mm, some are elongate. Minor oxidation. Blocks are angular to sub-rounded. Eruptive event entrained older lava flow?

Interpretation: Eruptive event entrained older lava flow, or hyaloclastite

Name: Pebble-sized vesicular slightly oxidized intermediate(?) volcanic talus

SAMPLE: MA13-009 **PARENT ID:** 2443 **SAMPLE DEPTH:** 6.00-6.10 mbsf	**DRILLHOLE:** TKAD019 **DRILLHOLE LOCATION:** 784760.22E/8649562.25N **WATER DEPTH:** 1109.44 mbsl

Hand Sample Description



Hand sample of MA13-009.

Black volcaniclastic sand with chunks of unaltered vesicular volcaniclastic extrusive. Vesicles are rounded, ~10%. Sample contains both sand and rock.

Interpretation: Hyaloclastic volcanic extrusive, separate eruptive event from above?

Name: Sand- to pebble-sized vesicular mafic intermediate(?) talus

Appendix E

Petrographic Reports – Sulfide-Sulfates

List of Samples

ROV GRAB SAMPLES 472

SAMPLE: GMA13-002 472

SAMPLE: GMA13-003a,b 475

SAMPLE: GMA13-004a,b 479

SAMPLE: GMA13-005 484

SAMPLE: GMA13-006 487

SAMPLE: GMA13-007 490

SAMPLE: GMA13-008 493

SAMPLE: GMA13-009a,b 496

SAMPLE: GMA13-010 501

SAMPLE: GMA13-012 503

SAMPLE: GMA13-017a,b 506

SAMPLE: GMA13-018a,b 511

SAMPLE: GMA13-019a,b 516

SAMPLE: GMA13-020 521

SAMPLE: GMA13-021 524

SAMPLE: GMA13-022 527

SAMPLE: GMA13-024 530

SAMPLE: GMA13-027 533

SAMPLE: GMA13-028 536

SAMPLE: GMA13-029 539

SAMPLE: GMA13-030a,b 542

SAMPLE: GMA13-031 547

SAMPLE: GMA13-032 550

SAMPLE: GMA13-033 553
SAMPLE: GMA13-034 554
SAMPLE: GMA13-038 557
SAMPLE: GMA13-040 560
SAMPLE: GMA13-041 563
SAMPLE: GMA13-042 566
SAMPLE: GMA13-045 569
SAMPLE: GMA13-046 572
SAMPLE: GMA13-048 575
SAMPLE: GMA13-049 578
SAMPLE: GMA13-050 581
SAMPLE: GMA13-051 584
SAMPLE: GMA13-052 587
SAMPLE: GMA13-053a,b 590
SAMPLE: GMA13-058 596
SAMPLE: GMA13-060 599
SAMPLE: GMA13-061 602
SAMPLE: GMA13-062 606

DRILLCORE SAMPLES 609

SAMPLE: MA13-003 609
SAMPLE: MA13-010 610
SAMPLE: MA13-011 611
SAMPLE: MA13-012 612
SAMPLE: MA13-013 613
SAMPLE: MA13-028 614
SAMPLE: MA13-029 615
SAMPLE: MA13-030 616
SAMPLE: MA13-031 617
SAMPLE: MA13-032 618
SAMPLE: MA13-033 619
SAMPLE: MA13-041 620
SAMPLE: MA13-043 621

SAMPLE: MA13-046 622
SAMPLE: MA13-048 623
SAMPLE: MA13-065 624
SAMPLE: MA13-066 625
SAMPLE: MA13-098 626
SAMPLE: P0010 627
SAMPLE: P0011 628
SAMPLE: P0042 629
SAMPLE: P0043 630

Notes:

Mineral abbreviations after Whitney and Evans (2010). Detailed whole rock geochemistry (this study) is reported in Appendix I.

+++ = abundant (>25%) ++ = major (10-25%); + = minor (1-9%); Tr = trace (<1%); - = none

**For samples not analyzed for whole rock geochemistry (this study), additional geochemistry on parent samples is provided by Neptune Minerals (including handheld XRF measurements of grab samples and limited whole-rock geochemistry of drillcore). This is used to guide petrographic interpretations and is not reported elsewhere.*

ROV GRAB SAMPLES

SAMPLE: GMA13-002 **PARENT ID:** 754	**LOCATION:** 784711.7E/8649565.6N **WATER DEPTH:** 1109 mbsl

Geochemical Notes

Whole rock: High Zn (228000 ppm), Cd (729 ppm), Ba (145000 ppm), Sr (3190 ppm); Low Fe, Cu.

Video Description

Sulphide piece from large blocks of sulphide talus and fallen chimney spires with irregular knobbly surfaces.

Hand Sample Description



Hand sample of GMA13-002.

Massive sphalerite-barite chimney with complex colloform banding and abundant pore space, including mm-size vugs and larger vugs up to 1.5 m wide, 25% pore space overall. The sample contains interstitial and vug-filling coarse-grained bladed barite (30%), and high-Fe (25%) and low-Fe (20%) sphalerite, coarse grained, with dendritic textures. Pyrite-marcasite (1%) and chalcopyrite (1%) aggregates on outer margin of the sample. The outer surface contains a cm-thick coating of clay (1%), iron oxide (3%), manganese oxide (<1%), and trace atacamite. Trace red vitreous mineral, likely iron oxides, in one vug.

Thin Section Description

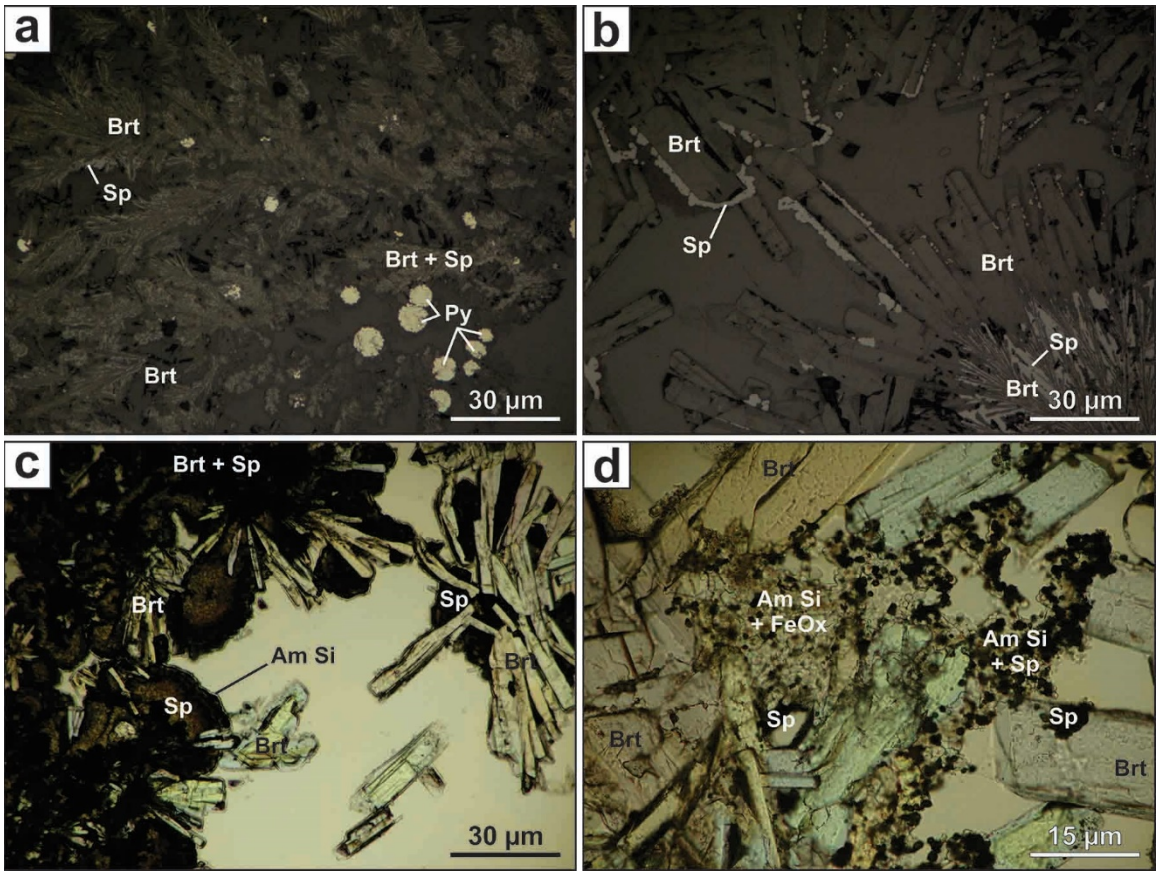


Thin section scan of GMA13-002.

Sample GMA13-002 has a very high porosity, with ~40-50% open space. The bottom quarter of the section is dominated by fine-grained needle-like dendritic barite, growing generally towards the top of the section, overgrown by moderate- to low-Fe sphalerite, with decreasing Fe content outwards. This is associated with local reddish hematite alteration. This is followed by the crystallization of minor spherulitic pyrite up to 0.75 mm in diameter, evenly distributed in this part of the section. A few of these pyrite crystals exhibit a subhedral cubic shape rather than the more-common rounded spherulitic shape. A second generation of coarse-grained tabular barite occurs in the open pore spaces. A thin coat of amorphous silica coats every phase.

Moving towards the top of the thin section, large areas of open space reflecting former vent conduits. These conduits are locally coated by a thin layer of low-Fe sphalerite, followed by ubiquitous mineralization of very coarse-grained radial tabular barite (up to 15 mm long). A third generation of fine- to very fine-grained sphalerite grows on top of the barite, which is intergrown with fine-grained “fish-egg” amorphous silica. Locally, very fine-grained pyrite is also present with the silica.

The top half of the section contains abundant dendritic barite-sphalerite, and former vent conduits. Here, the first phase to line the conduits is sphalerite, with variable Fe-concentrations ranging from moderate to very low, with Fe-concentrations either increasing or decreasing gradually outwards, and areas with multiple generations of sphalerite mineralization indicated by distinct growth zones. This is followed by coarse-grained tabular barite and a thin coat of amorphous silica, locally associated with very fine-grained sphalerite as above, and rare very fine-grained iron oxides/oxyhydroxides.



Photomicrographs of GMA13-002: ***(a)*** *reflected light (PPL) photomicrograph of dendritic fine-grained barite, overgrown by sphalerite and spherulitic pyrite;* ***(b)*** *reflected light (PPL) photomicrograph of multiple generations of barite and sphalerite, beginning with fine-grained dendritic barite, followed by sphalerite, followed by coarse-grained tabular barite and additional sphalerite;* ***(c)*** *transmitted light (PPL) photomicrograph of sphalerite and barite overgrown by a very thin layer of amorphous silica;* ***(d)*** *transmitted light (PPL) photomicrograph close-up of amorphous "fish-egg" silica with inclusions of sulfides and minor iron oxyhydroxides, associated with open-space fill between coarse-grained tabular barite.*

Mineral abundance: (modal %; not including pore space)

Sp	Ccp	Py	Mrc	Gn	Jd	Bn	Dg	Cv	Au	Brt	Anh	Am-Si	FeOx	Hem
+++	-	+	-	-	-	-	-	-	-	+++	-	+	Tr	+
25		1								68		1	<1	5

Paragenesis: Dendritic barite → sphalerite (mod-low Fe) → hematite → spherulitic pyrite → multiple pulses of sphalerite (mod-low Fe; variable) → coarse-grained tabular barite → amorphous "fish-egg" silica ± fine grained-sphalerite ± very fine-grained pyrite ± very fine-grained iron oxides/oxyhydroxides.

Name: Sphalerite-barite chimney (low-T) talus

SAMPLE: GMA13-003a,b **PARENT ID:** 632	**LOCATION:** 784724.0E/8649595.3N **WATER DEPTH:** 1109 mbsl

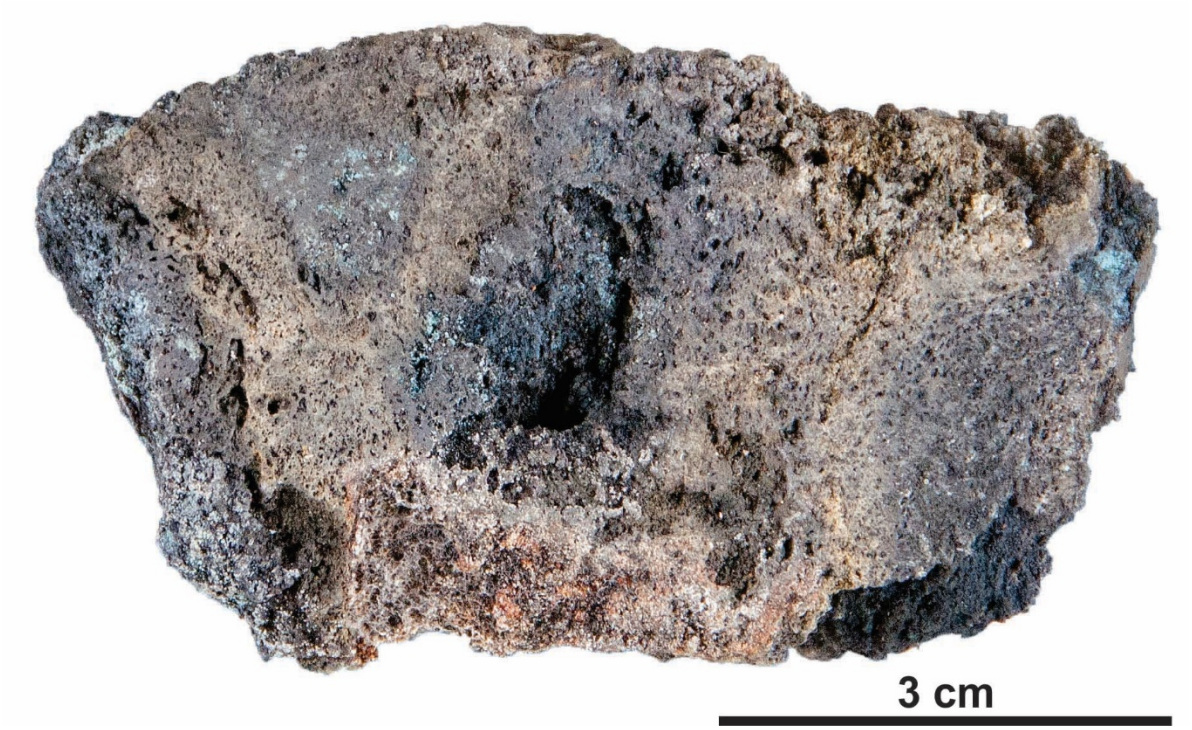
Geochemical Notes

**XRF (parent): Cu = 2.11%, Pb = 0.25%, Zn = 46.30%, Ag = 180.0 ppm; Au = 4.06 ppm.*

Video Description

Sample collected from inactive single-spired bulbous chimney, 1 m tall, surrounded by indurated sediments and talus and other small chimneys at edge of mound.

Hand Sample Description



Hand sample of GMA13-003.

Sphalerite-rich chimney sample with predominantly high-Fe sphalerite (40%) with lesser low-Fe sphalerite (30%), irregular distribution, generally with high-Fe sphalerite near vent conduits. Minor disseminated chalcopyrite (1%) and atacamite (<1%), white clay (1%) and trace iron oxide. Up to 5 mm thick crust of manganese oxide (5%). Possible central vent conduit 1 cm wide, pore space is mostly 1 mm wide, 25% overall.

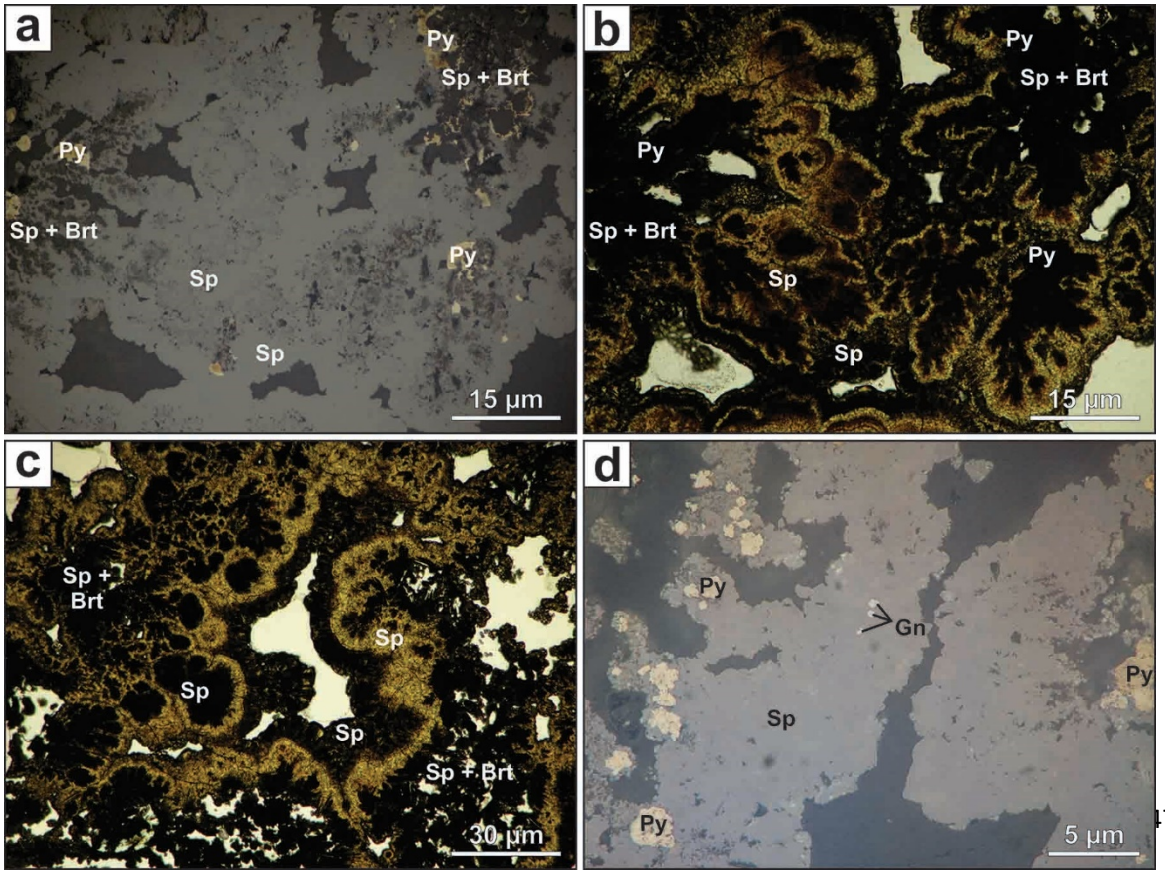
Thin Section Description



Thin section scan of GMA13-003a.

(a) This sample contains abundant pore space (~40-50%).

The earliest phase to crystallize is fine-grained radial to dendritic barite; most of these crystals relict or are too fine-grained or inclusion-filled to be easily identified. This is followed by abundant spherulitic pyrite up to ~1 mm in diameter. On larger pyrite spherules growth zones are identifiable. Most of this pyrite is highly porous, possibly indicating replacement of marcasite. Very little marcasite remains. This is followed by multiple phases of sphalerite, the most abundant mineral in this section, with both gradual and sharp changes in color (Fe-content), and multiple crystallization phases present. The earliest phase of sphalerite is high-Fe and dendritic (locally colloform), followed by a phase of sphalerite that has a gradual change from low to very low-Fe concentration (non-dendritic). Locally this trend is reversed. This phase is associated with minor fine-grained galena(?), which is included in the sphalerite. Minor fine-grained chalcopyrite occurs at the margins of this phase, locally associated with very minor covellite. This is followed by another phase of sphalerite that is tabular in form and changes quickly from high-Fe (black, minor), to very low-Fe (almost colorless, abundant), over very short distances.



Photomicrographs of GMA13-003a: ***(a)*** *reflected light (PPL) photomicrograph of dendritic fine-grained barite, overgrown by sphalerite and spherulitic pyrite (after marcasite?);* ***(b)*** *transmitted light (PPL) photomicrograph of the same view as (a) showing multiple generations of high- and low-Fe sphalerite;* ***(c)*** *transmitted light (PPL) photomicrograph of multiple generations of sphalerite;* ***(d)*** *reflected light (PPL) photomicrograph of spherulitic pyrite (after marcasite?) overgrown by sphalerite with galena inclusions.*

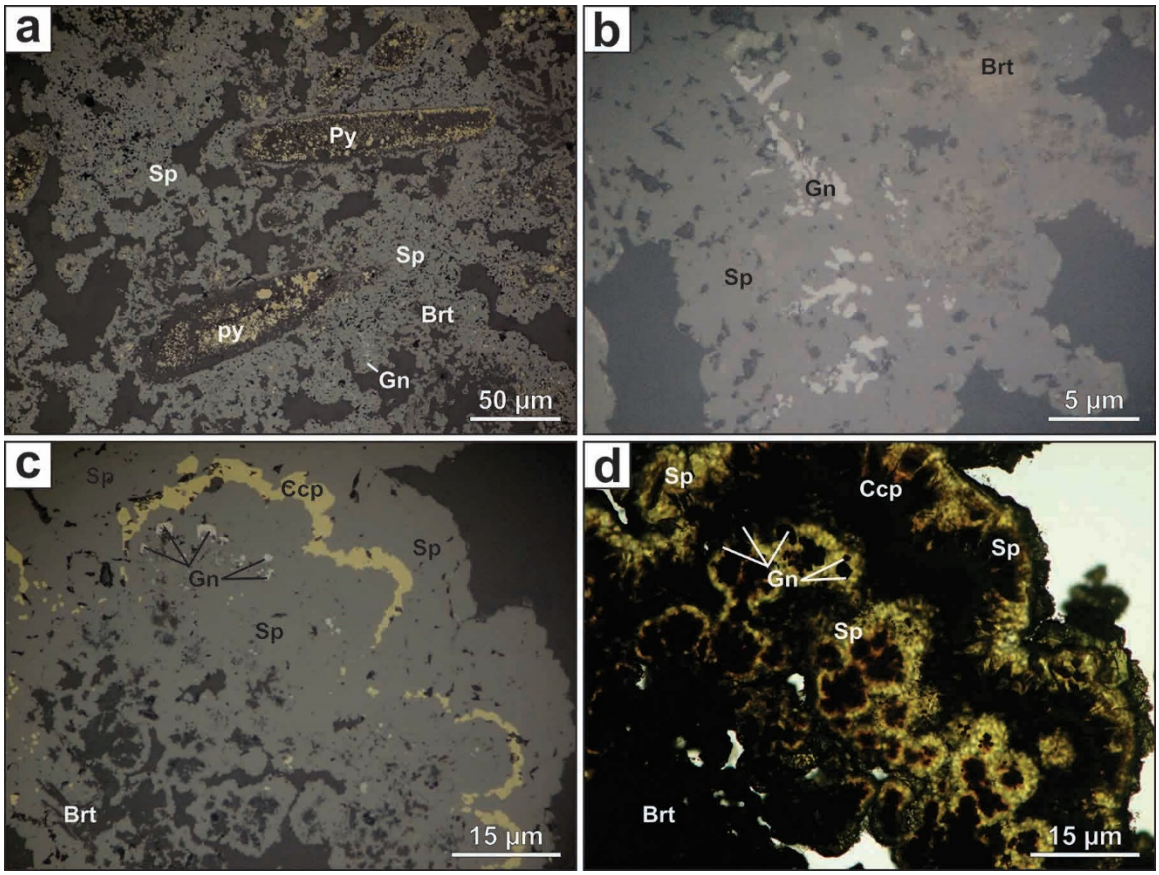
Mineral abundance: (modal %; not including pore space)

Sp	Ccp	Py	Mrc	Gn(?)	Jd	Bn	Dg	Cv	Au	Brt	Anh	Am-Si	FeOx	others
+++	Tr	++	+	Tr	-	-	-	Tr	-	++	-	-	-	-
77	<1	10	3	<1				<0.1		10				



Thin section scan of GMA13-003b.

(b) This section is cut from another part of the same rock as GMA13-003a; it also has a high porosity (~50%), with a similar mineralization sequence. The primary difference is the occurrence of former vent conduits that are generally lined by marcasite/pyrite, infilled by spherulitic marcasite/pyrite ± sphalerite. Interestingly, these vent conduits appear to pre-date the crystallization of the main sphalerite phases, which tend to grow outwards on these circular features. There is more marcasite (extensively inverted to secondary pyrite) in this sample overall. The barite in this sample is mostly relict, dendritic; it is hard to tell if the crystals are still there. The sphalerite phases are dendritic, crystalline, and locally colloform (as above). The final phase of sphalerite tends to have a higher proportion of high-Fe, with less very low-Fe (colorless) compared to above. There is slightly more chalcopyrite and galena(?) than above. At the bottom-left corner of the section there is a minor amount of bright-red iron oxyhydroxide.



Photomicrographs of GMA13-003b: ***(a)*** *reflected light (PPL) photomicrograph of pyrite lining and filling in former vent conduits, and abundant sphalerite overgrowing fine-grained barite, with galena inclusions;* ***(b)*** *reflected light (PPL) photomicrograph close-up of galena inclusions in sphalerite;* ***(c)*** *reflected light (PPL) photomicrograph of sphalerite with galena inclusions and chalcopyrite;* ***(d)*** *transmitted light (PPL) photomicrograph of the same view as (a) showing changing Fe-contents in sphalerite.*

Mineral abundance: (modal %; not including pore space)

Sp	Ccp	Py	Mrc	Gn(?)	Jd	Bn	Dg	Cv	Au	Brt	Anh	Am-Si	FeOx	others
+++	+	++	+	+	-	-	-	Tr	-	+	-	-	Tr	-
73	1	15	5	1				<1		5			<1	

Paragenesis: Dendritic barite → spherulitic and conduit-lining marcasite → secondary pyrite after marcasite + primary spherulitic pyrite → dendritic sphalerite (high-Fe) → sphalerite (low-Fe) + galena(?) → fine-grained chalcopyrite → covellite → tabular high- to very low-Fe sphalerite → Fe-oxyhydroxide.

Name: Sphalerite-barite chimney (low-T)

SAMPLE: GMA13-004a,b **PARENT ID:** 633	**LOCATION:** 784718.2N/8649637.3E **WATER DEPTH:** 1099 mbsl

Geochemical Notes

Whole rock: High S (34.6%), Fe (18.9%), Cu (67600 ppm), Zn (217000 ppm), Cd (895 ppm), Ga (91 ppm), Ge (99 ppm), Hg (95200 ppb), As (946 ppm); Low Ag.

Video Description

Large (5 m?) multi-spired chimney, not bulbous, covered in bacteria (active venting), no black smoke. Minor floc. Sample taken from tip of chimney. Surrounded by chimney talus, indurated sediments.

Hand Sample Description

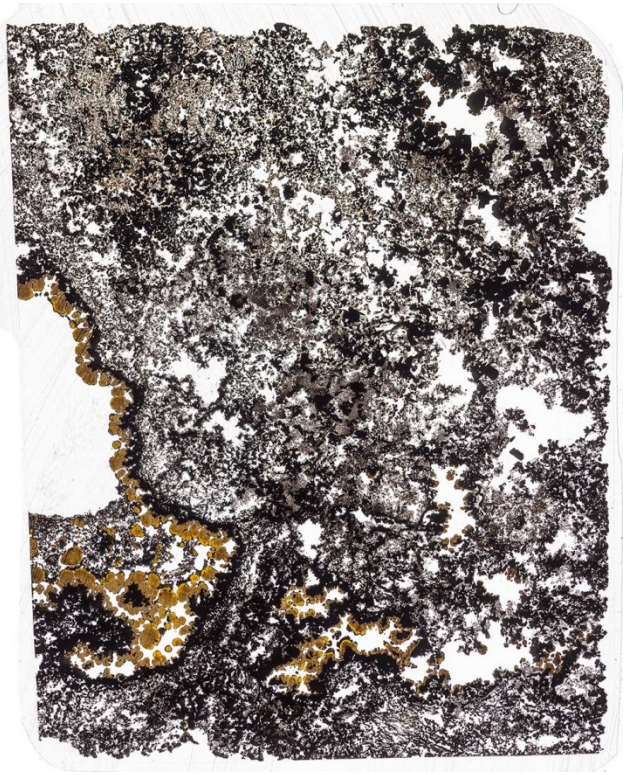


Hand sample of GMA13-004.

Zoned chimney with chalcopyrite (85-90%), sphalerite (5-10%), pyrite/marcasite (1%), and barite (1-5%) with multiple small orifices (<1 cm) that are lined by coarsely crystalline chalcopyrite. Outer surface has a mm-thick coat of iron and manganese oxide (<1%) and white clay (1%). Pore space is 5-15% overall.

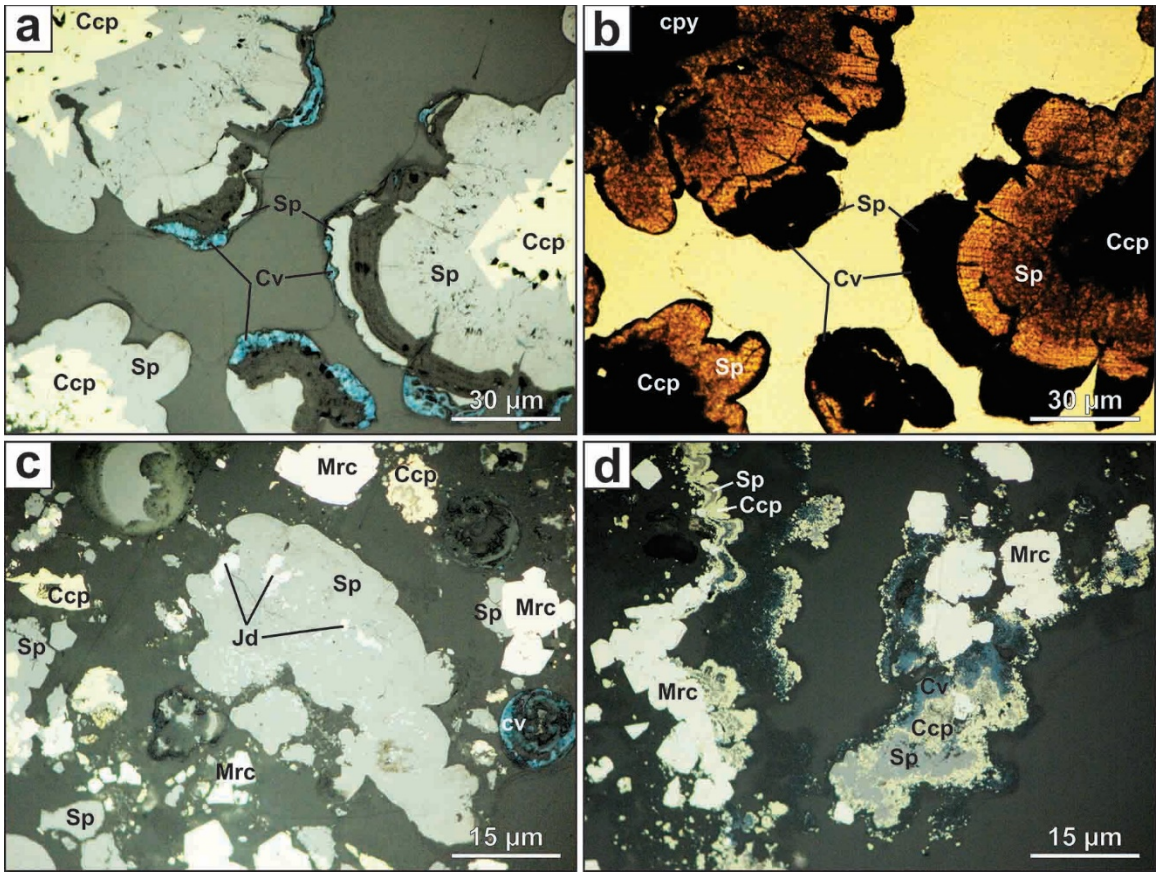
Thin Section Description

(a) This zoned chimney contains ~40% pore space. It is characterized by abundant coarse-grained subhedral to euhedral marcasite up to 10 mm long. The marcasite is locally porous, and rarely associated with secondary porous anhedral pyrite. Relict barite is indicated by dendritic patterns of sulfides, primarily at the bottom of this section. Large vent conduits are lined by fine- to coarse-grained chalcopyrite, which is locally altered to very fine-grained covellite. In some areas, the earliest phases of



Thin section scan of GMA13-004a.

chalcopyrite occur with alternating thin layers high-Fe sphalerite. The chalcopyrite is locally replacing marcasite (abundant embayment textures and fine inclusions of chalcopyrite in marcasite). The next phase precipitated within the vent conduits is low-Fe sphalerite, which grows as irregular rounded masses. These masses are mostly heterogeneous in color, or show a slight outward-decrease in Fe content. Locally, fine growth zones like tree-rings are present. Very fine-grained jordanite occurs as inclusions within this sphalerite. A thin layer of high-Fe sphalerite (black) coats this earlier sphalerite. A fine-grained colorless mineral fills in some of the remaining pore-space, thought to be amorphous silica. Tiny acicular needles (<0.02 mm long) of an unidentified mineral grow on top of this, which may be very fine-grained barite. A few crystals of coarse-grained barite are the last to precipitate.



Photomicrographs of GMA13-004a: ***(a)*** *reflected light (PPL) photomicrograph of sphalerite overgrowths on chalcopyrite, with secondary covellite;* ***(b)*** *transmitted light (PPL) photomicrograph of same view as (a) showing "tree-ring" laminae of low-Fe sphalerite with decreasing Fe-contents outwards, overgrown by high-Fe sphalerite (black);* ***(c)*** *reflected light (PPL) photomicrograph of jordanite inclusions in sphalerite, with early marcasite and chalcopyrite, secondary covellite;* ***(d)*** *reflected light (PPL) photomicrograph of marcasite, followed by sphalerite + chalcopyrite lamellae, and secondary covellite.*

Mineral abundance: (modal %; not including pore space)

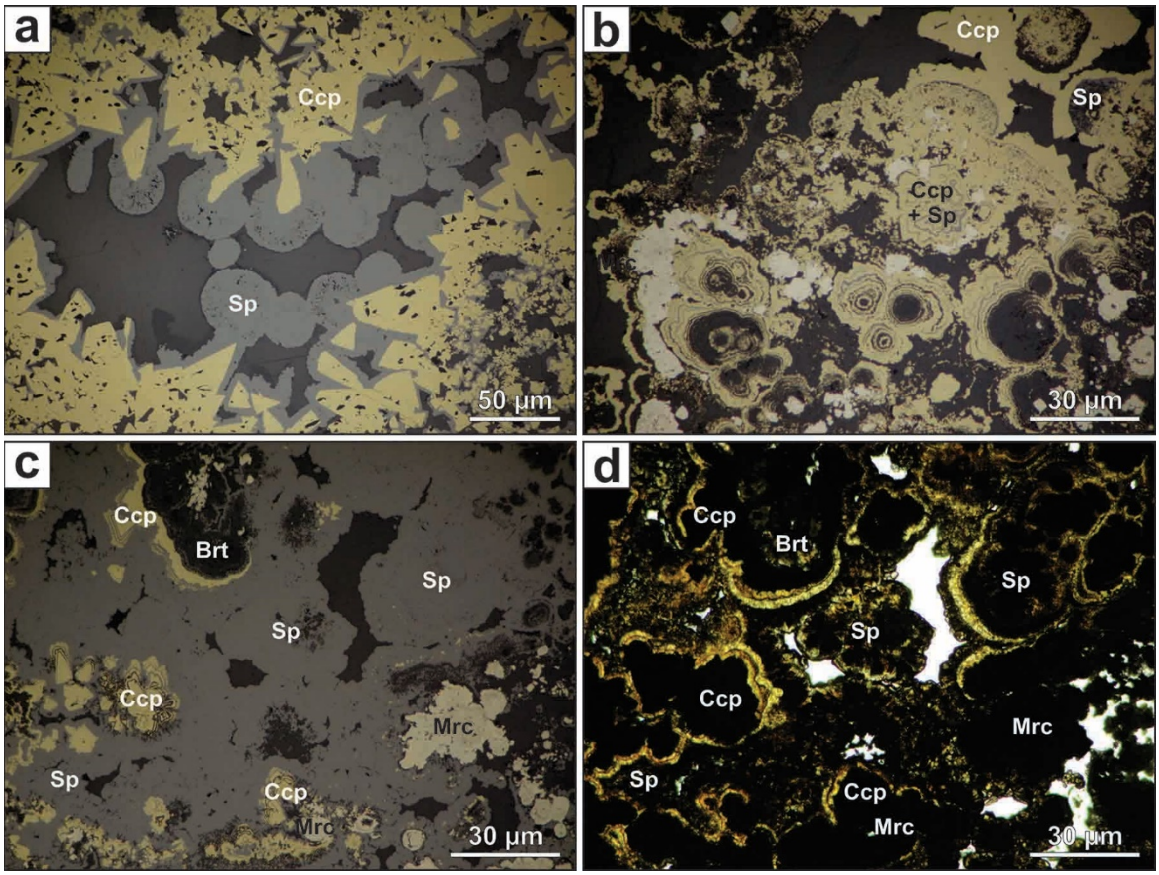
Sp	Ccp	Py	Mrc	Gn	Jd	Bn	Dg	Cv	Au	Brt	Anh	Am-Si	FeOx	others
++	+++	+	+++	-	Tr	-	-	+	-	+	-	++	-	-
10	34	1	40		<1			1		5		10		



Thin section scan of GMA13-004b.

(b) This section is cut from another part of the same rock as GMA13-004a; it has a slightly lower porosity than GMA13-004a at ~30%. The entire section shows a distinct zoning from top to bottom. The top quarter of the section shows a mineralization sequence similar to (a). It contains abundant coarse-grained marcasite that is fractured with minor porosity, rarely containing cores of highly-porous anhedral pyrite, indicating inversion of marcasite to secondary pyrite. This is followed by chalcopyrite and finely-laminated high-Fe sphalerite + chalcopyrite (locally replacing the marcasite along crystal margins). This is followed by low-Fe sphalerite with a slight decrease in Fe-content outwards. In some areas, this is followed again by chalcopyrite, and finally a third phase of tabular high- to low-Fe sphalerite, showing a considerable range in color from black to colorless over short distances. Secondary covellite is rare. Pore space is filled by amorphous silica(?) and tiny acicular barite(?) as above. Moving downwards along the section, there is a narrow zone dominated by marcasite and chalcopyrite growing on relict needles and dendrites of barite, with only minor chalcopyrite.

The bottom 2/3 of the section is dominated by chalcopyrite, with minor sphalerite. The small amount of marcasite remaining occurs as subhedral, often relict crystals. Locally, we see the sequence of laminated chalcopyrite → sphalerite → chalcopyrite. Near former vent conduits, the chalcopyrite crystals are very coarse-grained, up to 4 mm long. The next sulfide phase is always low to very low-Fe (almost colorless) sphalerite. In the vent conduits, this sphalerite is bulbous. No jordanite was observed. Amorphous silica(?) occurs as a thin, irregular coating.



Photomicrographs of GMA13-004b: ***(a)*** *reflected light (PPL) photomicrograph of coarse-grained chalcopyrite in a former vent conduit, lined by sphalerite;* ***(b)*** *reflected light (PPL) photomicrograph of layered chalcopyrite + sphalerite and marcasite;* ***(c)*** *reflected light (PPL) photomicrograph of early barite, marcasite (partially inverted to pyrite), and layered chalcopyrite + sphalerite, overgrown by sphalerite;* ***(d)*** *transmitted light (PPL) photomicrograph of the same view as (c) showing multiple generations of high- and low-Fe sphalerite.*

Mineral abundance: (modal %; not including pore space)

Sp	Ccp	Py	Mrc	Gn	Jd	Bn	Dg	Cv	Au	Brt	Anh	Am-Si	FeOx	others
++	+++	+	+++	-	-	-	-	Tr	-	+	-	++	-	-
20	40	1	26					<1		3		10		

Paragenesis: Marcasite → secondary pyrite → barite (relict, dendritic) → chalcopyrite + high-Fe sphalerite (finely laminated), locally replacing marcasite → chalcopyrite → Low-Fe sphalerite ± jordanite → chalcopyrite (local) → high-Fe sphalerite → covellite → amorphous silica(?)→ coarse-grained or tiny acicular barite (local).

Name: Zoned marcasite + chalcopyrite + sphalerite chimney

SAMPLE: GMA13-005 **PARENT ID:** 636	**LOCATION:** 784709.6E/8649654.2N **WATER DEPTH:** 1098 mbsl

Geochemical Notes

**XRF (parent): Cu = 0.49%, Pb = 0.11%, Zn = 30.00%, Ag = 97.2 ppm; Au = 2.18 ppm.*

Video Description

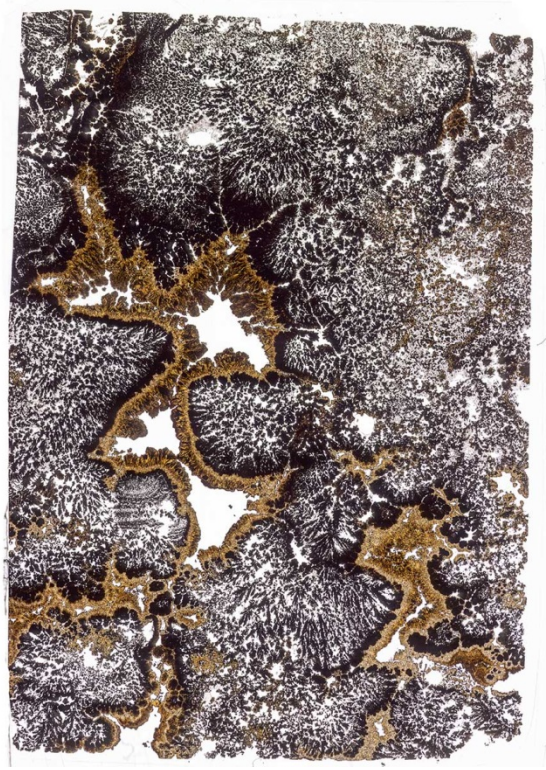
Small bulbous chimney (20 cm tall) at the edge of the mound, surrounded by sulfide talus and indurated sediment with MnOx and FeOx along fractures. Chimney has irregular shape, also follows fractures.

Hand Sample Description



Hand sample of GMA13-005.

Massive sphalerite-rich chimney with low-Fe sphalerite (45%) in the outer zones away from the conduits and high-Fe sphalerite (15%) lining the conduits. The low-Fe sphalerite has dendritic textures. Barite (10%) is interstitial to sphalerite and occurs as the final phase precipitated in the poor space, and also forms a thin 3 mm wide crust on the outer edge of the sample. Trace pyrite disseminated irregularly in sample. The pore spaces are evenly distributed through the sample, up to 1 cm wide, 30% overall. The weathered surface has a thin coat of iron oxide (2%), manganese oxide (<1%) and clay (1%).

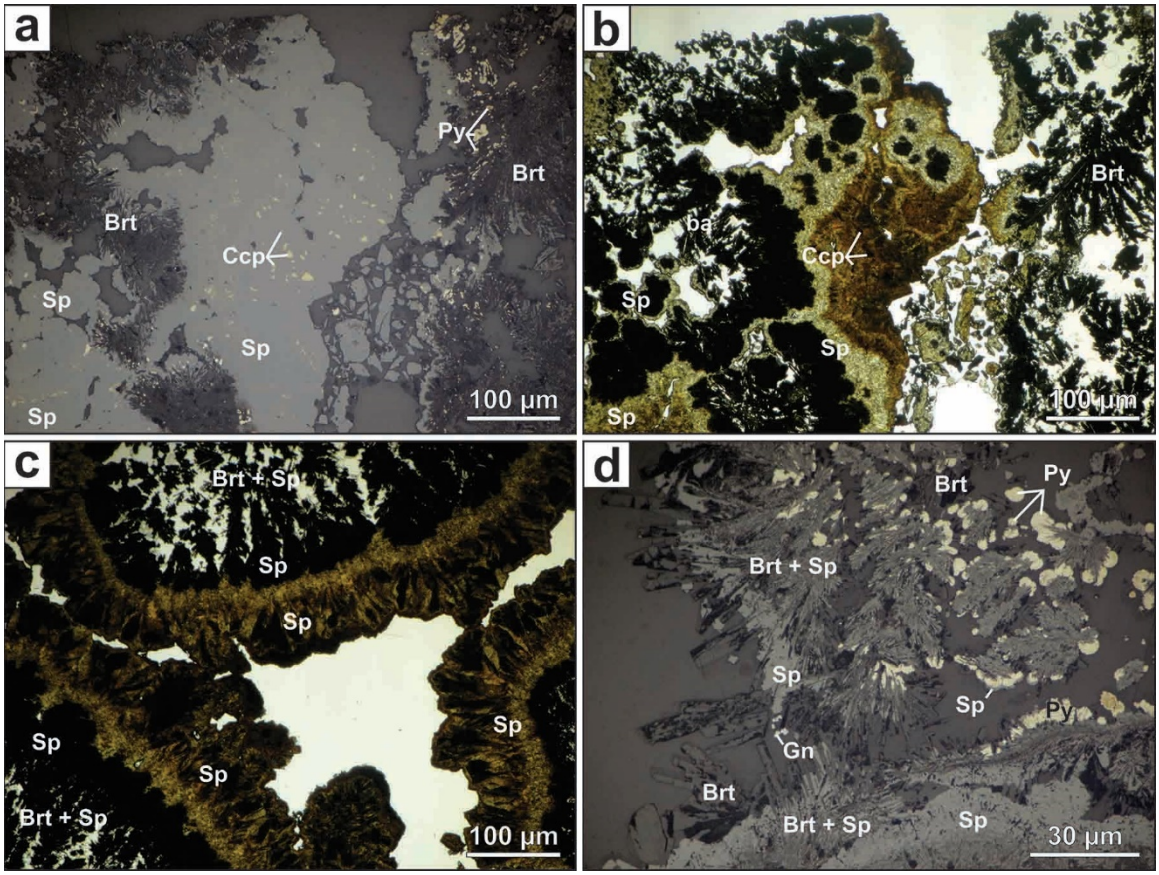


Thin section scan of GMA13-005.

Thin Section Description

This section has ~30% porosity, and is characterized by abundant dendritic textures and open-space fill. Dendritic barite occurs throughout the section, with fine overgrowths of high- to low-Fe sphalerite. This is

followed by abundant spherulitic pyrite, distributed throughout the section, with local increases in concentration. The spherulitic pyrite is up to ~2 mm in width, and displays growth zoning. Occasionally the spherules merge forming a botryoidal texture. This is followed by open-space fill of high-Fe (black) sphalerite that is also dendritic, and then minor medium-grained marcasite that has been partially inverted to secondary pyrite. This is followed by additional high-Fe sphalerite that contains chalcopyrite-exsolution (chalcopyrite disease). This is followed an abrupt zone of low-Fe sphalerite crystallization. This sphalerite has dark (high-Fe) dendritic cores, surrounded by a lighter brown. Coarse-grained inclusions of chalcopyrite occur locally within this sphalerite. Rarely, galena(?) (or jordanite?) occurs as fine inclusions within this sphalerite. An additional phase of moderate-Fe (darker brown) sphalerite coats this phase. Minor galena grows on top of all previous phases. Fine- to very coarse-grained tabular barite grows on the sulfide phases, filling in pore space.



Photomicrographs of GMA13-005: ***(a)*** *reflected light (PPL) photomicrograph of dendritic barite + sphalerite, minor spherulitic pyrite, and sphalerite with chalcopyrite inclusions;* ***(b)*** *transmitted light (PPL) photomicrograph of the same view as (a) showing the various high- and low-Fe sphalerite generations – chalcopyrite inclusions are associated with moderate-Fe (brown) sphalerite;* ***(c)*** *transmitted light (PPL) photomicrograph of various sphalerite generations with different Fe contents;* ***(d)*** *reflected light (PPL) photomicrograph of early dendritic barite, followed by sphalerite, spherulitic pyrite, late sphalerite, late coarse-grained tabular barite, and minor galena.*

Mineral abundance: (modal %; not including pore space)

Sp	Ccp	Py	Mrc	Gn	Jd	Dg	Cv	Au	Brt	Anh	Am-Si	FeOx	others
+++	+	++	+	+	-	-	-	-	+++	-	-	-	-
40	1	10	2	1					55				

Paragenesis: Dendritic barite → high- to low-Fe sphalerite → spherulitic pyrite → high-Fe dendritic sphalerite → marcasite → secondary pyrite after marcasite → high-Fe dendritic sphalerite ± chalcopyrite exsolution → low-Fe sphalerite with dendritic high-Fe sphalerite cores ± chalcopyrite ± galena(?)→ moderate-Fe sphalerite → galena → coarse-grained barite.

Name: Sphalerite-barite chimney (low-T)

SAMPLE: GMA13-006 **PARENT ID:** 634	**LOCATION:** 784732.8E/8649650.1N **WATER DEPTH:** 1099 mbsl

Geochemical Notes

**XRF (parent): Cu = 0.52%, Pb = 15.90%, Zn = 27.80%, Ag = 2700.0 ppm; Au =0.33 ppm.*

Video Description

Sulfide talus from side of mound, rounded, with thin oxidized rim.

Hand Sample Description

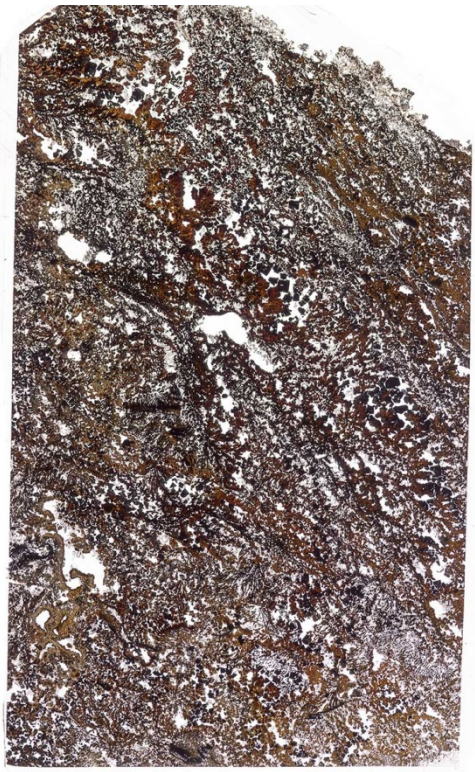


Hand sample of GMA13-006.

Sulphide talus from side of mound. Consists of weakly banded high-Fe sphalerite (65%) with lesser low-Fe sphalerite focused around vugs (2-3%). Abundant barite as crystalline vug fill and interstitial with sphalerite (20%). Minor chalcopyrite, irregularly distributed throughout (1%). Galena(?) occurs in a vug, <1%. Mostly massive and crystalline, weakly banded, with 5-10% pore space, small mm-wide vugs. Thin coat of iron oxide at surface (1-2%) with trace pyrite near weathered surface. Outer surface of the sample is smooth and knobby.

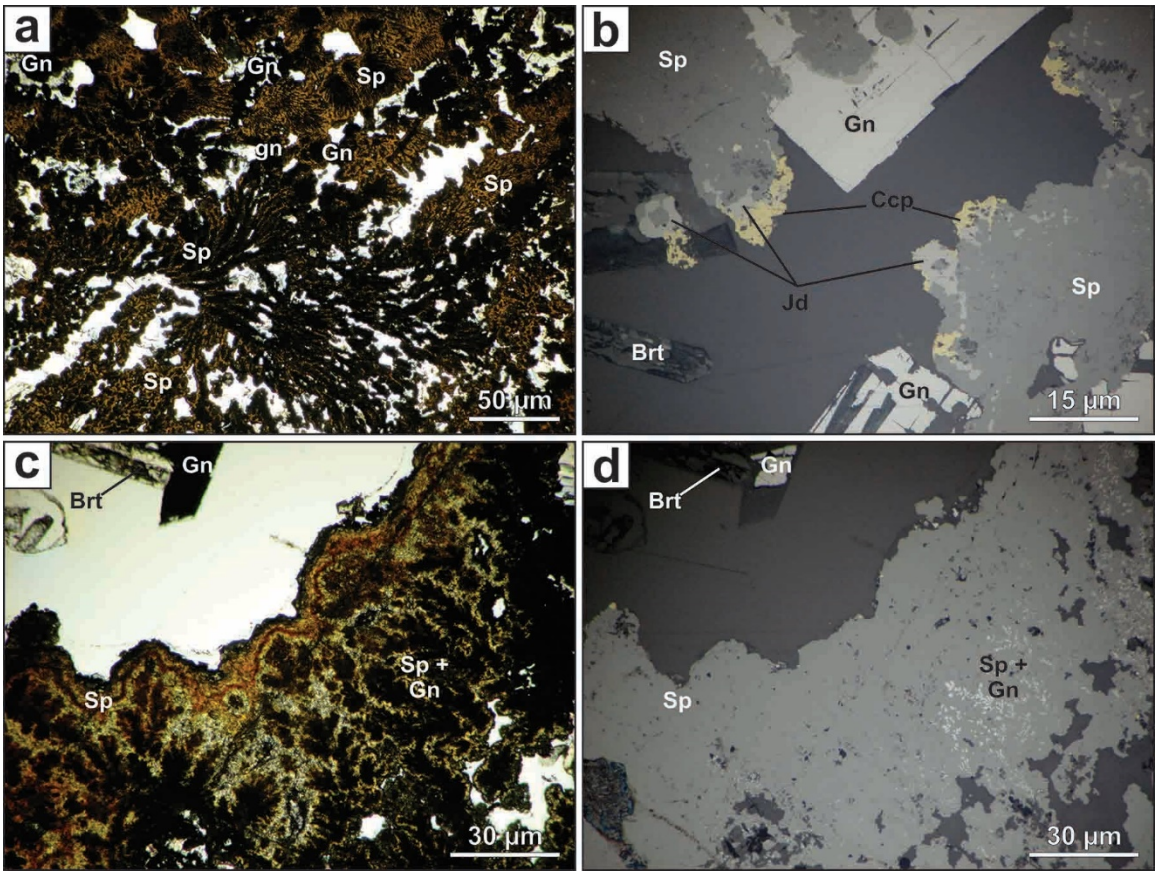
Thin Section Description

This section contains ~35% porosity. It is characterized by dendritic textures that appear to grow off of discrete layers. The dendrites are composed of black (high-Fe) sphalerite that contains abundant fine-grained inclusions of galena, which also display the same dendritic texture, and a few fine-grained inclusions of anhedral to euhedral pyrite. This is followed by the precipitation of coarse-grain subhedral to euhedral galena ± jordanite, and then low-Fe sphalerite that shows a slight decrease in iron content outwards. This sphalerite sometimes has a strong reddish hue. An additional layer of low-Fe sphalerite occurs locally directly on top of this sphalerite. This is followed by the crystallization of minor fine- to



medium-grained jordanite, fine- to medium grained chalcopyrite, and a second generation of abundant coarse- to very coarse-grained euhedral galena, up to ~7.5 mm long. Coarse-grained tabular (sometimes radial) barite crystalizes in the open spaces. Along one margin of the section, minor fine-grained iron oxyhydroxides are precipitated on top of the barite.

Thin section scan of GMA13-006.



Photomicrographs of GMA13-006: ***(a)*** *transmitted light (PPL) photomicrograph of dendritic sphalerite with variable Fe-contents;* ***(b)*** *reflected light (PPL) photomicrograph of sphalerite, jordanite, chalcopyrite, galena, and barite;* ***(c)*** *transmitted light (PPL) photomicrograph of dendritic sphalerite with variable Fe-contents;* ***(d)*** *reflected light (PPL) photomicrograph the same view as (c) showing galena inclusions in the high-Fe dendritic sphalerite.*

Mineral abundance: (modal %; not including pore space)

Sp	Ccp	Py	Mrc	Gn	Jd	Bn	Dg	Cv	Au	Brt	Anh	Am-Si	FeOx	others
+++	+	+	-	+++	+	-	-	-	-	++	-	-	+	-
52	2	1		30	4					10			1	

Paragenesis: dendritic galena → pyrite → dendritic high-Fe sphalerite → galena ± jordanite → low-Fe sphalerite (two generations locally present) → jordanite → chalcopyrite → coarse-grained galena → barite → iron oxyhydroxides (local).

Name: Sphalerite-galena-barite chimney (low T) talus

SAMPLE: GMA13-007 **PARENT ID:** 635	**LOCATION:** 784719.9E/8649659.5N **WATER DEPTH:** 1095 mbsl

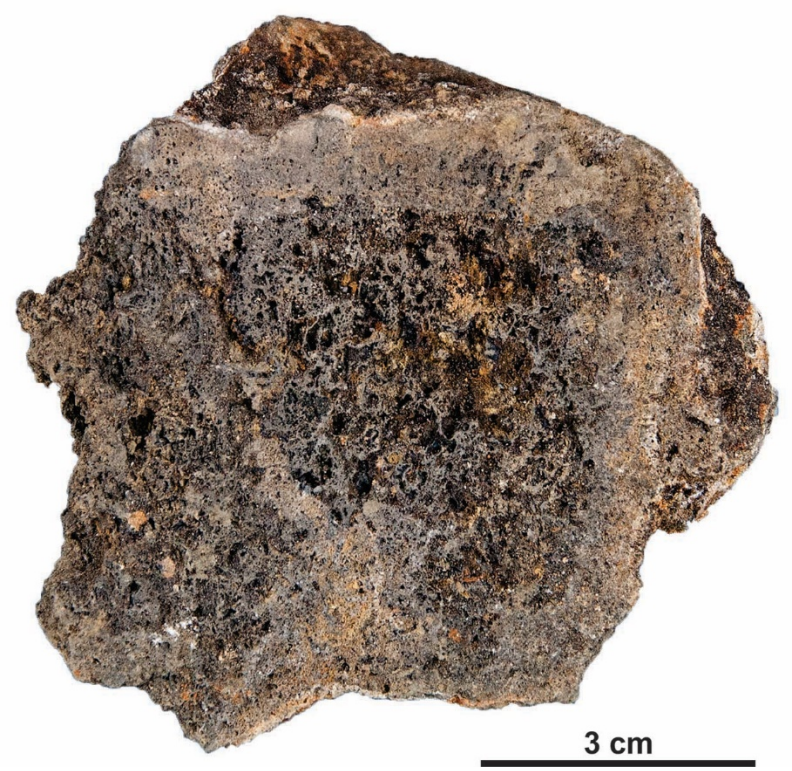
Geochemical Notes

**XRF (parent): Cu = 0.41%, Pb = 0.41%, Zn = 38.60%, Ag = 300.0 ppm; Au =1.02 ppm.*

Video Description

Small bulbous chimney (30 cm) in mound, very hard and difficult to sample. Inactive, minor bacterial floc. Minor FeOx around.

Hand Sample Description

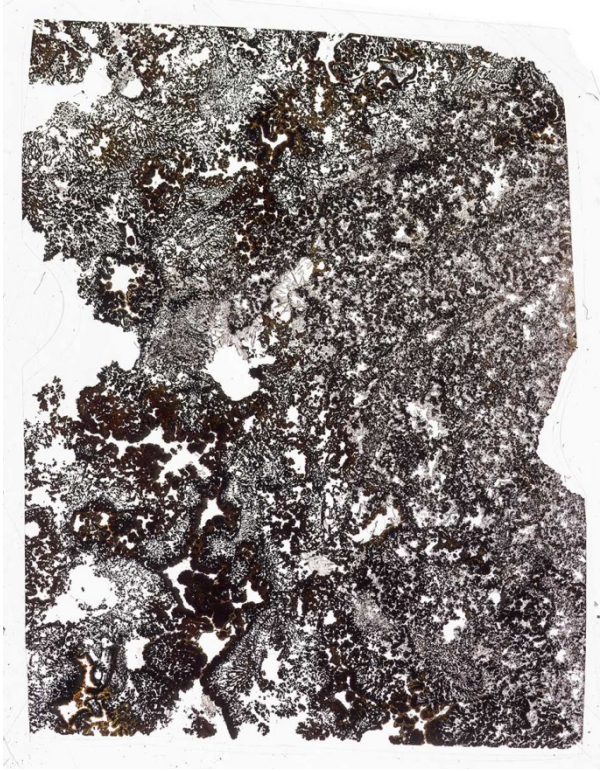


Hand sample of GMA13-007.

Massive sphalerite-barite chimney with no central conduits but abundant mm-size pore space, with higher pore space in the middle of the sample (35%) compared to the outer sample (5%), overall 20% pore space. High-Fe sphalerite (10%) lines vugs, low-Fe sphalerite (50%) comprises the outer zones with small dendritic textures. Barite is fine-grained and interstitial, 5% overall. Outer surface is composed of a thin surface of clay (1%), iron oxide (<1%), and Mn oxide (2%). Minor manganese oxide lining vugs.

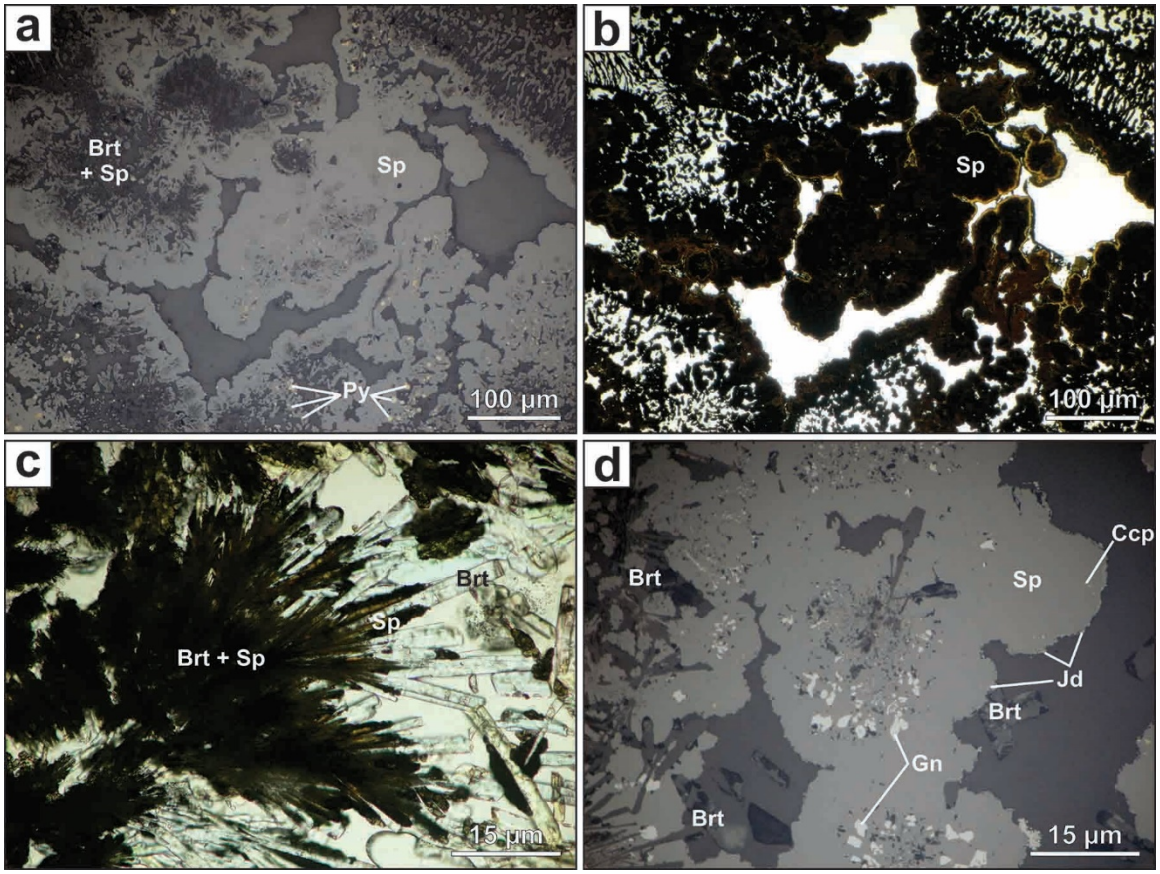
Thin Section Description

This sample is very porous, with ~40% total porosity. It is characterized by abundant dendritic high-Fe sphalerite, precipitated on radial (sometimes relict) needles of barite. This is followed by the precipitation of minor galena and spherulitic pyrite (irregularly distributed), which is then followed by two generations of lower-Fe sphalerite. The second generation is precipitates as a layer up to 3 mm thick, with decreasing Fe contents outwards, and has a slight reddish hue in some areas. It locally contains inclusions of fine-grained chalcopyrite. The third generation has a very low Fe content and is



Thin section scan of GMA13-007.

almost colorless, and occurs as a very thin layer (up to ~0.2 mm thick). Minor fine-grained galena, jordanite, and chalcopyrite crystallize next. Abundant medium-grained radial tabular barite fills in much of the pore space on the right half of the section; it is less common on the other side of the section, where it occurs as minor coarse-grained radial crystals. Locally, a fourth generation of sphalerite (low-Fe) crystallizes on top of the coarse-grained barite.



Photomicrographs of GMA13-007: ***(a)*** *reflected light (PPL) photomicrograph of dendritic barite with sphalerite, spherulitic pyrite, and late sphalerite;* ***(b)*** *transmitted light (PPL) photomicrograph of the same view of (a) showing multiple generations of multiple generations of sphalerite with various Fe-contents;* ***(c)*** *transmitted light (PPL) photomicrograph of dendritic barite and sphalerite, overgrown by coarse-grained tabular barite, and then sphalerite;* ***(d)*** *reflected light (PPL) photomicrograph of sphalerite with galena inclusions, and late jordanite.*

Mineral abundance: (modal %; not including pore space)

Sp	Ccp	Py	Mrc	Gn	Jd	Bn	Dg	Cv	Au	Brt	Anh	Am-Si	FeOx	others
+++	Tr	++	-	+	Tr	-	-	-	-	+++	-	-	-	-
58	<1	10		2	<1					30				

Paragenesis: Radial barite → dendritic high-Fe sphalerite → spherulitic pyrite + minor galena → low-Fe sphalerite ± chalcopyrite → low-Fe sphalerite → galena + jordanite + chalcopyrite → coarse-grained tabular barite → low-Fe sphalerite (local).

Name: Sphalerite-barite chimney (low-T)

SAMPLE: GMA13-008 **PARENT ID:** 646	**LOCATION:** 784692.8E/8649762.8N **WATER DEPTH:** 1082 mbsl

Geochemical Notes

Whole rock: High Hg (25200 ppm), Ba (154000 ppm), Ca (0.64%), Sr (5060 ppm), Co, W, Mg, Mn, Na, Al, Ti, V, Sc; Low Fe, Cu, Zn, Cd, Ga, As, Sb.

Video Description

Slabby rock from base of sulphide mound, mapped as either indurated sediments or hyaloclastite breccia.

Hand Sample Description

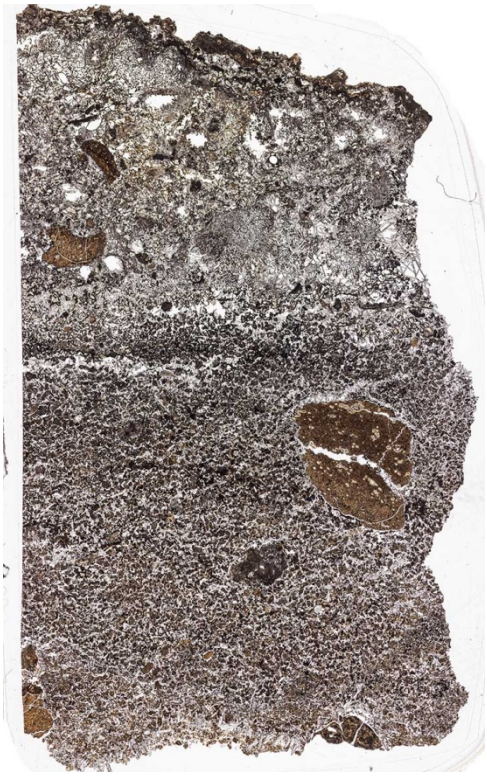


Hand sample of GMA13-008.

Matrix-supported breccia with angular clasts of clay-altered vesicular rock, up to 3 mm across, 3% overall. Few basalt clasts? Matrix is fine-grained Ba (saccharoidal) + minor Sph. Trace very fine grained Py, disseminated, mostly near exterior of sample. Sample looks bedded. Outer rind is FeOx + Clay and possibly amorphous silica, up to 1 cm wide, thin coating of MnOx. Sample is hydrothermally-cemented proximal volcaniclastic breccia.

Thin Section Description

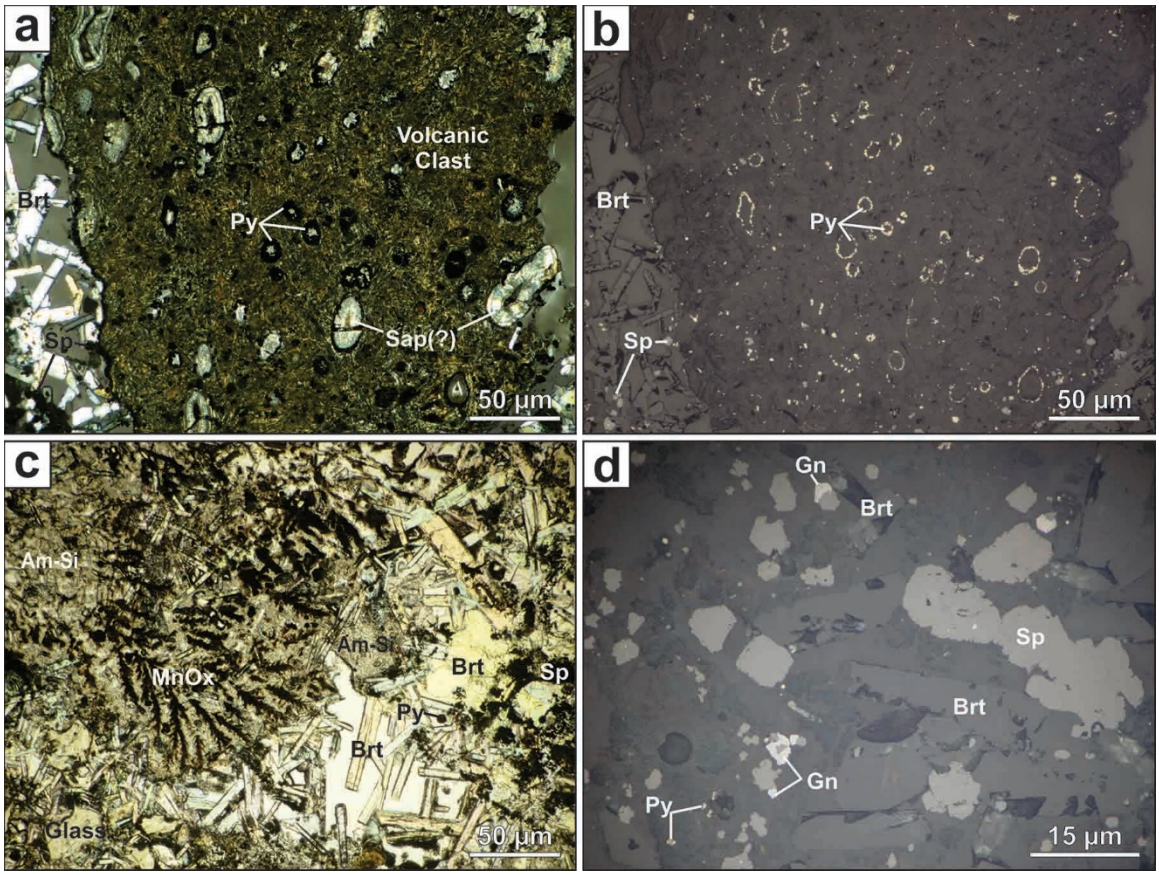
This section is stratified, with a change in mineralogy between the lower 2/3 of the section and the upper 1/3 of the section. The bottom 2/3 of the section has a porosity of ~15%, and contains abundant rounded volcanic clasts, ranging in size from 2 mm up to ~60 mm wide (dominantly mm-sized). These clasts contain relict mm-sized vesicles that are lined with a thin layer of pyrite, followed by fine-grained fibrous saponite (or zeolite?). They are crystal-rich, with abundant relict feldspar crystals up to ~1.5 mm long. In some clasts, feldspar phenocrysts show flow foliation. Intense alteration is pervasive throughout the clasts, altering them to clay and palagonite, which appears brown to dark brown or gray in thin



Thin section scan of GMA13-008.

section (white in hand sample), with finely-disseminated pyrite. Most of the clasts show large desiccation cracks resulting from dehydration of the clays. Differences in clast colors appear to arise from variations in alteration, and this breccia is interpreted to be monolithic. Inclusion-filled ("dirty"), fine-grained dendritic sulfate (barite?) appears to pseudomorph a few of the relict clasts. This part of the section contains abundant mm-sized altered clasts, with a few larger clasts (~35% overall), supported by a matrix of coarse-grained barite (~30%), and lined by a very thin layer of amorphous silica. This is followed by the precipitation of finely disseminated pyrite, followed by high-Fe sphalerite/wurtzite (locally hexagonal crystals) with low-Fe rims (~20%), and then minor fine-grained galena.

The upper 1/3 of the section contains fewer volcanic clasts overall, generally mm-size but up to ~25 mm long (5% overall), with a higher porosity (~30%), and abundant glass shards with curviplanar surfaces up to 5 mm long, with slightly orange color indicating minor palagonitization. These glass shards are concentrated on the left half of the section, ~6% overall. There is an increase in the size of barite crystals (~40%). There is also an increase in the amount of amorphous silica (15%), which is locally iron-stained and precipitated on an unknown black dendritic mineral (manganese oxide?, 3%). There is only minor pyrite, sphalerite, and galena (1% overall), occurring locally, with rare crystals of chalcopyrite at the very top of the section, altered to trace amounts of covellite. Minor iron oxides/oxyhydroxides are irregularly distributed in this part of the section.



Photomicrographs of GMA13-008: ***(a)*** *transmitted light (XPL) photomicrograph of the large clay-altered clast, with relict feldspar, pyrite-lined vesicles, and late saponite (or zeolite?);* ***(b)*** *reflected light (PPL) photomicrograph of the same view of (a) showing the pyrite-lined vesicles, and minor late sphalerite;* ***(c)*** *transmitted light (PPL) photomicrograph of the upper third of the section showing dendritic manganese oxide, glass, late barite, and amorphous silica;* ***(d)*** *reflected light (PPL) photomicrograph of sphalerite, galena, and pyrite.*

Mineral abundance: (modal %; not including pore space)

Volc. clasts	Glass (Pal.)	Py	Anh	Brt	Am-Si	Sp	Gn	Ccp	Cv	MnOx	FeOx	Sap(?)
+++	+	+	+	++	+	++	+	Tr	Tr	+	+	+
44	5	2	1	25	2	15	1	<0.01	<0.01	3	1	1

Paragenesis: Volcanic clasts + glass shards (stratified, palagonitized) → clay + pyrite alteration of clasts → saponite(?) lining vesicles → barite (+anhydrite?) → iron and manganese oxyhydroxides (top of section) → amorphous silica → pyrite (+ chalcopyrite, local) → sphalerite → galena → iron oxides/oxyhydroxides.

Name: Mineralized monolithic clay-altered volcaniclastic breccia

SAMPLE: GMA13-009a,b **PARENT ID:** 647	**LOCATION:** 784665.8E/8649759.3N **WATER DEPTH:** 1089 mbsl

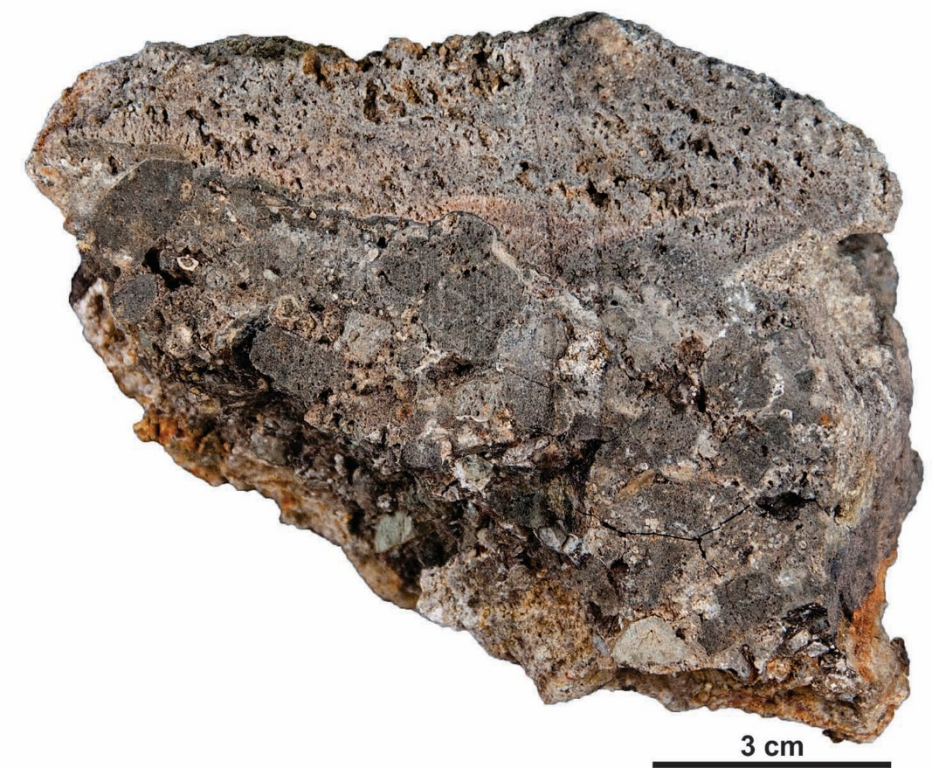
Geochemical Notes

**XRF (parent): Cu = 0.01%, Pb = 0.83%, Zn = 2.08%, Ag = 340.0 ppm; Au = 2.05 ppm.*

Video Description

Large sample, likely sulphide, knobby with Mn crust, loose piece from bottom of chimney in chimney + sulphide talus field.

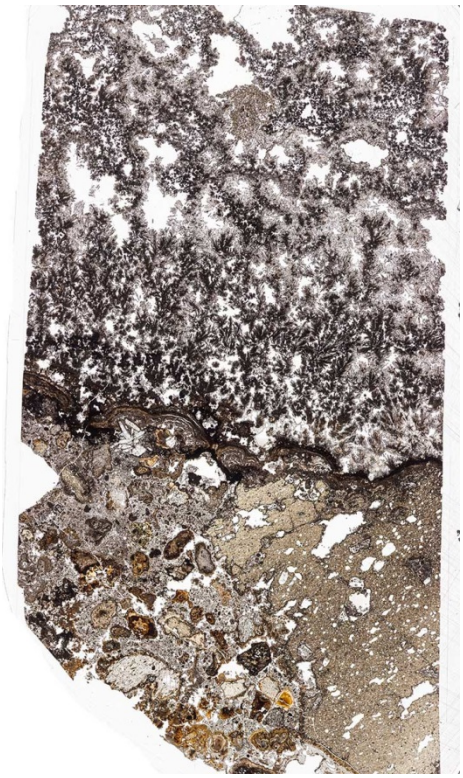
Hand Sample Description



Hand sample of GMA13-009.

At the contact between the matrix-supported volcaniclastic breccia, that has been cemented (silicified) and low-temperature barite-sphalerite chimney. The breccia consists of 40% clasts, angular to subrounded: 90% fine-grained vesicular mafic clasts, some with elongate vesicles, 5% white clay-altered vesicular clasts, 5% green clay altered vesicular clasts. Breccia represents reworked material. Matrix is indurated with clay, possible organic material + FeOx. surface of the sample is knobby. Possible orpiment on outer surface, along with native sulphur, hematite. FeOx surface, thin coat of MnOx. 10% small vugs overall. Weak grading, clast rich towards the bottom. At the bottom, contact with vuggy barite-rich chimney, consisting of 70% barite with dendritic textures and minor high-Fe sphalerite (10%), 15% small pore spaces.

Thin Section Description



Thin section scan of GMA13-009a.

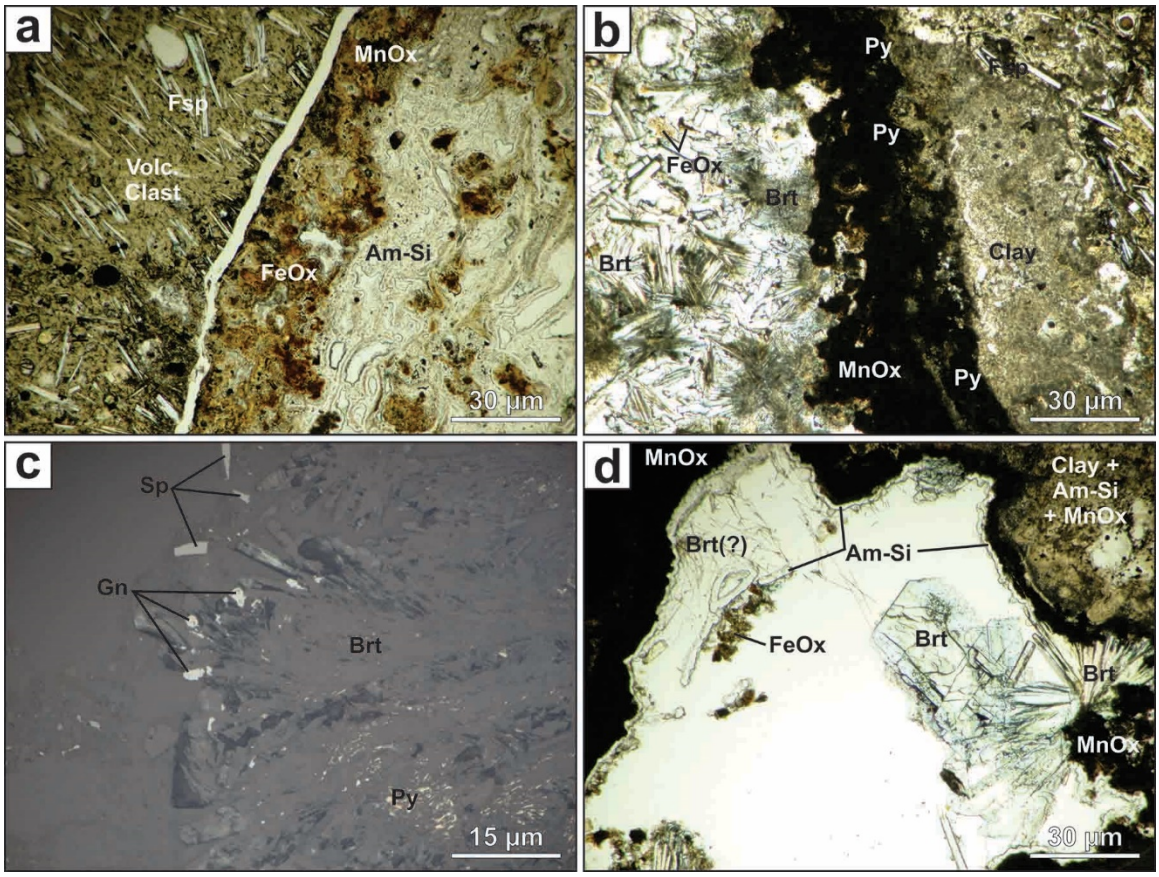
(a) This section is from the contact between the volcaniclastic substrate and the base of the chimney sulfides.

The bottom half of the section contains variably-altered volcanic clasts of a wide range of sizes, from 2 mm to >85 mm. The largest clast has abundant mm-sized feldspar phenocrysts and elongated vesicles showing flow direction. A few larger phenocrysts, up to 3 mm long, are also present. It is pervasively clay-altered, appearing dark brown in thin section (dark grey in hand sample), with a darker brown rim. Minor pyrite is disseminated throughout the clast. Other smaller clasts appear colorless, light to dark grey, or brown, with variable amounts of vesicles and phenocrysts. One clast has a glassy groundmass with perlitic fractures, with microlitic feldspar needles displaying a weak flow foliation. These polylithic clasts are subangular to rounded. Alteration at the clast margins is generally more intense than at the clast interiors. Iron oxide is common, altering the clasts, or forming at clast margins as part of the matrix, sometimes showing a colloform texture. This volcaniclastic breccia is matrix supported, with ~40% clasts and ~50% matrix, with the remaining ~10% pore space. Fine-grained manganese oxide is disseminated throughout the matrix. The clasts and iron and manganese oxides are coated with a layer of amorphous silica, displaying a "fish egg" texture.

Near the boundary between the polylithic volcaniclastic breccia at the bottom of the section and the chimney textures at the top of the section, there is the occurrence of a few clusters of coarse-grained, locally radiating barite, which is locally coated by amorphous silica, or growing on top of it. Tiny hair-like acicular needles of sulfide also grow on top of the amorphous silica locally. The boundary itself is marked by a thin layer of fine- to very fine-grained highly porous secondary pyrite (after marcasite), with minor coarse-grained marcasite, as well as manganese oxide over several mm, with local colloform textures.

Growing upwards from this boundary is inclusion-filled ("dirty" looking) dendritic barite (with possible iron and manganese oxide micro-inclusions), extending up to 10 mm, and radiating tabular barite with minor anhydrite. A mm-thick horizon of medium-grained pyrite is found a couple mm above this boundary on the left half of the section, growing on top of the sulfates. Minor fine-to medium grained pyrite is irregularly disseminated throughout the top half of this section, often as spherulites. This is followed by very fine- to medium-grained low-Fe sphalerite (with a few relict crystals) ± rare jordanite, and galena. These phases are all coated by a thin layer of amorphous fish-egg silica (as above), with local

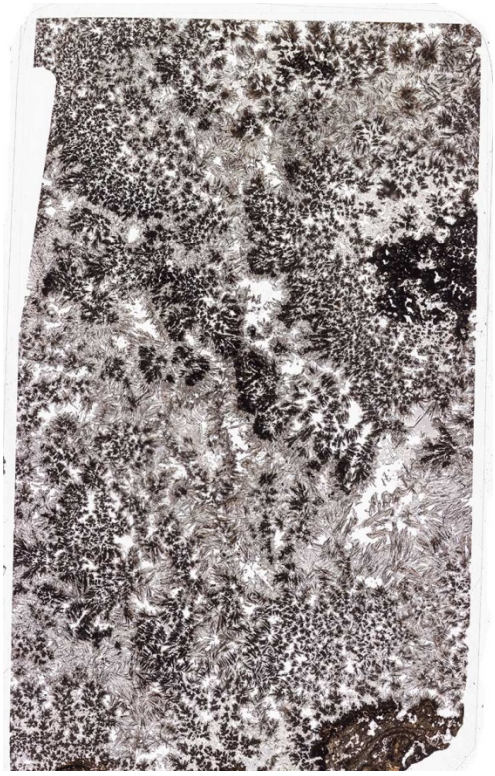
tiny acicular needles of sulfate (barite?). One relict ~3 mm wide clast with abundant iron oxide was observed in this part of the section.



Photomicrographs of GMA13-009a: ***(a)*** *transmitted light (PPL) photomicrograph of a clay-altered clast with relict feldspar from the bottom of the section in contact with amorphous silica and manganese and iron oxyhydroxides;* ***(b)*** *transmitted light (PPL) photomicrograph of the contact between the top (left) and bottom (right) of the section, marked by a thin layer of pyrite(after marcasite) and manganese oxide, with radiating fine- and coarse-grained barite growing from it;* ***(c)*** *reflected light (PPL) photomicrograph of the top of the section showing late sulfides on radiating barite;* ***(d)*** *transmitted light (PPL) photomicrograph a void space lined with manganese oxide, amorphous silica, barite, and iron oxyhydroxides.*

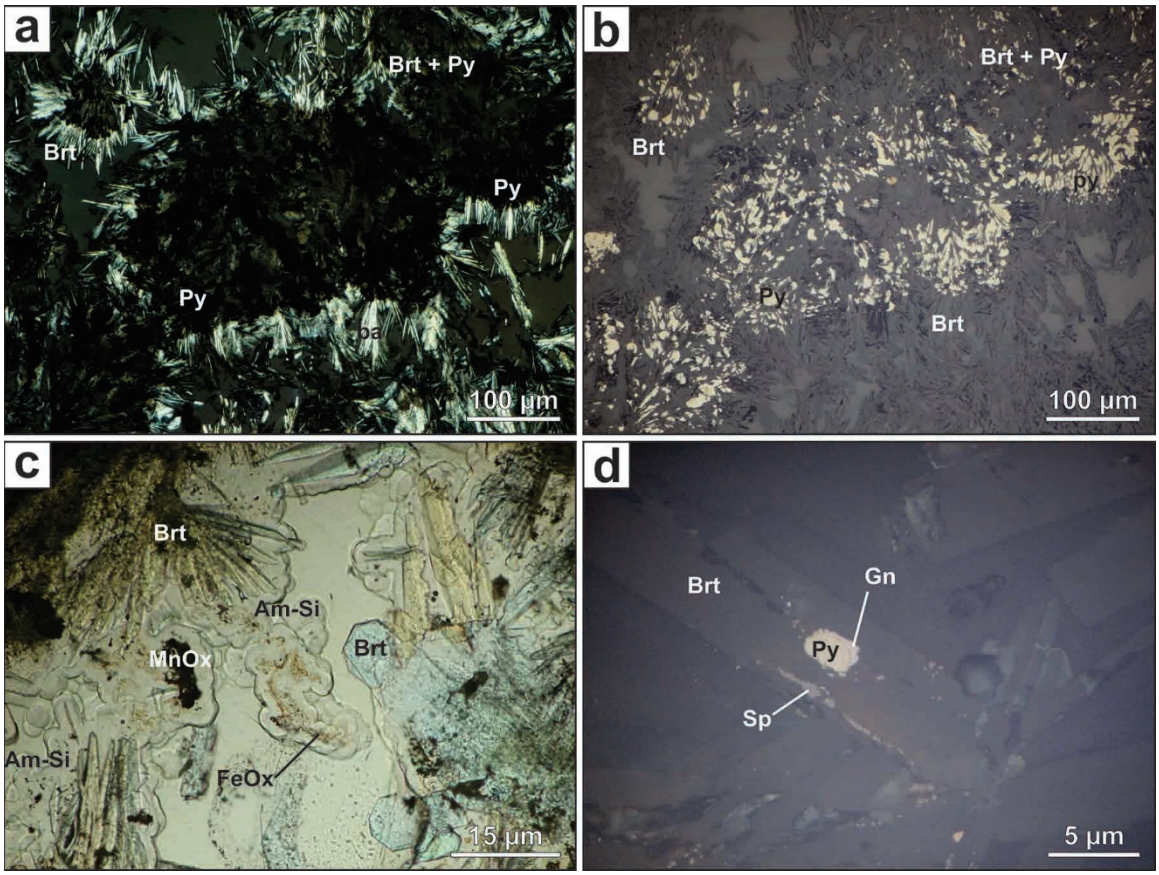
Mineral abundance: (modal %; not including pore space)

Volc. clasts	Mrc	Py	Anh	Brt(?)	Am-Si	Sp	Gn	Jd	MnOx	FeOx	Hem
+++	Tr	+	+	+++	+	++	Tr	Tr	+	+	+
25	<1	3	1	40	8	15	<1	<0.01	5	2	1



Thin section scan of GMA13-009b.

(b) This section is from the chimney at the top of the same sample. It has a porosity of ~25%. The bottom of the section is at the manganese-oxide + pyrite boundary with the volcaniclastic breccia, described above. The mineralization sequence begins with inclusion-filled dendritic barite, with possible manganese oxide micro-inclusions. The dendrites range in size from <1 mm to a few mm long. Directly on top of this is precipitated fine- to coarse-grained marcasite, with a concentration of marcasite at the right side of the section over ~60 mm, with evidence of recrystallization and only rare alteration to secondary pyrite, followed by several irregular "bands" of increased marcasite abundance. This is followed by coarse-grained, inclusion-free ('clear'), tabular, radiating barite. After this, there is the precipitation of minor fine grained pyrite (subhedral to spherulitic), followed by low-Fe sphalerite and galena. The sphalerite contains rare fine-grained inclusions of jordanite. The distribution of sulfides is irregular, with patchy pyrite throughout the section, and patchy disseminated sphalerite and galena on the left side of the section. There is a very low abundance of sulfides overall. All phases are overlain by a thin layer of amorphous "fish-egg" silica. The silica spheres appear to have tiny very-fine grained iron or manganese oxide nuclei.



Photomicrographs of GMA13-009b: ***(a)*** *transmitted light (XPL) photomicrograph of abundant radial barite with pyrite;* ***(b)*** *reflected light (PPL) photomicrograph of the same view as (a) showing distribution of pyrite;* ***(c)*** *transmitted light (PPL) photomicrograph of the amorphous "fish-egg" silica overgrowing radial barite, with FeOx or MnOx nuclei;* ***(d)*** *reflected light (PPL) photomicrograph fine-grained sulfides (pyrite, galena, sphalerite) included in barite.*

Mineral abundance: (modal %; not including pore space)

Volc. clasts	Glass	Py	Mrc	Brt(?)	Am-Si	Sp	Gn	Jd	Ccp	MnOx	FeOx
-	-	+	+	+++	++	+	Tr	Tr	-	+	+
		2	3	80	10	2	<1	<0.01		2	1

Paragenesis: Volcanic clasts → clay + pyrite alteration → iron + manganese oxides → dendritic barite → marcasite → secondary porous pyrite → tabular radiating barite (+minor anhydrite?) → spherulitic pyrite → low-Fe sphalerite + jordanite → galena → amorphous silica (fish-egg) → tiny acicular barite(?).

Name: Mineralized polylithic volcaniclastic breccia with barite chimney (low-T)

SAMPLE: GMA13-010 **PARENT ID:** 649	**LOCATION:** 784711.1E/8649704.6N **WATER DEPTH:** 1074 mbsl

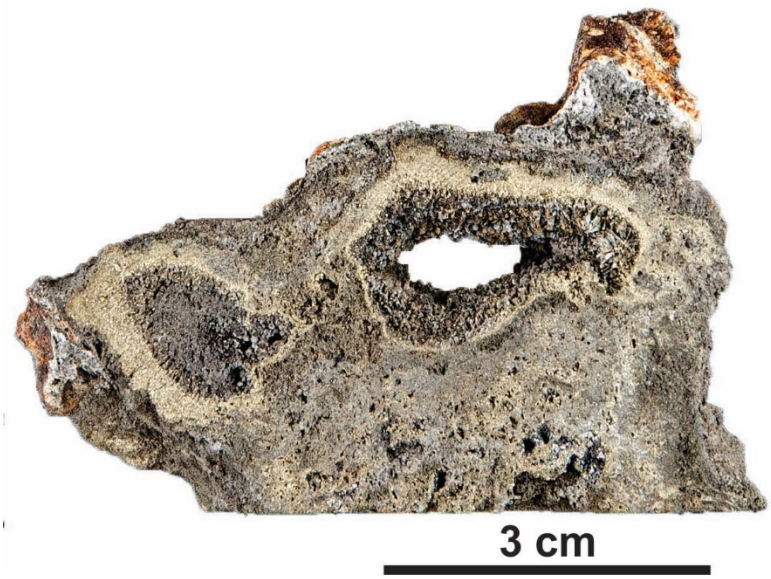
Geochemical Notes

Whole rock: High S (28.4%), Cu (113000 ppm), In (193 ppm), Zn (237000 ppm), Cd (1020 ppm), Ga (76 ppm), Ge (64 ppm), Sb (208 ppm), Ag (251 ppm).

Video Description

Large chimney fragment from blocky bulbous chimneys and talus, some sparkling sulfide, venting.

Hand Sample Description

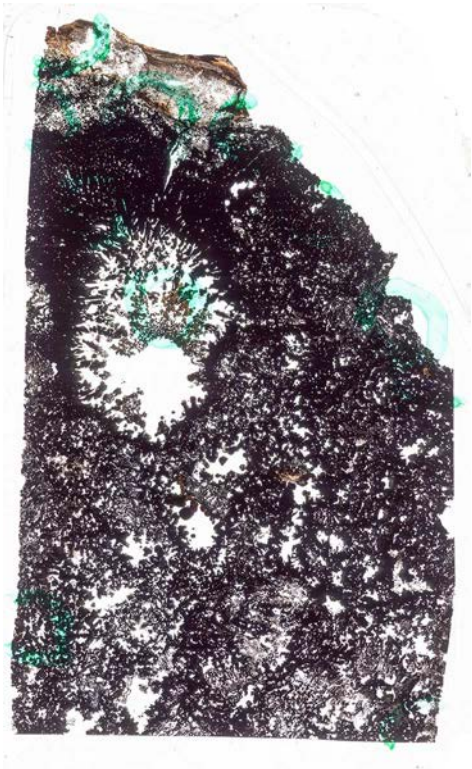


Hand sample of GMA13-010.

Large chimney fragment from a blocky bulbous chimney. With multiple conduits up to 1 cm wide and 8% pore space overall. The sample is zoned with chalcopyrite forming closest to conduits (15%) and minor pyrite (10%), with sphalerite (60%) and barite (5%) in the outer zone. The surface of the sample has a thin coat (1 mm- 1 cm thick) of clay and iron oxide (1%).

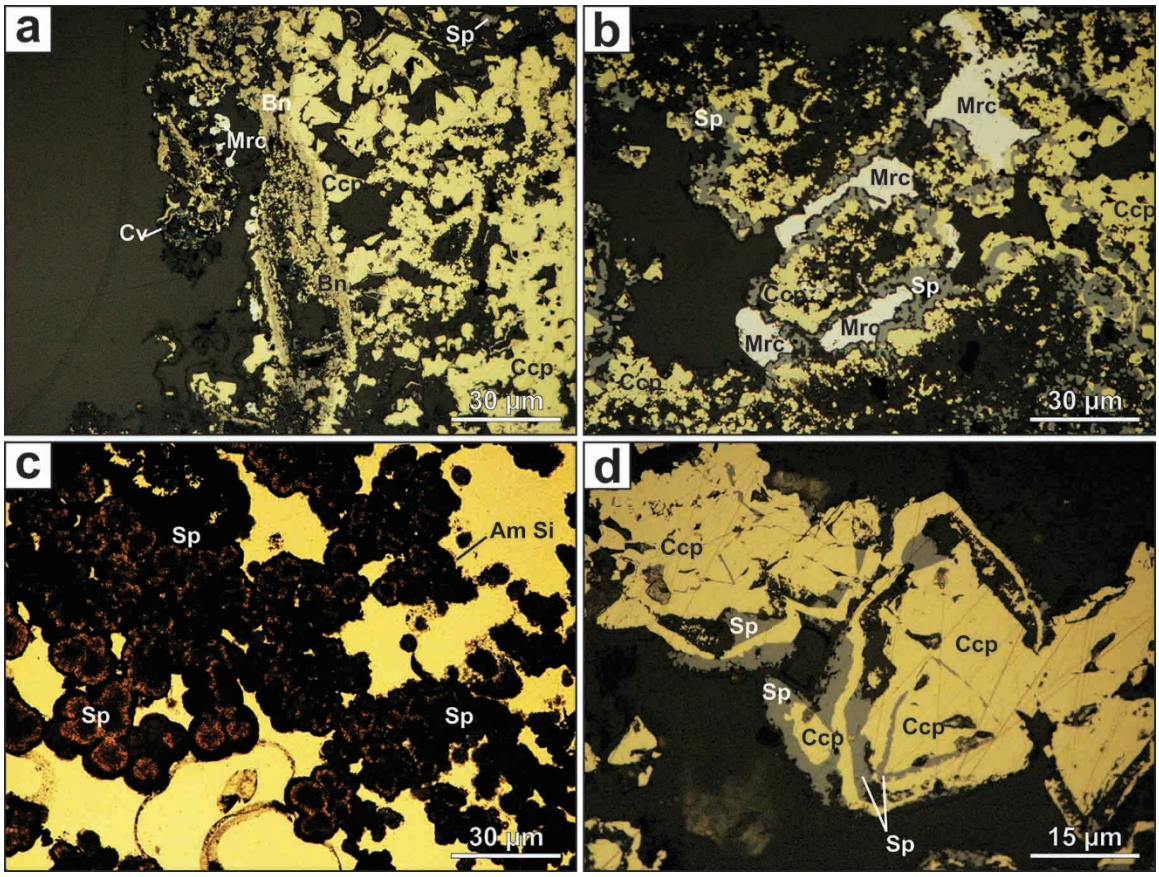
Thin Section Description

This section has a porosity of ~35%. It is composed primarily of coarse-grained chalcopyrite and has notable vent conduits. Locally, there is a repeated zonation of chalcopyrite with high-Fe sphalerite. Low-Fe sphalerite lines the central vent conduits, with a slight decrease in Fe-content outwards. A second generation of very low-Fe (almost colorless) sphalerite follows this. Near the top of the section, there is a horizon containing coarse-grained marcasite. At this horizon, the chalcopyrite is altered to bornite and minor covellite/digenite. Above this horizon, there is minor



Thin section scan of GMA13-010.

dendritic manganese and iron oxides, abundant radiating tabular coarse-grained barite, and layered iron oxy-hydroxides. There are almost no sulfides in this area, apart from the rare fine-grained chalcopyrite crystal. These phases are all covered by a thin layer of amorphous silica, which has a dusting of very fine grained sulfides (unidentifiable).



Photomicrographs of GMA13-010: ***(a)*** *photomicrograph in reflected light (PPL) at the upper limit of coarse-grained chalcopyrite, marked by alteration to bornite + covellite and the precipitation of marcasite;* ***(b)*** *photomicrograph in reflected light (PPL) of marcasite after chalcopyrite + sphalerite;* ***(c)*** *photomicrograph in reflected light (PPL) of low-Fe sphalerite (two generations) coated by a very thin layer of amorphous silica in a vent conduit;* ***(d)*** *photomicrograph in reflected light (PPL) of the repeating zones of chalcopyrite and sphalerite.*

Mineral abundance: (modal %; not including pore space)

Sp	Ccp	Py	Mrc	Gn	Jd	Bn	Dg	Cv	Brt	Anh	Am-Si	FeOx	MnOx
++	+++	-	+	-	-	+	Tr	Tr	+	-	+	+	+
10	70		6			1	<0.01	<1	5		4	2	2

Paragenesis: Chalcopyrite → layered chalcopyrite + high-Fe sphalerite → low-Fe sphalerite → very low-Fe sphalerite → bornite + covellite + digenite → marcasite → iron and manganese oxides/oxyhydroxides → barite → iron oxyhydroxides → amorphous silica.

Name: Zoned chalcopyrite + sphalerite chimney talus

SAMPLE: GMA13-012 **PARENT ID:** 659	**LOCATION:** 784802.0E/8649558.9N **WATER DEPTH:** 1128 mbsl

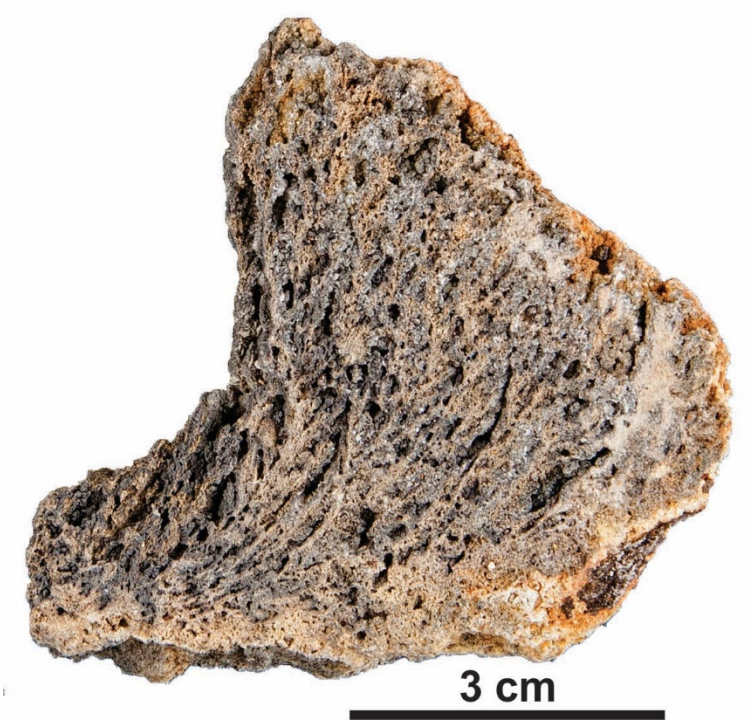
Geochemical Notes

Whole rock: High Zn (261000 ppm), Ge (76 ppm), Ba (152000 ppm), Sr (6700 ppm); Low Fe, Cu, Cd, Ga.

Video Description

Low mound of FeOx and MnOx chimneys, bulbous, mound that grows on hyaloclastite (volcaniclastic breccia), as in sample GMA13-014.

Hand Sample Description



Hand sample of GMA13-012.

Bulbous mound that grows on top of hyaloclastite. Characterized by dendritic high-Fe sphalerite (45%) and low-Fe sphalerite (5%), with abundant pore space (35-40%) up to 8 mm wide. Barite is interstitial with sphalerite and fills in vugs as coarse blades (5-10%). Thin coat of iron oxide on outer surface (1%).

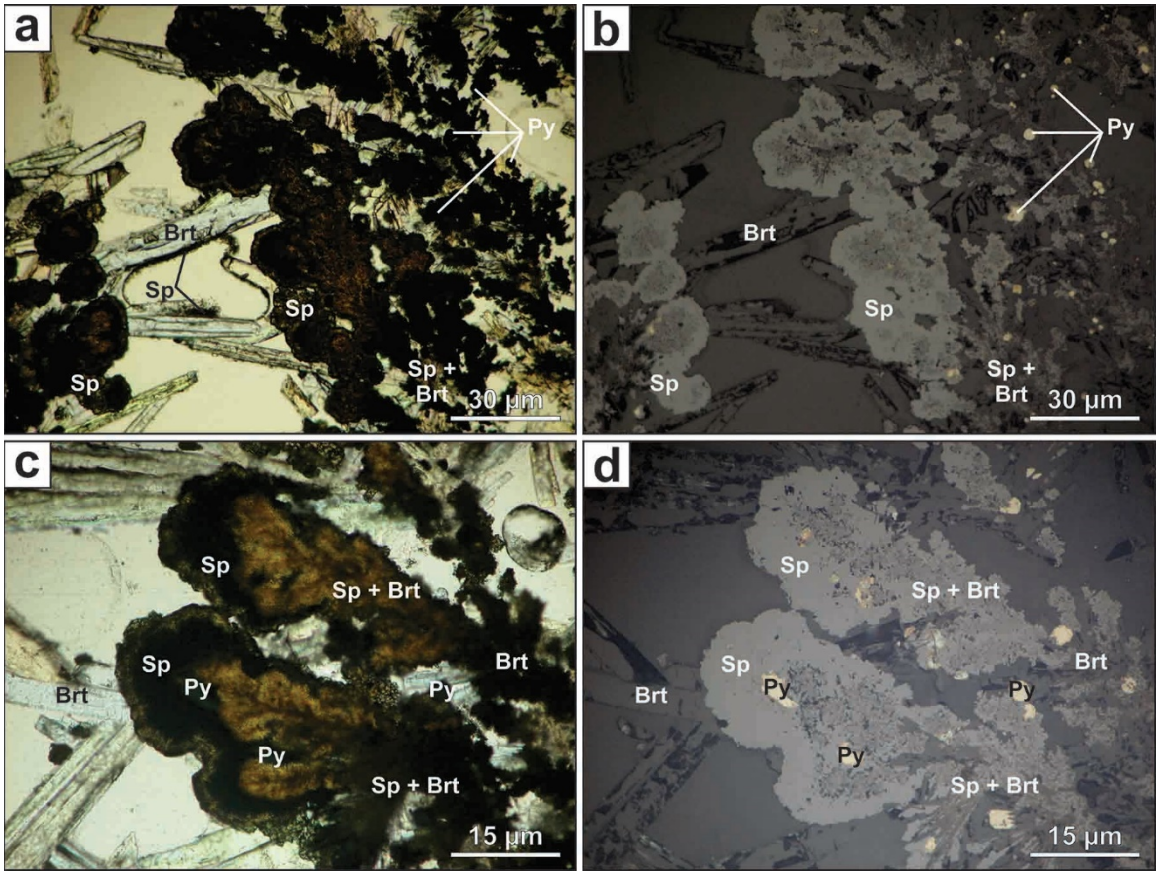
Thin Section Description

This section has ~50% porosity. It is characterized by dendritic high-Fe (black) sphalerite, followed by crystallization of fine- to medium grained spherulitic pyrite, irregularly distributed. Following this is several more generations of sphalerite. The second sphalerite generation is light brown, with decreasing Fe-contents outwards, and also displays a dendritic texture. This sphalerite appears to have many micro-inclusions or holes. This is followed by additional fine- to medium grained spherulitic to subhedral pyrite



Thin section scan of GMA13-012.

(few crystals with growth zones visible), and a third generation of high-Fe black sphalerite. The fourth sphalerite generation has very low Fe concentration (very light brown) and only occurs locally. This is followed by the crystallization of very coarse-grained tabular, often radiating barite. Additional minor fine-grained pyrite and low-Fe sphalerite crystallizes on top of the barite.



Photomicrographs of GMA13-012: ***(a)*** *transmitted light (PPL) photomicrograph of dendritic sphalerite growing on barite with late coarse-grained tabular barite;* ***(b)*** *reflected light (PPL) photomicrograph of the same view as (a) showing spherulitic pyrite growing on early generations of barite + sphalerite;* ***(c)*** *transmitted light (PPL) photomicrograph of dendritic barite and sphalerite, with different generations of sphalerite of variable Fe-contents;* ***(d)*** *reflected light (PPL) photomicrograph of the same view as (c) of dendritic barite overlain by dendritic sphalerite, followed by spherulitic pyrite, followed by several generations of pyrite, and late coarse-grained tabular barite.*

Mineral abundance: (modal %; not including pore space)

Sp	Ccp	Py	Mrc	Gn	Jd	Bn	Dg	Cv	Au	Brt	Anh	Am-Si	FeOx	others
+++	-	+	-	-	-	-	-	-	-	+++	-	-	-	-
65		5								30				

Paragenesis: High-Fe dendritic sphalerite → spherulitic pyrite → low-Fe sphalerite → spherulitic to subhedral pyrite → high-Fe sphalerite → very low-Fe sphalerite (local) → coarse-grained tabular barite → pyrite → low-Fe sphalerite.

Name: Sphalerite-barite chimney (low-T)

SAMPLE: GMA13-017a,b **PARENT ID:** 707	**LOCATION:** 784593.9E/8649858.1N **WATER DEPTH:** 1089 mbsl

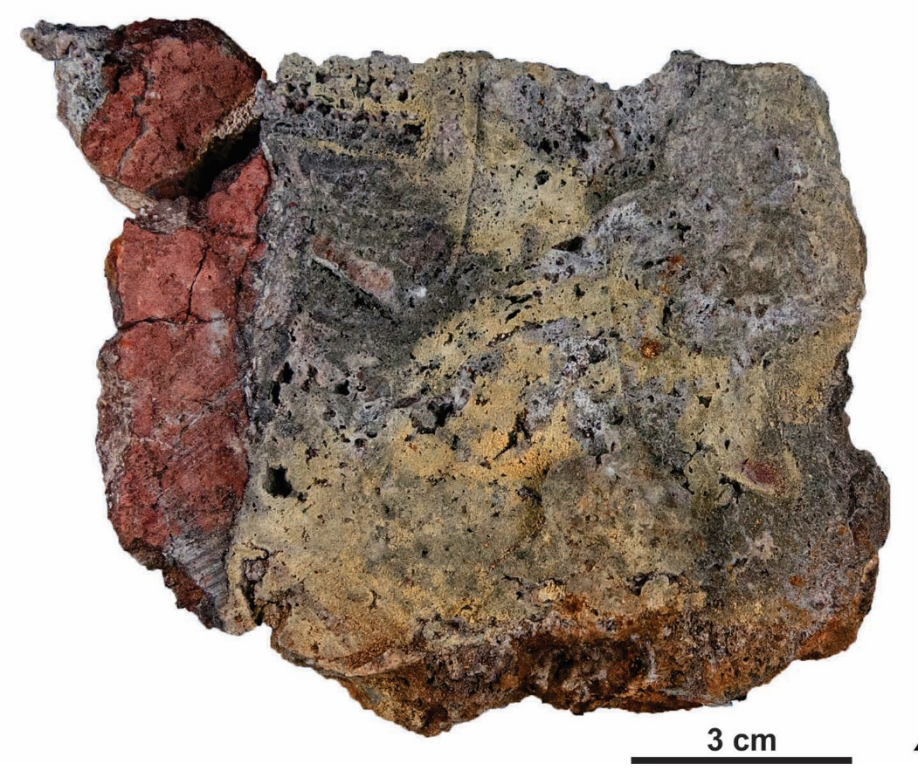
Geochemical Notes

Whole rock (17a): High Si (35.1%); Low S, Au, Fe, Cu, Zn, Cd, Ga, Ge, Hg, As, Ag.

Video Description

Chimney talus/cliff, scattered oxides.

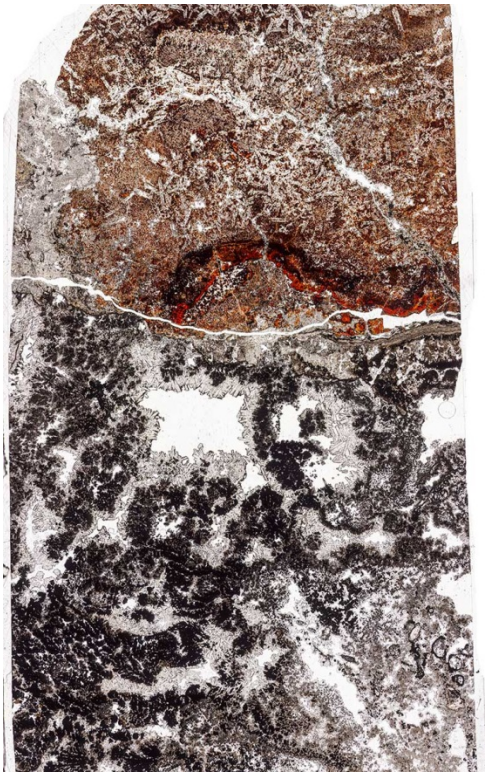
Hand Sample Description



Sample of talus from the base of a mound. The sample is pervasively silicified and contains abundant small vugs (up to 4 mm, 4-5%), likely biological in origin (worm casts), and complex banding. The sample is light grey with white infill, composed of abundant barite (20-25%), silicified. Grey coloration may be from silicified graphite (~60-65%). Near the edge of the sample is a layer of jasper-chert (5%), with a thin veneer of silicified graphite(?) at the contact. A small clast of jasper occurs in the matrix of the sample, with a few other rip-up clasts near this contact. There is trace disseminated pyrite + chalcopyrite near the contact. Yellow patchy iron oxy-hydroxides occur throughout (<1%).

Thin Section Description

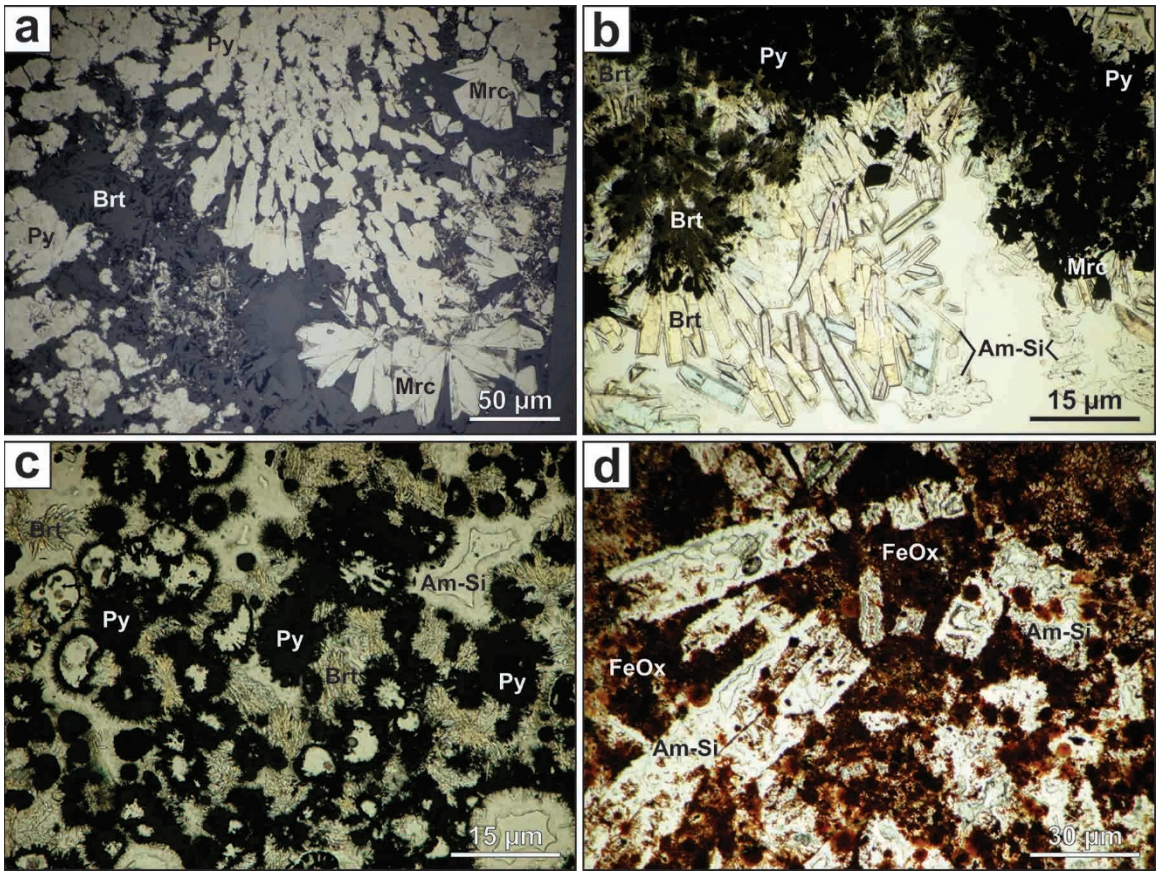
(a) This section has a porosity of ~20%. It encompasses the contact between a sulfide chimney with iron oxide. The bottom 2/3 of the section contains an early phase of coarse-grained dendritic pyrite/marcasite, primarily concentrated on the left side of the section. The dendrites tend to have porous, anhedral pyrite cores or rims, suggesting inversion of marcasite to pyrite. There is a higher proportion of marcasite relative to pyrite in these dendrites (70:30). This is followed by fine-grained



Thin section scan of GMA13-017a.

inclusion-filled (“dirty”) dendritic barite. A second generation of medium-grained spherulitic pyrite forms on top of this, with relict spherules observed in one area. Growth zoning of the pyrite is common, locally resulting in a colloform texture. This is followed by coarse-grained subhedral to euhedral marcasite, which locally displays a “starburst” pattern with fine-grained porous, anhedral pyrite forming along the crystal growth zones. The next mineralization phase is coarse- to very-coarse grained tabular, frequently radiating barite that is free from inclusions. A layer of amorphous silica coats everything, and ranges in thickness from ~0.1 to ~4.5 mm. This silica consistently displays a “fish-egg” texture. Locally, it contains very fine-grained black inclusions, likely sulfides (pyrite?), but is mostly inclusion-free. Minor very fine- to fine-grained pyrite + marcasite dusts the outside of the silica layer, locally forming crystals or spherules up to ~0.7 mm wide. Minor yellowish-brown iron oxides occur locally.

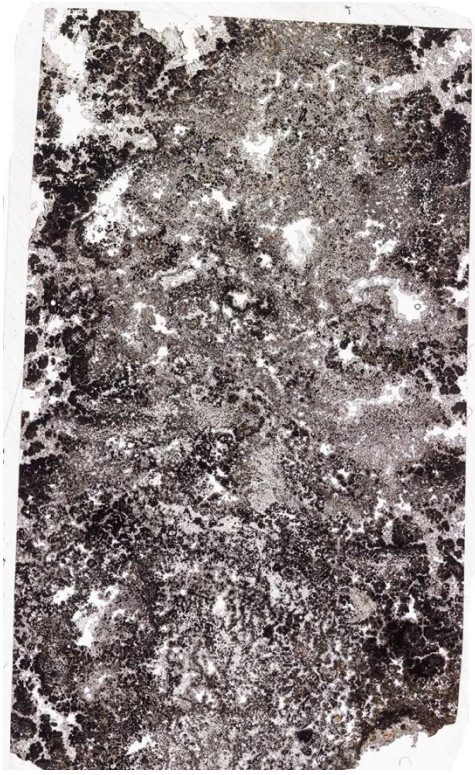
The contact with the upper 1/3 of the section is sharp and irregular. The fine-grained dendritic barite (described above) grows downward from it, suggesting that the upper part of the section formed first. Black manganese oxides and bright orange to brown iron oxides (including minor hematite) and oxyhydroxides form along the contact. The upper part of the section is composed of fine-grained amorphous silica with abundant black and orange inclusions, likely oxides. Much of the top of the section contains bright orange to red fine-grained iron oxy-hydroxides. These oxides locally coalesce, forming dendritic to colloform textures. Very coarse grained relict tabular crystals occur throughout this part of the section, up to ~15 mm long, with the highest abundance along the top of the section. These relicts are consistent with anhydrite, but none of the original mineral is preserved. Very minor fine-grained pyrite is disseminated throughout this part of the section. One crack in this part of the section is lined with manganese oxide; in general, the manganese oxides appear to post-date the iron oxides. Many of the pore spaces and cracks in this part of the section contain minor fine-grained dendritic barite and coarse-grained tabular barite, as described above. Lining everything in the top part of the section is a layer of relatively inclusion-free amorphous “fish-egg” silica, similar to the bottom part of the section; this also suggests that the top of the section formed first. Very fine cracks are filled with a late pyrite.



Photomicrographs of GMA13-017a: ***(a)*** *reflected light (PPL) photomicrograph of dendritic pyrite followed by marcasite with abundant growth zones, and late tabular barite;* ***(b)*** *transmitted light (PPL) photomicrograph of dendritic barite overgrown by pyrite, followed by coarse-grained tabular barite, and a thin coat of amorphous silica;* ***(c)*** *transmitted light (PPL) photomicrograph of radiating barite, infilled by pyrite and amorphous silica;* ***(d)*** *transmitted light (PPL) photomicrograph of relict coarse-grained crystals (anhydrite?), replaced by iron oxyhydroxides and amorphous silica.*

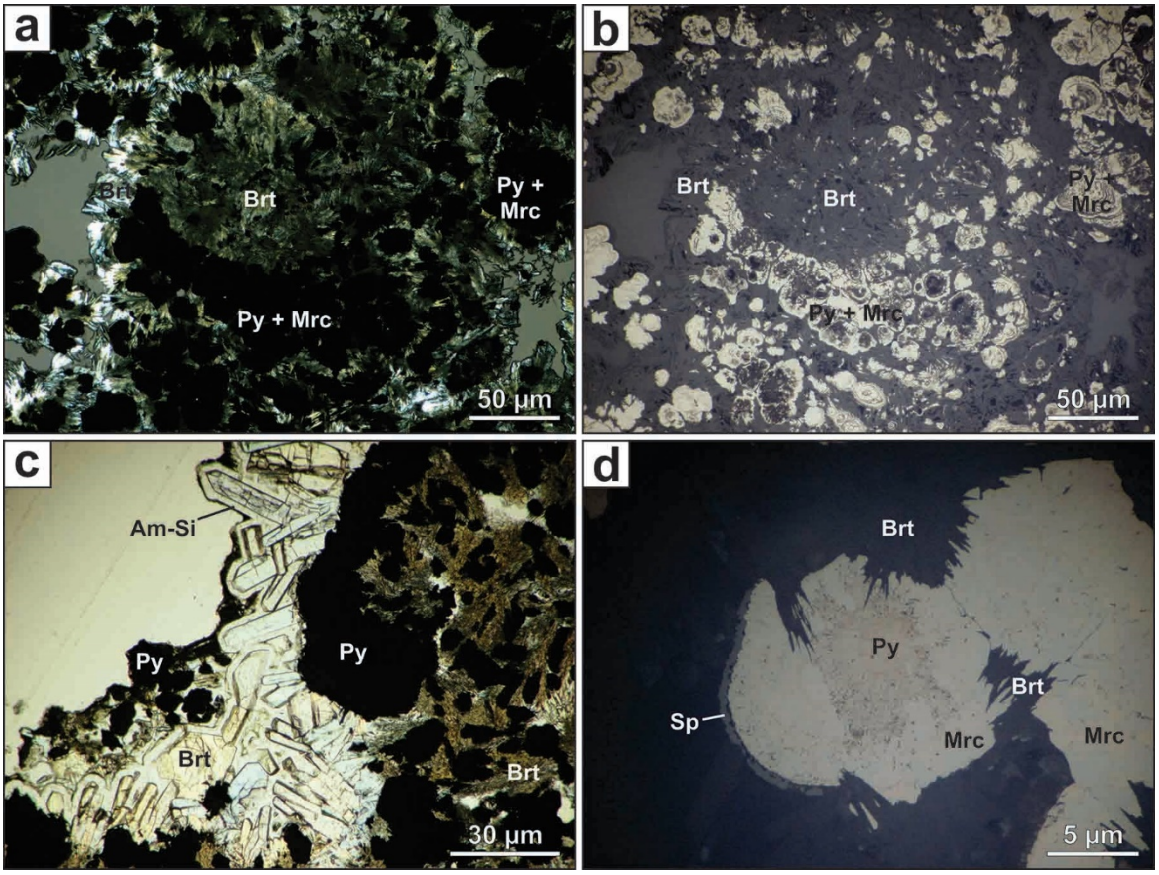
Mineral abundance: (modal %; not including pore space)

Sp	Ccp	Py	Mrc	Gn	Jd	Bn	Dg	Cv	Au	Brt	Am-Si	FeOx	Hem	MnOx
-	-	++	++	-	-	-	-	-	-	+++	+++	++	+	+
		10	15							30	30	10	2	3



Thin section scan of GMA13-017b.

(b) This section is from the bottom part of the same sample as GMA13-017a. It contains ~15% pore space. There is early crystallization of minor dendritic marcasite, irregularly distributed. As above, the dendrites generally have secondary pyrite cores, although this is not always the case. This is followed by fine-grained inclusion-filled dendritic barite. This barite occasionally appears orange, suggesting the presence of iron oxyhydroxide inclusions. Intergrown with this is medium-coarse grained marcasite/pyrite, generally with growth zones and locally showing colloform textures. Many of these crystals are spherulitic or donut-shaped with hollow centers, reflecting dissolution or increased porosity resulting from pyrite inversion. On top of this is a thin layer of minor fine-grained sphalerite. Crystallized next is abundant coarse-grained tabular barite, followed by a thin layer of amorphous silica and then fine-grained pyrite/marcasite, as above, in addition to rare tabular barite.



Photomicrographs of GMA13-017b: ***(a)*** *transmitted light (XPL) photomicrograph of dendritic/radiating barite, overgrown by pyrite and marcasite, followed by tabular, radiating barite;* ***(b)*** *reflected light (PPL) photomicrograph of the same view as (a) showing high porosity in pyrite/marcasite;* ***(c)*** *transmitted light (PPL) photomicrograph of dendritic/radiating barite, overgrown by pyrite, a second generation of tabular barite, a thin layer of amorphous silica, and additional pyrite;* ***(d)*** *reflected light (PPL) photomicrograph of early barite, followed by marcasite that is locally inverted to porous, anhedral pyrite, and late sphalerite.*

Mineral abundance: (modal %; not including pore space)

Sp	Ccp	Py	Mrc	Gn	Jd	Bn	Dg	Cv	Au	Brt	Anh	Am-Si	FeOx	others
+	-	++	++	-	-	-	-	-	-	+++	-	+++	Tr	-
1		15	10							50		24	<0.01	

Paragenesis: Anhydrite(?) relict crystals → iron oxyhydroxides → manganese oxides → inclusion-filled amorphous silica → dendritic coarse-grained marcasite → fine-grained dendritic barite + medium- to coarse-grained marcasite (locally colloform) → coarse-grained marcasite (locally 'starburst') → secondary pyrite (after marcasite)→ fine-grained sphalerite → coarse-grained tabular barite → amorphous "fish-egg" silica + sulfide inclusions → fine-grained pyrite + marcasite ± barite → iron oxyhydroxide (local).

Name: Silicified iron-oxide caprock with barite- pyrite chimney

SAMPLE: GMA13-018a,b **PARENT ID:** 706	**LOCATION:** 784594.1E/8649858.0N **WATER DEPTH:** 1089 mbsl

Geochemical Notes

**XRF (parent): Cu = 0.01%, Pb = 0.02%, Zn = 0.20%, Ag = 72.2 ppm; Au = 0.47 ppm.*

Video Description

Chimney talus/cliff, scattered oxides.

Hand Sample Description



Hand sample of GMA-018a.

(a) Large block of talus from base of sulphide mound. Sample is a silica-altered rock with banded heterogeneous dark and light grey areas (possibly containing graphite, 95%) that contain small (up to 4 mm wide) vugs that appear to have biological origin (2-3% overall). The silicified rock is cut by irregular (1-10 mm wide) white-orange veins with early needle-like barite (2%) and later silica (1%) precipitation, associated with orange cubic iron oxide (1%) likely replacing pyrite. On the surface there is a trace amount of orpiment(?).

(b) Complex silica-altered chimney (20% silica) containing abundant coarse-grained interstitial and vug-lining barite (55%), minor sphalerite (10%), possible black organic material? (3%), and siliceous 2 mm wide veins. Minor iron oxide associated with silica on outer surfaces and in veins (2%). Trace yellow material, possibly orpiment?. Small mm-size vugs, with 10% pore space overall.



Hand sample of GMA13-018b.

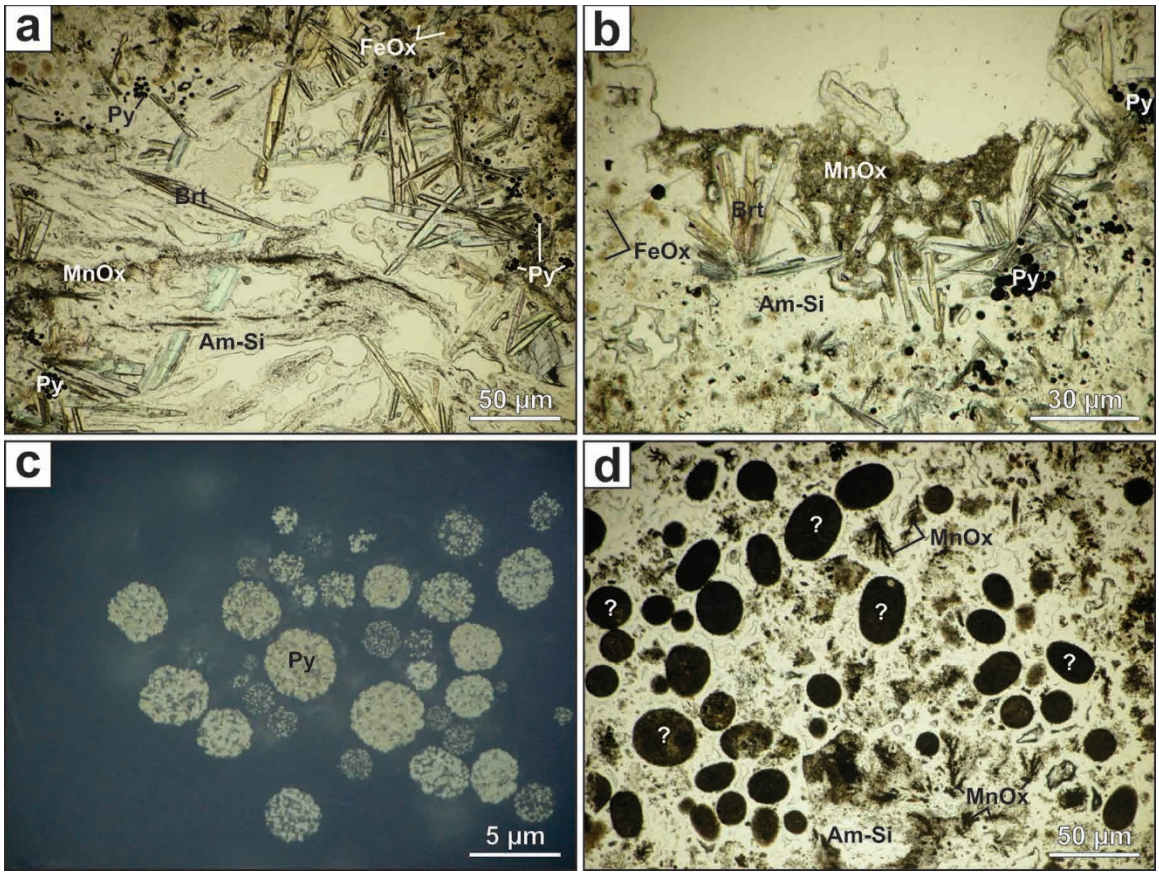
Thin Section Description



Thin section scan of GMA13-018a.

(a) This section has a porosity of ~10%. The top right corner contains abundant amorphous silica with fine- to very fine-grained brown to black inclusions, likely of oxides. There is very minor disseminated fine-grained spherulitic pyrite here. The oxide inclusions appear banded near the contact. This area appears mostly white with buff, orange, and black mottled colors in hand sample. The contact itself is sharp and irregular, and is characterized by black manganese oxide and minor bright-orange iron oxyhydroxides.

The bottom half of the section also contains amorphous silica with dark inclusions (fewer than above), with a few inclusions of dendritic manganese oxide. Despite the lower amount of inclusions, this area appears black in hand sample, possibly indicating that the inclusions are manganese oxide. There are no obvious hydrocarbons. This mineralogy grades upwards to the top left part of the section, which has a higher porosity. Here, there is also inclusion-filled amorphous silica, with additional dendritic iron oxides, apparent clasts of the inclusion-rich silica described in the first part, and strange dark brown to black oblate spheroids, up to ~3.2 mm long. These may be manganese concretions or replacements, possibly of biological origin. Hydrocarbons are not present. Grape-like collections of fine-grained framboidal pyrites are irregularly distributed, also possibly indicating biological activity. Very coarse-grained tabular to acicular, often radiating, barite grows in the open spaces. Everything is coated with a layer of relatively inclusion-free amorphous “fish-egg” silica, ranging from <1 mm to ~2.5 mm thick. Locally on top of this are additional minor very fine-grained manganese-iron oxyhydroxides.



Photomicrographs of GMA13-018a: ***(a)*** *transmitted light (XPL) photomicrograph of coarse-grained barite, framboidal pyrite, and iron and manganese oxides overgrown by amorphous silica;* ***(b)*** *transmitted light (PPL) photomicrograph of coarse-grained barite, framboidal pyrite, and iron and manganese oxides overgrown by amorphous silica, and late manganese oxide;* ***(c)*** *reflected light (PPL) photomicrograph close-up of framboidal pyrite;* ***(d)*** *transmitted light (PPL) photomicrograph of egg-shaped concretions manganese oxide(?), dendritic manganese oxide, and amorphous silica.*

Mineral abundance: (modal %; not including pore space)

Sp	Ccp	Py	Mrc	Gn	Jd	Bn	Dg	Cv	Brt	Anh	Am-Si	FeOx	MnOx
-	-	+	-	-	-	-	-	-	++	-	+++	+	+++
		2							10		58	5	25

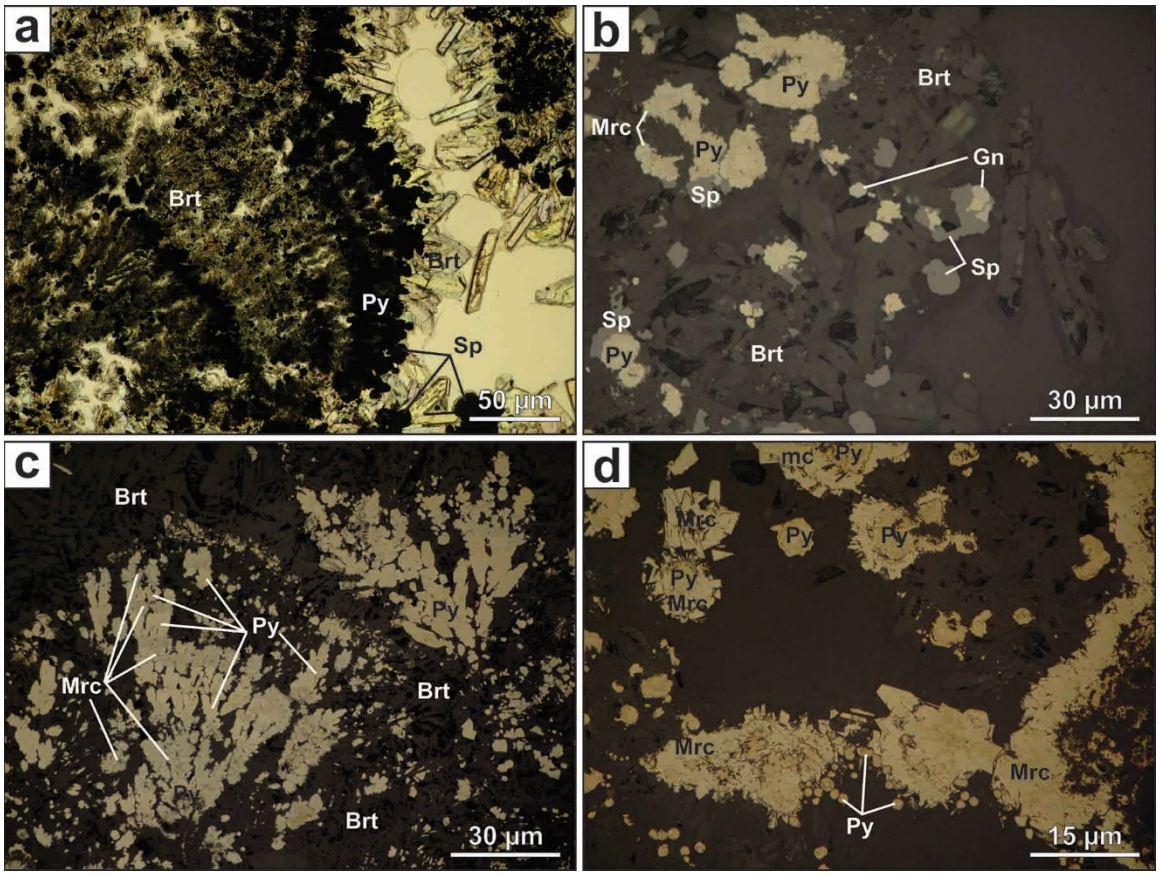
Paragenesis: [top of section] iron and manganese oxide (inclusions) → amorphous silica → [bottom of section] oblate spheroids (manganese oxide?) → dendritic manganese oxide and manganese(?) concretions + iron oxide (inclusions and dendrites) → amorphous silica → fine-grained framboidal pyrite → coarse-grained barite → inclusion-free amorphous "fish-egg" silica → minor fine-grained oxides

Name: Silicified biogenic(?) caprock



Thin section scan of GMA13-018b.

(b) This section is very different from GMA13-018A, suggesting that the two samples were collected in the same area but are not part of the same chimney. It has a porosity of ~20-25%. It is characterized by fine-grained dendritic barite with lots of fine inclusions ("dirty" looking; possibly with very fine-grained iron oxide or sulfide inclusions) and colloform to spherulitic marcasite (with minor porosity). The marcasite has been partially inverted to secondary porous, anhedral pyrite, which occurs as irregular cores to marcasite, or along crystal growth zones (giving it an 'etched' appearance). Primary (pore-free) medium-grained pyrite forms next, locally occurring as dendritic bands alternating with porous, partially pyritized marcasite. The sequence of dendritic barite and pyrite/marcasite repeats several times (at least three, locally). This pyrite/marcasite locally forms around former vent conduits, forming donut shapes. It is followed by coarser-grained crystalline marcasite, with less overall porosity, and only minor secondary pyrite. Minor fine-grained galena and high- Fe sphalerite are precipitated next, often intergrown with each other. The sphalerite is locally altered to secondary covellite ± digenite (trace), indicating the presence of copper. This is followed by coarse- to very coarse-grained tabular/radial barite. A very thin layer of amorphous "fish egg" silica (~0.1 mm thick) coats everything. This silica thickens to several mm at the very top of the section, where it also contains fine-grained inclusions of sulfides. A few very coarse-grained barite crystals up to ~6 mm wide form last in the former vent conduits; one notable crystal shows distinct growth zones and oscillatory extinction.



Photomicrographs of GMA13-018b: ***(a)*** *transmitted light (PPL) photomicrograph of sequential generations of dendritic barite and pyrite/marcasite, followed by sphalerite and coarse-grained tabular barite;* ***(b)*** *reflected light (PPL) photomicrograph of marcasite locally inverted to pyrite, followed by galena, and sphalerite;* ***(c)*** *reflected light (PPL) photomicrograph of dendritic primary pyrite, banded with porous marcasite that has been partially inverted to secondary pyrite (porous);* ***(d)*** *reflected light (PPL) photomicrograph of spherulitic pyrite(highly porous) after marcasite, overgrown by coarse-grained marcasite that is also locally inverted to pyrite.*

Mineral abundance: (modal %; not including pore space)

Sp	Ccp	Py	Mrc	Gn	Jd	Dg	Cv	Brt	Gr(?)	Am-Si	FeOx	MnOx
+	-	++	++	+	-	Tr	Tr	+++	-	+	Tr	-
5		20	12	1		<0.01	<0.01	60		2	<0.01	

Paragenesis: Fine-grained dendritic barite → spherulitic to colloform marcasite → primary medium-grained pyrite, locally dendritic and banded with marcasite [sequence locally repeated x3] → coarse-grained marcasite → secondary pyrite after marcasite → galena + high-Fe sphalerite → covellite + digenite → coarse-grained radial/tabular barite → amorphous “fish egg” silica → very coarse-grained barite.

Name: Pyrite/marcasite-barite chimney talus

SAMPLE: GMA13-019a,b **PARENT ID:** 701	**LOCATION:** 784567.2E/8649966.6N **WATER DEPTH:** 1101 mbsl

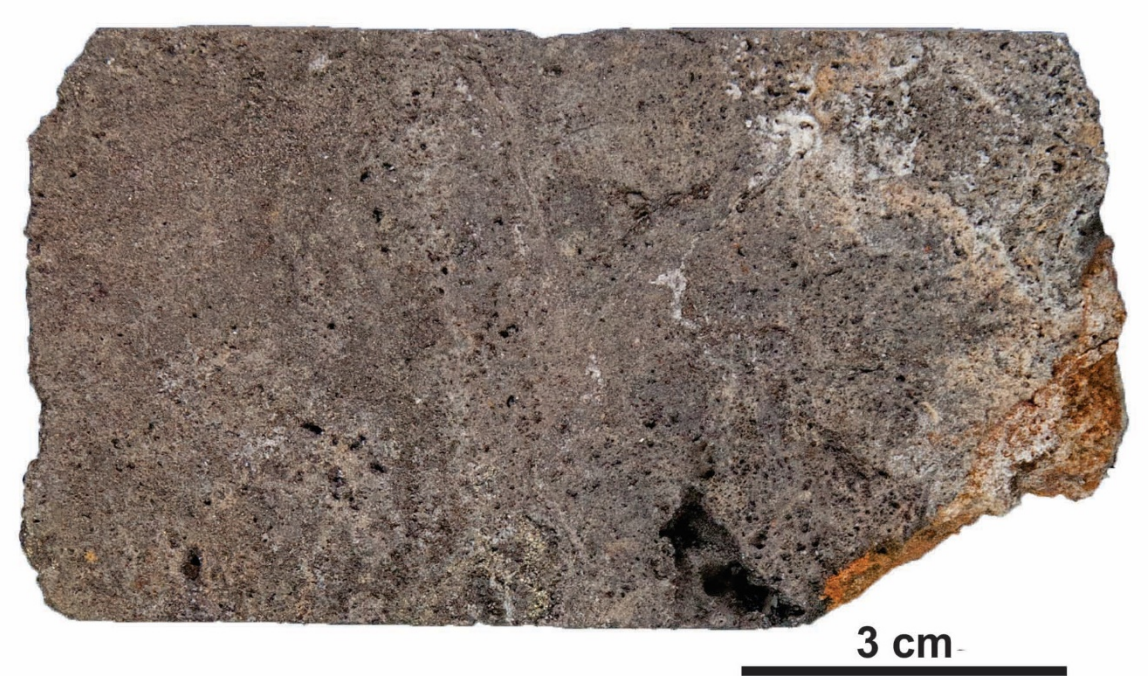
Geochemical Notes

(a) Whole rock (19a): High Zn (343000 ppm), Cd (1070 ppm), Ge (96 ppm), Ba (73400 ppm); Low Fe, Cu, Ga, Hg.

Video Description

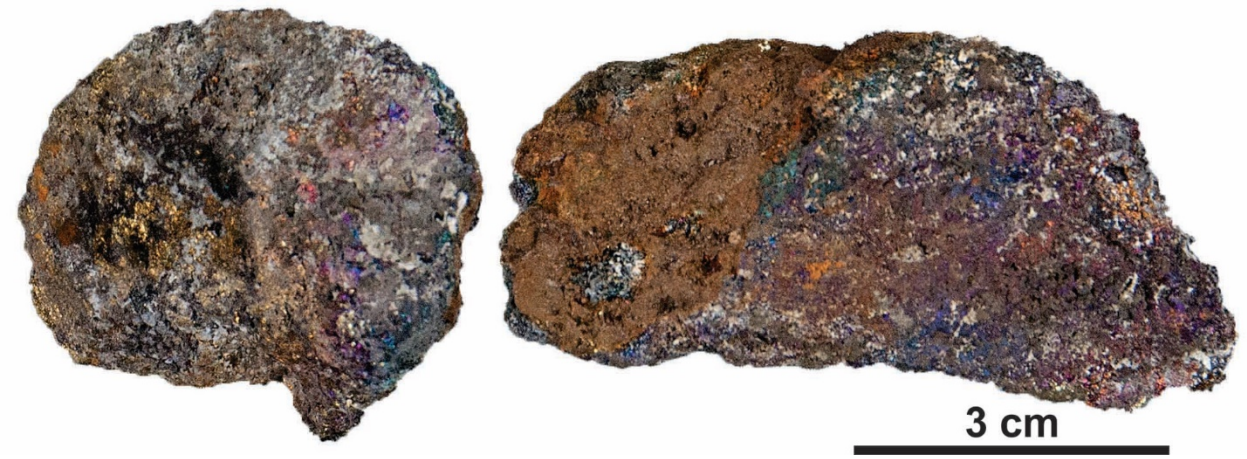
Boulder from talus in mound, rounded.

Hand Sample Description



Hand sample of GMA13-019a.

(a) Massive sphalerite-barite chimney with minor chalcopyrite (3%) around a former vent conduit that is now filled in with sphalerite and barite. The sphalerite is primarily low-Fe (40%) with lesser high-Fe (45%), displaying minor dendritic textures. The sample contains interstitial fine-grained barite and barite in vugs (10%). The vugs are generally small (mm-size), 10-15% overall. Weathered surface has an irregular thin layer, up to 6 mm wide, containing clay (1%) and iron oxide (<1%).



Hand sample of GMA13-019b.

(b) Chalcopyrite-rich chimney with coarse-grained crystals, very coarse crystals near former vugs, 90% chalcopyrite overall. Chalcopyrite is oxidized and contains 1% bornite and 1% covellite. Minor sphalerite, patchy, 2% overall. Pore space between chalcopyrite crystals is mm-size, 5% overall. Pore space is filled with white clay and/or anhydrite (2%). Trace iron oxide on outer surface.

Thin Section Description



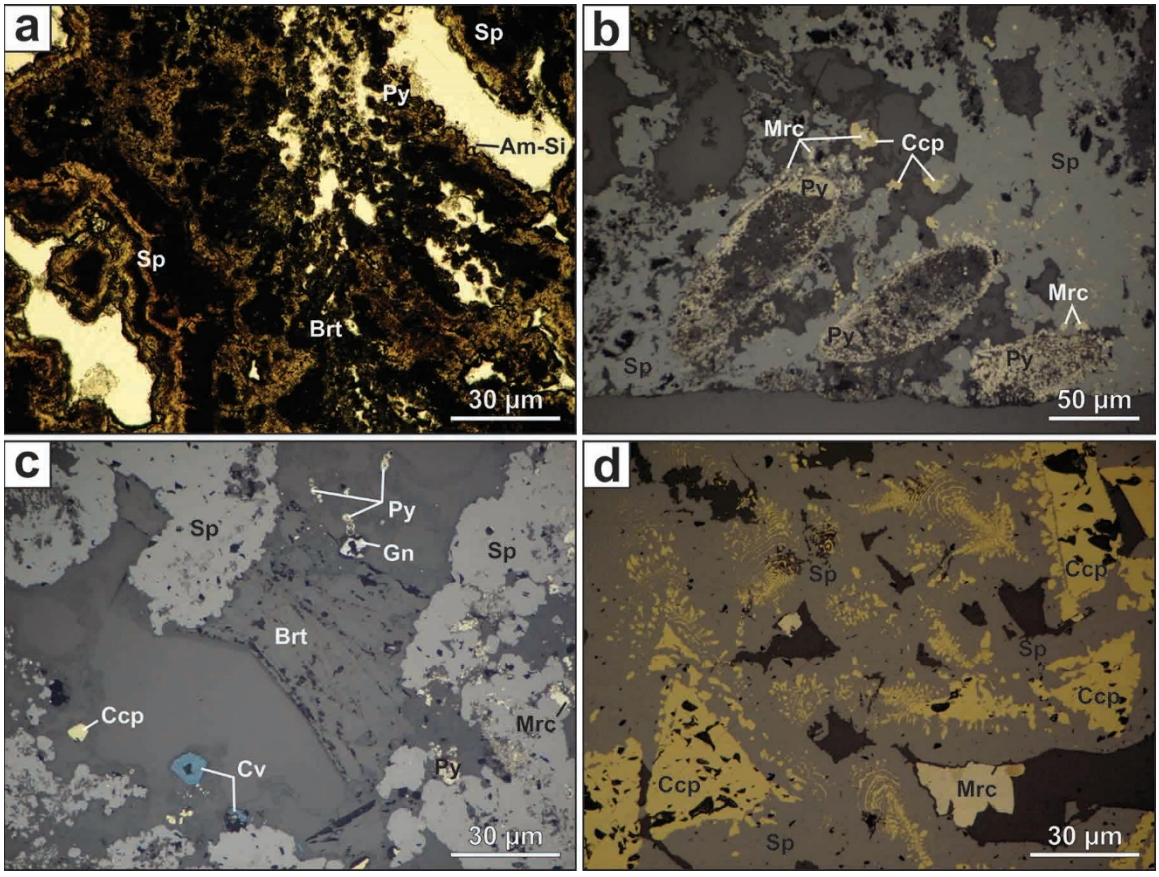
Thin section scan of GMA-019a.

(a) This sample has a porosity of ~35%. The mineralogy and textures vary between the bottom ¼ and top ¾ of the section. The bottom quarter contains abundant early fine-grained dendritic barite, overgrown by fine-grained spherulitic pyrite and dendritic high-Fe sphalerite. This dendritic sphalerite generally grows from left to right of the section. This is followed by several more generations of alternating low- and high-Fe sphalerite. The high-Fe sphalerite generations are associated with "chalcopyrite disease." This is followed by minor medium-grained pyrite and chalcopyrite. Bands of sulfides outline former vent conduits, generally lined by pyrite and partially filled by pyrite + sphalerite.

The border between the bottom quarter and the top of the section is loosely defined by an irregular band of fine- to medium grained pyrite. The previously-describe generation of fine- to very coarse-grained pyrite and chalcopyrite dominate the top ¾ of the section. The very coarse-grained chalcopyrite grows upwards from this border, indicating that the top of the section forms after the bottom dendritic part. Locally, repeated growth patterns of chalcopyrite with high-Fe sphalerite occur. Very coarse-grained low-Fe (light yellowish-brown, almost colorless) sphalerite occurs on top of this,

forming along bands mostly in the top quarter of the section. This sequence of pyrite/chalcopyrite followed by low-Fe sphalerite is repeated from the bottom part of the section. Minor coarse-grained marcasite and a few medium-grained crystals of galena form next. Scattered very fine-grained secondary covellite occurs throughout the top of the section. All of the sulfides have a generally banded, irregular distribution, typical of zoned chimneys. Very few late medium- to coarse-grained barite crystals are irregularly distributed, mostly associated with the sphalerite-rich bottom quarter of the section. Amorphous "fish-egg" silica with abundant sulfide inclusions irregularly fills in some of the remaining pore space (primarily in the top part of the section).

This section is interesting as it seems to encompass two chimney types: a sphalerite-barite (low-T) chimney type on the bottom, overgrown by a zoned chalcopyrite-sphalerite chimney type on the top. This demonstrates the changing temperature conditions at one location over time.



Photomicrographs of GMA13-019a: ***(a)*** *transmitted light (PPL) photomicrograph of sequential generations of high- and low-Fe sphalerite generations overgrowing dendritic barite, with a thin coat of amorphous silica;* ***(b)*** *reflected light (PPL) photomicrograph of pyrite lining former vent conduits, and sphalerite with chalcopyrite inclusions;* ***(c)*** *reflected light (PPL) photomicrograph of sphalerite associated with pyrite and marcasite inclusions, late chalcopyrite and galena, secondary covellite, and coarse-grained barite;* ***(d)*** *reflected light (PPL) photomicrograph of chalcopyrite, followed by fine layers of sphalerite-chalcopyrite, a thicker layer of sphalerite, and late marcasite.*

Mineral abundance: (modal %; not including pore space)

Sp	Ccp	Py	Mrc	Gn	Jd	Bn	Dg	Cv	Au	Brt	Anh	Am-Si	FeOx	others
+++	++	+	+	Tr	-	-	-	Tr	-	+++	-	+	-	-
60	15	5	2	<1				<1		15		3		

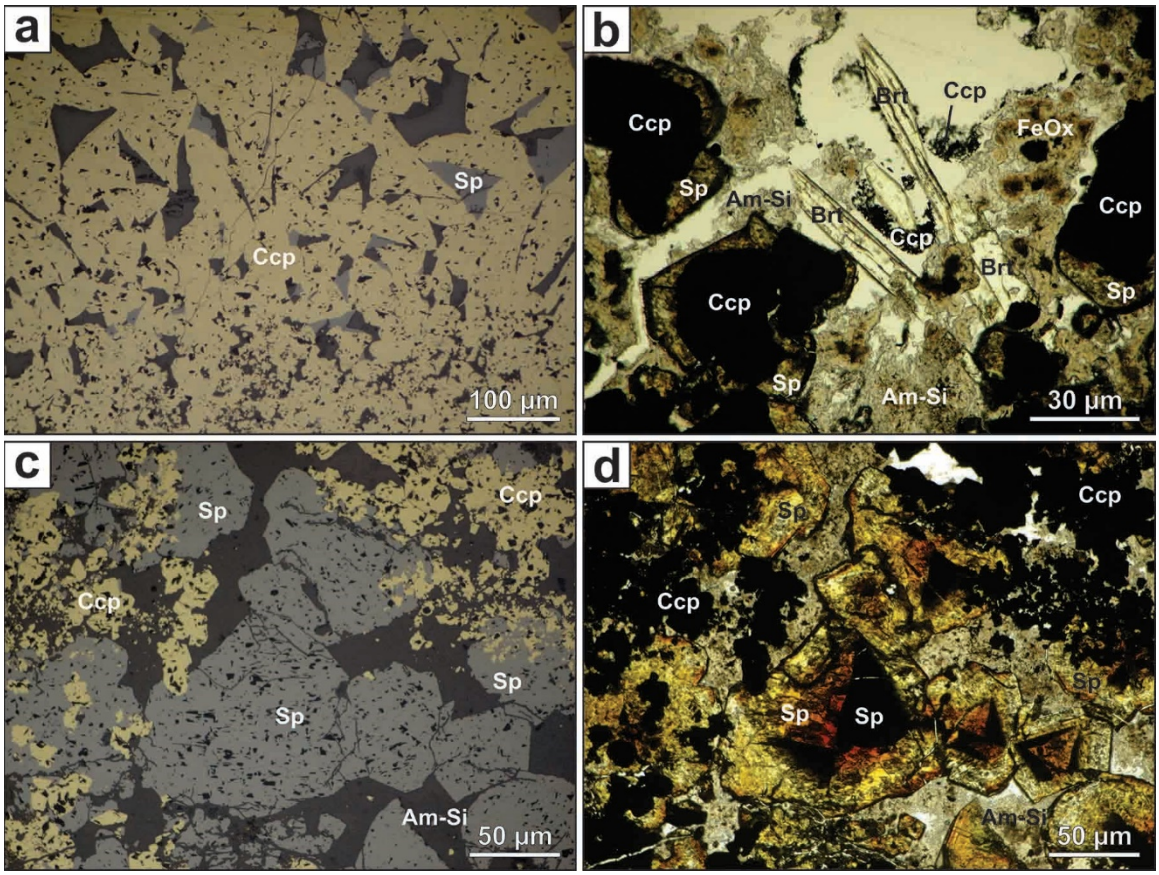
Paragenesis: Fine-grained dendritic barite → spherulitic pyrite → high-Fe dendritic sphalerite → alternating high-Fe sphalerite with chalcopyrite disease and low-Fe sphalerite → medium- to very coarse-grained grained pyrite + chalcopyrite → repeated chalcopyrite + high-Fe sphalerite zones → coarse-grained very low-Fe sphalerite → coarse-grained marcasite → secondary covellite → minor coarse-grained barite (local) → amorphous silica.

Name: Sphalerite-barite chimney talus overgrown by zoned chalcopyrite-sphalerite chimney



Thin section scan of GMA13-019b.

(b) This sample is very different from GMA13-019a, suggesting that they were recovered from the same area but are likely not part of the same chimney. This section has a porosity of ~20%. It has a very simple mineralogy, dominated by medium- to very coarse-grained chalcopyrite, with large tetrahedral crystals filling in a circular former vent conduit in the lower right corner of the section. The chalcopyrite is overgrown by low- to very-low Fe sphalerite, with a generally decreasing Fe-content outwards, ranging from reddish-orange to almost colorless. Much of the remaining pore space is filled by very fine-grained amorphous "fish egg" silica with abundant iron oxide(?) or sulfide inclusions. A few very coarse-grained tabular barite crystals occur in some of the pore spaces. Minor fine-grained chalcopyrite + sphalerite locally crystallizes last. Unlike the hand sample, no secondary sulfides (bornite or covellite) were observed. Minor bright orange-red iron oxyhydroxides occur at the very bottom of the section.



Photomicrographs of GMA13-019b: ***(a)*** *reflected light (PPL) photomicrograph of coarse-grained chalcopyrite overgrown by sphalerite;* ***(b)*** *transmitted light (PPL) photomicrograph of chalcopyrite overgrown by sphalerite, fine-grained amorphous silica with minor iron oxyhydroxides, coarse-grained barite, and late fine-grained chalcopyrite;* ***(c)*** *reflected light (PPL) photomicrograph of chalcopyrite with late sphalerite;* ***(d)*** *transmitted light (PPL) photomicrograph of the same view as (c), showing an early generation of high-Fe sphalerite, and a late generation of low-Fe sphalerite, with decreasing Fe-contents outwards, and late amorphous silica.*

Mineral abundance: (modal %; not including pore space)

Sp	Ccp	Py	Mrc	Gn	Jd	Bn	Dg	Cv	Au	Brt	Anh	Am-Si	FeOx	others
++	+++	-	-	-	-	-	-	-	-	+	-	++	Tr	-
15	74									1		10	<1	

Paragenesis: Coarse-grained chalcopyrite → low-Fe sphalerite → amorphous “fish egg” silica with FeOx inclusions → coarse-grained tabular barite → minor fine-grained chalcopyrite + sphalerite (local).

Name: Zoned chalcopyrite + sphalerite chimney talus

SAMPLE: GMA13-020 **PARENT ID:** 703	**LOCATION:** 784563.8E/8649943.2N **WATER DEPTH:** 1094 mbsl

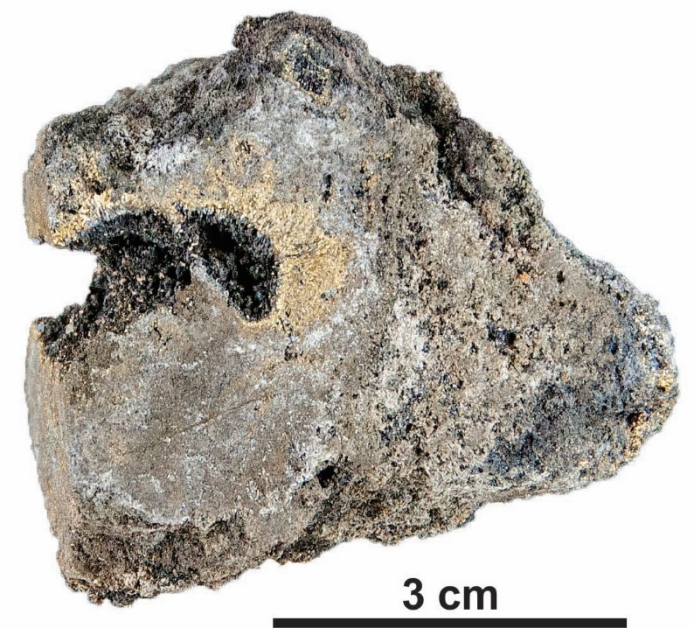
Geochemical Notes

**XRF (parent): Cu = 14.50%, Pb = 0.08%, Zn = 4.59%, Ag = 89.6 ppm; Au = 2.28 ppm.*

Video Description

From pipe organ chimney on sulphide mound. Towering chimneys protruding through indurated crust. Organ pipe chimney spires, popcorn chimneys, FeOx surficial coating on sulphides.

Hand Sample Description

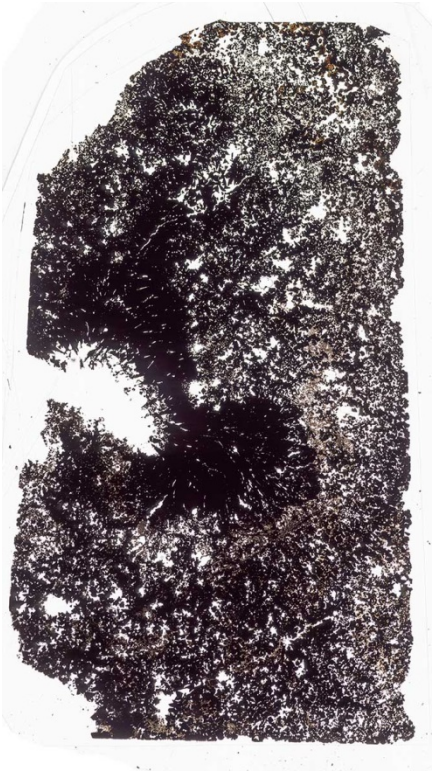


Hand sample of GMA13-020.

Small chimney fragment from the central orifice at the top of a chimney spire with an irregular axial conduit, with 10% pore space overall. Elongate chalcopyrite lines the conduits (10%) up to 1 cm thick, thinly coated by needle-like sphalerite (2-3%), with very fine grained barite as the final phase precipitated. The outer zone is pyrite/marcasite-rich, fine-grained (65%). Minor barite occurs in the outer zone as small granular white patches (6-7%).

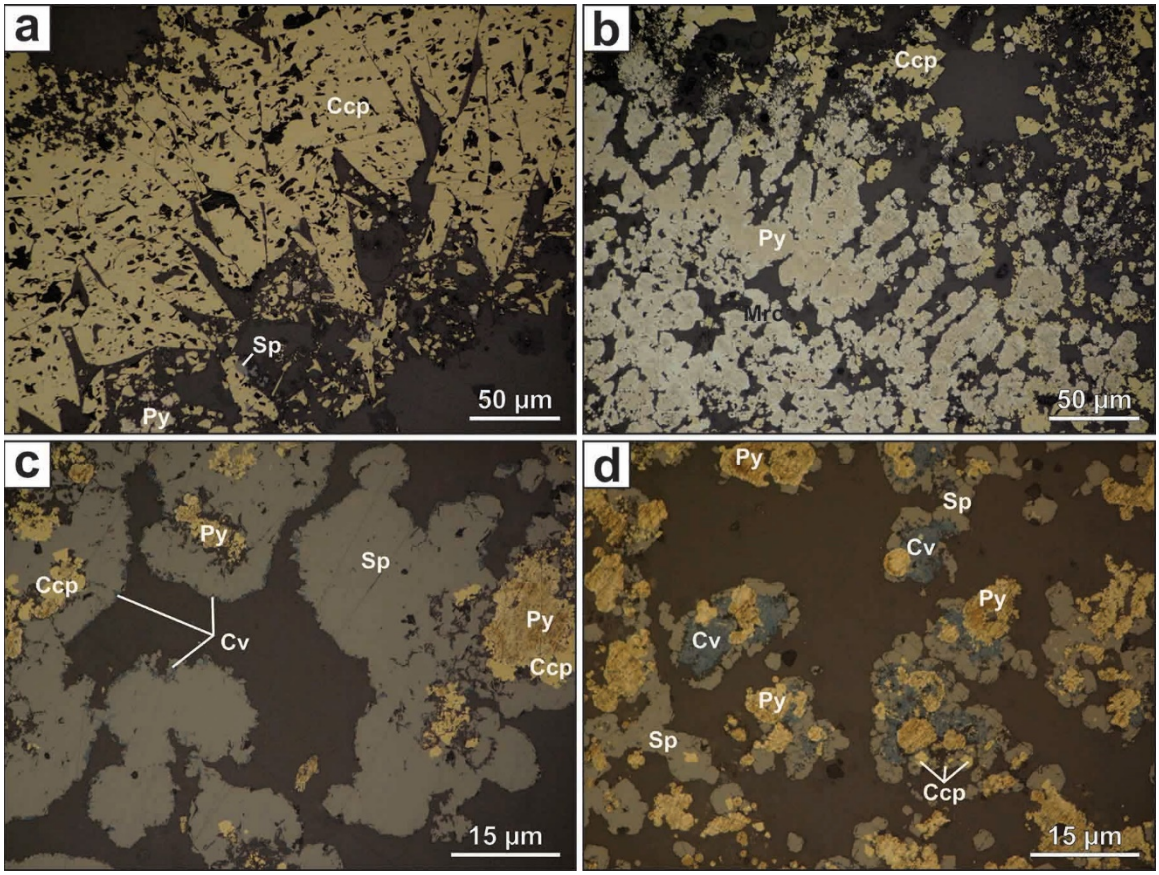
Thin Section Description

This sample has a high porosity of ~40%. The earliest phase to crystallize is dendritic to colloform (locally spherulitic) marcasite, which occurs primarily in the bottom part of the section, generally along a semi-circular band. It is extensively inverted to secondary anhedral pyrite. Locally, this replacement is complete, and is indicated only by the high porosity of the pyrite. This is followed by coarse- to very coarse-grained chalcopyrite, which also forms large tetragonal crystals that fill in most of the central vent conduit. High- to low-Fe sphalerite grows on top of both the chalcopyrite and



Thin section scan of GMA13-020.

marcasite/pyrite, with decreasing Fe-contents outwards, mostly forming in the top part of the section in a zone between the chalcopyrite-filling conduit and a band of dendritic marcasite. Locally, this sphalerite is associated with minor secondary fine-grained covellite. Fine-grained amorphous “fish-egg” silica with very-fine grained sulfide(?) inclusions irregularly fills in some of the remaining space, mostly in the bottom part of the section. The silica “fish-eggs” are locally arranged in a branching pattern. This silica has tiny acicular needles growing on top of it, possibly silica or barite(?). Rare radiating coarse-grained barite forms last.



Photomicrographs of GMA13-020: ***(a)*** *reflected light (PPL) photomicrograph of coarse-grained chalcopyrite in a former vent conduit, overgrown by minor sphalerite;* ***(b)*** *reflected light (PPL) photomicrograph of marcasite that has been extensively inverted to porous secondary pyrite, overgrown by chalcopyrite;* ***(c)*** *reflected light (PPL) photomicrograph of secondary pyrite (after marcasite), overgrown by chalcopyrite and sphalerite, with local alteration to covellite;* ***(d)*** *reflected light (PPL) photomicrograph of secondary pyrite (after marcasite), overgrown by chalcopyrite and sphalerite, altered to covellite, followed by another generation of sphalerite.*

Mineral abundance: (modal %; not including pore space)

Sp	Ccp	Py	Mrc	Gn	Jd	Bn	Dg	Cv	Au	Brt	Anh	Am-Si	FeOx	others
+	+++	++	+	-	-	-	-	+	-	+	-	++	-	-
5	68	10	5					1		1		10		

Paragenesis: Dendritic to colloform marcasite → secondary pyrite → chalcopyrite → high- to low-Fe sphalerite → covellite → amorphous “fish-egg” silica.

Name: Zoned chalcopyrite-marcasite/pyrite chimney.

SAMPLE: GMA13-021 **PARENT ID:** 704	**LOCATION:** 784551.0E/8649883.2N **WATER DEPTH:** 1088 mbsl

Geochemical Notes

Whole rock: High S (32.8%), Fe (27.3%), Cu (166000 ppm), Mo (123 ppm), In (87 ppm), As (760 ppm); Low Zn, Cd, Ge, Hg, Sb, Ag, Ba.

Video Description

Piece from large chimney with knobbly popcorn protrusions and patchy FeOx.

Hand Sample Description



Hand sample of GMA13-021.

Massive chimney with chalcopyrite and pyrite, with minor zonation and few vent conduits <1 cm wide, smaller vugs throughout sample, with 15% pore space overall. Chalcopyrite comprises 55% of the sample, with minor pyrite (20%), atacamite (3%). Only minor sphalerite (5%) and barite (2-3%). Iron oxide (<1%), manganese oxide (1%), and clay (<1%) on outer surface.

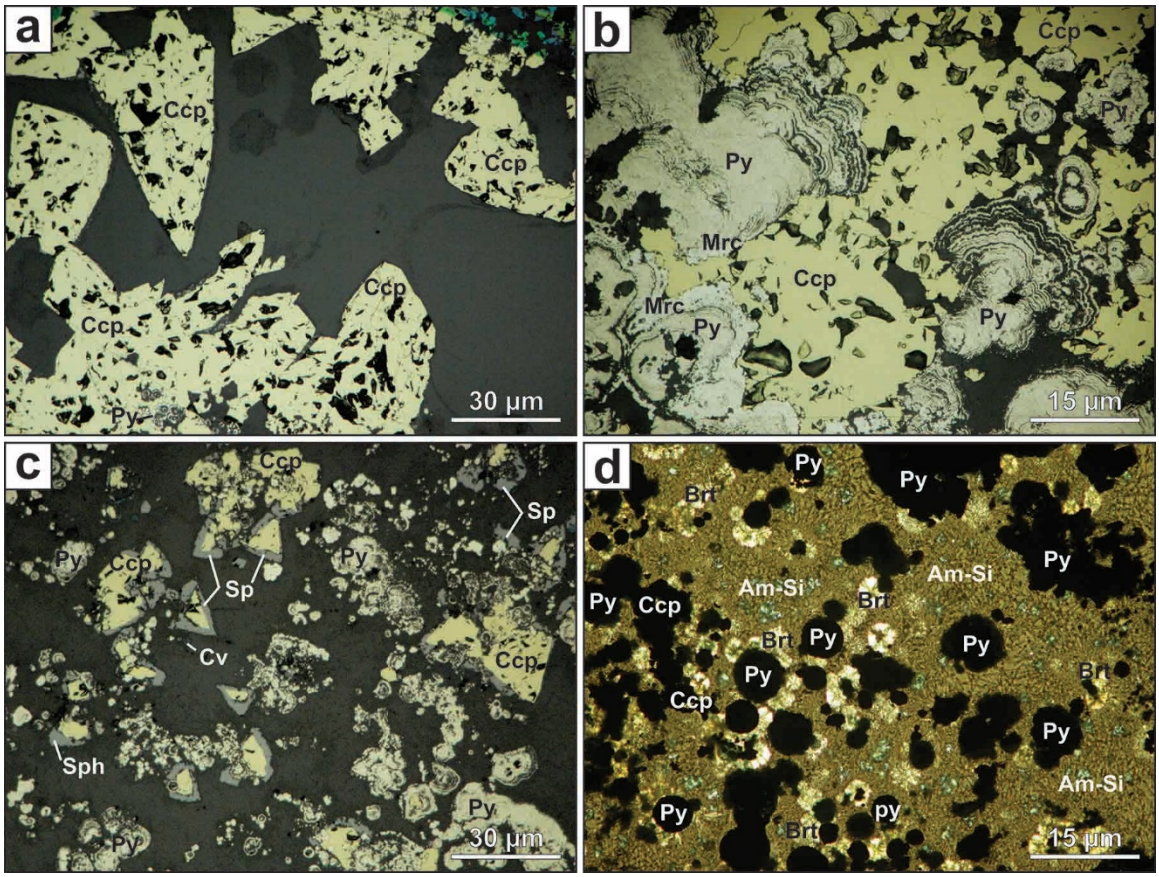
Thin Section Description

This section has a porosity of ~35%. It contains early fine- to medium-grained spherulitic to colloform marcasite that has almost been completely inverted to pyrite (indicated by high porosity) locally associated with fine-grained iron oxides (goethite?), overgrown by a second generation of medium-grained subhedral primary pyrite (also locally altered to fine-



Thin section scan of GMA13-021.

grained goethite?). The pyrite/marcasite is irregularly distributed along the section as bands, and occasionally outlines former round vent conduits. This is followed by medium- to very coarse-grained chalcopyrite, with the largest crystals growing in former vent conduits. A minor thin layer of low-Fe sphalerite crystallizes on top of the chalcopyrite, irregularly distributed. Minor secondary very fine-grained covellite is scattered throughout the section. Small spherules of radiating fine-grained barite(?), ~0.35 mm wide, are distributed unevenly throughout the section. These barite(?) spheroids are lightly stained orange (irregular) from the presence of iron oxyhydroxides. This is the first time this barite morphology has been observed in this sample set. Fine-grained spheroidal ("fish-egg") to acicular/branching amorphous silica unevenly fills in much of the remaining pore space. A fine dusting of very fine-grained sulfides (very minor amounts of pyrite + chalcopyrite) forms on top of the silica. At the margins of the amorphous silica there are occasional small light bluish-green amorphous accumulations, likely atacamite (or celadonite?). A few coarse-grained crystals of barite form last.



Photomicrographs of GMA13-021: ***(a)*** *Photomicrograph in reflected light (PPL) of coarse-grained chalcopyrite with early spherulitic pyrite (after marcasite) in a former vent conduit;* ***(b)*** *photomicrograph in reflected light (PPL) of colloform highly-porous secondary pyrite after marcasite (irregular) with growth zones , and late chalcopyrite;* ***(c)*** *photomicrograph in reflected light (PPL) early pyrite, followed by chalcopyrite, and then low-Fe sphalerite;* ***(d)*** *photomicrograph in transmitted light (XPL) of spherulitic pyrite and chalcopyrite, overgrown by radiating spheres of barite(?) (with minor Fe-staining), and late very fine-grained needles and "fish-eggs" of amorphous silica; faint bluish-green areas within the amorphous silica may be atacamite(?).*

Mineral abundance: (modal %; not including pore space)

Sp	Ccp	Py	Mrc	Gn	Jd	Bn	Dg	Cv	Au	Brt	Am-Si	Goe(?)	FeOx	Ata(?)
+	+++	++	+	-	-	-	-	+	-	+	++	+	+	+
3	53	15	5					1		5	15	1	1	1

Paragenesis: Spherulitic to colloform marcasite → secondary pyrite (porous) → primary subhedral pyrite → goethite(?) → chalcopyrite → low-T sphalerite → secondary covellite → radiating barite(?) spheroids + iron oxyhydroxides → amorphous "fish-egg" to branching/acicular silica → minor fine-grained chalcopyrite + pyrite + atacamite(?).

Name: Zoned chalcopyrite-pyrite chimney

SAMPLE: GMA13-022 **PARENT ID:** 705	**LOCATION:** 784597.3E/8649923.3N **WATER DEPTH:** 1090 mbsl

Geochemical Notes

Whole rock: High Zn (337000 ppm), Cd (1070 ppm), Ge (109 ppm), As (834 ppm); Ba (141000 ppm), Sr (2980 ppm); Low Au, Fe, Cu, Sb.

Video Description

From rim of crater - sulphide talus.

Hand Sample Description



Hand sample of GMA13-022.

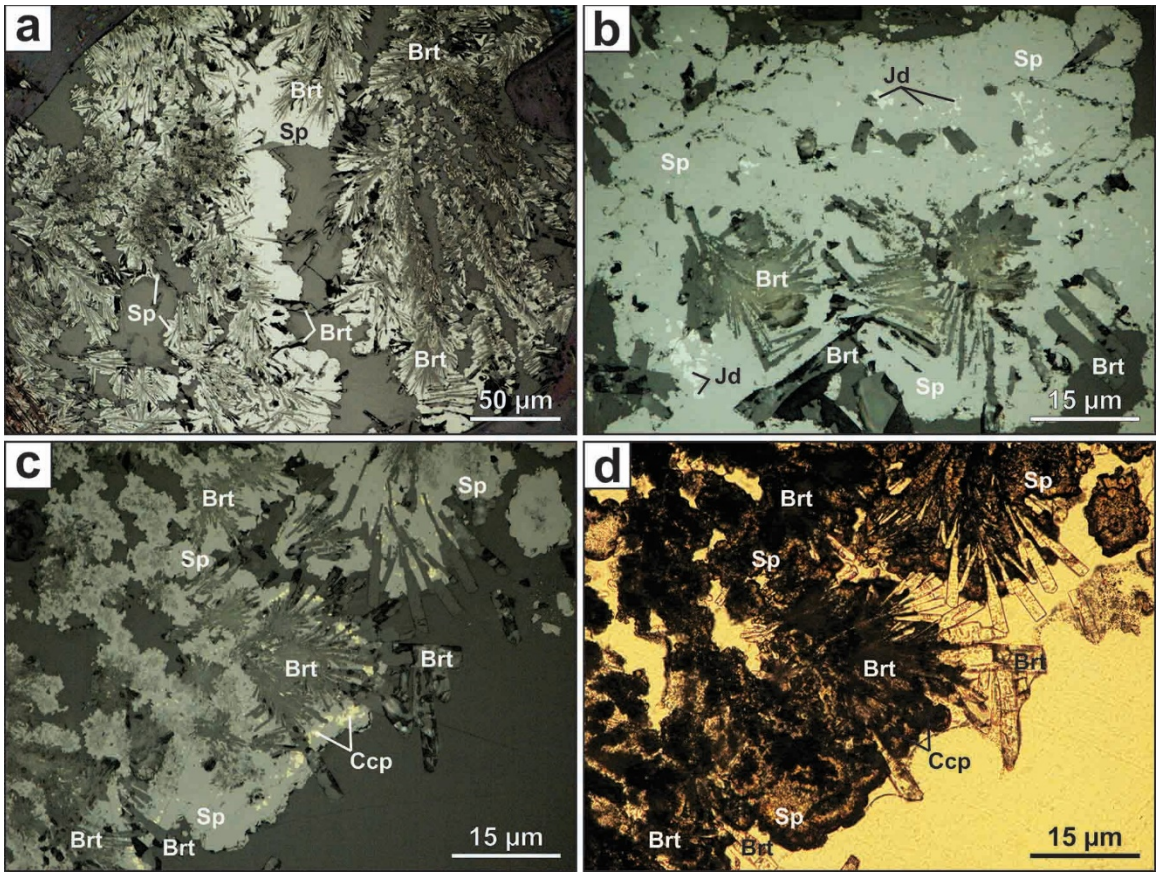
Massive sphalerite-barite chimney with no central conduits but abundant mm-size pore space, 30% overall. Sphalerite is mostly low-Fe (35%) mixed with high-Fe sphalerite (20%), displaying large dendritic (plumose) textures. Barite is interstitial and occurs in small cavities (15%). Patchy FeOx, and thin crust of Fe oxide (<1%), clay (<1%) and manganese oxide (<1%).

Thin Section Description



Thin section scan of GMA13-022.

This section has a very high porosity of ~40-45%. It is characterized by abundant dendritic textures, generally extending from the left to the right side of the section. The dendrites show a wide range in thickness and length. The dendrites have cores of dendritic to radial barite, overgrown by high-Fe (black) dendritic sphalerite. A few fine-grained crystals of pyrite and chalcopyrite form next, followed by two additional sphalerite generations that are irregularly distributed. The second sphalerite generation is light reddish brown (low-Fe), with decreasing Fe contents outwards. Locally, this generation contains fine-grained inclusions of jordanite. The third generation is generally a very thin layer of very low-Fe sphalerite that is almost colorless. Rare fine-grained galena forms next. Coarse-grained tabular to acicular/radiating barite crystals fill in some of the remaining pore space. A very fine-grained dusting of sulfides (primarily sphalerite) forms on top of this barite.



Photomicrographs of GMA13-022: ***(a)*** *Photomicrograph in reflected light (PPL) of dendritic barite overgrown by sphalerite, with late coarse-grained barite;* ***(b)*** *photomicrograph in reflected light (PPL) of early dendritic to radial barite, followed by sphalerite with fine-grained jordanite inclusions;* ***(c)*** *photomicrograph in reflected light (PPL) of early dendritic to radial barite, followed by several generations of sphalerite with interstitial chalcopyrite, and late barite;* ***(d)*** *photomicrograph in transmitted light (PPL) of the same view as (c) showing changing sphalerite colors (reflecting changing Fe-content) between subsequent generations.*

Mineral abundance: (modal %; not including pore space)

Sp	Ccp	Py	Mrc	Gn	Jd	Bn	Dg	Cv	Au	Brt	Anh	Am-Si	FeOx	others
+++	+	Tr	-	Tr	Tr	-	-	-	-	+++	-	-	-	-
59	1	<1		<1	<1					40				

Paragenesis: Dendritic barite → high-Fe sphalerite → minor chalcopyrite + pyrite → low-Fe sphalerite + jordanite → very low-Fe sphalerite → minor galena → coarse-grained tabular to acicular barite → very fine-grained sulfides (sphalerite?).

Name: Sphalerite-barite chimney (low-T) talus

SAMPLE: GMA13-024 **PARENT ID:** 588	**LOCATION:** 7847243E/8649655.5N **WATER DEPTH:** 1094 mbsl

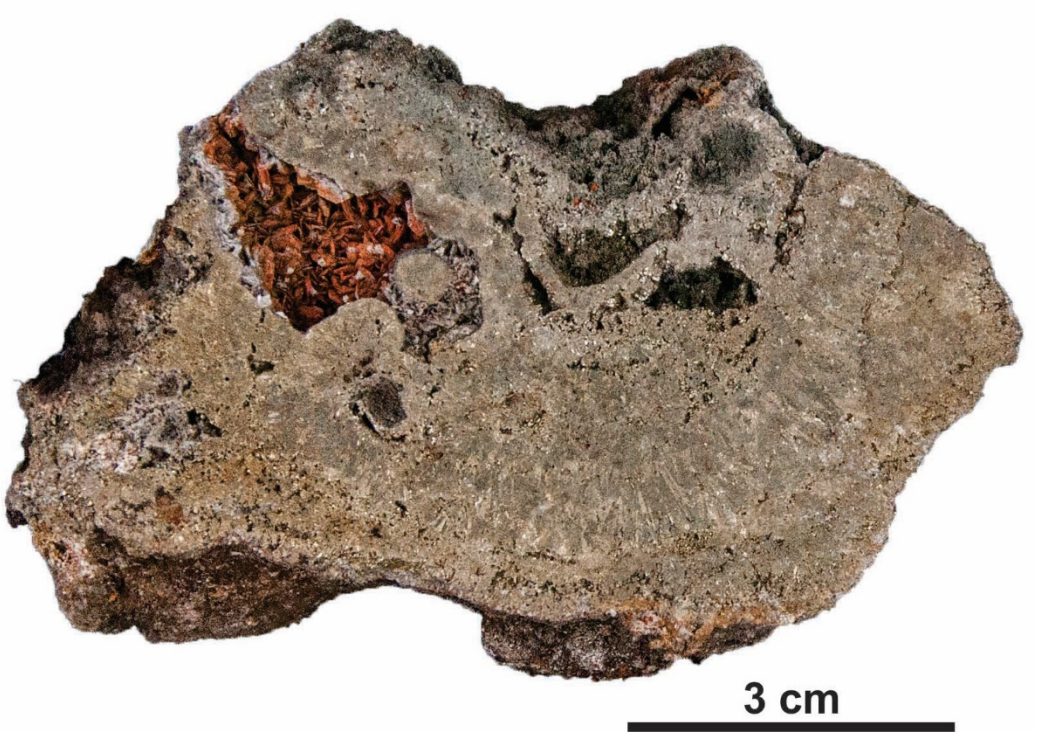
Geochemical Notes

Whole rock: High S (46.3%), Fe (31.8%), Au (5370 ppb), Hg (39500 ppb), Mn (1100 ppm); Low Cu, Zn, Ge.

Video Description

Stockwork fracture-controlled venting and bacterial matting - sample with knobby outer surface adjacent to venting area.

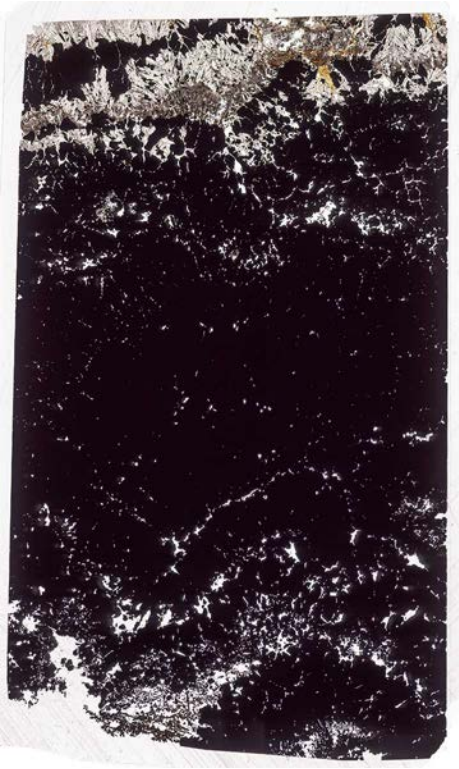
Hand Sample Description



Hand sample of GMA13-024.

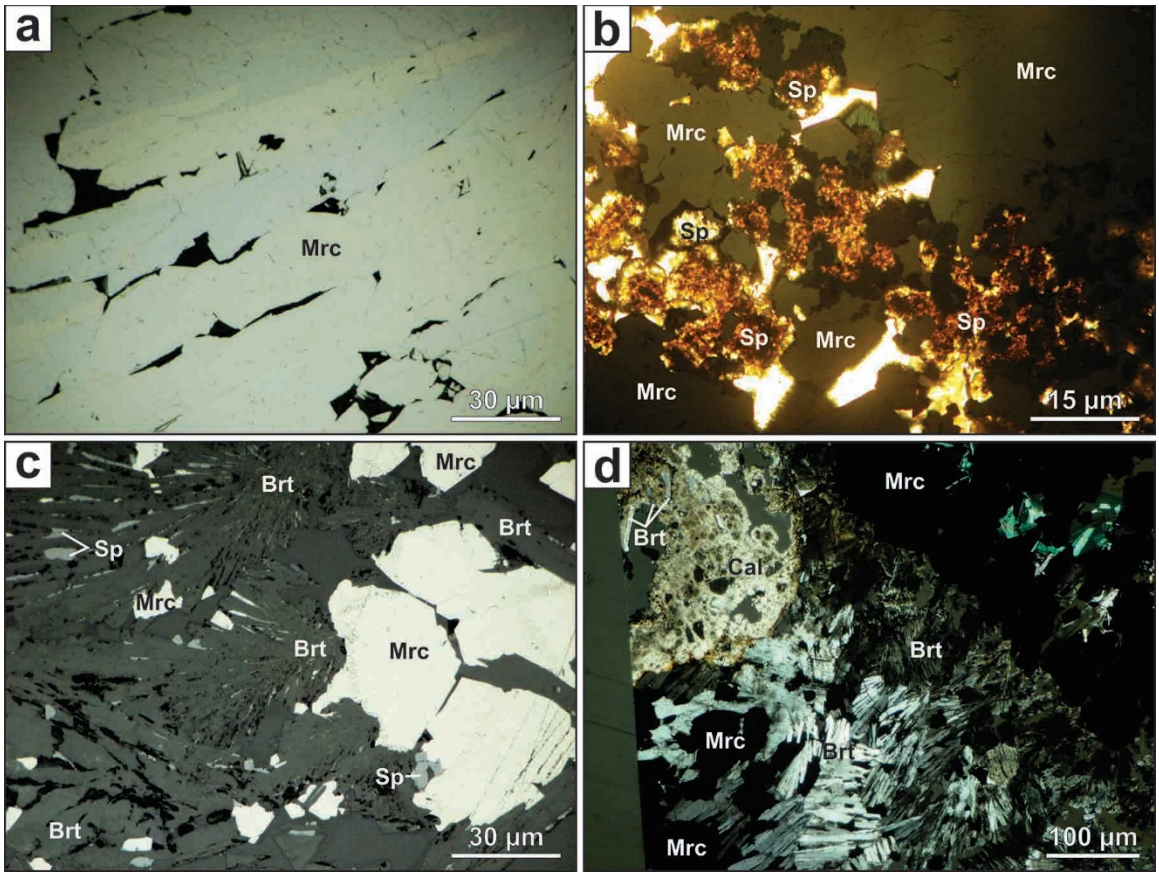
Massive chimney composed primarily of pyrite-marcasite (80%) with complex colloform banding and radial growth textures. Zoned with minor sphalerite (1-5%) and chalcopyrite (7-8%) in the outer zones. Several orifices up to 1 cm wide lined with bladed barite <1-2 mm (5-8%), with barite infill of pore space, thinly coated by iron oxide. Outer surface has thin <1-2 mm manganese oxide coating (1%), with lesser iron oxide (<1%). Pore space 2-6% overall.

Thin Section Description



Thin section scan of GMA13-024.

This section has a porosity of ~15%. It is characterized by a banded (repeating) mineralogy, with crystals growing upwards. It is dominated by very coarse-grained low-porosity marcasite, with minor fine-grained iron oxide alteration along the grain boundaries (goethite?). Locally, there are irregular horizons with minor fine-grained low-Fe sphalerite that line the marcasite, locally replacing the marcasite. Similarly, there is minor fine-grained and coarse-grained tabular and dendritic barite throughout most of the section, crystallizing both before and after the sphalerite. At the top of the section, there is a band of coarse-grained radial, tabular barite growing upwards from the marcasite and sphalerite, followed by a band of coarse-grained marcasite, followed by a band of fine-grained dendritic barite, locally iron-stained, and a layer of coarse-grained tabular/radial barite, followed by a band of coarse-grained dendritic marcasite (with increased alteration to goethite), followed again by coarse-grained tabular barite. The very top right of the section contains fine-grained calcite, with very fine-grained inclusions of sulfides and oxides. Late iron oxyhydroxides occur at the crystal margins, staining this part of the section orange-brown.



Photomicrographs of GMA13-024: ***(a)*** *Photomicrograph in reflected light (PPL) of coarse-grained marcasite;* ***(b)*** *photomicrograph in transmitted light (PPL) of low-Fe sphalerite replacin marcasite;* ***(c)*** *photomicrograph in reflected light (PPL) of multiple generations of marcasite + low-Fe sphalerite with dendritic to radiating tabular barite;* ***(d)*** *photomicrograph in transmitted light (XPL) of marcasite, followed by crystallization of dendritic to radiating barite, followed by coarse-grained radiating tabular barite, and late infill of calcite with minor iron staining.*

Mineral abundance: (modal %; not including pore space)

Sp	Ccp	Py	Mrc	Gn	Jd	Bn	Dg	Cv	Au	Brt	Anh	Goe	FeOx	Cal
+	-	-	+++	-	-	-	-	-	-	++	-	+	+	+
3			81							10		1	2	3

Paragenesis: Marcasite → low-T sphalerite (locally replacing marcasite) → tabular and dendritic barite → low-Fe sphalerite → marcasite → tabular barite → marcasite → dendritic, iron-stained barite → tabular barite → dendritic marcasite → tabular barite → calcite → iron oxyhydroxides + goethite.

Name: Marcasite-barite chimney

SAMPLE: GMA13-027 **PARENT ID:** 592	**LOCATION:** 784719.5E/8649655.6N **WATER DEPTH:** 1096 mbsl

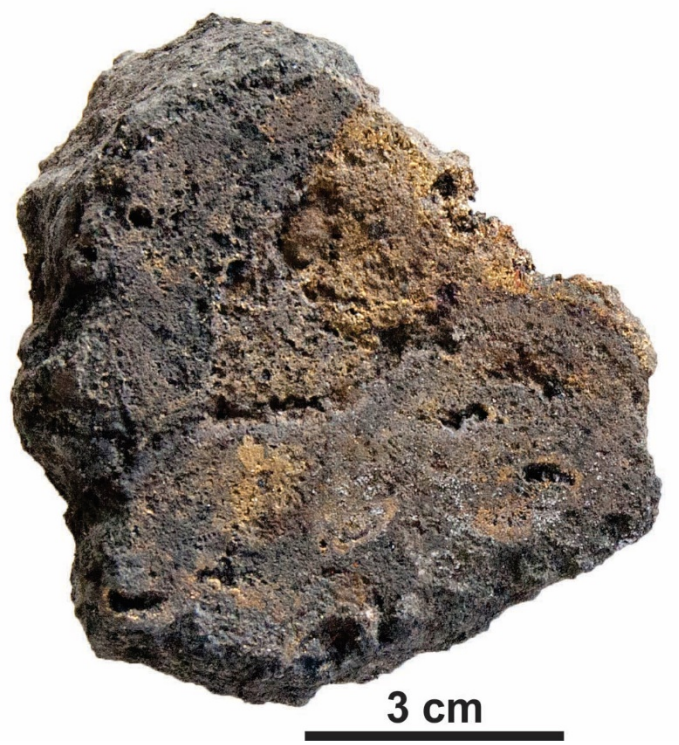
Geochemical Notes

**XRF (parent): Cu = 22.53%, Pb = 0.11%, Zn = 12.89%, Ag = 115.0 ppm; Au = 3.65 ppm.*

Video Description

Small pinnacle, multi spired.

Hand Sample Description



Hand sample of GMA13-027.

Small multi-spired zoned chimney with a central vent conduit, 1 cm wide, and smaller conduits >1 mm in width, with 5% pore space overall. The orifices are lined by chalcopyrite (30%), drusy and coarse-grained in the middle of the conduits. Chalcocite (1-2%) (or sphalerite?) is the final phase to line the central orifice, with trace bornite. Barite is granular/sugary infill in the central orifice and needle-like (10%). In the outer wall the barite is fine-grained (<1 mm). Trace hematite occurs along vugs. Dense fine-grained pyrite occurs as a narrow band on the outside of the chalcopyrite, < 1 cm thick (3%). Manganese oxide occurs up to 1 cm thick on the outer wall of the sample (55%), with trace iron oxide.

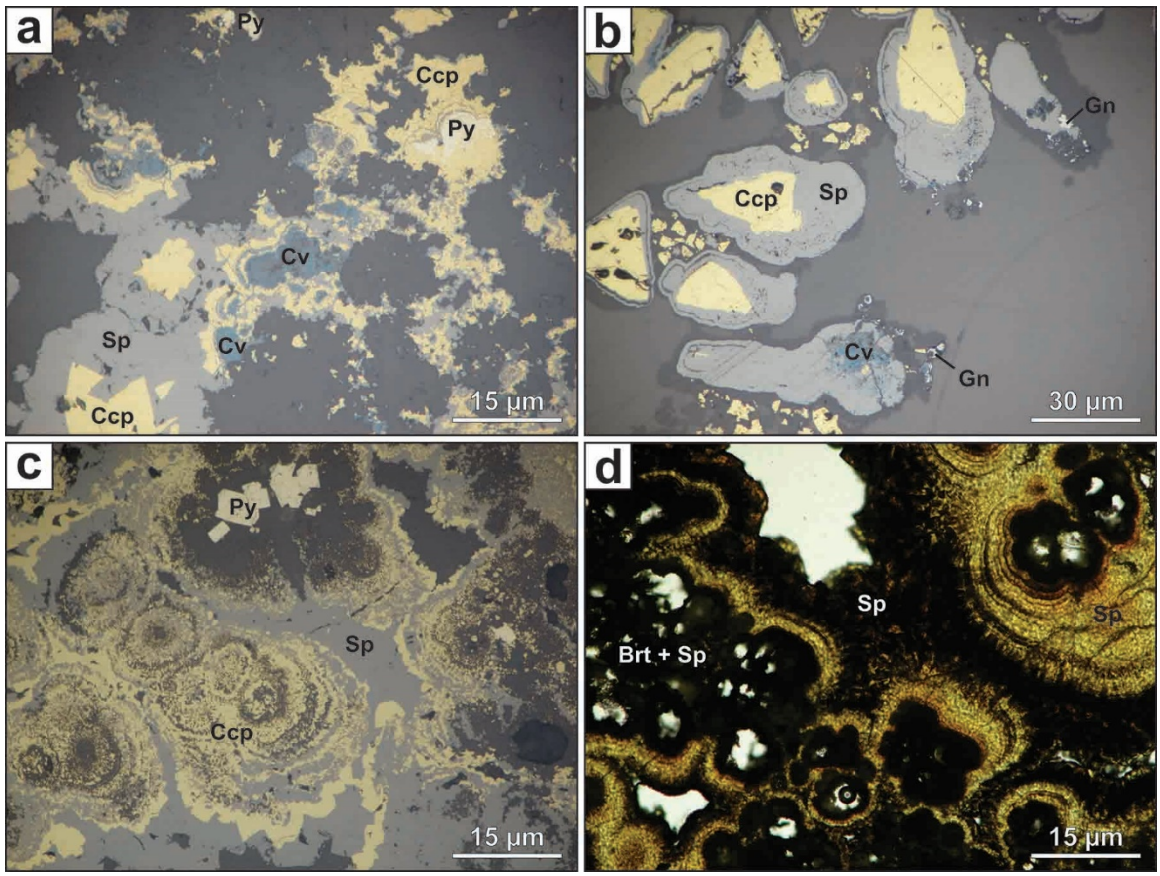
Thin Section Description

This sample has a porosity of ~30%. There are several former vent conduits, a few mm-across. The dominant mineral is chalcopyrite, which becomes very coarse-grained (euhedral) near these conduits. There are several irregular bands of fine- to medium-grained euhedral to anhedral pyrite following this. This pyrite ranges from spherulitic to colloform to dendritic. The dendritic and spherulitic pyrite grows on fine-grained dendritic (to relict) barite. This pyrite is locally porous, indicating that some of it may be inverted marcasite. Only minor marcasite was observed. This is locally followed by a repeated sequence of fine layers of chalcopyrite with high-Fe sphalerite, which is locally replacing the pyrite (and



Thin section scan of GMA13-027.

marcasite). The high-Fe sphalerite is locally altered to fine-grained covellite ± digenite. The dendritic barite is always overgrown by high-Fe sphalerite. Subsequent crystallization of low-Fe sphalerite locally shows tree-ring growth zones. It generally shows outward-decreasing Fe-contents, and locally contains fine-grained inclusions of jordanite(?). Locally, this is followed again by tabular high-Fe sphalerite, and finally a thin layer of very low-Fe (almost colorless) sphalerite. The sphalerite generations are concentrated along bands or lining vent conduits. Minor fine-grained chalcopyrite and galena are the final sulfide phases to grow, irregularly distributed. Amorphous silica, with very fine-grained "fish egg" texture and abundant sulfide (mostly chalcopyrite) inclusions irregularly fills in some of the remaining pore space. There are rare crystals of fine- to coarse-grained barite last.



Photomicrographs of GMA13-027: ***(a)*** *reflected light (PPL) photomicrograph of chalcopyrite, replacing marcasite, associated with sphalerite that is locally altered to covellite;* ***(b)*** *reflected light (PPL) photomicrograph of coarse-grained chalcopyrite, overgrown by sphalerite with local growth zoning, locally altered to covellite, and late fine-grained galena;* ***(c)*** *reflected light (PPL) photomicrograph of marcasite, and finely-layered chalcopyrite and sphalerite;* ***(d)*** *transmitted light (PPL) photomicrograph of multiple generations of high- and low-Fe sphalerite with fine growth zoning.*

Mineral abundance: (modal %; not including pore space)

Sp	Ccp	Py	Mrc	Gn	Jd	Bn	Dg	Cv	Au	Brt	Anh	Am-Si	FeOx	others
++	+++	+	+	Tr	+	-	Tr	+	-	+	-	+	-	-
10	70	5	1	<1	1		<1	2		5		6		

Paragenesis: Chalcopyrite → pyrite (euhedral) → dendritic barite → marcasite (minor) → spherulitic/colloform pyrite (primary and secondary) → high-Fe sphalerite + chalcopyrite (finely layered, replacing pyrite/marcasite) → covellite ± digenite → low-Fe sphalerite ± jordanite(?)→ very low-Fe sphalerite → fine-grained chalcopyrite + galena → amorphous silica → rare barite.

Name: Zoned chalcopyrite-sphalerite chimney

SAMPLE: GMA13-028 **PARENT ID:** 586	**LOCATION:** 784719.5E/8649655.6N **WATER DEPTH:** 1098 mbsl

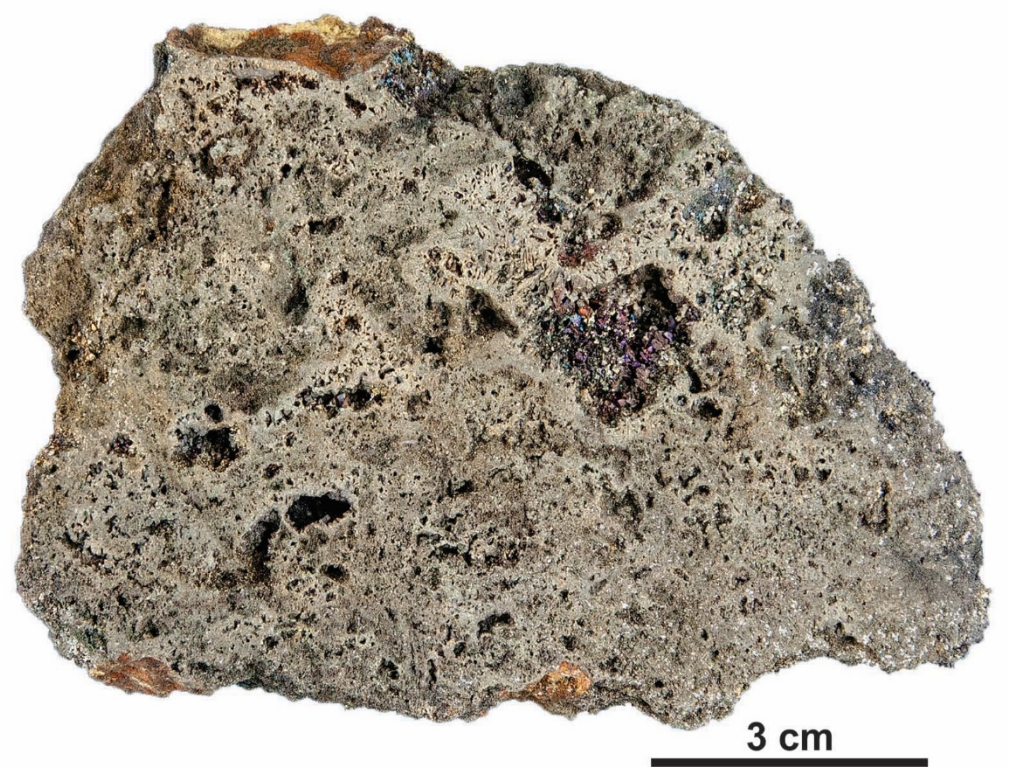
Geochemical Notes

N/A

Video Description

Small pinnacle, multi spired.

Hand Sample Description



Hand sample of GMA13-028.

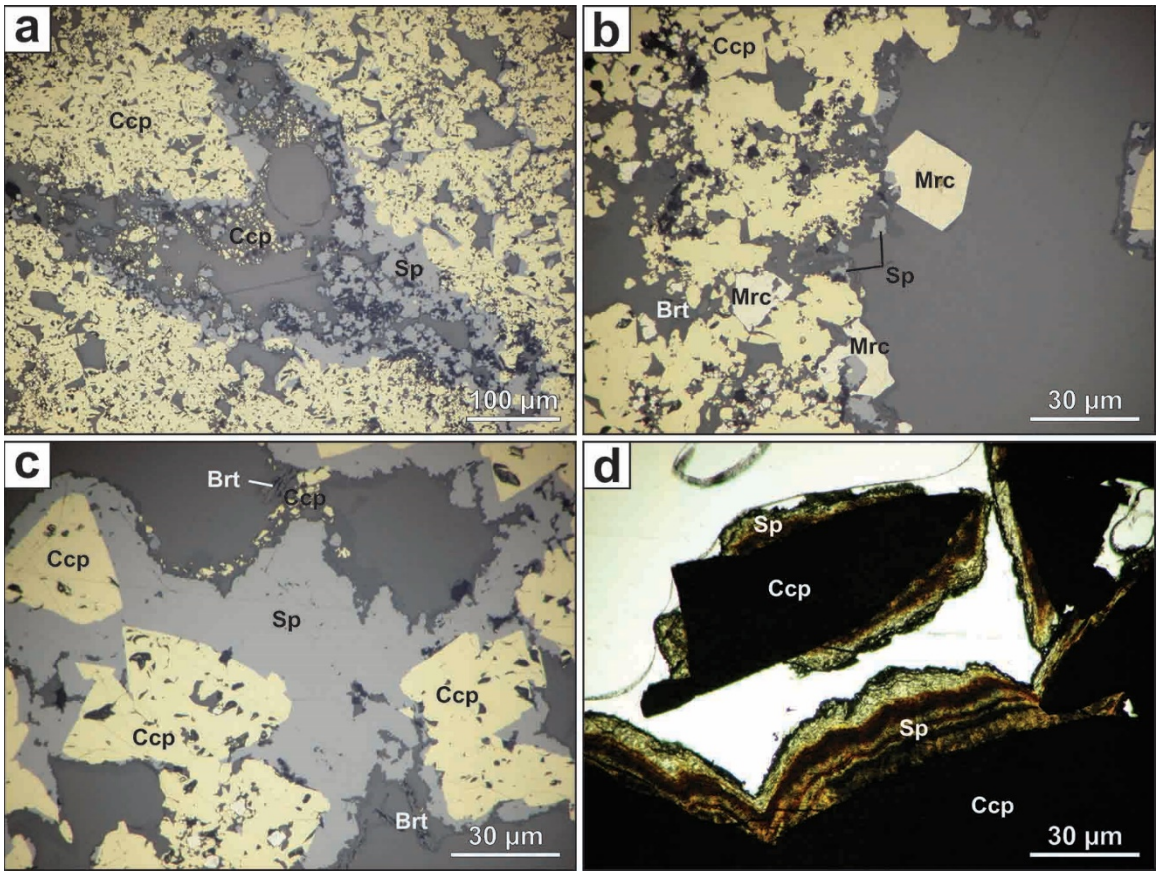
Chimney fragment from the same location as GMA13-027 (592). This sample is composed primarily of chalcopyrite (90-97%) with possible anhydrite (1%) along a fracture, minor pyrite (1%) and minor iron and manganese oxide (<1%) as a thin coat on the surface and trace atacamite and native sulfur or orpiment. The chalcopyrite has complex colloform banding and dendritic textures, and ranges from massive to vuggy with 2-10% pore space. Multiple small (up to 1 cm wide) orifices are characterized by drusy tetragonal manganese-coated and weakly oxidized chalcopyrite crystals. The sample is very heavy, possibly contains fine-grained barite.

Thin Section Description



Thin section scan of GMA13-028.

This section has a porosity of ~35%. It is comprised mainly of coarse- to very coarse-grained chalcopyrite and relict vent conduits. The chalcopyrite has minor inclusions of medium-grained pyrite, concentrated along specific horizons, and is locally overgrown by low-Fe sphalerite, also concentrated around certain former vent conduits. The color is variable and banded, but generally shows an outward-decreasing Fe-content, ending with very low-Fe (almost colorless) sphalerite. Locally the crystals are hexagonal, indicating wurtzite. The sphalerite is locally altered to minor fine-grained covellite. A later phase of minor medium- to coarse-grained subhedral-euhedral pyrite grows on top of this sphalerite. A final generation of fine- to medium-grained chalcopyrite is the last sulfide phase to form (locally). There are a few coarse-grained tabular barite crystals in some of the conduits. There is also minor very fine-grained iron oxyhydroxides irregularly distributed.



Photomicrographs of GMA13-028: ***(a)*** *reflected light (PPL) photomicrograph of sphalerite lining a former vent conduit in a chalcopyrite-rich chimney;* ***(b)*** *reflected light (PPL) photomicrograph of early marcasite, overgrown by chalcopyrite, followed by sphalerite, and a second generation of euhedral marcasite;* ***(c)*** *reflected light (PPL) photomicrograph of coarse-grained chalcopyrite, overgrown by sphalerite, with a later generation of finer-grained chalcopyrite and barite;* ***(d)*** *transmitted light (PPL) photomicrograph of multiple generations of high- and low-Fe sphalerite with fine growth zoning.*

Mineral abundance: (modal %; not including pore space)

Sp	Ccp	Py	Mrc	Gn	Jd	Bn	Dg	Cv	Au	Brt	Anh	Am-Si	FeOx	others
+	+++	+	-	-	-	-	-	+	-	+	-	-	+	-
7	83	5						1		3			1	

Paragenesis: Pyrite → chalcopyrite → low-Fe sphalerite/wurtzite → covellite → pyrite → chalcopyrite → barite → iron oxyhydroxides.

Name: Zoned chalcopyrite + sphalerite chimney

SAMPLE: GMA13-029 **PARENT ID:** 598	**LOCATION:** 784745.1E/8649583.1N **WATER DEPTH:** 1110 mbsl

Geochemical Notes

Whole rock: High Zn (214000 ppm), Cd (757 ppm), Hg (27700 ppb), Ba (169000 ppm), Sr (7690 ppm); Low Cu, Ga, Ge, As.

Video Description

Small YOUNG but not venting chimney, single orifice, part of large, mostly inactive mound.

Hand Sample Description

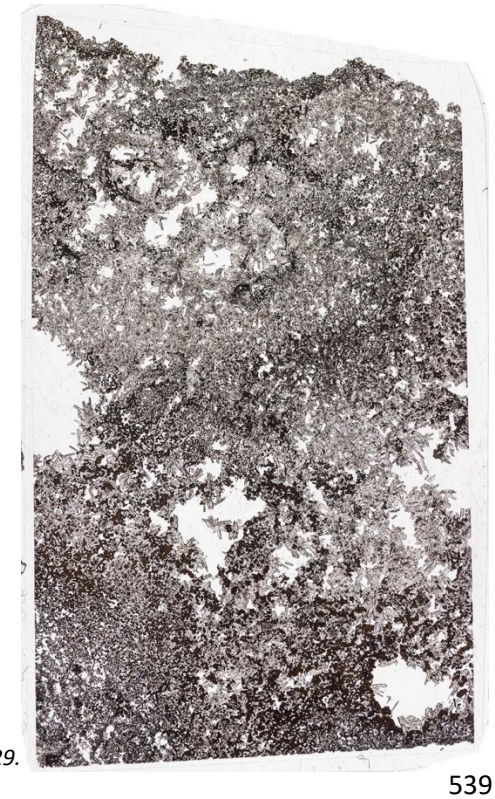


Hand sample of GMA13-029.

Massive chimney with high-Fe Sphalerite (35%) intergrown with barite (40%). Minor low-Fe sphalerite (1%) near vugs, with coarse barite as the final phase to precipitate. No obvious central conduits but abundant vug space (25%), up to 1 cm wide, mostly mm-scale. Outer rind of barite is 5-8 mm wide, with clay (1%) and iron oxide (<1%) on outer surface.

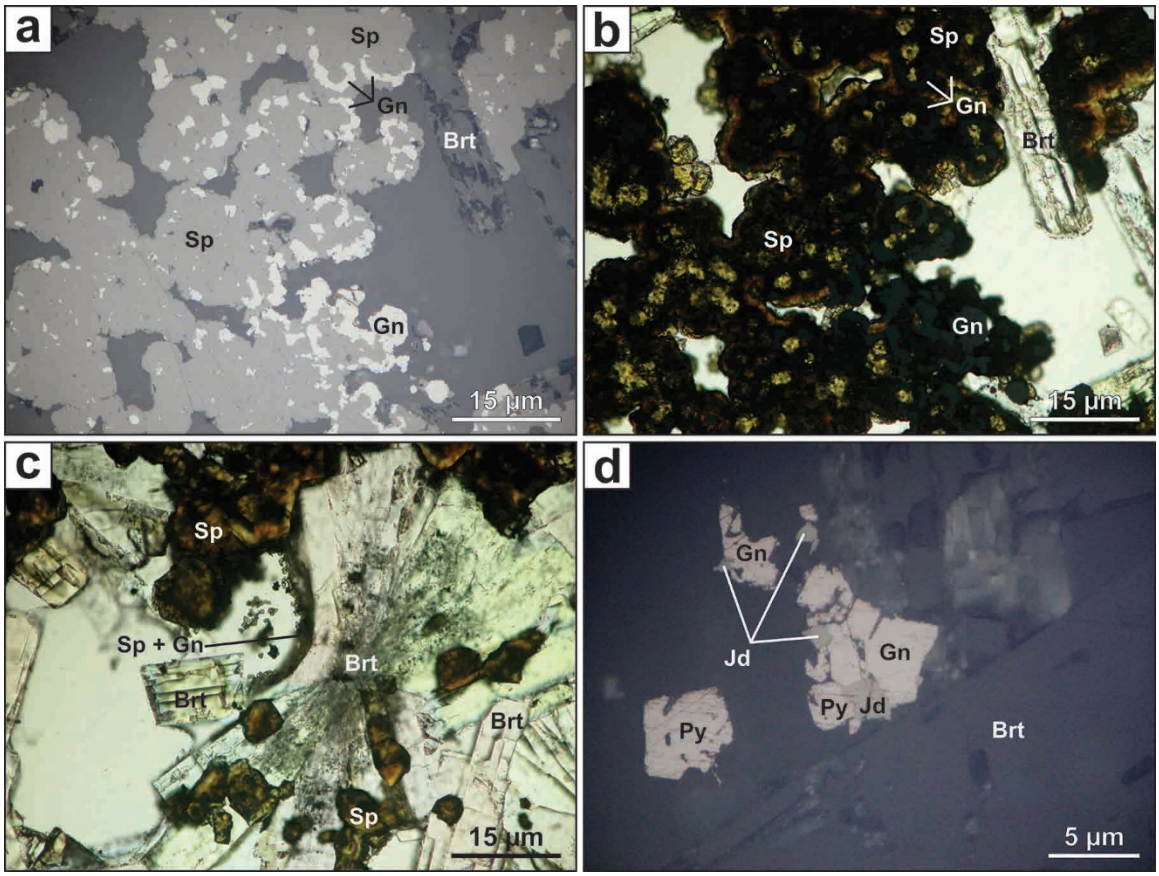
Thin Section Description

This section has ~35% porosity. It contains several former vent conduits. The main sulfide phase is fine- to medium-grained low-Fe sphalerite. Minor fine- to medium-grained galena forms locally at the margins of the sphalerite. Rare inclusions of fine-grained jordanite(?) is included in the sphalerite. Locally, this is overgrown by a second generation of medium-



Thin section scan of GMA13-029.

to low-Fe sphalerite, with decreasing Fe contents outwards. This sphalerite contains abundant inclusions of fine-grained euhedral to spherulitic pyrite, and a few inclusions of chalcopyrite. The pyrite is associated with the higher-Fe cores of the sphalerite. This is followed by more galena, and a third generation of low-Fe sphalerite. The sphalerite generations are 'blebby' in appearance, forming coalescing spherules, and is locally dendritic. Next in the mineralization sequence is abundant coarse- to very-coarse grained tabular, radiating barite. The cores of the radiating barite tend to have abundant very-fine inclusions. Several coarse crystals have second-order interference colors, possibly indicating the presence of anhydrite. There are several horizons where there are more abundant sulfates than sulfides. Additional fine- to medium-grained galena, pyrite, and very low-Fe sphalerite, along with rare fine-grained chalcopyrite, form last on top of the barite, locally. This late galena is most abundant near the margins of vent conduits, where it is locally intergrown with jordanite(?), which appears medium greenish-grey in reflected light.



Photomicrographs of GMA13-029: ***(a)*** *reflected light (PPL) photomicrograph of intergrown sphalerite and galena, with late coarse-grained barite;* ***(b)*** *transmitted light (PPL) photomicrograph of the same view as (a) showing different generations of sphalerite with high- and low-Fe contents;* ***(c)*** *transmitted light (PPL) photomicrograph of radiating fine-grained barite, sphalerite, and coarse-grained barite, with a late generation of fine-grained sphalerite + galena;* ***(d)*** *reflected light (PPL) photomicrograph close-up of galena, jordanite(?) and pyrite.*

Mineral abundance: (modal %; not including pore space)

Sp	Ccp	Py	Mrc	Gn	Jd(?)	Bn	Dg	Cv	Au	Brt	Anh(?)	Am-Si	FeOx
+++	Tr	+	-	+	Tr	-	-	-	-	+++	+	-	-
35	<1	2		5	<1					57	1		

Paragenesis: Pyrite (± rare chalcopyrite) → low-Fe sphalerite (± rare jordanite) → galena → medium- to low-Fe sphalerite + pyrite → galena → low-Fe sphalerite → coarse-grained tabular, radiating barite → pyrite → sphalerite → galena ± jordanite.

Name: Barite-sphalerite chimney (low-T)

SAMPLE: GMA13-030a,b **PARENT ID:** 604	**LOCATION:** 784717.4E/8649745.0N **WATER DEPTH:** 1075 mbsl

Geochemical Notes

**XRF (parent): Cu = 0.01%, Pb = 0.07%, Zn = 0.32%, Ag = 154.0 ppm; Au = 0.41 ppm.*

Video Description

Large piece of talus from base of mound.

Hand Sample Description



Hand sample of GMA13-030.

Angular talus boulder from base of mound. Siliceous chimney with colloform vent textures, 5-10% vugs. "Composite 'jasperoid' - barite spire." Many phases of sulphide/silica/barite deposition and giant botryoidal cavities. Minor Ba (vug-fill, disseminated), Py (disseminated). Colloform jasper (Silicified Hem) at margin of sample. "Wallrock jasper" varies from red to salmon pink, has many cavities, some with sulphides. Minor native sulphur. Fine-grained low-Fe Sph(?) finely disseminated throughout. Some surfaces coated by glassy red-brown chalcedony(?) and fine Py or Marc. Local grey vermicular fabrics. Does not appear like a biogenic oxide deposit.

Thin Section Description

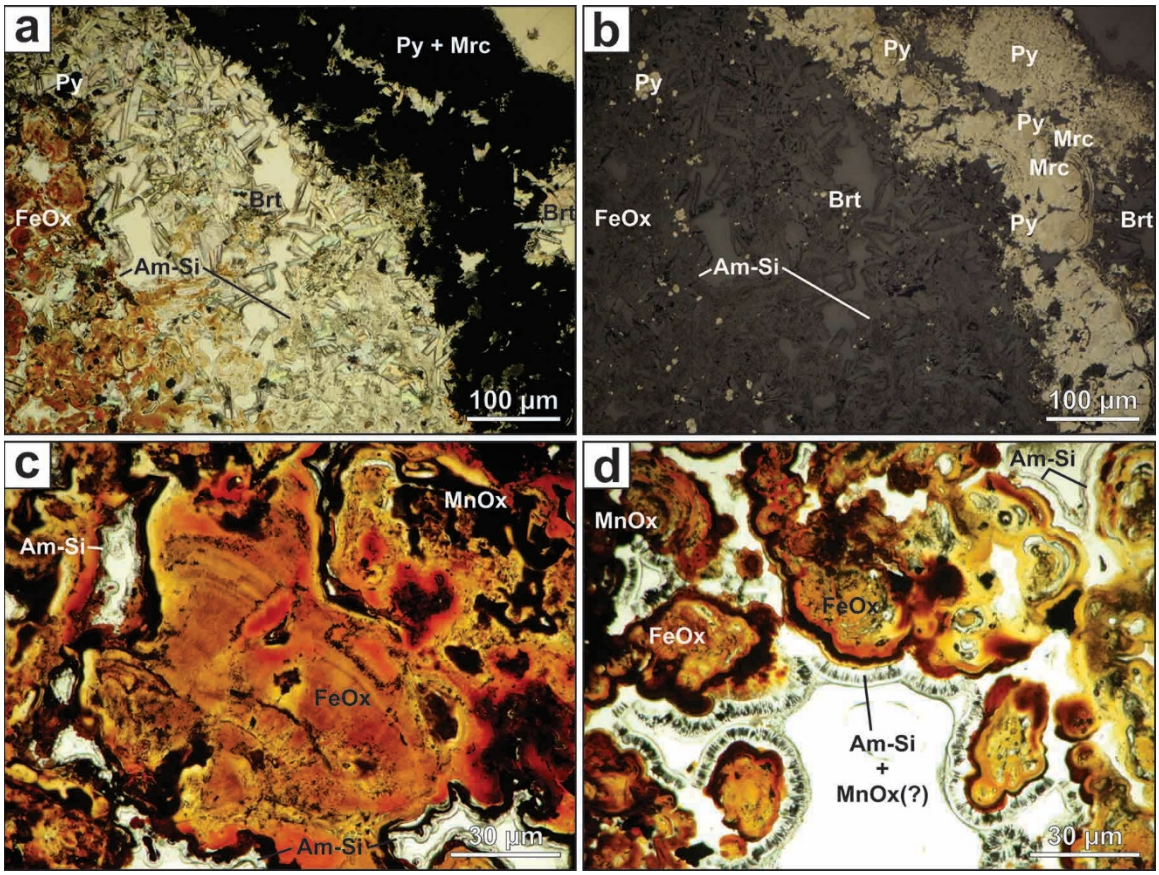
(a) This sample is similar to GMA13-017. It has a porosity of ~10%, not including the large vug at the bottom of the section. It is divided into two distinct parts; the top part of the section contains abundant iron oxyhydroxides, while the bottom contains sulfates and sulfides with chimney textures. In the oxide-rich upper portion of the section, there are several generations of iron oxides and oxyhydroxides, including an early dark brown generation that grades into light orange, locally displaying spherulitic,



Thin section scan of GMA13-030a.

colloform, and radiating textures and “tree-ring” growth zones (pseudomorphs?), with a bright orange rim, followed by a bright red to dark red generation of hematite. Locally, this is with black material, likely manganese oxide. In the top right part of the section, the oxides are brownish with abundant very-fine grained inclusions, likely manganese oxide. These oxides are locally filled in by coarse-grained marcasite. This is followed by a thick layer of amorphous silica, up to ~0.6 mm wide, locally containing abundant black inclusions (manganese oxide?), followed by a thin layer of amorphous silica, ~0.1 mm wide. Most of the oxides appear to be silicified.

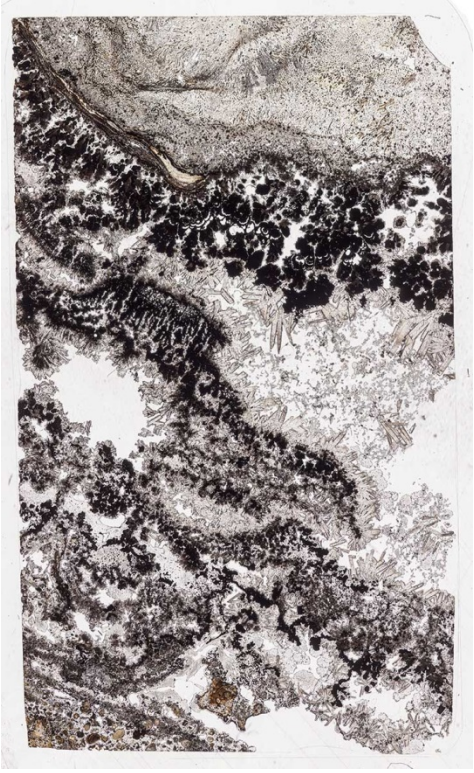
The contact with the bottom part of the section is marked by a thin, irregular layer of manganese oxide (locally dendritic) + fine- to medium grained pyrite, forming on the right half of the section. Following this is a thick horizon (~2-6 mm wide) containing abundant amorphous silica, generally showing a “fish-egg” texture with minor very fine-grained oxide inclusions, as well as abundant coarse-grained tabular, often radiating barite. These barites grow on top of the amorphous silica, and also have a thin layer of silica, indicating that it grows between the two silica generations. On the margin of this horizon is colloform primary pyrite growing downwards, followed by medium- to coarse-grained crystalline to dendritic marcasite. This marcasite is porous, and is partially altered to secondary pyrite, especially along grain boundaries giving it an ‘etched’ appearance. There are several bands of primary pyrite and marcasite. This is followed by additional coarse-grained tabular, often radiating barite. These phases are all covered by the thin layer of amorphous silica, followed by minor very fine-grained iron and manganese oxides, as well as pyrite/marcasite.



Photomicrographs of GMA13-030a: ***(a)*** *transmitted light (PPL) photomicrograph of the contact between the top and bottom of the section, characterized by a thick layer of pyrite + marcasite, a layer of barite, followed by the beginning of iron oxyhydroxides, with a fine coating of amorphous silica;* ***(b)*** *reflected light (PPL) photomicrograph of the same view as (a) showing different growth zoning in pyrite/marcasite;* ***(c)*** *transmitted light (PPL) photomicrograph of iron oxyhydroxides with relict colloform textures, followed by manganese oxide + hematite and a fine layer of amorphous silica;* ***(d)*** *transmitted light (PPL) photomicrograph of iron oxyhydroxides, irregular manganese oxide, a thick layer of amorphous silica with manganese oxide inclusions (?), and a second finer layer of amorphous silica.*

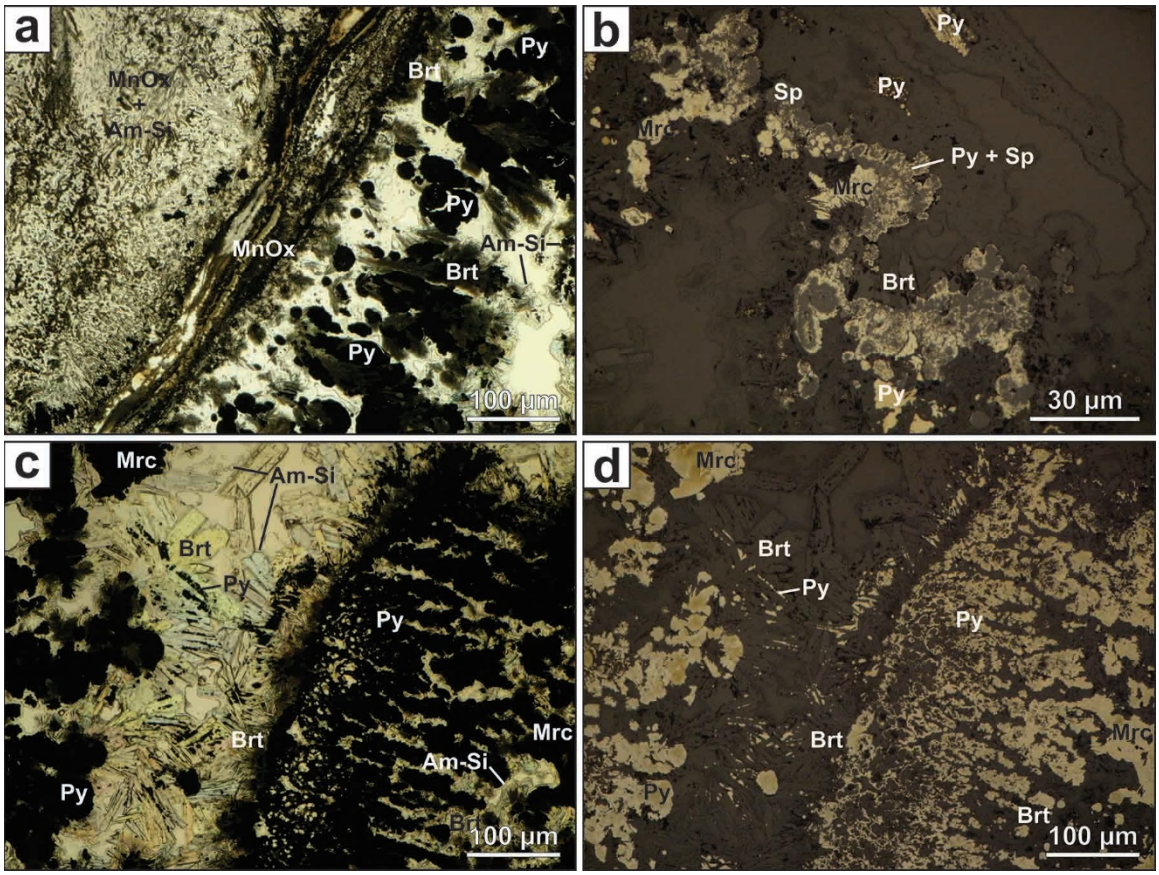
Mineral abundance: (modal %; not including pore space)

Sp	Ccp	Py	Mrc	Gn	Jd	Bn	Dg	Cv	Au	Brt	Am-Si	FeOx	Hem	MnOx
-	-	+	++	-	-	-	-	-	-	-	++	+++	+	+
		4	10								15	63	5	3



Thin section scan of GMA13-030b.

(b) This section is from the part of the sample with chimney textures. It has a porosity of ~30% and a banded appearance, with alternating sulfides and sulfates. The top of the section contains dendritic fine-grained manganese oxide that has been heavily silicified. Moving downwards, there is a distinct contact containing marcasite and banded manganese oxide. Fine-grained dendritic barite, locally very lightly iron-stained, grows downwards from this, followed by medium-grained tabular/radiating barite. This is followed by spherulitic to colloform pyrite with abundant growth zones. It contains abundant pore space, suggesting that it is inverted from marcasite. This is followed by crystalline to dendritic non-porous marcasite. Next, there is minor fine-grained radial acicular barite, followed by very coarse-grained tabular barite. Everything is covered by a fine layer of amorphous silica. There is a large void space next, partially filled by amorphous silica with fine-grained manganese oxide inclusions. The other side of the void space is a sharp contact, with inward(upward)-growing fine and coarse-grained barite. Minor pyrite/marcasite grows on top of the barite. The sulfide/sulfate mineralogy repeats on the other side of the contact, beginning with dendritic marcasite. Much of the pore space in the bottom part of the section is filled in with the amorphous silica + manganese oxide inclusions surrounding fine-grained pyrite/marcasite. There is very little iron oxide in this section. There is very minor fine-grained sphalerite intergrown with a late generation of marcasite near the bottom of the section. This locally overgrows the amorphous silica, before being covered by amorphous silica itself. Thus, the paragenesis of this sample (including GMA13-030a) is very repetitive.



Photomicrographs of GMA13-030b: ***(a)*** *transmitted light (PPL) photomicrograph of dendritic manganese oxide with amorphous silica, followed by a layer of manganese oxide, upon which dendritic barite and pyrite grows off of;* ***(b)*** *reflected light (PPL) photomicrograph of marcasite, overgrown by finely intergrown pyrite + sphalerite;* ***(c)*** *transmitted light (PPL) photomicrograph of dendritic pyrite/marcasite, with fine-grained dendritic barite growing off of it, followed by fine-grained pyrite + marcasite, and coarse-grained tabular barite, and a thin layer of amorphous silica;* ***(d)*** *reflected light (PPL) photomicrograph of the same view as (c), showing the high porosity of the pyrite, indicating that it is inverted marcasite.*

Mineral abundance: (modal %; not including pore space)

Sp	Ccp	Py	Mrc	Gn	Jd	Bn	Dg	Cv	Au	Brt	Anh	Am-Si	FeOx	MnOx
+	-	++	++	-	-	-	-	-	-	+++	-	++	+	+
1		15	15							50		15	1	3

Paragenesis: Brown to light orange iron oxyhydroxides → bright orange iron oxyhydroxides → bright to dark red hematite + manganese oxide → marcasite → secondary pyrite → amorphous silica → coarse-grained tabular barite → spherulitic to colloform primary pyrite → crystalline to dendritic marcasite → → secondary pyrite fine-grained radial barite → coarse-grained tabular barite → spherulitic to colloform primary pyrite → crystalline to dendritic marcasite → secondary pyrite → fine-grained radial barite → tabular barite → amorphous silica → fine-grained sphalerite + pyrite/marcasite (local, minor) → amorphous silica → fine-grained pyrite/marcasite + iron/manganese oxides.

Name: Silicified iron-oxide caprock talus with barite-pyrite chimney

SAMPLE: GMA13-031 **PARENT ID:** 603	**LOCATION:** 784671.0E/8649796.4N **WATER DEPTH:** 1103 mbsl

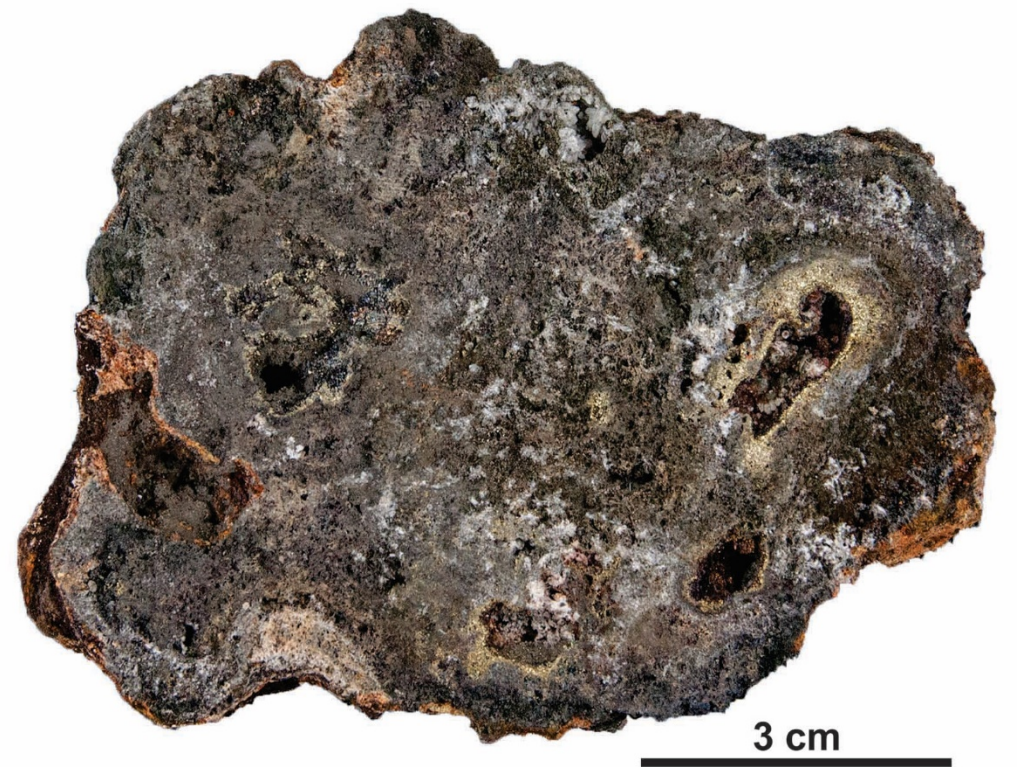
Geochemical Notes

Whole rock: High Zn (24000 ppm), Cd (1040 ppm), Ga (122 ppm), Ge (76 ppm), Sb (250 ppm), Ba (90400 ppm); Low Ag.

Video Description

Small spire from multi-spired chimney feature (~1 m tall), growing from indurated sheeted sediments - long skinny spire. Popcorn texture.

Hand Sample Description



Hand sample of GMA13-031.

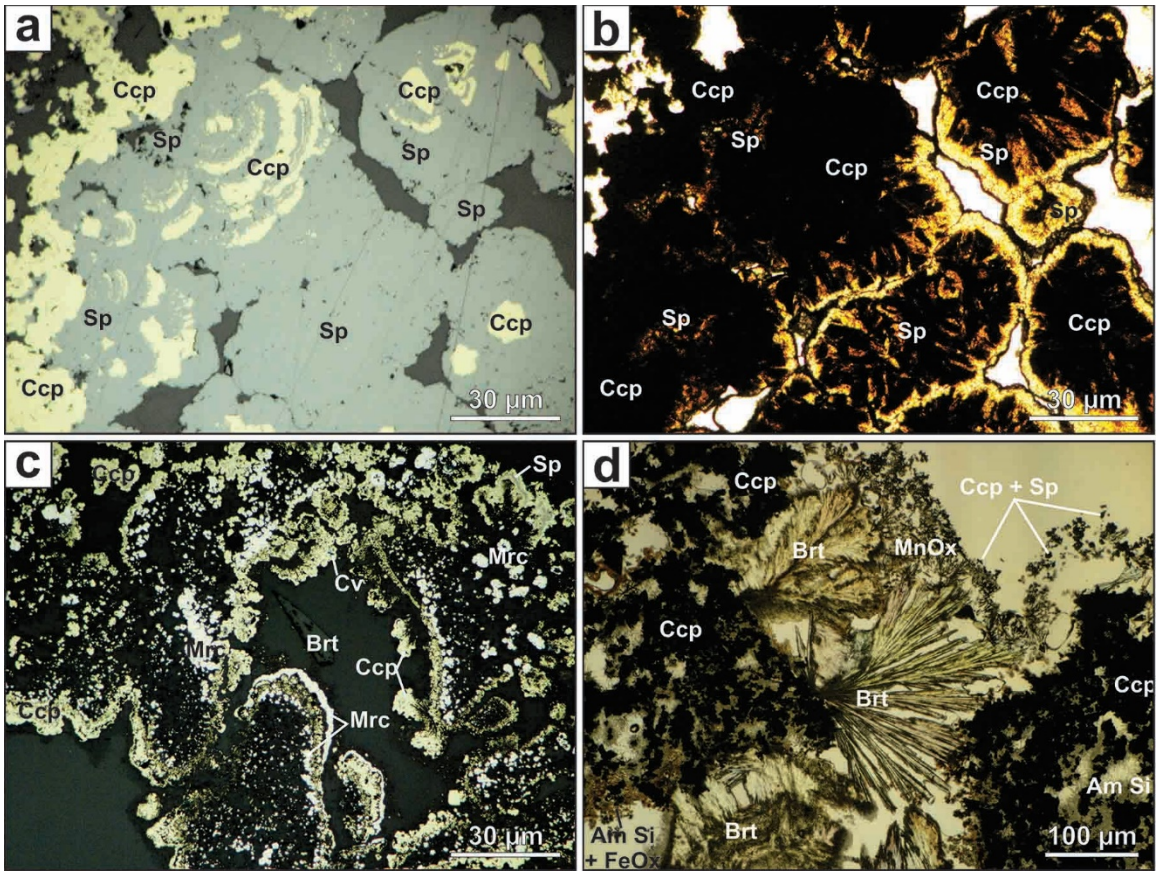
Zoned chimney, with multiple central vent conduits up to 2 cm wide lined by chalcopyrite (65%), minor pyrite (5%) and trace bornite. Sphalerite, mostly low-Fe (15%), occurs in outer zones with disseminated fine-grained chalcopyrite and barite (10%) that also fills vugs. Minor high-Fe sphalerite (5%) rims the chalcopyrite and is patchy in outer zones. Inner zones are less porous than outer zones. Pore space consists of central conduits and smaller vugs, 10%. Outer surface of sample has a very thin veneer of Fe oxide (<1%) and Mn oxide (3%).

Thin Section Description



Thin section scan of GMA13-031.

This section has a porosity of ~30%. It is a zoned chimney with several relict vent conduits. It has an early phase of fine- to medium-grained high-Fe sphalerite, followed by abundant fine- to coarse-grained chalcopyrite, with an increase in grain size near the vent conduits. This is followed by minor medium-grained marcasite, extensively inverted to secondary pyrite (porous). Locally, this is overgrown by a second layer of high-Fe sphalerite intergrown with chalcopyrite (replacing marcasite), and low-Fe sphalerite lining vent conduits. The sphalerite is locally associated with secondary fine-grained covellite ± digenite. This is followed by a second generation of fine- to coarse-grained chalcopyrite, locally overgrown by another generation of marcasite, partially inverted to secondary pyrite. Minor coarse-grained tabular radiating to dendritic barite forms next in the conduits. This is locally overgrown by silicified fine-grained dendritic manganese oxides (with minor iron oxides), extending up to ~6 mm into the conduits. Amorphous silica (with fine dendritic manganese oxide inclusions) fills in much of the remaining pore space. The amount of manganese oxide makes this section unique (so far). This in turn is overgrown by fine-grained marcasite, chalcopyrite, and sphalerite.



Photomicrographs of GMA13-031: ***(a)*** *Photomicrograph in reflected light (PPL) of early chalcopyrite followed by layered chalcopyrite + sphalerite, followed by additional sphalerite;* ***(b)*** *photomicrograph in transmitted light (PPL) of same view as (a), showing high-Fe sphalerite overgrown by low-Fe sphalerite;* ***(c)*** *photomicrograph in reflected light (PPL) of multiple generations of marcasite and chalcopyrite, with late coarse-grained barite;* ***(d)*** *photomicrograph in transmitted light (PPL) of chalcopyrite, followed by dendritic to radiating barite, overgrown by dendritic manganese oxide, amorphous silica, and iron oxyhydroxide, with late fine-grained sulfides (chalcopyrite + sphalerite).*

Mineral abundance: (modal %; not including pore space)

Sp	Ccp	Py	Mrc	Gn	Jd	Bn	Dg	Cv	Au	Brt	Anh	Am-Si	FeOx	MnOx
++	+++	+	+	-	-	-	Tr	+	-	+	-	+	+	+
11	60	1	5				<1	1		5		9	1	7

Paragenesis: High-Fe sphalerite → chalcopyrite → marcasite → secondary pyrite → high-Fe sphalerite + chalcopyrite → low-Fe sphalerite → covellite ± digenite → marcasite → secondary pyrite → coarse-grained barite → fine-grained dendritic manganese + iron oxyhydroxides → amorphous silica → fine-grained marcasite + chalcopyrite → fine-grained low-Fe sphalerite.

Name: Zoned chalcopyrite-sphalerite chimney

SAMPLE: GMA13-032 **PARENT ID:** 606	**LOCATION:** 784731.9E/8649743.1N **WATER DEPTH:** 1074 mbsl

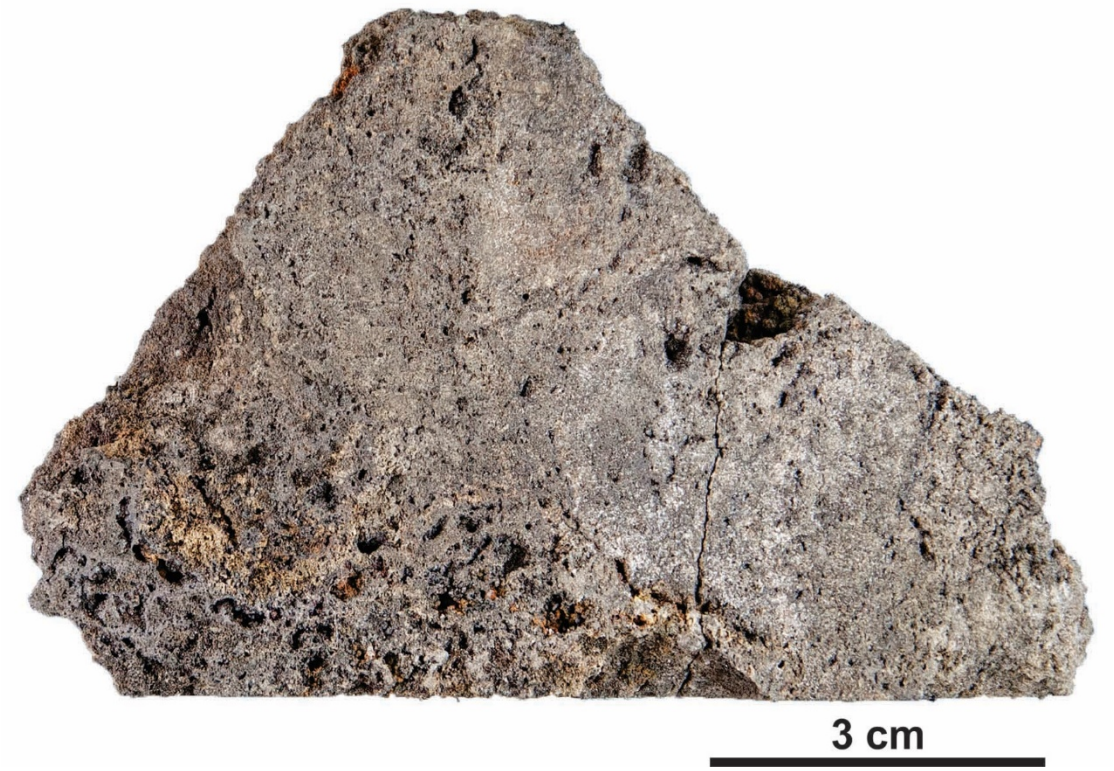
Geochemical Notes

Whole rock: High S (32.6%), Au (7260 ppb), Zn (454000 ppm), Cd (1030 ppm), Ge (91 ppm), Hg (30400 ppb), As (805 ppm), Sb (594 ppm), Ag (250 ppm); Low Cu, Ga.

Video Description

Top part of barite chimney. Small FeOx altered possible barite? Chimney on large protrusions - large protrusions may also be chimney/mound?

Hand Sample Description



Hand sample of GMA13-032.

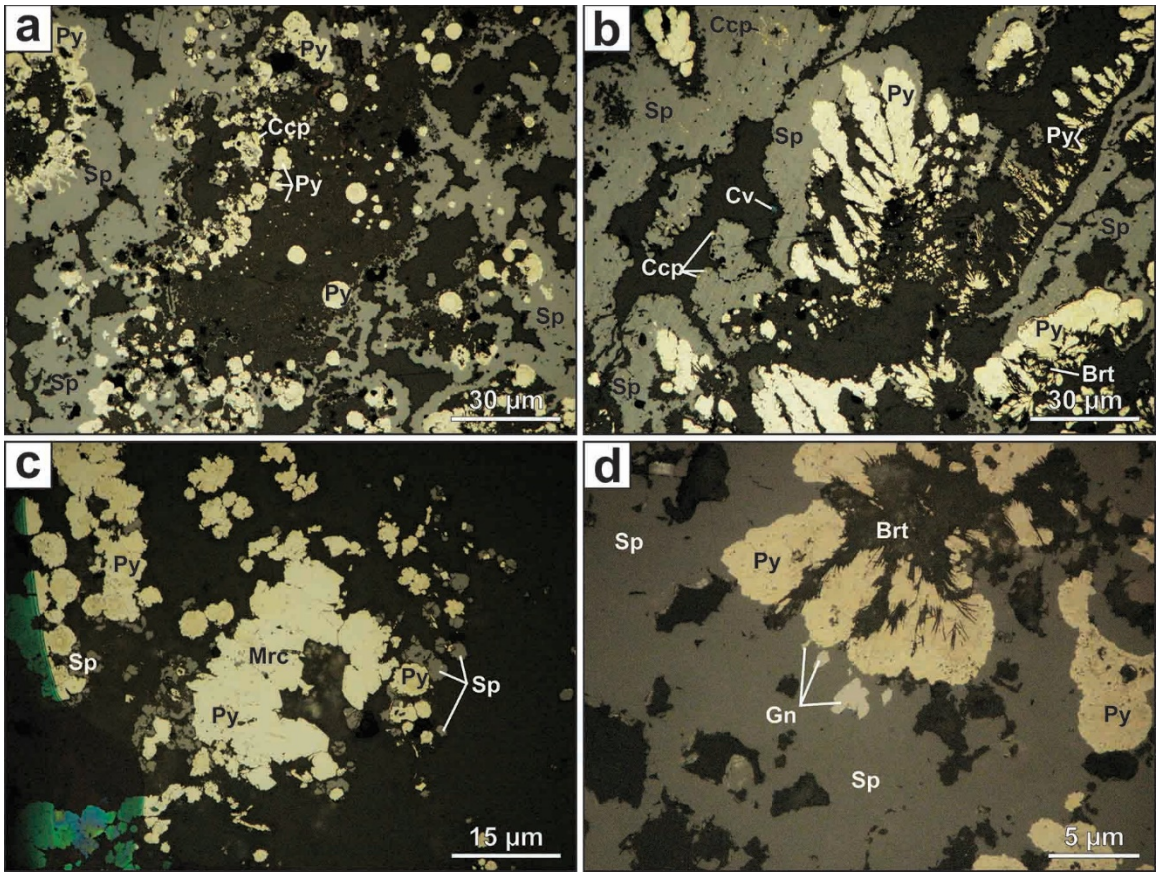
Massive sphalerite-rich chimney with mixed high-Fe sphalerite (35%) and low-Fe sphalerite (45%), with high-Fe sphalerite lining vent conduits. Irregular distribution of pore space, multiple small vent conduits up to 5 mm, 15% overall. Minor barite (5%) in vent conduits. Very thin veneer of manganese oxide on outer surface (<1%) and iron oxide (1%).

Thin Section Description



Thin section scan of GMA13-032.

This section has a porosity of ~30%. It is a zoned chimney with relict vent conduits and banded mineralogy. The earliest sulfide phase is spherulitic and dendritic pyrite, locally forming donut shapes that define former conduits. The dendritic pyrite locally grows on top of fine-grained dendritic barite. It is locally altered to goethite(?). This is overgrown by minor marcasite that has been extensively inverted to secondary pyrite. This is followed by high-Fe sphalerite (locally dendritic) with fine-grained chalcopyrite inclusions, grading outwards to low-Fe sphalerite. Locally, there are bands of changing color from dark reddish-brown to light orange-brown. This sphalerite has minor inclusions of fine-grained galena ± jordanite(?). This is followed by a generation of very low-Fe sphalerite (sharp contact), growing as a thin layer on previous generations. The sphalerite is locally altered to fine-grained covellite. Minor fine-grained chalcopyrite and galena ± jordanite form last. In the remaining pore space, there is fine-grained "fish-egg" amorphous silica with very fine-grained black inclusions (sulfides or manganese oxide?). Minor fine-grained sulfides (sphalerite, pyrite) grow on top of this. There are a few coarse-grained radiating barite crystals forming last, mostly near the bottom of the section.



Photomicrographs of GMA13-032: ***(a)*** *Photomicrograph in reflected light (PPL) of spherulitic pyrite and abundant sphalerite;* ***(b)*** *photomicrograph in reflected light (PPL) of pyrite, followed by sphalerite with chalcopyrite inclusions, locally altered to covellite;* ***(c)*** *photomicrograph in reflected light (PPL) of early pyrite overgrown by marcasite, followed by sphalerite;* ***(d)*** *photomicrograph in reflected light (PPL) of fine-grained barite, overgrown by pyrite, followed by sphalerite with galena inclusions.*

Mineral abundance: (modal %; not including pore space)

Sp	Ccp	Py	Mrc	Gn	Jd	Bn	Dg	Cv	Au	Brt	Anh	Am-Si	FeOx	Goe(?)
+++	+	+++	+	+	Tr	-	-	Tr	-	+	-	++	Tr	Tr
55	3	20	5	2	<1			<1		3		12	<0.01	<1

Paragenesis: Fine-grained dendritic barite → dendritic primary pyrite → minor marcasite → secondary pyrite → high-Fe sphalerite (locally dendritic) ± chalcopyrite → low-Fe sphalerite (alternating bands of color) ± galena ± jordanite(?) → minor very low-Fe sphalerite → covellite → fine-grained chalcopyrite + galena ± jordanite → amorphous silica (with fine sulfide or manganese oxide inclusions) → fine-grained pyrite → fine-grained sphalerite → coarse-grained barite.

Name: Zoned sphalerite-pyrite chimney

SAMPLE: GMA13-033 **PARENT ID:** 602	**LOCATION:** 784660.0E/8649788.9N **WATER DEPTH:** 1104 mbsl

Geochemical Notes

**XRF (parent): Cu = 0.41%, Pb = 0.82%, Zn = 36.10%, Ag = 146.0 ppm; Au = 7.28 ppm.*

Video Description

Sulphide boulder breccia at base of mound - oxide altered surface crust.

Hand Sample Description



Hand sample of GMA13-033.

Sample is a small boulder talus from the base of a chimney mound. The sample has an outer barite-rich zone with a sharp contact, likely a former central orifice that was lined by barite and is now filled in. The outer zone contains 20% barite and 75% high-Fe sphalerite, with small vugs (5%). The inner zone contains 10% barite and 80% low-Fe sphalerite, with slightly larger vugs up to 3 mm wide (most <1 mm), 10% vugs, with coarse-grained barite lining vugs. There are weakly developed colloform textures and minor dendritic textures.

Very fine grained pyrite is disseminated on outer rim and on walls of vugs (~3%), with <1% very fine grained galena in a vug. There is a thin coat of orange iron and manganese oxide on the outer surface of the sample (1%).

Mineral abundance: (modal %; not including pore space)

Sp	Ccp	Py	Mrc	Gn	Jd	Bn	Dg	Cv	Au	Brt	Anh	Am-Si	FeOx	MnOx
+++	-	+	-	Tr	-	-	-	-	-	++	-	-	+	+
75		3		<1						20			1	1

Name: Sphalerite-barite chimney (low-T) talus

SAMPLE: GMA13-034 **PARENT ID:** 608	**LOCATION:** 784759.0E/8649632.2N **WATER DEPTH:** 1108 mbsl

Geochemical Notes

Whole rock: High S (37.5%), Fe (28.8%), Cu (122000 ppm); Low Zn, Cd, Ga, Pb, Hg, Sb, Ag.

Video Description

Covered in bacterial matting, rounded in shape - mound with chimneys, spalled sulphides (?), cracks/fractures.

Hand Sample Description



Hand sample of GMA13-034.

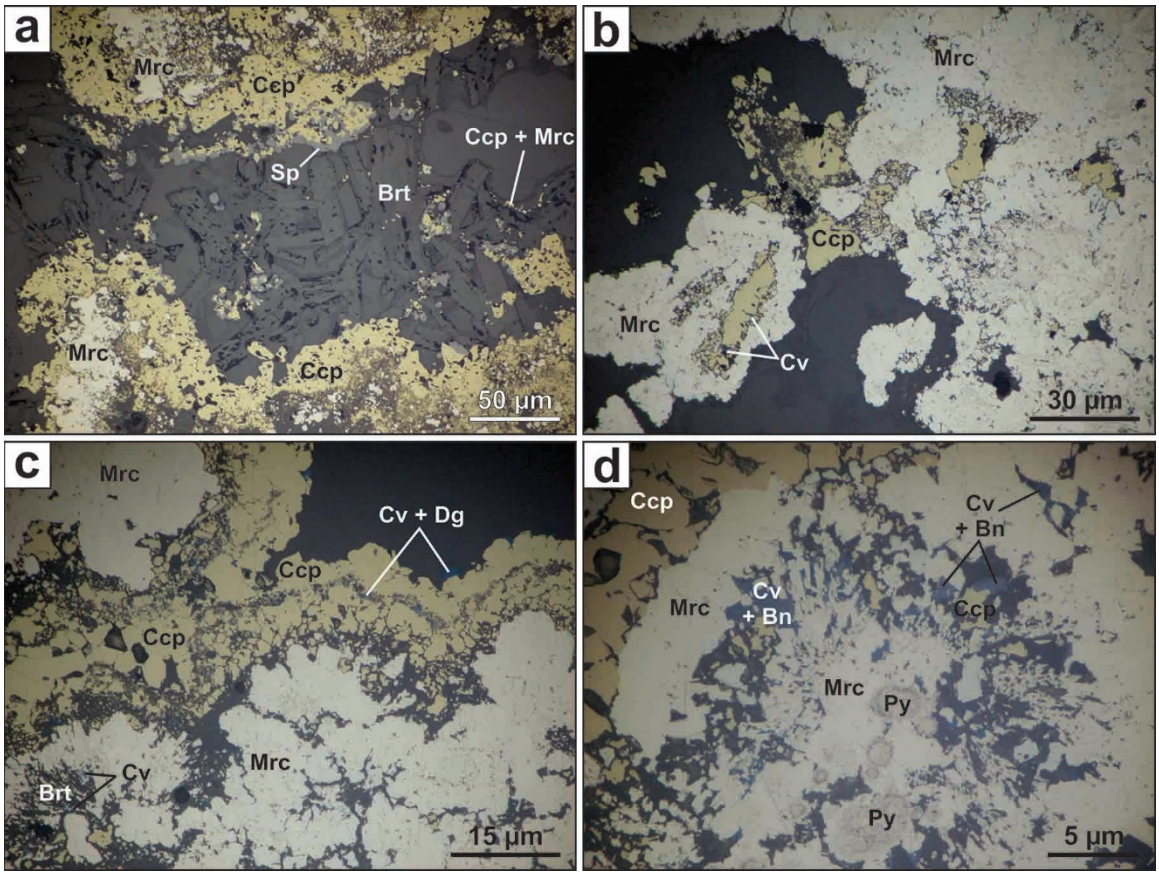
Dense chalcopyrite-rich chimney with massive chalcopyrite (75%), fine-grained to coarsely crystalline lining vent conduits. Bladed barite occurs as vent conduit fill and possibly fine-grained intergrown throughout (10%). Pyrite occurs as vent lining and very fine grained patches on outer rim of sample (1%) intergrown with chalcopyrite. Very minor sphalerite lining vent orifice (10%). Minor atacamite throughout (2%), with iron oxide (<1%) and manganese oxide (1%) on outer surface as a very thin coating, minor yellow orpiment(?) on outer surface (<1%). Trace bornite. Pore space irregularly distributed throughout, 5% overall.

Thin Section Description



Thin section scan of GMA13-034.

This section has a porosity of ~10-15%. The earliest phase to crystallize is abundant fine- to coarse-grained marcasite, which locally displays colloform and dendritic textures. The marcasite has been irregularly (but extensively) inverted to secondary pyrite, with minor alteration to goethite(?). This is followed by abundant fine- to coarse-grained chalcopyrite, locally altered to minor fine-grained covellite ± bornite ± digenite. Alteration of the chalcopyrite along bands, overgrown by additional chalcopyrite, which is also locally altered at the margins, indicates multiple chalcopyrite generations. Relict chalcopyrite crystals are rare. The crystal size increases near former vent conduits. Locally, this is followed by minor low-T sphalerite, which grows along some cracks / former vent conduits; primarily growing along one major crack near the right side of the section. This is locally overgrown by additional chalcopyrite. Along some of the fractures, coarse- to very-coarse grained tabular, often radiating barite forms, followed by minor fine- to coarse-grained marcasite + chalcopyrite + sphalerite. Near the top of the section, a second phase of coarse-grained tabular, radiating barite crystallizes. Minor iron oxyhydroxides, associated with amorphous silica, are distributed irregularly throughout the section.



Photomicrographs of GMA13-034: ***(a)*** *reflected light (PPL) photomicrograph of early marcasite, followed by chalcopyrite, then sphalerite, then coarse-grained barite, and additional fine-grained chalcopyrite + marcasite;* ***(b)*** *reflected light (PPL) photomicrograph of early and late chalcopyrite, locally altered to covellite, surrounded by marcasite that has been partially inverted to secondary pyrite;* ***(c)*** *reflected light (PPL) photomicrograph of marcasite, overgrowing barite, and two generations of chalcopyrite separated by a layer of secondary sulfides (covellite + digenite), with late covellite + digenite;* ***(d)*** *reflected light (PPL) photomicrograph marcasite, that has been partially inverted to secondary pyrite, followed by chalcopyrite locally altered to covellite + digenite + bornite, a second generation of marcasite, and finally chalcopyrite.*

Mineral abundance: (modal %; not including pore space)

Sp	Ccp	Py	Mrc	Gn	Jd	Bn	Dg	Cv	Au	Brt	Anh	Am-Si	FeOx	Goe
+	+++	++	+++	-	-	Tr	Tr	+	-	+	-	+	+	Tr
3	30	15	40			<1	<1	3		5		2	2	<1

Paragenesis: Marcasite → secondary pyrite + minor goethite(?)→ chalcopyrite → covellite ± digenite ± bornite → low-T sphalerite → chalcopyrite → covellite ± digenite ± bornite → coarse-grained tabular barite → minor marcasite + chalcopyrite + sphalerite → coarse-grained tabular barite → amorphous silica + iron oxyhydroxides

Name: Zoned pyrite/marcasite-chalcopyrite chimney

SAMPLE: GMA13-038 **PARENT ID:** 695	**LOCATION:** 784500.8E/8650057.7N **WATER DEPTH:** 1116 mbsl

Geochemical Notes

Whole rock: High S (34.4%), Fe (26.3%), Cu (270000 ppm), In (280 ppm); Low Ge, Pb, Hg, As, Sb, Ag.

Video Description

Top of central oxidised chimney spire.

Hand Sample Description

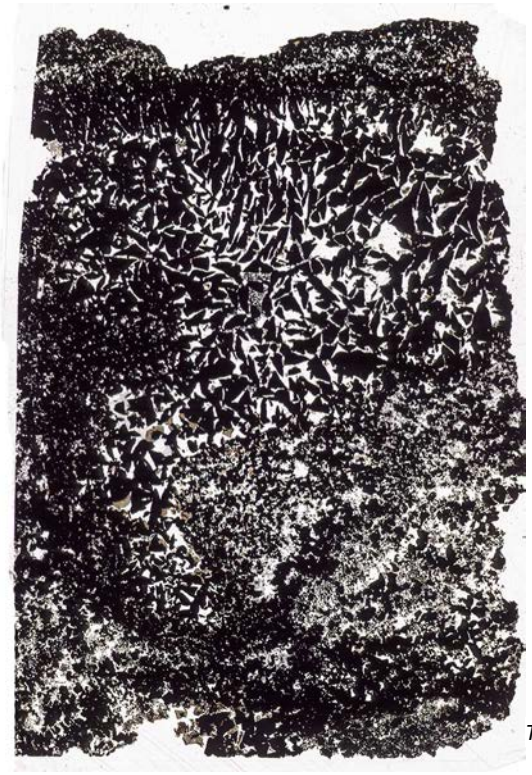


Hand sample of GMA13-038.

Zoned chalcopyrite-rich chimney with massive to coarsely crystalline chalcopyrite (65%), becoming very coarse near central conduits. Fine-grained massive high-Fe sphalerite (20%) in inner zones, and coarse sphalerite as final phase precipitated in conduits. Minor fine-grained pyrite intergrown with chalcopyrite (5%) and trace bornite. Iron oxide only on outer surfaces (1%). Well-formed banded textures with multiple vent conduits up to 2 cm wide, 10% pore space overall.

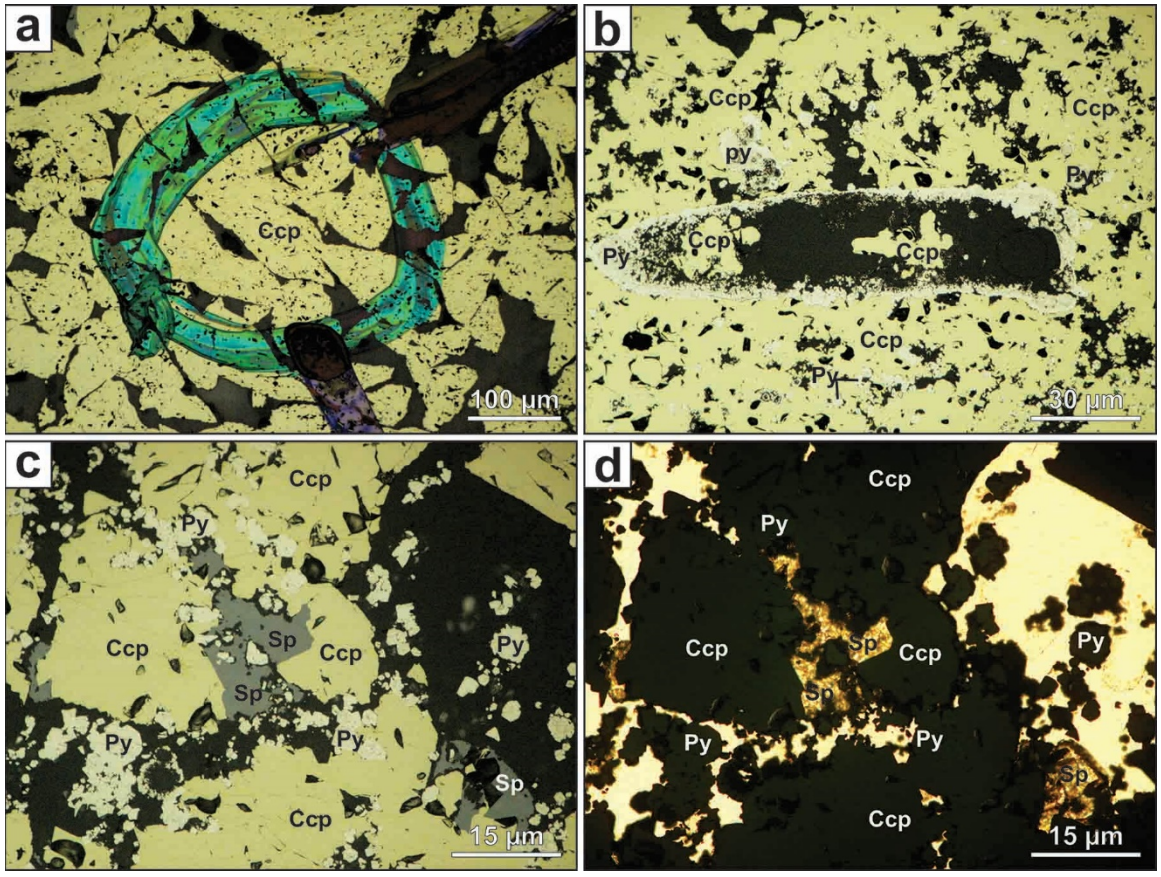
Thin Section Description

This section has a porosity of ~35%. It is dominated by medium- to very coarse-grained chalcopyrite, which crystallizes after early fine- to coarse-grained pyrite. The pyrite forms along discrete bands and around former rounded vent conduits. It is anhedral to euhedral, and locally displays growth zoning, spheroidal, and colloform textures. Following chalcopyrite, the next phase to crystallize is minor fine- to medium-grained sphalerite. The sphalerite is very light in color, almost colorless, indicating very low Fe-contents. It has an irregular distribution, forming in some former vent conduits. Near the top of the section, the sphalerite occurs within very fine cracks in the chalcopyrite. Minor very fine-grained



secondary covellite is irregularly distributed throughout the section, generally associated with sphalerite. Minor fine-grained radiating acicular barite, and medium-grained tabular barite form in some of the remaining pore spaces. The fine-grained radial barite masses are locally iron-stained, and fine-grained iron oxyhydroxides are scattered throughout the section, along with amorphous light-green atacamite. This section has the highest concentration of atacamite observed yet.

Thin section scan of GMA13-038.



Photomicrographs of GMA13-038: ***(a)*** *Photomicrograph in reflected light (PPL) of coarse-grained chalcopyrite;* ***(b)*** *photomicrograph in reflected light (PPL) of pyrite forming around a former vent conduit, followed by chalcopyrite;* ***(c)*** *photomicrograph in reflected light (PPL) of early pyrite overgrown by chalcopyrite, followed by sphalerite;* ***(d)*** *photomicrograph in transmitted light (PPL) of the same view as (c), showing the very light color of sphalerite, indicating low Fe contents.*

Mineral abundance: (modal %; not including pore space)

Sp	Ccp	Py	Mrc	Gn	Jd	Bn	Dg	Cv	Au	Brt	Anh	Am-Si	FeOx	Ata
+	+++	+	-	-	-	-	-	Tr	-	+	-	-	+	+
5	81	7						<1		5			1	1

Paragenesis: Pyrite → chalcopyrite → pyrite → low-T sphalerite → covellite → barite + iron oxyhydroxides + atacamite.

Name: Chalcopyrite chimney (high-T)

SAMPLE: GMA13-040 **PARENT ID:** 697	**LOCATION:** 784531.5E/8650094.1N **WATER DEPTH:** 1123 mbsl

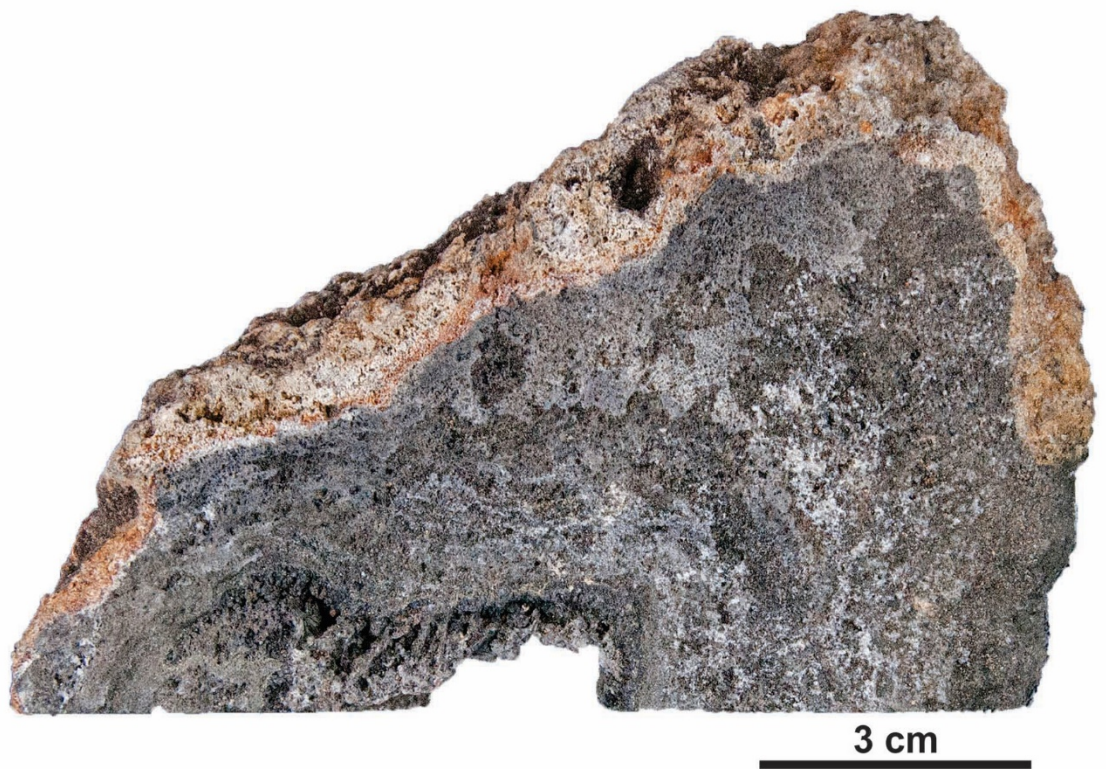
Geochemical Notes

Whole rock: High Zn (271000 ppm), Cd (1120 ppm), Ga (65 ppm), Ba (91500 ppm); Low Fe, Cu, Hg.

Video Description

Slabby sulphide sample from spired chimney, layered.

Hand Sample Description



Hand sample of GMA13-040.

Massive Sph-Ba chimney with a 2 cm wide central vent. The vent is lined first by pyrite + chalcopyrite (1%), followed by high-Fe sphalerite, and bladed coarse-grained barite. Outer part of chimney is composed of high-Fe sphalerite (50%), low-Fe sphalerite (20%) and interstitial barite (10%). Porous sample with sub-mm wide vugs, 15% overall. Outer surface has up to 1 cm thick coat of clay (5%), iron oxide (1%) and manganese oxide (<1%).

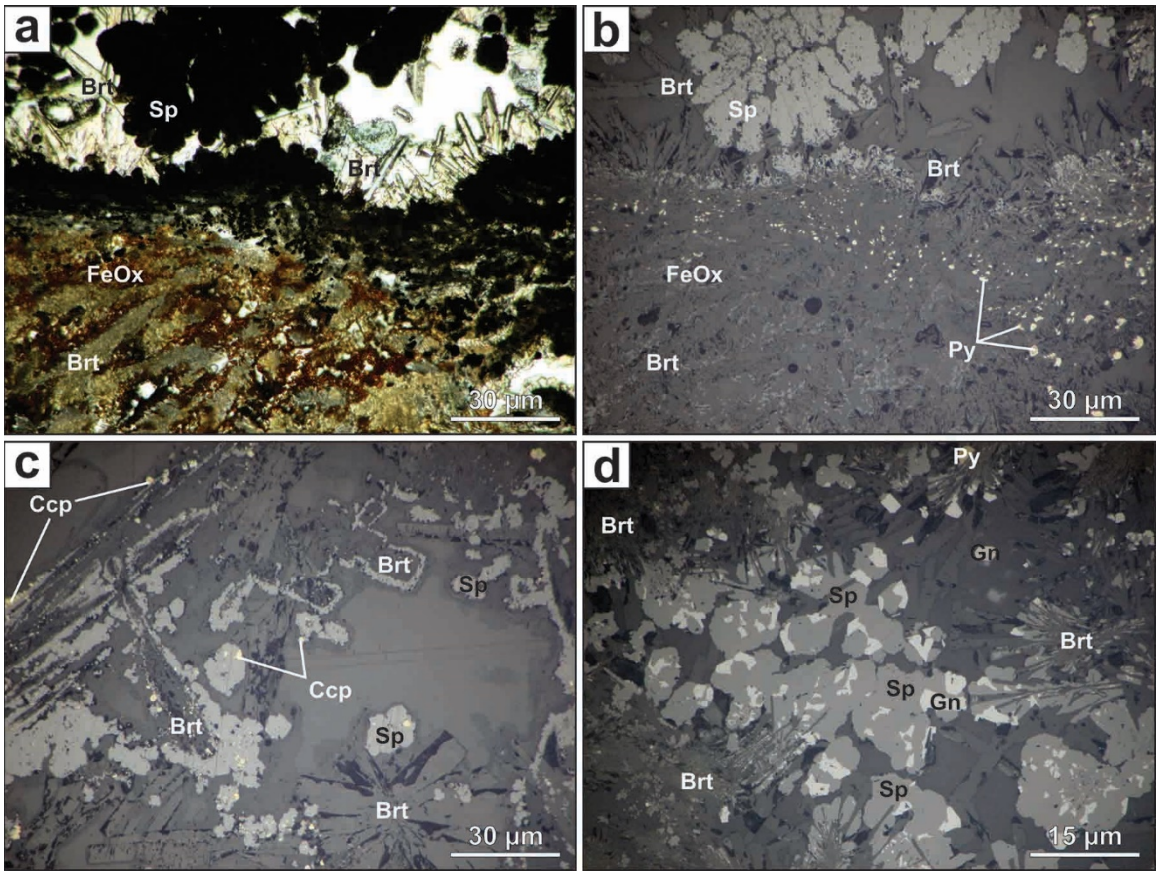
Thin Section Description



Thin section scan of GMA13-040.

This section has a porosity of ~35%. It is characterized by abundant dendritic textures with dendrites generally growing upwards. The mineralogy is similar to previous sphalerite-barite chimneys. It contains a contact between the chimney and its weathered outer surface, located at the top of the section. The earliest phase is fine- to medium-grained dendritic barite, followed by minor spherulitic pyrite up to ~1.2 mm wide. Pyrite also forms a discrete band in the bottom left corner of the section. The pyrite is overgrown by an early generation high-Fe (black) dendritic sphalerite, followed by a sharp contact with a second generation of sphalerite (low-Fe; generally decreasing outwards), and then a third generation sphalerite (high-Fe), which only forms locally. Fine- to medium-grained inclusions of galena and chalcopyrite are associated with the first generation of high-Fe sphalerite. Near the top of the section, the galena is more abundant and appears intergrown with the sphalerite; here, chalcopyrite inclusions are absent. This indicates local equilibrium conditions existed. Slightly larger inclusions of chalcopyrite also form in the second sphalerite generation (low-Fe); locally these are coarse-grained (e.g., lower left corner of the section). There are no chalcopyrite inclusions with the third generation of pyrite. Rare fine-grained covellite is locally present. The next sulfide phase to mineralize is minor fine- to medium-grained subhedral to euhedral galena. Next, fine-grained inclusion-filled (locally iron-stained) radiating to dendritic barite forms next, followed by coarse- to very-coarse grained tabular, radiating barite, which fills in most of the remaining pore space. This is locally coated by high-Fe sphalerite with chalcopyrite inclusions, followed by low-Fe sphalerite. This is again followed by coarse-grained tabular barite. Fine-grained amorphous “fish-egg” silica coats everything.

The contact with the top weathered horizon is irregular and somewhat gradual, characterized by the disappearance of sphalerite and galena first; spherulitic pyrite extends slightly further into this area. The top of the section is composed primarily of fine-grained inclusion-filled (“dirty” looking) dendritic barite, overgrown by coarser grained tabular barite. Abundant bright orange to blood-red iron oxides (including minor hematite) and oxyhydroxides form near the contact, infilling pore space and staining the late barite crystals and amorphous silica, which suggests that this is in fact a weathered horizon. At the very top of the section, discrete layers of dark red to black oxides occur, likely indicating the presence of manganese oxide. A few spherules of pyrite + sphalerite (intergrown) persist locally in this horizon.



Photomicrographs of GMA13-040: ***(a)*** *transmitted light (PPL) photomicrograph of dendritic barite with abundant iron oxyhydroxides, a band of spherulitic pyrite, followed by high-Fe sphalerite, minor fine-grained galena, and coarse-grained barite;* ***(b)*** *transmitted light (PPL) photomicrograph of the same view as (a);* ***(c)*** *reflected light (PPL) photomicrograph of a late generation of sphalerite with chalcopyrite inclusions overgrowing coarse-grained tabular barite, with a fine coating of amorphous silica;* ***(d)*** *reflected light (PPL) photomicrograph of dendritic/radiating barite, followed by intergrown sphalerite + galena, from the top of the section.*

Mineral abundance: (modal %; not including pore space)

Sp	Ccp	Py	Mrc	Gn	Jd	Bn	Dg	Cv	Au	Brt	Am-Si	FeOx	Hem	MnOx
+++	+	++	-	+	-	-	-	Tr	-	+++	+	+	Tr	+
35	1	10		2				<1		45	3	2	1	1

Paragenesis: Dendritic barite → spherulitic pyrite → high-Fe sphalerite + chalcopyrite + galena → low-Fe sphalerite + chalcopyrite → high-Fe sphalerite (local) → covellite → galena → dendritic barite → coarse-grained tabular barite → high-Fe sphalerite + chalcopyrite → low-Fe sphalerite → coarse-grained tabular barite → amorphous silica + iron oxides and oxyhydroxides → manganese oxide.

Name: Barite-sphalerite chimney (low-T)

SAMPLE: GMA13-041 **PARENT ID:** 700	**LOCATION:** 784565.3E/8649996.1N **WATER DEPTH:** 1109 mbsl

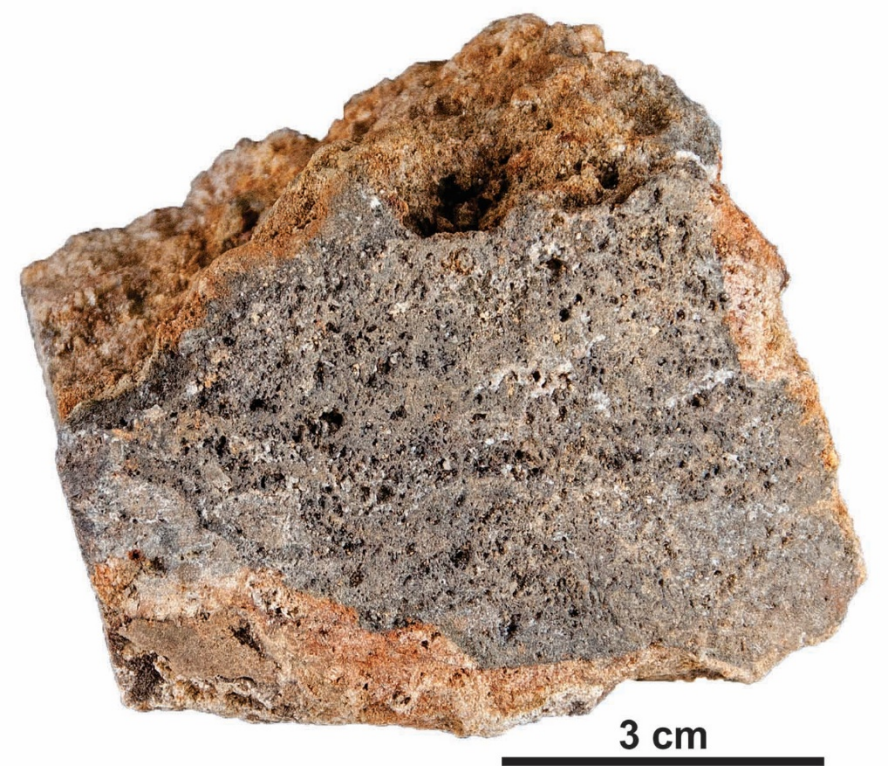
Geochemical Notes

**XRF (parent): Cu = 0.62%, Pb = 5.71%, Zn = 25.00%, Ag = 760.0 ppm; Au = 1.83 ppm.*

Video Description

Piece from base of chimney - knobby chimney spire grown sideways, largely inactive weakly oxidized.

Hand Sample Description



Hand sample of GMA13-041.

Massive Sph-Ba chimney. 10% fine vugs, no obvious vent orifice or colloform textures. Ba in vugs and cavities. Low and high Fe Sph, minor Gn. FeOx + clay weathering, mm to 0.5 mm thick, mottled orange with an outermost black crust, overlies a reasonably fresh grey to buff interior with a fine skeletal to globular structure and numerous small cavities. Cavities contain white globules and occasional barite blades. A large cavity (1 cm across and >2 cm long) lying mostly in the rind zone but also partly in the interior is lined by an earthy white-cream layer overgrown by rosettes of barite: within the outer rind these barites are stained brown. There is no axial conduit.

Thin Section Description

This section has a porosity of ~40%. It consists of a chimney with a weathered rind along the top of the section. The chimney portion is characterized by abundant dendritic to acicular, radiating high-Fe sphalerite overgrowing dendritic to tabular barite, with inclusions of euhedral to spherulitic pyrite (with minor growth zoning), and minor, irregular chalcopyrite disease. Near the bottom of the section, the spherulitic pyrite is overgrown by marcasite, which is partially altered to secondary pyrite and

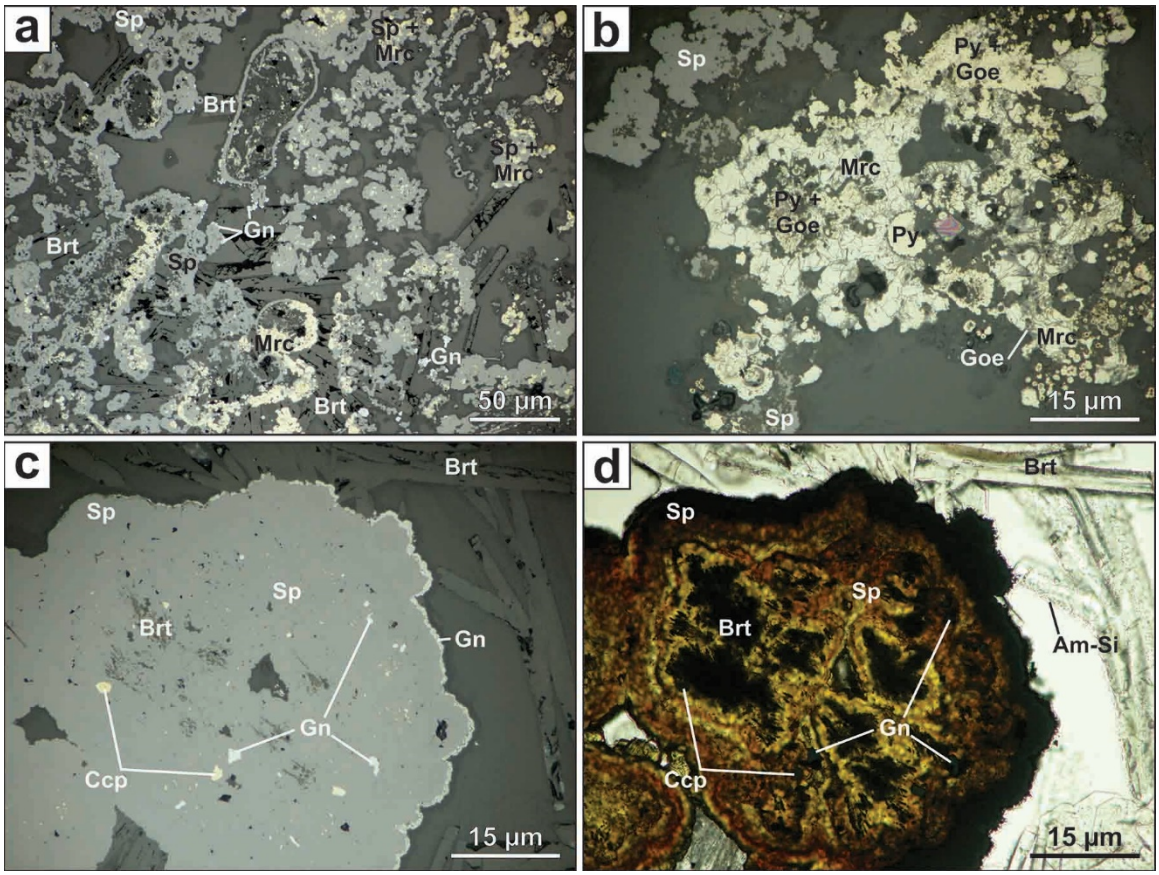


Thin section scan of GMA13-041.

goethite(?), occurring along a banded distribution. The early sphalerite is followed by minor fine-grained galena and medium-grained pyrite, and then at least two more generations of low-Fe sphalerite, irregularly distributed throughout the section. The first low-Fe generation ranges in color from light yellow-brown to medium red-brown, with increasing Fe-contents outwards. The second generation is light yellow-brown again. The low-Fe sphalerite generations have rare inclusions of fine-grained chalcopyrite and galena, and abundant inclusions of euhedral-spherulitic pyrite. Locally, additional generations of high- and low-Fe sphalerite are present. The next phase to precipitate is fine- to medium-grained anhedral to euhedral galena, which is locally coated by a very thin layer of very low-Fe (almost colorless) sphalerite. Small vent conduits are distinguished by the rounded lining of sulfides, primarily sphalerite + pyrite. The remaining pore space is partially filled by abundant coarse-grained radiating tabular barite, followed by intergrown galena + low-Fe sphalerite.

Near the contact with the weathered horizon, the sphalerite is altered to fine-grained covellite ± digenite, locally pseudomorphing sphalerite, and very few sulfides persist into the weathered surface. The contact is sharp, characterized by a layer of pyrite and bright-red iron oxides (including hematite) and oxyhydroxides. These oxides decrease in abundance away from the contact. Barite persists throughout this horizon, followed by a thick layer of amorphous silica containing iron oxide inclusions. This is followed locally by very fine-grained sulfides (sphalerite + chalcopyrite + pyrite), indicating renewed hydrothermal activity.

No jordanite was observed, despite the high Ag contents.



Photomicrographs of GMA13-041: ***(a)*** *reflected light (PPL) photomicrograph of sphalerite and marcasite lining vent conduits, with minor galena and late coarse-grained barite;* ***(b)*** *reflected light (PPL) photomicrograph of marcasite that has been partially inverted to pyrite, with minor late goethite(?);* ***(c)*** *reflected light (PPL) photomicrograph of sphalerite with inclusions of chalcopyrite and galena, with a thin coat of galena and late barite;* ***(d)*** *transmitted light (PPL) photomicrograph of the same view as (c) showing multiple generations of sphalerite, with late amorphous silica.*

Mineral abundance: (modal %; not including pore space)

Sp	Ccp	Py	Mrc	Gn	Jd	Bn	Dg	Cv	Brt	Am-Si	Goe(?)	FeOx	Hem
+++	+	++	+	+	-	-	Tr	+	+++	+	Tr	+	+
40	1	10	1	5			<1	1	35	2	<1	3	2

Paragenesis: Dendritic to radiating tabular barite → euhedral to spherulitic pyrite → marcasite (local, banded) → secondary pyrite + goethite → high-Fe sphalerite + chalcopyrite → galena + pyrite → low- to mod-Fe sphalerite → low-Fe sphalerite (+ additional sphalerite generations, locally) → galena → coarse-grained tabular barite → intergrown sphalerite + low-Fe galena → covellite ± digenite (local) → iron oxides (hematite) and oxyhydroxides → amorphous silica → very fine-grained sphalerite + chalcopyrite + pyrite.

Name: Sphalerite- barite chimney (low-T)

SAMPLE: GMA13-042 **PARENT ID:** 698	**LOCATION:** 784555.2E/8650074.9N **WATER DEPTH:** 1122 mbsl

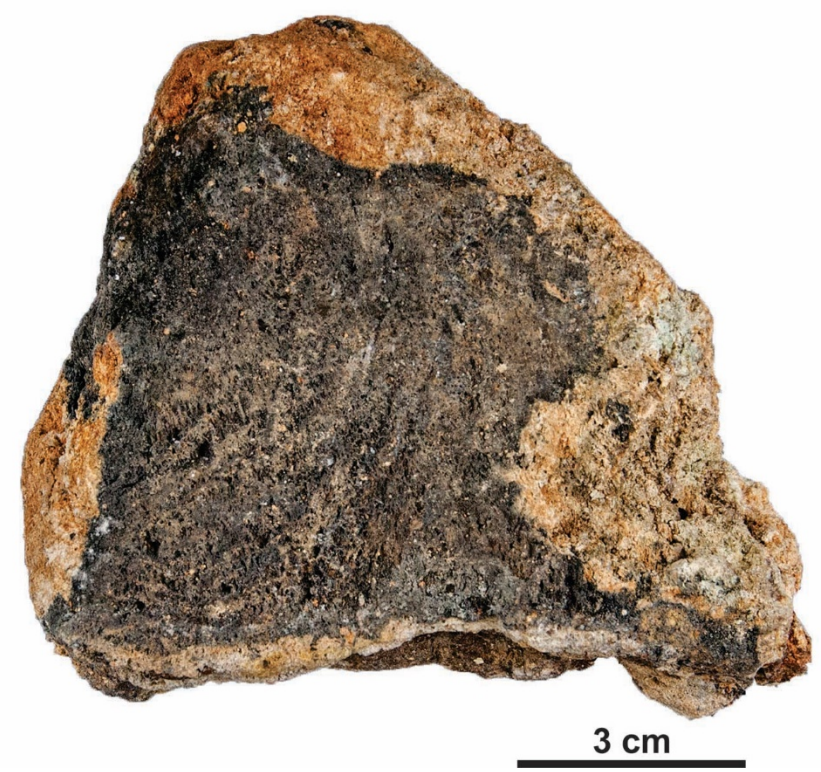
Geochemical Notes

Whole rock: High Zn (380000 ppm), Cd (1090 ppm), Ge (92 ppm), Pb (29300 ppm), As (1170 ppm), Ba (75200 ppm); Low Fe, Au, Cu, Ga.

Video Description

Piece from big chimney, 12 m high, off top, looks oxidized.

Hand Sample Description



Hand sample of GMA13-042.

Strongly weathered sphalerite-barite chimney with no central conduits, small mm-size vugs 25% overall. Strong dendritic textures in sphalerite, with both high-Fe (30%) and low-Fe (40%) sphalerite, alternating. Coarse grained barite in vugs, interstitial throughout (10%). Weathered rim is up to 4 cm thick composed of clay (10%), iron oxide (2%), and manganese oxide (10%). Barite crystals still survive in areas dominated by manganese oxide.

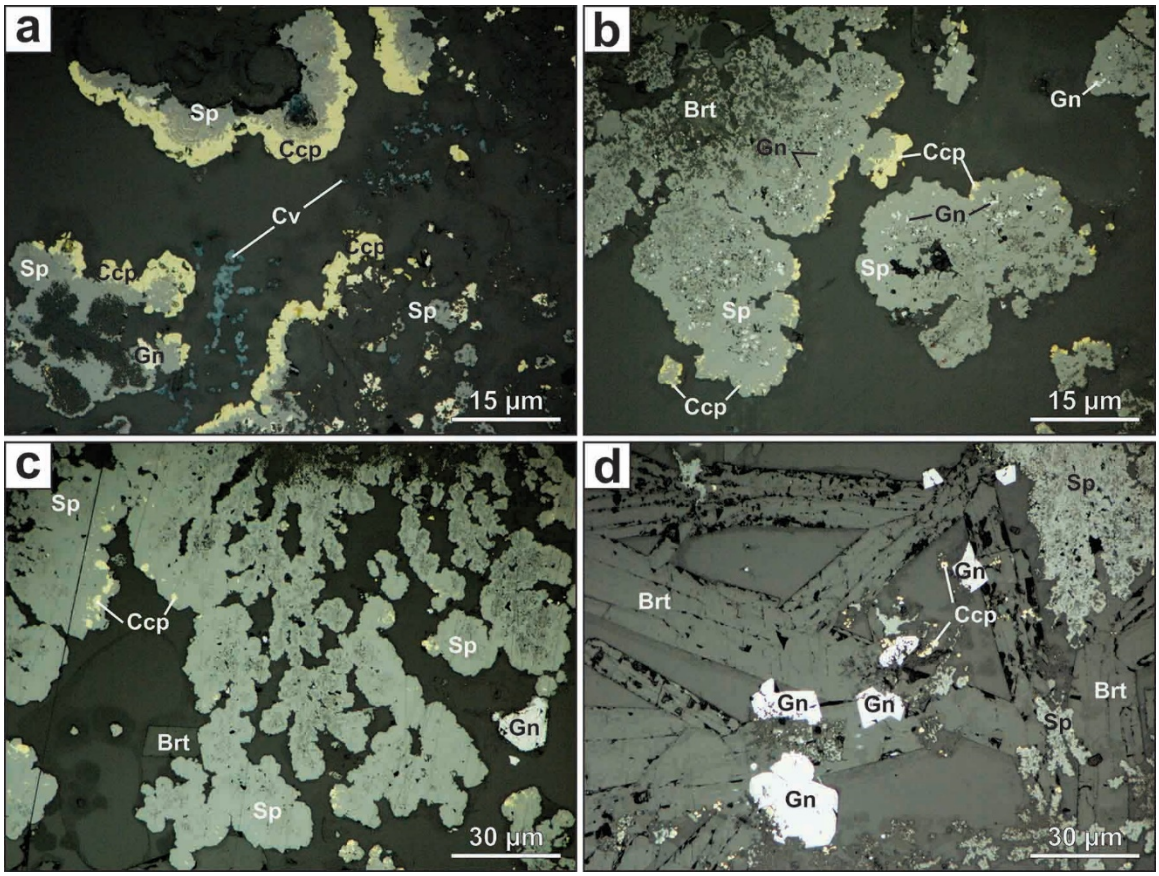
Thin Section Description

This section is very porous, with ~40-45% porosity. The earliest generation is dendritic barite followed by dendritic high-Fe sphalerite. This sphalerite contains abundant fine-grained inclusions of galena. Locally, there is secondary covellite. This is followed by minor spherulitic to euhedral pyrite, and a second generation of high-Fe sphalerite intergrown with chalcopyrite and minor galena. A lower-Fe phase of sphalerite precipitates next, followed by chalcopyrite, more low-Fe sphalerite, and more chalcopyrite.



This is then followed by medium-grained subhedral- to euhedral galena, irregularly distributed. A very thin layer of amorphous silica coats everything, locally displaying fish-egg texture with fine-grained sulfide nuclei. Very coarse-grained tabular barite forms next, sometimes radiating, growing in some pore spaces. It is particularly abundant near the top of the section where there is an irregular weathered horizon. Within the weathered horizon, there are few sulfides, but abundant light-orange iron oxyhydroxides associated with dendritic barite and amorphous silica. Dark red hematite appears to pseudomorph after pyrite, irregularly distributed in along this horizon. Minor fine-grained manganese oxides form last. The contact between the weathered and unweathered portions of the sample is fairly sharp, occurring over a few mm, but very irregular.

Thin section scan of GMA13-042.



Photomicrographs of GMA13-042: ***(a)*** *reflected light (PPL) photomicrograph of sphalerite with inclusions of galena, overgrown by chalcopyrite, with minor secondary covellite;* ***(b)*** *reflected light (PPL) photomicrograph of sphalerite overgrowing dendritic barite, with inclusions of galena, overgrown by chalcopyrite;* ***(c)*** *reflected light (PPL) photomicrograph of sphalerite overgrowing dendritic barite, followed by chalcopyrite, additional sphalerite, and late galena;* ***(d)*** *reflected light (PPL) photomicrograph subhedral galena and coarse-grained tabular barite.*

Mineral abundance: (modal %; not including pore space)

Sp	Ccp	Py	Mrc	Gn	Jd	Bn	Dg	Cv	Au	Brt	Am-Si	FeOx	Hem	MnOx
+++	+	+	-	+	-	-	-	+	-	+++	+	+	+	+
52	5	1		4				1		26	3	5	2	1

Paragenesis: Dendritic barite → high-Fe sphalerite + galena → covellite → pyrite → high-Fe sphalerite + chalcopyrite ± galena → low-Fe sphalerite → chalcopyrite → low-Fe sphalerite → covellite → chalcopyrite → galena → amorphous “fish-egg” silica → very coarse-grained tabular barite → Fe oxides (incl. hematite) and oxyhydroxides → manganese oxide.

Name: Sphalerite-barite chimney (low T)

SAMPLE: GMA13-045 **PARENT ID:** 708	**LOCATION:** 784650.5E/8649864.0N **WATER DEPTH:** 1090 mbsl

Geochemical Notes

Whole rock: High Fe (13.8%), Pb (23700 ppm), As (708 ppm), Ag (229 ppm), Ba (135000 ppm), Sr (6020 ppm); Low Cu, Cd, Ga.

Video Description

Large piece of sulphide talus, slightly oxidized on top of indurated sediments between knobby sulphide chimneys, scattered oxides nearby.

Hand Sample Description



Hand sample of GMA13-045.

Composed of high-Fe sphalerite (25%) and abundant barite (65%). The barite occurs as vent fill and has very well developed bladed textures in the central conduit where crystals are up to 5 mm long. Barite is also interstitial to sphalerite, which is very fine grained, with minor colloform textures, and is the latest vent fill. Minor pyrite around rims of vent conduits, up to 2 mm wide, 5-10% overall. The vent conduits are up to 1.5 cm wide, and there are small vugs distributed throughout the sample, ~1 mm wide, 3-4% overall. Very thin coat of Fe-MnOx on outside of sample (<1%) with trace orpiment(?).

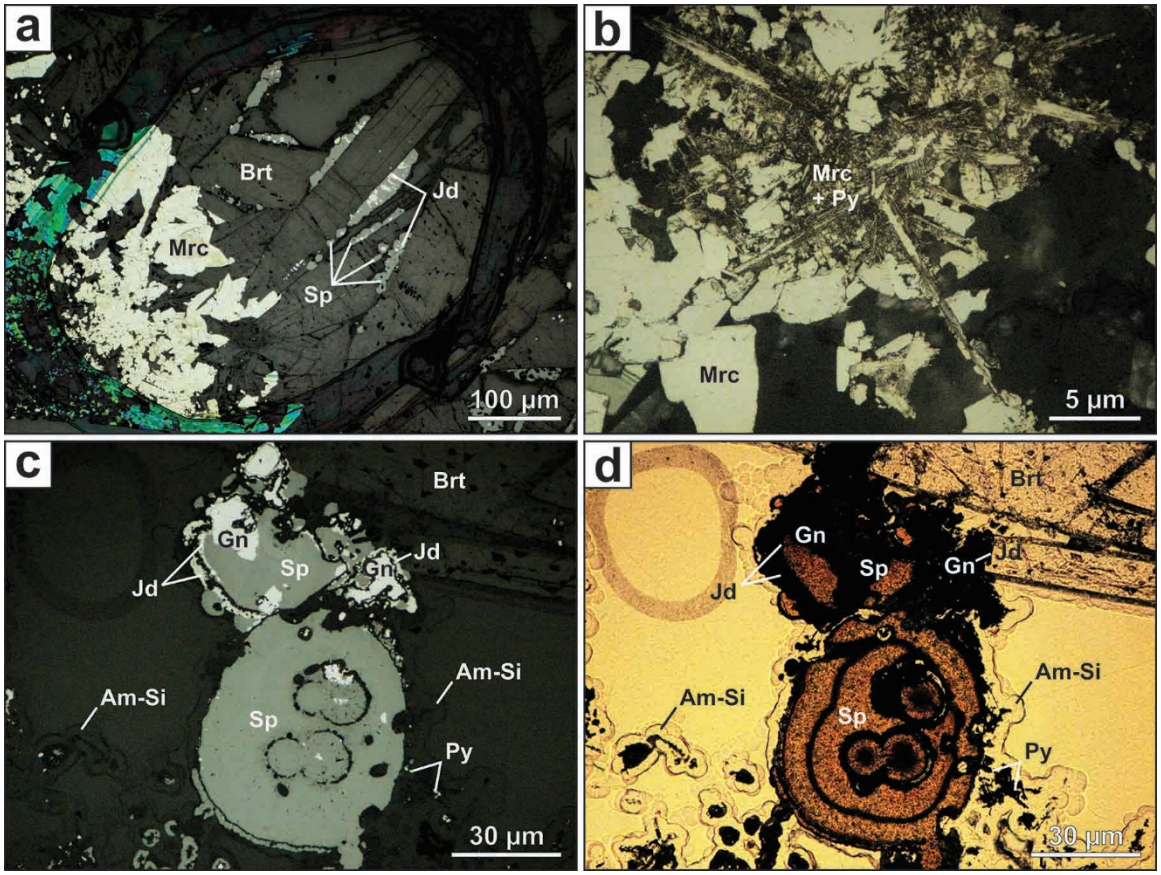
Thin Section Description

This section has a porosity of ~40-45%. It contains an early generation of dendritic barite with abundant very fine-grained black inclusions, likely sphalerite. This is overgrown by minor spherulitic to euhedral pyrite, followed by abundant coarse-grained marcasite is irregularly distributed, showing complicated growth zoning patterns that appear 'etched' due to alteration to secondary pyrite and goethite(?). This is followed by low-Fe sphalerite intergrown with galena.



The top half of the section marks a large infilled crack, lined by coarse-grained marcasite (partially altered to secondary pyrite and goethite), followed by sphalerite, and very-coarse grained tabular barite growing inwards. This coarse-grained barite is abundant throughout the section, and locally displays growth zoning. A later generation of spherulitic pyrite forms next, although a high porosity indicates that this may be secondary pyrite after marcasite. This followed by low-Fe sphalerite that grows as 'blebs' on top of the barite crystals. These blebs contain multiple sphalerite generations (at least four) intergrown with galena. Jordanite inclusions are common. There is minor late pyrite after this. Everything is covered by a thin layer of amorphous "fish-egg" silica. Locally, fine-grained radiating (colloform?) barite grows on top of this, locally associated with very minor iron oxyhydroxides. This is followed by 2-3 more layers of "fish-egg" amorphous silica. This silica is ubiquitous throughout the section, with a total thickness of 0.2 to 0.7 mm. It contains minor inclusions of fine black sulfides.

Thin section scan of GMA13-045.



Photomicrographs of GMA13-045: ***(a)*** *reflected light (PPL) photomicrograph of marcasite followed by coarse-grained barite, followed by late low-Fe sphalerite with abundant jordanite inclusions;* ***(b)*** *reflected light (PPL) photomicrograph of marcasite that has been partially inverted to pyrite, with minor late goethite(?);* ***(c)*** *reflected light (PPL) photomicrograph of sphalerite with inclusions of galena, and a generation of jordanite;* ***(d)*** *transmitted light (PPL) photomicrograph of the same view as (c) showing multiple generations of sphalerite, with late amorphous silica.*

Mineral abundance: (modal %; not including pore space)

Sp	Ccp	Py	Mrc	Gn	Jd	Bn	Dg	Cv	Au	Brt	Anh	Am-Si	FeOx	Goe(?)
+	-	+	++	+	+	-	-	-	-	+++	-	+	Tr	Tr
5		1	10	3	2					75		4	<1	<1

Paragenesis: Dendritic barite + high-T sphalerite → spherulitic marcasite → secondary pyrite + goethite(?)→ marcasite → low-Fe sphalerite + galena → very coarse-grained tabular barite → sphalerite + galena + jordanite → pyrite/marcasite → amorphous silica → radiating/colloform barite ± minor iron oxyhydroxides (local) → additional layers of amorphous "fish-egg" silica.

Name: Barite-marcasite chimney talus

SAMPLE: GMA13-046 **PARENT ID:** 710	**LOCATION:** 784546.0E/8649903.4N **WATER DEPTH:** 1090 mbsl

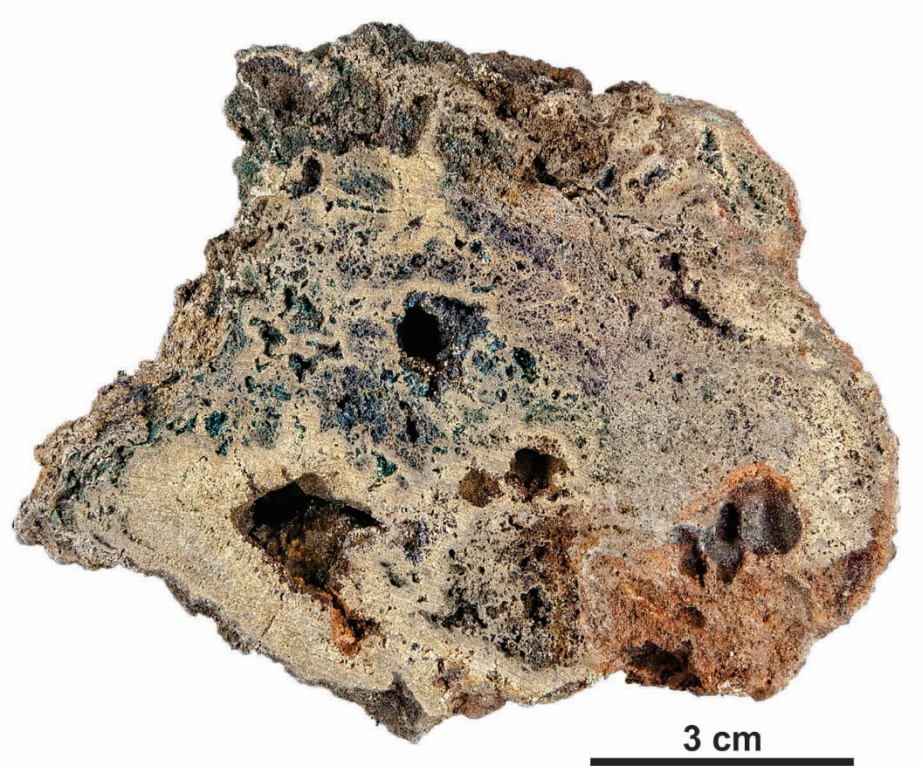
Geochemical Notes

Whole rock: High S (35.9%), Fe (27.8%), Cu (223000 ppm), Ba (22300 ppm); Low Cd, Ga, Pb, Sb, Ag, Ba.

Video Description

Sulphide chimney, orange oxide outer coating.

Hand Sample Description

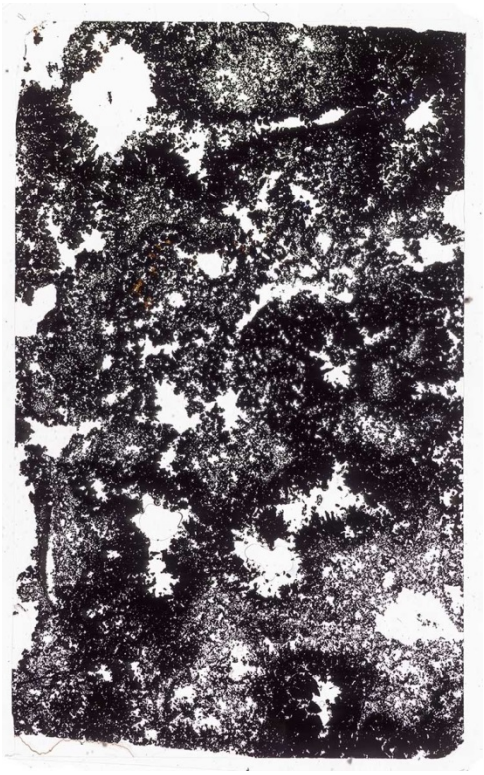


Hand sample of GMA13-046.

Sample from top of a chimney spire with multiple vent orifices up to 1.5 cm wide, with radial and colloform banding and 30% pore space overall. It is primarily composed of chalcopyrite (97%), which is coarse-grained near the vent orifices and fine-grained further away. Pyrite-marcasite occurs throughout the sample as a very fine grained dissemination and vug lining (1%). Minor sphalerite (1%) and barite (1%) lines the vugs. There is a very thin veneer of iron oxide at the surface of the sample (trace).

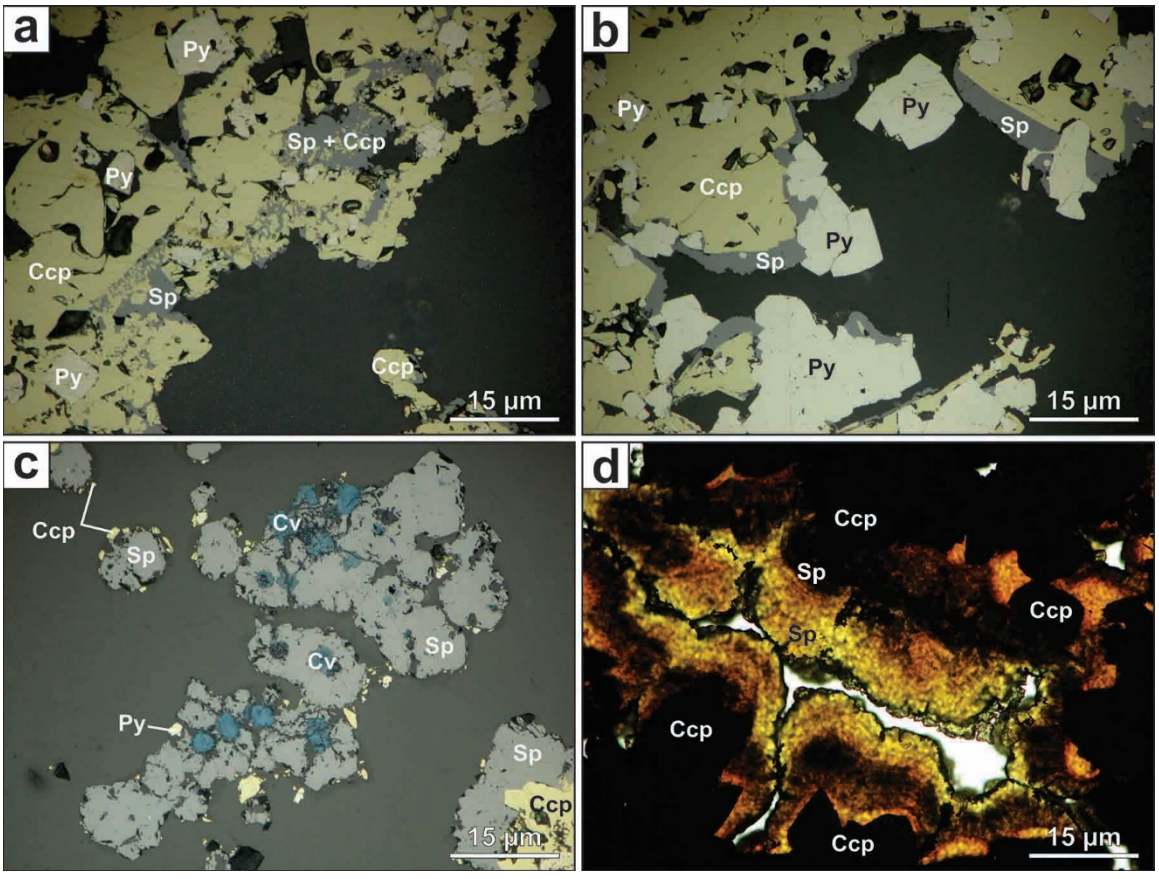
Thin Section Description

This section has a porosity of ~30-35%. It contains abundant vent conduits lined by an early phase of medium-grained anhedral pyrite, locally showing growth zoning and minor colloform textures. This followed by abundant fine- to coarse-grained chalcopyrite, with grain size increasing near the vent conduits. Rarely, this is followed by high-Fe sphalerite intergrown with chalcopyrite. A few vent



conduits are lined by low-Fe sphalerite. This sphalerite shows changing Fe-contents, rarely displaying growth zoning. This is followed by additional minor subhedral-euhedral pyrite, and minor fine-grained chalcopyrite. The chalcopyrite and sphalerite is rarely altered to secondary fine-grained covellite. In one vent conduit, there is abundant mixed chalcopyrite + pyrite + sphalerite grains (fine-grained), that are not in contact and appear milled. This may be a result of the thin section preparation process. In the remaining pore spaces, there are minor iron oxyhydroxides, and very few fine-grained crystals of barite. The absence of barite is surprising, given the high Ba contents in this sample.

Thin section scan of GMA13-046.



Photomicrographs of GMA13-046: ***(a)*** *reflected light (PPL) photomicrograph of early pyrite, followed by chalcopyrite, followed by sphalerite replacing chalcopyrite;* ***(b)*** *reflected light (PPL) photomicrograph of early pyrite and late pyrite, associated with chalcopyrite and sphalerite;* ***(c)*** *reflected light (PPL) photomicrograph of sphalerite partially altered to covellite, with late chalcopyrite and pyrite;* ***(d)*** *transmitted light (PPL) photomicrograph of sphalerite after chalcopyrite, with changing Fe contents.*

Mineral abundance: (modal %; not including pore space)

Sp	Ccp	Py	Mrc	Gn	Jd	Bn	Dg	Cv	Au	Brt	Anh	Am-Si	FeOx	others
+	+++	++	-	-	-	-	-	+	-	+	-	-	+	-
6	75	15						1		1			2	

Paragenesis: Pyrite → chalcopyrite → high-Fe sphalerite intergrown with chalcopyrite (local) → low-Fe sphalerite → euhedral pyrite → fine-grained chalcopyrite → covellite → barite → Fe oxyhydroxides.

Name: Chalcopyrite-pyrite chimney

SAMPLE: GMA13-048 **PARENT ID:** 750	**LOCATION:** 784714.6E/8649548.9N **WATER DEPTH:** 1109 mbsl

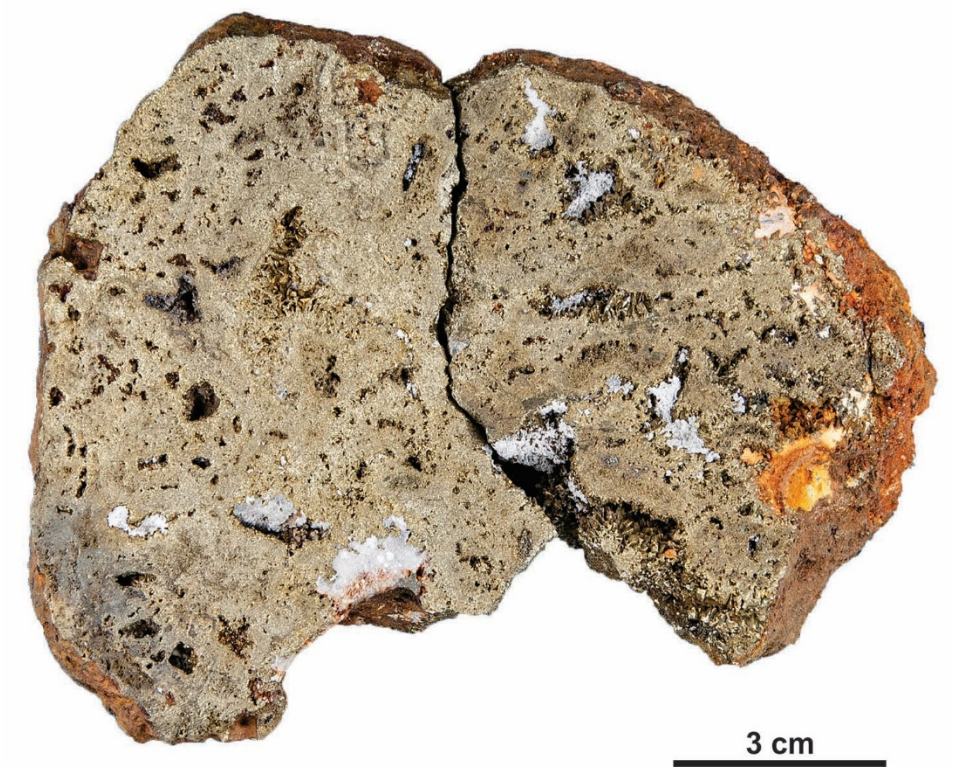
Geochemical Notes

Whole rock: High S (32.1%), Fe (25.0%), Au (9260 ppb), Cu (330000 ppm), Mo (620 ppm), In (243 ppm); Low Zn, Cd, Ga, Ge, Pb, Hg, As, Sb, Ag, Ba.

Video Description

Massive chalcopyrite/marcasite from area of talus. Large blocks of sulphide talus and fallen chimney spires with irregular knobbly surfaces.

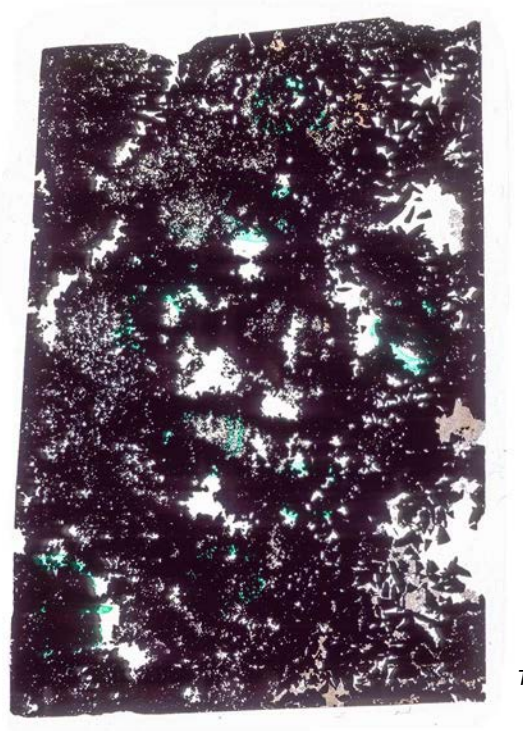
Hand Sample Description



Hand sample of GMA13-048.

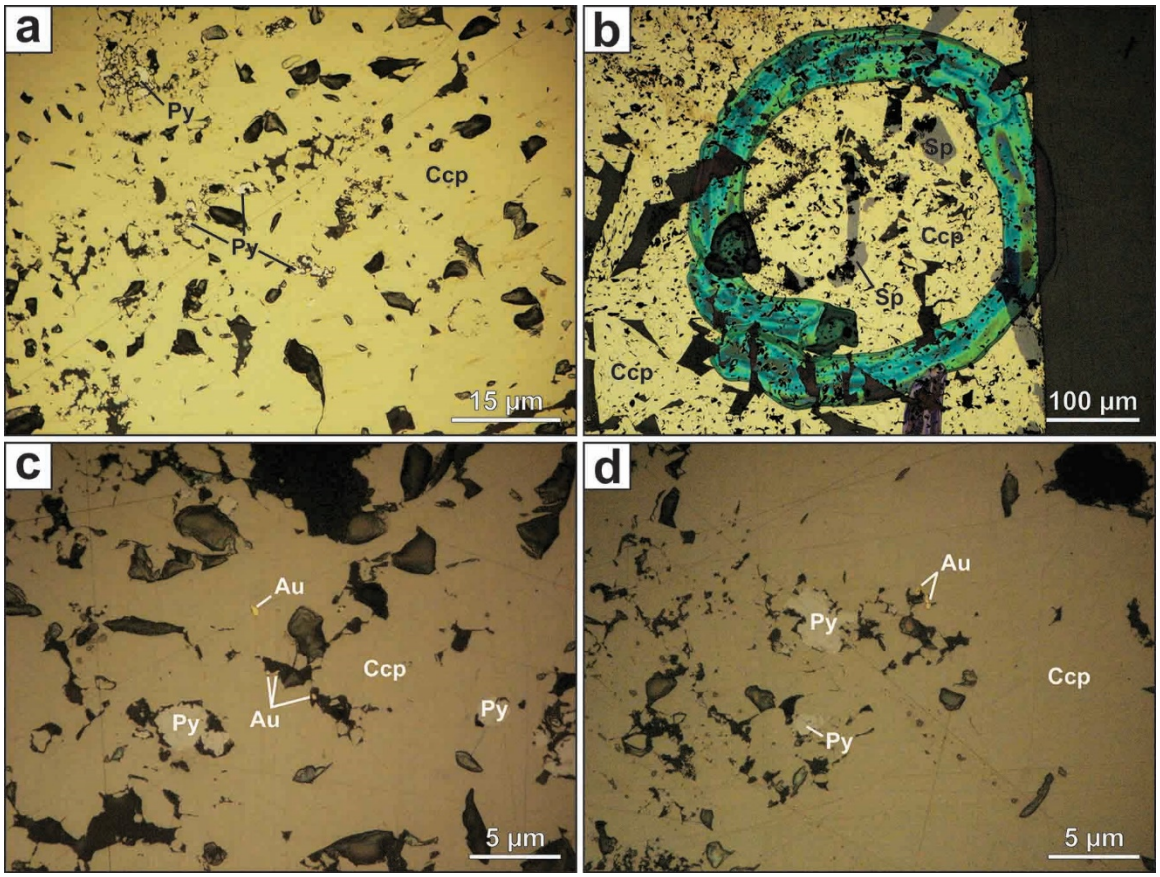
Massive chimney composed of chalcopyrite (85%) with minor pyrite-marcasite? (5%), with multiple small conduits up to 2 cm wide with 10% porosity overall. Crystals are massive, becoming coarse-grained near conduits. Pore space is filled by barite(?) (<1 %) + amorphous silica (3%). Trace sphalerite, patchy. Minor iron oxide on outer surface, 1-2%.

Thin Section Description



This section has a relatively low porosity of ~20%. It contains abundant coarse- to very coarse-grained chalcopyrite, forming around vent conduits. A total of 15 very fine-grained gold inclusions were observed, consistent with the high Au content of this rock. The chalcopyrite contains minor inclusions of anhedral pyrite. Subhedral pyrite also forms on top of the chalcopyrite. Minor very low-Fe sphalerite (almost colorless) forms in one corner, associated with minor fine-grained covellite and a few needles of radiating barite(?). Fine-grained amorphous "fish-egg" silica with very fine-grained iron oxide(?) inclusions occurs in many of the remaining pore spaces, growing as irregular branches rather than a coating.

Thin section scan of GMA13-048.



Photomicrographs of GMA13-048: ***(a)*** *reflected light (PPL) photomicrograph of chalcopyrite with pyrite inclusions;* ***(b)*** *reflected light (PPL) photomicrograph of chalcopyrite with minor late (low-Fe) sphalerite;* ***(c)*** *reflected light (PPL) photomicrograph of chalcopyrite with minor pyrite and gold inclusions;* ***(d)*** *reflected light (PPL) of chalcopyrite with minor pyrite and gold inclusions.*

Mineral abundance: (modal %; not including pore space)

Sp	Ccp	Py	Mrc	Gn	Jd	Bn	Dg	Cv	Au	Brt	Anh	Am-Si	FeOx	others
+	+++	+	-	-	-	-	-	Tr	Tr	Tr	-	+	Tr	-
2	88	5						<1	<1	<1		5	<1	

Paragenesis: Pyrite → chalcopyrite + gold → pyrite → Low-T sphalerite → covellite → barite (local, very minor) → amorphous “fish-egg” silica + Fe oxides.

Name: Chalcopyrite chimney talus (gold-rich)

SAMPLE: GMA13-049 **PARENT ID:** 742	**LOCATION:** 784706.5E/8649598.0N **WATER DEPTH:** 1112 mbsl

Geochemical Notes

Whole rock: High Fe (16.9%), Cu (155000 ppm), Cd (828 ppm), Ga (75 ppm), Ge (83 ppm), As (719 ppm); Low Hg, Ag.

Video Description

Sulphide chimney fragment.

Hand Sample Description



Zoned chimney predominantly composed of chalcopyrite (55%) that lines vent conduits, lesser patchy very fine grained pyrite (5%) intergrown with chalcopyrite in the next outer zone, and minor sphalerite (10%) in the outermost zone. Minor interstitial barite occurs (5%), no obvious large crystals. Pore space is composed larger vent conduits up to 1 cm wide and smaller vugs, 25-30% pore space overall. Only trace amounts of iron oxide.

Hand sample of GMA13-049.

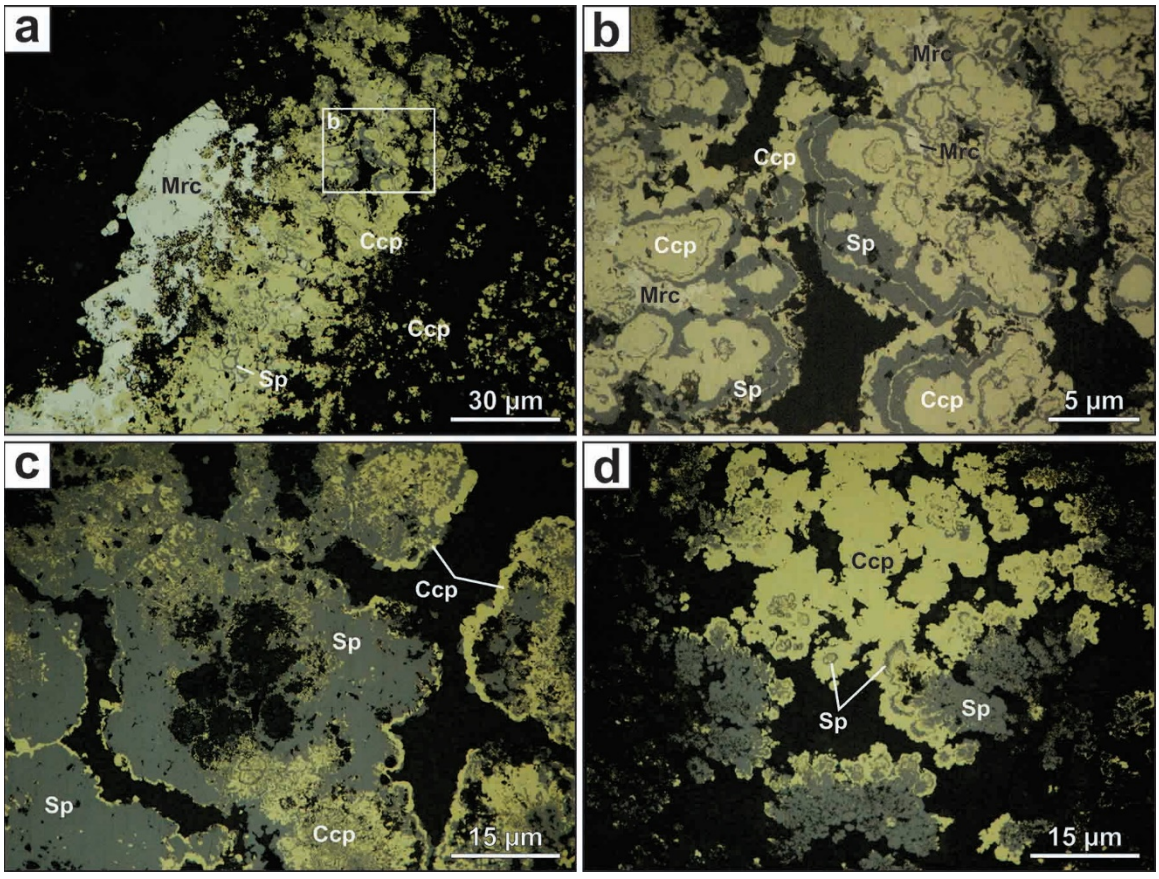
Thin Section Description

This section has a porosity of ~40-45%. It is characterized by abundant dendritic chalopyrite, observed here for the first time in this sample set. This is followed by complex replacement textures of chalcopyrite by high-Fe sphalerite, with variable proportions of each phase depending on the location in the section. This is also the first time that such extensive replacement textures have been observed in this study. This is followed by a phase of low-Fe sphalerite, a thin layer of chalcopyrite, and locally there is an adiditional thin layer of low-Fe sphalerite. Locally, near the top of the section this



sphalerite+chalcopyrite is replacing early marcasite, and is in turn overgrown by later marcasite. The marcasite is not altered to pyrite and has no pore space. This is overgrown by minor medium-grained radiating crystals of barite. Abundant amorphous “fish-egg” silica irregularly coats everything, and is most abundant around the dendritic chalcopyrite. Very fine-grained acicular needles of amorphous silica(?) or branches of tiney globules extend from some of the globules. Many of the amorphous silica globules contains very fine-grained nuclei of sulfides. The amount of silica is very high for this sample set. Globular sphalerite associated with the amorphous silica also forms locally. Jordanite was not observed, but high As whole-rock concentrations suggests that it may be present.

Thin section scan of GMA13-049.



Photomicrographs of GMA13-049: ***(a)*** *reflected light (PPL) photomicrograph of chalcopyrite and sphalerite with late marcasite;* ***(b)*** *reflected light (PPL) photomicrograph close-up of finely laminated sphalerite and chalcopyrite associated with marcasite;* ***(c)*** *reflected light (PPL) photomicrograph sphalerite that is replacing chalcopyrite, with late chalcopyrite;* ***(d)*** *reflected light (PPL) photomicrograph of dendritic sphalerite followed by laminated sphalerite + chalcopyrite, and late chalcopyrite.*

Mineral abundance: (modal %; not including pore space)

Sp	Ccp	Py	Mrc	Gn	Jd	Bn	Dg	Cv	Au	Brt	Anh	Am-Si	FeOx	others
++	+++	-	+	-	-	-	-	-	-	-	-	++	-	-
10	70		5									15		

Paragenesis: Dendritic chalcopyrite → minor marcasite (local) → high-Fe sphalerite replacing chalcopyrite → low-Fe sphalerite → chalcopyrite → low-Fe sphalerite → marcasite → minor radiating barite → abundant fine amorphous “fish-egg” silica.

Name: Zoned chalcopyrite-sphalerite chimney talus

SAMPLE: GMA13-050 **PARENT ID:** 741	**LOCATION:** 784712.1E/8649614.7N **WATER DEPTH:** 1101 mbsl

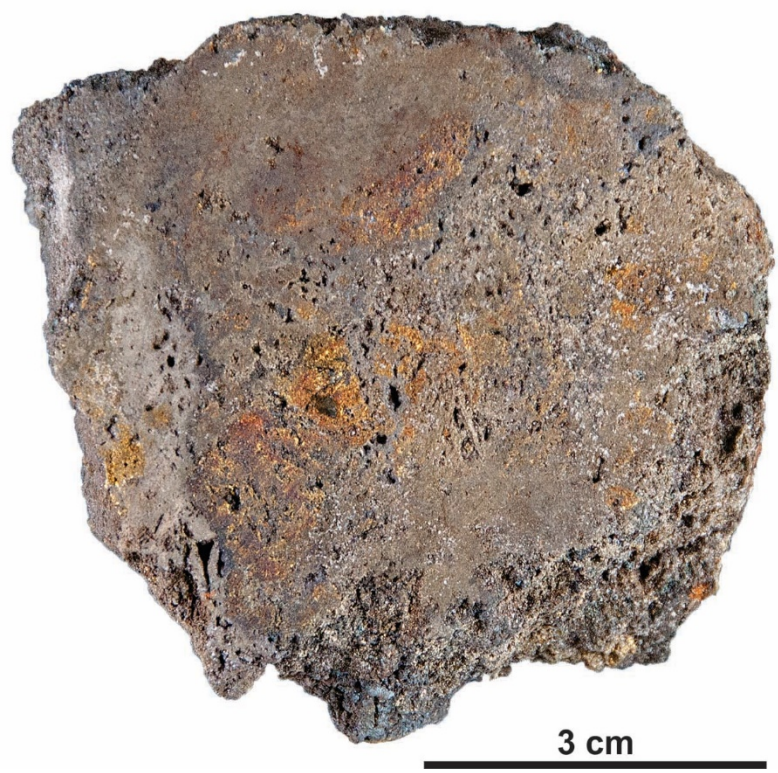
Geochemical Notes

Whole rock: High S (33.6%), Fe (15.9%), Au (5150 ppb), Cu (141000 ppm), Zn (290000 ppm), Cd (1540 ppm), Ga (172 ppm), Ge (73 ppm); Low Pb, Hg, Ba.

Video Description

Massive sulphide from base of mound.

Hand Sample Description

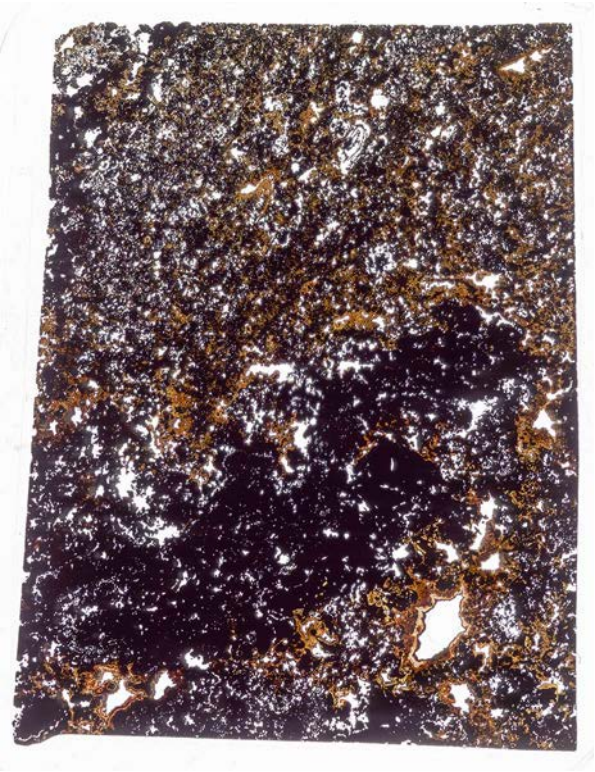


Sulphide chimney from base of mound. Zoned chimney with a chalcopyrite-rich core (10-15%), followed by pyrite (5%) with chalcopyrite, followed by high-Fe sphalerite in outer zone (45-50%). Minor anhydrite is interstitial (5%). Trace bornite. About 30% small vugs, mostly ~ 1 mm, up to 1 cm wide. A few small crystals of sphalerite formed last in the vugs. <1% iron oxide in central vugs and on outer surface, with thin Mn oxide crust (<1%).

Hand sample of GMA13-050.

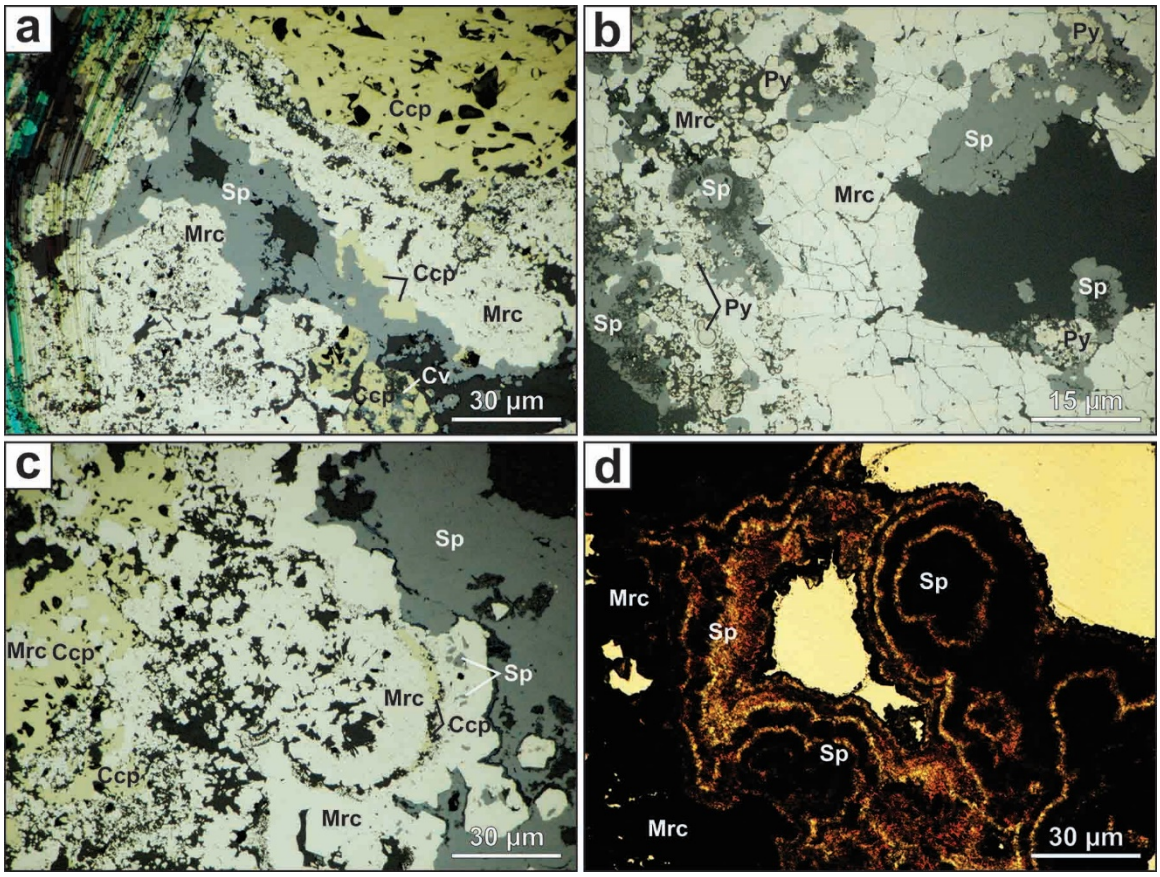
Thin Section Description

This section has a porosity of ~20%. It is a highly zoned chimney with abundant relict vent conduits lined by sulfides. The paragenesis is complicated by waxing and waning temperatures during hydrothermal activity. The sulfides are irregularly distributed throughout the section, generally Cu-rich in the bottom half of the section and Zn-rich in the top half. There is an early phase of coarse-grained marcasite, with locally spherulitic to colloform textures, which is being extensively altered to secondary pyrite. This is being overgrown and replaced by low-Fe sphalerite. Coarse-grained chalcopyrite contains inclusions of



Thin section scan of GMA13-050.

pyrite/marcasite and sphalerite, and often frequently has an altered rim of secondary covellite, up to 0.3 mm thick. The final sulfide phase is always sphalerite. This sphalerite shows large changes in color, forming a banded appearance resulting from changing Fe contents (i.e., temperatures). It generally follows a sequence of high-low-medium-very low-high Fe contents, but this varies considerably in different parts of the section. Inclusions of fine-grained jordanite are found locally in the high-Fe sphalerite. The Zn-rich top half shows less variation in Cu contents, generally showing an early generation of high-Fe and a late generation of low-Fe contents. In the top half of the section, sphalerite locally overgrows fine-grained dendritic barite.



Photomicrographs of GMA13-050: ***(a)*** *reflected light (PPL) photomicrograph showing porous, partially pyritized marcasite, chalcopyrite, and sphalerite;* ***(b)*** *reflected light (PPL) photomicrograph of spherulitic secondary pyrite after marcasite, overgrown by porous marcasite and sphalerite;* ***(c)*** *reflected light (PPL) photomicrograph of early porous marcasite, overgrown by chalcopyrite, followed by later marcasite + sphalerite, and a late generation of sphalerite;* ***(d)*** *transmitted light (PPL) of changing colors of sphalerite, resulting from changing Fe-contents, indicating fluctuating temperature conditions during crystallization.*

Mineral abundance: (modal %; not including pore space)

Sp	Ccp	Py	Mrc	Gn	Jd	Bn	Dg	Cv	Au	Brt	Anh	Am-Si	FeOx	others
+++	+++	+	+++	-	Tr	-	-	+	-	+	-	-	-	-
28	35	3	30		<1			2		2				

Paragenesis: Medium- to coarse-grained marcasite (locally spherulitic to colloform) → secondary pyrite → low-Fe sphalerite → coarse-grained marcasite → chalcopyrite → covellite → chalcopyrite → high-Fe sphalerite ± jordanite → chalcopyrite → marcasite → dendritic barite (local) → banded high-low-medium-very low-high-Fe sphalerite.

Name: Zoned chalcopyrite-marcasite-sphalerite chimney talus (gold-rich)

SAMPLE: GMA13-051 **PARENT ID:** 746	**LOCATION:** 784707.3E/8649570.0N **WATER DEPTH:** 1111 mbsl

Geochemical Notes

**XRF (parent): Cu = 0.44%, Pb = 0.01%, Zn = 23.40%, Ag = 25.4 ppm; Au = 3.27 ppm.*

Video Description

Piece of sulphide from talus - huge blocks of sulphide talus and fallen chimney spires with irregular knobbly surfaces (mound).

Hand Sample Description



Hand sample of GMA13-051.

Piece of sulphide talus that has been moderately oxidized. The outer sulphide zone contains very fine grained high-Fe sphalerite (65%) and barite(?) (5-7%). In vugs there is coarse-grained barite, and both high- and low-Fe sphalerite (1%). Pore space is 5% overall. Vein infill consists of clay-chalcedony-gypsum (2-3%). Outer rind of clay (20%) and iron oxide (2-3%) up to 3 cm thick.

Thin Section Description

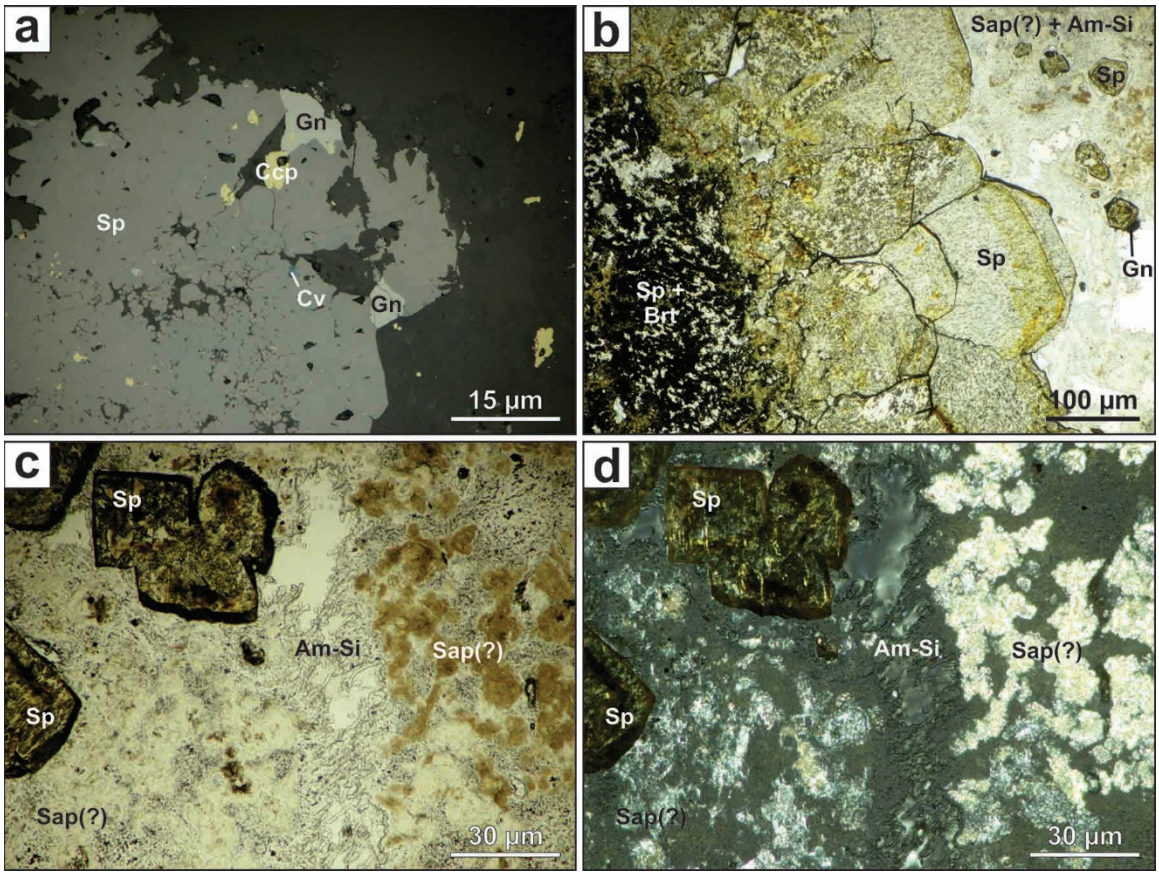


Thin section scan of GMA13-051.

This section has a porosity of ~25%, with porosity reduced by late silicification. This section consists of a banded chimney on the top half, and a weathered iron oxide-rich bottom half. The top half consists of upward-growing medium to fine-grained tabular radial barite with abundant black inclusions (sphalerite?), overgrown by fine- to medium-grained sphalerite (medium- to low-Fe) containing chalcopyrite and galena (rare) inclusions. An earlier phase of pyrite is locally present, surrounded by chalcopyrite and sphalerite. Minor covellite is irregularly distributed. Further up the section, there is a large crack, along which the low-Fe sphalerite also contains fine inclusions of jordanite, in addition to the chalcopyrite. Locally, the inclusions are aligned, suggesting multiple generations of sphalerite with jordanite in between. After this, there is coarse-grained inclusion-free very low-Fe sphalerite that is almost colorless, forming a layer up to ~8 mm thick. Minor late chalcopyrite forms next, followed by medium-grained jordanite forms with minor inclusions of chalcopyrite. This are the coarsest jordanite crystals observed in this sample set so far. Very coarse-grained tabular barite fills in some of the remaining open space along the fractures. This is followed by very fine-grained barite, with a feathery to radial texture, which is locally iron-stained. Finally, there is a thick layer of amorphous “fish-egg” silica with abundant very fine-grained opaque inclusions of sulfides. This layer of globules is around ~2 mm thick in places, showing a branching inward-growth along some pore spaces. Finally, there is minor fine-grained low-Fe sphalerite after the amorphous silica.

This pattern repeats along another fracture at the top of the slide, this time with even coarser-grained very low-Fe sphalerite, with individual crystals up to 22 mm long. In this fracture, there is also a late generation of galena after sphalerite and chalcopyrite.

There is a sharp, irregular contact with the weathered horizon at the mid-point of the section, marked by the disappearance of sulfides, and a layer of hematite and other iron oxyhydroxides ~ 5 mm thick. There are scattered fine-grained iron oxides and oxyhydroxides in the bottom half of the section, associated with amorphous silica. The dominant mineral though is tabular, radiating medium-grained barite, which comprises ~80% of the top of the section.



Photomicrographs of GMA13-051: ***(a)*** *reflected light (PPL) photomicrograph of sphalerite with inclusions of chalcopyrite, with late chalcopyrite and galena, and minor alteration to covellite;* ***(b)*** *transmitted light (PPL) photomicrograph of early high-Fe dendritic sphalerite + barite, followed by very low-Fe coarse-grained sphalerite and amorphous silica;* ***(c)*** *transmitted light (PPL) photomicrograph of sphalerite followed by fine-grained fibrous saponite(?) and late "fish-egg" silica;* ***(d)*** *transmitted light (XPL) photomicrograph of the same view as (d) highlighting the fine-grained fibrous saponite(?).*

Mineral abundance: (modal %; not including pore space)

Sp	Ccp	Py	Mrc	Gn	Jd	Bn	Dg	Cv	Au	Brt	Sap(?)	Am-Si	FeOx	Hem
+++	+	Tr	-	+	+	-	Tr	+	-	+++	++	++	+	+
29	3	<1		2	2		<1	1		35	10	10	5	3

Paragenesis: Radial tabular barite → pyrite → chalcopyrite → medium to low-Fe sphalerite + chalcopyrite + galena + jordanite → covellite ± digenite → jordanite → low-Fe sphalerite → very low-Fe (colorless) sphalerite → chalcopyrite → covellite ± digenite → medium-grained jordanite + pyrite + galena → very fine-grained saponite(?)→ amorphous "fish-egg" silica → fine-grained low-Fe sphalerite

Name: Barite-sphalerite chimney talus

SAMPLE: GMA13-052 **PARENT ID:** 727	**LOCATION:** 784650.6E/8649747.2N **WATER DEPTH:** 1092 mbsl

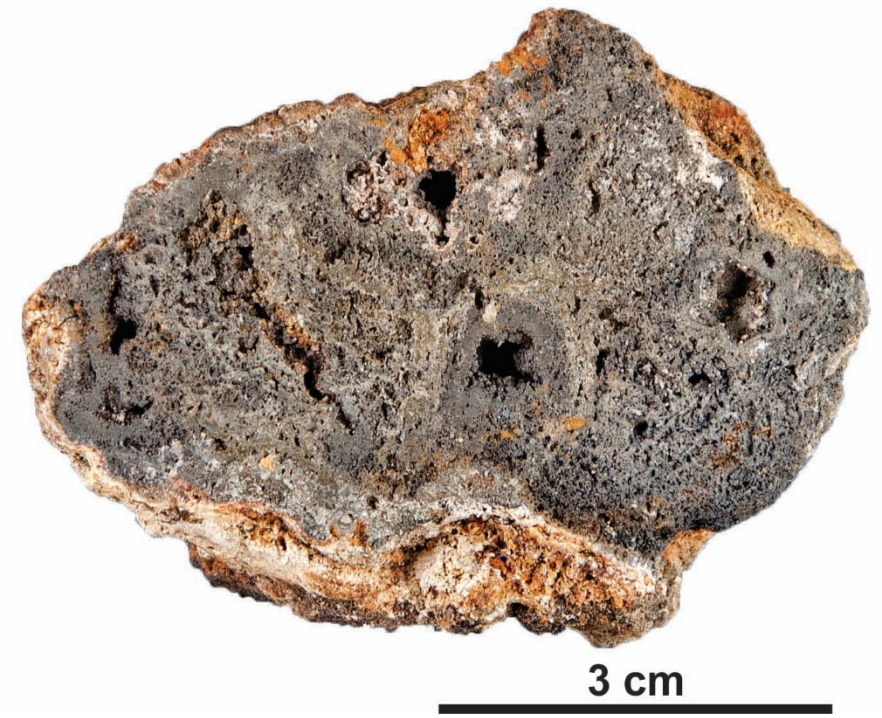
Geochemical Notes

Whole rock: High Zn (265000 ppm), Cd (1160 ppm), Ga (61 ppm), Hg (61800 ppb), As (828 ppm), Sb (272 ppm), Ba (64000 ppm), Sr (4490 ppm), Mn (6660 ppm); Low Cu, Ag.

Video Description

Sulphide chimney piece from sulphide chimney and mounded popcorn protrusions, sulphide talus debris, crusty oxide alteration.

Hand Sample Description



Hand sample of GMA13-052.

Chimney fragment with multiple vent conduits up to 1.5 cm wide, lined by high-Fe sphalerite (30%), with low-Fe sphalerite (25%) in outer zones. Abundant interstitial barite (20%). Very fine grained pyrite occurs next to vent conduits (1%). Pore space includes central vent conduits and smaller vugs (20% overall). Margin of clay (5%) and iron oxide (2%) up to 5 mm wide, with very thin veneer of manganese oxide (1%).

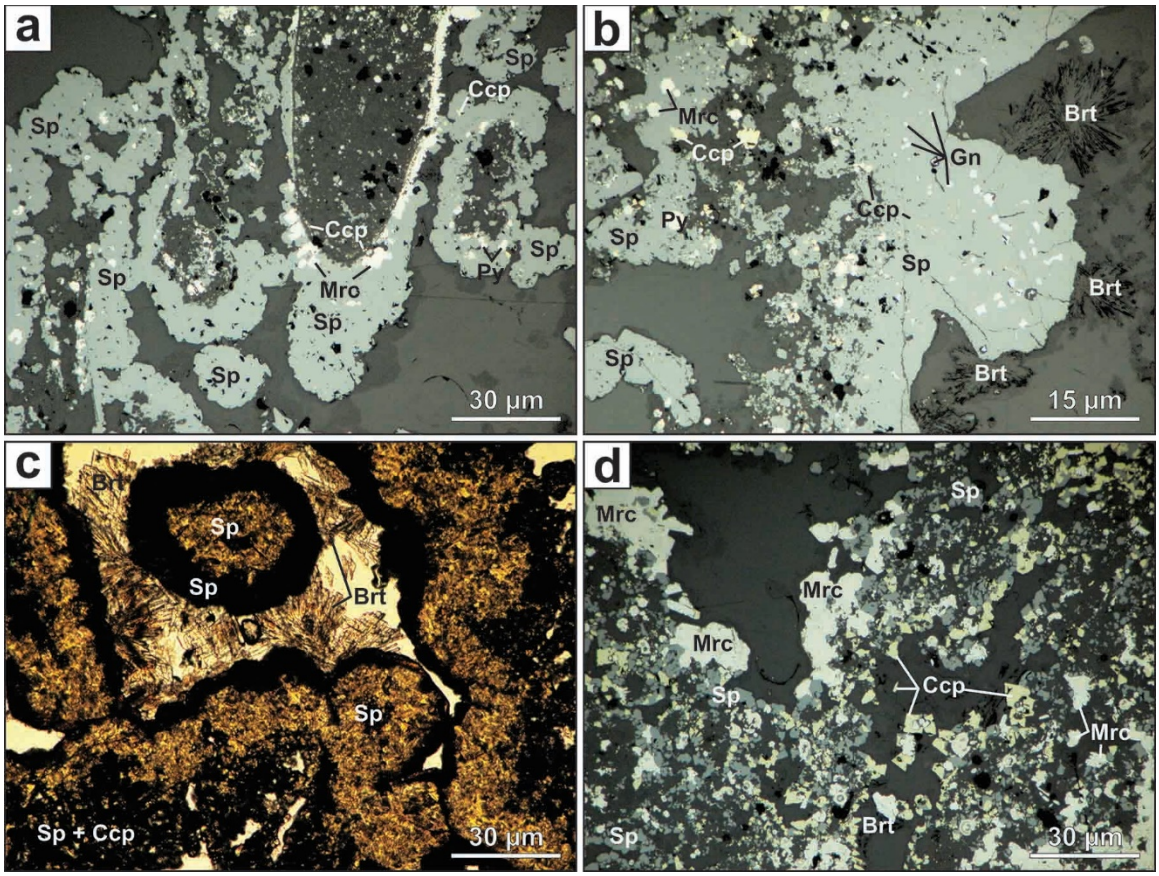
Thin Section Description

This sample has a porosity of ~40%. There are several large former vent conduits lined by sulfides and sulfates. The chimney shows a banded mineralogy, beginning with an early phase of minor high-Fe sphalerite and chalcopyrite. This early high-Fe sphalerite locally shows needle-like dendritic textures (middle left edge of the section). This is followed by marcasite. The marcasite is generally subhedral, but locally shows colloform or spherulitic textures with growth zoning, and only minor inversion to secondary pyrite. This is followed by intergrown very low-Fe sphalerite and chalcopyrite, with a higher



abundance of sphalerite relative to chalcopyrite. This in turn is overgrown by intergrown high- and low-Fe sphalerite. Around one vent conduit in the middle left of the section, this is overgrown by red-orange moderate-Fe sphalerite with abundant galena inclusions. Fine- to coarse-grained radiating barite grows off of this next, locally iron stained. This is followed locally by a thick layer of amorphous silica, irregularly distributed. This silica has a brownish tint, resulting from inclusions of oxides. Finally, there are additional fine-grained sulfides (marcasite, sphalerite, and chalcopyrite), and minor iron oxyhydroxides.

Thin section scan of GMA13-052.



Photomicrographs of GMA13-052: ***(a)*** *reflected light (PPL) photomicrograph of sphalerite and marcasite lining vent conduits, followed by late chalcopyrite;* ***(b)*** *reflected light (PPL) photomicrograph of sphalerite with inclusions of marcasite and galena;* ***(c)*** *transmitted light (PPL) photomicrograph of high-Fe sphalerite + chalcopyrite, followed by low-Fe sphalerite followed by high-Fe sphalerite and radial barite;* ***(d)*** *reflected light (PPL) of sphalerite and chalcopyrite, followed by late marcasite.*

Mineral abundance: (modal %; not including pore space)

Sp	Ccp	Py	Mrc	Gn	Jd	Bn	Dg	Cv	Au	Brt	Anh	Am-Si	FeOx	others
+++	+	+	++	+	-	-	-	-	-	+	-	+	+	-
64	4	3	12	2						7		7	1	

Paragenesis: Dendritic high-Fe sphalerite → chalcopyrite → marcasite (colloform to subhedral) → secondary pyrite → low-Fe sphalerite + chalcopyrite → moderate Fe-sphalerite + galena → radiating barite ± iron oxyhydroxides → amorphous “fish-egg” silica → minor sphalerite + chalcopyrite + marcasite → iron oxyhydroxides.

Name: Sphalerite-marcasite chimney

SAMPLE: GMA13-053a,b **PARENT ID:** 729	**LOCATION:** 784686.6E/8649749.0N **WATER DEPTH:** 1078 mbsl

Geochemical Notes

**XRF (parent): Cu = 0.19%, Pb = 1.75%, Zn = 14.50%, Ag = 186.0 ppm; Au = 1.04 ppm.*

Video Description

Piece from talus at base of large chimney.

Hand Sample Description



Hand sample of GMA13-053.

Heterogeneous sphalerite-barite chimney with a central area containing high concentrations of barite (65%), high-Fe sphalerite (20%), and 10% small pore spaces with a few siliceous grey-light grey subangular to subrounded clasts up to 5 mm wide, 5% overall. Surrounding this is an up to 4 cm wide dendritic sphalerite-barite chimney with sharp contacts. Contains few rounded clasts of the central material (1%). Contains more pore space with few central vent conduits up to 1.5 cm wide, mostly mm-sized, 15-20% overall. There are lower concentrations of fine-grained interstitial barite (15-20%), and higher concentrations of sphalerite, with 25% high-Fe and 30% low-Fe sphalerite, can be very coarse-grained. Outer surface has a very thin 2 mm-thick layer barite, clay (3%), iron oxide (1%), and manganese oxide (2%). Likely two generations of chimneys, one growing on top of older chimney talus.

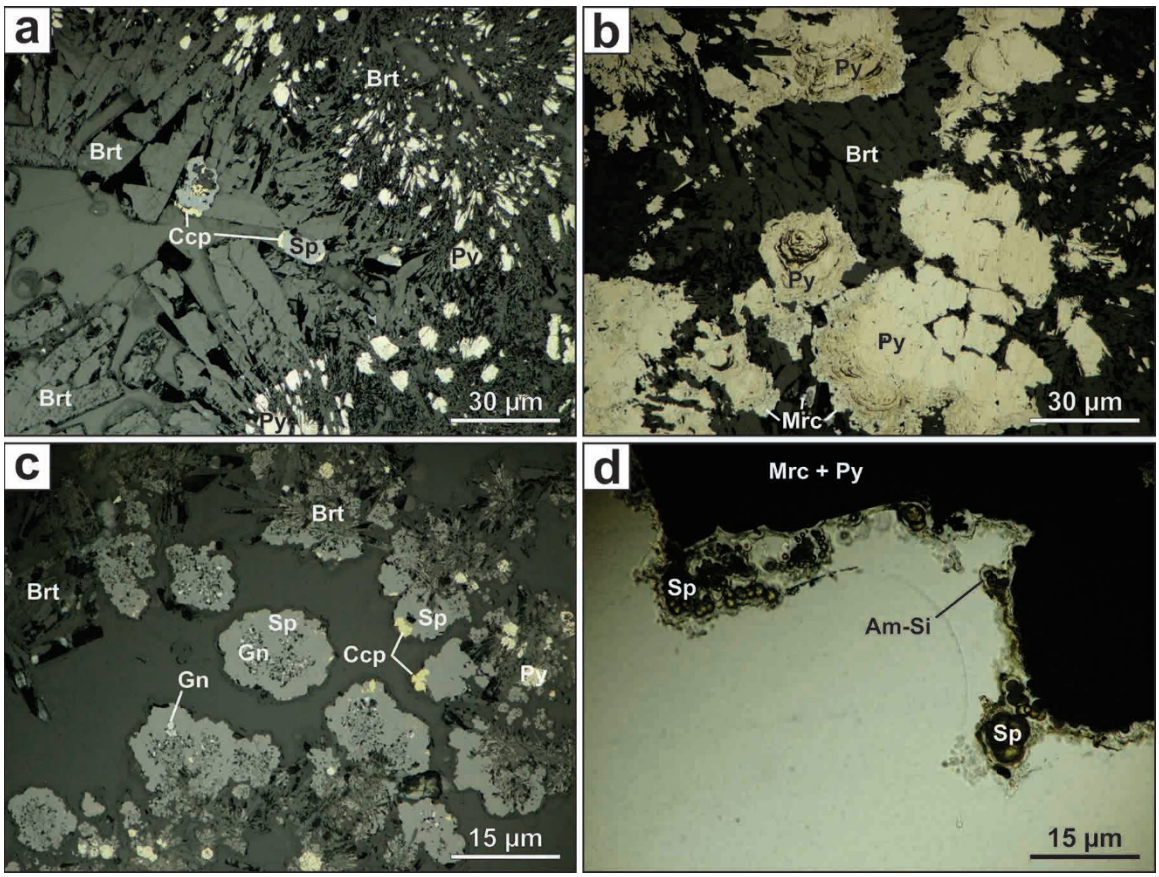
Thin Section Description

(a) This section has a porosity of ~35%. It contains abundant dendritic textures, beginning with fine-trained dendritic to radiating tabular barite overgrown by fine- to medium-grained spherulitic pyrite. The slightly porous nature of the pyrite suggests that it may be secondary after marcasite, although this is not certain. Abundant high-Fe sphalerite coats the barite dendrites. This is followed by low-Fe sphalerite (slightly increasing Fe-contents outwards) with inclusions of chalcopyrite. Minor medium-



Thin section scan of GMA13-053a.

grained galena follows. Locally, there is a second generation of very low-Fe sphalerite (almost colorless), intergrown with chalcopyrite, that envelopes the galena. Medium-grained tabular barite, locally radiating, form next in the remaining pore spaces. Medium-grained marcasite forms after the barite, locally encompassing pyrite spherules and high-Fe sphalerite. The marcasite locally coalesces into large masses, up to ~10 mm across, locally displaying colloform textures. It is partially altered to secondary pyrite and minor goethite(?). The marcasite is most abundant in the bottom third of the section, where it dominates over sphalerite, forming a banded appearance. This is locally overgrown by minor reddish moderate-Fe sphalerite. Additional very coarse-grained tabular barite forms again along the bottom of the section. Finally, this is followed by more reddish moderate-Fe sphalerite, locally coated by a very thin (~0.02 mm) layer of chalcopyrite, and minor galena. This late sphalerite is locally globular, with spheres ~0.05-0.50 mm in diameter. Everything is coated with a ~0.05 mm thick layer of amorphous “fish-egg” silica. There are minor scattered very fine-grained iron oxyhydroxides on top of the layer of silica.

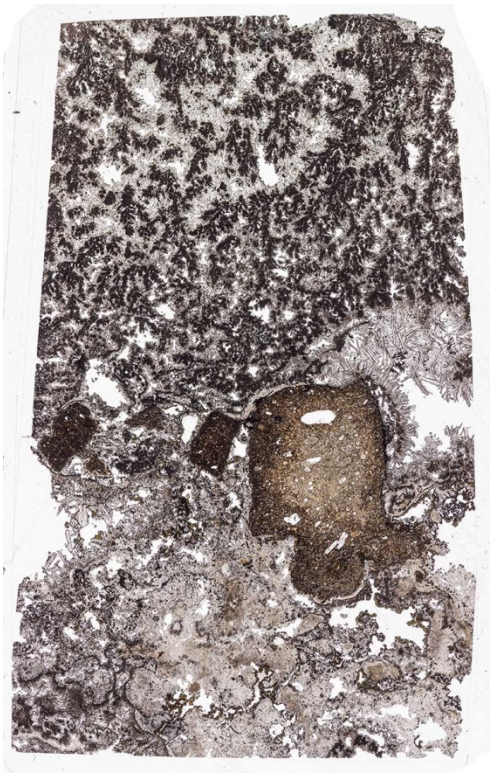


Photomicrographs of GMA13-053a: ***(a)*** *reflected light (PPL) photomicrograph of dendritic barite, followed by spherulitic pyrite, and late coarse-grained barite, with sphalerite and chalcopyrite;* ***(b)*** *reflected light (PPL) photomicrograph of primary pyrite, followed by secondary colloform porous pyrite, and marcasite;* ***(c)*** *reflected light (PPL) photomicrograph of sphalerite with inclusions of galena after barite, and late chalcopyrite and coarse-grained barite;* ***(d)*** *transmitted light (PPL) photomicrograph of marcasite/pyrite, followed by globular low-Fe sphalerite coated by amorphous "fish-egg" silica.*

Mineral abundance: (modal %; not including pore space)

Sp	Ccp	Py	Mrc	Gn	Jd	Bn	Dg	Cv	Au	Brt	Anh	Am-Si	FeOx	Goe
++	+	+	++	+	-	-	-	-	-	+++	-	+	Tr	Tr
20	1	3	10	2						62		2	<1	<1

Paragenesis: Dendritic to radiating tabular barite → spherulitic pyrite → high-Fe sphalerite → low-Fe sphalerite + chalcopyrite → medium-grained galena → very low-Fe sphalerite + chalcopyrite → medium-grained tabular barite → medium-grained, locally colloform marcasite → secondary pyrite + goethite(?) → reddish moderate-Fe sphalerite → very coarse-grained tabular barite → reddish moderate-Fe sphalerite + galena → fine-grained chalcopyrite → fine-grained low-Fe crystalline to "globular" sphalerite (not in direct contact with other crystals) → amorphous "fish-egg" silica → very fine-grained iron oxyhydroxides

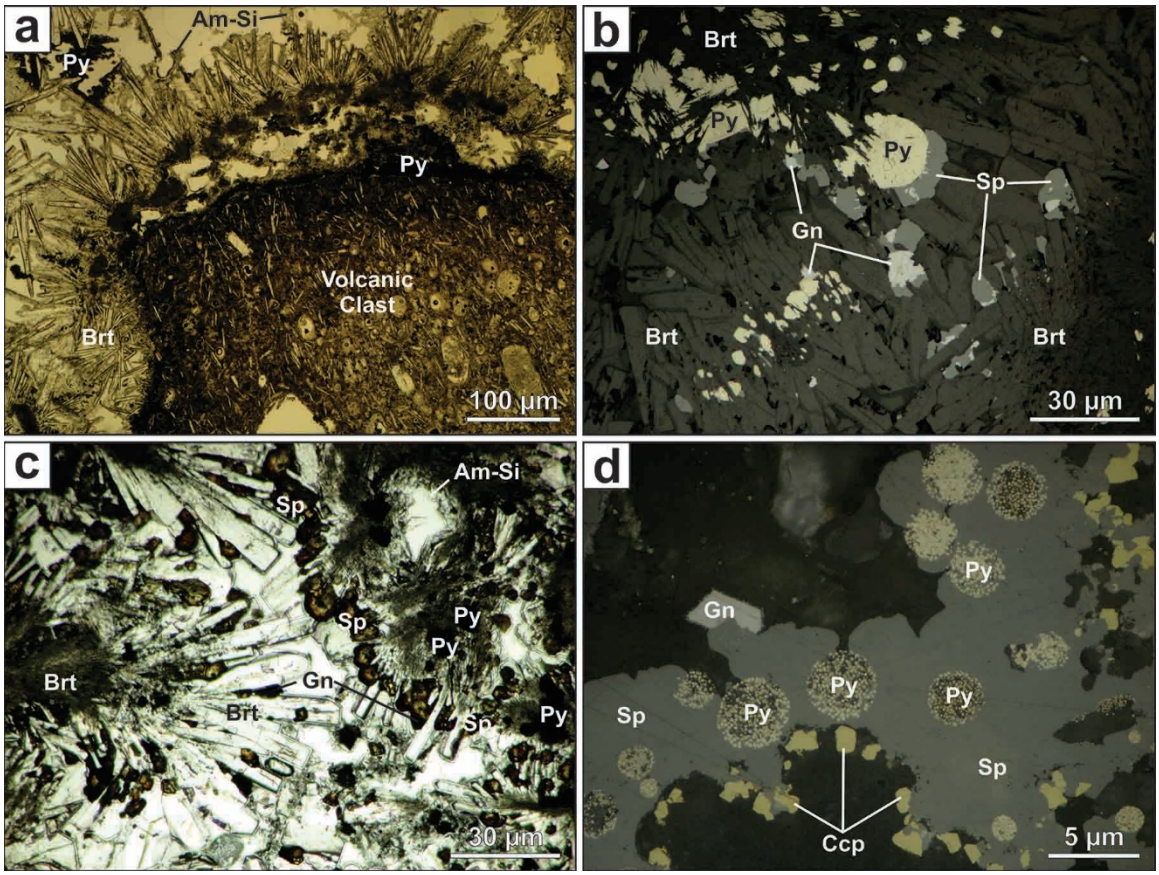


Thin section scan of GMA13-053b.

(b) This section has a porosity of ~30%. The top half of the section contains abundant dendritic fine-grained barite, which is overgrown by fine- to medium-grained spherulitic pyrite (secondary? Lower pore space than above), frequently displaying growth zoning. Very fine-grained sphalerite is associated with the barite dendrites, but there is very little sphalerite overall in comparison with GMA13-053a and other sphalerite-barite chimneys. A thicker layer of reddish moderate-Fe sphalerite, locally intergrown with galena, coats the spherulitic pyrite. Both the sphalerite and galena crystals contain rare inclusions of fine-grained chalcopyrite. This is followed by medium-grained tabular radiating barite, which becomes very coarse-grained near open pore space. Minor late reddish moderate-Fe sphalerite (+ minor galena and chalcopyrite), forms on top of the coarse barite crystals, similar to GMA13-053a. Very fine-grained crystals of sphalerite, completely enclosed in amorphous "fish-egg" silica, locally precipitate in the pore spaces, indicating crystallization in a fluid before being deposited inside the chimney structure.

The contact with the bottom half of the section is marked by an irregular <1 mm-thick layer very fine-grained radiating barite, followed by a ~2 mm-thick layer of amorphous ”fish-egg” silica containing abundant very fine-grained black inclusions. This is followed by fine-grained marcasite that has been intensively inverted to pyrite, along with minor fine-grained framboidal pyrite that is locally aligned along bands. Following this is moderate- to very low-Fe sphalerite that is beginning to replace the marcasite/prytie, with Fe-contents decreasing outwards, locally containing inclusions of fine-grained chalcopyrite. One pore space is lined by a few medium-grained crystals of chalcopyrite, followed by this low-Fe sphalerite, which encompasses the framboidal pyrite. There is a later phase of coarse-grained tabular barite, followed by galena. Everything is coated with another thin layer of amorphous “fish-egg” silica.

A notable feature of the bottom half of this section is the presence of altered subangular volcanic clasts. These clasts contain ~10-30% vesicles, up to a few mm-across. The vesicles are locally elongate, and are generally filled with a thin rim (0.1 mm thick) of very fine-grained iron-stained zeolite(?), followed by black to reddish high- to moderate-Fe sphalerite grains (up to 0.5 mm wide). Few vesicles also contain fine-grained tabular barite. Several small vesicles are lined with celadonite(or atacamite?). Some of the vesicles are almost completely filled in by amorphous “fish-egg” silica containing very fine-grained nuclei of iron oxides. There are ~35% flow-foliated mm-sized phenocrysts of plagioclase. The groundmass consists of cryptocrystalline feldspars (clay-altered?), abundant iron oxides, and abundant very-fine to medium grained sphalerite + chalcopyrite + pyrite + galena. Magnetite does not appear to be present. At the center of the largest clast, there is a less-altered core of palagonitized glass (40%) + plagioclase (50%) + vesicles (10%), with no sulfides in the groundmass. The phenocrysts are aligned with the flow foliation of the encompassing altered volcanic material. The clasts are surrounded by sulfides and amorphous silica, followed by dendritic barite and the mineralization sequence described in the above paragraph. It appears as though these clasts were entrained during the formation of the chimney. The very bottom of the section is dominated by amorphous silica, lined by sulfides (dominated by sphalerite) and barite.



Photomicrographs of GMA13-053b: ***(a)*** *transmitted light (PPL) photomicrograph of an vesicular altered volcanic clast, with increasing alteration intensity towards the clast margin, followed by pyrite and barite;* ***(b)*** *reflected light (PPL) photomicrograph of barite and pyrite, with later sphalerite + galena;* ***(c)*** *transmitted light (PPL) photomicrograph of early dendritic barite + pyrite, followed by later radial tabular barite and sphalerite;* ***(d)*** *transmitted light (PPL) photomicrograph of framboidal pyrite within sphalerite, with late chalcopyrite and galena.*

Mineral abundance: (modal %; not including pore space)

Sp	Ccp	Py	Mrc	Gn	Jd	Bn	Dg	Cv	Cel (?)	Brt	Zeo(?)	Am-Si	FeOx	Volc. clasts
++	+	+	+	+	-	-	-	-	Tr	+++	+	++	+	++
10	1	6	1	1					<1	54	1	15	1	10

Paragenesis: [Bottom] Altered volcanic clasts → very fine-grained zeolite(?) → fine-grained sphalerite + pyrite + chalcopyrite + marcasite + celadonite(?) → amorphous fish-egg silica → dendritic barite → chalcopyrite → spherulitic to framboidal pyrite → moderate- to very low-Fe sphalerite → coarse- to very coarse-grained tabular barite → low-Fe sphalerite → fine- to medium-grained galena + chalcopyrite

[Top] Dendritic to radiating tabular barite → spherulitic pyrite → high-Fe sphalerite → low-Fe sphalerite + chalcopyrite → medium-grained galena → very low-Fe sphalerite + chalcopyrite → medium-grained tabular barite → medium-grained, locally colloform marcasite → secondary pyrite → reddish moderate-Fe sphalerite → very coarse-grained tabular barite → reddish moderate-Fe sphalerite + galena → fine-grained chalcopyrite → fine-grained low-Fe crystalline to "globular" sphalerite (not in direct contact with other crystals) → amorphous "fish-egg" silica → very fine-grained iron oxyhydroxides

Name: Barite-sphalerite chimney**,** growing on silicified barite-sphalerite chimney talus with entrained volcanic clasts.

SAMPLE: GMA13-058 **PARENT ID:** 736	**LOCATION:** 784722.8E/8649648.6N **WATER DEPTH:** 1096 mbsl

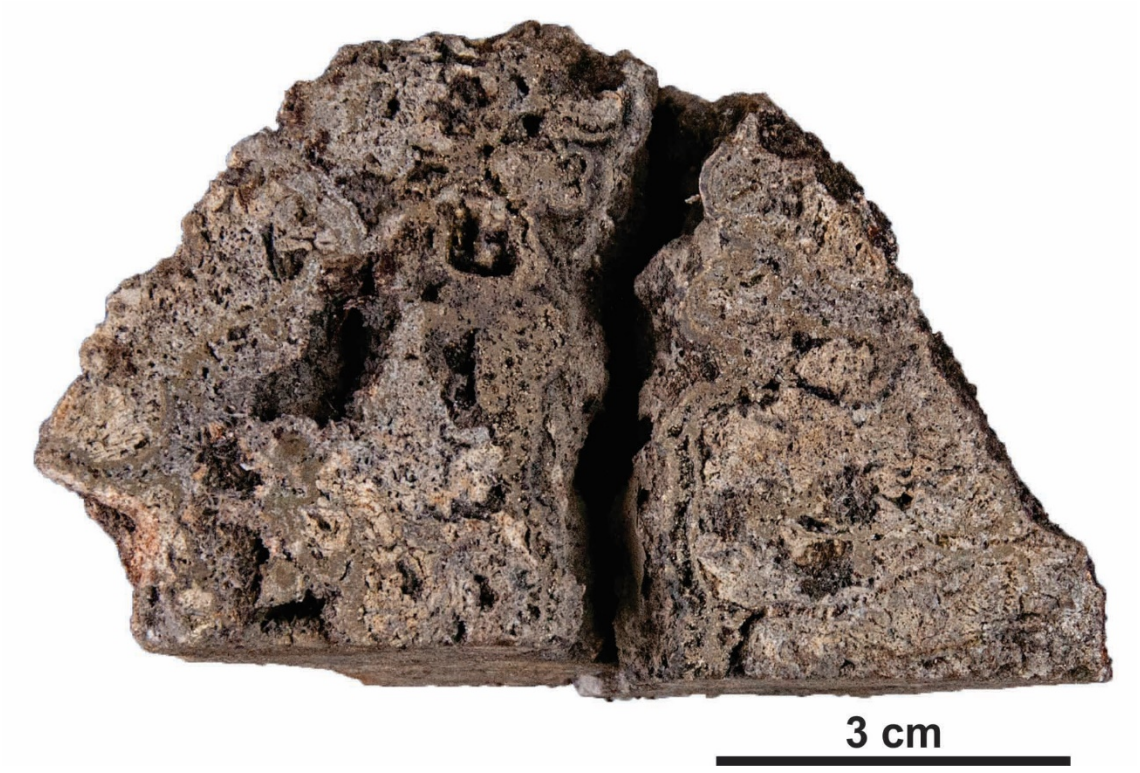
Geochemical Notes

Whole rock: High Au (7810 ppb), Sb (489 ppm), Ag (424 ppm), Ba (8530 ppm), Mn (427 ppm); Low Cu, Ga.

Video Description

Blocky sulphide talus.

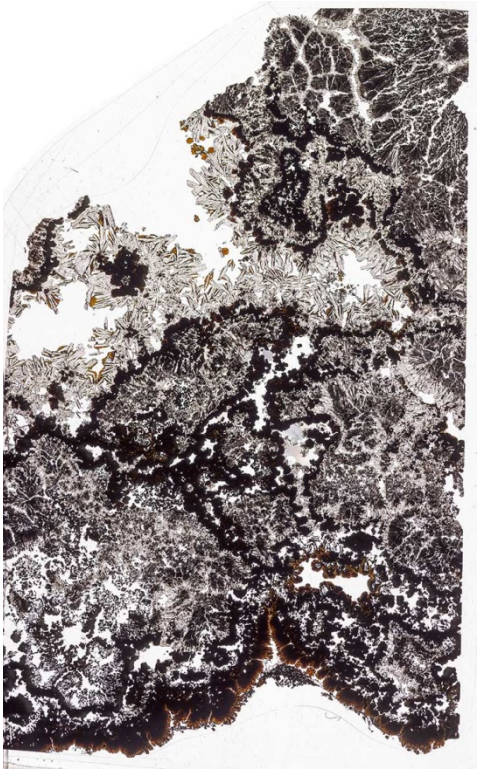
Hand Sample Description



Hand sample of GMA13-058.

Fragment of sphalerite-barite-pyrite chimney with central vent conduit, 1 cm wide, with well-developed colloform textures. Composed of high-Fe sphalerite (30-35%) lining vent conduits with low-Fe sphalerite (15-20%) in the outer zones. Abundant fine-grained barite throughout (20%), lining vent conduits. Pyrite-marcasite (5%) forms bands around vugs and occurs as very fine grained disseminations. Pore space consists of multiple vent conduits and mm-size vugs, 20% overall. Very thin coat of manganese oxide (<1%) on outer surface, underlain by iron oxide (<1%) and clay (<1%), 0.5 mm total thickness.

Thin Section Description



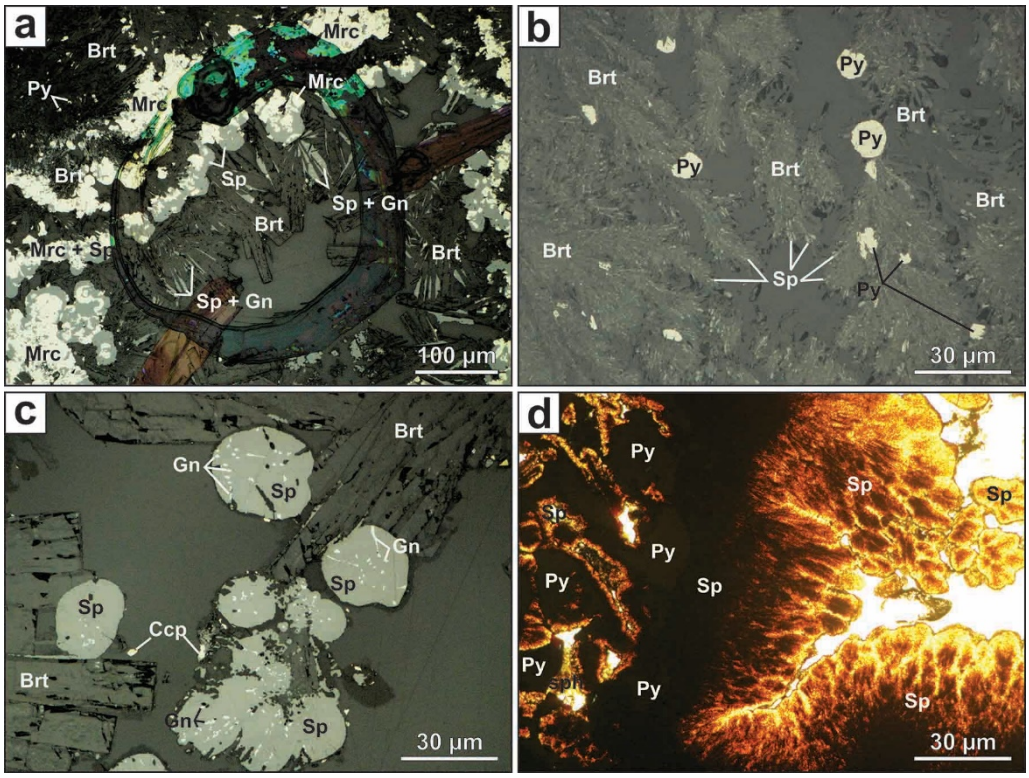
Thin section scan of GMA13-058.

This section has a porosity of 40%; much of the overall porosity is reduced by barite precipitation. It contains an early generation of fine-grained dendritic barite, locally showing growth rings (a feature not seen in this sample set yet), with very fine-grained low-Fe sphalerite on top. This is followed by euhedral to spherulitic pyrite (possibly secondary after marcasite?), and low-Fe sphalerite containing fine-grained inclusions of galena (± jordanite?). This is followed by coarse-grained tabular, locally radiating barite, which also occasionally displays growth rings. Along all of the remaining pore spaces, this is lined by marcasite, which appears a white-brassy color, with pinkish hues along laminae that follow the crystal form. It contains minor fine-grained inclusions of pyrite(?). It has a generally low porosity and only locally appears to be inverting to secondary pyrite (minor). This marcasite is being extensively replaced by moderate-Fe sphalerite, with slightly decreasing Fe-contents outwards. The sphalerite sometimes contains fine-grained inclusions of galena (± jordanite?). Rarely, galena is included in marcasite. At the crystal margins near pore spaces, the marcasite is locally being altered to iron oxide (goethite?).

After the marcasite + sphalerite horizon, there is a layer of intergrown high-Fe sphalerite with chalcopyrite. This is most common along the bottom of the section, where it is followed by dendritic high- to moderate-Fe sphalerite, with decreasing Fe-contents outwards.

There is minor medium-grained galena next, locally occurring in some pore spaces. This in turn is followed by additional coarse-grained tabular barite, and another generation of low-Fe sphalerite that also contains abundant fine-grained inclusions of galena (± jordanite?). This late sphalerite is locally spherical.

This sample is interesting because of the extensive replacement textures between marcasite and sphalerite. No gold was observed, so high Au concentrations suggest it is refractory. It is one of the few samples that does not contain late amorphous “fish-egg” silica.



Photomicrographs of GMA13-058: ***(a)*** *reflected light (PPL) photomicrograph of dendritic barite, followed by marcasite, with expensive replacement by sphalerite, followed by late barite and sphalerite + galena;* ***(b)*** *reflected light (PPL) photomicrograph of dendritic barite coated with fine-grained sphalerite, and spherulitic pyrite;* ***(c)*** *reflected light (PPL) photomicrograph of late spherical sphalerite after coarse-grained barite, containing abundant inclusions of galena;* ***(d)*** *transmitted light (PPL) photomicrograph of dendritic sphalerite ranging from high- to low-Fe, after pyrite.*

Mineral abundance: (modal %; not including pore space)

Sp	Ccp	Py	Mrc	Gn	Jd(?)	Bn	Dg	Cv	Au	Brt	Anh	Am-Si	FeOx	Goe(?)
+++	+	+	+++	+	Tr	-	-	-	-	+++	-	-	-	+
28	1	3	26	3	<1					38				1

Paragenesis: Dendritic barite (with growth rings) → low-Fe sphalerite → spherulitic pyrite → low-Fe sphalerite + galena → coarse-grained tabular barite → marcasite → minor secondary pyrite, local → replaced by moderate-Fe sphalerite ± galena and goethite(?) → medium-grained galena → intergrown high-Fe sphalerite + chalcopyrite → dendritic high- to moderate-Fe sphalerite → coarse-grained barite → low-Fe sphalerite + galena.

Name: Barite-sphalerite-marcasite chimney talus (gold-rich)

SAMPLE: GMA13-060 **PARENT ID:** 733	**LOCATION:** 784713.0E/8649643.7N **WATER DEPTH:** 1102 mbsl

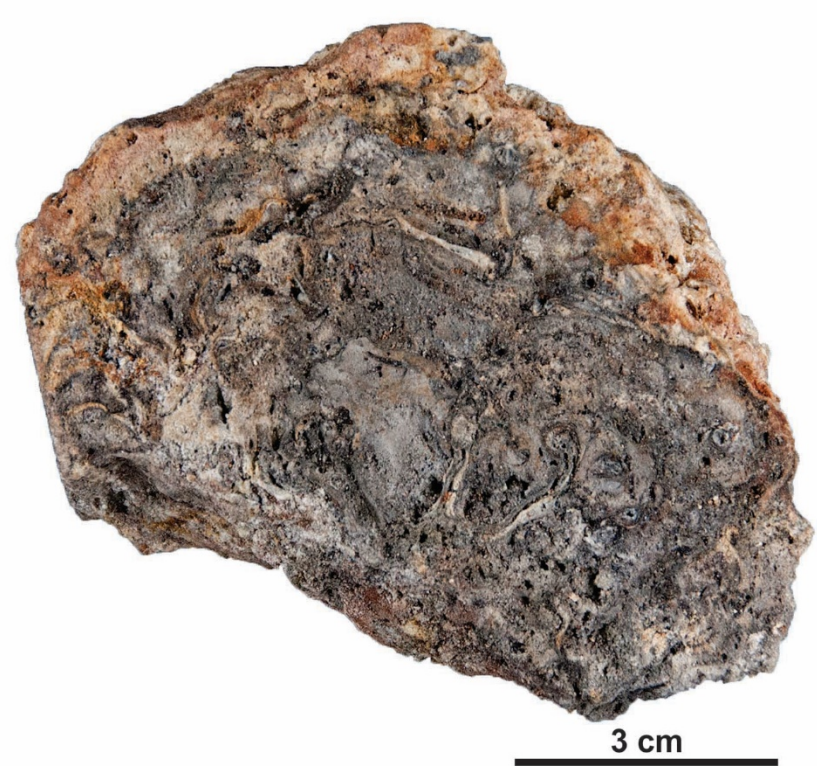
Geochemical Notes

N/A

Video Description

Sampled from top of bulbous sulphide chimney protruding through talus.

Hand Sample Description



Hand sample of GMA13-060.

Fragment from a multi-spire chimney, mottled chimney composed of barite (60%) and amorphous silica (20%), with minor sphalerite (5%), clay (3%), silica, and trace iron oxide. Manganese oxides may be present. The fabric of the chimney is complex with a framework of close-packed hollow grey lenticles likely formed from biological activity, 8-10% overall. The pore spaces are lined by small reflective white crystals (barite?). The pore spaces range in size from 1 mm in width in the interior to 1 cm near the surface of the sample.

The weathered surface has a light orange-tan crust composed of clay and iron oxide, 1 cm thick.

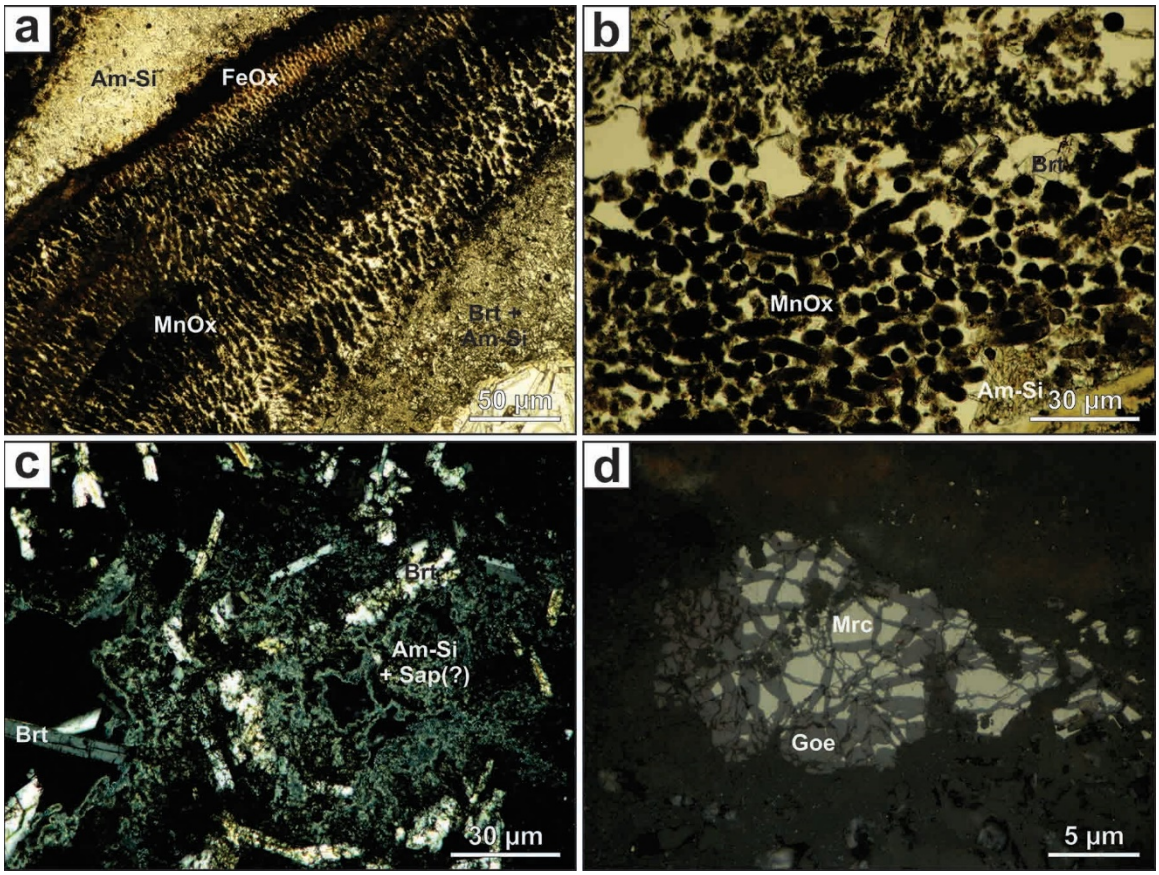
Thin Section Description

This section has a porosity of ~25%. The section has a wispy, banded appearance and is mostly composed of very fine- to coarse-grained barite and amorphous silica. Throughout the section (particularly at the top), amorphous “fish-egg” silica forms around holes, likely of biological origin (worm tubes?). The color of the silica is patchy, ranging from brownish to orange/reddish. The silica surrounds fine-grained marcasite and (rarer) sphalerite. A thin layer (~0.05 mm thick) layer of fibrous saponite (or



Thin section scan of GMA13-060.

barite?) locally forms next. Near the bottom of the section, there are bands of dendritic iron and manganese oxides and oxyhydroxides, with very fine-grained marcasite at the tips of the dendrites along bands. Along bands of iron oxyhydroxides, there is also minor hematite. Egg-shaped to spherical manganese oxide concretions form along one band. The bands appear broken and irregular. Dendritic manganese and iron oxides also form inside the worm burrows, lined by additional silica. There is minor medium-grained marcasite (highly porous), forming on top of the banded oxides. Locally, there is red goethite complexly replacing the marcasite. This is followed by additional amorphous silica with iron or manganese oxide nuclei. There is abundant medium- to coarse-grained tabular barite after this, throughout the section. A minor amount of fine- to medium-grained *unidentified mineral* forms after this, with fine-grained galena included. This mineral is radiating, tabular, and colorless in transmitted PPL light with high relief, fourth-order birefringence in transmitted XPL light (similar to calcite), and grey (typical of sphalerite) in reflected light, but shows anisotropism. Sulfides are most abundant in the bottom half of the section.



Photomicrographs of GMA13-060: ***(a)*** *transmitted light (PPL) photomicrograph of dendritic iron and manganese oxides, followed by barite and amorphous silica;* ***(b)*** *transmitted light (PPL) photomicrograph of spheroidal manganese oxide and late barite and amorphous silica;* ***(c)*** *transmitted light (XPL) photomicrograph of fine-grained fibrous saponite(?) and amorphous silica, along with coarse-grained tabular barite;* ***(d)*** *reflected light (PPL) photomicrograph of marcasite being replaced by goethite.*

Mineral abundance: (modal %; not including pore space)

Sp	Mrc	Gn	Brt	Am-Si	MnOx	FeOx	Hem	Goe	Sap(?)	Unident. Min.
+	+	Tr	+++	++	+	+	+	+	+	+
1	3	<1	57	20	5	5	1	2	5	1

Paragenesis: Fine- to coarse-grained barite + minor fine-grained marcasite + sphalerite → iron and manganese oxides → amorphous "fish-egg" silica → very fine-grained fibrous saponite(?) (local, surrounding Am-Si) → dendritic manganese and iron oxides (incl. hematite) and oxyhydroxides → medium-grained marcasite → goethite → amorphous silica → medium- to coarse-grained tabular barite → galena + *unidentified mineral*.

Name: Silicified barite chimney

SAMPLE: GMA13-061 **PARENT ID:** 738	**LOCATION:** 784678.2E/8649752.8N **WATER DEPTH:** 1082 mbsl

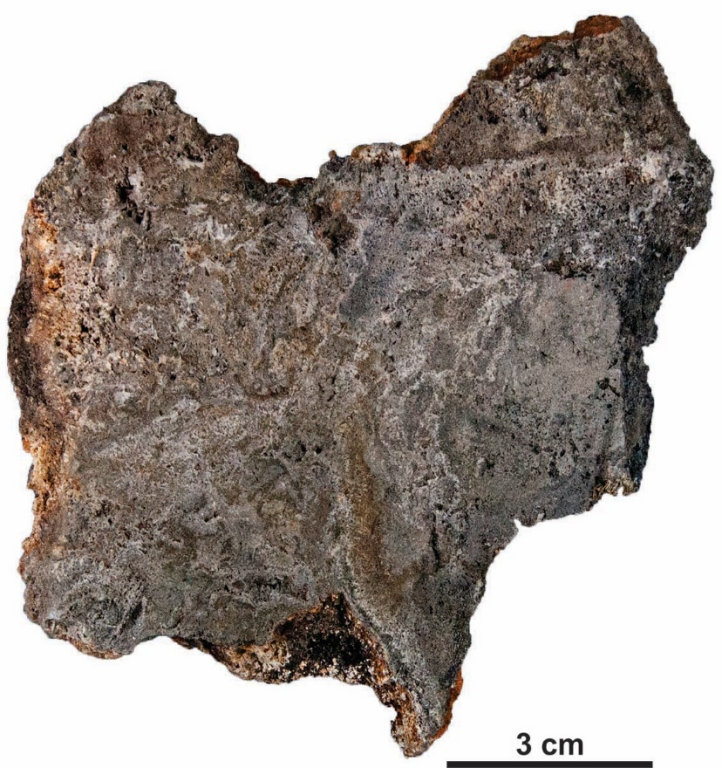
Geochemical Notes

Whole rock: High Zn (224000 ppm), Cd (762 ppm), Hg (25700 ppb), Sb (238 ppm), Ba (84800 ppm), Sr (3940 ppm); Low Cu.

Video Description

Large sulphide blocks/debris.

Hand Sample Description



Hand sample of GMA13-061.

Massive sphalerite-barite chimney collected from talus slope, with a heterogeneous distribution of minerals and no obvious central vent conduits. Abundant barite, irregularly distributed and banded, fine to coarse grained interstitial crystals and very coarse-grained vug fill (45%). The sample contains both high-Fe (25%) and low-Fe (15%) sphalerite. Pore space is mostly mm-size with a few larger 1 cm wide vugs, 15% overall. Minor patchy galena (1%), and trace amounts of pyrite, generally close to the larger vugs. Outer surface has a 5 mm thick rind of clay (1%), iron oxide (<1%) and manganese oxide (<1%).

Thin Section Description

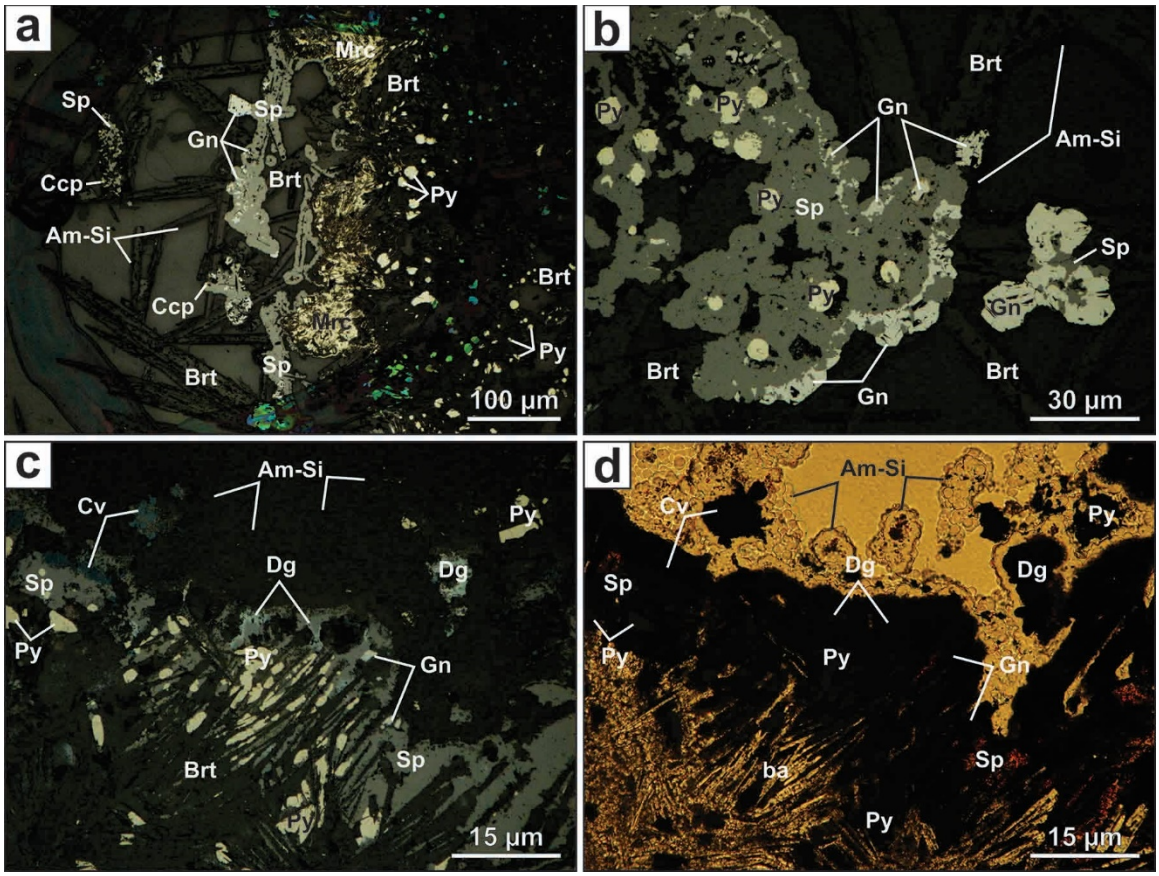
This section has a porosity of ~30%. It is characterized by both dendritic textures and banded mineralogy. It contains abundant fine-grained dendritic barite, with only minor very fine-grained sphalerite (high-Fe?). It is overgrown by abundant fine- to medium-grained spherulitic to colloform pyrite, followed by moderate-Fe sphalerite. Subsequently, there is coarse-grained tabular to acicular, locally radiating barite. This is coated by a layer of amorphous “fish-egg” silica, with minor iron-oxide inclusions, locally layered with high-Fe sphalerite. This is followed by another generation of dendritic,



Thin section scan of GMA13-061.

locally fibrous barite, forming a long layer on the right side of the section. This layer is banded with fine sulfides (sphalerite, and then pyrite). This barite has fine-inclusions (iron oxides?) but is not coated with sphalerite like the first generation of dendritic barite. This is followed by additional coarse-grained tabular barite. There is later pyrite (with fine-grained inclusions of sphalerite), and fine- to medium-grained crystalline marcasite, locally displaying growth zoning and colloform textures, located around some pore spaces and along bands. It is extensively inverted to secondary pyrite, with minor goethite(?) around grain boundaries. The next phase to precipitate is moderate- to low-Fe sphalerite with medium-grained inclusions of galena ± jordanite, and Fe-contents decreasing outwards (although this is locally reversed). This sphalerite is locally altered to covellite and/or digenite. It locally contains rare inclusions of chalcopyrite. Next, there is fine-grained galena that is being replaced by reddish moderate- to high-Fe sphalerite with rare chalcopyrite inclusions, forms next. This sphalerite is also locally altered to covellite ± digenite. Medium-grained galena forms on top of this. Another generation of coarse- to very coarse-grained tabular to acicular barite forms next. A very thin layer of amorphous “fish-egg” silica coats everything, followed by minor sulfides (marcasite + sphalerite) and additional amorphous silica.

This section is a good example of resurgent hydrothermal activity.



Photomicrographs of GMA13-061: ***(a)*** *reflected light (PPL) photomicrograph of dendritic barite, followed by spherulitic pyrite, marcasite partially inverted to pyrite, sphalerite, and galena;* ***(b)*** *reflected light (PPL) photomicrograph of spherulitic pyrite followed by sphalerite, followed by sphalerite + galena;* ***(c)*** *reflected light (PPL) photomicrograph of barite, spherulitic pyrite, and galena, with minor secondary digenite;* ***(d)*** *transmitted light (PPL) photomicrograph of the same view as (c) highlighting late amorphous "fish-egg" silica.*

Mineral abundance: (modal %; not including pore space)

Sp	Ccp	Py	Mrc	Gn	Jd	Bn	Dg	Cv	Au	Brt	Anh	Am-Si	FeOx	Goe(?)
++	+	+	++	+	Tr	-	+	+	-	+++	-	+	Tr	Tr
15	1	5	20	5	<1		1	1		47		5	<1	<1

Paragenesis: Fine-grained dendritic barite → high-Fe(?) sphalerite → spherulitic to colloform pyrite → moderate-Fe sphalerite → coarse-grained tabular to acicular barite → amorphous “fish-egg” silica + high-Fe sphalerite (local) + Fe-oxides(?) → dendritic, locally fibrous barite + sphalerite + pyrite + iron oxides(?)→ coarse-grained tabular barite → pyrite → fine- to medium-grained marcasite, locally colloform → secondary pyrite + goethite(?) → low- to moderate-Fe sphalerite + medium-grained galena ± jordanite + rare fine-grained chalcopyrite → fine-grained galena + reddish moderate- to high-Fe sphalerite + rare fine-grained chalcopyrite → covellite + digenite → medium-grained galena → coarse- to very coarse-grained tabular to acicular barite → amorphous “fish-egg” silica → minor fine grained marcasite + sphalerite → amorphous “fish-egg” silica.

Name: Barite-marcasite-sphalerite chimney talus

SAMPLE: GMA13-062 **PARENT ID:** 737	**LOCATION:** 784699.7E/8649651.0N **WATER DEPTH:** 1100 mbsl

Geochemical Notes

Whole rock: High Zn (351000 ppm), Cd (1770 ppm), Ga (141 ppm), Ge (75 ppm), Hg (>10000 ppb), Sb (211 ppm), Ba (63600 ppm).

Video Description

Active sulphide chimney mound, covered by abundant bacterial matting ('snot'). Piece of blocky massive sulphide talus from base of mound.

Hand Sample Description



Hand sample of GMA13-062.

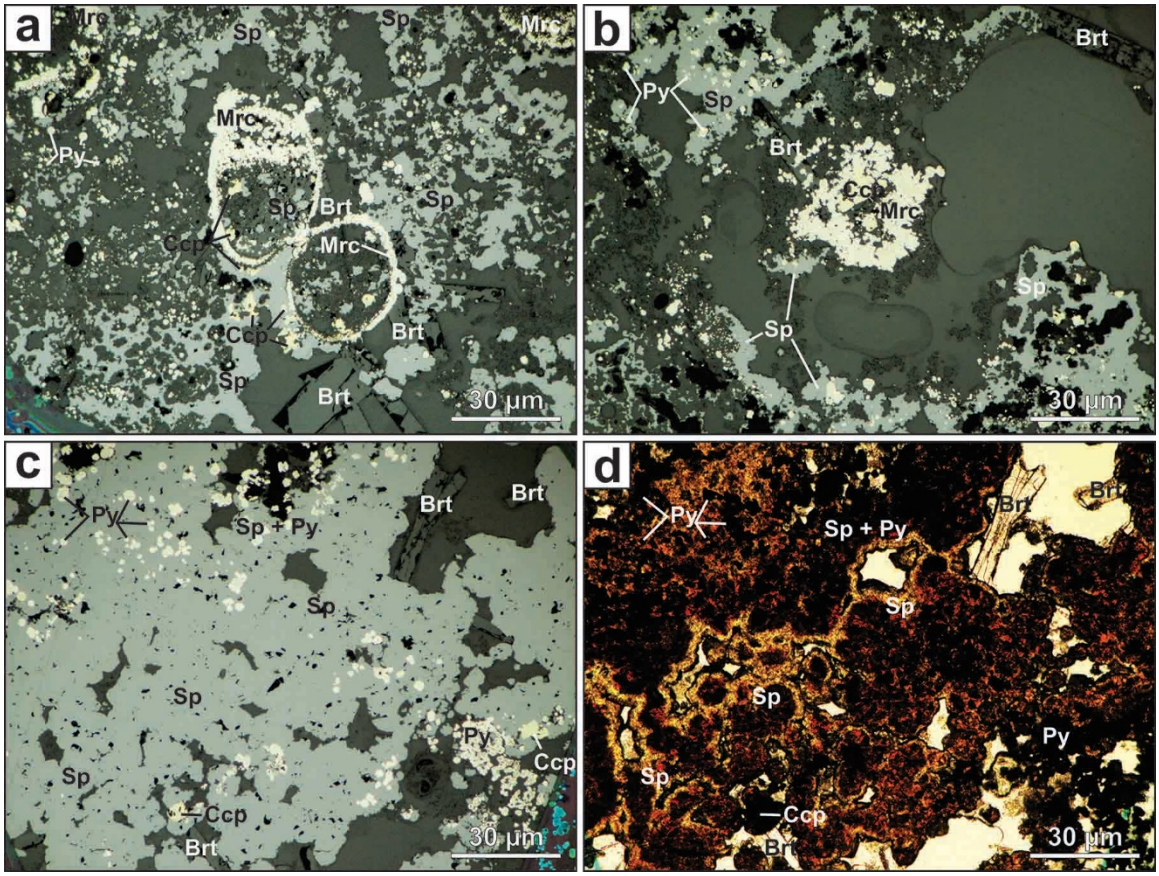
Massive sphalerite-barite chimney with mixed high- and low-Fe sphalerite, with high-Fe sphalerite predominantly lining vugs, 20% high-Fe and 35% low-Fe sphalerite overall. Minor patchy chalcopyrite (2%), irregularly distributed, generally close to vugs. Abundant interstitial barite (25%) and barite lining vugs, with the final phase of high-Fe sphalerite precipitating in vugs. Pore space is mostly mm-size, up to 4 mm wide, 20% overall. Weathered surface has very thin coat of iron oxide (<1%).

Thin Section Description



Thin section scan of GMA13-062.

This section has a porosity of ~35%, comprised mostly of fine pore spaces. The crystallization sequence begins with fine-grained marcasite, locally spherulitic, and fine-grained very low-Fe sphalerite, forming a cellular network. Locally, these sulfides outline relict vent conduits. The marcasite is highly porous and is extensively inverted to secondary pyrite. An irregular layer of high-Fe sphalerite locally follows this, followed by an abundant layer of low-Fe sphalerite that contains medium-grained inclusions of chalcopyrite. Rarely, this sphalerite contains cores of dendritic high-Fe sphalerite. This in turn is locally followed by another layer of high-Fe tabular sphalerite, growing inside low-Fe sphalerite as tabular crystals, locally displaying growth zoning that looks like feathers. This layer tends to have a reddish color. Rare fine-grained inclusions of galena(?) occur in this generation of sphalerite. An additional thin layer of low-Fe sphalerite is locally present. Minor medium-grained chalcopyrite is present as the last sulfide phase, irregularly distributed. Locally, fine-grained dendritic barite forms in the remaining pore space, followed by coarse-grained tabular, radiating barite. Patchy fine-grained amorphous “fish-egg” silica, with nuclei of iron oxides or sulfides(?) locally fill in some of the remaining pore space.



Photomicrographs of GMA13-062: ***(a)*** *reflected light (PPL) photomicrograph of marcasite lining vent conduits, associated with sphalerite and chalcopyrite, with late barite;* ***(b)*** *reflected light (PPL) photomicrograph of chalcopyrite, marcasite, and sphalerite with late barite;* ***(c)*** *reflected light (PPL) photomicrograph of sphalerite with inclusions of pyrite and chalcopyrite;* ***(d)*** *transmitted light (PPL) photomicrograph of the same view as (c) highlighting various generations of moderate- and low-Fe sphalerite.*

Mineral abundance: (modal %; not including pore space)

Sp	Ccp	Py	Mrc	Gn(?)	Jd	Bn	Dg	Cv	Au	Brt	Anh	Am-Si	FeOx	others
+++	+	+	+	Tr	-	-	-	-	-	++	-	+	Tr	-
67	5	8	2	<1						15		3	<1	

Paragenesis: Marcasite, locally spherulitic → secondary pyrite (porous) → very low-Fe sphalerite → high-Fe sphalerite (locally dendritic) → low-Fe sphalerite + chalcopyrite → high-Fe tabular, reddish sphalerite ± fine-grained galena(?) → low-Fe sphalerite → medium-grained chalcopyrite → fine-grained dendritic barite → coarse-grained tabular radiating barite → amorphous “fish-egg” silica, patchy.

Name: Sphalerite-barite chimney talus

DRILLCORE SAMPLES

SAMPLE: MA13-003	**DRILLHOLE:** TKAD030
PARENT ID: 2548	**DRILLHOLE LOCATION:** 784742.79E/8649607.79N
SAMPLE DEPTH: 2.41-2.55 mbsf	**WATER DEPTH:** 1107.72 mbsl

Geochemical Notes

**Whole rock (parent): High Zn (39.30%), Cd (1580 ppm), Sb (224 ppm), Ag (257 ppm).*

Hand Sample Description



Hand sample of MA13-003.

Massive sulphide chimney, no central conduit, weakly banded. Banded sphalerite, around 60% honey sphalerite (39% Zn), medium to fine grained. Heavy, ~15% coarse-grained barite (bladed), 2% chalcopyrite in vugs, <1% bornite, trace pyrite. 20% vugs, up to 1 cm across, filled with barite + chalcopyrite + low-Fe sphalerite + trace bornite. Possible trace orpiment?

Mineral abundance: (modal %; not including pore space)

Sp	Ccp	Py	Mrc	Gn	jd	Bn	Dg	Cv	Au	Brt	Anh	Am-Si	FeOx	others
+++	+	Tr	-	-	-	Tr	-	-	-	++	-	-	-	-
60	2	<1				<1				15				

Name: Sphalerite-barite chimney (low-T) talus

SAMPLE: MA13-010 **PARENT ID:** 2427 **SAMPLE DEPTH:** 0.74-0.84 mbsf	**DRILLHOLE:** TKAD018 **DRILLHOLE LOCATION:** 784756.43E/8649604.73N **WATER DEPTH:** 1110.18 mbsl

Geochemical Notes

Whole rock: High Zn (311000 ppm), Cd (951 ppm), Ga (48), Ba (70000 ppm); Low Fe, Pb, Hg, Sb, Ag.

Hand Sample Description



Hand sample of MA13-010.

Irregularly banded massive sulphides, 30% vugs lined with fine grained bladed barite and high-Fe sphalerite. There is more high-Fe than low-Fe sphalerite, 40% overall. 2% chalcopyrite, 1% pyrite. Matrix is barite-rich (heavy core), ~50%, with patchy silica alteration. Minor entrained clasts of altered (bleached) volcaniclastics, 3%. Represents base of chimney, with hydrothermally cemented volcaniclastic breccia.

Mineral abundance: (modal %; not including pore space)

Sp	Ccp	Py	Mrc	Gn	Jd	Bn	Dg	Cv	Au	Brt	Anh	Am-Si	FeOx	Volc. clasts
+++	+	+	-	-	-	-	-	-	-	+++	-	+	-	+
40	2	1								50		4		3

Name: Sphalerite-barite chimney (low-T) talus with volcanic clasts

SAMPLE: MA13-011	**DRILLHOLE:** TKAD018
PARENT ID: 2427	**DRILLHOLE LOCATION:** 784756.43E/8649604.73N
SAMPLE DEPTH: 1.10-1.19 mbsf	**WATER DEPTH:** 1110.18 mbsl

Geochemical Notes

Whole rock: High As (1520 ppm), Ba (128000 ppm), Si (11.8%); Low Fe, Cu, Ga, Hg, Sb.

Hand Sample Description



Hand sample of MA13-011.

Massive sulphide chimney with no central vent conduit. Abundant blackjack sphalerite (40%) weakly dendritic, 50% Ba, 10% vugs. Rind of barite (+silica?) represents chemical gradient, located at contact with volcaniclastics below, 3 cm wide. Thin dark rim where the barite-rind meets sphalerite-rich chimney, sharp contact (downhole in core). Large vug filled with coarse bladed barite, also has a 1 cm weathered rind. 1% chalcopyrite, 1% pyrite. High As indicates likely jordanite mineralization.

Mineral abundance: (modal %; not including pore space)

Sp	Ccp	Py	Mrc	Gn	Jd	Bn	Dg	Cv	Au	Brt	Anh	Am-Si	FeOx	others
+++	+	+	-	-	+	-	-	-	-	+++	-	+	Tr	-
40	1	1			1					54		3	<1	

Name: Sphalerite-barite chimney (low-T) talus

SAMPLE: MA13-012	**DRILLHOLE:** TKAD018
PARENT ID: 2428	**DRILLHOLE LOCATION:** 784756.43E/8649604.73N
SAMPLE DEPTH: 1.35-1.45 mbsf	**WATER DEPTH:** 1110.18 mbsl

Geochemical Notes

Whole rock: High Zn (348000 ppm), Cd (1270 ppm), Ge (144 ppm), As (1340 ppm), Sb (538 ppm), Si (16.8%); Low Fe, Cu, Hg.

Hand Sample Description



Hand sample of MA13-012.

Volcaniclastic sand-pebble sized breccia with moderate clay alteration (primarily altering clasts) and moderate silicification. Sulphide mineralization along veins (bioturbation), vugs (few), and disseminated. Contains 1% disseminated chalcopyrite (increasing downhole), 2% pyrite, 10% sphalerite. Clasts are angular, monomictic, matrix-supported, 1 - 5 mm long. Sulphate (barite) cement. High As and Sb indicates minor jordanite mineralizaiton. Represents stringer mineralization.

Mineral abundance: (modal %; not including pore space)

Sp	Ccp	Py	Mrc	Gn	Jd	Bn	Dg	Cv	Au	Brt	Anh	Am-Si	FeOx	Volc. clasts
++	+	+	-	-	+	-	-	-	-	+++	-	++	-	+++
10	1	2			1					36		15		35

Name: Mineralized, hydrothermally-altered volcaniclastic breccia (stringer zone)

SAMPLE: MA13-013	**DRILLHOLE:** TKAD018
PARENT ID: 2430	**DRILLHOLE LOCATION:** 784756.43E/8649604.73N
SAMPLE DEPTH: 1.67-1.83 mbsf	**WATER DEPTH:** 1110.18 mbsl

Geochemical Notes

Whole rock: High Si (25.5%), Al (2.95%), V (160 ppm); Low Cd, Pb, Hg, Sb, Ag, Ba.

Hand Sample Description



Hand sample of MA13-013.

Similar to MA13-012, located further downhole. At contact between moderately altered mineralized volcaniclastic breccia with strongly clay-altered monomictic volcaniclastic breccia below. Sample is at the transition. Very few vugs. Contains 2% disseminated chalcopyrite, 15% pyrite, 1% sphalerite. Represents altered stringer zone.

Mineral abundance: (modal %; not including pore space)

Sp	Ccp	Py	Mrc	Gn	Jd	Bn	Dg	Cv	Au	Brt	Anh	Am-Si	Clay	Volc. clasts
+	+	++	-	-	-	-	-	-	-	++	-	+	+++	++
1	2	15								12		5	50	15

Name: Mineralized, hydrothermally-altered volcaniclastic breccia (stringer zone)

SAMPLE: MA13-028 **PARENT ID:** 2382 **SAMPLE DEPTH:** 0.58-0.67 mbsf	**DRILLHOLE:** TKAD013 **DRILLHOLE LOCATION:** 784606.66E/9649845.93N **WATER DEPTH:** 1090.82 mbsl

Geochemical Notes

Whole rock: High S (35.9%), Fe (28.5%), As (1440 ppm); Low Cd, Ga, Ge, Pb, Hg, Ag, Ba.

Hand Sample Description



Hand sample of MA13-028.

Massive sulphide chimney with vent conduits, chalcopyrite (30%) + high-Fe sphalerite (15%) rich, <1% bornite, trace atacamite. 25% marcasite/pyrite(?). Beautiful banded textures. 10-15% vugs. Dominantly anhydrite, minor bladed barite.

Mineral abundance: (modal %; not including pore space)

Sp	Ccp	Py	Mrc	Gn	Jd	Bn	Dg	Cv	Au	Brt	Anh	Am-Si	FeOx	Ata
++	+++	-	+++	-	-	Tr	-	-	-	+	++	-	-	Tr
15	35		25			<1				5	20			<1

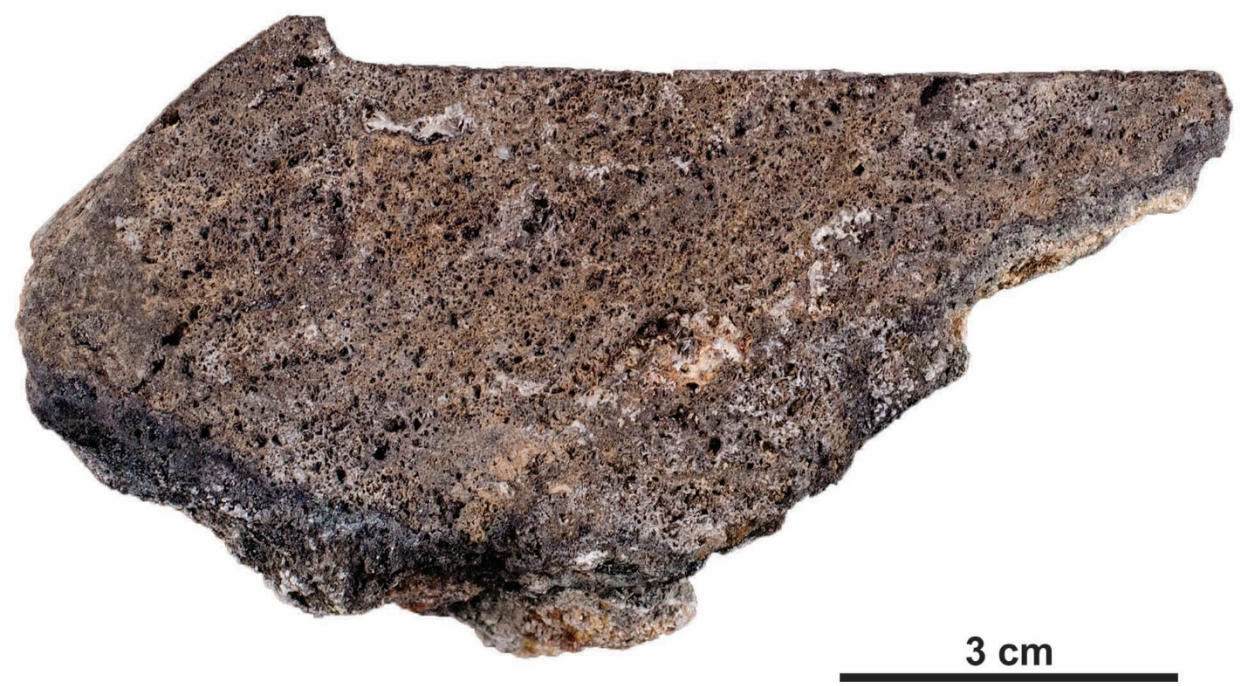
Name: Zoned chalcopyrite-sphalerite chimney talus

SAMPLE: MA13-029	**DRILLHOLE:** TKAD013
PARENT ID: 2384	**DRILLHOLE LOCATION:** 784606.66E/9649845.93N
SAMPLE DEPTH: 2.17-2.27 mbsf	**WATER DEPTH:** 1090.82 mbsl

Geochemical Notes

Whole rock: High Zn (313000 ppm), Cd (1130 ppm), Ga (58 ppm), Ge (61 ppm), As (777 ppm), Sb (381 ppm), Ag (262 ppm); Low Cu.

Hand Sample Description



Hand sample of MA13-029.

Massive sulphide chimney, no central vent conduit. 30% honey sphalerite, with minor chalcopyrite + pyrite (~5% overall). 10% vugs, smaller, some filled with bladed barite. Very heavy, high barite content (50%). Minor dendritic textures. High As and Sb, likely minor jordanite? Dark rind, weathering? Minor white mineral on weathered rind - clay?

Mineral abundance: (modal %; not including pore space)

Sp	Ccp	Py	Mrc	Gn	Jd	Bn	Dg	Cv	Au	Brt	Anh	Am-Si	FeOx	Clay
+++	+	+	-	-	+	-	-	-	-	+++	-	Tr	Tr	+
30	1	4			4					60		<1	<1	1

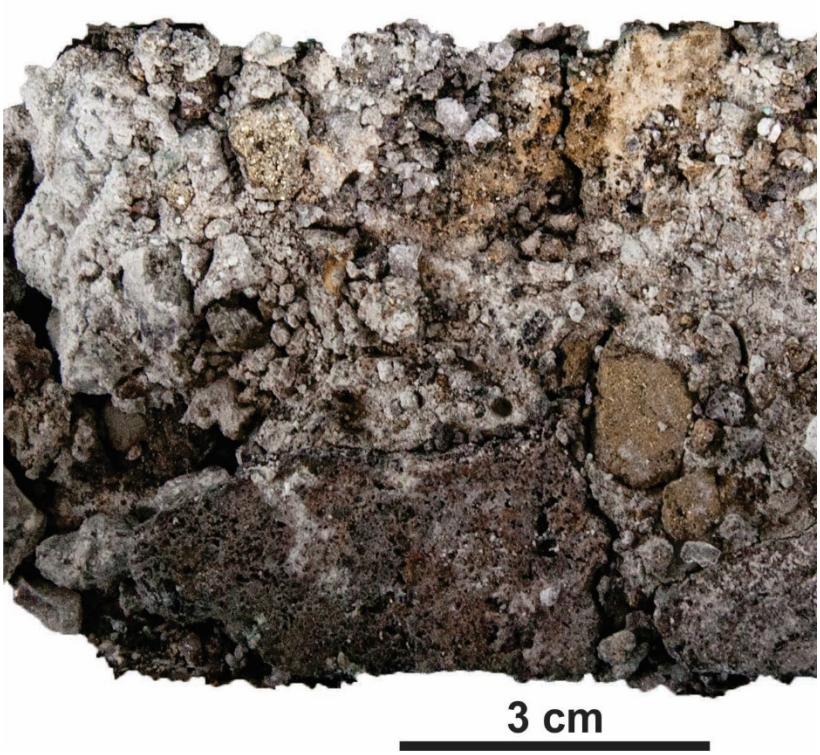
Name: Sphalerite-barite chimney (low-T) talus

SAMPLE: MA13-030 **PARENT ID:** 2386 **SAMPLE DEPTH:** 3.61-3.68 mbsf	**DRILLHOLE:** TKAD013 **DRILLHOLE LOCATION:** 784606.66E/9649845.93N **WATER DEPTH:** 1090.82 mbsl

Geochemical Notes

Whole rock: High Zn (356000 ppm), Cd (1610 ppm), Ge (66 ppm), Sb (530 ppm), Ag (401 ppm), Ba (94200 ppm); Low Fe, Cu, Ga, Pb.

Hand Sample Description



Hand sample of MA13-030.

Massive sulphide talus consisting of clasts of sphalerite-rich vuggy chimney fragments and massive pyrite (1 cm long) in an intensely clay-altered matrix with angular clay-altered clasts. Large gypsum crystals, 10 cm long. Additional disseminated sphalerite (18%) + pyrite (8%). High Sb indicates likely jordanite mineralization, high Ba indicates barite. Semi-lithified to unconsolidated sample.

Mineral abundance: (modal %; not including pore space)

Sp	Ccp	Py	Mrc	Gn	Jd	Bn	Dg	Cv	Au	Brt	Anh	Gp	FeOx	Clay
+++	+	++	-	-	+	-	-	-	-	++	+	++	-	++
30	2	15			1					20	5	12		10

Name: Mixed chimney talus

SAMPLE: MA13-031 **PARENT ID:** 2387 **SAMPLE DEPTH:** 4.88-4.95 mbsf	**DRILLHOLE:** TKAD013 **DRILLHOLE LOCATION:** 784606.66E/9649845.93N **WATER DEPTH:** 1090.82 mbsl

Geochemical Notes

Whole rock: High Fe (14.0%), Cu (137000 ppm), Mo (224 ppm), Si (16.2%), Al (1.78%), V (123 ppm); Low Ge, Pb, Hg, As, Sb, Ag.

Hand Sample Description



Hand sample of MA13-031.

Volcaniclastic sand- to pebble-sized breccia with moderate clay alteration (primarily altering clasts) and moderate silicification. Disseminated Sulphide mineralization, mainly pyrite (5%), chalcopyrite (15%) and 2% sphalerite. Clasts are 1-3 mm long, angular, 30% overall. Mineralization affects matrix only. 2% vugs. Barite cement. Represents stringer zone mineralization

Mineral abundance: (modal %; not including pore space)

Sp	Ccp	Py	Mrc	Gn	Jd	Bn	Dg	Cv	Au	Brt	Anh	Am-Si	FeOx	Volc. Clasts
+	++	+	-	-	-	-	-	-	-	+++	-	++	-	+++
2	15	5								33		15		30

Name: Mineralized, hydrothermally-altered volcaniclastic breccia (stringer zone)

SAMPLE: MA13-032 **PARENT ID:** 2405 **SAMPLE DEPTH:** 0.70-0.74 mbsf	**DRILLHOLE:** TKAD016 **DRILLHOLE LOCATION:** 784588.91E/8649829.11N **WATER DEPTH:** 1088.73 mbsl

Geochemical Notes

Whole rock: High Hg (23300 ppb), Ba (64300 ppm), Si (16.5%); Low Sb, Ag.

Hand Sample Description



Hand sample of MA13-032.

Clastic massive sulfides, hydrothermally cemented. Contains Blackjack sphalerite (10%), chalcopyrite (5%). Entrained angular volcanic fragments, angular, up to 1 cm across, variably altered (clay, chlorite). Some sphalerite-rich chimney clasts? 5-10% vugs. Barite cement and abundant bladed Ba (beveled crystal edges). Minor silicification. Minor FeOx straining. Possible worm casts (minor).

Mineral abundance: (modal %; not including pore space)

Sp	Ccp	Py	Mrc	Gn	Jd	Bn	Dg	Cv	Au	Brt	Anh	Am-Si	FeOx	Volc. clasts
++	+	+	-	-	-	-	-	-	-	+++	-	++	+	++
10	5	1								50		13	1	20

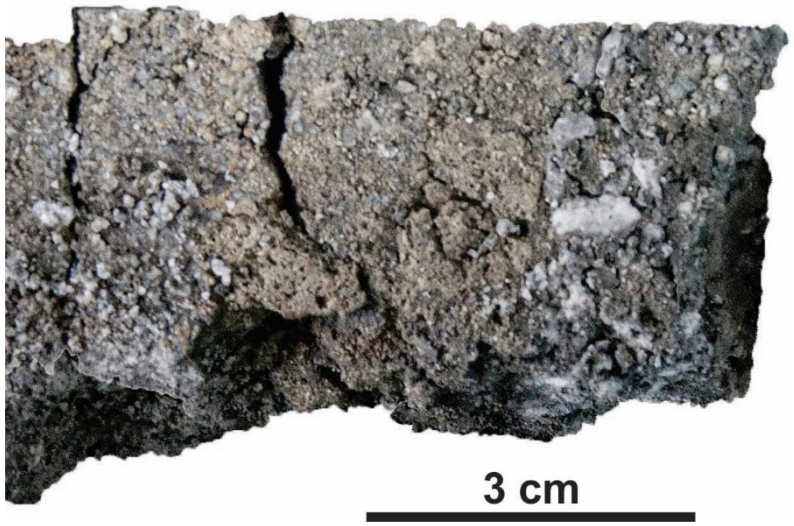
Name: Mineralized, hydrothermally-altered volcaniclastic breccia and chimney talus (stringer zone)

SAMPLE: MA13-033 **PARENT ID:** 2405 **SAMPLE DEPTH:** 0.91-1.00 mbsf	**DRILLHOLE:** TKAD016 **DRILLHOLE LOCATION:** 784588.91E/8649829.11N **WATER DEPTH:** 1088.73 mbsl

Geochemical Notes

**Whole rock (parent): High CaO (10.35 wt.%).*

Hand Sample Description



Hand sample of MA13-033.

Chalcopyrite- and sphalerite- rich sandy sulfide sediment, with larger clasts of chalcopyrite chimney talus. Moderate clay alteration, abundant anhydrite in matrix. Unconsolidated sample, original sample showed bedding, late sulphate veining.

Mineral abundance: (modal %; not including pore space)

Sp	Ccp	Py	Mrc	Gn	Jd	Bn	Dg	Cv	Au	Brt	Anh	Am-Si	FeOx	Gp
++	+++	++	-	-	-	-	-	-	-	-	++	-	-	+
20	35	10									30			5

Name: Mixed chimney talus

SAMPLE: MA13-041 **PARENT ID:** 2557 **SAMPLE DEPTH:** 0.78-0.90 mbsf	**DRILLHOLE:** TKAD031 **DRILLHOLE LOCATION:** 784726.04E/8649576.46N **WATER DEPTH:** 1110.26 mbsl

Geochemical Notes

Whole rock: High S (31.5%), Fe (18.9%), Cu (173000 ppm), Cd (610 ppm), Ge (61 ppm), Hg (37600 ppb), Sb (235 ppm); Low Pb, Ag.

Hand Sample Description



Hand sample of MA13-041.

Massive sulphide chimney boulder with banded chalcopyrite (35%), 15% blackjack sphalerite and minor marcasite/pyrite(?) filling vugs. Minor atacamite, 1%. 5% vugs. Sulphate + white clay matrix, abundant barite. High Sb indicates likely jordanite mineralization. Coarse bladed barite fills vugs, up to 5 mm long.

Mineral abundance: (modal %; not including pore space)

Sp	Ccp	Py	Mrc	Gn	Jd	Bn	Dg	Cv	Au	Brt	Anh	Ata	FeOx	Clay
++	+++	-	++	-	+	-	-	-	-	++	-	+	Tr	Tr
20	37		15		1					25		2	<1	<1

Name: Zoned chalcopyrite-sphalerite chimney talus

SAMPLE: MA13-043 **PARENT ID:** 2563 **SAMPLE DEPTH:** 4.91-5.00 mbsf	**DRILLHOLE:** TKAD031 **DRILLHOLE LOCATION:** 784726.04E/8649576.46N **WATER DEPTH:** 1110.26 mbsl

Geochemical Notes

Whole rock: High Zn (287000 ppm), Cd (916 ppm), Ge (70 ppm), Ba (81600 ppm); Low Cu, Pb, Hg, Sb, Ag.

Hand Sample Description



Hand sample of MA13-043.

Sphalerite-rich massive sulphide chimney breccia, fine-grained sulphides, bladed barite, banding/chimney textures not obvious. Abundant barite-filled fractures. Minor chalcopyrite, pyrite, trace bornite. 5% vugs. Hydrothermally lithified, minor silicification.

Mineral abundance: (modal %; not including pore space)

Sp	Ccp	Py	Mrc	Gn	Jd	Bn	Dg	Cv	Au	Brt	Anh	Am-Si	FeOx	others
+++	+	+	-	-	-	-	-	-	-	+++	-	++	-	-
32	3	5								50		10		

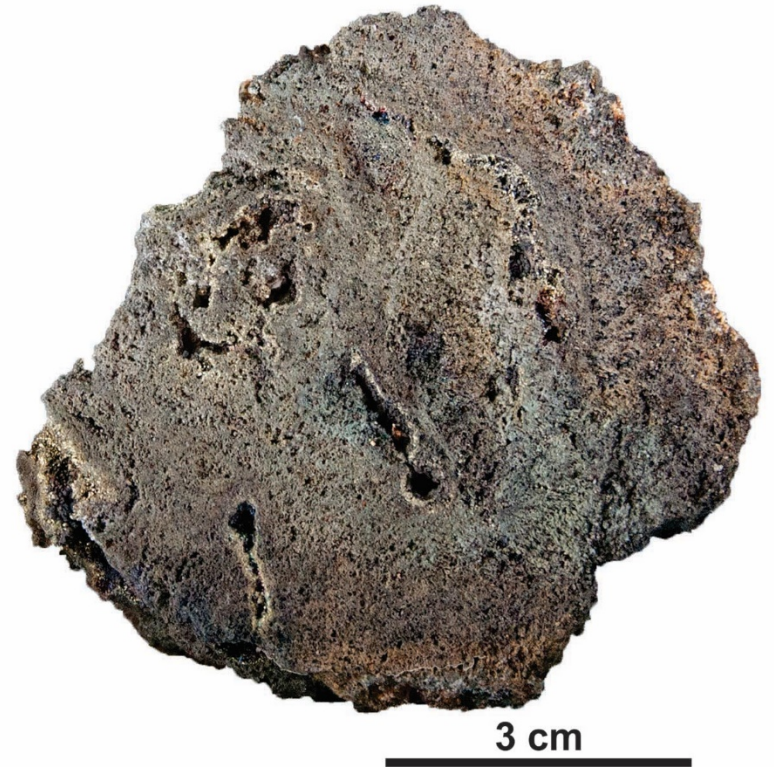
Name: Sphalerite-barite chimney talus

SAMPLE: MA13-046	**DRILLHOLE:** TKAD015
PARENT ID: 2392	**DRILLHOLE LOCATION:** 784561.08E/8649940.06N
SAMPLE DEPTH: 0.05-0.12 mbsf	**WATER DEPTH:** 1091.80 mbsl

Geochemical Notes

**Whole rock (parent): High FeO (23.80 wt.%), S (23.4%), Ni (217 ppm), Mo (116 ppm), As (1080 ppm).*

Hand Sample Description



Hand sample of MA13-046.

Fragments of chalcopyrite-rich chimneys, up to 5 cm long, with colloform banding and 10% vugs. Minor sphalerite. <1% atacamite, bornite. Patchy FeOx staining. Contained within coarse mafic volcaniclastic sand, minor patchy oxidation, with some Cpy-rich sand. High As contents suggest presence of jordanite. Sand-sized fragments of clay and FeOx. Sample contains chimney fragments and sand.

Mineral abundance: (modal %; not including pore space)

Sp	Ccp	Py	Mrc	Gn	Jd	Bn	Dg	Cv	Au	Brt	Anh	Clay	FeOx	Ata
++	+++	+	-	-	+	Tr	-	-	-	++	-	+	+	Tr
25	40	6			1	<1				25		3	1	<1

Name: Zoned chalcopyrite-sphalerite chimney talus

SAMPLE: MA13-048	**DRILLHOLE:** TKAD015
PARENT ID: 2394	**DRILLHOLE LOCATION:** 784561.08E/8649940.06N
SAMPLE DEPTH: 1.30-1.39 mbsf	**WATER DEPTH:** 1091.80 mbsl

Geochemical Notes

Whole rock: High S (36.4%), Fe (26.7%), Cu (79000 ppm), Ga (43 ppm) As (1940 ppm); Low Hg, Ag.

Hand Sample Description



Hand sample of MA13-048.

Barite-cemented sphalerite- and chalcopyrite-rich chimney fragments in massive sulphide sand. Chalcopyrite (20%), mostly blackjack sphalerite (30%), minor pyrite + bornite + atacamite. 15% vugs. Colloform banding and open space filling of vent conduit. Small amount of orpiment(?) on one fragment. High As contents also suggests presence of jordanite. Minor light grey clay alteration, also banded.

Mineral abundance: (modal %; not including pore space)

Sp	Ccp	Py	Mrc	Gn	Jd	Bn	Dg	Cv	Au	Brt	Orp(?)	Clay	FeOx	Ata
+++	+++	+	-	-	+	+	-	-	-	+++	Tr	+	+	Tr
30	26	4			1	1				33	<0.01	4	1	<1

Name: Zoned sphalerite-barite-chalcopyrite chimney talus

SAMPLE: MA13-065	**DRILLHOLE:** TKAD026
PARENT ID: 2526	**DRILLHOLE LOCATION:** 784609.20E/8649820.32N
SAMPLE DEPTH: 0.50-0.65 mbsf	**WATER DEPTH:** 1089.04 mbsl

Geochemical Notes

Whole rock: High Zn (344000 ppm), Cd (1210 ppm), Ga (44 ppm), As (933 ppm), Ba (81900 ppm); Low Fe, Cu, Ge, Hg.

Hand Sample Description



Hand sample of MA13-065.

Banded massive sulphide chimney, no central conduit. 15% vugs. Low- and high-Fe sphalerite (30%), dendritic. High-Fe sphalerite lines low-Fe sphalerite dendrites. Abundant barite (20%), minor FeOx. No chalcopyrite. Minor bladed barite fills void space. High As contents suggests presence of jordanite.

Mineral abundance: (modal %; not including pore space)

Sp	Ccp	Py	Mrc	Gn	Jd	Bn	Dg	Cv	Au	Brt	Anh	Am-Si	FeOx	others
+++	-	+	-	-	+	-	-	-	-	+++	-	-	+	-
54		5			1					40			1	

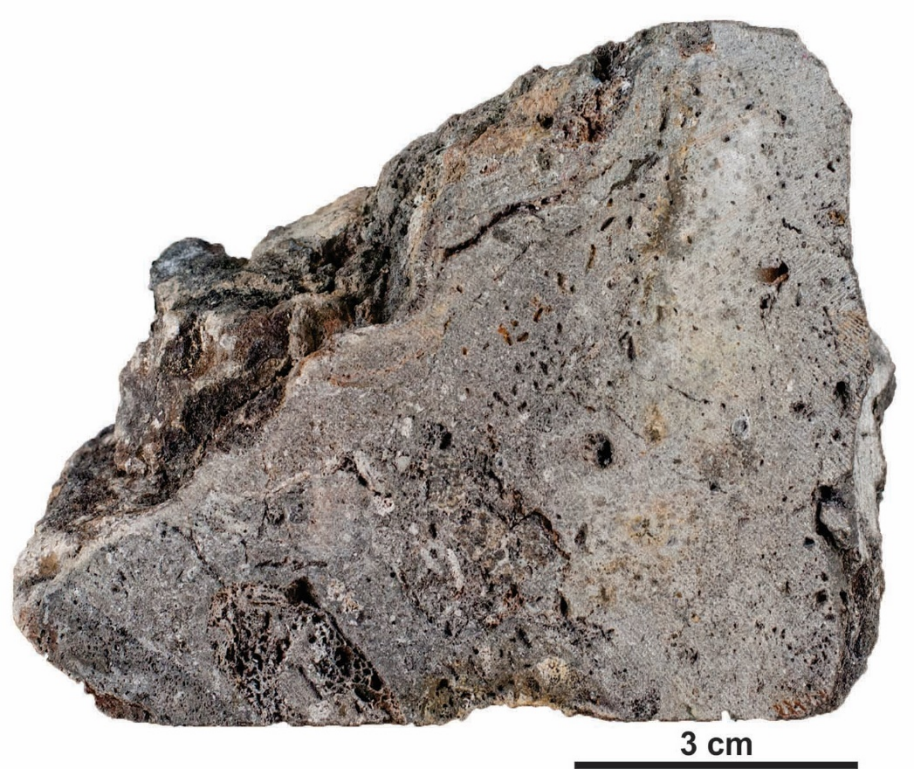
Name: Sphalerite-barite chimney (low-T) talus

SAMPLE: MA13-066	**DRILLHOLE:** TKAD026
PARENT ID: 2528	**DRILLHOLE LOCATION:** 784609.20E/8649820.32N
SAMPLE DEPTH: 1.18-1.27 mbsf	**WATER DEPTH:** 1089.04 mbsl

Geochemical Notes

Whole rock: High Pb (14800 ppm), Hg (37000 ppb), Ba (112000 ppm), Sr (3950 ppm) Si (13.4%); Low Fe, Cu, Ga, Sb.

Hand Sample Description



Hand sample of MA13-066.

Lithified chimney talus (former barite-sphalerite chimney) with bioturbated sediment containing worm casts and shell fragments, possible volcaniclastics. 5-10% vugs. Disseminated chalcopyrite (1%), pyrite (<1%). Blackjack sphalerite (12%) lines fractures. Minor bladed barite in vugs, also in matrix (heavy). Matrix may be sediment? Moderately silicified, looks saccharoidal. In contact with light grey volcanic extrusive with 5% small vesicles, may be a clast. Minor patchy FeOx, trace atacamite along fractures.

Mineral abundance: (modal %; not including pore space)

Sp	Ccp	Py	Mrc	Gn	Jd	Bn	Dg	Cv	Brt	Ata	Am-Si	FeOx	Volc. clasts
++	+	Tr	-	-	-	+++	-	-	-	Tr	++	-	+
10	1	<1				30				<1	10		5

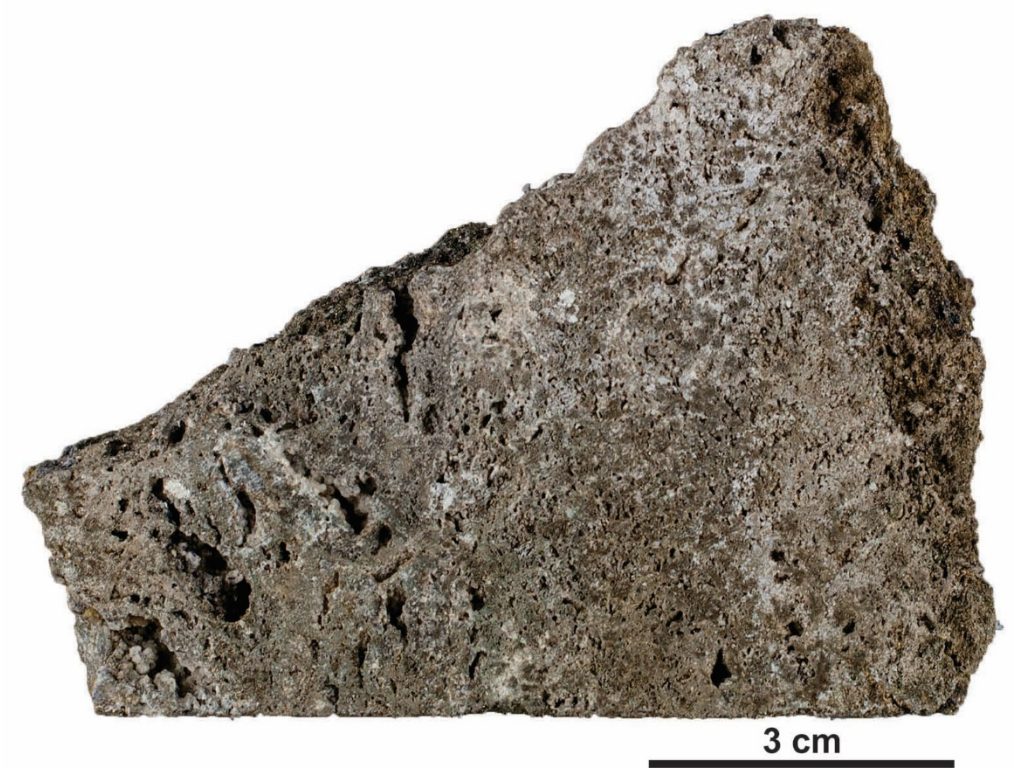
Name: Mineralized, hydrothermally-altered volcaniclastic breccia

SAMPLE: MA13-098	**DRILLHOLE:**TKAD028
PARENT ID: 2512	**DRILLHOLE LOCATION:** 784582.16E/8649932.63N
SAMPLE DEPTH: 1.56-1.65 mbsf	**WATER DEPTH:** 1091.00 mbsl

Geochemical Notes

Whole rock: High S (35.4%), Fe (28.0%), Si (10.5%); Low Cd, Ga, Ge, Pb, As, Sb, Ag.

Hand Sample Description



Hand sample of MA13-098.

Massive sulphide chimney with banded pyrite (35%) + honey sphalerite (20%) + chalcopyrite (10%) + bornite(<1%), 10% vugs, heterogeneous distribution of porosity. Minor barite, bladed in vugs (less than above sphalerite-rich interval). Minor clay alteration, white, interstitial to mineralization. Minor silicification. No central vent conduit.

Mineral abundance: (modal %; not including pore space)

Sp	Ccp	Py	Mrc	Gn	Jd	Bn	Dg	Cv	Au	Brt	Anh	Am-Si	FeOx	Clay
++	++	+++	-	-	-	-	-	-	-	++	-	++	Tr	+
20	10	35								20		10	<1	5

Name: Zoned pyrite-sphalerite chimney talus

SAMPLE: P0010	**DRILLHOLE:** TKAD003
PARENT ID: 2033	**DRILLHOLE LOCATION:** 784765.73E/8649281.14N
SAMPLE DEPTH: 0.99-1.10 mbsf	**WATER DEPTH:** 1113.84 mbsl

Geochemical Notes

Whole rock: High S (31.7%), Fe (22.2%), Mo (143 ppm), Mn (192 ppm), Si (10.9%); Low Pb, Hg, Sb, Ag.

Hand Sample Description



Hand sample of P0010.

A massive sulfide breccia with two large angular to subangular clasts, ~2 cm long, composed of pyrite-chalcopyrite and pyrite. Another irregular pyrite-rich area, ~1.5 cm across, is crossed by elongate fracture-like cavities. There are numerous smaller angular clasts in a pale to dark grey matrix (sulfide?) with pyrite or marcasite grains and abundant, with scattered grey blades of barite. Minor patchy silica and clay. The abundant matrix cavities, mostly 1mm or less in size, are rarely lined by crystals; rather they have black coatings, often smooth.

Mineral abundance: (modal %; not including pore space)

Sp	Ccp	Py	Mrc	Gn	Jd	Bn(?)	Dg	Cv	Au	Brt	Anh	Am-Si	FeOx	others
++	++	+++	-	-	-	+	-	-	-	++	-	++	-	-
10	15	40				5				15		15		

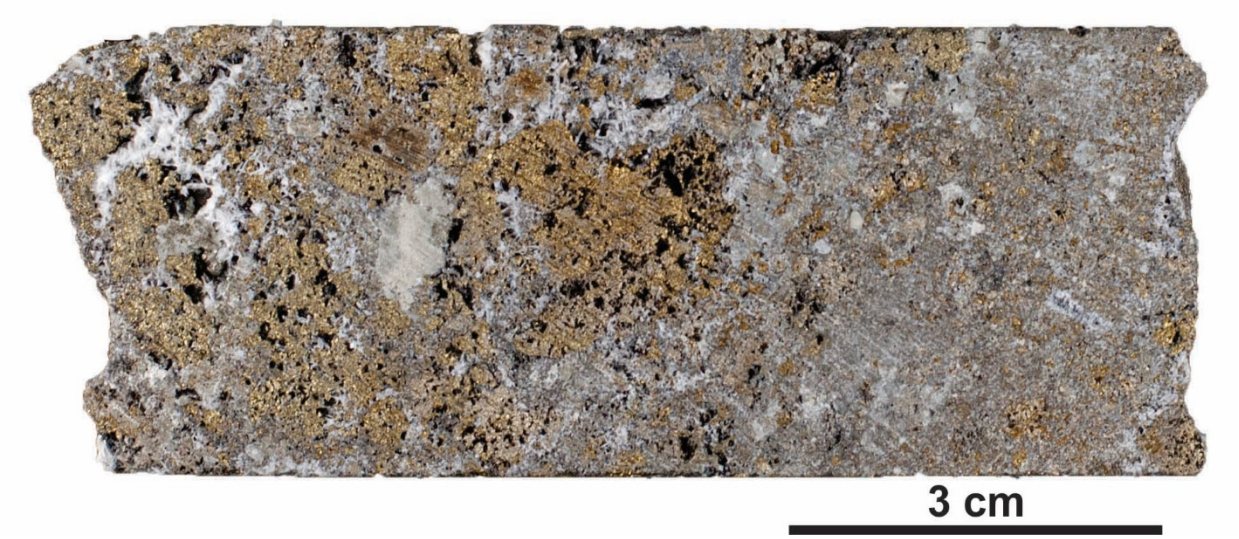
Name: Mixed chimney talus

SAMPLE: P0011 **PARENT ID:** 2037 **SAMPLE DEPTH:** 5.80-5.90 mbsf	**DRILLHOLE:** TKAD003 **DRILLHOLE LOCATION:** 784765.73E/8649281.14N **WATER DEPTH:** 1113.84 mbsl

Geochemical Notes

Whole rock: High S (30.2%), Fe (23.9%), Mo (102 ppm), Si (12.7%); Low Zn, Cd, Ga, Pb, Hg, Sb, Ag.

Hand Sample Description



Hand sample of P0011.

Barite-rich, silicified volcaniclastic breccia with abundant mineralization. Volcanic clasts are fine-grained, clay- and silica-altered, and hard to distinguish. There are several patches and discontinuous veinlets of white silica+barite, with mm-size crystals of barite projecting into cavities, associated with coarse-grained patchy chalcopyrite mineralization. Pyrite mineralization is also patchy.

Mineral abundance: (modal %; not including pore space)

Sp	Ccp	Py	Mrc	Gn	Jd	Bn	Dg	Cv	Au	Brt	Anh	Am-Si	FeOx	Volc. clasts
-	+++	++	-	-	-	Tr	-	Tr	-	+++	-	++	Tr	++
	25	15				<1		<1		30		20	<1	10

Name: Mineralized, hydrothermally-altered volcaniclastic breccia

SAMPLE: P0042 **PARENT ID:** 2557 **SAMPLE DEPTH:** 0.38-0.45 mbsf	**DRILLHOLE:** TKAD031 **DRILLHOLE LOCATION:** 784726.04E/8649576.46N **WATER DEPTH:** 1110.26 mbsl

Geochemical Notes

**Whole rock (parent): High FeO (40.14 wt.%), S (37.7%), Cu (14.50%).*

Hand Sample Description



Hand sample of P0042.

Chalcopyrite-rich chimney boulder with abundant cm-sized vent conduits and barite cement. Bladed barite infills former vent conduits, which are lined by dense chalcopyrite. Moderate sphalerite, locally dendritic, and minor pyrite. Patchy irregular clay(?) alteration.

Mineral abundance: (modal %; not including pore space)

Sp	Ccp	Py	Mrc	Gn	Jd	Bn	Dg	Cv	Au	Brt	Anh	Am-Si	FeOx	Clay
++	+++	+	-	-	-	Tr	-	Tr	-	++	-	-	+	Tr
25	44	5				<1		<1		25			1	<1

Name: Zoned chalcopyrite-sphalerite chimney talus (boulder)

SAMPLE: P0043 **PARENT ID:** 2560 **SAMPLE DEPTH:** 2.86-3.00 mbsf	**DRILLHOLE:** TKAD031 **DRILLHOLE LOCATION:** 784726.04E/8649576.46N **WATER DEPTH:** 1110.26 mbsl

Geochemical Notes

Whole rock: High Zn (526000 ppm), Cd (1920 ppm), Ga (52 ppm), Sb (433 ppm); Low Fe, Cu.

Hand Sample Description



Hand sample of P0043.

Complexly banded massive sulphide chimney, with opaline Silica (10%), bioturbated. Sphalerite-rich (20%) with high-Fe sphalerite lining vugs, minor low-Fe sphalerite, dendritic. 20% vugs, mostly small, few large 2 cm with botryoidal filling and minor bladed barite. Barite cement (heavy, 50%). Possible trace orpiment. Weak clay + FeOx alteration. High Sb contents suggest the presence of jordanite.

Mineral abundance: (modal %; not including pore space)

Sp	Ccp	Py	Mrc	Gn	Jd	Bn	Dg	Cv	Au	Brt	Orp(?)	Am-Si	FeOx	Clay
+++	-	+	-	-	+	-	-	-	-	+++	Tr	++	+	+
40		2			1					45	<0.01	10	1	1

Name: Sphalerite-barite chimney (low-T) talus

Appendix F

Petrographic Reports – Oxyhydroxides

List of Samples

ROV GRAB SAMPLES 632

SAMPLE: GMA13-011 632

SAMPLE: GMA13-013 634

SAMPLE: GMA13-014 636

SAMPLE: GMA13-016 638

SAMPLE: GMA13-025 640

SAMPLE: GMA13-026 642

SAMPLE: GMA13-037 644

SAMPLE: GMA13-047 646

SAMPLE: GMA13-054 648

SAMPLE: GMA13-055 650

SAMPLE: GMA13-056 652

SAMPLE: GMA13-059 654

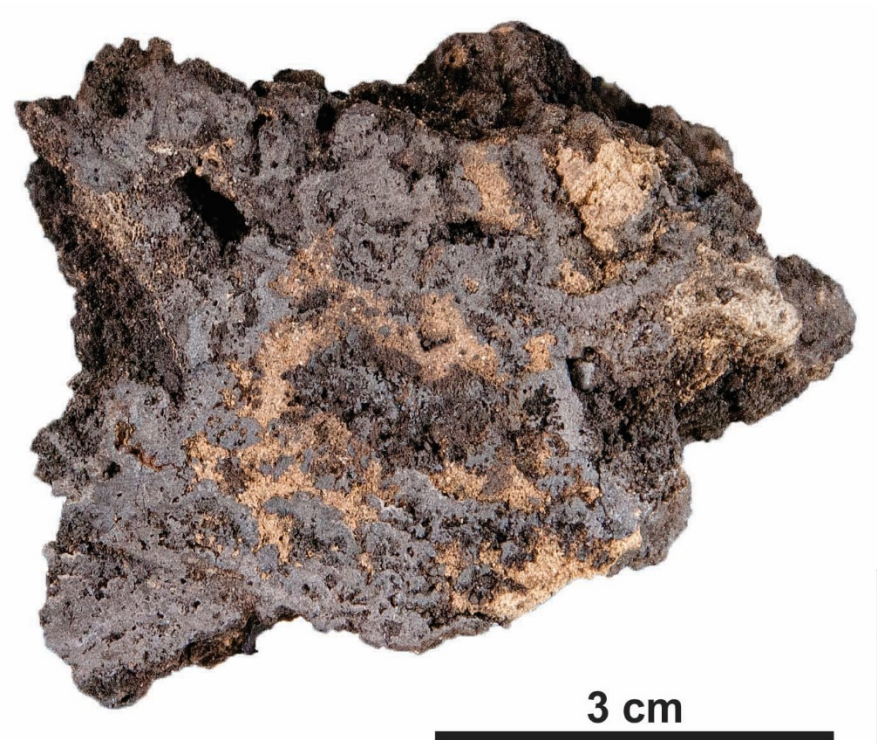
ROV GRAB SAMPLES

SAMPLE: GMA13-011 **PARENT ID:** 657	**LOCATION:** 784665.2E/8649570.8 **WATER DEPTH:** 1133 mbsl

Video Description

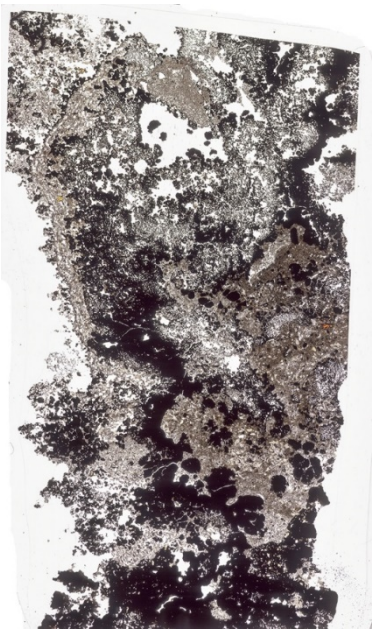
N/A

Hand Sample Description



Hand sample of GMA13-011.

This sample is a has an irregular outer surface. It is composed of an Mn-Oxide "chimney" fragment with bands of dense dendritic to colloform MnOx, and softer clay-FeOx infill. Sample is light/porous with no visible sulfides.

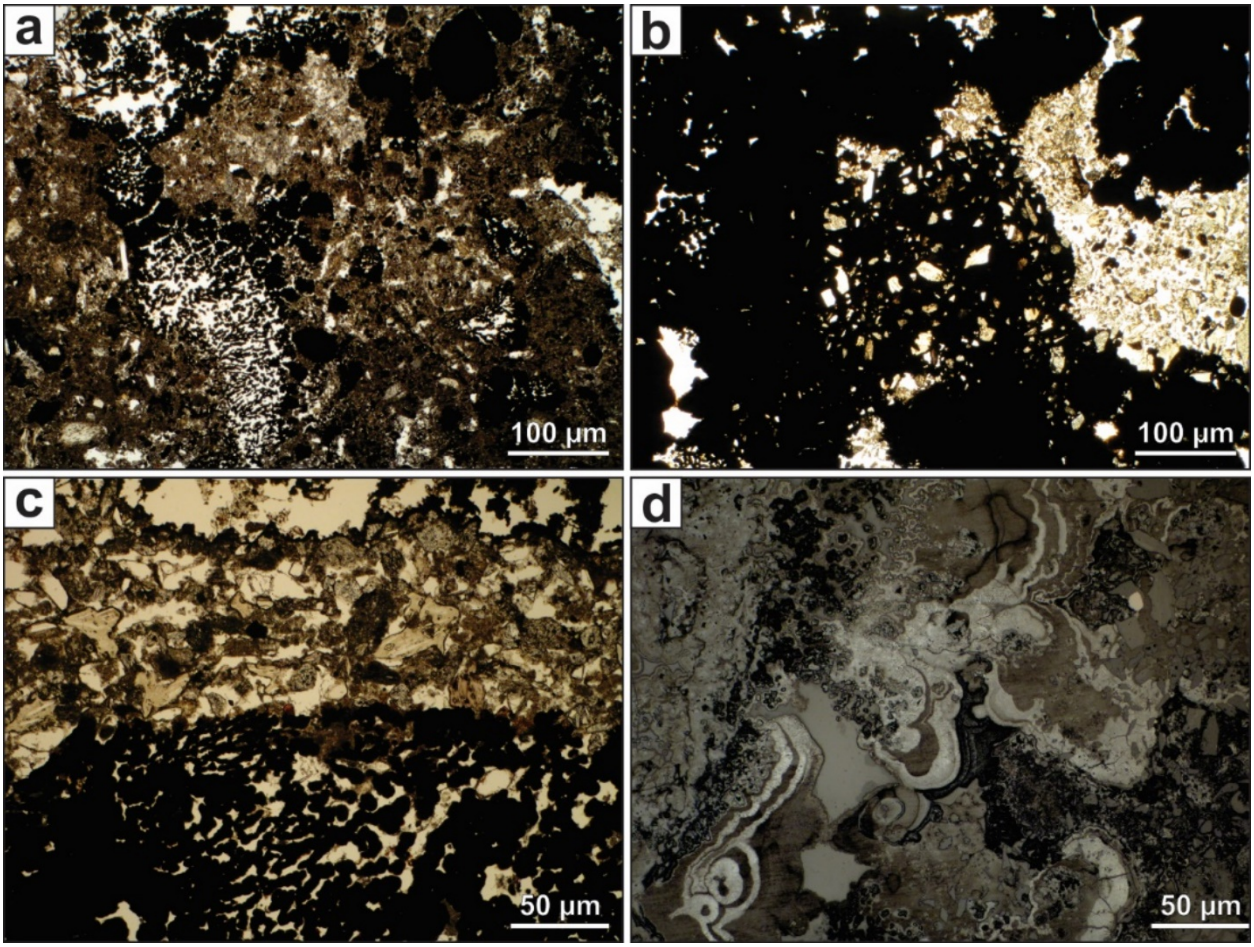


Thin section scan of GMA13-011.

Thin Section Description

This section has a porosity of 35%. It contains abundant broken-up relatively unaltered volcanic material comprising 40% of the section, with minor iron oxide staining. This volcanic material is microcrystalline to glassy, with abundant unaltered phenocrysts of plagioclase, orthopyroxene, and clinopyroxene. The clasts are fine-grained and are angular to subrounded. A few glass shards were identified. Abundant fine-grained manganese oxides with colloform and dendritic textures

constitute 15% of the section. In particular, pyrolusite was identified in reflected light, constituting 5% of the total manganese oxides. There are minor sulfides (pyrite and sphalerite) at the edge of the section associated with volcanic material (<1%). The MnOx dendrites appear to be growing from the volcanic material and filling in pore space.



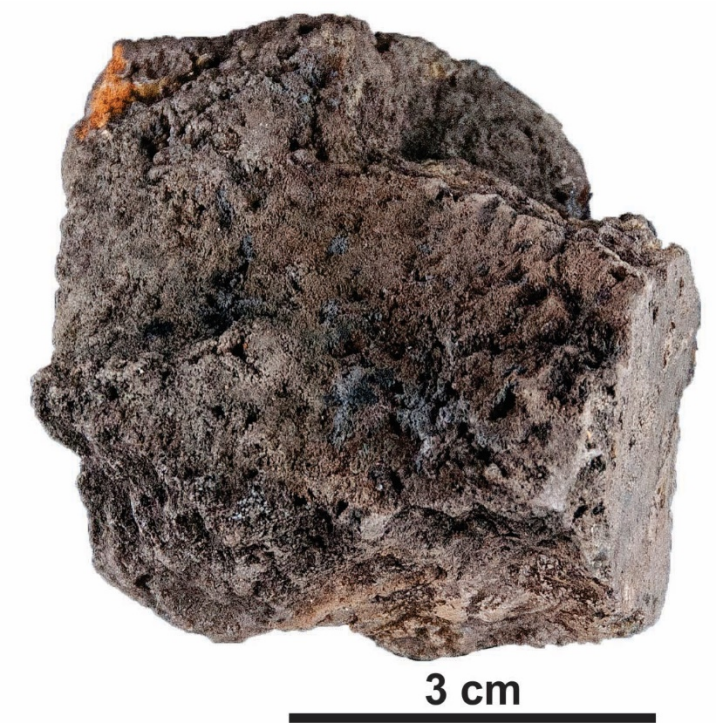
Photomicrographs of GMA13-011: ***(a)*** *transmitted light (PPL) showing small volcanic clasts, surrounded by dendritic MnOx;* ***(b)*** *transmitted light (PPL) showing close-up of volcanic clast;* ***(c)*** *transmitted light (PPL) showing contact between unaltered volcanic clasts and dendritic MnOx;* ***(d)*** *transmitted light (PPL) showing generations of colloform pyrolusite.*

SAMPLE: GMA13-013 **PARENT ID:** 651	**LOCATION:** 784884.0E8649703.3N **WATER DEPTH:** 1135 mbsl

Video Description

Dark Mn chunk of ropey formation, Mn oxide dendritic formation, from FeOx + MnOx chimney area, discrete chimneys with rippled and indurated sediments between. Chimneys are funky, dendritic.

Hand Sample Description



This black-colored sample is almost entirely composed of MnOx, with only minor FeOx, clay. Chimney textures are abundant, including a central 'vent' orifice and numerous smaller orifices. There are possible entrained volcanic glass fragments(?) The spaces between the MnOx bands are infilled by a lighter soft Mn (± Fe) oxide. The sample is very light, with at least 20 vol.% pore space.

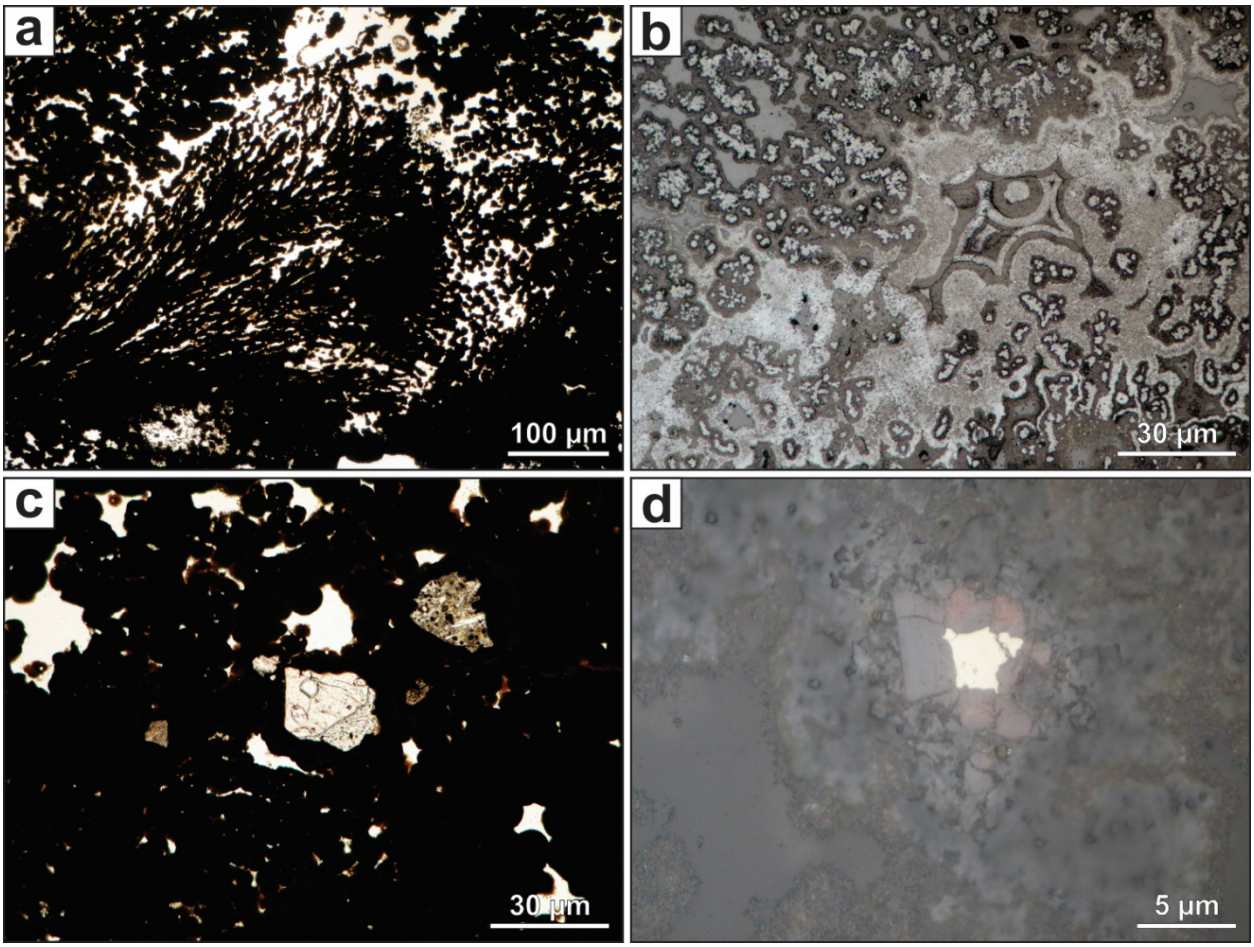
Hand sample of GMA13-013.

Thin Section Description

This section has a porosity of ~40%. It is dominated by dendritic manganese oxides (%), with minor fine-grained volcanic clasts that appear to be relatively unaltered (5% overall). There is minor red iron oxyhydroxides along one main horizon (10%). These oxyhydroxides are surrounded by manganese oxides and appear to pre-date them. Some of the iron oxides are identified as hematite in reflected light, and the manganese oxides may be pyrolusite. There are trace crystals of chalcopyrite (partly altered to iron oxide) and magnetite in open spaces.



Thin section scan of GMA13-013.



Photomicrographs of GMA13-013: ***(a)*** *transmitted light (PPL) showing dendritic MnOx;* ***(b)*** *reflected light (PPL) generations of hematite;* ***(c)*** *transmitted light (PPL) of a close-up of an unaltered volcanic clast surrounded by Fe-MnOx;* ***(d)*** *reflected light (PPL) showing pyrite altered into goethite(?).*

SAMPLE: GMA13-014 **PARENT ID:** 655	**LOCATION:** 784834.2E/8649561.3N **WATER DEPTH:** 1143 mbsl

Video Description

Bedded oxidized volcanic pebble breccia (hyaloclastite?), sample loose at bottom of outcrop.

Hand Sample Description



Hand sample of GMA13-014.

Bedded volcaniclastic sandstone with abundant FeOx and MnOx. Sand-sized particles, beds 5-8 mm thick. Moderately sorted, not graded. The upper surface (seafloor explosed) is MnOx altered, the bottom is pervasively FeOx altered.

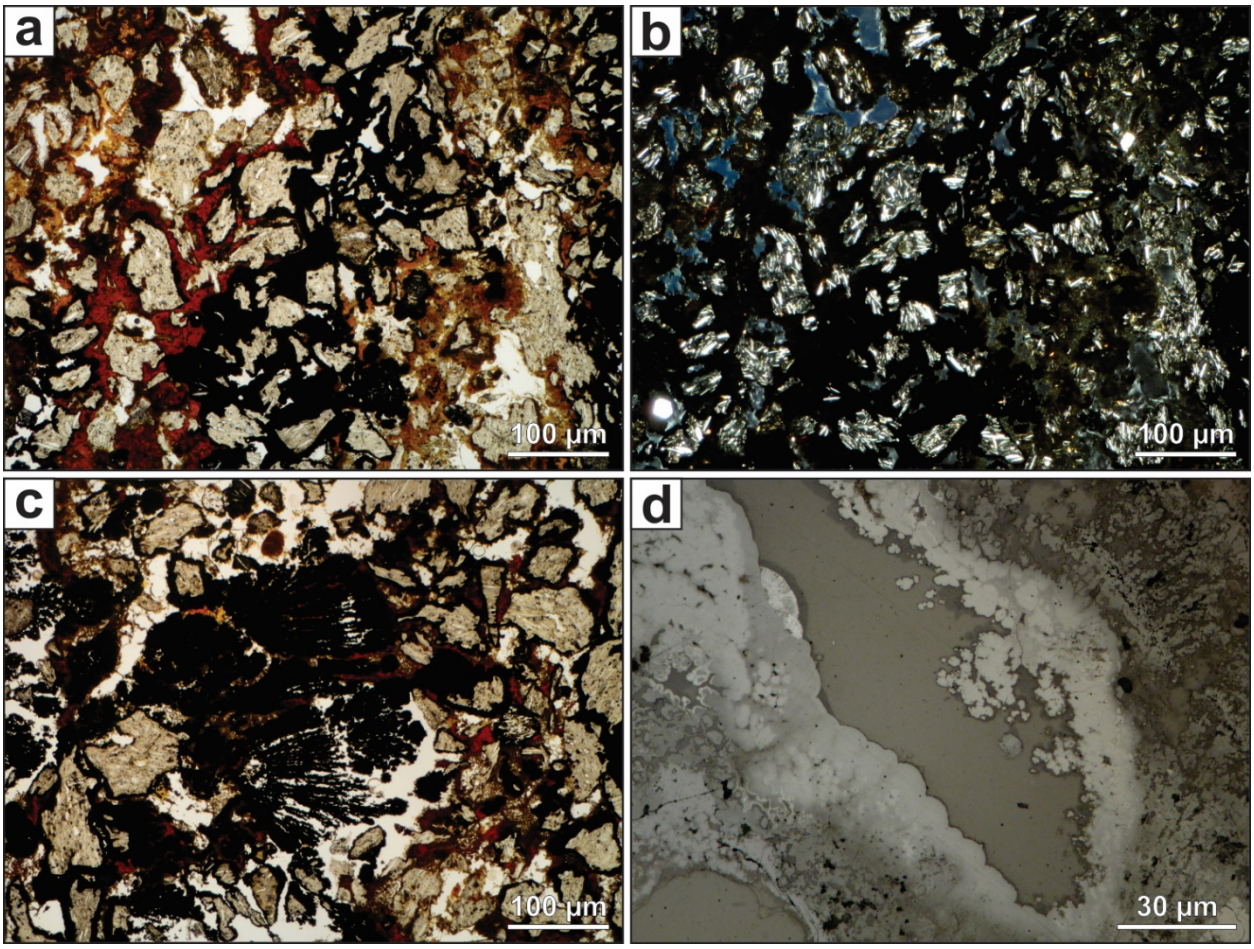


Thin section scan of GMA13-014.

Thin Section Description

This section has a porosity of 25% and contains abundant angular glassy volcanic fragments that contain abundant plagioclase microphenocrysts, and are unaltered. The volcanic fragments constitute 40% of the section, and appear to be monomictic. These fragments are surrounded by banded horizons of manganese and iron oxides of various colors. The MnOx is locally dendritic and pre-dates the iron oxides. Pyrolusite occurs locally. There are 20% iron

oxides and 15% manganese oxides overall. There are trace fine-grained magnetite crystals preserved in the volcanic fragments.



Photomicrographs of GMA13-014: ***(a)*** *transmitted light (PPL) showing small volcanic clasts, surrounded by layers of Fe-MnOx;* ***(b)*** *transmitted light (XPL) showing same view as (a), highlighting the unaltered crystal-rich volcanic clasts;* ***(c)*** *transmitted light (PPL) showing dendritic MnOx;* ***(d)*** *reflected light (PPL) showing generations of colloform pyrolusite(?).*

SAMPLE: GMA13-016 **PARENT ID:** 652	**LOCATION:** 784867.6E/8649732.4N **WATER DEPTH:** 1099 mbsl

Video Description

Mn oxide rich chimney sample, very friable and broken, from low lumpy chimney, aligned along fractures in indurated sediments.

Hand Sample Description



Fragments of an MnOx chimney, with abundant chimney textures (colloform banding) and dendritic MnOx. The outer surface appears smooth. The dense Mn-Ox bands are infilled with soft dendritic to granular MnOx. The bands appear to define former vent conduits. No sulphides observed. It is a high porosity sample, with no sulfides.

Hand sample of GMA13-016.

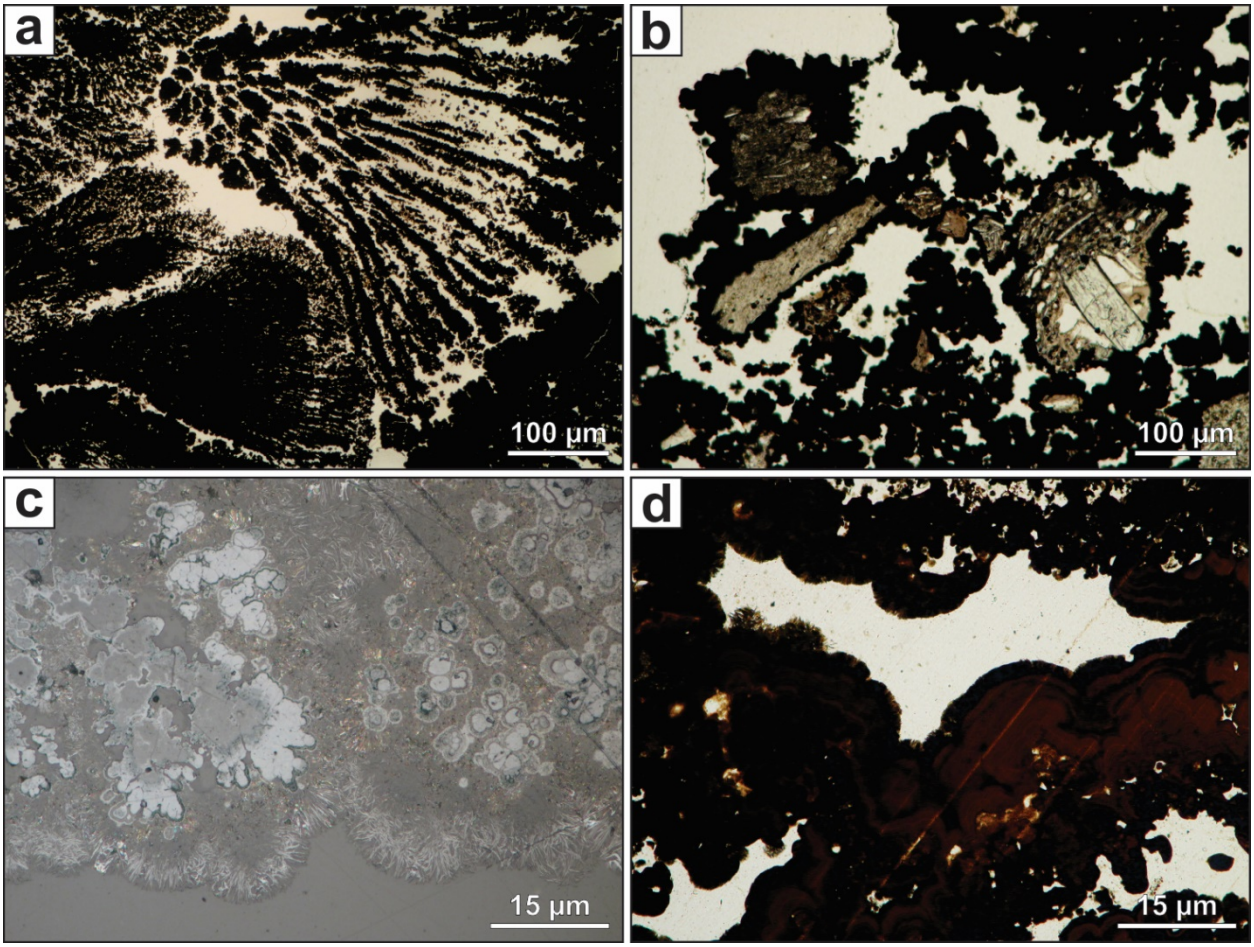
Thin Section Description

This section has a porosity of 40%. There are ~5% fine-grained glassy to microcrystalline angular volcanic clasts that appear unaltered. These clasts are locally scoriaceous. These clasts are surrounded by abundant manganese oxides with dendritic textures, constituting 45-50% of the sample. Along one horizon there are minor iron oxyhydroxides with colloform textures following MnOx, with an additional generation of intergrown needles of iron and manganese oxides precipitated on top of



Thin section scan of GMA13-016.

that. The iron oxides comprise 5-10% of the sample. The manganese oxides are dominantly pyrolusite.



Photomicrographs of GMA13-016: ***(a)*** *transmitted light (PPL) showing dendritic MnOx;* ***(b)*** *transmitted light (PPL) showing unaltered volcanic clasts surrounded by MnOxt;* ***(c)*** *reflected light (PPL) showing generations of oxides, with bright reflected minerals identified as pyrolusite;* ***(d)*** *transmitted light (PPL) colloform FeOx on top of MnOx, followed by an additional generation of MnOx.*

SAMPLE: GMA13-025 **PARENT ID:** 590	**LOCATION:** 784605.4E/8649877.1N **WATER DEPTH:** 1091 mbsl

Video Description

Oxidized piece of chimney from inactive, droopy chimneys, partly buried. Sample from talus at base of chimneys. Cluster/mound.

Hand Sample Description

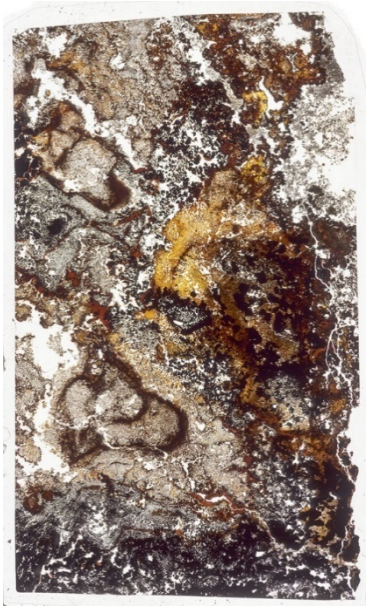


Hand sample of GMA13-025.

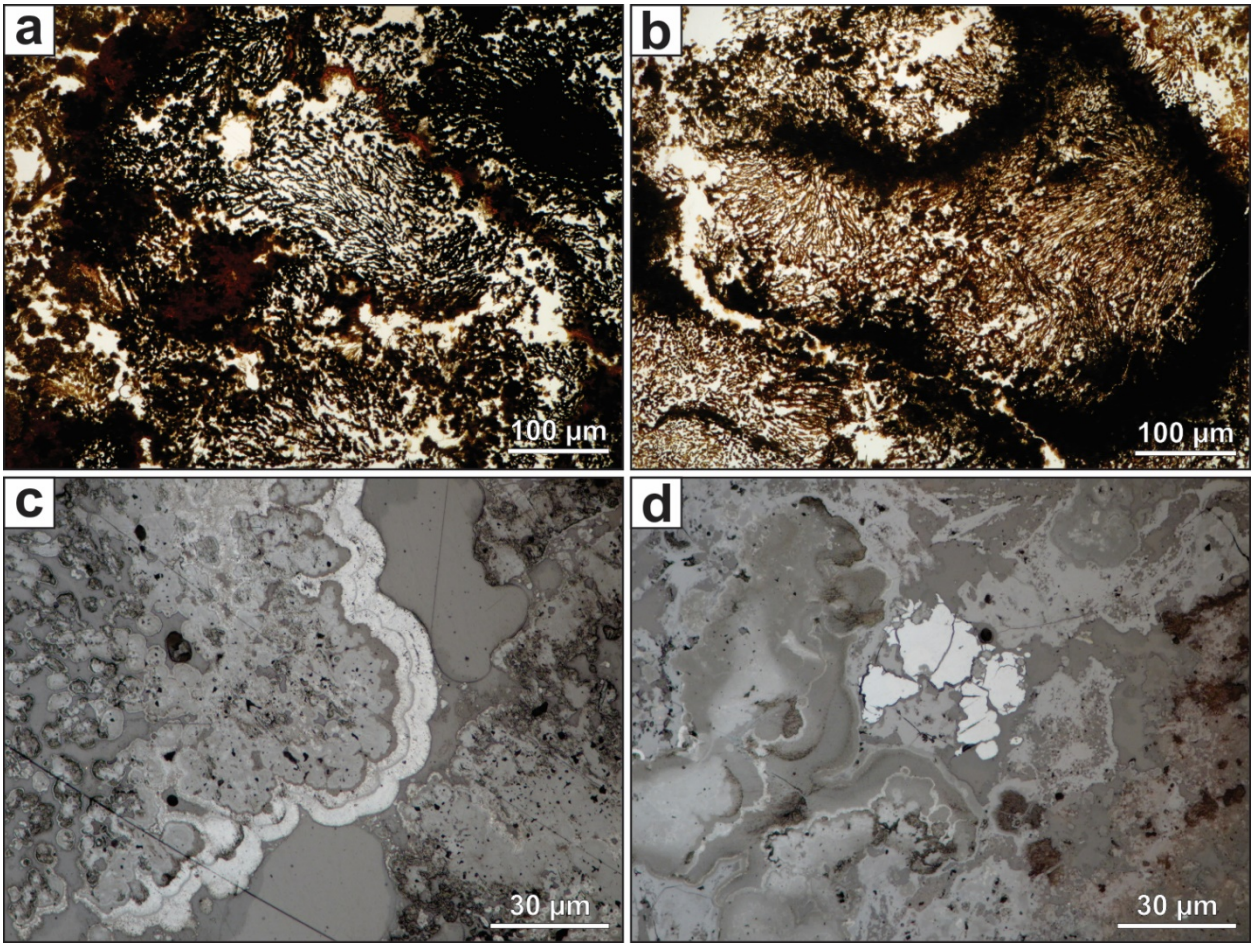
Intensely oxidized chimney fragment (orange-yellow-red FeOx and black MnOx). Original banding mostly preserved. 25% vugs. No primary sulphides observed. Minor hematite. Appears as a gossan stockwork.

Thin Section Description

This section has a porosity of 40% and contains multiple generations of dendritic to amorphous iron and manganese oxides. There are rare fine- to medium grained crystals of magnetite (<1%). Most of the oxides are unidentifiable, apart from a late generation of colloform pyrolusite that forms locally (2%). Overall, there are 40% iron oxides and 20% manganese oxides. No volcanic clasts or sulfides were identified.



Thin section scan of GMA13-025.



Photomicrographs of GMA13-025: ***(a)*** *transmitted light (PPL) showing dendritic MnOx and FeOx;* ***(b)*** *transmitted light (PPL) showing dendritic FeOx;* ***(c)*** *reflected light (PPL) showing bright generation of colloform pyrolusite;* ***(d)*** *reflected light (PPL) showing crystals of magnetite(?).*

SAMPLE: GMA13-026 **PARENT ID:** 595	**LOCATION:** 785157.4E/8649925.2N **WATER DEPTH:** 1147 mbsl

Video Description

Sample from boulder debris in dark grey rippled volcanic sand, very oxidized/altered.

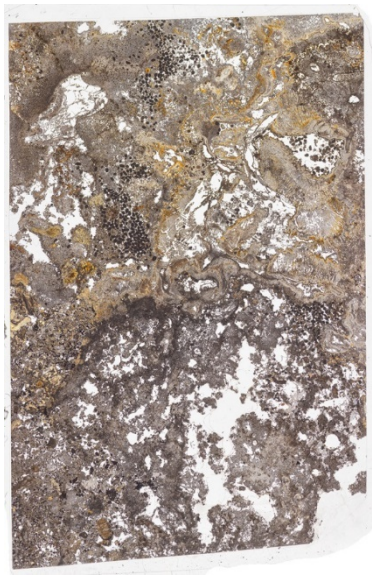
Hand Sample Description



Hand sample of GMA13-026.

Intensely oxidized and clay-altered chimney fragment, appears light grey & yellow. Primary finely-laminated colloform textures preserved. 25-30% vugs, filled by FeOx clay replacing bladed barite. Siliceous alteration in bands. Minor MnOx on outside of sample. Sample is friable.

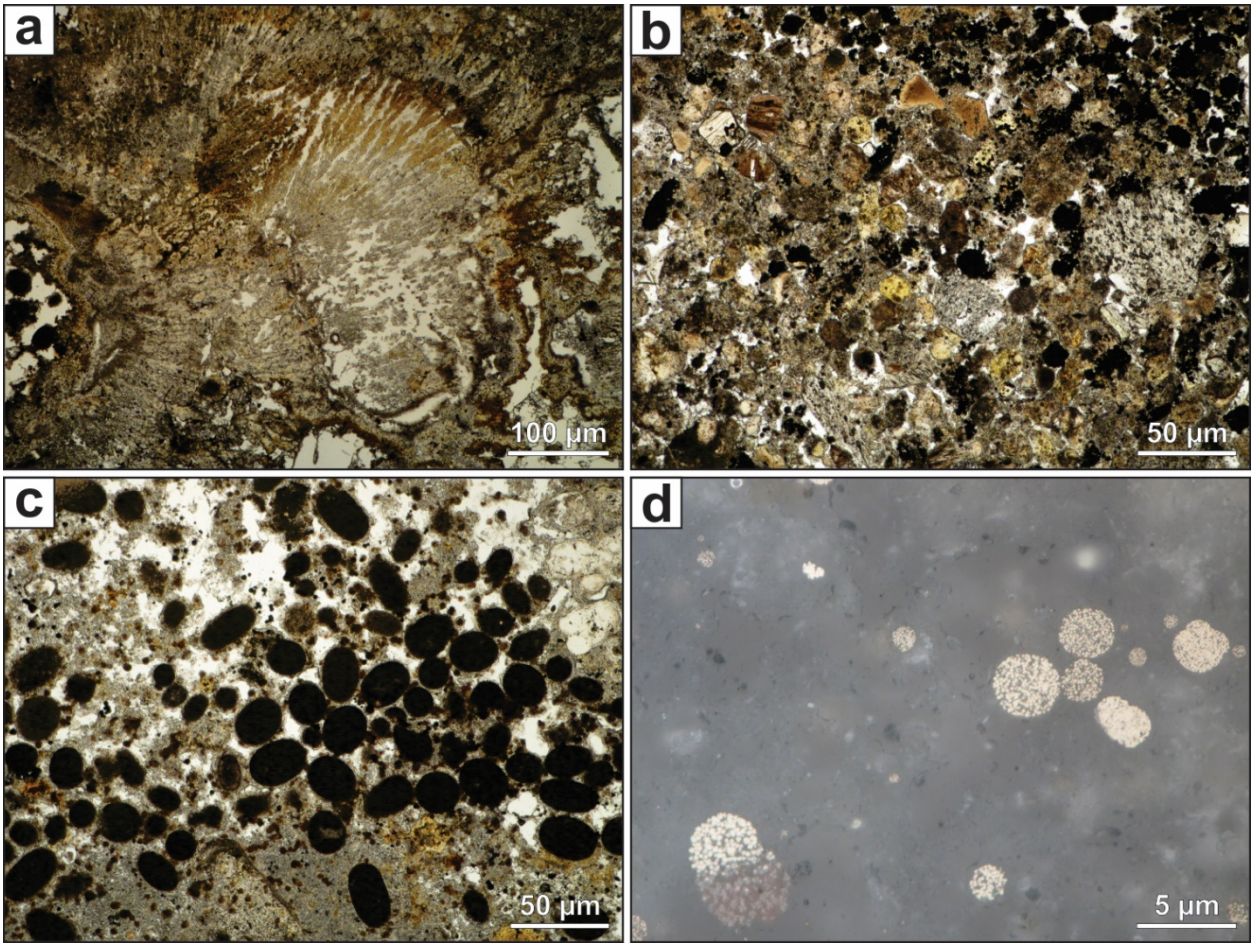
Thin Section Description



Thin section scan of GMA13-026.

This section has a porosity of 35-40%. It contains abundant amorphous silica that is locally dendritic, and is locally iron or manganese stained. This silica forms round features that appear to be relict worm tubes. Locally, there are egg-shaped concretions of manganese oxides. In one area there are abundant subangular to subrounded polymict volcanic fragments, including glassy, pumaceous, and microcrystalline fragments, and a few glass shards. These fragments appear unaltered. There is

minor dendritic to colloform amorphous iron oxyhydroxides that are light yellow-orange in color. Fine-grained framboidal pyrite is irregularly distributed throughout the section, further supporting a biological influence on theis sample. Overall, there are 5% volcanic fragments, 5% manganese oxides, 5-7% iron oxides, 2-3% framboidal pyrite, and 45% amorphous silica.



Photomicrographs of GMA13-026: ***(a)*** *transmitted light (PPL) showing dendritic amorphous silica, locally iron stained;* ***(b)*** *transmitted light (PPL) showing chaotic volcanic clasts with blebs of MnOx;* ***(c)*** *transmitted light (PPL) showing MnOx concretions;* ***(d)*** *reflected light (PPL) showing framboidal pyrite.*

SAMPLE: GMA13-037 **PARENT ID:** 687	**LOCATION:** 784572.3E/8649536.4N **WATER DEPTH:** 1145 mbsl

Video Description

Orange Fe oxidized outer surface of chimney spire.

Hand Sample Description



Hand sample of GMA13-037.

Extremely Si-altered chimney with original colloform banding / vugs preserved, 10-15% vugs. Jasperoidal (Si alteration of Hem). Sample is red-orange with dark core. Section across free-standing FeOx-Si chimney (inactive chimney complex). Sub-mm hematitic crust. Trace very fine grained Py around rims of vugs, minor fine grained Ba in vugs.

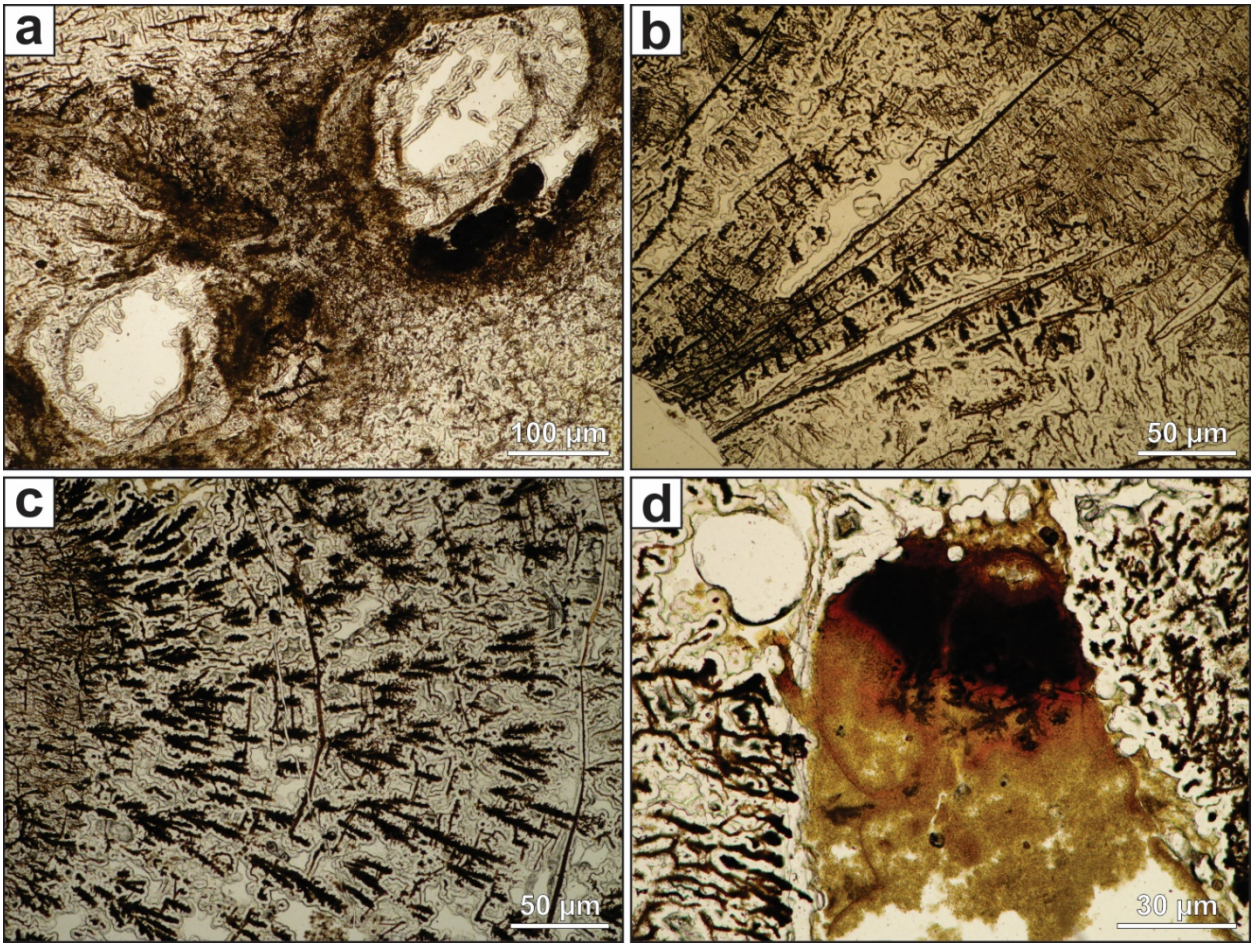
Thin Section Description

This section has a porosity of 35-40%. It consists of dendritic manganese oxides (5%) and amorphous iron oxides (2%) coated by abundant amorphous silica (50-55%). There are minor late amorphous iron oxides filling in pore space. The dendritic textures appear layered, with successive growth phases from a plane. There are abundant



Thin section scan of GMA13-037.

circular features that are locally lined by manganese oxide and infilled by additional silica, which are interpreted to have a biological origin. There are trace fine-grained crystals of sulfides (sphalerite, galena, Pb-As sulfosalts) irregularly disseminated, <1% overall. There are a few late crystals of coarse-grained barite after silica, ~1% overall.



Photomicrographs of GMA13-037: ***(a)*** *transmitted light (PPL) showing large holes surrounded by MnOx and amorphous silica, filled in by amorphous silica;* ***(b)*** *transmitted light (PPL) showing MnOx surrounded by amorphous silica;* ***(c)*** *transmitted light (PPL) showing dendritic MnOx in layers surrounded by amorphous silica;* ***(d)*** *transmitted light (PPL) showing late MnOx and amorphous FeOx.*

SAMPLE: GMA13-047 **PARENT ID:** 743	**LOCATION:** 784694.7E/8649577.9N **WATER DEPTH:** 1118 mbsl

Video Description

Oxide chimney fragment, blocky talus with scattered chimneys, active venting patchy.

Hand Sample Description

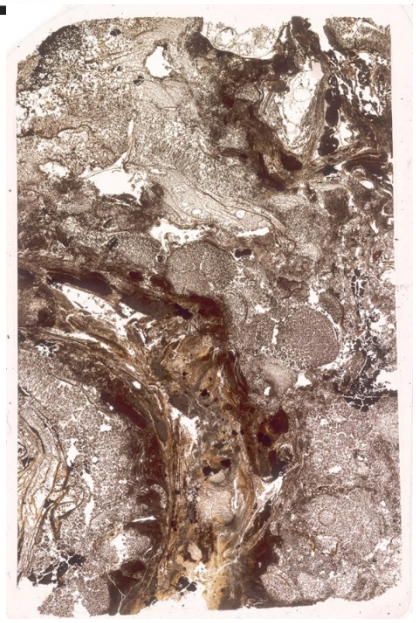


Very altered Fe-Ox chimney sample, from top of chimney. Very friable. Minor MnOx. Worm casts. Chimney textures. Relict Ba altered to clay throughout sample.

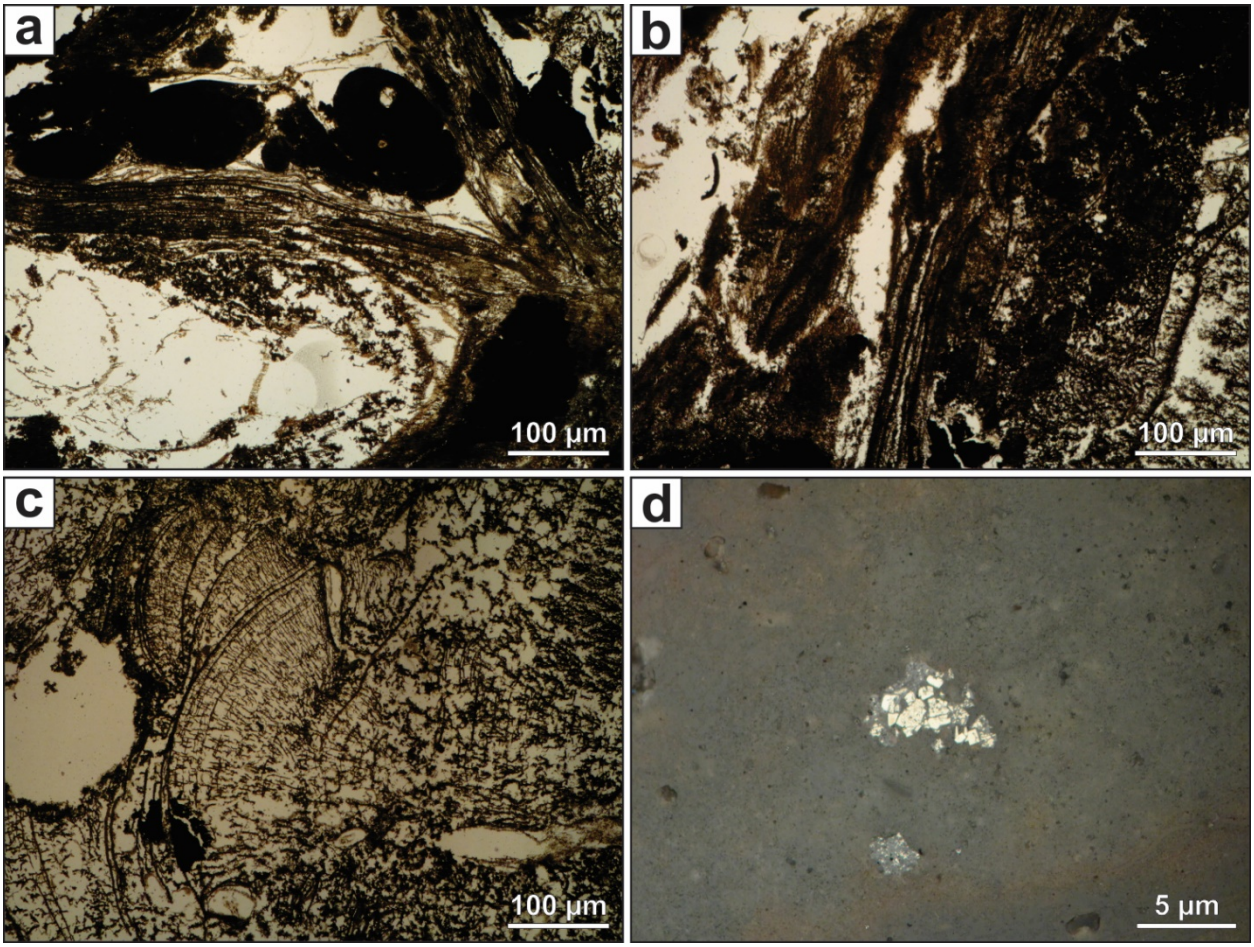
Hand sample of GMA13-047.

Thin Section Description

This section has a porosity of 35-40%. It contains abundant dendritic to wispy manganese oxides (%) grown in layers, and local manganese oxide concretions. Irregular iron oxides line major conduits in the sample, which are further infilled by iron and manganese oxides. The wispy areas may be associated with iron-stained silica, although none could be confidently identified. There are a few trace crystals of pyrite partly oxidized to goethite (<<1%). Overall there is 40% manganese oxides and 20% iron oxides. None of the oxides could be identified.



Thin section scan of GMA13-047.



Photomicrographs of GMA13-047: ***(a)*** *transmitted light (PPL) showing MnOx and wispy MnOx;* ***(b)*** *transmitted light (PPL) showing wispy MnOx and FeOx;* ***(c)*** *transmitted light (PPL) dendritic MnOx in layers;* ***(d)*** *reflected light (PPL) showing pyrite altered to goethite(?).*

SAMPLE: GMA13-054 **PARENT ID:** 723	**LOCATION:** 784671.9E/8649531.5N **WATER DEPTH:** 1137 mbsl

Video Description

Protruding chimney from cliff, oxide altered exterior sample.

Hand Sample Description

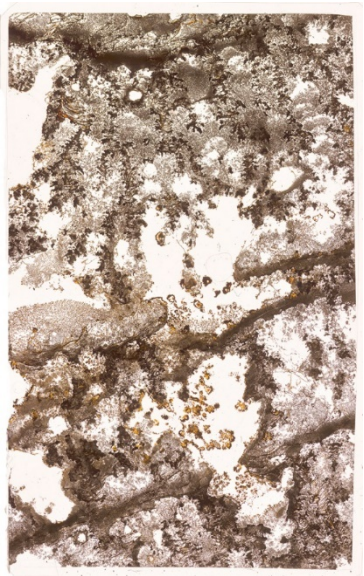


Hand sample of GMA13-054.

Extremely Fe-oxidized fragment from inactive chimney complex/mound. Contains abundant FeOx+clay, very friable, original colloform banding/vugs still visible. 20% vugs. Sample is bright orange. Pseudo-dendritic textures. Minor MnOx. Possible worm casts.

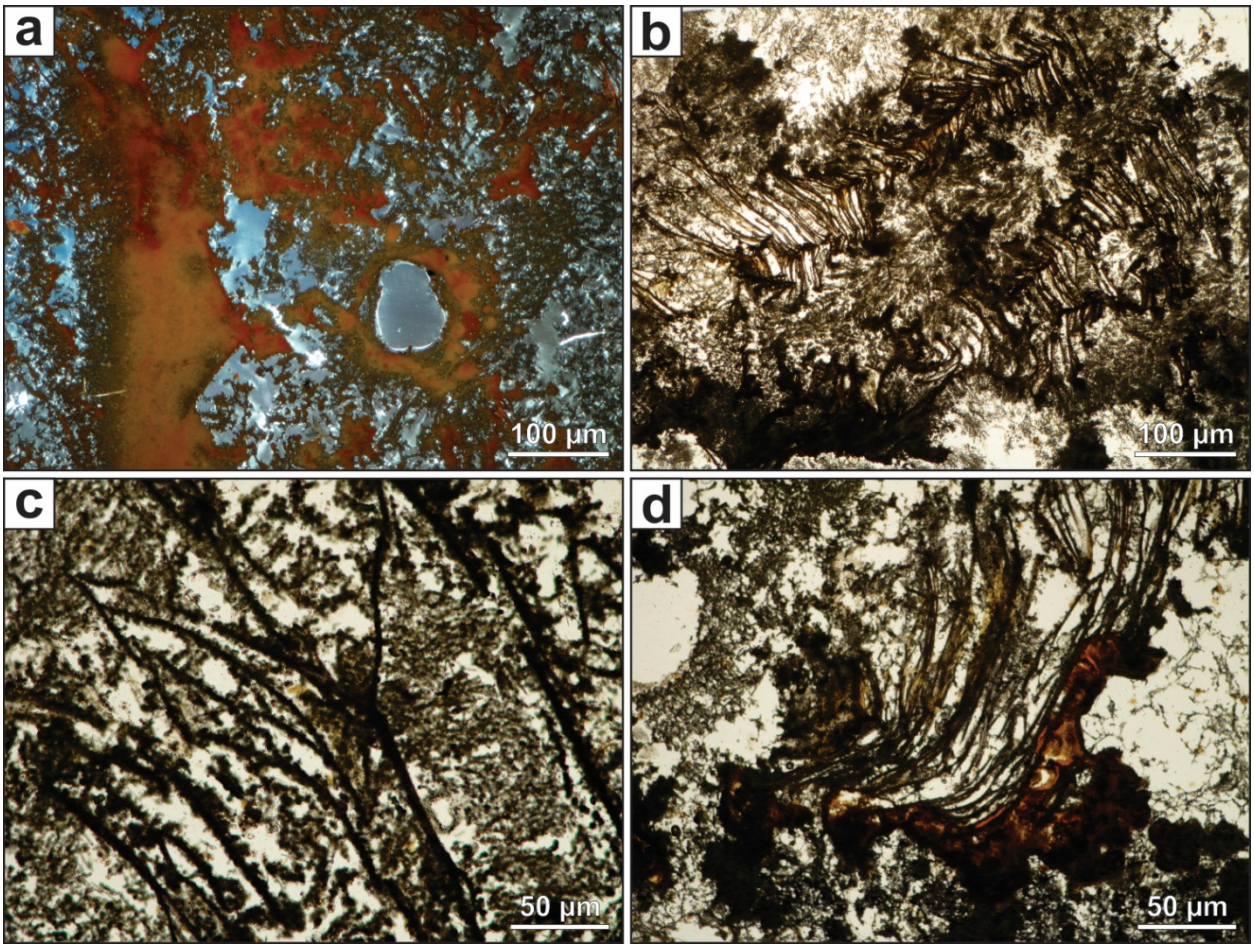
Thin Section Description

This section has a porosity of 50%. It also contains abundant fine-grained dendritic manganese oxides (%), with lesser amounts of iron oxides (30%), and minor late amorphous iron oxides (15%). There are locally feather-like textures of the oxides. There are a few holes that are



Thin section scan of GMA13-054.

interpreted to have a biological origin. There is a very fine coating of amorphous silica covering the dendrites, 3-5% overall. Areas of intergrown iron and manganese oxides are most easily distinguished in polarized light. No minerals appeared in reflected light.



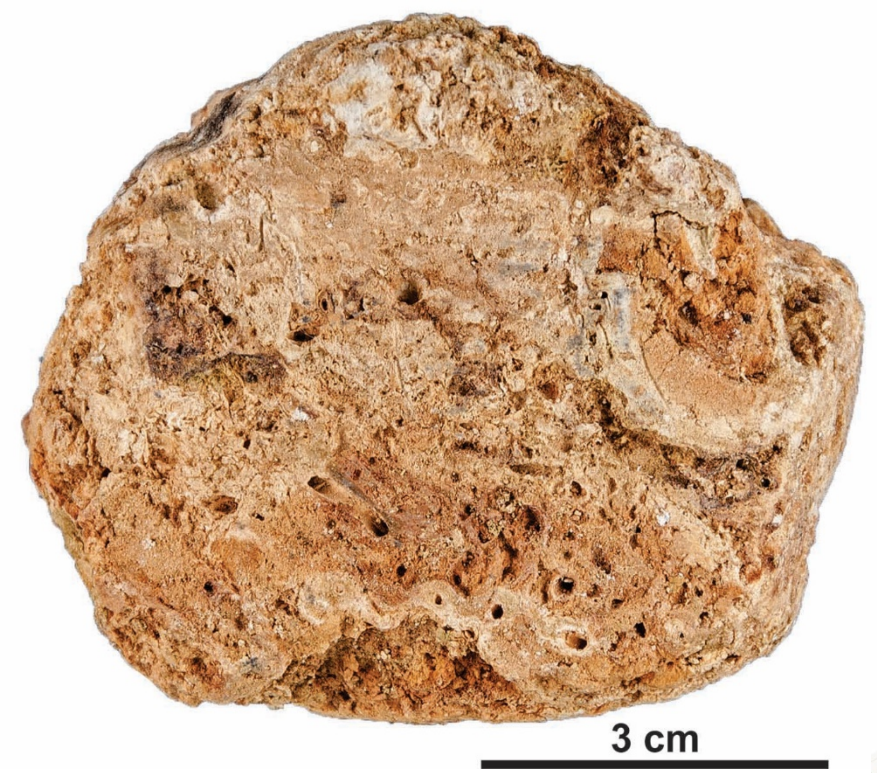
Photomicrographs of GMA13-054: ***(a)*** *transmitted light (XPL) distinguishing red FeOx from dark MnOx;* ***(b)*** *transmitted light (PPL) showing feature-like MnOx with minor FeOx;* ***(c)*** *transmitted light (PPL) showing close-up of MnOx feathers with dendritic textures;* ***(d)*** *transmitted light (PPL) showing wispy MnOx and late colloform amorphous FeOx.*

SAMPLE: GMA13-055 **PARENT ID:** 722	**LOCATION:** 784675.8E/8649494.2N **WATER DEPTH:** 1143 mbsl

Video Description

Irregular boulder - orange FeOx crusting.

Hand Sample Description



Strongly iron oxidized fragment from the base of a knobby chimney. Extremely friable, mostly FeOx + Clays, minor silicification. Minor MnOx. Heavily bioturbated.

Hand sample of GMA13-055.

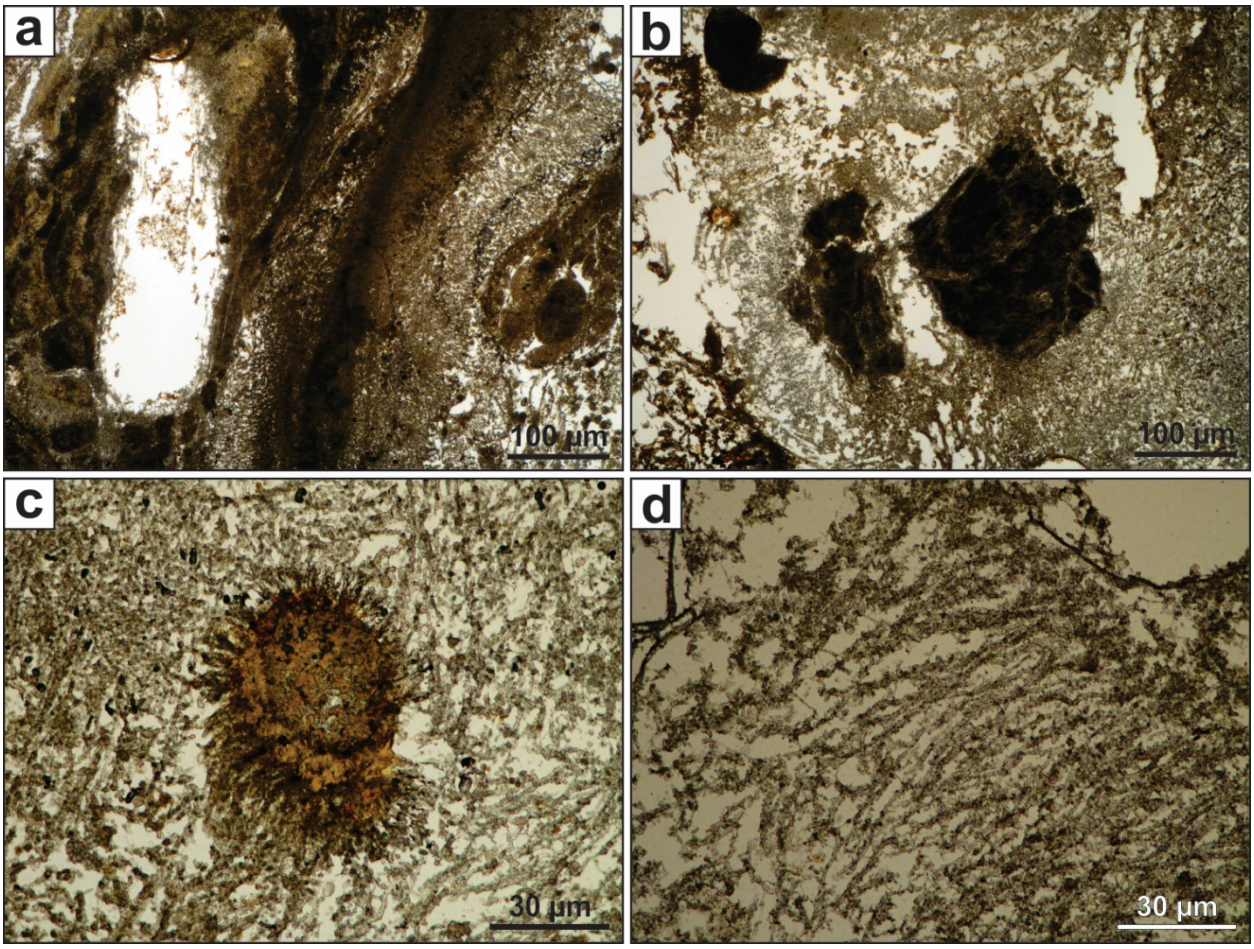
Thin Section Description



Thin section scan of GMA13-055.

This section also has a porosity of ~50-55%. It is dominated by amorphous silica (40%) that displays dendritic to wispy textures, and is variably stained by iron oxides (5%) and manganese oxides (2-3%). Large holes are interpreted to have a biological origin. There are a few blebs of amorphous iron oxides that the amorphous silica grows off of. There is one angular square clast in the middle that appears to be manganese oxide, but it could have a volcanic origin. Bands of iron and

manganese oxides are the most abundant near the bottom of the section. No minerals are revealed in reflected light.



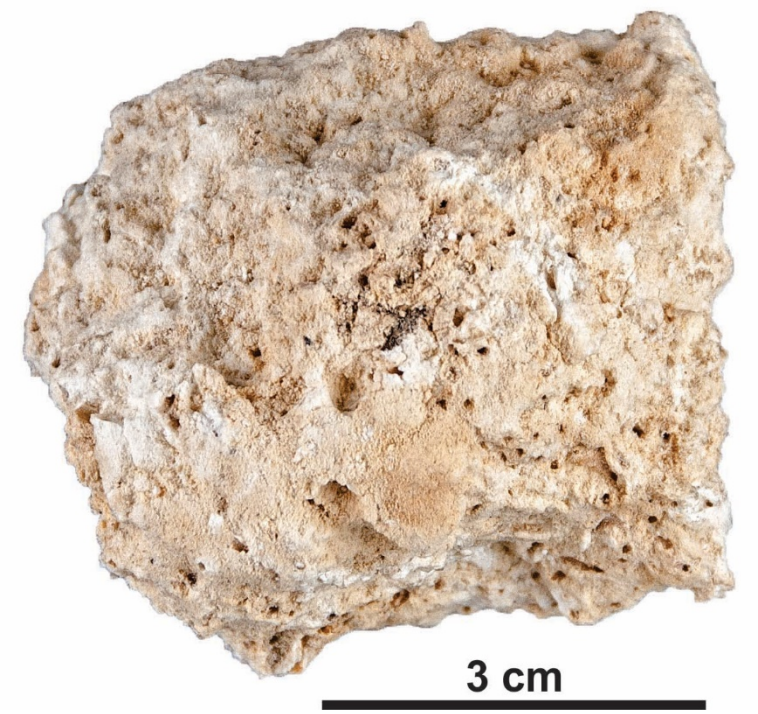
Photomicrographs of GMA13-055: ***(a)*** *transmitted light (PPL) showing banded oxides and a large hole, surrounded by amorphous silica;* ***(b)*** *transmitted light (PPL) showing dark colored clast of MnOx surrounded by Fe-Mn-stained amorphous silica;* ***(c)*** *transmitted light (PPL) showing amorphous FeOx, with amorphous silica dendrites growing off of it;* ***(d)*** *transmitted light (PPL) showing close-up of amorphous silica dendrites with minor oxides.*

SAMPLE: GMA13-056 **PARENT ID:** 725	**LOCATION:** 784607.8E/8649727.5N **WATER DEPTH:** 1107 mbsl

Video Description

Chimney with oxide and knobbly textures - white looking sample of bleached rind.

Hand Sample Description

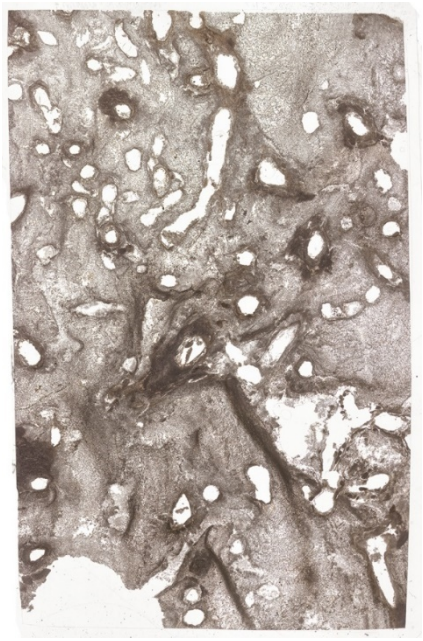


Light cream-orange rock with very fine grained disseminated Py, abundant holes (worm casts). Sample is soft, friable, consists of clay and chalcedony. Anhydrite? Fossiliferous.

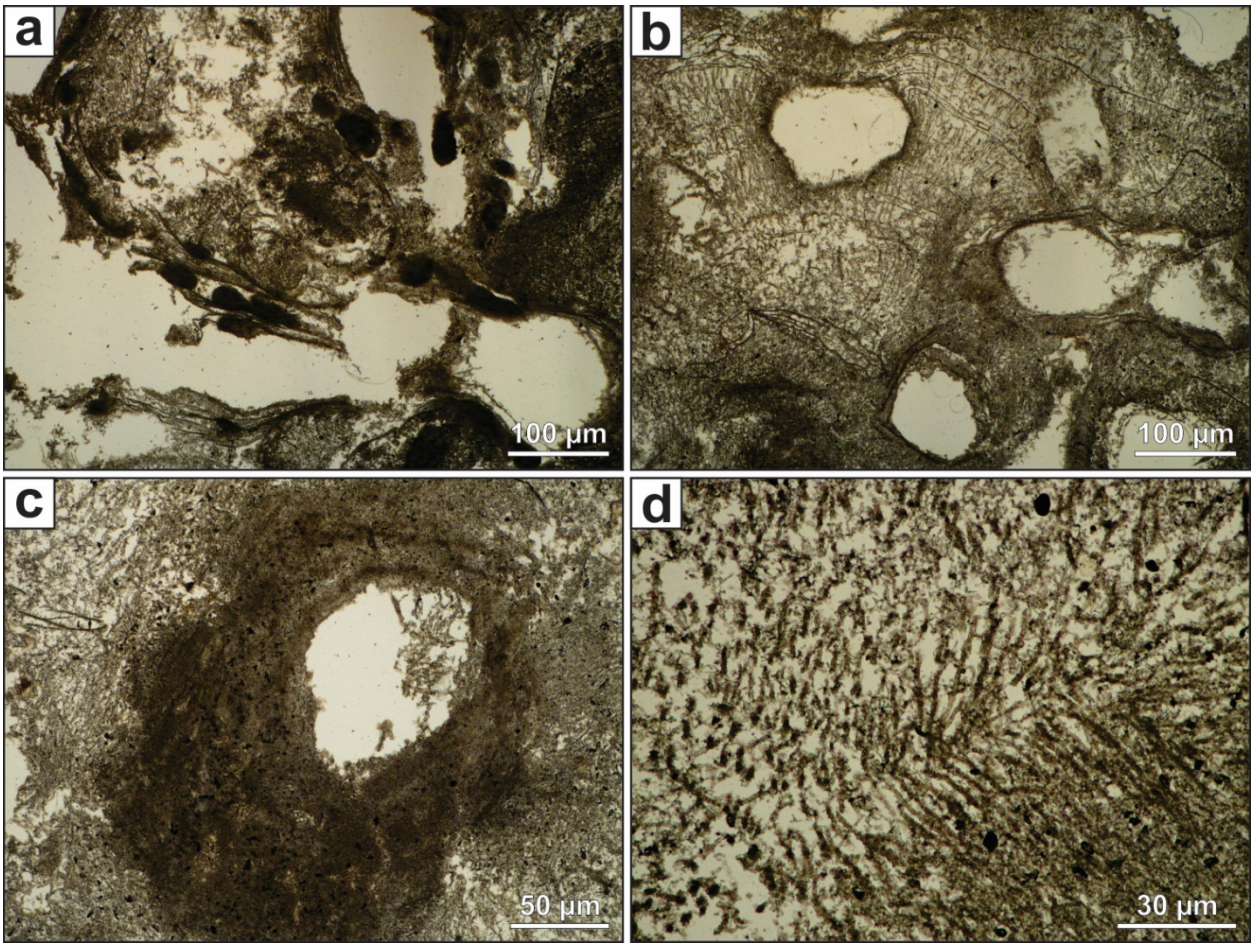
Hand sample of GMA13-056.

Thin Section Description

This section has a porosity of 50%. It is dominated by manganese- and iron oxide-stained amorphous silica that forms in dendritic textures. There are abundant holes of presumed biological origin that are lined by manganese oxides. There are areas of wispy oxides and silica. There are a few concretions of manganese oxide. There are a few late crystals of medium-grained barite (1%). No minerals were observed in reflected light. Overall, there is ~5% MnOx, ~5% FeOx, and 40% amorphous silica.



Thin section scan of GMA13-056.



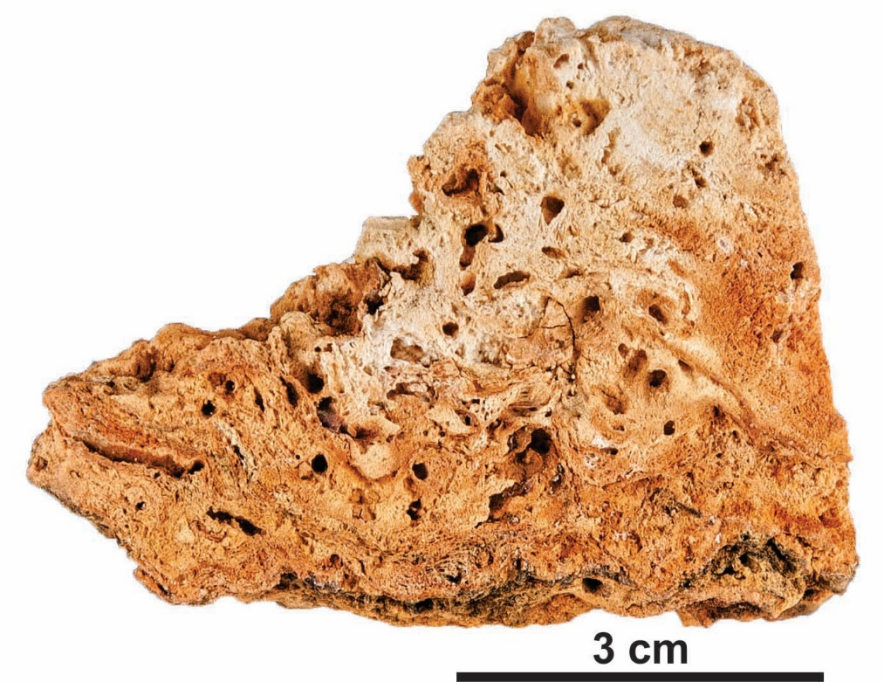
Photomicrographs of GMA13-056: ***(a)*** *transmitted light (PPL) showing irregular wispy MnOx with amorphous silica and a few dark concretions of MnOx;* ***(b)*** *transmitted light (PPL) showing numerous holes, and dendritic amorphous silica associated with MnOx growing in layers;* ***(c)*** *transmitted light (PPL) showing hole surrounded by oxides;* ***(d)*** *transmitted light (PPL) showing close-up of amorphous silica dendrites with minor MnOx.*

SAMPLE: GMA13-059 **PARENT ID:** 734	**LOCATION:** 784715.6E/8649686N **WATER DEPTH:** 1085 mbsl

Video Description

Oxidized top of bulbous chimney protruding through altered cemented talus / indurated crust.

Hand Sample Description

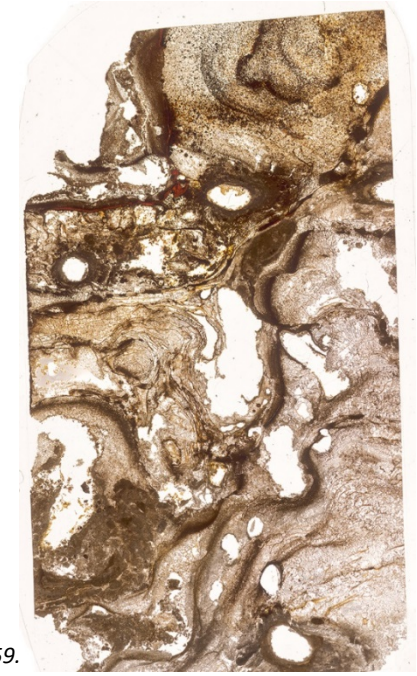


Collected from chimney-like protrusion. Sample is FeOx+clay-altered rock, very friable, minor silicification, thin MnOx crust. Abundant worm casts(?). Banded.

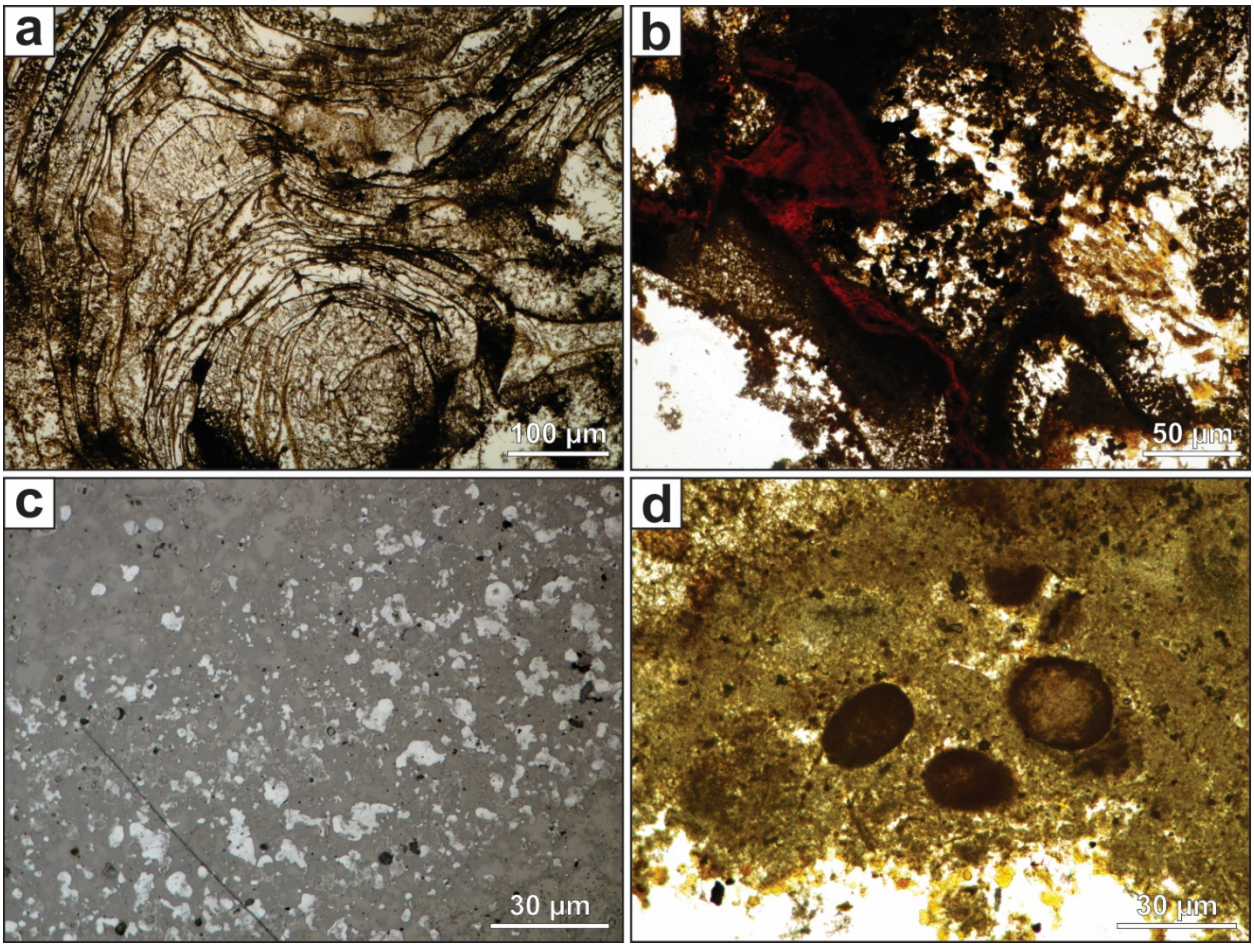
Hand sample of GMA13-059.

Thin Section Description

This section has a porosity of 40-50%. It is dominated by banded/wispy to dendritic manganese and iron oxides coated in amorphous silica, with an overall irregularly banded appearance. There are local accumulations of manganese concretions. There are abundant holes that are locally lined by manganese oxides, of interpreted biological origin. There is minor late amorphous iron oxyhydroxides lining some holes. There are a few horizons where the iron oxides are magnetite, identified in reflected light. Trace galena was found in one hole (<1%). Overall, there is 25-30% silica, 15-20% manganese oxides, and 10% iron oxides.



Thin section scan of GMA13-059.



Photomicrographs of GMA13-059: ***(a)*** *transmitted light (PPL) showing wispy, layered MnOx;* ***(b)*** *transmitted light (PPL) showing banded amorphous Fe and irregular MnOx;* ***(c)*** *reflected light (PPL) showing magnetite(?) crystals along one horizon;* ***(d)*** *transmitted light (PPL) showing MnOx concretions surrounded by Fe-stained amorphous silica.*

Appendix G

Petrographic Reports – Altered Volcaniclastic Rocks

List of Samples

ROV GRAB SAMPLES 659

SAMPLE: GMA13-064 659

DRILLCORE SAMPLES 660

SAMPLE: MA13-005 660

SAMPLE: MA13-006 662

SAMPLE: MA13-014 665

SAMPLE: MA13-015 667

SAMPLE: MA13-016 669

SAMPLE: MA13-019 672

SAMPLE: MA13-020 674

SAMPLE: MA13-023 675

SAMPLE: MA13-024 677

SAMPLE: MA13-025 680

SAMPLE: MA13-026 682

SAMPLE: MA13-027 684

SAMPLE: MA13-034 685

SAMPLE: MA13-035 687

SAMPLE: MA13-036 689

SAMPLE: MA13-038 692

SAMPLE: MA13-039 693

SAMPLE: MA13-040 696

SAMPLE: MA13-044 699

SAMPLE: MA13-045 701

SAMPLE: MA13-050 704

SAMPLE: MA13-051 707
SAMPLE: MA13-052 709
SAMPLE: MA13-053 712
SAMPLE: MA13-056 715
SAMPLE: MA13-057 717
SAMPLE: MA13-058 721
SAMPLE: MA13-062 723
SAMPLE: MA13-063 726
SAMPLE: MA13-064 727
SAMPLE: MA13-067 728
SAMPLE: MA13-068 731
SAMPLE: MA13-069 733
SAMPLE: MA13-072 735
SAMPLE: MA13-073 738
SAMPLE: MA13-074 741
SAMPLE: MA13-075 742
SAMPLE: MA13-078 745
SAMPLE: MA13-079 746
SAMPLE: MA13-080 747
SAMPLE: MA13-081 748
SAMPLE: MA13-082 749
SAMPLE: MA13-083 751
SAMPLE: MA13-084 752
SAMPLE: MA13-085 753
SAMPLE: MA13-086 754
SAMPLE: MA13-087 757
SAMPLE: MA13-088 760
SAMPLE: MA13-089 763
SAMPLE: MA13-090 766
SAMPLE: MA13-091 769
SAMPLE: MA13-092 770
SAMPLE: MA13-095 771

SAMPLE: MA13-099 772
SAMPLE: P002 773
SAMPLE: P003 774
SAMPLE: P004 775
SAMPLE: P005 776
SAMPLE: P012 777
SAMPLE: P013 780
SAMPLE: P014 781
SAMPLE: P020 784
SAMPLE: P021 785
SAMPLE: P022 788
SAMPLE: P023 789
SAMPLE: P024 790
SAMPLE: P025 791

Notes:

Mineral abbreviations after Whitney and Evans (2010). Detailed whole rock geochemistry (this study) is reported in Appendix K. SWIR results are reported in Appendix O and XRD results are reported in Appendix P.

Cham = chamosite; Corr = corrensite; I/S = illite/smectite; Mnt = montmorillonite; Non = nontronite; Pl = plagioclase; Py = pyrite

ROV GRAB SAMPLES

SAMPLE: GMA13-064 **PARENT ID:** 091	**LOCATION:** 781606.9E/8650201.1N (Big Starfish) **WATER DEPTH:** 630 mbsl

Mineralogy

N/A

Hand Sample Description



Clay-altered polymict volcaniclastic pebble breccia ("agglomerate"), clast supported with 70% clasts. Bimodal distribution of clast sizes: mm-scale and 5-15 mm (few clasts up to 4.5 cm). Subangular to angular, poorly sorted. Consists of variably altered clasts, some unaltered vesicular mafic volcanics. Some banded clasts. Most clasts have altered rims. Silica cement. Looks similar to altered footwall in core, less intense clay alteration.

Hand sample of GMA13-064.

Alteration Summary: Viariable alteration of clasts, late iron oxide
Interpretation: Transported/reworked volcanic breccia
Name: Variably clay-altered polymict clast-supported volcanic tephra, silicified

DRILLCORE SAMPLES

SAMPLE: MA13-005 **PARENT ID:** 2551/2552 **SAMPLE DEPTH:** 5.06-5.21 mbsf	**DRILLHOLE:** TKAD030 **DRILLHOLE LOCATION:** 784742.79E/8649607.79N **WATER DEPTH:** 1107.72 mbsl

Mineralogy

SWIR (powdered clast): Paragonite, montmorillonite(?)
XRD (clay-sized fraction): Nontronite, rectorite, illite
Assemblage: I/S + Py

Hand Sample Description

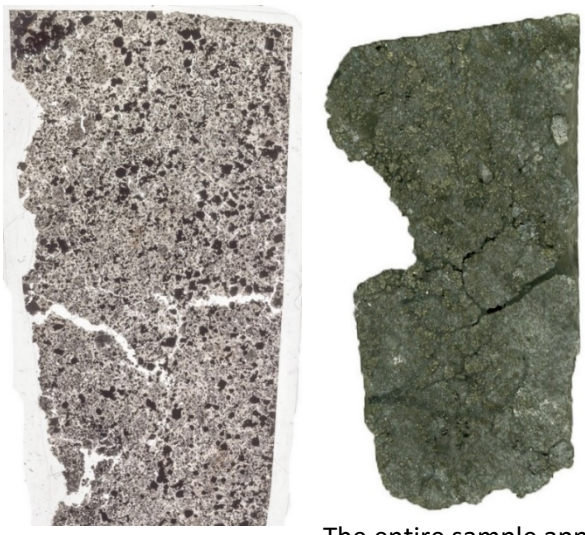


Hand sample of MA13-005.

Unconsolidated massive clay- to sand-sized sediment with abundant disseminated pyrite (10-20% pyrite), with fine-grained clasts (difficult to distinguish). There is pervasive very fine-grained white clay alteration. There is 2% porosity.

Thin Section Description

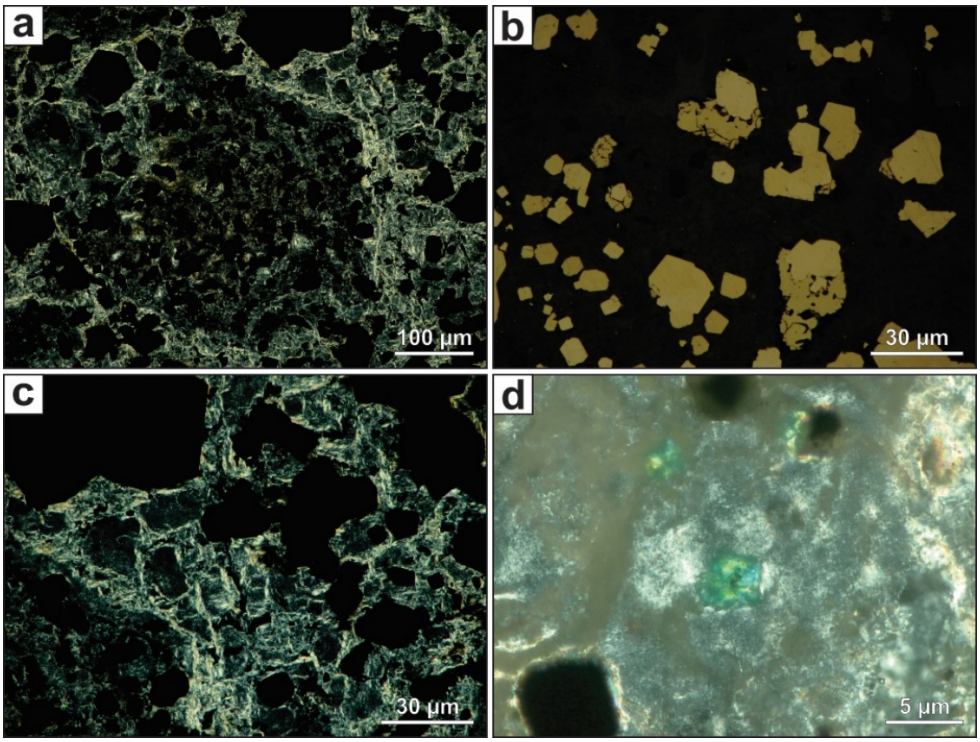
This section contains abundant fine- to medium-grained subhedral to euhedral pyrite disseminated throughout, ~20% overall, followed by minor chalcopyrite, irregularly distributed, ~3-5% overall, that has been slightly altered to chalcocite (<1%). These sulfides occur in both clasts and matrix, with a slightly higher abundance in the clasts. There is very minor iron oxide alteration associated with some of the pyrite. The clasts are difficult to distinguish from the matrix, as both are intensely altered to fine-grained clays (illite?). The clasts have a slightly darker color and is finer-grained than the matrix.



Thin section scan (left) and puck (right) of sample MA13-005.

The sample appears to be matrix-supported with ~40-50 % clasts. The clasts are subangular to rounded, with local jigsaw-fit brecciation. Clay alteration is intense and pervasive throughout, with no difference between the clast rims and the core. There are no preserved relict minerals. Some of the larger clasts have relict vesicles infilled by inward-growing fibrous clays. Rare vesicle-filling chlorite(?) (or atacamite?) is locally present. The clasts are mostly fine-grained and show no bedding. There is <1% anhydrite, comprised of a few medium-grained crystals occurring locally. The entire sample appears uncemented, with a total porosity of 10%. No glass shards or crystal fragments were identified.

Paragenesis: Volcanic clasts + ash(?) matrix → intense pervasive illite alteration → pyrite → chalcopyrite → FeOx + atacamite(?)
Interpretation: Mineralized hyaloclastite (monomict, jigsaw-fit brecciation)
Descriptive Lithological Name: Pervasively illitized massive monomict matrix-supported haloclastite sandstone, mineralized
Descriptive Alteration Facies: Intense, pervasive illite, abundant pyrite (clasts and matrix)



Photomicrographs of GMA13-005: (a) transmitted light (XPL) showing intensely clay-altered volcanic clast with clay-altered ash(?) matrix; (b) reflected light (PPL) showing pyrite surrounded by chalopyrite; (c) transmitted light (XPL) showing coarse-grained alteration minerals in the matrix; (d) transmitted light (XPL) showing close-up of chlorite filling in vesicles.

SAMPLE: *MA13-006* ***PARENT ID:*** *2554* ***SAMPLE DEPTH:*** *6.45-6.60 mbsf*	***DRILLHOLE:*** *TKAD030* ***DRILLHOLE LOCATION:*** *784742.79E/8649607.79N* ***WATER DEPTH:*** *1107.72 mbsl*

Mineralogy

SWIR (powdered clast): Paragonite, montmorillonite(?)
XRD (clay-sized fraction): Rectorite, I/S, illite
Assemblage: I/S + Py

Hand Sample Description

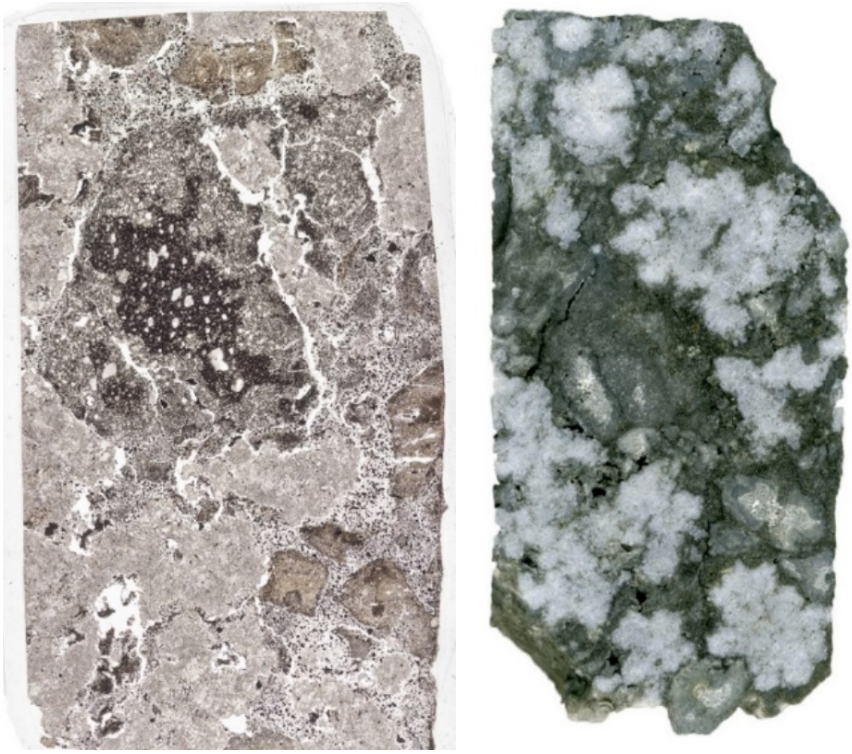


Hand sample of MA13-006.

This sample is a monomict matrix-supported volcanic breccia with rounded to sub-rounded grey-white clay-altered clasts and medium grey anhydrite patchy infill. There is 4% pyrite overall. There is weak bedding of the clasts. There is 30% clasts, which are clay-altered volcanics, with color ranging from grey to white (heterogeneous), <1.0-25.0 mm, poor sorting, high-sphericity. The clasts are aphanitic with a few sub-mm vesicles, 1% pyrite. There is 3% porosity.

Thin Section Description

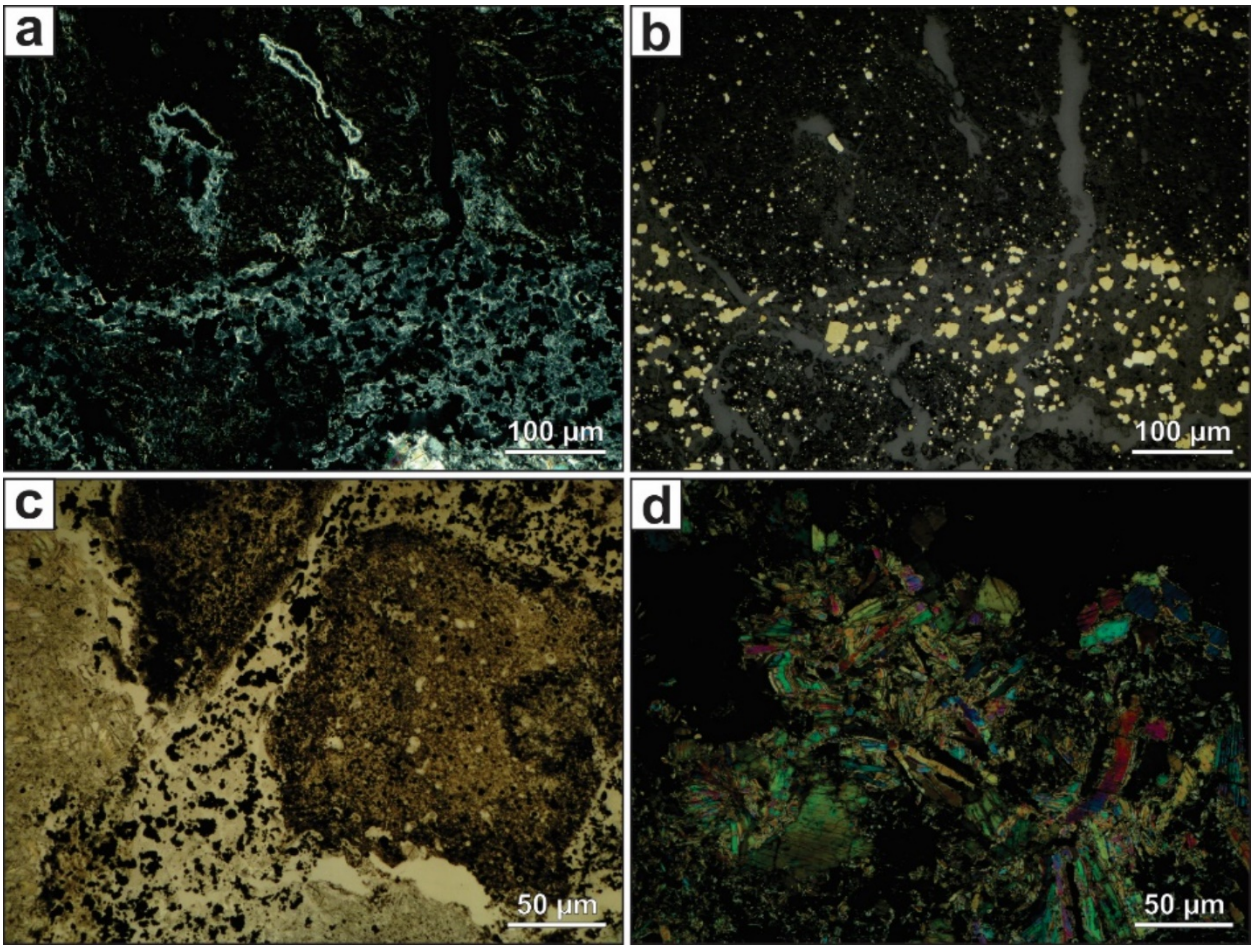
This sample is coarser-grained than MA13-005, with monomict subangular blocky clasts up to 20 mm wide, matrix-supported. The clasts are very vesicular, up to 20% vesicles that only locally show flow foliation. Several clast margins are curvi-planar. The clasts are pervasively altered to fine-grained clay (illite?), with clay lining vesicles. Weak iron oxide alteration occurs pervasively throught the clasts.



Thin section scan (left) and puck (right) of MA13-006.

There are rare relict plagioclase phenocrysts that have been entirely altered to sericite. The largest clast has an irregular core of darker color, possibly reflecting the difference between the original glassy rim and finely-crystalline core. This clast has less iron oxide compared to the other clasts and a slightly different color, but the original composition may be the same. The clasts are supported within an intensely altered matrix with coarser-grained illite(?). Very fine to fine-grained pyrite is disseminated throughout the clasts, making up 5-10% of the clasts. Coarser-grained and more abundant pyrite occurs throughout the altered matrix making up 15-20% of the matrix. Irregular patches of fine- to coarse-grained anhydrite occur irregularly throughout the sample, cementing it. The anhydrite has been weakly altered to gypsum, occurring locally, with 1% gypsum overall. The overall porosity is 5%, with 20% clasts, 35% clay-altered matrix, and 40% sulfate.

Paragenesis: Volcanic clasts + ash(?) matrix → pervasive alteration to illite → pyrite → iron oxide → patchy anhydrite → local hydration to gypsum
Interpretation: Hyaloclastite (monomict, jigsaw-fit blocky clasts), cemented by anhydrite
Descriptive Lithological Name: Pervasively illitized monomict matrix-supported hyaloclastite breccia, cemented
Descriptive Alteration Facies: Intense, pervasive illite, abundant pyrite (clasts and matrix)



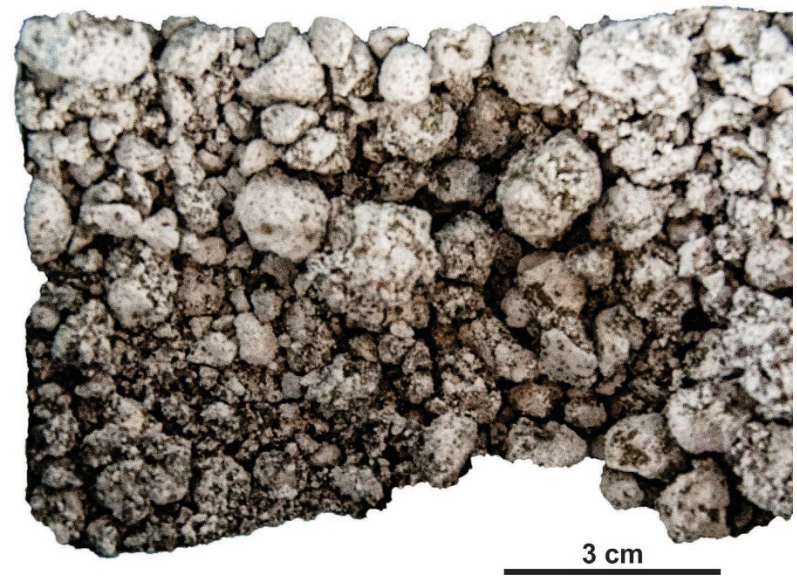
Photomicrographs of GMA13-006: (a) transmitted light (XPL) showing intensely clay-altered volcanic clast with clay-altered ash(?) matrix; (b) reflected light (PPL) showing fine-grained pyrite in the volcanic clasts and coarse-grained pyrite in the matrix; (c) transmitted light (PPL) showing light-brown weakly vesicular subangular clasts; (d) transmitted light (XPL) recrystallized anhydrite.

SAMPLE: MA13-014 **PARENT ID:** 2431 **SAMPLE DEPTH:** 3.00-3.10 mbsf	**DRILLHOLE:** TKAD018 **DRILLHOLE LOCATION:** 784756.43E/8649604.73N **WATER DEPTH:** 1110.18 mbsl

Mineralogy

XRD (clay-sized fraction): Montmorillonite, I/S, illite, pyrite, anhydrite
Assemblage: I/S + Py

Hand Sample Description



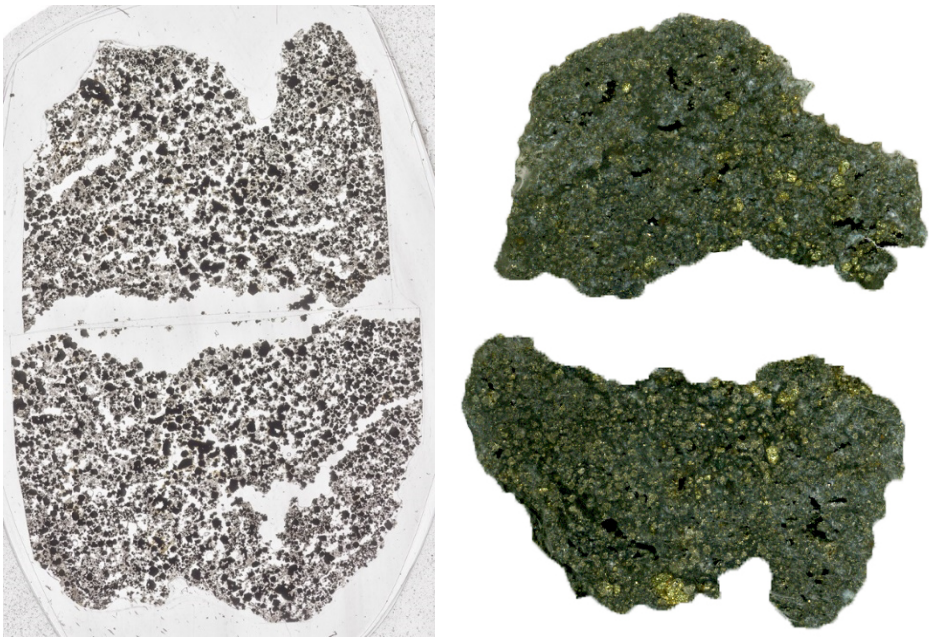
Unconsolidated white clay-sized sediment with abundant disseminated pyrite. The clay is lumpy but there are no obvious clasts. There is 30% pyrite overall, with minor patchy iron oxyhydroxides. There is 4% porosity.

Hand sample of MA13-014.

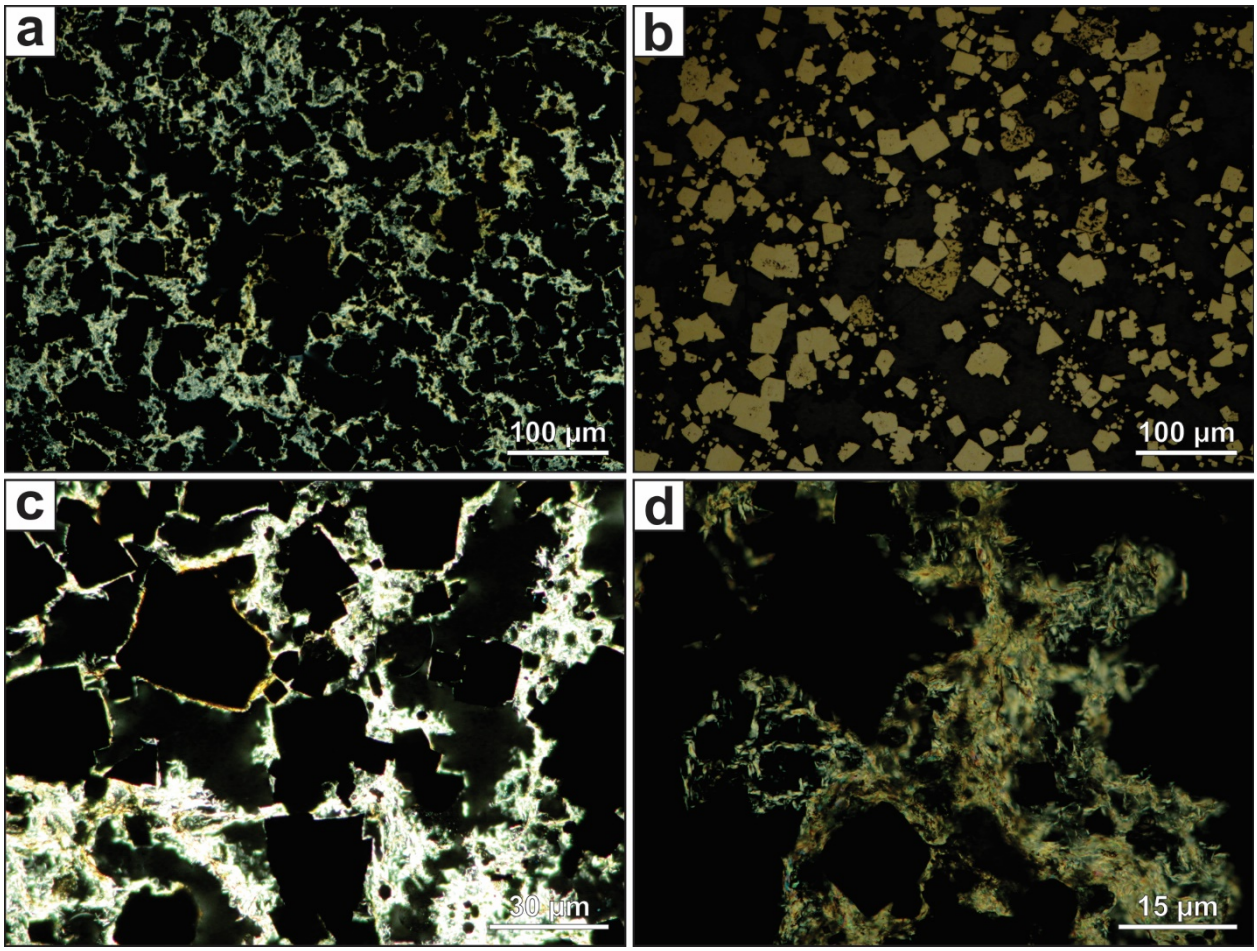
Thin Section Description

This sample is similar to MA13-005. It contains abundant fine- to coarse-grained subhedral to euhedral pyrite, 35% overall, followed by chalcopyrite, 5% overall. The section is very porous, with 35% overall porosity. The remaining matrix is very fine-grained clay (illite?, 25%), locally fibrous that is intense, pervasive. There are no relict minerals and no identifiable clasts. The sample is not cemented (no sulfates or silica). There are no other textures (massive facies).

Paragenesis: Volcanic mudstone → illite → pyrite → chalcopyrite → FeOx
Interpretation: Unknown origin: volcanic mudstone, mineralized
Descriptive Lithological Name: Pervasively illitized massive volcanic mudstone, mineralized
Descriptive Alteration Facies: Pervasive, intense illite, abundant pyrite



Thin section (left) and puck (right) of MA13-014.



Photomicrographs of GMA13-014: (a) transmitted light (XPL) showing intensely clay-altered ash(?) matrix; (b) reflected light (PPL) showing coarse-grained pyrite in the matrix surrounded by chalcopyrite; (c) transmitted light (XPL) showing coarse-grained alteration minerals in the matrix; (d) transmitted light (XPL) showing coarse-grained alteration minerals in the matrix.

SAMPLE: MA13-015 **PARENT ID:** 2433 **SAMPLE DEPTH:** 5.00-5.10 mbsf	**DRILLHOLE:** TKAD018 **DRILLHOLE LOCATION:** 784756.43E/8649604.73N **WATER DEPTH:** 1110.18 mbsl

Mineralogy

SWIR (powdered clast): Gypsum, paragonite
XRD (clay-sized fraction): Montmorillonite, rectorite, I/S, illite, hematite, anhydrite
Assemblage: I/S + Py

Hand Sample Description



Hand sample of MA13-015.

Chaotic monomict clast-supported volcanic breccia with small white-light grey clasts and a similar color clay matrix, yellow patches (iron oxide?), weakly cemented by patchy white anhydrite. It is difficult to distinguish the matrix from the clasts. There is 3% pyrite. There are 90% white to light-grey clasts with strong pervasive clay, patchy yellow iron oxide, <1.0-5.0 mm, poor sorting, subrounded shape, moderate sphericity, and a random fabric. There are abundant preserved sub-mm vesicles. There is 6% porosity.

Thin Section Description

This section contains a monomict matrix-supported breccia with ~15% pervasively-altered volcanic clasts, subrounded to subangular, variably vesicular, mostly aphanitic with up to 5% relict phenocrysts. The phenocrysts occur in the clast centers, surrounded by a dark brown rim, likely reflecting the change between a crystalline interior and glassy margin. The vesicles and clasts outline a weak flow foliation in some (but not all) clasts. The clast margins are irregular, jagged, and are distinguished from the matrix by their color, which ranges from light brown (minor FeOx) to dark grey. The clasts range in size from 2-6 mm. The clasts are pervasively and intensely altered to fine-grained clays, with clay lining the vesicles (illite?). The phenocrysts are also entirely altered to clay. The clasts area also associated with fine- to medium grey pyrite, disseminated throughout. The sample is strongly cemented by sulfates, comprising ~70% of the total sample, mostly constisting of fine-grained anhedral anhydrite, with a few coarser clasts, with minor gypsum, 5% overall.



Thin section scan (left) and puck (right) of MA13-015.

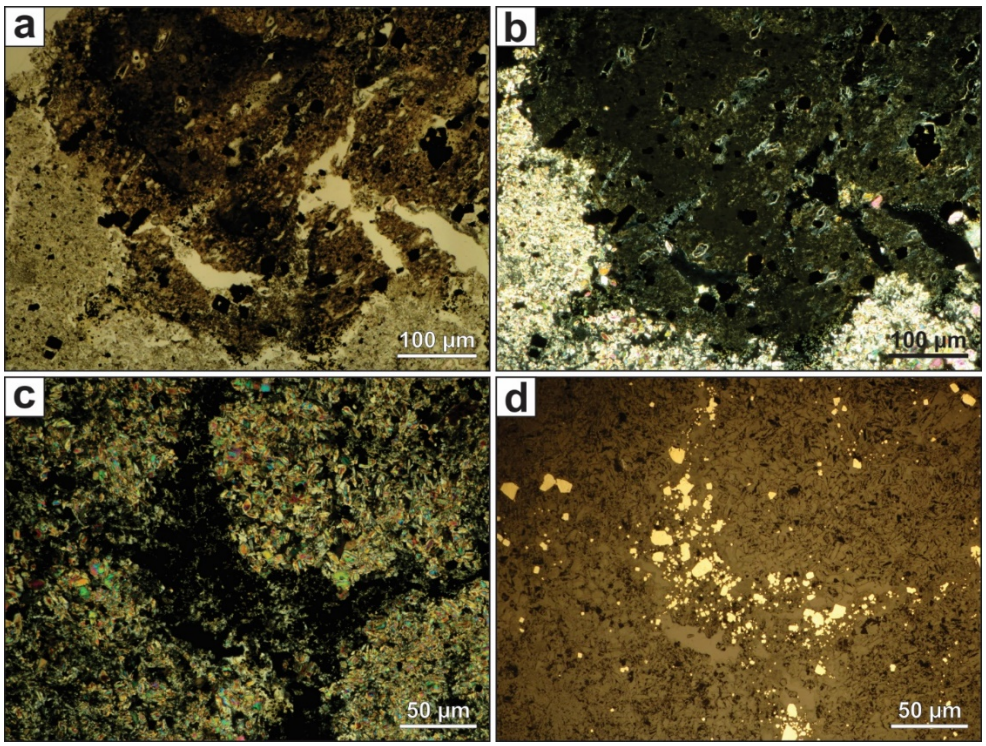
Between patches of anhydrite is wispy zones of illite + pyrite, likely representing the former matrix material (altered ash?). This altered matrix comprises 10% of the sample. Overall, there is 3-5% total porosity. No crystal fragments or glass shards were identified. This sample is similar to MA13-006, with finer clast sizes.

Paragenesis: Volcanic clasts + ash(?) matrix → pervasive alteration to illite → pyrite → iron oxide → abundant fine-grained anhydrite → local hydration to gypsum

Interpretation: Hyaloclastite (monomict, flow-foliation), cemented by anhydrite

Descriptive Lithological Name: Pervasively illitized monomict matrix-supported granular hyaloclastite, cemented

Descriptive Alteration Facies: Intense, pervasive illite, abundant pyrite (clasts and altered matrix)



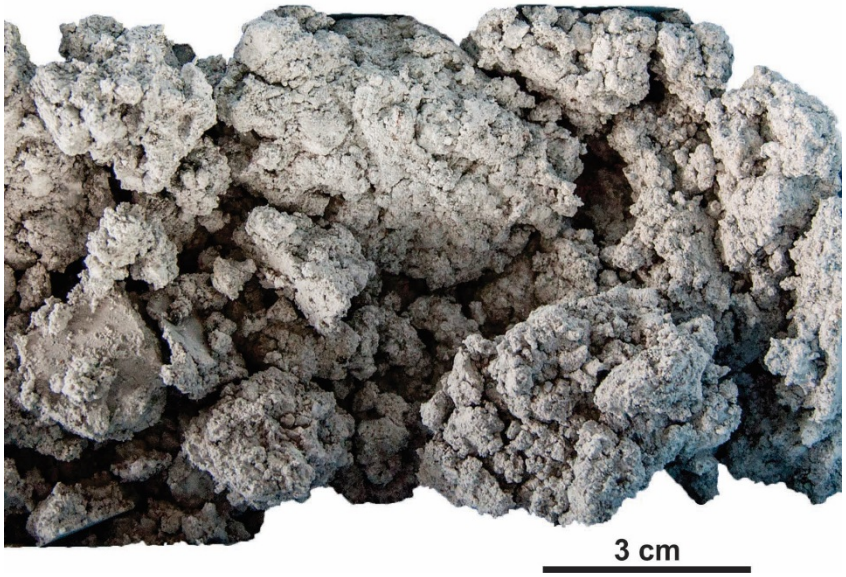
Photomicrographs of GMA13-015: (a) transmitted light (PPL) showing flow-foliated weakly vesicular volcanic clast; (b) transmitted light (XPL) of the same view as (a) showing clay minerals lining vesicles and recrystallized anhydrite matrix; (c) transmitted light (XPL) showing the recrystallized anhydrite matrix; (d)) reflected light (PPL) showing coarse-grained pyrite at the margin of a clast in the matrix with the same view as (c).

SAMPLE: MA13-016 **PARENT ID:** 2434 **SAMPLE DEPTH:** 6.60-6.71 mbsf	**DRILLHOLE:** TKAD018 **DRILLHOLE LOCATION:** 784756.43E/8649604.73N **WATER DEPTH:** 1110.18 mbsl

Mineralogy

XRD (clay-sized fraction): Montmorillonite, chamosite, I/S, illite, hematite, anhydrite
Assemblage: I/S + Cham

Hand Sample Description

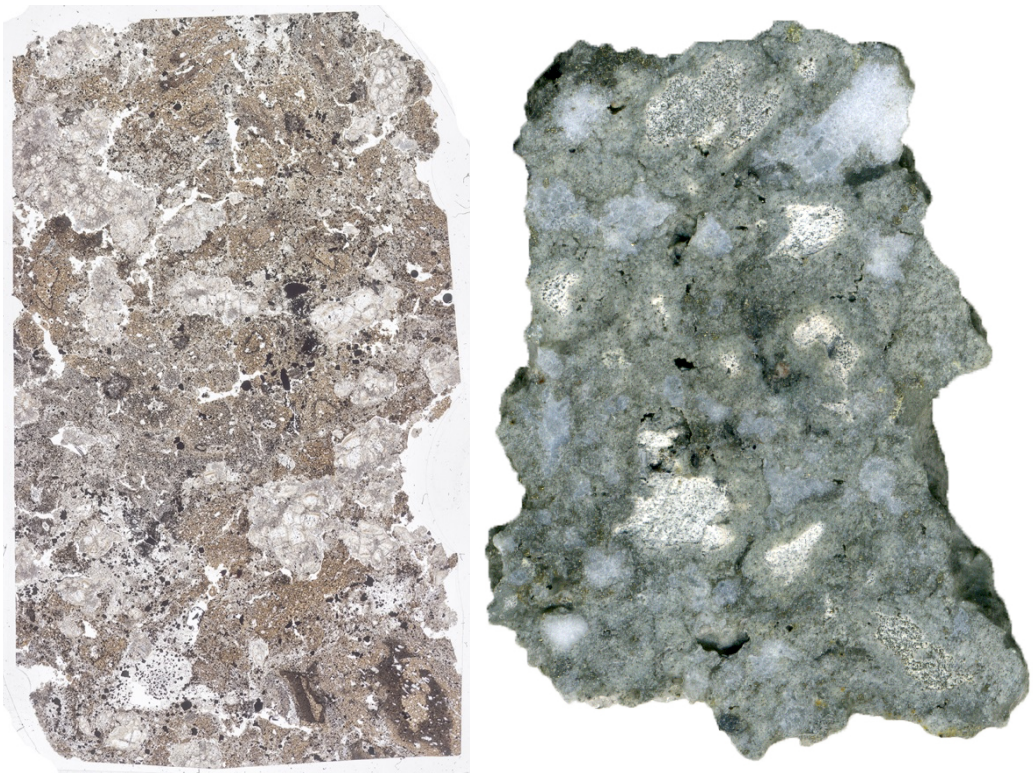


Hand sample of MA13-016.

Monomict clast-supported volcanic breccia with rounded to sub-rounded white clay-altered clasts and light grey clay-altered matrix with minor patchy white anhydrite. It is partially cemented and very friable. There is 2% pyrite, <1% sphalerite, finely disseminated. There are 80% clasts overall, white with strong pervasive clay alteration, <1.0-5.0 mm wide, poor sorting, rounded to subrounded shape, with moderate to high sphericity and random fabric. The clasts are aphanitic with rare sub-mm vesicles. There is 6% porosity.

Thin Section Description

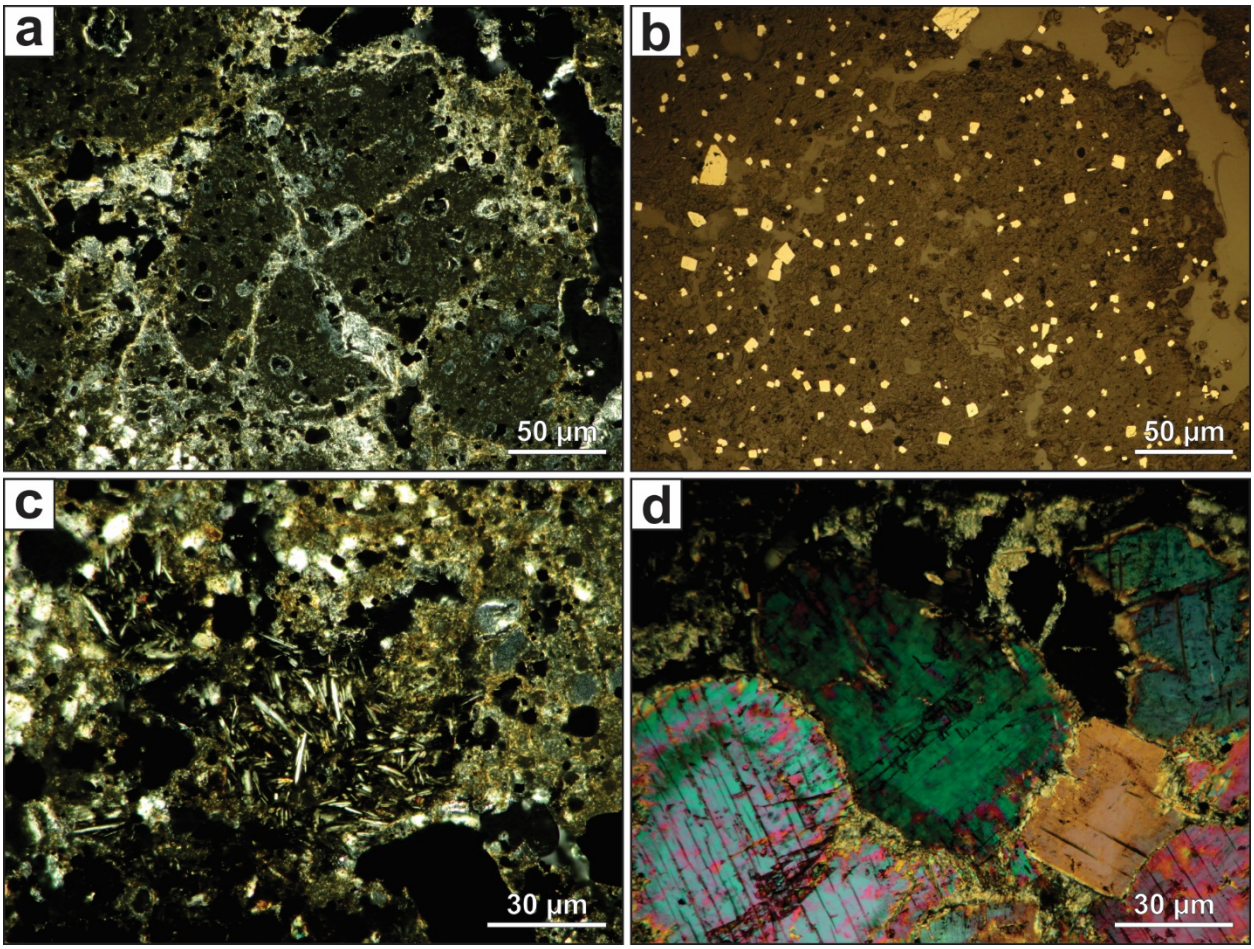
This section is a matrix-supported monomict breccia, with 40% subangular to subrounded clasts up to 20 mm long. The clasts have irregular margins and contain abundant irregular vesicles, comprising upt o 10% of each clast. These vesicles are aligned with a flow foliation in some (but not all) clasts. In these clasts, a few relict microphenocrysts (likely originally plagioclase) are also aligned with this foliation. The clasts are light-orange brown in PPL, although this color is not always uniform, and some clasts show an interior rim of darker brown, possibly reflecting a change from a microcrystalline core to glassy rim.



Thin section scan (left) and puck (right) of MA13-016.

The clasts are all intensely and pervasively altered to fine-grained clay (illite/smectite?), with clay lining the vesicles. There appears to be an early generation of vesicle lining clay that shows fourth-order interference colors, likely illite, followed by a second generation of clay with first-order grey interference colors, likely smectite. The clasts locally display jigsaw-fit. There are a few small glassy clasts that are altered to coarser-grained chlorite(?). The matrix is dominated by fine-grained clay minerals, likely smectite/illite, that may have altered a previously ash-dominated matrix. Within the matrix are patches of coarse-grained mica with a weak pale green pleochroism, with third to fourth order interference colors, possibly chlorite. Fine- to medium-grained euhedral pyrite is disseminated throughout the clasts and matrix, ~5% overall. Locally, there medium-grained high-Fe sphalerite and chalcopyrite, <1% overall. There is minor patchy gypsum within the matrix, mostly fine- medium grained and euhedral, resulting in weak overall cementation. The sample comprises ~5% porosity, 40% clasts, 10% coarse-grained chlorite, 3% gypsum, and ~40-45% clay-altered matrix. Compared to sample MA13-016, this sample has larger and more abundant clasts, less sulfate cement, and more variable alteration.

Paragenesis: Volcanic clasts + matrix (ash?) → illite + pyrite (+ sphalerite, chalcopyrite?) → smectite → gypsum → chlorite(?)
Interpretation: Hyaloclastite (monomict, flow-foliation, jigsaw fit)
Descriptive Lithological Name: Pervasively clay-altered (illite/smectite) monomict matrix-supported hyaloclastite breccia, unconsolidated
Descriptive Alteration Facies: Intense, pervasive illite and smectite, abundant pyrite (clasts and matrix), patchy late coarse-grained chlorite(?)



Photomicrographs of GMA13-016: (a) transmitted light (XPL) showing vesicular volcanic clast altered to clay, and clay alteration in the matrix (ash?); (b) reflected light (PPL) showing pyrite disseminated in a volcanic clast; (c) transmitted light (XPL) showing unaltered microphenocrysts in a volcanic clast, and a clay-altered matrix; (d) transmitted light (XPL) showing coarse-grained anhydrite being partially hydrated to gypsum at the margins.

SAMPLE: MA13-019 **PARENT ID:** 2421 **SAMPLE DEPTH:** 5.00-5.10 mbsf	**DRILLHOLE:** TKAD017 **DRILLHOLE LOCATION:** 784723.31E/8649601.46N **WATER DEPTH:** 1107.68 mbsl

Mineralogy

N/A

Hand Sample Description

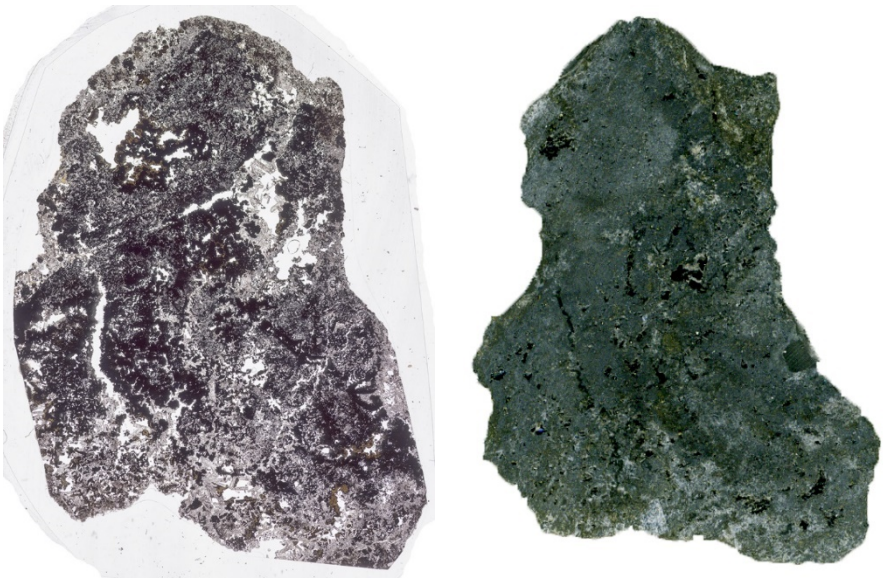


Hand sample of MA13-019.

Monomict clast-supported volcanic breccia with subrounded poorly-altered dary grey clasts with patchy anhydrite cement. This represents the transition area from chimney to footwall. It is unconsolidated, with local patchy cemented areas of dark grey anhydrite and possible silica. There is 2% disseminated pyrite, possible sphalerite(?). There are 80% less-altered volcanic clasts with minor patchy clay, <1.0-20.0 mm in size, poor sorting, subrounded shape, low sphericity, with random fabric. They are aphanitic with rare sub-mm vesicles. There is 2% porosity.

Thin Section Description

This sample contains no volcanic textures and appears to be a fragment of a chimney. It is comprised of 20% pore space, 40% early fine-grained barite, 35% sulfides, and 5% late coarse-grained barite. The sulfides are dominated by sphalerite, progressing from high-Fe to low-Fe outwards, showing vent conduit-lining textures. The sphalerite contains inclusions of fine-grained pyrite and chalcopyrite, with late fine- to medium-grained chalcopyrite after sphalerite. The late chalcopyrite appears to be locally replacing the sphalerite. Overall, there is 3% pyrite, 12% chalcopyrite, and 20% sphalerite.

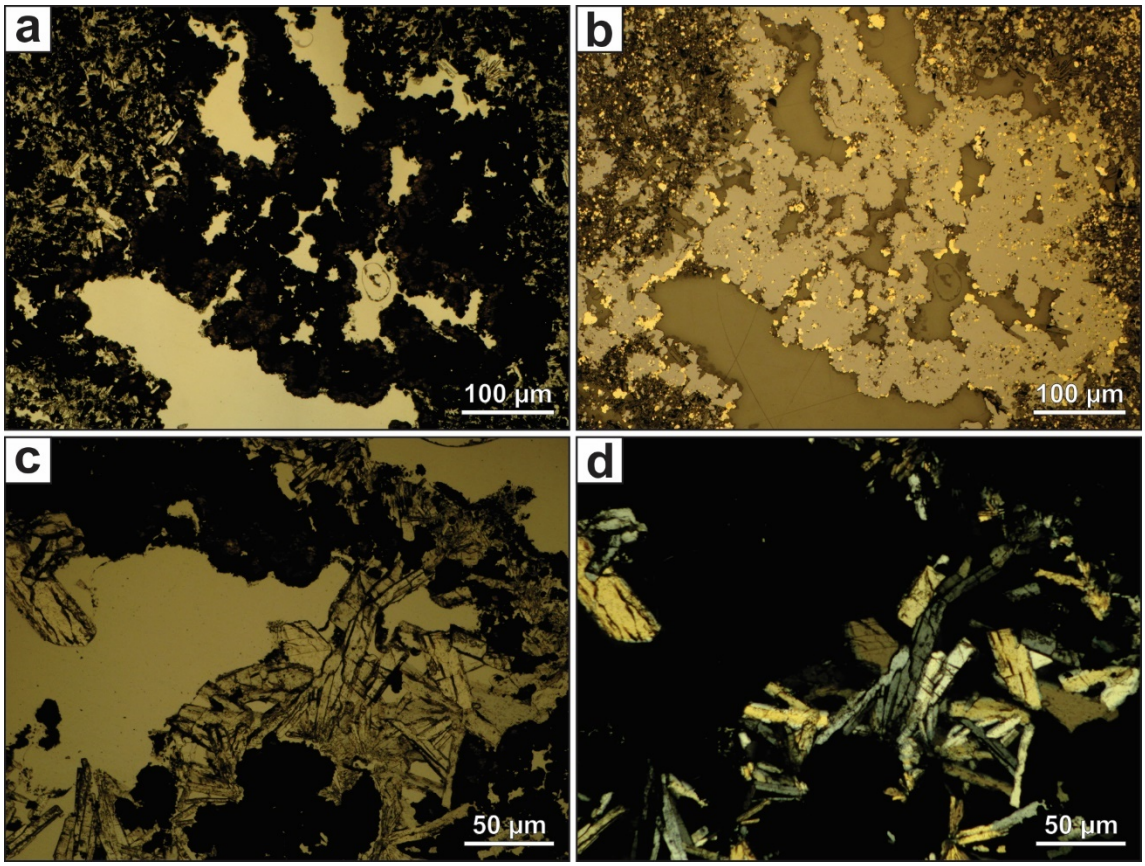


Thin section scan (left) and puck (right) of MA13-019.

Paragenesis: Barite → fine-grained pyrite + chalcopyrite → high-Fe sphalerite → low Fe-sphalerite → chalcopyrite → coarse-grained barite

Interpretation: Chimney fragment

Descriptive Lithological Name: Sphalerite+chalcopyrite+barite chimney fragment



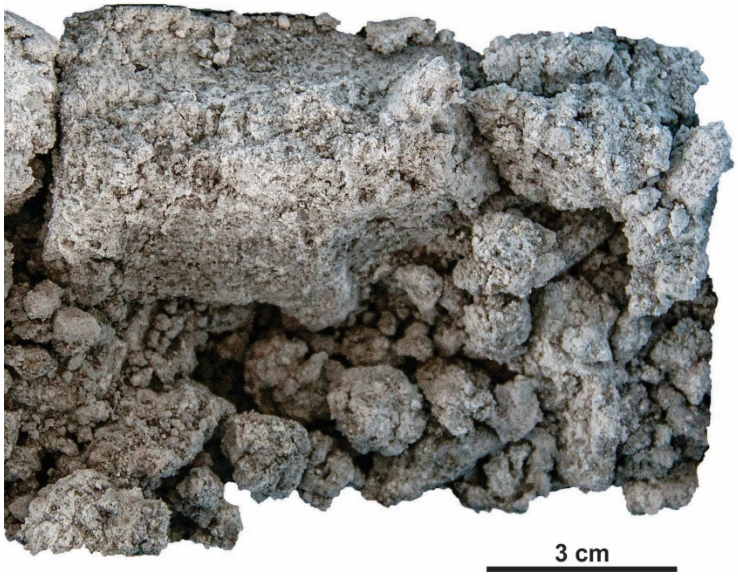
Photomicrographs of GMA13-019: (a) transmitted light (PPL) showing opaque sulfides; (b) reflected light (PPL) showing sphalerite with late pyrite, same view as (a); (c) transmitted light (PPL) showing bladed barite; (d) transmitted light (XPL) showing same view as (c).

SAMPLE: MA13-020	**DRILLHOLE:** TKAD017
PARENT ID: 2424	**DRILLHOLE LOCATION:** 784723.31E/8649601.46N
SAMPLE DEPTH: 6.90-7.00 mbsf	**WATER DEPTH:** 1107.68 mbsl

Mineralogy

XRD (clay-sized fraction): Montmorillonite, rectorite, I/S, illite, pyrite, anhydrite
Assemblage: I/S + Py

Hand Sample Description



Hand sample of MA13-020.

Monomict matrix-supported volcanic breccia with sub-rounded medium grey clay-altered clasts, friable with a white clay matrix and patchy white anhydrite cement. There is <1% disseminated pyrite. There are 35% clasts, with strong pervasive clay alteration, <1.0-10.0 mm, poor sorting, moderate sphericity, random fabric, aphanitic texture with rare sub-mm vesicles. There is 6% porosity.

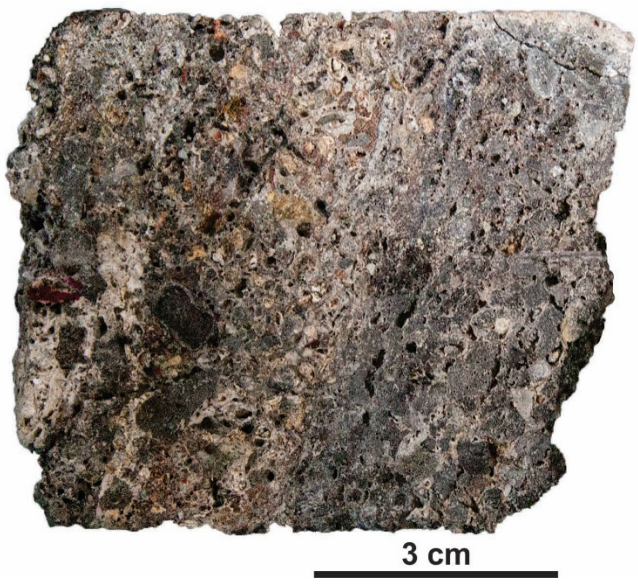
Alteration Summary: Pervasive intense clay (illite/smectite), abundant pyrite
Interpretation: Volcanic breccia (origin unknown)
Name: Intensely clay-altered volcaniclastic breccia, weakly cemented

SAMPLE: MA13-023 **PARENT ID:** 2581 **SAMPLE DEPTH:** 1.51-1.60 mbsf	**DRILLHOLE:** TKAD033 **DRILLHOLE LOCATION:** 784707.86E/8649726.84N **WATER DEPTH:** 1070.68 mbsl

Mineralogy

N/A

Hand Sample Description

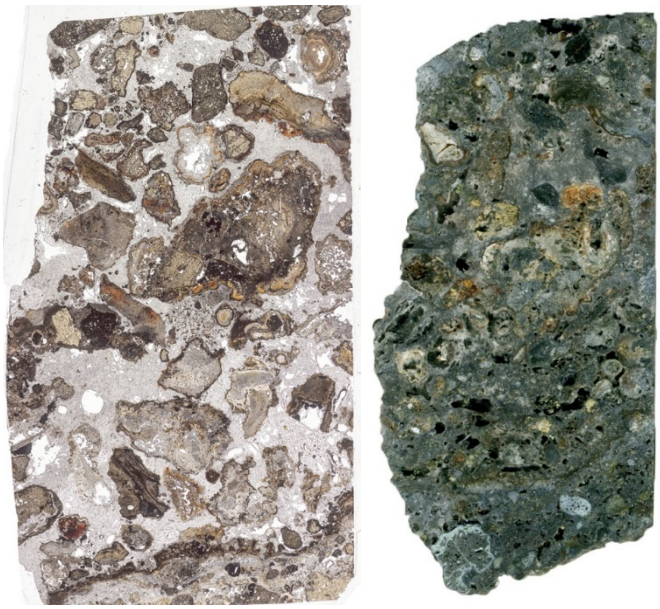


Hand sample of MA13-023.

Polymict clast-supported silicified volcanic breccia with small variably-altered white, green-yellow, and dark grey clasts, minor patchy iron oxides, with strong silica and anhydrite cement (well cemented), grey to white. There is trace pyrite. There are 80% clasts overall. Therea are 70% dark-grey volcanic clasts with inor clay, <1.0-10.0 mm in side, poor sorting, angular to sub-rounded, with low sphericity, random fabric, aphanitic, with a few sub-mm vesicles. There are 5% green-yellow clasts, with pervasive strong clay alteration, possible chlorite, and minor patchy iron oxide, <1.0-4.0 mm, poor sorting, subrounded-rounded, low sphericity, and random fabric. There are 5% light grey-white volcanic clasts with strong pervasive clay alteration, <1.0-3.0 mm, poor sorting, subrounded-rounded shape, low sphericity and random fabric. There is 8% porosity.

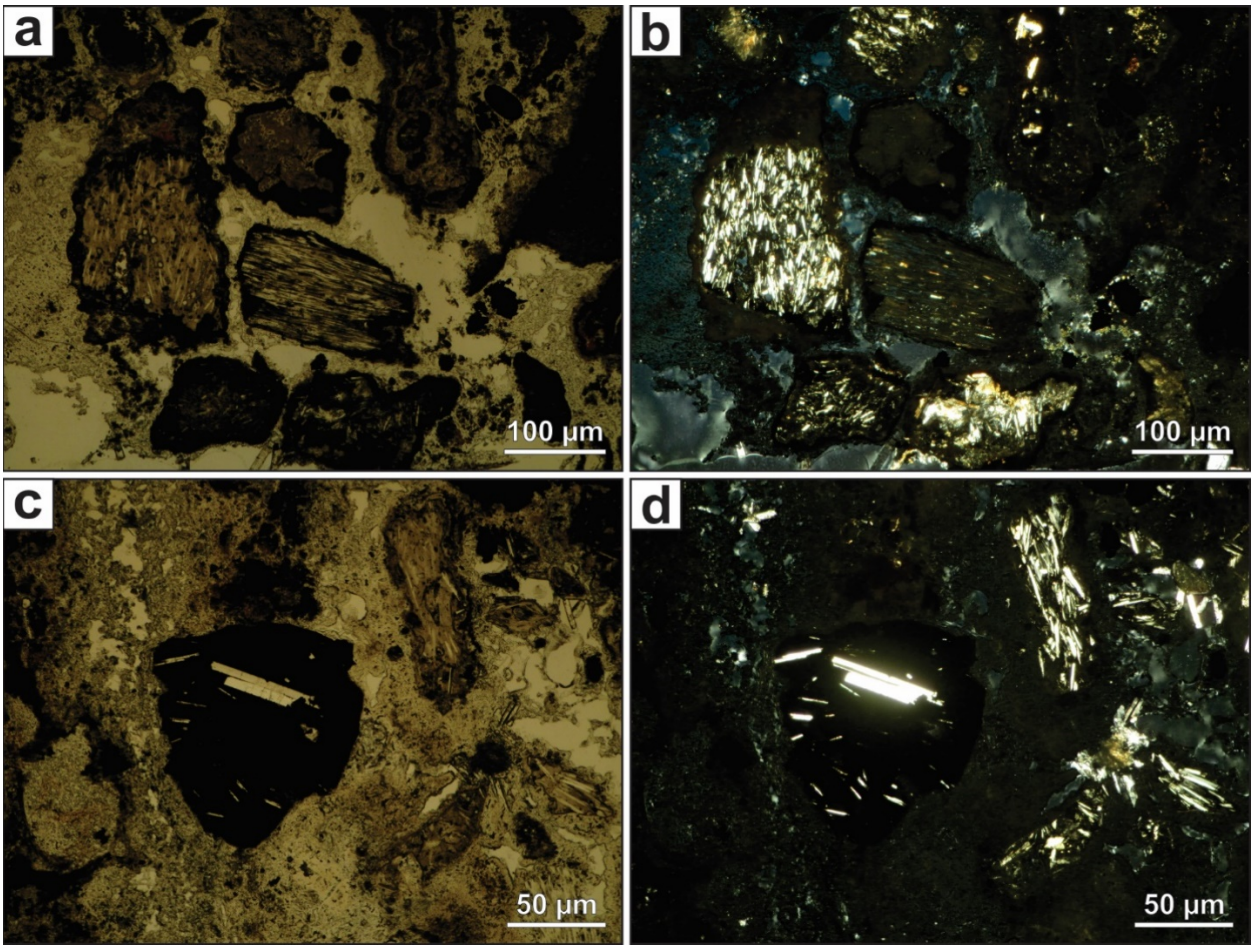
Thin Section Description

This section is a massive polymict matrix-supported breccia with 35% clasts, 45% matrix, and 20% pore space. The clasts are irregular with different colors and compositions, ranging from almost-black with relict plagioclast phenocrysts, to light-brown/glassy. They range in size from 1-12 mm. Many of the clasts are only weakly altered and still contain abundant isotropic class. They are variably vesicular and phenocrystic, with some unaltered microcrystalline clasts. At least one clast is composed of tube pumice. One glassy clast shows perlitic fractures. The main alteration is irregular patchy iron oxyhydroxides, which tends to concentrate at the clast margins. The matrix is dominated by amorphous ‘fish-egg’ silica that cements the sample. The silica is locally stained red from FeOx. The matrix contains irregular fine- to medium-grained anhydral pyrite (3-4%) and chalcopyrite (1%). No glass or crystal fragments were identified.



Thin section scan (left) and puck (right) of MA13-023.

Paragenesis: Volcanic clasts → pyrite + chalcopyrite → FeOx → amorphous silica
Interpretation: Resedimented volcanic breccia; volcanogenic sedimentary deposit (polymict, rounded, flow-foliated)
Descriptive Lithological Name: Silicified polymict matrix-supported resedimented volcanic breccia
Descriptive Alteration Facies: Weak, irregular FeOx, abundant amorphous silica



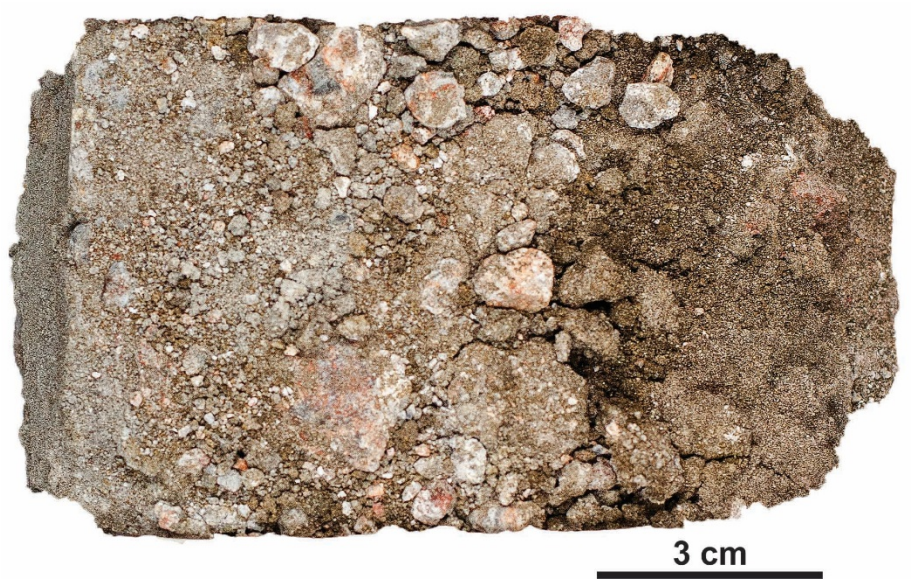
Photomicrographs of GMA13-023: (a) transmitted light (PPL) showing various clast types, including volcanic clasts and pumice; (b) reflected light (XPL) showing same view as (a) with unaltered crystals; (c) transmitted light (PPL) showing porphyritic clast; (d) transmitted light (XPL) showing same view as (c) showing unaltered phenocrysts.

SAMPLE: MA13-024 **PARENT ID:** 2582 **SAMPLE DEPTH:** 2.55-2.66 mbsf	**DRILLHOLE:** TKAD033 **DRILLHOLE LOCATION:** 784707.86E/8649726.84N **WATER DEPTH:** 1070.68 mbsl

Mineralogy

N/A

Hand Sample Description

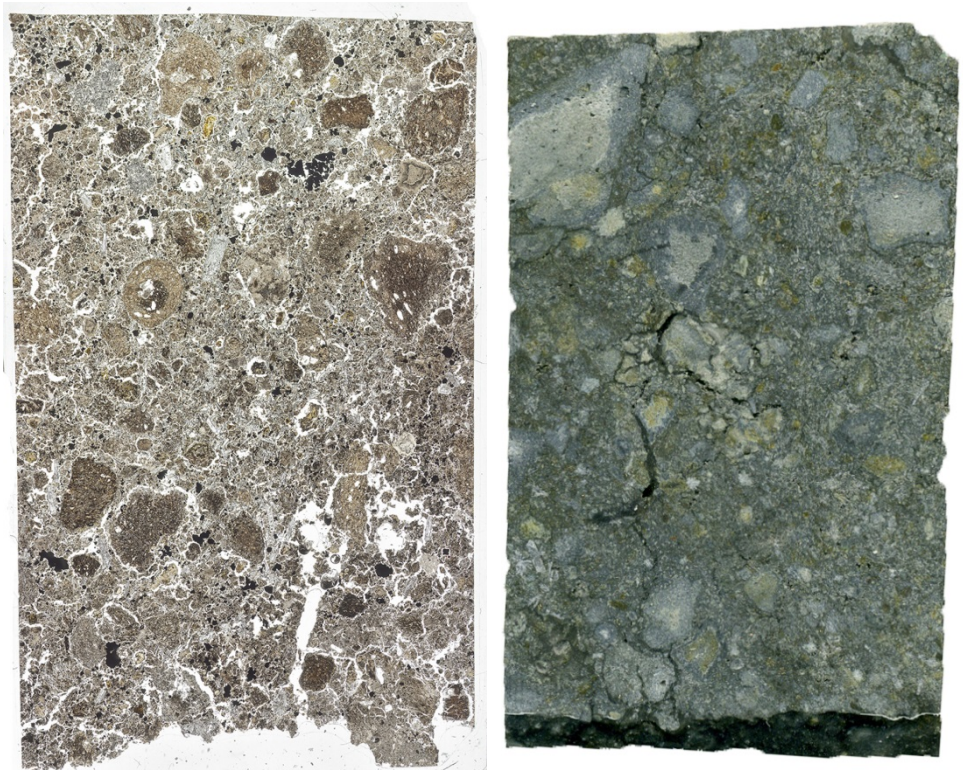


Hand sample of MA13-024.

This sample represents the stringer zone at the transition between sulfides and the altered footwall. It is a monomict(?) unconsolidated clast-supported volcanic breccia with small, siliceous, variably-altered fragments in a matrix of pyrite and clay (minor). There is 30% pyrite overall. There are 70% clasts that are medium grey and white, with patchy red (iron oxides?) with patchy to pervasive clay and abundant silica, 1.0-8.0 mm in size, poor sorting, angular shape, low sphericity, random fabric, and no preserved vesicles. There is 10% porosity.

Thin Section Description

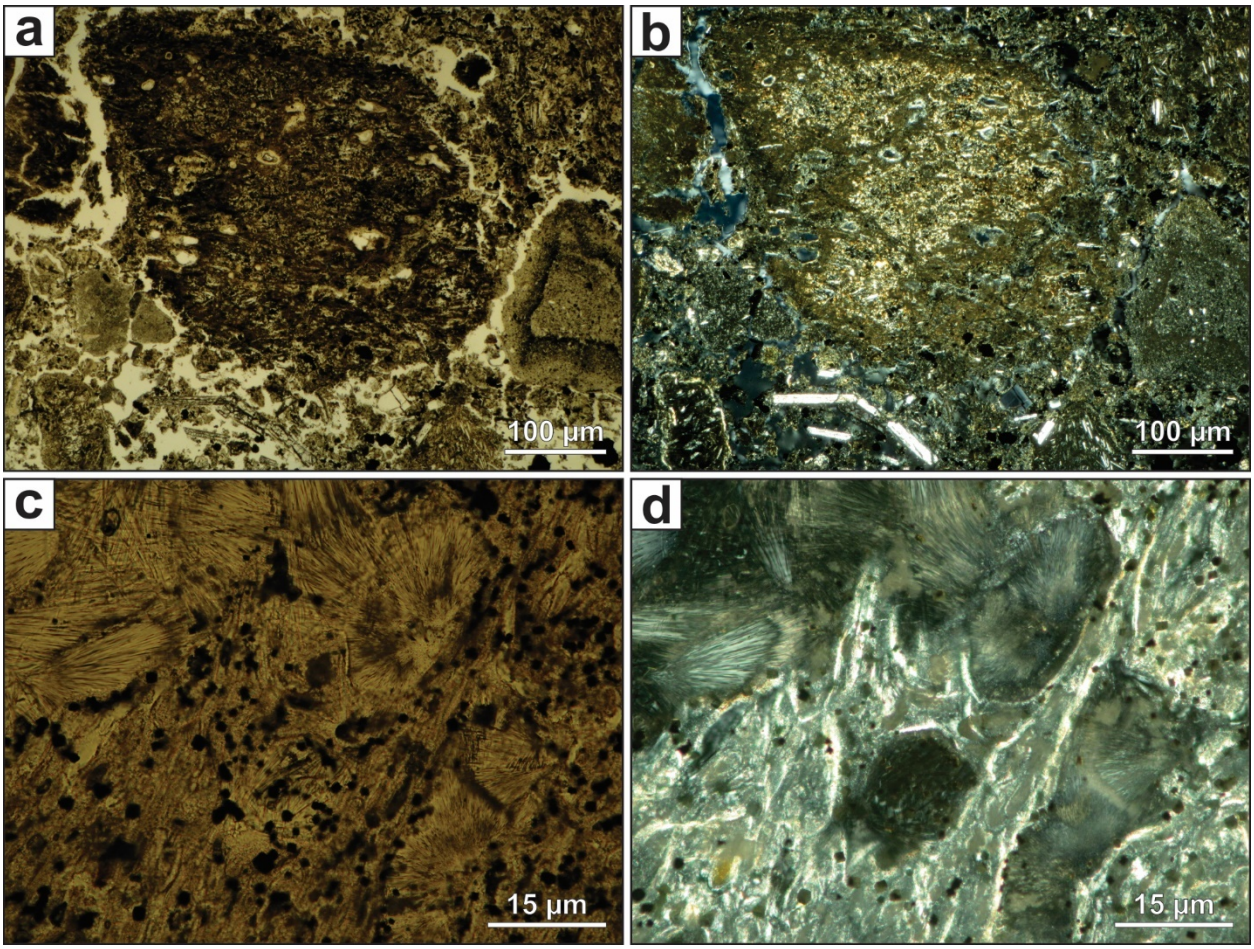
This section is a massive polymict clast-supported breccia with irregular clasts ranging in size from <1 mm to 10 mm. The clasts range from rounded to subangular, and are variably altered. Many of the clasts have relatively unaltered microphenocrysts and phenocrysts of plagioclase that show distinct flow foliation. Vesicles are also common. The clasts range in color from light brown (glassy) to very dark brown. The glassy groundmass is variably altered to fine-grained clays (illite/smectite?). Fine-grained pyrite is disseminated throughout most of the clasts. The clasts have variable FeOx alteration. Some clasts are



Thin section scan (left) and puck (right) of MA13-024.

wispy, composed of tube pumice, altered to chlorite(?), with late radiating to fibrous chlorite(?) filling in pore space. Clays variably fill in vesicles as well. It is difficult to distinguish clast from matrix as the clast margins are irregular and the clast size is variable. There is an estimated porosity of ~10%, with 65-70% clasts and 20-25% matrix. The matrix is composed of intensely clay-altered material (ash?), irregularly distributed gypsum (3% overall, weakly cemented), 9% fine- to coarse-grained subhedral to euhedral pyrite/marcasite, and 1% low-Fe sphalerite (anhedral) after pyrite.

Paragenesis: Volcanic clasts + matrix → illite/smectite/chlorite + pyrite altering clasts → pyrite + sphalerite mineralization → FeOx → patchy gypsum
Interpretation: Resedimented volcanic breccia; volcanogenic sedimentary deposit (polymict, rounded, flow-foliated)
Descriptive Lithological Name: Variably clay-altered (illite, smectite, chlorite?) polymict clast-supported resedimented volcanic breccia, weakly mineralized
Descriptive Alteration Facies: Irregular illite/smectite altering glassy groundmass and filling vesicles associated, local chlorite replacing tube pumice class and filling pore space, disseminated pyrite, irregular FeOx



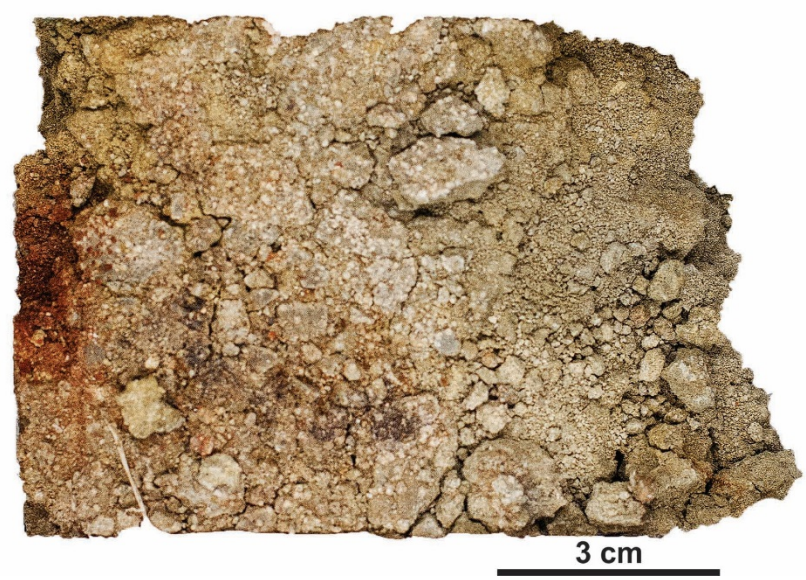
Photomicrographs of GMA13-024: (a) transmitted light (PPL) showing various clast types, including a flow-foliated weakly vesicular clast in the middle; (b) transmitted light (XPL) showing intense clay alteration of the clasts and matix, same view as (a); (c) transmitted light (PPL) showing radiating alteration minerals (chlorite?); (d) transmitted light (XPL) showing same view as (c).

SAMPLE: MA13-025 **PARENT ID:** 2583 **SAMPLE DEPTH:** 3.00-3.10 mbsf	**DRILLHOLE:** TKAD033 **DRILLHOLE LOCATION:** 784707.86E/8649726.84N **WATER DEPTH:** 1070.68 mbsl

Mineralogy

XRD (clay-sized fraction): Nontronite, plagioclase, pyrite, anhydrite
Assemblage: Mnt/Non + Pl

Hand Sample Description

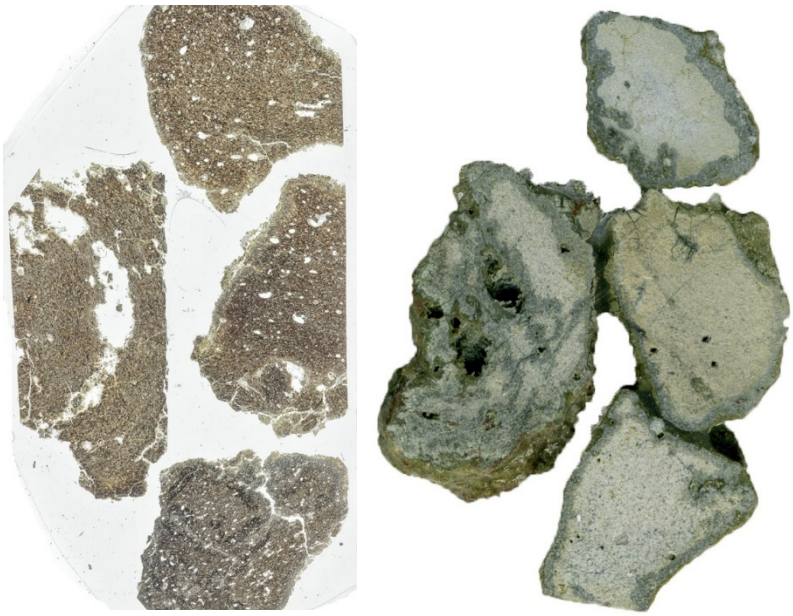


Hand sample of MA13-025.

Moderately-altered monomict clast-supported volcanic breccia with subangular to angular medium-dark grey clasts and an olive-green matrix with patchy red iron oxide, poorly consolidated. The clasts are not as altered as other footwall samples. There is 1% pyrite overall. The matrix has pervasive very fine grained clay, chlorite(?). There are 90% moderately-clay altered volcanic, with possible chlorite, with variable color (medium-dark grey). They are 1.0-18.0 mm, poor sorting, angular shape, low sphericity, random fabric, and abundant preserved sub-mm vesicles. There is 5% porosity.

Thin Section Description

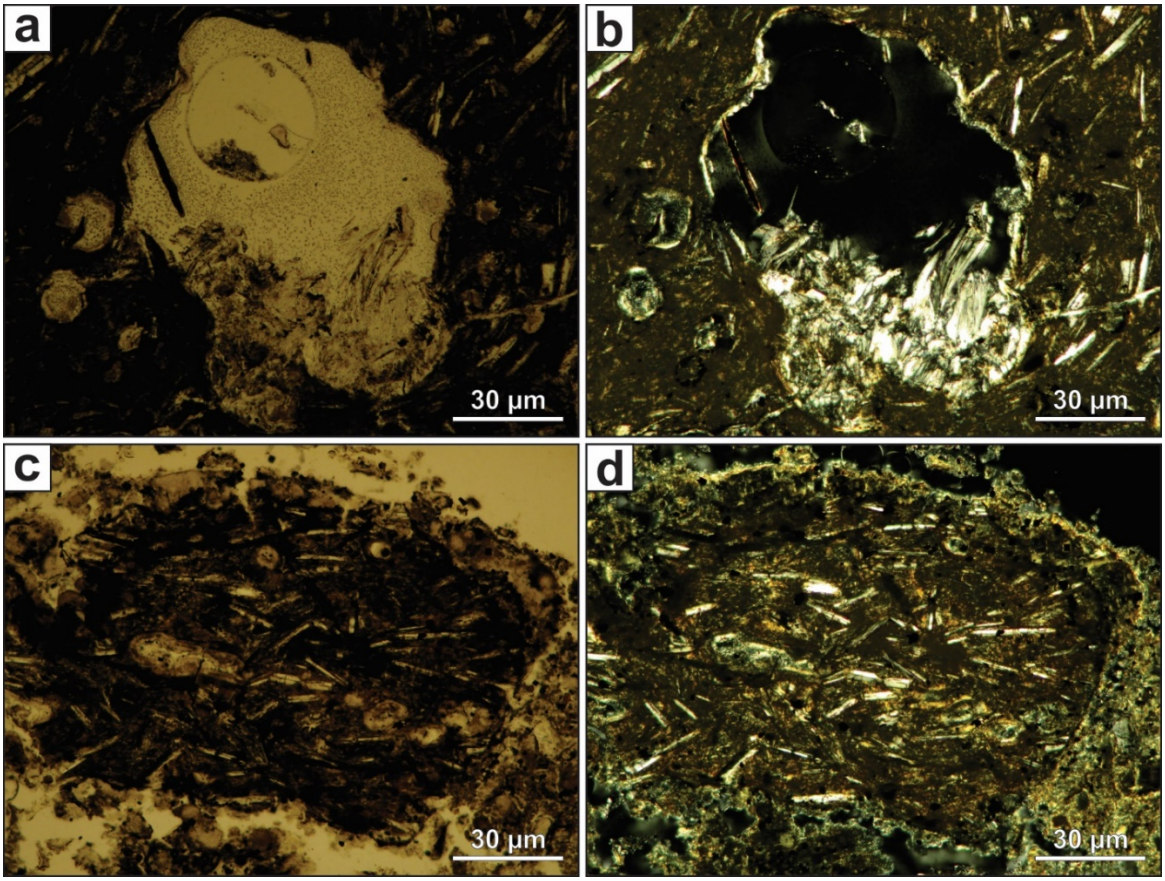
This sample is an unconsolidated monomict volcanic breccia. The section contains individual clasts up to 20 mm long and are subangular. They contain abundant flow-foliated microphenocrysts of plagioclase and are variably vesicular. They dark brown to grey in color (patchy), with minor iron oxide alteration. The formerly glassy groundmass has been altered to fine-grained clays with first-order interference colors (smectite?), with clays lining vesicles. The phenocrysts appear unaltered. The clast margins are surrounded by fine-grained clays, possibly representing altered quenched glassy margins. The clasts have minor finely-disseminated pyrite, 2-3% overall. Possible glass shards and matrix material at margins rather than quenched glass.



Thin section scan (left) and puck (right) of MA13-025.

Paragenesis: Volcanic clasts → alteration of glassy groundmass to smectite + minor pyrite → infill of vesicles by smectite
Interpretation: Lapilli tephra (flow-foliation, not rounded, glass shards)
Descriptive Lithological Name: Moderately smectite(?)-altered monomict shard-rich(?) lapilli tephra, unconsolidated

Descriptive Alteration Facies: Pervasive clay (smectite) alteration of glassy groundmass and glassy margins, unaltered phenocrysts



Photomicrographs of GMA13-025: (a) transmitted light (PPL) showing alteration minerals precipitating in a vesicle; (b) transmitted light (XPL) showing same view as (a); (c) transmitted light (PPL) showing flow-foliated volcanic clast; (d) transmitted light (XPL) showing same view as (c), with clay alteration of the glassy groundmass and ash(?) matrix, but unaltered microphenocrysts.

SAMPLE: MA13-026 **PARENT ID:** 2585 **SAMPLE DEPTH:** 4.76-4.88 mbsf	**DRILLHOLE:** TKAD033 **DRILLHOLE LOCATION:** 784707.86E/8649726.84N **WATER DEPTH:** 1070.68 mbsl

Mineralogy

SWIR (powdered clast, matrix): Nontronite
XRD (clay-sized fraction): Nontronite, clinochlore(?), plagioclase, hematite
Assemblage: Mnt/Non + Pl

Hand Sample Description

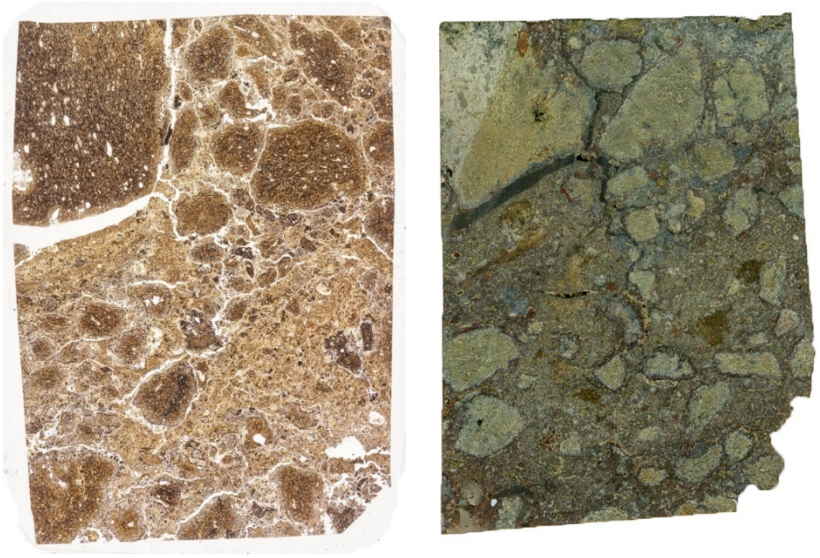


Hand sample of MA13-026.

Moderately-altered polymict clast-supported volcanic breccia with small to large angular clasts, a few less-altered clasts, poorly consolidated with a matrix of very fine-grained iron oxide and green-grey clay. The green clay coats the clasts. There is ~1% pyrite overall. There are 80% clasts overall. This includes 75% medium greenish-grey moderately clay- (and chlorite?)-altered volcanic clasts, <1.0-22.0 mm, poor sorting, angular, low sphericity, random fabric, with abundant sub-mm vesicles aligned along a flow foliation. There are 5% dark-grey slightly clay-altered volcanic clasts, up to 24.0 mm wide, angular shape, with low sphericity and random fabric with abundant sub-mm vesicles. There is 5% porosity.

Thin Section Description

This section is a matrix-supported polymict breccia with clasts up to 10 mm long. There is a narrow range of clast types defined by changing clast colors and degree of alteration. The clasts are subrounded to angular with irregular margins. They are porphyritic with unaltered plagioclase phenocrysts that display a strong flow-foliation. The clasts are also moderately-strongly vesicular. The clasts appear dark brown to grey in color, with FeOx staining. There are no jigsaw-fit textures. The groundmasss of the clasts is pervasively altered to fine-grained clays (illite/smectite?). The vesicles are lined by two generations of clays: fourth-order interference colors (illite?) followed by first-order grey interference colors (smectite?). There is <1% disseminated sulfides (pyrite, sphalerite?). There is 5-10% porosity, 30% clasts, and 60% matrix. The matrix is composed of fine-grained clays (mostly smectite?), with abundant clay-altered glass shards (20% overall), including bubble wall shards. Some of these shards are slightly green (chlorite alteration?).



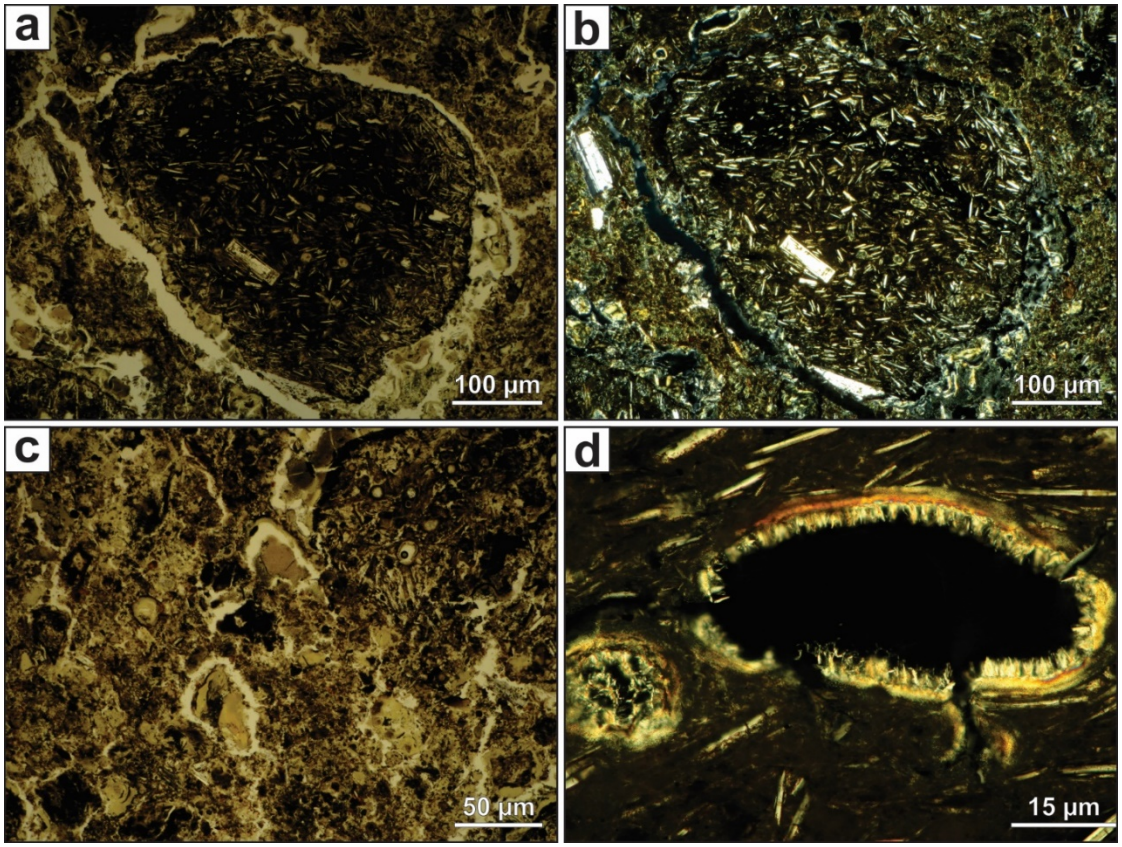
Thin section scan (left) and puck (right) of MA13-026.

Paragenesis: Clasts + matrix + glass shards → alteration of glassy groundmass and glass shards to clay (mostly smectite, minor chlorite) → infill of vesicles with minor illite(?) and smectite → minor pyrite + sphalerite → FeOx

Interpretation: Syn-eruptive lapilli tephra (flow-foliated, glass shards, angular)

Descriptive Lithological Name: Moderately clay-altered (smectite, chlorite?) polymict matrix-supported shard-rich lapilli tephra, unconsolidated

Descriptive Alteration Facies: Pervasive smectite(?) altering glassy groundmass and glass shards, local chlorite altering glass shards, vesicles lined by illite(?) followed by smectite. filling vesicles associated, irregular FeOx, unaltered plagioclase phenocrysts



Photomicrographs of GMA13-026: (a) transmitted light (PPL) showing large weakly-porphyritic volcanic clast; (b) transmitted light (XPL) showing same view as (a); (c) transmitted light (PPL) showing glass shards in volcaniclastic matrix; (d) transmitted light (XPL) showing clay minerals precipitating in a vesicle, and unaltered microphenocrysts.

SAMPLE: MA13-027 **PARENT ID:** 2588 **SAMPLE DEPTH:** 7.30-7.40 mbsf	**DRILLHOLE:** TKAD033 **DRILLHOLE LOCATION:** 784707.86E/8649726.84N **WATER DEPTH:** 1070.68 mbsl

Mineralogy

SWIR (powdered clast): Nontronite
XRD (clay-sized fraction): Montmorillonite, clinochlore, plagioclase, hematite(?)
Assemblage: Cham + Corr

Hand Sample Description



Hand sample of MA13-027.

Poorly consolidated polymict clast-supported volcanic breccia with large angular moderately-altered clasts, few less-altered clasts, and abundant dark red-brown iron oxide, primarily in the matrix. The matrix may also have minor very fine-grained clay. There is 1% pyrite overall. There are 80% clasts overall. This includes 78% medium greenish-grey moderately clay-altered volcanic clasts, with possible chlorite, <1.0-22.0 mm, poor sorting, angular clasts, low sphericity, random fabric, with abundant sub-mm vesicles and minor jigsaw fit. There are 2% dark grey slightly clay-altered volcanic clasts, <1.0-4.0 mm, poor sorting, low sphericity, random fabric, and an aphanitic texture. There is 1% porosity.

Alteration Summary: Viariable alteration of clasts, pervasive iron oxide.
Interpretation: Not transported far, similar to MA13-026 (lapilli tephra)
Name: Moderately clay-altered (smectite, chlorite?) polymict matrix-supported lapilli tephra, unconsolidated

SAMPLE: MA13-034 **PARENT ID:** 2406 **SAMPLE DEPTH:** 2.02-2.13 mbsf	**DRILLHOLE:** TKAD016 **DRILLHOLE LOCATION:** 784588.91E/8649829.11N **WATER DEPTH:** 1088.73 mbsl

Mineralogy

SWIR (powdered clast): Gypsum, diaspore* (*unreliable)
XRD (clay-sized fraction): Rectorite, aliettite(?), marcasite
Assemblage: I/S + Py

Hand Sample Description

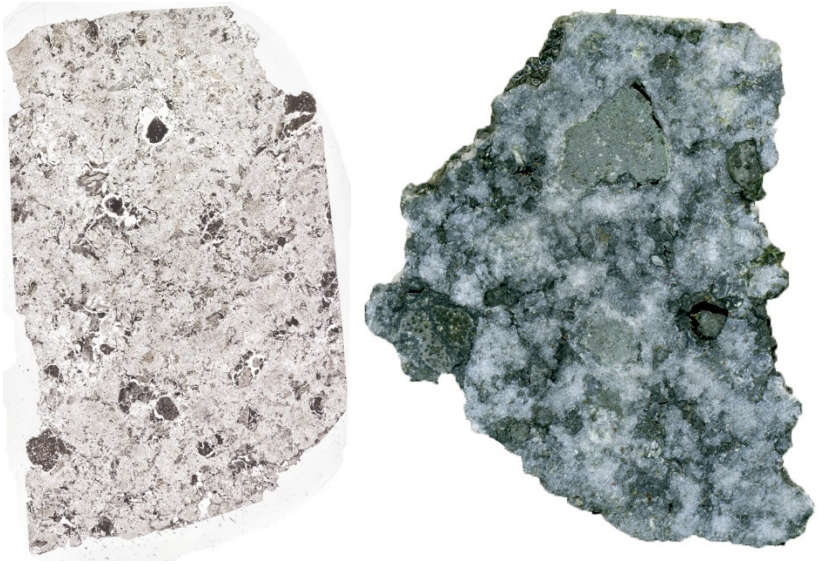


Hand sample of MA13-034.

Monomict matrix-supported volcanic breccia with small subangular clasts and white anhydrite infill (possible veining). There is only trace pyrite. There are 40% medium-grey clay-altered clasts, <1.0-8.0 mm clasts, with poor sorting, subangular shape, low sphericity, random fabric, and aphanitic texture. There is <1% porosity.

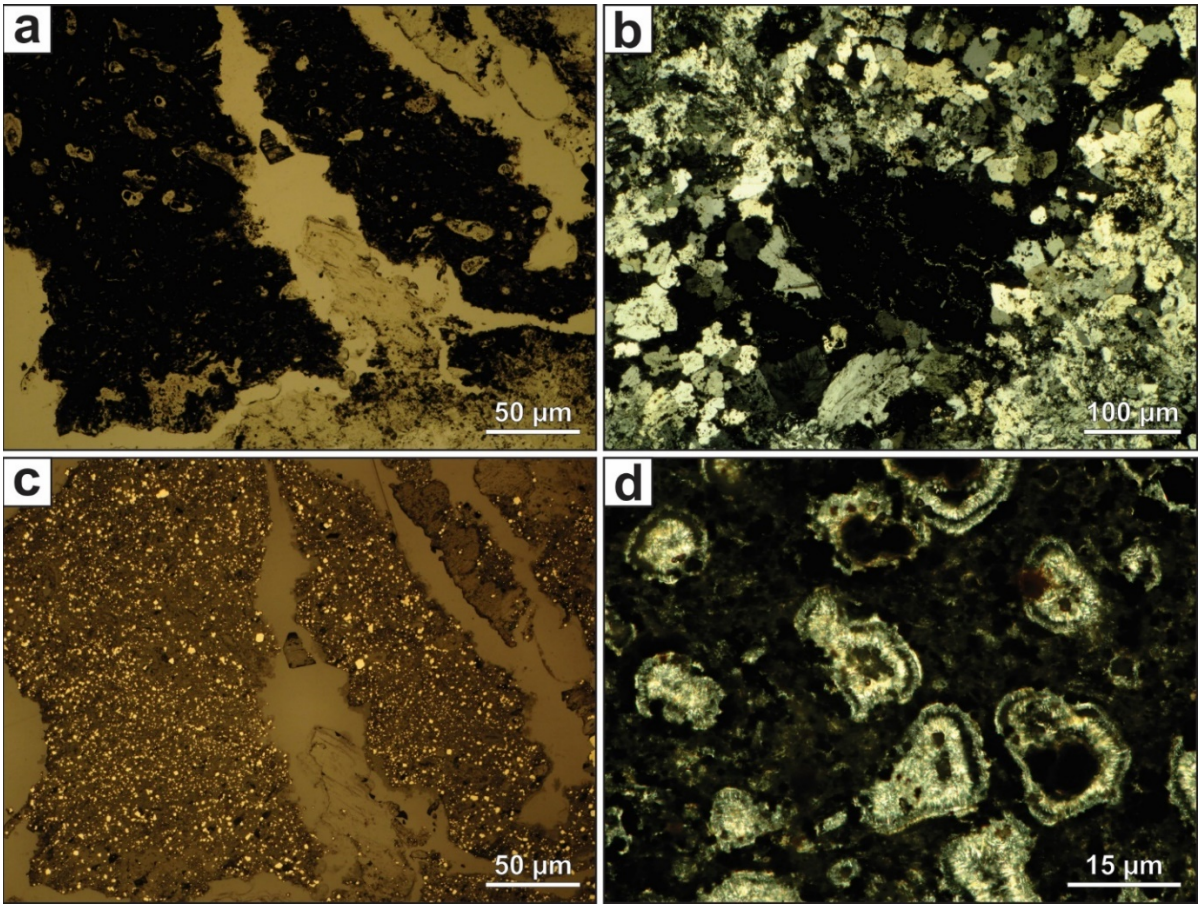
Thin Section Description

This section is a monomict matrix-supported breccia with only 10% clasts, 5% pore space, and 85% matrix. The clasts are subrounded to subangular. In thin section, they are up to 2 mm long, but are up to 8 mm long in hand sample. The clasts are light to dark brown and subrounded-subangular. The glassy groundmass is altered to fine-grained clays (illite/smectite?), with multiple generations of clays lining vesicles, generally beginning with a further-order interference color clay (illite), followed by a first-order interference clay (smectite), followed again by illite. Occasionally, a dark-colored unidentified mineral separates the two (MnOx?). The clasts also contain abundant fine- to medium-grained subhedral to euhedral pyrite. The matrix is dominated by medium- to coarse-grained gypsum, with minor relict anhydrite (1%). This gypsum is full of inclusions and looks 'dirty.' It is locally deformed. In between patches of gypsum is fine-grained clay and fine- to coarse-grained pyrite, likely representing the original matrix (ash?). This clay-altered matrix represents 5% of the matrix.



Thin section scan (left) and puck (right) of MA13-034.

Paragenesis: Volcanic clasts + matrix → alteration to illite/smectite + pyrite, plus vesicle lining I/S → cementation by anhydrite → pervasive hydration of anhydrite to gypsum
Interpretation: Coarse granular volcanic breccia, origin unknown (no glass shards, monomict)
Descriptive Lithological Name: Pervasively illite/smectite-altered monomict matrix supported coarse granular volcanic breccia, cemented
Descriptive Alteration Facies: Pervasive I/S + pyrite alteration of clasts + matrix, hydration of anhydrite to gypsum



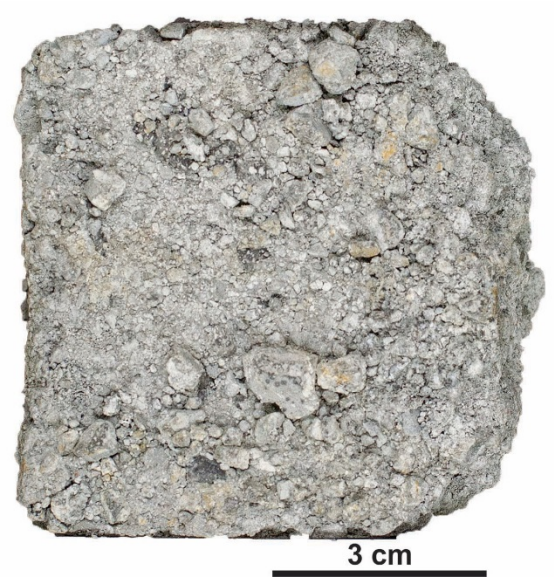
Photomicrographs of GMA13-034: (a) transmitted light (PPL) showing dark irregular volcanic clasts; (b) transmitted light (XPL) showing recrystallized gypsum; (c) reflected light (PPL) showing finely disseminated pyrite in a volcanic clast, same view as (a); (d) transmitted light (XPL) showing multiple generations of clay precipitating in vesicles.

SAMPLE: MA13-035	**DRILLHOLE:** TKAD016
PARENT ID: 2409	**DRILLHOLE LOCATION:** 784588.91E/8649829.11N
SAMPLE DEPTH: 5.65-5.71 mbsf	**WATER DEPTH:** 1088.73 mbsl

Mineralogy

XRD (clay-sized fraction): Chamosite, rectorite, I/S(?)
Assemblage: I/S + Cham

Hand Sample Description

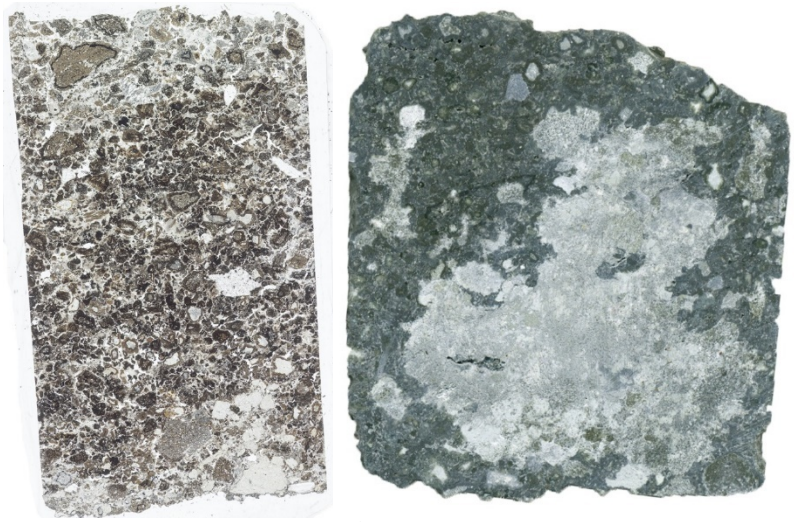


Semi-consolidated monomict(?) clast-supported volcanic breccia with sub-rounded white to medium-grey clasts and medium-grey clay matrix, with minor grey gypsum crystals, with a patchy distribution. It is difficult to distinguish clasts from matrix. There is <1% pyrite overall, mostly in the matrix (<<1% in vesicles). There are 80% volcanic clasts, with strong pervasive clay alteration, <1.0-9.0 mm (mostly <4.0 mm), poor sorting, subangular to rounded shape, low to moderate sphericity, random fabric, and rare sub-mm vesicles. There is 5% porosity.

Hand sample of MA13-035.

Thin Section Description

This section is a polymict clast-supported volcanic breccia, with clasts up to 4 mm in size. The clasts are subangular and show a variety of colors, textures, and degrees of alteration. Most clasts are vesicular with relict microphenocrysts that show a strong flow-foliation. These clasts are pervasively altered to fine-grained clays (illite/smectite?), with clays lining vesicles. These clasts have abundant fine-grained pyrite disseminated throughout, along with minor FeOx staining. There are also abundant tube pumice clasts that have been entirely altered to chlorite. Several glass shards(?) have also been altered to chlorite. Some glassy fragments remain isotropic. There are are 75% clasts (20% are tube pumice, 3% are glass shards, the remaining is porphyritic vesicular volcanic fragments), 20% matrix, and 5% porosity overall. The matrix is also comprised of fine-grained clays (illite/smectite), with fine-grained disseminated pyrite. There is 2% coarse-grained gypsum with <1% relict anhydrite.



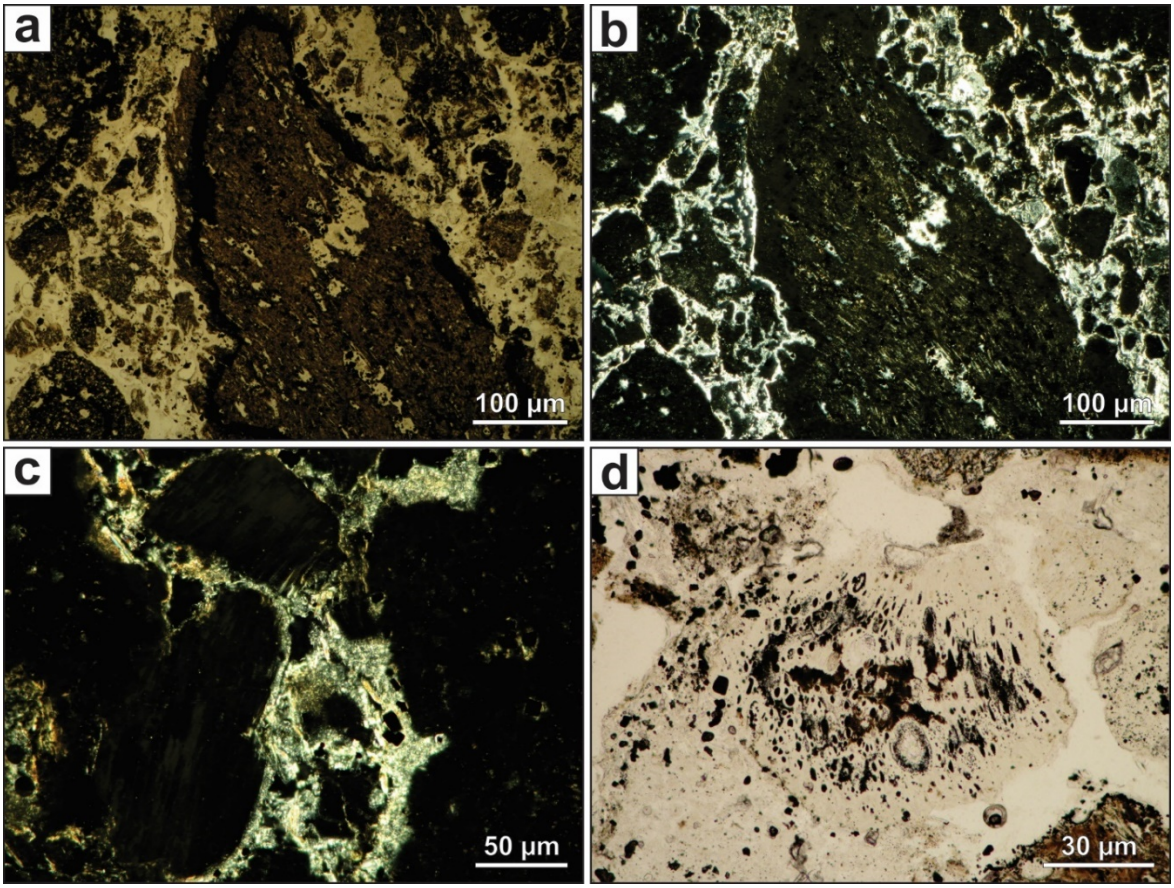
Thin section scan (left) and puck (right) of MA13-035.

Paragenesis: Volcanic clasts + matrix + glass shards → pervasive alteration to illite/smectite + pyrite, illite/smectite lining vesicles → alteration of tube pumice to chlorite, late chlorite lining vesicles → FeOx

Interpretation: Pumice lapillistone (glass shards, angular blocky clasts)

Descriptive Lithological Name: Pervasively clay-altered (illite/smectite + chlorite) polymict clast-supported pumaceous shard-rich lapillistone, weakly cemented

Descriptive Alteration Facies: Pervasive intense illite/smectite alteration of volcanic clasts, pervasive chlorite alteration of tube pumice.



Photomicrographs of GMA13-035: (a) transmitted light (PPL) showing dark irregular volcanic clasts; (b) transmitted light (XPL) showing abundant clay alteration of the matrix (ash?), same view as (a); (c) transmitted light (XPL) showing abundant clay alteration of the matrix (ash?); (d) reflected light (PPL) showing pumice fragment, altered to clay (chlorite?).

SAMPLE: MA13-036 **PARENT ID:** 2410 **SAMPLE DEPTH:** 7.00-7.05 mbsf	**DRILLHOLE:** TKAD016 **DRILLHOLE LOCATION:** 784588.91E/8649829.11N **WATER DEPTH:** 1088.73 mbsl

Mineralogy

SWIR (powdered clast): Chlorite, paragonite, montmorillonite(?)
XRD (clay-sized fraction): chamosite, corrensite(?), aliettite
Assemblage: Cham + Corr

Hand Sample Description

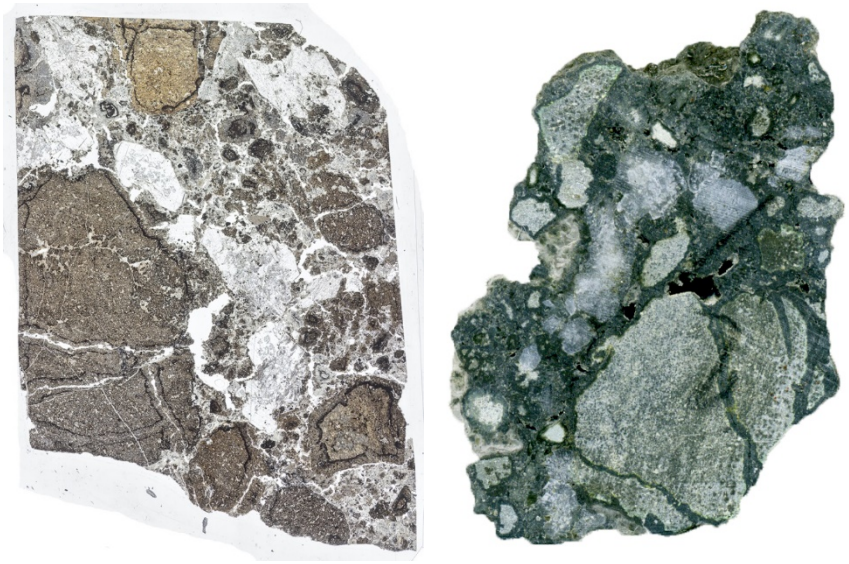


Polymict(?) clast-supported volcanic breccia with a wide range of clast sizes, mostly sub-angular. It is moderately consolidated, with a white-yellow clay-altered matrix, with patchy anhydrite and large gypsum crystals, and minor patchy iron oxide. There is 1% pyrite. There are 85% medium-grey volcanics, with strong pervasive clay alteration, <1.0-13.0 mm in size, poor sorting, subangular shape, low sphericity, random fabric, and relict sub-mm vesicles. There is 2% porosity.

Hand sample of MA13-036.

Thin Section Description

This section is a massive, polymict matrix-supported volcanic breccia. It has a porosity of 2%. There are 38% clasts, <1-15 mm in size, subrounded to angular with irregular margins. There are a variety of clast-types, including: (1) light to dark brown volcanic clasts; (2) light-grey clasts; (3) orange highly vesicular clasts; (4) glassy tube-pumice clasts; (5) other glassy clasts. Volcanic clast 1 (brown clasts) have dark bands between the core and the rim of the crystal (manganese oxide?). It has patchy iron oxides, resulting in uneven coloration. The clasts are massive, with no relict phenocrysts. Locally, there are relict plagioclase microphenocrysts that have been completely altered to clays that are locally aligned along a flow foliation (moderate). They are moderately to highly vesicular, with a wide range in vesicle size. Weak elongation of vesicles may indicate flow foliation. They contain abundant fine-grained pyrite crystals (10-20%). The groundmass is completely altered to clay. The vesicles are lined by a thin layer of chlorite, followed by opal-CT(?), and then illite ± chlorite. There is minor glass along fractures and in vesicles, completely altered to clays (chlorite + illite). XRD analysis indicates that the illite is likely a mixed-layer clay (rectorite). Clast



Thin section scan (left) and puck (right) of MA13-036.

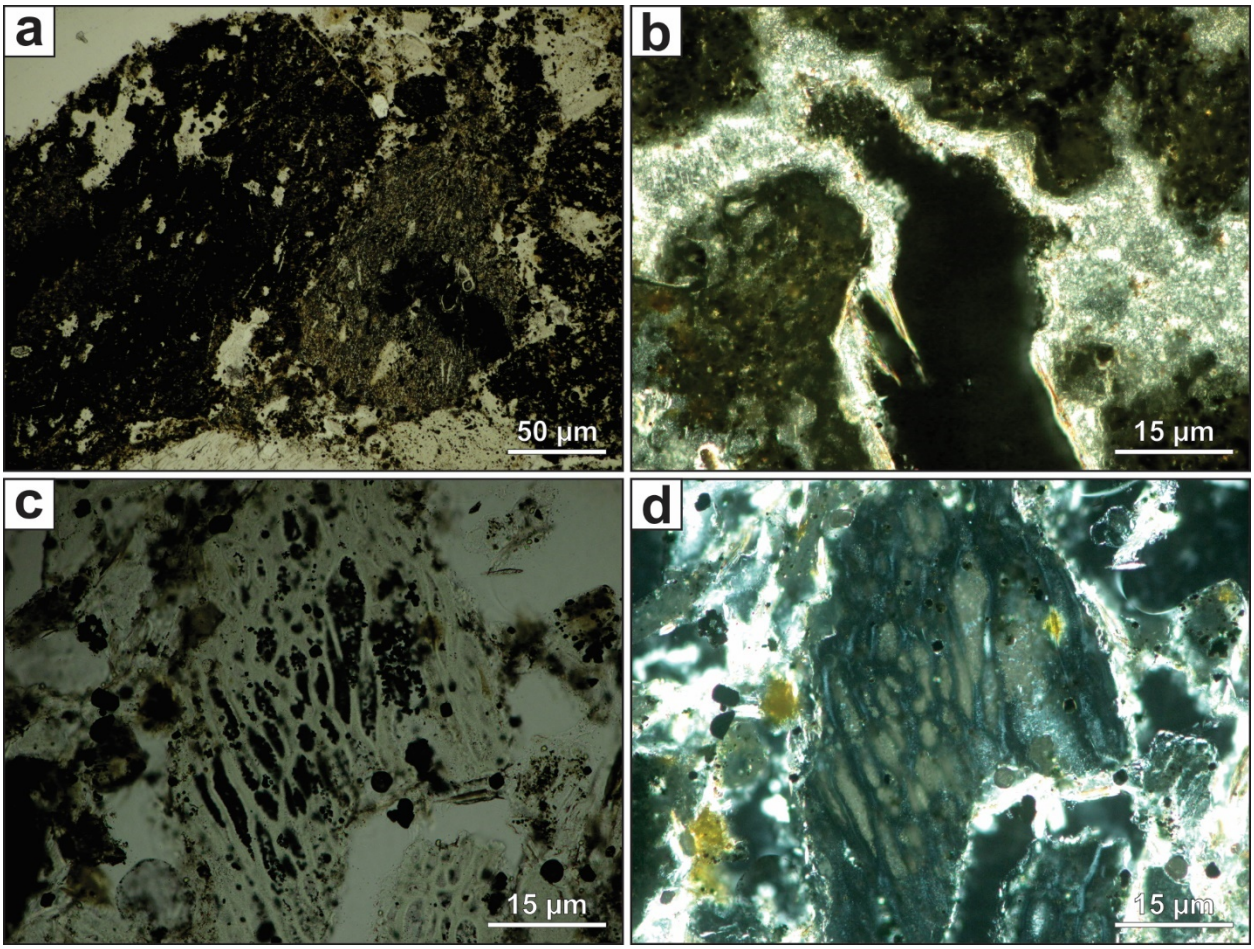
2 (light grey) are less vesicular, have more relict plagioclase microphenocrysts (completely altered), and contain very little pyrite (1%), associated with less iron oxide. The groundmass is also completely altered to clay, with vesicles filled in the same sequence as (1). These clasts also have dark bands of manganese oxide(?). There are light-grey clasts included in the brown clasts, which may be a xenolith or iron-rich and iron-poor parts of the same lava flow. Clast 3 (orange clasts) are highly vesicular/scoraceous, with abundant small vesicles that have been filled in by chlorite, giving the chlorite a globular appearance, separated by orange iron oxide. There are a few larger vesicles, filled in by chlorite → opal-CT(?) → illite + chlorite. Brecciation at the margin of a large clast displays jigsaw fit. This clast type also has a band of dark grey (Mn oxide?) between the core and the rim. It contains very little pyrite, restricted to minor fine-grained pyrite at the core (2%). Clast 4 (tube pumice) has irregular margins. The vesicles are elongate, possibly reflecting stretching during flow, but do not appear to be flattened after deposition. The glass is completely altered to chlorite. The vesicles are locally filled with dark brown material (Mn oxide?), mostly near the core of the clasts. There are also glass-rich clasts/shards (clast 5) that are light orange-brown in color, with subrounded margins, that have been completely altered to clay. There is 46% matrix. It is primarily composed of a combination of very fine- to fine-grained chlorite (25%) + fine-grained illite (rectorite) (14%). There may be opal-CT. The distribution of these phases is irregular, but chlorite generally forms first, followed by intergrown illite + chlorite.

There are patchy sulfates in the matrix, primarily very coarse-grained gypsum (5%), with inclusions of fine- to medium-grained anhedral anhydrite (3%). The matrix also contains fine- to medium-grained euhedral pyrite (3%), which is concentrated along clast margins. It locally contains chalcopyrite (1%) after pyrite, included in gypsum.

This sample is similar to MA13-035, with coarser-grained clasts and more abundant sulfate cement.

Paragenesis: Volcanic clasts (five types, including tube pumice) → clasts altered to Chl ± Py ± FeOx (+ Ill?) → chlorite lines vesicles → opal-CT(?) lines vesicles → intergrown Chl + Ill (+opal-CT?) → patchy anhydrite cementation + mineralization (Py → Ccp) → Anh is partially hydrated to Gp.
Interpretation: Pumice lapillistone (glass shards, angular blocky clasts)
Descriptive Lithological Name: Pervasively clay-altered (chlorite, illite?) massive scoriaceous and pumaceous polymict matrix-supported lapillistone, weakly mineralized and weakly cemented

Descriptive Alteration Facies: Early chlorite(chamosite) ± pyrite ± FeOx, minor opal-CT, late chlorite(chamosite) + illite(rectorite) (+opal-CT?)



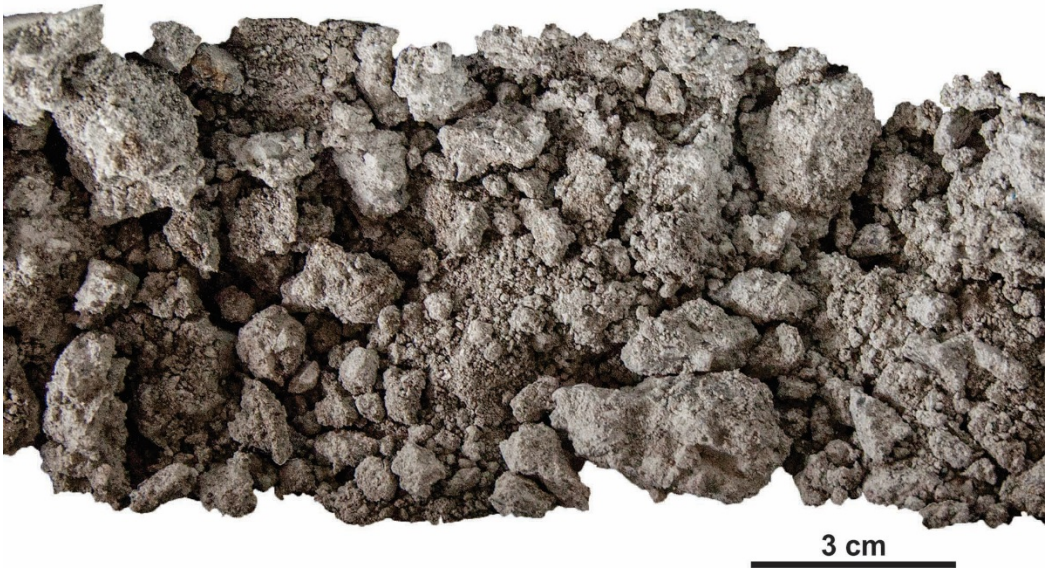
Photomicrographs of GMA13-036: (a) transmitted light (PPL) showing various volcanic clasts; (b) transmitted light (XPL) showing abundant clay precipitation in a void space; (c) transmitted light (PPL) showing a greenish pumice clast; (d) transmitted light (XPL) showing complete clay alteration of the pumice fragment from (c), and abundant clay-alteration in the matrix.

SAMPLE: MA13-038 **PARENT ID:** 2538 **SAMPLE DEPTH:** 3.54-3.70 mbsf	**DRILLHOLE:** TKAD025 **DRILLHOLE LOCATION:** 784605.04E/8649842.58N **WATER DEPTH:** 1090.91 mbsl

Mineralogy

N/A

Hand Sample Description



Hand sample of MA13-038.

Unconsolidated strongly clay-altered monomict(?) volcanic breccia, up to lapilli-sized. Rare pyrite crystals.

Alteration Summary: Pervasive white clay
Interpretation: Unknown origin
Name: Pervasively clay-altered monomict(?) volcanic breccia, unconsolidated

SAMPLE: MA13-039 **PARENT ID:** 2540 **SAMPLE DEPTH:** 5.50-5.60 mbsf	**DRILLHOLE:** TKAD025 **DRILLHOLE LOCATION:** 784605.04E/8649842.58N **WATER DEPTH:** 1090.91 mbsl

Mineralogy

SWIR (powdered clast): Gypsum, montmorillonite(?), chlorite(?)
XRD (clay-sized fraction): Chamosite, I/S
Assemblage: Cham + I/S

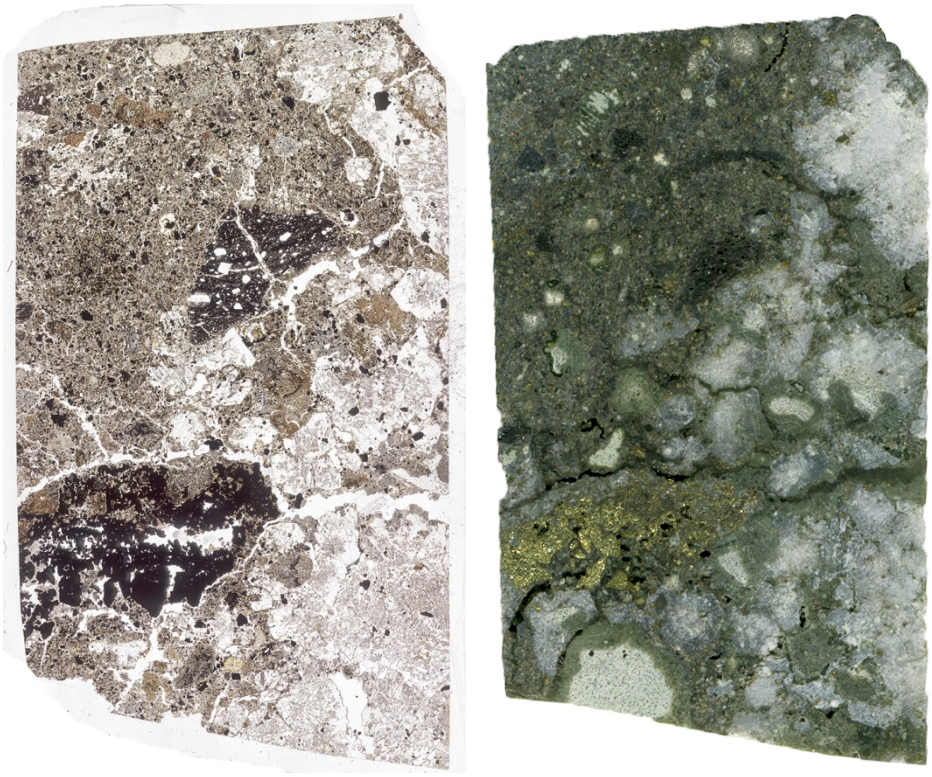
Hand Sample Description



Hand sample of MA13-039.

This sample represents the stringer zone. It is a polymict clast-supported volcanic breccia, with abundant sulfides, moderately consolidated with a pervasively clay-altered matrix and minor anhydrite cement. The matrix is light green-grey. It is difficult to distinguish fine-grained clasts from the matrix. There is 15% pyrite, 2% chalcopyrite, <1% atacamite, and <1% sphalerite. There is crude bedding of the sulfides in cross-section. There are 85% total clasts. This includes 79% light green-grey pervasively clay-altered clasts, <1.0-12.0 mm in size, with poor sorting, subrounded shape, low sphericity, random fabric, with relict sub-mm vesicles. There are 5% light-orange pervasively clay-altered volcanic with minor iron oxide, <1.0-14.0 mm, poor sorted, subrounded shate, low sphericity, random fabric, and aphanitic texture. There are 1% dark grey volcanic clasts with minor clay alteration, 3.0-4.0 mm in size, poor sorting, subrounded shape, low sphericity, random fabric, and aphanitic texture. There is 2% porosity.

Thin Section Description



*Thin section scan (left) and puck (right) of MA13-039***.**

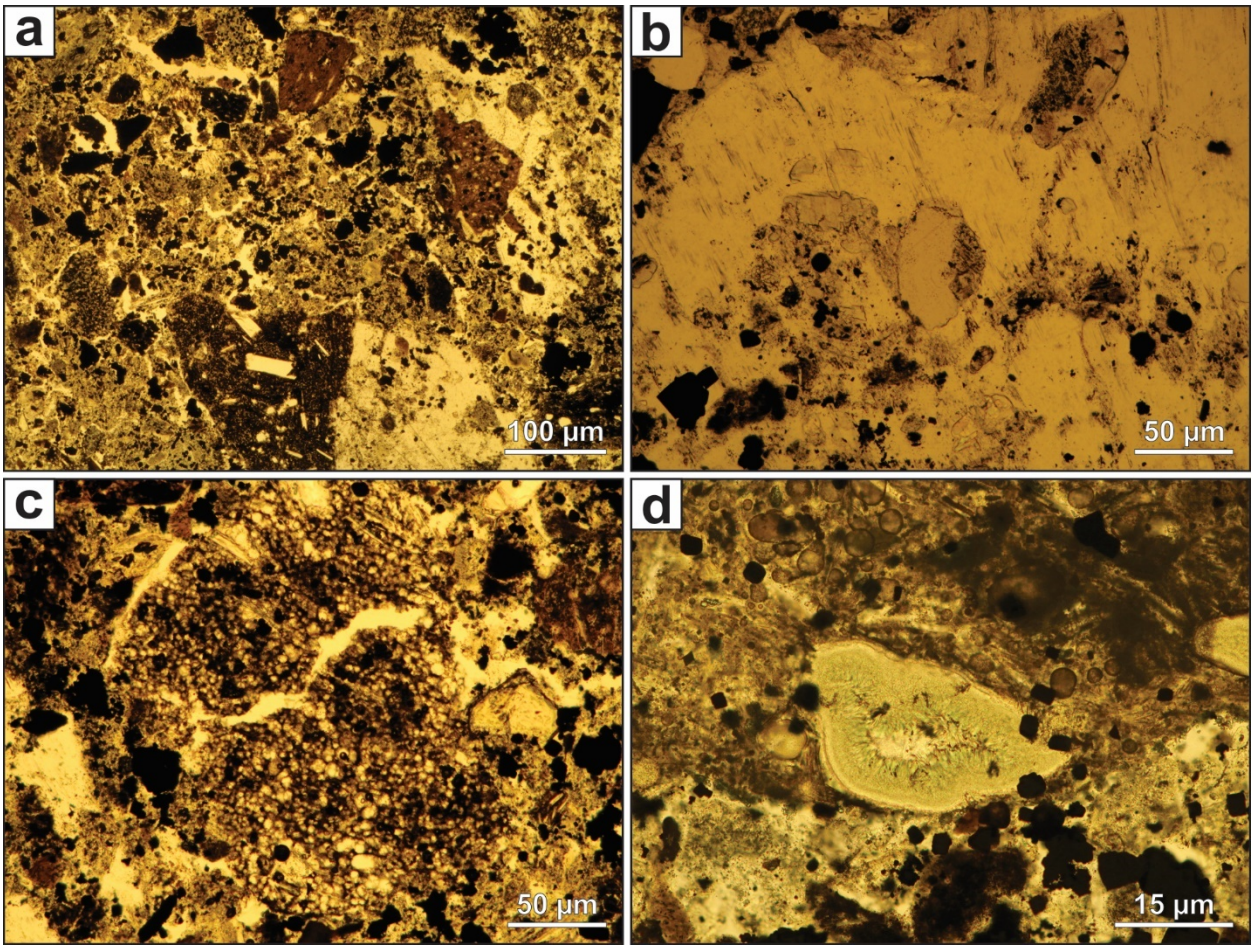
This section is a polymict clast-supported breccia with clasts ranging in size from <1 mm to 5 mm. The clasts are subangular to subrounded and show a variety of colors, textures, and degrees of alteration. The clasts are variably porphyritic, with unaltered plagioclase phenocrysts, and vesicular. The vesicles and phenocrysts locally display flow foliation. Some clasts are very vesicular (scoriaceous). The glassy groundmass is variably altered to fine-grained clays (illite/smectite), with vesicles lined by an early generation of clay (smectite?), followed by chlorite. There is minor disseminated fine-grained pyrite within the altered clasts. One dark grey porphyritic vesicular clast appears unaltered (juvenile fragment) There are also isotropic clasts of tube pumice and glass shards that may be slightly altered to chlorite (greenish). There is 3% total porosity, with 60% clasts and 37% matrix. The matrix is comprised of fine-grained clay-altered material (formerly ash; 16%), patchy sulfates (3% anhydrite, 10% gypsum), and disseminated and chimney-textured sulfides (5% pyrite, 3% chalcopyrite).

Paragenesis: Volcanic clasts (including scoria, tube pumice, and glass shards) and matrix (ash?) → clasts and matrix altered to illite/smectite, chlorite, pyrite and FeOx → chlorite lines vesicles → patchy anhydrite cementation → anhydrite is mostly altered to gypsum → late pyrite mineralization → late chalcopyrite mineralization.

Interpretation: Pumaceous lapillistone

Descriptive Lithological Name: Massive pumaceous shard-rich polymict matrix-supported lapillistone, moderately cemented and mineralized

Descriptive Alteration Facies: Variable in clasts and matrix; chlorite(chamosite) ± illite ± pyrite ± FeOx altering glassy groundmass, late chlorite(chamosite) lining vesicles



Photomicrographs of GMA13-038: (a) transmitted light (PPL) showing various volcanic clasts; (b) transmitted light (XPL) showing glass shard and sulfate cement; (c) transmitted light (PPL) showing a scoriaceous volcanic clast; (d) transmitted light (XPL) showing chlorite precipitation in a vesicle.

SAMPLE: MA13-040 **PARENT ID:** 2542 **SAMPLE DEPTH:** 6.91-7.00 mbsf	**DRILLHOLE:** TKAD025 **DRILLHOLE LOCATION:** 784605.04E/8649842.58N **WATER DEPTH:** 1090.91 mbsl

Mineralogy

SWIR (powdered clast): Chlorite, gypsum
XRD (clay-sized fraction): Montmorillonite, chamosite, corrensite(?)
Assemblage: Cham + Corr

Hand Sample Description



Hand sample of MA13-040.

This sample represents the stringer zone. It is a monomict clast-supported volcanic breccia with light-green-grey clasts , and minor patchy medium-grey to white anhydrite/gypsum cement, which may also include irregular veins up to 10 mm wide.There is 2% pyrite, <1% chalcopyrite, and trace atacamite. There are 80% clasts overall, composed of light green-grey volcanics, with strong pervasive clay alteration, minor chlorite(?), and possible atacamite, <1.0-10.0 mm (mostly <5.0 mm), poor sorting, subangular to subrounded shape, low sphericity, random fabric, with abundant sub-mm vesicles. There is 3% porosity.

Thin Section Description

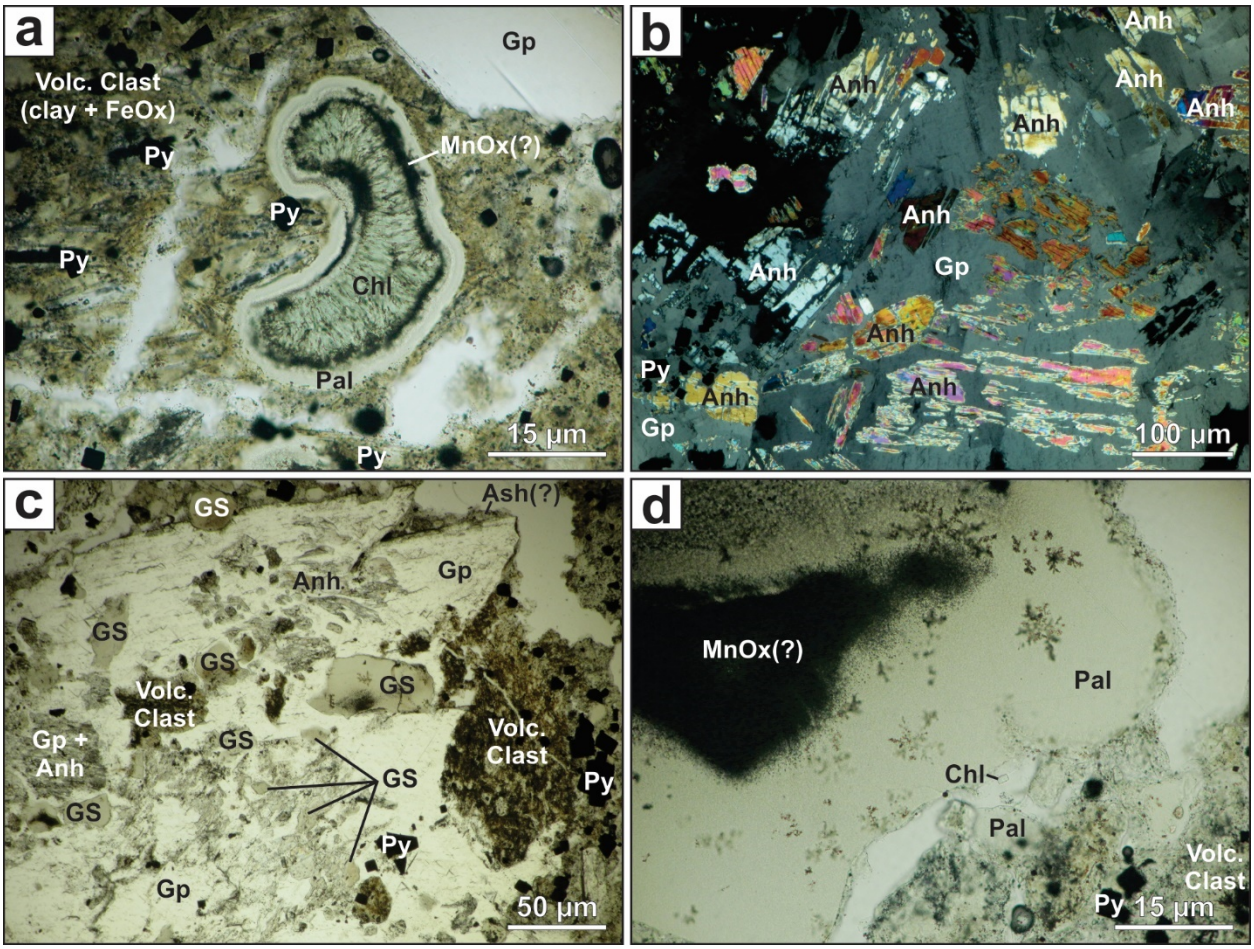
This section has a porosity of ~5%. It is a massive clast-supported (locally matrix-supported) monomict(?) volcaniclastic breccia with no observable bedding. It is from a part of the sample that is strongly cemented by sulfates (anhydrite/gypsum), with 10% fine- to coarse-grained skeletal/anhedral anhydrite at the core of coarse-grained euhedral gypsum (~30% overall). It contains ~25% obvious subrounded clay-altered volcanic clasts (irregular margins). There is also abundant clay-altered domains (irregular fine-grained volcanic clasts or ash?), comprising 10% of the sample. Associated with the clay-rich domains are glass shards that are subrounded to subangular, with curvi-margins, 10% overall. No crystals or crystal fragments were observed. Fine- to medium-grained euhedral pyrite occurs throughout the section, primariliy associated with the clay-altered volcanic clasts, 10% overall. A few of the pyrite cubes have minor dissolution pore space at the core. No other sulfides were observed.



Thin section scan (left) and puck (right) of MA13-040.

The volcanic clasts are dominated by isotropic glass, with patchy Fe,Mn-oxides. Relict plagioclase phenocrysts are completely replaced by very fine-grained clays with abundant dissolution. Microphenocrysts display relict flow foliation. The clasts are highly vesicular, with vesicles partially or completely infilled by gel-palagonite, with later fibrous chlorite. Some smaller clasts contain very large palagonite-chlorite lined vesicles. Palagonite also forms rims around some of the smaller clasts. Some of the coarser palagonite rims contains fine-grained plumose spherulites. The clasts also contain abundant euhedral cubes of pyrite, evenly distributed. The clasts are brown in transmitted light, with larger clasts displaying a blackened core, or a rim of black mineralization (Mn oxide) between the core and the rim of the clasts. Locally, there are medium-grained irregular clasts that closely resemble these darkened cores. Very fine-grained rutile is disseminated throughout the clasts, altered from titanomagentite.

Paragenesis: Volcanic clasts + glass shards + matrix → vesicles lined by gel-Pal → clasts altered to Chl + Py + FeOx → cemented by anhydrite → partially hydrated to Gp.
Interpretation: Shard-rich lapillistone (rounded clasts, abundant glass shards, no crystal fragments)
Descriptive Lithological Name: Massive shard-rich scoriaceous monomict clast-supported lapillistone, cemented
Descriptive Alteration Facies: Early gel-palagonite, later strong pervasive chlorite + pyrite, hydrothermally cemented by anhydrite → gypsum.



Photomicrographs of GMA13-040: (a) transmitted light (PPL) showing an palagonite around a vesicle, altered to clay, followed by minor MnOx(?) and chlorite infill; (b) transmitted light (XPL) showing hydration of anhydrite to gypsum; (c) transmitted light (XPL) showing various volcanic clasts and glass shards; (d) close-up of dendritic textures in a glass shard.

SAMPLE: MA13-044 **PARENT ID:** 2564 **SAMPLE DEPTH:** 5.64-5.69 mbsf	**DRILLHOLE:** TKAD031 **DRILLHOLE LOCATION:** 784726.04E/8649576.46N **WATER DEPTH:** 1110.26 mbsl

Mineralogy

SWIR (powdered clast): Paragoniticillite, nontronite
XRD (clay-sized fraction): Montmorillonite, I/S, illite, pyrite(?), anhydrite
Assemblage: I/S + Py

Hand Sample Description



Monomict matrix-supported volcanic breccia with white to light-grey clasts and medium to dark grey clay-altered matrix, poorly consolidated. The clasts are difficult than the matrix, which tends to be darker (from sulfides?). There are a few gypsum crystals in the matrix. There is 10% pyrite, trace chalcopyrite and trace atacamite. There are 45% volcanic clasts with strong pervasive clay alteration, <1.0-11.0 mm in size, poor sorting, rounded shape, moderate sphericity, random fabric, with patchy pyrite accumulations and minor green atacamite staining, and a few sub-mm vesicles. There is 4% porosity.

Hand sample of MA13-044.

Thin Section Description

This section is a mineralized monomict matrix-supported volcanic breccia, with 3-4% porosity, 25% clasts, and ~70% matrix. The clasts are somewhat difficult to distinguish from the matrix. They are light-medium brown to grey in color, and are up to 4 mm long. They are subrounded, variably vesicular and microporphyritic, generally displaying flow-foliation. The foliation in adjacent clasts is not in the same direction. The clasts are intensely pervasively altered to fine-grained clays (illite/smectite), including the relict phenocrysts, with clay lining the vesicles. There appears to be an early generation of vesicle lining clay with low-order interference colors (smectite?), followed by fibrous clay with fourth-order interference colors (illite?). Some (but not all) clasts appear to have relict glassy margins, although this is generally obscured by intense alteration and is only interpreted from the cocurrence of microphenocrysts. Fine- to coarse-grained euhedral pyrite is disseminated through the clasts and occur around the vesicle margins. Rare green crystals occur near some vesicles (chlorite or atacamite?). Fine-grained Ti-oxides (rutile?) occur within the clasts as an alteration product of magnetite. The matrix consists of fine-grained clays (after ash?), comprised of illite and smectite, with slightly more smectite than illite. The matrix also



Thin section scan (left) and puck (right) of MA13-044.

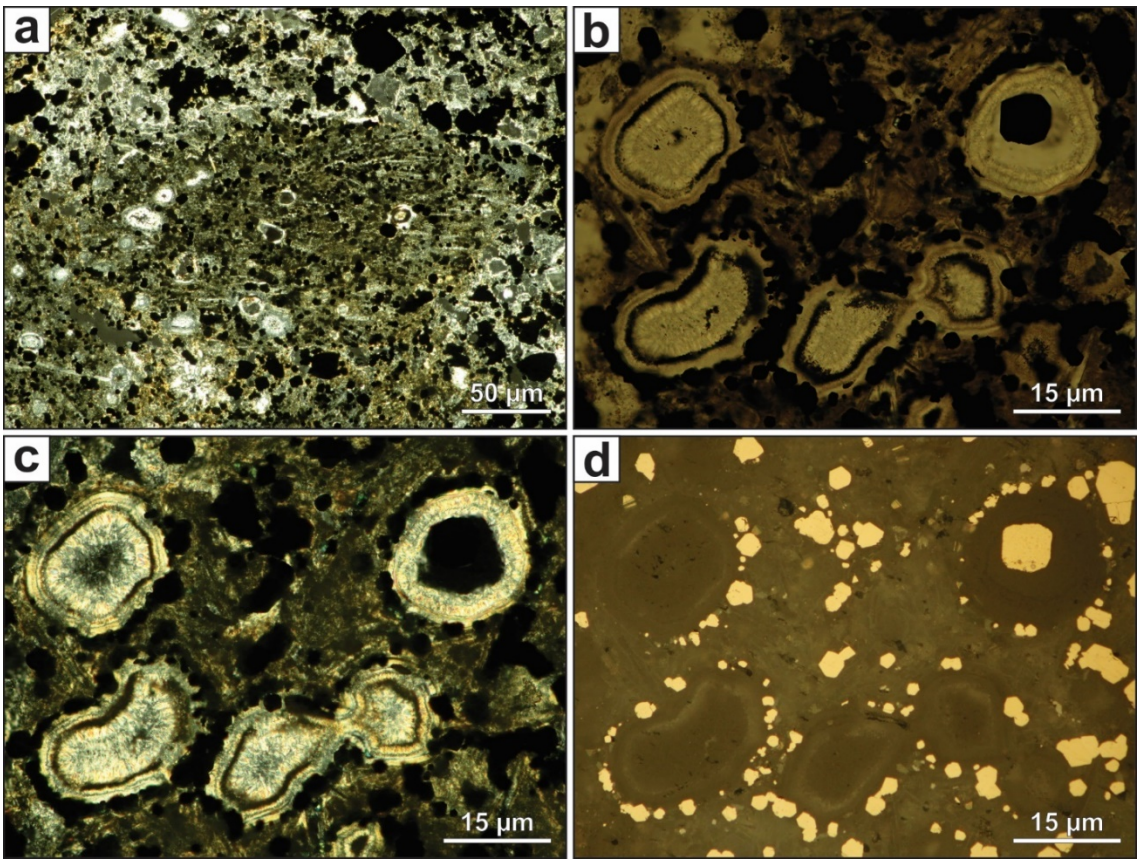
has abundant fine- to coarse-grained pyrite, locally followed by chalcopyrite. Of the 70% matrix, 30% is pyrite and 2% is chalcopyrite. The overall facies is massive and uncemented. No crystal fragments or glass shards were identified.

Paragenesis: Volcanic clasts + matrix (ash?) → smectite + Ti-oxides → illite + pyrite → chalcopyrite

Interpretation: Resedimented granular hyaloclastite (?) (rounding, flow foliation)

Descriptive Lithological Name: Pervasively smectite-illite-altered massive resedimented granular haloclastite, mineralized and unconsolidated

Descriptive Alteration Facies: Intense, pervasive smectite and illite, abundant pyrite (clasts and matrix)



Photomicrographs of GMA13-044: (a) transmitted light (XPL) showing intensely clay-altered volcanic clast and clay-altered matrix; (b) transmitted light (PPL) showing multiple generations of clay precipitation in vesicles; (c) transmitted light (XPL) showing a the same view as (b); (d) reflected light (PPL) showing coarse-grained pyrite around the vesicles, same view as (b) and (c).

SAMPLE: MA13-045 **PARENT ID:** 2565 **SAMPLE DEPTH:** 6.60-6.67 mbsf	**DRILLHOLE:** TKAD031 **DRILLHOLE LOCATION:** 784726.04E/8649576.46N **WATER DEPTH:** 1110.26 mbsl

Mineralogy

XRD (clay-sized fraction): Montmorillonite, I/S, illite, pyrite(?), anhydrite
Assemblage: I/S + Py

Hand Sample Description

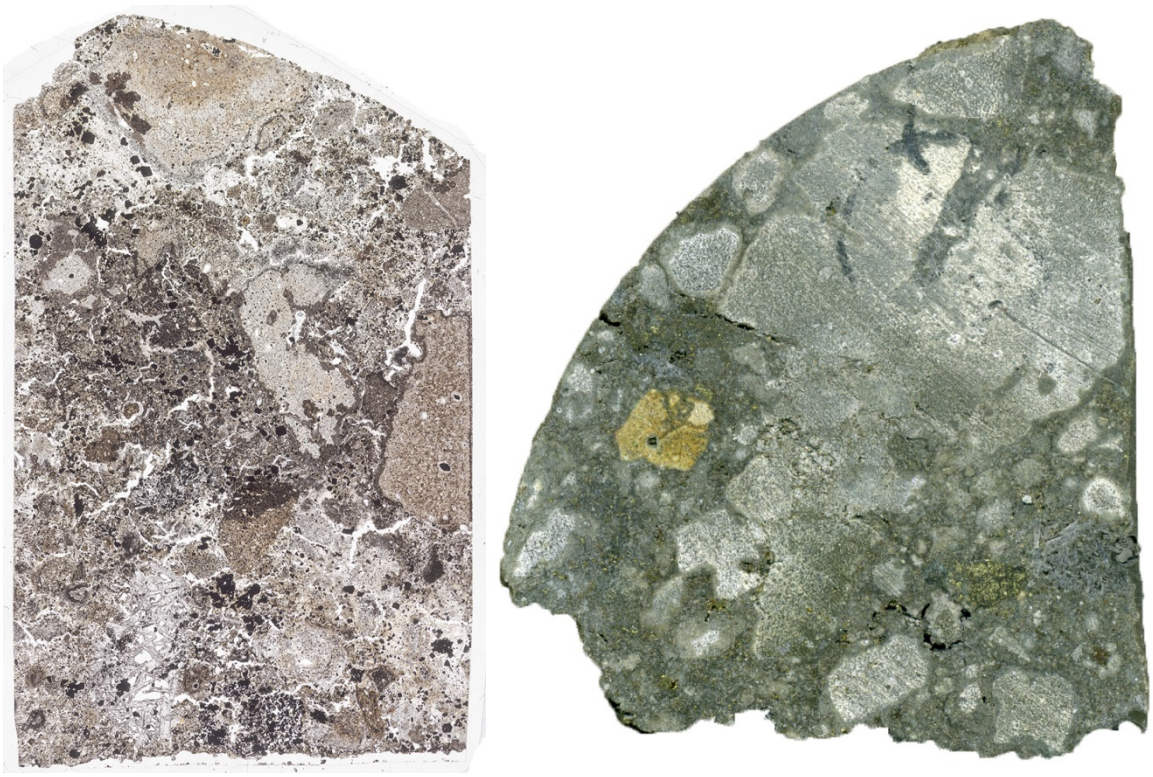


Hand sample of MA13-045.

This sample is a monomict matrix-supported volcanic breccia with white rounded clasts and abundant white to green-grey clay-altered matrix, with possible sulfates. There are abundant sulfides, 10% pyrite, 1% chalcopyrite, and trace atacamite. There are 10% clasts, with strong pervasive white clay alteration, 3.0-16.0 mm wide, with poor sorting, rounded shape, moderate sphericity, and a random fabric, with abundant preserved sub-mm vesicles and 1% pyrite. There is 5% porosity.

Thin Section Description

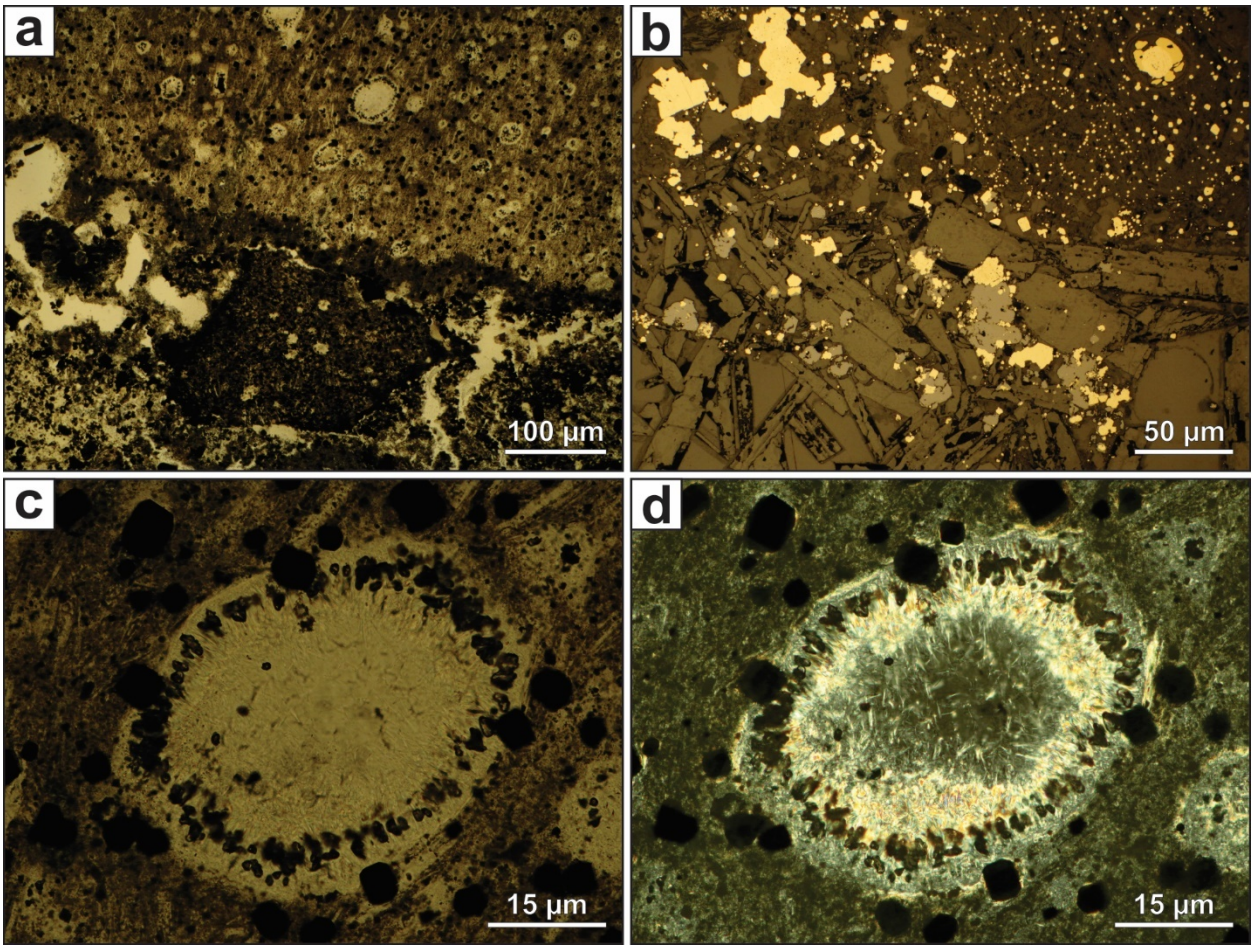
This sample constains a polymict(?) matrix supported volcanic breccia with clasts up to 13 mm long. The clasts are subrounded and show various textures and colors. The colors range from light grey to dark brown. The clasts are variably vesicular with local relict microphenicrysts of plagioclase, locally displaying flow-foliaiton. The foliation directions between adjacent clasts differ. The clast margins are irregular and locally are darker in color, possibly representing former glassy quenched margins. The clasts are pervasively and intensely altered to very fine-grained clays, mostly with first-order interference colors (smectite?). The vesicles are lined by two generations of clays, beginning with first-order grey clay (smectite), followed by a dark-brown-black mineral (Mn oxide?), followed by fourth-order clays (illite?). Fine- to medium-grained pyrite is also disseminated throughout the clasts, and there is variable minor iron oxide. There are 20% clasts overall, with 7-8% pore space, and the remainder matrix (~70%). The matrix is composed of fine-grained illite/smectite in equal proportions constituting 40% of the sample, along with abundant sulfides, constituting 25% of the sample, and late coarse-grained patchy gypsum (weak cement), constituting 5% of the sample. The sulfides are dominated by fine- to coarse-grained



Thin section scan (left) and puck (right) of MA13-045.

subhedral to anhedral pyrite (15-18%), followed by chalcopyrite (5-8%) and sphalerite (1-2%), with rare bornite and covellite (<1%). Compared to MA13-044, this sample has larger and more abundant clasts with more variable clast compositions. The original composition may be the same with variable degrees of alteration. No crystal fragments or glass shards were identified.

Paragenesis: Volcanic clasts + matrix (ash?) → smectite → MnOx? (local) → illite + pyrite → pyrite → chalcopyrite → sphalerite → bornite + covellite + FeOx → coarse-grained gypsum (patchy)
Interpretation: Resedimented hyaloclastite breccia (?) (polymict, rounding, flow foliation)
Descriptive Lithological Name: Pervasively smectite-illite-altered massive resedimented polymict haloclastite breccia, mineralized and unconsolidated
Descriptive Alteration Facies: Intense, pervasive smectite and illite, abundant pyrite (clasts and matrix)



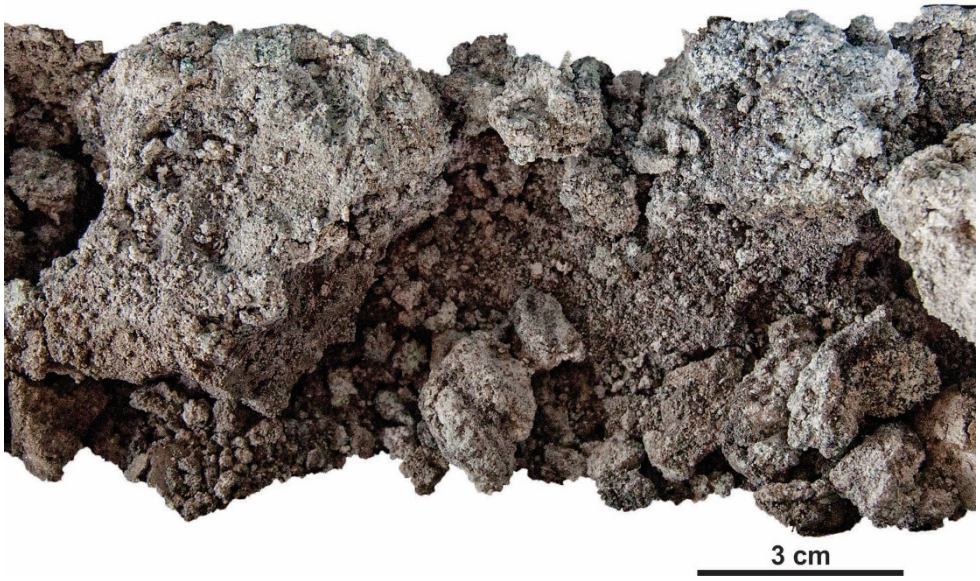
Photomicrographs of GMA13-045: (a) transmitted light (PPL) showing various volcanic clasts; (b) reflected light (PPL) showing finely disseminated pyrite in a volcanic clast (top right), and coarser-grained pyrite+sphalerite (with minor chalcopyrite+bornite+covellite) in the matrix associated with gypsum; (c) transmitted light (PPL) showing multiple generations of clay in a vesice, separated by MnOx(?); (d) transmitted light (XPL) showing the same view as (c).

SAMPLE: MA13-050 **PARENT ID:** 2398 **SAMPLE DEPTH:** 3.49-3.63 mbsf	**DRILLHOLE:** TKAD015 **DRILLHOLE LOCATION:** 784561.08E/8649940.06N **WATER DEPTH:** 1091.80 mbsl

Mineralogy

XRD (clay-sized fraction): Montmorillonite, chamosite, I/S, illite, paratacamite(?)
Assemblage: I/S + Cham

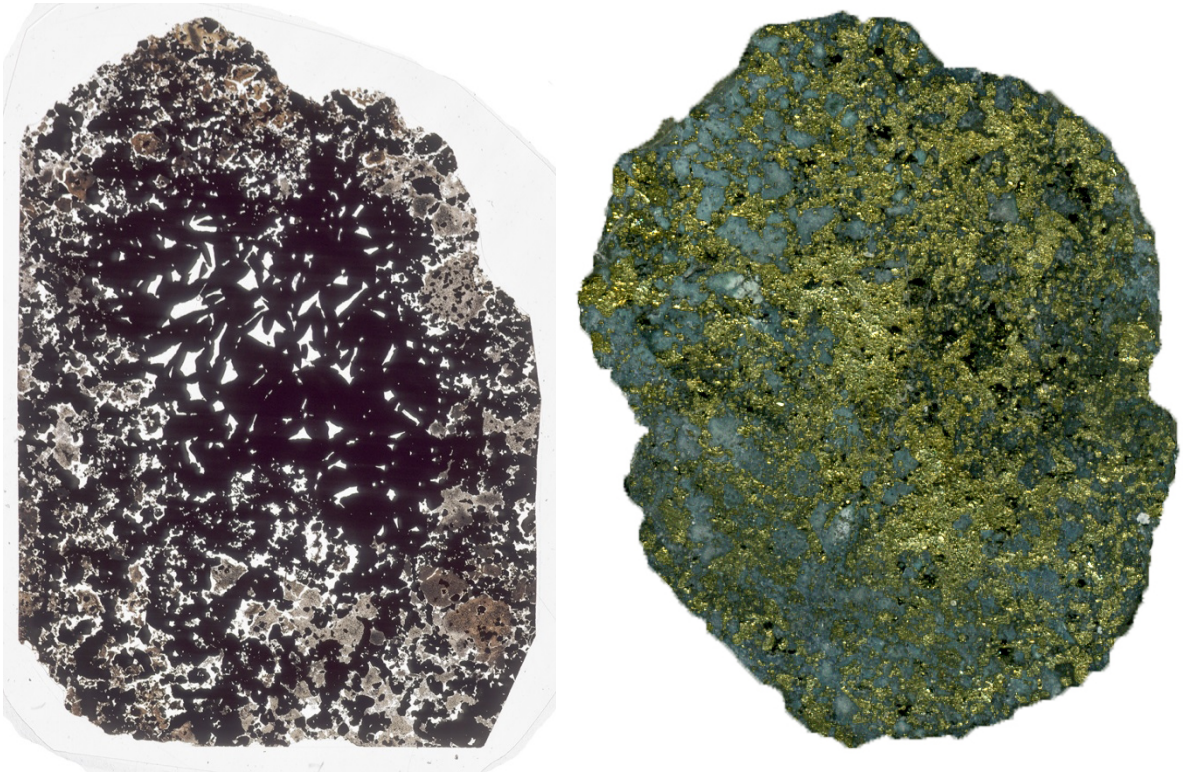
Hand Sample Description



Hand sample of MA13-050.

This sample represents the transition from chimney talus to the altered footwall (proximal to chimney). It is unconsolidated volcanic and chimney fragments with variably clay-altered clasts. The matrix is medium-grey very fine-grained clay. There are abundant sulfides, 5% chalcopyrite, 2% pyrite, trace atacamite. There are 70% clasts overall. This includes 45% medium-grey volcanic clasts with pervasive and variable clay alteration, <1.0-15.0 mm in size, very poor sorting, subrounded shape, low sphericity, and random fabric, and aphanitic texture. There are 35% chimney fragments, including fragments that are barite-rich (heavy) and chalcopyrite-rich with trace malachite. Alteration includes minor clay alteration and oxidation of sulfides. These clasts are <1.0-30.0 mm, with poor sorting, subangular shape, low sphericity, random fabric, and chimney growth textures. The porosity is 5%.

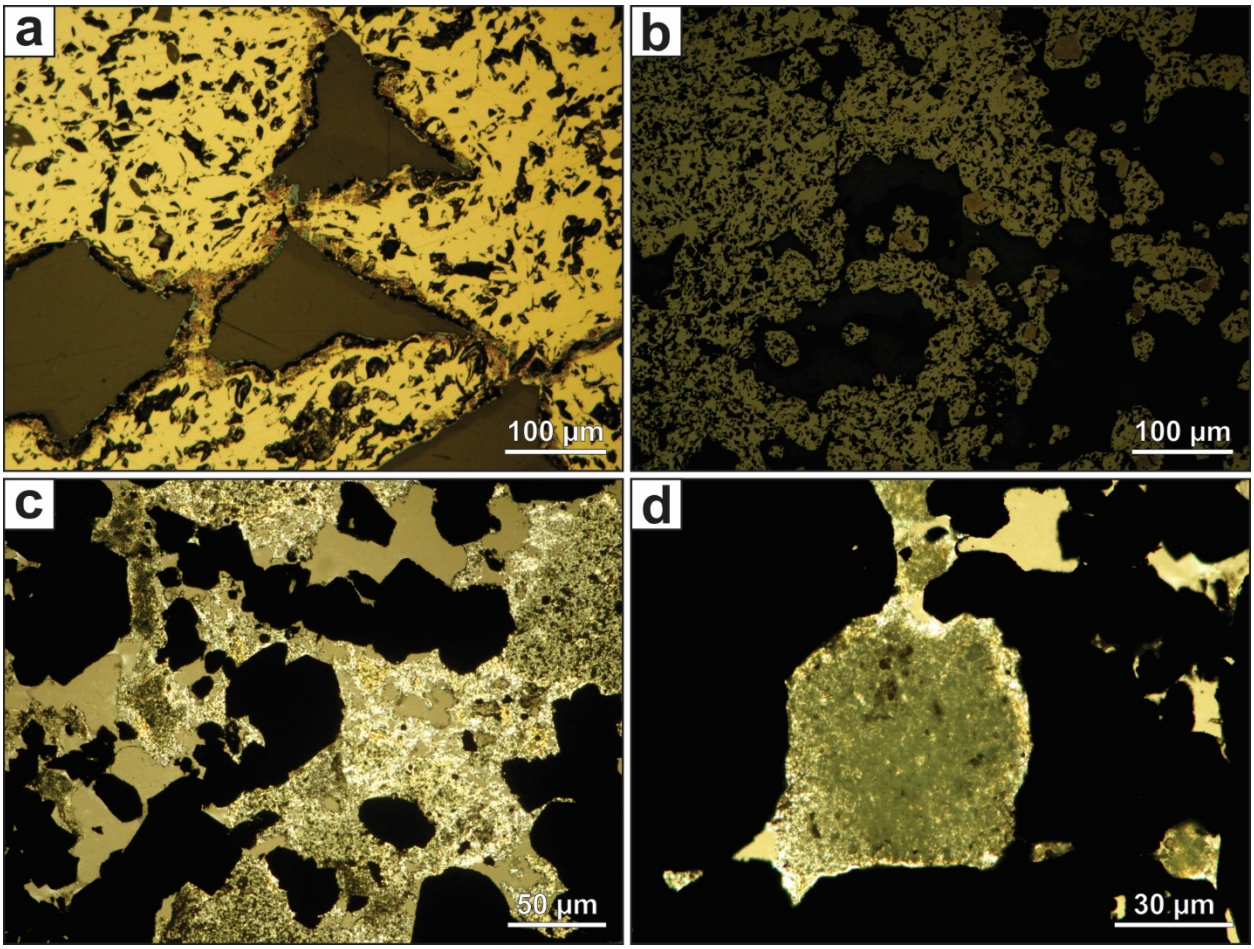
Thin Section Description



Thin section scan (left) and puck (right) of MA13-050.

This sample appears to be a chalcopyrite-rich chimney fragment, with 15% porosity, with 5% early medium-grained euhedral pyrite, and 50% coarse-grained chalcopyrite with dog-toothed texture and rare alteration to covellite (<1%). The remaining 30% consists of fine-grained unidentified material, likely clay minerals, and ~3% relict anhydrite crystals. The fine-grained material is translucent to muddy brown, and post-dates the sulfide material. There may be extremely altered relict volcanic clasts.

Paragenesis: Pyrite → chalcopyrite → covellite → anhydrite → clay
Interpretation: Chimney fragment
Descriptive Lithological Name: Chalcopyrite-rich chimney fragment
Descriptive Alteration Facies: Late clay alteration of matrix material



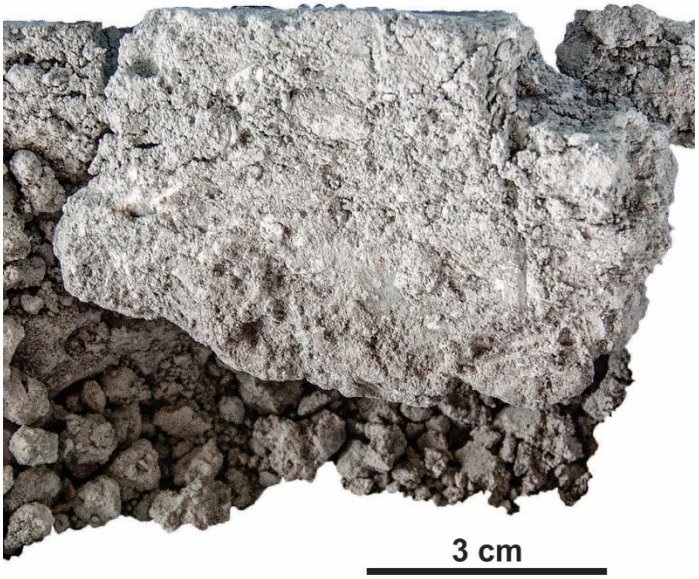
Photomicrographs of GMA13-050: (a) reflected light (PPL) showing coarse-grained chalcopyrite with minor alteration at the rims; (b) reflected light (PPL) showing chalcopyrite after pyrite; (c) transmitted light (XPL) showing clay minerals in the matrix; (d) transmitted light (XPL) showing a possible volcanic fragment that has been completely altered to clay.

SAMPLE: MA13-051 **PARENT ID:** 2400 **SAMPLE DEPTH:** 4.34-4.43 mbsf	**DRILLHOLE:** TKAD015 **DRILLHOLE LOCATION:** 784561.08E/8649940.06N **WATER DEPTH:** 1091.80 mbsl

Mineralogy

XRD (clay-sized fraction): Chamosite, I/S
Assemblage: Cham + Corr

Hand Sample Description

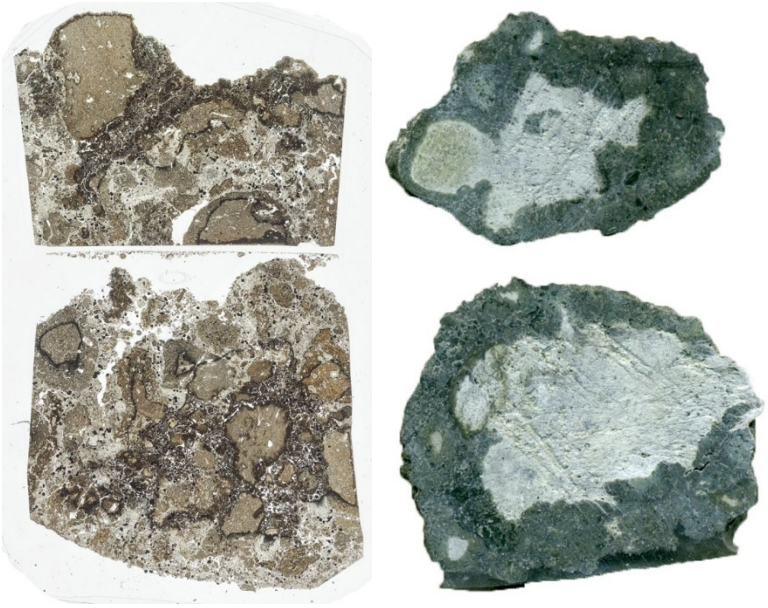


Hand sample of MA13-051.

This sample is a semi-consolidated clast-supported volcanic breccia with clay-altered clasts and matrix. The matrix is medium grey-green, with intense pervasive clay, and minor chlorite. There are 70% clasts overall, which appear to be polymict but may just reflect variable alteration intensities. There are 70% medium grey-green volcanic clasts, with intense pervasive clay alteration, minor chlorite and trace yellow mineral (sericite?), 1.0-10.0 mm wide, with poor sorting, subroudned-subangular shape, poor sphericity, random fabric, and aphanitic texture with 1% sub-mm vesicles and 1% pyrite. There is 10% porosity.

Thin Section Description

This section is a massive monomict(?) matrix-supported breccia, with ~15% pore space, with 5% tube pumice clasts, 10% glass shards, 55% of volcanic clasts, 5 % pyrite, 10% clay-altered matrix, and <1% anhydrite. The volcanic clasts are light reddish-brown to dark brown, and have 5-15% irregular vesicles, variable amounts of microphenocrysts, locally flow-foliated, and rare coarse-grained relict plagioclase phenocrysts. Several clasts have ~50% vesicles (scoria clasts) that are partly infilled by chlorite. The clasts are pervasively clay-altered, with clay and chlorite lining vesicles. The margins are irregular angular to sub-rounded, with locally preserved classy margins. Fine-grained pyrite is disseminated through the clasts, and occurs as coarse-grained euhedral crystals in the matrix. The matrix is shard-rich, with medium-grained pervasively clay-altered shards, and local dendritic features. The tube-pumice fragments are medium-grained and are also pervasively altered to clay-chlorite.



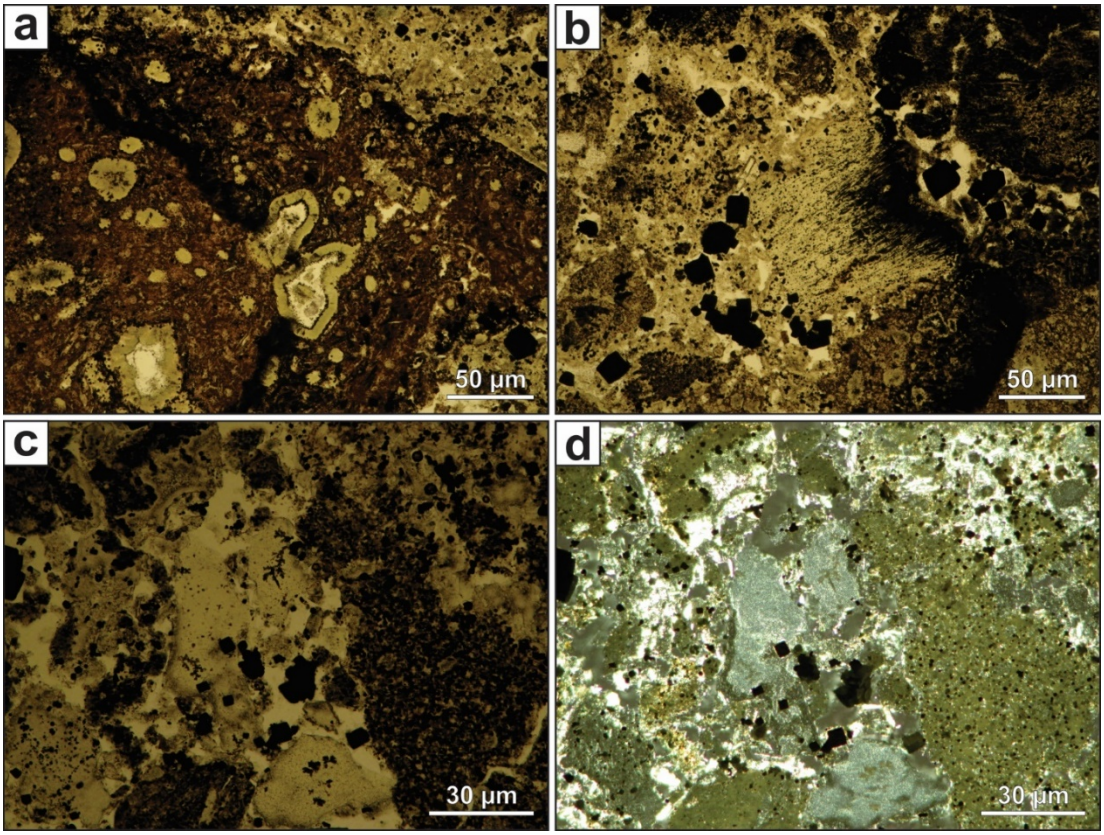
Thin section scan (left) and puck (right) of MA13-051.

Paragenesis: Volcanic clasts + pumice + glass shards → alteration of glassy groundmass and glass shards to clay (chlorite) and pyrite → infill of vesicles with chlorite → minor coarse-grained pyrite → FeOx

Interpretation: Syn-eruptive lapilli tephra (flow-foliated, glass shards, angular)

Descriptive Lithological Name: Intensely clay-altered (chlorite?) massive monomict(?) matrix-supported shard-rich pumaceous lapilli tephra, unconsolidated

Descriptive Alteration Facies: Pervasive clay altering clasts, pumice fragments, and glass shards, vesicles lined by chlorite.



Photomicrographs of GMA13-051: (a) transmitted light (PPL) showing a large volcanic clast with chlorite lining the vesicles; (b) transmitted light (PPL) showing a pumice fragment along with various volcanic fragments; (c) transmitted light (PPL) showing a glass shards; (d) transmitted light (XPL) showing complete clay alteration of the glass shards from (c), and abundant clay-alteration in the matrix.

SAMPLE: MA13-052 **PARENT ID:** 2402 **SAMPLE DEPTH:** 6.42-6.52 mbsf	**DRILLHOLE:** TKAD015 **DRILLHOLE LOCATION:** 784561.08E/8649940.06N **WATER DEPTH:** 1091.80 mbsl

Mineralogy

SWIR (powdered clast): Paragonite, gypsum, chlorite(?)
XRD (clay-sized fraction): Chamosite, I/S
Assemblage: Cham + Corr

Hand Sample Description

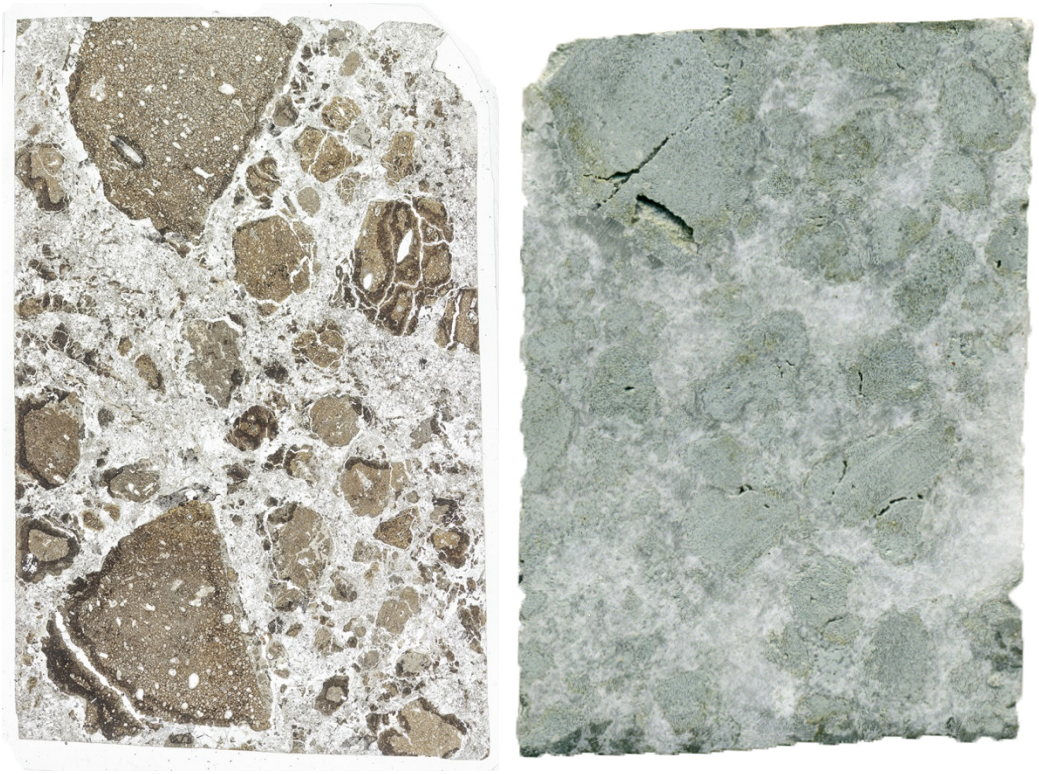


Hand sample of MA13-052.

This sample is a matrix-supported monomict volcanic breccia with light grey-green clay-altered clasts cemented by medium-grey to patchy-white anhydrite. There is possible clay alteration in the matrix. There is <1% pyrite. There is 40% clasts overall. This includes 38% pale green-grey volcanic clasts, with intense pervasive clay alteration, trace chlorite, and trace yellow at the clast edges (sericite?), <1.0-7.0 mm, poor sorting, subrounded-subangular shape, poor sorting, random fabric, aphanitic texture, 1% sub-mm vesicles, <1% fine-grained pyrite, and dessication cracks. There are 2% green clay- and chlorite-altered clasts, with a more intense color than the other clasts. The alteration is intense, pervasive. They are 4.0-10.0 mm wide, with poor sorted, subrounded to subangular shape, low sphericity, random fabric, and aphanitic texture. The clasts have a bimidal distribution: those between <1-2 mm and 3.7 mm (50:50). There is 1% porosity.

Thin Section Description

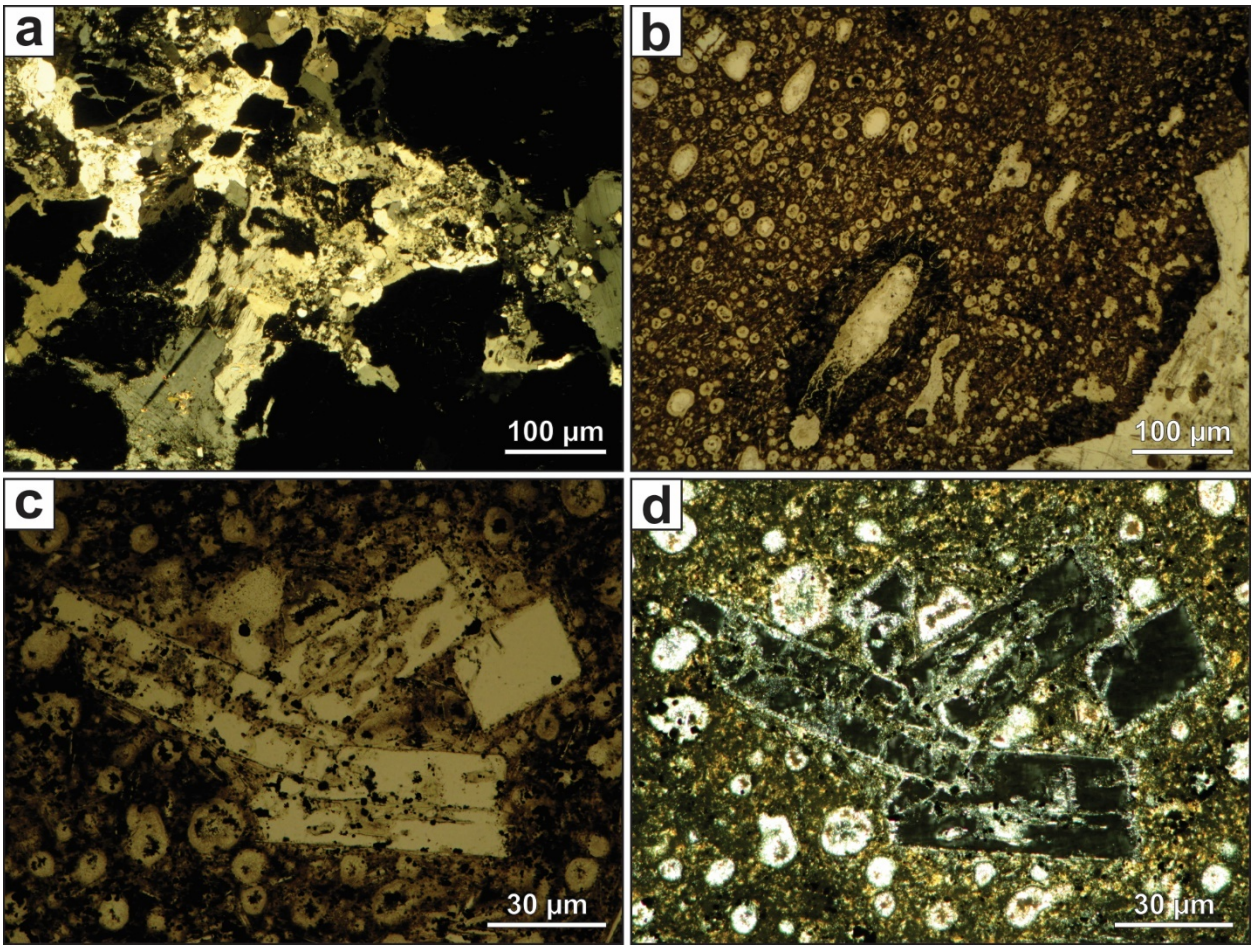
This sample is a matrix-supported monomict volcanic breccia with large scoriaceous volcanic clasts (30%), and abundant glass shards (10%), late clay infill (5%), cemented by gypsum (40%). The overall porosity is 5%. The volcanic clasts have irregular angular to subrounded margins, abundant small to



Thin section scan (left) and puck (right) of MA13-052.

large mostly rounded vesicles, abundant microphenocrysts, locally flow-foliated, and rare relict glomeroporphyritic coarse-grained plagioclase phenocrysts. The groundmass of the clasts is pervasively altered to clay (illite/chlorite) and minor fine-grained pyrite (~3%), with clay lining the vesicles. The clasts locally have glassy margins or domains that have been completely altered to clay. The glass shards have very irregular margins and are isotropic to pervasively clay-altered. The sulfate cement is dominantly gypsum, with rare relict anhydrite inclusions (3%), and abundant recrystallization textures.

Paragenesis: Scoria clasts + glass shards → alteration of glassy groundmass and glass shards to clay (illite/chlorite) and minor pyrite → infill of vesicles with clay → anhydrite cement → recrystallized to gypsum
Interpretation: Proximal lapilli tephra
Descriptive Lithological Name: Intensely clay-altered (illite/chlorite) massive monomict(?) matrix-supported shard-rich scoriaceous lapilli tephra, cemented
Descriptive Alteration Facies: Pervasive clay altering clasts, pumice fragments, and glass shards, vesicles lined by chlorite



Photomicrographs of GMA13-052: (a) transmitted light (XPL) showing recrystallized gypsum; (b) transmitted light (PPL) showing a vesicular/scoriaceous volcanic clast; (c) transmitted light (PPL) showing relict plagioclase phenocrysts; (d) transmitted light (XPL) showing clay precipitation in vesicles and relict phenocrysts, same view as (c).

SAMPLE: MA13-053 **PARENT ID:** 2403 **SAMPLE DEPTH:** 7.23-7.34 mbsf	**DRILLHOLE:** TKAD015 **DRILLHOLE LOCATION:** 784561.08E/8649940.06N **WATER DEPTH:** 1091.80 mbsl

Mineralogy

SWIR (powdered clast): Paragonite, gypsum, chlorite(?)
XRD (clay-sized fraction): chamosite, I/S
Assemblage: Cham + Corr

Hand Sample Description

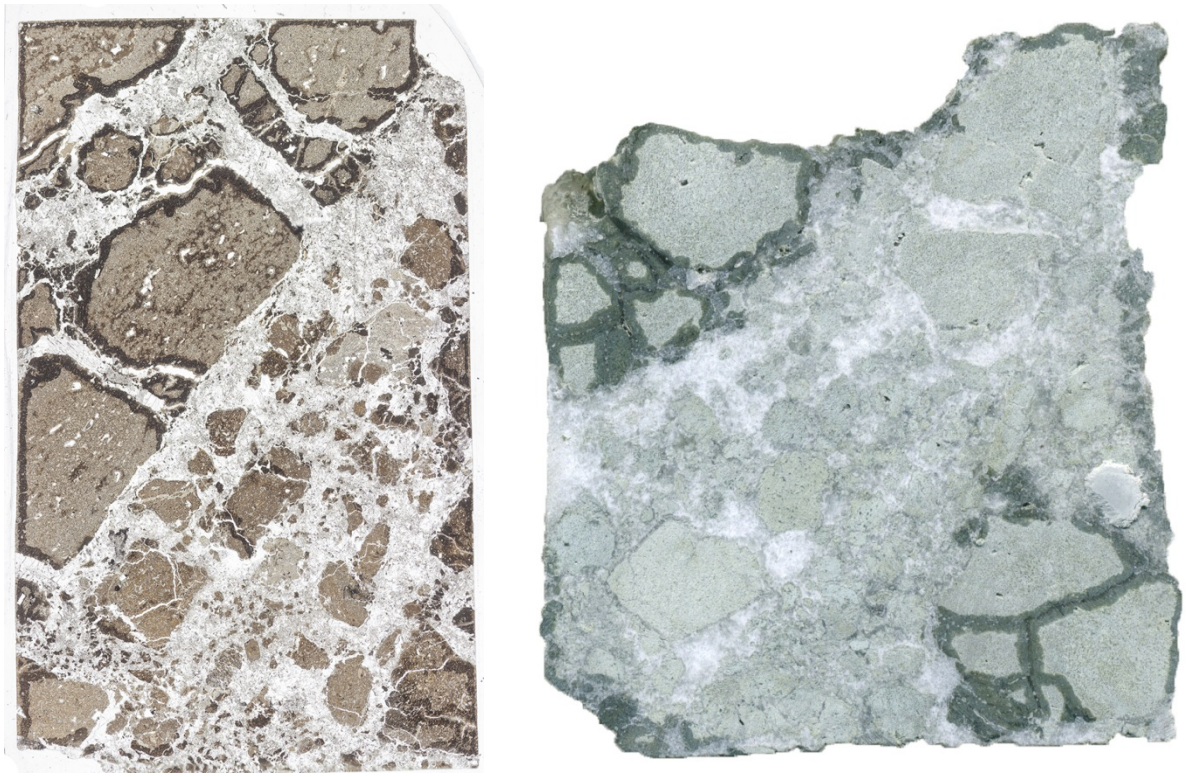


Hand sample of MA13-053.

This section is a matrix-supported monomict volcanic breccia with small light grey-green clay-altered clasts (few larger clasts), cemented by anhydrite/gypsum. The matrix is composed of medium grey- to white anhydrite/gypsum (and clay?). There are three irregular white anhydrite/gypsum veinlets, 1-3 mm wide at high angles to core axis (45-55° TCA). There is <1% pyrite overall. There are 35% pale green-gray volcanic clasts, with intense pervasive clay alteration (chlorite?). These clasts are <1.0-26.0 mm in size, with an abrupt decrease in grain size downhole. There is a bimidal grain size distribution: <1-2 mm and 6-26 mm (80:20). The clasts have poor sorting, a subrounded shape, moderate sphericity, random fabric, and aphanitic texture, very weakly vesicular with 1% sub-mm vesicles. The clasts are cut by the anhydrite/gypsum veins. The porosity is <1%.

Thin Section Description

This section has a porosity of ~2%. It is a monomict volcanic breccia with weak bedding according to grain size. It is matrix-supported, with 60% sulfate veins, dominated by gypsum (58%), with very little anhydrite remaining (2%). The gypsum is micropoikolitic, locally with sieve texture and displays extensive recrystallization. It is locally deformed. The matrix appears to be an infill or hydrothermal veining.



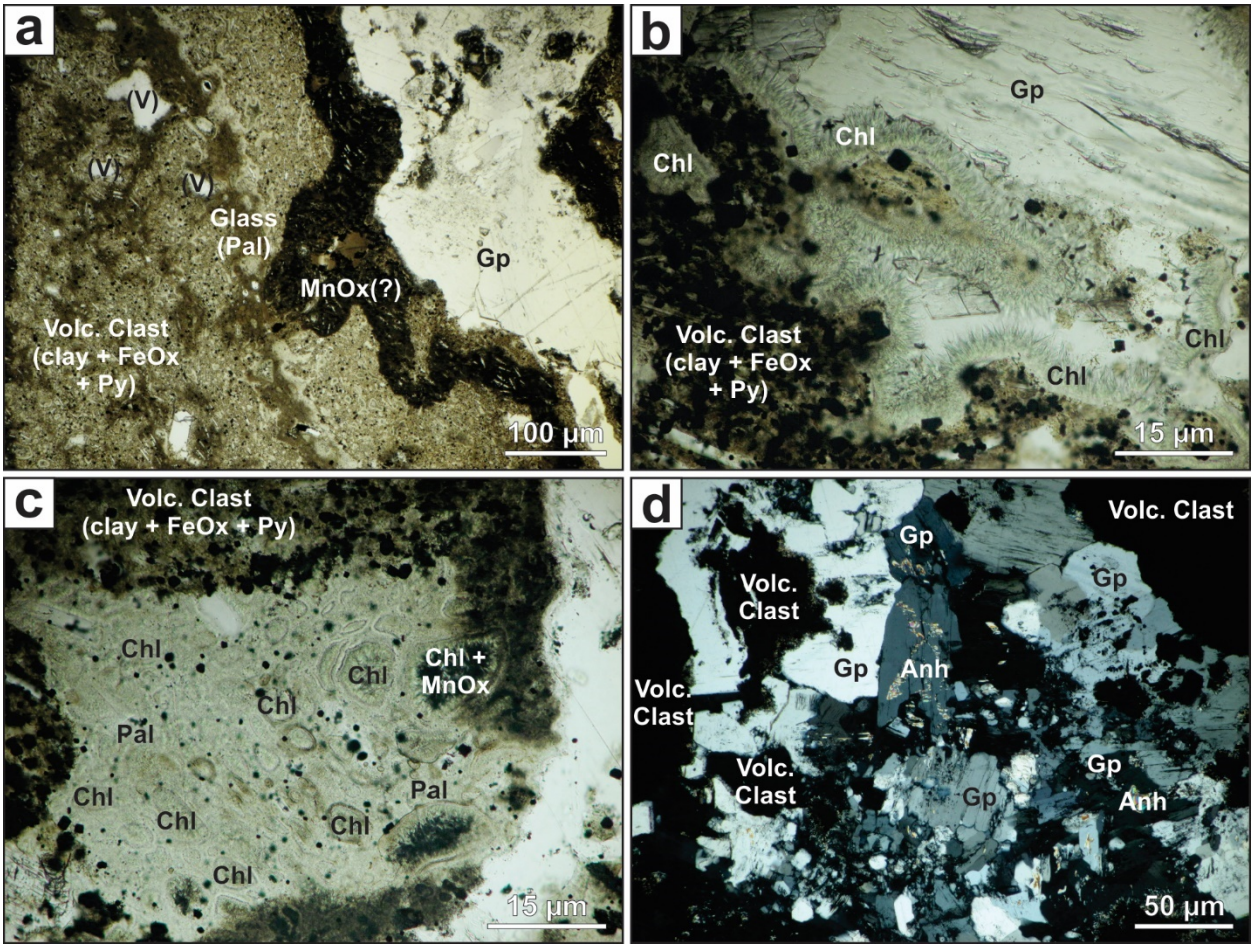
Thin section scan (left) and puck (right) of MA13-053.

There are two distinct varieties of volcanic clasts. Clast 1 appears medium-dark brown in thin section, with heterogeneous coloring (patchy Fe,Mn-oxides). The larger clasts have dark brown (oxidized?) rims. The clasts have irregular margins, and are subrounded to angular. There is minor jigsaw-fit brecciation. They are highly vesicular, with elongate irregular vesicles oriented along a flow foliation. Rare relict phenocrysts of plagioclase have been completely dissolved. Microphenocrysts of plagioclase have been completely altered to chlorite (clinochlore), but relict crystals also display a flow-foliation. The vesicles are also lined by transparent to very pale-green chlorite. Fibrous chlorite also locally grows outwards from the margins of the clasts. Locally, there are irregular zones of perlitic glass near the clast margins, which has also been pervasively altered to chlorite, with chlorite lining vesicles. Locally, some clasts contain elongate irregular areas of this glass cutting through the clast, ranging in color from light orange to dark brown. This may be small flows onlapping other flows. Mostly fine-grained euhedral pyrite is regularly distributed throughout the clasts, with a slight increase in abundance at the clast margins, with no pyrite in the glassy areas.

Clast 2 is finer-grained, with irregular sub-rounded to angular, locally curvi-planar margins. These clasts are lighter brown with less iron and manganese oxide. It is very highly vesicular. It contains less pyrite. It is completely pervasively altered to fine-grained chlorite. Chlorite also lines the vesicles. These clasts contain inclusions of clast 1. These clasts are interpreted to be glassy/pumaceous domains, but likely originating from the same flow as clast 1; therefore it is still considered a monolithic breccia. Clast 1 comprises 28% of the sample, and clast 2 comprises 5% of the sample.

There are few angular glass shards associated with the volcanic clasts, with irregular light to dark brown coloring (palagonite), 2% overall. Fine- to coarse-grained chalcopyrite forms in some of the pore spaces, including in dissolved relict plagioclase phenocrysts, <1% overall.

Paragenesis: Volcanic clasts → clasts altered to Chl + Py + FeOx → cemented by Anh → Anh hydrated to Gp → Gp recrystallized.
Interpretation: Hyaloclastite (curviplanar clasts, no crystal fragments)
Descriptive Lithological Name: Massive scoriaceous monomict matrix-supported hyaloclastite sand-pebble breccia, weakly mineralized, sulfate-cemented
Descriptive Alteration Facies: Strong pervasive chlorite + pyrite, hydrothermally cemented by anhydrite → gypsum



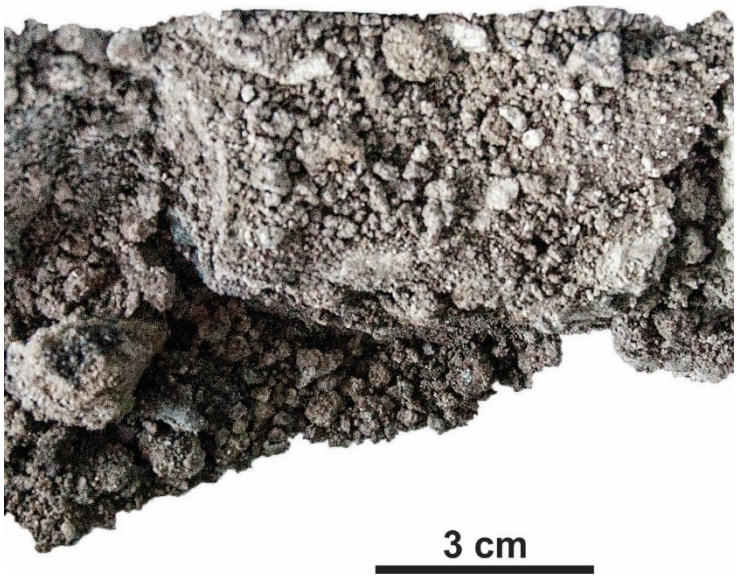
Photomicrographs of GMA13-053: (a) transmitted light (PPL) showing a dark rim along a volcanic clast; (b) transmitted light (PPL) showing chlorite precipitation along the margins of a clast; (c) transmitted light (PPL) showing a a chlorite-altered pumice fragment; (d) transmitted light (XPL) showing almost complete hydration of anhydrite to gypsum.

SAMPLE: MA13-056 **PARENT ID:** 2520 **SAMPLE DEPTH:** 2.50-2.60 mbsf	**DRILLHOLE:** TKAD027 **DRILLHOLE LOCATION:** 784562.04E/8649937.83N **WATER DEPTH:** 1091.36 mbsl

Mineralogy

XRD (clay-sized fraction): Chamosite, rectorite, paratacamaite, barite(?), barian celadonite(?)
Assemblage: I/S + Cham

Hand Sample Description

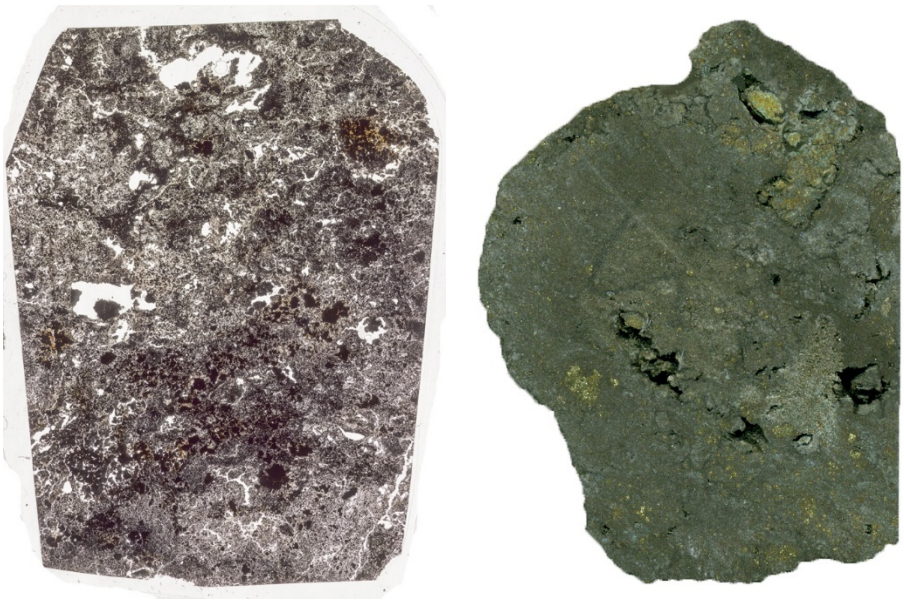


Hand sample of MA13-056.

This sample is altered chimney talus at the transition between the sulfides and the altered footwall. It is an unconsolidated breccia of chimney fragments and minor white to light-grey clay-altered clasts. It is partially cemented by sulfides and possible anhydrite. It is difficult to determine the % sulfides, as it consists of chimney fragments and unconsolidated sulfide sand. It contains an estimated 20% pyrite, 3% chalcopyrite, <1% atacamite. There are 90% total clasts, including 85% altered chimney fragments, with minor clay alteration and atacamite, <1.0-35.0 mm in size, with poor sorting, subrounded shape, moderate sphericity (from transportation), and a random fabric. 5% of the clasts are white to light grey volcanic clasts with intense pervasive clay alteration, <1.0-3.0 mm in size, poor sorting, subrounded shape, moderate sphericity, random orientation, and aphanitic texture. The porosity is <1%.

Thin Section Description

This sample appears to be a massive pyrite-rich sandstone with no obvious chimney textures, infilled by clay. There is an overall porosity of 20%. The pyrite is fine- to medium-grained, anhedral to euhedral, and accounts for 50-55% of the section. There is minor late anhedral chalcopyrite, 5% overall. There are rare anhydral relict crystals of anhydrite, 2% overall. The pyrite is infilled by fine- to very fine-grained clays, with up to fourth order birefringence (illite?), making up 20% of the section. There is minor iron oxyhydroxides in one part of the section, ~2% overall.



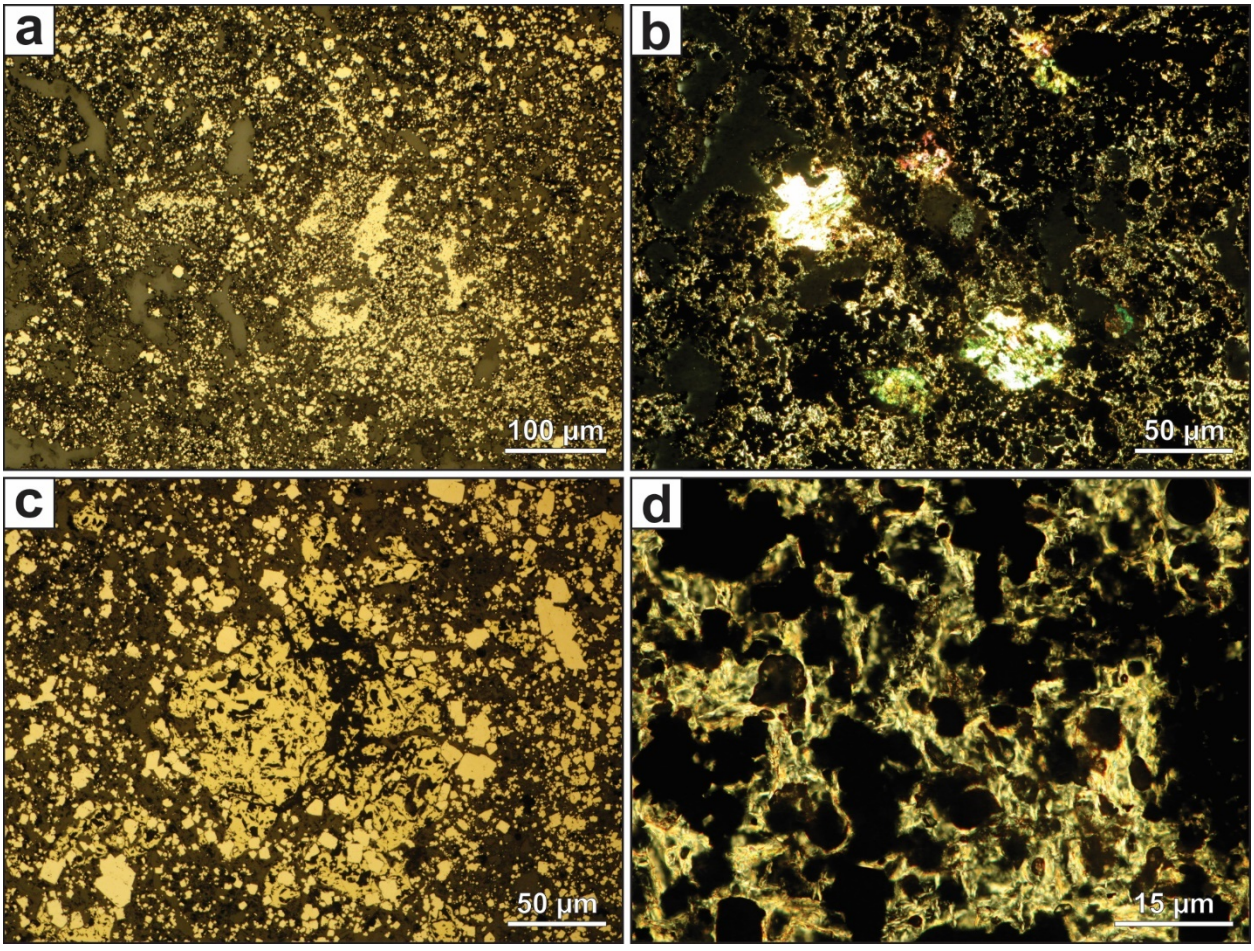
Thin section scan (left) and puck (right) of MA13-056.

Paragenesis: Pyrite → chalcopyrite → anhydrite → clay (illite) → FeOx

Interpretation: Resedimented pyrite sand

Descriptive Lithological Name: Sulfide sand with clay infill

Descriptive Alteration Facies: Clay infill, likely illite.



Photomicrographs of GMA13-056: (a) reflected light (PPL) showing fine-grained pyrite; (b) transmitted light (XPL) showing relict anhydrite crystals; (c) reflected light (PPL) showing chalcopyrite after pyrite; (d) transmitted light (XPL) clay precipitation in open spaces.

SAMPLE: MA13-057 **PARENT ID:** 2522 **SAMPLE DEPTH:** 4.60-4.70 mbsf	**DRILLHOLE:** TKAD027 **DRILLHOLE LOCATION:** 784562.04E/8649937.83N **WATER DEPTH:** 1091.36 mbsl

Mineralogy

XRD (clay-sized fraction): Chamosite, I/S
Assemblage: I/S + Cham

Hand Sample Description



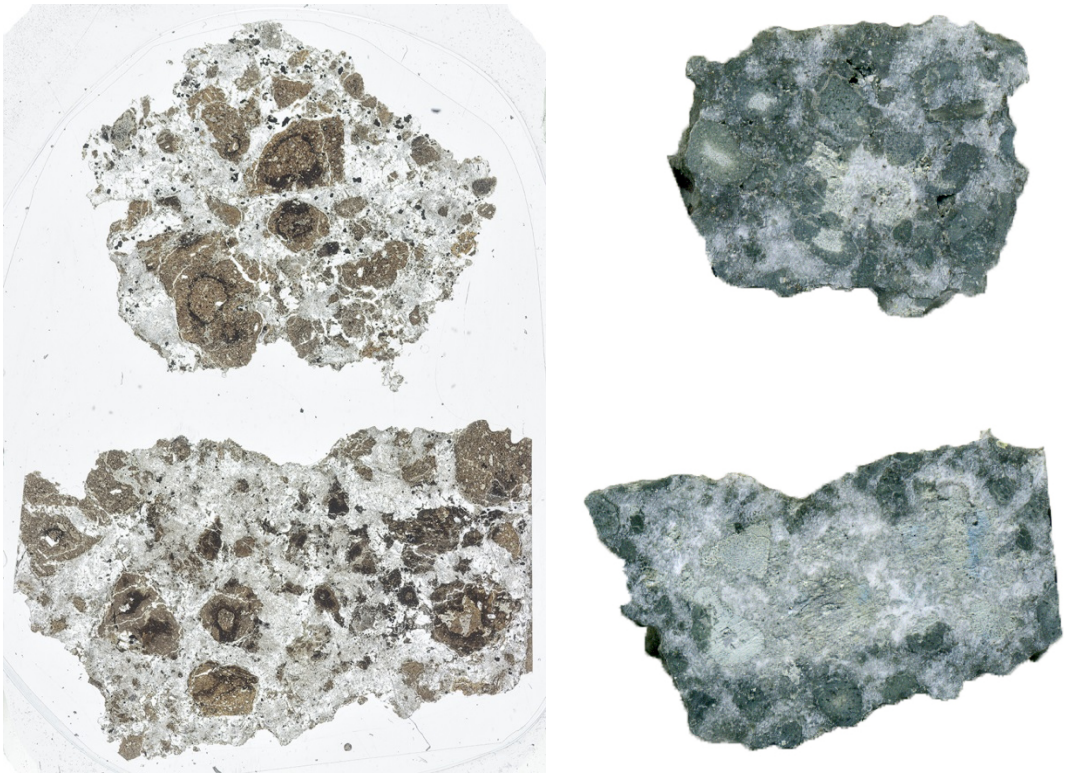
Hand sample of MA13-057.

Poorly consolidated polymict matrix-supported(?) volcanic breccia with rounded white and light grey clay-altered clasts, partially cemented by anhydrite. The matrix is composed of clay and patchy white anhydrite/gypsum. There is 1% pyrite. There are 75% clasts overall, consisting of 60% light greenish-grey volcanic clasts, with pervasive clay alteration (chlorite?), <1.0-9.0 mm in size, poor sorting, subrounded to rounded shape, moderate sphericity, random fabric, and aphanitic texture with abundant sub-mm vesicles and sub-mm phenocrysts, <1% pyrite. There are 15% medium-grey volcanic clasts with pervasive clay, <1.0-3.0 mm in size, poor sorting, rounded shape, moderate sphericity, random fabric, and aphanitic texture. There is <1% porosity.

Thin Section Description

This section is a massive monomict matrix-supported volcaniclastic, with 1% porosity. This section is from part of the sample that is strongly cemented by sulfates. There is very little anhydrite (1%), but abundant gypsum (60%) that has been strongly recrystallized, with micropoiklitic texture, inclusions of anhydrite

and volcanic clasts, and abundant sieve texture. Within the gypsum matrix, there is minor coarse-grained euhedral pyrite, regularly distributed.



Thin section scan (left) and puck (right) of MA13-057.

There are 33% light to medium-brown volcanic clasts, with dark brown-black cores, or horizons between the core and the rim of the clast. The coloring is heterogeneous and locally patchy. The clasts are subrounded to subangular, with irregular margins. The sizes range from <1 to 6 mm. There are relict plagioglase phenocrysts (minor), completely dissolved. Relict plagioclase microphenocrysts are completely altered to chlorite (clinochlore), locally aligned along a weak flow foliation. The groundmass of the clasts is strongly altered to chlorite, fine- to medium-grained euhedral pyrite, and patchy iron oxides. The amount of pyrite increases near the clast margins, associated with a slight increase in size. There is a higher abundance of pyrite in the volcanic clasts than in the matrix, with 5% pyrite overall. Rare relict phenocrysts of (titano)magnetite has been altered to rutile. The clasts are weakly to highly vesicular (variable), with a few clasts displaying elongated vesicles along the flow foliation. The vesicles are locally filled by a layer of fine-grained transparent to orange isotropic glass (gel-palagonite?), followed by fibrous pale-green chlorite (ubiquitous in all vesicles). Chlorite also locally grows outwards on the clast margins. The clasts locally contain irregular patches of light-brown glass (pumace), or glassy margins, that have been pervasively altered to intense chlorite.

This section is a massive monomict matrix-supported volcaniclastic, with 1% porosity. This section is from part of the sample that is strongly cemented by sulfates. There is very little anhydrite (1%), but abundant gypsum (60%) that has been strongly recrystallized, with micropoiklitic texture, inclusions of anhydrite

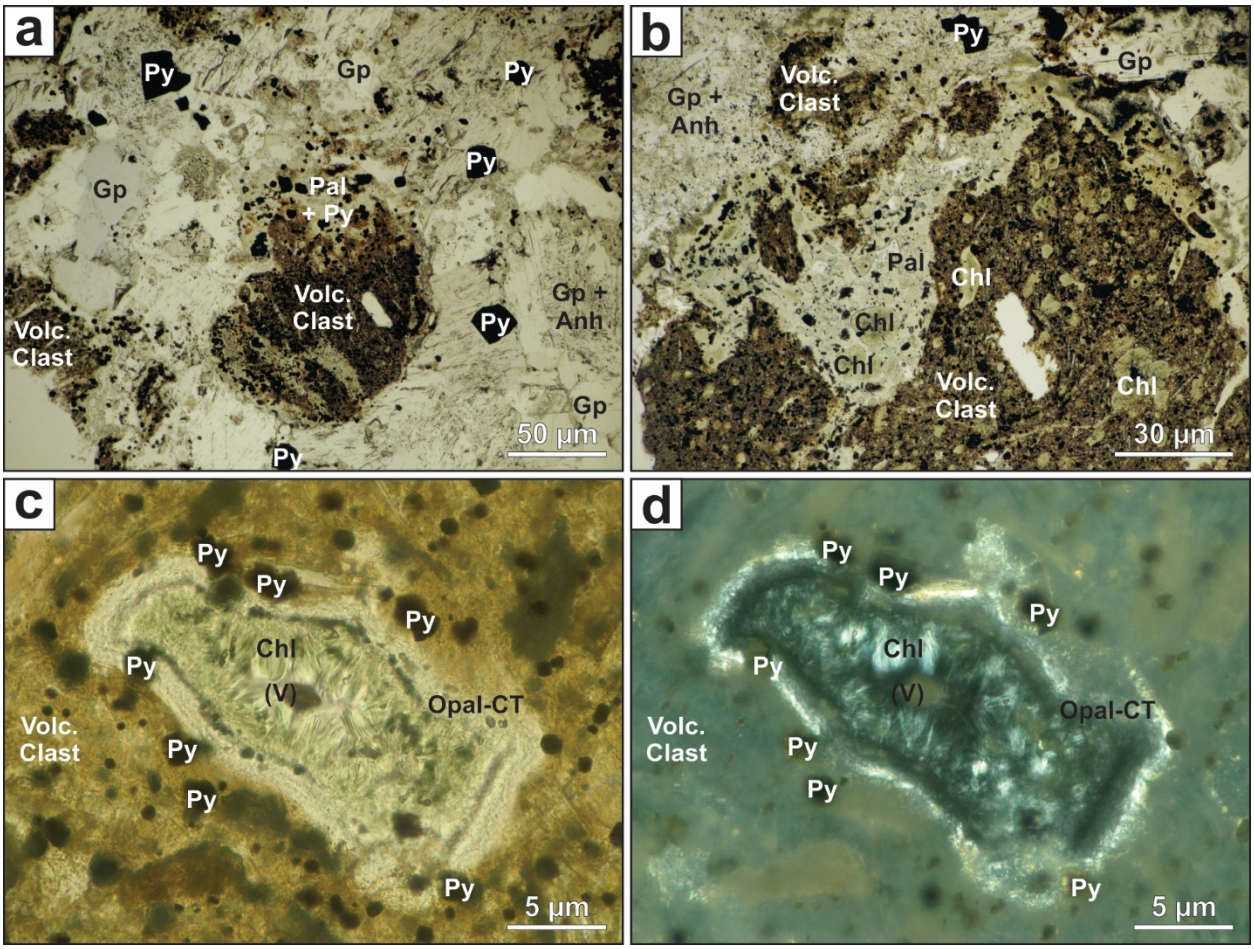
and volcanic clasts, and abundant sieve texture. Within the gypsum matrix, there is minor coarse-grained euhedral pyrite, regularly distributed.

There are 2% light to medium-brown volcanic clasts, with dark brown-black cores, or horizons between the core and the rim of the clast. The coloring is heterogeneous and locally patchy. The clasts are subrounded to subangular, with irregular margins. The sizes range from <1 to 6 mm. There are relict plagioglase phenocrysts (minor), completely dissolved. Relict plagioclase microphenocrysts are completely altered to chlorite (clinochlore), locally aligned along a weak flow foliation. The groundmass of the clasts is strongly altered to chlorite, fine- to medium-grained euhedral pyrite, and patchy iron oxides. The amount of pyrite increases near the clast margins, associated with a slight increase in size. There is a higher abundance of pyrite in the volcanic clasts than in the matrix, with 5% pyrite overall. Rare relict phenocrysts of (titano)magnetite has been altered to rutile. The clasts are weakly to highly vesicular (variable), with a few clasts displaying elongated vesicles along the flow foliation. The vesicles are locally filled by a layer of fine-grained transparent to orange isotropic glass (gel-palagonite?), followed by fibrous pale-green chlorite (ubiquitous in all vesicles). Chlorite also locally grows outwards on the clast margins. The clasts locally contain irregular patches of light-brown glass (pumace), or glassy margins, that have been pervasively altered to intense chlorite.

Some clasts (Volc. Clast 2) are composed entirely of light-brown glass that has been pervasively altered to intense chlorite. There are 3% of these glassy clasts. These are considered to be part of the same lava as the first clasts, so it is a monolithic breccia.

No glass shards or crystal fragments were observed. No other sulfides were observed. No palygorskite was identified.

Paragenesis: Volcanic clast → altered to Chl + Py + FeOx → cemented by Anh → Anh hydrated to Gp → Gp recrystallized.
Anhydrite is overprinted gypsum.
Interpretation: Resedimented hyaloclastite (?)
Descriptive Lithological Name: Massive scoriaceous monomict matrix-supported resedimented hyaloclastite sand-pebble breccia, sulfate-cemented
Descriptive Alteration Facies: Strong pervasive chlorite + pyrite, hydrothermally cemented by anhydrite → gypsum



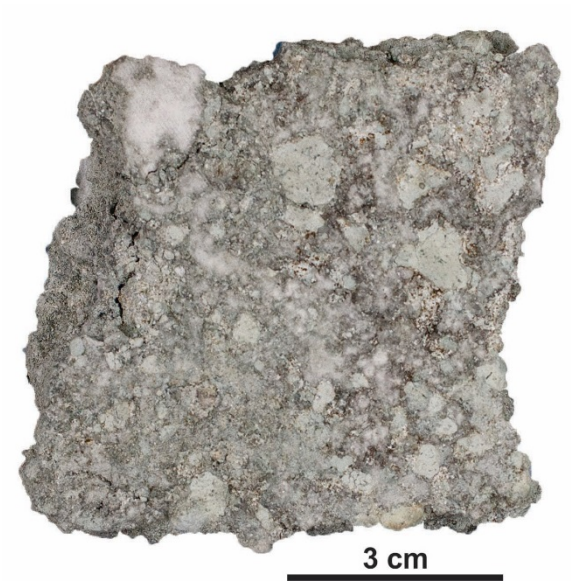
Photomicrographs of GMA13-057: (a) transmitted light (PPL) showing various volcanic clasts with glassy domains; (b) transmitted light (PPL) showing a closer look at the glassy domains, altered to chlorite; (c) transmitted light (PPL) showing a chlorite precipitation in a vesicle; (d) transmitted light (XPL) showing the same view as (c).

SAMPLE: MA13-058 **PARENT ID:** 2524 **SAMPLE DEPTH:** 6.50-6.59 mbsf	**DRILLHOLE:** TKAD027 **DRILLHOLE LOCATION:** 784562.04E/8649937.83N **WATER DEPTH:** 1091.36 mbsl

Mineralogy

XRD (clay-sized fraction): Chamosite, I/S
Assemblage: I/S + Cham

Hand Sample Description

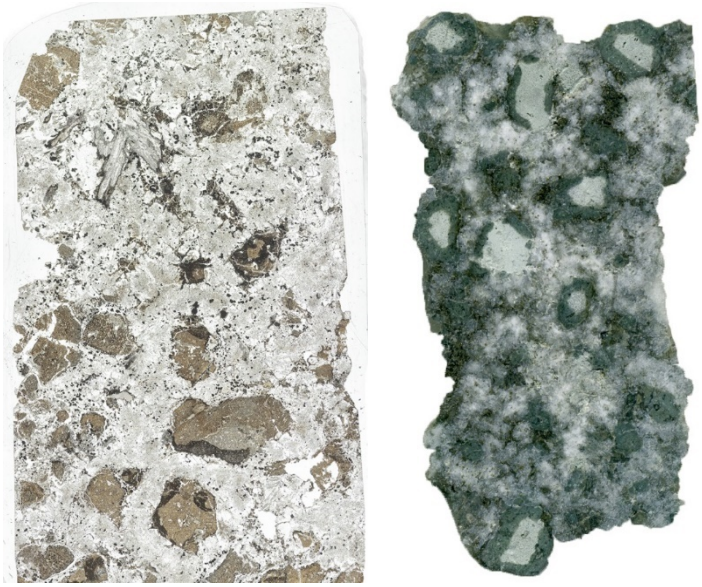


This section is a monomict matrix-supported volcanic breccia with sub-rounded green-grey clay-altered clasts with grey-white anhydrite patchy infill and diffuse veinlets. The anhydrite infill is mostly grey; where it is white it might be diffuse veinlets, 1 mm wide, anastomosing. There is 10% pyrite overall. There is 10% clasts composed of strong pervasively clay and chlorite-altered volcanics, <1.0-9.0 mm wide, with poor sorting, subrounded-rounded shape, moderate sphericity, random fabric, and an aphanitic texture with abundant sub-mm vesicles and sub-mm phenocrysts, with <1% pyrite in the clasts. There is 3% porosity overall.

Hand sample of MA13-058.

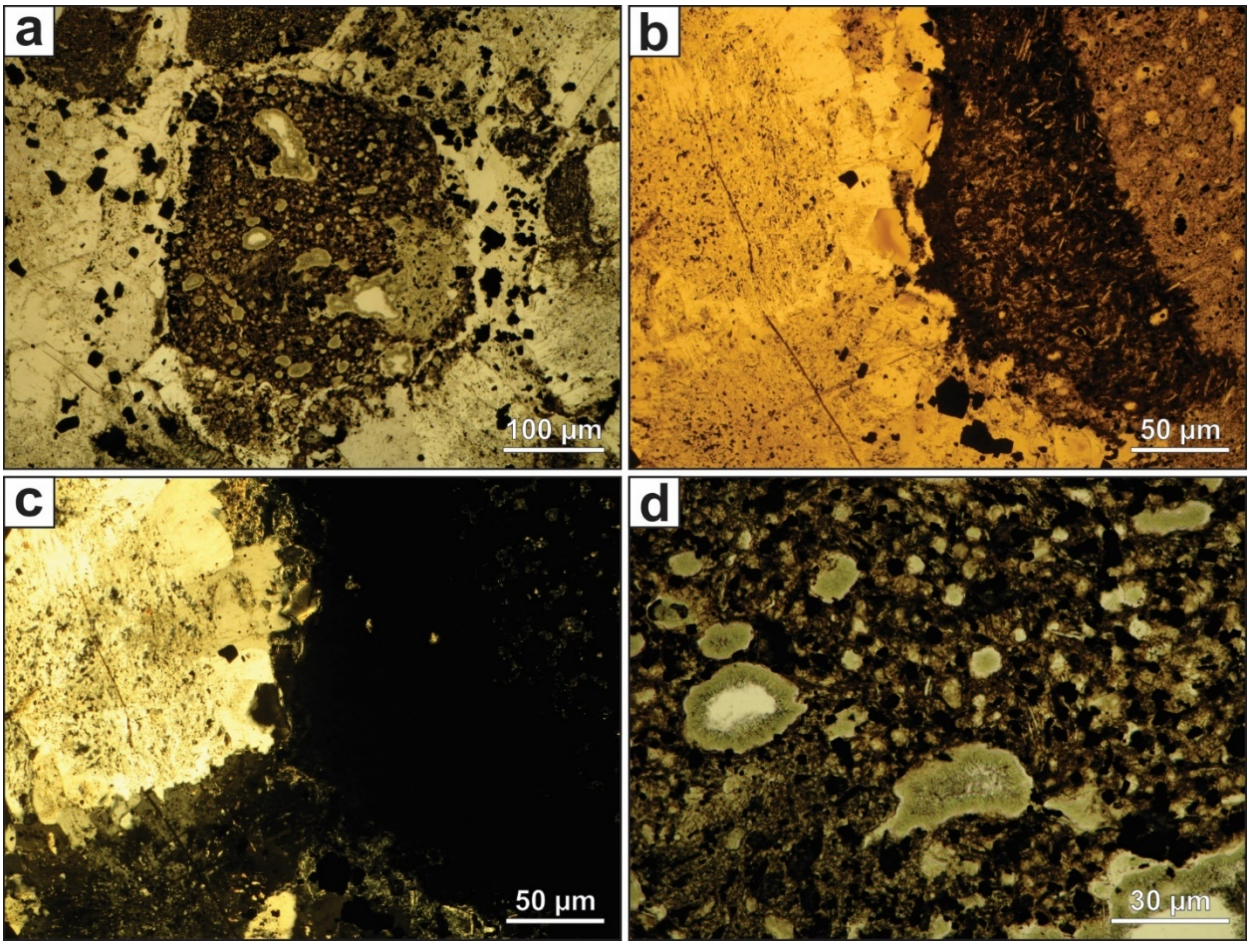
Thin Section Description

This section is a monomict matrix-supported volcanic breccia cemented by gypsum, with 5% porosity. The volcanic clasts are vesicular to scoriaceous, with irregular sub-rounded margins. Variable amounts of microphenocrysts show flow-foliation. The glassy groundmass is pervasively altered to clay, with two generations of clay filling in pore space – an early generation of high-birefringence clay (illite?) and later chlorite. The volcanic clasts comprise ~30% of the sample. There are several isotropic glass shards, 5% overall. Minor fine-grained pyrite is disseminated through the volcanic clasts, and ~5% medium-grained pyrite occurs in the matrix. The matrix is dominated by inclusion-filled gypsum, with rare relict anhydrite crystals, comprising ~55% of the sample.



Thin section scan (left) and puck (right) of MA13-058.

Paragenesis: Volcanic clasts + glass shards → altered to Ill + Chl + Py + FeOx → clays lining vesicles → cemented by Anh → Anh hydrated to Gp → Gp recrystallized.
Interpretation: Proximal lapilli tephra
Descriptive Lithological Name: Intensely clay-altered (illite/chlorite) massive monomict(?) shard-rich matrix-supported lapilli tephra, cemented
Descriptive Alteration Facies: Pervasive clay altering clasts and glass shards, vesicles lined by illite and chlorite



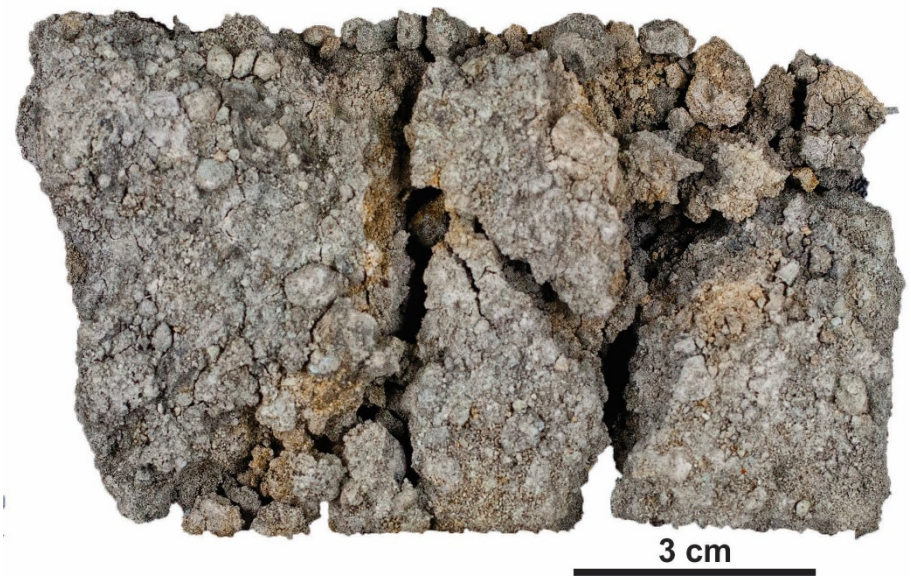
Photomicrographs of GMA13-058: (a) transmitted light (PPL) showing a vesicular volcanic clast with glassy domains; (b) transmitted light (PPL) showing a dark margin on a volcanic clast and glass shards in the matrix; (c) transmitted light (XPL) showing a gypsum precipitation, same view as (b); (d) transmitted light (PPL) showing chlorite precipitation in vesicles from the clast in (a).

SAMPLE: MA13-062 **PARENT ID:** 2374 **SAMPLE DEPTH:** 2.81-2.90 mbsf	**DRILLHOLE:** TKAD012 **DRILLHOLE LOCATION:** 784631.38E/8649842.16N **WATER DEPTH:** 1088.93 mbsl

Mineralogy

SWIR (powdered clast): Montmorillonite, paragoniticillite, chlorite(?)
XRD (clay-sized fraction): Chamosite, corrensite
Assemblage: Cham + Corr

Hand Sample Description

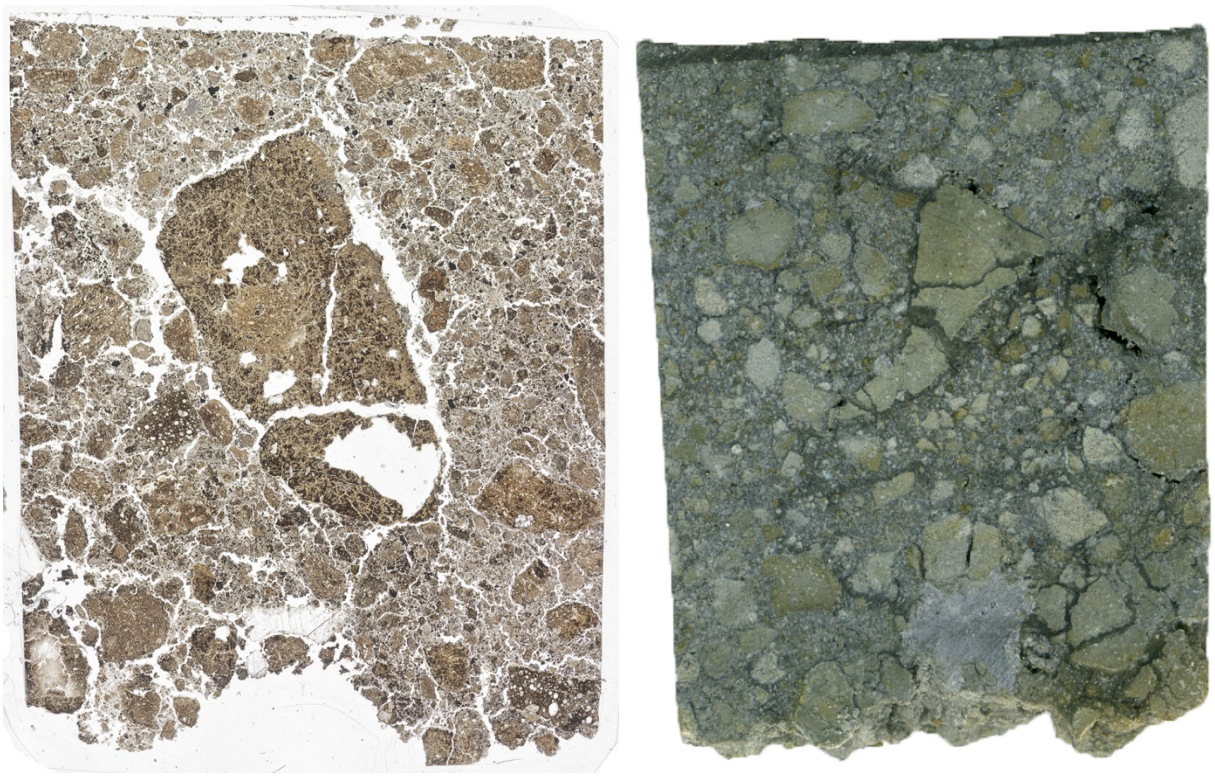


Hand sample of MA13-062.

This section is a monomict clast-supported volcanic breccia with subrounded-subangular small grey vesicular clasts, with a clay-altered matrix with patchy grey anhydrite infill (loosely consolidated) and minor orange-yellow iron oxide. There is 1% pyrite overall. There are 80% medium grey pervasively-clay altered clasts, with a few lighter-grey clasts, with minor iron oxide at the clast margins. The clasts are <1.0-8.0 mm, with poor sorting, low to moderate sphericity, a random fabric, and abundant preserved sub-mm vesicles. There is 5% porosity overall.

Thin Section Description

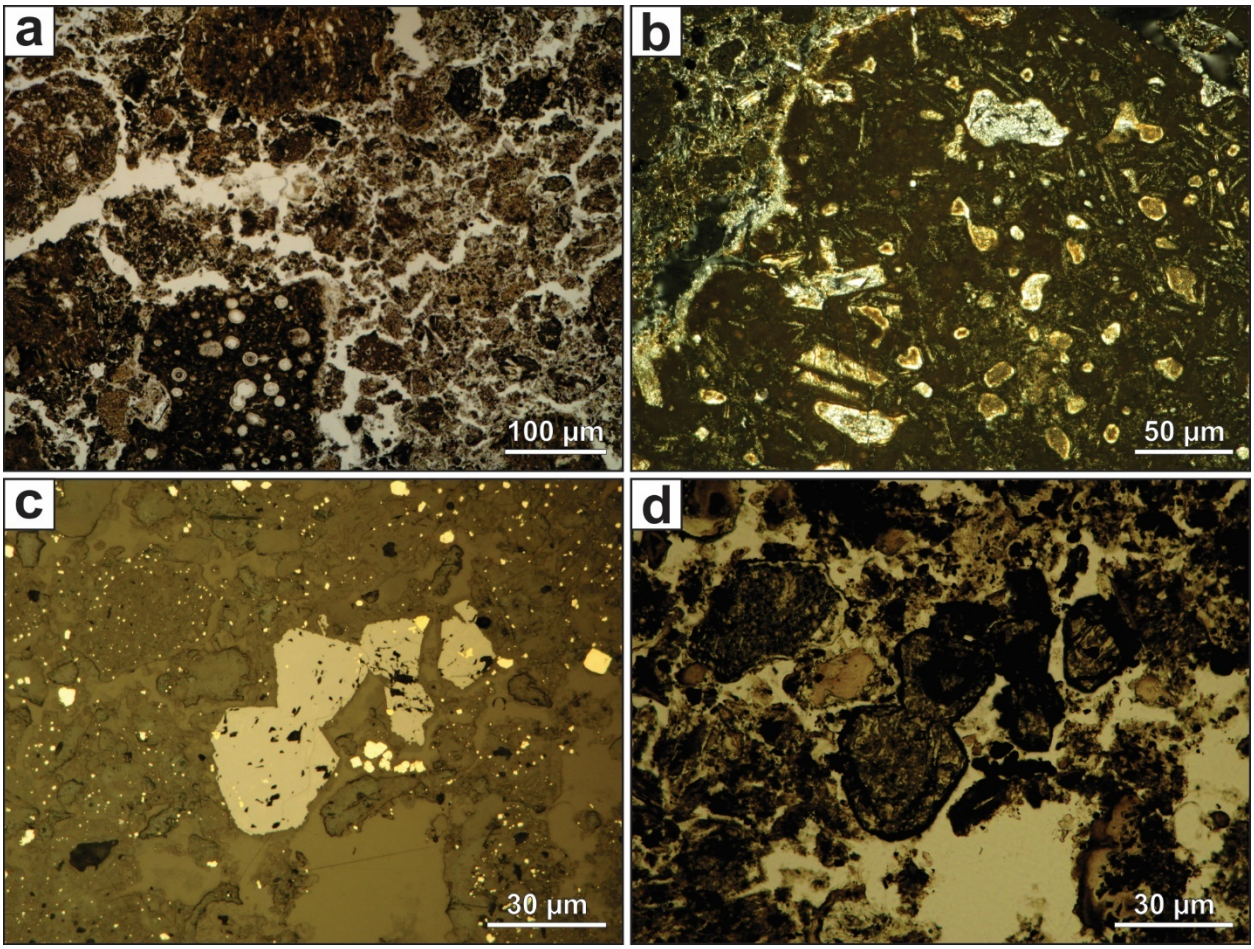
This section is a polymict(?) clast-supported volcanic breccia, with 10% porosity, 60% volcanic clasts, 20% clay-altered ash(?), 5% glass shards, 2% sphalerite mineralization, and 3% coarse-grained gysum crustals. The volcanic clasts are highly variable, with variable proportions of vesicles and microphenocrysts, with rare relict phenocrysts. The margins are generally sub-rounded. The clasts are pervasively altered to clay,



Thin section scan (left) and puck (right) of MA13-062.

with fine-grained clay partly filling some vesicles, beginning with an early generation of green clay (chlorite), followed by a later generation with up to 4th order birefringence (corrensite?). Larger phenocrysts have been completely altered to clay. The glass shards are isotropic. Medium-grained euhedral sphalerite is irregularly distributed in the matrix.

Paragenesis: Volcanic clasts + glass shards → altered to Chl + Py + FeOx → chlorite followed by corrensite(?) lining vesicles → cemented by Anh → Anh hydrated to Gp → Sp mineralization
Interpretation: Lapilli tuff
Descriptive Lithological Name: Intensely clay-altered (chlorite/corrensite) massive polymictmict(?) shard-rich clast-supported lapilli tuff, weakly mineralized and weakly cemented
Descriptive Alteration Facies: Pervasive clay altering clasts, glass shards, and matrix (ash?), vesicles lined by chlorite and corrensite(?)



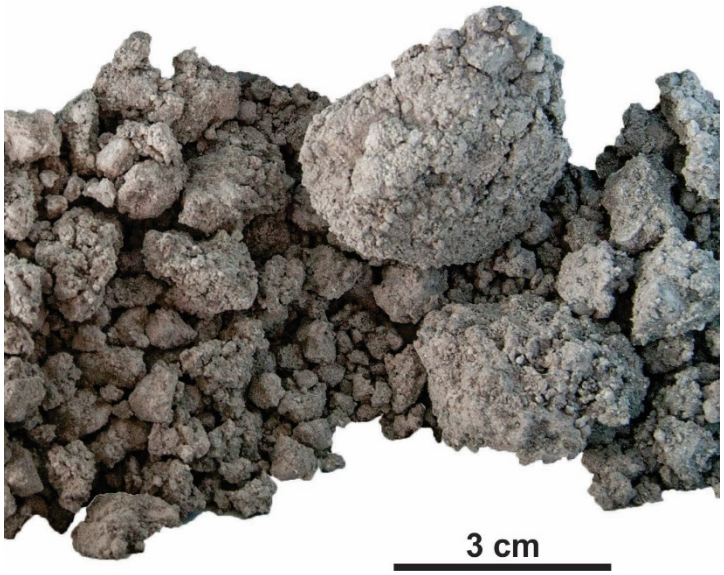
Photomicrographs of GMA13-062: (a) transmitted light (PPL) showing various volcanic clasts; (b) transmitted light (XPL) showing abundant clay alteration of clasts and matrix, and infilling of vesicles; (c) reflected light (PPL) showing sphalerite mineralization; (d) transmitted light (PPL) showing sphalerite mineralization, volcanic clasts, and glass shards, same view as (c).

SAMPLE: MA13-063 **PARENT ID:** 2376 **SAMPLE DEPTH:** 4.25-4.36 mbsf	**DRILLHOLE:** TKAD012 **DRILLHOLE LOCATION:** 784631.38E/8649842.16N **WATER DEPTH:** 1088.93 mbsl

Mineralogy

XRD (clay-sized fraction): Clinochlore, corrensite, paragonite
Assemblage: Cham + Corr

Hand Sample Description



Hand sample of MA13-063.

This section appears to be a polymict(?) unconsolidated volcanic breccia with small subrounded medium-grey, white, and few dark grey clasts, and no anhydrite. There is less than 1% pyrite overall. The clasts include medium greenish-grey pervasively clay+chlorite-altered volcanic clasts, ~94% overall, <1.0-5.0 mm in size, with poor sorting, subrounded shape, moderate sphericity, random fabric, and an aphanitic texture. There are 5% white to light-grey pervasively clay-altered volcanic clasts, <1.0-3.0 mm in size, with poor sorting, subrounded shape, low sphericity, random fabric, and an aphanitic texture. There are 1% dark grey volcanic clasts, with moderate pervasive clay alteration and trace iron oxide, 2.0-3.0 mm, poor sorting, subrounded to subangular shape, poor sorting, random fabric and aphanitic texture. There is 5% porosity overall.

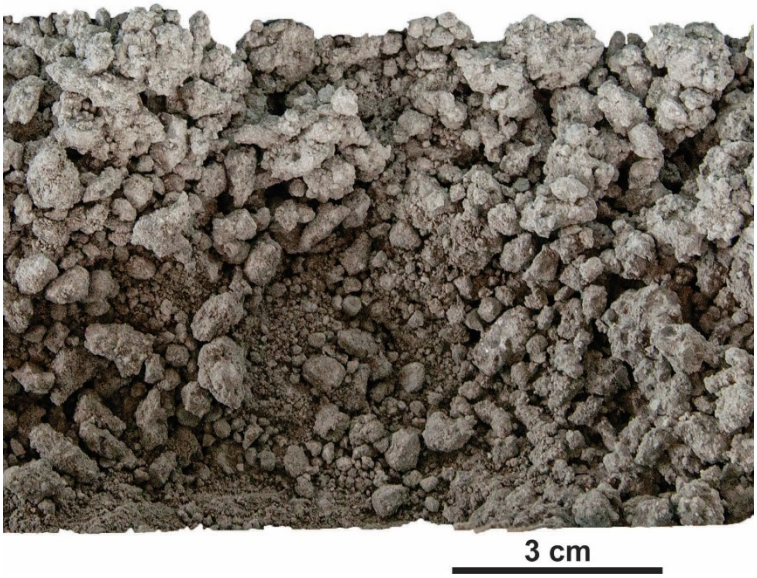
Alteration Summary: Variable white to medium-grey clay alteration
Interpretation: Origin unknown
Name: Variably clay-altered polymict(?) volcanic breccia, unconsolidated

SAMPLE: MA13-064 **PARENT ID:** 2378 **SAMPLE DEPTH:** 6.49-6.60 mbsf	**DRILLHOLE:** TKAD012 **DRILLHOLE LOCATION:** 784631.38E/8649842.16N **WATER DEPTH:** 1088.93 mbsl

Mineralogy

XRD (clay-sized fraction): Corrensite, I/S(?), hematite
Assemblage: Cham + Corr

Hand Sample Description



This sample is a monomict(?) unconsolidated volcanic breccia with 90% small sub-rounded medium-grey volcanic clasts, moderately clay-altered, <1.0-3.0 mm in size, with poor sorting, subrounded shape, moderate-high sphericity, random fabric, and aphanitic texture. There is minor gypsum infill (10%), and a few larger crystals of colorless gypsum. There is 5% porosity.

Hand sample of MA13-064.

Alteration Summary: Pervasive white to medium-grey clay alteration
Interpretation: Origin unknown
Name: Variably clay-altered monomict(?) volcanic sandstone, unconsolidated

SAMPLE: MA13-067 **PARENT ID:** 2530 **SAMPLE DEPTH:** 2.90-3.00 mbsf	**DRILLHOLE:** TKAD026 **DRILLHOLE LOCATION:** 784609.20E/8649820.32N **WATER DEPTH:** 1089.04 mbsl

Mineralogy

SWIR (powdered clast): Paragonite, montmorillonite
XRD (clay-sized fraction): Chamosite, rectorite, pyrite
Assemblage: I/S + Cham

Hand Sample Description

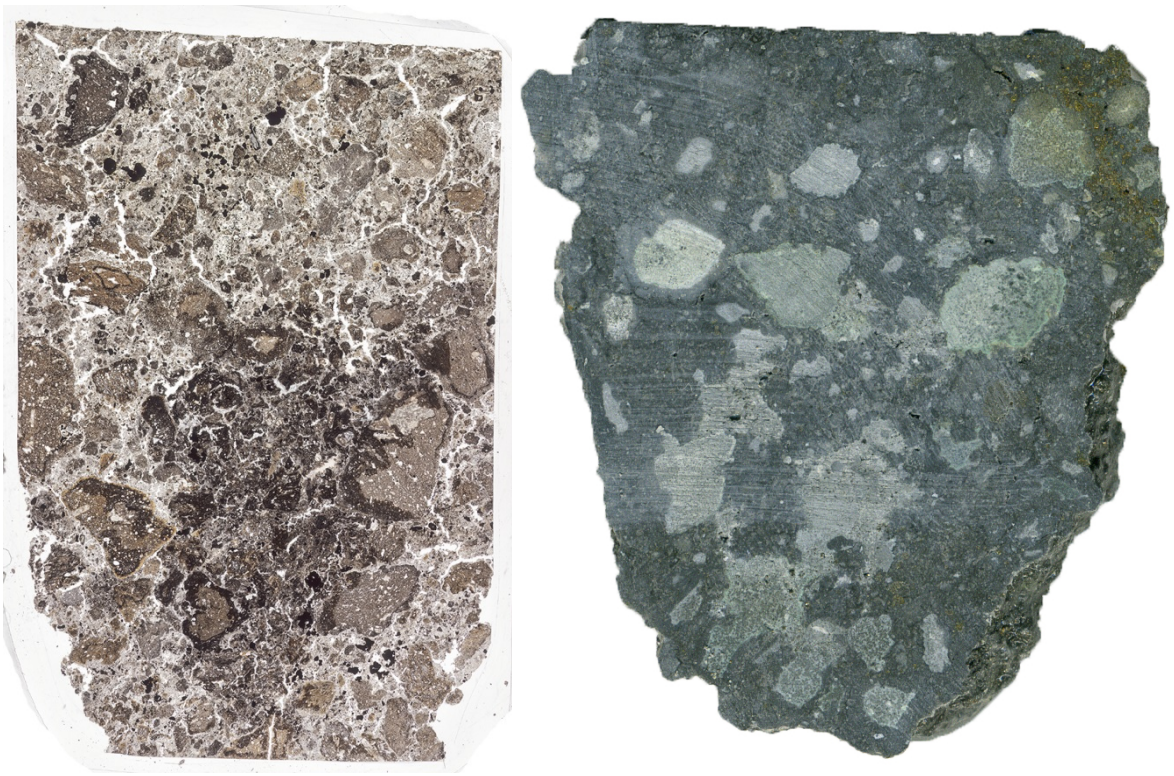


Hand sample of MA13-067.

This sample is a monomict(?) matrix-supported volcanic breccia, loosely consolidated with 20% medium-grey pervasively clay-altered matrix with minor white patchy anhydrite, minor orange iron oxide, patchy. It is difficult to distinguish the clasts from the matrix. There is 2% pyrite overall. There are 80% white to medium grey volcanic clasts with strong pervasive clay alteration and minor iron oxide. The clasts are <1.0-14.0 mm (mostly <6.0 mm), poor sorting, rounded-subrounded shape, moderate sphericity, random fabric, and abundant preserved sub-mm vesicles. There is 3% porosity.

Thin Section Description

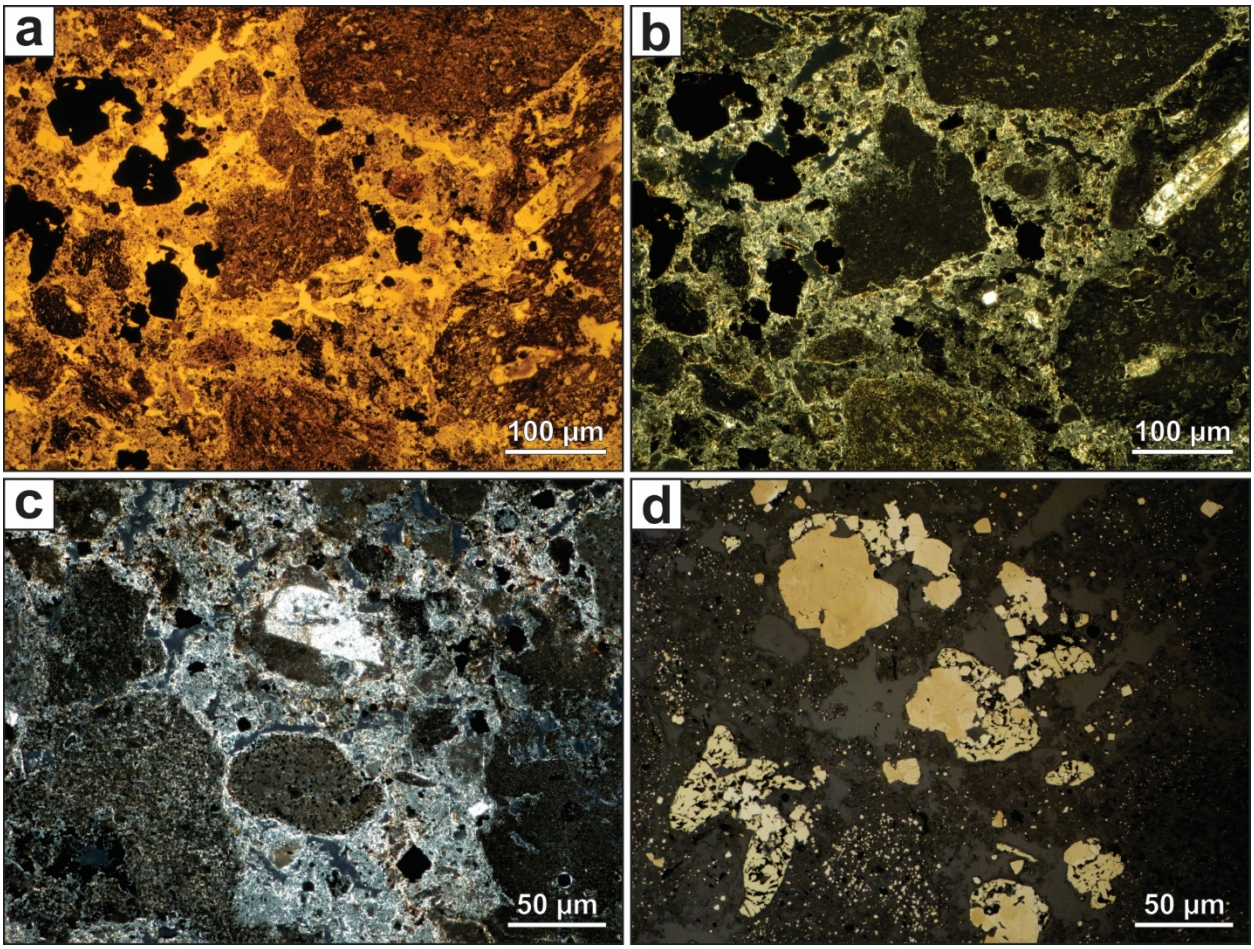
This section is a polymict matrix-supported breccia with subangular-subrounded clasts up to 6 mm in size. The clasts show various colors, textures, and degrees of alteration. Most clasts are vesicular, and some are even scoriaceous. Many have relict microphenocrysts and rare phenocrysts that show flow foliation. The clast margins are irregular. The glassy groundmass and phenocrysts are pervasively and intensely altered to fine-grained clay (illite/smectite?). The phenocrysts appear to be mostly altered to illite (fourth-order interference colors). Clays also line the irregular vesicles. The clasts also have variable amounts of fine-grained disseminated pyrite, and FeOx staining. There is one seemingly unaltered juvenile fragment that is mostly isotropic (glassy) with minor clay lining one vesicle. There are also tube pumice clasts that have been intensely altered to clay (chlorite?). Chlorite was not positively identified anywhere.



Thin section scan (left) and puck (right) of MA13-067.

Glass shards are rare. There is an overall porosity of 2%, with 40% clasts and 58% matrix. The matrix is mostly composed of fine-grained clay (illite/smectite), with 7% sulfides, including fine- to coarse-grained pyrite (5%), and minor late chalcopyrite (2%). No sulfates are present.

Paragenesis: Volcanic clasts + tube pumice + matrix (ash?) → pervasive intense alteration to illite/smectite/chlorite + pyrite + FeOx → late pyrite → late chalcopyrite
Interpretation: Pumaceous lapillistone
Descriptive Lithological Name: Intensely clay-altered massive polymict matrix-supported pumaceous lapillistone, mineralized
Descriptive Alteration Facies: Intense, pervasive clay altering clasts and phenocrysts, lining vesicles



Photomicrographs of GMA13-067: (a) transmitted light (PPL) showing various volcanic clasts; (b) transmitted light (XPL) showing abundant clay alteration of the matrix (ash?); (c) transmitted light (XPL) showing clay alteration of clasts and the matrix; (d) reflected light (PPL) showing pyrite and chalcopyrite mineralization in the matrix.

SAMPLE: MA13-068 **PARENT ID:** 2531 **SAMPLE DEPTH:** 3.60-3.68 mbsf	**DRILLHOLE:** TKAD026 **DRILLHOLE LOCATION:** 784609.20E/8649820.32N **WATER DEPTH:** 1089.04 mbsl

Mineralogy

SWIR (powdered clast): Paragonite, montmorillonite(?), chlorite(?)
XRD (clay-sized fraction): Montmorillonite, chamosite, rectorite(?), I/S
Assemblage: I/S + Cham

Hand Sample Description



Hand sample of MA13-068.

This sample is a muddy monomict(?) matrix-supported volcanic breccia, poorly consolidated with a medium-grey pervasively clay-altered matrix (80%), with patchy yellow iron oxide. There is less than 1% pyrite. It is somewhat difficult to distinguish clasts. There are 20% light to medium grey pervasively clay-altered volcanic clasts, with minor patchy yellow iron oxide. The clasts are <1.0-9.0 mm in size, with moderate sorting, rounded shape, moderate sphericity, random fabric, and a few sub-mm vesicles preserved. There is 3% porosity.

Thin Section Description

This section is a polymict matrix-supported breccia with clasts up to 3 mm in size. The clasts show various colors and textures. Some clasts are scoraceous, with abundant large rounded vesicles. Others have fewer vesicles and abundant flow-foliated phenocrystsl. The glassy matrix and phenocrysts are intensely and pervasively altered to fine-grained clays, associated with minor FeOx staining and variable finely disseminated pyrite. The vesicles are also lined by clay. The main vesicle-lining clay is chlorite. Some clasts are glassy, and isotorpic to clay-altered. There are rare clasts of tube pumice, altered to clay (chlorite?). Glass shards are rare. There is 5% porosity overall, with 40-45% clasts and 50-55% matrix. The matrix is dominated by fine-grained clays, and minor sulfides, including 5% pyrite and 5% late chalcopyrite. No sulfates are present.



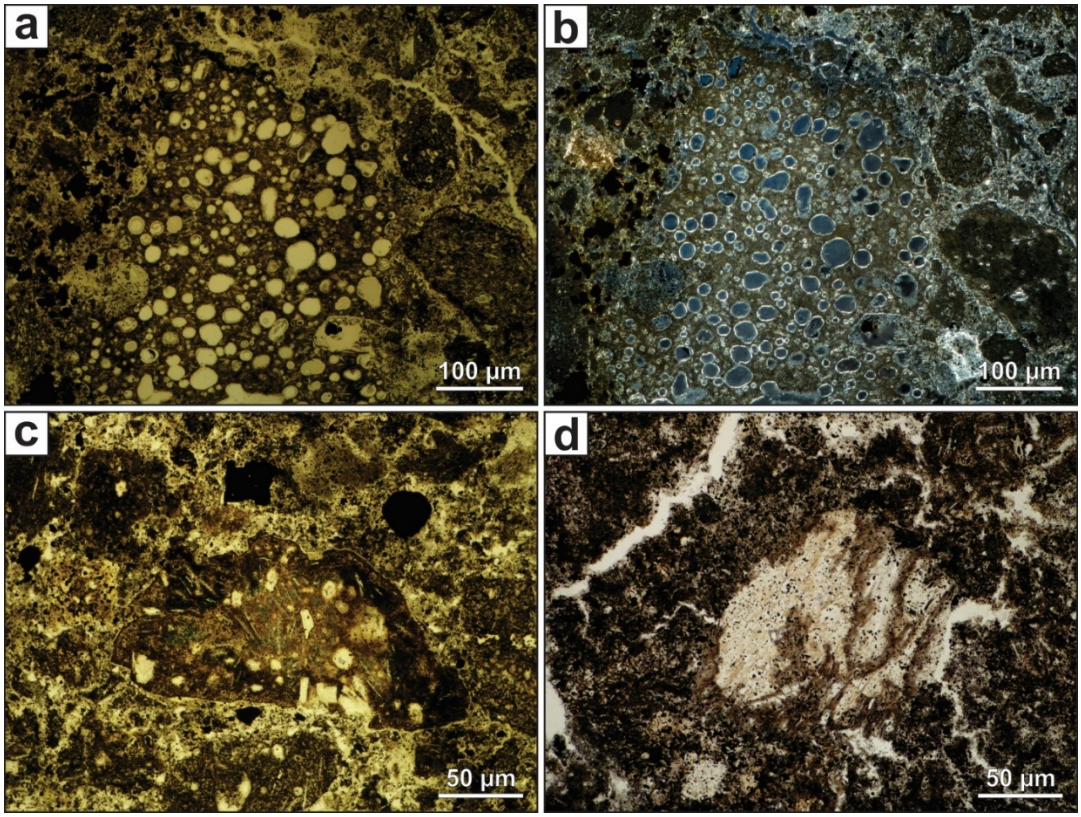
Thin section scan (left) and puck (right) of MA13-068.

Paragenesis: Volcanic clasts + matrix → pervasive intense alteration to clay (mostly chlorite) + pyrite + FeOx → late pyrite → late chalcopyrite

Interpretation: Coarse tuff to lapillistone

Descriptive Lithological Name: Intensely chloritized massive scoriaceous polymict matrix-supported coarse tuff, mineralized

Descriptive Alteration Facies: Intense pervasive clay (chlorite) altering clasts (with phenocrysts) and matrix, lining vesicles, minor pyrite



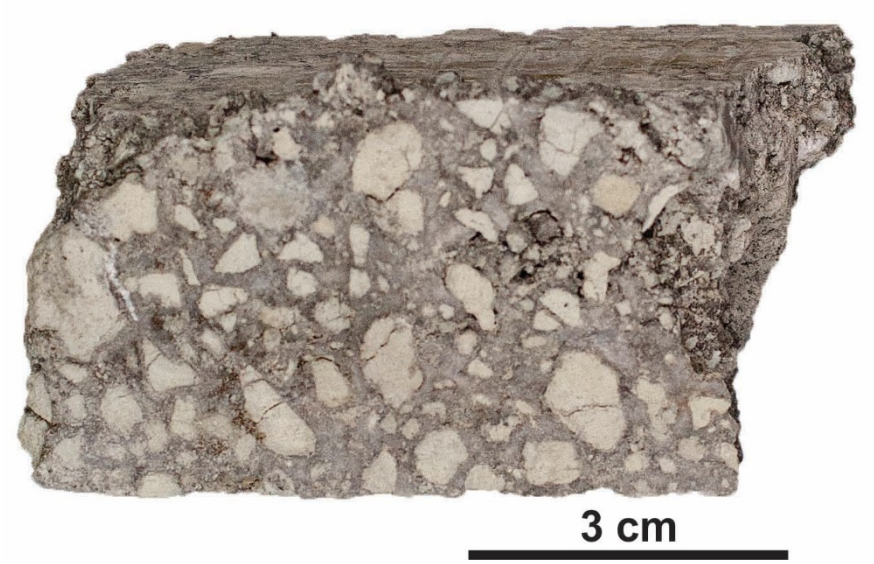
Photomicrographs of GMA13-068: (a) transmitted light (PPL) showing various volcanic clasts, including a large scoria fragment; (b) transmitted light (XPL) showing abundant clay alteration of the clasts and matrix, including precipitation in vesicles; (c) transmitted light (PPL) showing a poryphyritic volcanic clast with unaltered microphenocrysts; (d) transmitted light (PPL) showing a pumice fragment.

SAMPLE: MA13-069 **PARENT ID:** 2533 **SAMPLE DEPTH:** 5.64-5.75 mbsf	**DRILLHOLE:** TKAD026 **DRILLHOLE LOCATION:** 784609.20E/8649820.32N **WATER DEPTH:** 1089.04 mbsl

Mineralogy

SWIR (powdered clast): Gypsum(?), paragonite(?)
XRD (clay-sized fraction): Montmorillonite, chamosite, rectorite(?), I/S
Assemblage: I/S + Cham

Hand Sample Description



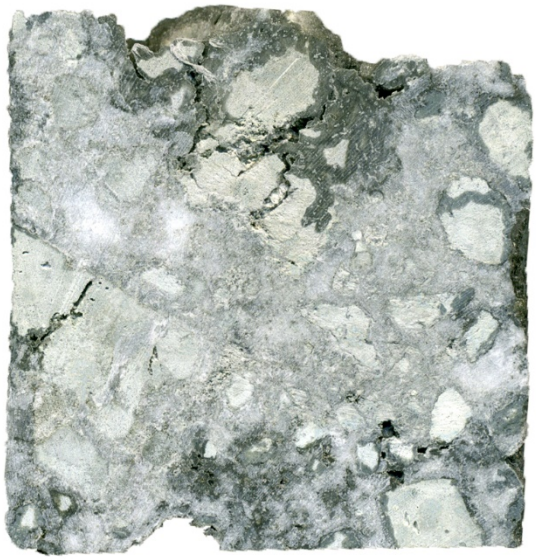
Hand sample of MA13-069.

This section is a monomict (?) matrix-supported volcanic breccia with a dark grey anhydrite matrix (75%), with drusy infill textures (veining?). The dark coloration may be fron very fine-grained sulfides. There are 25% light grey, slightly greenish volcanic clasts, pervasively clay-altered with minor chlorite. The clasts are 1.0-10.0 mm in size, with moderate sorting, subrounded-rounded shape, moderate sphericity, and random fabric, with rare preserved sub-mm vesicles. There is <1% pyrite overall, and 1% porosity.

Thin Section Description

This section is a polymict matrix-supported breccia with subrounded to subangular clasts up to 15 mm in size. There are three main clast types: Very vesicular scoria clasts, less-vesicular porphyritic clasts with flow-foliation, and glassy clasts. The scoriacous and porphyritic clasts are light brown in color with minor FeOx staining. The glassy groundmass is isotropic to clay-altered (chlorite, illite/smectite?), and the vesicles are lined by clays. All clasts have interior rims of MnOx(?). These glassy clasts also include smaller angular fragments, and are interpreted to represent the glassy margin of a flow as it picked up fragments of the flow. These glassy clasts are pervasively altered to chlorite. There is 2-3% overall porosity, 20% clasts (5% glassy clasts, 5% scoria clasts, 10% porphyritic clasts), and ~78% matrix. The matrix is contains 3% fine- to coarse-grained euhedral pyrite, ~5% clay-altered material, and 70% sulfates (10% relict anhydrite, 60% gypsum).





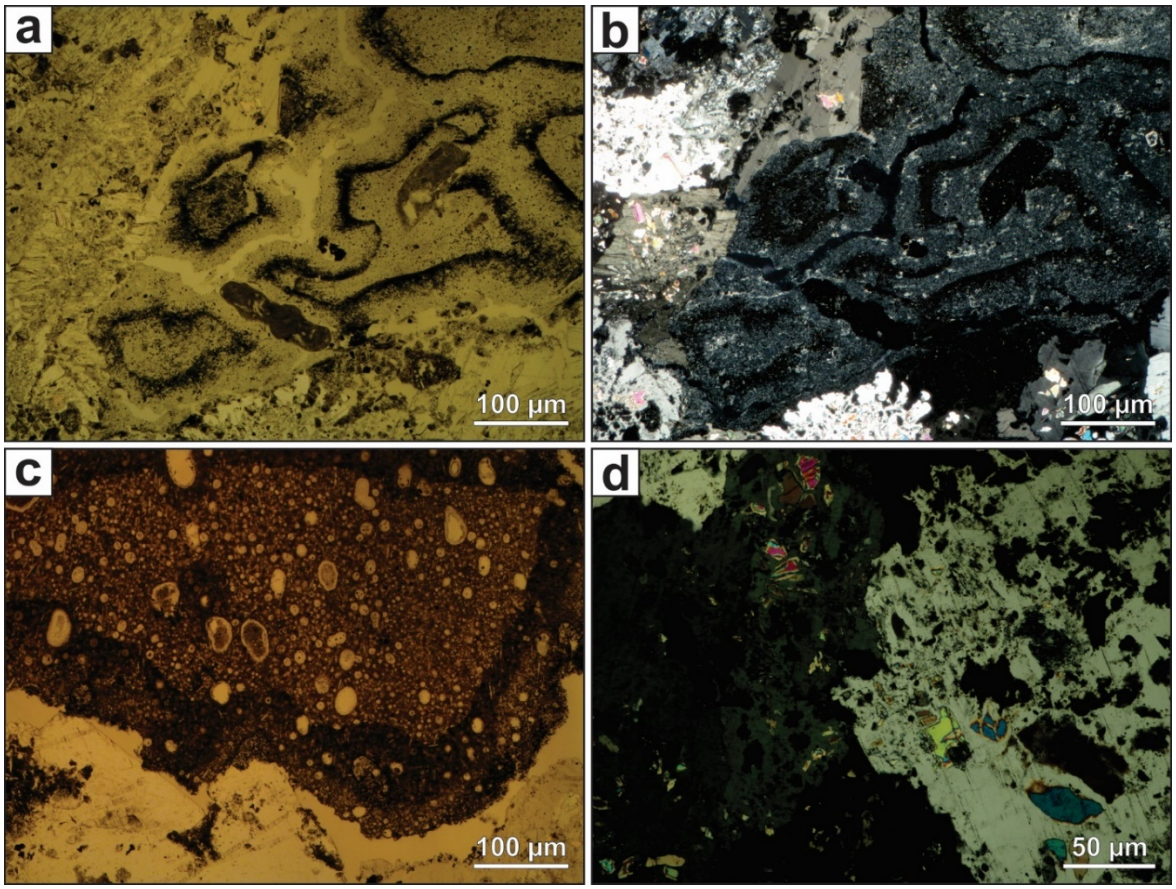
Thin section scan (left) and puck (right) of MA13-069.

Paragenesis: Volcanic clasts + matrix → moderate to intense pervasive alteration to chlorite (+ illite/smectite?), minor pyrite → anhydrite cement → hydration to gypsum

Interpretation: Lapillistone, scoriaceous (polymict)

Descriptive Lithological Name: Intensely chlorite-altered polymict matrix-supported scoriaceous lapillistone, cemented

Descriptive Alteration Facies: Pervasive chlorite with minor pyrite, chlorite lining vesicles



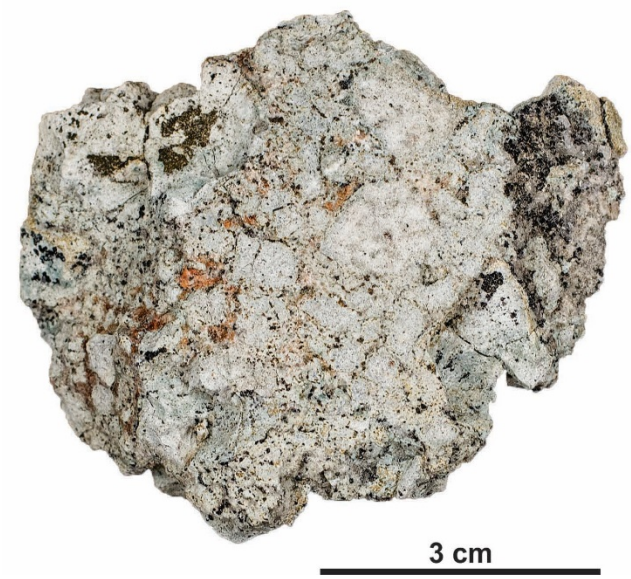
Photomicrographs of GMA13-069: (a) transmitted light (PPL) showing glassy clasts with dark rims; (b) transmitted light (XPL) showing abundant clay alteration of the glassy clast from (a); (c) transmitted light (PPL) showing a vesicular volcanic clast; (d) transmitted light (XPL) showing almost complete hydration of anhydrite to gypsum.

SAMPLE: MA13-072 **PARENT ID:** 2570 **SAMPLE DEPTH:** 2.05-2.17 mbsf	**DRILLHOLE:** TKAD032 **DRILLHOLE LOCATION:** 784672.04E/8649717.82N **WATER DEPTH:** 1084.40 mbsl

Mineralogy

SWIR (powdered clast): Montmorillonite
XRD (clay-sized fraction): Nontronite(?), corrensite, anhydrite
Assemblage: Mnt/Non + Pl

Hand Sample Description

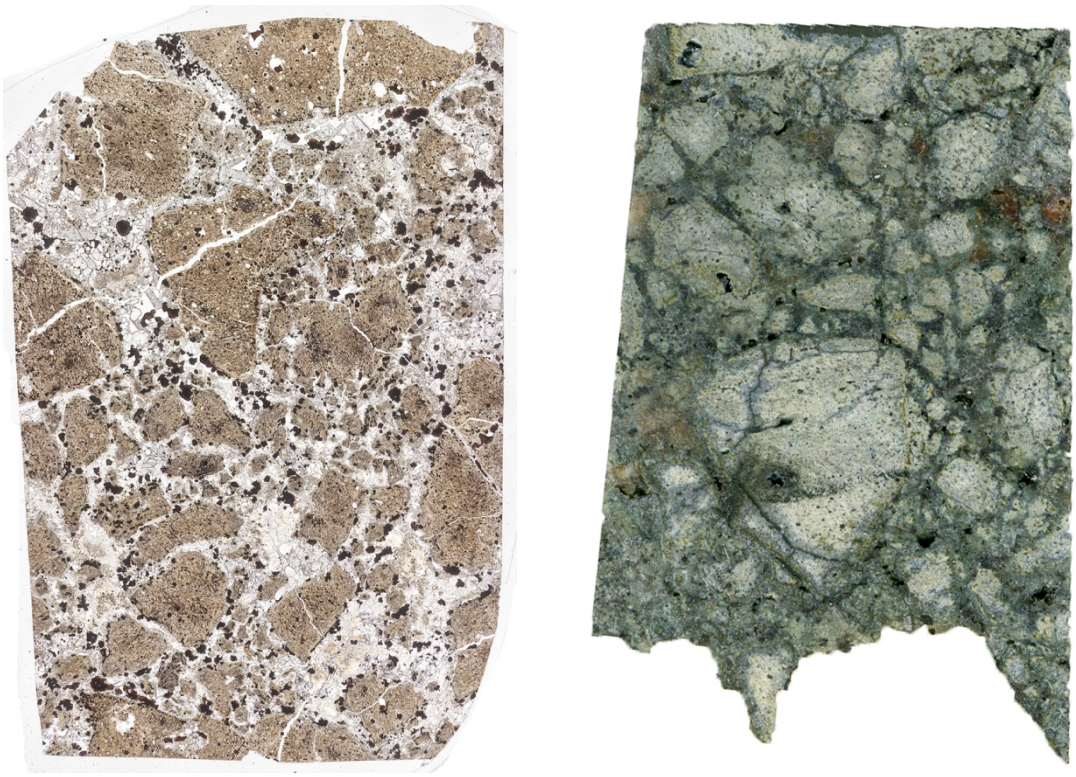


Hand sample of MA13-072.

This sample is from the stringer zone. It is a monomict matrix-supported volcanic breccia with a matrix of light green-grey clay, patchy orange iron oxide, and patchy anhydrite/gypsum + amorphous silica infill (possible veinlets?), 52% overall. There is 5% sphalerite, 3% pyrite, <1% chalcopyrite, and trace atacamite; the blackjack (mod-Fe) sphalerite forms primarly on the margins of the clasts, with some disseminated within the clasts. There are 40% light green-grey volcanic clasts, with minor patchy white coloration from strong pervasive clay alteration. The clasts are 1.0-13.0 mm in size, with poor sorting, subangular to angular shape, low sphericity, random fabric, and abundant mm-sized vesicles. There is 2% porosity.

Thin Section Description

This sample has a porosity of 2%. It is is a massive monolithic matrix-supported volcanic breccia, with 36% altered clasts, cemented by a matrix of amorphous silica and gypsum, 50% overall. There are three generations of amorphous silica. The first amorphous silica generation (opal-A) contains abundant very-fine grained inclusions of iron oxides and clay. The second generation (opal-A), with fewer inclusions of iron oxides and clay. This silica displays globular “fish-egg” texture at its margins. These generations locally display tree-ring growth zones. Vesicles are lined by smectite (nontronite) → opal-CT → smectite (local). Late euhedral to anhedral gypsum fills in the open spaces in the matrix, post-dating mineralization.



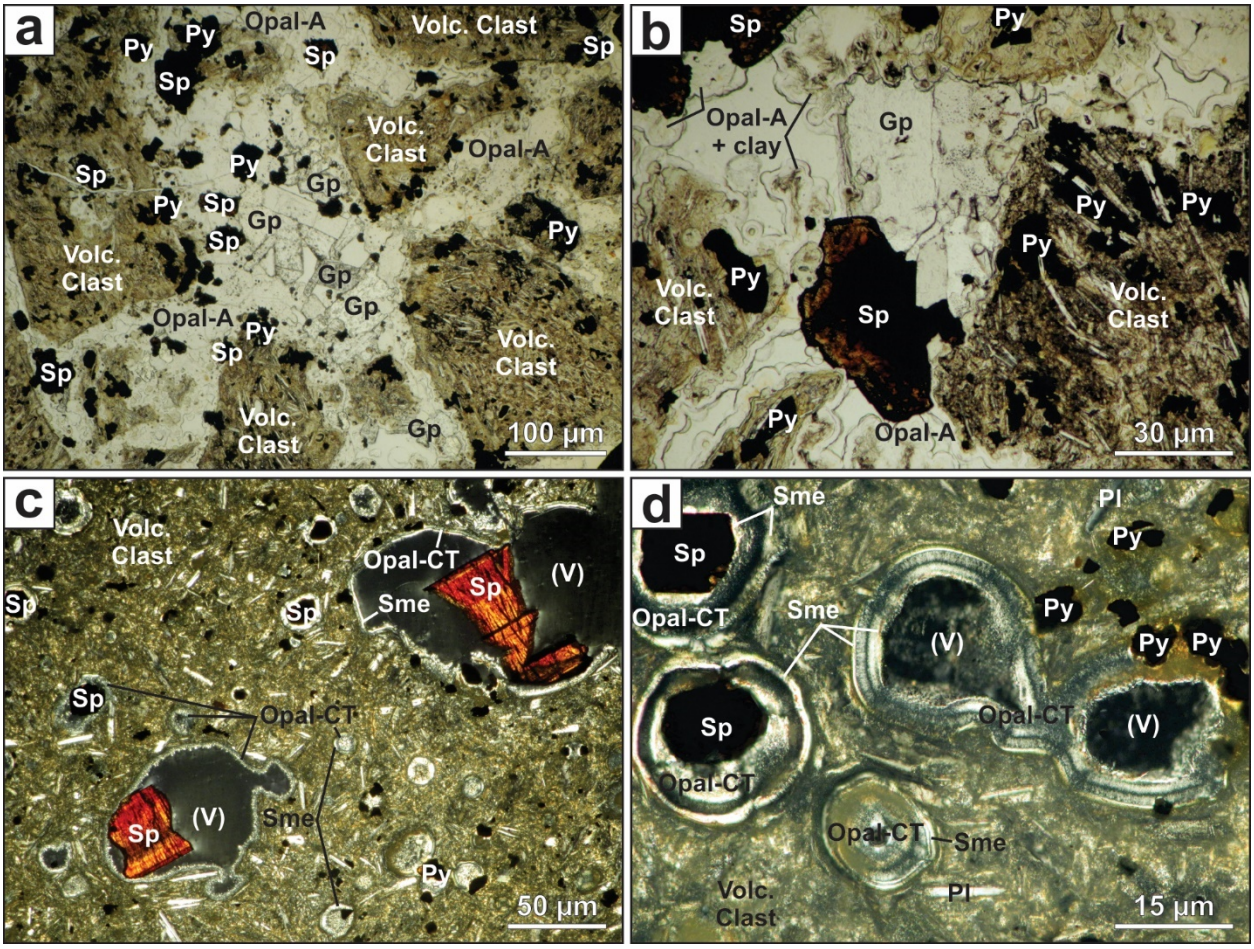
Thin section scan (left) and puck (right) of MA13-072.

The clasts have a wide range of sizes, from <1 mm to 13 mm. They are subrounded to angular, with minor dessication cracks. There is minor jigsaw-fit brecciation locally. The clasts appear light brown (patchy) in color from iron oxides, locally with an increase in iron oxides near the crystal margins. The clasts are vesicular, with a wide range of vesicle sizes, lined by very fine-grained clay (nontronite?), amorphous silica (opal-CT), n and sulfides. The clasts have have well-preserved phenocrysts of plagioclase (1%), locally glomeroporphyritic, and even rarer orthopyroxene. There are abundant preserved microphenocrysts of fine- to medium-grained plagioclase (15-25%), displaying weak to strong flow foliation. The flow directions change between clasts. The matrix of the clasts contains very fine-grained amorphous silica, iron oxide, and clay (nontronite), pervasively altering the former volcanic glass. There is minor disseminated fine-grained pyrite in the clasts, 1% overall. The locally have glassy (altered) quench margins. There is moderate mineralization of fine- to medium-grained anhedral to euhedral pyrite (5%), followed by moderate- to low-Fe sphalerite (5%), mostly associated with the matrix but also occurring in vesicles and pore spaces of the clasts. There is minor chalcopyrite (1%) included in the sphalerite, and trace galena (<1%) that is locally being altered and replaced by opal-CT. The sulfides form prior to silicification and gypsum crystallization. There are a few glass shards(?) that have been entirely altered to fine-grained chlorite (greenish) and silicified, with irregular margins, 2-3% overall.

Paragenesis: Volcanic clasts → hydrothermal mineralization (Py + Ccp → Sp + Gn) → Alteration of clast and matrix to opal-A + nontronite + FeOx + Py, alteration of glass shards to chlorite → Opal-A → Opal-CT lining vesicles → Nontronite (local) lining vesicles → Gp in open spaces.
Interpretation: Lapillistone (blocky angular clasts with glassy groundmass, quench margins, glass shards)

Descriptive Lithological Name: Moderately smectite-altered and silicified massive monomict matrix-supported shard-rich lapillistone, cemented and mineralized

Descriptive Alteration Facies: Opal-A and Opal-CT + nontronite + iron oxide + pyrite (multiple generations); pervasive chlorite altering glass shards



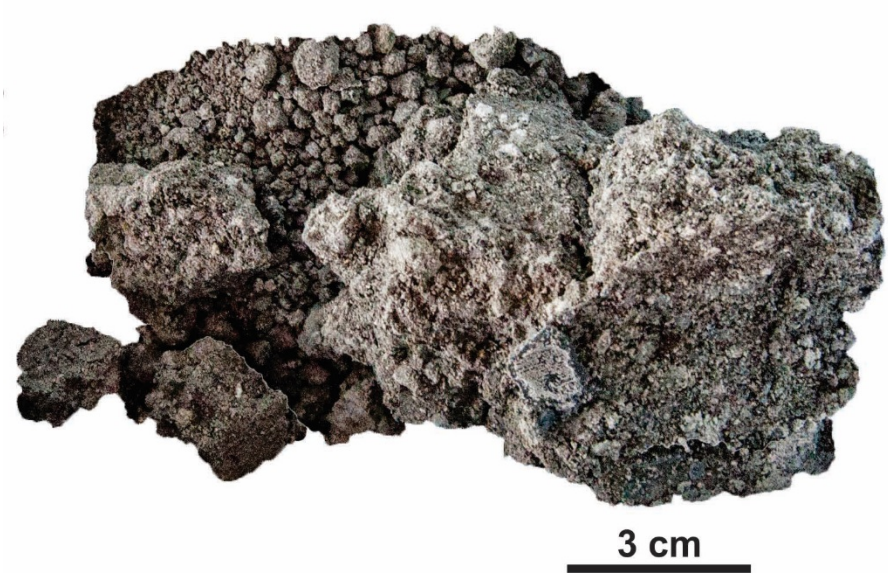
Photomicrographs of GMA13-072: (a) transmitted light (PPL) showing various volcanic clasts, sulfate matrix, and sulfides; (b) transmitted light (PPL) showing volcanic clasts, amorphous silica, and late sphalerite mineralization; (c) transmitted light (XPL) showing a vesicular clay-altered volcanic clast, with clay-lining vesicles and sphalerite mienralizaiton; (d) transmitted light (XPL) showing clay alteration in vesicles.

SAMPLE: MA13-073 **PARENT ID:** 2573 **SAMPLE DEPTH:** 3.90-4.00 mbsf	**DRILLHOLE:** TKAD032 **DRILLHOLE LOCATION:** 784672.04E/8649717.82N **WATER DEPTH:** 1084.40 mbsl

Mineralogy

SWIR (powdered clast): Montmorillonite
XRD (clay-sized fraction): Nontronite(?), corrensite, hematite, anhydrite
Assemblage: Non + Corr

Hand Sample Description

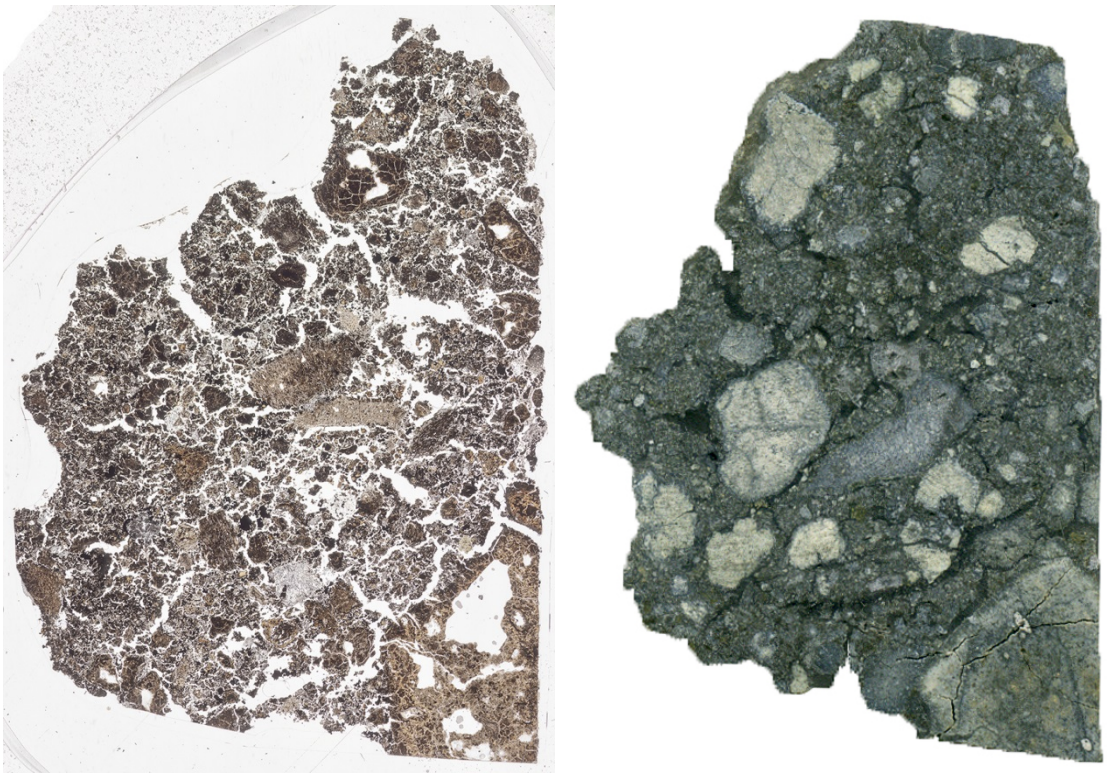


Hand sample of MA13-073.

This sample is a polymict(?) clast-supported(?) volcanic breccia with a strongly clay-altered matrix (20%) with dark red iron oxide (hematite) and minor patchy anhydrite cement (weakly cemented). There is 2% pyrite overall. There are 80% clasts overall. There are 78% medium grey moderately-clay altered clasts, <1.0-15.0 mm in size, with poor sorting, subangular-angular shape, low sphericity, random fabric, and a few mm-sized preserved vesicles. There are 2% white volcanic clasts, with strong pervasive clay alteration, <1.0-8.0 mm in size, with poor sorting, subangular shape, low sphericity, and random fabric. It is not clear if it is a polymict breccia, or a monomict breccia with variable alteration of the clasts. There is 2% porosity overall.

Thin Section Description

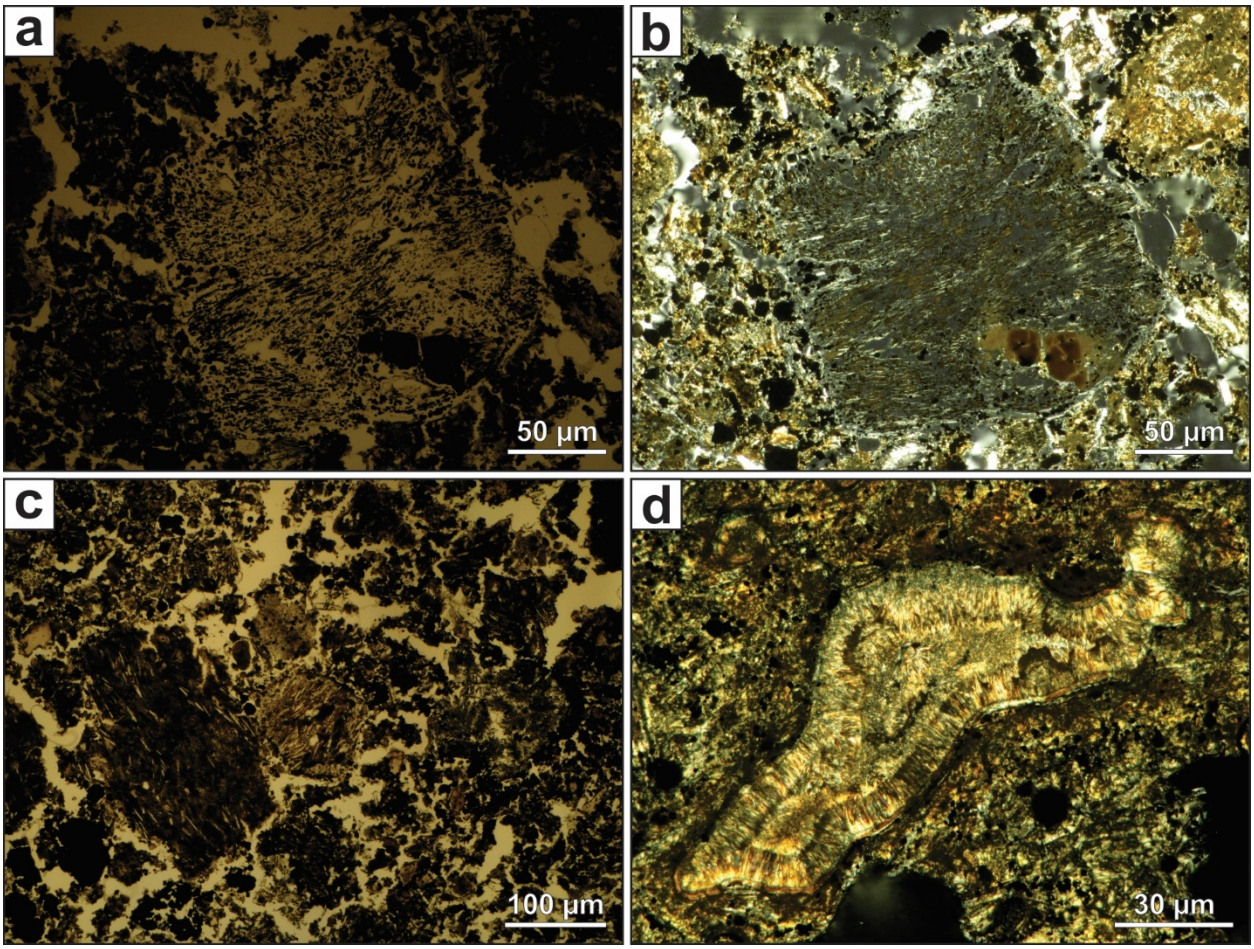
This section is difficult to distinguish clasts from matrix, with clasts ranging in size from <1 mm to 8 mm. The clasts are subrounded to subangular with a few curviplanar margins. The clasts are mostly medium to dark brown, with abundant phenocrysts displaying flow foliation. The phenocrysts range from clay-altered microphenocrysts to unaltered plagioclase phenocrysts. The clasts are variably vesicular. The clasts are pervasively and intensely altered to fine-grained clays with first-order interference colors (smectite?), and clay-lining vesicles. Rarely, vesicles are lined with late fine-grained chlorite. In addition, there are a few angular clasts of tube pumice, pervasively altered to clay. Open spaces are filled by inward-radiating



Thin section scan (left) and puck (right) of MA13-073.

fibrous clay.The clasts are variably altered to iron oxide, and contain minor fine-grained disseminated pyrite. The wide variety of clast colors, alteration intensities, and proportions of vesicles and phenocrysts suggests that this is a polymictic breccia, although the original composition of the clasts may be similar. The sample is comprised of 50% matrix material, 30% clasts, and 20% porosity. The matrix appears to consist of fine-grained clays and small broken clasts, along with sulfides and glass shards. Fine- to coarse-grained subhedral to euhedral pyrite is abundant in the matrix, comprising 10% of the total matrix material. There is also minor sphalerite (1%) and chalcopyrite (<1%), and rare bornite. Glass shards make up 5% of the matrix, minor irregular patchy coarse-grained gypsum comprises 5% of the matrix (weakly cemented), and the remaining 30% is fine-grained clays.

Paragenesis: Volcanic clasts + matrix (minor ash?) + glass shards → alteration of glassy groundmass and glass shards to smectite and vesicle-lining smectite → alteration of tube pumice to chlorite, minor chlorite infill of vesicles → pyrite + sphalerite → FeOx
Interpretation: Lapillistone (blocky angular clasts with glassy groundmass, glass shards)
Descriptive Lithological Name: Moderately smectite and chlorite-altered massive monomict matrix-supported shard-rich lapillistone, weakly cemented and mineralized
Descriptive Alteration Facies: Smectite altering glassy groundmass and glass shards, lining vesicles, minor chlorite altering tube pumice and later infilling vesicles, unaltered phenocrysts



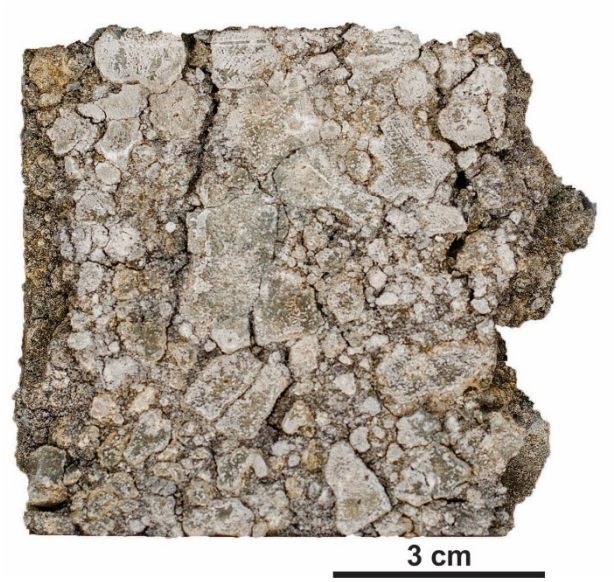
Photomicrographs of GMA13-073: (a) transmitted light (PPL) showing a pumice fragment; (b) transmitted light (XPL) showing clay alteration of the pumice fragment in (a) and alteration of the surrounding clasts and matrix; (c) transmitted light (PPL) showing various volcanic clasts; (d) transmitted light (XPL) showing clay alteration of the clast and infill of a vesicle.

SAMPLE: MA13-074 **PARENT ID:** 2575 **SAMPLE DEPTH:** 5.31-5.40 mbsf	**DRILLHOLE:** TKAD032 **DRILLHOLE LOCATION:** 784672.04E/8649717.82N **WATER DEPTH:** 1084.40 mbsl

Mineralogy

SWIR (powdered clast): Montmorillonite, paragoniticillite
XRD (clay-sized fraction): Nontronite, corrensite, anhydrite
Assemblage: Non + Corr

Hand Sample Description



Hand sample of MA13-074

This section is a monomict clast-supported volcanic breccia, weakly cemented with a matrix (25%) of dark grey and white clay and minor patchy anhydrite cement. There is patchy yellow iron oxide(?). There is <1% pyrite overall. There are 75% volcanic clasts, light grey with dark grey interiors, with moderate clay alteration (and possible sericite), <1.0-20.0 mm in size, poor sorting, angular shape, low sphericity, random fabric, with an aphanitic texture with abundant sub-mm vesicles. There is 3% porosity.

Alteration Summary: Moderate pervasive white clay primarily altering clast rims
Interpretation: Monomict(?) clast-supported volcanic breccia (pyroclastic or hyaloclastic?)
Name: Moderately clay-altered massive clast-supported volcanic breccia, weakly cemented

SAMPLE: MA13-075 **PARENT ID:** 2576 **SAMPLE DEPTH:** 6.42-6.54 mbsf	**DRILLHOLE:** TKAD032 **DRILLHOLE LOCATION:** 784672.04E/8649717.82N **WATER DEPTH:** 1084.40 mbsl

Mineralogy

SWIR (powdered clast): Montmorillonite, paragoniticillite, chlorite(?)
XRD (clay-sized fraction): Nontronite, corrensite, pyrite, anhydrite(?)
Assemblage: Non + Corr

Hand Sample Description

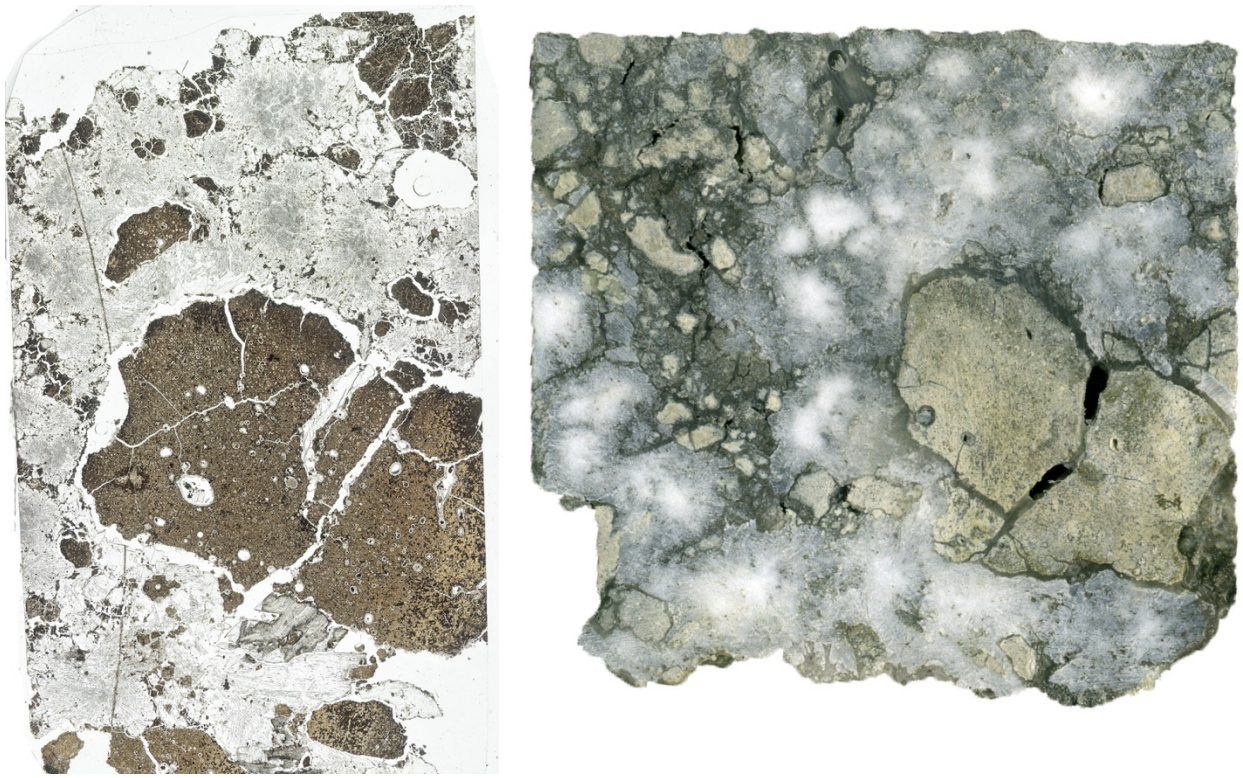


This sample is a monomict matrix-supported volcanic breccia, with a dark grey to white matrix composed of anhydrite (patchy infill) and minor yellow-grey clay. There is <1% pyrite overall. There are 15% pale yellowish-grey volcanic clasts, with strong pervasive clay alteration, with the highest alteration intensity near clast margins. The clasts are <1.0-20.0 mm in size, with poor sorting, rounded shape, moderate sphericity, random fabric, and an aphanitic texture with rare sub-mm vesicles. There is <1% pyrite in the clasts; the yellow coloring is likely from iron oxide weathering of pyrite. The porosity is 4%.

Hand sample of MA13-075.

Thin Section Description

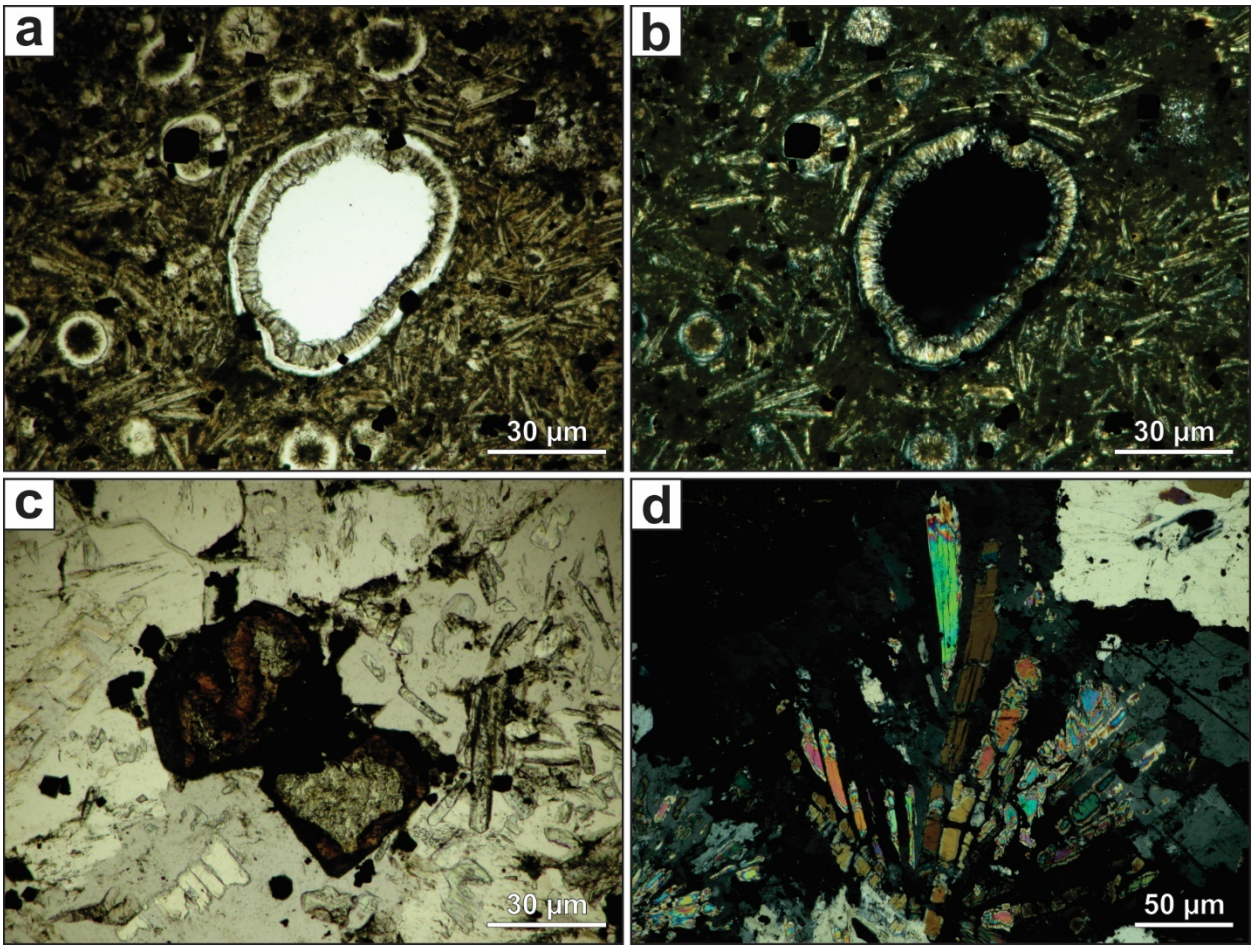
This sample has a porosity of 5%. It is a massive, monomict matrix-supported volcanic breccia. It is cemented by sulfates, with 60% matrix and 25% clasts. The clasts range in size from <1 mm to 20 mm. The clasts are subrounded to subangular, and appear medium orange-brown in transmitted light, with patchy dark brown areas (heterogeneous, patchy iron oxides). The clasts are poorly sorted and irregularly distributed throughout the section. The clasts are moderately vesicular with a wide range of vesicle sizes. There are rare relict phenocrysts of plagioclase, completely altered to clays. There are abundant microphenocrysts of plagioclase in the clast matrix, also completely altered to clays. There is no indication of flow foliation. The vesicles are lined with a thin rim of transparent fibrous-looking amorphous silica (opal-CT), followed by fribrous Fe-smectite (saponite), which partially or completely fills the vesicles. Locally, the saponite has traces of green chlorite. Locally, clasts are filled with chlorite, but there is very little overall chlorite identifiable (~1%). The groundmass and phenocrysts are also



Thin section scan (left) and puck (right) of MA13-075.

interpreted to be altered to smectite + iron oxide with disseminated pyrite. Fine- to medium-grained euhedral pyrite is irregularly disseminated throughout the clasts (5%). The matrix consists of coarse-grained lathe-like anhedral anhydrite, locally radiating, that has been extensively altered to coarse- to very coarse-grained gypsum, with abundant poikolitic, sieve, and recrystallization textures. The anhydrite also appears to be recrystallized in places. There is fine- to coarse-grained euhedral pyrite in the matrix (4%), along with minor sphalerite (1%) with inclusions of fine-grained chalcopyrite (<1%). The sulfide minerals are included in the sulfate minerals. Pyrite and sphalerite also form inside vesicles, with pyrite locally lining the vesicles. The sphalerite is colorless to light honey brown (low-Fe), increasing in iron content outwards. Pyrite is irregularly distributed throughout the section, with one pyrite-rich zone in the top right corner of the section. Here, medium-grained euhedral pyrite is up to 15% locally, and is associated with fine- to medium-grained (mostly ash- to sand-sized, few pebble-sized clasts) volcanic clasts and little sulfate cement. This combination of fine-grained clasts and sulfides occurs at the margins of large sulfate domains, suggesting that it may have been the primary matrix constituent prior to cementation. No crystal fragments or glass shards were observed.

Paragenesis: Volcanic clasts → Opal-CT lining some vesicles → Fe-smectite (saponite) alteration of clasts (groundmass and phenocrysts) → saponite ± chlorite lining vesicles → hydrothermal mineralization (Py → Sp + Ccp) → anhydrite cementation → anhydrite recrystallization and partial hydration to gypsum.
Interpretation: Hyaloclastite breccia? (no crystal fragments, blocky clasts)
Descriptive Lithological Name: Massive matrix-supported monomict hyaloclastite breccia, cemented and weakly mineralized
Descriptive Alteration Facies: Early opal-CT (vesicle-fill), intense pervasive smectite + iron oxide + pyrite, late Fe-smectite + chlorite (vesicle fill)



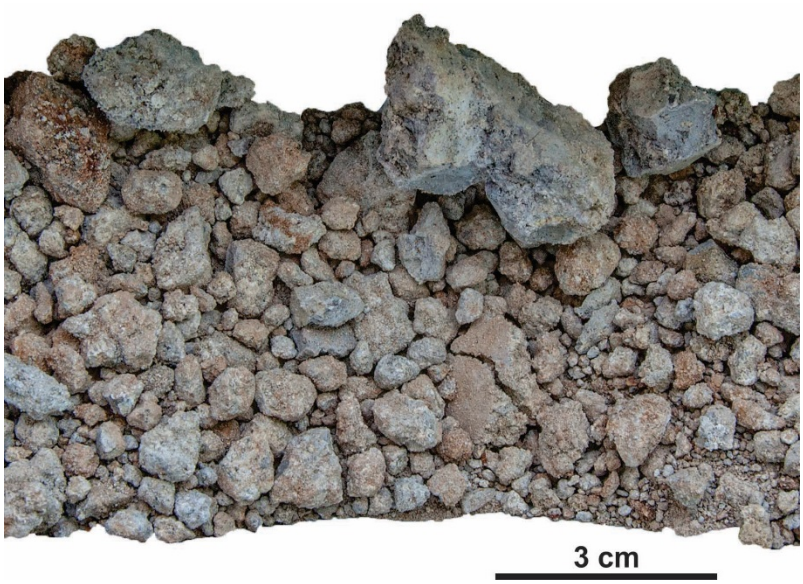
Photomicrographs of GMA13-075: (a) transmitted light (PPL) showing a large vesicle lined by clay; (b) transmitted light (XPL) showing clay alteration of the glassy groundmass and pheocrysts, and lining the vesicle; (c) transmitted light (PPL) showing a colorless to reddish sphalerite; (d) transmitted light (XPL) showing radial anhydrite, partially hydrated to gypsum.

SAMPLE: MA13-078 **PARENT ID:** 2006 **SAMPLE DEPTH:** 4.54-4.68 mbsf	**DRILLHOLE:** TKAD001 **DRILLHOLE LOCATION:** 784559.69E/8649995.52N **WATER DEPTH:** 1107.61 mbsl

Mineralogy

XRD (clay-sized fraction): Montmorillonite, plagioclase
Assemblage: Mnt/Non + Pl

Hand Sample Description



Hand sample of MA13-078.

This sample is composed of monomict unconsolidated volcanic fragments. The clasts are coherent medium-light grey moderately clay-altered volcanics (increased alteration intensity at clast margins), with yellow-orange iron oxide coating on the outside surface of the clasts. The clasts are <1.0-33.0 mm in size, with poor sorting, subangular shape, low sphericity, random fabric, and abundant mm-sized vesicles. There is 1% pyrite overall.

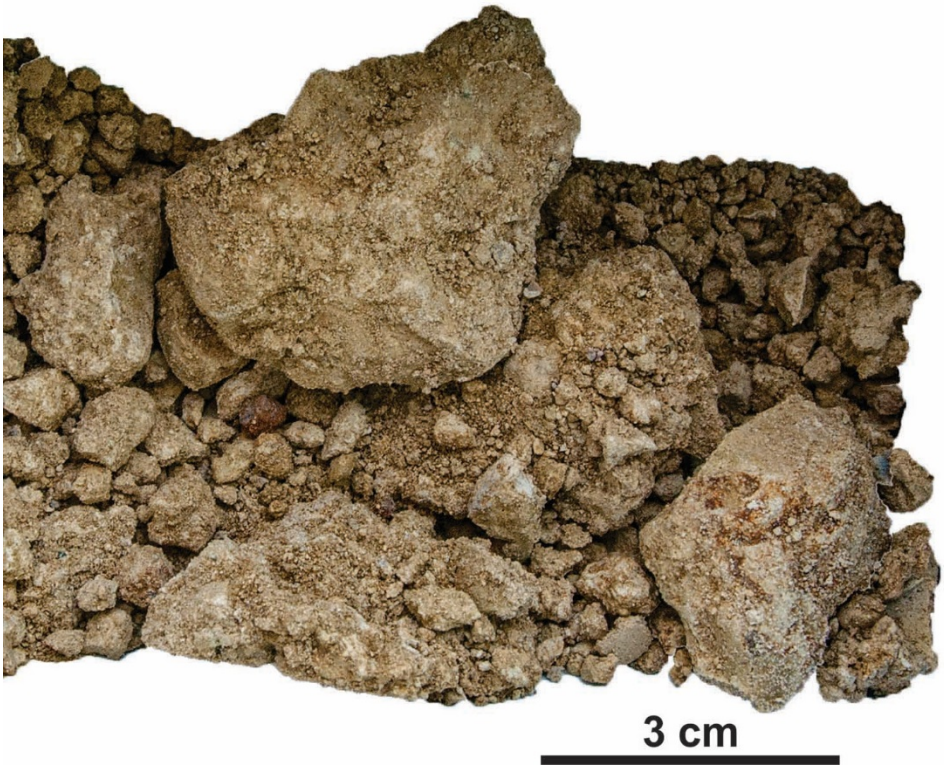
Alteration Summary: Intense, pervasive clay, minor FeOx
Interpretation: Origin unknown
Name: Monomict clay-altered volcanic breccia, unconsolidated

SAMPLE: MA13-079 **PARENT ID:** 2006 **SAMPLE DEPTH:** 4.90-5.00 mbsf	**DRILLHOLE:** TKAD001 **DRILLHOLE LOCATION:** 784559.69E/8649995.52N **WATER DEPTH:** 1107.61 mbsl

Mineralogy

N/A

Hand Sample Description



Hand sample of MA13-079.

Fine- to coarse-grained clay-altered volcanic breccia, monomict, low sphericity, low sorting, random fabric, moderate FeOx, minor pyrite, minor chalcopyrite, possible atacamite(?)

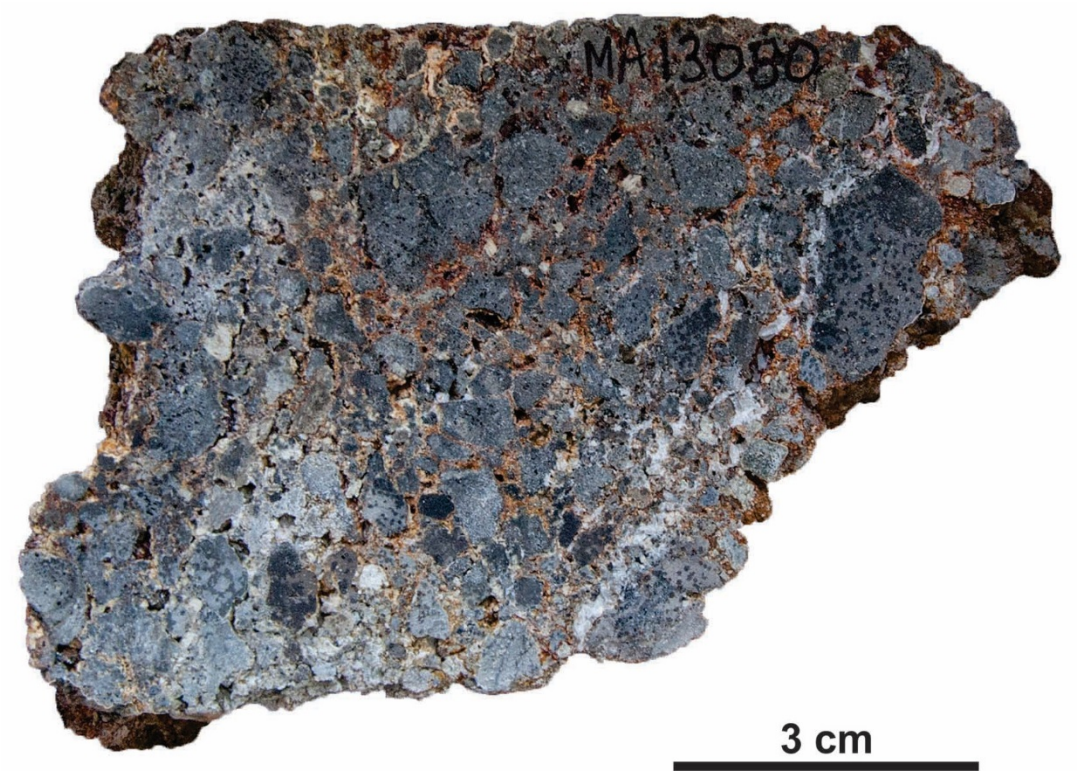
Alteration Summary: Intense pervasive white-grey clay, minor FeOx staining
Interpretation: Origin unknown
Name: Intensely clay-altered monomict volcanic breccia, unconsolidated

SAMPLE: MA13-080 **PARENT ID:** 2007 **SAMPLE DEPTH:** 5.50-5.60 mbsf	**DRILLHOLE:** TKAD001 **DRILLHOLE LOCATION:** 784559.69E/8649995.52N **WATER DEPTH:** 1107.61 mbsl

Mineralogy

N/A

Hand Sample Description



Hand sample of MA13-080.

This section is a variably-altered volcanic polymict clast-supported(?) breccia with clasts up to 10 mm, subrounded to subangular. The matrix consists of abundant FeOx and silica.

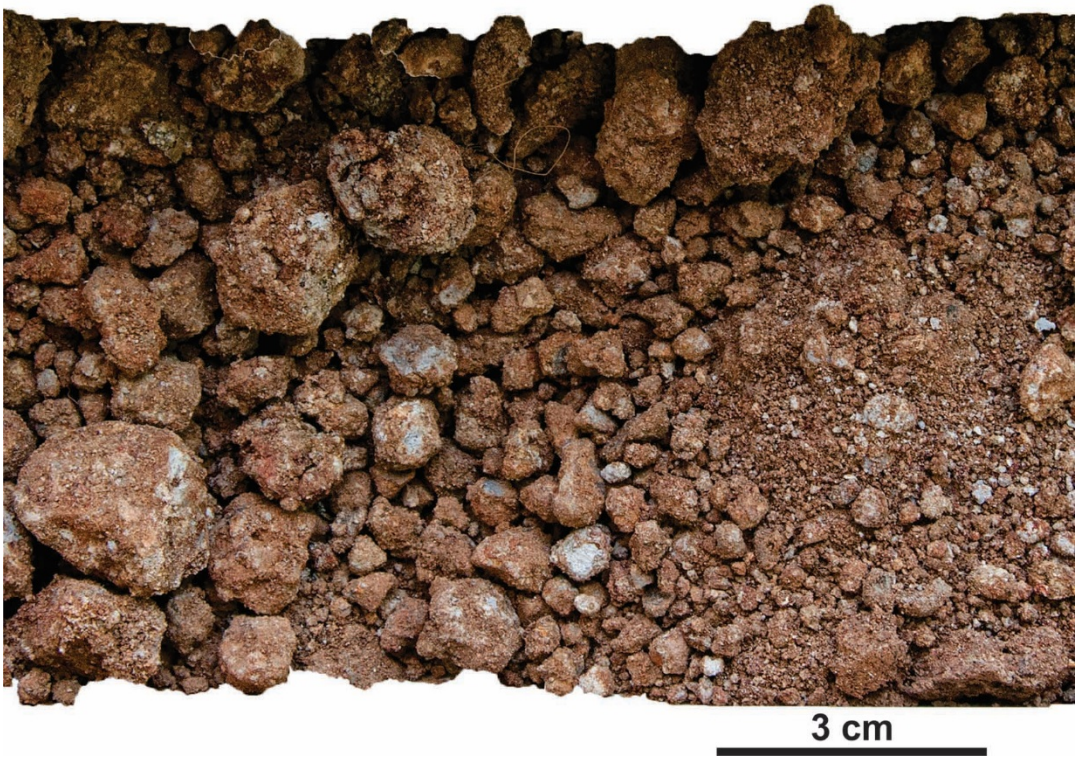
Alteration Summary: Variable light to dark grey clay
Interpretation: Volcaniclastic resedimented breccia(?)
Name: Weakly to moderately clay-altered polymict clast-supported volcanic breccia, silicified

SAMPLE: MA13-081 **PARENT ID:** 2008 **SAMPLE DEPTH:** 5.70-5.80 mbsf	**DRILLHOLE:** TKAD001 **DRILLHOLE LOCATION:** 784559.69E/8649995.52N **WATER DEPTH:** 1107.61 mbsl

Mineralogy

N/A

Hand Sample Description



Hand sample of MA13-081.

This sample consists of fine- to coarse-grained (up to 20 mm) unconsolidated monomict(?) volcanic breccia. It is poorly sorted, with subrounded to subangular clasts, with low sphericity and random fabric. The clasts are variably altered to light grey clay, with a thin coating of FeOx.

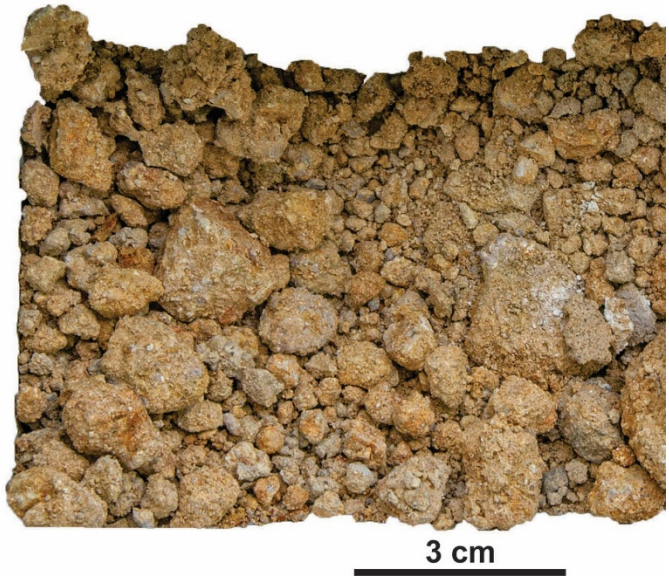
Alteration Summary: Moderate light grey clay, FeOx coating
Interpretation: Origin unknown
Name: Moderately clay-altered monomict(?) volcanic breccia, unconsoldiated

SAMPLE: MA13-082 **PARENT ID:** 2009 **SAMPLE DEPTH:** 7.00-7.10 mbsf	**DRILLHOLE:** TKAD001 **DRILLHOLE LOCATION:** 784559.69E/8649995.52N **WATER DEPTH:** 1107.61 mbsl

Mineralogy

XRD (clay-sized fraction): Montmorillonite, plagioclase
Assemblage: Mnt/Non + Pl

Hand Sample Description

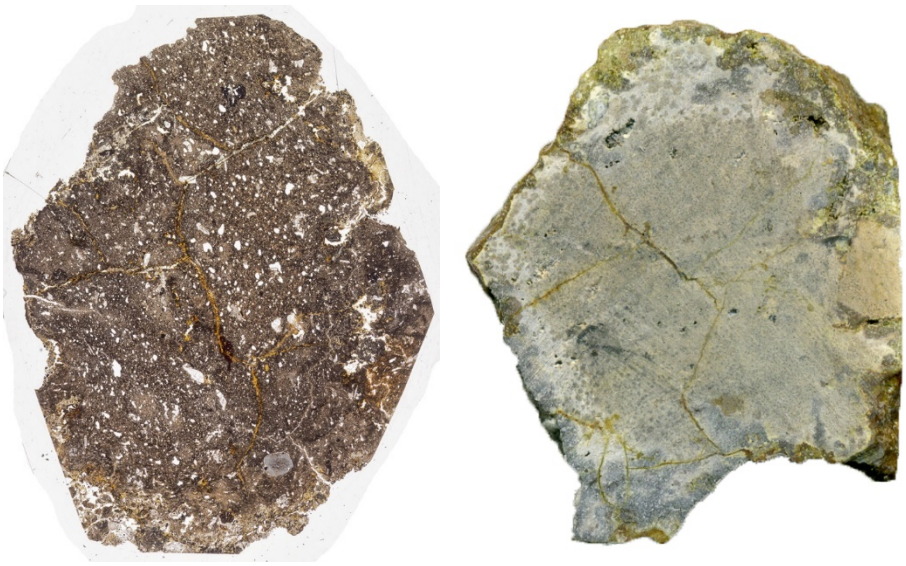


This sample consists of unconcolidated monomict volcanic fragments, with medium-light grey volcanic clasts with moderate pervasive clay alteration, and mm-thick orange iron oxide coating (more orange than sample MA13-078). The alteration is most intense at the clast margins. The clasts are <1.0-34.0 mm in size, with poor sorting, subangular-subrounded shape, low sphericity, random fabric, and abundant mm-sized clasts. There is 2% pyrite and 2% porosity.

Hand sample of MA13-082.

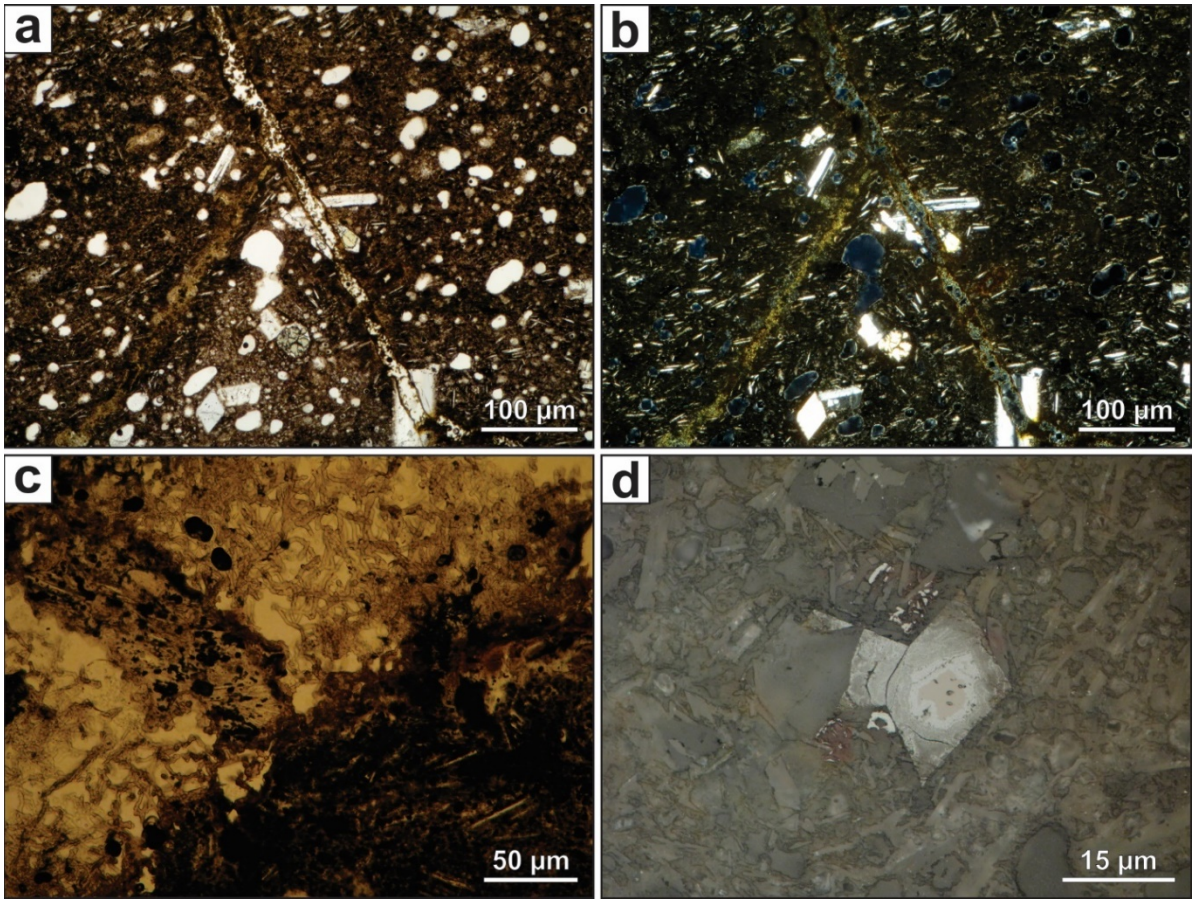
Thin Section Description

This sample consists of a single subangular 2.5 cm long clast from an unconsolidated monomict breccia. The clast contains ~15% large vesicles, ~20% flow-foliated microphenocrysts, and 5% plagioclase phenocrysts and 2% orthopyroxene phenocrysts The clast appears dark brown with patchy coloration. There is no pyrite, but there is trace magnetite altered to hematite. There is trace chalcopyrite in one vesicle. The glassy matrix of the clast is variably altered to fine-grained clays, with second to third order birefringence (smectite?). Clays rarely line vesicles. The microphenocrysts and phenocrysts are unaltered. The rim of the clast is locally glassy, and is overlain by iron-stained amorphous silica, with iron oxyhydroxides precipitating along fractures.



Thin section scan (left) and puck (right) of MA13-082.

Paragenesis: Clasts → smectite altering groundmass, magnetite altered to hematite → trace Ccp in vesicle → FeOx precipitation along fractures
Interpretation: Uknown origin
Descriptive Lithological Name: Weakly clay-altered vesicular volcanic clast
Descriptive Alteration Facies: Weak clay alteration of glassy groundmass



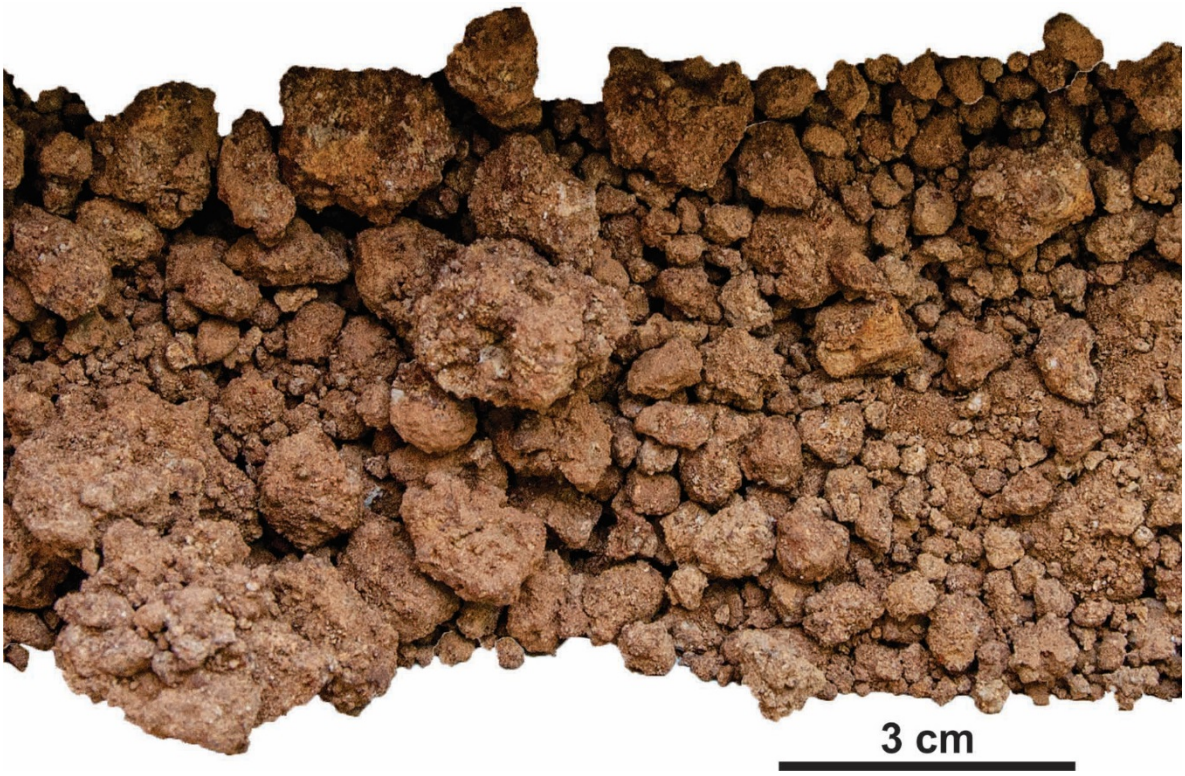
Photomicrographs of GMA13-082: (a) transmitted light (PPL) showing vesicular and weakly microporphyritic volcanic clasts; (b) transmitted light (XPL) showing clay alteration of the glassy groundmass and infilling a crack, with unaltered microphenocrysts, same view as (a); (c) transmitted light (PPL) showing Fe-stained amorphous silica; (d) reflected light (PPL) showing magnetite being altered to pyrite.

SAMPLE: MA13-083 **PARENT ID:** 2011 **SAMPLE DEPTH:** 8.40-8.50 mbsf	**DRILLHOLE:** TKAD001 **DRILLHOLE LOCATION:** 784559.69E/8649995.52N **WATER DEPTH:** 1107.61 mbsl

Mineralogy

N/A

Hand Sample Description



Hand sample of MA13-083.

This sample consists of fine- to coarse-grained (up to 25 mm) unconsolidated monomict(?) volcanic breccia. It is poorly sorted, with subrounded to subangular clasts, with low sphericity and random fabric. The clasts are variably altered to light grey clay, with a thin coating of FeOx.

Alteration Summary: Moderate light grey clay, FeOx coating
Interpretation: Origin unknown
Name: Moderately clay-altered monomict(?) volcanic breccia, unconsoldiated

SAMPLE: MA13-084 **PARENT ID:** 2013 **SAMPLE DEPTH:** 11.10-11.30 mbsf	**DRILLHOLE:** TKAD001 **DRILLHOLE LOCATION:** 784559.69E/8649995.52N **WATER DEPTH:** 1107.61 mbsl

Mineralogy

N/A

Hand Sample Description



Hand sample of MA13-084.

This sample consists of a variably-altered polymict volcanic breccia, unconsolidated. The clasts are angular to subangular, with low sphericity, poor sorting, and a random fabric. The clasts are variably altered to weak to moderate medium grey to white clay, and FeOx coating.

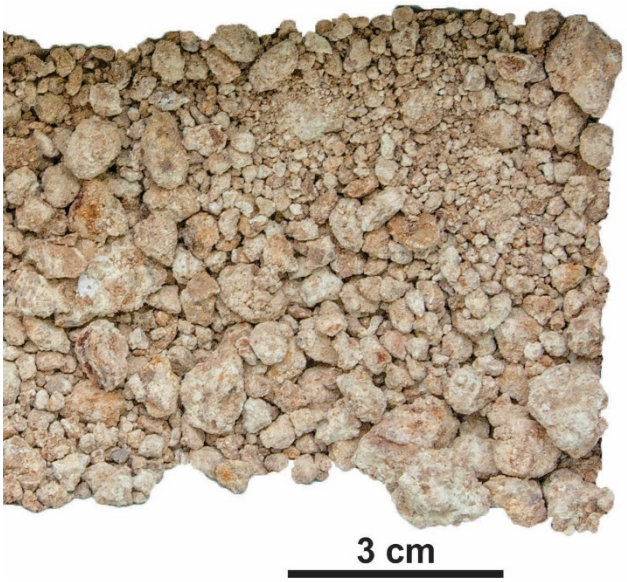
Alteration Summary: Variable, weak to moderate medium grey to white clay, FeOx coating.
Interpretation: Origin unknown
Coherent flow, hyaloclastic, hydraulic fracturing, autoclastic, pseudo-breccia, mass-flow emplaced polymict breccia, resedimented
Name: Variably clay-altered polymict(?) volcanic breccia, unconsoldiated

SAMPLE: MA13-085 **PARENT ID:** 2015 **SAMPLE DEPTH:** 12.90-13.00 mbsf	**DRILLHOLE:** TKAD001 **DRILLHOLE LOCATION:** 784559.69E/8649995.52N **WATER DEPTH:** 1107.61 mbsl

Mineralogy

XRD (clay-sized fraction): Nontronite, plagioclase
Assemblage: Mnt/Non + Pl

Hand Sample Description



This sample consists of unconcolidated monomict volcanic fragments, possibily with a siliceous (biological?) component. The clasts consist of orange-yellow (patchy red) volcanic clasts with strong pervasive clay, iron oxide, and possible silica, <1.0-13.0 mm in size, with poor sorting, subangular shape, low sphericity, random orientation, and an aphanitic texture. No sulfides were observed. There is 1% porosity.

Hand sample of MA13-085.

This sample consists of fine- to medium-grained (up to 10 mm) unconsolidated monomict(?) volcanic breccia, unconsolidated. It is poorly sorted, with subrounded to subangular clasts, with low sphericity and random fabric. The clasts are variably altered to light grey clay, with a thin coating of yellow-orange FeOx.

Alteration Summary: Moderate light grey clay, FeOx coating
Interpretation: Origin unknown
Name: Moderately clay-altered monomict(?) volcanic breccia, unconsoldiated

SAMPLE: MA13-086 **PARENT ID:** 2017 **SAMPLE DEPTH:** 16.05-16.22 mbsf	**DRILLHOLE:** TKAD001 **DRILLHOLE LOCATION:** 784559.69E/8649995.52N **WATER DEPTH:** 1107.61 mbsl

Mineralogy

SWIR (powdered clast): Montmorillonite, gypsum
XRD (clay-sized fraction): Montmorillonite(?), nontronite, hematite
Assemblage: Mnt/Non + Pl

Hand Sample Description

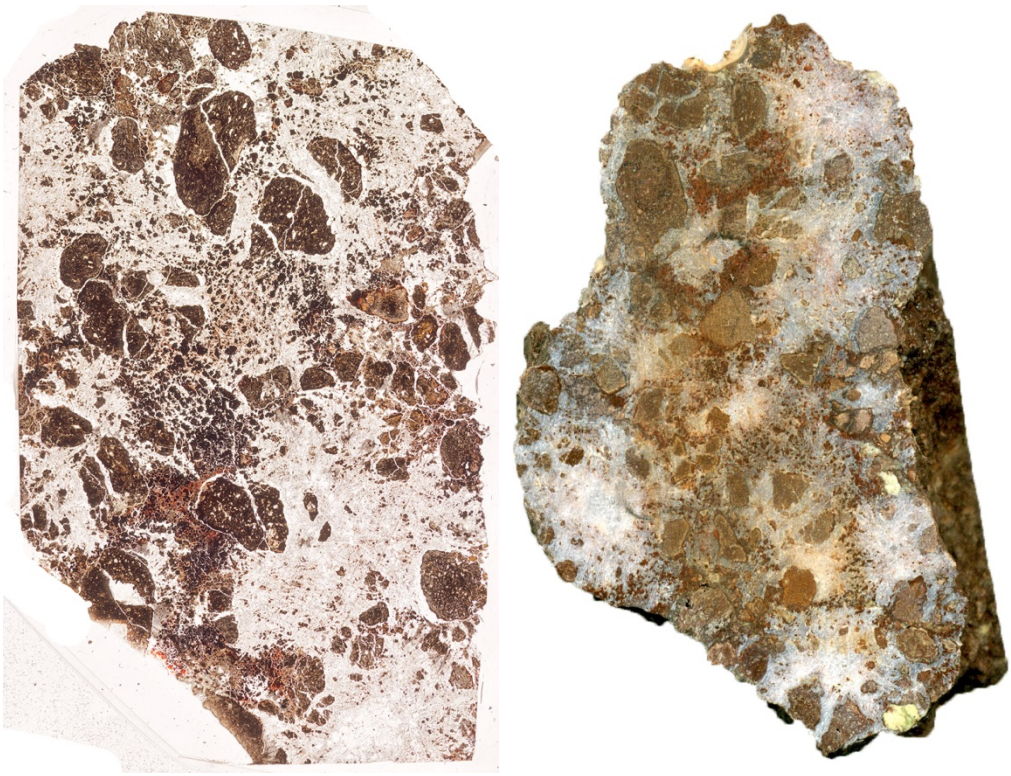


Hand sample of MA13-086.

This sample is a polylithic matrix-supported volcanic breccia, strongly cemented by anhydrite. The anhydrite matrix (75%) may be a hydrothermal vein, there is evidence for hydrothermal brecciation. There is minor iron oxide in the matrix. There are 25% volcanic clasts. This includes 21% red iron oxide-altered clasts with pervasive hematite, and possible minor clay alteration, with the strongest alteration at the clast margins. These clasts are <1.0-7.0 mm in size, with poor sorting, subangular shape, moderate sphericity, random fabric, and 1% sub-mm vesicles and a few sub-mm phenocrysts. Several of these clasts display jigsaw fit. There are 4% pale-green volcanic clasts, with pervasive intense clay alteration, with possible chlorite, 2.0-14.0 mm in size, with poor sorting, subangular shape, low sphericity, random fabric, and an aphanitic texture. There are a few inclusions of iron oxides. No sulfides were observed. The porosity is 1%.

Thin Section Description

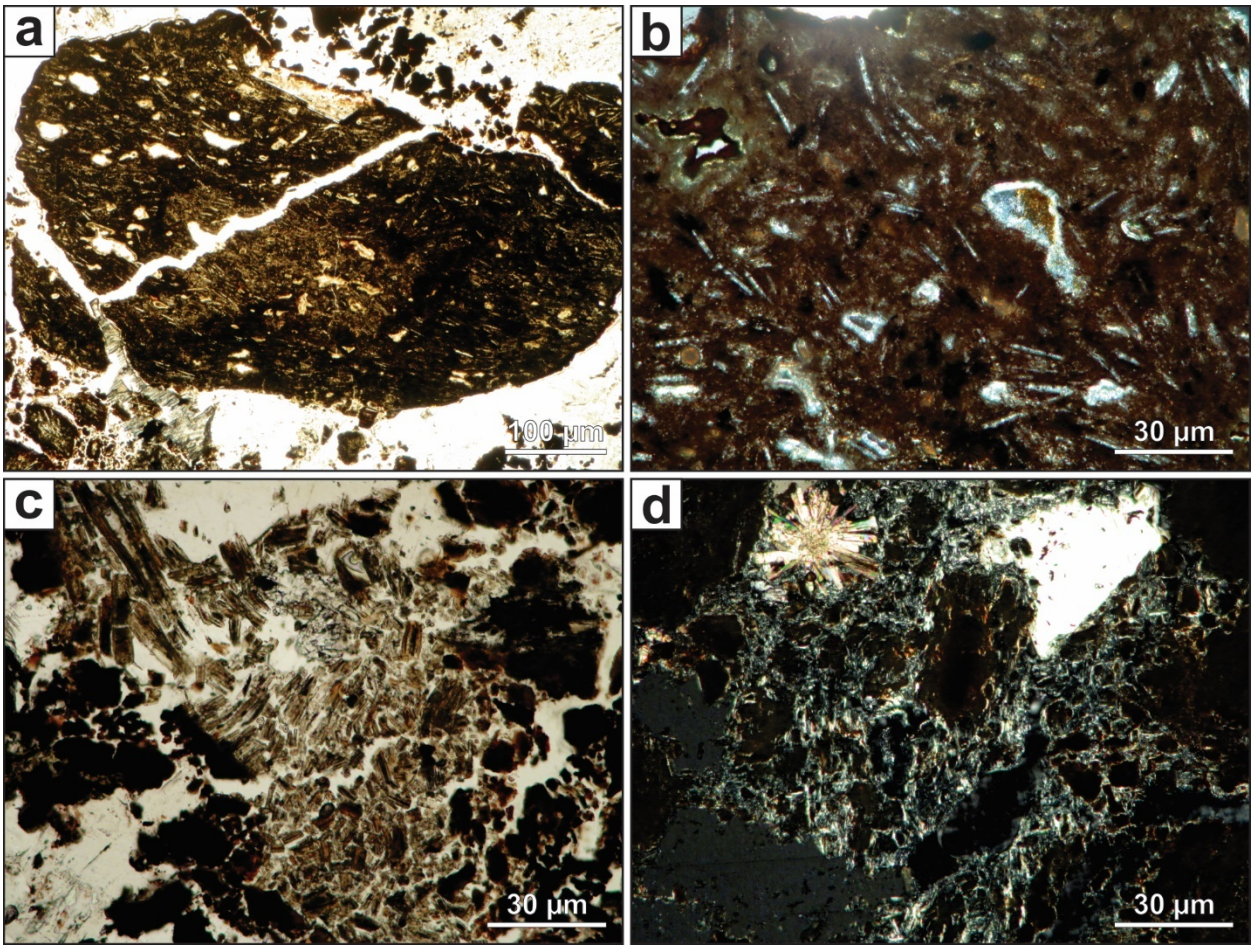
This sample is a strongly oxidized matrix-supported monomict volcanic breccia, cemented by gypsum, with 5% pore space. The volcanic clasts are rounded to subrounded and comprise 25-30% of the sample. The clasts appear dark brown to red, and contain up to 15% vesicles. There are a few fine- to locally coarse-grained crystals of hematite within the clasts. There are abundant microphenocrysts with strong flow-foliation. Some elongate vesicles also display flow-foliation. The volcanic clasts are pervasively altered to fine-grained clay with first-order birefringence colors (smectite?). The clay pervasively alters the clasts and microphenocrysts, and lines vesicles. There are some broken-up glass shards that may have been



Thin section scan (left) and puck (right) of MA13-086.

pumice fragments (2-3%), also pervasively altered to clay that is usually slightly coarser-grained. Muddy-looking gypsum comprises the rest of the sample (65-60%), with local inclusions of anhydrite (~2% overall).

Paragenesis: Volcanic clasts + pumice fragments → Fe-oxides → smectite pervasively altering clasts → smectite lining vesicles → anhydrite cementation → almost complete hydration of anhydrite to gypsum
Interpretation: Resedimented(?) lapilli tephra
Descriptive Lithological Name: Matrix-supported monomict resedimented(?) lapilli tephra, cemented
Descriptive Alteration Facies: Pervasive smectite alteration of clasts and phenocrysts, lining vesicles, intense pervasive iron oxide



Photomicrographs of GMA13-086: (a) transmitted light (PPL) showing a rounded flow-foliated volcanic clast; (b) transmitted light (XPL) showing clay alteration of a volcanic clast, including alteration of phenocrysts and infilling vesicles, and abundant FeOx; (c) transmitted light (PPL) showing broken glass shards (pumice?); (d) transmitted light (XPL) showing abundant clay alteration minerals in the matrix (altering ash?), and minor radiating anhydrite.

SAMPLE: MA13-087 **PARENT ID:** 2020 **SAMPLE DEPTH:** 14.00-14.12 mbsf	**DRILLHOLE:** TKAD001 **DRILLHOLE LOCATION:** 784559.69E/8649995.52N **WATER DEPTH:** 1107.61 mbsl

Mineralogy

SWIR (powdered clast): Montmorillonite, paragoniticillite
XRD (clay-sized fraction): Montmorillonite(?), nontronite, corrensite
Assemblage: Non + Corr

Hand Sample Description



Hand sample of MA13-087.

This sample is from the altered stringer zone. It is a monomict matrix-supported volcanic breccia, with 60% white anhydrite cement and 3 mm-wide irregular veinlets. The clasts show a wide range in sizes, with a large volcanic fragment (bomb?) that is at least 50 mm wide, cut by the anhydrite veins. There are 40% total light grey, slightly greenish volcanic clasts with strong pervasive clay alteration and minor chlorite alteration. The clasts are 1.0-90.0 mm wide, moderately sorted, rounded to subrounded shape, moderate-low sphericity, and possible bedding by clast size. The texture is aphanitic with a few sub-mm vesicles and abundant sulfides. The clasts display jigsaw fit near veins (hydrothermal brecciation?). The sulfides include sphalerite (3%) and pyrite (2%). It has a porosity of 2%.

Thin Section Description

This section is from the bedded area with fine volcanic clasts, but bedding is not obvious in the sample. It has a porosity of 1-2%. It is matrix supported, with 55% matrix and 20% volcanic clasts. There are ~5%

medium-grained blocky light orange-brown glass shards, subrounded to angular in shape, locally with curviplanar margins. The glass shards are completely altered to very fine-grained clays.



Thin section scan (left) and puck (right) of MA13-087.

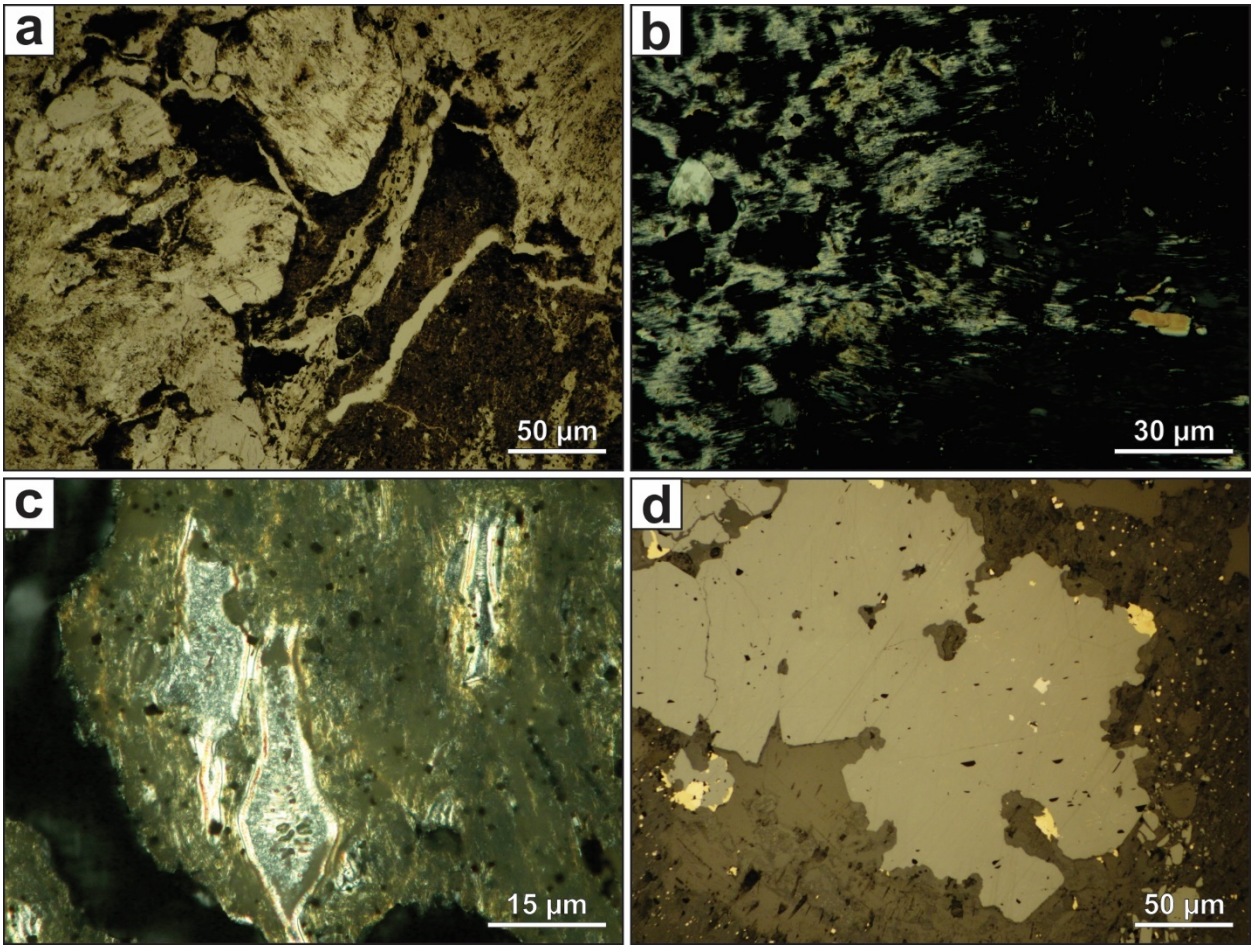
The clasts in this section range in size from <1 to 7 mm. They are blocky and subangular with some curviplanar surfaces. They are locally fine-grained and wispy. Larger clasts have glassy horizons, with zones of almost-transparent light brown glass that has been completely altered to very fine-grained clay. These glassy domains are irregular and patchy, and in some areas appears to form along a long stretch near the top of the lava surface. A few clasts have more glass than crystalline material. There are no preserved phenocrysts or microphenocrysts. There are minor elongate vesicles with irregular margins, possibly aligned along a flow foliation. The clasts appear light- to medium- orange-brown in transmitted light from patchy iron oxide. They contain fine-grained disseminated pyrite (2%). The groundmass is pervasively altered to fine-grained clays (nontronite?). The vesicles are lined with a thin layer of clay (nontronite?), followed by opal-CT, followed by additional clay (local).

The matrix is dominated by gypsum, displaying complex recrystallization textures, sieve textures, and poikolitic to micropoikolitic textures with inclusions of anhedral anhydrite. The gypsum locally appears fibrous and radiating. There is only 2% anhydrite preserved.

The matrix contains abundant sulfides. There is ~4% fine- to medium-grained pyrite, followed by ~10% medium-coarse grained sphalerite (very low Fe, almost colorless) that contains a few inclusions of fine-grained galena (1%). ~3% fine-medium grained chalcopyrite forms last. The sulfides are surrounded by

sulfates and have a few inclusions of sulfates, suggesting that they may have formed at the same time. This is a sulfide-rich part of the sample, so this abundance may not reflect the bulk sample abundance.

Paragenesis: Volcanic clasts → alteration of glass shards and clasts (nontronite + pyrite + iron oxide) + clay (nontronite) lining vesicles → Opal-CT lining vesicles → clay lining vesicles (nontronite) → hydrothermal mineralization (Py → Sp + Gn → Ccp) + anhydrite cementation → hydration of anhydrite to gypsum (almost complete).
Interpretation: Phreatic breccia, non-welded fall (bedded, glassy clasts, glass shards, large bomb), minor hydrothermal brecciation along veins.
Descriptive Lithological Name: Bedded matrix-supported monomict lappilistone, mineralized and sulfate-cemented
Descriptive Alteration Facies: Early nontronite (pervasive + vesicle-lining) + iron oxide + pryite, followed by opal-CT, and late nontronite (vesicle-lining)



Photomicrographs of GMA13-087: (a) transmitted light (PPL) showing irregular volcanic clasts with glassy domains; (b) transmitted light (XPL) showing complete alteration of the glassy groundmass of a volcanic clast to clay (chlorite?); (c) transmitted light (XPL) showing intense clay alteration of a volcanic clast and infilling vesicles; (d) reflected light (PPL) showing sphalerite, with inclusions of galena of Pb-As sulfodalts, and late chalcopyrite.

SAMPLE: MA13-088 **PARENT ID:** 2021 **SAMPLE DEPTH:** 17.40-17.50	**DRILLHOLE:** TKAD001 **DRILLHOLE LOCATION:** 784559.69E/8649995.52N **WATER DEPTH:** 1107.61 mbsl

Mineralogy

SWIR (powdered clast): Muscovite, muscoviticillite(?)
XRD (clay-sized fraction): Chamosite, corrensite, I/S, anhydrite
Assemblage: I/S + Cham

Hand Sample Description

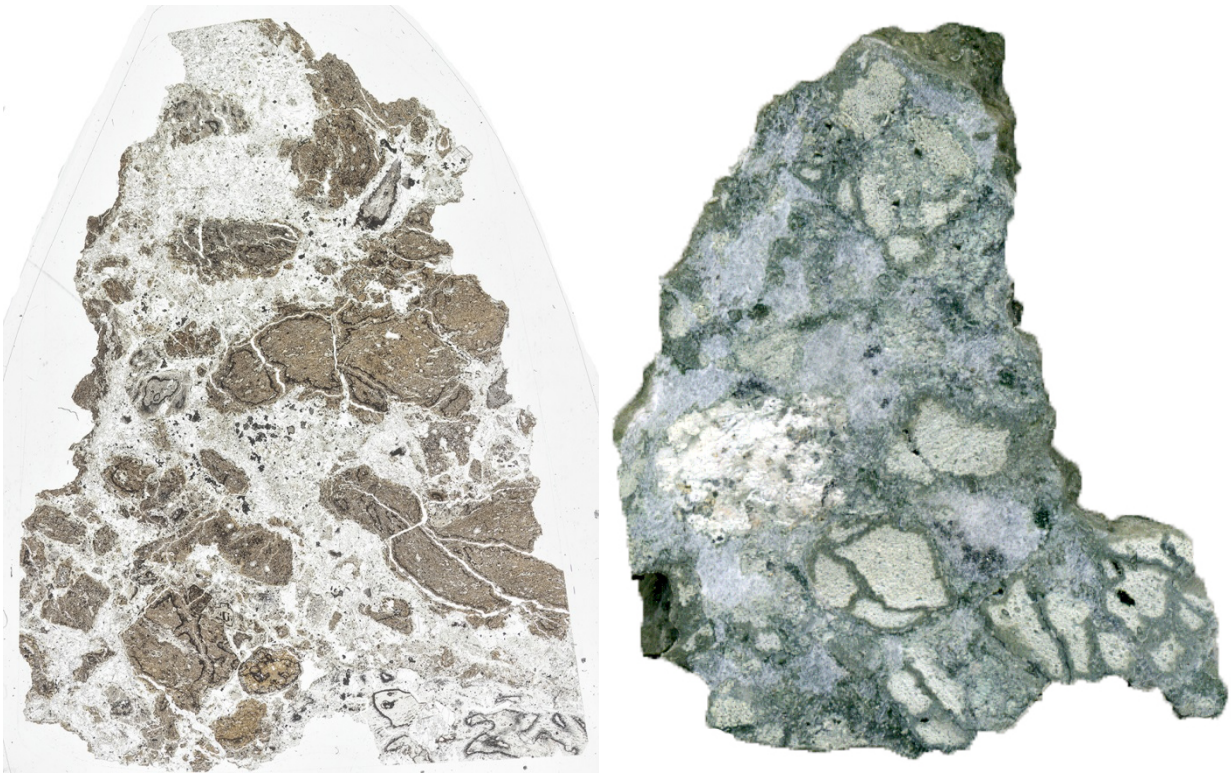


Hand sample of MA13-088.

This section is a polymict(?) matrix-supported volcanic breccia, cemented by a dark-grey matrix of anhydrite (50%), which may all be related to hydrothermal veining. The dark color may be from finely disseminated sulfides. One irregular 3-mm wide white anhydrite vein cuts the sample perpendicular to the core axis. There is 1% sphalerite (within anhydrite matrix), <1% pyrite, and trace atacamite at the clast margins. There are 50% clasts overall. These include 38% light greenish-grey volcanic clasts with strong pervasive clay alteration, minor chlorite, <1.0-12.0 mm in size, with poor sroting, subrounded shape, low sphericity, random fabric, aphanitic texture with rare sub-mm vesicles, and minor jigsaw fit (hydrothermal brecciation?). There are 10% white volcanic clasts that have strong pervasive clay alteration, 7.0-26.0 mm in size, with poor sorting, angular to subangular shape (irregular margins), low sphericity, random orientations, aphanitic texture with rare sub-mm vesicles, and minor jigsaw-fit (hydrothermal brecciation?). There are 2% grey volcanic clasts with moderate pervasive clay alteration (most intense at clast margins), 2.0-4.0 mm in size, with poor sorting, subrounded shape, moderate sphericity, random orientation, and aphanitic texture with minor sub-mm vesicles. The porosity is 1%.

Thin Section Description

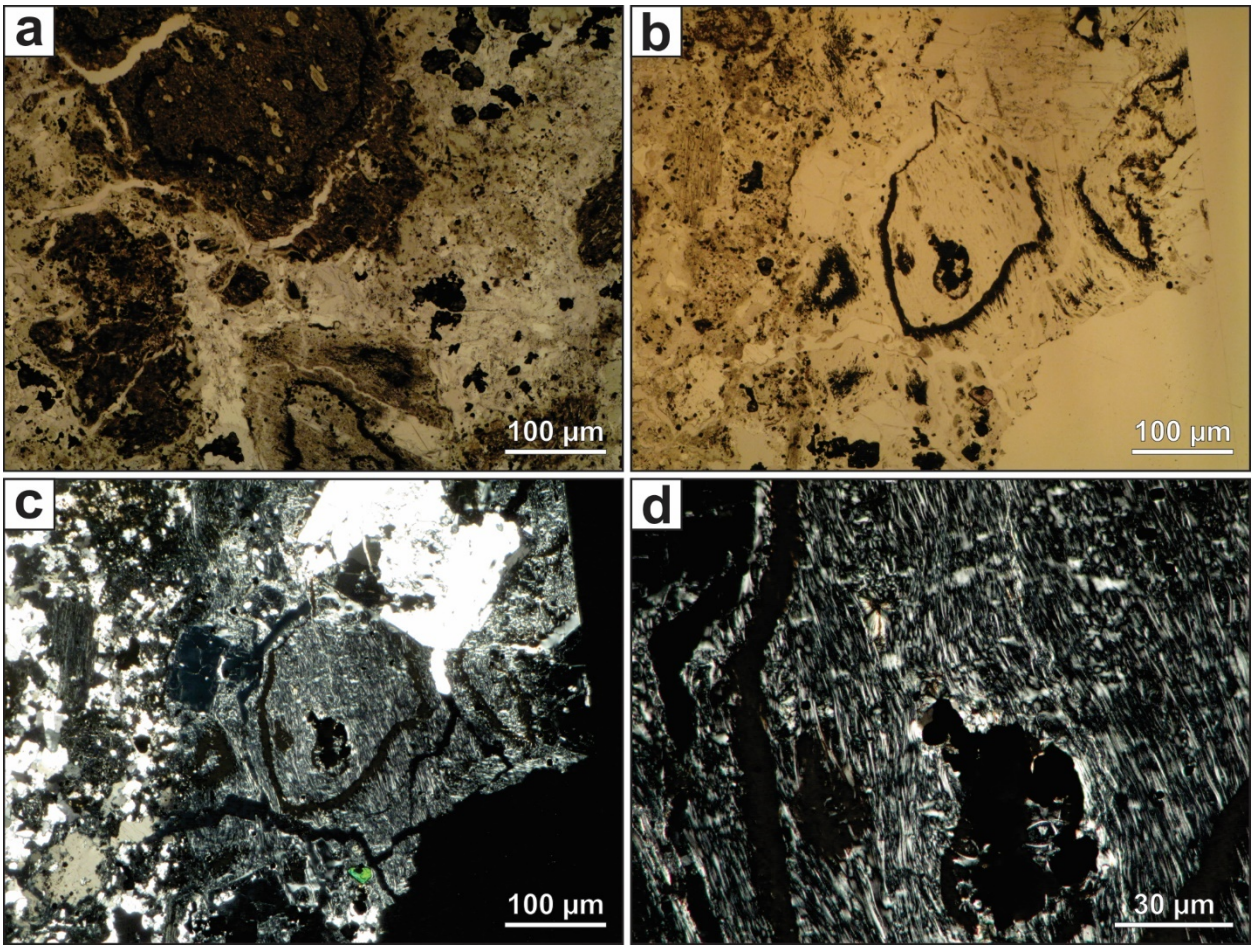
Despite appearances in hand-sample, section is a monomict pumice-rich matrix-supported volcanic breccia, cemented by intensely-recrystallized gypsum. The volcanic clasts are subangular, with slight variations in color. There are up to 10% vesicles and variable amounts of microphenocrysts that are locally flow-foliated. The glassy groundmass and microphenocrysts are pervasively altered to clay.



Thin section scan (left) and puck (right) of MA13-088.

The vesicles are lined by two generations of clay: an early high-birefringent generation (illite?) followed by chlorite. The pumice fragments are coarse-grained with irregular margins, and are pervasively altered to clay with first-order birefringence (smectite?). These clasts appear very white in hand sample, appearing polymict; however, these clasts may form simultaneously during the same eruption. The groundmass consists of recrystallized gypsum with no relict anhydrite. Fine-grained pyrite is disseminated throughout the volcanic clasts. Minor medium-grained sphalerite and pyrite crystals form in the matrix. Overall there is 3% porosity, 10% pumice clasts, 25% volcanic clasts, 60% gypsum, and 2% sphalerite.

Paragenesis: Volcanic clasts and pumice fragments → pervasive clay and pyrite alteration of clasts → illite/smectite lining vesicles followed by chlorite lining vesicles → hydrothermal mineralization of Sp →anhydrite cementation → complete hydration of anhydrite to gypsum and recrystallization
Interpretation: Lapilli tephra
Descriptive Lithological Name: Massive matrix-supported monomict pumaceous lapilli tephra, cemented and weakly mineralized
Descriptive Alteration Facies: Early illite/smectite + pryite, followed by chlorite



Photomicrographs of GMA13-088: (a) transmitted light (PPL) showing various volcanic clasts; (b) transmitted light (PPL) showing a pumice fragment; (c) transmitted light (XPL) showing complete alteration of the pumice fragment in (b) to clay, and clay alteration in the matrix; (d) transmitted light (XPL) showing a close-up of the clay alteration in (c).

SAMPLE: MA13-089 **PARENT ID:** 2022 **SAMPLE DEPTH:** 17.90-18.00 mbsf	**DRILLHOLE:** TKAD001 **DRILLHOLE LOCATION:** 784559.69E/8649995.52N **WATER DEPTH:** 1107.61 mbsl

Mineralogy

XRD (clay-sized fraction): Chamosite, rectorite, I/S, quartz
Assemblage: I/S + Cham

Hand Sample Description

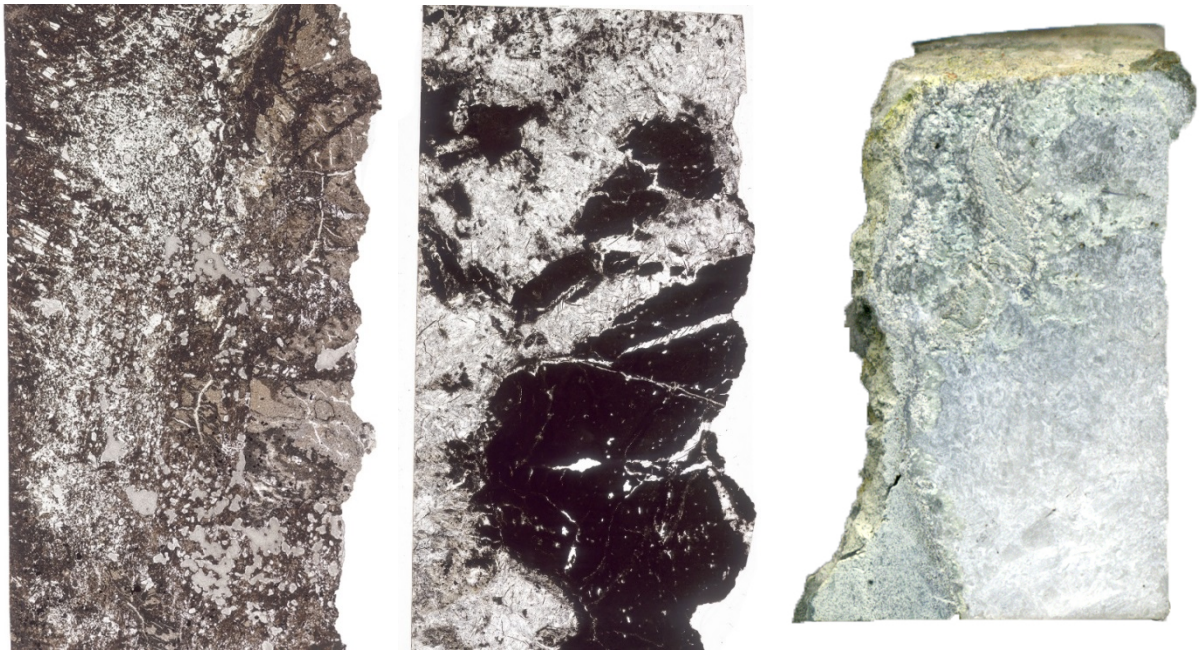


Hand sample of MA13-089.

This sample is a monomict matrix-supported volcanic breccia with early 2 mm-wide sulfate veins and brecciation, and later 2-3 cm-wide veins with sulfides (multiple vein fills). These veins are composed of anhydrite and gypsum, 70% overall. The sulfides include sphalerite (2%), pyrite (1%), and chalcopyrite (<1%). There are 30% light greenish-buff colored volcanic clasts, with strong pervasive clay and trace chlorite alteration. The clasts range in size from <1.0-75.0 mm (bomb sized), cut by sulfate veins, with moderate sorting, subangular shape, low sphericity, and possible bedding by clast size, aphanitic texture with abundant sub-mm vesicles, and minor jigsaw fit (hydrothermal brecciation?). There is <1% porosity.

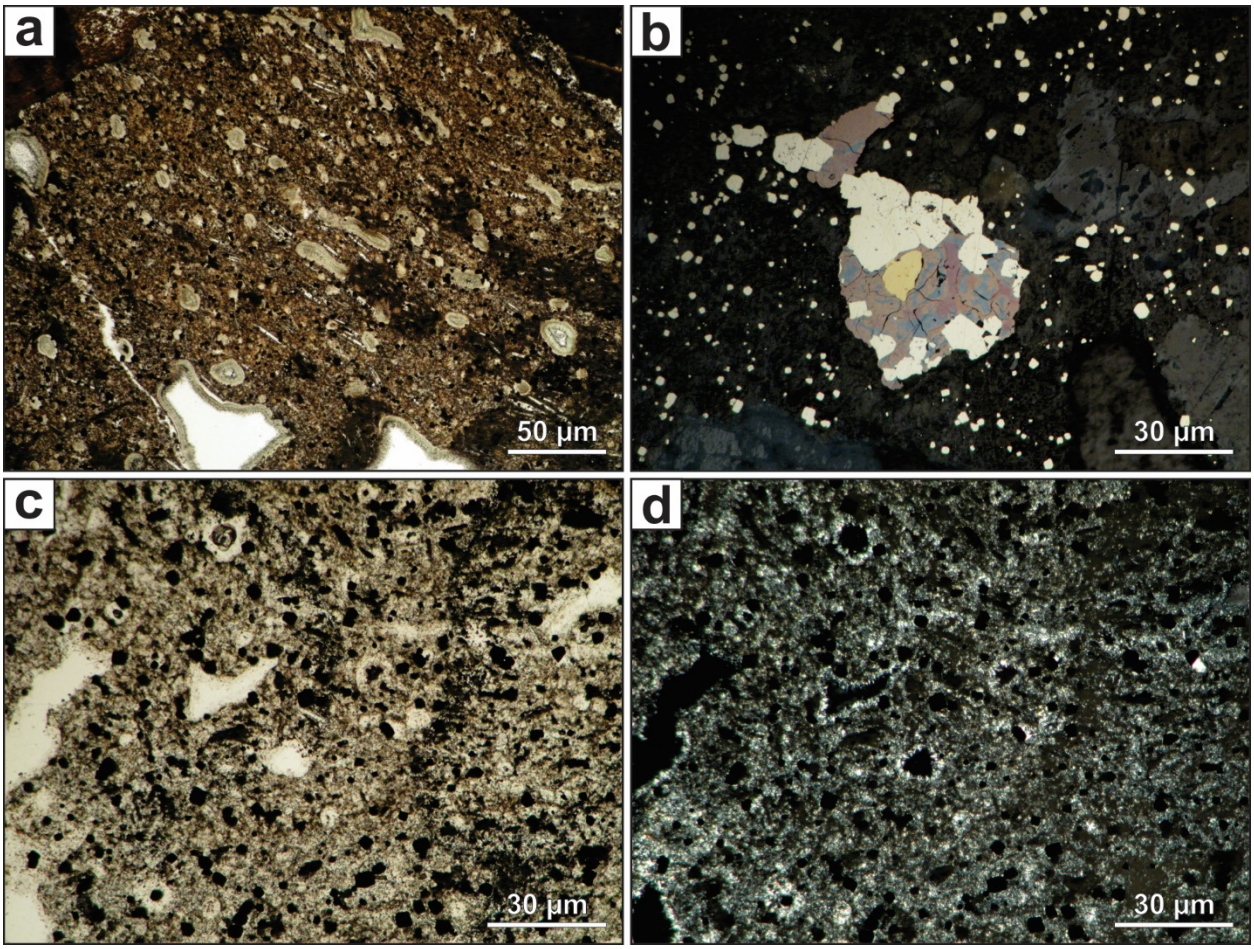
Thin Section Description

This section consists primarily of sulfate vein material (70-75%) with minor volcanic clasts (15%). There is 2% porosity overall. The clasts are subangular to subrounded, vesicular, and microporphyritic, with strong flow foliation. The clasts are intensely to pervasively altered to clay with first-order birefringence colors, with vesicles locally infilled by chlorite. The clasts contain fine- to medium-grained euhedral pyrite throughout. There is minor medium-grained pyrite associated with the vein sulfate material, followed by chalcopyrite and bornite/covellite, with 5% pyrite, 3% chalcopyrite, 2% bornite, and 1% covellite overall. Late iron oxide, including minor hematite, stains the slide. The sulfate vein material mostly consists of recrystallized gypsum, with 5% anhydrite. There are no pumice fragments, glass shards, or crystal fragments.



Thin section scan (left) with etched sulfates, thick section scan (middle), and puck (right) of MA13-089.

Paragenesis: Volcanic clasts → pervasive clay and pyrite alteration of clasts → clay lining vesicles → hydrothermal precipitation of anhydrite and sulfides (pyrite → chalcopyrite → bornite → covellite) → hydration of anhydrite to gypsum (almost complete) and iron oxides
Interpretation: Hyaloclastite breccia
Descriptive Lithological Name: Matrix-supported monomict hyaloclastite breccia, cemented and mineralized
Descriptive Alteration Facies: Intense clay and pyrite, pervasive and vesicle-lining, late iron oxide



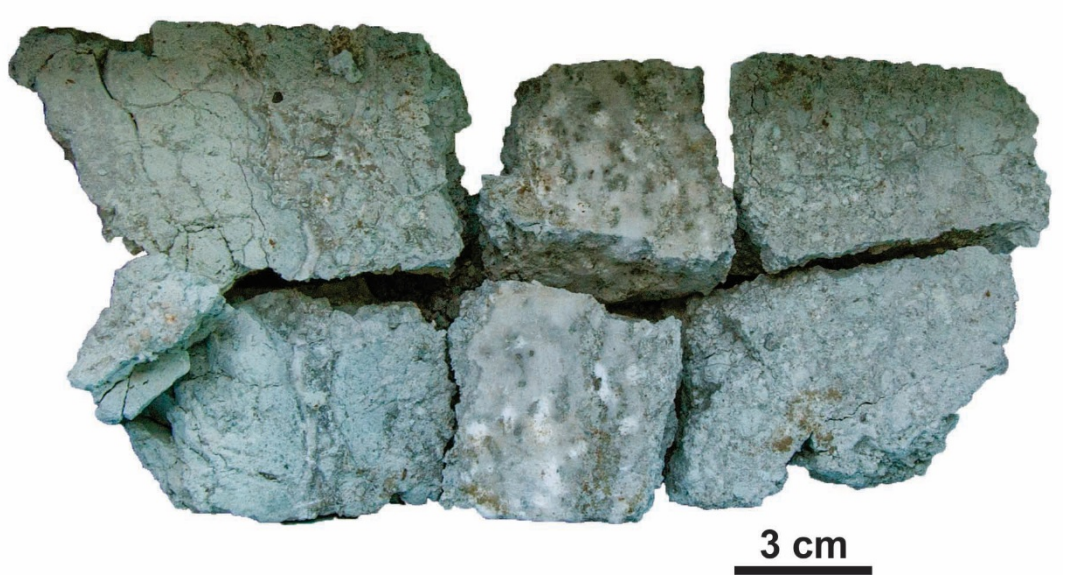
Photomicrographs of GMA13-089: (a) transmitted light (PPL) showing a vesicular volcanic clast, with vesicles infilled by chlorite; (b) reflected light (PPL) showing pyrite, chalcopyrite, bornite, and covellite mineralization in the matrix; (c) transmitted light (PPL) an irregular, vesicular glassy clast; (d) transmitted light (XPL) showing complete clay alteration of the clast from (c).

SAMPLE: MA13-090 **PARENT ID:** 2022/2023 **SAMPLE DEPTH:** 18.40-18.57 mbsf	**DRILLHOLE:** TKAD001 **DRILLHOLE LOCATION:** 784559.69E/8649995.52N **WATER DEPTH:** 1107.61 mbsl

Mineralogy

XRD (clay-sized fraction): Chamosite, rectorite, I/S, illite
Assemblage: I/S + Cham

Hand Sample Description

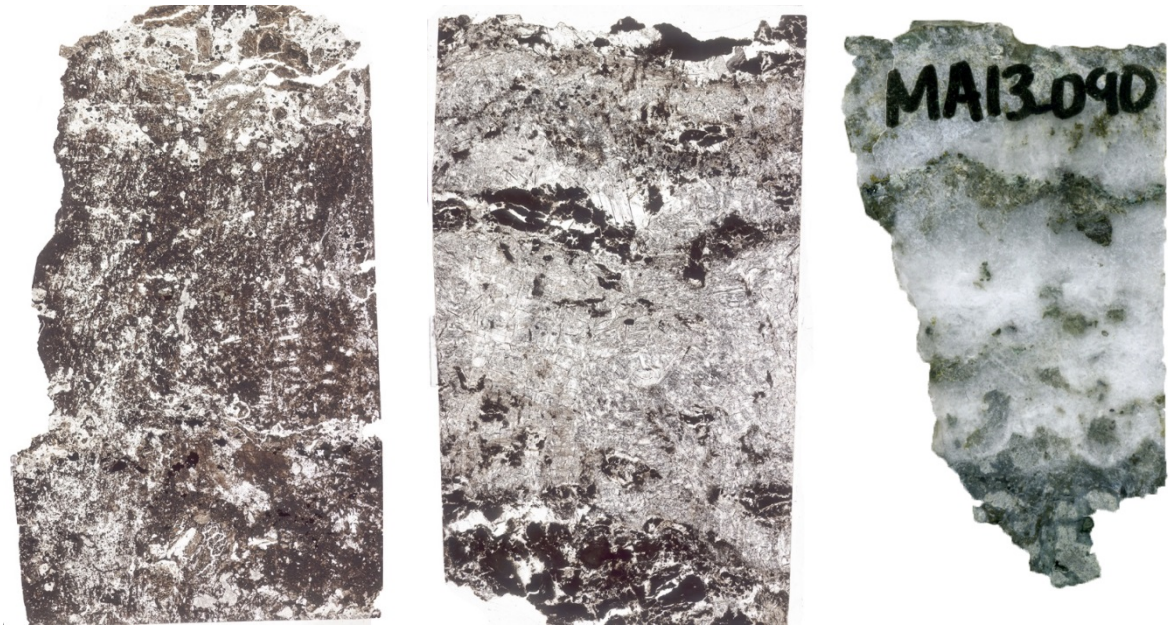


Hand sample of MA13-090.

This section is a monomict clast-supported volcanic breccia, with only 10% matrix, consisting of white to colorless anhydrite/gypsum patchy infill, and irregular mm-wide anhydrite veins that cut the clasts, oriented perpendicular to the core axis. The veins are associated iwht minor disseminated mineralization of <1% sphalerite and <1% pyrite. There are 90% light green-buff colored volcanic clasts, with strong pervasive clay and chlorite alteration. The clasts range in size from <1.0-18.0 mm, with a bed of fine-grained clasts, moderate sorting, subangular to subrounded shape, low-sphericity, and aphanitic texture with rare sub-mm vesicles. There is <1% porosity.

Thin Section Description

This section is from the sulfate-vein rich portion of the drillcore, with 80% sulfate material, 10% volcanic clasts, 2% pore space, and 5-8% sulfides. The vein material is dominantly gypsum, which has been intensely recrystallized and contains abundant inclusions, with 1-2% relict anhydrite. The volcanic clasts are irregular and difficult to distinguish in the slide that was accidently etched with acid. The clasts are generally small, subrounded to subangular, and are pervasively altered to clays with variable first- to



Thin section scan (left) with etched sulfates, thick section scan (middle,) and puck (right) of MA13-090.

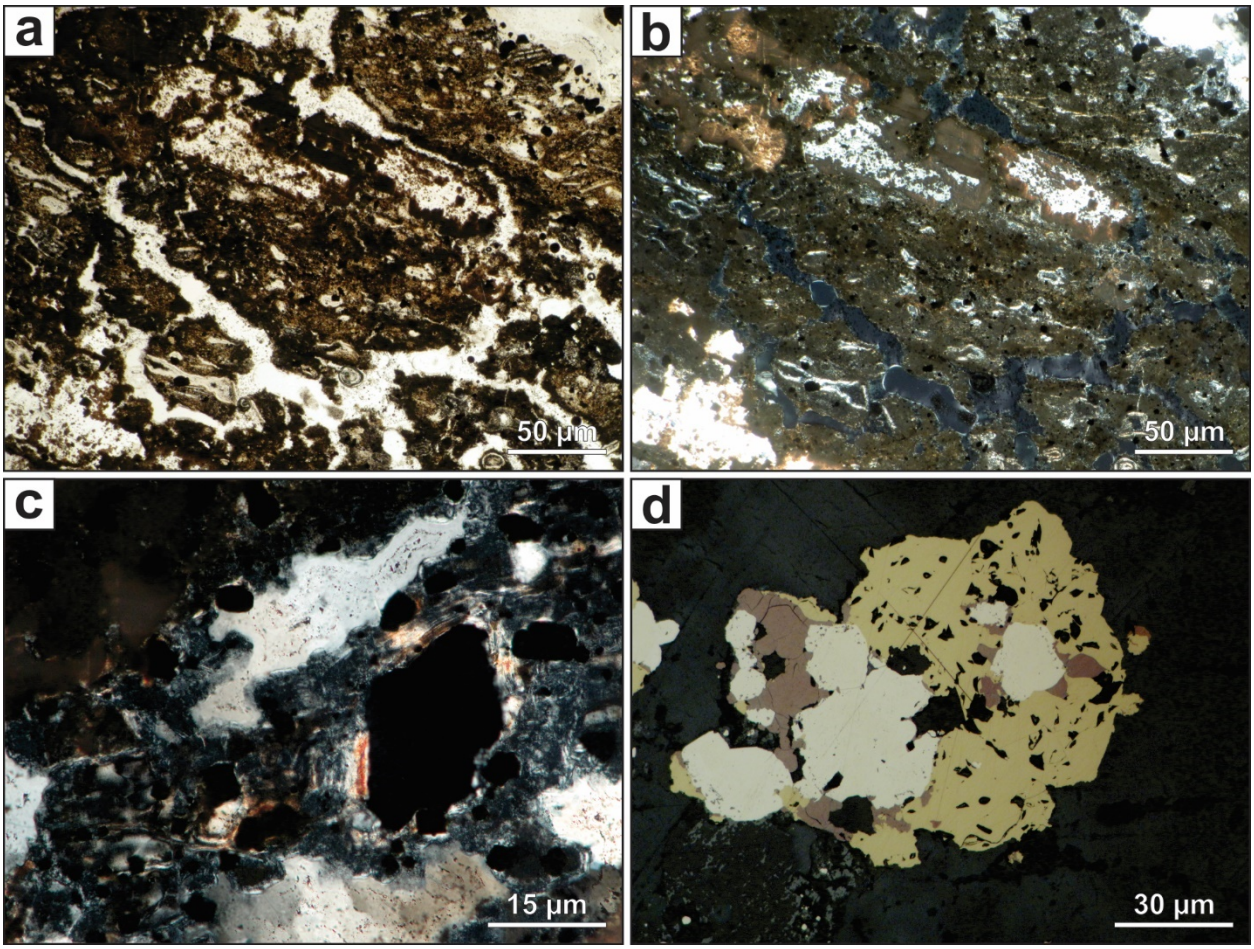
fourth-order birefringence (illite/smectite?). Clays also line the vesicles, beginning with the illite/smectite and followed by chlorite. Intense iron oxide stains the slide, and appears to result in part from the etching. Sulfides are precipitated along distinct horizons, suggesting generations of vein growth or fluid movement along relict bedding planes. They consist of medium-grained pyrite (4%), followed by medium- to coarse-grained chalcopyrite (3%), bornite (1%), and minor covellite (<1).

Paragenesis: Volcanic clasts → pervasive clay and pyrite alteration of clasts → clay lining vesicles (illite/smectite followed by chlorite) → hydrothermal precipitation of anhydrite and sulfides (pyrite → chalcopyrite → bornite → covellite) → hydration of anhydrite to gypsum (almost complete) and iron oxides

Interpretation: Lapilli tephra(?)

Descriptive Lithological Name: Bedded matrix-supported monomict lapilli tephra, cemented and mineralized

Descriptive Alteration Facies: Intense clay and pyrite, pervasive and vesicle-lining, late iron oxide



Photomicrographs of GMA13-090: (a) transmitted light (PPL) showing a browken-up volcanic clast with a relict phenocryst and abundant Fe-Oxide; (b) transmitted light (XPL) showing intense clay aleration of the clast from (a); (c) transmitted light (XPL) showing clay alteration of the glassy groundmass of a phenocryst, and clay precipitation within a vesicle; (d) reflected light (PPL) showing pyrite, chalcopyrite, and bornite mineralization in the matrix.

SAMPLE: MA13-091 **PARENT ID:** 2024 **SAMPLE DEPTH:** 20.77-21.00 mbsf	**DRILLHOLE:** TKAD001 **DRILLHOLE LOCATION:** 784559.69E/8649995.52N **WATER DEPTH:** 1107.61 mbsl

Mineralogy

SWIR (powdered clast + matrix): Chlorite, muscovite
XRD (clay-sized fraction): Montmorillonite, chamosite, I/S, pyrite(?)
Assemblage: I/S + Cham

Hand Sample Description



Hand sample of MA13-091.

This sample is a monomict clast-supported volcanic breccia with patchy dark grey anhydrite cementation (20%), and one irregular 10-mm wide white anhydrite vein at a high angle to the core axis. There are 80% white to light grey clay-altered volcanic clasts, <1.0-3.0 mm in size showing crude bedding at high angles to the core axis, moderate sorting, subrounded-rounded shape, and moderate sphericity. There is abundant pyrite (5% overall), which also forms as fine beds up to 5 mm thick, resulting in areas of high pyrite, up to 10% locally. There is 1% porosity.

Alteration Summary: Pervasive clay alteration, minor iron oxide
Interpretation: Lapilli tuff(?)
Name: Bedded, pervasively clay-altered monomict clast-supported lapilli tuff, cemented and mineralized

SAMPLE: MA13-092 **PARENT ID:** 2025 **SAMPLE DEPTH:** 21.30-21.45 mbsf	**DRILLHOLE:** TKAD001 **DRILLHOLE LOCATION:** 784559.69E/8649995.52N **WATER DEPTH:** 1107.61 mbsl

Mineralogy

XRD (clay-sized fraction): Chamosite, corrensite, I/S, illite
Assemblage: I/S + Cham

Hand Sample Description



Hand sample of MA13-092.

This sample is a monomict matrix-supported volcanic breccia with medium- to light-grey anhydrite infill (60%), with several sub-mm anhydrite veinlets that cut the clasts (looks similar to the matrix). There are 40% white to light grey volcanic clasts, with strong pervasive clay alteration, slightly yellowish in places (iron oxide?). The clasts are <1.0-12.0 mm in size, with moderate sorting, subangular to rounded shape, moderate sphericity, and crude bedding at high angles to the core axis, with a 20 mm thick bed ear the bottom of the core composed of smaller clasts and pyrite mineralization, up to 10% locally. Overall, there is 3% pyrite, trace chalcopyrite, and trace atacamite mineralization. There is <1% porosity.

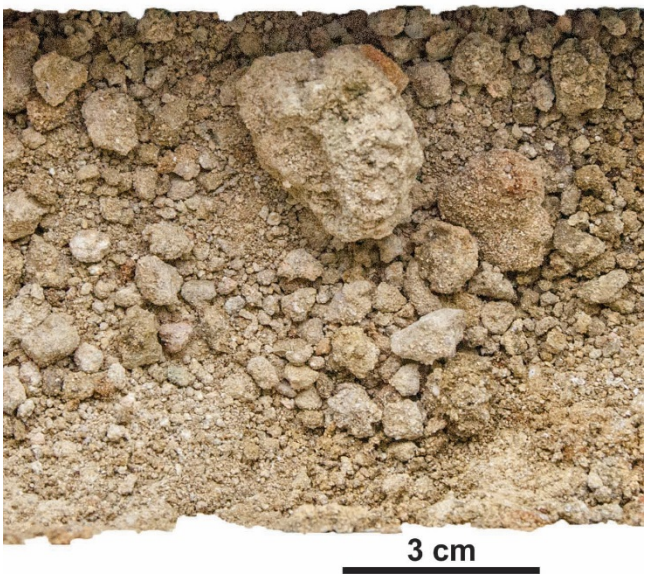
Alteration Summary: Pervasive clay alteration, minor iron oxide, slight greenish color from chlorite?
Interpretation: Lapilli tephra(?)
Name: Bedded pervasively clay-altered monomict matrix-supported lapilli tephra, cemented and mineralized

SAMPLE: MA13-095 **PARENT ID:** 2502 **SAMPLE DEPTH:** 3.60-3.70 mbsf	**DRILLHOLE:** TKAD029 **DRILLHOLE LOCATION:** 784611.16E/8649938.92N **WATER DEPTH:** 1091.81 mbsl

Mineralogy

XRD (clay-sized fraction): Nontronite, plagioclase
Assemblage: Non + Pl

Hand Sample Description



Hand sample of MA13-095.

This sample consists of unconsolidated polymict(?) volcanic fragments, variably altered. There are 90% orange volcanic fragments with strong pervasive clay alteration and moderate orange iron oxides, <1.0-10.0 mm in size, poor sorting, subrounded-subangular shape, low sphericity, random fabric, and an aphanitic texture. There are 5% white volcanic clasts with strong pervasive clay alteration, <1.0-4.0 mm in size, poor sorting, subrounded-subangular shape, low sphericity, random fabric, and aphanitic texture. There are also 5% medium-dark grey volcanic clasts with moderate pervasive clay alteration and trace iron oxides, <1.0-3.0 mm in size, with poor sorting, subrounded-subangular shape, low sphericity, random fabric, and aphanitic texture. No sulfides were observed. The porosity of the clasts are <1%.

Alteration Summary: Variable light grey clay, pervasive and strong, FeOx coating
Interpretation: Origin unknown
Name: Strongly clay-altered polymict(?) volcanic breccia, unconsoldiated

SAMPLE: MA13-099 **PARENT ID:** 2514 **SAMPLE DEPTH:** 4.50-4.60 mbsf	**DRILLHOLE:** TKAD028 **DRILLHOLE LOCATION:** 784582.16E/8649932.63N **WATER DEPTH:** 1091.00 mbsl

Mineralogy

SWIR (powdered clast): Diaspore(?), gypsum(?) (unreliable results)
XRD (clay-sized fraction): Chamosite, rectorite(?), I/S, pyrite
Assemblage: I/S + Cham

Hand Sample Description



Hand sample of MA13-099.

This sample is a matrix-supported monomict volcanic breccia with 60% dark grey to white anhydrite infill, and possible clay in the matrix. The dark color in the sulfates may come from finely-disseminated sulfides. There are 40% light to medium grey, slightly greenish volcanic clasts with intense pervasive clay alteration, and patchy yellow coloration (iron oxide? Primarily affects clasts), <1.0-5.0 mm in size (mostly <2.0 mm), with poor sorting, subrounded shape, low sphricity, random fabric, and aphanitic texture that is very weakly vesicular with dessication cracks. The clasts contain <1% fine-grained pyrite. The porosity is 1%.

Alteration Summary: Pervasive clay alteration, minor iron oxide
Interpretation: Unknown – lapilli tephra?
Name: Pervasively clay-altered monomict matrix-supported lapilli tephra(?), cemented

SAMPLE: P002 **PARENT ID:** 2013 **SAMPLE DEPTH:** 10.39-10.50 mbsf	**DRILLHOLE:** TKAD001 **DRILLHOLE LOCATION:** 784559.69E/8649995.52N **WATER DEPTH:** 1107.61 mbsl

Mineralogy

XRD (clay-sized fraction): Montmorillonite(?), nontronite, plagioclase
Assemblage: Mnt/Non + Pl

Hand Sample Description



Hand sample of P002.

This sample is a clast-supported polymict volcanic breccia, strongly cemented by anhydrite and dark green clay (chlorite?), 19% overall. It is difficult to distinguish the matrix, so the overall proportion may be lower. There are 81% clasts overall, variably altered. This includes 50% medium green volcanic clasts with strong pervasive chlorite (+ clay?) alteration, <1.0-30.0 mm in size, with poor sorting, angular to subangular shape, low sphericity, random fabric, and a porphyritic texture with 5% phenocrysts up to 1 mm in size, weakly vesicular. There are 20% dark green volcanic clasts, with very strong pervasive chlorite (+ clay?) alteration, <1.0-5.0 mm in size, subangular to subrounded shape, low sphericity, random fabric, and aphanitic texture that is weakly vesicular (<1% vesicles). There are 10% dark grey to black volcanic clasts, relatively unaltered with minor clay alteration, <1.0-17.0 mm in size, with poor sorting, angular shape, very low sphericity, random fabric, and aphanitic texture with 2% sub-mm vesicles. There are 1% medium grey to white volcanic clasts, with moderate to intense pervasive clay alteration, <1.0-3.0 mm in size, with poor sorting, angular shape, low sphericity, random fabric, and aphanitic texture that is weakly vesicular, with possible phenocrysts. This sample may be silicified. There is 2% total porosity.

Alteration Summary: Viariable alteration of clasts, greenish color from chlorite?
Interpretation: Resedimented volcanic breccia
Name: Variably clay-altered polymict clast-supported volcanic breccia, silicified

SAMPLE: P003 **PARENT ID:** 2018 **SAMPLE DEPTH:** 14.81-14.95 mbsf	**DRILLHOLE:** TKAD001 **DRILLHOLE LOCATION:** 784559.69E/8649995.52N **WATER DEPTH:** 1107.61 mbsl

Mineralogy

XRD (clay-sized fraction): Nontronite, chloritoid, corrensite
Assemblage: Non + Corr

Hand Sample Description



Hand sample of P003.

This section is a monomict matrix-supported breccia, with 60% white anhydrite infill with patchy red iron oxide and minor dark grey fine sulfides(?). The infill is vein-like, with minor hydrothermal brecciation of the clasts (jigsaw fit). There is 1% pyrite and trace sphalerite in the matrix. There is 40% medium-green volcanic clasts, with strong pervasive chlorite and clay, locally darker green in the center. The clasts are <1.0-15.0 mm in size, with poor sorting, subrounded-rounded shape, moderate sorting, crude bedding with grain size, and aphanitic texture with <1% sub-mm vesicles. The clasts contain 1% very fine-grained pyrite, and are cross-cut by anhydrite veinlets. There is 1% porosity.

Alteration Summary: Viariable alteration of clasts, greenish color from chlorite?, iron oxide in matrix
Interpretation: Hyaloclastite breccia
Name: Variably clay-altered monomict matrix-supported hyaloclastite breccia, cemented

SAMPLE: P004 **PARENT ID:** 2019 **SAMPLE DEPTH:** 15.65-15.80 mbsf	**DRILLHOLE:** TKAD001 **DRILLHOLE LOCATION:** 784559.69E/8649995.52N **WATER DEPTH:** 1107.61 mbsl

Mineralogy

XRD (clay-sized fraction): Chloritoid, corrensite, rectorite, illite
Assemblage: Non + Corr

Hand Sample Description



Hand sample of P004.

This sample is from the altered stringer zone. It is a monomict clast-supported breccia with 30% patchy white to colorless infill and minor clay in the matrix. There is 5 mm wide anhydrite vein with irregular margins at ~45° to the core axis, as well as additional mm-sized irregular anhydrite veinlets. There are 70% light-medium green, locally lighter grey volcanic clasts, with strong pervasive clay and chlorite(?). The clasts are <1.0-10.0 mm in size, with poor sorting, subrounded size, moderate rounding, random fabric, and an aphanitic texture with sub-mm vesicles. The clasts contain 1% pyrite and 3% sphalerite; however, most of the sulfides occur around the clasts or at the margins of the anhydrite vein, with a total of 4% sphalerite, 1% pyrite, and trace chalcopyrite. There is 2% porosity.

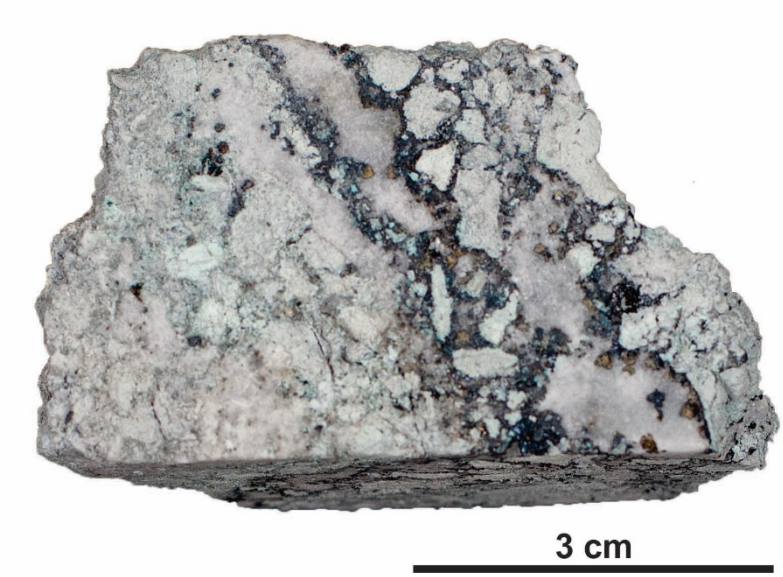
Alteration Summary: Pervasive clay alteration of clasts, slightly greenish color from chlorite
Interpretation: Unknown
Name: Pervasively clay-altered monomict clast-supported volcanic breccia, cemented and mineralized

SAMPLE: P005	**DRILLHOLE:** TKAD001
PARENT ID: 2023	**DRILLHOLE LOCATION:** 784559.69E/8649995.52N
SAMPLE DEPTH: 19.14-19.30 mbsf	**WATER DEPTH:** 1107.61 mbsl

Mineralogy

SWIR (powdered clast): Muscoviticillite, montmorillonite(?)
XRD (clay-sized fraction): Chamosite, rectorite, I/S, illite, pyrite(?)
Assemblage: I/S + Cham

Hand Sample Description



Hand sample of P005.

This sample is a clast-supported monomict volcanic breccia, with 20% white to colorless anhydrite infill and irregular branching veins up to 1 mm wide. There is also minor clay in the matrix. There are 80% light bright green to grey volcanic clasts, with strong pervasive chlorite and clay alteration. The clasts are <1.0-40.0 mm in size (mostly <10.0 mm in size), with poor sorting, rounded shape, high sphericity, random orientitaion, and aphanitic texture with rare sub-mm vesicles. The clasts contain 1% sphalerite and <1% pyrite. Euhedral sulfides also occur in the matrix, primarily associated with irregular veining, with 2% total sphalerite, 1% pyrite, trace chalcopyrite, and trace atacamite(?). There is 1% porosity.

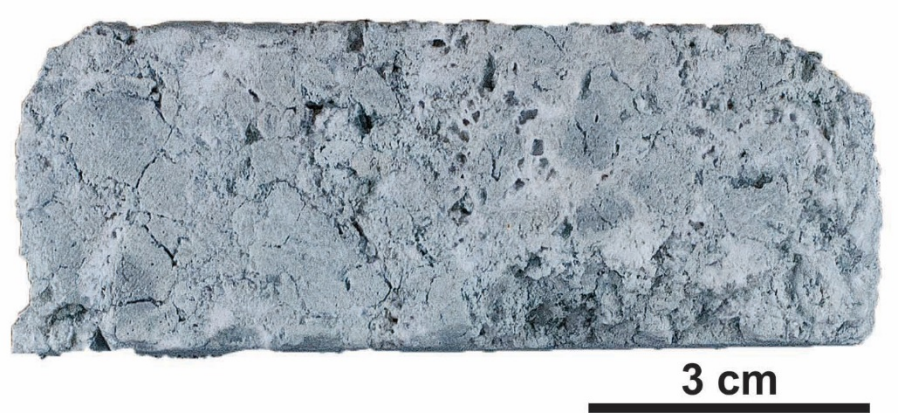
Alteration Summary: Pervasive clay alteration of clasts, slightly greenish color from chlorite
Interpretation: Unknown
Name: Pervasively clay-altered monomict clast-supported volcanic breccia, cemented and mineralized

SAMPLE: P012 **PARENT ID:** 2043 **SAMPLE DEPTH:** 11.11-11.20 mbsf	**DRILLHOLE:** TKAD003 **DRILLHOLE LOCATION:** 784765.73E/8649281.14N **WATER DEPTH:** 1113.84 mbsl

Mineralogy

XRD (clay-sized fraction): Montmorillonite(?), chamosite, I/S
Assemblage: I/S + Cham

Hand Sample Description



Hand sample photo of P012

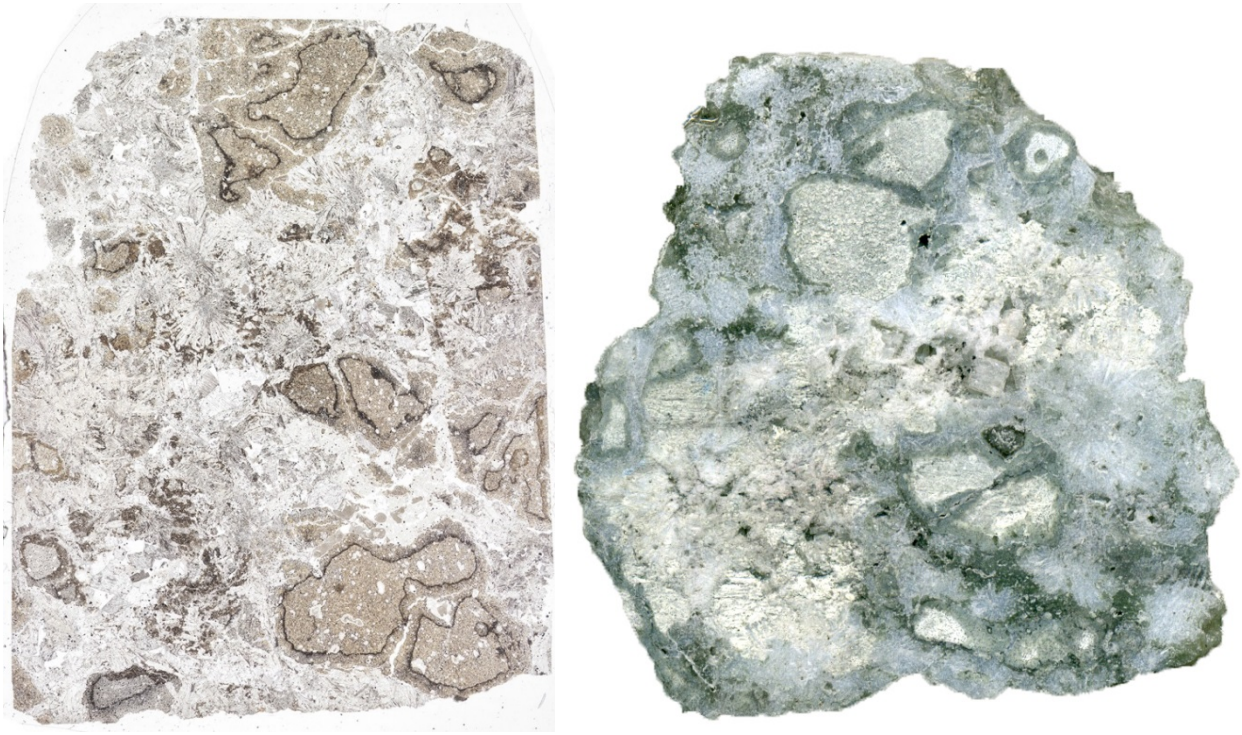
This sample is a matrix-supported polymict(?) volcanic breccia that has been cemented by white anhydrite (infill and veins), that shows a bladed texture in open spaces (57% overall). There is 1% very fine grained pyrite associated with the anhydrite. There are 43% clasts overall, including 40% pale greenish-grey volcanic clasts, with intense pervasive clay alteration and minor chlorite, 1.0-25.0 mm in size, with poor sorting, subrounded shape, low sphericity, random fabric, and aphanitic texture with dessication cracks and minor jigsaw-fit. There is 1% fine-grained pyrite associated with the clasts. There are also 3% white volcanic clasts (or anhydrite patches?), with pervasive intense clay alteration(?), 1.0-3.0 mm in size, with poor sorting, subangular shape, low sphericity, and random orientation. There is 3% total porosity.

Thin Section Description

This section is a massive volcaniclastic breccia with ~1% porosity. It is strongly cemented and matrix-supported, with ~30% clasts and 65% matrix.

There are three dominant clast types. The first (clast 1) is light brown to light grey (variable iron oxide content), with dark brown bands between the clast centers and rims (MnOx?), comprising ~25% of the sample. The clasts have irregular margins, and are subrounded to subangular, <1-10 mm in size. The clasts are locally relict, broken up and mixed in with the matrix. There are no relict phenocrysts in the clasts, but

there are relict fine- to medium grained plagioclase microphenocrysts (up to 15%) that have been completely dissolved and contain variable amounts of fine-grained needle-like chlorite growing inwards

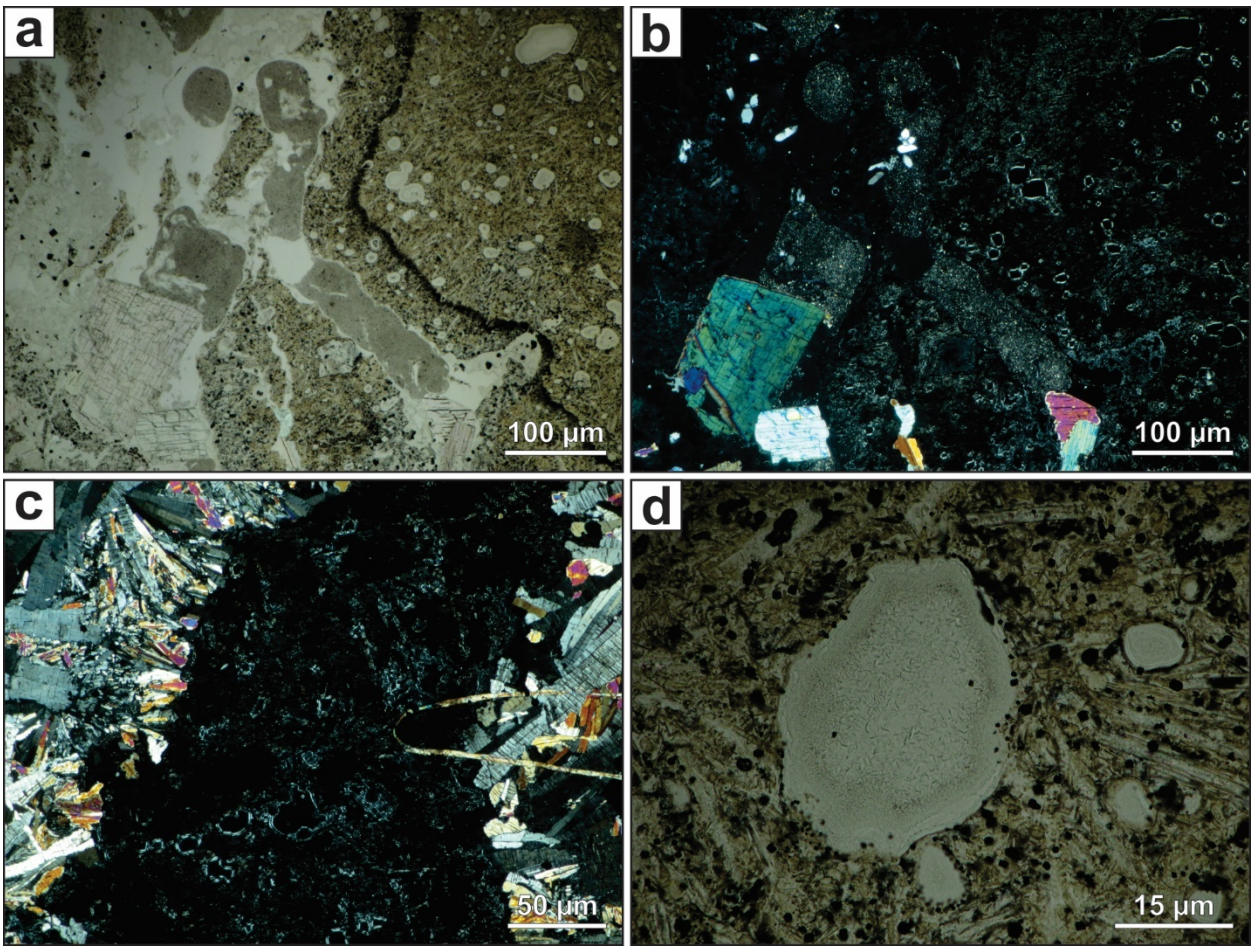


Thin section scan (left) and puck (right) of P012.

along dissolved relict crystals. These microphenecrysts are locally aligned along a moderate flow-foliation (with different directions in each clast). The clasts have a groundmass that is strongly altered to pervasive clay, with patchy/variable intensity, patchy iron oxide (including hematite), and fine- to medium-grained disseminated pyrite (~3% overall), locally concentrated at the clast margins. Irrregular glassy areas f the clasts have the most intense clay alteration. The clasts are moderately vesicular, with vesicles lined by a very thin layer of opal-CT(?), followed by a thicker layer of very pale green to transparent chlorite that appears isotropic with crossed nichols. This is locally followed by irregular fine-grained black material (Fe-MnOx?). Minor fine-grained needles of chlorite form last in the central part of the vesicles. Locally, the opal-CT is preceeded by a layer of iron-stained opal-CT(?) or illite(?). These clasts also frequently have glassy margins that grade into tube pumice, intensely and pervasively altered to chlorite. The second clast type is irregular translucent tube-pumice, with highly irregular margins, up to ~3 mm in size. The glass is intensely pervasively altered to chlorite. The tube pumice is locally associated with the volcanic clasts (type 1), suggesting that it is part of the same volcanic flow (monomict). There are 2% of clast 2.The third clast type is grey glassy clasts, with rounded margins, up to ~1 mm in size. These clasts are completely altered to fine-grained chlorite (darker green color), which also lines rare pore spaces. There is very minor iron oxide and fine disseminated pyrite (<1%). The clasts also appear to contain fine-grained sulfates (Anh + Gp). These clasts appear near the margins of clast 1, or within cracks of clast 1. It is not clear if they are genetically related or polymict. The origin of these clasts is unknown (volcanic?). There are 3% of these clasts.

The matrix is composed of coarse- to very coarse-grained radiating tabular anhydrite, locally recrystallized to fine-grained anhydrite + gypsum, or completely replaced by gypsum. There is ~ 54% anhydrite, 10% gypsum, and 1% fine- to medium-grained pyrite in the matrix.

Paragenesis: Volcanic clasts 1+2 → volcanic clast 3 → alteration of clast 1+2 to fine-grained clays (chlorite) + alteration of clast 3 to clay (chlorite) + sulfates? → thin layer of Opal-CT (± FeOx) lining vesicles → Fe-MnOx lining vesicles → chlorite lining vesicles → Fe-MnOx lining vesicles → needle-like chlorite filling vesicles → hydrothermal mineralization (Py) + anhydrite cementation → recrystallization of anhydrite and minor hydration of anhydrite to gypsum.
Interpretation: Reworked hyaloclastite breccia (glassy margins of clasts, minor flow foliation).
Descriptive Lithological Name: Massive matrix-supported polymict resedimented hyaloclastite sand-cobble breccia, sulfate-cemented
Descriptive Alteration Facies: Early chlorite + minor pyrite + FeOx, minor late opal-CT lining vesicles, followed by late chlorite



Photomicrographs of P012: (a) transmitted light (PPL) showing various volcanic clasts; (b) transmitted light (XPL) showing intense clay alteration, same view as (a), with a few anhydrite crystals; (c) transmitted light (XPL) showing anhydrite precipitates partially altered to galena, and intensely clay-altered volcanic fragment; (d) transmitted light (PPL) showing aciciular clay precipitation within a vesicle (chlorite?).

SAMPLE: P013 **PARENT ID:** 2045 **SAMPLE DEPTH:** 13.40-13.50 mbsf	**DRILLHOLE:** TKAD003 **DRILLHOLE LOCATION:** 784765.73E/8649281.14N **WATER DEPTH:** 1113.84 mbsl

Mineralogy

SWIR (powdered clast): Paragoniticillite, montmorillonite, chlorite(?)
XRD (clay-sized fraction): Chamosite, I/S
Assemblage: I/S + Cham

Hand Sample Description



Hand sample of P013.

This sample is a monomict clast-supported volcanic breccia, with 50% patchy white anhydrite infill, associated with <1% pyrite. The anhydrite infill is cut by irregular anhydrite veins, 0.5-7.0 mm in size.There are 50% pale green-grey volcanic clasts, with intense pervasive clay and trace chlorite, 1.0-13.0 mm in size, with poor sorting, subrounded texture, low sphericity, and random orientation, with an aphanitic texture and minor jigsaw fit. The grain size is slightly smaller than P0012, with similar rounding and an increase in clast abundance. There is 1% fine-grained pyrite associated with the clasts. There is 3% total porosity.

Alteration Summary: Pervasive clay alteration of clasts, uniformly light grey-white
Interpretation: Unknown
Name: Pervasively clay-altered monomict clast-supported volcanic breccia, cemented

SAMPLE: P014 **PARENT ID:** 2047 **SAMPLE DEPTH:** 16.41-16.50 mbsf	**DRILLHOLE:** TKAD003 **DRILLHOLE LOCATION:** 784765.73E/8649281.14N **WATER DEPTH:** 1113.84 mbsl

Mineralogy

SWIR (powdered clast): Chlorite, muscoviticillite, montmorillonite(?)
XRD (clay-sized fraction): Chamosite, I/S
Assemblage: I/S + Cham

Hand Sample Description



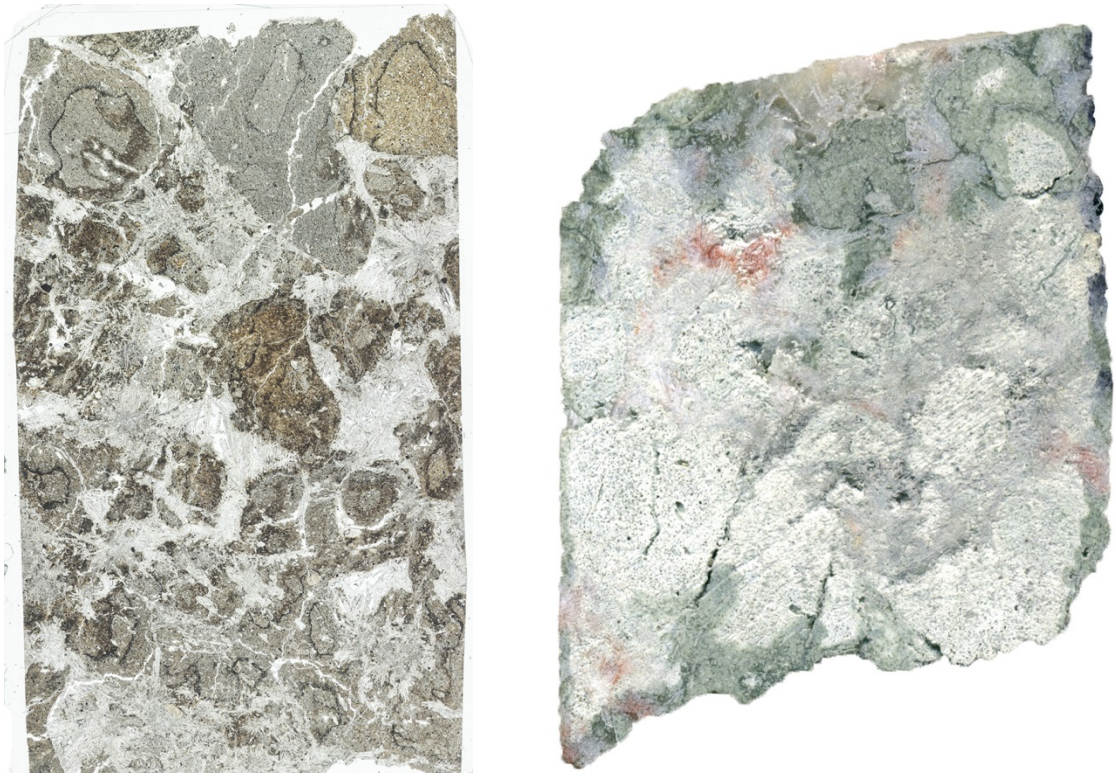
Hand sample of P014.

This sample is a clast-supported monomict volcanic breccia, with 50% white anhydrite infill, with minor patchy red iron oxide, and <1% fine-grained pyrite. There are 50% pale-green volcanic clasts, with intense pervasive clay and minor chlorite, with darker green coloration near the clast margins. The clasts also contain 2% fine-grained pyrite. The clasts are 1.0-20.0 mm in size, with poor sorting, angular-subrounded shape, low sphericity, random fabric, and aphanitic texture, weakly vesicular (sub-mm vesicles) and minor jigsaw fit brecciation. This sample is similar to P0012, but with iron oxide staining in the matrix only and slightly larger clasts.

Thin Section Description

This section is a massive volcaniclastic breccia with a porosity of of 2%. It is a matrix-supported monolithic breccia with ~50% volcanic clasts and ~46% matrix. The clasts have irregular shapes, subrounded to subangular with local jigsaw fit. They range in color from brown to grey in transmitted light, reflecting variable iron oxide contents. Most clasts have a thin black layer (MnOx?) separating the core from the rim. The clasts are <1-13 mm. Rare relict phenocrysts (plagioclase) are completely dissolved and partially lined by chlorite. There are abundant fine- to medium-grained plagioclase microphenocrsts (up to 20%)

that are completely dissolved, or locally replaced by fine-grained clay. These plagioclase laths display a strong flow foliation. The clasts are pervasively altered to intense clay (chlorite), patchy FeOx, and minor



Thin section scan (left) and puck (right) of P014.

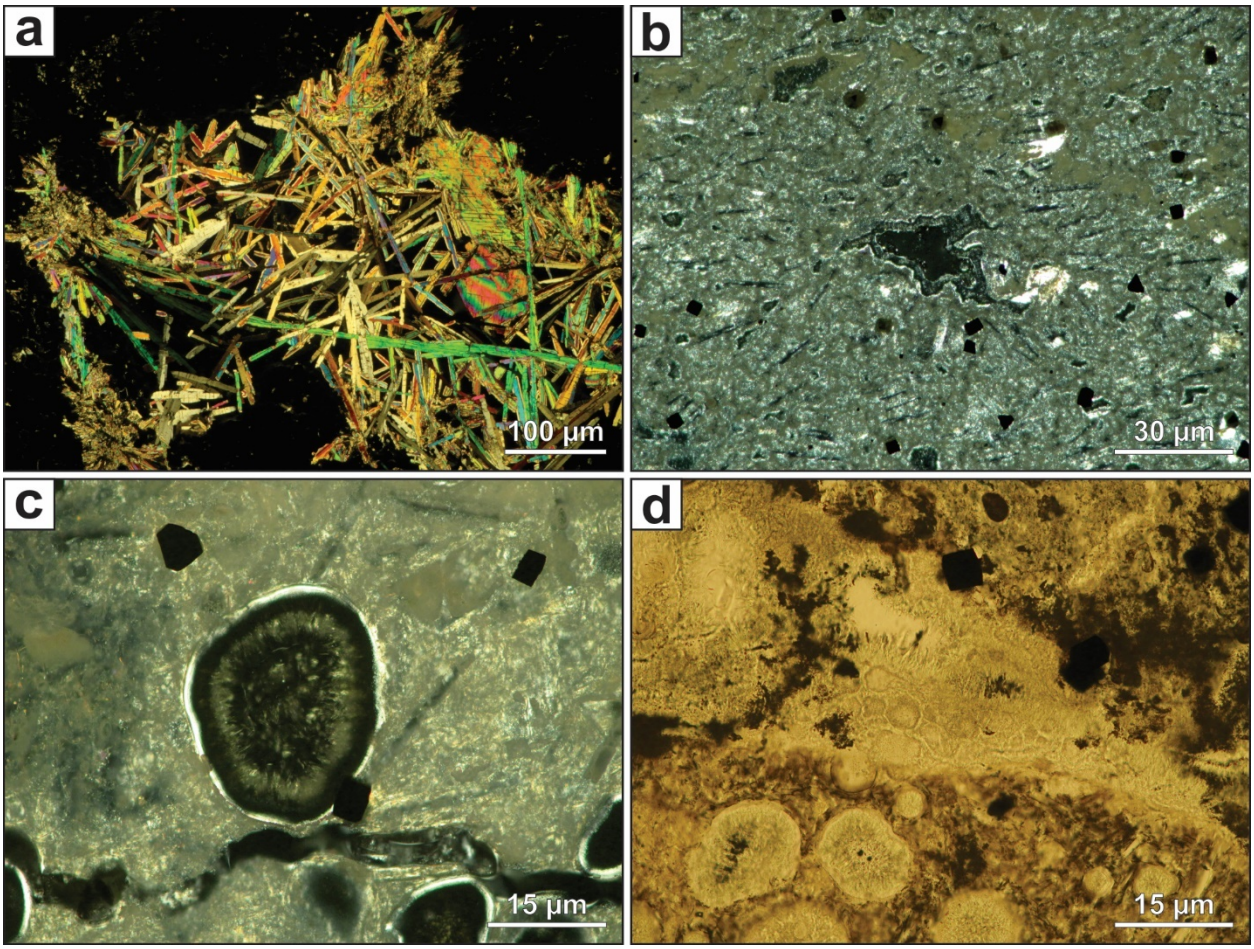
fine- to medium-grained euhedral pyrite (2%). The clasts are weakly to strongly vesicular, with irregular vesicals, locally elongate with the flow foliation. The vesicles are lined by a very thin layer of opal-CT(?), followed by partial to complete infill by chlorite. Locally, fine-grained black crystals (MnOx?) forms last in the vesicles. Chlorite also grows outwards from the clasts, replacing glassy margins. Locally, this outer chlorite appears to be replacing pumaceous domains.

The matrix is dominated by fine- to very coarse-grained tabular anhydrite, locally radiating, partially recrystallized to fine-grained anhydrite + gypsum. Locally gypsum occurs as coarse-grained tabular crystals (after anhydrite). There is 10% gypsum, 36% anhydrite, and <1% pyrite in the matrix.

There are no glass shards or crystal fragments.

Paragenesis: Volcanic clasts → alteration of clasts to chlorite + pyrite + FeOx (patchy) → thin layer of Opal-CT (± FeOx) lining vesicles → chlorite infilling vesicles → anhydrite cementation → recrystallization of anhydrite and minor hydration of anhydrite to gypsum.
Interpretation: Hyaloclastite breccia (glassy margins of clasts, strong flow foliation).
Descriptive Lithological Name: Massive matrix-supported monomict hyaloclastite sand-cobble breccia, sulfate-cemented

Descriptive Alteration Facies: Early chlorite + minor pyrite + FeOx, minor late opal-CT lining vesicles, followed by late chlorite



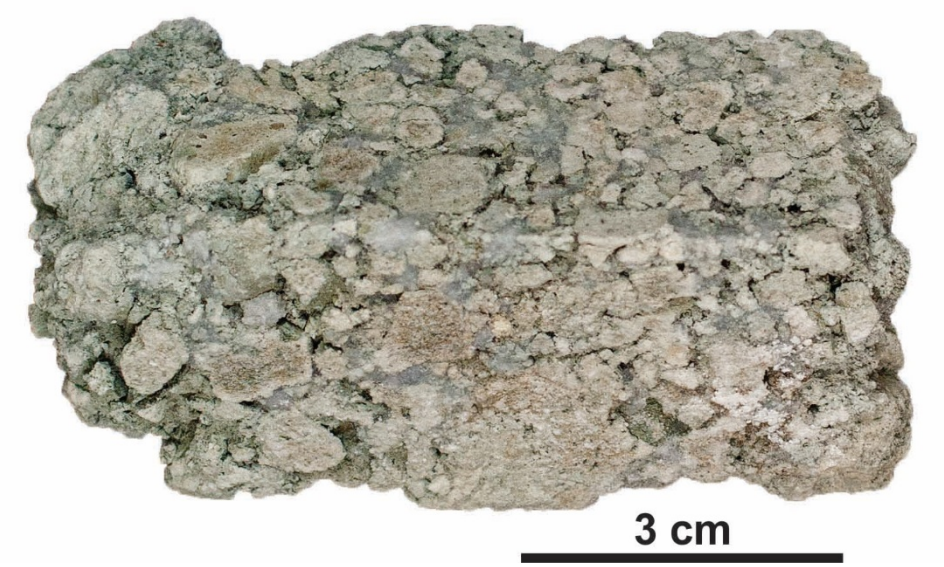
Photomicrographs of P014: (a) transmitted light (XPL) showing bladed anhydrite; (b) transmitted light (XPL) showing intense clay alteration of a volcanic clast, including altering microphenocrysts; (c) transmitted light (XPL) showing clay precipitation into a vesicle; (d) transmitted light (PPL) showing a glassy domain (pumaceous) and greenish chlorite precipitated into open spaces.

SAMPLE: P020 **PARENT ID:** 2132 **SAMPLE DEPTH:** 20.55-20.67 mbsf	**DRILLHOLE:** TKAD005 **DRILLHOLE LOCATION:** 784770.85E/8649318.94N **WATER DEPTH:** 1121.74 mbsl

Mineralogy

XRD (clay-sized fraction): Montmorillonite(?), chamosite, rectorite, I/S(?)
Assemblage: I/S + Cham

Hand Sample Description



Hand sample of P020.

This sample is a clast-supported monomict breccia, with 10% medium-grey anhydrite cement that may be irregular veining. The dark colors may be from fine-grained disseminated sulfides. There are 90% green-grey volcanic clasts with strong pervasive clay and chlorite alteration, <1.0-20.0 mm in size (chaotic distribution of clast sizes), with poor sorting, subangular to subrounded shape, low sphericity, random orientation, and aphanatic texture with abundant sub-mm vesicles and possible phenocrysts. There is <1% pyrite overall. There is abundant pore space between the clasts where there is no anhydrite, ~7% porosity overall.

Alteration Summary: Pervasive clay alteration of clasts, slightly greenish color from chlorite
Interpretation: Unknown
Name: Pervasively clay-altered monomict clast-supported volcanic breccia, irregularly cemented

SAMPLE: P021 **PARENT ID:** 2174 **SAMPLE DEPTH:** 3.50-3.60 mbsf	**DRILLHOLE:** TKAD007 **DRILLHOLE LOCATION:** 784469.39E/8649400.09N **WATER DEPTH:** 1161.27 mbsl

Mineralogy

XRD (clay-sized fraction): Corrensite, I/S(?), pyrite
Assemblage: I/S + Py

Hand Sample Description

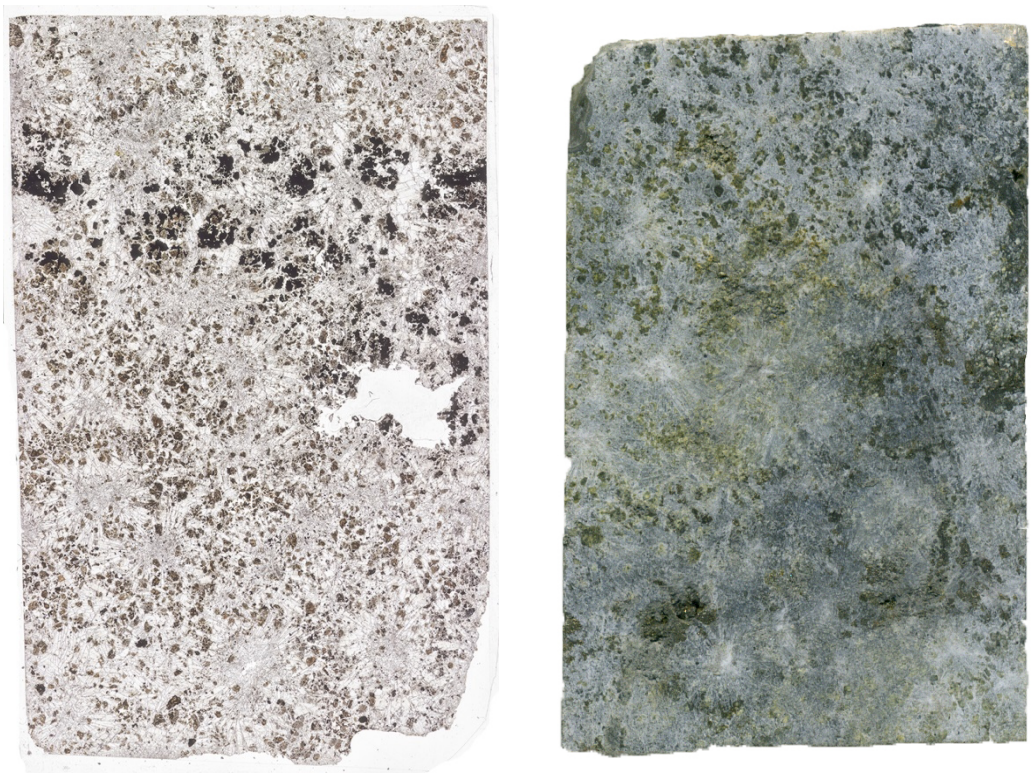


Hand sample of P021.

This sample is a monomict matrix-supported volcanic breccia, with 80% pervasive light-grey anhydrite infill (vein?), and possible silicification. There is 15% light grey volcanic clasts, with strong pervasive clay alteration, <1.0-6.0 mm in size (mostly small clasts), with poor sorting, subangular to subrounded shape, low sphericity, and a random fabric. There is trace pyrite, and 1% porosity.

Thin Section Description

This section is a massive matrix-supported volcanic breccia. It has a porosity of ~1%. The ratio of clasts:matrix is 20:80. The clasts are fine-grained, up to 2 mm in size (mostly <1 mm), There are two dominant clast types: volcanic clasts and glassy/pumaceous clasts. The volcanic clasts (1) make up 16% of the sample. They are orange-brown in color, angular to subrounded with irregular margins. Some clasts appear wispy. The clasts are intensely altered to pervasive clay, iron oxide, and minor fine-grained pyrite. There are few microphenocrysts of plagioclase, completely altered to clay. The clasts are too small to display flow-foliation. Glassy margins are also completely altered to clay (chlorite). Rare vesicles are lined by chlorite, locally by opal-CT(?). Chlorite also lines some of the vesicles, growing outwards, possibly replacing former glassy margins.



Thin section scan (left) and puck (right) of P021.

The second clast type is tube pumice, with stretched tubed, and glass that has been completely altered to chlorite. There is minor fine-grained pyrite, altered to iron oxide (incl. goethite) associated with these clasts. These clasts comprise ~1% of the sample, and are up to 1 mm in size. The pumice clasts may be genetically related to the volcanic clasts, so this is still considered a monomict breccia.

There are ~2% glass shards, with rounded to subangular margins, locally curviplanar. These shards are all <1 mm in size and are medium orange-brown from palagonitization.

Locally between clasts, there is fine-grained globular chlorite and scattered iron oxides, possibly representing altered ash(?), ~2% overall. The matrix is comprised of sulfates and sulfides. There is an early generation of sulfate (anhydrite and gypsum, variable) that lines the clasts. There are later generations of fine- to very coarse-grained tabular radiating anhydrite, with cores of fine-grained recrystallized anhydrite + gypsum. Gypsum has cojmpletely replaced some of the coarse-grained anhydrite. There is ~15% gypsum and ~53% anhydrite in the sample.

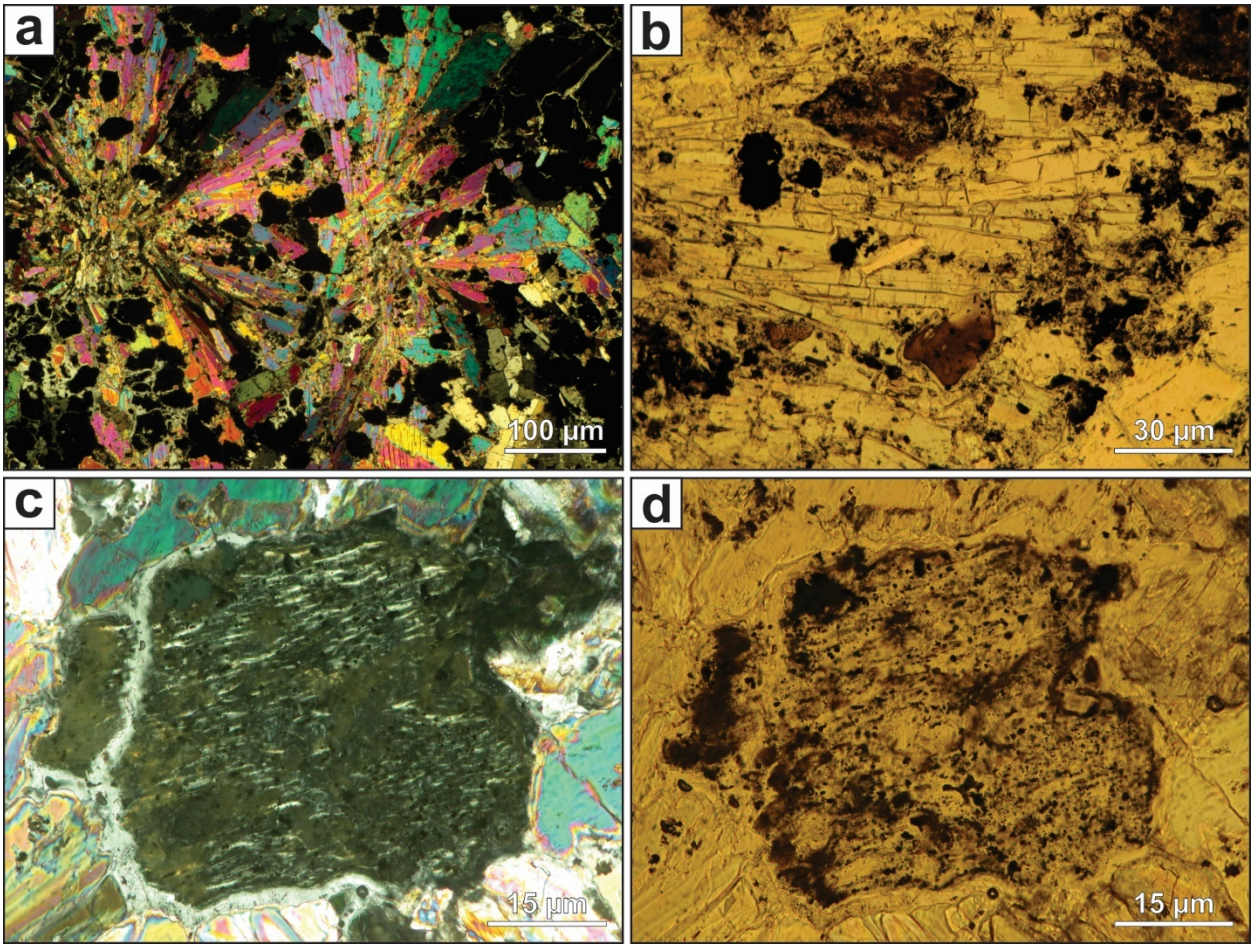
There is ~10% hydrothermal mineralization in the matrix of the sample, primarily forming along one horizon near the top third of the section. The mineralization consists of fine- to coarse-grained pyrite (5%), locally altered to goethite (+ hematite?), followed by fine- to medium-grained very low-Fe sphalerite (3%). The sphalerite contains inclusions of galena (1%), which also is included in the sulfate matrix, and is locally slightly altered at the margins. Rarely, sphalerite contains inclusions of fine-medium grained anhedral chalcopyrite (<1%). Secondary covellite is associated with sphalerite and galena (<1%).

Paragenesis: Volcanic clasts + pumice clasts → alteration of clasts to chlorite + pyrite + FeOx (patchy) → chlorite lining vesicles and clast exteriors + blebby chlorite in matrix → anhydrite cementation around clasts → second generation of anhydrite crystallization → recrystallization of anhydrite and minor hydration of anhydrite to gypsum.

Interpretation: Resedimented hyaloclastite breccia? (glassy margins of clasts, pumice fragments, glass shards).

Descriptive Lithological Name: Massive matrix-supported monomict resedimented hyaloclastite sand breccia, mineralized, sulfate-cemented

Descriptive Alteration Facies: Chlorite + minor pyrite + FeOx



Photomicrographs of P021: (a) transmitted light (XPL) showing radial anhydrite; (b) transmitted light (PPL) showing volcanic clasts and a glass shard surrounded by bladed anhydrite; (c) transmitted light (XPL) showing almost complete clay alteration of a pumice fragment; (d) transmitted light (PPL) showing the pumice fragment from (c).

SAMPLE: P022 **PARENT ID:** 2185 **SAMPLE DEPTH:** 11.23-11.34 mbsf	**DRILLHOLE:** TKAD007 **DRILLHOLE LOCATION:** 784469.39E/8649400.09N **WATER DEPTH:** 1161.27 mbsl

Mineralogy

SWIR (powdered clast): Paragoniticillite, chlorite, montmorillonite(?)
XRD (clay-sized fraction): Chamosite, rectorite(?), I/S
Assemblage: I/S + Cham

Hand Sample Description



Hand sample of P022.

This sample is a monomict matrix-supported volcanic breccia that is weakly cemented together, with 85% medium grey pervasive anhydrite infill and minor white clay n the matrix. There is 1% pyrite overall. There are 15% yellowish-grey volcanic clasts with strong pervasive clay, and patchy yellow iron oxide(?) mostly at the clast margins. The clasts are <1.0-14.0 mm in size, with a bimodal distribution of clast sizes: <2 mm and 6-14 mm in size. There is poor sorting, subrounded to subangular shape, with low-moderate sphericity, and random fabric. Very fine-grained pyrite (<1%) is associated with the clasts. There is 2% porosity.

Alteration Summary: Pervasive clay alteration of clasts, irregular iron oxide
Interpretation: Unknown
Name: Pervasively clay-altered monomict matrix-supported volcanic breccia, weakly cemented

SAMPLE: P023 **PARENT ID:** 2201 **SAMPLE DEPTH:** 22.35-22.45 mbsf	**DRILLHOLE:** TKAD007 **DRILLHOLE LOCATION:** 784469.39E/8649400.09N **WATER DEPTH:** 1161.27 mbsl

Mineralogy

XRD (clay-sized fraction): Chamosite, I/S, illite(?)
Assemblage: I/S + Cham

Hand Sample Description



Hand sample of P023.

This sample is a monomict clast-supported volcanic breccia, with 10% patchy white anhydrite infill. There are a couple irregular white anhydrite veins, one up to 12 mm wide, one 3 mm wide, at low angles to the core axis. The small vein is associated with sulfides, with 4% pyrite, and trace chalcopyrite. There are 90% greenish-yellowish-grey volcanic clasts, with strong pervasive clay alteration, and chlorite (or atacamite?). The clasts contain patchy orange iron oxides, and are locally coated by a thin layer of orange iron oxides. The clasts are 1.0-24.0 mm in size, poor sorting, angular to subrounded in shape (mix of rounded and elongate angular clasts), with low-moderate sphericity, random fabric, and aphanitic texture with rare sub-mm vesicles. The clasts contain <1% pyrite, trace atacamite(?). There is porosity around some of the clasts, 5% overall.

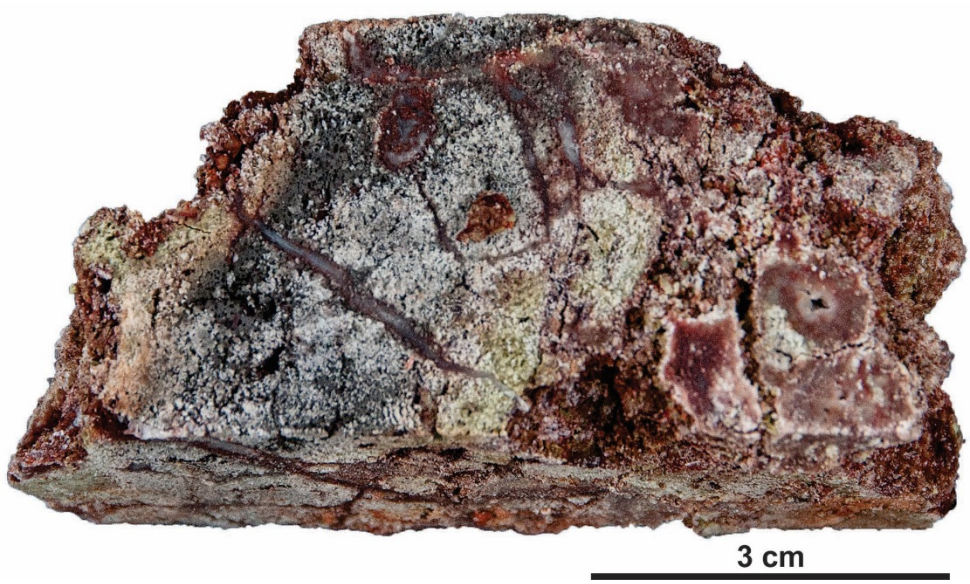
Alteration Summary: Pervasive clay alteration of clasts, slightly greenish color from chlorite, irregular iron oxide
Interpretation: Unknown
Name: Pervasively clay-altered monomict clast-supported volcanic breccia, cemented and mineralized

SAMPLE: P024 **PARENT ID:** 2229 **SAMPLE DEPTH:** 18.13-18.20 mbsf	**DRILLHOLE:** TKAD008 **DRILLHOLE LOCATION:** 784476.30E/8649298.22N **WATER DEPTH:** 1171.89 mbsl

Mineralogy

XRD (clay-sized fraction): Nontronite, hematite(?)
Assemblage: Mnt/Non + Pl

Hand Sample Description



Hand sample of P024.

This sample is a monomict clast-supported volcanic breccia, strongly cemented by white anhydrite, with pervasive red iron oxide staining (25%). There are several mm-wide white anhydrite veins with red iron oxide margins cutting the clasts. There are 75% volcanic clasts, with medium-dark grey interiors and light green exteriors, from pervasive clay alteration (and possible chlorite?) that is most intense at the clast margins. The clasts are 1.0-46.0 mm in size, up to bomb-sized, with poor sorting, subangular to subrounded in shape, with low sphericity, random fabric, and an aphanitic texture that is very vesicular with sub-mm vesicles. There is trace pyrite. There is 4% porosity.

Alteration Summary: Irregular clay alteration of clast margins, strong iron oxide
Interpretation: Hyaloclstite(?)
Name: Variably clay-altered monomict clast-supported hyaloclastite(?) breccia, cemented

SAMPLE: P025 **PARENT ID:** 2215 **SAMPLE DEPTH:** 7.50-7.56 mbsf	**DRILLHOLE:** TKAD008 **DRILLHOLE LOCATION:** 784476.30E/8649298.22N **WATER DEPTH:** 1171.89 mbsl

Mineralogy

XRD (clay-sized fraction): Montmorillonite, chamosite, corrensite, hematite(?)
Assemblage: Cham + Corr

Hand Sample Description



Hand sample of P025.

This section is a clast-supported monomict volcanic breccia, with strong anhydrite cement/infill that dispays radial growth patterns, and intense pervasive red iron oxide in the matrix, with 40% total matrix. There are 60% moderately-altered medium-dark grey volcanic clasts, and a few strongly-altered patchy green volcanic clasts. The alteration consists of moderate pervasive clay and strong chlorite alteration. The clasts are <1.0-16.0 mm in size, with poor sorting, subrounded shape, low-moderate sphericity, random fabric, and aphanitic texture with abundant sub-mm vesicles. There is trace pyrite and 2% porosity.

Alteration Summary: pervasive clay alteration of clasts, greenish color from chlorite, strong iron oxide
Interpretation: Unknown
Name: Variably clay-altered monomict clast-supported hyaloclastite(?) breccia, cemented

Appendix H

Whole-Rock Geochemistry of Volcanic Rocks – Starfish-Tinakula Area

Contents of this file:

1. Supplemental Tables:

   Table H1: Whole-rock geochemistry of ROV grab samples of volcanic rocks from the Tinakula-Starfish area (this study)

   Table H2: Whole-rock geochemistry of drillcore samples of volcanic rocks from the Tinakula-Starfish area (provided by Neptune Minerals Inc.)

   Table H3: Precision and accuracy of whole-rock geochemical data (standards)

   Table H4: Precision of whole-rock geochemical data (duplicates)

Notes:

D.L. = detection limit
bdl = below detection limit
Mg# = Mg/(Mg + Fe); atom %
AI = Alteration Index (Ishikawa et al., 1976): $100 \times (K_2O + MgO) / (K_2O + MgO + Na_2O + CaO)$
$FeO = Fe_2O_{3(T)} \times 0.8998$
RSD = relative standard deviation (ratio of the standard deviation to the mean)
Rel % Diff = relative % difference (absolute value of the change in value divided by the average)

1. Supplemental Tables

Table H1. Whole-rock geochemistry of ROV grab samples of volcanic rocks from the Starfish-Tinakula area (this study), normalized to 100% volatile-free

			GMA13-001	GMA13-015	GMA13-023	GMA13-035	GMA13-039	GMA13-043	GMA13-044	GMA13-057	GMA13-063	GMA13-065	P0015	P0016	P0040
			D	A	B-A	A	A	D	D	B-A	D	D	B-A	B-A	B-A
	D.L.	Method	Starfish	Tinakula	N Tinakula	Tinakula	Tinakula	Tinakula	W Tinakula	W Tinakula	Tinakula	N Tinakula	Starfish	Tinakula	Tinakula
SiO_2 - %	0.01	FUS-ICP	67.53	57.43	55.96	57.15	58.26	63.49	66.37	54.56	67.15	66.92	53.53	53.22	55.40
TiO_2	0.001	FUS-ICP	0.87	1.40	1.60	1.23	1.20	1.09	0.96	1.29	0.78	0.87	1.32	1.28	1.31
Al_2O_3	0.01	FUS-ICP	15.19	16.96	16.50	16.65	17.08	16.25	15.37	17.38	15.71	15.52	16.15	17.07	17.37
$Fe_2O_{3(T)}$	0.01	FUS-ICP	4.78	8.92	9.74	9.43	8.40	6.20	5.16	9.39	4.64	4.76	11.21	11.06	9.50
MnO	0.001	FUS-ICP	0.164	0.165	0.206	0.189	0.169	0.184	0.176	0.212	0.166	0.165	0.188	0.188	0.168
MgO	0.01	FUS-ICP	1.11	2.33	3.19	2.98	2.12	1.76	1.27	3.99	1.03	1.14	3.99	3.90	2.84
CaO	0.01	FUS-ICP	3.12	7.47	7.09	7.09	7.34	4.37	3.50	8.29	2.89	3.08	8.80	8.57	8.63
Na_2O	0.01	FUS-ICP	6.08	4.53	4.57	4.36	4.53	5.71	6.07	4.20	6.47	6.33	4.10	4.02	4.05
K_2O	0.01	FUS-ICP	0.97	0.62	0.80	0.69	0.67	0.73	0.85	0.55	1.02	0.98	0.52	0.52	0.60
P_2O_5	0.01	FUS-ICP	0.20	0.20	0.33	0.19	0.20	0.23	0.26	0.14	0.17	0.21	0.15	0.14	0.15
$FeO_{(T)}$			4.30	8.02	8.77	8.49	7.55	5.58	4.65	8.45	4.17	4.29	10.09	9.95	8.55
Mg#			20.4	22.5	26.7	26.0	21.9	24.0	21.4	32.1	19.8	21.0	28.3	28.1	24.9
AI			18.4	19.7	25.5	24.2	19.1	19.8	18.1	26.6	17.9	18.3	25.9	26.0	21.3
S - ppm	10	TD-ICP	60	200	140	170	120	50	80	120	20	40	250	310	220
Ag	0.3	TD-ICP	0.3	bdl	bdl	bdl	bdl	bdl	bdl	bdl	bdl	bdl	bdl	bdl	bdl
As	0.5	INAA	3.5	bdl	bdl	bdl	bdl	bdl	4.1	2.4	2.3	bdl	bdl	2.6	bdl
Bi	0.1	FUS-MS	bdl	bdl	bdl	bdl	bdl	bdl	bdl	bdl	bdl	bdl	bdl	bdl	bdl
Cd	0.5	TD-ICP	bdl	bdl	bdl	bdl	bdl	bdl	bdl	bdl	bdl	bdl	bdl	bdl	bdl
Cu	1	TD-ICP	7	57	9	47	76	3	3	86	3	6	109	95	39
Ga	1	FUS-MS	17	18	18	17	17	17	18	17	18	17	17	17	17
Ge	0.5	FUS-MS	1.6	1.2	1.0	1.3	1.0	1.3	1.3	1.2	1.2	1.3	1.1	1.1	1.5
Hg - ppb	5	1G	bdl	5	bdl	7	14	bdl	bdl	11	bdl	bdl	7	6	10
In - ppm	0.1	FUS-MS	0.1	0.1	0.1	bdl	bdl	0.1	0.1	0.1	0.1	0.1	bdl	0.1	0.1
Sb	0.2	FUS-MS	0.6	0.6	0.4	0.5	0.7	0.6	0.5	0.6	0.6	0.5	0.5	0.5	0.5
Se	3	INAA	bdl	bdl	bdl	bdl	bdl	bdl	bdl	bdl	bdl	bdl	bdl	bdl	bdl
Sn	1	FUS-MS	8	7	7	7	7	8	7	7	8	7	7	7	7
Tl	0.05	FUS-MS	0.09	0.06	bdl	0.06	bdl	0.06	0.06	0.08	0.07	0.08	bdl	bdl	0.09
Zn	1	TD-ICP	87	83	85	87	79	85	86	79	86	82	77	86	128

D = dacite; A = andesite; B-A = basaltic andesite

Table H1. Continued

			GMA13-001	GMA13-015	GMA13-023	GMA13-035	GMA13-039	GMA13-043	GMA13-044	GMA13-057	GMA13-063	GMA13-065	P0015	P0016	P0040
			D	A	B-A	A	A	D	D	B-A	D	D	B-A	B-A	B-A
	D.L.	Method	Starfish	Tinakula	N Tinakula	Tinakula	Tinakula	Tinakula	W Tinakula	W Tinakula	Tinakula	N Tinakula	Starfish	Tinakula	Tinakula
Au - ppb	2	INAA	bdl	9	bdl	bdl	bdl	bdl	bdl	bdl	bdl	bdl	bdl	bdl	bdl
Ir - ppm	5	INAA	bdl	bdl	bdl	bdl	bdl	bdl	bdl	bdl	bdl	bdl	bdl	bdl	bdl
Mo	2	FUS-MS	bdl	bdl	bdl	bdl	bdl	bdl	bdl	bdl	bdl	bdl	bdl	bdl	bdl
Co	1	FUS-MS	3	15	15	18	14	5	3	26	3	3	25	26	18
Cr	5	INAA	bdl	bdl	bdl	bdl	bdl	bdl	bdl	bdl	bdl	bdl	bdl	bdl	15
Ni	1	TD-ICP	2	3	3	3	5	1	1	10	***0.5***	2	10	9	5
Sc	0.1	INAA	10.6	23.5	19.4	21.4	20.1	13.9	11.9	26.6	9.4	10.6	24.2	23.9	24.0
V	5	FUS-ICP	36	299	202	232	229	66	43	354	30	37	356	353	347
Rb	1	FUS-MS	14	8	8	9	8	10	12	6	15	14	6	6	7
Cs	0.1	FUS-MS	0.3	0.2	0.2	0.2	bdl	0.2	0.3	0.2	0.3	0.3	0.2	0.1	0.2
Sr	2	FUS-ICP	166	269	263	266	258	210	179	278	159	172	286	278	278
Ba	3	FUS-ICP	218	136	100	126	130	166	192	105	222	219	106	107	112
Pb	3	TD-ICP	6	***1.5***	***1.5***	3	bdl	bdl	bdl	bdl	bdl	bdl	bdl	bdl	bdl
Zr	1	FUS-ICP	219	113	112	103	100	171	206	90	239	225	85	87	89
Hf	0.1	FUS-MS	4.9	2.4	2.6	2.6	2.6	3.7	4.4	2.0	5.4	4.9	2.0	2.0	2.0
Nb	0.2	FUS-MS	7.1	4.2	4.2	3.6	4.0	5.8	6.8	2.9	7.8	7.3	2.8	2.9	2.8
Ta	0.01	FUS-MS	0.43	0.25	0.25	0.23	0.20	0.32	0.43	0.19	0.48	0.47	0.18	0.17	0.18
Th	0.05	FUS-MS	1.61	0.84	0.69	0.78	0.90	1.24	1.43	0.63	1.71	1.65	0.62	0.66	0.75
U	0.01	FUS-MS	0.63	0.39	0.28	0.37	0.40	0.48	0.57	0.28	0.65	0.65	0.28	0.32	0.55
Be	1	FUS-ICP	1	1	1	bdl	bdl	1	1	bdl	2	1	bdl	bdl	bdl
Br	0.5	INAA	9.2	6.4	bdl	7.6	bdl	bdl	4.7	bdl	6.6	4.1	6.3	bdl	4.2
W	0.5	FUS-MS	0.9	bdl	bdl	bdl	bdl	bdl	1.6	bdl	bdl	1.9	bdl	1.2	bdl
Y	0.5	FUS-MS	56.3	34.3	39.0	32.8	36.0	50.7	57.2	28.1	59.1	55.9	28.2	29.2	30.4
La	0.05	FUS-MS	15.60	8.92	8.59	8.02	8.60	13.60	14.20	6.80	16.60	15.00	6.64	6.61	7.25
Ce	0.05	FUS-MS	34.9	20.8	21.6	18.9	20.3	30.1	33.5	15.6	37.4	34.8	15.3	15.9	16.8
Pr	0.01	FUS-MS	5.06	2.99	3.30	2.80	2.93	4.34	4.95	2.31	5.46	5.07	2.34	2.39	2.57
Nd	0.05	FUS-MS	22.7	13.6	15.6	13.3	13.3	18.8	22.7	10.7	23.5	23.4	10.8	11.0	11.3
Sm	0.01	FUS-MS	6.34	4.23	4.57	3.98	4.20	5.55	6.30	3.19	6.61	6.65	3.29	3.19	3.59
Eu	0.005	FUS-MS	1.86	1.48	1.75	1.43	1.52	1.87	1.88	1.24	1.95	1.86	1.22	1.21	1.35
Gd	0.01	FUS-MS	7.30	5.11	5.87	4.49	5.00	6.72	7.56	4.07	7.87	7.62	4.14	3.99	4.39
Tb	0.01	FUS-MS	1.36	0.90	1.03	0.81	0.90	1.23	1.36	0.70	1.45	1.34	0.72	0.75	0.74
Dy	0.01	FUS-MS	8.70	5.74	6.70	5.19	5.80	7.88	9.08	4.76	8.99	8.83	4.79	4.69	4.95
Ho	0.01	FUS-MS	1.85	1.16	1.38	1.11	1.10	1.64	1.87	0.99	1.92	1.87	0.96	1.00	1.02
Er	0.01	FUS-MS	5.31	3.31	3.75	3.22	3.50	4.93	5.63	2.78	5.76	5.58	2.80	2.77	3.00
Tm	0.005	FUS-MS	0.796	0.506	0.515	0.474	0.520	0.749	0.863	0.406	0.908	0.857	0.40	0.430	0.444
Yb	0.01	FUS-MS	5.45	3.35	3.52	3.25	3.50	5.00	5.61	2.72	5.80	5.95	2.69	2.86	2.97
Lu	0.002	FUS-MS	0.879	0.525	0.582	0.535	0.560	0.795	0.902	0.430	0.955	0.956	0.413	0.473	0.458
LOI	%	FUS-ICP	0.46	1.09	1.77	1.48	2.320	0.720	0.950	0.840	-1.17	0.45	0.4	0.15	1.14

D = dacite; A = andesite; B-A = basaltic andesite

D.L. = detection limit; bdl = below detection limit

Table H2. Whole-rock geochemistry of ROV grab samples of volcanic rocks from the Starfish-Tinakula area (data from Neptune Minerals Inc.) normalized to 100% volatile-free

		650A	660	813	TGS10-79B	93	601	624	763
		B-A	B-A	B-A	B-A	D	D	D	D
	Method	Tinakula	Tinakula	Tinakula	Tinakula	Starfish	Tinakula	Tinakula	Tinakula
SiO_2 - %	XRF	53.90	52.70	51.90	55.10	66.35	64.80	66.38	66.18
TiO_2	XRF	1.22	1.51	1.23	1.23	0.83	0.91	0.92	0.95
Al_2O_3	XRF	17.00	16.60	17.20	17.00	16.00	15.95	15.68	15.69
$Fe_2O_{3(T)}$	XRF	2.30	3.51	2.34	3.19	1.54	1.68	1.30	1.38
FeO	Titrations	8.06	7.61	8.01	6.58	2.88	3.50	3.46	3.48
MnO	XRF	0.20	0.67	0.19	0.18	0.17	0.18	0.18	0.18
MgO	XRF	3.97	3.93	4.93	3.23	1.29	1.59	1.26	1.29
CaO	XRF	8.44	8.28	10.00	8.06	3.40	3.89	3.49	3.56
Na_2O	XRF	4.32	4.72	3.62	4.57	6.47	6.40	6.27	6.21
K_2O	XRF	0.44	0.36	0.40	0.63	0.85	0.87	0.80	0.80
P_2O_5	XRF	0.16	0.16	0.14	0.16	0.22	0.22	0.27	0.28
Mg#		33.0	34.1	38.1	32.9	30.9	31.2	26.7	27.0
Al		25.7	24.8	28.1	23.4	17.8	19.3	17.4	17.6
S - ppm	ICPAES	152	405	202	202	50	255	101	50
Ag	ICPMS	0.51	0.51	bdl	bdl	bdl	bdl	bdl	bdl
As	ICPMS	2	1	1	1	1	2	1	2
Bi	ICPMS	bdl	bdl	bdl	bdl	bdl	bdl	bdl	bdl
Cd	ICPMS	bdl	bdl	bdl	bdl	bdl	bdl	bdl	bdl
Cu	ICPAES	81.0	28.0	121.0	83.0	8.1	14.3	14.1	10.1
Ga	ICPMS	19.4	20.3	19.4	19.2	19.2	18.6	19.2	19.8
In	ICPMS	0.06	0.06	0.06	0.06	0.08	0.08	0.08	0.10
Se	ICPMS	bdl	bdl	bdl	bdl	bdl	bdl	bdl	bdl
Sn	ICPMS	bdl	bdl	bdl	bdl	2	1	2	1
Zn	ICPAES	93	95	93	99	95	98	95	99
Au - ppb	ICPMS	2	2	2	2	1	3	2	1
Mo - ppm	ICPMS	0.91	12.30	0.61	0.81	1.70	1.60	1.60	1.60
Cr	ICPAES	bdl	bdl	30.4	bdl	70.6	30.6	10.1	bdl
Ni	ICPAES	14.1	10.1	20.2	10.1	6.0	10.2	8.1	6.1
Sc	ICPAES	28.3	28.4	34.4	26.3	12.1	12.2	12.1	16.1
V	ICPAES	343	345	374	323	40	61	30	30
Li	ICPMS	7.1	12.7	6.1	5.6	15.1	10.2	14.7	16.1
Rb	ICPMS	6.5	4.9	6.9	10.1	15.3	12.9	12.9	13.7
Sr	ICPMS	262	270	307	263	177	186	174	184
Ba	ICPMS	101	94	116	107	196	188	188	188
Pb	ICPMS	2.00	2.00	2.00	2.00	3.02	4.08	4.04	3.03
Zr	ICPMS	111	107	82	122	261	240	251	244
Hf	ICPMS	2.42	2.43	1.82	2.60	5.44	5.31	5.46	5.45
Nb	ICPMS	3.5	3.0	2.5	4.0	8.6	7.7	8.1	8.1
Ta	ICPMS	0.20	0.20	0.10	0.20	0.40	0.41	0.40	0.40
Th	ICPMS	0.81	0.71	0.71	1.11	1.81	1.63	1.62	1.72
U	ICPMS	0.30	0.30	0.20	0.40	0.60	0.61	0.61	0.61
Be	ICPMS	0.51	0.41	0.40	0.61	1.21	1.02	1.21	1.01
Y	ICPMS	28.3	29.3	23.9	30.5	52.1	48.0	54.6	55.3
La	ICPMS	6.57	5.98	5.36	7.38	13.81	12.86	14.35	14.22
Ce	ICPMS	16.06	16.32	13.26	19.00	34.89	31.64	34.55	33.90
Pr	ICPMS	2.40	2.45	2.00	2.71	5.04	4.70	4.97	5.12
Nd	ICPMS	11.01	11.86	9.51	12.63	22.89	21.33	22.63	23.51
Sm	ICPMS	3.38	3.55	2.83	3.69	6.40	5.97	6.47	6.61
Eu	ICPMS	1.31	1.47	1.21	1.36	2.02	1.89	2.12	2.12
Gd	ICPMS	4.04	4.86	3.64	4.85	7.86	7.35	8.08	8.47
Tb	ICPMS	0.71	0.81	0.61	0.81	1.41	1.28	1.41	1.41
Dy	ICPMS	5.05	5.37	4.20	5.41	9.23	8.42	9.24	9.38
Ho	ICPMS	1.05	1.13	0.89	1.15	2.00	1.84	1.96	2.06
Er	ICPMS	3.13	3.34	2.53	3.49	5.80	5.56	5.96	6.10
Tm	ICPMS	0.46	0.51	0.38	0.53	0.93	0.84	0.89	0.93
Yb	ICPMS	3.03	3.19	2.38	3.39	6.05	5.46	6.01	6.20
Lu	ICPMS	0.46	0.51	0.38	0.53	0.95	0.84	0.95	0.97
LOI	1000°C	0.84	1.51	0.91	1.73	1.22	4.08	1.63	1.52

D = dacite; A = andesite; B-A = basaltic andesite

Table H3: Precision and accuracy of whole-rock geochemical data (standards)

		Detection	Accepted	Measured		Accepted	Measured	
Element	Unit	Limit	GXR-1	GXR-1 (1)	*% Acc*	NIST 694	NIST 694 (1)	*% Acc*
V	ppm	5	-	-	-	1740	1619	*7*
V	ppm	5	-	-	-	1740	1619	*7*
Ni	ppm	1	41	40	*3*	-	-	-
Cu	ppm	1	1110	1210	*-8*	-	-	-
Zn	ppm	1	760	753	*1*	-	-	-
Cd	ppm	0.5	3.3	2.8	*18*	-	-	-
S	%	0.001	0.257	0.251	*2*	-	-	-
Ag	ppm	0.3	31	31.7	*-2*	-	-	-
Pb	ppm	3	730	733	*0*	-	-	-
Ag	ppm	0.05	31	27.6	*12*	-	-	-
Cu	ppm	0.2	1110	1100	*1*	-	-	-
Cd	ppm	0.1	3.3	2.3	*43*	-	-	-
Mn	ppm	1	852	870	*-2*	-	-	-
Pb	ppm	0.5	730	736	*-1*	-	-	-
Ni	ppm	0.5	41	37.7	*9*	-	-	-
Zn	ppm	0.5	760	770	*-1*	-	-	-
Ba	ppm	1	750	364	*106*	-	-	-
Be	ppm	0.1	1.22	1	*22*	-	-	-
Bi	ppm	0.02	1380	1440	*-4*	-	-	-
Ca	%	0.01	0.96	0.75	*28*	-	-	-
Co	ppm	0.1	8.2	6.9	*19*	-	-	-
Cs	ppm	0.05	3	2.36	*27*	-	-	-
Eu	ppm	0.05	0.69	0.48	*44*	-	-	-
Ga	ppm	0.1	13.8	< 0.1	-	-	-	-
In	ppm	0.1	0.77	0.6	*28*	-	-	-
Li	ppm	0.5	8.2	8.1	*1*	-	-	-
Mg	%	0.01	0.217	0.2	*8*	-	-	-
Nb	ppm	0.1	0.8	1	*-20*	-	-	-
Mo	ppm	0.05	18	16.6	*8*	-	-	-
Rb	ppm	0.2	14	2.4	*483*	-	-	-
Se	ppm	0.1	16.6	13.4	*24*	-	-	-
Sn	ppm	1	54	26	*108*	-	-	-
Sr	ppm	0.2	275	227	*21*	-	-	-
Ta	ppm	0.1	0.175	< 0.1	-	-	-	-
Te	ppm	0.1	13	12	*8*	-	-	-
Th	ppm	0.1	2.44	2.5	*-2*	-	-	-
Tl	ppm	0.05	0.39	0.4	*-3*	-	-	-
U	ppm	0.1	34.9	31.7	*10*	-	-	-
V	ppm	1	80	68	*18*	-	-	-
Y	ppm	0.1	32	23.7	*35*	-	-	-
Zr	ppm	1	38	24	*58*	-	-	-
La	ppm	0.1	7.5	5.9	*27*	-	-	-
K	%	0.01	0.05	0.05	*0*	-	-	-
Ce	ppm	0.1	17	13.2	*29*	-	-	-
Nd	ppm	0.1	18	8.1	*122*	-	-	-
Sm	ppm	0.1	2.7	2.8	*-4*	-	-	-
Gd	ppm	0.1	4.2	3.6	*17*	-	-	-
Dy	ppm	0.1	4.3	4.8	*-10*	-	-	-
Tb	ppm	0.1	0.83	0.6	*38*	-	-	-
Hg	ppb	10	3900	3720	*5*	-	-	-
Tm	ppm	0.1	0.43	0.3	*43*	-	-	-
Yb	ppm	0.1	1.9	2.2	*-14*	-	-	-
Lu	ppm	0.1	0.28	0.3	*-7*	-	-	-

Table H3: Continued

Element	Unit	Detection Limit	Accepted DNC-1	Measured DNC-1 (1)	% Acc	Accepted GXR-4	Measured GXR-4 (1)	% Acc
Hg	ppb	5	-	-	-	110	104	*6*
Ba	ppm	2	118	104	*13*	-	-	
Sr	ppm	2	144	141	*2*	-	-	
Y	ppm	1	18	16	*13*	-	-	
Zr	ppm	2	38	39	*-3*	-	-	
V	ppm	5	148	155	*-5*	-	-	
V	ppm	5	148	147	*1*	-	-	
V	ppm	5	148	155	*-5*	-	-	
Co	ppm	1	57	59	*-3*	-	-	
Ni	ppm	20	247	250	*-1*	-	-	
Ni	ppm	1	-	-	-	42	36	*17*
Cu	ppm	1	-	-	-	6520	6420	*2*
Cu	ppm	10	100	110	*-9*	-	-	-
Zn	ppm	1	-	-	-	73	70	*4*
Zn	ppm	30	70	70	*0*	-	-	-
Cd	ppm	0.5	-	-	-	0.86	< 0.5	-
S	%	0.001	-	-	-	1.77	1.77	*0*
Ga	ppm	1	15	14	*7*	-	-	-
Sr	ppm	2	144	151	*-5*	-	-	-
Sr	ppm	2	144	141	*2*	-	-	-
Y	ppm	0.5	18	17.3	*4*	-	-	-
Y	ppm	2	18	16	*13*	-	-	-
Zr	ppm	1	38	39	*-3*	-	-	-
Ag	ppm	0.3	-	-		4	3.3	*21*
Sb	ppm	0.2	0.96	0.9	*7*	-	-	-
Ba	ppm	3	118	104	*13*	-	-	-
La	ppm	0.05	3.6	3.8	*-5*	-	-	-
Nd	ppm	0.05	5.2	5	*4*	-	-	-
Eu	ppm	0.005	0.59	0.59	*0*	-	-	-
Yb	ppm	0.01	2	1.8	*11*	-	-	-
Pb	ppm	3	-	-	-	52	43	*21*
Ag	ppm	0.05	-	-	-	4	3.62	*10*
Cu	ppm	0.2	-	-	-	6520	6210	*5*
Cd	ppm	0.1	-	-	-	0.86	0.4	*115*
Mn	ppm	1	-	-	-	155	166	*-7*
Pb	ppm	0.5	-	-	-	52	46	*13*
Ni	ppm	0.5	-	-	-	42	38.2	*10*
Zn	ppm	0.5	-	-	-	73	68.9	*6*
Ba	ppm	1	-	-	-	1640	70	*2243*
Be	ppm	0.1	-	-	-	1.9	2.1	*-10*
Bi	ppm	0.02	-	-	-	19	18.7	*2*
Ca	%	0.01	-	-	-	1.01	0.91	*11*
Co	ppm	0.1	-	-	-	14.6	12.2	*20*
Cs	ppm	0.05	-	-	-	2.8	2.09	*34*
Eu	ppm	0.05	-	-	-	1.63	1.16	*41*
Ga	ppm	0.1	-	-	-	20	13.6	*47*
In	ppm	0.1	-	-	-	0.27	0.2	*35*
Li	ppm	0.5	-	-	-	11.1	11.7	*-5*
Mg	%	0.01	-	-	-	1.66	2.25	*-26*
Nb	ppm	0.1	-	-	-	10	16	*-38*
Mo	ppm	0.05	-	-	-	310	278	*12*
Rb	ppm	0.2	-	-	-	160	125	*28*
Se	ppm	0.1	-	-	-	5.6	3.4	*65*
Sn	ppm	1	-	-	-	5.6	8	*-30*
Sr	ppm	0.2	-	-	-	221	156	*42*
Ta	ppm	0.1	-	-	-	0.79	0.8	*-1*
Te	ppm	0.1	-	-	-	0.97	1.2	*-19*
Th	ppm	0.1	-	-	-	22.5	17.8	*26*
Tl	ppm	0.05	-	-	-	3.2	3.35	*-4*
U	ppm	0.1	-	-	-	6.2	5.5	*13*
V	ppm	1	-	-	-	87	75	*16*
Y	ppm	0.1	-	-	-	14	11.1	*26*
Zr	ppm	1	-	-	-	186	49	*280*
La	ppm	0.1	-	-	-	64.5	44.1	*46*
K	%	0.01	-	-	-	4.01	> 5.00	-
Ce	ppm	0.1	-	-	-	102	99.5	*3*
Nd	ppm	0.1	-	-	-	45	39.4	*14*
Sm	ppm	0.1	-	-	-	6.6	6.4	*3*
Gd	ppm	0.1	-	-	-	5.25	3.7	*42*
Dy	ppm	0.1	-	-	-	2.6	2.8	*-7*
Tb	ppm	0.1	-	-	-	0.36	0.5	*-28*
Hg	ppb	10	-	-	-	110	240	*-54*
Tm	ppm	0.1	-	-	-	0.21	0.2	*5*
Yb	ppm	0.1	-	-	-	1.6	1	*60*
Lu	ppm	0.1	-	-	-	0.17	0.1	*70*

Table H3: Continued

Element	Unit	Detection Limit	Accepted SDC-1	Measured SDC-1 (1)	% Acc	Accepted GXR-6	Measured GXR-6 (1)	% Acc	Accepted LKSD-3	Measured LKSD-3 (1)	% Acc
Hg	ppb	5	-	-	-	68	71	*-4*	-	-	-
V	ppm	5	-	-	-	-	-	-	82	87	*-6*
Cr	ppm	20	-	-	-	-	-	-	87	90	*-3*
Co	ppm	1	-	-	-	-	-	-	30	31	*-3*
Ni	ppm	20	-	-	-	-	-	-	47	50	*-6*
Ni	ppm	1	38	33	*15*	27	27	*0*	-	-	-
Cu	ppm	1	30	30	*0*	66	80	*-18*	-	-	-
Cu	ppm	10	-	-	-	-	-	-	35	30	*17*
Zn	ppm	1	103	96	*7*	118	135	*-13*	-	-	-
Cd	ppm	0.5	-	-	-	1	< 0.5	-	-	-	-
S	%	0.001	-	-	-	0.016	0.02	*-20*	-	-	-
As	ppm	5	-	-	-	-	-	-	27	25	*8*
Rb	ppm	1	-	-	-	-	-	-	78	77	*1*
Sr	ppm	2	-	-	-	-	-	-	240	258	*-7*
Y	ppm	0.5	-	-	-	-	-	-	30	29.1	*3*
Mo	ppm	2	-	-	-	-	-	-	2	2	*0*
Ag	ppm	0.3	-	-	-	1.3	0.4	*225*	-	-	-
Cs	ppm	0.1	-	-	-	-	-	-	2.3	2.3	*0*
Ba	ppm	3	-	-	-	-	-	-	680	658	*3*
Ce	ppm	0.05	-	-	-	-	-	-	90	88.1	*2*
Nd	ppm	0.05	-	-	-	-	-	-	44	43.5	*1*
Sm	ppm	0.01	-	-	-	-	-	-	8	7.6	*5*
Eu	ppm	0.005	-	-	-	-	-	-	1.5	1.4	*7*
Dy	ppm	0.01	-	-	-	-	-	-	4.9	4.7	*4*
Yb	ppm	0.01	-	-	-	-	-	-	2.7	2.6	*4*
Lu	ppm	0.002	-	-	-	-	-	-	0.4	0.39	*3*
Ta	ppm	0.01	-	-	-	-	-	-	0.7	0.68	*3*
La	ppm	0.05	-	-	-	-			-	-	-
Pb	ppm	3	25	22	*14*	101	100	*1*	-	-	-
U	ppm	0.01	-	-	-	-	-	-	4.6	4.2	*10*
Ag	ppm	0.05	-	-	-	1.3	0.26	*400*	-	-	-
Cu	ppm	0.2	30	28	*7*	66	66.1	*0*	-	-	-
Cd	ppm	0.1	-	-	-	1	< 0.1	-	-	-	-
Mn	ppm	1	880	811	*9*	1010	970	*4*	-	-	-
Pb	ppm	0.5	25	21.7	*15*	101	92	*10*	-	-	-
Ni	ppm	0.5	38	30.7	*24*	27	22.9	*18*	-	-	-
Zn	ppm	0.5	103	100	*3*	118	127	*-7*	-	-	-
Ba	ppm	1	630	334	*89*	1300	674	*93*	-	-	-
Be	ppm	0.1	3	2.8	*7*	1.4	1.2	*17*	-	-	-
Bi	ppm	0.02	-	-	-	0.29	0.2	*45*	-	-	-
Ca	%	0.01	1	0.91	*10*	0.18	0.14	*29*	-	-	-
Co	ppm	0.1	18	14.9	*21*	13.8	11.3	*22*	-	-	-
Cs	ppm	0.05	4	2.98	*34*	4.2	3.2	*31*	-	-	-
Eu	ppm	0.05	1.7	1.17	*45*	0.76	0.5	*52*	-	-	-
Ga	ppm	0.1	21	7.8	*169*	35	0.9	*3789*	-	-	-
In	ppm	0.1	-	-	-	0.26	< 0.1	-	-	-	-
Li	ppm	0.5	34	35.2	*-3*	32	37.1	*-14*	-	-	-
Mg	%	0.01	1.02	1.22	*-16*	0.609	0.77	*-21*	-	-	-
Nb	ppm	0.1	21	0.3	*6900*	7.5	0.2	*3650*	-	-	-
Mo	ppm	0.05	-	-	-	2.4	0.25	*860*	-	-	-
Rb	ppm	0.2	127	88	*44*	90	63.4	*42*	-	-	-
Se	ppm	0.1	-			0.94	< 0.1	-	-	-	-
Sn	ppm	1	3	1	*200*	1.7	2	*-15*	-	-	-
Sr	ppm	0.2	180	120	*50*	35	27.1	*29*	-	-	-
Ta	ppm	0.1	1.2	< 0.1	-	0.485	< 0.1	-	-	-	-
Te	ppm	0.1	-	-	-	0.018	< 0.1	-	-	-	-
Th	ppm	0.1	12	10.7	*12*	5.3	5	*6*	-	-	-
Tl	ppm	0.05	0.7	0.63	*11*	2.2	2.23	*-1*	-	-	-
U	ppm	0.1	3.1	2.7	*15*	1.54	1.4	*10*	-	-	-
V	ppm	1	102	40	*155*	186	89	*109*	-	-	-
Y	ppm	0.1	-	-	-	14	9.8	*43*	-	-	-
Zr	ppm	1	290	36	*706*	110	72	*53*	-	-	-
La	ppm	0.1	42	29.3	*43*	13.9	9.6	*45*	-	-	-
K	%	0.01	2.72	3.2	*-15*	1.87	2.29	*-18*	-	-	-
Ce	ppm	0.1	93	76.4	*22*	36	29.3	*23*	-	-	-
Nd	ppm	0.1	40	36.1	*11*	13	11.7	*11*	-	-	-
Sm	ppm	0.1	8.2	7.3	*12*	2.67	2.4	*11*	-	-	-
Gd	ppm	0.1	7	5.6	*25*	2.97	2	*49*	-	-	-
Dy	ppm	0.1	6.7	6.1	*10*	2.8	2.3	*22*	-	-	-
Tb	ppm	0.1	1.2	0.8	*50*	0.415	0.3	*38*	-	-	-
Ho	ppm	0.1	1.5	1.1	*36*	-	-	-	-	-	-
Hg	ppb	10	200	50	*300*	68	50	*36*	-	-	-
Er	ppm	0.1	4.1	3.3	*24*	-	-	-	-	-	-
Tm	ppm	0.1	0.65	0.5	*30*	-	-	-	-	-	-
Yb	ppm	0.1	4	3.2	*25*	2.4	1.6	*50*	-	-	-
Lu	ppm	0.1	-	-	-	0.33	0.3	*10*	-	-	-

Table H3: Continued

Element	Unit	Detection Limit	Accepted W-2a	Measured W-2a (1)	% Acc	Accepted DTS-2b	Measured DTS-2b (1)	% Acc
Ba	ppm	2	182	172	*6*	-	-	-
Sr	ppm	2	190	197	*-4*	-	-	-
Y	ppm	1	24	20	*20*	-	-	-
Sc	ppm	1	-	-	-	-	-	-
Zr	ppm	2	94	94	*0*	-	-	-
Be	ppm	1	-	-	-	-	-	-
V	ppm	5	262	273	*-4*	-	-	-
V	ppm	5	262	273	*-4*	-	-	-
Cr	ppm	20	-	-	-	15500	> 10000	-
Co	ppm	1	43	42	*2*	120	128	*-6*
Ni	ppm	20	70	80	*-13*	3780	3760	*1*
Cu	ppm	10	110	100	*10*	-	-	-
Ga	ppm	1	17	17	*0*	-	-	-
Ge	ppm	0.5	1	1.4	*-29*	-	-	-
Rb	ppm	1	21	19	*11*	-	-	-
Sr	ppm	2	190	194	*-2*	-	-	-
Sr	ppm	2	190	197	*-4*	-	-	-
Y	ppm	2	24	20	*20*	-	-	-
Zr	ppm	1	94	94	*0*	-	-	-
Mo	ppm	2	0.6	< 2	-	-	-	-
Sb	ppm	0.2	0.79	0.9	*-12*	-	-	-
Ba	ppm	3	182	159	*14*	-	-	-
Ba	ppm	3	182	172	*6*	-	-	-
La	ppm	0.05	10	10.4	*-4*	-	-	-
Ce	ppm	0.05	23	22.5	*2*	-	-	-
Nd	ppm	0.05	13	12.3	*6*	-	-	-
Sm	ppm	0.01	3.3	3	*10*	-	-	-
Eu	ppm	0.005	1	0.9	*11*	-	-	-
Dy	ppm	0.01	3.6	3.5	*3*	-	-	-
Ho	ppm	0.01	0.76	0.71	*7*	-	-	-
Lu	ppm	0.002	0.33	0.3	*10*	-	-	-
Hf	ppm	0.1	2.6	2.5	*4*	-	-	-
Ta	ppm	0.01	0.5	0.52	*-4*	-	-	-
W	ppm	0.5	0.3	0.8	*-63*	-	-	-
Tl	ppm	0.05	0.2	< 0.05	-	-	-	-
Bi	ppm	0.1	0.03	< 0.1	-	-	-	-
Th	ppm	0.05	2.4	2.3	*4*	-	-	-
U	ppm	0.01	0.53	0.49	*8*	-	-	-

Element	Unit	Detection Limit	Accepted SY-4	Measured SY-4 (1)	% Acc	Accepted CTA-AC-1	Measured CTA-AC-1 (1)	% Acc
Ba	ppm	2	340	354	*-4*	-	-	-
Sr	ppm	2	1191	1201	*-1*	-	-	-
Y	ppm	1	119	121	*-2*	-	-	-
Sc	ppm	1	-	-	-	-	-	-
Zr	ppm	2	517	538	*-4*	-	-	-
Be	ppm	1	-	-	-	-	-	-
V	ppm	5	8	9	*-11*	-	-	-
V	ppm	5	-	-	-	104	108	*-4*
V	ppm	5	8	9	*-11*	-	-	-
Sr	ppm	2	1191	1201	*-1*	-	-	-
Y	ppm	2	119	121	*-2*	-	-	-
Ba	ppm	3	340	354	*-4*	-	-	-
La	ppm	0.05	-	-	-	2176	> 2000	-
Ce	ppm	0.05	-	-	-	3326	> 3000	-
Nd	ppm	0.05	-	-	-	1087	1170	*-7*
Sm	ppm	0.01	-	-	-	162	168	*-4*
Eu	ppm	0.005	-	-	-	46.7	46.4	*1*
Gd	ppm	0.01	-	-	-	124	126	*-2*
Tb	ppm	0.01	-	-	-	13.9	14.7	*-5*
Yb	ppm	0.01	-	-	-	11.4	10.8	*6*
Th	ppm	0.05	-	-	-	21.8	22.3	*-2*

Table H3: Continued

Element	Unit	Detection Limit	Accepted BIR-1a	Measured BIR-1a (1)	% Acc	Accepted SdAR-M2	Measured SdAR-M2 (1)	% Acc
Hg	ppb	5	-	-	-	1440	1490	*-3*
Ba	ppm	2	6	6	*0*	-	-	-
Sr	ppm	2	110	108	*2*	-	-	-
Y	ppm	1	16	13	*23*	-	-	-
Sc	ppm	1	-	-	-	-	-	-
Zr	ppm	2	18	17	*6*	-	-	-
Be	ppm	1	-	-	-	-	-	-
V	ppm	5	310	330	*-6*	-	-	-
V	ppm	5	310	312	*-1*	-	-	-
V	ppm	5	310	330	*-6*	-	-	-
Cr	ppm	20	370	380	*-3*	-	-	-
Co	ppm	1	52	53	*-2*	-	-	-
Ni	ppm	20	170	180	*-6*	-	-	-
Ni	ppm	1	-	-	-	48.8	48	*2*
Cu	ppm	1	-	-	-	236	234	*1*
Cu	ppm	10	125	130	*-4*	-	-	-
Zn	ppm	1	-	-	-	760	758	*0*
Zn	ppm	30	70	70	*0*	-	-	-
Cd	ppm	0.5	-	-	-	5.1	5.4	*-6*
Ga	ppm	1	16	15	*7*	-	-	-
Sr	ppm	2	110	113	*-3*	-	-	-
Sr	ppm	2	110	108	*2*	-	-	-
Y	ppm	0.5	16	15.8	*1*	-	-	-
Y	ppm	2	16	13	*23*	-	-	-
Zr	ppm	1	18	17	*6*	-	-	-
Sb	ppm	0.2	0.58	0.6	*-3*	-	-	-
Ba	ppm	3	6	6	*0*	-	-	-
La	ppm	0.05	0.63	0.7	*-10*	-	-	-
Nd	ppm	0.05	2.5	2.5	*0*	-	-	-
Sm	ppm	0.01	1.1	1	*10*	-	-	-
Eu	ppm	0.005	0.55	0.51	*8*	-	-	-
Yb	ppm	0.01	1.7	1.6	*6*	-	-	-
Hf	ppm	0.1	0.6	0.6	*0*	-	-	-
Pb	ppm	3	-	-	-	808	806	*0*
Cu	ppm	0.2	-	-	-	236	220	*7*
Cd	ppm	0.1	-	-	-	5.1	4.9	*4*
Pb	ppm	0.5	-	-	-	808	784	*3*
Ni	ppm	0.5	-	-	-	48.8	47.9	*2*
Zn	ppm	0.5	-	-	-	760	789	*-4*
Ba	ppm	1	-	-	-	990	542	*83*
Be	ppm	0.1	-	-	-	6.6	7.1	*-7*
Bi	ppm	0.02	-	-	-	1.05	1.06	*-1*
Co	ppm	0.1	-	-	-	12.4	11.5	*8*
Cs	ppm	0.05	-	-	-	1.82	1.33	*37*
Eu	ppm	0.05	-	-	-	1.44	1.08	*33*
Ga	ppm	0.1	-	-	-	17.6	< 0.1	-
Li	ppm	0.5	-	-	-	17.9	18.7	*-4*
Nb	ppm	0.1	-	-	-	26.2	5.7	*360*
Mo	ppm	0.05	-	-	-	13.3	11.3	*18*
Rb	ppm	0.2	-	-	-	149	85.5	*74*
Sr	ppm	0.2	-	-	-	144	107	*35*
Ta	ppm	0.1	-	-	-	1.8	< 0.1	-
Th	ppm	0.1	-	-	-	14.2	13.4	*6*
U	ppm	0.1	-	-	-	2.53	2.4	*5*
V	ppm	1	-	-	-	25.2	22	*15*
Y	ppm	0.1	-	-	-	32.7	20.3	*61*
Zr	ppm	1	-	-	-	259	117	*121*
La	ppm	0.1	-	-	-	46.6	35.3	*32*
Ce	ppm	0.1	-	-	-	98.8	90.2	*10*
Pr	ppm	0.1	-	-	-	11	9	*22*
Nd	ppm	0.1	-	-	-	39.4	36.8	*7*
Sm	ppm	0.1	-	-	-	7.18	6.8	*6*
Gd	ppm	0.1	-	-	-	6.28	4.7	*34*
Dy	ppm	0.1	-	-	-	5.88	4.9	*20*
Tb	ppm	0.1	-	-	-	0.97	0.7	*39*
Ho	ppm	0.1	-	-	-	1.21	0.9	*34*
Hg	ppb	10	-	-	-	1440	1080	*33*
Er	ppm	0.1	-	-	-	3.58	2.7	*33*
Tm	ppm	0.1	-	-	-	0.54	0.4	*35*
Yb	ppm	0.1	-	-	-	3.63	2.7	*34*
Lu	ppm	0.1	-	-	-	0.54	0.4	*35*

Table H3: Continued

Element	Unit	Detection Limit	Accepted DMMAS 118	Measured DMMAS 118 (1)	*% Acc*	Measured DMMAS 118 (2)	*% Acc*	Measured DMMAS 118 (3)	*% Acc*	*% RSD*
Au	ppb	2	1729	1710	*1*	1700	*1*	1760	*-2*	*0*
As	ppm	0.5	1661	1580	*5*	1670	*-5*	-	-	*4*
Cr	ppm	5	83	83	*0*	86	*-3*	-	-	*3*
Sc	ppm	0.1	6.1	6.1	*0*	6.3	*-3*	6.2	*-2*	*2*
Sb	ppm	0.2	6.6	6.4	*3*	6.4	*0*			*0*
As	ppm	0.5	1661	1740	*-5*	-	-	-	-	-
Ba	ppm	50	1264	1250	*1*	-	-	-	-	-
Co	ppm	1	45	43	*5*	-	-	-	-	-
Cr	ppm	2	83	90	*-8*	-	-	-	-	-
Fe	%	0.01	3.25	3.33	*-2*	-	-	-	-	-
Na	%	0.01	2.21	2.16	*2*	-	-	-	-	-
Sb	ppm	0.1	6.6	6.9	*-4*	-	-	-	-	-
U	ppm	0.5	15.9	16.9	*-6*	-	-	-	-	-

Element	Unit	Detection Limit	Accepted TDB-1	Measured TDB-1 (1)	*% Acc*	Accepted BaSO4	Measured BaSO4 (1)	*% Acc*	Measured BaSO4 (2)	*% Acc*	*% RSD*
Total S	%	0.01	-	-	-	14	13.4	*4*	13.5	*4*	*1*
V	ppm	5	471	500	*-6*	-	-	-	-	-	-
Cr	ppm	20	251	270	*-7*	-	-	-	-	-	-
Ni	ppm	20	92	100	*-8*	-	-	-	-	-	-
Cu	ppm	10	323	300	*8*	-	-	-	-	-	-
Y	ppm	0.5	36	33.4	*8*	-	-	-	-	-	-
La	ppm	0.05	17	16.2	*5*	-	-	-	-	-	-
Ce	ppm	0.05	41	38.1	*8*	-	-	-	-	-	-
Nd	ppm	0.05	23	23.5	*-2*	-	-	-	-	-	-
Yb	ppm	0.01	3.4	3.1	*10*	-	-	-	-	-	-
Th	ppm	0.05	2.7	2.6	*4*	-	-	-	-	-	-

Table H4: Precision of whole-rock geochemical data (duplicates)

		Detection	Original	Duplicate		Original	Duplicate	
Element	Unit	Limit	GMA13_063	GMA13-063	*Rel % Diff*	GMA13_044	GMA13_0044	*Rel % Diff*
Hg	ppb	5	< 5	< 5	-	< 5	< 5	-
SiO2	%	0.01	67.94	66.70	*0.46*	65.94	66.99	*-0.39*
Al2O3	%	0.01	15.89	15.75	*0.22*	15.27	14.86	*0.68*
Fe2O3(T)	%	0.01	4.69	4.64	*0.27*	5.13	5.1	*0.15*
MnO	%	0.001	0.168	0.169	*-0.148*	0.175	0.174	*0.143*
MgO	%	0.01	1.04	1.01	*0.73*	1.26	1.24	*0.40*
CaO	%	0.01	2.92	2.92	*0.00*	3.48	3.49	*-0.07*
Na2O	%	0.01	6.55	6.49	*0.23*	6.03	5.8	*0.97*
K2O	%	0.01	1.03	1.01	*0.49*	0.84	0.81	*0.91*
TiO2	%	0.001	0.793	0.776	*0.542*	0.953	0.945	*0.211*
P2O5	%	0.01	0.17	0.17	*0.00*	0.26	0.23	*3.06*
LOI	%		-1.17	0.86	*327.42*	0.95	0.82	*3.67*
Total	%	0.01	100	100.5	*-0.1*	100.3	100.4	*0.0*
Y	ppm	1	11	10	*2*	13	13	*0*
Zr	ppm	2	2	2	*0*	1	1	*0*
Be	ppm	1	< 2	< 2	-	< 2	< 2	-
V	ppm	5	6.6	4.9	*7.4*	4.7	6.7	*-8.8*
Au	ppb	2	< 5	< 5	-	< 5	< 5	-
As	ppm	0.5	< 5	< 5	-	< 5	< 5	-
Br	ppm	0.5	9.4	8.1	*3.7*	11.9	12.4	*-1.0*
Cr	ppm	5	< 3	< 3	-	< 3	< 3	-
Ir	ppb	5	< 0.2	< 0.2	-	< 0.2	< 0.2	-
Sc	ppm	0.1	1.51	1.40	*1.89*	1.70	1.41	*4.66*
Se	ppm	3	< 0.01	< 0.01	-	< 0.01	< 0.01	-
Sb	ppm	0.2	30	26	*4*	43	43	*0*
Mass	g		< 20	< 20	-	< 20	< 20	-
Total S	%	0.01	3	3	*0*	3	3	*0*
V	ppm	5	< 1	2	-	1	3	*-25*
V	ppm	5	3	3	*0*	3	1	*25*
Cr	ppm	20	86	88	*-1*	86	89	*-1*
Co	ppm	1	< 0.5	< 0.5	-	< 0.5	< 0.5	-
Ni	ppm	20	0.002	0.004	*-16.667*	0.008	0.007	*3.333*
Ni	ppm	1	18	17	*1*	18	18	*0*
Cu	ppm	1	1.2	1.3	*-2.0*	1.3	1.4	*-1.9*
Cu	ppm	10	< 5	< 5	-	< 5	< 5	-
Zn	ppm	1	15	15	*0*	12	12	*0*
Zn	ppm	30	159	157	*0*	179	173	*1*
Cd	ppm	0.5	59.1	57.4	*0.7*	57.2	57.9	*-0.3*
S	%	0.001	239	234	*1*	206	199	*1*
Ga	ppm	1	7.8	7.8	*0.0*	6.8	6.4	*1.5*
Ge	ppm	0.5	< 2	< 2	-	< 2	< 2	-
As	ppm	5	< 0.3	< 0.3	-	< 0.3	< 0.3	-
Rb	ppm	1	0.1	0.1	*0.0*	0.1	0.1	*0.0*
Sr	ppm	2	8	8	*0*	7	7	*0*
Sr	ppm	2	0.6	0.5	*4.5*	0.5	0.5	*0.0*
Y	ppm	0.5	0.3	0.3	*0.0*	0.3	0.3	*0.0*
Y	ppm	2	222	219	*0*	192	186	*1*
Zr	ppm	1	16.6	15.5	*1.7*	14.2	14.3	*-0.2*
Nb	ppm	0.2	37.4	36.2	*0.8*	33.5	33.7	*-0.1*
Mo	ppm	2	5.46	5.21	*1.17*	4.95	5.04	*-0.45*
Ag	ppm	0.3	23.5	22.9	*0.6*	22.7	22.5	*0.2*
In	ppm	0.1	6.61	6.7	*-0.34*	6.3	6.45	*-0.59*
Sn	ppm	1	1.95	1.91	*0.52*	1.88	2.01	*-1.67*
Sb	ppm	0.2	7.87	7.62	*0.81*	7.56	7.95	*-1.26*
Cs	ppm	0.1	1.45	1.39	*1.06*	1.36	1.41	*-0.90*
Ba	ppm	3	8.99	8.86	*0.36*	9.08	9.08	*0.00*
Ba	ppm	3	1.92	1.92	*0.00*	1.87	1.85	*0.27*
La	ppm	0.05	5.76	5.6	*0.70*	5.63	5.7	*-0.31*
Ce	ppm	0.05	0.908	0.87	*1.069*	0.863	0.855	*0.233*
Pr	ppm	0.01	5.8	5.61	*0.8*	5.6	5.8	*-0.7*
Nd	ppm	0.05	0.955	0.881	*2.015*	0.902	0.929	*-0.737*
Sm	ppm	0.01	5.4	5.3	*0.5*	4.4	4.6	*-1.1*
Eu	ppm	0.005	0.48	0.46	*1.06*	0.43	0.42	*0.59*
Gd	ppm	0.01	< 0.5	< 0.5	-	1.6	< 0.5	-
Tb	ppm	0.01	0.07	0.07	*0.00*	0.06	0.06	*0.00*
Dy	ppm	0.01	< 3	< 3	-	< 3	< 3	-
Ho	ppm	0.01	< 0.1	< 0.1	-	< 0.1	< 0.1	-
Er	ppm	0.01	1.71	1.72	*-0.15*	1.43	1.42	*0.18*
Tm	ppm	0.005	0.65	0.65	*0.00*	0.57	0.56	*0.44*
Bi	ppm	0.1	2.3	< 0.5	-	4.1	< 0.5	-

Appendix I

Whole-Rock Geochemistry of Sulfide-Sulfates – Tinakula Deposit

Contents of this file:

1. Supplemental Figures

   Fig. I1: Box and whisker plots of whole-rock geochemistry of chimney samples (sulfide-sulfates) from the Tinakula deposit, including ROV grab samples and drillcore

2. Supplemental Tables:

   Table I1: Whole-rock geochemistry of ROV grab samples (sulfide-sulfates) from the Tinakula deposit

   Table I2: Whole-rock geochemistry of drillcore samples (sulfide-sulfates) from the Tinakula deposit

   Table I3: Precision and accuracy of whole-rock geochemical data (standards)

   Table I4: Precision of whole-rock geochemical data (duplicates)

Notes:

D.L. = detection limit
< = below detection limit
> = above detection limit
- = not analyzed
% Acc = percent accuracy
RSD = relative standard deviation (ratio of the standard deviation to the mean)
Rel % Diff = relative % difference (absolute value of the change in value divided by the average)

1. Supplemental Figures

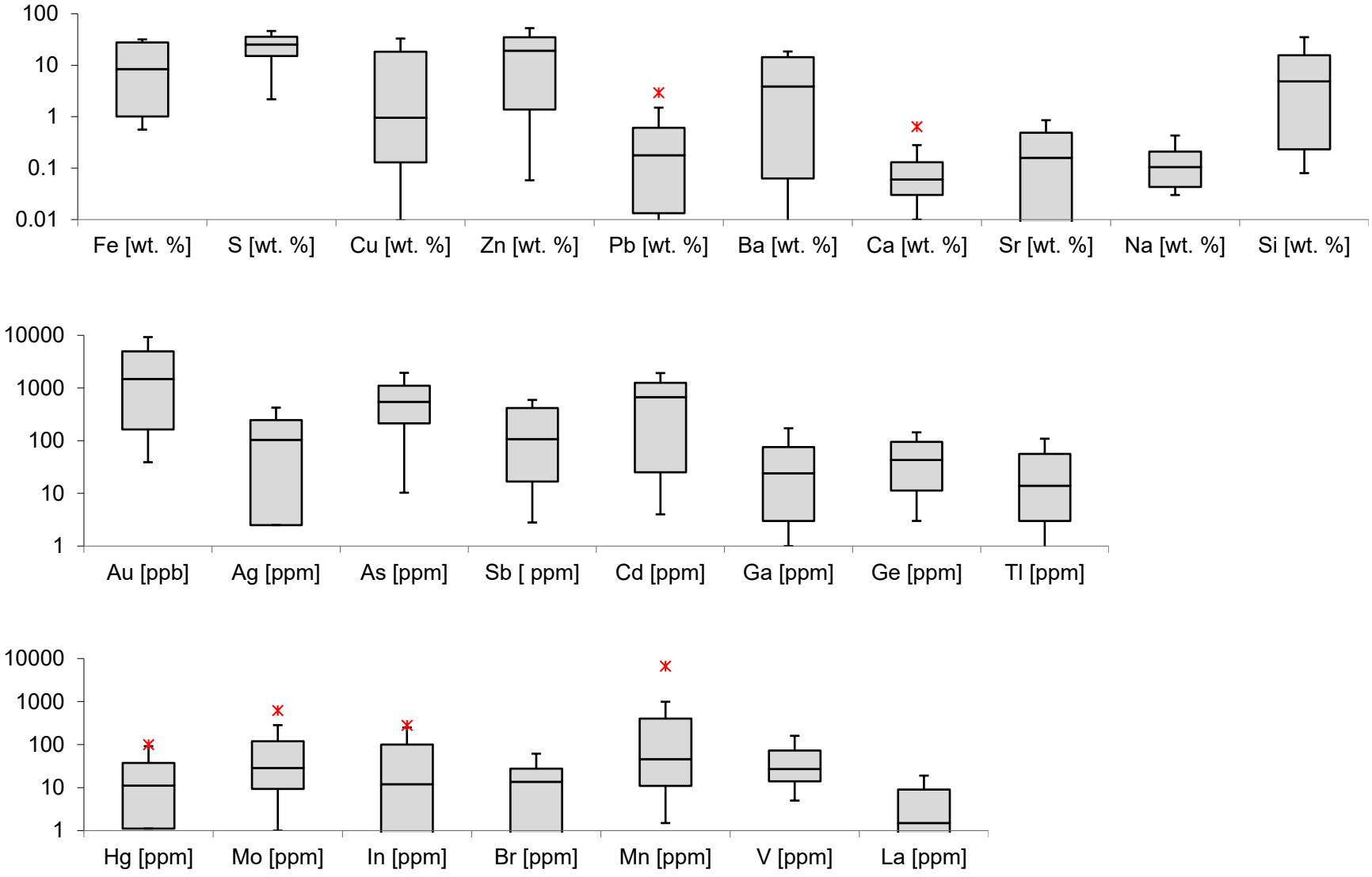


Fig. I1. Box-and-whisker plots of major and trace elements of chimney samples (sulfide-sulfates) from the Tinakula deposit (n = 30), plotted on a logarithmic scale; the top of the upper box represents the 90th percentile of data, the bottom of the lower box represents the 10th percentile, the middle line represents the median value, the error bars represent the range of data, and outliers are indicated by stars (*).

2. Supplemental Tables

Table I1. Whole-rock geochemistry of ROV grab samples (sulfide-sulfates) from the Tinakula deposit

	Total S	Au	Fe	Cu*	Mo	In	Ni	Bi	Co	Zn**	Cd	Ga	Ge	Se	Tl	Pb***
Units	%	ppb	%	ppm	ppm	ppm	ppm	ppm	ppm	ppm	ppm	ppm	ppm	ppm	ppm	ppm
Detection Limit	0.01	2	0.01	2	1	0.2	10	2	0.2	50	2	0.2	0.7	0.8	0.1	0.8
Method	CS	INAA	INAA	FUS-MS-Na2O2	FUS-MS-Na2O2	FUS-MS-Na2O2	FUS-MS-Na2O2	FUS-MS-Na2O2	FUS-MS-Na2O2	INAA	FUS-MS-Na2O2	FUS-MS-Na2O2	FUS-MS-Na2O2	FUS-MS-Na2O2	FUS-MS-Na2O2	FUS-MS-Na2O2
GMA13_002	19.5	243	0.66	1190	10	6	< 10	< 2	< 0.2	228000	729	4	58	9	9	2030
GMA13_004	34.6	2620	18.90	67600	30	42	< 10	< 2	3	217000	895	91	99	11	54	3790
GMA13_008	10.2	221	1.39	472	10	2	< 10	< 2	6	33900	20	9	22	5	6	3890
GMA13_010	28.4	4520	11.90	113000	73	193	< 10	< 2	< 0.2	237000	1020	76	64	9	14	1400
GMA13_012	22.6	191	2.12	1180	2	< 0.2	< 10	< 2	< 0.2	261000	147	2	76	10	25	3780
GMA13_017A	2.2	95	2.60	96	9	< 0.2	< 10	< 2	3	760	4	3	3	1	14	1840
GMA13_019A	26.9	906	3.87	2660	15	7	< 10	< 2	< 0.2	343000	1070	10	96	14	24	4690
GMA13_021	32.8	1350	27.30	166000	123	87	< 10	< 2	< 0.2	10700	44	41	13	7	57	697
GMA13_022	23.5	39	< 0.01	5060	1	< 0.2	< 10	< 2	< 0.2	337000	1070	2	109	14	3	1500
GMA13_024	46.3	5370	31.80	8680	10	< 0.2	< 10	< 2	1	30200	280	24	12	7	5	1500
GMA13_029	20.5	402	0.62	1190	5	< 0.2	< 10	< 2	< 0.2	214000	757	2	20	10	3	4080
GMA13_031	25.4	3970	7.35	47600	103	106	< 10	< 2	< 0.2	244000	1040	122	76	12	33	2070
GMA13_032	32.6	7270	8.61	6330	32	< 0.2	< 10	< 2	2	454000	1030	8	91	21	109	2650
GMA13_034	37.5	829	28.80	122000	106	34	< 10	< 2	< 0.2	4750	17	7	36	9	12	245
GMA13_038	34.4	124	26.30	270000	65	280	< 10	< 2	4	39300	280	40	11	10	1	70
GMA13_040	19.8	4270	2.10	8070	110	27	10	< 2	< 0.2	271000	1120	65	51	12	8	5300
GMA13_042	21.9	54	0.56	4900	11	5	10	< 2	< 0.2	380000	1090	3	92	20	10	29300
GMA13_045	25.2	2440	13.80	1530	11	< 0.2	10	< 2	< 0.2	37500	30	1	29	6	16	23700
GMA13_046	35.9	862	27.80	223000	27	56	< 10	< 2	< 0.2	30700	121	16	24	9	8	341
GMA13_048	32.1	9260	25.00	330000	620	243	< 10	< 2	< 0.2	580	7	5	7	8	< 0.1	18
GMA13_049	29.0	2060	16.90	155000	21	77	< 10	< 2	< 0.2	164000	828	75	83	13	49	2310
GMA13_050	33.6	5150	15.90	141000	82	107	< 10	< 2	< 0.2	290000	1540	172	73	20	8	410
GMA13_052	22.3	2980	7.80	6140	125	2	< 10	< 2	< 0.2	265000	1160	61	41	13	28	4310
GMA13_058	22.6	7810	7.72	2210	16	8	20	< 2	< 0.2	88100	439	7	24	10	15	6800
GMA13-060	8.0	247	2.09	216	8	< 0.2	< 10	< 2	1	3840	< 2	4	1	1	10	1250
GMA13_061	21.1	3100	5.47	5450	75	1	20	< 2	< 0.2	224000	762	29	35	12	61	6400
GMA13_062	27.8	4240	6.67	22200	23	54	10	< 2	< 0.2	351000	1770	141	75	15	17	1470

*Cu values >10000 measured by FUS-NA2O2 (D.L. 50 ppm)

**Zn values >100000 measured by FUS-NA2O2 (D.L. 100 ppm)

***Pb values >5000 measured by FUS-NA202 (D.L. 100 ppm)

Table I1. Continued

	Hg	As	Sb	Ag	Te	Sn	W	Br	Ba	Ca	Sr	Mg	Mn	K	Na	Si
Units	ppb	ppm	ppm	ppm	ppm	ppm	ppm	ppm	ppm	%	ppm	%	ppm	%	%	%
Detection Limit	5	0.5	0.1	5	6	0.5	0.7	0.5	50	0.01	3	0.01	3	0.1	0.01	0.01
Method	1G	INAA	INAA	INAA	FUS-MS-Na2O2	FUS-MS-Na2O2	FUS-MS-Na2O2	INAA	INAA	FUS-Na2O2	FUS-MS-Na2O2	FUS-Na2O2	FUS-MS-Na2O2	FUS-Na2O2	INAA	FUS-Na2O2
GMA13_002	16300	329	108.0	146	< 6	< 0.5	1	16.0	145000	0.02	3190	< 0.01	47	< 0.1	0.07	5.41
GMA13_004	95200	946	178.0	68	< 6	< 0.5	1	21.7	28600	0.03	1430	< 0.01	44	< 0.1	0.12	1.97
GMA13_008	25200	221	47.1	56	< 6	< 0.5	10	19.8	154000	0.64	5060	0.27	272	< 0.1	0.43	12.20
GMA13_010	17800	375	208.0	251	< 6	< 0.5	1	61.6	27200	0.03	1240	< 0.01	53	< 0.1	0.20	6.13
GMA13_012	18400	518	9.0	147	< 6	< 0.5	< 0.7	15.7	152000	0.13	6700	< 0.01	79	< 0.1	0.06	0.24
GMA13_017A	1860	123	52.3	28	< 6	< 0.5	1	13.5	17500	0.01	863	< 0.01	45	< 0.1	0.11	35.10
GMA13_019A	7770	631	114.0	196	< 6	< 0.5	5	< 0.5	73400	0.06	2140	< 0.01	20	< 0.1	0.10	4.85
GMA13_021	5930	760	82.7	54	< 6	1	< 0.7	31.2	360	0.03	11	0.04	71	< 0.1	0.25	6.78
GMA13_022	12300	834	39.5	146	< 6	< 0.5	2	19.8	141000	0.07	2980	< 0.01	9	< 0.1	0.09	< 0.01
GMA13_024	39500	267	108.0	190	< 6	< 0.5	< 0.7	< 0.5	36500	0.09	2250	< 0.01	1100	< 0.1	0.03	0.17
GMA13_029	27700	172	159.0	120	< 6	< 0.5	< 0.7	< 0.5	169000	0.08	7690	< 0.01	29	< 0.1	0.05	1.37
GMA13_031	9880	644	250.0	98	< 6	9	3	34.1	90400	0.05	2960	< 0.01	490	< 0.1	0.20	3.59
GMA13_032	30400	805	594.0	250	< 6	< 0.5	< 0.7	20.1	4560	0.03	110	< 0.01	346	< 0.1	0.14	3.57
GMA13_034	5010	384	19.0	< 5	< 6	1	1	23.2	18500	0.01	615	< 0.01	513	< 0.1	0.15	2.92
GMA13_038	989	97	15.8	52	< 6	17	< 0.7	11.3	580	< 0.01	< 3	0.01	< 3	< 0.1	0.14	0.70
GMA13_040	6480	425	179.0	124	< 6	4	1	28.3	91500	0.06	2730	< 0.01	227	< 0.1	0.21	9.13
GMA13_042	14000	1170	132.0	198	< 6	< 0.5	< 0.7	26.0	75200	0.05	1820	< 0.01	24	< 0.1	0.14	4.49
GMA13_045	15100	708	130.0	229	< 6	< 0.5	< 0.7	15.1	135000	0.07	6020	< 0.01	56	< 0.1	0.05	4.42
GMA13_046	22300	559	62.2	70	< 6	17	< 0.7	13.7	520	0.04	< 3	< 0.01	32	< 0.1	0.05	0.09
GMA13_048	81	10	2.8	32	< 6	10	13	9.9	440	0.04	5	< 0.01	19	< 0.1	0.04	0.56
GMA13_049	4410	719	120.0	64	< 6	6	2	16.8	4290	0.05	136	< 0.01	23	< 0.1	0.18	5.60
GMA13_050	3910	546	166.0	104	< 6	18	< 0.7	< 0.5	< 50	0.06	5	< 0.01	25	< 0.1	0.08	0.08
GMA13_052	61800	828	272.0	82	< 6	< 0.5	1	44.9	64000	0.16	4490	< 0.01	6660	< 0.1	0.26	6.01
GMA13_058	12400	518	489.0	424	< 6	< 0.5	< 0.7	20.4	185000	0.13	8530	< 0.01	427	< 0.1	0.09	0.23
GMA13-060	69900	99	39.4	36	< 6	< 0.5	1	14.7	286000	0.20	5410	0.05	82	< 0.1	0.35	18.80
GMA13_061	25700	615	238.0	120	< 6	1	< 0.7	< 0.5	84800	0.09	3940	< 0.01	194	< 0.1	0.10	9.71
GMA13_062	> 100000	550	211.0	142	< 6	60	6	20.9	63600	0.03	1790	< 0.01	28	< 0.1	0.05	2.88

Table I1. Continued

	Al	Ti	V	P	Cr	Ir	B	Be	Cs	Li	Rb	Nb	Ta	U	Hf	Th
Units	%	%	ppm	%	ppm	ppb	ppm	ppm	ppm	ppm	ppm	ppm	ppm	ppm	ppm	ppm
Detection Limit	0.01	0.01	5	0.005	5	5	10	4	0.1	3	0.4	2.4	0.2	0.1	1	0.1
Method	FUS-Na2O2	FUS-Na2O2	FUS-MS-Na2O2	FUS-Na2O2	INAA	INAA	FUS-MS-Na2O2	FUS-MS-Na2O2	FUS-MS-Na2O2	FUS-MS-Na2O2	FUS-MS-Na2O2	FUS-MS-Na2O2	FUS-MS-Na2O2	FUS-MS-Na2O2	INAA	FUS-MS-Na2O2
GMA13_002	< 0.01	< 0.01	29	< 0.005	< 5	< 5	< 10	< 4	< 0.1	< 3	< 0.4	< 2.4	< 0.2	< 0.1	< 1	< 0.1
GMA13_004	0.06	< 0.01	33	0.013	< 5	< 5	< 10	< 4	< 0.1	< 3	< 0.4	< 2.4	< 0.2	1	< 1	< 0.1
GMA13_008	1.79	0.11	109	0.019	< 5	< 5	20	< 4	< 0.1	< 3	2	< 2.4	< 0.2	2	< 1	1
GMA13_010	0.05	< 0.01	37	0.023	< 5	< 5	< 10	< 4	2	< 3	2	< 2.4	< 0.2	< 0.1	< 1	< 0.1
GMA13_012	< 0.01	< 0.01	31	< 0.005	< 5	< 5	< 10	< 4	< 0.1	< 3	1	< 2.4	< 0.2	< 0.1	< 1	< 0.1
GMA13_017A	0.01	< 0.01	34	< 0.005	< 5	< 5	< 10	< 4	< 0.1	< 3	1	< 2.4	< 0.2	2	< 1	< 0.1
GMA13_019A	0.02	< 0.01	26	< 0.005	< 5	< 5	< 10	< 4	1	< 3	1	< 2.4	< 0.2	< 0.1	< 1	< 0.1
GMA13_021	0.43	< 0.01	75	0.03	< 5	< 5	20	< 4	5	< 3	1	< 2.4	< 0.2	< 0.1	< 1	< 0.1
GMA13_022	< 0.01	< 0.01	27	< 0.005	< 5	< 5	< 10	< 4	< 0.1	< 3	1	< 2.4	< 0.2	< 0.1	< 1	< 0.1
GMA13_024	0.01	< 0.01	30	0.007	< 5	< 5	20	< 4	3	< 3	1	< 2.4	< 0.2	< 0.1	< 1	< 0.1
GMA13_029	0.02	< 0.01	27	< 0.005	< 5	< 5	< 10	< 4	< 0.1	< 3	1	< 2.4	< 0.2	< 0.1	< 1	< 0.1
GMA13_031	0.06	< 0.01	36	0.014	< 5	< 5	< 10	< 4	< 0.1	< 3	1	< 2.4	3.0	< 0.1	< 1	2
GMA13_032	0.04	< 0.01	21	< 0.005	< 5	< 5	< 10	< 4	6	< 3	4	< 2.4	< 0.2	< 0.1	< 1	< 0.1
GMA13_034	0.15	< 0.01	39	0.029	< 5	< 5	< 10	< 4	2	< 3	3	< 2.4	< 0.2	< 0.1	< 1	< 0.1
GMA13_038	0.41	< 0.01	53	0.047	< 5	< 5	20	< 4	< 0.1	< 3	1	< 2.4	< 0.2	< 0.1	< 1	< 0.1
GMA13_040	0.17	< 0.01	59	0.012	< 5	< 5	10	< 4	< 0.1	< 3	1	< 2.4	< 0.2	1	< 1	< 0.1
GMA13_042	0.01	< 0.01	15	< 0.005	< 5	< 5	< 10	< 4	< 0.1	< 3	1	< 2.4	< 0.2	< 0.1	< 1	< 0.1
GMA13_045	0.02	< 0.01	17	0.007	< 5	< 5	< 10	< 4	1	< 3	< 0.4	< 2.4	< 0.2	1	< 1	< 0.1
GMA13_046	0.04	< 0.01	14	0.041	< 5	< 5	20	< 4	< 0.1	< 3	< 0.4	< 2.4	< 0.2	1	< 1	< 0.1
GMA13_048	0.02	< 0.01	20	0.059	< 5	< 5	< 10	< 4	< 0.1	< 3	< 0.4	< 2.4	< 0.2	< 0.1	< 1	1
GMA13_049	0.20	< 0.01	33	0.029	< 5	< 5	10	< 4	< 0.1	< 3	< 0.4	< 2.4	< 0.2	1	< 1	< 0.1
GMA13_050	0.03	< 0.01	21	0.024	< 5	< 5	20	< 4	< 0.1	< 3	< 0.4	< 2.4	< 0.2	3	< 1	< 0.1
GMA13_052	0.07	< 0.01	87	0.153	< 5	< 5	20	< 4	1	< 3	2	< 2.4	< 0.2	5	< 1	< 0.1
GMA13_058	< 0.01	< 0.01	14	< 0.005	< 5	< 5	< 10	< 4	< 0.1	< 3	< 0.4	< 2.4	< 0.2	< 0.1	< 1	< 0.1
GMA13-060	0.26	0.02	19	< 0.005	69	< 5	< 10	< 4	< 0.1	< 3	1	< 2.4	< 0.2	1	< 1	< 0.1
GMA13_061	0.34	< 0.01	26	< 0.005	< 5	< 5	< 10	< 4	< 0.1	< 3	1	< 2.4	< 0.2	< 0.1	< 1	< 0.1
GMA13_062	0.05	< 0.01	17	< 0.005	< 5	< 5	< 10	< 4	< 0.1	< 3	1	4	10	1	< 1	1

Table I1. Continued

	Sc	Y	La	Ce	Pr	Nd	Sm	Eu	Gd	Tb	Dy	Ho	Er	Tm	Yb	Lu	Mass
Units	ppm	ppm	ppm	ppm	ppm	ppm	ppm	ppm	ppm	ppm	ppm	ppm	ppm	ppm	ppm	ppm	g
Detection Limit	0.1	0.1	0.4	0.8	0.1	0.4	0.1	0.1	0.1	0.1	0.3	0.2	0.1	0.1	0.1	0.05	
Method	INAA	FUS-MS-Na2O2	FUS-MS-Na2O2	FUS-MS-Na2O2	FUS-MS-Na2O2	FUS-MS-Na2O2	FUS-MS-Na2O2	FUS-MS-Na2O2	FUS-MS-Na2O2	FUS-MS-Na2O2	FUS-MS-Na2O2	FUS-MS-Na2O2	FUS-MS-Na2O2	FUS-MS-Na2O2	FUS-MS-Na2O2	INAA	INAA
GMA13_002	< 0.1	< 0.1	1	< 0.8	< 0.1	1	< 0.1	< 0.1	< 0.1	< 0.1	< 0.3	< 0.2	< 0.1	< 0.1	4	< 0.05	2.41
GMA13_004	< 0.1	< 0.1	< 0.4	< 0.8	< 0.1	2	< 0.1	< 0.1	< 0.1	< 0.1	< 0.3	< 0.2	< 0.1	< 0.1	1	< 0.05	2.28
GMA13_008	6.6	2	1	< 0.8	< 0.1	2	< 0.1	< 0.1	< 0.1	< 0.1	< 0.3	< 0.2	< 0.1	< 0.1	4	< 0.05	1.93
GMA13_010	< 0.1	< 0.1	< 0.4	< 0.8	< 0.1	1	< 0.1	< 0.1	< 0.1	< 0.1	< 0.3	< 0.2	< 0.1	< 0.1	< 0.1	< 0.05	1.70
GMA13_012	< 0.1	< 0.1	< 0.4	< 0.8	< 0.1	1	< 0.1	< 0.1	< 0.1	< 0.1	< 0.3	< 0.2	< 0.1	< 0.1	1	< 0.05	2.36
GMA13_017A	< 0.1	< 0.1	< 0.4	< 0.8	< 0.1	1	< 0.1	< 0.1	< 0.1	< 0.1	< 0.3	< 0.2	< 0.1	< 0.1	2	< 0.05	1.24
GMA13_019A	< 0.1	< 0.1	7	3	< 0.1	1	< 0.1	< 0.1	< 0.1	< 0.1	< 0.3	< 0.2	< 0.1	< 0.1	< 0.1	< 0.05	1.98
GMA13_021	< 0.1	< 0.1	< 0.4	< 0.8	< 0.1	1	< 0.1	< 0.1	< 0.1	< 0.1	< 0.3	< 0.2	< 0.1	< 0.1	< 0.1	< 0.05	2.01
GMA13_022	< 0.1	< 0.1	7	2	< 0.1	1	< 0.1	< 0.1	< 0.1	< 0.1	< 0.3	< 0.2	< 0.1	< 0.1	3	< 0.05	2.55
GMA13_024	< 0.1	< 0.1	1	< 0.8	< 0.1	1	< 0.1	< 0.1	< 0.1	< 0.1	< 0.3	< 0.2	< 0.1	< 0.1	< 0.1	< 0.05	3.32
GMA13_029	< 0.1	< 0.1	3	3	< 0.1	2	< 0.1	< 0.1	< 0.1	< 0.1	< 0.3	< 0.2	< 0.1	< 0.1	2	< 0.05	3.06
GMA13_031	< 0.1	< 0.1	5	3	< 0.1	4	< 0.1	< 0.1	< 0.1	< 0.1	< 0.3	< 0.2	< 0.1	< 0.1	< 0.1	< 0.05	2.33
GMA13_032	< 0.1	< 0.1	< 0.4	< 0.8	< 0.1	1	< 0.1	< 0.1	< 0.1	< 0.1	< 0.3	< 0.2	< 0.1	< 0.1	< 0.1	< 0.05	2.37
GMA13_034	< 0.1	< 0.1	< 0.4	< 0.8	< 0.1	1	< 0.1	< 0.1	< 0.1	< 0.1	< 0.3	< 0.2	< 0.1	< 0.1	2	< 0.05	2.56
GMA13_038	< 0.1	< 0.1	< 0.4	< 0.8	< 0.1	1	< 0.1	< 0.1	< 0.1	< 0.1	< 0.3	< 0.2	< 0.1	< 0.1	< 0.1	< 0.05	2.75
GMA13_040	< 0.1	< 0.1	9	8	< 0.1	1	< 0.1	< 0.1	< 0.1	< 0.1	< 0.3	< 0.2	< 0.1	< 0.1	1	< 0.05	1.96
GMA13_042	< 0.1	< 0.1	6	5	< 0.1	< 0.4	< 0.1	< 0.1	< 0.1	< 0.1	< 0.3	< 0.2	< 0.1	< 0.1	2	< 0.05	2.20
GMA13_045	< 0.1	< 0.1	12	7	< 0.1	< 0.4	< 0.1	< 0.1	< 0.1	< 0.1	< 0.3	< 0.2	< 0.1	< 0.1	3	< 0.05	2.67
GMA13_046	< 0.1	< 0.1	< 0.4	< 0.8	< 0.1	< 0.4	< 0.1	< 0.1	< 0.1	< 0.1	< 0.3	< 0.2	< 0.1	< 0.1	< 0.1	< 0.05	2.97
GMA13_048	< 0.1	< 0.1	< 0.4	2	< 0.1	2	< 0.1	< 0.1	< 0.1	< 0.1	< 0.3	< 0.2	< 0.1	< 0.1	< 0.1	< 0.05	2.74
GMA13_049	< 0.1	< 0.1	2	5	< 0.1	2	< 0.1	< 0.1	< 0.1	< 0.1	< 0.3	< 0.2	< 0.1	< 0.1	< 0.1	< 0.05	2.03
GMA13_050	< 0.1	< 0.1	< 0.4	< 0.8	< 0.1	< 0.4	< 0.1	< 0.1	< 0.1	< 0.1	< 0.3	< 0.2	< 0.1	< 0.1	< 0.1	< 0.05	2.26
GMA13_052	< 0.1	< 0.1	1	2	< 0.1	< 0.4	< 0.1	< 0.1	< 0.1	< 0.1	< 0.3	< 0.2	< 0.1	< 0.1	3	< 0.05	2.29
GMA13_058	< 0.1	< 0.1	10	8	< 0.1	1	< 0.1	< 0.1	< 0.1	< 0.1	< 0.3	< 0.2	< 0.1	< 0.1	1	< 0.05	2.70
GMA13-060	0.6	< 0.1	7	5	0.3	1	0.9	0.9	2.8	< 0.1	< 0.3	< 0.2	0.2	< 0.1	7	< 0.05	7.17
GMA13_061	< 0.1	< 0.1	6	5	< 0.1	< 0.4	< 0.1	< 0.1	< 0.1	< 0.1	< 0.3	< 0.2	< 0.1	< 0.1	1	< 0.05	2.28
GMA13_062	< 0.1	< 0.1	6	7	< 0.1	2	< 0.1	< 0.1	< 0.1	< 0.1	< 0.3	< 0.2	< 0.1	< 0.1	2	< 0.05	2.37

Table I2. Whole-rock geochemistry of drillcore samples (sulfide-sulfates) from the Tinakula deposit

	Total S	Au	Fe	Cu*	Mo	In	Ni	Bi	Co	Zn**	Cd	Ga	Ge	Se	Tl	Pb***
Units	%	ppb	%	ppm	ppm	ppm	ppm	ppm	ppm	ppm	ppm	ppm	ppm	ppm	ppm	ppm
Detection Limit	0.01	2	0.01	2	1	0	10	2	0.2	50	2	0	1	1	0	1
Method	CS	INAA	INAA	FUS-MS-Na2O2	FUS-MS-Na2O2	FUS-MS-Na2O2	FUS-MS-Na2O2	FUS-MS-Na2O2	FUS-MS-Na2O2	INAA	FUS-MS-Na2O2	FUS-MS-Na2O2	FUS-MS-Na2O2	FUS-MS-Na2O2	FUS-MS-Na2O2	FUS-MS-Na2O2
MA13_010	21.0	900	2.21	20000	36	49	< 10	< 2	< 0.2	311000	951	48	40	12	7	308
MA13_011	13.4	152	0.66	5610	8	< 0.2	< 10	< 2	< 0.2	124000	346	< 0.2	55	9	10	1780
MA13_012	20.5	3190	3.45	4870	27	3	< 10	< 2	2	348000	1270	33	144	16	18	854
MA13_013	13.7	1220	11.70	54000	17	48	< 10	< 2	7	20900	77	33	11	8	3	97
MA13_028	35.9	2100	28.50	46600	77	40	< 10	< 2	< 0.2	27900	131	20	15	6	33	549
MA13_029	24.5	1750	6.54	10400	19	5	< 10	< 2	< 0.2	313000	1130	58	61	9	75	4230
MA13_030	22.2	356	0.91	8570	22	< 0.2	< 10	< 2	< 0.2	356000	1610	3	66	12	< 0.1	539
MA13_031	19.5	307	14.00	137000	224	80	< 10	< 2	1	42400	195	33	10	9	17	81
MA13_032	17.8	2050	8.83	16000	40	22	< 10	< 2	3	67200	211	23	50	7	32	5100
MA13_041	31.5	1440	18.90	173000	47	45	< 10	< 2	< 0.2	170000	610	32	61	14	1	485
MA13_043	27.3	1520	8.41	4740	32	11	< 10	< 2	< 0.2	287000	916	31	70	13	13	265
MA13_048	36.4	2040	26.70	79000	30	49	< 10	< 2	1	51100	234	43	23	9	72	1770
MA13_065	22.5	3720	1.96	6610	11	46	< 10	< 2	1	344000	1210	44	109	14	6	2060
MA13_066	14.0	1950	2.98	2300	20	3	< 10	< 2	< 0.2	86900	204	4	44	7	30	14800
MA13_098	35.4	279	28.00	33200	43	13	< 10	< 2	< 0.2	31500	92	8	18	5	3	371
P0010	31.7	552	22.20	78600	143	30	< 10	< 2	2	51600	263	24	32	12	49	217
P0011	30.2	203	23.90	66600	102	7	< 10	< 2	21	6540	23	4	28	10	12	77
P0043	27.5	608	3.09	2810	15	< 0.2	< 10	< 2	< 0.2	526000	1920	52	42	17	18	2240

*Cu values >10000 measured by FUS-NA2O2 (D.L. 50 ppm)

**Zn values >100000 measured by FUS-NA2O2 (D.L. 100 ppm)

***Pb values >5000 measured by FUS-NA202 (D.L. 100 ppm)

Table I2. Continued

	Hg	As	Sb	Ag	Te	Sn	W	Br	Ba	Ca	Sr	Mg	Mn	K	Na	Si
Units	ppb	ppm	ppm	ppm	ppm	ppm	ppm	ppm	ppm	%	ppm	%	ppm	%	%	%
Detection Limit	5	1	0.1	5	6	0.5	0.7	0.5	50	0.01	3	0.01	3	0.1	0.01	0.01
Method	1G	INAA	INAA	INAA	FUS-MS-Na2O2	FUS-MS-Na2O2	FUS-MS-Na2O2	INAA	INAA	FUS-Na2O2	FUS-MS-Na2O2	FUS-Na2O2	FUS-MS-Na2O2	FUS-Na2O2	INAA	FUS-Na2O2
MA13_010	1730	309	21.4	< 5	< 6	14	8	< 0.5	70000	0.08	751	< 0.01	44	< 0.1	0.08	8.15
MA13_011	7250	1520	105.0	160	< 6	35	6	< 0.5	128000	0.10	1960	0.03	11	< 0.1	0.06	11.80
MA13_012	9010	1340	538.0	111	< 6	< 0.5	16	< 0.5	4440	0.09	133	< 0.01	40	< 0.1	0.17	16.80
MA13_013	1770	441	19.4	< 5	< 6	1	2	6.5	860	0.09	6	0.08	12	0.8	0.26	25.50
MA13_028	4060	1440	106.0	23	< 6	< 0.5	< 0.7	11.3	740	0.07	4	< 0.01	81	< 0.1	0.13	9.21
MA13_029	17300	777	381.0	262	< 6	< 0.5	1	18.5	40700	0.08	1950	< 0.01	54	< 0.1	0.13	7.75
MA13_030	13700	659	530.0	401	< 6	3	5	< 0.5	94200	0.04	1740	< 0.01	11	< 0.1	0.10	1.65
MA13_031	1230	210	20.4	< 5	< 6	2	6	< 0.5	6370	0.07	180	0.06	23	0.4	0.14	16.20
MA13_032	23300	722	94.9	72	< 6	< 0.5	7	< 0.5	64300	0.13	2030	0.01	79	< 0.1	0.21	16.50
MA13_041	37600	583	235.0	74	< 6	24	14	19.2	17500	0.04	413	0.03	8	< 0.1	0.07	0.97
MA13_043	5530	311	46.0	39	< 6	< 0.5	1	< 0.5	81600	0.09	2160	< 0.01	48	< 0.1	0.03	0.11
MA13_048	9840	1940	107.0	59	< 6	54	6	19.4	8310	0.07	318	< 0.01	49	< 0.1	0.17	4.01
MA13_065	5900	933	99.3	135	< 6	1	5	< 0.5	81900	0.04	2190	< 0.01	33	< 0.1	0.06	4.27
MA13_066	37000	429	97.3	148	< 6	< 0.5	11	19.6	112000	0.16	3950	0.01	55	< 0.1	0.18	13.40
MA13_098	13100	242	30.4	< 5	< 6	< 0.5	< 0.7	< 0.5	1370	0.05	17	< 0.01	7	< 0.1	0.08	10.50
P0010	1070	306	13.7	< 5	< 6	11	8	< 0.5	9740	0.02	303	< 0.01	192	< 0.1	0.04	10.90
P0011	579	299	5.7	< 5	< 6	< 0.5	4	< 0.5	7800	0.11	147	0.01	48	0.2	0.14	12.70
P0043	14700	280	433.0	119	< 6	< 0.5	< 0.7	< 0.5	12100	0.06	837	0.01	43	< 0.1	0.04	4.51

Table I2. Continued

	Al	Ti	V	P	Cr	Ir	B	Be	Cs	Li	Rb	Nb	Ta	U	Hf	Th
Units	%	%	ppm	%	ppm	ppb	ppm	ppm	ppm	ppm	ppm	ppm	ppm	ppm	ppm	ppm
Detection Limit	0.01	0.01	5	0.005	5	5	10	4	0.1	3	0.4	2.4	0.2	0.1	1	0.1
Method	FUS-Na2O2	FUS-Na2O2	FUS-MS-Na2O2	FUS-Na2O2	INAA	INAA	FUS-MS-Na2O2	FUS-MS-Na2O2	FUS-MS-Na2O2	FUS-MS-Na2O2	FUS-MS-Na2O2	FUS-MS-Na2O2	FUS-MS-Na2O2	FUS-MS-Na2O2	INAA	FUS-MS-Na2O2
MA13_010	0.16	< 0.01	25	< 0.005	< 5	< 5	< 10	< 4	< 0.1	< 3	< 0.4	< 2.4	3	< 0.1	< 1	1
MA13_011	< 0.01	< 0.01	14	< 0.005	< 5	< 5	< 10	< 4	< 0.1	< 3	< 0.4	4	9	1	< 1	3
MA13_012	0.54	0.08	50	< 0.005	< 5	< 5	< 10	< 4	< 0.1	< 3	4	< 2.4	< 0.2	5	< 1	< 0.1
MA13_013	2.95	0.33	160	0.009	< 5	< 5	< 10	< 4	1	< 3	15	< 2.4	< 0.2	5	< 1	< 0.1
MA13_028	0.34	< 0.01	23	0.006	< 5	< 5	< 10	< 4	< 0.1	< 3	2	< 2.4	< 0.2	< 0.1	< 1	< 0.1
MA13_029	0.03	< 0.01	8	< 0.005	< 5	< 5	< 10	< 4	< 0.1	< 3	< 0.4	< 2.4	< 0.2	2	< 1	< 0.1
MA13_030	0.09	< 0.01	18	< 0.005	< 5	< 5	< 10	< 4	< 0.1	< 3	< 0.4	< 2.4	< 0.2	< 0.1	< 1	< 0.1
MA13_031	1.78	0.11	123	0.027	< 5	< 5	< 10	< 4	< 0.1	< 3	8	< 2.4	< 0.2	4	< 1	< 0.1
MA13_032	0.76	0.06	67	< 0.005	< 5	< 5	< 10	< 4	< 0.1	< 3	3	< 2.4	< 0.2	9	< 1	< 0.1
MA13_041	0.23	< 0.01	15	0.028	< 5	< 5	< 10	< 4	< 0.1	< 3	< 0.4	< 2.4	< 0.2	< 0.1	< 1	< 0.1
MA13_043	0.09	< 0.01	19	< 0.005	< 5	< 5	< 10	< 4	< 0.1	< 3	1	< 2.4	< 0.2	1	< 1	< 0.1
MA13_048	0.25	< 0.01	42	0.013	< 5	< 5	< 10	< 4	1	< 3	1	< 2.4	6.0	< 0.1	< 1	1
MA13_065	0.04	< 0.01	5	< 0.005	< 5	< 5	< 10	< 4	< 0.1	< 3	< 0.4	< 2.4	< 0.2	< 0.1	< 1	< 0.1
MA13_066	0.35	0.02	16	< 0.005	< 5	< 5	< 10	< 4	< 0.1	< 3	1	< 2.4	< 0.2	3	< 1	< 0.1
MA13_098	0.15	< 0.01	8	< 0.005	< 5	< 5	< 10	< 4	1	< 3	2	< 2.4	< 0.2	< 0.1	< 1	< 0.1
P0010	0.13	< 0.01	66	0.012	< 5	< 5	< 10	< 4	< 0.1	< 3	< 0.4	< 2.4	1	8	< 1	< 0.1
P0011	0.81	0.09	64	0.012	< 5	< 5	< 10	< 4	2	< 3	9	< 2.4	< 0.2	37	< 1	< 0.1
P0043	0.01	< 0.01	5	< 0.005	< 5	< 5	< 10	< 4	1	< 3	2	< 2.4	< 0.2	< 0.1	< 1	< 0.1

Table I2. Continued

	Sc	Y	La	Ce	Pr	Nd	Sm	Eu	Gd	Tb	Dy	Ho	Er	Tm	Yb	Lu	Mass
Units	ppm	ppm	ppm	ppm	ppm	ppm	ppm	ppm	ppm	ppm	ppm	ppm	ppm	ppm	ppm	ppm	g
Detection Limit	0.1	0.1	0.4	1	0.1	0	0.1	0.1	0.1	0.1	0.3	0.2	0.1	0.1	0	0.05	
Method	INAA	FUS-MS-Na2O2	FUS-MS-Na2O2	FUS-MS-Na2O2	FUS-MS-Na2O2	FUS-MS-Na2O2	FUS-MS-Na2O2	FUS-MS-Na2O2	FUS-MS-Na2O2	FUS-MS-Na2O2	FUS-MS-Na2O2	FUS-MS-Na2O2	FUS-MS-Na2O2	FUS-MS-Na2O2	FUS-MS-Na2O2	INAA	INAA
MA13_010	< 0.1	< 0.1	3	4	< 0.1	2	< 0.1	< 0.1	< 0.1	< 0.1	< 0.3	< 0.2	< 0.1	< 0.1	1	< 0.05	2.19
MA13_011	< 0.1	< 0.1	7	13	1	9	2	< 0.1	1	< 0.1	< 0.3	< 0.2	< 0.1	< 0.1	2	< 0.05	1.98
MA13_012	< 0.1	1	< 0.4	2	< 0.1	1	< 0.1	< 0.1	< 0.1	< 0.1	< 0.3	< 0.2	< 0.1	< 0.1	1	< 0.05	2.07
MA13_013	7.4	8	1	4	1	2	1	1	1	< 0.1	1	< 0.2	1.0	< 0.1	1	< 0.05	1.57
MA13_028	0.4	< 0.1	< 0.4	< 0.8	< 0.1	< 0.4	< 0.1	< 0.1	< 0.1	< 0.1	< 0.3	< 0.2	< 0.1	< 0.1	< 0.1	< 0.05	1.76
MA13_029	< 0.1	< 0.1	9	11	1	5	< 0.1	< 0.1	1	< 0.1	< 0.3	< 0.2	< 0.1	< 0.1	2	< 0.05	1.91
MA13_030	< 0.1	< 0.1	2	1	< 0.1	< 0.4	< 0.1	< 0.1	< 0.1	< 0.1	< 0.3	< 0.2	< 0.1	< 0.1	1	< 0.05	2.50
MA13_031	3.7	1	19	28	3	9	1	< 0.1	1	< 0.1	< 0.3	< 0.2	< 0.1	< 0.1	1	< 0.05	1.39
MA13_032	1.9	2	7	6	< 0.1	1	< 0.1	< 0.1	1	< 0.1	< 0.3	< 0.2	< 0.1	< 0.1	2	< 0.05	1.65
MA13_041	< 0.1	< 0.1	2	1	< 0.1	1	< 0.1	< 0.1	< 0.1	< 0.1	< 0.3	< 0.2	< 0.1	< 0.1	1	< 0.05	2.31
MA13_043	< 0.1	< 0.1	1	1	< 0.1	< 0.4	< 0.1	< 0.1	1	< 0.1	< 0.3	< 0.2	< 0.1	< 0.1	3	< 0.05	2.59
MA13_048	< 0.1	< 0.1	2	2	< 0.1	1	< 0.1	< 0.1	< 0.1	< 0.1	< 0.3	< 0.2	< 0.1	< 0.1	< 0.1	< 0.05	2.11
MA13_065	< 0.1	< 0.1	10	9	1	1	< 0.1	< 0.1	< 0.1	< 0.1	< 0.3	< 0.2	< 0.1	< 0.1	1	< 0.05	2.16
MA13_066	0.4	2	8	6	< 0.1	1	< 0.1	< 0.1	< 0.1	< 0.1	< 0.3	< 0.2	< 0.1	< 0.1	1	< 0.05	1.95
MA13_098	< 0.1	< 0.1	< 0.4	< 0.8	< 0.1	< 0.4	< 0.1	< 0.1	< 0.1	< 0.1	< 0.3	< 0.2	< 0.1	< 0.1	< 0.1	< 0.05	2.01
P0010	< 0.1	< 0.1	1	1	< 0.1	1	< 0.1	< 0.1	< 0.1	< 0.1	< 0.3	< 0.2	< 0.1	< 0.1	1	< 0.05	1.98
P0011	2.2	1	7	11	1	4	1	< 0.1	< 0.1	< 0.1	< 0.3	< 0.2	< 0.1	< 0.1	1	< 0.05	2.03
P0043	< 0.1	< 0.1	1	1	< 0.1	< 0.4	< 0.1	< 0.1	< 0.1	< 0.1	< 0.3	< 0.2	< 0.1	< 0.1	< 0.1	< 0.05	2.18

Table I3. Precision and accuracy of whole-rock geochemical data (standards)

			Accepted	Measured		Measured		Measured		
Element	Unit	D.L.	CCU-1c	CCU-1c (1)	*% Acc*	CCU-1c (2)	*% Acc*	CCU-1c (3)	*% Acc*	*% RSD*
Hg	ppb	5	-	28300	-	29000	-	28500	-	*1*
Total S	%	0.01	33.3	33.0	*0.9*	31.5	*5.4*	31.4	*5.7*	*2.8*
Cu	%	0.005	25.620	25.10	*2.03*	25.10	*2.03*	24.90	*2.81*	*0.46*
Al	%	0.01	-	0.14	-	0.13	-	0.15	-	*7.14*
As	ppm	5	34	21	*38*	25	*26*	34	*0*	*25*
B	ppm	10	-	< 10	-	< 10	-	70	-	-
Ba	ppm	3	-	5	-	16	-	20	-	*57*
Be	ppm	4	-	< 4	-	< 4	-	< 4	-	-
Bi	ppm	2	-	78	-	68	-	69	-	*8*
Ca	%	0.01	0.1072	0.11	*-2.61*	0.15	*-39.93*	0.21	*-95.90*	*32.13*
Cd	ppm	2	136	131	*4*	125	*8*	131	*4*	*3*
Ce	ppm	0.8	-	1	-	6	-	3	-	*75*
Co	ppm	0.2	-	18	-	16	-	17	-	*6*
Cr	ppm	30	-	50	-	30	-	< 30	-	*35*
Cs	ppm	0.1	-	1	-	< 0.1	-	< 0.1	-	-
Cu	ppm	2	256200	> 10000	-	> 10000	-	> 10000	-	-
Dy	ppm	0.3	-	< 0.3	-	< 0.3	-	< 0.3	-	-
Er	ppm	0.1	-	< 0.1	-	< 0.1	-	< 0.1	-	-
Eu	ppm	0.1	-	< 0.1	-	< 0.1	-	< 0.1	-	-
Fe	%	0.05	29.34	29.40	*-0.20*	29.40	*-0.20*	29.00	*1.16*	*0.79*
Ga	ppm	0.2	-	6	-	3	-	3	-	*43*
Gd	ppm	0.1	-	< 0.1	-	< 0.1	-	< 0.1	-	-
Ge	ppm	0.7	-	4	-	3	-	4	-	*16*
Ho	ppm	0.2	-	< 0.2	-	< 0.2	-	< 0.2	-	-
Hf	ppm	10	-	< 10	-	< 10	-	< 10	-	-
In	ppm	0.2	-	24	-	21	-	22	-	*7*
K	%	0.1	-	< 0.1	-	< 0.1	-	< 0.1	-	-
La	ppm	0.4	-	< 0.4	-	3	-	1	-	*71*
Li	ppm	3	-	4	-	< 3	-	3	-	*20*
Mg	%	0.01	0.6152	0.54	*12.22*	0.52	*15.47*	0.54	*12.22*	*2.17*
Mn	ppm	3	120	115	*4*	107	*11*	123	*-3*	*7*
Mo	ppm	1	20	21	*-5*	21	*-5*	22	*-10*	*3*
Nb	ppm	2.4	-	< 2.4	-	< 2.4	-	< 2.4	-	-
Nd	ppm	0.4	-	3	-	2	-	2	-	*25*
Ni	ppm	10	-	10	-	< 10	-	< 10	-	-
P	%	0.005	-	0.043	-	0.042	-	0.041	-	*2.381*
Pb	ppm	0.8	-	3590	-	3140	-	3320	-	*7*
Pr	ppm	0.1	-	< 0.1	-	< 0.1	-	< 0.1	-	-
Rb	ppm	0.4	-	1	-	< 0.4	-	1	-	*0*
S	%	0.01	33.3	> 20.0	-	> 20.0	-	> 20.0	-	-
Sb	ppm	2	-	8	-	12	-	5	-	*42*
Se	ppm	0.8	107	143	*-34*	129	*-21*	137	*-28*	*5*
Si	%	0.01	1.1779	1.22	*-3.57*	1.20	*-1.88*	1.25	*-6.12*	*2.06*
Sm	ppm	0.1	-	< 0.1	-	< 0.1		< 0.1	-	-
Sn	ppm	0.5	-	36	-	34	-	34	-	*3*
Sr	ppm	3	-	3	-	< 3	-	6	-	*47*
Ta	ppm	0.2	-	< 0.2	-	< 0.2	-	< 0.2	-	-
Tb	ppm	0.1	-	< 0.1	-	< 0.1	-	< 0.1	-	-
Te	ppm	6	-	25	-	20	-	22	-	*11*
Th	ppm	0.1	-	< 0.1	-	1	-	< 0.1	-	-
Ti	%	0.01	-	< 0.01	-	< 0.01	-	< 0.01	-	-
Tl	ppm	0.1	-	2	-	1	-	2	-	*35*
Tm	ppm	0.1	-	< 0.1	-	< 0.1	-	< 0.1	-	-
U	ppm	0.1	-	1	-	1	-	1	-	*0*
V	ppm	5	-	22	-	15	-	6	-	*56*
W	ppm	0.7	-	1	-	6	-	9	-	*76*
Y	ppm	0.1	-	1	-	1	-	1	-	*0*
Yb	ppm	0.1	-	< 0.1	-	< 0.1	-	< 0.1	-	-
Zn	ppm	30	39900	> 10000	-	> 10000	-	> 10000	-	-
Au	ppb	2	4940	4400	*11*	4130	*16*	4180	*15*	*3*
Ag	ppm	5	129	157	*-22*	131	*-2*	136	*-5*	*10*
As	ppm	0.5	34	33.0	*3*	31.2	*8*	44.3	*-30*	*20*
Ba	ppm	50	-	< 50	-	< 50	-	630	-	-

Table I3. Continued

Element	Unit	D.L.	Accepted CCU-1c	Measured CCU-1c (1)	% Acc	Measured CCU-1c (2)	% Acc	Measured CCU-1c (3)	% Acc	% RSD
Br	ppm	0.5	0.1072	< 0.5	-	< 0.5	-	< 0.5	-	-
Ca	%	1	-	< 1	-	< 1	-	< 1	-	-
Co	ppm	1	-	19	-	19	-	18	-	*3*
Cr	ppm	5	-	40	-	23	-	18	-	*43*
Cs	ppm	1	-	< 1	-	< 1	-	< 1	-	-
Fe	%	0.01	29.34	27.5	*6.27*	24.60	*16.16*	25.30	*-303.43*	*5.87*
Hf	ppm	1	-	< 1	-	< 1	-	< 1	-	-
Hg	ppm	1	-	16	-	14	-	18	-	*13*
Ir	ppb	5	-	< 5	-	< 5	-	< 5	-	-
Mo	ppm	1	20	< 1	-	< 1	-	< 1	-	-
Na	%	0.01	-	0.03	-	0.02	-	0.02	-	*24.74*
Ni	ppm	20	-	< 20	-	< 20	-	< 20	-	-
Rb	ppm	15	-	< 15	-	< 15	-	< 15	-	-
Sb	ppm	0.1	-	4.4	-	3.8	-	4.3	-	*7.7*
Sc	ppm	0.1	-	< 0.1	-	0.3	-	< 0.1	-	-
Se	ppm	3	107	128	-	103	-	120	-	*11*
Sn	%	0.02	-	< 0.02	-	< 0.02	-	< 0.02	-	-
Sr	%	0.05	-	< 0.05	-	< 0.05	-	< 0.05	-	-
Ta	ppm	0.5	-	< 0.5	-	< 0.5	-	< 0.5	-	-
Th	ppm	0.2	-	< 0.2	-	< 0.2	-	< 0.2	-	-
U	ppm	0.5	-	< 0.5	-	< 0.5	-	< 0.5	-	-
W	ppm	1	-	< 1	-	< 1	-	< 1	-	-
Zn	ppm	50	39900	33200	*17*	36000	*10*	37800	*-225007*	*6*
La	ppm	0.5	-	1.6	-	1.6	-	1.7	-	*3.5*
Ce	ppm	3	-	< 3	-	< 3	-	< 3	-	-
Nd	ppm	5	-	< 5	-	< 5	-	< 5	-	-
Sm	ppm	0.1	-	0.3	-	0.4	-	0.2	-	*33.3*
Eu	ppm	0.2	-	< 0.2	-	< 0.2	-	< 0.2	-	-
Tb	ppm	0.5	-	< 0.5	-	< 0.5	-	< 0.5	-	-
Yb	ppm	0.2	-	< 0.2	-	< 0.2	-	< 0.2	-	-
Lu	ppm	0.05	-	< 0.05	-	< 0.05	-	< 0.05	-	-

Table I3. Continued

			Accepted	Measured		Measured		Measured		
Element	Unit	D.L.	CZN-3	CZN-3 (1)	% Acc	CZN-3 (2)	% Acc	CNZ-3 (3)	% Acc	% RSD
Hg	ppb	5	5000	4750	*5*	4690	*6*	4540	*9*	*2*
Total S	%	0.01	-	31.3	-	28.7	-	29.4	-	*4.5*
Cu	%	0.005	0.685	-	-	-	-	-	-	-
Al	%	0.01	0.10	0.10	*0.00*	0.11	*-10.00*	0.09	*10.00*	*10.00*
As	ppm	5	390	349	*11*	424	*-9*	366	*6*	*10*
B	ppm	10	-	< 10	-	< 10	-	< 10	-	
Ba	ppm	3	-	20	-	27	-	17	-	*24*
Be	ppm	4	-	< 4	-	< 4	-	< 4	-	-
Bi	ppm	2	-	7	-	7	-	7	-	*0*
Ca	%	0.01	0.058	0.06	*-3.45*	0.08	*-37.93*	0.08	*-37.93*	*15.75*
Cd	ppm	2	2480	2390	*4*	2640	*-6*	2560	*-3*	*5*
Ce	ppm	0.8	-	12	-	16	-	15	-	*14*
Co	ppm	0.2	90.0	90	*0*	90	*0*	87	-	*2*
Cr	ppm	30	-	40	-	< 30	-	< 30	-	-
Cs	ppm	0.1	-	1	-	< 0.1	-	< 0.1	-	-
Cu	ppm	2	6850	7160	*-5*	6980	*-2*	6810	*1*	*3*
Dy	ppm	0.3	-	1	-	1	-	1	-	*0*
Er	ppm	0.1	-	1	-	1	-	1	-	*0*
Eu	ppm	0.1	-	< 0.1	-	< 0.1	-	< 0.1	-	-
Fe	%	0.05	9.97	9.82	*1.50*	9.79	*1.81*	9.72	*2.51*	*0.52*
Ga	ppm	0.2	-	10	-	9	-	9	-	*8*
Gd	ppm	0.1	-	1	-	1	-	1	-	*0*
Ge	ppm	0.7	-	3	-	1	-	3	-	*48*
Ho	ppm	0.2	-	< 0.2	-	< 0.2	-	< 0.2	-	-
Hf	ppm	10	-	< 10	-	< 10	-	< 10	-	-
In	ppm	0.2	-	217	-	214	-	209	-	*2*
K	%	0.1	-	< 0.1	-	< 0.1	-	< 0.1	-	-
La	ppm	0.4	-	5	-	5	-	6	-	*11*
Li	ppm	3	-	< 3	-	3	-	< 3	-	-
Mg	%	0.01	0.051	< 0.01	-	< 0.01	-	< 0.01	-	
Mn	ppm	3	96	84	*13*	85	*11*	92	*4*	*5*
Mo	ppm	1	-	5	-	< 1	-	1	-	*94*
Nb	ppm	2.4	-	3	-	< 2.4	-	< 2.4	-	-
Nd	ppm	0.4	-	8	-	8	-	7	-	*8*
Ni	ppm	10	31	30	*3*	30	*3*	20	*35*	*22*
P	%	0.005	-	< 0.005	-	< 0.005	-	< 0.005	-	-
Pb	ppm	0.8	1130	1150	*-2*	1150	*-2*	1090	*4*	*3*
Pr	ppm	0.1	-	2	-	2	-	2	-	*0*
Rb	ppm	0.4	-	2	-	< 0.4	-	1	-	*47*
S	%	0.01	31.6	> 20.0	-	> 20.0	-	> 20.0	-	-
Sb	ppm	2	10	13	*-30*	17	*-70*	10	*0*	*26*
Se	ppm	0.8	-	145	-	144	-	140	-	*2*
Si	%	0.01	0.4394	0.43	*2.14*	0.44	*-0.14*	0.43	*2.14*	*1.33*
Sm	ppm	0.1	-	1	-	2	-	1	-	*43*
Sn	ppm	0.5	-	519	-	525	-	504	-	*2*
Sr	ppm	3	-	< 3	-	< 3	-	< 3	-	-
Ta	ppm	0.2	-	< 0.2	-	< 0.2	-	< 0.2	-	-
Tb	ppm	0.1	-	< 0.1	-	< 0.1	-	< 0.1	-	-
Te	ppm	6	-	< 6	-	< 6	-	< 6	-	-
Th	ppm	0.1	-	< 0.1	-	1	-	1	-	*0*
Ti	%	0.01	-	< 0.01	-	< 0.01	-	< 0.01	-	-
Tl	ppm	0.1	-	1	-	1	-	< 0.1	-	*0*
Tm	ppm	0.1	-	< 0.1	-	< 0.1	-	< 0.1	-	-
U	ppm	0.1	-	< 0.1	-	< 0.1	-	< 0.1	-	-
V	ppm	5	-	29	-	14	-	7	-	*67*
W	ppm	0.7	-	4	-	8	-	7	-	*33*
Y	ppm	0.1	-	6	-	6	-	6	-	*5*
Yb	ppm	0.1	-	1	-	1	-	1	-	*0*
Zn	ppm	30	509200	> 10000	-	> 10000	-	> 10000	-	-
Au	ppb	2	-	45	-	54	-	41	-	*14*
Ag	ppm	5	45	< 5	-	50	-	< 5	-	-
As	ppm	0.5	390	354	*9*	366	*6*	382	*2*	*4*
Ba	ppm	50	-	< 50	-	640	-	800	-	*16*

Table I3. Continued

Element	Unit	D.L.	Accepted CZN-3	Measured CZN-3 (1)	*% Acc*	Measured CZN-3 (2)	*% Acc*	Measured CNZ-3 (3)	*% Acc*	*% RSD*
Br	ppm	0.5	-	< 0.5	-	< 0.5	-	< 0.5	-	-
Ca	%	1	0.059	< 1	-	< 1	-	< 1	-	-
Co	ppm	1	90	86	*4*	83	*8*	86	*4*	*2*
Cr	ppm	5	-	< 5	-	< 5	-	< 5	-	-
Cs	ppm	1	-	< 1	-	< 1	-	< 1	-	-
Fe	%	0.01	9.97	9.34	*6.32*	8.83	*11.43*	8.72	*12.54*	*3.69*
Hf	ppm	1	-	< 1	-	< 1	-	< 1	-	-
Hg	ppm	1	-	3	-	< 1	-	< 1	-	-
Ir	ppb	5	-	< 5	-	< 5	-	< 5	-	-
Mo	ppm	1	-	< 1	-	< 1	-	< 1	-	-
Na	%	0.01	-	< 0.01	-	< 0.01	-	0.01	-	-
Ni	ppm	20	31	< 20	-	< 20	-	< 20	-	-
Rb	ppm	15	-	< 15	-	< 15	-	< 15	-	-
Sb	ppm	0.1	10	8.8	*12.0*	7.7	*23.0*	8.3	*17.0*	*6.7*
Sc	ppm	0.1	-	1	-	< 0.1	-	< 0.1	-	-
Se	ppm	3	-	109	-	124	-	91	-	*15*
Sn	%	0.02	-	< 0.02	-	< 0.02	-	< 0.02	-	-
Sr	%	0.05	-	< 0.05	-	< 0.05	-	< 0.05	-	-
Ta	ppm	0.5	-	< 0.5	-	< 0.5	-	< 0.5	-	-
Th	ppm	0.2	-	< 0.2	-	2.1	-	< 0.2	-	-
U	ppm	0.5	-	< 0.5	-	< 0.5	-	< 0.5	-	-
W	ppm	1	-	< 1	-	< 1	-	< 1	-	-
Zn	ppm	50	509200	> 100000	-	> 100000	-	> 100000	-	-
La	ppm	0.5	-	5.8	-	5.5	-	5.2	-	*5.5*
Ce	ppm	3	-	< 3	-	< 3	-	< 3	-	-
Nd	ppm	5	-	< 5	-	< 5	-	< 5	-	-
Sm	ppm	0.1	-	1.3	-	1.4	-	1.3	-	*4.3*
Eu	ppm	0.2	-	< 0.2	-	< 0.2	-	< 0.2	-	-
Tb	ppm	0.5	-	< 0.5	-	< 0.5	-	< 0.5	-	-
Yb	ppm	0.2	-	< 0.2	-	< 0.2	-	< 0.2	-	-
Lu	ppm	0.05	-	< 0.05	-	< 0.05	-	< 0.05	-	-
Pb	%	0.01	-	-	-	-	-	-	-	-
Zn	%	0.01	50.92	50.1	*1.6*	51.0	*-0.2*	50.4	*1.0*	*0.9*

Table I3. Continued

			Accepted	Measured		Measured		Measured		Measured		
Element	Unit	D.L.	GXR-4	GXR-4 (1)	*% Acc*	GXR-4 (2)	*% Acc*	GXR-4 (3)	*% Acc*	GXR-4 (4)	*% Acc*	*% RSD*
Hg	ppb	5	110	102	*7*	105	*5*	-	-	-	-	*2*
Cu	%	0.005	0.652	0.658	*-0.920*	0.677	*-3.834*	-	-	-	-	*2.013*
Al	%	0.01	7.2	7.54	*-4.72*	7.37	*-2.36*	7.54	*-4.72*	7.37	*-2.36*	*1.32*
As	ppm	5	98	90	*8*	66	*33*	-	-	-	-	*22*
Ba	ppm	3	1640	1590	*3*	1600	*2*	1730	*-5*	-	-	*5*
Bi	ppm	2	19	18	*5*	17	*11*	-	-	-	-	*4*
Ca	%	0.01	1.01	1	*1*	1	*1*	1	*1*	1	*1*	*0*
Ce	ppm	0.8	102	106	*-4*	101	*1*	-	-	-	-	*3*
Co	ppm	0.2	14.6	14	*4*	13	*11*	-	-	-	-	*5*
Cr	ppm	30	64	70	*-9*	70	*-9*	-	-	-	-	*0*
Cs	ppm	0.1	2.8	3	*-7*	2	*29*	-	-	-	-	*28*
Cu	ppm	2	6520	6430	*1*	5970	*8*	-	-	-	-	*5*
Dy	ppm	0.3	2.6	3	*-15*	3	*-15*	-	-	-	-	*0*
Eu	ppm	0.1	1.63	1	*39*	1	*39*	-	-	-	-	*0*
Fe	%	0.05	3.09	3.02	*2.27*	3.05	*1.29*	3.02	*2.27*	3.05	*1.29*	*0.57*
Ga	ppm	0.2	20	18	*10*	18	*10*	-	-	-	-	*0*
Gd	ppm	0.1	5.25	4	*24*	5	*5*	-	-	-	-	*16*
K	%	0.1	4.01	4.1	*-2.2*	4.2	*-4.7*	4.1	*-2.2*	4.2	*-4.7*	*1.4*
La	ppm	0.4	64.5	61	*5*	61	*5*	-	-	-	-	*0*
Li	ppm	3	11.1	15	*-35*	11	*1*	-	-	-	-	*22*
Mg	%	0.01	1.66	1.71	*-3.01*	1.75	*-5.42*	1.71	*-3.01*	1.75	*-5.42*	*1.33*
Mn	ppm	3	155	144	*7*	119	*23*	-	-	-	-	*13*
Mo	ppm	1	310	309	*0*	290	*6*	-	-	-	-	*4*
Nb	ppm	2.4	10	8	*20*	8	*20*	-	-	-	-	*0*
Nd	ppm	0.4	45	39	*13*	39	*13*	-	-	-	-	*0*
Ni	ppm	10	42	40	*5*	40	*5*	-	-	-	-	*0*
Pb	ppm	0.8	52	48	*8*	47	*10*	-	-	-	-	*1*
Rb	ppm	0.4	160	159	*1*	147	*8*	-	-	-	-	*6*
S	%	0.01	1.77	1.76	*0.56*	1.82	*-2.82*	1.76	*0.56*	1.82	*-2.82*	*1.94*
Sb	ppm	2	4.8	4	*17*	5	*-4*					*16*
Se	ppm	0.8	5.6	5	*11*	5	*11*	-	-	-	-	*0*
Sm	ppm	0.1	6.6	6	*9*	6	*9*	-	-	-	-	*0*
Sn	ppm	0.5	5.6	7	*-25*	5	*11*	-	-	-	-	*24*
Sr	ppm	3	221	222	*0*	201	*9*	-	-	-	-	*7*
Tb	ppm	0.1	0.36	1	*-178*	1	*-178*	-	-	-	-	*0*
Th	ppm	0.1	22.5	24	*-7*	22	*2*	-	-	-	-	*6*
Ti	%	0.01	0.29	0.29	*0.00*	0.30	*-3.45*	0.29	*0.00*	0.30	*-3.45*	*1.96*
Tl	ppm	0.1	3.2	3	*6*	3	*6*	-	-	-	-	*0*
U	ppm	0.1	6.2	6	*3*	6	*3*	-	-	-	-	*0*
V	ppm	5	87	85	*2*	77	*11*	-	-	-	-	*7*
W	ppm	0.7	30.8	31	*-1*	29	*6*	-	-	-	-	*5*
Y	ppm	0.1	14	14	*0*	14	*0*	-	-	-	-	*0*
Yb	ppm	0.1	1.6	1	*38*	1	*38*	-	-	-	-	*0*
Zn	ppm	30	73	80	*-10*	80	*-10*	-	-	-	-	*0*

Table I3. Continued

			Accepted	Measured		Measured		
Element	Unit	D.L.	GXR-1	GXR-1 (1)	*% Acc*	GXR-1 (2)	*% Acc*	*% RSD*
Hg	ppb	5	3900	4020	*-3*	4050	*-4*	*-1*
Ba	ppm	3	750	730	*3*	-	-	-
Au	ppb	2	3300	3290	*0*	-	-	-
Ag	ppm	5	31	37	*-19*	-	-	-
As	ppm	0.5	427	427	*0*	-	-	-
Ba	ppm	50	750	790	*-5*	-	-	-
Br	ppm	0.5	12	12	*0*	-	-	-
Cs	ppm	1	3.9	3	*23*	-	-	-
Hf	ppm	1	18	17	*6*	-	-	-
Hg	ppm	1	0.052	0.05	*3.85*	-	-	-
Na	%	0.01	122	122	*0*	-	-	-
Ni	ppm	20	1.58	1.7	*-7.6*	-	-	-
Rb	ppm	15	16.6	16	*4*	-	-	-
Sn	%	0.02	2.44	2.6	*-6.6*	-	-	-
Sr	%	0.05	34.9	34.2	*2.0*	-	-	-
Ta	ppm	0.5	164	162	*1*	-	-	-
Th	ppm	0.2	760	750	*1*	-	-	-
U	ppm	0.5	7.5	7.5	*0.0*	-	-	-
W	ppm	1	17	16	*6*	-	-	-
La	ppm	0.5	2.7	2.6	*3.7*	-	-	-
Ce	ppm	3	0.69	0.8	*-15.9*	-	-	-
Sm	ppm	0.1	1.9	1.9	*0.0*	-	-	-
Eu	ppm	0.2	0.28	0.28	*0.00*	-	-	-

Table I3. Continued

			Accepted	Measured		Measured		Measured		
Element	Unit	D.L.	MP-1b	MP-1b (1)	*% Acc*	MP-1b (2)	*% Acc*	MP-1b (3)	*% Acc*	*% RSD*
Cu	%	0.005	3.069	2.99	*2.57*	3.05	*0.62*	3.08	*-0.36*	*1.51*
As	ppm	5	23000	24200	*-5*	23600	*-3*	22900	*0*	*3*
Bi	ppm	2	954	967	*-1*	954	*0*	984	*-3*	*2*
Ca	%	0.01	2.47	2.45	*0.81*	2.51	*-1.62*	2.54	*-2.83*	*1.83*
Cd	ppm	2	527	516	*2*	498	*6*	490	*7*	*3*
Fe	%	0.05	8.19	7.97	*2.69*	8.02	*2.08*	8.04	*1.83*	*0.45*
In	ppm	0.2	565	573	*-1*	562	*1*	603	*-7*	*4*
Mo	ppm	1	285	293	*-3*	302	*-6*	313	*-10*	*3*
S	%	0.01	13.79	13.4	*2.8*	13.1	*5.0*	13.4	*2.8*	*1.3*
Sb	ppm	2	54	51	*6*	52	*4*	51	*6*	*1*
Si	%	0.01	16.79	16.8	*-0.1*	16.9	*-0.7*	17.0	*-1.3*	*0.6*
W	ppm	0.7	1100	1060	*4*	1060	*4*	1140	*-4*	*4*
Fe	%	0.01	8.19	8.81	*-7.57*	-	-	-	-	-
Mo	ppm	1	285	284	*0*	-	-	-	-	-
Sb	ppm	0.1	54	56.9	*-5.4*	-	-	-	-	-
Sn	%	0.02	1.61	1.62	*-0.62*	-	-	-	-	-
W	ppm	1	1100	1100	*0*	-	-	-	-	-
Pb	%	0.01	2.091	2.05	*1.96*	2.07	*1.00*	2.07	*1.00*	*0.56*
Zn	%	0.01	16.67	16.5	*1.0*	16.7	*-0.2*	16.3	*2.2*	*1.2*

Table I3. Continued

Element	Unit	D.L.	Accepted OREAS 101a	Measured OREAS 101a (1)	% Acc	Measured OREAS 101a (2)	% Acc	% RSD
Ce	ppm	0.8	1396	1490	*-7*	1470	*-5*	*1*
Co	ppm	0.2	48.8	51	*-5*	49	*0*	*4*
Cu	ppm	2	434	455	*-5*	461	*-6*	*-1*
Dy	ppm	0.3	33.3	34	*-2*	33	*1*	*3*
Er	ppm	0.1	19.5	20	*-3*	20	*-3*	*0*
Eu	ppm	0.1	8.06	8	*1*	8	*1*	*0*
Fe	%	0.05	11.06	11	*1*	11	*1*	*0*
Gd	ppm	0.1	43.4	41	*6*	44	*-1*	*-7*
Ho	ppm	0.2	6.46	7	*-8*	7	*-8*	*0*
K	%	0.1	2.34	2.3	*1.7*	2.3	*1.7*	*0.0*
La	ppm	0.4	816	855	*-5*	839	*-3*	*2*
Mg	%	0.01	1.23	1.2	*2.4*	1.2	*2.4*	*0.0*
Mn	ppm	3	964	1030	*-7*	915	*5*	*11*
Mo	ppm	1	21.9	21	*4*	20	*9*	*5*
Nd	ppm	0.4	403	412	*-2*	402	*0*	*2*
P	%	0.005	0	0.123	-	0.123	-	*0*
Pr	ppm	0.1	134	136	*-1*	134	*0*	*1*
Sm	ppm	0.1	48.8	52	*-7*	50	*-2*	*4*
Tb	ppm	0.1	5.92	6	*-1*	6	*-1*	*0*
Th	ppm	0.1	36.6	39	*-7*	38	*-4*	*3*
Ti	%	0.01	0.395	0.4	*-1.3*	0.4	*-1.3*	*0.0*
Tm	ppm	0.1	2.9	3	*-3*	3	*-3*	*0*
U	ppm	0.1	422	448	*-6*	432	*-2*	*4*
V	ppm	5	83	81	*2*	87	*-5*	*-7*
Y	ppm	0.1	183	187	*-2*	190	*-4*	*-2*
Yb	ppm	0.1	17.5	19	*-9*	18	*-3*	*5*

Table I3. Continued

Element	Unit	D.L.	Accepted CCU-1d	Measured CCU-1d (1)	% Acc	Measured CCU-1d (2)	% Acc	Measured CCU-1d (3)	% Acc	Measured CCU-1d (4)	% Acc	% RSD
Cu	%	0.005	23.93	23.6	*1.4*	23.1	*3.5*	23.2	*3.1*	23.6	*1.4*	*1.1*
Cd	ppm	2	245.9	275	*-12*	272	*-11*	-	-	-	-	*1*
Fe	%	0.05	29.26	29.5	*-0.8*	29.4	*-0.5*	29.5	*-0.8*	29.4	*-0.5*	*0.2*
Pb	ppm	0.8	2620	2750	*-5*	2760	*-5*	-	-	-	-	*0*
Pb	%	0.01	0.262	0.26	*0.76*	0.27	*-3.05*	-	-	-	-	*2.67*
Zn	%	0.01	2.63	2.67	*-1.5*	2.69	*-2.3*	-	-	-	-	*0.5*

Table I4. Precision of whole-rock geochemical data (duplicates)

Element	Unit	Detection Limit	Original GMA13_045	Duplicate GMA13_045	*Rel % Diff*	Original GMA13_002	Duplicate GMA13_002	*Rel % Diff*
Hg	ppb	5	15100	15200	*-0.7*	16300	16500	*-1*
Total S	%	0.01	25.2	27.2	*-7.6*	19.5	19.5	*0.0*
Cu	%	0.005	-	-	-	-	-	-
Al	%	0.01	0.02	0.02	*0.00*	< 0.01	< 0.01	-
As	ppm	5	849	782	*8*	345	344	*0*
B	ppm	10	< 10	< 10	-	< 10	< 10	-
Ba	ppm	3	> 10000	> 10000	-	> 10000	> 10000	-
Be	ppm	4	< 4	< 4	-	< 4	< 4	-
Bi	ppm	2	< 2	< 2	-	< 2	< 2	-
Ca	%	0.01	0.07	0.05	*33.33*	0.02	0.07	*-111.11*
Cd	ppm	2	30	25	*18*	729	716	*2*
Ce	ppm	0.8	7	4	*55*	< 0.8	< 0.8	-
Co	ppm	0.2	< 0.2	< 0.2	-	< 0.2	< 0.2	-
Cr	ppm	30	< 30	< 30	-	< 30	< 30	-
Cs	ppm	0.1	1	3	*-100*	< 0.1	< 0.1	-
Cu	ppm	2	1530	1510	*1*	1190	1120	*6*
Dy	ppm	0.3	< 0.3	< 0.3	-	< 0.3	< 0.3	-
Er	ppm	0.1	< 0.1	< 0.1	-	< 0.1	< 0.1	-
Eu	ppm	0.1	< 0.1	< 0.1	-	< 0.1	< 0.1	-
Fe	%	0.05	15.60	15.90	*-1.90*	0.70	0.70	*0.00*
Ga	ppm	0.2	1	3	*-100*	4	4	*0*
Gd	ppm	0.1	< 0.1	< 0.1	-	< 0.1	< 0.1	-
Ge	ppm	0.7	29	30	*-3*	58	59	*-2*
Ho	ppm	0.2	< 0.2	< 0.2	-	< 0.2	< 0.2	-
Hf	ppm	10	< 10	< 10	-	< 10	< 10	-
In	ppm	0.2	< 0.2	< 0.2	-	6	9	*-40*
K	%	0.1	< 0.1	< 0.1	-	< 0.1	< 0.1	-
La	ppm	0.4	12	12	*0*	1	< 0.4	-
Li	ppm	3	< 3	< 3	-	< 3	< 3	-
Mg	%	0.01	< 0.01	< 0.01	-	< 0.01	< 0.01	-
Mn	ppm	3	56	47	*17*	47	50	*-6*
Mo	ppm	1	11	9	*20*	10	13	*-26*
Nb	ppm	2.4	< 2.4	< 2.4	-	< 2.4	< 2.4	-
Nd	ppm	0.4	< 0.4	1	-	1	1	*0*
Ni	ppm	10	10	< 10	-	< 10	< 10	-
P	%	0.005	0.007	0.005	*33.333*	< 0.005	< 0.005	-
Pb	ppm	0.8	> 5000	> 5000	-	2030	1960	*4*
Pr	ppm	0.1	< 0.1	< 0.1	-	< 0.1	< 0.1	-
Rb	ppm	0.4	< 0.4	2	-	< 0.4	1	-
S	%	0.01	> 20.0	> 20.0	-	13.1	13.2	*-0.8*
Sb	ppm	2	138	130	*6*	113	107	*5*
Se	ppm	0.8	6	5	*18*	9	9	*0*
Si	%	0.01	4.42	4.41	*0.23*	5.41	5.45	*-0.74*
Sm	ppm	0.1	< 0.1	< 0.1	-	< 0.1	< 0.1	-
Sn	ppm	0.5	< 0.5	< 0.5	-	< 0.5	< 0.5	-
Sr	ppm	3	6020	5600	*7*	3190	3190	*0*
Ta	ppm	0.2	< 0.2	< 0.2	-	< 0.2	< 0.2	-
Tb	ppm	0.1	< 0.1	< 0.1	-	< 0.1	< 0.1	-
Te	ppm	6	< 6	< 6	-	< 6	< 6	-
Th	ppm	0.1	< 0.1	< 0.1	-	< 0.1	< 0.1	-
Ti	%	0.01	< 0.01	< 0.01	-	< 0.01	< 0.01	-
Tl	ppm	0.1	16	16	*0*	9	8	*12*
Tm	ppm	0.1	< 0.1	< 0.1	-	< 0.1	< 0.1	-
U	ppm	0.1	1	< 0.1	-	< 0.1	< 0.1	-
V	ppm	5	17	33	*-64*	29	29	*0*
W	ppm	0.7	< 0.7	< 0.7	-	1.0	5.0	*-133*
Y	ppm	0.1	< 0.1	< 0.1	-	< 0.1	< 0.1	-
Yb	ppm	0.1	3	< 0.1	-	4	1	*120*
Zn	ppm	30	> 10000	> 10000	-	> 10000	> 10000	-
Au	ppb	2	2440	2490	*-2*	243	215	*12*
Ag	ppm	5	229	238	*-4*	146	162	*-10*
As	ppm	0.5	708	756	*-7*	329	318	*3*
Ba	ppm	50	135000	123000	*9*	145000	151000	*-4*

Table I4. Continued

Element	Unit	Detection Limit	Original GMA13_045	Duplicate GMA13_045	*Rel % Diff*	Original GMA13_002	Duplicate GMA13_002	*Rel % Diff*
Br	ppm	0.5	15.1	18.2	*-18.6*	16.0	< 0.5	-
Ca	%	1	< 1	< 1		< 1	< 1	-
Co	ppm	1	< 1	< 1	-	< 1	< 1	-
Cr	ppm	5	< 5	< 5	-	< 5	< 5	-
Cs	ppm	1	< 1	< 1	-	< 1	< 1	-
Fe	%	0.01	13.80	14.90	*-7.67*	0.66	0.73	*-10.07*
Hf	ppm	1	< 1	< 1	-	< 1	< 1	-
Hg	ppm	1	10	14	*-33*	13	< 1	-
Ir	ppb	5	< 5	< 5	-	< 5	< 5	-
Mo	ppm	1	< 1	< 1	-	< 1	< 1	-
Na	%	0.01	0.05	0.06	*-18.18*	0.07	0.07	*0.00*
Ni	ppm	20	< 20	< 20	-	< 20	< 20	-
Rb	ppm	15	< 15	< 15	-	< 15	< 15	-
Sb	ppm	0.1	130.0	134.0	*-3.0*	108.0	106.0	*1.9*
Sc	ppm	0.1	< 0.1	< 0.1	-	< 0.1	< 0.1	-
Se	ppm	3	< 3	< 3	-	< 3	< 3	-
Sn	%	0.02	< 0.02	< 0.02	-	< 0.02	< 0.02	-
Sr	%	0.05	0.60	0.87	*-36.73*	< 0.05	< 0.05	-
Ta	ppm	0.5	< 0.5	< 0.5	-	< 0.5	< 0.5	-
Th	ppm	0.2	< 0.2	< 0.2	-	< 0.2	< 0.2	-
U	ppm	0.5	< 0.5	< 0.5	-	< 0.5	< 0.5	-
W	ppm	1	< 1	< 1	-	< 1	< 1	-
Zn	ppm	50	37500	34200	*9*	> 100000	> 100000	
La	ppm	0.5	15.2	14.7	*3.3*	3.3	3.1	*6.2*
Ce	ppm	3	< 3	< 3	-	< 3	< 3	-
Nd	ppm	5	< 5	< 5	-	< 5	< 5	-
Sm	ppm	0.1	< 0.1	< 0.1	-	0.1	< 0.1	-
Eu	ppm	0.2	< 0.2	< 0.2	-	< 0.2	< 0.2	-
Tb	ppm	0.5	< 0.5	< 0.5	-	< 0.5	< 0.5	-
Yb	ppm	0.2	< 0.2	< 0.2	-	< 0.2	< 0.2	-
Lu	ppm	0.05	< 0.05	< 0.05	-	< 0.05	< 0.05	-
Pb	%	0.01	2.37	2.31	*2.56*	-	-	-
Zn	%	0.01	-	-	-	22.8	22.6	*0.9*

Table I4. Continued

Element	Unit	Detection Limit	Original GMA13_034	Duplicate GMA13_034	*Rel % Diff*	Original MA13_030	Duplicate MA13_030	*Rel % Diff*
Hg	ppb	5	5010	5110	*-2*	13700	13400	*2*
Total S	%	0.01	37.5	35.5	*5.5*	22.2	22.6	*-1.8*
Cu	%	0.005	12.20	12.30	*-0.82*	-	-	-
Al	%	0.01	0.15	0.14	*6.90*	0.09	0.10	*-10.53*
As	ppm	5	388	440	*-13*	681	700	*-3*
B	ppm	10	< 10	< 10	-	< 10	< 10	-
Ba	ppm	3	> 10000	> 10000	-	> 10000	> 10000	-
Be	ppm	4	< 4	< 4	-	< 4	< 4	-
Bi	ppm	2	< 2	< 2	-	< 2	< 2	-
Ca	%	0.01	0.01	0.06	*-142.86*	0.04	0.08	*-66.67*
Cd	ppm	2	17	20	*-16*	1610	1590	*1*
Ce	ppm	0.8	< 0.8	< 0.8	-	1	1	*0*
Co	ppm	0.2	< 0.2	< 0.2	-	< 0.2	< 0.2	-
Cr	ppm	30	< 30	< 30	-	< 30	< 30	-
Cs	ppm	0.1	2	< 0.1	-	< 0.1	< 0.1	-
Cu	ppm	2	> 10000	> 10000	-	8570	8530	*0*
Dy	ppm	0.3	< 0.3	< 0.3	-	< 0.3	< 0.3	-
Er	ppm	0.1	< 0.1	< 0.1	-	< 0.1	< 0.1	-
Eu	ppm	0.1	< 0.1	< 0.1	-	< 0.1	< 0.1	-
Fe	%	0.05	33.20	32.90	*0.91*	0.77	0.80	*-3.82*
Ga	ppm	0.2	7	6	*15*	3	3	*0*
Gd	ppm	0.1	< 0.1	< 0.1	-	< 0.1	< 0.1	-
Ge	ppm	0.7	36	34	*7*	66	64	*3*
Ho	ppm	0.2	< 0.2	< 0.2	-	< 0.2	< 0.2	-
Hf	ppm	10	< 10	< 10	-	< 10	< 10	-
In	ppm	0.2	34	35	*-3*	< 0.2	< 0.2	-
K	%	0.1	< 0.1	< 0.1	-	< 0.1	< 0.1	-
La	ppm	0.4	< 0.4	< 0.4	-	2	1	*67*
Li	ppm	3	< 3	< 3	-	< 3	< 3	-
Mg	%	0.01	< 0.01	0.02	-	< 0.01	< 0.01	-
Mn	ppm	3	513	503	*2*	11	13	*-17*
Mo	ppm	1	106	119	*-11.6*	22	25	*-13*
Nb	ppm	2.4	< 2.4	< 2.4	-	< 2.4	< 2.4	-
Nd	ppm	0.4	1	< 0.4	-	< 0.4	< 0.4	-
Ni	ppm	10	< 10	< 10	-	< 10	< 10	-
P	%	0.005	0.029	0.030	*-3.390*	< 0.005	< 0.005	-
Pb	ppm	0.8	245	251	*-2*	539	572	*-6*
Pr	ppm	0.1	< 0.1	< 0.1	-	< 0.1	< 0.1	-
Rb	ppm	0.4	3	1	*100*	< 0.4	< 0.4	-
S	%	0.01	> 20.0	> 20.0	-	19.4	19.6	*-1.0*
Sb	ppm	2	19	27	*-34.8*	573	505	*13*
Se	ppm	0.8	9	12.5	*-32.6*	12	13	*-8*
Si	%	0.01	2.92	2.89	*1.03*	1.65	1.66	*-0.60*
Sm	ppm	0.1	< 0.1	< 0.1	-	< 0.1	< 0.1	-
Sn	ppm	0.5	1	1.5	*-40*	3	< 0.5	-
Sr	ppm	3	615	640	*-4*	1740	1800	*-3*
Ta	ppm	0.2	< 0.2	< 0.2	-	< 0.2	< 0.2	-
Tb	ppm	0.1	< 0.1	< 0.1	-	< 0.1	< 0.1	-
Te	ppm	6	< 6	< 6	-	< 6	< 6	-
Th	ppm	0.1	< 0.1	< 0.1	-	< 0.1	< 0.1	-
Ti	%	0.01	< 0.01	< 0.01	-	< 0.01	< 0.01	-
Tl	ppm	0.1	12	12	*0*	< 0.1	< 0.1	-
Tm	ppm	0.1	< 0.1	< 0.1	-	< 0.1	< 0.1	-
U	ppm	0.1	< 0.1	< 0.1	-	< 0.1	< 0.1	-
V	ppm	5	39	36	*8.0*	18	25	*-33*
W	ppm	0.7	1	< 0.7	-	5	2	*86*
Y	ppm	0.1	< 0.1	< 0.1	-	< 0.1	< 0.1	-
Yb	ppm	0.1	2	1	*67*	1	1	*0.0*
Zn	ppm	30	5190	5620	*-8*	> 10000	> 10000	-
Au	ppb	2	829	844	*-2*	356	360	*-1*
Ag	ppm	5	< 5	< 5	-	401	371	*8*
As	ppm	0.5	384	359	*6.7*	659	625	*5*
Ba	ppm	50	18500	18500	*0.0*	94200	92500	*2*

Table I4. Continued

Element	Unit	Detection Limit	Original GMA13_034	Duplicate GMA13_034	*Rel % Diff*	Original MA13_030	Duplicate MA13_030	*Rel % Diff*
Br	ppm	0.5	23.2	24.1	*-3.8*	< 0.5	< 0.5	-
Ca	%	1	< 1	< 1	-	< 1	< 1	-
Co	ppm	1	2	< 1	-	< 1	< 1	-
Cr	ppm	5	< 5	< 5	-	< 5	< 5	-
Cs	ppm	1	< 1	< 1	-	< 1	< 1	-
Fe	%	0.01	28.80	26.90	*6.82*	0.91	0.79	*14.12*
Hf	ppm	1	< 1	< 1	-	< 1	< 1	-
Hg	ppm	1	4	4	*0*	9	< 1	-
Ir	ppb	5	< 5	< 5	-	< 5	< 5	-
Mo	ppm	1	77	73	*5*	20	< 1	-
Na	%	0.01	0.15	0.10	*40.00*	0.10	0.10	*0.00*
Ni	ppm	20	< 20	< 20	-	< 20	< 20	-
Rb	ppm	15	< 15	< 15	-	< 15	< 15	-
Sb	ppm	0.1	19.0	17.4	*8.8*	530.0	523.0	*1.3*
Sc	ppm	0.1	< 0.1	< 0.1	-	< 0.1	< 0.1	-
Se	ppm	3	< 3	< 3	-	< 3	< 3	-
Sn	%	0.02	< 0.02	< 0.02	-	< 0.02	< 0.02	-
Sr	%	0.05	< 0.05	< 0.05	-	< 0.05	< 0.05	-
Ta	ppm	0.5	< 0.5	< 0.5	-	< 0.5	< 0.5	-
Th	ppm	0.2	< 0.2	< 0.2	-	< 0.2	< 0.2	-
U	ppm	0.5	< 0.5	< 0.5	-	< 0.5	< 0.5	-
W	ppm	1	< 1	< 1	-	< 1	19	-
Zn	ppm	50	4750	4620	*3*	> 100000	> 100000	-
La	ppm	0.5	0.6	< 0.5	-	3.0	2.4	*22.2*
Ce	ppm	3	< 3	< 3	-	< 3	< 3	-
Nd	ppm	5	< 5	< 5	-	< 5	< 5	-
Sm	ppm	0.1	0.1	< 0.1	-	< 0.1	< 0.1	-
Eu	ppm	0.2	< 0.2	< 0.2	-	< 0.2	< 0.2	-
Tb	ppm	0.5	< 0.5	< 0.5	-	< 0.5	< 0.5	-
Yb	ppm	0.2	< 0.2	< 0.2	-	< 0.2	< 0.2	-
Lu	ppm	0.05	< 0.05	< 0.05	-	< 0.05	< 0.05	-
Pb	%	0.01	-	-	-	-	-	-
Zn	%	0.01	-	-	-	35.6	35.3	*0.8*

Table I4. Continued

Element	Unit	Detection Limit	Original MA13_098	Duplicate MA13_098	*Rel % Diff*	Original GMA13_029	Duplicate GMA13_029	*Rel % Diff*
Hg	ppb	5	13100	13000	*1*	-	-	-
Total S	%	0.01	35.4	35.6	*-0.6*	-	-	-
Cu	%	0.01	3.32	3.38	*-1.79*	0.12	0.11	*0.87*
Al	%	0.01	0.15	0.15	*0.00*	0.02	0.02	*0.00*
As	ppm	5	219	219	*0*	190	191	*-1*
B	ppm	10	< 10	< 10	-	< 10	< 10	-
Ba	ppm	3	1200	1210	*-1*	> 10000	> 10000	-
Be	ppm	4	< 4	< 4	-	< 4	< 4	-
Bi	ppm	2	< 2	< 2	-	< 2	< 2	-
Ca	%	0.01	0.05	0.03	*50.00*	0.09	0.08	*11.76*
Cd	ppm	2	92	91	*1*	751	762	*-1*
Ce	ppm	0.8	< 0.8	1	-	3	2	*40*
Co	ppm	0.2	< 0.2	< 0.2	-	3	< 0.2	-
Cr	ppm	30	< 30	< 30	-	< 30	< 30	-
Cs	ppm	0.1	1	< 0.1	-	< 0.1	< 0.1	-
Cu	ppm	2	> 10000	> 10000	-	1200	1180	*2*
Dy	ppm	0.3	< 0.3	< 0.3	-	< 0.3	< 0.3	-
Er	ppm	0.1	< 0.1	< 0.1	-	< 0.1	< 0.1	-
Eu	ppm	0.1	< 0.1	< 0.1	-	< 0.1	1	-
Fe	%	0.05	30.60	30.70	*-0.33*	0.63	0.61	*3*
Ga	ppm	0.2	8	9	*-12*	2	2	*0*
Gd	ppm	0.1	< 0.1	< 0.1	-	< 0.1	< 0.1	-
Ge	ppm	0.7	18	18	*0*	20	20	*0*
Ho	ppm	0.2	< 0.2	< 0.2	-	< 0.2	< 0.2	-
Hf	ppm	10	< 10	< 10	-	< 10	< 10	-
In	ppm	0.2	13	13	*0*	< 0.2	< 0.2	-
K	%	0.1	< 0.1	< 0.1	-	< 0.1	< 0.1	-
La	ppm	0.4	< 0.4	< 0.4	-	3	2	*40*
Li	ppm	3	< 3	< 3	-	< 3	< 3	-
Mg	%	0.01	< 0.01	< 0.01	-	< 0.01	< 0.01	-
Mn	ppm	3	7	9	*-25*	27	31	*-14*
Mo	ppm	1	43	44	*-2*	5	5	*0*
Nb	ppm	2.4	< 2.4	< 2.4	-	< 2.4	< 2.4	-
Nd	ppm	0	< 0.4	1	-	2	2	*0*
Ni	ppm	10	< 10	< 10	-	< 10	< 10	-
P	%	0.005	< 0.005	< 0.005	-	< 0.005	< 0.005	-
Pb	ppm	0.8	371	380	*-2*	4110	4060	*1*
Pr	ppm	0.1	< 0.1	< 0.1	-	< 0.1	< 0.1	-
Rb	ppm	0.4	2	1	*67*	1	1	*0*
S	%	0.01	> 20.0	> 20.0	-	12.3	12.4	*-0.8*
Sb	ppm	2	40	39	*3*	157	159	*-1*
Se	ppm	0.8	5	6	*-18*	9	11	*-20*
Si	%	0.01	10.50	10.50	*0.00*	1.38	1.37	*0.73*
Sm	ppm	0.1	< 0.1	< 0.1	-	< 0.1	< 0.1	-
Sn	ppm	0.5	< 0.5	3	-	< 0.5	< 0.5	-
Sr	ppm	3	17	16	*6*	7680	7700	*0*
Ta	ppm	0.2	< 0.2	< 0.2	-	< 0.2	< 0.2	-
Tb	ppm	0.1	< 0.1	< 0.1	-	< 0.1	< 0.1	-
Te	ppm	6	< 6	< 6	-	< 6	< 6	-
Th	ppm	0.1	< 0.1	< 0.1	-	< 0.1	< 0.1	-
Ti	%	0.01	< 0.01	< 0.01	-	< 0.01	< 0.01	-
Tl	ppm	0.1	3	4	*-29*	3	3	*0*
Tm	ppm	0.1	< 0.1	< 0.1	-	< 0.1	< 0.1	-
U	ppm	0.1	< 0.1	< 0.1	-	< 0.1	< 0.1	-
V	ppm	5	8	8	*0*	28	26	*7*
W	ppm	0.7	< 0.7	10	-	1	< 0.7	-
Y	ppm	0.1	< 0.1	< 0.1	-	< 0.1	< 0.1	-
Yb	ppm	0.1	< 0.1	< 0.1	-	3	1	*100*
Zn	ppm	30	> 10000	> 10000	-	> 10000	> 10000	-
Au	ppb	2	279	273	*2*	-	- -	-
Ag	ppm	5	< 5	< 5	-	-	- -	-
As	ppm	0.5	242	218	*10*	-	- -	-
Ba	ppm	50	1370	1050	*26*	-	- -	-

Table I4. Continued

Element	Unit	Detection Limit	Original MA13_098		Duplicate MA13_098	*Rel % Diff*	Original GMA13_029	Duplicate GMA13_029	*Rel % Diff*
Br	ppm	0.5	< 0.5		9.3	-	-	-	-
Ca	%	1	< 1		< 1	-	-	-	-
Co	ppm	1	< 1		< 1	-	-	-	-
Cr	ppm	5	< 5		< 5	-	-	-	-
Cs	ppm	1	< 1		< 1	-	-	-	-
Fe	%	0.01	28.00		26.70	*4.75*	-	-	-
Hf	ppm	1	< 1		< 1	-	-	-	-
Hg	ppm	1	8		9	*-12*	-	-	-
Ir	ppb	5	< 5		< 5	-	-	-	-
Mo	ppm	1	28		37	*-28*	-	-	-
Na	%	0.01	0.08		0.09	*-11.76*	-	-	-
Ni	ppm	20	< 20		< 20	-	-	-	-
Rb	ppm	15	< 15		< 15	-	-	-	-
Sb	ppm	0.1	30.4		31.6	*-3.9*	-	-	-
Sc	ppm	0.1	< 0.1		< 0.1	-	-	-	-
Se	ppm	3	< 3		< 3	-	-	-	-
Sn	%	0.02	< 0.02		< 0.02	-	-	-	-
Sr	%	0.05	< 0.05		< 0.05	-	-	-	-
Ta	ppm	0.5	< 0.5		< 0.5	-	-	-	-
Th	ppm	0.2	< 0.2		< 0.2	-	-	-	-
U	ppm	0.5	< 0.5		< 0.5	-	-	-	-
W	ppm	1	< 1		< 1	-	-	-	-
Zn	ppm	50	31500		31500	*0.0*	-	-	-
La	ppm	0.5	< 0.5		< 0.5	-	-	-	-
Ce	ppm	3	< 3		< 3	-	-	-	-
Nd	ppm	5	< 5		< 5	-	-	-	-
Sm	ppm	0.1	< 0.1		< 0.1	-	-	-	-
Eu	ppm	0.2	< 0.2		< 0.2	-	-	-	-
Tb	ppm	0.5	< 0.5		< 0.5	-	-	-	-
Yb	ppm	0.2	< 0.2		< 0.2	-	-	-	-
Lu	ppm	0.05	< 0.05		< 0.05	-	-	-	-
Pb	%	0.01	-	-	-	-	0.39	0.39	*0*
Zn	%	0.01	-	-	-	-	21.5	21.4	*0.5*

Table I4. Continued

Element	Unit	Detection Limit	Original GMA13_053C	Duplicate GMA13_053C	*Rel % Diff*	Original MA13_028	Duplicate MA13_028	*Rel % Diff*
Hg	ppb	5	-	-	-	4140	3980	*4*
Total S	%	0.01	35.4	35.7	*-0.8*	-	-	-
Cu	%	0.005	12.30	12.30	*0.00*	4.60	4.73	*-2.79*
Al	%	0.01	0.14	0.14	*0.00*	0.34	0.34	*0.00*
As	ppm	5	441	439	*0*	1610	1400	*14*
B	ppm	10	< 10	10	-	< 10	< 10	-
Ba	ppm	3	> 10000	> 10000	-	33	31	*6*
Be	ppm	4	< 4	< 4	-	< 4	< 4	-
Bi	ppm	2	< 2	< 2	-	2	< 2	-
Ca	%	0.01	0.06	0.06	*0.00*	0.07	0.06	*15.38*
Cd	ppm	2	20	20	*0*	131	130	*1*
Ce	ppm	0.8	< 0.8	1	-	3	< 0.8	-
Co	ppm	0.2	< 0.2	2	-	< 0.2	< 0.2	-
Cr	ppm	30	< 30	< 30	-	< 30	< 30	-
Cs	ppm	0.1	< 0.1	< 0.1	-	< 0.1	< 0.1	-
Cu	ppm	2	> 10000	> 10000	-	> 10000	> 10000	-
Dy	ppm	0.3	< 0.3	< 0.3	-	< 0.3	< 0.3	-
Er	ppm	0.1	< 0.1	< 0.1	-	< 0.1	< 0.1	-
Eu	ppm	0.1	< 0.1	< 0.1	-	< 0.1	< 0.1	-
Fe	%	0.05	33.1	32.8	*0.9*	31.2	31.2	*0.0*
Ga	ppm	0.2	6	6	*0*	20	19	*5*
Gd	ppm	0.1	< 0.1	< 0.1	-	< 0.1	< 0.1	-
Ge	ppm	0.7	34	33	*3*	15	15	*0*
Ho	ppm	0.2	< 0.2	< 0.2	-	< 0.2	< 0.2	-
Hf	ppm	10	< 10	< 10	-	< 10	< 10	-
In	ppm	0.2	35	35	*0*	40	39	*3*
K	%	0.1	< 0.1	< 0.1	-	< 0.1	< 0.1	-
La	ppm	0.4	< 0.4	< 0.4	-	1	< 0.4	-
Li	ppm	3	< 3	< 3	-	< 3	< 3	-
Mg	%	0.01	0.01	0.02	*-66.67*	< 0.01	0.02	-
Mn	ppm	3	503	502	*0*	82	79	*4*
Mo	ppm	1	117	120	*-3*	78	76	*3*
Nb	ppm	2.4	< 2.4	< 2.4	-	< 2.4	< 2.4	-
Nd	ppm	0.4	< 0.4	< 0.4	-	2	< 0.4	-
Ni	ppm	10	< 10	< 10	-	< 10	< 10	-
P	%	0.005	0.031	0.03	*3.28*	0.006	0.006	*0.00*
Pb	ppm	0.8	251	250	*0*	559	538	*4*
Pr	ppm	0.1	< 0.1	< 0.1	-	< 0.1	< 0.1	-
Rb	ppm	0.4	1	1	*0*	2	1	*67*
S	%	0.01	> 20.0	> 20.0	-	> 20.0	> 20.0	-
Sb	ppm	2	27	26	*4*	101	100	*1*
Se	ppm	0.8	14	11	*24*	7	4	*55*
Si	%	0.01	2.89	2.89	*0.00*	9.12	9.31	*-2.06*
Sm	ppm	0.1	< 0.1	< 0.1	-	< 0.1	< 0.1	-
Sn	ppm	0.5	1	2	*-67*	11	< 0.5	-
Sr	ppm	3	639	641	*0*	4	3	*29*
Ta	ppm	0.2	< 0.2	< 0.2	-	< 0.2	< 0.2	-
Tb	ppm	0.1	< 0.1	< 0.1	-	< 0.1	< 0.1	-
Te	ppm	6	< 6	< 6	-	< 6	< 6	-
Th	ppm	0.1	< 0.1	< 0.1	-	1	< 0.1	-
Ti	%	0.01	< 0.01	< 0.01	-	< 0.01	< 0.01	-
Tl	ppm	0.1	12	12	*0*	33	32	*3*
Tm	ppm	0.1	< 0.1	< 0.1	-	< 0.1	< 0.1	-
U	ppm	0.1	< 0.1	1	-	< 0.1	< 0.1	-
V	ppm	5	37	35	*6*	23	22	*4*
W	ppm	0.7	< 0.7	1	-	11	< 0.7	-
Y	ppm	0.1	< 0.1	< 0.1	-	< 0.1	< 0.1	-
Yb	ppm	0.1	1	1	*0*	< 0.1	< 0.1	-
Zn	ppm	30	5690	5560	*2*	> 10000	> 10000	-
Zn	%	0.01	-	-	-	0.06	0.06	*0.00*
Pb	%	0.01	-	-	-	2.75	2.77	*-0.72*

Table I4. Continued

Element	Unit	Detection Limit	Original P0044C	Duplicate P0044C	*Rel % Diff*
Hg	ppb	5	4570	4510	*1*
Cu	%	0.005	0.688	0.688	-
Al	%	0.01	0.09	0.09	*0.00*
As	ppm	5	384	348	*10*
B	ppm	10	< 10	< 10	-
Ba	ppm	3	18	15	*18*
Be	ppm	4	< 4	< 4	-
Bi	ppm	2	7	6	*15*
Ca	%	0.01	0.09	0.08	*11.76*
Cd	ppm	2	2690	2420	*11*
Ce	ppm	0.8	15	14	*7*
Co	ppm	0.2	91	82	*10*
Cr	ppm	30	< 30	< 30	-
Cs	ppm	0.1	< 0.1	< 0.1	-
Cu	ppm	2	7180	6430	*11*
Dy	ppm	0.3	1	1	*0*
Er	ppm	0.1	1	1	*0*
Eu	ppm	0.1	< 0.1	< 0.1	-
Fe	%	0.05	9.73	9.71	*0.21*
Ga	ppm	0.2	9	8	*12*
Gd	ppm	0.1	1	1	*0*
Ge	ppm	0.7	2	3	*-40*
Ho	ppm	0.2	< 0.2	< 0.2	-
Hf	ppm	10	< 10	< 10	-
In	ppm	0.2	219	198	*10*
K	%	0.1	< 0.1	< 0.1	-
La	ppm	0.4	6	6	*0*
Li	ppm	3	< 3	< 3	-
Mg	%	0.01	< 0.01	< 0.01	
Mn	ppm	3	97	86	*12*
Mo	ppm	1	1	1	*0*
Nb	ppm	2.4	< 2.4	< 2.4	-
Nd	ppm	0.4	7	7	*0*
Ni	ppm	10	20	20	*0*
P	%	0.005	< 0.005	< 0.005	-
Pb	ppm	0.8	1150	1040	*10*
Pr	ppm	0.1	2	2	*0*
Rb	ppm	0.4	1	1	*0*
S	%	0.01	> 20.0	> 20.0	-
Sb	ppm	2	10	9	*11*
Se	ppm	0.8	149	131	*13*
Si	%	0.01	0.43	0.43	*0.00*
Sm	ppm	0.1	1	1	*0*
Sn	ppm	0.5	541	466	*15*
Sr	ppm	3	< 3	< 3	-
Ta	ppm	0.2	< 0.2	< 0.2	-
Tb	ppm	0.1	< 0.1	< 0.1	-
Te	ppm	6	< 6	< 6	-
Th	ppm	0.1	1	1	*0*
Ti	%	0.01	< 0.01	< 0.01	-
Tl	ppm	0.1	1	< 0.1	-
Tm	ppm	0.1	< 0.1	< 0.1	-
U	ppm	0.1	< 0.1	< 0.1	-
V	ppm	5	8	5	*46*
W	ppm	0.7	10	4	*86*
Y	ppm	0.1	6	5	*18*
Yb	ppm	0.1	1	1	*0*
Zn	ppm	30	> 10000	> 10000	-
Zn	%	0.01	0.1	0.11	*-10*
Pb	%	0.01	50.3	50.5	*-0.4*

Appendix J

Whole-Rock Geochemistry of Oxyhydroxides – Tinakula Deposit

Contents of this file:

1. Supplemental Tables:
   Table J1: Whole-rock geochemistry of ROV grab samples (oxyhydroxides) from the Tinakula deposit
   Table J2: Precision and accuracy of whole-rock geochemical data for oxides and altered volcanic rocks (standards)

Notes:

< = below detection limit
> = above detection limit
- = not analyzed
% Acc = Accuracy percent
RSD = Relative Standard Deviation (ratio of the standard deviation to the mean)

1. Supplemental Tables

Table J1. Whole-rock geochemistry of ROV grab samples (oxyhydroxides) from the Tinakula deposit

	Unit	D.L.	Analysis Method	GMA13-037	GMA13-025	GMA13-026	GMA13-047	GMA13-054	GMA13-055	GMA13-059
Si	%	0.01	FUS-Na2O2	43.10	11.10	> 30.0	29.60	> 30.0	> 30.0	25.60
Fe	%	0.01	INAA	2.37	11.10	4.75	8.77	6.91	6.72	12.90
Mg	%	0.01	FUS-Na2O2	0.02	0.80	0.18	0.28	0.14	0.36	0.32
Mn	ppm	3	FUS-MS-Na2O2	6	> 10000	451	9230	3340	247	> 10000
S	%	0.01	FUS-Na2O2	0.2	0.10	2.42	1.10	0.03	0.12	0.13
S_{Total}	%	0.01	CS	0.19	0.13	2.55	1.06	0.10	0.18	0.16
Au	ppb	2	INAA	< 2	< 2	24	< 2	26	37	< 2
Cu	ppm	2	FUS-MS-Na2O2	58	481	165	357	37	44	60
Mo	ppm	1	INAA	1	485	29	26	26	32	92
In	ppm	0.2	FUS-MS-Na2O2	< 0.2	0.3	< 0.2	< 0.2	< 0.2	< 0.2	< 0.2
Ni	ppm	10	FUS-MS-Na2O2	< 10	40	10	60	10	10	20
Bi	ppm	2	FUS-MS-Na2O2	7	< 2	< 2	< 2	< 2	< 2	< 2
Co	ppm	0.2	FUS-MS-Na2O2	< 0.2	62.7	16.0	2.9	1.0	2.5	49.4
Zn	ppm	30	FUS-MS-Na2O2	70	880	360	1090	90	100	620
Cd	ppm	2	FUS-MS-Na2O2	< 2	2	< 2	3	6	< 2	4
Ga	ppm	0.2	FUS-MS-Na2O2	2.0	33.3	6.3	4.6	1.6	0.9	4.5
Ge	ppm	0.7	FUS-MS-Na2O2	5.0	7.6	22.3	9.2	12.7	11.1	9.9
Se	ppm	0.8	FUS-MS-Na2O2	4.0	< 0.8	2.1	2.5	2.1	< 0.8	3.3
Tl	ppm	0.1	FUS-MS-Na2O2	2.0	9.3	61.0	0.7	0.9	0.1	4.0
Pb	ppm	0.8	FUS-MS-Na2O2	465.0	110.0	41.2	1330.0	65.1	171.0	1310.0
Hg	ppb	5	1G	2910	24	479	140	8980	2180	1250
As	ppm	0.5	INAA	105.0	159.0	189.0	415.0	444.0	71.2	292.0
Sb	ppm	0.1	INAA	14.7	7.6	25.6	21.6	39.9	13.3	31.9
Ag	ppm	5	INAA	< 5	< 5	< 5	< 5	< 5	< 5	< 5
Te	ppm	6	FUS-MS-Na2O2	< 6	< 6	< 6	< 6	< 6	< 6	< 6
Sn	ppm	0.5	FUS-MS-Na2O2	< 0.5	< 0.5	< 0.5	< 0.5	4.6	1.3	< 0.5
W	ppm	0.7	FUS-MS-Na2O2	2.0	2.9	< 0.7	2.5	2.5	0.8	3.0
Br	ppm	0.5	INAA	6.6	54.7	49.4	98.8	35.1	92.1	66.4
Ba*	ppm	3	FUS-Na2O2	2980	2080	56	29000	90	211	96
Ca	%	0.01	FUS-Na2O2	0.04	0.73	0.10	0.24	0.16	0.15	0.47
Sr	ppm	3	FUS-MS-Na2O2	89	354	34	2080	75	52	176
K	%	0.1	FUS-Na2O2	< 0.1	0.8	0.1	0.2	0.2	0.2	0.3
Na	%	0.01	INAA	0.10	1.75	0.87	1.78	1.01	1.76	1.68
Al	%	0.01	FUS-Na2O2	< 0.01	0.15	0.08	0.08	0.05	0.03	0.03
Ti	%	0.01	FUS-Na2O2	< 0.01	< 0.01	< 0.01	< 0.01	< 0.01	< 0.01	< 0.01

Table J1. Continued

	Unit	D.L.	Analysis Method	GMA13-037	GMA13-025	GMA13-026	GMA13-047	GMA13-054	GMA13-055	GMA13-059
V	ppm	5	FUS-MS-Na2O2	19	193	35	29	10	10	27
P	%	0.005	FUS-Na2O2	0.017	-	-	-	-	-	-
Cr	ppm	5	INAA	< 5	18	62	71	50	77	55
Ir	ppb	5	INAA	< 5	< 5	< 5	< 5	< 5	< 5	< 5
B	ppm	10	FUS-MS-Na2O2	< 10	110	20	60	90	40	120
Be	ppm	4	FUS-MS-Na2O2	< 4	< 3	< 3	< 3	< 3	< 3	6
Cs	ppm	0.1	FUS-MS-Na2O2	< 0.1	< 0.1	0.4	< 0.1	< 0.1	< 0.1	< 0.1
Li	ppm	3	FUS-MS-Na2O2	< 3	47	< 3	3	5	< 3	33
Rb	ppm	0.4	FUS-MS-Na2O2	< 0.4	5.5	2.8	1.9	1.6	2.1	1.9
Nb	ppm	2.4	FUS-MS-Na2O2	< 2.4	< 2.4	< 2.4	< 2.4	< 2.4	< 2.4	< 2.4
Ta	ppm	0.2	FUS-MS-Na2O2	< 0.2	< 0.2	< 0.2	< 0.2	< 0.2	< 0.2	< 0.2
U	ppm	0.1	FUS-MS-Na2O2	2.0	3.6	2.2	3.1	4.4	10.5	2.7
Hf	ppm	1	INAA	< 1	< 1	< 1	< 1	< 1	< 1	< 1
Th	ppm	0.1	FUS-MS-Na2O2	< 0.1	< 0.1	< 0.1	< 0.1	< 0.1	< 0.1	< 0.1
Sc	ppm	0.1	INAA	< 0.1	0.6	0.3	0.2	0.2	< 0.1	0.2
Y	ppm	0.1	FUS-MS-Na2O2	< 0.1	8.7	< 0.1	< 0.1	< 0.1	< 0.1	3.2
La	ppm	0.4	FUS-MS-Na2O2	< 0.4	2.2	0.7	0.6	< 0.4	< 0.4	1.6
Ce	ppm	0.8	FUS-MS-Na2O2	< 0.8	5.0	1.2	1.4	< 0.8	< 0.8	2.0
Pr	ppm	0.1	FUS-MS-Na2O2	< 0.1	0.6	0.1	0.2	< 0.1	< 0.1	0.2
Nd	ppm	0.4	FUS-MS-Na2O2	1.0	3.1	0.8	1.2	< 0.4	< 0.4	1.5
Sm	ppm	0.1	FUS-MS-Na2O2	< 0.1	0.6	< 0.1	0.3	< 0.1	< 0.1	0.1
Eu	ppm	0.1	FUS-MS-Na2O2	< 0.1	0.4	< 0.1	1.2	< 0.1	< 0.1	< 0.1
Gd	ppm	0.1	FUS-MS-Na2O2	< 0.1	1.2	0.2	0.9	< 0.1	0.1	0.4
Tb	ppm	0.1	FUS-MS-Na2O2	< 0.1	0.2	< 0.1	< 0.1	< 0.1	< 0.1	< 0.1
Dy	ppm	0.3	FUS-MS-Na2O2	< 0.3	1.1	< 0.3	< 0.3	< 0.3	< 0.3	0.5
Ho	ppm	0.2	FUS-MS-Na2O2	< 0.2	0.3	< 0.2	< 0.2	< 0.2	< 0.2	< 0.2
Er	ppm	0.1	FUS-MS-Na2O2	< 0.1	0.9	0.1	0.1	< 0.1	0.2	0.4
Tm	ppm	0.1	FUS-MS-Na2O2	< 0.1	0.1	< 0.1	< 0.1	< 0.1	< 0.1	< 0.1
Yb	ppm	0.1	FUS-MS-Na2O2	< 0.1	0.7	0.1	1.6	< 0.1	0.1	0.3
Lu	ppm	0.05	INAA	< 0.05	0.20	< 0.05	< 0.05	0.13	0.18	0.07

Table J2: Precision and accuracy of whole-rock geochemical data for oxides and altered volcanic rocks (standards)

		Detection	Accepted	Measured		Measured		Measured		Measured		
Element	Unit	Limit	GXR-1	GXR-1 (1)	*% Acc*	GXR-1 (2)	*% Acc*	GXR-1 (3)	*% Acc*	GXR-1 (4)	*% Acc*	*% RSD*
Hg	ppb	5	3900	3960	*-2*	3680	*6*	3510	*11*	4170	*-6*	*8*
Al	%	0.01	3.52	3.52	*0*	-	-	-	-	-	-	-
B	ppm	10	15	10	*50*	-	-	-	-	-	-	-
Ba	ppm	3	750	699	*7*	-	-	-	-	-	-	-
Be	ppm	3	1.22	< 3	-	-	-	-	-	-	-	-
Bi	ppm	2	1380	1520	*-9*	-	-	-	-	-	-	-
Ca	%	0.01	0.96	0.89	*7.87*	-	-	-	-	-	-	-
Cd	ppm	2	3.3	4	*-18*	-	-	-	-	-	-	-
Ce	ppm	0.8	17	16.3	*4.3*	-	-	-	-	-	-	-
Co	ppm	0.2	8.2	7.4	*10.8*	-	-	-	-	-	-	-
Cs	ppm	0.1	3	2.9	*3.4*	-	-	-	-	-	-	-
Cu	ppm	2	1110	1120	*-1*	-	-	-	-	-	-	-
Dy	ppm	0.3	4.3	4.4	*-2.3*	-	-	-	-	-	-	-
Eu	ppm	0.1	0.69	0.7	*-1.4*	-	-	-	-	-	-	-
Ga	ppm	0.2	13.8	13.2	*4.5*	-	-	-	-	-	-	-
Gd	ppm	0.1	4.2	4.5	*-6.7*	-	-	-	-	-	-	-
In	ppm	0.2	0.77	0.8	*-3.8*	-	-	-	-	-	-	-
K	%	0.1	0.05	< 0.1	-	-	-	-	-	-	-	-
La	ppm	0.4	7.5	8.5	*-11.8*	-	-	-	-	-	-	-
Li	ppm	3	8.2	11	*-25*	-	-	-	-	-	-	-
Mg	%	0.01	0.217	0.21	*3.33*	-	-	-	-	-	-	-
Mn	ppm	3	852	832	*2*	-	-	-	-	-	-	-
Nb	ppm	2.4	0.8	3.7	*-78.4*	-	-	-	-	-	-	-
Nd	ppm	0.4	18	10.2	*76.5*	-	-	-	-	-	-	-
Ni	ppm	10	41	50	*-18*	-	-	-	-	-	-	-
Pb	ppm	0.8	730	714	*2*	-	-	-	-	-	-	-
Rb	ppm	0.4	14	2.9	*382.8*	-	-	-	-	-	-	-
S	%	0.01	0.257	0.26	*-1.15*	-	-	-	-	-	-	-
Se	ppm	0.8	16.6	22.1	*-24.9*	-	-	-	-	-	-	-
Sm	ppm	0.1	2.7	2.8	*-3.6*	-	-	-	-	-	-	-
Sn	ppm	0.5	54	52.8	*2.3*	-	-	-	-	-	-	-
Sr	ppm	3	275	284	*-3*	-	-	-	-	-	-	-
Ta	ppm	0.2	0.175	< 0.2	-	-	-	-	-	-	-	-
Tb	ppm	0.1	0.83	0.8	*3.7*	-	-	-	-	-	-	-
Te	ppm	6	13	14	*-7*	-	-	-	-	-	-	-
Th	ppm	0.1	2.44	2.6	*-6.2*	-	-	-	-	-	-	-
Ti	%	0.01	0.036	0.03	*20.00*	-	-	-	-	-	-	-
Tl	ppm	0.1	0.39	0.4	*-2.5*	-	-	-	-	-	-	-
Tm	ppm	0.1	0.43	0.4	*7.5*	-	-	-	-	-	-	-
U	ppm	0.1	34.9	33.3	*5*	-	-	-	-	-	-	-
V	ppm	5	80	83	*-4*	-	-	-	-	-	-	-
W	ppm	0.7	164	159	*3*	-	-	-	-	-	-	-
Y	ppm	0.1	32	33.5	*-4*	-	-	-	-	-	-	-
Yb	ppm	0.1	1.9	2.1	*-9.5*	-	-	-	-	-	-	-
Zn	ppm	30	760	770	*-1*	-	-	-	-	-	-	-

		Detection	Accepted	Measured		Measured		Measured		Measured		
Element	Unit	Limit	GXR-6	GXR-6 (1)	*% Acc*	GXR-6 (2)	*% Acc*	GXR-6 (3)	*% Acc*	GXR-6 (4)	*% Acc*	*% RSD*
Hg	ppb	5	68	70	*-3*	67	*1*	76	*-11*	78	*-13*	*7*
Ni	ppm	1	27	26	*4*	28	*-4*	-	-	-	-	-
Cu	ppm	1	66	67	*-1*	76	*-13*	-	-	-	-	-
Zn	ppm	1	118	123	*-4*	132	*-11*	-	-	-	-	-
Cd	ppm	0.5	1	< 0.5	-	< 0.5	-	-	-	-	-	-
S	%	0.001	0.016	0.021	*-23.810*	0.033	*-51.515*	-	-	-	-	-
Ag	ppm	0.3	1.3	0.5	*160.0*	0.5	*160.0*	-	-	-	-	-
Pb	ppm	3	101	89	*13*	122	*-17*	-	-	-	-	-

		Detection	Accepted	Measured		Measured		Measured		Measured		
Element	Unit	Limit	BaSO4	BaSO4 (1)	*% Acc*	BaSO4 (2)	*% Acc*	BaSO4 (3)	*% Acc*	BaSO4 (4)	*% Acc*	*% RSD*
Total S	%	0.01	14.0	14.0	*0.0*	14.1	*-0.7*	14.3	*-2.1*	14.1	*-0.7*	*0.9*

Table J2: Continued

Element	Unit	Detection Limit	Accepted GXR-4	Measured GXR-4 (1)	% Acc	Measured GXR-4 (2)	% Acc	Measured GXR-4 (3)	% Acc	Measured GXR-4 (4)	% Acc	% RSD
Hg	ppb	5	110	111	*-1*	103	*7*	< 5	-	117	*-6*	*6*
Al	%	0.01	7.2	7.35	*-2.04*	-	-	-	-	-	-	-
B	ppm	10	4.5	< 10	-	-	-	-	-	-	-	-
Ba	ppm	3	1640	1420	*15*	-	-	-	-	-	-	-
Be	ppm	3	1.9	< 3	-	-	-	-	-	-	-	-
Bi	ppm	2	19	19	*0*	-	-	-	-	-	-	-
Ca	%	0.01	1.01	1.08	*-6.48*	-	-	-	-	-	-	-
Cd	ppm	2	0.86	< 2	-	-	-	-	-	-	-	-
Ce	ppm	0.8	102	114	*-11*	-	-	-	-	-	-	-
Co	ppm	0.2	14.6	13.8	*5.8*	-	-	-	-	-	-	-
Cs	ppm	0.1	2.8	2.2	*27.3*	-	-	-	-	-	-	-
Cu	ppm	2	6520	6100	*7*	-	-	-	-	-	-	-
Dy	ppm	0.3	2.6	2.6	*0.0*	-	-	-	-	-	-	-
Eu	ppm	0.1	1.63	1.4	*16.4*	-	-	-	-	-	-	-
Ga	ppm	0.2	20	17.6	*13.6*	-	-	-	-	-	-	-
Gd	ppm	0.1	5.25	4.2	*25.0*	-	-	-	-	-	-	-
In	ppm	0.2	0.27	< 0.2	-	-	-	-	-	-	-	-
K	%	0.1	4.01	3.9	*2.8*	-	-	-	-	-	-	-
La	ppm	0.4	64.5	57	*13*	-	-	-	-	-	-	-
Li	ppm	3	11.1	5	*122*	-	-	-	-	-	-	-
Mg	%	0.01	1.66	1.75	*-5.14*	-	-	-	-	-	-	-
Mn	ppm	3	155	119	*30*	-	-	-	-	-	-	-
Nb	ppm	2.4	10	10.8	*-7.4*	-	-	-	-	-	-	-
Nd	ppm	0.4	45	39	*15*	-	-	-	-	-	-	-
Ni	ppm	10	42	80	*-48*	-	-	-	-	-	-	-
Pb	ppm	0.8	52	48.3	*7.7*	-	-	-	-	-	-	-
Rb	ppm	0.4	160	128	*25*	-	-	-	-	-	-	-
S	%	0.01	1.77	1.59	*11.32*	-	-	-	-	-	-	-
Se	ppm	0.8	5.6	< 0.8	-	-	-	-	-	-	-	-
Si	%	0.01	30.89	> 30.0	-	-	-	-	-	-	-	-
Sm	ppm	0.1	6.6	5.7	*15.8*	-	-	-	-	-	-	-
Sn	ppm	0.5	5.6	6.4	*-12.5*	-	-	-	-	-	-	-
Sr	ppm	3	221	190	*16*	-	-	-	-	-	-	-
Ta	ppm	0.2	0.79	0.3	*163.3*	-	-	-	-	-	-	-
Tb	ppm	0.1	0.36	0.6	*-40.0*	-	-	-	-	-	-	-
Te	ppm	6	0.97	< 6	-	-	-	-	-	-	-	-
Th	ppm	0.1	22.5	23.7	*-5.1*	-	-	-	-	-	-	-
Ti	%	0.01	0.29	0.28	*3.57*	-	-	-	-	-	-	-
Tl	ppm	0.1	3.2	3.1	*3.2*	-	-	-	-	-	-	-
Tm	ppm	0.1	0.21	0.2	*5.0*	-	-	-	-	-	-	-
U	ppm	0.1	6.2	6.7	*-7.5*	-	-	-	-	-	-	-
V	ppm	5	87	78	*12*	-	-	-	-	-	-	-
W	ppm	0.7	30.8	30.5	*1.0*	-	-	-	-	-	-	-
Y	ppm	0.1	14	14.5	*-3.4*	-	-	-	-	-	-	-
Yb	ppm	0.1	1.6	1	*60*	-	-	-	-	-	-	-
Zn	ppm	30	73	80	*-9*	-	-	-	-	-	-	-

Element	Unit	Detection Limit	Accepted SGR-1b	Measured SGR-1b (1)	% Acc	Measured SGR-1b (2)	% Acc	Measured SGR-1b (3)	% Acc	% RSD
Total S	%	0.01	1.53	1.56	*-1.92*	1.58	*-3.16*	1.55	*-1.29*	*0.98*

Element	Unit	Detection Limit	Accepted NIST 696	Measured NIST 696 (1)	% Acc	Measured NIST 696 (2)	% Acc	% RSD
Al	%	0.01	28.9	> 25.0	-	-	-	-
Cr	ppm	30	321	300	*7*	300	*7*	*0*
V	ppm	5	403	354	*14*	360	*12*	*1*

Table J2: Continued

Element	Unit	Detection Limit	Accepted LKSD-3	Measured LKSD-3 (1)	% Acc
V	ppm	5	82	76	*8*
Cr	ppm	20	87	90	*-3*
Co	ppm	1	30	29	*3*
Ni	ppm	20	47	50	*-6*
Cu	ppm	10	35	30	*17*
Zn	ppm	30	152	150	*1*
As	ppm	5	27	26	*4*
Rb	ppm	1	78	75	*4*
Sr	ppm	2	240	240	*0*
Y	ppm	0.5	30	29	*3*
Mo	ppm	2	2	< 2	-
Sn	ppm	1	3	3	*0*
Ba	ppm	3	680	654	*4*
La	ppm	0.05	52	48.6	*7.0*
Ce	ppm	0.05	90	91.4	*-1.5*
Nd	ppm	0.05	44	43.1	*2.1*
Sm	ppm	0.01	8	7.6	*5.3*
Eu	ppm	0.005	1.5	1.4	*7.1*
Dy	ppm	0.01	4.9	4.8	*2.1*
Yb	ppm	0.01	2.7	2.8	*-3.6*
Lu	ppm	0.002	0.4	0.36	*11.11*
Hf	ppm	0.1	4.8	4.5	*6.7*
Ta	ppm	0.01	0.7	0.6	*16.7*
W	ppm	0.5	2	< 0.5	-
U	ppm	0.01	4.6	4.2	*9.5*

Element	Unit	Detection Limit	Accepted TDB-1	Measured TDB-1 (1)	% Acc
V	ppm	5	471	491	*-4*
Cr	ppm	20	251	250	*0*
Ni	ppm	20	92	100	*-8*
Cu	ppm	10	323	330	*-2*
Zn	ppm	30	155	160	*-3*
Rb	ppm	1	23	21	*10*
Y	ppm	0.5	36	35	*3*
La	ppm	0.05	17	18.2	*-6.6*
Ce	ppm	0.05	41	41	*0*
Nd	ppm	0.05	23	24.6	*-6.5*
Eu	ppm	0.005	2.1	2.1	*0.0*
Yb	ppm	0.01	3.4	3.3	*3.0*
Th	ppm	0.05	2.7	2.9	*-6.9*

Element	Unit	Detection Limit	Accepted GBW 07239	Measured GBW 07239 (1)	% Acc
As	ppm	5	1	< 5	-
Bi	ppm	2	1	< 2	-
Ce	ppm	0.8	60.3	60.4	*-0.2*
Co	ppm	0.2	13.5	14.4	*-6.3*
Cu	ppm	2	48.6	59	*-18*
Ga	ppm	0.2	23.1	23.7	*-2.5*
Ge	ppm	0.7	12.4	13.7	*-9.5*
La	ppm	0.4	37.4	44.7	*-16.3*
Mn	ppm	3	11540	> 10000	-
Mo	ppm	1	1100	1000	*10*
Nd	ppm	0.4	29.8	29.1	*2.4*
Ni	ppm	10	20.9	30	*-30*
Pb	ppm	0.8	26.1	28.2	*-7.4*
Pr	ppm	0.1	7.4	7.1	*4.2*
Sn	ppm	0.5	33.2	32	*4*
W	ppm	0.7	1000	954	*5*
Y	ppm	0.1	34.2	39.9	*-14.3*
Zn	ppm	30	120	130	*-8*

Element	Unit	Detection Limit	Accepted SY-4	Measured SY-4 (1)	% Acc
SiO2	%	0.01	49.9	50.3	*-0.8*
Al2O3	%	0.01	20.69	20.65	*0.19*
Fe2O3(T)	%	0.01	6.21	6.2	*0.2*
MnO	%	0.001	0.108	0.11	*-1.82*
MgO	%	0.01	0.54	0.5	*8.0*
CaO	%	0.01	8.05	8.16	*-1.35*
Na2O	%	0.01	7.1	6.97	*1.87*
K2O	%	0.01	1.66	1.67	*-0.60*
TiO2	%	0.001	0.287	0.29	*-1.03*
P2O5	%	0.01	0.131	0.11	*19.09*
Sc	ppm	1	1.1	1	*10*
Be	ppm	1	2.6	3	*-13*
V	ppm	5	8	8	*0*
Sr	ppm	2	1191	1207	*-1*
Y	ppm	1	119	114	*4*
Zr	ppm	1	517	530	*-2*
Ba	ppm	2	340	347	*-2*

Element	Unit	Detection Limit	Accepted DNC-1a	Measured DNC-1a (1)	% Acc
Ni	ppm	1	247	259	*-5*
Cu	ppm	1	100	106	*-6*
Pb	ppm	3	6.3	< 3	-
Zn	ppm	1	70	57	*23*

Table J2: Continued

Element	Unit	Detection Limit	Accepted W-2a	Measured W-2a (1)	% Acc
SiO2	%	0.01	52.4	52.29	*0.21*
Al2O3	%	0.01	15.4	15.26	*0.92*
Fe2O3(T)	%	0.01	10.7	10.65	*0.47*
MnO	%	0.001	0.163	0.17	*-4.12*
MgO	%	0.01	6.37	6.21	*2.58*
CaO	%	0.01	10.9	11.08	*-1.62*
Na2O	%	0.01	2.14	2.16	*-0.93*
K2O	%	0.01	0.626	0.61	*2.62*
TiO2	%	0.001	1.06	1.06	*0.00*
P2O5	%	0.01	0.13	0.12	*8.33*
Sc	ppm	1	36	35	*3*
Be	ppm	1	1.3	< 1	-
V	ppm	5	262	279	*-6*
V	ppm	5	262	271	*-3*
Cr	ppm	20	92	90	*2*
Co	ppm	1	43	43	*0*
Ni	ppm	20	70	80	*-13*
Cu	ppm	10	110	110	*0*
Zn	ppm	30	80	70	*14*
Ga	ppm	1	17	17	*0*
Ge	ppm	0.5	1	1.4	*-29*
Rb	ppm	1	21	20	*5*
Sr	ppm	2	190	193	*-2*
Sr	ppm	2	190	193	*-2*
Y	ppm	0.5	24	21	*14*
Y	ppm	1	24	19	*26*
Zr	ppm	1	94	96	*-2*
Nb	ppm	0.2	7.9	7	*13*
Mo	ppm	2	0.6	< 2	-
Sb	ppm	0.2	0.79	0.8	*-1.3*
Cs	ppm	0.1	0.99	0.9	*10.0*
Ba	ppm	3	182	167	*9*
Ba	ppm	2	182	172	*6*
La	ppm	0.05	10	10.8	*-7.4*
Ce	ppm	0.05	23	23.9	*-3.8*
Nd	ppm	0.05	13	12.9	*0.8*
Sm	ppm	0.01	3.3	3.3	*0.0*
Tb	ppm	0.01	0.63	0.62	*1.61*
Dy	ppm	0.01	3.6	3.9	*-7.7*
Ho	ppm	0.01	0.76	0.78	*-2.56*
Yb	ppm	0.01	2.1	2.1	*0.0*
Lu	ppm	0.002	0.33	0.31	*6.45*
Hf	ppm	0.1	2.6	2.5	*4.0*
Ta	ppm	0.01	0.5	0.45	*11.11*
W	ppm	0.5	0.3	1	*-70.0*
Tl	ppm	0.05	0.2	0.07	*185.71*
Bi	ppm	0.1	0.03	< 0.1	-

Element	Unit	Detection Limit	Accepted OREAS 101a	Measured OREAS 101a (1)	% Acc
V	ppm	5	83	76	*9*
Co	ppm	1	48.8	44	*11*
Cu	ppm	10	434	410	*6*
Y	ppm	0.5	183	168	*9*
Mo	ppm	2	21.9	21	*4*
La	ppm	0.05	816	821	*-1*
Ce	ppm	0.05	1396	1430	*-2*
Pr	ppm	0.01	134	132	*2*
Nd	ppm	0.05	403	403	*0*
Sm	ppm	0.01	48.8	51.1	*-4.5*
Eu	ppm	0.005	8.06	7.89	*2.15*
Dy	ppm	0.01	33.3	32.4	*2.8*
Ho	ppm	0.01	6.46	6.34	*1.89*
Er	ppm	0.01	19.5	19.5	*0.0*
Tm	ppm	0.005	2.9	2.7	*7.4*
Yb	ppm	0.01	17.5	18.6	*-5.9*
Lu	ppm	0.002	2.66	2.54	*4.72*
Th	ppm	0.05	36.6	35.5	*3.1*
U	ppm	0.01	422	414	*2*
Ce	ppm	0.8	1396	1190	*17*
Co	ppm	0.2	48.8	46.9	*4.1*
Cu	ppm	2	434	399	*9*
Dy	ppm	0.3	33.3	30.3	*9.9*
Er	ppm	0.1	19.5	19.8	*-1.5*
Eu	ppm	0.1	8.06	8.8	*-8.4*
Fe	%	0.05	11.06	11.4	*-3.0*
Gd	ppm	0.1	43.4	43.2	*0.5*
Ho	ppm	0.2	6.46	7.3	*-11.5*
K	%	0.1	2.34	2.2	*6.4*
La	ppm	0.4	816	752	*9*
Mg	%	0.01	1.23	1.21	*1.65*
Mn	ppm	3	964	915	*5*
Mo	ppm	1	21.9	19	*15*
Nd	ppm	0.4	403	416	*-3*
Pb	ppm	0.8	19	8.2	*131.7*
Pr	ppm	0.1	134	131	*2*
Sm	ppm	0.1	48.8	50.7	*-3.7*
Tb	ppm	0.1	5.92	6.1	*-3.0*
Th	ppm	0.1	36.6	39.2	*-6.6*
Ti	%	0.01	0.395	0.41	*-3.66*
Tm	ppm	0.1	2.9	3.2	*-9.4*
U	ppm	0.1	422	416	*1*
V	ppm	5	83	77	*8*
Y	ppm	0.1	183	197	*-7*
Yb	ppm	0.1	17.5	16.4	*6.7*

		Detection	Accepted	Measured		Measured		Measured		Measured		
Element	Unit	Limit	DMMAS 120	DMMAS 120 (1)	*% Acc*	DMMAS 120 (2)	*% Acc*	DMMAS 120 (3)	*% Acc*	DMMAS 120 (4)	*% Acc*	*% RSD*
Au	ppb	2	727	678	*7*	660	*10*	752	*-3*	628	*16*	*8*
As	ppm	0.5	1790	1750	*2*	1790	*0*	1790	*0*	1890	*-5*	*3*
Ba	ppm	50	1270	1420	*-11*	-	-	-	-	-	-	-
Co	ppm	1	47	46	*2*	-	-	-	-	-	-	-
Cr	ppm	5	138	136	*1*	156	*-12*	153	*-10*	156	*-12*	*6*
Fe	%	0.01	3.54	3.51	*0.85*	-	-	-	-	-	-	-
Na	%	0.01	2.16	2.03	*6.40*	-	-	-	-	-	-	-
Sb	ppm	0.1	7.3	6.1	*19.7*	-	-	-	-	-	-	-
Sc	ppm	0.1	6.5	6.3	*3.2*	-	-	-	-	-	-	-
U	ppm	0.5	11.7	12.7	*-7.9*	-	-	-	-	-	-	-
La	ppm	0.5	17.6	17.1	*2.9*	-	-	-	-	-	-	-
Ce	ppm	3	32	34	*-5.9*	-	-	-	-	-	-	-
Sm	ppm	0.1	2.7	2.2	*22.7*	-	-	-	-	-	-	-
Sc	ppm	0.1	6.5	6.2	*4.8*	6.8	*-4*	6.7	*-3*	-	-	*5*
Sb	ppm	0.2	7.3	6.2	*17.7*	6.3	*16*	5.5	*33*	-	-	*7*

Table J2: Continued

		Detection	Accepted	Measured	
Element	Unit	Limit	OREAS 131a	OREAS 131a (1)	*% Acc*
As	ppm	5	91	89	*2*
Ba	ppm	3	865	892	*-3*
Cd	ppm	2	80	75	*7*
Co	ppm	0.2	25	23.2	*8*
Cu	ppm	2	324	317	*2*
Fe	%	0.05	5.9	5.93	*-0.51*
Pb	ppm	0.8	17400	> 5000	-
S	%	0.01	4.82	4.41	*9.30*
Sb	ppm	2	49	50	*-2*
Zn	ppm	30	28400	> 10000	-

		Detection	Accepted	Measured	
Element	Unit	Limit	OREAS 131b	OREAS 131b (1)	*% Acc*
As	ppm	5	90	83	*8*
Ba	ppm	3	803	779	*3*
Cd	ppm	2	93	98	*-5*
Co	ppm	0.2	19.4	20.6	*-5.8*
Cu	ppm	2	217	223	*-3*
Fe	%	0.05	5.85	5.83	*0.34*
Pb	ppm	0.8	19000	> 5000	-
S	%	0.01	5.01	5.08	*-1.38*
Sb	ppm	2	54	51	*6*
Zn	ppm	30	30500	> 10000	-

		Detection	Accepted	Measured	
Element	Unit	Limit	CTA-AC-1	CTA-AC-1 (1)	*% Acc*
V	ppm	5	104	103	*1*
Cu	ppm	10	54	60	*-10*
Zn	ppm	30	38	40	*-5*
Y	ppm	0.5	272	298	*-9*
La	ppm	0.05	2176	> 2000	-
Ce	ppm	0.05	3326	> 3000	-
Nd	ppm	0.05	1087	1190	*-9*
Sm	ppm	0.01	162	171	*-5*
Eu	ppm	0.005	46.7	46.3	*0.9*
Gd	ppm	0.01	124	133	*-7*
Tb	ppm	0.01	13.9	14.5	*-4*
Yb	ppm	0.01	11.4	11	*4*
Lu	ppm	0.002	1.08	1.06	*1.89*
Ta	ppm	0.01	2.65	2.71	*-2.21*
Th	ppm	0.05	21.8	23.4	*-6.84*

		Detection	Accepted	Measured	
Element	Unit	Limit	NCS DC86312	NCS DC86312 (1)	*% Acc*
Y	ppm	0.5	976	999	*-2*
La	ppm	0.05	2360	> 2000	-
Ce	ppm	0.05	190	184	*3*
Nd	ppm	0.05	1600	1620	*-1*
Gd	ppm	0.01	225	245	*-8*
Tb	ppm	0.01	34.6	33.6	*3.0*
Dy	ppm	0.01	183	189	*-3*
Ho	ppm	0.01	36	35.9	*0.3*
Er	ppm	0.01	96.2	101	*-5*
Tm	ppm	0.005	15.1	14	*8*
Yb	ppm	0.01	87.79	88.7	*-1.0*
Lu	ppm	0.002	11.96	12.2	*-2.0*
Th	ppm	0.05	23.6	24.9	*-5.2*

Element	Unit	Detection Limit	Accepted MP-1b	Measured MP-1b (1)	% Acc	Measured MP-1b (2)	% Acc	Measured MP-1b (3)	% Acc	% RSD
As	ppm	5	23000	> 10000	-	-	-	-	-	-
Bi	ppm	2	954	928	*3*	-	-	-	-	-
Ca	%	0.01	2.47	2.53	*-2.37*	2.43	*1.65*	2.61	*-5.36*	*3.57*
Cd	ppm	2	527	570	*-8*	-	-	-	-	-
Cu	ppm	2	30690	> 10000	-	-	-	-	-	-
Fe	%	0.05	8.19	8.27	*-0.97*	8.14	*0.61*	8.07	*1.49*	*1.24*
In	ppm	0.2	565	582	*-3*	-	-	-	-	-
Mg	%	0.01	0.024	0.03	*-20.00*	0.02	*20.00*	0.03	*-20.00*	*21.65*
Mo	ppm	1	285	287	*-1*	-	-	-	-	-
Pb	ppm	0.8	20900	> 5000	-	-	-	-	-	-
S	%	0.01	13.79	14.1	*-2.2*	13.8	*-0.1*	13.1	*5.3*	*3.8*
Sb	ppm	2	54	48	*13*	-	-	-	-	-
Si	%	0.01	16.79	17.2	*-2.4*	16.7	*0.5*	17.0	*-1.2*	*1.5*
Sn	ppm	0.5	16100	> 10000	-	-	-	-	-	-
W	ppm	0.7	1100	1000	*10*	-	-	-	-	-
Zn	ppm	30	166700	> 10000	-	-	-	-	-	-
Cu	%	0.001	3.069	3.16	*-2.88*	-	-	-	-	-

Element	Unit	Detection Limit	Accepted OREAS 13b	Measured OREAS 13b (1)	% Acc	Measured OREAS 13b (2)	% Acc	% RSD
Al	%	0.01	8.41	8.28	*1.57*	8.22	*2.31*	*0.51*
Ca	%	0.01	5.57	5.66	*-1.59*	5.84	*-4.62*	*2.21*
Fe	%	0.05	8.41	8.55	*-1.64*	8.56	*-1.75*	*0.08*
K	%	0.1	2.3	2.3	*0.0*	2.2	*4.5*	*3.1*
Mg	%	0.01	3.01	3.06	*-1.63*	2.96	*1.69*	*2.35*
S	%	0.01	1.19	1.22	*-2.46*	1.14	*4.39*	*4.79*
Si	%	0.01	22.9	23.2	*-1.29*	22.9	*0.00*	*0.92*
Ti	%	0.01	0.711	0.7	*1.6*	0.71	*0.14*	*1.00*

Table J2: Continued

Element	Unit	Detection Limit	Accepted BIR-1a	Measured BIR-1a (1)	% Acc
SiO2	%	0.01	47.96	47.84	*0.25*
Al2O3	%	0.01	15.5	15.61	*-0.70*
Fe2O3(T)	%	0.01	11.3	11.28	*0.18*
MnO	%	0.001	0.175	0.17	*2.94*
MgO	%	0.01	9.7	9.58	*1.25*
CaO	%	0.01	13.3	13.58	*-2.06*
Na2O	%	0.01	1.82	1.82	*0.00*
K2O	%	0.01	0.03	0.02	*50.00*
TiO2	%	0.001	0.96	0.97	*-1.03*
P2O5	%	0.01	0.021	0.01	*110.00*
Sc	ppm	1	44	44	*0*
Be	ppm	1	0.58	< 1	-
V	ppm	5	310	325	*-5*
V	ppm	5	310	315	*-2*
Cr	ppm	20	370	370	*0*
Co	ppm	1	52	51	*2*
Ni	ppm	20	170	180	*-6*
Cu	ppm	10	125	130	*-4*
Zn	ppm	30	70	70	*0*
Ga	ppm	1	16	16	*0*
As	ppm	5	0.44	< 5	-
Sr	ppm	2	110	107	*3*
Sr	ppm	2	110	109	*1*
Y	ppm	0.5	16	15	*7*
Y	ppm	1	16	14	*14*
Zr	ppm	1	18	17	*6*
Nb	ppm	0.2	0.6	0.6	*0*
Ba	ppm	2	6	8	*-25*
La	ppm	0.05	0.63	0.59	*6.78*
Ce	ppm	0.05	1.9	2	*-5*
Nd	ppm	0.05	2.5	2.3	*8.7*
Sm	ppm	0.01	1.1	1	*10*
Yb	ppm	0.01	1.7	1.6	*6*
Lu	ppm	0.002	0.3	0.2	*50*
Hf	ppm	0.1	0.6	0.6	*0*

Element	Unit	Detection Limit	Accepted NCS DC70009	Measured NCS DC70009 (1)	% Acc
Cr	ppm	20	30	30	*0*
Cu	ppm	10	960	890	*8*
Zn	ppm	30	100	100	*0*
Ga	ppm	1	16.5	16	*3*
Ge	ppm	0.5	11.2	10.2	*10*
As	ppm	5	69.9	67	*4*
Rb	ppm	1	500	485	*3*
Y	ppm	0.5	128	133	*-4*
In	ppm	0.1	1.3	1	*30*
Sn	ppm	1	1701	> 1000	-
Sb	ppm	0.2	3.1	2.9	*6.9*
Cs	ppm	0.1	41	39.6	*3.5*
La	ppm	0.05	23.7	23.4	*1.3*
Ce	ppm	0.05	60.3	59.6	*1.2*
Pr	ppm	0.01	7.9	7.8	*1.3*
Nd	ppm	0.05	32.9	31.3	*5.1*
Sm	ppm	0.01	12.5	12	*4*
Eu	ppm	0.005	0.16	0.15	*6.67*
Gd	ppm	0.01	14.8	15	*-1*
Dy	ppm	0.01	20.7	21.3	*-2.8*
Ho	ppm	0.01	4.5	4.1	*9.8*
Er	ppm	0.01	13.4	13.3	*0.8*
Tm	ppm	0.005	2.2	2.1	*4.8*
Yb	ppm	0.01	14.9	16	*-7*
W	ppm	0.5	2200	2110	*4*
Tl	ppm	0.05	1.8	1.9	*-5.3*
Th	ppm	0.05	28.3	27.7	*2.2*

Element	Unit	Detection Limit	Accepted JR-1	Measured JR-1 (1)	% Acc
Ni	ppm	20	1.67	< 20	-
Zn	ppm	30	30.6	30	*2*
Ga	ppm	1	16.1	16	*1*
Ge	ppm	0.5	1.88	2	*-6*
As	ppm	5	16.3	16	*2*
Rb	ppm	1	257	244	*5*
Sr	ppm	2	29.1	28	*4*
Y	ppm	0.5	45.1	43	*5*
Nb	ppm	0.2	15.2	13.9	*9*
Mo	ppm	2	3.25	3	*8*
In	ppm	0.1	0.028	< 0.1	-
Sn	ppm	1	2.86	3	*-5*
Cs	ppm	0.1	20.8	19.1	*8.9*
Ba	ppm	3	50.3	47	*7*
La	ppm	0.05	19.7	20.3	*-3.0*
Ce	ppm	0.05	47.2	49.6	*-4.8*
Pr	ppm	0.01	5.58	6	*-7*
Nd	ppm	0.05	23.3	23.7	*-1.7*
Sm	ppm	0.01	6.03	5.85	*3.08*
Eu	ppm	0.005	0.3	0.27	*11.11*
Ho	ppm	0.01	1.11	1.16	*-4.31*
Yb	ppm	0.01	4.55	4.94	*-7.89*
Lu	ppm	0.002	0.71	0.65	*9.23*
Hf	ppm	0.1	4.51	4.6	*-2.0*
Ta	ppm	0.01	1.86	1.75	*6.29*
W	ppm	0.5	1.59	1.7	*-6.5*
Tl	ppm	0.05	1.56	1.39	*12.23*
Bi	ppm	0.1	0.56	0.6	*-6.7*
Th	ppm	0.05	26.7	26.3	*1.52*
U	ppm	0.01	8.88	8.77	*1.25*

Element	Unit	Detection Limit	Accepted OREAS 100a	Measured OREAS 100a (1)	% Acc
Co	ppm	1	18.1	18	*1*
Cu	ppm	10	169	170	*-1*
Y	ppm	0.5	142	133	*7*
Mo	ppm	2	24.1	24	*0*
La	ppm	0.05	260	270	*-4*
Ce	ppm	0.05	463	486	*-5*
Pr	ppm	0.01	47.1	48.3	*-2.5*
Nd	ppm	0.05	152	154	*-1*
Sm	ppm	0.01	23.6	24.6	*-4.1*
Eu	ppm	0.005	3.71	3.66	*1.37*
Gd	ppm	0.01	23.6	21.7	*8.8*
Tb	ppm	0.01	3.8	3.44	*10.47*
Dy	ppm	0.01	23.2	24	*-3*
Ho	ppm	0.01	4.81	4.92	*-2.24*
Er	ppm	0.01	14.9	15.8	*-5.7*
Tm	ppm	0.005	2.31	2.19	*5.48*
Yb	ppm	0.01	14.9	15.7	*-5.1*
Lu	ppm	0.002	2.26	2.05	*10.24*
Th	ppm	0.05	51.6	51.8	*-0.4*
U	ppm	0.01	135	136	*-1*

Table J2: Continued

Element	Unit	Detection Limit	Accepted OREAS 101b	Measured OREAS 101b (1)	
V	ppm	5	80	80	*0*
Co	ppm	1	47	46	*2*
Ni	ppm	20	9	< 20	-
Cu	ppm	10	416	430	*-3*
Y	ppm	0.5	178	183	*-3*
Mo	ppm	2	20.9	21	*0*
La	ppm	0.05	789	811	*-3*
Ce	ppm	0.05	1331	1420	*-6*
Pr	ppm	0.01	127	128	*-1*
Nd	ppm	0.05	378	388	*-3*
Sm	ppm	0.01	48	50	*-4*
Eu	ppm	0.005	7.77	8.29	*-6.27*
Tb	ppm	0.01	5.37	5.42	*-0.92*
Dy	ppm	0.01	32.1	32.7	*-1.8*
Ho	ppm	0.01	6.34	6.42	*-1.25*
Er	ppm	0.01	18.7	19.3	*-3.1*
Tm	ppm	0.005	2.66	2.8	*-5.0*
Yb	ppm	0.01	17.6	18.5	*-4.9*
Lu	ppm	0.002	2.58	2.73	*-5.49*
Th	ppm	0.05	37.1	37.8	*-1.9*
U	ppm	0.01	396	418	*-5*
Ce	ppm	0.8	1331	1360	*-2*
Co	ppm	0.2	47	49.8	*-5.6*
Cu	ppm	2	416	404	*3*
Dy	ppm	0.3	32.1	29.8	*7.7*
Er	ppm	0.1	18.7	18.4	*1.6*
Eu	ppm	0.1	7.77	7.7	*0.9*
Fe	%	0.05	10.8	10.8	*0.0*
Gd	ppm	0.1	41	33.4	*22.8*
Ho	ppm	0.2	6.34	6.3	*0.6*
K	%	0.1	2.42	2.3	*5.2*
La	ppm	0.4	789	829	*-5*
Mg	%	0.01	1.23	1.24	*-0.8*
Mn	ppm	3	931	899	*4*
Mo	ppm	1	20.9	18	*16*
Nd	ppm	0.4	378	393	*-4*
Ni	ppm	10	9	20	*-55*
Pb	ppm	0.8	18	6.7	*168.7*
Pr	ppm	0.1	127	118	*8*
Sm	ppm	0.1	48	52	*-8*
Tb	ppm	0.1	5.37	6.2	*-13.4*
Th	ppm	0.1	37.1	36.7	*1.1*
Ti	%	0.01	0.386	0.39	*-1.03*
Tm	ppm	0.1	2.66	3	*-11*
U	ppm	0.1	396	413	*-4*
Y	ppm	0.1	178	198	*-10*
Yb	ppm	0.1	17.6	16.3	*8.0*

Appendix K

Whole-Rock Geochemistry of Altered Volcaniclastic Rocks – Tinakula Deposit

Contents of this file:

1. Supplemental Tables:
   Table K1: Whole-rock geochemistry of drillcore samples (clasts and matrix separates of altered volcaniclastic rocks) from the Tinakula deposit, normalized to 100% LOI-free
   Table K2: Mass balance changes associated of altered volcaniclastic rocks relative to least-altered basaltic-andesite precursor
   Table K3: Precision of whole-rock geochemical data (duplicates)

Notes:

D.L. = detection limit
< = below detection limit
> = above detection limit (O.L)
- = not analyzed
Rel % Diff = Relative % Difference (absolute value of the change in value divided by the average)
Precision and accuracy determined through measurements of standards are reported in Table J2

1. Supplemental Tables

Table K1. Whole-rock geochemistry of drillcore samples (clasts and matrix separates of altered volcaniclastic rocks) from the Tinakula deposit, normalized to 100% LOI-free

			MA13-005-M	MA13-006-C	MA13-014-C	MA13-015-C	MA13-016-C	MA13-019-CM	MA13-020-CM	MA13-023-C
	D.L.	Method	TKAD030	TKAD030	TKAD018	TKAD018	TKAD018	TKAD017	TKAD017	TKAD033
SiO_2 - %	0.01	FUS-ICP	20.29	41.65	22.09	37.85	26.93	9.62	30.81	76.31
TiO_2	0.001	FUS-ICP	1.195	2.467	0.965	2.153	1.446	0.721	1.563	0.638
Al_2O_3	0.01	FUS-ICP	12.35	27.00	14.16	23.86	17.39	9.37	20.53	8.76
$Fe_2O_{3(T)}$	0.01	FUS-ICP	38.70	20.24	57.91	24.21	19.93	70.37	36.05	7.21
MnO	0.001	FUS-ICP	0.026	0.010	0.011	0.012	0.036	0.061	0.008	0.067
MgO	0.01	FUS-ICP	0.30	0.63	0.24	0.69	0.71	8.23	0.62	1.01
CaO	0.01	FUS-ICP	0.23	0.69	0.48	3.93	29.13	0.37	4.35	3.41
Na_2O	0.01	FUS-ICP	1.05	1.50	1.18	1.93	1.46	0.77	1.29	2.15
K_2O	0.01	FUS-ICP	2.26	5.72	2.96	5.20	2.93	0.33	4.76	0.36
P_2O_5	0.01	FUS-ICP	0.06	0.07	<0.01	0.15	0.06	0.16	0.03	0.08
$S_{(T)}$	0.01	CS	27.70	13.30	31.80	16.70	19.70	25.40	23.70	2.85
Cu - ppm	1	TD-ICP*	3090	128	51500	1050	455	14800	432	359
Zn	1	TD-ICP*	935	135	175	169	229	79600	295	675
Ag	0.3	TD-ICP	1.2	1.3	3.1	1.3	0.7	8.5	1.0	0.6
As	0.5	INAA	160.0	226.0	148.0	148.0	126.0	188.0	44.8	82.9
Bi	0.1	FUS-MS	<0.1	<0.1	<0.1	<0.1	<0.1	<0.1	0.1	<0.1
Cd	0.5	TD-ICP	1.5	<0.5	<0.5	0.6	0.6	224.0	1.3	1.8
Ga	1	FUS-MS	20	28	17	25	15	19	21	10
Ge	0.5	FUS-MS	1.2	<0.5	0.8	<0.5	<0.5	8.3	<0.5	3.8
Hg - ppb	5	1G	49	14	47	21	44	1570	182	1040
In - ppm	0.1	FUS-MS	3.0	0.3	11.9	0.6	0.4	24.5	0.7	0.5
Sb	0.2	INAA	2.4	3.4	8.4	6.1	1.7	21.1	2.3	5.9
Se	3	INAA	<3	<3	<3	<3	<3	<3	<3	<3
Sn	1	FUS-MS	1	<1	1	<1	<1	<1	1	<1
Tl	0.05	FUS-MS	0.14	0.40	0.21	0.24	<0.05	<0.05	0.08	10.50
Au - ppb	2	INAA	162	94	155	119	88	727	98	54
Ir - ppm	5	INAA	<5	<5	<5	<5	<5	<5	<5	<5
Mo	2	FUS-MS	20	8	22	14	5	21	38	9
Co	1	FUS-MS	4	11	5	10	8	1	31	12
Cr	5	INAA	<5	<5	<5	<5	<5	52	95	<5
Ni	1	TD-ICP	11	5	4	6	5	12	13	6
Sc	0.1	INAA	21.1	32.6	12.8	25.7	14.8	2.4	21.5	11.2
V	5	FUS-ICP	224	350	155	226	161	164	289	180
Rb	1	FUS-MS	26	64	26	51	40	3	44	8
Cs	0.1	FUS-MS	0.3	0.3	0.2	0.3	0.4	<0.1	0.2	1.1
Sr	2	FUS-ICP	45	234	22	190	769	2543	220	501
Ba	2	FUS-ICP	418	2228	259	702	1139	233300	2593	16100
Pb	3	TD-ICP	20	40	90	119	34	10	15	315
Zr	1	FUS-ICP	78	163	97	133	83	28	95	41
Hf	0.1	FUS-MS	1.8	3.6	2.1	3.0	1.7	0.7	2.1	0.9
Nb	0.2	FUS-MS	5.5	6.6	3.7	5.3	2.9	0.9	3.7	1.5
Ta	0.01	FUS-MS	5.14	0.43	<0.01	0.70	0.08	0.24	0.09	0.11
Th	0.05	FUS-MS	0.43	1.25	0.68	1.05	0.56	0.15	0.68	0.35
U	0.01	FUS-MS	6.51	16.6	7.75	14.70	3.79	49.00	8.19	6.70
Be	1	FUS-ICP	<1	<1	<1	<1	<1	<1	<1	1
Br	0.5	INAA	37.2	39.1	26.5	42.9	26	17.4	29.3	14.7
W	0.5	FUS-MS	98.8	178.0	74.1	89.0	188.0	220.0	163.0	1.8
Y	0.5	FUS-MS	8.1	38.4	35.1	32.4	17.6	3.7	23.4	12.2
La	0.05	FUS-MS	16.40	75.50	26.90	10.80	2.53	9.00	5.43	3.61
Ce	0.05	FUS-MS	31.10	157.00	57.40	23.20	7.08	9.45	12.60	8.42
Pr	0.01	FUS-MS	3.91	18.80	7.51	3.13	1.13	0.90	1.69	1.16
Nd	0.05	FUS-MS	16.30	74.00	32.50	13.80	5.92	3.26	7.85	5.31
Sm	0.01	FUS-MS	3.12	13.60	7.04	4.03	2.18	1.01	2.60	1.42
Eu	0.005	FUS-MS	3.99	7.58	4.28	3.44	1.48	<0.005	2.36	1.35
Gd	0.01	FUS-MS	2.28	8.24	6.39	5.14	2.80	0.67	3.71	2.04
Tb	0.01	FUS-MS	0.31	1.13	1.05	0.93	0.50	0.10	0.68	0.32
Dy	0.01	FUS-MS	1.76	7.48	6.52	6.22	3.14	0.44	4.37	2.03
Ho	0.01	FUS-MS	0.33	1.45	1.42	1.27	0.67	0.09	0.89	0.44
Er	0.01	FUS-MS	0.97	4.50	4.22	3.78	1.95	0.32	2.57	1.27
Tm	0.005	FUS-MS	0.140	0.656	0.625	0.566	0.305	0.052	0.380	0.192
Yb	0.01	FUS-MS	1.00	4.39	4.14	3.72	2.02	0.33	2.51	1.29
Lu	0.002	FUS-MS	0.179	0.726	0.682	0.616	0.333	0.055	0.407	0.204

*O.L. = 4acid ICP-OES

Table K1. Continued

			MA13-024-C	MA13-025-C	MA13-026-C	MA13-027-CM	MA13-034-C	MA13-035-C	MA13-036-C	MA13-039-C
	D.L.	Method	TKAD033	TKAD033	TKAD033	TKAD033	TKAD016	TKAD016	TKAD016	TKAD016
SiO_2 - %	0.01	FUS-ICP	89.40	56.72	53.95	57.00	34.88	38.06	35.27	27.17
TiO_2	0.001	FUS-ICP	0.063	1.541	1.592	1.662	1.762	1.764	1.804	1.600
Al_2O_3	0.01	FUS-ICP	1.15	20.56	22.48	22.07	20.58	23.95	22.85	18.18
$Fe_2O_{3(T)}$	0.01	FUS-ICP	8.48	9.16	7.69	6.99	25.97	19.00	23.18	22.85
MnO	0.001	FUS-ICP	0.007	0.026	0.041	0.020	0.022	0.073	0.079	0.110
MgO	0.01	FUS-ICP	0.17	3.35	2.72	3.11	1.01	8.20	9.11	12.32
CaO	0.01	FUS-ICP	0.31	4.49	6.06	5.33	10.79	4.10	3.43	15.63
Na_2O	0.01	FUS-ICP	0.31	3.35	4.97	3.50	1.60	1.54	1.33	1.00
K_2O	0.01	FUS-ICP	0.07	0.68	0.32	0.24	3.35	3.15	2.85	1.05
P_2O_5	0.01	FUS-ICP	0.03	0.13	0.16	0.09	0.03	0.15	0.11	0.07
$S_{(T)}$	0.01	CS	6.56	2.49	0.56	0.09	18.90	11.30	12.70	13.10
Cu - ppm	1	TD-ICP*	195	206	83	42	1660	65	2250	2410
Zn	1	TD-ICP*	5660	135	117	87	81	61	120	638
Ag	0.3	TD-ICP	4.3	3.2	0.6	< 0.3	0.8	0.4	0.6	1.2
As	0.5	INAA	231.0	21.8	11.8	< 0.5	46.4	13.2	28.4	64.9
Bi	0.1	FUS-MS	< 0.1	< 0.1	< 0.1	< 0.1	< 0.1	< 0.1	< 0.1	0.4
Cd	0.5	TD-ICP	5.4	< 0.5	< 0.5	< 0.5	< 0.5	< 0.5	< 0.5	2.3
Ga	1	FUS-MS	3	19	22	22	19	23	22	22
Ge	0.5	FUS-MS	0.5	3.0	2.3	1.8	< 0.5	< 0.5	< 0.5	1.1
Hg - ppb	5	1G	782	373	82	39	277	76	51	359
In - ppm	0.1	FUS-MS	< 0.1	< 0.1	< 0.1	0.1	0.9	0.2	0.6	2.3
Sb	0.2	INAA	10.3	1.5	0.5	0.3	1.3	0.3	< 0.2	2.2
Se	3	INAA	< 3	< 3	< 3	< 3	< 3	< 3	< 3	< 3
Sn	1	FUS-MS	< 1	< 1	< 1	< 1	< 1	< 1	1	< 1
Tl	0.05	FUS-MS	7.03	0.71	0.66	0.17	1.45	1.04	0.34	< 0.05
Au - ppb	2	INAA	97	26	< 2	< 2	47	< 2	30	60
Ir - ppm	5	INAA	< 5	< 5	< 5	< 5	< 5	< 5	< 5	< 5
Mo	2	FUS-MS	23	3	< 2	< 2	34	11	7	18
Co	1	FUS-MS	9	26	9	9	14	18	17	12
Cr	5	INAA	< 5	9	< 5	< 5	< 5	< 5	< 5	23
Ni	1	TD-ICP	5	8	8	4	7	7	6	10
Sc	0.1	INAA	1.2	24.2	28.2	29.3	17.7	21.4	21.2	15.6
V	5	FUS-ICP	59	407	361	364	234	248	283	181
Rb	1	FUS-MS	2	20	5	5	28	28	28	13
Cs	0.1	FUS-MS	0.2	1.1	0.4	0.5	0.3	0.3	0.2	0.1
Sr	2	FUS-ICP	246	1071	414	215	245	60	58	354
Ba	2	FUS-ICP	9501	40070	8162	151	722	514	395	1801
Pb	3	TD-ICP	367	66	39	27	32	< 3	< 3	63
Zr	1	FUS-ICP	7	81	884	95	101	194	139	115
Hf	0.1	FUS-MS	< 0.1	1.8	2.2	2.4	2.3	4.4	3.3	2.5
Nb	0.2	FUS-MS	< 0.2	2.4	3.8	3.7	4.3	7.5	5.8	4.6
Ta	0.01	FUS-MS	< 0.01	0.02	0.18	0.19	0.28	0.43	0.22	0.10
Th	0.05	FUS-MS	0.05	0.53	0.78	0.78	0.83	1.59	1.03	0.85
U	0.01	FUS-MS	5.32	18.50	4.68	4.77	7.48	8.49	8.15	4.34
Be	1	FUS-ICP	< 1	3	2	1	< 1	< 1	< 1	< 1
Br	0.5	INAA	2.8	22.3	18.4	15.9	18.1	37.4	26.3	24.9
W	0.5	FUS-MS	2.7	156.0	1.1	< 0.5	1.4	0.9	124.0	180.0
Y	0.5	FUS-MS	5.0	26.2	21.2	24.7	11.7	43.9	37.1	32.3
La	0.05	FUS-MS	1.74	5.08	6.18	5.49	26.90	15.80	15.20	14.80
Ce	0.05	FUS-MS	3.34	11.60	14.40	14.40	40.10	34.10	33.90	31.40
Pr	0.01	FUS-MS	0.46	1.63	2.17	2.26	4.39	4.59	4.45	4.10
Nd	0.05	FUS-MS	2.01	8.20	9.93	10.20	16.10	21.70	20.10	18.30
Sm	0.01	FUS-MS	0.73	2.63	2.89	3.33	2.56	5.52	5.23	4.53
Eu	0.005	FUS-MS	1.11	1.81	1.40	1.54	1.52	2.97	2.67	1.71
Gd	0.01	FUS-MS	0.69	3.30	3.36	3.82	2.15	6.44	5.90	4.69
Tb	0.01	FUS-MS	0.15	0.62	0.61	0.67	0.37	1.19	1.01	0.82
Dy	0.01	FUS-MS	1.05	4.03	3.82	4.25	2.29	7.85	6.61	5.14
Ho	0.01	FUS-MS	0.21	0.89	0.78	0.93	0.46	1.62	1.37	1.07
Er	0.01	FUS-MS	0.60	2.64	2.42	2.77	1.39	4.86	4.11	3.35
Tm	0.005	FUS-MS	0.095	0.407	0.357	0.444	0.208	0.719	0.608	0.494
Yb	0.01	FUS-MS	0.66	2.72	2.34	2.87	1.38	4.85	4.12	3.11
Lu	0.002	FUS-MS	0.116	0.446	0.361	0.465	0.217	0.784	0.655	0.512

*O.L. = 4acid ICP-OES

Table K1. Continued

			MA13-040-C	MA13-044-C	MA13-044-M	MA13-045-C	MA13-050-C	MA13-051-CM	MA13-052-C	MA13-052-M
	D.L.	Method	TKAD025	TKAD031	TKAD031	TKAD031	TKAD015	TKAD015	TKAD015	TKAD015
SiO_2 - %	0.01	FUS-ICP	25.19	33.73	20.01	34.58	32.04	32.13	31.29	9.56
TiO_2	0.001	FUS-ICP	1.633	1.850	0.977	1.572	0.766	1.688	1.818	0.417
Al_2O_3	0.01	FUS-ICP	18.69	20.76	12.73	19.19	14.86	22.73	22.41	6.93
$Fe_2O_{3(T)}$	0.01	FUS-ICP	26.65	37.39	62.11	38.10	46.95	28.70	18.53	7.19
MnO	0.001	FUS-ICP	0.159	0.011	0.013	0.017	0.015	0.118	0.136	0.049
MgO	0.01	FUS-ICP	18.51	0.79	0.50	0.83	0.53	9.93	11.60	3.75
CaO	0.01	FUS-ICP	6.90	0.13	0.14	0.46	0.41	0.57	10.55	71.43
Na_2O	0.01	FUS-ICP	1.39	1.08	0.94	1.29	1.25	1.32	1.26	0.23
K_2O	0.01	FUS-ICP	0.17	4.25	2.55	3.78	3.18	2.53	2.13	0.34
P_2O_5	0.01	FUS-ICP	0.69	0.03	0.01	0.21	<0.01	0.30	0.30	0.13
$S_{(T)}$	0.01	CS	11.70	23.70	35.70	20.80	29.10	12.20	8.35	17.40
Cu - ppm	1	TD-ICP*	682	2340	19100	19500	196000	1510	121	72
Zn	1	TD-ICP*	375	425	1970	17900	50	140	154	33
Ag	0.3	TD-ICP	0.5	1.7	2.3	5.7	1.5	0.9	0.4	<0.3
As	0.5	INAA	47.5	226.0	267.0	182.0	129.0	299.0	23.6	8.8
Bi	0.1	FUS-MS	0.3	<0.1	<0.1	<0.1	0.1	0.3	0.3	<0.1
Cd	0.5	TD-ICP	5.2	1.3	11.5	52.8	<0.5	<0.5	<0.5	<0.5
Ga	1	FUS-MS	23	21	13	25	9	24	20	4
Ge	0.5	FUS-MS	0.6	<0.5	0.8	4.2	<0.5	0.6	<0.5	<0.5
Hg - ppb	5	1G	90	78	293	958	1480	1450	219	41
In - ppm	0.1	FUS-MS	0.7	0.9	3.2	11.3	8.9	0.6	0.2	<0.1
Sb	0.2	INAA	0.7	5.3	6.1	8.9	4.1	8.4	0.9	0.4
Se	3	INAA	<3	<3	<3	<3	24	<3	<3	<3
Sn	1	FUS-MS	<1	<1	1	1	2	<1	<1	<1
Tl	0.05	FUS-MS	0.68	0.30	0.32	0.70	2.52	5.39	1.13	<0.05
Au - ppb	2	INAA	16	412	534	364	72	69	23	<2
Ir - ppm	5	INAA	<5	<5	<5	<5	<5	<5	<5	<5
Mo	2	FUS-MS	8	15	15	23	>100	26	7	4
Co	1	FUS-MS	20	15	10	11	4	37	21	3
Cr	5	INAA	<5	7	<5	10	10	<5	17	<5
Ni	1	TD-ICP	7	7	5	8	1	11	7	2
Sc	0.1	INAA	16.0	23.0	11.7	18.2	6.5	21.1	21.8	3.6
V	5	FUS-ICP	206	331	187	275	192	423	274	44
Rb	1	FUS-MS	1	44	28	37	14	23	18	2
Cs	0.1	FUS-MS	<0.1	0.2	0.2	0.2	0.1	0.2	0.1	<0.1
Sr	2	FUS-ICP	165	15	31	391	31	23	204	587
Ba	2	FUS-ICP	105	1395	1184	35880	517	469	314	89
Pb	3	TD-ICP	35	109	105	51	14	57	16	7
Zr	1	FUS-ICP	114	115	70	94	48	146	102	19
Hf	0.1	FUS-MS	2.5	2.7	1.3	2.2	1.1	3.3	2.5	0.4
Nb	0.2	FUS-MS	5.3	4.8	2.0	3.8	2.0	5.6	4.4	0.2
Ta	0.01	FUS-MS	0.23	0.13	<0.01	0.06	0.08	0.30	0.23	<0.01
Th	0.05	FUS-MS	0.95	0.83	0.41	0.71	0.37	1.15	0.80	0.12
U	0.01	FUS-MS	3.35	6.47	3.34	17.70	6.88	12.20	3.84	0.50
Be	1	FUS-ICP	<1	<1	<1	<1	<1	<1	<1	<1
Br	0.5	INAA	40.1	25.6	16.4	27.1	16.5	34	29.6	6.1
W	0.5	FUS-MS	1.1	206.0	193.0	160.0	1.0	2.0	1.8	134.0
Y	0.5	FUS-MS	32.7	26.2	13.6	22.4	25.7	38.2	32.3	5.2
La	0.05	FUS-MS	6.98	10.50	13.20	9.94	16.10	16.30	4.34	0.92
Ce	0.05	FUS-MS	16.70	21.90	25.10	19.90	33.50	34.50	9.22	2.64
Pr	0.01	FUS-MS	2.59	3.02	3.28	2.67	4.32	4.48	1.28	0.44
Nd	0.05	FUS-MS	14.00	13.90	13.60	12.50	18.20	19.60	7.58	2.36
Sm	0.01	FUS-MS	5.07	3.19	2.58	3.67	3.93	4.95	3.21	0.83
Eu	0.005	FUS-MS	2.83	3.40	2.13	3.29	1.76	2.10	1.64	0.47
Gd	0.01	FUS-MS	5.74	3.85	1.93	3.85	4.04	5.72	4.79	1.02
Tb	0.01	FUS-MS	0.98	0.73	0.36	0.63	0.69	1.03	0.84	0.16
Dy	0.01	FUS-MS	5.99	4.74	2.34	3.94	4.38	6.63	5.54	0.93
Ho	0.01	FUS-MS	1.17	0.97	0.51	0.79	0.87	1.34	1.13	0.18
Er	0.01	FUS-MS	3.33	2.90	1.55	2.44	2.49	3.95	3.23	0.51
Tm	0.005	FUS-MS	0.496	0.447	0.235	0.365	0.353	0.600	0.482	0.074
Yb	0.01	FUS-MS	3.23	3.07	1.49	2.41	2.31	4.31	3.26	0.47
Lu	0.002	FUS-MS	0.533	0.495	0.233	0.392	0.378	0.713	0.522	0.080

*O.L. = 4acid ICP-OES

Table K1. Continued

			MA13-053-C	MA13-056-CM	MA13-057-C	MA13-058-C	MA13-062-C	MA13-063-CM	MA13-064-C	MA13-067-C
	D.L.	Method	TKAD015	TKAD027	TKAD027	TKAD027	TKAD012	TKAD012	TKAD012	TKAD026
SiO_2 - %	0.01	FUS-ICP	17.76	13.08	32.44	32.64	54.28	48.66	28.92	42.41
TiO_2	0.001	FUS-ICP	0.793	0.261	1.319	1.741	2.015	1.568	1.302	1.986
Al_2O_3	0.01	FUS-ICP	11.75	8.19	17.16	19.67	25.03	23.61	16.08	27.07
$Fe_2O_{3(T)}$	0.01	FUS-ICP	10.17	74.59	17.89	25.80	7.19	11.36	13.67	19.67
MnO	0.001	FUS-ICP	0.090	0.022	0.098	0.128	0.027	0.051	0.108	0.015
MgO	0.01	FUS-ICP	5.32	0.41	5.96	7.98	7.62	10.25	11.87	1.59
CaO	0.01	FUS-ICP	52.76	0.64	21.85	8.42	0.33	1.15	26.05	0.38
Na_2O	0.01	FUS-ICP	0.47	1.07	1.19	1.23	2.53	2.71	1.20	1.98
K_2O	0.01	FUS-ICP	0.77	1.57	1.80	2.16	0.91	0.52	0.47	4.86
P_2O_5	0.01	FUS-ICP	0.13	0.15	0.29	0.23	0.04	0.15	0.30	0.02
$S_{(T)}$	0.01	CS	15.50	40.10	12.00	12.30	2.52	4.13	10.50	14.00
Cu - ppm	1	TD-ICP*	119	19900	98	98	899	666	278	6240
Zn	1	TD-ICP*	44	256	60	81	2650	3940	403	60
Ag	0.3	TD-ICP	<0.3	2.4	0.5	1.4	1.4	1.2	0.3	3.3
As	0.5	INAA	17.0	633.0	58.8	166.0	69.2	52.3	79.0	213.0
Bi	0.1	FUS-MS	<0.1	0.2	0.4	0.8	<0.1	<0.1	<0.1	<0.1
Cd	0.5	TD-ICP	<0.5	0.8	<0.5	<0.5	7.1	13.8	0.9	<0.5
Ga	1	FUS-MS	7	11	14	19	26	23	11	24
Ge	0.5	FUS-MS	<0.5	0.5	<0.5	<0.5	1.1	1.9	<0.5	0.5
Hg - ppb	5	1G	27	1380	297	198	214	393	16	590
In - ppm	0.1	FUS-MS	<0.1	4.8	2.3	0.7	0.4	0.3	0.2	1.1
Sb	0.2	INAA	0.6	24.4	2.0	8.0	4.1	2.5	1.2	5.8
Se	3	INAA	<3	<3	<3	<3	<3	<3	<3	<3
Sn	1	FUS-MS	<1	<1	<1	<1	1	1	<1	<1
Tl	0.05	FUS-MS	<0.05	0.06	<0.05	<0.05	0.56	0.55	<0.05	4.90
Au - ppb	2	INAA	<2	210	22	26	36	39	27	96
Ir - ppm	5	INAA	<5	<5	<5	<5	<5	<5	<5	<5
Mo	2	FUS-MS	3	56	13	9	18	26	5	65
Co	1	FUS-MS	6	18	12	25	19	16	6	22
Cr	5	INAA	<5	17	<5	17	<5	8	<5	12
Ni	1	TD-ICP	4	12	6	5	8	5	4	17
Sc	0.1	INAA	7.2	4.5	13.7	19.9	26.1	19.5	12.5	24.5
V	5	FUS-ICP	84	267	171	253	305	226	160	505
Rb	1	FUS-MS	8	18	20	22	12	6	7	44
Cs	0.1	FUS-MS	<0.1	0.2	0.2	0.2	0.6	0.2	0.1	0.3
Sr	2	FUS-ICP	770	21	367	137	44	199	246	58
Ba	2	FUS-ICP	130	211	319	346	97	2453	128	1427
Pb	3	TD-ICP	7	118	36	38	69	52	31	119
Zr	1	FUS-ICP	41	31	71	99	122	178	76	144
Hf	0.1	FUS-MS	1.0	0.7	1.6	2.5	3.1	4.1	1.8	3.3
Nb	0.2	FUS-MS	1.1	1.4	2.6	7.9	5.2	7.3	2.9	5.4
Ta	0.01	FUS-MS	0.28	<0.01	<0.01	6.67	0.25	0.43	<0.01	0.30
Th	0.05	FUS-MS	0.26	0.18	0.51	0.74	0.96	1.60	0.56	1.10
U	0.01	FUS-MS	1.06	32.30	3.08	4.99	6.74	6.51	2.76	45.10
Be	1	FUS-ICP	<1	<1	<1	<1	2	1	1	1
Br	0.5	INAA	8.2	28.6	27.9	31.1	35.4	36.5	21.3	39.2
W	0.5	FUS-MS	49.1	64.2	155.0	188.0	2.1	1.3	243.0	1.1
Y	0.5	FUS-MS	10.1	21.8	16.3	31.2	28.4	36.1	19.9	25.5
La	0.05	FUS-MS	3.26	22.30	5.62	7.04	9.36	11.60	6.01	7.42
Ce	0.05	FUS-MS	7.81	43.20	13.60	18.30	20.70	27.60	13.80	17.00
Pr	0.01	FUS-MS	1.11	5.10	1.99	2.62	2.80	3.70	1.97	2.44
Nd	0.05	FUS-MS	5.47	20.80	9.07	13.30	13.60	17.50	9.09	10.8
Sm	0.01	FUS-MS	1.54	4.32	2.71	4.21	4.09	4.66	2.64	3.17
Eu	0.005	FUS-MS	0.70	2.49	1.30	1.72	3.10	3.37	3.73	2.41
Gd	0.01	FUS-MS	1.77	3.98	2.96	5.20	4.58	5.64	3.13	3.77
Tb	0.01	FUS-MS	0.29	0.61	0.51	0.88	0.83	1.00	0.56	0.77
Dy	0.01	FUS-MS	1.74	3.68	3.03	5.50	5.20	6.45	3.47	5.14
Ho	0.01	FUS-MS	0.34	0.74	0.63	1.15	1.06	1.33	0.72	1.00
Er	0.01	FUS-MS	1.03	2.19	1.95	3.34	3.16	3.94	2.19	2.87
Tm	0.005	FUS-MS	0.151	0.313	0.283	0.489	0.482	0.593	0.326	0.445
Yb	0.01	FUS-MS	1.02	2.05	1.82	3.17	3.25	4.24	2.13	3.00
Lu	0.002	FUS-MS	0.166	0.330	0.299	0.507	0.508	0.684	0.351	0.494

*O.L. = 4acid ICP-OES

Table K1. Continued

			MA13-068-C	MA13-069-C	MA13-072-C	MA13-073-C	MA13-074-C	MA13-075-C	MA13-078-C	MA13-082-C
	D.L.	Method	TKAD026	TKAD026	TKAD032	TKAD032	TKAD032	TKAD032	TKAD001	TKAD001
SiO_2 - %	0.01	FUS-ICP	41.66	38.51	60.02	51.72	44.54	44.55	58.30	57.33
TiO_2	0.001	FUS-ICP	1.955	2.364	1.642	1.718	1.721	1.804	1.592	1.574
Al_2O_3	0.01	FUS-ICP	26.57	25.38	21.27	21.93	21.54	22.50	22.09	21.12
$Fe_2O_{3(T)}$	0.01	FUS-ICP	15.71	14.19	7.80	13.69	15.57	10.77	5.04	7.80
MnO	0.001	FUS-ICP	0.049	0.084	0.019	0.045	0.059	0.043	0.030	0.024
MgO	0.01	FUS-ICP	8.07	12.66	0.86	7.65	14.13	17.95	1.78	2.14
CaO	0.01	FUS-ICP	0.49	2.97	4.93	0.65	0.57	0.62	5.71	5.01
Na_2O	0.01	FUS-ICP	1.76	1.06	3.02	2.34	1.67	1.64	4.98	4.51
K_2O	0.01	FUS-ICP	3.60	2.58	0.43	0.24	0.14	0.06	0.31	0.46
P_2O_5	0.01	FUS-ICP	0.13	0.21	0.03	0.04	0.06	0.06	0.17	0.07
$S_{(T)}$	0.01	CS	8.16	5.96	6.46	7.00	8.40	5.65	0.54	0.12
Cu - ppm	1	TD-ICP*	491	86	648	237	74	43	325	25
Zn	1	TD-ICP*	114	155	48200	1080	643	1390	1090	425
Ag	0.3	TD-ICP	2.0	2.8	19.7	3.1	1.1	1.5	43.7	<0.3
As	0.5	INAA	74.3	83.5	115.0	56.3	31.6	88.5	35.4	9.4
Bi	0.1	FUS-MS	<0.1	<0.1	<0.1	<0.1	<0.1	<0.1	<0.1	<0.1
Cd	0.5	TD-ICP	<0.5	<0.5	164.0	1.4	<0.5	1.3	<0.5	<0.5
Ga	1	FUS-MS	26	26	22	17	20	19	24	20
Ge	0.5	FUS-MS	<0.5	0.6	6.1	0.9	<0.5	0.5	3.3	4.1
Hg - ppb	5	1G	203	106	1330	902	485	542	2110	44
In - ppm	0.1	FUS-MS	0.5	0.4	4.4	0.3	<0.1	<0.1	0.1	<0.1
Sb	0.2	INAA	2.9	2.9	21.1	10.4	4.7	6.7	4.8	2.4
Se	3	INAA	<3	<3	<3	<3	<3	<3	<3	<3
Sn	1	FUS-MS	1	<1	<1	<1	<1	<1	1	1
Tl	0.05	FUS-MS	2.47	3.51	0.45	1.14	0.92	1.14	1.68	0.19
Au - ppb	2	INAA	65	<2	207	42	44	18	5	<2
Ir - ppm	5	INAA	<5	<5	<5	<5	<5	<5	<5	<5
Mo	2	FUS-MS	13	9	5	12	3	13	4	<2
Co	1	FUS-MS	62	39	22	27	18	28	11	4
Cr	5	INAA	18	<5	<5	26	<5	<5	<5	<5
Ni	1	TD-ICP	15	12	7	24	7	9	4	5
Sc	0.1	INAA	27.2	26.9	26.4	24.8	25.0	27.9	23.7	23.2
V	5	FUS-ICP	376	356	315	316	288	375	308	302
Rb	1	FUS-MS	34	26	8	4	2	2	3	7
Cs	0.1	FUS-MS	0.3	0.2	0.3	0.2	0.2	0.2	0.5	0.8
Sr	2	FUS-ICP	78	54	328	202	79	46	288	250
Ba	2	FUS-ICP	1558	881	19580	7194	1920	838	247	45
Pb	3	TD-ICP	69	23	372	522	156	526	433	61
Zr	1	FUS-ICP	157	176	84	91	91	94	116	108
Hf	0.1	FUS-MS	3.7	4.6	2.1	2.1	2.4	2.6	3.1	2.8
Nb	0.2	FUS-MS	6.3	8.1	3.0	3.8	3.7	3.8	5.3	4.2
Ta	0.01	FUS-MS	0.34	0.44	<0.01	0.18	0.18	0.20	0.26	0.24
Th	0.05	FUS-MS	1.15	1.49	0.63	0.67	0.73	0.77	1.03	0.92
U	0.01	FUS-MS	20.10	48.50	6.92	13.20	1.91	7.33	18.50	6.88
Be	1	FUS-ICP	2	1	<1	2	3	2	1	1
Br	0.5	INAA	35.7	26.3	10.3	27.5	26.7	24.3	36.7	29.9
W	0.5	FUS-MS	0.5	1.5	5.1	0.6	0.6	<0.5	0.9	1.1
Y	0.5	FUS-MS	25.8	39.9	27.4	20.8	25.1	28.5	38.6	25.9
La	0.05	FUS-MS	4.07	6.19	11.30	4.98	5.35	6.19	11.90	7.54
Ce	0.05	FUS-MS	10.30	15.40	24.40	12.10	13.80	15.20	28.40	17.70
Pr	0.01	FUS-MS	1.78	2.46	3.23	1.76	2.05	2.21	4.35	2.73
Nd	0.05	FUS-MS	9.53	13.30	14.30	8.86	10.40	10.50	20.80	13.10
Sm	0.01	FUS-MS	3.38	4.98	3.98	2.89	3.21	3.23	5.97	3.87
Eu	0.005	FUS-MS	3.23	3.19	3.73	1.41	2.58	2.96	2.56	1.49
Gd	0.01	FUS-MS	4.53	6.05	4.57	3.25	3.84	4.00	6.85	4.49
Tb	0.01	FUS-MS	0.78	1.08	0.77	0.6	0.68	0.71	1.18	0.77
Dy	0.01	FUS-MS	5.02	7.01	4.88	3.91	4.48	4.73	7.43	4.81
Ho	0.01	FUS-MS	1.01	1.47	1.02	0.77	0.96	1.03	1.46	0.97
Er	0.01	FUS-MS	3.04	4.45	3.04	2.25	2.75	3.16	4.23	2.80
Tm	0.005	FUS-MS	0.467	0.679	0.438	0.333	0.407	0.456	0.612	0.387
Yb	0.01	FUS-MS	3.16	4.68	2.79	2.27	2.75	3.05	3.76	2.70
Lu	0.002	FUS-MS	0.499	0.731	0.448	0.365	0.462	0.497	0.570	0.398

*O.L. = 4acid ICP-OES

Table K1. Continued

			MA13-085-CM	MA13-086-C	MA13-086-M	MA13-087-C	MA13-088-C	MA13-090-C	MA13-091-CM
	D.L.	Method	TKAD001	TKAD001	TKAD001	TKAD001	TKAD001	TKAD001	TKAD001
SiO_2 - %	0.01	FUS-ICP	54.18	47.03	18.13	41.70	52.34	58.48	58.35
TiO_2	0.001	FUS-ICP	1.630	1.586	0.496	1.598	1.983	1.204	1.335
Al_2O_3	0.01	FUS-ICP	21.37	19.28	6.75	19.16	23.80	15.65	18.01
$Fe_2O_{3(T)}$	0.01	FUS-ICP	11.90	11.89	4.96	5.69	8.99	12.66	12.29
MnO	0.001	FUS-ICP	0.025	0.078	0.032	0.027	0.253	0.114	0.090
MgO	0.01	FUS-ICP	1.58	13.38	4.71	1.97	6.42	3.81	3.83
CaO	0.01	FUS-ICP	4.60	4.20	63.77	6.35	1.16	4.66	1.96
Na_2O	0.01	FUS-ICP	3.97	1.58	0.70	1.06	1.05	0.77	0.90
K_2O	0.01	FUS-ICP	0.66	0.85	0.37	3.15	3.94	2.52	3.20
P_2O_5	0.01	FUS-ICP	0.07	0.14	0.09	0.19	0.06	0.12	0.05
$S_{(T)}$	0.01	CS	0.05	1.34	15.50	5.96	2.73	7.11	6.65
Cu - ppm	1	TD-ICP*	29	11	9	1330	141	525	656
Zn	1	TD-ICP*	245	625	131	20800	928	359	181
Ag	0.3	TD-ICP	<0.3	<0.3	<0.3	5.2	0.6	2.0	0.6
As	0.5	INAA	23.0	8.8	4.1	38.9	24.5	140.0	129.0
Bi	0.1	FUS-MS	<0.1	<0.1	<0.1	<0.1	<0.1	<0.1	<0.1
Cd	0.5	TD-ICP	<0.5	<0.5	<0.5	52.8	2.1	0.9	<0.5
Ga	1	FUS-MS	21	17	3	17	23	15	20
Ge	0.5	FUS-MS	11.4	1.7	<0.5	1.5	1.0	1.2	0.5
Hg - ppb	5	1G	14	5	<5	580	298	682	1190
In - ppm	0.1	FUS-MS	<0.1	<0.1	<0.1	<0.1	0.3	0.4	0.3
Sb	0.2	INAA	3.7	11.3	2.4	2.6	1.3	11.6	8.9
Se	3	INAA	<3	<3	<3	<3	<3	<3	<3
Sn	1	FUS-MS	1	<1	<1	<1	1	2	<1
Tl	0.05	FUS-MS	<0.05	<0.05	<0.05	0.46	0.76	1.67	2.74
Au - ppb	2	INAA	<2	<2	7	83	82	614	24
Ir - ppm	5	INAA	<5	<5	<5	<5	<5	<5	<5
Mo	2	FUS-MS	<2	<2	<2	13	<2	9	5
Co	1	FUS-MS	3	9	<1	22	17	15	17
Cr	5	INAA	16	<5	<5	<5	13	25	<5
Ni	1	TD-ICP	4	5	1	7	7	9	8
Sc	0.1	INAA	23.6	21.6	4.2	23.5	28.8	16.6	22.6
V	5	FUS-ICP	102	90	21	296	360	188	551
Rb	1	FUS-MS	11	14	4	44	56	33	40
Cs	0.1	FUS-MS	1.6	0.9	0.2	0.2	0.3	0.3	<0.1
Sr	2	FUS-ICP	232	354	1170	371	88	248	90
Ba	2	FUS-ICP	45	130	103	1242	1559	1084	734
Pb	3	TD-ICP	9	67	12	675	30	155	16
Zr	1	FUS-ICP	165	101	22	123	156	97	89
Hf	0.1	FUS-MS	4.1	2.4	0.5	2.9	3.9	2.5	2.5
Nb	0.2	FUS-MS	5.5	4.6	0.3	5.1	6.7	4.0	3.6
Ta	0.01	FUS-MS	0.35	0.22	<0.01	0.07	0.36	0.31	0.24
Th	0.05	FUS-MS	1.10	0.84	0.14	0.92	1.35	0.80	0.74
U	0.01	FUS-MS	5.95	6.29	1.23	16.70	12.90	5.01	10.40
Be	1	FUS-ICP	1	2	<1	<1	1	1	<1
Br	0.5	INAA	17.2	15.7	2.9	18.6	25.2	10.5	21.9
W	0.5	FUS-MS	0.6	1.0	2.9	3.8	2.8	2.7	1.6
Y	0.5	FUS-MS	23.4	27.8	6.6	24.5	33.3	21.8	26.6
La	0.05	FUS-MS	8.32	6.16	1.74	8.39	14.90	8.00	8.76
Ce	0.05	FUS-MS	17.00	14.90	4.19	18.30	31.90	18.00	18.30
Pr	0.01	FUS-MS	3.27	2.19	0.6	2.57	4.37	2.56	2.40
Nd	0.05	FUS-MS	16.10	11.00	2.82	11.80	19.20	11.70	10.10
Sm	0.01	FUS-MS	4.28	3.04	0.87	3.31	4.89	3.31	3.01
Eu	0.005	FUS-MS	1.63	1.32	0.30	2.42	2.53	1.80	1.47
Gd	0.01	FUS-MS	4.93	3.90	0.93	3.85	5.58	3.62	4.07
Tb	0.01	FUS-MS	0.85	0.69	0.17	0.70	0.95	0.63	0.74
Dy	0.01	FUS-MS	5.14	4.71	1.10	4.40	6.12	4.01	4.74
Ho	0.01	FUS-MS	0.98	1.04	0.23	0.91	1.31	0.82	1.00
Er	0.01	FUS-MS	2.96	2.98	0.70	2.70	3.77	2.39	2.89
Tm	0.005	FUS-MS	0.432	0.468	0.096	0.426	0.545	0.357	0.422
Yb	0.01	FUS-MS	2.80	3.10	0.68	2.83	3.39	2.40	2.78
Lu	0.002	FUS-MS	0.431	0.485	0.108	0.439	0.521	0.402	0.425

*O.L. = 4acid ICP-OES

Table K2: Mass balance changes associated of altered volcaniclastic rocks relative to least-altered basaltic-andesite precursor

	MA13-086-C	MA13-086-M	MA13-087-C	MA13-088-C	MA13-090-C	MA13-091-CM	MA13-050-C	MA13-051-CM	MA13-052-C	MA13-052-M	MA13-053-C
Location	North	North	North	North	North	North	Site A	Site A	Site A	Site A	Site A
Drillhole	TKAD001	TKAD001	TKAD001	TKAD001	TKAD001	TKAD001	TKAD015	TKAD015	TKAD015	TKAD015	TKAD015
Depth	14.00	14.00	16.05	17.40	18.40	20.80	3.49	4.34	6.42	6.42	7.23
	MC [%]	MC [%]	MC [%]	MC [%]	MC [%]	MC [%]	MC [%]	MC [%]	MC [%]	MC [%]	MC [%]
SiO_2	-13.11	18.66	-24.33	-24.64	-0.94	3.74	4.78	-34.88	-27.19	-9.79	-15.99
TiO_2	0.096	0.703	-0.144	-0.169	-0.195	0.034	0.119	-0.271	0.284	0.648	0.420
Al_2O_3	-0.35	9.91	-3.46	-3.75	-2.96	0.67	10.18	-3.47	2.21	15.05	8.14
$Fe_2O_{3(T)}$	0.45	10.01	-5.88	-4.87	1.59	2.26	76.74	7.44	6.13	23.56	12.00
MnO	-0.121	-0.058	-0.170	-0.045	-0.085	-0.100	-0.161	-0.117	-0.071	0.042	0.006
MgO	8.17	15.39	-2.15	0.08	-0.09	0.24	-2.59	2.45	6.51	13.93	7.93
CaO	-4.81	248.51	-3.92	-7.84	-4.23	-6.54	-7.75	-8.15	0.67	324.85	105.59
Na_2O	-2.70	-1.29	-3.33	-3.49	-3.39	-3.19	-1.79	-3.29	-3.00	-3.00	-3.07
K_2O	0.20	0.94	1.72	1.69	1.75	2.63	5.32	0.99	1.30	1.03	1.12
$S_{(T)}$	1.15	62.45	4.27	1.53	6.48	6.60	53.73	7.39	7.24	81.18	33.50
Cu	-63.68	-37.06	885.42	6.81	406.56	580.21	361982.22	843.70	31.85	262.67	184.02
Zn	451.01	430.30	14896.37	429.79	230.49	82.66	-5.31	-12.64	36.20	56.33	-2.51
Ag	-0.02	0.45	3.60	0.19	1.68	0.45	2.62	0.40	0.20	0.55	0.17
As	6.0	14.8	26.3	12.2	126.2	126.8	236.5	179.8	18.8	39.3	35.0
Bi	-0.01	0.15	-0.01	-0.02	0.00	0.00	0.13	0.13	0.21	0.18	0.06
Cd	-0.03	0.76	37.81	0.94	0.57	0.00	0.21	-0.10	-0.03	0.92	0.29
Ga	-2.08	-4.91	-4.75	-3.93	-3.29	2.93	-0.38	-2.42	0.39	1.67	-1.86
Ge	0.23	-0.26	-0.19	-0.70	-0.17	-0.77	-0.80	-0.90	-1.05	-0.10	-0.73
Hg	-4.61	1.08	409.10	160.38	614.41	1176.54	2724.89	871.59	181.37	182.33	49.39
In	-0.1	0.1	-0.1	0.1	0.3	0.2	16.3	0.3	0.1	0.1	0.0
Sb	9.39	9.14	1.34	0.21	10.07	8.33	7.04	4.57	0.25	1.33	0.76
Se	-0.18	4.55	-0.42	-0.65	-0.13	-0.01	42.83	-0.59	-0.20	5.50	1.74
Sn	-6.56	-4.98	-6.64	-6.43	-5.17	-6.50	-3.31	-6.70	-6.57	-4.67	-5.92
Tl	-0.04	0.04	0.27	0.37	1.46	2.66	4.59	3.21	0.92	0.05	-0.01
Au	-0.12	27.21	58.83	45.61	560.25	22.91	132.00	40.90	18.99	3.67	1.16
Ir	-0.31	7.58	-0.70	-1.08	-0.21	-0.01	2.12	-0.98	-0.33	9.17	2.91
Mo	-0.12	3.03	8.37	-0.43	7.23	3.98	183.72	14.79	5.08	17.67	5.49
Co	-15.43	-21.32	-7.47	-13.67	-9.62	-6.40	-15.94	-0.86	-5.08	-9.33	-10.36
Cr	-4.47	3.41	-4.86	0.72	16.19	-4.18	11.81	-5.15	8.11	5.00	-1.26
Ni	-3.61	-3.97	-2.95	-4.02	0.23	-0.03	-6.15	-1.32	-1.92	1.33	0.65
Sc	-5.87	-7.91	-7.89	-8.46	-9.66	-2.32	-12.83	-12.02	-5.88	-8.03	-9.26
V	-272.32	-266.70	-137.96	-146.72	-179.48	197.60	3.33	-94.44	-113.15	-146.00	-169.67
Rb	5.96	9.79	25.38	25.50	23.83	33.52	19.53	7.63	9.31	3.00	10.97
Cs	0.62	0.64	-0.02	0.00	0.11	-0.12	0.02	-0.05	-0.08	0.07	-0.06
Sr	32.77	4437.45	-10.56	-227.98	-51.31	-188.34	-220.74	-264.03	-100.67	2461.33	1387.20
Ba	6.13	307.12	787.32	778.10	882.87	623.25	847.01	176.83	164.95	307.33	173.14
Pb	57.32	46.86	485.09	15.55	140.18	14.44	24.36	33.12	12.41	31.17	13.64
Zr	88.67	88.67	88.67	88.67	88.67	88.67	88.67	88.67	88.67	88.67	88.67
Hf	0.11	0.02	0.09	0.22	0.29	0.49	0.03	0.00	0.17	-0.13	0.16
Nb	1.17	-1.66	0.81	0.94	0.79	0.72	0.83	0.53	0.96	-1.93	-0.49
Ta	0.01	0.02	-0.13	0.02	0.10	0.06	-0.03	0.00	0.02	-0.16	0.43
Th	0.06	-0.12	-0.02	0.09	0.05	0.06	0.00	0.02	0.02	-0.12	-0.12
U	5.14	4.57	11.66	6.95	4.20	9.98	12.33	7.03	2.95	1.95	1.91
Be	1.26	1.52	-0.14	0.07	0.41	0.00	0.42	-0.20	-0.07	1.83	0.58
Br	12.22	10.12	11.84	12.76	8.03	20.25	28.91	19.08	24.16	26.90	16.17
W	0.31	11.12	2.17	1.02	1.90	1.03	1.28	0.65	1.00	624.77	105.62
Y	-4.83	-2.63	-11.57	-10.31	-9.31	-2.73	18.24	-6.03	-1.16	-4.97	-7.39

Table K2: Continued

	MA13-056-CM	MA13-057-C	MA13-058-C	MA13-034-C	MA13-035-C	MA13-036-C	MA13-039-C	MA13-040-C	MA13-067-C	MA13-068-C	MA13-069-C	MA13-062-C	MA13-063-CM	MA13-064-C
Location	Site A	Site A	Site A	Site B	Site B	Site B	Site B	Site B	Site B	Site B	Site B	Site B	Site B	Site B
Drillhole	TKAD027	TKAD027	TKAD027	TKAD016	TKAD016	TKAD016	TKAD016	TKAD025	TKAD026	TKAD026	TKAD026	TKAD012	TKAD012	TKAD012
Depth	2.50	4.60	6.50	2.02	5.65	7.00	5.50	6.91	2.90	3.60	5.64	2.81	4.25	6.49
	MC [%]	MC [%]	MC [%]	MC [%]	MC [%]	MC [%]	MC [%]	MC [%]	MC [%]	MC [%]	MC [%]	MC [%]	MC [%]	MC [%]
SiO_2	-16.97	-13.88	-25.16	-23.77	-37.00	-31.90	-33.44	-34.80	-28.28	-30.87	-34.99	-14.94	-30.16	-20.66
TiO_2	-0.550	0.351	0.263	0.250	-0.490	-0.145	-0.063	-0.026	-0.073	-0.192	-0.105	0.168	-0.515	0.223
Al_2O_3	6.15	4.16	0.34	0.80	-6.33	-2.70	-3.25	-2.74	-0.61	-2.27	-4.48	0.92	-5.51	1.49
$Fe_2O_{3(T)}$	203.37	12.36	13.13	12.81	-1.30	4.80	7.63	10.74	2.13	-1.11	-2.84	-4.76	-4.32	5.97
MnO	-0.126	-0.067	-0.074	-0.170	-0.156	-0.139	-0.104	-0.066	-0.180	-0.161	-0.147	-0.170	-0.164	-0.063
MgO	-2.40	3.87	3.57	-2.69	0.18	2.23	5.92	10.82	-2.60	0.98	2.80	1.96	1.53	10.28
CaO	-6.65	18.79	-0.96	0.97	-6.63	-6.31	3.55	-3.13	-8.26	-8.22	-7.00	-8.26	-7.93	21.90
Na_2O	-1.03	-2.60	-2.99	-2.68	-3.39	-3.24	-3.32	-3.00	-2.87	-3.09	-3.56	-2.25	-2.74	-2.69
K_2O	3.93	1.69	1.39	2.39	0.89	1.26	0.26	-0.42	2.44	1.48	0.75	0.11	-0.29	0.00
$S_{(T)}$	114.67	14.96	10.99	16.57	5.14	8.08	10.08	9.08	8.60	4.59	2.98	1.81	2.04	12.23
Cu	56844.95	49.05	14.44	1383.96	-43.63	1361.92	1784.81	457.11	3768.89	203.96	-30.01	580.04	258.42	251.00
Zn	634.55	-22.74	-25.12	-26.56	-69.79	-21.12	394.24	194.00	-60.72	-33.28	-19.58	1828.29	1864.96	372.50
Ag	6.71	0.47	1.10	0.55	0.03	0.23	0.78	0.24	1.88	0.98	1.26	0.87	0.45	0.20
As	1808.8	71.7	146.9	39.0	4.3	16.4	48.3	35.2	129.4	40.2	40.3	48.5	24.3	90.4
Bi	0.52	0.45	0.67	-0.01	-0.03	-0.02	0.26	0.18	-0.02	-0.02	-0.02	-0.01	-0.03	0.01
Cd	2.04	0.06	-0.03	-0.03	-0.14	-0.09	1.52	3.79	-0.10	-0.11	-0.12	4.91	6.62	0.80
Ga	14.46	0.48	0.02	-0.32	-6.49	-2.97	-0.04	0.89	-2.22	-2.32	-3.90	1.90	-5.54	-4.17
Ge	0.16	-0.95	-1.04	-1.05	-1.15	-1.11	-0.42	-0.80	-0.96	-1.13	-0.96	-0.47	-0.32	-0.98
Hg	3938.10	361.90	168.33	234.17	25.74	23.53	267.79	61.00	354.29	105.65	44.40	146.53	186.76	9.67
In	13.6	2.8	0.5	0.7	0.0	0.3	1.7	0.4	0.6	0.2	0.1	0.2	0.0	0.1
Sb	69.26	1.96	6.63	0.61	-0.40	-0.47	1.16	0.01	3.04	1.10	0.93	2.45	0.71	0.87
Se	2.79	0.37	-0.16	-0.18	-0.81	-0.54	-0.34	-0.33	-0.58	-0.65	-0.74	-0.41	-0.75	0.25
Sn	-5.57	-6.38	-6.55	-6.56	-6.77	-6.36	-6.61	-6.61	-6.69	-6.44	-6.75	-6.27	-6.50	-6.42
Tl	0.11	-0.03	-0.04	1.21	0.41	0.15	-0.05	0.46	2.95	1.33	1.70	0.34	0.21	-0.04
Au	599.65	26.47	22.29	40.26	-0.54	18.14	45.26	11.44	58.11	35.71	-0.50	25.16	18.43	30.50
Ir	4.65	0.62	-0.26	-0.31	-1.36	-0.91	-0.57	-0.56	-0.96	-1.09	-1.24	-0.68	-1.25	0.42
Mo	159.17	15.23	7.06	28.85	4.03	3.47	12.88	5.22	39.02	6.34	3.53	12.08	11.95	4.83
Co	28.15	-8.35	-0.94	-11.04	-15.11	-12.49	-14.08	-7.78	-9.79	11.68	-3.69	-9.52	-15.36	-16.33
Cr	41.96	-3.54	8.56	-4.47	-5.52	-5.07	11.07	-4.72	0.72	3.50	-5.41	-4.85	-2.68	-3.75
Ni	26.32	-0.51	-3.52	-1.85	-4.80	-4.17	-0.29	-2.56	2.47	0.47	-1.95	-2.19	-5.51	-3.33
Sc	-11.96	-7.72	-7.01	-9.29	-15.05	-11.31	-12.81	-12.39	-9.75	-9.47	-11.28	-5.86	-15.12	-10.25
V	412.34	-137.78	-124.74	-145.91	-237.99	-170.81	-211.78	-191.11	-40.38	-138.99	-171.98	-129.67	-238.76	-164.67
Rb	45.15	18.64	13.37	18.25	6.46	11.53	3.69	-5.56	20.76	12.87	6.77	2.39	-3.34	1.83
Cs	0.41	0.08	0.01	0.10	-0.03	-0.04	-0.09	-0.13	0.02	0.00	-0.07	0.27	-0.07	-0.05
Sr	-217.94	180.32	-155.30	-62.92	-250.58	-241.00	-5.06	-149.67	-242.29	-233.95	-250.80	-246.02	-178.87	9.00
Ba	495.51	290.38	201.89	525.83	126.92	143.97	1280.60	-26.33	770.66	771.89	335.84	-37.50	1113.91	41.33
Pb	336.01	43.46	32.53	26.59	-0.81	-0.54	47.07	25.72	71.77	37.47	10.09	48.65	24.40	34.67
Zr	88.67	88.67	88.67	88.67	88.67	88.67	88.67	88.67	88.67	88.67	88.67	88.67	88.67	88.67
Hf	0.00	0.00	0.24	0.02	0.01	0.11	-0.07	-0.06	0.03	0.09	0.32	0.25	0.04	0.10
Nb	1.14	0.38	4.21	0.91	0.56	0.83	0.68	1.26	0.46	0.69	1.21	0.91	0.77	0.52
Ta	-0.17	-0.17	5.79	0.07	0.02	-0.04	-0.10	0.00	0.00	0.01	0.04	0.00	0.03	-0.17
Th	-0.17	-0.04	-0.02	0.05	0.05	-0.02	-0.02	0.06	0.00	-0.03	0.07	0.02	0.12	-0.03
U	92.00	3.46	4.09	6.18	3.50	4.82	2.96	2.22	27.39	10.97	24.05	4.52	2.86	2.84
Be	0.93	0.12	-0.05	-0.06	-0.27	-0.18	-0.11	-0.11	0.12	0.63	0.00	0.95	0.00	0.67
Br	80.24	33.28	26.29	14.32	15.53	15.21	17.63	29.62	22.57	18.60	11.68	24.16	16.61	23.28
W	183.06	193.00	167.81	0.66	-0.16	78.53	138.22	0.29	0.11	-0.28	0.19	0.96	0.08	282.93
Y	33.12	-8.88	-1.29	-18.96	-9.17	-5.57	-4.33	-3.80	-13.53	-14.66	-9.13	-8.59	-11.25	-6.02

Table K2: Continued

	MA13-072-C	MA13-073-C	MA13-074-C	MA13-075-C	MA13-023-C	MA13-024-C	MA13-025-C	MA13-026-C	MA13-027-CM	MA13-019-CM	MA13-020-CM	MA13-044-C	MA13-044-M	MA13-045-C
Location	Site C	Site C	Site C	Site C	Site C	Site C	Site C	Site C	Site C	Site D	Site D	Site D	Site D	Site D
Drillhole	TKAD032	TKAD032	TKAD032	TKAD032	TKAD033	TKAD033	TKAD033	TKAD033	TKAD033	TKAD017	TKAD017	TKAD031	TKAD031	TKAD031
Depth	2.05	3.90	5.31	6.42	1.51	2.55	3.00	4.76	7.30	5.00	6.90	5.64	5.64	6.60
	MC [%]	MC [%]	MC [%]	MC [%]	MC [%]	MC [%]	MC [%]	MC [%]	MC [%]	MC [%]	MC [%]	MC [%]	MC [%]	MC [%]
SiO_2	8.96	-4.00	-11.00	-12.37	110.63	1077.97	7.70	-48.98	-1.20	-23.94	-25.63	-28.39	-29.05	-21.78
TiO_2	0.438	0.378	0.381	0.405	0.083	-0.501	0.391	-1.137	0.255	0.988	0.162	0.130	-0.059	0.186
Al_2O_3	5.18	4.10	3.71	3.95	1.66	-2.65	5.23	-15.02	3.33	12.41	1.89	-1.27	-1.14	0.83
$Fe_2O_{3(T)}$	-1.75	3.36	5.19	0.17	5.61	97.49	0.04	-9.21	-3.46	212.87	23.66	18.84	68.70	25.95
MnO	-0.169	-0.146	-0.132	-0.148	-0.044	-0.104	-0.160	-0.185	-0.171	0.004	-0.181	-0.180	-0.173	-0.174
MgO	-2.67	3.88	10.19	13.36	-1.39	-1.44	0.09	-3.30	-0.67	22.49	-2.99	-2.97	-2.94	-2.79
CaO	-3.29	-7.87	-7.94	-7.91	-1.13	-4.52	-3.59	-7.89	-3.53	-7.34	-4.44	-8.40	-8.32	-8.07
Na_2O	-0.91	-1.81	-2.46	-2.54	0.57	-0.11	-0.43	-3.59	-0.82	-1.64	-2.89	-3.26	-2.90	-2.87
K_2O	-0.10	-0.32	-0.42	-0.49	0.22	0.30	0.19	-0.52	-0.33	0.48	3.89	2.72	2.68	3.02
$S_{(T)}$	6.80	6.80	8.16	5.31	6.14	83.07	2.70	0.03	0.06	80.41	22.10	18.25	45.20	19.60
Cu	610.67	157.59	-1.23	-32.77	703.04	2396.67	152.16	-65.01	-34.13	46793.33	329.87	1730.84	24120.00	18320.28
Zn	50780.11	954.64	528.85	1213.47	1362.09	71595.67	50.11	-85.93	-16.47	251969.00	177.67	230.01	2397.67	16786.73
Ag	20.64	2.87	0.92	1.26	1.15	54.32	3.35	-0.09	-0.01	26.77	0.78	1.16	2.76	5.23
As	119.6	53.1	29.0	81.7	177.5	2924.3	22.1	-0.6	-1.5	593.6	40.1	172.5	336.5	169.9
Bi	0.00	0.00	0.00	0.00	0.06	0.58	0.00	-0.04	0.00	0.11	0.04	-0.01	0.01	0.00
Cd	172.86	1.11	-0.01	0.98	3.64	68.15	0.02	-0.22	-0.02	709.08	0.96	0.75	14.32	49.55
Ga	6.22	-0.44	2.49	0.92	4.63	21.00	3.80	-14.79	3.53	43.17	2.60	-0.81	-0.53	6.58
Ge	5.17	-0.39	-1.02	-0.80	6.95	5.07	2.02	-1.04	0.41	25.02	-1.03	-1.07	-0.25	2.70
Hg	1394.89	869.87	463.56	502.25	2240.11	9896.33	399.30	-0.78	27.40	4962.67	160.87	51.14	362.13	894.65
In	4.5	0.2	-0.1	-0.1	1.0	0.5	0.0	-0.1	0.0	77.5	0.6	0.6	4.0	10.6
Sb	21.74	9.60	4.05	5.79	12.23	129.93	1.11	-0.48	-0.25	66.28	1.61	3.55	7.19	7.86
Se	0.08	-0.04	-0.04	-0.09	1.74	17.50	0.14	-1.35	-0.10	3.25	0.83	-0.34	0.40	-0.09
Sn	-6.47	-6.51	-6.51	-6.53	-5.92	-0.67	-6.45	-6.95	-6.53	-5.42	-6.07	-6.61	-5.73	-6.06
Tl	0.41	1.05	0.83	1.01	22.64	88.98	0.71	0.00	0.09	0.01	0.01	0.17	0.34	0.60
Au	217.50	39.92	41.87	15.98	115.78	1227.67	27.46	-0.90	-0.07	2301.17	90.47	316.66	675.40	342.35
Ir	0.14	-0.06	-0.06	-0.14	2.91	29.17	0.24	-2.25	-0.17	5.42	-0.17	-0.57	0.67	-0.14
Mo	4.28	10.69	1.92	11.26	18.46	290.33	2.28	-0.90	-0.07	65.50	34.47	10.57	18.00	20.70
Co	-0.11	2.97	-5.79	3.08	2.62	90.67	5.13	-22.43	-14.93	-20.17	5.60	-11.77	-10.67	-12.96
Cr	-4.03	18.67	-4.23	-4.31	-1.26	25.00	3.19	-6.42	-4.33	158.00	82.00	-1.27	-3.50	2.77
Ni	-0.61	15.38	-1.18	0.49	4.98	55.33	0.76	-7.20	-4.27	30.00	4.13	-2.60	-1.67	-0.45
Sc	3.03	-0.67	-0.47	1.48	-0.61	-9.63	1.66	-22.00	2.51	-17.23	-4.77	-7.10	-10.01	-7.67
V	-18.83	-43.44	-70.72	2.39	37.93	396.00	94.19	-315.12	-11.60	168.00	-81.60	-96.13	-114.47	-91.94
Rb	2.11	-2.44	-4.38	-4.45	10.97	19.00	15.56	-5.83	-1.67	3.17	34.73	27.59	29.13	28.57
Cs	0.15	0.03	0.03	0.02	2.21	2.37	1.04	-0.13	0.30	-0.01	0.02	-0.01	0.09	0.02
Sr	68.22	-81.18	-201.03	-234.61	805.46	2838.00	894.37	-236.48	-77.33	7774.83	-72.67	-266.43	-238.73	90.82
Ba	20559.78	6901.54	1762.77	682.45	34709.89	120238.00	43754.63	710.66	32.93	738675.33	2312.13	967.57	1391.73	33736.26
Pb	391.17	507.12	150.50	494.66	679.72	4647.17	70.75	2.41	23.70	30.17	12.50	82.54	131.50	46.61
Zr	88.67	88.67	88.67	88.67	88.67	88.67	88.67	88.67	88.67	88.67	88.67	88.67	88.67	88.67
Hf	0.22	0.05	0.34	0.45	-0.05	-1.37	-0.03	-1.78	0.24	0.22	-0.04	0.08	-0.35	0.08
Nb	0.30	0.84	0.74	0.72	0.38	-1.60	-0.24	-2.49	0.59	-0.02	0.59	0.83	-0.33	0.72
Ta	-0.17	0.00	0.00	0.01	0.06	-0.12	-0.16	-0.16	0.00	0.58	-0.10	-0.08	-0.17	-0.12
Th	-0.02	-0.03	0.03	0.05	0.08	-0.05	-0.10	-0.60	0.05	-0.21	-0.05	-0.04	-0.16	-0.01
U	6.92	12.48	1.48	6.53	14.11	67.00	19.87	0.09	4.07	154.78	7.26	4.61	3.85	16.31
Be	0.03	1.45	2.42	1.39	1.66	5.83	2.78	-0.30	0.43	1.08	-0.03	-0.11	0.13	-0.03
Br	9.31	25.23	24.45	21.35	30.22	33.90	22.84	0.28	13.27	53.53	25.78	18.17	19.21	24.00
W	4.82	0.02	0.02	-0.33	3.33	33.63	170.20	-0.46	-0.33	696.10	151.57	158.26	243.90	150.36
Y	-0.31	-8.97	-4.78	-2.35	-2.85	34.10	-0.55	-27.11	-6.18	-17.52	-7.39	-9.03	-12.01	-8.10

Table K2: Continued

	MA13-005-M	MA13-006-C	MA13-014-C	MA13-015-C	MA13-016-C
Location	Site D	Site D	Site D	Site D	Site D
Drillhole	TKAD030	TKAD030	TKAD018	TKAD018	TKAD018
Depth	5.06	6.45	3.00	5.00	6.60
	MC [%]	MC [%]	MC [%]	MC [%]	MC [%]
SiO_2	-31.33	-31.74	-34.20	-29.16	-25.63
TiO_2	0.062	0.046	-0.414	0.139	0.248
Al_2O_3	-3.24	-2.58	-4.33	-1.36	1.30
$Fe_2O_{3(T)}$	34.01	1.03	42.95	6.16	11.30
MnO	-0.159	-0.184	-0.179	-0.182	-0.151
MgO	-3.23	-3.23	-3.36	-3.11	-2.81
CaO	-8.23	-8.12	-8.06	-5.88	22.62
Na_2O	-2.90	-3.27	-3.01	-2.80	-2.53
K_2O	2.02	2.56	2.15	2.91	2.57
$S_{(T)}$	31.47	7.21	29.05	11.11	21.02
Cu	3439.23	-3.71	47002.27	626.67	412.73
Zn	965.20	-24.23	62.30	15.00	146.97
Ag	1.21	0.56	2.68	0.72	0.60
As	180.1	121.2	133.5	96.9	132.9
Bi	0.01	0.22	0.41	0.28	0.00
Cd	1.46	-0.11	-0.02	0.15	0.39
Ga	5.74	-1.77	-1.46	-0.33	-0.98
Ge	0.10	-1.13	-0.54	-1.10	-1.00
Hg	46.70	-1.38	33.96	5.00	38.00
In	3.3	0.1	10.8	0.3	0.3
Sb	2.19	1.32	7.15	3.53	1.28
Se	0.21	-0.68	-0.13	-0.50	0.10
Sn	-5.86	-6.73	-6.09	-6.67	-6.47
Tl	0.09	0.15	0.13	0.10	-0.04
Au	183.15	50.13	140.68	78.33	93.01
Ir	0.34	-1.14	-0.21	-0.83	0.17
Mo	21.74	3.35	19.11	8.33	4.34
Co	-18.79	-17.35	-18.76	-16.67	-14.79
Cr	-3.82	-5.31	-4.38	-5.00	-4.00
Ni	4.50	-5.28	-4.34	-4.00	-2.66
Sc	-0.85	-7.10	-13.13	-7.70	-9.02
V	-96.70	-160.94	-209.65	-200.67	-179.34
Rb	23.22	28.48	17.43	27.67	36.40
Cs	0.17	0.00	0.02	0.03	0.26
Sr	-226.85	-150.71	-257.89	-151.33	543.50
Ba	367.16	1103.96	128.75	360.00	1108.76
Pb	21.24	20.26	80.77	77.83	34.82
Zr	0.00	88.67	88.67	88.67	88.67
Hf	0.05	-0.04	-0.08	0.00	-0.18
Nb	3.39	0.72	0.52	0.67	0.23
Ta	5.66	0.05	-0.18	0.29	-0.09
Th	-0.19	0.00	-0.06	0.02	-0.08
U	7.02	8.65	6.70	9.42	3.67
Be	0.07	-0.23	-0.04	-0.17	0.03
Br	40.72	19.70	22.66	27.03	26.21
W	111.74	96.26	67.17	58.77	200.27
Y	-20.03	-8.34	2.85	-7.63	-10.43

Table K3: Precision of whole-rock geochemical data (duplicates)

		Detection	Original	Duplicate		Original	Duplicate	
Element	Unit	Limit	MA13-027-CM	MA13-027-CM	*Rel % Diff*	MA13-035-C1	MA13-035-C1	*Rel % Diff*
Hg	ppb	5	39	39	*0*	-	-	-
SiO2	%	0.01	-	-	-	29.82	30.02	*-0.17*
Al2O3	%	0.01	-	-	-	18.89	18.76	*0.17*
Fe2O3(T)	%	0.01	-	-	-	14.95	14.93	*0.03*
MnO	%	0.001	-	-	-	0.056	0.057	*-0.44*
MgO	%	0.01	-	-	-	6.4	6.5	*-0.4*
CaO	%	0.01	-	-	-	3.21	3.23	*-0.16*
Na2O	%	0.01	-	-	-	1.2	1.23	*-0.62*
K2O	%	0.01	-	-	-	2.47	2.49	*-0.20*
TiO2	%	0.001	-	-	-	1.385	1.388	*-0.054*
P2O5	%	0.01	-	-	-	0.13	0.12	*2.00*
LOI	%		-	-	-	19.46	19.46	*0.00*
Total	%	0.01	-	-	-	97.97	98.19	*-0.06*
Sc	ppm	1	-	-	-	23	24	*-1*
Be	ppm	1	-	-	-	< 1	< 1	-
V	ppm	5	-	-	-	233	242	*-1*
V	ppm	5	-	-	-	247	250	*0*
Cr	ppm	20	-	-	-	< 20	< 20	-
Co	ppm	1	-	-	-	17	18	*-1*
Ni	ppm	20	-	-	-	< 20	< 20	-
Cu	ppm	10	-	-	-	50	60	*-5*
Zn	ppm	30	-	-	-	60	60	*0*
Ga	ppm	1	-	-	-	22	23	*-1*
Ge	ppm	0.5	-	-	-	0.7	< 0.5	-
As	ppm	5	-	-	-	6	6	*0*
Rb	ppm	1	-	-	-	27	28	*-1*
Sr	ppm	2	-	-	-	54	56	*-1*
Sr	ppm	2	-	-	-	59	60	*0*
Y	ppm	0.5	-	-	-	43.1	44.8	*-1.0*
Y	ppm	1	-	-	-	42	41	*1*
Zr	ppm	1	-	-	-	198	191	*1*
Nb	ppm	0.2	-	-	-	7.5	7.5	*0.0*
Mo	ppm	2	-	-	-	10	11	*-2*
In	ppm	0.1	-	-	-	0.2	0.2	*0.0*
Sn	ppm	1	-	-	-	< 1	< 1	-
Sb	ppm	0.2	-	-	-	< 0.2	< 0.2	-
Cs	ppm	0.1	-	-	-	0.3	0.3	*0.0*
Ba	ppm	3	-	-	-	516	535	*-1*
Ba	ppm	2	-	-	-	512	516	*0*
La	ppm	0.05	-	-	-	15.1	16.5	*-2.2*
Ce	ppm	0.05	-	-	-	33.3	35	*-1*
Pr	ppm	0.01	-	-	-	4.58	4.6	*-0.1*
Nd	ppm	0.05	-	-	-	21.3	22.1	*-0.9*
Sm	ppm	0.01	-	-	-	5.44	5.6	*-0.7*
Eu	ppm	0.005	-	-	-	2.86	3.08	*-1.85*
Gd	ppm	0.01	-	-	-	6.53	6.34	*0.74*
Tb	ppm	0.01	-	-	-	1.17	1.21	*-0.84*
Dy	ppm	0.01	-	-	-	7.69	8	*-1*
Ho	ppm	0.01	-	-	-	1.59	1.65	*-0.93*
Er	ppm	0.01	-	-	-	4.87	4.84	*0.15*
Tm	ppm	0.005	-	-	-	0.714	0.723	*-0.313*
Yb	ppm	0.01	-	-	-	4.91	4.79	*0.62*
Lu	ppm	0.002	-	-	-	0.793	0.775	*0.574*
Hf	ppm	0.1	-	-	-	4.5	4.4	*0.6*
Ta	ppm	0.01	-	-	-	0.42	0.43	*-0.59*
W	ppm	0.5	-	-	-	0.7	1	*-9*
Tl	ppm	0.05	-	-	-	1.06	1.03	*0.72*
Bi	ppm	0.1	-	-	-	< 0.1	< 0.1	-
Th	ppm	0.05	-	-	-	1.61	1.57	*0.63*
U	ppm	0.01	-	-	-	8.39	8.58	*-0.56*

Table K3: Continued

		Detection	Original	Duplicate		Original	Duplicate	
Element	Unit	Limit	MA13-062-C1	MA13-062-C1	*Rel % Diff*	MA13-064-C1	MA13-064-C1	*Rel % Diff*
Au	ppb	2	-	-	-	31	23	*7*
As	ppm	0.5	-	-	-	79.5	78.5	*0.3*
Cr	ppm	5	-	-	-	< 5	< 5	-
Ir	ppb	5	-	-	-	< 5	< 5	-
Br	ppm	0.5	-	-	-	21.9	20.8	*1.3*
Sc	ppm	0.1	-	-	-	12.5	12.5	*0.0*
Se	ppm	3	-	-	-	< 3	< 3	-
Sb	ppm	0.2	-	-	-	1.2	1.1	*2.2*
Total S	%	0.01	2.66	2.37	*2.88*	-	-	-
SiO2	%	0.01	-	-	-	17.25	17.1	*0.2*
Al2O3	%	0.01	-	-	-	9.52	9.59	*-0.18*
Fe2O3(T)	%	0.01	-	-	-	8.16	8.09	*0.22*
MnO	%	0.001	-	-	-	0.064	0.064	*0.000*
MgO	%	0.01	-	-	-	7.05	7.06	*-0.04*
CaO	%	0.01	-	-	-	15.42	15.52	*-0.16*
Na2O	%	0.01	-	-	-	0.72	0.7	*0.7*
K2O	%	0.01	-	-	-	0.29	0.28	*0.88*
TiO2	%	0.001	-	-	-	0.768	0.778	*-0.323*
P2O5	%	0.01	-	-	-	0.21	0.15	*8.33*
LOI	%		-	-	-	30.53	30.53	*0.00*
Total	%	0.01	-	-	-	89.96	89.86	*0.03*
Sc	ppm	1	-	-	-	13	13	*0*
Be	ppm	1	-	-	-	1	1	*0*
V	ppm	5	-	-	-	172	169	*0*
V	ppm	5	-	-	-	160	160	*0*
Cr	ppm	20	-	-	-	< 20	< 20	-
Co	ppm	1	-	-	-	5	6	*-5*
Ni	ppm	20	-	-	-	< 20	< 20	-
Cu	ppm	10	-	-	-	300	320	*-2*
Zn	ppm	30	-	-	-	450	510	*-3*
Ga	ppm	1	-	-	-	11	11	*0*
Ge	ppm	0.5	-	-	-	< 0.5	< 0.5	-
As	ppm	5	-	-	-	73	81	*-3*
Rb	ppm	1	-	-	-	7	7	*0*
Sr	ppm	2	-	-	-	232	232	*0*
Sr	ppm	2	-	-	-	245	248	*0*
Y	ppm	0.5	-	-	-	19.9	19.9	*0*
Y	ppm	1	-	-	-	18	18	*0*
Zr	ppm	1	-	-	-	77	76	*0*
Nb	ppm	0.2	-	-	-	3	2.8	*1.7*
Mo	ppm	2	-	-	-	5	5	*0*
In	ppm	0.1	-	-	-	0.2	0.2	*0.0*
Sn	ppm	1	-	-	-	< 1	< 1	-
Sb	ppm	0.2	-	-	-	0.6	1.6	*-22.7*
Cs	ppm	0.1	-	-	-	0.1	0.1	*0.0*
Ba	ppm	3	-	-	-	136	133	*1*
Ba	ppm	2	-	-	-	130	126	*1*
La	ppm	0.05	-	-	-	6.07	5.95	*0.50*
Ce	ppm	0.05	-	-	-	13.8	13.8	*0.0*
Pr	ppm	0.01	-	-	-	1.98	1.95	*0.38*
Nd	ppm	0.05	-	-	-	9.11	9.08	*0.08*
Sm	ppm	0.01	-	-	-	2.63	2.65	*-0.19*
Eu	ppm	0.005	-	-	-	3.75	3.72	*0.20*
Gd	ppm	0.01	-	-	-	3.11	3.14	*-0.24*
Tb	ppm	0.01	-	-	-	0.54	0.57	*-1.35*
Dy	ppm	0.01	-	-	-	3.43	3.5	*-0.5*
Ho	ppm	0.01	-	-	-	0.7	0.74	*-1.39*
Er	ppm	0.01	-	-	-	2.21	2.17	*0.46*
Tm	ppm	0.005	-	-	-	0.329	0.322	*0.538*
Yb	ppm	0.01	-	-	-	2.16	2.1	*0.7*
Lu	ppm	0.002	-	-	-	0.357	0.346	*0.782*
Hf	ppm	0.1	-	-	-	1.8	1.7	*1.4*
Ta	ppm	0.01	-	-	-	0.09	< 0.01	-
W	ppm	0.5	-	-	-	250	236	*1*
Tl	ppm	0.05	-	-	-	< 0.05	< 0.05	-
Bi	ppm	0.1	-	-	-	< 0.1	< 0.1	-
Th	ppm	0.05	-	-	-	0.58	0.55	*1.33*
U	ppm	0.01	-	-	-	2.75	2.77	*-0.18*

Table K3: Continued

		Detection	Original	Duplicate		Original	Duplicate	
Element	Unit	Limit	MA13-090-C1	MA13-090-C1	*Rel % Diff*	MA13-095-C1	MA13-095-C1	*Rel % Diff*
Total S	%	0.01	-	-	-	0.17	0.13	*6.67*
SiO2	%	0.01	48.9	48.89	*0.01*	-	-	-
Al2O3	%	0.01	13.13	13.05	*0.15*	-	-	-
Fe2O3(T)	%	0.01	10.52	10.66	*-0.33*	-	-	-
MnO	%	0.001	0.095	0.096	*-0.262*	-	-	-
MgO	%	0.01	3.19	3.19	*0.00*	-	-	-
CaO	%	0.01	3.88	3.92	*-0.26*	-	-	-
Na2O	%	0.01	0.65	0.63	*0.78*	-	-	-
K2O	%	0.01	2.12	2.1	*0.2*	-	-	-
TiO2	%	0.001	1.002	1.013	*-0.273*	-	-	-
P2O5	%	0.01	0.1	0.11	*-2.38*	-	-	-
LOI	%		14.95	14.95	*0.00*	-	-	-
Total	%	0.01	98.53	98.61	*-0.02*	-	-	-
Sc	ppm	1	17	17	*0*	-	-	-
Be	ppm	1	1	1	*0*	-	-	-
V	ppm	5	183	182	*0*	-	-	-
V	ppm	5	188	187	*0*	-	-	-
Cr	ppm	20	30	30	*0*	-	-	-
Co	ppm	1	15	15	*0*	-	-	-
Ni	ppm	20	30	20	*10*	-	-	-
Cu	ppm	10	490	500	*-1*	-	-	-
Zn	ppm	30	380	370	*1*	-	-	-
Ga	ppm	1	15	14	*2*	-	-	-
Ge	ppm	0.5	1.4	1	*8*	-	-	-
As	ppm	5	98	89	*2*	-	-	-
Rb	ppm	1	33	33	*0*	-	-	-
Sr	ppm	2	233	232	*0*	-	-	-
Sr	ppm	2	248	248	*0*	-	-	-
Y	ppm	0.5	21.8	21.7	*0.1*	-	-	-
Y	ppm	1	20	20	*0*	-	-	-
Zr	ppm	1	99	95	*1*	-	-	-
Nb	ppm	0.2	3.8	4.2	*-2.5*	-	-	-
Mo	ppm	2	9	9	*0*	-	-	-
In	ppm	0.1	0.4	0.3	*7.1*	-	-	-
Sn	ppm	1	2	2	*0*	-	-	-
Sb	ppm	0.2	9.6	8.4	*3.3*	-	-	-
Cs	ppm	0.1	0.3	0.3	*0.0*	-	-	-
Ba	ppm	3	1110	1110	*0*	-	-	-
Ba	ppm	2	1096	1072	*1*	-	-	-
La	ppm	0.05	7.91	8.09	*-0.56*	-	-	-
Ce	ppm	0.05	17.8	18.2	*-0.6*	-	-	-
Pr	ppm	0.01	2.57	2.55	*0.20*	-	-	-
Nd	ppm	0.05	12.5	10.9	*3.4*	-	-	-
Sm	ppm	0.01	3.18	3.44	*-1.96*	-	-	-
Eu	ppm	0.005	1.72	1.89	*-2.35*	-	-	-
Gd	ppm	0.01	3.76	3.47	*2.01*	-	-	-
Tb	ppm	0.01	0.65	0.61	*1.59*	-	-	-
Dy	ppm	0.01	4.09	3.92	*1.06*	-	-	-
Ho	ppm	0.01	0.78	0.86	*-2.44*	-	-	-
Er	ppm	0.01	2.26	2.53	*-2.82*	-	-	-
Tm	ppm	0.005	0.346	0.368	*-1.54*	-	-	-
Yb	ppm	0.01	2.36	2.45	*-0.94*	-	-	-
Lu	ppm	0.002	0.385	0.42	*-2.17*	-	-	-
Hf	ppm	0.1	2.5	2.5	*0.0*	-	-	-
Ta	ppm	0.01	0.33	0.29	*3.23*	-	-	-
W	ppm	0.5	2.6	2.7	*-0.9*	-	-	-
Tl	ppm	0.05	1.55	1.8	*-3.7*	-	-	-
Bi	ppm	0.1	< 0.1	< 0.1	-	-	-	-
Th	ppm	0.05	0.78	0.82	*-1.25*	-	-	-
U	ppm	0.01	4.84	5.17	*-1.65*	-	-	-

Table K3: Continued

Element	Unit	Detection Limit	Origina P014-M	Duplicate P014-M	*Rel % Diff*	Original P022-C1	Duplicate P022-C1	*Rel % Diff*
Hg	ppb	5	< 5	< 5	-	-	-	-
Total S	%	0.01	17.4	17.2	*0.3*	-	-	-
SiO2	%	0.01	-	-	-	38.2	37.97	*0.15*
Al2O3	%	0.01	-	-	-	19.7	20.11	*-0.51*
Fe2O3(T)	%	0.01	-	-	-	10.16	10.26	*-0.24*
MnO	%	0.001	-	-	-	0.085	0.085	*0.000*
MgO	%	0.01	-	-	-	7.06	6.99	*0.25*
CaO	%	0.01	-	-	-	2.92	2.9	*0.2*
Na2O	%	0.01	-	-	-	1.29	1.27	*0.39*
K2O	%	0.01	-	-	-	2.28	2.27	*0.11*
TiO2	%	0.001	-	-	-	1.453	1.482	*-0.494*
P2O5	%	0.01	-	-	-	0.02	0.03	*-10.00*
LOI	%		-	-	-	15.93	15.93	*0.00*
Total	%	0.01	-	-	-	99.08	99.29	*-0.05*
Sc	ppm	1	-	-	-	37	37	*0*
Be	ppm	1	-	-	-	< 1	< 1	-
V	ppm	5	-	-	-	369	371	*0*
V	ppm	5	-	-	-	369	371	*0*
Cr	ppm	20	-	-	-	40	40	*0*
Co	ppm	1	-	-	-	20	20	*0*
Ni	ppm	20	-	-	-	< 20	< 20	-
Cu	ppm	10	-	-	-	40	40	*0*
Zn	ppm	30	-	-	-	530	530	*0*
Ga	ppm	1	-	-	-	22	22	*0*
Ge	ppm	0.5	-	-	-	< 0.5	< 0.5	-
As	ppm	5	-	-	-	30	28	*2*
Rb	ppm	1	-	-	-	26	26	*0*
Sr	ppm	2	-	-	-	189	187	*0*
Sr	ppm	2	-	-	-	192	195	*0*
Y	ppm	0.5	-	-	-	21.1	21.3	*0*
Y	ppm	1	-	-	-	20	20	*0*
Zr	ppm	1	-	-	-	97	97	*0*
Nb	ppm	0.2	-	-	-	4.1	4.1	*0*
Mo	ppm	2	-	-	-	9	9	*0*
In	ppm	0.1	-	-	-	< 0.1	< 0.1	-
Sn	ppm	1	-	-	-	< 1	< 1	-
Sb	ppm	0.2	-	-	-	1.1	1	*2*
Cs	ppm	0.1	-	-	-	0.1	< 0.1	-
Ba	ppm	3	-	-	-	1610	1610	*0*
Ba	ppm	2	-	-	-	1701	1698	*0*
La	ppm	0.05	-	-	-	8.37	8.63	*-0.76*
Ce	ppm	0.05	-	-	-	19.9	20.2	*-0.4*
Pr	ppm	0.01	-	-	-	2.78	2.85	*-0.62*
Nd	ppm	0.05	-	-	-	11.9	12.1	*-0.4*
Sm	ppm	0.01	-	-	-	2.92	2.82	*0.87*
Eu	ppm	0.005	-	-	-	1.44	1.39	*0.88*
Gd	ppm	0.01	-	-	-	3.38	3.44	*-0.44*
Tb	ppm	0.01	-	-	-	0.61	0.63	*-0.81*
Dy	ppm	0.01	-	-	-	3.82	3.85	*-0.20*
Ho	ppm	0.01	-	-	-	0.78	0.78	*0.00*
Er	ppm	0.01	-	-	-	2.35	2.39	*-0.42*
Tm	ppm	0.005	-	-	-	0.36	0.365	*-0.345*
Yb	ppm	0.01	-	-	-	2.52	2.47	*0.50*
Lu	ppm	0.002	-	-	-	0.377	0.375	*0.133*
Hf	ppm	0.1	-	-	-	2.5	2.6	*-1.0*
Ta	ppm	0.01	-	-	-	0.25	0.25	*0.00*
W	ppm	0.5	-	-	-	1	0.9	*2.6*
Tl	ppm	0.05	-	-	-	< 0.05	< 0.05	-
Bi	ppm	0.1	-	-	-	< 0.1	< 0.1	-
Th	ppm	0.05	-	-	-	0.73	0.75	*-0.68*
U	ppm	0.01	-	-	-	7.41	7.51	*-0.34*

Table K3: Continued

Element	Unit	Detection Limit	Original MA13-014-C	Duplicate MA13-014-C	*Rel % Diff*	Original MA13-024-C1	Duplicate MA13-024-C1	*Rel % Diff*
Total S	%	0.01	-	-	-	6.53	6.59	*-0.23*
Cu	%	0.001	5.07	5.23	*-0.78*	-	-	-

Element	Unit	Detection Limit	Original MA13-044-M	Duplicate MA13-044-M	*Rel % Diff*	Original MA13-057-C	Duplicate MA13-057-C	*Rel % Diff*
Hg	ppb	5	-	-	-	296	299	*0*
Total S	%	0.01	35.8	35.6	*0.1*	-	-	-

Element	Unit	Detection Limit	Original MA13-075-C1	Duplicate MA13-075-C1	*Rel % Diff*	Original MA13-078-C1	Duplicate MA13-078-C1	*Rel % Diff*
Total S	%	0.01	-	-	-	0.53	0.55	*-0.93*
Ni	ppm	1	9	9	*0*	-	-	-
Cu	ppm	1	45	41	*2*	-	-	-
Zn	ppm	1	1390	1390	*0*	-	-	-
Cd	ppm	0.5	1.4	1.2	*3.8*	-	-	-
S	%	0.001	5.24	5.04	*1*	-	-	-
Ag	ppm	0.3	1.5	1.5	*0.0*	-	-	-
Pb	ppm	3	516	535	*-1*	-	-	-

Element	Unit	Detection Limit	Original MA13-082-C	Duplicate MA13-082-C	*Rel % Diff*	Original MA13-086-C1	Duplicate MA13-086-C1	*Rel % Diff*
Hg	ppb	5	-	-	-	5	5	*0*
Ni	ppm	1	4	6	*-10*	-	-	-
Cu	ppm	1	22	28	*-6*	-	-	-
Zn	ppm	1	417	433	*-1*	-	-	-
Cd	ppm	0.5	< 0.5	< 0.5	-	-	-	-
S	%	0.001	0.066	0.071	*-1.825*	-	-	-
Ag	ppm	0.3	< 0.3	< 0.3	-	-	-	-
Pb	ppm	3	60	62	*-1*	-	-	-

Element	Unit	Detection Limit	Original P024-C1	Duplicate P024-C1	*Rel % Diff*
Au	ppb	2	< 2	< 2	-
As	ppm	0.5	10	9.6	*1.0*
Cr	ppm	5	47	51	*-2*
Ir	ppb	5	< 5	< 5	-
Br	ppm	0.5	13.8	14	*0*
Sc	ppm	0.1	36.1	35.7	*0.3*
Se	ppm	3	< 3	< 3	-
Sb	ppm	0.2	3.2	3.2	*0.0*

Appendix L

EPMA Analyses on Sulfide Minerals of the Tinakula Deposit

Contents of this file:

1. Supplemental Figures:

   Fig. L1. CuS versus FeS ratios for EPMA analyses of sphalerite from the Tinakula deposit (n = 598)

2. Supplemental Tables:

   Table L1: Results of EPMA analyses on sulfide minerals in sample GMA13-004A

   Table L2: Results of EPMA analyses on sulfide minerals in sample GMA13-010

   Table L3: Results of EPMA analyses on sulfide minerals in sample GMA13-021

   Table L4: Results of EPMA analyses on sulfide minerals in sample GMA13-024

   Table L5: Results of EPMA analyses on sulfide minerals in sample GMA13-031

   Table L6: Results of EPMA analyses on sulfide minerals in sample GMA13-032

   Table L7: Results of EPMA analyses on sulfide minerals in sample GMA13-038

   Table L8: Results of EPMA analyses on sulfide minerals in sample GMA13-042

   Table L9: Results of EPMA analyses on sulfide minerals in sample GMA13-04

   Table L10: Results of EPMA analyses on sulfide minerals in sample GMA13-048A

   Table L11: Results of EPMA analyses on sulfide minerals in sample GMA13-049

   Table L12: Results of EPMA analyses on sulfide minerals in sample GMA13-050

   Table L13: Results of EPMA analyses on sulfide minerals in sample GMA13-052

   Table L14: Results of EPMA analyses on sulfide minerals in sample GMA13-058

   Table L15: Results of EPMA analyses on sulfide minerals in sample GMA13-061

   Table L16: Results of EPMA analyses on sulfide minerals in sample GMA13-062

   Table L17: Summary of EPMA analyses of sphalerite with mole% FeS and CuS calculations (all samples, this study)

   Table L18: Summary of EPMA analyses of sphalerite with mole% FeS from footwall samples (from Anders, 2016)

   Table L19: Average mineral formulas calculated from EPMA data (Table 4.7)

Notes:

EPMA = Electron Probe Micro-Analyzer
All values expressed as percent (%)
- = below detection limit
NA = not analyzed
Highlighted values in red are totals that are high or low (± 2%)

1. Supplemental Figures

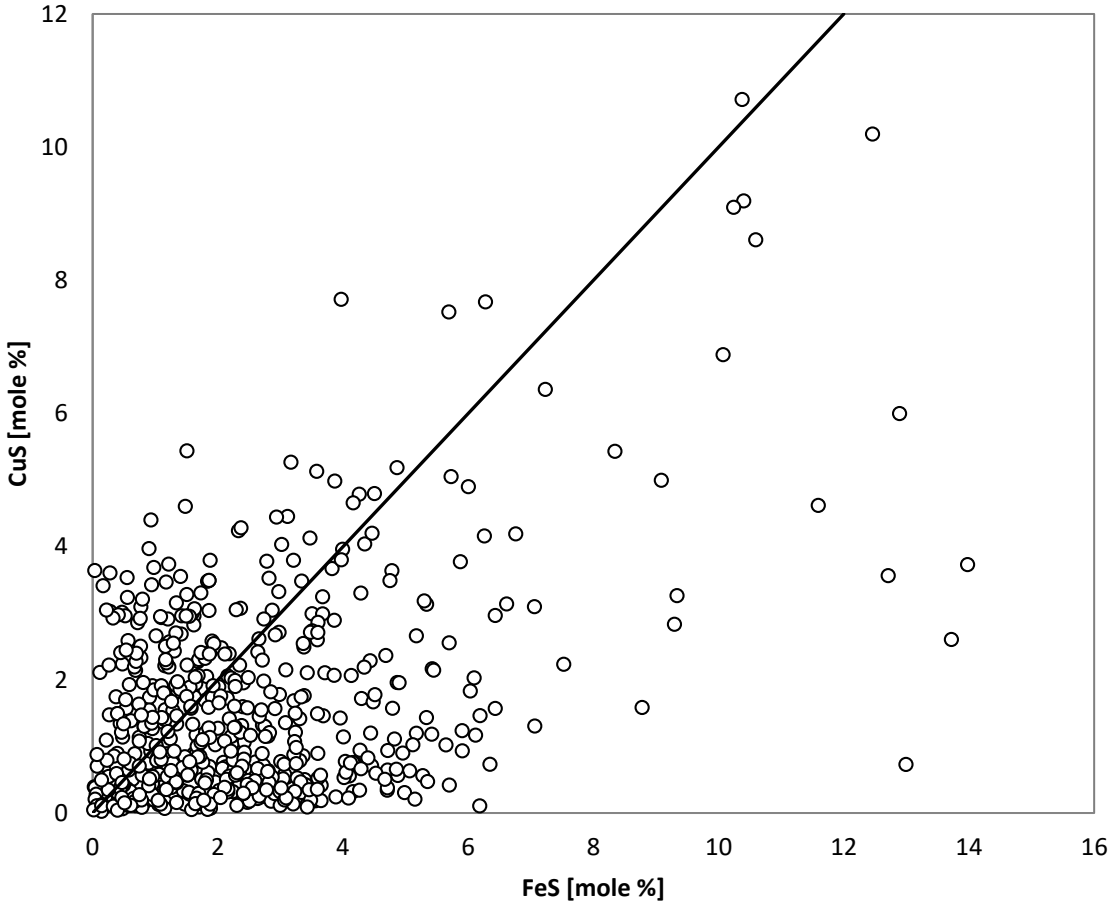


Fig. L1. CuS versus FeS ratios for EPMA analyses of sphalerite from the Tinakula deposit (n = 598).

1. Supplemental Tables

Table L1. Results of EPMA analyses on sulfide minerals in sample GMA13-004A

Sample	Fe	S	Cu	In	Zn	Cd	Ga	Hg	Pb	As	Sb	Ag	Au	Mn	Total	Comment
4A_C1_ccp1	30.47	35.15	34.43	-	-	0.0127	0.0007	-	0.0996	-	-	NA	NA	NA	100.1629	
4A_C1_ccp2	30.4	34.9	34.57	-	0.0244	-	0.0178	-	0.0936	-	0.0008	NA	NA	NA	100.0065	
4A_C1_ccp3	29.94	35.04	34.13	-	0.5331	-	-	0.0054	0.095	-	0.0012	NA	NA	NA	99.7448	early
4A_C1_ccp4	30.44	35.08	34.49	-	0.2097	-	0.0192	0.0163	0.1262	-	0.0072	NA	NA	NA	100.3885	late
4A_C1_ccp5	11.94	33.43	13.88	-	38.7	0.2143	0.125	0.1263	0.1963	-	0.0877	NA	NA	NA	98.6996	mixed with sp
4A_C1_ccp6	29.53	34.96	34.17	-	0.5035	0.0101	-	-	0.104	0.2551	0.0247	NA	NA	NA	99.5574	
4A_C1_ccp7	29.69	34.82	33.74	-	0.3783	0.0048	-	0.0345	0.141	-	0.002	NA	NA	NA	98.8107	
4A_C1_ccp8	12.32	33.5	14.06	-	36.73	0.097	0.1228	0.0621	0.3658	0.4814	0.0479	NA	NA	NA	97.787	mixed with sp
4A_C1_ccp9	30.25	34.91	34.35	-	0.5546	0.0149	0.0445	-	0.0966	-	-	NA	NA	NA	100.2206	late
4A_C1_mrc1	46.24	52.91	1.79	-	0.1146	-	-	0.0326	0.1863	0.3414	-	NA	NA	NA	101.6149	
4A_C1_mrc2	47.29	53.42	0.3107	-	0.2949	-	-	-	0.7143	-	-	NA	NA	NA	102.0298	
4A_C1_mrc3	46.95	53.39	0.3563	-	0.5367	0.0036	-	-	0.8203	-	0.0058	NA	NA	NA	102.0626	
4A_C1_mrc4	46.17	53	1.21	-	0.1589	0.0155	-	-	0.1281	0.768	-	NA	NA	NA	101.4504	
4A_C1_sp1	1.92	32.77	1.34	0.0167	61.07	0.5675	0.3514	0.0346	0.2167	-	0.1523	NA	NA	NA	98.4392	
4A_C1_sp2	0.9589	32.78	1.47	0.0178	62.63	0.4875	0.2439	-	0.5974	0.4775	0.1917	NA	NA	NA	99.8548	
4A_C1_sp3	0.9078	33.11	1.19	-	63.95	0.0987	0.1642	-	0.9201	-	0.0045	NA	NA	NA	100.3453	
4A_C1_sp4	1.22	33.08	1.32	-	62.75	0.0714	0.1389	-	0.4779	0.2031	0.0606	NA	NA	NA	99.322	
4A_C2_ccp1	30.78	34.88	34.86	-	-	0.0047	0.0278	-	0.196	-	0.0084	NA	NA	NA	100.7569	
4A_C2_ccp2	27.09	34.52	32	-	5.45	0.0488	0.081	0.0018	0.2179	-	0.1161	NA	NA	NA	99.5257	early
4A_C2_ccp3	30.05	34.83	34.5	-	0.1642	0.0001	0.0476	-	0.1579	1.25	0.0529	NA	NA	NA	101.0526	late
4A_C2_ccp4	30.72	34.73	33.37	-	0.1802	0.0154	-	-	0.1186	-	0.0414	NA	NA	NA	99.1757	early
4A_C2_ccp5	22.7	34.12	27.64	0.0151	14.58	0.1491	0.1153	0.0055	0.2241	0.1064	0.0459	NA	NA	NA	99.7015	mixed with sp
4A_C2_ccp6	29.94	35.13	34.27	-	0.1775	0.0031	-	-	0.1262	-	0.0251	NA	NA	NA	99.6719	late
4A_C2_ccp7	26.19	33.76	26.97	-	0.2114	0.0194	-	-	0.2964	-	0.0189	NA	NA	NA	87.4661	altered
4A_C2_mrc1	40.06	45.77	7.24	-	0.1057	0.0074	-	-	0.9905	0.2114	0.0514	NA	NA	NA	94.4365	small grain in ccp
4A_C2_mrc2	46.89	53.38	1.6	-	0.1858	0.0052	0.0015	0.0034	0.1364	-	-	NA	NA	NA	102.2022	
4A_C2_mrc3	47.33	53.29	0.5056	-	0.0772	0.0084	-	-	0.1362	-	-	NA	NA	NA	101.3474	
4A_C2_sp1	1.03	33.32	1.1	-	64.35	0.3651	0.2278	-	0.1345	-	0.0348	NA	NA	NA	100.5621	
4A_C2_sp2	3.6	32.9	2.72	0.0023	59.53	0.5003	0.2746	-	0.4791	-	0.1359	NA	NA	NA	100.1422	gen1
4A_C2_sp3	15.63	33.86	19.81	0.0106	29.69	0.6209	0.2044	-	0.3939	-	0.1292	NA	NA	NA	100.349	gen2
4A_C2_sp4	16.44	32.59	19.2	-	28.02	0.3611	0.1566	-	0.7637	-	0.1402	NA	NA	NA	97.6717	gen3
4A_C2_sp5	10.9	33.26	12.82	-	40.98	0.4971	0.1689	-	0.9479	-	0.1496	NA	NA	NA	99.7235	gen4
4A_C2_sp6	8.89	33.12	11.3	-	44.4	0.876	0.2561	0.0246	0.4428	-	0.2057	NA	NA	NA	99.5153	mixed with ccp
4A_C2_sp7	0.5805	32.48	1.73	-	63.55	0.2001	0.2137	-	0.7037	0.4211	0.0214	NA	NA	NA	99.9006	
4A_C2_sp8	3.1	32.94	6.04	0.0065	56.71	0.8312	0.2594	0.0134	0.303	-	0.131	NA	NA	NA	100.3344	mixed with ccp
4A_C2_cov1	3.32	23.49	57.55	-	1.6	0.0238	0.0209	-	0.1015	-	0.0422	NA	NA	NA	86.1485	
4A_C3_ccp1	30.6	34.94	34.56	-	0.0555	0.0145	0.0071	0.0309	0.0877	-	-	NA	NA	NA	100.2956	late
4A_C3_ccp2	21.17	30.63	41.2	-	3.09	0.0229	0.0176	-	0.2978	-	0.0016	NA	NA	NA	96.43	mixed with sp
4A_C3_ccp3	29.8	34.7	34.52	-	0.0553	0.0021	-	-	0.2065	-	0.0064	NA	NA	NA	99.2903	late
4A_C3_ccp4	29.39	34.27	34.18	-	0.0488	0.008	0.0222	-	0.1262	-	0.0024	NA	NA	NA	98.0477	late
4A_C3_mrc1	46.77	53.24	1.37	-	-	-	-	0.029	0.1448	-	0.0062	NA	NA	NA	101.56	
4A_C3_mrc2	47.53	53.24	0.447	-	0.0455	0.0125	-	0.0051	0.1063	-	-	NA	NA	NA	101.3863	
4A_C3_mrc3	46.24	52.8	2.08	-	0.1506	0.011	-	0.0206	0.1992	0.5285	0.0157	NA	NA	NA	102.0456	
4A_C3_sp1	0.946	32.81	0.7593	-	64.26	0.3903	0.2577	0.0212	0.735	-	0.0598	NA	NA	NA	100.2393	early crystal1 prof
4A_C3_sp2	0.3622	32.47	0.3241	-	64.83	0.3968	0.1987	-	0.8926	-	0.0666	NA	NA	NA	99.541	crystal1 profile
4A_C3_sp3	0.1502	32.28	0.4022	0.0037	63.77	0.397	0.2038	-	1.69	-	0.0739	NA	NA	NA	98.9709	crystal1 profile
4A_C3_sp4	0.1492	32.12	0.187	-	63.55	0.222	0.1888	0.0366	1.82	-	0.0562	NA	NA	NA	98.3298	crystal1 profile
4A_C3_sp5	0.1277	32.03	0.4384	0.0034	62.97	0.3998	0.2006	0.0096	2.21	-	0.1148	NA	NA	NA	98.5043	crystal1 profile
4A_C3_sp6	0.103	31.66	0.2027	-	61.46	0.271	0.1783	-	3.38	0.6652	0.0749	NA	NA	NA	97.9951	crystal1 profile
4A_C3_sp7	0.0722	31.56	0.2365	-	58.23	0.328	0.176	-	5.26	1.19	0.1333	NA	NA	NA	97.1861	late crystal1 prof
4A_C3_sp8	7.34	24.77	44.3	0.0033	3.68	0.0114	-	-	1.34	-	0.0883	NA	NA	NA	81.5331	mixed with ccp
4A_C4_ccp1	31.32	35.78	32.5	-	-	0.0013	-	-	0.0873	-	0.0179	NA	NA	NA	99.7066	early incl in Mrc
4A_C4_ccp2	29.03	34.95	35.44	-	0.7558	0.0044	-	-	0.0476	-	0.0091	NA	NA	NA	100.2368	
4A_C4_ccp3	29.75	34.98	34.47	-	0.0634	0.0004	0.0016	-	0.141	0.2879	0.0386	NA	NA	NA	99.7329	latest
4A_C4_mrc1	47.85	53.41	0.1032	-	0.0585	0.0183	0.0005	0.0307	0.0878	-	0.0079	NA	NA	NA	101.5668	
4A_C4_mrc2	47.52	53.34	0.3314	-	0.1739	0.0061	-	-	0.1857	0.2051	0.0409	NA	NA	NA	101.803	
4A_C4_mrc3	46.92	52.53	0.1467	-	0.1295	0.01	-	0.0153	0.2651	-	0.0385	NA	NA	NA	100.055	early
4A_C4_mrc4	48.02	53.65	0.2106	-	0.0433	0.0181	-	-	0.2607	-	0.0323	NA	NA	NA	102.2349	late
4A_C4_sp1	2.26	32.67	4.99	-	57.71	0.7746	0.274	-	0.7503	0.0974	0.1057	NA	NA	NA	99.632	
4A_C4_cov1	0.2504	21.06	52.55	-	0.5837	0.0184	0.0238	0.0208	0.2045	-	0.0218	NA	NA	NA	74.7334	
4A_C4_cov2	2.05	25	61.95	-	0.4585	0.0005	0.0653	-	0.0845	-	0.0352	NA	NA	NA	89.6441	
4A_C5_ccp1	27.35	34.64	32.38	-	4.68	0.0339	0.0445	-	0.1237	-	-	NA	NA	NA	99.2522	gen1
4A_C5_ccp2	29.43	34.83	34.64	-	0.194	0.0182	0.0241	-	0.1218	-	0.0498	NA	NA	NA	99.308	gen2
4A_C5_ccp3	16.18	33.25	25.26	0.0349	19.17	0.2244	0.1651	-	0.3249	-	0.0759	NA	NA	NA	94.6853	gen3
4A_C5_ccp4	29.83	34.81	34.42	-	0.1999	0.0079	-	-	0.1336	-	0.0239	NA	NA	NA	99.4253	gen2
4A_C5_ccp5	29.96	34.63	34.26	-	0.3506	0.004	-	-	0.1771	0.7641	0.0271	NA	NA	NA	100.1728	gen1
4A_C5_ccp6	15.5	33.61	18.35	-	30.38	0.1374	0.078	-	0.3028	-	0.016	NA	NA	NA	98.3743	gen2, mixed w sp
4A_C5_ccp7	30.14	34.83	34.58	-	0.4281	0.0129	-	-	0.2495	-	-	NA	NA	NA	100.2404	gen3
4A_C5_ccp8	29.73	34.69	34.46	-	0.4452	0.0072	0.0305	0.0181	0.1679	-	-	NA	NA	NA	99.549	early
4A_C5_ccp9	28.29	35.65	33.23	-	0.2299	0.0076	-	-	0.1171	-	-	NA	NA	NA	97.5247	late
4A_C5_mrc1	43.66	50.41	6.93	-	0.1598	0.0182	-	-	0.1631	0.1612	-	NA	NA	NA	101.5023	
4A_C5_mrc2	46.76	53.12	1.4	-	-	0.0156	-	0.0273	0.054	-	-	NA	NA	NA	101.3768	
4A_C5_mrc3	46.64	52.42	1.82	-	0.0304	0.0042	-	-	0.2744	0.3408	-	NA	NA	NA	101.5297	
4A_C5_sp1	11.57	32.87	15.08	-	38.41	0.2185	0.176	-	0.3037	-	0.0522	NA	NA	NA	98.6805	gen1, mixed w ccp
4A_C5_sp2	9.21	32.78	15.06	0.0011	39.2	0.2086	0.1371	-	0.3471	-	0.0652	NA	NA	NA	97.0092	gen2, mixed w ccp
4A_C5_sp3	12.85	32.91	14.24	0.0016	38.12	0.1802	0.1173	0.0471	0.3753	-	0.0417	NA	NA	NA	98.8832	gen1, mixed w ccp

Table L1. Continued

Sample	Fe	S	Cu	In	Zn	Cd	Ga	Hg	Pb	As	Sb	Ag	Au	Mn	Total	Comment
4A_C5_sp4	4.91	33.3	7.5	-	54.54	0.3799	0.2387	0.0441	0.2437	-	-	NA	NA	NA	101.1563	gen2, mixed w ccp
4A_C5_sp5	2.38	33.07	1.35	0.0032	62.35	0.7304	0.3465	0.0384	0.1433	-	0.0771	NA	NA	NA	100.4888	early
4A_C5_cov1	1.74	28.45	63.78	-	0.7357	0.0094	0.0025	-	0.1778	-	-	NA	NA	NA	94.8955	
4A_C6_ccp1	30.68	34.73	34.74	-	-	0.0026	0.0003	-	0.1202	-	0.0402	NA	NA	NA	100.3132	
4A_C6_ccp2	30.54	34.89	34.54	-	-	0.006	-	0.0417	-	-	-	NA	NA	NA	100.0176	
4A_C6_mrc1	47.13	53.04	0.4886	-	0.0258	0.0058	-	-	0.1351	0.8874	0.0083	NA	NA	NA	101.7209	early crystal1
4A_C6_mrc2	47.98	53.41	0.0742	-	0.1158	0.0066	0.0058	-	0.1207	0.5461	0.0115	NA	NA	NA	102.2706	late crystal1
4A_C6_mrc3	48.07	53.32	0.2324	-	0.0451	0.0061	-	-	0.1459	-	0.0223	NA	NA	NA	101.8417	early crystal2
4A_C6_mrc4	46.38	52.82	1.31	-	0.0469	0.0174	-	-	0.0852	0.1365	0.0041	NA	NA	NA	100.8	early crystal2
4A_C6_mrc5	47.25	53.08	0.4134	-	0.07	0.0048	-	0.0017	0.1077	-	0.0116	NA	NA	NA	100.9391	late crystal2
4A_C6_sp1	1.05	32.23	2.24	-	61.21	0.9546	0.2682	-	1.23	-	0.1663	NA	NA	NA	99.3491	early crystal1
4A_C6_sp2	0.1578	31.71	1.92	-	61.51	0.5904	0.2421	-	2.26	0.3857	0.084	NA	NA	NA	98.86	late crystal1
4A_C6_sp3	1.33	32.58	1.43	-	62.54	0.3403	0.2526	-	0.8103	-	0.0573	NA	NA	NA	99.3406	early
4A_C6_sp4	2.11	32.82	0.9485	-	62.88	0.347	0.2621	0.0675	0.2591	0.1379	0.0307	NA	NA	NA	99.8629	
4A_C6_cov1	0.0165	11.44	18.78	0.002	3.92	0.0262	0.0757	0.0753	0.2711	-	-	NA	NA	NA	34.6068	
4A_C7_ccp1	30.41	34.99	34.59	-	-	0.0052	-	-	0.1469	-	-	NA	NA	NA	100.1421	
4A_C7_ccp2	30.09	34.81	34.76	-	0.0497	0.0099	-	-	0.0995	-	-	NA	NA	NA	99.8192	
4A_C7_ccp3	30.59	34.72	34.62	-	0.0827	-	-	0.0237	0.1367	0.1645	-	NA	NA	NA	100.3375	
4A_C7_ccp4	30.17	34.56	34.76	-	-	-	-	-	0.1321	0.1396	0.0084	NA	NA	NA	99.7702	
4A_C7_ccp5	30.58	34.99	34.5	-	0.0936	0.0064	-	-	0.0995	-	-	NA	NA	NA	100.2694	
4A_C7_mrc1	47.01	53.37	1.07	-	0.092	0.0001	-	-	0.1772	-	-	NA	NA	NA	101.7192	
4A_C7_mrc2	47.37	53.59	1.01	-	0.0723	0.0046	-	-	0.1206	-	-	NA	NA	NA	102.1674	
4A_C7_mrc3	47.4	53.5	0.1703	-	0.0704	0.0045	-	-	0.1517	0.2905	-	NA	NA	NA	101.5873	
4A_C7_mrc4	46.64	52.54	1.1	-	0.0278	0.0133	-	-	0.1376	-	0.0351	NA	NA	NA	100.4938	
4A_C7_mrc5	47.5	53.37	0.2195	-	0.1247	0.0151	0.0011	-	0.1545	-	0.0129	NA	NA	NA	101.3977	
4A_C7_sp1	3.47	32.83	3.22	-	59.73	0.1968	0.2218	0.0941	0.5166	-	0.0326	NA	NA	NA	100.3119	
4A_C7_sp2	1.72	32.91	1.78	0.0089	63.25	0.0377	0.2165	0.0598	0.5309	-	0.0355	NA	NA	NA	100.5492	early
4A_C7_sp3	1.06	32.56	0.1546	0.0184	63.78	0.0173	0.1862	0.0309	1.14	-	0.0113	NA	NA	NA	98.9588	early crystal1
4A_C7_sp4	0.0934	31.72	0.2716	-	62.48	0.1804	0.1983	-	2.26	-	-	NA	NA	NA	97.2038	late crystal1
4A_C7_sp5	0.9388	32.32	0.3805	-	62.64	0.1552	0.1413	-	1.25	0.4851	-	NA	NA	NA	98.311	
4A_C8_ccp1	30.42	34.94	34.66	-	0.2461	0.0066	-	0.0835	0.0817	-	0.0024	NA	NA	NA	100.4403	
4A_C8_ccp2	33.37	38.09	29.31	-	-	0.0006	0.0052	0.0179	0.1222	-	0.0301	NA	NA	NA	100.9459	
4A_C8_ccp3	30.56	35.46	34.76	-	-	0.0144	-	-	0.1764	-	-	NA	NA	NA	100.9707	
4A_C8_mrc1	47.36	53.22	0.6854	-	0.05	0.0062	-	-	0.1658	-	-	NA	NA	NA	101.4874	
4A_C8_sp1	0.8073	32.36	1.74	0.0149	62.6	0.8525	0.3315	-	1.17	0.0888	0.2017	NA	NA	NA	100.1666	early crystal1 prof
4A_C8_sp2	0.4873	32.4	1.03	-	63.29	0.5968	0.2431	-	1.38	-	0.0533	NA	NA	NA	99.4806	crystal1 profile
4A_C8_sp3	0.3207	32.13	1.66	0.0031	62.39	1.03	0.3437	-	1.57	-	0.2423	NA	NA	NA	99.6899	crystal1 profile
4A_C8_sp4	0.2696	32.29	1.43	0.0096	62.72	0.9391	0.2506	-	1.37	-	0.2056	NA	NA	NA	99.4846	crystal1 profile
4A_C8_sp5	0.2538	32.02	1.54	0.0046	62.54	0.8757	0.2877	0.0709	1.66	-	0.1695	NA	NA	NA	99.4223	crystal1 profile
4A_C8_sp6	0.1781	31.91	0.2348	0.0015	64.07	0.3893	0.1949	-	1.52	-	0.0162	NA	NA	NA	98.5148	crystal1 profile
4A_C8_sp7	0.0765	31.29	0.4062	0.0035	62.2	0.4136	0.2281	-	2.75	-	0.044	NA	NA	NA	97.4119	crystal1 profile
4A_C8_sp8	0.0621	31.23	0.1702	-	61.56	0.2123	0.1977	-	3.66	-	0.0238	NA	NA	NA	97.1162	crystal1 profile
4A_C8_sp9	0.0445	31.09	0.1737	0.0054	61.15	0.1806	0.1344	-	4.21	0.2395	0.0348	NA	NA	NA	97.263	crystal1 profile
4A_C8_sp10	0.052	31.03	0.2272	-	60.48	0.2032	0.2394	0.0133	4.25	0.6145	0.0521	NA	NA	NA	97.1618	crystal1 profile
4A_C8_sp11	0.0259	30.09	6.68	-	53.07	0.1123	0.163	-	4.42	1.14	0.0165	NA	NA	NA	95.7178	crystal1 profile
4A_C8_sp12	0.0392	30.19	6.97	0.0106	52.86	0.0902	0.1658	0.0152	4.61	0.9402	0.0165	NA	NA	NA	95.9078	late crystal1 prof
4A_C8_sp13	0.0365	30.39	5.51	0.0014	54.03	0.1895	0.1857	-	4.39	-	0.0315	NA	NA	NA	94.7647	late
4A_C8_cov1	0.0451	30.71	61.44	-	1.24	0.0309	-	-	2.67	-	-	NA	NA	NA	96.1361	
4A_C8_cov2	0.016	33.03	64.68	0.019	0.4951	0.0031	-	-	0.1952	-	-	NA	NA	NA	98.4385	
4A_C8_cov3	0.0221	32.67	65.45	0.0018	-	-	-	-	0.2805	0.2109	-	NA	NA	NA	98.6353	
4A_C8_cov4	0.0061	33.26	66.41	-	-	0.005	0.0132	-	0.2332	-	-	NA	NA	NA	99.9276	dark blue
4A_C8_cov5	0.003	33.39	64.22	0.0163	1.38	-	0.0107	-	0.3046	-	0.0016	NA	NA	NA	99.3263	light blue
4A_C9_ccp1	30.56	34.95	34.75	-	-	0.011	0.0061	0.0091	0.1009	0.2053	0.0171	NA	NA	NA	100.6094	
4A_C9_ccp2	28.41	34.15	29.38	-	0.1665	0.0024	0.016	-	0.4692	-	0.0176	NA	NA	NA	92.6118	
4A_C9_ccp3	30.22	34.86	34.63	-	0.1733	0.0065	0.0055	-	0.1351	-	0.0175	NA	NA	NA	100.0479	late
4A_C9_mrc1	46.48	53.02	1.53	-	0.0576	0.0214	-	-	0.1348	-	0.012	NA	NA	NA	101.2558	
4A_C9_mrc2	47.44	53.36	0.5653	-	0.0767	0.0038	-	0.0205	0.234	0.4006	0.0186	NA	NA	NA	102.1194	
4A_C9_sp1	0.9316	33.03	0.5806	-	65.26	0.0603	0.2273	-	0.5918	-	0.048	NA	NA	NA	100.7295	early
4A_C9_sp2	0.3138	32.5	0.2288	-	63.9	0.0595	0.1862	-	2.04	0.4509	0.063	NA	NA	NA	99.7423	late
4A_C9_sp3	0.054	31.27	0.1544	0.0238	61.32	0.134	0.1495	-	4.22	0.4152	0.0658	NA	NA	NA	97.8068	
4A_C9_sp4	0.0373	31.01	0.2713	-	54.96	0.1594	0.1192	-	7.47	1.41	0.0609	NA	NA	NA	95.4982	
4A_C9_sp5	0.5813	32.44	0.8656	0.0195	63.02	0.0426	0.2673	0.0135	1.38	0.0809	0.0101	NA	NA	NA	98.7208	
4A_C9_cov1	0.1988	16.55	30.02	0.0465	0.9683	0.0338	0.0533	-	0.1903	0.4218	0.0072	NA	NA	NA	48.49	
4A_C10_ccp1	29.09	34.9	33.24	-	2.69	0.0257	-	-	0.1976	-	-	NA	NA	NA	100.1433	late crystal1
4A_C10_ccp2	29.33	34.85	33.69	-	1.69	0.0138	0.0003	0.0127	0.1307	-	0.0203	NA	NA	NA	99.7379	early crystal1
4A_C10_ccp3	30.62	34.97	34.51	-	-	0.0016	-	-	0.0861	-	-	NA	NA	NA	100.1876	
4A_C10_ccp4	30.63	34.66	34.78	-	-	0.0004	0.0339	-	-	-	0.0278	NA	NA	NA	100.132	
4A_C10_mrc1	47.61	53.2	0.4232	-	0.0698	0.0059	-	-	0.1459	-	0.0169	NA	NA	NA	101.4716	
4A_C10_mrc2	46.56	53.04	1.16	-	0.159	0.0022	-	-	0.3231	-	0.0178	NA	NA	NA	101.262	
4A_C10_mrc3	47.72	53.46	0.1346	-	0.0589	0.0145	-	-	0.218	-	0.024	NA	NA	NA	101.63	
4A_C10_sp1	0.0745	31.01	0.1041	0.0046	59.31	0.3187	0.227	0.0132	5.73	-	0.0522	NA	NA	NA	96.8444	
4A_C10_sp2	0.9029	32.72	0.4777	0.0056	64.8	0.5708	0.2489	-	0.3714	-	0.0935	NA	NA	NA	100.1907	early crystal1 prof
4A_C10_sp3	0.1626	32.2	0.3394	-	63.12	0.4142	0.2304	0.0632	1.97	-	0.1329	NA	NA	NA	98.6328	crystal1 profile
4A_C10_sp4	0.0624	30.71	0.3914	0.0123	58.33	0.1675	0.2336	-	6.8	0.5457	0.0223	NA	NA	NA	97.2753	late crystal1 prof
4A_C10_sp5	0.6687	32.62	0.295	-	65.14	0.4419	0.2137	0.0039	0.7016	-	0.0794	NA	NA	NA	100.1641	early crystal2
4A_C10_sp6	0.0805	31.08	0.0988	0.0053	57.66	0.2304	0.1795	-	7.24	1.83	0.0922	NA	NA	NA	98.4968	late crystal2
4A_C10_Jd1	0.0563	16.68	0.1668	-	1.96	0.0565	-	0.0998	74.88	6.11	0.1012	NA	NA	NA	100.1105	included in sp
4A_C10_Jd2	0.0058	18.21	0.0774	-	3.61	0.032	-	0.0045	71.14	10.67	0.8042	NA	NA	NA	104.5538	included in sp
4A_C10_Jd3	-	17.71	0.0413	-	2.65	0.0417	-	-	72.08	9.34	0.1408	NA	NA	NA	102.0037	included in sp
4A_C10_cov1	0.2519	33.46	64.2	0.0306	1.56	0.0111	0.0222	-	0.1341	-	-	NA	NA	NA	99.67	

Table L2. Results of EPMA analyses on sulfide minerals in sample GMA13-010

Sample	Fe	S	Cu	In	Zn	Cd	Ga	Hg	Pb	As	Sb	Ag	Au	Mn	Total	Comment
10_C2_ccp1	30.43	33.85	34.67	-	-	0.004	0.0043	0.0418	NA	-	0.0091	0.0059	0.037	-	99.0522	early, weathered area
10_C2_mrc1	47.37	51.26	0.3317	-	0.0411	-	-	-	NA	-	0.0207	0.0031	-	0.0153	99.0419	
10_C2_bn1	15.71	32.18	48.46	-	-	0.0104	-	-	NA	-	0.0111	0.1173	0.1852	0.0222	96.6963	late, mixed Bn + ccp
10_C3_ccp1	30.58	33.94	34.53	-	-	0.0026	-	-	NA	-	0.0298	0.0005	0.1162	0.003	99.2022	sample interior
10_C3_ccp2	30.85	33.83	34.62	0.024	-	0.003	-	-	NA	-	0.0342	0.0078	0.2794	0.0273	99.6758	
10_C4_ccp1	30.52	34.07	34.48	0.1342	-	0.0071	0.003	-	NA	-	0.0334	0.0094	-	-	99.2571	weathered area
10_C4_ccp2	28	33.32	35.64	-	0.2613	0.0195	0.0102	-	NA	-	-	0.0267	-	0.0157	97.2935	late, altered
10_C4_mrc1	47.72	52.05	0.2829	-	0.0279	-	-	-	NA	-	0.0244	-	0.0822	-	100.1873	
10_C4_mrc2	48.05	52.15	0.4376	-	0.0238	0.0104	0.0007	-	NA	-	-	0.0051	0.022	-	100.6995	
10_C4_cov1	1.71	24.84	52.32	0.0013	0.1721	0.0208	0.0362	-	NA	-	0.0112	0.0496	-	0.0424	79.2036	
10_C4_bn1	15.52	32.8	49.62	-	-	0.0107	0.0052	-	NA	0.2041	0.0307	0.0604	0.0629	0.0155	98.3296	mixed bn + ccp
10_C5_ccp1	30.78	33.95	35	0.0472	-	0.0097	0.0335	-	NA	-	0.0112	-	0.0281	-	99.8598	weathered area, late
10_C5_mrc1	47.04	51.51	0.3986	-	0.0429	0.0095	-	-	NA	-	0.0004	-	-	-	99.0014	
10_C5_sp1	1.53	32.1	1.71	0.0013	62.69	1.19	0.2511	0.0481	NA	-	0.1496	0.0132	0.2322	0.016	99.9315	
10_C5_bn1	16.19	33.24	49.7	-	-	0.0098	0.0252	-	NA	-	0.018	0.1551	-	-	99.3382	mixed bn + ccp
10_C5_bn2	15.28	33.43	51.22	-	-	-	0.0151	-	NA	-	0.0012	0.1683	-	0.0106	100.1251	mixed bn + ccp
10_C5_cov1	2.15	32.61	63.89	-	-	-	-	-	NA	0.6984	0.0292	0.066	0.0452	0.0191	99.508	
10_C6_ccp1	30.72	34.28	34.6	-	-	0.004	-	0.0218	NA	-	0.0087	0.0151	0.0088	-	99.6584	slightly weathered area
10_C6_ccp2	28.43	33.75	37.53	0.0194	-	0.0035	0.0342	-	NA	-	-	0.043	0.0212	0.005	99.8363	early
10_C6_ccp3	29.93	33.92	34.37	-	-	0.0084	0.023	0.06	NA	-	-	0.0376	0.0353	0.0077	98.3921	late
10_C6_mrc1	47.77	52.2	0.1181	-	-	-	0.0142	-	NA	-	-	0.0132	0.1077	0.0064	100.2295	
10_C6_mrc2	48.09	52.17	0.4793	-	-	0.0097	0.0025	-	NA	-	-	0.0014	-	0.0045	100.7573	
10_C6_sp1	1.21	32.61	1.1	0.0011	62.53	0.5822	0.225	-	NA	-	0.0937	-	0.2034	0.0088	98.5642	
10_C7_ccp1	30.67	34.08	34.41	0.0214	0.4146	0.0101	-	-	NA	-	-	0.0018	0.0141	-	99.622	sample interior, Late
10_C7_ccp2	30.15	34.1	34.29	0.0486	0.9098	0.0054	0.0043	-	NA	-	0.0135	0.0043	-	-	99.526	early
10_C7_ccp3	30.07	33.6	34.31	0.1799	0.0161	-	0.0466	-	NA	-	0.0044	-	-	-	98.2271	late
10_C7_mrc1	47.82	52.51	0.0486	-	0.1219	0.0139	-	-	NA	-	-	-	0.1077	-	100.622	
10_C7_mrc2	47.95	52.09	0.0124	-	0.0473	0.0061	-	-	NA	-	0.0182	-	0.0547	-	100.1787	
10_C7_sp1	2.14	32.43	1.38	0.1196	62.21	1.09	0.4448	0.0365	NA	-	0.2229	0.0013	0.2391	0.0019	100.316	dark
10_C7_sp2	1.39	32.29	1.05	-	64.66	0.2988	0.2248	0.06	NA	-	0.0133	-	0.0139	-	100.0007	light
10_C8_ccp1	30.69	33.95	34.69	0.0102	0.069	0.0148	0.016	-	NA	-	-	0.0006	-	-	99.4407	sample interior
10_C8_sp1	0.5257	32.03	1.14	0.0137	65.19	0.4996	0.1986	-	NA	-	0.1262	0.0008	0.2289	0.0112	99.9648	
10_C8_sp2	1.28	31.96	0.6094	-	63.83	2.04	0.1984	-	NA	-	0.2532	0.0079	-	0.0247	100.2035	
10_C9_sp1	0.0976	31.49	2.23	0.0153	64.32	0.4265	0.192	-	NA	-	0.0533	0.0269	0.1822	-	99.0339	light center
10_C9_sp2	0.0418	31.51	0.1129	-	63.72	0.0061	0.2108	0.0621	NA	0.6412	0.0432	0.0074	-	0.0061	96.3617	dark rim
10_C9_sp3	0.161	31.36	2.35	0.0087	63.93	0.4066	0.2189	-	NA	-	0.0512	0.0489	0.1491	0.0308	98.7153	light center
10_C9_sp4	0.0867	31.74	0.3469	-	64.77	0.0077	0.2084	-	NA	-	-	0.0689	-	-	97.2286	dark rim
10_C9_sp5	0.1769	31.48	2.06	0.0155	62.99	0.2907	0.1836	0.0309	NA	-	0.0452	0.0281	0.307	-	97.608	dark
10_C10_ccp1	30.6	33.99	34.64	0.0429	-	0.0009	0.0046	-	NA	-	0.0072	-	0.1197	-	99.4054	gen1
10_C10_ccp2	30.53	34.11	34.66	-	0.3647	0.0088	-	-	NA	-	-	0.0123	-	0.0149	99.7008	gen2
10_C10_ccp3	30.38	34.17	34.52	-	0.633	-	-	-	NA	0.074	0.0087	0.0097	0.051	-	99.8464	gen3
10_C10_sp1	4.39	32.58	1.48	0.0056	60.53	1.28	0.2258	-	NA	-	0.1063	0.0023	0.1422	0.0027	100.7448	gen1
10_C10_sp2	1.73	32.24	1.17	0.0065	63.7	0.7687	0.2981	-	NA	-	0.1728	0.0011	0.1579	0.0015	100.2465	gen2
10_C10_sp3	0.7521	32.13	1.18	0.0027	65.41	0.0763	0.2441	-	NA	-	0.0004	-	0.1164	0.0322	99.9443	gen3
10_C10_sp4	1.17	32.14	1.25	-	64.74	0.4738	0.1992	0.0174	NA	-	0.0274	0.0013	0.1007	-	100.1197	gen3 early
10_C10_sp5	0.5375	31.75	2.22	-	63.47	-	0.2169	0.0058	NA	0.0647	-	0.0478	0.0035	-	98.3163	gen3 late
10_C11_ccp1	30.59	33.95	34.62	0.0353	0.2979	-	0.0374	0.0054	NA	0.0493	-	0.0039	-	0.0265	99.6157	
10_C11_ccp2	30.06	34.3	34.42	0.0039	0.7488	0.0087	-	-	NA	0.074	0.0083	0.0014	0.088	-	99.7132	
10_C11_ccp3	30.81	34.14	34.71	-	-	0.0038	-	-	NA	-	0.0087	0.0019	0.2023	-	99.8767	
10_C11_ccp4	30.6	33.95	34.59	0.0065	-	0.0062	0.0315	-	NA	0.5751	0.0211	0.0081	-	0.0107	99.7993	
10_C11_sp1	0.7689	32.14	2.06	0.0385	62.52	1.22	0.4435	-	NA	0.2426	0.4391	0.0149	0.1731	0.0055	100.066	
10_C11_sp2	0.6368	32.2	0.9054	0.0022	65.51	0.1875	0.2298	-	NA	0.5347	-	0.0017	0.314	-	100.522	early crystal1
10_C11_sp3	0.7486	32.21	0.3108	-	65.49	0.4348	0.1915	-	NA	-	-	-	0.0486	-	99.4343	late crystal1
10_C11_sp4	23.59	32.04	26.65	-	9.55	0.0144	0.0044	-	NA	-	0.0208	0.0033	-	-	91.873	edge of ccp + sp grains
10_C11_cov1	0.2004	26.79	63.88	-	1.37	0.0397	0.0131	0.0493	NA	0.2093	0.0143	0.315	0.2257	0.0063	93.1132	
10_C12_ccp1	30.79	34.26	34.59	-	-	-	0.0269	-	NA	-	-	0.0126	0.1003	-	99.7799	
10_C12_py1	46.33	51.76	1.93	-	0.0993	0.0056	-	0.012	NA	-	0.0277	0.0118	-	0.027	100.2033	included in ccp, mrc?
10_C12_sp1	1.36	32.13	2.01	-	63.17	0.2772	0.2203	0.0212	NA	-	0.0286	0.0284	0.2862	-	99.532	

Table L3. Results of EPMA analyses on sulfide minerals in sample GMA13-021

Sample	Fe	S	Cu	In	Zn	Cd	Ga	Hg	Pb	As	Sb	Ag	Au	Mn	Total	Comment
21_C1_ccp1	30.96	34.4	34.19	-	-	0.0111	0.0063	0.0108	0.0764	-	-	NA	NA	0.0169	99.6716	
21_C1_ccp2	30.93	34.43	34.3	-	-	0.0108	0.0008	-	0.0897	-	-	NA	NA	0.0199	99.7813	
21_C1_ccp3	30.91	34.77	34.54	-	-	0.0082	-	-	0.116	-	0.0334	NA	NA	0.0142	100.3917	early crystal1
21_C1_ccp4	29.88	34.25	34.02	-	0.0367	0.0017	-	-	0.3509	-	0.0299	NA	NA	0.0013	98.5705	late crystal1
21_C1_py1	46.29	51.87	0.4051	-	0.0949	0.0035	0.0008	0.005	0.3102	-	0.0066	NA	NA	0.0272	99.0134	colloform, early crystal1 prof
21_C1_py2	46.72	52.07	0.3417	-	0.0428	0.0137	0.001	-	0.3311	-	-	NA	NA	0.0268	99.5472	crystal1 profile
21_C1_py3	46.74	51.85	0.3079	-	0.0837	-	0.0016	-	0.2346	0.1706	0.007	NA	NA	0.0207	99.4162	crystal1 profile
21_C1_py4	45.87	50.51	0.4682	-	0.0445	0.0075	0.0039	-	0.2276	-	0.0054	NA	NA	0.0186	97.1558	crystal1 profile
21_C1_py5	46.31	51.53	0.33	-	0.1194	0.013	0.0025	-	0.3441	0.1706	0.0215	NA	NA	0.0266	98.8678	crystal1 profile
21_C1_py6	45.6	50.02	0.4451	-	0.0703	0.0159	0.0012	0.0084	0.1671	-	0.0107	NA	NA	-	96.3387	crystal1 profile
21_C1_py7	39.09	40.59	0.4683	-	0.0392	-	0.0001	-	0.2151	-	0.0024	NA	NA	0.0074	80.4126	crystal1 profile
21_C1_py8	33.35	35.1	0.5205	-	0.0642	0.0068	0.0086	-	0.159	-	0.0086	NA	NA	0.0049	69.2226	crystal1 profile
21_C1_py9	44.93	49.36	0.6902	-	0.0739	0.0031	0.0062	-	0.2388	-	-	NA	NA	0.0101	95.3124	crystal1 profile
21_C1_py10	45.8	50.99	0.8074	-	0.0353	0.009	0.0049	-	0.2638	-	0.0149	NA	NA	0.0148	97.9402	late crystal 1 profile
21_C1_py11	46.84	52.3	0.2653	-	0.0231	0.0097	-	-	0.2554	-	-	NA	NA	0.0317	99.7253	colloform pyrite, middle
21_C1_mrc1	47.79	52.66	0.2154	-	0.0423	0.0114	-	-	0.1952	-	0.0025	NA	NA	0.0001	100.9168	
21_C2_ccp1	31.02	34.59	34.52	-	-	0.0065	0.0068	-	0.0368	0.1315	0.0354	NA	NA	0.0194	100.3663	
21_C2_ccp2	30.99	34.51	34.31	-	-	-	-	-	0.1073	0.3864	-	NA	NA	0.0064	100.31	
21_C2_py1	47.92	53.29	0.0803	-	0.0688	0.013	0.0013	-	0.4918	-	-	NA	NA	-	101.8652	
21_C2_py2	47.92	52.79	0.0272	-	0.0602	0.0063	0.006	-	0.2076	-	-	NA	NA	0.0281	101.0454	
21_C2_py3	42.59	50.68	0.1101	-	6.02	0.0179	0.0251	-	0.8184	-	0.0169	NA	NA	0.0143	100.2926	
21_C2_py4	3.98	31.92	0.4546	-	59.65	0.1647	0.2094	-	1.05	-	0.0722	NA	NA	0.2206	97.7215	slightly tarnished
21_C2_sp1	1.75	32.57	0.8735	-	62.94	0.229	0.2364	-	0.3816	-	0.0622	NA	NA	0.0253	99.068	
21_C3_ccp1	30.91	34.79	34.1	-	-	0.013	0.0041	-	0.1806	-	0.0012	NA	NA	0.0066	100.0054	
21_C3_ccp2	30.7	33.54	33.43	-	-	0.006	0.0119	-	0.0764	-	0.0095	NA	NA	0.0043	97.7782	
21_C3_py1	47.64	52.08	0.1822	-	0.0891	0.0134	-	-	0.1726	-	-	NA	NA	0.0023	100.1795	colloform, early crystal1 prof
21_C3_py2	47.09	52	0.236	-	0.079	0.0111	-	-	0.3915	-	0.0108	NA	NA	0.0126	99.8311	crystal1 profile
21_C3_py3	47.69	52.33	0.0492	-	0.0085	0.0166	0.0022	0.005	0.2572	0.6908	-	NA	NA	0.0112	101.0607	crystal1 profile
21_C3_py4	47.25	52.53	0.0125	-	0.0219	0.0167	0.0007	-	0.3757	-	0.0137	NA	NA	0.0148	100.2359	crystal1 profile
21_C3_py5	46.67	52.25	0.3087	-	0.1092	-	-	-	0.3241	-	0.0331	NA	NA	0.0385	99.7336	crystal1 profile
21_C3_py6	46.89	52.03	0.3537	-	0.0907	0.0108	0.0072	0.0167	0.2161	-	0.0174	NA	NA	0.0334	99.6661	crystal1 profile
21_C3_py7	47.61	52.56	0.3716	-	0.0551	0.0045	-	-	0.5944	-	0.0211	NA	NA	0.0031	101.2197	late crystal 1 profile
21_C4_ccp1	31.01	34.49	34.67	-	-	0.0021	-	0.0249	0.1044	-	0.0127	NA	NA	0.0176	100.3316	
21_C4_ccp2	30.81	34.52	34.76	-	-	-	0.0058	-	0.0868	-	-	NA	NA	0.0011	100.1836	
21_C4_ccp3	29.82	34.33	34.2	-	0.12	-	0.0018	-	0.1029	-	0.0215	NA	NA	-	98.5963	
21_C4_py1	44.38	51.14	0.847	-	0.2518	0.0034	0.012	-	0.2118	-	0.0224	NA	NA	0.0354	96.9039	slightly tarnished
21_C4_sp1	2.42	32.6	1.1	0.0024	60.58	0.7403	0.5964	0.0547	0.2327	0.2025	0.2154	NA	NA	0.0113	98.7558	
21_C4_cov1	0.112	32.21	64.38	-	0.6045	0.0102	-	-	0.1314	-	0.0048	NA	NA	-	97.4529	
21_C4_cov2	0.2251	27.07	63.25	-	-	0.0001	0.0171	-	0.3201	-	0.0112	NA	NA	0.0173	90.911	
21_C4_cov3	0.3289	32.46	65.02	-	-	0.0011	0.0106	0.0222	0.1435	0.4866	0.0324	NA	NA	-	98.5054	
21_C5_ccp1	30.85	34.5	34.41	-	-	0.0079	0.0123	0.0071	0.1732	-	-	NA	NA	-	99.9606	
21_C5_ccp2	30.8	34.12	34.31	-	-	0.006	0.0012	0.0498	0.1366	-	0.0342	NA	NA	0.0066	99.4644	
21_C5_ccp3	30.43	34.38	34.12	-	-	-	0.0037	-	0.1321	-	0.0139	NA	NA	0.0009	99.0807	
21_C5_ccp4	30.84	34.49	34.42	-	-	0.0005	0.0022	-	0.1117	0.4025	0.0028	NA	NA	0.027	100.2966	
21_C5_ccp5	30.29	34.61	34.52	-	0.2988	0.0106	0.0143	-	0.1203	-	-	NA	NA	0.0143	99.8783	
21_C5_py1	44.45	52.27	0.5386	-	0.7312	0.0123	0.0022	-	0.4783	-	0.0012	NA	NA	0.1127	98.5965	early
21_C5_py2	47.91	53.05	0.1668	-	0.0897	0.0069	0.0023	-	0.2636	-	-	NA	NA	0.1452	101.6344	
21_C5_py3	45.31	53.28	1.07	-	0.2158	0.0185	0.0002	-	0.3406	-	0.0062	NA	NA	0.0703	100.3115	late
21_C5_py4	45.55	53.34	0.2842	-	0.8739	0.0084	0.0061	-	0.3154	-	0.0261	NA	NA	0.99	101.3941	
21_C5_py5	47.04	52.5	0.1415	-	0.1414	0.0078	-	-	0.2215	-	-	NA	NA	0.0091	100.0612	
21_C5_py6	46.04	51.43	0.2515	-	0.0529	0.0047	-	-	2.4	0.2538	-	NA	NA	-	100.4329	
21_C5_sp1	3.49	32.79	1.32	0.0083	61.07	0.2305	0.2461	0.0283	0.1649	-	0.0866	NA	NA	0.0032	99.438	
21_C5_sp2	1.08	32.98	0.2792	0.0033	64.66	0.1342	0.2464	-	0.286	-	0.0287	NA	NA	0.0169	99.7148	
21_C6_ccp1	30.84	34.53	34.57	-	-	0.0012	0.0056	-	0.0896	-	0.0095	NA	NA	-	100.0458	
21_C6_py1	47.76	52.75	0.1428	-	0.1202	0.0032	-	-	0.1795	-	0.002	NA	NA	-	100.9576	
21_C6_sp1	1.19	32.49	0.4903	-	64.13	0.1443	0.2271	-	0.6825	-	0.0331	NA	NA	0.0007	99.3881	
21_C7_ccp1	30.94	34.52	34.51	-	-	0.0086	0.0075	0.0053	0.091	0.0822	-	NA	NA	0.0167	100.1813	

Table L3. Continued

Sample	Fe	S	Cu	In	Zn	Cd	Ga	Hg	Pb	As	Sb	Ag	Au	Mn	Total	Comment
21_C7_ccp2	30.79	34.53	34.54	-	-	0.0072	0.0083	-	0.1395	-	-	NA	NA	-	100.015	
21_C7_py1	46.87	52.27	0.2277	-	0.0973	0.0113	0.0119	-	1.1	-	0.0273	NA	NA	0.0389	100.6543	
21_C7_py2	42.43	44.46	0.335	-	0.1656	0.0065	0.0016	-	0.2585	-	0.0111	NA	NA	0.0169	87.6853	collo., crystal 1 profile
21_C7_py3	46.69	52.64	0.2802	-	0.1919	0.0044	0.0022	-	0.2089	-	0.0054	NA	NA	0.036	100.059	crystal1 profile
21_C7_py4	47.34	51.29	0.1995	-	0.1065	-	-	0.0017	0.2091	0.0511	-	NA	NA	0.0065	99.2045	late crystal1 profile
21_C7_sp1	1.36	32.67	0.6492	0.0116	63.8	0.2147	0.2191	0.0113	0.3399	-	0.067	NA	NA	0.0204	99.3633	
21_C7_sp2	1.85	32.63	0.7845	-	63.3	0.2976	0.23	-	0.2964	-	0.0669	NA	NA	0.0095	99.465	
21_C8_ccp1	30.74	34.63	34.52	-	-	-	0.0004	-	0.0837	-	0.025	NA	NA	-	99.9992	
21_C8_ccp2	28.46	34.17	32.08	-	4.38	0.0382	0.2974	-	0.1268	-	0.0044	NA	NA	0.021	99.5779	
21_C8_py1	46.78	51.64	0.2989	-	0.1464	0.0106	0.0042	-	0.4539	-	0.0136	NA	NA	0.023	99.3707	early
21_C8_py2	47.74	52.57	0.1447	-	0.0077	0.0076	-	-	0.4425	-	0.0417	NA	NA	-	100.9541	late
21_C8_py3	46.13	52.79	0.3493	-	0.143	-	0.0036	-	0.8424	0.1448	0.0128	NA	NA	0.0432	100.459	early
21_C8_py4	47.33	52.35	0.271	-	0.1003	0.0081	-	0.0017	0.2248	0.6986	0.0182	NA	NA	0.0138	101.0165	late
21_C8_sp1	1.86	32.91	1.58	0.0017	60.01	0.1609	0.2064	-	0.376	0.5923	0.0259	NA	NA	0.0006	97.7239	
21_C9_ccp1	30.25	34.53	34.41	-	0.6302	0.0111	-	0.0107	0.0824	-	-	NA	NA	0.0179	99.9423	
21_C9_ccp2	28.59	33.82	26.01	-	-	0.0052	0.0109	-	0.665	-	0.0473	NA	NA	-	89.1485	late, mixed with py?
21_C9_ccp3	31.01	34.65	33.74	0.0289	-	0.0033	0.0421	-	0.0821	-	0.004	NA	NA	-	99.5605	early
21_C9_py1	45.8	52.4	0.2446	-	1.02	0.0079	0.0006	-	0.1936	-	0.0198	NA	NA	0.0874	99.7739	early
21_C9_py2	47.35	52.3	0.0775	-	0.1524	-	-	-	0.5028	-	0.024	NA	NA	0.0074	100.414	late
21_C9_py3	45.48	52.65	1.96	-	0.0763	0.0098	-	0.005	0.4543	-	0.0136	NA	NA	0.0312	100.6802	late
21_C9_py4	47.85	52.84	0.0775	-	0.0225	0.0084	-	-	0.2845	-	0.0186	NA	NA	-	101.1014	early
21_C9_py5	48.09	52.99	0.1887	-	0.051	0.0175	-	-	0.2215	0.2045	0.0338	NA	NA	-	101.7969	
21_C9_sp1	1.03	32.86	0.7819	0.0061	64.36	0.14	0.2475	-	0.1052	-	0.0213	NA	NA	0.0081	99.5602	
21_C9_cov1	0.3152	24.41	59.78	-	1.04	-	0.0258	-	0.184	-	0.023	NA	NA	0.0219	85.7999	
21_C10_ccp1	30.4	34.32	34.31	-	0.3592	0.0053	0.0228	-	0.075	0.8859	0.0309	NA	NA	0.0098	100.4189	
21_C10_py1	47.22	52.97	1.46	-	0.4741	0.0068	0.0042	-	0.2009	-	-	NA	NA	0.0149	102.3508	
21_C10_py2	45.52	52.13	0.3984	-	0.2904	0.0107	-	0.0351	0.6229	-	0.0306	NA	NA	0.0369	99.0751	early
21_C10_py3	47.16	52.9	0.1446	-	0.2175	0.0168	0.0056	-	0.3236	-	0.0079	NA	NA	0.0012	100.7771	late
21_C10_py4	40.35	48.2	3.17	-	0.7939	0.01	-	-	4.48	1.23	0.04	NA	NA	-	98.274	
21_C10_py5	45.14	51.36	1.11	-	0.3681	0.0169	-	-	2.62	0	0.0116	NA	NA	0.0168	100.6433	
21_C10_sp1	0.8831	32.94	0.8181	-	64.03	0.3837	0.2632	-	0.5848	0	0.186	NA	NA	0.0306	100.1194	
21_C10_sp2	1.61	33.04	0.7523	0.0171	64.1	0.0661	0.1991	-	0.1406	0.154	0.0375	NA	NA	0.0029	100.1195	

Table L4. Results of EPMA analyses on sulfide minerals in sample GMA13-024

Sample	Fe	S	Cu	In	Zn	Cd	Ga	Hg	Pb	As	Sb	Ag	Au	Mn	Total	Comment
24_C1_mrc1	47.94	53.97	0.0844	-	-	-	-	0.0051	NA	-	-	-	-	0.0015	102.0009	late, edge of slide
24_C1_mrc2	47.78	54.38	0.1998	-	0.0156	-	-	-	NA	-	-	-	0.0621	-	102.4375	late, edge of slide
24_C1_mrc2_2	47.52	52.79	0.4033	-	0.012	-	-	-	NA	-	-	-	-	-	100.7252	late, edge of slide
24_C1_sp1	1.45	33.57	0.4833	-	62.95	-	-	0.208	NA	-	-	-	0.0837	0.0111	98.7562	
24_C1_sp2	0.4542	34.04	0.8074	-	63.1	-	-	-	NA	-	-	-	0.3612	-	98.7629	
24_C1_sp3	0.4782	32.54	1.34	-	59.35	-	-	0.0289	NA	-	-	-	0.2775	0.0126	94.0272	
24_C1_sp3_2	0.4752	33.72	1.57	-	61.02	-	-	0.2475	NA	-	-	-	0.0982	0.026	97.157	
24_C1_sp4	0.8357	33.04	0.8813	0.0044	61.95	-	-	0.1405	NA	-	-	-	0.282	0.0344	97.1684	
24_C2_mrc1	45.37	53.76	0.1331	-	1.19	-	-	-	NA	-	-	-	-	0.1	100.553	
24_C2_mrc1_2	45.58	53.59	0.1185	-	1.19	-	-	-	NA	-	-	-	0.1003	0.1268	100.7056	
24_C2_mrc2	47.49	54.54	0.0332	-	0.0342	-	-	-	NA	-	-	-	-	-	102.0974	
24_C2_mrc2_2	47.8	52.95	0.0243	-	0.0335	-	-	-	NA	-	-	-	0.2389	0.0098	101.0564	
24_C2_mrc3	47.65	54.21	0.3126	-	0.0237	-	-	-	NA	-	-	-	-	0.0124	102.2086	
24_C2_sp1	1.21	33.38	0.4465	-	64.59	-	-	0.1504	NA	-	-	-	0.3497	0.0052	100.1317	replacing mrc
24_C2_sp2	1.6	33.26	0.4099	-	64.33	-	-	0.0213	NA	-	-	-	0.1551	0.0106	99.7869	
24_C2_sp3	1.4	32.75	1.67	0.0091	61.09	-	-	0.1062	NA	-	-	-	0.1412	0.0302	97.1968	
24_C3_mrc1	47.45	54.56	0.2311	-	0.0041	-	-	-	NA	-	-	-	-	-	102.2451	c.g., early, base of crystal
24_C3_mrc1_2	47.6	52.74	0.355	-	0.0071	-	-	-	NA	-	-	-	-	-	100.702	
24_C3_mrc2	46.95	54.25	0.6932	-	0.0107	-	-	-	NA	-	-	-	-	0.0177	101.9215	end of crystal
24_C3_mrc3	46.98	54.73	0.8951	-	-	-	-	-	NA	-	-	-	0.2338	0.0048	102.8437	
24_C4_mrc1	46.05	54.46	1.91	-	0.0022	-	-	-	NA	-	-	-	-	0.0097	102.4318	
24_C4_mrc1_2	43.9	52.8	4.46	-	-	-	-	-	NA	-	-	-	-	0.0158	101.1757	
24_C4_mrc2	47.52	54.65	0.9025	-	-	-	-	-	NA	-	-	-	-	0.0237	103.0961	
24_C4_mrc3	47.01	54.12	0.7123	-	0.0009	-	-	-	NA	-	-	-	0.0767	-	101.9198	
24_C4_sp1	3.34	33.75	0.5984	-	61.58	-	-	0.0153	NA	-	-	-	0.1934	-	99.4771	
24_C5_mrc1	46.42	54.14	1.42	-	0.1804	-	-	-	NA	-	-	-	-	-	102.1603	late edge of slide
24_C5_mrc2	46.77	53.88	0.5432	-	0.3178	-	-	-	NA	-	-	-	0.0839	-	101.5948	
24_C5_mrc3	44.14	54.66	3.75	-	0.8671	-	-	-	NA	-	-	-	0.0931	-	103.5102	
24_C5_mrc3_2	44.51	52.91	3.63	-	0.8797	-	-	0.0017	NA	-	-	-	-	0.0147	101.946	
24_C5_sp1	1.03	33.18	0.339	-	64.47	-	-	-	NA	-	-	-	0.0835	-	99.1026	replacing mrc
24_C5_sp2	0.5813	33.46	0.1851	-	65.15	-	-	0.0347	NA	-	-	-	0.0418	0.0244	99.4773	
24_C5_sp3	3.02	33.76	0.3642	-	63.01	-	-	-	NA	-	-	-	0.1691	0.0208	100.344	
24_C5_sp4	0.3935	33.99	0.0693	0.0045	65.91	-	-	-	NA	-	-	-	0.0662	-	100.4334	
24_C6_mrc1	46.62	54.31	1.5	-	0.0044	-	-	-	NA	-	-	-	0.0766	-	102.5109	coarse-grained, early
24_C6_mrc2	44.97	54.82	3.11	-	0.0034	-	-	-	NA	-	-	-	0.1751	-	103.0785	coarse-grained, early
24_C6_mrc3	46.81	54.23	1.11	-	0.0163	-	-	-	NA	-	-	-	-	0.0215	102.1877	later
24_C6_mrc3_2	47.1	52.55	0.4259	-	0.0386	-	-	0.0239	NA	-	-	-	0.0692	-	100.2075	
24_C6_sp1	1.3	33.57	0.414	-	64.16	-	-	-	NA	-	-	-	-	0.0137	99.4578	replacing mrc
24_C7_mrc1	47.14	54.43	0.8328	-	0.0311	-	-	-	NA	-	-	-	0.1369	0.006	102.5767	greenish
24_C7_mrc1_2	47.06	52.4	1.01	-	0.0484	-	-	0.0103	NA	-	-	-	0.0985	-	100.6272	
24_C7_mrc2	47.4	54.66	0.6772	-	-	-	-	-	NA	-	-	-	0.1917	0.002	102.9308	
24_C7_mrc3	46.4	54.19	1.42	-	0.5177	-	-	-	NA	-	-	-	-	-	102.5276	
24_C7_mrc4	47.12	54.34	0.2883	-	1.45	-	-	-	NA	-	-	-	0.0585	0.0216	103.2783	
24_C7_sp1	0.5361	33.89	0.474	-	65.34	-	-	-	NA	-	-	-	0.4278	0.0122	100.68	replacing mrc
24_C7_sp2	0.2869	33.91	0.2041	0.0044	65.51	-	-	0.0425	NA	-	-	-	0.1863	-	100.1442	
24_C7_sp3	0.3868	33.69	0.5765	0.0093	65.79	-	-	0.0714	NA	-	-	-	-	0.0255	100.5494	
24_C7_sp4	0.6069	33.79	0.374	0.0116	65.66	-	-	0.027	NA	-	-	-	-	0.0008	100.4702	
24_C7_sp5	1.78	34.61	0.3465	-	64.8	-	-	0.0077	NA	-	-	-	0.2959	0.0224	101.8624	
24_C7_sp6	0.9775	33.88	0.5058	0.0087	64.82	-	-	0.0212	NA	-	-	-	0.0906	-	100.3037	

Table L5. Results of EPMA analyses on sulfide minerals in sample GMA13-031

Sample	Fe	S	Cu	In	Zn	Cd	Ga	Hg	Pb	As	Sb	Ag	Au	Mn	Total	Comment
31_C1_ccp1	29.3	34.77	33.67	-	2.08	-	-	0.0109	0.1337	-	0.0131	NA	NA	NA	99.9778	
31_C1_ccp2	30.02	34.81	34.4	-	0.0406	0.007	0.0167	-	0.08	-	0.0115	NA	NA	NA	99.3859	
31_C1_ccp3	30.06	34.62	34.34	-	0.822	-	-	-	0.1439	-	0.0076	NA	NA	NA	99.9936	
31_C1_ccp4	29.96	33.68	33.37	-	0.4445	0.0045	0.0376	-	0.3886	0.3115	0.0187	NA	NA	NA	98.2155	with ccp
31_C1_ccp5	30.7	34.75	34.8	-	0.1691	0.0104	-	0.0471	0.1544	-	-	NA	NA	NA	100.6309	with ccp
31_C1_ccp6	30.33	34.81	34.67	-	-	0.0011	-	-	0.1439	-	0.0243	NA	NA	NA	99.9793	late
31_C1_ccp7	28.74	33.33	33.51	-	0.5018	0.0104	0.0152	-	0.3342	-	0.0107	NA	NA	NA	96.4524	earlier
31_C1_mrc1	47.69	53.19	0.1125	-	0.0186	-	-	-	0.15	-	0.0228	NA	NA	NA	101.1838	
31_C1_mrc2	47.42	53.1	0.7985	-	0.0585	0.0165	-	0.0017	0.1106	-	-	NA	NA	NA	101.5058	
31_C1_mrc3	47.64	53.08	0.2947	-	0.0695	0.0158	0.0146	-	0.1232	-	0.0145	NA	NA	NA	101.2523	
31_C1_sp1	2.22	32.97	1.89	0.0041	61.79	0.4141	0.3465	-	0.2598	-	0.5006	NA	NA	NA	100.3951	
31_C1_sp2	3.13	33.04	1.42	-	61.72	0.509	0.185	0.0326	0.4106	-	0.1224	NA	NA	NA	100.5695	ccp disease
31_C1_sp3	2.82	32.93	1.29	-	62.57	0.3286	0.236	-	0.3645	0.0811	0.0584	NA	NA	NA	100.6786	ccp disease
31_C1_sp4	5.46	33.47	2.17	0.0115	59.09	0.5756	0.3122	0.0287	0.1397	-	0.0962	NA	NA	NA	101.3539	with ccp
31_C1_sp5	5.37	33.45	1.86	0.0101	58.77	0.6166	0.2076	0.0115	0.107	-	0.0761	NA	NA	NA	100.4789	
31_C2_ccp1	28.9	34.79	32.97	0.0035	3.65	0.0494	0.0373	-	0.2557	-	0.0398	NA	NA	NA	100.6956	gen1
31_C2_ccp2	30.46	34.97	34.38	0.0201	0.2998	0.0106	0.0234	-	0.0697	-	0.0175	NA	NA	NA	100.251	gen2
31_C2_ccp3	29.79	34.75	34.15	0.0354	0.113	0.0053	0.0431	-	0.1423	-	0.0127	NA	NA	NA	99.0419	gen3
31_C2_ccp4	30.59	34.8	34.45	-	0.0947	-	0.0055	-	0.1112	-	-	NA	NA	NA	100.0514	gen1
31_C2_ccp5	29.52	34.8	33.9	-	0.4348	0.0112	0.0067	-	0.1023	-	-	NA	NA	NA	98.7751	gen3
31_C2_ccp6	30.49	34.76	34.3	-	0.6314	0.0143	0.0216	-	0.0801	-	0.0282	NA	NA	NA	100.3255	
31_C2_ccp7	22.62	34.1	26.73	-	14.67	0.1773	0.025	-	0.2939	-	0.1118	NA	NA	NA	98.7281	ccp inclusion in sp
31_C2_ccp8	18.12	26.33	22.23	-	6.86	0.0205	-	-	0.1865	-	0.02	NA	NA	NA	73.7671	late, with sp
31_C2_ccp9	30.45	34.66	34.72	-	0.05	-	-	0.0018	0.1675	-	0.021	NA	NA	NA	100.0703	
31_C2_sp1	16.17	34.23	19.46	-	30.82	0.1446	0.1163	0.0355	0.1005	-	0.0236	NA	NA	NA	101.1004	gen1
31_C2_sp2	2.48	32.84	2.62	-	60.61	0.1454	0.186	-	0.6435	-	0.1676	NA	NA	NA	99.6926	gen2
31_C2_sp3	2.82	33.43	1.28	-	62.02	0.533	0.2234	-	0.2815	-	0.2539	NA	NA	NA	100.8417	
31_C2_sp4	6.71	33	3.04	-	56.25	0.173	0.1762	-	0.7441	-	0.033	NA	NA	NA	100.1262	early crystal1
31_C2_sp5	4.81	32.88	3.56	0.0174	57.26	0.6842	0.259	0.0631	0.2915	-	0.2752	NA	NA	NA	100.1003	late crystal1
31_C2_sp6	1.26	32.95	1.31	-	63.46	0.0959	0.1956	-	0.2824	-	0.0286	NA	NA	NA	99.5826	
31_C2_sp7	13	33.56	14.7	0.001	37.26	0.1042	0.1493	-	0.4599	-	0.0461	NA	NA	NA	99.2805	light color, early with ccp
31_C2_sp8	0.503	32.29	0.4766	-	62.88	0.0002	0.1649	0.092	2.32	0.732	-	NA	NA	NA	99.4588	late
31_C2_cov1	0.3211	32.97	62.58	-	1.01	0.0063	-	-	0.4593	0.3081	0.0112	NA	NA	NA	97.6661	
31_C3_ccp1	30.84	34.84	34.69	-	-	-	-	-	0.1142	-	-	NA	NA	NA	100.4841	
31_C3_ccp2	30.54	34.76	34.57	0.0566	-	0.0015	0.0018	-	0.1616	0.3119	0.021	NA	NA	NA	100.4243	
31_C3_ccp3	29.24	34.66	34.22	-	1.25	0.0007	-	0.0363	0.196	-	0.0398	NA	NA	NA	99.6429	
31_C3_ccp4	29.72	34.64	33.97	0.0004	0.4523	0.0031	0.0119	-	0.1571	-	0.0072	NA	NA	NA	98.9621	late
31_C3_ccp5	21.1	31.08	39.82	-	0.131	0.0146	0.021	-	0.2716	-	0.0994	NA	NA	NA	92.5377	gen 1 colloform
31_C3_ccp6	19.5	29.87	37.41	-	0.1711	0.0189	0.0581	0.0165	0.2718	-	0.0422	NA	NA	NA	87.3587	gen2
31_C3_ccp7	20.27	30.71	38.96	-	0.1711	0.0129	-	-	0.278	0.0081	0.0593	NA	NA	NA	90.4695	gen3
31_C3_ccp8	30.01	34.75	34.6	-	0.1344	0.0031	0.021	-	0.0623	-	-	NA	NA	NA	99.5808	gen4
31_C3_mrc1	47.08	52.84	0.4172	-	-	0.0223	-	-	0.1685	-	-	NA	NA	NA	100.5279	
31_C3_sp1	2	32.83	1.94	0.0164	61.69	0.5094	0.2403	-	0.4791	-	0.0999	NA	NA	NA	99.8052	ccp inclusions?
31_C3_sp2	0.6661	33.32	1.01	-	64.79	0.4263	0.1913	-	0.2402	-	0.0911	NA	NA	NA	100.7349	
31_C3_sp3	2.45	32.87	3.13	0.1444	59.85	1.21	0.3923	-	0.253	-	0.2489	NA	NA	NA	100.5485	
31_C4_ccp1	30.47	34.58	34.68	0.0126	0.3021	0.012	0.0603	-	0.1349	-	0.052	NA	NA	NA	100.3039	gen1 banded w sp
31_C4_ccp2	29.6	34.62	34.48	-	1.34	0.0012	0.0764	-	0.1054	-	0.0759	NA	NA	NA	100.2988	gen2
31_C4_ccp3	30.23	34.91	34.52	0.1614	0.3908	0.0169	0.0346	-	0.0934	0.1068	0.0803	NA	NA	NA	100.5441	gen3
31_C4_ccp4	29.47	34.33	34.16	0.0272	1.71	0.024	0.0415	-	0.1634	0.4177	0.2234	NA	NA	NA	100.5672	gen4
31_C4_ccp5	1.82	32.17	3.27	0.0163	61	0.5668	0.2221	-	1.35	-	0.101	NA	NA	NA	100.5161	gen5
31_C4_ccp6	29.91	34.71	34.51	0.0746	0.5908	0.0073	0.0795	-	0.101	0.4676	0.1323	NA	NA	NA	100.583	gen6
31_C4_ccp7	27.28	34.35	31.67	0.0016	5.74	0.0905	0.0456	-	0.1697	0.0575	0.1412	NA	NA	NA	99.5462	gen7
31_C4_ccp8	29.99	34.63	34.7	0.0117	0.8168	0.0037	0.0532	0.1123	0.1722	-	0.0929	NA	NA	NA	100.5828	gen8
31_C4_ccp9	28.82	34.73	34	-	2.8	0.0156	0.0061	-	0.1114	-	0.1212	NA	NA	NA	100.6042	gen9
31_C4_sp1	1.65	32.76	1.99	-	62.58	0.4425	0.2386	0.0288	0.5696	-	0.0789	NA	NA	NA	100.3383	gen1 banded w ccp
31_C4_sp2	1.99	32.43	2.69	-	61.07	0.6104	0.2645	0.0058	0.653	-	0.1546	NA	NA	NA	99.8684	gen2 ccp inclusions
31_C4_sp3	2.58	32.62	2.76	0.0081	60.72	0.8754	0.2561	-	0.5869	-	0.187	NA	NA	NA	100.5934	gen3
31_C4_sp4	1.79	32.26	2.91	0.0002	60.99	0.9401	0.2907	0.0153	0.8262	-	0.1738	NA	NA	NA	100.1963	gen4
31_C4_sp5	2.24	32.16	3.28	0.0032	60.62	0.8522	0.2484	0.0364	0.941	-	0.1419	NA	NA	NA	100.523	gen5
31_C4_sp6	1.74	32.58	2.64	0.0038	61.68	0.5668	0.2455	-	1.13	-	0.0419	NA	NA	NA	100.6279	gen6
31_C4_sp7	1.7	32.2	2.92	-	61.82	0.6293	0.2509	-	0.6564	-	0.0623	NA	NA	NA	100.2389	gen7

Table L5. Continued

Sample	Fe	S	Cu	In	Zn	Cd	Ga	Hg	Pb	As	Sb	Ag	Au	Mn	Total	Comment
31_C4_sp8	2.12	32.76	2.13	0.0095	61.49	1.43	0.2834	-	0.3881	-	0.2512	NA	NA	NA	100.8621	gen8
31_C4_sp9	1.09	32.73	1.59	-	63.99	0.4415	0.2504	-	0.2978	-	0.0664	NA	NA	NA	100.456	gen9
31_C4_sp10	0.7056	32.57	1.68	0.0094	63.82	0.6785	0.3639	-	0.3428	-	0.1972	NA	NA	NA	100.3673	gen10
31_C4_sp11	0.437	32.85	0.0937	0.0004	65.76	0.0154	0.2094	-	0.3483	-	0.0077	NA	NA	NA	99.722	gen11 latest, light
31_C5_ccp1	28.71	34.69	33.23	0.01	0.5996	0.0146	0.0045	0.0489	0.1037	0.0246	0.0434	NA	NA	NA	97.4793	
31_C5_ccp2	30.22	34.59	34.77	-	-	-	0.0028	-	0.1022	-	0.2119	NA	NA	NA	99.8969	
31_C5_ccp3	30.3	34.59	34.67	0.0018	0.4413	-	0.0049	-	0.1541	-	0.2393	NA	NA	NA	100.4013	gen1 banded w sp
31_C5_ccp4	30.07	34.43	34.27	-	0.9413	0.0126	0.0159	-	0.1335	-	0.1834	NA	NA	NA	100.0567	gen2
31_C5_ccp5	29.97	34.35	34.56	0.0101	0.3153	0.007	0.0058	-	0.0785	-	0.376	NA	NA	NA	99.6728	gen3
31_C5_sp1	1.06	32.18	2.28	0.0191	62.72	0.9689	0.2798	-	0.4416	-	0.2937	NA	NA	NA	100.243	early crystal1 profile
31_C5_sp2	0.3926	32.29	1.39	0.0122	63.92	0.4789	0.2211	0.0096	1.63	-	0.0455	NA	NA	NA	100.3898	crystal1 profile
31_C5_sp3	0.2627	32.31	0.8534	0.0059	63.95	0.4819	0.2619	0.0863	1.63	-	0.1213	NA	NA	NA	99.9635	crystal1 profile
31_C5_sp4	0.4974	32.92	0.1959	-	65.67	0.0045	0.1891	-	0.1472	-	0.0145	NA	NA	NA	99.6387	late crystal1 profile
31_C5_sp5	2.05	32.17	3.34	-	60.19	0.7138	0.2467	-	0.857	-	0.1251	NA	NA	NA	99.6926	gen1 banded w ccp
31_C5_sp6	2.29	32.76	2.58	-	60.75	0.7616	0.2785	-	0.7388	-	0.0841	NA	NA	NA	100.2429	gen2 banded w ccp
31_C6_ccp1	28.26	32.02	33.26	-	0.0744	0.0116	0.0339	-	0.5985	-	0.0087	NA	NA	NA	94.2672	
31_C6_ccp2	28.59	33.89	33.13	-	-	0.001	-	-	0.086	0.8287	-	NA	NA	NA	96.5257	
31_C6_ccp3	28.81	33.59	34.03	-	0.2578	0.0093	0.0104	-	0.2179	-	0.0493	NA	NA	NA	96.9748	
31_C6_ccp4	30.48	34.77	34.45	-	0.3592	0.0001	0.0285	-	0.1244	-	0.0099	NA	NA	NA	100.2221	
31_C6_ccp5	27.4	32.13	30.98	-	-	0.0111	-	-	0.2869	-	0.0064	NA	NA	NA	90.8145	
31_C6_ccp6	30.6	34.71	34.13	-	-	0.0085	-	-	0.1495	-	0.0004	NA	NA	NA	99.5984	
31_C6_mrc1	45.62	52.43	2.19	-	0.0517	-	-	0.0051	0.548	-	0.0223	NA	NA	NA	100.867	early
31_C6_mrc2	47.25	52.89	0.1951	-	0.1069	0.0081	-	-	0.4112	-	0.0194	NA	NA	NA	100.8807	late
31_C6_mrc3	47.26	52.75	0.3063	-	0.0594	0.0076	-	-	0.2758	-	-	NA	NA	NA	100.659	
31_C6_mrc4	43.66	49.07	0.4671	-	0.0498	0.0089	-	-	0.2433	0.0598	-	NA	NA	NA	93.559	late
31_C6_sp1	13.94	32.79	15.19	0.0086	36.75	0.0765	0.1832	-	1.11	-	0.0312	NA	NA	NA	100.0794	
31_C7_ccp1	29.33	34.89	33.7	-	2.53	0.0161	-	-	0.1411	-	0.0461	NA	NA	NA	100.6532	early
31_C7_ccp2	30.48	34.67	34.36	-	0.1389	-	0.0051	0.0036	0.2	0.1393	-	NA	NA	NA	99.9969	late
31_C7_ccp3	26.97	30.97	32.83	-	0.2195	0.0084	0.0163	-	0.233	-	0.0278	NA	NA	NA	91.2751	tarnished
31_C7_ccp4	30.4	34.92	34.63	-	-	0.0042	0.0042	-	0.1228	-	0.0294	NA	NA	NA	100.1106	
31_C7_sp1	5.31	33.3	3.32	0.0481	57.75	0.8051	0.2731	-	0.1286	0.1457	0.1933	NA	NA	NA	101.2738	with ccp
31_C7_sp2	3.1	32.95	2.07	-	61.76	0.3421	0.1737	-	0.2876	-	0.047	NA	NA	NA	100.7303	inside ccp
31_C8_ccp1	29.93	34.54	34.31	-	1.66	-	0.0177	0.0109	0.0935	0.3601	0.0052	NA	NA	NA	100.9274	
31_C8_ccp2	26.53	34.37	32.03	0.0009	5.64	0.1119	0.0273	-	0.1799	-	0.2603	NA	NA	NA	99.1504	
31_C8_ccp3	29.71	34.87	34.26	0.0096	1.74	0.0027	-	0.0362	0.0594	-	-	NA	NA	NA	100.6879	
31_C8_mrc1	46.75	53.53	0.414	-	1.84	0.005	0.0018	-	0.1989	1	0.0083	NA	NA	NA	103.7479	
31_C8_mrc2	41.63	49.01	3.36	-	3.68	0.0148	0.0157	-	0.3225	0.0507	0.0222	NA	NA	NA	98.106	
31_C8_sp1	9.96	32.8	7.98	-	46.21	0.4735	0.1198	-	0.3115	-	0.0381	NA	NA	NA	97.893	early with ccp
31_C8_sp2	1.1	32.32	1.69	0.0064	63.79	0.3518	0.2547	-	0.3539	-	0.0997	NA	NA	NA	99.9666	early crystal2
31_C8_sp3	0.2589	33.12	0.2639	0.0019	65.88	0.0125	0.2144	-	0.1608	-	-	NA	NA	NA	99.9124	late crystal2
31_C8_sp4	3.31	33.07	3.32	-	59.63	0.6152	0.1937	-	0.3986	-	0.115	NA	NA	NA	100.6524	early with ccp
31_C8_sp5	1.19	32.6	1.63	0.014	63.81	0.4878	0.2917	0.0077	0.243	-	0.2585	NA	NA	NA	100.5326	late
31_C8_sp6	3.75	33.16	1.04	-	62.21	0.4137	0.2306	-	0.1461	-	0.0784	NA	NA	NA	101.0287	early with ccp
31_C8_sp7	1.16	33.02	0.8358	-	65.1	0.1625	0.1857	-	0.407	-	0.0555	NA	NA	NA	100.9264	early crystal3
31_C8_sp8	0.4666	24.52	10.56	-	31.53	0.0232	0.036	-	0.8786	-	0.032	NA	NA	NA	68.0465	late crystal 3, edge
31_C8_cov1	1.06	30.12	57.3	-	3.31	0.095	0.0111	-	0.2466	-	0.0698	NA	NA	NA	92.2126	
31_C9_ccp1	30.58	34.6	34.7	-	-	-	-	-	0.157	-	-	NA	NA	NA	100.0369	c.g. vent conduit
31_C9_ccp2	30.09	34.77	34.58	0.0039	-	0.0016	0.0092	0.0235	0.1628	-	-	NA	NA	NA	99.6411	
31_C9_sp1	1.54	33.05	0.1567	0.0002	64.51	0.0129	0.1835	-	0.5683	-	0.0125	NA	NA	NA	100.034	very late after brt
31_C9_sp2	2.55	33	0.4601	0.0101	63.16	-	0.1916	-	0.4416	-	0.002	NA	NA	NA	99.8154	very late after brt
31_C9_gn1	0.0319	13.24	0.1736	-	0.0472	0.0403	-	-	86.42	-	0.0893	NA	NA	NA	100.0422	
31_C9_gn2	0.0197	13.37	0.1971	0.0073	0.0676	0.0533	0.0211	0.0835	86.69	0.3007	0.0666	NA	NA	NA	100.8768	
31_C10_ccp1	29.64	34.37	34.3	0.0012	1.4	0.0088	0.0166	0.0471	0.2121	-	-	NA	NA	NA	99.9958	
31_C10_ccp2	30.58	34.58	34.67	-	0.0878	0.0151	0.0046	0.0036	0.1244	-	-	NA	NA	NA	100.0654	
31_C10_ccp3	29.7	34.61	33.99	-	1.78	-	0.0039	-	0.1379	-	0.0131	NA	NA	NA	100.2348	
31_C10_mrc1	46.36	52.75	0.7376	-	1.29	0.002	-	0.0068	0.1445	-	-	NA	NA	NA	101.2908	
31_C10_sp1	12.97	33.48	16.2	0.0129	36.25	0.575	0.25	0.0637	0.3399	0.2271	0.1852	NA	NA	NA	100.5537	
31_C10_sp2	0.9302	32.74	1.13	0.0025	64.17	0.2776	0.1782	0.0251	0.3863	-	-	NA	NA	NA	99.84	
31_C10_sp3	7.37	32.92	2.35	-	56.03	0.7614	0.2568	-	0.2254	-	0.0699	NA	NA	NA	99.9836	light, early in ccp
31_C10_sp4	0.5355	32.96	0.6036	0.0064	65.66	0.1554	0.2321	-	0.1809	-	0.0362	NA	NA	NA	100.37	late
31_C10_cov1	0.7812	32.87	64.43	0.0127	0.3286	0.0051	0.0235	0.0299	0.1552	0.6467	0.0068	NA	NA	NA	99.2898	altering sp/ccp
31_C11_ccp1	30.65	34.63	34.71	-	0.0777	-	0.0201	0.0109	0.1258	-	0.0277	NA	NA	NA	100.2522	
31_C11_ccp2	30.67	34.61	34.7	-	-	0.0037	-	-	0.1317	-	-	NA	NA	NA	100.1153	
31_C11_sp1	5.92	33.22	4.6	-	56.48	0.4317	0.2959	-	0.2058	-	0.0919	NA	NA	NA	101.2453	early in ccp
31_C11_sp2	4.11	33	2.05	-	60.67	0.2124	0.2258	-	0.5118	-	0.09	NA	NA	NA	100.8699	early in ccp

Table L6. Results of EPMA analyses on sulfide minerals in sample GMA13-032

Sample	Fe	S	Cu	In	Zn	Cd	Ga	Hg	Pb	As	Sb	Ag	Au	Mn	Total	Comment
32_C1_ccp1	29.61	35.25	33.87	-	2.13	0.0027	-	-	0.0105	-	-	0.0483	0.1285	-	101.0499	
32_C1_ccp2	29.46	35.42	34	-	2.22	0.0068	-	0.029	0.1525	-	0.0367	0.024	0.0721	-	101.421	included in sp
32_C1_ccp3	29.3	34.87	33.92	-	2.46	0.0111	-	-	0.0937	-	0.0159	0.0227	0.0071	-	100.7004	included in sp
32_C1_py1	46.73	53.52	0.0778	-	0.2336	0.0036	-	-	0.4393	0.4184	0.0129	0.0089	-	-	101.4445	colloform, gen1
32_C1_py2	46.24	54.11	0.036	-	1.36	0.0086	-	-	0.7901	-	0.0178	-	-	-	102.5625	gen2
32_C1_py3	45.79	53.51	0.0839	-	1.12	0.015	-	-	1.28	-	-	0.0068	-	-	101.8056	gen3
32_C1_py4	46.03	53.26	0.0394	-	1.97	0.0018	-	-	0.6186	-	-	-	-	-	101.9197	gen4
32_C1_py5	44.72	53.25	0.4742	-	1.28	0.0152	-	0.0051	0.3968	0.3156	0.0191	0.0752	0.244	-	100.7951	sperulitic
32_C1_sp2	1.27	33.49	0.3495	-	64.5	0.0988	0.253	-	0.1462	-	0.1661	0.0247	0.5122	-	100.8104	
32_C1_sp3	1.39	33.47	0.6919	-	64.1	0.0656	0.2368	-	0.3505	-	0.3509	0.0614	0.3142	-	101.0312	late, with ccp inclusions
32_C1_sp4	0.728	32.44	1.54	0.0012	60.75	0.1142	0.176	-	4.86	-	0.2092	0.165	0.1212	-	101.1047	vent lining, bright interior BSE
32_C1_sp5	0.8022	33.8	0.1629	-	65.79	0.0142	0.1939	-	0.1145	-	0.0295	0.0723	0.1044	-	101.0839	vent lining, dark rim BSE
32_C1_sp6	1.06	33.68	0.044	-	64.1	0.081	0.2077	-	0.1397	0.1464	0.0255	0.0135	0.1219	-	99.6198	
32_C1_sp7	0.9664	33.44	0.0567	-	64.68	0.0067	0.191	-	0.4413	-	-	0.0296	0.3301	-	100.1417	
32_C1_gn1	0.4487	19.59	0.1447	-	24.07	0.0534	0.0417	-	62.33	-	0.1044	0.0095	0.0535	-	106.8458	High total from heavy Pb
32_C1_gn2	0.1658	14.56	0.1038	-	9.03	0.0515	0.0269	0.0304	84.29	-	0.0268	0.0032	-	-	108.2883	
32_C2_py1	46.72	53.61	0.0579	-	0.3368	0.0079	-	-	0.6156	-	0.0062	0.0058	0.0346	-	101.3947	sperulitic
32_C2_py2	42.51	51.91	0.503	-	4.14	0.0044	-	0.0343	2.54	-	0.0257	0.1014	0.2055	-	101.9743	sperulitic, sp inclusions?
32_C2_py3	46.67	53.91	0.0498	-	1.37	0.0024	-	-	0.4664	-	0.0178	0.0094	0.02	-	102.5157	
32_C2_py4	45.33	53.24	0.0717	-	1.14	0.0117	-	-	1.43	0.0852	0.0037	-	0.1016	-	101.4139	
32_C2_py5	43.04	51.65	0.3278	-	1.84	0.0011	-	-	3.61	2.57	0.0343	0.0557	-	-	103.1288	relict sperulitic
32_C2_py6	43.87	51.69	0.3546	-	1.25	0.0158	-	-	4.02	0.655	-	0.0737	0.0019	-	101.9309	sperulitic
32_C2_sp1	1.63	33.67	0.1136	0.0119	64.51	-	0.2038	0.0539	0.2252	-	0.0061	0.0281	-	-	100.4525	
32_C2_sp2	1.11	33.55	0.3522	0.0019	63.47	0.0322	0.2342	0.0519	0.6516	0.8018	0.078	0.1051	0.1924	-	100.6313	
32_C2_sp3	1.89	33.17	0.5463	0.0065	62.11	0.0257	0.2305	0.0325	1.42	-	0.0412	0.1374	0.1662	-	99.7764	
32_C2_sp4	0.5176	31.54	1.17	-	58.7	0.0859	0.1812	-	6.69	0.1032	0.0839	0.11	0.1747	-	99.3566	bright interior BSE
32_C2_sp5	2.85	33.52	0.198	-	62.85	-	0.1874	0.0557	0.8113	-	-	0.0044	0.2863	-	100.7631	dark rim BSE
32_C2_sp6	0.5149	30.53	1.1	-	56.09	0.0831	0.1667	-	9.59	-	0.0774	0.1814	0.3235	-	98.6571	early
32_C2_sp7	2	33.53	0.115	0.0047	62.86	0.0297	0.1923	-	0.3326	-	0.0235	0.0186	0.0992	-	99.2057	late
32_C3_ccp1	28.96	35.32	33.28	-	2.72	0.0005	0.0009	-	0.0815	-	0.0219	0.037	-	-	100.4217	very late after sp
32_C2_gn1	0.3487	13.73	0.4594	-	2.81	0.0508	0.0054	-	88.39	-	0.3501	0.1106	-	-	106.2549	
32_C3_py1	44.96	53.34	0.1923	-	1.31	0.0038	-	-	0.278	-	-	-	-	-	100.084	sperulitic
32_C3_py2	46.17	53.44	0.0379	-	0.0635	0.0153	-	-	0.2818	-	-	0.0084	0.1078	-	100.1246	sperulitic
32_C3_py3	44.63	51.97	0.234	-	0.7721	0.0099	0.0152	-	0.5136	-	-	0.0059	0.0911	-	98.2419	sperulitic/colloform
32_C3_py4	45.47	52.95	0.2904	-	0.1124	0.0054	-	-	0.2344	-	-	0.0252	-	-	99.0878	sperulitic within mrc
32_C3_py6	44.54	52.1	0.2777	-	0.0701	0.0171	-	-	0.3321	0.2647	0.0269	0.0273	-	-	97.656	early colloform
32_C3_py7	45.38	52.73	0.2357	-	0.0495	0.019	-	-	0.593	-	-	0.0341	0.0164	-	99.0578	late colloform
32_C3_mrc1	47.38	54.05	0.0234	-	0.2142	0.009	0.0149	-	0.1655	0.2394	-	-	-	-	102.0964	surrounding sperulitic py
32_C3_mrc2	47.49	53.7	0.0001	-	0.026	0.0148	-	-	0.2688	-	0.019	-	-	-	101.5186	late after py
32_C3_sp1	1.96	33.75	0.0838	0.0049	64.09	0.1324	0.2105	0.0077	0.1776	-	-	-	0.3477	-	100.7645	
32_C3_sp2	1.73	34.01	0.0734	0.013	65.02	0.1405	0.2066	-	0.0888	-	0.0093	0.0027	0.1861	-	101.4803	
32_C3_sp3	28.83	46.13	0.051	-	24.99	0.0612	0.0916	-	0.2214	-	0.0308	-	0.1882	-	100.5941	included in mrc
32_C3_sp4	2.38	33.36	0.2065	0.002	63.61	0.0807	0.1821	-	0.1315	-	0.1348	0.0147	-	-	100.1023	late after mrc
32_C3_sp5	1.36	33.79	0.8498	-	63.8	0.0145	0.1989	-	0.7407	-	-	0.0764	0.1094	-	100.9396	late, interior crystal1
32_C3_sp6	1.52	33.62	0.14	0.0006	65.02	0.2056	0.1915	-	0.1841	-	0.0424	-	0.231	-	101.1551	late crystal1 rim
32_C3_gn1	0.8374	18.71	0.1656	-	20.25	0.0186	0.0191	0.0662	66.45	-	0.1194	0.0334	-	-	106.6696	included in sp
32_C3_gn2	0.2346	14.03	0.0664	-	6.87	0.0412	-	-	88.07	0.2267	0.1257	0.0206	-	-	109.6851	included in sp
32_C4_ccp1	16.34	34.94	17.74	-	30.68	0.0737	0.1056	-	0.0987	-	-	0.005	0.2364	-	100.2193	mixed ccp + sp
32_C4_ccp2	30.31	35.21	34.19	-	1.04	0.0131	0.0435	-	0.1011	-	0.0111	0.0046	0.1459	-	101.0692	late c.g.
32_C4_ccp3	29.74	35.67	33.9	-	0.9938	-	0.0345	-	0.1115	-	-	0.0109	-	-	100.4606	late c.g.
32_C4_py1	42.11	51.38	1.26	-	0.6279	0.0192	-	-	1.17	-	0.0369	0.3045	-	-	96.9086	sperulitic
32_C4_py2	43.49	51.77	0.4696	-	0.4008	0.0209	-	0.0323	1.04	-	0.015	0.0333	-	-	97.272	sperulitic
32_C4_py3	46.23	53.79	0.2938	-	0.8312	0.0094	-	-	0.4098	-	0.0058	0.0335	0.0037	-	101.6071	early sperulitic, tarnished?
32_C4_sp1	11.06	34.16	0.2147	-	54.06	0.0449	0.1516	-	0.5118	-	0.0141	0.0206	0.2631	-	100.5007	included in py
32_C4_sp2	0.8275	32.54	2.92	-	59.98	0.0247	0.1694	-	2.62	-	0.0372	0.3905	0.2529	-	99.7623	brighter BSE
32_C4_sp3	0.9656	33.74	0.6572	-	64.51	0.0084	0.1611	0.0212	0.3174	0.3652	0.0796	0.0341	0.1772	-	101.037	
32_C4_sp4	1.2	33.67	0.4134	0.0074	64.88	0.0229	0.2189	-	0.1713	-	0.0113	0.0157	0.1077	-	100.7186	

Table L6. Continued

Sample	Fe	S	Cu	In	Zn	Cd	Ga	Hg	Pb	As	Sb	Ag	Au	Mn	Total	Comment
32_C4_sp5	1.32	33.89	0.2638	0.0047	64.45	-	0.2016	0.0058	0.1668	0.7703	0.0073	0.0175	0.3195	-	101.4173	
32_C4_spy6	1.39	33.58	0.4269	-	64.32	0.0005	0.2358	-	0.2046	-	0.04	0.0314	0.1304	-	100.3596	
32_C4_gn1	0.1321	13.67	0.1217	-	3.37	0.0393	0.0276	0.0184	88.13	0.2815	0.0663	-	0.0062	-	105.863	included in sp
32_C4_gn2	0.7713	17.85	0.3741	-	16.8	0.061	0.0226	0.0821	67.03	-	0.4221	0.0433	-	-	103.4564	included in sp
32_C4_gn3	0.7865	13.71	0.0988	-	3.2	0.0506	-	-	87.39	1.24	0.0044	0.0047	0.0087	-	106.4936	
32_C4_gn4	0.5055	17.66	0.2559	-	18.02	0.0448	0.0326	-	67.32	-	0.0478	-	0.1547	-	104.0413	
32_C4_gn5	0.4258	13.87	0.2491	-	6.29	0.0528	-	0.04	87.59	-	0.071	0.0283	-	-	108.6169	
32_C5_py1	45.73	53.97	0.2738	-	0.7062	0.0122	0.0096	0.0017	0.354	-	0.0257	0.0582	0.2769	-	101.4182	sperulitic
32_C5_sp1	0.7347	32.94	0.1994	-	63	0.0095	0.161	-	2.65	-	-	0.1721	0.1323	-	99.9991	
32_C5_sp2	1.56	33.78	0.2685	0.009	64.01	0.0291	0.1555	-	0.2614	0.1461	0.1273	0.0457	0.0539	-	100.4465	
32_C5_gn1	0.3012	14.05	0.1593	-	2.39	0.0244	-	-	54.65	1.27	13.79	0.0654	-	-	86.7004	off grain
32_C6_py1	45.01	52.89	0.4648	-	0.3225	0.0046	-	-	0.7394	-	0.0075	0.0453	-	-	99.4842	sperulitic
32_C6_py2	44.97	52.31	0.1861	-	3.01	0.0059	-	-	0.5563	0.102	-	0.0269	0.1526	-	101.3197	mrc
32_C6_py3	47	53.93	0.4357	-	0.9546	0.0096	-	-	0.2004	0.4858	0.0012	0.0183	-	-	103.0355	intergrown w sp
32_C6_sp1	1.58	33.34	1.3	0.0011	63.65	0.0847	0.1992	-	0.7218	-	0.3202	0.0289	0.2478	-	101.4737	
32_C6_sp2	7.56	34.33	0.4805	-	58.14	0.2117	0.1766	-	0.4919	-	0.0343	0.0217	0.4032	-	101.8498	early, intergrown w py
32_C6_sp3	1.12	33.66	0.3439	-	65.24	0.0005	0.1774	-	0.2792	-	0.0396	0.0295	0.1598	-	101.0498	late
32_C6_gn1	0.1687	13.87	0.1256	-	6.36	0.0565	0.0124	0.0057	87.81	-	0.1662	0.0171	-	-	108.5921	
32_C7_ccp1	29.94	35.19	34	-	1.24	0.006	-	0.0091	0.2412	0.1971	0.1361	0.0117	-	-	100.9711	c.g., included in sp
32_C7_ccp2	11.81	33.81	12.16	-	40.56	0.2885	0.1268	0.1463	0.939	-	0.6461	0.1067	0.158	0	100.7514	mix of ccp + sp, later
32_C7_ccp3	29.14	35.32	33.4	-	2.89	0.0035	-	-	0.1147	-	0.0119	-	-	-	100.8801	c.g., included in sp
32_C7_py1	36.71	49.65	0.2839	-	13.73	0.0151	0.0378	-	1.96	-	0.0177	0.0214	0.1363	-	102.5621	mix of py + sp
32_C7_py2	46.71	53.62	0.0452	-	0.3747	0.0167	0.0114	-	0.4725	-	-	-	0.0018	-	101.2523	dendritic
32_C7_py3	22.04	41.59	0.4745	-	31.23	0.0088	0.0868	0.0161	5.14	-	0.0188	0.058	0.0524	-	100.7153	dendritic, mixed w sp, greyis
32_C7_py4	43.6	53.08	0.4052	-	2.67	0.0123	0.0239	-	1.12	-	-	0.0325	0.176	-	101.1199	
32_C7_py5	44.69	53.52	0.2073	-	1.32	0.0102	0.0046	-	2.58	0.5157	0.0079	0.0072	0.027	-	102.8898	early
32_C7_sp1	2.47	32.33	0.7567	-	59.65	0.0567	0.1503	-	3.92	0.2803	0.0715	0.0806	-	-	99.7662	
32_C7_sp2	1.8	33.8	0.1167	0.0072	64.17	0.145	0.1568	0.0404	0.1773	-	0.0186	-	0.1895	-	100.6214	different shade of grey BSE
32_C7_sp3	2.44	33.57	0.6106	0.0022	62.67	0.041	0.1641	-	0.5567	-	0.1154	0.1015	0.5665	-	100.8379	late, after gn
32_C7_sp4	2.31	33.81	0.5018	0.0004	63.12	0.1458	0.2143	0.0134	0.2959	-	0.2156	0.0158	0.2414	-	100.8843	latest, tiny inclusion of jd
32_C7_sp5	1.61	33.76	0.2593	0.0049	64.24	0.2165	0.1925	-	0.1362	-	0.1497	0.0069	0.1599	-	100.7358	early, inclusions of ccp
32_C7_sp6	1.27	32.85	1.02	-	61.72	0.1181	0.2229	-	2.28	-	0.1877	0.156	0.3666	-	100.1912	late, inclusions of ccp
32_C7_sp7	3.37	33.14	2.46	-	59.24	0.3058	0.2175	0.0457	1.28	-	0.79	0.1608	0.228	-	101.2377	gen2
32_C7_sp8	7.21	33.49	6.71	-	51.18	0.3842	0.1801	0.0341	0.9087	-	0.785	0.1069	0.085	-	101.074	gen1
32_C7_sp9	1.95	33.87	0.3263	-	64.09	0.2932	0.1949	0.0327	0.1474	-	0.2149	0.0034	0.2484	-	101.3711	gen3
32_C7_sp10	3.83	33.03	2.7	-	57.65	0.1844	0.1952	0.0418	2.06	-	0.6428	0.1321	0.0638	-	100.53	
32_C7_gn1	0.3348	14.22	0.1588	-	7.45	0.0598	-	-	86.62	-	0.122	0.0301	0.2367	-	109.2321	
32_C7_gn2	1.01	15.69	0.1584	-	10.33	0.0448	-	0.0248	78.26	-	0.1135	0.0549	0.0038	-	105.6901	included in gn
32_C8_py1	44.16	52.72	0.6041	-	1.75	-	-	-	1.32	0.4328	0.0087	0.058	-	-	101.0536	sperulitic
32_C8_py2	46.48	53.41	0.2065	-	0.9353	0.0033	-	-	0.3743	-	0.0162	0.0129	0.0292	-	101.4676	
32_C8_py3	47.31	53.6	0.0513	-	0.4788	0.0147	0.0143	-	0.2345	-	-	0.0037	-	-	101.7072	
32_C8_sp1	1.38	33.49	1.27	-	62.75	0.0195	0.1467	-	0.8772	0.6952	0.2431	0.0687	0.3151	-	101.2554	
32_C8_sp2	1.28	33.68	0.6708	-	64.22	0.0007	0.23	-	0.4202	0.6001	0.0997	0.0388	-	-	101.2402	
32_C8_sp3	1.35	33.75	0.3965	-	64.83	0.0166	0.2384	-	0.45	-	0.0299	0.048	0.2359	-	101.3452	
32_C8_sp4	1.08	33.7	1.11	-	63.04	0.015	0.1491	0.0499	0.7074	-	0.0494	0.0979	0.3139	-	100.3126	
32_C8_gn1	0.0203	13.68	0.0455	-	3.3	0.036	0.04	0.0254	88.42	-	0.0016	-	0.1606	-	105.7293	included in sp
32_C8_gn2	0.0788	13.83	0.0951	-	4.76	0.0428	0.0122	-	88.86	-	0.0503	-	0.3018	-	108.031	included in sp
32_C8_gn3	0.1033	13.89	0.0933	0.001	4.81	0.0361	0.0215	0.0014	88.59	-	0.1677	0.0229	0.0926	-	107.8297	included in sp
32_C8_gn4	0.0631	13.87	0.0583	-	5.53	0.0447	0.0384	0.0228	88.85	-	0.0471	-	-	-	108.5243	included in sp
32_C9_py1	45.4	53.29	0.1337	-	1.74	0.0041	-	-	0.7892	-	-	0.0211	0.1673	-	101.5453	dendritic early crystal1
32_C9_py2	44.77	53.22	0.1951	-	2.14	-	0.0068	-	1.03	-	-	0.0149	0.2233	-	101.6	dendritic crystal1 dark BSE
32_C9_py3	41.63	51.35	0.174	-	6.14	0.0113	-	-	2.16	-	0.0103	0.0011	-	-	101.4766	dendtiric crystal1 light BSE
32_C9_py4	45.15	53.06	0.0563	-	1.69	0.0118	-	-	1.41	-	0.0179	-	0.0728	-	101.4688	dentritic crystal1 dark BSE
32_C9_py5	44.12	52.19	0.0708	-	2.82	0.0084	-	-	1.96	-	0.0236	0.0016	0.1246	-	101.3189	dendritic crystal 1 light BSE
32_C9_py6	33.36	46.3	0.3422	-	14.18	0.0138	0.0279	-	5.78	0.3297	0.0107	0.03	0.2484	-	100.6226	dendritic crystal 1 light BSE, edge
32_C9_py7	44.35	53.05	0.7578	-	1.44	0.0159	-	-	0.8162	-	-	0.0743	0.0836	-	100.5877	
32_C9_py8	44.92	52.81	0.2138	-	1.87	0.0078	-	-	1.54	-	0.019	0.0223	0.0109	-	101.4137	dendritic
32_C9_py9	47.08	54.08	0.0417	-	0.395	0.0126	-	0.0562	0.3088	-	-	0.0018	-	-	101.9761	
32_C9_sp1	1.69	33.6	0.2891	0.0056	64.32	0.2321	0.1836	-	0.1822	-	0.2067	0.0094	-	-	100.7187	
32_C9_sp2	2.74	33.25	2.37	-	60.34	0.1778	0.1774	-	1.32	-	0.5207	0.0657	0.2384	-	101.2	
32_C9_sp3	1.76	33.53	0.3747	-	63.76	0.2048	0.2111	-	0.1982	0.3078	0.2078	0.016	0.4387	-	101.009	
32_C9_sp4	1.55	33.52	0.4591	-	63.61	0.1063	0.2015	-	0.0745	-	0.2692	0.0288	0.3265	-	100.1459	
32_C9_sp5	2.56	33.77	1.5	-	62.42	0.2177	0.1862	0.0077	0.1915	-	0.2566	0.0173	0.2519	-	101.3788	

Table L7. Results of EPMA analyses on sulfide minerals in sample GMA13-038

Sample	Fe	S	Cu	In	Zn	Cd	Ga	Hg	Pb	As	Sb	Ag	Au	Mn	Total	Comment
38_C1_ccp1	30.48	34.67	34.63	-	-	0.002	-	NA	NA	NA	NA	NA	0.0596	NA	99.8417	
38_C1_ccp2	30.69	34.78	34.83	-	-	0.0162	-	NA	NA	NA	NA	NA	-	NA	100.3161	
38_C1_ccp3	30.8	34.8	34.6	-	-	0.0224	0.0184	NA	NA	NA	NA	NA	0.2083	NA	100.449	
38_C1_py1	45.84	52.08	0.8428	-	0.131	0.0016	0.0007	NA	NA	NA	NA	NA	0.0508	NA	98.9469	early, mrc?
38_C1_py2	46.11	52.57	0.7434	-	0.1254	0.0088	-	NA	NA	NA	NA	NA	0.2524	NA	99.8101	early
38_C2_ccp1	30.49	34.8	34.64	-	-	0.0025	-	NA	NA	NA	NA	NA	-	NA	99.9326	late
38_C2_ccp2	30.58	34.64	34.6	-	-	0.0118	0.0148	NA	NA	NA	NA	NA	0.1068	NA	99.9535	
38_C2_ccp3	30.75	34.57	34.65	-	-	0.0091	-	NA	NA	NA	NA	NA	0.0227	NA	100.0017	early
38_C2_ccp4	30.41	35.33	34.53	-	0.7075	0.0058	0.0024	NA	NA	NA	NA	NA	0.0997	NA	101.0853	
38_C2_py1	46.29	52.95	1.73	-	0.0714	0.016	0.0108	NA	NA	NA	NA	NA	0.1433	NA	101.2115	early
38_C2_py2	45.25	52.64	0.5122	-	0.2101	0.006	-	NA	NA	NA	NA	NA	0.1018	NA	98.7201	colloform vent lining2
38_C2_py3	47.3	53.23	0.6689	-	0.039	0.0154	-	NA	NA	NA	NA	NA	-	NA	101.2533	colloform vent lining1
38_C2_py4	46.65	52.92	0.7766	-	0.0407	0.0145	0.0069	NA	NA	NA	NA	NA	-	NA	100.4087	colloform near vent gen1
38_C2_py5	44.61	49.01	0.4188	-	0.0563	-	-	NA	NA	NA	NA	NA	-	NA	94.0951	colloform near vent gen2
38_C2_py6	46.47	53.15	0.3994	-	0.0899	0.0051	0.0007	NA	NA	NA	NA	NA	0.1698	NA	100.2848	colloform near vent gen3
38_C2_py7	47.49	53.29	0.7837	-	0.0349	0.0009	0.017	NA	NA	NA	NA	NA	-	NA	101.6164	
38_C2_sp1	0.5321	33.14	0.213	0.0014	66.07	0.3056	0.2465	NA	NA	NA	NA	NA	-	NA	100.5085	
38_C3_ccp1	30.92	34.79	34.81	-	-	0.0196	-	NA	NA	NA	NA	NA	0.0752	NA	100.6148	v.c.g. early crystal1 profile
38_C3_ccp2	30.68	34.7	34.53	-	-	0.0138	-	NA	NA	NA	NA	NA	0.0734	NA	99.9973	crystal1 profile
38_C3_ccp3	30.55	34.65	34.63	-	-	0.0093	0.0167	NA	NA	NA	NA	NA	-	NA	99.8561	crystal1 profile
38_C3_ccp4	30.66	34.69	34.76	-	-	0.0061	-	NA	NA	NA	NA	NA	0.2397	NA	100.3558	crystal1 profile
38_C4_ccp1	30.55	34.76	34.78	-	0.1731	0.018	0.0537	NA	NA	NA	NA	NA	0.1993	NA	100.534	
38_C4_ccp2	30.65	34.64	34.86	-	-	0.0137	-	NA	NA	NA	NA	NA	0.0489	NA	100.2125	
38_C4_py1	47.5	53.18	0.2013	-	0.8498	-	0.0089	NA	NA	NA	NA	NA	-	NA	101.74	
38_C4_py2	46.84	52.84	0.3539	-	0.0824	0.0128	0.0055	NA	NA	NA	NA	NA	0.0164	NA	100.1509	early sperulitic
38_C4_py3	47.58	53.44	0.2721	-	0.0296	0.0082	-	NA	NA	NA	NA	NA	0.1271	NA	101.457	later
38_C4_py4	45.57	52.86	2.1	-	0.0718	0.0021	-	NA	NA	NA	NA	NA	-	NA	100.6038	
38_C4_sp1	0.847	33.12	0.1413	-	65.53	0.3789	0.1924	NA	NA	NA	NA	NA	0.3368	NA	100.5463	
38_C5_ccp1	30.39	34.67	34.55	-	0.3403	0.0156	-	NA	NA	NA	NA	NA	0.2482	NA	100.214	included in sp
38_C5_ccp2	30.51	34.68	34.68	-	-	0.0128	-	NA	NA	NA	NA	NA	0.1469	NA	100.0296	
38_C5_ccp3	30.68	34.62	34.63	-	-	0.0076	0.0039	NA	NA	NA	NA	NA	0.0998	NA	100.0413	
38_C5_ccp4	30.66	34.63	34.53	-	-	0.0146	0.0258	NA	NA	NA	NA	NA	0.028	NA	99.8885	
38_C5_ccp5	30.57	34.67	34.73	-	-	0.0046	-	NA	NA	NA	NA	NA	-	NA	99.9746	
38_C5_sp1	1.13	33.34	0.6703	0.0056	64.95	0.4392	0.2125	NA	NA	NA	NA	NA	0.1815	NA	100.929	
38_C5_sp2	1.58	33.33	0.8727	0.0026	64.85	0.2715	0.2577	NA	NA	NA	NA	NA	0.2886	NA	101.453	
38_C5_sp3	1.96	33.38	1.16	-	63.84	0.4744	0.2432	NA	NA	NA	NA	NA	-	NA	101.0576	
38_C5_sp4	0.6161	33.23	0.1666	-	65.92	0.415	0.1675	NA	NA	NA	NA	NA	0.2349	NA	100.75	very light
38_C5_sp5	0.6049	33.18	0.0819	-	65.69	0.5133	0.2148	NA	NA	NA	NA	NA	0.026	NA	100.3108	
38_C5_sp6	0.7246	33.36	0.1707	0.005	65.68	0.3817	0.26	NA	NA	NA	NA	NA	0.0587	NA	100.6406	
38_C5_sp7	0.6631	33.06	0.11	0.001	65.63	0.546	0.1995	NA	NA	NA	NA	NA	0.209	NA	100.4185	
38_C5_cov1	0.2834	31.29	64.11	0.0082	1.38	0.0054	-	NA	NA	NA	NA	NA	-	NA	97.0771	
38_C5_cov2	0.2759	33.51	54.31	-	12.38	0.1277	0.034	NA	NA	NA	NA	NA	-	NA	100.6376	
38_C6_ccp1	30.55	34.87	34.7	-	-	0.0095	-	NA	NA	NA	NA	NA	-	NA	100.1294	
38_C6_ccp2	30.41	34.67	34.68	-	-	-	-	NA	NA	NA	NA	NA	-	NA	99.7601	
38_C6_py1	47.81	53.02	0.0417	-	-	0.0174	0.013	NA	NA	NA	NA	NA	-	NA	100.9021	c.g. mrc
38_C6_py2	47.82	52.87	0.3606	-	0.0333	0.0011	-	NA	NA	NA	NA	NA	0.0164	NA	101.1014	c.g. mrc
38_C6_py3	45.52	49.78	0.5431	-	0.1236	0.0072	-	NA	NA	NA	NA	NA	-	NA	95.974	interior, sec py?
38_C6_py4	46.63	53.28	0.9318	-	-	0.0055	0.0095	NA	NA	NA	NA	NA	-	NA	100.8567	later mrc
38_C7_ccp1	29.6	34.85	34.04	-	2.05	0.0184	-	NA	NA	NA	NA	NA	0.2691	NA	100.8274	incl. in sp
38_C7_ccp2	29.66	34.23	34.69	-	0.0635	-	0.0307	NA	NA	NA	NA	NA	-	NA	98.6742	
38_C7_ccp3	30.37	34.74	35.05	-	-	-	0.0233	NA	NA	NA	NA	NA	0.1312	NA	100.3144	
38_C7_ccp4	30.75	34.75	34.8	-	-	0.0008	-	NA	NA	NA	NA	NA	0.292	NA	100.5928	
38_C7_py1	47.64	52.9	0.4885	-	0.3076	0.0093	-	NA	NA	NA	NA	NA	-	NA	101.3454	
38_C7_py2	47.1	53.07	0.5839	-	0.0624	-	-	NA	NA	NA	NA	NA	0.0671	NA	100.8833	
38_C7_py3	45.07	51.86	0.7155	-	0.0851	0.0053	-	NA	NA	NA	NA	NA	-	NA	97.736	
38_C7_py4	43.92	51.66	0.5995	-	4.1	0.016	0.0265	NA	NA	NA	NA	NA	0.0778	NA	100.3997	
38_C7_sp1	1.2	33.23	0.4387	-	65.26	0.5582	0.2065	NA	NA	NA	NA	NA	-	NA	100.8933	very light
38_C7_sp2	0.6886	33.37	0.357	-	65.94	0.3966	0.2014	NA	NA	NA	NA	NA	0.026	NA	100.9795	
38_C7_sp3	0.7619	33.08	0.4246	0.0994	65.23	0.6667	0.2392	NA	NA	NA	NA	NA	-	NA	100.5018	
38_C7_cov1	0.8082	31.1	64.44	-	0.8396	0.0049	-	NA	NA	NA	NA	NA	-	NA	97.1928	

Table L8. Results of EPMA analyses on sulfide minerals in sample GMA13-042

Sample	Fe	S	Cu	In	Zn	Cd	Ga	Hg	Pb	As	Sb	Ag	Au	Mn	Total	Comment
42_C1_ccp1	29.9	34.77	34.59	-	-	0.0017	-	-	0.1413	-	0.034	NA	NA	NA	99.437	late
42_C1_ccp2	28.96	34.62	33.92	-	0.2087	0.0132	-	-	0.1027	-	0.0204	NA	NA	NA	97.845	late
42_C1_ccp3	29.55	34.96	34.03	-	0.2196	0.0067	-	-	0.0595	-	-	NA	NA	NA	98.8258	
42_C1_ccp4	30	34.98	34.39	-	0.0316	0.0134	-	-	0.1176	-	0.0232	NA	NA	NA	99.5558	
42_C1_ccp5	26.62	34.84	32.07	-	4.65	0.0509	0.0296	-	0.0732	-	0.038	NA	NA	NA	98.3718	
42_C1_py1	45.95	53.1	0.7705	-	0.8832	0.0147	-	-	0.9575	0.111	-	NA	NA	NA	101.7868	
42_C1_py2	44.57	52.92	2.09	-	1.52	0.0084	0.0211	-	1.04	-	-	NA	NA	NA	102.1694	
42_C1_sp1	2.73	32.93	2.28	-	60.69	0.6927	0.2473	-	0.7557	0.0893	0.1173	NA	NA	NA	100.5322	ccp inclusions
42_C1_sp2	1.23	33.21	0.7247	-	61.88	0.9911	0.2219	-	0.2294	-	0.077	NA	NA	NA	98.5642	
42_C1_sp3	4.09	33.39	4.09	0.008	56.44	0.5673	0.173	0.0479	0.6012	-	0.0793	NA	NA	NA	99.4867	ccp inclusions
42_C1_sp4	7.33	32.04	9.45	0.0008	44.89	0.2229	0.1287	0.0434	2.46	-	0.0145	NA	NA	NA	96.5804	
42_C1_sp5	0.9586	32.59	1.48	-	62.23	0.4162	0.1759	-	1.04	0.5508	0.0639	NA	NA	NA	99.5055	early crystal1
42_C1_sp6	1.49	32.57	1.55	-	61.58	0.7714	0.1649	0.0999	1.36	-	0.0789	NA	NA	NA	99.6652	late crystal1
42_C1_gn1	-	18.42	3.28	-	0.0213	0.0346	-	-	65.93	9.59	0.0215	NA	NA	NA	97.2974	
42_C1_gn2	0.0626	13.66	0.3549	-	4.69	0.0496	0.0264	-	85.61	-	0.0156	NA	NA	NA	104.469	
42_C1_gn3	0.0663	14.15	0.5941	-	7.51	0.0484	-	-	82.97	0.2587	0.0389	NA	NA	NA	105.6364	
42_C1_cov1	0.0612	29.62	63.06	-	6.09	0.0403	0.0407	-	0.4328	-	0.0012	NA	NA	NA	99.3463	altering sp
42_C1_cov2	0.2598	15.59	26.4	0.019	1.48	0.0461	0.1017	0.0317	1.28	0.646	0.0549	NA	NA	NA	45.9093	
42_C2_ccp1	29.46	34.97	33.98	-	0.6035	0.0042	0.0153	0.0309	0.1399	-	0.032	NA	NA	NA	99.2358	
42_C2_sp1	0.241	31.99	0.8308	-	60.89	0.4083	0.1694	-	3.89	-	0.0179	NA	NA	NA	98.4375	gn inclusions
42_C2_sp2	1.9	33.11	2.25	-	60.81	1.23	0.1705	0.0172	0.419	-	0.3266	NA	NA	NA	100.2332	spy (+gn?) inclusions
42_C2_sp3	0.4015	31.9	0.6438	-	58.2	0.0897	0.1921	-	0.8533	-	0.0085	NA	NA	NA	92.289	
42_C2_sp4	0.6015	33.22	0.5704	-	63.74	0.3083	0.1854	-	0.3146	0.6175	0.0376	NA	NA	NA	99.5953	
42_C2_sp5	1.13	33.27	0.2747	-	63.23	0.7615	0.2	0.0096	0.1407	-	0.0186	NA	NA	NA	99.0351	
42_C2_sp6	0.2188	32.16	0.9418	0.0017	63.14	0.1663	0.1913	-	1.38	0.0486	0.0433	NA	NA	NA	98.2918	
42_C2_gn1	0.4491	15.04	1.14	-	7.83	0.0969	-	-	77.96	0.0596	0.1191	NA	NA	NA	102.6946	included in sp
42_C2_gn2	0.0367	13.69	0.3046	-	4.98	0.0713	0.0275	-	86.81	-	0.0865	NA	NA	NA	106.0065	included in sp
42_C2_gn3	0.5894	13.98	1.07	-	5.34	0.0382	0.0225	-	85.2	0.5552	0.0052	NA	NA	NA	106.8004	
42_C3_ccp1	29.04	34.97	33.99	-	1.41	0.008	0.0204	-	0.1146	0.1154	0.0271	NA	NA	NA	99.6956	late
42_C3_ccp2	29.54	34.98	34.36	-	0.7932	0.0105	-	-	0.0848	-	-	NA	NA	NA	99.7686	late
42_C3_ccp3	29.92	34.99	34.49	-	0.223	0.0013	-	-	0.1517	-	0.0036	NA	NA	NA	99.7797	
42_C3_ccp4	30.13	35.05	34.27	-	0.4759	0.0076	0.0212	-	0.0461	0.4117	0.0307	NA	NA	NA	100.4431	
42_C3_py1	45.96	52.84	0.4588	-	0.4429	-	-	-	1.48	-	0.0054	NA	NA	NA	101.1871	
42_C3_sp1	0.8523	32.49	2.11	0.0033	61.79	0.7926	0.212	-	1.39	-	0.3059	NA	NA	NA	99.9462	gn inclusions
42_C3_sp2	0.2715	32.34	0.7294	0.001	64.28	0.072	0.1969	-	1.23	-	0.0093	NA	NA	NA	99.1302	gn inclusions
42_C3_sp3	0.4348	31.89	1.49	-	62.69	0.3907	0.2235	-	2.02	-	0.0829	NA	NA	NA	99.2219	gn inclusions
42_C3_sp4	2.46	33.31	1.41	-	61.45	0.4605	0.2068	0.0212	0.1827	-	0.0275	NA	NA	NA	99.5288	
42_C3_gn1	0.051	15.83	0.5289	-	13.51	0.0415	0.0081	0.0388	73.93	-	0.0345	NA	NA	NA	103.9728	incl. in sp
42_C3_gn2	0.1	14.1	0.2635	-	6.52	0.0776	-	-	86.1	-	0.0252	NA	NA	NA	107.1862	incl. in sp
42_C3_gn3	0.0679	15.1	0.5139	-	10.17	0.0586	0.013	-	80.1	-	0.0084	NA	NA	NA	106.0317	incl. in sp
42_C3_gn4	-	12.35	0.1794	-	1.46	0.0552	0.0098	0.0295	84.25	-	0.0864	NA	NA	NA	98.4204	
42_C3_jd1	0.0026	6.05	0.0249	-	0.8827	0.0304	-	0.036	67.52	-	-	NA	NA	NA	74.5467	
42_C3_jd2	0.0336	0.0551	0.0217	-	1.06	0.0497	0.0222	0.0041	74.89	-	-	NA	NA	NA	76.1364	
42_C3_jd3	0.0026	0.0262	0.0214	-	1.93	0.0641	0.0025	0.0316	88.77	-	0.0468	NA	NA	NA	90.8952	
42_C3_jd4	0.005	0.0331	0.0431	-	2.27	0.0762	0.0308	0.0509	88.61	-	0.0113	NA	NA	NA	91.1305	
42_C3_jd5	-	0.0254	0.0347	-	1.5	0.061	-	0.0932	84.73	-	0.009	NA	NA	NA	86.4534	
42_C3_jd6	0.0345	0.03	0.1598	-	0.4607	0.0569	0.0224	-	84.84	-	-	NA	NA	NA	85.6043	
42_C3_jd7	0.0818	0.04	0.1979	-	0.736	0.0638	-	0.0411	84.48	-	0.032	NA	NA	NA	85.6727	
42_C4_ccp1	30.16	35	34.33	-	0.0626	-	-	-	0.043	-	0.0112	NA	NA	NA	99.6069	
42_C4_ccp2	29.54	34.83	33.98	-	0.5056	0.0034	0.0143	-	0.0984	-	0.0168	NA	NA	NA	99.8946	
42_C4_ccp3	28.27	34.98	33.04	-	3.27	0.055	0.0274	0.0312	0.217	-	0.1249	NA	NA	NA	101.8554	early gen1 lam w sp
42_C4_ccp4	29.89	34.98	34.19	-	0.6745	-	0.0007	-	0.0923	-	0.016	NA	NA	NA	99.8436	late gen2 lam w sp
42_C4_ccp5	29.43	34.89	34.02	-	0.3614	0.0116	0.0082	-	0.1308	-	0.0084	NA	NA	NA	98.8604	late
42_C4_py1	41.23	50.87	1.53	-	2.83	0.0161	0.0275	-	4.3	-	0.0008	NA	NA	NA	100.8044	
42_C4_sp1	1.58	33.27	0.8479	-	63.97	0.4443	0.1768	-	0.1392	-	0.0526	NA	NA	NA	100.4807	
42_C4_sp2	0.7809	33.03	1.19	-	64.09	0.5913	0.2207	-	0.5063	-	0.0991	NA	NA	NA	100.5082	
42_C4_sp3	1.42	32.8	1.32	0.0168	62.11	1.88	0.2007	0.0288	0.553	-	0.4287	NA	NA	NA	100.7579	early crystal 1 lam w ccp
42_C4_sp4	1.85	33.15	1.1	-	63.29	0.6023	0.1888	0.0366	0.2952	-	0.0817	NA	NA	NA	100.5946	late crystal1 lam w ccp
42_C4_sp5	1	33.43	0.3281	-	65.07	0.4391	0.2154	-	0.2019	-	0.0122	NA	NA	NA	100.6966	gn inclusions?
42_C4_gn1	0.5663	13.45	1.03	0.0114	0.4256	0.061	-	0.0324	87.92	0.8717	0.0576	NA	NA	NA	104.4259	
42_C4_gn2	0.078	13.72	0.5514	-	3.78	0.0456	0.0238	-	85.75	-	0.0148	NA	NA	NA	103.9635	incl. in sp
42_C4_jd1	0.0701	0.0289	0.1961	-	1.48	0.0702	0.0339	0.0261	87.52	-	0.0285	NA	NA	NA	89.4538	
42_C4_jd2	0.1898	0.0287	0.3827	-	0.4329	0.0443	-	0.0793	87.38	-	0.0191	NA	NA	NA	88.5568	
42_C5_ccp1	29.54	34.93	34.02	-	1.24	0.0135	-	-	0.058	-	-	NA	NA	NA	99.8016	late

Table L8. Continued

Sample	Fe	S	Cu	In	Zn	Cd	Ga	Hg	Pb	As	Sb	Ag	Au	Mn	Total	Comment
42_C5_ccp2	29.77	34.86	34.23	-	0.2312	0.0115	-	-	0.0728	-	0.0215	NA	NA	NA	99.1971	late
42_C5_py1	45.65	53.08	1.17	-	0.6577	0.0081	-	-	0.8413	-	0.0157	NA	NA	NA	101.4228	
42_C5_sp1	1.77	32.96	1.4	0.0113	62.85	0.5636	0.172	-	0.6071	-	0.0344	NA	NA	NA	100.3683	
42_C5_sp2	1.81	33.31	0.6819	0.0043	62.19	0.7064	0.1495	-	0.17	-	0.0437	NA	NA	NA	99.0658	
42_C5_sp3	1.31	32.43	1.98	-	61.97	0.8966	0.1874	-	1.4	-	0.2226	NA	NA	NA	100.3966	early crystal1 ccp inclusions
42_C5_sp4	0.8095	33.48	0.2104	0.0072	63.73	0.3542	0.1503	0.0714	0.111	-	0.028	NA	NA	NA	98.9521	late cyrstal1 ccp inclusions
42_C5_cov1	0.1483	29.9	64.78	-	1.85	0.0474	0.0085	-	1.49	-	0.0263	NA	NA	NA	98.2505	altering sp
42_C6_ccp1	28.58	35.02	32.48	-	2.84	0.0186	0.008	-	0.1681	-	0.0148	NA	NA	NA	99.1296	
42_C6_ccp2	30.03	34.98	34.07	-	-	0.0049	-	-	0.1678	-	-	NA	NA	NA	99.2528	
42_C6_ccp3	29.97	35.04	34.2	-	0.2456	0.0088	0.0194	0.0091	0.1145	-	-	NA	NA	NA	99.6075	late
42_C6_py1	46.38	53.24	0.6508	-	0.0237	0.0086	-	-	0.6433	-	0.0145	NA	NA	NA	100.9609	
42_C6_py2	44.57	52.78	0.6316	-	0.0307	0.0044	-	-	2.96	-	-	NA	NA	NA	100.9766	
42_C6_sp1	1.53	33.03	0.9457	-	63.58	0.6157	0.2154	-	0.7301	-	0.11	NA	NA	NA	100.7569	
42_C6_gn1	0.0821	17.7	0.3799	-	2.63	0.063	-	-	72.21	8.53	-	NA	NA	NA	101.5949	late
42_C7_ccp1	28.88	34.93	33.27	-	2.4	0.0136	-	-	0.1205	-	0.0275	NA	NA	NA	99.6417	
42_C7_ccp2	28.84	35.04	33.82	-	1.42	0.0132	-	-	0.0565	-	0.0208	NA	NA	NA	99.2106	late
42_C7_ccp3	29.21	35.49	33.99	-	0.9636	0.0011	-	-	0.0624	-	-	NA	NA	NA	99.7172	
42_C7_sp1	0.1513	32.37	0.9366	-	63.52	0.4723	0.208	-	1.18	-	0.034	NA	NA	NA	98.8722	gn inclusions
42_C7_sp2	0.1464	29.4	0.9649	-	57.24	0.0893	0.1356	-	7.81	-	0.019	NA	NA	NA	95.8052	gn inclusions
42_C7_sp3	0.8306	33.31	0.0836	0.0131	64.12	0.273	0.2333	0.0193	0.1424	0.3578	0.0279	NA	NA	NA	99.4111	gn inclusions?
42_C7_sp4	1.15	32.22	1.61	0.0034	60.99	0.1953	0.1829	0.0077	0.8045	-	0.027	NA	NA	NA	97.1908	gn inclusions?
42_C7_gn1	-	16	0.076	-	0.1401	0.0339	-	0.0088	70.72	8.15	0.0366	NA	NA	NA	95.1654	very late
42_C7_gn2	0.012	13.65	0.1197	-	3.71	0.0375	0.0047	0.0185	87.55	0.8819	0.0228	NA	NA	NA	106.007	or jd? Incl. in sp
42_C7_jd1	0.0745	0.027	0.2171	-	0.2056	0.0423	-	0.0218	84.89	-	0.0281	NA	NA	NA	85.5065	included in sp
42_C7_jd2	0.0345	0.0465	0.0746	-	1.85	0.0551	0.0213	0.0371	91.32	-	-	NA	NA	NA	93.4392	
42_C7_jd3	0.051	17.9	0.1761	-	2.63	0.0457	-	0.0798	72.96	10.01	0.07	NA	NA	NA	103.9226	included in sp
42_C8_ccp1	30.41	35.49	34.47	0.0453	-	0.0131	0.0055	-	0.0683	-	-	NA	NA	NA	100.5022	latest
42_C8_ccp2	30.34	34.94	34.45	0.0618	0.0206	0.0121	0.0316	-	0.1351	-	-	NA	NA	NA	99.9912	latest
42_C8_sp1	1.25	33.17	0.918	0.0055	63.45	1.12	0.1469	-	0.4548	-	0.1988	NA	NA	NA	100.714	latest
42_C8_sp2	1.13	33.3	0.3021	0.0094	65.12	0.5179	0.3019	-	0.1704	-	0.0037	NA	NA	NA	100.8553	latest
42_C9_ccp1	29.08	35.08	33.63	-	2.24	0.0135	0.0048	-	0.1652	-	-	NA	NA	NA	100.2134	late incl in sp
42_C9_ccp2	0.173	21.63	1.05	-	30.78	0.2972	0.0462	-	47.45	-	0.0372	NA	NA	NA	101.4636	
42_C9_sp1	1.24	33.35	0.32	-	64.34	1.15	0.1497	-	0.1515	0.3323	0.0841	NA	NA	NA	101.1175	
42_C9_sp2	0.1415	29.1	0.1085	-	60.61	0.005	0.1745	-	0.721	-	0.0283	NA	NA	NA	90.8888	
42_C9_sp3	0.9469	33.36	0.5703	-	64.65	0.6408	0.1987	-	0.1953	-	0.0659	NA	NA	NA	100.6278	early phase1
42_C9_sp4	0.0943	31.98	0.2836	-	62.7	0.0061	0.1807	-	1.05	-	-	NA	NA	NA	96.2948	late phase2
42_C9_sp5	0.2109	32.07	1.11	0.0183	63.5	0.0584	0.2093	-	1.26	-	-	NA	NA	NA	98.437	early gen1
42_C9_sp6	0.2608	32.31	0.7729	0.0024	63.65	0.5066	0.1635	-	1.45	0.0404	0.0158	NA	NA	NA	99.1725	gen2
42_C9_sp7	0.4291	31.86	1.59	-	61.56	1.03	0.1671	0.021	2.57	-	0.2457	NA	NA	NA	99.473	gen3
42_C9_sp8	1.06	33.35	0.4485	0.0023	64.22	0.3818	0.2238	-	0.1344	-	0.0348	NA	NA	NA	99.8556	gen4
42_C10_ccp1	25.38	32.73	26.87	-	5.95	0.0441	0.003	-	0.3185	-	0.0376	NA	NA	NA	91.3332	incl. in sp
42_C10_sp1	0.3247	32.44	1.21	-	62.22	0.292	0.1578	-	1.39	-	0.0502	NA	NA	NA	98.0848	
42_C11_ccp1	29.76	35.09	34.07	-	1.44	0.008	-	-	0.1441	-	0.0012	NA	NA	NA	100.5132	
42_C11_sp1	0.6489	32.72	1.41	-	62.8	0.1027	0.1801	-	1.33	-	0.0336	NA	NA	NA	99.2254	
42_C11_sp2	0.9619	33.34	0.6551	-	64.86	0.5799	0.2099	-	0.303	-	0.1123	NA	NA	NA	101.022	
42_C11_sp3	0.9678	33.19	0.0905	-	65.6	0.5013	0.2288	-	0.122	-	0.0263	NA	NA	NA	100.7266	early dendritic
42_C11_sp4	0.5002	33.14	0.6695	0.0102	64.23	0.498	0.1866	-	0.2235	-	0.2794	NA	NA	NA	99.7375	late dendritic
42_C11_sp5	0.301	31.96	0.9926	-	61.4	0.4604	0.1634	-	4.13	0.6313	0.0202	NA	NA	NA	100.0589	
42_C11_sp6	0.9484	33.81	0.1744	-	65.3	0.6512	0.2034	-	0.0266	-	0.0247	NA	NA	NA	101.1386	
42_C11_gn1	-	13.48	0.0693	-	0.0203	0.0547	-	0.0585	86.26	-	0.0104	NA	NA	NA	99.9533	late c.g. after sp
42_C12_ccp1	27.72	34.68	32.46	-	4.69	0.0378	0.0037	-	0.1222	-	0.0311	NA	NA	NA	99.7449	incl. in sp
42_C12_sp1	0.6235	32.66	1.23	0.0073	63.66	0.3498	0.2042	-	0.8223	-	0.0444	NA	NA	NA	99.6016	early dendritic
42_C12_sp2	0.9103	33.38	0.0318	0.0014	64.91	0.5474	0.2171	-	0.0892	0.8359	0.0263	NA	NA	NA	100.9494	late dendritic
42_C12_sp3	0.7492	32.6	1.23	0.0006	62.7	0.769	0.1786	-	1.47	-	0.08	NA	NA	NA	99.7775	gen1 dark
42_C12_sp4	0.6564	33.43	0.0428	0.0029	65.14	0.3304	0.1964	-	0.0469	0.2356	0.0065	NA	NA	NA	100.0879	gen2 light
42_C12_sp5	0.0715	33.31	0.0498	0.0042	65.27	0.0166	0.2755	-	0.1457	-	-	NA	NA	NA	99.1433	gen3 light
42_C12_gn1	0.0038	13.69	0.0864	-	0.014	0.0128	-	-	84.94	0.9366	0.018	NA	NA	NA	99.7017	late c.g., interior crystal1
42_C12_gn2	-	13.43	0.03	-	-	0.0405	0.0071	0.1003	86.84	0.017	-	NA	NA	NA	100.4648	late c.g., rim crystal1
42_C12_gn3	0.0033	13.58	0.124	-	0.0632	0.0479	-	-	86.02	2.4	-	NA	NA	NA	102.2383	late c.g., interior
42_C12_gn4	-	13.54	0.0549	-	0.043	0.0517	-	0.0014	86.21	0.4557	0.0773	NA	NA	NA	100.434	late c.g., interior
42_C12_gn5	0.12	15.93	0.5652	-	14.47	0.1193	0.0183	-	75.64	-	0.0369	NA	NA	NA	106.8997	early incl. in sp.
42_C12_gn6	0.1263	15.89	0.673	-	13.58	0.1438	0.0429	-	73.16	-	0.067	NA	NA	NA	103.683	early, incl. in sp
42_C12_gn7	-	13.3	0.074	-	0.8474	0.0476	-	-	86.79	-	0.0176	NA	NA	NA	101.0765	late c.g.
42_C13_ccp1	29.49	35.09	33.7	-	0.9682	0.0177	0.0215	-	0.1203	-	0.012	NA	NA	NA	99.4198	latest
42_C13_sp1	0.9275	32.98	1.24	-	62.5	0.911	0.1521	0.0519	0.6698	-	0.038	NA	NA	NA	99.4704	late dendritic
42_C13_sp2	0.5919	33.06	0.5343	0.0024	64.55	0.3798	0.1894	-	0.2706	0.673	0.0445	NA	NA	NA	100.2959	latest
42_C13_gn1	0.0084	13.69	0.0543	-	-	0.048	-	0.0463	85.43	1.08	-	NA	NA	NA	100.3569	late c.g.
42_C13_gn2	0.0141	13.72	0.0684	-	-	0.0441	-	0.038	85.62	1.62	0.0244	NA	NA	NA	101.1489	late c.g.

Table L9. Results of EPMA analyses on sulfide minerals in sample GMA13-045

Sample	Fe	S	Cu	In	Zn	Cd	Ga	Hg	Pb	As	Sb	Ag	Au	Mn	Total	Comment
45_C1_mrc1	47.09	53.49	0.0232	-	0.3557	0.0073	-	-	0.1397	0.959	0.0075	-	-	NA	102.0723	
45_C1_mrc2	47.08	53.12	0.0242	-	0.3134	0.0121	-	-	0.1267	-	0.0096	0.0051	0.0732	NA	100.7642	latest after brt
45_C1_mrc3	46.75	53.39	0.6024	-	-	0.0071	-	-	0.2154	-	0.0341	0.0142	0.0202	NA	101.0334	
45_C1_mrc4	47	52.8	0.2548	-	0.0049	0.0099	-	-	0.2154	-	-	0.0275	-	NA	100.3124	latest after brt
45_C1_sp1	3.16	32.52	1.61	-	57.87	0.0692	0.2001	-	0.729	0.3165	1.21	0.3172	0.3091	NA	98.3111	latest after brt, gn incl.
45_C1_sp2	0.9684	32.89	0.1601	-	62.93	0.0091	0.2175	-	1.13	-	0.0735	0.1588	0.233	NA	98.7705	latest after brt, gn incl.
45_C1_sp3	2.37	33.1	0.4826	-	62.29	0.0135	0.1783	-	0.483	-	0.3422	0.1403	0.2475	NA	99.6474	latest after brt, gn incl.
45_C1_sp4	1.09	32.64	0.2794	-	60.55	0.01	0.1783	-	1.71	-	0.0878	0.2157	0.2674	NA	97.0287	latest after brt, gn incl.
45_C1_sp5	2.23	32.76	0.912	-	61.25	0.0412	0.2356	0.0152	0.9189	-	0.6343	0.3789	0.1564	NA	99.5326	latest after brt, gn incl.
45_C1_gn1	0.0597	13.61	0.1385	-	3.67	0.047	0.0173	-	85.91	0.1967	0.6448	0.0345	0.0062	NA	104.3346	latest after brt, incl. in sp
45_C1_gn2	0.0863	13.53	0.0897	-	3.71	0.0491	0.0022	-	83.96	-	1.68	0.2903	-	NA	103.3975	latest after brt, incl. in sp
45_C1_gn3	0.0289	13.53	0.1127	-	3.68	0.036	-	0.0295	84.12	1.11	0.3361	0.2442	0.0595	NA	103.2868	latest after brt, incl. in sp
45_C1_gn4	-	13.68	0.0737	-	0.915	0.0465	0.0237	-	84.38	-	1.64	0.2984	0.1806	NA	101.2378	latest after brt, incl. in sp
45_C2_mrc1	46.53	52.85	0.0006	-	0.1512	0.0146	-	-	0.7529	-	-	-	0.1026	NA	100.4018	
45_C2_mrc2	47.25	52.87	0.175	-	-	0.0094	-	-	0.1902	0.06	0.0245	0.0374	0.0109	NA	100.6273	late, crystal1 interior
45_C2_mrc3	46.79	52.94	0.3608	-	-	0.0183	-	-	0.1564	-	-	0.0047	0.0074	NA	100.2775	late, crystal1 rim
45_C2_sp1	1.84	32.53	0.4954	-	61.25	0.0238	0.1661	-	1.36	-	0.2886	0.521	0.1164	NA	98.5914	latest after brt, early crystal1 prof
45_C2_sp2	1.33	32.32	0.7757	-	62.13	0.0386	0.1791	-	1.74	-	0.4898	0.6226	0.2805	NA	99.9064	latest after brt, crystal1 profile
45_C2_sp3	0.5234	32.16	0.2721	-	61.09	0.0066	0.1922	-	2.97	0.8145	0.1218	0.2026	-	NA	98.3533	latest after brt, late crystal1 prof
45_C2_sp4	2.17	33.01	1.32	-	60.72	0.064	0.1673	-	0.8027	-	0.8758	0.3631	0.0974	NA	99.5903	latest after brt, early crystal2 prof
45_C2_sp5	2.65	32.59	1.52	-	60.08	0.0534	0.2022	-	0.9291	-	1.15	0.3354	0.3939	NA	99.9041	latest after brt, crystal2 profile
45_C2_sp6	2.31	33.03	0.7473	-	62.5	0.0361	0.1743	-	0.6058	0.878	0.4087	0.2236	-	NA	100.9137	latest after brt, crystal2 profile
45_C2_sp7	1.37	31.69	0.3315	-	60.25	0.0151	0.1964	0.0247	2.8	-	0.0931	0.1002	0.2416	NA	97.1126	latest after brt, late crystal2 prof
45_C2_gn1	0.0147	13.62	0.1097	-	0.9364	0.038	0.0229	-	83.39	-	1.59	0.325	-	NA	100.0466	incl. in sp
45_C2_gn2	-	13.51	0.0757	-	0.4706	0.0522	0.0099	0.1048	84.86	-	1.11	0.0861	0.1103	NA	100.3895	incl. in sp
45_C2_gn3	0.1274	13.67	0.1326	-	5.15	0.0447	0.0102	-	84.81	-	1.12	0.28	0.2116	NA	105.5564	incl. in sp
45_C2_gn4	0.0017	13.66	0.1254	-	0.0798	0.0754	0.0284	-	81.14	-	2.84	1.23	0.0062	NA	99.187	incl. in sp
45_C2_gn5	0.0025	13.41	0.1303	-	-	0.0403	0.0098	-	85.07	-	0.8182	0.1959	-	NA	99.6771	
45_C2_gn6	0.0216	13.27	0.1064	-	-	0.0537	0.0024	-	84.5	-	1.27	0.2126	-	NA	99.4368	incl. in brt
45_C3_sp1	0.0454	31.76	0.2523	-	61.56	0.0213	0.2271	0.0587	1.84	-	-	0.0785	0.1284	NA	95.9717	latest after brt, early crystal1 prof
45_C3_sp2	0.1035	32.05	0.2583	-	62.24	0.0215	0.185	0.0736	2.86	-	0.0012	0.1347	0.3421	NA	98.27	crystal1 profile
45_C3_sp3	0.1145	32.19	0.1494	0.001	62.93	0.0331	0.1682	0.0794	2.36	-	0.0004	0.0236	0.1627	NA	98.2123	crystal1 profile
45_C3_sp4	0.2588	32.52	0.2861	-	63.67	0.0455	0.2044	-	1.69	-	0.0532	0.0864	0.2984	NA	99.1129	crystal1 profile
45_C3_sp5	0.2088	32.52	0.2275	0.0079	63.12	0.0789	0.2043	0.0075	2.19	-	0.0748	0.0831	-	NA	98.7229	crystal1 profile
45_C3_sp6	0.3079	32.65	0.1545	-	63.92	0.0405	0.1882	-	1.58	1.14	0.0337	0.055	0.0659	NA	100.1357	crystal1 profile
45_C3_sp7	0.1893	31.22	0.235	0.0063	58.48	0.1077	0.15	0.1396	6.44	0.8423	0.4912	0.1687	0.1122	NA	98.5824	crystal1 profile
45_C3_sp8	0.042	32.22	0.4465	0.0078	63.54	0.0066	0.1939	0.0037	1.03	0.6247	0.3763	0.2865	0.1616	NA	98.9397	late crystal1 profile
45_C3_sp9	0.0937	31.07	0.0909	-	56.11	0.0117	0.1073	0.0705	7.22	1.78	0.0359	0.0545	0.2122	NA	96.8567	later crystal 2 profile
45_C3_sp10	0.1259	31.55	0.0591	-	57.68	0.0048	0.1178	0.0337	5.62	1.41	0.0057	-	0.1846	NA	96.7917	latest crystal 2 profile
45_C3_sp11	0.021	31.95	2.3	-	60.56	0.0341	0.2097	-	1.24	-	1.87	0.7696	-	NA	98.9545	
45_C3_sp12	0.0934	31.71	0.1052	0.0022	57.94	0.0403	0.1588	0.1839	3.6	0.8369	-	0.1159	0.2395	NA	95.0261	
45_C3_sp13	0.0089	32.51	1.22	-	61.12	0.0224	0.1823	0.0834	0.6885	-	1.02	0.4395	0.1148	NA	97.4098	after gn
45_C3_sp14	0.0156	31.13	0.2851	-	61.13	0.1394	0.2296	0.0569	1.12	-	0.0918	0.1177	0.2382	NA	94.5544	early profile1
45_C3_sp15	0.0502	33.16	0.1942	-	65.31	0.0084	0.1963	-	0.3047	-	0.0491	0.0682	0.1047	NA	99.4458	profile1
45_C3_sp16	0.1939	31.91	0.0862	0.0002	59.86	-	0.1607	0.0207	4.25	0.8754	0.0155	0.0085	0.2355	NA	97.6166	profile1
45_C3_sp17	0.3733	32.51	0.0934	-	62.61	0.0015	0.1871	-	2.2	-	-	-	0.047	NA	98.0223	profile1
45_C3_sp18	0.4689	33.19	0.1091	0.0019	63.83	0.0056	0.1838	0.0873	0.9086	-	0.0378	0.0087	0.202	NA	99.0338	late profile1
45_C3_gn1	0.0005	13.26	0.0851	-	2.83	0.0382	0.0073	0.1266	85.64	-	0.055	0.1238	0.2671	NA	102.4335	gen1, incl. in sp.
45_C3_gn2	0.0366	13.37	0.3602	-	3.75	0.0417	0.0115	0.1205	83.63	0.2841	0.0948	0.5887	0.1896	NA	102.4776	gen1, incl. in sp.
45_C3_gn3	0.029	13.16	0.1827	-	3.83	0.0633	-	0.0308	84.59	-	0.0261	0.124	-	NA	102.0358	gen1, incl. in sp.
45_C3_gn4	0.0201	13.87	0.9084	-	5.32	0.0652	0.0134	0.068	81.16	-	1.24	0.5308	-	NA	103.1958	gen2 sp rim
45_C3_gn5	0.0424	14.84	0.1563	-	8.32	0.0491	-	-	76.92	1.26	0.0447	-	-	NA	101.6325	gen3
45_C3_gn6	-	13.44	0.1924	-	0.1099	0.0469	0.0006	-	84.17	-	0.2068	0.2077	0.1946	NA	98.569	gen4 latest
45_C3_gn7	-	13.1	0.1343	-	0.57	0.0477	0.0041	-	84.38	-	0.1479	0.1412	-	NA	98.5253	interior large crystal
45_C3_gn8	-	13.33	0.0548	-	0.0197	0.0572	0.0034	0.0111	85.2	0.1028	0.3091	0.121	0.1893	NA	99.3985	rim large crystal
45_C3_gn9	0.0009	13.27	0.1386	-	1.1	0.0477	0.0088	-	85.54	0.0287	0.4445	0.0787	-	NA	100.6579	
45_C3_jd1	-	12.78	0.1739	-	0.8499	0.0486	-	-	71.67	6.43	0.0707	0.7503	0.0929	NA	92.8663	after gn
45_C3_jd2	0.0092	16.82	0.0946	-	1.69	0.0403	-	0.0413	69.32	8.97	0.0947	0.3698	-	NA	97.45	after gn

Table L9. Continued

Sample	Fe	S	Cu	In	Zn	Cd	Ga	Hg	Pb	As	Sb	Ag	Au	Mn	Total	Comment
45_C3_jd3	-	17.3	0.1328	-	0.597	0.0374	-	0.0705	70.16	8.95	0.06	0.1249	-	NA	97.4327	after gn
45_C3_jd4	0.0119	16.71	0.0923	-	0.3967	0.038	-	-	69.99	8.31	0.0457	0.1296	-	NA	95.7243	after gn
45_C4_sp1	0.1103	31.84	0.2376	0.0049	59.92	0.0397	0.1818	0.0752	3.66	0.266	0.0244	0.0235	0.0137	NA	96.3972	early crystal1 profile
45_C4_sp2	0.1626	32.1	0.1651	0.0024	60.76	0.0227	0.1975	0.0056	3.5	0.7492	0.0224	0.0118	0.1346	NA	97.8339	crystal1 profile
45_C4_sp3	0.601	33.09	0.0819	-	63.5	0.0143	0.165	-	1.04	-	-	-	-	NA	98.4923	late crystal1 profile
45_C4_sp4	0.3062	32.2	0.0947	-	62.61	0.0021	0.2127	-	2.6	0.3474	0.0138	0.0011	0.1936	NA	98.5817	crystal2 interior
45_C4_sp5	0.6202	32.48	0.1272	0.0109	61.88	-	0.2277	-	0.7681	-	0.0223	-	0.4165	NA	96.5529	crystal2 rim
45_C4_sp6	0.3345	32.43	0.2026	-	61.97	0.0151	0.1854	-	2.84	1.2	0.0033	-	0.1746	NA	99.3556	crystal3 interior
45_C4_sp7	1.37	33.12	0.0991	0.0011	62.5	-	0.2133	-	0.9226	-	-	0.0029	0.2266	NA	98.4557	crystal3 rim
45_C4_gn1	0.0124	17.75	0.238	-	-	0.0565	-	0.081	69.93	9.88	0.1524	0.1337	-	NA	98.234	interior sperulitic crystal1
45_C4_gn2	0.003	16.53	0.0927	-	0.0558	0.0417	-	0.0294	71.41	10.16	0.1156	0.1138	-	NA	98.5521	late sperulitic crystal1
45_C4_gn3	0.013	17.55	0.1433	-	0.0806	0.0484	-	0.1223	70.14	10.06	0.1259	0.2532	0.2625	NA	98.7992	sperulitic
45_C4_gn4	0.043	17.2	0.1249	-	0.3185	0.0442	-	-	71.05	9.93	0.0809	0.0715	-	NA	98.8631	
45_C4_gn5	0.0087	16.95	0.626	-	0.9071	0.0431	-	0.0646	68.7	8.15	0.4067	0.2377	-	NA	96.0939	raggedy sperulitic
45_C4_gn6	0.0437	18.01	0.0915	-	5.49	0.0348	-	-	72.32	9.75	0.0262	0.0014	-	NA	105.7675	incl. in sp
45_C5_sp1	0.0309	31.91	0.2404	-	61.86	0.0586	0.1798	0.0378	2.49	-	0.0411	0.1064	0.1487	NA	97.1038	early crystal1 profile
45_C5_sp2	0.0154	32.23	0.2432	0.0023	62.83	0.0502	0.2033	0.0075	2.54	-	0.0155	0.2018	-	NA	98.3393	crystal1 profile
45_C5_sp3	0.0769	32.32	0.181	-	64.19	0.039	0.1879	0.0493	1.67	-	0.0138	0.1072	0.1198	NA	98.955	crystal1 profile
45_C5_sp4	0.1588	32.01	1.16	-	61.41	0.1186	0.1903	0.1173	1.5	0.1458	0.1674	0.2276	0.2359	NA	97.4417	crystal1 profile
45_C5_sp5	0.2817	32.54	0.4897	0.0047	63.37	0.0804	0.2135	-	2.01	-	0.1174	0.1671	-	NA	99.2746	crystal1 profile
45_C5_sp6	0.2665	32.47	1.94	-	62.35	0.0534	0.2152	0.1004	1.12	-	1.45	0.3526	-	NA	100.318	crystal1 profile
45_C5_sp7	0.373	32.92	0.1407	-	64.91	0.0268	0.1927	0.0685	0.8402	0.3656	-	0.0369	0.1617	NA	100.0361	crystal1 profile
45_C5_sp8	0.0657	32.4	1.32	-	61.33	0.0584	0.2152	0.1851	1.07	-	1.42	0.3381	0.0883	NA	98.4909	crystal1 profile
45_C5_sp9	0.2368	32.38	0.0644	-	59.13	0.0023	0.1658	-	3.89	1.49	0.0143	-	0.0258	NA	97.3994	crystal1 profile
45_C5_sp10	0.1071	31.96	0.0642	0.001	60.48	0.0142	0.1793	0.0754	3.44	0.926	0.0333	-	-	NA	97.2806	crystal1 profile
45_C5_sp11	0.1082	31.9	0.16	-	58.37	0.0364	0.1611	0.1087	3.89	0.6118	-	0.0233	-	NA	95.3696	late crystal1 profile
45_C5_sp12	0.0237	32.3	0.2372	-	63.5	0.0508	0.1942	0.0359	1.98	-	0.0207	0.1119	0.0727	NA	98.5271	early crystal2 profile
45_C5_sp13	0.0327	32.44	0.1761	-	63.48	0.0159	0.1976	-	2.13	-	0.0231	0.1616	0.1629	NA	98.82	crystal2 profile
45_C5_sp14	0.0219	30.25	0.2796	0.0073	59.11	0.0329	0.1993	-	2.92	1.21	0.0609	0.123	0.2378	NA	94.4528	crystal2 profile
45_C5_sp15	0.2215	32.65	0.5657	0.007	63.51	0.1022	0.1688	0.0474	1.63	-	0.0784	0.1918	0.0052	NA	99.1781	crystal2 profile
45_C5_sp16	0.2107	32.37	0.4437	-	63.02	0.0906	0.1908	0.1191	1.99	-	0.0943	0.1797	0.2667	NA	98.9757	crystal2 profile
45_C5_sp17	0.2224	32.25	0.943	-	62.44	0.1225	0.1946	0.134	2.15	0.1292	0.1701	0.2419	0.394	NA	99.3917	crystal2 profile
45_C5_sp18	0.5519	32.41	2.36	-	60.98	0.0892	0.1956	0.2382	0.6981	-	2.1	0.3356	-	NA	99.9586	crystal2 profile
45_C5_sp19	0.1908	32.55	0.5367	-	63.1	0.0682	0.1577	-	1.91	-	0.0894	0.2068	0.312	NA	99.1217	crystal2 profile
45_C5_sp20	0.2756	32.37	0.263	-	63.05	0.0646	0.1766	-	2.06	0.2672	0.0552	0.0923	0.0191	NA	98.6936	crystal2 profile
45_C5_sp21	0.0353	26.61	0.8546	-	46.68	0.0205	0.1632	0.1018	29.9	-	0.7199	0.363	-	NA	105.4482	late crystal2 profile
45_C5_gn1	-	13.42	0.1735	-	0.3243	0.0524	0.0055	0.0551	85.38	-	-	0.156	0.1125	NA	99.6794	gen4
45_C5_gn2	-	13.47	0.1844	-	0.1021	0.0567	0.0054	0.0028	83.76	-	0.9014	0.305	0.0025	NA	98.7904	gen3
45_C5_gn3	0.0004	13.63	0.4915	-	1.88	0.0516	0.0048	0.1196	83.59	-	1.18	0.6291	-	NA	101.5769	gen3
45_C5_gn4	0.0095	13.24	0.1877	-	0.9486	0.0425	-	-	84.33	-	0.0157	0.1236	-	NA	98.8977	gen2
45_C5_gn5	-	13.97	0.4444	-	7.25	0.0493	0.0007	0.0843	80.67	0.9376	0.0927	0.2453	-	NA	103.7442	gen1 incl. in sp
45_C5_gn6	0.0156	13.18	0.1687	-	3.91	0.0502	0.0386	-	83.47	-	1.04	0.1713	-	NA	102.0443	gen3
45_C5_gn7	-	13.48	0.2144	-	3.81	0.0594	0.0148	0.0517	85.36	-	0.0305	0.0916	-	NA	103.1123	new crystal gen1
45_C5_gn8	0.0062	13.89	0.2235	-	5.91	0.0497	-	-	84.76	0.8529	0.1403	0.0134	-	NA	105.8459	new crystal gen2
45_C5_gn9	-	13.54	0.1402	-	3.88	0.0616	0.003	-	86.36	-	0.1746	0.0431	-	NA	104.2024	new crystal gen3
45_C5_jd1	0.0007	14.56	0.1463	-	0.9177	0.0544	-	-	70.71	10.24	0.2809	0.3101	0.2067	NA	97.4269	after gn
45_C5_jd2	0.0173	18.21	0.1113	-	1.86	0.0377	-	-	69.67	11.91	0.034	0.1173	-	NA	101.9675	after gn
45_C5_jd3	0.0199	17.28	0.1191	-	1.34	0.0497	-	-	71.19	9.1	0.0586	0.1682	-	NA	99.3256	after gn
45_C5_jd4	0.0284	16.7	0.1179	-	0.3079	0.0446	-	0.1173	71.77	9.41	0.0392	0.1088	-	NA	98.6441	after gn
45_C5_jd5	0.0429	15.63	0.1449	-	0.8725	0.0462	-	-	72.49	6.45	0.1376	0.204	-	NA	96.0182	after gn
45_C5_jd6	0.025	13.73	0.151	-	0.637	0.0602	0.0142	-	82.18	-	2.63	0.6133	-	NA	100.0406	after gn
45_C6_sp1	0.0994	32.39	0.0502	-	63.6	0.016	0.1803	-	2	-	0.0329	0.0015	0.1146	NA	98.485	early crystal1 profile
45_C6_sp2	0.0617	32.3	0.0381	0.0096	63.53	0.0172	0.2031	0.0473	2.25	-	0.0191	0.003	0.0867	NA	98.5658	crystal1 profile
45_C6_sp3	0.0011	32.12	0.0555	0.0081	63.29	0.024	0.1993	0.0246	2.04	-	0.015	-	0.1664	NA	97.944	crystal1 profile
45_C6_sp4	0.0228	32.29	0.1295	-	63.85	0.0334	0.2151	-	1.88	-	0.1198	0.0297	0.0659	NA	98.6363	crystal1 profile
45_C6_sp5	0.0369	30.31	0.0633	0.0047	56.11	0.0382	0.2282	0.6398	8.39	1.8	0.0627	0.076	0.2559	NA	98.0158	crystal1 profile, bright BSE
45_C6_sp6	0.0796	32.43	0.0139	-	62.81	0.0055	0.1801	0.0322	2.72	0.4199	-	-	0.0727	NA	98.764	crystal1 profile
45_C6_sp7	0.5601	33.16	0.1272	0.0251	65.73	0.008	0.2165	0.0801	0.2628	-	0.0122	0.0177	-	NA	100.1997	crystal1 profile
45_C6_sp8	0.0665	32.23	0.0475	-	61.28	0.0064	0.1557	0.015	3	0.3713	0.0187	0.0131	0.0622	NA	97.2664	crystal1 profile
45_C6_sp9	0.2489	32.8	0.0804	-	64.5	0.0278	0.1982	0.0056	1.47	0.6802	0.0288	0.005	0.2462	NA	100.291	crystal1 profile

Table L9. Continued

Sample	Fe	S	Cu	In	Zn	Cd	Ga	Hg	Pb	As	Sb	Ag	Au	Mn	Total	Comment
45_C6_sp10	0.0879	33	0.0806	-	64.95	0.0091	0.261	0.038	0.6162	-	0.1084	0.0637	0.0766	NA	99.2915	late crystal1 profile
45_C6_sp11	0.2369	32.36	0.0472	0.0143	64.03	0.0173	0.2004	0.0512	1.7	-	0.019	0.0333	0.1509	NA	98.8606	
45_C6_sp12	0.0822	19.52	0.0888	-	23.91	0.0257	0.0592	0.0359	55.66	1.24	0.585	0.0109	0.1702	NA	101.3878	
45_C6_gn1	0.0068	17.14	0.0798	-	2.19	0.0524	-	0.1082	71.76	10.37	0.0674	0.0425	0.2084	NA	102.0255	gen1, incl. in sp.
45_C6_gn2	0.0429	21.98	0.0557	-	30.47	0.028	0.0507	0.0936	45.15	-	0.3493	0.0054	-	NA	98.2257	gen2
45_C6_gn3	-	13.9	0.0898	-	6.61	0.0494	0.0147	0.1026	82.51	1.34	0.1106	-	-	NA	104.7271	gen3
45_C6_gn4	-	13.36	0.1218	-	1.68	0.0345	0.0146	0.018	85.34	-	0.2115	0.0146	-	NA	100.7949	gen4
45_C6_gn5	-	13.4	0.1317	-	1.44	0.0201	0.0051	0.0608	87	-	0.3287	0.0056	-	NA	102.3919	gen5
45_C6_gn6	-	13.29	0.0893	-	0.4699	0.0444	0.0011	0.0055	86.46	-	0.0461	-	-	NA	100.4062	gen6
45_C6_gn7	0.004	13.3	0.0627	-	3.27	0.047	0.0141	0.1002	85.89	-	0.0345	-	0.2105	NA	102.9329	gen4
45_C7_ccp1	29.15	34.51	33.41	-	1.09	-	-	0.0537	0.1946	-	0.0004	0.0125	0.0371	NA	98.4584	
45_C7_sp1	0.0099	31.83	0.0278	0.0127	62.24	0.0347	0.1831	0.0321	2.99	0.3543	0.0081	0.0053	0.2759	NA	98.004	early crystal1 profile
45_C7_sp2	0.0261	31.75	0.0442	0.0074	62.56	0.0309	0.2247	-	2.71	-	0.0065	0.0139	0.2453	NA	97.6191	crystal1 profile
45_C7_sp3	0.0272	31.85	0.0404	0.0065	62.21	0.0336	0.2349	-	2.81	-	-	-	0.1106	NA	97.3232	crystal1 profile
45_C7_sp4	0.0626	31.93	0.0419	-	62.65	0.0144	0.1602	-	2.53	0.5167	0.0154	0.0037	-	NA	97.925	crystal1 profile
45_C7_sp5	0.0336	32.19	0.0363	0.0244	62.9	0.0303	0.1937	0.0095	2.27	-	0.0016	-	0.1818	NA	97.8713	crystal1 profile
45_C7_sp6	0.0303	31.48	0.0405	-	60.59	0.0201	0.2139	0.017	2.65	-	0.0439	-	0.102	NA	95.1878	crystal1 profile
45_C7_sp7	0.0811	32.22	0.0673	-	63.91	0.0121	0.2217	-	2.16	-	0.0446	0.0174	-	NA	98.7343	crystal1 profile
45_C7_sp8	0.0616	30.59	0.1028	0.0054	55.83	0.0348	0.1898	0.4182	8.22	1.6	0.0232	0.0777	-	NA	97.1535	crystal1 profile
45_C7_sp9	0.446	32.89	0.0537	0.0002	65.26	0.0229	0.1969	0.0476	0.4428	-	0.0126	-	0.0348	NA	99.4076	crystal1 profile
45_C7_sp10	0.4375	33.02	0.1578	0.0162	64.78	0.0135	0.1698	0.019	0.1476	-	0.1298	0.0778	0.1239	NA	99.0929	late crystal1 profile
45_C7_sp11	2.83	32.98	0.5829	-	62.28	0.0446	0.1969	0.0496	0.4382	-	0.2719	0.0966	0.2222	NA	99.993	f.g., dark, late
45_C7_sp12	2.34	32.78	0.4838	0.0004	61.9	0.0275	0.1765	0.0321	0.6629	-	0.2917	0.2504	-	NA	98.9454	f.g., dark, late
45_C7_gn1	-	18.17	0.0565	-	4.48	0.0291	-	0.0255	69.78	10.38	0.082	0.0793	0.1207	NA	103.203	gen1, incl. in sp.
45_C7_gn2	-	13.39	0.1405	-	3.22	0.0456	-	0.1184	85.05	-	0.0658	-	-	NA	102.0303	gen1
45_C7_gn3	0.0153	13.51	0.1692	-	5.41	0.0674	0.0057	0.0661	83.19	-	0.0329	0.1379	0.0796	NA	102.684	gen2
45_C7_gn4	0.0055	13.2	0.1222	-	2.3	0.0576	0.0196	-	85.22	-	0.0638	0.0156	0.0676	NA	101.0718	gen3
45_C7_gn5	-	15.33	0.1013	-	5.63	0.0496	-	0.097	78.29	4.39	0.1519	-	0.0852	NA	104.1249	gen1
45_C8_mrc2	41.14	50.82	0.0376	-	0.2985	0.0024	0.0039	-	2.81	-	0.0113	-	0.0272	NA	95.1509	
45_C8_mrc3	25.59	31.28	29.87	-	1.03	0.0051	-	-	2.41	-	0.1131	0.0104	0	NA	90.3087	
45_C8_sp1	0.0416	31.32	0.0396	0.0084	60.67	0.0503	0.1762	0.1166	3.34	-	0.0256	0.0006	0.2894	NA	96.0783	
45_C8_sp2	0.0964	32.66	0.0796	0.0149	62.18	0.0066	0.2089	0.1605	2	0.1298	0.0378	0.0149	-	NA	97.5895	
45_C8_sp3	0.0371	31.61	0.0469	0.0103	61.58	0.0245	0.1765	-	3.24	-	0.0155	-	0.3016	NA	97.0424	
45_C8_sp4	0.0544	32.06	0.0775	-	62.24	0.011	0.2039	-	2.27	0.1292	0.05	0.0117	0.2509	NA	97.3587	
45_C8_sp5	0.1848	32.88	0.063	0.0064	64.12	0.0118	0.1902	0.1006	0.9209	-	0.03	0.0289	0.101	NA	98.6377	
45_C8_sp6	0.0054	31.84	0.0772	0.0072	61.59	0.0122	0.1837	-	3.04	-	-	-	0.1157	NA	96.8715	gen1
45_C8_sp7	0.2684	32.96	0.0382	0.0022	64.17	-	0.1878	0.0854	0.7433	-	-	0.0071	0.3654	NA	98.8279	gen2, light
45_C8_gn1	-	12.87	0.0678	-	-	0.049	0.0198	0.0467	85.59	0.0512	0.1522	-	-	NA	98.8467	c.g., after sp
45_C8_gn2	0.0007	13.18	0.0599	-	0.3096	0.053	0.0127	0.1209	87.02	-	0.1782	-	-	NA	100.9349	c.g., after sp
45_C8_gn3	0.1628	11.69	0.0751	-	0.1376	0.0595	0.0086	0.0788	79.67	1.11	0.6441	0.1536	0.0134	NA	93.8036	c.g., after sp
45_C8_py1	45.68	52.97	0.0213	-	0.0657	0.0161	0.0015	-	1.73	-	-	0.0055	-	NA	100.4901	c.g., after sp
45_C8_gn4	0.0113	13.08	0.0585	-	0.1586	0.0531	0.0199	0.1003	86.18	-	0.0904	-	-	NA	99.7522	c.g., after sp
45_C8_gn5	0.0201	13.34	0.1006	-	1.17	0.0412	0.0021	-	85.61	0.5564	0.0747	0.0247	-	NA	100.9397	incl. in sp
45_C9_mrc1	47.71	52.79	0.1485	-	0.0106	0.0107	0.0071	-	0.1677	0.1542	0.049	0.0003	0.0659	NA	101.1139	crystal1 interior, gen1
45_C9_mrc2	47.56	53.28	0.0196	-	0.2296	0.0115	-	-	0.2293	-	-	0.0093	-	NA	101.3392	crystal1 rim, gen1
45_C9_mrc3	47.19	53.18	0.0242	-	0.2068	0.018	-	-	0.2856	-	0.0249	0.0029	0.0788	NA	101.0111	gen3
45_C9_mrc4	44.89	51.53	0.0489	-	0.3728	0.0085	0.0055	-	1.3	-	0.0175	0.0188	0.2441	NA	98.4362	gen4
45_C9_mrc5	43.94	48.65	0.0196	-	0.2113	0.0131	0.0014	-	0.8026	-	-	0.0279	-	NA	93.666	gen4
45_C9_mrc6	47.13	53.38	0.0271	-	0.1978	0.006	-	-	0.1519	-	0.0062	0.0125	0.1593	NA	101.0707	
45_C9_mrc7	46.35	52.58	0.0366	-	0.3644	0.0084	-	0.0454	0.228	-	0.0075	-	-	NA	99.6204	
45_C9_mrc8	47.51	52.88	0.0002	-	0.3352	0.0058	0.0031	0.0186	0.1452	0.4026	-	-	-	NA	101.3006	crystal2 rim, gen1
45_C9_mrc9	47	52.58	0.0437	-	0.3365	0.0128	0.0029	-	0.2575	-	0.0265	-	0.0146	NA	100.2745	gen2
45_C9_sp1	4.98	32.94	1.02	-	58.58	0.031	0.2091	0.0094	0.3653	-	0.6669	0.2146	0.31	NA	99.3263	
45_C9_sp2	2.53	32.77	1.07	-	60.95	0.0523	0.1811	-	0.7929	-	0.7451	0.2683	0.0678	NA	99.4276	
45_C9_sp3	3.52	32.89	0.7631	-	61.59	0.0249	0.1924	0.0019	0.4158	0.1544	0.4731	0.1341	0.1028	NA	100.2625	
45_C9_sp4	2.31	33.05	0.3541	0.0002	62.32	0.0063	0.2096	-	0.3114	-	0.1918	0.0843	0.1432	NA	98.981	
45_C9_sp5	2.67	33.08	0.4141	-	62.26	0.0132	0.1968	0.019	0.2461	-	0.2896	0.0643	0.0245	NA	99.2776	
45_C10_mrc1	47.16	52.51	0.1371	-	-	0.0076	-	0.0084	0.2779	0.8982	0.0174	0.0149	0.0019	NA	101.0333	crystal1 interior
45_C10_mrc2	46.73	52.49	0.0454	-	0.0953	0.0165	0.0045	-	0.2954	-	0.0241	-	-	NA	99.7013	crystal1 rim
45_C10_sp1	2.71	32.88	1.01	-	60.95	0.0489	0.2028	0.0075	0.5748	-	0.7219	0.1804	0.3739	NA	99.6602	
45_C10_sp2	4.04	32.77	0.8486	-	60.55	0.0393	0.1998	0.0038	0.366	-	0.5967	0.1495	0.1585	NA	99.7223	

Table L10. Results of EPMA analyses on sulfide minerals in sample GMA13-048A

Sample	Fe	S	Cu	In	Zn	Cd	Ga	Hg	Pb	As	Sb	Ag	Au	Mn	Total	Comment
48A_C1_ccp1	30.78	34.31	34.79	-	-	-	-	0.0146	NA	-	-	-	-	-	99.8947	
48A_C1_py1	47.23	52.75	0.5267	-	-	-	-	-	NA	-	-	-	-	-	100.5066	
48A_C1_py2	47.88	52.56	0.9728	-	-	-	-	-	NA	-	-	-	-	-	101.4128	
48A_C2_ccp1	30.9	34.24	34.56	-	-	-	-	-	NA	-	-	-	0.3056	-	100.0055	
48A_C2_ccp2	30.44	34.19	34.8	0.0052	-	-	-	0.0091	NA	-	-	-	0.1391	-	99.5835	
48A_C2_ccp3	30.6	34.14	34.7	-	-	-	-	-	NA	-	-	-	-	-	99.4401	
48A_C2_Au1	10.73	13.52	9.89	-	-	-	-	-	NA	-	-	-	69.13	-	103.2699	
48A_C2_py1	47.27	52.37	1.06	-	-	-	-	-	NA	-	-	-	-	0.0035	100.7034	
48A_C2_py2	47.47	52.26	0.8714	-	-	-	-	-	NA	-	-	-	-	-	100.6013	
48A_C3_ccp1	30.54	34.53	35.01	-	-	-	-	0.0508	NA	-	-	-	0.165	-	100.2957	
48A_C3_ccp2	30.7	34.14	34.69	-	-	-	-	-	NA	-	-	-	-	-	99.5301	
48A_C3_ccp3	30.6	34.01	34.57	-	-	-	-	0.129	NA	-	-	-	-	-	99.3091	
48A_C3_Au2	26.79	31.89	31.41	-	-	-	-	-	NA	-	-	-	7.43	0.0207	97.5408	
48A_C3_py1	46.54	51.39	1.45	-	0.0076	-	-	-	NA	-	-	-	-	-	99.3876	
48A_C3_py2	47.39	52.67	1.33	-	-	-	-	0.0172	NA	-	-	-	0.0292	0.0207	101.457	
48A_C4_ccp1	30.97	34.21	34.74	-	-	-	-	-	NA	-	-	-	-	-	99.9201	
48A_C4_ccp2	30.64	33.87	34.84	-	-	-	-	-	NA	-	-	-	-	-	99.35	
48A_C4_ccp3	30.46	34.45	34.66	-	-	-	-	-	NA	-	-	-	-	-	99.5701	
48A_C4_ccp4	30.49	34.5	34.8	-	-	-	-	-	NA	-	-	-	0.1039	0.0193	99.9132	
48A_C4_py1	47.85	52.76	0.5062	-	-	-	-	-	NA	-	-	-	0.2446	0.0258	101.3866	
48A_C4_py2	47.14	51.6	1.48	-	0.015	-	-	-	NA	-	-	-	0.3554	-	100.5903	
48A_C5_py1	47.29	52.53	0.6367	-	-	-	-	-	NA	-	-	-	0.0933	0.0024	100.5524	
48A_C5_ccp1	30.57	34.5	34.46	-	-	-	-	0.0491	NA	-	-	-	-	0.0059	99.5851	
48A_C5_ccp2	30.41	34.51	34.53	-	-	-	-	-	NA	-	-	-	-	-	99.4501	
48A_C5_ccp3	30.19	34.17	34.35	-	-	-	-	-	NA	-	-	-	0.0017	0.0316	98.7434	
48A_C6_py1	47.22	52.49	1.69	-	-	-	-	-	NA	-	-	-	0.0584	-	101.4584	
48A_C5_py2	47.64	53.33	0.9911	-	-	-	-	-	NA	-	-	-	0.1699	0.0037	102.1346	
48A_C6_ccp1	30.52	34.61	34.81	-	-	-	-	-	NA	-	-	-	0.0864	-	100.0264	
48A_C6_ccp2	30.41	34.28	34.47	-	-	-	-	-	NA	-	-	-	0.2147	-	99.3748	
48A_C6_sp1	3.82	32.57	2.06	-	60.95	-	-	0.0424	NA	-	-	-	0.0366	0.0115	99.4905	
48A_C7_ccp1	30.53	34.17	34.53	-	-	-	-	-	NA	-	-	-	0.0529	0.0101	99.2931	
48A_C7_Au1	22.77	28.02	27.26	-	0.0994	-	-	0.0218	NA	-	-	-	1.12	0.0296	79.3209	
48A_C7_MinA1	27.48	32.75	24.17	0.0058	2.65	-	-	-	NA	-	-	-	0.1471	0.007	87.21	
48A_C7_py1	47.71	52.33	0.6873	-	-	-	-	-	NA	-	-	-	-	-	100.7272	
48A_C8_ccp1	30.43	34.22	34.67	-	-	-	-	-	NA	-	-	-	0.1849	-	99.505	
48A_C8_ccp2	30.39	34.24	34.42	-	-	-	-	-	NA	-	-	-	0.2515	0.0265	99.3281	
48A_C8_py1	46.57	51.12	0.8758	-	0.0045	-	-	-	NA	-	-	-	0.0932	0.0008	98.6644	
48A_C8_py2	47.38	52.69	0.6774	-	-	-	-	0.0223	NA	-	-	-	0.1406	0.006	100.9162	
48A_C9_ccp1	30.56	34.38	34.81	-	-	-	-	-	NA	-	-	-	-	0.0021	99.7522	
48A_C9_Au1	22.19	27.37	20.4	-	-	-	-	0.1616	NA	-	-	-	43.4	0.0485	113.5701	
48A_C9_py1	47.82	52.65	0.3507	-	-	-	-	-	NA	-	-	-	-	-	100.8206	
48A_C10_ccp1	30.76	34.37	34.57	-	-	-	-	-	NA	-	-	-	0.0599	-	99.7599	
48A_C10_ccp2	29.87	33.56	34.23	-	-	-	-	-	NA	-	-	-	0.7776	0.0214	98.4591	
48A_C10_py1	47.32	52.82	0.8833	-	0.0037	-	-	-	NA	-	-	-	0.1534	-	101.1803	
48A_C10_sp1	7.39	34.54	3.91	0.0342	54.3	-	-	-	NA	-	-	-	0.2481	0.0124	100.4346	
48A_C11_ccp1	30.27	34.39	34.58	-	-	-	-	-	NA	-	-	-	-	0.0113	99.2514	
48A_C11_sp1	1.2	33.03	0.6969	-	64.41	-	-	-	NA	-	-	-	0.0487	-	99.3857	
48A_C11_sp2	0.9619	32.7	0.1885	-	65.27	-	-	-	NA	-	-	-	0.0992	-	99.2197	

Table L11. Results of EPMA analyses on sulfide minerals in sample GMA13-049

Sample	Fe	S	Cu	In	Zn	Cd	Ga	Hg	Pb	As	Sb	Ag	Au	Mn	Total	Comment
49_C1_ccp1	28.64	32.44	33.25	-	0.1054	0.0065	0.0243	-	0.401	-	0.0842	0.0237	0.0195	NA	94.9947	weathered area
49_C1_ccp2	29.95	34.44	34.01	-	-	0.0123	0.0071	-	0.1252	-	0.0092	0.0106	0.0406	NA	98.605	weathered area
49_C1_ccp3	29.84	34.23	33.91	-	0.8796	0.0038	-	0.0036	0.2904	-	0.0642	0.0261	-	NA	99.2477	layered w sp, gen1
49_C1_ccp4	30.05	34.09	33.97	-	0.8284	0.0073	0.0098	-	0.2081	0.1239	0.0574	0.0125	-	NA	99.3575	gen2
49_C1_ccp5	29.64	34.42	33.77	-	1.61	0.0107	0.0108	0.0322	0.093	-	0.0212	0.0081	0.0248	NA	99.6409	gen3
49_C1_ccp6	25.78	34.08	29.78	-	9.1	0.1096	0.049	-	0.1396	-	0.0536	0.0058	0.0193	NA	99.117	gen4
49_C1_ccp7	28.24	34.3	32.91	-	3.02	0.0515	0.0176	-	0.1993	-	0.034	-	0.0688	NA	98.8413	gen5
49_C1_ccp8	6.37	30.83	6.89	0.0231	50.59	0.6978	0.1857	-	0.7013	0.6486	0.05	-	0.1458	NA	97.1323	gen6
49_C1_ccp9	6.6	32.79	8.04	-	52.02	0.2966	0.1774	-	0.5072	-	0.05	0.0129	0.2229	NA	100.717	gen7
49_C1_ccp10	28.84	34.3	30.75	-	1.19	0.0074	-	0.0339	0.2442	-	0.0317	0.0033	0.1308	NA	95.5314	gen8
49_C1_mrc1	47.22	52.06	1.32	-	0.0135	0.0209	-	-	0.1986	-	-	-	-	NA	100.8329	late after ccp
49_C1_mrc2	47.87	52.5	0.082	-	0.1096	0.0126	0.0047	-	0.1717	-	0.0224	-	0.0751	NA	100.848	
49_C1_sp1	13.82	33.49	15.61	-	36.26	0.3149	0.1268	-	0.484	-	0.0318	0.0044	0.1172	NA	100.2591	layered w ccp, gen1
49_C1_sp2	18.92	32.75	22.51	-	21.16	0.1796	0.0615	0.0091	0.7913	0.0081	0.0462	0.0188	0.1453	NA	96.6	gen2
49_C1_sp3	3.61	32.42	5.02	-	57.29	0.37	0.1986	-	0.4896	-	0.019	-	0.2176	NA	99.6348	gen3
49_C1_sp4	1.82	31.87	3.44	0.0113	60.86	0.5259	0.2149	-	0.4367	-	0.0654	0.0085	-	NA	99.2528	gen4
49_C1_sp5	5.96	32.57	7	-	52.24	0.536	0.2161	0.0413	0.3892	-	0.025	0.0034	0.4437	NA	99.4248	gen5
49_C1_sp6	2.61	32.83	3.16	0.0006	60.41	0.0789	0.1713	-	0.8851	0.6005	-	-	0.2572	NA	101.0036	gen6
49_C2_ccp1	30.32	34.3	34.43	-	0.0428	0.0121	0.0115	-	0.1062	0.1402	-	0.0034	-	NA	99.3663	
49_C2_ccp2	30.78	34.56	34.49	-	0.0649	0.0097	0.0013	-	0.109	-	0.0131	0.0059	-	NA	100.0339	
49_C2_ccp3	29.81	34.35	33.29	-	-	0.0118	0.0105	-	0.1973	-	-	0.0044	0.0813	NA	97.7554	
49_C2_ccp4	30.49	34.61	34.39	-	-	-	0.0076	-	0.1398	-	0.0172	0.0014	-	NA	99.6561	
49_C2_ccp5	29.75	33.89	34.23	-	0.0053	0.0033	0.0295	-	0.2138	-	0.0431	0.0053	0.2026	NA	98.3729	
49_C2_ccp6	29.9	34.62	34.14	-	0.4395	0.0077	0.0003	0.0143	0.1136	-	0.0212	-	0.1852	NA	99.4418	
49_C2_ccp7	30.21	34.61	34.19	-	0.1362	0.0077	-	-	0.1369	-	0.0024	-	-	NA	99.2933	
49_C2_ccp8	29.81	34.22	33.91	-	1.45	-	0.0296	-	0.1107	-	0.0024	-	0.0053	NA	99.5381	
49_C2_ccp9	30.1	34.18	33.8	-	0.3277	-	0.019	-	0.0884	-	0.0087	0.0071	-	NA	98.5309	
49_C2_ccp10	29.13	33.77	33.31	-	1.14	0.0067	0.0088	0.0053	0.2225	-	0.0562	0.0002	0.0846	NA	97.7344	
49_C2_ccp11	29.97	34.57	34.03	-	0.5182	0.0078	-	0.0214	0.1122	0.5352	0.0391	0.0031	0.1761	NA	99.9832	conduit lining
49_C2_sp1	0.93	32.56	1.93	0.002	62.79	0.7951	0.2593	0.0494	0.5482	0.2675	0.1724	0.0008	0.1025	NA	100.4072	
49_C2_sp2	0.5164	32.3	1	-	64.29	0.1822	0.1443	-	0.435	0.2433	0.0453	0.0028	0.4013	NA	99.5607	
49_C2_sp3	1.04	32.54	1.33	0.0041	63.55	0.0999	0.2281	-	1.01	-	-	0.0073	0.1685	NA	99.978	
49_C2_sp4	2.95	31.82	3.59	-	56.51	0.3269	0.1824	-	0.452	-	0.0497	0.005	-	NA	95.886	
49_C2_sp5	0.8854	32.47	1.22	0.0023	62.84	0.9581	0.2121	-	0.5297	0.3726	0.1203	0.002	0.2811	NA	99.8937	
49_C2_sp6	1.31	32.72	1.3	0.0172	63.19	0.1899	0.1745	-	0.3307	0.9429	0.0057	0.0043	-	NA	100.1852	
49_C2_sp7	1.53	32.53	1.85	-	61.31	0.0785	0.1926	0.0285	0.401	-	0.03	0.02	0.0749	NA	98.0455	
49_C2_sp8	1.56	32.99	1.5	-	63.45	0.3181	0.1775	0.038	0.33	-	-	-	0.073	NA	100.4366	
49_C2_sp9	0.8618	32.47	1.44	-	63.73	0.3443	0.186	-	0.4633	-	0.0267	0.006	0.0435	NA	99.5717	
49_C3_ccp1	25.43	28.97	33.92	-	2.05	0.0086	0.0008	-	0.476	-	0.0175	0.0045	0.063	NA	90.9405	
49_C3_ccp2	30.35	34.67	34.3	-	-	0.0089	0.0065	0.0126	0.1489	0.6421	0.0072	0.0005	0.1215	NA	100.2682	
49_C3_ccp3	30.15	34.56	33.98	-	0.6854	0.0108	-	-	0.0913	-	0.0945	0.0115	0.1392	NA	99.7228	gen1
49_C3_ccp4	28.75	34.73	33.28	-	2.67	0.0302	0.0281	-	0.2008	0.1976	0.018	0.0167	0.0829	NA	100.0042	gen2
49_C3_ccp5	30.34	34.6	34.45	-	0.2161	-	0.014	0.0036	0.1503	0.4118	0.0243	0.0014	-	NA	100.2114	w sp
49_C3_mrc1	47.79	52.73	0.041	-	0.0104	0.004	-	0.0134	0.1772	0.2394	-	-	-	NA	101.0053	
49_C3_mrc2	47.25	53.02	0.23	-	0.0192	0.0118	0.0011	-	0.1672	-	0.0008	-	-	NA	100.7001	
49_C3_sp1	3.06	32.39	2.09	-	60.78	1.05	0.2729	0.1285	0.2718	-	0.1325	-	0.0556	NA	100.2312	w ccp
49_C3_sp2	2.78	32.55	3.37	0.008	59.53	0.3166	0.1915	0.0246	0.61	-	0.0425	-	0.1218	NA	99.5451	w ccp
49_C3_sp3	20.6	33.1	23.96	-	19.52	0.0291	0.0854	-	0.4041	-	0.0104	0.0159	0.1001	NA	97.8251	w ccp
49_C3_sp4	0.8901	32.82	1.01	-	63.58	0.2395	0.2263	-	0.1722	-	0.0535	-	0.2126	NA	99.2043	w ccp, late
49_C4_ccp1	21.83	33.9	25.26	-	17.08	0.0993	0.0192	0.0564	0.2166	-	0.0036	0.0085	0.0931	NA	98.5667	
49_C4_ccp2	30.27	34.52	34.57	-	0.5444	0.0062	0.0072	0.0536	0.1712	-	0.0176	0.004	0.3485	NA	100.5127	
49_C4_ccp3	30.5	34.43	34.74	-	0.4261	0.0091	0.0099	0.0322	0.1872	-	0.0144	0.0022	-	NA	100.3511	
49_C4_ccp4	25.14	33.83	29.74	-	8.91	0.0568	0.0232	0.0306	0.3412	-	0.0156	0.0021	-	NA	98.0896	sp incl., gen 1
49_C4_ccp5	26.3	33.29	30.38	-	5.96	0.0836	0.0472	-	0.3004	-	0.0328	-	0.0247	NA	96.4187	gen2
49_C4_ccp6	11.56	33.54	14.88	0.0033	37.39	0.1105	0.0974	-	0.7737	0.2528	0.0222	0.0111	0.1222	NA	98.7632	gen3

Table L11. Continued

Sample	Fe	S	Cu	In	Zn	Cd	Ga	Hg	Pb	As	Sb	Ag	Au	Mn	Total	Comment
49_C4_sp1	4.99	31.59	7.7	-	52.32	0.3213	0.1671	0.0075	0.3697	-	0.0476	-	0.207	NA	97.7202	
49_C4_sp2	6.09	32.81	6.12	0.0011	54.4	0.607	0.1802	-	0.3291	-	0.0686	-	0.1166	NA	100.7226	
49_C4_sp3	0.9771	32.68	2.12	-	61.71	0.4089	0.3536	-	0.5681	-	0.1809	0.0141	0.4167	NA	99.4295	
49_C4_sp4	2.11	32.35	1.95	-	61.76	0.8073	0.2351	0.0606	0.4841	-	0.087	0.0076	0.0573	NA	99.909	w ccp incl, gen1
49_C4_sp5	1.03	32.72	1.51	0.0001	63.35	0.3773	0.2139	0.053	1.17	-	0.047	0.0079	0.1231	NA	100.6022	gen2
49_C4_sp6	1.3	32.61	1.23	-	62.91	1.03	0.188	-	0.6089	-	0.0656	0.0061	0.0746	NA	100.0231	gen3
49_C4_sp7	0.9106	32.69	1.95	-	62.99	0.6044	0.1842	-	0.8911	-	0.0121	0.017	0.1527	NA	100.402	gen4
49_C4_sp8	1.05	32.42	1.95	-	62.15	0.3402	0.2103	-	0.6653	-	0.0376	0.007	-	NA	98.8305	gen5
49_C5_ccp1	29.98	34.25	34.12	-	0.4272	0.0214	0.0119	-	0.2829	-	0.0319	0.0201	-	NA	99.1455	early, w sp
49_C5_ccp2	30.39	34.72	34.49	-	0.031	0.0089	0.0303	-	0.1223	-	0.0271	0.0074	-	NA	99.8271	late
49_C5_ccp3	28.02	34.31	31.53	-	5.67	0.032	0.042	0.018	0.2176	-	0.1038	0.045	0.0211	NA	100.0094	early, w sp
49_C5_ccp4	30.34	34.16	34.71	-	-	-	0.0264	0.0108	0.0664	-	0.0742	0.0096	0.0846	NA	99.4821	late
49_C5_ccp5	26.45	34.41	30.33	-	8.6	0.1525	0.0499	0.0721	0.1231	-	0.0548	0.0074	0.0511	NA	100.3008	sp incl?
49_C5_ccp6	30.14	34.63	34.42	-	0.1947	0.0095	0.0127	-	0.1738	-	0.0124	0.0066	0.0529	NA	99.6526	sp incl?
49_C5_mrc1	47.16	52.8	0.4957	-	0.4564	0.0089	0.0001	-	0.1815	-	-	0.0031	-	NA	101.1056	
49_C5_sp1	2.35	32.8	2.99	-	59.72	0.2015	0.1837	-	0.4896	-	0.0437	0.0067	0.1549	NA	98.9401	dendritic, ccp incl. gen1
49_C5_sp2	8.93	32.77	10.77	-	45.26	0.199	0.1539	0.0392	0.416	-	0.0423	0.0123	0.2565	NA	98.8493	gen2
49_C5_sp3	5.89	31.73	6.68	-	50.54	0.3452	0.1689	-	0.2569	-	0.0363	0.0093	0.3086	NA	95.9653	gen3
49_C5_sp4	15.05	33.16	17.91	-	32.01	0.3913	0.125	-	0.3023	-	0.0703	0.0026	0.1033	NA	99.1248	gen4
49_C5_sp5	0.9932	32.83	1.57	-	63.75	0.3229	0.1878	-	0.3393	-	0.0417	0.0108	0.0661	NA	100.1118	ccp inclusions
49_C5_sp6	2.21	32.83	2.41	0.0271	61.86	0.2906	0.2251	-	0.3158	-	0.118	0.0019	0.3494	NA	100.6379	ccp inclusions
49_C5_sp7	1.23	32.55	1.53	-	61.94	0.7524	0.2163	-	0.4423	-	0.1558	0.0006	0.2744	NA	99.0919	ccp inclusions
49_C6_ccp1	23.94	28.57	22.78	-	-	0.0025	-	0.0071	0.5697	-	0.0341	0.0212	-	NA	75.9247	
49_C6_ccp2	22.52	25.67	21.67	-	0.279	0.0053	0.0044	-	0.3737	-	0.0232	0.0135	-	NA	70.5592	
49_C6_ccp3	11.61	14.38	13.69	-	-	0.0026	-	-	0.1573	-	0.0136	0.0099	-	NA	39.8634	
49_C6_ccp4	21.54	25.19	26.23	-	0.0801	-	0.0137	-	3.13	-	0.0211	-	-	NA	76.205	
49_C6_ccp5	20.26	23.8	24.14	-	-	-	0.0003	0.0214	0.212	-	0.0219	0.0152	-	NA	68.4708	
49_C6_ccp6	30	34.52	34.53	-	-	0.007	0.0085	-	0.084	-	-	0.0064	0.2484	NA	99.4044	
49_C6_ccp7	32.88	38.2	23.7	-	-	0.0068	-	-	0.2702	-	0.0214	0.0087	-	NA	95.0872	
49_C6_ccp8	30.72	34.58	34.78	-	-	0.0067	0.0139	-	0.1664	-	0.0052	0.0009	-	NA	100.273	
49_C6_ccp9	28.29	33.63	34.85	-	-	-	0.0076	0.0018	0.1637	-	0.0355	0.0043	0.1198	NA	97.1028	
49_C6_ccp10	28.47	33.6	34.78	-	-	0.0025	0.0029	0.0358	0.2711	-	0.0526	0.0106	-	NA	97.2255	
49_C6_ccp11	27.78	31.36	31.38	-	-	0.0146	0.0012	0.0464	0.1149	-	0.0431	0.0058	0.1339	NA	90.88	
49_C6_ccp12	30.55	34.69	34.48	-	-	0.0135	0.0139	-	0.025	-	0.0435	0.0012	0.0124	NA	99.8296	
49_C7_ccp1	30.28	34.63	34.32	-	0.4558	0.0071	-	-	0.0649	-	0.0327	0.006	-	NA	99.7966	gen1
49_C7_ccp2	30.43	34.45	34.13	-	0.4846	-	0.0124	-	0.1885	-	0.0036	-	0.1163	NA	99.8155	gen2
49_C7_ccp3	30.24	34.71	34.22	-	0.3194	0.0034	0.0163	-	0.1267	-	0.0056	-	0.164	NA	99.8106	gen3
49_C7_ccp4	30.36	34.57	34.27	-	0.3037	0.002	0.0106	0.0197	0.1782	-	0.0124	0.0036	-	NA	99.7303	second gen1
49_C7_ccp5	30.25	34.89	34.51	-	0.1167	0.0098	-	-	0.0957	-	0.0328	0.0057	-	NA	99.9108	second gen2
49_C7_ccp6	30.22	35.06	34.32	-	-	-	-	-	0.1132	-	-	0.014	-	NA	99.7272	
49_C7_sp2	2.06	32.91	1.86	0.0106	61.53	1.06	0.2278	-	0.5845	-	0.0582	-	0.0364	NA	100.3374	
49_C7_sp3	1.83	32.65	2.46	-	61.55	0.0728	0.2218	-	0.5185	-	-	0.0045	0.2816	NA	99.5893	
49_C7_sp4	1.93	32.6	1.62	-	62.26	0.6519	0.2276	-	0.2459	-	0.0918	0.004	-	NA	99.6312	
49_C7_sp5	1.92	32.54	1.65	-	62.01	0.6381	0.2241	-	0.3141	-	0.089	-	0.1982	NA	99.5835	
49_C7_sp5	2.29	32.74	2.49	-	61.66	0.2944	0.192	-	0.4003	-	0.0178	0.0192	0.0678	NA	100.1715	
49_C8_ccp1	30.3	34.59	34.47	-	-	0.0174	0.0016	0.0499	0.1251	-	0.0247	0.0134	-	NA	99.5921	gen1
49_C8_ccp2	29.32	34.66	31.63	-	0.3507	0.0093	0.0051	0.0071	0.2922	-	0.0436	-	0.0265	NA	96.3446	gen2
49_C8_ccp3	29.64	34.25	33.99	-	0.8453	0.0097	0.0538	0.0232	0.1961	-	0.0243	0.008	0.2094	NA	99.2498	gen3
49_C8_ccp4	30.61	34.61	34.38	-	-	0.0019	0.0375	-	0.1824	-	0.0283	0.0029	-	NA	99.8531	gen4
49_C8_sp1	5.96	30.97	6.02	0.0074	54.04	0.7535	0.2618	0.0114	0.5015	-	0.0555	-	0.0918	NA	98.6729	gen1
49_C8_sp2	2.96	32.87	1.73	-	60.28	1.62	0.2903	-	0.4032	-	0.1342	-	0.0798	NA	100.3675	gen2
49_C9_ccp1	30.57	34.9	34.4	-	-	0.0103	0.0043	-	0.0648	0.1894	0.0032	0.0147	0.222	NA	100.3786	
49_C9_ccp2	30.59	34.71	34.49	-	-	0.0023	0.0131	0.0446	0.1266	-	-	0.0119	0.0458	NA	100.0342	
49_C9_ccp3	29.48	34.74	33.69	-	2.01	0.0109	0.0121	0.0376	0.149	-	-	0.0043	-	NA	100.1339	
49_C9_sp1	0.7333	32.51	0.9988	0.0034	63.47	0.7441	0.3136	-	0.6175	0.5179	0.1443	0.0725	0.1525	NA	100.2779	
49_C9_sp2	0.6446	32.81	1.16	0.0034	63.76	0.2284	0.2149	0.0171	0.7719	-	0.0008	0.0222	0.0191	NA	99.6525	
49_C10_sp1	8.21	33.2	2.49	-	55.84	0.5971	0.1824	0.045	0.1259	-	0.0774	0.0045	0.3499	NA	101.1221	
49_C10_sp2	8.06	33.43	1.74	-	56.8	0.4592	0.1908	-	0.1291	0.2281	0.0645	-	0.0314	NA	101.133	
49_C10_ccp3	30.24	34.77	34.5	-	0.4354	0.0041	0.0153	-	0.1267	-	0.018	-	0.3081	NA	100.4175	

Table L12. Results of EPMA analyses on sulfide minerals in sample GMA13-050

Sample	Fe	S	Cu	In	Zn	Cd	Ga	Hg	Pb	As	Sb	Ag	Au	Mn	Total	Comment
50_C1_ccp1	29.91	34.61	34.86	-	0.5104	0.0015	-	NA	NA	NA	NA	NA	0.1748	NA	100.0667	
50_C1_ccp2	30.08	34.5	34.8	-	0.6079	0.004	-	NA	NA	NA	NA	NA	0.0848	NA	100.0767	
50_C1_ccp3	30.43	34.7	34.56	-	0.1529	0.0097	-	NA	NA	NA	NA	NA	-	NA	99.8527	
50_C1_ccp4	29.62	34.5	34.11	-	1.67	0.0061	-	NA	NA	NA	NA	NA	0.1201	NA	100.0262	
50_C1_mrc1	47.62	52.84	0.1297	-	0.1332	0.0125	-	NA	NA	NA	NA	NA	-	NA	100.7353	
50_C1_mrc2	45.11	51.97	0.3124	-	2.39	0.009	-	NA	NA	NA	NA	NA	0.1701	NA	99.9616	
50_C1_mrc3	47.36	53.2	0.1982	-	0.8633	0.0073	0.0114	NA	NA	NA	NA	NA	-	NA	101.6401	
50_C1_sp1	1.57	33.31	0.3915	-	64.84	0.3278	0.2086	NA	NA	NA	NA	NA	0.1519	NA	100.7997	
50_C1_sp2	3.41	33.39	0.8108	-	61.49	0.5494	1.03	NA	NA	NA	NA	NA	-	NA	100.6801	
50_C1_sp3	0.5395	33.05	0.811	0.0081	64.32	0.0311	0.1712	NA	NA	NA	NA	NA	0.1014	NA	99.0323	
50_C1_sp4	2.05	33.14	0.1213	-	64.71	0.3933	0.2216	NA	NA	NA	NA	NA	0.0892	NA	100.7253	
50_C1_sp5	1.06	33.19	0.3965	0.0047	65.28	0.1682	0.1802	NA	NA	NA	NA	NA	0.1886	NA	100.4681	
50_C1_sp6	1.96	33.07	0.276	0.0094	64.36	0.3428	0.1987	NA	NA	NA	NA	NA	0.1344	NA	100.3512	
50_C2_py1	46.8	52.82	0.0838	-	0.9546	0.0049	0.012	NA	NA	NA	NA	NA	-	NA	100.6752	sperulitic, early
50_C2_py4	45.72	52.54	0.2592	-	1.3	0.0105	-	NA	NA	NA	NA	NA	-	NA	99.8298	sperulitic
50_C2_py5	43.7	52.45	1.46	-	0.4092	0.0186	-	NA	NA	NA	NA	NA	0.0733	NA	98.1112	sperulitic crystal1 rim
50_C2_py6	43.06	49.75	0.3396	-	2.56	0.0184	0.0314	NA	NA	NA	NA	NA	0.2778	NA	96.0373	sperulitic crystal1 interior
50_C2_py8	46.98	52.94	0.0629	-	0.4151	0.0165	-	NA	NA	NA	NA	NA	0.1739	NA	100.5883	sperulitic interior
50_C2_py9	44.5	51.72	0.6389	-	0.6435	0.013	0.0146	NA	NA	NA	NA	NA	0.1227	NA	97.6528	sperulitic crystal2 rim
50_C2_py13	46.41	51.98	0.1871	-	0.057	0.0065	-	NA	NA	NA	NA	NA	0.1592	NA	98.7999	
50_C2_py10	41.54	45.2	0.7217	-	1.39	0.0127	-	NA	NA	NA	NA	NA	0.0183	NA	88.8828	sperulitic crystal2 interior
50_C2_mrc2	47.73	53.13	0.0175	-	0.0281	0.0155	0.0106	NA	NA	NA	NA	NA	-	NA	100.9317	after py
50_C2_mrc3	47.93	53.42	0.0115	-	0.0415	0.0218	-	NA	NA	NA	NA	NA	-	NA	101.4247	after py
50_C2_mrc7	47.3	53.39	0.0393	-	0.4076	0.0154	0.0102	NA	NA	NA	NA	NA	-	NA	101.1624	after py
50_C2_mrc11	47.4	53.28	0.0619	-	0.1504	0.0076	-	NA	NA	NA	NA	NA	-	NA	100.8998	after py
50_C2_mrc12	47.36	53.21	0.013	-	0.0525	0.01	-	NA	NA	NA	NA	NA	-	NA	100.6454	or mrc?
50_C2_sp1	2.89	33.36	0.1303	-	61.68	0.2066	0.2834	NA	NA	NA	NA	NA	0.2866	NA	98.837	
50_C2_sp2	0.7181	33.21	0.2466	-	65.25	0.0271	0.2022	NA	NA	NA	NA	NA	0.3823	NA	100.0362	
50_C2_sp3	2.22	33.41	0.1551	-	63.78	0.1557	0.173	NA	NA	NA	NA	NA	0.063	NA	99.9569	
50_C2_sp4	1.28	32.67	0.4188	-	64.02	0.0242	0.2305	NA	NA	NA	NA	NA	0.3106	NA	98.9541	
50_C2_sp5	1.35	32.37	0.5034	-	62.73	0.0484	0.1513	NA	NA	NA	NA	NA	-	NA	97.1532	
50_C2_sp6	1.28	33.1	0.2064	-	64.87	-	0.2624	NA	NA	NA	NA	NA	0.0488	NA	99.7677	
50_C2_sp7	1.92	31.85	0.0378	0.0095	62.5	0.2488	0.2334	NA	NA	NA	NA	NA	0.0698	NA	96.8694	
50_C2_sp8	0.8903	33.03	0.4132	0.0158	64.5	0.0163	0.1854	NA	NA	NA	NA	NA	0.1047	NA	99.1557	
50_C3_ccp1	30.19	34.8	34.61	-	0.52	0.0263	-	NA	NA	NA	NA	NA	0.1919	NA	100.3381	incl. in sp
50_C3_py2	47.66	53.31	0.063	-	0.2173	0.0066	-	NA	NA	NA	NA	NA	-	NA	101.2569	
50_C3_py3	45.52	51.88	0.5063	-	0.715	0.0022	0.0065	NA	NA	NA	NA	NA	0.0129	NA	98.643	sperulitic, early
50_C3_py5	44.61	51.28	0.8034	-	0.667	0.0093	-	NA	NA	NA	NA	NA	-	NA	97.3698	sperulitic crystal1 interior
50_C3_py6	44.33	51.17	1.3	-	1.02	-	-	NA	NA	NA	NA	NA	-	NA	97.8201	sperulitic crystal1 rim
50_C3_mrc1	45.8	52.78	0.5783	-	1.03	0.0161	0.0076	NA	NA	NA	NA	NA	-	NA	100.2119	sp inclusions
50_C3_mrc4	47.79	53.37	0.1001	-	0.2339	-	0.0025	NA	NA	NA	NA	NA	0.0164	NA	101.5128	
50_C3_sp1	1.8	33.05	0.5559	-	62.47	0.154	0.1962	NA	NA	NA	NA	NA	0.211	NA	98.4372	
50_C3_sp2	1.3	32.97	0.834	-	64.05	0.097	0.2306	NA	NA	NA	NA	NA	0.162	NA	99.6437	crystal1 rim, light
50_C3_sp3	3.27	33.29	0.2719	-	62.48	0.4857	0.2174	NA	NA	NA	NA	NA	0.1882	NA	100.2031	crystal1 interior, light
50_C3_sp4	0.9992	33.05	0.49	-	64.36	0.1157	0.1889	NA	NA	NA	NA	NA	0.1829	NA	99.3867	
50_C4_ccp1	30.48	34.54	34.85	-	-	0.0119	0.0135	NA	NA	NA	NA	NA	0.1089	NA	100.0042	
50_C4_ccp2	30.44	34.69	34.77	-	-	0.0079	-	NA	NA	NA	NA	NA	0.1339	NA	100.0417	
50_C4_ccp3	30.64	34.65	35	-	-	0.0105	0.0037	NA	NA	NA	NA	NA	0.1656	NA	100.4697	
50_C4_mrc1	47.43	53.56	0.6645	-	0.0546	0.0118	-	NA	NA	NA	NA	NA	-	NA	101.7209	early gen1
50_C4_mrc2	47.24	52.71	0.221	-	0.0078	0.0096	-	NA	NA	NA	NA	NA	0.1481	NA	100.3364	early gen1
50_C4_mrc3	47.88	53.28	0.0948	-	0.0179	0.0042	0.008	NA	NA	NA	NA	NA	0.1535	NA	101.4384	gen2
50_C4_mrc4	47.77	53.06	0.0435	-	0.5789	0.0067	0.0011	NA	NA	NA	NA	NA	0.0146	NA	101.4748	gen3 vent lining
50_C4_mrc5	47.68	52.72	0.0984	-	0.4148	0.0101	-	NA	NA	NA	NA	NA	0.2793	NA	101.2025	crystalline gen1
50_C4_mrc6	46.41	52.13	1.06	-	1.29	0.0107	-	NA	NA	NA	NA	NA	-	NA	100.9006	crystalline gen2
50_C4_mrc7	47.17	53.48	0.0814	-	1.3	0.011	-	NA	NA	NA	NA	NA	-	NA	102.0423	gen3 vent lining
50_C4_sp1	3.28	33.48	0.674	0.0008	62.71	0.589	0.4227	NA	NA	NA	NA	NA	0.0141	NA	101.1705	gen1 (may be later)
50_C4_sp2	1.68	33.11	1.75	-	63.21	0.2477	0.2075	NA	NA	NA	NA	NA	0.1219	NA	100.3271	gen2
50_C4_sp3	1.39	33.17	0.5921	0.0029	64.32	0.4472	0.2348	NA	NA	NA	NA	NA	0.134	NA	100.2909	early crystal1 prof
50_C4_sp4	1.72	33.12	0.5	-	63.82	0.6876	0.2042	NA	NA	NA	NA	NA	-	NA	100.0517	crystal1 profile
50_C4_sp5	2.45	33.21	0.2212	0.0029	63.6	0.4404	0.2988	NA	NA	NA	NA	NA	-	NA	100.2232	crystal1 profile
50_C4_sp6	0.7616	33.13	0.8588	-	64.09	0.123	0.2234	NA	NA	NA	NA	NA	0.3898	NA	99.5767	crystal1 profile
50_C4_sp7	0.9756	33.06	0.5495	-	64.62	0.0748	0.1475	NA	NA	NA	NA	NA	0.1515	NA	99.5789	late crystal1 prof
50_C4_sp8	1.04	31.91	1.8	-	59.22	0.0745	0.1765	NA	NA	NA	NA	NA	0.176	NA	94.3971	bright spot BSE
50_C4_sp9	1.72	28.34	1.1	-	45.17	0.052	0.138	NA	NA	NA	NA	NA	0.5289	NA	77.049	bright spot BSE
50_C4_sp10	1.32	18.76	0.4956	-	8.08	0.053	0.0299	NA	NA	NA	NA	NA	0.0572	NA	28.7957	bright spot BSE
50_C4_sp11	0.3912	18.81	0.3198	-	9.61	0.0666	-	NA	NA	NA	NA	NA	-	NA	29.1976	bright spot BSE
50_C4_sp12	1.06	33.15	2.26	0.0036	62.67	0.1979	0.2143	NA	NA	NA	NA	NA	0.24	NA	99.7959	
50_C4_cov1	2.02	23.37	67.08	-	-	-	0.0003	NA	NA	NA	NA	NA	-	NA	92.4704	

Table L12. Continued

Sample	Fe	S	Cu	In	Zn	Cd	Ga	Hg	Pb	As	Sb	Ag	Au	Mn	Total	Comment
50_C5_ccp1	30.89	34.72	33.98	-	-	0.0008	-	NA	NA	NA	NA	NA	-	NA	99.5909	early gen1
50_C5_ccp2	30.61	34.41	33.94	-	-	0.0021	-	NA	NA	NA	NA	NA	0.102	NA	99.0642	gen2
50_C5_ccp3	30.34	34.85	34.95	-	-	0.0035	-	NA	NA	NA	NA	NA	0.3236	NA	100.467	
50_C5_ccp4	30.3	34.71	35.02	-	-	0.0017	0.0018	NA	NA	NA	NA	NA	0.1953	NA	100.2287	
50_C5_ccp5	29.34	33.82	35.15	-	-	0.0199	-	NA	NA	NA	NA	NA	0.2406	NA	98.5706	
50_C5_ccp6	30.31	34.67	35.22	-	0.032	0.0046	-	NA	NA	NA	NA	NA	-	NA	100.2365	
50_C5_ccp7	30.72	34.74	35.16	-	-	-	-	NA	NA	NA	NA	NA	0.0282	NA	100.6481	early c.g. gen1, incl. in sp
50_C5_ccp8	29.86	34.59	34.16	-	1.59	0.0077	-	NA	NA	NA	NA	NA	0.1017	NA	100.3093	later f.g. gen2
50_C5_ccp9	29.95	34.71	35.16	-	0.1151	0.0152	0.021	NA	NA	NA	NA	NA	0.4432	NA	100.4144	
50_C5_mrc1	47.93	53.18	0.1053	-	0.0686	0.0068	-	NA	NA	NA	NA	NA	0.022	NA	101.3127	colloform early gen1
50_C5_mrc2	47.46	52.5	0.0683	-	0.007	0.0005	-	NA	NA	NA	NA	NA	-	NA	100.0358	gen2
50_C5_mrc3	47.77	52.65	0.0358	-	-	0.0128	0.0045	NA	NA	NA	NA	NA	0.1808	NA	100.6538	gen3
50_C5_mrc4	47.51	52.73	0.076	-	0.0056	0.0171	0.0126	NA	NA	NA	NA	NA	0.053	NA	100.4042	gen4
50_C5_mrc5	47.54	52.64	0.0369	-	0.1026	0.0065	0.0122	NA	NA	NA	NA	NA	0.0055	NA	100.3437	gen5
50_C5_mrc6	47.59	53.13	0.2354	-	0.4185	0.0028	-	NA	NA	NA	NA	NA	0.0493	NA	101.4259	gen6
50_C5_mrc6_2	47.06	52.9	1.57	-	0.2223	0.0093	0.0117	NA	NA	NA	NA	NA	-	NA	101.7732	
50_C5_mrc7	47.37	52.72	1.07	-	0.0269	0.0192	-	NA	NA	NA	NA	NA	0.1583	NA	101.3643	new gen1
50_C5_mrc8	47.61	52.44	0.1267	-	0.04	0.0159	-	NA	NA	NA	NA	NA	0.0382	NA	100.2708	new gen2
50_C5_mrc9	47.45	52.94	0.1894	-	0.7953	-	-	NA	NA	NA	NA	NA	0.0892	NA	101.4639	new gen3
50_C5_sp1	19.53	29.25	45.87	-	-	0.0034	0.0205	NA	NA	NA	NA	NA	-	NA	94.674	grain edge
50_C5_sp2	3.28	32.51	4.93	-	58.24	0.0113	0.2062	NA	NA	NA	NA	NA	0.2382	NA	99.4157	
50_C5_sp3	2.49	33.27	2.18	-	62.48	0.2127	0.2088	NA	NA	NA	NA	NA	0.1077	NA	100.9491	
50_C5_sp4	21.19	32.57	44.48	-	0.0835	0.0058	0.0154	NA	NA	NA	NA	NA	0.0017	NA	98.3465	
50_C5_sp5	2.02	33.06	1.79	-	62.93	0.1188	0.1507	NA	NA	NA	NA	NA	0.0849	NA	100.1544	earliest
50_C5_sp6	1.34	32.8	2.77	-	62.68	0.0325	0.1456	NA	NA	NA	NA	NA	-	NA	99.7682	late, early crystal1 prof
50_C5_sp7	1.89	33.23	0.3451	-	64.57	0.3816	0.2097	NA	NA	NA	NA	NA	0.3292	NA	100.9556	crystal1 profile
50_C5_sp8	0.6755	33.2	0.6589	-	65.63	0.0906	0.2391	NA	NA	NA	NA	NA	0.2512	NA	100.7452	crystal1 profile
50_C5_sp9	0.7733	33.25	0.2945	-	65.77	0.0763	0.2139	NA	NA	NA	NA	NA	0.2999	NA	100.6778	crystal1 profile
50_C5_sp10	0.5883	33.28	0.5125	-	65.63	0.0816	0.1918	NA	NA	NA	NA	NA	0.2288	NA	100.5129	crystal1 profile
50_C5_sp11	0.3322	33.07	0.4202	-	66.09	0.0005	0.2084	NA	NA	NA	NA	NA	0.2564	NA	100.3776	late crystal1 prof
50_C5_sp12	1.62	33.06	2.5	0.0137	63.26	0.2432	0.1867	NA	NA	NA	NA	NA	0.078	NA	100.9615	
50_C6_ccp1	30.53	34.8	34.88	-	0.1416	0.0114	-	NA	NA	NA	NA	NA	0.1173	NA	100.4802	incl. in sp
50_C6_ccp2	30.47	35.25	35.08	-	-	0.0158	0.0168	NA	NA	NA	NA	NA	-	NA	100.8326	
50_C6_py1	46.27	52.39	0.2137	-	0.9618	0.0006	-	NA	NA	NA	NA	NA	0.0872	NA	99.9234	colloform
50_C6_mrc2	47.28	53.3	0.3416	-	1.12	0.0003	-	NA	NA	NA	NA	NA	0.1415	NA	102.1833	
50_C6_sp1	0.6753	33.27	0.4817	0.0018	65.26	0.064	0.2015	NA	NA	NA	NA	NA	0.0935	NA	100.0477	late crystal1 prof
50_C6_sp2	1.29	33.3	0.5182	-	64.69	0.3618	0.1844	NA	NA	NA	NA	NA	0.2425	NA	100.5869	crystal1 profile
50_C6_sp3	1.52	33.23	0.4348	0.0056	64.79	0.2841	0.2157	NA	NA	NA	NA	NA	0.1178	NA	100.5979	early crystal1 prof
50_C6_sp4	0.3858	33.15	0.1109	0.0073	66.15	-	0.2431	NA	NA	NA	NA	NA	-	NA	100.0471	late crystal2 prof
50_C6_sp5	1.3	33.01	0.8378	-	64.5	0.218	0.1996	NA	NA	NA	NA	NA	0.1921	NA	100.2574	crystal2 profile
50_C6_sp6	2.99	33.21	0.7854	-	62.66	0.5592	0.2853	NA	NA	NA	NA	NA	0.2092	NA	100.699	early crystal2 prof
50_C6_sp7	2.09	33.18	1.72	0.0015	63.53	0.1135	0.2361	NA	NA	NA	NA	NA	0.2023	NA	101.0733	
50_C6_cov1	2.42	27.25	48.84	0.0171	0.1898	-	-	NA	NA	NA	NA	NA	-	NA	78.717	
50_C7_ccp1	30.27	34.61	34.77	-	0.389	0.0216	0.0137	NA	NA	NA	NA	NA	-	NA	100.0742	late, incl. in sp
50_C7_ccp2	30.88	34.64	35.01	-	-	0.0022	-	NA	NA	NA	NA	NA	0.0997	NA	100.6318	
50_C7_ccp3	30.28	34.72	34.68	-	0.5571	-	0.0109	NA	NA	NA	NA	NA	0.0788	NA	100.3267	
50_C7_mrc1	46.47	51.48	1.12	-	0.027	0.0125	-	NA	NA	NA	NA	NA	0.2573	NA	99.3669	
50_C7_mrc2	47.29	52.74	0.6479	-	-	0.0132	-	NA	NA	NA	NA	NA	0.1198	NA	100.8108	
50_C7_mrc3	47.2	52.72	0.8057	-	0.448	0.0148	0.0174	NA	NA	NA	NA	NA	-	NA	101.2058	
50_C7_sp1	1.59	33.16	0.7696	-	62.85	0.0927	0.2286	NA	NA	NA	NA	NA	0.0728	NA	98.7637	late crystal1 prof
50_C7_sp2	0.269	33.22	0.2655	-	66.18	0.0134	0.1306	NA	NA	NA	NA	NA	0.2336	NA	100.312	crystal1 profile
50_C7_sp3	0.5503	33.13	0.1803	0.0282	66.33	0.0525	0.1631	NA	NA	NA	NA	NA	-	NA	100.4343	early crystal1 prof
50_C7_sp4	1.07	33.23	0.8365	-	65.03	0.0774	0.2228	NA	NA	NA	NA	NA	0.3043	NA	100.7709	
50_C7_sp5	1.59	33.15	0.7516	0.0019	64.47	0.091	0.1939	NA	NA	NA	NA	NA	0.0952	NA	100.3436	
50_C7_cov1	1.26	23.55	34.71	0.0054	15.26	0.026	0.0787	NA	NA	NA	NA	NA	0.0465	NA	74.9367	
50_C8_ccp1	30.79	34.63	34.34	-	-	0.0081	0.0067	NA	NA	NA	NA	NA	-	NA	99.7749	vent lining
50_C8_ccp2	30.47	34.85	34.78	-	-	0.0076	-	NA	NA	NA	NA	NA	0.1822	NA	100.2897	
50_C8_ccp3	29.31	34.68	34.03	-	2.47	-	0.0042	NA	NA	NA	NA	NA	0.1559	NA	100.65	f.g., incl. in sp
50_C8_mrc1	47.48	52.93	0.0275	-	0.0492	0.0194	0.011	NA	NA	NA	NA	NA	-	NA	100.5171	gen4 vent lining
50_C8_mrc2	47.53	52.61	0.0564	-	-	0.0173	-	NA	NA	NA	NA	NA	0.0055	NA	100.2191	gen3 vent lining
50_C8_mrc3	47.61	53.22	0.0574	-	0.1959	0.0062	0.0104	NA	NA	NA	NA	NA	-	NA	101.0999	gen2 w sp
50_C8_mrc4	47.56	53.08	0.0717	-	0.15	0.011	-	NA	NA	NA	NA	NA	-	NA	100.8727	gen1 w sp
50_C8_mrc5	47.46	52.71	0.2183	-	0.1484	0.002	-	NA	NA	NA	NA	NA	-	NA	100.5386	
50_C8_mrc6	47.61	53.17	0.7359	-	0.0214	0.0109	-	NA	NA	NA	NA	NA	-	NA	101.5481	
50_C8_sp1	3.55	33.2	0.0686	-	62.57	0.251	0.2033	NA	NA	NA	NA	NA	0.1438	NA	99.9868	incl. in mrc
50_C8_sp2	0.9646	32.92	1.34	-	64.02	0.1967	0.2023	NA	NA	NA	NA	NA	0.0502	NA	99.6938	
50_C8_sp3	1.1	33.1	1.24	-	63.77	0.3552	0.2195	NA	NA	NA	NA	NA	0.3147	NA	100.0993	late crystal1 prof
50_C8_sp4	0.5475	32.88	0.3522	0.0092	65.34	0.0076	0.2223	NA	NA	NA	NA	NA	0.1385	NA	99.4973	crystal1 profile
50_C8_sp5	1.08	33.02	0.7418	-	65.11	0.0737	0.2194	NA	NA	NA	NA	NA	0.1419	NA	100.3867	crystal1 profile
50_C8_sp6	0.4279	33.21	0.7397	-	65.54	-	0.2034	NA	NA	NA	NA	NA	0.1022	NA	100.2232	crystal1 profile
50_C8_sp7	0.4449	33.42	0.1239	-	65.56	-	0.185	NA	NA	NA	NA	NA	0.078	NA	99.8119	early crystal1 profile

Table L13. Results of EPMA analyses on sulfide minerals in sample GMA13-052

Sample	Fe	S	Cu	In	Zn	Cd	Ga	Hg	Pb	As	Sb	Ag	Au	Mn	Total	Comment
52_C1_ccp1	30.17	34.63	33.93	-	0.959	-	-	-	0.183	-	0.0104	NA	NA	-	99.8825	
52_C1_ccp2	29.44	34.69	33.63	-	2.57	0.0015	0.013	-	0.1406	0.5936	-	NA	NA	-	101.0787	
52_C1_py1	46.37	53.08	0.1781	-	1.96	0.0132	0.0021	0.0017	0.8305	-	0.0096	NA	NA	0.0107	102.4558	
52_C1_py2	44.94	52.67	1.41	-	1.27	0.0188	0.0042	-	0.729	-	-	NA	NA	0.095	101.1369	sperulitic
52_C1_sp1	1.43	33.08	0.162	0.0392	64.82	0.4158	0.2122	-	0.1971	-	0.0109	NA	NA	-	100.3672	earliest?
52_C1_sp2	1.45	32.97	0.1154	-	65.5	0.0524	0.2084	0.0476	0.1538	-	0.0652	NA	NA	0.0131	100.5759	early crystal1 prof
52_C1_sp3	2.07	32.83	0.5836	0.0119	63.77	0.3037	0.2097	-	0.2062	-	0.149	NA	NA	0.0039	100.138	crystla1 prof
52_C1_sp4	0.8514	32.28	0.362	0.0061	63.31	0.0198	0.1928	0.0152	2.45	-	0.1103	NA	NA	0.034	99.6316	crystla1 prof
52_C1_sp5	0.218	31.99	0.1975	-	63.39	0.0283	0.2092	-	3.29	0.3061	0.0223	NA	NA	0.0216	99.673	crystla1 prof
52_C1_sp6	0.2881	31.52	1.86	-	60.99	0.1238	0.1696	0.0338	3.6	-	0.1164	NA	NA	0.0169	98.7187	late crystal1 prof
52_C1_sp7	1.93	33.23	0.2005	-	64.49	0.4336	0.3559	-	0.1799	-	-	NA	NA	0.0151	100.8349	early crystal2 prof dark
52_C1_sp8	1.91	32.92	0.3035	0.0085	64.22	0.1176	0.2473	0.0285	0.1971	-	0.1349	NA	NA	0.0048	100.0921	crystal2 prof dark
52_C1_sp9	0.8765	32.25	0.1811	0.0118	64.45	0.0276	0.2071	0.0304	1.22	-	0.0125	NA	NA	0.024	99.2911	crystal2 prof light
52_C1_sp10	0.591	32.21	0.1212	0.0057	64.3	0.0146	0.2282	-	1.62	-	0.0539	NA	NA	0.0198	99.1645	crystal2 prof light
52_C1_sp11	0.3189	32.12	0.0683	-	63.86	0.0162	0.179	-	2.27	-	0.0069	NA	NA	0.0079	98.8472	crystal2 prof light
52_C1_sp12	0.3418	32.12	0.0714	-	64.15	0.0277	0.2048	-	2.04	-	0.0223	NA	NA	0.0193	98.9974	crysta2 prof dark
52_C1_sp13	0.2479	32	0.2361	0.0118	63.42	0.0411	0.2064	0.0529	2.78	-	0.0321	NA	NA	0.0076	99.0359	crstyal2 prof light
52_C1_sp14	0.2936	31.69	1.07	-	61.98	0.0863	0.2125	-	3.39	-	0.0636	NA	NA	0.0319	98.818	late crystal 2 prof light
52_C1_gn1	0.0169	13.39	0.0977	-	3.29	0.0342	-	-	87.12	-	0.1821	NA	NA	0.0179	104.1488	incl. in sp
52_C1_gn2	0.0205	13.31	0.0759	-	2.76	0.0433	-	0.0917	87.16	-	0.1035	NA	NA	0.0147	103.5796	incl. in sp
52_C1_gn3	0.0012	13.53	0.0706	-	3.18	0.0616	-	0.0056	86.25	0.1038	0.3016	NA	NA	-	103.5043	incl. in sp
52_C2_ccp1	28.27	33.73	32.54	-	1.49	0.0127	0.002	-	0.4526	-	0.0436	NA	NA	0.0021	96.5431	incl. in sp
52_C2_ccp2	29.37	34.48	33.62	-	1.14	0.0166	0.0122	0.0286	0.2549	-	-	NA	NA	0.0267	98.9491	edge of sp
52_C2_ccp3	29.01	34.49	33.36	-	2.27	0.0202	0.0163	-	0.2169	-	0.0419	NA	NA	-	99.4254	edge of sp
52_C2_py1	46.13	53.11	0.2799	-	3.13	0.0018	0.0036	-	0.3463	-	-	NA	NA	-	103.0015	incl. in sp
52_C2_py2	47.07	53.02	0.0698	-	2.34	0.0093	-	-	0.4052	-	0.0182	NA	NA	0.0079	102.9403	incl. in sp
52_C2_py3	46.56	52.9	0.1981	-	2.66	0.0083	0.004	-	0.6366	-	0.0244	NA	NA	-	102.9913	incl. in sp
52_C2_sp1	1.26	32.98	0.3616	0.0056	65.12	0.1966	0.2351	0.0361	0.4807	0.0568	0.0065	NA	NA	0.002	100.741	dendritic interior
52_C2_sp2	1.39	32.98	0.1892	-	65.35	0.0884	0.1995	-	0.1444	-	0.0697	NA	NA	-	100.4111	dendritic rim
52_C2_sp3	2.29	32.97	0.3427	-	63.09	0.4624	0.1823	-	0.3235	-	0.0409	NA	NA	0.0224	99.7243	dendritic
52_C2_sp4	1.04	32.86	0.2147	-	65.44	0.2485	0.2382	-	0.205	-	0.0263	NA	NA	0.0223	100.2949	dendritic
52_C2_sp5	2.09	32.88	0.2693	-	63.56	0.6073	0.2147	-	0.2833	-	0.0401	NA	NA	0.0153	99.9601	dendritic
52_C3_ccp1	27.23	32.31	29.89	-	2	-	0.0111	0.0659	1.29	-	0.036	NA	NA	0.0071	92.8402	incl. in sp
52_C3_ccp2	29.41	34.62	33.6	-	1.2	0.0012	0.0122	-	0.0575	0.1072	0.0148	NA	NA	0.0159	99.0388	incl. in sp
52_C3_ccp3	29.09	34.53	33.31	-	2.1	0.0107	-	-	0.18	-	0.03	NA	NA	0.001	99.2518	incl. in sp
52_C3_ccp4	29.8	34.69	33.81	-	1.87	0.0015	-	0.052	0.1417	-	-	NA	NA	0.0155	100.3807	incl. in sp
52_C3_py1	47.97	53.4	0.406	-	0.6793	0.0021	0.0085	0.0219	0.1958	-	0.0149	NA	NA	0.0094	102.7078	vent lining
52_C3_py2	47.24	52.97	0.5376	-	0.6919	0.0048	-	-	0.217	-	-	NA	NA	0.0145	101.6758	vent lining
52_C3_py3	46.99	52.9	0.1823	-	1.22	-	0.0057	-	0.5857	-	0.0357	NA	NA	0.0438	101.9632	
52_C3_sp1	2.04	33	0.9617	0.0011	62.45	0.0794	0.2295	-	0.4955	0.1873	0.0336	NA	NA	0.0115	99.4896	early crystal1 prof dark
52_C3_sp2	1.38	32.91	0.5232	-	64.23	0.1188	0.2002	-	0.1521	0.0733	0.0656	NA	NA	0.0096	99.6628	crystal1 prof dark
52_C3_sp3	2.6	33.49	0.3889	-	63.1	0.5238	0.2219	-	0.317	-	0.0944	NA	NA	0.0198	100.7557	crystal1 prof dark
52_C3_sp4	1.05	32.98	0.324	-	65.63	0.2513	0.168	-	0.1397	-	-	NA	NA	0.0018	100.5447	crystal2 prof dark
52_C3_sp5	1.7	32.95	0.2289	-	64.47	0.5353	0.1994	-	0.1565	-	0.1215	NA	NA	0.0296	100.3911	crystal2 prof light
52_C3_sp6	1.44	32.87	0.2412	-	65.44	0.1351	0.2281	-	0.1196	-	0.0275	NA	NA	0.0062	100.5077	crystal2 prof light
52_C3_sp7	1.76	32.96	0.3355	-	64.98	0.0149	0.1894	-	0.253	-	0.0579	NA	NA	0.0005	100.5512	
52_C4_ccp1	29.18	34.75	33.37	-	2.84	0.0011	0.0038	-	0.1815	-	0.0184	NA	NA	-	100.3447	incl. in sp
52_C4_ccp2	29.73	34.51	34	-	2.41	0.0337	-	-	0.1004	-	0.0076	NA	NA	0.022	100.8137	gen2
52_C4_ccp3	30.24	34.42	34.22	-	1.4	0.0038	0.0042	-	0.1667	-	-	NA	NA	0.001	100.4557	gen3
52_C4_ccp4	28.4	34.64	33.03	-	4.19	0.0241	0.0003	-	0.1286	-	0.0351	NA	NA	0.008	100.4561	gen4 small incl.
52_C4_ccp5	29.87	34.46	33.6	-	1.67	0.0005	0.0051	-	0.0841	-	0.0036	NA	NA	0.0184	99.7118	gen1
52_C4_ccp6	29.16	35.03	33.44	-	3.23	0.0063	0.0088	0.0771	0.1344	-	0.0204	NA	NA	-	101.107	small incl.
52_C4_ccp7	30.37	34.47	34.2	-	1.61	-	0.0094	-	0.1346	-	0.042	NA	NA	-	100.836	
52_C4_py1	44.53	51.63	0.8348	-	1.95	0.022	0.0051	-	0.9977	-	0.0104	NA	NA	0.0857	100.0657	
52_C4_py2	46.37	52.79	0.5644	-	2.53	0.0119	0.0018	-	0.7183	0.8769	0.0116	NA	NA	0.0235	103.8983	later, incl. in sp
52_C4_py3	46.46	51.7	0.3171	-	2.57	0.014	-	-	0.2797	-	-	NA	NA	-	101.3408	later, incl. in sp
52_C4_py4	47.37	52.34	0.0189	-	0.6765	0.0085	-	-	0.2918	0.5128	0.0104	NA	NA	0.0035	101.2323	early

Table L13. Continued

Sample	Fe	S	Cu	In	Zn	Cd	Ga	Hg	Pb	As	Sb	Ag	Au	Mn	Total	Comment
52_C4_sp1	1.32	31.95	0.1414	-	62.1	0.4114	0.2168	-	1.04	-	0.0515	NA	NA	0.0142	97.2454	early
52_C4_sp2	1.68	32.92	0.1907	0.0047	64.88	0.4856	0.242	0.0208	0.1658	-	-	NA	NA	0.0214	100.6109	early crystal1 prof
52_C4_sp3	1.74	32.75	0.212	-	65.13	0.504	0.271	0.0247	0.0916	-	0.0158	NA	NA	0.0217	100.7607	crystal1 prof
52_C4_sp4	2.08	32.66	0.3411	0.0243	64.01	0.7447	0.2981	-	0.1595	-	0.0247	NA	NA	0.0117	100.354	red gen early crystal2 prof
52_C4_sp5	1.42	32.73	1.03	-	63.6	0.0514	0.2181	0.2124	0.6475	-	0.4983	NA	NA	0.0467	100.4543	crystal2 prof, red
52_C4_sp6	0.1273	31.52	0.4954	-	61.16	0.0465	0.1579	0.0452	4.39	1.44	0.0547	NA	NA	0.0165	99.4536	late crystal2 prof, red
52_C4_sp7	1.24	32.64	0.2036	-	64.95	0.0197	0.1956	-	0.9402	-	0.0255	NA	NA	0.0216	100.2361	early crystal3 prof, medium
52_C4_sp8	1.42	32.62	0.3157	0.049	64.07	0.5193	0.2664	-	0.3532	-	0.0401	NA	NA	0.006	99.6598	crystal3 prof, dark
52_C4_sp9	2.96	33.02	0.6722	-	63	0.4475	0.2198	-	0.1115	-	0.0413	NA	NA	0.02	100.4922	crystal3 prof, dark - ccp incl?
52_C4_sp10	0.5073	32.37	0.2617	0.0044	64.37	0.0342	0.1862	-	1.63	-	0.0603	NA	NA	0.0479	99.4721	crystal3 prof, medium
52_C4_sp11	0.3742	31.74	1.39	-	62.23	0.0803	0.1886	0.0208	2.99	-	0.1049	NA	NA	0.0051	99.1239	crystal3 prof, light
52_C4_sp12	0.3412	31.88	0.8743	0.0086	62.61	0.0777	0.179	0.0283	2.86	-	0.1373	NA	NA	0.0106	99.007	late crystal3 prof, light
52_C4_gn1	0.0393	13.45	0.1161	-	4.2	0.0425	0.0123	0.0028	87.1	-	0.0545	NA	NA	0.001	105.0184	incl. in sp
52_C4_gn2	0.0548	13.35	0.0765	-	3.57	0.0384	-	-	85.42	-	0.288	NA	NA	-	102.7976	incl. in sp
52_C4_gn3	0.0378	13.19	0.0636	-	2.02	0.0361	0.0207	0.0553	86.53	-	0.3378	NA	NA	-	102.2912	incl. in sp
52_C5_ccp1	30	34.38	34.02	-	0.9528	0.0087	0.0058	-	0.2374	-	0.0168	NA	NA	0.0066	99.6281	after sp
52_C5_ccp2	30.03	34.68	33.73	-	1.67	-	0.0045	-	0.1313	-	-	NA	NA	0.0034	100.2492	after py
52_C5_ccp3	28.98	34.61	33.21	-	3.21	0.0093	0.0234	-	0.1846	-	-	NA	NA	0.0365	100.2637	
52_C5_ccp4	29.76	34.55	33.7	-	1.82	0.0067	0.0075	-	0.1579	-	0.004	NA	NA	-	100.006	
52_C5_py1	46.16	53.28	0.0218	-	1.51	0.0101	0.0059	-	1.02	-	0.0042	NA	NA	0.0821	102.094	
52_C5_py2	38.69	49.11	8.35	-	0.9899	0.0038	0.0107	0.0508	3.84	-	0.0166	NA	NA	0.0698	101.1315	sperulitic interior
52_C5_py3	45.99	52.8	1.26	-	1.25	0.0115	-	-	0.8537	-	0.0174	NA	NA	0.0512	102.2337	sperulitic rim
52_C5_sp1	1.24	32.86	0.3317	0.454	64.83	0.6636	0.2519	0.0647	0.1039	0.2597	0.0246	NA	NA	0.0116	101.0956	early
52_C5_sp2	1.32	32.79	0.3711	0.1251	65	0.4178	0.2249	-	0.2605	-	0.0607	NA	NA	-	100.57	early crystal1 prof
52_C5_sp3	1.54	32.96	0.1649	0.0041	65.24	0.2542	0.2304	-	0.1194	-	0.0271	NA	NA	0.0296	100.5696	crystal1 prof
52_C5_sp4	2.72	33.12	0.2224	-	63.86	0.0877	0.202	0.0019	0.1101	-	0.0364	NA	NA	0.0467	100.4071	crystal1 prof
52_C5_sp5	1.46	32.32	0.2877	-	64.14	0.0268	0.1986	-	1.41	-	0.0194	NA	NA	0.0301	99.8927	crystal1 prof
52_C5_sp6	0.4231	32.36	0.1751	0.0042	64.59	0.0339	0.1974	-	1.79	-	0.0774	NA	NA	0.0353	99.6864	crystal1 prof
52_C5_sp7	0.3379	32.23	0.474	-	63.73	0.0524	0.2016	-	2.48	-	0.0433	NA	NA	-	99.5492	late crystal1 prof
52_C5_sp8	3.09	32.96	0.3079	0.0099	63.25	0.1353	0.2365	0.038	0.0759	-	0.0425	NA	NA	0.009	100.155	crystal2 interior
52_C5_sp9	0.1418	31.92	0.3411	-	61.56	0.0263	0.1708	0.0207	3.94	0.9547	0.015	NA	NA	-	99.0905	crystal2 rim
52_C5_sp10	1.85	32.81	0.2089	-	63.78	0.5855	0.3119	-	0.1348	0.1628	0.0518	NA	NA	-	99.8958	
52_C5_sp11	1.49	33.08	0.3151	0.0448	64.33	0.4483	0.4477	-	0.1456	-	0.034	NA	NA	0.0308	100.3662	
52_C5_gn1	0.0213	13.85	0.0725	-	4.98	0.0404	-	0.0482	85.76	2.07	0.2446	NA	NA	0.0069	107.0938	incl. in sp
52_C5_gn2	0.0374	13.12	0.0942	-	1.14	0.037	0.0103	0.0772	86.22	-	0.1643	NA	NA	-	100.9003	c.g. after sp
52_C5_gn3	0.0238	12.97	0.0816	-	1.45	0.0622	0.0234	-	86.82	-	0.1042	NA	NA	0.0183	101.5534	
52_C6_ccp1	30.46	34.73	34.07	-	0.2912	0.0173	0.0131	-	0.1281	-	0.0164	NA	NA	0.0158	99.742	
52_C6_ccp2	29.39	34.51	33.51	-	2.65	0.0052	0.0076	-	0.1432	-	0.0028	NA	NA	0.0055	100.2243	
52_C6_ccp3	30.22	34.48	34	-	1.65	0.0059	0.0036	0.009	0.1048	-	0.0116	NA	NA	-	100.4848	
52_C6_py1	47.65	53.39	0.1055	-	0.1032	0.0106	-	0.0438	0.4483	-	0.0211	NA	NA	0.0354	101.8079	
52_C6_py2	46.99	53.3	0.5521	-	2.13	0.0234	0.016	-	0.181	0.453	-	NA	NA	0.0021	103.6475	
52_C6_sp1	1.64	32.66	0.3492	0.0053	63.88	0.4797	0.3991	0.0152	0.1333	-	0.0502	NA	NA	0.0013	99.6133	
52_C6_sp2	2.35	32.91	0.4023	0.0397	63.97	0.5166	0.4309	-	0.1332	-	0.0283	NA	NA	-	100.7809	
52_C6_sp3	1.85	33.11	0.0877	-	64.62	0.5819	0.2527	-	0.155	-	0.0518	NA	NA	0.0063	100.7154	
52_C6_sp4	1.04	33.13	0.0326	0.005	64.52	0.1256	0.2132	-	0.197	-	0.0503	NA	NA	0.0323	99.3461	
52_C6_sp5	1.41	32.68	0.2762	0.0509	64.07	0.4592	0.3933	0.0153	0.1769	-	0.0121	NA	NA	-	99.544	
52_C6_gn1	-	13.09	0.0172	-	0.7	0.0546	0.0011	-	86.24	-	0.0533	NA	NA	0.0116	100.1677	c.g., late after sp
52_C6_gn2	0.0243	13.23	0.0687	-	1.53	0.0423	0.0012	-	86.64	-	0.2152	NA	NA	-	101.7516	c.g., late after sp
52_C7_ccp1	29.53	34.43	33.43	-	0.4145	0.0047	0.0159	-	0.1476	0.9645	0.0152	NA	NA	0.0006	98.953	late after brt?
52_C7_ccp2	29.44	34.26	33.55	-	0.379	0.0107	0.0137	-	0.2047	-	0.012	NA	NA	0.0085	97.8786	late after brt?
52_C7_sp1	1.71	31.65	0.3261	-	61.33	0.0263	0.21	0.1589	1.29	-	0.0947	NA	NA	0.0162	96.8123	late after brt?
52_C7_sp2	1.57	32.61	0.2878	0.0129	62.62	0.0749	0.1839	0.0076	0.6191	-	0.0268	NA	NA	0.0064	98.0195	late after brt?
52_C7_gn1	0.0213	13.1	0.0442	-	1.85	0.0535	0.0248	-	86.96	-	0.0016	NA	NA	-	102.0553	c.g., late after sp
52_C7_gn2	-	13.1	0.0429	-	0.2277	0.0498	0.0249	-	86.43	-	0.0221	NA	NA	-	99.8975	c.g., late after sp
52_C7_gn3	0.1135	13.28	0.0496	-	1.94	0.0512	0.0116	-	86.92	0.4874	0.0072	NA	NA	0.0294	102.8898	c.g., late after sp
52_C8_ccp1	29.48	34.36	33.91	-	2.57	0.0038	0.0127	-	0.1594	-	0.0283	NA	NA	-	100.5241	incl. in sp
52_C8_ccp2	29.7	34.53	33.93	-	0.4555	-	0.0108	0.0214	0.2548	-	0.0292	NA	NA	-	98.9317	incl. in sp
52_C8_ccp3	29.18	34.44	33.66	-	2.83	0.0179	0.0182	-	0.2201	0.0741	-	NA	NA	-	100.4402	incl. in sp
52_C8_ccp4	28.45	33.91	32.83	-	4.29	0.0406	0.02	-	0.176	-	0.0036	NA	NA	-	99.7203	incl. in sp
52_C8_py1	41.9	49.16	4.73	-	3.99	0.0336	0.0116	0.0171	0.2633	-	0.0235	NA	NA	0.0029	100.1319	incl. in sp

Table L13. Continued

Sample	Fe	S	Cu	In	Zn	Cd	Ga	Hg	Pb	As	Sb	Ag	Au	Mn	Total	Comment
52_C8_py2	44.6	52.6	1.36	-	3.73	0.0107	0.0109	0.0051	0.4074	-	-	NA	NA	0.011	102.735	incl. in sp
52_C8_sp1	1.33	32.76	0.0727	-	65.21	0.5901	0.2728	0.0019	0.2048	-	0.015	NA	NA	0.0009	100.4582	crystal1 interior, dark
52_C8_sp2	3.57	32.56	0.9568	-	61.84	0.1216	0.1802	0.1041	0.4267	-	0.1709	NA	NA	-	99.9304	crystal1 rim, light
52_C8_sp3	1.77	32.55	0.1268	-	64.58	0.8162	0.1919	-	0.2354	-	0.0449	NA	NA	0.0132	100.3283	crystal2 interior, dark
52_C8_sp4	0.6643	32.31	1.62	-	63.41	0.1111	0.1913	-	1.53	-	0.1481	NA	NA	0.0042	99.9891	crystal2 rim, light
52_C8_sp5	3.13	32.49	1.4	-	61.19	0.151	0.2038	0.0834	0.5072	0.3494	0.3151	NA	NA	-	99.82	crystal3 rim, light
52_C8_sp6	1.1	32.44	1.64	0.0085	62.65	0.1451	0.1845	0.072	1.15	-	0.2145	NA	NA	0.019	99.6236	crystal3 rim, dark
52_C8_sp7	1.24	32.69	0.23	0.0069	64.78	0.4622	0.2498	0.0362	0.152	-	0.0898	NA	NA	-	99.937	crystal3 interior, dark
52_C8_sp8	6.07	32.89	5.61	-	53.53	0.4997	0.2335	0.0169	0.3179	-	0.0517	NA	NA	0.0163	99.236	
52_C8_sp9	1.46	32.84	0.2461	-	64.38	0.4062	0.2717	-	0.1504	-	0.0153	NA	NA	0.0017	99.7714	
52_C8_sp10	1.59	32.58	0.2247	-	64.19	0.4262	0.3202	-	0.3578	-	0.0517	NA	NA	0.0119	99.7526	
52_C8_sp11	2.01	32.89	0.1424	-	63.94	0.5461	0.2373	-	0.1332	-	-	NA	NA	0.0175	99.9166	
52_C9_ccp1	30.65	34.54	34.29	-	0.3053	-	0.0017	0.0161	0.193	-	-	NA	NA	-	99.9961	intergrown w sp, mrc
52_C9_ccp2	30.77	34.35	34.52	-	0.0645	0.0089	0.0164	-	0.084	-	0.0131	NA	NA	-	99.827	intergrown w sp, mrc
52_C9_ccp3	30.35	34.52	34.21	-	0.2132	0.0046	0.0044	-	0.1737	-	0.0283	NA	NA	-	99.5043	intergrown w sp, mrc
52_C9_mrc1	47.5	52.16	0.0506	-	0.0731	0.0054	-	-	0.5903	0.1965	-	NA	NA	-	100.5759	intergrown w sp, ccp
52_C9_mrc2	45.18	51.85	0.3672	-	0.5511	-	0.0006	-	1.23	0.8855	0.0066	NA	NA	0.1327	100.2036	intergrown w sp, ccp
52_C9_mrc3	48	53.11	0.8021	-	0.2043	0.0081	0.002	-	0.1676	-	0.0145	NA	NA	0.0036	102.3122	intergrown w sp, ccp
52_C9_mrc4	47.74	52.57	0.0835	-	0.0515	0.0129	0.0052	0.0168	0.1561	-	0.0285	NA	NA	-	100.6645	intergrown w sp, ccp
52_C9_mrc6	46.14	51.77	1.37	-	0.3376	0.0091	0.0029	-	0.4055	-	0.0174	NA	NA	0.0093	100.0618	after py
52_C9_mrc7	46.69	50.57	0.8677	-	0.3458	0.0113	-	-	0.2962	0.4524	0.0206	NA	NA	-	99.2541	intergrown w sp, ccp
52_C9_py5	45.79	53.09	1.04	-	0.3438	0.0091	0.017	0.0253	0.6313	-	0.0016	NA	NA	0.1019	101.05	early colloform
52_C9_sp1	1.77	32.82	0.1459	-	63.92	0.5161	0.2384	-	0.158	0.2763	0.0215	NA	NA	0.0156	99.8818	intergrown w ccp, mrc
52_C9_sp2	2.1	32.88	0.3713	0.0195	63.99	0.428	0.3249	-	0.1672	-	0.0117	NA	NA	0.0039	100.2965	intergrown w ccp, mrc
52_C9_sp3	2.52	32.78	0.5382	-	63.02	0.3655	0.2691	-	0.195	-	0.0186	NA	NA	-	99.7065	intergrown w ccp, mrc
52_C9_sp4	2.75	33.08	0.7185	0.0021	62.48	0.0602	0.175	-	0.1331	-	0.019	NA	NA	0.0213	99.4393	intergrown w ccp, mrc
52_C10_ccp1	28.03	34.37	32.4	-	4.57	0.0752	0.0478	0.0072	0.2541	-	0.0403	NA	NA	0.0082	99.8029	gen1, incl. in sp.
52_C10_ccp2	22.21	33.97	26.44	-	14.1	0.2601	0.0369	-	0.186	-	0.0513	NA	NA	0.0052	97.2596	gen2, incl. in sp
52_C10_ccp3	28.99	34.61	33.58	-	3.25	0.009	0.0029	-	0.1182	-	-	NA	NA	-	100.5601	incl. in sp
52_C10_mrc1	46.91	52.03	0.5433	-	0.9361	0.0069	-	0.005	0.3464	-	0.0136	NA	NA	-	100.7912	incl. in sp
52_C10_mrc2	46.15	53.15	0.4137	-	2.28	0.0164	-	-	0.7116	-	0.029	NA	NA	0.012	102.7626	incl. in sp
52_C10_sp1	2.38	32.54	0.492	-	63.53	0.7842	0.2122	-	0.2151	-	0.0796	NA	NA	0.017	100.25	early crystal1 prof, ccp incl.
52_C10_sp2	2.72	32.55	0.6131	-	62.86	0.744	0.2163	-	0.2118	-	0.1826	NA	NA	0.0363	100.134	crystal1 prof
52_C10_sp3	1.77	32.7	0.4789	-	64.62	0.2788	0.1848	0.0494	0.3178	-	0.0622	NA	NA	0.041	100.5029	crystal1 prof
52_C10_sp4	0.8806	32.76	0.2003	-	65.37	0.1752	0.1721	-	0.1723	-	0.1104	NA	NA	0.0105	99.8515	late crystal1 prof
52_C10_sp5	3.15	32.98	0.7802	0.001	62.4	0.3129	0.205	0.0436	0.4084	0.6581	0.0335	NA	NA	0.0269	100.9995	early crystal2 prof, ccp incl.
52_C10_sp6	2.48	32.83	0.4344	-	63.7	0.4733	0.2105	0.0171	0.2508	-	0.074	NA	NA	0.0159	100.4859	crystal2 prof
52_C10_sp7	2.93	32.84	0.414	0.0134	63.16	0.6366	0.1859	0.0834	0.1902	-	0.0327	NA	NA	0.025	100.5111	crystal2 prof
52_C10_sp8	2.04	33.19	0.1695	-	63.86	0.3461	0.185	-	0.2491	-	0.1044	NA	NA	0.0257	100.1697	late crystal2 proc
52_C10_sp9	3.08	32.68	0.9398	-	62.2	0.715	0.2192	0.0322	0.2427	-	0.0966	NA	NA	0.0263	100.2317	early crystal3 prof, ccp incl.
52_C10_sp10	3.48	32.63	1.2	0.0033	61.29	0.9049	0.2887	-	0.1837	-	0.0796	NA	NA	-	100.0601	crystal3 prof
52_C10_sp11	11.03	33.23	12.42	-	39.89	0.5946	0.1509	0.0464	0.0821	-	0.0303	NA	NA	0.0036	97.478	crystal3 prof
52_C10_sp12	2.81	32.77	0.3678	-	63.01	0.7167	0.2243	-	0.2273	-	0.0566	NA	NA	0.0319	100.2145	crystal3 prof
52_C10_sp13	1.55	32.59	0.5795	-	64.21	0.1028	0.2252	-	0.138	-	0.0255	NA	NA	-	99.421	crystal3 prof
52_C10_sp14	0.9099	32.25	0.859	-	63.91	0.1157	0.1939	-	1.13	-	0.0352	NA	NA	-	99.4038	late crystal3 prof, bright
52_C11_ccp1	29.74	34.54	34.02	-	1.7	0.0161	0.0066	-	0.1624	-	-	NA	NA	0.0103	100.1953	incl. in sp
52_C11_mrc1	47.11	53.02	0.2539	-	1.85	0.0169	-	-	0.4562	0.9291	-	NA	NA	0.0275	103.6635	incl. in sp
52_C11_mrc2	47.51	51.54	0.143	-	0.1774	0.0019	-	-	0.2754	1.33	0.0198	NA	NA	-	100.9974	
52_C11_mrc3	47.42	52.51	0.0016	-	0.0892	0.0092	-	-	0.6556	0.5805	0.0174	NA	NA	-	101.2834	crystal1 interior
52_C11_mrc4	46.72	53.16	0.0251	-	0.154	0.0192	-	0.0319	0.2261	-	0.01	NA	NA	0.0299	100.3762	crystal1 rim
52_C11_mrc5	42.54	51.01	0.2376	-	5.14	0.0193	0.0101	0.0034	1.81	-	0.0133	NA	NA	0.0687	100.8524	crystal2 interior
52_C11_mrc6	45.23	51.03	0.0812	-	0.2498	0.003	-	-	0.7829	0.128	0.0427	NA	NA	0.0083	97.5559	crystal2 rim
52_C11_mrc7	7.97	35.92	0.5777	-	56.22	0.0616	0.217	0.0392	0.7764	0.2369	0.03	NA	NA	0.0295	102.0782	crystal3 interior, bright
52_C11_mrc8	47.64	52.49	0.2499	-	0.0272	0.0134	-	-	0.2375	-	0.0277	NA	NA	0.0046	100.6903	early crystal4 prof
52_C11_mrc9	45.58	51.31	-	-	0.0387	0.0059	-	-	2.88	1.57	0.0286	NA	NA	-	101.4131	crystal4 prof
52_C11_mrc10	47.23	53.17	0.03	-	0.0444	-	-	0.0302	0.3508	-	0.0066	NA	NA	-	100.8619	late crystal4 prof
52_C11_mrc11	47.84	52.59	0.0287	-	0.0739	0.0097	-	0.0219	0.5788	0.2903	0.0112	NA	NA	-	101.4444	earliest
52_C11_sp1	0.9764	32.63	0.1911	0.0095	65.32	0.6076	0.253	-	0.1629	-	0.0061	NA	NA	0.0149	100.1715	crystal1 interior
52_C11_sp2	2.69	33.08	0.2443	0.0066	63.09	0.1014	0.1918	-	0.1161	-	0.0158	NA	NA	0.0346	99.5707	crystal1 rim

Table L14. Results of EPMA analyses on sulfide minerals in sample GMA13-058

Sample	Fe	S	Cu	In	Zn	Cd	Ga	Hg	Pb	As	Sb	Ag	Au	Mn	Total	Comment
58_C1_py1	45.43	53.7	0.0024	-	0.1753	0.0036	-	-	1.31	1.11	-	0.0432	-	-	101.7745	spherulitic
58_C1_py2	45.54	53.66	0.0335	-	0.1348	0.0249	-	0.0137	1.04	-	-	0.0094	-	-	100.4563	spherulitic
58_C2_mrc1	46.91	53.64	0.367	-	0.1077	0.0174	0.0058	0.0377	0.6727	0.2821	0.0353	0.0373	0.0311	-	102.144	early, intergrown w sp
58_C2_mrc2	45.4	52.84	-	-	0.3168	0.0082	-	-	1.69	0.0084	0.0279	0	0.0327	-	100.324	
58_C2_mrc3	46.12	53	0.7925	-	0.1216	0.0173	0.0011	-	1.08	-	0.0574	0.104	0.1295	-	101.4233	late, intergrown w sp
58_C2_sp1	1.44	33.02	0.7554	-	62.87	0.3474	0.2355	-	0.8503	0.3322	0.5481	0.1594	0.2445	-	100.8027	early, intergrown w mrc
58_C2_sp2	0.4498	33.14	0.3645	0.0141	64.7	0.3602	0.2397	0.0773	0.4154	-	0.2363	0.0787	0.2696	-	100.3455	
58_C2_sp3	1.93	32.01	1.71	-	58.41	0.5795	0.1783	0.1933	3.54	-	0.8924	0.3268	0.2247	-	99.995	late, intergrown w sp
58_C3_ccp1	29.55	34.69	33.69	-	0.1535	0.0093	0.0107	-	0.1027	-	0.0044	0.0122	0.0158	-	98.2387	
58_C3_mrc1	46.59	53.1	-	-	0.5439	0.0144	0.0022	-	0.1414	-	-	0.0107	-	-	100.4025	after sp
58_C3_sp1	0.0402	31.86	0.5433	0.0129	61.11	0.1913	0.1517	0.0381	3.92	0.3205	0.2386	0.15	0.1853	-	98.762	latest after brt, crystal1 interior
58_C3_sp2	0.0444	31.57	0.1505	0.0112	60.82	0.1022	0.143	0.0305	4.5	-	0.117	0.0517	0.1047	-	97.6452	crystal1 rim
58_C3_sp3	0.1786	32.22	0.0949	0.0105	61.5	0.0734	0.1937	0.0842	3.36	-	0.0703	0.0212	-	-	97.8069	crystal2 rim
58_C3_sp4	0.1413	32.83	0.2172	0.0081	63.83	0.0403	0.1764	0.0983	1.39	-	0.0243	0.0611	0.0174	-	98.8344	crystal2 interior
58_C3_jd1	-	14.1	0.0705	-	4.92	0.054	0.0082	0.0116	85.77	1.71	0.4801	0.0784	0.0885	-	107.2912	early incl. in sp
58_C3_jd2	0.0302	14.33	0.0745	-	3.4	0.0366	-	0.0703	83.81	1.77	0.2659	0.0432	-	-	103.8306	late, incl. in sp
58_C3_jd3	-	13.91	0.0662	-	3.68	0.0673	-	-	85.29	0.469	0.1688	0.0346	0.057	-	103.7429	late, incl. in sp
58_C3_jd4	-	13.94	0.1067	-	4.65	0.0462	-	-	84.94	-	1.05	0.3901	-	-	105.1229	early, incl. in sp
58_C3_jd5	0.0051	13.97	0.1441	-	4.69	0.0633	0.0124	-	84.58	-	0.7454	0.2896	-	-	104.4998	late, incl. in sp
58_C4_mrc1	47.09	53.42	0.0032	-	0.4307	0.0115	-	-	0.4056	-	0.0498	0.0105	0.1991	-	101.6203	
58_C4_mrc2	46.86	53.26	0.2198	-	0.1606	0.0089	-	-	0.437	-	0.0066	0.0085	0.1097	-	101.071	early before sp
58_C4_mrc3	46.41	53.06	0.124	-	0.8885	0.0213	0.0098	-	0.7548	-	0.0216	0.0195	-	-	101.3094	
58_C4_sp1	0.6905	32.88	1.41	-	62.49	0.4429	0.2314	0.0653	1.2	-	0.8168	0.1685	0.2388	-	100.6342	crystal1 interior, replacing mrc
58_C4_sp2	1.16	32.81	1.13	-	62.5	0.3327	0.2276	0.0616	0.8418	-	0.7304	0.1697	0.1716	-	100.1353	crystal1 rim
58_C4_sp3	1.05	33.1	1.02	-	62.72	0.578	0.2298	0.2849	0.5724	-	0.6858	0.1423	-	-	100.3831	early, replacing mrc
58_C4_sp4	0.7064	32.89	0.7193	-	63.8	0.2099	0.1357	0.0096	1.46	-	0.3504	0.2266	0.1714	-	100.6792	latest after brt
58_C4_sp5	0.2142	32.56	0.3733	-	63.14	0.1748	0.2058	-	2.82	-	0.2039	0.1343	0.05	-	99.8764	
58_C4_gn1	0.0791	15.51	0.1924	-	11.27	0.0653	0.037	-	78.38	-	0.7076	0.0405	0.1232	-	106.405	incl. in sp
58_C4_gn2	0.2011	21.34	0.5917	-	27.89	0.1878	0.0638	0.0785	44.63	-	0.7642	0.1312	-	-	95.8783	incl. in sp
58_C4_gn3	-	13.54	0.0355	-	2.47	0.0523	0.0175	-	86.78	-	0.5448	0.058	-	-	103.498	incl. in sp
58_C4_gn4	0.0088	13.58	0.0645	-	2.17	0.0322	0.0329	-	86.25	-	0.7705	0.1143	-	-	103.0231	incl. in sp
58_C5_mrc1	46.57	53.33	0.823	-	0.1826	0.0175	-	0.0017	0.2109	-	-	0.0218	-	-	101.1574	
58_C5_mrc2	46.75	53.26	0.8517	-	0.0123	0.0145	-	-	0.2571	0.2567	0.0124	0.0453	-	-	101.4599	
58_C5_sp1	0.7887	32.89	1.19	-	62.46	0.5351	0.2007	0.1249	0.9535	-	0.7945	0.1427	0.2217	-	100.3018	replacing mrc
58_C5_sp2	0.8401	33.06	0.5451	-	64.33	0.3315	0.2186	0.027	0.4892	-	0.3056	0.0927	0.0783	-	100.318	replacing mrc
58_C5_sp3	0.6391	32.33	0.8768	-	61.41	0.5642	0.2106	0.1152	1.2	-	0.6154	0.126	0.4116	-	98.499	replacing mrc
58_C5_gn1	0.0412	13.26	0.0224	-	0.0902	0.0568	0.0278	0.0139	87.09	-	0.1864	-	-	-	100.7886	c.g. after sp
58_C5_gn2	-	13.28	0.0208	-	0.1927	0.0635	-	-	87.67	-	0.154	-	-	-	101.3809	c.g. after sp
58_C5_gn3	0.0986	13.58	0.0163	-	1.01	0.0564	0.0208	0.0127	87.25	-	0.3872	-	0.3753	-	102.8073	early, after marc?
58_C5_gn4	-	13.29	-	-	0.2069	0.0378	0.0239	0.0182	87.42	-	0.2341	-	-	-	101.2308	c.g. after sp
58_C6_py1	42.31	53.43	5.7	-	0.1451	-	0.0029	-	0.3147	0.2645	0.0075	0.0296	0.0183	-	102.2226	
58_C6_mrc2	47.58	53.9	0.0441	-	0.1028	0.0003	0.0005	-	0.2451	-	0.0573	0.0065	-	-	101.9365	interior crystal1
58_C6_mrc3	46.11	52.53	0.3465	-	0.1821	0.0028	-	-	0.746	-	0.0374	0.084	-	-	100.0387	rim crystal1
58_C6_sp1	0.9824	32.97	0.6805	0.0038	63.37	0.1819	0.1922	-	1.42	0.0323	0.3379	0.2114	0.2131	-	100.5954	vent lining? replacing mrc
58_C6_sp2	0.7971	32.42	2.29	-	60.41	0.5002	0.2348	0.0804	2.48	0.6744	1.02	0.2595	0.2201	-	101.3864	replacing mrc
58_C6_jd1	0.2952	13.89	0.196	-	4.57	0.0616	-	0.0415	86.75	-	1.33	0.216	0.1729	-	107.5231	
58_C6_jd2	0.2386	19.2	0.6837	-	22.14	0.1778	0.0647	-	63.78	-	1.05	0.155	0.1843	-	107.674	
58_C7_py1	44.86	53.16	1.53	-	0.7989	0.0013	-	-	1.12	0.3835	0.054	0.0876	-	-	101.9952	
58_C7_sp1	0.437	32.76	1.99	-	61.52	0.967	0.2245	0.3832	0.9225	-	1.3	0.1687	0.3038	-	100.9767	crystal1 interior
58_C7_sp2	0.4198	33.11	0.6869	-	63.36	0.1579	0.2155	0.0327	1.76	-	0.2193	0.1576	0.1194	-	100.239	crystlal1 rim
58_C7_sp3	0.0793	32.49	0.3088	0.004	62.25	0.1683	0.1925	-	3.62	-	0.1627	0.0968	0.2321	-	99.6046	crystal2 rim
58_C7_gn1	0.0163	13.78	0.051	-	1.67	0.0324	-	-	85.48	-	0.7508	0.074	-	-	101.8545	gen3, incl. in sp
58_C7_gn2	-	13.54	0.0585	-	3.11	0.052	-	-	86.83	-	0.1045	-	-	-	103.6949	gen3, incl. in sp
58_C7_gn3	-	13.8	0.0408	-	1.71	0.0425	0.0073	-	86.85	1.5	0.2712	0.0349	0.0258	-	104.2824	gen2, incl. in sp
58_C7_gn4	0.0304	13.64	0.055	-	2.6	0.0274	0.0358	-	87.9	-	0.5084	0.0247	0.2198	-	105.0415	gen1 incl in sp
58_C7_gn5	-	13.66	0.091	-	4.35	0.0405	-	0.0754	87.42	-	0.6502	0.0088	-	-	106.2958	incl. in sp
58_C7_gn6	0.065	13.66	0.0516	0.0056	3.82	0.0378	0.0096	0.0326	86.63	-	0.6011	-	-	-	104.9132	incl. in sp
58_C8_mrc1	46.77	53.35	0.4646	-	0.0516	0.0078	0.0166	-	0.5953	-	0.0316	0.0582	0.0585	-	101.4041	crystal1 rim
58_C8_mrc2	47.16	53.48	0.5328	-	0.2007	0.0115	-	-	0.1359	0.7688	0.0133	0.0244	0.0731	-	102.4004	crystal1 interior
58_C8_mrc3	47.09	53.44	0.0992	-	0.5027	-	-	-	0.3423	0.1538	0.0116	0.0224	0.2191	-	101.881	crystal1 interior

Table L14. Continued

Sample	Fe	S	Cu	In	Zn	Cd	Ga	Hg	Pb	As	Sb	Ag	Au	Mn	Total	Comment
58_C8_mrc4	46.9	54.02	0.0758	-	2.29	0.007	-	-	0.1404	0.1369	0.0472	0.0032	-	-	103.6205	
58_C8_sp1	0.4708	33.03	0.8415	-	63.33	2.01	0.2159	0.3801	0.4469	-	0.4249	0.0274	0.2612	-	101.4386	replacing mrc
58_C8_sp2	0.8621	32.92	1.14	-	63.53	0.5882	0.288	0.1348	0.6136	-	0.7322	0.1137	0.2217	-	101.1443	replacing mrc
58_C8_sp3	1.16	33.32	1.08	-	63.6	0.3929	0.2628	0.0481	0.5039	-	0.7844	0.1405	0.0331	-	101.3257	replacing mrc
58_C8_sp4	0.6905	33.02	0.7949	-	63.92	1.14	0.2587	0.3464	0.5835	-	0.4047	0.0811	0.0035	-	101.2432	replacing mrc
58_C8_sp5	2.75	33.24	0.4223	-	61.35	0.3577	0.2008	0.197	1.65	-	0.2803	0.1067	0.3288	-	100.8835	replacing mrc
58_C8_gn1	1.91	15.13	0.2714	-	4.79	0.0443	-	0.0359	83.33	-	0.8715	0.1941	0.1987	-	106.7758	incl. in sp
58_C9_mrc1	47.7	53.84	0.0474	-	0.2725	0.0231	0.0051	-	0.1401	0.2737	-	-	0.19	-	102.4918	
58_C9_mrc2	46.04	53.9	1.74	-	0.108	0.0144	-	-	0.1803	-	-	0.0496	-	-	102.0322	
58_C9_sp1	0.424	33.33	1.06	0.0063	64.27	0.3234	0.1874	0.0385	0.7408	-	0.4183	0.1211	0.1959	-	101.1156	replacing mrc, crystal1 interior
58_C9_sp2	0.4228	33.12	0.4521	-	64.41	0.2076	0.1677	0.0925	1.05	-	0.2071	0.1546	0.3208	-	100.6052	replacing mrc, crystal1 rim
58_C9_sp3	2.09	33.26	0.1198	-	64.01	0.1151	0.2003	-	0.3637	-	0.0429	0.0363	0.0314	-	100.2694	replacing mrc
58_C9_sp4	2.77	32.48	1.88	-	58.78	0.6354	0.2099	0.294	1.69	-	0.8135	0.1986	-	-	99.7514	replacing mrc, mixed w mrc
58_C9_sp5	0.5407	32.95	0.8748	-	64.45	0.2945	0.1951	-	0.7114	-	0.3536	0.1175	0.1632	-	100.6507	replacing mrc
58_C9_sp6	2.34	33.44	0.1444	0.0178	63.58	0.1659	0.2091	-	0.246	-	0.0473	0.0308	0.1759	-	100.3972	replacing mrc
58_C9_sp7	1.25	32.96	0.5961	-	63.03	0.2049	0.1924	0.1056	1.29	-	0.3195	0.1417	0.1627	-	100.2528	replacing mrc, crystal2 rim
58_C9_sp8	0.8486	32.34	3.48	0.0056	58.57	1.06	0.2555	0.2461	1.14	-	2.14	0.2904	0.2733	-	100.6494	replacing mrc, crystal2 interior
58_C9_sp9	0.8918	32.04	1.77	-	59.47	0.4039	0.1751	0.021	4.11	-	0.5306	0.337	0.0017	-	99.7512	
58_C9_gn1	0.0135	13.59	-	-	2.44	0.0627	-	-	88.02	-	0.1349	-	0.087	-	104.348	incl. in sp
58_C9_gn2	0.0994	13.84	0.0603	-	6.46	0.0387	0.0088	-	87.79	-	0.6661	-	0.1167	-	109.0799	incl. in sp
58_C9_gn3	0.0421	13.67	0.0404	-	4.3	0.049	0.0015	0.132	88.51	-	0.2691	-	0.4187	-	107.4327	incl. in sp
58_C10_ccp1	29.03	34.96	34.59	-	0.9959	0.0067	-	-	0.2071	0.4192	0.5522	0.0254	-	-	100.7864	incl. in sp
58_C10_ccp2	28.7	34.97	34.75	-	0.9461	0.0157	0.0098	-	0.2731	-	0.7368	0.0587	0.0124	-	100.4726	incl. in sp, c.g.
58_C10_ccp3	29.28	34.81	34.05	-	1.99	0.022	-	-	0.1527	-	0.2697	0.0288	0.1951	-	100.7983	incl. in sp
58_C10_ccp4	29.64	35.16	33.92	-	1.74	0.0108	0.0076	0.0345	0.0166	-	0.1555	0.01	-	-	100.695	incl. in sp
58_C10_mrc1	45.79	53.31	0.5132	-	1.16	0.001	-	-	0.4413	-	0.0605	0.1097	-	-	101.3857	
58_C10_mrc2	47.64	53.61	0.0371	-	0.4009	0.0088	-	-	0.1385	0.1368	0.017	0.0205	-	-	102.0095	
58_C10_mrc3	46.97	53.51	0.6685	-	0.1159	0.0049	-	-	0.248	-	0.0447	0.0765	0.042	-	101.6804	
58_C10_mrc4	47.37	53.89	0.4091	-	0.0449	-	-	-	0.2564	-	0.0141	0.0149	-	-	101.9993	
58_C10_mrc5	44.1	53.63	3.11	-	0.2232	0.0132	0.0096	0.012	0.3723	-	0.0195	0.1256	-	-	101.6153	
58_C10_sp1	0.5095	32.54	2.55	-	60.69	0.8719	0.2631	0.2278	1.01	-	1.64	0.2563	0.0775	-	100.6361	replacing mrc
58_C10_sp2	0.6213	32.38	0.9141	-	62.36	0.2604	0.2092	0.023	2.86	-	0.2935	0.2408	0.4452	-	100.6074	replacing mrc
58_C10_sp3	2.02	32.58	1.73	0.0008	59.75	0.5219	0.2317	0.1735	1.97	-	0.7884	0.1916	0.1999	-	100.1577	replacing mrc
58_C10_sp4	0.6761	31.97	2.36	-	59.55	0.5964	0.1752	-	3.49	-	0.7557	0.3148	0.1455	-	100.0336	replacing mrc, gn incl.
58_C10_sp5	0.5281	32.76	2.83	-	60.27	1.1	0.2584	0.2334	1.08	0.1367	1.55	0.2248	-	-	100.9714	early crystal1 prof, dend, dark
58_C10_sp6	0.3953	32.76	1.47	-	62.9	0.4782	0.2203	-	1.87	0.0807	0.4103	0.2684	0.4051	-	101.2583	crystal1 profile, dendritic
58_C10_sp7	0.4115	32.79	1.85	0.0053	62.55	0.5725	0.2116	0.0057	1.8	-	0.5709	0.2525	0.4461	-	101.466	crystal1 profile, dendritic
58_C10_sp8	0.6234	32.47	1.89	-	61.92	0.6646	0.2386	0.0135	1.77	-	0.6007	0.2344	0.1999	-	100.625	crystal1 profile, dendritic
58_C10_sp9	0.3124	32.5	2.27	-	61.55	0.7677	0.1556	0.0745	2.09	-	0.6916	0.2503	0.1703	-	100.8323	crystal1 profile, dendritic
58_C10_sp10	0.7593	32.51	1.75	0.0059	62.43	0.5539	0.2116	0.0883	1.58	-	0.5619	0.2211	0.1069	-	100.7788	crystal1 profile, dendritic
58_C10_sp11	0.235	32.35	1.93	0.0015	62.34	0.5121	0.2018	0.0057	2.74	0.3771	0.3964	0.3111	0.2903	-	101.6909	crystal1 profile, dendritic
58_C10_sp12	0.1839	32.37	1.87	-	61.77	0.531	0.163	-	2.82	-	0.4419	0.3378	0.153	-	100.6405	crystal1 profile, dendritic
58_C10_spy13	0.1244	32.55	0.6994	0.0033	63.5	0.237	0.2068	0.0172	2.21	0.2813	0.2091	0.1499	0.3393	-	100.5277	late crystal 1 prof, dend, light
58_C11_ccp1	28.19	34.72	35.18	-	0.8993	0.004	0.0039	0.0073	0.0589	-	1.11	0.0488	-	-	100.2221	c.g., incl. in sph
58_C11_ccp2	27.52	34.75	35.24	-	1.23	0.0105	-	0.0145	0.1361	0.6633	1.4	0.0349	-	-	100.9992	c.g., incl. in sph
58_C11_mrc1	45.9	53.3	1.51	-	0.0738	0.0111	-	0.0017	0.3834	-	0.0133	0.0714	-	-	101.2646	
58_C11_mrc2	46.44	53.83	1.01	-	0.3247	0.0184	-	0.0102	0.4123	-	-	0.1038	0.1167	-	102.2661	
58_C11_mrc3	46.66	53.54	0.8404	-	0.3793	0.0079	-	0.0308	0.7725	0.0343	0.0415	0.0876	0.0219	-	102.4161	
58_C11_mrc4	46.31	53.95	0.8541	-	1.08	0.0199	0.0005	-	0.2366	-	0.0099	0.088	-	-	102.549	
58_C11_sp1	2.57	33.23	1.15	-	61.3	0.4199	0.2001	0.0364	0.9684	-	0.4644	0.1349	0.3171	-	100.7912	gen1
58_C11_sp2	1.05	32.12	2.41	-	58.96	0.6298	0.1822	0.1006	3.52	0.4235	0.813	0.3264	0.1095	-	100.6449	gen1 incl. of gn
58_C11_sp3	0.9151	32.46	1.96	-	60.64	0.4857	0.2185	0.0457	2.89	-	0.7048	0.3132	0.2833	-	100.9163	gen1, incl. in mrc
58_C11_sp4	0.7992	32.81	1.89	-	61.03	0.4224	0.1969	0.0401	2.43	-	0.6361	0.3569	0.0586	-	100.6702	gen1
58_C11_sp5	0.6562	32.17	2.2	-	60.09	0.5522	0.1931	0.0209	3.45	-	0.677	0.3489	0.1027	-	100.4609	gen2
58_C11_sp6	1.2	32.78	1.54	-	62.1	0.5917	0.194	-	0.9192	-	0.5062	0.179	0.4701	-	100.4801	gen3 early crystal1 prof, dark
58_C11_sp7	0.3156	32.6	2.08	0.0024	61.65	0.6669	0.1902	-	2.04	0.1687	0.7041	0.2473	0.3836	-	101.0488	gen3 crystal1 prof
58_C11_sp8	0.7104	32.66	1.07	-	62.66	0.4423	0.1611	-	1.39	-	0.3041	0.2505	-	-	99.6485	gen3 crystal1 prof
58_C11_sp9	0.3959	32.66	1.54	-	61.88	0.5287	0.2471	0.0076	2.27	0.514	0.4302	0.2692	0.196	-	100.9386	gen3 crystal1 prof
58_C11_sp10	0.1246	32.1	1.93	-	60.98	0.5798	0.2271	0.0209	3.51	-	0.4025	0.379	-	-	100.2538	gen3 crystal1 prof
58_C11_sp11	0.1446	32.16	1.38	-	59.63	0.3751	0.1748	0.0284	4.72	0.5501	0.3909	0.3107	0.0206	-	99.8852	gen3 late crystal1 prof, light

Table L15. Results of EPMA analyses on sulfide minerals in sample GMA13-061

Sample	Fe	S	Cu	In	Zn	Cd	Ga	Hg	Pb	As	Sb	Ag	Au	Mn	Total	Comment
61_C1_py1	46.46	53.15	-	-	0.0495	0.0075	-	0.005	0.2581	-	0.0025	NA	NA	0.229	100.1615	colloform gen1
61_C1_py2	46.41	52.37	0.0164	-	0.0674	0.0091	-	-	0.2709	-	0.0025	NA	NA	0.1116	99.258	colloform gen2
61_C1_py3	44.32	48.68	0.0215	-	0.0672	0.0006	-	0.0168	0.4186	-	0.075	NA	NA	0.1775	93.7773	colloform gen3
61_C1_py4	46.77	52.55	0.0287	-	0.0297	0.0157	-	-	0.1068	0.2908	0.0033	NA	NA	0.0911	99.8862	colloform gen4
61_C1_py5	45.73	51.15	0.0162	-	0.104	0.0047	0.0023	-	0.4057	-	0.0165	NA	NA	0.1201	97.5496	crystal1 interior
61_C1_py6	46.31	52.52	0.0055	-	0.2262	0.0164	0.0007	-	0.2625	-	0.0199	NA	NA	0.1389	99.5002	crystal1 rim
61_C2_py1	46.21	52.46	0.0426	-	0.3305	0.0161	0.0054	-	1.14	-	0.0286	NA	NA	0.1369	100.37	colloform gen1
61_C2_py2	43.29	51.74	0.0657	-	1.45	0.0209	-	0.0688	3.1	0.5155	0.0407	NA	NA	0.0965	100.388	colloform gen2
61_C2_py3	44.23	51.68	0.0773	-	0.4943	0.0049	-	0.0518	3.12	-	0.0378	NA	NA	0.1121	99.8083	colloform gen3
61_C2_py4	45.1	51.33	0.3444	-	0.1194	0.0193	-	-	2.72	0.2545	0.042	NA	NA	0.0698	99.9995	colloform gen4
61_C2_py5	45.63	52.5	0.0425	-	0.1076	0.0171	-	0.0017	1.21	1.13	0.0175	NA	NA	0.1102	100.7665	
61_C2_sp1	1.67	32.25	2.12	0.0004	60.56	0.0468	0.2196	0.0508	1.84	-	0.217	NA	NA	0.0155	98.9902	crystal2 interior, gn incl
61_C2_sp2	1.53	32.76	0.997	-	62.92	0.0975	0.1877	0.0417	0.8909	-	0.1718	NA	NA	0.0206	99.6173	crystal2 interior, gn incl
61_C2_sp3	1.07	31.4	1.84	0.0146	58.2	0.0459	0.188	-	2.85	-	0.208	NA	NA	0.0317	95.8483	crystal3 rim, gn incl
61_C2_sp4	0.6689	29.11	1.25	0.0064	55.53	0.0283	0.215	0.0882	3.19	-	0.0421	NA	NA	0.0242	90.1532	crystal1 rim, gn incl
61_C2_sp5	1.59	32.03	2.26	-	60.64	0.0943	0.1791	-	2.32	-	0.324	NA	NA	0.0214	99.4589	crystal1 rim, gn incl
61_C2_sp6	1.32	31.67	2.71	-	59.23	0.0793	0.1736	-	3.76	-	0.3272	NA	NA	0.0151	99.2853	crystal1 rim, gn incl
61_C2_sp7	1.24	28.54	1.93	-	52.77	0.0624	0.1138	0.0428	18.87	-	0.2121	NA	NA	0.0233	103.8044	crystal1 interior, gn incl
61_C3_py1	47.01	52.47	0.0142	-	0.0825	-	-	-	0.5881	-	0.0162	NA	NA	0.0631	100.244	spherulitic
61_C3_py2	47.27	52.35	0.0007	-	0.0717	0.0136	-	0.0218	0.5207	-	0.0149	NA	NA	0.0278	100.2911	spherulitic
61_C3_py3	47.34	52.45	0.0126	-	0.043	0.008	0.0033	0.0335	0.7224	-	0.036	NA	NA	0.0406	100.6894	spherulitic
61_C4_mrc1	43.34	46.5	0.0299	-	0.1025	0.0225	-	-	0.1167	-	-	NA	NA	-	90.1116	gen1
61_C4_mrc2	48	52.71	0.0113	-	0.0296	0.0118	-	-	0.3093	0.1795	0.0191	NA	NA	0.0466	101.3171	gen2
61_C4_mrc3	47.74	53.22	0.0289	-	0.1301	0.0129	-	0.005	0.1985	0.9477	0.0177	NA	NA	0.3147	102.6154	gen4
61_C4_mrc4	47.58	52.99	0.0307	-	0.1556	0.0114	-	-	0.1826	-	-	NA	NA	-	100.9503	gen5
61_C4_mrc5	48	52.79	0.0235	-	0.0897	0.0118	0.0105	-	0.2486	0.0598	0.002	NA	NA	0.0687	101.3046	gen5
61_C4_mrc6	46.89	51.17	0.0746	-	0.0875	0.0068	-	-	0.3264	2	0.019	NA	NA	-	100.5742	gen3 bright
61_C4_mrc7	47.3	51.23	0.1146	-	0.0551	0.0046	-	-	0.293	2.71	0.0491	NA	NA	0.0177	101.774	gen3 bright
61_C4_mrc8	48.26	53.23	0.0227	-	0.0545	0.0016	0.0154	-	0.1658	-	0.0195	NA	NA	0.117	101.8864	gen5
61_C4_mrc9	47.18	51.66	0.0342	-	0.0746	0.0157	-	0.0017	0.2675	2.54	0.0062	NA	NA	0.0018	101.7817	gen3 bright
61_C5_py1	44.06	52.1	0.5796	-	1.02	0.0177	0.0011	-	2.63	0.1524	0.0386	NA	NA	0.1698	100.7691	
61_C5_sp1	0.8009	32.27	0.4313	-	61.58	0.0348	0.1873	-	1.7	0.4047	0.177	NA	NA	0.0418	97.6279	
61_C5_sp2	0.8796	32.11	1.23	-	60.48	0.0788	0.1747	0.0301	2.19	-	0.4504	NA	NA	0.0122	97.6359	bright, gn/jd incl.?
61_C5_sp3	0.7335	32.28	0.1287	0.0036	63.15	0.01	0.2055	0.0682	0.602	-	0.0494	NA	NA	0.0313	97.2623	
61_C5_sp4	0.9451	32.45	0.5368	-	63.05	0.0229	0.1836	-	1.53	0.2266	0.1808	NA	NA	0.0483	99.1742	
61_C5_sp5	0.5277	32.06	0.897	-	61.37	0.0406	0.1693	-	2.92	0.3057	0.276	NA	NA	0.016	98.5824	brighter
61_C5_sp6	0.7473	32.09	0.2961	-	62.92	0.0089	0.1892	-	3.61	-	0.1574	NA	NA	0.0459	100.0648	bright incl. in sp
61_C5_sp7	0.717	31.38	2.48	-	56.62	0.1085	0.1422	0.1498	2.75	-	0.7241	NA	NA	0.0109	95.0826	gn/jd incl?
61_C5_jd1	0.0181	13.48	0.1979	-	1.62	0.0492	0.0022	0.0761	84.15	-	1.36	NA	NA	-	100.9535	incl. in sp
61_C5_jd2	0.0441	13.64	0.3038	-	2.94	0.0442	0.0027	0.0293	84.62	0.0462	1.47	NA	NA	-	103.1403	incl. in sp
61_C5_cov1	0.1439	26.1	41.51	-	2.77	0.0772	0.0246	0.2959	0.7991	0.1383	0.4619	NA	NA	0.0266	72.3476	or dig
61_C6_mrc1	43.24	50.45	0.7228	-	1.44	0.0122	-	0.0501	4.82	0.1842	0.1095	NA	NA	0.0239	101.0527	incl. in sp
61_C6_mrc2	44.25	52.42	0.3035	-	2.02	0.0088	-	-	2.78	0.8951	0.0161	NA	NA	0.1975	102.8909	
61_C6_sp1	1.02	31.37	1.59	-	60.58	0.0397	0.2048	0.2731	2.16	0.1851	0.4517	NA	NA	0.0164	97.8909	early crystal 1 prof, dark red
61_C6_sp2	0.857	32.27	1.86	-	60.04	0.0768	0.1731	0.0095	1.34	0.8321	0.9515	NA	NA	0.0074	98.4174	crystal 1 prof, dark red
61_C6_sp3	0.7377	31.92	0.9091	-	61.06	0.0497	0.1669	-	2.84	-	0.342	NA	NA	0.0262	98.0517	crystal 1 prof, dark red
61_C6_sp4	0.5073	31.88	0.3231	-	62.21	0.0287	0.1897	-	2.8	0.9162	0.1617	NA	NA	0.0222	99.039	crystal 1 prof, med red, dark BSE band
61_C6_sp5	0.3124	30.31	0.3906	-	61.31	0.0397	0.1638	-	1.47	-	0.1854	NA	NA	0.0118	94.1938	late crystal 1 prof, very light
61_C6_sp6	0.4883	27.72	0.3544	-	54.57	0.0305	0.1422	-	6.11	-	0.1869	NA	NA	0.0039	89.6063	crystal2 interior, light grey
61_C6_sp7	0.2728	31.95	0.2464	-	61.75	0.0341	0.2078	-	0.8995	-	0.1154	NA	NA	0.0102	95.4863	crystal2 rim, light grey
61_C6_sp8	2.64	33.27	0.324	-	62.1	0.016	0.2267	0.0396	0.9645	-	0.1419	NA	NA	0.0168	99.7395	dark grey
61_C6_sp9	1.56	32.58	0.3928	-	62.46	0.0343	0.193	0.0132	0.7077	-	0.1125	NA	NA	0.0349	98.0885	very light grey, bluish
61_C6_gn1	0.407	18.94	0.7333	-	17.37	0.0665	0.0653	0.0786	64.42	0.6945	2.53	NA	NA	-	105.3051	incl. in sp, gen2
61_C6_gn2	-	13.36	0.0392	-	2.37	0.0533	0.0022	0.0403	84.34	0.3965	0.2422	NA	NA	-	100.8436	after sp, gen3
61_C6_gn3	0.0103	13.55	0.0699	-	0.7179	0.0452	0.0128	-	82.87	-	2.36	NA	NA	-	99.6362	incl. in sp, gen2
61_C6_gn4	0.1216	13.61	0.1644	-	4.62	0.0519	0.0089	0.0099	83.71	-	0.5333	NA	NA	0.0037	102.8336	incl. in sp, gen1.5
61_C6_gn5	0.104	13.35	0.0478	-	1.42	0.061	-	0.0911	85.37	-	0.8802	NA	NA	-	101.3241	incl. in sp, gen1
61_C6_gn6	41.22	48.04	0.3136	-	0.9068	0.012	-	-	4.01	0.2773	0.0494	NA	NA	0.0366	94.8658	
61_C6_gn7	0.0434	13.66	0.114	-	3.63	0.0505	-	-	83.02	-	1.34	NA	NA	0.0201	101.8779	
61_C6_gn8	0.0175	13.44	0.05	-	0.9663	0.0598	0.0001	-	83.75	0.7969	0.7371	NA	NA	0.0193	99.8371	
61_C7_py1	45.09	52.44	0.0198	-	1.34	0.0088	-	-	2.4	0.2288	0.0125	NA	NA	0.1056	101.6454	spherulitic
61_C7_py2	44.58	51.36	0.0852	-	0.404	0.0193	-	0.0117	3.49	0.8344	0.1356	NA	NA	0.089	101.0091	spherulitic
61_C7_py3	46.87	52.74	0.0667	-	0.3724	0.0005	-	-	1.17	-	0.0555	NA	NA	0.0768	101.3518	spherulitic, crystal1 interior
61_C7_py4	43.2	49.7	0.7807	-	0.645	0.0126	-	-	4.57	1.31	0.2645	NA	NA	-	100.4827	spherulitic, crystal1 rim
61_C7_sp1	0.6802	32.27	1.87	-	61.73	0.0903	0.1575	0.0133	1.34	0.452	1.1	NA	NA	0.0206	99.724	gen1
61_C7_sp2	0.8537	32.24	1.92	-	61.74	0.1467	0.158	-	1.02	1	1.22	NA	NA	0.0188	100.3171	gen2
61_C7_sp3	0.6759	32.71	0.5732	0.0165	64.47	0.0568	0.1508	-	0.3313	-	0.4493	NA	NA	-	99.4339	gen3, with gn
61_C7_sp4	0.4514	32.62	1.24	-	62.36	0.2274	0.1987	0.1608	0.5945	-	0.9367	NA	NA	-	98.7895	gen4, with gn
61_C7_sp5	0.4734	32.17	1.75	-	60.73	0.0531	0.1947	-	0.7616	-	1.35	NA	NA	0.0061	97.489	with gn
61_C7_sp6	0.7216	32.22	1.62	-	61	0.0597	0.2425	-	0.5608	0.8332	1.31	NA	NA	0.0109	98.5788	with gn
61_C7_sp7	1.17	32.86	0.2205	-	64.98	0.0099	0.2242	-	0.6274	0.6728	0.1555	NA	NA	0.0219	100.9422	crystal1 interior
61_C7_sp8	0.7298	32.78	0.4854	-	64.88	0.0274	0.2039	-	0.3068	-	0.3338	NA	NA	0.0277	99.7748	crystal1 rim
61_C7_sp9	0.9279	32.42	1.31	-	62.74	0.0739	0.1828	-	0.9458	-	0.791	NA	NA	-	99.3914	gen2
61_C7_sp10	0.8897	32.76	1.03	-	63.38	0.0446	0.1825	0.0625	0.3943	0.0489	0.7919	NA	NA	0.011	99.5955	gen3, with gn

Table L15. Continued

Sample	Fe	S	Cu	In	Zn	Cd	Ga	Hg	Pb	As	Sb	Ag	Au	Mn	Total	Comment
61_C7_sp11	0.7636	32.32	1.26	-	62.52	0.0821	0.1709	0.0207	1.56	0.1858	0.4772	NA	NA	0.0094	99.3698	gen2
61_C7_sp12	0.6692	32.52	1.45	-	62.81	0.0401	0.1889	-	0.6672	0.1214	1.13	NA	NA	0.0128	99.6096	gen3, with gn
61_C7_gn1	-	13.08	0.0611	-	1.03	0.0507	0.0153	-	85.25	-	0.6265	NA	NA	-	100.1135	gen3, incl. in sp as band
61_C7_gn2	-	13.11	0.0412	-	-	0.0526	-	-	85.32	-	0.5229	NA	NA	0.0097	99.0564	gen4, after sp
61_C7_gn3	0.0031	13.2	0.0474	-	0.0168	0.039	0.0039	-	84.82	-	1.19	NA	NA	-	99.3203	gen4, after sp
61_C7_gn4	45.28	51.91	0.0403	-	1.6	0.0126	-	0.0388	1.38	0.739	0.0518	NA	NA	0.0017	101.0542	gen1, incl. in sp.
61_C7_gn5	0.0706	13.59	0.0741	-	3.23	0.0376	0.0244	0.0069	83.72	-	1.97	NA	NA	0.0019	102.7254	gen2, incl. in sp
61_C7_gn6	0.0857	13.75	0.1384	-	5.8	0.0466	0.0002	-	84.81	-	1.7	NA	NA	0.0059	106.3367	early, incl. in sp
61_C7_gn7	-	13.13	0.0678	-	0.1828	0.0364	0.0036	0.0028	85.83	-	0.4183	NA	NA	-	99.6718	late, rim of sp
61_C8_ccp1	15.34	23.66	16.53	-	0.4944	0.0314	-	-	42.08	-	0.5142	NA	NA	0.0016	98.6517	mix of ccp and gn!
61_C8_ccp2	28.96	34.41	33.96	-	-	0.0183	-	0.0875	0.1118	-	0.0044	NA	NA	-	97.5521	late after gn
61_C8_py1	46.39	51.81	0.0853	-	0.2867	0.0125	0.0013	-	1.9	0.5003	0.036	NA	NA	0.047	101.069	spherulitic, early
61_C8_py2	45.98	51.67	0.3298	-	1.49	0.0081	-	-	1.41	-	0.1419	NA	NA	0.0324	101.0621	spherulitic, late
61_C8_sp1	0.6484	32.21	1.45	-	61.6	0.0501	0.1909	0.0888	1.37	-	0.6033	NA	NA	0.0193	98.2309	with gn
61_C8_sp2	0.5779	32.79	0.6516	-	64.63	0.0413	0.196	-	0.3686	-	0.1669	NA	NA	0.0049	99.4272	with gn
61_C8_sp3	1.02	32.7	0.29	-	64.46	0.0168	0.1965	-	0.5306	-	0.1362	NA	NA	0.007	99.3572	early crystal1 prof
61_C8_sp4	0.8194	32.66	0.4391	-	64.75	0.0334	0.2237	-	0.3794	-	0.1838	NA	NA	0.0082	99.4971	crystal1 prof
61_C8_sp5	0.612	32.71	0.5079	0.0024	63.46	0.0147	0.1784	0.0247	0.6014	-	0.3037	NA	NA	0.0335	98.4488	late crystal1 prof
61_C8_gn1	0.021	13.27	0.0249	-	-	0.0468	0.0102	-	84.13	-	1.67	NA	NA	-	99.173	late, c.g. after sp
61_C8_gn2	0.0566	13.8	0.1031	-	3.8	0.0595	0.0021	-	81.7	-	1.97	NA	NA	0.0121	101.5033	late, c.g. after sp
61_C8_gn3	0.0384	13.24	0.0687	-	2.06	0.0516	0.0187	0.0526	86.42	-	0.5387	NA	NA	0.0114	102.5	early, incl. in sp
61_C8_gn4	0.037	13.38	0.0578	-	4.02	0.0344	0.0103	0.0126	85.68	0.6929	0.8626	NA	NA	-	104.7876	early, incl. in sp
61_C9_ccp1	29.36	34.25	33.9	-	0.4796	0.0057	-	-	0.1663	-	0.0929	NA	NA	-	98.2546	late, incl. in sp
61_C9_ccp2	29.31	34.62	33.62	-	1.24	0.0057	-	-	0.1294	-	0.0359	NA	NA	0.0029	98.9639	late, incl. in sp
61_C9_py3	46.32	53.41	0.0319	-	0.0191	0.0063	-	-	0.3787	0.0683	-	NA	NA	0.1897	100.4239	early crystal1 prof, spherulitic?
61_C9_py4	47.67	52.95	0.035	-	0.0373	0.0099	-	-	0.2596	-	0.0352	NA	NA	0.1144	101.1114	crystal1 prof
61_C9_py5	46.75	52.57	0.1534	-	0.0426	0.0058	-	0.0067	0.2748	1.42	0.0124	NA	NA	0.053	101.2886	late crystal1 prof
61_C9_py6	45.49	51.32	0.08	-	0.1203	0.0058	0.0069	-	1.36	-	0.0228	NA	NA	0.0361	98.442	
61_C9_py7	48.32	52.7	0.0155	-	0.0074	0.0091	-	-	0.2274	-	0.0111	NA	NA	0.0001	101.2906	
61_C9_py8	47.13	53.25	0.031	-	0.0315	-	-	0.0118	0.2833	-	0.099	NA	NA	0.0301	100.8667	
61_C9_py9	43.31	47.51	0.0701	-	0.2573	0.0109	0.0053	0.0169	0.295	-	0.0434	NA	NA	0.0082	91.5272	
61_C9_py10	46.85	52.91	0.0387	-	0.0951	0.0079	-	0.0151	0.2146	-	0.0079	NA	NA	0.0495	100.1887	
61_C9_py11	45.7	51.55	0.0301	-	-	0.0031	-	-	0.4655	-	-	NA	NA	0.0047	97.7534	
61_C9_py12	44.19	50.39	0.0367	-	0.1059	-	-	0.0436	0.4067	-	0.0112	NA	NA	-	95.1842	
61_C9_sp1	0.9973	32.65	0.71	-	64.02	0.0183	0.1862	0.0418	0.5615	-	0.3474	NA	NA	0.0339	99.5665	crystal1 prof (early or late?)
61_C9_sp2	0.7345	32.74	0.5921	-	63.79	0.0305	0.2113	0.0342	0.2832	0.0487	0.3984	NA	NA	0.0431	98.9061	crystal1 prof
61_C9_sp3	0.8747	32.59	0.4928	-	63.98	0.0093	0.2174	-	0.3377	-	0.2551	NA	NA	0.031	98.788	crystal2 prof (early or late)
61_C9_sp4	1.09	32.34	0.1753	-	63.57	0.0241	0.2084	0.0435	0.9846	-	0.15	NA	NA	0.0579	98.6439	crystal2 prof
61_C9_sp5	1.69	32.58	0.2385	-	62.71	0.0172	0.2349	0.1852	0.9898	-	0.1351	NA	NA	0.0368	98.8176	crystal2 prof
61_C9_sp6	0.6068	32.22	1.87	-	60.85	0.0481	0.2039	0.1058	1.26	0.6137	1.05	NA	NA	0.0312	98.8596	crystal2 prof
61_C9_sp7	0.2966	32.03	1.53	-	60.75	0.0647	0.3235	1.28	1.14	-	1.17	NA	NA	0.0091	98.5939	crystal2 prof
61_C9_sp8	1.04	33.46	0.0814	-	63.1	0.0147	0.1888	-	0.232	-	0.0507	NA	NA	0.0044	98.1721	
61_C9_gn1	0.0241	13.46	0.1147	-	2.73	0.0558	0.0213	-	85.79	-	1.02	NA	NA	-	103.2158	incl. in sp
61_C9_gn2	-	13.36	0.0798	-	1.02	0.0404	0.0007	0.1063	84.93	-	1.66	NA	NA	0.0046	101.2018	incl. in sp
61_C9_gn3	0.0069	13.39	0.0919	-	0.9116	0.0623	0.0195	0.0055	84.34	-	1.16	NA	NA	0.0082	99.996	incl. in sp
61_C9_gn4	-	13.3	0.0741	-	-	0.0649	0.0115	-	84.57	-	1.21	NA	NA	-	99.2306	
61_C10_mrc1	47.25	52.41	0.027	-	0.055	0.0004	0.011	0.0034	0.5932	-	0.0405	NA	NA	0.0341	100.4246	complex banded, gen1
61_C10_mrc2	47.14	52.44	0.0288	-	0.2267	-	-	-	0.8511	-	0.0195	NA	NA	0.0565	100.7626	gen2
61_C10_mrc3	47.01	52.67	0.0166	-	0.0857	-	0.0034	-	0.5817	-	0.0203	NA	NA	0.0373	100.4249	gen3
61_C10_mrc4	45.35	51.26	0.0084	-	0.0538	0.0005	-	-	0.3953	-	0.046	NA	NA	0.0557	97.1698	gen4
61_C10_mrc5	46.44	52.87	0.0263	-	0.183	0.0081	-	-	0.1824	-	-	NA	NA	0.1778	99.8877	gen5
61_C10_mrc6	47.54	52.84	0.032	-	0.0315	0.011	0.0019	-	0.125	-	-	NA	NA	0.0447	100.626	gen6
61_C10_mrc7	46.37	52.7	0.0062	-	0.0115	0.0092	0.0012	0.0084	0.1656	-	-	NA	NA	0.0246	99.2968	gen7
61_C10_mrc8	48.07	52.65	0.0046	-	0.0433	0.0056	-	0.0353	0.1712	-	-	NA	NA	0.0067	100.9866	gen8, py?
61_C10_mrc9	46.16	51.28	0.0507	-	0.0325	0.0065	-	0.0434	1.97	-	-	NA	NA	0.0047	99.5479	gen9, py?
61_C10_mrc10	45.12	51.29	0.0459	-	0.0849	-	0.0044	-	0.6976	-	0.0071	NA	NA	0.0063	97.2563	gen10, py?
61_C10_mrc11	46.79	52.45	-	-	0.1052	0.0135	-	-	0.4779	-	-	NA	NA	0.1163	99.953	new gen1
61_C10_mrc12	47.87	52.91	0.0174	-	0.0275	0.0135	-	-	0.066	-	0.0004	NA	NA	0.031	100.9357	new gen2
61_C10_mrc13	47.2	52.37	0.0305	-	0.0513	0.0166	-	-	0.1741	-	0.0236	NA	NA	-	99.8662	new gen3
61_C10_mrc14	42.85	51.48	0.0222	-	0.1853	-	-	0.0134	0.1544	0.7447	0.0574	NA	NA	0.0738	95.5813	new gen4
61_C11_py1	43.44	51.01	0.0519	-	2.6	0.0026	0.0125	0.0269	2.3	-	0.0129	NA	NA	0.1211	99.578	spherulitic, sp incl, crystal1 interior
61_C11_py2	45.14	51.2	0.3153	-	0.4414	0.0161	-	0.1828	1.91	0.5167	0.0377	NA	NA	0.0947	99.8548	spherulitic, crystal1 rim
61_C11_py3	45.95	52.42	0.0444	-	0.3122	0.0087	-	-	1.83	0.1783	0.0365	NA	NA	0.137	100.917	colloform, early crystal1 prof
61_C11_py4	42.81	50.93	0.0729	-	3.92	0.0151	0.0199	0.0084	2.45	-	0.0472	NA	NA	0.1528	100.4262	crystal1 prof
61_C11_py5	45.06	51.82	0.0633	-	1.42	0.009	0.0007	-	2.09	-	0.0497	NA	NA	0.1194	100.632	crystal1 prof
61_C11_py6	45.79	52.04	0.0348	-	0.9635	0.003	0.0089	0.0268	1.04	-	0.0335	NA	NA	0.0964	100.0368	crystal1 prof
61_C11_py7	42.93	50.94	0.0253	-	4.91	0.0268	0.0112	0.0135	1.9	-	0.0054	NA	NA	0.1115	100.8736	crystal1 prof
61_C11_py8	34.9	47.67	0.1181	-	15.06	0.0246	0.0234	-	3.26	0.0583	0.1141	NA	NA	0.118	101.3464	late crystal1 prof
61_C11_py9	46.78	52.62	0.0174	-	0.0891	-	-	-	1.17	-	0.0228	NA	NA	0.1139	100.8131	early crystal2 prof, collo (dark BSE)
61_C11_py10	45.31	51.57	0.0909	-	0.6561	0.0111	-	-	3.07	-	0.0315	NA	NA	0.1613	100.9008	crystal2 prof (light BSE)
61_C11_py11	46.55	51.87	0.1538	-	0.4656	0.0146	-	0.0084	1.39	-	0.0202	NA	NA	0.0569	100.5294	late crystal2 prof (dark BSE)
61_C11_sp1	3.56	32.73	0.4651	-	60.34	0.0329	0.2263	0.0547	0.6942	-	0.2782	NA	NA	0.0306	98.4121	after spherulitic py
61_C11_sp2	1.87	32.7	0.9079	-	62.24	0.1076	0.2235	-	0.4412	-	0.5838	NA	NA	0.0118	99.0859	

Table L16. Results of EPMA analyses on sulfide minerals in sample GMA13-062

Sample	Fe	S	Cu	In	Zn	Cd	Ga	Hg	Pb	As	Sb	Ag	Au	Mn	Total	Comment
62_C1_ccp1	30.67	34.2	34.23	-	0.2593	0.0016	0.0097	-	NA	-	0.0116	0.0285	-	0.0001	99.4109	
62_C1_py1	45.93	51.83	0.2191	-	2.5	0.0168	0	-	NA	-	-	0.0235	0.0292	-	100.5485	incl. in sp
62_C1_py2	44.39	50.49	0.5126	-	2.49	0.0075	0.0012	-	NA	-	0.0371	0.0253	0.202	-	98.1558	
62_C1_sp1	0.9466	32.44	0.1414	-	64.73	0.6318	0.2495	-	NA	-	0.1372	0.0019	-	-	99.2785	
62_C1_sp2	0.4361	32.76	1.9	-	63.92	0.0863	0.1321	0.0097	NA	0.3165	0.0141	0.0665	0.1165	-	99.7579	dark
62_C1_sp3	0.6187	32.67	0.5984	0.0089	65.74	0.014	0.1973	-	NA	-	0.0419	0.0194	-	0.0033	99.912	
62_C1_sp4	0.2294	32.39	0.0263	-	66.34	-	0.229	-	NA	0.527	0.0189	0.0079	0.0747	0.0017	99.8449	
62_C1_sp5	0.274	32.68	0.3005	0.0033	66.21	-	0.1734	0.0116	NA	0.989	0.0053	0.0548	-	-	100.7019	
62_C2_py1	43.06	47.25	0.9884	-	1.84	0.008	-	0.0172	NA	-	0.235	0.0504	-	0.0989	93.548	
62_C2_sp1	0.4599	32.32	2.1	-	63.55	0.1141	0.1941	-	NA	0.8341	0.0181	0.0785	0.1839	-	99.8527	crystal1 interior, dark
62_C2_sp2	0.2696	32.7	0.1511	-	66.66	0.0065	0.2054	-	NA	-	0.0383	0.1146	0.0347	0.0126	100.1928	crystal1 rim, light
62_C2_sp3	0.294	32.28	0.0972	0.0089	66.58	-	0.2199	-	NA	-	0.0246	0.079	0.0694	0.0062	99.6593	crystal1 rim, light
62_C2_jd1	0.0139	18.73	0.1865	-	10.45	0.0661	0.0014	0.1261	NA	-	-	0.0518	-	0.043	29.6688	incl. in sp
62_C3_ccp1	30.64	33.82	34.34	0.0077	-	0.0063	0.05	-	NA	0.6896	0.0075	0.0342	-	0.0092	99.6046	
62_C3_ccp2	30.3	34.24	34.31	-	0.0969	0.0038	0.0326	0.0072	NA	-	0.0429	0.0049	0.26	0.002	99.3004	
62_C3_ccp3	30.23	33.77	34.57	-	0.0842	0.0094	0.0125	-	NA	-	0.0246	0.0153	0.195	0.0132	98.9242	
62_C4_ccp2	29.58	33.98	33.9	-	1.89	0.0023	0.0211	-	NA	-	0.0183	0.0156	0.1648	-	99.5722	
62_C3_py1	46.71	51.65	0.1357	-	1.02	0.0041	-	-	NA	0.1023	0.0062	0.0169	0.1166	0.0103	99.7721	
62_C3_py2	45.41	50.53	1.39	-	0.1993	0.0029	-	0.0325	NA	-	0.0099	0.0282	-	0.0402	97.6431	incl. in cpy
62_C3_py3	45.41	51.23	0.2393	-	0.2774	0.008	-	-	NA	-	0.036	0.0142	0.3225	0.0467	97.5842	
62_C3_py4	44.41	50.01	0.7961	-	1.55	0.0162	-	-	NA	-	0.0359	0.0457	0.0928	0.1189	97.0756	
62_C3_sp1	0.7217	32.49	0.4169	-	65.81	0.1123	0.2161	-	NA	-	-	0.0079	0.1927	-	99.9677	
62_C3_sp2	1.85	32.34	0.9711	1.31	62.1	0.5328	0.516	0.0058	NA	-	0.0057	0.0001	0.1056	0.0068	99.7439	
62_C4_ccp1	30.91	34.52	34.88	-	0.3056	0.011	-	0.0417	NA	-	0.0278	0.0194	-	0.0067	100.7222	c.g. w sp
62_C4_py1	47.31	52.15	0.8713	-	0.8956	0.0066	-	-	NA	-	0.0119	-	-	0.0124	101.2578	
62_C4_sp1	0.6849	32.25	0.2303	0.0029	66.66	0.111	0.1896	-	NA	-	0.025	0.0018	-	-	100.1554	crystal1 interior, dark
62_C4_sp2	0.9366	32.56	0.0899	0.0038	64.91	0.2642	0.2952	0.0289	NA	-	0.0399	0.0011	0.352	0.0007	99.4823	crystal1 rim, light
62_C4_sp3	3.72	32.1	1.95	-	60.26	1	0.2237	-	NA	0.0728	0.3139	0.0219	0.0693	0.0019	99.7335	crystal2 interior, dark
62_C4_sp4	1.21	32.69	0.2505	0.0264	64.97	0.2186	0.2552	-	NA	-	0.0125	-	0.3451	-	99.9783	crystal2 rim, light
62_C5_sp1	1.02	32.75	0.1235	-	65.27	0.3342	0.1934	-	NA	-	0.0468	-	0.4714	-	100.2092	
62_C5_sp2	1.92	32.15	1.14	-	63.18	0.6324	0.2153	0.0173	NA	-	0.1621	0.0158	0.2683	0.0269	99.7282	
62_C5_sp3	1.99	32.34	0.1239	-	63.25	1.52	0.196	-	NA	-	0.0331	-	-	0.0322	99.4853	
62_C5_sp4	1.06	32.5	1.54	0.0058	62.84	0.6483	0.1752	-	NA	-	0.0589	0.1165	0.3847	0.0194	99.3489	
62_C6_ccp1	29.88	34.45	34.17	-	1.61	0.0128	-	0.0291	NA	-	0.0254	0.022	0.1158	-	100.315	incl. in sp
62_C6_py1	47.74	50.96	0.0376	-	0.6574	-	-	-	NA	-	0.0095	0.0054	0.2419	-	99.6518	framboidal
62_C6_sp1	1.38	32.75	0.191	0.0006	64.5	0.5065	0.2286	-	NA	-	0.0818	0.0055	0.1942	0.0299	99.8682	after fram py
62_C6_sp2	1.38	32.64	0.46	-	65.03	0.3201	0.1981	0.0251	NA	-	0.068	-	0.1352	0.0368	100.2932	
62_C7_ccp1	30.33	33.85	34.15	-	0.4464	0.011	-	0.0309	NA	0.1804	0.0107	0.0117	-	-	99.0212	c.g.
62_C7_ccp2	29.78	34.09	33.87	-	1.37	0.0072	-	-	NA	-	0.002	0.0181	0.193	0.0261	99.3565	c.g. incl. in sph
62_C7_ccp3	29.83	34.03	34.06	-	0.0309	0.0048	-	-	NA	-	0.0191	0.0084	0.1599	0.008	98.1511	c.g. incl. in sph
62_C7_py1	47.22	52.62	0.0329	-	0.7656	0.007	0.0089	-	NA	-	-	-	0.2094	0.0172	100.8809	vent lining
62_C7_py2	46.49	51.88	0.3071	-	1.14	0.0163	-	-	NA	-	-	0.0132	0.0055	-	99.8521	vent lining
62_C7_py3	45.87	51.94	0.662	-	0.5097	0.0117	-	-	NA	-	0.0058	0.0312	0.113	0.0742	99.2177	vent lining
62_C7_py4	46.27	51.11	0.2475	-	0.7843	0.0086	0.0009	-	NA	-	-	0.0372	-	0.0317	98.4903	spherulitic
62_C7_sp1	2	32.47	0.2286	-	64.55	0.3631	0.2294	-	NA	-	0.0016	0.01	0.1519	0.0009	100.0055	
62_C7_sp2	0.8842	32.53	0.3752	0.0014	65.8	0.1339	0.1995	-	NA	0.534	0.0737	0.0039	0.1629	-	100.6987	
62_C7_sp3	1.99	32.35	0.0581	-	64.75	0.4406	0.2209	0.0154	NA	0.267	-	0.0066	0.1075	-	100.206	
62_C8_ccp1	30.62	34.12	34.58	-	0.3616	0.0102	0.0125	0.0073	NA	-	-	0.0354	-	-	99.7471	c.g., incl. in sph
62_C8_py1	46.28	51.23	0.1315	-	2.54	0.0189	0.0052	-	NA	-	0.0498	0.0106	0.0418	0.0004	100.3081	incl. in sph
62_C8_sp1	1.89	32.24	0.6485	0.0376	64.02	0.6453	0.6492	-	NA	-	0.1496	-	0.0017	-	100.2818	
62_C9_ccp1	29.8	34.23	34.17	-	1.9	0.0126	0.0016	-	NA	-	0.0072	0.0107	-	0.0019	100.1339	
62_C9_sp1	1.64	32.6	1.19	0.0192	63.44	0.7237	0.2397	-	NA	-	0.1244	0.0103	0.1768	0.0241	100.1881	
62_C9_sp2	1.67	32.16	1.02	-	63.15	0.9108	0.1966	0.0635	NA	-	0.1541	0.0013	0.2784	-	99.6047	
62_C10_ccp1	30.52	34.13	34.89	-	0.3266	0.0029	-	-	NA	0.2379	0.0373	0.0064	0.0771	-	100.2281	c.g.
62_C10_py1	45.55	50.91	0.3599	-	0.3774	0.0206	-	-	NA	0.0511	0.0359	0.0493	-	0.0824	97.4367	fill in former vent
62_C10_py2	44.15	50.78	0.1899	-	2.86	0.0156	0.0248	-	NA	-	0.0182	0.0289	0.0891	0.0035	98.1601	spherulitic
62_C10_sp1	2.06	33.03	0.2313	-	63.56	0.8932	0.3291	-	NA	-	0.0576	0.0121	0.1161	0.0091	100.2985	vent lining
62_C11_ccp1	30.32	34.12	34.54	-	0.5126	0.0127	-	-	NA	-	-	0.0065	-	0.0238	99.5357	c.g.
62_C11_py1	47.76	52.26	0.0648	-	0.4247	0.0117	-	0.0444	NA	-	0.0169	0.0027	0.2437	-	100.8288	framboidal
62_C11_sp1	0.7573	32.06	0.0988	-	64.55	0.2739	0.1853	-	NA	-	0.0371	0.0011	0.35	0.0114	98.325	late crystal1 prof, light
62_C11_sp2	0.2868	32.59	0.8775	-	65.87	0.0138	0.2296	0.0174	NA	-	0.0447	0.0642	0.2981	0.0074	100.2995	crystal1 prof, red
62_C11_sp3	0.4493	32.22	0.9626	-	65.54	0.0656	0.167	-	NA	-	0.0322	0.044	0.3776	-	99.8584	early crystal1 prof, red darker
62_C12_sp1	0.2902	32.42	0.5291	0.0152	66.22	0.0042	0.2277	0.0019	NA	-	-	0.0194	0.1456	-	99.8734	
62_C12_jd1	0.4301	26.96	0.2224	-	51.68	0.0112	0.158	0.0347	NA	-	0.0149	0.0401	0.1391	-	79.6905	incl. in sp
62_C13_ccp1	30.27	33.96	34.62	-	0.2053	-	0.0095	0.02	NA	-	-	0.0115	0.0824	0.0288	99.2075	
62_C13_py1	45.79	52.29	0.2678	-	1.26	0.0179	-	-	NA	-	0.0091	0.0199	0.1002	0.0259	99.7809	spherulitic
62_C13_sp1	1.18	32.57	0.1502	0.0331	65.35	0.3813	0.3703	-	NA	-	0.0258	-	0.0295	-	100.0901	
62_C14_ccp1	31.03	34.28	34.42	-	-	0.0119	-	-	NA	-	0.0202	0.0097	0.0158	0.0158	99.8035	
62_C14_py1	46.96	51.87	0.2063	-	0.0083	0.0119	-	-	NA	-	0.0309	0.014	-	0.033	99.1345	framboidal?
62_C14_sp1	1.33	32.63	0.3941	0.0015	64.72	0.5215	0.3126	-	NA	-	0.1977	0.0206	-	0.0041	100.132	
62_C14_sp2	1.87	32.59	0.4825	0.0021	63.74	0.7125	0.2737	-	NA	-	0.221	0.0043	0.0589	0.0007	99.9557	

Table L17. Summary of EPMA analyses of sphalerite (wt.%) with mole % FeS and CuS calculations

Sample	Zn	S	Fe	Cu	FeS	CuS	FeS*
4A_C1_sp1	61.07	32.77	1.92	1.34	3.43	2.10	1.33
4A_C1_sp2	62.63	32.78	0.9589	1.47	1.69	2.27	-0.59
4A_C1_sp3	63.95	33.11	0.9078	1.19	1.59	1.83	-0.24
4A_C1_sp4	62.75	33.08	1.22	1.32	2.16	2.06	0.11
4A_C2_sp1	64.35	33.32	1.03	1.1	1.80	1.68	0.11
4A_C2_sp2	59.53	32.9	3.6	2.72	6.26	4.16	2.10
4A_C2_sp7	63.55	32.48	0.5805	1.73	1.02	2.66	-1.64
4A_C3_sp1	64.26	32.81	0.946	0.7593	1.66	1.17	0.49
4A_C3_sp2	64.83	32.47	0.3622	0.3241	0.64	0.50	0.14
4A_C3_sp3	63.77	32.28	0.1502	0.4022	0.27	0.63	-0.36
4A_C3_sp4	63.55	32.12	0.1492	0.187	0.27	0.30	-0.03
4A_C3_sp5	62.97	32.03	0.1277	0.4384	0.23	0.70	-0.47
4A_C4_sp1	57.71	32.67	2.26	4.99	3.97	7.71	-3.74
4A_C5_sp5	62.35	33.07	2.38	1.35	4.14	2.06	2.07
4A_C6_sp1	61.21	32.23	1.05	2.24	1.86	3.49	-1.63
4A_C6_sp2	61.51	31.71	0.1578	1.92	0.28	3.02	-2.74
4A_C6_sp3	62.54	32.58	1.33	1.43	2.35	2.22	0.13
4A_C6_sp4	62.88	32.82	2.11	0.9485	3.69	1.46	2.23
4A_C7_sp1	59.73	32.83	3.47	3.22	6.01	4.90	1.11
4A_C7_sp2	63.25	32.91	1.72	1.78	2.98	2.71	0.27
4A_C7_sp3	63.78	32.56	1.06	0.1546	1.89	0.24	1.65
4A_C7_sp5	62.64	32.32	0.9388	0.3805	1.69	0.60	1.09
4A_C8_sp1	62.6	32.36	0.8073	1.74	1.42	2.68	-1.27
4A_C8_sp2	63.29	32.4	0.4873	1.03	0.86	1.61	-0.74
4A_C8_sp3	62.39	32.13	0.3207	1.66	0.57	2.59	-2.02
4A_C8_sp4	62.72	32.29	0.2696	1.43	0.48	2.23	-1.76
4A_C8_sp5	62.54	32.02	0.2538	1.54	0.45	2.41	-1.96
4A_C8_sp6	64.07	31.91	0.1781	0.2348	0.32	0.37	-0.05
4A_C9_sp1	65.26	33.03	0.9316	0.5806	1.62	0.89	0.73
4A_C9_sp2	63.9	32.5	0.3138	0.2288	0.56	0.36	0.20
4A_C9_sp5	63.02	32.44	0.5813	0.8656	1.04	1.36	-0.32
4A_C10_sp2	64.8	32.72	0.9029	0.4777	1.58	0.73	0.84
4A_C10_sp3	63.12	32.2	0.1626	0.3394	0.29	0.54	-0.24
4A_C10_sp5	65.14	32.62	0.6687	0.295	1.17	0.45	0.72
4A_C10_sp6	57.66	31.08	0.0805	0.0988	0.15	0.16	-0.01
10_C5_sp1	62.69	32.1	1.53	1.71	2.66	2.61	0.05
10_C6_sp1	62.53	32.61	1.21	1.1	2.15	1.72	0.43
10_C7_sp1	62.21	32.43	2.14	1.38	3.71	2.10	1.61
10_C7_sp2	64.66	32.29	1.39	1.05	2.40	1.59	0.81
10_C8_sp1	65.19	32.03	0.5257	1.14	0.91	1.73	-0.82
10_C8_sp2	63.83	31.96	1.28	0.6094	2.22	0.93	1.29
10_C9_sp1	64.32	31.49	0.0976	2.23	0.17	3.41	-3.24
10_C9_sp3	63.93	31.36	0.161	2.35	0.28	3.60	-3.32
10_C10_sp1	60.53	32.58	4.39	1.48	7.53	2.23	5.30
10_C10_sp2	63.7	32.24	1.73	1.17	2.99	1.78	1.21
10_C10_sp3	65.41	32.13	0.7521	1.18	1.30	1.79	-0.49
10_C10_sp4	64.74	32.14	1.17	1.25	2.02	1.89	0.12
10_C10_sp5	63.47	31.75	0.5375	2.22	0.94	3.43	-2.48
10_C11_sp1	62.52	32.14	0.7689	2.06	1.34	3.15	-1.81
10_C11_sp2	65.51	32.2	0.6368	0.9054	1.09	1.37	-0.27
10_C11_sp3	65.49	32.21	0.7486	0.3108	1.31	0.48	0.83
10_C12_sp1	63.17	32.13	1.36	2.01	2.36	3.07	-0.71
21_C2_sp1	62.94	32.57	1.75	0.8735	3.08	1.35	1.73
21_C4_sp1	60.58	32.6	2.42	1.1	4.30	1.72	2.58
21_C5_sp1	61.07	32.79	3.49	1.32	6.10	2.03	4.07
21_C5_sp2	64.66	32.98	1.08	0.2792	1.90	0.43	1.47
21_C6_sp1	64.13	32.49	1.19	0.4903	2.09	0.76	1.34
21_C7_sp1	63.8	32.67	1.36	0.6492	2.39	1.00	1.39
21_C7_sp2	63.3	32.63	1.85	0.7845	3.24	1.21	2.03
21_C9_sp1	64.36	32.86	1.03	0.7819	1.81	1.21	0.60
21_C10_sp2	64.1	33.04	1.61	0.7523	2.81	1.15	1.65
24_C1_sp1	62.95	33.57	1.45	0.4833	2.60	0.76	1.84
24_C1_sp2	63.1	34.04	0.4542	0.8074	0.82	1.29	-0.46
24_C2_sp1	64.59	33.38	1.21	0.4465	2.13	0.69	1.44
24_C2_sp2	64.33	33.26	1.6	0.4099	2.81	0.63	2.18
24_C4_sp1	61.58	33.75	3.34	0.5984	5.91	0.93	4.98
24_C5_sp1	64.47	33.18	1.03	0.339	1.83	0.53	1.30
24_C5_sp2	65.15	33.46	0.5813	0.1851	1.03	0.29	0.74
24_C5_sp3	63.01	33.76	3.02	0.3642	5.28	0.56	4.72
24_C5_sp4	65.91	33.99	0.3935	0.0693	0.69	0.11	0.59
24_C6_sp1	64.16	33.57	1.3	0.414	2.30	0.64	1.66
24_C7_sp1	65.34	33.89	0.5361	0.474	0.94	0.73	0.21
24_C7_sp2	65.51	33.91	0.2869	0.2041	0.51	0.32	0.19
24_C7_sp3	65.79	33.69	0.3868	0.5765	0.68	0.89	-0.21
24_C7_sp4	65.66	33.79	0.6069	0.374	1.06	0.58	0.49
24_C7_sp5	64.8	34.61	1.78	0.3465	3.09	0.53	2.56
24_C7_sp6	64.82	33.88	0.9775	0.5058	1.72	0.78	0.94
31_C1_sp1	61.79	32.97	2.22	1.89	3.86	2.89	0.97
31_C1_sp2	61.72	33.04	3.13	1.42	5.43	2.16	3.26
31_C1_sp3	62.57	32.93	2.82	1.29	4.87	1.96	2.91
31_C1_sp4	59.09	33.47	5.46	2.17	9.34	3.26	6.08
31_C1_sp5	58.77	33.45	5.37	1.86	9.30	2.83	6.47
31_C2_sp2	60.61	32.84	2.48	2.62	4.35	4.04	0.31
31_C2_sp3	62.02	33.43	2.82	1.28	4.90	1.95	2.95
31_C2_sp4	56.25	33	6.71	3.04	11.59	4.62	6.98
31_C2_sp5	57.26	32.88	4.81	3.56	8.35	5.43	2.92
31_C2_sp6	63.46	32.95	1.26	1.31	2.21	2.02	0.19
31_C2_sp8	62.88	32.29	0.503	0.4766	0.90	0.75	0.15
31_C3_sp1	61.69	32.83	2	1.94	3.51	2.99	0.52
31_C3_sp2	64.79	33.32	0.6661	1.01	1.16	1.55	-0.39
31_C3_sp3	59.85	32.87	2.45	3.13	4.26	4.78	-0.52
31_C4_sp1	62.58	32.76	1.65	1.99	2.87	3.04	-0.17
31_C4_sp2	61.07	32.43	1.99	2.69	3.47	4.13	-0.65
31_C4_sp3	60.72	32.62	2.58	2.76	4.47	4.20	0.27
31_C4_sp4	60.99	32.26	1.79	2.91	3.12	4.45	-1.34
31_C4_sp5	60.62	32.16	2.24	3.28	3.87	4.98	-1.11
31_C4_sp6	61.68	32.58	1.74	2.64	3.02	4.03	-1.01
31_C4_sp7	61.82	32.2	1.7	2.92	2.94	4.44	-1.50
31_C4_sp8	61.49	32.76	2.12	2.13	3.68	3.25	0.43
31_C4_sp9	63.99	32.73	1.09	1.59	1.89	2.42	-0.53
31_C4_sp10	63.82	32.57	0.7056	1.68	1.23	2.57	-1.34
31_C4_sp11	65.76	32.85	0.437	0.0937	0.77	0.14	0.62
31_C5_sp1	62.72	32.18	1.06	2.28	1.84	3.48	-1.64
31_C5_sp2	63.92	32.29	0.3926	1.39	0.69	2.14	-1.45
31_C5_sp3	63.95	32.31	0.2627	0.8534	0.46	1.32	-0.86
31_C5_sp4	65.67	32.92	0.4974	0.1959	0.87	0.30	0.57
31_C5_sp5	60.19	32.17	2.05	3.34	3.58	5.13	-1.55
31_C5_sp6	60.75	32.76	2.29	2.58	4.00	3.96	0.04
31_C7_sp1	57.75	33.3	5.31	3.32	9.09	4.99	4.09
31_C7_sp2	61.76	32.95	3.1	2.07	5.34	3.13	2.21
31_C8_sp2	63.79	32.32	1.1	1.69	1.91	2.58	-0.67
31_C8_sp3	65.88	33.12	0.2589	0.2639	0.45	0.41	0.05
31_C8_sp4	59.63	33.07	3.31	3.32	5.73	5.05	0.68
31_C8_sp5	63.81	32.6	1.19	1.63	2.06	2.48	-0.42
31_C8_sp6	62.21	33.16	3.75	1.04	6.44	1.57	4.87
31_C8_sp7	65.1	33.02	1.16	0.8358	2.00	1.27	0.74
31_C9_sp1	64.51	33.05	1.54	0.1567	2.70	0.24	2.46
31_C9_sp2	63.16	33	2.55	0.4601	4.46	0.71	3.75
31_C10_sp2	64.17	32.74	0.9302	1.13	1.63	1.74	-0.11
31_C10_sp3	56.03	32.92	7.37	2.35	12.71	3.56	9.15
31_C10_sp4	65.66	32.96	0.5355	0.6036	0.93	0.92	0.01
31_C11_sp1	56.48	33.22	5.92	4.6	10.08	6.88	3.20
31_C11_sp2	60.67	33	4.11	2.05	7.06	3.10	3.97
32_C1_sp2	64.5	33.49	1.27	0.3495	2.22	0.54	1.68
32_C1_sp3	64.1	33.47	1.39	0.6919	2.42	1.06	1.36
32_C1_sp4	60.75	32.44	0.728	1.54	1.31	2.43	-1.12
32_C1_sp5	65.79	33.8	0.8022	0.1629	1.40	0.25	1.15
32_C1_sp6	64.1	33.68	1.06	0.044	1.88	0.07	1.82

Table L17. Continued

Sample	Zn	S	Fe	Cu	FeS	CuS	FeS*
32_C1_sp7	64.68	33.44	0.9664	0.0567	1.71	0.09	1.62
32_C2_sp1	64.51	33.67	1.63	0.1136	2.85	0.17	2.68
32_C2_sp2	63.47	33.55	1.11	0.3522	1.96	0.55	1.41
32_C2_sp3	62.11	33.17	1.89	0.5463	3.37	0.86	2.51
32_C2_sp4	58.7	31.54	0.5176	1.17	0.96	1.91	-0.95
32_C2_sp5	62.85	33.52	2.85	0.198	4.98	0.30	4.68
32_C2_sp6	56.09	30.53	0.5149	1.1	0.98	1.85	-0.86
32_C2_sp7	62.86	33.53	2	0.115	3.56	0.18	3.38
32_C3_sp1	64.09	33.75	1.96	0.0838	3.43	0.13	3.30
32_C3_sp2	65.02	34.01	1.73	0.0734	3.00	0.11	2.89
32_C3_sp4	63.61	33.36	2.38	0.2065	4.16	0.32	3.84
32_C3_sp5	63.8	33.79	1.36	0.8498	2.38	1.31	1.08
32_C3_sp6	65.02	33.62	1.52	0.14	2.64	0.21	2.43
32_C4_sp2	59.98	32.54	0.8275	2.92	1.48	4.60	-3.12
32_C4_sp3	64.51	33.74	0.9656	0.6572	1.69	1.01	0.68
32_C4_sp4	64.88	33.67	1.2	0.4134	2.10	0.63	1.46
32_C4_sp5	64.45	33.89	1.32	0.2638	2.30	0.40	1.89
32_C4_spy6	64.32	33.58	1.39	0.4269	2.44	0.66	1.78
32_C5_sp1	63	32.94	0.7347	0.1994	1.32	0.31	1.00
32_C5_sp2	64.01	33.78	1.56	0.2685	2.74	0.41	2.33
32_C6_sp1	63.65	33.34	1.58	1.3	2.74	1.98	0.76
32_C6_sp2	58.14	34.33	7.56	0.4805	13.00	0.73	12.27
32_C6_sp3	65.24	33.66	1.12	0.3439	1.95	0.53	1.42
32_C7_sp1	59.65	32.33	2.47	0.7567	4.44	1.20	3.25
32_C7_sp2	64.17	33.8	1.8	0.1167	3.16	0.18	2.98
32_C7_sp3	62.67	33.57	2.44	0.6106	4.28	0.94	3.33
32_C7_sp4	63.12	33.81	2.31	0.5018	4.04	0.77	3.27
32_C7_sp5	64.24	33.76	1.61	0.2593	2.82	0.40	2.42
32_C7_sp6	61.72	32.85	1.27	1.02	2.27	1.60	0.67
32_C7_sp7	59.24	33.14	3.37	2.46	5.88	3.77	2.11
32_C7_sp8	51.18	33.49	7.21	6.71	12.46	10.19	2.27
32_C7_sp9	64.09	33.87	1.95	0.3263	3.39	0.50	2.89
32_C7_sp10	57.65	33.03	3.83	2.7	6.76	4.19	2.57
32_C8_sp1	62.75	33.49	1.38	1.27	2.41	1.95	0.46
32_C8_sp2	64.22	33.68	1.28	0.6708	2.22	1.02	1.20
32_C8_sp3	64.83	33.75	1.35	0.3965	2.35	0.61	1.74
32_C8_sp4	63.04	33.7	1.08	1.11	1.92	1.73	0.19
32_C9_sp1	64.32	33.6	1.69	0.2891	2.95	0.44	2.51
32_C9_sp2	60.34	33.25	2.74	2.37	4.78	3.64	1.15
32_C9_sp3	63.76	33.53	1.76	0.3747	3.07	0.57	2.50
32_C9_sp4	63.61	33.52	1.55	0.4591	2.73	0.71	2.02
32_C9_sp5	62.42	33.77	2.56	1.5	4.44	2.28	2.15
38_C2_sp1	66.07	33.14	0.5321	0.213	0.93	0.33	0.60
38_C4_sp1	65.53	33.12	0.847	0.1413	1.48	0.22	1.26
38_C5_sp1	64.95	33.34	1.13	0.6703	1.96	1.02	0.94
38_C5_sp2	64.85	33.33	1.58	0.8727	2.72	1.32	1.40
38_C5_sp3	63.84	33.38	1.96	1.16	3.38	1.76	1.62
38_C5_sp4	65.92	33.23	0.6161	0.1666	1.07	0.25	0.82
38_C5_sp5	65.69	33.18	0.6049	0.0819	1.06	0.13	0.93
38_C5_sp6	65.68	33.36	0.7246	0.1707	1.26	0.26	1.00
38_C5_sp7	65.63	33.06	0.6631	0.11	1.16	0.17	0.99
38_C7_sp1	65.26	33.23	1.2	0.4387	2.08	0.67	1.41
38_C7_sp2	65.94	33.37	0.6886	0.357	1.19	0.54	0.65
38_C7_sp3	65.23	33.08	0.7619	0.4246	1.33	0.65	0.68
42_C1_sp1	60.69	32.93	2.73	2.28	4.75	3.49	1.26
42_C1_sp2	61.88	33.21	1.23	0.7247	2.22	1.15	1.07
42_C1_sp3	56.44	33.39	4.09	4.09	7.24	6.36	0.88
42_C1_sp5	62.23	32.59	0.9586	1.48	1.70	2.30	-0.61
42_C1_sp6	61.58	32.57	1.49	1.55	2.64	2.42	0.23
42_C2_sp1	60.89	31.99	0.241	0.8308	0.44	1.34	-0.90
42_C2_sp2	60.81	33.11	1.9	2.25	3.34	3.48	-0.14
42_C2_sp4	63.74	33.22	0.6015	0.5704	1.07	0.89	0.18
42_C2_sp5	63.23	33.27	1.13	0.2747	2.02	0.43	1.59
42_C2_sp6	63.14	32.16	0.2188	0.9418	0.39	1.49	-1.09

Sample	Zn	S	Fe	Cu	FeS	CuS	FeS*
42_C3_sp1	61.79	32.49	0.8523	2.11	1.51	3.28	-1.77
42_C3_sp2	64.28	32.34	0.2715	0.7294	0.48	1.14	-0.66
42_C3_sp3	62.69	31.89	0.4348	1.49	0.77	2.33	-1.55
42_C3_sp4	61.45	33.31	2.46	1.41	4.34	2.19	2.16
42_C4_sp1	63.97	33.27	1.58	0.8479	2.75	1.30	1.45
42_C4_sp2	64.09	33.03	0.7809	1.19	1.36	1.83	-0.46
42_C4_sp3	62.11	32.8	1.42	1.32	2.49	2.03	0.46
42_C4_sp4	63.29	33.15	1.85	1.1	3.22	1.68	1.54
42_C4_sp5	65.07	33.43	1	0.3281	1.74	0.50	1.24
42_C5_sp1	62.85	32.96	1.77	1.4	3.09	2.15	0.94
42_C5_sp2	62.19	33.31	1.81	0.6819	3.23	1.07	2.16
42_C5_sp3	61.97	32.43	1.31	1.98	2.30	3.05	-0.75
42_C5_sp4	63.73	33.48	0.8095	0.2104	1.45	0.33	1.12
42_C6_sp1	63.58	33.03	1.53	0.9457	2.67	1.45	1.22
42_C7_sp1	63.52	32.37	0.1513	0.9366	0.27	1.47	-1.20
42_C7_sp3	64.12	33.31	0.8306	0.0836	1.47	0.13	1.34
42_C8_sp1	63.45	33.17	1.25	0.918	2.19	1.41	0.78
42_C8_sp2	65.12	33.3	1.13	0.3021	1.96	0.46	1.50
42_C9_sp1	64.34	33.35	1.24	0.32	2.16	0.49	1.67
42_C9_sp3	64.65	33.36	0.9469	0.5703	1.65	0.88	0.78
42_C9_sp5	63.5	32.07	0.2109	1.11	0.38	1.74	-1.37
42_C9_sp6	63.65	32.31	0.2608	0.7729	0.46	1.21	-0.75
42_C9_sp7	61.56	31.86	0.4291	1.59	0.77	2.50	-1.73
42_C9_sp8	64.22	33.35	1.06	0.4485	1.87	0.69	1.17
42_C10_sp1	62.22	32.44	0.3247	1.21	0.59	1.93	-1.34
42_C11_sp1	62.8	32.72	0.6489	1.41	1.16	2.21	-1.05
42_C11_sp2	64.86	33.34	0.9619	0.6551	1.67	1.00	0.67
42_C11_sp3	65.6	33.19	0.9678	0.0905	1.68	0.14	1.54
42_C11_sp4	64.23	33.14	0.5002	0.6695	0.88	1.04	-0.16
42_C11_sp5	61.4	31.96	0.301	0.9926	0.54	1.57	-1.03
42_C11_sp6	65.3	33.81	0.9484	0.1744	1.65	0.27	1.39
42_C12_sp1	63.66	32.66	0.6235	1.23	1.10	1.91	-0.81
42_C12_sp2	64.91	33.38	0.9103	0.0318	1.58	0.05	1.53
42_C12_sp3	62.7	32.6	0.7492	1.23	1.33	1.92	-0.59
42_C12_sp4	65.14	33.43	0.6564	0.0428	1.15	0.07	1.09
42_C12_sp5	65.27	33.31	0.0715	0.0498	0.13	0.08	0.05
42_C13_sp1	62.5	32.98	0.9275	1.24	1.65	1.94	-0.29
42_C13_sp2	64.55	33.06	0.5919	0.5343	1.04	0.82	0.21
45_C1_sp1	57.87	32.52	3.16	1.61	5.70	2.55	3.15
45_C1_sp2	62.93	32.89	0.9684	0.1601	1.74	0.25	1.49
45_C1_sp3	62.29	33.1	2.37	0.4826	4.19	0.75	3.44
45_C1_sp5	61.25	32.76	2.23	0.912	3.96	1.42	2.54
45_C2_sp1	61.25	32.53	1.84	0.4954	3.31	0.78	2.53
45_C2_sp2	62.13	32.32	1.33	0.7757	2.36	1.21	1.15
45_C2_sp3	61.09	32.16	0.5234	0.2721	0.96	0.44	0.52
45_C2_sp4	60.72	33.01	2.17	1.32	3.86	2.06	1.80
45_C2_sp5	60.08	32.59	2.65	1.52	4.69	2.36	2.32
45_C2_sp6	62.5	33.03	2.31	0.7473	4.01	1.14	2.87
45_C3_sp2	62.24	32.05	0.1035	0.2583	0.19	0.42	-0.23
45_C3_sp3	62.93	32.19	0.1145	0.1494	0.21	0.24	-0.03
45_C3_sp4	63.67	32.52	0.2588	0.2861	0.46	0.45	0.01
45_C3_sp5	63.12	32.52	0.2088	0.2275	0.38	0.36	0.02
45_C3_sp6	63.92	32.65	0.3079	0.1545	0.54	0.24	0.30
45_C3_sp7	58.48	31.22	0.1893	0.235	0.36	0.39	-0.03
45_C3_sp8	63.54	32.22	0.042	0.4465	0.08	0.70	-0.63
45_C3_sp11	60.56	31.95	0.021	2.3	0.04	3.64	-3.60
45_C3_sp15	65.31	33.16	0.0502	0.1942	0.09	0.30	-0.21
45_C3_sp17	62.61	32.51	0.3733	0.0934	0.68	0.15	0.53
45_C3_sp18	63.83	33.19	0.4689	0.1091	0.84	0.17	0.67
45_C4_sp3	63.5	33.09	0.601	0.0819	1.09	0.13	0.96
45_C4_sp4	62.61	32.2	0.3062	0.0947	0.56	0.15	0.40
45_C4_sp6	61.97	32.43	0.3345	0.2026	0.60	0.32	0.28
45_C4_sp7	62.5	33.12	1.37	0.0991	2.48	0.16	2.32
45_C5_sp2	62.83	32.23	0.0154	0.2432	0.03	0.39	-0.36

Table L17. Continued

Sample	Zn	S	Fe	Cu	FeS	CuS	FeS*
45_C5_sp3	64.19	32.32	0.0769	0.181	0.14	0.29	-0.15
45_C5_sp5	63.37	32.54	0.2817	0.4897	0.51	0.77	-0.27
45_C5_sp6	62.35	32.47	0.2665	1.94	0.47	3.01	-2.54
45_C5_sp7	64.91	32.92	0.373	0.1407	0.66	0.22	0.44
45_C5_sp8	61.33	32.4	0.0657	1.32	0.12	2.11	-1.99
45_C5_sp12	63.5	32.3	0.0237	0.2372	0.04	0.38	-0.33
45_C5_sp13	63.48	32.44	0.0327	0.1761	0.06	0.28	-0.22
45_C5_sp15	63.51	32.65	0.2215	0.5657	0.40	0.89	-0.49
45_C5_sp16	63.02	32.37	0.2107	0.4437	0.38	0.70	-0.32
45_C5_sp17	62.44	32.25	0.2224	0.943	0.40	1.49	-1.09
45_C5_sp18	60.98	32.41	0.5519	2.36	0.98	3.68	-2.70
45_C5_sp19	63.1	32.55	0.1908	0.5367	0.34	0.85	-0.51
45_C5_sp20	63.05	32.37	0.2756	0.263	0.50	0.42	0.08
45_C6_sp1	63.6	32.39	0.0994	0.0502	0.18	0.08	0.10
45_C6_sp2	63.53	32.3	0.0617	0.0381	0.11	0.06	0.05
45_C6_sp4	63.85	32.29	0.0228	0.1295	0.04	0.21	-0.16
45_C6_sp5	56.11	30.31	0.0369	0.0633	0.07	0.11	-0.04
45_C6_sp6	62.81	32.43	0.0796	0.0139	0.14	0.02	0.12
45_C6_sp7	65.73	33.16	0.5601	0.1272	0.98	0.20	0.78
45_C6_sp9	64.5	32.8	0.2489	0.0804	0.44	0.12	0.32
45_C6_sp10	64.95	33	0.0879	0.0806	0.16	0.13	0.03
45_C6_sp11	64.03	32.36	0.2369	0.0472	0.43	0.07	0.35
45_C7_sp1	62.24	31.83	0.0099	0.0278	0.02	0.04	-0.03
45_C7_sp7	63.91	32.22	0.0811	0.0673	0.15	0.11	0.04
45_C7_sp9	65.26	32.89	0.446	0.0537	0.79	0.08	0.71
45_C7_sp10	64.78	33.02	0.4375	0.1578	0.78	0.25	0.53
45_C7_sp11	62.28	32.98	2.83	0.5829	4.96	0.90	4.06
45_C7_sp12	61.9	32.78	2.34	0.4838	4.16	0.76	3.40
45_C8_sp5	64.12	32.88	0.1848	0.063	0.33	0.10	0.23
45_C8_sp7	64.17	32.96	0.2684	0.0382	0.48	0.06	0.42
45_C9_sp1	58.58	32.94	4.98	1.02	8.78	1.58	7.20
45_C9_sp2	60.95	32.77	2.53	1.07	4.48	1.67	2.82
45_C9_sp3	61.59	32.89	3.52	0.7631	6.12	1.17	4.95
45_C9_sp4	62.32	33.05	2.31	0.3541	4.10	0.55	3.55
45_C9_sp5	62.26	33.08	2.67	0.4141	4.72	0.64	4.07
45_C10_sp1	60.95	32.88	2.71	1.01	4.79	1.57	3.22
45_C10_sp2	60.55	32.77	4.04	0.8486	7.07	1.30	5.76
48A_C6_sp1	60.95	32.57	3.82	2.06	6.62	3.14	3.48
48A_C10_sp1	54.3	34.54	7.39	3.91	12.90	6.00	6.90
48A_C11_sp1	64.41	33.03	1.2	0.6969	2.11	1.08	1.03
48A_C11_sp2	65.27	32.7	0.9619	0.1885	1.69	0.29	1.40
49_C1_sp3	57.29	32.42	3.61	5.02	6.28	7.67	-1.39
49_C1_sp4	60.86	31.87	1.82	3.44	3.17	5.27	-2.10
49_C1_sp5	52.24	32.57	5.96	7	10.38	10.71	-0.33
49_C1_sp6	60.41	32.83	2.61	3.16	4.51	4.79	-0.29
49_C2_sp1	62.79	32.56	0.93	1.93	1.62	2.96	-1.34
49_C2_sp2	64.29	32.3	0.5164	1	0.91	1.54	-0.64
49_C2_sp3	63.55	32.54	1.04	1.33	1.82	2.05	-0.23
49_C2_sp5	62.84	32.47	0.8854	1.22	1.56	1.89	-0.33
49_C2_sp6	63.19	32.72	1.31	1.3	2.28	1.99	0.29
49_C2_sp7	61.31	32.53	1.53	1.85	2.74	2.91	-0.17
49_C2_sp8	63.45	32.99	1.56	1.5	2.71	2.29	0.42
49_C2_sp9	63.73	32.47	0.8618	1.44	1.51	2.22	-0.71
49_C3_sp1	60.78	32.39	3.06	2.09	5.30	3.18	2.12
49_C3_sp2	59.53	32.55	2.78	3.37	4.87	5.18	-0.32
49_C3_sp4	63.58	32.82	0.8901	1.01	1.57	1.57	0.00
49_C4_sp2	54.4	32.81	6.09	6.12	10.40	9.19	1.22
49_C4_sp3	61.71	32.68	0.9771	2.12	1.73	3.30	-1.57
49_C4_sp4	61.76	32.35	2.11	1.95	3.68	2.99	0.69
49_C4_sp5	63.35	32.72	1.03	1.51	1.80	2.32	-0.52
49_C4_sp6	62.91	32.61	1.3	1.23	2.28	1.90	0.38
49_C4_sp7	62.99	32.69	0.9106	1.95	1.59	3.00	-1.40
49_C4_sp8	62.15	32.42	1.05	1.95	1.86	3.04	-1.18
49_C5_sp1	59.72	32.8	2.35	2.99	4.16	4.66	-0.49

Sample	Zn	S	Fe	Cu	FeS	CuS	FeS*
49_C5_sp5	63.75	32.83	0.9932	1.57	1.73	2.41	-0.67
49_C5_sp6	61.86	32.83	2.21	2.41	3.83	3.67	0.16
49_C5_sp7	61.94	32.55	1.23	1.53	2.18	2.39	-0.20
49_C7_sp2	61.53	32.91	2.06	1.86	3.60	2.86	0.74
49_C7_sp3	61.55	32.65	1.83	2.46	3.21	3.79	-0.58
49_C7_sp4	62.26	32.6	1.93	1.62	3.38	2.49	0.89
49_C7_sp5	62.01	32.54	1.92	1.65	3.37	2.54	0.82
49_C7_sp5	61.66	32.74	2.29	2.49	3.98	3.80	0.18
49_C8_sp1	54.04	30.97	5.96	6.02	10.24	9.09	1.15
49_C8_sp2	60.28	32.87	2.96	1.73	5.17	2.66	2.52
49_C9_sp1	63.47	32.51	0.7333	0.9988	1.28	1.54	-0.25
49_C9_sp2	63.76	32.81	0.6446	1.16	1.14	1.80	-0.66
49_C10_sp1	55.84	33.2	8.21	2.49	13.98	3.73	10.25
49_C10_sp2	56.8	33.43	8.06	1.74	13.72	2.60	11.12
50_C1_sp1	64.84	33.31	1.57	0.3915	2.72	0.60	2.13
50_C1_sp2	61.49	33.39	3.41	0.8108	5.91	1.23	4.67
50_C1_sp3	64.32	33.05	0.5395	0.811	0.96	1.26	-0.31
50_C1_sp4	64.71	33.14	2.05	0.1213	3.55	0.18	3.36
50_C1_sp5	65.28	33.19	1.06	0.3965	1.85	0.61	1.24
50_C1_sp6	64.36	33.07	1.96	0.276	3.41	0.42	2.98
50_C2_sp1	61.68	33.36	2.89	0.1303	5.15	0.20	4.95
50_C2_sp2	65.25	33.21	0.7181	0.2466	1.26	0.38	0.88
50_C2_sp3	63.78	33.41	2.22	0.1551	3.89	0.24	3.65
50_C2_sp4	64.02	32.67	1.28	0.4188	2.26	0.65	1.61
50_C2_sp6	64.87	33.1	1.28	0.2064	2.24	0.32	1.92
50_C2_sp8	64.5	33.03	0.8903	0.4132	1.57	0.64	0.93
50_C3_sp1	62.47	33.05	1.8	0.5559	3.22	0.87	2.34
50_C3_sp2	64.05	32.97	1.3	0.834	2.28	1.29	0.99
50_C3_sp3	62.48	33.29	3.27	0.2719	5.70	0.42	5.29
50_C3_sp4	64.36	33.05	0.9992	0.49	1.76	0.76	1.00
50_C4_sp1	62.71	33.48	3.28	0.674	5.65	1.02	4.63
50_C4_sp2	63.21	33.11	1.68	1.75	2.92	2.67	0.25
50_C4_sp3	64.32	33.17	1.39	0.5921	2.43	0.91	1.52
50_C4_sp4	63.82	33.12	1.72	0.5	3.01	0.77	2.24
50_C4_sp5	63.6	33.21	2.45	0.2212	4.27	0.34	3.93
50_C4_sp6	64.09	33.13	0.7616	0.8588	1.35	1.33	0.01
50_C4_sp7	64.62	33.06	0.9756	0.5495	1.72	0.85	0.87
50_C4_sp12	62.67	33.15	1.06	2.26	1.86	3.49	-1.63
50_C5_sp2	58.24	32.51	3.28	4.93	5.69	7.52	-1.83
50_C5_sp3	62.48	33.27	2.49	2.18	4.29	3.30	0.99
50_C5_sp5	62.93	33.06	2.02	1.79	3.51	2.73	0.78
50_C5_sp6	62.68	32.8	1.34	2.77	2.33	4.24	-1.90
50_C5_sp7	64.57	33.23	1.89	0.3451	3.27	0.52	2.75
50_C5_sp8	65.63	33.2	0.6755	0.6589	1.17	1.00	0.17
50_C5_sp9	65.77	33.25	0.7733	0.2945	1.34	0.45	0.89
50_C5_sp10	65.63	33.28	0.5883	0.5125	1.03	0.79	0.24
50_C5_sp11	66.09	33.07	0.3322	0.4202	0.58	0.64	-0.06
50_C5_sp12	63.26	33.06	1.62	2.5	2.79	3.78	-0.99
50_C6_sp1	65.26	33.27	0.6753	0.4817	1.18	0.74	0.44
50_C6_sp2	64.69	33.3	1.29	0.5182	2.25	0.79	1.45
50_C6_sp3	64.79	33.23	1.52	0.4348	2.64	0.66	1.98
50_C6_sp4	66.15	33.15	0.3858	0.1109	0.67	0.17	0.50
50_C6_sp5	64.5	33.01	1.3	0.8378	2.26	1.28	0.98
50_C6_sp6	62.66	33.21	2.99	0.7854	5.18	1.19	3.98
50_C6_sp7	63.53	33.18	2.09	1.72	3.59	2.60	0.99
50_C7_sp1	62.85	33.16	1.59	0.7696	2.83	1.20	1.63
50_C7_sp2	66.18	33.22	0.269	0.2655	0.47	0.41	0.06
50_C7_sp3	66.33	33.13	0.5503	0.1803	0.96	0.28	0.68
50_C7_sp4	65.03	33.23	1.07	0.8365	1.86	1.28	0.58
50_C7_sp5	64.47	33.15	1.59	0.7516	2.76	1.15	1.62
50_C8_sp1	62.57	33.2	3.55	0.0686	6.19	0.11	6.08
50_C8_sp2	64.02	32.92	0.9646	1.34	1.69	2.06	-0.37
50_C8_sp3	63.77	33.1	1.1	1.24	1.93	1.91	0.02
50_C8_sp4	65.34	32.88	0.5475	0.3522	0.96	0.54	0.42

Table L17. Continued

Sample	Zn	S	Fe	Cu	FeS	CuS	FeS*
50_C8_sp5	65.11	33.02	1.08	0.7418	1.88	1.13	0.74
50_C8_sp6	65.54	33.21	0.4279	0.7397	0.75	1.14	-0.39
50_C8_sp7	65.56	33.42	0.4449	0.1239	0.78	0.19	0.59
52_C1_sp1	64.82	33.08	1.43	0.162	2.49	0.25	2.24
52_C1_sp2	65.5	32.97	1.45	0.1154	2.51	0.18	2.33
52_C1_sp3	63.77	32.83	2.07	0.5836	3.60	0.89	2.71
52_C1_sp4	63.31	32.28	0.8514	0.362	1.52	0.57	0.95
52_C1_sp5	63.39	31.99	0.218	0.1975	0.39	0.31	0.08
52_C1_sp6	60.99	31.52	0.2881	1.86	0.52	2.96	-2.44
52_C1_sp7	64.49	33.23	1.93	0.2005	3.34	0.31	3.04
52_C1_sp8	64.22	32.92	1.91	0.3035	3.33	0.46	2.86
52_C1_sp9	64.45	32.25	0.8765	0.1811	1.55	0.28	1.27
52_C1_sp10	64.3	32.21	0.591	0.1212	1.05	0.19	0.86
52_C1_sp11	63.86	32.12	0.3189	0.0683	0.57	0.11	0.46
52_C1_sp12	64.15	32.12	0.3418	0.0714	0.61	0.11	0.50
52_C1_sp13	63.42	32	0.2479	0.2361	0.45	0.37	0.07
52_C1_sp14	61.98	31.69	0.2936	1.07	0.53	1.70	-1.17
52_C2_sp1	65.12	32.98	1.26	0.3616	2.18	0.55	1.63
52_C2_sp2	65.35	32.98	1.39	0.1892	2.41	0.29	2.12
52_C2_sp3	63.09	32.97	2.29	0.3427	4.02	0.53	3.49
52_C2_sp4	65.44	32.86	1.04	0.2147	1.81	0.33	1.48
52_C2_sp5	63.56	32.88	2.09	0.2693	3.65	0.41	3.24
52_C3_sp1	62.45	33	2.04	0.9617	3.59	1.49	2.11
52_C3_sp2	64.23	32.91	1.38	0.5232	2.42	0.81	1.61
52_C3_sp3	63.1	33.49	2.6	0.3889	4.53	0.60	3.93
52_C3_sp4	65.63	32.98	1.05	0.324	1.82	0.49	1.33
52_C3_sp5	64.47	32.95	1.7	0.2289	2.96	0.35	2.61
52_C3_sp6	65.44	32.87	1.44	0.2412	2.49	0.37	2.12
52_C3_sp7	64.98	32.96	1.76	0.3355	3.04	0.51	2.53
52_C4_sp2	64.88	32.92	1.68	0.1907	2.91	0.29	2.62
52_C4_sp3	65.13	32.75	1.74	0.212	3.00	0.32	2.67
52_C4_sp4	64.01	32.66	2.08	0.3411	3.60	0.52	3.08
52_C4_sp5	63.6	32.73	1.42	1.03	2.48	1.58	0.90
52_C4_sp6	61.16	31.52	0.1273	0.4954	0.23	0.79	-0.56
52_C4_sp7	64.95	32.64	1.24	0.2036	2.16	0.31	1.85
52_C4_sp8	64.07	32.62	1.42	0.3157	2.49	0.49	2.00
52_C4_sp9	63	33.02	2.96	0.6722	5.12	1.02	4.10
52_C4_sp10	64.37	32.37	0.5073	0.2617	0.90	0.41	0.49
52_C4_sp11	62.23	31.74	0.3742	1.39	0.67	2.19	-1.52
52_C4_sp12	62.61	31.88	0.3412	0.8743	0.61	1.38	-0.77
52_C5_sp1	64.83	32.86	1.24	0.3317	2.14	0.50	1.64
52_C5_sp2	65	32.79	1.32	0.3711	2.29	0.57	1.72
52_C5_sp3	65.24	32.96	1.54	0.1649	2.66	0.25	2.41
52_C5_sp4	63.86	33.12	2.72	0.2224	4.71	0.34	4.37
52_C5_sp5	64.14	32.32	1.46	0.2877	2.56	0.44	2.11
52_C5_sp6	64.59	32.36	0.4231	0.1751	0.75	0.27	0.48
52_C5_sp7	63.73	32.23	0.3379	0.474	0.60	0.74	-0.14
52_C5_sp8	63.25	32.96	3.09	0.3079	5.35	0.47	4.89
52_C5_sp9	61.56	31.92	0.1418	0.3411	0.26	0.55	-0.29
52_C5_sp10	63.78	32.81	1.85	0.2089	3.23	0.32	2.91
52_C5_sp11	64.33	33.08	1.49	0.3151	2.60	0.48	2.11
52_C6_sp1	63.88	32.66	1.64	0.3492	2.87	0.54	2.33
52_C6_sp2	63.97	32.91	2.35	0.4023	4.05	0.61	3.44
52_C6_sp3	64.62	33.11	1.85	0.0877	3.21	0.13	3.07
52_C6_sp4	64.52	33.13	1.04	0.0326	1.84	0.05	1.79
52_C6_sp5	64.07	32.68	1.41	0.2762	2.47	0.43	2.05
52_C7_sp2	62.62	32.61	1.57	0.2878	2.82	0.45	2.37
52_C8_sp1	65.21	32.76	1.33	0.0727	2.31	0.11	2.20
52_C8_sp2	61.84	32.56	3.57	0.9568	6.19	1.46	4.73
52_C8_sp3	64.58	32.55	1.77	0.1268	3.07	0.19	2.87
52_C8_sp4	63.41	32.31	0.6643	1.62	1.17	2.50	-1.33
52_C8_sp5	61.19	32.49	3.13	1.4	5.45	2.14	3.31
52_C8_sp6	62.65	32.44	1.1	1.64	1.94	2.54	-0.60
52_C8_sp7	64.78	32.69	1.24	0.23	2.16	0.35	1.81

Sample	Zn	S	Fe	Cu	FeS	CuS	FeS*
52_C8_sp8	53.53	32.89	6.07	5.61	10.60	8.61	1.99
52_C8_sp9	64.38	32.84	1.46	0.2461	2.56	0.38	2.18
52_C8_sp10	64.19	32.58	1.59	0.2247	2.78	0.35	2.43
52_C8_sp11	63.94	32.89	2.01	0.1424	3.51	0.22	3.29
52_C9_sp1	63.92	32.82	1.77	0.1459	3.09	0.22	2.87
52_C9_sp2	63.99	32.88	2.1	0.3713	3.64	0.57	3.08
52_C9_sp3	63.02	32.78	2.52	0.5382	4.40	0.83	3.57
52_C9_sp4	62.48	33.08	2.75	0.7185	4.83	1.11	3.72
52_C10_sp1	63.53	32.54	2.38	0.492	4.12	0.75	3.37
52_C10_sp2	62.86	32.55	2.72	0.6131	4.72	0.93	3.78
52_C10_sp3	64.62	32.7	1.77	0.4789	3.06	0.73	2.33
52_C10_sp4	65.37	32.76	0.8806	0.2003	1.54	0.31	1.23
52_C10_sp5	62.4	32.98	3.15	0.7802	5.42	1.18	4.24
52_C10_sp6	63.7	32.83	2.48	0.4344	4.29	0.66	3.63
52_C10_sp7	63.16	32.84	2.93	0.414	5.07	0.63	4.44
52_C10_sp8	63.86	33.19	2.04	0.1695	3.57	0.26	3.31
52_C10_sp9	62.2	32.68	3.08	0.9398	5.34	1.43	3.91
52_C10_sp10	61.29	32.63	3.48	1.2	6.04	1.83	4.21
52_C10_sp12	63.01	32.77	2.81	0.3678	4.88	0.56	4.32
52_C10_sp13	64.21	32.59	1.55	0.5795	2.71	0.89	1.82
52_C10_sp14	63.91	32.25	0.9099	0.859	1.60	1.33	0.27
52_C11_sp1	65.32	32.63	0.9764	0.1911	1.70	0.29	1.41
52_C11_sp2	63.09	33.08	2.69	0.2443	4.71	0.38	4.34
58_C2_sp1	62.87	33.02	1.44	0.7554	2.52	1.16	1.36
58_C2_sp2	64.7	33.14	0.4498	0.3645	0.79	0.56	0.23
58_C2_sp3	58.41	32.01	1.93	1.71	3.48	2.71	0.77
58_C3_sp1	61.11	31.86	0.0402	0.5433	0.07	0.88	-0.80
58_C3_sp4	63.83	32.83	0.1413	0.2172	0.25	0.34	-0.09
58_C4_sp1	62.49	32.88	0.6905	1.41	1.22	2.19	-0.97
58_C4_sp2	62.5	32.81	1.16	1.13	2.05	1.75	0.29
58_C4_sp3	62.72	33.1	1.05	1.02	1.85	1.58	0.27
58_C4_sp4	63.8	32.89	0.7064	0.7193	1.24	1.11	0.13
58_C4_sp5	63.14	32.56	0.2142	0.3733	0.38	0.59	-0.20
58_C5_sp1	62.46	32.89	0.7887	1.19	1.40	1.85	-0.46
58_C5_sp2	64.33	33.06	0.8401	0.5451	1.47	0.84	0.63
58_C5_sp3	61.41	32.33	0.6391	0.8768	1.16	1.40	-0.24
58_C6_sp1	63.37	32.97	0.9824	0.6805	1.73	1.05	0.68
58_C6_sp2	60.41	32.42	0.7971	2.29	1.41	3.55	-2.14
58_C7_sp1	61.52	32.76	0.437	1.99	0.77	3.09	-2.32
58_C7_sp2	63.36	33.11	0.4198	0.6869	0.75	1.08	-0.33
58_C7_sp3	62.25	32.49	0.0793	0.3088	0.14	0.49	-0.35
58_C8_sp1	63.33	33.03	0.4708	0.8415	0.83	1.30	-0.47
58_C8_sp2	63.53	32.92	0.8621	1.14	1.50	1.75	-0.24
58_C8_sp3	63.6	33.32	1.16	1.08	2.02	1.65	0.37
58_C8_sp4	63.92	33.02	0.6905	0.7949	1.21	1.22	-0.01
58_C8_sp5	61.35	33.24	2.75	0.4223	4.86	0.66	4.20
58_C9_sp1	64.27	33.33	0.424	1.06	0.74	1.63	-0.89
58_C9_sp2	64.41	33.12	0.4228	0.4521	0.75	0.70	0.04
58_C9_sp3	64.01	33.26	2.09	0.1198	3.65	0.18	3.47
58_C9_sp5	64.45	32.95	0.5407	0.8748	0.95	1.35	-0.40
58_C9_sp6	63.58	33.44	2.34	0.1444	4.09	0.22	3.87
58_C9_sp7	63.03	32.96	1.25	0.5961	2.21	0.93	1.28
58_C9_sp8	58.57	32.34	0.8486	3.48	1.51	5.44	-3.93
58_C9_sp9	59.47	32.04	0.8918	1.77	1.62	2.82	-1.20
58_C10_sp1	60.69	32.54	0.5095	2.55	0.90	3.97	-3.07
58_C10_sp2	62.36	32.38	0.6213	0.9141	1.11	1.43	-0.32
58_C10_sp3	59.75	32.58	2.02	1.73	3.60	2.71	0.89
58_C10_sp4	59.55	31.97	0.6761	2.36	1.22	3.73	-2.52
58_C10_sp5	60.27	32.76	0.5281	2.83	0.93	4.40	-3.47
58_C10_sp6	62.9	32.76	0.3953	1.47	0.70	2.27	-1.58
58_C10_sp7	62.55	32.79	0.4115	1.85	0.72	2.86	-2.13
58_C10_sp8	61.92	32.47	0.6234	1.89	1.10	2.93	-1.83
58_C10_sp9	61.55	32.5	0.3124	2.27	0.55	3.53	-2.98
58_C10_sp10	62.43	32.51	0.7593	1.75	1.33	2.70	-1.37

Table L17. Continued

Sample	Zn	S	Fe	Cu	FeS	CuS	FeS*
58_C10_sp11	62.34	32.35	0.235	1.93	0.41	2.97	-2.56
58_C10_sp12	61.77	32.37	0.1839	1.87	0.33	2.93	-2.60
58_C10_spy13	63.5	32.55	0.1244	0.6994	0.22	1.09	-0.87
58_C11_sp1	61.3	33.23	2.57	1.15	4.51	1.77	2.74
58_C11_sp2	58.96	32.12	1.05	2.41	1.88	3.79	-1.91
58_C11_sp3	60.64	32.46	0.9151	1.96	1.63	3.06	-1.44
58_C11_sp4	61.03	32.81	0.7992	1.89	1.42	2.96	-1.54
58_C11_sp5	60.09	32.17	0.6562	2.2	1.18	3.46	-2.29
58_C11_sp6	62.1	32.78	1.2	1.54	2.11	2.38	-0.27
58_C11_sp7	61.65	32.6	0.3156	2.08	0.56	3.23	-2.68
58_C11_sp8	62.66	32.66	0.7104	1.07	1.26	1.67	-0.41
58_C11_sp9	61.88	32.66	0.3959	1.54	0.70	2.40	-1.70
58_C11_sp10	60.98	32.1	0.1246	1.93	0.22	3.04	-2.82
58_C11_sp11	59.63	32.16	0.1446	1.38	0.26	2.22	-1.95
61_C2_sp1	60.56	32.25	1.67	2.12	2.98	3.32	-0.34
61_C2_sp2	62.92	32.76	1.53	0.997	2.70	1.55	1.15
61_C2_sp5	60.64	32.03	1.59	2.26	2.82	3.52	-0.70
61_C2_sp6	59.23	31.67	1.32	2.71	2.37	4.28	-1.91
61_C5_sp4	63.05	32.45	0.9451	0.5368	1.68	0.84	0.84
61_C5_sp5	61.37	32.06	0.5277	0.897	0.96	1.43	-0.47
61_C5_sp6	62.92	32.09	0.7473	0.2961	1.33	0.46	0.87
61_C6_sp2	60.04	32.27	0.857	1.86	1.55	2.95	-1.40
61_C6_sp3	61.06	31.92	0.7377	0.9091	1.35	1.46	-0.11
61_C6_sp4	62.21	31.88	0.5073	0.3231	0.91	0.51	0.40
61_C6_sp8	62.1	33.27	2.64	0.324	4.67	0.50	4.17
61_C6_sp9	62.46	32.58	1.56	0.3928	2.80	0.62	2.18
61_C7_sp1	61.73	32.27	0.6802	1.87	1.20	2.91	-1.71
61_C7_sp2	61.74	32.24	0.8537	1.92	1.50	2.96	-1.46
61_C7_sp3	64.47	32.71	0.6759	0.5732	1.19	0.89	0.30
61_C7_sp4	62.36	32.62	0.4514	1.24	0.81	1.96	-1.15
61_C7_sp6	61	32.22	0.7216	1.62	1.29	2.55	-1.26
61_C7_sp7	64.98	32.86	1.17	0.2205	2.02	0.34	1.69
61_C7_sp8	64.88	32.78	0.7298	0.4854	1.28	0.75	0.53
61_C7_sp9	62.74	32.42	0.9279	1.31	1.64	2.04	-0.40
61_C7_sp10	63.38	32.76	0.8897	1.03	1.57	1.60	-0.03
61_C7_sp11	62.52	32.32	0.7636	1.26	1.36	1.97	-0.61
61_C7_sp12	62.81	32.52	0.6692	1.45	1.18	2.25	-1.07
61_C8_sp1	61.6	32.21	0.6484	1.45	1.17	2.30	-1.13
61_C8_sp2	64.63	32.79	0.5779	0.6516	1.02	1.01	0.01
61_C8_sp3	64.46	32.7	1.02	0.29	1.80	0.45	1.35
61_C8_sp4	64.75	32.66	0.8194	0.4391	1.44	0.68	0.76
61_C8_sp5	63.46	32.71	0.612	0.5079	1.10	0.80	0.30
61_C9_sp1	64.02	32.65	0.9973	0.71	1.76	1.10	0.66
61_C9_sp2	63.79	32.74	0.7345	0.5921	1.31	0.92	0.38
61_C9_sp3	63.98	32.59	0.8747	0.4928	1.55	0.77	0.78
61_C9_sp4	63.57	32.34	1.09	0.1753	1.94	0.27	1.67
61_C9_sp5	62.71	32.58	1.69	0.2385	3.01	0.37	2.64
61_C9_sp6	60.85	32.22	0.6068	1.87	1.09	2.95	-1.86
61_C9_sp7	60.75	32.03	0.2966	1.53	0.54	2.44	-1.90
61_C9_sp8	63.1	33.46	1.04	0.0814	1.88	0.13	1.75
61_C11_sp1	60.34	32.73	3.56	0.4651	6.35	0.73	5.62
61_C11_sp2	62.24	32.7	1.87	0.9079	3.31	1.41	1.90
62_C1_sp1	64.73	32.44	0.9466	0.1414	1.66	0.22	1.44
62_C1_sp2	63.92	32.76	0.4361	1.9	0.76	2.92	-2.16
62_C1_sp3	65.74	32.67	0.6187	0.5984	1.08	0.91	0.16
62_C1_sp4	66.34	32.39	0.2294	0.0263	0.40	0.04	0.36
62_C1_sp5	66.21	32.68	0.274	0.3005	0.47	0.46	0.02
62_C2_sp1	63.55	32.32	0.4599	2.1	0.80	3.21	-2.41
62_C2_sp2	66.66	32.7	0.2696	0.1511	0.47	0.23	0.24
62_C2_sp3	66.58	32.28	0.294	0.0972	0.51	0.15	0.36
62_C3_sp1	65.81	32.49	0.7217	0.4169	1.25	0.64	0.62
62_C3_sp2	62.1	32.34	1.85	0.9711	3.24	1.49	1.75
62_C4_sp1	66.66	32.25	0.6849	0.2303	1.18	0.35	0.83
62_C4_sp2	64.91	32.56	0.9366	0.0899	1.64	0.14	1.51
62_C4_sp3	60.26	32.1	3.72	1.95	6.43	2.96	3.47
62_C4_sp4	64.97	32.69	1.21	0.2505	2.11	0.38	1.73
62_C5_sp1	65.27	32.75	1.02	0.1235	1.78	0.19	1.59
62_C5_sp2	63.18	32.15	1.92	1.14	3.34	1.74	1.59
62_C5_sp3	63.25	32.34	1.99	0.1239	3.49	0.19	3.30
62_C5_sp4	62.84	32.5	1.06	1.54	1.87	2.38	-0.52
62_C6_sp1	64.5	32.75	1.38	0.191	2.41	0.29	2.12
62_C6_sp2	65.03	32.64	1.38	0.46	2.39	0.70	1.69
62_C7_sp1	64.55	32.47	2	0.2286	3.46	0.35	3.12
62_C7_sp2	65.8	32.53	0.8842	0.3752	1.52	0.57	0.95
62_C7_sp3	64.75	32.35	1.99	0.0581	3.43	0.09	3.34
62_C8_sp1	64.02	32.24	1.89	0.6485	3.25	0.98	2.27
62_C9_sp1	63.44	32.6	1.64	1.19	2.85	1.82	1.03
62_C9_sp2	63.15	32.16	1.67	1.02	2.92	1.56	1.35
62_C10_sp1	63.56	33.03	2.06	0.2313	3.59	0.35	3.24
62_C11_sp1	64.55	32.06	0.7573	0.0988	1.34	0.15	1.19
62_C11_sp2	65.87	32.59	0.2868	0.8775	0.50	1.34	-0.84
62_C11_sp3	65.54	32.22	0.4493	0.9626	0.78	1.47	-0.69
62_C12_sp1	66.22	32.42	0.2902	0.5291	0.50	0.81	-0.30
62_C13_sp1	65.35	32.57	1.18	0.1502	2.05	0.23	1.82
62_C14_sp1	64.72	32.63	1.33	0.3941	2.31	0.60	1.71
62_C14_sp2	63.74	32.59	1.87	0.4825	3.26	0.74	2.52

Table L18. Summary of EPMA analyses of sphalerite with mole% FeS from footwall samples (from Anders, 2016)

Sample	Zn	S	Fe	Cd	Cu	FeS
MA13-090_07_sph_cr01	65.76	32.75	1.49	0.22	<0.01	2.65
MA13-090_07_sph_cr02	66.14	32.65	1.36	0.20	<0.01	2.40
MA13-090_07_sph_cr03	65.79	32.61	1.37	0.22	0.09	2.43
MA13-090_07_sph_cr04	65.44	33.13	1.31	0.27	0.09	2.33
MA13-090_07_sph_cr05	65.98	33.17	1.42	0.24	<0.01	2.51
MA13-090_07_sph_cr06	65.44	32.73	1.36	0.27	<0.01	2.43
MA13-090_07_sph_cr07	66.35	33.08	0.73	0.30	0.06	1.28
MA13-090_07_sph_cr08	66.17	32.58	0.83	0.30	0.07	1.46
MA13-090_07_sph_cr09	66.41	32.61	0.81	0.28	0.19	1.42
MA13-090_07_sph_cr10	64.31	32.71	1.25	0.33	1.17	2.23
MA13-090_09_sph_cr01	65.97	32.92	1.06	0.24	<0.01	1.88
MA13-090_09_sph_cr02	66.37	32.72	1.07	0.25	<0.01	1.88
MA13-090_09_sph_cr03	66.28	33.14	1.20	0.22	<0.01	2.12
MA13-090_09_sph_cr04	65.76	33.12	1.30	0.20	<0.01	2.31
MA13-090_09_sph_cr05	66.06	33.12	1.35	0.18	<0.01	2.39
MA13-090_09_sph_cr06	66.29	32.65	0.82	0.27	0.06	1.44
MA13-090_09_sph_cr07	66.28	33.14	1.05	0.23	<0.01	1.85
MA13-090_09_sph_cr08	65.6	32.81	1.12	0.26	0.08	1.99
MA13-090_09_sph_cr09	66.28	32.77	1.12	0.34	<0.01	1.97
MA13-090_09_sph_cr10	65.26	33.15	1.16	0.39	0.34	2.06
MA13-090_11_sph_rr02	65.72	33.10	1.24	0.62	0.22	2.19
MA13-090_11_sph_rr03	66.03	32.82	1.08	0.57	0.19	1.90
MA13-090_11_sph_rr04	65.91	33.06	1.09	0.63	0.05	1.92
MA13-090_11_sph_rr05	65.94	32.87	0.98	0.61	<0.01	1.73
MA13-090_11_sph_rr06	66.29	32.95	1.04	0.60	<0.01	1.83
MA13-090_11_sph_rr07	66.15	33.41	1.04	0.66	<0.01	1.83
MA13-090_11_sph_rr08	65.96	32.73	1.03	0.63	0.09	1.82
MA13-090_11_sph_rr09	65.8	33.02	1.04	0.64	0.14	1.84
MA13-090_11_sph_rr10	65.27	33.19	0.88	0.55	0.21	1.57
P0005_04_sph_cr01	62.89	33.19	3.76	0.30	0.09	6.97
P0005_04_sph_cr03	64.29	32.83	2.61	0.16	<0.01	4.75
P0005_04_sph_cr04	64.64	33.17	1.84	0.22	0.08	3.32
P0005_04_sph_cr05	65.39	32.97	1.74	0.20	<0.01	3.11
P0005_04_sph_cr06	65.19	33.30	1.54	0.18	<0.01	2.76
P0005_04_sph_cr07	64.95	32.72	1.88	0.15	<0.01	3.38
P0005_04_sph_cr08	66.41	32.81	0.82	0.07	0.13	1.44
P0005_04_sph_cr09	67.19	32.58	0.24	0.24	<0.01	0.42
P0005_07_sph_cr01	64.76	32.79	1.23	0.13	1.38	2.17
P0005_07_sph_cr02	63.60	33.10	1.69	0.11	1.85	3.02
P0005_07_sph_cr03	65.02	33.24	2.12	0.11	0.09	3.81
P0005_07_sph_cr04	65.71	33.17	1.16	0.10	0.99	2.03
P0005_07_sph_cr05	62.87	33.00	2.77	0.27	1.50	5.02
P0005_07_sph_cr06	63.25	33.12	3.05	0.20	<0.01	5.63
P0005_07_sph_cr07	64.35	33.08	2.39	0.21	<0.01	4.34
P0005_07_sph_cr08	61.52	33.33	3.32	0.29	1.55	6.14
P0005_07_sph_cr09	63.99	33.13	1.34	0.20	1.30	2.40
P0005_09_sph_cr01	63.97	33.00	2.90	0.16	0.06	5.29
P0005_09_sph_cr02	64.52	33.12	2.49	0.11	<0.01	4.51
P0005_09_sph_cr03	64.73	33.44	2.19	0.08	<0.01	3.96
P0005_09_sph_cr04	62.83	33.32	3.41	0.34	<0.01	6.33
P0005_09_sph_cr05	62.83	33.49	3.52	0.37	<0.01	6.54
P0005_09_sph_cr06	63.09	33.39	3.03	0.34	<0.01	5.60
P0005_09_sph_cr07	65.06	33.21	1.75	0.23	<0.01	3.14
P0005_09_sph_cr08	65.60	33.36	1.30	0.26	0.34	2.30
P0005_09_sph_cr09	65.78	33.27	1.17	0.15	<0.01	2.08
P0005_09_sph_cr10	64.53	33.54	1.21	0.17	1.24	2.15
P0005_11_sph_cr01	64.42	32.92	0.75	0.19	1.06	1.34
P0005_11_sph_cr02	64.35	32.58	1.07	0.20	1.25	1.91
P0005_11_sph_cr03	62.34	32.62	1.76	0.25	2.59	3.16
P0005_11_sph_cr04	63.84	33.11	1.43	0.21	1.59	2.55
P0005_11_sph_cr05	65.55	32.61	0.83	0.18	0.53	1.47
P0005_11_sph_cr06	65.50	32.91	1.15	0.13	<0.01	2.05
P0005_11_sph_cr07	65.51	32.84	1.13	0.24	<0.01	2.02
P0005_11_sph_cr08	65.56	33.11	1.24	0.20	<0.01	2.21
P0005_11_sph_cr09	64.40	32.72	1.49	0.14	0.68	2.68
P0005_11_sph_cr10	65.94	32.75	1.07	0.17	<0.01	1.90
P0005_11_sph_cr11	66.30	32.85	0.55	0.22	0.06	0.97
P0005_11_sph2_cr01	64.06	33.10	1.33	0.19	1.33	2.38
P0005_11_sph2_cr02	65.38	33.02	1.12	0.24	0.18	2.00
P0005_11_sph2_cr03	65.48	32.58	1.03	0.19	0.09	1.84
P0005_11_sph2_cr04	65.64	33.18	0.95	0.29	<0.01	1.69
P0005_11_sph2_cr05	65.59	32.98	0.87	0.21	0.07	1.55
P0005_11_sph2_cr06	65.81	32.80	1.03	0.22	<0.01	1.83
P0005_11_sph2_cr07	65.55	33.05	1.20	0.15	<0.01	2.14
P0005_11_sph2_cr08	65.69	32.77	0.85	0.27	0.22	1.51
P0005_12_sph_cr01	65.54	33.10	0.26	0.25	0.62	0.46
P0005_12_sph_cr02	65.15	33.63	1.20	0.05	0.20	2.15
P0005_12_sph_cr03	65.99	32.95	0.21	0.19	<0.01	0.37
P0005_12_sph_cr04	64.94	32.88	1.60	0.16	0.07	2.88
P0005_12_sph_cr05	65.70	33.10	1.26	0.32	0.10	2.24
P0005_12_sph_cr06	65.45	32.96	1.15	0.38	0.07	2.05
P0005_12_sph_cr08	65.26	33.16	1.26	0.30	<0.01	2.25
P0005_12_sph_cr09	65.02	32.60	1.26	0.19	<0.01	2.26
P0005_12_sph_cr10	65.46	32.59	0.63	0.24	<0.01	1.12
P0005_12_sph_cr11	65.37	32.95	0.93	0.30	<0.01	1.66
P0005_13_sph_cr01	60.02	32.80	3.26	0.23	3.35	6.00
P0005_13_sph_cr02	63.99	33.07	2.13	0.23	0.09	3.88
P0005_13_sph_cr03	64.25	32.68	1.98	0.20	<0.01	3.60
P0005_14_sph_cr04	66.42	32.91	0.96	0.04	<0.01	1.69
P0005_14_sph_cr05	66.28	32.67	0.23	0.14	0.08	0.41
P0005_14_sph_cr06	65.72	32.79	1.27	0.33	<0.01	2.26
P0005_14_sph_cr07	65.37	32.34	1.07	0.44	0.13	1.91
P0005_14_sph_cr08	65.44	32.66	1.08	0.19	<0.01	1.93
P0005_14_sph_cr09	65.94	32.62	0.76	0.25	<0.01	1.35
P0005_16_sph_rr07	63.23	32.44	3.01	0.19	0.12	5.55
P0005_17_sph_c03	64.17	33.13	0.90	0.31	0.32	1.63
P0005_18_sph_c02	66.17	33.17	1.19	0.28	<0.01	2.10
P0005_18_sph_c03	65.53	32.6	1.26	0.28	0.16	2.24
P0005_19_sph_rr01	62.93	33.26	1.17	0.23	2.12	2.10
P0005_19_sph_rr04	64.67	33.21	1.20	0.24	1.40	2.12
P0005_19_sph_rr013	65.01	33.15	1.52	0.32	0.58	2.70
P0005_19_sph_rr014	65.39	33.09	1.30	0.30	0.13	2.32
P0005_19_sph_rr015	65.02	32.98	1.13	0.17	0.58	2.01
P0005_20_sph_rr08	65.86	32.57	0.71	0.28	0.24	1.25
P0005_20_sph_rr09	65.77	32.89	0.53	0.28	0.36	0.94
P0005_20_sph_rr10	66.03	32.49	0.38	0.29	0.39	0.67
P0005_20_sph_rr11	65.27	33.10	0.63	0.28	0.98	1.11

Table L18. Average mineral formulas calculated from EPMA data (Table 4.7)

Mineral	Chimney Type	Avg. Mineral Formula
Chalcopyrite - $CuFeS_2$		
	Ccp-rich	$Cu_{0.55}Fe_{0.55}S_{1.08}$
	Zoned Ccp-rich	$Cu_{0.54}Fe_{0.54}S_{1.08}$
	Dendritic Sp-rich	$Cu_{0.54}Fe_{0.53}S_{1.08}$
	Dendritic Brt-rich	$Cu_{0.53}Fe_{0.52}S_{1.08}$
Pyrite - FeS_2		
	Ccp-rich	$Fe_{0.84}S_{1.64}$
	Zoned Ccp-rich	$Fe_{0.84}S_{1.63}$
	Dendritic Sp-rich	$Fe_{0.82}S_{1.63}$
Marcasite - FeS_2		
	Ccp-rich	$Fe_{0.85}S_{1.65}$
	Dendritic Sp-rich	$Fe_{0.84}S_{1.64}$
	Dendritic Brt-rich	$Fe_{0.84}S_{1.67}$
Sphalerite - (Zn,Fe)S		
	Ccp-rich	$(Zn_{0.98},Fe_{0.03})S_{1.04}$
	Zoned Ccp-rich	$(Zn_{0.96},Fe_{0.03})S_{1.02}$
	Dendritic Sp-rich	$(Zn_{0.97},Fe_{0.02})S_{1.02}$
	Dendritic Brt-rich	$(Zn_{0.96},Fe_{0.02})S_{1.02}$
Galena - PbS		
	Zoned Ccp-rich	$Pb_{0.42}S_{0.42}$
	Dendritic Sp-rich	$Pb_{0.41}S_{0.43}$
	Dendritic Brt-rich	$Pb_{0.40}S_{0.42}$
Jordanite - $Pb_{14}As_6S_{23}$		
	Zoned Ccp-rich	$Pb_{0.35}As_{0.10}S_{0.54}$
	Dendritic Sp-rich	$Pb_{0.34}As_{0.13}S_{0.56}$
	Dendritic Brt-rich	$Pb_{0.34}As_{0.13}S_{0.52}$
Covellite - CuS		
	Ccp-rich	$Cu_{0.96}S_{1.00}$
	Zoned Ccp-rich	$Cu_{1.02}S_{1.03}$
	Dendritic Sp-rich	$Cu_{1.01}S_{0.93}$
Bornite - Cu_5FeS_4		
	Zoned Ccp-rich	$Cu_{0.78}Fe_{0.28}S_{1.03}$

Appendix M

Supplementary Information for Chapter 5: Mineralogical and geochemical characteristics of hydrothermal alteration in the volcaniclastic-hosted Tinakula seafloor massive sulfide deposit (New Hebrides back-arc, SW Pacific)

Contents of this file:

1. Comparison between SWIR spectroscopy and XRD methods
2. Supplementary Figures:
    - **Fig. M1.** Downhole changes in whole-rock concentrations of selected major and trace elements for drillhole TKAD001.
    - **Fig. M2.** Downhole changes in whole-rock concentrations of selected major and trace elements for drillhole TKAD015.
    - **Fig. M3.** Downhole changes in whole-rock concentrations of selected major and trace elements for drillhole TKAD027
    - **Fig. M4.** Downhole changes in whole-rock concentrations of selected major and trace elements for drillhole TKAD016.
    - **Fig. M5.** Downhole changes in whole-rock concentrations of selected major and trace elements for drillhole TKAD025.
    - **Fig. M6.** Downhole changes in whole-rock concentrations of selected major and trace elements for drillhole TKAD026.
    - **Fig. M7.** Downhole changes in whole-rock concentrations of selected major and trace elements for drillhole TKAD012
    - **Fig. M8.** Downhole changes in whole-rock concentrations of selected major and trace elements for drillhole TKAD032.
    - **Fig. M9.** Downhole changes in whole-rock concentrations of selected major and trace elements for drillhole TKAD033.
    - **Fig. M10.** Downhole changes in whole-rock concentrations of selected major and trace elements for drillhole TKAD017.

Fig. M11. Downhole changes in whole-rock concentrations of selected major and trace elements for drillhole TKAD031.

Fig. M12. Downhole changes in whole-rock concentrations of selected major and trace elements for drillhole TKAD030.

Fig. M13. Downhole changes in whole-rock concentrations of selected major and trace elements for drillhole TKAD018.

Comparison between SWIR spectroscopy and XRD methods

Identifications of clay minerals using SWIR spectroscopy on bulk-rock samples and XRD analyses on clay-sized fractions are generally in good agreement. While both smectite and micas were identified using SWIR spectroscopy, this technique could not distinguish some phases in the bulk rock from mixed-layer I/S clays, resulting in an over-estimation of the amount of montmorillonite. Slight increases in the wavelength of the Al-OH absorption feature track progressive decreases in aluminum content, often interpreted to reflect changes in mica composition from paragonite to muscovitic illite (e.g., Velde, 1980). At Tinakula, interstratified mixed-layer I/S clays are associated with higher Al in the octahedral layers, resulting in shifts to lower wavelengths. This explains the abundance of paragonite identified by SWIR spectroscopy that was not identified by XRD analysis. Therefore, co-existing montmorillonite + paragonite/paragonitic-illite indicated by SWIR spectroscopy on the bulk samples is actually mixed layer I/S clays. In the bulk rock, the presence of anhydrite/gypsum dominates the SWIR spectrum and disguises other phases. Despite the careful hand-picking of clay-altered clasts from the sulfate-rich matrix and dry-sieving to <63 μm, almost a third of all samples contained sulfates. The TSG 7 software used to identify mineral phases works best for mixtures of only two minerals, further limiting the application of SWIR spectroscopy in this study where alteration is dominated by assemblages of polyminerallic clays. Finally, SWIR spectroscopy is relatively insensitive to small amounts of chlorite in such complex mixtures, with positive identification only possible in samples that contain more than ~50% of poorly crystallized chlorite.

The process of particle-size separation for XRD analysis was effective in removing sulfate phases and also detecting chlorite in samples with very low concentrations as indicated by whole-rock geochemistry. The main limitation of XRD analysis is that it requires a time-consuming process of particle-size separation in order to collect noise-free profiles, and it is uncertain whether the resulting clay-size fraction is reflective of the mineralogical composition of the bulk sample.

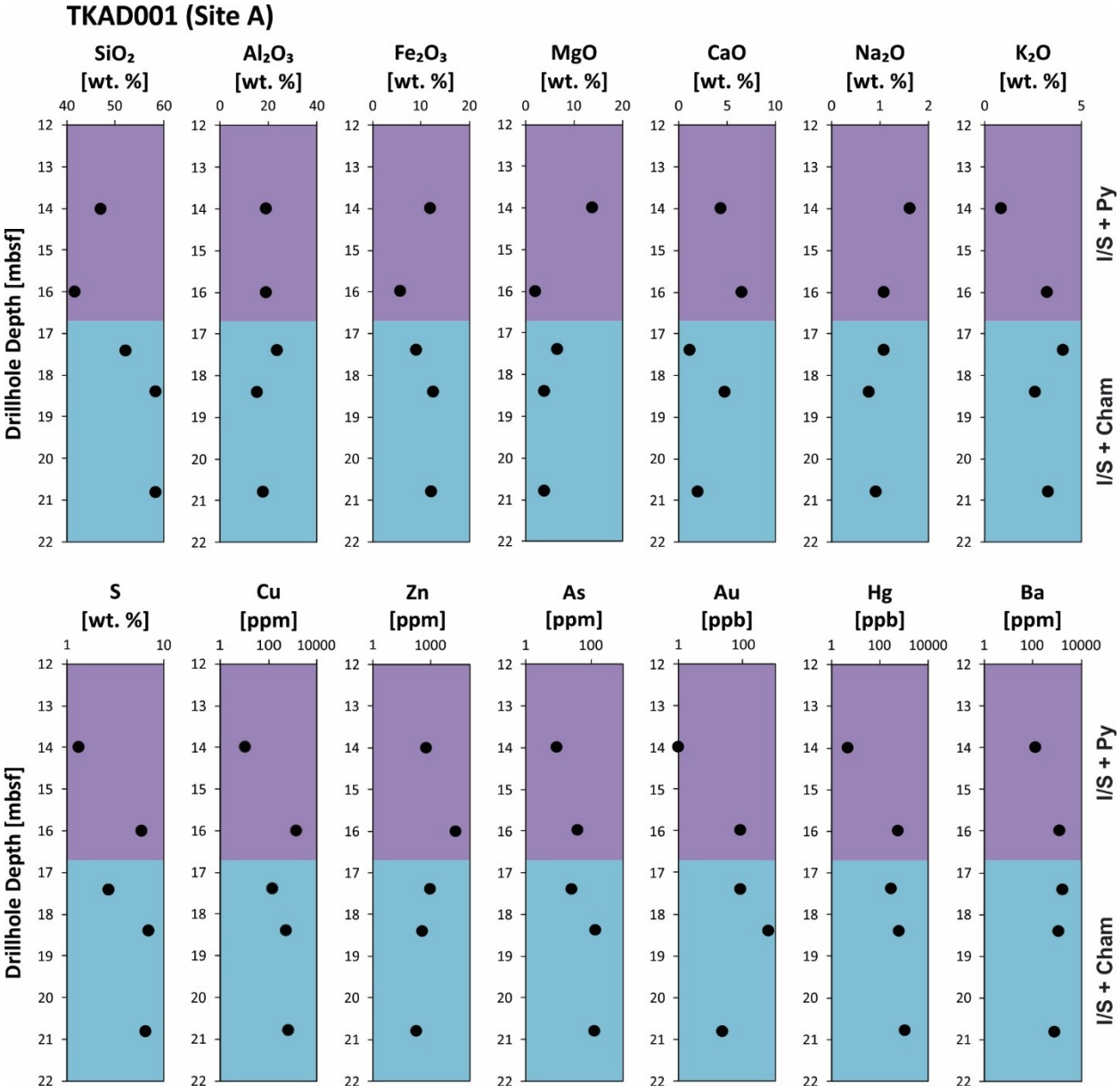


Fig. M1. Downhole changes in whole-rock concentrations of selected major and trace elements for drillhole TKAD001, with main alteration assemblages. Cham = chamosite; I/S = illite/smectite; Non = nontronite; Pl = plagioclase; Py = pyrite.

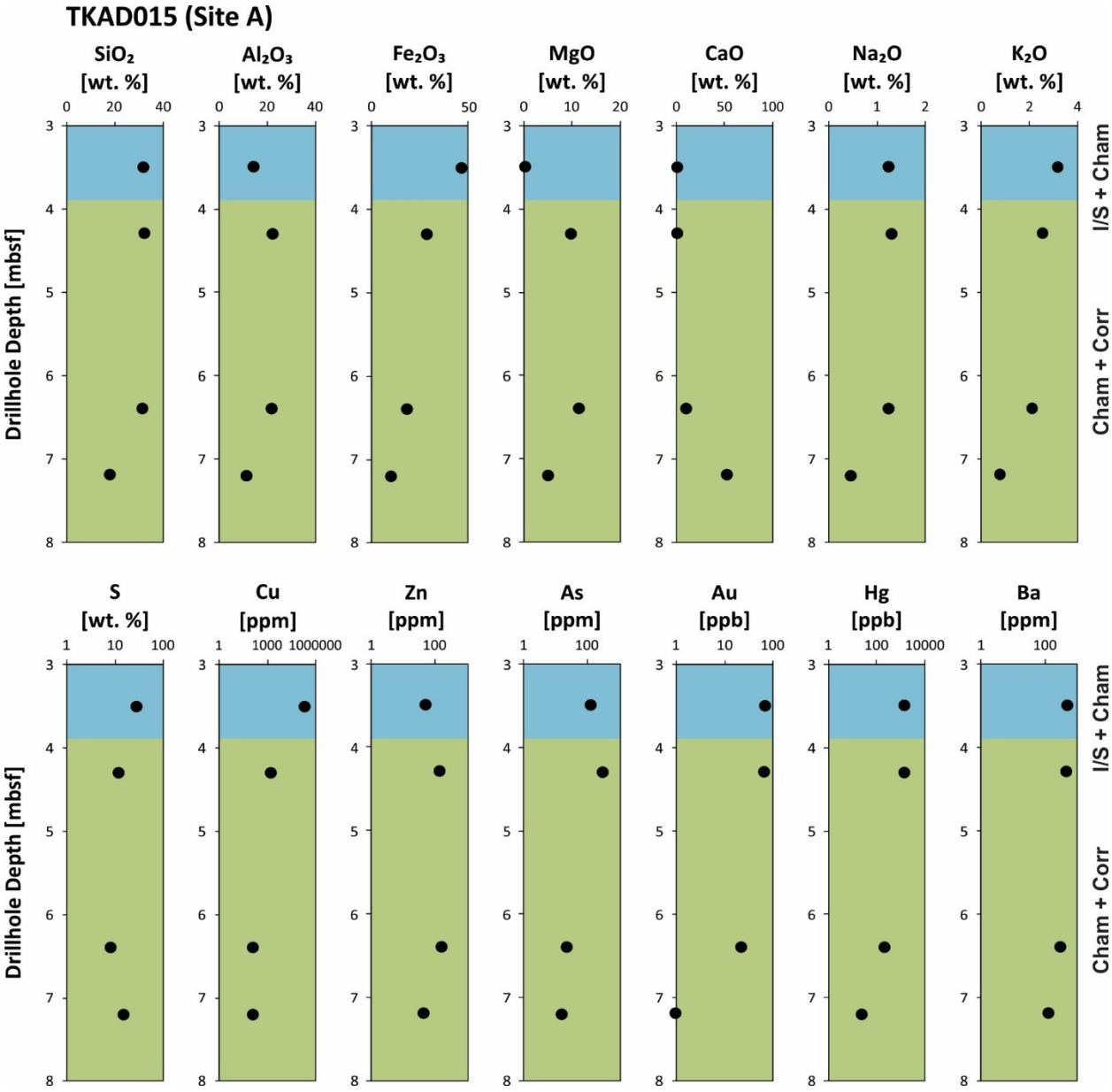


Fig. M2. Downhole changes in whole-rock concentrations of selected major and trace elements for drillhole TKAD015, with main alteration assemblages. Cham = chamosite; Corr = corrensite; I/S = illite/smectite.

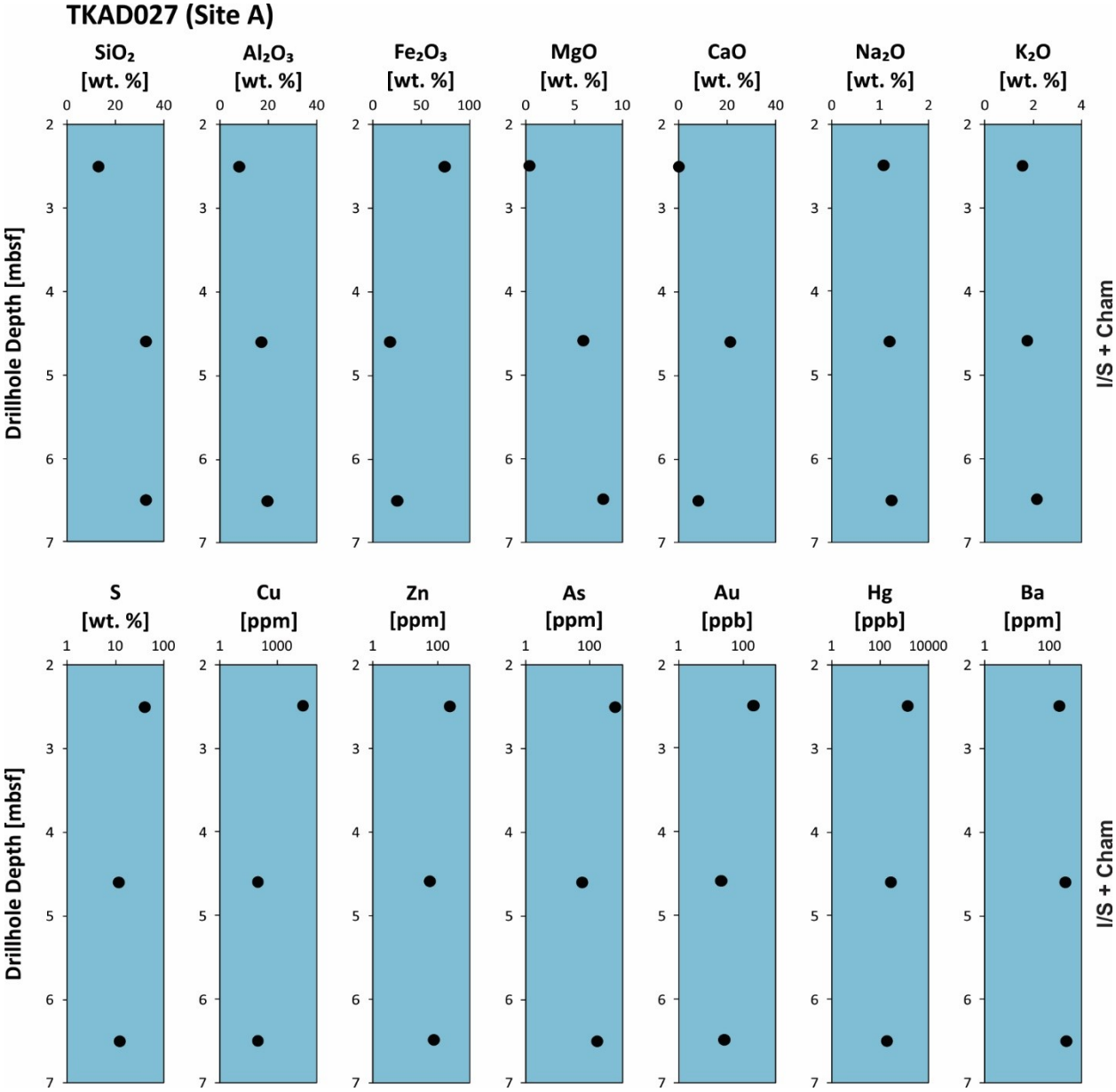


Fig. M3. Downhole changes in whole-rock concentrations of selected major and trace elements for drillhole TKAD027, with main alteration assemblages. Cham = chamosite; I/S = illite/smectite.

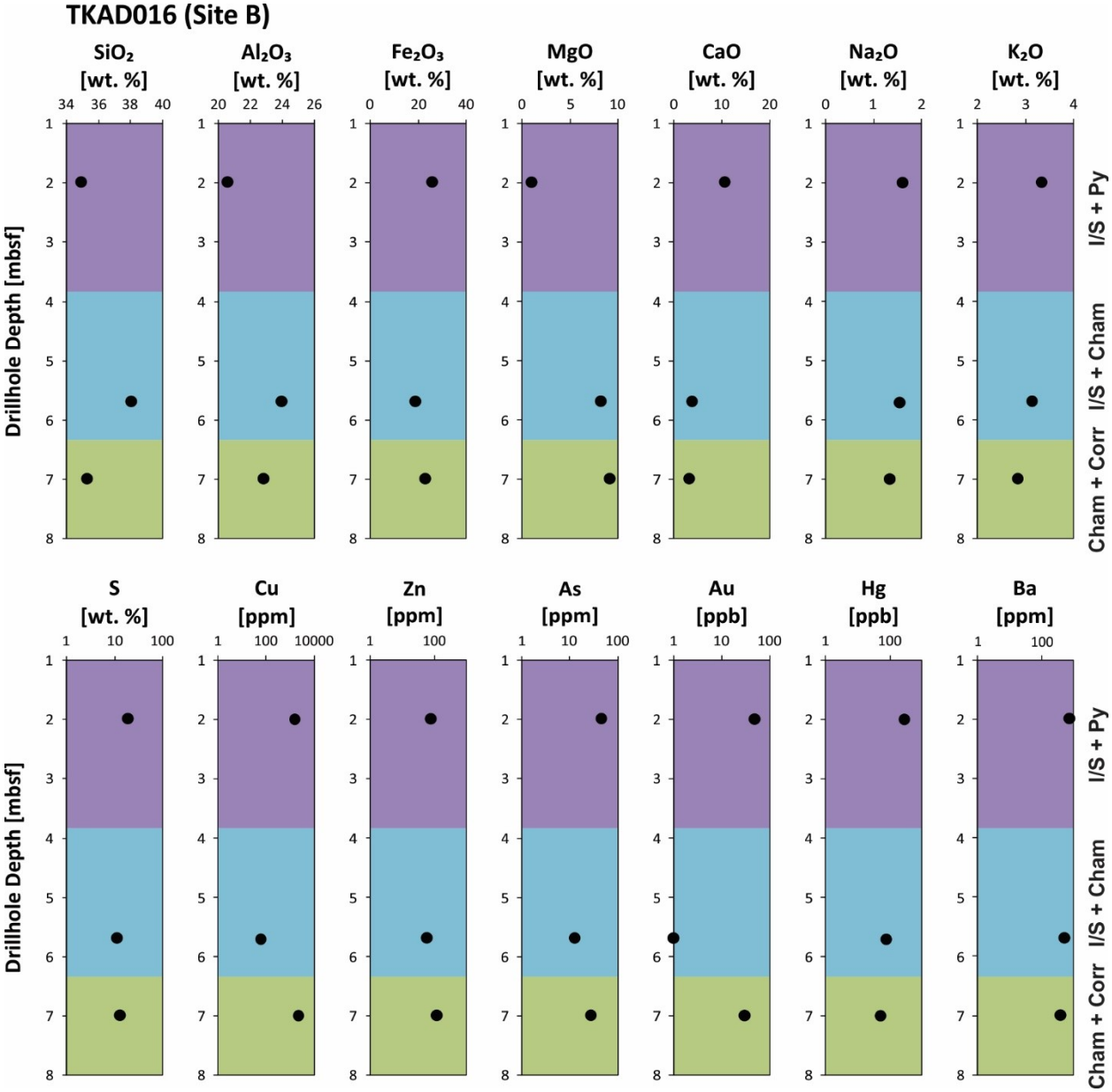


Fig. M4. Downhole changes in whole-rock concentrations of selected major and trace elements for drillhole TKAD016, with main alteration assemblages. Cham = chamosite; Corr = corrensite; I/S = illite/smectite; Py = pyrite.

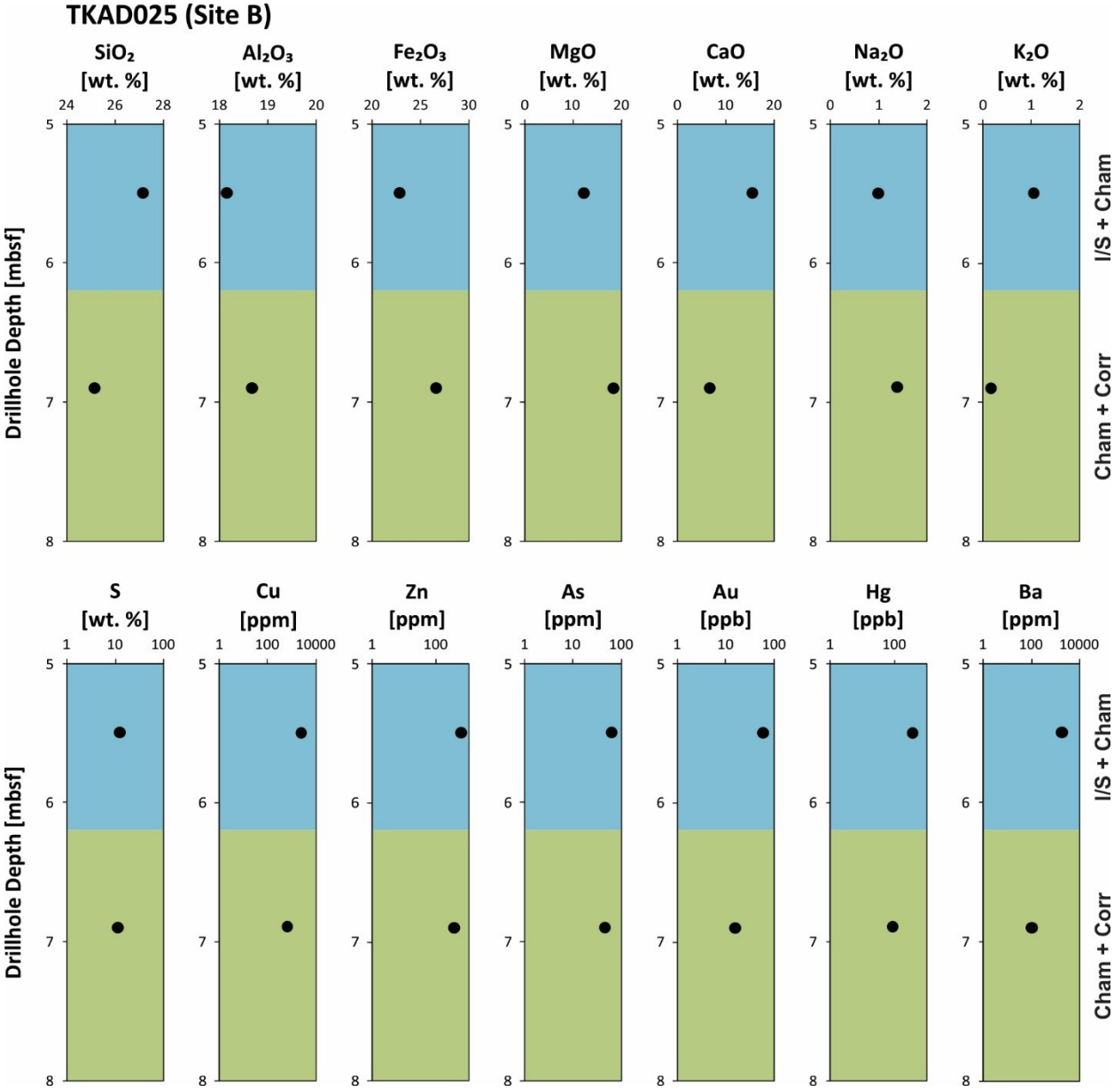


Fig. M5. Downhole changes in whole-rock concentrations of selected major and trace elements for drillhole TKAD025, with main alteration assemblages. Cham = chamosite; Corr = corrensite; I/S = illite/smectite.

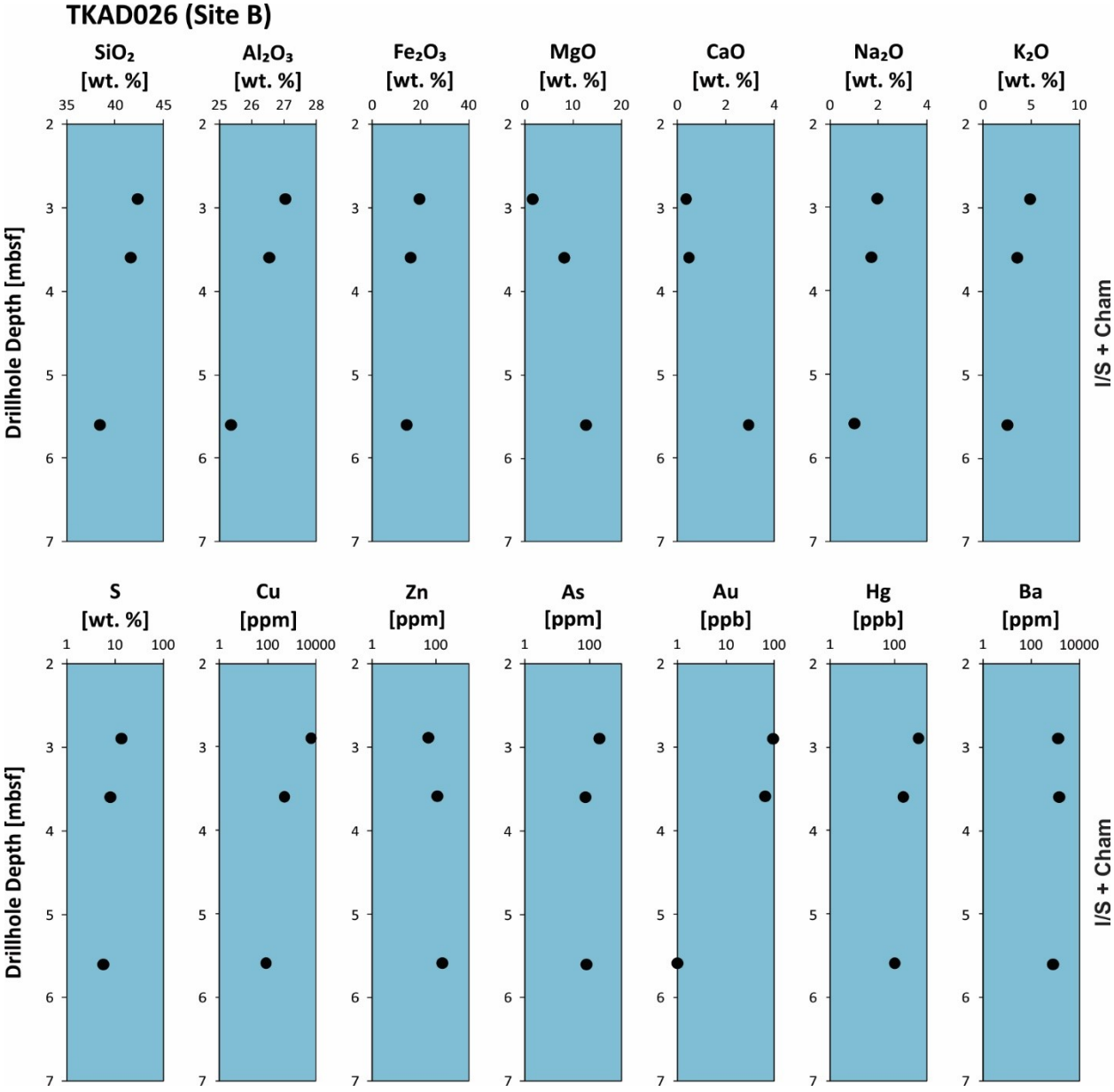


Fig. M6. Downhole changes in whole-rock concentrations of selected major and trace elements for drillhole TKAD026, with main alteration assemblages. Cham = chamosite; I/S = illite/smectite.

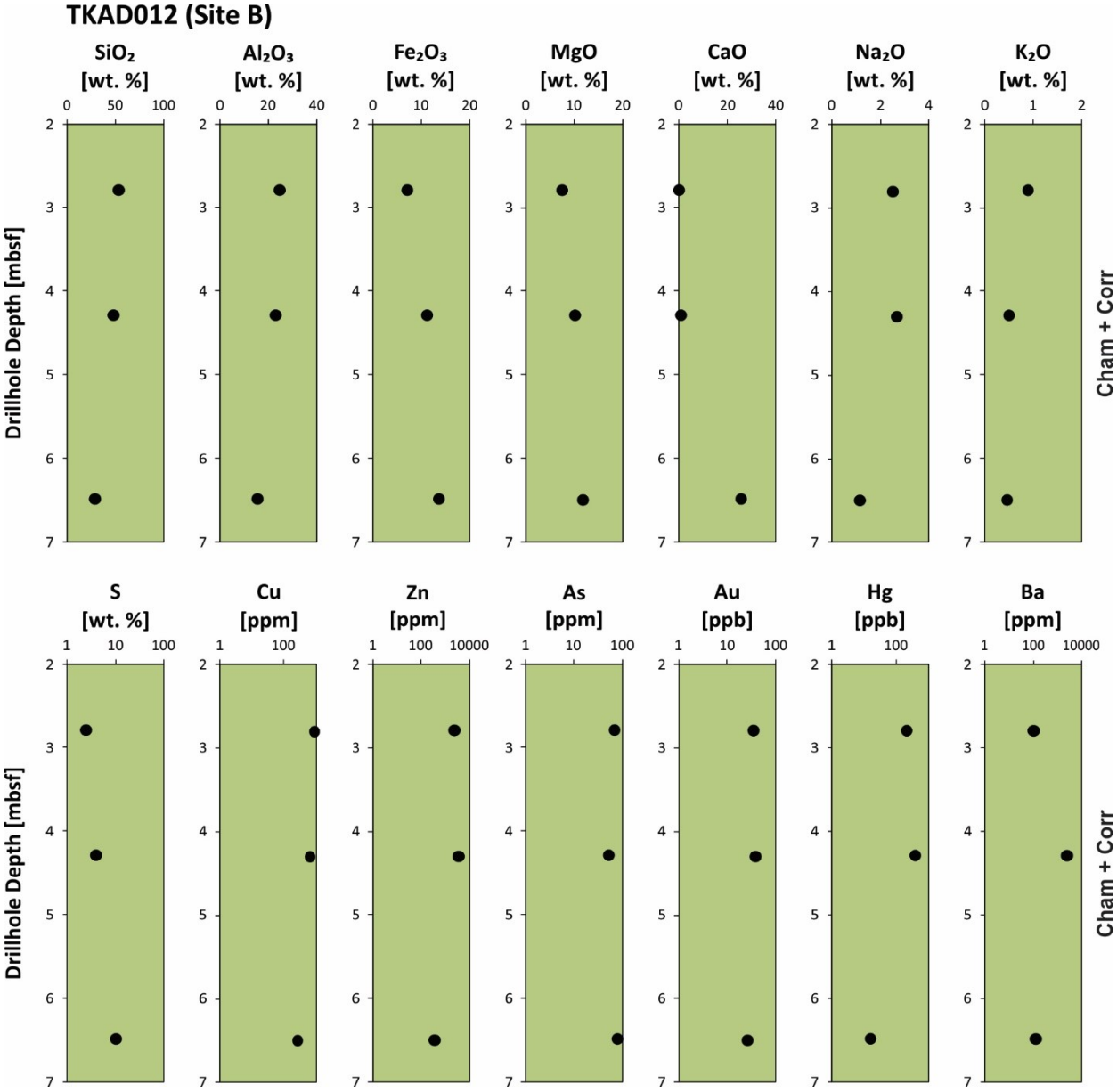


Fig. M7. Downhole changes in whole-rock concentrations of selected major and trace elements for drillhole TKAD012, with main alteration assemblages. Cham = chamosite; Corr = corrensite.

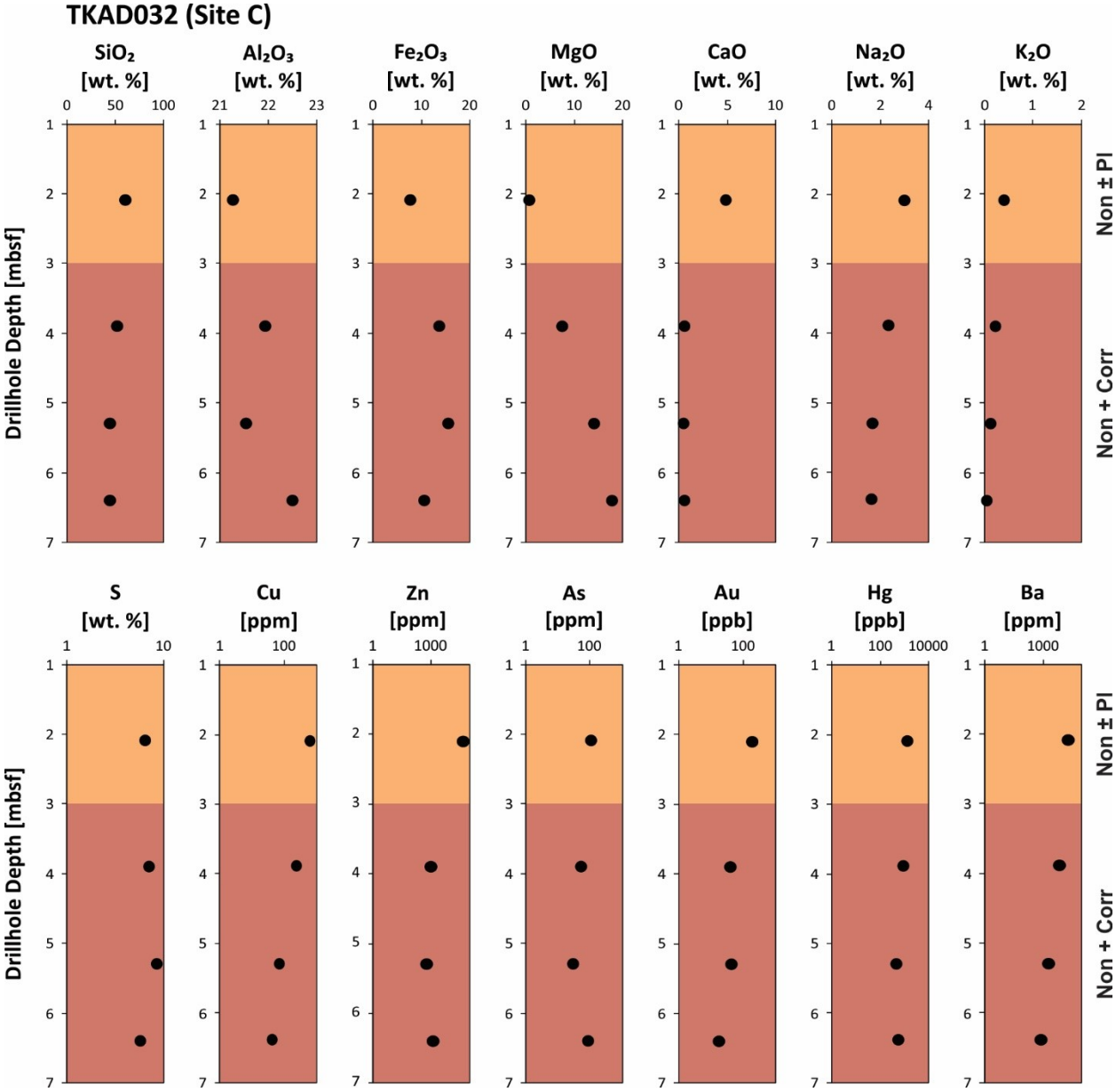


Fig. M8. Downhole changes in whole-rock concentrations of selected major and trace elements for drillhole TKAD032, with main alteration assemblages. Corr = corrensite; Non = nontronite; Pl = plagioclase.

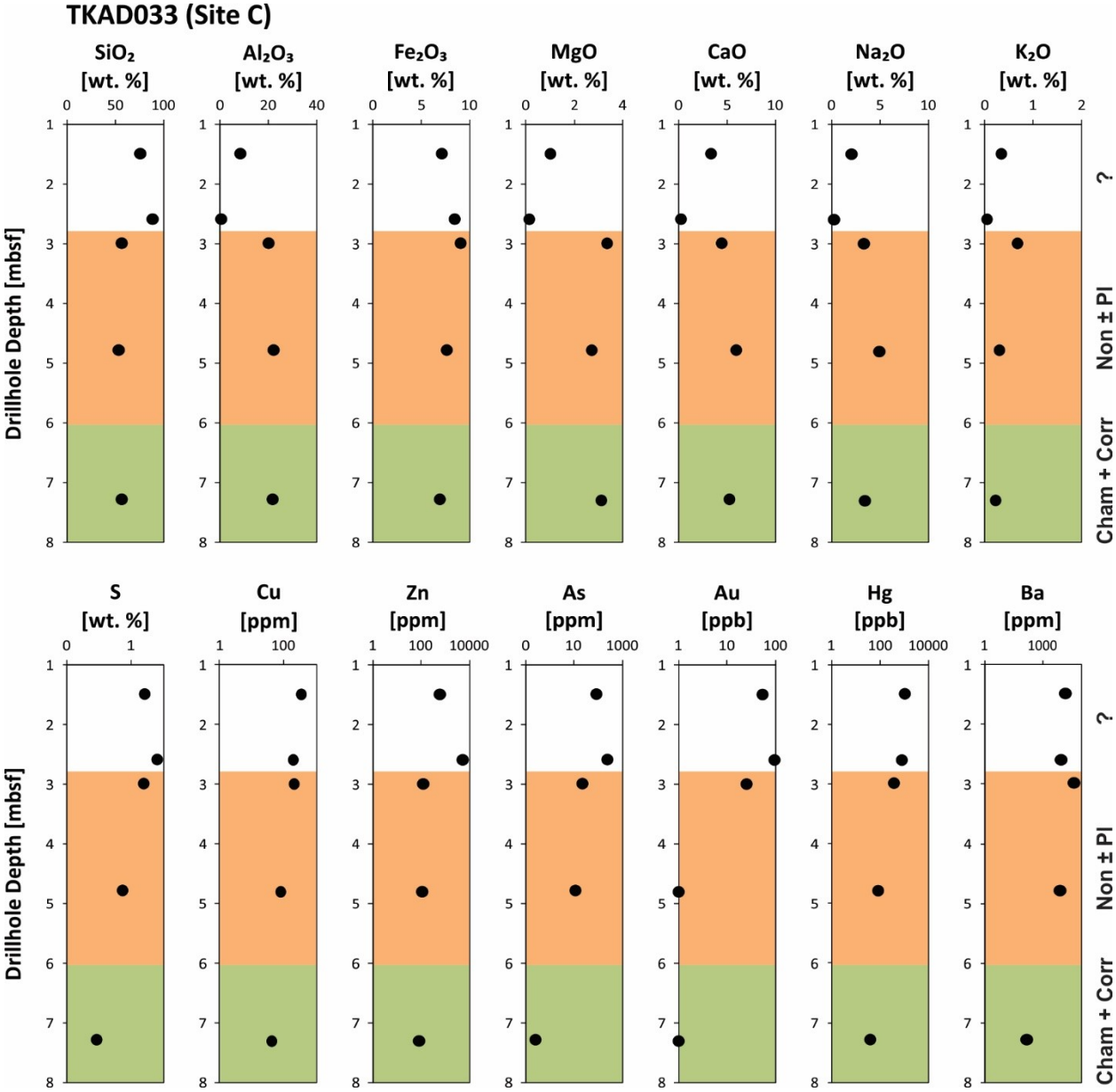


Fig. M9. Downhole changes in whole-rock concentrations of selected major and trace elements for drillhole TKAD033, with main alteration assemblages. Cham = chamosite; Corr = corrensite; Non = nontronite; Pl = plagioclase.

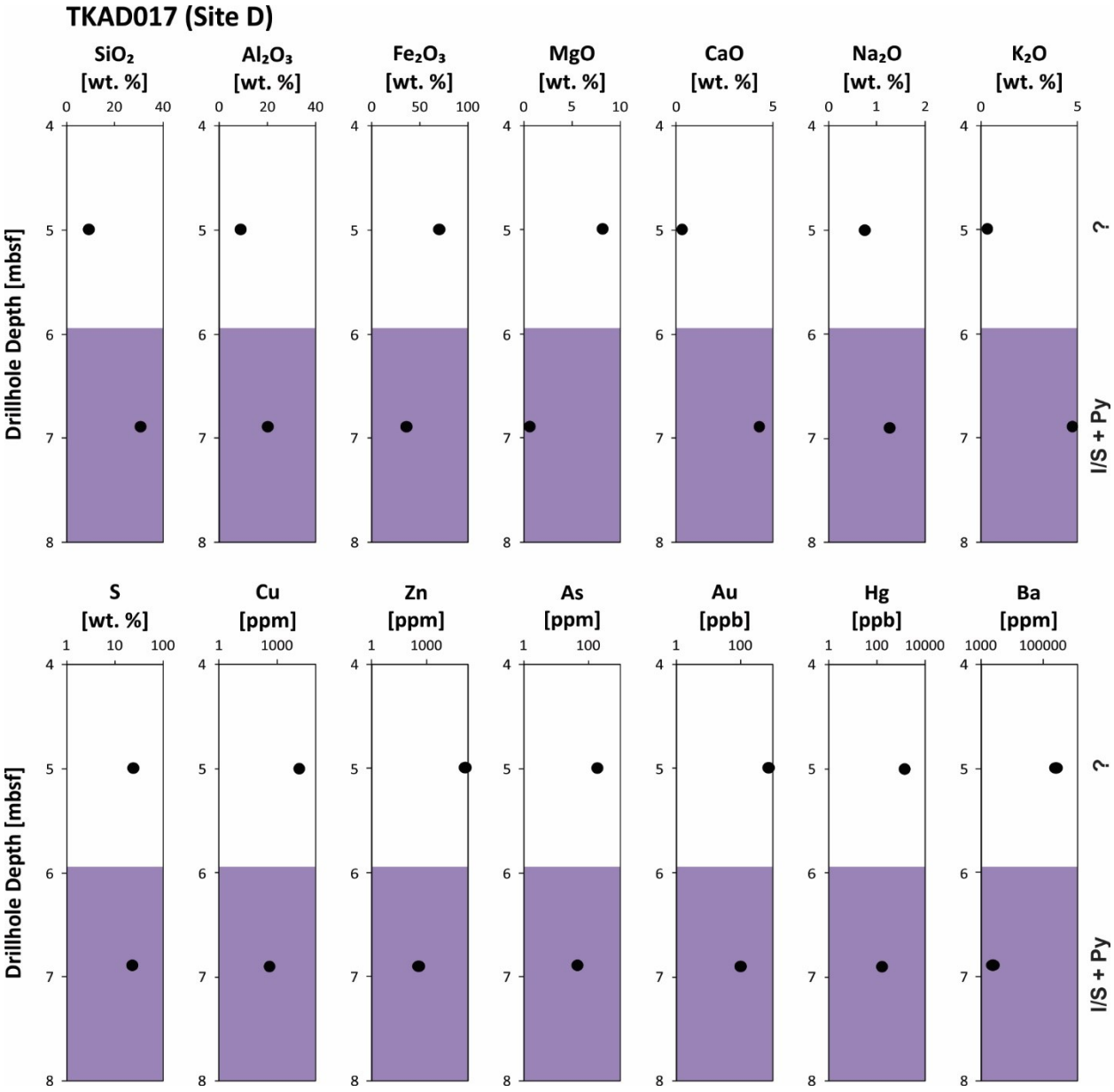


Fig. M10. Downhole changes in whole-rock concentrations of selected major and trace elements for drillhole TKAD017, with main alteration assemblages. I/S = illite/smectite; Py = pyrite.

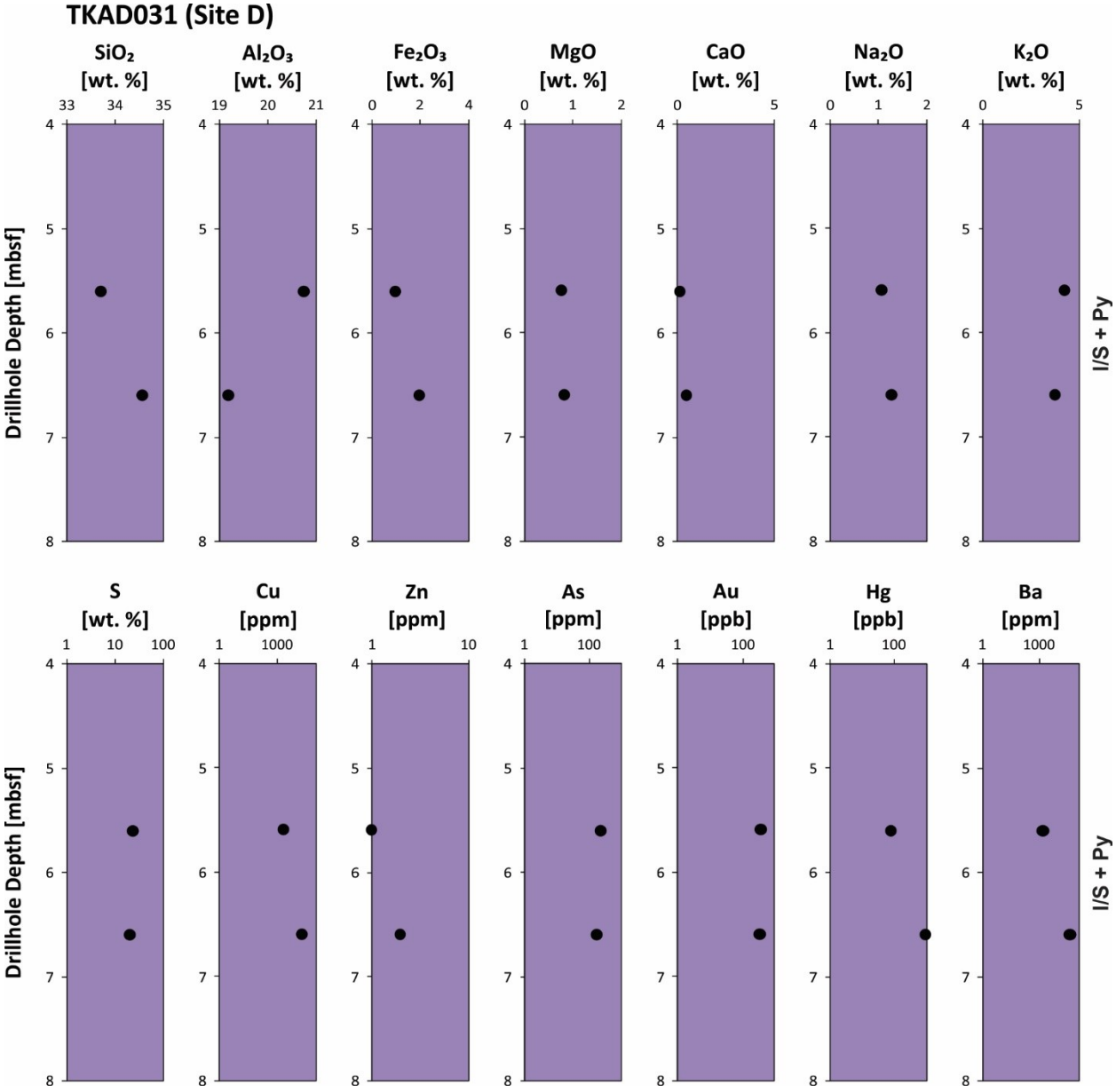


Fig. M11. Downhole changes in whole-rock concentrations of selected major and trace elements for drillhole TKAD031, with main alteration assemblages. I/S = illite/smectite; Py = pyrite.

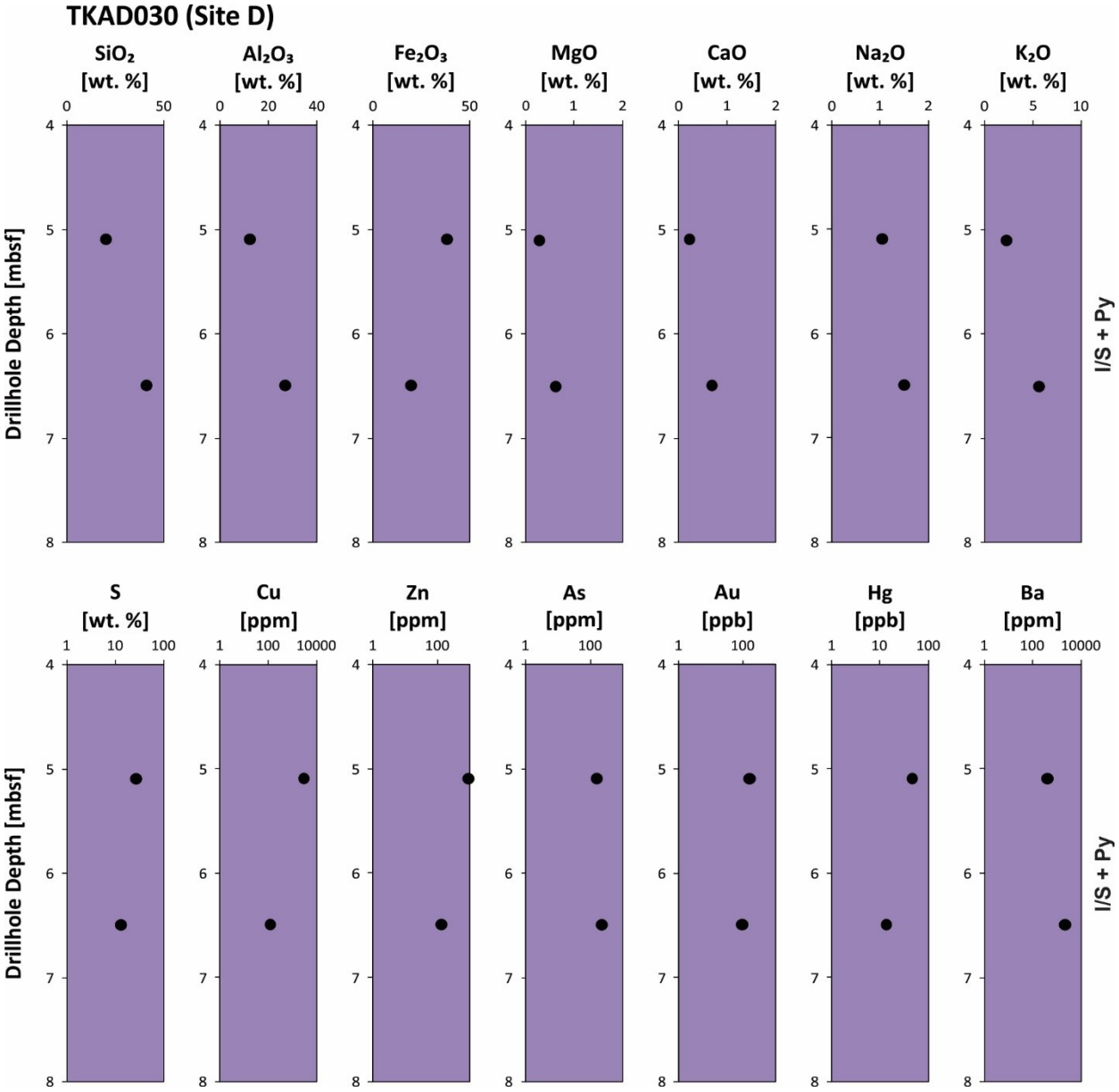


Fig. M12. Downhole changes in whole-rock concentrations of selected major and trace elements for drillhole TKAD030, with main alteration assemblages. I/S = illite/smectite; Py = pyrite.

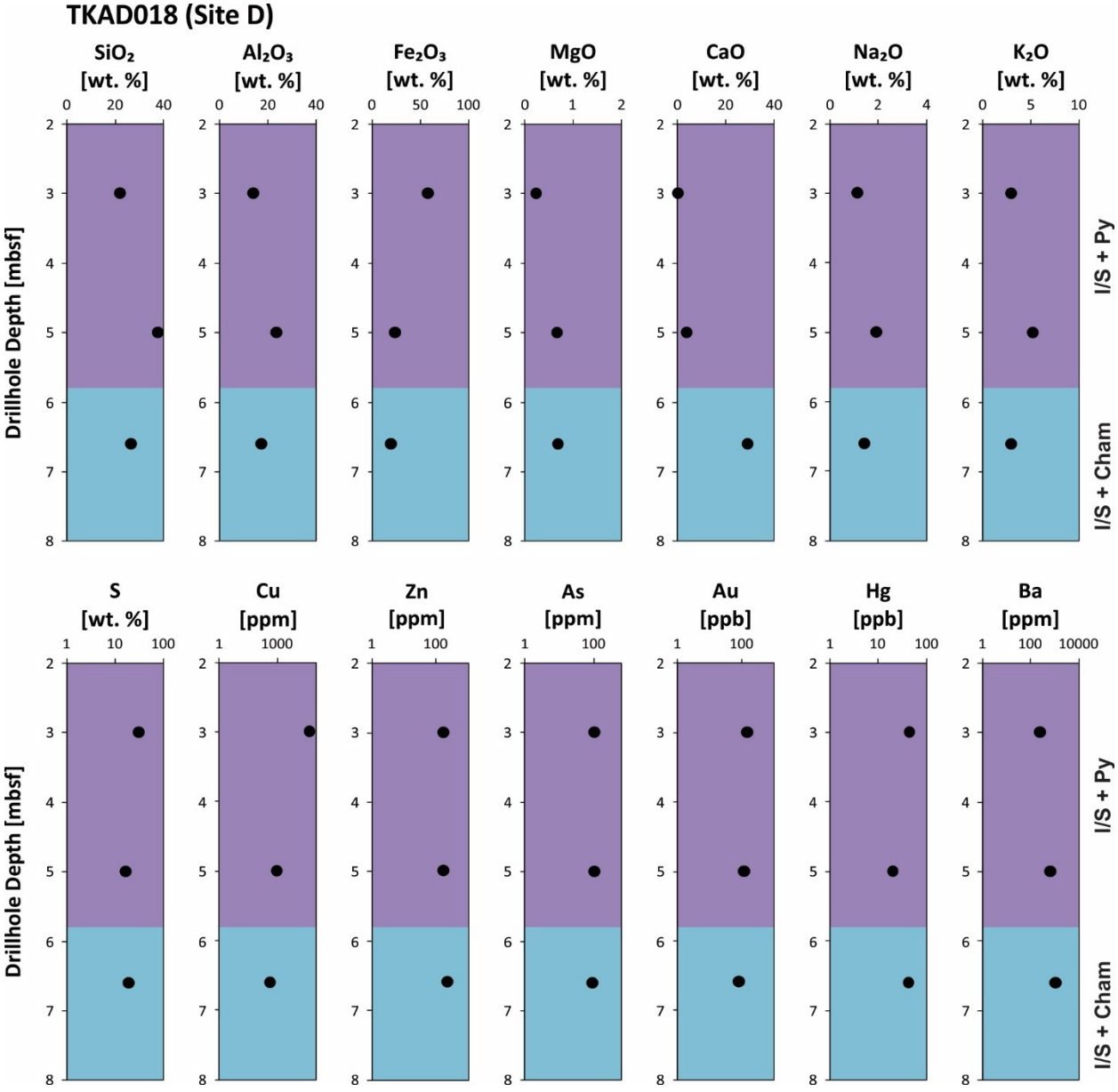


Fig. M13. Downhole changes in whole-rock concentrations of selected major and trace elements for drillhole TKAD018, with main alteration assemblages. Cham = chamosite; I/S = illite/smectite; Py = pyrite.

Appendix N

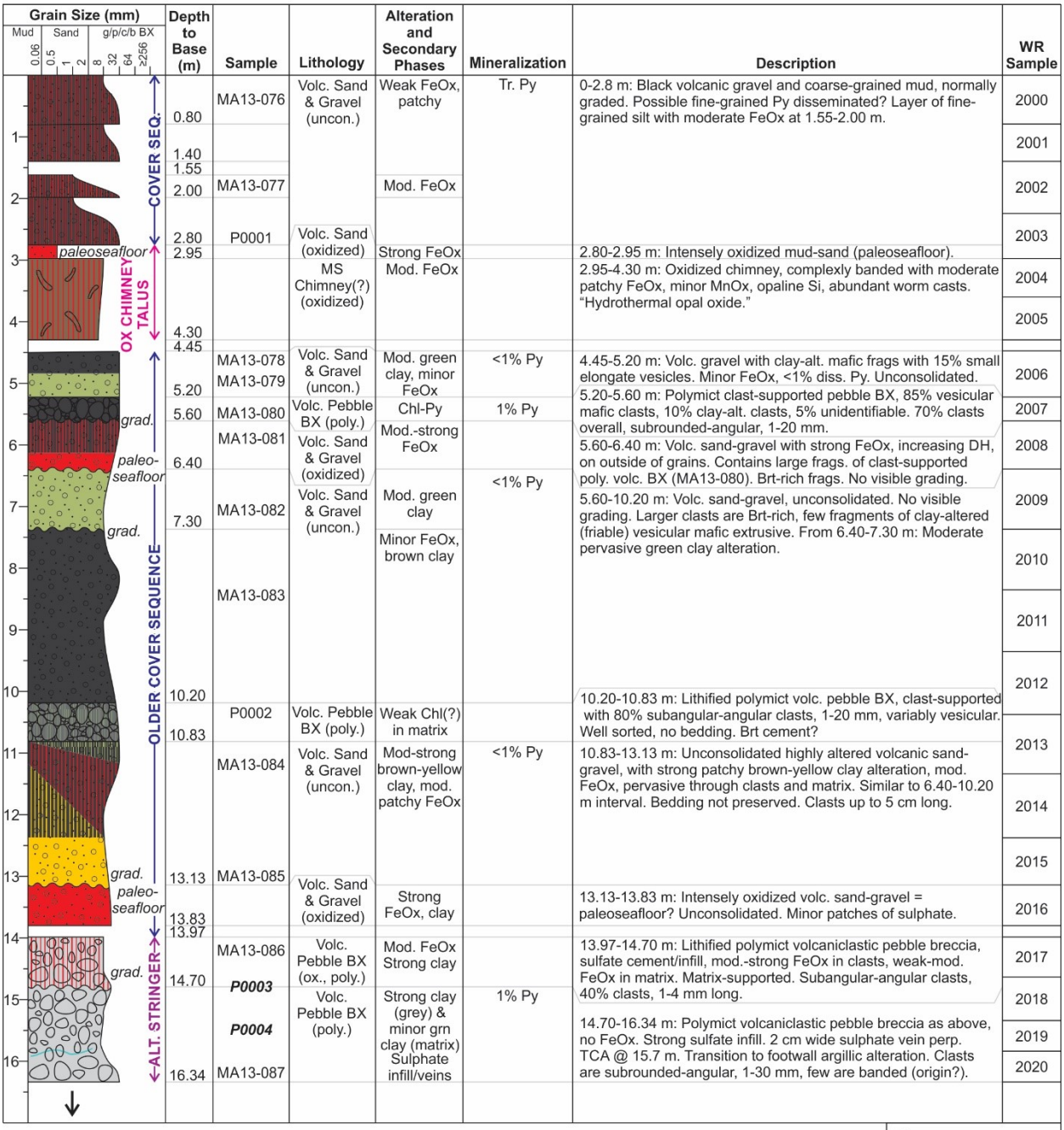
Graphical Drillcore Summary Logs – Tinakula Deposit

GRAPHICAL DRILLCORE SUMMARY LOGS 911
Drillhole TKAD001 911
Drillhole TKAD012 913
Drillhole TKAD013 914
Drillhole TKAD015 915
Drillhole TKAD016 916
Drillhole TKAD017 917
Drillhole TKAD018 918
Drillhole TKAD019 919
Drillhole TKAD025 920
Drillhole TKAD026 921
Drillhole TKAD027 922
Drillhole TKAD028 923
Drillhole TKAD029 924
Drillhole TKAD030 925
Drillhole TKAD031 926
Drillhole TKAD032 927
Drillhole TKAD033 928

GRAPHICAL DRILLCORE SUMMARY LOGS

Date: 16-Nov-2013 **Hole ID**: TKAD001 **Deposit**: Tinakula

Geologist: M.O. Anderson **EOH Depth**: 22.32 m **Area**: North "Site A"



Depth to Base (m)	Sample	Lithology	Alteration and Secondary Phases	Mineralization	Description	WR Sample
0.80	MA13-076	Volc. Sand & Gravel (uncon.)	Weak FeOx, patchy	Tr. Py	0-2.8 m: Black volcanic gravel and coarse-grained mud, normally graded. Possible fine-grained Py disseminated? Layer of fine-grained silt with moderate FeOx at 1.55-2.00 m.	2000
1.40						2001
1.55						
2.00	MA13-077		Mod. FeOx			2002
2.80	P0001	Volc. Sand (oxidized)				2003
2.95			Strong FeOx		2.80-2.95 m: Intensely oxidized mud-sand (paleoseafloor).	
4.30		MS Chimney(?) (oxidized)	Mod. FeOx		2.95-4.30 m: Oxidized chimney, complexly banded with moderate patchy FeOx, minor MnOx, opaline Si, abundant worm casts. "Hydrothermal opal oxide."	2004
4.45						2005
5.20	MA13-078 MA13-079	Volc. Sand & Gravel (uncon.)	Mod. green clay, minor FeOx	<1% Py	4.45-5.20 m: Volc. gravel with clay-alt. mafic frags with 15% small elongate vesicles. Minor FeOx, <1% diss. Py. Unconsolidated.	2006
5.60	MA13-080	Volc. Pebble BX (poly.)	Chl-Py	1% Py	5.20-5.60 m: Polymict clast-supported pebble BX, 85% vesicular mafic clasts, 10% clay-alt. clasts, 5% unidentifiable. 70% clasts overall, subrounded-angular, 1-20 mm.	2007
6.40	MA13-081	Volc. Sand & Gravel (oxidized)	Mod.-strong FeOx		5.60-6.40 m: Volc. sand-gravel with strong FeOx, increasing DH, on outside of grains. Contains large frags. of clast-supported poly. volc. BX (MA13-080). Brt-rich frags. No visible grading.	2008
7.30	MA13-082	Volc. Sand & Gravel (uncon.)	Mod. green clay	<1% Py	5.60-10.20 m: Volc. sand-gravel, unconsolidated. No visible grading. Larger clasts are Brt-rich, few fragments of clay-altered (friable) vesicular mafic extrusive. From 6.40-7.30 m: Moderate pervasive green clay alteration.	2009
			Minor FeOx, brown clay			2010
	MA13-083					2011
10.20						2012
10.83	P0002	Volc. Pebble BX (poly.)	Weak Chl(?) in matrix		10.20-10.83 m: Lithified polymict volc. pebble BX, clast-supported with 80% subangular-angular clasts, 1-20 mm, variably vesicular. Well sorted, no bedding. Brt cement?	2013
13.13	MA13-084	Volc. Sand & Gravel (uncon.)	Mod-strong brown-yellow clay, mod. patchy FeOx	<1% Py	10.83-13.13 m: Unconsolidated highly altered volcanic sand-gravel, with strong patchy brown-yellow clay alteration, mod. FeOx, pervasive through clasts and matrix. Similar to 6.40-10.20 m interval. Bedding not preserved. Clasts up to 5 cm long.	2014
	MA13-085					2015
13.83		Volc. Sand & Gravel (oxidized)	Strong FeOx, clay		13.13-13.83 m: Intensely oxidized volc. sand-gravel = paleoseafloor? Unconsolidated. Minor patches of sulphate.	2016
13.97						
14.70	MA13-086	Volc. Pebble BX (ox., poly.)	Mod. FeOx Strong clay		13.97-14.70 m: Lithified polymict volcaniclastic pebble breccia, sulfate cement/infill, mod.-strong FeOx in clasts, weak-mod. FeOx in matrix. Matrix-supported. Subangular-angular clasts, 40% clasts, 1-4 mm long.	2017
	P0003	Volc. Pebble BX (poly.)	Strong clay (grey) & minor grn clay (matrix) Sulphate infill/veins	1% Py		2018
	P0004				14.70-16.34 m: Polymict volcaniclastic pebble breccia as above, no FeOx. Strong sulfate infill. 2 cm wide sulphate vein perp. TCA @ 15.7 m. Transition to footwall argillic alteration. Clasts are subrounded-angular, 1-30 mm, few are banded (origin?).	2019
16.34	MA13-087					2020

Continued Next Page

Pebble-sized clasts
Sand/gravel clasts
Worm casts
Sulfate veins

Date: 16-Nov-2013 **Hole ID**: TKAD001 - Cont'd **Deposit**: Tinakula

Geologist: M.O. Anderson **EOH Depth**: 22.32 m **Area**: North "Site A"

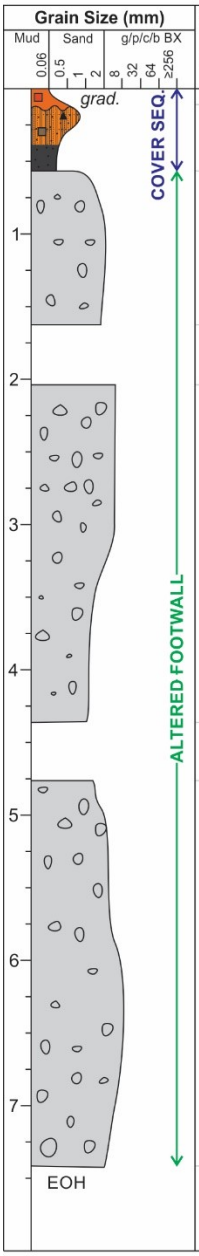
Grain Size (mm) Mud / Sand / g/p/c/b BX (0.06, 0.5, 1, 2, 8, 32, 64, ≥256)	Depth to Base (m)	Sample	Lithology	Alteration and Secondary Phases	Mineralization	Description	WR Sample
Continued From Prev. Page	16.71						
ALTERED FOOTWALL		MA13-088	Volcanic Pebble BX (poly.)	Strong clay (pervasive)	Tr. Py	16.71-19.48 m: Polymictic volcaniclastic pebble breccia, lithified, clast-supported, subrounded-subangular clasts, 1-50 mm long, 75% clasts overall. Larger clasts have altered rims. Patchy alternating green clay and FeOx (mod-minor) altering matrix. Few sulfate veins up to 5 mm wide, perpendicular to high angle to core axis. Larger vein at 15.70 m has Sp along margins. Crudely bedded. Patchy sulfate in matrix.	2021
		MA13-089		Mod. grn clay & FeOx, patchy, alternating, matrix only			2022
		MA13-090			2% Py		
	19.48	***P0005***		Sulfate infill/veins	5% Py+Sp <1% Ccp		2023
	20.05						
		MA13-091	Volcanic Pebble BX (poly.)	Strong clay (pervasive)	5% Py	20.05-22.32 m: Polylithic volcaniclastic pebble breccia, lithified, matrix-supported. Clasts are smaller than above (1-5 mm), ~40%, subrounded-subangular. Py is disseminated, concentrated along bedding at high angles to core axis. 1 cm-wide Anh vein at high angle to core axis at 20.77 m.	2024
		MA13-092		Minor grn clay & FeOx, matrix only, dec. DH	2% Py		2025
	22.32			Sulfate infill/veins			2026
EOH							

Notes/Interpretation:
Very deep drillhole in far north area. Three main lithologies include unconsolidated volcaniclastic sand to gravel (cover sequence), Fe-oxidized chimney (described as hydrothermal silica-oxide layer by Neptune geos), and polymict, clast- to matrix-supported moderatedly sorted volcaniclastic pebble breccia with crude bedding. FeOx chimney contains very low Au, Ag, Zn, Pb, and Cu. Alteration consists of Fe-oxide (red to brown), green clays, and white clays (argillic alteration).
Strongly clay-altered footwall contains variable sulfate infill/cement, with late veins of Anh (+/- Sp along margins), at high angles to core axis. Veins generally occur at boundaries between different alteration. Fe-oxide and green clay alteration in footwall is limited to the matrix.
Sulfide mineralization is associated with late sulfate infill and veins, with Py disseminated through footwall.
Several oxidized layers may be paleoseafloor horizons.

Pebble clasts
Sand/gravel clasts
Worm casts
Sulfate veins

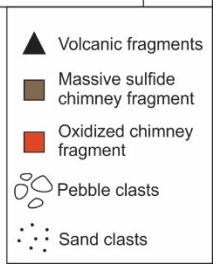
Date: 15-Nov-2013 **Hole ID**: TKAD012 **Deposit**: Tinakula

Geologist: M.O. Anderson **EOH Depth**: 7.51 m **Area**: North "Site B"



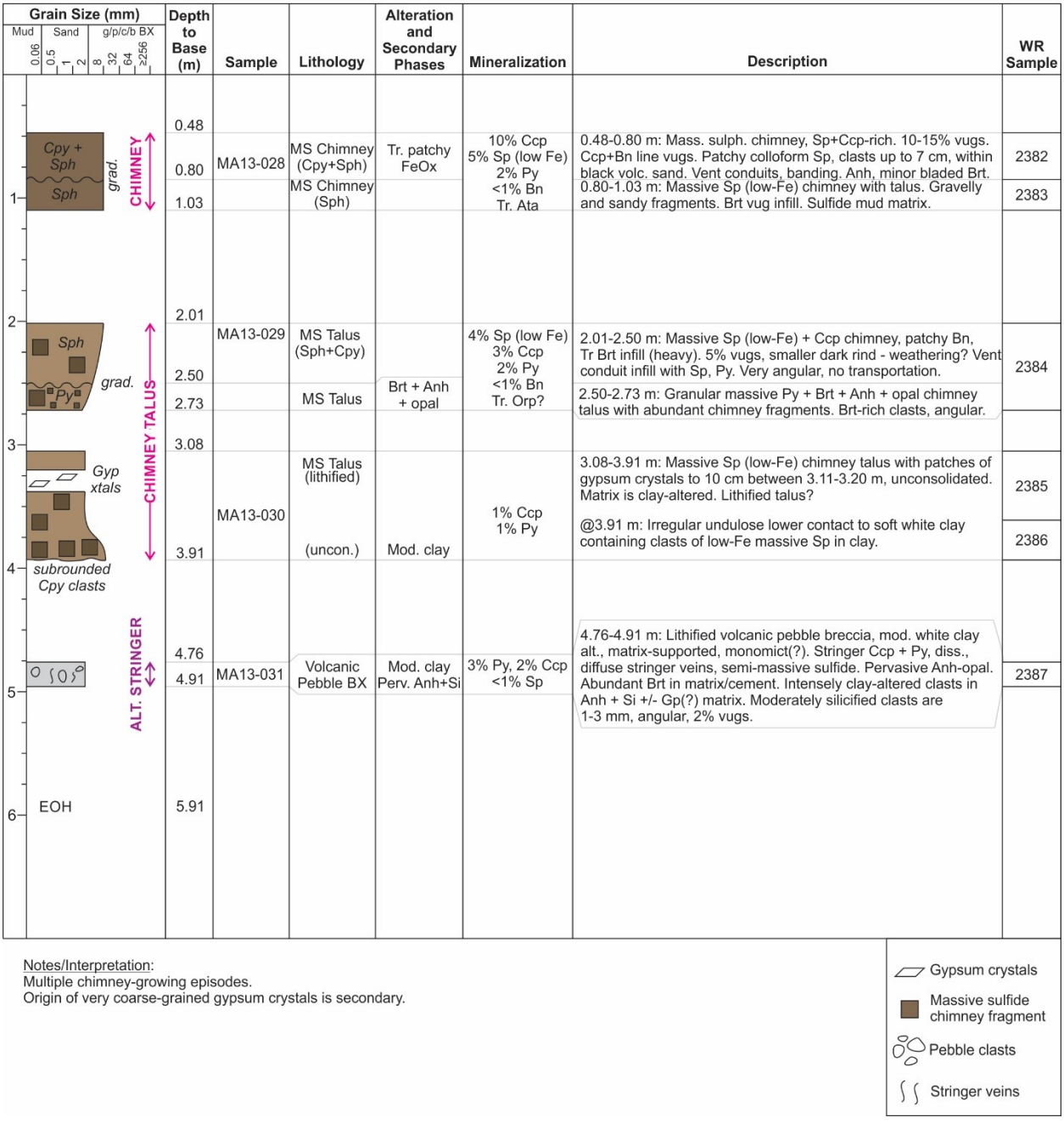
Depth to Base (m)	Sample	Lithology	Alteration and Secondary Phases	Mineralization	Description	WR Sample
0.10	MA13-059	Volc. Sand (oxidized)	Strong FeOx		0-0.1 m: MnOx crust with oxidized chimney fragments, subang.	
	MA13-060	Volcanic Sand	Patchy FeOx	2% Py	0.1-0.62 m: Mafic volc. sand with clasts of Brt (chimney), patchy FeOx mud. Some Opal A. Mud at base contains v.c.g. ~5 cm euh. Gyp crystals. Minor chimney clasts and volcanic frags, uncons.	2370
0.62	MA13-061	Volcanic Pebble BX (uncon.)	Strong clay Minor patchy green opaline to smectite (?) clay	3% Sp (high Fe) 1% Py	0.62-1.66 m: Intensely clay-altered polymict volcanic pebble breccia. Green opal A and clay matrix. Fine disseminated sulfides. 25% clay-altered subrounded clasts, matrix-supported. Clasts are 1-10 mm long, vesicles in clasts preserved. Unconsolidated. Moderately sorted. Variably altered. Clasts (black, grey, white) = polymict? Reworked?	2371
1.66						2373
2.01						
	MA13-062	Volcanic Pebble BX (uncon.)	Strong clay Weak FeOx Variable Gp Clay alt. slightly dec. downhole	3% Py 1% Sp (low Fe)	2.01-4.36 m: Intensely clay-altered volcanic pebble breccia as above, less Sp, more Py. Decreasing Brt downhole. Slight increase in clast size and abundance. Variably altered clasts - polymict or reworked? Subrounded to subangular, few angular, up to 1 cm. 30% clasts.	2374 2375 2376
4.36	MA13-063				@4.25 m: Clasts are slightly smaller, 1-5 mm, 10-15% clasts overall. Unconsolidated.	
4.76						
	MA13-064	Volcanic Pebble BX	Strong clay dec. with depth Anh infill + Gp crystals	3% Py <1% Sp (low Fe)	4.76-7.42 m: Intensely clay-altered volcanic pebble breccia, as above. Clay alteration slightly decreasing with depth. Development of Gp crystals at 5.60 m depth, ~2% overall. 30-35% clasts overall.	2377 2378 2379
7.42						
7.51						

Notes/Interpretation:
Footwall has consistent alteration with mineralized drillholes.
Cover sequence has few fragments of Brt-rich chimneys, subangular, transported from nearby.
Locally reworked mass flow facies in footwall.



Date: 14-Nov-2013 **Hole ID**: TKAD013 **Deposit**: Tinakula

Geologist: M.O. Anderson **EOH Depth**: 5.91 m **Area**: North "Site B"



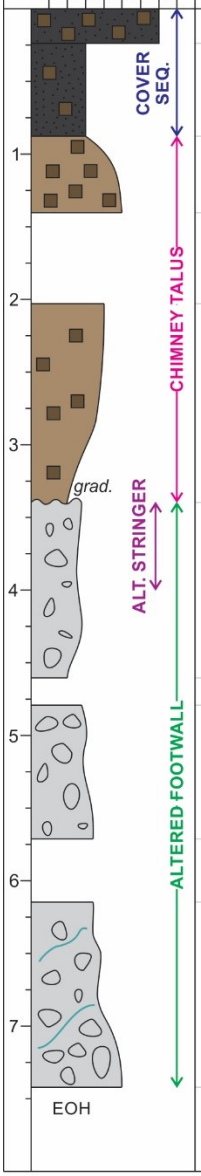
Depth to Base (m)	Sample	Lithology	Alteration and Secondary Phases	Mineralization	Description	WR Sample
0.48						
0.80	MA13-028	MS Chimney (Cpy+Sph)	Tr. patchy FeOx	10% Ccp 5% Sp (low Fe) 2% Py <1% Bn Tr. Ata	0.48-0.80 m: Mass. sulph. chimney, Sp+Ccp-rich. 10-15% vugs. Ccp+Bn line vugs. Patchy colloform Sp, clasts up to 7 cm, within black volc. sand. Vent conduits, banding. Anh, minor bladed Brt.	2382
1.03		MS Chimney (Sph)			0.80-1.03 m: Massive Sp (low-Fe) chimney with talus. Gravelly and sandy fragments. Brt vug infill. Sulfide mud matrix.	2383
2.01						
2.50	MA13-029	MS Talus (Sph+Cpy)		4% Sp (low Fe) 3% Ccp 2% Py <1% Bn Tr. Orp?	2.01-2.50 m: Massive Sp (low-Fe) + Ccp chimney, patchy Bn, Tr Brt infill (heavy). 5% vugs, smaller dark rind - weathering? Vent conduit infill with Sp, Py. Very angular, no transportation.	2384
2.73		MS Talus	Brt + Anh + opal		2.50-2.73 m: Granular massive Py + Brt + Anh + opal chimney talus with abundant chimney fragments. Brt-rich clasts, angular.	
3.08						
	MA13-030	MS Talus (lithified)		1% Ccp 1% Py	3.08-3.91 m: Massive Sp (low-Fe) chimney talus with patches of gypsum crystals to 10 cm between 3.11-3.20 m, unconsolidated. Matrix is clay-altered. Lithified talus?	2385
3.91		(uncon.)	Mod. clay		@3.91 m: Irregular undulose lower contact to soft white clay containing clasts of low-Fe massive Sp in clay.	2386
4.76						
4.91	MA13-031	Volcanic Pebble BX	Mod. clay Perv. Anh+Si	3% Py, 2% Ccp <1% Sp	4.76-4.91 m: Lithified volcanic pebble breccia, mod. white clay alt., matrix-supported, monomict(?). Stringer Ccp + Py, diss., diffuse stringer veins, semi-massive sulfide. Pervasive Anh-opal. Abundant Brt in matrix/cement. Intensely clay-altered clasts in Anh + Si +/- Gp(?) matrix. Moderately silicified clasts are 1-3 mm, angular, 2% vugs.	2387
5.91						

Notes/Interpretation:
Multiple chimney-growing episodes.
Origin of very coarse-grained gypsum crystals is secondary.

Gypsum crystals
Massive sulfide chimney fragment
Pebble clasts
Stringer veins

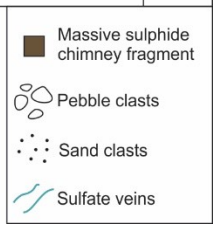
Date: 15-Nov-2013 **Hole ID**: TKAD015 **Deposit**: Tinakula

Geologist: M.O. Anderson **EOH Depth**: 7.35 m **Area**: North "Site A"



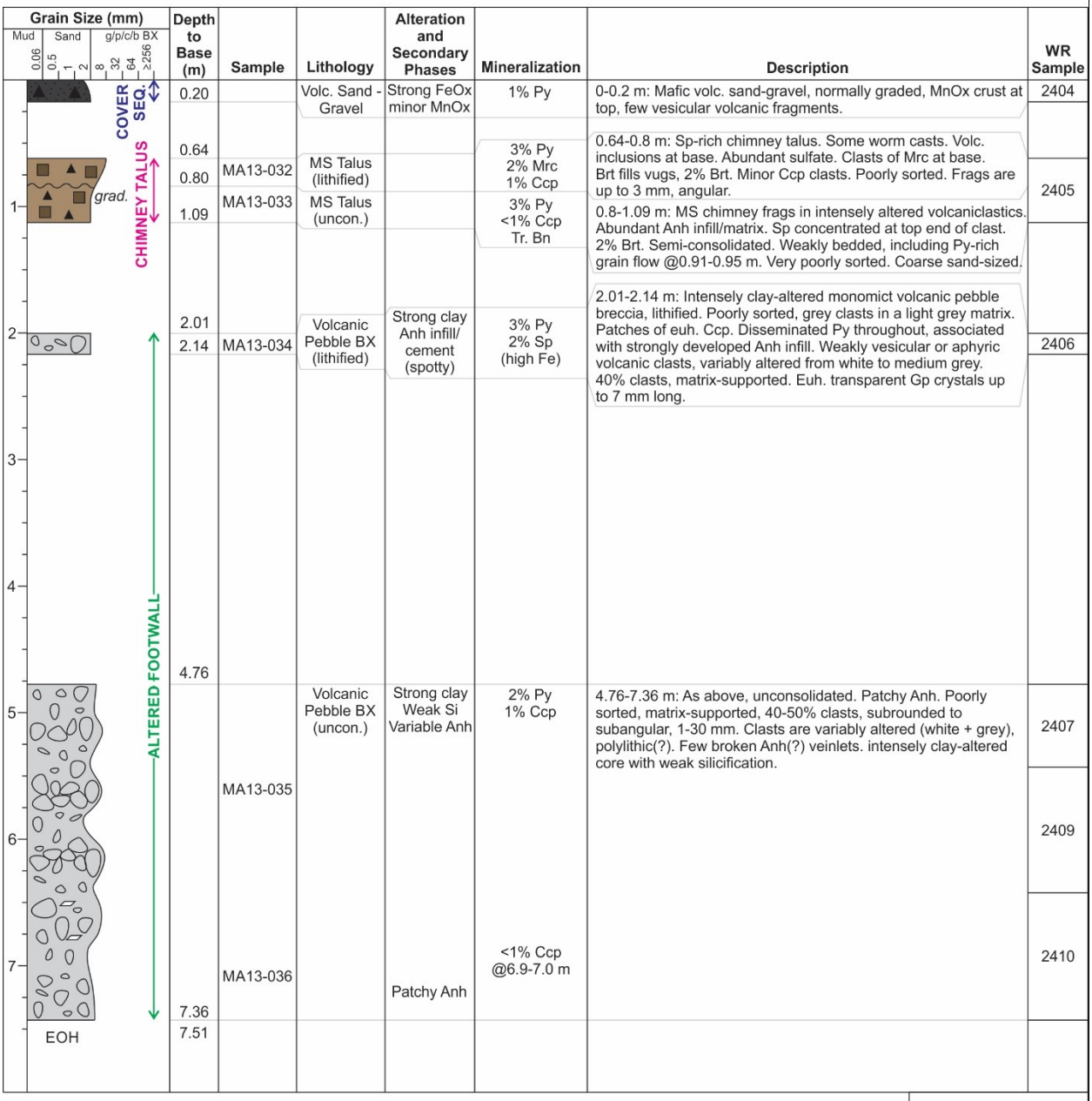
Depth to Base (m)	Sample	Lithology	Alteration and Secondary Phases	Mineralization	Description	WR Sample
0.24	MA13-046	Volc. Sand	Minor FeOx patchy	3% Ccp, 2% Py, 2% Sp	0-0.24 m: C.g. mafic volc. sand with abundant Ccp-rich chimney frags, up to 5 cm long. Colloform banding, 10% vugs. Minor Sp, <1% Ata, Bn, minor patchy FeOx. Some Ccp sand. Few sand-sized clasts of FeOx and clay.	2392
0.82	MA13-047	Volcanic Sand		<1% Ccp <1% Sp <1% Py	0.24-0.82 m: C.g. mafic volc. sand with few clasts of clay + FeOx Occasional Ccp + Py grains. Few relatively unaltered frags of vesicular mafic extrusive with quenched margins, ~40% vesicles, ~1 cm long. Occasional Ccp + Sp chimney frags.	2393
1.40	MA13-048	MS Talus		3% Ccp 2% Sp 2% Py	0.82-1.40 m: Brt-cemented Sp + Ccp-rich chimney fragments in massive sulphide sand. Minor Bn + Ata. 15% vugs, colloform banding + open space filling of vent conduit. Fragments are subangular to rounded.	2394
2.01						
3.40	MA13-049	MS Talus		4% Ccp 2% Sp 2% Py 1% Bn	2.01-3.40 m: Coarse-grained Ccp + Py massive sulfide sand with coarse pebble clasts. Unconsolidated. Abundant chimney fragments of massive Ccp + Bn, minor Sp, Brt cement. Brt-rich frags appear to have better survival. Some fragments are rounded (transported). Sp decreases downhole.	2395 2396 2397
4.58	MA13-050 MA13-051	Volcanic Pebble BX	Intense clay alt.	5%Py 2% Ccp <1% Sp Tr. Py	3.40-4.58 m: Intensely clay-altered volcanic pebble-mud breccia. Monomict, matrix-supported, muddy matrix. 20% pebble-sized clasts, subrounded-subangular, altered to clay. Tr. disseminated Py. Unconsolidated. Original volcanic textures almost completely obliterated. Poorly sorted.	2398 2400
4.76						
5.71		Volcanic Pebble BX	Intense clay alt.	Tr. Py	4.76-5.71 m: Similar to above, slightly larger clasts (less textural destruction?)	2401
6.15						
7.35	MA13-052 MA13-053	Volcanic Pebble BX	Strong clay alt. Sulfate infill/veins (late)	Tr. Py	6.15-7.35 m: Intensely clay-altered volcanic pebble breccia, lithified by late sulfate (Anh) infill cement. Few Anh veins, 2-5 mm wide, at high angles to core axis. Clay-altered clasts are sand-pebble sized (1 - 10 mm long), with increasing clast size downhole. Clasts are subrounded to angular. Original vesicles? Tr. disseminated Py. Friable. Few euhedral gypsum crystals. Decreasing clay alteration downhole.	2402 2403

Notes/Interpretation:
Twinned hole of TKAD027.
Contains volcanic sand cover sequence with "fresh" chimney talus, overlying second sequence of volcanic sand.
Massive sulfde chimney talus has rounded fragments, indicating transport.
Multiple episodes of mass wasting of nearby chimneys (reworking?)
Footwall is locally reworked. Contains late sulfate infill/veins, unmineralized.



Date: 14-Nov-2013 **Hole ID**: TKAD016 **Deposit**: Tinakula

Geologist: M.O. Anderson **EOH Depth**: 7.51 m **Area**: North "Site B"



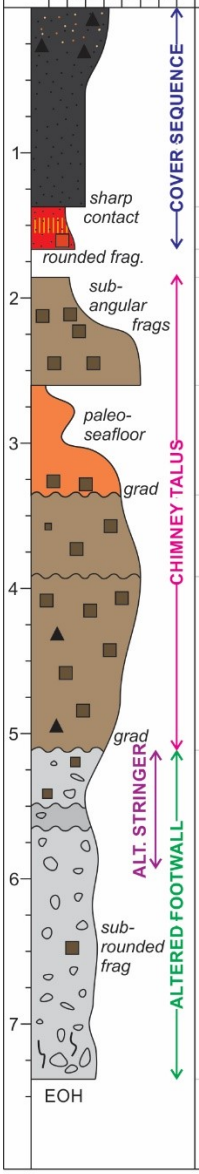
Depth to Base (m)	Sample	Lithology	Alteration and Secondary Phases	Mineralization	Description	WR Sample
0.20		Volc. Sand - Gravel	Strong FeOx minor MnOx	1% Py	0-0.2 m: Mafic volc. sand-gravel, normally graded, MnOx crust at top, few vesicular volcanic fragments.	2404
0.64				3% Py 2% Mrc 1% Ccp	0.64-0.8 m: Sp-rich chimney talus. Some worm casts. Volc. inclusions at base. Abundant sulfate. Clasts of Mrc at base. Brt fills vugs, 2% Brt. Minor Ccp clasts. Poorly sorted. Frags are up to 3 mm, angular.	2405
0.80	MA13-032	MS Talus (lithified)				
1.09	MA13-033	MS Talus (uncon.)		3% Py <1% Ccp Tr. Bn	0.8-1.09 m: MS chimney frags in intensely altered volcaniclastics. Abundant Anh infill/matrix. Sp concentrated at top end of clast. 2% Brt. Semi-consolidated. Weakly bedded, including Py-rich grain flow @0.91-0.95 m. Very poorly sorted. Coarse sand-sized.	
2.01		Volcanic Pebble BX (lithified)	Strong clay Anh infill/ cement (spotty)	3% Py 2% Sp (high Fe)	2.01-2.14 m: Intensely clay-altered monomict volcanic pebble breccia, lithified. Poorly sorted, grey clasts in a light grey matrix. Patches of euh. Ccp. Disseminated Py throughout, associated with strongly developed Anh infill. Weakly vesicular or aphyric volcanic clasts, variably altered from white to medium grey. 40% clasts, matrix-supported. Euh. transparent Gp crystals up to 7 mm long.	
2.14	MA13-034					2406
4.76		Volcanic Pebble BX (uncon.)	Strong clay Weak Si Variable Anh	2% Py 1% Ccp	4.76-7.36 m: As above, unconsolidated. Patchy Anh. Poorly sorted, matrix-supported, 40-50% clasts, subrounded to subangular, 1-30 mm. Clasts are variably altered (white + grey), polylithic(?). Few broken Anh(?) veinlets. intensely clay-altered core with weak silicification.	2407
	MA13-035					2409
	MA13-036		Patchy Anh	<1% Ccp @6.9-7.0 m		2410
7.36						
7.51						

Notes/Interpretation:
Chimney talus contains polylithic variably altered volcanic and massive sulphide fragments.
Fragments are angular and small (<3 mm). Indicative of transport from nearby source.
Low relief area. No stringer zone (due to low core recovery?).

- Volcanic fragments
- Massive sulfide chimney fragment
- Gypsum crystals
- Pebble clasts
- Sand clasts

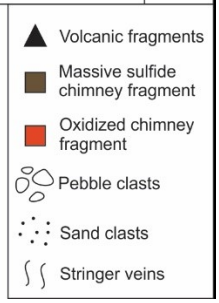
Date: 13-Nov-2013 **Hole ID**: TKAD017 **Deposit**: Tinakula

Geologist: M.O. Anderson **EOH Depth**: 7.36 m **Area**: Central "Site D"



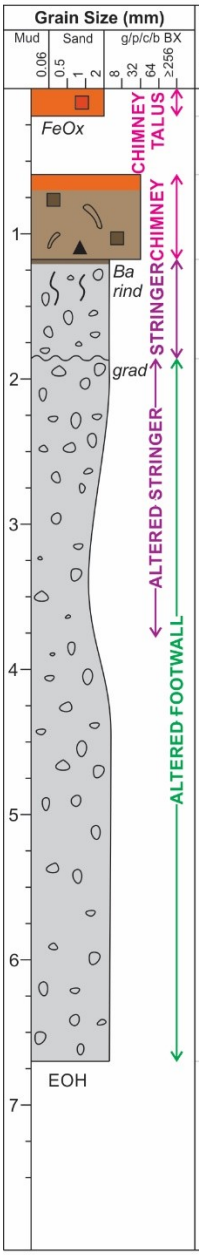
Depth to Base (m)	Sample	Lithology	Alteration and Secondary Phases	Mineralization	Description	WR Sample
	MA13-100	Volcanic Sand	Minor FeOx + clay clasts		0-1.39 m: Black mafic volcaniclastic sand, monomict. Coarse-grained for first 40 cm with 2-8 cm long fragments of vesicular mafic extrusive, more abundant at top of interval. Volc. frags are subrounded - subangular. No grading below 0.40 m. 5-10% clasts of FeOx + clay over first 20 cm. Unconsolidated.	2413
						2414
1.39						
		Volc. Sand (oxidized)	Mod-Strong FeOx		1.39-1.70 m: Same as above, with finer-grained FeOx (possibly hydrothermal deposition?). Sulfide clast at 1.6 m, rounded (transported). Unconsolidated.	2415
1.70						
1.86						
	MA13-017	MS Talus (Sph + Cpy)		4% Py 3% Sp (low Fe) 2% Ccp	1.86-2.58 m: Massive sulfide mud-sand with chimney frags (talus). Abundant disseminated Sp + Ccp + Gn(?). Rare bladed Brt. Clastic material decreases and sulfate content increases downhole. Chimney fragments are subangular (not transported far). Unconsolidated.	2416
2.58						
	MA13-018	MS Talus (oxidized)	Mod FeOx Rare clay-altered clasts	1% Py <1% Sp (high Fe) Tr Ccp	2.58-3.34 m: Oxidized fine-grained sulfide mud, unconsolidated. Bright reddish-orange. Few volcanic clasts, altered to clay. Few Brt-rich chimney fragments, subangular. Short-lived time as paleoseafloor horizon? Looks similar to massive sulfide mud, just oxidized. Variable oxidation intensity.	2417
3.34						
		MS Talus (Sph)		4% Py 3% Sp (low Fe)	3.34-3.83 m: Massive sulfide mud-sand talus, unconsolidated, poorly sorted. Similar to 1.86-2.58 m interval. Few volc. frags.	2418
3.93						
	MA13-101	MS Talus (Sph + Cpy)		4% Py 2% Sp (high Fe) 2% Ccp	3.83-5.15 m: Massive sulfide talus, similar to above. Sulfide chimney fragments increase in size and abundance with depth. Minor Bn in some clasts. Few volcanic fragments, subrounded to subangular. Gradational contact with altered footwall.	2419
						2421
5.15	MA13-019					
		Volcanic Pebble BX	Intense clay	3% Py-Mrc 2% Ccp Inc. sulfides	5.15-7.36 m: Strongly clay-altered monomict volcanic pebble breccia, unconsolidated. Original volcanic textures obscured. white in color. Py+Mrc disseminated throughout (2-3%) + Ccp veins towards base, associated with very white clay alteration, gypsum crystals. 6 cm subrounded Ccp-rich chimney fragment at 6.5 m, fine-grained, 75% Py 15% Ccp, 10% Brt, weakly banded. Altered volcanic clasts are completely clay altered (white), subrounded, sub-cm size. Matrix supported? Variable alteration, increases downhole. Increasing Ca content from 5.9 m to EOH.	2422
						2423
	MA13-020					2424
7.36				Inc. Ccp		
EOH						

Notes/Interpretation:
Chimney talus contains rounded chimney fragments, fine sulfides.
May contain in-situ hydrothermal precipitation(?) as well as chimney talus.
Overlies intensely altered reworked volcanic pile with obscured volcanic textures.
Highly altered stringer zone from 5.15 - 5.90 m indicated by whole-rock chemistry.
Oxidized intervals may be paleoseafloor horizons - second interval likely short lived.
Overlain by predictable cover sequence.



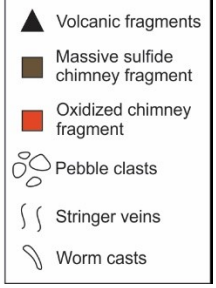
Date: 13-Nov-2013 **Hole ID**: TKAD018 **Deposit**: Tinakula

Geologist: M.O. Anderson **EOH Depth**: 6.71 m **Area**: Central "Site D"



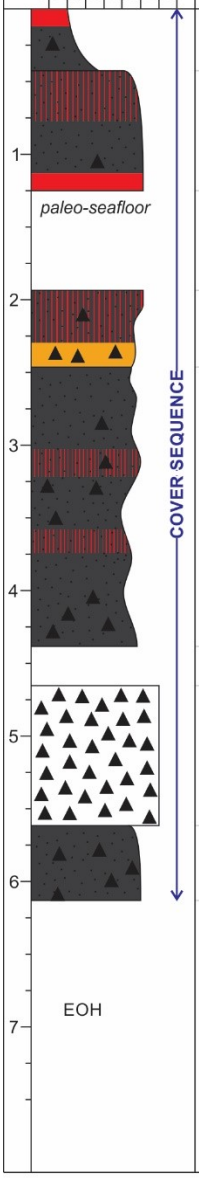
Depth to Base (m)	Sample	Lithology	Alteration and Secondary Phases	Mineralization	Description	WR Sample
0.20		MS Talus (oxidized)	FeOx, Si	Tr. Sp	0-0.2 m: Oxidized chimney talus, unconsolidated. SiO crust, biological fragments(?) in top 5 cm, polylithic. Few fragments of oxidized chimney.	2426
0.57	MA13-010	MS Chimney (Sph)	Patchy Si, weak patchy FeOx	4% Sp (low Fe) 3% Py 2% Ccp	0.57-1.19 m: Massive sulfide chimney with banded Sph, 10% vugs lined with Brt, Ccp (2%), Sp. Matrix is Brt-rich. Minor entrained clasts of altered (bleached) volcaniclastics, 5%. Hydrothermally cemented chimney talus? Weathered rind of Brt-Si alteration at lower contact.	2427
1.19	MA13-011	Volcanic Sand-Pebble BX (mineralized)	Mod-strong clay, mod Si, minor patchy FeOx	2% Sp (low Fe) 2% Py 1% Ccp	1.19-1.83 m: Volcaniclastic sand-pebble breccia with moderate to strong clay alteration (mainly altering clasts), sulfide mineralization along veins, vugs (few), and disseminated. Clasts are angular, monomict, matrix-supported, 1-5 mm long. Lithified by silica alteration (cement).	2428
1.83	MA13-012					
	MA13-013	Volcanic Pebble BX	Strong clay	3% Py 2% Ccp <1% Sp (dec. DH)	1.83-6.71 m: Strongly clay-altered, monomict(?) volcanic pebble breccia (footwall), unconsolidated. Original volcanic textures obscured. Abundant disseminated Py + Ccp +/- Sp to 3.85 m, decreasing downhole. Below 3.85 m there is minor anhydrite (cement). Breccia is clast-supported, moderately sorted. Difficult to tell facies changes.	2430
	MA13-014					2431
				2% Py 1% Ccp Tr. Sp		2432
	MA13-015			2% Py <1% Ccp		2433
						2434
6.71	MA13-016					

Notes/Interpretation:
Massive sulphide chimney talus is oxidized at the seafloor, overlies Sp-rich massive sulfide chimney.
Preserved stringer zone, variable alteration increasing downhole.
Grades into intensely clay-altered footwall volcanic pebble breccia.
Intervals that are sulfide-rich (Py + Ccp) suggests that the stringer zone persists to ~3.85 m.



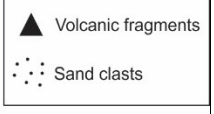
Date: 13-Nov-2013 **Hole ID**: TKAD019 **Deposit**: Tinakula

Geologist: M.O. Anderson **EOH Depth**: 6.88 m **Area**: Central "Site D"



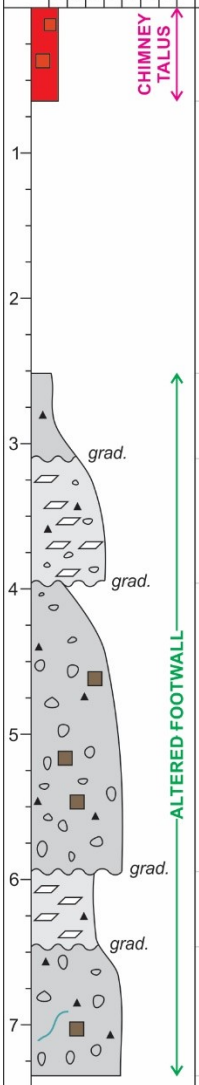
Depth to Base (m)	Sample	Lithology	Alteration and Secondary Phases	Mineralization	Description	WR Sample
0.41		Volcanic Sand (uncon.)	Weak FeOx patchy		0-0.41 m: Dark grey medium-grained volcaniclastic sand, patchy FeOx at top - weathered sulphides?	2436
1.25		Volcanic Sand (uncon.)	Mod. FeOx patchy, clay-alt volc. frags.		0.41-1.25 m: Brown-black volcaniclastic sand with fresh volcanic (vesiuclar, aphanitic, aphyric, black) and red-brown oxidized mud. Volcanic clasts are variably clay altered, angular to subangular. Traces of blood red and yellow minerals on volcanic clasts (arsenic mineral?). Disaggregated volcanic autobreccia - hyaloclastite(?).	2437
1.91						
2.45	MA13-007	Volcanic Sand (uncon.)	Mod. FeOx patchy, minor clay dec. DH		1.91-2.45 m: Coarse-grained orange-brown volcaniclastic sand. Contains fresh to slightly oxidized volcanic fragments (similar to above). Hyaloclastite rubble and quenched formerly glassy margins to lava fragments (strongly jointed).	2439
4.35			Inc. MnOx DH Minor FeOx Minor FeOx		2.45-4.35 m: Sharp contact between FeOx mud and relatively unoxidized sediment. Increasing MnOx downhole. Volcanic fragments are subrounded-subangular. Vesicles are elongate. Grain sizes cover a wide range from sandy to 1 cm clasts. Clasts are hard between 2.45-3.65 m, soft at 3.65 m, increasing hardness to 4.35 m.	2440 2441
4.65						
5.60	MA13-008	Volcanic Gravel (uncon.)	Weak FeOx on outside of clasts		4.65-5.60 m: Similar to 2.45-4.35 m, with sand washed out. Unconsolidated fragments of vesicular mafic extrusive, black, 5-15% vesicles, 1-5 mm long, elongate. Eruptive event entrained older lava flow?	2442
6.14	MA13-009	Volcanic Sand (uncon.)	Tr. FeOx		5.60-6.14 m: Black volcaniclastic sand with fragments of unaltered vesicular volcanic mafic extrusive. Vesicles are round, ~10%. Less sandy component than 0-4.35 m.	2443
6.88						

Notes/Interpretation:
No sulfides or altered footwall volcanic pebble-breccia encountered.
Represents thick cover sequence in "saddle" feature, drilling did not penetrate cover sequence.
Distal volcanics with multiple episodes of deposition.
Angular volcanic fragments with elongate vesicles, quenched margins indicate pyroclastic eruption.
Sharp contacts with oxidized horizons (control?) demonstrate no mixing.
Overall general increase in size of volcanic fragments towards bottom, variable overall.
No fine interbedded fine-grained and coarse-grained sequences.
No peperitic textures.



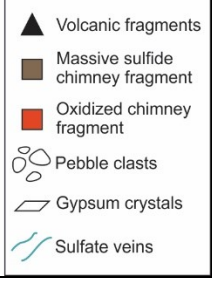
Date: 14-Nov-2013 **Hole ID**: TKAD025 **Deposit**: Tinakula

Geologist: M.O. Anderson **EOH Depth**: 7.31 m **Area**: North "Site B"



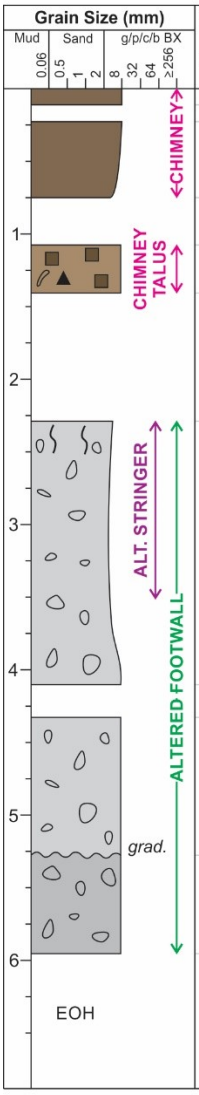
Depth to Base (m)	Sample	Lithology	Alteration and Secondary Phases	Mineralization	Description	WR Sample
0.67	MA13-037	MS Talus (oxidized)	Strong FeOx MnOx	2% Py	0-0.67 m: FeOx mud with pieces of MnOx crust and few frags of massive sulfide chimney fragments, subrounded, some Sp-rich, some Ccp+Bn-rich, up to 8 cm long. Patches of sulfate mud (contacts destroyed by drilling and extraction).	2536
2.51		Volcanic Mud BX	Strong clay, patchy grn opal A, sulfate	4% Py (diss., fine) Tr. Ccp Tr. Bn	2.51-3.09 m: Fine-grained sulfate mud with patches of green opal A and fine euhedral white patch of gypsum crystal clusters, up to 3 cm wide. Fine-grained disseminated Py, Tr. Ccp + Bn. Detrital or in-situ Ccp?	2537
3.09	MA13-038	Volcanic Mud-Sand BX	Strong clay, sulfate infill/cement	3% Py 2% Sp	3.09-3.98 m: Fine-grained sulfate mud with abundant (~50%) gypsum crystals up to 3 cm long, often forming clusters. Much lighter than previous interval and less sulfides. Gradual lower contact with increasing lithic fragments.	2538
3.98	MA13-039	Volcanic Pebble BX (polymictic)	Strong clay, sulfate infill/cement	3% Py 2% Ccp 2% Sp	3.98-5.91 m: Polymictic volcanic pebble breccia with subangular to subrounded clasts, 1-20 mm, Clasts of intensely altered volcanics, relatively unaltered volcanics, massive Py+Cpy, "detrital grains." Green Si in matrix of lithic sulfate mud. Poorly sorted, weakly bedded(?), matrix-supported. Few small fragments of Sphrich chimney talus.	2539 2540
5.94		Volcanic Mud-Sand BX	Strong clay, sulfate infill/cement	3% Py 2% Sp	5.94-6.47 m: Sulfate mud with gypsum crystals, similar to 3.09-3.98 m interval. Gradual lower contact with increasing lithic content. Very high Ca content, no grade.	2541
6.47	MA13-040	Volcanic Pebble BX (polymictic)	Strong clay, sulfate infill/cement	3% Py 3% Ccp 2% Sp	6.47-7.31 m: Volcanic pebble breccia, polymictic, similar to 3.98-5.94 m interval. Fewer mafic clasts, no sulfide clasts. Clasts are less abundant. Broken sulfate vein material.	2542
7.31						

Notes/Interpretation:
Twinned hole of TKAD013
Reworked polymictic footwall breccia with chimney talus and late sulfate infill/cement/veins.
Strongly oxidized mud at top of hole.
Relatively high Ca content throughout.
Interpreted to be explosive hydrothermal reworking.



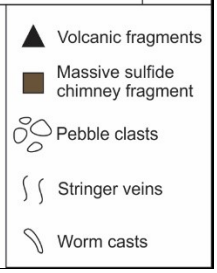
Date: 15-Nov-2013 **Hole ID**: TKAD026 **Deposit**: Tinakula

Geologist: M.O. Anderson **EOH Depth**: 6.31 m **Area**: North "Site B"



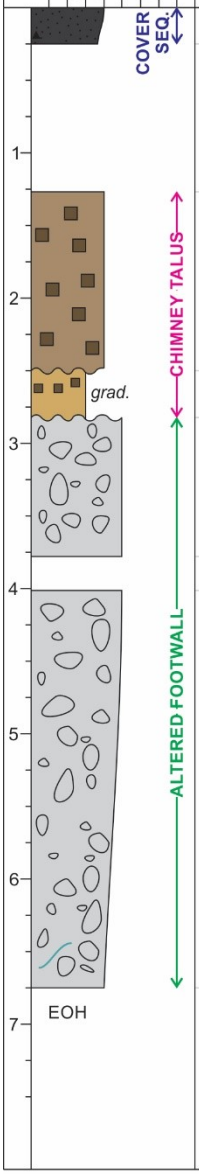
Depth to Base (m)	Sample	Lithology	Alteration and Secondary Phases	Mineralization	Description	WR Sample
0.10		MS Chimney	Weak FeOx	4% Sp (low Fe) 3% Py	0-0.75 m: Massive Sp-Brt chimney. Brt is interstitial and forms undulose bands. Sp is banded, dendritic. Few worm casts. 10% vugs. Brt fills void space, minor bladed Brt.	2526
0.21	MA13-065	MS Chimney				
0.75						
1.18				4% Py 1% Gn 1% Sp Tr. Ccp	1.18-1.41 m: Fragments of massive sulfide in lithified very fine-grained sulfides, too fine to identify. Gn forms in void. Cemented by sulfide. Brt-Sp-rich chimney talus, bioturbated sediments with worm casts and shell fragments, volcaniclastics(?)	
1.41	MA13-066	MS Talus (lithified)	Weak FeOx Minor Si Tr. Ata		5-10% vugs. Disseminated Py, Tr Ccp. Sp lines fractures. Saccharoidal texture - silicification. In contact with light grey volcanic extrusive(?) with 5% small vesicles, may be clast. Minor patchy FeOx, trace green alteration mineral along fractures. Angular fragments.	2528
2.27						
	MA13-067	Volcanic Pebble BX (uncon.)	Intense clay decreasing downhole	3% Ccp 1% Bn 2% Py 1% Ccp 1% Py	2.27-4.16 m: Footwall volcaniclastic pebble breccia (dark grey), monomictic, matrix-supported, moderately rounded, intensely clay-altered with alteration decreasing downhole. Ccp+Bn veinlet at top (stringer) of interval. Ccp disseminated throughout, decreasing downhole. Ungraded. Angular to subangular clasts proximal to locally reworked. Anh in matrix. @2.9 m: 35% clay-altered clasts, subrounded, 1-5 mm. @3.6 m: 20% clasts, subrounded, finer-grained, 1-3 mm long.	2529 2530 2531
4.16	MA13-068			<1% Py		
4.30						
		Volcanic Pebble BX (uncon.)		1% Ccp 1% Py	4.3-5.26 m: Same as above interval (2.27-4.16 m).	2532
5.26						
	MA13-069	Volcanic Pebble BX (lithified)	Intense clay Anh infill/ cement Tr. FeOx	<1% Py	5.26-5.9 m: Lithified clay-altered footwall volcanic pebble breccia with late Anh infill cement. Clasts are sand-pebble sized, 1-10 mm, subrounded to angular, original vesicles in clasts are preserved.	2533
5.96						
6.31						

Notes/Interpretation:
Chimney growth on top of chimney talus mound.
Strongly altered stringer zone.
Bottom interval of footwall is cemented by sulphate.
Volcanic pebble breccia clasts are angular - proximal facies.



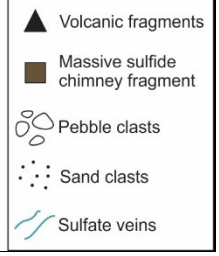
Date: 15-Nov-2013 **Hole ID**: TKAD027 **Deposit**: Tinakula

Geologist: M.O. Anderson **EOH Depth**: 6.75 m **Area**: North "Site A"



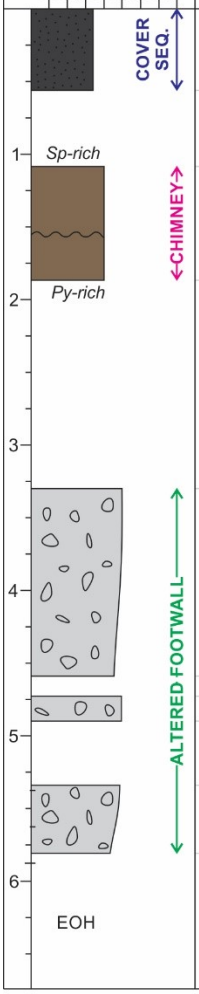
Depth to Base (m)	Sample	Lithology	Alteration and Secondary Phases	Mineralization	Description	WR Sample
0.25	MA13-054	Volc. Sand	Minor FeOx		0-0.25 m: C.G. mafic volc. sand (uncon.) with few sand-sized frags of clay and FeOx. Dec. grainsize downhole. Few clasts of vesicular mafic extrusive with variable FeOx.	2517
1.26						
2.50	MA13-055	MS Talus (Py+Sp + Ccp)		4% Py 4% Sp 2% Ccp Tr. Bn	0-2.50 m: Coarse-grained Ccp + Py massive sulphide sand with coarse pebble clasts. Unconsolidated. Occasional small massive sulfde chimney fragments (Sp-rich) and fragments of barite, subangular-subrounded. 3% Brt in matrix.	2519
2.80	MA13-056	MS Talus (transition)	Mod-strong clay	2% Py, 2% Sp 1% Ccp	2.5-2.8 m: Intensely clay-altered chimney talus (transition). 70% alteration to clay minerals. Mud- to sand-sized grains.	2520
3.76		Volcanic Pebble BX	Intense clay	4% Py	2.80-3.76 m: Intensely clay-altered volcanic pebble breccia (footwall) with very fine grained Py and minor Sp, Brt. Altered stringer zone. Monomict, matrix-supported.	2521
4.01						
	MA13-057	Volcanic Pebble BX	Intense clay	2% Py	4.016.75 m: Intensely clay-altered footwall volcanic pebble breccia, similar to above, with coarser euhedral Py, no Sp, no Brt. Minor Anh infill in matrix, partially lithified. Matrix-supported with a muddy matrix, 20% pebble-sized subrounded to sub-angular clasts, altered to clay. Original volcanic textures almost completely obliterated.	2522
						2523
				2% Py	Increasing Anh cement downhole, few Anh veins, 2-5 mm wide, at high angles to core axis. Clay-altered clasts are sand-pebble sized, 1 - 10 mm long, subrounded. Original vesicles in clasts are preserved(?), 2% disseminated Py increasing downhole. Rock is friable.	
			Sulfate infill/cement			2524
6.75	MA13-058					

Notes/Interpretation:
Twinned hole of TKAD015.
Rounding of chimney fragments suggests some transport.
Gradual transition to altered footwall.
Stringer zone indicated by presence of minor disseminated Sp and depletion of Ca.
Footwall is fairly homogenous in terms of facies changes.
Anh infill and high angle veins are late, unmineralized.



Date: 16-Nov-2013 **Hole ID**: TKAD028 **Deposit**: Tinakula

Geologist: M.O. Anderson **EOH Depth**: 5.77 m **Area**: North "Site A"



Depth to Base (m)	Sample	Lithology	Alteration and Secondary Phases	Mineralization	Description	WR Sample
0.52	MA13-097	Volcanic Sand	Weak FeOx		0.0.52 m: Mafic medium-grained volcaniclastic sand, no grading observed. Unconsolidated.	2510
1.11						
1.84	MA13-098	MS Chimney (Py + Sp)		4% Sp(low Fe) 4% Py, 3% Ccp	1.11-1.84 m: Massive sulpfide chimney with banded high-Fe Sp + Py + Ccp. 10% vugs. Minor barite.	2511
				4% Py, 2% Ccp 2% Sp(high Fe)	1.56-1.84 m: Massive pyrite, high temperature fluid pathway.	2512
3.31						
4.63	MA13-099	Volcanic Pebble BX	Intense clay Brt-infill	2% Py 1% Sp (high Fe) 1% Py	3.31-5.77 m: Strongly clay-altered volcanic pebble breccia with sulfate cement. Breccia is matrix-supported with subrounded to subangular clay-altered clasts, 30% clasts, 1-3 mm long. Trace disseminated Py. Patchy anhydrite infill. Monomict, moderately sorted.	2513
			Brt + Anh infill	2% Py <1% Sp (high Fe)		2514
4.76						
4.89			Brt infill			
5.29						
5.77			Brt infill	2% Py 1% Sp		2515

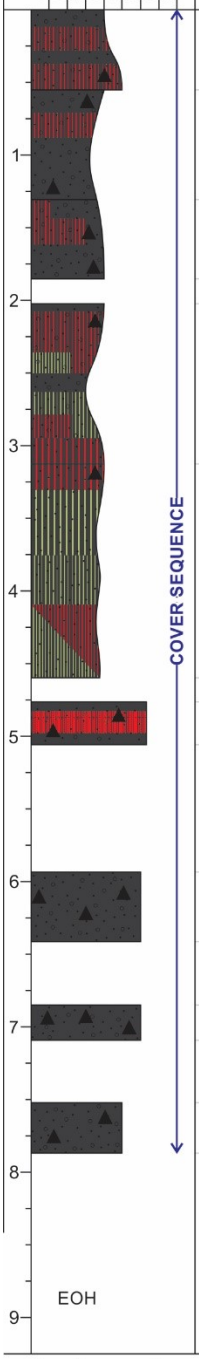
Notes/Interpretation:
No stringer zone preserved due to core loss.
Massive sulfide interval is Py-rich at base - high temperature fluid pathway.

Pebble clasts

Sand clasts

Date: 16-Nov-2013 **Hole ID**: TKAD029 **Deposit**: Tinakula

Geologist: M.O. Anderson **EOH Depth**: 8.79 m **Area**: North "Site A"



Depth to Base (m)	Sample	Lithology	Alteration and Secondary Phases	Mineralization	Description	WR Sample
0.53		Volc. Sand (oxidized)	Strong FeOx		0-0.53 m: Black (mafic) volcaniclastic sand, grading to gravel with increasing FeOx intensity.	2496
1.28	MA13-093	Volc. Sand & Gravel	Strong MnOx		0.53-1.28 m: As above with abundant MnOx in matrix. Coarse-grained. Weakly graded. Unconsolidated.	2497
1.79		Volc. Sand & Gravel	Strong FeOx		1.28-1.79 m: As above (volc. sand/gravel). Clasts of vesicular mafic extrusives, mm-cm scale.	2498
2.01						
3.13	MA13-094	Volc. Sand & Gravel	Mod-strong FeOx, Minor patchy green clay		2.01-3.13 m: As above (volc. sand/gravel), with patches of alternating FeOx/brown clay with green clay alteration. Clasts are softened. Coarse-grained.	2499 2500
4.63	MA13-095	Volc. Sand	Green clay, Mod FeOx		3.13-4.63 m: Volcanic sand/gravel with strong green clay alteration in matrix + pervasive through clasts. Original volcanic textures obscured in clasts.	2502 2503
4.76						
5.06		Volc. Sand & Gravel	Mod patchy Fe+MnOx		4.76-5.06 m: Volcanic sand/gravel, minor FeOx staining.	2504
5.92						
6.42	MA13-096	Volc. Sand & Gravel	Mod patchy oxide & clay		5.92-7.07 m: As above, increase in proportion of gravel fragments (vesicular extrusives).	2505
6.84						
7.07						2506
7.51						
7.84		Volc. Sand & Gravel	Minor green clay in clasts FeOx in matrix		7.51-7.84 m: Volcanic sand/gravel with minor green alteration in clasts and FeOx stains in matrix.	2507
8.79						

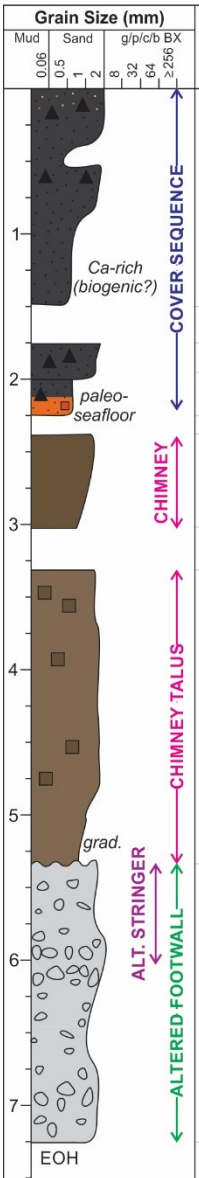
Notes/Interpretation:
Sequence of unconsolidated volcaniclastic sand/pebbles with no sulphides or footwall alteration.
Represents distal volcanics or thick cover sequence.
Multiple episodes of deposition, similar to TKAD019.

▲ Volcanic fragments

Sand/gravel clasts

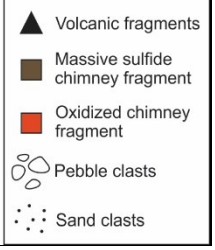
Date: 19-Nov-2013 **Hole ID**: TKAD030 **Deposit**: Tinakula

Geologist: M.O. Anderson **EOH Depth**: 7.26 m **Area**: Central "Site D"



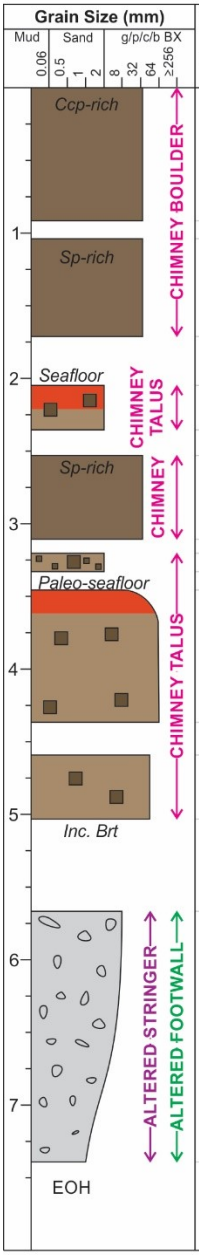
Depth to Base (m)	Sample	Lithology	Alteration	Mineralization	Description	WR Sample
	MA13-001	Volcanic Sand (uncon.)	Minor FeOx + clay clasts		0-2.0 m: Black mafic monomict volcaniclastic sand with few clasts of soft white clay and hematite. Few intervals of silt. Weakly magnetic. Grain size decreases downhole. Few FeOx + clay clasts to 0.4 m. Fine grained to silt-sized interval from 0.4-0.7 m (coarse-grained at 0.7 m, decreasing downhole to 1.5 m. Coarse-grained with volcanic fragments at 1.76 m. three eruptive sequences.	2545
						2546
1.50						
1.76						
2.00		Volc. Sand		Tr Ccp + Sp		2547
2.25	MA13-002	Volc. Sand-Mud (Ox.)	Mod. FeOx + clay		2-2.25m: Ox. volc. sed. Sharp upper contact. Ox. chimney frags?	
2.31						
	MA13-003	MS Chimney (Sph)		3% Sp (low Fe) 1% Ccp (vugs) <1% Bn Tr Py Tr Orp(?)	2.31-3.05m: Massive sulfide chimney with banded honey Sp, medium- to fine-grained, 5% Brt, 5% vugs up to 1 cm. Minor open-space fill. Heavy. Low Fe-Sp.	2548
3.05						
3.28						
	MA13-004	MS Talus (Sph)	Minor patchy FeOx + clay 4 - 5 m	3% Sp 2% Ccp	3.28-5.32m: Massive sulfide mud, mostly Sp, minor Ccp (inc. downhole), disseminated. Clasts of massive sulphide chimney, mostly at top. Patchy FeOx concentrated along beds. Chimney clasts are angular, no evidence for transport.	2549
						2550
	MA13-005					2551
5.32						
		Footwall Volcanic Pebble BX	Strong clay (white) Sulfate infill/veins (anh?)	3% Py 2% Ccp Tr Sp	5.32-7.26m: Strongly clay-altered volcaniclastic pebble breccia, mostly sandy to pebble-sized clasts up to 1 cm. Infilled by sulfate (Anh?) with minor sulfate veins. Sulfides disseminated, concentrated along grain boundaries. Clasts are bleached, bedded, monomictic, 1-2% small vesicles, aligned. Minor sulfate, varies downhole. Moderate sorting. Matrix-supported, locally clast-supported.	2552
6.00						
	MA13-006		Tr FeOx	1-3% Py	Altered stringer zone from 5.32-6..0 m? Inc. in Cu+Ca. Two grain sizes of sulfides: pervasive fine-grained pyrite/marcasite + coarse-grained crystalline Py+Mrc (0.5 mm) along grain boundaries.	2554
						2555
7.26						

Notes/Interpretation:
Sp-rich chimney talus on volcanic pile, not transported far.
Growth of massive sulphide chimney above talus, becomes oxidized at seafloor.
Stringer zone in strongly altered footwall indicated by higher Cu concentration, low Ca.
~3 episodes of volcanic sand with volcanic fragments deposited at top (pyroclastic).



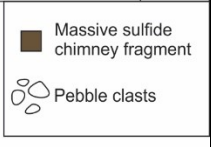
Date: 14-Nov-2013 **Hole ID**: TKAD031 **Deposit**: Tinakula

Geologist: M.O. Anderson **EOH Depth**: 7.33 m **Area**: Central "Site D"



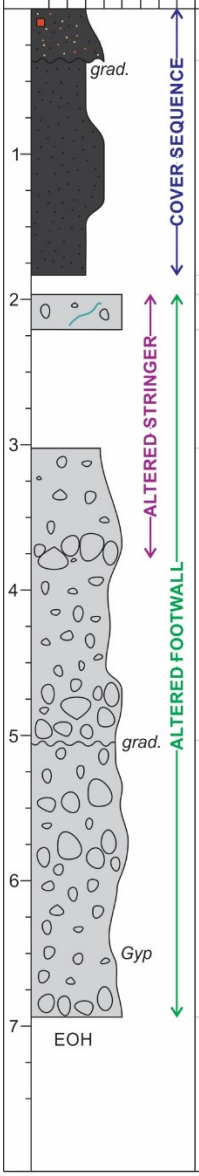
Depth to Base (m)	Sample	Lithology	Alteration and Secondary Phases	Mineralization	Description	WR Sample
	P0042	MS Chimney (Ccp + Sp) Boulder	Patchy clay top 30 cm	4% Ccp 3% Sp 2% Py Tr. Ata	0-1.71 m: Massive sulfide (Ccp + Sp) chimney *boulder*. 0-0.96 m is the core of the chimney, outer sp-rich zone between 1.02-1.71 m. Anh lining pore spaces and conduits, bladed barite vug fill, 5% vugs. Minor atacamite. Minor clay alteration over first 30 cm. Beautiful open-space fill with Ccp -> Sp -> Brt. Lots of banding. Not many biological indicators.	2557
0.96	MA13-041					
1.02						
				4% Sp 3% Ccp 2% Py		2558
1.71						
2.06					2.06-2.30 m: Black Sp-rich massive sulfide sediment, silty to sandy sized with few coarse fragments. Patchy FeOx near top (weathered sulfides). Disseminated Sp + Ccp throughout. Unconsolidated. Minor massive sulphide chimney fragments.	
2.30	MA13-042	MS Talus (Sp)	Mod Patchy FeOx	3% Sp 2% Ccp		2559
2.55					2.55-3.12 m: Massive sulfide chimney with low and high Fe Sp chimney fragments with visible former zones of weathering. Si flooding of pore spaces. Sp is complexly banded, dendritic. Brt cement (heavy). 10% vugs, infilled by Brt, lined by Sp. Opaline Si wisps.	
	P0043	MS Chimney (Sp)	Si infill Minor clay + FeOx	4% Sp (low Fe) 2% Ccp		2560
3.12						
3.20						
3.30		MS Talus (Sp)			3.20-3.30 m: Sulfide sand/mud, Sp-rich.	
3.45						
	P0044	MS Talus (Sp) Lithified Breccia	Mod FeOx alt. of clasts @ 3.45-3.70 m	3% Sp 2% Ccp 2% Py	3.45-5.04 m: Massive sulfide chimney breccia cemented by Brt + Sp. FeOx affects clasts. 5-10% vugs. Bands of low and high Fe Sp, upper ~18 cm is bright red oxidized sillica (jasper). Increasing abundance of 1-2 cm clasts of Anh + vein infill towards bottom. Bladed Brt and botryoidal Sp vein fill. Not simple chimney textures, appears to be lithified chimney talus, hydrothermally cemented. Brt content increases downhole. Not transported far.	2561
4.34						
4.58						
	MA13-043	MS Talus (Sp) Lithified BX		4% Sp 3% Ccp 2% Py		2563
5.04						
5.64						
	MA13-044	Volcanic Pebble BX	Intense clay	2% Py Tr. Ccp	5.64-7.33 m: Intensely clay-altered matrix-supported volcaniclastic pebble breccia. 30% subrounded clasts, 1-10 mm long, decreasing in abundance and size downhole. Matrix is light grey, muddy. Unconsolidated. Abundant disseminated euh. Py, decreasing downhole. Tr. disseminated Ccp. Minor sulfate cementing clasts. Monolithic. No obvious grading.	2564
	MA13-045					2565
7.33						

Notes/Interpretation:
Massive sulfide chimney (Ccp+Sp) boulder sits on moderately oxidized seafloor chimneys (very different, Sp-rich), lithified chimney talus (hydrothermal cement).
Grades into matrix-supported strongly clay-altered footwall.
Small, rounded clasts in footwall = distal volcaniclastics?
Footwall alteration is likely altered stringer zone (low Ca content).
Origin of FeOx from 3.45-3.70 m: paleoseafloor? Short lived, prior to pulse of hydrothermal fluids causing another chimney building episode, lithified talus.



Date: 15-Nov-2013 **Hole ID**: TKAD032 **Deposit**: Tinakula

Geologist: M.O. Anderson **EOH Depth**: 6.92 m **Area**: North "Site C"



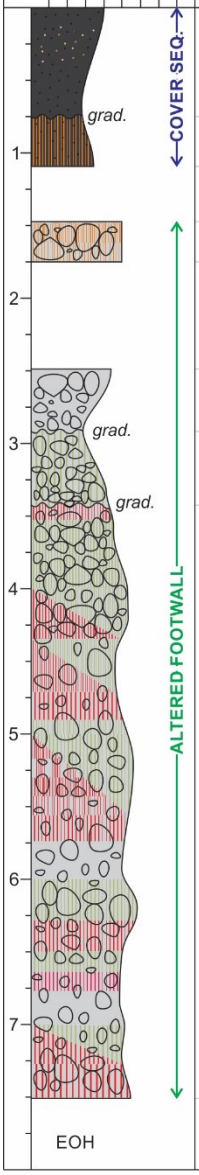
Depth to Base (m)	Sample	Lithology	Alteration and Secondary Phases	Mineralization	Description	WR Sample
0.31	MA13-070	Volc. Sand (uncon.)	Minor FeOx strong Anh (40%) minor MnOx minor Chl		0-0.31 m: Black volc. sand, very c.g. Thin MnOx crust. Weakly magnetic. Very few clasts of jasperoid and clear Gp xtals. Tr. green altered clasts (chl?). Possible FeOx chimney fragment.	2567
1.85	MA13-071	Volc. Sand (uncon.)	Minor FeOx	<1% Py-Mrc	0.30-1.85 m: Black volc. sand, medium-grained, increase in grain size downhole. Minor clasts of FeOx and clay. Reverse grading towards bottom, possibly 2 depositional events. Tr. Anh. 5% grains of oxide/sulfate. No volcanic fragments observed. Few fragments of Py-Mrc (<1%). Poorly sorted, subrounded to rounded = reworking.	2568 2569
1.96						
2.20	MA13-072	Volcanic Pebble BX	Mod-strong clay weak FeOx	3% Sp (high Fe) 3% Py, 1% Ccp	1.96-2.20 m: Footwall volc. pebble breccia with veins of sulfate, Py-Mrc, opaline Si (4%), barite (3%). Green chalcedony(?) in matrix with fine Py + Sp disseminated throughout matrix and clasts. Clasts are weakly clay-altered, 2-20 mm long, 15-20%, subrounded-subangular, vesicular. Matrix-supported, monomict.	2570
3.01						
5.02	MA13-073	Volcanic Pebble BX	Strong clay in matrix	3.02-3.77m: 4% Py 2% Ccp 1% Sp	3.01-5.02 m: Monomict mildly vesicular volcaniclastic pebble breccia (agglomerate) in dark grey clay + Anh matrix. Abundant v.f.g. subhedral Py + Ccp in matrix. Clasts are variably altered with white-grey clay. Clast size varies from sub-mm to 20 mm. Strong clay alteration of matrix, weaker alteration of clasts. Matrix-supported, 10% subrounded-subangular clasts. Clasts have altered rims and are variably fractured (fractures infilled by late sulfides). Disseminated low-grade Zn mineralization at 3.65 m, very fine.	2572 2573 2574
6.92	MA13-074	Volcanic Pebble BX	Strong clay Anh infill and veins	4% Py	5.02-6.92 m: As above, with v.f.g. sulfides (Py + Ccp? + Gn?) in matrix. Abundant Py mineralization in intensely clay altered matrix, variable. 3% Anh infill and veins. Facies vary from clast-supported (angular, 1-20 mm, vesicular, 60% clasts, muddy matrix, 5% disseminated Py) to matrix-supprted (subangular, 1-20 mm, 30-40% clasts). Patchy sulfate, locally up to 25%.	2575
	MA13-075		Gp @ 6.40-6.60 m		6.40-6.60 m: ~50% gypsum, botryoidal. Clasts have darker rims and lighter cores, vary in size from 2-30 mm. Zones of Anh from like diffuse veins or relict fluid pathways.	2576

Notes/Interpretation:
Sequence of volcaniclastic breccia (subrounded-subangular, poorly sorted), overall matrix-supported (proximal facies of small volcano), altered to clay and infilled with sulfate (Anh).
Covered by at least 2 sequences of distal volcanic sand (reworked).
Located at intersection of 2 big structures, providing conduit for magma = volcano.

Oxidized chimney fragment
Pebble clasts
Sand clasts
Sulfate veins

Date: 14-Nov-2013 **Hole ID**: TKAD033 **Deposit**: Tinakula

Geologist: M.O. Anderson **EOH Depth**: 7.51 m **Area**: North "Site C"



Depth to Base (m)	Sample	Lithology	Alteration and Secondary Phases	Mineralization	Description	WR Sample
0.75	MA13-021	Volc. Sand (uncon.)	Weak FeOx		0-0.75 m: Black volcanic gravel grading to sand, patchy FeOx from 0.78 m. Few intervals of silt-sized material, ~5 cm wide.	2578
1.10	MA13-022	Volc. Sand (oxidized)	Mod. FeOx patchy Si + clay	1% Py	0.75-1.10 m: Lithified volcanic pebble breccia with clasts of Opal A, jasper, barite, finer-grained crust of underlying interval. Abundant worm clasts in lithified fragments.	2579
1.49					1.49-1.75 m: Silicified volcanic pebble breccia, weakly clay-altered, polymict(?), clast-supported, moderately sorted, moderately rounded volcanic clasts, with minor jasper(?) and green opal A clasts. Clasts are 1-10 mm, mafic (vesicular), silicified and clay-altered (protolith?), weakly bedded. Anh-Si in matrix. Brt = 3%. 5-10% pore space, 4% disseminated Py, <1% native sulphur(?).	
1.75	MA13-023	Volcanic Pebble BX (polymict)	Mod. Si weak clay	4% Py <1% Sp		2581
2.49					2.49-2.90 m: Volcanic pebble BX with intensely clay-altered matrix and weakly clay-altered clasts. Polymict, clast-supported, poorly sorted, volcanic autobreccia facies(?). Arcuate margins and strongly jointed clasts. Clay-altered equivalent of above, increase in jasper(?) clasts, fewer mafic clasts. Disseminated Py, locally concentrated in matrix with FeOx.	
2.90	MA13-024	Volcanic Pebble BX (polymict)	Strong clay in matrix, weak in clasts	4% Py		2582
3.40	MA13-025	Volcanic Pebble BX (polymict)	Strong clay, green alt.	5% Py	2.90-3.40 m: Volc. pebble BX, intensely clay-alt. matrix, weakly clay-alt. clasts. Matrix is soft, dark green (Opal A?). Alt. version of above. Matrix infill = Anh + opal +/- palagonite rims. Some clasts have aligned vesicles. Trace Py.	2583
		Volcanic Pebble BX (monomict)	Strong clay, green alt., patchy Mod-minor FeOx	Tr. Py	3.40-7.51 m: Volc. pebble breccia, similar to above, green matrix has patchy FeOx staining, dark brown to orange, minor-mod. Monomictic? Increasing angularity of clasts. Bimodal distribution of clasts; small 1-3 mm and larger cm-scale clasts. Trace Py at top of interval.	2584
	MA13-026			No Py		2585
			Patchy green alt. + FeOx, intense clay			2586
						2587
7.51	MA13-027					2588

Notes/Interpretation:
Sequence of volcaniclastic breccia, similar to TKAD032.
Clast-supported, polymict (variably altered clasts) to monomict autobreccia facies.
Variable alteration, patchy green alternating with FeOx, mod-intense clay.
Possibly 2 episodes of cover sequence with oxidation at paleoseafloor surface?

Pebble clasts
Sand clasts

Appendix O

SWIR Spectroscopy Analyses on Altered Volcaniclastic Rocks of the Tinakula Deposit

Contents:

Summary All Drillholes **932**

Fig. O1. Summary of all minerals identified by SWIR spectroscopy. 932

Fig. O2. Summary of all mineral groups identified by SWIR spectroscopy. 933

Drillhole TKAD001 ..... **934**

Fig. O3. Stacked SWIR spectra (normalized hull quotient) of samples from drillhole TKAD001. 934

Fig. O4. SWIR spectra (normalized hull quotient) of sample MA13-086-C, drillhole TKAD001 (14.00–14.12 mbsf), composed of 82% Mnt + 18% Gp. 935

Fig. O5. SWIR spectra (normalized hull quotient) of sample MA13-087-C, drillhole TKAD001 (16.05–16.22 mbsf), composed of 69% Mnt + 31% Pgl. 935

Fig. O6. SWIR spectra (normalized hull quotient) of sample MA13-088-C, drillhole TKAD001 (17.40–17.50 mbsf), composed of 100% Ms. 936

Fig. O7. SWIR spectra (normalized hull quotient) of sample P005-C, drillhole TKAD001 (19.14–19.30 mbsf), composed of 100% Msl. 936

Fig. O8. SWIR spectra (normalized hull quotient) of sample MA13-091-CM, TKAD001 (20.80–21.00 mbsf), composed of 50% Chl and 50% Ms. 937

Drillhole TKAD003 ..... **938**

Fig. O9. Stacked SWIR spectra (normalized hull quotient) of samples from drillhole TKAD003. 938

Fig. O10. SWIR spectra (normalized hull quotient) of sample P013-C, drillhole TKAD003 (13.40–13.50 mbsf), composed of 67% Pgl and 33% Mnt. 939

Fig. O11. SWIR spectra (normalized hull quotient) of sample P014-C, drillhole TKAD003 (16.41–16.50 mbsf), composed of 50% Chl-FeMg + 50% Msl. 939

Drillhole TKAD007 ..... **940**

Fig. O12. Stacked SWIR spectra (normalized hull quotient) of samples from drillhole TKAD007. 940

Fig. O13. SWIR spectra (normalized hull quotient) of sample P022-C, drillhole TKAD007 (11.23–11.34 mbsf), composed of 51% Pg1 + 49% Chl-FeMg. 941

Drillhole TKAD012 ..... **942**

Fig. O14. Stacked SWIR spectra (normalized hull quotient) of samples from drillhole TKAD012. 942

Fig. O15. SWIR spectra (normalized hull quotient) of sample MA13-062-C, drillhole TKAD012 (2.81–2.90 mbsf), composed of 72% Mnt + 28% Pgl. 943

Drillhole TKAD015 ..... **944**

Fig. O16. Stacked SWIR spectra (normalized hull quotient) of samples from drillhole TKAD015. 944

Fig. O17. SWIR spectra (normalized hull quotient) of sample MA13-052-C, drillhole TKAD015 (6.42–6.52 mbsf), composed of 77% Pg + 23% Gp. 945

Fig. O18. SWIR spectra (normalized hull quotient) of sample MA13-053-C, drillhole TKAD015 (7.23–7.34 mbsf), composed of 52% Pg + 48% Gp. 945
Drillhole TKAD016 946
Fig. O19. Stacked SWIR spectra (normalized hull quotient) of samples from drillhole TKAD016. 946
Fig. O20. SWIR spectra (normalized hull quotient) of sample M13-034-C, drillhole TKAD016 (2.02–2.13 mbsf), composed of 74% Dsp + 26% Gp, with a high degree of uncertainty. 947
Fig. O21. SWIR spectra (normalized hull quotient) of sample MA13-036-C, drillhole TKAD016 (7.00–7.05 mbsf), composed of 60% Chl and 40% Pg. 947
Drillhole TKAD018 948
Fig. O22. Stacked SWIR spectra (normalized hull quotient) of samples from drillhole TKAD018. 948
Fig. O23. SWIR spectra (normalized hull quotient) of sample MA13-015-C, drillhole TKAD018 (5.00–5.10 mbsf), composed of 59% Gp + 41% Pg. 949
Drillhole TKAD025 950
Fig. O24. Stacked SWIR spectra (normalized hull quotient) of samples from drillhole TKAD025. 950
Fig. O25. SWIR spectra (normalized hull quotient) of sample MA13-039-C, drillhole TKAD025 (5.50–5.60 mbsf), composed of 100% Gp. 951
Fig. O26. SWIR spectra (normalized hull quotient) of sample MA13-040-C, drillhole TKAD025 (6.91–7.00 mbsf), composed of 90% Chl-FeMg + 10% Gp. 951
Drillhole TKAD026 952
Fig. O27. Stacked SWIR spectra (normalized hull quotient) of samples from drillhole TKAD026. 952
Fig. O28. SWIR spectra (normalized hull quotient) of sample MA13-067-C, drillhole TKAD026 (2.90–3.00 mbsf), composed of 63% Pg and 37% Mnt. 953
Fig. O29. SWIR spectra (normalized hull quotient) of sample MA13-068-C, drillhole TKAD026 (3.60–3.68 mbsf), composed of 100% Pg. 953
Fig. O30. SWIR spectra (normalized hull quotient) of sample MA13-069-C, drillhole TKAD026 (5.64–5.75 mbsf), with an unreliable result. 954
Drillhole TKAD027 955
Fig. O31. Stacked SWIR spectra (normalized hull quotient) of samples from drillhole TKAD027 955
Fig. O32. SWIR spectra (normalized hull quotient) of sample P022-C, drillhole TKAD027 (11.3–11.34 mbsf), composed of 51% Pgl + 49% Chl-FeMg. 956
Drillhole TKAD028 957
Fig. O33. Stacked SWIR spectra (normalized hull quotient) of samples from drillhole TKAD028. 957
Fig. O34. SWIR spectra (normalized hull quotient) of sample MA13-099-C, drillhole TKAD028 (4.50–4.60 mbsf), composed of 72% Dsp + 28% Gp. 958
Drillhole TKAD030 959
Fig. O35. Stacked SWIR spectra (normalized hull quotient) of samples from drillhole TKAD030. 959
Fig. O36. SWIR spectra (normalized hull quotient) of sample MA13-005-C, drillhole TKAD030 (5.06–5.21 mbsf), composed of 100% Pg. 960
Fig. O37. SWIR spectra (normalized hull quotient) of sample MA13-006-C, drillhole TKAD030 (6.45–6.60 mbsf), composed of 100% Pg. 960
Drillhole TKAD031 961
Fig. O38. Stacked SWIR spectra (normalized hull quotient) of samples from drillhole TKAD031. 961

Fig. O39. SWIR spectra (normalized hull quotient) of sample MA13-044-C, drillhole TKAD031 (5.64–5.69 mbsf), composed of 72% Pgl and 28% Non. 962

Drillhole TKAD032 963

Fig. O40. Stacked SWIR spectra (normalized hull quotient) of samples from drillhole TKAD032. 963

Fig. O41. SWIR spectra (normalized hull quotient) of sample MA13-072-C, drillhole TKAD032 (2.05–2.1 mbsf), composed of 100% Mnt. 964

Fig. O42. SWIR spectra (normalized hull quotient) of sample MA13-073-C, drillhole TKAD032 (3.90–4.00 mbsf), composed of 100% Mnt. 964

Fig. O43. SWIR spectra (normalized hull quotient) of sample MA13-074-C, drillhole TKAD032 (5.31–5.40 mbsf), composed of 67% Mnt + 33% Pgl. 965

Fig. O44. SWIR spectra (normalized hull quotient) of sample MA13-075-C, drillhole TKAD032 (6.42–6.54 mbsf), composed of 71% Mnt + 29% Pgl. 965

Drillhole TKAD033 966

Fig. O45. Stacked SWIR spectra (normalized hull quotient) of samples from drillhole TKAD033. 966

Fig. O46. SWIR spectra (normalized hull quotient) of sample MA13-026-C, drillhole TKAD033 (4.76–4.88 mbsf), composed of 100% Mnt. 967

Fig. O47. SWIR spectra (normalized hull quotient) of sample MA13-026-M, drillhole TKAD033 (4.76–4.88 mbsf), composed of 100% Mnt. 967

Fig. O48. SWIR spectra (normalized hull quotient) of sample MA13-027-C, drillhole TKAD033 (7.30–7.40 mbsf), composed of 100% Mnt. 968

Fig. O49. SWIR spectra (normalized hull quotient) of sample MA13-027-M, drillhole TKAD033 (7.30–7.40 mbsf), composed of 100% Dsp. 968

Notes:

All analyses performed on fine powders (< 63 μm), separated by clast (-C), matrix (-M), or both clast and matrix (-CM) components; see Methods. Reference spectra are shown, colored according to the error scale indicated in each figure.
SWIR = ShortWave InfraRed Spectroscopy
Asp = aspectral; Chl = chlorite; Dsp = diaspore; Gp = gypsum; Mnt = montmorillonite; Ms = muscovite; Msl = muscoviticillite; Pg = paragonite; Pgl = paragoniticillite

Summary All Drillholes

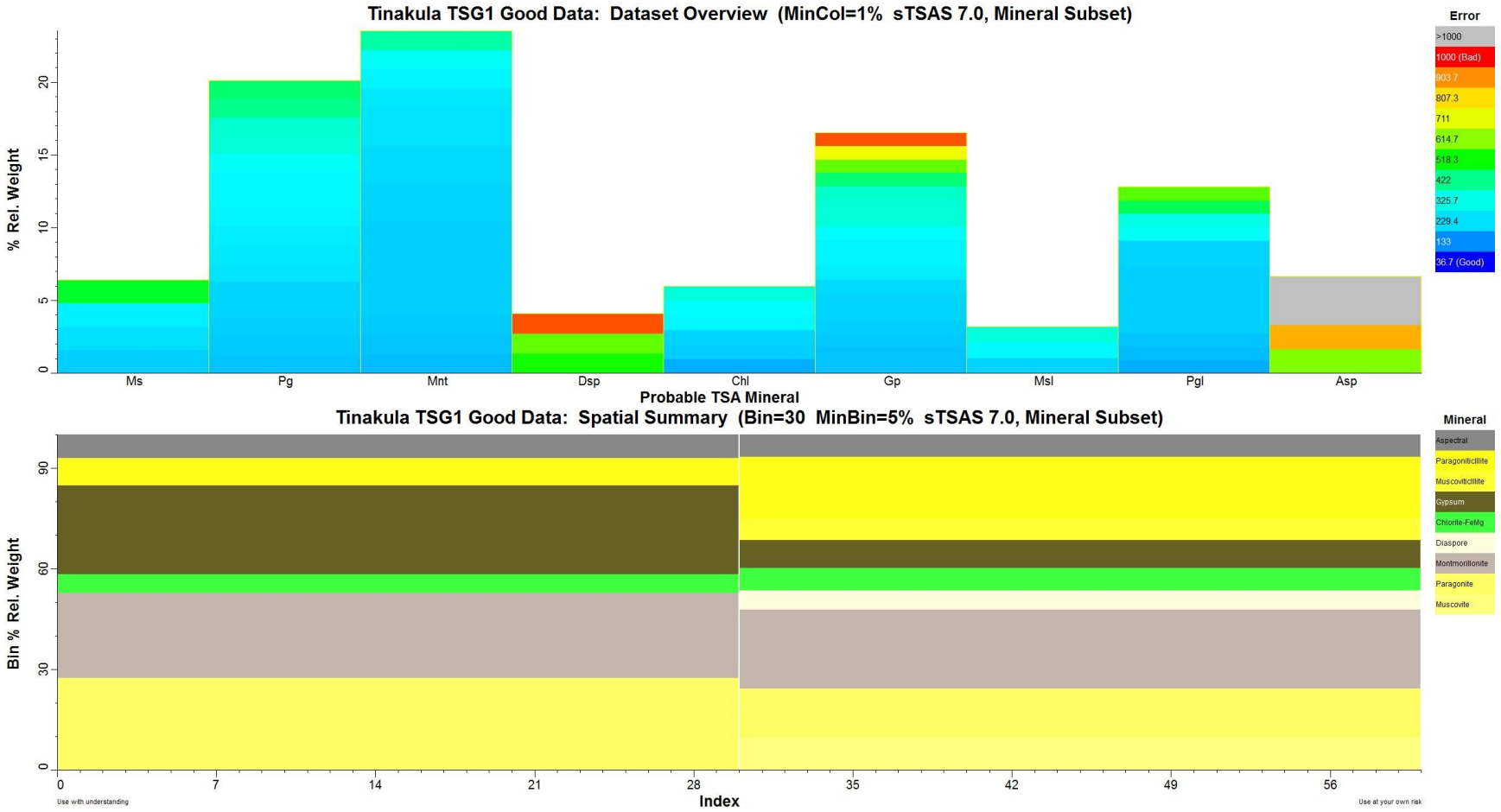


Fig. O1. Summary of all minerals identified by SWIR spectroscopy.

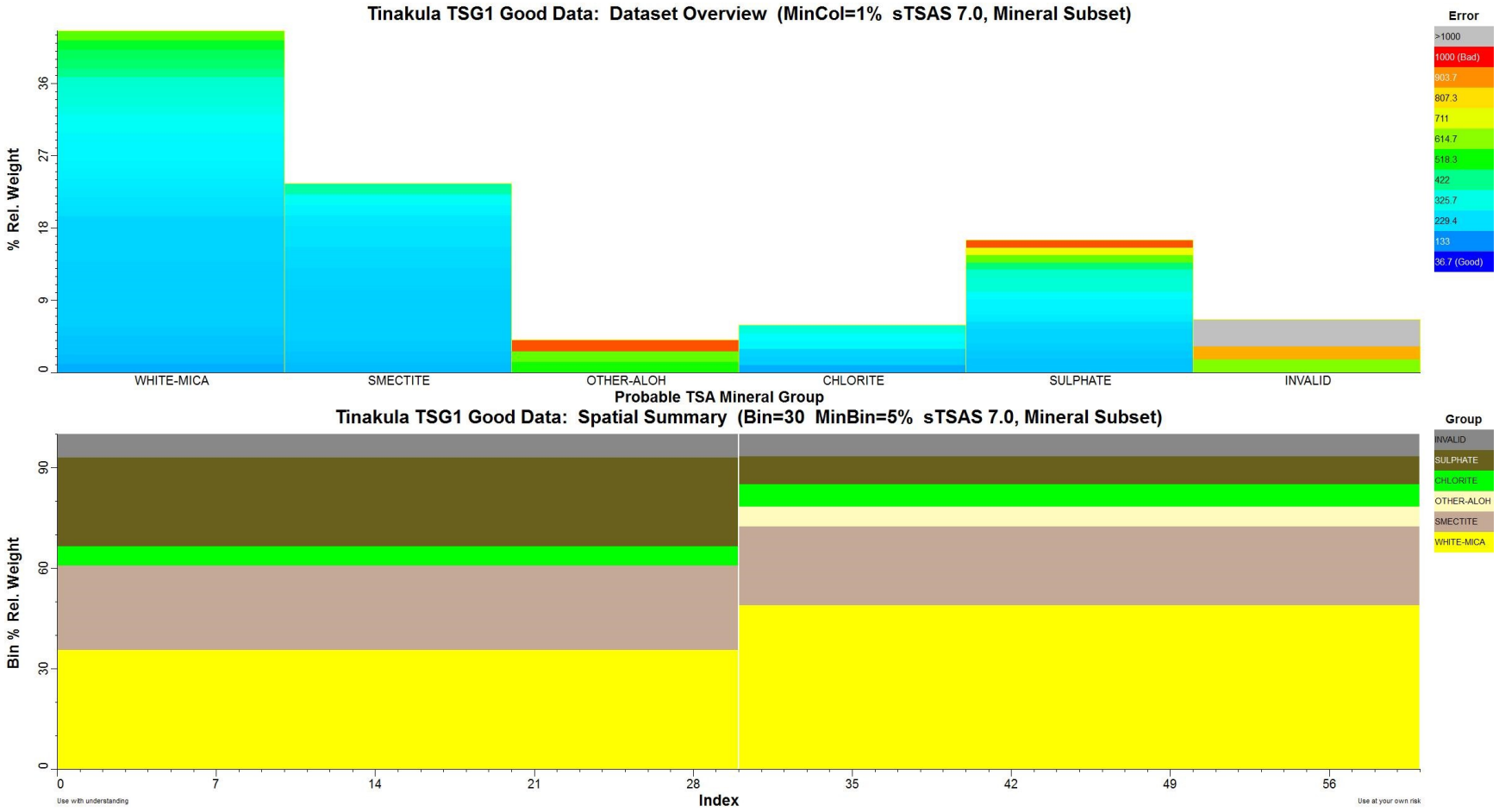


Fig. O2. Summary of all mineral groups identified by SWIR spectroscopy.

Drillhole TKAD001

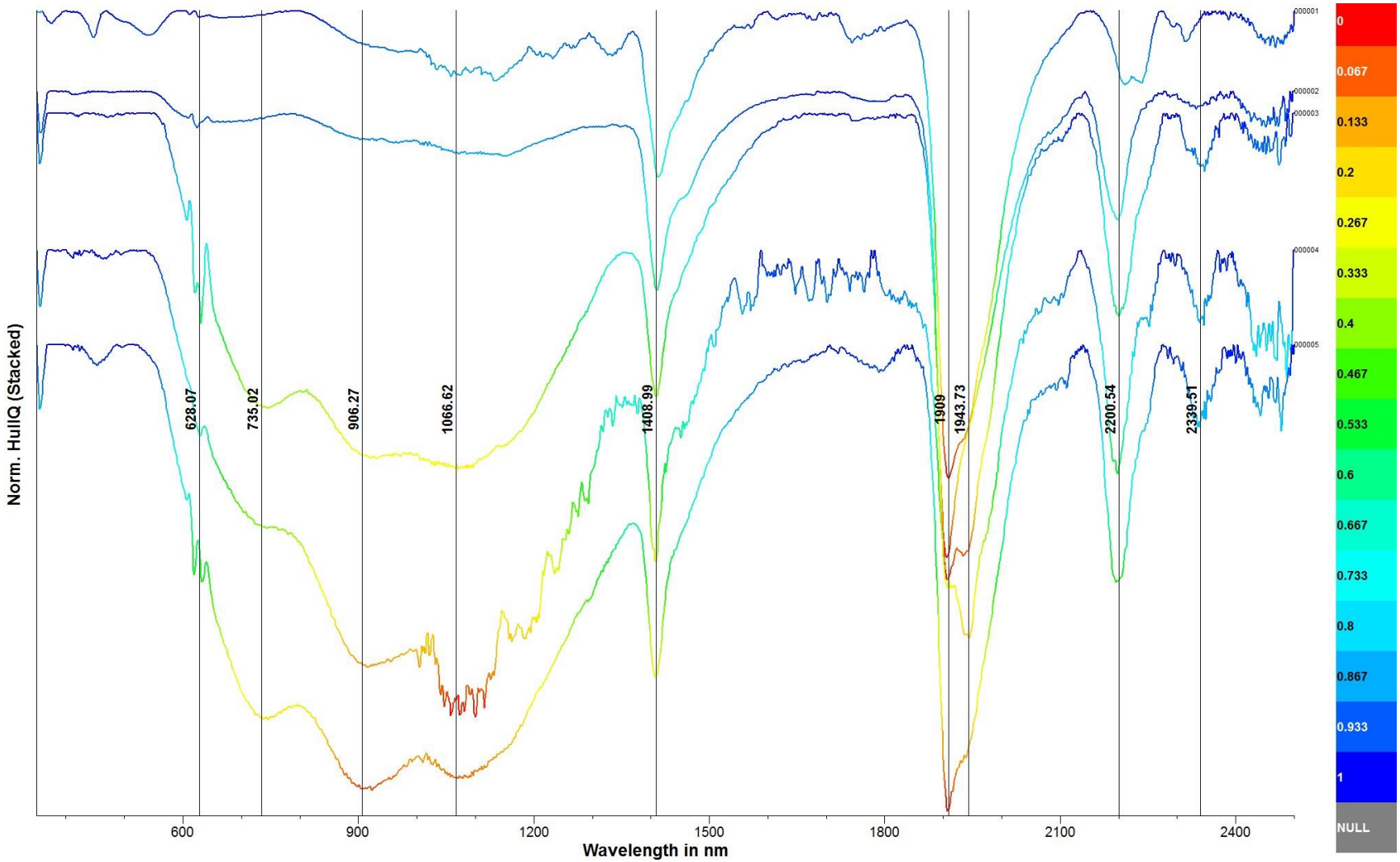


Fig. O3. Stacked SWIR spectra (normalized hull quotient) of samples from drillhole TKAD001.

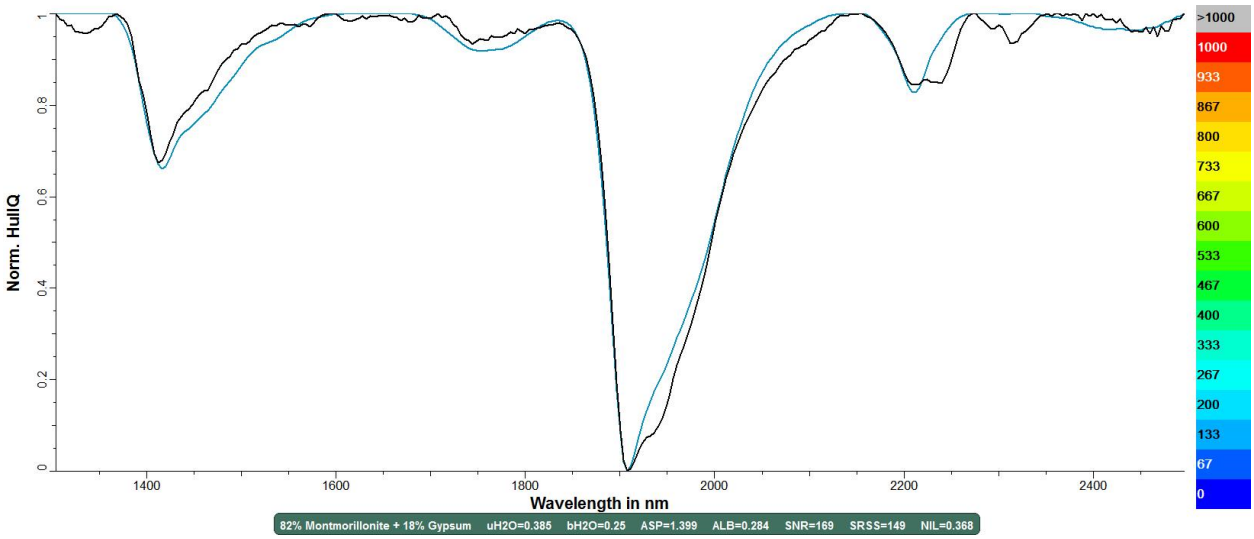


Fig. O4. SWIR spectra (normalized hull quotient) of sample MA13-086-C, drillhole TKAD001 (14.00–14.12 mbsf), composed of 82% Mnt + 18% Gp.

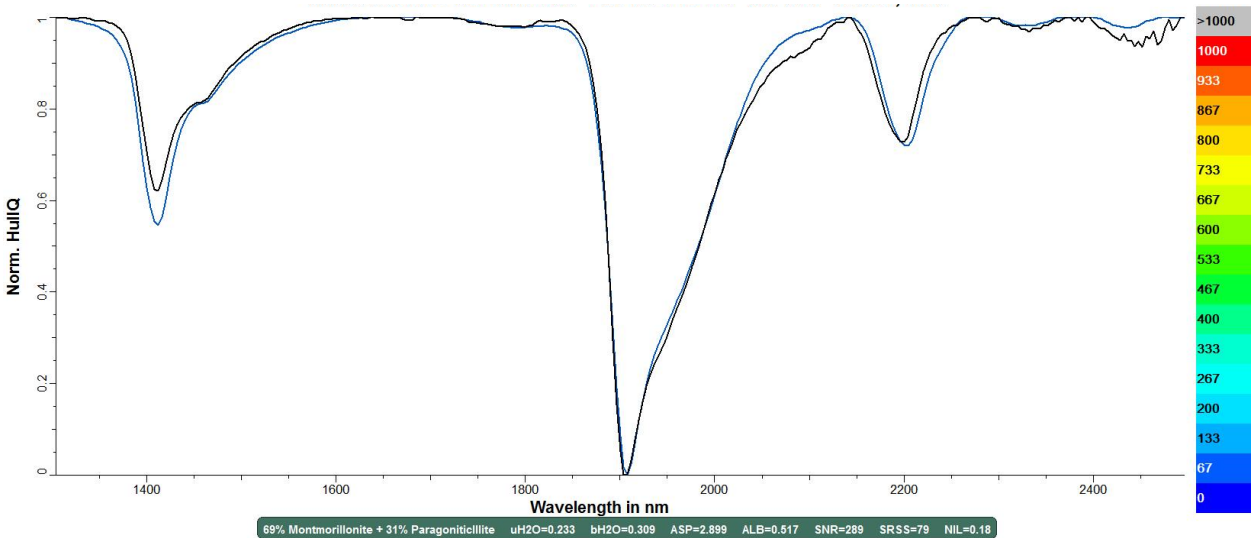


Fig. O5. SWIR spectra (normalized hull quotient) of sample MA13-087-C, drillhole TKAD001 (16.05–16.22 mbsf), composed of 69% Mnt + 31% Pgl.

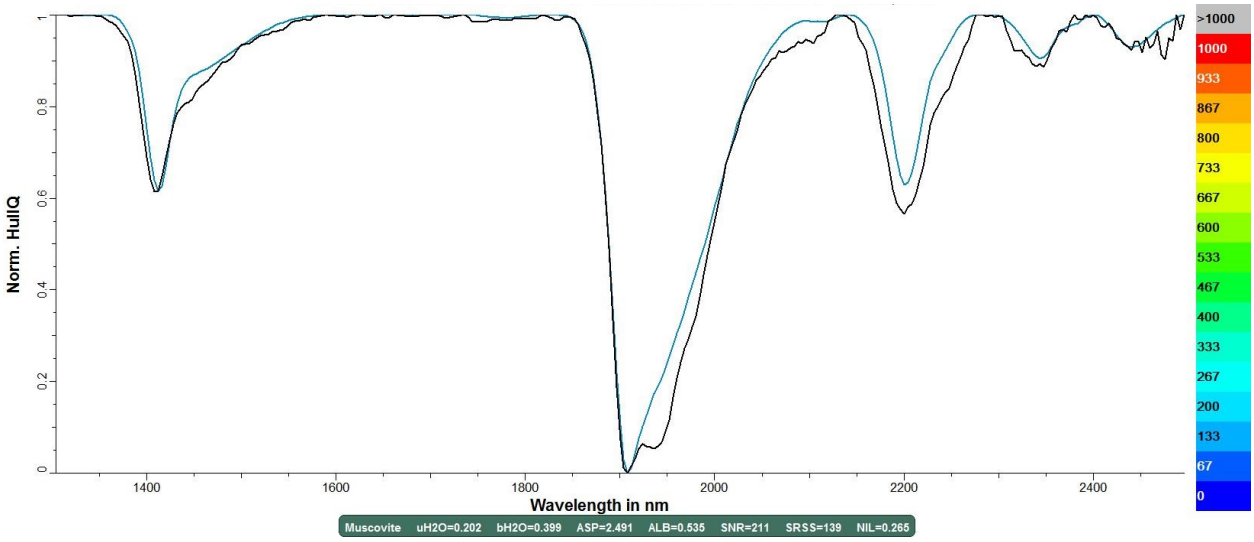


Fig. O6. SWIR spectra (normalized hull quotient) of sample MA13-088-C, drillhole TKAD001 (17.40–17.50 mbsf), composed of 100% Ms.

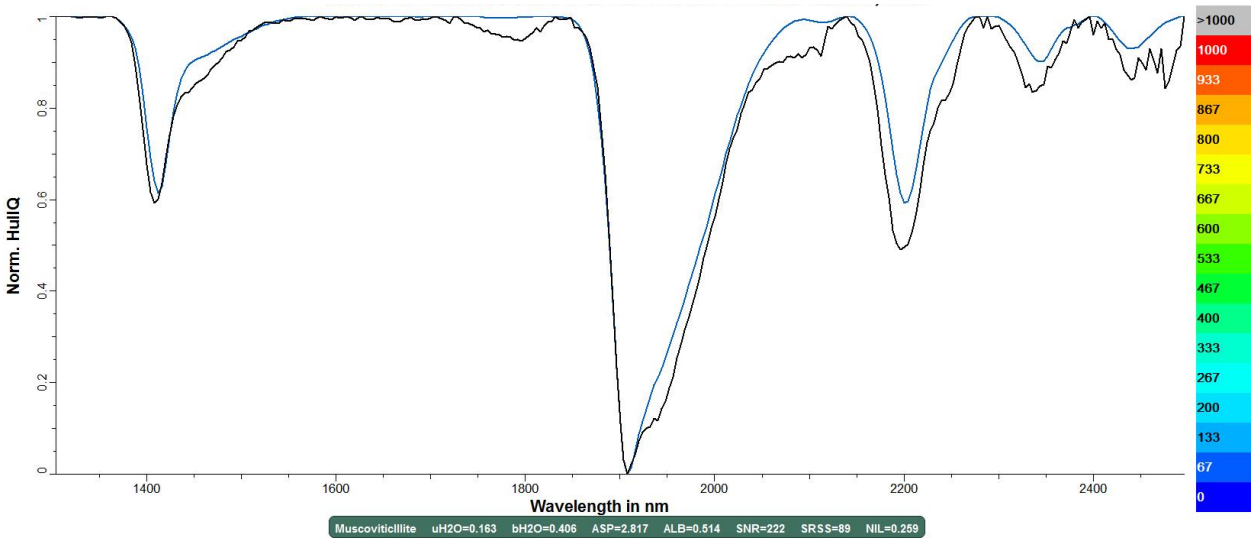


Fig. O7. SWIR spectra (normalized hull quotient) of sample P005-C, drillhole TKAD001 (19.14–19.30 mbsf), composed of 100% Msl.

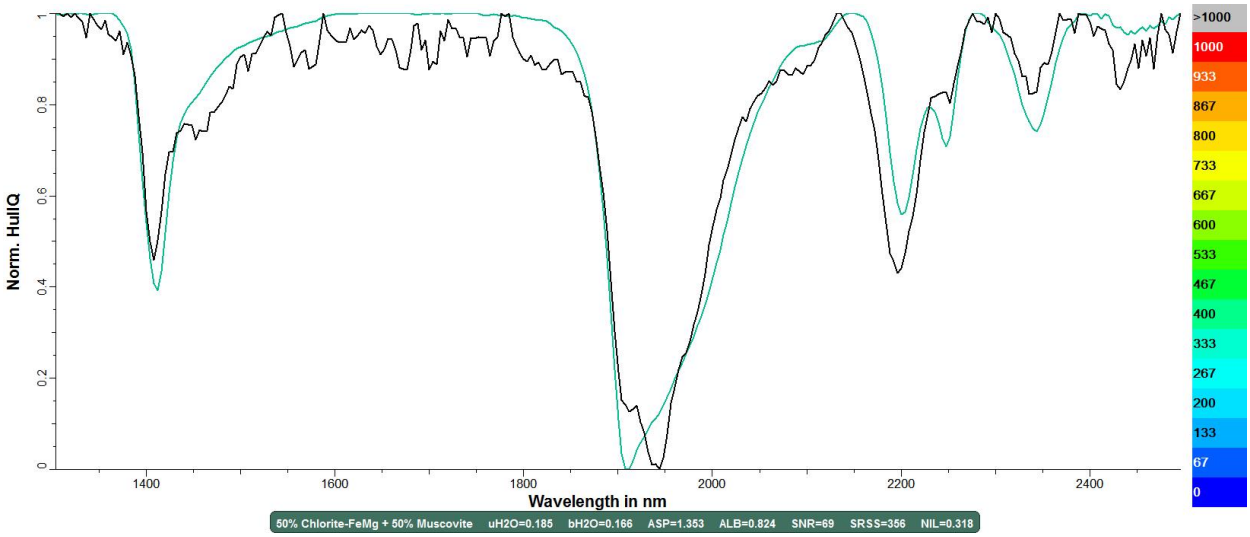


Fig. O8. SWIR spectra (normalized hull quotient) of sample MA13-091-CM, TKAD001 (20.80–21.00 mbsf), composed of 50% Chl and 50% Ms.

Drillhole TKAD003

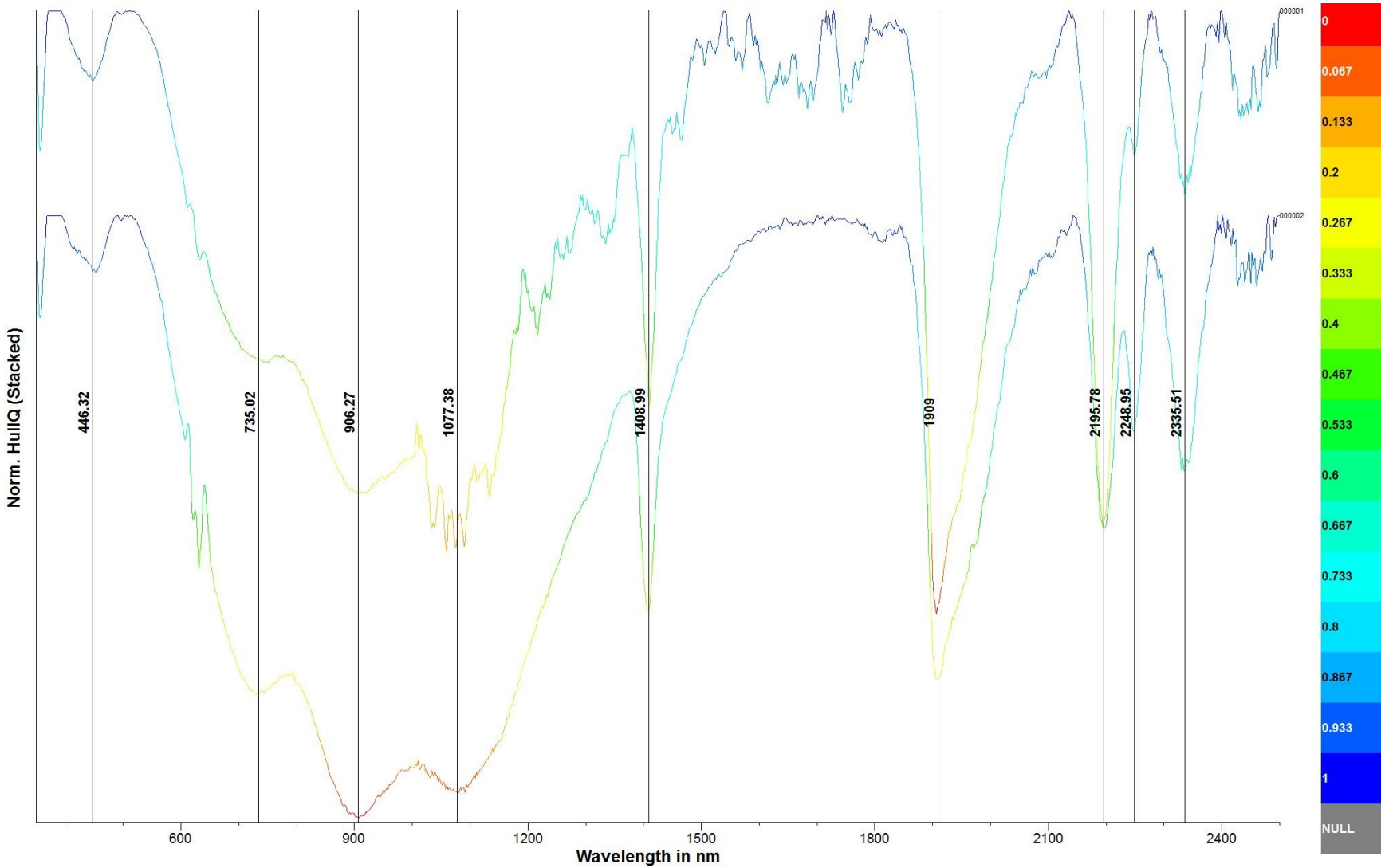


Fig. O9. Stacked SWIR spectra (normalized hull quotient) of samples from drillhole TKAD003.

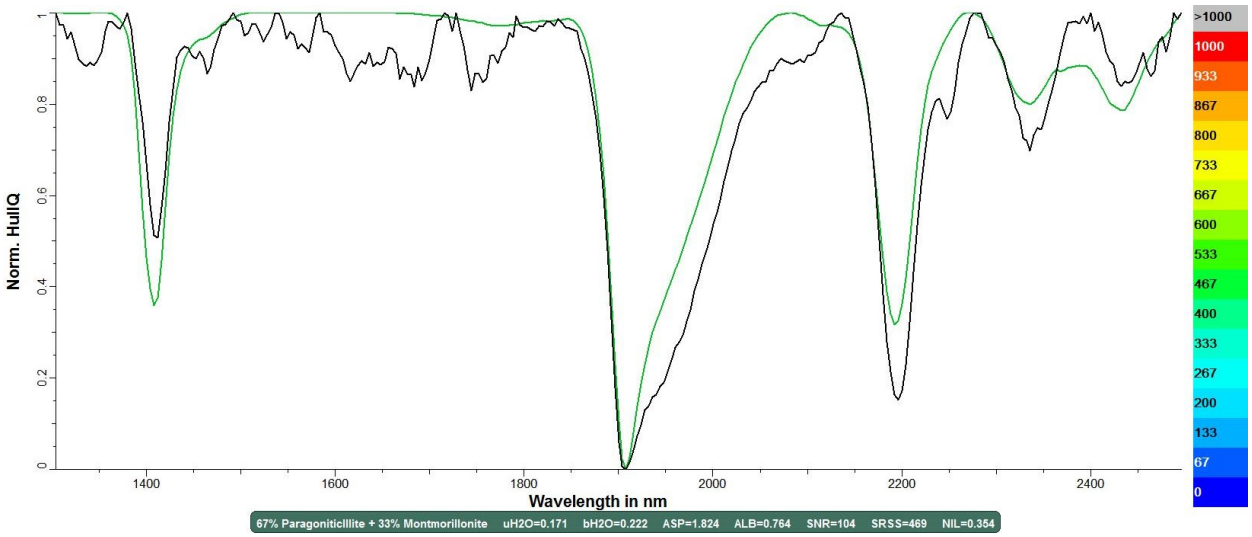


Fig. O10. SWIR spectra (normalized hull quotient) of sample P013-C, drillhole TKAD003 (13.40–13.50 mbsf), composed of 67% Pgl and 33% Mnt.

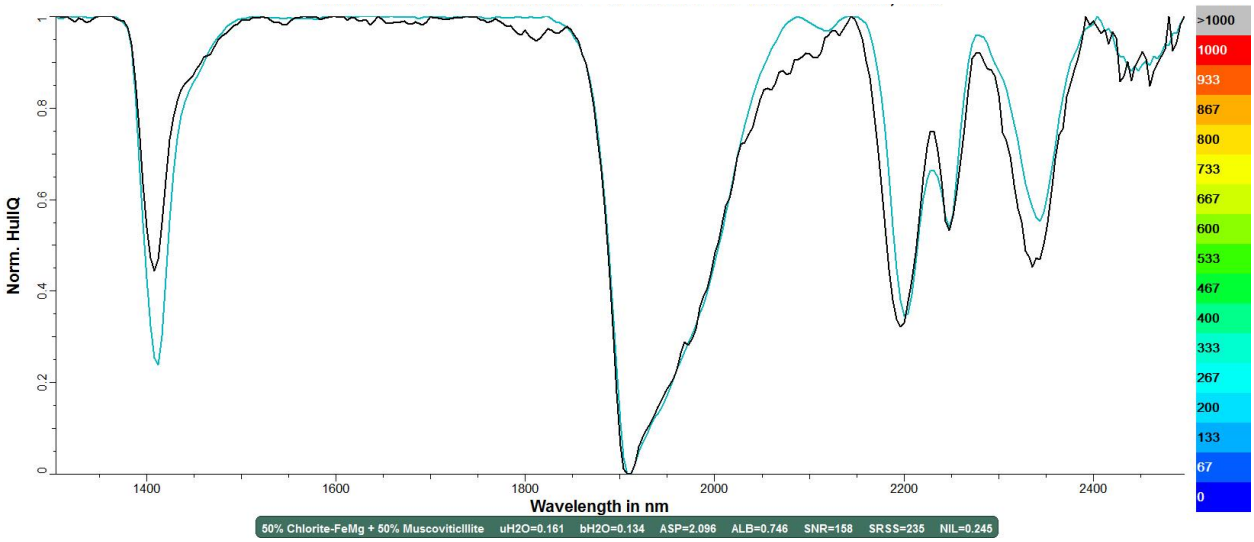


Fig. O11. SWIR spectra (normalized hull quotient) of sample P014-C, drillhole TKAD003 (16.41–16.50 mbsf), composed of 50% Chl-FeMg + 50% Msl.

Drillhole TKAD007

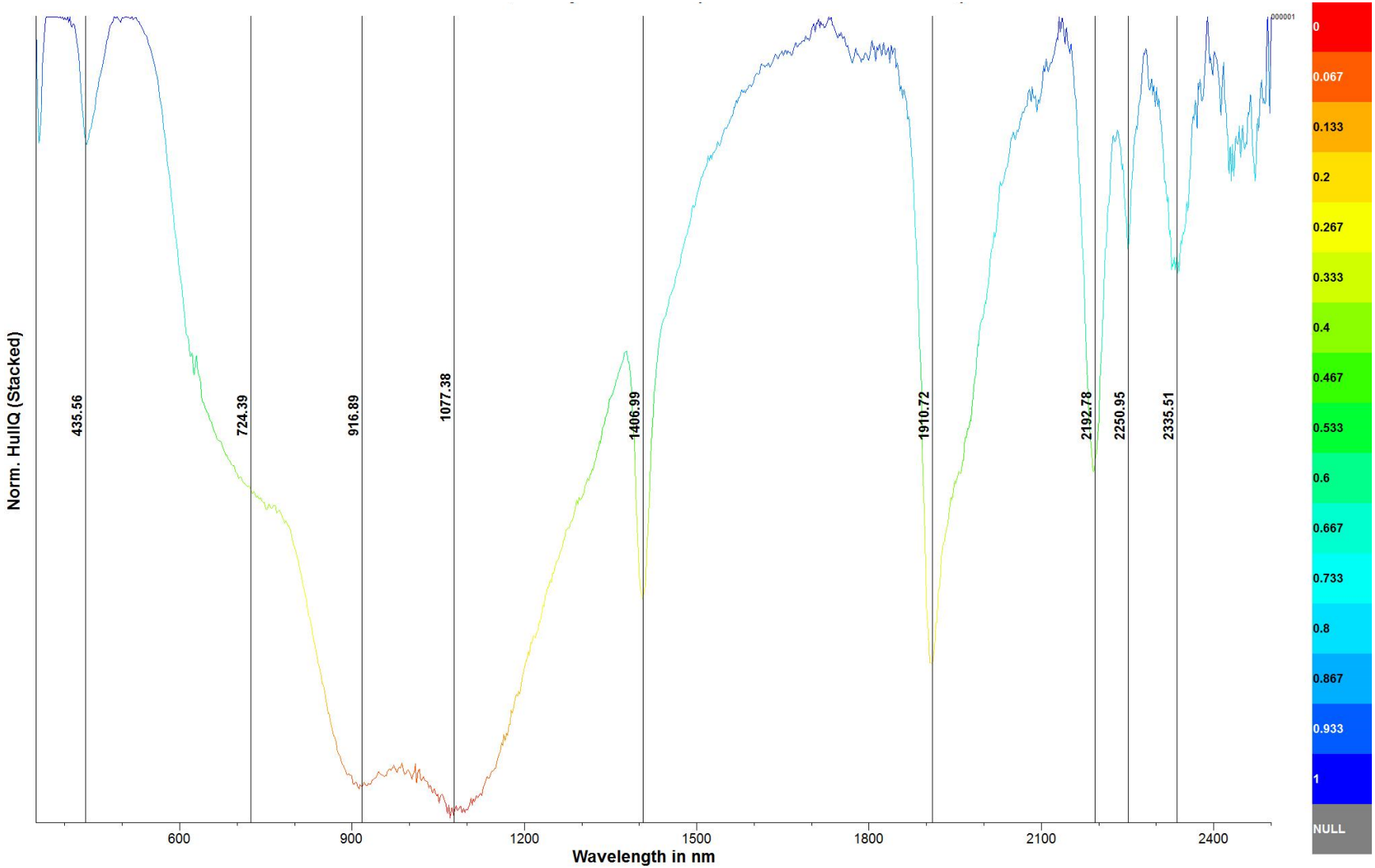


Fig. O12. Stacked SWIR spectra (normalized hull quotient) of samples from drillhole TKAD007.

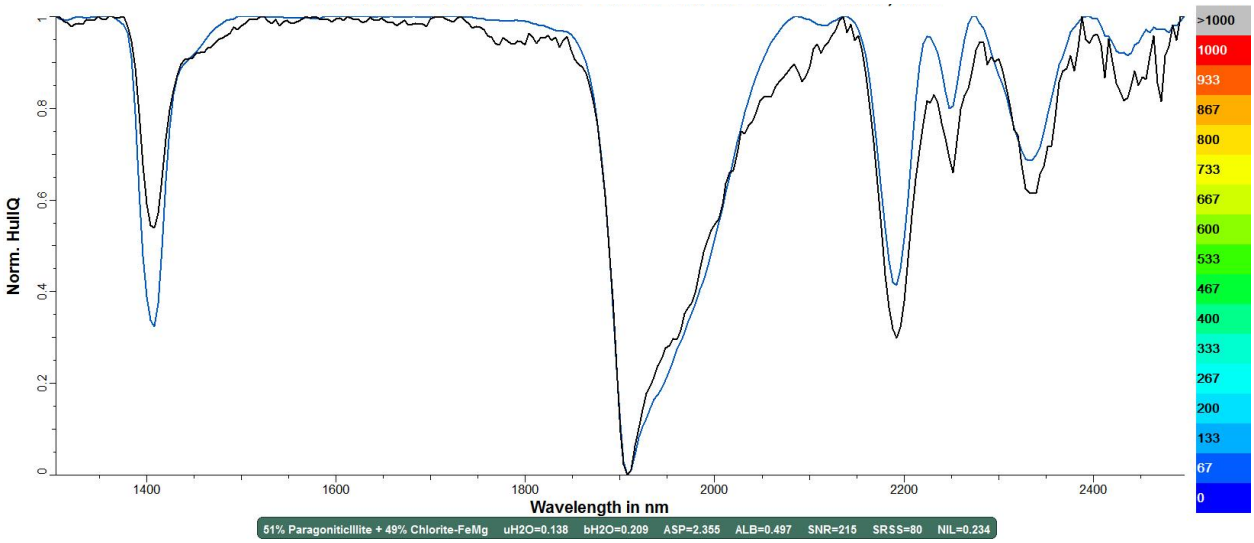


Fig. O13. SWIR spectra (normalized hull quotient) of sample P022-C, drillhole TKAD007 (11.23–11.34 mbsf), composed of 51% Pg1 + 49% Chl-FeMg.

Drillhole TKAD012

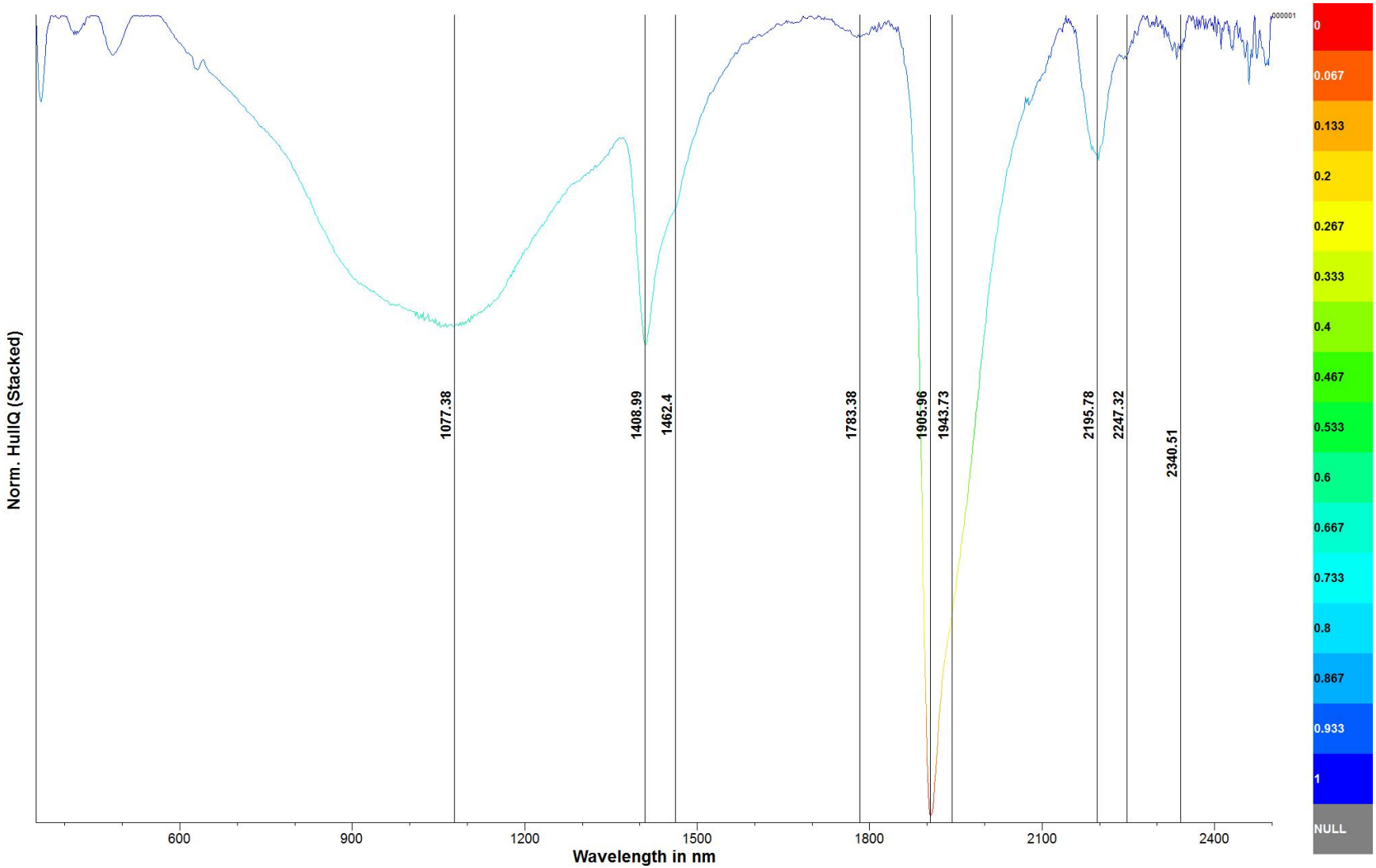


Fig. O14. Stacked SWIR spectra (normalized hull quotient) of samples from drillhole TKAD012.

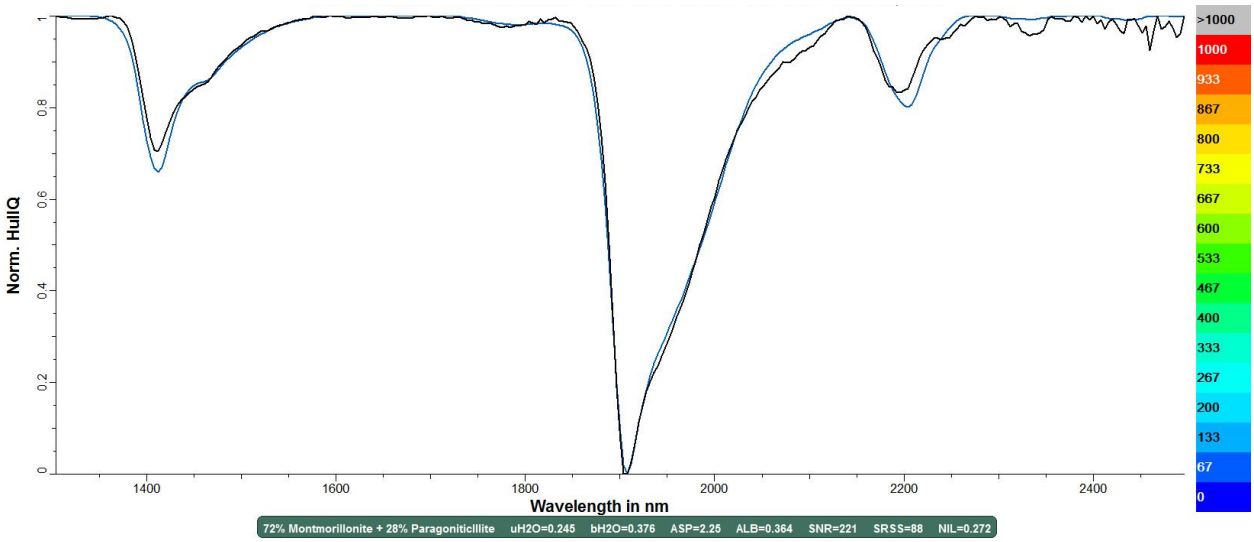


Fig. O15. SWIR spectra (normalized hull quotient) of sample MA13-062-C, drillhole TKAD012 (2.81–2.90 mbsf), composed of 72% Mnt + 28% Pgl.

Drillhole TKAD015

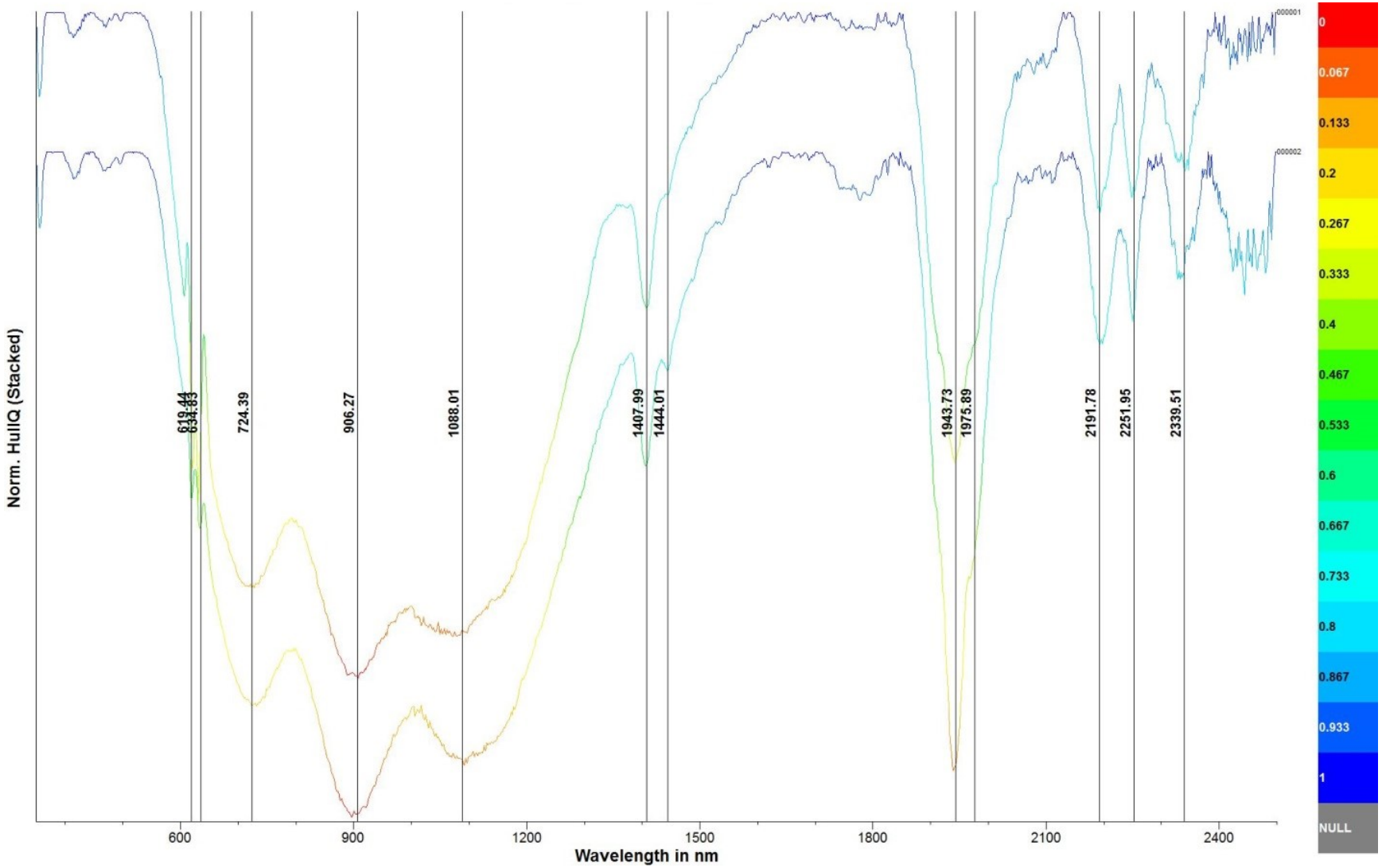


Fig. O16. Stacked SWIR spectra (normalized hull quotient) of samples from drillhole TKAD015.

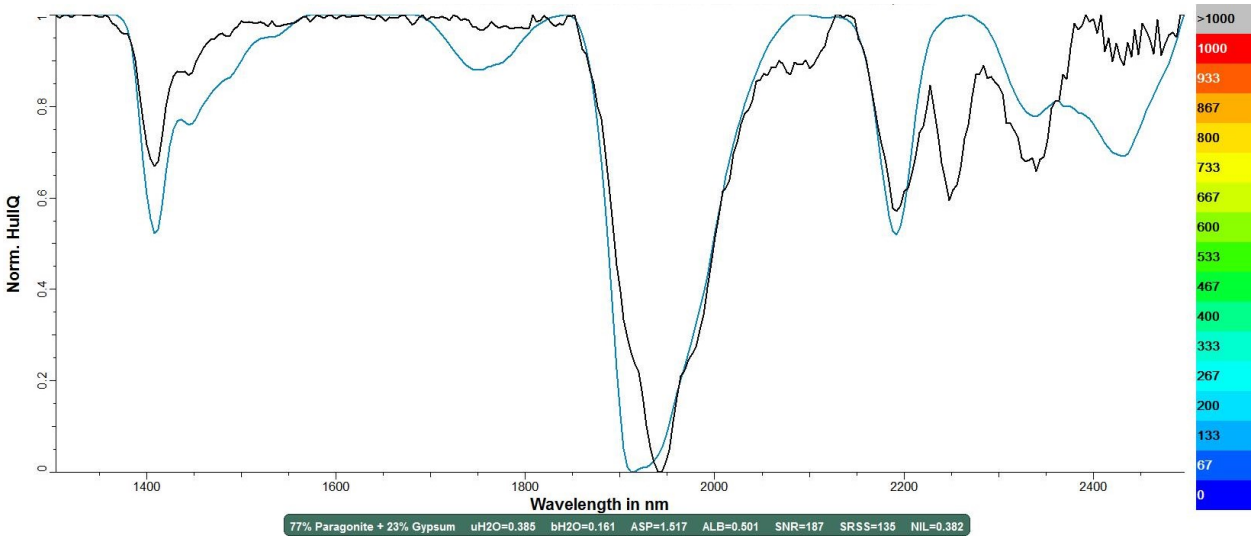


Fig. O17. SWIR spectra (normalized hull quotient) of sample MA13-052-C, drillhole TKAD015 (6.42–6.52 mbsf), composed of 77% Pg + 23% Gp.

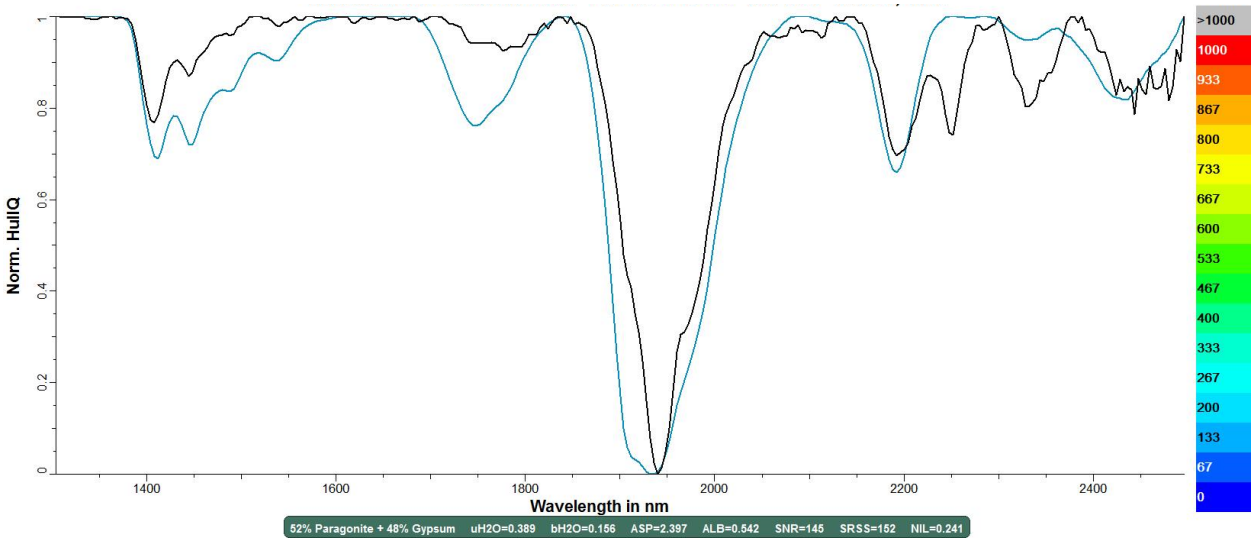


Fig. O18. SWIR spectra (normalized hull quotient) of sample MA13-053-C, drillhole TKAD015 (7.23–7.34 mbsf), composed of 52% Pg + 48% Gp.

Drillhole TKAD016

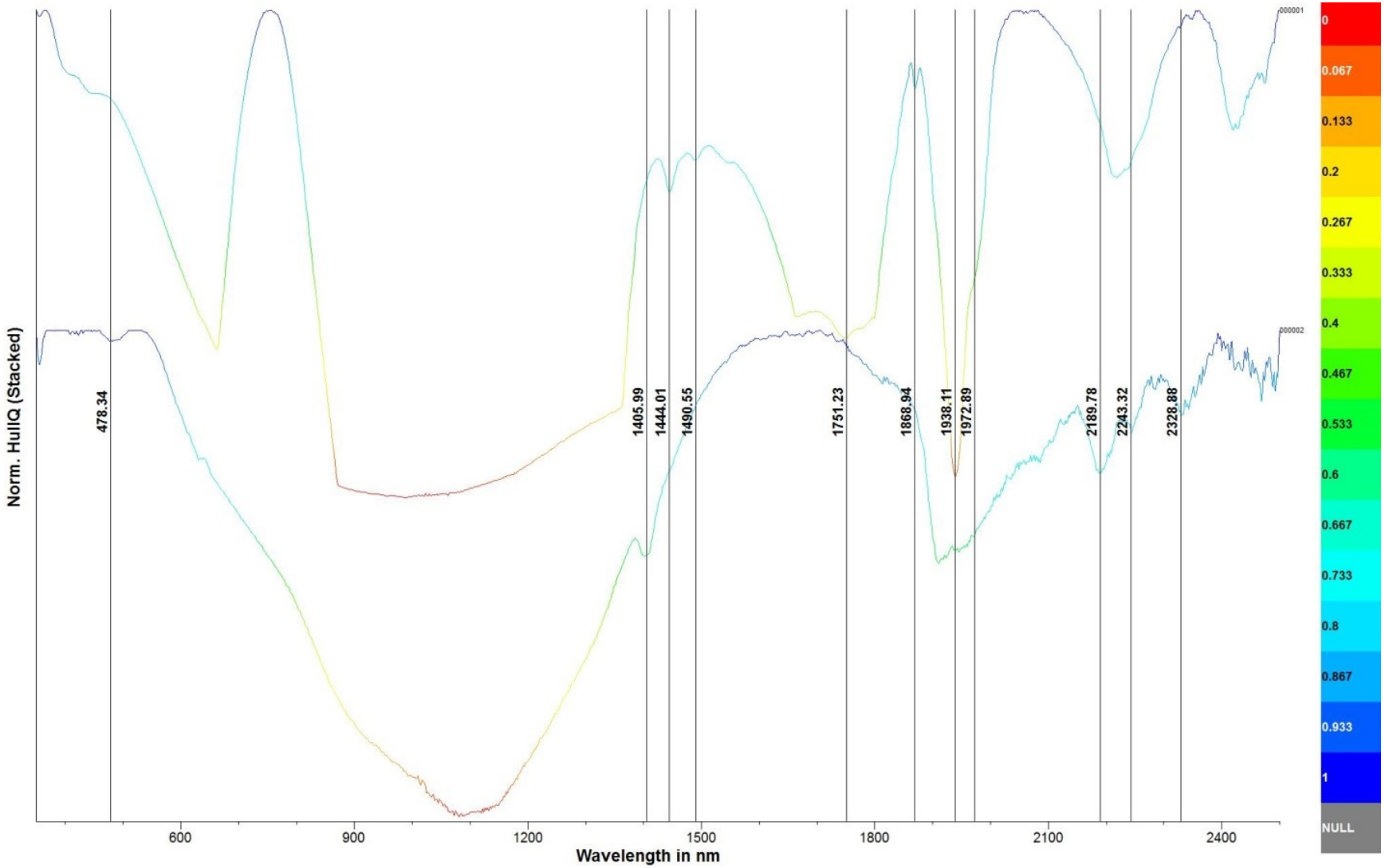


Fig. O19. Stacked SWIR spectra (normalized hull quotient) of samples from drillhole TKAD016.

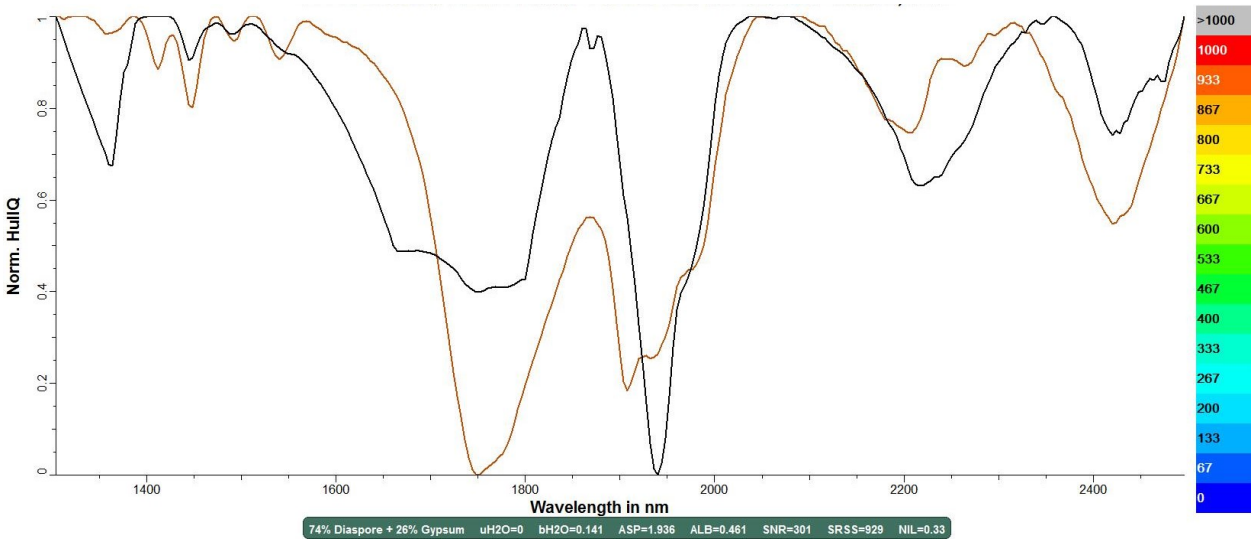


Fig. O20. SWIR spectra (normalized hull quotient) of sample M13-034-C, drillhole TKAD016 (2.02–2.13 mbsf), composed of 74% Dsp + 26% Gp, with a high degree of uncertainty.

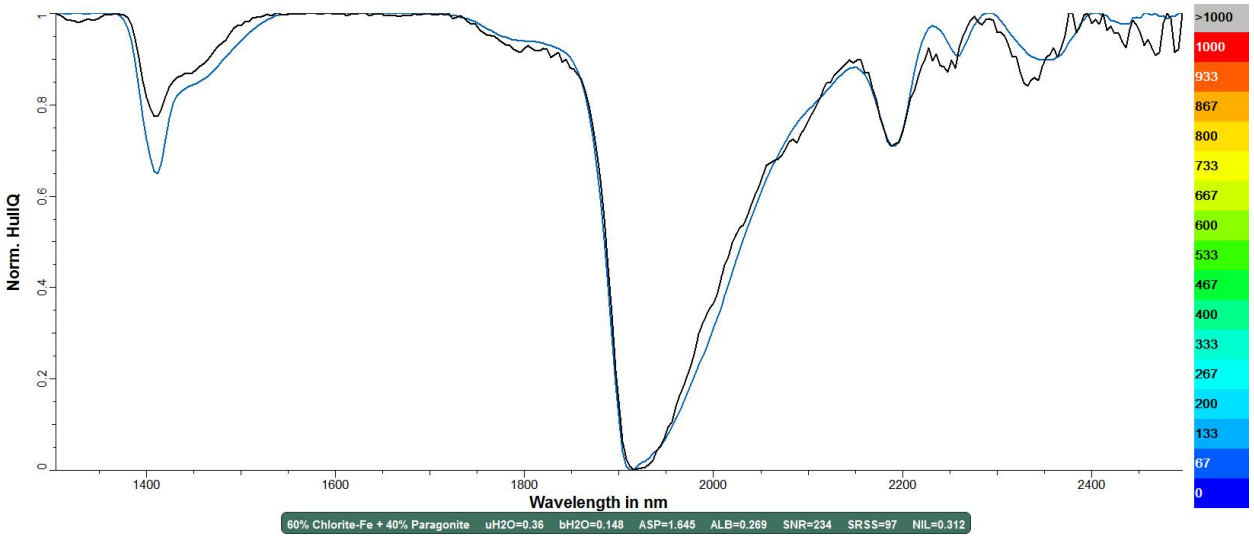


Fig. O21. SWIR spectra (normalized hull quotient) of sample MA13-036-C, drillhole TKAD016 (7.00–7.05 mbsf), composed of 60% Chl and 40% Pg.

Drillhole TKAD018

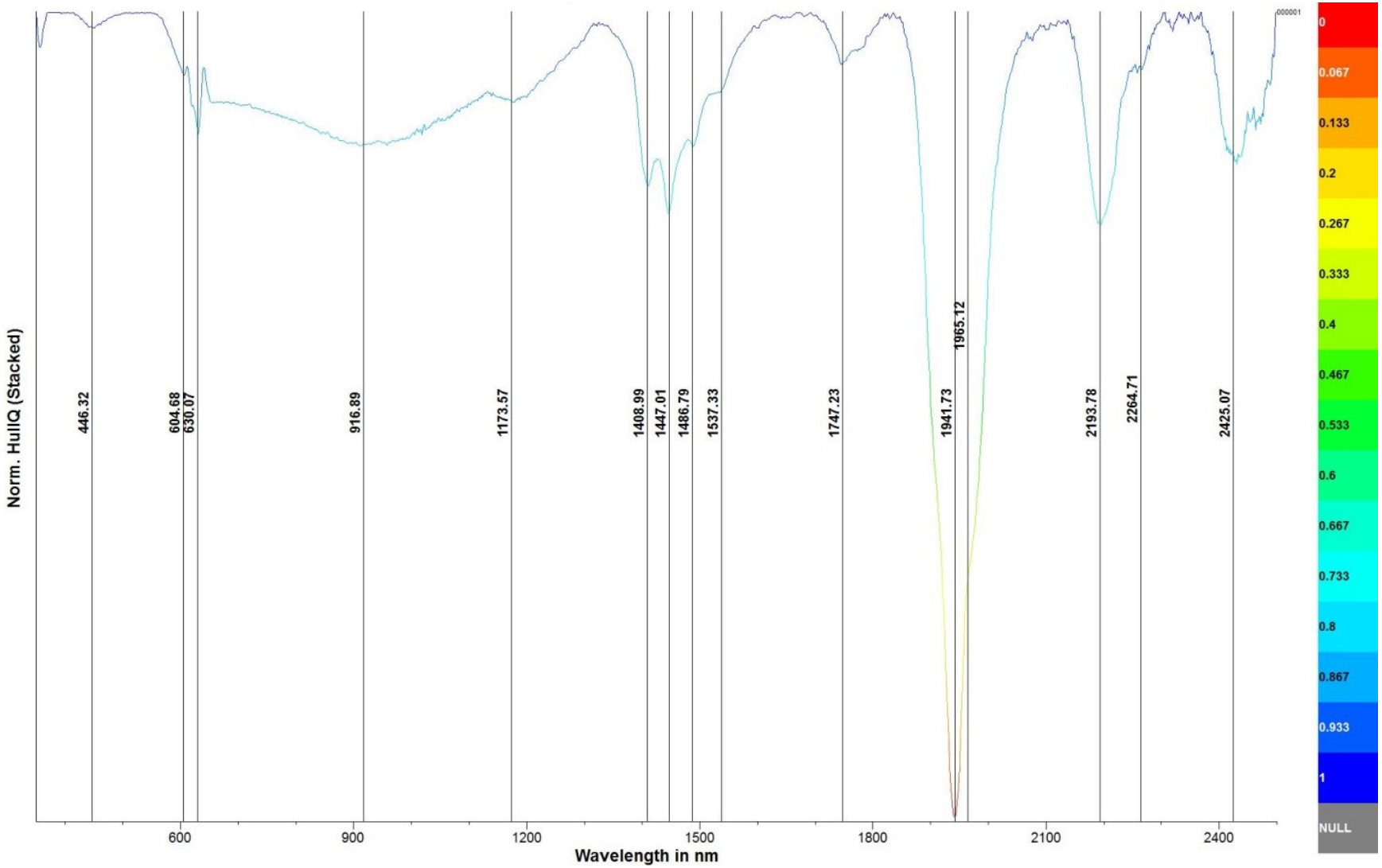


Fig. O22. Stacked SWIR spectra (normalized hull quotient) of samples from drillhole TKAD018.

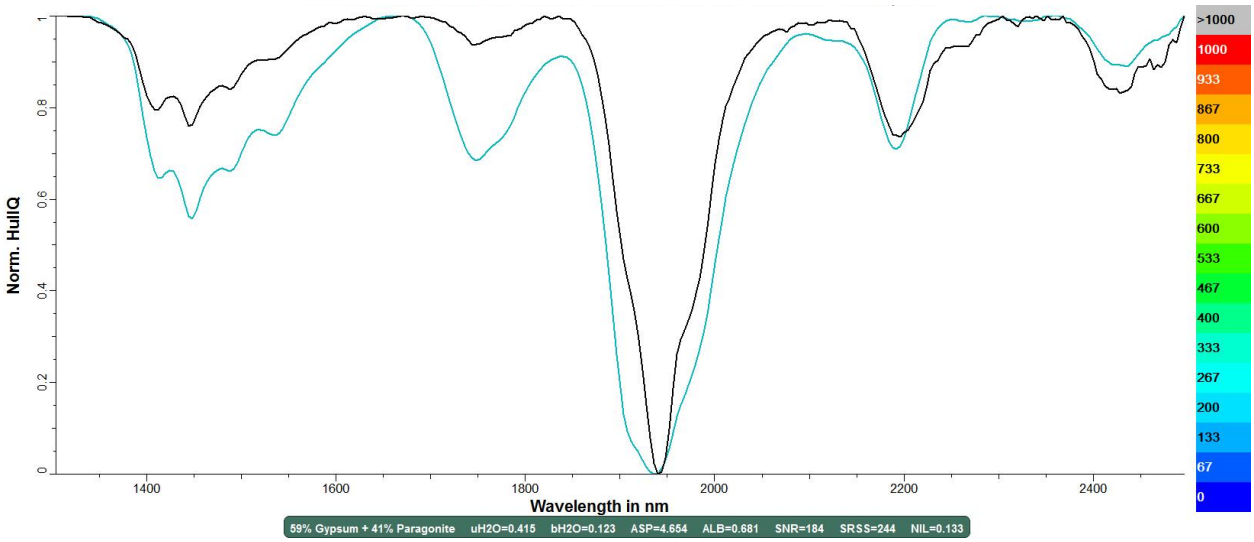


Fig. O23. SWIR spectra (normalized hull quotient) of sample MA13-015-C, drillhole TKAD018 (5.00–5.10 mbsf), composed of 59% Gp + 41% Pg.

Drillhole TKAD025

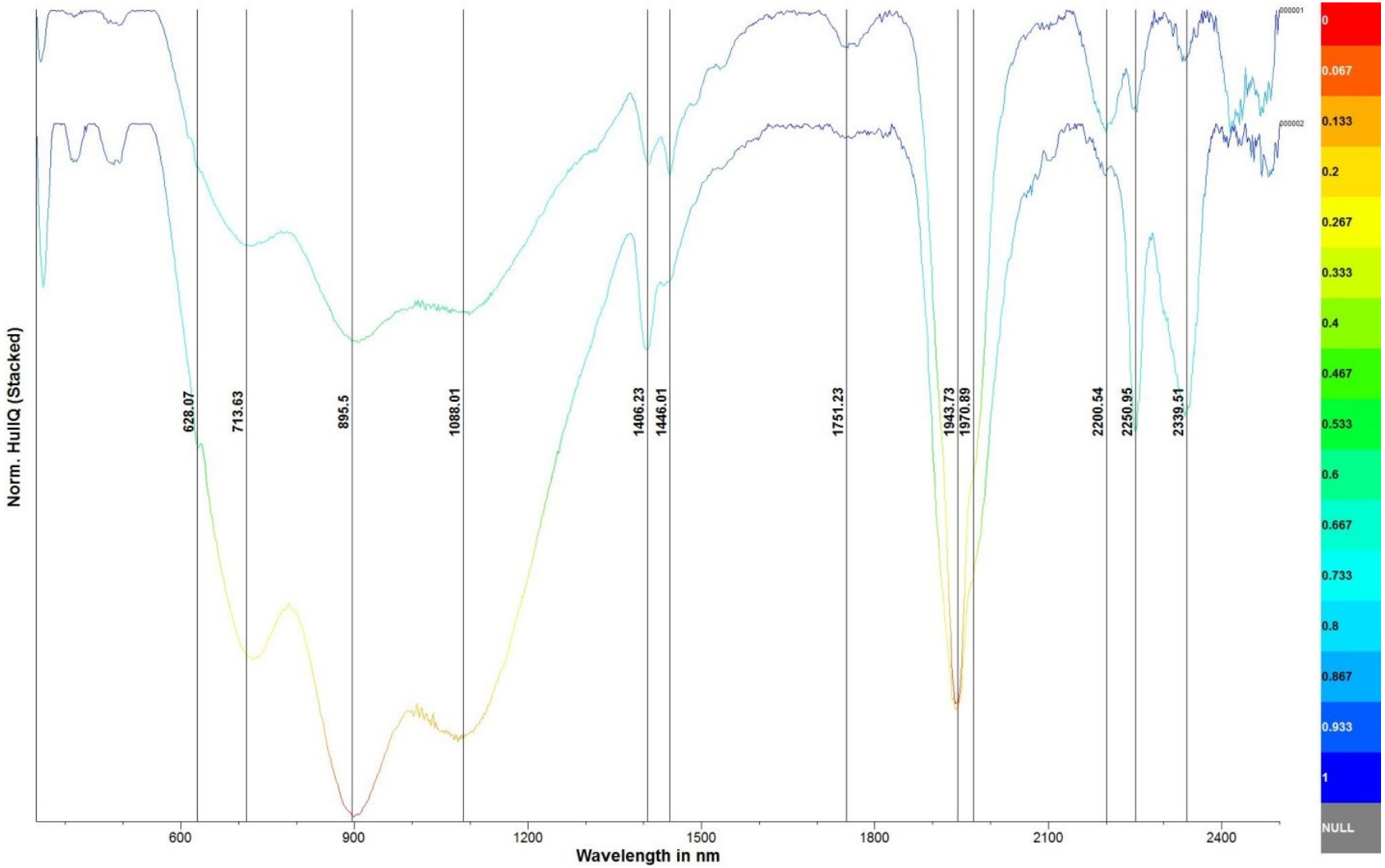


Fig. O24. Stacked SWIR spectra (normalized hull quotient) of samples from drillhole TKAD025.

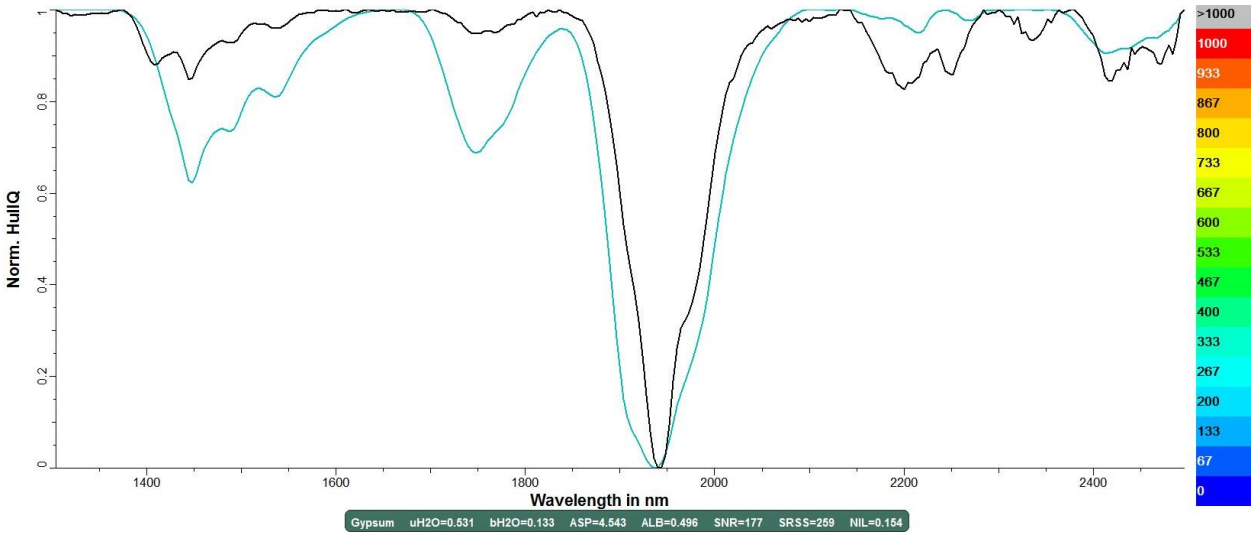


Fig. O25. SWIR spectra (normalized hull quotient) of sample MA13-039-C, drillhole TKAD025 (5.50–5.60 mbsf), composed of 100% Gp.

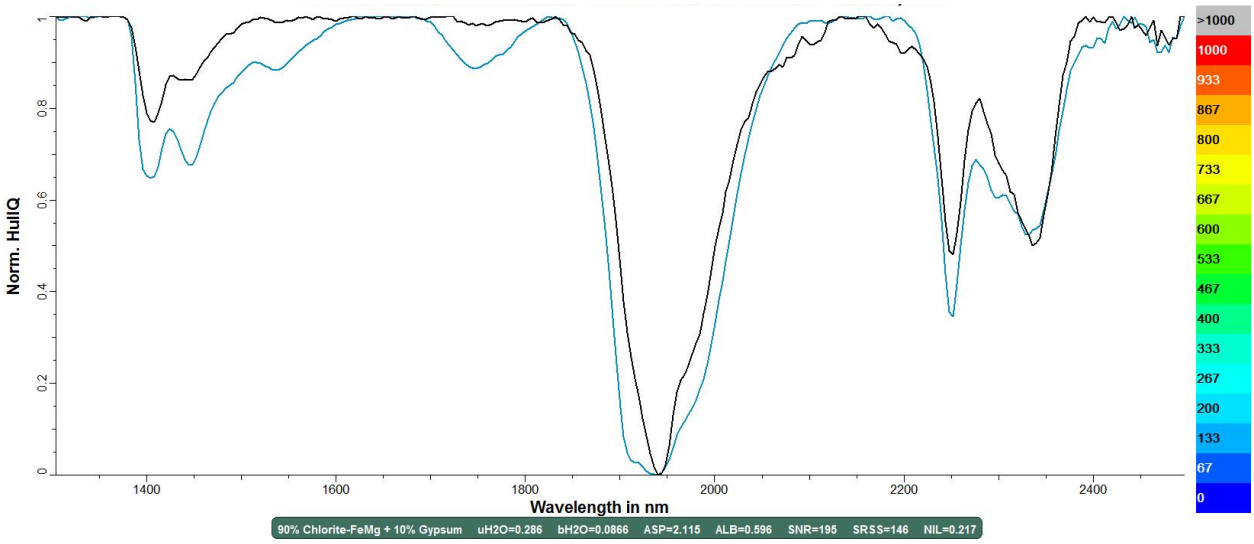


Fig. O26. SWIR spectra (normalized hull quotient) of sample MA13-040-C, drillhole TKAD025 (6.91–7.00 mbsf), composed of 90% Chl-FeMg + 10% Gp.

Drillhole TKAD026

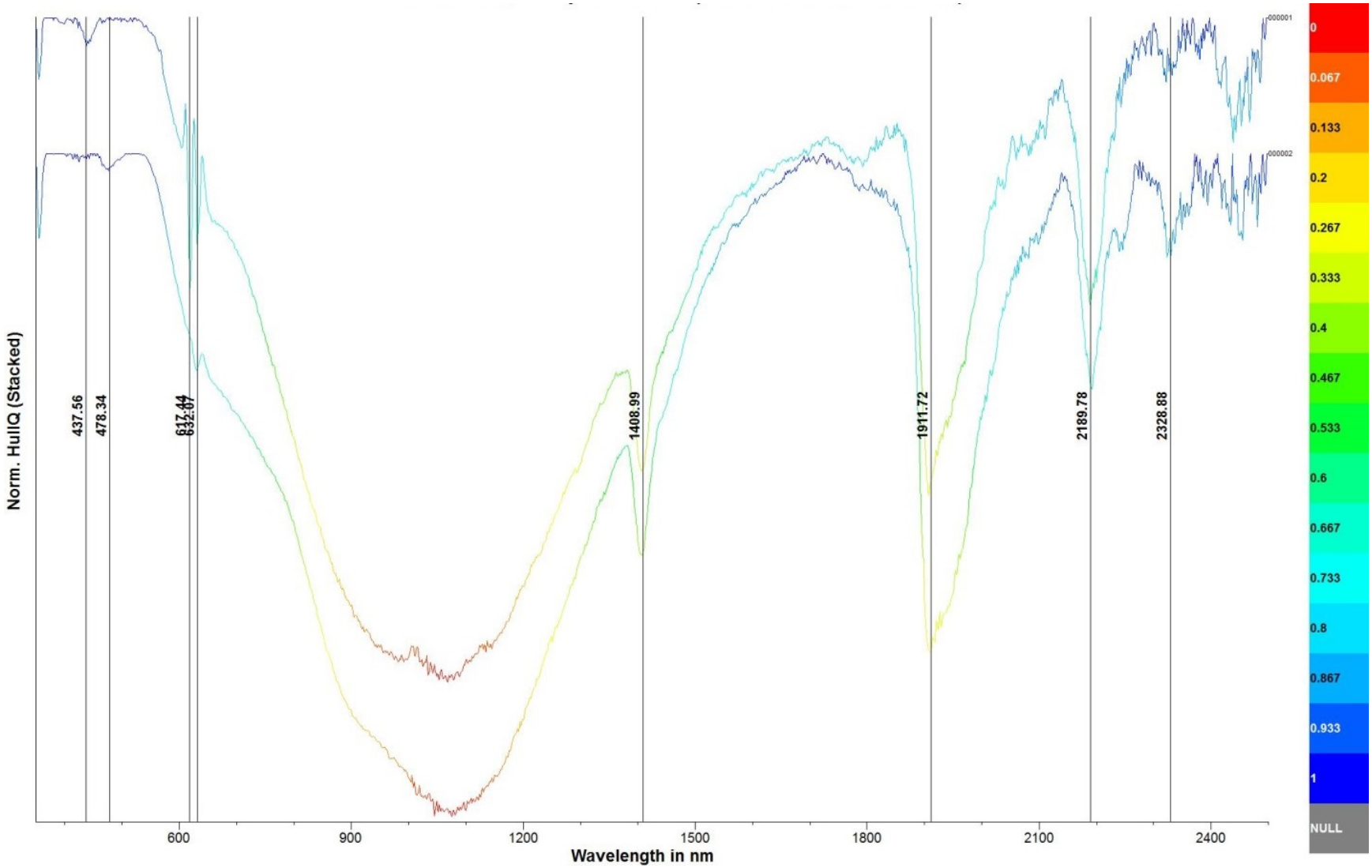


Fig. O27. Stacked SWIR spectra (normalized hull quotient) of samples from drillhole TKAD026.

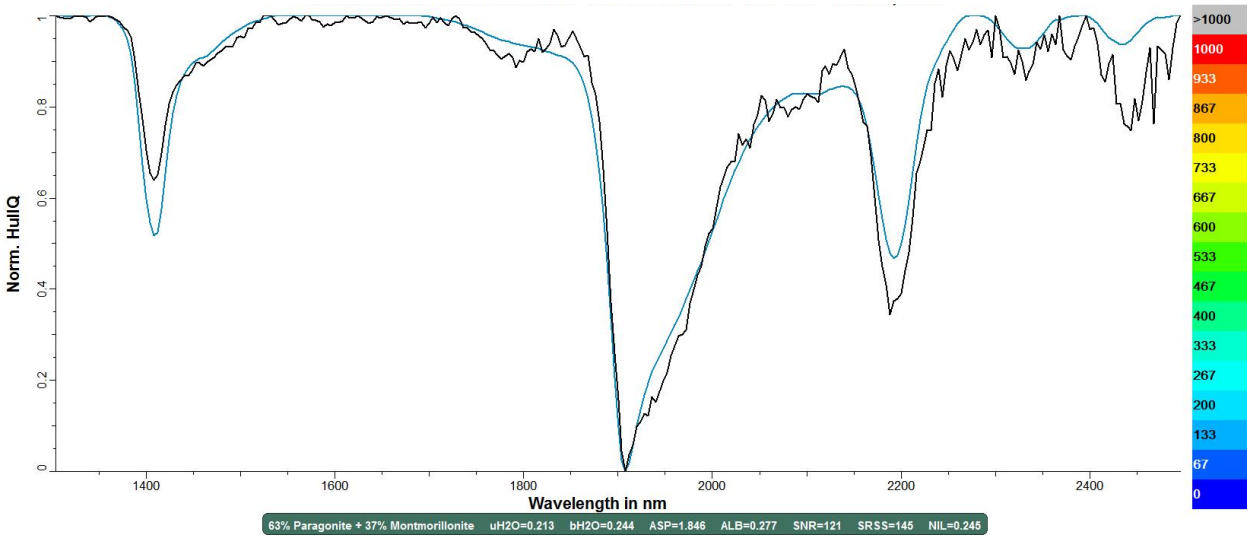


Fig. O28. SWIR spectra (normalized hull quotient) of sample MA13-067-C, drillhole TKAD026 (2.90–3.00 mbsf), composed of 63% Pg and 37% Mnt.

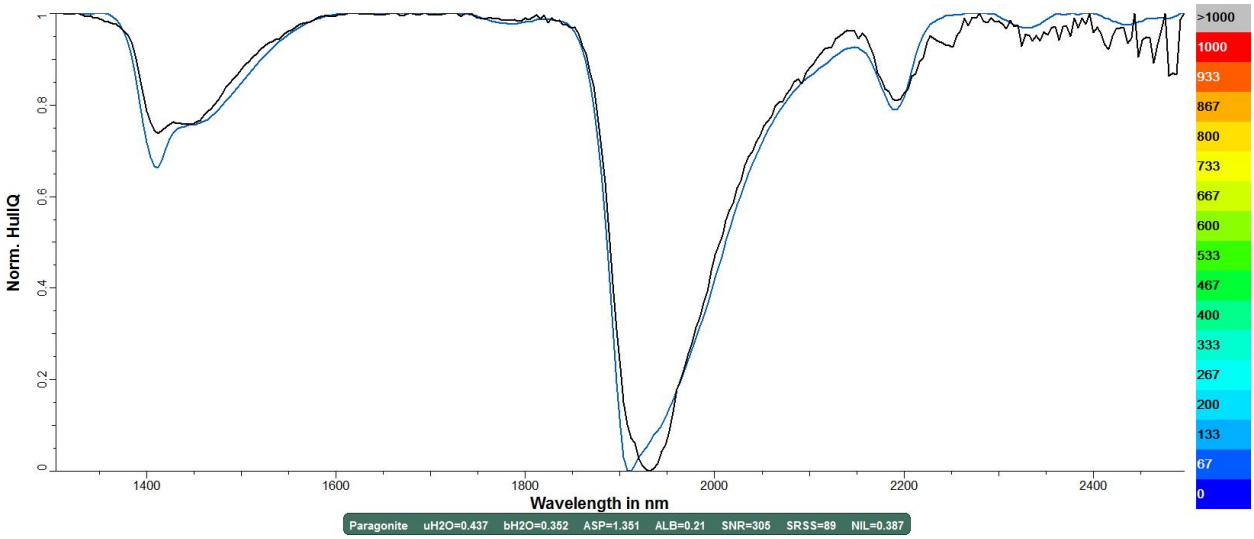


Fig. O29. SWIR spectra (normalized hull quotient) of sample MA13-068-C, drillhole TKAD026 (3.60–3.68 mbsf), composed of 100% Pg.

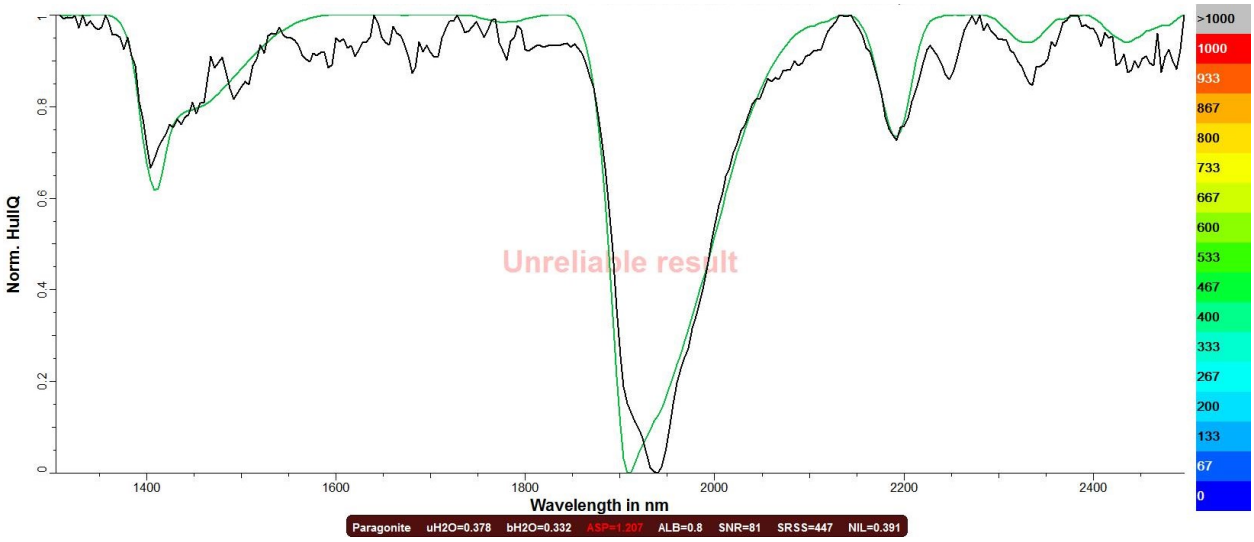


Fig. O30. SWIR spectra (normalized hull quotient) of sample MA13-069-C, drillhole TKAD026 (5.64–5.75 mbsf), with an unreliable result.

Drillhole TKAD027

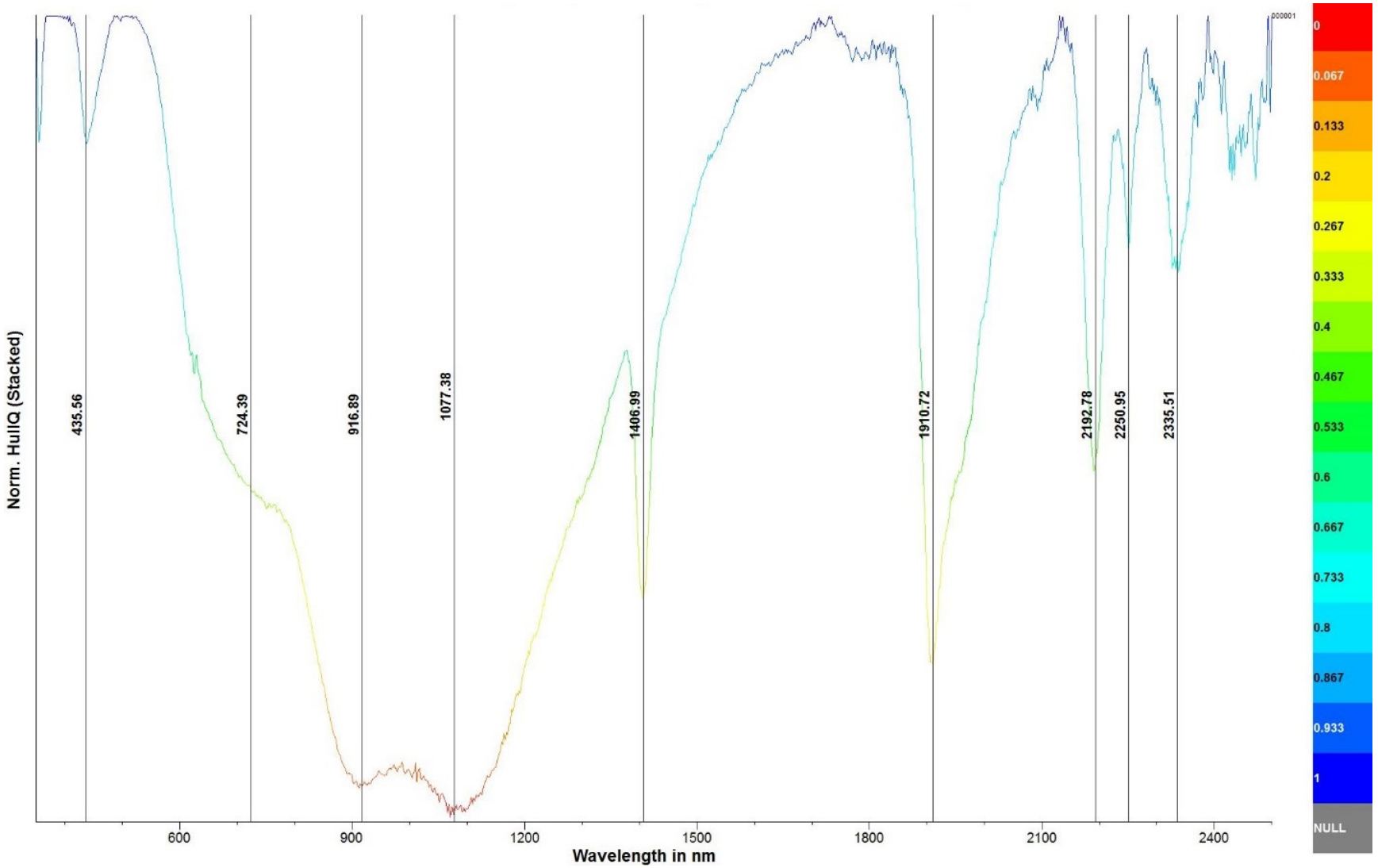


Fig. O31. Stacked SWIR spectra (normalized hull quotient) of samples from drillhole TKAD027

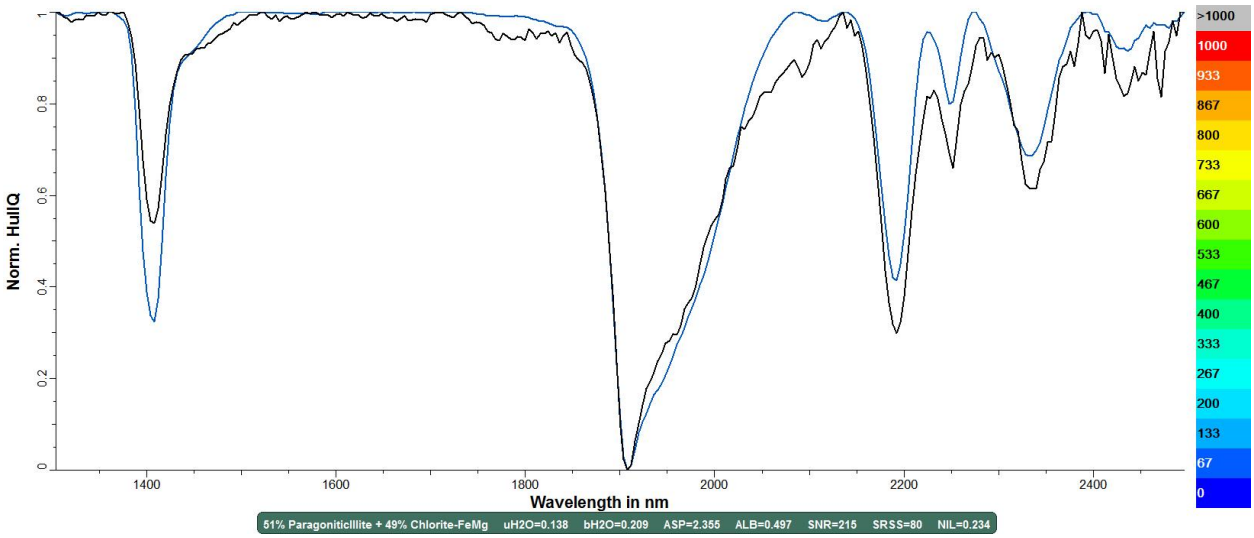


Fig. O32. SWIR spectra (normalized hull quotient) of sample P022-C, drillhole TKAD027 (11.3–11.34 mbsf), composed of 51% Pgl + 49% Chl-FeMg.

Drillhole TKAD028

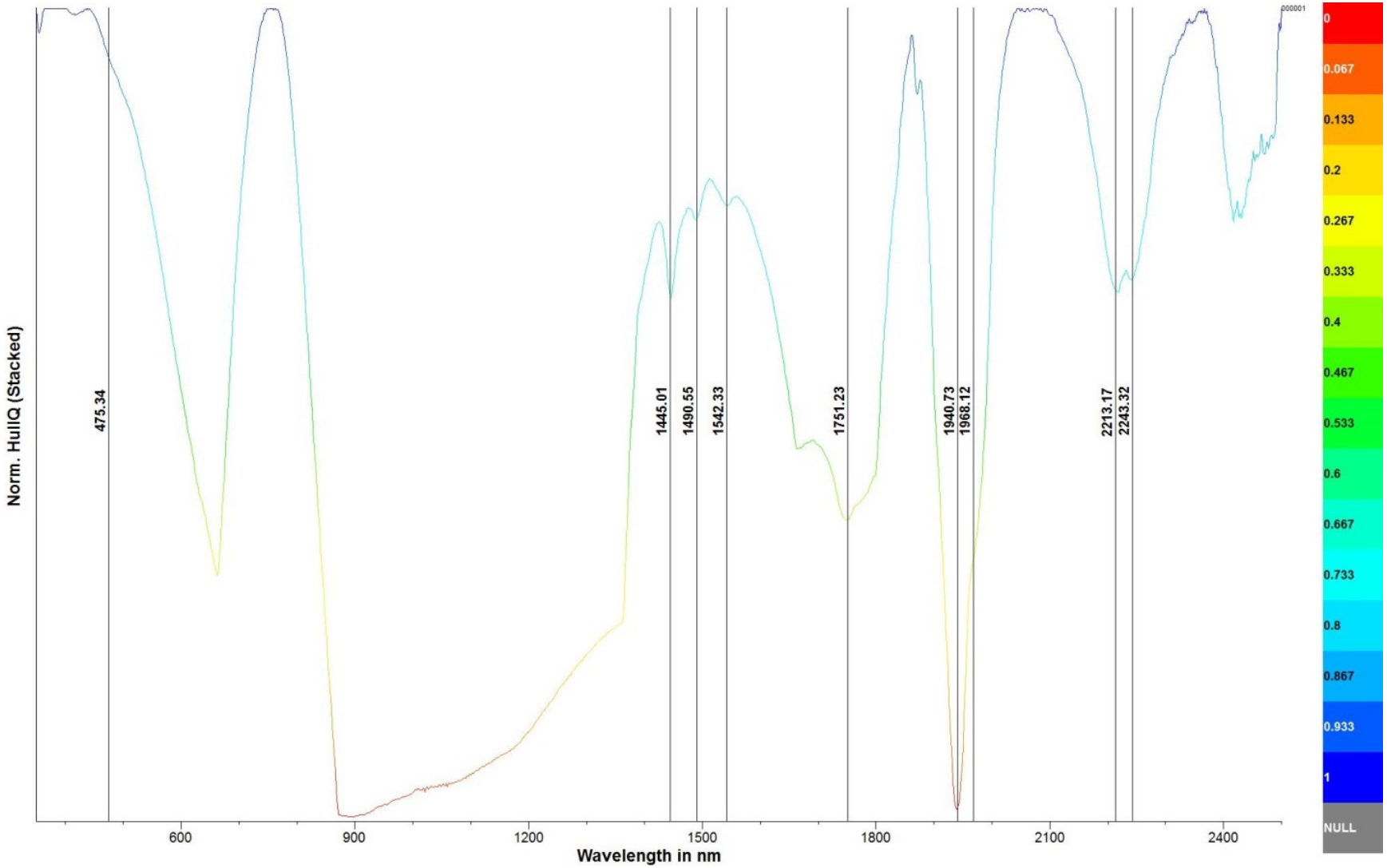


Fig. O33. Stacked SWIR spectra (normalized hull quotient) of samples from drillhole TKAD028.

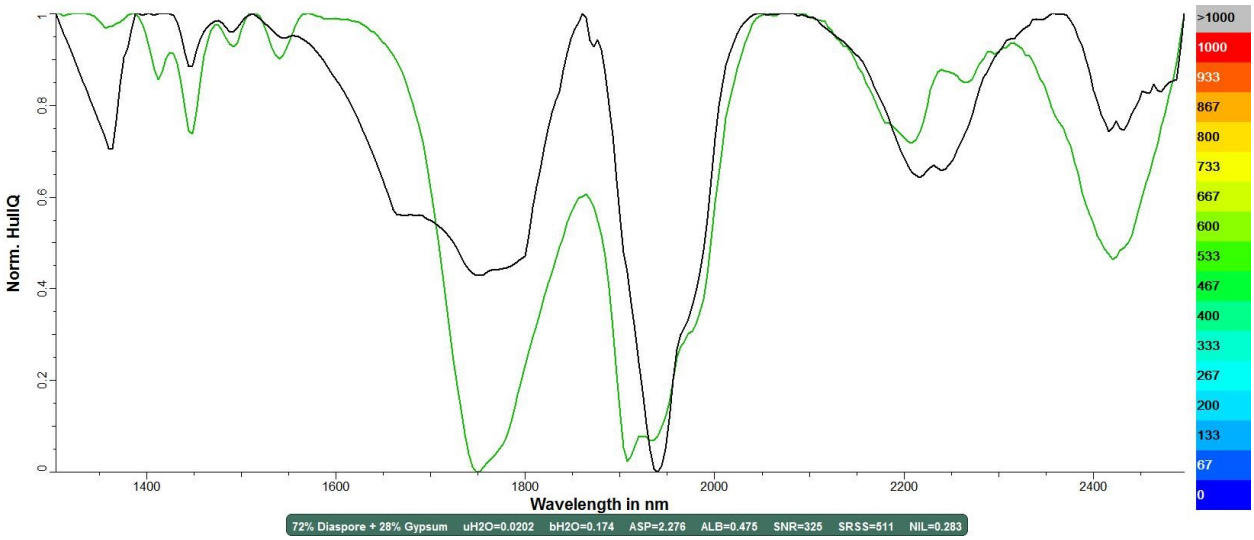


Fig. O34. SWIR spectra (normalized hull quotient) of sample MA13-099-C, drillhole TKAD028 (4.50–4.60 mbsf), composed of 72% Dsp + 28% Gp.

Drillhole TKAD030

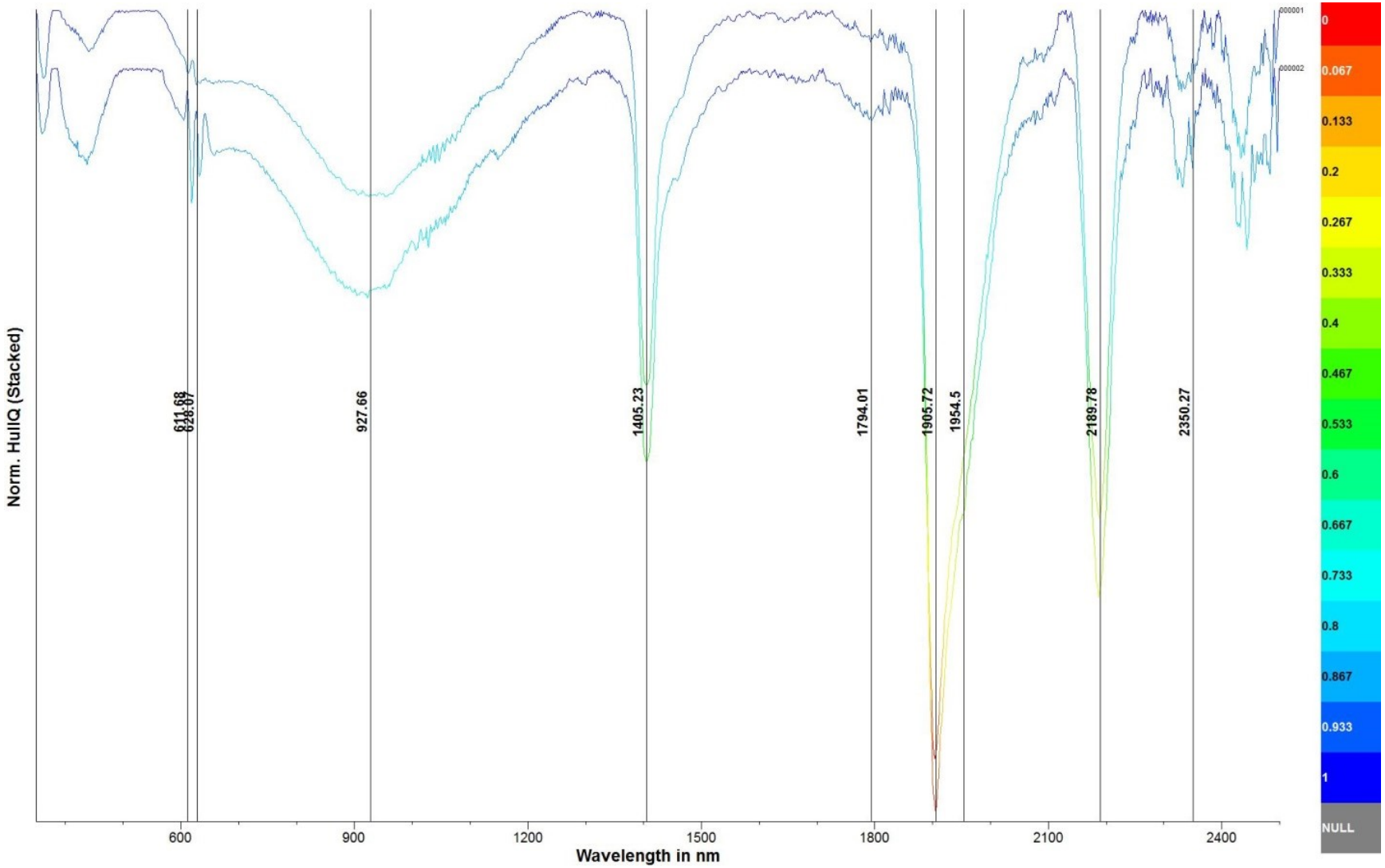


Fig. O35. Stacked SWIR spectra (normalized hull quotient) of samples from drillhole TKAD030.

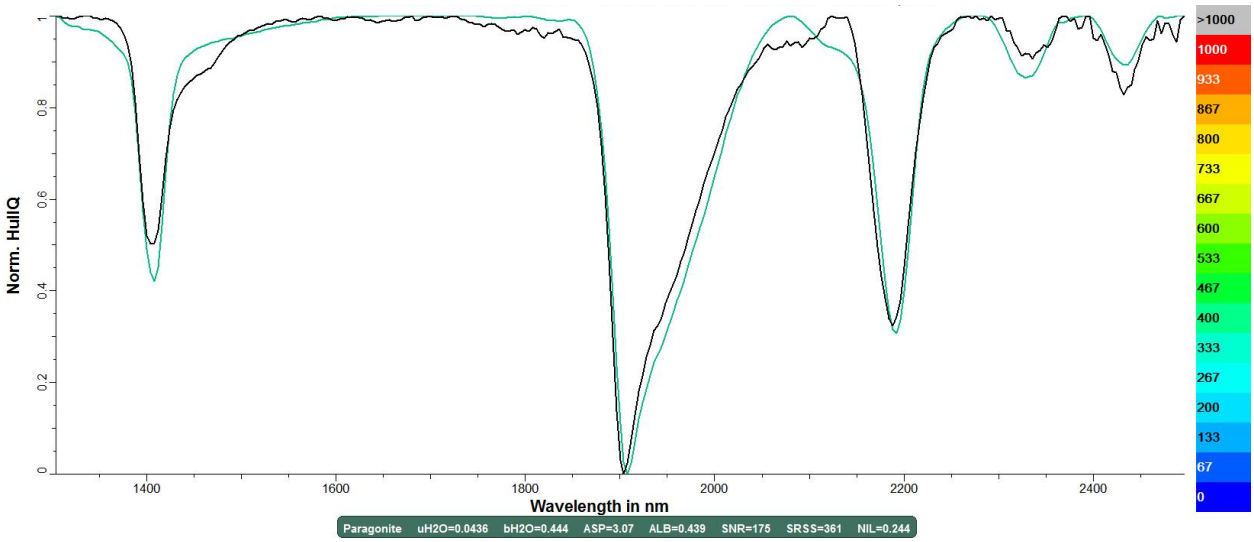


Fig. O36. SWIR spectra (normalized hull quotient) of sample MA13-005-C, drillhole TKAD030 (5.06–5.21 mbsf), composed of 100% Pg.

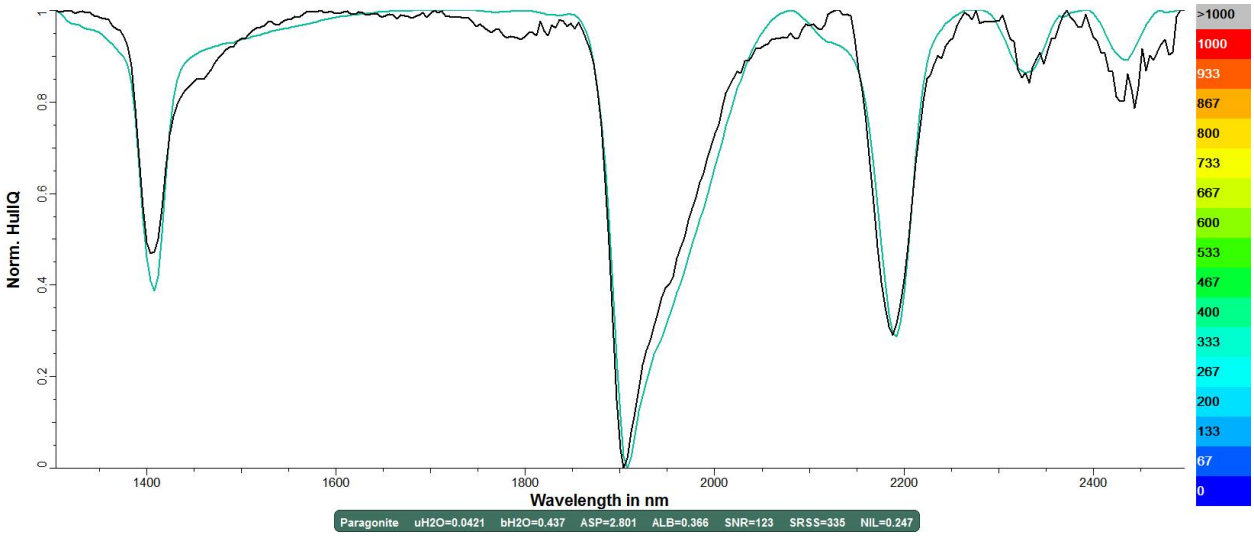


Fig. O37. SWIR spectra (normalized hull quotient) of sample MA13-006-C, drillhole TKAD030 (6.45–6.60 mbsf), composed of 100% Pg.

Drillhole TKAD031

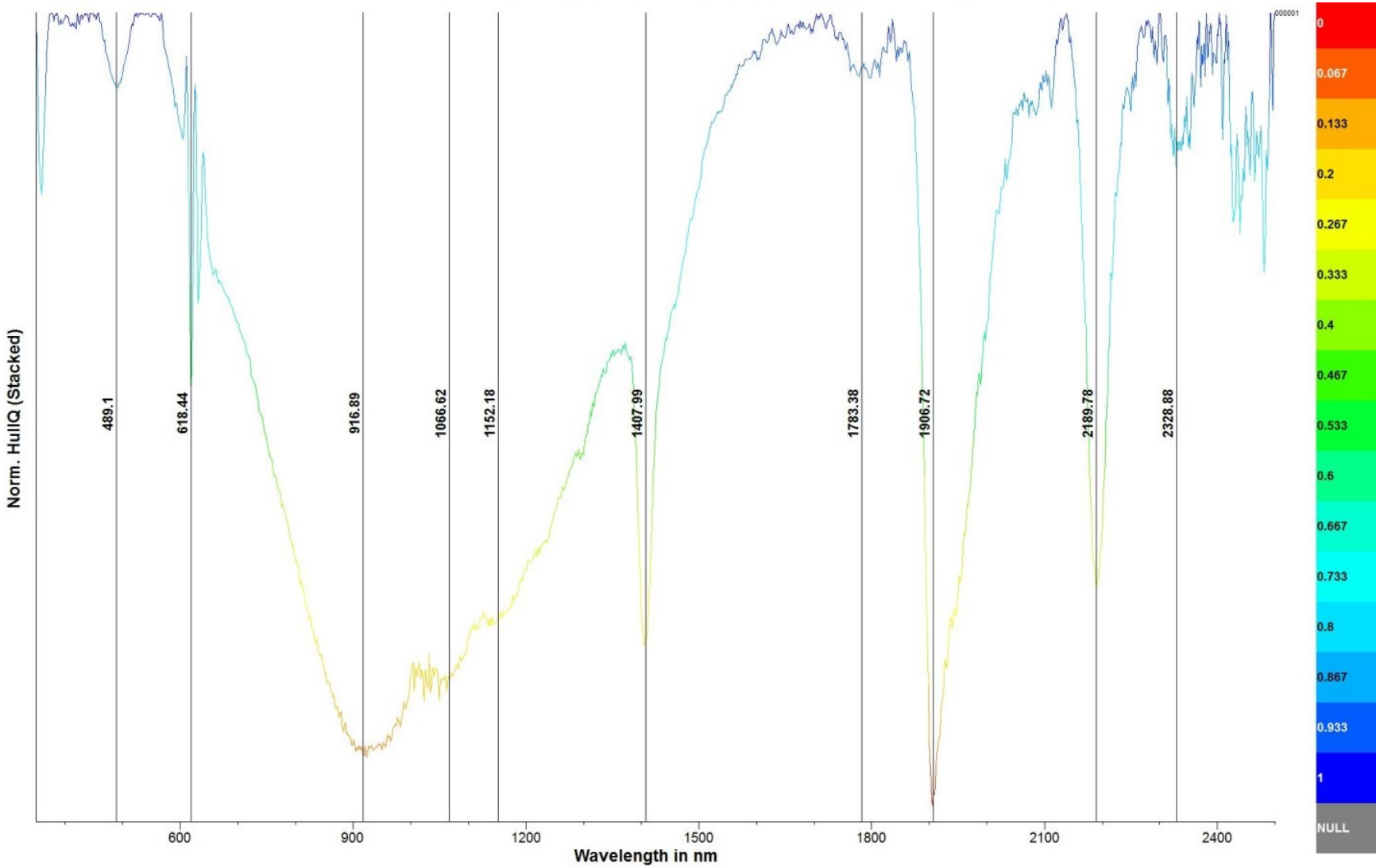


Fig. O38. Stacked SWIR spectra (normalized hull quotient) of samples from drillhole TKAD031.

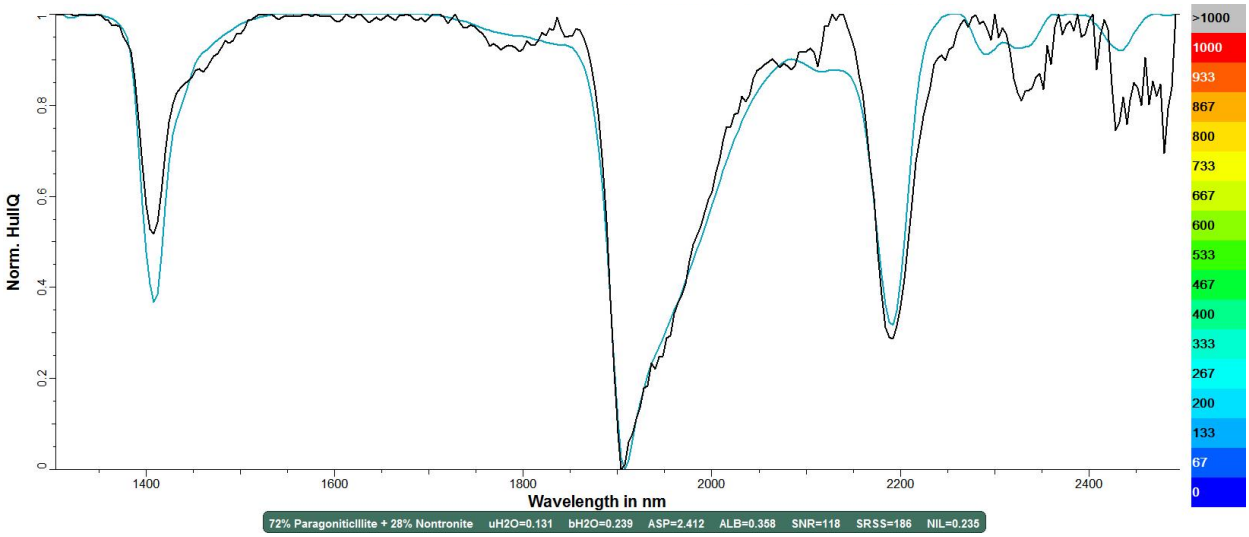


Fig. O39. SWIR spectra (normalized hull quotient) of sample MA13-044-C, drillhole TKAD031 (5.64–5.69 mbsf), composed of 72% Pgl and 28% Non.

Drillhole TKAD032

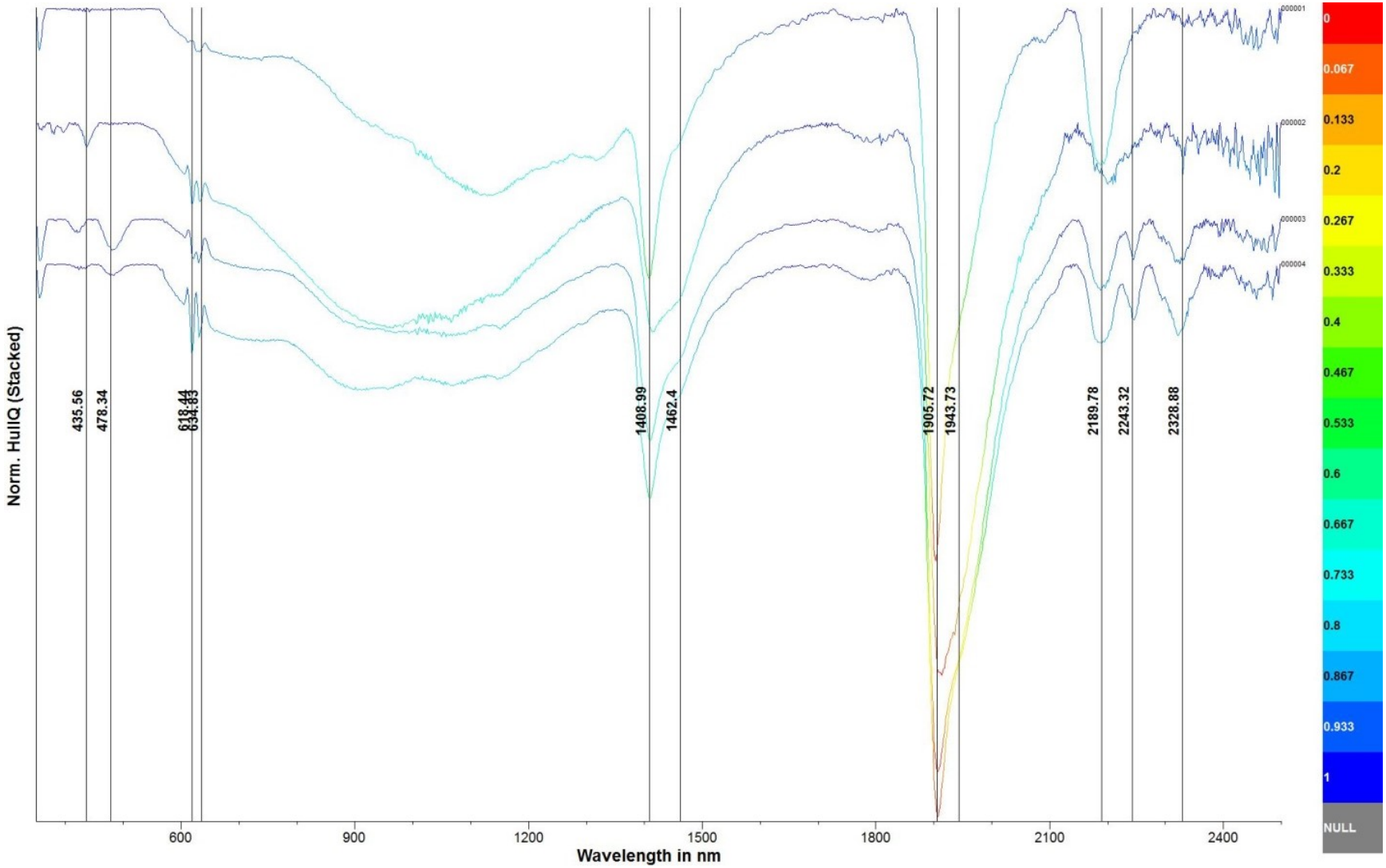


Fig. O40. Stacked SWIR spectra (normalized hull quotient) of samples from drillhole TKAD032.

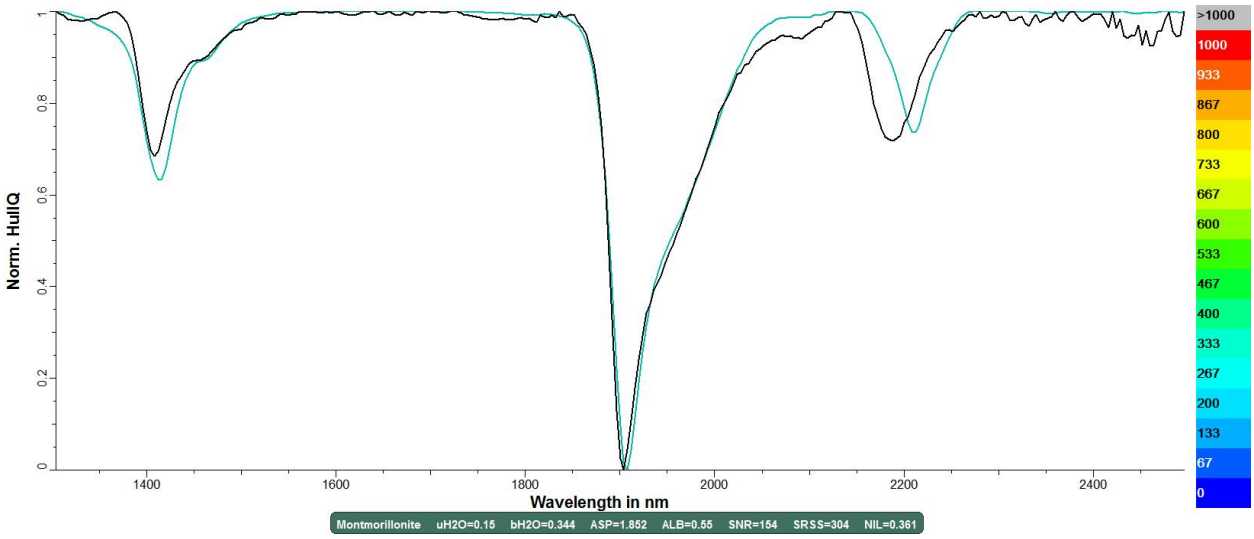


Fig. O41. SWIR spectra (normalized hull quotient) of sample MA13-072-C, drillhole TKAD032 (2.05–2.1 mbsf), composed of 100% Mnt.

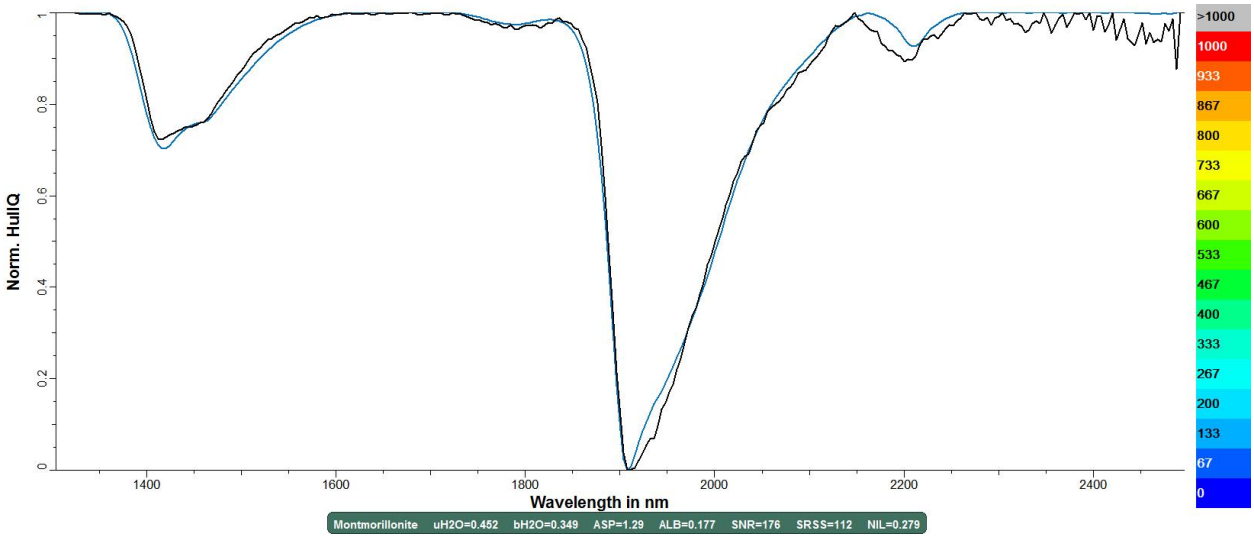


Fig. O42. SWIR spectra (normalized hull quotient) of sample MA13-073-C, drillhole TKAD032 (3.90–4.00 mbsf), composed of 100% Mnt.

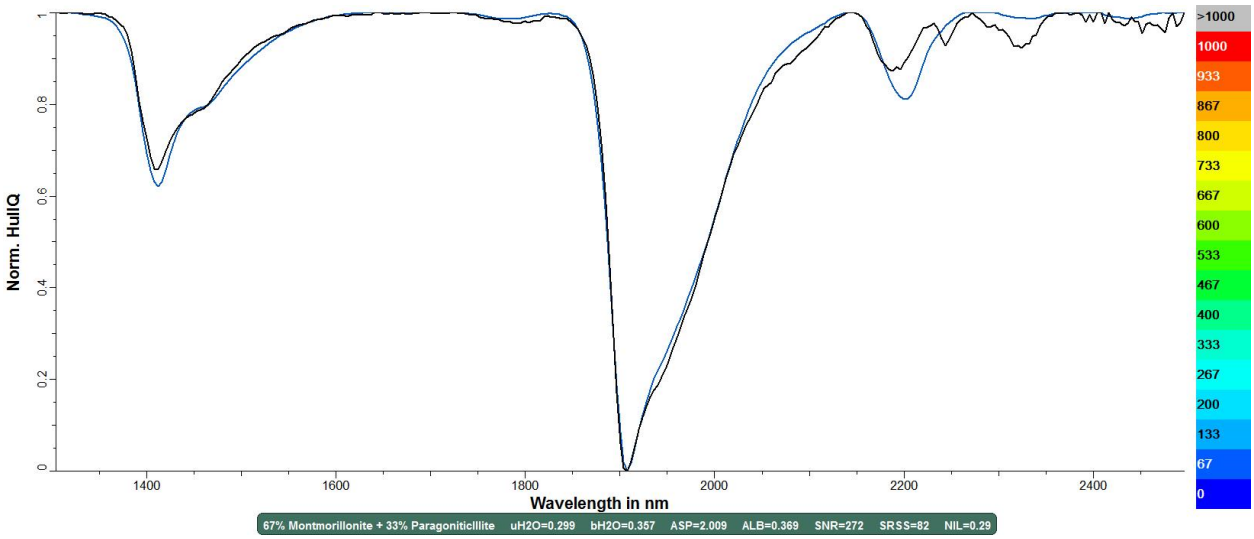


Fig. O43. SWIR spectra (normalized hull quotient) of sample MA13-074-C, drillhole TKAD032 (5.31–5.40 mbsf), composed of 67% Mnt + 33% Pgl.

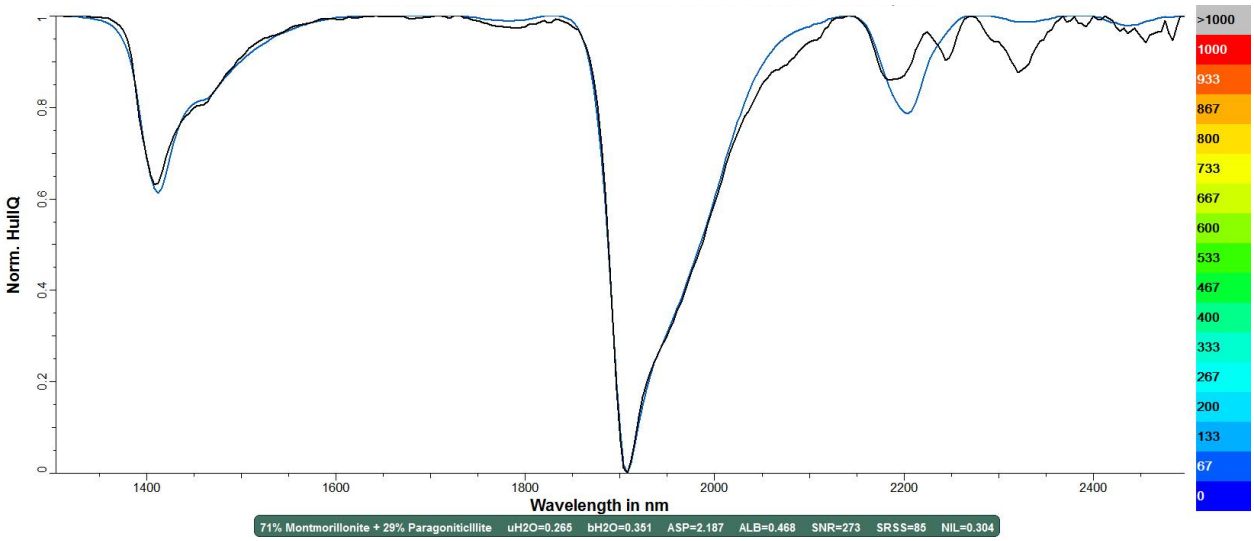


Fig. O44. SWIR spectra (normalized hull quotient) of sample MA13-075-C, drillhole TKAD032 (6.42–6.54 mbsf), composed of 71% Mnt + 29% Pgl.

Drillhole TKAD033

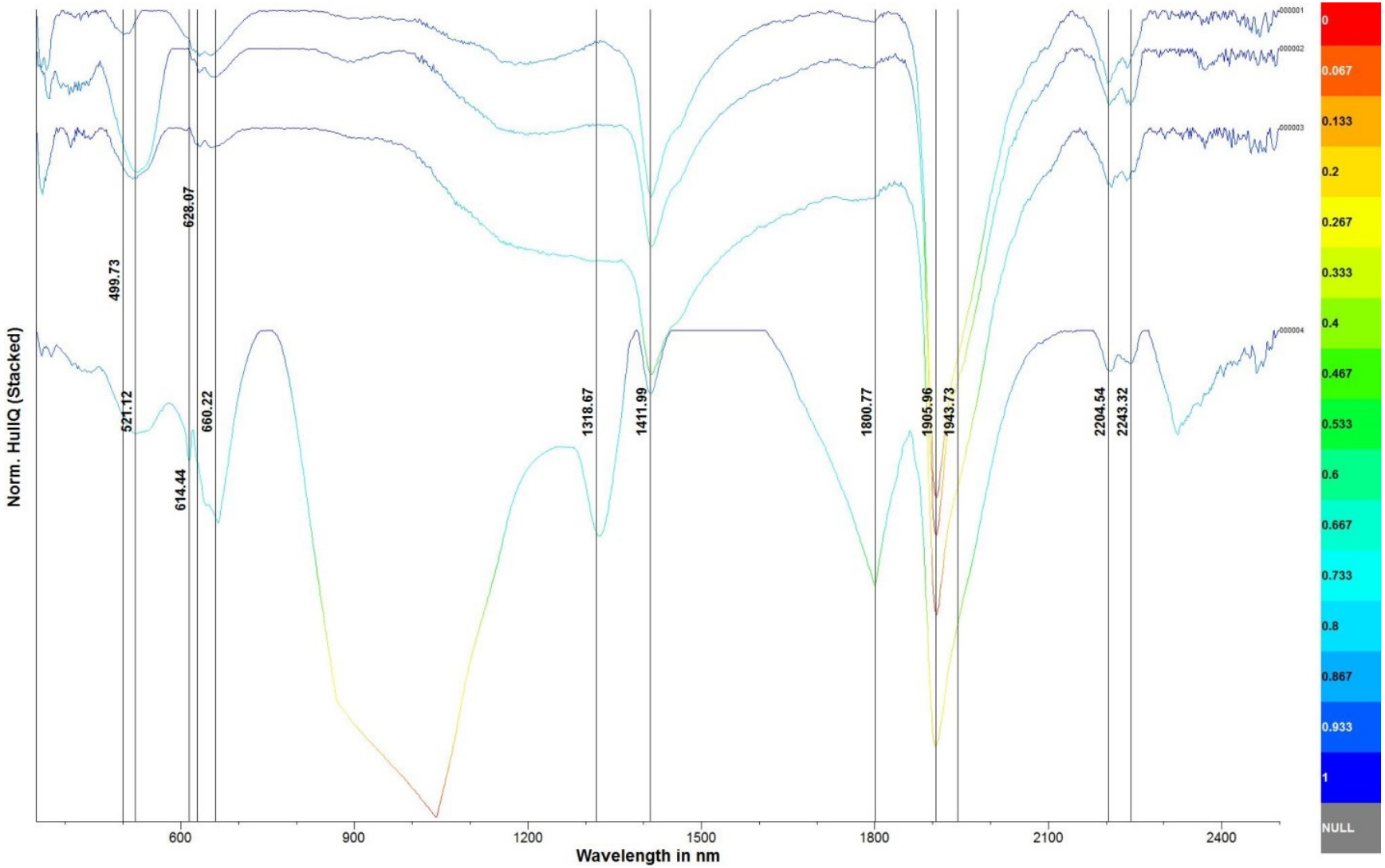


Fig. O45. Stacked SWIR spectra (normalized hull quotient) of samples from drillhole TKAD033.

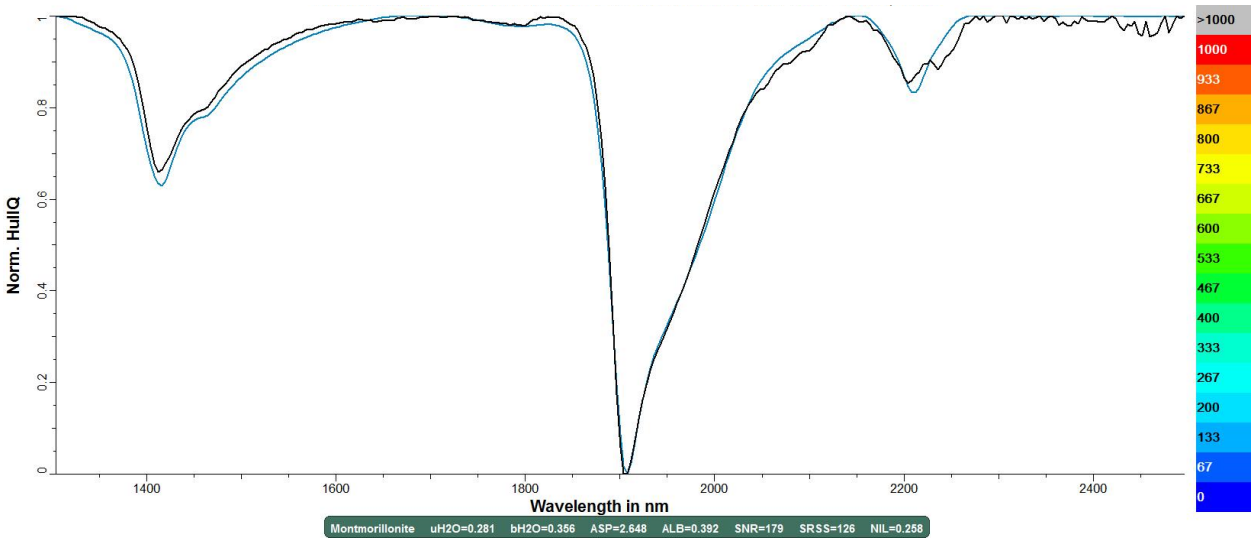


Fig. O46. SWIR spectra (normalized hull quotient) of sample MA13-026-C, drillhole TKAD033 (4.76–4.88 mbsf), composed of 100% Mnt.

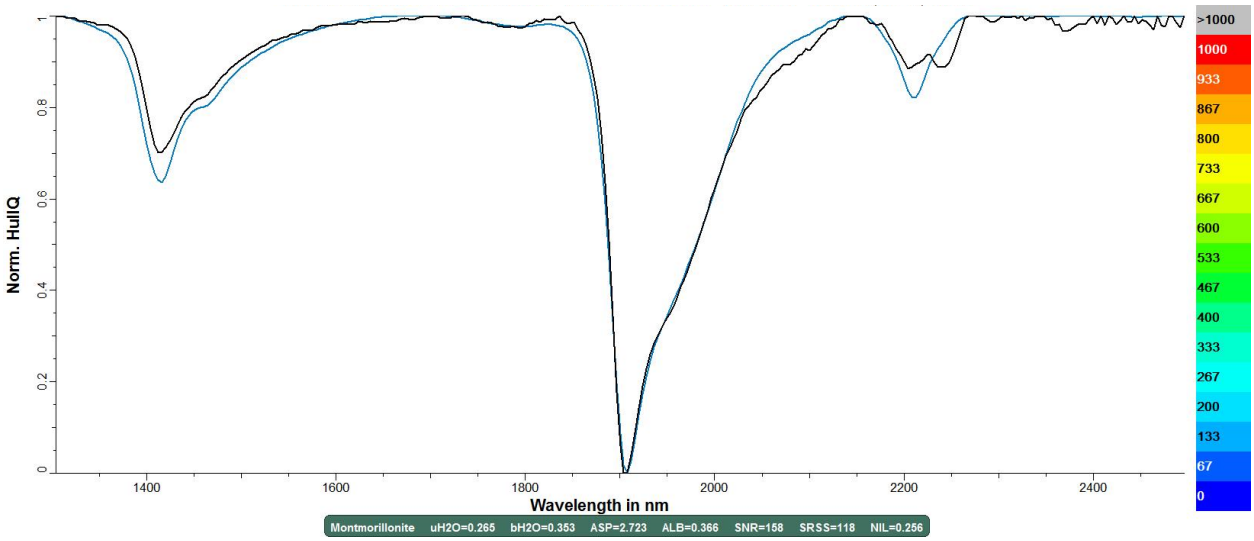


Fig. O47. SWIR spectra (normalized hull quotient) of sample MA13-026-M, drillhole TKAD033 (4.76–4.88 mbsf), composed of 100% Mnt.

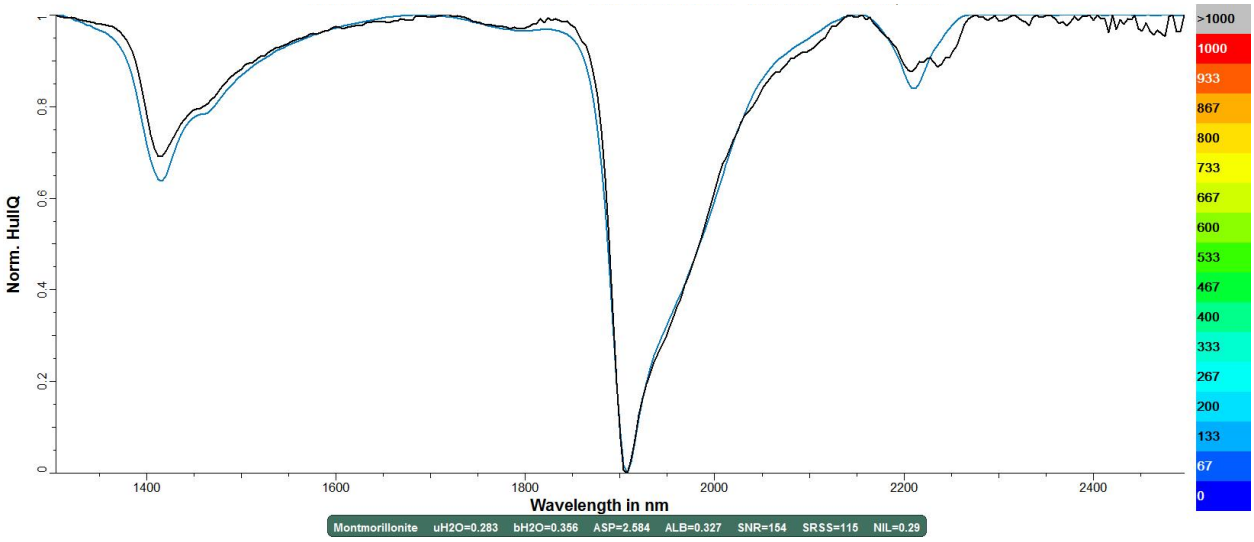


Fig. O48. SWIR spectra (normalized hull quotient) of sample MA13-027-C, drillhole TKAD033 (7.30–7.40 mbsf), composed of 100% Mnt.

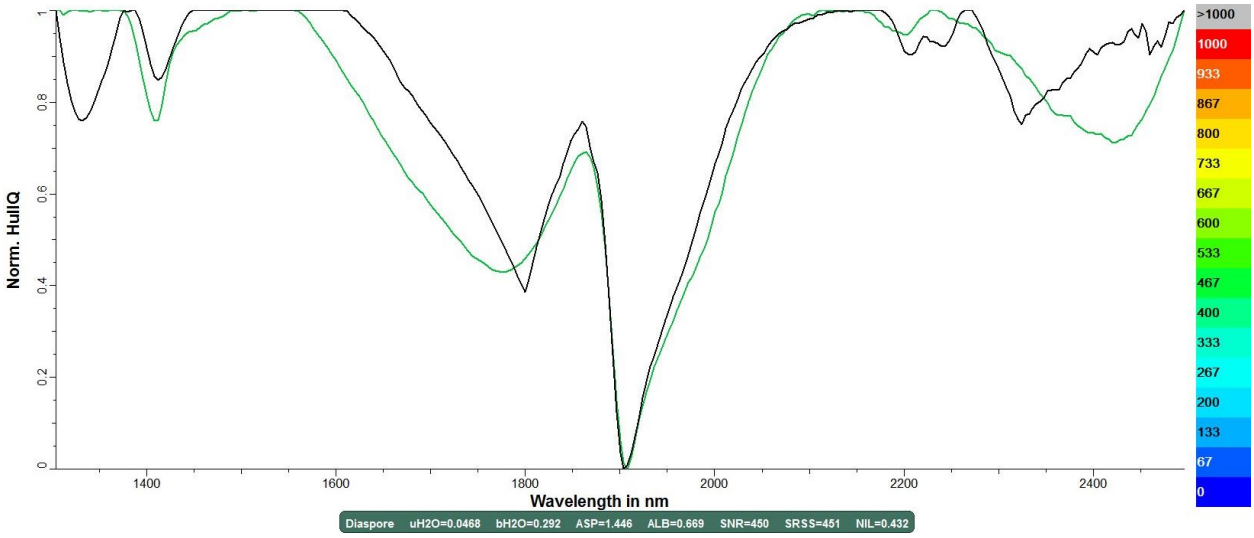


Fig. O49. SWIR spectra (normalized hull quotient) of sample MA13-027-M, drillhole TKAD033 (7.30–7.40 mbsf), composed of 100% Dsp.

Appendix P

XRD Analyses of Altered Volcaniclastic Rocks of the Tinakula Deposit

Contents:

Drillhole TKAD001 973

Fig. P1. Air-dried (red) and glycol-saturated (black) oriented XRD spectra of sample MA13-078, drillhole TKAD001 (4.54–4.68 mbsf). 973

Fig. P2. Air-dried (red) and glycol-saturated (black) oriented XRD spectra of sample MA13-082, drillhole TKAD001 (7.00–7.10 mbsf). 973

Fig. P3. Air-dried (red) and glycol-saturated (black) oriented XRD spectra of sample P002, drillhole TKAD001 (10.39–10.50 mbsf). 974

Fig. P4. Air-dried (red) and glycol-saturated (black) oriented XRD spectra of sample MA13-085, drillhole TKAD001 (12.90–13.00 mbsf). 974

Fig. P5. Air-dried (red) and glycol-saturated (black) oriented XRD spectra of sample MA13-086, drillhole TKAD001 (14.00–14.12 mbsf). 975

Fig. P6. Air-dried (red) and glycol-saturated (black) oriented XRD spectra of sample P003, drillhole TKAD001 (14.81–14.95 mbsf). 975

Fig. P7. Air-dried (red) and glycol-saturated (black) oriented XRD spectra of sample P004, drillhole TKAD001 (15.65–15.80 mbsf). 976

Fig. P8. Air-dried (red) and glycol-saturated (black) oriented XRD spectra of sample MA13-087, drillhole TKAD001 (16.05–16.22 mbsf). 976

Fig. P9. Air-dried (red) and glycol-saturated (black) oriented XRD spectra of sample MA13-088, drillhole TKAD001 (17.40–17.50 mbsf). 977

Fig. P10. Air-dried (red) and glycol-saturated (black) oriented XRD spectra of sample MA13-089, drillhole TKAD001 (17.90–18.00 mbsf). 977

Fig. P11. Air-dried (red) and glycol-saturated (black) oriented XRD spectra of sample MA13-090, drillhole TKAD001 (18.40–18.60 mbsf). 978

Fig. P12. Air-dried (red) and glycol-saturated (black) oriented XRD spectra of sample P005, drillhole TKAD001 (19.14–19.30 mbsf). 978

Fig. P13. Air-dried (red) and glycol-saturated (black) oriented XRD spectra of sample MA13-091, drillhole TKAD001 (20.80–21.00 mbsf). 979

Fig. P14. Air-dried (red) and glycol-saturated (black) oriented XRD spectra of sample MA13-092, drillhole TKAD001 (21.30–21.45 mbsf). 979

Drillhole TKAD003 980

Fig. P15. Air-dried (red) and glycol-saturated (black) oriented XRD spectra of sample P012, drillhole TKAD003 (11.11–11.20 mbsf). 980

Fig. P16. Air-dried (red) and glycol-saturated (black) oriented XRD spectra of sample P013, drillhole TKAD003 (13.40–13.50 mbsf). 980

Fig. P17. Air-dried (red) and glycol-saturated (black) oriented XRD spectra of sample P014, drillhole TKAD003 (16.41–16.50 mbsf). 981

Drillhole TKAD005 ..... **981**

Fig. P18. Air-dried (red) and glycol-saturated (black) oriented XRD spectra of sample P020, drillhole TKAD005 (20.55–20.67 mbsf). 981

Drillhole TKAD007 ..... **982**

Fig. P19. Air-dried (red) and glycol-saturated (black) oriented XRD spectra of sample P021, drillhole TKAD007 (3.50–3.60 mbsf). 982

Fig. P20. Air-dried (red) and glycol-saturated (black) oriented XRD spectra of sample P022, drillhole TKAD007 (11.23–11.34 mbsf). 982

Fig. P21. Air-dried (red) and glycol-saturated (black) oriented XRD spectra of sample P023, drillhole TKAD007 (22.35–22.45 mbsf). 983

Drillhole TKAD008 ..... **983**

Fig. P22. Air-dried (red) and glycol-saturated (black) oriented XRD spectra of sample P025, drillhole TKAD008 (7.50–7.56 mbsf). 983

Fig. P23. Air-dried (red) and glycol-saturated (black) oriented XRD spectra of sample P024, drillhole TKAD008 (18.13–18.20 mbsf). 984

Drillhole TKAD012 ..... **984**

Fig. P24. Air-dried (red) and glycol-saturated (black) oriented XRD spectra of sample MA13-062, drillhole TKAD012 (2.81–2.90 mbsf). 984

Fig. P25. Air-dried (red) and glycol-saturated (black) oriented XRD spectra of sample MA13-063, drillhole TKAD012 (4.25–4.36 mbsf). 985

Fig. P26. Air-dried (red) and glycol-saturated (black) oriented XRD spectra of sample MA13-064, drillhole TKAD012 (6.49–6.60 mbsf). 985

Drillhole TKAD015 ..... **986**

Fig. P27. Air-dried (red) and glycol-saturated (black) oriented XRD spectra of sample MA13-050, drillhole TKAD015 (3.49–3.63 mbsf). 986

Fig. P28. Air-dried (red) and glycol-saturated (black) oriented XRD spectra of sample MA13-051, drillhole TKAD015 (4.34–4.43 mbsf). 986

Fig. P29. Air-dried (red) and glycol-saturated (black) oriented XRD spectra of sample MA13-052, drillhole TKAD015 (6.42–6.52 mbsf). 987

Fig. P30. Air-dried (red) and glycol-saturated (black) oriented XRD spectra of sample MA13-053, drillhole TKAD015 (7.23–7.34 mbsf). 987

Drillhole TKAD016 ..... **988**

Fig. P31. Air-dried (red) and glycol-saturated (black) oriented XRD spectra of sample MA13-034, drillhole TKAD016 (2.02–2.13 mbsf). 988

Fig. P32. Air-dried (red) and glycol-saturated (black) oriented XRD spectra of sample MA13-035, drillhole TKAD016 (5.65–5.71 mbsf). 988

Fig. P33. Air-dried (red) and glycol-saturated (black) oriented XRD spectra of sample MA13-036, drillhole TKAD016 (7.00–7.05 mbsf). 989

Drillhole TKAD017 ..... **989**

Fig. P34. Air-dried (red) and glycol-saturated (black) oriented XRD spectra of sample MA13-020, drillhole TKAD017 (6.90–7.00 mbsf). 989

Drillhole TKAD018 ..... **990**

Fig. P35. Air-dried (red) and glycol-saturated (black) oriented XRD spectra of sample MA13-014, drillhole TKAD018 (3.00–3.10 mbsf). 990

Fig. P36. Air-dried (red) and glycol-saturated (black) oriented XRD spectra of sample MA13-015, drillhole TKAD018 (5.00–5.10 mbsf). 990

Fig. P37. Air-dried (red) and glycol-saturated (black) oriented XRD spectra of sample MA13-016, drillhole TKAD018 (6.60–6.71 mbsf). 991

Drillhole TKAD025 991

Fig. P38. Air-dried (red) and glycol-saturated (black) oriented XRD spectra of sample MA13-039, drillhole TKAD025 (5.50–5.60 mbsf). 991

Fig. P39. Air-dried (red) and glycol-saturated (black) oriented XRD spectra of sample MA13-040, drillhole TKAD025 (6.91–7.00 mbsf). 992

Drillhole TKAD026 992

Fig. P40. Air-dried (red) and glycol-saturated (black) oriented XRD spectra of sample MA13-067, drillhole TKAD026 (2.90–3.00 mbsf). 992

Fig. P41. Air-dried (red) and glycol-saturated (black) oriented XRD spectra of sample MA13-068, drillhole TKAD026 (3.60–3.68 mbsf). 993

Fig. P42. Air-dried (red) and glycol-saturated (black) oriented XRD spectra of sample MA13-069, drillhole TKAD026 (5.64–5.75 mbsf). 993

Drillhole TKAD027 994

Fig. P43. Air-dried (red) and glycol-saturated (black) oriented XRD spectra of sample MA13-056, drillhole TKAD027 (2.50–2.60 mbsf). 994

Fig. P44. Air-dried (red) and glycol-saturated (black) oriented XRD spectra of sample MA13-057, drillhole TKAD027 (4.60–4.70 mbsf). 994

Fig. P45. Air-dried (red) and glycol-saturated (black) oriented XRD spectra of sample MA13-058, drillhole TKAD027 (6.50–6.59 mbsf). 995

Drillhole TKAD028 995

Fig. P46. Air-dried (red) and glycol-saturated (black) oriented XRD spectra of sample MA13-099, drillhole TKAD028 (4.50–4.60 mbsf). 995

Drillhole TKAD029 996

Fig. P47. Air-dried (red) and glycol-saturated (black) oriented XRD spectra of sample MA13-095, drillhole TKAD029 (3.60–3.70 mbsf). 996

Drillhole TKAD030 997

Fig. P48. Air-dried (red) and glycol-saturated (black) oriented XRD spectra of sample MA13-005, drillhole TKAD030 (5.06–5.21 mbsf). 997

Fig. P49. Air-dried (red) and glycol-saturated (black) oriented XRD spectra of sample MA13-006, drillhole TKAD030 (6.45–6.60 mbsf). 997

Drillhole TKAD031 998

Fig. P50. Air-dried (red) and glycol-saturated (black) oriented XRD spectra of sample MA13-044, drillhole TKAD031 (5.64–5.69 mbsf). 998

Fig. P51. Air-dried (red) and glycol-saturated (black) oriented XRD spectra of sample MA13-045, drillhole TKAD031 (6.60–6.67 mbsf). 998

Drillhole TKAD032 999

Fig. P52. Air-dried (red) and glycol-saturated (black) oriented XRD spectra of sample MA13-072, drillhole TKAD032 (2.05–2.17 mbsf). 999

Fig. P53. Air-dried (red) and glycol-saturated (black) oriented XRD spectra of sample MA13-073, drillhole TKAD032 (3.90–4.00 mbsf). 999

Fig. P54. Air-dried (red) and glycol-saturated (black) oriented XRD spectra of sample MA13-074, drillhole TKAD032 (5.31–5.40 mbsf). 1000

Fig. P55. Air-dried (red) and glycol-saturated (black) oriented XRD spectra of sample MA13-075, drillhole TKAD032 (6.42–6.54 mbsf). 1000

Drillhole TKAD033 1001

Fig. P56. Air-dried (red) and glycol-saturated (black) oriented XRD spectra of sample MA13-025, drillhole TKAD033 (3.00–3.10 mbsf). 1001

Fig. P57. Air-dried (red) and glycol-saturated (black) oriented XRD spectra of sample MA13-026, drillhole TKAD033 (4.76–4.88 mbsf). 1001

Fig. P58. Air-dried (red) and glycol-saturated (black) oriented XRD spectra of sample MA13-027, drillhole TKAD033 (7.30–7.40 mbsf). 1002

Notes:

All analyses performed on oriented clay-sized fractions (< 2 μm), air-dried and glycol-saturated (GL); see Methods (*Chapter 5, Section 3.4*).
Peaks for reference spectra are shown, see **Table 5.2** for interpreted mineralogy.
Locations of drillholes are shown in **Fig. 5.2**.
XRD = X-Ray Diffraction; I = illite; S = smectite; C = chlorite

Drillhole TKAD001

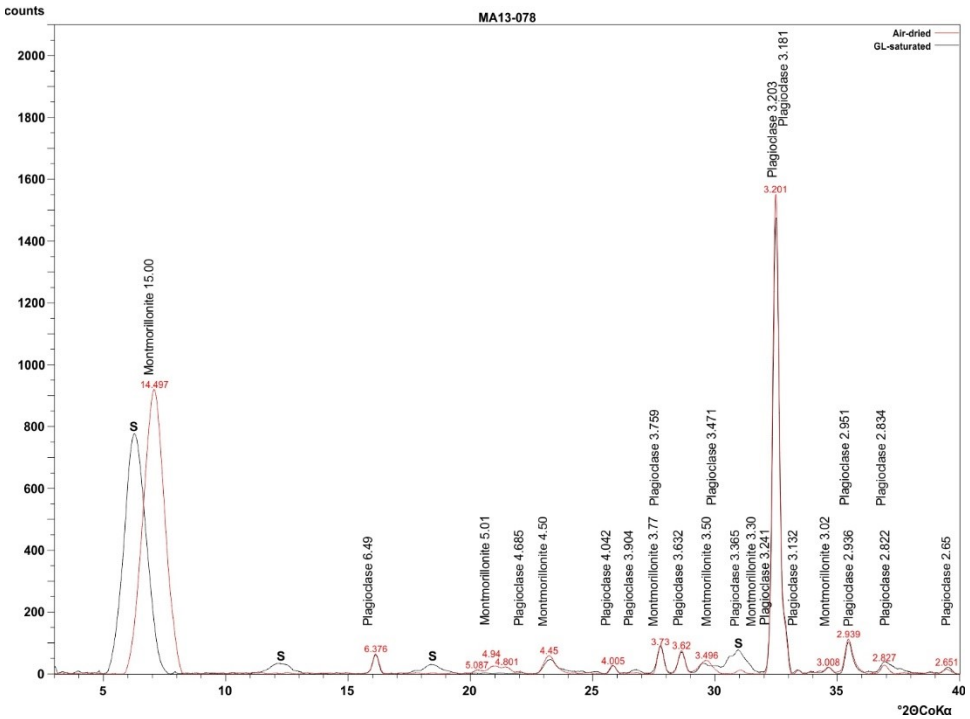


Fig. P1. Air-dried (red) and glycol-saturated (black) oriented XRD spectra of sample MA13-078, drillhole TKAD001 (4.54–4.68 mbsf).

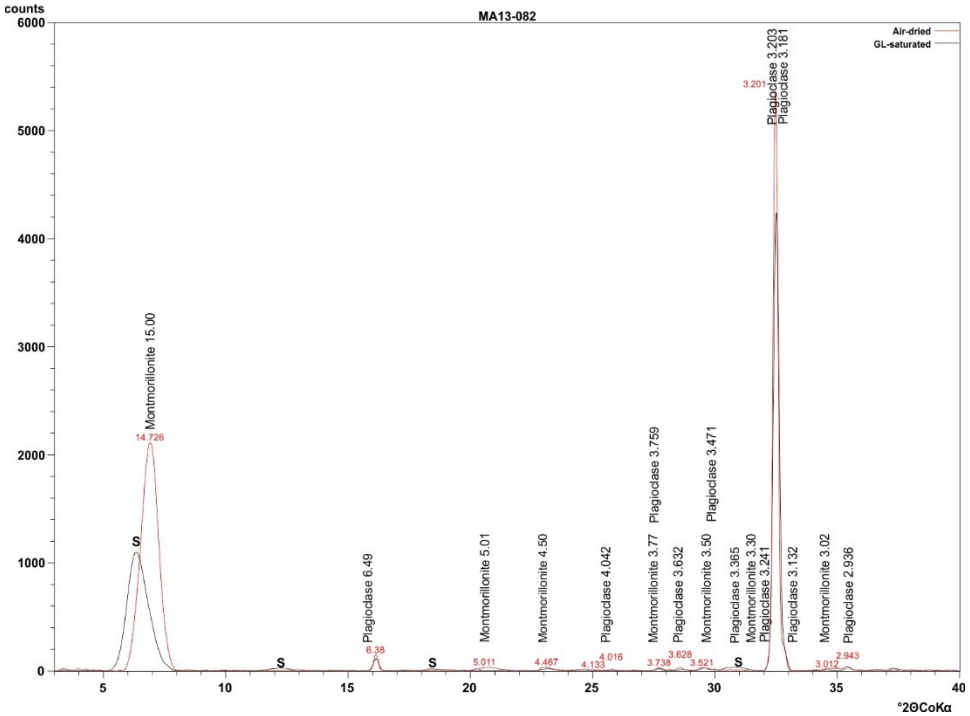


Fig. P2. Air-dried (red) and glycol-saturated (black) oriented XRD spectra of sample MA13-082, drillhole TKAD001 (7.00–7.10 mbsf).

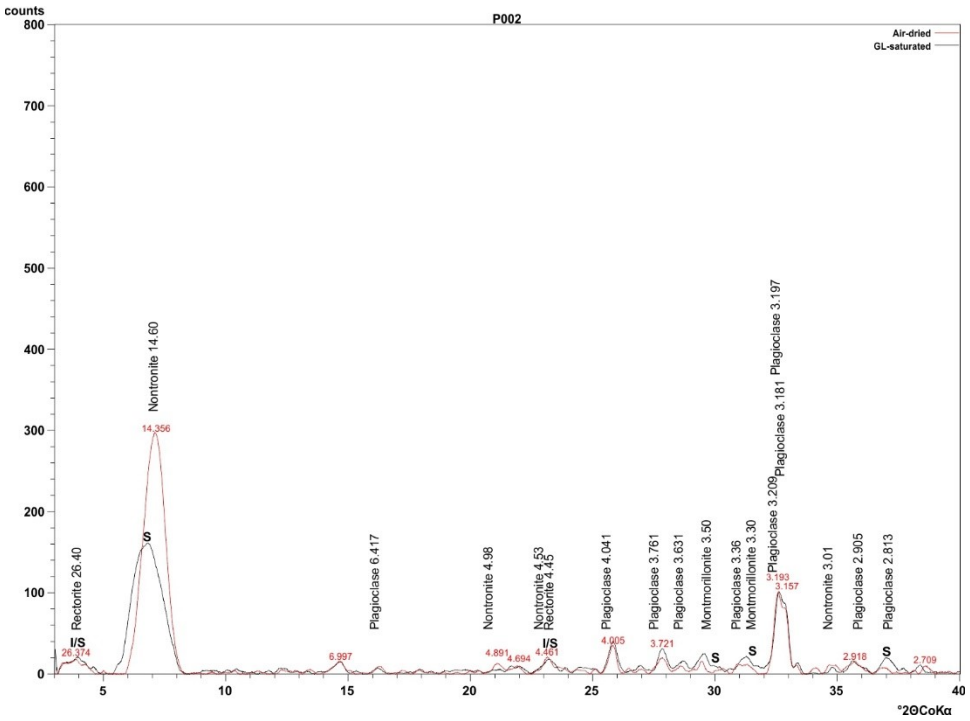


Fig. P3. Air-dried (red) and glycol-saturated (black) oriented XRD spectra of sample P002, drillhole TKAD001 (10.39–10.50 mbsf).

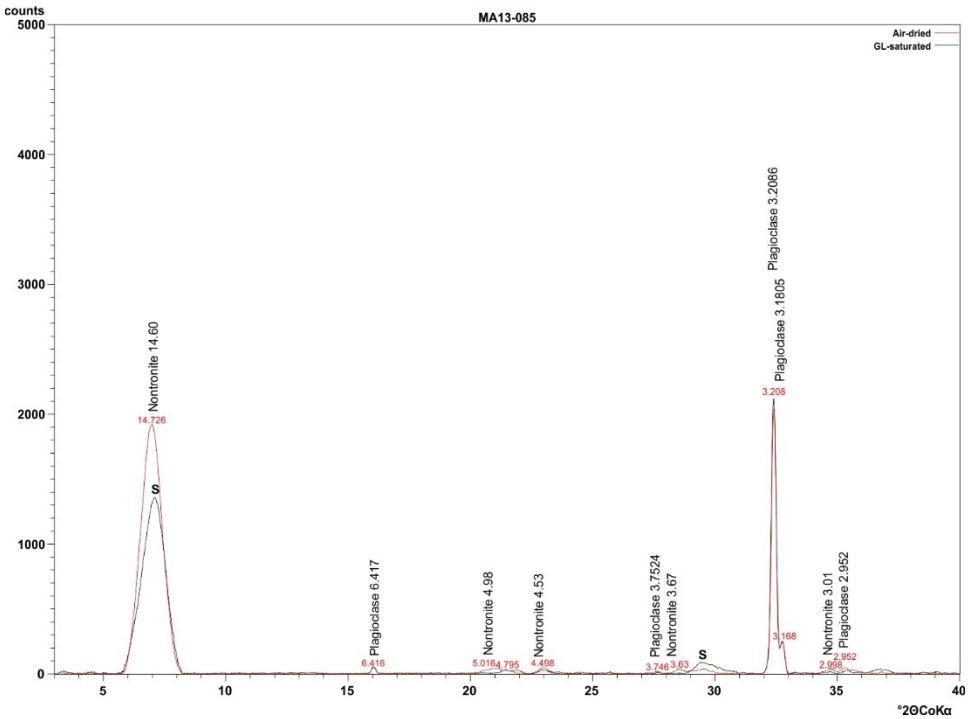


Fig. P4. Air-dried (red) and glycol-saturated (black) oriented XRD spectra of sample MA13-085, drillhole TKAD001 (12.90–13.00 mbsf).

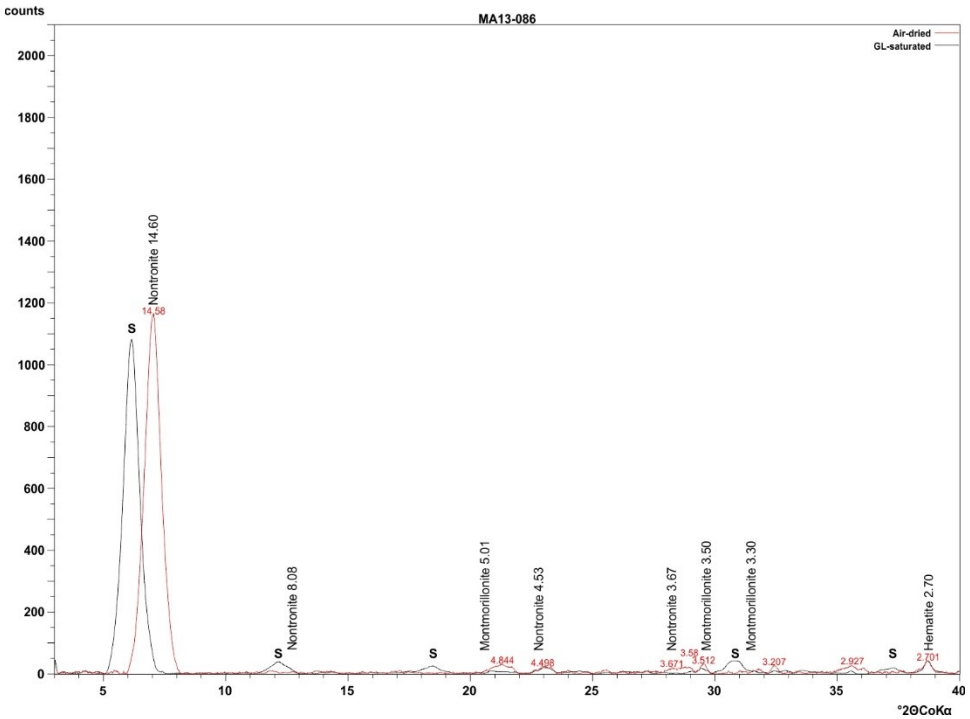


Fig. P5. Air-dried (red) and glycol-saturated (black) oriented XRD spectra of sample MA13-086, drillhole TKAD001 (14.00–14.12 mbsf).

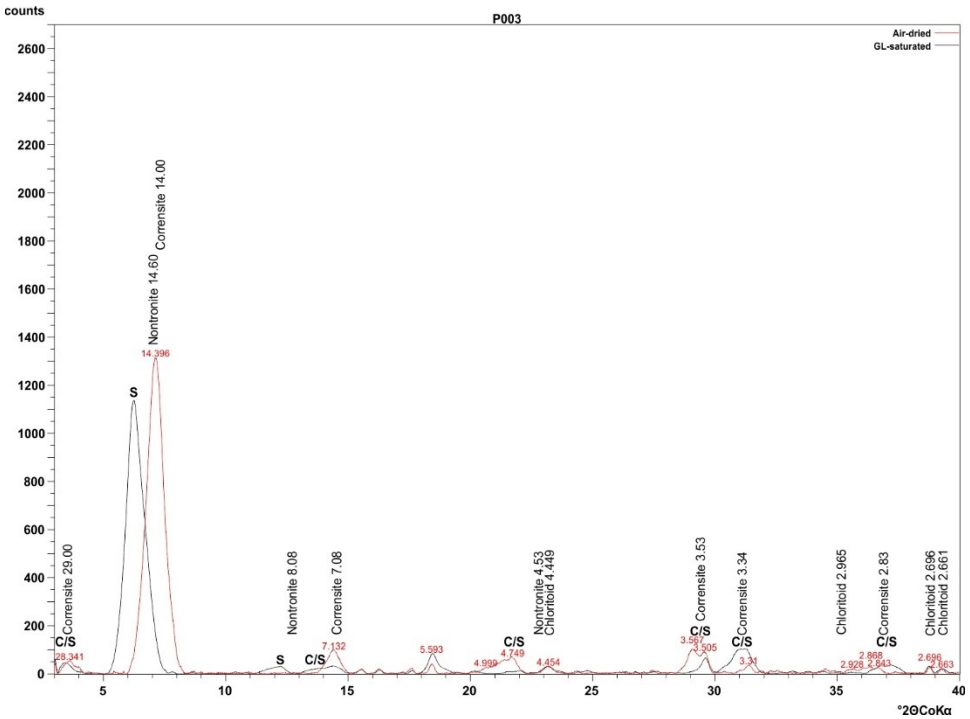


Fig. P6. Air-dried (red) and glycol-saturated (black) oriented XRD spectra of sample P003, drillhole TKAD001 (14.81–14.95 mbsf).

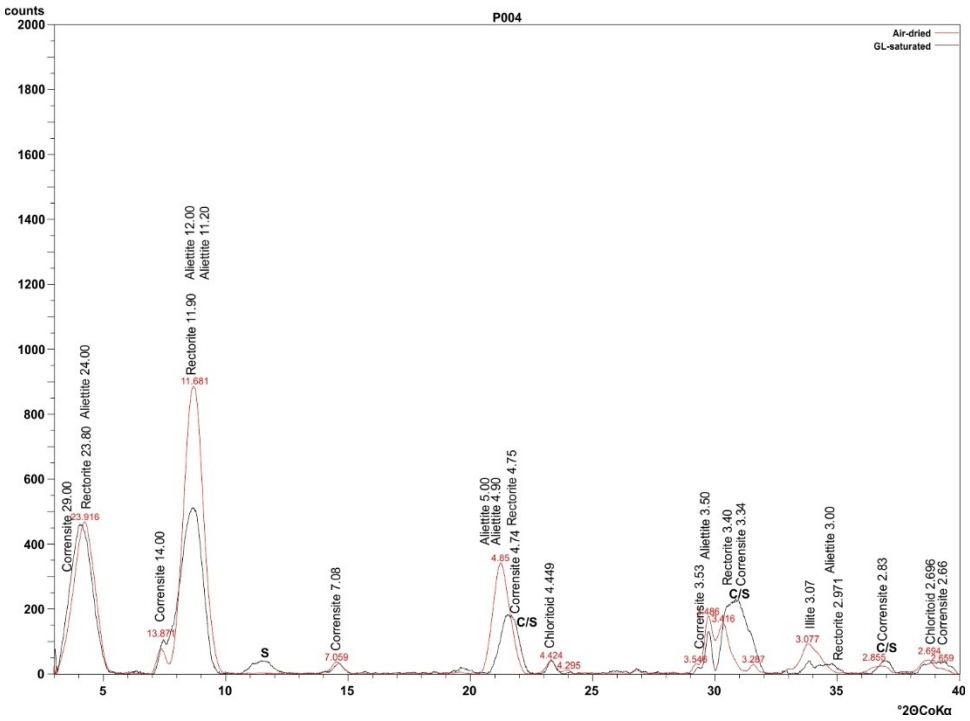


Fig. P7. Air-dried (red) and glycol-saturated (black) oriented XRD spectra of sample P004, drillhole TKAD001 (15.65–15.80 mbsf).

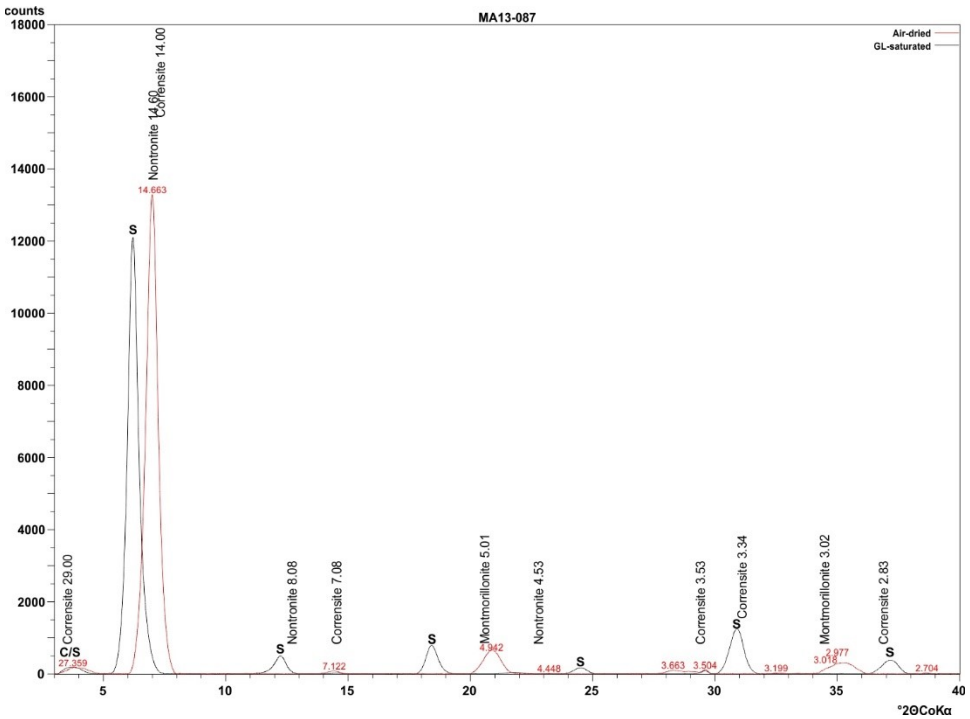


Fig. P8. Air-dried (red) and glycol-saturated (black) oriented XRD spectra of sample MA13-087, drillhole TKAD001 (16.05–16.22 mbsf).

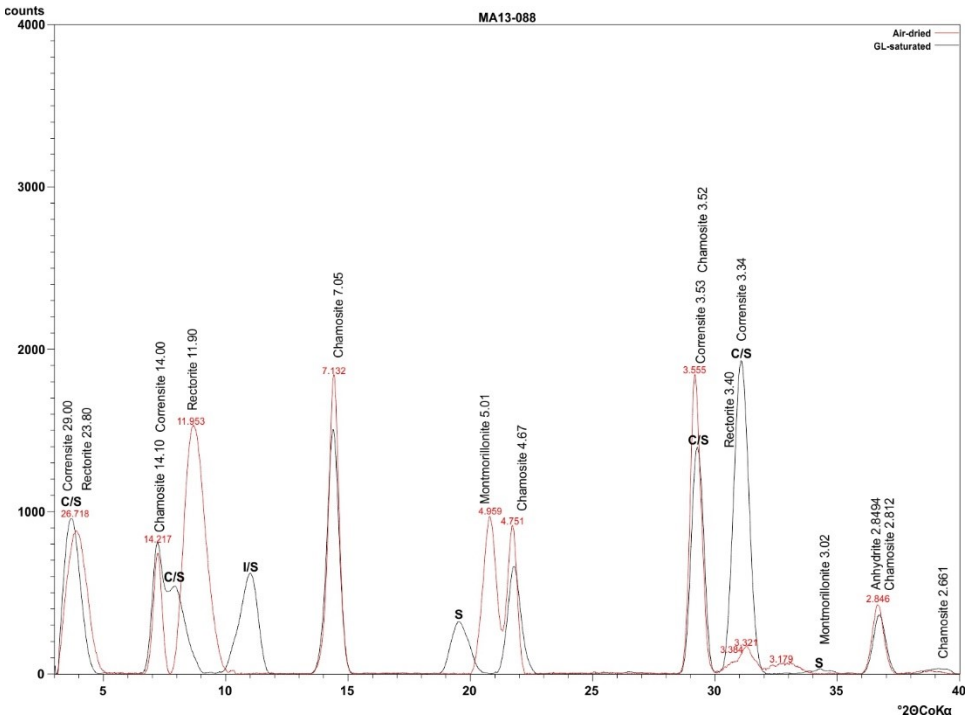


Fig. P9. Air-dried (red) and glycol-saturated (black) oriented XRD spectra of sample MA13-088, drillhole TKAD001 (17.40–17.50 mbsf).

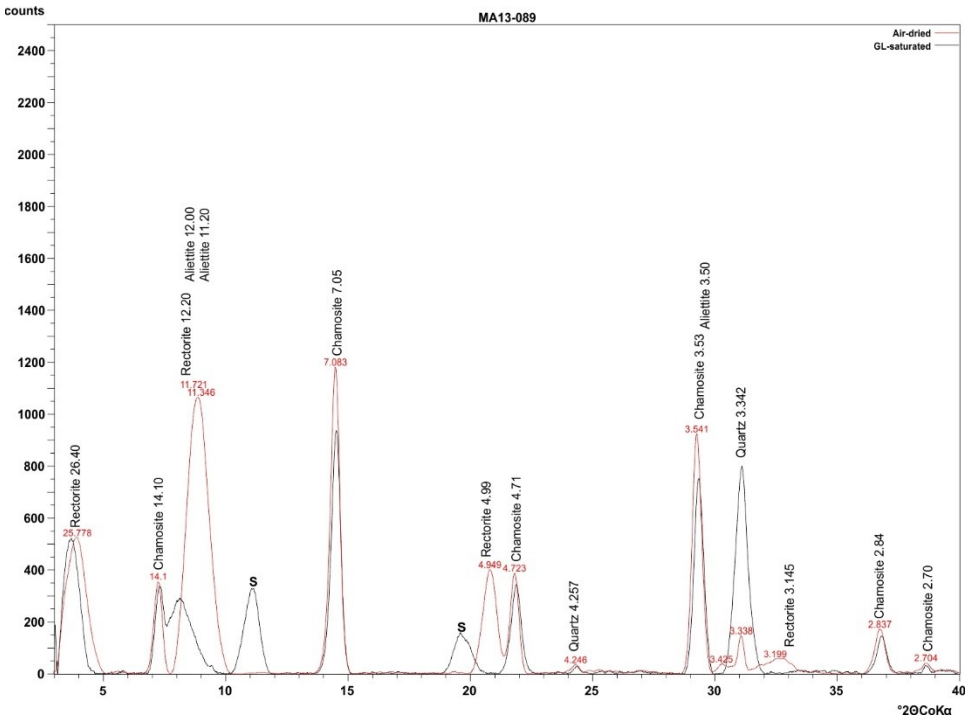


Fig. P10. Air-dried (red) and glycol-saturated (black) oriented XRD spectra of sample MA13-089, drillhole TKAD001 (17.90–18.00 mbsf).

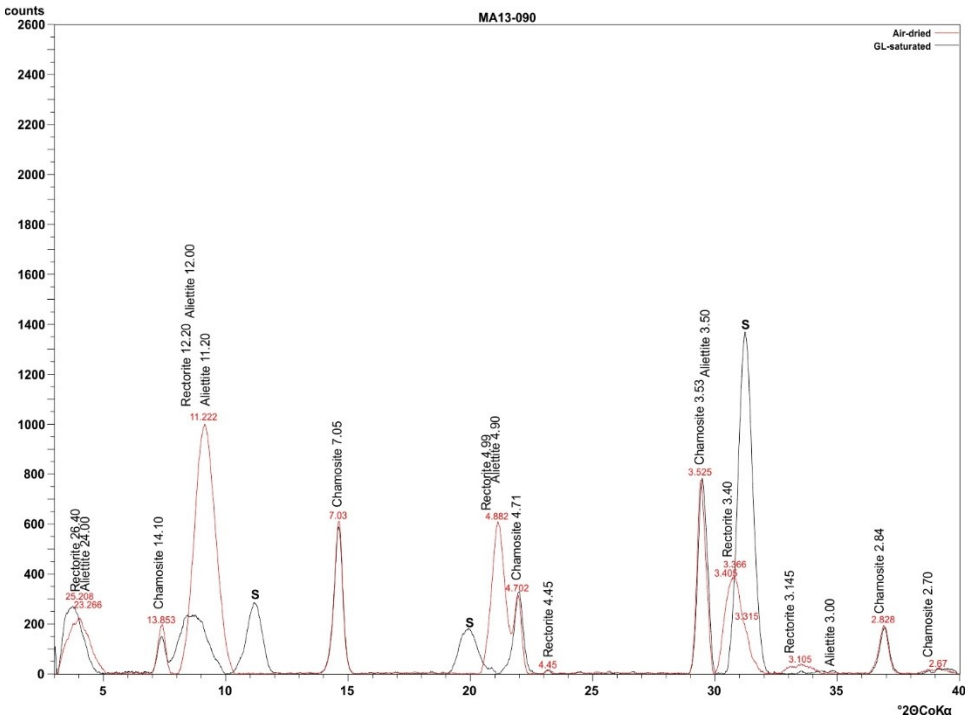


Fig. P11. Air-dried (red) and glycol-saturated (black) oriented XRD spectra of sample MA13-090, drillhole TKAD001 (18.40–18.60 mbsf).

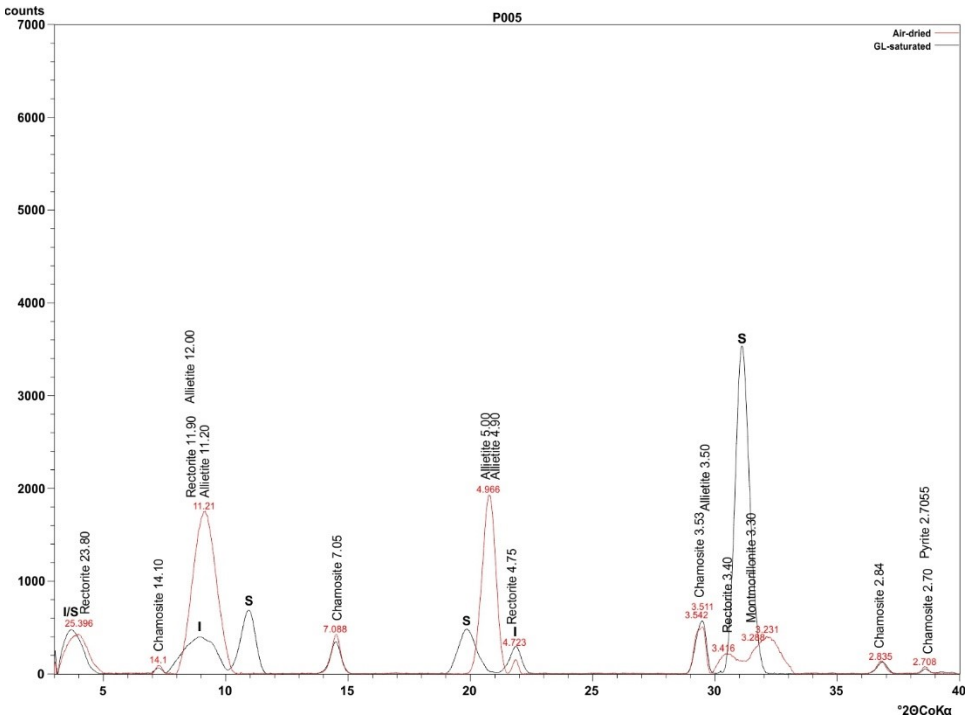


Fig. P12. Air-dried (red) and glycol-saturated (black) oriented XRD spectra of sample P005, drillhole TKAD001 (19.14–19.30 mbsf).

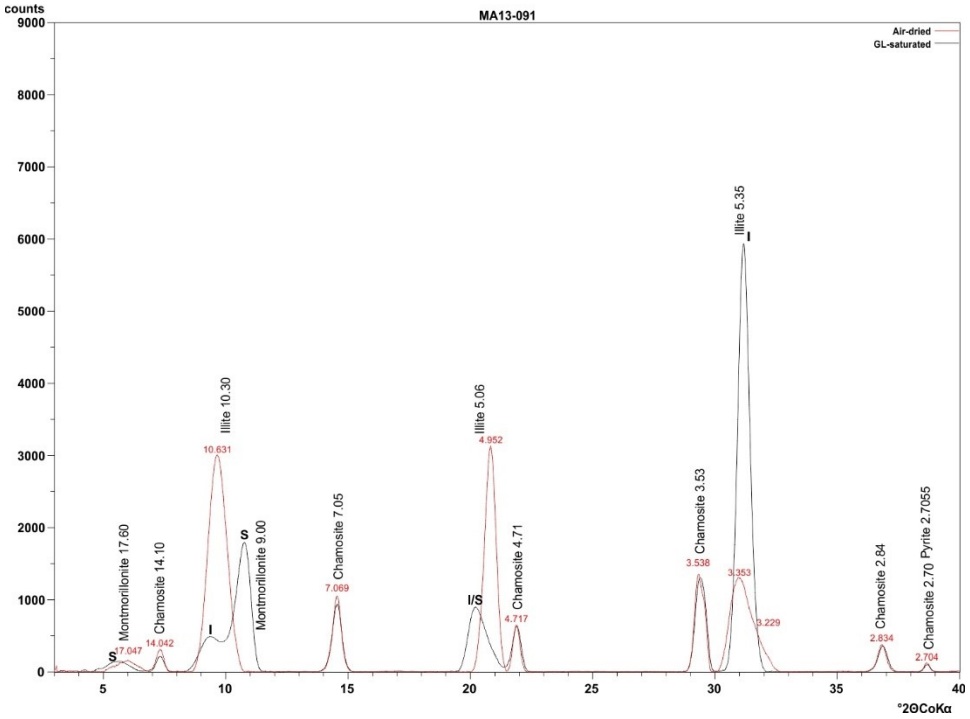


Fig. P13. Air-dried (red) and glycol-saturated (black) oriented XRD spectra of sample MA13-091, drillhole TKAD001 (20.80–21.00 mbsf).

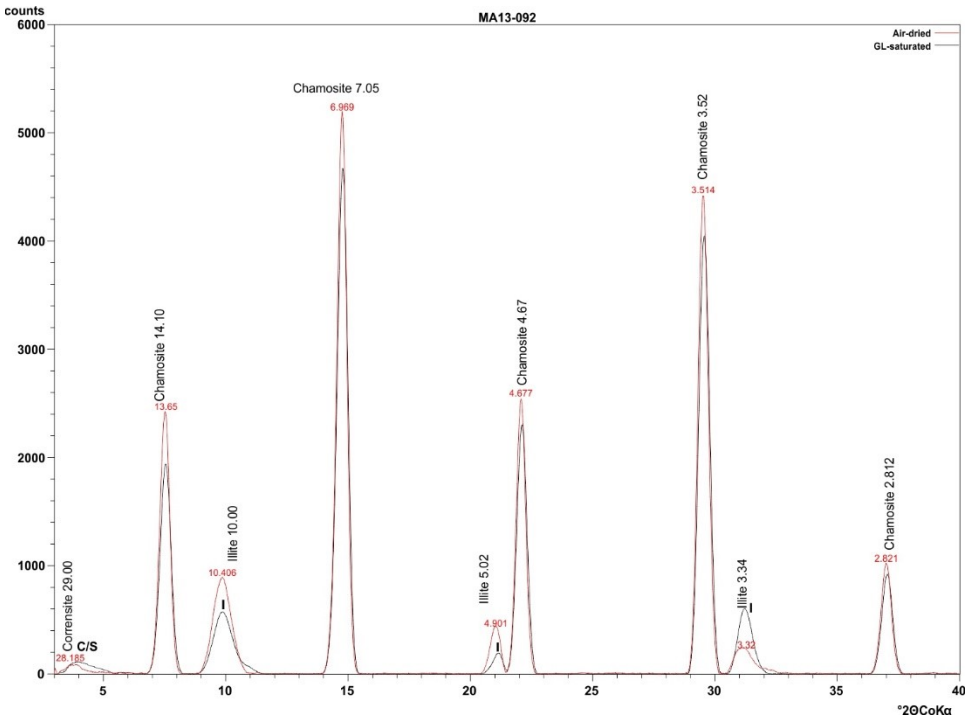


Fig. P14. Air-dried (red) and glycol-saturated (black) oriented XRD spectra of sample MA13-092, drillhole TKAD001 (21.30–21.45 mbsf).

Drillhole TKAD003

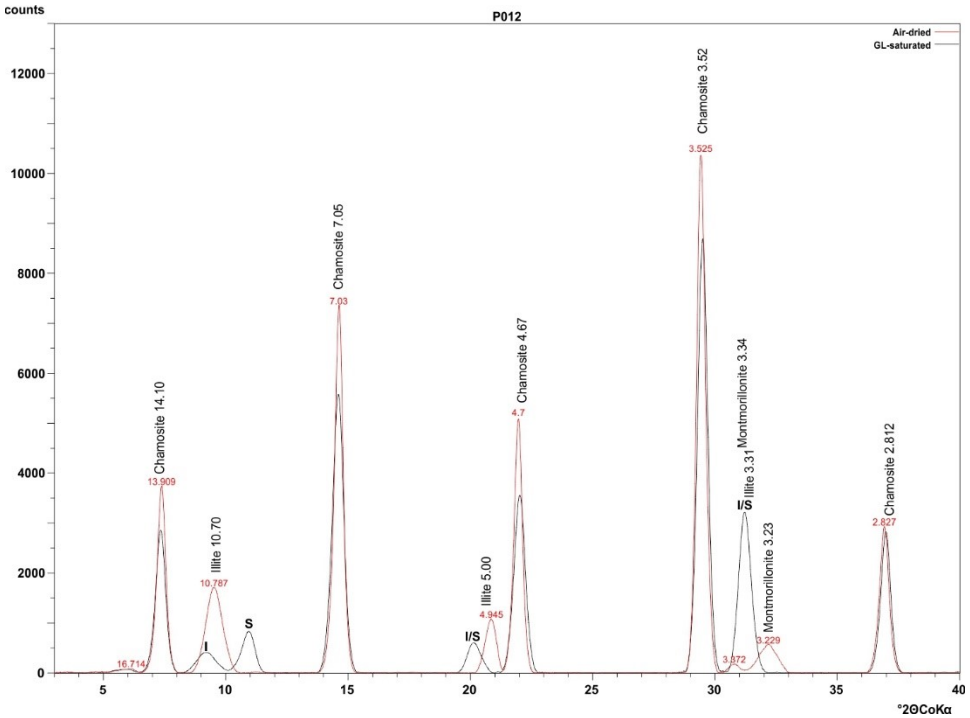


Fig. P15. Air-dried (red) and glycol-saturated (black) oriented XRD spectra of sample P012, drillhole TKAD003 (11.11–11.20 mbsf).

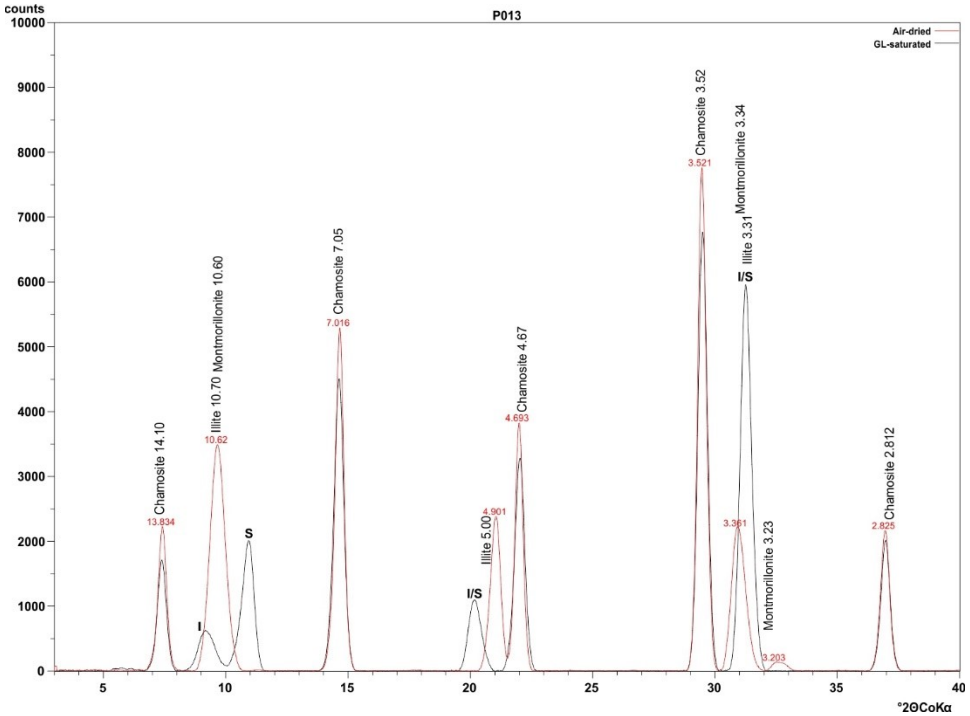


Fig. P16. Air-dried (red) and glycol-saturated (black) oriented XRD spectra of sample P013, drillhole TKAD003 (13.40–13.50 mbsf).

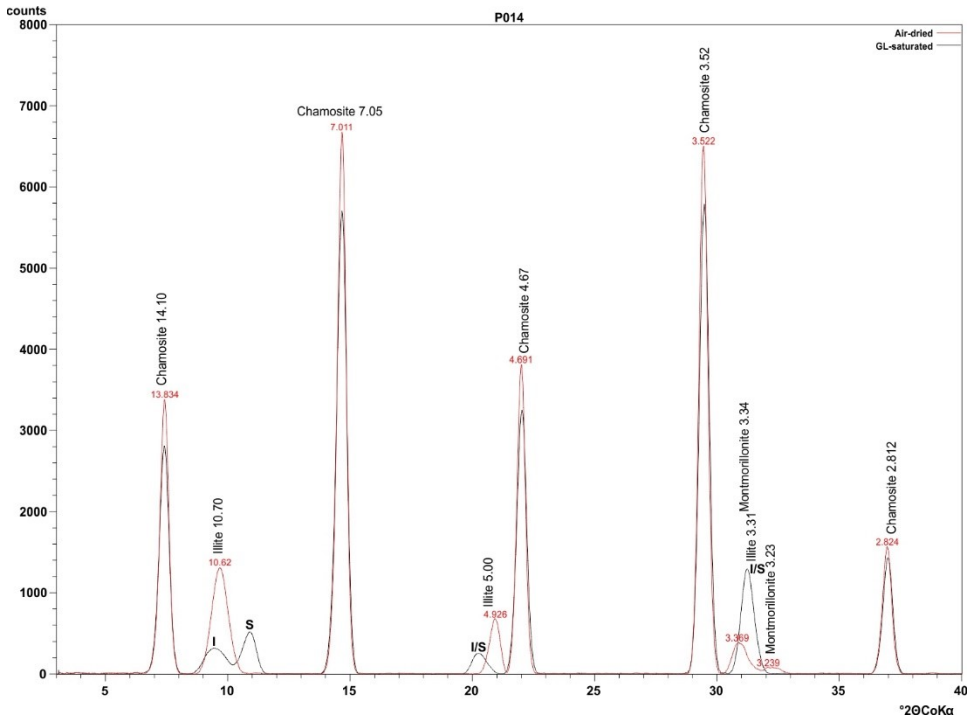


Fig. P17. Air-dried (red) and glycol-saturated (black) oriented XRD spectra of sample P014, drillhole TKAD003 (16.41–16.50 mbsf).

Drillhole TKAD005

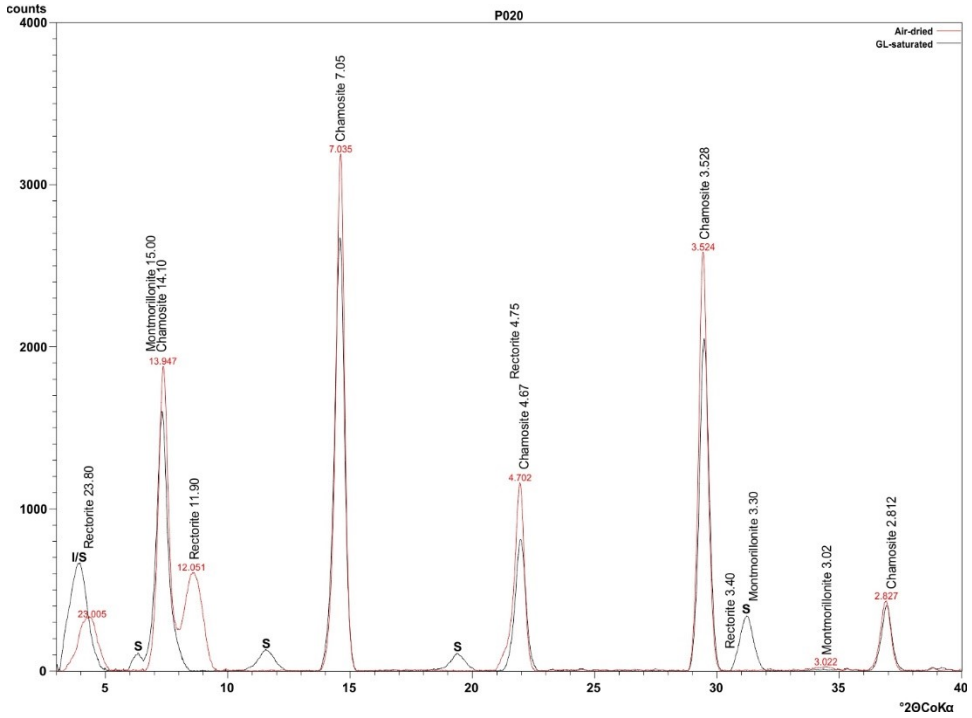


Fig. P18. Air-dried (red) and glycol-saturated (black) oriented XRD spectra of sample P020, drillhole TKAD005 (20.55–20.67 mbsf).

Drillhole TKAD007

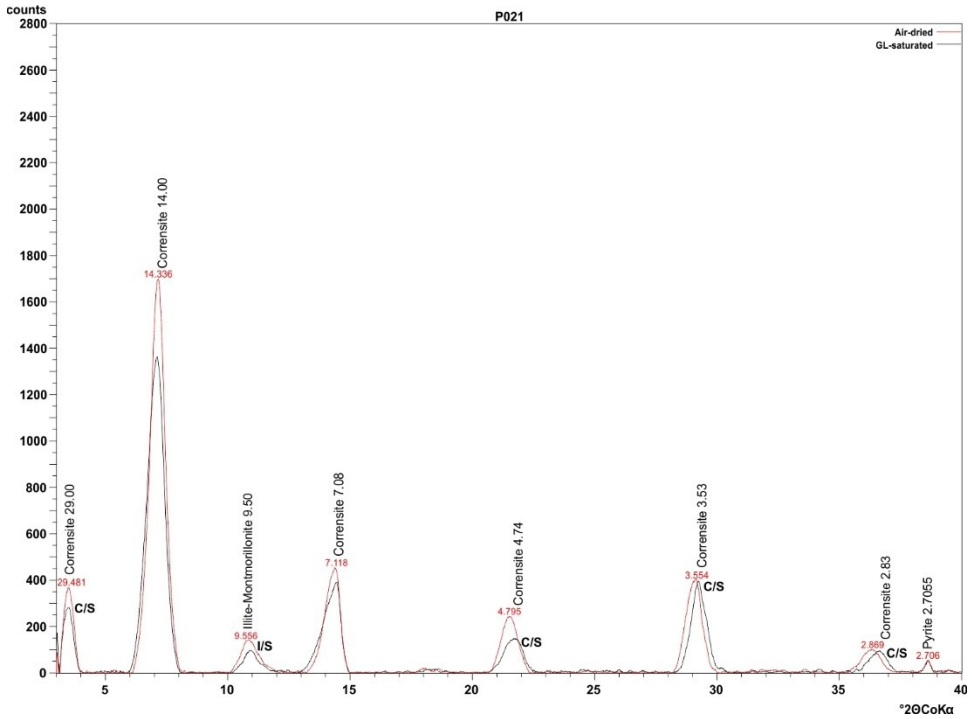


Fig. P19. Air-dried (red) and glycol-saturated (black) oriented XRD spectra of sample P021, drillhole TKAD007 (3.50–3.60 mbsf).

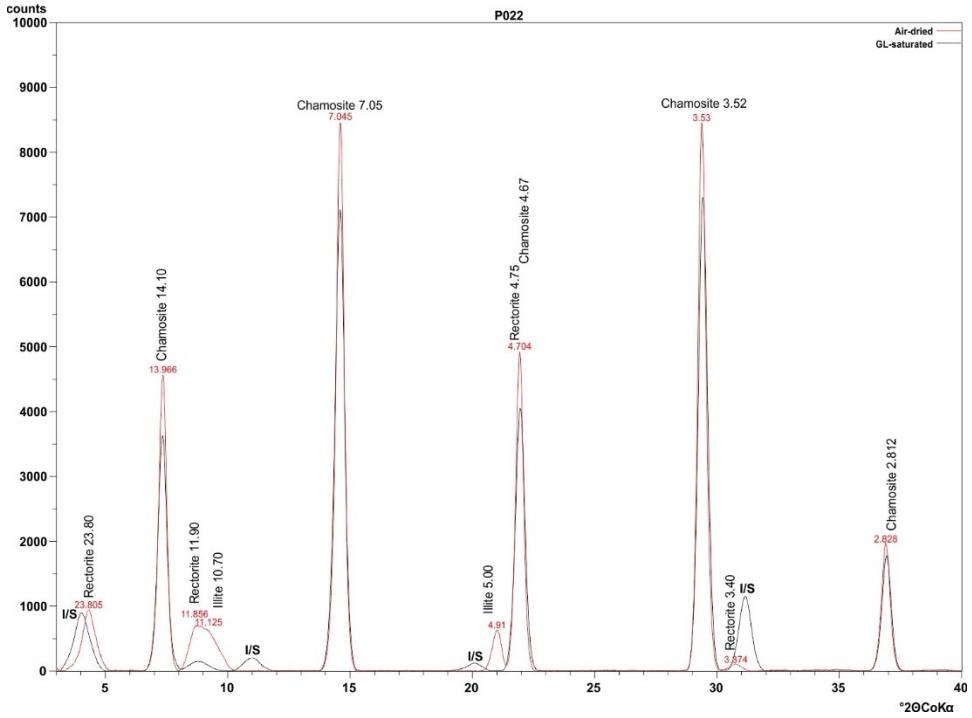


Fig. P20. Air-dried (red) and glycol-saturated (black) oriented XRD spectra of sample P022, drillhole TKAD007 (11.23–11.34 mbsf).

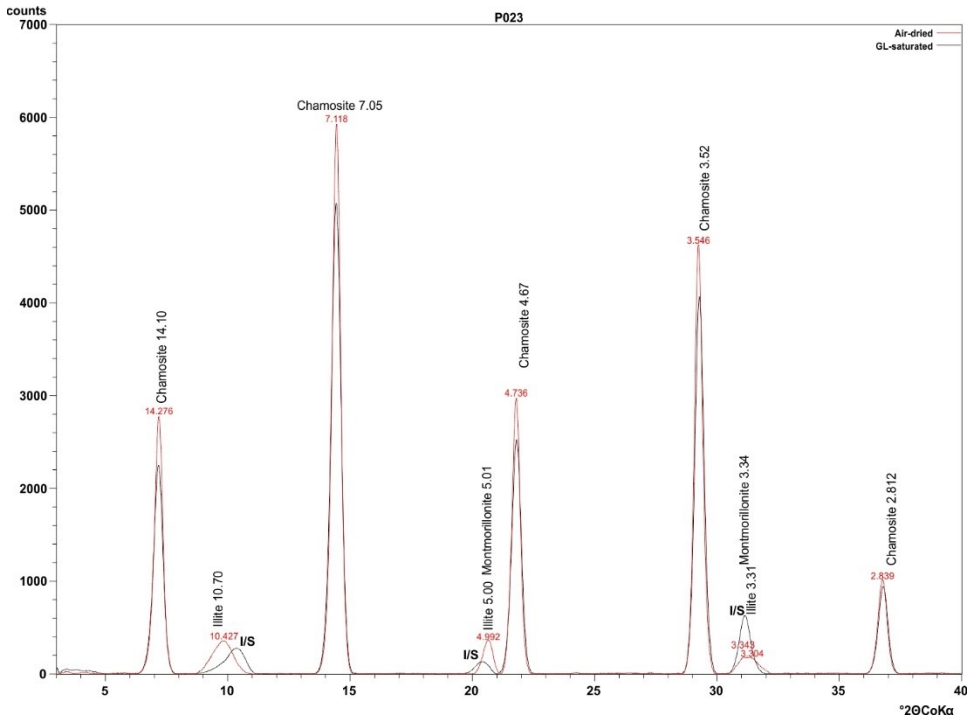


Fig. P21. Air-dried (red) and glycol-saturated (black) oriented XRD spectra of sample P023, drillhole TKAD007 (22.35–22.45 mbsf).

Drillhole TKAD008

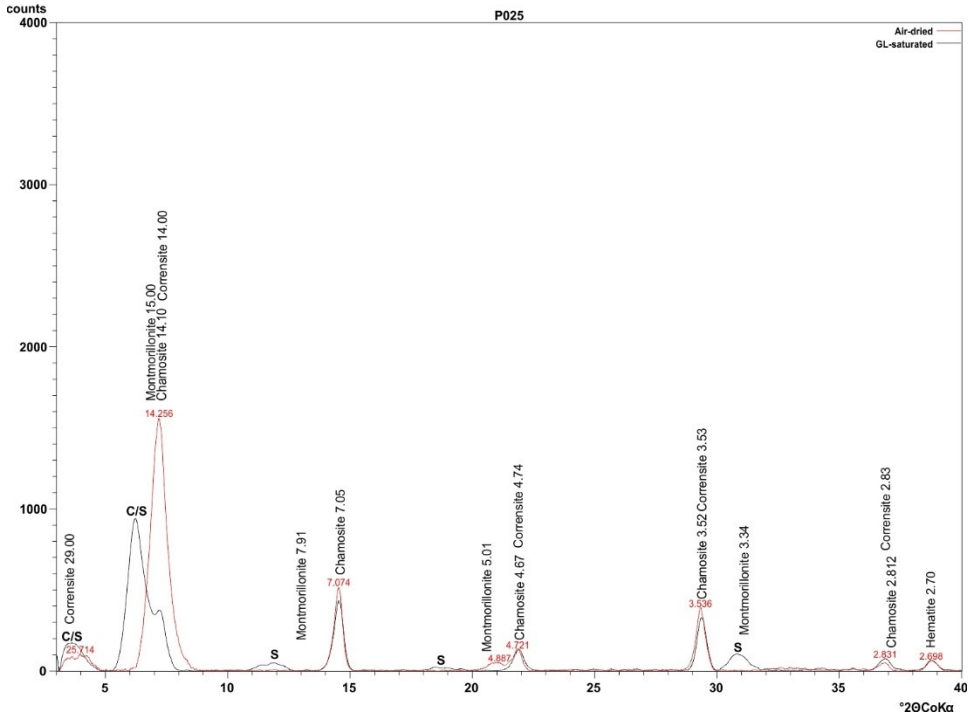


Fig. P22. Air-dried (red) and glycol-saturated (black) oriented XRD spectra of sample P025, drillhole TKAD008 (7.50–7.56 mbsf).

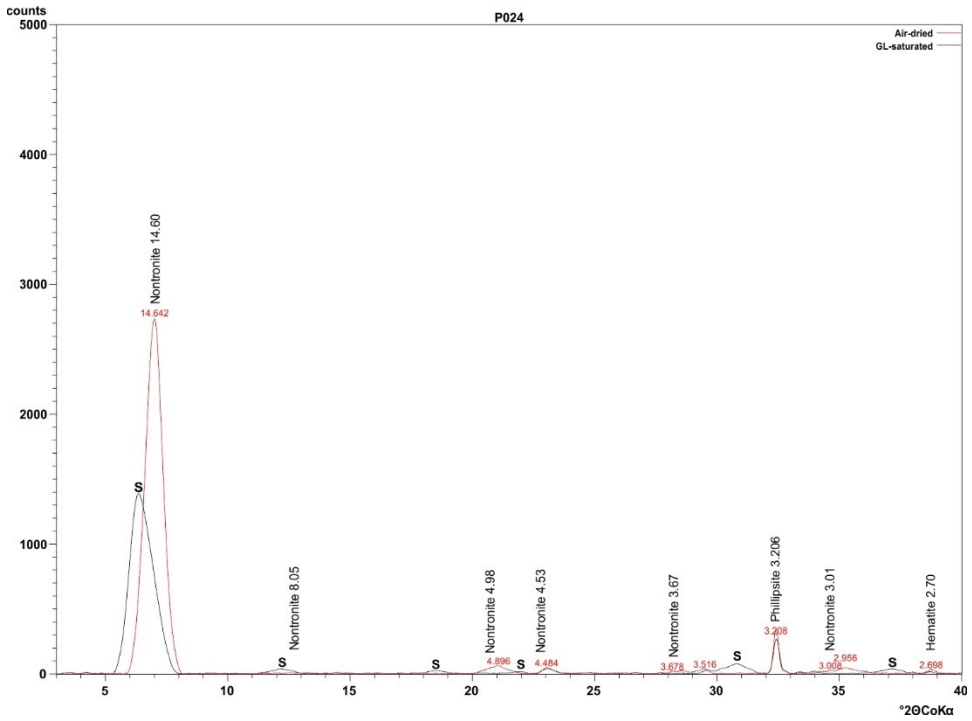


Fig. P23. Air-dried (red) and glycol-saturated (black) oriented XRD spectra of sample P024, drillhole TKAD008 (18.13–18.20 mbsf).

Drillhole TKAD012

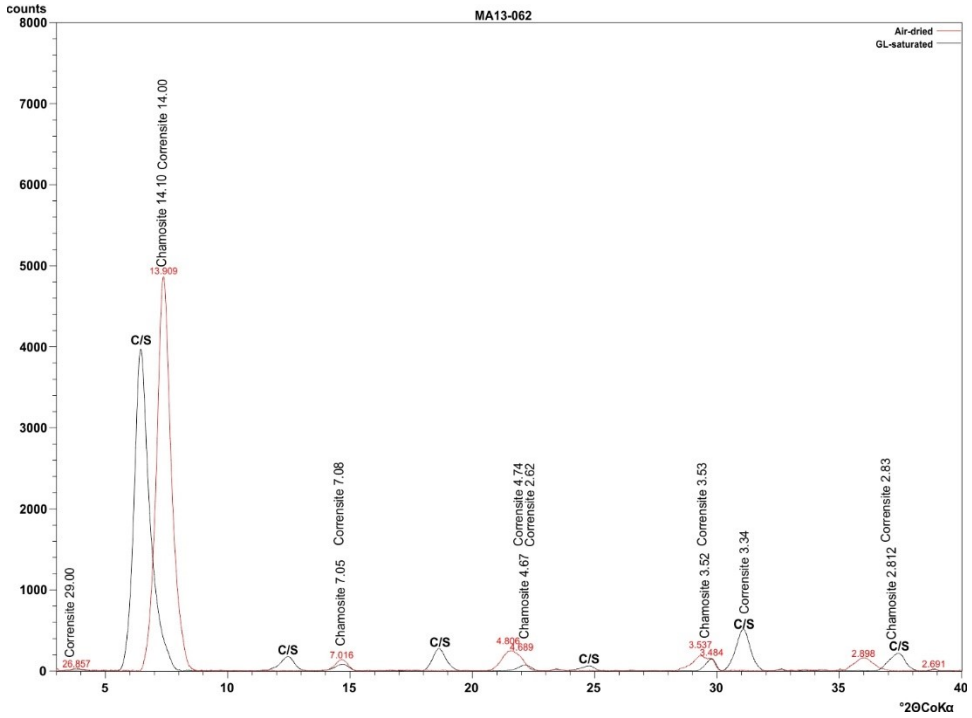


Fig. P24. Air-dried (red) and glycol-saturated (black) oriented XRD spectra of sample MA13-062, drillhole TKAD012 (2.81–2.90 mbsf).

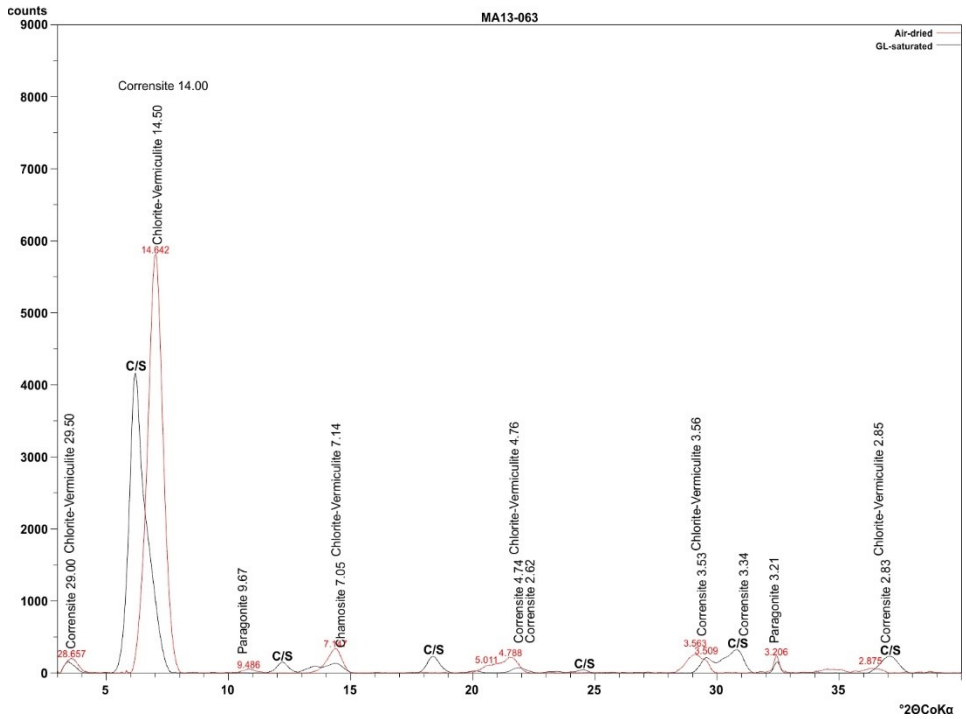


Fig. P25. Air-dried (red) and glycol-saturated (black) oriented XRD spectra of sample MA13-063, drillhole TKAD012 (4.25–4.36 mbsf).

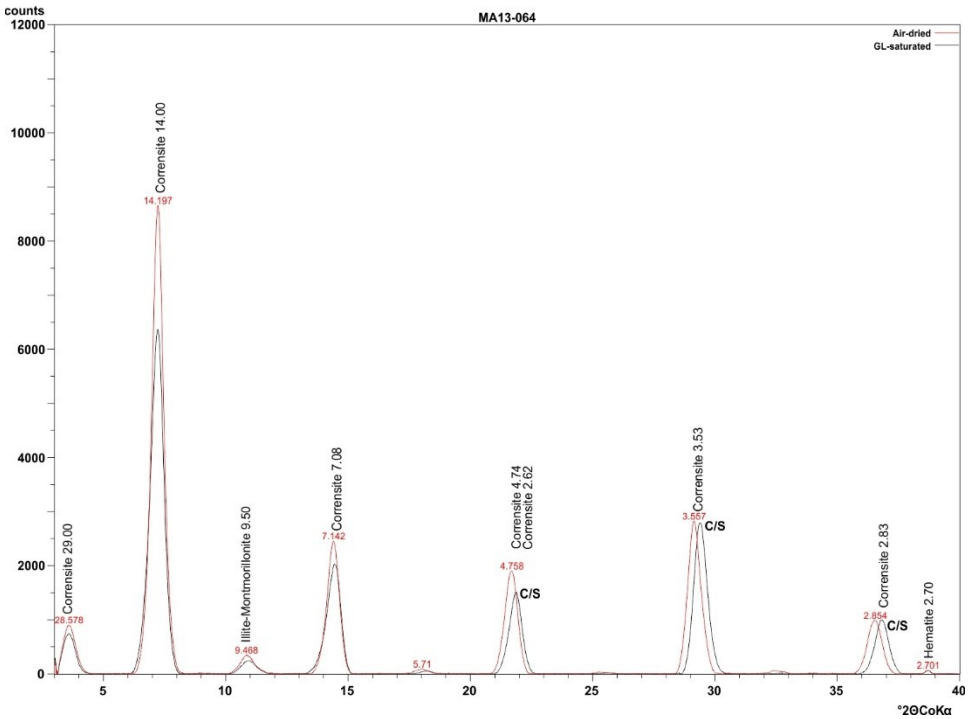


Fig. P26. Air-dried (red) and glycol-saturated (black) oriented XRD spectra of sample MA13-064, drillhole TKAD012 (6.49–6.60 mbsf).

Drillhole TKAD015

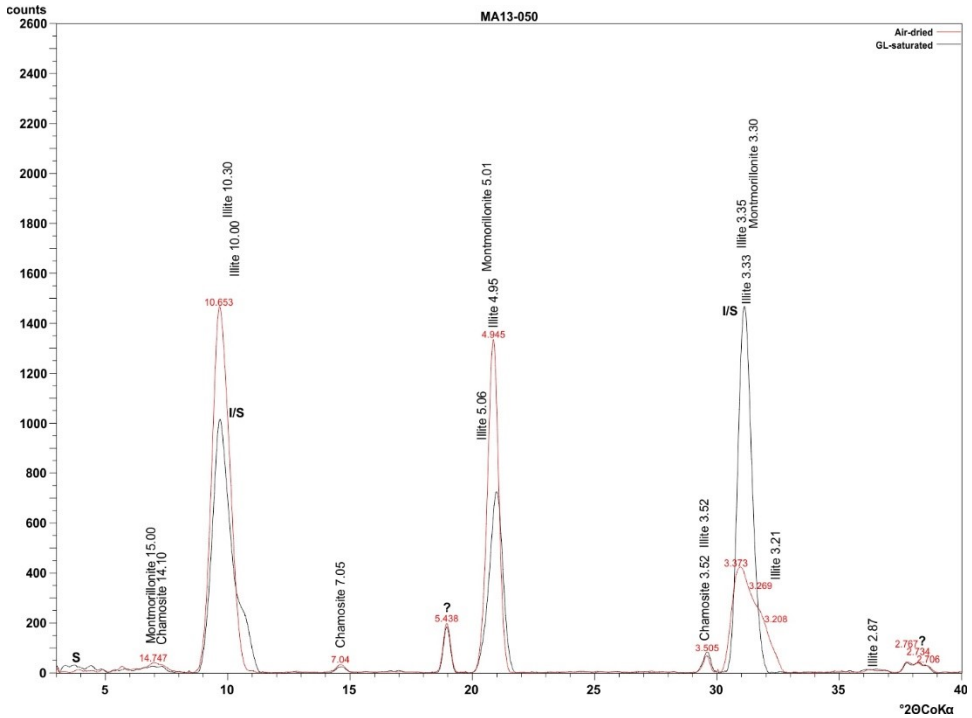


Fig. P27. Air-dried (red) and glycol-saturated (black) oriented XRD spectra of sample MA13-050, drillhole TKAD015 (3.49–3.63 mbsf).

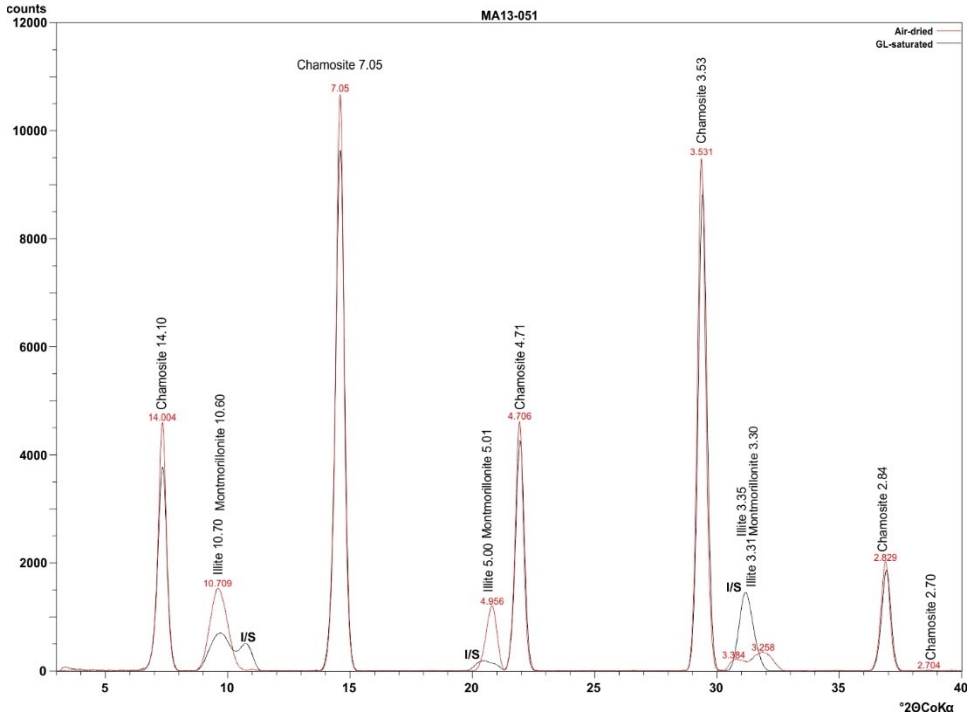


Fig. P28. Air-dried (red) and glycol-saturated (black) oriented XRD spectra of sample MA13-051, drillhole TKAD015 (4.34–4.43 mbsf).

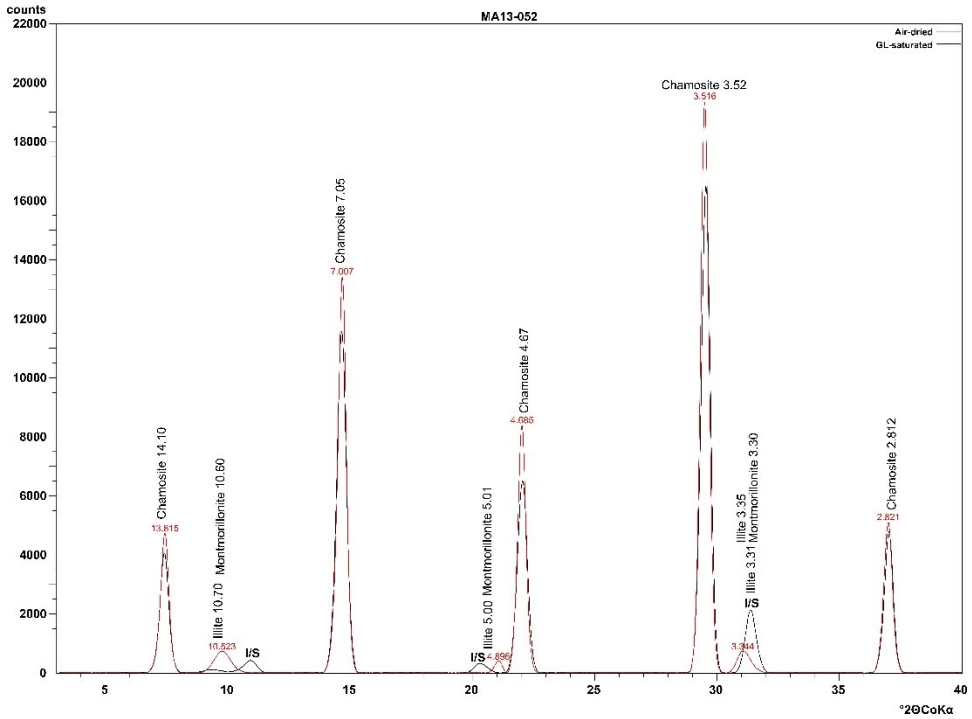


Fig. P29. Air-dried (red) and glycol-saturated (black) oriented XRD spectra of sample MA13-052, drillhole TKAD015 (6.42–6.52 mbsf).

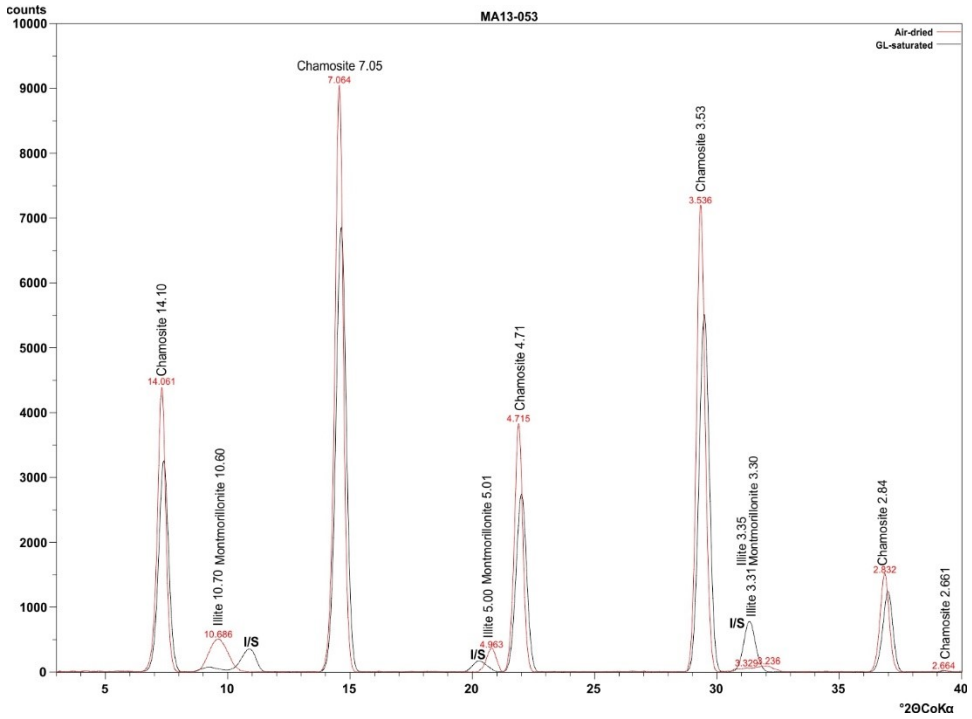


Fig. P30. Air-dried (red) and glycol-saturated (black) oriented XRD spectra of sample MA13-053, drillhole TKAD015 (7.23–7.34 mbsf).

Drillhole TKAD016

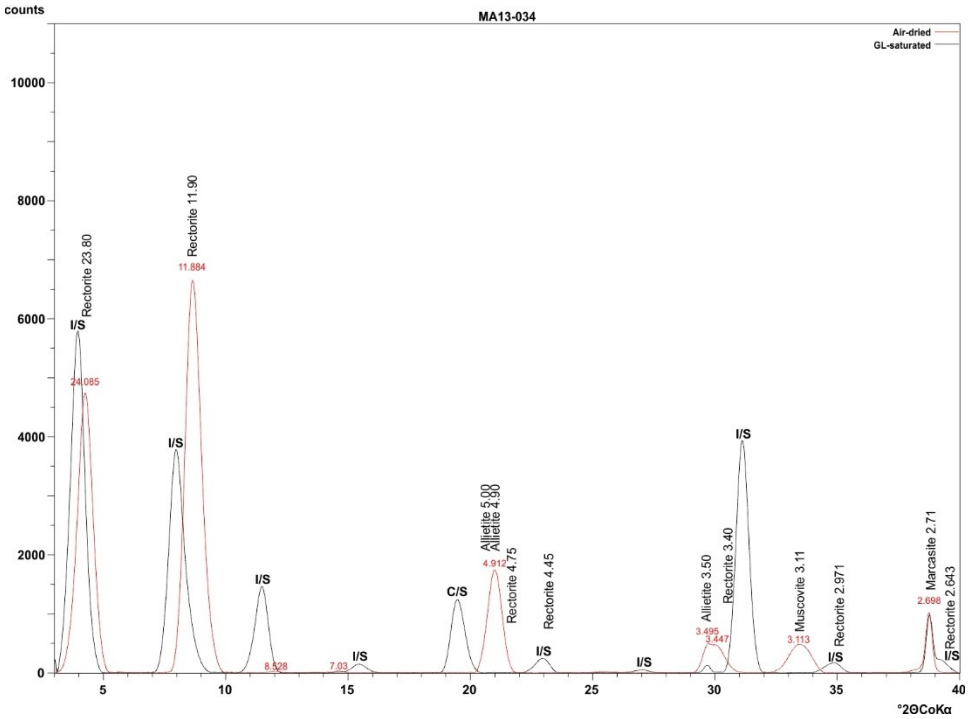


Fig. P31. Air-dried (red) and glycol-saturated (black) oriented XRD spectra of sample MA13-034, drillhole TKAD016 (2.02–2.13 mbsf).

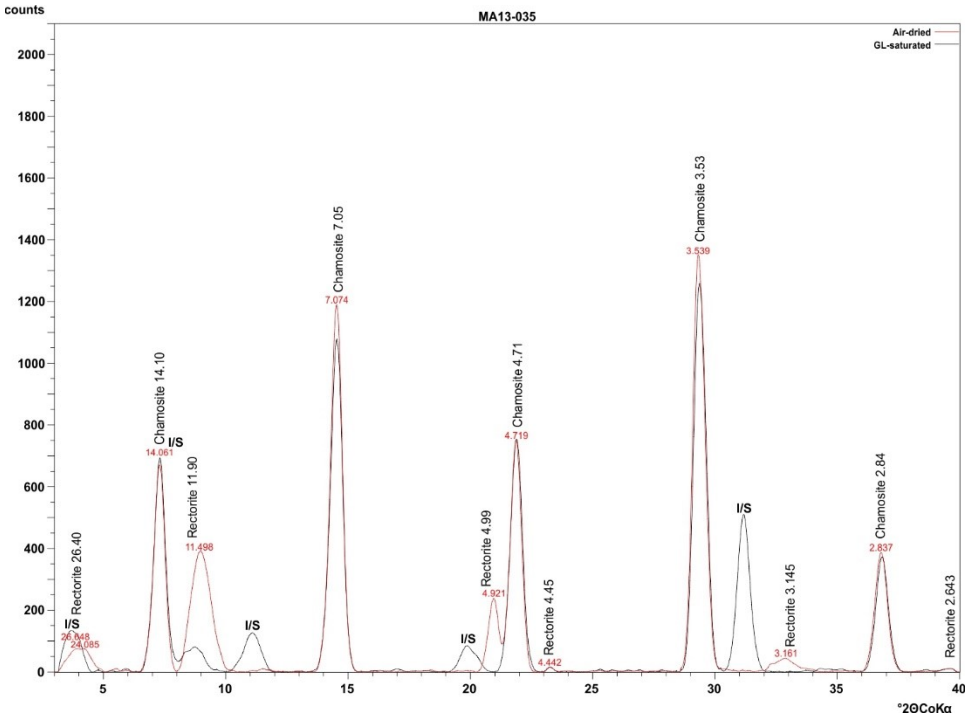


Fig. P32. Air-dried (red) and glycol-saturated (black) oriented XRD spectra of sample MA13-035, drillhole TKAD016 (5.65–5.71 mbsf).

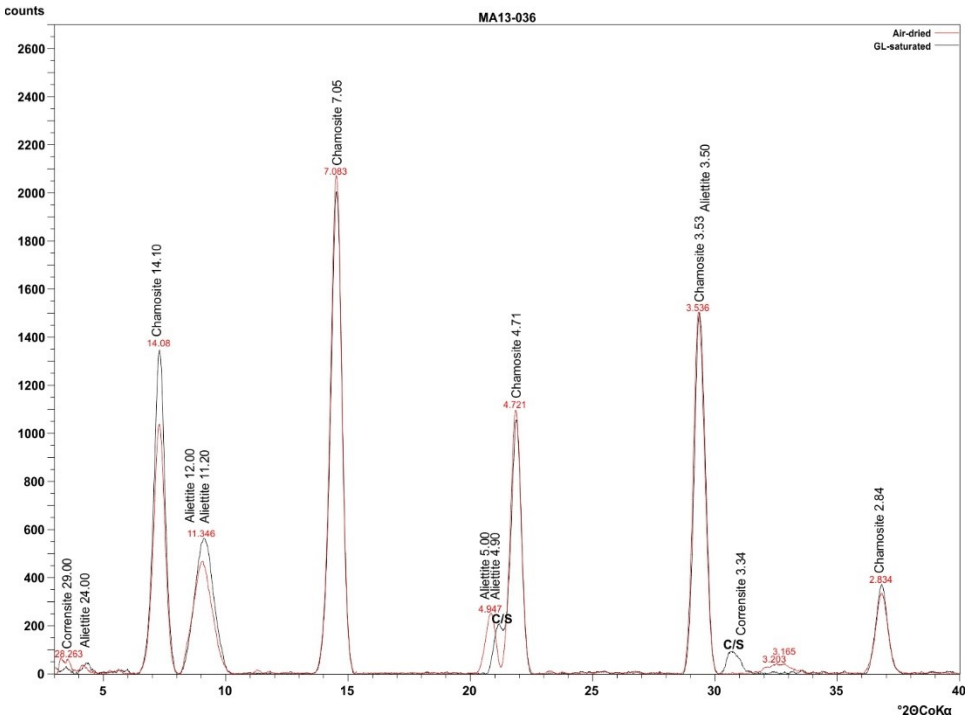


Fig. P33. Air-dried (red) and glycol-saturated (black) oriented XRD spectra of sample MA13-036, drillhole TKAD016 (7.00–7.05 mbsf).

Drillhole TKAD017

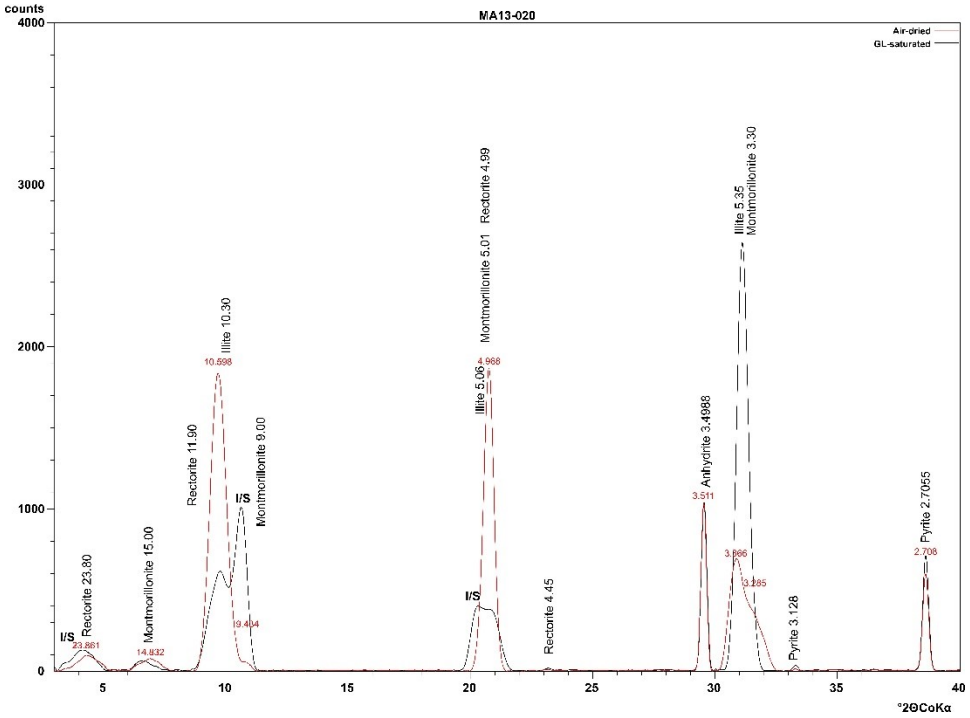


Fig. P34. Air-dried (red) and glycol-saturated (black) oriented XRD spectra of sample MA13-020, drillhole TKAD017 (6.90–7.00 mbsf).

Drillhole TKAD018

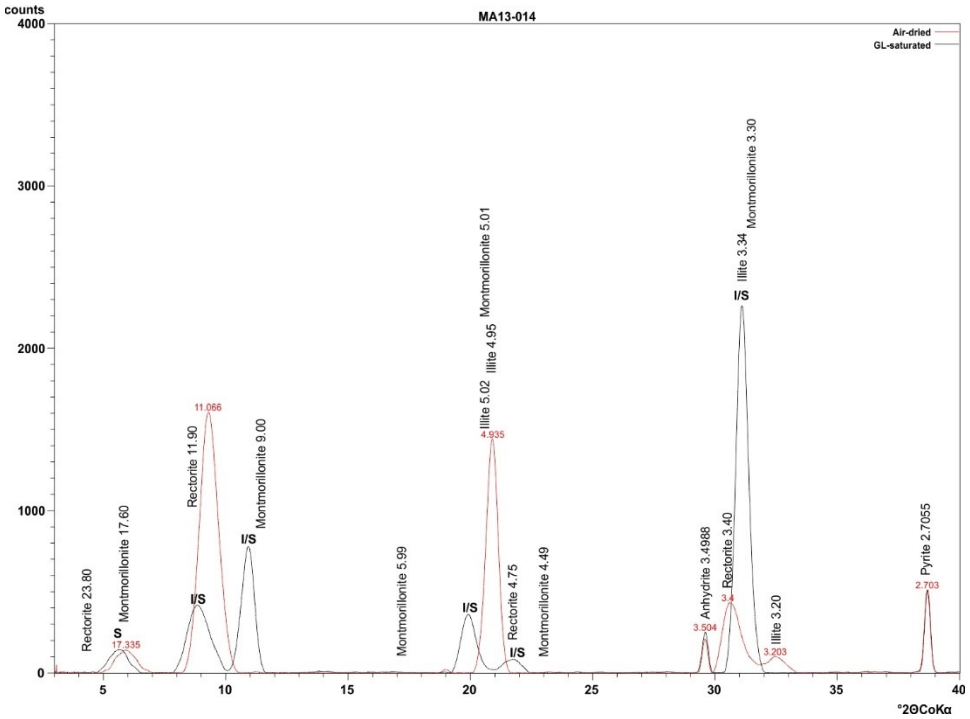


Fig. P35. Air-dried (red) and glycol-saturated (black) oriented XRD spectra of sample MA13-014, drillhole TKAD018 (3.00–3.10 mbsf).

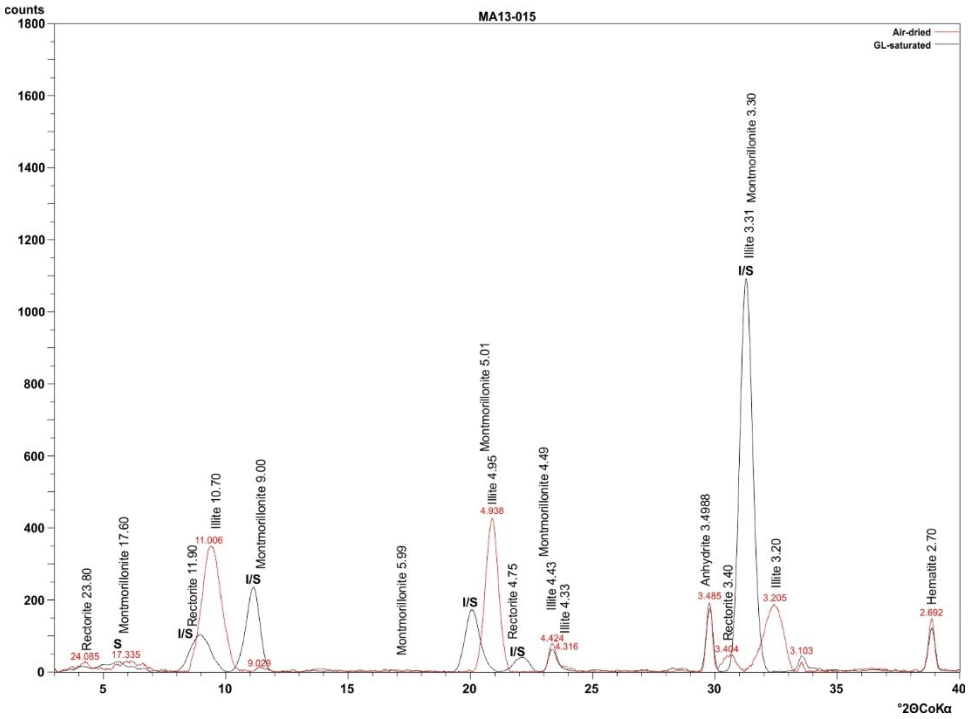


Fig. P36. Air-dried (red) and glycol-saturated (black) oriented XRD spectra of sample MA13-015, drillhole TKAD018 (5.00–5.10 mbsf).

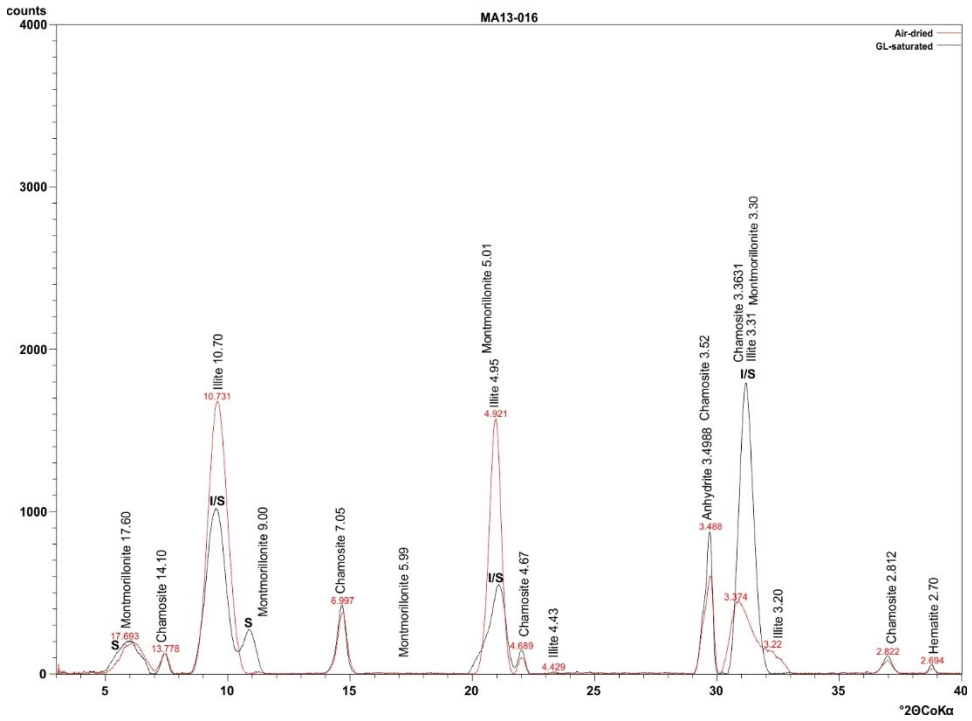


Fig. P37. Air-dried (red) and glycol-saturated (black) oriented XRD spectra of sample MA13-016, drillhole TKAD018 (6.60–6.71 mbsf).

Drillhole TKAD025

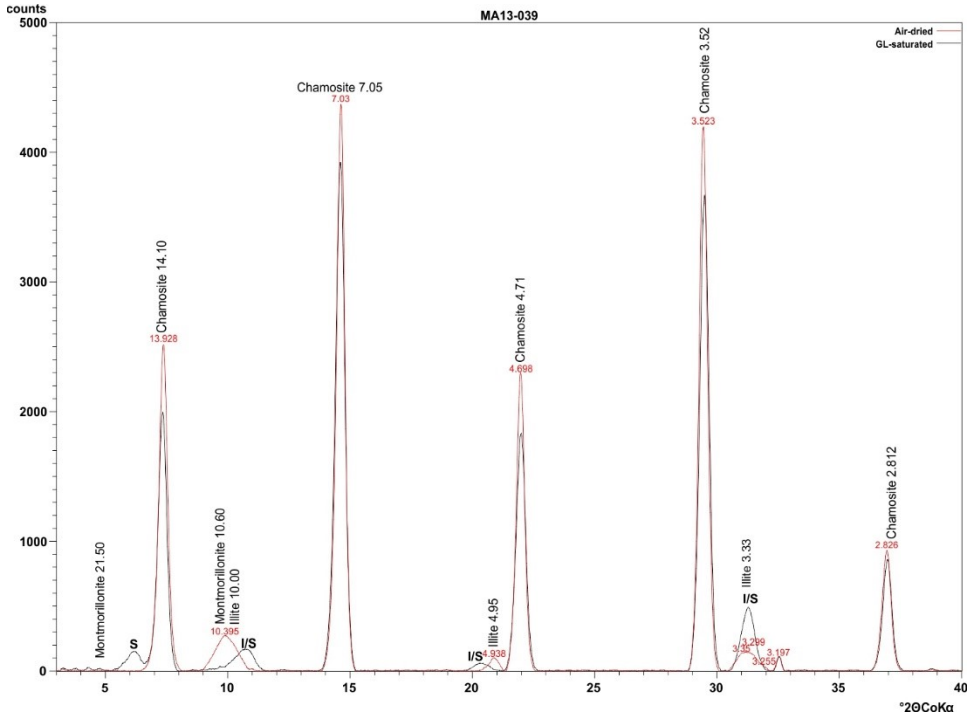


Fig. P38. Air-dried (red) and glycol-saturated (black) oriented XRD spectra of sample MA13-039, drillhole TKAD025 (5.50–5.60 mbsf).

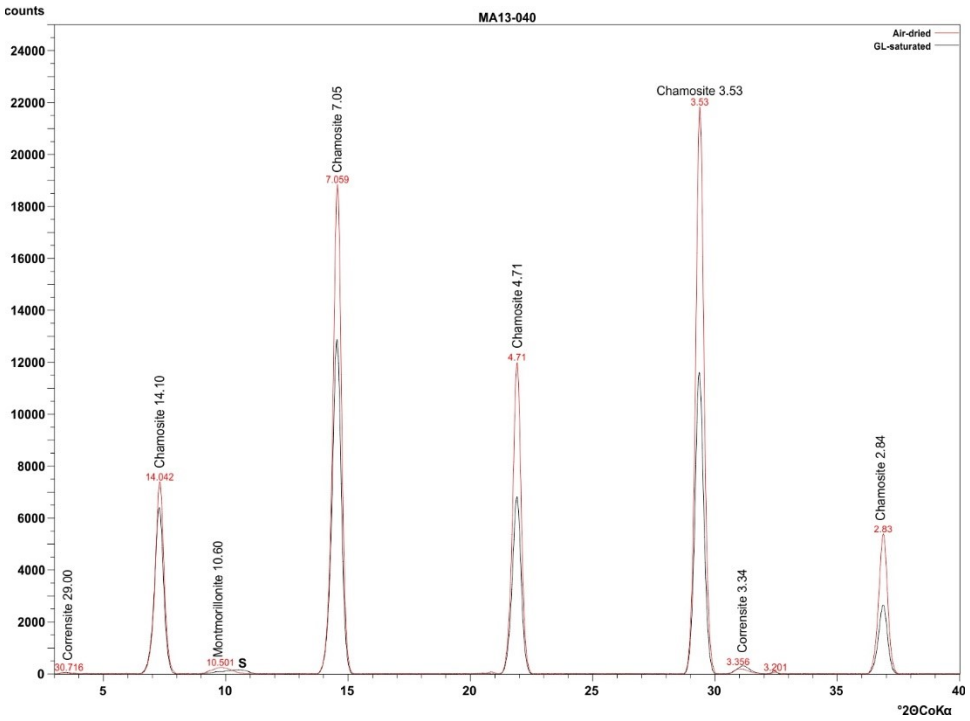


Fig. P39. Air-dried (red) and glycol-saturated (black) oriented XRD spectra of sample MA13-040, drillhole TKAD025 (6.91–7.00 mbsf).

Drillhole TKAD026

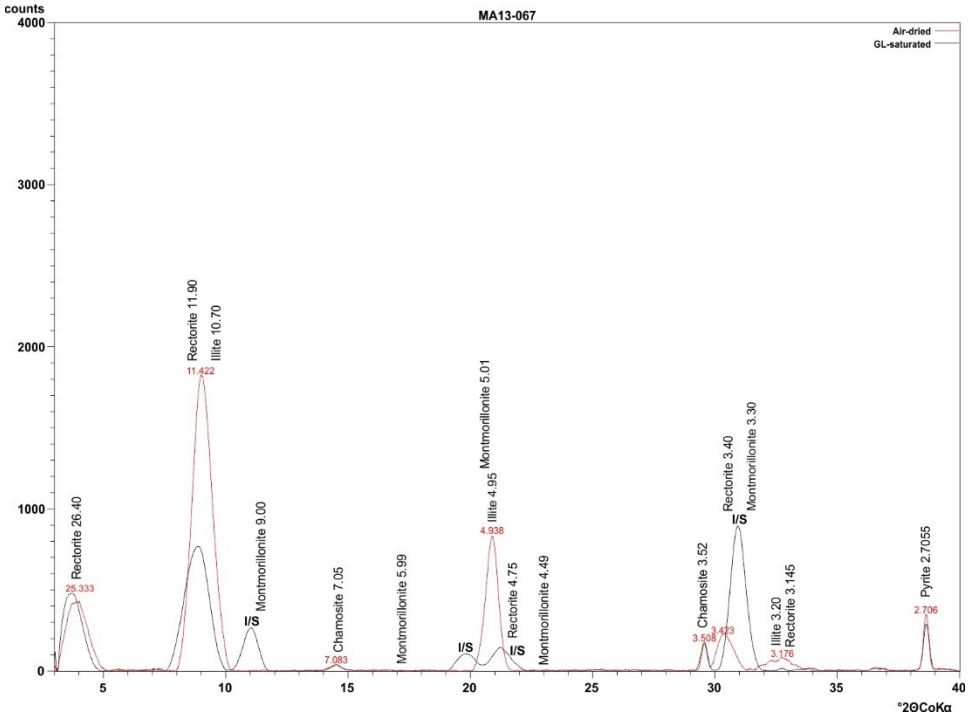


Fig. P40. Air-dried (red) and glycol-saturated (black) oriented XRD spectra of sample MA13-067, drillhole TKAD026 (2.90–3.00 mbsf).

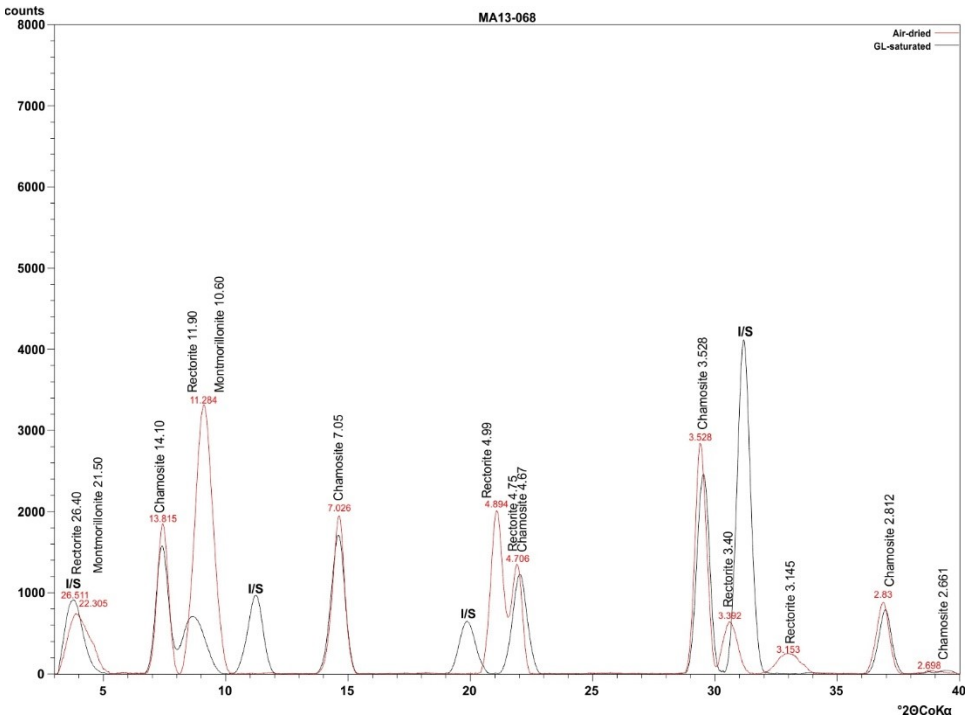


Fig. P41. Air-dried (red) and glycol-saturated (black) oriented XRD spectra of sample MA13-068, drillhole TKAD026 (3.60–3.68 mbsf).

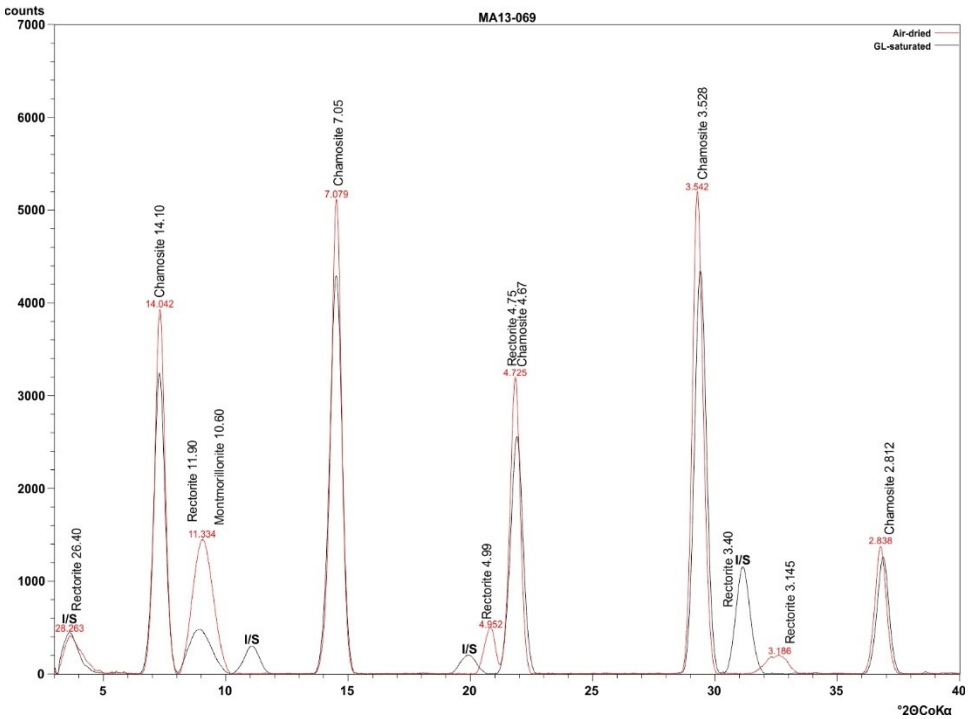


Fig. P42. Air-dried (red) and glycol-saturated (black) oriented XRD spectra of sample MA13-069, drillhole TKAD026 (5.64–5.75 mbsf).

Drillhole TKAD027

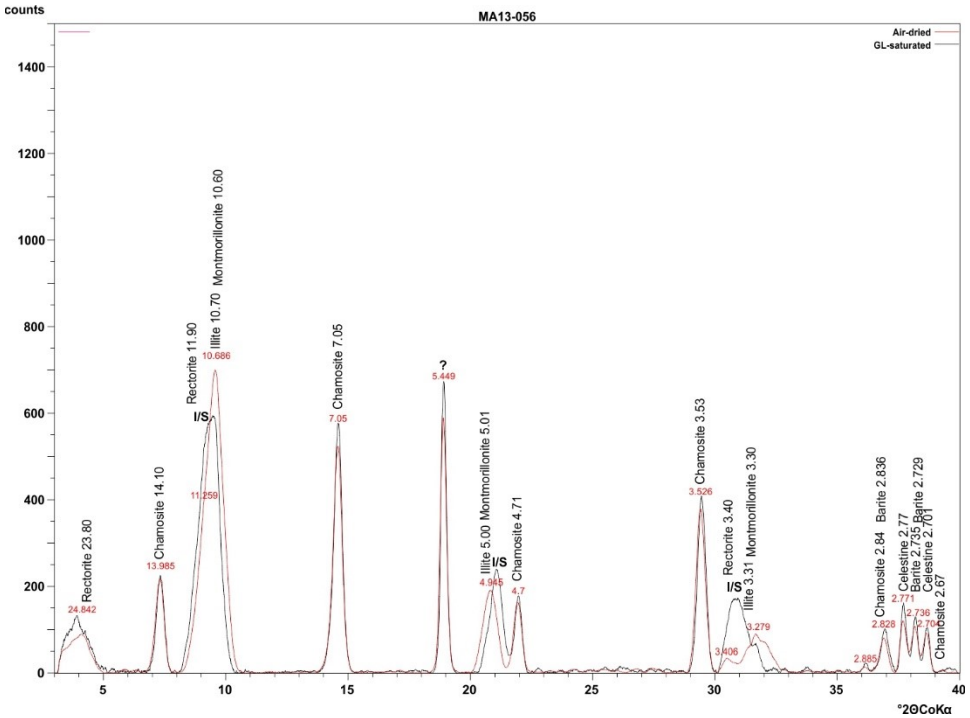


Fig. P43. Air-dried (red) and glycol-saturated (black) oriented XRD spectra of sample MA13-056, drillhole TKAD027 (2.50–2.60 mbsf).

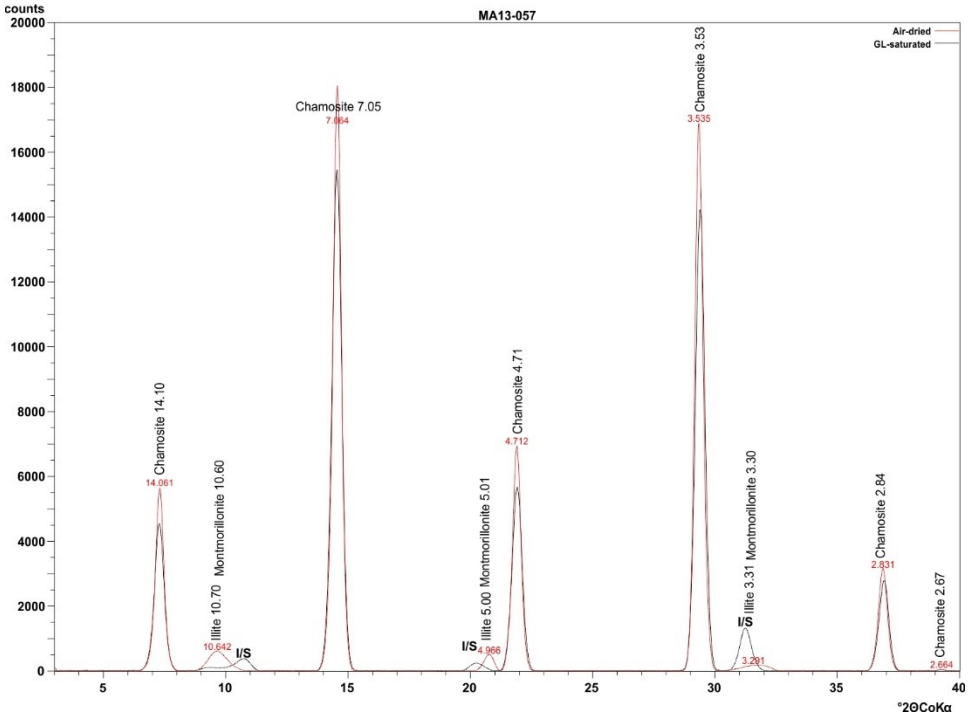


Fig. P44. Air-dried (red) and glycol-saturated (black) oriented XRD spectra of sample MA13-057, drillhole TKAD027 (4.60–4.70 mbsf).

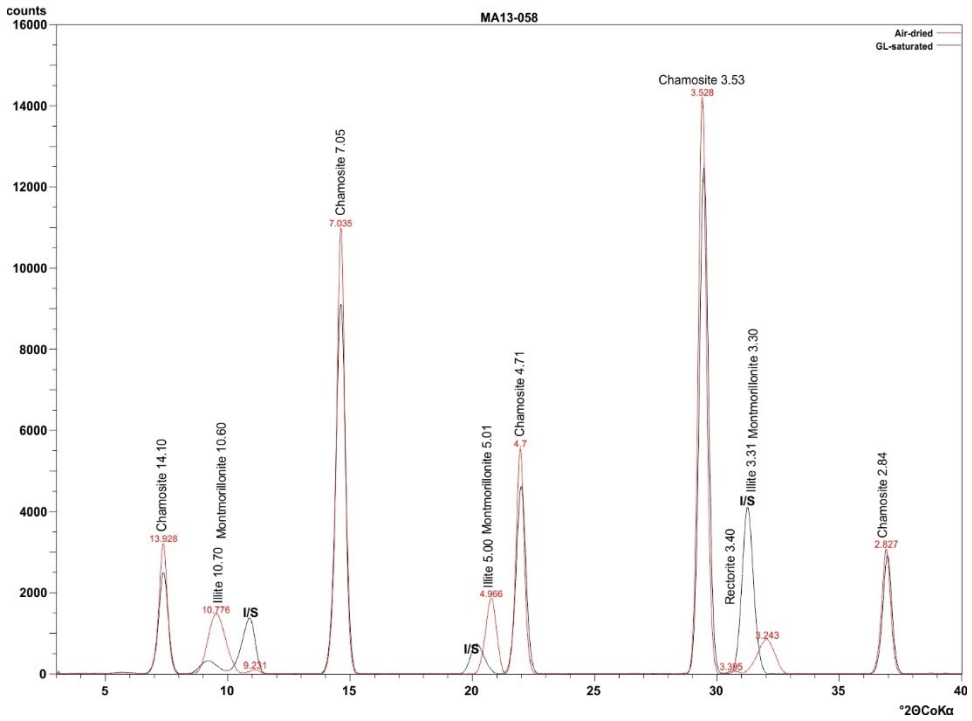


Fig. P45. Air-dried (red) and glycol-saturated (black) oriented XRD spectra of sample MA13-058, drillhole TKAD027 (6.50–6.59 mbsf).

Drillhole TKAD028

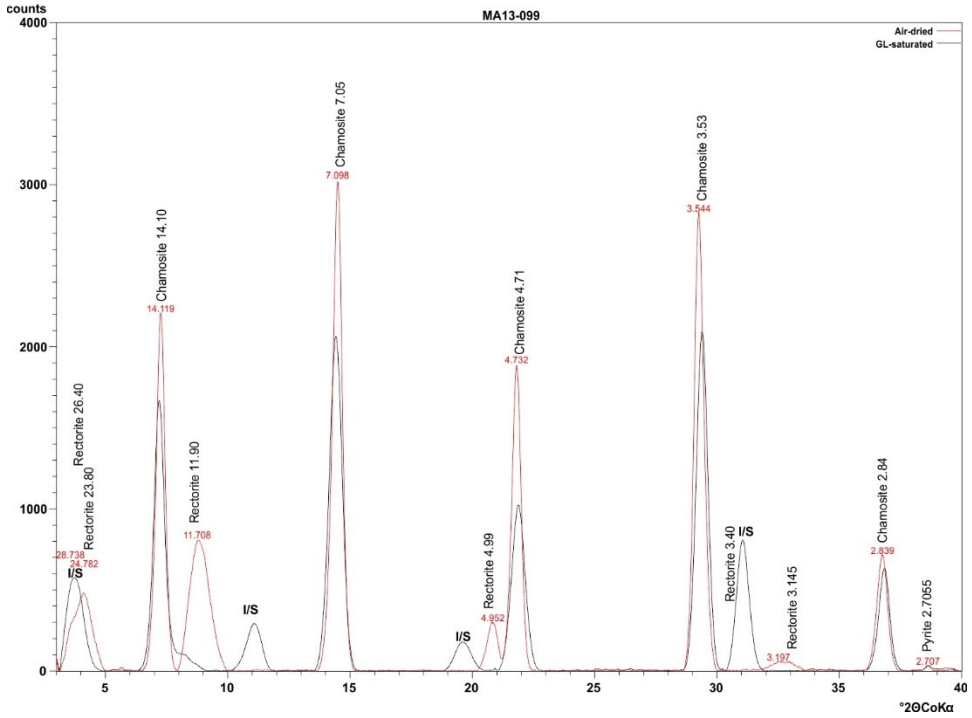


Fig. P46. Air-dried (red) and glycol-saturated (black) oriented XRD spectra of sample MA13-099, drillhole TKAD028 (4.50–4.60 mbsf).

Drillhole TKAD029

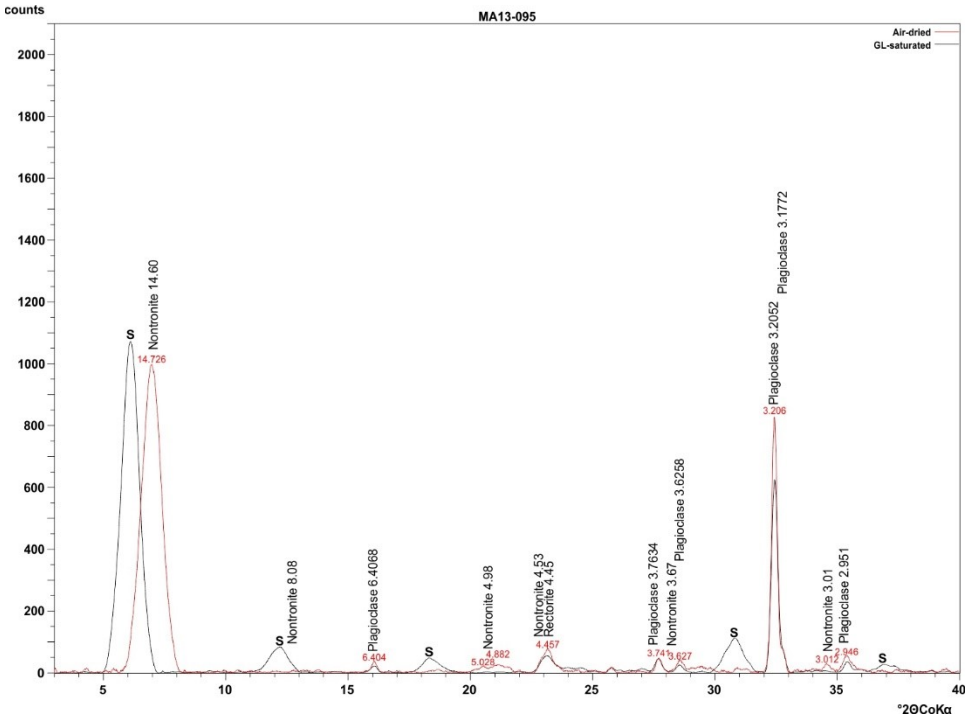


Fig. P47. Air-dried (red) and glycol-saturated (black) oriented XRD spectra of sample MA13-095, drillhole TKAD029 (3.60–3.70 mbsf).

Drillhole TKAD030

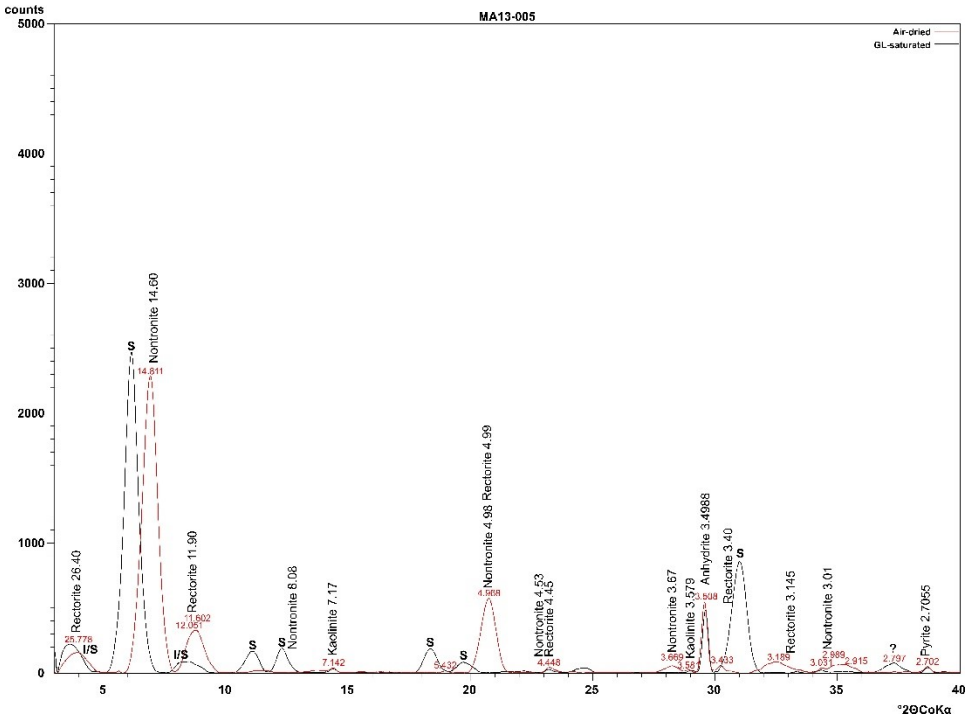


Fig. P48. Air-dried (red) and glycol-saturated (black) oriented XRD spectra of sample MA13-005, drillhole TKAD030 (5.06–5.21 mbsf).

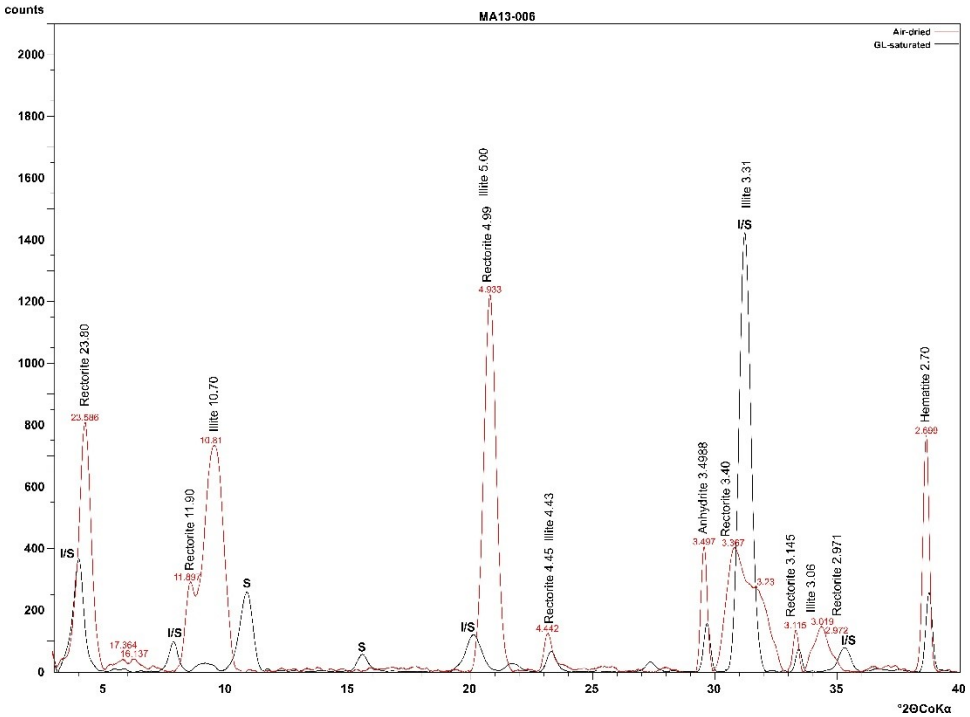


Fig. P49. Air-dried (red) and glycol-saturated (black) oriented XRD spectra of sample MA13-006, drillhole TKAD030 (6.45–6.60 mbsf).

Drillhole TKAD031

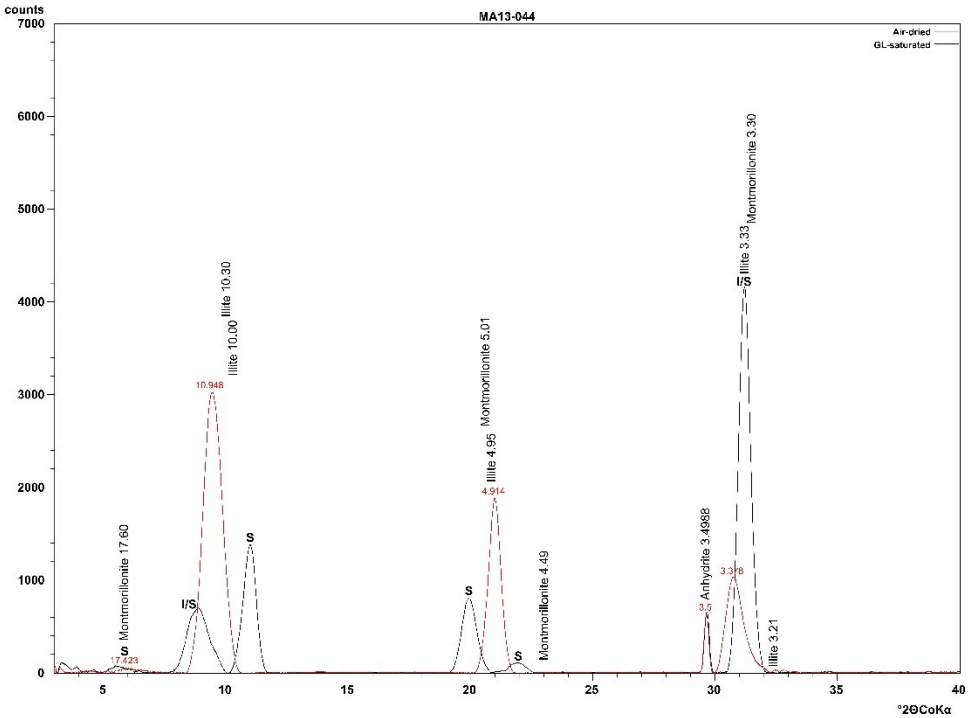


Fig. P50. Air-dried (red) and glycol-saturated (black) oriented XRD spectra of sample MA13-044, drillhole TKAD031 (5.64–5.69 mbsf).

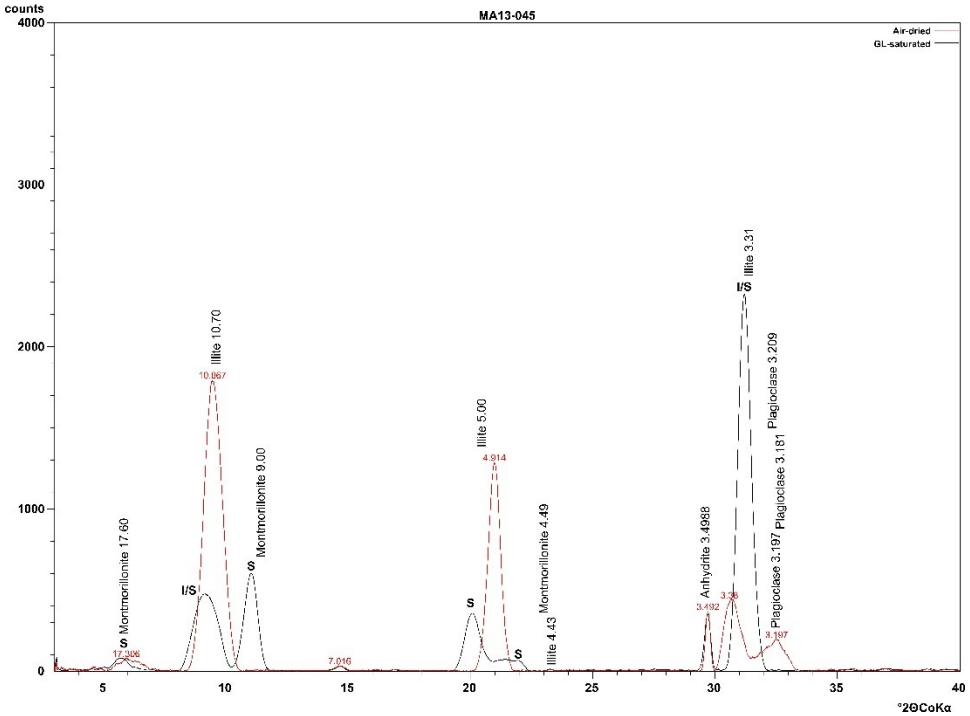


Fig. P51. Air-dried (red) and glycol-saturated (black) oriented XRD spectra of sample MA13-045, drillhole TKAD031 (6.60–6.67 mbsf).

Drillhole TKAD032

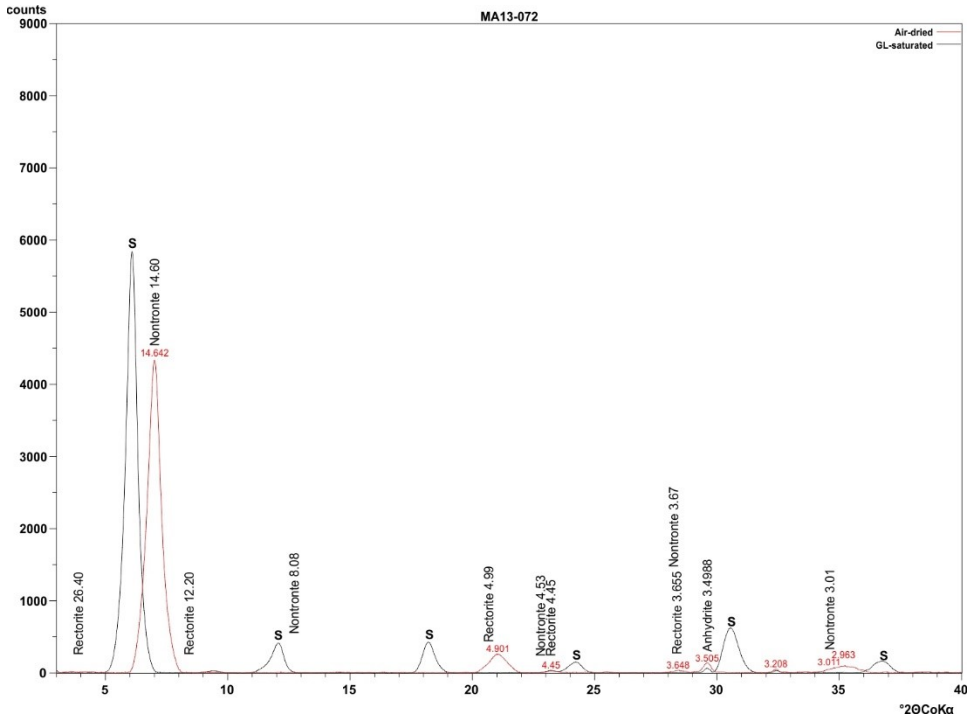


Fig. P52. Air-dried (red) and glycol-saturated (black) oriented XRD spectra of sample MA13-072, drillhole TKAD032 (2.05–2.17 mbsf).

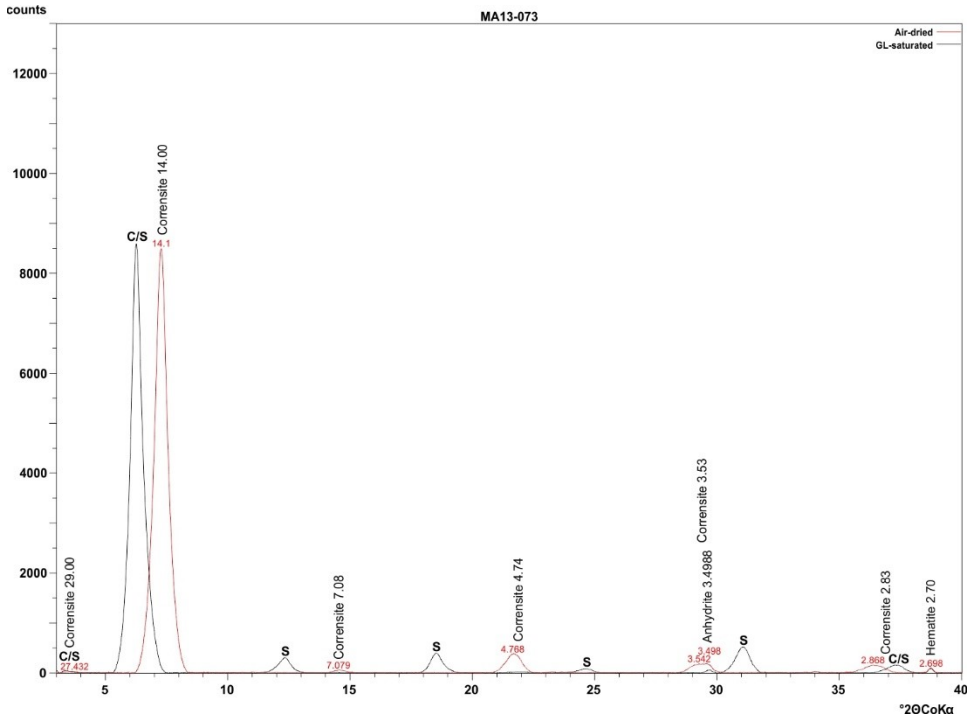


Fig. P53. Air-dried (red) and glycol-saturated (black) oriented XRD spectra of sample MA13-073, drillhole TKAD032 (3.90–4.00 mbsf).

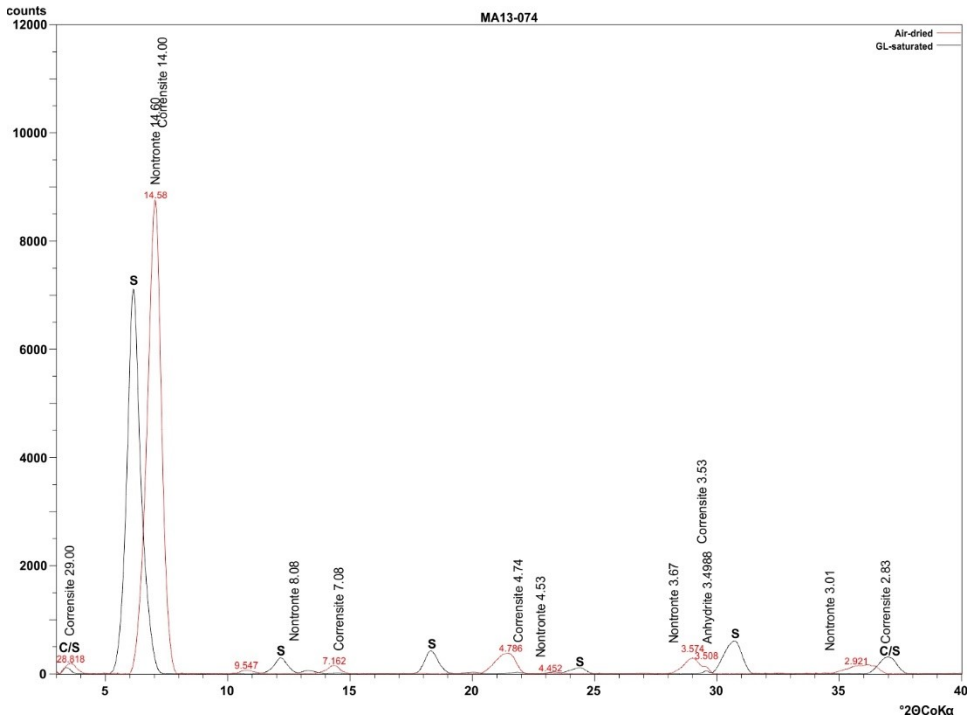


Fig. P54. Air-dried (red) and glycol-saturated (black) oriented XRD spectra of sample MA13-074, drillhole TKAD032 (5.31–5.40 mbsf).

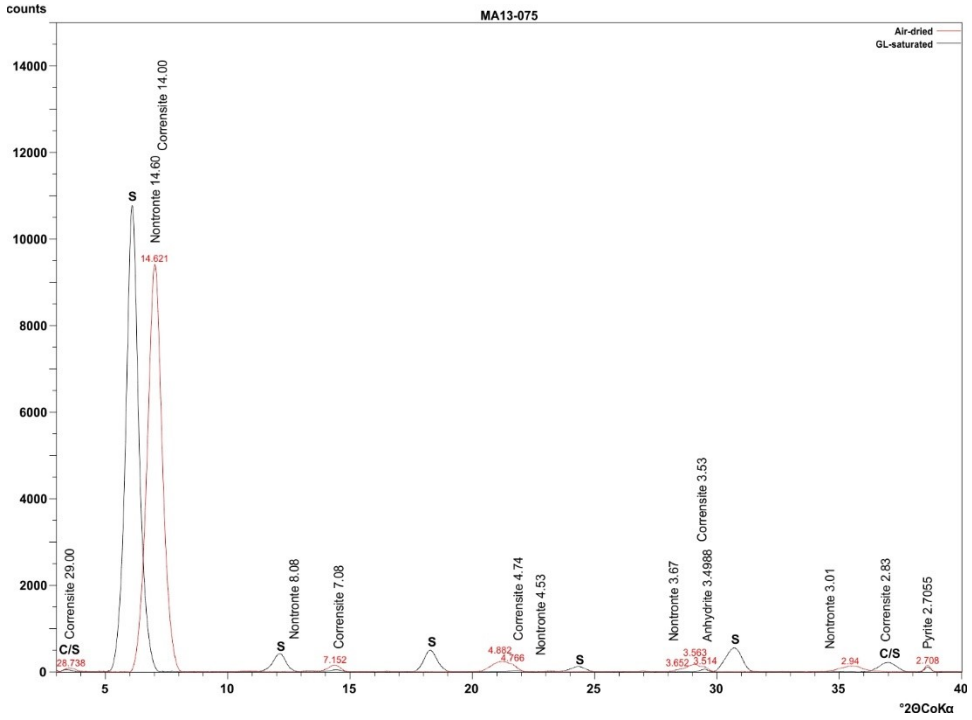


Fig. P55. Air-dried (red) and glycol-saturated (black) oriented XRD spectra of sample MA13-075, drillhole TKAD032 (6.42–6.54 mbsf).

Drillhole TKAD033

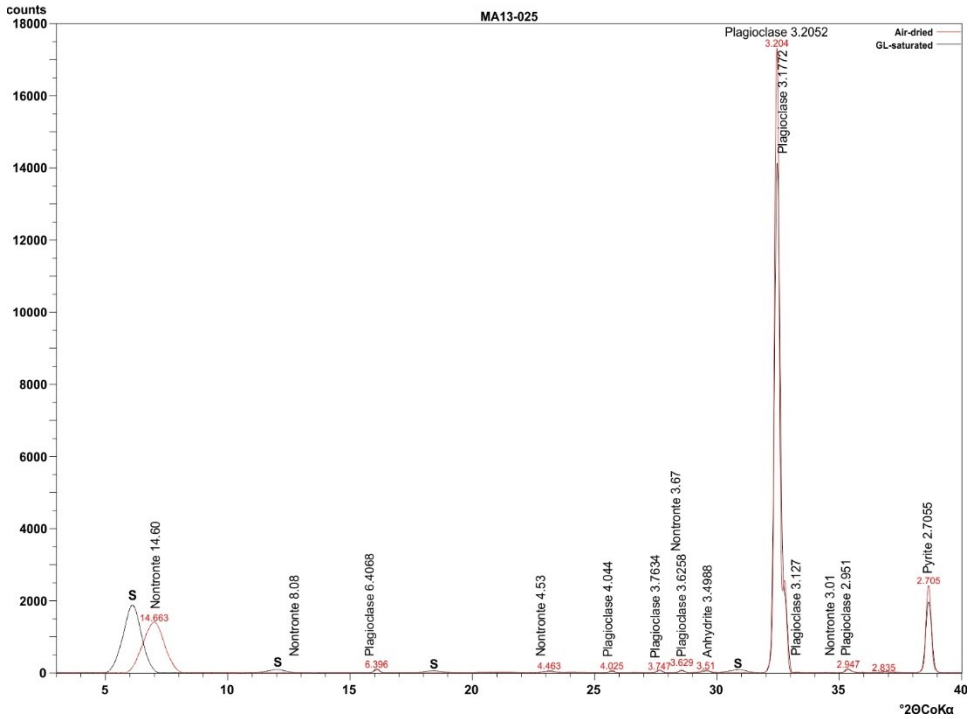


Fig. P56. Air-dried (red) and glycol-saturated (black) oriented XRD spectra of sample MA13-025, drillhole TKAD033 (3.00–3.10 mbsf).

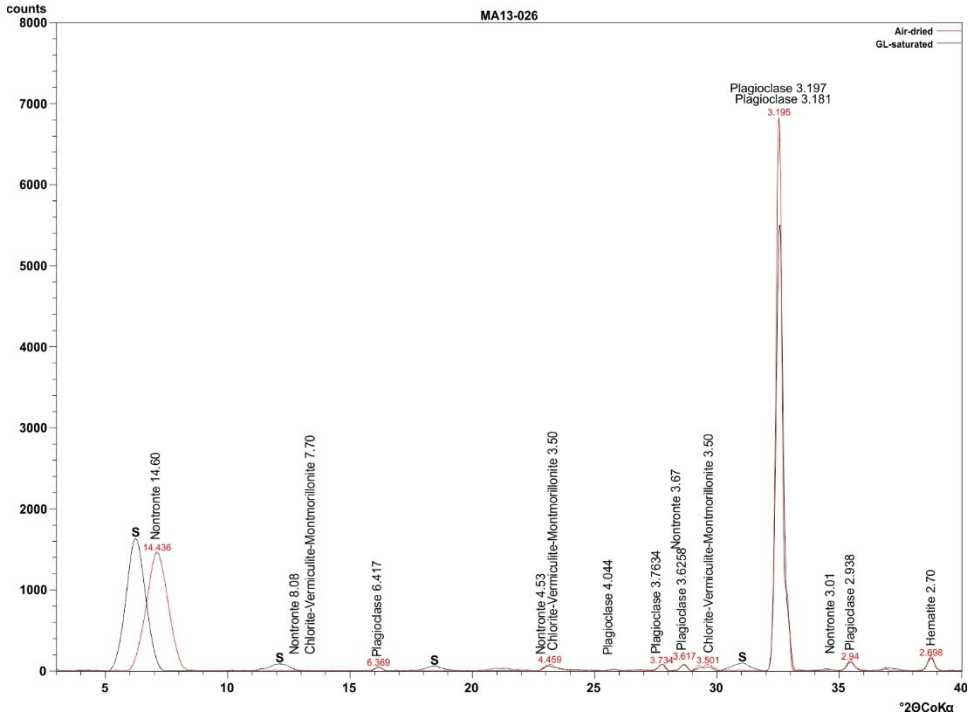


Fig. P57. Air-dried (red) and glycol-saturated (black) oriented XRD spectra of sample MA13-026, drillhole TKAD033 (4.76–4.88 mbsf).

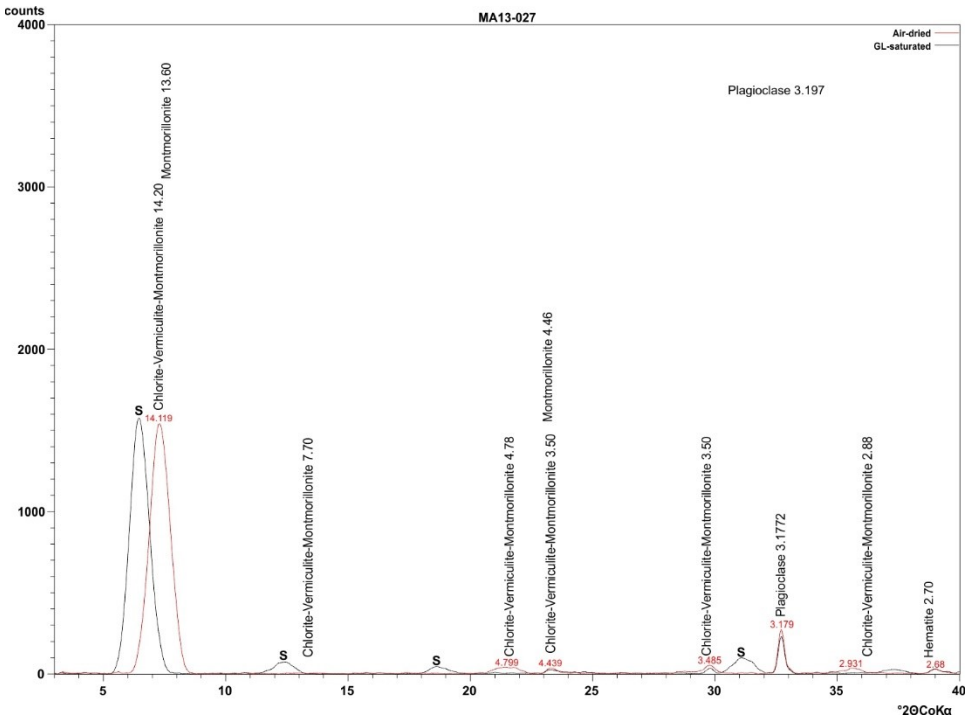


Fig. P58. Air-dried (red) and glycol-saturated (black) oriented XRD spectra of sample MA13-027, drillhole TKAD033 (7.30–7.40 mbsf).

Appendix Q

Supplementary Information for Chapter 6: Geological interpretation of volcanism and segmentation of the Mariana back-arc spreading center between 12.7°N and 18.3°N

Contents of this file:

1. Introduction
2. Neovolcanic volume calculations
3. Eruption rate calculations
4. Supplemental Figures Q1 to Q15
5. Supplemental Tables Q1 to Q2

1. Introduction

This supporting information includes an example of the types of remote sensing data used for geological interpretations (Fig. Q1), larger-sized geological legend and maps (Figs. Q2 to Q12), a closer look at the bathymetric features that further support the arguments made in the main text (Figs. Q13 and Q14), and methodologies used to calculate neovolcanic volumes (Fig. Q15; Table Q1) and eruption rates (Table Q2) along each of the segments.

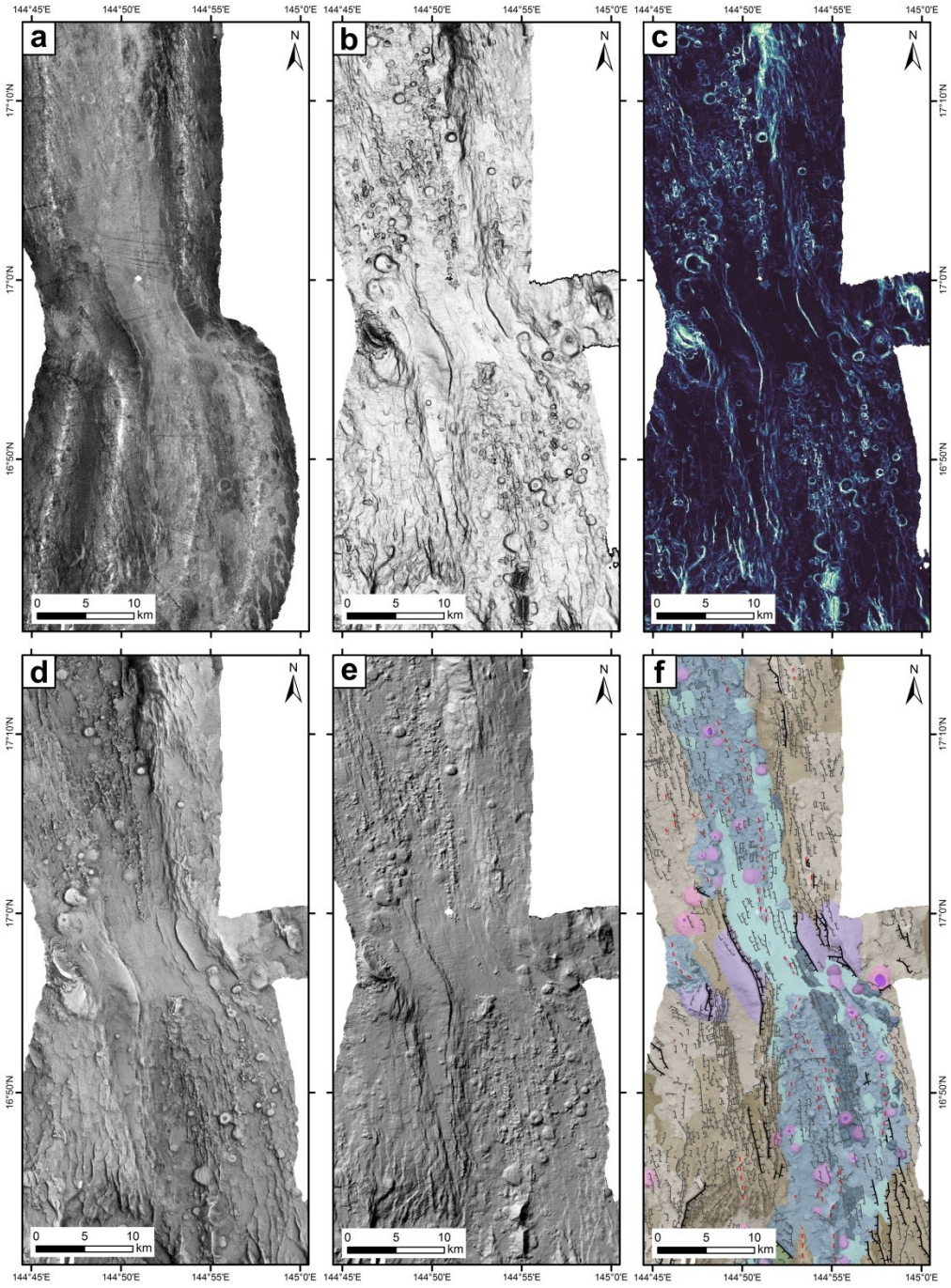


Figure Q1. Examples of bathymetric data used to support the geological interpretations (segment 18.1°N): (a) acoustic backscatter, with high intensities in white and low intensities in black; (b) slope, with high slopes in black, to a maximum slope of 40°, and flat areas in white; (c) seafloor roughness calculated as the standard deviation of elevation, with rough terrains in lighter colors and flat terrain in dark colors (GIS script from Evans et al., 2014); (d) terrain-texture-shaded bathymetry that uses a diffuse light source (see text for details); (e) traditional hill-shaded bathymetry; and (f) geological interpretations (50% transparency) overlayed on a basemap that combines TTS-processed bathymetry (50% transparency) and hill-shaded bathymetry, following the legend in Figs. 5.5–5.14 (main text).

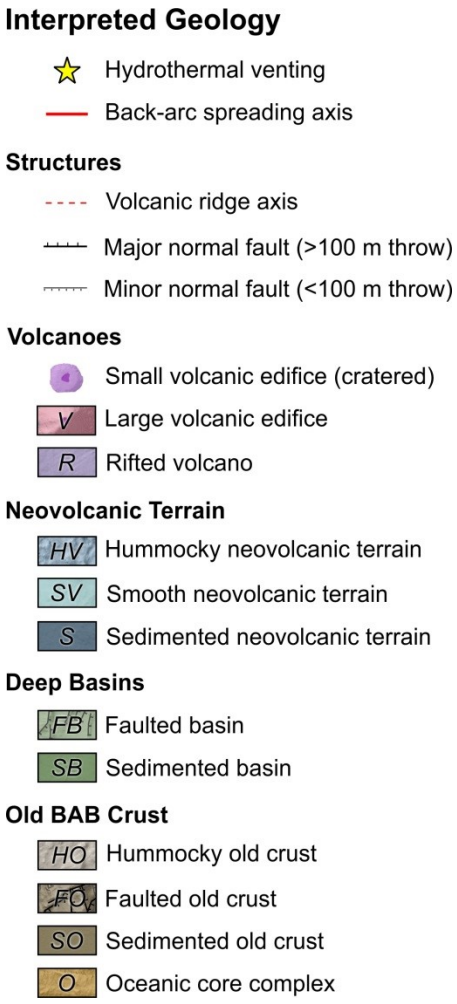


Figure Q2. Legend of the structures and mapped units for all subsequent geological maps (Figs. Q3-Q12) in order of generally increasing relative age. Locations of hydrothermal vent sites from Resing et al. (2016) and Baker et al. (2016).

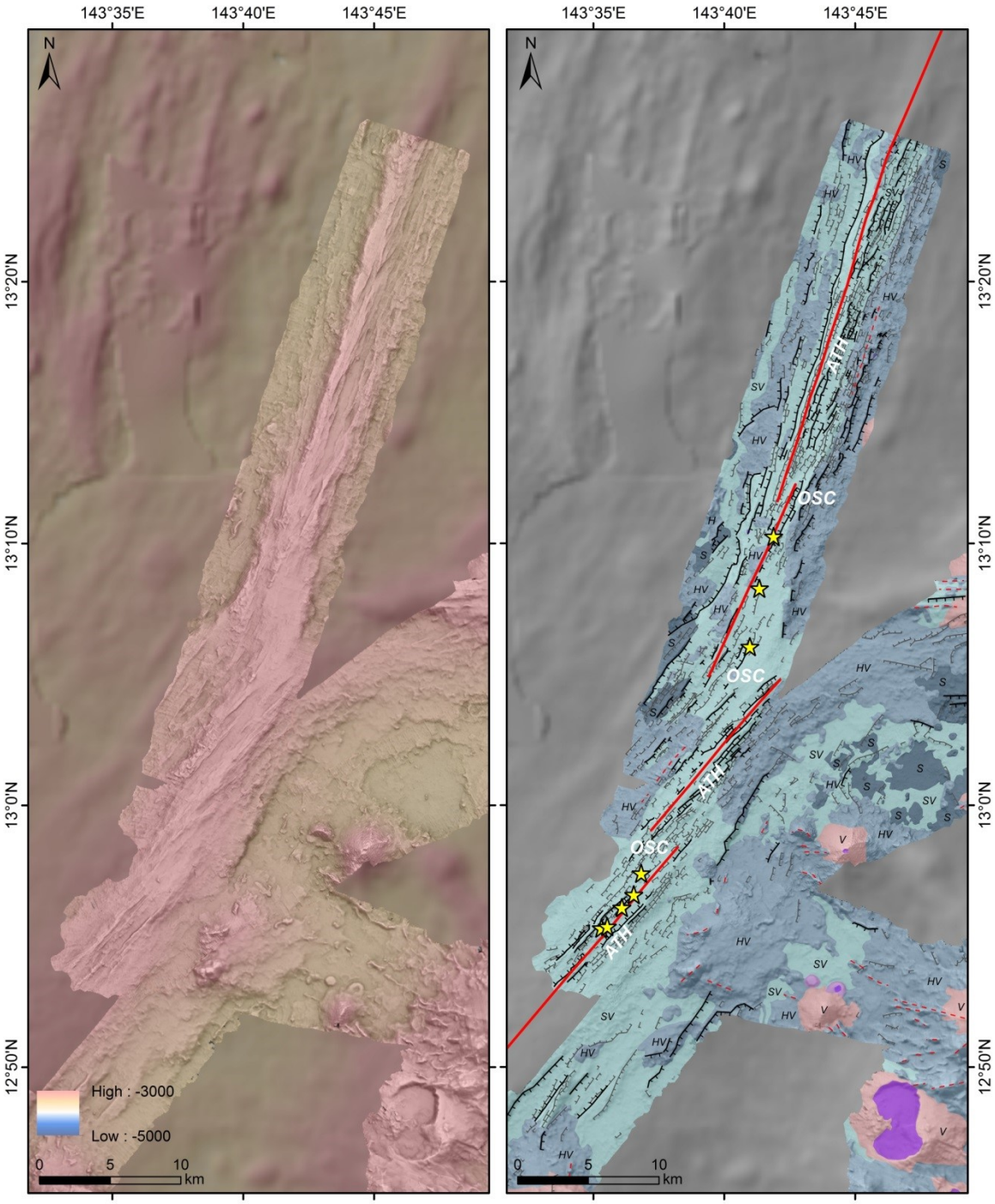


Figure Q3. Bathymetry (left) and interpreted geology (right) of the 12.8°N and 13.3°N segments, following the legend in Fig. Q2. ATH = axial topographic high; OSC = overlapping spreading center. See Figure 5.5 (main text) for more information.

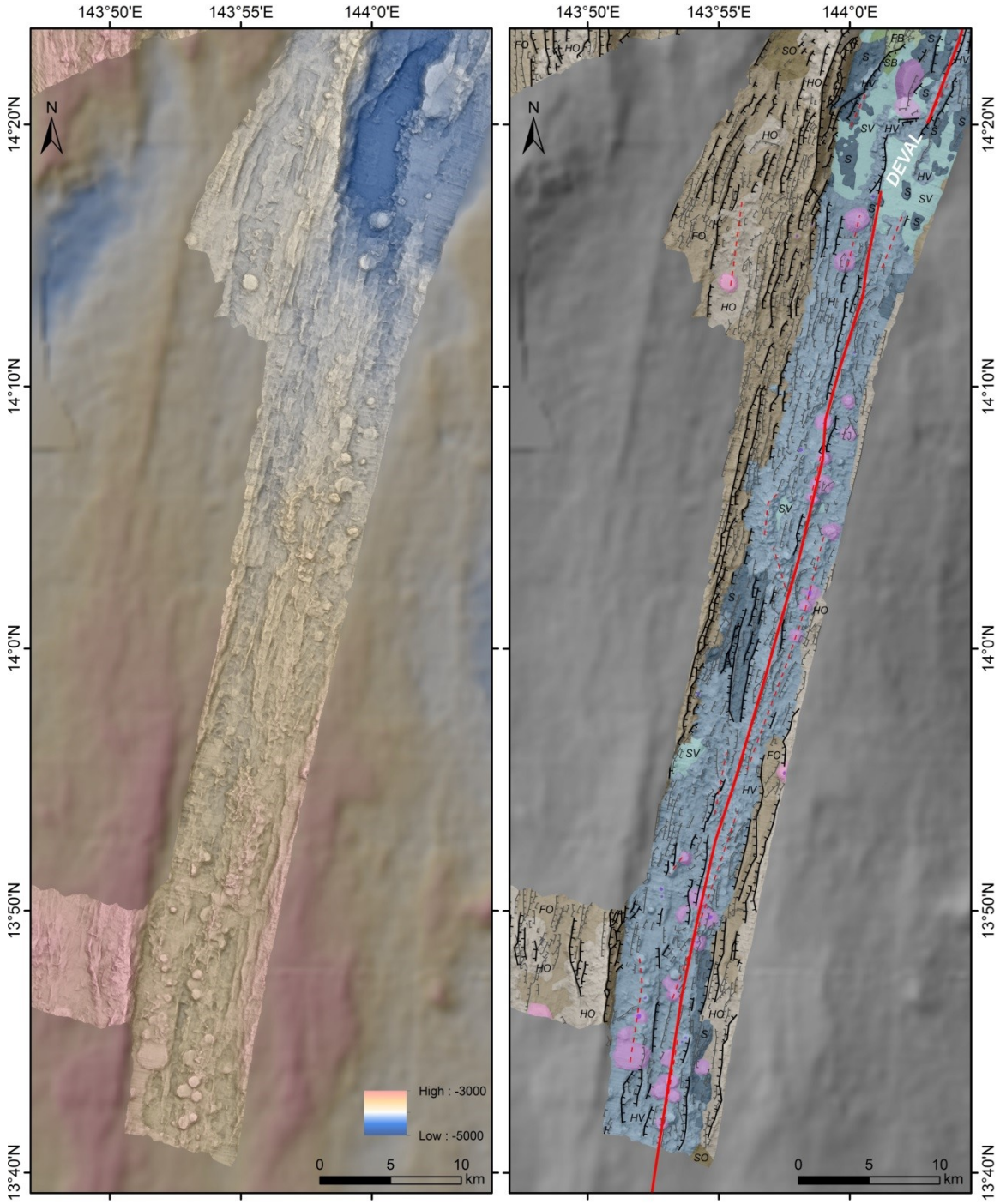


Figure Q4. Bathymetry (left) and interpreted geology (right) of the 13.9°N segment, following the legend in Fig. Q2. DEVAL = deviation in axial linearity. See Figure 5.6 (main text) for more information.

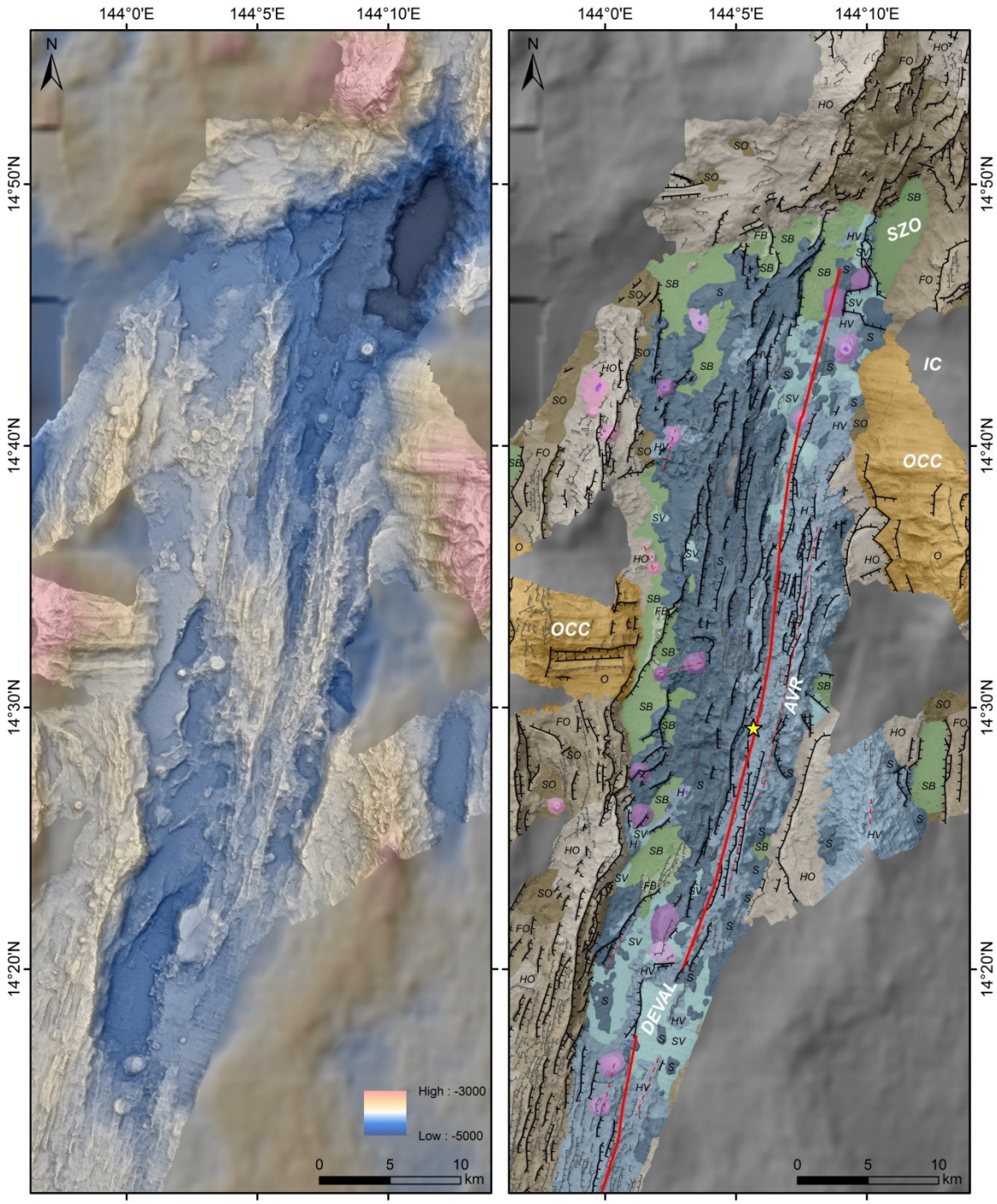


Figure Q5. Bathymetry (left) and interpreted geology (right) of the 14.5°N segment, following the legend in Fig. Q2. AVR = axial volcanic ridge; DEVAL = deviation in axial linearity; IC = inside corner high; OCC = oceanic core complex. See Figure 5.7 (main text) for more information.

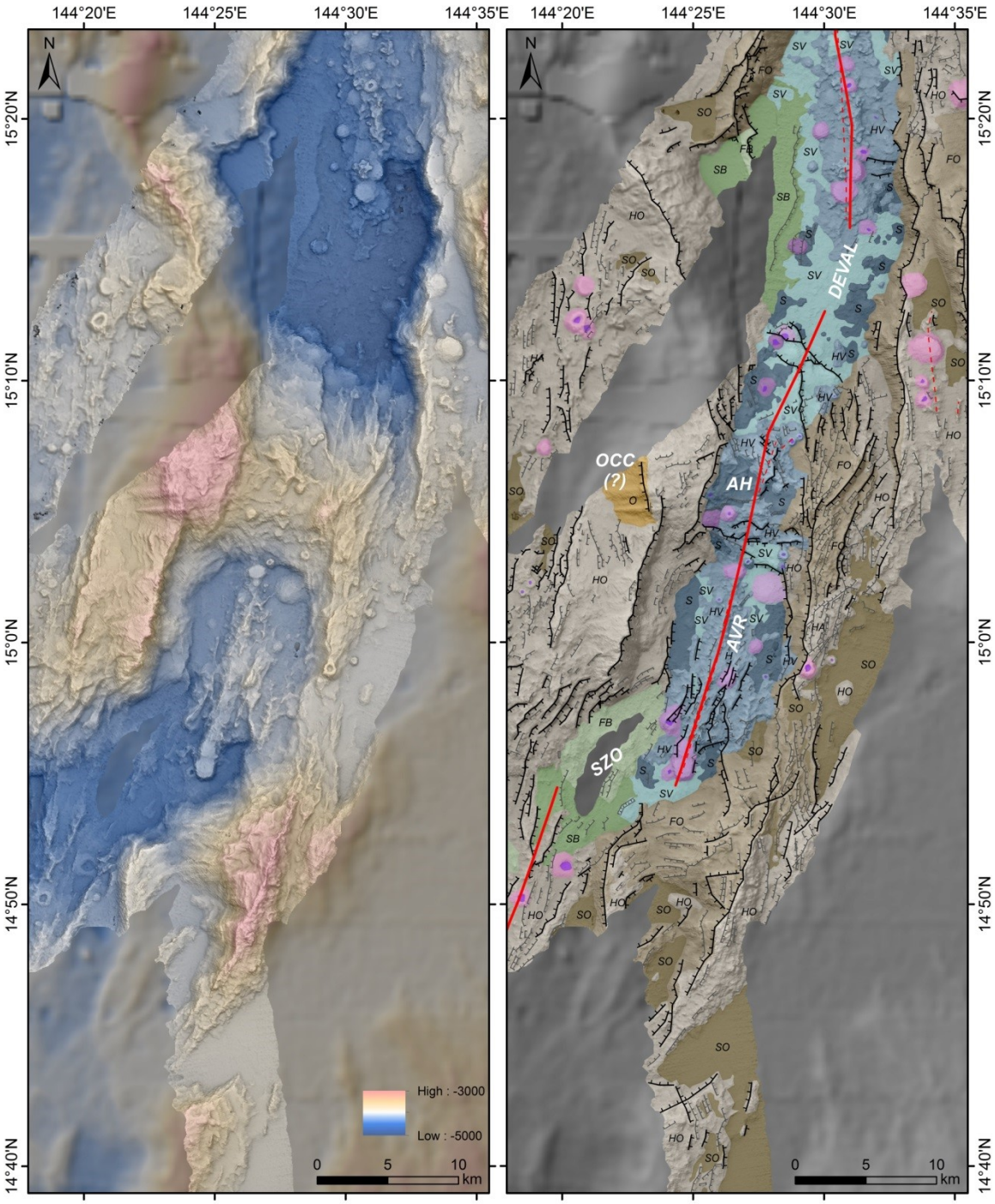


Figure Q6. Bathymetry (left) and interpreted geology (right) of the 15.1°N segment, following the legend in Fig. Q2. AH = axial high; AVR = axial volcanic ridge; DEVAL = deviation in axial linearity; OCC(?) = possible oceanic core complex. See Figure 5.8 (main text) for more information.

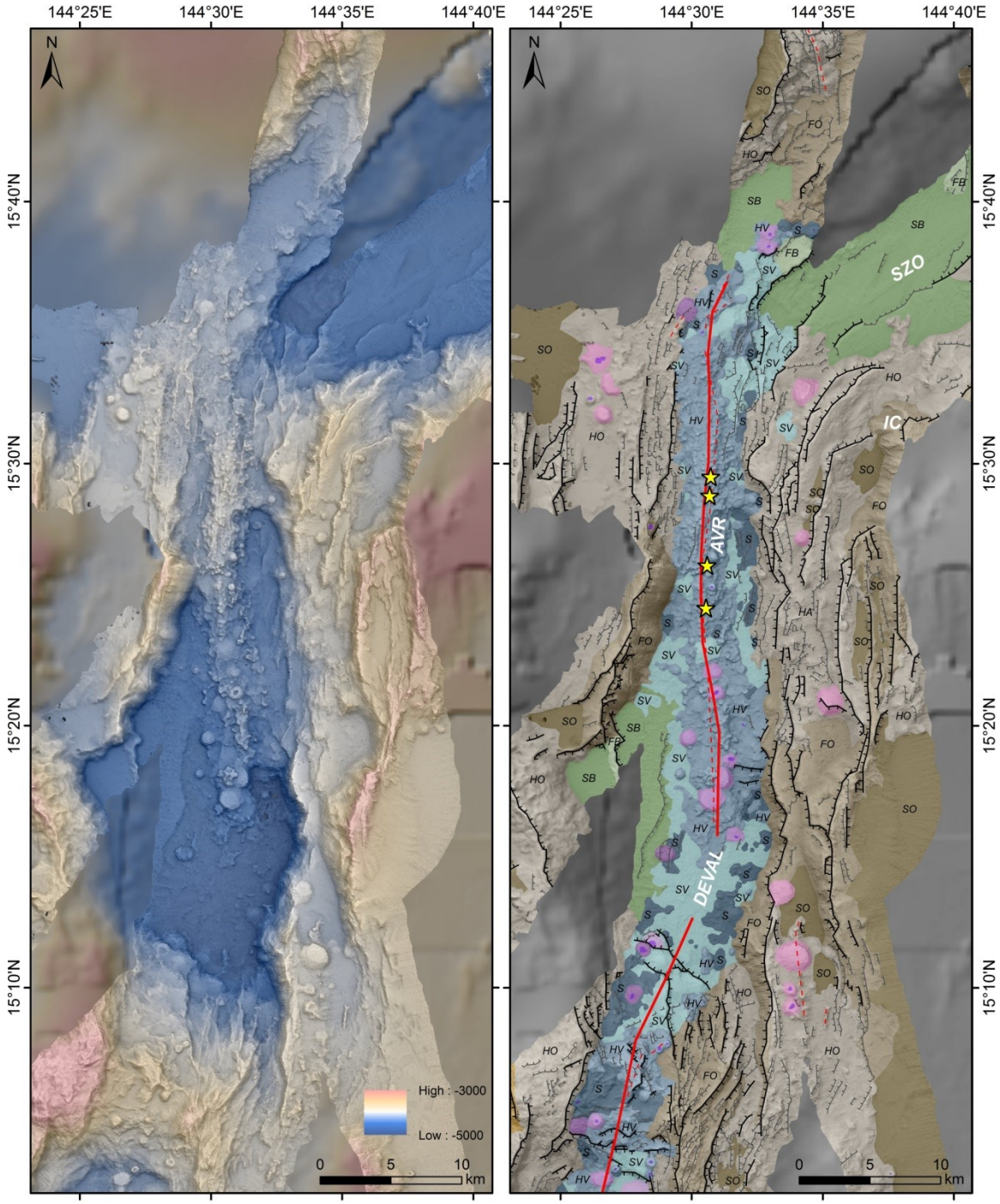


Figure Q7. Bathymetry (left) and interpreted geology (right) of the 15.5°N segment, following the legend in Fig. Q2. AVR = axial volcanic ridge; DEVAL = deviation from axial linearity; IC = inside corner high. See Figure 5.9 (main text) for more information.

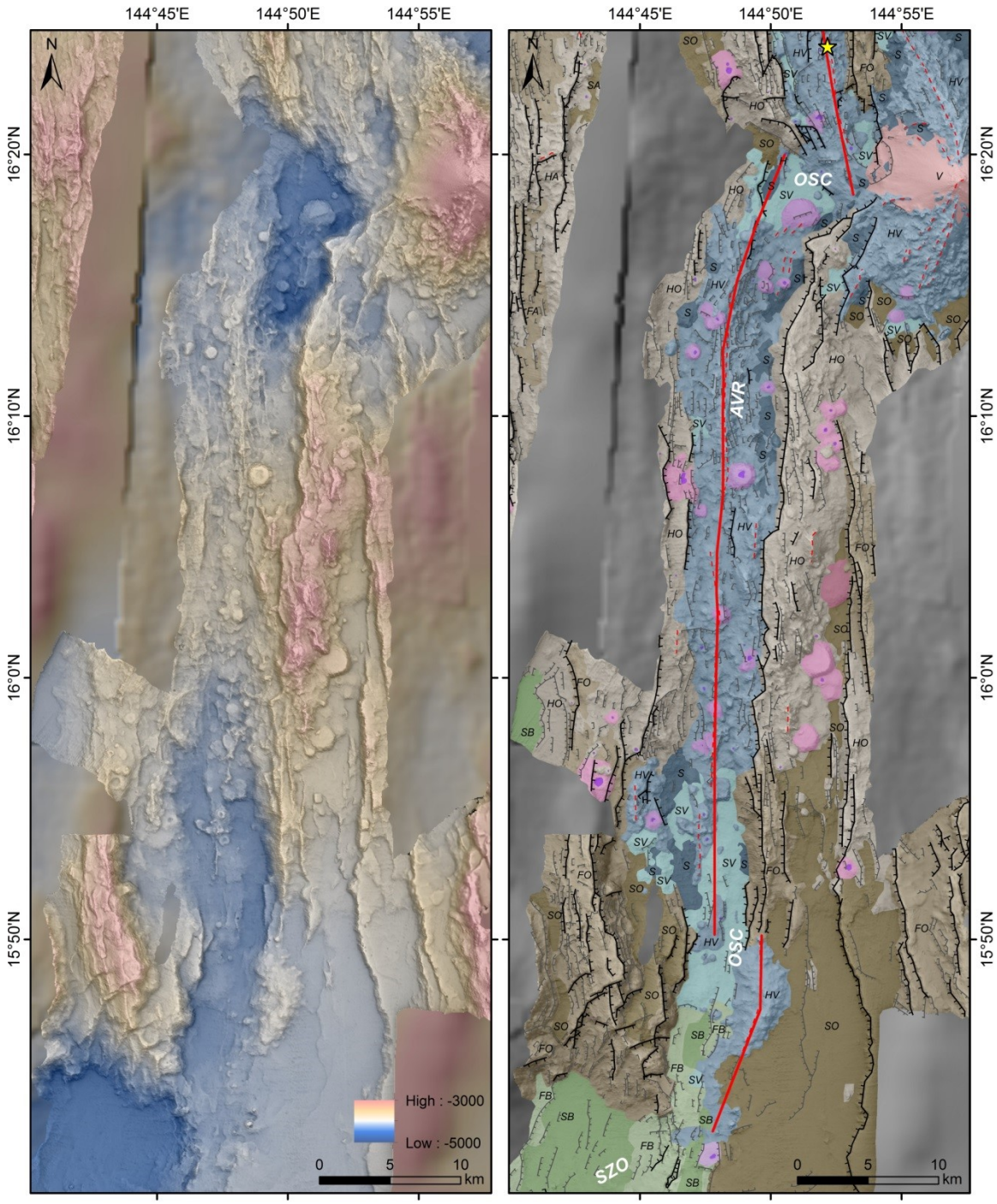


Figure Q8. Bathymetry (left) and interpreted geology (right) of the 16.1°N segment, following the legend **in Fig. Q2. AVR = axial volcanic ridge; OSC = overlapping spreading center. See Figure 5.10** (main text) for more information.

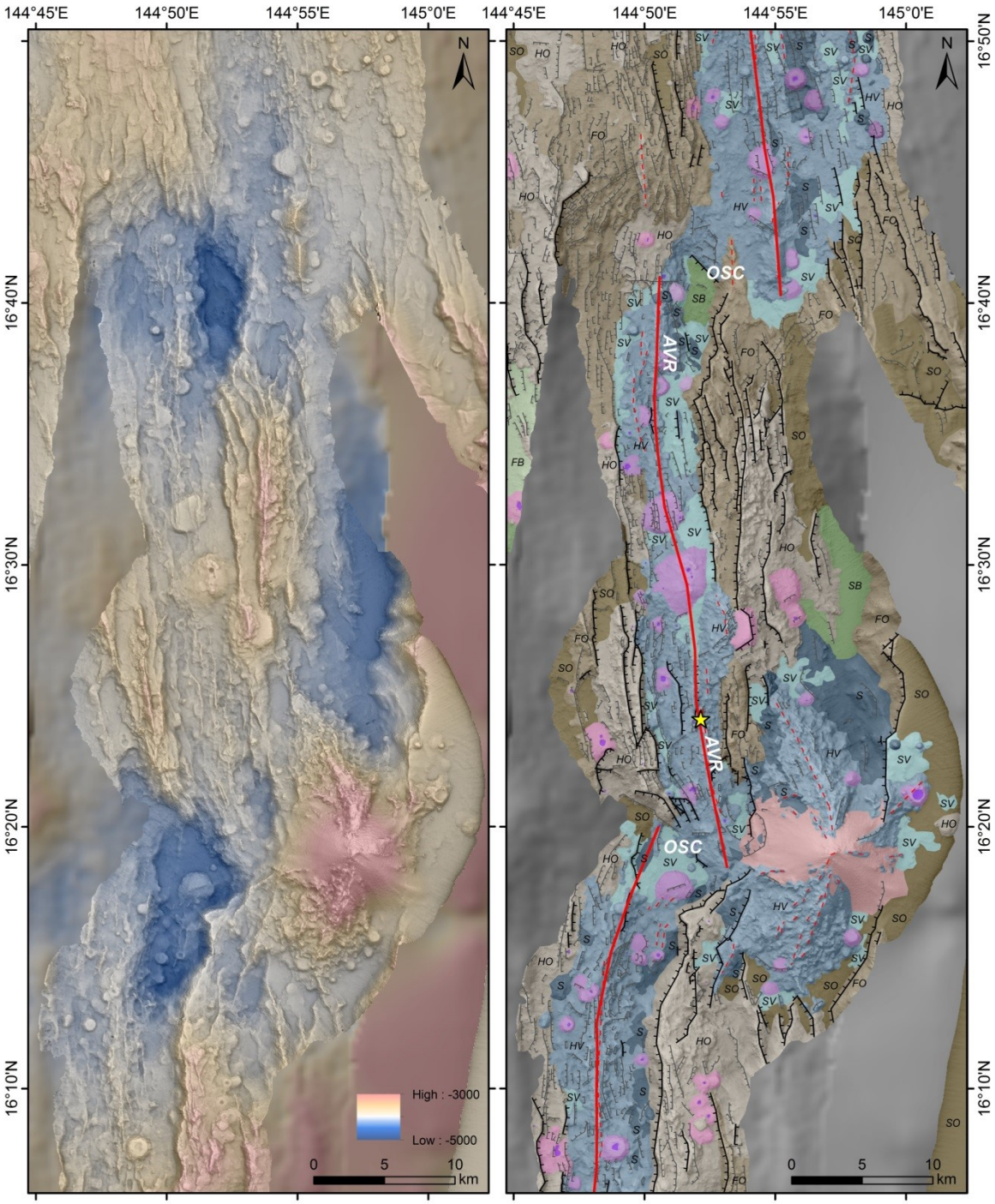


Figure Q9. Bathymetry (left) and interpreted geology (right) of the 16.5°N segment, following the legend in Fig. Q2. AVR = axial volcanic ridge; OSC = overlapping spreading center. See Figure 5.11 (main text) for more information.

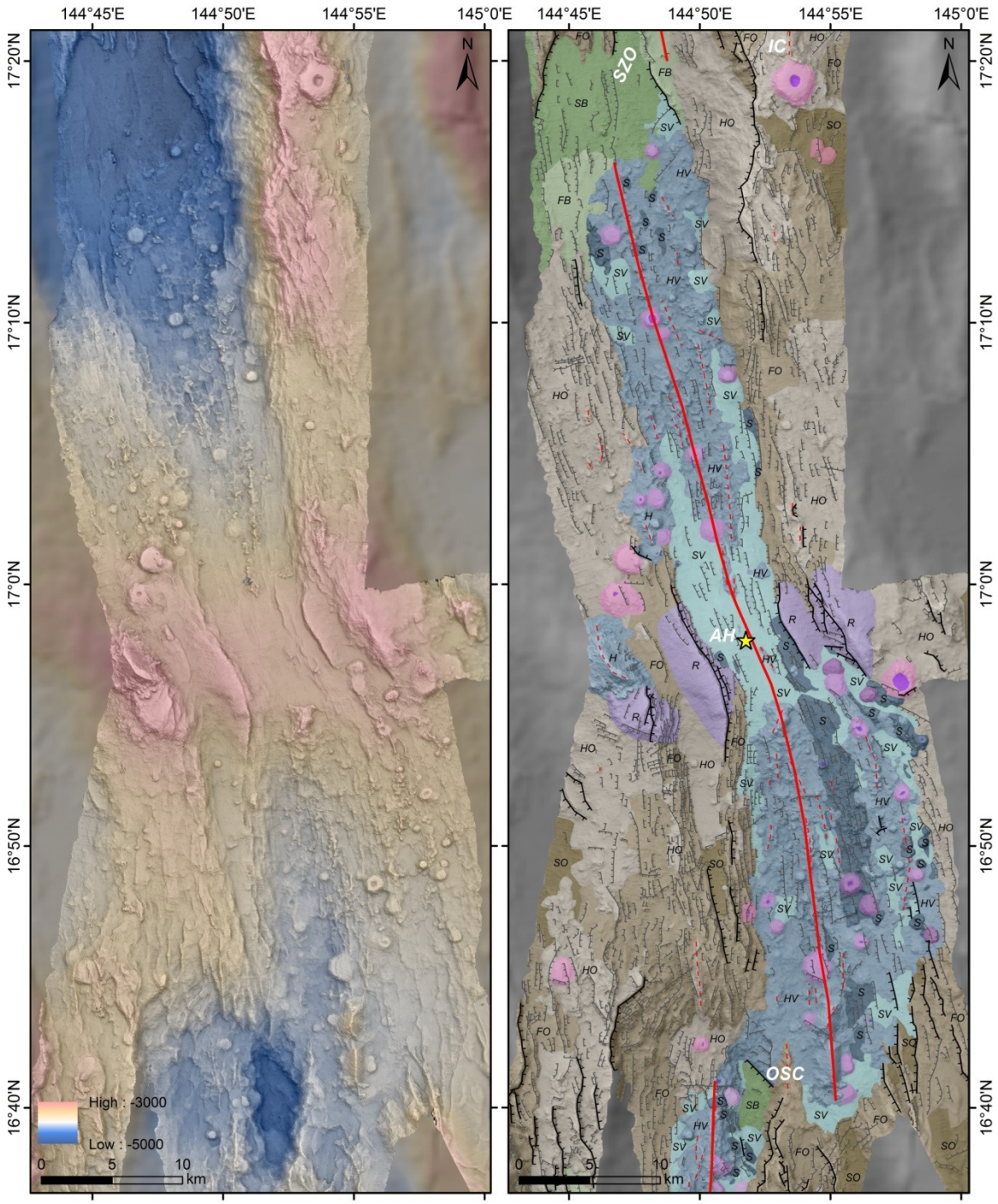


Figure Q10. Bathymetry (left) and interpreted geology (right) of the 17.0°N segment, following the legend in Fig. Q2. AH = axial high; IC = inside corner high; OSC = overlapping spreading center. See Figure 5.12 (main text) for more information.

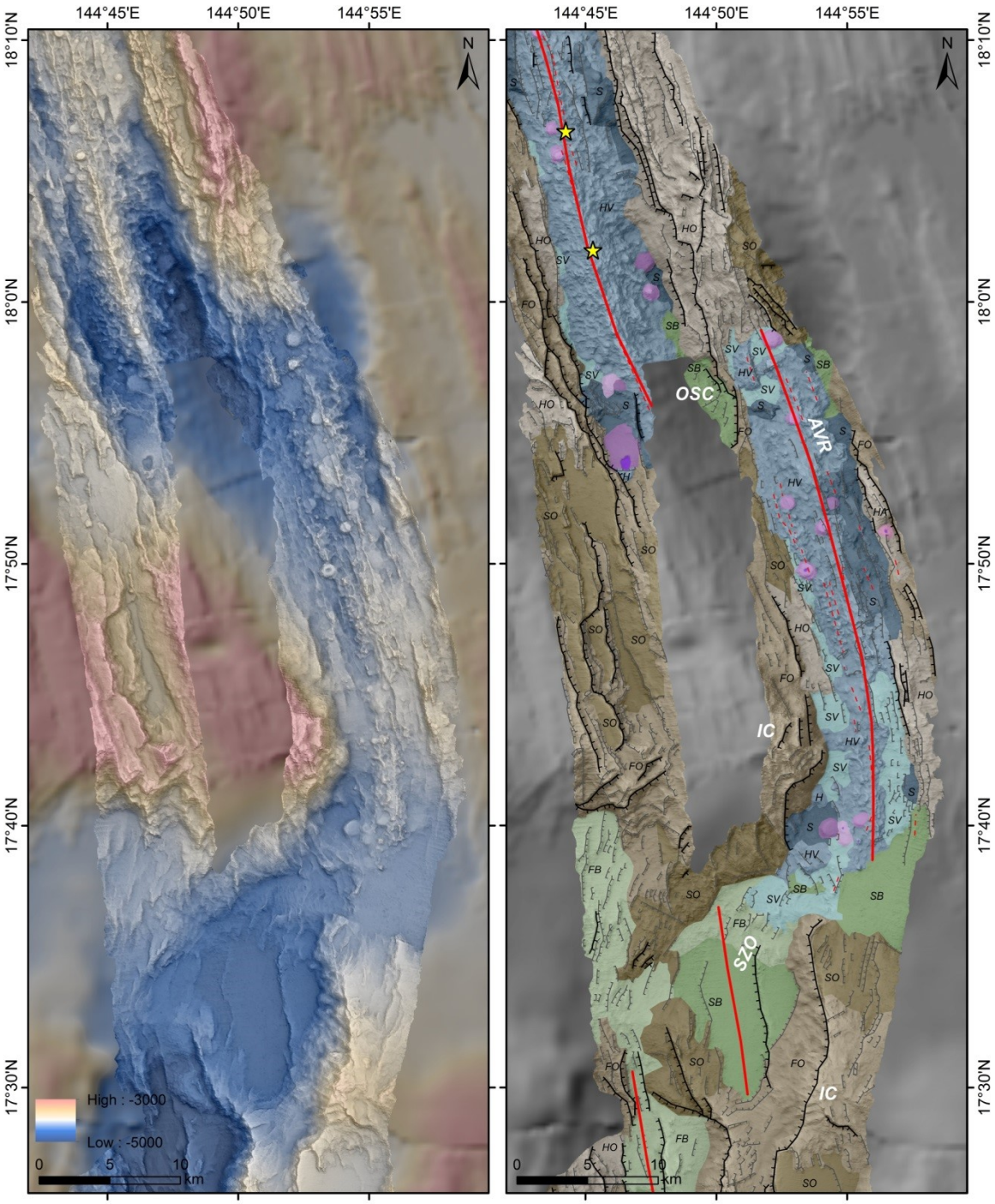


Figure Q11. Bathymetry (left) and interpreted geology (right) of the 17.8°N segment, following the legend in Fig. Q2. AVR = axial volcanic ridge; IC = inside corner high; OSC = overlapping spreading center. See Figure 5.13 (main text) for more information.

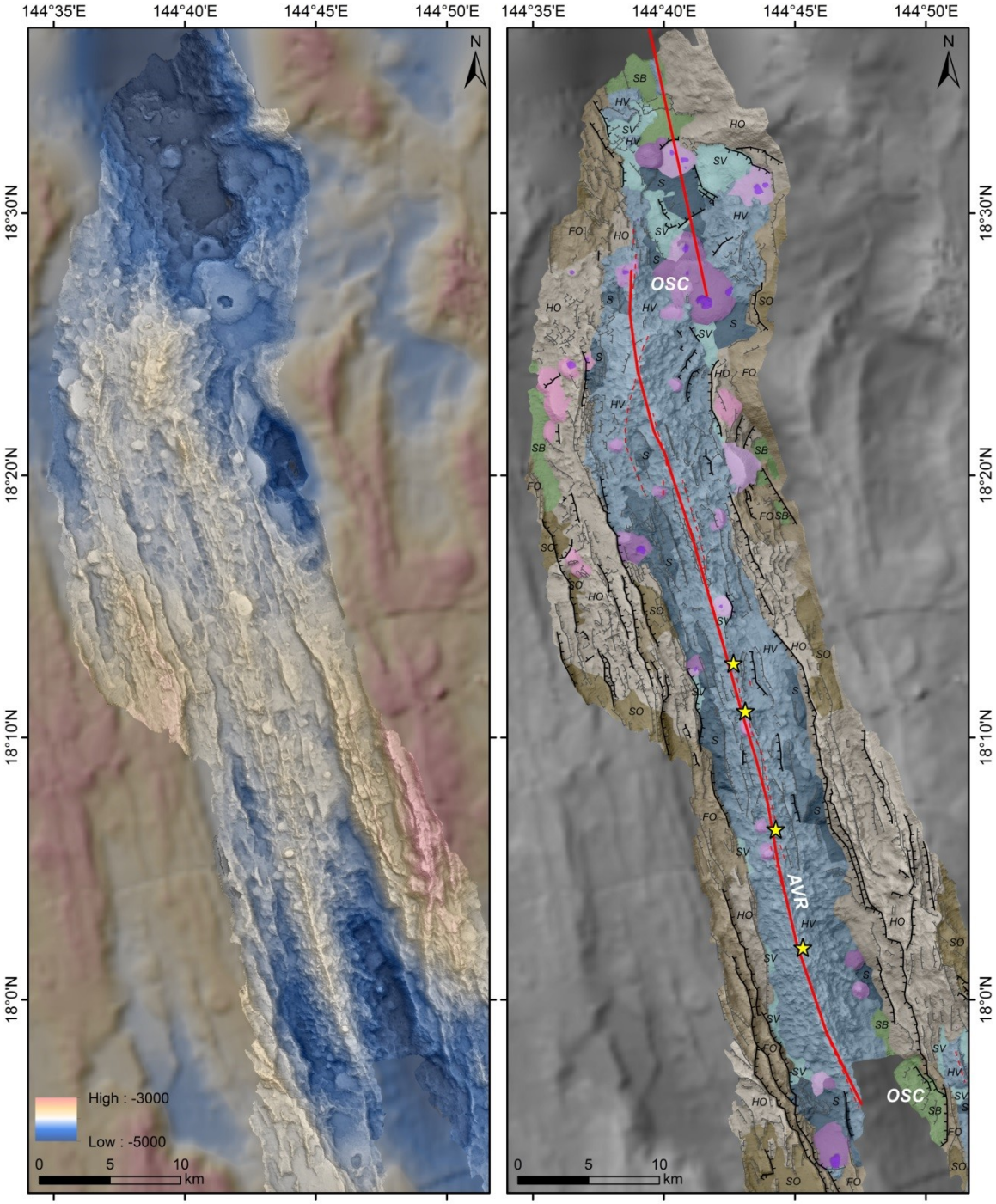


Figure Q12. Bathymetry (left) and interpreted geology (right) of the 18.2°N segment, following the legend in Fig. Q2. AVR = axial volcanic ridge; OSC = overlapping spreading center. See Figure 5.14 (main text) for more information.

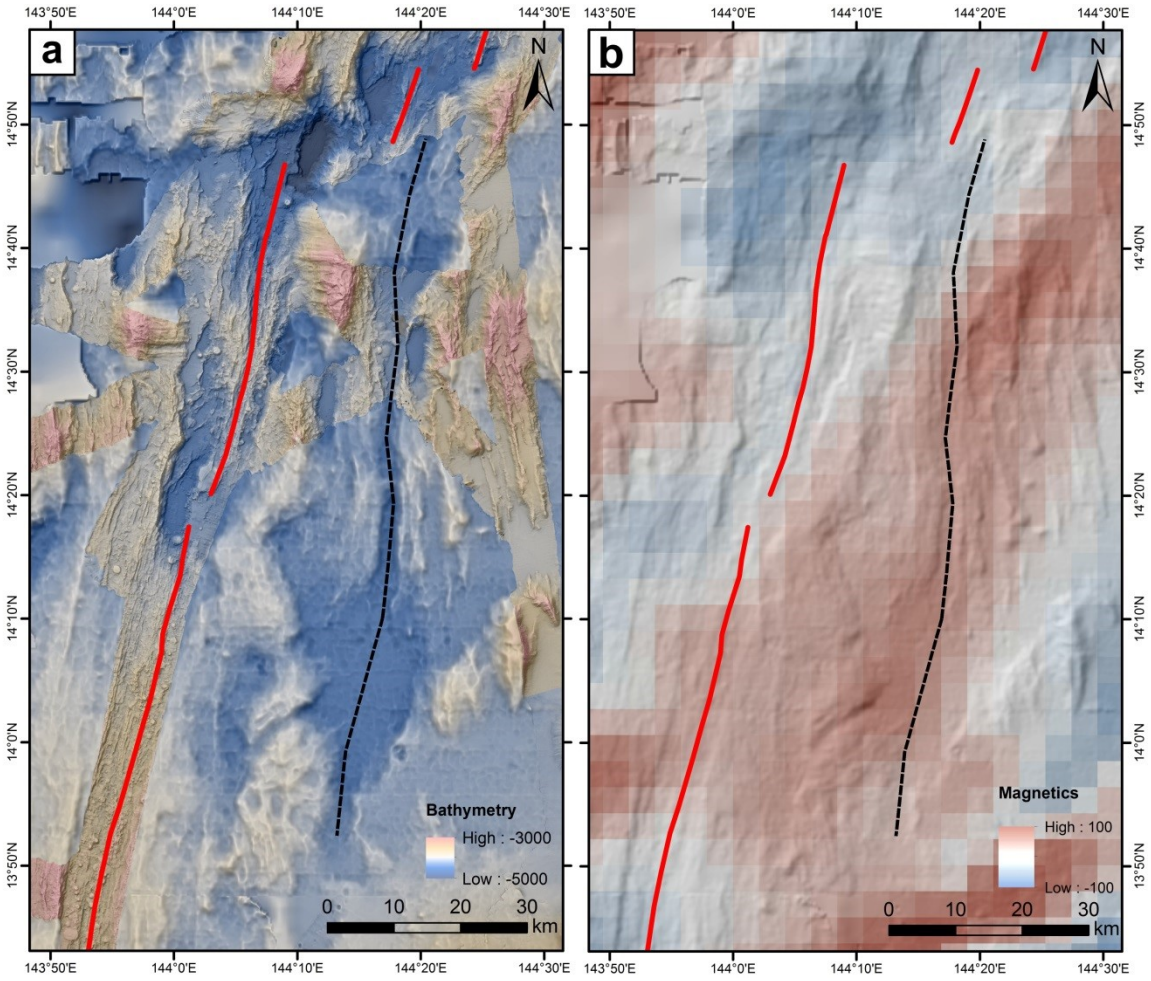


Figure Q13. A closer look at the bathymetry east of the 14.5°N segment, supporting a westward jump of the back-arc spreading axis in the southern back-arc: (a) TTS-shaded bathymetry showing a deep rift basin (paleo-rift zone) east of the active spreading center, and (b) strong magnetic anomaly along the paleo-rift zone, similar to that found along most of the active spreading center (Fig. 5.16c; 2-arc min Earth Magnetic Anomaly Grid; Maus et al., 2009). The modern back-arc spreading axis is shown as a solid red line, and the inferred paleo-spreading axis is shown as a dashed black line.

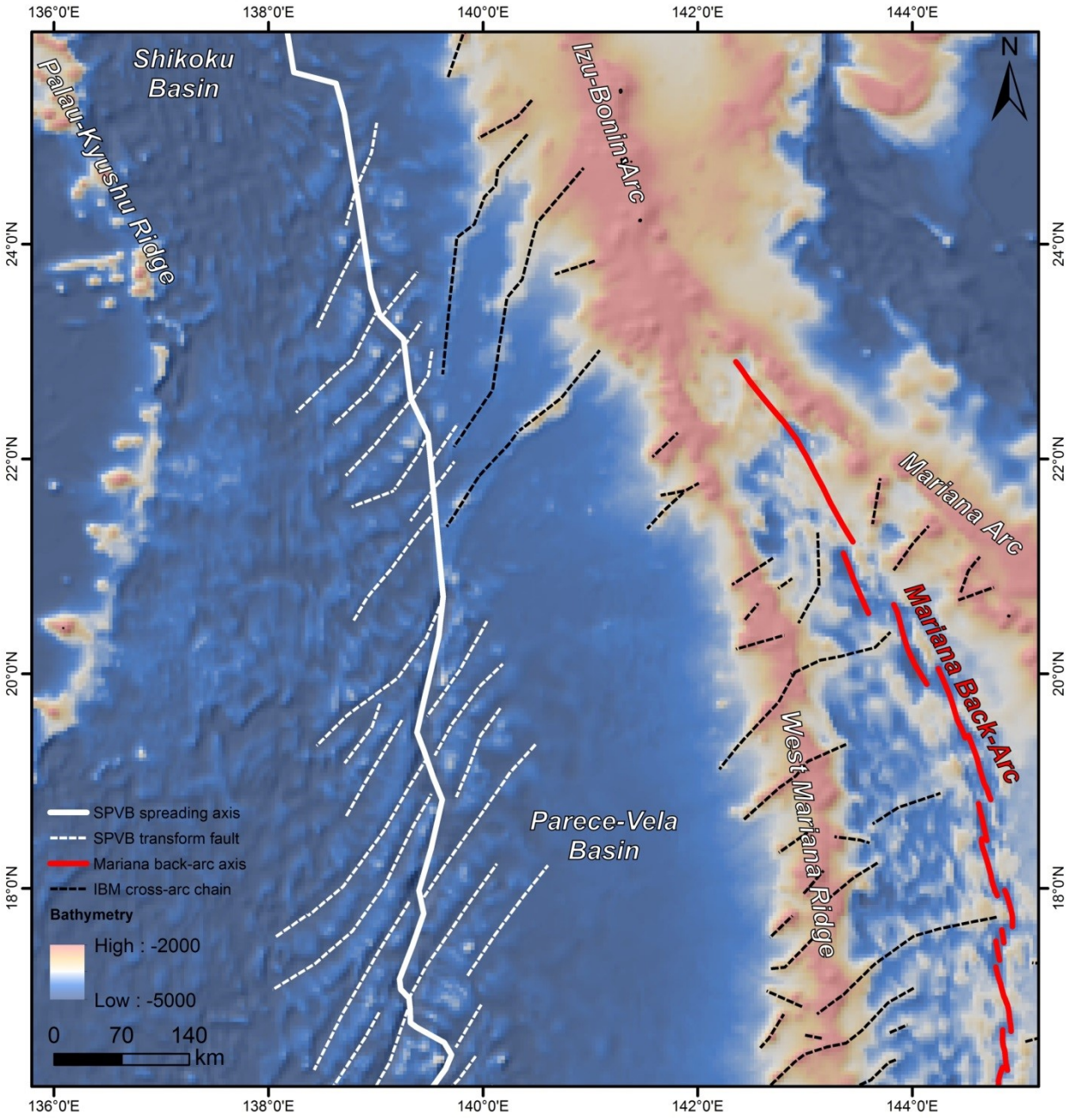


Figure Q14. Regional bathymetry (GMRT v3.2; Ryan et al., 2009) along the northern Mariana back-arc, showing volcanic cross-chains (black dashed lines) extending west of the northern West Mariana Ridge to the Shikoku-Parece Vela Basin (SPVB), closely following the orientation of the NNE-trending transform faults (white dashed lines) in the SPVB. These structures may be long-lived basement structures inherited during successive episodes of back-arc opening, modified by subsequent rotation of the Philippine Sea plate. Seafloor fractures modified from Matthews et al. (2011). IBM = Izu-Bonin Mariana.

2. Neovolcanic volume calculations

Bathymetric data collected during the FK151121 "Hydrothermal Hunt in the Marianas" cruise was first analyzed to interpret the geology of the seafloor (see main text), from which the extent of the neovolcanic zone could be determined. The neovolcanic units included "smooth volcanic terrain," "hummocky volcanic terrain," and "sedimented volcanic terrain. The bathymetry along each segment was clipped to the extent of the neovolcanic units (Fig. Q15), and projected into UTM coordinates (WGS 1984 World Mercator projection). Volume calculations were done using the "Surface Volume" tool in ArcGIS®v.10.1 (3D Analysist plugin) to calculate the volumetric difference between each clipped bathymetric surface and a reference plane (Fig. Q15; Table Q1). Reference planes were individually set for each segment at the average depth of the segment ends through qualitative analysis. The depths of the segment ends were similar for most of the segments (within ~500 m) apart from segment 13.9°N, where the northern end was significantly deeper than the southern end. In addition, this segment continues further to the south of the mapped area by ~9.5 km. As a result, the volume calculation along this segment should be considered with caution. Since the reference plane is a flat surface, this method will under-estimate the volume of neovolcanic material if it infills a bowl-shaped depression along the rift axis, and an over-estimate if it infills a saddle-shaped rift axis.

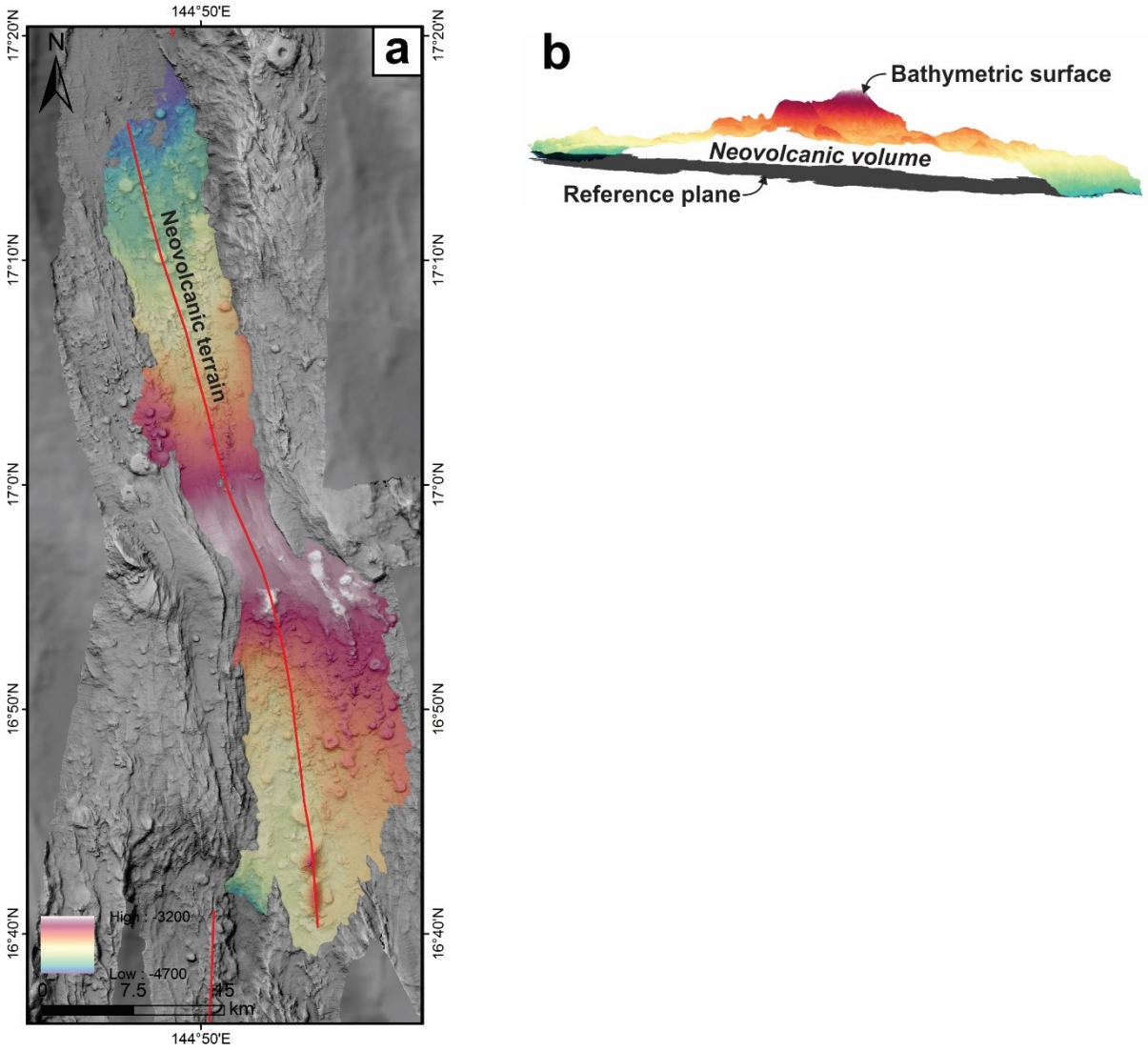


Figure Q15. An example of the method used to calculate the neovolcanic volumes (segment 17.0°N): (a) clipped bathymetry (colored) to include just the neovolcanic zone, as determined by geological mapping (see Fig. 5.12, main text); (b) an oblique view facing ENE of the clipped bathymetry (5x vertical exaggeration) and a reference plane (black surface) set at the mid-point of the depths at the segment ends. The "Surface Volume" tool in ArcGIS was used to calculate the volumetric difference between these two surfaces (Table Q1).

Table Q1. Segment features and reference plane heights used in "surface differencing" volume calculations

Segment (Mid-Latitude)	Min. Elevation [mbsl]	Max. Elevation [mbsl]	Area [km^2]	Reference Plane [mbsl]	Volume [km^3]
13.9°N	4510	3191	468	3950*	145*
14.5°N	5099	3655	608	4700	599
15.1°N	4693	3231	228	4630	118
15.5°N	4727	3826	272	4630	84
16.1°N	4627	3236	400	4450	163
16.5°N	4578	3198	219	4400	108
17.0°N	3074	4773	652	4550	474
17.8°N	4610	3752	269	4500	83
18.2°N	5326	3465	560	4850	401

* Due to a large difference in segment-end heights along 13.9°N, there is a large uncertainty associated with the reference plane height and subsequent volume calculation.

3. Eruption rate calculations

Rough age estimates were first calculated using the spreading rates determined by GPS by Kato et al. (2003) for some segments (extrapolated for intervening segments), divided by the mid-segment widths, measured along profiles summarized in Table 5.1 (main text). Spreading rates are assumed to be the same over the history of back-arc spreading. By dividing the neovolcanic volumes calculated earlier (Table 5.1; Table Q1) by these age estimates, rough eruption rates for the entire segment were calculated, as well as eruption rates per kilometer along the segment. The width at the mid-segment points were used (rather than the segment ends) as they are generally the narrowest point of the segment, providing the oldest age estimate, and therefore lowest eruption rates. These calculations could be further refined by precise age determinations of the neovolcanic rocks in the axial valleys.

Table Q2. Calculation of eruption rates of neovolcanic material along each segment

Segment (Mid-Latitude)	Segment Length [km]	Spreading Rate [mm yr^{-1}]*	Mid-Segment Width [km]	Age [yr]	Neovolcanic Volume [m^3]	Eruption Rate [m^3 yr^{-1}]	Eruption rate per km [m^3 yr^{-1} km^{-1}]
13.9°N	82	~42.5	8	188235	1.45+11	768932	9377
14.5°N	49	~41.5	23	554217	2.71E+11	488978	9979
15.1°N	33	40	23	575000	1.18E+11	205217	6219
15.5°N	34	~38	24	631579	8.40E+10	133000	3912
16.1°N	64	35	8	228571	1.63E+11	713125	11143
16.5°N	42	~32	8	250000	1.08E+11	432000	10286
17.0°N	70	28	6	214286	4.74E+11	2212000	31600
17.8°N	39	~26	16	615385	8.3E+10	134875	3458
18.2°N	61	25	14	560000	4.01E+11	716071	11739

* Full spreading rates determined by GPS for some latitudes (Kato et al., 2003); extrapolated for intervening segments (indicated by ~)